NANOTECHNOLOGICAL APPROACHES TO AMPLIFICATION IN BIOLOGICAL AND CHEMICAL DETECTION SYSTEMS

Chad A. Mirkin

Department of Chemistry and International Institute for Nanotechnology, Northwestern University, 2145 Sheridan Road, Evanston, IL 60208-3113, USA

chadnano@northwestern.edu

ABSTRACT

Recent advances in the development and miniaturization of highly sensitive and selective enzyme-free assays for protein and nucleic acid detection will be presented. Gold nanoparticles loaded with a large number of barcode DNA strands are part of a recently developed homogeneous bio-barcode assay that exhibits attomolar sensitivity for a variety of protein and nucleic acid targets without the need for enzymatic amplification of the target prior to detection. The bio-barcode assay offers several advantages. Due to the large number of discernable oligonucleotides the assay allows researchers to (1) use new biomarkers for diagnosis that cannot be detected with conventional technology due to sensitivity limitations; (2) assess and study disease recurrence using existing markers, and (3) detect a panel of markers simultaneously with high sensitivity. The bio-barcode assay has been used in a clinical pilot study to assess PSA levels in the serum of men who have undergone prostate removal. Following surgery, PSA is typically undetectable when measured by conventional assays. The ability to detect a PSA baseline in each man post-surgery, and to follow the rise in PSA levels would represent a significant advantage for detecting disease recurrence and implementing intervening measures at the earliest possible time. Using the bio-barcode assay, we could detect a PSA baseline in all the men tested following prostate removal. Furthermore, our data suggest that the bio-barcode assay detects disease recurrence years earlier than conventional assays. Advances in the development of a fully integrated, chip-based microfluidic system for carrying out highly selective multiplexed detection of protein cancer markers in buffer and serum media also will be presented.

Keywords: DNA, Bio-Barcode, Nanoparticles, Diagnosis

978-0-9798064-0-7/μTAS2007/$20©2007CBMS

HIGH-THROUGHPUT DNA MICROFRACTIONATOR USING SELF-PATTERNED LARGE-SCALE CRYSTALLINE NANOARRAYS

Y. Zeng and D. J. Harrison

Department of Chemistry, University of Alberta, Canada

ABSTRACT

This paper reports a high-throughput DNA microfractionator based on the use of regular colloidal nanoarrays to define the nanofluidic environment. A facile microfluidic large-scale colloidal self-patterning strategy has been developed to create large-area crack-free colloidal nanoarrays within microfluidic devices, with which continuous separation of DNA can be achieved using asymmetric pulsed electric fields.

Keywords: colloidal self-assembly, large-area patterning, DNA, continuous separation

1. INTRODUCTION

Nanofabricated structures for biomolecular separation, dubbed artificial gels, have received increasing interest because they offer improved separation performance and easy integration with multifunctional microsystems [1]. Applications of such nanosieves, however, are dramatically limited by current technical challenges in nano-lithography which is very expensive, time-consuming, and difficult to perform at ~10-nm length scales. In our previous work, we have demonstrated that colloidal self-assembly offers a simpler and cheaper alternative to conventional nanofabrication of sieving structures [2]. We developed a single-channel microfluidic colloidal self-assembly strategy to overcome the challenge associated with lattice cracking. In this paper, we report on self-patterning of large-area crack-free colloidal nanoarrays using multiple evaporation channels. A 2-D microsystem based on this method is demonstrated as a high-throughput DNA fractionator.

2. EXPERIMENTAL

Fig. 1 elucidates our method of crack-avoiding large-scale colloidal patterning using microchannel arrays. The colloidal solution fills the PDMS chip spontaneously and evaporates from the open channel outlets. Evaporation triggers colloidal nucleation at the air-liquid interface, creating a one-directional flux for continuous growth of the bed to pack the device. 4× TBE buffer containing 4% 2-mercaptoethanol was used to reduce EOF and photobleaching during electrophoretic separation and fluorescence detection of DNA.

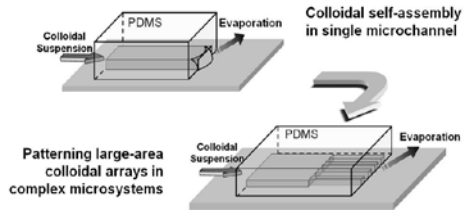

Figure 1. Schematic of microfluidic colloidal self-assembly using micro-channel array for patterning large-scale crack-free crystalline nanoarrays in 2-D microdevices.

3. RESULTS AND DISCUSSION

Large crack-free colloidal structures are much more challenging to prepare than narrow 1D colloidal bands, because heterogeneous capillary stress builds across large areas, causing severe film fracture during evaporation-driven assembly. When packing a fluidic

978-0-9798064-0-7/μTAS2007/$20©2007CBMS

cell, cracks were observed in a periodic array vertical to the drying edge, which reflects the balance between drying-induced capillary pressure and stress relaxation by crack opening [3]. Here we use multiple parallel microchannels with appropriate width (~100 μm) to guide the colloidal self-assembly within large-scale microdevices. The microchannels serve two functions: (A) they reduce the stress nonuniformity by separating long open edges into segments shorter than the characteristic length scale above which cracks occur; (B) microchannels prevent a drying front from entering the bulk, thus avoiding cracks due to bead and contact volume shrinkage [2].

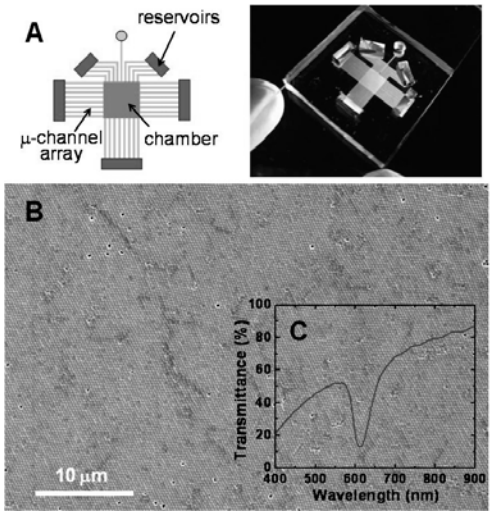

Figure 2. 2-D DNA microfractionator based on self-patterned crystalline arrays. A) Chip design and digital photo of a PDMS chip packed with 900-nm silica spheres. B, C) SEM image and normal incidence transmission spectrum of ordered 330-nm silica nanoarrays packed in microdevices.

Fig. 2A shows the design of a 2-D microdevice and a photograph of a packed PDMS chip. The microchannel contacts to the bed generate a uniform electric field across the packed chamber [4]. Both SEM and optical characterizations confirm a crystalline structure extends across a large area (Fig. 2B and C). Fig. 3A illustrates the mechanism of DNA separation using a pulsed field [4]. Separation is operated in a continuous-flow manner (Figure 3B-D), giving much higher throughput of sample processing than single-channel separation. Compared to nanofabricated 2-D structures, our approach greatly increases throughput simply because we incorporate a 3-D lattice that is nanoporous. The interplay of the molecular size, the crystal planes of the lattice, the electric field vectors and pulsing frequencies all play a role in the angular deflection of DNA, as evident in Fig. 4A-C. Fig. 4D clearly shows that the maximum deflection angle, θ_{max}, is a characteristic measure of the size for DNA larger than 6 kbp. This may be attributed to size-dependent relaxation and fluctuation of DNA conformations during electromigration [5,6]. Fig. 5A displays a separation that gives the best peak capacity across the size range of 2-20 kbp under the optimum field conditions in

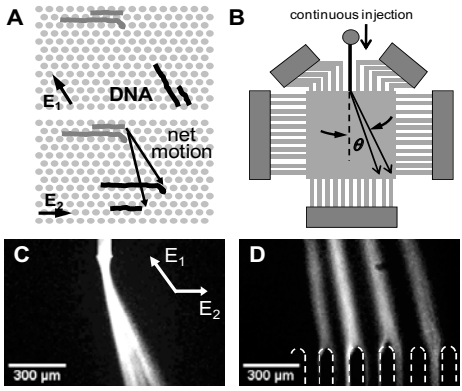

Figure 3. Pulsed-field separation of DNA. A) Biased reorientation mechanism. When the field direction is switched, DNA reorient at different spots because of their size difference. With $E_1 > E_2$, DNA net motion is biased to size-dependent direction. B) Sample is continuously injected and separated into DNA streams with distinct deflection angle θ from the injection direction. C, D) Fluorescence images of separating four DNA fragments of 2, 6, 10, and 20 kbp in a 330-nm silica array taken from top and bottom of the chamber ($E_1 = \sim 1.4E_2$). The collecting channels are outlined for clarity.

Fig. 4C. It shows greatly improved size selectivity compared to that achieved with a lower field strength (Fig. 4A and 5B). This could be due to enhanced DNA stretching under higher electric force and reduced relaxation within shorter pulse duration, especially for smaller DNA.

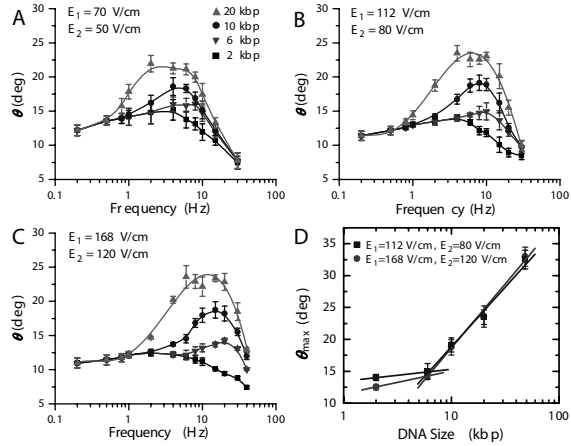

Figure 4. Effects of pulsed field on deflection angle θ. A-C) Frequency spectra of various DNA show distinct maximum θ dependent on molecular size, pulse frequency, and field strength. Lines are drawn to guide the eye. D) Semi-log plot of θ_{max} against DNA size under various field conditions. All measurements were performed in 330-nm silica arrays. Error bars are standard deviation (n=3).

4. CONCLUSIONS

To summarize, we have successfully extended the single-channel microfluidic colloidal self-assembly approach to simple, fast, and economic patterning of large-area crack-free crystalline nano-sieves into complex microfluidic systems. As an example of its potential applications, we devised a 2D DNA microfractionator operated in a continuous separation manner. Our studies on the separation behavior clearly point out the roadmap to achieve the optimum separation for given targets. Moreover, this approach offers great flexibility in choosing various pore sizes to target certain molecular size range to achieve the best separation efficiency.

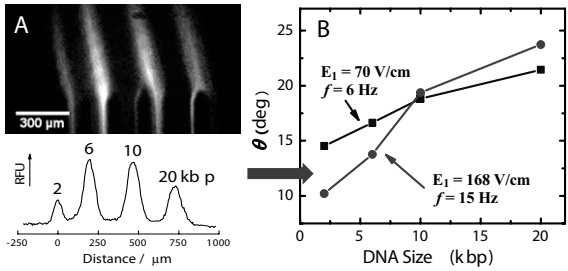

Figure 5. A) Fluorescence image (top) and intensity profile (bottom) of the separation of 2–20 kbp DNA under the optimum field conditions obtained from Figure 4C. B) Comparison of size selectivity under the optimum pulsed-field conditions shown in Figure 4 A and C.

ACKNOWLEDGEMENTS

We thank the Nanofab at University of Alberta for the facilities and the Natural Sciences and Engineering Research Council of Canada (NSERC) for funding.

REFERENCES

[1] J. Han, and H. C. Craighead, Science, 288, 1026-1029 (2000).
[2] Y. Zeng, and D. J. Harrison, Anal. Chem., 79, 2289 - 2295 (2007).
[3] C. Allain, and L. Limat, Phys. Rev. Lett., 74, 2981-2984 (1995).
[4] L. R. Huang, et al. Nat. Biotechnol., 20, 1048-1051 (2002).
[5] J.-L. Viovy, Electrophoresis, 10, 429-441 (1989).
[6] S. Ferree, and H. W. Blanch, Biophys. J., 87, 468-475 (2004).

A CELL DELIVERY AND FIXING SYSTEM UTILIZING MICRO-PUMPS/VALVES AND NEGATIVE-DEP DEVICES FOR ON-CHIP DUAL-BEAM OPTICAL TRAP APPLICATIONS

Chia-Wei Lai[1], Suz-Kai Hsiung[1], Chen-Min Chung[1], Yin-Quan Chen[2], Arthur Chiou[2] and Gwo-Bin Lee[1*]

[1]Department of Engineering Science, National Cheng Kung University, Tainan, TAIWAN
[2]Institute of Biophotonics, National Yang-Ming University, Taipei, TAIWAN

ABSTRACT

This study reports a new cell delivery and fixing microfluidic system integrating micro-pumps, micro-valves, dielectrophoretic electrodes and micro-coupler devices for on-chip dual-beam optical trap applications. After focusing and delivering cells to the detection area, the cell can be fixed at the top side of a micro flow channel by micro-valves and a negative dielectrophoretic (N-DEP) force for optical trapping and manipulation. The fiber micro-coupler can be used to promote the probability in trapping cells. Results show the proposed system can trap the cell successfully by a dual-beam optical trap. It is promising for applications of a single cell/particle optical trapping, manipulation and analysis.

Keywords: micro-pump, micro-valve, DEP, optical manipulation, MEMS

1. INTRODUCTION

Optical trap has been widely used for trapping, manipulating, and analyzing a single cell and a single biological molecule [1]. In addition, compact chip-based optical trap systems were demonstrated recently [2]. However, separating and delivering a single cell for the optical trap still remains an issue. In this study, we report a microfluidic chip capable of cell delivery and manipulation system for optical trap applications. Pneumatic micro-pumps were employed to generate a focusing flow to orderly deliver the cell samples to a designated detection area. When a cell was transported into the detection area, a pair of micro-valves and DEP microelectrodes were employed to fix the cell on top of the detection area to increase the catching efficiency of the dual-beam optical trap. Moreover, an active micro-coupler capable of active alignment of two buried optical fibers was used to increase the coupling efficiency for optical trapping. Trapping and manipulation of cells has been successfully demonstrated.

2. DESIGN

Figure 1(a) shows a schematic illustration of the proposed system composed of four major components including micro-channels, micro-pumps, indium tin oxide (ITO) electrodes and a detection area. Three pneumatic micro-pumps [3] were integrated for transporting sample and sheath flows to generate flow focusing effect such that cell samples can be delivered to the detection area orderly (Fig. 1(b)). A photograph of the detection area is shown in Fig. 1(c). A pair of active micro-couplers was used to align the head-on optical fibers inside the detection area. The working principle of the micro-coupler is schematically shown in Fig. 2. The optical fiber can be adjusted horizontally and vertically while compressed air was injected to deform the moving wall and membrane structures. After optical fibers alignment was completed and a cell was transported to the detection area, a pair of micro-valves driven by compressed air can be used to fix the cell in the detection

978-0-9798064-0-7/μTAS2007/$20©2007CBMS

area (Fig. 3a). However, the cell can not be trapped efficiently by dual-beam optical trap since the cell may stay at the bottom of the flow channel which is too far from the optical axis for the cells to be trapped by the laser beam. In order to increase the catching efficiency of the dual-beam optical trap, the negative-DEP force was applied to push the cell sample to the top of the flow channel (Fig. 3b).

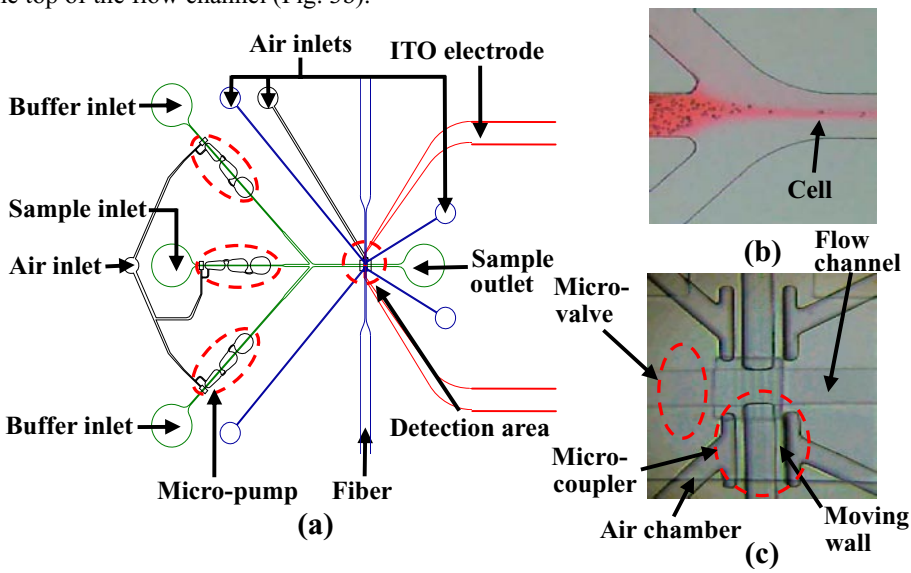

Figure 1 (a) Schematic representation of the microfluidic chip integrated with micro-channels, micro-pumps, ITO electrodes and a detection area. (b) Photograph of hydrodynamic focusing effect. (c) A close-up view of the detection area integrated with fiber channels, micro-valves and micro couplers.

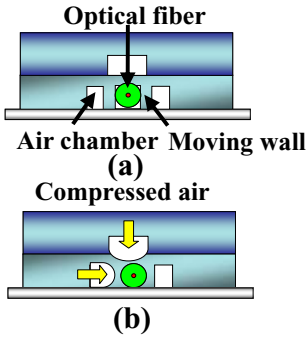

Figure 2 Illustration of the working principle of the micro-coupler.

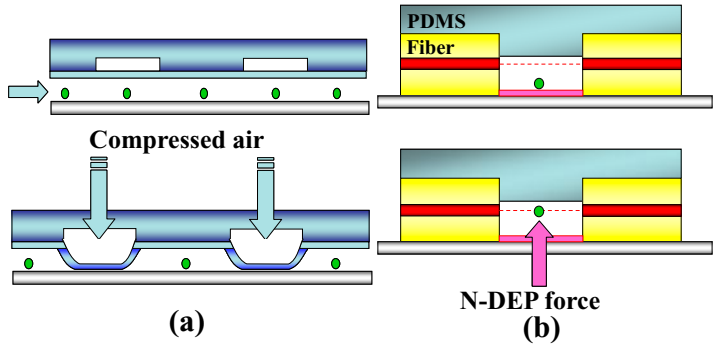

Figure 3 Schematic illustration about the working principle of (a) micro-valves and (b) Negative-DEP forces.

3. RESULTS AND DISCUSSION

Figure 4 shows that the micro-couplers, the flow channel with different depths, and optical fiber channels were fabricated successfully by 2-layer SU-8 and PDMS replica fabrication process. It can allow alignment of optical axes completely through the top of flow channel which improve the catching efficiency of the dual-beam optical trap. Figure 5 shows a lung cancer cell can be successfully fixed at the top of ITO electrodes in the detection area by micro-valves and the N-DEP force. Finally, the cell was trapped

successfully by the dual-beam optical trap in the proposed system, as shown in Fig. 6. By adjusting the power of the laser light, the shape of the trapped cell also could be stretched along the axis of the laser beams. With this approach, the cell optical manipulation and cell mechanics can be investigated thoroughly.

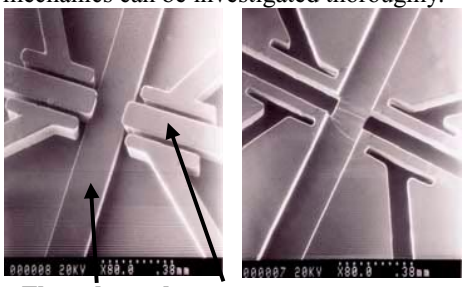

Figure 4 SEM images of detection area for (a) SU-8 template and (b) PDMS replica after de-molding process.

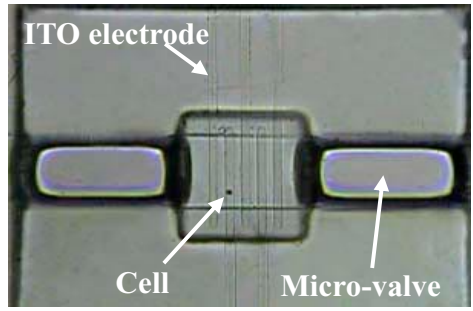

Figure 5 Image showing a lung cancer cell can be successfully trapped by micro-valves and the negative-DEP force.

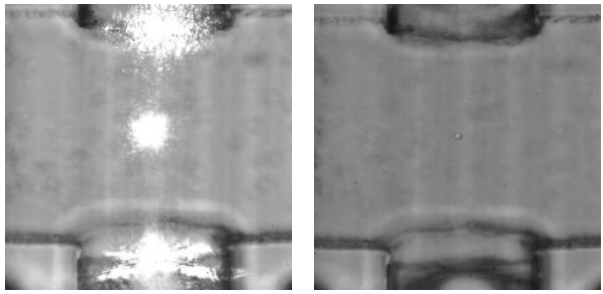

Figure 6 A red blood cell can be successfully trapped by dual-beam optical trap: (a) image without a laser line filter (Notch filter-1064nm) and (b) image with a laser line filter.

4. CONCLUSIONS

We have developed a new cell delivery and fixing system for dual-beam optical trap application. Cell samples can be delivered to the detection area orderly and then fixed at the top of ITO electrodes in the detection area by micro-valves and N-DEP forces. Finally, the cell/particle can be trapped successfully by dual-beam optical trap.

ACKNOWLEDGEMENTS

The authors would like to thank financial support from the National Science Council in Taiwan.

REFERENCES

[1] C.T. Lim, E.H. Zhou, A. Li, S.R.K. Vedula and H.X. Fu, Experimental techniques for single cell and single molecule biomechanics, Materials Science and Engineering C, 26, pp.1278-1288 (2006).

[2] F.U. Gast, P.S. Dittrich, P. Schwille et al., The microscopy cell (MicCell), a versatile modular flowthrough system for cell biology, biomaterial research, and nanotechnology, Microfluid Nanofluid, 2, pp.21-36 (2006).

[3] C.W. Huang, S.B Huang and G.B. Lee, *Pneumatic micropumps with serially connected actuation chambers*, J. Micromech. Microeng, 16, pp.2265-2272 (2006).

DIELECTROPHORETICALLY SWITCHABLE MICROFLUIDIC WEIR STRUCTURES FOR EXCLUSION-BASED SINGLE-CELL MANIPULATION

B. M. Taff, S. P. Desai, and J. Voldman
Massachusetts Institute of Technology, USA

ABSTRACT

We offer the first known platform for parallelized single-cell manipulation that combines negative dielectrophoretic (n-DEP) sorting with the efficient loading behavior of hydrodynamic traps. Our devices provide manipulations using ejection- and/or exclusion-based techniques. In ejection operations we unload targeted sites by driving their associated electrodes and displacing held beads or cells from the hydrodynamic capture faces. In exclusion operations we prevent site loading altogether by activating selected electrodes before introducing microparticles into the system. In our work, we have formed multi-colored patterns of interwoven dyed beads and cells. This platform thus enables scalable dielectrophoretically modulated single-cell manipulation in culture media.

Keywords: Dielectrophoresis, Hydrodynamic Trap, Weir, Single Cell Manipulation

1. INTRODUCTION

DEP is regularly used for both cell patterning [1] and sorting applications [2]. Most platforms incorporate positive dielectrophoretic (p-DEP) strategies to capture cells at electrode sites, capitalizing on associated high-magnitude capture forces and a complementary design ease. Unfortunately, this approach requires operation with low-conductivity buffers, thus presenting cell health complications. N-DEP methods, which function in cell culture media, are more difficult to develop because they are better suited for pushing cells away from localized sites instead of enabling trapping. Passive microfluidic weir structures as presented by Lee [3] demonstrate excellent single-cell loading characteristics but cannot manipulate or sort cells following capture. We have created an architecture that combines the effective capture of weir geometries with active n-DEP manipulations thus enabling active cell arrays that function in standard cell culture media (Figure 1).

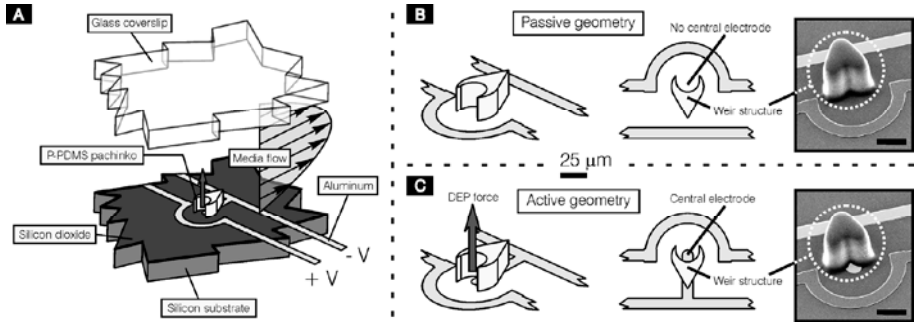

Figure 1: **(A)** provides an outline of our electrically active hydrodynamic weir platform. We use patterned electrodes to dielectrophoretically modulate site loading. **(B)** and **(C)** show passive and active weir architectures. The central electrode in the active geometries enables the DEP exclusion force (arrows). Scale bar = 25 µm.

978-0-9798064-0-7/µTAS2007/$20©2007CBMS

2. DEVICE OPERATION AND FUNCTIONALITY

Our active traps prevent weir site loading by using n-DEP to push cells away from the device capture crevices such that passing fluid flow sweeps ejected cells out of the device. This capability demanded a revised approach where weir structures are well-separated from the flow chamber ceiling. We thus implemented the structures using free-standing photopatternable silicone [4], taking advantage of its low autofluorescence as compared to SU-8. As shown in Figure 2, this revised approach still enables effective single-particle capture.

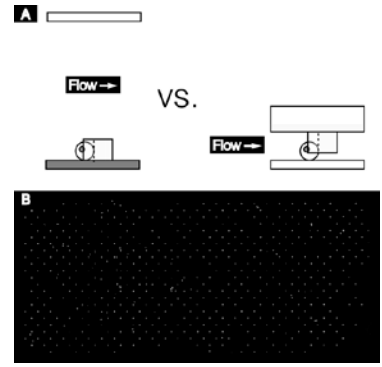

Figure 2: (A) compares our strategy (left) to the approach by Lee [3] (right). **(B)** presents the loading response of our designs, showing effective single-bead capture in a large array.

Our manipulation architecture provides two methods for loading. In one approach, we initially load all sites (Figure 3) by deactivating the electrodes and flushing microparticle-laced fluid through our devices. We then turn on active array sites (Figure 1C) by applying voltages to their affiliated electrodes. This procedure exerts vertical n-DEP forces on particles held in active cell-capture sites causing them to levitate above the capture surface where they cascade out of the array. Alternatively (Figure 4) we can prevent loading at active sites altogether by injecting particles into the chamber and repelling them from the capture surfaces while electrodes are ON. This approach offers benefits for cell-based assays by minimizing the potential for cells to non-specifically attach to active sites. Both approaches use n-DEP to *exclude* cells from sites, retaining for examination cells that nominally witness no DEP forces.

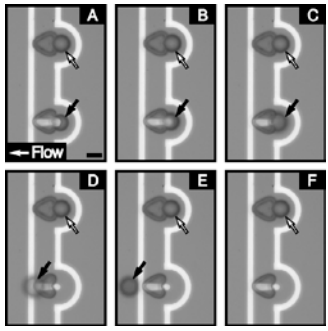

Figure 3: (A-F) show images detailing the site-specific ejection response of an active weir geometry (black arrow) as compared to a passive structure (white arrow). This approach enables the unloading of specific filled sites. Scale bar = 25 μm.

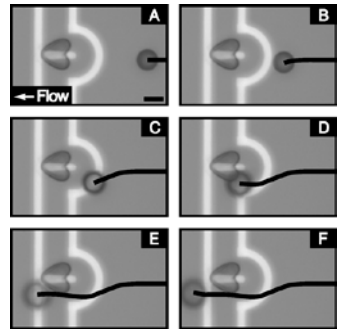

Figure 4: Instead of unloading specific sites after the fact, as shown in Figure 3, **(A-F)** demonstrate a method for preventing site loading by means of electrode activation. Throughout this sequence the electrodes are ON. Scale bar = 25 μm.

3. RESULTS AND DISCUSSION

In Figure 5 we show a checkerboard pattern formed from two different particle types. This demonstration advertises the key functionalities that our *active* array adds to prior mechanically based *passive* manipulation strategies. In scaled implementations we can approach the placement of multiple cell types at distinct locations across the chip and we can utilize the row/column site addressing schemes detailed earlier [2] for sorting operations. With BA/F3 cells we further examine device operation (Figure

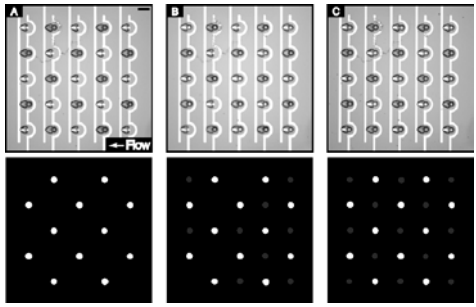

Figure 5: In **(A)** we selectively load the passive weir structures with orange beads (shown in white) using the loading approach demonstrated in Figure 4, where we apply voltages to prevent beads from loading in active sites (top – merged with bright field, bottom – fluorescent signal alone). In **(B)** we inject green fluorescent beads (shown in grey) and begin backfilling the remaining sites by turning off all applied voltages. **(C)** shows a 5×5 "checkerboard" pattern of fluorescent beads. Scale bar = 50 μm.

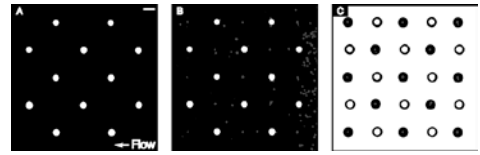

Figure 6: We first load the passive sites with green beads (shown in white) **(A)** and then backfill the grounded active sites with DsRED-expressing BA/F3 cells (shown in grey) **(B)**. In **(C)** we more closely examine the data provided in **(B)** by combining it with a post-processing screening layer showing that all target sights are loaded despite the fact that non-specific surface binding leaves residual cells in other locations. Future work will take advantage of the wide variety of published methods available for effectively managing binding interactions between cells and device surfaces. Scale bar = 50 μm.

6). Though non-specific binding hindered perfect loading in initial tests, individual cells did load into every prescribed array site (6C). In continuing work, known strategies should alleviate this binding effect. We thus present a novel approach to single-cell manipulations enabling loading and sorting in standard cell culture media.

4. CONCLUSIONS

In our work we have introduced a novel approach to manipulating single cells that capitalizes upon the efficient trapping characteristics of weir-style hydrodynamic traps and further augments that functionality using active negative dielectrophoretic sorting. In a single platform we offer means for ejecting and/or excluding particles from targeted subsets of arrayed system traps. We thus provide a unique scalable technology for sorting and positioning groups of single cells that functions effectively in standard culture media.

ACKNOWLEDGEMENTS

This work was supported in part by the NIH (RR19652), the Singapore-MIT Alliance, and graduate fellowship funding from the NSF. We thank both the Microsystems Technology Laboratories and the Cell Decision Process Center at MIT and the WM Keck Foundation at the Whitehead Institute for valuable discourse and facilities access.

REFERENCES

[1] Albrecht D. R., V. L. Tsang, R. L. Sah, S. N. Bhatia, Lab Chip, 2005. **5**(1): p. 111-118.
[2] Taff, B. M. and J. Voldman, Anal. Chem., 2005. **77**(24): p.7976-7983.
[3] Di Carlo, D., L. Y. Wu, and L. P. Lee, Lab Chip, 2006. **6**(11): p. 1445-1449.
[4] Desai, S. P., B. M. Taff., and J. Voldman, Paper ID No.: 0967, MicroTAS 2007

OPTOFLUIDIC SPECTROMETER FOR MICROCHIP FLOW CYTOMETRY

W. Z. Song[1], L. A. G. Lin[1], A. Q. Liu[1†], C. S. Lim[1], P. H. Yap[2]

[1]School of Electrical & Electronic Engineering
Nanyang Technological University, Singapore 639798
[2]DSO National Laboratories, Singapore 639798
(Tel: +65-67904336, Fax: +65-3-67933318, E-mail: eaqliu@ntu.edu.sg)

ABSTRACT

A compact optofluidic spectrometer is demonstrated for the fluorescence detection of moving particles in a microfluidic chip. The object is excited within an integrated liquid-liquid waveguide and its fluorescence spectrum is recorded in real time with resolution of 10 nm. Three different types of fluorescence beads were tested and distinguished by this spectrometer. This micro-optical-fluidic-systems (MOFS) hold a promising new concept of the multi-color fluorescence detection in microchip flow cytometry. Besides the low cost and compact, it also bears the advantages of self-reference, high sensitivity, high speed and accuracy.

Keywords: Optofluidic, liquid-liquid waveguide, spectrometer, microchip flow cytometry

1. INTRODUCTION

Fluorescence activated flow cytometry is one of the most powerful tools for analyzing chemicals, particles and cells in clinical diagnostic, biochemistry and biology. In the past decades, microfluidics and micro-fabrication opened new opportunities for miniaturizing flow cytometry. However, nearly all of these micro-devices still rely on bulky external optical detection system which uses several filters and PMTs for multi-color fluorescence detection [1].

To simplify the optical system and reduce its cost, a time-multiplexing method is exploited in this paper. We present a compact optofluidic spectrometer which use single photon-detector to obtain the full fluorescence spectrum of the particles in time-domain. It preserves the high sensitivity of the PMT while avoids to use individual photon-detectors to monitor the different fluorescence colors.

2. DESIGN AND WORK PRINCIPLE

The schematic diagram of the chip is shown in Figure 1. The chip consists of three parts, the microfluidic structures, liquid waveguide and optical encoder. The microfluidic structures are for cell focusing and sorting with external valves. As the core liquid has a higher refractive index than the cladding with the optically smooth liquid interface, the laminar flows also work as liquid-core liquid-cladding waveguide [2,3]. The pumping light being confined in the core liquid ensures the fluorescence excitation of the samples with high efficiency and self-alignment. An opaque mask with grating pattern underneath the channel was deposited on the substrate to act as the optical encoder.

Figure 2 shows the work principle of the optofluidic spectrometer. The sample passes through the detection area and the fluorescence light transmits into the collection lens through the optical encoder. Thus the output signal from the photomultiplier tube (PMT) is

978-0-9798064-0-7/μTAS2007/$20©2007CBMS

a train of pulses for each sample and different pulses correspond to the different wavelength, namely the envelope curve of the pulse train represents the optical spectrum of the sample. As the modulated fluorescence signal can be easily extracted from the background noise, the optical encoder can also enhance the detection sensitivity.

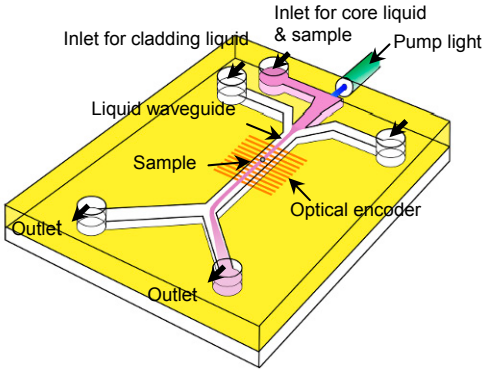

Figure 1

. *Figure 1*. The schematic diagram of the microchip.

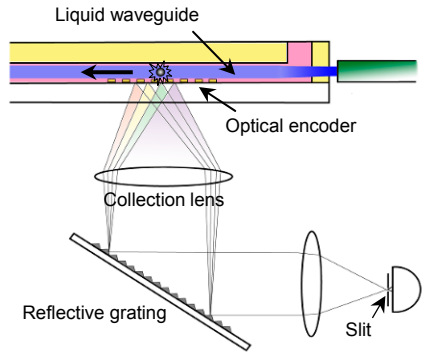

Figure 2

Figure 2. The working principle of the optofluidic spectrometer.

3. EXPERIMENT RESULT AND DISCUSSIONS

The chip shown in Figure 3(a) was fabricated by replica molding with PDMS which was then bonded on the glass slide. The glass substrate is firstly coated 100 nm Al film by electron beam evaprotor. Then the grating pattern on the substrate was defined by wet etching with the recipe of H_3PO_4 : Water : Acetic Acid : HNO_3 = 16:2:1:1 in weight. The grating has the lines of 600/mm and blaze angle at 500 nm. The two identical micro lens in Figure 3(b) have the same foucs length of 5 mm. The signal of PMT is recorded by Labview system. To reduce the background noise, the optical system is sealed in a dark box.

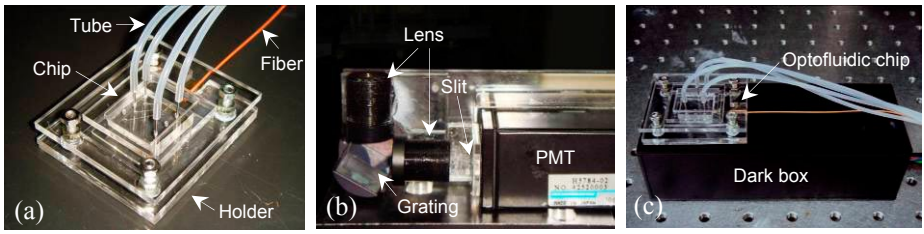

Figure 3. The photograph of the device. (a) Photograph of the package of the microchip; (b) External optical system of the optofluidic spectrometer; (c) The microchip under experiment.

A multimode optical fiber which is connected to the Argon laser (λ = 488 nm) couples the pumping light into the liquid waveguide. By adding small amount of ethylene glycol into the pure water, the core liquid has a slight high refractive index (n = 1.35) than the pure water (n = 1.33) in the cladding. Figure 4(a) shows the microscope picture of the microchip and Figure 3(b) shows the a fast moving fluorescene bead inside the liquid waveguide.

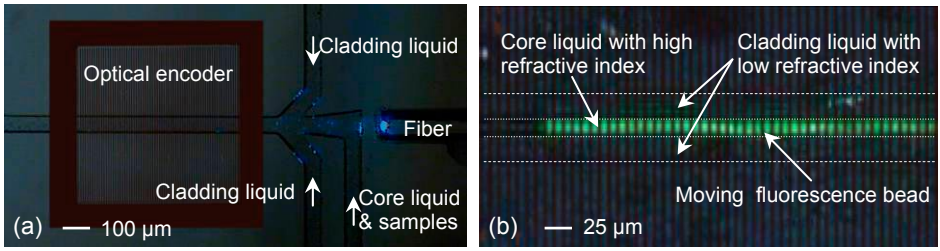

Figure 4. The micrograph of the microchip. (a) The main abbreviated view of the chip; (b). The micrograph of the a fluorescence beads moving inside the liquid waveguide.

Three different types of the fluorescence beads (AlignFlow Plus flow cytometry alignment beads, diameter of 6 μm, max excitation at 488 nm). Figure 5 compares the typical measurement spectrum of three different fluorescence beads. The spectrums are all self-referenced since the peaks with the highest intensity in each spectrum correspond to the scattering light with λ = 488 nm. The smaller peaks correspond to the fluorescence. The three different color fluorescence beads can be obvious distinguished. A resolution of $\Delta\lambda$ = 10 nm can be obtained from this optofluidic spectrometer while its screening speed is estimated to be 1000 particles per second at least due to the high working bandwidth of the PMT.

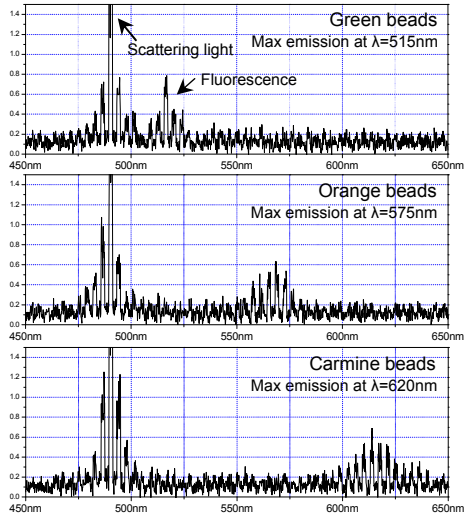

Figure 5. The measurement spectrum of three different fluorescence beads.

4. CONCLUSIONS

An optofluidic spectrometer with integrated liquid-liquid waveguide is demonstrated. Compared with the previous methods that use several PMTs and filters to distinguish the fluorescence colors, this design employs only one PMT to measure the fluorescence spectrum with high resolution of $\Delta\lambda$ = 10 nm. Besides low cost and ultra compact, it also bears the advantages of self-reference, high sensitivity, high speed and accuracy. This method holds a promising new concept for multi-color fluorescent detection in microchip flow cytometry.

REFERENCES

[1] D. Huh, *et al*., "Microfluidics for flow cytometric analysis of cells and particles," Physiol. Meas. 26(2005) R73-R98.

[2] Daniel B. Wolfe, *et al*., "Dynamic control of liquid-core /liquid-cladding optical waveguides," Proc. Nat. Acad. Sci. USA, 2004, 101: 12434-12338.

[3] Brlan T. Mayers, Dmltri V. Vezenov, *et al*., "Arrays and cascades of fluorescent liquid-liquid waveguides: Broadband light sources for spectroscopy in microchannels," Anal. Chem. 2005, 77:1310-1316.

A COMPLETE ON-CHIP HIGH RESOLUTION MICROSCOPE SYSTEM BASED ON THE OPTOFLUIDIC MICROSCOPY METHOD

Xiquan Cui, Xin Heng, Lapman Lee, and Changhuei Yang
Electrical Engineering, California Institute of Technology, Pasadena, CA 91125, USA

ABSTRACT

We report the implementation of a complete on-chip high resolution microscope system based on the Optofluidic Microscopy (OFM) method. This microscope does not use any lens elements and yet is capable of resolution comparable to a conventional microscope. We demonstrate the use of the microscope for C. elegans imaging at a resolution of ~ 1 μm with an imaging time of 0.5 sec for C. elegans.

Key words: microscope, optofluidic, cytometry, C. elegans

1. INTRODUCTION

This paper reports on the implementation of a complete on-chip high resolution microscope system based on the Optofluidic Microscopy (OFM) method, which can form a vital imaging component in a wide range of lab-on-a-chip (LOC) systems. Currently the microscopy imaging needs associated with LOC systems are still generally fulfilled through the use of bulky conventional microscopes. Despite the need, a commercially viable approach for miniaturizing microscopes did not exist until recently because 1) there does not exist an efficient way to fabricate precise optical lenses on chips, 2) the space requirements of conventional microscopes for image magnification conflict with the size constraints of chip-based devices.

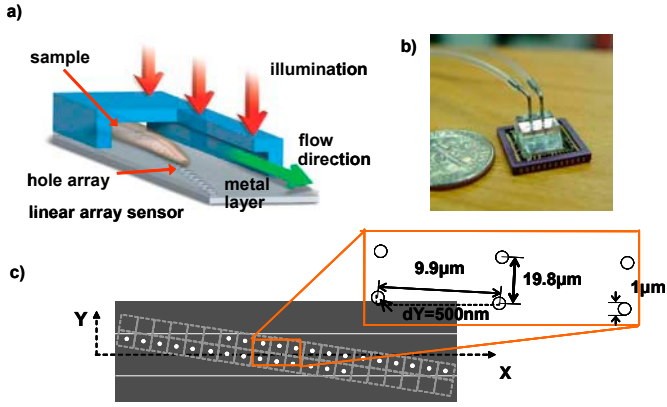

Figure 1: a) The OFM scheme. The device is uniformly illuminated from the top. The sample passes over the hole array and blocks the light transmissions through the holes. b) A completed prototype. c) The physical dimensions of the prototype. The holes are spaced 9.9μm apart so that each hole maps uniquely onto an individual CMOS pixel. Two lines of holes are used.

The OFM method abandons the conventional microscope design and, instead, shares similarities with direct shadow imaging methods where the target object is directly placed

978-0-9798064-0-7/μTAS2007/$20©2007CBMS

on top of a CCD or CMOS imaging sensor chip. In direct shadow imaging, the image resolution is not better than the sensor pixel size. As the typical sensor pixel dimension is ~10x10 micron^2, direct shadow imaging systems have poor resolution. The OFM method overcomes this by flowing the target over a line of submicron holes that is etched onto a metal coated CMOS imaging sensor array; each hole transmits light to a unique pixel on the array (see Fig. 1a,c). As the object passes over each hole along a microfluidic channel, it interrupts light transmissions through the hole. The time varying transmission trace represents a line scan across the object. The slanted hole arrangement ensures that adjacent line scans overlap and the object is fully scanned. By stacking the line traces together appropriately, we can then construct an object's image with resolution equal to the hole size (see Fig. 2).

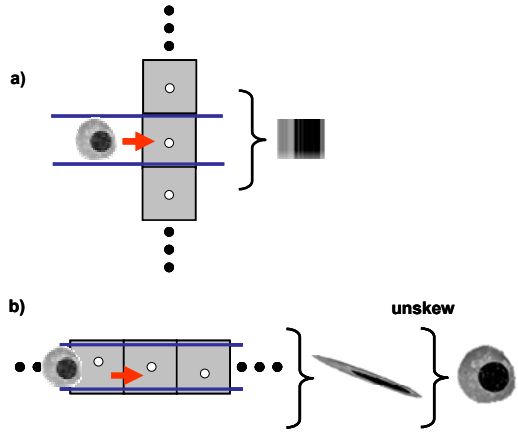

Figure 2: a) Non-OFM technique. A transmission image of the object can be obtained by simply stacking the transmission time traces collected as the object passes over the holes. This particular arrangement gives poor resolution as we cannot space the holes closer than a sensor pixel wide. (b) OFM technique. The line of holes along the channel is skewed. This way, we can space the holes as closely across the channel as we want (in latitude), while at the same time ensuring that there is a unique 1-to-1 mapping of holes to sensor pixels. As the object will pass over each hole at different time, we need to correct for the time delays in the transmission prior to image construction. This is easily done by unskewing the traces based on the flow velocity of the sample. Note that in the actual implementation, the line of holes and pixel array are parallel to each other and the microfluidic channel is simply emplaced at an angle with respect to the chip.

2. EXPERIMENTAL

Progressing from our initial proof-of-principle experiments [1-3], we recently implemented a complete on-chip OFM system. In this device, the base sensor chip is a 640×480 CMOS imaging sensor with pixel size of 9.9µm (Fig. 2(a)). We planarized the die with a 2µm thick layer of SU8 photoresist, and plated it with an aluminum layer of thickness 300nm. Holes of diameter 1µm were then fabricated on the metal layer via FIB. Finally, a 15 µm high and 50µm width channel in PDMS is placed on top of the hole array. The separation between adjacent holes across the channel is 500nm; this ensures that passing objects are fully scanned and sufficiently sampled. Two hole arrays are fabricated. The chip is reconfigured to output line scans from the pixel array directly beneath each hole array at a rate of 1000 fps. We demonstrated the system by imaging C. elegans.

C. elegans were flowed through the channel at an average speed of 500μm/s. The two hole arrays serves two functions. First, by knowing the time difference between the passage of each C. elegans across each hole array and the separation between the two array, we can determine the C. elegans' speed. Second, the two images acquired by the two hole arrays can be compared and correlated. If the images appear different, it implies that the C. elegans had rotated or changed form during the image acquisition process. This allows us to screen out images that have motional artifacts. Fig. 3 shows a typical set of C. elegans images acquired with our prototype.

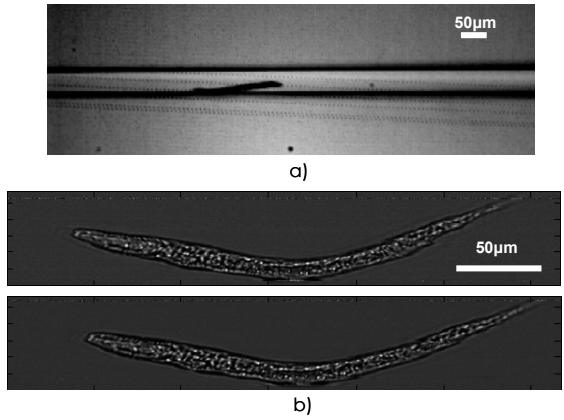

Figure 3: (a) *C. elegans* flowing through the on-chip OFM device. The holes separation is 9.9μm (or every CMOS pixels) along the channel and 500 nm across the channel. The holes are 1μm. b) An OFM image of a *C. elegans*.

The OFM's dual advantages of compactness and low cost open up a wide range of possible applications. For example, the OFM can be used in white-blood-cell-counting cytometry devices as image-based cell-type discriminators. Clinicians can use such units as disposable, point-of-care microscopes. Health workers in rural areas can use cheap, compact OFMs as part of their regular toolkit for malaria diagnosis. Further, the OFM can change the way a bioscientist tackles imaging problems. Potentially tens or even hundreds of OFMs can be fabricated onto a single chip. Such a device can be used to parallelize the imaging of a large number of microorganisms and dramatically improve throughput.

In summary, to our knowledge, this system is the first complete on-chip lensless high resolution microscope system ever reported. The simplicity of the system design and the absence of precision optical elements make the OFM highly suitable for inclusion in LOC systems. Finally, OFM variants that have super-resolution, fluorescence sensitivity and/or phase imaging capability can be readily implemented.

3. REFERENCES

[1] X. Heng, X. Cui, D. W. Knapp, J. Wu, Z. Yaqoob, E. J. McDowell, D. Psaltis, and C. Yang, *Optics Express*, vol. 14, pp. 10410-10425, 2006.

[2] X. Heng, L. R. Baugh, D. Erickson, Z. Yaqoob, P. W. Sternberg, D. Psaltis, and C. Yang, *Lab On A Chip*, vol. 6, pp. DOI: 10.1039/b604676b, 2006.

[3] X. Cui, X. Heng, J. Wu, Z. Yaqoob, A. Scherer, D. Psaltis, and C. Yang, *Optics Letters*, vol. 31, pp. 3161-3163 2006.

A MONOLITHIC EVANESCENT EXCITATION (EE)-BASED BIOCHIP FOR HIGHLY-SENSITIVE AND REAL-TIME FLUORESCENT DETECTION

Dzung Viet Dao, Nam Cao Hoai Le, Ryuji Yokokawa, John Wells, and Susumu Sugiyama

Graduate School of Science and Engineering, Ritsumeikan University, JAPAN

ABSTRACT

This paper presents a novel EE-based biochip for highly-sensitive and real-time fluorescent detection. The chip is monolithically mass-fabricated using low-cost Si micromachining and PDMS molding. The slide-format and monolithic chip can be utilized with both inverted and upright fluorescent microscope. Various sample delivery platforms, namely flow-cells, microchannels etc., can be attached to the chip by van-der-Waals contact. We then report the application of our chip with upright fluorescent microscope to detect real-time events including Brownian motion of Nile-red carboxylate-modified nanobeads and photobleaching of Tetramethylrhodamine (TMR) dye. Our miniaturized chip could be potentially integrated into a micro-total analysis system (μ-TAS).

Keywords: Evanescent Wave, Total Internal Reflection, Biochip, Fluorescent Detection

1. INTRODUCTION

The ability of evanescent illumination generated by total internal reflection (TIR) to detect real-time events has recently drawn the interest of researchers for studying the dynamics of biological systems from cell membrane to single bio-molecules [1]. Miniaturized and low-cost EE-based optical systems which can be integrated to μ-TAS could be an alternative to the expensive, conventional total internal reflection fluorescent microscopy (TIRFM) systems [2]. We propose a method to integrate miniaturized optical components, namely cylindrical microlens and prism into one single PDMS chip; thus assembly is unnecessary, and misalignment is eliminated, compared to previous work [2].

2. DESIGN AND FABRICATION

Figure 1(a) shows the cross sectional view of the EE-based chip in van-der-Waals contact with a flow-cell [3] which is used for sample delivery. The design, fabricarion and evaluation of the chip with an inverted fluorescent microscope have been reported elsewhere [3]. In brief, laser from an optical fiber is collimated by a cylindrical microlens, refracted twice at air/PDMS and PDMS/glass interfaces, respectively, and finally TIR at glass/water interface. The incident angle $\theta_i = 69.5^0$ is larger than the critical angle $\theta_C = 61^0$ (for the case of glass/water interface) satisfying the condition for TIR. The penetration depth of the evanescent field is approximately 300 nm based on our analytical calculation [3]. The Si mold is fabricated using 300 μm-thick wafers. From front-side, TMAH anisotropic etching of Si is used to form cavity of the prism and V-groove with side surfaces inclined 54.7º. The through-wafer DRIE from backside forms the cavity of the cylindrical microlens. The chip is then cast in PDMS using the fabricated Si mold (figure 1(b)). The dimensions (L × W × T) of the chip are 15 x 12 x 0.8 mm³ (Figure 1(c)).

978-0-9798064-0-7/μTAS2007/$20©2007CBMS

3. EXPERIMENTAL

The set-up for experiments using the EE-based chip with an upright fluorescent microscope is shown in figure 2. Laser beam from a laser diode (Melles Griot, 543.2 nm, 2 mW) is positioned perpendicularly into the coupling-lens by 2 adjustable mirrors (Sigma Koki, Japan). The coupling-lens focuses the beam into one end of an FC-connector single mode fiber (Sumitomo, Japan) while the other cleaved end is inserted into the PDMS chip. The friction force of the V-groove and the glass slide fixes the optical fiber inside the chip. The chip is then placed with the flow-cell facing an objective lens of an upright fluorescent microscope (NikonE600-FN) equipped with a Hamamatsu Orca-AG CCD camera. In each experiment, 10 μl of fluorescent aqueous samples are injected into the flow-cell. For observation of evanescent spots, TMR (C-1711, Molecular Probes, USA) solution in methanol with concentration from 1 mM down to 10 nM is evaporated on the glass slides of the flow-cell after 30 min of injection. For Brownian motion observations, Nile red carboxylate-modified 500 nm beads (CFP-0556-2, Spherotech, USA) suspended in Tween20/DI water at 0.05% volume fraction is used.

4. RESULTS AND DISCUSSION

Figure 3(a) shows the fluorescent image of the evanescent wave spot of TMR dye at 10X magnification and 1 mM concentration. As expected from the 1-D collimation capability of the cylindrical microlens, the evanescent spot is broadly extended in the longitudinal direction of the chip. The fluorescent intensity scan profile of figure 3(a) is shown in figure 3(b). As can be seen, the intensity in the center of the spot is very high compared to the outside background, i.e. more than 10 times higher. From figure 3(b), the width of the evanescent spot is measured to be 50 µm. Figure 4 shows the real-time photobleaching curves of TMR dye at 100nM and 10nM concentration detected by the chip. The 10nM concentration of TMR dye is also the limit of detection for our biochip. The capability of the chip to detect dynamic events is demonstrated by observing the Brownian motion of 500nm nanobeads. In contrast to the low signal-to-noise ratio (SNR) of the wide-field fluorescent image (figure 5(b), the EE-based image (figure 5(a)) has a very high SNR

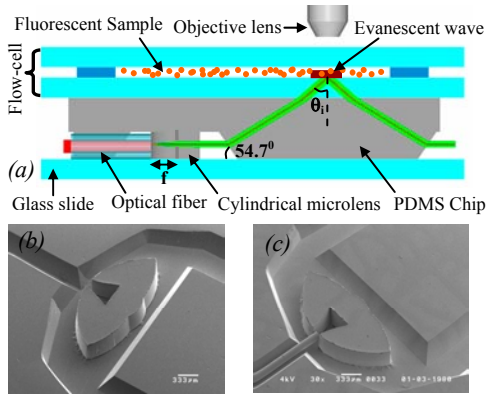

Figure 1(a). Cross sectional view of the monolithic EE-based biochip with flow cell attached (b) SEM micrograph of the PDMS chip (c) Picture of the PDMS EE-based chip.

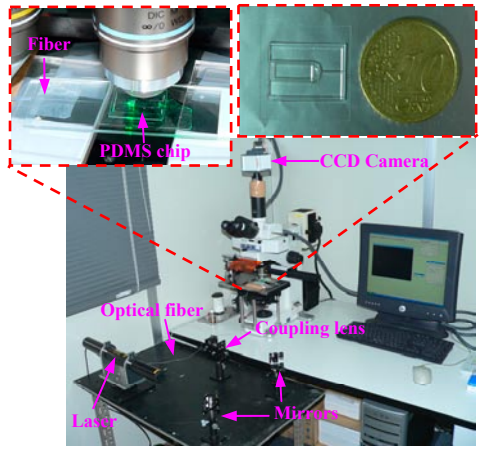

Figure 2. Experimental set-up for fluorescent detection

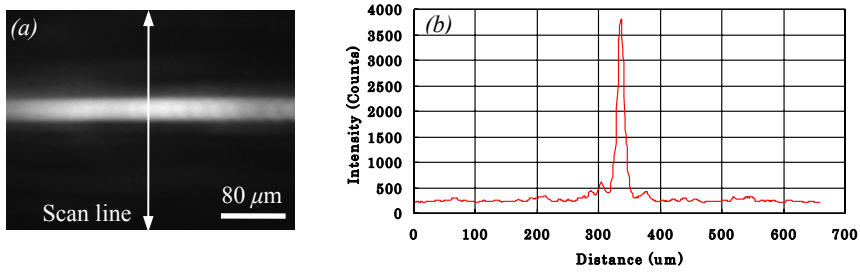

Figure 3. (a) Evanescent spot image of TMR dye and (b) its fluorescent intensity scan profile

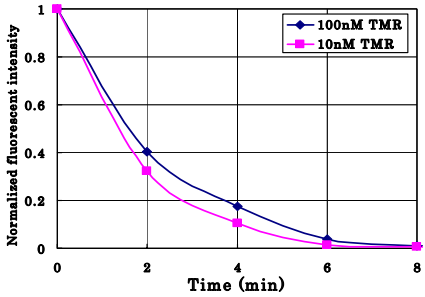

Figure 4. Photobleaching curves of TMR dye

due to evanescent illumination. It, therefore, allows us to detect the Brown motion of a single bead. Figure 5(c-f) show a frame sequence of real-time motion of 3 individual nanobeads relatively to the field of view of 16 μm x 16 μm and the 300 nm depth of the evanescent field.

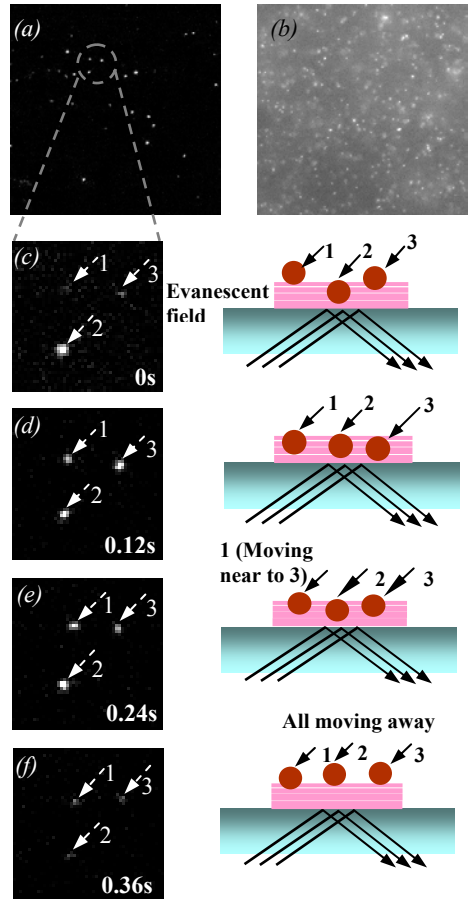

Figure 5. Brownian motion Nile red carboxylate-modified nanobeads

5. CONCLUSIONS

The design and fabrication of the novel EE-based biochip have been presented. The evaluation of the biochip with fluorescent detection of TMR dye and Brownian motion of nanobeads have also been performed. Our biochip would be a useful evanescent illumination platform integrated into a μ-TAS.

ACKNOWLEDGEMENTS

This study was partially supported by the MEXT of Japan.

REFERENCES

[1] Y Sako et al. *Nat. Rev. Mol. Cell. Bio.* September supplement, pp. SS1-SS5, 2003
[2] N Chronis et al. *Proceedings of 7th μTAS 2003*, pp. 1323-26, 2003
[3] NCH Le et al. *J. Micromech. Microeng.* Vol 17, pp. 1139-1146, 2007

DIRECT DETECTION OF BIOMOLECULAR INTERACTIONS WITH BIOACTIVATED NANOPORES

AmirAli H. Talasaz[1,2], Rod M. Aliabadi[2], Baback Gharizadeh[2], Shadi Shokralla[2], Mostafa Ronaghi[2], Fabian Pease[1] and Ronald W. Davis[2]

[1] *Electrical Engineering Department, Stanford, CA*

[2] *Stanford Genome Technology Center, Stanford, CA*

ABSTRACT

We have developed a versatile nanopore device for numerous analytical and detection applications that benefits medical and pharmaceutical fields. We have demonstrated the electrical detection of single immunocomplex formation and DNA hybridization.

Keywords: Bioactivated nanopores, label-free detection, immunodetection, DNA-hybridization detection

1. INTRODUCTION

Bioactivated nanopores have been introduced as one of the most promising approaches for label-free and electronic monitoring of biochemical bindings at the single-molecule level [1]. Here, we have shown the application of this platform by detecting a single human chorionic gonadotropin (hCG) immunocomplex and also by detecting DNA hybridization.

2. THEORY

Bioactivated nanopores are customized nanopore devices with a biological macromolecule attached in the pore as the probe. Any chemical binding to the biomolecule can be detected by monitoring the ionic current passing through the nanopores. To detect a single-molecule of hCG and DNA hybridization, we used a single nanopore activated with primary antibody against hCG and an array of nanopores activated with primers respectively.

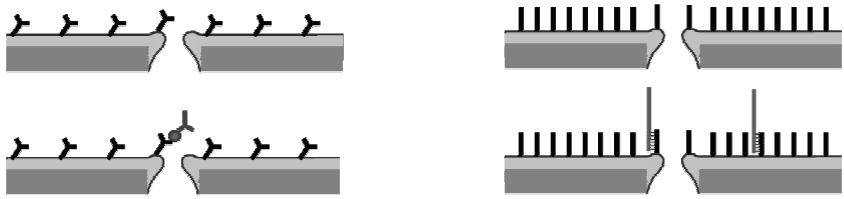

Figure 1. (Left) View of the experimental steps for monitoring immunocomplex formation. First, the nanopore is bioactivated with the primary antibody. Then the premixed antigen-secondary antibody is added. (Right) For detecting the hybridization of DNA, first the nanopores are bioactivated with primers. Then the hybridization is detected by monitoring the rectification of ionic current.

3. RESULTS AND DISCUSSION

The nanoscale holes (about 10nm diameter, see Fig. 2) are fabricated in a freestanding silicon nitride membrane made with silicon micromachining techniques similar to earlier approaches [2]. The nanopore is bioactivated via the immobilization of a biomolecular probe on the pore. Subsequently, these devices can be used to study the interactions

978-0-9798064-0-7/μTAS2007/$20©2007CBMS

between probe molecules and solutes being investigated by monitoring the ionic current passing through the nanopore.

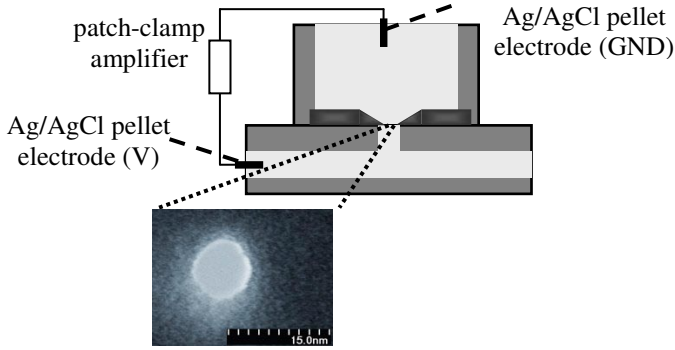

Figure 2. The single nanopore apparatus and TEM image of the nanopore.

By using single synthetic bioactivated nanopores, we have been able to monitor the formation of a single immunocomplex; consequently, allowing us to demonstrate the ability to detect molecular interactions at single molecular levels. Specifically we have been able to monitor the interactions of hCG and a matched antibody pair. First, the primary hCG monoclonal antibody is introduced into the nanopore with a concentration of 0.5mg/ml (~5 nM) in pH 6 buffer. The current is monitored until an antibody is captured at the opening of the nanopore. Subsequently, the chambers are washed and the secondary antibody with concentration of 4 mg/ml (~20 nM) is added as a control experiment. During 30 minutes, no further sudden blockage in ionic current was detected. Finally, the pre-mixed solution of antigen and secondary antibody, with concentrations of 0.2 μg/ml (~5 nM) and 4 μg/ml (~20 nM) respectively, is added. Within 30s of injection, current reduces by about 50% as shown in Fig. 3, indicating another binding event. No more sudden changes in current are observed during one hour of incubation. After washing, the current level remains unchanged confirming the detection of a single immunocomplex.

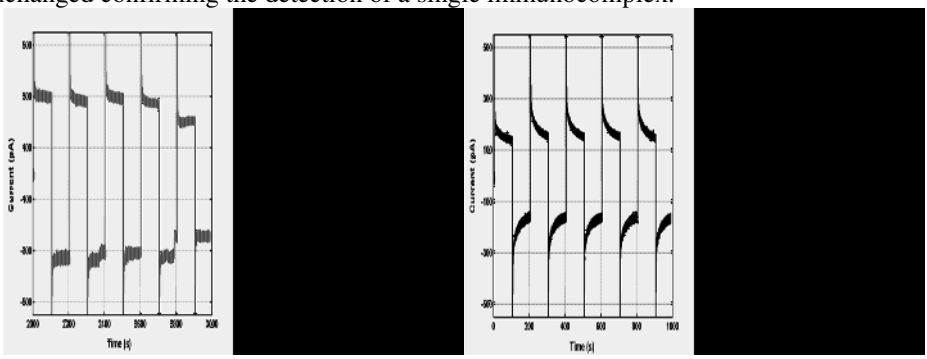

Figure 3. (Left) The recorded ionic current passing through the nanopore during the bioactivation phase where a square-wave voltage is applied across the pore. After forty minutes, a partial blockage was detected followed by a more substantial blockage due to the antibody immobilization on the nanopore. (Right) The current passing through the bioactivated nanopore after the injection of the premixed antigen-secondary antibody solution.

By using an array of synthetic bioactivated nanopores, we have directly detected the hybridization of single stranded target DNA to the immobilized primers. These nanopores have been bioactivated using short length primers (20-base) and then incubated with single stranded target DNA (303-base long) molecules with concentration of 65 nM. Thereafter, the ionic current passing through nanopores is monitored in a buffered solution of 100mM KCl with pH 6.0. As shown in Fig. 4, the amplitude and rectification of the current change by hybridization of the introduced DNA.

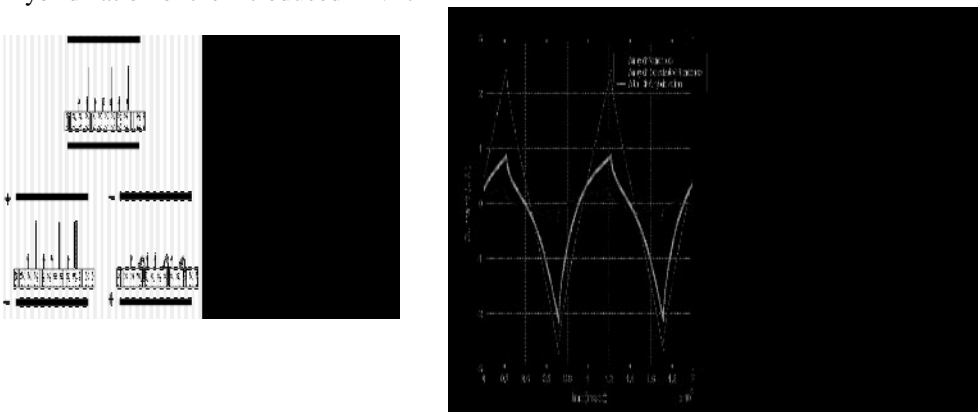

Figure 4. (Left) The hybridized DNA strands are pulled inside the nanopores in one voltage polarity and pulled toward top electrode in the opposite polarity. (Right) The current passing through an array of nanopores, the array of nanopores bioactivated with primers before and after DNA hybridization are shown.

4. CONCLUSIONS

The bioactivated nanopores have the advantages of real-time, label-free electrical detection of biomolecular interactions. A portable handheld device is envisioned for multiplex high throughput analysis using an array of nanopores and spotting different probe molecules. The method opens new avenues for numerous applications in proteomics and genomics such as protein-protein interactions, characterization of candidate proteins and molecules for development of new drugs, microbial and viral detection, mutation analysis and general diagnostics.

REFERENCES

[1] "Fabrication of Customized Bioactivated Nanopore Devices," A. H. Talasaz, D. Pantelis, M. Ronaghi, F. Pease, and R. W. Davis, Proceedings of uTAS, (2005).

[2] “Formation of nanopores in a SiN/SiO2 membrane with an electron beam,” M. Y. Wu, D. Krapf, M. Zandbergen, and H. Zandbergen, Applied Physics Letters, **87**, (2005).

ULTRA-SENSITIVE MAGNETIC IMMUNOSENSING PLATFORM BASED ON THE COMBINED MANIPULATION AND DETECTION OF MAGNETIC PARTICLES

G. Reekmans, C. Liu, R. De Palma, R. Wirix-Speetjens, W. Laureyn* and L. Lagae

NEXT-Nano-enabled Systems, Interuniversity Microelectronics Center (IMEC), Belgium

ABSTRACT

We report on a novel magnetic biosensing concept based on the positioning of magnetic particles towards the most sensitive location on the magneto-resistive sensors. Exploiting this concept, we have constructed an immunosensing platform that allows highly sensitive detection of proteins over a wide range of target concentrations.

Keywords: Magnetic sensor, spin-valve, magnetic particle, immuno-assay, S100ββ

1. INTRODUCTION

Non-optical biosensors based on microelectronics are gaining increasing attention for μTAS as they offer a number of advantages such as small size, fast in use, simplicity in operation, and eventually low cost. Within this area, magnetic biosensors are a suitable candidate for highly sensitive biosensing. In this approach, the classical optical reporters (*e.g.* fluorescent labels) are replaced by superparamagnetic particles, which can be detected by micro-magnetic sensors, *e.g.* magneto-resistive sensors.

The pioneering work in the field of magneto-resistive biosensors was performed by the Naval Research Laboratory [1], followed by other research groups [2, 3, 4]. Such state-of-the-art has mainly focused on the detection of DNA hybridization. Although many of these studies have proven the high physical sensitivity of magneto-resistive sensors, the establishment of dose-response curves for the detection of proteins is largely unexplored and their capability to sensitively detect low concentrations of target molecules for diagnostic applications remains unproven.

In this work, our aim was to increase the sensitivity of magneto-resistive immunosensors, based on spin-valves, by combining manipulation and detection of magnetic particles.

3. EXPERIMENTAL

A spin valve sensor consists of multiple magnetic and non-magnetic metal layers. The resistance of the spin valve sensor changes in response to the external magnetic field and hence an output voltage change can be measured. Our magnetic chips consist of two rows of 12 sensors and each sensor is made of 9 parallel spin-valves that function both as the alignment and the detection elements.

To allow for immunosensing, a sandwich assay was built up on the surface of the magnetic chips (Figure 1). As a model analyte we targeted S100ββ, a diagnostic marker for

* E-mail: wim.laureyn@imec.be

978-0-9798064-0-7/μTAS2007/$20©2007CBMS

stroke and minor head injury. Packaged chips were first cleaned and their gold surface was coated with a mixed SAM of the alkane thiols SH-C_{16}-COOH and SH-C_{11}-OH [5]. The thiol modified surfaces were activated with EDC/NHS, followed by the covalent immobilisation of the primary antibody (*i.e.* S53) and blocking steps with 5% BSA and 1M triethylene-glycol monoamine. Next, the antibody-modified samples were incubated with different S100ββ concentrations followed by the biotinylated secondary antibody (*i.e.* S36). Finally, the samples were incubated with 300 nm streptavidin-coated magnetic particles from Ademtech. Incubations with S100ββ, secondary antibody and magnetic particles were performed in HBS containing 5 % BSA and 0.1 % Tween-20® to suppress non-specific adsorption.

4. RESULTS AND DISCUSSION

For spin valve sensors, the sensor signal shows a clear dependence on the position of the magnetic particles relative to the sensor location [6]. In order to increase the sensitivity of magneto-resistive sensors for immunosensing we have combined the manipulation and detection of magnetic particles using a "link-cut-move" methodology (Figure 1). Following the sandwich assay formation, specifically bound particles were released by applying 10 mM NaOH. The current-induced magnetic field then allows to attract the released magnetic particles to the sensor edges, where the field is maximal [6]. This way, the particle is maximally magnetized and hence the stray field is most effectively collected by the spin valve sensor. Figure 2 shows microscopic images of magnetic particles bound via a sandwich assay and after alignment, proving the feasibility of our approach.

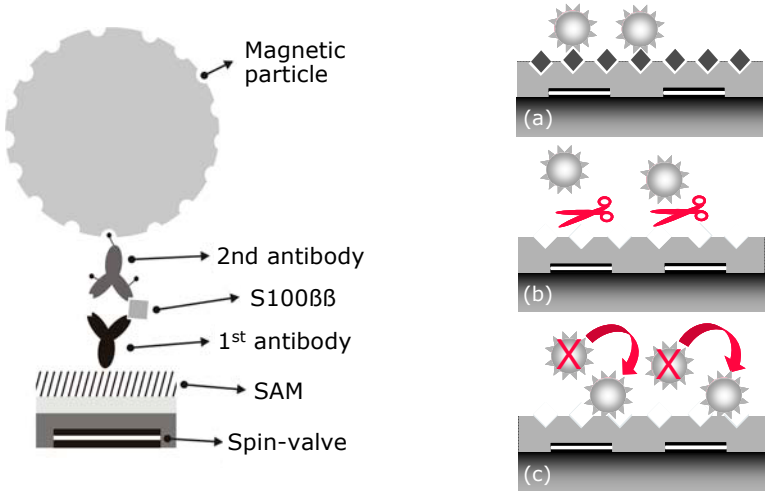

Figure 1. Left: scheme of the sandwich assay on the device surface. Right: scheme of the "link-cut-move" method. (a - link) the magnetic particles are bound onto the sensor area in a random fashion; (b - cut) the particles are released from the surface; (c - move) the particles are positioned to the edge of the spin valve sensor, where the magnetic field is maximal [6].

Based on the approach outlined above we have constructed a dose-response curve for the detection of S100ββ (Figure 2). As expected, the sensor signal for a random distribution of particles approaches zero. Following the "link-cut-move" scheme, the sensor signal was

strongly enhanced allowing us to specifically detect S100ββ from ~1 ng/mL down to ~25 pg/mL (~1 pM). In future work, we will exploit this concept further to e.g. DNA sensing. In addition, the impact of integration with microfluidics and the use of magnetic attenuation principles will be investigated.

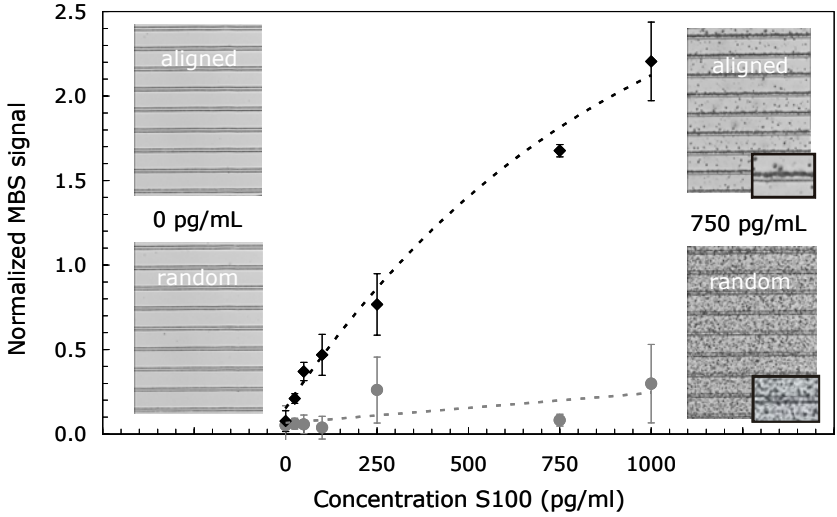

Figure 2. Center: dose-response curve for the detection of S100ββ before (*random-grey circles*) and after (*aligned-black diamonds*) particle regeneration and alignment. Left and right: microscopic images for magnetic particles bound to the surface in a sandwich assay format (*random*) and following particle regeneration and alignment (aligned).

5. CONCLUSIONS

We established a dose-response curve that proofs our magnetic biosensing platform can specifically detect S100ββ, a diagnostic marker for brain damage, down to ~1pM, while maintaining a broad dynamic detection range of ~2 decades. We believe this will provide a universal tool for the highly sensitive and specific detection of biomolecules, with potential for combination with immunomagnetic isolation.

ACKNOWLEDGEMENTS

The authors thank Stijn de Jonge and Erwin Vandenplas for assistance in processing and INESC-MN (Portugal) for the deposition of spin-valve structures. The authors would also like to thank the members of the biosensor group in IMEC for their scientific support.

REFERENCES

[1] J.C. Rife et al. *Sensors and Actuators A* **107** (2003) pp. 209-218.
[2] J. Schotter et al. *Biosensors & Bioelectronics* **19** (2004) pp. 1149-1156.
[3] D.L. Graham et al. *TRENDS in Biotechnology* **22** (2004) pp. 455-462.
[4] R. Wirix-Speetjens et al. *Encyclopedia of Sensors*, Eds. C.A. Grimes, E.C. Dickey, M.V. Pishko, American Scientific Publishers, 5 (2006) pp 403-414.
[5] F. Frederix et al. *Langmuir* **19** (2003) pp. 4351-4357.
[6] R. Wirix-Speetjens et al. *Journal of Applied Physics* **99** (2006) 103903.

ULTRASENSITIVE IMMUNOASSAY ON A POWER-FREE MICROCHIP WITH LAMINAR FLOW-ASSISTED SIGNAL AMPLIFICATION

Kazuo Hosokawa, Masaki Omata, and Mizuo Maeda
Bioengineering Laboratory, RIKEN, JAPAN

ABSTRACT

This paper demonstrates ultrasensitive immunoassay on a microchip which needs no external pumping systems. Fluorescence signal was amplified with a newly devised method: laminar flow-assisted dendritic amplification (LFDA). Specifically, FITC-labeled streptavidin and biotinylated antibody were simultaneously but separately supplied to the captured analyte molecule using laminar flow to construct a dendritic structure there. We have achieved analysis of C-reactive protein in human serum with analysis time of 23 min, a sample volume of 0.5 μL, and a limit of detection of 0.15 pM (equivalent to 75 zmol) under a common fluorescence microscope.

Keywords: immunoassay, laminar flow, dendritic amplification, power-free microchip

1. INTRODUCTION

Recently, we demonstrated immunoassay on a "power-free" microchip [1]. This microchip exploits the high gas solubility in PDMS, and does not require external power sources or mechanical connections for fluid pumping. However, the limit of detection (LOD) was not very low (sub-nM) because of the lack of signal amplification. To improve the LOD, we first tried enzyme-linked immunosorbent assay (ELISA) without success.

In this paper, we report a new signal amplification method: laminar flow-assisted dendritic amplification (LFDA), in which a dendritic structure is constructed on the captured analyte molecule by supplying two building blocks, FITC-labeled streptavidin and biotinylated antibody in this paper, from laminar streams (Figure 1). We adopted human C-reactive protein (CRP) as a model analyte in accordance with the previous report [1]. With LFDA, we have improved the LOD by 3 orders of magnitude.

Dendritic amplification schemes have been reported by several groups [2], but these schemes have not yet become popular, probably due to the need for iterative incubation steps for layer-by-layer growth of the dendritic structure. We have reduced the incubation steps by employing the continuous reaction at the contact line among two laminar streams and the solid surface. So far, such laminar flow-assisted, 3-phase reactions have been utilized mainly for fabrication purposes [3], but rarely for analytical purposes [4].

2. EXPERIMENTAL

Figure 1 illustrates the scheme of LFDA. The PDMS-glass hybrid microchip containing Y-shaped microchannels (100 μm wide, 25 μm deep, and 12 mm long) was fabricated through the soft lithography process. Immunoassay was carried out at room temperature. The power-free sequential injection technique [1] was used for pumping the necessary solutions listed in Table 1. In advance, CRP was diluted with CRP-free human serum (HyTest), anti-CRP was dissolved in PBS (pH 7.5), and other components were dissolved in 1% BSA in PBS. Steps 1 through 3 in Table 1 were carried out to form the sandwich

978-0-9798064-0-7/μTAS2007/$20©2007CBMS

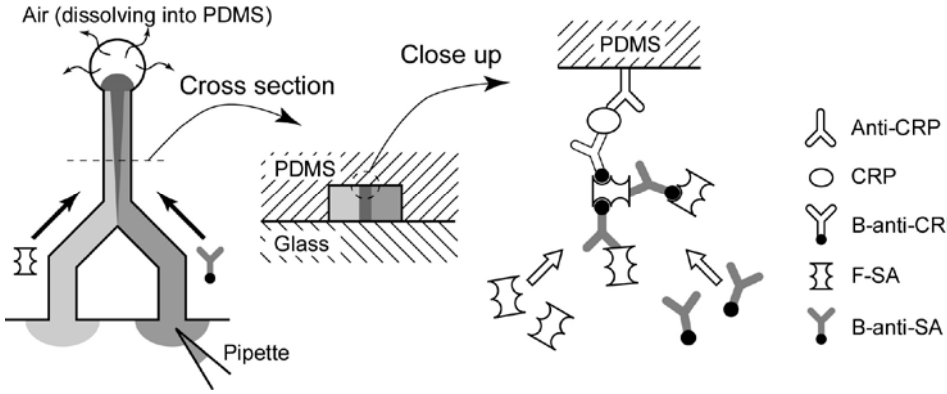

Figure 1. LFDA on a power-free microchip. After construction of the sandwich immunocomplex (anti-CRP)–CRP–(B-anti-CRP), F-SA and B-anti-SA are supplied using laminar flow. Abbreviations: CRP, C-reactive protein; B-anti-CRP, biotinylated anti-CRP; F-SA, FITC-labeled streptavidin; B-anti-SA, biotinylated anti-streptavidin.

immunocomplex onto the PDMS surface, using biotinylated secondary antibody (B-anti-CRP). We then introduced FITC-labeled streptavidin (F-SA) and biotinylated anti-streptavidin (B-anti-SA) at the same time for LFDA. The two components were continuously supplied onto the sandwich immunocomplex to grow a dendritic structure. During the flow (without washing), the fluorescence images of the microchannel were taken using an inverted fluorescence microscope (TE2000-U, Nikon), and analyzed using image analysis software (ImageJ, NIH).

3. RESULTS AND DISCUSSION

Figure 2 shows a typical fluorescence image during the LFDA with a high CRP dose (20 nM). As expected, a bright line appeared in the middle of the microchannel, where the 3-phase (F-SA, B-anti-SA, and the PDMS surface) contact line should be formed. Fluorescence from the bulk F-SA stream was not discernible under this imaging condition. We set a detection point at 200 μm downstream from the confluent point. The peak intensity was defined as the signal.

Figure 3A shows the time course of the signals generated by the LFDA for the immunoassay of CRP with various concentrations. In this time scale, a general tendency of signal evolution is shown best by the intermediate concentration (0.20 nM, dashed line).

Table 1. Summary of the assay procedure.

	Left inlet	Right inlet
Step 1 (~7 min)	anti-CRP 0.5 mg/mL, 0.5 μL	anti-CRP 0.5 mg/mL, 0.5 μL
Step 2 (~4 min)	Blocking buffer [a] 0.5 μL	Blocking buffer [a] 0.5 μL
Step 3 (~4 min)	CRP in human serum 0–20 nM, 0.5 μL	B-anti-CRP 75 μg/mL, 0.5 μL
Step 4 (10 min)	F-SA 75 μg/mL, 3 μL	B-anti-SA 75 μg/mL, 3 μL

[a] 0.1% Roche Blocking Regent (#1096176) with 1% BSA.

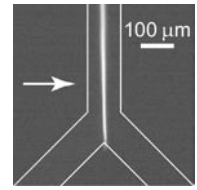

Figure 2. Representative fluorescence image of the microchannel executing LFDA. The arrow indicates the detection point. CRP concentration, 20 nM; amplification time, 10 min.

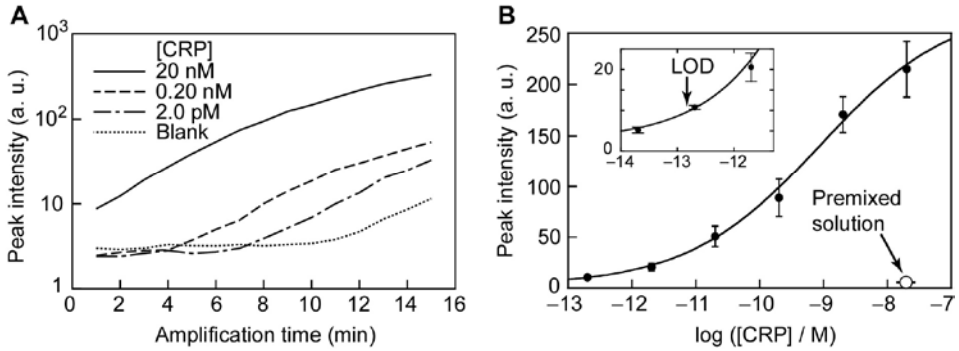

Figure 3. (A) Time course of the peak intensities during the LFDA for the immunoassay of CRP. (B) Calibration curve of the immunoassay of CRP with the LFDA for 10 min. The inset shows the low concentration range. The open circle indicates the data from another experiment using a premixed solution of F-SA and B-anti-SA. The error bars indicate ±1 σ ($n \geq 3$).

Namely, the signal is negligible at the beginning (< 5 min). Once it rises, it exponentially grows (5–11 min), and then gradually saturates (> 11 min). For the blank sample (dotted line), the exponential growth seeded by nonspecific adsorption began at 11 or 12 min. Therefore, we decided that the optimal amplification time was 10 min. The total assay time was ~23 min including the antibody immobilization step.

Figure 3B shows the calibration curve of this immunoassay followed by the LFDA for 10 min. The LOD was calculated as 0.15 pM (17 pg/mL). This value favorably compares with those of the previously published ELISA methods for CRP, 1–10 pM [5,6]. Furthermore, we consumed only 0.5 μL of the sample solution without dead volume. This means that we were able to detect 75 zmol of CRP.

Incidentally, we also tried another amplification method using a premixed solution of F-SA and B-anti-SA, and obtained negative results (Figure 3B, open circle). After formation of the sandwich immunocomplex, we mixed F-SA and B-anti-SA off-chip, and immediately (< 15 s) injected into the microchannel. The resulting signal was surprisingly low. We have proven that F-SA and B-anti-SA must be supplied separately.

4. CONCLUSIONS

The LOD of immunoassay on the power-free microchip has dramatically been improved by the LFDA, which exploits the advantage inherent to the microchip format. No specialized chemicals or instruments were required. The LFDA would be possible with other building blocks such as gold nanoparticles and quantum dots. The combination of the power-free microchip and the LFDA will provide a new opportunity for point-of-care testing.

REFERENCES

[1] K. Hosokawa, M. Omata, K. Sato, M. Maeda, *Lab Chip* 6, 236–241, (2006).
[2] F. Lucarelli, G. Marrazza, M. Mascini, *Langmuir* 22, 4305–4309, (2006).
[3] P. J. A. Kenis, R. F. Ismagilov, G. M. Whitesides, *Science* 285, 83–85, (1999).
[4] Y. Sato, K. Sato, K. Hosokawa, M. Maeda, *Anal. Biochem.* 355, 125–131, (2006).
[5] W. L. Roberts, et al. *Clin. Chem.* 46, 461–468, (2000).
[6] H. R. Zhang, M. E. Meyerhoff, *Anal. Chem.* 78, 609–616, (2006).

MICROFLUIDIC PWM GENERATION OF CHEMICAL SIGNALS

Farouk Azizi, Li Chen and Carlos H. Mastrangelo
Electrical Engineering and Computer Science Department
Case Western Reserve University, USA

ABSTRACT

We demonstrate on-chip generation of chemical signals using pulse width modulation (PWM) and filtering. In PWM, solvent and concentrated analyte streams are switched rapidly to produce a single, constant velocity, digitally encoded analyte flow stream. The code is then filtered and averaged out by Taylor dispersion producing an output concentration proportional to the code. A two-bit PWM signal generator chip was implemented with two-level PDMS technology. The chip was tested at 4-15 Hz switching rates for output flows of 15 μL/min. Several time-dependent analyte waveforms have been generated with this chip.

Keywords: Microfluidics mixer, Chemical signal, PWM

1. INTRODUCTION

Dynamic chemical signals have many applications in life sciences ranging from analyte-ligand analysis, to the regulation and probing of complex cellular response. This paper discusses a method for generation of chemical signals with microfluidic chips. In [1-3] we used static microfluidic mixing networks [1-3] to produce a series of binary weighted analyte dilutions [5]. Corresponding weighted network outputs are selectively tapped with flow multiplexers, and the multiplexer outputs are mixed to produce a single flow output that encodes the multiplexer digital code into a corresponding output concentration.

In this paper we discuss a signal generation technique that does not require dilution networks. The concentration of the output flow is instead determined by a rapidly pulsing sequentially encoded flow stream. Figure 1 shows the basic 1-bit scheme. The output flow of a 1-bit multiplexer (MUX) is rapidly switched between a fixed analyte flow of concentration $C = C_o$ or a pure solvent flow with $C = 0$. The flow switching is controlled by digitally encoded clock signal ϕ. The stream of analyte and solvent pulses travels through a long resistive network where the pulses are rapidly mixed and averaged by Taylor dispersion. The wider the pulse stream is over a fixed period cycle the higher its average is; hence this technique is known as PWM. In frequency domain, the long resistor exhibits a low pass filter (LPF) characteristic that smoothens out the high speed digital encoded pulses quickly producing an output signal proportional to the PWM code.

2. CHIP DESIGN AND FABRICATION

Figure 2 shows a simplified schematic of the fabricated two-bit PWM signal generation chip. Each bit multiplexer has of four input and two output paths and eight flow control valves. Three input paths of MUX_B1 are connected to the solvent and the fourth path to the analyte (a fluorescent dye of concentration C_o) and two input paths of MUX_B0 are

978-0-9798064-0-7/μTAS2007/$20©2007CBMS

connected to the analyte and the other two to the solvent. The multiplexers in the chip are driven by a sequence of binary bit pulse signals of $b_0(t)$, $\overline{b_0}(t)$, $b_1(t)$ and $\overline{b_1}(t)$ which depend on the desired digital code. When mixing the output flows of the two multiplexers the output flow has concentration $C_{out}(t) = \frac{C_o}{2} \cdot [b_0(t) + \frac{b_1(t)}{2}]$; hence a two-bit concentration digital to analog conversion (C-DAC) can realized in a single pulse cycle.

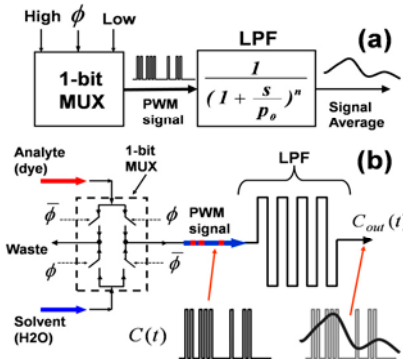

Figure 1. (a) Basic idea of PWM. (b) PWM C-DAC in more details.

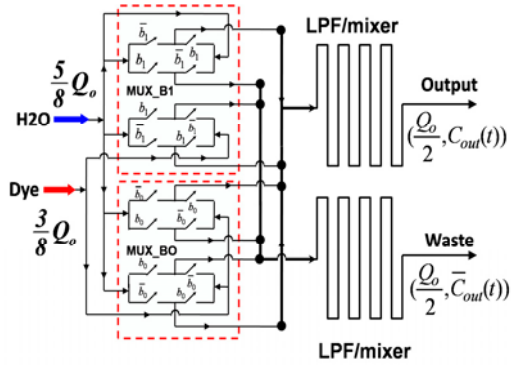

Figure 2. Schematic of microfluidic circuit for a two-bit PWM C-DAC.

More discrete output levels for conversion of codes with higher number of bits require more pulses per cycle. If each pulse has exactly the same width, for an N-cycle converter we obtain the discrete equation

$$C_{out} = \frac{C_o}{2N} \cdot \sum_{i=1}^{N} [b_0(i) + \frac{1}{2} \cdot b_1(i)] \qquad (1)$$

For example, to obtain sixteen distinct discrete concentration levels, the two-bit chip must use $N=5$. Figure 3 shows an example of PWM signals for a 16-level (4-bit) conversion. The top two signals correspond to least and most significant bits of the code. The bottom signal is the average of the output concentration over the cycle.

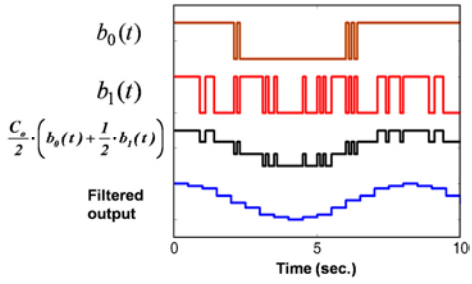

Figure 3. Signals in 5-cycle, two-bit PWM C-DAC.

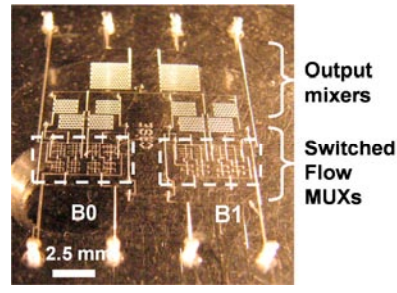

Figure 4. Photograph of the PWM C-DAC chip

3. EXPERIMENTAL RESULTS

Figure 4 shows a photograph of the two-bit PWM chip constructed using a two-level PDMS process [7]. All flow channels were 25 μm wide. Figure 5 illustrates a time

sequence of the device switching in operation. All measurements were recorded using a Hamamatsu EM-CCD camera. Fluorescein disodium salt (0.1 mg/ml) and water were used as analyte and solvent, respectively. The average flow rate was constant at ~12.5 μL/min. Figure 6 shows examples of synthesized sawtooth, ramp and sinusoidal fluorescein signals with a four bit digital to analog conversion scheme which was used with five clock cycles. At a PWM pulse rate of 5 Hz a single conversion requires 1 sec. Repeated cycles (holds) were introduced to maintain a steady level for an arbitrary time duration. Pulse rates as high as 15 Hz were used in this chip. Through careful design of the LPF the high frequency ripples of the stream pulses can be effectively eliminated.

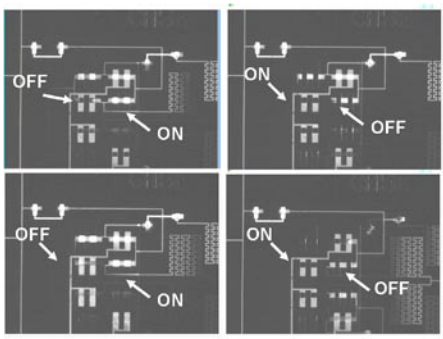

Figure 5. Demonstration of flow switching in PWM signal generation showing mixing for different sequential digital codes.

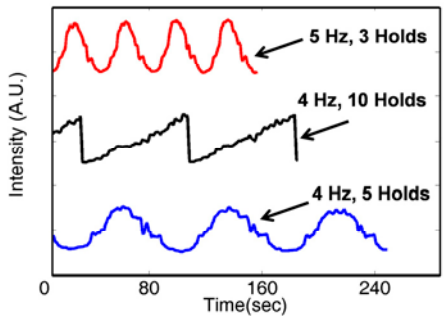

Figure 6. PWM generated fluorescein waveforms for different frequencies and holds (repeated cycles).

REFERENCES

[1] X. Jiang, J. M. K. Ng, A. D. Stroock, S. K. W. Dertinger and G. M Whitesides, *A miniaturized, parallel, serially diluted immunoassay for analyzing multiple antigens*, J. Am. Chem. Soc., Vol. 125, pp. 5294-5295, (2003).

[2] S. C. Jacobson, T. E. McKnight, and J. M. Ramsey, *Microfluidic devices for electrokinetically driven parallel and serial mixing*, Anal. Chem., Vol. 71, pp. 4455-4459, (1999).

[3] S. K. W. Dertinger, D. T. Chiu, N. L. Jeon and G. M. Whitesides, *Generation of gradients having complex shapes using microfluidic networks*, Anal. Chem., Vol. 73, pp. 1240-1246, (2001).

[4] F. Lin, W. Saadi, S. W. Rhee, S.-J. Wang, S. Mittal, and N. J. Leon, *Generation of dynamic temporal and spatial concentration gradients using microfluidic devices*, Lab-on-a-chip, Vol. 4, pp. 164-167, (2004).

[5] L. Chen, F. Azizi and C. H. Mastrangelo, *The digital generation of analog chemical signals*, MicroTAS 2006, pp. 1109-1111, (2006).

[6] I. Glasgow, S. Lieber and N. Aubry, *Parameters influencing pulsed flow mixing in microchannels*, Anal. Chem., 76, 4825-4832, (2004).

[7] M. A. Unger, H. P. Chou, T. Thorsen, A. Acherer, S. R. Quake, *Monolithic Microfabricated Valves and Pumps by Multilayer Soft Lithography*, Science, Vol. 288, pp. 113-116, (2000).

EFFICIENT ADDRESSABLE FLUID CONTROL SYSTEM USING PNEUMATIC VALVE ARRAY

Kentaro Kawai[1], Masaki Kanai[1,2] and Shuichi Shoji[1]

[1] *Major in Nanoscience and Nanoengineering, Waseda University, Japan*

[2] *Technology Research Laboratory, Shimadzu Corporation, Japan*

ABSTRACT

An efficient control method of a large number of valves is proposed. This method can control (m * n) valve matrix with (m + n) control pressure lines. With this method, the number of off-chip valve controller and world-to-chip connector are reduced remarkably. Using a fabricated device of 16 * 16 microvalve array, 256 valves controlled by 32 off-chip valve successfully. The switching speed of the valves in a selected line is 200 msec.

Keywords: micro valve, pneumatic valve, valve control

1. INTRODUCTION

Microvalves are one of most important fluidic components for the fluid control and widely-used for switching, valving and pumping of fluid in the field of μTAS. Various structures and methods of on-chip valve had been reported for realizing on-chip fluid control. On-chip pneumatic actuation is employed in many microvalves due to its simple structure and easy fabrication. High efficient multi arrayed microfluidic systems using pneumatic valves have been developed for high throughput screening or multi synthesis [1-4]. However, the operation of pneumatic valve is given by off-chip solenoid valve in fact, a large number of valve array increases the number of off-chip control valves and world-to-chip connectors. To solve this problem, we propose a novel valve control method which can control a large number of channel flows using a small number of off-chip control valves.

2. CONCEPT

Fig. 1 shows the structure of the proposed valve array. The valve control is symmetrical for the C-MOS memory-like matrix addressing which consists of the pressure inputs of column channels and line channels. The on-chip valves are driven by the compressed air from the column channels called “drive channel”. The line channels called “gate channel” select the line of activate valves. To make the valve ON, applied the compressed air to the drive channel and open the gate channel as shown in Fig. 2(a). To make the valve OFF, open the drive channel and the gate channel as shown in Fig. 2(b). The gate channels are the pinched signal lines which keep the state of ON/OFF. The state can be changed only after the gate channel is opened.

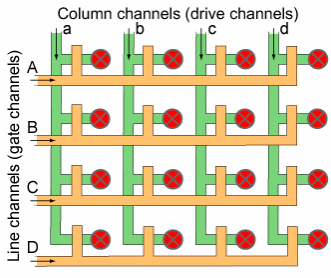

Fig.1 Structure of the addressable fluid control system with 4 * 4 valve array.

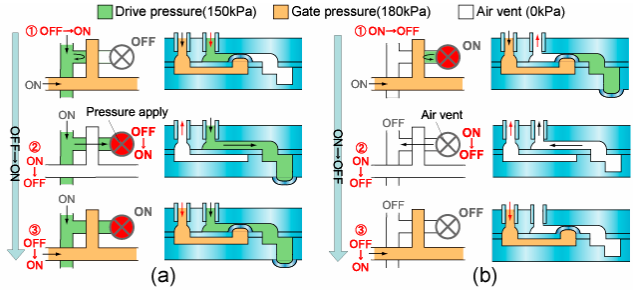

Fig.2 Schematic valve membrane operation. (a) OFF to ON and (b) ON to OFF.

978-0-9798064-0-7/μTAS2007/$20©2007CBMS

3. EXPERIMENTAL AND RESULTS

A prototype device of 4 * 4 and 16 * 16 microvalve array was fabricated and tested. The device has a laminated structure consist of four layers of PDMS as shown in Fig. 3. Fig. 4 shows the operation of an on-chip valve switching of 4 * 4 valve array. The inert liquid (Fluorinert™, 3M) was filled in all drive and gate channels instead of the compressed air. The applied pressure to drive channels and gate channel are 150 kPa and 180 kPa respectively. Fig. 4(a-c) show the operation of OFF to ON and Fig. 4(e-g) show the operation of ON to OFF. Fig. 4(d) and Fig. 4(h) show the images of OFF and ON injecting 1μm fluorescent beads suspension. Fig. 5(a-d) show the 4 * 4 valve matrix operation. The switching speed of the valves of the selected line is 200 msec. Sixteen valves can be controlled within 800 msec successfully.

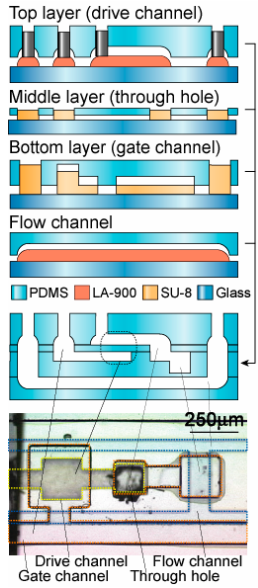

Fig.3 Fabrication process of the four PDMS layers and top view of the stacked device.

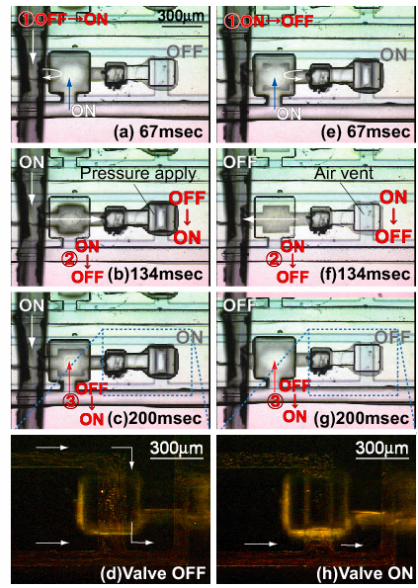

Fig.4 Images of the switching sequence of the on-chip valve. (a-c) OFF to ON and (e-g) ON to OFF. (d) and (h) the images of 1μm fluorescent beads injection.

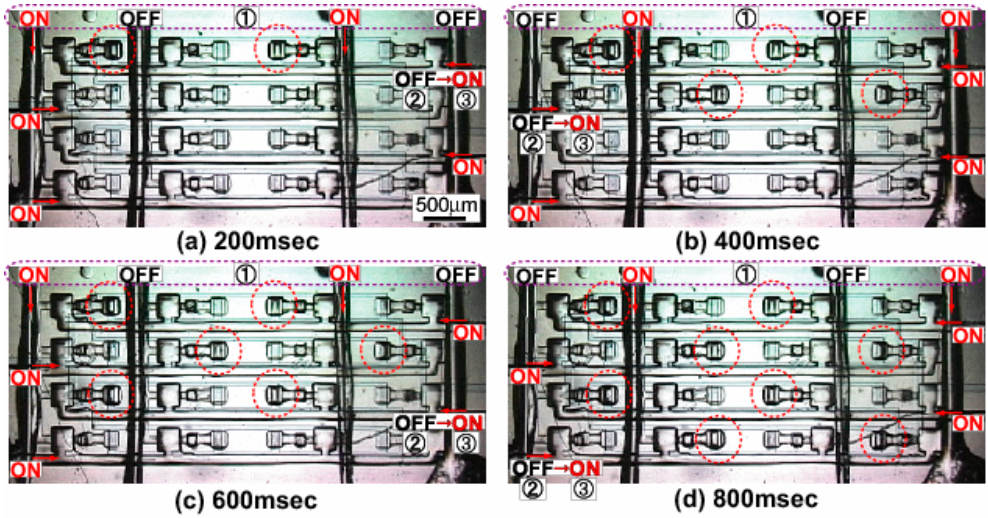

Fig.5 Images of 4 * 4 valve operation. Each image shows the every switching of valves in a line after three steps. (a) First gate port OFF to ON, (b) Second gate port OFF to ON, (c) Third gate port OFF to ON, (d) Fourth gate port OFF to ON.

Fig. 6(a-d) show the SEM images of the molds of the 16 * 16 microvalve array. In order to shut the valves without leakage, Molds of the drive channels and the flow channel are made by resist reflow of positive photoresist (PMER P-LA 900, Tokyo Ohka). Molds of the through holes and the gate channels are made by negative photoresist (SU-8 3000, MicroChem) to realizing high aspect structures. Fig. 7 shows the overview of the device. The valve operation of 256 valves is shown in Fig. 8. Each 16 gate channel which has 16 valves can be controlled within 200 msec and 256 valves are controlled by 32 off-chip control valves respectively.

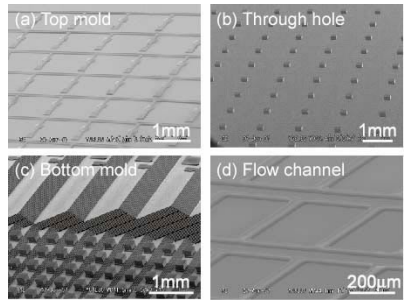

Fig.6 SEM images of the molds of the four layers. (a) top, (b) through hole, (c) bottom, (d) flow channel.

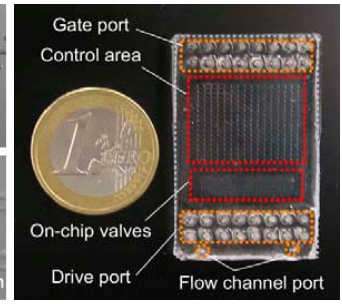

Fig.7 Overview of the 16 * 16 valve matrix consist of the 256 microvalves.

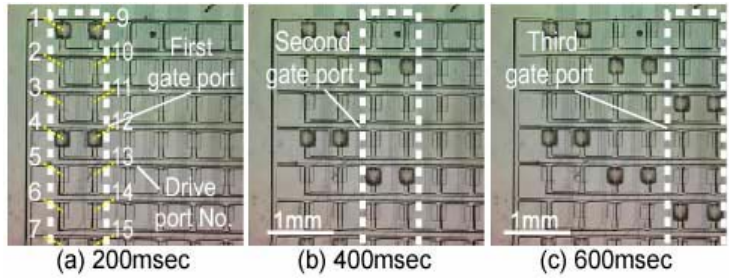

Fig.8 Operation images of 16 * 16 valves. (a) First gate port OFF to ON, (b) Second gate port OFF to ON, (c) Third gate port OFF to ON.

4. CONCLUSION

In order to control a large number of arrayed valves efficiently, a new method of valve controlling system was proposed. Using a fabricated device of 16 * 16 microvalve array, 256 valves can controlled by 32 off-chip control valves. Gas leak problem originated PDMS gas permeability is solved by filling inert liquid in the pneumatic channels. This structure can be applicable for large number of arrayed microvalves.

ACKNOWLEDGEMENTS

This work is partly supported by Japan Ministry of Education, Culture, Sports Science & Technology, Scientific Basic Research A07113700, and SCOE ASMeW.

REFERENCES

[1] T. Thorsen, SJ Maerkl, and SR Quake, Science, Vol. 298, No. 5593, 2002, pp. 580-584.

[2] C.C. Lee, G. Sui, A. Elizarov, C. J. Shu, Y.-S. Shin, A. N. Dooley, J. Huang, A. Daridon, P. Wyatt, D. Stout, H. C. Kolb, O. N. Witte, N. Satyamurthy, J. R. Heath, M. E. Phelps, S. R. Quake, and H.-R. Tseng, Science, Vol. 310, No. 5755, 2005, pp.1793-1796.

[3] M Kanai, S Ikeda, J Tanaka, J Sang Go, H Nakanishi and S Shoji, Sens. Act. A, Vol.111, Issue 1, 2004, pp.32-36.

[4] M.Kanai, T. Munaka, H. abe, Y. Fujiyama, D. Uchida, H. Mikado, H Nakanishi and S Shoji, μTAS'04, 2004, pp.126-128.

CHARACTERIZATION OF FLOW REVERSAL IN ANODICALLY BONDED GLASS-BASED AC ELECTROKINETIC MICROPUMPS

Misha Marie Gregersen, Laurits Højgaard Olesen, Anders Brask, Mikkel Fougt Hansen, and Henrik Bruus

MIC – Department of Micro and Nanotechnology, Technical University of Denmark
DTU bldg. 345 east, DK-2800 Kongens Lyngby, Denmark

ABSTRACT

Microfluidic chips have been fabricated to study electrokinetic pumping generated by a low voltage AC signal applied to an asymmetric electrode array. A measurement procedure has been established and followed carefully resulting in a high degree of reproducibility of the measurements. Depending on the ionic concentration as well as the amplitude of the applied voltage, the observed direction of the DC flow component is either forward or reverse.

Keywords: AC electroosmosis, Reverse flow, Electrokinetics, Micropump.

1. INTRODUCTION

During the recent years several groups have fabricated and tested AC electrokinetic micropumps [1–6]. We have improved the design of the microfluidic system, and by devoting special attention to the low-voltage regime (below 2 V) we have found a new phenomenon, which cannot be explained by the standard theory: In contrast to previous observations by other groups [2, 5, 6], the flow direction in our system can be reversed as a function of both driving voltage as well as electrolyte concentration.

2. MATERIALS AND METHODS

The chip consisted of two 500 µm thick Pyrex glass wafers anodically bonded together. The flow-generating electrodes were placed in one part of the channel, while the flow velocities were measured in an electrode-free part, see Fig. 1(a). The electrodes, made by e-beam evaporated Ti(10 nm)/Pt(400 nm), were defined on the bottom wafer by a photolithographic lift-off process. The channel of width 967 µm and height 33.6 µm was etched into the surface of the top Pyrex wafer. After bonding the two wafers, holes were drilled for the in- and outlet ports. This construction ensured an electrical insulated chip with fully transparent channels.

During flow-velocity measurements the two ends of the main on-chip channel were connected in an outer pumping loop by a teflon tube with low hydraulic resistance. This eliminated the unwanted hydrostatic pressure differences, see Fig. 1(b). Flow velocities were measured by introducing fluorescent tracer particles in the measurement channel and recording their positions at regular time intervals using a digital camera attached to a stereo microscope.

978-0-9798064-0-7/µTAS2007/$20©2007CBMS

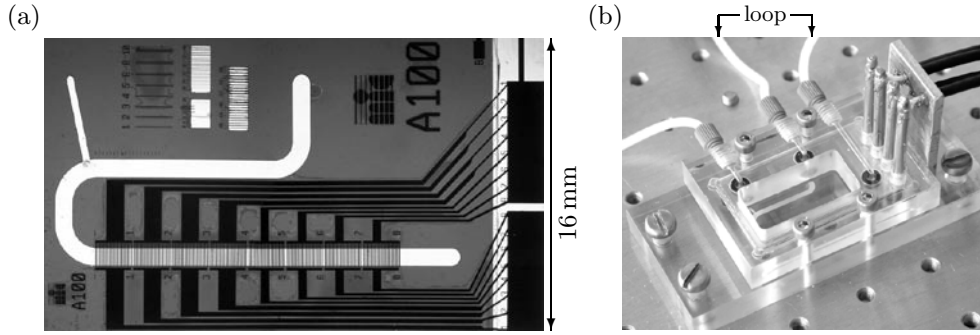

Figure 1: (a) Micrograph of the full chip containing a channel (white) with flow-generating electrodes (black) and a narrow side channel for bead injection (upper left corner). The electrode array is divided into eight sub arrays, each having its own connection to the electrical contact pad. The flow-generating electrodes are restricted to lower channel section, while the upper channel section is reserved for measuring the flow velocity across a number of ruler lines defined on the channel bottom. (b) Chip holder constructed to connect external tubing and electrical wiring with the microfluidic chip.

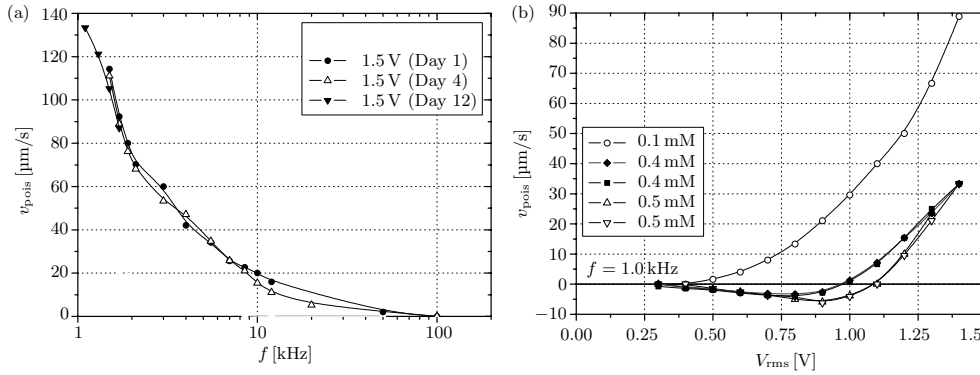

Figure 2: (a) Reproducible induced flow-velocities in a 0.1 mM KCl solution observed at different days as a function of frequency at a fixed rms voltage of 1.5 V. Lines have been added to guide the eye. (b) Reversed flow observed for repeated measurements of two concentrations of KCl at 1.0 kHz.

3. RESULTS AND DISCUSSION

Our microfluidic chips were stable both structurally and functionally. This combined with a careful measurement procedure have led to flow velocity measurements with a high degree of reproducibility as shown in Fig. 2(a). By storing the chips in milli-Q water between measurements kept them functional over time periods extending up to a year.

To check the electrical properties of the micropumps we have made full impedance characterizations extending over eight frequency decades and successfully analyzed them in terms of an equivalent circuit model.

By letting the electrodes cover as much as 40% of the total on-chip channel length, we have obtained a ratio between the maximum Poiseuille flow velocity in the measurement channel and the electro-osmotic flow velocity at the electrodes as high as 0.29. This made it possible to observe the reversal of the flow direction at low voltages ($V_{\rm rms} \lesssim 1\,{\rm V}$) and low frequencies ($f \lesssim 20\,{\rm kHz}$), see Fig. 2(b). It is clearly seen that for concentrations $c = 0.1\,{\rm mM}$, the velocity as function of voltage exhibits the known exclusively forward and increasing pumping velocity. However, for slightly increased electrolyte concentrations, $c = 0.4\,{\rm mM}$ and $0.5\,{\rm mM}$, an unambiguous reversal of the flow direction is observed. This flow reversal has an almost constant magnitude between $1\,{\rm kHz}$ and $10\,{\rm kHz}$. This differs from usual AC electroosmosis, which peaks around the inverse RC-time of the device.

The trends of our flow velocity measurements are accounted for by a previously published theoretical model [10], but the quantitative agreement is lacking. Most important, the predicted velocities do not depend on electrolyte concentration, yet the concentration seems to be one of the causes of our measured flow reversal.

4. CONCLUSION

We have produced an integrated AC electrokinetic micropump using MEMS fabrication techniques. Due to careful measurement procedures it has been possible over weeks to reproduce the observed flow velocities. An hitherto unobserved reversal of the pumping direction has been measured in a regime, where the applied voltage is low ($V_{\rm rms} < 1.5$ V) and the frequency is low ($f < 20$ kHz) compared to earlier investigated parameter ranges. This reversal depends on the exact electrolytic concentration and the applied voltage. The observed strong dependence on electrolyte concentration is not accounted for by present theoretical models [7–10] showing the need for further theoretical work on the electro-hydrodynamics of these systems.

REFERENCES

[1] A. B. D. Brown, C. G. Smith and A. R. Rennie, Phys. Rev. E **63**, 016305 (2000).
[2] V. Studer, A. Pépin, Y. Chen and A. Ajdari, The Analyst **129**, 944 (2004).
[3] B. P. Cahill, L. J. Heyderman, J. Gobrecht and A. Stemmer, Phys. Rev. E **70**, 036305 (2004).
[4] S. Debesset, C. J. Hayden, C. Dalton, J. C. T. Eijkel and A. Manz, Lab Chip **4**, 396 (2004).
[5] A. Ramos, H. Morgan, N. G. Green, A. Gonzalez and A. Castellanos, J. Appl. Phys. **97**, 084906 (2005).
[6] P. García–Sánchez, A. Ramos, N. G. Green and H. Morgan, IEEE Trans. Dielect. El. In. **13**, 670 (2006).
[7] A. Ajdari, Phys. Rev. E **61**, R45 (2000).
[8] A. Ramos, A. Gonzalez, A. Castellanos, N. G. Green and H. Morgan, Phys. Rev. E **67**, 056302 (2003).
[9] L. H. Olesen, H. Bruus and A. Ajdari, Phys. Rev. E **73**, 056313 (2006).
[10] L. H. Olesen, *AC Electrokinetic micropumps*, PhD Thesis, MIC - Dept. of Micro and Nanotechnology, DTU (2006), www.mic.dtu.dk/mifts

CELLULAR-SCALE HYDRODYNAMICS

Howard A. Stone

School of Engineering and Applied Sciences, Harvard University,USA

ABSTRACT

We summarize several approaches for learning about cellular-scale hydrodynamics using microfluidic methods. In particular, we consider the response of suspensions of red blood cells to flows in constrictions, and the mechanical response of individual cells to confinement while flowing. In addition, we present some ideas and results for multiphase flows (liquid-liquid and gas-liquid) in part because of their potential for controlled studies of individual cells or small numbers of cells.

Keywords: Red-blood cells, drift, separation, pressure measurement, drop formation

1. INTRODUCTION

Microfluidic systems offer many practical routes for studying research problems at the scale of individual cells. The field is rapidly evolving. Needs include handling suspensions of cells, isolating individual cells, controlling the chemical environment of the cells, making mechanical and other physical measurements on individual cells, obtaining and reporting genetic information on the cells, etc. In this paper we report a few of our efforts in these directions.

2. EXPERIMENTAL

We have considered several types of studies. In one set of investigation we examined the influence of a constriction on the flow of a suspension of red-blood cells (RMCs); see Figure 1a,b and [1]. Upstream of a constriction the cells are basically uniformly distributed with a small layer of pure fluid – the "cell-free layer" associated with the name of Fahraeus, adjacent to the wall. Downstream of the constriction the cell-free layer is significantly amplified (Figure 1b). This effect can then be used to separate cells from the plasma and some analysis of the drift of the cells away from the wall is given in [1].

Second, we have developed an approach to measure the approximate pressure change when a red blood cell enters and leaves a small channel of comparable dimension; see Figure 1c,d and [2]. The device uses parallel streams of viscous fluid, where the deflection of the interface indicates a change in volumetric flow rate which is calibrated to the pressure change produced when a small object, such as a cell, partially blocks the channel (Figure 1c). Typical results are shown in Figure 1d where the signature of the cell is recorded with a high-speed camera and yields a response at the scale of tens of milliseconds.

We have also been involved with developments for the controlled formation of drops and bubbles, e.g. [3] and [4]. These approaches with multiphase fluid dynamics are finding a large set of applications, including those targeting the studies of individual cells.

978-0-9798064-0-7/μTAS2007/$20©2007CBMS

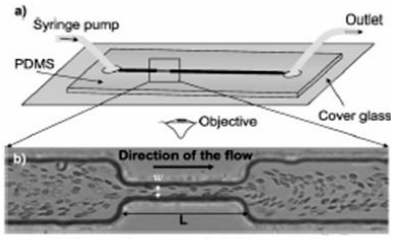

Shear in constriction: cell-free layer downstream

(c) Deflection of the downstream interface is a signature of a pressure change

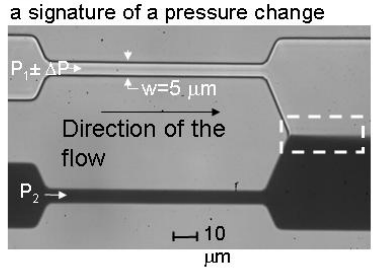

(d) Example: Pressure change when a red then a white cell flows through the device

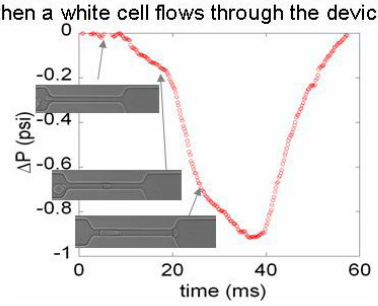

Figure 1. (a), (b) Pressure-driven flow of a suspension of cells in a microfluidic section. Upstream of a constriction the cells are basically uniformly distributed with a small layer of pure fluid – the "cell-free layer" associated with the name of Fahraeus, adjacent to the wall. Downstream of the constriction the cell-free layer is significantly amplified. This effect can then be used to separate cells from the plasma. (c), (d) Measuring the pressure change when a red blood cell enters and leaves a small channel of comparable dimensions. The device uses (c) parallel streams of viscous fluid, where the deflection of the interface indicates a change in volumetric flow rate which is calibrated to the pressure change produced when a small object, such as a cell, partially blocks the channel.

3. CONCLUSIONS

The area of microfluidic approaches to cellular-scale hydrodynamics is growing and developing at a rapid rate. The references given here provide citations to those studies that have influenced our work. In addition, there are many new ideas for using multiphase flows – bubbles and drops – for chemical and biological studies. The presentation will hopefully summarize some of these ideas.

ACKNOWLEDGEMENTS

We thank the Harvard MRSEC and NSEC for partial support of this research. My research group has been responsible for all of the work reported in Figure 1. In particular, most of the work we will discuss in the presentation was done by M. Faivre, M. Abkarian, and K. Bikraj. The work on multiphase flows was done in collaboration with S. Anna, N. Bontoux, D. Link, P. Garstecki, M. Fuerstman, and A. Lai, and E. Kumacheva, G.

Whitesides, D. Weitz and their fabulous research groups. Over the years I have also benefited a lot from conversations on microfluidics with A. Ajdari, A. Stroock and R. Ismagilov.

REFERENCES

[1] M. Faivre, M. Abkarian, K. Bikraj and H.A. Stone, *Geometrical focusing of cells in microfluidic devices: A route to separate blood plasma.* Biorheology. Vol 43, pp. 147-159 (2006).

[2] M. Abkarian, M. Faivre, and H.A. Stone, *High-speed microfluidic differential manometer for cellular-scale hydrodynamics.* Proc. Nat. Acad. Sci. USA. 103, pp. 538-542 (2006).

[3] S.L. Anna, N. Bontoux, and H.A. Stone, *Formation of dispersions using "flow focusing" in microchannels.* Appl. Phys. Lett. 82, pp. 364-366 (2003).

[4] P. Garstecki, M.J. Fuerstman, H.A. Stone and G.M. Whitesides, *Formation of droplets and bubbles in a microfluidic T-junction – scaling and mechanism of breakup.* Lab on a Chip, 6, pp. 437-446 (2006).

ENHANCED SPATIAL RESOLUTION OF MALDI IMAGES USING SILICON MASKS

N. Verplanck[1], M. Wisztorski[2], J. Stauber[2], J.C. Camart[1], M. Salzet[2], I. Fournier[2] and V. Thomy[1]

[1]*Institut d'Electronique, de Microélectronique et de Nanotechnologie (IEMN) - UMR 8520*
[2]*Laboratoire de Neuroimmunologie des Annélides (LNA) - FRE CNRS 2933*

ABSTRACT

This paper reports on simple, efficient and economical methods to increase MALDI image resolution. It is not currently possible to focus the diameter of a MALDI laser down to 50x50µm², i.e. 2500µm², without decreasing signal intensity. But using Silicon masks openings features, it might even be decreased to about 15x50µm², i.e. 750µm². Furthermore, the presence of a mask on the tissue section sample may result in a significant increase in the signal intensity for high m/z ratios. Finally, a huge advantage of the masks is their ease of adaptability on any MALDI mass spectrometer.

Keywords: MALDI imaging, mass spectrometry, silicon mask, tissue analysis

1. INTRODUCTION

MALDI is well adapted to the introduction of raw samples such as tissue cuts. For tissue imaging, the minimum distance between two points must be superior to the laser beam diameter, which corresponds to the irradiation of several cells in the tissue using focalisation systems available on classical commercial instruments. Ideally, the image definition should be at the scale of the cell (10-20 µm for small cells). In the art, various methods have been tried to decrease the area irradiated by the laser beam for MALDI analysis (optical techniques [1], aperture [2], etc). In view of the various drawbacks of known methods to increase MALDI imaging resolution, there is clearly a need for new alternative, simple, efficient and economical methods to increase MALDI image resolution.

2. EXPERIMENTAL

The masks were engineered in silicon substrates (<100> orientation). Several masks of various openings, forms and sizes were fabricated using standard microfabrication techniques. According to the technique used (wet and dry etching), two geometries of masks have been obtained. Dry etching (50 µm) has been performed using Bosch process (ICP) through a photoresist mask: Mask A (Figure 1). For wet etching, we used KOH through a Si_xN_y mask which leads to V-grooves formation (following <111> orientation): Mask B (Figure 2). Both substrates were reduced in thickness to obtain a perforated membrane around 50-100 µm.

978-0-9798064-0-7/µTAS2007/$20©2007CBMS

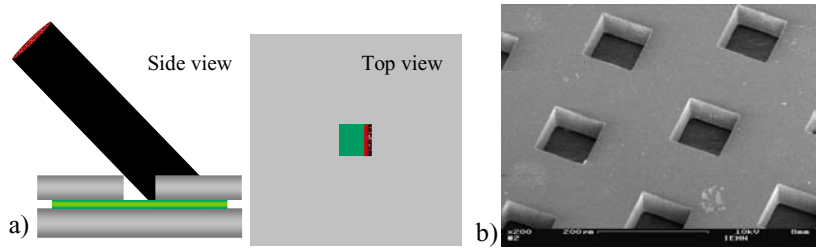

Figure 1 a) Schematic view of the irradiated area through a DRIE mask, b) View of the mask.

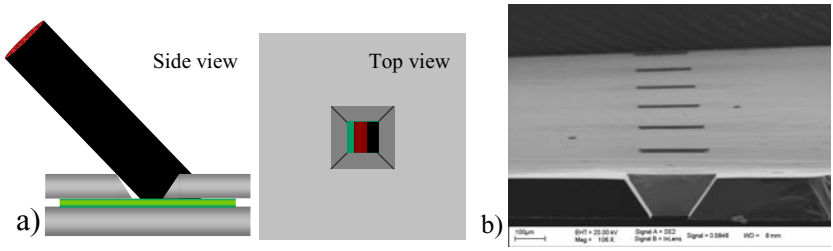

Figure 2 a) Schematic view of the irradiated area through a V-groove mask, b) View of the mask.

3. RESULTS AND DISCUSSION

Masks were evaluated for MALDI analysis of standard peptide solutions and tissue sections. Mass spectra were either acquired on a Voyager DE-STR (Applied Biosystems) equipped with a nitrogen laser or on an Ultraflex II TOF/TOF (Bruker Daltonics) equipped with a Smartbeam laser.

First tests on standard peptides solutions and tissue sections show that the apposition of masks does not disturb the desorption/ionization process and significantly decrease the dimensions of the irradiated area by the MALDI laser without decreasing the signal intensity of the observed ions. These results demonstrate that it is possible to decrease the analyzed areas down to about 15x75 µm², i.e. 1125 µm². Using other masks openings features, it might even be decreased to about 15x50 µm², i.e. 750 µm². Without masks, it is not currently possible to focus the diameter of a MALDI laser down to 50x50µm², i.e. 2500µm², without decreasing signal intensity. Figure 3 describes such results through mask A with different dimensions of openings (500 µm, 240µm, 100 µm and 50µm). Figure 4 shows results without mask (Figure 4.a) and through mask B with internal openings respectively of 100 µm (Figure 4.b) and 185 µm (Figure 4.c).

In addition, it has even been observed that the presence of a mask on the tissue section sample may result in a significant increase in the signal intensity, in particular for high m/z ratios (results obtained both on standard peptide mixtures and on rat brain tissue sections).

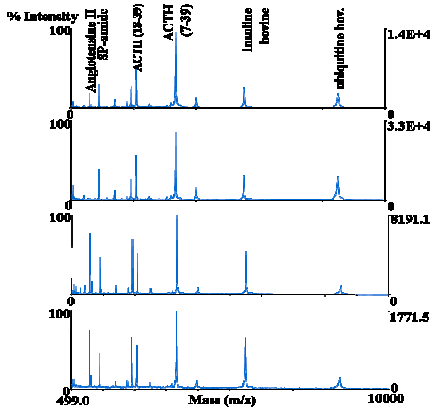

Figure 3 MALDI analysis of peptide standards through mask A with opening of a) 500µm, b) 240µm, c) 100µm and d) 50µm.

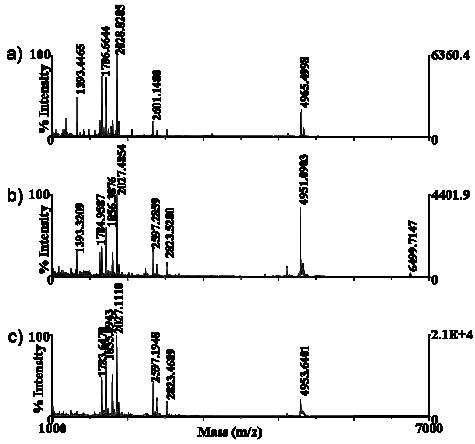

Figure 4 MALDI Direct analysis of rat brain a) without mask, b) and c) through mask B with internal opening of respectively 100µm and 185µm

4. CONCLUSIONS

Although the precise mechanism leading to this surprising increase in signal intensity is not completely elucidated, this result is particularly interesting for tissue section MALDI imaging, since most of the prior art technologies used to improve the resolution tend to result in a signal decrease. Finally, a huge advantage of the masks is certainly their ease of adaptability on any MALDI mass spectrometer, since their use does not involve any material modification or new equipment [3].

The next step will be the realization of a matrix of openings allowing MALDI imaging by point-to-point mass spectrometry.

ACKNOWLEDGEMENTS

We thank for its technical support Mr. Christophe Boyaval (SEM imaging). The European Union, the Centre National de la Recherche Scientifique (CNRS) and the Nord-Pas de Calais region are gratefully acknowledged for financial support.

REFERENCES

[1] "Desorption lasers in mass spectrometry: choices and selections", F. Hillenkamp and K. Dreisewerd, 49th ASMS Conference on Mass Spectrometry and Allied Topics, Chicago, USA (2001).

[2] "Molecular imaging of biological samples: localization of peptides and proteins using MALDI-TOF MS", R.M. Caprioli, T.B. Farmer, and J. Gile, Anal. Chem, **69**, 4751 (1997). 69(23): p. 4751-60.

[3] "Masks useful for MALDI imaging of tissue sections, processes of manufacture ans uses thereof ", M. Wisztorski, N. Verplanck, V. Thomy, I. Fournier and M. Salzet, Deposited patent CNRS n° DI 00047-03 (2005) *US Provisional*.

INTEGRATION OF MONOLITHIC VALVES INTO MICROFLUIDIC DEVICE FOR PROTEOMIC ANALYSIS

Qingye Lu, Jian-Bin Bao, D. Jed Harrison

Department of Chemistry, University of Alberta, Edmonton, Alberta, Canada T6G 2G2

ABSTRACT

A microfluidic poly(dimethylsiloxane) (PDMS) proteome analysis device is developed here to integrate electrokinetic separation, protein fractionation, solid phase extraction (SPE), protein digestion on packed reaction beds and subsequent electrospray ionization mass spectral (ESI-MS) analysis, using a multiplexed, hydraulically valved system.

Keywords: Proteomics, Mass spectrometry, Multiplexing, Valve

1. INTRODUCTION

Multiplexing of microfluidic systems for protein analysis provides a powerful route to more rapid, less costly proteomics research. We have explored electrokinetically controlled systems, but the challenge of making many channels with solid phase extraction (SPE) or chromatographic beds identical in terms of flow resistance has encouraged us to explore mechanical valve-based systems. Pneumatically actuated valves, introduced by VerLee [1] and developed into complex systems by Quake [2] provide a powerful alternative actuation system. The design and operation of a system (a schematic shown in Figure 1) that performs electrokinetic separation, followed by fractionation into multiple channels for protein digestion and SPE on packed reaction beds, using a multiplexed, hydraulically valved system, with subsequent mass spectral analysis of the digested peptides is described here.

2. RESULTS AND DISCUSSION

The proteome chip consists of two PDMS layers on a glass substrate, as shown in the optical micrograph in Fig. 1. The valve design of Quake [2] gives the low dead volume required for protein separation and fractionation. The bottom layer provides hydraulic valve control and the control ports are later connected to an array of Lee-solenoid-valves. The top layer is the fluidic path and the solution inputs are

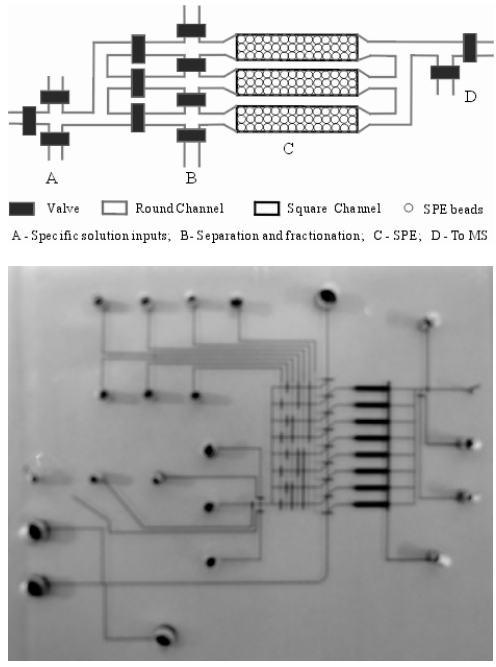

Figure 1. The schematic drawing (upper) and optical micrograph of a PDMS proteomic analysis system (lower)

978-0-9798064-0-7/μTAS2007/$20©2007CBMS

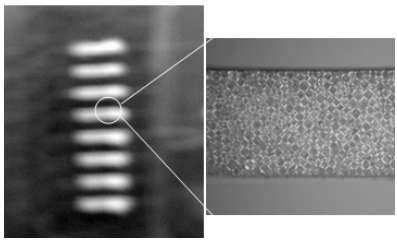

Figure 2. Optical micrograph of eight packed beds with Oasis® HLB beads

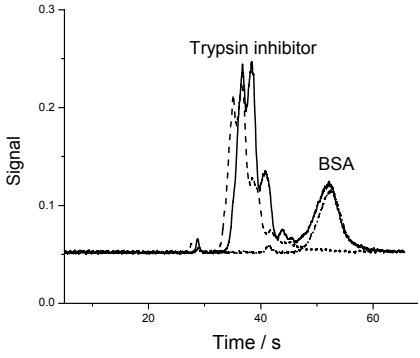

Figure 3. Electrophoretic separation of proteins (dash – trypsin inhibitor; dash dot – BSA; solid – mixture of the two)

connected to a stable pressurized source. The layers were bonded using plasma oxidation treatments. An injection method, loading beads through the wall of the PDMS device by syringe was developed to load beds defined by weirs. The weirs consisted of 10 µm deep zones connected to 100 µm deep beds. Another method is to punch small holes into the bed region for direct loading under vacuum. An optical micrograph of a packed bed is shown in Fig. 2. A capillary tip was inserted into the exit channel of the PDMS structure for electrospray to an MS.

Electrophoresis was used for protein separation. *N*-Dodecyl *β*-D-maltoside and methylcellulose were added to decrease protein adsorption and minimize electroosmotic flow [3]. A typical separation of trypsin inhibitor protein and bovine serum albumin (BSA) in the device is shown in Fig. 3. Based on the volumes within the chip, about 10 pg of fractionated protein is collected in a bed volume of 0.15 µL, starting with a 0.05 mg/mL sample. Given a free volume of the packed bed of 60 nL, protein is concentrated to 0.16 mg/L, which is sufficient for MS detection [4].

Cytochrome c was loaded into different channels on the chip with SPE beds and detected by sequentially opening valves that release each bed's contents to the MS. The total ion chromatograms (TIC) of multiple elutions are shown in Fig. 4. As can be seen, a well separated elution can be controlled using the multiplexing valve system. Digestion within SPE beds by flowing trypsin across the trapped protein sample has been developed previously, and tests on this device show the method works well. Fig. 5 presents a protein digest released from one channel of the device.

3. CONCLUSIONS

In summary, this hydraulically valved PDMS microfluidic device is the first to integrate electrophoresis, sample fractionation, packed beds with weir-style trapping, trypsin digestion, and interfacing to electrospray mass spectrometry in one complex system. The experimental results show that this device is functional, and that the concepts are very promising for on-chip sample preparation for proteomics.

ACKNOWLEDGEMENTS

We acknowledge the support from the Natural Sciences and Engineering Research Council of Canada (NSERC) and thank Waters for the free Oasis HLB beads.

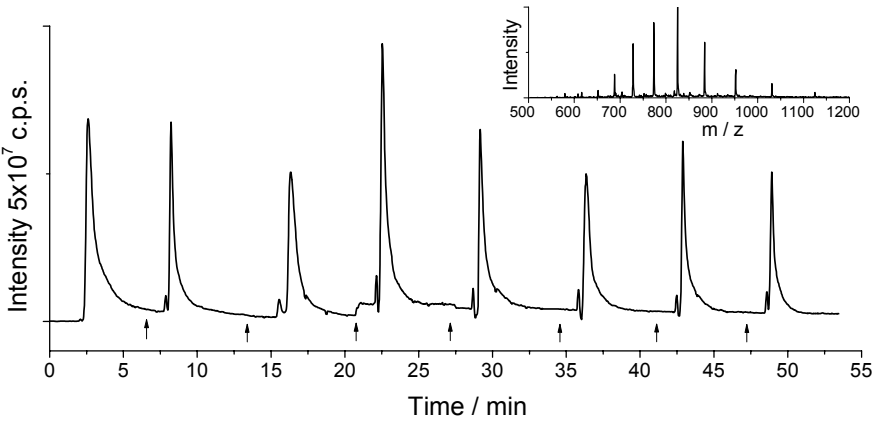

Figure 4. The TICs from multiple elutions of cytochrome c from eight separate channels with SPE beds (inset - corresponding cytochrome c mass spectrum; elution solution: 75% methanol + 1% formic acid)

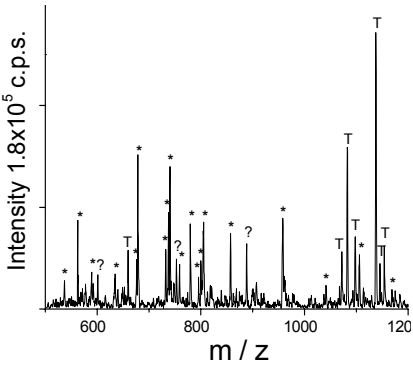

Figure 5. The mass spectrum of cytochrome c digest with an SPE bed (- cytochrome c peptides, T - trypsin autodigestion peaks, ? – unidentified peaks; sequence coverage is 87%.)*

REFERENCES

[1] J. Pan, D. VerLee, M. Mehregany, "Latched Valve Manifolds for Efficient Control of Pneumatically Actuated Valve Arrays," Transducers 97, 817 (1997).

[2] T. Thorsen, S.J. Maerkl, S.R. Quake, "Microfluidic Large-Scale Integration," Science, **298**, 580 (2002).

[3] F. Dang, K. Kakehi, J. Cheng, O. Tabata, M. Kurokawa, K. Nakajima, M. Ishikawa, Y. Baba, "Hybrid Dynamic Coating with *n*-Dodecyl *β*-D-Maltoside and Methyl Cellulose for High-Performance Carbohydrate Analysis on Poly(methyl methacrylate) Chips," Analytical Chemistry, **78**, 1452 (2006).

[4] F.W. McLafferty, E.K. Fridriksson, D.M. Horn, M.A. Lewis, R.A. Zubarev, "Biochemistry: Biomolecule Mass Spectrometry," Science, **284**, 1289 (1999).

NON-PCR LINEAR AMPLIFICATION OF mRNA TOWARD SINGLE CELL WHOLE TRANSCRIPTOME ANALYSES

J.G. Kralj[1], A. Player[2], D. Petersen[2], S.P. Forry[1], M.S. Munson[1], E. Kawasaki[2], and L.E. Locascio[1]

[1]*National Institute of Standards and Technology, USA*

[2]*National Cancer Institute/National Institutes of Health, USA*

ABSTRACT

We demonstrate whole transcriptome (mRNA) amplification of Jurkat T-cells near the single-cell level. A microfluidic packed bed was made of T7-oligo(dT) functionalized microbeads with immobilized cDNA from mRNA. Linear amplification of global mRNA was performed using the "Eberwine" method. The packed bed approach effectively concentrates the mRNA/cDNA into a ≈0.5 nL volume using a partially-closed pneumatic valve. The amplified samples were then analyzed by reverse transcription polymerase chain reaction (RT-PCR) for specific genes or reamplified off-chip to further increase global mRNA concentration for gene expression microarrays.

Keywords: whole-transcriptome amplification, single-cell assays

1. INTRODUCTION

Single-cell analysis is a growing need in biology and medicine, especially to study rare cells from small samples such as tissue biopsies and laser capture microdissected tissue. Previous microfluidic mRNA analyses utilized RT-PCR [1, 2]. However, methods that amplify mRNA continuously from a T7 primer without thermocycling (linear amplification) have an advantage over RT-PCR because a single primer is used for global full-length transcription [3]. Thus, linear amplification is a powerful supplementary tool to PCR, allowing the researcher to analyze the whole transcriptome rather than being limited to specific genes. This is critical for comparative cell studies and discovery of biomarkers.

In particular, linear amplification reactions of single-cell mRNA are challenging because the template cDNA amplifies less than the background. By immobilizing single-cell mRNA onto 1 nL packed beds, the local concentration reaches ≈0.4 ng/μL, or approximately $8 \cdot 10^4$ higher than standard benchtop protocols. Linear amplification of mRNA requires reverse transcription to cDNA, followed by an isothermal in vitro transcription reaction (IVT) to make antisense-RNA (aRNA) (Figure 1).

2. EXPERIMENTAL

The mRNA from Jurkat T-cells were immobilized and cDNA transcribed onto 6 μm beads conjugated with a T7 primer off-chip, then packed into the device in 0.2 nL to 1 nL volumes. Typical on-chip amounts of mRNA ranged from 1 pg to 20 pg, or 10 to 200 cell equivalents. The microfluidic device was fabricated using multilayer soft-lithography techniques, utilizing a sieve-valve to retain the beads (Figure 2) [2]. A Peltier unit controls the temperature; fluidic/pneumatic lines were connected by inserting capillary tubing directly into holes punched in the silicone rubber; and a syringe pump delivered fluid from 50-μL syringes to the device. The microvalves were actuated using 250 kPa air with an off-chip computer-controlled manifold. Flowrates were maintained at 37 nL/min to 75 nL/min for 2 h to 16 h. Using a continuous flow over a packed bed, fresh reagents are introduced

978-0-9798064-0-7/μTAS2007/$20©2007CBMS

while product aRNA is convected away and collected. In this way, the reaction proceeds until sufficient material is collected for further processing.

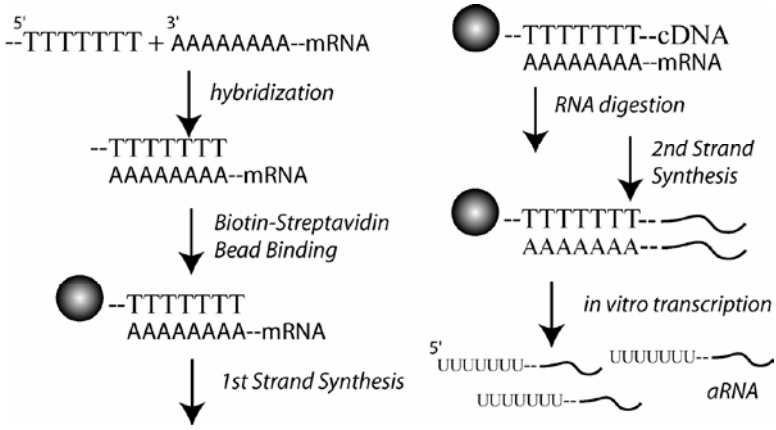

Figure 1 T7-based linear amplification requires 5 steps, the final product of which is aRNA. Here, we studied the IVT reaction. Others have previously demonstrated mRNA capture on beads [4] and cDNA synthesis [1, 2].

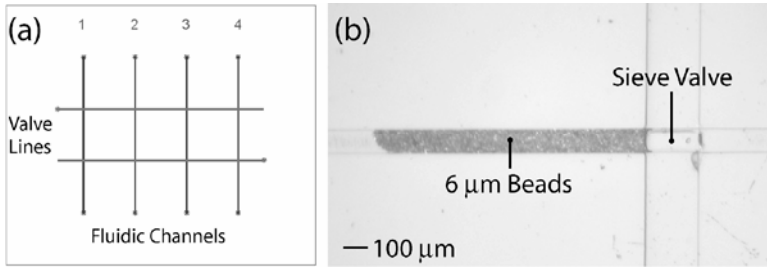

Figure 2 (a) The device schematic shows a two-layer design with valve lines (horizontal) arranged perpendicular to the fluid channels (vertical). (b) The packed bed of microbeads is realized with a nearly-closed sieve valve. Column size is controlled by injecting measured volumes of bead suspensions.

3. RESULTS & CONCLUSIONS

Samples from 2 pg and 20 pg mRNA were first analyzed for specific genes (GAPDH, ITPG) to confirm amplification using RT-PCR and electrophoresis (Figure 3a,b). The average aRNA length after microfluidic amplification was 1.0 kilobases (kb) as measured by electrophoresis (Figure 3c), indicating good quality and full length transcription. Global expression can be analyzed using a microarray after a second round of amplification (Figure 4). Though variations were observed between the microfluidic and benchtop techniques requiring further work, this demonstrates the potential for whole transcriptome studies ($\approx 10^4$ genes) using microfluidic linear amplification of single cell samples.

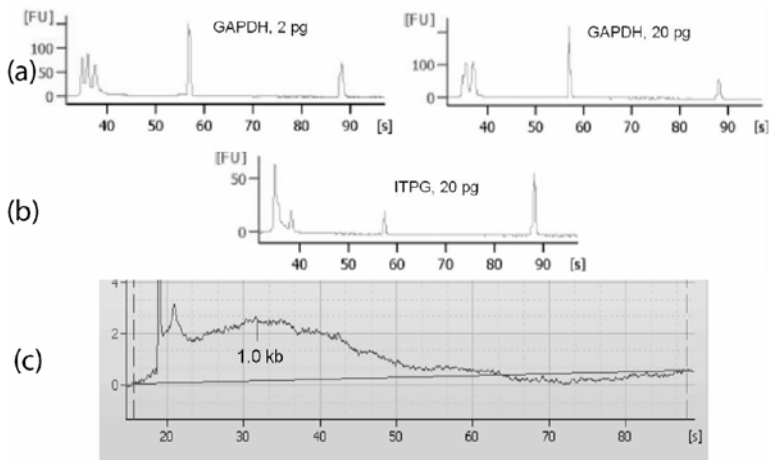

Figure 3 Electropherograms indicating on-chip amplification of Jurkat mRNA – (a) GAPDH from 2 pg and 20 pg samples, and (b) ITPG from 20 pg samples. The aRNA was purified, reverse transcribed, and subjected to 35 cycles of PCR. (c) Measurement of the average length of the transcriptome (1.0 kb).

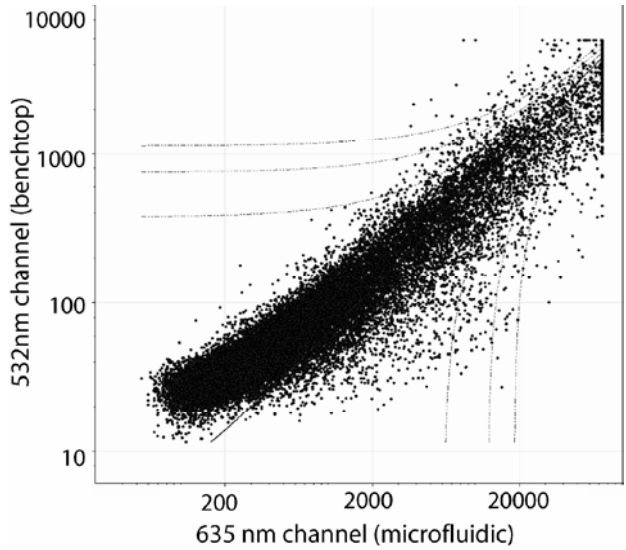

Figure 4 Preliminary microarray data show variation between the benchtop and individual on-chip amplifications. In the microdevice, 10 pg samples were amplified, purified, and re-amplified off-chip to raise the aRNA concentration. From 35024 genes with features >1000, 10789 were found using microfluidics, 9635 features using traditional methods with an overlap of 9071. Lines indicate statistical average and 1, 2, and 3 standard deviations.

REFERENCES

1. Bontoux, N., et al. *Micro Total Analysis Systems 2006*. 2006. Tokyo, Japan.
2. Marcus, J.S., W.F. Anderson, and S.R. Quake, Analytical Chemistry, 2006. **78**(9).
3. van Gelder, R., et al., PNAS, 1990. **87**.
4. Jiang, G. and D. Harrison, The Analyst, 2000. **125**.

ON-CHIP TRYPTIC DIGEST WITH DIRECT-COUPLING TO ESI/MS USING MAGNETIC NANOPARTICLES

A. Le Nel[1,2*], J. Krenkova[3*], K. Kleparnik[3], C. Smadja[2], M. Taverna[2], J.-L. Viovy[1], F. Foret[3]

[1]Laboratoire PCC, Institut Curie (UMR CNRS/IC 168), Paris Cedex 05, France, [2]JE2495 Protéines et Nanotechnologies en Sciences Séparatives, Université Paris XI, Châtenay-Malabry, France, [3] Institute of Analytical Chemistry, Brno, Czech Republic

Contact email: foret@iach.cz

** These authors contributed equally to this work.*

ABSTRACT

As a step towards further integration and automation, we propose here the first system to our knowledge able to perform online tryptic digest and ESI, using a replaceable on-chip digestion microcolumn.

Keywords: magnetic beads, self-assembly, trypsin, mass spectrometry, proteomics

1. INTRODUCTION

After the success of the human genome project, and the sequencing of an increasing number of genomes of various organisms, the focus of methodological research is progressively shifting towards proteomics. The conventional tools for proteomics, 2D-electrophoretic separation followed by tryptic digest of individual spots, peptide mass measurements and database interrogation, are very labor-intensive. Thus, numerous efforts are devoted to the development of more automated strategies involving e.g. liquid chromatography coupled to Mass Spectrometry. Online coupling of in-capillary digestion on monolith phases to ESI-MS has also been proposed [1]. Microfabricated systems are especially suitable for further integration, and chips combining LC separation and electrospray ionization (ESI/MS) are now developed [2]. The main goal of this study was to develop an interface to enable the coupling of on-chip enzymatic degradation and mass spectrometry analysis.

2. EXPERIMENTAL

Enzymatic microreactor: The enzymatic reactor is based on self-assembled magnetic nanoparticles [3]. Native trypsin is covalently grafted on the –COOH functional groups of the particles (500 nm). A plug of these nanoparticles is then immobilized between two magnets in a PDMS microchannel for flow-through enzymatic digestion. An original magnets layout allows the formation of a labyrinth-like structure parallel to the flow, yielding low-hydrodynamic resistance, and high reaction rates.

Interface: The enzymatic microreactor was connected to the MS apparatus through a new microspray interface (see figure 1) adapted from previous work [4]. The inlet and outlet of the microchannel are connected to syringe pump and microspray interface, respectively, via fused silica tubing (10cm*75µm id). For more efficient and reproducible ionization, the eluent from the microreactor was continuously mixed with $2\mu L.h^{-1}$ spray solution, consisting of 50% aqueous ACN and 1% formic acid, using a T-union.

978-0-9798064-0-7/µTAS2007/$20©2007CBMS

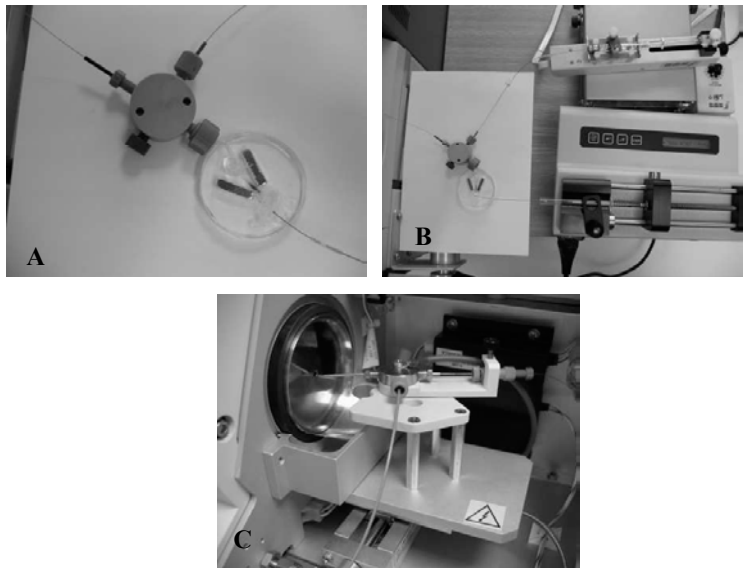

Figure 1. Experimental setup.
A: Detail of the microdevice with the embedded magnets and the T-union for coupling with the ESI interface; B: connection of the syringe pumps; C: the MS interface.

3. RESULTS AND DISCUSSION

Solutions of Cytochrome C in ammonium acetate buffer were passed through the trypsin-microreactor at different flow rates. The results (figure 2) show an increase of digestion efficiency while decreasing the flow rate. From 40 to 25 $\mu L.h^{-1}$, the peaks corresponding to multiply-ionized entire protein are decreasing, while new peaks (from digested fragments) appear. At 10 $\mu L.h^{-1}$, no more intact Cytochrome C is detected, demonstrating full digestion within experimental sensitivity. The matched peptides cover 92% (96/104 aminoacids') of the protein sequence.

4. CONCLUSIONS

We demonstrated online peptide mapping using a microfluidic microreactor based on self-assembled magnetic nanoparticles and direct ESI/MS coupling. This new arrangement presents several advantages as compared to permanent packings such as monolith or non magnetic particles. The beads bed can be refreshed by a strong hydrodynamic flush, but in ESI injection conditions, no particle leaks out to the MS machine. Performances equal or superior to conventional off-line digestion are achieved with a short residence time in the microreactor, compatible e.g. with "on flight" digestion coupled to the outlet of capillary electrophoresis. These developments pave the route for the development of a fully integrated Micro Total Analysis System dedicated to proteomics analysis.

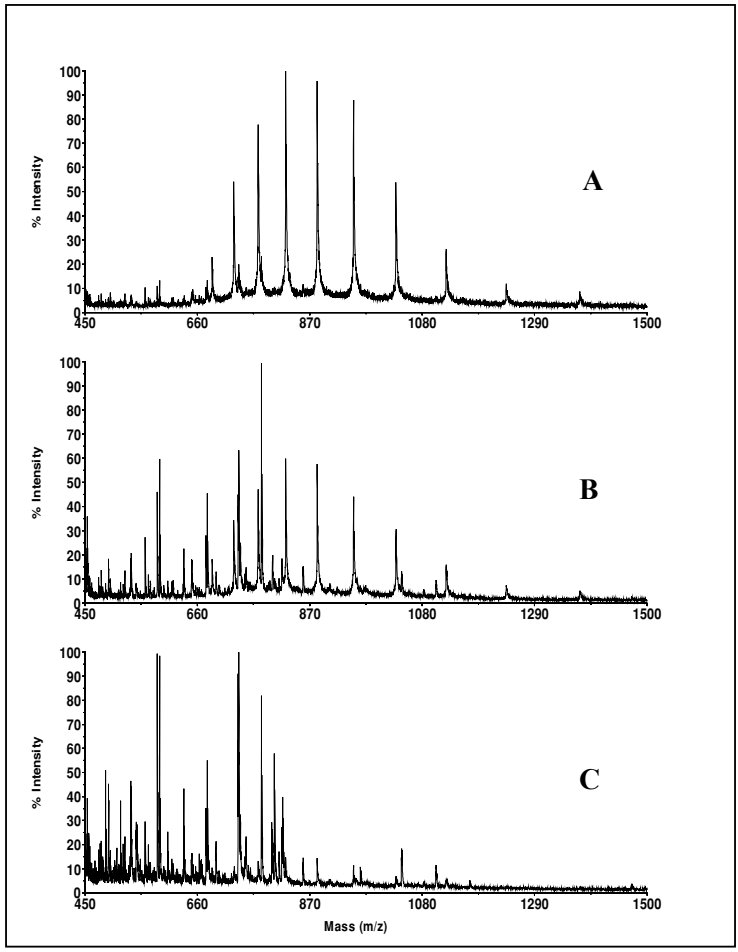

Figure 2: ESI/MS spectra of the Cytochrome C tryptic digest obtained in the on-line mode at different flow rates: 40 µL/h (A), 25 µL/h (B), 10 µL/h (C). The ESI-TOF measurements have been carried out in positive ion mode with a scan range of 450-2500 m/z.

REFERENCES

[1] D.S. Peterson, T. Rohr, F. Svec, J.M.J. Fréchet, *Proteome Res*., 2002, 1, 563-568
[2] W.C. Sung, H. Makamba, S.H. Chen, *Electrophoresis*, 2005, 9, 1783-1791
[3] M. Slovakova, N. Minc, Z. Bilkova, C. Smadja, W. Faigle, C. Fütterer, M. Taverna, J.I Viovy, *Lab on a Chip* 2005, pp. 935-942
[4] J. Krenková; Z. Bilkova; F. Foret; *J. Sep. ci*. 2005, 28, pp. 1675-1684

SINGLE DNA MOLECULE DETECTION BY ON-BEAD ROLLING CIRCLE AMPLIFICATION IN A MICROCHIP

Atsuki Tachihara[1], Kae Sato[1], Kiichi Sato[1], Yuki Tanaka[2], Jonas Jarvius[2], Mats Nilsson[2] and Takehiko Kitamori[1]

[1]The University of Tokyo, JAPAN and
[2]Uppsala University, SWEDEN

ABSTRACT

This paper reports a single DNA molecule detection by on-bead rolling circle amplification (RCA) in a microchip. RCA was successfully done in the microchip, and individual RCA products on beads were visible with a fluorescence microscope as a bright object, and they could be easily counted.

Keywords: DNA, rolling circle amplification, solid-phase amplification

1. INTRODUCTION

Genomic analysis is the most important technique for biology, medical diagnostics, food production etc. There are a lot of reports on microchips for DNA analysis, which is based on a PCR technology. Even though quantitative PCR provides single-molecule sensitivity in principle, the technique only allows for averaged measurements. The number of DNA molecules cannot be counted by the methods. On the other hand, single molecule counting system based on padlock probes and RCA was reported [1, 2]. To count the individual RCA products, microscale chamber was necessary, because the RCA product had a diameter of approximately 1 μm, and it is difficult to analyze it in a bulk scale. We thought that on-bead DNA enrichment and the solid-phase amplification in a microspace is preferable to detect and count very small amount of microscale analytes. We have realized miniaturization of immunosorbent assay systems, in which antigen and antibodies are fixed on a bead surface in a microchip [3]. By applying the knowledge and technique, we developed a microchip-based RCA system.

2. THEORY

Molecular recognition of DNA targets through padlock probe ligation results in the formation of a unique circular DNA molecule with a diameter of approximately 20 nm. The circular molecule acts as an endless template for a RCA reaction. This produces a long single-stranded concatemer DNA molecule complementary in sequence to the DNA circle, repeated approximately 1,000 times, which spontaneously collapses into a random coil of DNA. Fluorescent molecule–tagged probes are hybridized to the repeated sequence, resulting in a confined cluster of up to 1,000 fluorophores, visible in a fluorescence microscope as a bright object with a diameter of approximately 1 μm.

3. EXPERIMENTAL

The fabrication procedures were described previously [4]. The microchip was composed of two glass plates (30 mm × 70 mm), which were fabricated by wet etching methods. The microchannels had Y-shape with 210 μm in width and 100 μm in depth (Fig.1). A dam structure with 10-20 μm opening was fabricated in the microchannel. Beads can be

978-0-9798064-0-7/μTAS2007/$20©2007CBMS

retained one side of the dam region. DNA primer (35-mer) was immobilized on NHS-activated agarose gel beads of 34 μm in diameter (Fig. 2).

The beads were pre-immobilized with primer and padlock probe (Fig. 3A). Sample DNA solution was introduced from one inlet into the channel with the packed beads, and then primer, padlock probe and sample DNA formed a complex on the beads (Fig. 3B). Next, ligase was injected into the microchannel, and padlock primer was circularized (Fig. 3C). Extension of the primer hybridized to the DNA circle, *i.e.* RCA, was performed by DNA polymerase in the presence of excess dNTPs in a solution (Fig. 3D). The RCA products were labeled by adding fluorescence DNA probe (Fig. 3E). The resulting product was detected using a fluorescence microscopy.

4. RESULTS AND DISCUSSION

First, efficiencies of the primer immobilization and DNA hybridization on the beads were examined. By addition of an FITC labeled DNA (20-mer), which was complementary to immobilized primer, to the beads, specific fluorescence signal could be observed on the beads. The results indicated that the primer was successfully immobilized and DNA hybridization was not inhibited on the beads. Next, we examined on-beads RCA reaction using ligase, phi29 polymerase and fluorescence DNA probe in a microtube. The enzymatic reactions were also realized on the beads successfully. Finally, on-beads RCA reaction in a microchip was examined. RCA was successfully done in the microchip, and individual RCA products on beads were visible with a fluorescence microscope as a bright object, and they could be easily counted (Fig. 4B, 4C).

5. CONCLUSIONS

In this research, we demonstrate a single DNA molecule detection by on-bead RCA in a microchip. It is the first report of RCA realized in a microchip. This system helps us counting DNA easily. System optimization and detection of pathogenic bacteria using this system are under investigation.

REFERENCES

[1] M. Nilsson, H. Malmgren, M. Samiotaki, M. Kwiatkowski, B.P. Chowdhary, U. Landegren, *Padlock probes: circularizing oligonucleotides for localized DNA detection,* Science. **265,** pp2085-2058, (1994).

[2] J. Jarvius, J. Melin, J. Goransson, J. Stenberg, S. Fredriksson, C. Gonzalez-Rey, S. Bertilsson, M. Nilsson, *Digital quantification using amplified single-molecule detection, ,* Nat Methods. **3,** pp725-727, (2006).

[3] K. Sato, M. Tokeshi, T. Odake, H. Kimura, T. Ooi, M. Nakao, T. Kitamori, *Integration of an immunosorbent assay system: analysis of secretory human immunoglobulin A on polystyrene beads in a microchip,* Anal Chem. **72,** pp1144-1147, (2000).

[4] K. Sato, M. Yamanaka, T. Hagino, M. Tokeshi, H. Kimura, T. Kitamori, *Microchip-based enzyme-linked immunosorbent assay (microELISA) system with thermal lens detection,* Lab Chip. **4,** pp570-575, (2004).

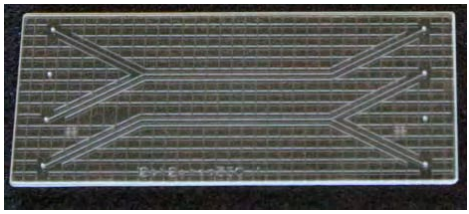

Figure 1. Rolling circle amplification (RCA) Chip.

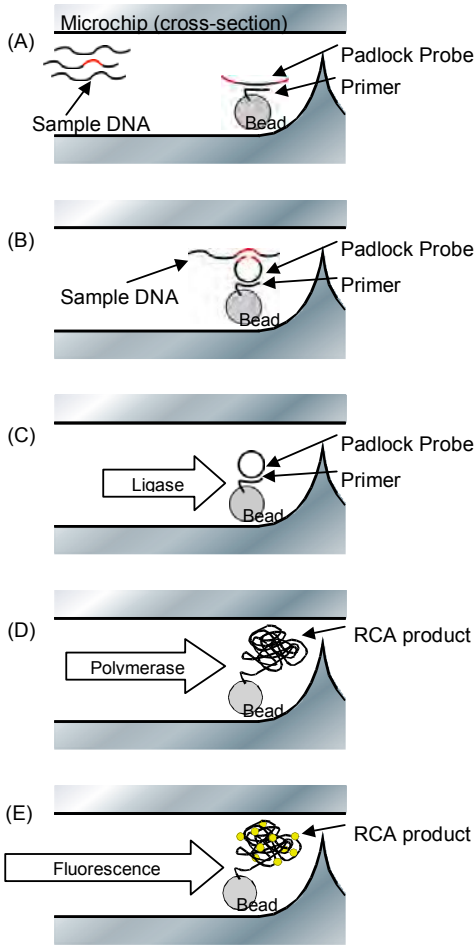

Figure 3. RCA using agasose gel beads.

(A) Sample intruduction. (B) Target recognition.
(C) Circle creation. (D) Amplification.
(E) Specific labeling.

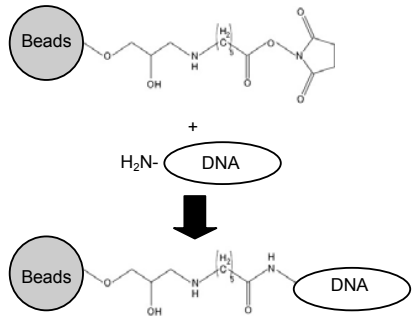

Figure 2. DNA-immobilized agarose gel bead.

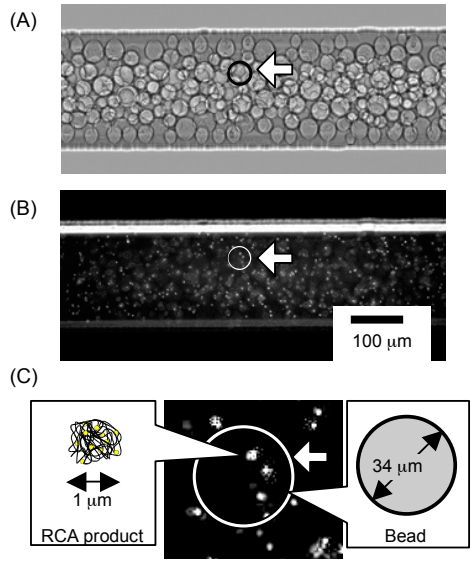

Figure 4. Detection of a single RCA product on bead in microchip.

(A) Phase-contrast image.
(B) Fluorescence image.
(C) Enlarged image of (B).

TOWARDS ON-CHIP ISOTHERMAL POLYMERASE CHAIN REACTION

Alexandre Persat[1], Tomoyuki Morita[2] and Juan G. Santiago[1]
[1] *Stanford Uiniversity, USA*
[2]*Ebara Research Co., Ltd., JAPAN*

ABSTRACT

We present a novel technique for on-chip polymerase chain reaction (PCR) where temperature is held constant and uniform in the reactor. Specific chemicals, known as denaturants, have the ability to melt DNA. A flow control scheme establishes spatio-temporal fluctuations in the concentration of denaturants along a microchannel, while electromigration drives DNA through this spatially varying denaturant concentration field. Preliminary results show amplification of a 200 base pairs (bp) DNA template.

Keywords:Polymerase chain reaction, DNA amplification, isotachophoresis

1. INTRODUCTION

PCR is the technique of choice for DNA amplification throughout biology and medicine. In the last decade, microfluidic PCR devices have been competing for miniaturization and faster amplification [1]. Still, thermal cycling limits speed and design flexibility. A few isothermal methods have been reported, such as helicase dependant amplification [2], strand displacement amplification [3], and rolling circle amplification [4]. So far, isothermal methods are slow, restricted to short DNA and/or require additional process proteins. We here propose and demonstrate preliminary experiments for an isothermal PCR technique that can simplify device design and speed up amplification.

In classical PCR, double stranded DNA (dsDNA) is subjected to a three-step thermal cycle. The first step is the denaturation, where a temperature of 95°C disrupts all hydrogen bonds between the two strands of DNA. This is followed by the annealing step at which the temperature of the reactor is lowered (typically to 55°C) allowing binding of primers to the parent single-stranded DNA (ssDNA). Primers are specifically designed short ssDNA that are complementary to the 5' extremities flanking the targeted gene on the template. Finally, increasing the temperature to 72°C allows *Taq* DNA polymerase to bind to the priming sites and synthesize the new strand by elongating the primer.

Chemical denaturants can also melt DNA (converting dsDNA to ssDNA), and are commonly used in separation techniques like denaturant gradient gel electrophoresis [5]. So far, denaturants have not been used in PCR as they inhibit polymerase activity.

Isotachophoresis (ITP) is widely used as a pre-concentrator step prior to separation and detection by capillary electrophoresis. In ITP, leading and trailing ions are selected to have respectively higher and lower electrophoretic mobility than the samples of interest. Under the influence of an electric field, analyte ions concentrate in successive, sharp zones bounded by the leading electrolyte (LE) and the trailing electrolyte (TE).

2. EXPERIMENTAL

We performed a series of calibration experiments to optimize the chemistry and flow conditions of our method. We have demonstrated the efficacy of *Taq* Polymerase for a

978-0-9798064-0-7/μTAS2007/$20©2007CBMS

relatively low extension temperature of 55°C. We compared final concentrations of three-step classical PCR products of a 200 bp template from *E.Coli* by agarose gel electrophoresis. The PCR trials show very similar yields for extension temperatures of 55°C and 72°C demonstrating high *Taq* activity at 55°C for the tested template (data not shown). This result shows that annealing and extension are possible at 55°C.

In a second set of experiments, we verified that the ITP conditions can result in a buffer compatible with PCR. Buffer type, buffer concentration, and DNA concentration can have a strong effect on PCR efficiency. We varied ionic concentration by changing the PCR buffer concentration of a three-step classical PCR from 1x to 6x (1x PCR buffer corresponds to 50 mM KCl, 20 mM Tris-HCl) and compared PCR yields for each concentration by agarose gel electrophoresis. PCR yield decreases dramatically for buffer concentrations greater than about 3x (data not shown). Similar experiments suggest that PCRs in Tris-HEPES buffer with concentrations ranging from 25 mM to 100 mM have similar yields to PCR in a 1x PCR buffer (data not shown).

In our technique, we leverage the high free-solution electrophoretic mobility of DNA to drive polynucleotide samples through a counter flow stream with alternately high and low denaturant concentration. The experiment is depicted in Figure 1. The counterflow stream can be pressure driven and/or electroosmotic. Double-stranded DNA (dsDNA) concentration is monitored via SYBR Green I intercalating dye fluorescence and ssDNA concentration by SYBR Green II fluorescence. We performed experiments in a fused silica microchip with silanized channels and added Tween 20 to all solutions to minimize protein adsorption.

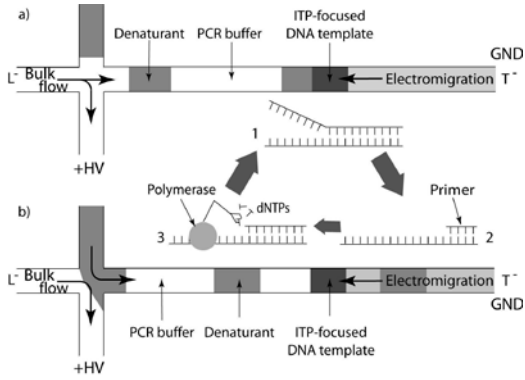

Figure 1. Schematic of on-chip isothermal PCR. PCR buffer is shown in white. Buffer with trailing ions (T^-) is light grey. DNA sample/template is focused between these and held approximately stationary by balancing ITP flux with bulk flow. Discrete pulses of denaturant containing leading ions (L^-) are injected from the north well via gated pressure or electroosmotic injection. a) Focused DNA encounters discrete clouds of high denaturant concentration and melts (1). b) The next denaturant cloud is injected at the intersection while ssDNA is annealed with a primer (2) and extended by a polymerase in the PCR (3).

3. RESULTS AND DISCUSSION

In ITP, trailing ion concentration reaches the same order of magnitude as leading ion concentration at the interface between electrolytes. We successfully performed ITP

preconcentration of 200 bp DNA using a 3x PCR buffer as leading electrolyte (chloride is the leading ion) and 5 mM to 25 mM Tris-HEPES as trailing electrolyte (HEPES is the trailing ion). Calibration experiments show compatibility of ITP with PCR. We also performed ITP using a 3x PCR buffer 100% denaturant solution as leading electrolyte and observed a sharp, fluorescent zone of SYBR Green II-labeled DNA.

We built and tested a device capable of exposing an ITP-focused DNA template to cycles of denaturant. We verified melting of dsDNA in <1 s via SYBR Green I fluorescence. SYBR Green I has a lower quantum yield as a ssDNA intercalator versus a dsDNA intercalator. Figure 2 shows a sample result of a fluorescent DNA plug experiencing a high denaturant concentration in a 34 μm wide microchannel.

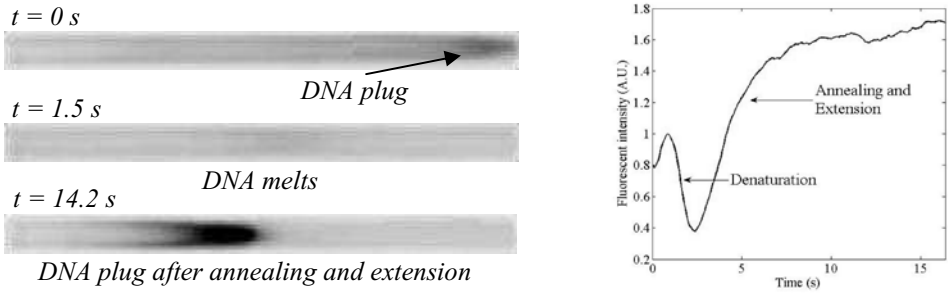

Figure 2. On-chip isothermal DNA denaturation, annealing and extension in a 34 μm wide channel. DNA concentration is monitored via SYBR Green I fluorescence plotted versus time on the right. Under conditions of balanced electromigration and bulk flow velocity, DNA plug oscillates within about a 1 mm region. Fluorescent intensity decreases dramatically during denaturing before amplifying via annealing and extension.

4. CONCLUSIONS

Preliminary experiments show that ITP conditions are compatible with PCR for specific ionic concentrations. Although high DNA concentration remains an issue, we successfully showed isothermal denaturation, annealing and extension of a 200 bp DNA template in a microchannel using our ITP/denaturant cycle strategy. We are currently pushing toward 30 cycle PCR amplification demonstration. On-chip isothermal PCR has a great potential in biology and medical research lab as a fast and compact DNA amplification technique.

REFERENCES

[1] Kopp, M.U., A.J. de Mello, and A. Manz, *Chemical amplification: Continuous-flow PCR on a chip.* Science, Vol. 280, pp. 1046-1048, (1998).

[2] Vincent, M., Y. Xu, and H.M. Kong, *Helicase-dependent isothermal DNA amplification.* Embo Reports, Vol. 5, pp. 795-800, (2004).

[3] Andras, S.C., et al., Molecular Biotechnology, Vol. 19, pp. 29-44, (2001).

[4] Fire, A. and S.Q. Xu, *Rolling Replication of Short DNA Circles.* Proceedings of the National Academy of Sciences of the United States of America, Vol. 92, pp. 4641-4645, (1995).

[5] Fischer, S.G. and L.S. Lerman, *Length-Independent Separation of DNA Restriction Fragments in 2-Dimensional Gel-Electrophoresis.* Cell, Vol. 16, pp. 191-200, (1979).

A SIMPLE AND EFFICIENT METHOD FOR ON-CHIP STORAGE OF REAGENTS: TOWARDS LAB-ON-A-CHIP SYSTEMS FOR POINT-OF-CARE DNA DIAGNOSTICS

Monica Brivio,[1] Yiping Li,[2] Annika Ahlford, [3] Bastian Gaardsvig Kjeldsen,[1] Jakob Leffland Reimers,[1] Minqiang Bu,[1] Ann-Christine Syvänen, [3] Dang Duong Bang[2] and Anders Wolff[1]

[1]Dept. of Micro and Nanotechnology, Technical University of Denmark, DENMARK,
[2]National Veterinary Institute, Technical University of Denmark, DENMARK and
[3]Molecular Medicine, Dept. Medical Sciences, University Hospital, Uppsala, SWEDEN

ABSTRACT

A method for on-chip storage of reagents for point-of-care diagnostics is presented. The method is based on on-chip freeze-drying of reagents for lab-on-a-chip applications. The stability of three enzymes, *viz.* Polymerase, Exonuclease I and Shrimp Alkaline Phosphatase throughout freeze drying and storage were investigated. As a proof of concept, on-chip DNA amplification was carried out using on-chip freeze-dried reagents. The results reported here are a key step towards the development of a ready to use tool for point-of-care genetic diagnostics.

Keywords: lab-on-a-chip, diagnostics, genotyping, freeze-drying.

1. INTRODUCTION

Current state-of-the-art genotyping techniques used in centralized laboratories require bulky equipment and laborious procedures. By integrating miniaturized components and automating functionalities, lab-on-a-chip technologies offer a valuable tool to perform fast, cost-effective and efficient point-of-care DNA analysis [1].

In the EC-funded SMART-BioMEMS project a microfluidic platform for genotyping of single nucleotide polymorphisms (SNPs) is being developed. Genotyping is based on PCR-amplification followed by minisequencing [2]. Three independent enzymatic steps, *i.e.* PCR, PCR clean-up and minisequencing are carried out on polymer chips, where the freeze-dried reagents are stored, see Figure 1.

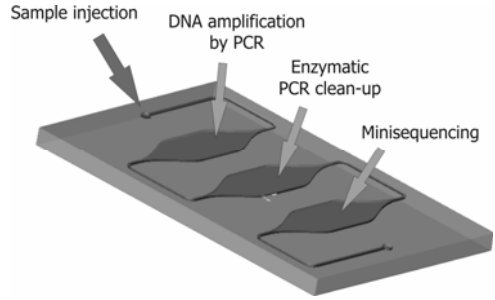

Figure 1. Schematic representation of a generic polymer chip with reaction chambers for storage of freeze-dried reagents.

2. EXPERIMENTAL

A premixed solution of all PCR reagents was introduced into the reaction chambers of three different polymer chips. After filling, the chips were stored overnight at –80 ºC and then transferred to a freeze-drier. Photographs of three 200 µm deep polymer chambers with freeze-dried PCR reagents are displayed in Figure 2.

978-0-9798064-0-7/µTAS2007/$20©2007CBMS



Figure 2. Freeze-drying for on-chip storage of reagents has been investigated in two European projects: OPTOLABCARD and SMART-BioMEMS. Pictures of PCR reagents freeze-dried in (a) a 7 µL chamber milled in Topas, (b) a 10 µL SU-8 chamber microfabricated on a Pyrex substrate and (c) a 6 µL SU-8 chamber.

The freeze-dried PCR reagents stored in the polymer chambers were redissolved upon addition of DNA solution. The chips were then transferred to a flat bed where PCR was carried out. Examples of results of on-chip freeze-drying and subsequent PCR are displayed in Figure 3.

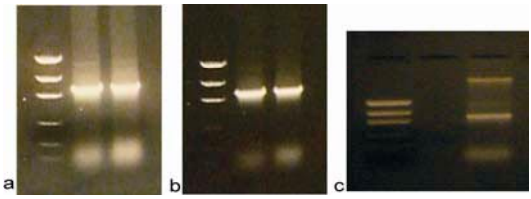

Figure 3. Gel chromatogram of on-chip PCR carried out in the closed SU-8 PCR chips of (a and b) Figure 2b and (c) Figure 2c, respectively.

3. RESULTS AND DISCUSSION

The stability of freeze-dried reagents during storage is a key issue. The activity of PCR reagents after six months of storage at room temperature (RT), at 4 ºC and at –20 ºC was measured by real-time PCR. No Polymerase activity was left after storage at room temperature. However, about half or complete polymerase activity was recovered after storage at 4 ºC and –20 ºC, respectively (Figure 4).

Unlike the thermo-stable polymerrase, used for the PCR, the enzymes used for the PCR clean-up, Exonuclease I (Exo) and Shrimp Alkaline Phosphatase (SAP), are thermo-labile. Accelerated stability tests were carried out for these enzymes, using TaqMan probe and fluorescein diphosphate as substrates for Exo and SAP, respectively. Samples prepared with “low” and “high” lyoprotectant concentration (Table 1) were freeze-dried and incubated at 37 ºC and 60 ºC. The residual enzyme activity was evaluated by end-point fluorescence measurements. With “low” lyoprotectant concentration the activity of both Exo (Figure 5) and SAP (Figure 6) was rapidly lost, regardless of the storage temperature. With “high”

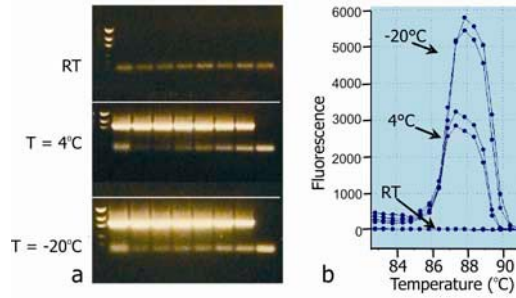

Figure 4. Stability tests of freeze-dried PCR reagents after six months storage at room temperature (RT), 4 °C and –20 ºC. (a) Gel chromatogram and (b) and melting curve measurements of real-time PCR at various concentration of DNA template.

lyoprotectants concentration no residual activity of SAP was measured whereas that of Exo decreased of about 20% after 5 days at 60 ºC. Remarkably, the activity of both Exo and SAP stored at 37 ºC for 5 days remained virtually unchanged, demonstrating the feasibility of the method for labile enzymes.

Table 1. Lyoprotectants used to stabilize EXO and SAP during freeze-drying.

lyoprotactants	**Lyoprotactants concentration (%w/vol)**	
	high	*low*
Threalose	5%	1%
Mannitol	2%	0.5%
PEG	1.5%	0.5%
Dextran	1.5%	0.5%

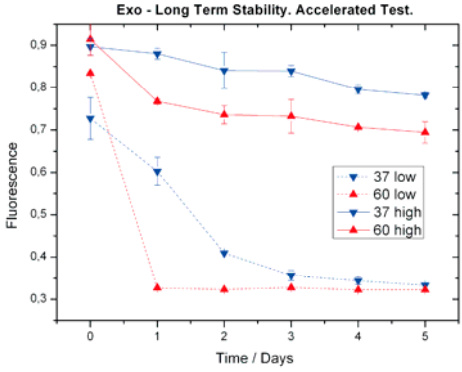

Figure 5. Accelerated stability tests of freeze-dried Exo. Samples with "low" (dashed lines) and "high" (solid lines) lyoprotectant concentration (Table 1) were stored at both 37 ºC (▼) and 60 ºC (▲).

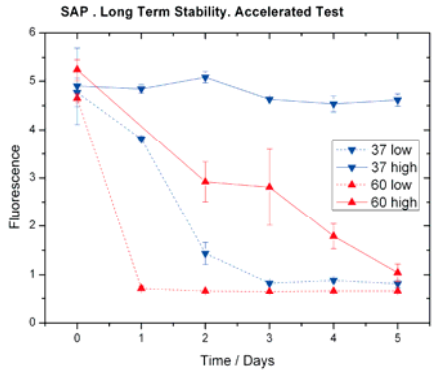

Figure 6. Accelerated stability tests of freeze-dried SAP. Samples with "low" (dashed lines) and "high" (solid lines) lyoprotectant concentration (Table 1) were stored at both 37 ºC (▼) and 60 ºC (▲).

4. CONCLUSIONS

Our results clearly demonstrate the feasibility of storing freeze-dried reagents on-chip for point-of-care diagnostics. After testing each step of the genetic analysis, we are currently working on the integration and automation of all steps on a single platform.

ACKNOWLEDGEMENTS

The authors would like to thank Ikerlan for providing the structures of Figure 2c and both SMART-BioMEMS and OPTOLABCARD European projects for financial support.

REFERENCES

[1] C. H. Mastrangelo *et al.*, *Microfabricated Devices for Genetic Diagnostics*, Proceedings if IEEE, **86**, 1769 (1998).

[2] A. C. Syvanen, *et al.*, *Quantitative evaluation by minisequencing and microarrays reveals accurate multiplexed SNP genotyping of whole genome amplified DNA*, Nucleic Acid Research, **31**, 1 (2003).

AN IMMUNOASSAY USING SILVER NANOPARTICLE, SILVER ENHANCEMENT AND A FLATBED SCANNER

Keng-Shiang Huang[1], Wei-Ting Chen[1], I-Long Wang[1], Hong-Ping Lin[2], Tsung Chain Chang[3], Yu-Cheng Lin[1]*

[1]Dept. of Engineering Science, [2]Dept. of Chemistry, [3]Dept. of Medical Laboratory Science and Biotechnology,
National Cheng Kung University, Taiwan
**Email: yuclin@mail.ncku.edu.tw*

ABSTRACT

This paper reports a novel immunoassay using antibody-silver nanoparticles (Ab-AgNPs) conjugates as a reporter, the silver enhancement reaction to magnify the detection signal, a flatbed scanner to scan and detect the immuno-reaction signal. This study is based on the sandwich immunoassay which contained a primary antibody, a secondary antibody and antigens. The results show that the silver precipitation was catalyzed by Ab-AgNPs conjugates. The changing color of reaction could be observed by naked eye or commercial scanner. And the detection limit was 1 ng/mL.

Keywords: Immunoassay, silver nanoparticles, commercial scanner

1. INTRODUCTION

Immunoassay based on the materials of labeling, it can be classified as chemiluminescence immunoassay, enzyme-linked immunosorbent assay (ELISA), and so on [1, 2]. Recently, the immunogold silver staining (IGSS) technique was found to have the capability to increase the sensitivity of DNA array [3, 4]. To date no effort has been made to apply IGSS technique coupled with AgNPs to improve the performance and sensitivity of immunoassays.

2. EXPERIMENTAL

Our strategy is that the immunoglobulin G-silver nanoparticles (IgG-AgNPs) conjugates immobilized on the slide were employed to catalyze the reduction of silver ion to silver metal (resulting in a particle-size enlargement and color change). After the immuno-reaction signal being amplified, the change of color was easily detected and captured by a scanner, and the gray level data were then analyzed by a personal computer. The proposed model is shown in (Figure 1). Figure 2 shows: (a) reaction well using polydimethylsiloxane (PDMS) as the material on glass slide was patterned with a circular area, (b) the scanner (Scanjet 3400C) was used to scan and capture the reaction signal, and (c) a personal computer with Adobe Photoshop installed was used to analyze the gray level data. The IgG-AgNPs conjugates need to be identified. Figure 3 (a) shows a TEM image of IgG-AgNPs conjugates which the black dots were AgNPs and gray parts around the black dot were IgG. Moreover, the IgG-AgNPs conjugates show red shift from 390 nm to 400 nm in UV-Vis spectrum (Figure 3 (b)).

978-0-9798064-0-7/μTAS2007/$20©2007CBMS

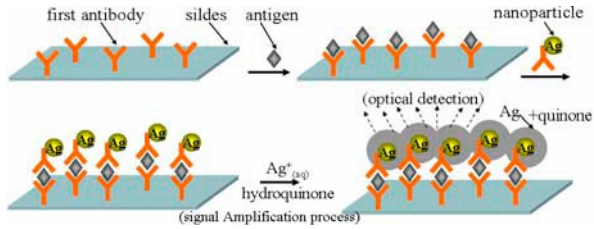

Figure 1. Schematic drawings of the signal amplification method for immunoassay, in which silver ions are reduced by hydroquinone to bulk silver metals.

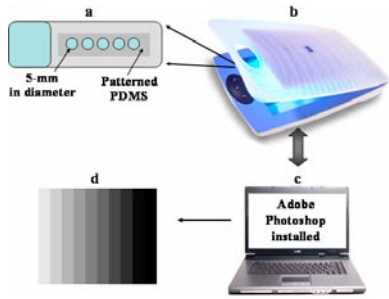

Figure 2. The whole detection instrumentation is silver-precipitation immunoassay.

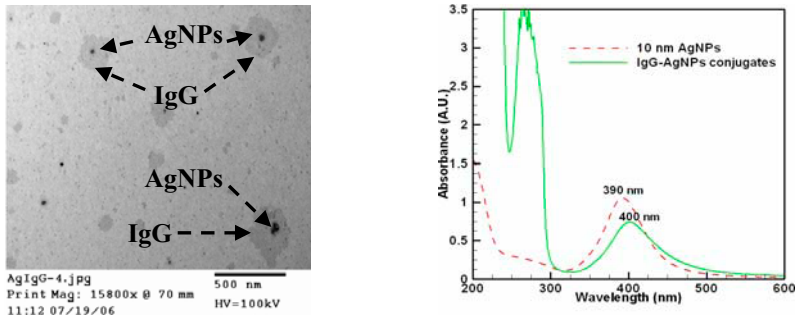

(a) (b)

Figure 3. (a) TEM images of IgG-AgNPs conjugates. (b) The UV-Vis absorption spectrums of 10 nm AgNPs and IgG-AgNPs conjugates.

3. RESULTS AND DISCUSSION

The ability of IgG-AgNPs conjugates catalyzed ionic silver to metal silver was studied. Figure 4 (a) shows the real-time color change of the IgG-AgNPs conjugates in the presence of the silver enhancement solution. The reaction could be observed by the naked eye even at an IgG-AgNPs concentration of 30 μM. For the highest concentration, the gray level values reached the saturation point promptly after about 13 minutes, indicating that all silver ions appeared to be reduced to the silver metal (Figure 5 (b)). Obviously, the time of the whole detection (within 13 minutes) was shorter than the conventional ELISA (approximately 60 minutes). In experiments, the concentration of first antibody was 10 μg/mL, and the concentration of antigen was from 10^{-4} μg/mL to 10 μg/mL.

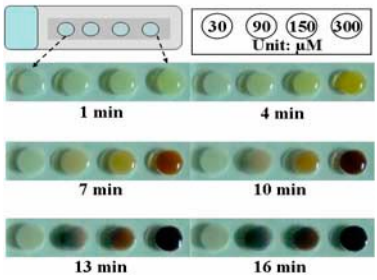

(a)

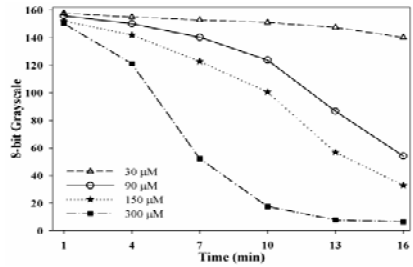

(b)

Figure 4. (a) Real-time color change of IgG-AgNPs conjugates in the silver enhancement. (b) Dynamic 8-bit gray-scale values indicate that IgG-AgNPs conjugates can successful catalyze the reduction of silver ion to silver metal.

4. CONCLUSION

The antigen concentration was respectively mapped to each gray level, provides the relation between the sample concentrations and the detection signals (Figure 5 (a)). The gray level value of 0.1 ng/mL approached the negative control. According to the results, the detection limit is 1 ng/mL (Figure 5 (b)) which is similar to the sensitivity of ELISA. We have successfully developed a novel immunoassay. This method has advantages of rapid, low cost and convenient than convention immunoassay ELISA.



(a)

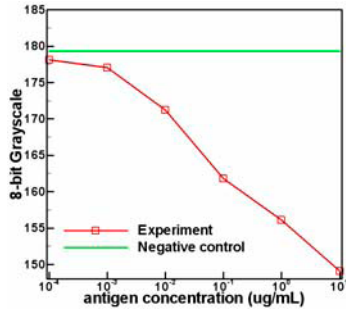

(b)

Figure 5. (a) The difference among protein A ($10\sim10^{-4}$ μg/mL) concentrations can be easily observed by the naked eye. (b) Graph of 8-bit gray-scale values of sandwich format as a function of reaction time.

ACKNOWLEDGEMENTS

The authors would like to thank the Center for Micro/Nano Technology Research, National Cheng Kung University, Tainan, for their equipment.

REFERENCES

[1] J.S. Rossier and H.H. Girault, Lab on a Chip, Vol. **1**, pp. 153-157, (2001).
[2] S. Lai, S.N. Wang, J. Luo, L.J. Lee, S.T. Yang and M.J. Madou, Analytical Chemistry, Vol. **76**, pp. 1832-1837, (2004).
[3] T.A. Taton, C.A. Mirkin and R.L. Letsinger, Science, Vol. **289**, pp. 1757-1760, (2000).
[4] S.J. Park, T.A. Taton and C.A. Mirkin, Science, Vol. **295**, pp. 1503-1506, (2002).

DETERMINATION OF TOTAL AND PANCREATIC AMYLASE ACTIVITIES IN HUMAN BLOOD BY USE OF MICROCHIP ELECTROPHORESIS

Eiki Maeda[1], Masatoshi Kataoka[2], Yasuo Shinohara[1, 2], Noritada Kaji[3, 4], Manabu Tokeshi[3, 4] and Yoshinobu Baba[2, 3, 4, 5]

[1] Graduate School of Pharmaceutical Sciences, The University of Tokushima, JAPAN
[2] Health Technology Research Center, AIST, JAPAN
[3] Department of Applied Chemistry, Graduate School of Engineering, [4] MEXT Innovative Research Center for Preventive Medical Engineering, Nagoya University, JAPAN
[5] Institute for Molecular Science, JAPAN

ABSTRACT

In this study, a high-performance determination system for isoenzyme activities of human α-amylase was developed using microchip electrophoresis (ME) with a plastic chip. The combination of ME for substrate/hydrolysate separation and immunoinhibition method for differentiation of isoenzymes using anti human salivary amylase (S-AMY) monoclonal antibody, Tu88E8, realized the highly selective determination of amylase isoenzyme activities even in a complex matrix such as a blood sample. This paper demonstrates that this system enables us to determine amylase isoenzyme activities with easy operation and high accuracy, and it will be applicable to clinical diagnosis for acute pancreatic disorders.

Keywords: amylase activity, isoenzyme, microchip electrophoresis, clinical diagnosis

1. INTRODUCTION

Alpha-amylase in human blood consists of two major isoenzymes which originated either from the pancreas or salivary glands [1]. Assaying the pancreatic amylase (P-AMY) and S-AMY activities in blood is valuable for accurate diagnoses of various diseases because changes in the activity can reveal pancreatic and parotid disorders, so differential assay is necessary. Over the past decades, many methods for differential assay of each amylase have been developed. However, these methods needed adding several reagents for chromophore-release, such as auxiliary enzyme [2] and stimulant [3], and this caused troublesome liquid-handling procedures. Therefore, a novel method for differential assay which realizes convenient, sensitive and accurate determination of amylase isoenzyme activities is required, especially in clinical field.

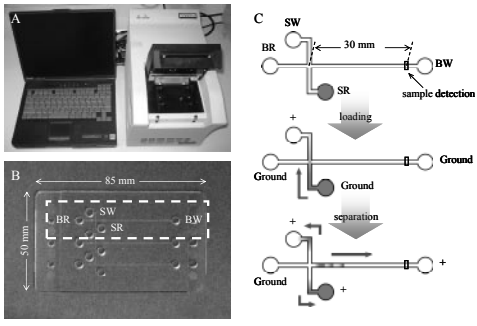

2. EXPERIMENTAL

All experiments were carried out using a Hitachi SV1100 ME system, and performed on a microfabricated polymethylmethacrylate chip (Figure 1). Several maltooligosaccha-

Figure 1: A) Hitachi SV1100 ME system. B) Plastic chip with a simple cross-channel was used in determination of amylase activity. C) Electrokinetic sample injection process.

978-0-9798064-0-7/μTAS2007/$20©2007CBMS

rides were used as reaction substrate after derivatization with 8-aminopyrene-1,3,6-trisulfonate (APTS) via reductive amination (Figure 2) [4]. Total amylase (T-AMY) and P-AMY activities in thirteen specimens were calculated using standard curve obtained from amylase standard solutions. Furthermore, as comparison of the quantitative accuracy, clinical assay using the same specimens was requested to SRL Inc.

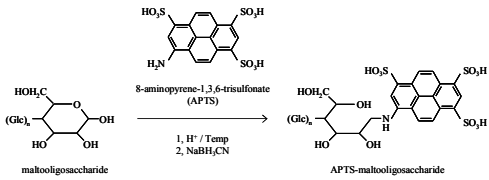

Figure 2: Reaction scheme for the derivatization of maltooligosaccharides. (Glc, glucose; n=2-6)

3. RESULTS AND DISCUSSION

By using ME, this system could be performed with easy operation and negligible troublesome liquid-handling procedures, because it does not need chromophore-release from reaction substrate. Enzymatic reactions using substrates prepared from several length maltooligosaccharides were performed for investigation of cleavage pattern of amylase isoenzymes (Figure 3), and APTS-maltohexaose was decided as a reaction substrate. As shown in Figure 4, 98% of S-AMY activity was inhibited by Tu88E8 and P-AMY was not. In Figure 5, T-AMY activity in the range of 5-500 U/L showed good linearity to the fluorescent intensity of

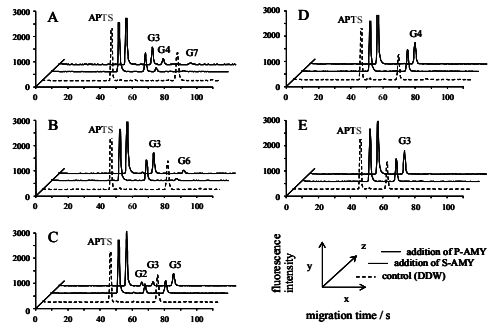

**G2, maltose; G3, maltotriose; G4, maltotetraose; G5, maltopentaose; G6, maltohexaose; G7, maltoheptaose*

*Figure 3: Cleavage pattern of several length APTS-maltooligosaccharides. *A) APTS-G7, B) APTS-G6, C) APTS-G5, D) APTS-G4 and E) APTS-G3 were used as a reaction substrate.*

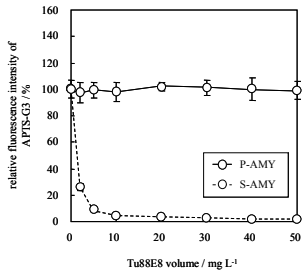

Figure 4: Effect of anti S-AMY monoclonal antibody.

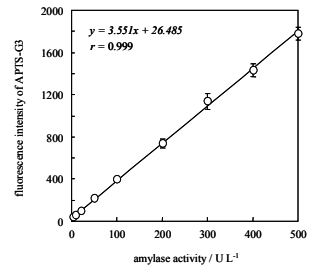

Figure 5: Relationship between fluorescence intensity of hydrolysate, APTS-G3, and amylase activity.

hydrolysate (APTS-maltotriose). Furthermore, good relationship was observed between both determination values of T- and P-AMY activities obtained by using the proposed method and clinical diagnostic method by linear regression analysis (Figure 6). The obtained values by use of ME exhibited high reproducibility (Table 1) in the same day (coefficient of variation, CV<6.4%) and during five days (CV<5.7%). This system enables

us to determine not only T-AMY but also both isoenzyme activities in human blood with high accuracy and high reproducibility.

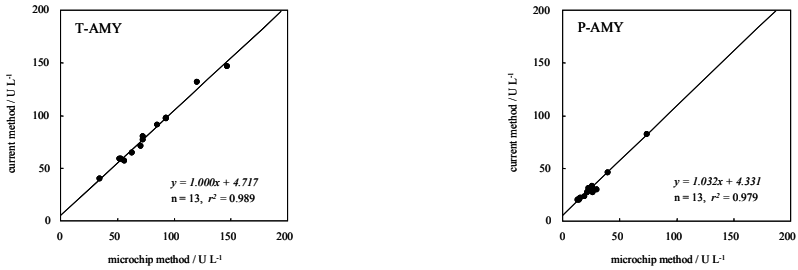

Figure 6: Linear regression analysis on determination values obtained by microchip method and current clinical method

Table 1. Reproducibilities of T- and P-AMY assay.

Sample	T-AMY assay		P-AMY assay	
	mean ± SD, U/L	CV, %	mean ± SD, U/L	CV, %
Within day, n=10				
A	97.46 ± 6.11	6.27	42.12 ± 1.96	4.66
B	159.53 ± 4.75	2.98	66.89 ± 3.27	4.89
C	93.10 ± 3.04	3.27	28.53 ± 1.82	6.39
D	69.36 ± 3.95	5.69	33.76 ± 1.29	3.83
Between days, n=5				
A	98.42 ± 5.24	5.33	40.78 ± 1.76	4.33
B	163.19 ± 7.65	4.69	70.32 ± 2,56	3.64
C	94.76 ± 2.73	2.88	29.76 ± 1.68	5.63
D	70.32 ± 3.98	5.66	34.11 ± 1.53	4.47

CV, coefficient of variation

4. CONCLUSIONS

We have presented a high-performance determination system for amylase isoenzyme activities, using ME with a plastic chip. These results serve as a good basis for further research towards a real highly-integrated chip format, like the diagnostic chip which can perform clinical assay on one sheet.

REFERENCES

[1] J.E. Berk, S. Hayashi, R.L. Searcy, N.C. Hightower, Jr., Am. J. Dig. Dis., **9**, 695-701 (1966).
[2] I. Warshawsky, G.L. Hortin, J. Clin. Lab. Anal. **15**, 64-70 (2001).
[3] Y. Morishita, Y. Iinuma, N. Nakashima, K. Majima, K. Mizuguchi, Y. Kawamura, Clin. Chem., **46**, 928-933 (2000).
[4] F. Dang, L. Zhang, H. Hagiwara, Y. Mishina, Y. Baba, Electrophoresis, **24**, 714-721 (2003).

HYBRID CERAMIC/PDMS microLAB WITH TWO INDEPENDENT DETECTION SYSTEMS FOR ON-LINE DIALYSIS' PARAMETERS MONITORING

Ilona Grabowska[1], Iwona Wyżkiewicz[2], Michał Chudy[1], Artur Dybko[1] and Zbigniew Brzózka[1]

[1] Warsaw University of Technology, POLAND
[2]Institute of Electronic Materials and Technology, POLAND

ABSTRACT

The paper describes the construction of a hybrid (ceramic/polymer) miniaturized system which allows carrying out determination of a few very important bioanalytes (urea, creatinine, uric acid, and NH_4^+) using two various and independent analytical methods: i.e. electrochemical and spectrophotometric. The application of dual detection configuration makes obtained results more reliable. Additionally, it creates opportunities for monitoring urea, creatinine and uric acid concentration during hemodialisis course.

Keywords: dual detection, hybrid technology, ceramic, PDMS

1. INTRODUCTION

Up to now, there are only several microsystems with dual detection published in the literature. Wang [1] used both amperometric and potentiometric detection built-in one system for organophosphorus neurotoxins determination. Together with Pumera [2] he reported also a microCE chip with conductometric and amperometric detection for explosives analysis. Manica and co-workers [3] published a microchip for photobleaching evaluation based on amperometric measurements. Because of its transparency, fluorescence measurements through the chip were also possible using an inverted microscope. Detection in all pointed systems was based on electrochemical measurements, whereas optical signal was measured because the chip was transparent.

2. EXPERIMENTAL

Proposed by our group system was fabricated using a new hybrid technology - ceramic and polymer – see Fig. 1 and Fig. 2. The microsystem consists of three layers:

1) a ceramic plate – support for screen printing of electrodes and a self calibrating heater on the opposite side;
2) a PDMS thin layer with small holes (determining size of obtained ion selective membranes on the surface of electrodes)
3) a PDMS plate with 50 cm long (50x100 μm) mixing microchannel fabricated using capillary film stamp, inlets, outlet and fiber optics are placed here as well. At the end of the channel, there was a special microvolume optical flow-cell for absorbance measurements of the analytical reaction product.

The ceramic support and PDMS layers were sealed using plasma bonding technique [4] following by the membrane deposition on the microelectrodes. The electroactive components of potentiometric membranes are showed in table 1. The main advantage of the constructed microsystem is the application of the glazed ceramic support with screen-printed both sensors and the heater. It made the technology easier and repeatable. Up to

978-0-9798064-0-7/μTAS2007/$20©2007CBMS

now, microsystems developed in our group consisted of separate modules (microreactor, potentiometric or spectrophotometric detector) in different configurations and they were fabricated mostly in PDMS. Many steps during their fabrication were difficult and acceptable only in a laboratory. Fabrication of potentiometric sensors directly on the PDMS surface was impossible at all.

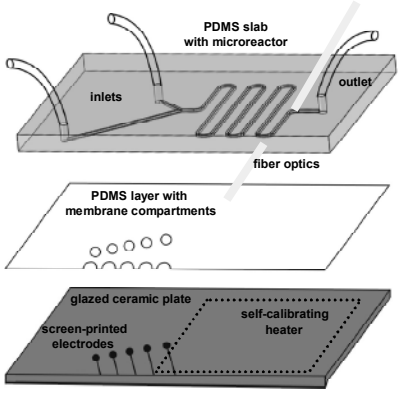

Figure 1: Scheme of the hybrid microsystem for bioanalytes determination

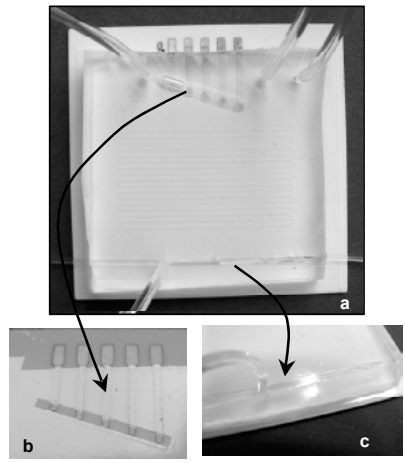

Figure 2. a) photograph of the microsystem; b) close-up of the potentiometric screen-printed electrodes with membranes; c) close-up of the spectrophotometric cell.

2. DISCUSSION AND RESULTS

Patients with renal disorders are treated with dialysis as a life-saving therapy. During kidney disfunction it is the only way to purify their organism from various toxins. Such a therapy must be controlled and for this purpose several parameters are examined. Urea, creatinine as well as uric acid and NH_4^+ levels are measured to estimate the efficiency of detoxification and the hemodialysis profile. The statement of the analytical methods that are applied in the fabricated microsystem is presented in table 1.

Table 1. Analytical methods applied in the microsystem

bioanalyte	potentiometry	spectrophotometry
NH_4^+	nonactine/PVC membrane	-
uric acid	-	phosphotungstenic acid λ_{max} 710 nm
creatinine	nonactine/creatinine deiminase membrane	Jaffe reaction λ_{max} 510 nm
urea	nonactine/urease membrane	o- ftalate aldehyde / N-naphtyl-(ethylenediamine) λ_{max} 505 nm

The microsystem allows for the determination of all listed analytes or one bioanalyte by two various methods, which can be carried out simultaneously and independently. Obtained calibration curves for all bioanalytes are showed in Fig. 3. Therefore it is possible to compare the obtained results and reliability of the results is ensured.

NH_4^+

LOD 0.28mg/l
lin.range
0.5 – 18.0 mg/l
slope 54 mV/dec

urea

LOD 42.0 mg/l
lin.range
53,1 – 1060 mg/l
slope 42 mV/dec

creatinine

LOD 35.7 mg/l
lin.range
63,5 – 2255 mg/l
slope 53.9 mV/dec

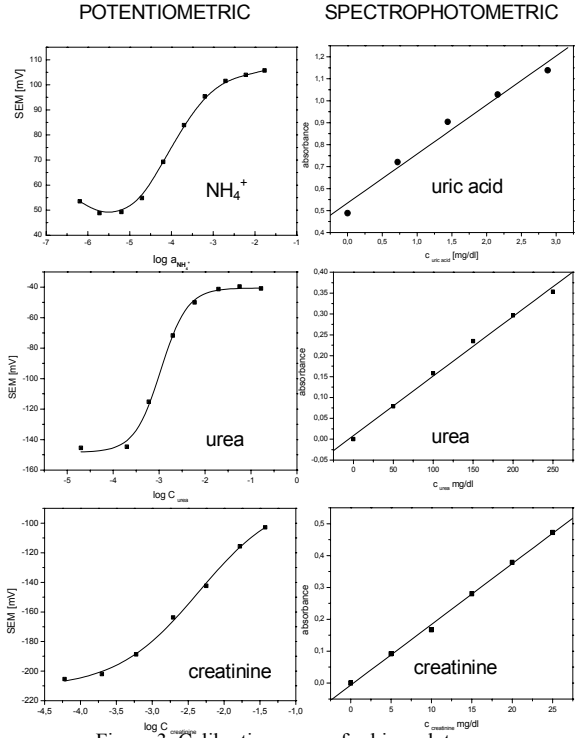

Figure 3. Calibration curves for bioanalytes.

uric acid

LOD 1.0 mg/l
lin.range
0.0 – 30.0 mg/l

urea

LOD 52 mg/l
lin.range
0.0 – 2500 mg/l

creatinine

LOD 12.0 mg/l
lin.range
0.0 – 250 mg/l

CONCLUSIONS

The paper describes the new construction of novel microsystem for carrying out determination of very important analytes. Its main advantage is flexibility in bionalayte selection for analysis and easiness to operate. Moreover, all applied methods are sensitive enough for measuring wide range of all analytes' concentrations which are present in real samples. Materials which were used allow for rapid system preparation and also cost of system preparation is relatively low.

ACKNOWLEDGEMENTS

The author wish to thank Rector of Warsaw University of Technology for financial support.

REFERENCES

[1] J. Wang, R. Krause, K. Block, M. Musameh, A. Mulchandani, P. Mulchandani, W. Chen, M. J. Schoning, "Dual amperometric-potentiometric biosensor detection system for monitoring organophosphorus neurotoxins", Anal. Chim. Acta, 469, 197-203, (2002)

[2] J. Wang, M. Pumera, "Dual conductivity/amperometric detection system for microchip capillary electrophoresis" Anal. Chem., 74, 5919-5923, (2002)

[3] D.P. Manica, J.A. Lapos, A.D. Jones, A.G. Ewing, "Dual electrochemical and optical detection on a microfabricated electrophoretic chip", Micro Total Analysis Systems, 262-264, (2001),

[4] L. Golonka, K. Malecha, H. Roguszczak, D. Stadnik, I. Grabowska, M. Chudy, A. Dybko, Z. Brzozka, "LTCC technology for various microsystem applications" microTAS 2005, Boston, USA, 9-14 Oct. 2005.

LABEL-FREE OPTICAL DETECTION OF DNA BY REVERSIBLE ELECTRIC FIELD CONFINEMENT IN FREE SOLUTION

Faisal A. Shaikh and Victor M. Ugaz

Artie McFerrin Department of Chemical Engineering, Texas A&M University, College Station, TX, USA

ABSTRACT

We introduce a new technique to enable label-free detection of charged biomolecules (DNA, proteins) that harnesses a microfluidic on-chip electrode array to generate localized zones where the biomolecules become ultra-concentrated, resulting in formation of a mesophase that is clearly visible under ordinary white light. This phenomenon is made possible by a synergistic combination of (i) the closely spaced electrodes within the array (225 μm) that permit sufficiently high electric field strengths (50–100 V/cm) to be imposed upon application of low potentials (~1–2 V), and (ii) 2-dimensional compaction that confines the biomolecules within a layer at the electrode surface that is only a few microns thick. Using this arrangement, we demonstrate that it is possible to detect DNA in free solution by simply illuminating the electrode surface with white light and observing the accompanying strong increase in reflected intensity

Keywords: DNA detection, mesophase, diffraction, label free detection

1. INTRODUCTION

Optical detection of DNA in free solution is generally carried out by labelling the DNA with intercalating dyes or fluorescent probes. The ability to quantitatively detect the presence of charged and unlabelled biomolecules like DNA and proteins in free solution provides opportunities for the simplification of the physical and operational design of integrated lab-on-a-chip devices. Pre-concentration strategies for such charged biomolecules are generally required given the minute amounts of sample used at the microscale. The progress of such on-chip pre-concentration strategies such as PCR-reactions or electrical methods could be regulated in real-time in free solution using this technique which involves focusing and compaction of DNA present in free solution onto the surface of a microfabricated electrode, resulting in the formation of a light diffracting mesophase (Figure 1).

2. THEORY

The cornerstone of our approach is a microfluidic system incorporating an array of individually addressable microfabricated electrodes capable of sequentially concentrating a DNA sample and focusing it into a narrow zone (Figure 2) [1]. Computational simulations of the single electrode capture process reveal that, in this arrangement, the collected DNA experiences simultaneous concentration in both the axial and vertical planes so that the sample becomes confined within a very narrow layer (< 5 μm) at the electrode surface (Figure 3). The high degree of confinement in this zone can become sufficient to promote formation of a mesophase owing to a combination of high concentration and excluded volume interactions [2].

978-0-9798064-0-7/μTAS2007/$20©2007CBMS

The potential for mesophase formation under these conditions is supported by Semenov-Khokhlov theory for semi-flexible polymers, where the critical volume fraction ϕ required to form a fully nematic liquid crystalline phase scales as $\phi = 5.7\ d/L_p$ (d is the diameter of the molecule and L_p is its persistence length). This corresponds to a value of about $\phi = 0.22$ for double-stranded DNA ($d \sim 2$ nm, $L_p \sim 50$ nm), while we estimate that values of $\phi = 0.25$ or higher are possible within the compaction zone at the electrode surface.

3. EXPERIMENTAL

We illustrate this phenomenon in a series of experiments that involve injecting DNA into a glass microchannel glued to a silicon device with microfabricated gold electrodes (50 μm wide with 225 μm spacing). A 100-bp ladder suspended in supplied, 1X Tris-Borate EDTA and Histidine (50 mM) buffers was used as the sample. The concentration process is initiated by applying a 2 V DC potential between a pair of electrodes on the floor of the microchannel. The DNA present between the electrode pair, being intrinsically poly-anionic, migrates toward the anode in response to the electric field and becomes focused there. The DNA can be concentrated further by sequentially switching the applied voltages to subsequent electrodes in the electrode array (Figure 2).

4. RESULTS AND DISCUSSION

When the anode is viewed under white light illumination it becomes very bright due to the formation of a DNA mesophase and is clearly distinguishable (Figure 4). For a DNA sample initially at a concentration of 12 μg/ml, the typical timescale for mesophase formation is in the vicinity of 10–20 s. We have also directly characterized the mesophase using an optically transparent indium tin oxide (ITO) electrode array. Here, distinct textures are evident under transmitted polarized light illumination (Figure 5). The dramatic magnitude of this effect combined with the extremely low actuation voltages required make this technique a robust label-free method to enable minute sample quantities to be detected in portable bioanalysis systems without the use of chemical fluorophores.

REFERENCES

[1] F.A. Shaikh and V.M. Ugaz, *Collection, focusing, and metering of DNA in microchannels using addressable electrode arrays for portable low-power bioanalysis*, Proc. Natl. Acad. Sci. USA, **103**, pp. 4825-4830, (2006).

[2] F. Livolant and A. Leforestier, *Condensed phases of DNA: structures and phase transitions*, Prog. Polym. Sci. **21**, 1115 (1996).

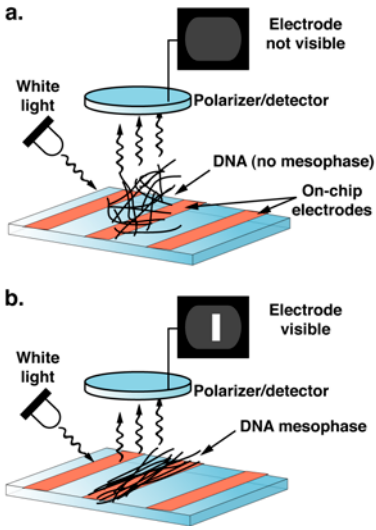

Figure 1: Schematic illustration of label-free detection scheme. (a) Initially, DNA is isotropically oriented. (b) When DNA is compacted to an ultra-high concentration at an electrode, a mesophase is formed that is visible under white light.

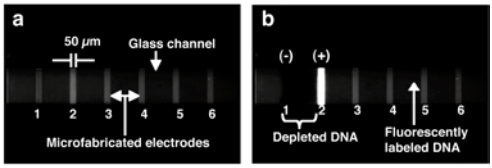

Figure 2. Top view of an electrode array in a glass microchannel that allows DNA to move and become more concentrated and focused at an anode [1].

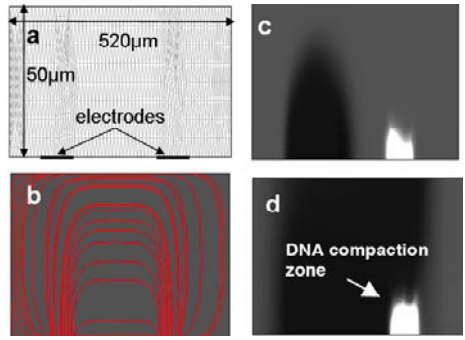

Figure 3. Side view of the electrode capture process in Fig. 2 simulated for DNA initially at 12 μg/ml under a 1 V applied potential. (a) Mesh generated within the geometry, and (b) resulting electric field lines. Simulation results depicting the migration and capture of DNA after elapsed times of (c) 10 s, and (d) 200 s.

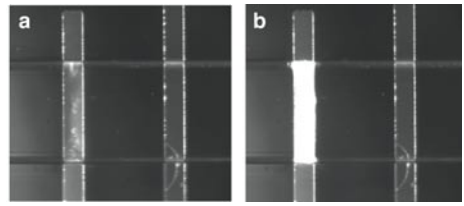

Figure 4. DNA detection under white light (100 bp dsDNA ladder; same device layout as in Fig. 2). (a) No voltage applied to electrodes. (b). Reflected band is evident after applying a 1.5 V potential between electrodes for ~1 min.

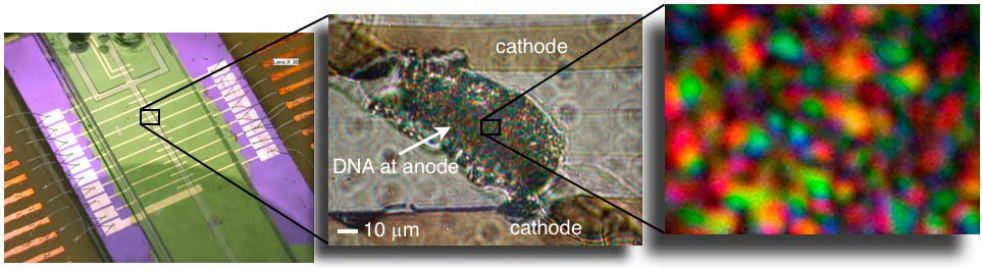

Figure 5. The lab-chip on the left shows the addressable electrode array along the microchannel floor. Zooming into the microchannel reveals the DNA mesophase visible under polarized white light which forms on application of an electric field, and reveals brilliant colors under 400X magnification on the far right.

MICROFLUIDIC COMPACT DISC PLATFORMS FOR RAPID AND SENSITIVE DETECTION AND IDENTIFICATION OF *CANDIDA* YEASTS FROM BLOOD.

I. Martineau[1], D.K. Boudreau[1], L. Monfort[1], F. Bégin[1], M.-J. Fiola[1], G. Stewart[1], H. Morin[1], A. Huletsky[1], R. Peytavi[1], M. Boissinot[1], F.J. Picard[1], J.V. Zoval[2], H. Kido[2], G. Jia[2], M.J. Madou[2] and M.G. Bergeron[1].

[1]*Centre de Recherche en Infectiologie de l'Université Laval, CHUQ (Pavillon CHUL), Québec, PQ, CANADA*

[2]*University of California, Irvine, CA, USA*

ABSTRACT

We present the design and application of novel microfluidic platforms for extraction of genomic DNA and hybridization on microarrays for the rapid detection and identification of *Candida* species associated with septicemia. The lysis CD platform successfully extracted high quality yeast DNA from treated spiked blood samples in less than 10 minutes. The multiplex PCR coupled with microfluidic microarray hybridization could detect the equivalent of as few as 8 CFUs of *Candida* cells per ml of blood.

Keywords: *Candida*, microfluidic, microarray, DNA extraction

1. INTRODUCTION

Invasive infections caused by *Candida* yeasts are associated with high mortality rates. Current phenotype-based methods for the detection and identification of yeasts from clinical samples are time-consuming and often unreliable. In this study, we show that molecular diagnostics can be achieved directly from blood samples using novel automated compact disc (CD)-based platforms for the rapid and sensitive detection of clinically relevant *Candida* species.

2. DESIGN

For the lysis of blood-infecting *Candida* yeasts, we used mechanical cell disruption induced by the relative motion of a ferromagnetic metal disc, actuating a grinding matrix into a liquid medium in the presence of an oscillating magnetic field (Fig. 1). For rapid microarray hybridization, we developed a microfluidic flow cell consisting of a network of chambers and channels molded into polydimethylsiloxane (PDMS), overlaid above a DNA microarray printed onto a glass slide. These units were installed on a rotational device. Centrifugal forces drove the sample and buffers directly on the microarray surface (Fig. 2).

3. EXPERIMENTAL

The assay was designed using a combination of rapid blood sample preparation process starting with 5 ml of spiked blood and concentrating the yeast cells into a 60 µL volume which was further treated by an automated microfluidic CD platform for the cell lysis and DNA extraction [1]. Multiplex PCR reactions were carried out on a Rotor-Gene™ thermocycler (Corbett Life Science) with specific primers that were designed upon *tef*-1 gene nucleotide sequences unique to *Candida* species. An automated microfluidic

978-0-9798064-0-7/µTAS2007/$20©2007CBMS

microarray hybridization CD platform was used to identify each PCR amplicon by hybridization onto a DNA microarray spotted with species-specific capture probes [3].

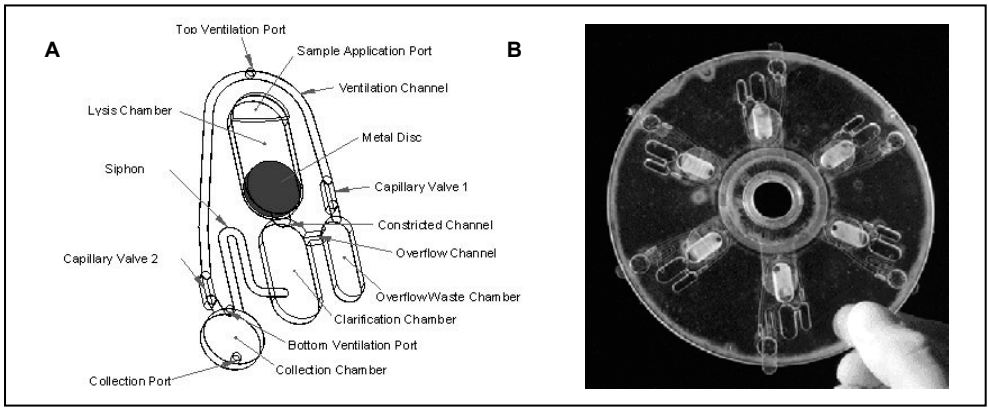

Figure 1. Cell lysis and microfluidic nucleic acid extraction. A) Schematic of the cell lysis and purification microfluidic module. B) Cell lysis plastic CD assembly. CD rotation at different speeds allows sequential control of fluid movements. Magnets staggered on the stator plate impede movement to the metal disc incorporated into the lysis chamber.

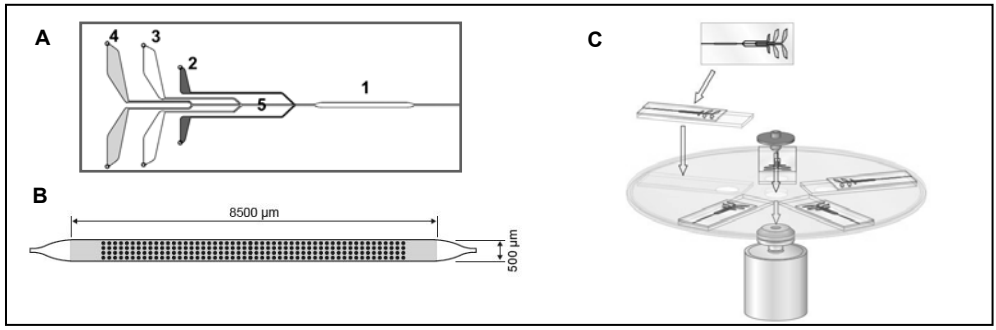

Figure 2. Microfluidic microarray hybridization. A) Molded PDMS microfluidic unit juxtaposed onto a glass slide where capture probes are arrayed. Reservoir chambers are filled with PCR-amplified samples (2), washing buffer, (3) and rinsing buffer (4). These reagents sequentially flow through the central microchannel (5) to reach the hybridization chamber (1). B) Schematic view of the 425 nL hybridization chamber (1) covering up to 192 capture probes. C) Up to 5 glass slides overlaid with PDMS can be accomodated on this CD system.

4. RESULTS AND DISCUSSION

The lysis and DNA extraction CD platform successfully extracted high quality yeast DNA from treated spiked blood samples in less than 10 minutes. PCR-amplified sample was flowed through a 425 nL hybridization chamber containing *Candida*-specific capture probes immobilized onto a 0.5 mm x 8.5 mm array. The automated microfluidic microarray hybridization platform yielded results within 15 minutes. Strong and specific fluorescent signals were observed with all selected species-specific capture probes, in the presence of their respective targeted *Candida* DNA (Fig. 3). This system could detect the equivalent of as few as 8 CFUs of *Candida* cells per ml of blood.

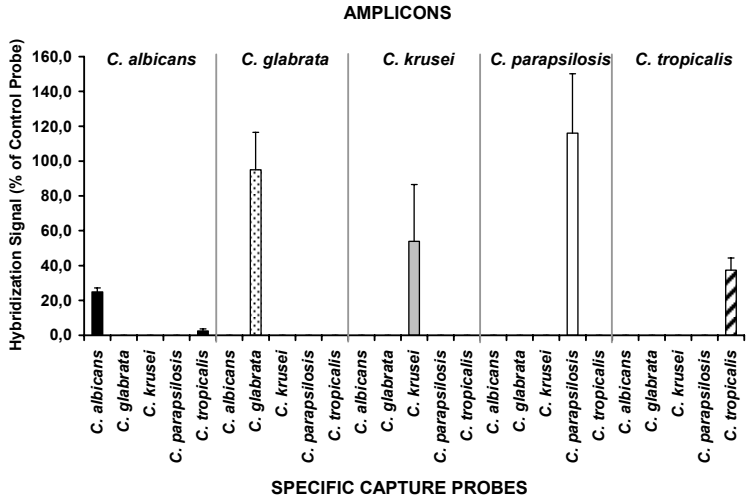

Figure 3. **Microfluidic microarray detection of *Candida* specific amplicons**. Graph illustrating the intensity and specificity of the microarray detection of PCR-amplified blood samples spiked with *Candida* cells (range of 8 to 40 CFUs of *Candida* per ml of blood). Standard deviation for at least 4 replicates from 2 independent experiments. There was no significant cross hybridization between capture probes and non-targeted *Candida* PCR amplicons.

5. CONCLUSIONS

Using a combination of automated microfluidic CD platforms, we were able to achieve rapid, specific, and sensitive detection of 5 clinically relevant *Candida* species from spiked blood samples. These microfluidic devices not only represent significant design improvements over our previous systems [2-4], but for the first time, they have all been made compatible with each other for integration into a single CD to create a μTAS. Further development and miniaturization will include the addition of a microfluidic thermocycler and a portable microarray fluorescence scanning device.

ACKNOWLEDGEMENTS

This research project was supported by grants from Genome Canada and Génome Québec.

REFERENCES

[1] H. Kido, M. Micic, D. Smith, J. Zoval, J. Norton and M. Madou. *A novel, compact disk-like centrifugal microfluidic system for cell lysis and sample homogenization,* Colloids Surf B Biointerfaces, **58**: pp. 44-5, (2007).

[2] J. Kim, H. Kido, J.V. Zoval, D. Gagné, R. Peytavi, F.J. Picard, M. Bastien, M. Boissinot, M.G. Bergeron and M.J. Madou. *Rapid and automated sample preparation for nucleic acid extraction on a microfluidic CD (compact disk),* Microfluidics, BioMEMS, and Medical Microsystems IV. Edited by Papautsky, Ian; Wang, Wanjun. Proceedings of the SPIE, **6112**: pp. 24-31, (2006).

[3] R. Peytavi, F.R. Raymond, D. Gagné, F.J. Picard, G. Jia, J. Zoval, M. Madou, K. Boissinot, M. Boissinot, L. Bissonnette, M. Ouellette and M.G. Bergeron. *Microfluidic device for rapid (<15 min) automated microarray hybridization*, Clin Chem, **51**: pp. 1836-44, (2005).

[4] G. Jia, K.S. Ma, J. Kim, J.V. Zoval, R. Peytavi, M.G. Bergeron and M.J. Madou. *Dynamic automated DNA hybridization on a CD (compact disc) fluidic platform*, Sens and Actuators B, **114**: pp. 173-181, (2006).

MICROFLUIDICS FOR CLINICAL DIAGNOSTICS: DNA PURIFICATION FROM LARGE-VOLUME BLOOD SAMPLES USING A MICRO-TWO-DIMENSIONAL SOLID PHASE EXTRACTION SYSTEM

Jian Wen[1,2], Travis M. Hartberger[2], Jerome P. Ferrance[2] and James P. Landers[1, 2,3,4]

[1]Department of Molecular Physiology and Biological Physics and Departments of [2]Chemistry and [3]Mechanical Engineering and [4]Pathology, University of Virginia, Charlottesville, VA 22904

ABSTRACT

A multiphase microscale two-dimensional (2-D) microfluidic solid phase extraction (SPE) device system design was developed by multiplexing to increase the loading capacity of whole blood to at least 160 μL human whole blood. Approximately 60% of the protein (15 ± 1.3 mg) present in the 160 μL blood was captured by the C18 phase but allowed more than 98% of the DNA (6.03 ± 0.98 μg) to pass on to monolith for DNA purification. An overall extraction efficiency of 50-60% was demonstrated on this credit card-sized microdevice for handling crude large-volume samples for clinical diagnostics.

Keywords: Microfluidic, DNA Purification, Blood, Clinical diagnostics

1. INTRODUCTION

At microTAS-06, we described a microscale two-dimensional (2-D) microfluidic solid phase extraction (SPE) device containing a C18 phase for protein capture, followed by a grafted organic monolith for DNA extraction. The system showed unprecedented microscale capability, accepting 10 μL of human whole blood and extracting DNA with an efficiency of ~70% [1]. Microchip purification of DNA from blood, to remove chemical species known to interfere with the polymerase chain reaction (PCR), is an important development owing to the value of whole blood as a universal source of genomic DNA for diagnostic applications. Extraction of DNA from rare cells in blood (Minimal Residual Disease-MRD) in patients undergoing cancer treatment or in remission requires that larger blood volumes be extracted than are typically possible on microchips. This work expanded the micro-two-dimensional solid phase extraction (μ2D-SPE) device exploiting eight parallel C18 phase four-channel units to capture the blood proteins (stage 1) with a single extended monolithic column for DNA extraction (stage 2) from blood volumes up to 160 μL for minimal residual disease (MRD) detection.

2. EXPERIMENTAL

DNA purification from a blood lysate (0.4 μL blood/μL lysate) was performed on the multiplex two-stage device shown in **Figure 1**. The 400 μL of lysate containing 160 μL of blood was split into eight load syringes and flowed onto the eight parallel C18 pre-column units packed with 15 μm C18 beads. The C18 pre-columns were then rinsed with a total of 640 μL equilibration buffer (6M Gu.HCl, pH 6) to remove the DNA from the C18 phase and transfer it to the monolithic DNA capture phase. For protein capture studies, fractions were collected before the monolith at the interfacing reservoir to determine the amounts of

978-0-9798064-0-7/μTAS2007/$20©2007CBMS

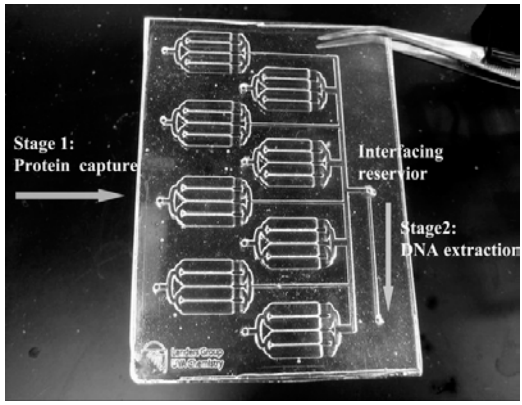

Figure 1. Microdevice deign showing an 8-unit protein capture section (stage 1) connecting with a TMOS-grafted monolith (stage 2) for DNA extraction. Arrows show the flow from stage 1 to stage 2.

protein and DNA which passed through the C18 phase. For DNA extraction studies, elution of the DNA from the monolith was achieved by flowing elution buffer (10 mM Tris, 1 mM EDTA, pH 8) through the DNA extraction channel from the interfacing reservoir after DNA loading.

3. RESULTS AND DISCUSSION

We had determined [1] that DNA momentarily retained by the C18 phase will be rapidly displaced by proteins that bind more avidly as loading continues, allowing the vast majority of the loaded DNA to be recovered from the loaded sample. Selectivity achieved with an unprecedented load of 160 μL of whole blood (6.14 ± 0.7 μg of DNA) showed retention of 60% (15 ± 1.3 mg) of the protein on stage 1 with >98% of the DNA (6.03 ± 0.98 μg) exiting to the stage 2 monolithic phase (**Figure 2**).

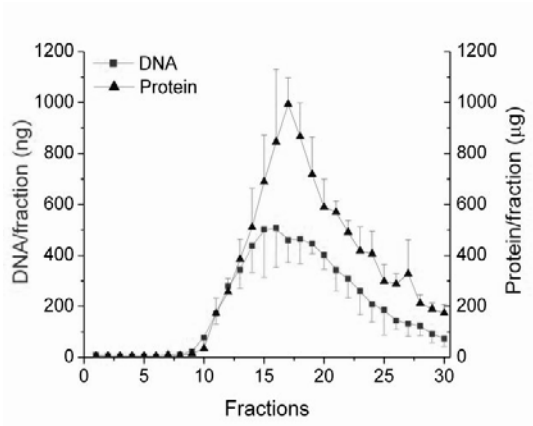

Figure 2. Elution of DNA and proteins from stage 1 with160 μL of whole blood loaded. 16 μL whole blood was loaded pre fraction.

To confirm the DNA monolith in stage 2 can accommodate the large amount of

DNA from stage 1, DNA extractions were performed while loading 7 μg or 14 μg of λ-phage DNA. Typical elution profiles from the first extraction on a fresh prepared monolith are shown in **Figure 3**. Up to 4.2 μg and 8.7 μg DNA, respectively, were extracted from the loading of 7 μg and 14 μg, representing an extraction efficiency of ~60%. A majority of the DNA (64 ± 4%) was eluted in just 20 μL with most of the DNA (77 ± 6%) released in only 30 μL.

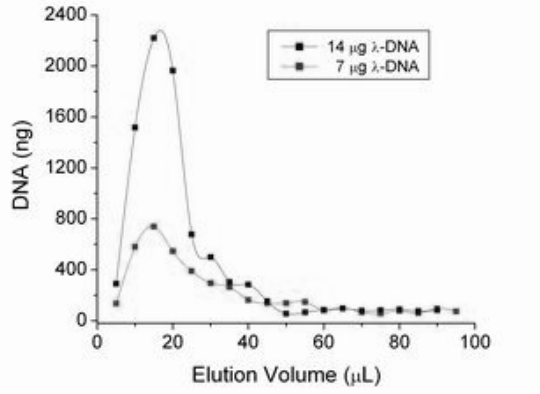

Figure 3. DNA extractions from loads of 7 μg and 14 μg λ-phage DNA.

The high protein capture stage and efficient DNA extraction stage were next evaluated together for DNA recovery from up to 160 μL of whole blood. The results showed that an unprecedented 50-60% extraction efficiency was achieved with 160 μL of blood in a microfluidic device comparable in size to a credit card. This has provided a very promising method for DNA purification with high capacity, high efficiency and a low elution volume, providing a significant 'concentration' effect.

4. CONCLUSIONS

A high capacity/high efficiency microscale 2-D SPE device for DNA extraction was developed utilizing two phases connected serially in an integrated device. The combination of these two phases allows for the purification of DNA from 160 μL of whole blood with PCR amplification of the extracted DNA without a protein wash step. This yields a microdevice for DNA extractions from whole blood suitable for clinical and biomedical applications.

REFERENCES

[1] J. Wen, C. Guillo, J. P. Ferrance and J. P. Landers, *Microfluidic-based DNA purification in a two-stage, dual-phase microchip containing a reverse phase and a photo-polymerized monolith*, Proc. Micro Total Analysis Systems 2006, Tokyo, Japan, p 272-274, (2006).

PDMS-BASED MICROLITER VISCOMETER FOR BLOOD PLASMA AND OTHER NEWTONIAN FLUIDS

Zuoyan Han, Xiaoju Tang and Bo Zheng

Department of Chemistry, The Chinese University of Hong Kong, Shatin, Hong Kong

ABSTRACT

This paper describes a poly(dimethylsiloxane) (PDMS) microfluidic device for measuring the viscosity of Newtonian fluid. The high solubility and permeability of air in PDMS generated Poiseuille flow in the degassed PDMS microfluidic device. By measuring the travel distance and the flow velocity of the fluids in the PDMS microchannel, the ratio of the viscosity of the sample fluid to the viscosity of a reference fluid was determined, and the viscosity of the sample fluid was then obtained. The PDMS viscometer consumed 5 μL or less fluid, and was accurate and applicable to a broad range of fluids.

Keywords: viscometer, Poiseuille flow, microfluidic, blood plasma

1. INTRODUCTION

This paper describes a poly(dimethylsiloxane) (PDMS) microfluidic device for measuring the viscosity of Newtonian fluids. Viscosity is generally measured in mechanical viscometers, such as capillary viscometer, cone and plate viscometer, and falling-ball viscometer. A major limitation of these viscometers is that milliliter or more volume of fluid is needed, which is not appropriate for biological and medical samples. To address this issue, many miniaturized viscometers have been developed.[1, 2]

In the present work, we used degassed PDMS to generate vacuum and aspirate fluid into the microchannels. By characterizing the flow of the fluid, the viscosity of the fluid could be determined. The viscosities of many fluids, including aqueous solutions, several organic solvents as well as blood plasma were successfully measured on the PDMS viscometer.

2. EXPERIMENTAL

The PDMS viscometer device was fabricated by soft lithography (Figure 1).[3] The device contained a chamber (height 60 μm) connected with three microchannels. The height (h) of all the three channels was 60 μm. The width (w) was 100 μm for the SC and the RC, and 50 μm for the CC. The PDMS viscometer was then placed in a vacuum desiccator, and kept for about 15 min under a vacuum of 10 kPa.[4] After the degassing process, the PDMS viscometer was placed under a stereomicroscope equipped with a CCD camera. Two droplets (5 μL each), one with the unknown viscosity (sample fluid) and the other with known viscosity (reference fluid, deionized water in the experiment), were added separately by micropipette to the inlets of the SC and the RC. When the inlet of the CC was blocked, the CCD camera started to capture the images at an interval of 1 second. The conventional viscosity measurement was performed in a series of Ubbelohde viscometers for comparison.

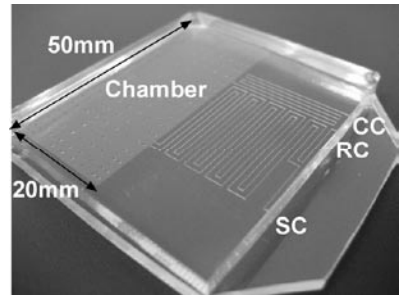

Figure 1. A photograph of a PDMS viscometer. The chamber's dimension was 50 mm × 20 mm × 60 μm. The chamber was connected with three channels: sample channel (SC), reference channel (RC), and control channel (CC).

978-0-9798064-0-7/μTAS2007/$20©2007CBMS

3. RESULTS AND DISCUSSION

The pressure-driven laminar flow inside microchannels can be described by the Hagen-Poiseuille equation. The pressure drop between the inlet and the moving front of the fluid, $\Delta P = P_o - P_i + P_c$ (Figure 2), where P_o is the atmosphere pressure and P_i is the air pressure inside the PDMS channel; P_c is the pressure contributed by capillary force, θ is the dynamic contact angle of the fluid with PDMS. In the viscometer, P_i (t) was the same value for both fluids at any time t; therefore, by replacing ΔP in Hagen-Poiseuille equation with $P_o - P_i$ (t) + P_c for both the sample and the reference fluids, we could obtain:

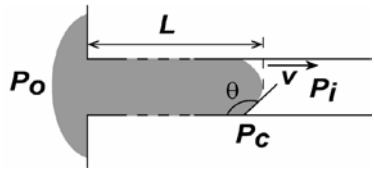

Figure 2. Pressures in the degassed PDMS viscometer.

$$L_{reference}(t)v_{reference}(t) = \frac{\mu_{sample}}{\mu_{reference}} L_{sample}(t)v_{sample}(t) + d_h^{\,2} \frac{P_{c,reference} - P_{c,sample}}{S\mu_{reference}} \quad (1)$$

L_{sample} and $L_{reference}$ were measured directly from the experimental images. v_{sample} and $v_{reference}$ were equal to the increase of the L_{sample} and $L_{reference}$ in two images with 1 second time interval. According to Equation 1, by linearly fitting the curve of $L_{reference}v_{reference}$ versus $L_{sample}v_{sample}$, the slope, $\mu_{sample}/\mu_{reference}$, was obtained (Figure 3). The viscosity of the sample μ_{sample} was calculated by the slope value multiplying the reference viscosity $\mu_{reference}$.

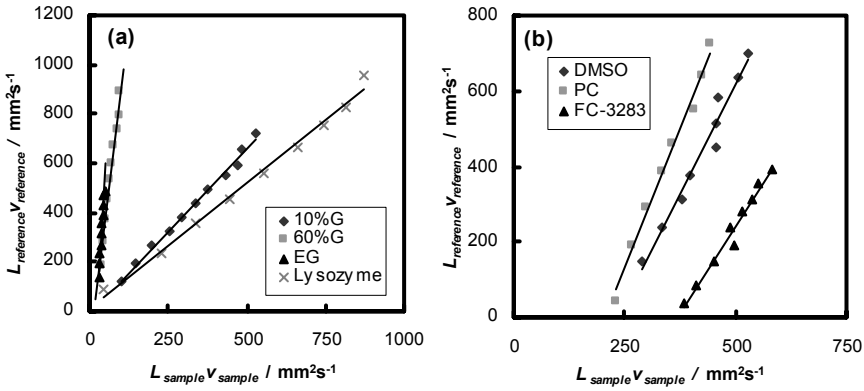

Figure 3. (a) The plot of $L_{reference}v_{reference}$ versus $L_{sample}v_{sample}$ of the fluids that did not wet PDMS. (b) The plot of $L_{reference}v_{reference}$ versus $L_{sample}v_{sample}$ of the fluids that wet PDMS.

By using water as the only reference fluid, we measured a series of glycerol solutions with different concentration, protein solution (1.0 mg mL^{-1} lysozyme in 50 mM sodium acetate buffer, pH 6.0), organic solvents and fluorocarbon on the PDMS viscometer at room temperature (ranging from 21.5 ^{o}C to 22.5 ^{o}C) (Table 1). We also measured the viscosity of blood plasma at 37 ^{o}C. The result from the PDMS viscometer matched the value obtained from the Ubbelohde viscometer (Table 1).

The measurement using the PDMS viscometer was improved by using a second method of data analysis. By replacing v with dL / dt in Equation 1, followed by the integral of both sides of the equation over t from t_1 to t_2 ($t_2 > t_1$), we could obtain:

$$\frac{L_{reference}^{\,2}(t_2) - L_{reference}^{\,2}(t_1)}{t_2 - t_1} = \frac{\mu_{sample}}{\mu_{reference}} \frac{L_{sample}^{\,2}(t_2) - L_{sample}^{\,2}(t_1)}{t_2 - t_1} + 2d_h^{\,2} \frac{P_{c,reference} - P_{c,sample}}{S\mu_{reference}} \quad (2)$$

The viscosities obtained through the second method of analysis were almost identical with the viscosities from the first method of analyzing *Lv* (Table 1). The advantage of the second method of analysis is that it does not involve the velocity *v* of the fluid flow; therefore sequential images with short time interval (1 second in the current work) are no longer needed. Through the second method of analysis, a consumer digital camera with a timer will suffice to measure the viscosity on the PDMS viscometer.

Table 1. Viscosities of various fluids measured by Ubbelohde viscometer and PDMS viscometer.

Sample	Ubbelohde viscometer [a]	PDMS viscometer [a]	
	μ (mPa s)	μ (mPa s) [b]	μ (mPa s) [c]
10.0% glycerol	1.25±0.01	1.24±0.02	1.23±0.02
60.0% glycerol	9.89±0.02	10.1±0.1	10.1±0.1
85.0% glycerol	86.5±0.6	83.0±1.7	83.8±2.5
ethylene glycol	17.2±0.1	17.3±0.3	17.3±0.2
lysozyme solution	0.923±0.001	0.91±0.01	0.91±0.02
DMSO	2.08±0.01	2.20±0.06	2.20±0.06
propylene carbonate	2.60±0.01	2.58±0.10	2.54±0.12
FC-3283	1.56±0.01	1.64±0.03	1.64±0.03
blood plasma	1.27±0.01	1.30±0.02	1.31±0.01

[a] Each sample was measured five times by both Ubbelohde viscometer and PDMS viscometer.
[b] Measured by using equation (1). [c] Measured by using equation(2).

4. CONCLUSIONS

We have developed and validated a PDMS-based microliter viscometer. In addition to the ultralow consumption of the sample and high accuracy and precision, the PDMS viscometer has the following attractive points: (1) The PDMS viscometer is easy to fabricate, and the low cost (US$ 0.5 per chip) makes it possible to be disposable; (2) The measurement is simple and fast, and the transparency of PDMS facilitate the observation of the fluid flow; (3) A variety of fluids, including aqueous solutions, PDMS non-swelling organic solvents, fluorinated hydrocarbon, are applicable on the PDMS viscometer. An important application would be measuring the viscosity of blood plasma; (4) The PDMS viscometer is able to measure viscosity from 1 mPa s to at least 80 mPa s with water as the reference fluid. Higher viscosity can be measured by using a high-viscosity reference fluid. We believe that the PDMS viscometer will be useful in industrial applications where many fluids are tested quickly in disposable devices, or in medical diagnosis where only minute amount of fluid is available.

ACKNOWLEDGEMENTS

This work was supported by the Chinese University of Hong Kong and the Research Grants Council of Hong Kong (Direct Allocation 2060283). We thank Gang Wang for the preparation of blood plasma. We thank Jimmy Yu for invaluable experimental assistance.

REFERENCES

[1] N. Srivastava, R. D. Davenport, and M. A. Burns, Anal. Chem., **77**, 383-392, (2005).
[2] P. Guillot, P. Panizza, J. B. Salmon, M. Joanicot, A. Colin, C. H. Bruneau, and T. Colin, Langmuir, **22**, 6438-6445, (2006).
[3] J. C. McDonald, and G. M. Whitesides, Acc. Chem. Res., **35**, 491-499, (2002).
[4] K. Hosokawa, K. Sato, N. Ichikawa, and M. Maeda, Lab Chip, **4**, 181-185, (2004).

SENSITIVITY ENHANCEMENT OF THE NANOMECHANICAL DYNAMIC CANTILEVER BY TWO TYPES OF SANDWICH IMMUNOASSAYS BASED ON POLYCLONAL ANTIBODY AND POLYCLONAL ANTIBODY CONJUGATED SILICA NANOPARTICLES : FEMTOMOLAR PSA DETECTION AS MODEL STUDY

Sang-Myung Lee[1], Kyo Seon Hwang[2], Hyo-Jin Yoon[1], Yoon-Sik Lee[1] and Tae Song Kim[2]

[1]School of Chemical and Biological Engineering, Seoul National University, KOREA and
[2]Nano Bio Research Center, Korea Institute of Science and Technology, KOREA

ABSTRACT

We report on the sensitivity enhancement of nanomechanical dynamic cantilever by the two types of sandwich immunoassay using the polyclonal antibody and the silica nanoparticles-conjugated polyclonal antibody, which successfully leaded to detect PSA in femtomolar scale.

Keywords: Dynamic cantilever, sensitivity enhancement, sandwich assay, silica nanoparticle

1. INTRODUCTION

As a 'biosensor', high sensitivity and high selectivity is very important goal to be achieved. The sensitivity is largely depends on the character of electrical or physical transduction element. Many research groups have tried to achieve the high sensitivity by developing a new device. Biological or chemical approaches, such as surface modification, orientation control of bio-receptors and developing novel bio-receptors were also tried to enhance the sensitivity [1]. Among them, the sandwich-type immunoassay is a well-known signal amplification technique, and has been successfully applied to the biosensor system such as QCM, SPR, etc. In this regard, we firstly report on the sensitivity enhancement of nanomechanical dynamic cantilever by the sandwich-type immunoassay based on polyclonal antibody and silica nanoparticles-conjugated polyclonal antibody, which leads to detect PSA in femtomolar scale.

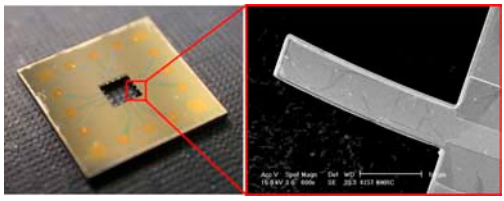

Figure 1. Images of nanomechanical dynamic cantilever. (a) snapshot image of a device containing 12 cantilevers, and (b) SEM image.

2. EXPERIMENTAL

The fabricated nanomechanical dynamic cantilevers (50×150×2 μm) are shown in the Figure 1, and the fabrication process was already reported in the previous papers [2]. The sandwich immunoassay on the cantilever was performed *via* two pathways, using RITC (Rhodamine B isothiocyanate) conjugated PSA

978-0-9798064-0-7/μTAS2007/$20©2007CBMS

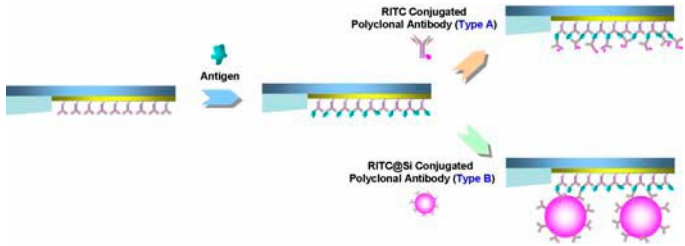

Figure 2. Procedure of two types of sandwich immunoassay

polyclonal antibody (PSA pAb-RITC conjugate, Type A) and RITC-doped silica nanoparticle conjugated PSA polyclonal antibody (PSA pAb-RITC@Si conjugate, Type B). The procedures of two types of sandwich immunoassay using the cantilever are the same as below (Figure 2). The calixcrown SAM was built up on the gold surface of cantilevers. Monoclonal PSA antibody as the receptor was immobilized on them, and then PSA immunoassay was performed on antibody-immobilized cantilevers at 3.6 fM ~ 3.6 pM concentrations. Thereafter, the cantilevers were treated with 10 μg/mL of PSA pAb-RITC conjugates (Type A) and 10 μg/mL of PSA pAb-RITC@Si conjugate (Type B) respectively. The measurement of resonant frequency was performed at each step.

3. RESULTS AND DISCUSSION

RITC, fluorescent dye, was used for cross-checking and confirming the immunoassay together with the resonant frequency shift. For Type A assay, RITC was labeled to the PSA pAb, and for Type B assay, it was doped into the silica nanoparticles, which were labeled to the PSA pAb later. RITC@Sis were synthesized according to the previous report [3].

We could successfully confirm the dramatic sensitivity enhancement of the nanomechnical dynamic cantilevers through both Type A and Type B in the femtomolar range. As shown in Figure 3(a) and 4(a), simple PSA immunoassay didn't work well under 36 fM of PSA, showing the error ranged shift in 3.6 fM or a little shift in 36 fM. However, the sandwich immunoassay by type A and type B showed the improved results, which give meaningful and reasonable shift under 36 fM, and 2~4 fold more sensitive over 360 fM.

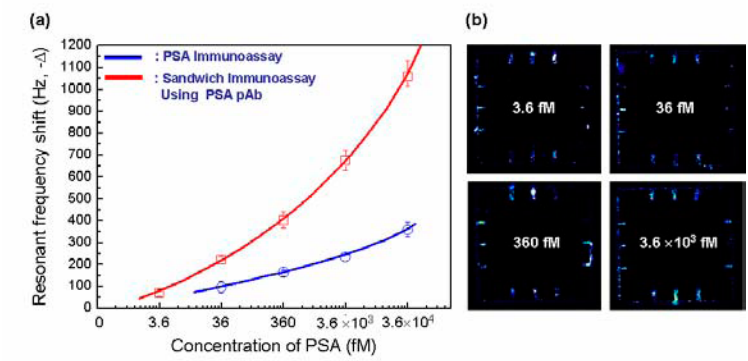

Figure 3. The results of Type A sandwich immunoassay. (a) the resonant frequency shifts of simple PSA immunoassay and sandwich immunoassay, and (b) fluorescence scanning images at each PSA concentration.

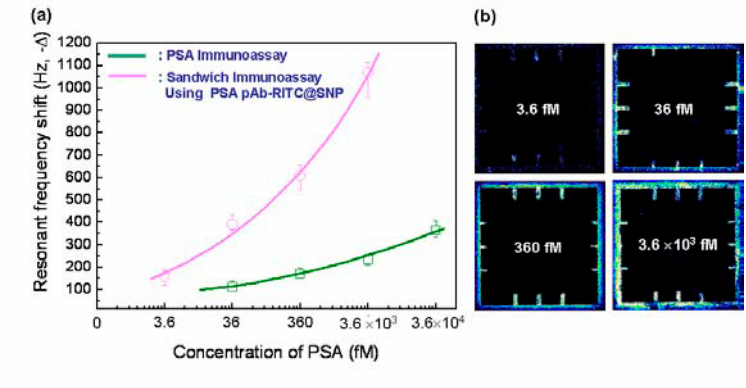

Figure 4. The results of Type B sandwich immunoassay. (a) the resonant frequency shifts of simple PSA immunoassay and nanoparticle-based PSA sandwich immunoassay, (b) fluorescent scanning images at each PSA concentration.

The fluorescent support the results from the cantilever (Figure 3(b) and 4(b)). The additional theoretical study on this work is in progress based on the consideration that the results of Type A stem from the enhanced stress effect and those of Type B stem from the enhanced mass effect.

6. CONCLUSIONS

The sandwich assay is one of the well-known methods for improving the performance of the biosensor. In this respect, we applied the simple concept of sandwich assay to orgins, mass and stress, of dynamic cantilever signaling appropriately, and could successfully detect PSA of the femtomolar level. We expect these methods for the dynamic cantilever will be useful for the detection of biomolecules in the extremely low level and the diagnosis of the disease marker proteins by amplified and well-resolved signals in the clinical range.

ACKNOWLEDGEMENTS

The authors are grateful for the financial support by Intelligent Microsystem Center sponsored by Korea Ministry of Science and Technology as a part of the 21st century's Frontier R&D Projects (Grant MS-01-133-01) and National Core Research Center for Nanomedical Technology sponsored by KOSEF (Grant R15-2004-024-00000-0).

REFERENCES

[1] R. Baron, B. Willner, I. Willner, *Biomolecule–nanoparticle hybrids as functional units for nanobiotechnology*, Chemical Communications, 323, (2007).

[2] K. S. Hwang, J. H. Lee, J. Park, D. S. Yoon, J. H. Park, T. S. Kim, *In-situ quantitative analysis of a prostate-specific antigen (PSA) using a nanomechanical PZT cantilever*, Lab on a Chip, **4**, 547, (2004).

[3] L. Wang, W. Tan, *Multicolor FRET silica nanoparticles by single wavelength excitation*, Nano Letters, **6**, 84, (2006).

GOLD SURFACE-BASED GLYCOARRAYS: A GENERIC PLATFORM FOR HIGH THROUGHPUT INTERROGATION OF CARBOHYDRATE-PROTEIN INTERACTIONS

Zheng-liang Zhi, Andrew K. Powell and Jeremy E. Turnbull
School of Biological Sciences, The University of Liverpool, Liverpool, L69 7ZB, UK.
Email: zzhi@liv.ac.uk.

ABSTRACT

This paper describes a simple and generic microarray platform for presenting multiple oligosaccharides to protein targets, with utility as innovative tools for mapping out the specific interactions between carbohydrate and protein partners. The approach is based on the use of self-assembled monolayer of a hydrazide-derivatized PEGylated alkyl-thiolate linker on gold surfaces for direct attachment of nonderivatized glycans. The feasibility of this analytical platform was tested for diverse biophysical exploitation including fluorescence microarrays, quartz crystal microbalances (QCM), and surface plasmon resonance (SPR) biosensors.

Keywords: Glycoarrays, carbohydrate and protein interactions, biophysical interrogation techniques.

1. INTRODUCTION

Carbohydrates expressed on cell surfaces interact specifically with proteins and regulate a wide range of biological processes. An understanding of the cell's glycome-protein interactions complements data from studies of the proteome and represents an essential facet of post-genome technology development that will underpin discovery of novel glycotherapeutics and biomarkers in diverse applications such as cancer, infectious diseases, inflammation, neurodegeneration, wound healing and tissue engineering. The elucidation of structure-function relations of the biologically active carbohydrates has proved problematic largely because of their high structural diversity and low availability of many pure cell-expressed sugars.[1]

Carbohydrazide microarrays, also called glycoarrays, have been used in glycomics research to examine the interactions of carbohydrates with other molecules. The miniaturized microarray chip offers important advantages over common screening techniques, because many binding events can be screened on a single slide and only very small amounts of analyte and ligand are required. Available strategies for carbohydrate probe immobilization on surfaces require postsynthetic derivatization and postpurification of each individual probe that complicates the microarray fabrication procedure.[2]

This paper describes a simple and generic microarray platform for presenting multiple oligosaccharides to protein targets, with utility as innovative tools for mapping out the carbohydrate and protein partners in the highly specific interactions of the 'glycome' –the complete set of glycan structures expressed by specific cells, tissues or organisms.

978-0-9798064-0-7/μTAS2007/$20©2007CBMS

2. EXPERIMENTAL

The approach is based on the use of self-assembled monolayer of a hydrazide-derivatized PEGylated alkyl-thiol linker on gold surfaces for direct attachment of nonderivatized glycans. The hydrazide linkage chemistry provides an efficient and chemoselective anchoring of oligosaccharide probes on surfaces via their reducing ends.[2] To produce natural saccharide probes from heparin and heparan sulphate (HS), the tissue-derived polysaccharides were first digested using partial depolymerisation (enzymic or chemical), the oligosaccharides generated were then size- fractionated by gel-filtration chromatography and finally resolved by ion-exchange and reverse phase-HPLC. Libraries consisting of ~200 fractions (dp 6-12) from commercially available HS products were used for microarray generation. The oligosaccharides in 1 M betaine were arrayed (1 nl/spot) on derivatized gold-coated glass slides using a MicroGrid II compact arrayer (Biorobotics). The microarrays were read using a Genepix 400 microarray scanner.

3. RESULTS AND DISCUSSION

The feasibility of this analytical platform was tested using diverse surface binding-based biophysical interrogation techniques, including fluorescence microarrays, quartz crystal microbalances, and surface plasmon resonance biosensors. We found that a certain adjustment of the hydrazide density on the monolayer using a 'dilutor' HS-alkyl-PEG-OH could minimize the nonspecific protein adsorption to the chip surface. The fluorescence quenching due to gold surface was minimized by using a long hydrocarbon chain self-assembled monolayer and multiple binding-protein layers.

As a proof-of-principle we demonstrate here that oligosaccharide probes derived from natural (heparin and HS) and synthetic sources (*N*-liked saccharides) could be effectively and covalently attached without prior derivatization onto the gold-coated slide surfaces in a microarray format. The generated microarrays were used to assess binding of several saccharide-binding protein targets (FGF1, FGF2, GDNF, HGF, Siglec, ConA and anti-heparin antibodies) at very high sensitivity. Several positive protein binding fractions purified from heparan sulphate oligosaccharides were thus identified using this approach in a high-throughput format.

4. CONCLUSIONS

We have developed a gold surface-based platform for direct covalent attachment of non-derivatized oligosaccharides via their reducing ends. We demonstrated that the platform could be usful for fluorescence detection at very high sensitivity (femtomoles of sugar spotted and detected); SPR and QCM can also be exploited. The microarray platform can be applicable to interrogation of both heparin type and other glycan-lectin interactions (data not shown), and has potential for integrated applications in large-scale study of glycan-protein interactions. Future experiments will include the generation and structure analysis of highly structurally diverse HS-analogues (natural/synthetic) and exploition for deciphering the HS information code.

ACKNOWLEDGEMENTS

We thank UK Glycochips Consortium (RCUK Basic Technology Programme) for funding this project; assistance from Liverpool BioArray Consortium & Functional Genomics Facility; assistance for SPR experiments from Dr Rositsa Karamanska, and advice from Prof Rob Field and Prof Jonathan Blackburn (Capetown University).

REFERENCES

[1] J. E. Turnbull and R. Field. *Nature Chemical Biology*, 2007, 3, 74.
[2] Z.-L. Zhi, A. K. Powell and J. E. Turnbull. *Anal. Chem*., 2006, 78, 4786.

MICROPATTERNED MATRIGEL FOR THREE-DIMENSIONAL EPITHELIAL CULTURES

T.R. Sodunke[1], K.W. McBride[2], M.J. Reginato[1], and H. Noh[1]

[1]*Drexel University, USA and*

[2]*Texas Tech University, USA*

ABSTRACT

This paper presents general strategies for creating bulk micropatterns of Matrigel (most widely used biomatrix hydrogel for three-dimensional (3D) epithelial culture). Both buried and free-standing patterns of Matrigel were created using modified soft lithography techniques such as microtransfer molding (μTM) and dry lift-off. Surface modification of polydimethylsiloxane (PDMS) membranes with oxygen plasma and poly-2-hydroxy-ethyl-methacrylate (poly-HEMA) was sufficient to promote deformation-free release of Matrigel patterns. Moreover, we show that the micropatterned Matrigel can support 3D culture of single normal mammary epithelial (MCF-10A) cells and breast cancer cells (MDA-MB-231) with comparable phenotypes to standard 3D culture techniques.

Keywords: Micropatterned Matrigel, 3D Culture, MCF-10A, Microtransfer Molding

1. INTRODUCTION

3D epithelial culture models are widely used to promote a physiologically relevant microenvironment for the study of normal and aberrant epithelial organization [1]. Studies in 3D cultures have also provided model systems to study how cancer genes disrupt the biological interactions of individual cells with their immediate surroundings and have become valuable tools for understanding cancer initiation and progression. However, conventional 3D models do not allow for single spheroid or 'acinus' analysis as cells are randomly distributed within the Matrigel matrix (Figure 1a). In addition, Matrigel and other reagents used for 3D studies are very expensive, making these systems less amenable to large-scale cellular studies. To address these limitations, micropatterns of Matrigel were created to serve as housing for single epithelial cells during 3D culture and to control the spatial organization of the cells within the gel environment (Figure 1b).

2. EXPERIMENTAL

Bulk micropatterns of Matrigel were fabricated using modified soft lithography techniques such as microtransfer molding and dry lift-off (Figure 2). First, PDMS mold with microwells and PDMS membranes with through-holes were fabricated using replica molding technique from SU-8 micropatterns. The PDMS molds were then treated with oxygen plasma and poly-HEMA prior to Matrigel patterning in order to achieve deformation-free patterning. To create buried or free-standing micropatterns of Matrigel, we have modified and used microtransfer molding and dry lift-off techniques. The final Matrigel patterns had dimensions of 100-800 μm in diameter and 80-200 μm in thickness.

Patterned Matrigel was then used for the subsequent 3D cell culture step. Normal mammary epithelial cells (MCF-10A) and Breast cancer cell line (MDA-MB-231) were grown using standard 3D culture techniques as previously described [1]. Phase contrast and confocal microscopies were used to verify the morphologies of the cells.

978-0-9798064-0-7/μTAS2007/$20©2007CBMS

3. RESULTS AND DISCUSSION

Hydrogel patterning using soft lithography techniques has been previously reported [2, 3]. However, the use of PDMS stamp to mold and release gel structures is often hindered by the tendency of gels molded against them to adhere to the hydrophobic membranes resulting in difficulty releasing patterns without deformation. We investigated several surface treatments for PDMS including modification using bovine serum albumin (BSA) [3] and poly-HEMA Matrigel is a very soft hydrogel and surface treatment of PDMS membranes with BSA alone did not preclude deformation of Matrigel structures following membrane release. We found instead, that plasma treatment of PDMS membranes followed by coating with poly-HEMA was sufficient to promote deformation-free release of Matrigel patterns. Figure 3 shows Matrigel micropatterns created using both μTM and dry lift-off techniques.

In order to ensure that the micropatterning process did not perturb the biological properties of Matrigel and thus did not alter the normal development of cells cultured on them, we compared different stages of the morphogenetic process in mammary cells grown on our micropatterned Matrigel to cells placed in conventional 3D assays. As expected, the normal cells placed in the micropatterned template adopted the usual spherical polarized morphology (Figure 4a-b). We used confocal microscopy to verify the programmed death of centrally located cells and hollow lumen formation (Figure 4e-f), another key feature of normal acini grown in 3D. Furthermore, the carcinoma cell line showed their characteristic formation of disorganized invasive cellular clusters, lacking normal epithelial architecture on micropatterned Matrigel (Figure 4c). Hence, micropatterned Matrigel can serve as a 3D culture platform for a variety of applications in cancer biology, tissue engineering, and drug screening.

4. CONCLUSIONS

We have constructed bulk micropatterns of Matrigel that can be used as a platform for 3D epithelial cell-based assays. Our novel platform can be used as 3-D cell based assay in conjunction with microfluidic (e.g. drug/gene screening using multiple laminar streaming in a microchannel) or with automated high-throughput screening systems.

ACKNOWLEDGEMENTS

The authors would like to acknowledge the support of NSF Grant: DGE-022164 and funds provided by Drexel University College of Medicine.

REFERENCES

[1] K.L. Schmeichel and M.J. Bissell, *Modeling tissue-specific signalling and organ function in three dimensions*, Journal of Cell Science 2003, Vol.116, pp. 2377- 2388.

[2] G.M. Whitesides, E. Ostuni, S. Takayama, X. Jiang, and D.E. Inger. *Soft lithography in biology and biochemistry*. Ann. Rev. Biomed. Engineering 2001, Vol. 3, pp. 335-373

[3] M.D. Tang, A.P. Golden, and J. Tien, *Molding of three-dimensional microstructures of gels*. Journal of American chemical society 2003, Vol. 125, pp. 12988-12989

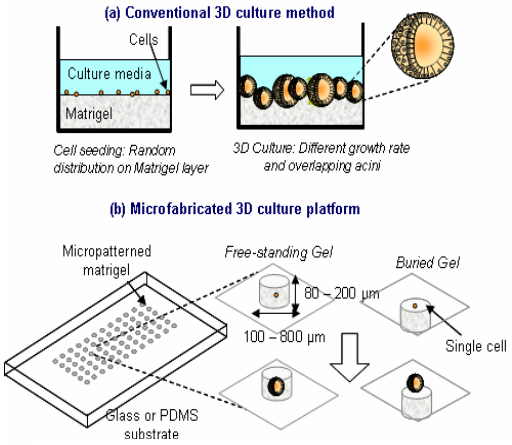

Figure 1. Schematic diagram comparing conventional 3D culture system to a microfabricated 3D culture platform. In a microfabricated setting, we can achieve an organized array of cells on patterned Matrigel.

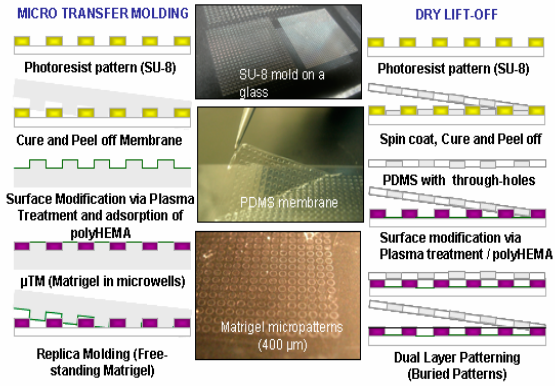

Figure 2. Fabrication process flow for bulk micropatterns of Matrigel. Microtransfer molding and dry lift-off techniques were modified and used to create buried and free-standing micropatterns of Matrigel.

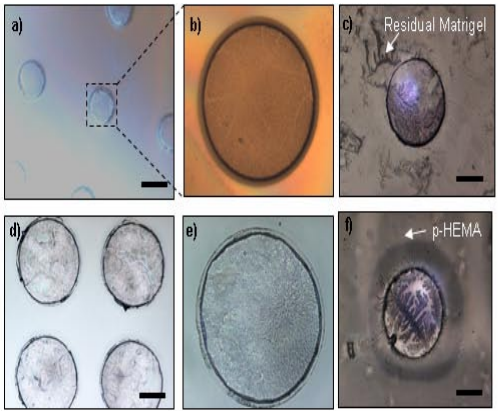

Figure 3. Matrigel micropatterns made via microtransfer molding (a-c) and dry lift-off techniques (d-f). (a,b) buried patterns of Matrigel in microwells and (c) free standing pattern. (d-e) free standing patterns of Matrigel and (f) buried pattern of Matrigel. Scale bar: 100µm

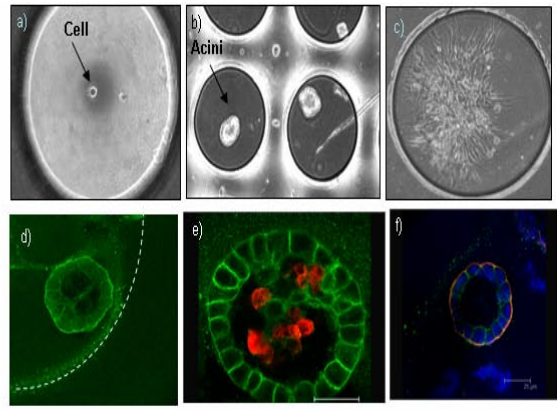

Figure 4. Phase contrast images of (a) single cell on patterned Matrigel (b) mammary acini after 10 days of culture (c) carcinoma cell after 8 days of culture. (d-f) confocal images of mammary acini (d) (green) alpha-5 antibody to show outer layer of epithelial cell in a microwell, (e), (red) antibody to active-caspase 3 to show center cells undergoing programmed cell death and (f), (blue) dapi nuclear stain to show organized layer of viable outer cells. Scale bar: 100µm

PROTEIN PATTERNING THROUGH SELECTIVE FLUOROCARBON PLASMA-INDUCED DEPOSITION ON SILICON

Pinelopi Bayiati[1], Angeliki Tserepi[1], Panagiota S. Petrou[2], Sotirios E. Kakabakos[2], Evrimahos Matrozos[1], Evangelos Gogolides[1]

[1]*Institute of Microelectronics-NCSR "Demokritos", Greece*

[2]*Institute of Radioisotopes & Radiodiagnostic Products-NCSR "Demokritos", Greece*

ABSTRACT

This study presents a method for selective protein adsorption on substrates with hydrophilic/hydrophobic patterning, created via selective plasma deposition. Using C_4F_8 plasma, hydrophobic fluorocarbon films (FC) are selectively deposited on patterned Si substrates, versus SiO_2 or Si_3N_4 areas that are simultaneously etched retaining their hydrophilicity. Plasma parameters were optimized for selective deposition on Si versus SiO_2 and Si_3N_4 areas. Plasma-treated substrates were immersed, without further modification, in IgG protein solutions. Highly selective protein adsorption was demonstrated by staining the surface bound protein through reaction with a fluorescently labeled anti-IgG antibody. This simple and fast method can be applied to the fabrication of protein microarrays of high spot density and increased signal to noise ratio.

Keywords: selective deposition, fluorocarbon, hydrophobic/hydrophilic patterning, protein microarrays

1. INTRODUCTION

Microarrays consist of immobilized biomolecules spatially addressed on surfaces that allow fast, easy, and parallel detection of thousands of addressable elements in a single experiment using minimum sample volumes. Recently, microarrays have become an invaluable tool for large-scale and high-throughput bioanalytical applications, and have been used for basic research, diagnostics and drug discovery [1].

The simplest way to bind biomolecules onto a surface is through surface adsorption either by electrostatic forces on charged surfaces [2] or by hydrophobic interactions [3]. Another approach to immobilize proteins is through covalent binding [4]. In spite of their simplicity, most adsorption methods present several drawbacks one of which is the high background level due to protein adsorption on non-designated areas. This is overcome, in some studies, by spatial modification of the substrate, and adsorption of proteins only onto the hydrophilic [5] or hydrophobic areas [6]. In few cases, the modification is achieved by plasma treatment but, in most cases, the treated surfaces require further chemical modification for inducing protein adsorption.

In this study, we have developed a simple and fast process for selective protein adsorption using hydrophilic SiO_2 or Si_3N_4 patterns on hydrophobically modified Si substrates. The hydrophobic/hydrophilic patterning resulted from a standard lithographic /etching process and subsequent treatment in C_4F_8 plasma, where, under appropriate conditions, a hydrophobic fluorocarbon film was selectively deposited on Si while, at the same time, SiO_2 or Si_3N_4 patterns were etched retaining their hydrophilicity. The plasma-treated patterned substrates were then immersed in protein solutions without any further chemical or other modification, and selective protein adsorption took place. The proteins

978-0-9798064-0-7/μTAS2007/$20©2007CBMS

were adsorbed only on the hydrophilic etched SiO_2 or Si_3N_4 patterns but not on the Si surface covered by the deposited hydrophobic fluorocarbon film.

The proposed method can be used for the fabrication of biomolecule microarrays with very small spot size (depending on the resolution of the lithographic method), high spot density, and increased signal to noise ratio due to elimination of non-specific adsorption.

2. EXPERIMENTAL

Conventional negative photolithography with resist AZ 5214, followed by etching of SiO_2/Si_3N_4 exposed areas and photoresist removal, was used to make arrays of spots or lines of SiO_2/Si_3N_4 on Si substrates. The high-density plasma reactor used for the C_4F_8 plasma treatment was an Alcatel ICP etcher. The deposition and etching rates were measured by means of *in situ* ellipsometry using a M2000 Woolam spectroscopic ellipsometer, and the wettability of the treated samples was characterized by water contact angle measurements using a Digidrop Contact Angle Measurement System from GBX.

The protein binding on the surfaces was determined through a model binding-assay. After plasma treatment, the hydrophilic/hydrophobic patterned substrates were immersed in rabbit IgG solutions (0.5, 1.0 or 2 μg/mL) in 10 mM phosphate buffer, pH 7.0, for 1 h at room temperature (RT), washed with distilled water and blocked with a 1% bovine serum albumin (BSA) solution for 1 h at RT. Then, they were immersed in a 5 μg/mL AlexaFluor 488-anti-rabbit IgG antibody solution in 50 mM phosphate buffer, pH 7.0, 1% BSA, for 1 h at RT. Finally, the surfaces were washed with 10 mM phosphate buffer, pH 7.0, 0.05 % (v/v) Tween 20 and distilled water. Fluorescence images of the surfaces were acquired with Axioskop 2 Plus epifluorescence microscope (Carl Zeiss) facilitated with a digital camera.

3. RESULTS AND DISCUSSION

We conducted experiments with plasma power in the range 800–1800 Watts, bias voltage in the range (-100)–(- 250) Volts, gas pressure in the range 2–10 mTorr, gas flow rate at 25 sccm and temperature at 0 ^oC. The etching rates achieved were in the range 40–270 nm/min for SiO_2 and 39–223 nm/min for Si_3N_4. At plasma conditions where low etching rates of SiO_2 (<70 nm/min) or Si_3N_4 (<130 nm/min) are achieved, contact angle measurements indicate that hydrophobic fluorocarbon layer deposition occurs on all surfaces. However, when the etching rates increase, selective deposition is achieved on Si, while, in contrary, SiO_2/Si_3N_4 surfaces are etched, leading to hydrophobic/hydrophilic patterning (Table I).

Table I. *Contact angles on Si and SiO_2/ Si_3N_4 surfaces, and etching rates of SiO_2/ Si_3N_4 for samples treated under different plasma conditions*

Samples	**1**	**2**	**3**	**4**		**Samples**	**5**	**6**
Etching Rate of SiO_2 (nm/min)	172	185	140	268		**Etching Rate of Si_3N_4 (nm/min)**	145	223
θ (Si) (^{o})	90	90	90	92		**θ (Si) (^{o})**	92	91
θ (SiO_2) (^{o})	65	57	52	48		**θ (Si_3N_4) (^{o})**	77	81
θ (Si) – θ (SiO_2) (^{o})	25	33	38	44		**θ (Si) – θ (Si_3N_4) (^{o})**	15	10

Samples bearing hydrophilic/hydrophobic patterns were immersed in IgG solutions of different concentration (0.5, 1 and 2 mg/ml). Representative microscope images of the treated samples are shown in Figure 1. In all samples tested, the protein was selectively adsorbed on the hydrophilic SiO_2/Si_3N_4 surfaces and not on the hydrophobic Si surfaces.

The adsorption of IgG increases with protein concentration, as shown in Figure 2. In the case of SiO_2, increased protein adsorption was observed with increased hydrophilicity. On the other hand, concerning Si_3N_4 surfaces such a tendency was not observed possibly due to the small differences of the surface hydrophilicity between the samples tested.

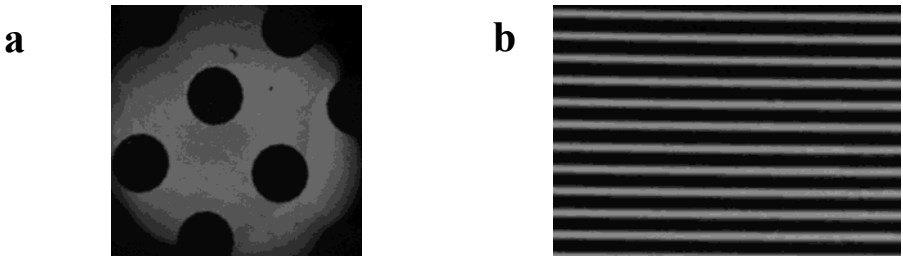

***Figure 1**. Fluorescent images of rabbit IgG adsorption on plasma-treated surfaces consisted of (a) hydrophilic SiO_2 area (gray) interrupted by 1 mm-diameter hydrophobic Si spots (black) and (b) 3 μm-wide hydrophilic SiO_2 lines (gray) on hydrophobic Si surface (black).*

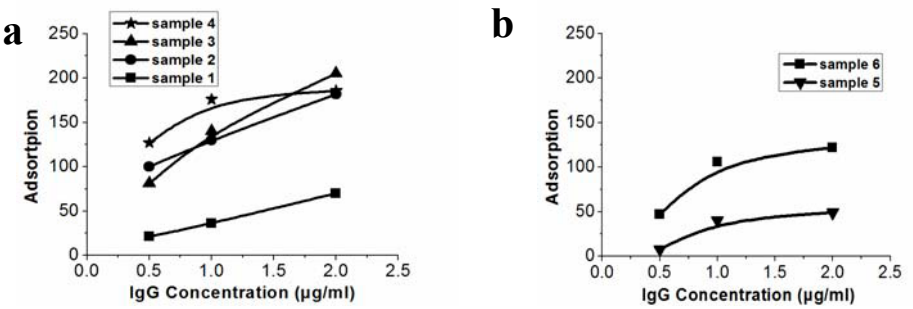

***Figure 2**. Protein adsorption as a function of its concentration on (a) SiO_2 and (b) Si_3N_4 samples treated under different plasma conditions*

4. CONCLUSIONS

Highly selective protein adsorption was demonstrated by hydrophilic/hydrophobic patterning achieved through optimized fluorocarbon plasma treatment followed by simple immersion of substrates in protein solution, leading to a simple method for protein microarray fabrication.

6. REFERENCES

1. M. Cretich, F. Damin, G. Pirri, M. Chiari, *Biomolecular Engineering* **23**, 77 (2006)
2. B. B. Haab, M. J. Dunham, and P. O. Brown, *Genome Biol.* **2**(2), 4 (2001)
3. D. J. Cahill, *J. Immunol. Methods* **250**, 81 (2001)
4. B. Guilleaume, A. Buness, C. Schmidt, F. Klimek, G. Moldenhauer, W. Huber, D. Arlt, U. Korf, S. Wiemann, A. Poustka, *Proteomics* **5**(18), 4705 (2005)
5. S.-H. Lee, C.-S. Lee, D.-S. Shin, B.-G. Kim, Y.-S. .Lee, Y.-K. Kim, *Sensors and Actuators B* **99**, 623 (2004)
6. J. Kai, Y. S. Sohn, and C. H. Ahn, *7th International Conference on Miniaturized Chemical and Biochemical Analysis Systems*, 2003, p.p. 1101 and related patent US2005130226

A HANDHELD MICROFLUIDIC PHOTOMETER BASED ON LIQUID-CORE WAVEGUIDE ABSORBANCE DETECTION

Jian-Zhang Pan, Qun Fang*

Institute of Microanalytical Systems, Department of Chemistry, Zhejiang University, Hangzhou, CHINA, 310058

ABSTRACT

This paper reports a handheld microfluidic photometer with a size of 10 cm×4.5 cm×1.8 cm. Whole assembly including sample introduction device, LED light source, flow-cell, photodiode, single chip microcomputer (SCM) control system, data processing and display system and power source were integrated in the photometer. Liquid core waveguide (LCW) technique was employed to construct the absorption detection system with long optical path length of 5 mm and low sample consumption of 250 nL. The photometer was powered by a rechargeable Li-ion battery and can continuously work for 20 hours.

Keywords: absorption detection, liquid-core waveguide, handheld, microfluidics

1. INTRODUCTION

Recently, there has been a large demand for the development of a point-of-care (POC) diagnostic kit for the rapid diagnostic of disease in remote settings. Ever since the modern inception of microfluidic technologies around 1990, use in remote settings has been perceived as potentially one of the most powerful applications of the technology by taking advantage of its small size, low volume requirement for samples, and rapid analysis. Absorbance measurement is one of the most commonly used methods in the clinical diagnosis. A number of microfluidic absorption detection systems [1-3] have been developed. In most of these systems, sample introduction system and electrical control unit were rarely integrated with the detection systems, which may limit the application of the whole systems in real POC testing. In this work, a fully integrated photometer with a liquid core waveguide (LCW) flow cell and a simple sample introduction system was developed.

2. EXPERIMENTAL

All components of the photometer were integrated into a case with the size of 10 cm×4.5 cm×1.8 cm, as shown in Fig.1. A lab-made SCM control system based on the mix-signal processor MSP430F169 (Texas Instruments) was developed to collect and process data. A keyboard and a liquid crystal display (LCD) were used to control the measurement operation and display the analysis results.

The schematic diagram of the photometer layout is shown in Fig.2. The LCW flow-cell was made of a Teflon AF 2400 capillary (5-cm-long, 90-μm i.d., 345-μm o.d. Random Tech.). The capillary was bent at point A and B into U-shape to facilitate the transmission of light. A blue LED served as light source was positioned 1 mm from the U-shape tip (point A) without further focusing. A photodiode (OPT301, Texas Instruments) served as detector was fixed 1 mm from the other U-shape tip (point B) with the detection window facing to the tip.

978-0-9798064-0-7/μTAS2007/$20©2007CBMS

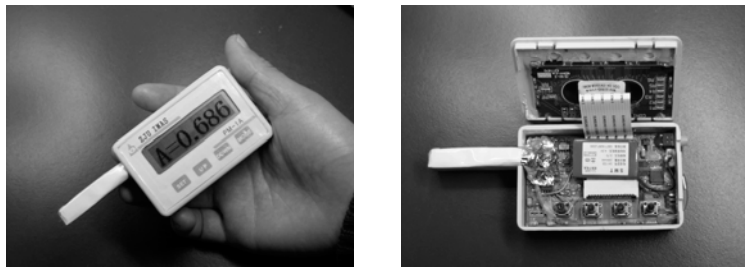

Figure 1. Handheld microfluidic photometer

Sample introduction system using negative pressure or gravity driving system was employed to draw the sample solution from the inlet of the capillary into the LCW flow cell for measurement. In the former system, an elastic Tygon tube (7-cm-long, 1.2-mm i.d.) with one end blocked was used as a thumb-powered sample introduction pump. Sample solution was drawn into the LCW flow cell by simply pressing the Tygon tube and then releasing it (as shown in Fig.2). In the latter system, a Tygon tube was connected to the outlet of the flow cell, and its distal end was connected to a horizontal waste reservoir. Hydrostatic pressure produced from difference in liquid levels between the flow cell and the waste reservoir was employed to provide driving power for sample introduction.

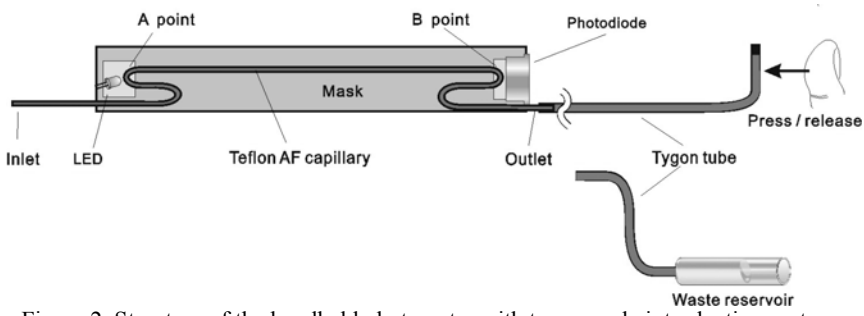

Figure 2. Structure of the handheld photometer with two sample introduction systems

3. RESULTS AND DISCUSSION

In this work, a LCW flow cell with a bending configuration (as shown in Figure 2) was employed to integrate the function of sampling probe, light coupler, and flow cell for absorption detection in a single LCW capillary without any connection. The bending radius and light incident angle were optimized using computer simulation and experimental testing. The bending radius of 0.3 mm and LED incident angle of 20° demonstrated the best performance.

Potentials for applying the system in clinical diagnostics were demonstrated in the measurement of cholesterol with the cholesterol oxidase phenol 4-aminoantipyrine peroxidase (CHOD-PAP) method. The results are as shown in Figure 3. A linear response in the range of 2.61×10^{-4}-5.22×10^{-3} M cholesterol was obtained with a detection limit of 3.57×10^{-7} M (S/N=3). The precision of the system was 1.3% RSD (n=5) for 2.61×10^{-3} M cholesterol standard. The effective optical path length of the photometer was 5 mm with a sample consumption of 250 nL.

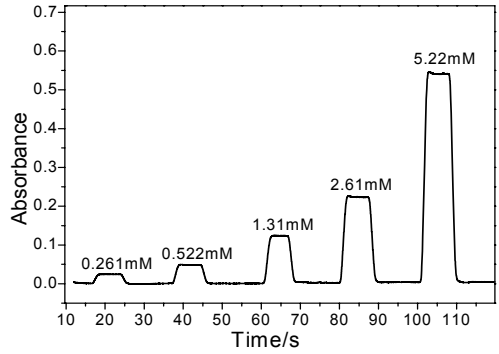

Figure 3. Recordings of absorbance of cholesterol standards using sample introduction system with gravity-driven flows.

4. CONCLUSIONS

In conclusion, we have designed, fabricated and demonstrated a simple and robust handheld photometer based on LCW absorption detection. The present photometer could be used as a portable instrument which has great potentials in clinical diagnosis and environmental analysis, such as Point of Care (POC) and on-site analysis. In addition to these applications, the photometer could also be coupled to a microfluidic system to serve as an absorption detector.

REFERENCES

[1] "High-throughput nanoliter sample introduction microfluidic chip-based flow injection analysis system with gravity-driven flows," W. B. Du, Q. Fang, Q. H. He and Z. L. Fang, Analytical Chemistry, 77, 1330 (2005).

[2] "Portable flow-injection analyzer with liquid-core waveguide based fluorescence, luminescence, and long path length absorbance detector," Q. Y. Li, K. J. Morris, P. K. Dasgupta, I. M. Raimundo and H. Temkin, Analytica Chimica Acta, 479, 151 (2003).

[3] "Microfluidic liquid-liquid extraction system based on stopped-flow technique and liquid core waveguide capillary," M. Sun, W. B. Du and Q. Fang, Talanta, 70, 392 (2006).

CLINICAL MOLECULAR DIAGNOSTICS USING AN INTEGRATED MICROCHIP WITHIN A FULLY PORTABLE PLATFORM

G.V. Kaigala*[1], V.H. Hoang*[1], A. Stickel[1], D. Manage[1], L.M. Pilarski[2] and C.J. Backhouse[1]

[1]Electrical and Computer Engineering, University of Alberta, Edmonton T6G2V4 CANADA, [2]Oncology and Cross Cancer Institute, University of Alberta, Edmonton T6G1Z2 CANADA

* contributed equally

ABSTRACT

We present a fully portable, microfluidic chip-based platform for performing reverse transcription (RT), polymerase chain reaction (PCR), and capillary electrophoresis (CE) on clinical samples. The microchip consists of integrated pneumatically actuated valves and pumps for fluid handling and a thin film resistive element for thermal cycling. The platform also includes a high voltage system for CE and an optical system for the excitation and detection of fluorescently labeled analytes. The system presented is a significant step towards the practical realization of genetic tests within a clinic or as a point-of-care device.

Keywords: Integration, genetic amplification (PCR), capillary electrophoresis, sample preparation.

1. INTRODUCTION

Molecular testing for genetic analysis on microchips can provide valuable insights into the diagnostics and monitoring of a wide range of diseases and is highly suitable for use in a clinical setting. However, there is a pressing need for microfluidic systems that are able to perform entire protocols yet be inexpensive and portable. Although there have been major advances in microfluidic technologies, a factor that often limits the applications of these technologies is the need for considerable supporting equipment, whether for temperature control (e.g. Peltiers or IR lasers), high voltage, electronics interfacing, valve control or analyte detection. Recent demonstrations of combined genetic amplification and analysis (PCR-CE) by Mathies[2] and Landers[3] show systems of great functionality, but which are far from portable. We present here a novel platform coupled with integrated microchips. We believe that our cost-effective integration of microfluidics, optics, and electronics will result in affordable systems with wide applicability in the clinic.

2. MICROCHIP

A critical element for an integrated microchip is the development of appropriate microvalve technology. Here, we implement a valve based on the Mathies valves[1] for fluid handling. Both the pressure and vacuum necessary to actuate the valves are generated within the platform using mini-pumps (Virtual Industries, Inc., Colorado Springs, CO, USA). The microchip also includes a platinum thin-film resistive element designed for simultaneous heating and instantaneous temperature sensing. Within this microchip, reverse transcription (RT), polymerase chain reaction (PCR), and capillary electrophoresis (CE) have been seamlessly integrated and sample preparation is being integrated as well. We differ from[2] in that we use a single resistive element approach to perform both heating and temperature sensing (as opposed to two separate elements for heating and sensing),

978-0-9798064-0-7/μTAS2007/$20©2007CBMS

while[3] employs IR heating. We employ a three layer chip architecture, as opposed to four layers in[2,3]. The top glass layer consists of fluid-carrying channels, the PCR chamber, and the CE channels, while the bottom layer consists of etched regions for actuating the valves. We have adapted CE to use short distances and moderate voltages. The system described here provides good performance with several hundred volts and 1-2 cm CE chips using 4% LPA (Polysciences Inc., PA (MW 600,000-1,000,000) with 1xTTE buffer. Prior to the first filling of the polymer, the CE channels are filled with Dynamic coating (The Gel Co., San Francisco, CA, cat# DEH-100) to improve the separation efficiencies.

3. GENETIC ANALYSIS PLATFORM

The platform (Fig. 1) is based on robust and inexpensive CCD detection, laser diodes, optimized resistive heating/sensing for genetic amplification, integrated fluidic control, and moderate voltage/short distance electrophoresis for compact microfluidics. The entire system can be built for less than $1000 and has performance comparable to commercial systems. By actuating the valves, RT-PCR mix is pumped with bubble-free loading into the reaction chamber for thermal cycling. After the genetic amplification is completed, the product is pumped into the input well of the CE section of the microchip where the PCR product is separated and detected.



Figure 1. Portable diagnostic platform for fluid handling, RT, PCR and CE.

Although the maximum potential available for electrophoresis is 6 kV for the separation of the DNA fragments, in Fig. 2 a DNA separation voltage of only 1000 V was sufficient for excellent CE resolution. Optical detection is performed at 24 mm from the CE channel intersection. We have also demonstrated detection at 10 mm with comparable separation efficiencies, using this system (not shown). The optics consist of a single emission filter and a laser diode focused on the CE channel. Fluorescence detection of PCR products is performed using CCD detection. Image processing can be performed externally on a PC to produce an electropherogram or by using the microcontroller in the portable system itself. All the electronics and optics required for performing RT-PCR and CE are integrated within this compact platform.

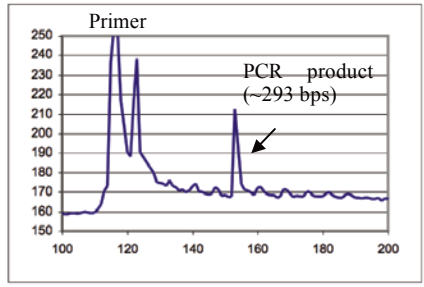

Figure 2. On-chip single step RT-PCR-CE performed within the portable platform to detect the β2M gene (small peaks are from DNA ladder)

4. RESULTS AND DISCUSSION

The system described here has been used to perform RT-PCR detection of beta 2 microglobulin gene expression (b2M) (Fig. 2). This seamless integration of a single step RT with PCR and subsequent detection using CE within a portable platform provides a highly versatile and a powerful diagnostic tool for performing viral, baterial, or gene

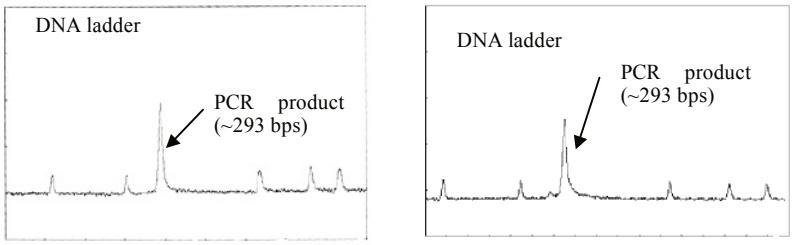

Figure 3. (a) On-chip magnetic beads-based DNA purification achieved from (a) whole blood (b) and from buccal cells in the buffer used to elute buccal epithelial cells from the cotton swabs used to collect them. The microchip-based purification was followed by microchip PCR-CE (to identify the beta 2 microglobulin gene). An external magnet was used to transport the beads across the micro-channel.

expression tests. We have also performed microchip genotyping from whole blood and from buccal swabs (Figs. 3a and b; x- axis is time in seconds, and y-axis is fluorescence units). The DNA from these samples was purified on a microchip using a magnetic bead-based technique that is currently being integrated with the RT-PCR-CE platform of Fig 1. This will enable a range of genetic tests using cells, tissues and bodily fluids as the starting material. Using a similar microchip PCR-CE platform we earlier tested for cancer biomarkers[4] and viral infections from unprocessed fluids[5].

5. CONCLUSIONS

The microchip-based tests and platform developed here are ideally suited to personalized biomarker screening and "in the field"-based viral load assessment. The RT-PCR-CE protocol implemented here on an integrated microfluidic chip holds great potential for point-of-care testing. With the on-going integration of sample preparation techniques coupled with our thermal responsive polymer filled microvalves, we envisage a highly advanced portable genetic analysis system that will be versatile and sensitive, with low power consumption, making it ideally suited to widespread use in a clinical setting.

REFERENCES

[1] Grover, W. H.; Skelley, A. M.; Liu, C. N.; Lagally, E. T.; Mathies, R. A., *Sensors and Actuators B-Chemical*, **2003,** 89(3), p. 315-323.

[2] Liu, P.; Sep, T. S.; N., B.; Shin, K.; Scherer, J. R.; Mathies, R. A., *Analytical Chemistry*, 2007, 79, p. 1881-1889.

[3] Easley, C. J.; Karlinsey, J. M.; Bienvenue, J. M.; Legendre, L. A.; Roper, M. G.; Feldman, S. H.; Hughes, M. A.; Hewlett, E. L.; Merkel, T. J.; Ferrance, J. P.; Landers, J. P., *PNAS*, **2006** 103, p. 19272-19277.

[4] VanDijken, J.; Kaigala, G. V.; Lauzon, J.; Atrazhev, A.; Adamia, S.; Taylor, B. J.; Reiman, T.; Belch, A. R.; Backhouse, C. J.; Pilarski, L. M., *Journal of Molecular Diagnostics,* 2007, 9(3).

[5] Kaigala, G. V.; Huskins, R. J.; Preiksaitis, J.; Pang, X. L.; Pilarski, L. M.; Backhouse, C. J., *Electrophoresis,* 2006, 27, (19), p. 3753-3763.

FULLY AUTONOMOUS MICROFLUIDIC CAPILLARY SYSTEMS FOR FAST AND SENSITIVE SURFACE IMMUNOASSAYS

J. Ziegler[*,1,2], M. Zimmermann[*,1,2], P. Hunziker[1], E. Delamarche[2]

[1] *University Hospital Basel, Petersgraben 4, CH-4031 Basel, Switzerland*

[2] *IBM Research GmbH, Zürich Research Laboratory, Säumerstrasse 4, CH-8803 Rüschlikon, Switzerland*

ABSTRACT

This paper reports a method for performing fast and sensitive surface immunoassays using fully autonomous microfluidic capillary systems (CSs). A surface immunoassay for C-reactive protein (CRP) having a sensitivity of 0.9 ng mL^{-1} (30 pM), done in only 10 min and with 1 µL of human serum sample exemplifies the power of CSs.

Keywords: microfluidic, immunoassay, autonomous capillary system

1. INTRODUCTION

In autonomous CSs, samples and reagents are displaced only due to capillary forces. [1] Such CSs are independent of peripherals for moving liquids but nevertheless have very uniform flow conditions and can efficiently replenish analytes to detection sites therefore enabling fast surface immunoassays. [2, 3]

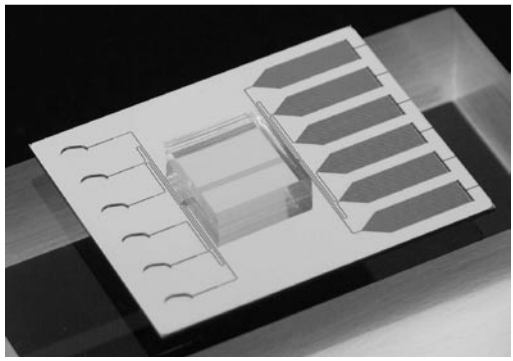

Figure 1. Photograph of Si microfluidic chip (coated with Au) having 6 independent CSs. A block of PDMS (8 × 8 mm^2) having immobilised capture antibodies seals the reaction chamber of the CSs.

2. EXPERIMENTAL

Capture antibody (cAb) lines are immobilised on a PDMS block and placed orthogonally on the reaction chamber of wettable CSs (Figure 1). Human serum having various concentrations of CRP and fluorescence labelled detection Ab dissolved in CRP-free human serum were pipetted sequentially into the loading pads.

Table 1. Characteristic flow rates of liquids in the passive microfluidic chip. The contact angles of these liquids on the walls of the CS are similar.

Flow Rates in the Reaction Chambers	Viscosity	20 µm deep Reaction Chamber		30 µm deep Reaction Chamber	
	[mPa s]	[nL s^{-1}]	CV (%)	[nL s^{-1}]	CV (%)
Water	1	1.9	4.7	4.2	4.8
PBS + 1% BSA	1	1.9	5.0	4.0	3.4
Solution of 20% hum. albumin	4	0.5	12.0	1.5	11.9

978-0-9798064-0-7/µTAS2007/$20©2007CBMS

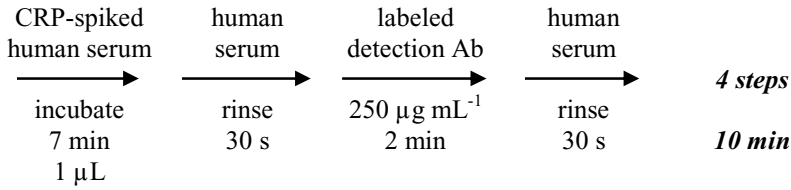

Figure 2. Steps performed for the detection of CRP using surface fluorescence immunoassays and CSs.

3. RESULTS AND DISCUSSION

Figure 1 shows a photograph of a fully autonomous microfluidic chip having 6 independent CSs. The CSs are microfabricated in Si, Au-coated and have wettable flow paths. Each CS has a loading pad, a reaction chamber, a capillary pump and can be used for one surface immunoassay. The reaction chamber is 30-µm-wide and 20-µm-deep but other dimensions can be used. Capillary pumps provide a constant flow rate of 1.9 nL s^{-1} (CV ≤ 5.0 %), for liquids having a viscosity similar to water (1 mPa s), Table 1. A solution of 20% human albumin has a higher viscosity than water and thus fills with a smaller flow rate. The 2 µL capillary pump can accommodate the total volume of the different solutions

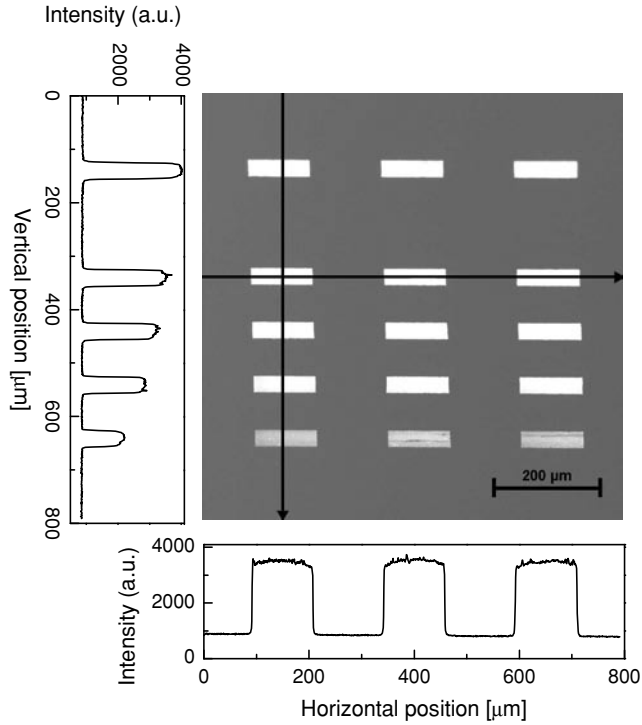

Figure 3. Fluorescence microscope image of a PDMS block revealing the concentration of CRP in human serum CRP concentrations are (top to bottom) 10, 0, 3, 1, 0.3, and 0.1 µg mL^{-1}. The horizontal intensity profile shows the intra-channel fluorescence intensity for equivalent CRP concentration whereas the vertical intensity profile shows the inter-channel fluorescence intensity for different CRP concentration values.

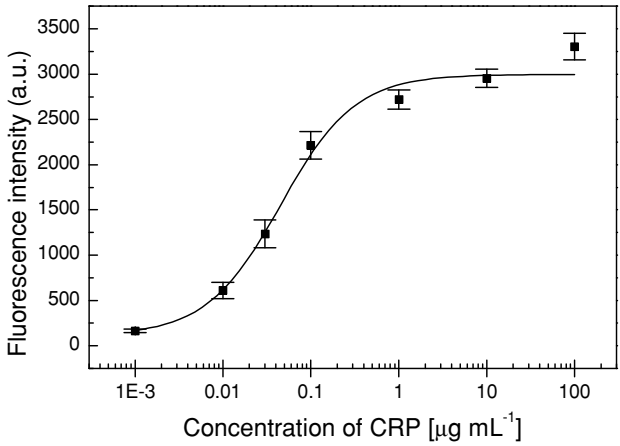

Figure 4. Reference curve for CRP-free human serum spiked with CRP and its expected sigmoidal fitting curve. Error bars correspond to the standard deviation. This assay has a calculated sensitivity of 0.9 ng mL^{-1}.

that need to pass through one CS for effecting a surface immunoassay.

The steps needed for performing a surface immunoassay in a CS are shown in Figure 2. cAb against CRP is patterned as lines on a block of poly-(dimethylsiloxane) (PDMS) and rinsed. The PDMS surface is blocked with a 1%-solution of bovine serum albumin (BSA), rinsed and dried under a stream of N_2. The block of PDMS is then placed on CSs so as to orient the lines of cAb orthogonally to the rectangular reaction chambers. 1 μL of CRP-spiked CRP-free human serum is filled into loading pads, from where it flows during 7 min in the reaction chambers. After a brief rinsing step with CRP-free human serum, the captured CRP is detected by flowing an Alexa-647-labelled detection Ab through the reaction chamber. After a final rinsing step with CRP-free human serum, the PDMS is separated from the CSs, rinsed and dried under a stream of N_2. The antibody patterns on the PDMS are imaged using a fluorescence microscope, Figure 3. The reference curve for CRP spiked CRP-free human serum is displayed in Figure 4. The coefficient of variation (CV) ranges from 8 to 15 %. Based on a sigmoidal fit of a logistic model [4], the sensitivity (minimal concentration of CRP giving a fluorescence signal of 3 standard deviations above the background signal) for detecting CRP in human serum is calculated to be 0.9 ng mL^{-1}.

4. CONCLUSIONS

The results presented here demonstrate that fully autonomous microfluidic CSs can detect antigens from human serum rapidly, accurately, with high sensitivity, and using low volumes of samples. These microfluidics therefore represent a promising platform for quantitative point-of-care diagnostics.

REFERENCES:

1. D. Juncker et al. Autonomous microfluidic capillary system, Anal. Chem. **74**, 2002, 6139–6144.
2. M. Zimmermann et al. Capillary pumps for autonomous capillary systems, Lab Chip **7**, 2007, 119–125.
3. S. Cesaro-Tadic et al. High sensitivity miniaturized immunoassays for TNF-α using microfluidic systems, Lab Chip **4**, 2004, 563–569.
4. D. Wild, Ed. The Immunoassay Handbook, Elsevier Science, Amsterdam, 2005.

HIGH REYNOLDS NUMBER MICROFLUIDICS FOR DRUG DELIVERY

J. C. Stachowiak[1] T. H. Li[1], D. L. Richmond[2], A. P. Liu[2], S. H. Parekh[3], and D. A. Fletcher[2,3]

University of California, Berkeley, USA, [1]Department of Mechanical Engineering, [2]Biophysics Graduate Group, and [3]Department of Bioengineering.

ABSTRACT

We use piezoelectric actuators to propel and control high Reynolds number microfluidic jet flows for two drug delivery applications: transdermal jet injection and jet-induced deformation of lipid bilayers to encapsulate solutes in giant vesicles.

Keywords: jet, vortex, drug delivery, needle-free, lipid, vesicle

1. INTRODUCTION

We report the development and application of a piezoelectric-driven device capable of controlling the velocity of high Reynolds number (Re) microfluidic jets (30-50μm diameter) in real-time for two applications (Figure 1): (i) penetrating the skin to deliver drugs (demonstrated using surrogate materials) and (ii) deforming liquid/liquid interfaces to form lipid vesicles. While the great majority of microfluidic devices employ low Re flows, the potential to deform and penetrate surfaces enabled by our high Re jet flows (10-10,000) is critical for the biomedical applications we explore.

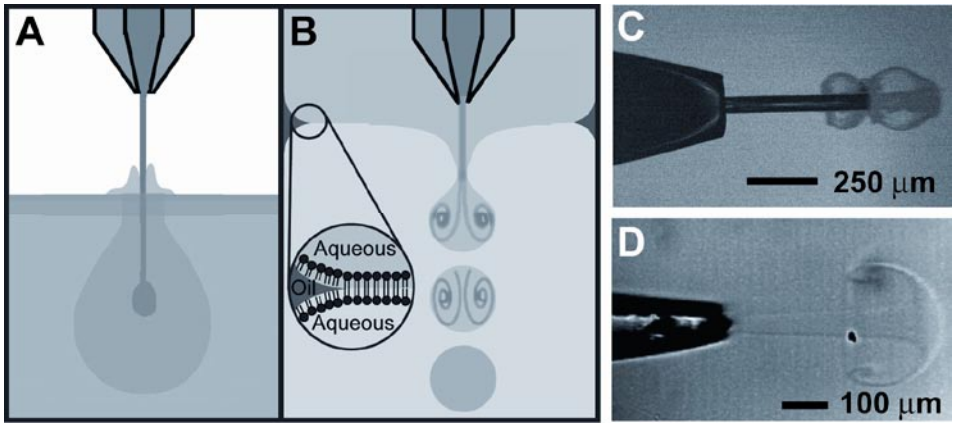

Figure 1. High Re microfluidic jets are used to (A) penetrate the skin to deliver drugs and (B) deform liquid-liquid interfaces to form lipid vesicles. (C) Image of two-phase jet (liquid in air) used for skin penetration, Re ~ 7500, strobe microscopy. (D) Image of single-phase jet used for interface deformation, Re ~ 25, high speed imaging, brightfield with refractive index contrast.

2. EXPERIMENT

At MicroTAS 2006 we reported a first-generation device capable of generating high-speed liquid jets using a piezoelectric actuator [1]. Here we describe the development of a second-generation device, which achieves continuous jet velocity control by varying actuator (DSM, Franklin, TN, USA) expansion rate against the plunger of a conventional syringe (Hamilton, Reno, NV, USA) in real-time. A closed-loop control simulation based

978-0-9798064-0-7/μTAS2007/$20©2007CBMS

on a simple fluid dynamics model predicts the voltage profile necessary for achieving the desired expansion profile (Figure 2A-top). When this profile is applied, the consequent actuator motion (Figure 2A-center) and jet force production (Figure 2A-bottom, for jets in air only) are measured using laser-based tracking and impingement upon a load cell, respectively. In this way, we demonstrate the repeatable production of multiple distinct jet velocities within a single actuator motion.

3. RESULTS AND DISCUSSION – DRUG DELIVERY

Conventional needle-free drug delivery is achieved by penetrating the skin using a high-speed liquid jet driven by springs or gases [2]. In contrast, our piezo-driven device is capable of tailoring the temporal jet velocity profile to the varying mechanical properties of the skin, potentially increasing control over the depth and dose of drug delivery and reducing pain associated with the injection. Using two distinct jet velocities, we show that control of penetration depth into skin surrogate materials is possible while maintaining a constant injected volume, Figure 2B. An initial high velocity (180m/s) penetrates the material, defining the depth, while a second lower velocity (30m/s) delivers additional fluid without increasing the depth of penetration, Figure 2C. In this way, increasing the fraction of total volume delivered at high velocity increases the depth of penetration.

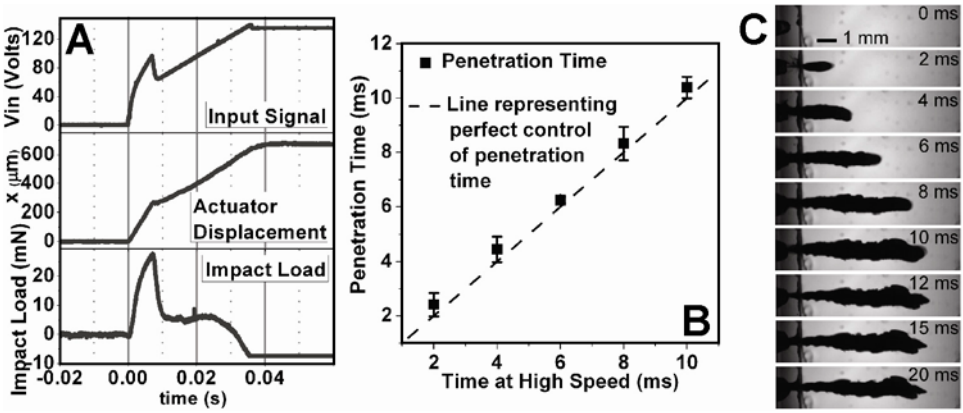

Figure 2. (A) Input voltage signal, resulting actuator displacement (from laser-based tracking), and impact force of jet (against load cell). (B) Variation of high speed period duration to control length of penetration period. (C) Penetration of 15 w/v% polyacrylamide gel, where high speed period lasted 10 ms.

4. RESULTS AND DISCUSSION – VESICLE FORMATION

Encapsulation of large molecule solutes, such as proteins, in lipid vesicles of controlled size is desirable for a variety of applications from fundamental synthetic biology to drug delivery. However, the primary existing techniques for vesicle formation (swelling, electroformation) severely limit large solute encapsulation and provide little control of vesicle size. At MicroTAS 2006, Funakoshi et al. [3] presented a new technique in which a solute-containing fluid jet impacts and deforms a solvent-stabilized lipid bilayer [4], resulting in the formation of multiple giant lipid vesicles containing the solute. We follow this approach but employ our piezo-electric driven device as the means of jet propulsion. The high rates of acceleration achieved by this device enable precise metering of small liquid volumes and careful control of fluid jet velocities. Using this approach, we have

formed multiple vesicles (~10) from a single bilayer, Figure 3. A high-speed camera (10 kfps) records the jet-induced deformation of the bilayer and subsequent vesicle formation. The bilayer is observed to reseal after each shot. The vesicles have a uniform size of approximately 200 μm, which represents approximately a 15-fold volume reduction in comparison to the vesicles produced by Funakoshi, et al. These smaller vesicles more closely approach the cellular scale and show limited solvent encapsulation in the membrane. We are currently conducting experiments to determine whether biological transport across vesicle boundaries is possible. Additionally, we are exploring the variation of the piezoelectric expansion profile towards controlling vesicle size.

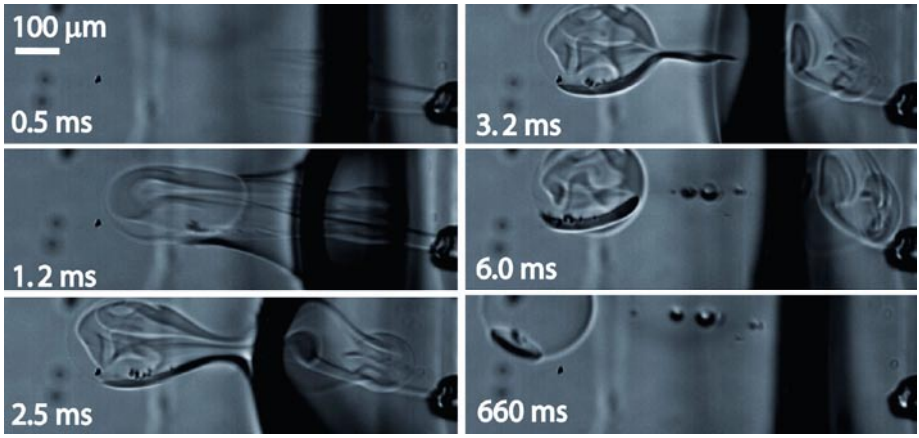

Figure 3. High-speed image sequence of encapsulation of sucrose solution in a lipid vesicle surrounded by glucose solution. Dark region of the vesicle, especially apparent in the final image, is thought to be a small amount of solvent encapsulated in its lipid membrane. Brightfield contrast was achieved using collimated illumination and refractive index contrast.

5. CONCLUSIONS

We demonstrate dynamic control of high Re microfluidic flows and utilize them for novel applications including penetration depth control in transdermal drug delivery and vesicle formation.

ACKNOWLEGEMENTS

We thank NXP Co. for financial support. J.C.S. thanks the NSF and ARCS foundation.

REFERENCES

[1] "Development of a piezoelectric microjet injector for transdermal drug delivery," J. C. Stachowiak, T. H. Li, J. Rasooly, W. A. Lam, D. A. Fletcher, MicroTAS , **1**, 308 (2006).

[2] “Innovation - Current status and future prospects of needle-free liquid jet injectors,” S. Mitragotri, Nature Reviews Drug Discovery, **5**, 543 (2006).

[3] “Blowing vesicles, a simple method for direct microencapsulation in lipid vesicles,” K. Funakoshi, H. Suzuki, S. Takeuchi, MicroTAS, **1**, 534 (2006).

[4] “Lipid bilayer formation by contacting monolayers in a microfluidic device for membrane protein analysis,” K. Funakoshi, H. Suzuki, S. Takeuchi, Analytical Chemistry, **78**, 8169 (2006).

IMMUNOASSAY UTILIZING MAGNETIC BEADS FOR RAPIDVIRUS DETECTION IN THE MICROFLUIDIC FLOW CYTOMETER SYSTEM

Sung-Yi Yang[1], Kang-Yi Lien[2], Kao-Jean Huang[3], Huan-Yao Lei[3] and Gwo-Bin Lee[1,2]

[1]Department of Engineering Science, [2]Institute of Institute of Nanotechnology and Microsystems Engineering, [3]Department of Microbiology and Immunology, National Cheng Kung University, Tainan, Taiwan

ABSTRACT

The study presents a new microfluidic flow cytometer system integrated with functional micro-devices for bead-based immunoassay capable of viral samples pretreatment and detection. Several essential components are integrated into a single chip including a microfluidic flow cytometer device, a bio-samples pretreatment module with the microcoils for concentration by using antibody-conjugated magnetic beads and an optical control device to perform the functions of virus sample injection, optical signal detection, and virus collection. The virus sample with a concentration of 10^4 pfu/ml can be detected successfully by the optical control device in the proposed system. Consequently, the miniature microfluidic flow cytometer system may provide a powerful platform for future biological applications.

Keywords:Immunoassay, magnetic beads, microfluidics, flow cytometer

1. INTRODUCTION

In the past decade, dye synthesis and high-speed analytical technology have advanced flow cytometry technology and have brought this powerful analytical tool into routine clinical and laboratory use in the field of gene diagnosis, bacteria analysis, clinical hematology diagnosis and environmental microbial sensing [1]. Recently, micro-electro-mechanical-systems (MEMS) technology and micromachining techniques have enabled the miniaturization of biomedical devices and microfluidic systems to perform the transportation, mixing and separation of fluids in the micro-systems. Hence, the micro-fabricated rotary pump has been demonstrated to transport the fluids and to enhance the mixing performance in the microchannels [2]. Purification of bio-samples using magnetic beads bound with target protein/antigen/DNA segments have also been demonstrated in literatures [3]. Consequently, pretreatment of bio-samples including sample purification and enrichment using the magnetic bead-based rotary microfluidic system has been proposed by the current research group [4]. Instead of using complex and time-consuming polymerase chain reaction (PCR) techniques for biological diagnosis, the proposed hand-held system provide a promising approach to detect the target virus with a higher sensitivity and specificity in an automatic fashion.

2. DESIGN AND FABRICATION

The whole operation procedures of the proposed device were performed on a microfluidic system. The target viruses were first captured by mixing with the magnetic beads conjugated with specific antibodies, followed by conjugated 2nd detective specific

978-0-9798064-0-7/μTAS2007/$20©2007CBMS

antibodies labeled with fluorescent dye in the incubation process utilizing a rotary microfluidic pump (Fig. 1(a)). The target virus can be bound onto the surface of the magnetic beads specifically with the fluorescent signals generated from the dye-labeled 2nd antibody. Then, the on-chip bio-separators consisting of copper (Cu) microcoils were used to generate the required magnetic field to attract the virus-bound magnetic beads onto the surface of the microchip while the washing buffer still flew through the chamber for purification and of the target virus. Next, sample flow with the purified beads and sheath flows were injected into the microfluidic channel utilizing the rotary micropump to perform microfluidic focusing and subsequent optical detection of fluorescent signals by using a PMT (Photomultiplier Tube) module (Fig. 1(b)). Finally, a sorting module with active microvalves can be used to sort and collect the magnetic beads in the collection chambers by using the feedback signals from the PMT module. Figure 2 shows a schematic illustration of the integrated microfluidic flow cytometer system. Note that three major components including the bio-separators comprised of 2-D spiral microcoils, a microfluidic control module with the rotary micropump and a sorting module consisting of active microvalves are integrated onto a single micro chip. The microfluidic structures are formed using the polydimethylsiloxane (PDMS) and the Cu microcoils are fabricated by the standard electroplating techniques. The dimensions of the microfluidic chip are measured to be 46 mm x 66 mm x 5 mm.

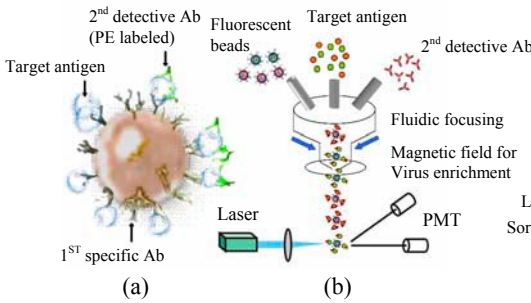

Fig 1. (a) Conceptual illustration of a sandwich immunoassay on the bead-based flow cytometer. (b) Experimental process of the integrated flow cytometer

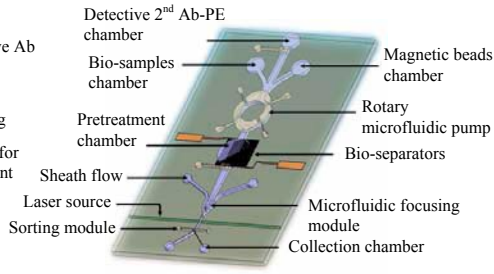

Fig 2. Schematic diagram of the integrated flow cytometer system.

3. RESULTS AND DISCUSSION

The characterization of the integrated microfluidic flow cytometer system is shown in Fig. 4. The relation between the pumping rate and the driving frequency at three different driving air pressures are shown in Fig. 3(a). The maximum pumping rate of the rotary micropump is measured to be 170 μl/min at a driving frequency of 18Hz. The magnetic field and the temperature at different applied currents are shown in Fig. 3(b). When a current of 500 mA was applied into the microcoils, the bio-separator can generate the magnetic field with 25 Gauss and the temperature of 38.9°C. The low temperature of the bio-separator is crucial to assure that the bio-samples may not become non-active during the operation of pretreatment process. Figure 4 shows the successful detection of the target virus in the microfluidic flow cytometer system while the virus-bound magnetic bead sample flows through the optical detection region. Each peak in this figure indicates that one particle flows through the counting region and is detected by the optical detection

device. An average signal-to-noise (S/N) ratio of 30 was obtained. that dengue virus serotype 2 can be successfully detected by the optical detection module in the micro system. The data show that the signals of the 2nd antibodies decay with the decreasing concentration of the dengue virus. The virus sample with a concentration of 10^4 pfu/ml can be successfully detected by the developed system. Detection of virus samples with lower concentration is still undergoing.

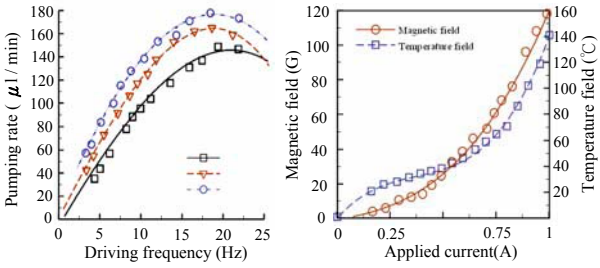

(a) (b)

Fig.3(a) Relation between the pumping rate and the driving frequency (b) The magnetic and temperature fields generated by the bio-separator at different applied DC currents.

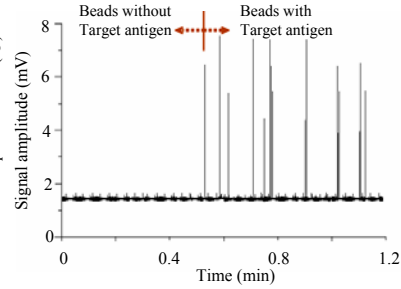

Fig 4. Fluorescent signals collected by a PMT module while bead samples flow through the optical detection region.

4. CONCLUSIONS

The current study has successfully demonstrated a hand-held, integrated bead-based microfluidic flow cytometer system. Bio-samples have been effectively mixed, purified, detection and collected in the automatic one-step process. Moreover, the developed microfluidic flow cytometer system may pre-treat and analyze the samples in a short period of time when compared with the traditional PCR technique and may provide a powerful platform for rapid diagnosis.

ACKNOWLEDGEMENTS

The authors would like to thank partial financial supports from the National Science Council in Taiwan.

REFERENCES

[1] S.Y. Yang, S. K. Hsiung, Y. C. Hung,C. M. Chang, T. L. Liao and G. B. Lee, Meas. Sci. Technol., Vol.17, pp. 2001-2009 (2006).

[2] M. A. M. Gijs, Magnetic bead handling on-chip: new opportunities for analytical applications, Microfluid Nanofluid, Vol. 1, pp. 22-40 (2004).

[3] H. Miyachi et al., Automated Specific Capture of Hepatitis C Virus RNA with Probes and Paramagnetic Particle Separation, J. Clin. Microbio., Vol. 38, pp. 18-21 (2000).

[4] K. Y. Lien, J. L. Lin, C. Y. Liu, H. Y. Lei and G. B. Lee, Purification and enrichment of virus samples utilizing magnetic beads on a microfluidic system, Lab Chip, DOI: 10.1039/b700516d, (2007).

MICROWAVE-MEDIATED MICROCHIP THERMOCYCLING: PATHWAY TO AN INEXPENSIVE, HANDHELD REAL-TIME PCR INSTRUMENT

D.J. Marchiarullo[1], A. Sklavounos[2], N.S. Barker[2], J.P. Landers[1,3,4]

Departments of Chemistry[1], Electrical and Computer Engineering[2], Pathology[3] and Mechanical Engineering[4], University of Virginia, Charlottesville, VA 22904 USA

ABSTRACT

Miniature wireless communications components were utilized to generate and amplify microwave power between 5-6 GHz to up to 1.5 W. This system was used to rapidly thermocycle solution with two different types of control, frequency and power-dependent cycling. The thermocycling was applied to the PCR amplification of a fragment from the λ-phage genome and demonstrated a functional polymerase after exposure to microwave radiation.

Keywords: microwave dielectric heating, polymerase chain reaction, transmission line, thermocycling

1. INTRODUCTION

At the previous μTAS conference, low-power microwave dielectric heating was demonstrated using a microstrip transmission line matching network delivering 1 W of power between 4-6 GHz to a 1 μl chamber, rapidly bringing the solution to a boil [1]. By operating in this frequency range, inexpensive miniaturized microwave components created for the wireless communications industry can be exploited and, coupled with inexpensive light sources and detectors, the creation of a portable real-time PCR device is feasible (Table 1). This paper presents advances made with this particular method of dielectric heating and its application to PCR. Some of these advances include: 1) the use of commercially-available miniaturized microwave source and amplifiers, 2) a computer-controlled thermocycling program with thermocouple temperature feedback, 3) chip design enhancements including an entirely polycarbonate (PC) chip, and, 4) altered chamber dimensions. Several temperature sensing methods were also examined before defining the best current method to be a thermocouple-based temperature sensing mode.

Table 1: Component costs for a portable real-time microwave PCR system

Component	Cost
1 W Power Amp	$5
Driver Amp	$6
VCO	$7.50
SPST	$2.25
LED	$10
Optics	$20
Filter Stacks	$50
APDs	$50
Total	$151

2. EXPERIMENTAL

Microchips were machined from PC sheets with a CNC milling machine. Initial designs used a 1 mm diameter and 1 mm deep chamber with square channels 200-300 μm wide and deep leading to the chamber - the chip was sealed on top and bottom with polyimide tape. Later chip designs used a 2 mm diameter and 254 μm deep chamber with 150-200 μm wide and 254 μm deep channels leading to the chamber. The chip was sealed with 127 μm thick polycarbonate by two thermal bonding steps (top and bottom covers) at

978-0-9798064-0-7/μTAS2007/$20©2007CBMS

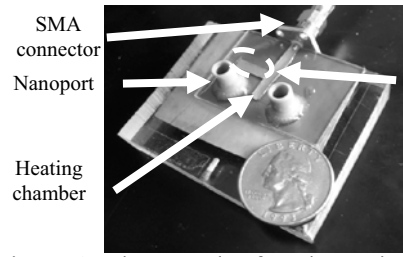

Figure 1: Photograph of a glass microchip with microfluidic channel and integrated microstrip transmission line matching network.

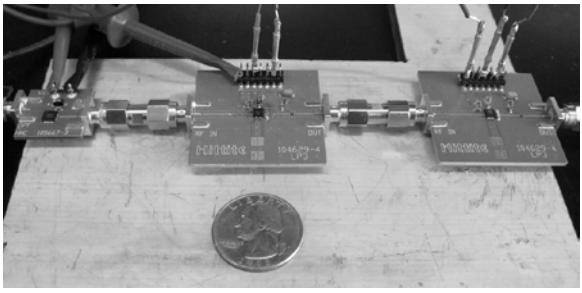

Figure 2: Photograph of microwave source (left) and amplifiers (center and right).

200 ºC for 1.5 hours under ~15 lb weight. Access holes were drilled between the first and second bonding step.

The microwave transmission lines were designed from the model previously developed allowing for optimal transmission of power (<-20 dB reflection or 99% transmission of power) at a predetermined frequency, usually between 5-6 GHz. The lines were cut from copper tape and applied to the top of the chip. A plexiglass stage with copper tape acting as a ground plane and an SMA connector were used to couple the microwave power to the chip completing the circuit (Figure 1).

Initially, microwave power was generated with a microwave generator coupled to a 1 W (30 dB) amplifier and temperature controlled by manually varying the microwave frequency away from the matched frequency. Currently, a miniature voltage-controlled oscillator coupled to two miniature 20 dB amplifiers is used to generate microwave power between 5-6 GHz and up to 1.5 W (Figure 2). Thermocycling is controlled through an in-house Labview program by varying the amplifier power with a thermocouple placed inside the chamber for temperature feedback.

PCR amplification of a 500 bp fragment of the λ-phage genome was attempted. The thermocycling program has an initial denaturation at 95 ºC and then 30 cycles between 94 ºC for denaturation and 68 ºC for annealing and extension and a final extension at 72 ºC. Capillary gel electrophoresis was used to separate the products.

3. RESULTS

This chip design was modified from a polyimide bound PC chip to a thermally-bonded PC chip. This was due to bubbling issues in the chamber likely due to the adhesive and eventual leakage from the chamber after repeated rinsing of the chip. The PC chip did reduce bubbling from the adhesive resulting in steadier temperature sensing and more consistent heating and cooling profiles.

Several methods of temperature monitoring were examined. The use of a pyrometer for non-contact temperature sensing was attempted and then ruled out due to the poor emissivity from the copper transmission line above the chamber and interference from radiated microwave energy. Varying thermocouple placements were attempted including in channels and chambers near but not inside of the heating chamber. Unfortunately, calibration was difficult due to the chip substrate's solvent incompatibility. Ultimately, the only method that gave reasonable results was placement of the thermocouple directly inside the chamber, or in the channel leading into the chamber. Figure 3 shows thermocycling by

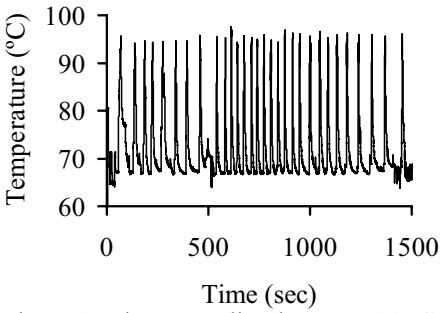

Figure 3: Thermocycling between 94 ºC and 68 ºC by manually varying microwave frequency.

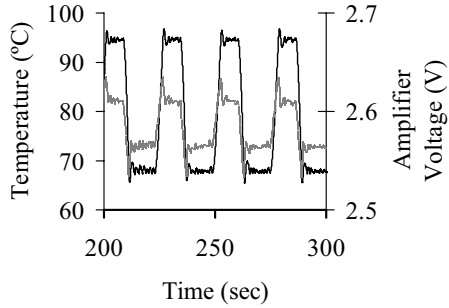

Figure 4: Thermocycling between 94 ºC and 68 ºC (black) by computer control of the amplifier voltage (gray).

manually altering the applied microwave frequency while Figure 4 shows computer-controlled thermocycling by adjusting the amplifier power.

The microwave heating and thermocycling capability was applied to the PCR amplification of a 500 bp fragment of the λ-phage genome. Initial attempts have yielded dimer, a non-specific PCR product (Figure 5) which indicates a functional polymerase, and conditions are being optimized to produce the desired product.

4. CONCLUSIONS

This paper has demonstrated microwave-mediated thermocycling through two different control mechanisms, frequency and amplifier power. A computer controlled cycling program with thermocouple temperature feedback has been developed producing more consistent and accurate thermocycling. Also, the system has been substantially miniaturized through use of inexpensive, commercially available wireless communications components.

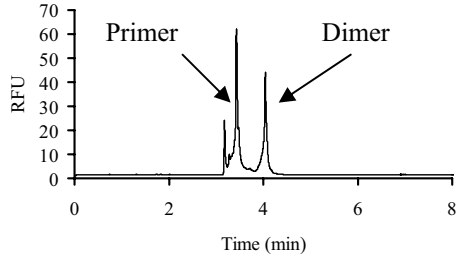

Figure 5: Electropherogram of PCR products after microwave thermocycling. Presence of dimer indicates a functional polymerase.

5. REFERENCES

1. A. Sklavounos, D.J. Marchiarullo, S.L.R. Barker, J.P. Landers, N.S. Barker, "Efficient Miniaturized Systems for Microwave Heating on Microdevices" in *Proceedings of μTAS 2006 Conference*. Editors: Kitamori, T. Fujita, H. Hasebe, S. Society for Chemistry and Micro-Nano Systems. 2006. Vol 2, 1238-1240.

BIOMARKER DETECTION BY ENZYMATIC AMPLIFICATION IN DROPLETS – TOWARDS HIGH THROUGHPUT DETECTION OF LOW COPY NUMBER CELL SURFACE BIOMARKERS

Haakan N. Joensson[1], Eric R. Brouzes[2], Michael Samuels[3], Mathias Uhlén[4], Helene Andersson Svahn[1] and Darren R. Link[3]

[1]Royal Institute of Technology, Dept of Nano Biotechnology, Stockholm, SWEDEN,
[2]Genetics Dept, Harvard Medical School, Boston, MA, USA,
[3]RainDance Technologies, Guilford, CT, USA and
[4]Royal Institute of Technology, Dept of Proteomics, Stockholm, SWEDEN

ABSTRACT

We report the development of a microfluidic droplet-based assay for detecting very low numbers of surface biomarkers on single cells. The method hinges on an enzymatic amplification whose product is confined in each droplet. The device generates droplets [1] containing individual cells for analysis at rates up to 10^6 cells per hour. The CD45 biomarker on the cell surface of human T lymphocytes is used as a model system for the assay.

Keywords: Droplets, Enzymes, Antibodies, Cell Surface Biomarkers

1. INTRODUCTION

Low copy number cell surface proteins, typically fewer than ~1000 copies per cell, are important for many cell functions, particularly cell signaling [2]. Flow cytometry is routinely used to detect highly expressed cell surface markers at a single cell level using antibodies directly coupled to fluorophores. However, its sensitivity is limited because only a few fluorophores are bound to each antibody [3]. To overcome this limitation, we encapsulate cells in droplets and detect cell surface proteins with an antibody coupled to the Beta-Galactosidase enzyme. Hence the fluorescent signal resulting from the processing of the fluorogenic substrate is confined in a finite volume; thousands of fluorophores are produced per antibody molecule, amplifying the cell surface biomarker signal. The narrow distribution in droplet size facilitates quantitative analysis of the fluorescent assay [4].

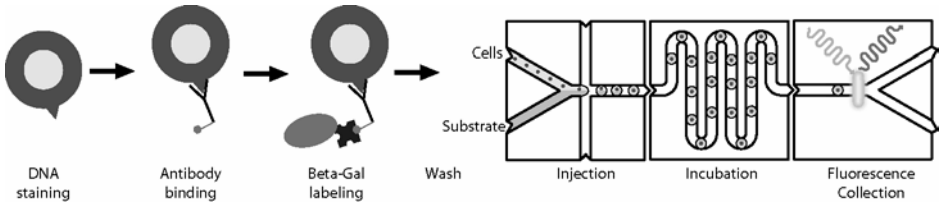

Figure 1. Droplet-based enzymatic amplification assay for biomarker detection.

2. EXPERIMENTAL

Microfluidic devices were manufactured in polydimethylsiloxane (PDMS) using standard soft lithography techniques [5]. Human T lymphocytes (Jurkat E6.1 cell line,

978-0-9798064-0-7/μTAS2007/$20©2007CBMS

ATCC) were cultured in suspension, collected and stained with one of two DNA stains (SYTO61-85, Invitrogen) for visualization. Cells were then incubated with antibodies coupled to biotin: anti-CD45 antibody for the assay, and an isotype antibody as a negative control (BD Biosciences) and subsequently labeled with streptavidin conjugated Beta-Gal (Rockland). After several washes to remove unbound reagents the cells were injected into the microfluidic chip. The fluorogenic substrate fluorescein beta-digalactopyranoside, (FDG (Invitrogen)) and cells were encapsulated to produce monodisperse aqueous droplets in the carrier oil phase (fig.1). Droplets were incubated either on-chip or off-chip and further analyzed on-chip with a 488nm laser through a detection module. The fluorescence signal was collected by two photomultipliers associated with specific filters, and corrected for fluorescent cross-talk.

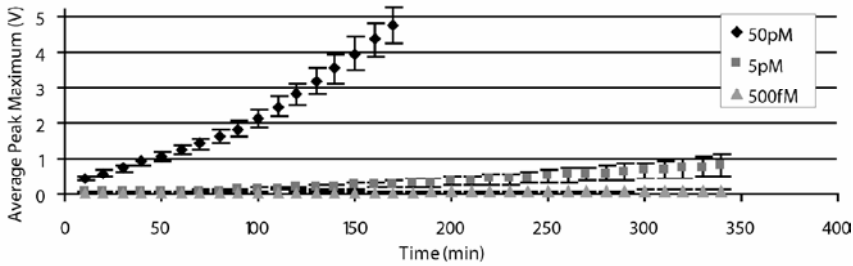

Figure 2. Kinetics of the fluorescence signal generated by three different Beta-Gal concentrations (50, 5 and 0.5 pM) encapsulated with 100µM FDG in 30µm droplets.

3. RESULTS AND DISCUSSION

To characterize the detection limit of the system we assayed the kinetics of the fluorescent signal generated by a series of decreasing Beta-Gal concentrations in 30µm droplets (fig. 2). Within hours, enzyme concentrations as low as 5pM can be detected, equivalent to an average of 43 Beta-Galactosidase molecules per droplet. Coupling Beta-Gal molecules to primary antibodies should allow this detection limit to be achieved for cell surface proteins.

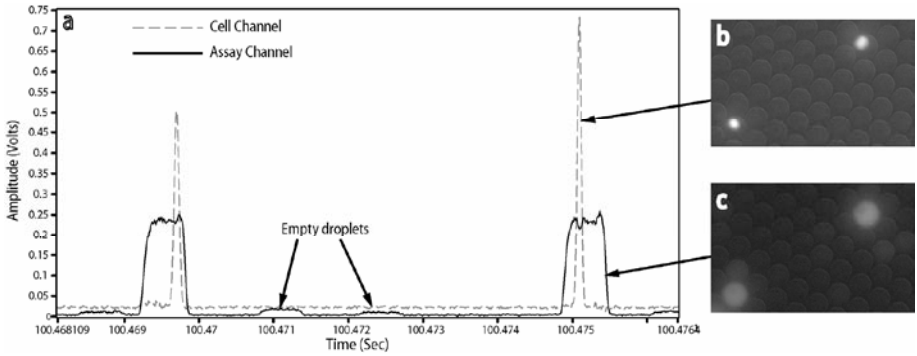

Figure 3.a) Data trace showing empty droplets and two droplets containing the cell presence and assay signals; b)-c) Microscopy images of a field of droplets where cell (b) and assay (c) signals are co-localized to two cell-containing droplets.

As a model system we have assayed human T lymphocytes for the abundant surface marker CD45. A typical data trace (fig 3a) and microscope images (fig3b-c) show that encapsulation couples the amplified fluorescent assay signal to the analyzed single cell. The histogram (fig. 4) shows the data for 10,000 cells assayed for CD45. The signal from the assay can be clearly distinguished from noise as assessed with the negative control.

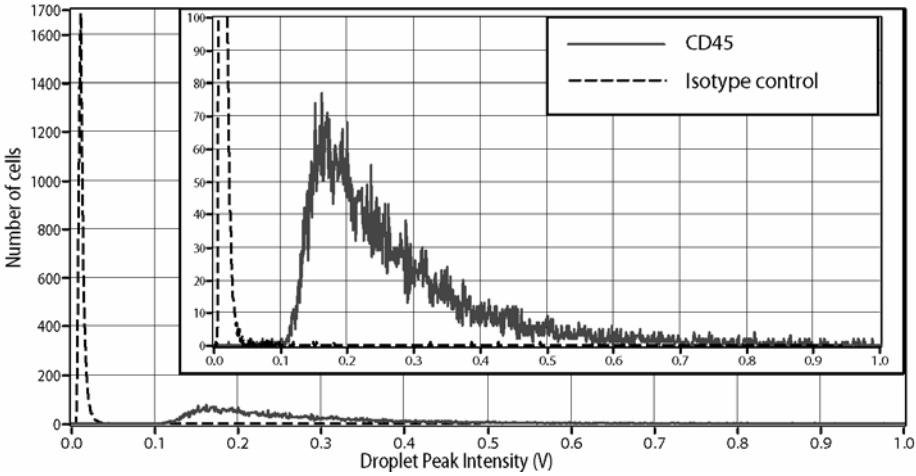

Figure 4. Histogram of fluorescent intensity maxima from Jurkat cells assayed for the CD45 biomarker (10,000 cells encapsulated in 50µm droplets) with inset: magnification of the lower part of the histogram. The result from the assay is represented by the solid line, and the negative control corresponding to an isotype antibody by the dashed line. Average fluorescent signals and standard deviations were 0.27V (std: 0.145 V) for CD45 and 0.013V (std: 0.0095 V) for the negative control.

4. CONCLUSIONS

We have developed a droplet-based assay for detecting cell surface biomarkers using enzymatic amplification in a microfluidic device. To illustrate the capability of the assay to detect low copy number biomarkers we showed that as few as 43 enzyme molecules per droplet can be detected. In addition, we documented the use of this assay by detecting CD45 on human lymphocyte. We are currently expanding our investigation to several mammalian cell lines assaying for low abundant cell surface biomarkers.

REFERENCES

[1] S.L. Anna, N. Bontoux, and H.A. Stone, *Formation of dispersions using "flow focusing" in microchannels*, Applied Physics Letters, Vol. 82, pp. 364-366, (2003)

[2] B. Huang, H. Wu, D. Bhaya, A. Grossman, S. Granier, B.K. Kobilka, and R.N. Zare, *Counting Low-Copy Number Proteins in a Single Cell*, Science, Vol. 315, pp. 81-82, (2007).

[3] E. Lundberg, M. Sundberg, T. Graslund, M. Uhlen and H. Andersson Svahn, *A novel method for reproducible fluorescent labeling of small amounts of antibodies on solid phase*, J. Immunol. Meth., Vol 322, pp. 40-49 (2007)

[4] A. Huebner, M. Srisa-Art, D. Holt, C. Abell, F. Hollfelder, A. J. deMello and J. B. Edel, *Quantitative detection of protein expression in single cells using droplet microfluidics*, Chem. Commun., pp 1218-1220 (2007)

[5] J.C. McDonald, D.C. Duffy, J.R. Anderson, D.T. Chiu, H Wu, O.J.A. Schueller, G.M. Whitesides, *Fabrication of microfluidic systems in poly(dimethylsiloxane)*, Electrophoresis, Vol 21, pp. 27-40, (2000)

CELL SORTING OF LIVE AND DEAD CELLS BY LASER RADIATION PRESSURE AND SHEATH FLOW IN MICROCHANNEL

Masaya Murata[1], Noritada Kaji[1,2], Manabu Tokeshi[1,2], Yoshinobu Baba[1, 2,3,4]

[1]*Department of Applied Chemistry, Nagoya University, JAPAN*
[2]*MEXT Innovative Research Center, Nagoya University, JAPAN*
[3]*Health Technology Research Center, AIST, JAPAN*
[4]*Institute for Molecular Science, JAPAN*

ABSTRACT

We have developed a novel cell sorting technique for live and dead cells by using optical tweezers (1064 nm Nd; YAG Laser) and sheath flow in a PDMS microchip. The dead cells stained by Trypan Blue have low refraction index than the live cells. Therefore, by using appropriate laser power and flow rate only, the live cells could be trapped by optical tweezers.

Keywords: Optical tweezers, Sheath flow, Polydimethylsiloxane, Trypan Blue

1. INTRODUCTION

Although current cell sorting techniques are still the standard for high speed, multi-parametric cell sorting, these include two steps of fluorescence detection and cell isolation and also require complex equipments [1]. In contrast to current techniques, our technique includes one step and does not require fluorescent labeling because the optical tweezers can isolate target cells without a detection step by utilizing the difference absorption wavelength of cells. Resulting this paper, we demonstrated that the optical tweezers would be used for not only cell manipulation [2] but also cell sorting.

Optical tweezers are the tools which enable us to trap the small particle having different refraction factor against surrounding solvent. So we can say that the trapping force depend on the refraction factor of the small particle. Therefore we have tried a novel cell sorting techniques by utilizing the difference of trapping force based on the difference of refraction factor caused by the difference of absorption wavelength of the cells.

2. EXPERIMENTAL

First, we evaluated the trapping ability for live HeLa cells and dead HeLa cells stained by Trypan Blue and Erythrosine B with maximum absorption at 450 nm and 930~1170 nm, respectively. The results showed that by using the optical tweezers (1064 nm) the dead cells stained by Trypan Blue can not be trapped while the live cells and the dead cells stained by Erythrosine B could be trapped. Since the refraction factor of the dead cells stained by Trypan Blue may not arise the local heat results from absorption of the laser of the optical tweezers, dead cells stained by Trypan Blue were not trapped by the optical tweezers.

Taking these results into consideration, we fabricated a PDMS microchip for cell sorting of live and the dead cells (Fig.1a,b). The microchip has two branch channels at cross point. By applying sheath flow, the cells can pass through a narrow line at the center of the microchannel (Fig.1c). If the laser of the optical tweezers is irradiated at the side of the cells flow, only live cells could be trapped and changed their lines of flow while the dead cells flowed downstream without any trapping (Fig.2,3).

978-0-9798064-0-7/μTAS2007/$20©2007CBMS

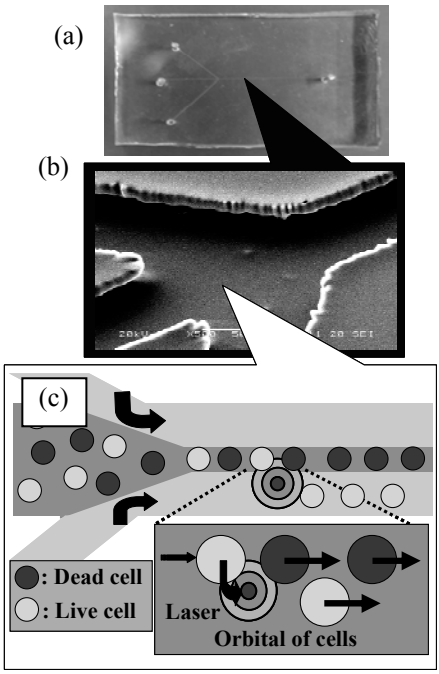

Figure 1. The microscopic images of the microchip (a) and the SEM images of the microchip (b) and the schematic illustration of cell sorting in sheath flow (c).

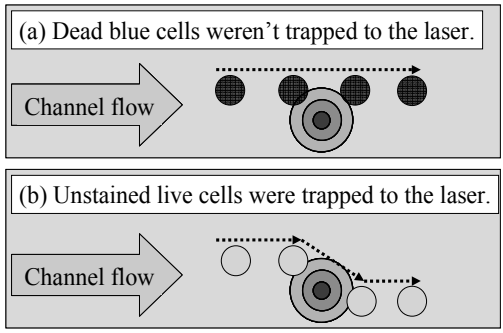

Figure 2. The schematic illustration of difference movement of live and dead cells.

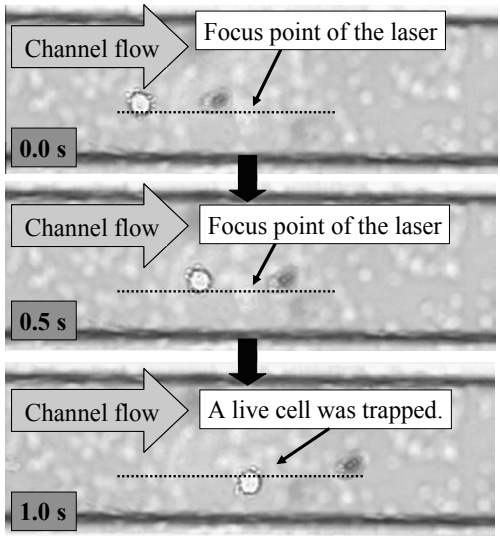

Figure 3. The microscopic images of cells in channel flow (0.0s, 0.5s, 1.0s).

4. RESULTS AND DISCUSSION

In order to evaluate the separation efficiency, we compared the dependence of the flow rate on the trapping efficiency of live cells and dead cells stained by Trypan Blue, respectively (Fig.4a,b: These results were given by using ready-made PMMA microchip). In this method of evaluation, we can say that it is a good separation as the difference between the trapped percentage of live cells and the trapped percentage of dead cells become larger. As show in Fig.4a at 90 μm/s and Fig.4b at 130 μm/s, the live cells and dead cells stained by Trypan Blue could be separated completely. We think that we could accomplish cell sorting when the laser power and the flow velocity were optimum balance because the separated cells were mainly affected from these two parameters in microchanel.

This consideration is supported by the results that optimum flow velocity to separate the

cells becomes faster as the laser power becomes higher (Fig.4a,b). In addition to, these results clearly shows the relationship between the laser power and the flow velocity. When the flow velocity is very slow against the laser power, the trapping force relatively become larger and both sorts of cells are trapped by the laser. By contraries, when the flow velocity is very fast against the laser power, the trapping force relatively become smaller and both sorts of cells are not trapped by the laser. These results show that the relationship between the laser power and the flow velocity is very important to accomplish cell sorting, too.

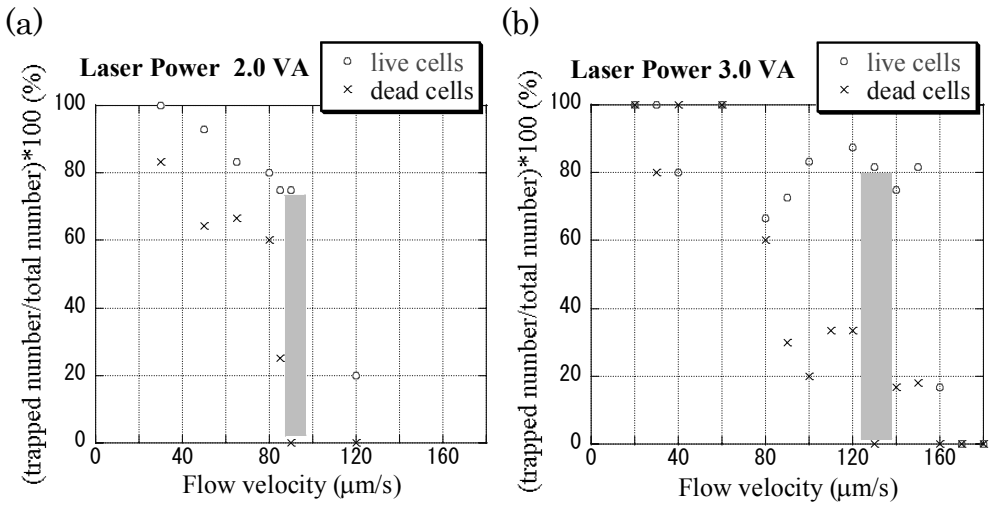

Figure4. The quantitative analysis of the trap efficiency against flow velocity. (a,) A plot of trap percentage of live and dead cells at 2.0 VA. (b,) A plot of trapped percentage of live and dead cells at 3.0 VA.

These results demonstrated alternative cell sorting technique of live and dead cells by optical tweezers and sheath flow in the microchip, however, the sorting precision should be more and more risen. Therefore, we will exert ourselves into performing a series of experiments by using PDMS microchip which enables us to make a very narrow line of cells flow because hydrodynamic focusing is very important to accomplish a accurate cell sorting. Furthermore, we will have to go next step to take up the live cells isolated by the optical tweezers. For that purpose, we are now trying to separate live and dead cells by using a newly designed glass microchip which enable us to take up the live cells isolated by the optical tweezers at the cross point of backward microchannel.

5. CONCLUSIONS

We have developed a novel cell sorting technique for live and dead cells by using optical tweezers (1064 nm Nd; YAG Laser) and sheath flow in a PDMS microchip. And our results indicated that anything which has different absorbance can be separated by this principle.

REFERENCES

[1] Wang MM, and Butler WF. *Nature. Biotech*., 2005, *23*, 83-87
[2] Nigel R. Munce, and Lothar Lilge, *Anal. Chem*., 2004, *76*, 4983-4989

CELL TRAPPING VIA COUNTER-ROTATING MICRO-VORTICES

Cheng-Ming Lin, Yu-Shiang Lai, Hsin-Ping Liu, and Andrew M. Wo
Institute of Applied Mechanics, National Taiwan University, Taiwan

ABSTRACT

Trapping of suspended cells is fundamentally important for cellular studies. This work presents a suspended oscillating micro-plate, actuated by Lorentz force law, and generated a pair of counter-rotating micro-vortices to trap bioparticles. In contrast to other approaches, this microfluidic device allows bio-particles to flow freely through unobstructed region, trapped, and controlled release. The trapping force is in pico-Newton range, and varies linearly with the flow. This hydrodynamic approach should be useful for controllable trap/release of bioparticles.

Keywords: Micro-vortices, Microfluidics, Lorentz force, Trapping of cells

1. INTRODUCTION

Recent interests in cellular studies, microfluidic devices play an important role for providing the platform for biological applications because microfluidic devices are easy to fabricate, convenient to controll, and fast to process of detection. Cell trapping devices are based on mechanical and electrical principles. However, little is done on cell trapping in a local region using gentle environment without perturbing the properties of cells. Although the optical tweezers (OT), dielectrophoresis (DEP), acoustical tweezers (AT) methods can trap cells in suspension, they might harm the cells. Recently, some have utilized hydrodynamic approaches, particularly vortical flow. Shelby et al. [1] utilized microvortices to manipulate a bioparticle and measured its rotation rate within a confined region, and applied the technique to nano-particles [2]. Lutz et al. [3] trapped cells using microeddies behind circular cylinder. The purpose of this study is to present an entirely new device leveraging on a pair of counter-rotating micro-vortices to trap bioparticles. In contrast to other approaches, this device allows bioparticles to flow freely through unobstructed region, trapped, and controlled released.

2. EXPERIMENTAL

The device is in resonance and actuated based on Lorentz law. Alternating current (140kHz) flows along a suspended microelectrode thin-plate structure with direction normal to an external magnetic field (~1 Tesla), forcing the structure to oscillate in the third direction (Fig. 1). The oscillatory structure induces flow non-linearity at the two plate edges (parallel to its centerline) causing an adverse time-mean pressure gradient in the direction outward from its centerline. The net result is inducing a pair of counter-rotating micro-vortices.

978-0-9798064-0-7/μTAS2007/$20©2007CBMS

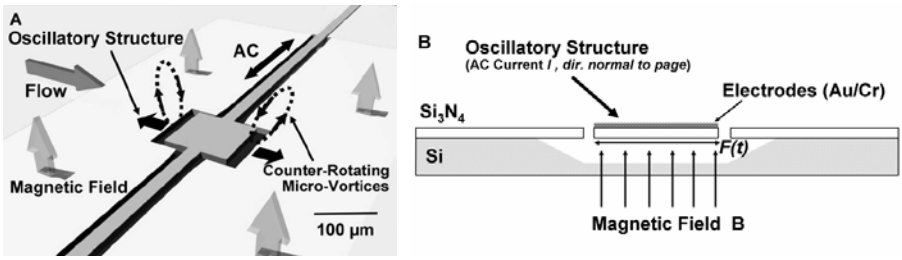

Figure 1. Sketch of the device. (A) The suspended thin (1μm thick) square plate (100μm*100μm) in resonance (140kHz.) induced a pair counter-rotating micro-vortices at plate edges. The total length of the suspended beam is 750μm and the width is 20μm. (B) Edge-on view of the oscillatory structure.

Fabrication methods utilized conventional lithography. Silicon wafer coded with silicon nitride (~1μm) was sputtered with metallic layer (0.15μm thickness of Cr/Au). Photoresist (Shipley 1813) was patterned to define the microelectrode structure. Unnecessary metal was removed by etchant. By repeating the procedure of coating photoresist and developing, the cavity underneath the oscillatory structure was formed. Reactive ionic etch (RIE) removed the silicon nitride unprotected by photoresist. Potassium hydroxide (KOH) performed bulk micromachining to remove unwanted silicon to suspend the structure, as shown in Fig. 1B.

3. RESULTS AND DISCUSSION

Results in Fig. 2A shows the counter-rotating micro-vortices above the two edges of the oscillatory structure. The fluid was drawn by low pressure in the center of the plate (from simulation) and flows outward, loops upward (adverse pressure gradient at the edges), and returns to the plate. Moreover, this swirling velocity is easily controllable by adjusting the input voltage to the microelectrode structure (via changing the oscillatory displacement). Figure 2B shows the relation between the angular velocity of the flow and input voltage is distinct and parabolic.

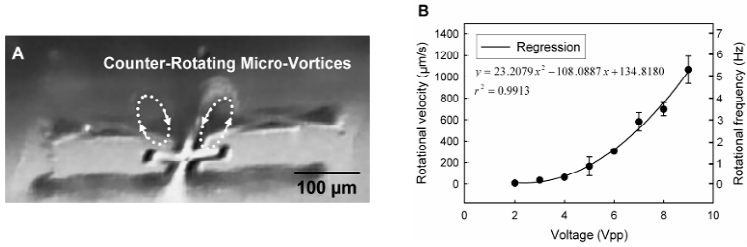

Figure 2. (A) Micrograph of counter-rotating micro-vortices above the two-edges of the structure at resonant (140kHz) at an instant in time. Trapped particles in the right vortex is evident. Left vortex also trapped particles as clearly seem in the movie. (Dotted lines are to guide the eyes.) (B) The parabolic relation between the velocity of vortex above the resonant structure and the input voltage. The data indicated the minimum trapping voltage around the 2 Volts (peak to peak).

Trapping study used polystyrene particles (10μm) injected into the PDMS channel by a syringe pump. Figure 3A shows a particle approached the structure (left trajectory) and eventually trapped by the micro-vortices. By increasing the background flow velocity, controlled release of the trapped particle is demonstrated. Quantitatively, for example, the micro-vortices can trap the particles under 140μm/s background flow at 7V (peak to peak)

input voltage (Fig. 3B). Using Stokes drag on a sphere ($F= 6\pi\eta Ua$, where η is the viscosity, U the velocity, and a the particle radius), the maximum trapping force is calculated against a fixed vortex velocity (expressed as $Re\Gamma= \Gamma/\eta$, where $\Gamma= \oint V \bullet dl$ or the circulation of a vortex) as the background flow is increased.

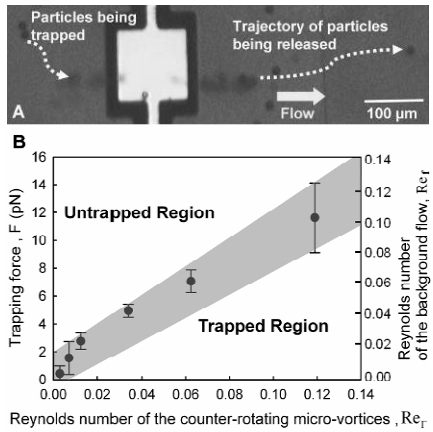

Figure 3. Trapping of 10μm particles by micro-vortices. (A) Trajectory of a particle being trapped (left dotted line) and upon release (right dotted line). When the background flow velocity is greater than the trapping force, the particle is released. (B) Map of trapping force verse Reynolds number of micro-vortices (as defined in the text). The gray region illustrates the boundary between trapped and untrapped regions. The Reynolds number scale ($Re_f= U*h/\eta$) on the far right ordinate characterizes the flow in the microchannel.

4. CONCLUSIONS

This research describes a non-contact approach of rotating, controlling, and quantifying suspended microparticles via micro-vortices generated by an oscillating thin plate. This device combined with the simple theory, controllable trapping strength, and small trapping region identify the oscillating plate as a potential candidate may be integrated easily for other applications, such as cell cultural platform, drug detection, and various bioassays.

ACKNOWLEDGEMENTS

This work was supported by the National Science Council (Grant No. 95-2120-M-002-006), Taiwan.

REFERENCES

[1] J.P. Shelby, S.A. Mutch, and D.T. Chiu, *Direct manipulation and observation of the rotational motion of single optically trapped microparticles and biological cells in microvortices.* Analytical Chemistry, 2004. 76(9): p. 2492-2497.

[2] J.P. Shelby and D.T. Chiu, *Controlled rotation of biological micro- and nano-particles in microvortices.* Lab on a Chip, 2004. 4(3): p. 168-170.

[3] B.R. Lutz, J. Chen, and D.T. Schwartz, *Hydrodynamic tweezers: 1. Noncontact trapping of single cells using steady streaming microeddies.* Analytical Chemistry, 2006. 78(15): p. 5429-5435.

CONTINUOUS MAGNETOPHORETIC ENRICHMENT OF RARE TUMOR CELLS

D. Nawarathna[1], P. Kumaresan[2], Y. Zhang[3], B. Ferguson[1], S-H Oh[4], K. S. Lam[2] and H.T. Soh[1,5]

[1]Dept. of Mech. Eng., University of California, Santa Barbara, CA, USA 93106
[2] UC-Davis Cancer Research Center, Sacramento, CA, USA 95817
[3]CytomX, LLC, 460 Ward Drive, Suite E1, Santa Barbara, CA, USA 93111
[4]Dept. of Electrical Engineering, University of Minnesota, Minneapolis, MN, USA 55455
[5]Dept. of Materials, University of California, Santa Barbara, CA, USA 93106

ABSTRACT

We present the Continuous-flow Magnetic Activated Cell Sorter (CMACS) device which is capable of enriching rare magnetic particles with high purity. The microfabricated ferromagnetic strips within the microfluidic channels create high magnetic field gradients, which generate the magnetophoretic separation forces. We report on the effective separation of magnetically labeled Human Lymphoma (Jurkat) cells from non-target cells and compare its performance against commercially available macro-scale systems.

Keywords: Magnetic separation, rare cell sorting

1. INTRODUCTION

Accurate assessment of disease progression has a critical influence on the therapeutic outcome of the patient. However, for diseases such as cancer, such methods of quantitative prognosis are critically lacking. Recently, there have been many promising reports of utilizing circulating tumor cells (CTCs) as a quantitative marker for cancer prognosis [1]. In order to isolate the rare CTCs with high purity and recovery, batch processed, magnetophoretic enrichment techniques have been shown to be effective [2]. On the other hand, continuous methods of rare-cell enrichment offer an important advantage in that multiple sorting stages can be integrated monolithically. Toward this end, we have developed the Continuous-flow Magnetic Activated Cell Sorter (CMACS) device.

2. RESULTS

The CMACS device (Fig 1a) is fabricated similarly to our previous work [3], and it consists of two inlets (sample / buffer) and two outlets (collection / waste). The labeled target cells in the sample are magnetophoretically separated continuously by Magnetic Field-gradient Generators (MFG), ferromagnetic micro-patterns within the sorting chamber (Fig 1b). The MFGs precisely shape the B field gradients in a reproducible manner thereby providing an accurate magnetophoretic force - a challenging task in conventional, macro-scale devices. The particle saturation magnetization and the external magnet field strength, which drives the MFG, are measured at 0.05T and 0.1T respectively. A magnetophoretic force of a few nN is thus exerted, directing the labeled cells toward the collection channel.

CMACS separation performance is tested with a binary bead mixture (Fig 2a) consisting of 1 μm magnetic beads (0.01% of mixture, Invitrogen) and 2.8 μm polystyrene beads (99.99% of mixture, Duke Scientific). The beads are sorted at ~ 2 mL/hr and the eluted sample, from the collection port, is analyzed using flow cytometry (FacsAria, BD Biosciences). CMACS demonstrates > 9000 fold enrichment in a single pass (Fig 2b).

978-0-9798064-0-7/μTAS2007/$20©2007CBMS

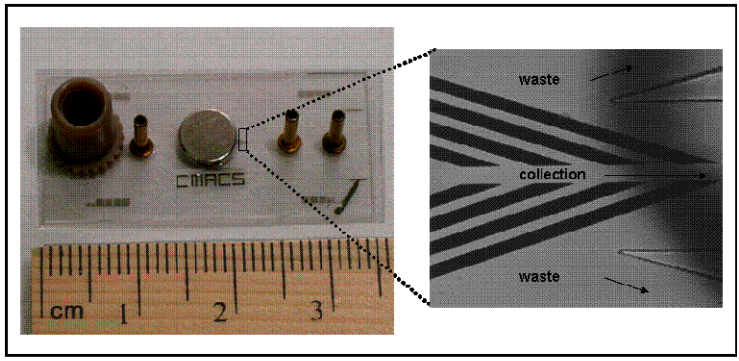

Figure 1: *Micrographs of the CMACS device a) The device consists of two inlets (sample / buffer) and two outlets (collection / waste). A low-loss microfluidic interface (Nanoport, Upchurch Scientific) is used at the sample inlet. The external neodymium permanent magnet activates the MFGs which create a controlled B field gradient within the micro channel. (b) The resulting magnetophoretic force deflects the magnetically labeled cells into the collection port, where as unlabeled cells flow into the waste port.*

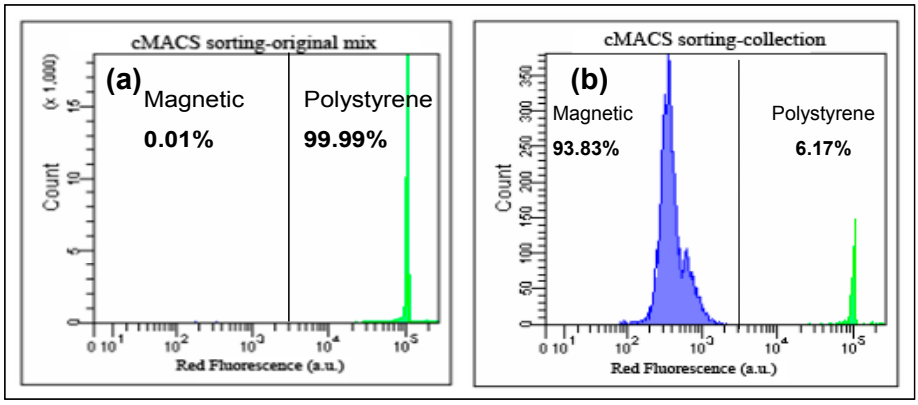

Figure 2: *CMACS separation performance for binary bead mixtures The bead mixture is sorted at ~ 2 mL/hr and the eluted sample from the collection port is analyzed using flow cytometry (FacsAria, BD Biosciences) a) The initial binary bead mixture consists of 0.01% 1-μm magnetic beads (Invitrogen) and 99.99% 2.8-μm polystyrene beads (Duke Scientific) b) After 1 round of sorting, the collected sample consists of 93.83% magnetic beads and 6.17% polystyrene beads, representing > 9000-fold enrichment.*

Next, enrichment of mammalian cells is tested with a binary mixture of positive control (Jurkat) and negative control (K-562) cells. The Jurkat cells are engineered to express the green fluorescent protein (GFP) inter-cellularly, and α4β1 integrin on its cell surface [4]. The K-562 cells do not express either protein. Using a high affinity peptidemimetic affinity ligand (Bio 1211), the Jurkat cells are labeled in the mixture (Fig 3a). The initial ratio of the cells (positive control: negative control) ranged from 1:1000 and 1:10,000. The

analysis of the collected cells through flow cytometry revealed that significantly higher enrichment is achieved through the CMACS device compared to the commercially available, macroscale, bead concentration system for the same mixture (Fig 3b).

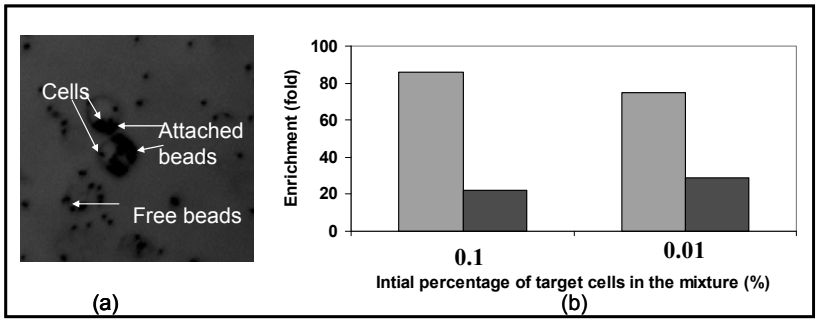

Figure 3: *Comparative rare mammalian cell sorting performance for CMACS and commercially available macroscale, magnetic bead concentrators. a) An optical micrograph of the positive control (Jurkat) cells labeled with 1 um magnetic beads. The Jurkat cells are grown (anaerobically at 370C) in RPMI- 1640 medium with 10% fetal bovine serum (FBS), 1% penicillin, 0.5mg/ml Geneticin, 1mM non-essential amino acids, 25mM HEPES buffer. b) Comparative enrichment results for Jurkat and K-562 (negative control) cells demonstrate significantly higher performance of the CMACS (light shade) device compared to commercially available magnetic bead concentrators (dark shade).*

3. CONCLUSIONS

We report on the microfluidic separation of magnetically labeled Human Lymphoma (Jurkat) cells from non-target cells and compare its performance against commercially available macroscale systems. The use of ferromagnetic strips offers significant advantages in that accurate magnetophoretic forces can be generated with the precision of microfabricated features inside the microfluidic channels. The continuous-flow mode of magnetic separation used in the CMACS device offers very high enrichment capability of rare magnetic particles, which seems to be superior in comparison to macro-scale magnetic bead concentrators.

REFERENCES

[1] M. Cristofanilli, G. T. Budd, M. J. Ellis, A. Stopeck, J. Matera, M. C. Miller, J.M. Reuben, G. V. Doyle, W. J. Allard, L.W.M.M. Terstappen and D.Hayes, *Circulating Tumor Cells, Disease Progression, and Survival in Metastatic Breast Cancer*, New England Journal of Medicine 351, pp.2453-2454 (2004).

[2] W. J. Allard, J. Matera, M. C. Miller, M. Repollet, M. C. Connelly, C. Rao, A. G. J. Tibbe, J. W. Uhr and L. W. M. M. Terstappen, *Tumor Cells Circulate in the Peripheral Blood of All Major Carcinomas but not in Healthy Subjects or Patients With Nonmalignant Diseases* **,** Clin. Cancer Res, 10, pp. 6897-6904 (2004).

[3] S.H Oh, A. K. Singh, P. H. Bessette, S. A. Kenrick, J. J. Rice, J. Qian, P. S. Daugherty, and H. T. Soh, *Screening of Molecular Libraries Using The Continuous-Flow Micro-Magnetic Cell Sorter*, Micro Total Analysis Systems Tech. Digest, pp. 975,(2006).

[4] L. Peng, R. Liu, J. Marik, X. Wang, Y. Takada & K. S. Lam, *Combinatorial chemistry identifies high-affinity peptidomimetics against α4β1 integrin for in vivo tumor imaging*, nature chemical biology, 2, pp. 381-389 (2006).

CONTINUOUS SEPARATION OF CELLS IN A MICROFLUIDIC DEVICE USING LATERAL DIELECTROPHORESIS

Nicolas Demierre, Thomas Braschler, Robin Muller and Philippe Renaud
Laboratory of Microsystems, Ecole Polytechnique Fédérale de Lausanne EPFL, 1015 Lausanne, SWITZERLAND

ABSTRACT

We have fabricated a microfluidic device with a lateral arrangement of patterned metal electrodes and insulator to achieve a continuous separation of cells in flow by opposing dielectrophoretic force fields. The novelty in this device is the control of several DEP forces which define a position of equilibrium for the particles as a function of their dielectric properties. We demonstrate the efficiency of our method in a continuous separation of viable and non-viable yeast cells by taking advantage of their different responses to high frequency electric fields.

Keywords: Microfluidics, Dielectrophoresis, Flow Cytometer, Continuous Separation

1. INTRODUCTION

A fundamental issue in biology is the separation and isolation of a cell population of interest as pure as possible. Due to the recent developments in the field of BioMEMS, such prerequisite operations of biological assays can be performed on chip. The advantages are portability, low cost, low volumes of sample and small time constants. In dielectrophoresis-based separation a DEP force is generally opposed to gravity, drag force or diffusion and has already been used for the separation of viable and non-viable yeast cells [1-3].
We propose a method of continuous separation obtained by opposing DEP-forces. Lateral arrangements of metal electrodes and patterned insulator are used to shape electric fields and generate DEP-forces with the principle of insulator-based electrodeless dielectrophoresis [4]. The opposition of forces create an equilibrium position for the particles flowing through the channel. The cell separation is obtained since particles with different dielectric properties end up at distinct positions of equilibrium. Our microfabricated flow cytometer has demonstrated an improvement in the separation efficiency compare to previous work by operating the similar separation of viable and nonviable yeast cells.

2. EXPERIMENTAL

The chip design consists of an array of 2x15 planar and metal electrodes located on both sides of a microchannel (Fig. 1c) through which liquids are driven by a pneumatic system [5]. Metal electrodes made of Ti/Pt were patterned by a lift-off process on a pyrex wafer (Fig. 1ab) and channels were structured in a SU-8 layer by standard photolithography. The metal electrodes located on both sides of the channel are connected to it through narrow access channels which guide the electric field. The vertical surface boundaries between access channels and the main channel behave like vertical metal electrodes [6]. DEP-forces parallel to the channel bottom are produced from both sides, hence the term lateral dielectrophoresis.

978-0-9798064-0-7/μTAS2007/$20©2007CBMS

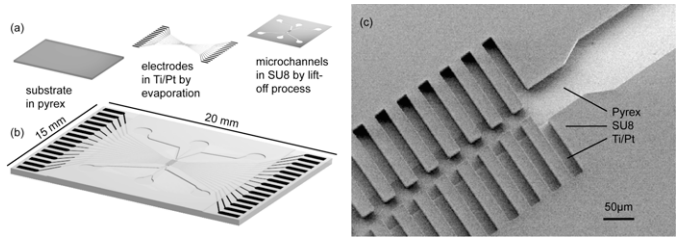

Figure 1. (a) Microfabrication process: patterning of Ti/Pt electrodes on a pyrex substrate by lift-off and standard photolithography of SU8 for the channels. (b) 3D drawing of the device with external dimensions of 20x15mm. (c) SEM picture of the electrode array located on both sides of a main fluidic channel.

3. RESULTS AND DISCUSSION

A mixture of 5µm beads and yeast cells are separated into pure sub-populations. A low frequency signal (<100 kHz) was applied on each side of the electrode array (up and down in Fig. 2) and a third signal at high frequency (2 MHz) was added to the upper side. When this high frequency signal is switched off, the populations are mixed but focused due to the opposite nDEP from both sides as shown in the left part of Fig. 2. However, the beads and yeasts appeared clearly separated when the high frequency was switched on since the high frequency exerted a negative DEP on beads and a positive DEP on yeast cells.

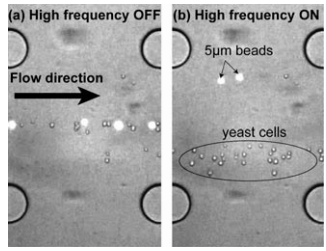

Figure 2. Video captures of separation of yeast cells and 5µm beads. (a) they appear focused and mixed when the high frequency is off and (b) clearly separated when the high frequency is on. pDEP is exerted on beads while nDEP is exerted on yeast cells.

We also apply our method to the separation of viable and nonviable yeast cells suspended in phosphate buffer saline with a conductivity of 60mS/m. The nonviable cells were stained with propidium iodide as shown in Fig. 3ab. Again signals at low frequencies (50 and 60 kHz) and one additional signal on the left side at variable high frequency (1.5 and 5 MHz) were used. Fig. 3c shows the positions of the sub-populations across the channel right after the separation for two different high frequencies (1.5 and 5MHz). The channel can be split into up to 3 zones and cells flowing in these specific zones can be collected at the 3 fluidic outlets with nearly 100% purities. The positions of nonviable yeast cells are not affected by the high frequency increase revealing a constant frequency response over all frequency range used (50kHz to 20MHz). Inversely, the viable yeast cells turned from nDEP to increasing pDEP with the increasing high frequency revealing a dielectric dispersion with a crossover frequency experimentally observed around 860kHz.

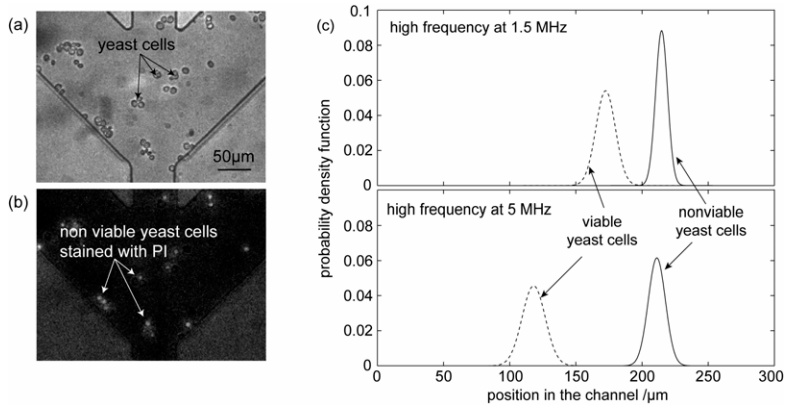

Figure 3. Image of flowing viable yeast cells (a) and nonviable stained yeast cells (b). (c) Positions of viable and non-viable yeast cells for two high frequencies (1.5 and 5MHz) added on the left side. pDEP is exerted on viable yeast cells while nDEP is exerted on nonviable yeast cells.

4. CONCLUSION

The arrangement of electrodes and insulator permits to generate and oppose DEP-forces which facilitate the observation of cell manipulation on chip. The resulting equilibrium avoid the deviation to be dependent on the time spent in the structure. The method allows characterizing dielectric properties of cells and reveals a high efficiency in continuous cell separation with fraction purities near 100%. We intend to use this method for separating infected cell samples [7].

ACKNOWLEDGEMENTS

This work was supported by the European Community-funded CellPROM project under the 6th Framework Programme, contract no. NMP4-CT-2004-500039

REFERENCES

[1] I. Doh and Y. H. Cho, "A continuous cell separation chip using hydrodynamic dielectrophoresis (DEP) process," *Sensors and Actuators, A: Physical*, vol. 121, pp. 59-65, 2005.

[2] Y. Li, et al., "Continuous dielectrophoretic cell separation microfluidic device," *Lab Chip*, vol. 7, pp. 239-248, 2007.

[3] G. H. Markx, et al., "Separation of viable and non-viable yeast using dielectrophoresis," *Journal of Biotechnology*, vol. 32, pp. 29-37, 1994.

[4] C.-F. Chou and F. Zenhausern, "Electrodeless Dielectrophoresis for Micro Total Analysis Systems," *IEEE Engineering in Medicine and Biology Magazine*, vol. 22, pp. 62-67, 2003.

[5] T. Braschler, et al., "A simple pneumatic setup for driving microfluidics," *Lab Chip*, 2007.

[6] N. Demierre, et al., "Characterization and optimization of liquid electrodes for lateral dielectrophoresis," *Lab Chip*, vol. 7, pp. 355-365, 2007.

[7] C. Küttel, et al., "Label-free detection of Babesia bovis infected red blood cells using impedance spectroscopy on a microfabricated flow cytometer," *Acta Tropica*, vol. 102, pp. 63-68, 2007.

EIS-ASSISTED IMPEDANCE ASSAY FOR IN SITU MONITORING CARDIOMYOCYTE APOPTOSIS

Yiling Qiu[1], Ronglih Liao[2] and Xin Zhang[1]

[1]Department of Manufacturing Engineering, Boston University, USA and
[2]Brigham and Women's Hospital, Harvard Medical School, USA

ABSTRACT

In this work, we report to develop an impedance assay for in situ monitoring cardiomyocyte apoptosis which is determined by recording the change in cardiomyocyte adhesion to extracellular matrix (ECM) by electrical cell-substrate impedance sensing (ECIS) and electrochemical impedance spectroscopy (EIS). The time course of the resistance of cell-substrate gap is presented here to describe the adhesion change during apoptosis process.

Keywords: ECIS, EIS, cardiomyocyte, apoptosis

1. INTRODUCTION

The research on cardiomyocyte apoptosis has gained great attention recently because it has been proved to involve in heart failure, ischemic heart deceases, atherosclerosis [1], etc. In the cell model, the adhesion of cardiomyocytes to ECM is one of the most basic cell behaviors seen in the primary culture. When cardiomyocytes undergo some biological processes, especially apoptosis in this case, the elimination or formation of cell focal adhesion acts as side tracks of signaling pathways, leading to the weakening or strengthening of cell adhesion. In other words, the change in cell adhesion is cellular level response of cardiomyocytes to various stimuli, which makes the in situ monitoring of the cell adhesion available in providing instant information of the biological processes.

2. THEORY

An emerging sensor technology referred to as ECIS has been extended for monitoring the morphology, viability and environmental change for the adherent cells in which cells are assumed to behave essentially like insulating particles hindering current flow from the electrode into the bulk electrolyte [2]. ECIS is a non-invasive and sensitive detecting technique for cell adhesion which provides equivalent cell-substrate distance as the quantitative indicator in the advanced analysis [3]. However, in this analysis, the cell membrane impedance and the junctional resistance between adjacent cells have been provided by previous research on the specific commercialized cells, such as fibroblasts and endothelial cells. On the contrary, these parameters are unknown and various for our primary cells, cardiomyocyte, which makes the advanced ECIS analysis of cardiomyocytes unreliable. That invokes EIS, a powerful approach to the study of electrolyte- electrode interface, into the cell adhesion study.

As cardiomyocytes are cultured on electrodes, cell-related impedance (Z_c), which are obtained by calculating the impedance values with and without cardiomyocytes, can be considered as the combination of several elements (Figure 1a). Simplifying the model in Figure 1a, the quantitative indicator for cell adhesion is resistance of the thin medium layer between cardiomyocytes and laminin (R_t) (Figure 1b) which is determined by occupation of

978-0-9798064-0-7/μTAS2007/$20©2007CBMS

cell body to the thin medium layer. The following equation describes the relationship between the real and imaginary components of Z_c in a circle function of Nyquist plots.

$$\left(Z_{c,\mathrm{Re}} - R_t - \frac{R_c}{2}\right)^2 + Z_{c,\mathrm{Im}}^2 = \left(\frac{R_c}{2}\right)^2 \quad (1)$$

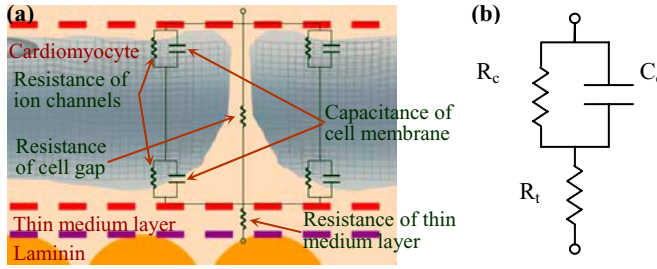

Figure 1: (a) Impedance components of cardiomyocyte layer. (b) Simplified equivalent circuit model of cell-related impedance (Z_c). C_c is the capacitance of cell layer caused by dielectric properties of cell membrane whereas R_c is the resistance across cell layer owing to the gap between cells and ion channels on individual cells. R_t is the resistance of thin medium layer between cells and substrate.

When cardiomyocytes are undergoing apoptosis, the activation of caspase family will chop off some essential protein including focal adhesion kinase (FAK). Inactivation of FAK is presumed to disrupt cell adhesion, leading to detachment of the apoptotic cells from their neighbors, leading the increase of cell-substrate distance which is to be reflected in the descent of R_t.

3. EXPERIMENTAL

Figure 2a shows the schematic diagram and photo of our impedance-sensing system. The configuration of our biosensors is shown in Figure 2b where the electrode material is gold and insulating layer is made of SiN_x. The testing electrodes were coated with laminin, an ECM protein, before injecting in the isolated cardiomyocytes of rats. The cardiomyocytes formed a confluent cell layer by adjusting the cell concentration. A home-made air-tight chamber was prepared for the hypoxia treatment to cardiomyocytes. After cultured for 3 days, cardiomyocytes were subjected to hypoxia in the air-tight chamber for 1 h.

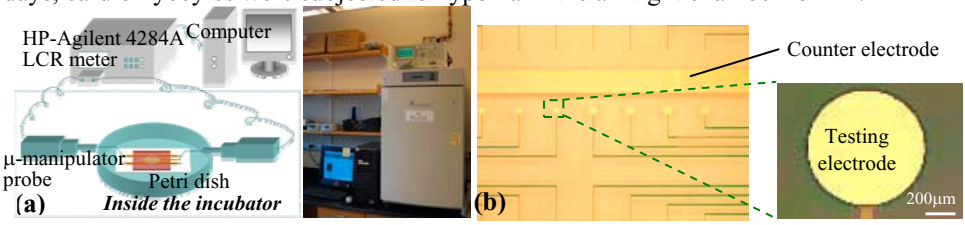

Figure 2. (a) Schematic diagram and photo of the impedance measurement system. The part surrounded by dash lines is inside the incubator (37 ºC, 5% CO_2). (b) Top view of the biosensing chip and Close view of the gold-coated testing electrode. A laminin (an ECM protein) layer was coated before cardiomyocytes were injected in.

The extraction of R_t was performed by dividing the impedance value obtained from ECIS to its real and imaginary parts and plotting it in a Nyquist plot. Nyquist plots recorded

in frequency scanning every 10 min were used in determining components of the cell-related impedance in a least square curve fitting to equivalent circuit model in Figure 1.

4. RESULTS AND DISCUSSION

Figure 3a shows the typical Nyquist plots of cardiomyocyte impedance which were then been processed and connected to form a time course (Figure 3b) showing the typical cell adhesion change at the beginning of primary culture in terms of the increasing of R_t. The change of R_t within 27 h after the hypoxia treatment is shown in a time course (Figure 4) with that of a control sample. R_t of the apoptotic samples dropped after a lag phase of about 3.3 h and slowly reaches its saturation while the control kept relative constant values.

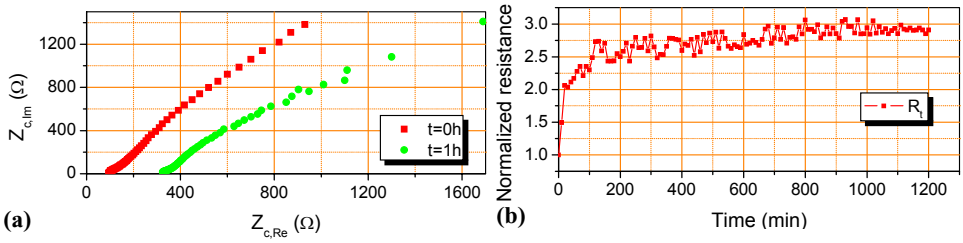

Figure 3. (a) Typical Nyquist plots of the cardiomyocyte layer impedance. (b) Normalized R_t changes in the first 20 h of cardiomyocyte culture. The initial R_t value is set as the normalizing unit.

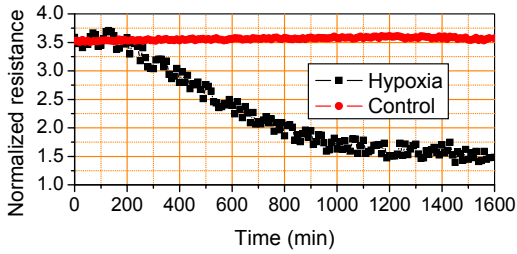

Figure 4. Normalized R_t change of hypoxia-treated sample and control in the first 27 h after hypoxia.

5. CONCLUSIONS

The R_t decrease of apoptotic sample indicates weakening of cardiomyocyte adhesion to ECM which matches to the biological hypothesis. Moreover, compared with the smooth curve of control, larger fluctuation of the apoptotic sample also shows larger micromotion of cardiomyocytes due to the change in cell adhesion.

ACKNOWLEDGEMENTS

This work is in part supported by NSF CAREER Award (No. 0239163) and NSF NER Award (No. 0609147).

REFERENCES

[1] A. Haunstetter and S. Izumo, *Apoptosis: Basic Mechanisms and Implications for Cardiovascular Disease,* Circulation Research, vol. 82, pp. 1111-1129, 1998.

[2] I. Giaever and C. R. Keese, *Monitoring fibroblast behavior in tissue culture with an applied electric field,* Proc Natl Acad Sci U S A, vol. 81, pp. 3761-4, Jun 1984.

[3] I. Giaever and C. R. Keese, *Micromotion of mammalian cells measured electrically,* Proc Natl Acad Sci U S A, vol. 88, pp. 7896-900, Sep 1 1991.

ENHANCED LOCOMOTION *CAENORHABDITIS ELEGANS* IN STRUCTURED MICROFLUIDIC ENVIRONMENTS

Hyejin Hwang[1], Seong-Won Nam[1], Fernando Martinez[2], Robert H. Austin[2], William S. Ryu[3], Sungsu Park[1]

[1] Division of Nano Sciences, Ewha Womans University, Seoul 120-750, Korea.
[2] Department of Physics, Princeton University, Princeton, NJ 08544, USA.
[3] Lewis-Sigler Institute for Integrative Genomics, Princeton University, Princeton, NJ 08544, USA.

ABSTRACT

Behavioral studies of *Caenorhabditis elegans* traditionally are done on the smooth surface of agar plates, but the natural habitat of *C. elegans* and other nematodes is the soil, a complex and structured environment. In order to investigate how worms move in complex environments, we have developed a technique to study *C. elegans* locomotion in structures fabricated from agar. A microfluidic structure containing an array of posts was designed and the movement of worms in these structures was studied by video microscopy. We discovered that worms are capable of a novel mode of locomotion - a combination of the fast oscillatory movements of swimming with the efficiency of crawling. When the wavelength of the worms matched the spatial scale of the post array, the microstructure directed and increased the swimming speed *C. elegans* ten-fold. However, we found that the swimming speed of mutants defective in mechanosensation (*mec-4*, *mec-10*) did not increase, which suggests this enhanced locomotion depends in part on mechanosensory feedback. The worms sense of touch is likely important in how *C. elegans* navigate complex, structured environments.

Keywords: C. elegans, soft lithography, micropattern, mechanosensation

1. INTRODUCTION

Determining patterns of movement has been important in the characterization of *C. elegans* behavior, including in the studies of chemotaxis, thermotaxis, and mechanosensation [1][2]. Traditionally these experiments have been done on the smooth surface of agar plates, where the general mechanics of locomotion is well understood [3]. On laboratory plates, worms typically move without slip, and so speed is equal to the wavelength (~ 1 mm) times the oscillation frequency (~ 0.5 Hz), which is about 0.1 mm/s. In the wild, worms live in the soil, and so are challenged with a more heterogeneous environment than the smooth agar plates of the laboratory. In order to investigate how worms move through complex and confined spaces - like the interstitial areas between soil particles - we introduced worms into microfluidic structures cast with agar. We found that this enhanced swimming on micro-pattern and a mutant defective in generating the correct pattern swam poorly in the microstructure.

2. EXPERIMENTAL

The PDMS (polydimethylsiloxane, Dow-Corning, Cortland, NY, USA) mold was prepared with a ratio of 1:10 (curing agent: PDMS) and 4% agar was poured onto PDMS

978-0-9798064-0-7/μTAS2007/$20©2007CBMS

mold. After 1-hour the agar was cut and lifted from the mold, and placed structure-side up onto a petri-dish. The Agar grid structure was soaked in distilled water and kept at 100% humidity until ready to use. Just before use, surface of structure filled with NGM buffer (50 mM NaCl, 1mM $CaCl_2$, 1mM $MgSO_4$, 25 mM KH_2PO_4).]. Movies of worms moving in the microstructures were taken using a stereomicroscope (MZ-APO; Leica Microsystems, Wetzlar, Germany) with an IEEE 1394 CMOS camera (Basler A601; Basler, Exton, PA).

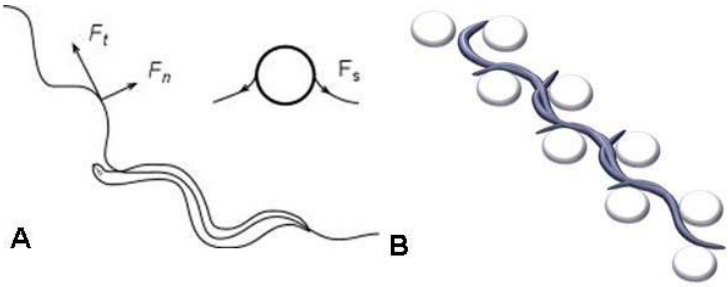

Fig.1. A simplified view of nematode locomotion. (A) on an agar plate. (B) In the grid microstructures.

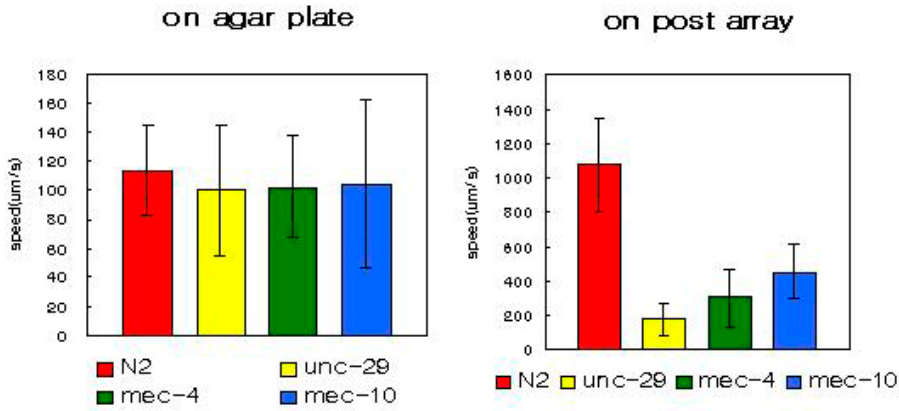

Fig.2. Motility of *C. elegans* strains on agar plates and in the grid microstructures.

3. RESULTS AND DISCUSSION

The structures consisted of a chamber (20 mm x 20 mm x 0.11 mm) containing circular posts (300 μm in dia.) in a square grid configuration with a range of center-to-center distances (350 to 550 μm). The chambers were filled with buffer, and single worms synchronized for size (900 ± 40 μm in length) were placed in the structures and tested for motility. In the microstructures with center-to-center post spacings of 425 to 475 μm, locomotion became strikingly more efficient and directed (Fig.1). Both *mec-4* and *mec-10* show no differences in movement on agar or in bulk fluids when compared to wild-type worms, yet they moved much more slowly in the post array (Fig.2).

4. CONCLUSIONS

Here we show that a simple our simple agar microstructures can differentiate mechanosensory mutants that show no locomotion phenotype under normal laboratory conditions. The failure of mechanosensory mutants to navigate the microstructures in the same manner as wild-type worms suggests that this pathway is important in how worms navigate the complicated structures of soils.

ACKNOWLEDGEMENTS

This research was equally supported by the Nano/Bioscience & Technology Program (M10536090002-05N3609-00210) of the Ministry of Science and Technology (MOST), the SRC program of the Korea Science and Engineering Foundation (KOSEF) through the Center for Intelligent Nano-Bio Materials at Ewha Womans University (Grant R11-2005-008-02003-0), and the Korean Research Foundation Grant (MOEHRD, Basic Research Promotion Fund) (KRF-2006- 005-J04002).

REFERENCES

[1] Bargmann, C. I. and Kaplan, J. M. (1998). Signal transduction in the *Caenorhabditis elegans* nervous system. Annu. Rev. Neurosci. 21, 279-308.

[2] Chalfie, M., Sulston, J. E., White, J. G., Southgate, E., Thomson, J. N. and Brenner, S. (1985). The neural circuit for touch sensitivity in *Caenorhabditis elegans*. J. Neurosci. 5, 956-64.

[3] Gray, J. and Lissmann, H. W. (1964). The Locomotion of Nematodes. J. Exp. Biol. 41, 135-54.

ESTIMATION OF MECHANICAL ROLE OF INTRACELLULAR STRUCTURES IN SMOOTH MUSCLE CELLS BY USING TRACTION FORCE MEASUREMENTS

Toshiro Ohashi[1], Shouji Nakamura[2], Naoya Sakamoto[1] and Masaaki Sato[1]
[1]*Graduate School of Engineering, Tohoku University, JAPAN*
[2]*Tohoku University, JAPAN (Present: PENTAX Corporation)*

ABSTRACT

Although several studies have estimated traction forces, little is known of how intracellular structures contribute to traction forces. In this study, microfabricated substrates were used to explore contribution of microtubules to traction forces. A triton cytoskeleton model (TC model) was introduced to remove mictotubules. Traction forces for TC model significantly decreased compared to control whereas nocodazole treatment induced an increase in traction forces. Myosin light chain phosphorylation was fluorescently observed both for TC model and the nocodazole-treated cells. It is possible that contribution of microtubules is not only as a force balance but also as a modulator of actomyosin mechanism.

Keywords: Traction forces, Micropillars, Force balance, Phosphorylation

1. INTRODUCTION

Although several studies have estimated cellular traction forces with implications for mechanical role of cytoskeletal structures using microfabrication techniques [1], little is still known of how intracellular structures, particularly cytoskeletal structures, contribute to cell mechanics. This study addresses a technique to explore mechanical role of intracellular structures by using a triton cytoskeleton model (TC model [2]) for traction force measurements. So far, our group [3] and other groups [4] have reported that disruption of microtubules induces an increase in traction forces. One possible idea to explain this change may be that tensional forces generated by actin filaments and intermediate filaments are balanced by microtubules that resist compression. In contrast, an alternative explanation is that disruption of microtubules may be attributable mainly to activation of the contractile machinery. However, this is still controversial. In this study, the TC model was introduced for further investigations of traction force measurements. Inhibition of signaling pathways of myosin light chain phosphorylation, possibly being induced by disruption of mictotubules, was also addressed.

2. MATERIALS AND METHODS

Smooth muscle cells were obtained from bovine thoracic aortas. Cells were seeded in tissue culture flasks with Dulbecco's modified Eagle medium (DMEM, Gibco, MD, USA) supplemented with 10% heat-inactivated fetal bovine serum (JRH Biosciences, KS, USA), penicillin and streptomycin (Gibco). Cultures were grown in a 37˚C humidified atmosphere of 95% air and 5% CO_2 gas. Cell populations from the 4th to 9th generation were studied.

A mold of silicon substrates with arrays of micropillars (3 μm in diameter, 10 μm in height, and 8 μm spacing) was fabricated using micromachining techniques (Figure 1), and

978-0-9798064-0-7/μTAS2007/$20©2007CBMS

polydimethylsiloxane (PDMS) was poured into it to produce a substrate membrane with micropillars. A scanning electron microscope (SEM) image of the mold is shown in Figure 2. Prior to experiments, cells were transfected with GFP-actin to visualize actin filament structures, and plated on the substrates. Cell spreading produces deflection of microposts, showing subcellular distribution of tractions forces. Deflection of microposts was measured from brightfield images with an image analysis technique using the public domain NIH Image software version 1.62 (National Institute of Health, MD, USA). Traction forces F were then determined using the simple equation $F=kx$, where k is spring constant and x the deflection of microposts. The spring constant was determined using a cross-calibration technique prior to experiments.

Cells were then treated with 10 μg/ml nocodazole for 15 min to disrupt microtubules. The TC model was prepared by treating cells with 0.125% Triton X-100 buffer for 1 min. In the TC model, microtubules, plasma membrane, and cytoplasm were removed while actin filaments and intermediate filaments were remained. For inhibition of Rho/Rho kinase (ROCK pathway), cells were treated with 20 μM Y27632 for 15 min prior to microtubules disruption.

3. RESUTLTS AND DISCUSSION

It was confirmed that actin filament networks were preserved whereas microtubule networks were disrupted for the TC model. Traction forces for the TC model significantly decreased compared to control (Figure 3). In contrast, traction forces significantly increased from 10.3 ± 2.5 nN to 13.3 ± 3.7 nN after treatment of nocodazole (Figure 4 for the comparison), which is well consistent with previous studies. From these results, it is supposed that not only cytoskeletal structures but also other cellular components such as cytoplasm should be involved in cell mechanics or the TC model could damage . Separate fluorescence studies showed that microtubules disruption induced myosin light chain phosphorylation. Exposure to Y27632 showed that traction forces decreased by 80% compared to control within 15 min and the following treatment with nocodazole showed only 40% recovery from the prior decreased forces. This result indicates that microtubules disassembly may modulate the actomyosin mechanism leading to the increase in traction forces, mainly through the ROCK pathway.

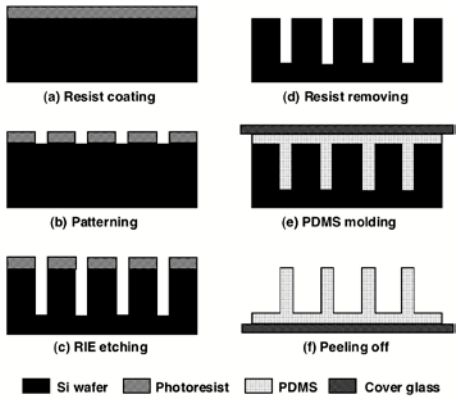

Figure 1. Fabrication process of PDMS substrate with arrays of micropillars.

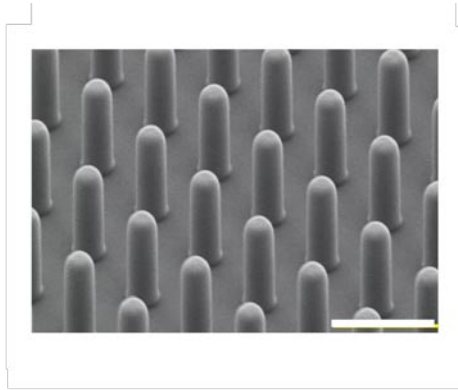

Figure 2. SEM image of the silicon mold with arrays of micropillars. Bar = 10 μm.

4. CONCLUSIONS

Microfabricated substrates with arrays of micropillars were used to estimate cellular traction forces of smooth muscle cells, particularly exploring contribution of microtubules to traction forces. It is indicated that contribution of microtubules is not only as a structural element involved in intracellular force balance but also as a modulator to activate actomyosin mechanism.

ACKNOWLEDGEMENTS

This work was supported financially in part by the Grants-in-Aid for Scientific Research (No. 18650119), the 21st Century Program "Future Medical Engineering Based on Bio-nanotechnology" and Grant-in-Aid for Scientific Research on Priority Areas "System Cell Engineering by Multi-scale Manipulation", by the Ministry of Education, Culture, Sports, Science and Technology (MEXT) in Japan.

REFERENCES

[1] J.L. Tan, J. Tien, D.M. Pirone, D.S. Gray, K. Bhadriaju, C.S. Chen, *Cells lying on a bed of microneedles: An approach to isolate mechanical force*, Proc Natl Acad Sci, Vol. 100, pp. 1484-1489, (2003).

[2] M. Tamada, M.P. Sheetz, Y. Sawada, *Activation of a signaling cascade by cytoskeleton stretch*, Dev. Cell, Vol. 7, pp. 709-718, (2004).

[3] T. Ohashi, J. Yamazaki, N. Kameda, and M. Sato, *Mechanical role of cytoskeletal structures in traction forces of smooth muscle cells using different configuration of micropillars*, Abstract of the 5th World Congress of Biomechanics, in CD-ROM, (2006).

[4] N. Wang, K. Naruse, D. Stamenovic, J.J. Fredberg, S.M. Mijailovich, I.M. Tolic-Norrelykke, T. Polte, R. Mannix, D.E. Ingber, *Mechanical behavior in living cells consistent with the tensegrity model*, Proc. Natl. Acad. Sci., Vol. 98, pp. 7765-7770 (2001).

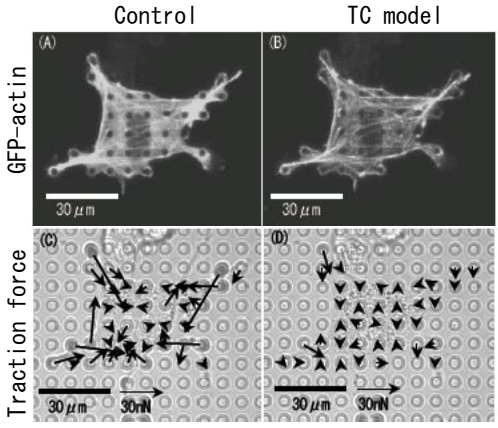

Figure 3. Fluorecsence images GFP-actin for control (A) and TC model (B). traction forces for control (C) and TC model (D).

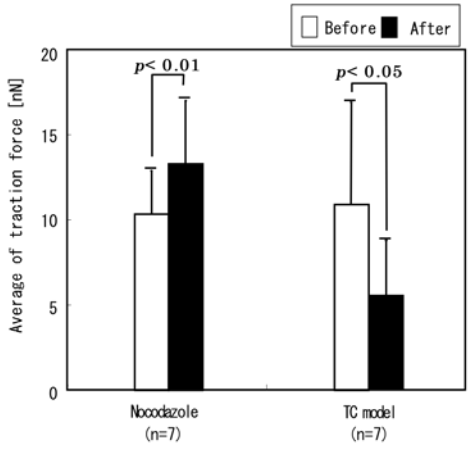

Figure 4. Change in average of traction forces of nocodazole-treated cells and TC model.

GLASS MICROCHIP-BASED BIOASSAY SYSTEM USING HUMAN ARTERIAL ENDOTHELIAL CELLS

Yo Tanaka[1], Yuji Kikukawa[1], Kae Sato[1], Yasuhiko Sugii[2] and Takehiko Kitamori[1]

[1] The University of Tokyo, JAPAN

[2] Kogakuin University, JAPAN

ABSTRACT

We have fabricated a culture and bioassay system using human arterial endothelial cells (HAECs) in a thermally fused-glass microchip which is chemically stable and favorable for optical detections. HAECs reached confluence within 4 days and responded to inflammatory cytokine, tumor necrosis facor-α (TNF-α) and attached to more leukocyte cell line, HL-60 cells than unstimulated HAECs.

Keywords: endothelial cell, leukocyte, vascular model, glass microchip

1. INTRODUCTION

ECs lining all blood vessels have various functions to contribute to the homeostasis of the circulatory system, and they are related to vascular diseases, such as atherosclerosis and thrombosis. By culturing ECs in a microchip, vascular models have been fabricated recently [1,2]. However, most of the microchips are made of polydimethylsiloxane (PDMS), and PDMS microchips would be difficult to be applied for our developed glass microchip-based cell analysis systems [3,4] in which all procedures for cell analysis including chemical reactions and Thermal Lens Microscope (TLM) detection [5] can be performed. This is mainly because TLM detection requires glass microchips' advantages such as transparency with flat surfaces, and transmitting visible and UV light. Here, we construct a glass microchip-based EC culture and bioassay system that could be combined with various analytical operations on one microchip [6].

2. EXPERIMENTAL

Firstly, to determine which cell adhesion protein is useful for attaching HAECs to the glass surface quickly, we measured the cell attachment rates to slide glasses coated with several cell adhesion proteins 2 h after seeding. Secondly, we cultured HAECs in a microchannel coated with the determined protein. Design of a microchannel and liquid introduction method are described in Figure 1.

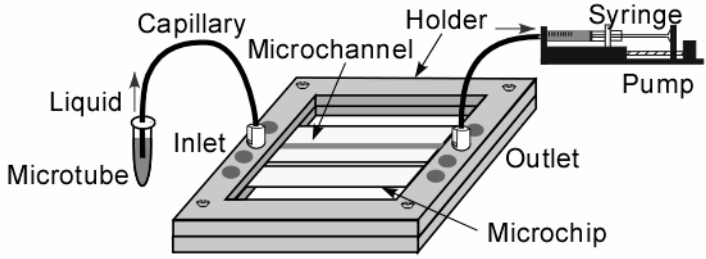

Figure 1. Liquid introduction method into a microchannel.

978-0-9798064-0-7/μTAS2007/$20©2007CBMS

After introducing HAECs, we observed cells periodically. Finally, to demonstrate that HAECs in a microchannel are useful for a leukocyte adhesion assay, we measured the adhesion number of fluorescently labeled leukocyte cell line, HL-60 cells to HAECs with and without recombinant TNF-α which is an inflammatory cytokine promoting leukocyte adhesion at inflammatory sites.

3. RESULTS AND DISCUSSION

From the cell attachment rate for several cell adhesive proteins (Figure 2), "poly-L-lysine + matrigel (coated with matrigel after coating with poly-L-lysine)" was found to have the largest cell attachment rate (94 %) among the six types of coating conditions.

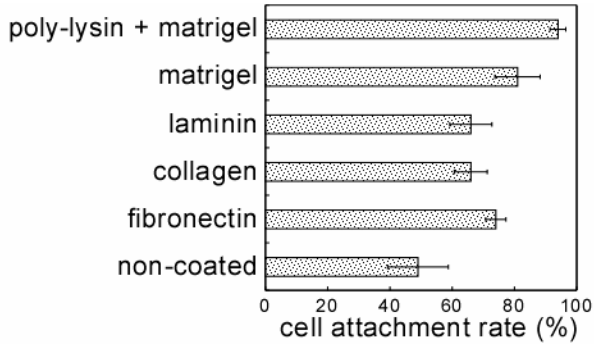

Figure 2. Cell attachment rates 2 h after seeding for 6 coating conditions.

After culturing HAECs in a microchannel, the number of HAECs increased continuously and became confluent within 96 h as shown in Figure 3a. It is apparent from a HAECs' nuclei stained fluorescent image (Figure 3b) that the HAECs attached to the microchannel walls confluently and uniformly including on the microchannel edges. From HAECs' mitochondria stained fluorescent image (Figure 3c), it was found that HAECs were surviving because only living cells emit fluorescence.

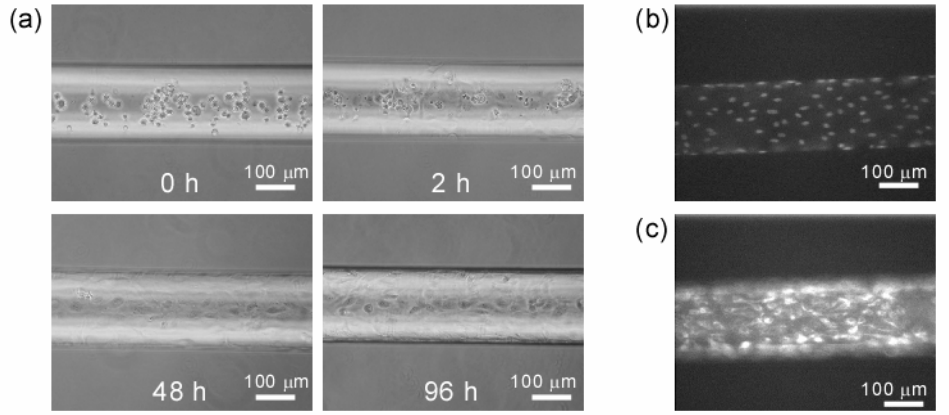

Figure 3. Actual photos of HAECs cultured in a glass microchannel. (a) Phase contrast images at 0 h (just after introducing cells), 2h (just before pumping medium), 48 h and 96 h after introducing cells. (b),(c) Fluorescent images of nuclei (b) and mitochondria (c) stained HAECs after culturing them for 4 days in a microchannel.

Figure 4 shows the results of the leukocyte adhesion assay. The cell concentration in TNF-α stimulated HAECs cultured microchannel is higher than that in unstimulated HAECs cultured or blank microchannel. This is the first demonstration of a confluent HAEC culture and bioassay in a thermally fused-glass microchip. As example of the application, it can be applied for monitoring of the time course of EC-derived nitric oxide (NO) release proportional to shear stress by combining with our previously developed ultrasensitive cell-derived NO detection system using chemical reactions and TLM [3]. It also could be applied to fabricate a component of a cardiovascular circulatory system micro-model.

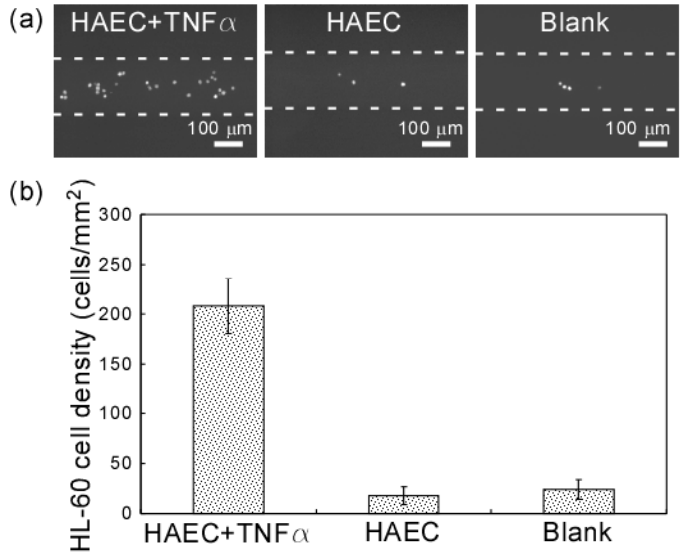

Figure 4. Results of leukocyte adhesion assay. (a) Fluorescent images of the three types of microchannels (HAEC cultured and TNF-α stimulated, HAEC cultured, blank) after introduction and washing of HL-60 cells. (b) The density of attached HL-60 cells to each microchannel. Values are means ± S.D.; n = 5.

REFERENCES

[1] J. W. Song, W. Gu, N. Futai, K. A. Warner, J. E. Nor, and S. Takayama, Anal. Chem., 77, 3993-3999 (2005).

[2] P. Mulder, S. Koster, H. J. van der Linden, G. Molema, and E. Verpoorte, Proc. Micro Total Analysis Systems 2005, 1383-1385. (2005).

[3] M. Goto, K. Sato, A. Murakami, M. Tokeshi, and T. Kitamori, Anal. Chem., 77, 2125-2131 (2005)

[4] E. Tamaki, K. Sato, M. Tokeshi, K. Sato, M. Aihara, and T. Kitamori, Anal. Chem., 74, 1560-1564 (2002).

[5] T. Kitamori, M. Tokeshi, A. Hibara, and K. Sato, Anal. Chem., 76, 52A-60A (2004).

[6] Y. Tanaka, Y. Kikukawa, K. Sato, Y. Sugii, and T. Kitamori, Anal. Sci., 23, 261-266 (2007).

HEAT-POLISHING INTEGRATED GLASS PATCH CAPILLARIES FOR ENHANCED GIGASEALS

Wee-Liat Ong, Lian-Wee Luo, Agarwal Ajay, Nagarajan Ranganathan, Kum-Cheong Tang, and Levent Yobas

Institute of Microelectronics, 11 Science Park Road, S117685, SINGAPORE

Corresponding Author: leventy@ime.a-star.edu.sg

ABSTRACT

We improved on a previous method of forming fully-round integrated patch capillaries in a glass layer for lateral patch clamping. Surface finish of the improved devices was clearly much smoother and their capacitive current was also drastically reduced. We tested these devices with rat basophilic leukaemia (RBL-1) cells and obtained 34 gigaseals out of 59 attempts. Many of the gigaseals were stable enough for whole-cell current recordings.

Keywords: patch clamp, glass, round, gigaseal

1. INTRODUCTION

In an effort to provide a high-throughput ion channel assay, researchers have been developing chips that can automate patch-clamping which is the "gold" standard for studying cellular ion channels but at the same time labor intensive and low throughput technique [1], [2]. Among the proposed concepts, lateral architecture uses single side of a chip substrate and thus may lead to simpler microfluidic integration and packaging [3]. Nevertheless, realizing a lateral aperture which mimics the round opening of a glass patch pipette by applying planar fabrication methods is non-trivial. Moving forward, researchers have built lateral architectures based on rectangular and semi-circular apertures that are replica molded in elastomer poly(dimethylsiloxane) (PDMS) [3]. These devices mostly produced substandard seals.

Our group recently demonstrated a method of forming fully-round integrated patch capillaries in glass layer for lateral patch clamping [4]. This method exploits a well-known problem in Microelectronics identified by void (keyhole) formation in isolation trenches due to incomplete filling of dielectric layer. In our method, we turn such void into a round patch capillary by choosing dielectric layer as phosphosilicate glass (PSG) and then subjecting it to thermal reflow. In this paper, we describe improvements made on the above process to achieve a thicker insulation layer and smoother surface finish on the device to address the challenges of large capacitive currents that are difficult to compensate and poor GΩ seal success rate (<5% GΩ) seen in our earlier attempts [4].

2. EXPERIMENTAL

We modified the process to allow for deposition of an extra layer of PSG insulation and a final step of heat polishing glass surface without clogging the aperture (Figure 1). This was achieved by dry etching about 20 μm deep into the exposed silicon to raise the apertures and 1 min buffered oxide etching to enlarge them. Directly on these structures, an additional layer of 3 μm PSG was uniformly deposited and annealed at 1150 ºC for 30 mins.

978-0-9798064-0-7/μTAS2007/$20©2007CBMS

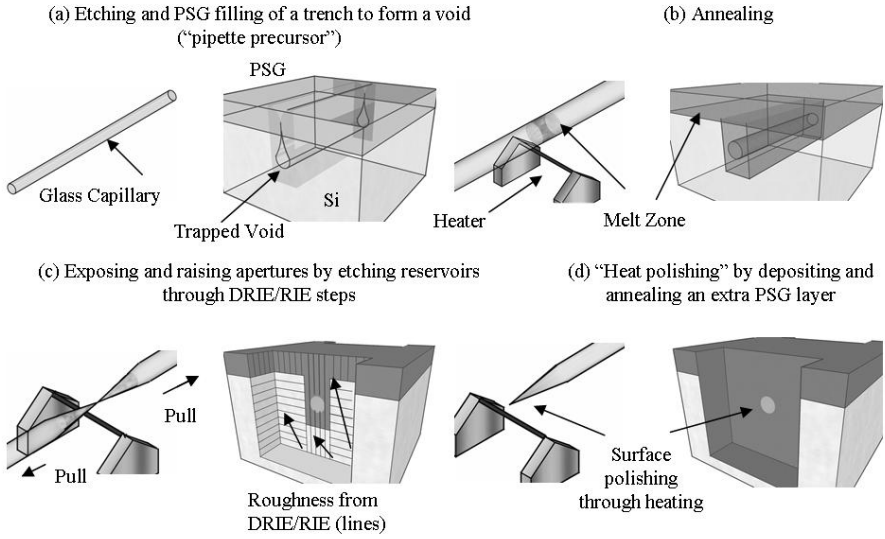

Figure 1. Major fabrication steps comparing our approach to heat-pulling conventional patch pipettes.

3. RESULTS AND DISCUSSION

Figure 2 compares typical devices obtained from the original and modified processes in terms of their surface finish and electrical characteristics. Surface finish of the improved device is clearly much smoother with no protrusions threatening cells. The capacitive currents are also drastically reduced to levels that can be compensated. As can be seen, the additional fabrication steps did not seal off the aperture which remained circular within a diameter of 1-2µm ideal for patch clamping.

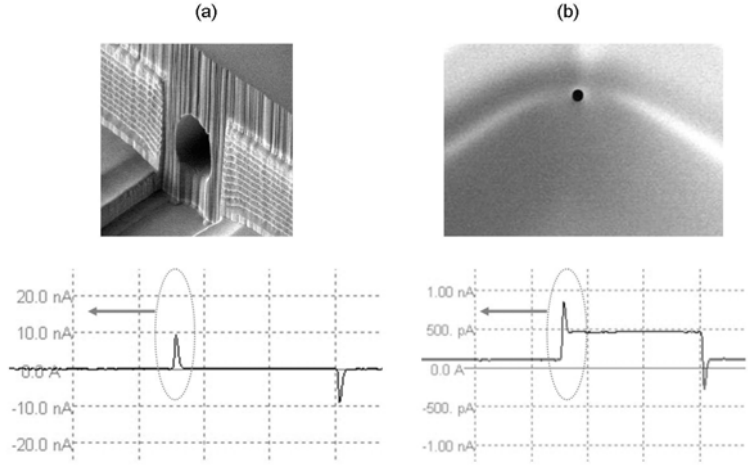

Figure 2. Comparison of the devices obtained by (a) the original and (b) the modified processes. Electron microscope images (above) and electrical current recordings across the devices filled with buffer solution (18mS/cm) in response to test pulses (5mV, 5ms) across 50µm long capillaries.

After capping them with layer of PDMS, we tested heat-polished devices using suspended rat basophilic leukaemia (RBL-1) cells for seal quality assessment and whole-cell recording. Out of 59 heat-polished devices that were able to capture single cell, 34 exceeded 1 GΩ seal resistance (56%) while the remaining 25 returned <250 MΩ (Figure 3). We found many of the gigaseals stable enough to be able to record whole-cell currents (Figure 4). The results indicate significant improvement over those from earlier devices.

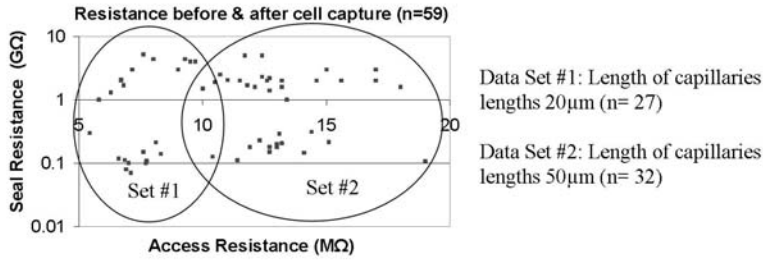

Figure 3. Test results of the modified patch apertures: Access resistance (without a cell) versus seal resistance after capturing a single RBL-1 cell.

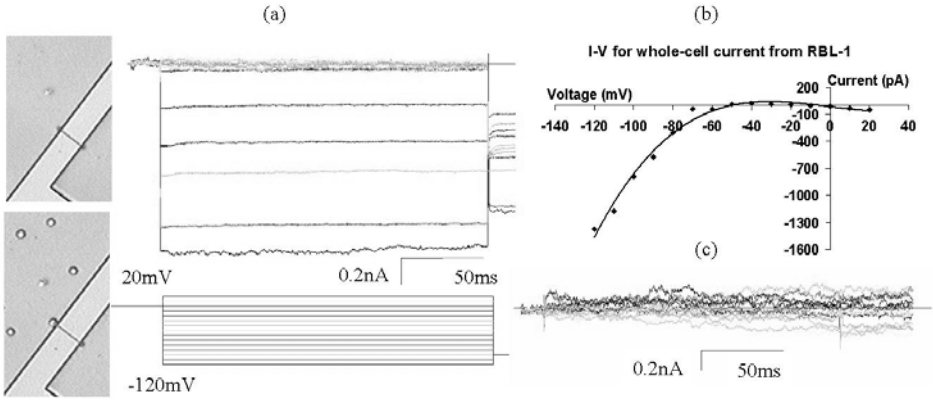

Figure 4. (a) A set of whole-cell currents recorded from RBL-1 cell using our device (b) the corresponding I-V curve confirming the behavior of inward-rectifying voltage-gated potassium channels (c) successful suppression of whole-cell currents after the application of known channel blocker (CsCl).

REFERENCES

[1] B. Sakmann, and E. Neher (Eds). *Single Channel Recording*, 2nd Ed., New York: Plenum, (1995)

[2] C. Schmidt, M. Mayer, and H. Vogel, "A chip-based biosensor for the functional analysis of single ion channels," *Angew Chem. Int. Ed Eng*,39, pp. 3137–3140, (2000).

[3] J. Seo, C. Ionescu-Zanetti, R. Lai, and L.P. Lee, "Integrated multiple patch-clamp array chip via lateral cell trapping junctions," *Appl. Phys. Lett.*, 84(11), pp.1973-1975, (2004).

[4] W.L. Ong, J.S. Kee, A. Agarwal,, R. Nagarajan, K.C. Tang, and L. Yobas, "Buried microfluidic channel for integrated patch-clamping assay," *Appl. Phys. Lett.,* 89, 093902 (2006).

HIGH-THROUGHPUT ENZYMATIC ASSAYS OF WHOLE CELLS ENCAPSULATED IN MICRODROPLETS

Luis F. Olguin[1], Ansgar Huebner[1], Daniel Bratton[1], Graeme Whyte[1], Wilhelm Huck[1], Chris Abell[1] and Florian Hollfelder[2]

[1]Department of Chemistry, University of Cambridge, UK

[2]Department of Biochemistry, University of Cambridge, UK

ABSTRACT

We describe the design and testing of a device that permits the quantification of alkaline phosphate activity of encapsulated *E. coli* cells in aqueous microdroplets. The system enables us to do this in a high-throughput manner.

Keywords: Droplets, cells, enzyme, high-throughput

1. INTRODUCTION

Microfluidic techniques have been applied successfully to analyze and quantify the dynamics of gene expression on high-content single cell assays [1, 2]. However, to study single cell enzymatic activities it is necessary to enclose the cells to prevent the diffusion of substrates and products between them, as it is observed in continuous flow microfluidics.

Different methods have been used in microfluidics to isolate cells and quantify one of their enzymatic activities. Cai *et al*. constructed a device in which a series of valves allow specific channels to be closed to create microchambers with single *E. coli* cells trapped inside [3]. Chiu D. T. *et al*. used optical trapping to manipulate single mammalian cells in a device that produces droplets in such a way that the cells are enclosed within a droplet during the droplet formation process [4]. However, these methods were not designed to suit high-throughput analysis (i.e. <104 cells). Recently, our research group has used droplet microfluidics technology to encapsulate and quantify *E. coli* cells in a high-throughput manner [5]. In this submission, we have extended this application to measure the enzymatic activities of the encapsulated cells.

2. EXPERIMENTAL

The device was constructed using soft lithographic methods [6]. The microchannels measure 75 μM in height and 75 μM in diameter. We use mineral oil with span-80 (2%) as the continuous phase and 100 mM TRIS buffer pH 8.0 with 100 mM NaCl as the aqueous phase. *E. coli* cells harbouring a plasmid for overexpression of alkaline phosphatase were grown and induced overnight outside the device. They were then centrifuged and washed to remove extra cellular enzyme and were loaded in one of the microchannels. The fluoregenic substrate 3-O-methylfluorescein phosphate (OMFP) was used to detect the alkaline phosphatase activity using an Ar^+ laser at 488 nm and a photomultiplier (PMT).

3. RESULTS AND DISCUSSION

To measure the enzymatic activity of cells inside microdroplets we designed a three-inlet device that enables us to dilute cells on-chip overexpressing alkaline phosphatase with buffer and the OMFP substrate (Figure 1A). This aqueous mixture was encapsulated in homogenous droplets using a flow-focusing device. The droplets then flowed through an

978-0-9798064-0-7/μTAS2007/$20©2007CBMS

extended channel where we detected the increase in the fluorescence intensity at various points. The analysis of the content of each individual droplet was done by recording the data trace and analyzing the height of each peak with Labview software (Figure 1B). With this information, we generated time courses of the first 40 seconds of the reaction averaging the values of more than 1,000 droplets for each time point (Figure 2A).

The use of three aqueous inlet channels allowed us to change the substrate concentration by dilution while keeping the amount of cells constant. We used this feature to follow the reaction at different initial substrate concentrations, and found that the results showed saturation kinetics similar to those observed in bulk solution (Figure 2B). To further characterize the dynamic range of our system, we measure the activity of cells expressing an alkaline phosphatase mutant (R166S) with 30-fold less activity (Figure 3).

Our aim is to decrease the number of cells by dilution on-chip [5] to arrive at single cell measurements, but at the moment this is out of reach of our detection limit. The devices and methods described in this work could be used in the future to analyze thousands of mutants in a short time, allowing screening of large populations of single cells, which is a requirement in diverse fields such as directed evolution and quantitative dynamics of gene expression [6, 7].

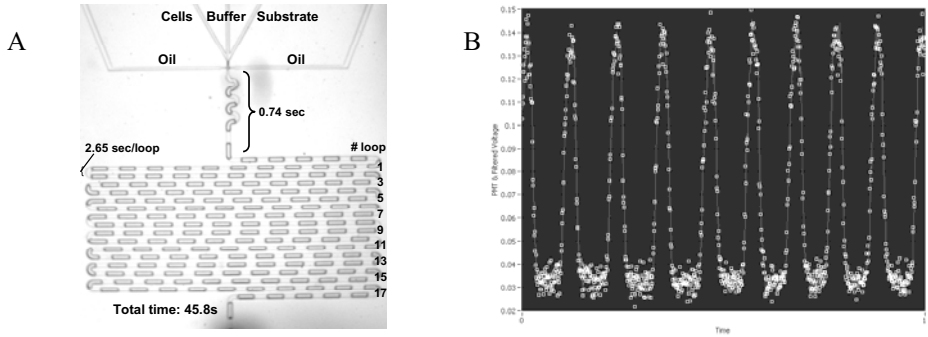

Figure 1. A) Image of the PDMS device used to generate droplets containing cells and the fluorogenic substrate. B) Data trace of raw signal of one second.

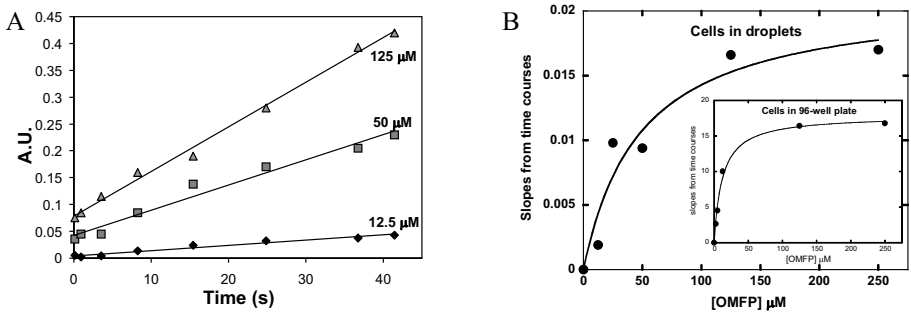

Figure 2. A) Time course of the hydrolysis reaction of OMFP by cells expressing alkaline phosphatase in microdroplets at three different concentrations. B). Activity of cells at different substrate concentration. For comparison the results of the same experiment but made in a 96-well plate are shown in the insert.

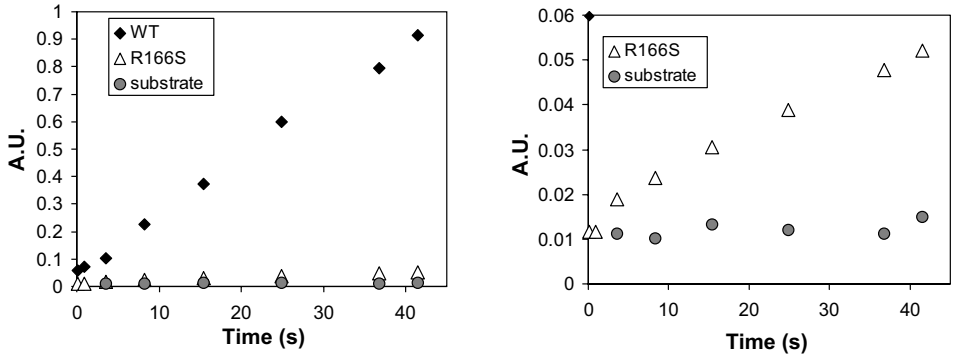

Figure 3. Hydrolysis of OMFP in microdroplets by cells expressing wild-type alkaline phosphatase or the 30-fold less active mutant R166S.

4. CONCLUSIONS

We have designed and demonstrated a microfluidic device capable of encapsulating *E. coli* cells and fluorogenic substrates in homogenous droplets. By using a laser and a PMT, the specific activity of alkaline phosphatase inside each droplet was measured in high-throughput manner. In the future, with a more sensitive setup, we hope to determine the enzymatic activity of individual encapsulated cells.

REFERENCES

[1] El-Ali, J., P. K. Sorger, *et al.*, *Cells on chip*s, Nature 442(7101): 403-11, (2006).
[2] King, K. R., S. Wang, *et al.*, *A high-throughput microfluidic real-time gene expression living cell array,* Lab Chip 7(1): 77-85, (2007).
[3] Cai, L., N. Friedman, *et al*., *Stochastic protein expression in individual cells at the single molecule level,* Nature 440(7082): 358-62, (2006).
[4] He, M., J. S. Edgar, *et al*., *Selective encapsulation of single cells and subcellular organelles into picoliter- and femtoliter-volume droplets*. Anal Chem 77(6): 1539-44, (2005).
[5] Huebner, A., M. Srisa-Art, *et al*., *Quantitative detection of protein expression in single cells using droplet microfluidics*. Chem Commun (Camb)(12): 1218-20, (2007).
[6] McDonald, J. C., Duffy, D. C. *et al*., *Fabrication of microfluidic systems in poly(dimethylsiloxane*), Electrophoresis, 21, 27-40, (2000).
[7] Griffiths, A. D. and D. S. Tawfik, *Miniaturising the laboratory in emulsion droplets.* Trends Biotechnol 24(9): 395-402, (2006).
[8] Longo, D. and J. Hasty, *Dynamics of single-cell gene expression*. Mol Syst Biol 2: 64, (2006).

HIGH-THROUGHPUT μFLUIDIC CELLULAR ASSAYS

Jay Warrick[1], Keil Regehr[1], Maribella Domenech[1], Ivar Meyvantsson[1], Caroline Wagner[2], Caroline Alexander[2], David J. Beebe[1]

[1]Department of Biomedical Engineering, University of Wisconsin – Madison, USA
[2]Department of Oncology, University of Wisconsin – Madison, USA

ABSTRACT

We present results of three cell culture experiments that show the basic functionalities and utility of a high-throughput microfluidic platform for cellular assays. The platform utilizes a method of fluid delivery termed passive pumping. The experiments show the ability of the platform to support both manual and automated cellular assays with low reagent use and large sample sizes. Future goals with the platform are to investigate more extensive factorial experimental designs and design assays for cell migration and cellular differentiation.

Keywords: Co-culture, high-throughput, growth factor, microfluidic

1. INTRODUCTION

Cell signaling via soluble factors play a critical role in regulation of cell behavior and the way we treat disease. Drugs diffuse their way to locations for transport or directly to their active site. Soluble signals are implicated in numerous critical cellular behaviors such as proliferation, differentiation, cell survival, as well as maintenance and activations of stem cells within their niche and cancer progression. Despite the importance of soluble signals, current technology is not well suited to soluble factor study. Macro-scale technology often puts cells into a highly convective environment that can sweep soluble signals away from their targets, minimizing local concentrations of important factors. Microfluidics addresses this issue by reducing the scale of the local environment to microns. The cellular microenvironment can be controlled to minimize convection and allow diffusion to establish significant concentrations and gradients for more natural cell-cell signaling.

However, in order to study soluble factor effects using microfluidics, an accurate method is needed for delivery of the factors and patterning of cells. We use a method of surface-tension based pumping termed passive-pumping, to introduce cells and soluble factors to the microchannels[1]. This method introduces fluid to microchannels using only a pipette. Thus, we were able to automate the experiments using pipetting robots. The method of fluid delivery proves to be ten times less sensitive to errors in dispense-volume compared to wells or dishes, which are the current standard in cell assays[2]. Further, simple patterning of cells is accomplished using a method we term fixed-volume loading. When a very small volume of fluid containing cells is introduced to a microchannel port, the flow will stop shortly after entering the port, creating a local seeding of cells for culture. Cell patterning is then achieved via strategic placement of the ports and small volumes of cells. Not only, can cells be seeded and treated with factors, the cells can be stained in the microchannels providing a nearly unlimited range of readouts. We present results of three cell culture experiments that show some of the basic functionalities of the platform.

2. EXPERIMENTAL

SU8 masters molds were made using standard soft lithography procedures and devices were cast using polydimethylsiloxane (Sylgard 184, Dow Corning).

978-0-9798064-0-7/μTAS2007/$20©2007CBMS

3. RESULTS AND DISCUSSION

Tri-Culture Experiment: In passive pumping, liquid droplets with a small radius of curvature are driven to droplets with a larger radius of curvature due to surface tension-based forces. Small volumes of cells are seeded into the device shown in Fig 1 using this method. Each of the three lobes of the device contains a group cells held in close proximity but in non-contact with the other lobes. Cells are kept from contact by limiting the volume of cell suspension that is allowed to flow into each lobe towards the output (labeled in Fig 1A). Live and dead cell staining was quantified in an automated fashion using image processing. Algorithms were created to locate the channels, mask non-channel regions, and integrate intensity for each chamber and for each fluorescent probe.

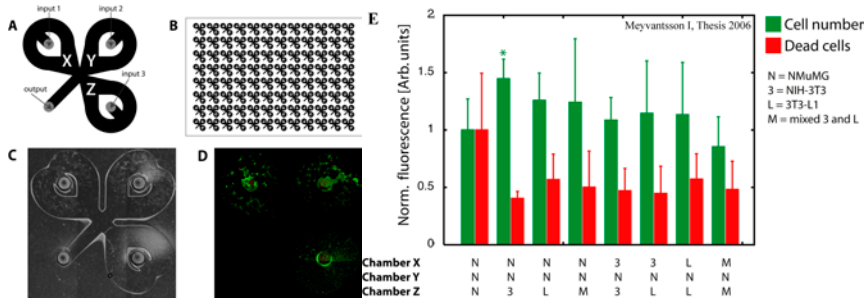

Figure 1. Three chamber co-culture structure. A) Schematic representation of structure with arrows indicating three inputs and a common output, and labels X, Y and Z indicating the three cell culture chambers. B) 96 structures in array format with port locations according to microtiter plate standards. C) Phase contrast image of cells at day 3, NMuMG, NMuMG and 3T3-L1 cells in chambers X, Y and Z, respectively. D) Same structure with cells stained with nuclear (green) and dead cell (red) dyes. E) Total cell quantity and dead cell quantity in chamber Y (NMuMG cells) at day 3. Two-sided T-test was used to test the null hypothesis of equal means (* = $p < 0.05$).

Penta-Culture: This experiment is an expansion of the previous to include up to 5 chambers instead of 3. A slightly different method of determining cell number is used here to obtain results. An Odyssey scanner (Licor - Lincoln Nebraska) was used to scan for Syto 60 stained cells (NMuMG and FVB) in the penta-culture device. Cells were seeded manually using passive pumping and cultured for 24 hours. The cells were stained with Syto-60 and 5 chambers in the array of devices were chosen for their range of intensities. Cell number versus intensity was plotted to determine if the scanning technique is a viable one for determining cell proliferation in a high-throughput format. The high correlation suggests good sensitivity and linearity (see Fig 2).

Growth Factor Effects: Two growth factors were tested for there effects on HC11 proliferation compared to standard culture. The standard media consists of RPMI with 10% FBS, 10 µg/mL of insulin, and 10 ng/mL of EGF. Standard media was used on all cells from time 0 hrs to time 24 hrs. The cells were treated at 24 hours with RPMI with 2% FBS, 10 µg/mL of insulin, and either 100 ng/mL of EGF, 50 ng/mL of FGF, or 10 ng/mL of EGF (control). After treatment the cells were incubated for another 24 hrs. Confluency was determined using an image processing technique where areas covered with cells are colored

white, and other areas colored black. Error propagation was used to determine error bars based on a single standard error on the mean of the confluency.

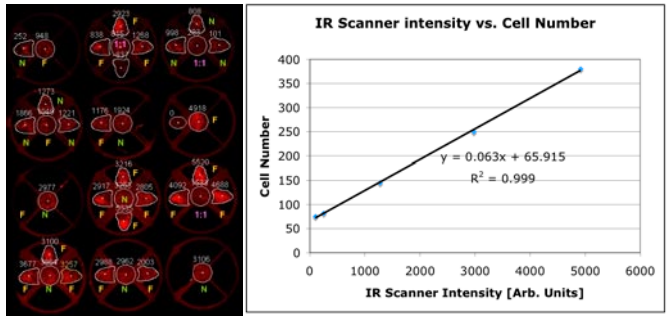

Figure 2. Multiple versions of the Pent-Culture device seeded with NMuMG and FVB cells. 5 chambers showing a range of intensities were chosen and the number of cells counted. The correlation between intensity and cell number is plotted showing that this method can provide an accurate method of determining cell number and proliferation.

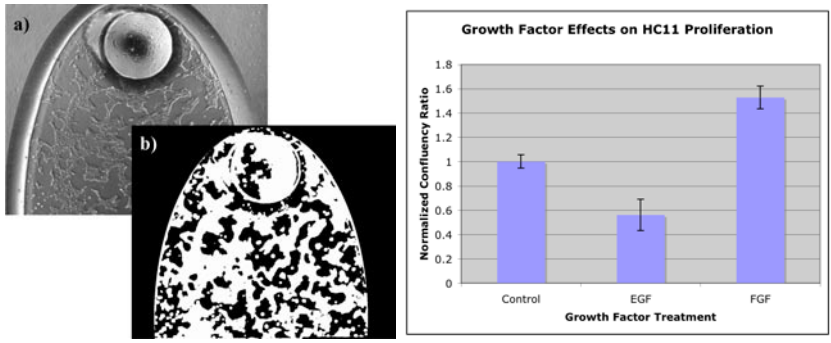

Figure 3. Growth factor effects on HC11 cell proliferation. a) Phase image of a channel. b) Image processed to obtain confluency. Right) confluency at 48 hours over confluency at 24 hours normalized to the ratio obtained for the control group.

4. CONCLUSIONS

This work demonstrates the ability of the platform to perform automated cellular assays working towards more extensive factorial experimental designs. Factorial design will help to elucidate the cross-talk between soluble signaling pathways that effect cell behavior. This platform helps to achieve the necessary number of samples required of factorial experiments yet with very efficient use of expensive reagents and micro-scale control of cell patterning and soluble factor delivery.

ACKNOWLEDGEMENTS

We thank the Army Breast Cancer Research Program (W81XWH-04-1-0572) & National Institutes of Health (K25 CA104162).

REFERENCES

[1] Walker, G. M. & Beebe, D. J. (2002) *Lab Chip* **2,** 131-134.
[2] Warrick, Meyvantsson, Ju, & Beebe, D.J. (2007) *Lab Chip* **3**, 316-321.

MAGNETOPHORETIC TRAPPING OF MICROPARTICLES

Hichem Chetouani[1,2], Christian Jeandey[1], Vincent Haguet[1], Franąois Chatelain[1], Gilbert Reyne[2]

[1]*Commissariat à l'Energie Atomique (CEA), Grenoble, FRANCE*

[2]*Laboratoire de Génie Electrique de Grenoble, INPG-UJF-CNRS, Saint-Martin-d'Hères, FRANCE*

ABSTRACT

On-chip passive contactless magnetophoresis was produced at both the millimeter and micrometer scales by using permanent magnets. Linear magnetic wells were manufactured to achieve stable magnetic trapping and translation of diamagnetic and paramagnetic microbeads in liquids. The magnetophoretic capture and alignment of cells was also demonstrated. A very efficient restoring force maintains the levitating particles inside the magnetic wells. This technology may appear useful for contactless particle handling on a chip.

Keywords: magnetophoresis, levitation, permanent magnet, microparticle, cell

1. INTRODUCTION

We demonstrated in 2006 the possibility to trap unlabelled 3µm-large latex beads within punctual magnetic wells produced by permanent micro-magnets [1]. Magnetophoresis (magnetic force due to an inhomogeneous magnetic field) allows contactless and passive particle handling in microgravity conditions. The microparticles are trapped and move in a liquid in the situation of magnetic levitation. No magnetic labelling of the particles is required: magnetophoresis applies directly upon diamagnetic and paramagnetic particles by adjusting the magnetic susceptibility of the liquid. This new manipulation technique in microgravity conditions could find various applications such as particle trapping, guiding and arraying, protein crystal growth or cell analysis. For instance, at the cellular level, weightlessness is known to have an effect on gene expression and microtubule organisation.

This paper shows magnetophoretic trapping and motion of diamagnetic and paramagnetic microbeads as well as cells in appropriate media. A microarray of permanent magnets was developed to provide linear magnetic traps with a restoring force having a high stiffness constant. As a result, the particles are efficiently maintained inside the magnetic traps. The confined particles can align and move along the grooves between the permanent magnets.

2. FABRICATION OF PERMANENT MAGNETS

Linear magnetic wells were achieved by two techniques which provided similar results concerning the magnetic trapping of particles. In the first technique, large linear traps were realized by electro-discharge micromachining of grooves in bulk planar NdFeB permanent magnets. The resulting devices are magnetic substrates having centimeter-long and ~150µm-wide grooves and a vertical magnetization direction.

Micron-scale magnet arrays were then produced by using microfabrication technology. After a deep etching of silicon wafers by ICP-RIE, permanent magnet microarrays were

978-0-9798064-0-7/µTAS2007/$20©2007CBMS

fabricated collectively by sputtering deposition of thick NdFeB layer (Fig. 1). Several NdFeB thicknesses from 12 µm to 60 µm were successfully deposited onto the silicon microstructures. Finally, the magnet microarrays were magnetised vertically (throughout the plane). The resulting micromagnets have a residual magnetisation of ~1.2 T [2].

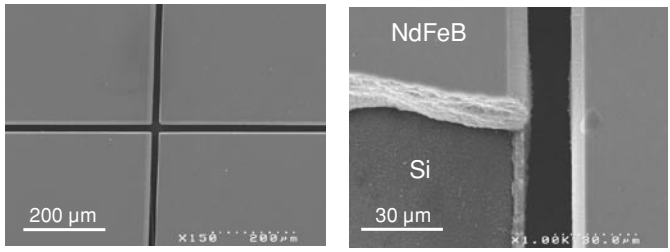

Fig. 1. SEM views of ~30µm-thick NdFeB micromagnets.

3. EXPERIMENTAL RESULTS

Capture of (diamagnetic) cells in the magnetic grooves was investigated using the magnet microarrays (Fig. 2). The chosen medium was Phosphate Buffer Saline (PBS) whose volume magnetic susceptibility of -8.95×10^{-6} was enhanced to $+4.8 \times 10^{-5}$ by adding 0.17 M Gd-DOTA in order to achieve magnetophoretic trapping of cells while maintaining biocompatible conditions. Gd-DOTA is a contrast agent commonly used in magnetic resonance imaging (MRI). Proliferation of Retinal Pigmented Epithelium (RPE1) human cells during 72 h in Gd-DOTA was verified in a separate experiment. The Figure 2 shows an alignment of RPE1 cells and a S2 cell extracted from drosophila magnetically trapped within 30µm-wide grooves. Displacement of the cells levitating along the linear wells was also observed.

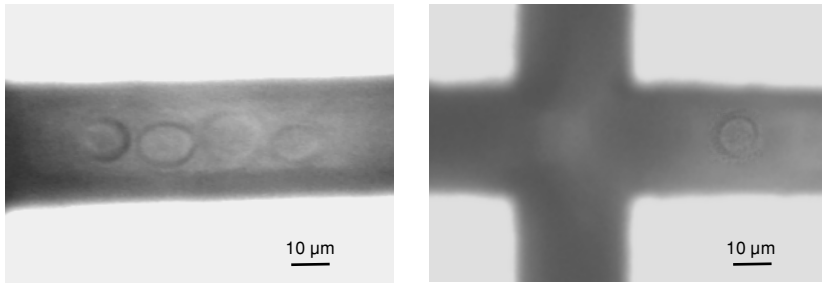

Fig. 2. Alignment of RPE1 cells (left) and a S2 cell from drosophila (right) levitating between permanent micromagnets.

The possibility of contactless trapping of paramagnetic microparticles by magnetophoresis was also demonstrated. The slightly paramagnetic feature of 9-13µm hollow glass spheres was measured at $+2.2 \times 10^{-7}$ with a Superconducting QUantum Interference Device (SQUID). The susceptibility contrast between the particles and the aqueous medium was increased by addition of 0.17 M Gd-DOTA in order to amplify the magnetophoretic effect on the particles. The Figure 3 shows a group of 3 glass microbeads trapped and moving in a linear magnetic well between the micromagnets. During the

experiments, the displacement of the beads within the grooves was always observed from right to left, which is likely due to a gravitational effect onto a slightly tilted device. This unidirectional mode of displacement may appear helpful to perform passive contactless translation of levitating bodies.

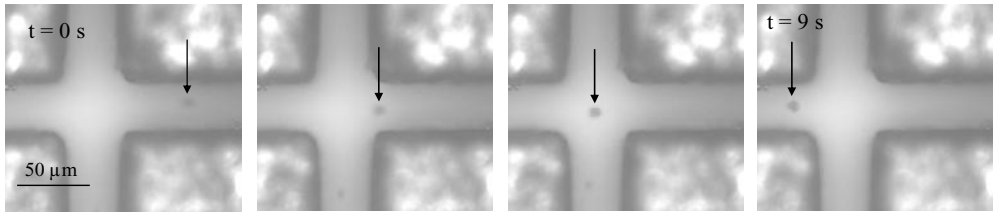

Fig. 3. A group of three paramagnetic glass microbeads moving along a linear magnetic well between micro-magnets.

The efficiency of the magnetic trapping was examined using the 9-13µm hollow glass beads and the micromachined magnetic substrate (Fig. 4). The glass microbeads suspended in a medium similar to the one in Fig. 3, were deposited randomly above the permanent magnet with a pipette. The linear magnetic wells were materialised by using a high density of glass beads, forming "white clouds" within the grooves. The glass beads gathered inside the magnetic wells in less than one minute. During the experiment, the magnet substrate was rapidly displaced in order to investigate the stability of the magnetic traps. The particle clouds oscillate around their equilibrium position and are rapidly damped, and then return to their initial position within few seconds. We thus consider the magnetic wells produced by this magnet as very efficient.

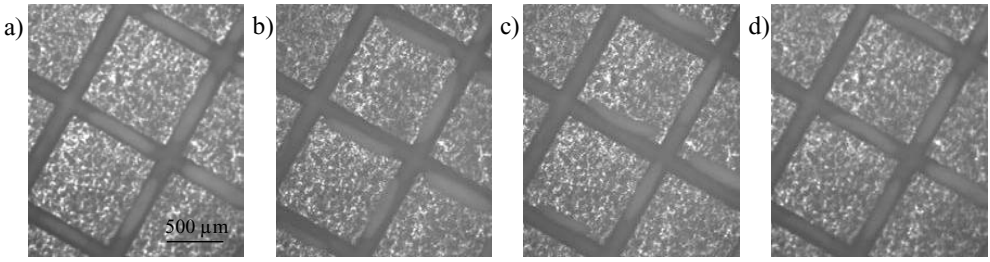

Fig. 4. a) Glass beads magnetically trapped in the linear grooves between the permanent magnets. b-c-d) When the magnet device is agitated, the glass spheres oscillate around their stable position and finally stabilise in their initial position.

REFERENCES

[1] H. Chetouani, C. Jeandey, V. Haguet, H. Rostaing, C. Dieppedale, J.-F. Jacquot, T. Kerlin, and G. Reyne, "Principle and analysis of a two-dimensional on-chip magnetophoresis of bioparticles for contamination-free biochemical reactors", IEEE Trans. Magn., vol. 43, n° 4, 1673, 2007.

[2] N.M. Dempsey, A. Walther, F. May, D. Givord, K. Khlopkov, and O. Gutfleisch, "High performance hard magnetic NdFeB thick films for integration into micro-electro-mechanical systems", Appl. Phys. Lett., vol. 90, 092509, 2007.

MICROFLUIDIC BIOCHIP FOR THE ELECTROCHEMICAL CELL ACTIVITY ANALYSIS

N. Pereira Rodrigues[1], H. Kimura[2], Y. Sakai[1,3] and T. Fujii[1,2]

[1] *LIMMS/CNRS-IIS, Institute of Industrial Science, University of Tokyo, JAPAN*
[2] *Institute of Industrial Science, University of Tokyo, JAPAN*
[3] *Center for Disease Biology and Integrative Medicine, University of Tokyo, JAPAN*

ABSTRACT

We developed a new cell-based biochip dedicated to the real-time and on-line monitoring of transient effluxes of glucose and oxygen. This microfluidic device "on a chip" will realize a real-time monitoring of the composition of cell medium. The microdevice is composed of arrays of amperometric microsensors integrated in the inlet and the outlet of a polydimethylsiloxane (PDMS) cell chamber. The present study focuses on the design of this microfluidic biochip and on the performances of the both inlet and outlet integrated electrochemical glucose and oxygen microsensors in the dynamic flow conditions.

Keywords: integrated amperometric microsensors, PDMS microfluidic biochip, glucose, oxygen

1. INTRODUCTION

Recently, there has been intensive research in the field of medical diagnostics aimed at the fabrication of reliable analytical systems for multiple and accurate analysis of *in-vitro* steady-state and transient fluxes of molecules involved in cellular metabolism [1,2]. These cell-based biochips are expected to perform *in-vitro* analysis by mimicking *in-vivo* conditions. Microfluidic devices obtained by photolithographic and planar techniques are now widely used because of their numerous advantages [1,2], and electrochemical miniaturized sensors are particularly adapted to *in-vivo* and *ex-vivo* biomedical applications [3]. However, no cell-based devices dedicated to the electrochemical detection of one (or more) analytes implied in cell activity as been reported so far.

We report here the fabrication and the performances of a cell-based biochip devoted to the on-line continuous monitoring of fluxes of glucose and oxygen during cell growth and development.

2. EXPERIMENTAL

The developed miniaturized device "on a chip" (Figure 1) is fabricated by microfabrication techniques and is composed of a biocompatible PDMS microfluidic chamber in which miniaturized glucose and oxygen amperometric biosensors are integrated. All the microelectrodes are fabricated by thin film technology.

Working microelectrodes are modified in surface to achieve a selective and sensitive amperometric detection of glucose and oxygen:

- *Oxygen microsensors* are obtained by modifying the gold surface with a layer of Nafion®, which is an O_2 permeable perfluorinated cation-exchange polymer [4]
- *Glucose microsensors* are based on the immobilization of glucose oxidase (GOx) within

978-0-9798064-0-7/μTAS2007/$20©2007CBMS

a matrix of Nafion®.

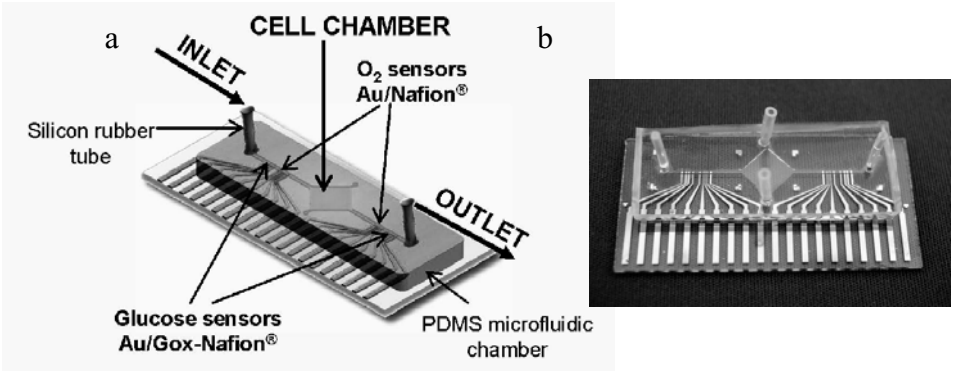

Figure 1: Schematic diagram (a) and photograph (b) of the developed biochip composed of arrays of glucose and oxygen microsensors integrated in the microchannels of a PDMS microfluidic device

This cell-based biochip was designed to compare the effluxes of O_2 and glucose before and after contact with the cells, which are inoculated directly inside the cell chamber (Figure 1). Here we show the performances of the integrated sensors during calibration and validate the design of the biochip for cell activity monitoring.

3. RESULTS AND DISCUSSION

Previous studies put in evidence the good performances of the integrated Au/GOx-Nafion® and Au/Nafion® sensors of the developed biochip [4]. We showed the good sensitivity and stability of glucose and oxygen monitoring in the dynamic flow conditions. Here we compare the inlet and outlet electrochemical responses of each group of microsensors and local variations of glucose and oxygen concentrations are measured simultaneously before and after going to the cell chamber.

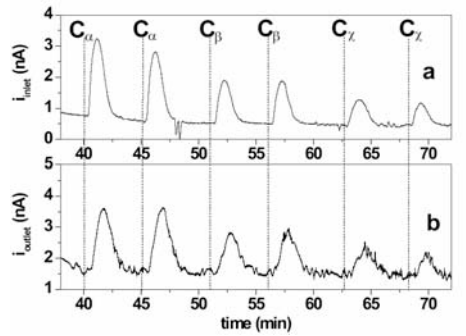

Figure 2. Simultaneous amperometric detection of glucose (E = 0.65 V vs Ag/AgCl) at the inlet (a) and outlet (b) microchannels: injections of C_α=5.00 mmol.L^{-1}, C_β = 2.50 mmol.L^{-1} and C_χ = 1.25 mmol.L^{-1}.

Figures 2 and 3 show the on-line simultaneous monitoring of glucose and oxygen respectively both at the inlet and outlet microchannels connected to the cell chamber. A good concordance between both inlet and outlet amperometric responses was observed.

Therefore, we have shown here the great potential of a new biochip dedicated to perform toxicological studies during cell culture by monitoring the composition of culture medium during cell perfusion (e.g. O_2 and glucose consumption by cells).

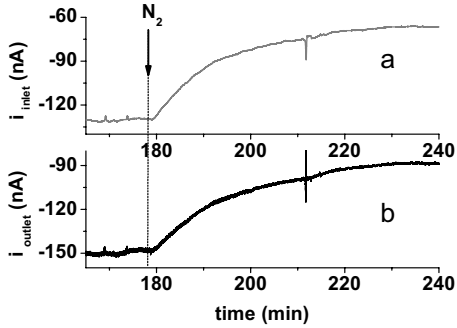

Figure 3. Simultaneous real-time detection of O_2 (E = -0.60 V vs Ag/AgCl) at the inlet (a) and outlet (b) Au/Nafion® from 235 µmol.L^{-1}(air) to 0 µmol.L^{-1}(after bubbling with N_2).

Oxygen and glucose monitoring have been also done at 37°C and showed no degradation of the Gox layer and Nafion®. Studies on the multidetection in cell culture medium with the presence of cells are currently in progress.

4. CONCLUSION

In summary, we have shown here the great potential of a new biochip dedicated to perform toxicological studies during cell culture by monitoring the composition of culture medium during cell perfusion (e.g. O_2 and glucose consumption by cells).

Studies on the multidetection in cell culture medium with the presence of liver cells (Hep-G2) are currently in progress.

ACKNOWLEDGEMENTS

We would like to acknowledge CNRS, JSPS and MEXT for their financial support.

REFERENCES

[1] "Biology on a chip: microfabrication for studying the behaviour of cultured cells", N. Li, A. Tourovskaia, and A. Folch, Crit. Rev. Biomed. Eng., **31**(5-6), 423 (2003)

[2] "Lab-on-a-chip for drug development", B.H. Weigl, R.L. Bardell and C.R. Cabrera, Adv. Drug Deliv. Rev., **55**, 349 (2003)

[3] "Biosensors for real-time in vivo measurements", G.S. Wilson and R. Gifford, Bios. Bioelectron. **20**, 2388 (2005)

[4] "Cell-based microfluidic biochip for electrochemical real-time monitoring of glucose and oxygen", N. Pereira-Rodrigues, H. Kimura, Y. Sakai and T. Fujii, Proc. of Transducers 2007, **1,** 843 (2007)

MICROFLUIDIC CASSETTE FOR RAPID ISOLATION AND PROCESSING OF LEUKOCYTE SUBPOPULATIONS FROM WHOLE BLOOD

Kenneth T. Kotz[1], Aman Russom[1], Daniel Irimia[1], Michael N. Mindrinos[2], Lyle L. Moldawer[3], Ronald G. Tompkins[1], and Mehmet Toner[1]

[1]Massachusetts General Hospital, Shriners Hospital for Children, and Harvard Medical School, Boston, MA 02144 USA

[2]Stanford Genome Technology Center, Palo Alto, CA 94304, USA

[2]University of Florida College of Medicine, Gainesville, FL 32610, USA

ABSTRACT

We report a microfluidic device capable of rapidly separating CD66b+ granulocytes directly from whole blood within a clinical environment. We use immunoaffinity capture combined with well defined shear stress within microfluidic channels to isolate >300K granulocytes from 150 μL of blood in less than 5 minutes. Furthermore we demonstrate that these captured cells can be rapidly lysed on chip to obtain ~100 ng of high quality RNA for microarray studies.

Keywords: neutrophil, immunoaffinity positive selection, cell lysis, RNA isolation

1. INTRODUCTION

We are interested in developing cell processing technologies in order to understand the role of the immune system in chronic and systemic inflammation at a transcriptional level. As part of the immune system, neutrophils are the first cells recruited to injured tissues within the body because of their important role in host defence against invading pathogens. Thus, obtaining gene expression profiles of neutrophils following major burns or trauma is critical to understanding the inflammatory response. It was recently shown that it is necessary to isolate and separately analyze different leukocyte subpopulations in order to understand the complex regulatory networks involved in inflammation [1]. Unfortunately, it is difficult to obtain high-quality RNA from some leukocyte subpopulations such as neutrophils using established protocols, because of high levels of endogenous nucleases present in blood as well as the long processing times associated with leukocyte fractionation. While established methods exist for blood fractionation and RNA processing, these techniques typically require that a trained technician serially process 10's of milliliters of blood over a period of hours making them difficult to implement in the clinic [2]. To address the shortcomings of bulk processing protocols, we have developed a microfluidic platform for the rapid isolation of neutrophils from whole blood as described below. It combines capture, counting, and on-chip processing of burn patient samples.

2. EXPERIMENTAL

The device presented here, efficiently captures neutrophils directly from whole blood using anti-CD66b monoclonal antibodies in a microfluidic device fabricated from PDMS using standard molding techniques [3]. The well-defined fluid flow within microfluidic channels allows precise control of the shear forces experienced by cells at the surface of the device. This combined with the specificity of monoclonal antibodies for cell surface

978-0-9798064-0-7/μTAS2007/$20©2007CBMS

antigens provides optimal conditions for highly specific cell capture from whole blood [3, 4]. The optimized device geometry (Figure 1) maximizes the width of the capture chambers on a small footprint in order to reduce the total processing time to 10 minutes. Device functionalization and cell capture characterization were performed using established protocols [4]. To isolate total RNA, cells captured on the microfluidic cassette were directly lysed on-chip using guanadinium isothiocyanate, and the RNA was extracted using a standard, commercially available kit (Qiagen). The bulk isolation was performed using established density gradient centrifugation protocols. Granulocytes were separated from mononuclear and red blood cells followed by cell lysis and RNA extraction using another Qiagen kit.

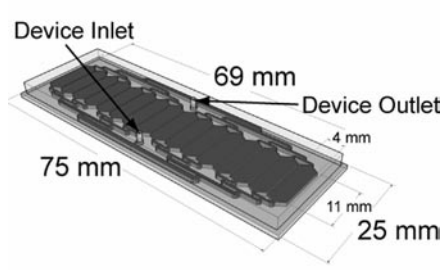

Figure 1. Device geometry used for granulocyte capture. The channel height is 50 μm.

3. RESULTS AND DISCUSSION

Cell capture efficiency and purity were first optimized by finding the correct flow rate and monoclonal antibody. The device geometry shown in Figure 1 exhibits excellent linearity from 50K-2M cells captured (Figure 2a). The purity of CD66b+ granulocytes was determined by immunofluorescence and Wright-Giemsa (Figure 2b) staining to be 94% ± 5% for healthy normal volunteers and 96% ± 1% for burn patients. Using flow cytometry, we found that it was possible to deplete 80% ± 7% of the total circulating granulocytes from blood (data not shown).

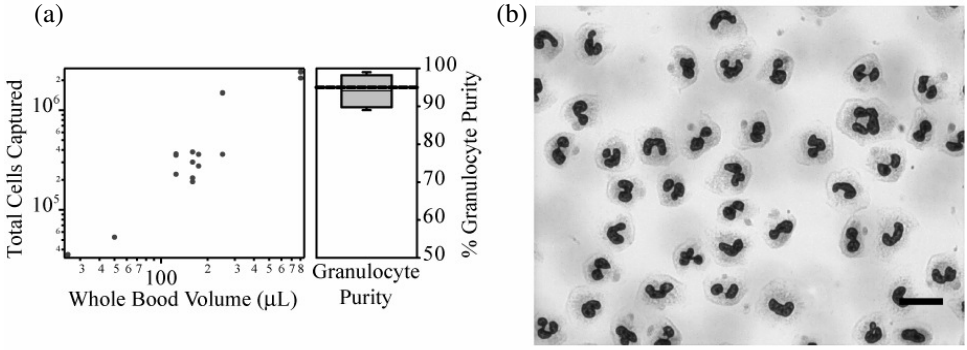

Figure 2. (a) Device loading of the microfluidic immunoaffinity capture cassette; (b) Wright-Giemsa stain of captured CD66b+ granulocytes. Scale bar represents 20 μm.

Following device characterization, we tested the feasibility of these devices to isolate total RNA from the isolated cells for genomic analysis. We characterized the RNA extracted

by direct on-chip lysis of the cells and compared it with the RNA extracted from the standard bulk isolation of neutrophils from different healthy volunteers. We also examined RNA extracted from burn patients. The results are summarized in Table 1 below. Although the overall RNA yield is lower for the microfluidic cassette, when normalized to the blood sample volume the RNA extraction is actually a factor of six greater than for the bulk methods. More importantly, we can obtain extremely high-quality RNA from the direct on-chip sample processing for both healthy normal controls and clinically relevant samples. The yield is sufficient for processing on Affymetrix GeneChips.

Table 1. Summary of RNA isolation from healthy normal samples and burn patients

	Microfluidic Processing		Bulk Processing
	Healthy Normals (N=12)	Burn Patients (N=6)	Healthy Normals (N=8)
Blood volume per sample (μL)	160	150	8000
Average RNA Yield (ng)	190	50	1700
Total RNA/ml blood (ng/ml)	718	317	213
Agilent RIN Score	8.8 ± 0.3	9.2 ± 0.1	7.2 ± 0.2

5. CONCLUSIONS

The simplicity of the single inlet-single outlet cassette described above makes this microfluidic technology accessible to doctors, nurses, and technical staff. We are currently working with clinical researchers to deploy these devices for genomic analysis of the immune response to injury.

ACKNOWLEDGEMENTS

The authors of this paper would like to thank Chey Collura and Drs. Amit Gupta and Alan Rosenbach for help in device fabrication.

REFERENCES

[1] K. Laudanski et al. “Cell-specific expression and pathway analysis revel alterations in trauma-related human T cell and monocyte pathways,” *Proc. Natl. Acad. Sci. USA,* **103**, 15564 (2006).

[2] A. K. De, S. E. Roach, M. De, R. C. Minielly, K. Laudanski, C. L. Miller-Graziano, P. E. Bankey, “Development of a simple method for rapid isolation of polymorphonuclear leukocytes from human blood,” *J. Immunoassay Immunochem.* **26**, 35 (2005).

[3] S. K. Murthy, A. Sin, R. G. Tompkins, and M. Toner, “Effect of flow and surface conditions on human lymphocyte isolation using microfluidic chambers,” *Langmuir*, **20**, 11649 (2004).

[4] X. Cheng, D. Irimia, M. Dixon, K. Sekine, U. Demirci, L. Zamir, R. G. Tompkins, W. Rodriguez, M. Toner, "A microfluidic device for practical label-free CD4(+) T cell counting of HIV-infected subjects," *Lab on a Chip*, **7**, 170 (2007).

MICROFLUIDIC DEVICES FOR STUDYING THE RESPONSE OF ADHERENT CELLS UNDER SHORT TIME STIMULI TREATMENT

Linlin YE[1], Mingsheng Zhang[2], L.G. Alexopoulos[2], Peter Sorger[2], and K.F. Jensen[1]

[1] Massachusetts Institute of Technology, Cambridge, MA 02139, USA and
[2] Harvard Medical School, Boston, MA 02115, USA

ABSTRACT

This paper reports a microfluidic method for studying protein pathways of adherent cells under short stimulation times. The device is capable of performing all the steps needed in stimulus-signal response analysis of signalling pathways by an immunocytochemical assay (In-Cell Western), including cell culture, cell stimulus, cell fix, and protein analysis. The main contributions of this study are: 1) ability for analyzing short time stimuli response of adherent cells; 2) integration of cell culture, stimulation, with protein analysis in one device; 3) multiple time points are obtained from a single experiment.

Keywords: adherent cell, early response, In-Cell Western

1. INTRODUCTION

Some protein response events involved in cell signalling in mammalian cells exhibit fast transient responses [1]. Analysis of such responses requires very short treatment times and well-controlled and reproducible stimulus conditions. The pathways can be difficult to reproducibly probe with conventional laboratory techniques as even small fluctuations in the manual handling become significant at short times. Microfluidic systems offer the potential for reproducible and automated analysis with good control over experimental parameters such as volume, concentration, and temperature. Our overall aim is to achieve cell culture, cell stimulation, and protein analysis in microfluidic devices and thereby expand greatly the number and reliability of experiments designed to collect information on signalling pathways.

2. EXPERIMENTAL

The microfluidic device consists of a fluidic channels defined in a poly(dimethylsiloxane) (PDMS) layer fabricated by soft lithography and subsequently bonded to a glass slide. Schematics of the device and the fluidic system are shown in Fig.1. All fluidic features are 300 μm deep and 50 μm wide. A typical process flow in these experiments starts with cell culture. Prior to seeding, the device was sterilized and filled with culture media. Suspended cells were seeded at ~ 10^6 cells/mL. The cells were cultured at 37°C in a humidified incubator with 5% CO_2 in air. After 5-6 days cell culture in the devices, fresh cell medium and stimuli to cells (cytokines or growth factors) under controlled conditions of concentration, time, and temperature were added. An air segmentation of liquid streams was used to separate the fresh medium and stimuli, and to trace the position and time of the head of the stimuli treatment. The time needed for the head of the stimuli to pass a specific positions in the device and reach the end of the channel defined the stimulation time for cells in that position. Consequently, spatial

978-0-9798064-0-7/μTAS2007/$20©2007CBMS

positions along the channel corresponded to time points. After the stimulus, the cells were fixed and a primary antibody added. After incubating for several hours, a fluorescently labelled second antibody was added with an additional one hour of incubation. Finally, the fluorescence ass measured along the length of the channel.

3. RESULTS

Three types of cell lines (Hela cells, HT-29 cells, and HepG2 cells) have be tested for cultivating in the devices. Fig.2 shows the three cell types growing in the devices after 2 days. Hela cells and HT-29 cells are cultured in batch reactor mode. HepG2 cells are grown under feed-batch model.

One advantage of microfluidic devices used for the immunocytochemical assay over the convention methods is reducing the incubation time for the antibody binding [2]. Fig.3 shows the p-AKT signal of the HT-29 cells under insulin-like growth factor (IGF) treatment by different incubation times. Under flow condition, the cell signals measured by the fluorescence after half an hour or one hour incubation of the primary antibody are comparable with that after overnight incubation without flow, but the cell signals are relatively lower after half an hour or one hour incubation of the primary antibody without flow. The main reason is the enhanced mass transfer in the microfluidic device relative to conventional stationary batch procedures.

Fig.4 shows In-Cell Western results of AKT, ERK, and JNK signalling in HT-29 cells stimulated with IGF, epidermal growth factor (EGF) and tumour necrosis factor-alpha (TNFα) for different times in the microfluidic devices and 96-wells. Stimulation of cells performed in the device results in pathway activations comparable to those observed when using conventional methods. However, the error bars of the microfluidic data are relatively smaller than in the conventional method, which suggests that the microfluidic system provides better time control and correspondingly reproducible analysis of fast transient responses in the cell signalling pathways. Furthermore, additional information about the early stage of the cell signal responses are achieved by this technique.

4. CONCLUSIONS

HT-29 cells have been studies for cytokine early response under short time stimuli treatment. The AKT, ERK, and JNK signalling stimulated with IGF, EGF, and TNFα in the micrfluidic device are comparable with those from conventional methods. However, a single microfluidic experiment produces a complete temporal response curve, while conventional approaches would have required multiple experiments and manual immunocytochemical assays by standard 96 well and pipetting techniques.

ACKNOWLEDGEMENTS

This research was funded by the National Institutes of Health (NIH) (NIGMS GM-68762).

REFERENCES

1. Kholodenko, B. N.; Demin, et.al, **"**Quantification of short term signalling by the epidermal growth factor receptor," J. Biol. Chem., 274, 30169 (1999)
2. Gervais, T, and Jensen, K.F, "Mass transport and surface reactions in microfluidic systems," Chem. Eng. Sci. 61, 1102 (2006).

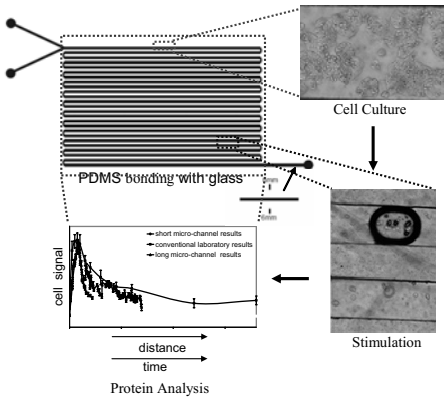

Figure 1. Schematic of the fluidic system layout

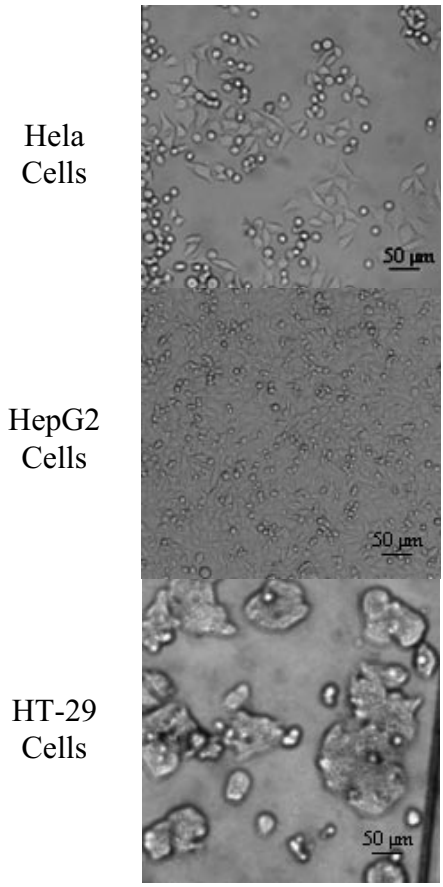

Figure 2. Cell growing in the device after 2 days

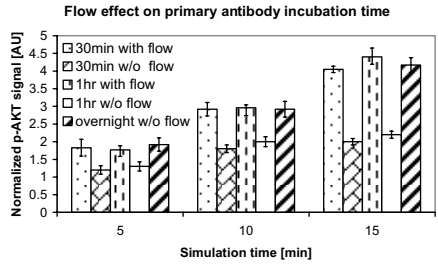

Figure 3. p-AKT signal of HT-29 cells under IGF treatment by different incubation times

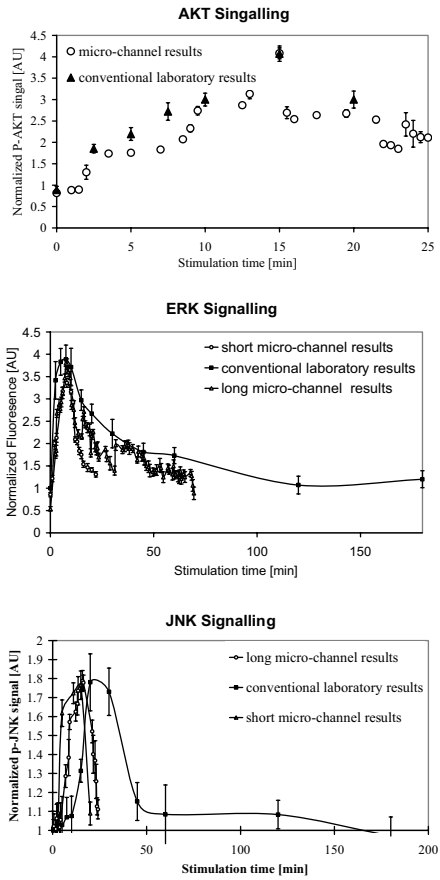

Figure 4. p-AKT, p-ERK and p-JNK signalling in HT-29 cells under IGF, EGF and TNFα treatment for different times

MICROFLUIDIC STICKERS FOR QUANTITATIVE STUDIES OF CULTURED CELLS.

Mathieu Morel [1], Denis Bartolo [2], Maxime Dahan [1], Vincent Studer [3]

[1] *Laboratoire Kastler Brossel- ENS, France.*

[2] *Physique et Mécanique des Milieux Hétérogènes- ESPCI, France.*

[3] *Laboratoire de Neurobiologie- ESPCI, France.*

ABSTRACT

We propose a new approach to prepare live cells in a microfluidic environment without cultivating cells in microchannels. We use microfluidic stickers that are tightly sealed over cells, cultured on glass coverslips. By greatly simplifying the conditions in which cells can be placed into a microchip, our method opens new prospects for quantitative investigation of the cell response to controlled external stimulation.

Keywords: Microfabrication, Live cells, Biological imaging, Systems biology.

1. INTRODUCTION

Systems biology seeks to develop a complete understanding of cellular mechanisms by unravelling the dynamic properties of molecular networks. A key requirement for the development of systems-based approach is the ability to apply controlled perturbations and monitor the cell response. In this context, microfluidic technologies appear as a powerful tool for real time chemical stimulations of biological samples. For instance, microcircuits have already been used to apply biologically active compounds at a cellular or subcellular level [1, 2] or to generate a controlled gradient of a signalling molecule [3, 4]. Such devices have the potential to significantly impact systems biology by enabling a methodical and quantitative investigation of the cell response to controlled spatial and temporal changes in its environment.

Nevertheless microfluidic technologies are not part of the standard toolbox of every cell biology or developmental biology lab. This can be largely attributed to the operating difficulties encountered when trying to obtain cultured cells in a microchannel, particularly for primary culture cells or multicellular systems such as tissues or neuronal slices. Indeed this requires to precisely control gas exchanges, temperature and the flux of nutrients inside the microsystem for couples of days.

3. EXPERIMENTAL

In our approach, cells are cultured on glass coverslips using standard techniques. Subsequently, a microfluidic circuit is placed above the coverslip and sealed over the cell culture. The microfluidic circuits are made out of UV-polymerizable material (NOA 81, Norland Optical) by a method described in [5]. Briefly, a thin layer of monomer is photopolymerized between a glass slide with holes for fluidic connections, and a PDMS mold. Since the polymerization is inhibited by oxygen, the PDMS mold can be easily removed and an ultra-thin layer of un-polymerized monomers remains at the surface. The pre-formed sticker is then pressed against the glass coverslip on which cells are cultured, and a second short UV illumination allows for a tight sealing between the microstructured layer and the cover slip (Figure 1.).

978-0-9798064-0-7/μTAS2007/$20©2007CBMS

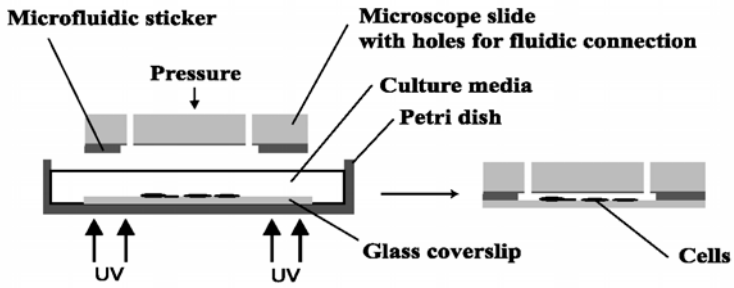

Figure 1. Fabrication scheme of a functionnal microfluidic device, using a microfluidic sticker.

3. RESULTS AND DISCUSSION

We demonstrated the feasibility and interest of our approach using different cell lineages. Cells were cultured in standard conditions and a microfluidic sticker was subsequently sealed over the coverslip. We first used primary cultured neurons: spinal cord interneurons at 2 days in vitro. A sticker was sealed over the neuronal cells, and the device was used to immunolabel membrane receptors. For instance, we tagged NCAM receptors in the soma and the growth cones and tracked them at the single molecule level using quantum dots as a fluorescent probes. This points out the high optical sensitivity that can be achieved in our devices (Figure 2).

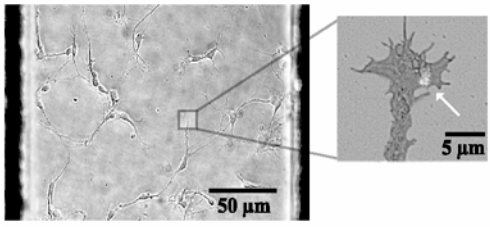

Figure 2. Spinal cord interneurons sealed with a microfluidic sticker. Single molecule tracking of a NCAM membrane receptor (zoom and arrow).

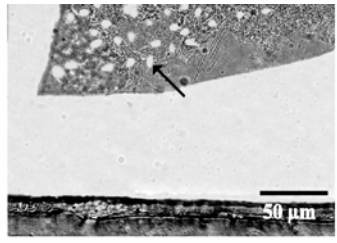

Figure 3. Drosophila dorsal tissu near the channel border (in black, at the bottom). White points are SOP cells expressing eGFP.

Then we applied microfluidic sticker to dissected *D. melanogaster* notum (larva dorsal epithelium), with Sensory Organ Precursor (SOP) cells expressing GFP (Figure 3). Preliminary treatment allowed us to follow cellular vesicles trafficking, directly in the channel. We also showed that we could monitor in real time the dynamics of intra-cellular components in the channel, using Hela cells transfected with fluorescent microtubule end binding proteins (Figure 4). Moreover by applying a trypsin flow in the device, we could then selectively detach regions of the confluent culture (Figure 5).

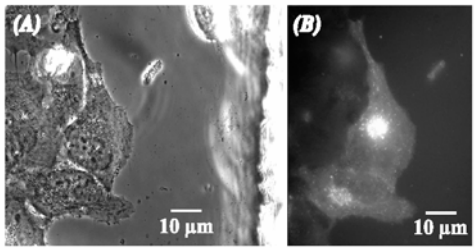

Figure 4. Microtubule End Binding EB1-eGFP transfected HeLa cells in a sticked channel. 60x phase contrast, with the channel border to the right (A) ; and fluorescence (B) microscopy.

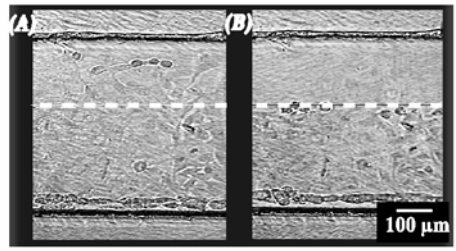

Figure 5. Trypsin/MEM medium coflow applied in the channel (white crossed line). HeLa cells culture before (A) and after (B) the selective detachment.

5. CONCLUSIONS

Altogether, these experiments demonstrate that microfluidic circuits can be sealed on cell samples from various cultures, including neurons or tissues. We have also demonstrated the compatibility of microfluidic stickers with standard cell biology tools such as transfection and immunolabelling before positioning the microcircuit. In the near future, we expect to take advantage of this technique to make advanced devices such as gradient generators. This will open new prospects for the quantitative study of complex biological problems such as chemotaxis or axonal guidance.

We emphasize the numerous advantages of microfluidic stickers over conventional PDMS devices. The coupling between cellular biology, imaging and microfluidic will be substantially simplified: (i) There is no need to adapt the culture conditions to the microfluidic environment. (ii) Cell manipulation can be performed before placing the cell into the microchannel. (iii) The position and orientation can be adjusted as a function of the cells. (iv) Cells do not flow inside the channels. This eliminates the risk of clogging with cellular aggregates. (v) The microfluidic sticker is very thin and has excellent optical properties compatible with high quality microscopy for cell based studies.

REFERENCES

[1] Takayama S, Ostuni E, Leduc P, Naruse K, Ingber DE, Whitesides GM, "Subcellular positioning of small molecules", Nature, 411, 1016 (2001).

[2] Tourovskaia A, Fettah Kosar T, Folch A, "Local induction of acetylcholine receptor clustering in myotube cultures using microfluidic application of agrin", Biophysical Journal, 90, 2192 (2006).

[3] Jeon NL, Baskaran H, Dertinger SKW, Whitesides GM, Van De Water L, Toner M, "Neutrophil chemotaxis in linear and complex gradients of interleukin-8 formed in a microfabricated device", Nature Biotech, 20, 826 (2002).

[4] Paliwal S, Iglesias PA, Campbell K, Hilioti Z, Groisman A, Levchenko A, "MAPK-mediated bimodal gene expression and adaptative gradient sensing in yeast", Nature, 446, 7131 (2007).

[5] Bartolo, D., Degré G., Nghe P., Studer, V, "Stick and flow: fast simple prototyping method for performance microfluidic device", Submitted to MicroTAS 2007.

MICROFLUIDIC TOXICOLOGICAL PLATFORM FOR THE MONITORING OF EXTRACELLULAR IONIC ACTIVITIES

Silvia Generelli[1,2], Francois Berthiaume[3], Martin L. Yarmush[3], Mario Jolicoeur[4], Milena Koudelka-Hep[2] and Olivier T. Guenat[1]

[1]Ecole Polytechnique de Montréal, Eng. Physics, CANADA
[2]University of Neuchâtel, Institute of Microtechnology, SWITZERLAND
[3]Harvard Medical School, Massachusetts General Hospital, USA
[4]Ecole Polytechnique de Montréal, Chemical Eng., CANADA

ABSTRACT

A microfluidic toxicological platform aimed at the real-time monitoring of ionic cellular responses is being developed. These responses are assessed with ion-selective microelectrodes integrated in the platform. First cellular assays were successfully performed by monitoring the increasing K^+ concentration generated by induced cell necrosis.

Keywords : toxicological platform, ion-selective microelectrodes, cell necrosis

1. INTRODUCTION

The use of cell and tissue culture techniques in research and industry is increasing rapidly due to a demand for biological test systems and the drive to avoid the use of animals for experimentation [1]. A regulation law recently adopted by the EU Parliament [2], expressing the obligation for testing the toxicity of all the currently employed chemicals, is an example of the increasing need for fast, reliable, high throughput screening assays. Similarly, the pharmaceutical industry is looking for tools which can be used to assess the cytotoxicity of drugs in early stage drug development [3].

To tackle this problem, we are developing a toxicological platform capable of generating concentration gradients and monitoring cell responses in real time as a function of chemical or drug exposure. Our objective is to monitor extracellular potassium and ammonium in a culture of hepatocytes. Potassium, which is present at high levels in intact viable cells, leaks out of dying cells, thus elevation of extracellular potassium can be used as a marker of cell death. Ammonium (the protonated form of ammonia) is taken up by hepatocytes and converted to urea, leading to a decrease of its extracellular concentration. Modification of the ammonium uptake rate will be used as a degradation indicator of hepatocytes detoxification function.

2. EXPERIMENTAL

The presented platform (Fig.1) is equipped with an array of 16 ion-selective microelectrodes (μISE) having a diameter of 6 μm and separated by a gap of 150 μm. This array is located at the bottom of a 200 μm wide and 350 μm deep microchannel, in which the cells are cultured. Side microchannels are implemented to deliver a concentration gradient of the chemicals/drugs to be tested. The fabrication process of the platform was described earlier [4].

978-0-9798064-0-7/μTAS2007/$20©2007CBMS

Extended characterization of the arrays in different standard and physiological solutions was carried out. Nernstian slopes were obtained for both K^+ and NH_4^+, after more than one week of use, with detection limits in the order of 10^{-6} M. The calibration curves were highly reproducible and showed very little drift (in average 4 mV/h, n=10) [5].

3. RESULTS AND DISCUSSION

Cell assays performed using the platform equipped with potassium-selective μISE arrays are reported here for the first time. 3T3 NIH fibroblasts necrosis was induced by osmotic shock provoked by deionized (DI) water and monitored in real time by measuring extracellular potassium activity. The cells (about 10^4 cells) trapped in the microwell by the mean of a porous membrane (Fig. 2) were either in suspension or cultured on such a membrane. In the presence of cells, a sharp increase in potassium concentration could be clearly identified (Fig. 3). After the assay a calibration was performed by flowing standard solutions through the manifold.

4. CONCLUSIONS

This first attempt to use this μISE platform for toxicology studies is a promising way to provide high throughput screening assays to respond to the needs of the research and industry.

ACKNOWLEDGEMENTS

The authors thank the SAMLAB technical team. This work was supported by the Swiss National Science Foundation (project 205321-103961 and advanced researcher grant PA00A-105032), the National Institutes of Health, grants R01DK43371 and P41EB002503, and the Shriners Hospitals for Children.

REFERENCES

[1] G. N. Stacey, A. Doyle, M. Ferro, (ed.), *Cell Culture Methods for In Vitro Toxicology*, Kluwer Academic Press (2001).

[2] REACH Regulation (Registration, Evaluation and Authorisation of Chemicals) (Dec. 06): http://ec.europa.eu/environment/chemicals/reach/reach_intro.htm

[3] G. Eisenbrand, B. Pool-Zobel, V. Baker, M. Balls, B.J. Blaauboer, A. Boobis, A. Carere, S. Kevekordes, J.-C. Lhuguenot, R. Pieters, J. Kleiner, *Methods of In Vitro Toxicology*, Food Chem. Toxicol., **40**, 193 (2002).

[4] O. T. Guenat, S. Generelli, M. Dadras, L. Berdondini, N. F. de Rooij, M. Koudelka-Hep, *Generic Technological Platform for Microfabricating Silicon Nitride Micro- and Nanopipette Arrays*, J. Micromech. Microeng., **15**, 2372 (2005).

[5] O. T. Guenat, S. Generelli, N. F. de Rooij, M. Koudelka-Hep, F. Berthiaume, M. T. Yarmush, *Development of an Array of Ion-Selective Microelectrodes Aimed for the Monitoring of Extracellular Ionic Activities*, Anal. Chem., **78**, 7453 (2006).

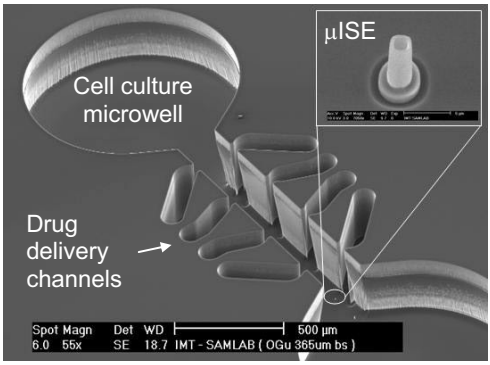

Figure 1. SEM photograph of the cell culture microwell, and a close-up of a silicon nitride-based ion-selective electrode, located at the bottom of the well.

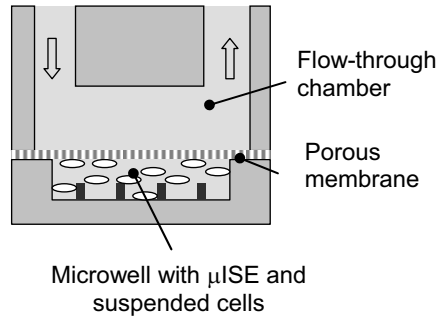

Figure 2. Schematic cross-section of the cell culture microwell. Cells are trapped in the microwell by the mean of a porous membrane. Solutions are pumped through the porous membrane.

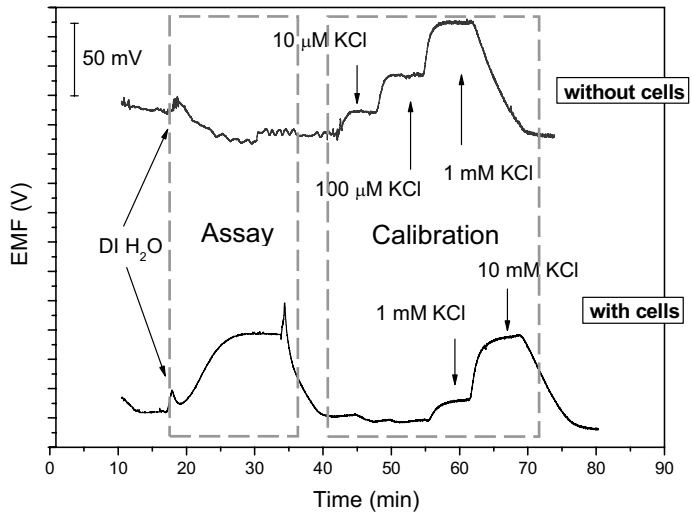

Figure 3. Cell necrosis assay carried out with suspended fibroblasts. The K^+ concentration increase due to cell lysis is clearly visible on the cell-containing assay (lower curve), while no potential step is registered in the blank assay (upper curve).

PERFUSED MULTIWELL TISSUE CULTURE PLATES FOR DRUG AND DISEASE MODEL DEVELOPMENT

K. Domansky[1], W. Inman[1], M. H. M. Lim[1,3], J. Serdy[1,2], B. Owens[1,2], S. Karackattu[1], J. R. Llamas Vidales[1], R. Littrell[1], L. Vineyard[1], and L. G. Griffith[1,2]

[1]*Biological Engineering Division and Biotechnology Process Engineering Center*
[2]*Mechanical Engineering Dept., MIT, Cambridge, MA 02139, USA*
[3]*Department of Chemical Engineering, University of Cambridge, Cambridge CB2 3RA, UK*

ABSTRACT

We have developed a perfused three-dimensional microbioreactor array in the format of multiwell tissue culture plate. Both theoretical and experimental data for the distribution of fluid flow and dissolved oxygen transport within the reactor are presented. Multi-day culture of rat hepatocytes with high cell viability is demonstrated.

Keywords: Cell-based assays, microbioreactor, multiwell tissue culture plates

1. INTRODUCTION

It costs ~ 1 billion dollars to bring a drug to market. Nearly 90% of the lead candidates identified by current *in vitro* screens fail to become drugs. One reason for the high failure rate is the lack of adequate drug screening models. Similarly, there is a shortage of robust *in vitro* models for studying many human diseases. To address this issue, we have developed a more physiologically relevant tissue culture system in the format of a standard multiwell tissue culture plate. It allows the cells to be cultured in 3D instead of the conventional 2D format and provides the necessary *in vivo*-like biomechanical forces by culturing the cells under flow conditions.

2. EXPERIMENTAL

The perfused multiwell plate contains an array of microbioreactors and reservoir pairs (Fig. 1). Cell culture medium is re-circulated between reactors and reservoirs by built-in diaphragm pumps actuated in parallel by three common pneumatic inputs [1]. An electro-pneumatic controller (Fig. 1) sets the timing. Each microbioreactor/reservoir pair is fluidically isolated from all the other reactors on the plate [2]. A cross-section of a single microbioreactor/reservoir pair is shown in Fig. 2a. Ruthenium-based fiber optic oxygen sensors are mounted in a custom multiwell plate lid and inserted into the reactor and reservoir wells. Computational fluid dynamic flow simulation shows the effectiveness of the microporous filter in the reactor well in uniformly distributing flow of cell culture medium through all channels in the scaffold (Fig. 2b). It also maps stagnant fluid flow zones that can be minimized by altering the bioreactor design. Flow pulsatility is controlled by fluidic capacitors [1]. Filtering out flow pulses is critical during the cell attachment period. Cells are seeded by pipetting cell suspension onto the scaffolds in reactor wells. Cells attach to the collagen-coated channel walls of the scaffold and form an array of 3D microtissue units. During cell culture, temperature and pH of the cell culture medium are maintained by placing the multiwell plate into a CO_2 incubator. In the experiments described in this paper, we used silicon scaffolds microfabricated by the deep reactive ion etching. The reactor plates were fabricated by CNC machining.

978-0-9798064-0-7/μTAS2007/$20©2007CBMS

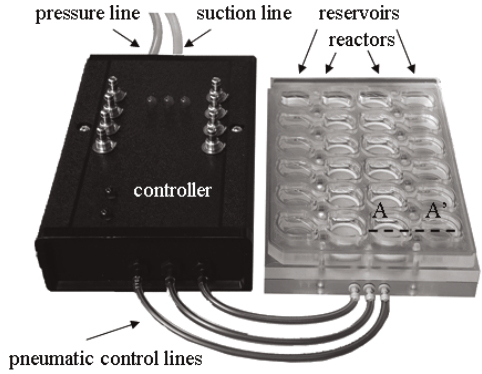

Figure 1. 12-microbioreactor array in the multiwell tissue culture plate format.

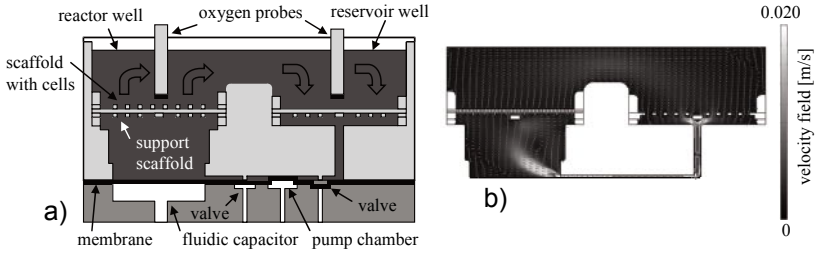

Figure 2. a) A schematic cross-section (A-A') of a reactor/reservoir pair. b) A computational fluid dynamic flow simulation showing the effectiveness of the filter in providing a stable flow across the scaffold containing the cultured cells.

3. RESULTS AND DISCUSSION

Phase contrast and fluorescent live-dead images of rat hepatocytes 5 days after seeding are shown in Fig. 3. It can be seen that vast majority of cells are viable. The size of the channels is approximately 300 x 300 x 230 microns. Each channel typically contains 500-1000 cells. Measurement of dissolved oxygen in a reactor well as a function of the flowrate is illustrated in Fig. 4. During the measurement, oxygen sensor was placed approximately 1 mm above the scaffold with cells. Therefore, under the upward flow of cell culture medium it indicates the concentration of oxygen depleted by cells before medium is re-oxygenated in the return loop by a mass transfer from the ambient gas phase. It can be seen that concentration of oxygen increases with increasing flowrate and the response gets slower. The trends are reversible as shown by stepping the flowrate down. By simultaneously measuring the concentration of oxygen in the reservoir well (data not presented), oxygen consumption of the cells can be calculated. We used both the computational fluid dynamic flow simulation and oxygen measurements as tools for improving the bioreactor design and optimizing cell culture conditions.

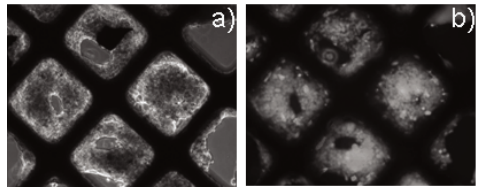

Figure 3. Phase contrast (a) and fluorescent live (green) – dead (red) staining images (b) of rat hepatocytes 5 days after seeding.

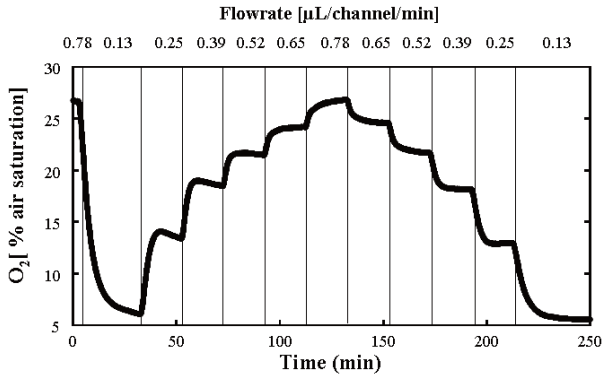

Figure 4. Oxygen concentration downstream from the cell in the reactor well as a function of flowrate. Rat hepatocytes 7 days after seeding.

4. CONCLUSIONS

A perfused 3D tissue culture plate has been developed. Simulation of fluid flow and measurements of dissolved oxygen were performed to give us objective parameters for device operation and design optimization. A viable multi-day cell culture was demonstrated. The system provides a means to conduct higher throughput assays for toxicology and metabolism. It can be also used for evaluation of long-term exposure to drugs or environmental agents or as a model to study viral hepatitis, cancer metastasis, and other diseases and pathological conditions.

ACKNOWLEDGEMENT

We want to thank DuPont – MIT Alliance, Pfizer, and NSF Biotechnology Process Engineering Center for financial support.

REFERENCES

[1] W. Inman, K. Domansky, J. Serdy, B. Owens, D. Trumper, and L. G. Griffith, Design, Modeling and Fabrication of a Constant Flow Pneumatic Micropump, J. Micromech. Microeng. 17 (2007) 891-899.

[2] K. Domansky, W. Inman, J. Serdy, and L. G. Griffith, Multiwell Cell Culture Plate Format with Integrated Microfluidic Perfusion System, Proceedings of SPIE, Microfluidics, BioMEMS, and Medical Microsystems IV, Vol. 6112, pp. 61120F-1 - 61120F-7, San Jose, January 23-25, (2006).

GROWTH RATE AND STRESS-RESPONSE ANALYSES OF MICRO-CONTACT PRINTED BACTERIAL ARRAYS AND SINGLE BACTERIA IN MICROFLUIDIC CHAMBERS

Lydia Robert[1,2], Luping Xu[2], François Taddei[1], Yong Chen[2], Ariel Lindner[1] and Damien Baigl[2]

[1]Inserm U571 and Univ. Paris Descartes, Fac. Med. Necker, Paris, FRANCE and
[2]Department of Chemistry, Ecole Normale Supérieure, Paris, FRANCE

ABSTRACT

We report on two novel methodologies to respectively position and culture living bacteria (*E. coli*) with a single-cell resolution under controlled micro-environment. The first one is based on micro-contact printing technology and the second one is achieved using microfluidic manipulations. It should allow us to measure the single-cell responses to perturbations and their propagation through the lineage of a growing population of bacteria.

Keywords: Systems biology, microfluidics, cell culture, single-cell response

1. MICROCONTACT PRINTING OF LIVING BACTERIA ARRAYS WITH SINGLE-CELL RESOLUTION

First, we developed a novel methodology to print arrays of living bacteria with a single-cell resolution. [1] It consists of the microcontact printing of living bacteria from an agarose 'inkpad' to an agarose substrate with PDMS stamps having high aspect ratio. (Figure 1A) PDMS stamps were fabricated by introducing an improved UV lithography protocol, called reverse *in situ* lithography (RISL).

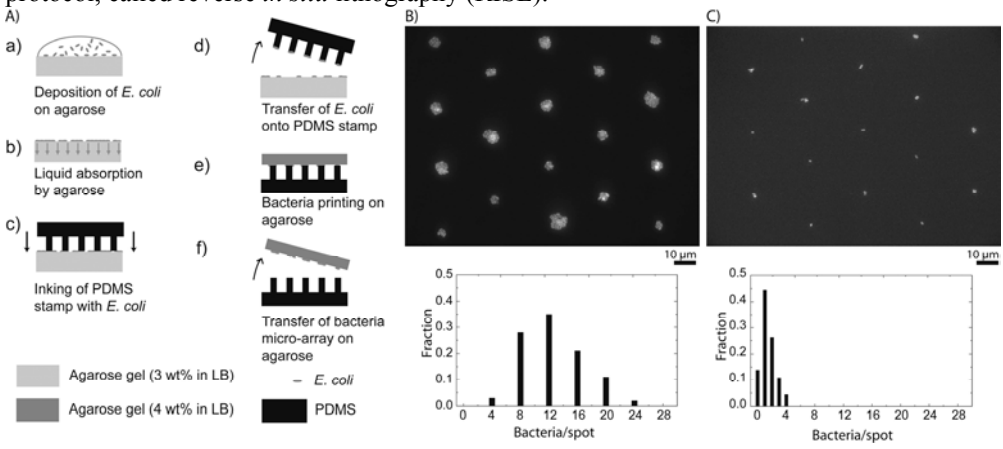

Figure 1. A) Principle of the method to print arrays of living *E. coli* bacteria. B) and C) Arrays of living *E. coli* printed on an agarose gel with a PDMS stamp (diameter 6 µm, period 30 µm, height 12 µm)). Top: Fluorescence microscopy. Bottom: Number of bacteria per spot. Bacteria concentrations are 10^9 cells/mL (B) and 10^8 cells/mL (C), respectively.

978-0-9798064-0-7/µTAS2007/$20©2007CBMS

Figures 1B and 1C show that the printed bacteria arrays reproduce perfectly the original patterns of the stamp. We found that the arrays were very regular for various kinds of patterns and over a very large area (typically cm^2). Figures 1B and 1C shows that, for initial concentrations of 10^9 and 10^8 cells/mL, the average number of printed bacteria per spot is 12.1 and 1.4, respectively. For the lower concentration, the distribution is very narrow, with 44.6% of spots having exactly a single *E. coli* cell and other 40.1% having 0 or 2. These results demonstrate that our methodology can produce very regular arrays of single bacteria over a large scale.

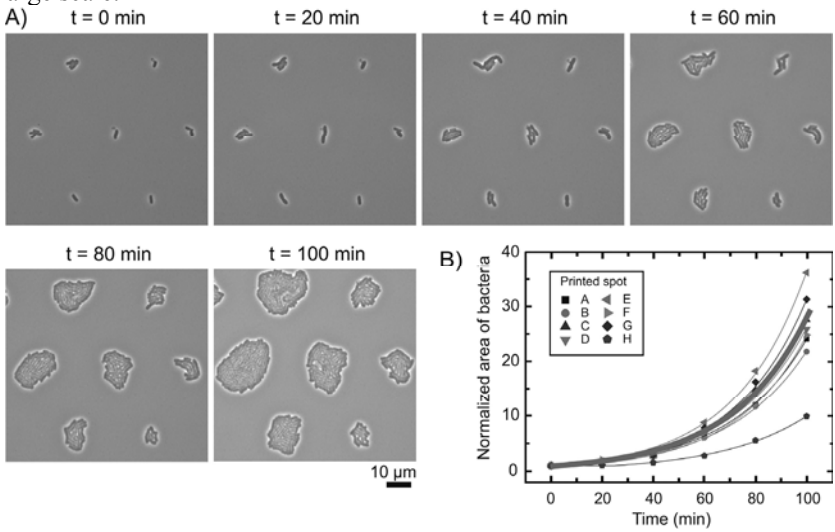

Figure 2. A) Growth of patterned bacteria at T = 37 °C (conditions of fig. 1C) B) Growth curves of printed bacteria. Each symbol corresponds to one printed spot. Thin lines are single exponential fittings for each printed spot. The thick line is a single exponential averaged fitting curve providing an average division time of 20.6 ± 1.3 min.

Figure 2 shows that patterned bacteria keep living, dividing and growing after printing on the agarose gel. Figure 2B shows the total area of printed bacteria as a function of time. The exponential fit provides a characteristic division time of 20.6 ± 1.3 min per generation, which corresponds well to that in bulk culture conditions (21.4 ± 0.9 min). This demonstrates that bacteria keep their normal physiological behavior after printing. This new method is thus suitable for further biological investigations such as cell-cell interaction, competition, evolution, or population dynamics.

2. CULTURE OF BACTERIA ARRAYS UNDER DYNAMICAL MICROFLUIDIC CONDITIONS

Then, we elaborated a microfluidic device, in which bacteria were grown in a 2D monolayer under dynamical microfluidic conditions. It is based on the confinement of bacteria in a sandwich configuration between an agarose gel and a microscopy glass slide. The microfluidic flow (which can bring nutrients, drugs, stress molecules, etc…) is above the gel, *i.e.*, the bacteria are hydrodynamically isolated from the flow (Fig. 3A). Phase contrast and fluorescence microscopy (Fig. 3B) coupled with an automated image analysis system [2] allowed the single-cell tracking of all individuals. Bacteria growing under a flow

of nutriments had an average characteristic division time of 21.5 min (Fig. 3C), showing that bacteria kept their normal physiological behaviour inside the microsystem.

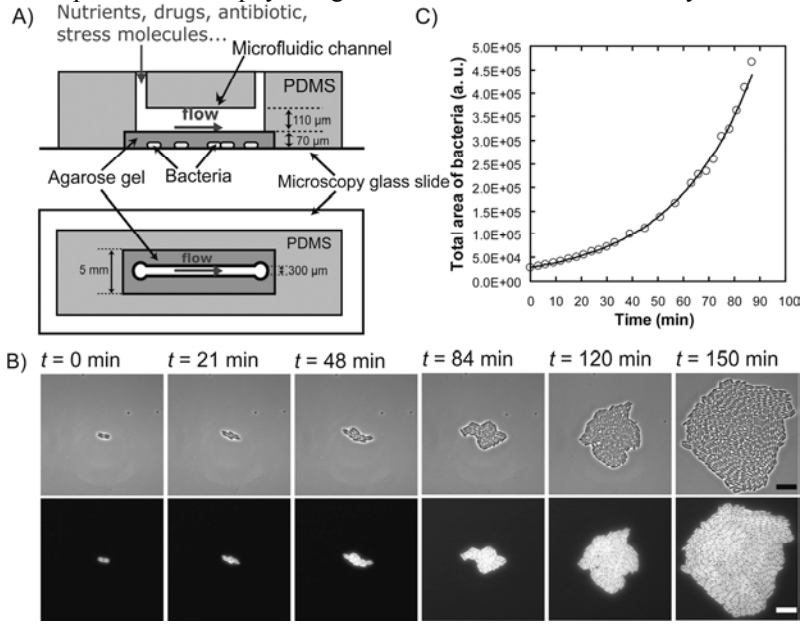

Figure 3. A) Device for 2D-culture of bacteria under a flow. B) Time-lapse microscopy images (phase contrast and fluorescence) of *E. coli* under a flow of nutrients (LB culture medium) of 60 µL/min. C) Growth curve of bacteria. The solid line is an eponential fitting curve providing a characteristic division time of 21.5 min.

3. LINEAGE-DEPENDENT SINGLE-CELL RESPONSES TO ENVIRONMENTAL PERTURBATION

Using the methodology described above, we established the distribution of single-cell responses to the injection of IPTG of wild type strain of *E. coli* modified to express the gene encoding yellow fluorescent protein (YFP) under the control of $P_L$lacO promoter (induced by IPTG). We found that individual time-responses were directly correlated to initial fluctuations in bacteria before induction and established the signal propagation through successive generations. These results will be published in a forthcoming paper.

4. CONCLUSION AND PERSPECTIVES

We developed two novel methodologies, which allow cell positioning, bacteria culture, automated cell tracking, and response detection, all being performed with single-cell resolution. Their combination should provide a powerful and versatile platform to investigate the ecological and evolutionary properties of living systems.

REFERENCES

[1] L. Xu et al., *Micro-Contact Printing of Living Bacteria Arrays with Cellular Resolution*, Nano Lett. (in press, 2007)

[2] E.J. Stewart et al., *Aging and death in an organism that reproduces by morphologically symmetric division*, PloS Biology, e45, pp. 295-300, (2005)

REAL TIME DETECTION OF CELL BINDING ON BIOCHIPS USING SPR IMAGING

Yoann Roupioz*, Emmanuel Suraniti*, Roberto Calemczuk*, Thierry Livache*, Patrice Marche and Marie-Bernadette Villiers****

**UMR 5819, CNRS-CEA-UJF, Grenoble, FRANCE*

***INSERM Unité 548, Grenoble, FRANCE*

ABSTRACT

We demonstrate the use of SPR imaging for detection if site-specific binding of either B or T lymphocyte populations on an electrochemically-grafted antibody array. With low concentration samples, individual cells are visualized on SPR images as discrete objects. With higher cell concentrations, grey levels on microarray spots are used to follow cell binding.

Keywords: antibody microarray – SPR imaging – cell sorting - biochip

1. INTRODUCTION

Biochips dedicated to cell analysis have generated tremendous interests in developing new tools for both diagnostic and research purposes. The goals sought after are based on rapid analysis, high throughput, small sample volumes and the use of biology compatible materials to increase efficiencies of detection.

Among usual biological samples, blood is a major source of data for diagnostic purposes. This complex material is composed of a large number of different cell types, present at various concentrations. Red blood cells constitute about 99% of the blood cells, whereas platelets and leucocytes are present at much lower levels (about 0.6-1% and 0.2% respectively). Among leucocytes, B and T lymphocytes are key actors within immune responses. Any variation of the lymphocyte concentrations is important to track as it may be linked to immune disorders. To mimic such a biological sample, we used B-type lymphocyte and T-type lymphocyte murine cell lines. The samples were prepared as pure cell populations or as mixed B and T lymphocyte populations before loading in the biochip reactor (Figure 1).

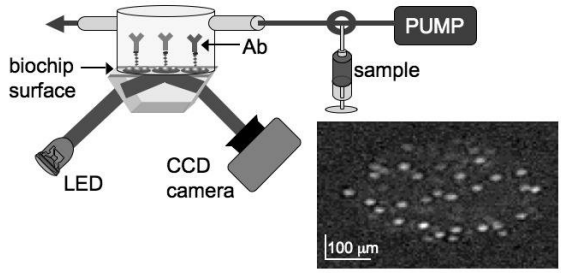

Figure 1: Schematic view of the SPR imaging setup. Inset: SPR differential image of an anti-CD19 antibody (Ab) spot after binding of B-type lymphocytes.

In the scope of functionalizing active surfaces toward biological samples (such as blood), pyrrole coupling to biomolecules (used as probes) and subsequent electro-

978-0-9798064-0-7/µTAS2007/$20©2007CBMS

polymerization on gold surfaces has been shown to be a versatile approach for designing biochip.[1, 2] Such electrochemically arrayed gold films can easily be coupled to Surface Plasmon Resonance imaging (SPRi) for detection of biological interactions in the vicinity of the biochip surface. This surface-sensitive technique is of increasing interest for bioanalysis as it allows label-free and real-time analysis of biomolecule interactions on functionalized surfaces.

3. EXPERIMENTAL

Materials and reagents: Prisms bearing a 48 nm thick gold layer above a 2 nm thick chromium layer were provided by Genoptics (Orsay, France). Purified monoclonal antibodies were supplied by BD Pharmingen (Le Pont-de-Claix, France); LS102.9 B cell hybridoma and 13G7 T cell hybridoma were kindly provided by L. Vidard (Institut Curie, France).[3]

Sample preparation: Cells were centrifuged for 5 minutes at 400 g and resuspended in DMEM (Dubelco's Modified Eagles Medium) supplemented with 5% heat inactivated FCS (Fetal Calf Serum). The cell concentration was then determined and adjusted to $1x10^6$ cells.mL^{-1}.

Preparation of pyrrole–protein conjugates: N-hydroxysuccinimidyl 6-(pyrrol-yl)-caproate (NHS–pyrrole) was prepared as previously described.[1] Antibodies (1.5 µM) were conjugated to NHS–pyrrole (15 µM) in phosphate-buffered saline (PBS) pH 7 overnight at room temperature.

Biochip functionalization: Biochips are glass prisms covered with a gold layer used as a working electrode. Pyrrole conjugated proteins were arrayed on the biochip as described elsewhere.[1]

Cell binding on the chip: The reactions were carried out in a 200 µL PEEK reactor connected to a peristaltic pump (100 µL/min) and a waste vial. The prism was placed in a SPR imager (Genoptics SA, Orsay, France). Then, the reactor was filled with DMEM and plasmon curves were plotted. Cellular samples were injected through a syringe into the circuit and moved with the peristaltic pump. Cell–antibody interactions induced a modification in the refractive index near the gold surface, resulting in a change of the reflectivity which was monitored using a 12-bit CDD camera as a grey level contrast.[2] Images were recorded every 0.02 seconds and analyzed with a dedicated software (Genovision, Genoptics).

4. RESULTS AND DISCUSSION

Gold surfaces were arrayed with several monoclonal antibodies known for efficient binding of antigens present in lymphocyte cellular membranes. Most of these proteins are used as cell-type specific markers in Fluorescence-Activated Cell Sorting (FACS) experiments (e.g. CD3, CD90, CD19, IA/IE, IA^b). The antibodies were covalently pyrrole-modified and electro-polymerized on gold films lying on glass prisms. Such functionalized biochips were then mounted on a SPR imager. SPR images were recorded in real time and allowed monitoring of label-free cell surface binding (Figure 1, inset). Binding events were successfully detected within minutes after cells injection. Our experimental setup allowed visualization of single cell binding events with low concentration cell samples but also quantification of grey level variations on regions of interest with more concentrated cellular samples. The cell surface binding responses were highly specific to the grafted antibodies and to the injected cell type, with poor non-specific or cross-reacted binding (Figure 2).

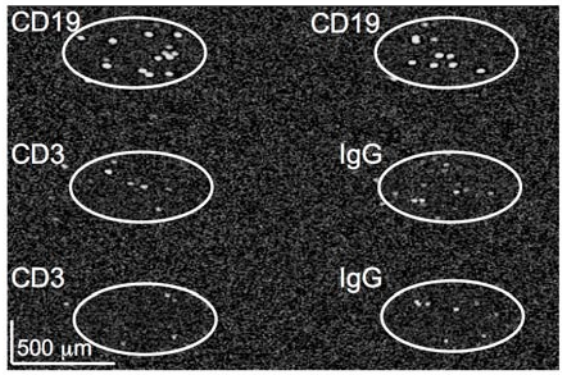

Figure 2. SPR image of an antibody microarray after cell binding. Individual cells can be seen on B-lymphocyte targeting spots (anti-CD19 antibodies) and T-lymphocyte targeting spots (anti-CD3 antibodies). Control IgG spots have also been spotted to assess the antibody non-specific cell binding.

5. CONCLUSIONS

As a conclusion, we designed electrochemically functionalized antibody microarrays dedicated to cell sample analysis. Using SPR imaging, we detected single cell binding as well as cell binding of mixed cell populations mimicking blood cell samples. These interactions were monitored in real-time and with no labelling of the sample to be analyzed. The versatility of this approach opens up several fields of applications and should be useful in designing new miniaturized systems for rapid diagnostic analysis or cell-surface adhesion kinetic studies.

ACKNOWLEDGMENTS

The authors are grateful to the Nanobio program for funding part of this work.

REFERENCES

[1]L. Grosjean, B. Cherif, E. Mercey, A. Roget, Y. Levy, P. N. Marche, M. B. Villiers and T. Livache, "A polypyrrole protein microarray for antibody-antigen interaction studies using a label-free detection process," Anal Biochem, Vol.347, pp.193-200 (2005)

[2]P. Guedon, T. Livache, F. Martin, F. Lesbre, A. Roget, G. Bidan and Y. Levy, "Characterization and optimization of a real-time, parallel, label-free, polypyrrole-based DNA sensor by surface plasmon resonance imaging," Anal Chem, Vol.72, pp.6003-9 (2000)

[3]L. Vidard, K. L. Rock and B. Benacerraf, "Diversity in MHC class II ovalbumin T cell epitopes generated by distinct proteases," J Immunol, Vol.149, pp.498-504 (1992)

SINGLE CELL ANALYSIS BY NATIVE UV LASER INDUCED FLUORESCENCE DETECTION IN A PDMS MICROFLUIDIC CHIP

Dominik Greif, Dario Anselmetti, Alexandra Ros

Experimental Biophysics and Applied Nanoscience, Physics Department, Bielefeld University, Universitätsstr. 25, 33615 Bielefeld, Germany

ABSTRACT

We present an extension of our studies on single cell analysis with native label-free UV-LIF detection [1], in order to improve separation efficiency and detection sensitivity. We significantly reduced the background fluorescence by the fabrication of new PDMS-Quartz-Window-chips (PQW-chips) by at least 75 percent. Furthermore, the pH of the separation buffer was optimized for maximum signal intensity of the aromatic amino acid tryptophan. Based on these improvements we exemplarily present two single cell protein electropherograms from *Spodoptera frugiperda* (Sf9) insect cells with five times more and four times higher peaks as compared to our previous single cell studies [2].

Keywords: single cell, label-free UV-LIF detection, PDMS microfluidic chip, proteome

1. INTRODUCTION

Future single cell analysis allows individual expression studies, which are not limited by ensemble averaging effects from cell-cycle dependent states, the different and inhomogeneous cellular response to external stimuli, or the introduction of genomic and proteomic variability during cell proliferation. Experiments have shown that significant cellular phenotypes are only resolvable when studying single cells, emphasizing the importance of studying individual cells rather than heterogeneous populations [3]. For proteome research, effective, sensitive and quantitative separation and detection techniques are essential. Microfluidic devices have the potential to fulfil these requirements, which is impressively demonstrated by the transfer of proteome relevant separation techniques to the microfluidic format [4]. We could recently demonstrate a detection limit of 25 nM tryptophan (Trp) realised in a polydimethylsiloxane (PDMS) microfluidic device coupled to a sensitive label-free UV laser induced fluorescence (UV-LIF) detection system [2]. Thus we were able to perform single cell electropherograms on chip combined with UV-LIF detection [2].

2. EXPERIMENTAL

Chemicals and reagents were purchased from Sigma. Detailed chip design and operations are adapted from [1, 5] as well as an earlier proposed method for single cell analysis combining navigation and steering of single cells with optical tweezers, on-chip cell lysis and electrophoretic separation of proteins with subsequent LIF detection. For the production of PQW-chips, copper weights were used, which push down small fused silica windows onto the microchannel at the point of detection before the PDMS is cured. Fluorescence spectra were taken with an LS 45 luminescence spectrometer (PerkinElmer).

978-0-9798064-0-7/μTAS2007/$20©2007CBMS

3. RESULTS AND DISCUSSION

a) Chip enhancement: We significantly reduced the background fluorescence by at least 75 percent for native UV-LIF detection with the fabrication of new PQW-chips as compared to our previous PDMS-chips (Figure 2).

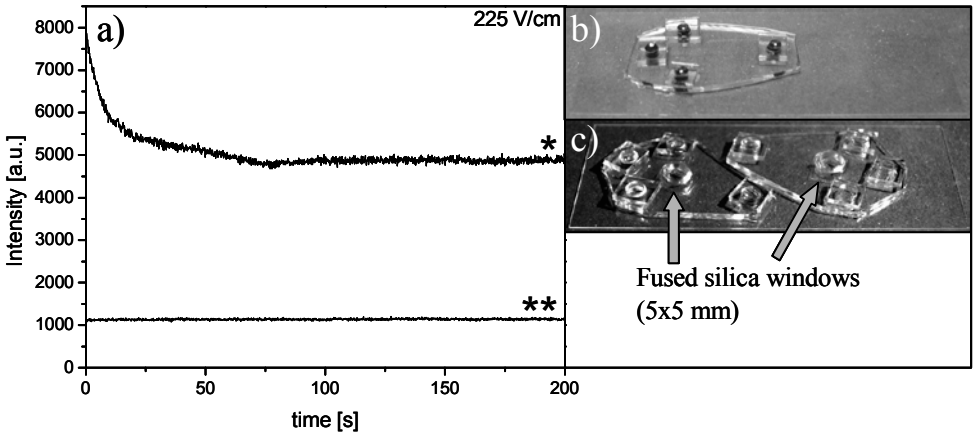

Figure 2. Fluorescence background reduction: (a) Fluorescence background of the microchannels filled with separation buffer (100 mM TRIS, 100 mM CHES, 4 % Pullulan, pH = 11,0), with 1000 µm pinhole and 500 µW laser power, λ_{ex} = 266 nm, (*) within the PDMS-chip and (**) within a PQW-chip. (b) Photograph of a PDMS-chip and c) two PQW-chips.

b) Increased signal intensity at basic pH: The investigation of the fluorescence intensity for the aromatic amino acid tryptophan in dependence of the separation buffer pH revealed an optimum pH value at ~11 for maximum intensity (Figure 3).

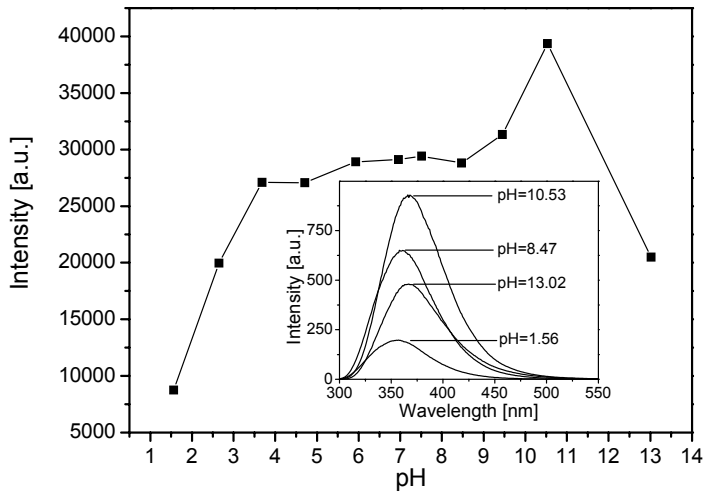

Figure 3. Increased signal intensity at basic pH: dependence of fluorescence intensity on pH for 10 mM tryptophan (Trp) solutions (in PBS), (λ_{ex} = 280 nm, λ_{det} = 335-385 nm). Inset: Selected emission spectra of the same Trp solutions from pH 1.6 to 13.0 (λ_{ex} = 280 nm).

c) Single cell electropherograms: Two single cell protein electropherograms from Sf9 cells are shown in Figure 4. These electropherograms exhibit five times more and four times higher peaks as compared to our previous single cell studies (total number of peaks: ~50-55) [2].

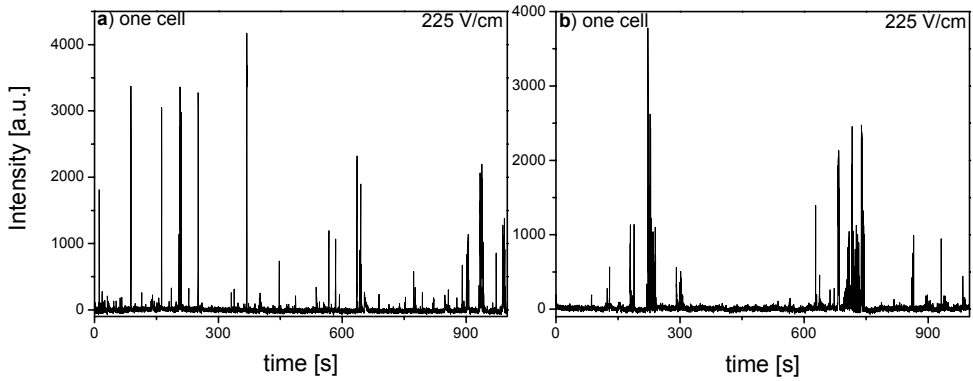

Figure 4. (a) Baseline corrected electropherogram from a single Sf9 cell with native UV-LIF detection (λ_{ex} = 266 nm). Separation buffer (100 mM TRIS, 100 mM CHES, 4 % Pullulan, pH = 11,0), 1000 µm pinhole and 500 µW laser power. The cells were electrically lysed with an electric field pulse (1800 V/cm, 50 ms). The channels in the PQW-chip were coated with F108. (b) Electropherogram of a single Sf9 cell with equal conditions as in (a).

4. CONCLUSIONS

The background fluorescence in native UV-LIF detection was significantly reduced by the production of the new PQW-chips. These PQW-chips integrate fused silica windows in the PDMS-microdevice at the point of detection. Thus, the advantages of normal PDMS-chips, like gas permeability and low costs were combined with those of full-body quartz glas chips, especially the high detection sensitivity. Further, the fluorescence intensity of the aromatic amino acid tryptophan, which is mainly responsible for the fluorescence signal in UV-LIF detection, could be raised by the use of a basic pH. With those amendments the UV-LIF detection was explicitly improved for single cell analysis. In the future, we will strive towards single cell fingerprinting with label-free UV-LIF detection.

ACKNOWLEDGEMENT

Financial support from the Deutsche Forschungsgemeinschaft (Project: An 370/1-2) is gratefully acknowledged.

REFERENCES

[1] W. Hellmich, C. Pelargus, K. Leffhalm, A. Ros, D. Anselmetti, Electrophoresis 26 (2005) 3689.
[2] W. Hellmich, D. Greif, C. Pelargus, D. Anselmetti, A. Ros, J. Chromatogr. A 1130 (2006) 195.
[3] David N. Breslauer, Philip J. Lee, Luke P. Lee, Mol. Biosyst. 2 (2006) 97-112.
[4] N. Lion, et al., Electrophoresis 24 (2003) 3533.
[5] A. Ros, W. Hellmich, J. Regtmeier, T.T. Duong, D. Anselmetti, Electrophoresis 27 (2006) 2651.

SINGLE CELL ISOLATIONS BY TAMDEM MICRO-CHAMBERS ON A CENTRIFUGAL FLOW DEVICE

H. Nagai[1], S. Furutani[2] and I. Kubo[2]

[1]National Institute of Advanced Industrial Science and Technology (AIST), JAPAN and
[2]Soka University, Japan

ABSTRACT

We developed a convenient method for simultaneous isolation of a large number of cells using "tandem microchambers" on a centrifugal microfluidic device. Small "pockets" were periodically arranged along the sidewall of a microchannel and used as tandem microchambers. Each microchamber individually trapped the microvolume of cell suspension during centrifugal flow, and then the dispersing cells could be isolated into these microchambers followed by Poisson distribution. When micro-beads and microorganisms were separated on the device, the efficiency of isolation depended on the shape of microchambers and the number of beads or cells. Using the optimized condition and the tamdem microchannels, the cells could be successfully isolated.

Keywords: Single Cell, isolation, centrifugal microfluidics, microchamber array

1. INTRODUCTION

For single cell assay, cell manipulation devices based on electrokinetic/magnetic forces and optical tweezers have been developed instead of a conventional cell sorter [1-3], but they need complicated fabrication and control system. Takeuchi et al. proposed a simple cell-trapping concept based on hydro-dynamic traps, which consisted of a loop channel and many narrow trap channels choked with a cell, in μTAS 2006 [4]. However, the throughput of single cell assay using these devices would be limited because the isolated cells need to be individually transported for the subsequent assay after the cell isolation process. In order

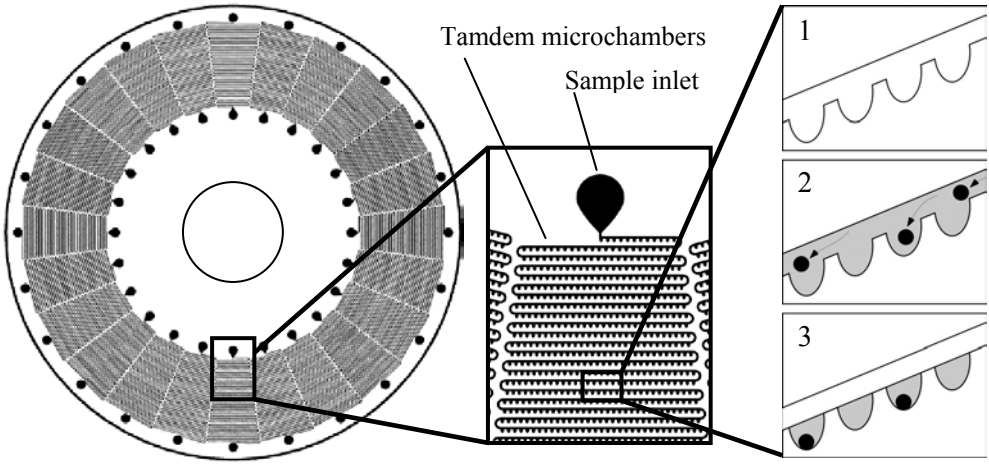

Figure 1. Design of the tandem microchambers on a centrifugal flow device and the scheme of the single cell isolation. A large number of microchambers align along a main channel (1), and the cells flow through the microchambers (2) and are distributed into the individual microchamber (3).

978-0-9798064-0-7/μTAS2007/$20©2007CBMS

to realize the high throughput of single cell assay, we aim the common use of highly integrated microchambers for the trap in cell isolation and reaction chambers in cell assay.

2. EXPERIMENTAL

As shown in Figure 1, a disk-shaped microfluidic device was designed and fabricated of PDMS. A large number of microchambers were aligned in tandem along the main channel on the device. The sample solution containing beads or microorganisms was injected into the inlets, and then the microchannel was filled by centrifugal force. Subsequently, the excess solution in the main channel flowed out except for the solution in each microchamber. To prevent drying of the solutions, mineral oil or fluoride solvent were immediately injected by capillary effect. The distributed parts of the solution in the microchambers were absorbed with a microscope and a imaging scanner. Thus, the number of the microchambers containing isolated cells or beads were counted.

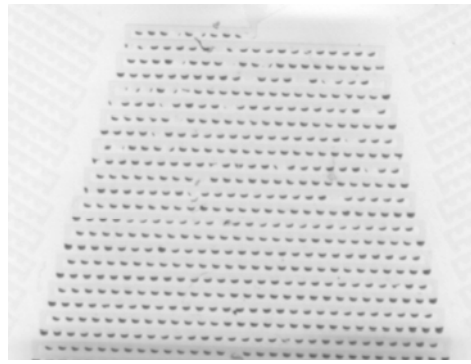

Figure 2. Distribution using tamdem microchambers on a Disk-shaped microfluidics. Red ink was successfully distributed into the microchambers.

3. RESULTS AND DISCUSSION

Figure 2 shows the distribution of ink solution using the tamdem microchambers. Thus, the solution was easily separated into a large number of microchambers with the almost same volume, and the contents was randomly distributed within the tandem microchambers. Especially, it was expected that each cell could be isolated by the tandem microchambers when the amount of cells was by far fewer than the whole number of the microchambers.

To estimate the efficiency of cell isolation, the geometrical structure of the tandem microchambers was examined by using beads suspension. Two types of microchambers were designed as square-shape and curved-shape; the sizes were 150 x 150 μm. Compared with the square-shaped microchambers, the curved-shaped microchambers could efficiently isolate the single bead after the rotation of the device at 3,000 rpm (Figure 3). When there was a dead-volume in the microchamber such as the square-shape, it was considered that the flowing cells were dominantly trapped in the microchambers on the upstream of the

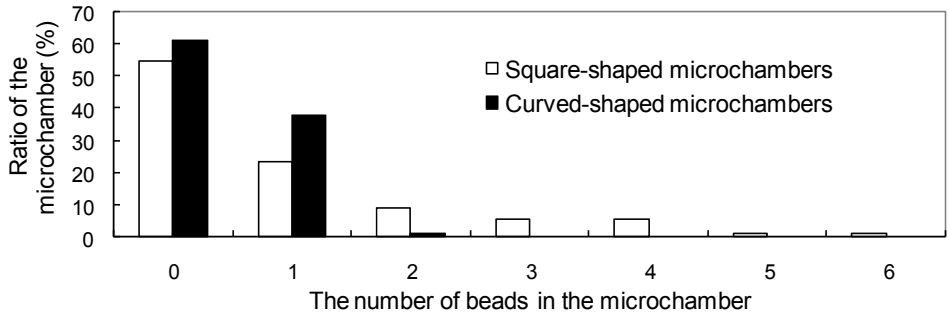

Figure 3. Ratio of the microchamber containing various numbers of beads after beads separation.

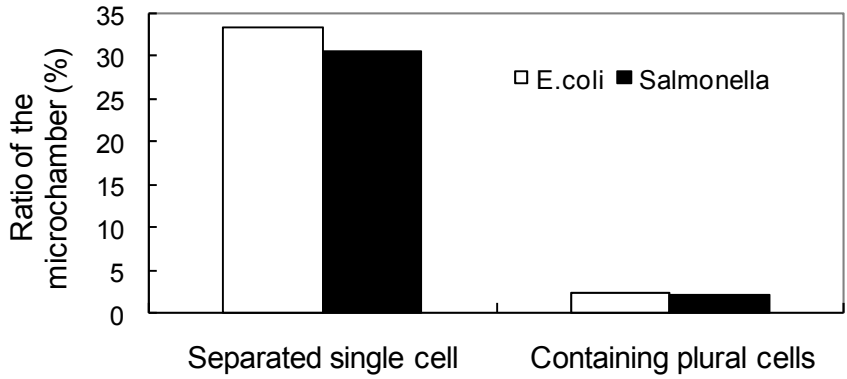

Figure 4. Single cell isolation for two kinds of microorganisms by the tandem microchambers.

channel and would clog the channel at the worst case. Hence, it was important that the behavior of cell in microfluidic flow would contribute to the efficiency of single cell isolation. Using the tandem microchambers with the curved shape, single cell isolation for microorganisms was examined as shown in Figure 4. Although the size and the shape of E.coli were different from those of Salmonella, these microorganisms could be individually separated with the same efficiency of the single cell isolation (≈ 95%). It was also observed that the probability of the existence of cells in each microchamber depended upon Poisson distribution, regardless of the cell size.

4. CONCLUSIONS

We successfully demonstrated the single cell isolation by using the tandem microchambers and centrifugal microfluidics. The efficient of cell isolation depended on Poisson distribution. This concept for cell isolation are very simple and useful to perform single cell analysis on a compact system. Especially, since all of the isolated cells were enclosed into the individual solution, it was expected that each cell could be continuously identified by PCR.

REFERENCES

[1] N. Manaresi, A. Romani, G. Medoro, L. Altomare, A. Leonardi, M. Tartagni, and R. Guerrieri, “A CMOS chip for individual cell manipulation and detection”, IEEE J. Solid-State Circuits, **38**, 2297 (2003).

[2] H. Lee, A.M. Purdon, and R.M. Westervelt, “Manipulation of biological cells using a microelectromagnet matrix”, Appl. Phys. Lett., **85**, 1063 (2004).

[3] P.Y. Chiou, A.T. Ohta, and M.C. Wu, “Massively parallel manipulation of single cells and microparticles using optical images”, Nature, **436**, 370 (2005).

[4] W.-H. Tan and S. Takeuchi, “An optical retrieval microfluidic system for microarray applications”, Micro Total Analysis Systems 2006, **1**, 509 (2006).

AN INTEGRATED MICROFLUIDIC SYSTEM FOR LONG-TERM CULTURE AND CONTINUOUS MONITORING OF INTESTINAL CELLS

H. Kimura, T. Yamamoto, Y. Sakai and T. Fujii
Institute of Industrial Science, University of Tokyo, Japan

ABSTRACT

We developed an integrated microfluidic device with on-chip pumping and optical detection functionalities for cell culture and assay. The microfluidic structure in the device is divided into two compartments separated by a semipermeable membrane on which cells are inoculated and cultured. The performance of the device was examined through long-term culture and monitoring of polarized transportation activity of gastrointestinal cells, Caco-2. The cells were cultured for more than two weeks, and transportation of rhodamine 123 by Caco-2 cells during cell culture was successfully monitored by continuous fluorescence measurement.

Keywords: Cell culture and assay, on-chip perfusion, 2-compartment, Caco-2 cell

1. INTRODUCTION

Although there has been enormous efforts made to improve *in vitro* cell-based assays for life science and medical applications, the conventional methods still have many problems in keeping and monitoring the activity and functionality of cells for a longer time-period. Microfluidics is the emerging technologies that have potentials to culture the cells in good condition like *in vivo* by integrating functional elements necessary for continuous perfusion and monitoring cells activities into a single microfluidic device.

Here, we have developed an on-chip micro perfusion cell culture device for long-term cell culture and on-line monitoring. The microfluidic structure is divided into two compartment separated by a polyester semipermeable membrane, on which cells are inoculated and cultured. Polarized transportation activity of Caco-2 cells, as a function of gastrointestinal cells, is examined to demonstrate the performance of the device.

2. EXPERIMENTAL

The overall structure of the device is schematically shown in Figure 1. The microfluidic structure in the device is divided into two compartments. The upper and lower compartments are denoted as apical (AP)-side and basolateral (BL)-side corresponding to the polarity of the cells cultured on the semipermeable membrane. Both compartments consist of a culture chamber and a pumping chamber connected with microchannels. The photograph of the device is shown in Figure 2. A stir-bar enclosed in the pumping chamber is energized by the external magnetic field generated by a motor-controlled permanent magnet placed just beneath of the pumping chamber. Pulsative but unidirectional continuous flow is generated as the rotational motion of stir-bar, which rakes up a liquid from the inlet to the outlet of the pumping chamber. The flow rate versus rotational frequency of the stir-bar is shown in Figure 3. This result shows that the stirrer-based micropump can circulate the culture medium with keeping enough slow to prevent the cells from peeling off the semipermeable membrane [2]. Additionally, both of the AP-side and

978-0-9798064-0-7/μTAS2007/$20©2007CBMS

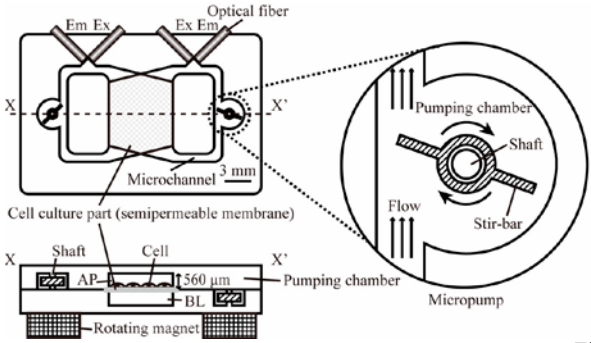

Figure 1. Schematic of the on-chip micro perfusion cell culture device.

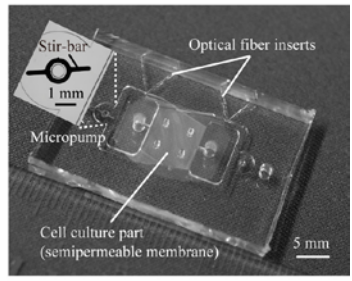

Figure 2. Photograph of the microfluidic device.

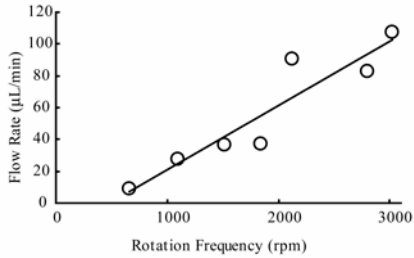

Figure 3. Flow rates measured by PIV plotted vs. rotation frequency of the stir-bar.

the BL-side has two optical fiber inserts for fluorescence measurement; one is for excitation, the other is for detection, where commercially available optical fibers are inserted.

The transportation assay on Caco-2 cells was conducted by measuring the fluorescent intensity difference between the AP-side and BL-side using rhodamine 123, which is a fluorescent dye to be transported by P-glycoprotein of Caco-2 cells [3]. To monitor the fluorescent intensity of rhodamine 123, the optical fibers for excitation were connected to a homemade LED light source of 470 nm in wavelength, while the ones for detection were connected to a spectrophotometer to detect the emission light of 530 nm in wavelength.

Rhodamine 123 (10 μM final concentration) was premixed with the culture medium prior to the experiment, and fed into the AP-side and the BL-side simultaneously. The fluorescent intensities were continuously recorded at 50 ms interval for 24 h after injecting the rhodamine 123 solution. In this work, transportation assays were conducted from day 14 to day 21.

3. RESULTS AND DISCUSSION

Figure 4 shows the time course of the intensity of rhodamine 123 during the transportation assay. In order to display only the variation from the equilibrium, all the data were normalized by subtracting the intensity obtained in the negative control experiment with no cells (not displayed). All plotted points were the mean values of four data sets independently obtained from four devices under the same experimental conditions. As expected from the literature[3], rhodamine 123 is apparently transported from the BL-side to the AP-side.

The apparent permeability coefficient (P_{app} [cm/sec]) is commonly used to characterize transportation through a membrane, which can be calculated as;

$$P_{app} = \frac{dQ}{dt}\frac{1}{C_0 A} \quad (1)$$

where Q [mol] is the increased amount of fluorescent molecule transported over time dt [sec], A [cm^2] is the area of the semipermeable membrane, and C_0 [mol/mL] is the initial concentration of fluorescent molecule. Here, P_{app} is calculated from the parameters used in the experiments; Q=0.18×10^{-9} [mol] was derived from the measured intensity data, A=0.72 [cm^2], and C_0=10×10^{-9} [mol/mL]. The resulting calculated value of P_{app} is 3.47×10^{-6} cm/sec, which is as same as the value obtained from conventional culture methods using commercially available culture inserts [3]. This result shows the capability of the device for long-term culture coupled transportation assay of Caco-2 cells.

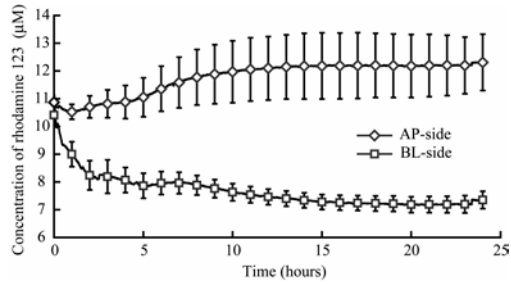

Figure 4. Time course of rhodamine 123 concentration in the AP-side and the BL-side. The fluorescent intensity in both the AP-side and the BL-side are continuously measured for 24 h through optical fibers in the device. The graph shows that the intensity in the AP-side is increasing while it is decreasing in the BL-side over time, which corresponds to the polarized transportation of rhodamine 123 from the BL-side to the AP-side.

4. CONCLUSIONS

Thanks to the integrated functionality of culture medium perfusion and fluorescence measurement, the on-chip micro perfusion cell culture device could provide useful platforms for drug screening and toxicity testing for cells forming layer-like structures. The system could potentially be extended to realize complicated culture systems containing a network of miniaturized culture chambers to study dynamic mutual interactions between various types of cells and tissues with much simpler setups compared to existing works.

ACKNOWLEDGEMENTS

This work is partially supported by the Grand-in-Aid for Scientific Research on Priority Areas, System Cell Engineering by Multi-scale Manipulation (MEXT), Center for NanoBio Integration (MEXT), and Bioarchitect Research Program (RIKEN).

REFERENCES

[1] J.T. Borenstein, H. Terai, J.P. Vacanti et al., *A microfabricated array bioreactor for perfused 3D liver culture*, Biomed Microdevices, vol. 4, pp. 167-175, (2002).

[2] A. Sin, M. L. Shuler et al., *The design and fabrication of three-chamber microscale cell culture analog devices with integrated dissolved oxygen sensors*, Biotechnol Prog, vol. 20, pp. 338-345, (2004).

[3] B. D. Rege, J. E. Polli et al., *Effects of nonionic surfactants on membrane transporters in Caco-2 cells monolayers*, Eur J Pharm Sci, vol. 16, pp. 237-246, (2002).

MICROPATTERNED HYDROGEL TISSUE SCAFFOLDS WITH CONTROLLED ELECTROKINETIC PROPERTIES FOR INVESTIGATION OF CHONDROCYTE MECHANOTRANSDUCTION

A.D. Rouillard, Y. Tsui, L.J. Bonassar and B.J. Kirby
College of Engineering, Cornell University, Ithaca, NY

ABSTRACT

Microparticle doping and micropatterning of hydrogel materials allow unique control of the electrical, mechanical, and chemical cellular environment in tissue scaffolds. This enables study of the role that individual electrical and mechanical effects play in mechanotransduction. In this work, key hydrogel fabrication techniques have been identified that allow electrokinetic decoupling of hydrogel materials. Micropatterning will allow these decoupled materials to be tested on chondrocytes in a consistent chemical environment and enable further understanding of chondrocyte mechanotransduction.

Keywords: electrokinetic, mechanotransduction, micropatterning, tissue engineering

1. INTRODUCTION

The present work uses microfabrication techniques and microparticle doping to pattern hydrogel tissue scaffolds with microscale spatial resolution to control the electrokinetic scaffold environment for the study of chondrocyte (cartilage cell) mechanotransduction (Fig. 1). Mechanical signals are extremely important factors driving cell differentiation and tissue generation. As a consequence of the complex poroelastic (solid/aqueous) environment of many tissues, externally applied mechanical forces may be sensed by cells in a variety of ways: pressure, deformation, shear, material flux, or streaming potential. The complexity of these systems beckons the use of microscale engineering approaches for more controlled study. Micropatterning of composite hydrogel materials uniquely allows independent control of the electrical, mechanical, and chemical cellular environment.

Cartilage tissue is a complex, electrokinetically coupled poroelastic material. Dynamic mechanical loading has been shown to stimulate chondrocyte biosynthesis of glycosaminoglycans (GAG) [1]. Negatively charged GAG carbohydrate polymers found in the cartilage extracellular matrix provide cartilage with its compressive resistance [2]. As a consequence of the high negative charge density, mechanical stresses applied externally to cartilage cause both high pressurization of the tissue and the generation of streaming potentials due to fluid flow. This coupling of electrical (streaming potential) and mechanical (pressurization, fluid flow) effects confounds more detailed understanding of chondrocyte mechanotransduction.

We are using microparticle doping and micropatterning in order to control flow-induced streaming potentials by layering hydrogel materials with different fixed charge densities, while maintaining a consistent chemical and mechanical cellular environment (Fig. 1). Specifically, we have investigated the use of ionic and covalent crosslinking of alginate in conjunction with silica microparticle doping as a means of manipulating streaming potential, modulus, and permeability. Successful formulations have delineated a clear path toward creating layered hydrogel constructs with electrokinetically decoupled cellular environments.

978-0-9798064-0-7/μTAS2007/$20©2007CBMS

2. METHODS

Layered hydrogel materials with different fixed charge densities can be used to manipulate flow-induced electric fields in the bulk material by changing the microscale spatial patterning of the layers. For successful electrokinetic decoupling, these materials must have similar mechanical properties (modulus and permeability). Seeding cells within a single layer then achieves a consistent chemical environment. Choice of ionic or covalent crosslinking with the addition of silica microparticles was studied as a means of creating electrokinetically decoupled hydrogel materials for micropatterning.

The electrokinetic properties of the hydrogels were characterized via stress relaxation and dynamic compression in a radially confined geometry. Stress (σ), strain (ε), and streaming potential (ΔV) were measured and modulus (H_A) and permeability (k_p) were calculated according to models from poroelastic theory.

3. RESULTS AND DISCUSSION

The electromechanical properties of alginate hydrogels were probed as a function of alginate concentration, silica concentration, and choice of crosslinker. Modulus and permeability were changed by an order of magnitude by varying alginate concentration (Fig. 2). The addition of silica microparticles increased modulus independently of permeability (Fig. 2). Streaming potentials varied by an order of magnitude between ionically and covalently crosslinked hydrogels (Fig. 3). This parameter space allows modulus and permeability to be selected with low or high streaming potentials, depending upon choice of crosslinker.

Electrokinetically decoupled hydrogels (similar mechanical characteristics, different electrical characteristics) were successfully produced. This was achieved by using choice of crosslinker as a means of changing the alginate fixed charge density. Ionic crosslinking, in which Ca^{2+} binds negative charges on alginate polymers, effectively reduced the alginate charge density. Covalent crosslinking, on the other hand, left the charged groups on alginate unperturbed. This difference in fixed charge density gave rise to different streaming potentials.

Micropatterning of these materials in a layered construct is the key to achieving a consistent chemical environment in addition to a consistent mechanical environment. Chondrocytes can be seeded into a single material type. The degree of averaging of the hydrogels with high and low electrical response in the bulk material can then be manipulated through choice of layering duty cycle (Fig. 1). Such a construct allows study of how chondrocytes respond to dynamic electric fields, with all other chemical and mechanical factors constant.

4. CONCLUSION

Microparticle doping and micropatterning of hydrogel materials allow unique control of the electrical, mechanical, and chemical cellular environment in tissue scaffolds. This enables independent manipulation of individual electrical and mechanical responses to loading for mechanotransduction studies. In this work, key hydrogel fabrication techniques have been identified that allow electrokinetic decoupling of hydrogel materials. Micropatterning will allow these decoupled materials to be tested on chondrocytes in a consistent chemical environment. Such study will further understanding of chondrocyte mechanotransduction and direct more intelligent design of tissue scaffold properties.

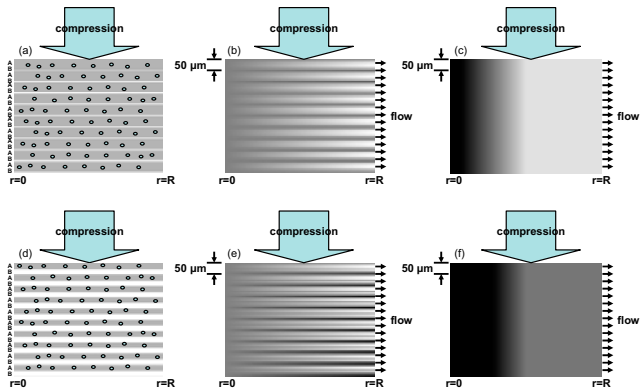

Fig. 1 Spatial patterning allows control of streaming current and streaming potential. Two materials (e.g., ionically and covalently crosslinked alginate) lead to streaming current of different magnitudes, and the duty cycle of the micropatterning controls the resulting streaming potential. Results shown for compression of an axisymmetric disk with high duty cycle (a-c) and low duty cycle (d-f). Left: patterning of ionically (A) and covalently (B) crosslinked alginate; chondrocytes are seeded into a single type for a consistent chemical environment. Middle: streaming current field; grayscale indicates current density magnitude. Right: streaming potential field; grayscale indicates local electrical potential.

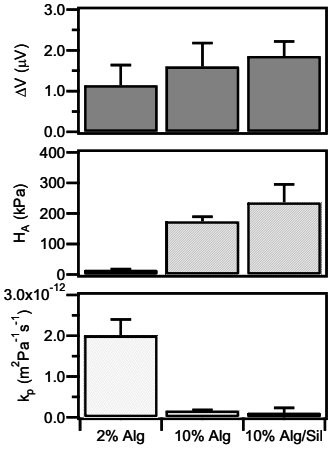

Fig. 2 Micropatterned alginate hydrogels fabricated by layering and ionically crosslinking 100 µm thick films. H_A and k_p changed by an order of magnitude between 2% and 10% w/v alginate with constant ΔV. H_A was changed independently of k_p by adding 10% w/v silica microparticles.

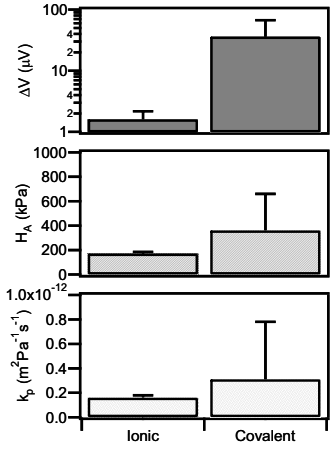

Fig. 3 10% w/v ionically crosslinked alginate (left) and covalently crosslinked alginate (right). Modulus (H_A) and permeability (k_p) differed by a factor of 2, while streaming potential (ΔV) differed by a factor of 20.

REFERENCES

[1] Kim, Y. *et al.* (1995) Journal of Biomechanics **28**, 1055-1066.
[2] Lee, R.C. *et al.* (1981) Journal of Biomechanical Engineering **103**, 280-291.

PERIODIC PRESSURE PULSE GENERATOR IN CELL CULTURE CHIP

Y. F. Yu[1] , X. Zhang[1], R. Chua[2], P. H. Yap[2] and A. Q. Liu[1†]

[1]School of Electrical & Electronic Engineering,
Nanyang Technological University, Singapore.
[2] Defence Medical & Environmental Research Institute,
DSO National Laboratories, Singapore.
([†]Corresponding author. Tel: +65-6790 4336; Fax: +65-6793 3318; Email: aqliu@ntu.edu.sg)

ABSTRACT

For studying the effect of stress on cell growth, this paper presents a design of cell culture chip, which can generate periodic pressure pulses via fluidic control system and generate pressure pulses with different amplitudes via hydrodynamic pressure. Pressure pulses ranging from 180 mmHg to 80 mmHg are obtained. This chip features wide frequency range (from 0 to 100 pulses/min), tunable duty cycle (from 0 to 1) and no shear stress effect, making the cell culture chip promising for many applications, for example, biological research on the relation between hypertension and cancer.

Keywords: Cell culture, stress, pressure pulse, microfluidic chip

1. INTRODUCTION

In order to simulate on-chip in vivo microenvironments for cell culture, microfluidic chip with accurate fluidic control system is applied recently [1]. Compared with the traditional cell culture research, microfluidic cell culture systems focus on regulating the fluid mechanical environment but not the chemical environment. In prior studies, the shear stress is mainly considered for endothelial cells lining the inner lumen of blood vessels [1,2]. This paper presents a design of microfluidic cell culture chip, which has no shear stress effect on cells, can generate periodic pressure pulses via fluidic control system and generate pressure pulses with different amplitudes via hydrodynamic pressure. These features make the microfluidic chip possible for the culture of most cells under periodic pressure. It's significant for many applications, for example, to research on the relationship between hypertension and cancer [3] in the cell level.

2. THEORY AND DESIGN

In micro channel, the typical flow is a Poiseuille flow. In a steady-state Posieuille flow, there is a simple relationship between the flow rate Q and the pressure drop Δp as given by

$$Q = \Delta p / R \tag{1}$$

where R is the fluidic resistance, which is dependent on the channel's cross-section, the length L and the viscosity of the liquid η. For a rectangular channel with a width w and a height h ($w > h$), the fluidic resistance is

$$R = \frac{12\eta L}{h^3 w} \Bigg/ \left[1 - \sum_{n,odd}^{\infty} \frac{192}{\pi^5} \frac{h}{w} \frac{1}{n^5} \tanh\left(n\pi \frac{w}{2h} \right) \right] \tag{2}$$

978-0-9798064-0-7/μTAS2007/$20©2007CBMS

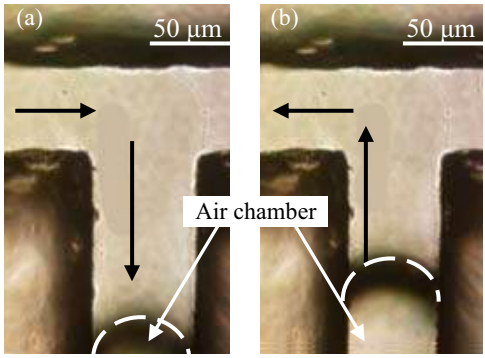

Figure 3. The region close to the air chamber. (a) high pressure; (b) low pressure.

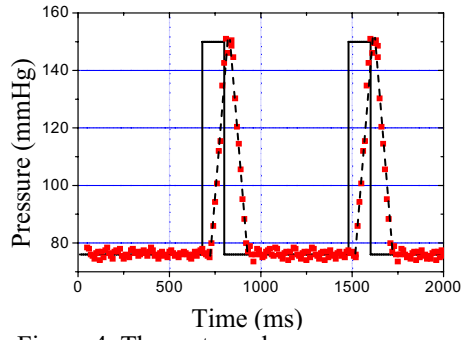

Figure 4. The rectangular pressure wave and the pressure in the air chamber.

Therefore, along the direction of Posieuille flow in a channel, the pressure is decreased continuously. A suspended branch (no flow) connecting to the channel at different locations can achieve different pressures.

Fig. 1a presents the schematic of the microfluidic cell culture chip with integral fluidic systems. The chamber a, b and c are filled with air. An air chamber functions as a capacitor, and the micro channel resembles a resistance. They are combined together to form the integral fluidic system, and similar to the integral circuit. Inlet 1, 2 and 3 are used for cell loading, and after that, they are clamped to stop the flow in the cell culture chambers. Periodic flow of cell culture medium from the inlet to the outlet generates periodic pressures with different amplitudes on different suspended branches. But shear stresses caused by the flow will be kept out of the cell culture chambers by the integral fluidic system, and only the stress caused by the pressure will affect the cell functions. Nutritional exchange between the flow of cell culture medium and the medium in cell culture chambers is mainly dependent on diffusion. Fig. 1b is the related circuit model, in which the differences of pressure pulse shape and amplitudes at different locations are shown.

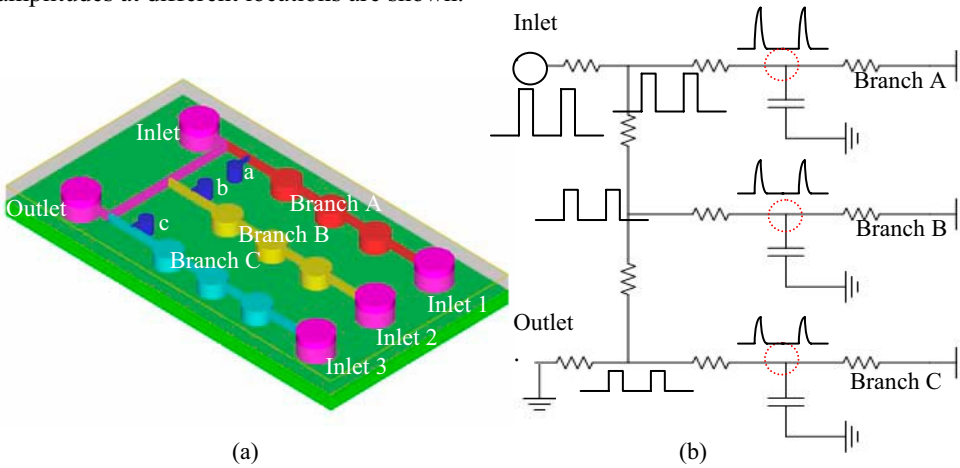

Figure 1. (a) The schematic of cell culture array chip with the integral fluidic system. (b) the circuit model and the shape of pressure pulse at several key points.

3. EXPERIMENTS AND RESULTS

The microfluidic cell culture chip (Fig. 2) fabricated by three PMMA layers through laser engraving and thermal bonding. UV glue is used for the sealing of the connection between the chip and the tubes. Syringe pump controlled by computer is used to generate initial rectangular wave with arbitrary period and duty cycle. The time resolution of the syringe pump is 1 ms. Micro-sized water droplets in air chamber a, b and c are used to monitor the real time pressures on different branches through interferometry method. The capacitor-like functions of air chamber are observed under microscope through the shift of air-liquid interface, as enhanced by dash lines in Fig. 3. Under a high pressure (Fig. 3a), the liquid flow into the air chamber and its pressure is increased. Under a low pressure (Fig. 3b), the compressed air push the liquid to flow out. Velocity distribution can also be measured by a μPIV system.

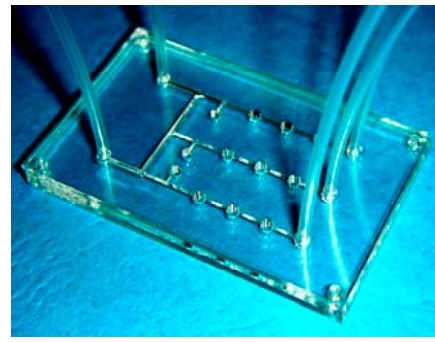

Figure 2. The chip fabricated by PMMA.

Pressure pulses with ranging amplitudes from 80 to 180 mmHg can be obtained by changing location and volume flow rate. A typical rectangular wave, with a period of 800 ms and a duty circle of 0.15, is shown in Fig. 4, and is deformed into a triangular wave. There is a delay about 30 ms between the two pressure waves. Frequency can be adjusted in the range from 0 to 100 pulses/min, and duty cycle from 0 to 1.

MDCK cells with cell culture medium (Dulbecco's modified eagle media with 10% fetal bovine serum) were loaded into the chambers through inlet 1, 2 and 3. After 2 days, cell monolayer is formed and attached on the base of the chambers (Fig. 5).

5. CONCLUSIONS

In summary, microfluidic cell culture chip with periodic pressure pulses is developed for studying the effect of pressure/stress on cell morphology and pathology, which has advantages as easy design, simple microfluidic manipulation and no shear stress caused by flow.

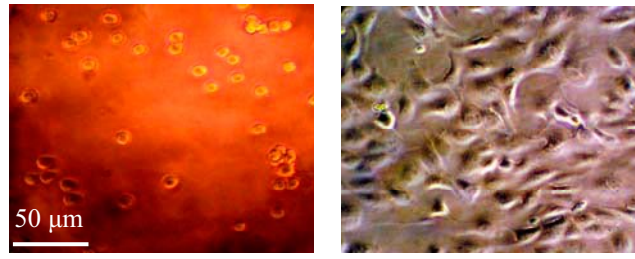

(a) (b)

Figure 5. MDCK Cell culture. (a) after loading; (b) after 48 hours.

REFERENCES

[1] J. W. Song, W. Gu, N. Futai, K. A. Warner, J. E. Nor, and S. Takayama, *Computer-controlled micro-circulatory support system for endothelial cell culture and shearing,* Anal. Chem., Vol. 77, pp. 3993-3999, (2005).
[2] Y. Tanaka, M. Yamato, T. Okano, T. Kitamori and K. Sato, *Evaluation of effects of shear stress on hepatocytes by a microchip-based systenm*, Meas. Sci. Technol., Vol. 17, pp. 3167-3170, (2006).
[3] E. Grossman, F. H. Messerli, V. Boyko, U. Goldbourt, *Is there an association between hypertension and cancer mortality?,* Am. J. Med., Vol. 112, pp. 479-486, (2002).

MANUFACTURE OF DUAL-LAYER MICROBUBBLE LIPOSPHERES AS DRUG DELIVERY VEHICLES IN MICROFLUIDIC DEVICES

Kanaka Hettiarachchi[1], Esra Talu[2], Marjorie L. Longo[2], Paul A. Dayton[2], Abraham P. Lee[1]

[1]University of California, Irvine, USA and [2]University of California, Davis, USA

ABSTRACT

An improved method utilizing microfluidic systems for the controlled generation of dual-layer microbubble lipospheres for drug delivery is demonstrated. These gas-filled vehicles have a lipid shell and an additional layer of oil just beneath the lipid shell. The PDMS-based microfluidic devices feature a combined dual flow-focusing region and expanding nozzle geometry with a 15μm orifice width. We are able to produce 10μm lipospheres, which is an ideal size for carrying large drug payloads.

Keywords: Drug Delivery, Lipospheres, Microbubbles, Microfluidics

1. INTRODUCTION

The utilization of acoustically active lipospheres (AALs) (Fig. 1a) capable of delivering bioactive substances at high concentrations in the lipid-oil complex has been reported [1]. The oil layer is capable of carrying highly hydrophobic drugs such as the chemotherapeutic drug Paclitaxel, which is currently delivered to cancer patients intravenously. Paclitaxel can be dissolved at high concentrations (70 mg/ml) in the lipid-oil complex of the AALs [2]. Such vehicles can provide an alternative method of delivery of therapeutic drugs that have poor oral bioavailability.

2. THEORY

The commonly used production technique of mechanical shaking creates a highly polydisperse microbubble population, with varying amounts of oil within many of the microbubble vehicles. Thus, the drug dosages within each vehicle are also not consistent. Microfluidic chambers provide an ideal platform for the controlled production of monodisperse double emulsions [3] and microbubble contrast agents [4] with a much smaller size distribution. Our device (Fig. 1b) combines two hydrodynamic flow-focusing regions together and features expanding nozzle geometry to generate gas-filled dual-layer lipospheres.

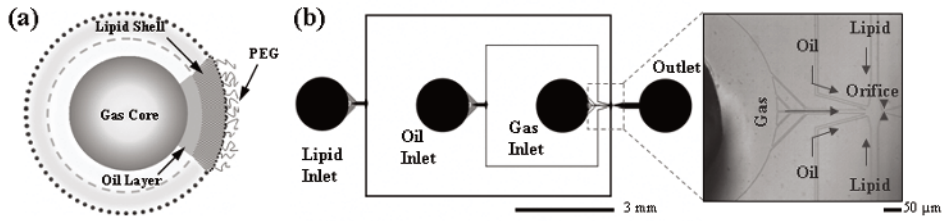

Figure 1. (a) Schematic of an AAL and (b) PDMS-based microfluidic flow-focusing device

978-0-9798064-0-7/μTAS2007/$20©2007CBMS

3. EXPERIMENTAL

The devices were fabricated from a SU-8 master with the channels molded in poly(dimethylsiloxane) (PDMS) using standard soft lithography and rapid prototyping techniques. A high resolution 20,000 dpi photomask enabled designs having critical channel widths such as a 15μm orifice and closely spaced filtering channels.

The recipe for lipid preparation consisted of adding to a vial containing a 9:1 molar ratio of phospholipid to emulsifier a 10% aqueous glycerol/propylene glycol mixture. An oil soluble blue dye was added at 1mg/mL for microscopy studies. Table 1 defines the lipid shell, oil, and gas core components of the lipospheres.

Table 1. Liposphere composition

Component	Abbreviation	Name	Category
Shell	DSPC	1,2-distearoyl-*sn*-glycero-3-phosphocholine	Phospholipid
Shell	DSPE-PEG2000	1,2-distearoyl-sn-glycero-3-phoshoethanolamine-N-[Poly(ethylene glycol)2000]	Lipopolymer emulsifier
Oil layer	Triacetin	Glyceryl triacetate	Drug carrier
Gas core	N_2	Nitrogen	Osmotic agent

Gas-filled lipospheres were produced by flow-focusing (Fig. 2a), forcing a central stream of nitrogen gas and two (lipid and oil) double-sided liquid sheath flows through a narrow 15 micron orifice. The outer sheath flow stream contains an aqueous glycerol/propylene glycol mixture with the stabilizing lipids DSPC and DSPE-PEG2000. The inner sheath flow stream consists of the oil triacetin, capable of carrying bioactive substances. The viscosity of triacetin (28.0 cP) is considerably less compared to other oils, making it ideal for use at the desired liquid flow rate regimes of 0.5-1.0 μL/sec in the microchannels.

The gas is supplied from a pressurized tank via flexible tubing and delivered into the chamber using a micro flow meter. The continuous lipid and oil phase mixtures are pumped at constant flow rates using two digitally controlled syringe pumps. A Nikon inverted microscope and high-speed camera is used to capture images and record movies of the dual-layer microbubble lipospheres in the microfluidic device.

4. RESULTS AND DISCUSSION

Microfluidic generated lipospheres are visible in brightfield (Fig. 2b), and the inner blue layer confirms the existence of the additional triacetin oil layer (Fig. 2c). The outer DSPC lipid shell stabilizes the vehicle and the inner triacetin oil layer can contain dissolved therapeutics. The gas interior makes the vehicle acoustically active to ultrasound pulses.

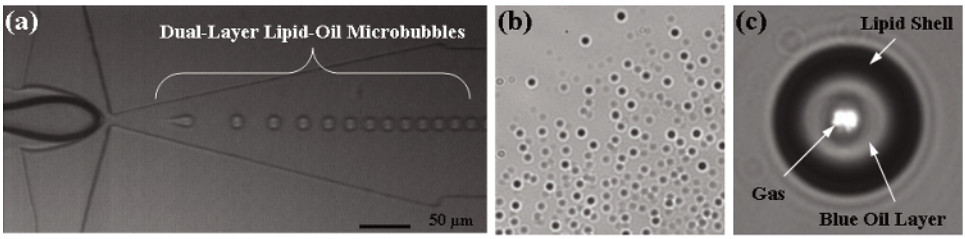

Figure 2. (a) Production by flow-focusing and (b) generated AALs. (c) Close-up of AAL

Microbubble size and production rate are highly prone to downstream pressure conditions. The large viscosity difference between the oil and gas makes the production of dual-layer lipospheres particularly challenging. Channel geometry in addition to the liquid and gas flow rates are the main factors used to control the liposphere sizes.

Paclitaxel is a poorly water soluble drug and its large size prevents it from being accommodated within the phospholipid bilayers in liposomes. In a dual-layer vehicle, a high volume fraction of the oil phase can be used and paclitaxel exhibits good solubility in triacetin. The production method will enable more precise dosages of drug to be delivered. Conjugating a cyclic-RGD peptide to the shell due to over-expression of $\alpha v\beta 3$ integrin in the tumor blood vessel endothelium is a possibility for targeted delivery.

The issue of creating long-lasting dual-layer microbubble lipospheres for drug delivery in microfluidic systems poses interesting studies concerning the impact of device geometry and scale, flow parameters, and the synergy between shell, internal components, and surrounding medium on the stabilization.

5. CONCLUSIONS

With microfluidics technology, we can produce monodisperse dual-layer microbubbles in a suitable size range for oral drug delivery or direct injection into the circulation (10μm or less). The composition makes them ultrasonically active and able to carry a large and precise drug payload to the target site. On-going and immediate experiments are to demonstrate drug loading in the manufactured dual-layer vehicles, targeted delivery to cancer cells, and to demonstrate that the drug Paclitaxel can remain, or be slowly released over time.

ACKNOWLEDGEMENTS

The authors would like to acknowledge funding from UC Discovery Grant BIO-ELE04-10462 and by the National Institutes of Health through the NIH Roadmap for Medical Research, Grant # 1 R21 EB005325-01.

REFERENCES

[1] Evan C. Unger, Thomas P. McCreery, Robert H. Sweitzer, Veronica E. Caldwell, and Yunqiu Wu, "Acoustically Active Lipospheres Containing Paclitaxel: A New Therapeutic Ultrasound Contrast Agent," Investigative Radiology, Vol. 33, pp. 886-892 (1998).

[2] M. J. Shortencarier, P. A. Dayton, S. H. Bloch, P. A. Schumann, T. O. Matsunaga, and K. W. Ferrara, "A method for radiation-force localized drug delivery using gas-filled lipospheres," IEEE Trans Ultrason Ferroelectr Freq Control, Vol. 51, pp. 822-831 (2004).

[3] T. Nisisako, S. Okushima and T. Torii, "Controlled formulation of monodisperse double emulsions in a multiple-phase microfluidic system," Soft Matter, Vol. 1, pp. 23-27 (2005).

[4] K. Hettiarachchi, E. Talu, M. L. Longo, P. A. Dayton, and A. P. Lee, "On-chip generation of microbubbles as a practical technology for manufacturing contrast agents for ultrasonic imaging," Lab Chip, Vol. 7, pp. 463-468 (2007).

MICROFLUIDIC ELECTROPORATIVE DELIVERY OF SMALL MOLECULES AND GENES INTO CELLS USING A COMMON DC POWER SUPPLY

Hsiang-Yu Wang, Chang Lu*
Department of Agricultural and Biological Engineering, School of Chemical Engineering, Purdue University, West Lafayette, Indiana 47907

ABSTRACT

We present a microfluidics-based technique, which delivers small molecules and genes into cells under constant direct current (DC) voltage (provided by a common DC power supply), taking advantage of the field intensity variation in a microfluidic channel due to its geometry. In this study, we demonstrated the delivery of two molecules into Chinese hamster ovary (CHO-K1) cells: a membrane impermeable nucleic acid dye (SYTOX® Green) and a plasmid vector carrying the gene for green fluorescent protein (pEGFP-C1). By tuning the electrical parameters and other conditions, we were able to conduct the electroporative delivery with performance comparable to that of electropulsation. Our technique provides a simple solution to electroporation-based drug and gene delivery by eliminating the need for a pulse generator. This new electroporative delivery technique paves the way to high throughput drug and gene screening on a microfluidic platform.

Keywords: microfluidics, electroporation, drug delivery, transfection

1. INTRODUCTION

Electroporation is an efficient method of introducing foreign impermeant molecules such as drugs and genes into cells since first demonstrated in 1982 [1]. Conventional electroporation has been based on the application of short electrical pulses (electropulsation). Electropulsation requires specialized equipment and is not compatible with techniques such as electrophoresis which is based on constant voltage. In this study, we demonstrate the delivery of impermeant small molecules (SYTOX Green) and plasmid vectors (pFGFP-C1) into cells using this microfluidics-based electroporation technique under constant DC voltage provided by a common DC power supply. Devices with different geometries were applied to gene delivery. We report the effects of the device geometry and the electrical parameters on the delivery efficiency in detail.

2. EXPERIMENTAL SECTION

The devices were fabricated based on Polydimethylsiloxane (PDMS) using standard soft lithography. The detailed procedures for experiments were provided in our previous publication [2].

3. RESULTS AND DISCUSSION

Figure 1a shows one part of the fabricated channel with the width reduction connecting a wide section with a narrow section. As shown in Figure 1b, devices with different designs (configurations A, B, and C) were applied in this study. The modeling of the field strength inside the devices suggests that the field strength in the narrow section is around 8-fold higher than that in the bulk of the wide sections (Figure 1b). In our experiments, Chinese hamster ovary cells (CHO-K1) in a buffer which contained impermeant small molecules or plasmid DNA, flowed through the channel when a constant DC voltage was applied across

978-0-9798064-0-7/μTAS2007/$20©2007CBMS

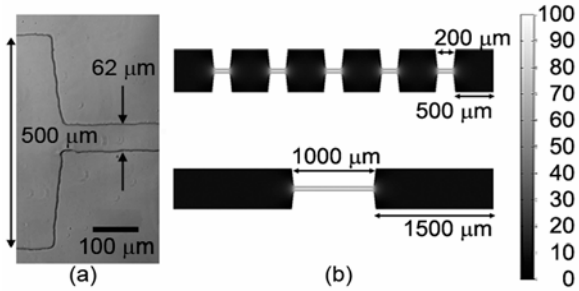

Figure 1. The design of the electroporation devices and the modeling of the field intensity distribution inside the devices. **(a)** The optical image of the device. **(b)** Mathematical modeling (Comsol 3.2) of the field intensity distribution in devices of different configurations. The high intensity is assigned to be 100.

the channel. Cells experienced pulse-like electric field variation(s) while flowing through the channel with alternating wide and narrow sections. We tested devices with a variety of layouts which were analogous to the application of single or multiple pulses with different pulse patterns.

We tested the delivery of SYTOX® Green, which was a nucleic acid stain impermeant to live cells and became fluorescent upon binding to DNA (Figure 2). We also demonstrated the transfection of CHO cells with a plasmid DNA. The pEGFP-C1 plasmid (4.7 Kb, coding enhanced green fluorescent protein) was chosen to facilitate the observation of the delivery (Figure 3). We found that the efficacy of the delivery was strongly dependent on the electrical parameters including the field intensity and duration in the narrow section(s), and the number of the narrow sections in the device. Our results indicate that the devices with multiple narrow sections can yield significantly better results in the final transfection yield than the devices with single narrow section, when the electrical parameters are well tuned in both cases.

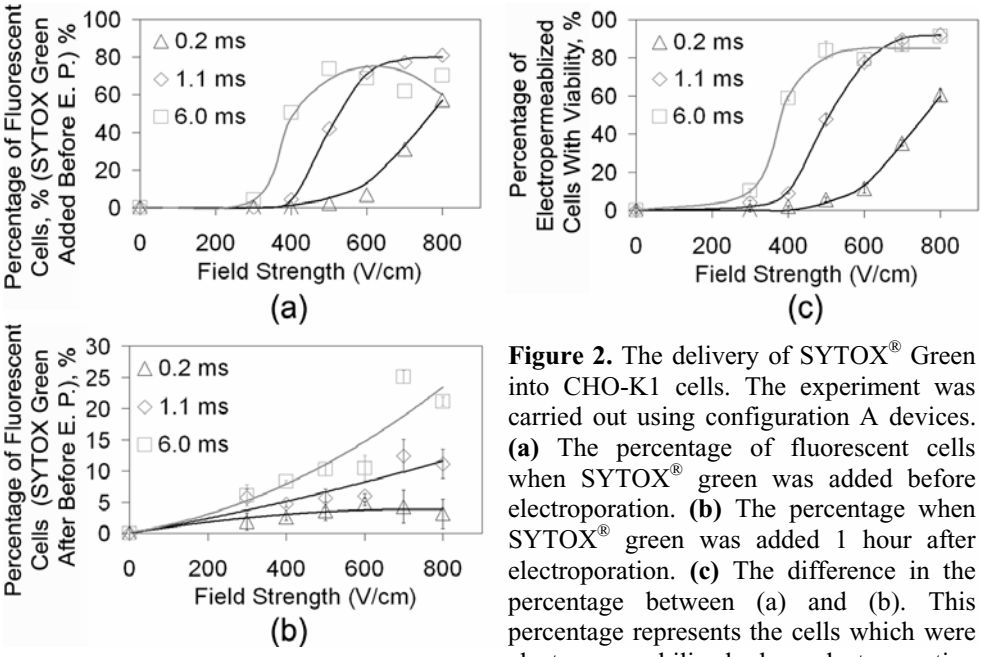

Figure 2. The delivery of SYTOX® Green into CHO-K1 cells. The experiment was carried out using configuration A devices. **(a)** The percentage of fluorescent cells when SYTOX® green was added before electroporation. **(b)** The percentage when SYTOX® green was added 1 hour after electroporation. **(c)** The difference in the percentage between (a) and (b). This percentage represents the cells which were electropermeabilized by electroporation and remained viable after the delivery.

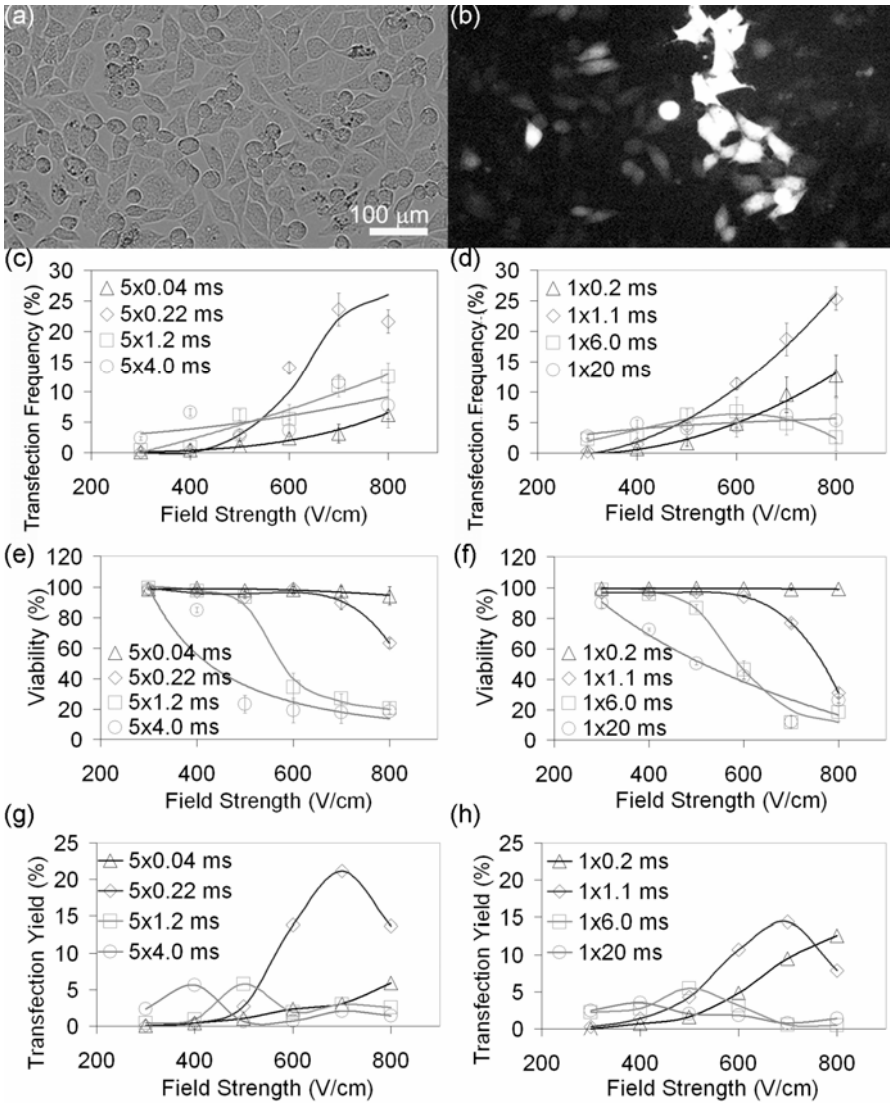

Figure 3. The transfection of CHO-K1 cells with the plasmid vector pEGFP-C1. **(a)** The phase contrast image. **(b)** The fluorescent image. **(c)** and **(d)** The transfection rates among viable cells with varying field intensities and durations in the narrow section(s) in devices with 5 and 1 narrow sections, respectively. **(e)** and **(f)** The percentage of viable cells in the starting cell population in devices with 5 and 1 narrow sections, respectively. **(g)** and **(h)** The percentage of transfected cells in the starting cell population (the transfection yield) in devices with 5 and 1 narrow sections, respectively. (e.g. 5×1.2 ms means that the device has 5 narrow sections and the duration in each is 1.2 ms).

REFERENCES

[1] E. Neumann, *et al*., Embo. J., Vol.1, pp 841-845 (1982).
[2] H. Y. Wang and C. Lu, Anal. Chem., Vol. 78, pp 5158-5164 (2006).

CONTROLLING HIGHER-ORDER STRUCTURES OF GIANT GENOMIC DNA MOLECULES IN MICROFLUIDIC CHANNEL

H. Oana[1, 2], M. Ohuchi[1] and M. Washizu[1, 2]

[1]*Department of Mechanical Engineering, The University of Tokyo*

[2]*CREST of JST, JAPAN*

ABSTRACT

This paper presents a new methodology for the observation and the artificial control of higher-order structures of genomic DNA molecules, and reversible folding and unfolding of over 250 μm-long DNA were demonstrated with a high reproducibility.

Keywords: Chromosomal DNA, Higher-order structures, Microfluidic device, PDMS

1. INTRODUCTION

In eukaryotic cells, DNA with the aid of polycations such as histone are folded to form a highly ordered chromosome structures, and the gene expression is influenced by how tightly it is folded around a particular gene, which is controlled by such a process as histone acetylation or methylation. However, the mechanism and the dynamics of DNA folding, such as the speed of folding on a DNA strand, or how much cooperativity influences the folding of very long DNA strand, is not well understood.

2. EXPERIMENTAL

To study folding/unfolding dynamics of DNA in single molecular level, a method which enables to stretch DNA strands, hold it in a solution, which can be quickly replaced the solutions having different cationic or salt concentrations is required. For this purpose, we have developed a microfluidic device schematically depicted in Figure 1. The device is fabricated by a standard soft lithography with PDMS. The main channel of the device has micro-pillars to hook and stretch DNA by hydrodynamic force [1]. There are inlets on the upstream side of the pillars, from which yeast chromosomal DNA, 1 mM spermidine (DNA condensing polycationic agent), and 500 mM NaCl (de-condensing salt) are fed. Each solution contains 1 mM YO-PRO-1 for fluorescence visualization of DNA and 1 mM dithiothreitol as a deoxidizer.

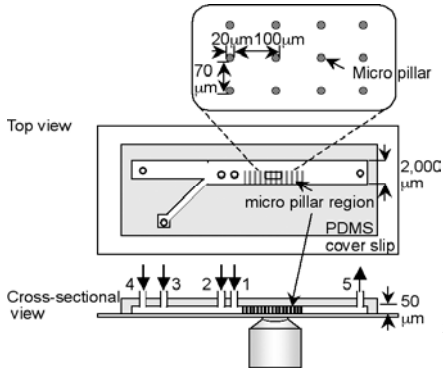

Figure 1. Schematic illustration of the microfluidic device for the observation of individual DNA molecules under various solution conditions. Kinetic conformational changes of the DNA are observed by an inverted microscope. Inset: Pattern of the micro-pillars for immobilization of DNA molecules. The region of pillars is 5 mm x 1 mm.

978-0-9798064-0-7/μTAS2007/$20©2007CBMS

3. RESULTS AND DISCUSSION

First yeast chromosomal DNA (*S. pombe*) was fed, hooked to the pillar, and stretched by flow (Figure 2). By carefully controlling the feeding speed in the microfluidics, we can obtain DNA strands longer than several hundred μm on the pillars, which is substantially longer than in a previous work (20-80 μm [2]), and which is long enough for the observation of long-range cooperativity of folding. Then, the introducing solution was switched to Mili-Q water when appropriate number of DNAs were hooked on the pillars.

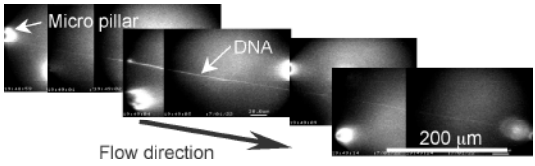

Figure 2. Example fluorescence image of DNA molecule hooked on the micro-pillar. *S. pombe* chromosomal DNA molecules were obtained from a piece of agarose gel block containing the DNA as size markers.

After immobilizing DNA molecules, the spermidine solution was fed. As soon as the condensing agent reached the immobilized DNA, the folding started, whose snap shots are shown in Figure 3a. In many cases, DNA condensation started from the free end, because the hydrodynamic tensile stress is minimal there. But in other cases, nucleation occurred in the middle of the DNA fibre, to which more and more strands are condensed cooperatively from both sides to form ball-like structure as shown by a white arrow in the Figure 3a (3 s). After complete folding of the DNA, the solution was switched to 500 mM NaCl. The folded DNA molecules seemed to swell first (presumably due to the relaxation of condensation), and then started to be extended by the flow (Figure 2b). The unfolding process was more than ten times slower than the folding. It was observed that where nucleation started in folding was slow in unfolding. The folding and unfolding was repeatable for several times by switching solutions (spermidine/NaCl) until photo bleaching of the fluorescent dye.

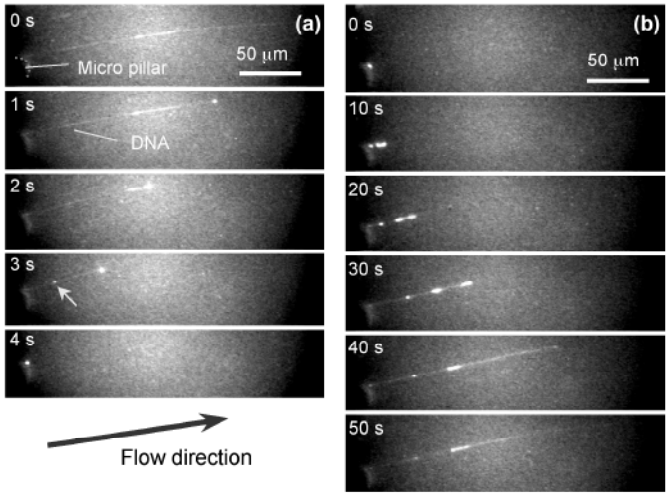

Figure 3. Example of folding process (a) and unfolding process (b) of the same DNA molecule. Since the length of this DNA was too long (over 250 μm) and there was a limitation of the optical setup, the free end was out of the frame. a) 1 mM spermidine, flow rate is ca. 80 μm/s. The white arrow indicates a nucleation point in the middle of the DNA fibre (3 s). b) 500 mM NaCl, flow rate is ca. 90 μm/s. These flow rates were estimated by the drifting DNA fragments across the observation field.

Figure 4 shows time developments of folding and unfolding of the same molecule shown in Figure 3. In the folding process, one can see a start-and-stop motion at around 2.5 s. This motion seems to indicate nucleation (slow folding) and growth (fast folding) process. In the slow folding process, DNA may be folded in ordered structure, and in the fast folding process, disordered folded structure may be formed [3]. In the unfolding process, in contrast to the folding process, the start-and-stop motion is not seen. One can see that at first, the unfolding is slow and then, it becomes faster. This phenomenon has been also observed under dilution of a neutral polymer (polyethylene glycol; PEG) solution [4]. PEG solution above a certain concentration also folds DNA and prior to that unfolding experiment, 57 μm long DNA was folded by PEG [4]. It is to be noted that the time course of the unfolding are quite similar although properties of these condensing agents, spermidine and PEG, are different.

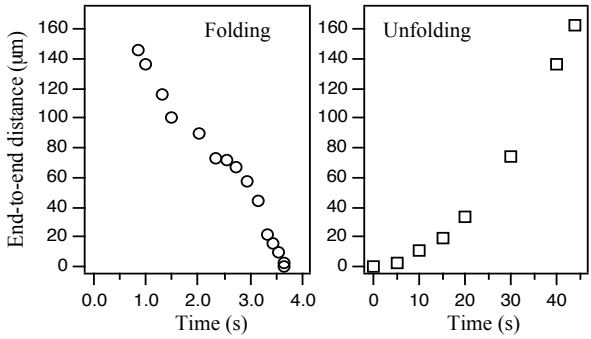

Figure 4. Time development of apparent end-to-end distance of DNA during folding/unfolding. Data points were obtained from the same molecule shown in Figure 3.

4. CONCLUSIONS

We visualized the DNA folding and unfolding along over several hundred-kilo base pairs by on-site control of solution conditions using the microfuluidic device. The method developed here not only contributes to the basic biochemical researches, but may also open a way for the DNA handling towards single-molecule sequencing, or control of cellular activity through artificially induced higher-order changes.

ACKNOWLEDGEMENTS

This work was supported in part by Grant-in-Aid for Scientific Research (B) from the JSPS of Japan and Industrial Technology Research Grant Program from NEDO of Japan. Photography masks were fabricated using EB lithography apparatus of VLSI Design and Education Centre (VDEC), the University of Tokyo.

REFERENCES

[1] K. Terao, H. Kabata, H. Oana, and M. Washizu, *Complete extension of chromosomal DNA and its manipulation using optically-driven micro-fabricated hooks*, Proc. Micro TAS 2005, **1**, pp. 715-717, (2005).

[2] L. R. Brewer, M. Corzett and R. Balhorn, *Protamine-Induced Condensation and Decondensation of the Same DNA Molecule*, Science, **286**, pp. 120-123 (1999).

[3] K. Yoshikawa and Y. Matsuzawa, *Discrete Phase Transition of Giant DNA Dynamics of Globule Formation from a Single Molecular Chain*, Physica D, **84**, pp. 220-237 (1995).

[4] K. Yoshikawa and Y. Matsuzawa, *Nucleation and Growth in Single DNA Molecules*, J. Am. Chem. Soc., **118**, pp. 929-930 (1996).

MICROFLUIDIC GENE SYNTHESIS

David S. Kong[1], Peter A. Carr[1], Lu Chen[2], Kelly Chang[3], Shuguang Zhang[4], and Joseph M. Jacobson[1]

Media Laboratory, Center for Bits and Atoms[1], Department of Chemical Engineering[2], Department of Biological Engineering[3], Center for Biomedical Engineering[4], Massachusetts Institute of Technology, 77 Massachusetts Avenue, Cambridge, MA 02139, USA

ABSTRACT

It has long been recognized that the capacity to design and synthesize genes and longer DNA constructs can be enabling to a broad array of applications within traditional biological research and more recently synthetic biology, including the design of genetic circuitry, the engineering of entire metabolic pathways, and even the construction and re-engineering of viral and bacterial genomes. However, current per-base synthesis costs limit wide access to such synthetic constructs. Thus, to reduce such costs microfluidic devices have been utilized to reduce gene synthesis reaction volumes to at least one order of magnitude smaller than those used in conventional bench-top techniques. Furthermore, parallel synthesis was conducted for the fabrication of a variety of genes with length up to 1 kb using minute amounts (femtomoles) of oligonucleotide building blocks, thus demonstrating that such an approach should be compatible with high density DNA microarrays. Lastly, progress in a device designed for integrated microfluidic gene and protein synthesis in is reported.

Keywords: Gene synthesis, gene assembly, synthetic biology, microfluidic

1. INTRODUCTION

The core technology for DNA synthesis involves the assembly of pools of oligonucleotides (oligos), typically less than 50 nucleotides in length, into increasingly larger DNA molecules. The most widely reported methods for building long DNA molecules involve variations of the polymerase-mediated assembly technique collectively termed Polymerase Construction and Amplification (PCA). Here, much like in Polymerase Chain Reaction (PCR), three temperature steps are employed to denature, anneal, and elongate the various overlapping oligos until, after multiple rounds of thermocycling, the desired full length DNA construct is obtained. Using such techniques, researchers have successfully synthesized DNA constructs larger than 10 kb [1].

Despite these promising results considerable challenges remain, particularly reducing the cost and time of synthesizing long constructs. Currently, the cost for custom gene synthesis services is significant, on the order of $0.65-$1.10 dollars per base pair, with the major expenditures being attributable to reagents and sample handling. Microfluidic technology provides an elegant means to overcome these limitations. By scaling reactions down to volumes less than a microliter, reagent costs can be substantially reduced. Thus, the parallel synthesis of genes has been demonstrated in a microfluidic device utilizing 500 nL reactor volumes [2]. These volumes are at least an order of magnitude smaller than those utilized in standard bench-top techniques. Furthermore, microfluidic technology enables automated sample handling and process integration. Toward this end, a microfluidic device integrating gene synthesis and protein synthesis has been designed, and the individual process modules have been successfully tested.

978-0-9798064-0-7/μTAS2007/$20©2007CBMS

2. EXPERIMENTAL

Microfluidic devices composed of poly(dimethylsiloxane) (PDMS) for gene synthesis and integrated gene and protein synthesis were fabricated utilizing multilayer soft lithography [3]. Protocols for synthesizing genes in a microfluidic environment are reported in [2]. Protein synthesis was accomplished in microfluidic devices by loading commercially available transcription/translation mixture (Roche, RTS 100 *E. coli* HY Kit) with control GFP and visualized utilizing confocal microscopy.

3. RESULTS

Parallel gene syntheses were successfully conducted in the PDMS-based microfluidic device. The synthesis of four constructs, a GFP construct (993 bp), OR128-1 (942 bp), DsRed (733 bp), and ble (461 bp) was accomplished and visualized in the gels shown in figure 1, and the identity of each construct was verified by sequencing. Furthermore, the resultant error rate for microfluidic gene synthesis was determined to be 1 per 560 bases, in agreement with theoretical predictions and other results reported in the literature for fabricating genes from commercially available oligonucleotides. In other reports oligos for gene synthesis were synthesized *in situ* in a microarray, cleaved from the substrate and subsequently assembled in macroscopic ($\geq$ 5 µl) reactions [1]. In contrast, we have synthesized these DNA constructs in parallel within four 500 nanoliter reactors of a microfluidic device. The minute oligo concentrations utilized (10-25 nM each oligo) are significantly lower than concentrations expected to be attainable (without amplification) from high density oligonucleotide microarrays. Thus, such a microfluidic approach should be compatible with DNA microarray-derived oligonucleotides, further reducing the cost of this crucial reagent.

Lastly, progress in an integrated gene and protein synthesis device is reported. The design for an integrated gene and protein synthesis device is shown in Figure 2A. This device features three 45 nL gene synthesis reactors and three 12 nL protein synthesis reactors. To verify the expression of fluorescent protein in a microfluidic device, GFP has been successfully expressed, as visualized in the confocal microscopy image shown in Figure 2B.

4. CONCLUSIONS

The parallel synthesis of genes in a microfluidic device has been successfully demonstrated. All constructs were verified by gel electrophoresis and sequencing. Furthermore, the minute amounts of oligonucleotides utilized for synthesis (femtomoles) suggest that microfluidic gene synthesis should be compatible with high density DNA microarrays. Lastly, an integrated gene and protein synthesis module has been designed, and individual process components have been successfully tested.

REFERENCES

[1] Tian, J. et al. (2004) Accurate *Nature*, **432**, 1050-1054.
[2] Kong D.S. et al. (2007) *Nucleic Acids Research*, **35**, e61.
[3] Unger, M.A. et al. (2000) *Science* **288**, 113-6.

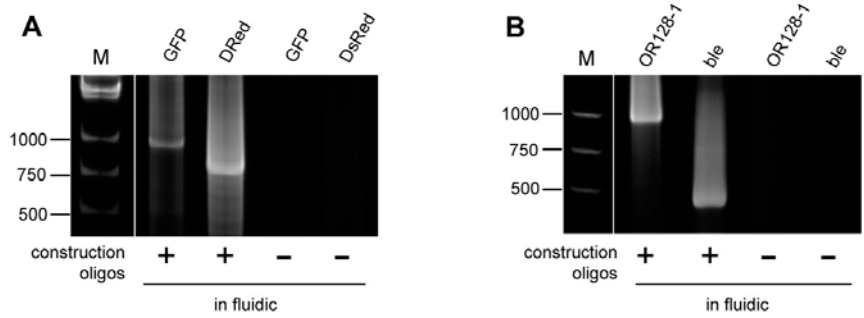

Figure 1. PAGE showing successful parallel synthesis of genes along with negative controls. In the presence of construction oligos, DNA constructs GFP and DsRed (figure 1A) and OR128-1 and ble (figure 1B) are synthesized and amplified. Without construction oligos, no product bands are generated.

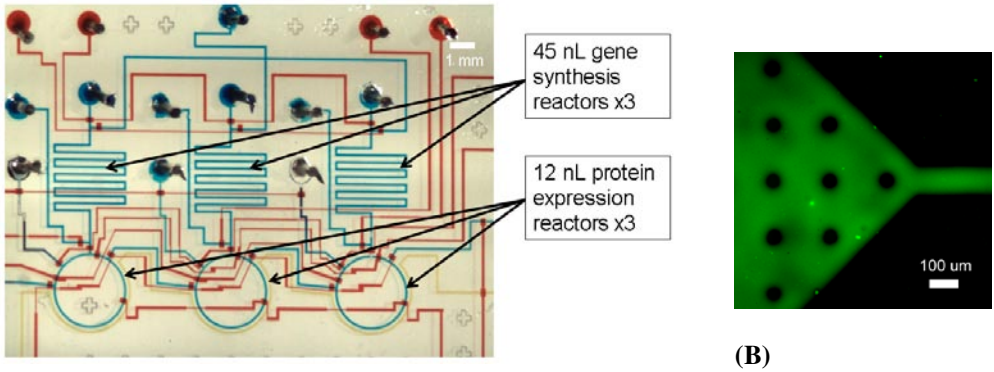

(A)

(B)

Figure 2A. Optical image of a microfluidic device designed for the integrated synthesis of genes and proteins. **2B.** A fluorescence microscope image indicating the successful expression of GFP in a microfluidic reactor.

MICROFLUIDIC GRADIENT GENERATOR FOR STEM CELL DIFFERENTIATION

T.M. Keenan[1,2], K. Feyereisen[1], C.N. Svendsen[3], and D.J. Beebe[1]

[1]Department of Biomedical Engineering, [2]Stem Cell Training Program, and [3]Waisman Center, University of Wisconsin-Madison, U.S.A.

ABSTRACT

Microfluidic gradient generators can provide a more quantitative understanding of key developmental events. Critical to this aim is the ability to create stable, well-defined gradients without fluid flow that would otherwise destroy essential paracrine signaling. We have developed a robust gradient generator that can create stable and tunable gradients using a "no-flow" design. Gradients are tunable and reach steady-state within 6 minutes. Human neural stem cells seeded within the device were viable for 3 days with no obvious morphological differences from controls.

Keywords: microfluidics, gradient, development

1. INTRODUCTION

Chemical gradients are a dominant signaling mechanism in many biological phenomena including development, inflammation, wound healing, and cancer. In human development, a long cascade of highly-orchestrated signaling protein gradients dictate the fate and organization of all cells and tissues in the body. Our understanding of development is severely limited by our inability to expose cells to well-defined gradients in a controlled, *in vitro* setting. The precise dimensions and well-understood physics of microfluidic devices make them adept at generating *in vitro* gradients that are reproducible and easily quantified. However, most microfluidic gradient generators cannot provide the spatial or temporal control required to induce differentiation of human stem cells. The gradients they generate evolve continuously, with lifetimes far shorter than the 7-10 days it can take to induce differentiation. Only microfluidic gradient generators that rely upon continuous flow for gradient formation [2-4] are able to maintain user-defined gradients for a week or more. Unfortunately, continuous-flow gradient generators constantly perfuse cells with fresh, chemically-defined medium, eliminating all autocrine and paracrine signaling resulting from the applied gradient. Abnormal or non-biologically relevant differentiation can result. A microfluidic gradient generator described in [5] creates dynamically-tunable, steady-state gradients without continuous cell perfusion. Unfortunately, the complicated design and susceptibility to clogging prevents the device from maintaining user-defined gradients for more than just a few hours. A more robust "no-flow" gradient generator is needed.

2. EXPERIMENTAL

The gradient generator we have developed (schematized in *Figure 1A)* creates gradients by pneumatically ejecting fluids through polyester track etch membranes containing 0.2 um diameter pores into a cell culture chamber. The device consists of four PDMS layers individually molded from photolithographically-defined SU-8 masters and bonded together using oxygen plasma exposure (*Figure 1B)*. Layer 1 comprises the gradient/cell culture chamber. Layers 2 and 3 seal the perimeter of the polyester membrane and provide it mechanical support. Layer 4 is a two-level PDMS layer comprising the

978-0-9798064-0-7/μTAS2007/$20©2007CBMS

microchannels which deliver gradient fluids to the cell culture chamber. Gradient formation was characterized by filling the gradient chamber with water and then loading one microchannel with fluoroscein isothiocyanate (FITC) and the other with water. Compressed gas and low pressure regulators (1-5 psi) where used to apply unique pressures to each microchannel. Gradient formation was documented using time-lapse fluorescence microscopy at 15 second intervals for 40 minutes. To test the biocompatibility of the device for neural stem cell culture, fetal-derived human neural stem cells (hNSCs) were dissociated and seeded within a polyornithine- (100 ug/mL, 60 min), and laminin- (100 ug/mL, 90 min) coated cell culture chamber and on polyornithine- and laminin-coated glass coverslips. Cells were cultured for 3 days in a humidified 37°C, 5% CO_2 incubator and then imaged with phase contrast microscopy.

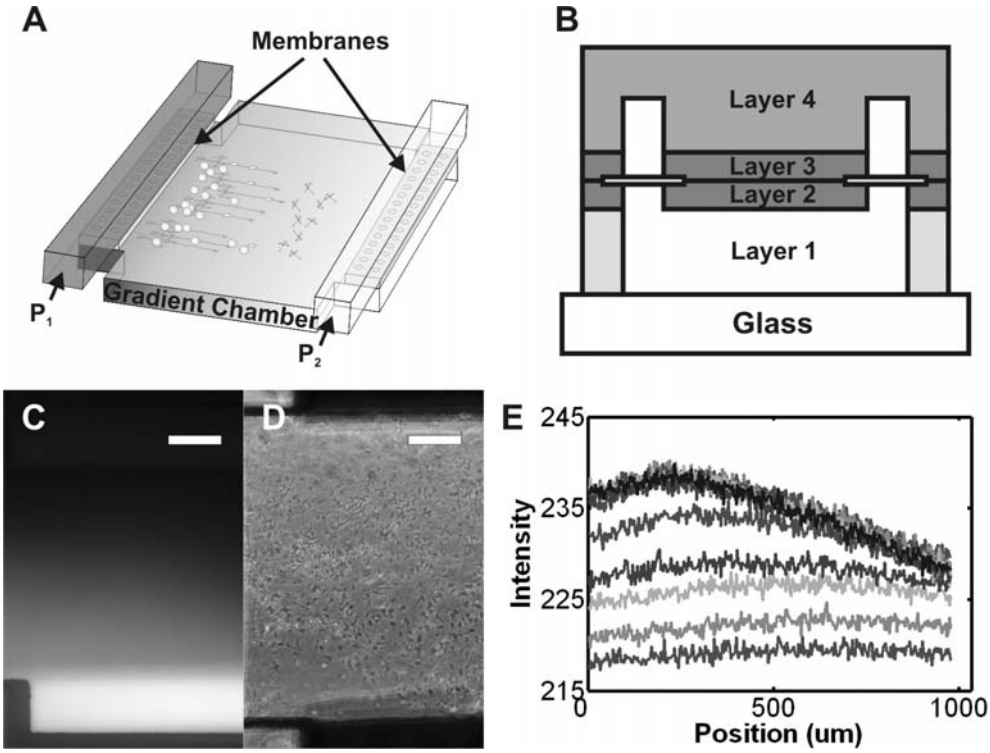

Figure 1. (A) 3D schematic of the device. (B) Cross-section schematic of the device showing 4-layer architecture. (C) Stable, tunable FITC gradient generated in the device. (D) Human neural stem cells after 3 days in culture within the cell culture chamber. (E) Concentration profiles of gradient shown in (C) at 1 minute intervals showing gradient stability within 6 minutes and maintenance of stable gradient for 34 minutes. (Scale bar = 200 um)

3. RESULTS AND DISCUSSION

Gradient formation experiments showed the rapid formation of a pressure-tunable FITC gradient in the cell culture chamber (*Figure 1C)*. The gradient reached a steady-state profile within 6 minutes and stayed stable for the rest of the 40 minute experiment (*Figure 1E).* Biocompatibility experiments showed that hNSCs grow well in the gradient generator

with morphologies indistinguishable from those on polyornithine/laminin-coated glass controls.

4. CONCLUSION

We have developed a gradient generator that has a more robust design than other no-flow gradient generators. The gradient generator forms stable, tunable gradients and supports hNSC culture. The device we have developed can begin to probe the intricacies of developmental phenomena which utilize chemical gradients and paracrine signaling for proper cell differentiation and migration.

ACKNOWLEDGMENTS

REFERENCES

[1] Chung, B.G., et al., *Human neural stem cell growth and differentiation in a gradient-generating microfluidic device.* Lab Chip, 2005. **5**(4): p. 401-6.

[2] Irimia, D., D.A. Geba, and M. Toner, *Universal microfluidic gradient generator.* Analytical Chemistry, 2006. **78**(10): p. 3472-3477.

[3] Mao, H., P.S. Cremer, and M.D. Manson, *A sensitive, versatile microfluidic assay for bacterial chemotaxis.* Proc Natl Acad Sci U S A, 2003. **100**(9): p. 5449-54.

[4] Jeon, N.L., et al., *Generation of solution and surface gradients using microfluidic systems.* Langmuir, 2000. **16**(22): p. 8311-8316.

[5] Keenan, T.M., C.H. Hsu, and A. Folch, *Microfluidic "jets" for generating steady-state gradients of soluble molecules on open surfaces.* Applied Physics Letters, 2006. **89**(11): p. -.

SONOPORATION OF SUSPENSION CELLS IN A MICROFLUIDIC FORMAT BY USE OF A SINGLE CAVITATION BUBBLE

Séverine Le Gac[1], Albert van den Berg[1] and Claus-Dieter Ohl[2]

[1]*BIOS the Lab-on-a-Chip group, MESA+ Institute for Nanotechnology, The Netherlands.*
[2]*Physics of Fluids, University of Twente, The Netherlands and Department of Physics and Applied Physics, Nanyang Technical University, Singapore.*

ABSTRACT

We report here on both viable and permanent poration of (suspension) cells by combining microfluidics and cavitation bubbles. Cells to be porated are introduced in a PDMS-based microchamber and a single cavitation bubble is created by means of a highly focused laser pulse. The expansion and collapse of this circa 100-µm sized bubble results in high shear stress on cells leading eventually to poration of their membrane. Transient poration of cells is demonstrated using a fluorescent marker, calcein, which is released out of the cells upon poration, while permanent poration is shown with uptake of Trypan Blue present in the medium. The experiments presented here have enabled us to determine a killing radius corresponding to the distance below which cell death is observed (> 50%).

Keywords: cell poration, cavitation bubble, microfluidics, molecular delivery.

1. INTRODUCTION

Delivery of foreign substances into cells which has great importance for several research areas, e.g. drug synthesis, food industry or stem cell research requires transient poration of the cellular membrane. A common technique to achieve this is electroporation that uses short pulses of a high electric field [1]. However, performing electroporation in a microchip implies the integration of electrodes and complex fabrication techniques [2]. S*onoporation is* an alternative technique whereby poration results from the flow induced by oscillating bubbles [3]. Without confinement this method is restricted to adherent cells [4] while in combination with microfluidics it can be applied to suspension cells, and a higher shear stress on cells is expected from this microfluidics confinement. We describe here a novel method for (sono)poration of cells with a single cavitation bubble in a microchip with minimal requirements regarding system fabrication.

2. EXPERIMENTAL

Microfluidics confinement of cells is achieved with a PDMS microsystem fabricated using conventional molding techniques and bonded to a thin glass slide. The microsystem includes a shallow ($h < 40$ µm) chamber of a few hundreds of microns diameter (100-1000 µm) where cells are collected and the bubble created. The set-up used for sonoporation experiments is illustrated in fig. 2; it includes a microscope equipped with a laser (Nd:YAG laser, 532 nm) generating short pulses (6 ns), two illumination systems (bright field and fluorescence) and a camera to record bubble dynamics and the motion of cells.

978-0-9798064-0-7/µTAS2007/$20©2007CBMS

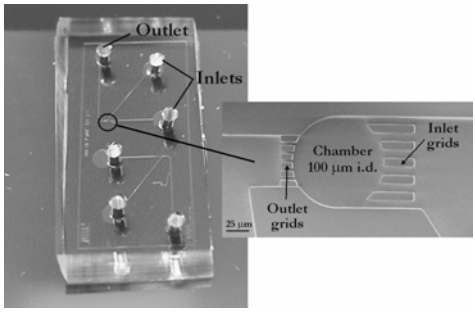

Figure 1. Microsystem used for sonoporation experiments. *Left*: PDMS microsystem; *Right*: SEM photograph of the microchamber.

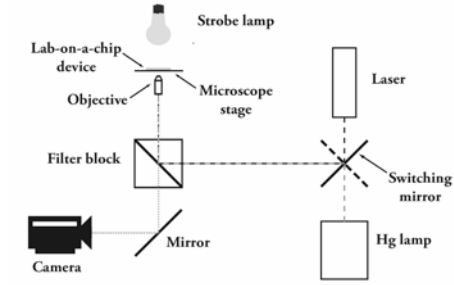

Figure 2. Set-up to generate cavitation bubbles in a microfluidic device.

The microsystem containing the cells is placed on the microscope stage. Explosively expanding cavitation bubbles result from absorption of the laser energy by the liquid supplemented with appropriate compounds [5]. Before being introduced in the microchamber cells are loaded with Calcein AM (few hours incubation with a 1 µM Calcein AM solution followed by thorough washing) and resuspended in fresh medium supplemented with Trypan blue (1%). This compound is not only used as viability probe here but also as light-absorbing compound to generate cavitation bubbles. Suspension (human leukemia HL60 cells) and adherent cells (macrophages, RAW 264.7) (data not shown) are tested for sonoporation experiments in a microchip.

3. RESULTS AND DISCUSSION

We firstly used a 100-µm microchamber and calcein-loaded cells, and a bubble was shot in the chamber, as illustrated on fig.3. As the bubble is created close to a boundary, a jetting flow ressembling the phenomena obtained 3D cavitation is observed [6]. This leads to a net motion of cells located in the vicinity of the bubble towards the other side of the chamber.

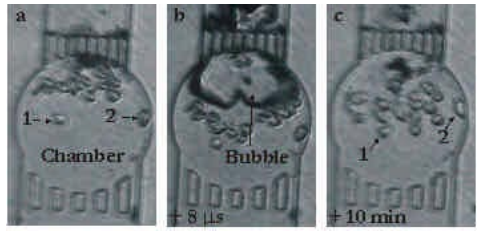

Figure 3. Creation of a cavitation bubble in a microchamber (160 µm diam.; 20 µm height) loaded with cells and motion of cells initially located close to the bubble

Fluorescence inspection (fig. 4) of the chamber after cavitation reveals calcein leakage out of the cells with both a decrease in the fluorescence level in the cells and an increase of the background fluorescence. Nonetheless, both phenomena (cell motion and calcein leakage) are limited to cells located close to the bubble, while cells numbered 1 & 2 remain mildly affected by the bubble. Figure 5 represents the fluorescence intensity as a function of the distance from the position indicated with a cross in fig. 4 before and after the bubble; a net increase in the background fluorescence is observed in the chamber after the bubble.

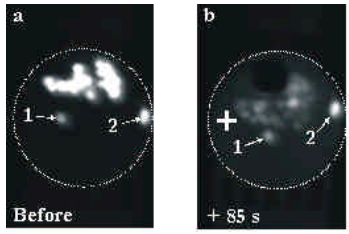

Figure 4. Fluorescent imaging of the microchamber before and after the bubble showing calcein leakage out of cells initially located close to the bubble.

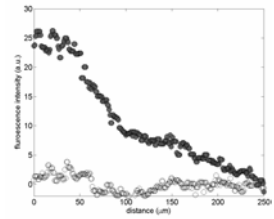

Figure 5. Intensity of fluorescence as a function of the distance from the cross (see fig. 4) before and after the bubble.

We secondly used larger microchambers (> 400 µm) so as to alleviate any jetting phenomena and motion of the suspension cells; the flow induced by the bubble becomes purely radial. We studied cell death as a function of the initial position of the cells respective to the bubble center. Data collected on 10 different microsystems and 170 cells enabled us to determine a killing radius for the cells; cells placed closer than 1.5 R_{max} from the bubble center (R_{max} being the maximal radius of the bubble) die (>50% cell death) after exposure to the cavitation bubble.

5. CONCLUSIONS

Laser-induced sonoporation in microfluidics is a novel and very advantageous method for transient (or permanent) poration of cells. Simple PDMS microsystems can be used, no wiring is necessary and any optical accessible area in the chip can be used. By adjusting the laser spot with respect to the cells selective drug delivery can be done and we determined an effective killing radius as a distance below which cell death (>50%) is observed.

ACKNOWLEDGEMENTS

C.D.O. is supported by N.W.O. (The Netherlands) through a VIDI grant. We thank Jiajie Li for his help in the fabrication of the silicon masters.

REFERENCES

[1] E. Neumann et al., *Gene-transfer into mouse lyoma cells by electroporation in high electric-fields*, EMBO J., **1**, pp. 841, (1982).

[2] M.B. Fox, D.C. et al., *Electroporation of cells in microfluidic devices: a review*, Anal. Bioanal. Chem., **3**, pp. 474, (2006).

[3] M.W. Miller et al., *A review of in vitro bioeffects of inertial ultrasonic cavitation from a mechanistic perspective* Ultrasound. Med. Biol., **22**, pp. 1131, (1996).

[4] C.D. Ohl et al., *Sonoporation from jetting cavitation bubbles*, Biophys, J., **11**, pp. 4285, (2006).

[5] E. Zwaan, S. Le Gac, K. Tsuji, C.D. Ohl, *Controlled cavitation in microfluidics*, Phys. Rev. Let., 98, 250201, (2007).

[6] A. Vogel et al., *Investigation of the dynamics of laser-produced cavitation bubbles near a solid boundary*, J. Fluid Mech., 206, pp. 299 (1989).

CONTINUOUS AND SELECTIVE SEPARATION TECHNIQUE OF SUSPENDED PARTICLES BY UTILIZING ACOUSTIC RADIATION AND ELECTROSTATIC FORCES

Y. Sato, H. Ishida and K. Hishida

Keio University, JAPAN

ABSTRACT

A particle separation technique in a sub-mili channel has been developed by utilizing the acoustic radiation and electrostatic forces, which will be applicable to microfluidic devices. When the acoustic radiation force was applied by an ultrasound transducer, large and small particles were trapped at nodal positions in the standing field, which was equal to half of the wavelength in the transverse direction. On simultaneous application of electric field to the channel, both forces acted on particles. The relationship between the acoustic radiation and electrostatic force acting on particles was investigated in order to separate particles in the flow field.

Keywords : Separation, acoustic radiation force, electrostatic force, PTV

1. INTRODUCTION

Non-intrusive and continuous separation techniques of microscopic objects in a microchannel flow were developed by utilizing the acoustic radiation and electrostatic forces. The advantages of techniques are that (1) only the suspended particles are affected by the forces, (2) the selective particle separation is achieved based on the particle diameter and (3) it is easy to apply to various types of microchannel. The present study focuses on two types of separation techniques, i.e., (i) small particles are collected when large particles are trapped at nodal positions in a standing wave field and (ii) large and small particles are separated in downstream by operating the frequency sweep, as illustrated in Figure 1.

2. PRINCIPLE OF SEPARATION

When the acoustic radiation force is applied by an ultrasound transducer, the large and small particles in a buffer solution are trapped at the nodal positions in the

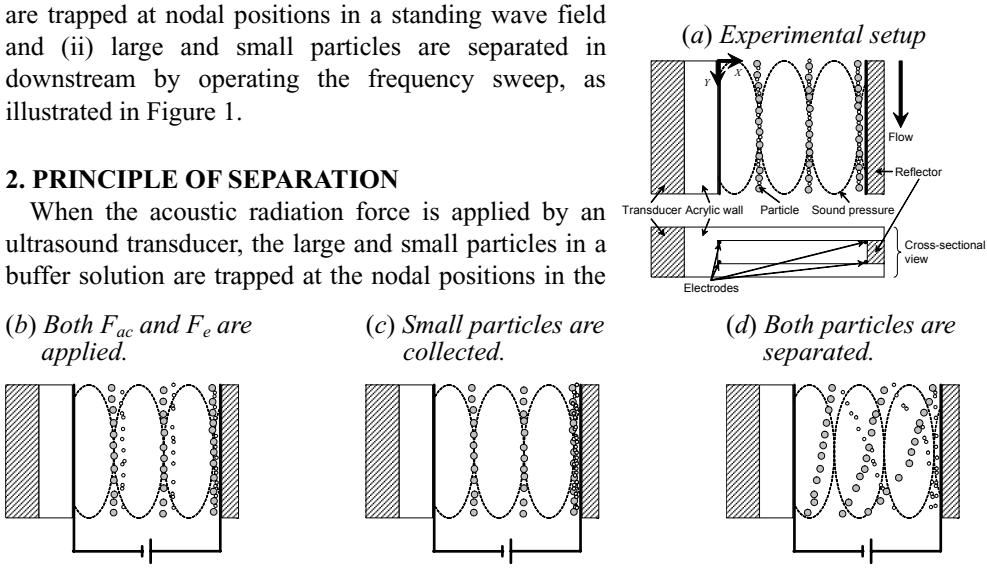

Figure 1. Schematic concept of non-intrusive and selective separation techniques of suspended particles.

978-0-9798064-0-7/μTAS2007/$20©2007CBMS

Table 1. Acoustic impedance of material

Medium	Acoustic impedance [$\times 10^6$ kg/(m^{2}s)]
Acrylic	3.26
Glass	12.8
Water @317 K	1.48

Table 2. Properties of particles

Diameter	[μm]	2.0	4.0	9.6
Density	[g/cm^3]	1.055	1.055	1.055
Volume		0.02	0.02	0.08
Concentration	[%]			
Fluorescence		with	with	without

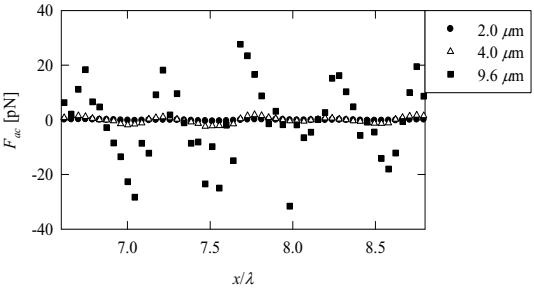

Figure 2. Profiles of F_{ac}.

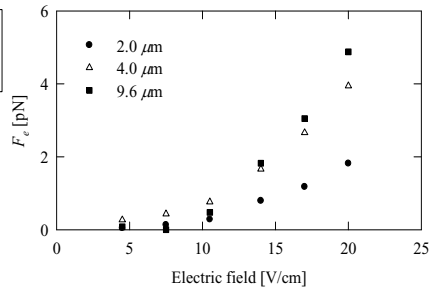

Figure 3. Relationship between electric field and F_e.

standing wave field, which is equal to half of the wavelength in the transverse direction (Figure 1(*a*)). On simultaneous application of electric field to the channel, both forces acted on particles. When the relationship between the acoustic radiation force, F_{ac}, and electrostatic force, F_e, acting on particles are optimized, the large particles are trapped at the nodes by F_{ac} without being affected by F_e, while the small particles are moved toward anode by F_e (Figure 1(*b*)). The mechanism of this separation is that the motion of particles is determined by the dominant force. In this study, F_{ac} and F_e were measured by particle tracking velocimetry (PTV)[1] to investigate quantitatively the balance between both forces. It is possible to move the nodal positions by changing the sound frequency (Figure 1(*c*)). When the period and the frequency range of the sweep operation in the electrostatic field are controlled, the large particles are migrated toward the reflector, while the small particles are electrophoresed toward anodes (Figure 1(*d*)).

Schematic of experimental setup is shown in Figure 1(*a*). The acoustic impedance of materials used in a set of experiments is listed in Table 1. Fluorescent particles, as summarized in Table 2, were selected to detect easily by using a CCD camera attached to an inverted microscope. A 5mM HEPES buffer solution was injected into the channel at pH 9.8 and the conductivity of 111.6 μs.

3. RESULTS AND DISCUSSION

The PTV technique was employed to calculate F_{ac} acting on each particle, whose profiles are plotted in Figure 2. It is noted that F_{ac} is dependent on the particle diameter[2]. F_e is also calculated by PTV and plotted against the applied electric field in Figure 3. By using these results, the relationship between both forces was optimized to separate particles based on the particle diameter.

The present techniques were applied to the flow field. Figure 4 depicts the instantaneous velocity vector map of the large and small particles. As mentioned above, only the small particles moved toward bottom right, which means that only the small particles were collected in downstream. On application of the sweep operation, the large particles that

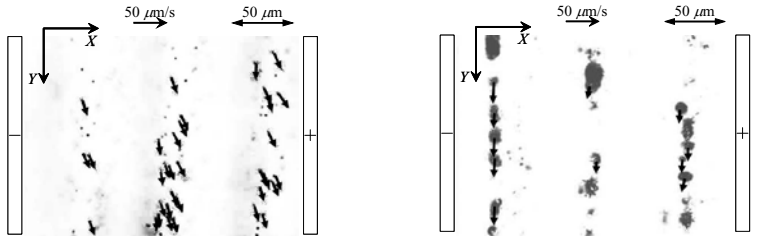

Figure 4. Velocity vector map of (a) 2.0 μm and (b) 9.6 μm particles measured simultaneously by PTV with the 3CCD camera.

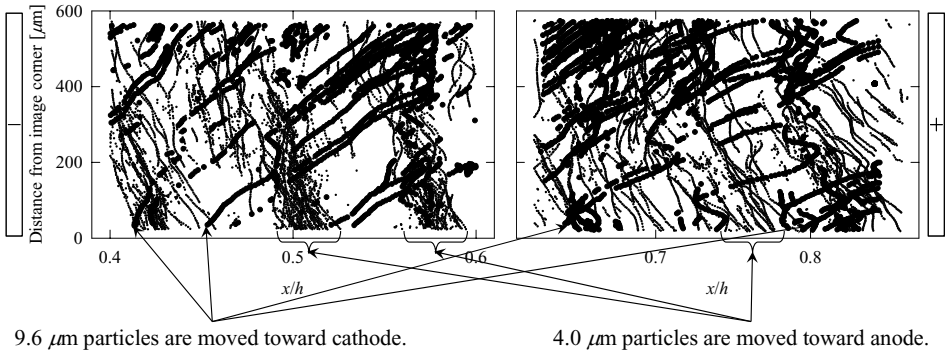

Figure 5. Migration of 4.0 and 9.6 μm particles by moving the standing wave within 3.0 s.

traced nodes migrated toward bottom left, while the small particles were electrophoresed toward bottom right, as shown in Figure 5. The migration of each particle in the opposite direction was observed.

4. CONCLUSIONS

Non-intrusive and continuous particle separation techniques were proposed. The acoustic radiation and electrostatic forces acted on particles, thus large and small particles were separated continuously perpendicular to the flow direction.

ACKNOWLEDGEMENT

This work was subsidized by the Grant-in-Aid for Scientific Research (No. 15206024).

REFERENCES

[1] Y. Sato, S. Inaba, K. Hishida and M. Maeda, *Spatial averaged time-resolved particle tracking velocimetry in microspace considering Brownian motion of sub-micron particles*, Exp. Fluids, **35**, pp. 167–177 (2003).

[2] L.N. Wesley, *Radiation pressure on a small rigid sphere*, Acout. Soc. Am., **42**, pp. 947–953 (1967).

CONTINUOUS FLOW SORTING OF POLYMER MICROPARTICLES BY DIAMAGNETIC REPULSION

Noriyuki Horita[1], Alexander Iles[2] and Nicole Pamme[2]

[1] *National Institute for Materials Science (NIMS), Tsukuba, 305-0051 Ibaraki, JAPAN*

[2] *The University of Hull, Department of Chemistry, Hull HU6 7RX, UK*

ABSTRACT

We explore the potential of strong magnetic fields for the on-chip sorting of polymer microparticles based on diamagnetic repulsion.

Keywords: diamagnetic repulsion, microparticles, continuous flow

1. INTRODUCTION

It is quite intuitive that ferromagnetic objects such as iron oxide containing particles can be manipulated with magnetic fields. This phenomenon has been explored extensively in microfluidic devices.[1] However, it is less commonly known that non-magnetic or, more specifically, diamagnetic materials can also be manipulated with magnetic forces. Diamagnetic substances are repelled from magnetic fields. This repulsion force is generally too weak to be noticed and thus diamagnetic materials such as glass, water, wood or polymers are commonly considered as non-magnetic. However, using the strong magnetic forces generated by superconducting magnets, diamagnetic repulsion has been used to levitate gold particles,[2] organic materials[3] or even frogs[4] against gravity. Here we investigate the diamagnetic repulsion of polystyrene microparticles within microfluidic devices for continuous flow sorting.

2. THEORY

The magnetic force ($\mathbf{F}_{mag}$) acting on a polymer particle can be estimated according to equation 1, where χ is the magnetic suspectibility of the particle and surrounding buffer medium, V refers to the particle volume and B to the magnetic flux.

$$F_{mag} = \frac{1}{\mu_0} \cdot \left(\chi_{particle} - \chi_{medium}\right) \cdot V \cdot B \cdot \frac{dB}{dz} \qquad \text{(equation 1)}$$

For a polystyrene particle of 1 μm diameter (χ= -8.21 x 10^{-6}) in a paramagnetic $MnCl_2$ solution (χ = 7.99 x 10^{-4}) in a magnetic field with B dB/dz = 500 T^2 m^{-1}, the magnetic force is -1.34 pN, the negative sign indicating that the force is directed away from the magnetic field. This calculated force is comparable to forces acting on magnetic particles in microchannels that are manipulated with permanent magnets.[1]

3. EXPERIMENTAL

A schematic of the microfluidic glass chip is shown in figure 1. This chip was mounted onto a holder featuring a prism, a CCD camera and LEDs (figure 2). The holder was inserted into the bore of a superconducting magnet (Jastec, B ≤ 13 T, dB/dz ≤ 586 T^2 m^{-1}) (figure 3). The microchip was interfaced via tubing to a syringe containing the particle suspension. Liquid was introduced into the chip by applying positive pressure to the syringe.

978-0-9798064-0-7/μTAS2007/$20©2007CBMS

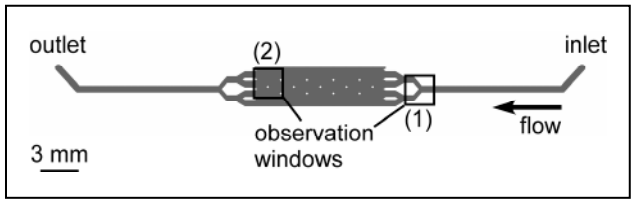

Figure 1: The chip featured a branched network of inlet and outlet channels as well as a 3 mm by 10 mm central chamber of 20 µm depth. Observations were made either at the branching point (1) or in the central chamber (2).

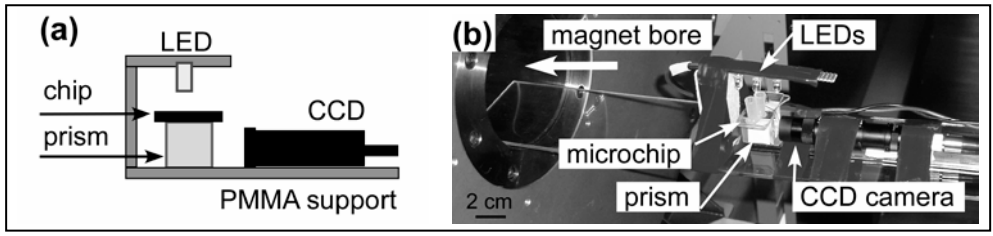

Figure 2. A PMMA support was used to slide the chip and periphery into the magnet bore. The chip itself was placed onto a 45° prism, which allowed for image acquisition through the bottom of the chip by a small CCD camera. Illumination was achieved with LEDs.

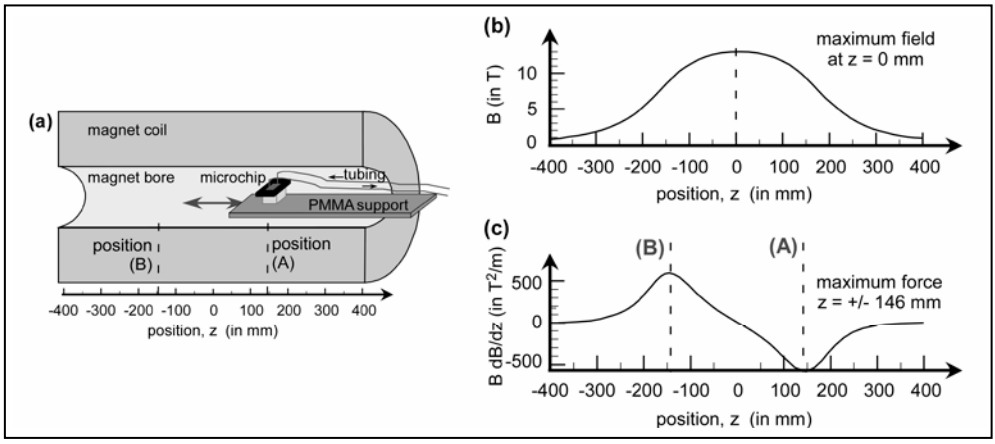

Figure 3. (a) Schematic of chip inside the magnet bore. (b-c) In the bore centre (z = 0 mm), the field strength is at its maximum (13 T), but the gradient of the magnetic field dB/dz equals 0 T m^{-1}. The product of magnetic field strength and gradient is at its maximum of 586 T^2 m^{-1} at positions A and B.

4. RESULTS AND DISCUSSION

Initially, polystyrene particles (6 µm, Polysciences) were suspended in 40 % $MnCl_2$ solution (χ = 7.99 x 10^{-4}) and observed at a channel branching point. Outside the magnet, the particles were found to flow through both branches, whereas inside the magnet, the particles were deflected into one branch (figure 4). In a second series of experiments, the particles were suspended in 6 % $MnCl_2$ solution (χ = 8.14 x 10^{-5}) and the flow behaviour inside the microchamber was observed. The chip was shifted between two bore positions, where the repulsion force acted in opposite directions. At position (A) the particles were observed to be deflected towards their left (figure 5a). When the chip was moved to position (B), the particles were observed to be deflected into the opposite direction (figure 5b).

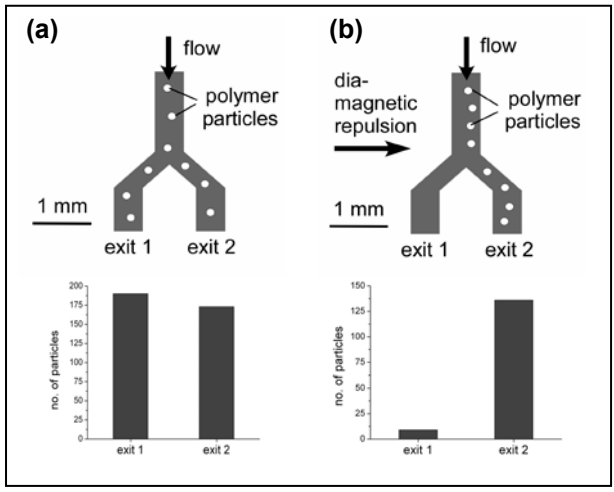

Figure 4: Flow path taken by 6 µm diameter polystyrene particles in an aqueous solution of 40 % $MnCl_2$. (a) Outside the magnet bore (B dB/dz = 0 T^2 m^{-1}), the particles were observed to flow through both branches. (b). Inside the magnet bore (B dB/dz = 500 T^2 m^{-1}), the diamagnetic repulsion force led to the particles taking almost exclusively one branch.

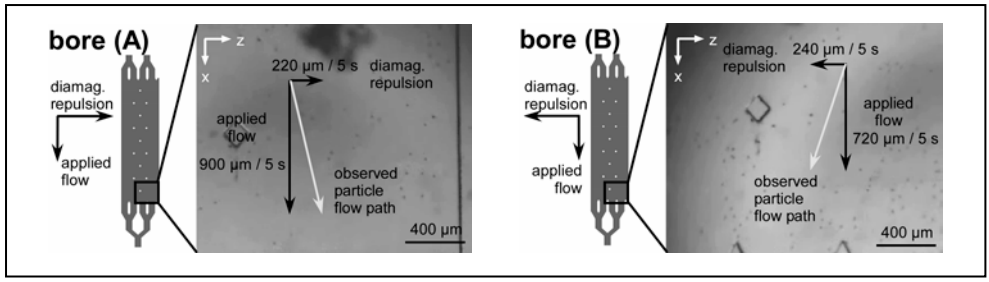

Figure 5: Diamagnetic repulsion in continuous flow of 6 µm polystyrene particles suspended in 6 % $MnCl_2$ solution at two different positions in the magnet bore (see figure3): (left) Particle repulsion at bore position (A); (right) particle repulsion at bore position (B). In both cases, the particles are deflected away from the field maximum.

5. CONCLUSIONS

We have demonstrated the diamagnetic repulsion of polystyrene microparticles for continuous on-chip sorting. These first experiments open the door to further investigations including the sorting and manipulation of different polymer materials and the on-chip study of biological materials using strong magnetic fields.

ACKNOWLEDGEMENTS

The authors would like to thank the Royal Society (UK) for funding.

REFERENCES

(1) N. Pamme, *Lab on a Chip* **2006**, *6*, 24-38.
(2) T. Takayama; Y. Ikezoe, et al., *Applied Physics Letters* **2005**, *86*, 234103.
(3) E. Beaugnon; R. Tournier, *Nature* **1991**, *349*, 470-470.
(4) M. V. Berry; A. K. Geim, *Eur. J. Phys.* **1997**, *18*, 307-313.

CONTINUOUS SEPARATION OF WHITE BLOOD CELLS BY HYDROPHORETIC FILTRATION

Sungyoung Choi and Je-Kyun Park

Department of Bio and Brain Engineering, Korea Advanced Institute of Science and Technology (KAIST), KOREA

ABSTRACT

We propose a new hydrophoretic method for continuous blood cell separation using a microfluidic device composed of slanted obstacles and filtration obstacles. In principle, the height and gap of the filtration obstacles with a filtration pore are set between the diameters of small and large particles and define the critical separation diameter. The particles smaller than the criterion freely pass through the gap. In contrast, the particles larger than the criterion collide against the filtration obstacle and move into the filtration pore.

Keywords: Hydrophoresis, blood cells, filtration, microfluidics

1. INTRODUCTION

Blood is a very complex mixture containing red blood cells (RBCs), white blood cells (WBCs), and platelets. For the proteomic or genomic analysis of WBCs, blood samples need to be separated prior to the analysis. To address this need, several passive approaches have been carried out with splitting and recombining channel network [1], and cross-flow filtration [2]. However, their complex channel networks make it difficult to integrate with downstream analysis and to multiply the networks on a single chip for increasing separation throughput.

2. FILTRATION PRINCIPLE

Hydrophoresis is the first proposed concept to explain the horizontal deflection of particles around slanted and filtration obstacles [3]. The microfluidic device for hydrophoretic filtration consists of the first region for focusing and the second region for filtration (Figure 1). Following the focusing flow of the rotating flow induced by the slanted obstacle, particles are focused to a sidewall. The height and gap of the filtration obstacle are set between the small and large particle diameters. The obstacle forms a filtration pore through which the large particle can pass. Therefore, the particle smaller than the gap freely passes through it and keeps its focused position (focusing mode). In contrast, the particle larger than the gap collides against the obstacles and moves into the

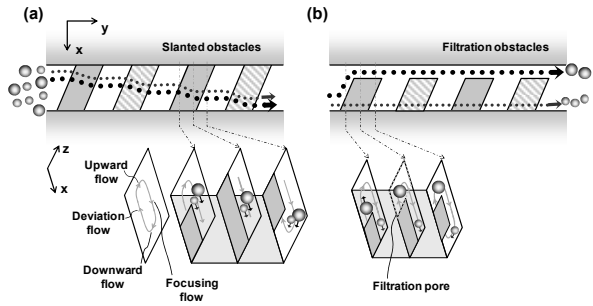

Figure 1. Hydrophoretic filtration. (a) Focusing and (b) filtration process. Shaded- and lined-areas denote lower and upper obstacles, respectively. A flow direction is along the y-axis.

978-0-9798064-0-7/μTAS2007/$20©2007CBMS

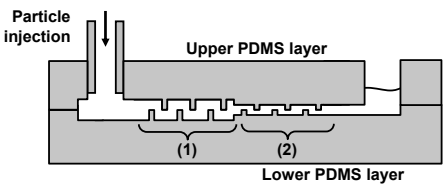

Figure 2. Schematic microfluidic device for hydrophoretic filtration. The height of the slanted obstacles in (1) is higher than that of filtration obstacles in (2).

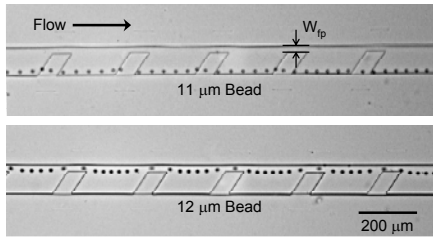

Figure 3. Optical micrographs showing trajectories of beads passing the 11.6 μm filtration obstacles at 0.1 μL min^{-1}.

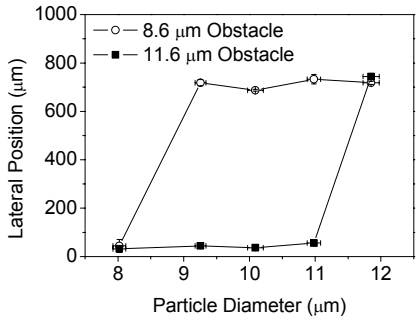

Figure 4. Lateral position of particles as a function of microsphere diameters, measured in the expanded outlet region of 1 mm.

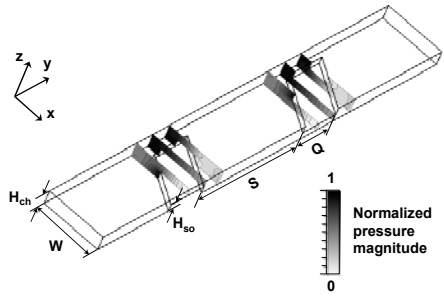

Figure 5. Simulated pressure fields. The simulation geometry composed of lower and upper filtration obstacles and the cross-sectional plots of pressure distributions.

filtration pore (filtration mode).

3. EXPERIMENTAL

To demonstrate the principle, we microfabricated slanted obstacles and filtration obstacles with poly(dimethylsiloxane) (PDMS). Patterns of upper and lower obstacles were formed on silicone wafer with SU-8 photoresist. Molded PDMS layers with upper and lower obstacles put with each other and bonded after oxygen plasma treatment (Figure 2).

4. RESULTS AND DISCUSSION

To demonstrate the hydrophoretic filtration, we tested whether particles larger than the gaps of filtration obstacles can bump against the obstacles and change their flow direction. The filtration device was characterized with several beads ranging from 8 to 12 μm in diameter (Figure 3,4). The width of the filtration pore (W_{fp}) was 20 μm. In the device with 8.6 μm-height filtration obstacles, only 8 μm beads flowed in the focusing mode. In contrast, only 12 μm beads flowed in the filtration mode in the device with 11.6 μm-height filtration obstacles. The pressure field intensity is higher at the filtration pore and it becomes lower going to the right sidewall (Figure 5). The lateral flow induced by the transverse pressure gradient focuses small particles in the focusing mode to the rightmost sidewall.

Applying the hydrophoretic filtration method, we isolated WBCs from RBCs. The microfluidic device was designed with slanted obstacles of 13.0 μm-height and filtration

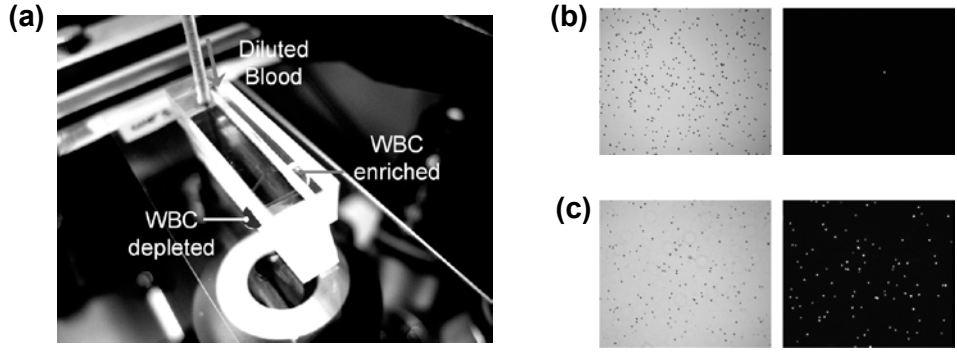

Figure 6. (a) Blood cell separation by hydrophoretic filtration. (b, c) Blood cells before separation (b) and after separation (c) are shown in bright-field (left) and fluorescence (right) images.

obstacles of 4.0 μm-height. In our device, RBCs were aligned parallel to the filtration obstacles of 4.0 μm-height due to their thin thickness of 1.7~2.6 μm and deformability. In contrast, WBCs collided against the filtration obstacles and moved into the filtration pore. By the filtration process, WBCs were isolated with a purity of ~ 58% at a throughput of 4×10^3 cells s^{-1} (Figure 6). Up to 85% of WBCs were recovered compared with their initial concentration. Our hydrophoretic filtration device enriched WBCs to ~ 210-fold from RBCs in just a single round of separation.

5. CONCLUSIONS

In conclusion, we have proposed a new hydrophoretic filtration method using slanted obstacles and filtration obstacles. The filtration obstacles as a filter play not only the filtration role of large particles blocked by the obstacles but also the focusing role of small particles being able to pass through the gap of the obstacles. These results show that the presented device can be useful for the binary separation of a wide range of biological particles by size. The hydrophoretic filtration as a sample preparation unit offers potential for a power-free cell sorter to be integrated in disposable lab-on-a-chip devices.

ACKNOWLEDGEMENTS

This work was supported by Chung Moon Soul Center for BioInformation and BioElectronics, KAIST. The microfabrication work was performed at the Digital Nanolocomotion Center.

REFERENCES

[1] M. Yamada, M. Seki, *Hydrodynamic filtration for on-chip particle concentration and classification utilizing microfluidics*, Lab Chip, Vol. 5, pp. 1233-1239, (2005).

[2] V. VanDelinder, A. Groisman, *Perfusion in microfluidic cross-flow: separation of white blood cells from whole blood and exchange of medium in a continuous flow*, Anal. Chem., Vol. 79, pp. 2023-2030, (2007).

[3] S. Choi, J.-K. Park, *Continuous hydrophoretic separation and sizing of microparticles using slanted obstacles in a microchannel*, Lab Chip, Vol. 7, 890- 897, (2007).

CONTROLLED PATTERNINGS OF THE TARGET PROTEINS BASED ON THE STRUCTURAL TRANSITION OF A HEAT-SENSITIVE POLYMER

Dae-Sik Lee[1], Jun Hwang Lee[2], Kwang Hyo Chung[2], Hyeon-Bong Pyo[2], Mun Yeon Jung[2] and Hyun C. Yoon[2]

[1]BioMEMS Team, IT-BT group, ETRI, KOREA

[2] Department of Molecular Science & Technology, Ajou University, KOREA

(dslee@etri.re.kr)

ABSTRACT

This paper reports a novel method for the actively controlled micropatterning of a protein, anti-6-(2,4-dinitrophenyl)aminohexanoic acid (DNP) antibody, with a smart polymer (poly(N-isopropylacrylamide), PNIPAAm)-modified temperature-controllable electrode, fabricated using MEMS protocols, in a sample preparation microfluidic device.

Keywords: Heat-controlled Microelectrode, PNIPAAm polymer, Protein separation

1. INTRODUCTION

Because there is no PCR-equivalent amplification in proteomics, sample preparation coupled with advanced sample separation and purification steps is a must for detecting low-abundance protein species. Many techniques have been developed, including chemical modification of channel surfaces, packing with biochemical-coated beads, and packing with a biochemical-bearing porous monolithic slab [1-2]. These methods share several disadvantages like clogging or difficulty in packaging. However, the novel integrated microfluidic device employing the heat-sensitive polymer, PNIPAAm on the temperature-addressable electrodes, can overcome the problems and is very suitable for a portable bio-separation system [2]. Here, the controlled micropatterning of biointerface in the microfluidic device by an external stimulus with an intelligent polymer-modified electrode is described.

2. EXPERIMENTAL

The device is composed of a bulk-micromachined Si component and a hot-embossed cyclo-olefin copolymer (COC) component. The 5-in wafer-level Si bulk-micromachined fabrication processes were utilized for the implementation of the Si components, including the micropatterning of electrodes both for the temperature control (microheater and temperature sensor) and for electroanalysis, and the casting of a thin polymer membrane. The microfluidic components with chamber, channel, and valve for a leak-free device are also fabricated using hot embossing protocols (Fig. 1) [3]. For the controlled patterning and analysis of a model protein, DNP, NHS-esterified PNIPAAm was synthesized [4] and functionalized on the gold electrode with dendrimer-conjugated self assembly monolayer (SAM). Then, the electrode surface was manipulated based on the structural transition (shrinkage/extention) of PNIPAAm polymer by changing the surface temperature of electrodes across its lower critical solution temperature (LCST, it is about 26~28 ℃), as shown in Figure 2.

978-0-9798064-0-7/μTAS2007/$20©2007CBMS

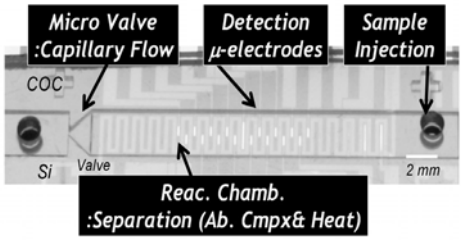

Figure1. Photograph of the protein separation Microfluidic device.

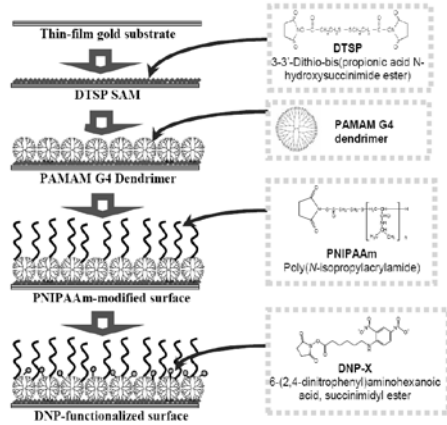

Figure 2. Schematic representation of the bottom-up construction of dendrimer/DTSP monolayer and surface modification with NHSPNIPAAm.

3. RESULTS AND DISCUSSION

The temperature as a function of electrical power consumption on a micro hot plate shows the very low power consumption as shown in Fig. 3. Only 36 mW was used to heat the hot diaphragm area of 2 mm×16 mm to 40℃ and it takes about 0.2~0.3 sec. The controlled patterning of FITC-labeled anti-DNP antibody as forms of controlled one (mode A) and uncontrolled one (mode B), shown in Fig. 4, was confirmed by fluorescence microscopy on a micrometer scale shown in Fig. 5. With in situ temperature control, the results indicated that the extended form of PNIPAAm below LCST on the surface inhibited the molecular approach strongly and selective separation of DNP proteins on the on-chip interface is working very well by the easy and simple manipulating turn-on and turn-off switching of the electric voltage for temperature control.

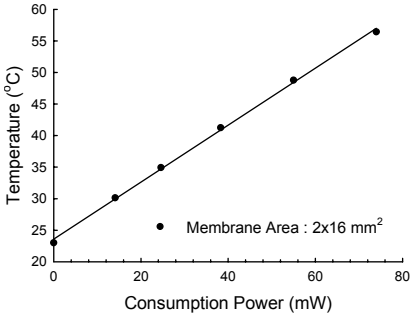

Figure 3. The temperature as a function of electrical power consumption on a micro hot plate.mode.

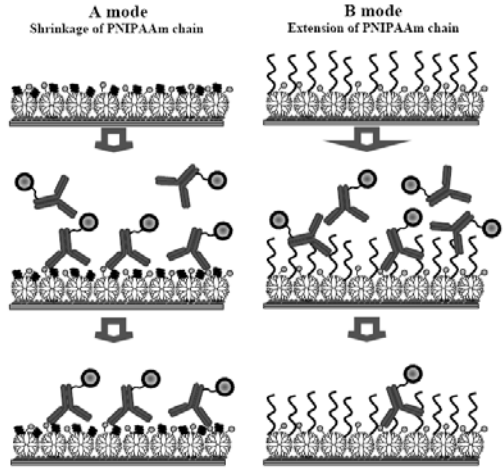

Figure 4. Diagram showing process for selective DNP patternings evaluation, with A mode and B mode.

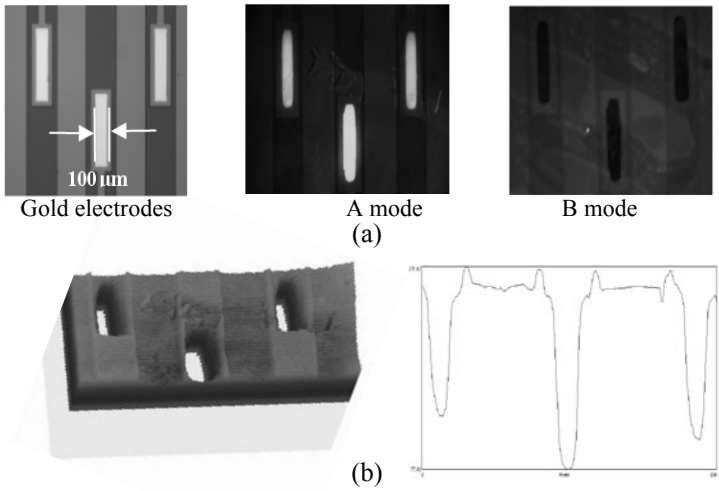

Figure 5. Original photograph of the micropatterned gold electrode, fluorescence microscopy images of the two microelectrodes sequentially reacted with FITC-labeled anti-DNP antibody on the DNP-coated surfaces formed by A and B modes (a) and 3-D image with a line of mode A (b).

4. CONCLUSIONS

A novel temperature-controllable microelectrode array for active biomolecular immobilizing was fabricated through standard microfabrication protocols using a heat-sensitive polymer, PNIPAAm, in a microfluidic device. An anti-DNP antibody micropatterning on the microelectrodes was carried out as a model affinity test on the microelectrodes, estimated by patterns generated from fluorophores-tagged antibodies. The smart microdevice is applicable for portable devices that must rapidly and precisely regulate biochemical reactions like bio-separations.

ACKNOWLEDGEMENTS

This work was supported by the IT R&D program of MIC/IITA. [2006-S007-01, Ubiquitous Health Monitoring Module and System Development]

REFERENCES

[1] Malmstadt, A. S. Hoffman, and P. S. Stayton, *Smart mobile affinity matrix for microfluidic immunoassays*, Lab Chip 4**,** pp. 412-415 (2004).

[2] D. L. Huber, R. P. Manginell, B. Kim, B. C. Bunker, Programmed Adsorption and release of proteins in a microfluidic Device, Science 301, pp. 352-354 (2003).

[3] D. Lee, K Chung, H. Yoon, *A Microfluidic device based on the heat-sensitive structural transition of poly(isopropylacrylamide)*, Proc. Micro Total Analysis Systems 2006, Tokyo, Japan, pp. 311-313 (2006).

[4] B. Won, H. Choi, K. Kim, S. Byun, H. Kim, H. Yoon, Bioelectrocatalytic Signaling From Immunosensors With Back-Filling Immobilization of Glucose Oxidase on Biorecognition Surfaces, Biotechnol. Bioeng., **89**, p. 815 (2005).

FREE-FLOW DIELECTROPHORESIS – A NUMERICAL STUDY

G.O.F. Parikesit[1], A.P. Markesteijn[2], J. Westerweel[2], I.T. Young[1], and Y. Garini[1,3],

[1]Quantitative Imaging group, Delft University of Technology, The Netherlands
[2]Lab for Aero and Hydrodynamics, Delft University of Technology, The Netherlands, and [3]Physics Department, Bar-Ilan University, Israel.

ABSTRACT

This paper presents the numerical simulation analysis of particle separation, using insulator-based dielectrophoresis (iDEP), in a branched U-turn 2D-like nanofluidic device. Particle pathlines under positive and negative dielectrophoresis are studied. The results demonstrate the device capability to continuously separate free-flowing particles. Because the proposed separation is done across the channel width, instead of along channel length (like in capillary electrophoresis), separation quality degradation usually associated with U-turn geometries can be avoided.

Keywords: free-flow, separation, dielectrophoresis, nanofluidics.

1. INTRODUCTION

Recently we develop a novel branched U-turn nanofluidic device, designed to separate particles based on their physical properties. Figure 1(a) shows the scheme of the fabricated device. The fluidic channel's depth is ~100 nanometers, much less than the length and the width (~100 microns). Therefore the device can be analyzed as a 2D-like device. Previously we reported the electroosmotic flow analysis in the device [1], showing excellent agreement between our numerical simulation results and the experimental pathlines and velocity data. We now extend our 2D numerical simulation to include the effects of insulator-based dielectrophoresis (iDEP) on the particle pathlines in the device.

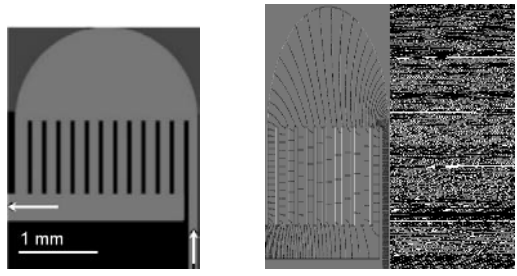

(a) (b)

Figure 1. *(a) A scheme of the device. (b) Electric field distribution in the branched U-turn geometry, when an electric field is applied using a pair of electrodes in the device inlet and outlet. Solid lines are equipotential lines. In this plot, the directions of the insulator-based dielectrophoretic forces are along the density gradient of the equipotential lines.*

978-0-9798064-0-7/μTAS2007/$20©2007CBMS

2. METHODS

We perform the 2D numerical simulation using the software Femlab (Comsol, USA). We calculate the distribution of particle velocity in the device, which is governed by combination of velocities due to electroosmosis, electrophoresis, and dielectrophoresis:

$$\mathbf{v} = \mathbf{v}_{\mathbf{EO}} + \mathbf{v}_{\mathbf{EP}} + \mathbf{v}_{\mathbf{DEP}} = \mu_{EK}\mathbf{E} + \mu_{DEP}\nabla|\mathbf{E}|^2 , \quad (1)$$

with μ_{EK} and μ_{DEP} as the electrokinetic (electroosmotic plus electrophoretic) and dielectrophoretic mobilities [2], respectively. The ratio of μ_{EK} and μ_{DEP} is varied in our simulation to study how the strengths of positive and negative dielectrophoresis influence the particle pathlines.

3. RESULTS AND DISCUSSIONS

Figure 1(b) shows the distribution of equipotential lines in the device, where the directions of iDEP forces are along the *density gradient* of the lines. We then use equation (1), with various values of ratio between μ_{EK} and μ_{DEP}, to plot the particle pathlines along the device. The separation is performed around the sharp corner in the U-turn geometry, as shown in Figure 2. In positive dielectrophoresis, the pathlines are attracted to the highest electric field density, and eventually all particles enter the first sub-outlet, as shown in the zoom-in of Figure 2(a). In negative dielectrophoresis, the pathlines are repelled from the highest electric field density, such that all particles enter the last sub-outlet, as shown in the zoom-in of Figure 2(b).

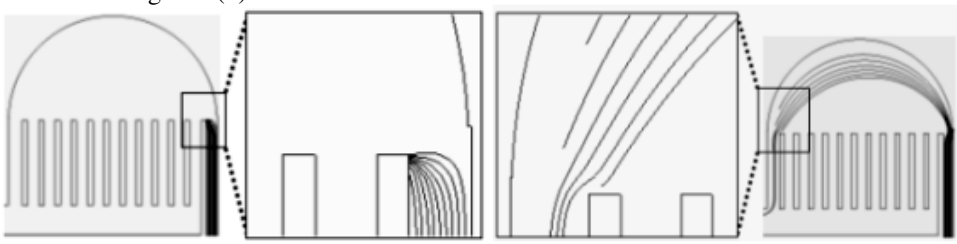

(a) (b)

Figure 2. *Typical particle pathlines under (a) positive- and (b) negative-dielectrophoresis, where the particle enter the nearest and the furthest outlets from the inlet, respectively.*

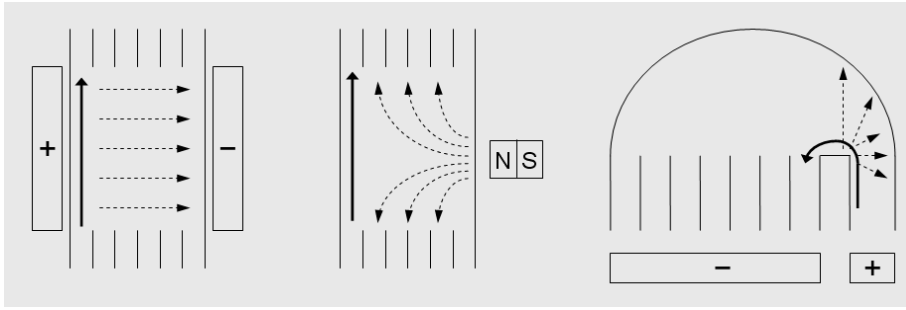

(a) (b) (c)

Figure 3. *Schematic comparison between (a) Free-Flow Electrophoresis, (b) Free-Flow Magnetophoresis, and (c) Free-Flow Dielectrophoresis.*

Previously iDEP has been used to separate particles (but not continuously) [2], to continuously separate particles (but by using insulators that protrude and disrupt the flow) [3], and to trap (but not continuously separate) DNA molecules [4]. A circular chamber has also been proposed for continuous particle separation [5], but the electric field gradient in this device is not sufficiently high for nano-scale particle manipulation, due to lack of sharp corners in their device geometry. Our method, termed Free-Flow Dielectrophoresis (FF-DEP), use the inherent sharp corners in the branched U-turn geometry to continuously separate particles using a high electric field gradient. Figure 3 schematically compares FF-DEP with Free-Flow Electrophoresis (FF-EP) and Free-Flow Magnetophoresis (FF-MP), which have been established before but are only applicable on charged and magnetic particles, respectively. In Figure 3, solid arrows indicate the general particle path, while the dashed arrows illustrate forces ((a) electrophoretic, (b) magnetic, and (c) dielectrophoretic) that induce the free-flow separation

In separation methods using Lab-on-a-Chip, the U-turn geometry is frequently used for allowing the separation length sufficiently long while keeping the device length sufficiently short. A U-turn, however, usually causes the so-called "race-track" effect, where sample flowing along the inner radius move faster than sample flowing along the outer radius. FF-DEP allows us to perform separation across the channel width, instead of along the channel length, hence giving us two advantages: (1) the separation quality becomes independent from the "race-track" effect, and (2) separation could be run continuously, allowing for high-throughput analysis. We foresee the application of FF-DEP, using alternating current (AC) voltage, direct current (DC) voltage, and combination of both, for continuous separation of particles and biomolecules.

4. CONCLUSIONS

In summary, we propose a novel free-flow separation method based on insulator-based dielectrophoresis. Our 2D numerical analysis shows the feasibility of the method to continuously separate free-flowing particles under positive and negative dielectrophoresis. The proposed method, termed Free-Flow Dielectrophoresis, complements Free-Flow Electrophoresis and Free-Flow Magnetophoresis, which have been established before but are only applicable on charged and magnetic objects, respectively. Moreover, because the separation in our device is done across the channel width, instead of along channel length, the separation quality becomes independent from the "race-track" effect and separation could be run continuously to allow a high-throughput analysis.

REFERENCES

[1] G.O.F. Parikesit et.al., "Electroosmotic flow analysis of a branched U-turn nanofluidic device", Lab Chip, 2005, 5: 1067–1074.

[2] E.B. Cummings et.al., "Dielectrophoresis in Microchips Containing Arrays of Insulating Posts: Theoretical and Experimental Results", Anal. Chem., 2003, 75: 4724-4731.

[3] K.H. Kang et.al., "Continuous Separation of Microparticles by Size with DC-dielectrophoresis", Electrophoresis, 2006, 27: 694–702.

[4] Chia-Fu Chou et.al., "Electrodeless Dielectrophoresis of Single- and Double-Stranded DNA", Biophysical Journal, 2002, 83: 2170-2179.

[5] L. Zhang et.al., "Continuous Electrodeless Dielectrophoretic Separation in a Circular Channel", Journal of Physics: Conference Series, 2006, 34: 527–532.

Authors' contact: g.o.f.parikesit@tudelft.nl

HIGH SPEED ORGANELLES SORTING MICROSYSTEM DRIVEN BY A SINGLE PRESSURE SOURCE

Tokihiko Aoki[1], Yoshitaka Shirasaki[2], Takahiro Arakawa[1], Hirokazu Sugino[3], Takashi Funatsu[3], and Shuichi Shoji[1]

[1]Major in Nano-science and Nano-engineering, Waseda University
[2] Lab. of Genome Tech., Dep. of Human Genome Res., KAZUSA DNA Res. Inst.
[3]Graduate School of Pharmaceutical Sciences, The University of Tokyo

ABSTRACT

High performance biomolecules sorting microsystem was realized using the thermosensitive hydrogel (block copolymer of poly *N*-isopropylacrylamide and poly oxyethylene: Mebiol Gel^{TM}). High speed switching of about 5 msec was performed by the 3-D sheath flow and flow resistance change caused by the sol-gel transfrormation of the hydrogel with the focused infrared (IR) laser. Considering the actual applications, the microchannel structure was designed to control sample and carriers with only one pressure source. 1.5 millions of mitochondria were successfully separated by this system with accuracy of more than 92.5 % during 60 hours.

Keywords: Organelle Sorter, Mitochondria Separation, High Speed Sorter, 3-D Sheath Flow

1. INTRODUCTION

Separation of organelles to identify their components is required to characterize their functions. For this purpose, general method for separating organelles is required because the size of organelles distributes from several nano-meters to micro-meters in diameter. Conventional fluorescence-activated cell sorter (FACS) is used to sort biological specimen such as fluorescence-labeled mammalian cells with diameter of several micro-meters [1]. However, it cannot separate organelles of which diameter is several nano-meters. Many separation techniques were developed so far, however, most of their applications are to separate cells and proteins. In this paper, we present an improved high speed organelles sorting microsystem which succeed in separating mitochondria.

2. PRINCIPLE AND DESIGN

The sorting mechanism of our sorter is shown in Fig.1. The device has 3 inlets (two carriers and one sample flow) and 2 outlets (waste port and collection port). Thermosensitive hydrogel containing samples is introduced from the center channel, while carrier flows of thermosensitive hydrogel from both sides. When the target molecules are detected, focused IR laser is irradiated and a part of the waste port side hydrogel changes from sol to gel by thermal effect. This changes the flow direction of the sample flow and the target molecule flows to the collection port.

In the previous work, we used three different syringe pumps to control a sample flow and two carrier flows [2]. The stability of the sample flow position was strongly influenced by the balance between right carrier and left carrier. To stabilize the sample flow position at the initial mode, the flow system was designed so that sample and carriers are driven by a single pressure source. To realize an accurate sorting, the sample flow is finely focused using 3-D sheath flow. This realizes that single sample material can always flow in the detection area. The outlet flow channels are designed so that the sample flow is directed to the waste port at the initial mode.

Using CFD simulation, the microchannel structures are optimized to satisfy these conditions. Flow ratio of sample and whole carriers is kept 2/98. Total flow ratio to the waste outlet is 73%, while that to the collection outlet is 27% at the initial state. Optimum separating condition was automatically realized by a single pressure source. (Fig. 2)

978-0-9798064-0-7/μTAS2007/$20©2007CBMS

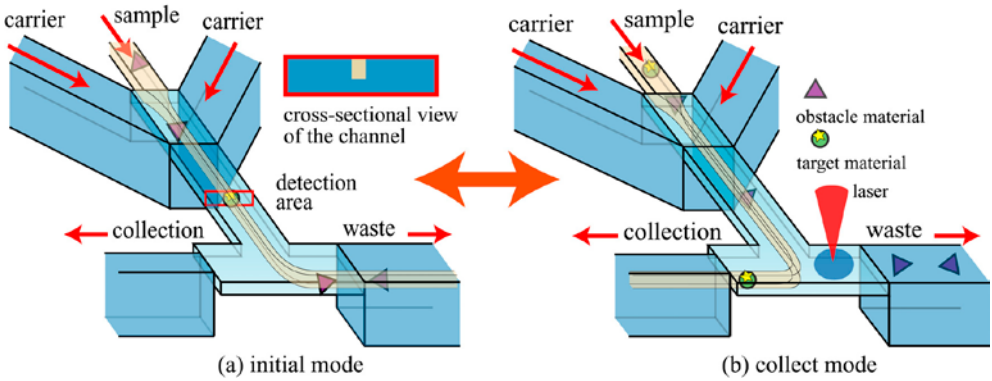

Figure1. Principle of the proposed organelle sorter using thermosensitive hydrogel

3. EXPERIMENTAL SECTION

To establish low cost disposable device, the channel structure was formed by PDMS. At first, positive photoresist of OFPR-800 LB 200CP was spin-coated and the sample channel pattern was transferred to the silicon substrate. 5 μm deep sample channel was etched by CCP-RIE. After the photoresist was removed using acetone, negative photoresist of SU-8 was spin-coated and patterned for 20 μm deep carrier channels. The double-deck structure was realized by the silicon and the photoresist mold. Before transferring these patterns to PDMS, surface treatment chemical (EGC-1720^{TM}) was coated on the substrate in order to transfer fine patterns to PDMS precisely. After this process, the liquid PDMS was casted. To fabricate microchannels having a small cross-sectional area, the casting PDMS of 5:1 ratio of resin to curing agent, was used instead of the normally used one (10 : 1). The PDMS microchannel and 170 μm-thick glass substrate were bonded after O_2 plasma treatment. Fig.3 shows the microchannel having double-deck structure made by PDMS.

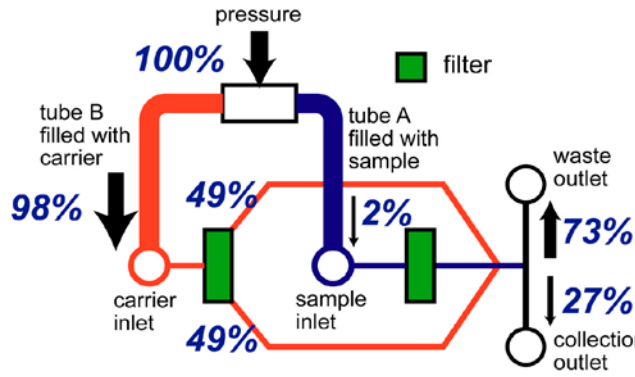

Figure2. Flow ratio of the sample flows and the carrier flow (tube A and B is filled with sample and carrier in advance)

Fig.4 shows the sample flow distribution. Using Rhodamine B as the sample flow, sample was focused to about 2.0 μm in the lateral direction and 1.5 μm in the vertical direction. Contamination around the collect port was not observed at the initial state.

Sorting results of the fabricated device are shown in Fig.5. The fluorescent signals of mitochondria passing the detection area and the reference area are shown in Fig.5(a). Fig.5(b) shows the areas in which signals were obtained. Sample flow is consisted of hydrogel and cell lysis containing fluorescent mitochondria. From the results, the switching speed is estimated within 5 msec and the sorting accuracy is more than 92.5 %. During 60 hours operation, 1.5 million mitochondria were separated. We are now going to analyze the separated mitochondria using mass spectrometry and 2-D electrophoresis. Since this system is automatically controlled, longer time operation is promised from the results.

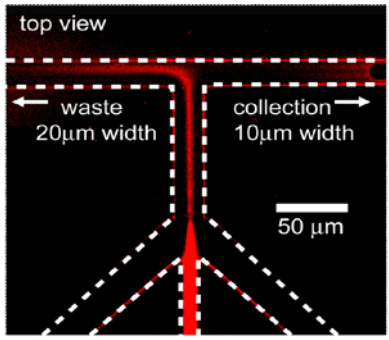

(a) top view

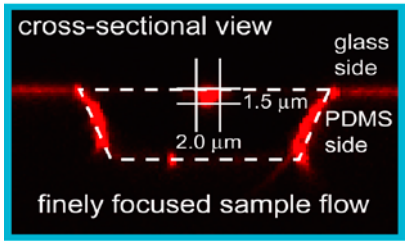

(b) cross-sectional view

Figure4. Confocal images of the 3-D sheath flow at the initial mode (Rhodamine B as the sample flow)

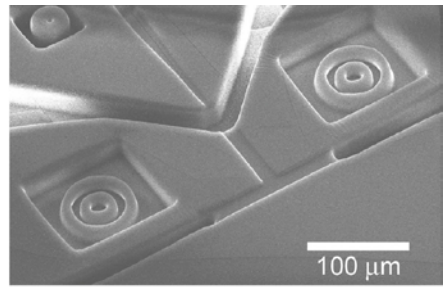

Figure3. Photomicrographs of the fabricated microchannel

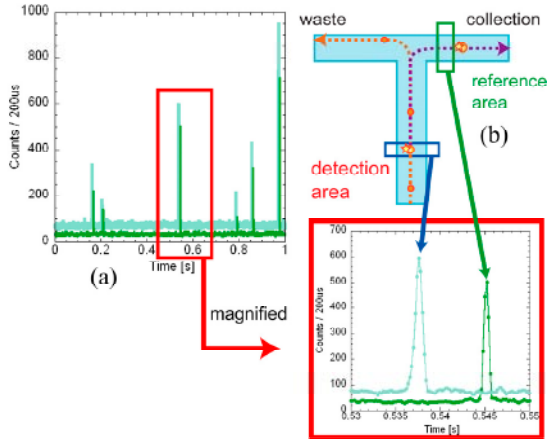

Figure5. Fluorescent signals of the detection area and the reference area at the collect mode

4. CONCLUSION

High performance organelle sorter using 3-D sheath flow was fabricated. Fast and reproducible sorting was obtained by optimizing the microchannel structure. Maximum sorting speed is about 5 ms and remarkable errors were not observed during 60 hours. Millions of mitochondria which quantity is enough to analyze by a mass spectrometry and 2-D electrophoresis were separated.

This system will be a useful tool to analyze the components of organelles. It is also applicable for the high-speed protein and biomolecule separation which is expected in biological and medical research field.

ACKNOWLEDGEMENT

This development was partly supported by SENTAN, JST and Grants-in-Aid for COE Research "Molecular Nano-engineering and Its Development into Microsystem" and SCOE "ASMew" from the Ministry of Education, Culture, Sports Science & Technology of Japan..

REFERENCES

[1] Bonner et al., Review of Scientific Instruments 43: pp.404-409, 1972
[2] T.Arakawa et al., Micro Total Analysis Systems 2006, pp.512-514

INDIRECT DETECTION AND SEPARATION OF NON-FLUORESCENT ANALYTES USING FLUORESCENT ISOTACHOPHORETIC SPACERS

Tarun Khurana and Juan G. Santiago
Department of Mechanical Engineering, Stanford University, USA

ABSTRACT

We present a method to achieve separation and indirect detection of non-fluorescent species using fluorescent spacers. This technique leverages isotachophoresis (ITP) and employs a leading electrolyte (LE), trailing electrolyte (TE) and a set of fluorescent spacers to separate non-fluorescent analytes of interest. We easily achieve ~10 μM detection sensitivity with this technique, and we currently extending the sensitivity to <100 nM.

Keywords: Isotachophoresis, Indirect detection, Spacers, Non fluorescent detection.

1. INTRODUCTION

On-chip electrophoresis has proven a powerful tool for rapid, low-sample volume chemical and biological assays. However, most of the success is limited to fluorescently-labeled analytes as UV-absorbance and electrochemical detection lack sufficient sensitivity and/or are difficult to implement on microfluidic platforms. Traditional indirect detection of non-fluorescent/non-absorbing analytes is performed using fluorescent/UV-absorbing background electrolytes.[1] However, these methods suffer from low sensitivity and resolution due to dispersion; lack of preconcentration; and ambiguity due to so-called false system peaks. We here present a new indirect detection technique that uses isotachophoresis[2] (ITP) and a set of fluorescent electrophoretic "spacers" to achieve high sensitivity indirect detection of unlabeled analytes.

2. THEORY

As in standard ITP, we employ a high mobility leading electrolyte (LE) and a low mobility trailing electrolyte (TE). As shown in Fig. 1, we inject a mixture of non-fluorescent analytes and fluorescent spacers between the LE and TE in a microchannel. Under the influence of an applied electric field, the unlabeled analytes and fluorescent spacers segregate into concentrated, contiguous zones arranged in order of reducing mobility from LE to TE, and move at identical speed. The non-fluorescent analyte zones are unambiguously detectable as dark regions or "gaps" between the fluorescent spacer zones. As shown by both our models and experiments, the known mobilities of fluorescent spacers bounding each analyte zone provide an upper and lower bound of analyte mobility. Further, the width of the "gap" between spacers is a linear measure of initial analyte concentration.

3. EXPERIMENTAL

We have performed extensive ITP/fluorescent-spacer separation and detection with a variety of non-fluorescent analytes. We used 5mM Tris-HCl (pH 8.1) and 5 mM sodium tetraphenyl-borate (TPB) as the LE and TE, respectively and a three-fluorescent-spacer

978-0-9798064-0-7/μTAS2007/$20©2007CBMS

ladder composed of Oregon Green carboxylic acid (OGCA), Fluorescein and Bodipy (~100 nM concentration each). We used an NS-95 microchip (Caliper, Mountain View, CA) with a simple cross pattern and 34 μm wide and 12 μm deep channels. We obtained images using an inverted epifluorescent microscope (Olympus, IX70) and captured images using a 12 bit, 1300 x 1030 pixel array CCD camera (Coolsnap, fx16). We applied ~600 V across the microchannel using a high voltage power supply (Labsmith, HVS-300D) to initiate ITP focusing of analyte and spacer zones.

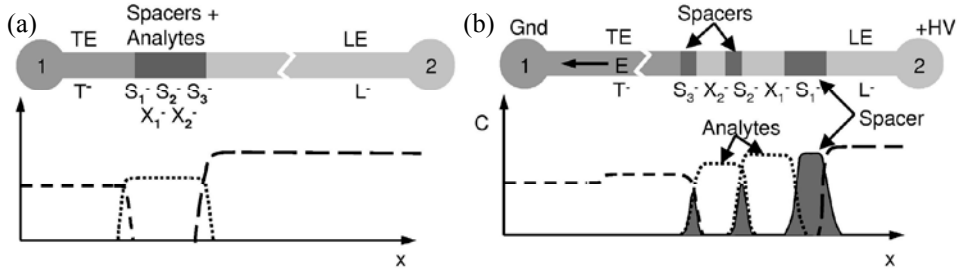

Figure 1: Schematic of our ITP/spacer assay for injection, pre-concentration, separation, and indirect fluorescence detection of unlabeled analytes. (a) An injection plug containing fluorescent spacers and unlabeled analytes is inserted between the leading (LE) and the trailing electrolyte (TE). (b) Isotachophoresis (ITP) is initiated upon application of an electric field and analytes and spacers segregate between LE and TE in order of decreasing mobility.

4. RESULTS AND DISCUSSION

Figure 2 shows measured spatio-temporal plot of the evolution of fluorescent spacer intensity in the separation and detection of two amino acids phenylalanine and serine in a 34 μm wide microchannel. The three parallel (dark) bands correspond to three fluorescent spacers; migrate at identical speed as per ITP; and unambiguously show the presence of the two amino acids.

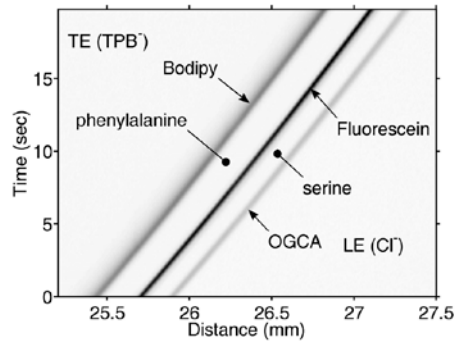

Figure 2. Measured fluorescence intensity as a function of distance and time. ITP-focused migration of three fluorescent spacers inside a 34 μm by 12 μm deep glass microchannel is shown. The three parallel bands are the OGCA, Fluorescein, and Bodipy spacers moving at identical speed. The three spacer bands bound two zones of unlabeled amino acids (serine and phenylalanine) among them.

In figure 3, we show detection and separation of (non-fluorescent) acetic acid and phenylpropionic acid using the same set of spacers. The spacing between OGCA and

fluorescein increases approximately linearly with the acetate concentration. In figure 4, we show quantitatively that the gap width between fluorescent spacers increases linearly with the concentration of analyte bound among them. Hence, the spacing between adjacent spacers is a linear measure of the concentration of analyte bracketed between them.

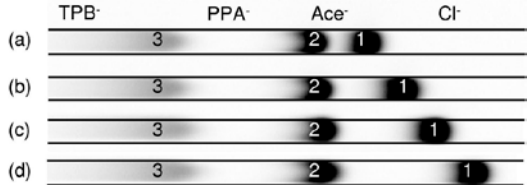

Figure 3. CCD images of the fluorescent spacers in a microchannel demonstrating separation of acetate (Ace^-) and phenylpropionate (PPA) ions in four different experiments. The initial concentration of Ace^- is increased linearly from 12 µM to 48 µM in (a)-(d) resulting in a linear increase in the spacing between fluorescent spacer peaks 1 and 2. PPA^- concentration is held constant at 40 µM. 1: OGCA, 2: Fluorescein, 3: Bodipy

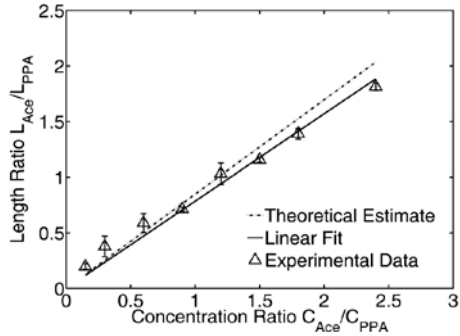

Figure 4. Measured ratio of the length of unlabeled Ace^- and PPA^- sample zones (the "gap width" ratio) after ITP separation/detection vs. the Ace^--to-PPA^- initial concentration ratio. This plot validates that the length of an unlabeled analyte zone at steady state is a measure of its initial concentration.

5. CONCLUSIONS

We have demonstrated the indirect detection of unlabeled analytes with a technique combining isotachophoresis with fluorescent spacers. We have demonstrated separation and detection of unlabeled analytes with sensitivity of ~200 nM. This is, to our knowledge, the highest ever achieved sensitivity for indirect detection (by ~500 fold).The resolution of the technique is limited only by the mobilities of the "spacer ladder" (which we are now expanding) and, even for a small ladder, the technique can provide exquisite specificity.

REFERENCES

[1] N. J. Munro, Z. L. Huang, D. N. Finegold, and J. P. Landers, *Indirect fluorescence detection of amino acids on electrophoretic microchips,* Analytical Chemistry, 72(13), pp. 2765-2773, (2000).

[2] F. M. Everaerts, J. L. Beckers, and T. P. E. M. Verheggen, *Isotachophoresis : Theory, Instrumentation, and Application*, New York, Amsterdam. 1976.

MICROFLUIDIC TEMPERATURE GRADIENT FOCUSING FOR *IN SITU* CHIRAL AMINO ACIDS ANALYSIS ON MARS

Grégoire Danger and David Ross
National Institute of Standards and Technology, USA

ABSTRACT

In this paper, we present the application of scanning temperature gradient focusing (TGF) for the chiral separation of amino acid biomarkers. Using a mixture of seven amino acids including five chiral amino acids, we show that scanning TGF is a simple and efficient method for chiral separations. The modulation of TGF parameters (temperature window, scan rate pressure, temperature range, chiral selector concentration) allow optimization of peak efficiencies and analyte resolutions. The use of hydroxypropyl-β-cyclodextrin (HPβCD) as chiral selector at low concentration provides chiral TGF separations with high resolution between enantiomers (Rs > 1.5) using a short silica capillary (4 cm). With these new results, the scanning TGF method appears to be a viable method for *in situ* biomarker analysis for future missions to Mars or other solar system bodies.

Keywords: Scanning TGF, *in situ* analysis, chiral analysis, low detection limit, high resolution

1. INTRODUCTION

Future National Aeronautics and Space Administration (NASA) space missions will have the objective to perform *in situ* analysis of amino acids biomarkers and their chirality in extraterrestrial environments. For the miniaturization of analytical systems, the use of microchip based on electrophoresis process is one possible solution.[1, 2] The concentration of amino acids in samples from extraterrestrial environments is not well known, but it is expected to be very low (below the detection limit for the Viking lander, for example). Consequently, it is important to develop methods with the lowest possible detection limits. With this in mind, we are exploring the feasibility of using TGF [3] for *in situ* amino acid analysis. With this method, a buffer with a temperature-dependent ionic strength is used. When a temperature gradient is applied across channel, a gradient in electrophoretic velocity of analytes is formed. By balancing the electrophoretic motion of the analytes with a counter bulk flow, it is possible to adjust the value of the bulk flow in order to obtain a total velocity of the analyte equal to zero only at a single point along the gradient. Analytes move toward its own zero velocity point where they are focused. With the addition of a chiral selector to the run buffer, it is possible to obtain chiral separation of amino acids.[4] Furthermore, the bulk counter flow can be scanned over the time in order to provide separations with high resolution and peak capacity.[5] In addition to high resolution, scanning TGF provides simultaneous concentration enhancement for low detection limits.[5, 6]

In this paper we present results for chiral separation with scanning TGF on the Mars7 Standard (a mixture of seven amino acids including five chiral amino acids that are expected to be found on Mars).[7] We show that the application of scanning TGF to chiral separation of amino acids is easily optimized to provide good resolution of nearly all the amino acid

978-0-9798064-0-7/μTAS2007/$20©2007CBMS

enantiomers while keeping very low detection limits, and only using a short, simple separation column.

2. RESULTS AND DISCUSSION

The optimized conditions for chiral separation with HP□CD as chiral selector are presented in Figure 1. The resolutions obtained between enantiomers are very high due to the strong interaction between amino acids and cyclodextrin. The average resolution between enantiomers is 6.1. The lowest resolution is obtained with aspartic acid (1.7) and the highest resolution with valine (9.9). With these conditions, for the Mars7 standard sample separation just one co-migration is observed between L enantiomers of alanine and serine. All others analytes are resolved with the lowest resolution observed between glycine and D-alanine (0.8).

Pressure scan rate effects on peak heights and resolutions for Mars7 standard sample with chiral separation are shown in Figure 2. Compared with the optimized result of Figure 1, peak heights and resolutions are lower. At lower scan rate pressure (Figure 1), the time allowed for each amino acid to focus is increased which improves the peak shape and detection limit.

Figure 3 show the influence of the applied temperature gradient on separation. At a higher average temperature and larger gradient (3 °C to 50 °C), resolutions are lower and peak heights higher than the optimized result (3 °C to 25 °C). A higher temperature range over a fixed gradient length is thus roughly equivalent to the use of a shorter separation channel with conventional capillary electrophoresis: peak concentrations are higher, but resolution is lower. Thus by adjusting the temperature range, it is possible to tune the separation according to the needs of each sample without any change in the device hardware.

5. CONCLUSIONS

With the optimized chiral TGF separation conditions thirteen of the fourteen analytes (including the two by-products of the labelling reaction with 5-carboxyfluorescein succinimidyl ester) can be resolved with an average resolution between neighbouring peaks of 4.6. This is accomplished with a very simple microfluidic device with no injection structure and a separation column only 4 cm long. Furthermore, the method provides approximately 100-fold enhancement of the analyte concentration at the detection point (after high-resolution separation) relative to the input concentration.

ACKNOWLEDGEMENTS

This research was supported by the NASA Astrobiology Science and Technology Instrument Development (ASTID) program grant number NNH06AE121.

REFERENCES

[1] Belder, D., Ludwig, M., *Electrophoresis*, **2003**, 24, 2422-2430.
[2] Piehl, N. *et al*., *Electrophoresis*, **2004** 25, 3848-3852.
[3] Ross, D., Locascio, L., *Analytical Chemistry*, **2002** 74, 2556-2564.
[4] Balss, K., *et al.*, *Analytical Chemistry*, **2004** 76, 7243-7249.
[5] Hoebel, S. *et al.*, *Analytical Chemistry*, **2006** 78, 7186-7190.

[6] Munson, M., *et al.* to be published in *Analytical Chemistry*, **2007**.
[7] Skelley, A. M., Mathies, R. A., *Journal of Chromatography A*, **2003** 1021, 191-199.

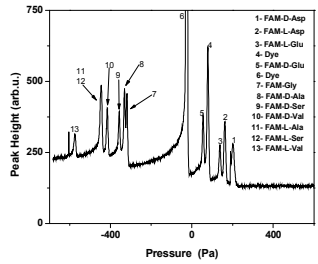

Figure 1: High-resolution chiral TGF. With a moderate temperature gradient and slower pressure scan rate, 12 of the 13 species present can be resolved and quantitatively measured. Sample: 10 nmol L^{-1} concentration of each amino acid enantiomer in 0.5 mol L^{-1} tris-borate buffer. Separation conditions: -4000V, 4 cm total column length, temperature gradient from 3 °C to 25 °C over 1 cm length, 0.5 mol L^{-1} tris-borate buffer, pH 8.3 with 1.5 mmol L^{-1} HPCD, pressure scan from 1000 Pa to -700 Pa at -0.25 Pa/s.

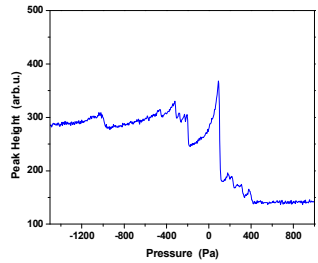

Figure 2: Rapid chiral TGF result. The measurement was produced by scanning the pressure applied to the channel outlet from 1000 Pa to -1500 Pa at a rate of -2.5 Pa/s. The weakly focused peaks/steps give a rapid indication of which chiral species are present. For others conditions see Figure 1.

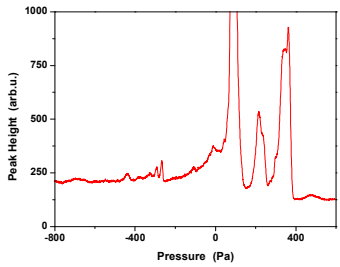

Figure 3: Chiral TGF with large temperature gradient. A larger temperature gradient gives enhanced focusing for the acidic amino acids (large peaks at ≈200 Pa and ≈350 Pa), but does not give the optimal resolution. Temperature gradient from 3 °C to 50 °C, for others conditions see Figure 1.

ON-CHIP CONTINUOUS CELL SEPARATOR USING POSITIVE AND NEGATIVE DIELECTROPHORESIS

J. Avian, S. Kostner, and M.J. Vellekoop
Vienna University of Technology, Austria

ABSTRACT

In this work a microfluidic device for the continuous separation of particles based on positive and negative dielectrophoresis was developed.

The particles are first focused hydrodynamically and then separated due to their dielectrophoretic response. Experiments with yeast cells (d ~ 5 µm) and polystyrene beads (d = 8 µm) at a voltage of 11.3 V_{RMS} and a frequency of 1 kHz showed positive dielectrophoretic behavior with a mean deviation of 46.5 µm and negative dielectrophoretic behavior with a mean deviation of –35 µm for yeast and beads, respectively.

Keywords: dielectrophoresis, cells, separation

1. INTRODUCTION

In this paper we present a novel design for a continuous separation device for particles and cells based on dielectrophoresis (DEP). Compared to other DEP separators, which rely on negative dielectrophoretic particle behavior [1] or particle traps [2], the separator presented in this contribution works continuously with negative as well as positive DEP forces without trapping the particles at the electrode edges. This is effective for direct sorting of particles or cells and prevents them from sticking to electrodes or channel wall.

2. THEORY

The dielectrophoretic force moves polarizable particles in an inhomogeneous electric field according to

$$F_{DEP} = 2\pi\varepsilon_m R^3 \cdot \mathrm{Re}[\underline{K}] \cdot \nabla E_0^2 \quad \text{with} \quad \underline{K} = \frac{\underline{\varepsilon}_p - \underline{\varepsilon}_m}{\underline{\varepsilon}_p + 2\underline{\varepsilon}_m},\ \mathrm{Re}[\underline{K}] \in [-0.5..1],\ \underline{\varepsilon}_x = \varepsilon_x - j\frac{\sigma_x}{2\pi f}.$$

The Clausius Mossotti factor K depends on permittivity and conductivity of the medium (ε_m, σ_m), the particle (ε_p, σ_p), and the frequency f. R is the particle radius and E_0 is the electric field.

3. SEPARATION PROCESS

The basic idea of the separation process is outlined in Figure 1. After injection of the particles they are hydrodynamically focused and then separated along a microfluidic channel with electrodes on either side. To prevent the particles from being trapped at the electrodes the separation process has to take place in a certain distance from the maxima of the field gradient at the metal surface. In the actual separation zone the isosurface planes for the electric potential are vertically orientated and the dielectrophoretic force is independent of the vertical position of the particles. Therefore it is sufficient to realize the electrodes as plane electrodes on the bottom of the channel. The small electrodes opposite to the straight electrode cause the inhomogeneity of the electric field.

978-0-9798064-0-7/µTAS2007/$20©2007CBMS

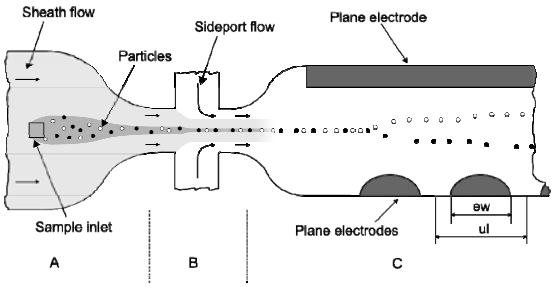

Figure 1. Schematic function of separation process (top view): (A) Particle injection, (B) focusing, and (C) separation due to their differing size and electrical properties that cause a different dielectrophoretic force.

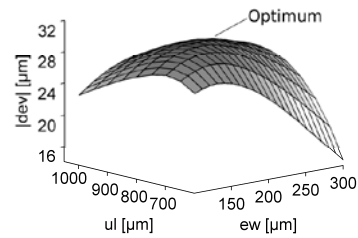

Figure 2. Geometry optimization for the electrodes. The parameters are electrode width (ew) and DEP unit length (ul), see Figure 1.

The geometry of those electrodes provides a uniform current density distribution at the electrode edges to minimize erosion. The optimal electrode dimensions were found by simulating the particle displacement |dev| along the channel for varying size (ew) and spacing (ul) of those electrodes. The maximum particle deviation denotes the best ratio of those parameters, see Figure 2.

4. DEVICE

The channel boundaries of the device are defined by silicon substrate, glass and SU8 for the bottom, top and side walls, respectively [3]. The channel height is 30 µm. The fabricated device is shown in Figure 3. Particles are injected through the sample inlet (1), transported to the taper by the sheath flow (2) and focused by the side port flows (3). After passing the separation channel (4) the particle positions are determined (5) and the waste leaves the chip through the outlet (6). The electrodes are made of platinum with an titanium undercoating (7).

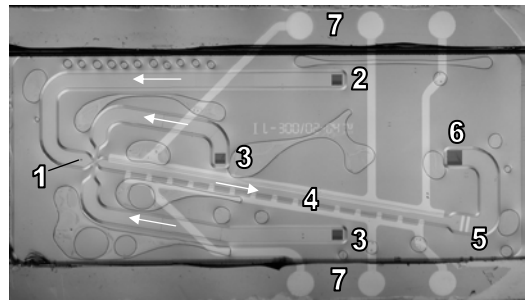

Figure 3. Fabricated device (11x19mm²).
1: sample inlet, 2: sheath inlet, 3: sideport inlets, 4: separation region, 5: detection area, 6: outlet, 7: bond pads for electric contacts.

4. EXPERIMENTAL

Micromer®-blue beads and yeast cells (Saccharomyces cerevisiae) were used to evaluate the design principle. Beads and cells were suspended in 0.4M mannitol solution and injected separately through the sample inlet of the chip mounted on a DELRIN® device holder. With a digital camera (Sony Cybershot DSC-S75) attached to a stereo microscope (Zeiss Stemi SV11) the particle trajectories through the detection area for applied root-mean-square voltages of 0 V_{RMS} and 11.3 V_{RMS} at a frequency of 1 kHz and a flow rate in the separation channel of 1.2 µl/min were recorded and analyzed afterwards.

4. RESULTS AND DISCUSSION

The relative frequency of the particle count for polystyrene beads (a) and yeast cells (b) are shown in Figure 4. Obviously the distribution of the beads is moved to the left of the diagram for applied voltage due to their negative DEP response. The yeast cells show a wider distribution without applied voltage because the hydrodynamically focusing capability is limited for small particles. Due to the varying diameter of 2-5 µm and therefore varying DEP force acting on the cells the distribution for applied voltage is broadened in comparison to the distribution for no applied voltage. The mean deviation of the beads and cells is –35 µm and 46.5 µm, respectively.

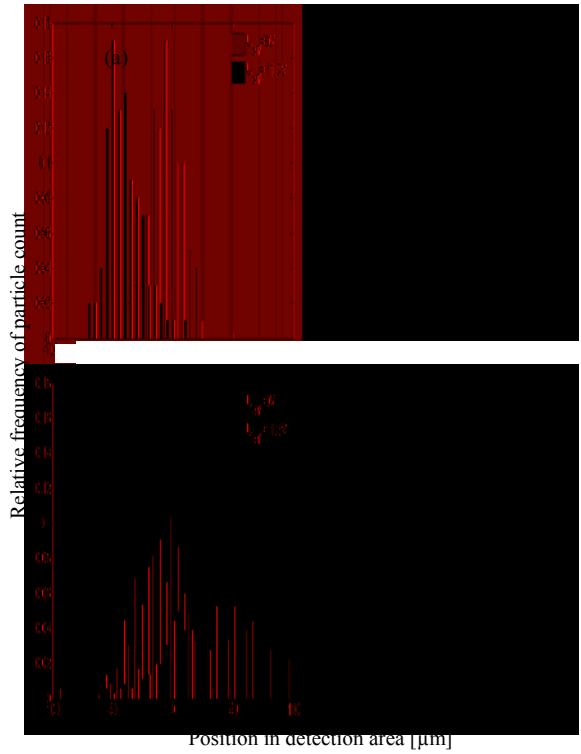

Figure 4. Particle distribution with (black) and without (gray) applied voltage for polystyrene beads (a) and yeast cells (b).

5. CONCLUSIONS

The function of the design principle has successfully been proved by the separation of yeast cells and polystyrene beads and the separation efficiency was evaluated. In future devices the particle focusing will be improved since the separation efficiency depends heavily on a common starting position of the particles in the separation channel.

REFERENCES

[1] J. Rousselet, G.H. Markx, and R. Pethig, *Separation of erythrocytes and latex beads by dielectrophoretic levitation and hyperlayer field-flow fractionation*, Colloids and Surfaces (A), 140, p. 209-216 (1998).

[2] G. Zhou, M. Imamura, J. Suehiro, and M. Hara, *A Dielectrophoretic Filter for Separation and Collection of Fine Particles Suspended in Liquid*, Industry Applications Conference, 2002. 37th IAS Annual Meeting. Conference Record of the, 2, p. 1404-1411 (2002).

[3] P. Svasek, E. Svasek, B. Lendl, and M. Vellekoop, *Fabrication of miniaturized fluidic devices using SU-8 based lithography and low temperature wafer bonding*, Sensors and Actuators A: Physical, Volume 115, Issues 2-3, p. 591-599 (2004).

POINT MUTATION DETECTION BY ON-CHIP DIFFUSION COEFFICIENTS MEASUREMENT

A. Estévez-Torres,[1] T. Le Saux,[1] H. Berthoumieux,[1]
A. Georges,[1] S. Fernandez,[1] J.-F. Allemand,[2] V. Croquette,[2]
A. Lemarchand,[3] L. Jullien,[1] and C. Gosse.[4]

[1]Département de Chimie, École Normale Supérieure, Paris, France
[2]Laboratoire de Physique Statistique, École Normale Supérieure, Paris, France
[3]Laboratoire de Physique Théorique de la Matière Condensée, Université Paris 6, France
[4]Laboratoire de Photonique et de Nanostructures, LPN – CNRS, Marcoussis, France

ABSTRACT

A stationary migration-diffusion concentration pattern for a binary mixture is analyzed by 1D-Fourier transform and diffusion coefficients are straightforwardly extracted using an exact analytical model. As this approach also allows species titration, it is used to measure the extent of hybridization reactions between complementary oligonucleotides. Any point mutation can then be detected within 20 s, in free solution and without separation.

Keywords: Fourier transform, oligonucleotide, hybridization, SNP, electrophoresis.

1. INTRODUCTION

Because it does not depend on molecular structure details, diffusion is a scarcely used criterion in separation science. However, in a binary mixture, Brownian motion can efficiently discriminate components that significantly differ in size. One can for instance access the relative proportion of a ligand during titrations, free or bound to a macromolecule [1]. We propose here to detect single nucleotide polymorphism (SNP) by injecting and analyzing on-chip an equilibrium mixture of fluorescent probe and non-fluorescent target, 9 and 100 nucleotides long, respectively. The diffusion-based quantification of the respective amounts of free probe **1** and probe-target duplex **2** yields information on the hybridization thermodynamics and hence on any mismatch presence.

2. EXPERIMENTAL

Fluidic structures, 10 μm high, are molded in PDMS and closed with a glass cover-slip (Fig. 1a). Upon applying a permanent electric field, the **1** + **2** mixture is continuously introduced through a 20 μm narrow channel into a 7.5 mm wide chamber (Fig. 1b). To ensure a homogeneous potential drop over the analysis area, arrays of highly resistive microfluidic channels are used to connect the electrodes reservoirs [2]. These resistors, 20 μm large and 7.5 mm long, are separated by 20 μm thick PDMS walls.

Solutes exit the microscope field of view within ~ 3 s, i.e. well before the hybridization chemistry has relaxed (τ_{match} ~ 50 s). Thus, the **1** and **2** molecular motions are independent and the recorded stationary fluorescent image, $I(x,y)$, only accounts for both components migration along the injection axis and diffusion in two-dimensions (Fig. 2a). The resulting concentration profiles superposition is next Fourier transformed along y, yielding the x-dependence of the normalized Fourier modes $\tilde{I}(x,n)/\tilde{I}(x,0)$ (Fig. 2b) [3]. Finally, a bi-exponential fit, $\tilde{I}(x,n)/\tilde{I}(x,0) = a_{1,n}\ exp(-l_{1,n}\ x) + a_{2,n}\ exp(-l_{2,n}\ x)$, is performed to extract each component **j** diffusion coefficient D_j from the corresponding exponential decays $l_{j,n}$. Indeed, in the Fourier space, concentration profiles write $\tilde{A}_j(x,n) = \tilde{A}_j(0,n)$ x $exp(-l_{j,n}\,x)$ with $l_{j,n} = D_j\ q_n^2/v_{x,j}$ and $q_n = 2\pi\, n\ /L_y$ (for an image of width L_y along y).

978-0-9798064-0-7/μTAS2007/$20©2007CBMS

Additionally, the pre-exponential amplitudes $a_{j,n}$ are plotted as a function of the mode spatial frequency q_n and fitted with a Gaussian function (Fig. 2c). One can hence determine the $a_{j,0}$ and measure the ratio between both species concentrations in the sample reservoir : $\alpha = [\mathbf{2}]/[\mathbf{1}] = a_{2,0}/a_{1,0} \times Q_1/Q_2$ where Q_j is the component **j** brightness. The proportion of hybridized probe in the injected mixture is finally computed as $h = \alpha / (1+\alpha)$.

In independent experiments, h is determined by using fluorescence spectroscopy to monitor the bulk titration of a 50 nM probe solution with increasing target concentrations.

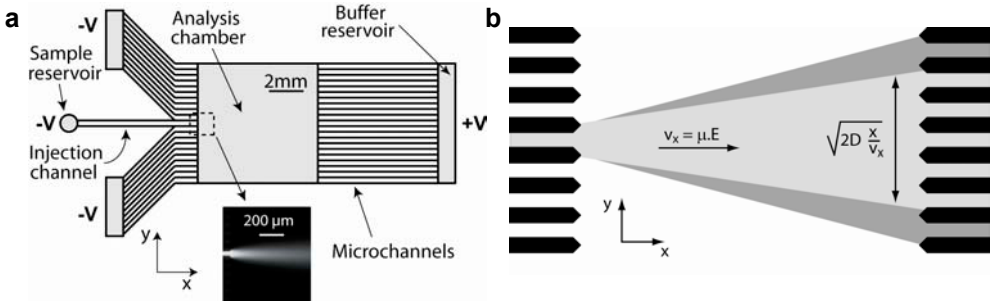

Figure 1. (a) Microchip top-view. (b) Principle of the migration-diffusion concentration pattern generation. Under electric field, analytes (■ and ■) are continuously injected along x at speed $v_{x,j}$ and their transverse diffusion yields parabola-like patterns which width depends on the $D_j/v_{x,j}$ ratio.

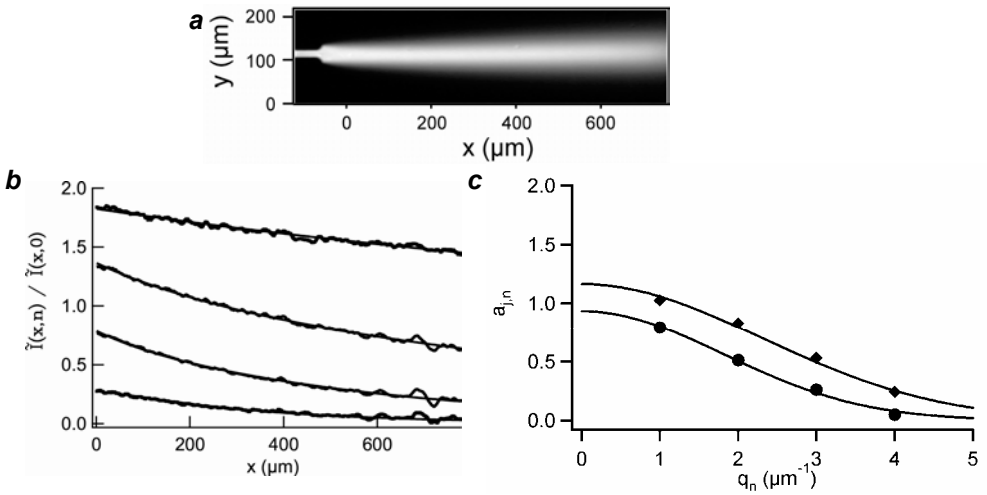

Figure 2. Successive steps of the 1-D Fourier transform analysis performed on a mixture of 1 µM Texas-Red labeled probe, Tex-TGT9$_{match}$, and 5 µM non-labeled target, ACA100. An 8 x 10^3 Vm^{-1} electric field is applied in NaOH/Hepes 25/50 mM pH 7.5, 0.1% (w/w) PDMA buffer at 10°C. (a) Stationary migration-diffusion pattern. (b) Dependence along x of the normalized Fourier mode resulting from the Fourier transform along y of the preceding image. (c) Pre-exponential amplitudes $a_{j,n}$ as a function of the mode spatial frequency q_n for the free probe (●) and the probe-target duplex (◆).

3. RESULTS

When using T-sensors, transport phenomena are complex due to Poiseuille hydrodynamic flow and several approximations must be performed to measure D [4]. Here, in contrast, electromigration results in a uniform plug-like velocity field, which allows to derivate an exact analytical model for the concentration profiles relaxation. Moreover, whereas bi-Gaussian fitting in the direct space was unsuccessful, a robust bi-exponential analysis in the Fourier space yields the diffusion coefficients and the relative concentrations for both free short probe **1** and long hybridized target **2** (Table 1). A single mismatch is then easily detected; it corresponds to a much lower amount of the slowest diffusing species, i.e. almost no probe-target formation.

Table 1. Proportion of hybridized probe h (10^{-2}), either measured on-chip or computed using the duplex association constants determined by control bulk titrations. Diffusion coefficients D_f (10^{-12} m^2s^{-1}) were extracted from the bi-exponential decays associated to the concentration profiles relaxation.

Mixture	h_{chip}	h_{bulk}	$D_{Tex\text{-}TGT9}$	$D_{Tex\text{-}TGT9\,+\,ACA100}$
Tex-TGT9 alone	-	-	106 ± 3	-
Tex-TGT9$_{match}$ + ACA100	55 ± 5	60 ± 5	106 ± 3	32.5 ± 3
Tex-TGT9$_{mismatch}$ + ACA100	<6 ± 5	5 ± 2	117 ± 5	0 ± 5

4. CONCLUSION

Fourier analysis is a powerful tool for studying diffusion, one of the most relevant physical phenomena in microdevices. Indeed, D can be extracted in less than a minute by observing the Brownian motion at the 200 μm scale. Our application to SNP detection demonstrates that simple diffusion analysis in free solution can compete favorably with separation-based methods (e.g. electrochromatography [5], DNA chips [6]) which often rely on complex procedures to achieve oligonucleotides immobilization.

ACKNOWLEDGEMENTS

We thank J.-L. Mergny, L. Lacroix, and A. Bourdoncle for insightful discussions. This work was supported by two research fellowships and the ACN 2003 “Cargos Moléculaires” and ACI-MNAC 2003 “Puces Cinétiques” grants from the Ministère de la Recherche et de la Technologie.

REFERENCES

[1] A. Chen and M. J. Shapiro, *Anal. Chem.*, **71**, 669A (1999); A. Hatch, *et al.*, *Nat. Biotechnol.*, **19**, 461 (2001).
[2] L. R. Huang, *et al.*, *Nat. Biotechnol.*, **20**, 1048 (2002); C.-X. Zhang and A. Manz, *Anal. Chem.*, **75**, 5759 (2003).
[3] T.-T. Tsay and K. A. Jacobson, *Biophys. J.*, **60**, 360 (1991); D. A. Berk, *et al.*, *Biophys. J.*, **65**, 2428 (1993).
[4] R. F. Ismagilov, *et al.*, *Appl. Phys. Lett*., **76**, 2376 (2000); A. E. Kamholz and P. Yager, *Biophys. J.*, **80**, 155 (2001); J.-B. Salmon and A. Ajdari, *J. Appl. Phys.*, **101**, 074902 (2007).
[5] T. Ito, *et al.*, *Anal. Chem.*, **77**, 4759 (2005).
[6] J. G. Hacia. *Nat. Genet.*, **21**, 42 (1999).

SEMI-PACKED MICRO GAS CHROMATOGRAPHY COLUMNS

Syed A. Ali[1], Mohammad A. Zareian-Jahromi[1], Mehdi Ashraf-Khorassani[2], Larry T. Taylor[2], and Masoud Agah[1]

[1]VT MEMS Laboratory, Department of Electrical & Computer Engineering
[2]Department of Chemistry
Virginia Tech, Blacksburg, USA

ABSTRACT

This paper reports, for the first time, a new class of gas chromatographic separation columns, named "semi-packed." These 1 m-long columns have yielded 10,000 theoretical plates which is the highest separation efficiency reported to date on microfabricated separation columns.

Keywords: Gas chromatography, μGC, MEMS, Semi-Packed

1. INTRODUCTION

Gas chromatography is used to separate different compounds of a gas mixture based on the mass transfer principle between a mobile phase (carrier gas) and a stationary phase (coating). The relative amount of time spent in the stationary phase with respect to the mobile phase varies for different components in the gas mixture, and hence they get separated as they travel though the column. A detector at the column outlet generates an electronic signal based on the concentration of the components as they exit the column. Conventional GCs are too bulky and power consuming, making them unsuitable for portable applications. Microelectromechanial systems (MEMS) technology promises the development of micro gas chromatography systems (μGCs) with faster analysis times, lower power consumption, and higher portability. Open tubular MEMS based microfabricated columns have been reported in [1,2]. This paper reports the fabrication and performance of semi-packed columns which are fabricated with embedded microposts in the separation channel. The posts improve the separation efficiency of the semi-packed columns by a factor of two as compared to the open tubular MEMS columns. The posts also increase the overall surface area of the column giving them higher sample capacity.

2. FABRICATION

Fig. 1 shows the fabrication process for semi-packed silicon-glass columns. After cleaning the substrate, a 10μm-thick layer of AZ9260 photoresist is spun and patterned on the wafer (Fig. 1a). Silicon is then selectively etched using deep reactive ion etching (DRIE) technique, forming microfluidic channels and microposts (Fig. 1b). The resist is stripped and the channels are sealed by anodically bonding

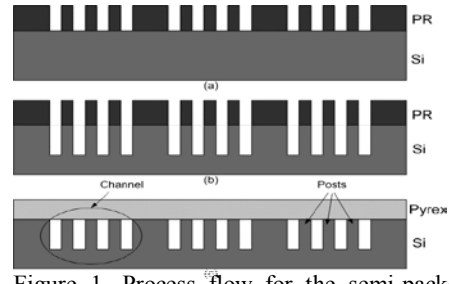

Figure 1. Process flow for the semi-packed chip. (a) Patterned PR, (b) DRIE, and (c) Anodic Bonding

978-0-9798064-0-7/μTAS2007/$20©2007CBMS

the silicon substrate to a Pyrex 7740 wafer (Fig. 1c). After dicing the wafer, epoxy is used to glue fused silica capillary tubing to the microfluidic ports in order to connect the MEMS columns to a conventional GC system for evaluation.

Fig. 2 shows an SEM image of a section of a column and its embedded posts. The column has a width, depth, and length of 150µm, 180µm, and 1m, respectively, and is fabricated on an 18mm square die. The square posts are 20µm on the side giving the semi-packed chip about twice the surface as compared to that of rectangular open tubular MEMS columns, thus providing a larger sample capacity.

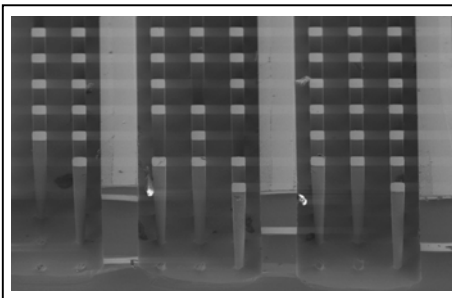

Figure 2. SEM image of a section of the semi-packed column

In order to compare the performance of semi-packed columns with open tubular MEMS columns, both were coated statically using a 6mg/mL concentration of OV-1 stationary phase dissolved in n-pentane. In this method, the column was first filled with the solution, and then, one end of the column was sealed with wax. Next, vacuum was applied to the other end to evaporate the solvent leaving behind a thin layer of the OV-1 coating.

3. RESULTS AND DISCUSSION

The separation efficiency of GC columns is quantified by height-equivalent-to-a-theoretical plate (HETP) which is given by [3]:

$$H = A + \frac{B}{\bar{u}} + C \cdot \bar{u} + D \cdot \bar{u}^2 \qquad (1)$$

Here, $\bar{u}$ is the average linear flow velocity of the mobile phase. The A term is used to explain eddy diffusion in packed columns in which analytes travel different distances. The B and C terms arise from longitudinal gas-gas diffusion and resistance to mass transfer, respectively. The D term is significant in short columns at high linear velocities due to the effects of the instrumentation [3]. To experimentally determine the HETP of open tubular and semi-packed MEMS colums, the theoretical plate number was measured at different gas velocities using injections of nonane at 28°C. The HETP was then found by dividing the total length of the column by the number of theoretical plates. The HETP curves versus the average linear carrier gas flow velocity are shown in Fig. 3. The open tubular MEMS column showed a minimum HETP of ~0.02cm (5000 plates/m), which was comparable to the

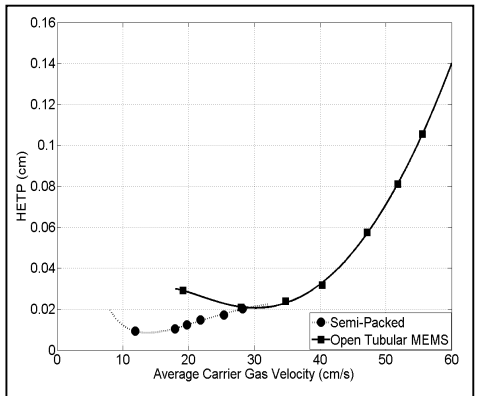

Figure 3. HETP plot for the semi-packed and the open tubular MEMS column

efficiency reported in [2]. The semi-packed column showed a minimum HETP of ~0.01cm (10,000 plates/m), the highest efficiency achieved with MEMS-based columns.

The enhancement of the separation efficiency is likely to be attributed to the minimization of the variation in the gas velocity profile across the channel width in the semi-packed column as well as the reduction in the mass transfer distances (decrease in the *C* term). It should be noted that in these semi-packed columns, as opposed to conventional packed columns, eddy diffusion has a minimal effect on brand broadening because of the uniform size and distribution of the posts.

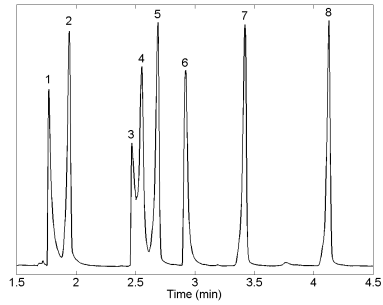

Figure 4. Chromatogram showing the separation of the compounds achieved by the semi-packed column

Fig. 4 shows the separation results of a gas mixture containing four polar and four non-polar compounds, listed in Table 1, performed under a temperature programming rate of 30°C/min. The chromatogram demonstrates the accepatable resovling power of semi-packed columns for these polar and non-polar analytes.

Table 1. List of components in the test mixture

	Component	Boiling Point (°C)		Component	Boiling Point (°C)
1	2-Octanone	173	5	Undecane	196
2	Decane	174	6	2,6-Dimethylaniline	214
3	1-Octanol	195	7	Dodecane	216
4	2,6-Dimethylphenol	201	8	Tridecane	234

4. CONCLUSION

The paper introduced a new class of gas chromatographic columns developed by the use of MEMS technology. These columns, named as "semi-packed," have no conventional counterpart. The separation efficiency of these columns were measured to be 10,000 plates per column length, which is the highest efficiency achieved using MEMS columns to date. Theoretically, semi-packed columns should provide a higher sample capacity as well. Work is under way to study the effect of different configurations of microposts on both separation efficiency and sample capacity.

ACKNOWLEDGEMENT

This work has been supported partially by the National Science Foundation under Award Number ECCS-0601456.

REFERENCES

[1] M. Agah, J. A. Potkay, G. Lambertus, R. Sacks and K. D. Wise, *J. Microelectromech. Syst.*, 2005, **14**, 1039-1050.

[2] S. Reidy, G. Lambertus, J. Reece and R. Sacks, *Anal. Chem.*, 2006, **78**, 2623-2630.

[3] G. Gaspar, R. Annino, C. Vidal-Madjar and G. Guiochon, *Anal. Chem.*, 1978, **50**, 1512-1518.

SEPARATION AND POLARIZABILITY OF DNA BY DIELECTROPHORESIS

Jan Regtmeier*, Henning Höfemann*, Ralf Eichhorn, Dario Anselmetti* and Alexandra Ros***

** Biophysics & Applied Nanoscience, Bielefeld University, Germany*

*** Condensed Matter Theory, Bielefeld University, Germany*

ABSTRACT

Although separation of polymers based on the combination of dielectrophoretic trapping and electrophoretic forces has already been proposed 15 years ago [1], the experimental realization has only recently been demonstrated [2]. Here, we address the fast separation of biotechnologically relevant DNA by utilizing electrodeless dielectrophoresis in a simple, structured microfluidic chip. In addition, we demonstrate how the same chip and the same experimental setup can be used to determine the polarizability of DNA.

Keywords: microfluidics, DNA, polarizability, separation

1. INTRODUCTION

Using electric fields for transport and separation of biomolecules is a standard technique in lab-on-a-chip systems. A detailed understanding of the polarizability of DNA in an AC electric field is still lacking, although there have been proposals of how this polarizability could be exploited for separation [1]. A quantitative access to the length dependent polarizability is an important prerequisite for the development of effective and predictable separation procedures. Here, we demonstrate the separation of supercoiled DNA by the combination of electrophoresis and electrodeless dielectrophoresis in a microfluidic device. Additionally, we show that the same setup can be used to determine the polarizability of DNA using rate theory description of the escape process from a dielectrophoretic trap.

2. THEORY

Applying an electric AC field $U_{ac}\cdot\sin\omega t$ (frequency ω) to a channel structured with non-conducting posts leads to an inhomogenoues electric field $\boldsymbol{E}\cdot\sin\omega t$ therein. Subjecting DNA to this field, the trapping of DNA in the constrictions between two posts [3] can be observed under appropriate experimental conditions, an effect known as positive dielectrophoresis. The potential energy of an object of polarizability α can be calculated as

$$W = -(1/2)\,\alpha\,\boldsymbol{E}^2 \,. \qquad (1)$$

The additional application of a DC voltage induces the migration of DNA and thus tilts the potential landscape. Assuming a quasi-stationary globular configuration of the DNA molecule during the migration process, the escape time τ out of dielectrophoretic trap is then given by the inverse Kramers rate [4]

$$\tau \propto exp\,(\Delta W/kT) \qquad (2)$$

where ΔW denotes the depth of the potential well and kT the thermal energy. With eq. 1 and 2 and a simple geometric equivalent circuit diagram, which allows the calculation of $\boldsymbol{E}^2$ in the traps from the applied U_{ac}, one can calculate α . More precisely, we plot $ln\ \tau$ vs. U_{ac}^2 and obtain α from the adequate fitting of the data for each DNA length (see ref [2]).

978-0-9798064-0-7/μTAS2007/$20©2007CBMS

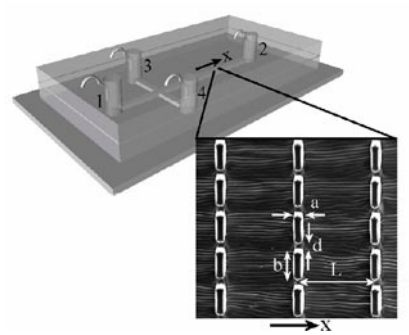

Figure 1. Schematic drawing of the microfluidic chip with reservoirs and Pt electrodes. The magnification is a SEM image of the separation channel (a=2.2 µm, b=7.4 µm, d=2.3 µm, L=21.1 µm; channel (2) is 5 mm long (structured region 3.8 mm), channels (1), (3) and (4) are 2 mm long and the channels are 6 µm high.).

3. EXPERIMENTAL

The microfluidic chip is made using a PDMS (poly(dimethylsiloxane)) soft lithography process [2]. A scheme of the final device is depicted in Fig. 1. After replica moulding from a structured wafer, the PDMS device is oxidized, assembled and subsequently coated with a PEG-silane. The DNA (in 10 mM phosphate buffer pH 8.3, 2 mM NaCl, 1 mM EDTA, 0.2% 2-mercaptoethanol, 0.1% POP-6) is stained with YOYO-1 (1 molecule per 10 base pairs), stored in reservoir 3 and injected via pinched injection.

For the determination of α, the migration of a DNA plug is observed via fluorescence video microscopy for constant U_{dc} =12V and different U_{ac}. From these data the escape times of 30 molecules for every U_{ac} are determined via visual tracking.

For DNA separation, a mixture of the two DNA species is injected and driven through the channel by U_{dc} =12V. During the migration the U_{ac} is increased stepwise up to a final value. Then the U_{dc} is switched off and the channel is scanned for fluorescence intensity.

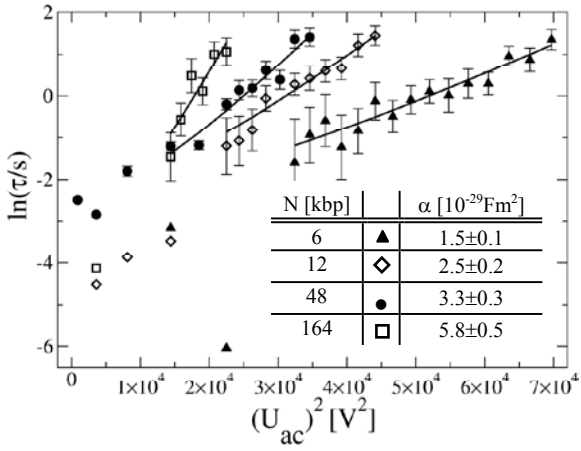

Figure 2: Plot of the experimentally measured trapping times τ versus U_{ac}^2 (symbols with error bars). The solid lines represent data fits from which the polarizabilities are deduced quantitatively. The inset table shows the resulting values of α for the four investigated DNA lengths.

4. RESULTS AND DISCUSSION

Fig. 2 shows the observed escape times versus the applied U_{ac} for linear DNA with 6, 12, 48.5 and 164 kbp. The linear fits with logarithmic corrections [2] have significantly different slopes resulting in increasing α with increasing DNA length (see inset Fig. 2).

For briefly exemplifying the separation performance of the device, we here focus on supercoiled DNA. As demonstated with Fig. 3, a supercoiled 7 kbp monomer can be separated from its 14 kbp dimer within only 210 seconds with base line resolution.

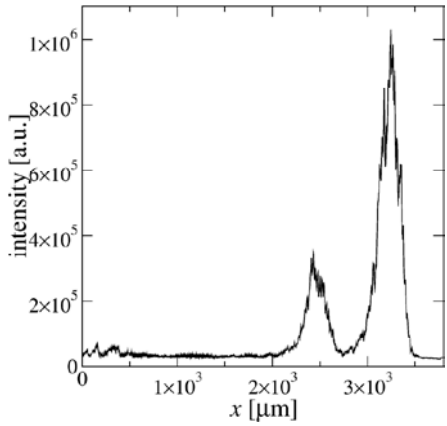

Figure 3. Scanned electropherogram of separated supercoiled 7 kbp (right peak) and 14 kbp (left peak) DNA. Parameters of the separation: U_{dc} = 12 V, U_{start} = 198 V, U_{inc} = 6 V, τ_{inc} = 30 sec, U_{end} = 240 V, ω = 60 Hz, scan speed 10 µm/s at 3 frames per s.

5. CONCLUSIONS

In summary, we demonstrated the separation of supercoiled DNA based on dielectrophoretic trapping. Moreover, we are able to deduce the molecular polarizability from the trapping times. With this quantitative information a systematic choice of the separation parameters will be possible in the future. The demonstrated separation technique is of high potential for the fast and cheap quality control of biotechnologically relevant plasmid DNA for applications such as in DNA vaccination.

ACKNOWLEDGEMENTS

Supply of plasmid samples from PlasmidFactory, Bielefeld, and financial support from the Deutsche Forschungsgemeinschaft within SFB 613 is gratefully acknowledged.

REFERENCES

[1] "Free-flow electrophoresis with trapping by a transverse inhomogeneous field," A. Ajdari and P. Prost, PNAS, **88**, 4468 (1991).

[2] "Dielectrophoretic manipulation of DNA: Separation and polarizability," J. Regtmeier et al., Anal. Chem., **79**, 3925 (2007)

[3] "Electrodeless Dielectrophoresis of Single- and Double-stranded DNA," C.-F. Chou et al., Biophys. J., **83**, 2170 (2002)

[4] "Dynamics of a polymer surmounting a potential barrier. The Kramers problem for polymers," P. Park and W. Sung, J. Chem. Phys., **111**, 5259 (1999).

SIZE-SELECTIVE SEPARATION OF GLASS BEADS USING THE SECONDARY FLOW IN A CURVED MICROCHANNEL

J. B. Ha[1], D. H. Yoon[1], S. Y. Park[1], Y. K. Bahk[1], T. Arakawa[2], Shuichi Shoji[2], and Jeung Sang Go[1]

[1]*School of mechanical Eng. Pusan National Univ., 609-735, South Korea*

[2]*Major in Nano-science and Nano-Engineering, Waseda Univ., 169-8555, Japan*

ABSTRACT

This paper presents a use of the micro-scale benefit of a secondary flow obtained in a curved microchannel, which is unfavorable and negligible in the conventional flow. In specific, we have demonstrated the size-selective separation and sorting of glass beads for biomolecular assays. Their numerical and experimental evaluation has been performed.

Keywords: Bead separation, curved channel, secondary flow, centrifugal acceleration

1. INTRODUCTION

The study of viscous flow in a curved duct constitutes a problem of fundamental interest in the field of internal fluid mechanics [1]. There are numerous applications, which include the flows through turbomachinery blade passages, aircraft intakes, diffusers, and heat exchangers [2]. However, to our knowledge, no previous studies have used the benefit of these secondary flows to separate of different size of particles in microfluidic channel. Herein, we have performed a number of numerical computations and experimentation to study on the size-selective separation of particles in the micro curved duct.

2. WORKING PRINCIPLE AND DESIGN

When a fluid flows through the curved channel, the secondary flow is generated on the cross-sectional plane of the channel due to the centrifugal acceleration in the axial direction. A dimensionless parameter equivalent to the centrifugal acceleration is the Dean number, $K = \mathrm{Re}\sqrt{D/R}$ defined by the function of Reynolds number related with fluid and its inlet velocity, hydraulic diameter D and the radius of channel curvature, R (Fig. 1). The Dean number increases rapidly with decreasing the radius of curvature.

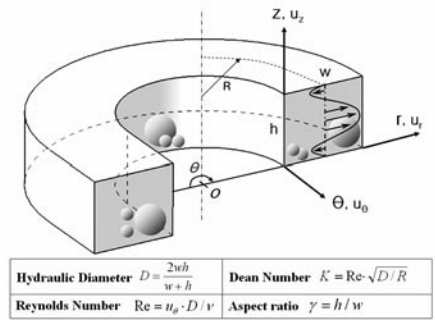

Figure 1. The geometry of a curved microchannel in the cylindrical coordinate and important variables for glass beads movements

978-0-9798064-0-7/μTAS2007/$20©2007CBMS

Figure 2 shows the numerical analysis of the velocity distribution on the cross-sectional plane for the various Dean numbers. The strong secondary flow can be obtained in the curved microchannel. Also, around the middle of the microchannel, the high velocities are directed outward to the channel, while near at the top and bottom, the weak velocities are distributed inward to satisfy the mass conservation. Especially, the position of the zero velocity at the moment of change in velocity direction was obtained constant at 0.27 in symmetry for the various Dean numbers and different cross-sections (Fig. 3).

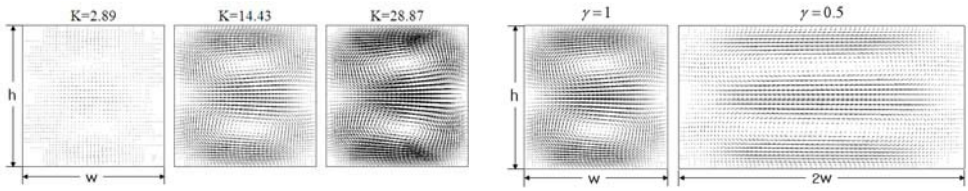

(a) (b)

Figure 2. Secondary flow velocity fields for (a) various Dean numbers K and (b) different aspect ratios γ, fixed at K=14.43

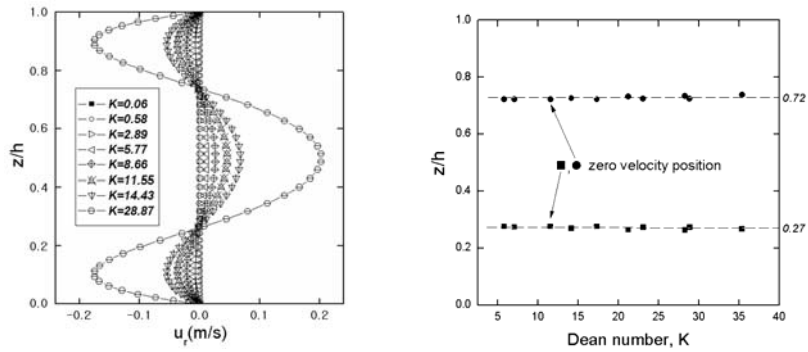

(a) (b)

Figure 3. (a) Velocity distribution for the various Dean numbers K at θ=90°, γ=1, (b) Constant position of the zero velocity for the various Dean numbers K, θ=90°, γ=0.5 and the different aspect ratios

This characteristic velocity distribution provides the size-selective separation of glass beads. When larger glass beads than the height of the zero velocity position are introduced into the microchannel, the outward velocity distribution is acted strongly on surface so that they are moved outward to the microchannel and in similar, for smaller glass beads, they are moved to the inward due to the inward velocity distribution compared with the outward velocity distribution. Finally, the glass beads are separated size-selectively. Figure 4 describes the schematic view of the size-selective separation of the mixed glass beads in the curved microchannel and their sorting into two different outlet channels.

3. EXPERIMENTAL RESULTS

For the experimental evaluation, the curved microchannel was bonded with the transparent glass substrate and a high speed CCD camera was installed in a microscope for the quantitative visualization. Fig. 5 shows the perfect separation of the glass beads with

the diameter of 20 μm and 40 μm, respectively in the condition of K = 14.43 and γ = 0.5 (w = 150 μm, h = 75 μm and R = 200 μm). As expected, the 40 μm-diameter glass beads showed the movement of the outward direction to the cross section but the 20 μm-diameter glass beads moved inward. For the two mixed glass beads, it was identically visualized that they were separated and sorted into two different outlet channels.

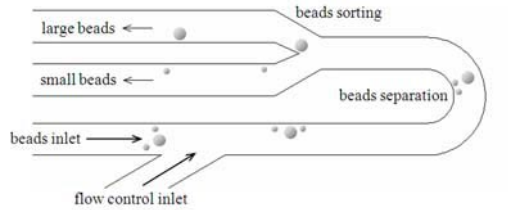

Figure 4. Size-selective separation of different glass beads in the curved microchannel

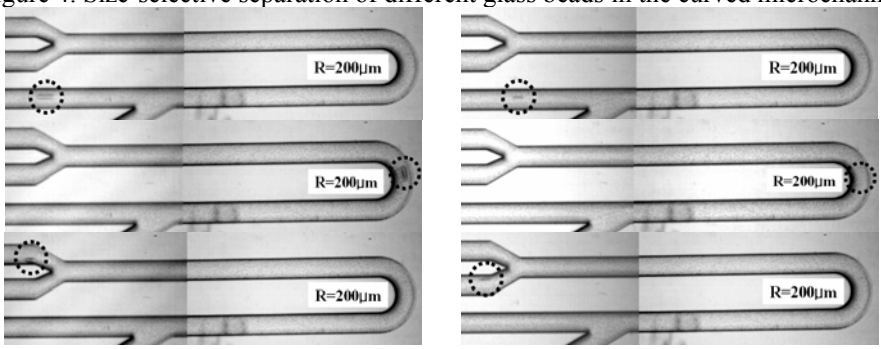

(a) (b)

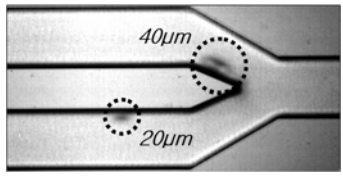

(c)

Figure 5. Visualization of size-selective separation for (a) the diameter of 40 μm, (b) the diameter of 20 μm and (c) their simultaneous size-selective sorting at K=14.43

4. CONCLUSIONS

In conclusion, the size-selective separation of micro glass beads was demonstrated successfully. For the further works, the various sizes of glass beads will be separated and an application linking with biomolecular assemblies will be developed.

REFERENCES

[1] K. C. Cheng, R. C. Lin, J. W. Ou, *Fully Developed Laminar Flow in Curved Rectangular Channels*, J. Fluids Eng., 3, pp. 41-48 (1976).

[2] K. N. Ghia, J. S. Sokhey, *Laminar Incompressible Viscous Flow in Curved Ducts of Regular Cross-Sections,* J. Fluids Eng. 99, 640-648 (1977).

[3] S. P. Vanka, G. Luo, and C.M. Winkler, *Numerical Study of Scalar Mixing in Curved Channels at Low Reynolds Numbers*, J. AIChE, 50, 10, (2004).

USE OF MICRO- AND NANO-FABRICATED ORDERED PILLAR ARRAYS FOR PRESSURE-DRIVEN REVERSED PHASE LIQUID CHROMATOGRAPHY SEPARATIONS

Wim De Malsche[1, 2], Hamed Eghbali[1], David Clicq[1], Joris Vangelooven[1], Deniz Tezcan[3], Piet De Moor[3], Vincent Verdoold[2], Han Gardeniers[2], Gert Desmet[1]

[1]Department of Chemical Engineering, Vrije Universiteit Brussel, Belgium
[2]Research Programme Mesofluidics, Twente University, The Netherlands
[3]IMEC, Belgium

ABSTRACT

In the present contribution, an account is given of the different solutions for injection, detection and retentive layer coating that needed to be developed to bring Fred Regnier's dream of a completely microfabricated HPLC column[1] to reality. These developments enabled the achievement of the first high resolution reversed phase liquid chromatography separations in ordered pillar array columns.

Keywords: Pillar array, liquid chromatography, collocated monolithic support structure, reversed phase

1. INTRODUCTION

As a radical solution to the tedious problem of column-to-column packing reproducibility of HPLC columns[2], Regnier proposed in 1998 to leave the conventional approach to slurry pack HPLC columns with micron sized-spherical particles for the high-precision etching technologies of the micro-electronics industry[1]. Given that these techniques also offer a perfect control over the position of each individual "particle", this novel manufacturing approach should also allow eliminating all possible sources of eddy-diffusion. Unfortunately, separations were thus far only performed in CEC mode, whereas it is the pressure-driven mode that is currently preferred by the analytical community.

2. EXPERIMENTAL

In a first series of experiments, thermally oxidized silicon pillars with a diameter of 4.3 μm and an external porosity of 55 % were coated with a C8 dimethyloctylchlorosilane phase. Using an in situ injection system (Figure 1) and varying the mobile phase composition and the pH, coumarin plugs were generated and subsequently followed by a fluorescence camera mounted on an automated translation stage.

3. RESULTS AND DISCUSSION

After optimalization of the mobile phase composition, very fast and high resolution separations of the coumarins C440, C460, C480 were demonstrated (Figure 2).
Van Deemter curves of the 3 components could be established (Figure 3), showing that minimal plate heights as low as 4 μm are possible for the most retained components C460 and C480. In pure methanol, unretained component plate heights as low as 1 μm could be obtained[3]. Aiming for a separation of these components at 1 cm in the channel, even lower plate heights of 2 and 2.4 μm were obtained (respective k' values of 0.13 and 0.23),

978-0-9798064-0-7/μTAS2007/$20©2007CBMS

yielding 4000-5000 plates over a column length of 1 cm. The separation impedance E of the array was as small as E=150, which is of the same order as the best currently existing monolithic columns.

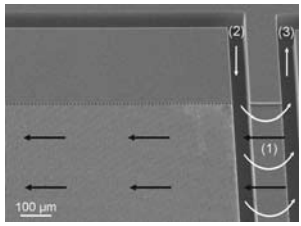

Figure 1: Injection mechanism of the pillar array. (1) injection zone, (2) inlet of injection channel, (3) outlet of injection channel.

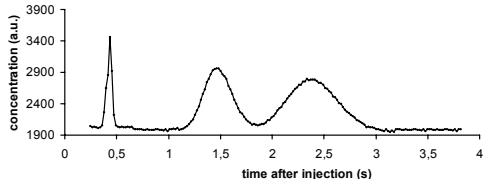

Figure 2: Chromatogram of a separation of the coumarins C440 (0.25 mM), C460 (0.40 mM) and C480 (1 mM) in an array of non-porous pillars (diameter=4.3 µm, spacing between pillars=1.7 µm), obtained at 1.7 mm downstream the injection zone.

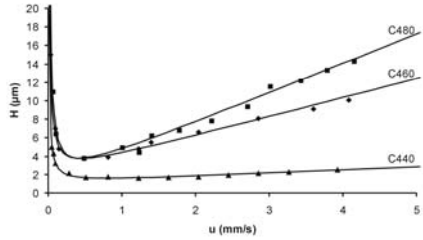

Figure 3. Van Deemter plots of the coumarins C440, C460 and C480 in the same channel as in Fig. 2, with respective retention coefficients of 0, 0.65 and 1.2. The respective concentrations are 0.75 10^{-4} M, 0.75 10^{-4} M and 3 10^{-4} M.

Subsequently, pillar arrays with different pillar dimensions and shapes were produced to seek the optimal pillar array architecture. The smallest pillars that were produced using deep-UV lithography had an inter pillar distance of about 400 nm and a pillar diameter of 570 nm (Figure 4).

Besides producing smaller pillars, another point of interest was the production of porous pillars, because practical applications in liquid chromatography require a high mass loadability and retention capacity. For this purpose, the available surface was increased several orders of magnitudes by an anodisation technique with HF using highly doped silicon. In this way, pillars with different porous layer thicknesses could be produced (Figure 5).

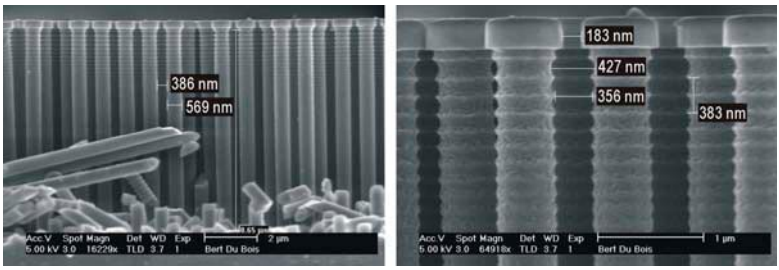

Figure 4. Silicon pillars with (d=570 nm) etched by Bosch-type deep reactive ion etching (depth is 8.7 µm). The SiO_2 hard mask is still present on top of the pillars, but is removed before the anodic bonding. The lithography was done with a deep UV lithography stepper (λ=193 nm).

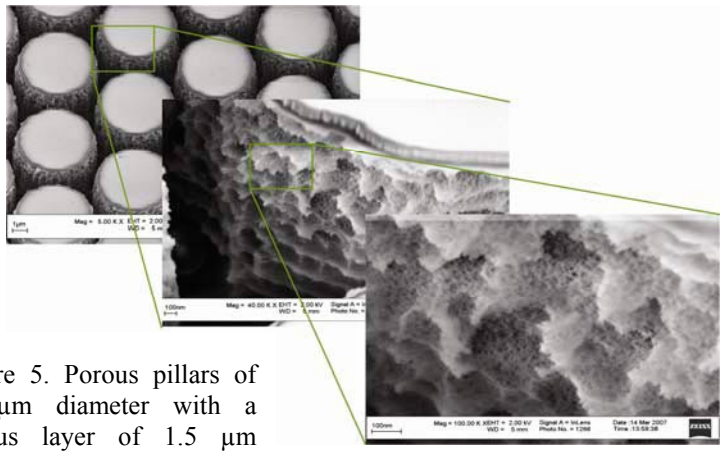

Figure 5. Porous pillars of 10 µm diameter with a porous layer of 1.5 µm thick. The pores sizes vary between 5 and 20 nm.

Using a thorough optimization procedure of the anodization process parameters, the porous layers appear highly uniform, both on the local scale as on the scale of a whole wafer (Figure 6). Performing band broadening experiments with these porous pillars show that the porous layers only minimally increase the band broadening, while offering a large increase in surface area of the columns.

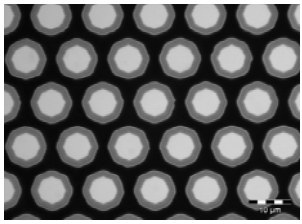

Figure 6: Top-view optical microscope picture of 10 µm pillars with a porous shell of 1.5 µm. On top of the pillars is a layer of 300 nm LPCVD deposited SiN, that has a mask function for both the Bosch-etching as for the anodisation. The porous zone is clearly visible through the SiN.

4. CONCLUSIONS

Very fast separation characteristics of the pillar array are demonstrated. Inter pillar distances of about 400 nm were achieved using deep UV-lithography. Large increases in specific pillar surface were created by anodisation in HF, leading to homogenous porous layers on the wafer scale.

REFERENCES

[1] B. He, N. Tait, F.E. Regnier, *Fabrication of Nanocolumns for Liquid Chromatography*, Anal. Chem., **70**, 3790 (1998).

[2] J. Kirkland, J.J. DeStefano, *The Art and Science of Forming Packed Analytical High- performance Liquid Chromatography Columns*, J. Chromatogr. A, **1126**, 50 (2006).

[3] M. De Pra, W.Th. Kok, J.G.E. Gardeniers, G. Desmet,; S. Eeltink,; J.W. van Nieuwekasteele, P.J. Schoenmakers, *Experimental Study on Band Dispersion in Channels Structured with Micropillars*, Anal.Chem., **78**, 6519 (2006).

ENVIRONMENTALLY-FRIENDLY DISPOSABLE HEAVY METAL ION SENSORS USING PLANAR BISMUTH MICROELECTRODES FOR IN SITU ENVIRONMENTAL MONITORING

Zhiwei Zou, Am Jang*, Pei-Ming Wu, Jaephil Do, Jungyoup Han, Paul L. Bishop*, and Chong H. Ahn

MicroSystems and BioMEMS Laboratory,
Department of Electrical and Computer Engineering,
[*]Department of Civil and Environment Engineering, University of Cincinnati, Ohio, USA

ABSTRACT

This paper presents an environmentally-friendly heavy metal ion sensor using microfabricated planar bismuth (Bi) electrodes in place of the traditional mercury electrodes. In this work, the heavy metal ion sensors using non-toxic Bi electrode have been designed, fabricated, and characterized for the detection of lead (Pb) and cadmium (Cd) ion in non-deaerated solution using anodic stripping voltammetry (ASV).

Keywords: Heavy metal ion, bismuth electrode, anodic stripping voltammetry

1. INTRODUCTION

Heavy metal pollution in soil, pore water, and ground water has received significant attention because of its toxicity and adverse biological and ecological effects. In our previous work, an on-chip-generated mercury microelectrode was developed for the detection of Pb^{2+} and Cd^{2+} [1]. However, the toxicity and volatility of the mercury electrode limits its applicability for *in situ* measurements as a platform of disposable sensor. Several plated Bi film-electrodes have been reported as an alternative electrode to mercury electrodes because Bi is an environmentally-friendly material and has a similar performance compared with mercury in the measurement of heavy metals using anodic stripping voltammetry (ASV) [2]. When carbon electrodes were used as one of the substituted electrodes to mercury, Bi ions were usually added to the sample liquid to improve the detection sensitivity. Although this approach was adopted for overcoming the generic problems caused by the mercury electrode, the addition of Bi ions into the sample liquid usually hindered the *in situ* measurement of the target heavy metals. In this work, miniaturized planar Bi microelectrodes were fabricated using e-beam evaporation and wet etching techniques, while both Bi ions and target metals were simultaneously deposited over the carbon electrode in the previously developed method [2]. This new method can provide the *in situ* metal measurement in the natural or biochemical environment.

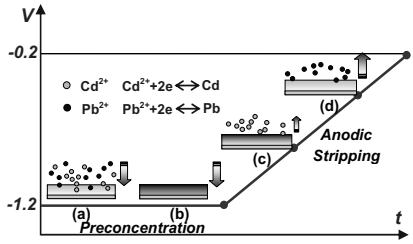

Figure 1: ASV measurement of heavy metal using planar Bi electrode. (a) Pb^{2+} and Cd^{2+} start to deposit on the electrode at preconcentration potential; (b) deposited metals form multi-component alloys with Bi; (c) Cd^{2+} is first stripped from the electrode, and generates a peak current at its reduction potential, and (d) Pb^{2+} is stripped off and generates another peak current.

978-0-9798064-0-7/μTAS2007/$20©2007CBMS

2. DESIGN AND FABRICATION

The schematic illustration of the device and the ASV sensing principle using planar Bi electrode are presented in Fig. 1. While amalgam formation is responsible for the stripping performance of mercury electrodes, the attractive and unique behavior of Bi electrode is attributed to the formation of multi-component Bi alloys with numerous heavy metals [2]. The design of the on-chip sensor is shown in Fig. 2 and the fabrication process is summarized in Fig. 3. A 300-nm thick planar Bi working electrode was fabricated on top of the gold (Au) conductive layer on the polymer substrate of cyclic olefin copolymer (COC). A three-electrode sensor configuration was adopted by including an Au counter electrode and an Ag/AgCl reference electrode. Fig. 4 shows the photographs of the fabricated sensor chip.

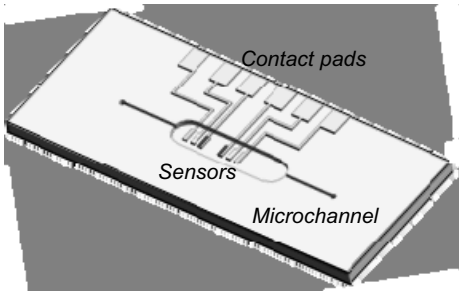

Figure 2: Design of the disposable on-chip sensor.

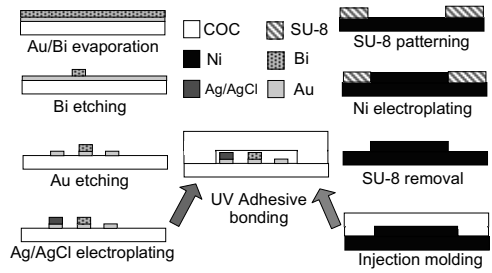

Figure 3: Summary of the fabrication process.

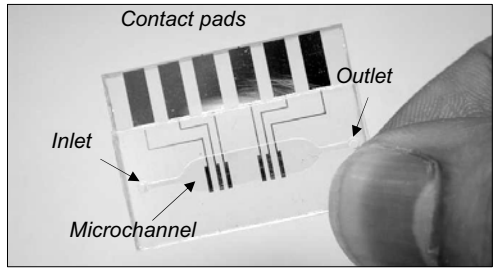

Figure 4: Photograph of the fabricated disposable heavy metal ion sensors with integrated polymer micro fluidic chips.

3. RESULTS AND DISCUSSION

The ASV was performed to calibrate the peak currents at different Pb^{2+} concentrations, and a linear response was obtained in Fig. 5. The sensing performance of the Au electrode and our proposed Bi/Au electrode is compared in Fig. 6a. The evaporated Bi thin film layer on Au has a dramatically increased output current due to the formation of alloys which facilitate the nucleation process during the target heavy metals deposition. The undesired second peak caused by underpotential deposition (UPD) at the Au electrode is also eliminated by the Bi layer. Thus, our sensor's performances are attributed to the microfabricated Bi layer. Using ASV to detect multiple heavy meal ions using Bi electrode is also demonstrated in Fig. 6b. Two current peaks have been clearly recorded, which correspond with Cd^{2+} at -0.75 V and Pb^{2+} at -0.48 V.

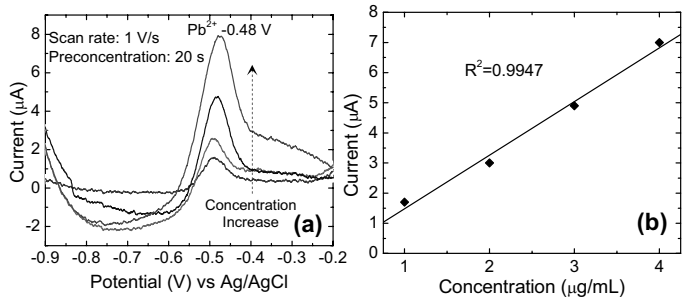

Figure 5: (a) ASV for Pb^{2+} (1, 2, 3, and 4 μg/mL respectively) in 0.1 M KCl buffer acidified using HNO_3 (*p*H=1.5), and (b) calibration of the peak current.

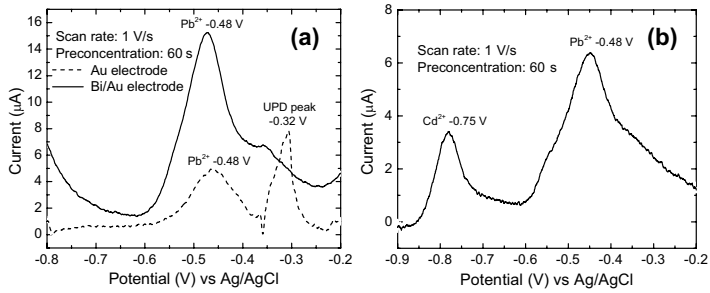

Figure 6: (a) Compare of ASV for Pb^{2+} (4 μg/mL) in 0.1 M KCl buffer acidified using HNO_3 (*p*H=1.5) by using Au electrode and Bi/Au electrode, and (b) ASV for Pb^{2+} and Cd^{2+} mixture (both of 1 μg/mL) in 0.1 M KCl buffer acidified using HNO_3 (*p*H=3).

4. CONCLUSIONS

This environmentally-friendly heavy metal ion sensor in a disposable platform using microfabricated planar Bi electrodes provides a fast and effective detection for *in situ* ASV measurement of various heavy metal ions without generating toxic waste. Microfabrication technology has been utilized in this work to realize a new fully integrated sensor with planar Bi microelectrodes, which can be used in applications such as detecting trace metal from *in situ* environmental samples, or *in vivo* and *in vitro* biological samples, where using mercury or adding plating Bi ions is undesirable.

ACKNOWLEDGEMENTS

This work was fully supported from the National Institute of Environmental Health Sciences (NIEHS, R01 ES015446) in the National Institute of Health (NIH).

REFERENCES

[1] X. Zhu, C. Gao, J.W. Choi, and C.H. Ahn, "On-chip generated mercury microelectrode for heavy metal ion detection," Lab Chip, Vol. 5, pp. 212-217, (2005).

[2] J. Wang, J. Lu, S.B. Hocevar, P.A.M. Farias, and B. Ogorevc, "Bismuth-coated carbon electrodes for anodic stripping voltammetry," Anal. Chem. Vol. 72, pp. 3218-3222, (2000).

THE UREY INSTRUMENT: AN INTEGRATED END-TO-END *in situ* ANALYTICAL SYSTEM DESIGNED FOR THE ULTRA-SENSITIVE CHEMICAL DETECTION OF EXTANT OR EXTINCT LIFE ON MARS

Frank J. Grunthaner[1], Jeffrey L. Bada[2], Alison M. Skelley[3], Richard A. Mathies[3], Richard Quinn[4], Aaron Zent[5], Peter Willis[1], Xenia Amashukeli[1], Allen Farrington[1], Andrew Aubrey[2] and Pascale Ehrenfreund[6]

[1]Caltech/Jet Propulsion Laboratory, USA, [2]Scripps Institution of Oceanography, UCSD, USA, [3]UC Berkeley, USA, [4]SETI Institute, NASA Ames Research Center, USA, [5]NASA Ames Research Center, USA, [6]Leiden Institute of Chemistry, NL.

ABSTRACT

The Urey Instrument is an integrated suite of *in situ* instruments which is designed to search the Martian regolith for chiral biomarkers at terrestrial laboratory state-of-the-art detection levels (part-per-trillion sensitivity) while profiling the presence and chemical reactivity of surface and atmospheric oxidants that might have reactively degraded organic compounds using chemo-resistor oxidant sensors. The Urey instrument suite has been selected for the Pasteur payload in the European Space Agency's (ESA's) ExoMars rover mission and is considered a fundamental instrument to achieve the mission's scientific objectives. *The instrument is named Urey in recognition of Harold Clayton Urey's seminal contributions to cosmochemistry, geochemistry and the study of the origin of life.* This integrated end-to-end suite consists of two analytical systems, one (a lab-on-a-chip system) for the measurement of trace organics and the other to measure the reactivity of the regolith and atmosphere. The weight of the full package as delivered to the ExoMars rover is approximately 4.4 kg, with external dimensions of 21 x 20 x 16 cm.

Keywords: Mars, in situ, microfluidics, microchip, CE, sensor, chemi-resistor, biomarker, oxidant, integrated system

1. INTRODUCTION

The search for evidence of extinct or extant life outside of the Earth has fired the imagination of scientists as well as philosophers for generations. In recent time, this search has lead to the development new multidisciplinary fields including Astrobiology and Exobiology. As scientists have struggled with questions such as the mechanism of the origin of life on the Earth and the probability of life on other planetary systems, we have looked closely at the other planets in our solar system for the evidence of the presence of liquid water and complex organic chemistry. Studies of Mars by robotic spacecraft show a surface with many chemical, mineralogical and physical features that are consistent with the presence of liquid water in the distant past. In 1976, the Viking Landers searched two areas of the Martian surface with an impressive suite of instruments for evidence of life. The experimental results suggested that the Martian regolith was chemically oxidizing, and no organic carbon compounds were detected within the sensitivity limits of the instruments. Since Viking, Mars has been studied with a series of rovers and orbiters with high resolu-

978-0-9798064-0-7/μTAS2007/$20©2007CBMS

tion imaging spectrographs that have studied the chemical composition of the accessible surface and established the presence of key minerals that are consistent with the extended presence of liquid water. The recently launched Phoenix mission will study the northern polar region of Mars searching for organic compounds trapped or preserved in icy permafrost material. In 2009, NASA will launch the Mars Science Laboratory mission with a large rover carrying analytical instruments to search for generic organic compounds (GCMS) and to carefully identify mineralogy. In 2013, ESA will launch the ExoMars rover with Pasteur instrument package specifically designed to search for evidence of extinct or extant life. The ExoMars mission brings an array of complementary instruments focused on organic detection, measurement of surface chemical reactivity and establishing the mineralogical context together with drill sampling system that is designed to acquire samples from as deep as 2 meters below the surface. One of the primary ExoMars/Pasteur organic detection systems, the Urey instrument is a miniaturized total analytical system designed to search for organic biomarkers at unprecedented detection levels while simultaneously characterizing the chemical reactivity of surface and subsurface samples.

Our team has developed the Urey instrument package to detect organic biomarkers at the part per trillion (mass/mass) level using Laser Induced Fluorescence detection (LIF). We have chosen a family of biomarkers for our search that contain a primary amino group. These biomarkers include amino acids, amines, certain nucleobases and amino-sugars. The amino acids are the key materials of our search. Using microchip capillary electrophoresis implemented an integrated lab-on-a-chip analyzer, we are able to detect the full range of biotic and abiotic amino acids, establish composition ratios and, with the addition of a cyclodextrin buffer, we can measure the enantiomeric ratio of individual amino acids. Our system also detects polycyclic aromatic hydrocarbons (PAHs) at similar levels. The Urey instrument consists of a fully functional module that accepts a powdered solid from the ExoMars sampling system, measures the soil reaction chemistry, uses liquid phase extraction to remove trace organics from the soil, employs focused sublimation to concentrate the volatile organics on a sample stage, reacts primary amines with fluorescamine to form the fluorescent adduct, microfluidically transports the extracted sample to the microchip CE analyzer and completes a variety of analyses at different dilution ratios and pH values. The instrument module includes all liquids, gases and reagents required to complete the extraction, processing and analysis along with all control electronics within its 4.4 kg. mass. In the following, we will describe the components of the Urey instrument and several of the results from field trials in the Chilean Atacama Desert that establish its performance and sensitivity.

2. FUNCTIONAL DESCRIPTION

The Urey Instrument is comprised of five primary components. These include the 1) Sample Handling System, 2) the Mars Oxidant Instrument (MOI), 3) the Sub-Critical Water Extractor (SCWE), 4) the Mars Organic Detector (MOD) and 5) Mars Organic Analyzer (MOA). The complete Urey module is assembled at the Jet Propulsion Laboratory under stringent contamination control and Planetary Protection approved procedures and then sealed in a bio-barrier container. This bio-barrier system remains sealed throughout the integration of the instrument with the Pasteur payload, spacecraft assembly and test as well as launch and cruise to Mars. On the Martian surface, a mechanical tab is opened as the rover is deployed from the landing carrier, giving sample access to the package. This procedure is required by the high sensitivity of the instrument and the need to minimize back-

ground contamination from terrestrial sources. The instrument is shown in a CAD drawing in Figure 1.

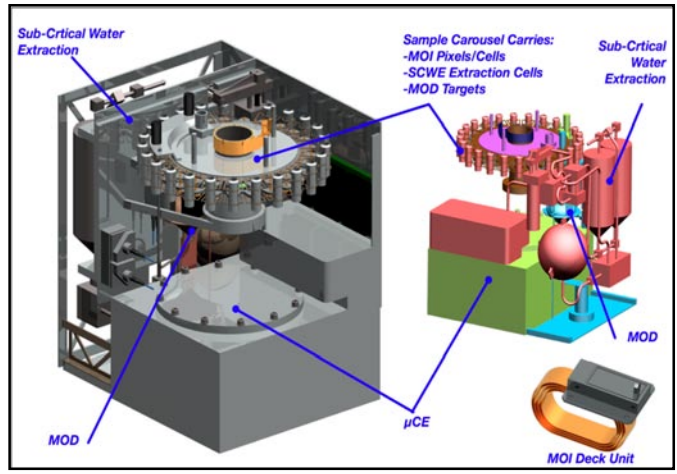

Figure 1: Urey instrument with labeling of key components. µCE system is contained within a sealed chamber to maintain 1 bar pressure for microfluidic operation and to minimize issues with the 15 keV power supply. MOI deck unit measures reactivity of atmosphere and dust.

1.) Sample Handling System The sample handling system consists of two inlet funnels to direct 0.5 gm. samples delivered by the ExoMars distribution system to either the SCWE sample extraction cells or to the MOI chemi-resistor cells for analysis. The handling system aligns individual sample cups as needed for an experiment and aligns MOD sample deposition targets for preliminary LIF analysis. There are 24 individual sample cells.

2.) Mars Oxidant Instrument The oxidant instrument consists of arrays of thin film compounds including self assembled monolayers bound to thin gold films, thin films of reactive metals and organic semiconductors as well as organic reference compounds deposited on electrode arrays to make chemi-resistor sensor arrays. Sealed until exposed to Martial regolith, the changes in film resistivity are used to establish the kinetics of reaction with the unknown oxidants. We control the temperature of the interface between sensor film and soil and the relative humidity in the enclosed reaction cell. The resistivity of the sensor is monitored rapidly at the start of the experiment and then at longer time intervals as the reactions progress. Samples are taken from the surface to 2 m. depth to profile oxidants.

3.) Sub-Critical Water Extractor The organic biomarkers addressed by Urey range from small highly polar organics to complex non-polar aromatic structures. To extract these compounds at the anticipated trace levels in Martian soils, we have developed a highly efficient water-based extraction system. The dielectric constant of liquid water is a strong function of temperature. At 120 to 200 C, it is a very polar solvent and readily extracts amino acids; at 325 C, it has a dielectric constant approaching that of benzene and readily extracts PAHs. Water is an ultra-high purity solvent compared to the highest quality organic solvents available. In the SCWE system, the soil sample is added to a cell with integral frit, flow restric-tor and high temperature seals. Liquid water is injected at pressure and temperature and permitted to interact with sample for 5 to 15 minutes. The extract is then sent to the MOD sublimator. Operating parameters have been established through careful study of extraction yield, compound decomposition and temperature-induced racemization.

4.) Mars Organic Detector The water sample extracted in the SCWE (about 1 ml. total) is directed to a pyrolytic boron nitride sublimation oven. The extract is then freeze-dried to leave the extracted organic residues. The oven is heated to temperatures of 150C to 450C to sublime these organics at Mars ambient pressures. The sublimation oven has a tapered

Knudsen nozzle to focus evolved volatile organics onto a cold finger maintained at about –25C. Individual sample substrates, each coated with fluorescamine reagent, are provided for each sublimed extract. The dry reagent reacts with the condensed primary amine giving a labelled product. A LIF system is used to detect the presence of adduct as a screen to determine whether the sample should be analyzed by the µCE system.

5.) Mars Organic Analyzer The MOA is an integrated µCE system with fluid control microfluidics as developed by the Mathies group to provide for automated operation, sample and reagent mixing and dilution, sample selection and injection. As described in Skelley et al [2], the MOA analyzer used in Urey consists of 8 independent channels, two of which are dedicated to PAH analysis and the remainder to chiral primary amine separation. Detection is by LIF with a solid state GaN laser operating at ~395 nm.

3. FIELD DEMONSTRATIONS

Through the experimental results of our Atacama Desert (Chile) and Panoche Creek (California) field campaigns, we have demonstrated the sensitivity (pp trillion) [2] of our Amino Acid biomarker detection system to be several orders of magnitude greater than the pyrolytic GCMS systems utilized by Viking; established direct measurements of unique acid-derived oxidation systems triggered by molecular films of water that are consistent with Viking observations of Martian soils [1]; and showed the extreme variation of detectable organics over lateral distances of decimeters and depths from the surface of centimeters. See Figure 2.

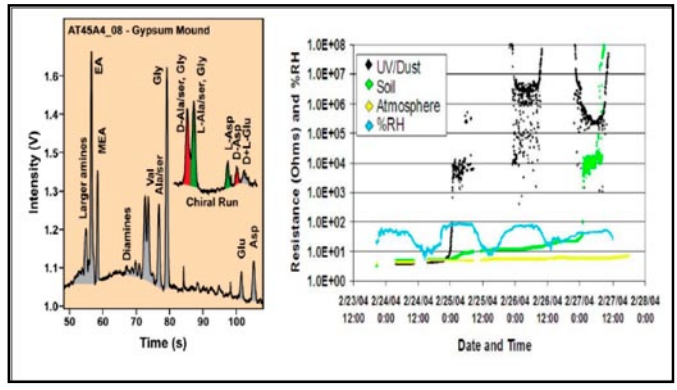

Figure 2. Electropherogram and oxidant results from Atacama field studies

5. CONCLUSIONS

We have offered a terse description of a fully integrated in situ planetary instrument to provide terrestrial laboratory quality data to probe exciting novel chemical questions. Future developments will find extensive use of *in situ* instruments based on lab-on-a-chip and chemical sensor technologies to explore Europa, Titan, Enceledus and other unique extreme environments.

REFERENCES

[1].Quinn, R. C., Zent, A. P., Grunthaner, F. J., Ehrenfreund, P., Taylor, C. L., and Garry, J. R. C.: 2005, 'Detection and Characterization of Oxidizing Acids in the Atacama Desert Using the Mars Oxidation Instrument', *Planetary and Space Science* 53, 1376–1388.

[2].Skelley, A. M., Scherer, J. R., Aubrey, A. D., Grover, W. H., Ivester, R. H. C., Ehrenfreund, P., Grunthaner, F. J., Bada, J. L., and Mathies, R. A.: 2005, 'Development and Evaluation of a Microdevice for Amino Acid Biomarker Detection and Analysis on Mars', *Proc. Natl. Acad. Sci. U.S.A.* 102, 1041–1046.

For additional detail and papers describing the technology of Urey and the field validation experiments, see: http://astrobiology.berkeley.edu

A STRIPLINE BASED MICROFLUIDIC PROBE FOR NMR SPECTROSCOPY

J. Bart[1], J.W.G. Janssen[2], P.J.M. van Bentum[2], A.P.M Kentgens[2] and J.G.E. Gardeniers[1]

[1]MESA+ Institute for Nanotechnology, University of Twente, THE NETHERLANDS
[2]Department of Physical Chemistry, Radboud University, THE NETHERLANDS

ABSTRACT

This paper describes the fabrication and measurement results of a newly developed microfluidic Nuclear Magnetic Resonance (NMR) chip. The excitation/detection mechanism on this chip is based on a stripline configuration. It is developed for high sensitivity, high resolution NMR on small sample volumes of less than a microliter which allows to follow chemical reactions on-line in a microfluidics environment. With this chip we demonstrate a 600 nl ethanol sample spectrum with a Signal-to-Noise-ratio (SNR) of 5500 and a linewidth of 1 Hz.

Keywords: NMR, stripline, microfluidic, reaction-monitoring

1. INTRODUCTION

NMR is a powerful analytical tool not only for determining complex (bio)molecular structures, but also for monitoring molecular dynamics and reaction kinetics. Despite its versatility, NMR analyses currently require relatively large amounts of highly concentrated samples because of its intrinsic low sensitivity. We here report on the design, fabrication and measurement results of a microdevice that can analyze small samples (< 1 µl).

2. THEORY

Currently, NMR on small sample volumes is performed by use of small solenoids wrapped around a capillary [1], or planar coils on glass chips containing microfluidic channels [2] [3] [4]. The NMR sensitivity is still the main limiting factor when working at room temperature. One method to enhance the sensitivity is maximizing the filling factor of the excitation coil. This can be realized by positioning the coil closer to the sample. However, positioning of the coil closer to the sample will lead to susceptibility distortion, due to the different susceptibilities of the coil material (copper) and the sample, resulting in a lower resolution. When using a stripline based configuration the filling factor is intrinsically better, and the susceptibility distortion is low due to the simple structure of the copper stripline.

The stripline configuration investigated consists of a flat wire confined between two metal shielding planes, resulting in a coax type transmission line, as shown in figure 1. In this configuration, the RF excitation field is very homogeneous at the position of a microfluidic channel that is located between the strip and one of the metallic planes.

Furthermore, this structure can be equipped easily with a susceptibility matching mechanism, which will result in higher resolution. This geometry has no topological pole, which means that all electrical connections can be made in the same plane, which simplifies the fabrication process.

978-0-9798064-0-7/µTAS2007/$20©2007CBMS

3. EXPERIMENTAL

Figure 2 shows a schematic view of the stripline based chip as it was developed. On the carrier silicon substrate a copper stripline is electroplated. The width of this line is decreased in the centre to increase the RF field strength locally. A microfluidic channel and

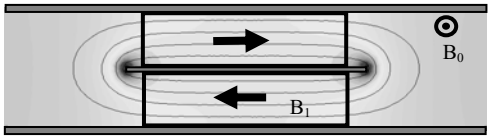

Figure 1. Schematic cross-section of a stripline. The RF field B_1 circulates around the strip as is indicated by the field lines. Because of the boundary conditions imposed by the metallic planes above and beneath the strip, the magnetic field lines are forced parallel to the surface. The result is a homogeneous B_1 as well as a homogeneous current distribution in the strip, minimizing the electrical losses. The static field B_0 can be oriented perpendicular to the cross section shown in the figure (along the stripline axis). Areas suitable for sample analysis, viz. where the RF field is homogeneous within about 10%, are indicated by the two black rectangles.

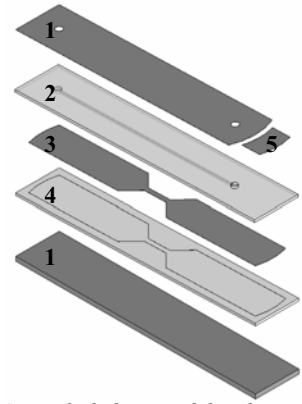

Figure 2. Exploded view of the chip:
1. Copper shielding to confine RF field
2. Substrate containing microfluidic channel
3. Copper stripline
4. Carrier substrate
5. Capacitive RF coupling to external electrical circuit

accessholes are etched by Deep Reactive Ion Etching (DRIE) in the top silicon substrate. The effective sample volume underneath the central part (detection area) is 600 nl. Both substrates are bonded together by a fluorocarbon film intermediate layer bonding. The stack is covered with copper at both sides by electroplating to confine the RF magnetic field. The chip was designed for NMR equipment operating at 600 MHz ^{1}H resonance, which implies that the length of the stripline, being equal to half the wavelength of the RF radiation used, amounts to 5 cm. A full-silicon chip, realized in silicon is shown in figure 3. A probe was designed which contains the fluidic and electrical connections, see figure 4.

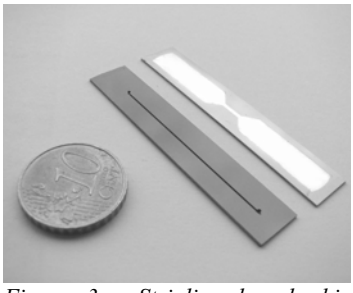

Figure 3. Stripline based chip realized in silicon, showing the copper stripline on one part, and the microfluidic channel in the other part.



Figure 4. Photograph of the home-built probe. The chip is positioned vertically in the aluminium cylinder. The microfluidic channel is connected with fused silica capillaries (right). The matching and tuning capacitors are closely to the chip, to minimize noise (left).

4. RESULTS AND DISCUSSION

The chip was implemented in the probe and connected to a syringe and filled with a 100% ethanol sample. Figure 5 shows a single-shot spectrum of the sample as it was obtained with this probe. An excellent SNR of 5500, and a linewidth of 0.0017 ppm (1 Hz) full-width-at-half-maximum were achieved. The spectrum shows a flat baseline and J-coupling is clearly visible. It has to been mentioned that no susceptibility matching or shimming is performed at the moment, which will likely enhance the resolution.

Especially for kinetics monitoring, where samples stay for a limited time in the detection area, this high SNR is necessary.

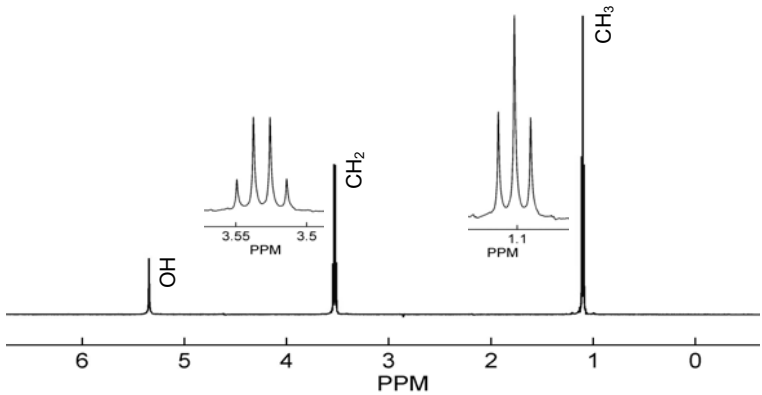

Figure 5. Single scan proton spectrum of a 600 nl 100% ethanol sample. SNR=5500, linewidth=1 Hz.

5. CONCLUSIONS

We have shown the first measurement results of a newly developed NMR detection method based on a stripline configuration. The excellent SNR combined with the good resolution demonstrate the high potential of this new configuration for both elucidating complex biomolecular structures as well as fast monitoring of reaction kinetics.

ACKNOWLEDGEMENTS

We acknowledge the Netherlands Organization for Scientific Research (NWO) and the Advanced Chemistry and Technologies for Sustainability foundation (ACTS) for the financial support.

REFERENCES

[1] D.L. Olson, M.E. Lacey, J.V. Sweedler, *High-resolution microcoil NMR for analysis of mass-limited, nanoliter samples*, Anal. Chem. 70, pp. 645-650, (1998).

[2] J.D. Trumbull, I.K. Glasgow, D.J. Beebe, R.L. Magin, *Integrating Microfabricated Fluidic Systems and NMR Spectroscopy*, IEEE Trans. Biomed. Eng. 47, pp. 3-7, (2000).

[3] C. Massin, F. Vincent, A. Homsy, K. Ehrmann, G. Boero, P.A. Besse, A. Daridon, E. Verpoorte, N.F. de Rooij, R.S. Popovic, *Planar microcoil-based microfluidic NMR probes*, J. Magn. Reson. 164, pp. 242-255, (2003).

[4] H. Wensink, F. Benito-Lopez, D.C. Hermes, W. Verboom, J.G.E. Gardeniers, D.N. Reinhoudt, A. van den Berg, *Measuring reaction kinetics in a lab-on-a-chip by microcoil NMR*, Lab Chip 5, pp. 280-284, (2005).

A TRI-PHASE CATALYTIC MICROFLUIDIC REACTOR FOR THE GENERATION OF SINGLET OXYGEN USING A NOVEL IMMOBILISED *SECO*-PORPHYRAZINE CATALYST

Christopher Cullen[1], Matthew J. Fuchter[1], Robert C.R.Wootton[2], Anthony G.M. Barrett[1] and Andrew J. de Mello[1]

[1]Imperial College London, United Kingdom and [2]University of Cambridge, United Kingdom

ABSTRACT

A *seco*-porphyrazine photooxygenation catalyst was co-polymerised within a norbornene based Ring Opening Metathesis Polymerisation (ROMP) gel coating the internal surfaces of a microfluidic reactor. Subsequently, continuous flow photooxidations of α-terpinene were performed in space time yields 100 times faster than bulk equivalent reactions.

Keywords: microreactor, channel derivatisation, catalysis, photooxidation, triphasic reactions

1. INTRODUCTION

Singlet oxygen is a versatile reagent for oxidation reactions with applications including cycloadditions with dienes producing endoperoxides and ene reactions providing allylic hydroperoxides. Currently, the most effective method for singlet oxygen generation is the dye-sensitized photoexcitation of ground-state triplet oxygen. Previous work has focussed on the increased process safety afforded by the generation and use of singlet oxygen within a microfluidic structure using soluble photosensitising dyes.[1] Herein we report the development of an advanced catalytic microfluidic reaction system for the production of singlet oxygen using a tri-phasic system. This incorporates both the oxygen flow and the substrate solution along with a solid supported photosensitizing catalyst confined within the microfluidic structure. Continuous-flow reactions across a polymer immobilised photosensitizing dye produce cleaner transformations with simplified purification.

2. THEORY

Singlet oxygen production using *seco*-porphyrazines has previously been demonstrated with high quantum yields, establishing them as photooxygenation catalysts for the synthesis of endoperoxides from the corresponding dienes. Furthermore, these macrocycles have been reported to be successfully immobilised on resin beads which have efficiently catalysed singlet oxygen production under mild conditions.[2] In many cases the *seco*-porphyrazines proved themselves to be superior catalysts compared with to traditional dyes sensitizers, such as Rose Bengal.

In recent years, several techniques for mounting catalysts within chip systems have been developed, and the advantages of catalyst immobilisation within microfluidic devices is well established.[3, 4] However, these systems have not been shown to be resistant to photooxidation, whereas ring opening metathesis polymerisation gels (ROMP gels) are

978-0-9798064-0-7/μTAS2007/$20©2007CBMS

known to be stable under these conditions. Subsequently, we report a *seco*-porphyrazine catalyst mounted within a microfluidic reactor network using ROMP gel as a solid support.

3. EXPERIMENTAL

The microfluidic reactor featured a network of isotropically etched glass channels, typically with depths of 80 μm and widths of 210 μm. Protruding motifs intermittently dispersed along the channel length enhanced the physical attachment of the ROMP gel to channel surfaces by bulk forces. Functionalised ROMP gel was mounted into the microfluidic channels using localised thermal polymerisation controlled by a resistive heating network (Figure 1).

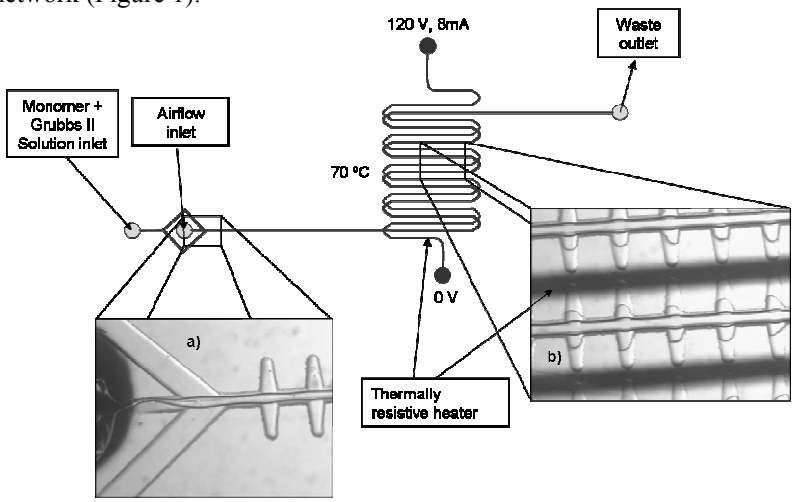

Figure 1. Experimental Schematic for ROM polymerisation derivatisation. a) Interface between air flow and "jacketing" polymerisation solution b) Micro channels illustrating tri-phasic system as polymer forms, polymer in "motifs" extremities then liquid co-monomer solution jacketing air flow.

The channel was maintained by flowing monomer solution in annular flow with a concurrent flow of compressed air. Visualisation by the co-polymerisation of a fluorescent monomer within the ROMP gel illustrated an even and continuous channel coating (Figure 2).

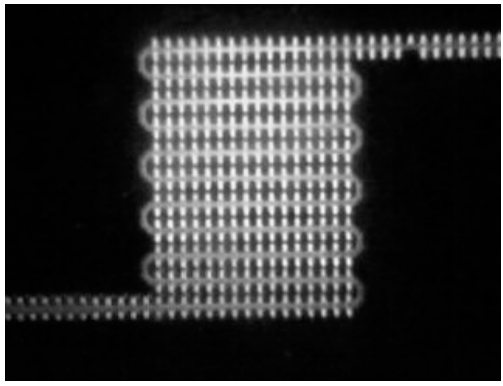

Figure 2. Wall coating of microfluidic device visualised using a fluorescent marker.

4. RESULTS AND DISCUSSION

Incorporation of *seco*-porphyrazine labelled gel (Figure 3) resulted in a wall coating averaging 7 µm.

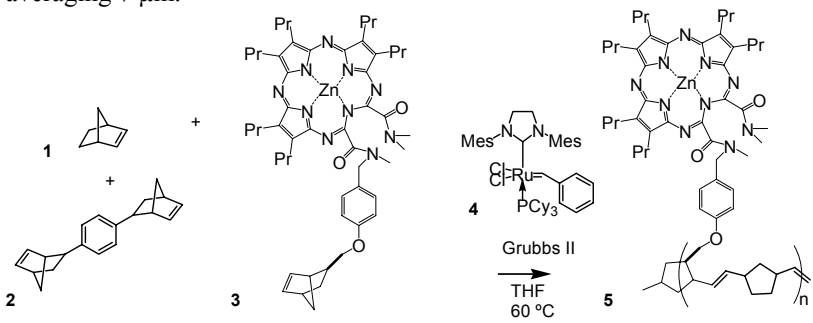

Figure 3. Synthesis ROM polymer functionalised with *seco*-porphorazine.

Oxygen and a solution containing 0.021M α-terpinene in dichloromethane were combined in slug flow at an overall flow rate of 7.7 µl min^{-1} giving a residence time on chip of 15.5s. Transformation of α-terpinene to ascaridole (Figure 4) was monitored by GC and gave space time yields in excess of 0.45% s^{-1}. Reactions carried out in bulk using the same polymer gave space time yields of 0.0041% s^{-1}. The increase in relative space time yields can be attributed to the increased rate of mass transport of oxygen into the catalytic system in a microfluidic environment.

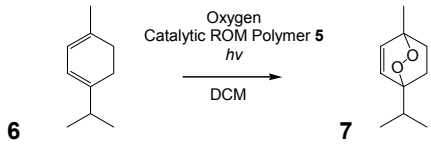

Figure 4. Photooxygenation of α-terpinene to ascaridole.

5. CONCLUSIONS

The increase in relative space time yields can be attributed to the increased rate of mass transport of oxygen into the catalytic system in a microfluidic environment. Coating microfluidic reactors with this *seco*-porphyrazine labelled polymer, and performing continuous flow photo-oxidations provided significant increases in efficiency relative to bulk scale reactivity. This improved reactivity demonstrates the benefits of continuous flow microfluidic reactors for multiphase catalysis and photocatalytic applications.

ACKNOWLEDGEMENTS

The authors would like to thank GlaxoSmithKline and the EPSRC for their support.

REFERENCES

1. Wootton, R.C.R., R. Fortt, and A.J. de Mello, *A microfabricated nanoreactor for safe, continuous generation and use of singlet oxygen.* Organic Process Research & Development, 2002. **6**(2): p. 187-189.
2. Fuchter, M.J., B.M. Hoffman, and A.G.M. Barrett, *Ring-opening metathesis polymer sphere-supported seco-porphyrazines: Efficient and recyclable photooxygenation catalysts.* Journal of Organic Chemistry, 2006. **71**(2): p. 724-729.
3. Wootton, R.C.R. and A.J. deMello, *A one-step protocol for the chemical derivatisation of glass microfluidic devices.* Lab on a Chip, 2006. **6**(4): p. 471-473.
4. Kobayashi, J., et al., *A microfluidic device for conducting gas-liquid-solid hydrogenation reactions.* Science, 2004. **304**(5675): p. 1305-1308.

INFLUENCE OF PRESSURE ON DIELS-ALDER REACTIONS PERFORMED IN GLASS MICROREACTORS

F. Benito-López[1], R.M. Tiggelaar[2], A.J. Kettelarij[1], R.J.M. Egberink[1], J.G.E. Gardeniers[2], D.N. Reinhoudt[1] and W. Verboom[1]

[1]Supramolecular Chemistry and Technology Group (SMCT)
[2]Mesoscale Chemical Systems Group (MCS)
MESA+ Institute for Nanotechnology, University of Twente,
Enschede, THE NETHERLANDS

ABSTRACT

A microreactor platform that resists pressures up to 150 bar has been constructed and used to study the influence of pressure on the Diels-Alder reaction of cyclopentadiene with methyl-, phenyl- and benzylmaleimides. The reaction of cyclopentadiene with phenylmaleimide and benzylmaleimide showed 1.7-fold and 1.3-fold higher conversions, respectively, compared with batch experiments, whereas the reaction of cyclopentadiene with methylmaleimide was alsmost not accelerated.

Keywords: high-pressure, Diels-Alder, glass microreactor, rate enhancements

1. INTRODUCTION

Nowadays, Lab-on-a-Chip systems are used for the improvement of chemical processes, as well as for the production of new/specialty products that are difficult to produce in conventional systems [1]. The use of high pressure in chemistry is usually inaccessible for many research laboratories, because it requires specialized, expensive equipment with strict safety precautions [2]. Due to their small characteristic dimensions microreactors offer a solution to these issues. In this contribution it is described that glass microreactors can be used to study the influence of pressure (up to 150 bar) on the Diels-Alder reaction of cyclopentadiene (**1**) with methyl (**2a**), benzyl- (**2b**) and phenylmaleimide (**2c**) (scheme 1) in an easy, fast and safe way.

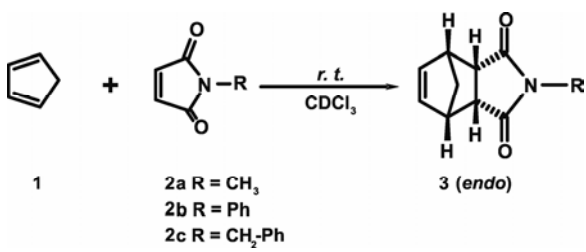

*Scheme 1. Diels-Alder reaction of cyclopentadiene (**1**) with maleimides (**2a-c**)*

2. MICROREACTOR LAYOUT

In the microreactor, shown in Figure 1a, the fiber interface geometries for the inlets (1,2) and outlet (6) are fabricated using hydrofluoric acid. It is shown that microreactors equipped with these inlet/outlet interface structures are suitable for working pressures up to

978-0-9798064-0-7/μTAS2007/$20©2007CBMS

600 bar [3]. Via inlets 1 and 2 reactants can be pumped separately into the reaction zone (3), where they join, mix and react at high pressures under continuous flow conditions.

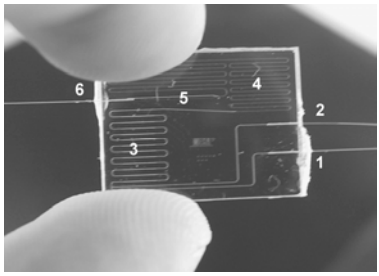

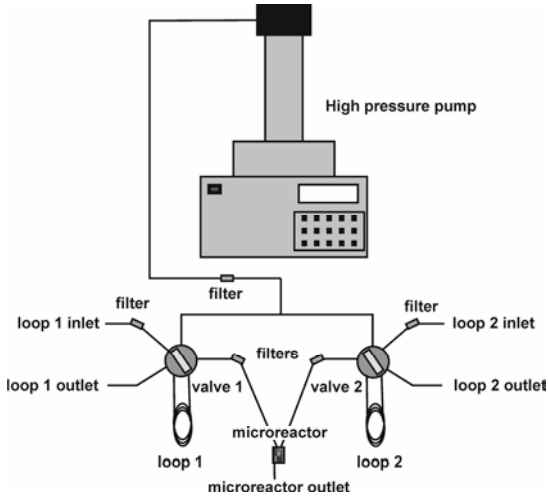

(a) (b)

Figure 1. (a) Picture of the microreactor. The fibers have an external diameter of 110 µm and an internal diameter of 50 µm. Legend: 1 inlet for cyclopentadiene, 2 inlet for maleimides, 3 reaction zone, 4 fluidic resistor, 5 expansion zone, 6 outlet. (b) Set-up for continuous flow operation of a high-pressure glass microreactor.

3. SET-UP

Figure 1b shows a schematic representation of the set-up used in this study. Two stainless steel loops and two six-port valves are used to flow the pressurized reactants independently and/or simultaneously into the microreactor. After reacting in the reaction zone of the microreactor, fluid is collected from the outlet fiber and the reaction is quenched by diluting it in 400 µL deuterated chloroform at -20 ºC. Reaction times depend on the applied pressure, and are in the range 6-10 seconds.

4. RESULT AND DISCUSSION

Figure 2 shows that the reactions of **1** with **2a-c** are influenced by pressure. The reaction with **2c** is most positively affected by pressure, and the reaction with **2a** the least. This is in agreement with the estimated reaction volumes (ΔV) as obtained with a molecular modelling program (-11.0, -12.7 and -13.4 $cm^3\ mol^{-1}$ for the reactions of **1+2a**, **1+2b** and **1+2c** respectively): reactions with high negative ΔV are more affected by pressure. For batch experiments at atmospheric pressure the order of reactivity of **1** with the **2a-c** is **2b** > **2a** > **2c**. This can be explained by taking into account the pressure as well as the very efficient and fast mixing in the microreactor [4]: these two issues improve the reaction rates significantly, probably also a synergistic effect plays a role.

The reaction of **1** with **2a** is the least affected in the microreactor, only a 1.1-fold higher conversion was obtained compared to batch experiments, since it has the less negative ΔV value. The reaction of **1** with **2b** shows a 1.7-fold higher conversion, because it has a high negative ΔV value. A 1.3-fold higher conversion was obtained for the reaction

of **1** with **2c**. Although **1**+**2c** has the highest negative ΔV value, its reaction kinetics are slower than for the reaction of **1**+**2b**, therefore the difference in conversion between microreactor and batch experiments is less pronounced.

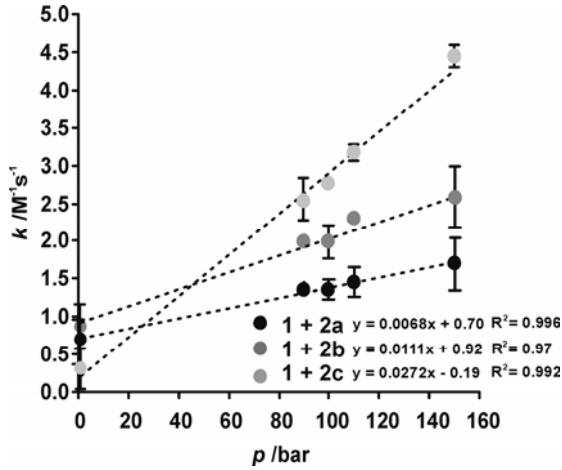

*Figure 2. Second order rate constants as function of pressure for the Diels-Alder reaction of cyclopentadiene **1** with the maleimides **2a-c** performed in the microreactor at pressures up to 150 bar. Data points at 1 bar are from batch experiments in a silica fiber. All points are average values from duplicate experiments.*

5. CONCLUSIONS

A set-up is realized to study organic reactions under high pressure and continuous flow conditions in a fast and safe way. Pressurized reactants are introduced in a glass microreactor independently and/or simultaneously via stainless steel loops, valves and a high pressure pump.

Pressure affects all three investigated Diels-Alder reactions. The effect of pressure, fast and efficient mixing of the reactants in the microreactor and probably a synergistic effect between these 2 issues are believed to be the reasons for the observed rate enhancements.

REFERENCES

[1] P. Watts and C. Wiles, *Chem. Commun*., pp. 443-467, (2007).

[2] R. van Eldik and F.-G. Klärner, in: "High pressure chemistry", Wiley-VCH, Weinheim, Germany, (2002).

[3] R.M. Tiggelaar, F. Benito-López, D.C. Hermes, H. Rathgen, R.J.M. Egberink, F.G. Mugele, D.N. Reinhoudt, A. van den Berg, W. Verboom and J.G.E. Gardeniers, *Chem. Eng. J.* 131, pp. 163-170, (2007).

[4] F. Benito-López, R.M. Tiggelaar, R.J.M. Egberink, J.G.E. Gardeniers, W. Verboom, A. van den Berg, D.N. Reinhoudt, *Pressure and supercritical CO_2 conditions improve the esterification reaction of phthalic anhydride with methanol in glass microreactors,* Proc. Micro Total Analysis Systems 2006, November 4-9, Tokyo, Japan, pp. 873-875, (2006).

MICROREACTOR FOR JANUS BEADS PRODUCTION USING MICROCHANNEL INTEGRATION TECHNIQUES

Toru Torii[1], Takanori Takahashi[2], Youich Takizawa[2], Takasi Nisisako[3]

[1] The University of Tokyo, JAPAN,

[2] Soken Chemical & Engineering Co., Ltd., JAPAN,

[3] Tokyo Institute of Technology, JAPAN

ABSTRACT

This paper describes the Janus beads production for electronic paper by using various microchannel techniques. 16 microchannels were parallelized in one glass chip for Janus beads production fabricated by press work. The C.V. of the products was less than 5% which indicated that the products were well mono disperse. The Janus beads showed good rotating performance in a flat panel display. Integration of microchannel was also applied for Janus beads production up to 128.

Keywords: droplet formation, electronic paper, twist ball, parallelization

1. INTRODUCTION

We had produced various kinds of droplets in microchannels [1], which were applied to the polymeric beads production, such as Janus beads production for electronics papers [2,3], core shell structured beads [4], and anisotropic polymeric beads [5]. Janus beads are hemispherically black-and-white balls with different electrical charges for the electronic paper. We had realized 16-microchannels integration in a glass chip for Janus beads to increase the production rate with the coefficient of variation (C.V.) less than 5% [4], and 256-microchannels parallelization for normal beads production with C.V. less than 2% (Fig.1) [6].

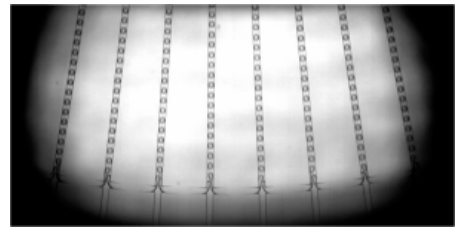

Fig.1 Droplet formation in 256-integrated microchannels

A new glass chip fabricated by press work was used for the Janus beads production. Microchannel integration by dry etching was also achieved up to 128- microchannels for Janus droplets formation.

2. EXPERIMENTAL

A new glass chip of 16-parallelized microchannels with bump structure by press work on fused silica (Covalent Materials Co. Ltd.) was used, in which the height of the channel was varied from 85 to 170 μm. Figure 2 shows the microchannel chips fabricated by press work (a) and dry etching (b and c) on fused silica. The structure of

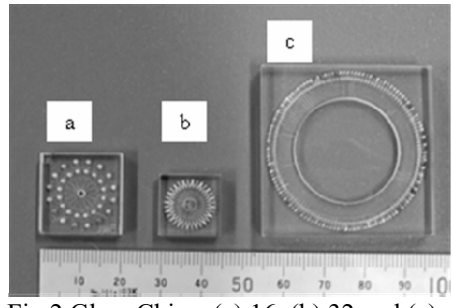

Fig.2 Glass Chips: (a) 16, (b) 32 and (c) 128 channels parallelized chips

978-0-9798064-0-7/μTAS2007/$20©2007CBMS

the glass chip holder is shown in Fig. 3. Only three inlets (black monomer, white monomer, PVA solution) and one output were used to supply materials to each microchannel. The materials were transferred to the microchannel by using syringe pumps, and Janus droplets were polymerized in a hot bath. Droplet formation was observed using a high speed camera.

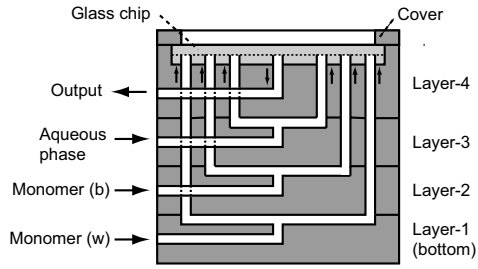

Fig.3 Microchannel holder structure

3. RESULTS AND DISCUSSION

Figure 4 shows the Janus beads obtained and their microscopic image. The boundary of the Janus beads were more clear than the previously used methods, suggesting that the bump structure affected the break-up of the droplets. Figure 5 shows the relationships between continuous-phase flow rate and droplet diameter. The droplet diameter varied from 90 to 130 μm. The C.V. of the droplets was less than 5%. A flat panel for the electrical display was fabricated using these Janus beads, where smooth rotation of the beads was observed (Fig. 6). It was also found that the contrast of the display was the best in the microchannels having bump structure as compared to the other structures.

We had produced a microchannel parallization for the plain beads up to 256-integrated microchannels with monodispersed droplet formation having a production rate of 300 g/h [6]. Microchannel integration for Janus droplet formation was performed for 32 and 128 microchannels. Figure 5 also shows the diameter variations according to the continuous flow rate for a 32 microchannels assembly. It was found that the variation in the droplets diameter was same in the both integrated microchannels. Figure 7 shows the droplet formations in 32 and 128 integrated microchannels. The mean diameter was 135 μm with the C.V. of 1.9 % (continuous-phase flow rate 256 ml/h, and dispersed-phase flow rate 32 ml/h) for 32 integrated microchannels, and 140 μm with C.V. 1.7 % (continuous-phase flow rate 1024 ml/h, and dispersed-phase flow rate 128 ml/h) for 128 integrated microchannels. Our results showed that the droplets were well mono disperse, which mean that the both dispersed-phase and continuous-phase were uniformly sent to every microchannel. These techniques would contribute to fabricate the microreactors for Janus beads production.

REFERENCES

[1] T. Nisisako, T. Torii, and T. Higuchi, *Droplet Formation in a Microchannel Network,* Lab on a Chip, **2**, 24-26, (2002).

[2] T. Nisisako, T. Torii, and T. Higuchi, *Novel Microreactors for Functional Polymer Beads*, Chem. Eng. J., **101**, 23-29,(2004).

[3] T. Nisisako T. Torii, T. Takahashi, and Y. Takizawa, *Synthesis of Monodisperse Bicolored Janus Particles with Electrical Anisotropy Using a Microfluidic Co-flow System*, Adv. Mater. **18**, 1152-1156, (2006).

[4] S. Okushima, T. Nisisako, T. Torii, and T. Higuchi, *Controlled Production of Monodisperse Double Emulsions by Two-Step Droplet Breakup in Microfluidic Devices*, Langmuir **20**, 9905-9908, (2004)

[5] T. Nisisko and T. Torii, *Formation of biphasic Janus Droplets in a microfabricated channel for the synthesis of shape-controlled polymer microparticles,* Adv. Mater.19.1489-1493, (2007)
[6] T. Nisisako and T. Torii, *Scaled-Up Production of Monodisperse Droplets by Multiple-Channel Integration on a Chip*, IMRET 9 Abstracts, 216-217, (2006).

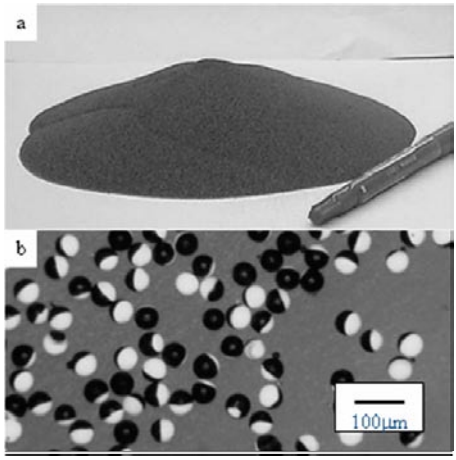

Fig.4 Janus beads (a) and microscope image (b)

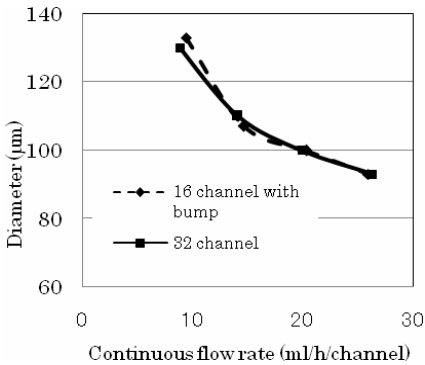

Fig. 5 Continuous flow rate vs. droplet diameter



Fig.6 Rotating ball display

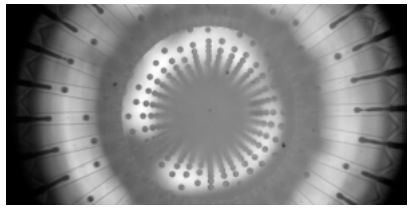

(a) 32-parallelized microchannel

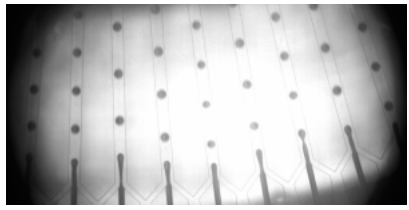

(b) 128-parallelized microchannel

Fig.7 Janus droplet formation in integrated microchannels

SOLID CATALYZED HYDROGENATION IN A SI/GLASS MICROREACTOR USING SUPERCRITICAL CO_2 AS THE REACTION SOLVENT

F. Trachsel, B. Tidona and Ph. Rudolf von Rohr
Institute of Process Engineering, ETH Zurich, Switzerland

ABSTRACT

In this study we present the reduction of mass transfer limitations in the case of the hydrogenation of cyclohexene over Pd/Al_2O_3 catalyst in a Si/Glass microreactor by using supercritical CO_2 ($scCO_2$) as the reaction solvent. The combination of the advantages of microreaction technology and the unique fluid properties of supercritical reaction media lead to a significant increase in reaction performance of the heterogeneously catalyzed model reaction. The comparison of the reaction at sub- and supercritical conditions shows an increase of the reaction rate of about one order of magnitude. This leads to the conclusion that the mass transfer resistance is decreased.

Keywords: Microreactor, high pressure, supercritical fluids, hydrogenation

1. INTRODUCTION

The small characteristic length scales of microreactors enable safe operation at high pressures. Excessive wall thicknesses necessary for the relatively demanding and heavy constructions of macroscale high pressure reactors can be avoided using microchannels as reactors. A high surface-to-volume-ratio increases the heat and mass transfer and the interfacial area at multiphase operating conditions. Since microreactors have a low thermal mass it is possible to obtain stable temperature control and minimal temperature gradients in the reactor. It has been shown previously that microreactors have a better performance in the case of a three phase solid catalyzed hydrogenation than their macroscale counterpart [1]. But the reaction in the gas-liquid-solid case is still mass transfer limited in a packed bed microreactor even at high pressures [2].

To decrease the mass transfer limitation in heterogeneously catalyzed hydrogenation supercritical fluids (SCFs) as reaction solvent are used at high pressure conditions [3]. SCFs are fluids at conditions above their critical pressure and temperature. Their properties are typically in the range between the one of gases and liquids. In heterogeneous catalysis SCFs have significant advantages. In particular the low viscosity in combination with relatively high diffusivities leads to high diffusion rates and is advantageous eliminating mass transfer limitations. Additionally the solubility of reactants is increased in the supercritical reaction mixture. The gas-liquid phase boundary is eliminated which means that all reactants are present in one homogeneous phase. A reaction with SCFs is accelerated in comparison to three phase systems since diffusion of the gaseous species is often the rate limiting step these reactions. It can be said that SCF increase the reaction rates due to the enhanced heat and mass transfer and the higher reactant solubilities. CO_2 (T_c = 31°C, p_c = 73.8 bar) is the most widely used SCF in chemistry, because it has mild critical properties, is non-toxic, non-flammable and inexpensive.

Only few studies of high pressure microreactors or the combination of microreactors and $scCO_2$ are available in literature [4, 5]. Difficulties are the mechanical strength of the microreactor and the sophisticated equipment needed for the control of continuous flow at low flow rates (~µl/min) and high pressure.

978-0-9798064-0-7/µTAS2007/$20©2007CBMS

2. EXPERIMENTAL

Standard photolithography, dry etching and anodic bonding methods were used for the Si/Glass microreactor fabrication. The high pressure microfluidic connections were realized by soldering stainless steel capillaries onto the microreactor chip. The microreactor design is shown in Fig. 1. It consists of three reactant inlets, one catalyst inlet/outlet, a meandering mixing section, a packed bed and a common outlet. Micromachined filter elements prevent the catalyst to leave the packed bed section. The channel width is 400 µm and the depth 250 µm respectively. Commercially available catalyst particles (2 wt-% Pd on Al_2O_3, d_{50} = 115 µm) were inserted via a side channel. A typical catalyst weight in the packed bed was about 1 mg.

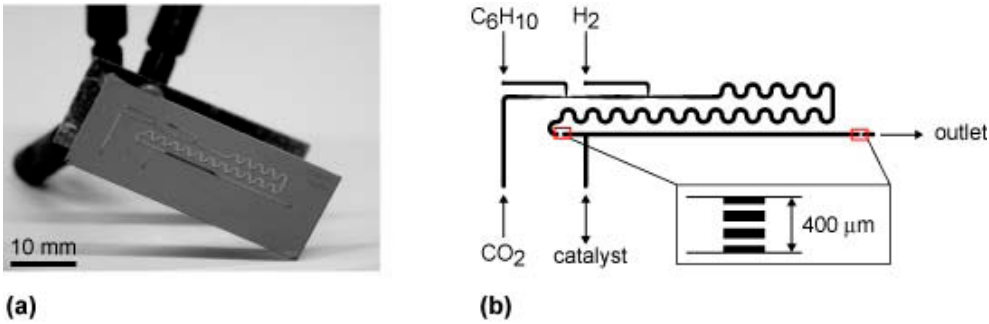

Figure 1. High pressure microreactor design. (a) Photograph of the Si/Glass microreactor. (b) Schematic of the single microchannel design. The meandering mixing and the packed bed section are 65 mm and 26.5 mm in length respectively.

The reactions under supercritical conditions were conducted at flow rates of V*CO_2 = 200 µl/min, V*C_6H_{10} = 23 µl/min and V*H_2 = 5.6 sccm corresponding to a molar ratio of 90:5:5 at 136 bar and 70 °C. The three phase reactions were conducted at the same conditions without CO_2. Residence times in the packed bed were in the range of 0.1 – 0.5 s. Conversion was analyzed by GC-MS. No cooling was needed during the exothermal reaction. Temperature control of the microreactor is realized by two different methods. For chemical experiments the microreactor is placed in an oil bath. A resistive heating, directly evaporated on the Si surface, is used for precise local heating of the microreactor. The later heating method allows the optical characterization of the phase behavior of the reaction mixture at high pressure in the reaction channel on an inverse microscope.

3. RESULTS AND DISCUSSION

Tab. 1. shows selected data of the results obtained in the high pressure microreactor.

Table 1. Selected averaged values of reaction results

Experiment series	Pressure [bar]	Temperature [°C]	Reaction rate [mol/g_{cat}min]
Three phase reaction			
1	50	54	0.038
2	50	73	0.046
Supercritical phase reaction			
3	136	70	0.300
4	136	100	0.320

The three phase reactions at 50 bar show an increase in the observed reaction rate with increasing temperature. This corresponds to the increased solubility of H_2 in C_6H_{10} and kinetic effects at higher temperature. The supercritical phase reactions show the same effect with increasing temperature less pronounced. Comparing the three phase with the supercritical phase reaction, an increase of the reaction rate of about one order of magnitude is observed. It must be stated that the supercritical phase reaction was conducted at a higher pressure that the comparing three phase case. Although the higher solubility of H_2 at 136 bar cannot only account for the reported increase in reaction rate. As the reaction is mass transfer limited in the three phase case [2], the mass transfer resistance must be reduced in the supercritical phase case.

Following terms contribute to an increased observed reaction rate at supercritical conditions. (1) No gas-liquid mass transfer resistance. The gas-liquid phase boundary vanishes as the reaction mixture is in supercritical state at operating conditions. (2) The fluid-solid mass transfer is increased by two reasons. The combination of low fluid viscosity and high diffusivity of the reactants in the SCF reduce the mass transfer resistance. The concentrations of the reactants are higher due to the higher solubility. (3) The diffusion within the catalyst pore is accelerated. This is predominantly to the higher diffusivity of reactants in the supercritical reaction mixture. Also a good wetting of the catalyst pores is expected because of the lower surface tension of the SCF.

4. CONCLUSION AND OUTLOOK

A versatile high pressure microreactor setup is presented for the analysis of heterogeneously catalyzed reactions using $scCO_2$ as the reaction solvent. Experiments with a model hydrogenation reaction show an increase of the reaction rate at supercritical conditions of about one order of magnitude compared to subcritical reaction conditions. This indicates an increased mass transfer of the reactants to the active sites of the catalyst. The presented setup is also used for in-situ phase studies of the reaction mixture during reaction in the Si/Glass microreactor.

ACKNOWLEDGEMENTS

This work was supported by ETH Research Grant TH-32/05-2 and the Emil Barell foundation.

REFERENCES

[1] M.W. Losey, et al., *Microfabricated multiphase packed-bed reactors: Characterization of mass transfer and reactions,* Industrial & Engineering Chemistry Research, **40**, pp. 2555-2562. (2001).

[2] F. Trachsel, et al., *Transparent Silicon/glass microreactor for high pressure and high temperature reactions,* Chemical Engineering Journal, accepted for publication, (2007).

[3] A. Baiker, *Supercritical fluids in heterogeneous catalysis,* Chemical Reviews, **99**, pp. 453-473. (1999).

[4] J. Kobayashi, et al., *Hydrogenation reactions using scCO(2) as a solvent in microchannel reactors,* Chemical Communications, 2567-2568. (2005).

[5] R.M. Tiggelaar, et al., *Fabrication, mechanical testing and application of high-pressure glass microreactor chips,* Chemical Engineering Journal, **131**, pp. 163-170. (2007).

OBSERVATION OF BIOFILM IN MICROCHANNEL WITH THERMAL LENS MICROSCOPY

T. T. J. Rossteuscher[1,2], A. Hibara[1,3,4], K. Mawatari[3], T. Kitamori[1,3,4]

[1]*Department of Applied Chemistry, University of Tokyo, JAPAN*

[2]*Institute of Hydrochemistry, Technische Universität München, GERMANY*

[3]*Kanagawa Academy of Science and Technology, JAPAN*

[4] *Japan Science and Technology Agency, JAPAN*

ABSTRACT

In this paper, for the first time, *in situ*, staining-free biofilm observation with high spatial resolution over a sufficient depth is presented. Biofilm was grown in a well-defined and reproducible way. The application of microfluidics and thermal lens microscopy (TLM) will provide a new powerful tool for the investigation of biofilm control and biofilm removal strategies.

Keywords: biofilm, in situ, photothermal, microscopy

1. INTRODUCTION

Biofilms are bacterial aggregates embedded in gel matrices, forming at interfaces [1]. Biofilms are utilized in wastewater treatment plants, but they also have adverse effects like pipe plugging, corrosion, or biofouling. Biofilm growth depends on environment, nutrient supply and many further conditions. While biofilm research on plates offer detailed observation in micrometer scale, it is difficult to investigate biofilm in flowing reactors, where biofilm occurs in a more natural state. Observation of biofilm under flowing conditions and their *in situ* measurements are still challenging. Current methods either lack sufficient three-dimensional resolution or require dye staining like confocal laser-scan microscopy (CLSM), which is the standard method for biofilm observation. Staining-free observation of biofilm with optical methods is furthermore hampered by the strong scattering nature of the biofilm structure. Photothermal methods are less affected by scattering and can be applied to biofilm research [2]. However, spatial resolution of the present photothermal method is restricted.

2. THEORY

Microchannels offer defined flow conditions and the possibility of microstructure observation, making them a good choice for biofilm experiments. Thermal lens microscopy (TLM) offers high spatial resolution and can be applied to three-dimensional structure observation. TLM observation of single cell has been carried out before [3]. Figure 1 presents the advantages of biofilm observation in microchannels with TLM.

TLM experiments are carried out with an excitation and a probe beam. During TLM measurements, a part of the excitation beam is absorbed by the biofilm sample. The main part of absorbed light energy is released to matrix to generate a temperature gradient around the beam. Since temperature coefficient of refractive index is negative, the temperature gradient acts as a transient concave lens, which is called thermal lens effect. The degree of the lens on the probe beam is directly proportional to absorption. In this paper, by using an excitation wavelength of 532 nm, biofilm pigment structure is elucidated within the biofilm structure. The information can be compared with results obtained by other microscopic methods.

978-0-9798064-0-7/μTAS2007/$20©2007CBMS

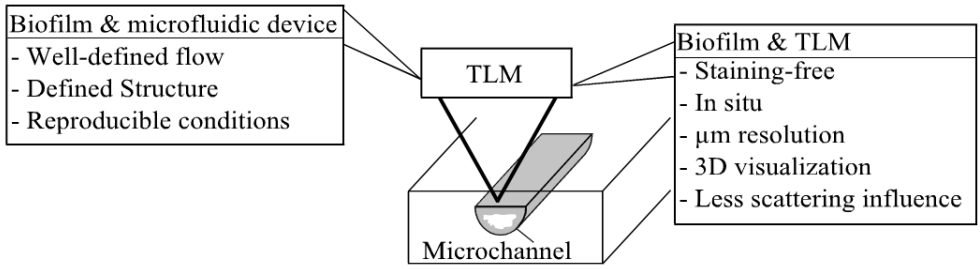

Figure 1: Biofilm research in the microchannel with TLM has several benefits, making detailed on-line, in situ observation of biofilm growth, control and removal possible

3. EXPERIMENTAL

Biofilm suspension was flown into an S-shaped microchannel and left for initial adhesion over night. Afterwards a nutrient solution of D-glucose (510 mg/L), NH_4Cl (150 mg/L), KH_2PO_4 (60 mg/L), Na_2SO_4 (100 mg/L) and yeast extract (4 mg/L) was driven through the channel continuously for biofilm growth at a speed of 23 mm/s. After 20 days of growth at room temperature biofilm was taken for observation with transmission microscopy and TLM.

In this paper, TLM measurements were carried out with a modulated excitation beam at 532 nm and a continuous probe beam at 633 nm. For three-dimensional data acquisition, a scanning stage was applied. TLM observation was carried out by horizontally scanning layers of biofilm growth in different depths of the channel.

4. RESULTS AND DISCUSSION

Figure 2 illustrates the S-shaped microchannel and the region of the main biofilm occurrence. Figure 3a shows a picture of the biofilm taken with a phase-contrast microscope. The observation with TLM is presented as topview over all recorded layers in Figure 3b. The difference in biofilm signal within each layer is furthermore highlighted in the Figure 3c, showing that biofilm also has grown in vertical direction within the channel. The appearance of the main biofilm colony at the inner wall of the second curve in the microchannel shows the tendency of bacteria for initial adhesion in regions of small shear stress.

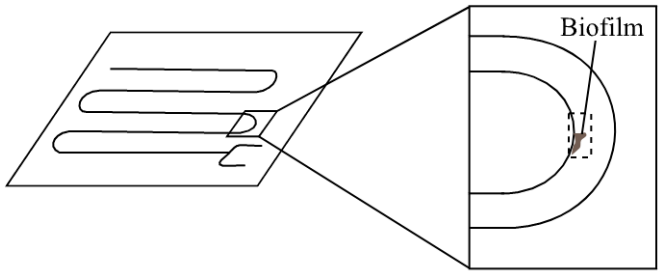

Figure 2: Illustration of microchannel design and location of biofilm growth in the second curve of the S-channel; biofilm was grown under constant flow with constant nutrient supply; dotted square shows observation area in figure 3

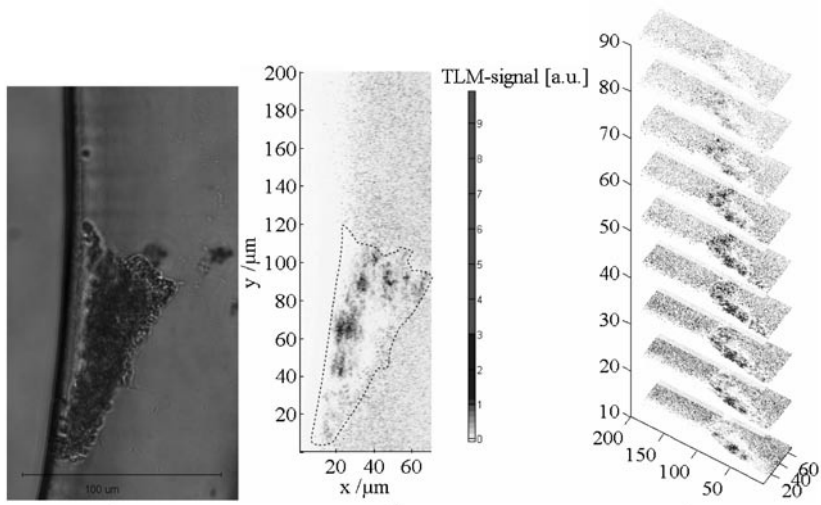

Figure 3: Phase-contrast photograph of biofilm in microchannel (a; scalebar at bottom represents 100 µm); overlay of 9 layers of the same biofilm in topview observed with thermal lens microscopy, layers being vertically 10 µm apart (dashed line represents assumed area of biofilm growth): biofilm absorption is found at the same positions as in the DIC picture (b; white areas represent no absorption); the layered view of the TLM picture observed from the left side of figure 3b shows that the biofilm at the tip is found in lower layers than the broader biofilm in the middle

5. CONCLUSION

Biofilm growth under defined, controllable conditions as well as online, *in situ* observation with TLM have been demonstrated. Biofilm growth in a tubular flowing environment under reproducible conditions without a need of disassembly prior to experiment will provide a new and powerful tool for the examination of biofilm removal strategies with different chemicals as well as different naturally, locally occurring biofilm species.

ACKNOWLEDGEMENTS

Biofilm for experiments has been kindly provided by Ohgaki-laboratory, University of Tokyo. T. T. J. R. acknowledges a scholarship provided by the Ministry of Education, Science, Sports and Culture of Japan.

REFERENCES

[1] S. S. Branda et al., Trends Microbiol. **13**, 20-26, 2005.
[2] T. Schmid et al., Rev. Sci. Instr. **74**, 755-757, 2003.
[3] E. Tamaki et al., Anal. Chem. **74**, 1560-1564, 2002.

A PARTICULE IMAGE ANEMOMETRY TECHNIQUE FOR A NON INVASIVE, QUICK DETERMINATION OF AVERAGE FLOW RATES IN MICROCHANNELS

A. Plecis, L. Malaquin and Y. Chen
LPN-CNRS, France

ABSTRACT

In this work, we propose an original method to measure the flow rate of liquids in microchannels. Accurate determinations of flow rates can be achieved in most of microfluidic devices using conventional epifluorescence setups and very simple algorithms. We demonstrate that it is possible to measure flow rates ranging from 1 $\mu m.s^{-1}$ up to $1mm.s^{1}$ in microchannels within a few seconds. The limits of this Particle Image Anemometry (PIA) technique are also discussed theoretically and experimentally.

Keywords: Particle Image Anemometry (PIA), Microfluidics, Flow measurement.

1. INTRODUCTION

Different micro-anemometers have been reported for the monitoring of the flow rate in microchannels [1,2]. In most of them, heavy clean room processes, calibration steps, additional connections to the macro-world and suitable measurement units are usually required. Particle Image Velocimetry (PIV) techniques have also been adapted to microfluidic systems for the non invasive monitoring of micro flows [3]. Despite the inherent difficulties induced by the downscaling of the system (particule diffusion, adsorption on wall surfaces, etc...), impressive cartographies of velocity fields were obtained using complex algorithms, or combining PIV techniques with Particle Tracking Velocimetry techniques [4]. Nevertheless, these techniques are quite sophisticated and do not seem to be well adapted to adress such a simple question as: what is the average flow rate in this microchannel?

2. METHODS

We have designed the PIA technique in order to measure the flow rates in straight microchannels with Poiseuille or plug-like flows oriented along the axis of the channel (see figure 1). The cross correlation C is calculated from the intensity of two successive images I of a flow seeded with fluorescent particles.

$$C(u) = \sum_{y,x} I(x-u, y, t) * I(x, y, t+\Delta t)$$

The interval Δt between two images defines the dynamic working range of the measure. The cross correlation is calculated for the displacement u in the direction of the flow x. The fact that images are not divided in subregions makes the crosscorrelation algorithm very simple to implement. As shown in figure 1, the shape of the crosscorrelation peak in the direction of the flow depends on the type of flow. A mathematical developpment leads to the following expression for C when averaged over the time:

$$\langle C(u) \rangle = A. \sum_{v} P(-v/\Delta t) * L(u-v)$$

978-0-9798064-0-7/μTAS2007/$20©2007CBMS

where A is a constant, P the probability density of velocities (PDV) in the channel and L a function that depends on the particle intensity profile. If particles are considered as punctual, this expression is drastically simplified and the cross correlation becomes proportionnal to the PDV:

$$\langle C(u) \rangle = A.P(-u/\Delta t)$$

The averaged flow rate can be deduced from the value of the most probable displacement V_{max} of the particles.

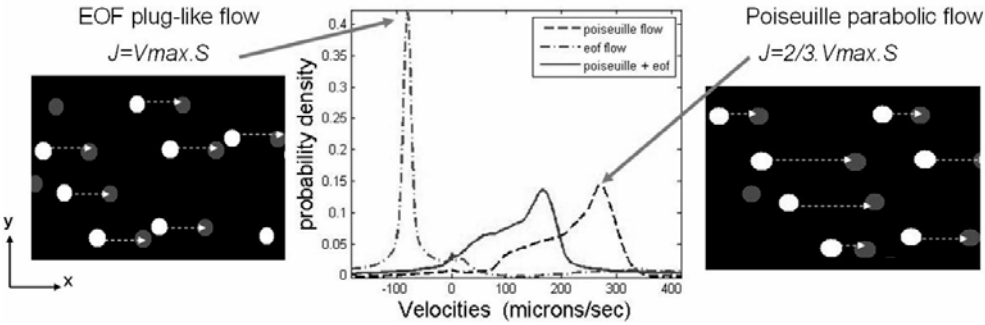

Figure 1. Principle of the PIA technique. The cross-correlation is done on successive images of a flow seeded with fluorescent beads. For plug like flows, images can be superimposed as the beads have all the same velocity, which results in a sharp peak for the PDV. For Poiseuille flows, the shape of the crosscorrelation curve results from the distribution of velocities among the beads. The averaged velocity is in this case 2/3 of the most probable velocity. For the flow rate determination J of electro-osmotic flows (EOF), the electrophoretic velocity of the beads has to be taken into account.

3. RESULTS AND DISCUSSION

This technique was experimentally applied on rectangular microchannels (figure 2) microfabricated with a glass-PDMS-glass technique [5]. As expected, the measured velocities showed a linear dependance with the pressure difference applied across the microchannel.

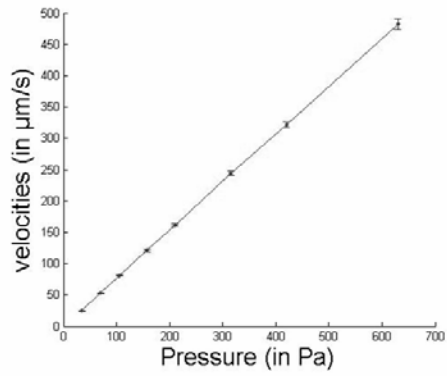

Figure 2. Experimental validation of the PIA technique. The error bars correspond to the standard deviation for 10 measurements. This standard deviation was below 5% for all the experiments.

The influence of the particle shape on both the cross-correlation result and the flow rate measurement was investigated theoretically (figure 3.A) and confirmed experimentally (figure 3.B). These results show that when V_{max} is in the order of the bead size Φ, a systematic shift toward lower values is measured for the velocity. However, when Δt is increased so that $V_{max} >> \Phi$, the measured value is in good agreement with the real velocity value and no correction is necesssary.

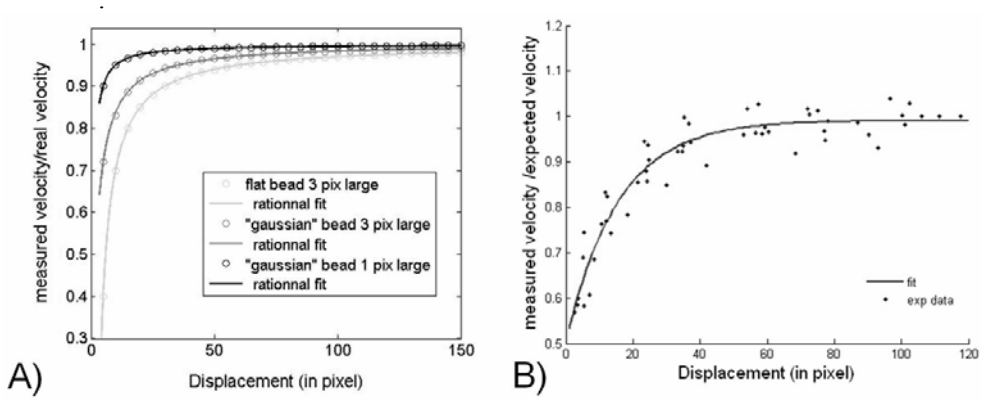

Figure 3. A) Influence of particule size and shape in the image plan of the camera on the measured velocity. The convolution term in equation [2] is responsible for a systematic shift in the measured velocity at low displacements. Different particle geometries were numerically investigated. B) Experimental measurement of the velocities shift at low displacements. In this experiment, each velocity value reported in figure 1 (in the range of 50 to 500 $\mu m.s^{-1}$) was measured for different Δt values varying from 33 ms to 3s. The ratio between measured and real velocities is plotted as a function of the most probable displacement. The curves confirm the good accuracy of the measurement methods when the interval between image pairs is kept sufficiently long.

In these experiments, all measurements were performed within a few of seconds and thus they give an access to real-time monitoring of flow rates. We believe that this fast, simple and reliable method which can be used on conventional epifluorescence setups is perfectly adapted for a wide range of microfluidic applications that require an accurate and continuous monitoring of microflows.

REFERENCES

[1] C. Amatore, M. Belotti, Y. Chen, E. Roy, C. Sella, L. Thouin, *Using electrochemical coupling between parallel microbands for in situ monitoring of flow rates in microfluidic channels*, Journal of Electroanalytical Chemistry 573 (2) (2004) 333-343.

[2] N.T. Nguyen, *Micromachined flow sensors - a review*, Flow Measurement and Instrumentation 8 (1) (1997) 7-16.

[3] C.D. Meinhart, S.T. Wereley, J.G. Santiago, *PIV measurements of a microchannel flow*, Experiments in Fluids 27 (5) (1999) 414-419.

[4] S. Devasenathipathy, J.G. Santiago, K. Takehara, *Particle tracking techniques for electrokinetic microchannel flows*, Analytical Chemistry 74 (15) (2002) 3704-3713.

[5] A. Plecis, Y. Chen, *Fabrication of microfluidic devices based on glass-PDMS-glass technology*, Microelectronic Engineering 84 (5-8) (2007) 1265-1269.

CHAOTIC MIXING INDUCED BY A MAGNETIC CHAIN IN A ROTATING MAGNETIC FIELD

T.G. Kang, M.A. Hulsen, P.D. Anderson, J.M.J. den Toonder, and H.E.H. Meijer

Eindhoven University of Technology, Materials Technology, The Netherlands

ABSTRACT

A magnetic chain, self-assembling from magnetic particles, may act as an intelligent micro-stirrer, inducing chaotic mixing in a well-chosen rotating magnetic field. We investigate this using a 2D circular cavity with magnetic particles. The motion of the chain is dependent on the Mason number. At a lower Mason number, the chain rotates like a rigid body. We observe break-up of the chain at a certain range of the Mason number. The detached chains either assemble into a single chain again or remain as separate chains depending on the Mason number. The alternating break-up and reformation of the chain lead to better mixing.

Keywords: Chaotic Mixing, Magnetic Chain, Rotating Magnetic Field

1. INTRODUCTION

We investigate the possibility of using self-assembling chains of magnetic particles, which act as active micro stirrers under the influence of a rotating magnetic field, to actively induce chaotic mixing in a liquid-filled circular cavity. This has attractive applications in diagnostic lab-on-a-chip devices [1,2]. Our main focus is on the dynamics of the chain and the route to induce chaotic mixing. The progress of mixing characterized by the length stretch will be introduced, with an emphasis on the effect of Mason number, the ratio of the viscous force to the magnetic force. The Mason number is defined by

$$\mathrm{Ma} = \frac{\eta\omega}{\mu_0 \chi_\mathrm{p} H_0^2}, \tag{1}$$

where η is the viscosity, ω the angular frequency of the rotating magnetic field, μ_0 the magnetic permeability in vacuum, χ_p the magnetic susceptibility of the particles, and H_0 the magnitude of the magnetic field intensity.

2. MODELING

The problem chosen is a 2D flow in a circular cavity with 17 circular paramagnetic particles subjected to a rotating magnetic field, initially forming a chain aligned horizontally. The particles are circular with the same radius a. The fluid flow is governed by viscous forces and magnetic interactions between the particles. The governing equations for the magnetostatic problem are given by the two Maxwell's equations,

$$\nabla \times \mathbf{H} = \mathbf{J}, \quad \nabla \cdot \mathbf{B} = 0, \tag{2}$$

where $\mathbf{H}$ is the magnetic field intensity, $\mathbf{J}$ the current density, and $\mathbf{B}$ the magnetic flux density. In a two-dimensional Cartesian coordinate system, the governing equation for magnetic potential A is represented by

978-0-9798064-0-7/μTAS2007/$20©2007CBMS

$$-\frac{\partial}{\partial x}\left(\frac{1}{\mu_r}\frac{\partial A}{\partial x}\right)-\frac{\partial}{\partial y}\left(\frac{1}{\mu_r}\frac{\partial A}{\partial y}\right)=\mu_0 J, \tag{3}$$

where μ_r denotes the relative magnetic permeability and A the z-component of the magnetic vector potential **A**. Once A is found, the magnetic flux density **B** is computed by taking the curl of **A**. Then, the body force acting on materials in the magnetic field is given by the divergence of the Maxwell stress tensor **T,** which is added to the Stokes equations, as follows:

$$\begin{aligned} -\eta\nabla^2\mathbf{u}+\nabla p &= \nabla\cdot\mathbf{T} \quad \text{in } \Omega, \\ \nabla\cdot\mathbf{u} &= 0 \quad \text{in } \Omega, \end{aligned} \tag{4}$$

where **u** is the velocity and p the pressure. Here, we solve the same governing equations for both fluid and particle domains, with the rigid body constraints imposed on the particle boundaries [1].

3. NUMERICAL METHODS

We solved the magnetic problem using the standard finite element method with bi-quadratic interpolation for A. The flow problem is solved by using a fictitious domain method and the finite element method. The rigid body constraints are treated by a rigid-ring description implemented by Lagrange multipliers [1]. The resulting matrix equations for both magnetic and flow problems are solved using a direct sparse matrix solver, HSL/MA57.

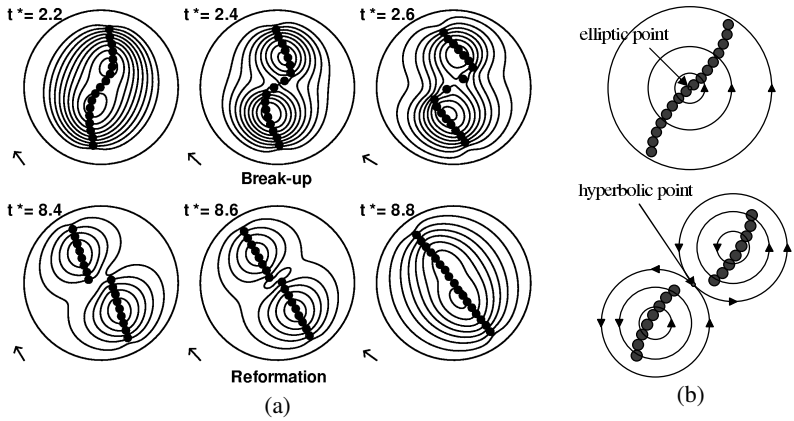

Figure 1. Flow characteristics at Ma=0.002. (a) Streamlines at the moment of break-up (upper) and reformation (lower) of the chain, (b) two typical flows: single rotating flow and two co-rotating flows. The shape of the chain at break-up, a reverse S-like structure, is similar to that observed experimentally by Melle et al. [3]. The arrows in Fig. 1(a) indicate the direction of the magnetic field.

4. RESULTS AND DISCUSSION

The dynamics of particle motion is highly influenced by the Mason number. At Ma=0.001, the chain rotates almost like a rigid body, but lags behind the field. We observe chain break-up at Ma=0.002 and 0.003. At Ma=0.002, the detached chains join together

again, forming a single again, which take place in an alternating manner. The alternating flows create two flow portraits (see Fig. 1 for the flow characteristics), which act as two-stirrers. At Ma=0.003, however, the two split chains remain as separate chains without joining together. We tracked the interface of a circular blob in time. The length stretch at Ma=0.002 increases faster than the others due to stretching and folding induced by the topological changes of the chain.

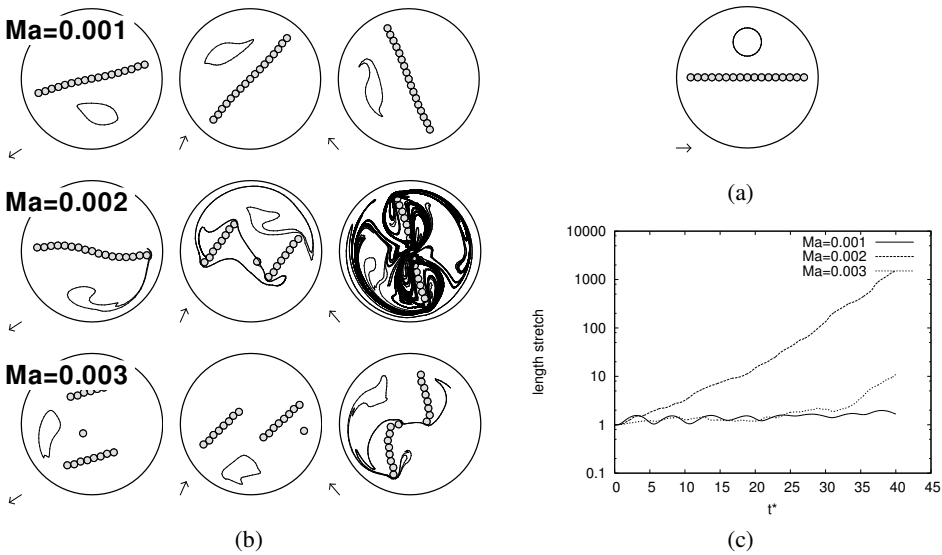

Figure 2. Interface tracking of a circular blob of fluid. (a) Initial shape of the blob, (b) deformation at the non-dimensional time t*=10, 20, and 40 for the three Mason numbers, Ma=0.001 (top), 0.002 (middle), and 0.003 (bottom), and (b) the evolution of the length stretch. The non-dimensional time is defined as, $t^*=\omega t$.

5. CONCLUSIONS

We investigated the dynamics of a magnetic chain and subsequent mixing under the influence of a rotating magnetic field. The dynamics of the chain and resulting fluid flow are significantly influenced by the Mason number. We conclude that, within a limited range of the Mason number, a magnetic chain rotates and breaks into smaller chains, and the detached chains connects again, yielding chaotic mixing by stretching at break-up and folding due to the rotational flows.

REFERENCES

[1] T. G. Kang, M. A. Hulsen, J. M. J. den Toonder, P. D. Anderson, H. E. H. Meijer, J. Comput. Phys. A direct simulation method for flows with suspended paramagnetic particles, submitted.

[2] R. Calhoun, A. Yadav, P. Phelan, A. Vuppu, A. Garciab, M. Hayes, Paramagnetic particles and mixing in micro-scale flows, Lab. Chip. **6** (2006) 247–257.

[3] S. Melle, O. G. Calderon, M. A. Rubio, G. G. Fuller, Microstructure evolution in magnetorheological suspensions governed by Mason number Phys. Rev. E **68** (2003) 041503.

COMPUTATIONAL SIMULATION OF DROPLET JETTING OF PIEZOELECTRIC DRIVEN INKJET HEAD WITH INK COMPRESSIBILITY

J.H. Park[1], W.C Sim[2], Y.J. Kim[2], P.J. Kang[2], C.S. Park[2], Y.S. Yoo[2] and J.W. Jeong[2]

[1]CAE Group, Samsung Electro-Mechanics, South Korea and
[2] eMD Center, Samsung Electro-Mechanics, South Korea

ABSTRACT

Computational simulation model using FLUENT, commercial CFD software, has been developed in order to design robust inkjet head and understand the mechanisms of droplet jetting. Generally, liquid flow is regarded as incompressible. In inkjet flow, however, ink compressibility should be considered because of pressure wave effect by sudden PZT deformation. PLIC-VOF method is adopted for simulating free surface flow. Since FLUENT cannot solve PZT deformation, PZT displacement based on simulation data by ANSYS is applied to moving wall condition in FLUENT. Simulation results agree well with experimental results, and profiles of pressure and mass flow rate in inkjet head have very similar waveforms.

Keywords: inket, slightly compressible, VOF(Volume of Fluid), CFD(Computational Fluid Dynamics)

1. INTRODUCTION

Inkjet printing technology is very versatile, simple and low-cost manufacturing tools for electronic products. So many theoretical and experimental researches have been performed. Especially, to design robust inkjet head is very essential element for precise printing process because jetting performances mainly depend on the quality of inkjet head. However, it is very difficult to examine design factor of head using experimental method, due to long time and high cost. Therefore, we performed numerical computer simulation of droplet jetting in order to design head and predict jetting performances. Jetting process of piezo-electric driven inkjet head is very complicated, including PZT deformation by applied voltage, ink flow, free surface flow of droplet in air, and so on. In this study, the analysis model considering these phenomena was established to simulate droplet jetting.

2. THEORY

Continuum assumption is valid in micro to millimeter scale. So, CFD(Computational Fluid Dynamics) analysis can be applied to present study. Generally, most liquid flow is regarded as incompressible [1]. In inkjet flow, however, ink compressibility should be considered because of pressure wave generated by sudden PZT deformation [2], [3], [4], [5]. In order to express liquid compressibility, we introduced slightly compressible model. In slightly compressible model, density is a function of pressure and sound speed [2], [4]. In addition, PLIC-VOF method is adopted for simulation of free surface flow. Continuity, momentum, state and volume fraction equation in present study is as follows:

978-0-9798064-0-7/μTAS2007/$20©2007CBMS

$$\frac{\partial \rho}{\partial t} + \nabla \bullet (\rho \vec{v}) = S_m$$
$$\frac{\partial}{\partial t}(\rho \vec{v}) + \nabla \bullet (\rho \vec{v} \vec{v}) = -\nabla p + \nabla \bullet \bar{\tau} + \rho \vec{g} + F$$
$$c^2 = \frac{\partial p}{\partial \rho} \qquad (1)$$
$$\frac{1}{\rho_q}\left[\frac{\partial \alpha_q}{\partial t} + \nabla \bullet \left(\alpha_q \rho_q \overrightarrow{v_q}\right)\right] = 0$$

FLUENT, commercial CFD code is used in this study. Because PZT deformation is simulated by ANSYS, and PZT displacement based on simulation data is applied to boundary condition of FLUENT.

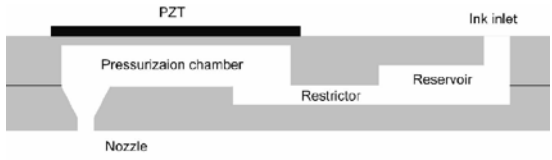

Figure 1. Schematic structure of piezoelectric driven inkjet head

3. Results

Jetting simulations with and without ink compressibility have been compared, as shown in Table 1. The simulation results with ink compressibility are well matched with experimental results. On the contrary, simulation results without ink compressibility have much difference from experimental results. Figure 2 presents image of droplet formation by experiment and simulation with ink compressibility. Simulation described the phenomena that droplet ejected from nozzle was shaped into sphere by surface tension.

Table 1. Jetting performances by experiments and simulations

Case	Droplet velocity (m/s)	Droplet volume (pl)
Experiment	2.8~3.3	17~22
Simulation with ink compressibilty	3.0	18.5
Simulation without ink compressibility	15.2	18.5

The ink pressure in chamber and mass flow rate at nozzle entrance were obtained by simulation. As shown in Fig. 4, the profiles of pressure and mass flow rate have very similar waveforms. As a result, it is found that ink flow is governed by pressure wave generated by

PZT deformation and acoustic characteristics of inkjet head are very important factors of jetting performances [3], [4], [5].

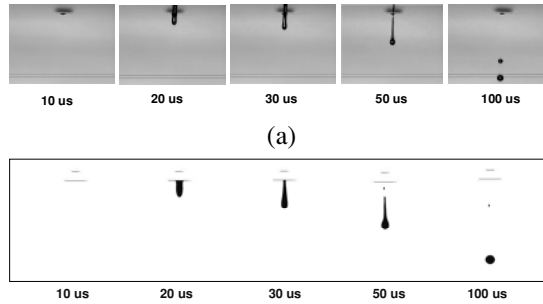

Figure 2. Images of droplet formation by (a) experiment (b) simulation

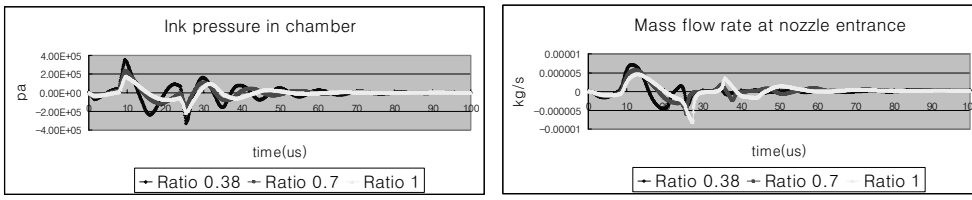

Figure 3. Ink pressure in chamber and mass flow rate at nozzle entrance as functions of time by simulation with ink compressibility

4. CONCLUSIONS

We performed computational simulations of droplet jetting process of piezoelectric driven inkjet head. According to simulation results, pressure wave is generated by sudden PZT deformation and plays an important role in inkjet flow. We are performing multi-nozzle and sequential jetting simulations in order to design robust inkjet head and understand the mechanisms of droplet jetting.

REFERENCES

[1] F.M. White, *Fluid Mechanics 4th edition*, McGraw Hill, pp. 575-577, (1999).

[2] J.F. Dijksman, *Hydro-Acoustics of Piezoelectrically Driven Ink-Jet Print Heads*, Flow, Turebulence and Combustion, Vol. 61, pp.211-237, (1999).

[3] J.T. Yeh, *VOF-FEM Coupled Inkjet Simulation*, in 2001 ASME Fluids Engineering Division Summer Meeting, New Orleans, May 29-June 1, (2001).

[4] S.K. Wee, S.Y. Oh, and J.W. Chung, *Hydro-Acoustics of Piezoelectrically Driven Ink-Jet Print Heads*, in 2001 in Proceedings of KSME annual spring conference, pp. 4181-4186, (2006).

[5] J.F. Djijksman, P.C. Duineveld, M.J.J. Hack, A. Pierik, J. Rensen, J.E. Rubingh, I. Schram, and M.M. Vernhout, *Precision Ink Jet Printing of Polymer Light Emitting Displays*, Journal of Materials chemistry, pp.511-522, (2006).

ELECTROLYTE DEPENDENCE OF AC ELECTRO-OSMOSIS

Martin Z. Bazant[1] , John Paul Urbanski[1], Jeremy A. Levitan[1], Kapil Subramanian[1], Mustafa Sabri Kilic[1], Andrew Jones[1] and Todd Thorsen[1]

[1]*Massachusetts Institute of Technology, USA*

ABSTRACT

This paper reports the first investigation of the dependence of AC electro-osmosis (ACEO) on the solution chemistry. It is argued that classical dilute-solution theory breaks down in ACEO, since the large applied voltage leads to ion crowding near the electrode surfaces. A modified theory is proposed with steric effects (finite ion sizes) and a charge-dependent viscoelectric effect, which predicts that ACEO flow depends on the salt concentration, ion sizes and valences. Experiments demonstrate significant variations in ACEO pumping upon varying salt concentration (μM – mM KCl) or ionic species (μM NaCl, $CaCl_2$, $MgCl_2$, KI, KOH), which merit further experimental and theoretical study.

Keywords: AC electro-osmosis, nonlinear electrokinetics, micropumps

1. INTRODUCTION

Nonlinear "induced-charge" electro-osmotic (ICEO) flows offer promising methods for manipulating fluids and colloids in portable or implantable microfluidic devices [1]. The potential advantages include the lack of moving parts or mechanical actuation, precise local flow control, ease of fabrication, and low voltage (a few volts) and low power (milliwatts), which could be provided by standard miniature batteries. In particular, the design of AC electro-osmotic (ACEO) pumps [2,3] has advanced to the point where fast mm/sec velocities are now possible at a few volts [4], at least in water [5] and dilute KCl [6].

Two prior experiments have shown the decay of ICEO flow with increasing salt concentration above 0.1 mM and effectively vanishing above 10 mM, which is not predicted by the existing theory. For ACEO pumps, this effect has only been reported once in KCL using an asymmetric planar electrode array at high voltage (>2 V) and high frequency (>10 kHz), where the flow is in the reverse direction from the theory [3]. Recently, a similar concentration dependence has been observed in NaCl in the induced-charge electrophoresis (ICEP) of metallo-dielectic Janus particles at lower voltages (< 0.5 V across the particles) and lower frequencies (< 1 kHz) [7]. It has been suggested that this concentration dependence is a universal feature of ICEO flows, associated with ion crowding in highly charged double layers [8]. The theory also predicts that ICEO flows depend on the ionic species, but this has never been studied experimentally.

2. THEORY

Classical Poisson-Boltzmann theory assumes a dilute solution of point-like ions in thermal equilibrium in the mean potential. There clearly exists a concentration $c_{\max}$, which depends (at least) on the size a and valence z of each counter-ion, above which this approximation breaks down. This limit is reached at a diffuse-layer voltage $\psi_c = (kT/ze)\log(c_{\max}/c)$ of order the thermal voltage kT/e = 25 mV, which is 100 times smaller than typical voltages applied to the double layer in ACEO. At such large voltages, ions become crowded in the double layer [9]. One consequence of steric repulsion is that

978-0-9798064-0-7/μTAS2007/$20©2007CBMS

the differential capacitance decays at large voltage, the opposite prediction of PB theory (Fig. 1). This alters the "RC time" and thus the frequency dependence of ICEO flows in a way that depends on the counterion size and valence. Steric effects alone, however, cannot predict strong dependence on the salt concentration. This can be explained by postulating that the viscosity η increases (and permittivity ε decreases) with increasing counter-ion charge density ρ and diverges at close packing. The simplest assumption, $\varepsilon/\eta \propto (1-\rho/c_{\max})$, yields a modified induced electro-osmotic slip formula [8],

$$u_s = -\frac{\varepsilon E}{\eta}\left(\psi - \mathrm{sgn}(\psi)\frac{kT}{ze}\log\left[1+4\frac{c}{c_{\max}}\sinh^2\frac{ze\psi}{2kT}\right]\right) \sim -\mathrm{sgn}(\psi)\frac{\varepsilon kT}{\eta ze}E\log\frac{c_{\max}}{c} \qquad (1)$$

in which the ICEO mobility saturates at large voltage as $u_s/E \propto \log(c_{\max}/c)/z$.

3. EXPERIMENTAL

Using the methods of Ref 6, ACEO pumps consisting of 5mm-long interdigitated Au electrode arrays of two designs (planar [3] and non-planar [6]) were tested using 20mm-long multilayer soft-lithographic loops, which served to isolate the pumps from external pressure gradients. Each electrolyte was prepared in reagent-grade de-ionized (DI) water (0.56 S/cm, pH=5). Each pump was operated in DI water at 2 Vpp, 1 kHz for 30 min prior to testing and for 2 min. between electrolytes. A dilute fluorescent bead solution was loaded and not allowed to reach the electrodes in each case. Digital movies were analyzed in custom PIV software built around the shareware uraPIV. The resulting parabolic flow profile was analyzed to determine peak mid-channel stream velocity reported in the figures.

In the first experiment, the velocity versus frequency was carefully measured for a range of concentrations of KCl from 1.0 μM to 1.0 mM in a single planar device [3] at 3 Volt peak-to-peak (Vpp). In the second, preliminary set of experiments, the ionic species were varied at 1 μM in the sequence NaCl, $CaCl_2$, $MgCl_2$, KI, NaI, KOH, NaOH in a single non-planar 3D ACEO pump [6] with 3.0 μm step height at 2 Vpp. The NaI and NaOH data showed irregular scatter and were not included in the comparison in Figure 2.

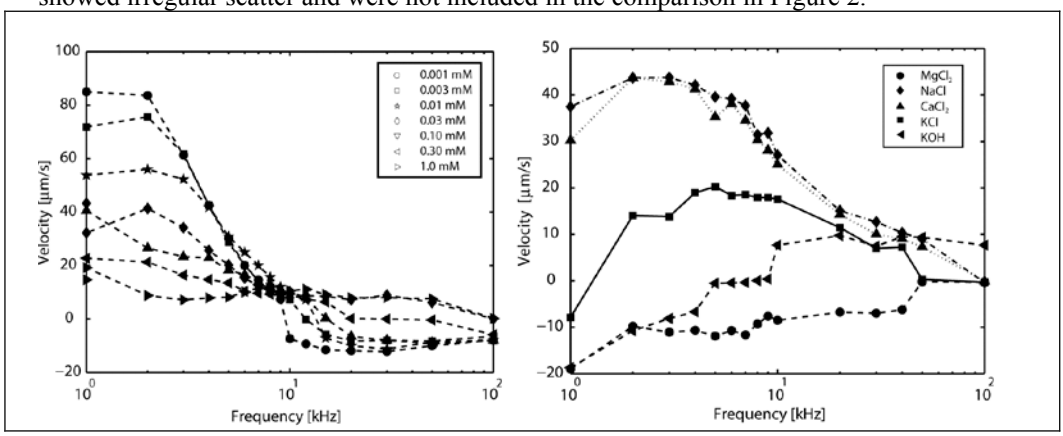

Figure 2. Left: Velocity from the planar ACEO pump [3] at 3 Vpp versus AC frequency in KCl at different concentrations, 1.0 μM – 1.0 mM, in DI water. Right: Velocity from the non-planar 3D ACEO pump [8] (3 μm steps) at 2 Vpp for different electrolytes at 1.0 μM.

4. RESULTS AND DISCUSSION

The KCl data for the planar pumps in Fig. 2 (left) is consistent with prior measurements [3]. At all concentrations, there is single peak around 1 kHz with flow reversal at high frequency > 10 kHz, which can be reproduced in simulations using the nonlinear capacitance with steric effects in Fig. 1 [8]. The concentration dependence is roughly logarithmic for all frequencies, $u(\omega) \propto \log(c_{\max}/c)$, and extrapolates to zero around $c_{\max} \approx 10$ mM (similar to ICEP in NaCl [7]), as in the large-voltage limit of (1).

The second data set shows a strong dependence on the ionic species, but it is difficult to interpret. The data shows little difference between NaCl and $CaCl_2$, which were tested first; both exhibit a single peak of forward pumping, as expected for the non-planar pumps. The salt concentration is so low (1mM) that crowding effects could mainly involve the common H^+ and OH^- ions, which are more abundant in the bulk at pH=5. The next electrolyte, $MgCl_2$, exhibited only reverse flow, inversely proportional to the frequency. Such low-frequency flow reversal is new and could be due to Faradaic reactions at the gold electrodes. Subsequent solution either showed erratic flow (NaI, NaOH) or more low-frequency flow reversal (KI, KOH, KCl). Prior experiments in KCl [3,6] have not seen this behavior, which suggests that the electrodes may have been electrochemically altered.

5. CONCLUSIONS

We have shown that ICEO flow depends on solution chemistry, which can adversely affect microfluidic applications, such as ACEO pumps. More experiments are planned.

ACKNOWLEDGEMENTS

This research was supported by the U.S. Army through the Institute for Soldier Nanotechnologies, under Contract DAAD-19-02-0002 with the Army Research Office.

REFERENCES

[1] M. Z. Bazant and T. M. Squires, *Induced-charge electro-kinetic phenomena: Theory and microfluidic applications*, Physical Review Letters 92, art. no. 066101 (2004).

[2] A. Ajdari, *Pumping liquids using asymmetric electrode arrays*, Physical Review E 61, R45-R48 (2000).

[3] V. Studer, A. Pepin, Y. Chen, and A. Ajdari, *An integrated AC electrokinetic pump in a microfluidic loop for fast and tuneable flow control*, Analyst, 129, 944 (2004).

[4] M. Z. Bazant and Y. Ben, *Theoretical prediction of fast 3D AC electro-osmotic pumps*, Lab on a Chip, **6**, 1455 (2006).

[5] J. P. Urbanski, T. Thorsen, J. A. Levitan, and M. Z. Bazant, *Fast AC electro-osmotic pumps with non-planar electrodes*, Applied Physics Letters **89**, 143508 (2006).

[6] J. P. Urbanski, J. A. Levitan, D. Burch, M. Z. Bazant, and T. Thorsen, *The effect of step height on the performance of three-dimensional ac electro-osmotic microfluidic pumps*, Journal of Colloid and Interface Science 309, pp. 332-341 (2007).

[7] S. Ganghwal, O. J. Cayre, M. Z. Bazant, and O. Velev, *Induced-charge electrophoresis of metallo-dielectric particles*, submitted.

[8] M. Z. Bazant, M. S. Kilic, B. Storey, and A. Adjari, *Nonlinear electrokinetics at large applied voltages*, submitted. Preprint: http://www.arxiv.org/abs/cond-mat/0703035

[9] M. S. Kilic, M. Z. Bazant, and A. Ajdari, *Steric effects in the dynamics of electrolytes at large applied voltages*, Physical Review E, **75**, 021502 (2007).

THE MECHANICS OF FREQUENCY-SPECIFIC MICROFLUIDIC NETWORKS

Daniel C. Leslie[1] and Christoper J. Easley[2], James P. Landers[1], Marcel Utz[3] and Matthew R. Begley[3]

[1]*Department of Chemistry, University of Virginia, USA*
[2]*Molecular Physiology and Biophysics, Vanderbilt University Medical Center, USA*
[3]*Department of Mechanical and Aerospace Engineering, University of Virginia, USA*

ABSTRACT

This paper describes the mechanics of microfluidic networks that combine fluidic capacitors (deformable elements that store fluid) with fluidic resistors (microchannels that induce pressure changes proportional to flow rate). An elementary analysis of microchannel fluid flow illustrates the relationships between microchannel dimensions and frequency response characteristics (e.g. characteristic frequency and bandwidth). These relationships can be used to assess the potential of flow control strategies based on modulation of the excitation frequency of a single pump.

Keywords: frequency response, fluidic resistance, fluidic capacitance

1. INTRODUCTION

It has been shown that microfluidic networks can be created whose flow characteristics depend on the frequency of periodic input pressure applied to a deformable elastomer membrane [1]. Figure 1 illustrates such a network, which consists of two essential features: microchannels which introduce fluidic resistance (i.e. pressure drops proportional to flow rate), and deformable elastomer membrances which introduce fluidic capacitance (i.e. fluid storage proportional to pressure). The essential frequency-specific response of three such networks – each with membranes of different dimension (and hence capacitance) – is shown in Figure 2. Figure 2 plots the "output" pressure at the membrane which is not directly pressurized: this pressure is calculated from the membrane deflections, which were measured optically [1]. The results in Figure 2 suggest that these networks are analogous to "bandpass" filters which regulate flow amplitudes through modulation of a single excitation frequency.

This paper describes an elementary analysis of the flow/pressure characteristics of such networks, which provides the

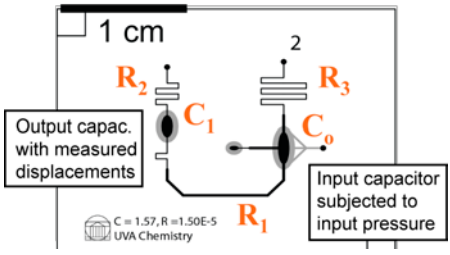

Figure 1: Layout of frequency-dependent network.

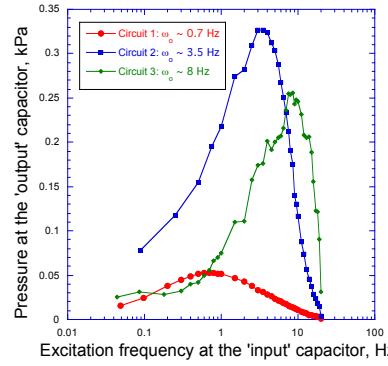

Figure 2: Measurements of pressure at output capacitor (C_1)

978-0-9798064-0-7/μTAS2007/$20©2007CBMS

foundation to quantitatively evaluate the range of possible performance of such filters. Ultimately, the goal is to combine multiple networks (each with different characteristic frequencies) with fluidic diodes [2] to achieve 'valveless' switches that regulate flow by exploiting the inherent dynamic performance of the network.

2. THEORY

The relationship between pressure drop and flow rate defines fluidic resistance, i.e. $\Delta p = Rq$, where Δp is the pressure drop along a channel, R is the fluidic resistance (a function of channel cross-section), and q is the volume flow rate. Capacitance is related to the volume change of an element as a function of pressure. If density changes are negligible, $q = C\dot{p}$, where $C = \partial V / \partial p$ and can be determined from a solid mechanics analysis of the valve film. Here, we neglect fluidic inductance, which arises from the inertia associated with moving fluid, and relates pressure drops to increases in the the flow rate: $\Delta p = L\dot{q}$, where $L = \rho A / l$: for low excitation frequencies relative to *R/L*, inductance has a negligible effect on the dynamic response of the circuit.

The circuit shown in Figure 1 is represented by the circuit shown in Figure 3. By combining these relationships between pressure changes and flow rate with a statement of mass conservation (i.e. the fluidic equivalent to Kirchoff's Law in electronic analysis), one can derive the following governing equation for the pressure acting on the 'output' capacitor (C_1):

$$m\ddot{p}(t) + c\dot{p}(t) + kp(t) = C_o \dot{p}_{in}(t) = C_o p_o \omega \cos \omega t \tag{1}$$

where the coefficients m, c and k are functions of the resistances and capacitance values introduced by the channel and membrane dimensions:

$$m = R_1 C,\ c = 1 + \frac{R_1}{R_3} + \frac{R_1}{R_2} + \frac{C}{C_o} \text{ and } k = \frac{1}{R_2 C_o}\left(1 + \frac{R_1}{R_3} + \frac{R_2}{R_3}\right) \tag{2}$$

Here, we assume a sinusoidal input pressure signal and examine steady-state harmonic behavior. The pressure amplitude at a given excitation frequency is given by:

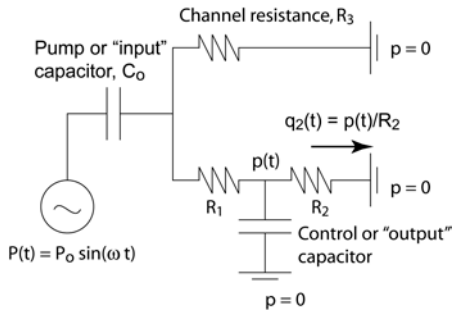

Figure 3: Equivalent circuit of the network shown in Fig. 1.

$$\Delta p(r) = 2p_o c^{-1} \cdot \xi r\left(\left(1 - r^2\right)^2 + \left(2\xi r\right)^2\right)^{-1/2} \tag{3}$$

where $r = \omega / \omega_o$, and ω_o is the characteristic frequency at which peak flow amplitude is obtained. The damping ratio ξ dictates the 'bandwidth' of the response, i.e. the frequency range over which the flow is at least half the maximum is $\Delta\omega = 2\sqrt{3}\xi$. These two characteristics are given by: $\omega_o = \sqrt{k/m}$ and $\xi = c / \left(2\sqrt{km}\right)$.

3. RESULTS AND DISCUSSION

Using resistance and capacitance values computed from elementary fluid and solid mechanics, one predicts theoretical characteristic frequencies for three circuits shown in Figure 2 that are in close agreement with the experiments: 0.8, 3.5 and 8.0 Hz. The maximum pressure amplitude at peak frequency are predicted to be 0.04, 0.6 and 0.3 kPa, as compared to the measured values of 0.05, 0.32 and 0.25 kPa (respectively). It is clear that the model is a useful design tool to identify effective combinations of channel and membrane dimensions. Comparisons between predicted and measured bandwidth are not currently feasible, due to the limited frequency range of the displacement measurement: it is clear there is an aliasing problem in the experiments, as the measured response clearly falls off at the sampling frequency of 40 Hz. These experiments are being repeated with a new system.

The circuits utilized in the experiments modulate the characteristic frequency by changing the relative dimensions of the input and output capacitors, while holding the channel dimensions fixed. The model provides the foundation to establish more effective parameter combinations, which produce identical peak flow amplitudes at different frequencies. Figure 4 illustrates the theoretical response of three circuits, wherein the flow resistances are modulated instead of the capacitances. There is strong indication that one can construct fluidic bandpass filters that exhibit prescribed and clearly distinguishable flow rates at different frequencies. Two limitations of resistor-capacitor circuits are readily apparent: first, despite the similarity with resonators, one cannot construct underdamped circuits with narrow bandwidth. Inspection of equations (1)-(3) reveals that as peak frequency is increased, the bandwidth also increases (as indicated in Figure 4). Secondly, non-linear elements such as fluidic diodes are needed to generate frequency-specific flow rates that are not oscillatory, i.e. diodes are needed to modulate the steady-flow component of dynamic response.

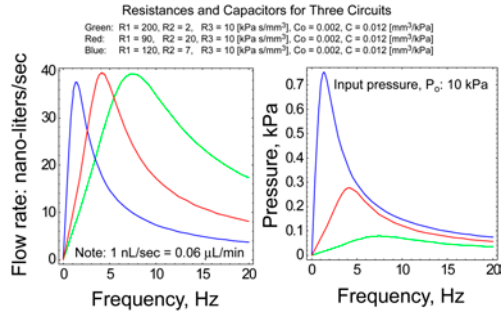

Figure 4: Examples of near optimal networks with different characteristic frequencies and narrow bandwidth.

5. CONCLUSIONS

Elementary circuit analysis, combined with straight-forward fluid and solid mechanics, can provide general and highly useful insight regarding the design of dynamic fluidic circuits; the indications are that relatively simple components can be used to generate useful frequency-specific response, which ultimately may lead to 'valveless' systems driven by a single pressure source.

REFERENCES

[1] C. J. Easley, J.M. Karlinsey, D. C. Leslie, M.R. Begley and J.P. Landers, *Directional and frequency-dependent flow control in microfluidic circuits using passive elastomeric components*, Proc. Micro Total Analysis Systems 2006, Kluwer Academic Publisher, Dordrecht, The Netherlands, pp. 1064-1066, (2006).

NONLINEAR PHENOMENA IN INDUCED-CHARGE-ELECTROOSMOSIS: A NUMERICAL AND EXPERIMENTAL INVESTIGATION

G. Soni, T.M. Squires and C.D. Meinhart
University of California, Santa Barbara, USA

ABSTRACT

Induced-charge-electroosmotic (ICEO) flow was produced on a planar micro electrode using an AC electric field with applied voltages much higher than the linear limit of Debye Huckel, 25 mV. At voltages higher than this limit, several detrimental nonlinear phenomena may take place, yielding much lower experimental slip velocities than those predicted by the linear theory of the double layer. In our experiments, the slip velocity is found to be two and a half orders of magnitude lower than those predicted by linear simulations. To over come this, we incorporate two possible nonlinear effects, namely, the nonlinear capacitance of the double layer and the surface conduction of the double layer charge. The nonlinear simulations produce lower velocities reducing the discrepancy by an order of magnitude.

Keywords: ac electroosmosis, double layer, nonlinear capacitance, surface conduction

1. INTRODUCTION

Recent applications of microfluidic devices in biology have revived the interest in the study of electrokinetic transport of ionic fluids and suspended species such as cells, DNA and proteins. AC electroosmotic flow can be utilized to create micropumps for micro-bio-chips [1]. As a result, a lot of work has been done on experimental and numerical estimation of electroosmotic slip velocities [2]. The linear theory of electrokinetics is valid only for very low driving voltages ($\phi \ll k_B T / e = 25\,\mathrm{mVolt}$) whereas the experiments are generally performed for several volts. As a result, the experiments yield much lower slip velocities than those predicted by the linear theory. This emphasizes the need for inclusion of nonlinear effects in the existing theory. Olesen et al., 2006 [3] considered presence of nonlinear capacitance of double layer along with faradaic injections in their analysis of ac electroosmotic micropumps. ICEO [4] refers to a phenomenon in which a DC or AC electric field induces charge on a polarizable surface (metal or dielectric) immersed in an ionic liquid (figure 1a), and leads to formation of electrical double layer (figure 1b). The double layer screens the induced charge yielding some tangential electric field (E_o) which sets the double layer into motion (figure 1c).

2. EXPERIMENTAL

ICEO experiments were performed in a micro-chamber with three equispaced microelectrodes on its bottom (figure 2). The chamber was filled with 1 mM KCl solution seeded with flow tracing particles utilized for microPIV measurements. An AC voltage was applied between the two outer electrodes leaving the central electrode (denoted 'gate electrode') at a floating potential. As a result, a symmetric ICEO slip profile developed on the gate electrode (figure 1c).

978-0-9798064-0-7/μTAS2007/$20©2007CBMS

3. NONLINEAR SIMULATIONS

The nonlinear electrokinetic model solves Laplace's equation for bulk potential, ϕ, in the chamber (figure 3). The chamber walls are insulated and the two outer electrodes are assigned sinusoidal and ground potentials respectively. On the central gate electrode, a PDE is solved for the double layer charge, q. The surface conduction current is characterized by *Dukhin* number, a nonlinear function of the zeta potential, ζ. Zeta potential, ζ, is calculated from q using a nonlinear capacitance formula (figure 3). This value of ζ is then used for calculating the bulk boundary condition on the gate electrode. Finite element simulations were performed in COMSOL multiphysics version 3.3 (Stockholm, Sweden).

4. RESULTS AND DISCUSSION

Experimentally measured slip velocity has been compared with the linear and the nonlinear simulation results (figure 4). The experimental values are two and a half orders of magnitude smaller than the linear values but only one and half orders smaller than the nonlinear values (figure 4). This indicates that the nonlinear phenomena have a detrimental effect on the slip velocity. The detrimental impact of nonlinear phenomena can be understood by plotting ζ, on the central electrode (figure 5). The two said nonlinear phenomena cause significant loss both in ζ and in the tangential electric field, E_x, leading to a larger cumulative loss in the slip velocity as the slip velocity is proportional to the product of ζ and E_x.

5. CONCLUSIONS

For high voltages, the linear theory predicts slip velocities two and half order of magnitude higher than the experiments. Incorporation of nonlinear capacitance and surface conduction helps reduce this discrepancy by an order of magnitude. However, these nonlinear effects do not eliminate the discrepancy completely. A large difference still exists and opens up the scope for other nonlinear effects.

ACKNOWLEDGEMENTS

This work was supported by the US army research office.

REFERENCES

1. Ajdari, A., *Pumping liquids using asymmetric electrode arrays.* Physical Review E, 2000. **61**(1): p. R45-R48.
2. Green, N.G., et al., *Fluid flow induced by nonuniform ac electric fields in electrolytes on microelectrodes. III. Observation of streamlines and numerical simulation.* Physical Review E, 2002. **66**(2): p. 11.
3. Olesen, L.H., H. Bruus, and A. Ajdari, *ac electrokinetic micropumps: The effect of geometrical confinement, Faradaic current injection, and nonlinear surface capacitance.* Physical Review E, 2006. **73**(5).
4. Squires, T.M. and M.Z. Bazant, *Induced-charge electro-osmosis.* Journal of Fluid Mechanics, 2004. **509**: p. 217-252.

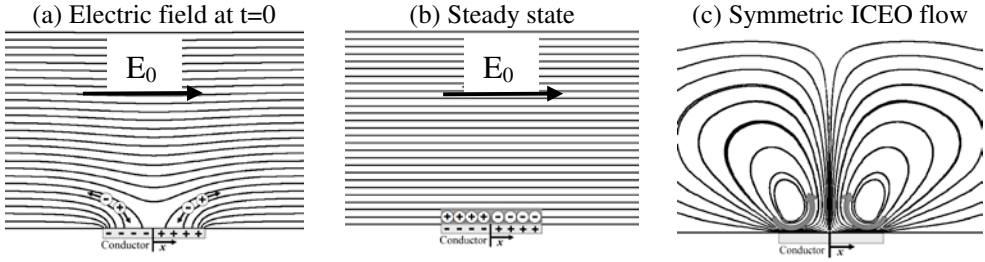

Figure 1: ICEO flow on a flat conducting surface

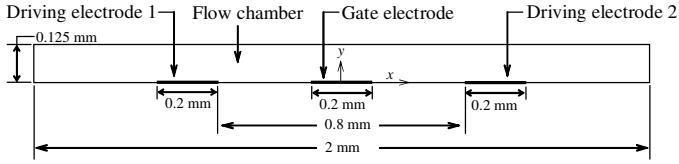

Figure 2: Cross section of the ICEO flow chamber

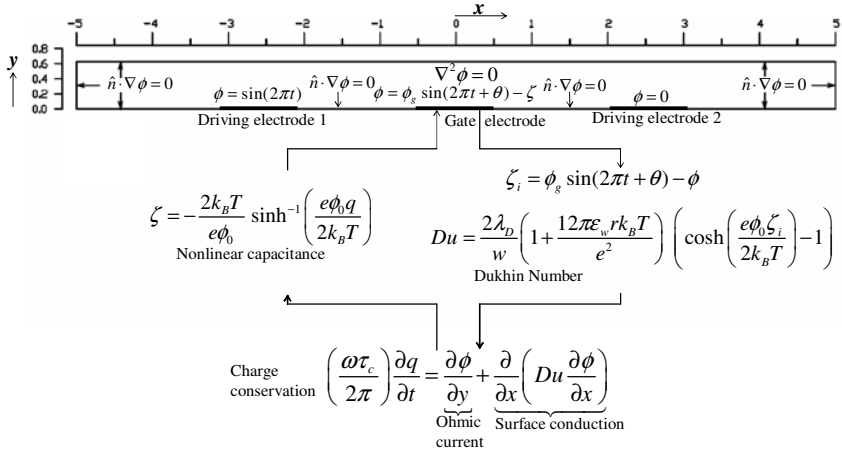

Figure 3: Nondimensional model with surface conduction and nonlinear capacitance

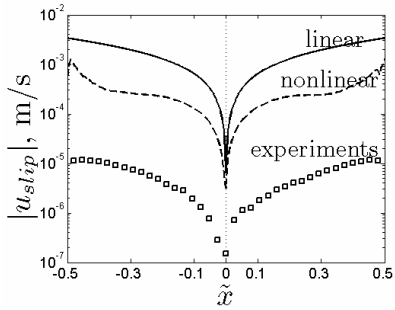

Figure 4: Slip speed on the gate for 9 Volt (amplitude) at 163 Hz

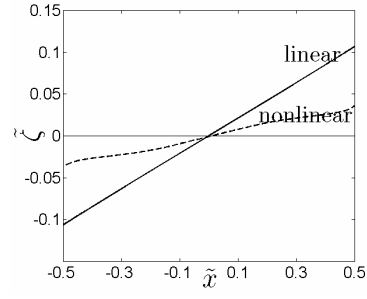

Figure 5: Nondimensional peak ζ on the gate for 9 Volt at 163 Hz

SURFACE ACOUSTIC WAVE μSTREAMING TO ENHANCE BIOSENSING IN A DROPLET-BASED μTAS PLATFORM

Olivier Ducloux[1] Elisabeth Galopin[1] Jean-Christophe Camart[1]
Vincent Thomy[1] and Farzam Zoueshtiagh[2]
[1] *IEMN – Institut d'Electronique, Microélectronique et Nanotechnologie, FRANCE*
[2] *LML – Laboratoire de Mécanique de Lille, FRANCE*

ABSTRACT

This paper describes a droplet based microTAS platform involving biosensing performance enhancement by integrated Surface Acoustic Wave streaming. Such a system allows an important decrease of the response time by bringing fresh analyte to the sensing surface. Performance improvement has been pointed out using speed carthographies and finite element simulation.

Keywords: surface acoustic waves, streaming, droplet, biosensing enhancement

1. INTRODUCTION

It has been recently pointed out that μfluidic nanobiosensing performances can be limited in both response time and sensitivity by the diffusion of the analyte species near the sensing surface [1]. In the case of low Peclet number hydrodynamic flows, individual molecule displacements are mainly governed by diffusive effects. Reaction rate are then mass transport limited, affecting time scales and sensitivity. To overcome this problem in integrated systems, enhancement of biosensors activity by electrothermal stirring within μchannels has been reported by Meinhart et. al. [2]. However, encapsulated devices present some disadvantages in liquid handling (such as dead volumes, important pressure drop, irreversible encapsulation…) that digitalized μfluidics can overcome.

The use of Surface Acoustic Wave (SAW) in microfluidic systems is currently being increasingly investigated [3], especially for the enhancement of liquid/surface interaction [4]. In this paper, we present a droplet-based μTAS platform integrating a SAW based microstirring layout. We show that such a technology can be adapted to obtain reproducible vortex-like circular flows with a controlled flow speed. The system permits the enhancement of the biosensing performances by the continous renewal of the analyte-carrying fluid near the sensing surface. Mean flow speeds up to 1800 μm/s have been measured, permitting the adaptation to a large set of analyte/ligand interactions.

First, we present the SAW-based micromixing layout and its characterization. Then, a FEM simulation of the enhanced biosensing performances within a SAW bioreactor is described.

2. SAW GENERATION

Rayleigh surface acoustic waves are generated using interdigitated transducers (IDT) laid on a X-cut LiNbO3 substrate, with an interdigit of 50 μm. Such waves are radiated on one half of the studied microchambers consisting in microliter droplets situated between a hydrophobic substrate and a cover. Fluid flow results from the absorption of the

978-0-9798064-0-7/μTAS2007/$20©2007CBMS

longitudinal pressure wave radiated into the droplet under the Rayleigh angle θ, as shown in Figure 1.

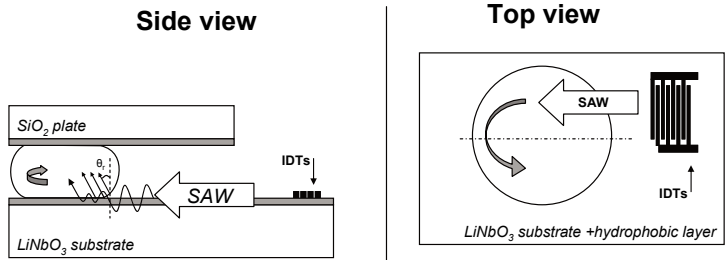

Figure 1. SAW propagation at the substrate/ µdroplet interface side view (a), top view (b).

Speed cartographies are realized within the droplet using the Particle Image Tracking technique for different SAW generation powers. Instantaneous images of the flow are taken with a high-speed video camera (240 frames per second, 500µs aperture time) on 0,25 µl droplets containing 1µm diameter fluorescent particles. The resulting speed cartographies shown in Figure 2 show that the mean stirring speed is greatly dependent on the inlet power.

(a)

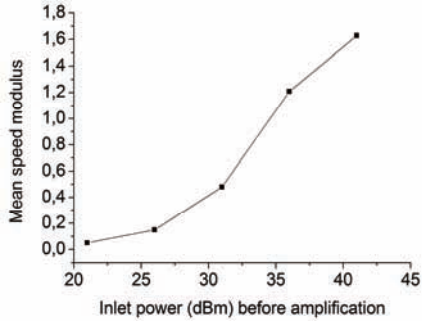

(b)

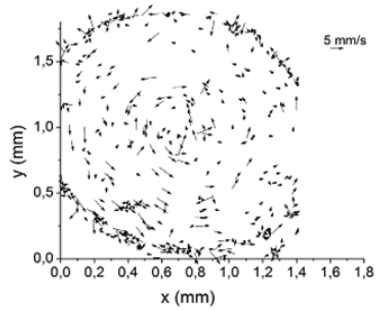

Figure 2. (a) Mean value of the measured speeds within the droplet as a function of the inlet power before amplification (b) exemple of speed cartography for 41 dBm inlet power

3. BIOSENSING ENHANCEMENT

Comsol numerical simulations were undertaken to show the efficiency of the SAW stirring in the case of a cylindrical microbioreactor of 1mm diameter (cf. Figure 3).

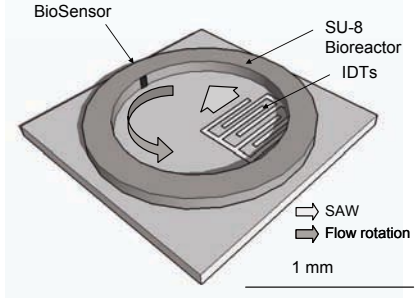

Figure 3. General layout of the simulated bioreactor. SAW stirring, provided by the IDT allow a one vortex like stirring of the analyte-carrying fluid

Supposing the flow to be 2D, the simulated model takes into account the convective and diffusive effects in the analyte carrying fluid and the binding kinetics on the biosensor surface.

Results show that a depleted zone is formed near the biosensor in the case of an interaction without stirring. Sensing performances are then limited by the diffusion of the analyte from the center towards the peripheral layer. Thanks to the stirring, the depleted zone is transformed in an analyte-poor layer on the vicinity of the biosensor perimeter.

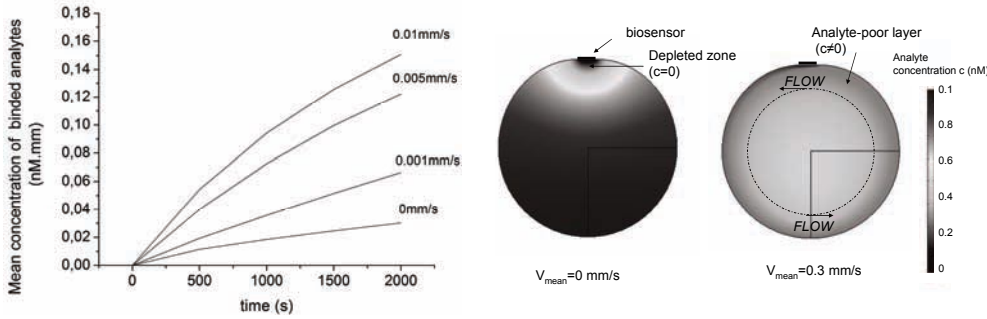

(a) (b)

Figure 4. Mean concentration of bound analytes vs. time for different mean flow speeds (a). Obtained concentration profiles with and without circular stirring, t=10000s (b).

Initial analyte and receptor concentrations are respectively 0.1 nM and 3.3 10-3nM m, diffusion coefficient is D=10-11 m²s-1 and reaction constants are kon=106 M-1s-1, koff=10-3s-1. Simulations show that the mean concentration of bound analytes highly increases with the flow speed, improving the efficiency of the biosensing device. These results are presented in Figure 4.

4. CONCLUSIONS

We show in this paper that surface loading of typical analytes on a droplet-based biosensor can be highly increased by the help of surface acouctic wave microstirring. In addition to the yield biosensing performance improvement, such a method is highly integrable on microTAS systems, which makes it a convenient tool for liquid handling in future biochips.

REFERENCES

[1] P. Nair and A. Alam, *Performance limits of nanobiosensors*, Applied Physics Letters, 88, 233120 (2006).

[2] M. Sigurdson, D. Wang, C. D. Meinhart, *Electrothermal stirring for heterogenous immunoassays*, Lab Chip, 5, pp. 1366-1373 (2005).

[3] A. Wixforth, C. Strobl, Ch. Gauer, A. Toegl, J. Scriba, Z. Guttenberg, *Acoustic manipulation of small droplets*, Anal. Bioanal. Chem., 379, 982 (2004).

[4] E. Galopin, A. Renaudin, V. Thomy, J.C. Camart, P. Tabourier, C. Druon, *Enhanced protein capture by ultrafast SAW droplet µmixing*, MicroTAS'06, pp. 651-653 (2006).

THEORETICAL AND EXPERIMENTAL INVESTIGATION OF THE VALVELESS MICROPUMP WITH A LEAKAGE BARRIER

Il-Han Hwang, Byung-Phil Moon, Sang-Mo Shin and Jong-Hyun Lee

MEMS Lab., Dept. Mechatronics, GIST, South Korea, jonghyun@gist.ac.kr

ABSTRACT

The valveless micropump is one of the essential components in self-contained microfluidic systems to handle the liquid volume precisely in Lab-on-a-Chips (LoCs). However, conventional valveless micropumps are susceptible to leakage flow even at low-pressure differences between the inlet and the outlet because the channels are normally open. In this paper, a leakage barrier was suggested in the chamber of the valveless micropump to reduce leakage flow without interfering the flow rectification. The coupled dynamic equations for the flow and the diaphragm oscillation were obtained and numerically analyzed to predict the flow characteristics of the valveless micropump, which matched well with the experiment results.

Keywords: Micropump, leakage barrier, valveless, diffuser, PZT

1. INTRODUCTION

Recent technical progress in microelectromechanical systems (MEMS) has been incorporated into design and fabrication of biomedical and chemical devices [1]. These devices deal typically with microfluid for system operation. To handle small volume of liquid precisely, the micropump is one of the essential components in self-contained microfluidic systems [2]. Among many types of micropumps, valveless micropumps have great advantages such as simple structures and easy fabrication for the application to LoCs [3]. However, conventional valveless micropumps are susceptible to leakage flow even at low pressure difference between the inlet and the outlet because the channels remain normally open state when the pumps are not in operation.

In this paper, a leakage barrier was suggested in the chamber of the valveless micropump to reduce leakage flow without interfering the net positive flow of the diffuse/nozzle channels. To estimate the actuation force of PZT driving, the theoretical analysis of the membrane deflection was performed. The coupled dynamic equations for the flow and diaphragm oscillation were obtained and numerically analyzed to predict the flow characteristics of the valveless micropumps. The simulation results were compared with the experimental results.

2. OPERATION PRINCIPLE

The operation principle of valveless micropumps with a leakage barrier is shown in Figure 1. Due to the higher flow resistance of the nozzle, more liquid flows through the diffuser than the nozzle generating the net positive flow toward the outlet. Figure 2 shows

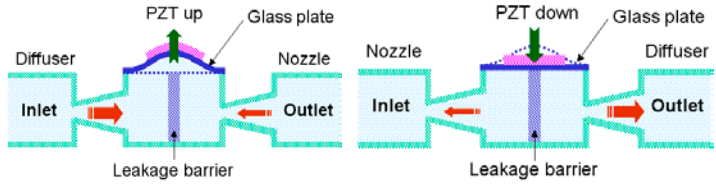

(a) PZT up (b) PZT down

Figure 1. Schematic of the valveless micropump with a leakage barrier for low leakage flow.

978-0-9798064-0-7/μTAS2007/$20©2007CBMS

the configuration of the suggested valveless micropump with a leakage barrier. The channels and the chamber were fabricated on the silicon substrate by KOH etching (80 μm deep) and the glass plate (200 μm thick) was anodically bonded with the silicon substrate. A separation layer of Ti/Au (30 nm/3 nm) was deposited on the surface of leakage barrier to prevent the bonding of the glass with the leakage barrier. PZT disk (8mm diameter) was bonded on the glass plate by epoxy. The chamber diameter and the width of the leakage barrier were designed at 12 mm and 0.5 mm, respectively. Figure 3 shows the fabricated valveless micropump with a leakage barrier.

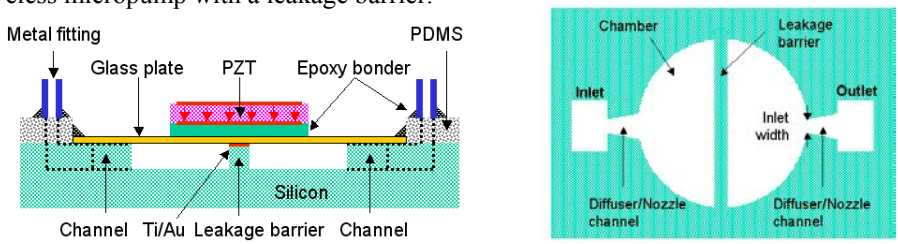

(a) the side view (b) the front view

Figure 2. Configuration of the valveless micropump with a leakage barrier.

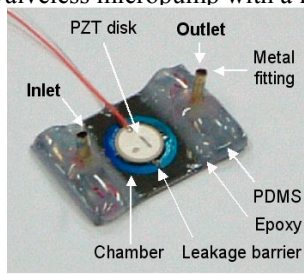

Figure 3. Photo image of the fabricated valveless micropump with a leakage barrier.

3. THEORETICAL/EXPERIMENTAL ANALYSIS

Figure 4 shows simulation results for water with the sine voltage input to PZT disk. The peak-to-peak (V_{pp}) voltage was 150 V at 225 Hz as shown in Figure 4(a). Figure 4(b) shows the net positive flow at the outlet. The flow rate experiments were performed for the valveless micropump with and without a leakage barrier. Figure 5 shows their experiment and simulation results with V_{pp} of 150 V. In numerical simulations, the leakage barrier was modeled as an internal pressure loss in the chamber; however, it generated a small decrease in flow rate compared to the conventional pump. The optimum frequency was measured at around 225 Hz for the flow rate of around 6.75 μL/min, which was close to the simulation results. Figure 6 shows the experimental results of leakage flow with the pressure at the inlet higher than the outlet by 600 Pa. Leakage flow could be reduced by more than 5 times compared to the micropump without a leakage barrier. Leakage flow was reduced further by applying the holding voltage to reduce the gap between the plate and the leakage barrier.

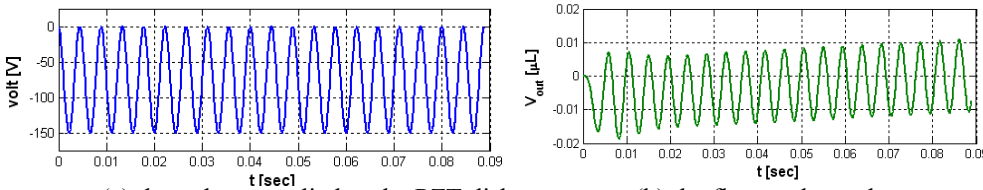

(a) the voltage applied to the PZT disk (b) the flow at the outlet

Figure 4. Numerical analysis for the transient response of the valveless micropump with V_{pp} of 150 V at 225 Hz.

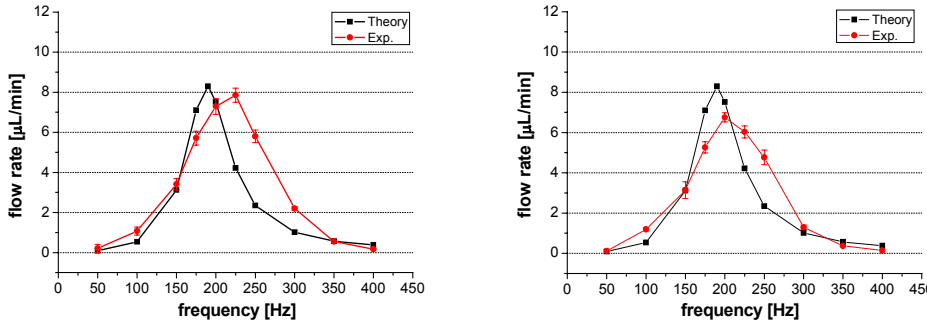

Figure 5. Experimental results of the flow rate with V_{pp} of 150 V: (a) without a leakage barrier and (b) with a leakage barrier.

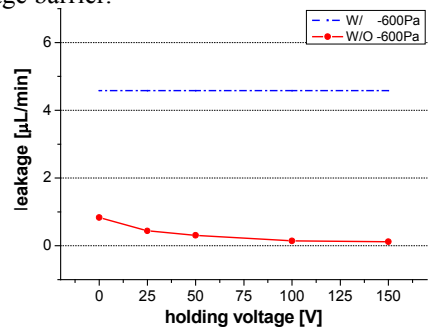

Figure 6. Experimental results of leakage flow for the valveless micropump with and without the leakage barrier at the pressure difference of 600 Pa.

4. CONCLUSION

A novel valveless micropump was proposed with a leakage barrier in the chamber to reduce leakage flow without interfering the net positive flow of the diffuse/nozzle channels. To estimate the flow characteristics, theoretical analysis of the flow characteristics was performed. At V_{pp} of 150 V, the maximum flow rate of around 6.75 μL/min was obtained at 225 Hz in experiments, which was close to the flow rate estimated by the numerical simulations. Leakage flow was decreased by around 5 times compared to the conventional valveless micropump without a leakage barrier. Leakage flow could be reduced further by applying the holding voltage to the PZT disk to decrease the gap between the membrane and the leakage barrier.

ACKNOWLEDEGMENT

This work was supported by the Center for Distributed Sensor Network (CDSN) at GIST, Korea.

REFERENCES

[1] C. Ahn, et al., *Disposable smart lab on a chip for point-of-care clinical diagnostics*, Proceedings of IEEE, vol. 92, no. 1, pp. 154-173, (2004).
[2] S. Yang, et al., *A microfluidic device for continuous, real-time blood plasma separation*, Lab on a Chip, vol. 6, pp. 871-880, (2006).
[3] D. J. Laser, et al., *A review of micropumps*, J. Micromech. Microeng., vol. 14, pp. 35-64, (2004).
[4] A. Olsson, et al., *A valve-less planar pump isotropically etched in silicon*, J. Micromech. Microeng., vol. 6, pp. 87-91, (1996).

A NEW MICROPUMPING PRINCIPLE BY ACOUSTICALLY EXCITED OSCILLATING BUBBLE

Kyungjoo Ryu, Sang Kug Chung, and Sung Kwon Cho*

Department of Mechanical Engineering and Materials Science, University of Pittsburgh, USA

ABSTRACT

This paper describes a recently discovered pumping principle using a micro oscillating bubble excited by an acoustic wave. A maximum flow rate of 0.25 μl/s and a maximum pressure generation of 67 Pa have been achieved through a micro capillary tube in non-optimized configurations.

Keywords: Oscillating Bubble, Micro Pump, Acoustic Streaming

1. INTRODUCTION

Since gaseous bubbles in liquid are compressible, they oscillate (expand and shrink) in the presence of acoustic waves, thus generating strong circulating flows (Fig. 1) around them, which is called "acoustic streaming". Recently, increasing attention to oscillating bubbles has spawned many potential applications such as ultrasonic imaging contrast agents, drug carriers, micro fluid steering, cell deformation/lysis [1], vortex generator and micro particle carrier [2, 3]. However, to authors' knowledge, fluid pumping through capillary tubes using oscillating bubbles has never been reported to date.

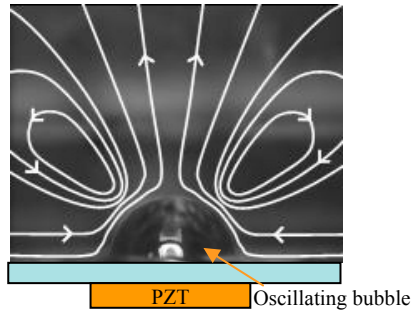

Fig. 1 Streamlines of acoustic streaming. The bubble is acoustically excited at its resonance frequency, and as a result vortical flows are generated around the bubble.

2. PRESSURE GENERATION AT ZERO FLOW RATE

The key concept of the present pumping principle is to collect only upward flows in the acoustic streaming into a straight or U-type capillary tube. To do so, we placed a capillary tube above the center of the capped bubble sitting on the solid surface, varying the distance (δ) between the tube inlet and the substrate surface (Fig. 2a). An acoustic wave was applied to the bubble by a piezoelectric disk actuator mounted underneath the testing chamber. The applied frequency was set at the resonance frequency of the bubble (4 kHz) in all the testing conditions to maximize bubble oscillation.

In order to examine how much the pressure can be generated by an oscillating bubble, the inlet of a straight capillary tube is placed above the bubble in water with its outlet open to the atmosphere (Fig. 2a). We observed a change in curvature of the top meniscus and a slight water level rise when the bubble is acoustically excited (Fig. 2b, c). Since this

978-0-9798064-0-7/μTAS2007/$20©2007CBMS

configuration is a zero-flow rate state, the total water weight in the tube is balanced with the surface tension plus the pressure generation by bubble oscillation. By measuring the height of rise Δh and the radius of curvature R, the maximum pressure generated by the oscillating bubble is measured at 67 Pa. Here the inner diameter of capillary tube D is 1 mm, the bubble base diameter r 1.6 mm, and the distance between the inlet and the substrate surface δ 0.6 mm.

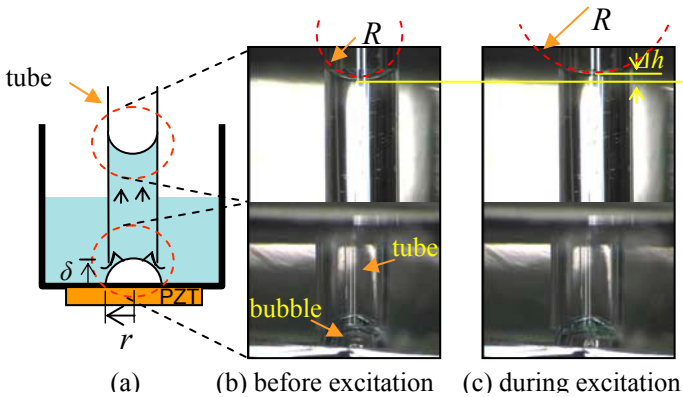

Fig. 2 Pressure generation in a zero flow rate condition. ***(a)*** *Experimental setup of bubble pump. A capillary tube is placed above the oscillating bubble to collect only upward flows in acoustic streaming* ***(b)*** *Before acoustic excitation.* ***(c)*** *During acoustic excitation, the curvature of the top meniscus inside the tube decreases with a slight increase in water height, showing the excited bubble generating a pressure.*

3. MICRO PUMPING

We measured the flow rate through capillary U-type tubes, of which both ends were immersed in a reservoir (Fig. 3a), by tracing seeded microparticles in the tubes. From sequential images of particle tracing in Fig. 3c, it is clearly confirmed that the oscillating bubble can pump the liquid into the capillary tube. In this pumping configuration, many parameters such as the tube diameter D and the distance δ come into play on the flow rate.

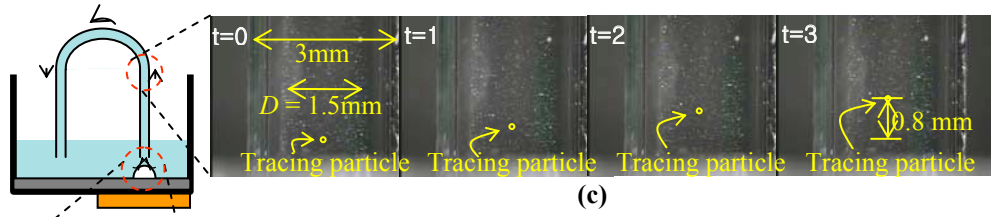

Fig. 3 Flow generation by bubble pump ***(a)*** *Experimental setup of bubble pump. The inlet of the U-tube is placed above the oscillating bubble while the outlet is immersed in the water reservoir.* ***(b)*** *Configuration of the tube inlet and bubble. The bubble diameter is 1.6 mm and the tube inner diameter is 1.5 mm.* ***(c)*** *Particle were seeded and traced to measure the flow velocity and the flow rate in the tube. The measured flow rate in the tube is 0.24 µl/s.*

Figure 4 shows the flow rate (velocity) vs. the inner tube diameter D. As D increases, the flow velocity in the tube decreases. However, the flow rates are comparable among the three different diameters. The effect of the distance δ on the flow velocity was also investigated (Fig. 5). As the distance δ increases, the velocity monotonically decreases. The assumption of the Poiseuille flow in the tube allows calculation of the pressure drop at the corresponding velocity, which also monotonically decreases as the distance δ increases (Fig. 6). When the bubble was in contact with the tube rim, the velocity as well as pressure drop were maximized.

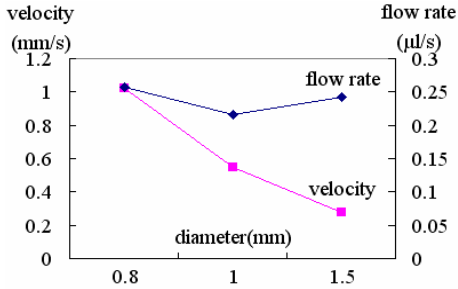

Fig. 4 The effect of the inner diameter of the tube on velocity and flow rate. In all cases, bubbles are in contact with the tube inlet rim.

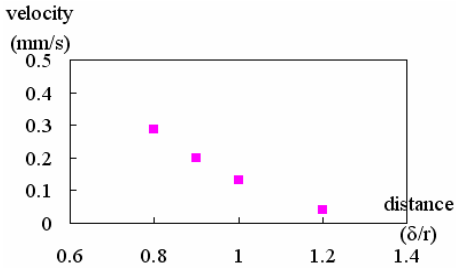

Fig. 5 The effect of the vertical position of the tube inlet (δ /r) on the velocity. When δ /r = 0.8 (the bubble is in contact with the tube rim), the velocity is maximum.

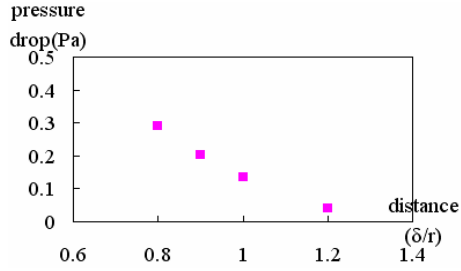

Fig. 6 Pressure drop in the tube. The data were reproduced from Fig. 5 based on the Poiseuille flow assumption in the U tube.

4. CONCLUSION

The present new pumping principle generates a maximum flow rate of 0.25 μl/s and a maximum pressure generation of 67 Pa with neither mechanical moving parts nor wiring for signal and power inputs, implicating potential applications for implantable drug releasing agents or pumps which can be easily switched on and off by a remote acoustic source.

ACKNOWLEDGEMENTS

The work was supported by the National Science Foundation (NSF ECS-0601470).

REFERENCES

[1] P. Marmottant and S. Hilgenfeldt, *Controlled vesicle deformation and lysis by single oscillating bubbles*, Nature, **23**, pp.153-156, (2003).

[2] Y. Zhao and S. K. Cho, *Micro Bubble Manipulation by Electrowetting on Dielectric: transporting, splitting, merging and eliminating of bubbles*, Lab Chip, **7**, pp.273-280, (2007).

[3] S. K. Chung, Y. Zhao, U.-C. Yi and S. K. Cho, *Micro Bubble Fluidics by EWOD and Ultrasonic Excitation for Micro Bubble Tweezers*, MEMS 2007 Conference, pp.31-34, (2007).

AC ELECTROKINETIC ENHANCEMENT FOR BIOSENSORS

Marin Sigurdson, Hope Feldman and Carl Meinhart
University of California, Santa Barbara, USA

ABSTRACT

A device is developed to improve binding rates in heterogeneous immunosensors by augmenting diffusive transport with microstirring. AC electric fields generate fluid motion through electrothermal forces on the fluid. The resulting circulation redirects or stirs the fluid, providing more binding opportunities between suspended and wall-immobilized molecules. Experiments and numerical simulations show up to a 9-fold increase in bound concentration with this microstirring.

Keywords: AC electrokinetics, electrothermal, immunoassay

1. INTRODUCTION

AC electric fields have previously been used in fluid suspensions to trap or redirect particles through dielectrophoresis [1], and to pump low conductivity fluid with electroosmotic forces [2]. This device, however, exploits a force that is effective in high conductivity buffer, the electrothermal force. Joule heating produces temperature inhomogeneities and therefore temperature-dependent conductivity and permittivity inhomogeneities, which interact with the applied electric field to produce fluid motion, typically in circulation patterns. Because the electric field is alternating, electrolysis can be avoided even in high conductivity solutions. Additionally, because the flow is driven by Joule heating, the electrothermal force scales with fluid conductivity, a characteristic which makes this technique well suited for reactions in buffers of physiological conductivity and higher. Electrothermal microstirring has been measured and described by Ramos et al [3], investigated numerically for biosensor enhancement by the authors [4], and combined with dielectrophoresis for virus capture by Docoslis et al [5].

2. MICROSTIRRING DEVICE AND EXPERIMENTS

The microstirring device (Fig. 1) consists of a silicon base with two parallel metal electrodes separated by 60 μm; a 165 μm thick Parafilm gasket which defines the 4mm x 4mm reaction cavity, and a glass coverslip. In our test assay, fluorescently labeled streptavidin in a phosphate buffer (1.0 Sm^{-1}) binds to biotin patterned on the base. The electrodes are driven at 10 V_{rms} and 200 kHz. The reaction is allowed to proceed for durations between 1 and 15 minutes. Bound concentration is assessed through measurement of fluorescent intensity with a CCD camera and epi-fluorescent microscope. Both microstirred binding ($B_{stirred}$) and non-stirred binding (B_{static}, taken far from the electrodes) are measured, and their ratio, the *Binding Enhancement Factor*, is reported in Fig. 2. Electrothermal microstirring increased binding for the longer test durations by nearly an order of magnitude.

978-0-9798064-0-7/μTAS2007/$20©2007CBMS

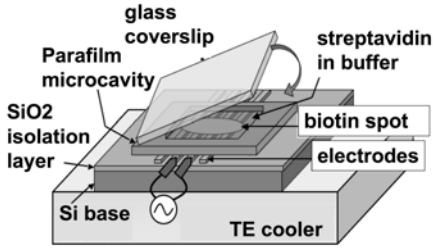

Figure 1. Microfabricated electrodes (separated by 60 μm) generate electrothermal microstirring to allow more binding opportunities. The thermally conductive silicon base, together with the thermostated thermoelectric cooler, allows precise control of thermal gradient that drives the flow. The reaction microcavity, defined by the Parafilm gasket, is 4mm x 4mm x 165 μm.

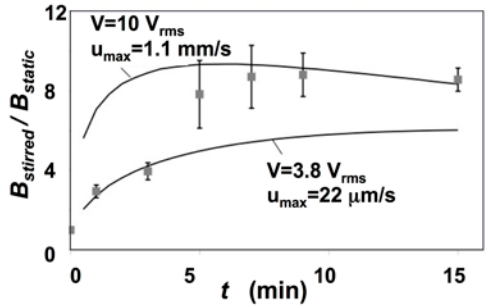

Figure 2. Binding Enhancement factor ($B_{stirred}$ /B_{static}); numerical simulations (solid lines) and experimental measurement (squares). Because measured velocity magnitude differs significantly from numerically predicted velocity, simulation results are shown both for actual potential (10Vrms) and reduced potential which corresponds to measured velocity (22 μm/s). Experimental results show electrothermal microstirring increases binding by up to a factor of 9.

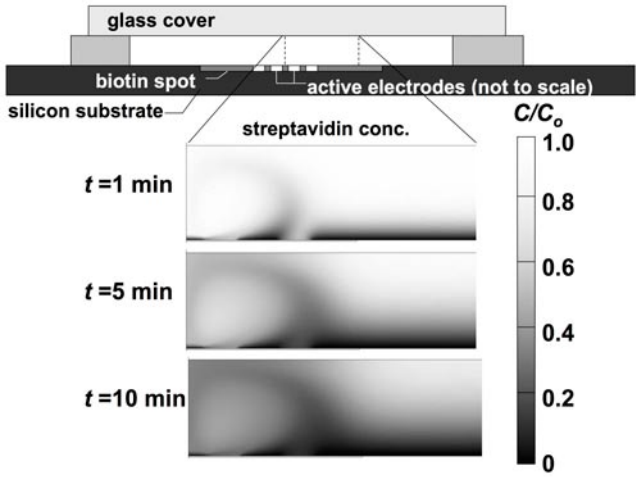

Figure 3. Numerical model of analyte concentration within the microcavity. Concentration is depleted at the wall through specific binding with immobilized biotin. Above the electrodes (left side of figure), electrothermal microstirring circulates this depleted concentration away. Near the electrodes, the binding rate is therefore increased, compared with the static region (right side of figure) where streptavidin can only reach the binding surface through diffusion. Cavity height is 165 μm.

3. SIMULATIONS

A 2-D numerical model of the electric, temperature, velocity, and analyte concentration fields was developed [4]. Fig. 3 shows the concentration of streptavidn in the microcavity subject to convection through electrothermal microstirring and depletion through binding at the wall. The circulation pattern formed by the electrothermal flow draws depleted concentration away from the binding region, and circulates fresh analyte back in. The model velocity simulation, while agreeing with experimental measurements on how velocity varies in space, and with several other parameters, significantly overpredicts velocity *magnitude* in each case. The source of this discrepancy is under investigation, therefore binding simulation results based on both velocity extremes – numerically predicted and experimentally measured – are reported on the binding improvement plot (Fig. 2). Nonetheless, the model can be a helpful tool in device optimization. Simulations suggest that reducing the interelectrode gap from 60 μm to 2 μm can as much as double the binding rate. With this modification, we expect electrothermal microstirring to increase bound concentration by well over an order of magnitude.

4. CONCLUSIONS

Experimental measurements have shown that electrothermal microstirring can increase binding in diffusion limited heterogeneous immunoassays by a factor of 9; numerical simulations suggest improvement may be considerably more with optimization. This can significantly decrease test time in microTAS devices, and is adaptable to microfluidic as well as microarray formats.

ACKNOWLEDGEMENTS

This work is supported by the Institute for Collaborative Biotechnologies through grant DAAD19-03-D-004 from the US Army Research Office.

REFERENCES

[1] X. Hu, P. Bessette, J. Qian, C.D. Meinhart, P. Daugherty, and T. Soh, "Marker-specific sorting of rare cells using dielectrophoresis", *Proc. of the Natl. Acad. Sci*, USA, 2005, **102**(44), 15757-15761.

[2] T. Squires and M.Z. Bazant, "Induced-charge electro-osmosis", *J. Fluid Mech*., 2004, **509**, 217-252.

[3] A. Ramos, H. Morgan, N.G. Green, and A. Castellanos, "Ac electrokinetics: a review of forces in mircroelectrode structures", *J. Phys. D: Appl. Phys*., 1998, **31**, 2338-2353.

[4] M. Sigurdson, D. Wang, and C.D. Meinhart, "Electrothermal stirring for heterogeneous immunoassays", *Lab on a Chip*, 2005, **5**, 1366-1373.

[5] A. Docoslis et al, "Using Nonuniform Electric Fields To Accelerate the Transport of Viruses to Surfaces from Media of Physiological Ionic Strength," *Langmuir* **2007,** *23,* 3840-3848.

EWOD STABILIZATION OF TWO LIQUID STREAMS ALONG A MICROCHANNEL AND EHD-INDUCED ENHANCEMENT OF INTERFACIAL MASS TRANSFER

Y. Ishida[1], L. Davoust[2], A. Glière[1], J. Gratier[1] and N. Sarrut[1]
[1] *CEA – LETI, MINATEC, 17, rue des Martyrs, 38054 Grenoble cedex 9, FRANCE*
[2] *CNRS, LEGI, BP 53, 38041 Grenoble cedex 9, FRANCE*

ABSTRACT

This paper presents a new micro-device for liquid-liquid extraction in which two immiscible liquids flow in parallel along a microchannel located after a T-junction. Two electrical phenomena, electrowetting on dielectrics (EWOD) and electrohydrodynamics (EHD), respectively allow for the stabilization of the meniscus between the two liquid streams and the enhancement of interfacial mass transfer.

Keywords: Electrowetting, Electrohydrodynamics, Interface, Micro-extractor

1. INTRODUCTION

A large number of microchips using both microfluidic and electrical fluid control for performing chemical analyses have been demonstrated. For instance, electrical processes have been used for handling reagents, dispensing liquid samples, separating or transferring chemical species [1]. This paper presents a new micro-device for liquid-liquid extraction in which two immiscible liquids flow along a micro-channel located after a T-junction. Our approach to enhance mass transfer differs from usual strategies developed in the literature [1, 4-7] since both electrohydrodynamics (EHD) [2] and electrowetting on dielectrics (EWOD) [3] are involved. The top and bottom walls of the micro-channel are made of ITO-coated glass and silicon, respectively. The side walls are made of dry resin (Ordyl, Elga Europe). The whole inner surface of the channel is hydrophobically coated.

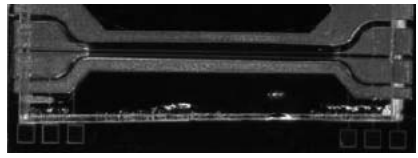

Figure 1. A snapshot of the micro-extractor.

3. EWOD STABILIZATION

Chemical transfer in integrated microfluidic devices strongly depends upon the possibility to stabilize fluidic streams in microchannels. The stability of the meniscus separating liquid streams is usually dictated by their internal geometry and the pressure heads applied between the ends of the channels. Here, by properly designing the microchannel manifold, one provides EWOD stabilization of the interface using a simple voltage-control circuit (Figures 1, 2, 5a). A gold electrode is patterned on one half of the microchannel silicon substrate and then covered with a thin dielectric film. The contact line at the bottom of the meniscus is electrically pinned and Laplace jump pressure is balanced by capillary and electrostatic pressure. It is thus possible to stabilize the location of the liquid-liquid interface during microchannel filling (Figure 3). When EWOD actuation is turned off, the water/cyclohexane interface is proven to be unstable and a plug flow arises.

978-0-9798064-0-7/μTAS2007/$20©2007CBMS

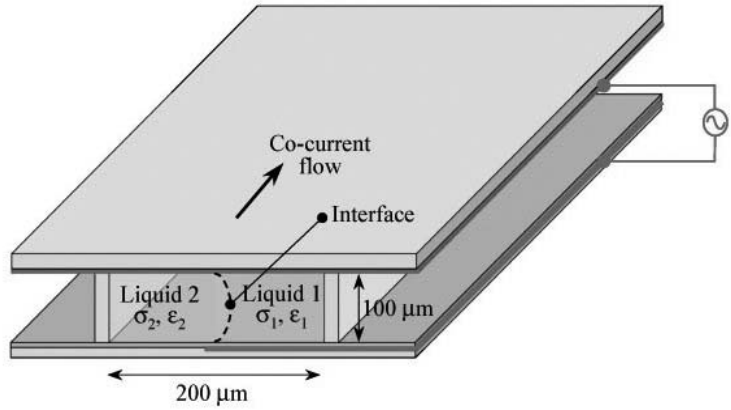

Figure 2. Geometry of the micro-extractor as sketched. Both liquids are in contact with the top electrode while the half-width bottom electrode is buried under a thin dielectric film.

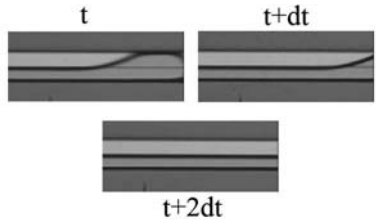

Figure 3. EWOD stabilization of the liquid streams (cyclohexane/colored water) along the micro-channel observed through the transparent top electrode during filling process.

4. EHD-INDUCED MIXING

Interfacial EHD is used to enhance mass transfer across the meniscus. Here, mixing within the micro-extractor typically occurs by the interplay of molecular diffusion and EHD-driven convection at the interface. In usual applications, the Schmidt number is so large that even a weak convective flux is capable of enhancing significantly interfacial mass transfers. Considering the approximation of electro-quasistatics in moving fluids and assuming that the Ohmic current is much larger than the displacement current, it can be shown that the only non-vanishing electric charges accumulate at the liquid-liquid interface, provided the dielectric permittivities of the liquids are different. The bottom electrode occupies only one half of the cross-section whereas the upper electrode is standing all over the channel. Therefore, the electric field at the interface exhibits both tangential and normal components responsible for the arising of a tangential electric stress along the interface. This surface electric stress balances a viscous stress and this gives rise to a recirculating fluid motion within the bulks. By considering that the ratio of the EHD velocity to the axially pressure-driven velocity is a small number, a perturbation technique is carried out, which allows for calculating the axial flow independently of the EHD recirculating motion, provided that the electric Reynolds number remains small. EHD-induced mixing is shown in figures 4 and 5b when the interface is perfectly plane or curved. Regarding mixing efficiency, a realistic situation is proposed with a 70° wetting angle and an AC voltage whose peak amplitude and frequency are 50V and 3 KHz.

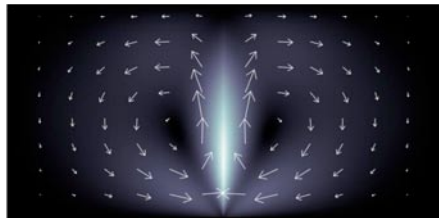

Figure 4. EHD recirculating flow when a perfectly plane liquid-liquid interface is assumed. The velocity module is represented by the background grayscale colormap. (max. velocity: 0.0175 mm/s, applied bias: 50V, frequency: 3 KHz).

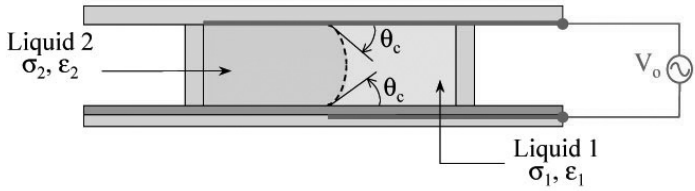

Figure 5a. The case of a EWOD-driven meniscus with a wetting angle θ_c=70°.

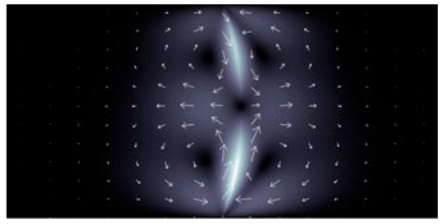

Figure 5b. EHD vortices as computed with the curved meniscus sketched in Figure 5a. The velocity scales favorably (max. velocity: 0.16 mm/s, applied bias: 50V, frequency: 3 KHz).

REFERENCES:

1. L. Dongquing, Electrokinetics in microfluidics, Elsevier (2007)
2. J.R. Melcher & G.I. Taylor, Electrohydrodynamics: a review of the role of interfacial shear stresses, Ann. Rev. Fluid. Mech, 1, 111 (1969)
3. Y. Fouillet, D. Jary, A.G. Brachet, J-M. Roux, L. Davoust, R. Blervaque, J-L. Achard & C. Peponnet, EWOD digital microfluidics for lab on a chip, ASME, ICNMM2006, Limerick, Irlande (2006)
4. A.Yu. Gelfgat, A.L. Yarin & P.Z. Bar-Yoseph, Dean vortices-induced enhancement of mass transfer through an interface separating two immiscible liquids, Phys. Fluids, 15, 330 (2003)
5. M.J. Gross & J.E. Porter, Electrically Induced Convection in Dielectric Liquids, Nature, 212, 1343 (1966)
6. A. Ramos, H. Morgan, N.G. Green & A. Castellanos, AC electrokinetics: a review of forces in microelectrode structures, J. Phys. D Appl. Phys., 31, 2338 (1998)
7. I. Glasgow, J. Batton & N. Aubry, Electroosmotic mixing in microchannels, Lab Chip, 4, 558, (2004)

MICROMIXER BASED ON BAKER'S TRANSFORMATION

Keiko Osato[1], Manabu Tokeshi[1,2], Noritada Kaji[1,2], Yusuke Omoto[3], Norikazu Suzuki[3], Yasuhiko Sakai[3], Eiji Shamoto[3] and Yoshinobu Baba[1,2,4,5]

[1]Department of Applied Chemistry, Nagoya University, JAPAN
[2]MEXT Innovative Research Center for Preventive Medical Engineering, Nagoya University, JAPAN
[3]Department of Mechanical Science & Engineering, Nagoya University, JAPAN
[4]Health Technology Research Center, AIST, JAPAN
[5]Institute for Molecular Science, JAPAN

ABSTRACT

Herein we report the development of a new passive micromixer with 3-D structure based on Baker's transformation. The 3-D structure was fabricated on an oxygen-free copper block by using an ultrasonic elliptical vibration cutting method [1] and was used as a mold master. Using this master mold, we fabricated a PDMS micromixer chip. The mixing efficiency of the micromixer was evaluated by measuring the fluorescence image that results from mixing of two liquids (FITC solution and water). From these measurements, we found that the mixing efficiency at relatively high flow rate conditions is much better than that of low flow rate conditions. The mixing behavior in the microchannel was observed by a confocal fluorescence microscopy.

Keywords: Micromixer, Baker's transformation, 3-D structure

1. INTRODUCTION

In microfluidic-based (bio)chemical analysis systems, mixing of the liquid samples is considered as one of the most challenging tasks to achieve an appropriate reaction in a short period of time. Since mixing in microfluidic systems is typically dominated by diffusion due to the low Reynolds number, mixing by diffusion only is very time-consuming and inefficient. Therefore, the works concerning micromixers for micro total analyses systems (μTAS) have been developed by many groups around the world [2]. In this paper, we have proposed and demonstrated a new passive micromixer based on Baker's transformation.

2. CONCEPT AND FABRICATION OF MICROMIXER

Figure 1 shows an illustration of the principle of a new passive micromixer based on Baker's transformation. The 7-mm special structure as shown in Figure 1was repeated five times. Figure 2 shows a photograph of a mold master and SEM images of the roll out and fold area parts which correspond with the illustrations in Figure 1. The ultrasonic elliptical vibration cutting used here enables us to fabricate the complex 3-D micro structure which can be hardly obtained [1].

3. RESULTS AND DISCUSSION

The mixing efficiency of a PDMS chip fabricated by using a mold mater was evaluated by measuring fluorescent images of the microchannel using a confocal fluorescence microscope. FITC solution and water were introduced into the microchannel by a syringe

978-0-9798064-0-7/μTAS2007/$20©2007CBMS

pump at constant flow rates. The dependence of mixing efficiency on the flow rate is shown in Figure 3. The micromixer developed in this work has achieved better mixing performance at a higher flow rate. The reason why such a result was obtained may be derived from increasing contact area between FITC solution and water. Figure 4 shows the fluorescence images of vertical cross sections of the microchannel such as in Figure 1. It is clear from Figure 4 that the mixing performance at the flow rate of 20 mm/s was better than that of 4 mm/s. Moreover, our results had strongly supported by numerical simulation that used CFD (Computational Fluid Dynamics, ANSYS CFX). Typical examples of simulation are shown in Figure5. The mixing performance of a cross section of the microchannel in the vicinity of the outlet at the flow rate of 20 mm/s (Figure 5(b)) was worse than that of 40 mm/s (Figure 5(c)).

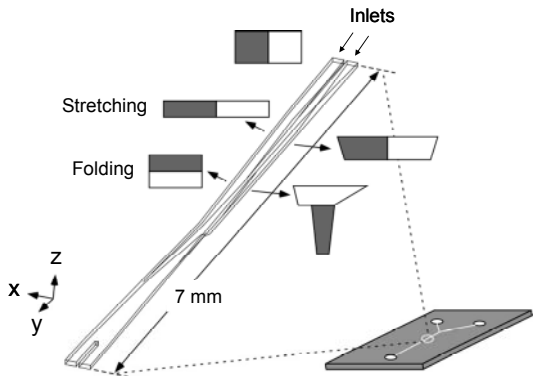

Figure 1. Schematic illustration of the principle of a new micromixer based on Baker's transformation.

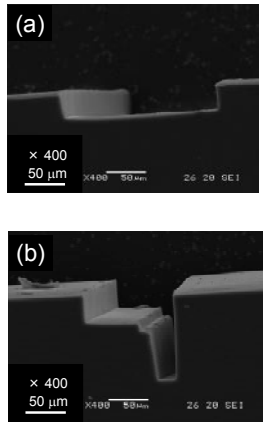

Figure 2. SEM micrographs of the micromixer mold. (a) Stretching part. (b) Folding part.

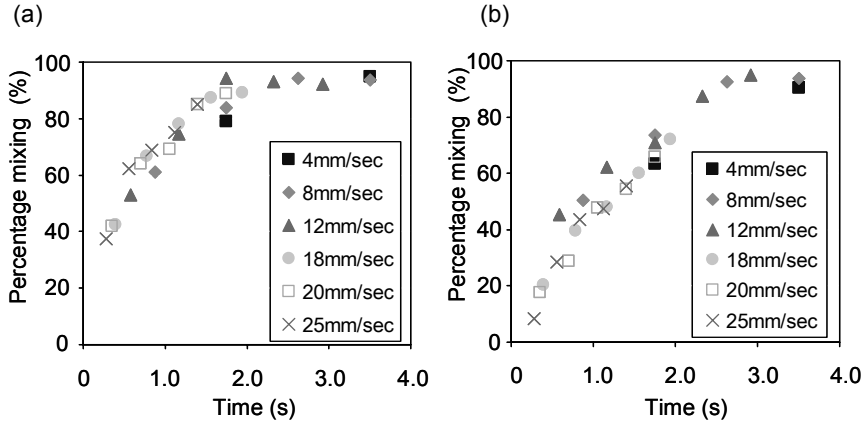

Figure 3. Dependence of mixing efficiency on the flow rate. (a) Micromixer. (b) T-shape microchannel.

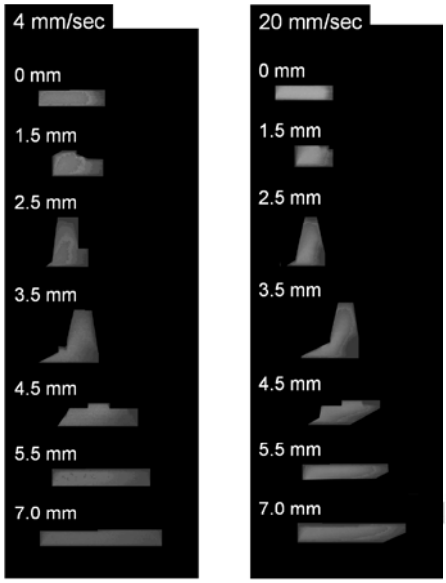

Figure 4. Fluorescence images of vertical cross section of the microchannel such as Figure 1. (a) Flow rate: 4 mm/s. (b) Flow rate: 20 mm/s.

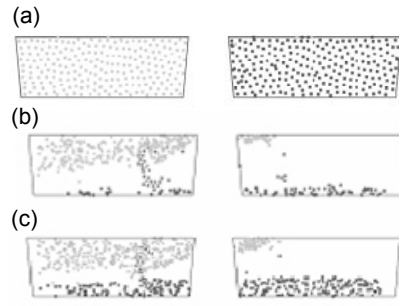

Figure 5. Mixing behaviour of numerical simulation analysis. (a) No flow. (b) Outlet at the flow rate of 20 mm/s. (c) Outlet at the flow rate of 40 mm/s.

4. CONCLUSIONS

We have developed a new 3-D micromixer based on Baker's transformation. The mixing performance was evaluated by measuring fluorescence intensity using a confocal fluorescence microscopy. Although the mixing performance was limited in this stage, it can be improved by shortening an interval of the special 3-D structures or increasing number of the 3-D structures. The micromixer developed here will be useful for most μTAS devices.

ACKNOWLEDGEMENTS

This work was partially supported by Nature COE, Nagoya University.

REFERENCES

[1] E. Shamoto, N. Suzuki, E. Tsuchiya, Y. Hori, H. Inagaki and K. Yoshino, *Development of 3 DOF ultrasonic vibration tool for elliptical vibration cutting of sculpture surfaces*, CIRP Annals, 54, 321 (2005).

[2] N. -T. Nguyen, S. T. Wereley, *Fundamentals and applications of microfluidics*, Artech House, (2006).

MICROPUMP AND MICROMIXER BASED ON ELECTRICALLY INDUCED BUOYANCY

Shuzo Hirahara, Tomoyuki Tsuruta, Yoshinori Matsumoto, Norihisa Miki, and Haruyuki Minamitani

Keio University, Japan

ABSTRACT

A fast buoyant flow occurs along the gap between electrodes aligned in the vertical direction in a microchannel filled with isotonic saline. A micropump and a micromixer have been realized by applying this phenomenon in two types of device: an upright chip and a horizontally oriented upright chip, respectively. These devices have very simple structures and can be made from cheap materials by uncomplicated manufacturing processes. Because the devices work efficiently in the range of solution conductivities that includes isotonic saline, we expect them to be useful in biochemical assays and medical tests.

Keywords: Micropump, Micromixer, Isotonic saline, Buoyant flow

1. INTRODUCTION

Buoyancy was widely believed to be an insignificant and negligible factor in microfluidic devices, because the Rayleigh number is far less than the value of 1708, claimed be the boundary as to whether convection does or does not occur, and because the Peclet number, which is the thermal energy ratio of convective to diffusive transport, is less than unity. Recently, however, it has been shown by means of algebraic estimation [1] and computational fluid dynamics [2] that buoyant flow as a result of Joule heating is less slow. Even so, it is difficult to find any reports of experimental studies on, or applications of, microfluidic buoyancy.

2. EXPERIMENTAL

In an experiment using isotonic saline, we found that a fast buoyant flow arises along a narrow gap between AC electrodes aligned in the plumb-bob vertical direction. We proposed two types of device that utilize this phenomenon, a micropump [Figure 1 (a)] and a micromixer [Figure 1 (b)], and we examined them to define their characteristics.

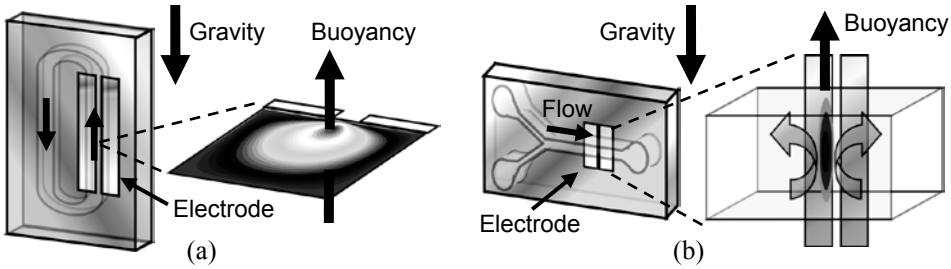

Figure 1. (a) Upright chip with a circular-type micropump, and its cross-sectional thermal distribution. (b) Horizontal upright chip with a Y-shaped micromixer, and a close-up of the near electrode.

978-0-9798064-0-7/μTAS2007/$20©2007CBMS

2.1 MICROPUMP

For an experiment to confirm micropumping operation, we fabricated an upright chip in which the channel is aligned in the vertical direction and a pair of electrodes is aligned with the longitudinal direction to form a microchannel [Figure 1 (a)]. When an AC voltage (up to 20 V_{PP}, 5 MHz) is applied through the pair of electrodes, the liquid moves upward along the gap between electrodes, as shown in the right half of Figure 2(a), and a circulating flow is induced in the ring-structured channel. The resulting flow should be considered as a laminar flow, because the velocity of the flow passing through the channel cross-section has a parabolic distribution.

The pumping flow rate could be controlled by varying the applied voltage over the range tested up to 20 V_{PP}, as shown in Figure 2(b). Furthermore, the broader the channel cross-section, the faster the fluid flowed through it.

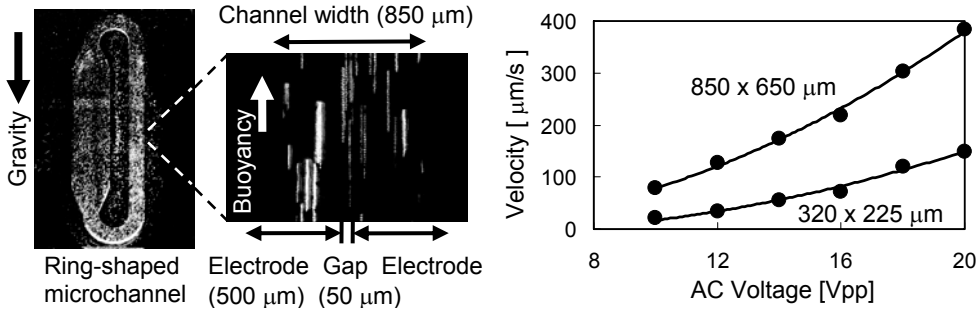

Figure 2. (a) Circulating flow and trajectories of fluorescent beads moving with buoyant flow in 1 s. (b) Characteristics of flow velocity versus AC voltage with cross-sectional size as a parameter.

2.2 MICROMIXER

Next, to confirm micromixing operation, we fabricated a horizontal upright chip device in which the channel is aligned with the horizontal direction and a pair of electrodes is aligned with the vertical direction at right angles to the channel [Figure 1(b)].

Trajectories of fluorescent beads dispersed in isotonic saline at 5-s time intervals are shown in Figure 3. These photographs show that different flows that are formed under conditions of: (a) horizontal flow and no applied voltage, (b) no horizontal flow and applied voltage, and (c) both horizontal flow and applied voltage.

3. RESULTS

The micropumping flow rate in a cross section of 850 × 650 μm at an applied voltage of 20 V_{PP} reached 110 nL/sec, which is approximately a hundred times more than that of a pumping device driven by AC electroosmotic flow [3].

Mixing in a microchannel can be achieved by a single transition of an inter-laminar flow. In the case of the proposed mixing device, the flow transition is achieved in very short distance that is almost equivalent to the gap between the electrodes, which is approximately

100 μm. The distance needed for mixing may be slightly shorter than that for an AC electroosmotic flow-mixing device [4].

Other characteristics of this flow have been clarified as follows: the flow appears predominantly in liquids with conductivities of more than 0.01 S/m; the flow velocity is independent of the applied AC frequency; and, of course, the liquid flow is always generated in the direction opposite to gravity.

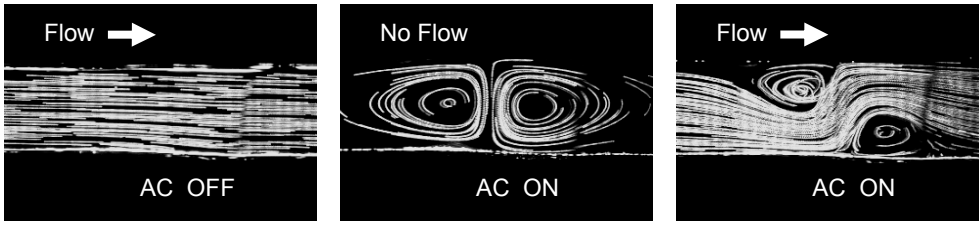

(a) (b) (c)

Figure 3. Trajectories for: (a) horizontal flow and no applied voltage, (b) no horizontal flow and applied voltage, and (c) both horizontal flow and applied voltage.

4. CONCLUSION

Our newly developed devices have very simple structures, and can handle highly conductive liquids containing isotonic saline (conductivity 1.6 S/m) in which AC electroosmosis cannot be generated. Furthermore, the devices can be made from cheap materials, such as polydimethylsiloxane (PDMS) or glass plates, by applying simple manufacturing techniques such as photolithography, wet etching, or molding. These microfluidic devices are expected to contribute to biochemical researches and medical tests on various biological substances.

REFERENCES

[1] A. Castellanos, A. Ramos, A. Gonzalez, N. G. Green, and H. Morgan: "*Electrohydrodynamics and dielectrophoresis in microsystems: scaling laws*", Journal of Physics D: Applied Physics, vol.36, pp.2584-2597 (2003).

[2] S. Hirahara, T. Tsuruta, Y. Matsumoto, and H. Minamitani: "*Analysis of Electrically Induced Swirling Flow of Isotonic Saline in a Mixing Microchannel*", IEEJ Transaction on Sensors and Micromachines, vol.127-E, no.3, pp.121-125 (2007).

[3] V. Studer, A. Pepin, Y. Chen, and A. Ajdari: "*An integrated ac electrokinetic pump in a microfluidic loop for fast and tunable flow control*", Analyst, vol.129, pp.944-949 (2004).

[4] N. Sasaki, T. Kitamori, and H. Kim: "*AC electroosmotic micromixer for chemical processing in a microchannel*", Lab on a Chip, vol.6, pp.550-554 (2006).

NUMERICAL STUDY ON FLOW AND HEAT TRANSFER CHARACTERISTICS OF PERISTALTIC PUMP

K. Tatsumi[1], Y. Miwa[1], Y. Matsunaga[2] and K. Nakabe[1]

[1] *Department of Mechanical Engineering and Science, Kyoto University, Kyoto, Japan*
[2] *Department of Mechanical Engineering, Osaka Prefecture University, Osaka, Japan*

ABSTRACT

The present study focuses on a peristaltic micro pump [1]. Flow and heat transfer characteristics of a channel accompanying a wall with peristaltic motions are evaluated by numerical simulations, and the effects of the travelling wave amplitude, velocity, phase and shapes on the pump performance are discussed.

Keywords: Numerical simulation, Peristaltic pump, Pump performance, Heat transfer

1. INTRODUCTION

A proto-type device of peristaltic micro pump was manufactured and presented by Kanno et al.[1]. Its active part consisted of piezoelectric elements was attached to the channel from the outside of the channel wall as illustrated in Fig. 1(a). This contributes to a simplification of the device structure, and, moreover, makes it available in multi-test cases to replace only the test-section channel but not the pump, resulting in cost and time reductions. To design an effective peristaltic pump for practical use, however, detail information of the flow and heat transfer characteristics of such pumps is required. Therefore, in the present article, effects of the parameter of the periodically-moving wall on the flow characteristics and pump performance are evaluated together with the discussion of the thermal field of flow and heat transfer rate at walls.

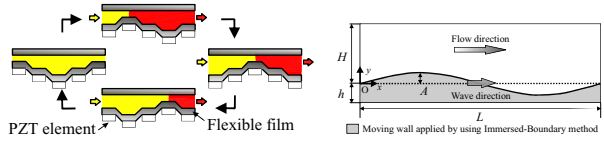

(a) Schematic view of pump *(b) Computational domain*

Figure 1. Schematic view of peristaltic micro-pump.

2. NUMERICAL PROCEDURE AND CONDITIONS

Figure 1(b) shows the computational domain and coordinates. The channel height, H, and streamwise wavelength, L, were fixed at a constant value as H=100μm and L/H=10, respectively. Other geometric parameters are tabulated in Table 1 with their labels. In the sawtooth case, the wall is consisted of two sinusoidal functions so that steep and moderate slopes are respectively obtained in the leading and trailing part of the convex surface.

The present code was on the basis of Finite-Volume Method (FVM) and the governing equations solved were two-dimensional, time-dependent and incompressible continuity, Navier-Stokes and energy equations. To represent the peristaltic motion of the wall, Immersed Boundary Method [2] was adopted in the computation. No-slip and periodic conditions were applied to the walls and streamwise boundaries, respectively. To evaluate the heat transfer characteristics, the upper wall of the channel in the region of $3.75 \le x/H \le 6.75$ was heated under

Table 1. Computational conditions

Label	A/H	c [m/s]
A1c01~A9c01	0.01~0.9	0.1
A1c001~A1c10	0.1	0.01~10
A1c01s (sawtooth)	0.1	0.1

978-0-9798064-0-7/μTAS2007/$20©2007CBMS

isothermal wall condition. The working fluid was water and the physical properties were kept constant.

3. RESULTS AND DISCUSSION

Figures 2(a) and (b) show how the wave amplitude, A, and wave travelling velocity, c, affect the mean streamwise flow velocity, U_m. As shown in Fig. 2(a), the relation between U_m and A matches well with the fitting function of a parabolic curve under small A/H conditions. This agrees well with the results predicted by Yun and Fung [3], indicating the validity of the present code. Under larger A/H conditions, U_m/c deviates from the parabolic profile and approaches to unity. On the other hand, in Fig. 2(b), U_m/c remains almost constant under the conditions of c=0.01~1.0m/s.

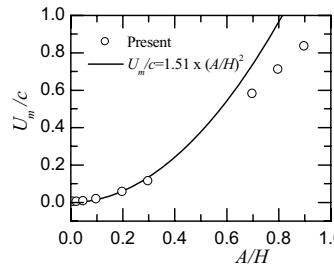

(a) Effects of A/H

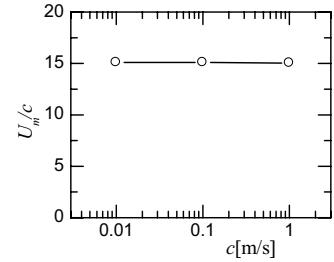

(b) Effects of c

Figure 2. Relations between U_m/c, A/H and c.

Figure 3 shows the pathlines of the flow obtained in the cases, A1c01 and A8c01. Figures 3(a) and (c) are illustrated in absolute coordinates, and (b) and (d) in relative coordinates on the bases of the moving wall, respectively. In Fig. 3(a), the fluid flows in the streamwise direction moving back and forth in one period, while in (b), the flow moves in opposite direction drawing a sinusoidal pathlines in respect to the moving wall. In the case of larger A/H, as shown in Fig. 3 (c) and (d), a different flow characteristic is obtained. Namely, most of the fluids is apparently trapped between the concave walls and is convected at a velocity identical with that of the travelling wave. In Fig. 3(d), a pair of counter-rotating circulations appears in the center area, and reverse flows relative to the travelling wave are obtained near the top and bottom walls.

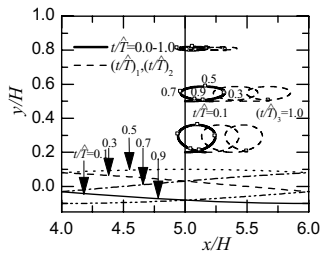

(a) Absolute coordinates (A1c01)

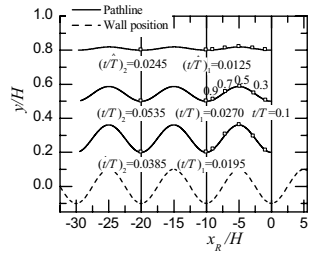

(b) Relative coordinates (A1c01)

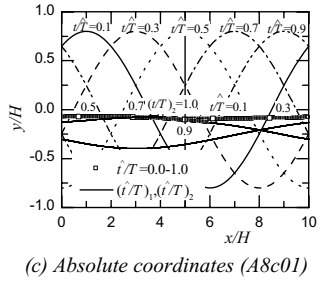

(c) Absolute coordinates (A8c01)

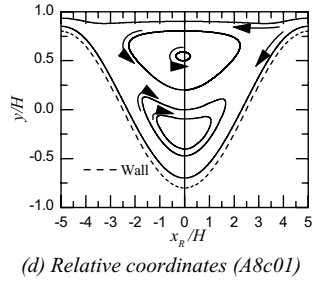

(d) Relative coordinates (A8c01)

Figure 3. Pathlines in the cases, A1c01 and A8c01.

Figure 4 shows the relation between the U_m and mechanical work supplied from the wall to the fluid during one period. The values in the figure are normalized with that obtained in case A1c01. The work is defined by Eq. (1) using the pressure, y component

of shear stress and velocity at the wall.

$$W = \frac{\int_0^L \int_0^{\Delta T} (p_w(x,t) + \tau_{w,y}) v_w(x,t) dt dx}{L \Delta T} \quad (1)$$

In comparison with the case A1c01, both U_m and W increase with respect to A (cases A1c01~A9c01) and c (cases A1c01~A1c10). However, the gradient of the latter case is larger than the former one indicating that a higher efficiency is obtained by increasing the peristaltic amplitude than the wave speed. In the case of sawtooth wave pattern, both U_m and W do not differ much with those of case A1c01 (3% increase with W in case A1c01S). This indicates that pumping efficiency depends more significantly on the wave amplitude and speed than on the wall shape pattern.

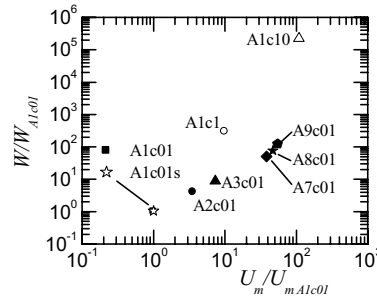

Figure 4. Mechanical work, W vs U_m.

Figure 5 shows the time history of the Nusselt number spatially averaged along the heated area at the channel top wall. Nu_m is defined as $Nu_m = q_w H/\lambda(T_w - T_0)$, where q_w, T_w, T_0 and λ are the wall heat flux, wall temperature, flow inlet bulk mean temperature and fluid thermal conductivity. By the influence of the flow motion, Nu_m fluctuates periodically and possesses maximum and minimum values at $t/T \cong 0.5$ and 1.0, respectively. On the contrary, the maximum streamwise velocity is obtained at $t/T \cong 0.3$. Therefore, a phase difference appears between the velocity of the mean flow and heat transfer profiles.

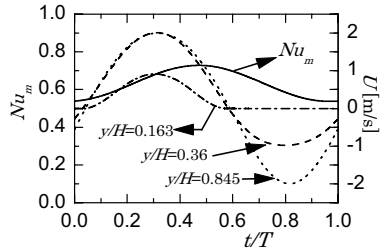

Figure 5. Nusselt number at heated wall surface and streamwise velocity at x/H=0.5.

4. CONCLUSIONS

Two-dimensional unsteady computation was conducted for a peristaltic pump. The mean flow velocity increased in a quadratic form against the peristaltic wave amplitude, and linearly to the travelling wave speed, respectively. Under large amplitude conditions, the velocity profile deviates from the quadratic form, and a pair of counter-rotating circulation was observed in the concave part of the moving wall. A phase shift between the profiles of the mean velocity and Nusselt number was obtained at the heated wall.

ACKNOWLEDGEMENTS

This study was carried out as a part of Advancing Technology Excellence "Nano-Medicine" project, which is under Kyoto City Collaboration of Regional Entities assigned by JST.

REFERENCES

[1] I. Kanno, T. Suzuki, H. Hata, H. Shintaku, S. Kawano and H. Kotera, *Development and Characterization of a Travelling Wave Micropump Driven by Piezoelectric Actuators*, 2nd Int. Symp. Micro & Nano Tech. (ISMNT-2), 226 (2006).

[2] C. S. Peskin, *Numerical Analysis of Blood Flow in the Heart*, J. Comp. Physics, **25**, 220 (1977).

[3] F.C.P. Yin and Y.C. Fung, J., *Comparison of Theory and Experiment in Peristaltic Transpor*", J. Fluid Mech, **47**, 93, (1971).

PARTICLE TRANSPORT AND MIXING IN MICRODEVICES WITH RIDGES

Louise M. Barrett, Gregory J. Fiechtner* and Anup K. Singh
Sandia National Laboratories, Livermore, CA. 94550, USA

ABSTRACT
This paper presents a novel microdevice for the manipulation of particles. Particle manipulation is achieved by controlling the applied field and hydrodynamic pressure in a microdevice containing ridges of varying angle and number. This device uses multi parameter particle control and multiple functions can be performed, in both continuous and batch mode, using the same device. Using this device in different modes of operation we have shown the integration of cell focusing, trapping, lysis, and mixing of bioparticles such as macrophages and T-cells in a single device.

Keywords: dielectrophoresis, cell focusing, mixing and trapping.

1. INTRODUCTION
New and improved techniques for processing microliter samples containing micron sized particles and cells are in high demand for a wide range of applications in areas such as biomedical research, clinical diagnostics, and environmental analysis. Ridge structures, such as Stroock's herringbone[1], have previously been used for fluid mixing.[2, 3] A recent paper[4] has shown that a similar ridge design can be used to bring the particles closer to an electrode surface of a electrode based DEP device improving the concentration efficiency. Here we present a device where particle mixing and manipulations is achieved by controlling the applied field, hydrodynamic pressure, ridge geometry and ridge number.

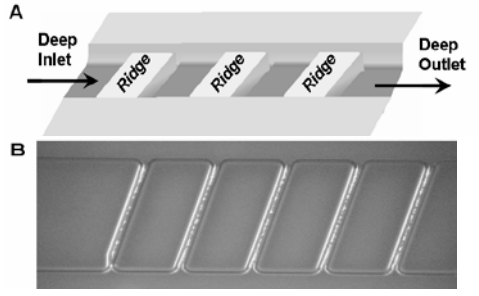

Figure 1 A: 3D representation of ridges, the channels were 10.2 mm long, 1 mm wide and 73μm deep, with ridges that were 52 μm high. Electrodes were located in reservoirs immediately above drilled access holes located in the cover at each end of the channel. **B:** Photograph of glass channel with ridges

2. EXPERIMENTAL
A standard two step isotropic etch of a glass substrate was used to create three dimensional ridge-like structures in micrometer-sized channels. (Figure 1) The resulting ridge structures were designed to pattern localized regions of electric field gradients in electrokinetic flows. A sample of labelled cells or inert polystyrene beads was introduced at the inlet reservoir. The 10μm polystyrene particles were obtained from Duke Scientific (Fremont, California). Murine macrophage cell J774A.1 were obtained from the American Type Culture Collection (ATCC, Manassas, VA). The cells were cultured as in Dulbecco's Modified Essential Medium (DMEM) serum, 100 mg/mL

* Current affiliation: Chemical Sciences, Geosciences, and Biosciences Division, Office of Basic Energy Sciences, , U.S. Department of Energy, Washington, D.C. 20585-129, USA.

978-0-9798064-0-7/μTAS2007/$20©2007CBMS

penicillin/streptomycin, and 2mM L-glutamine (Mediatech, Inc., Herndon, VA). Cultures were grown in an incubator at 37.0C with air, 95%, carbon dioxide 5%. The orginal culture was grown for one week, the cells were then split every two days, 1:10 ratio. The cells were labelled using CellTracker^{TM} Green CMFDA, (Molecular Probes, Eugene, Oregon) and suspended in 300mM Mannitol. Electroosmotic flow was induced at the walls of the channel by electrodes located in the channel fluid reservoirs. Care was taken to minimize pressure driven flow produced by liquid-level differences in the reservoirs before each run. A high-voltage power supply (Stanford Research Systems, PS350, Palo Alto, CA) was used to apply electric fields by employing platinum-wire electrodes with a 0.5mm diameter (Omega Engineering INC, Stamford, CT). The behaviour of the cells and inert particles was imaged using an inverted fluorescence microscope (model IX-70, Olympus, Napa, CA) and an Olympus U-MNB (Olympus, Napa, CA) filter set. The data was collected in the form of videos that were captured from a Sony digital camera (Sony, San Diego, CA) using a program written in house.

4. RESULTS AND DISCUSSION

Increasing the applied field, in the absence of opposing hydrodynamic pressure, results in particles being deflected to one side of the channel until they stream out the outlet. (Figure 2 A, B). As the field is increased the particles are restricted to an increasingly narrow region of the channel, however, an optimal field was found for each particle size and type. If this

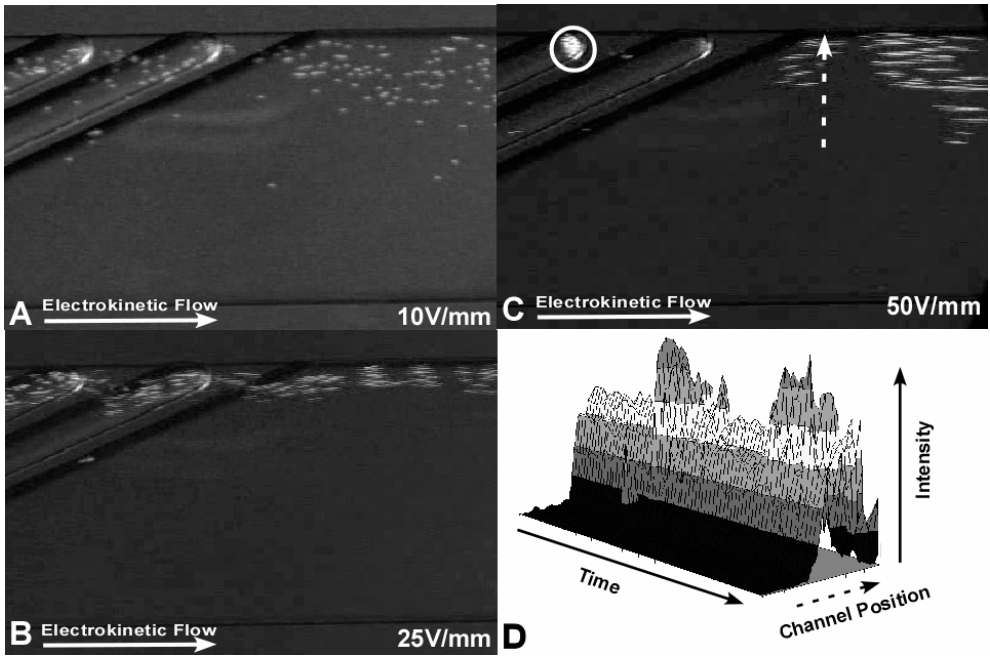

Figure 2: A: Particles are confined to one half of the channel, **B:** Particles are confined to one tenth of the channel, with increase in applied field**,** optimal field. **C:** Applied field is above the optimal field causing instability in the operation. Particles start to trap but can still overcome the field when critical saturation point is reached**. D:** Graph showing the particles release in pulses

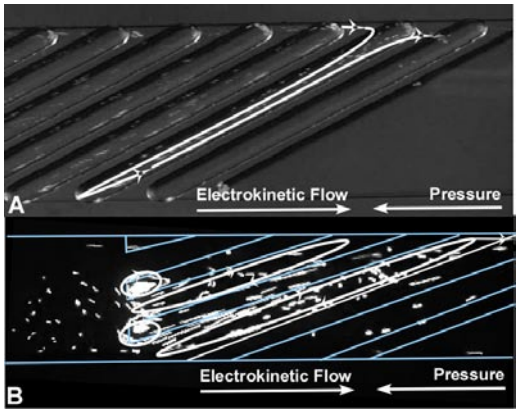

Figure 3: Mixing of particles (10μm) using parallel ridges. Applied field, 25V/mm. **A:** Hydrodynamic pressure opposes electrokinetic flow, the beads travel across the ridge (top of picture), travel across the trailing edge of that ridge and then travel back across the front edge of the next ridge until it can cross over that ridge. This process repeats until the particles reach the last ridge at which point they travel over the ridge and file out of the channel. **B:** Recirculation evident at partial ridges (ridges that do not complete traverse entire channel). A pressure gradient is not necessary for mixing to occur.

optimal field is exceeded, particles start to trap at the ridges and instabilities in particle flow are evident (Figure 2 C). The particles can still overcome the dielectrophoretic trapping force when a critical saturation point is reached but pulsed flow of the particles results. (Figure 2 D). Another operational regime was found to exist when a hydrodynamic force, opposing the electrokinetic flow, was present. This regime was found to occur, after 40 seconds using an applied field of 25V/mm, as a pressure gradient developed due to the increase in the outlet fluid reservoir volume. The two opposing forces cause transverse flow and recirculation to occur before each ridge which in turn causes mixing of the particles. (Figure 3). It is very important to note that instabilities in the electric field are evident at the corners of partial ridges (ridges that do not transverse the entire channel) even when a pressure gradient is not present. Therefore, using partial ridges, mixing can be performed using low applied fields in the absence of a pressure gradient.

5. CONCLUSIONS

In summary we have shown a device that can be operated under various regimes to perform reversible trapping, lysis deflection and mixing of particles. Most importantly the use of partial ridges can be used to provide mixing and a concentrated stream using only an electric field.

REFERENCES

[1] A.D. Stroock, S.K.W. Dertinger, A. Ajdari, I. Mezic, H.A. Stone, and G.M. Whitesides, Chaotic Mixer for Microchannels, Science,. 295, 647-651, (2002).

[2] P.B. Howell, Jr., D.R. Mott, S. Fertig, C.R. Kaplan, J.P. Golden, E.S. Oran, F.S. Ligler, A microfluidic mixer with grooves placed on the top and bottom of the channel, Lab Chip, 5, 524-530, 2005.

[3] T.J. Johnson, and L.E. Locascio, Characterization and optimization of slanted well designs for microfluidic mixing under electroosmotic flow, Lab Chip, 2, 135-140, 2002.

[4] Gadish, N. and J. Voldman, High-Throughput Positive-Dielectrophoretic Bioparticle Microconcentrator, Analytical Chem., 78, 7870-7876, (2006).

SLUG MIXING BY ACOUSTIC STREAMING IN LAB-CHIPS

F. Schönfeld, J. Pinzón, M. Weniger

Institut für Mikrotechnik Mainz –(IMM), Carl-Zeiss-Str. 18-20, 55129 Mainz, GERMANY

ABSTRACT

We present a method for mixing of minute liquid plugs relying on acoustic streaming induced by oscillating air slugs. Firstly, an FEM-based model has been developed allowing to study the interplay between the oscillating air and the adjacent liquid. The model shows good agreement with published experimental data. Secondly, an experimental realization is presented featuring a single actuation chamber and a turning valve for switching between different mixing chambers to achieve efficient mixing of multiple liquid slugs. Finally, we present an acoustic stirrer, being an alternative to the widely-used magnetic stirrers.

Keywords: Micro mixing, Flow rectification, Acoustic streaming

1. INTRODUCTION

Common biological Lab-on-a-chip (LOC) applications typically require mixing of minute liquid slugs. However, most passive droplet-based mixing methods such as utilizing meandering channels (see e.g. [1,2]) are adversarial. Because of the inevitable intense sample-to-wall contact unwanted binding of sample molecules to the wall may occur. Moreover, many conventional passive mixing concepts designed for continuous mixing do not ensure a complete drainage of the channel structures if finite slugs are processed. Active mixing can overcome these drawbacks. In the present work we investigate how acoustic streaming can be utilized in integrated LOC systems. Several studies have been published on the subject (see e.g. [3,4]). In our present investigation we go beyond these studies in various respects: a closed numerical simulation framework is developed; the mixing of finite slugs is investigated; a distributor valve allowing switching between different resonators is presented and acoustic stirrers are discussed.

2. THEORY AND SIMULATION

Acoustic streaming relies on the fact that periodic motion is rectified by the inertial non-linearity of the governing Navier-Stokes equations. One, especially simple appealing realization of such an acoustic pump has been presented, by Dijkink et al. [4]. The basic working principle relying on the asymmetry of flow exiting and entering a tube is shown in Fig. 1. For not too low Re the liquid exits the tube as a jet while it enters almost isotropically from the half solid angle. Thus, averaging over a cycle of an oscillating flow one finds a net momentum input from the tube into the liquid. Fig. 2a shows the present FEM-model [5]

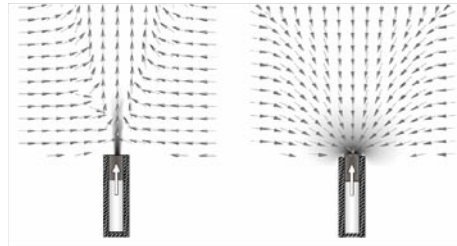

Figure 1: FEM simulation of flow fields exiting and entering a capillary. Arrows denote the normalized liquid velocity field. The velocity magnitude is grayscale encoded.

978-0-9798064-0-7/µTAS2007/$20©2007CBMS

which basically represents a Helmholtz resonator [6]. For the structural part (lower part with regular mesh in Fig. 2a) to resemble the compressible entrained air with the speed of sound equalling c_{air} = 344 m/s the Young module was set to 1.18 bar and the Poisson ratio was set to zero. Water like fluid properties have been applied in the upper part of the model. The coupling between both domains occurs via the moving boundary which models the interface between water and air. Within the given framework structural properties as well as the dynamics of the flow field was analyzed. Exemplarily, a characteristic resonance curve and typical forces are given in Fig. 2b,c. In both cases the FEM model is found to reproduce the experimental data without any additional fit parameter with a reasonable accuracy. Hence, the simulation approach is appropriate to design more complex resonant-bubble devices, which is the subject of future work.

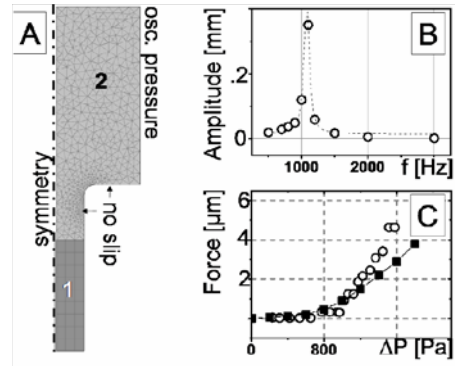

Figure 2: A: FEM model for simulation of fluid dynamics induced by an oscillating air bubble. Domain 1 describes the compressible gas, domain 2 represents the incompressible liquid; boundary conditions are as indicated. B: Simulated resonance curve (circles) and fit of a Lorentz curve. C: Simulation results (squares) and experimental data (circles) taken from [3] for the force excerted on the tube as function of the exciting pressure amplitude.

3. EXPERIMENTAL

Several acoustic-driven micro mixers have been reported so far (see e.g. refs. given in [4]). Yet, especially in the case of acoustic actuation in polymer µ-fluidic systems the transducer/liquid coupling is not trivial due to impedance mismatches and among others relative complex set-ups have been reported. We aim for a simple and yet reliable set-up which allows the use of disposable polymer chips in combination with a piezo actuator to be mounted in the respective LOC handling system. Details are given in [7].

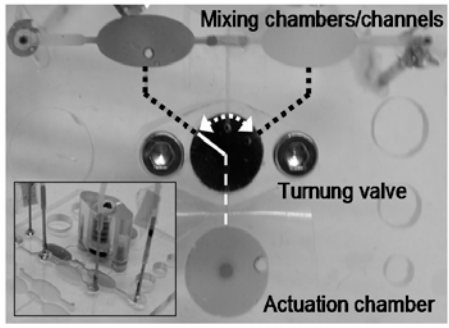

Figure 3: LOC system showing two oval mixing chambers. Air, is entrained in the connected channels (black short-dashed lines). Depending on the valve position, either channel is connected to the chamber (bottom) which is actuated by a piezo actuator (not shown).

Mixing of finite slugs: While a huge number of mixing concepts have been developed for continuous liquid streams, fast mixing of finite slugs with minimum sample-to-wall contact still remains challenging. In order to induce acoustic streaming within finite slugs care has to be taken regarding the transducer/liquid coupling. One realization where pressure oscillations are directly applied to the sample is given in [7]. Yet, performing more complex assays within a LOC slug mixing needs to be performed at different positions, preferably using a single (piezo) actuator only. This is realized in the system shown in Fig. 3, comprising a distributor valve interconnecting the actuation chamber with different resonators and mixing chambers.

Acoustic Stirrer: Magnetic stirrers have their limits when it comes to miniaturization or handling of magnetic beads. Here, we introduce a miniaturized analogue of a magnetic stirrer based on the above mentioned principle. Consider a tube as shown in Fig. 4a containing an air slug (which arises naturally for poor wetting materials). If the immersed tube experiences an acoustic field the oscillating air plug causes an off-axis momentum input. The resulting spinning could be utilized for mixing the same way magnetic stirrers are used for mixing of macroscopic batch systems.

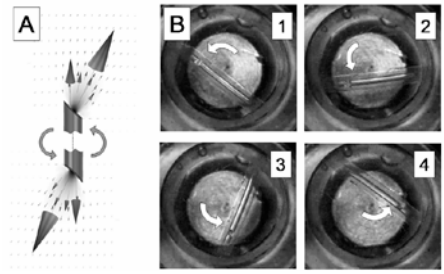

Figure 4: A: Sketch and preliminary simulation of an acoustic stirrer. The inclined end faces lead to an off-axis momentum input causing the tube to spin. B: Consecutive snapshots ($\Delta t \approx 0.2$ s) taken from a video of a corresponding experiment.

5. SUMMARY AND CONCLUSIONS

It has been shown how acoustic streaming – induced by oscillating air slugs – can be utilized for mixing of liquid slugs. A corresponding FEM-model has been implemented and validated. The numerical simulation reliably predicts resonance frequencies, damping and momentum input in the studied models. Furthermore, experiments with respect to mixing of different sample plugs have been conducted. Finally, an acoustic analogue of a magnetic stir bar is discussed. Future work is dedicated to quantitative evaluation of the approach using chemical reactions, to miniaturization and to integration of the approach into further complex disposable LOC systems.

ACKNOWLEDGEMENTS

This paper partly describes work undertaken in the context of EC IST project 027652 MASCOT (http://www.imec.be/mascot). The IST programme is partially funded by the European Commission. Moreover, FS acknowledges financial support by the DFG-Forschergruppe FOR 516/1

REFERENCES

[1] S. Hardt, K.S. Drese, V. Hessel, F. Schönfeld, Micro- Nanofluidics 1 (2), 108, 2005.
[2] H. Son, D. L. Chen and R.F. Ismagilov, Angew. Chem. Int. Ed. 45, 7336, 2006.
[3] R. H. Liu, J. Yang, M. Z. Pindera, M. Athavale, P. Grodzinski, Lab Chip 2, 151, (2002).
[4] R.J. Dijkink, J.P. van der Dennen, C. D. Ohl, A. Prospereti, J. Micromech. Microeng. 16, 1653, 2006.
[5] The model uses the FSI module of COMSOL (www.comsol.com)
[6] http://www.phys.unsw.edu.au/jw/Helmholtz.html
[7] F. Schönfeld, D. Dadic, J. Pinzón, F. Schmitz, M. Weniger, Technical Proceedings Nanotech 2007 Vol. 3, 312, (2007).

THERMAL ACTUATION FOR A CROSS-CHANNEL MICROMIXER

Bertrand Selva[1], Olivier Franąais[2], Lionel Rousseau[3], Patrick Poulichet[3], Serge Desportes[4], Jacques Delaire[4], Damien Grenier[1], Marie-Caroline Jullien[1]

[1]SATIE, CNRS, ENS Cachan Antenne de Bretagne, Bruz, FRANCE
[2]CNAM Pôle STI - ESCPI, Paris, FRANCE
[3]Groupe ESIEE, Noisy-le - Grand, FRANCE
[4]PPSM, ENS Cachan, CNRS, Cachan, FRANCE

ABSTRACT

We report the study of liquid volumetric expansion by mean of a thermal actuation leading to mixing in a cross-channel.

Keywords: thermal, actuation, heating resistance, micromixer, chaotic, cross-channel

1. INTRODUCTION

In microfluidic, flows are laminar due to low Reynolds number (<1). Consequently, mixing between two liquids is mainly obtained by natural diffusion which may take a long time or equivalently requires centimeter length channels. This problem is well known in the community, and several micromixers have already been proposed. The most efficient ones generate chaotic like flows by either modifying the channel geometry [1] or by external perturbation of the flow [2,3]. In this paper, we present a new active micromixer, based on thermal actuation which is very easy to integrate and control in a microsystem. In order to disturb the liquid flow, an oscillating transverse flow is generated by a thermal volumetric expansion of the liquid controlled by heating resistors. The configuration is identical to the one of Dodge *et al.* [3], but the transversal oscillating flow is created by a thermal actuation instead of pneumatic one. A chaotic mixing is then induced under particular conditions depending on volume expansion, liquid velocity, frequency of actuatio This solution presents the advantage to achieve mixing in a very short time (1 s) and along a short length (channel width).

2. EXPERIMENTAL SET-UP

a) b)

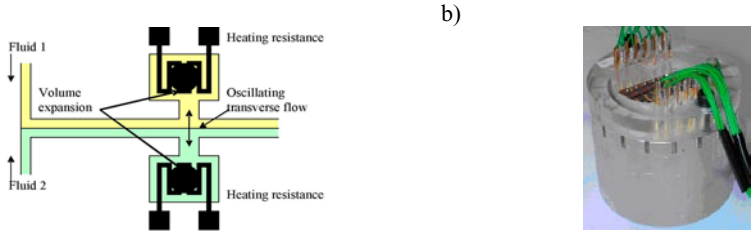

Figure 1 : a) Sketch of the microsystem integrating electrical resistances leading to volumetric expansion of the liquid; b) : Complete experimental setup, including electrical connections and the thermal drain preventing from energy storage.

The micromixer is based on classical microfluidic obtained by PDMS moulding. The microfluidic device is then bounded on a substrate on which the thermal actuator has been

978-0-9798064-0-7/μTAS2007/$20©2007CBMS

previously integrated. The thermal actuator consists of a heating resistor deposited on silicon wafers, wich has a high thermal conductivity. It is in contact with a cavity filled by a liquid and connected to the microfluidic channel.
By heating this liquid, a volumetric expansion is generated and causes a transverse flow across the main channel where two liquids are to be mixed (figure 1.a). Two thermal cavities are used in opposition and are located on each side of the main channel. The addition of a thermal drain prevents from the storage of energy in the microsystem, and thus allows to control temperature of the liquid (figure 1.b). The liquid is a mixture of 70% water plus 30% glycerol.

2. RESULTS

In order to get orders of magnitude of volumetric expansion, liquid expansion (no state change) as a function of temperature in the cavity is given by :

$$\Delta V = V_0(\alpha \Delta T - \chi \Delta P) \tag{1}$$

where α is the dilation coefficient, and χ is the compressibility coefficient. Pressure effects are negligeable compared to temperature variation effects due to viscosity and inertial effects. This leads to :

$$Q = \frac{\partial \Delta V}{\partial t} \tag{2}$$

represented on figure 2.a, showing both, as a function of time, the flow rate in the transverse channel as well as the liquid temperature increase. It is noticeable that the flow rate evolves as the temperature time derivative, i.e. it is a transient process. This means that, in order to be used efficiently, this microsystem requires temperature evolving rapidly.

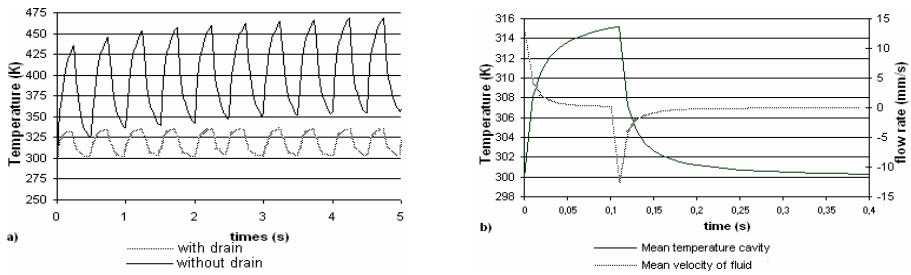

Figure 2 : a) Thermal response of liquid and fluid velocity in the actuation canal for a power of 10W during 0.1s. b) Mean temperature in the cavity with and without thermal drain, frequency = 2Hz, cyclic ratio = 0.5, power = 10W, a layer of PDMS of 3.5mm, a cavity's height of 100µm, a silicon layer of 350µm

It is shown on Figure 2.b that a thermal drain is compulsory in order to prevent energy storage. Indeed, it is seen that without thermal drain, mean temperature incresases while it keeps constant with the addition of the thermal drain.

Figure 3 shows an example of achieved mixing at 3 Hz and 25 V for a flow rate of 10 µl/h. More generally, efficient mixing is achieved for frequencies of approximatively 1 Hz (low frequency) and applied power about 4.5 W (high amplitude). The efficiency of mixing

as a function of both frequency and applied voltage is done by image processing as in Ref. [3] and is represented on Figure 4.b. Mixing efficiency is characterized by measuring, the root mean square σ of concentration fluctuations at the exit of intersection. For poor mixing, σ is high (bimodal distribution of concentration fluctuations) ; and for hight mixing efficiency σ is low (gaussian distribution of concentration fluctuations). The structure of the result is closed to the one obtained by [3].

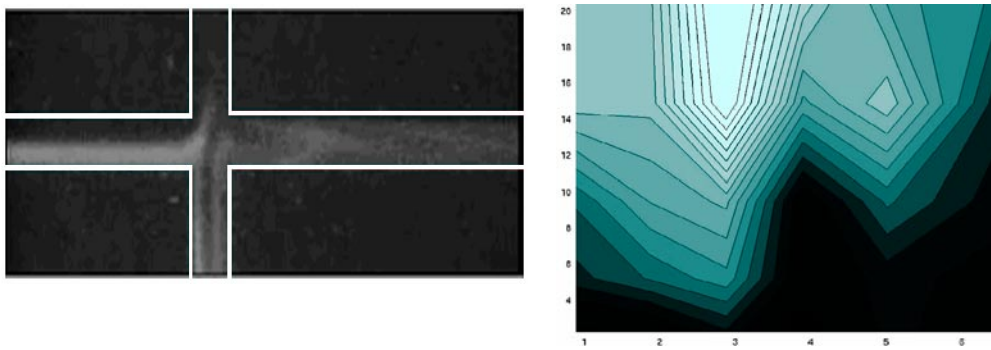

Figure 4 : a) Example of an efficient mixing achieved for a frequency of 3 Hz, a potential of 25 V,a resistance of 88 Ω , flow rate is 10 µl/h. b) Mixing efficiency, σ (red: good mixing, blue: poor mixing), as a function of both amplitude (ordinate) and frequency (abscisse).

3. CONCLUSION

In this paper, we have shown that thermal actuation is feasible in microsystems, due to the high surface/volume ratio, leading to a very fast diffusion of heat. Modelisation and numerical simulations of volumetric expansion has been performed and show that volumetric expansion/contraction is maximum (successively minimum) for high temperature gradient (successively low). Furthermore, in order to keep controle on the mean temperature in the microsystem, the adition of a thermal drain is compulsory to prevent from energy storage. The application that has been chosen to validate this actuation processs is mixing, using an already well documented micromixer, the cross channel one. We have shown that it is possible to controle both frequency and amplitude of the transversal flow, leading to the same behaviour as [3].
This system has the advantage to be easy to manufacture and also easy to integrate.

REFERENCES

[1] A. Stroock, S. Dertinger, A. Ajdari, I. Mezic, H. Stone, G. Whiteside, *Chaotic Mixer for Microchannels*, Science **295**, pp. 647, (2002).
[2] H. Chou, M. Unger and S. Quake, *A Microfabricated Rotary Pump*, Biomed. Microdevices **3:4** pp. 323, (2001).
[3] A. Dodge, A. Hountondji, M. C. Jullien, and P. Tabeling, *Spatiotemporal Resonances in a Microfluidic System*, Phys. Rev. *E* **72**, 056312, (2005).
[4] B. Stoeber, E. Espanol and D. Liepmann *Operational Limits of Suspension Flows through Sudden Contractions*, ASME, New-York (2001).
[5] Y. R. Thorstenson, S. P. Hunicke-Smith, P. J. Oefner, and R. W. Davis, *An Automated Hydrodynamic Process for Controlled Unbiased DNA Shearing*, Genome Research, **8**, pp. 848-855, (1998)

3D DROPLET ACTUATION IN DIGITAL MICROFLUIDICS DEVICES: TOWARDS INTEGRATION WITH MASS SPECTROMETRY

Sergio L. S. Freire,[1] M. Abdelgawad,[2] H. Yang,[1] and A. R. Wheeler[1]

[1]Department of Chemistry and [2]Department of Mechanical and Industrial Engineering, University of Toronto, Toronto, CANADA

ABSTRACT

We developed a method for 3D droplet actuation in digital microfluidics, called All Terrain Droplet Actuation (ATDA), in which droplets are manipulated on inclined, declined, vertical, twisted and upside down architectures. ATDA enables discrete processes on a single platform without thermal, chemical, or biological interference between them. To illustrate this capacity, we developed sensors capable of cycling droplets between distinct temperatures and oxygen milieu, as well as an automated platform for liquid-liquid extraction (LLE). We anticipate that ATDA will have significant impact in the field of microfluidics and laboratory miniaturization

Keywords: Digital microfluidics, flexible devices, liquid-liquid extraction

1. INTRODUCTION

We introduce a new method for fluid transport, called All-Terrain Droplet Actuation (ATDA), in which droplets containing biochemical samples and reagents are manipulated on non-planar microfluidic devices. The new format enables straightforward integration of distinct physicochemical environments on monolithic platforms, which may render it a useful new tool in the lab-on-a-chip field. While conventional digital microfluidics devices are formed on a rigid plane, ATDA devices are formed using our recently developed rapid prototyping method [1], a side-benefit of which is the use of flexible substrates that can be bent into topographies with radii as small as 2 mm.

2. THEORY

Digital microfluidics is a micro-scale fluid handling technique that enables manipulation of discrete droplets on an array of electrodes by means of electrowetting [2,3] or dielectrophoresis [4,5].

3. EXPERIMENTAL

Electrode arrays used for ATDA were patterned by photolithography on flexible copper coated polyimide substrates (Pyralux® AP7156E, DuPont Electronic Materials, Research Triangle Park, NC) followed by wet etching in ferric chloride (CE-100, Transene Company Inc., Danvers, MA). Electrodes were then covered with poly(dimethyl siloxane) (PDMS) and Teflon-AF by spin-coating. Electrodes (1 mm x 1 mm each) were formed in two lines separated by 60 μm. Devices were bent into 3D shapes by hand and 1.5 – 5.5 μL droplets were actuated by applying voltage to successive pairs of electrodes. Details of the fabrication process and droplet actuation can be found in reference [1].

For liquid-liquid extraction (LLE), aqueous stock solutions of calf muscle type IIA histone and 20-mer pre-desalted DNA oligonucleotide (5′AGCAGAGCGACCTCA-ATGAT3′) (Sigma Aldrich, Oakville, ON) were prepared by dissolving them individually

978-0-9798064-0-7/μTAS2007/$20©2007CBMS

in DI water. A working solution was prepared (20 μM DNA, 440 μg/mL protein), and a 2 μL droplet was pipetted onto a device similar to the one shown in Figure 1b. The droplet was driven into a solution of phenol (2.5% by weight in silicone oil), and then cycled on submerged electrodes for few moments before being driven back to the air-oil interface. The processed droplet and an equal volume of non-processed (control) solution were diluted into 40 μL water-methanol (50% vol/vol) for analysis. Samples were injected into an LTQ linear ion trap mass spectrometer in positive ion mode (ThermoElectron, Waltham, MA). Samples were delivered via a transfer capillary (100 μm ID) mated to a nanoelectrospray emitter tip (30 μm ID) at a flow rate of 0.5 μL/min, with an applied voltage of 1.6 kV and capillary temperature of 250°C.

4. RESULTS AND DISCUSSION

ATDA makes the process of integrating distinct physicochemical environments on a single, monolithic device very straightforward in comparison to the alternatives, which typically require significant microfabrication. To illustrate this principle, we developed sensors relying on ATDA to cycle droplets between distinct (a) temperature or (b) oxygen milieus. A colorimetric temperature sensor is shown in Figure 1a – a droplet containing a thermo-responsive dye (black < 29°C < white) can sample multiple thermal conditions simply by driving it onto an air-cooled open structure or down to a warm hot plate. A colorimetric oxygen sensor is shown in Figure 1b – in this geometry, an ATDA device is partially submerged in a chamber containing silicone oil. When a droplet containing methylene blue dye is exposed to an aerobic environment, it remains colored blue, and when driven into an anaerobic chamber (submersed in oil), the dye is reduced and the droplet is colorless.

The most promising application that we have developed for ATDA is an automated method for enrichment of oligonucleotides from a solution containing histones by liquid-liquid extraction (LLE). To implement LLE by ATDA, we used a platform similar to the one shown in Figure 1b to drive droplets containing DNA and histones from an open surface into a water-immiscible extractant solution for approximately one minute. Droplets were subsequently driven out of the extractant, collected manually, and analyzed by mass spectrometry. The data shown in Figure 2 are representative of multiple identical spectra. We attribute the peak at m/z 1372 to the oligonucleotide (also observed in spectra of samples containing only DNA, not shown).

5. CONCLUSION

In conclusion, ATDA represents a new mode for microfluidics with unique capacities, and we speculate that it may be useful for applications that require cycling samples and reagents between distinct conditions, such as PCR or recombinant synthesis.

6. ACKNOWLEDGMENTS

We thank the Natural Sciences and Engineering Council (NSERC) and the Canada Foundation for Innovation (CFI) for financial support.

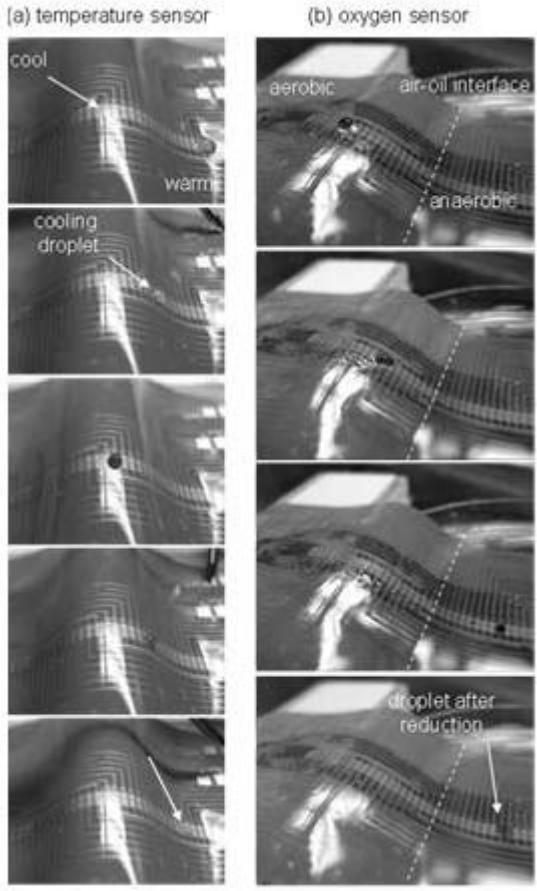

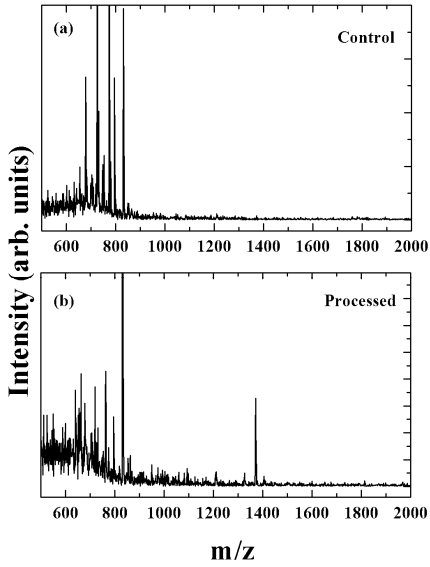

Fig. 2: Mass spectra of samples containing DNA and histones. (a) spectrum of non-processed (control) sample; (b) spectrum of sample enriched by ATDA-driven liquid-liquid extraction in phenol

Fig. 1: Multi-environmental ATDA devices, (a) droplet containing thermo-responsive dye (black < 29°C < white) is driven up and down an air-cooled bridge structure, (b) droplet containing methylene blue dye and glucose is driven from an aerobic chamber to an anaerobic chamber (submerged in silicone oil). In anaerobic conditions, the dye is reduced and the droplet becomes colorless

7. REFERENCES

[1] Adelgawad, M., Wheeler, A. R., Adv. Mater. 2007, 19, 133-137.
[2] Lee, J., Moon, H., Fowler, J., Schoellhammer, T., Kim, C.-J., Sens. Actuators, A 2002, 95, 259-268.
[3] Pollack, M. G., Fair, R. B., Shenderov, A. D., Appl. Phys. Lett. 2000, 77, 1725-1726.
[4] Washizu, M., IEEE Trans. Ind. Appl. 1998, 34, 732-737.
[5] Velev, O. D., Prevo, B. G., Bhatt, K. H., Nature 2003, 426, 515-516.

FABRICATION AND CHARACTERIZATION OF MAGNETIC ALGINATE BEAD CARRIER FOR MULTIPLE SORTING OF CELLS OR MULTIFLEXED IMMUNOASSAY

Kangsun Lee[1], Choong Kim[1], Jung Rak Lee[1], Jong Hyun Kim[1]
Ji Yoon Kang[1] and Tae Song Kim[1]
[1]Nanobio Research Center, Korea Institute of Science and Technology, Korea

ABSTRACT

This paper reports fabrication and characterization of nanoporpous hydrogel beads embedded with magnetic particles as a new class of functional carriers for magnetic separation. The embedding process was carried out by the gelation of alginate solution with calcified oil in two-phase microfluidic chip. The doping of magnetic particle was quantitatively controlled by adjusting their concentration in alginate solution. The fabricated magnetic alginate bead carrier (MABC) was applied to magnetophoretic device yielding magnetic separation efficiencies higher than 99%. When the quantity of embedding was differentiated by three levels, mixed solutions were separated into 3 levels with more than 95% efficiencies.

Keywords: Cell sorting, MACS, Magnetophoresis, Mutiplexed Immunoassay

1. INTRODUCTION

Magnetic separation of biological samples such as cells, DNA's, and proteins provides convenient tools in biological or biochemical experiments. MACS (Magnetically Activated cell separation) is simple and inexpensive compared to FACS (Fluorescence Activated Cell Sorter) but it can not simultaneously separate various types of biological samples. Although free flow magnetophoretic separations of magnetic beads were studied for multiple cell sorting [1,2], their separation efficiency is still low because the method can not quantitatively control the magnetic moments of beads attached on the surface of cells [2]. Therefore, MABC material is suitable for multiple sorting of cells since it is easy to control the magnetic moment of beads.

2. FABRICATION OF MABC USING 2-PHASE MICROFLUIDIC DEVICE

Monodisperse MABC's were produced by 2-phase microfluidic device (Figure 1) [3]. This device could fabricate three types of carriers with concentrations of 0X (none magnetic beads: alginate solution 1mL), 1X (magnetic beads 0.5mg: alginate solution 1mL), and 2X (magnetic beads 1.0mg: alginate solution). The average sizes were respectively 110μm, 130μm, and 100μm with standard deviation belw 10% (Figure 1b).

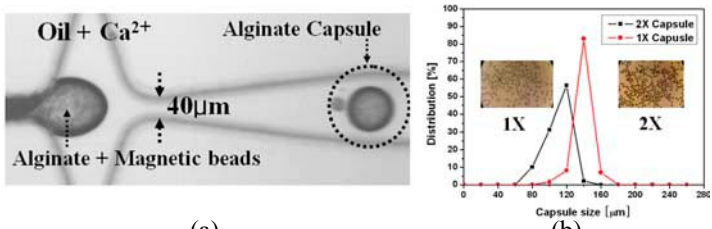

(a) (b)

978-0-9798064-0-7/μTAS2007/$20©2007CBMS

Figure 1. Fabrication process of various types of carriers, (a) the image capturing the process of the capsule fabrication using 2-phase microfluidic chip, (b) the fabricated alginate carriers containing magnetic beads with 1X and 2X concentration of magnetic beads and their size distribution.

3. SEPARATION EXPERIMENT USING MABC

Figure 2 shows the working principle of the sorting several kinds of cells at once. When a carrier containing magnetic beads went through a magnetic field, the carrier was deflected by magnetic force actuation on magnetic beads. That is, we can control the deflection distance vertically if a number of magnetic beads in a single carrier is controlled. When a cell is captured by the surface marker antibodies on the surface of these carriers, several types of cells could to be separated in one process.

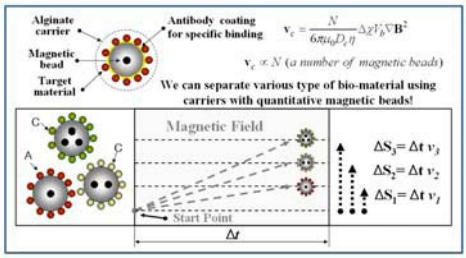

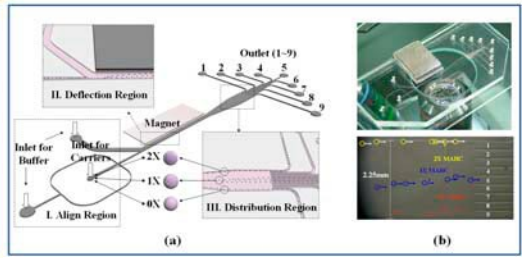

Figure 2. The concept of multiple sorting device

Figure 3. (a) The schematic of the proposed device for multiple sorting using magnetophoresis, which consists of three parts such as align region, deflection region, and distribution region, (b) the practically fabricated PDMS device through soft-lithography process.

Using these carriers, we investigated the deflection distance of MABC by appliying magnetic field. MABC's with 3 concentrations were injected respectively with the flow rates ranging from 3 mL/h to 30 mL/h (Figure 4). We could see that the deflection distance of 2X carrier was about two times larger than that of 1X in same flow rate.

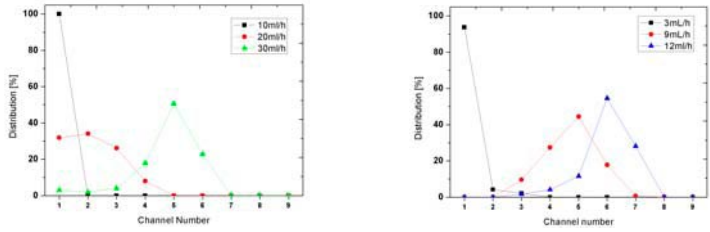

(a) (b)

Figure 4. A distribution of carriers in function of flow rate, a concentration of magnetic beads in a single carrier are (a) 5mg per 1mL alginate solution, and (b) 10mg per 1mL alginate solution.

This means the displacement in vertical direction can be controlled by the number of magnetic beads in a single carrier. Magnetophoretic separation of mixed MABC's

was tested in PDMS device. 0X and 2X capsules were separated with high separation and recovery ratio above 99%. When 3 types of capsules (0X, 1X and 2X) were sorted, the separation efficiency was about 95%.

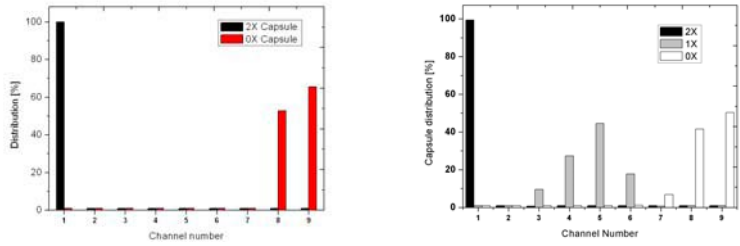

(a) (b)

Figure 5. The results of separation experiment of different kinds of carriers at the flow rate of 10 mL/h, (a) the result of separation experiment of 0X and 2X capsule and (b) 0X, 1X, and 2X.

Table 1. The separation and recovery efficiency in the experiment with 2 kinds of carriers and 3 kinds of carriers.

Separation experiment of 2 types carrier			
Types of carriers	Concentration	Separation efficiency	Recovery efficiency
0X	0×10^9/mL	99.90%	99.90%
2X	2×10^9/mL	99.90%	99.90%
Separation experiment of 2 types carrier			
Types of carriers	Concentration	Separation efficiency	Recovery efficiency
0X	0×10^9/mL	99.90%	91.93%
1X	1×10^9/mL	98.50%	89.73%
2X	2×10^9/mL	99.90%	99.34%

4. CONCLUSIONS

The experimental results showed that the microfluidic device is highly efficient in sorting several types of magnetic alginate bead carriers. Thus, we expect that the sorting device will be able to be applicable to cell sorting as well as multiplexed immunoassay.

ACKNOWLEDGEMENTS

This research has been supported by the Intelligent Microsystem Center(IMC; http://www.microsystem.re.kr), which carries out one of the 21st century's Frontier R&D Projects sponsored by the Korea Ministry Of Commerce, Industry and Energy.

REFERENCES

[1] "Continuous sorting of magnetic cells via on-chip free-flow magnetophoresis", N. Pamme et al, Lab on a chip, **6**, 974(2006)

[2] "Combined microfluidic-micromagnetic separation of living cells in continuous flow", N. Xia et al, Biomed Microdevices, **8**, 299(2006)

[3] "Three Dimensional Perfusion Culture of Encapsulated Stem Cells in Microfluidic Chip", Choong Kim et al , Transducers 2007, Lyon, France, June 10-14 (2007)

GENERATION OF MONODISPERSE NONSPHERICAL DROPLETS VIA MICROCHANNEL ARRAYS WITH A STEP

I. Kobayashi[1], K. Uemura[1] and M. Nakajima[1,2]

[1]National Food Research Institute, Japan and [2]University of Tsukuba, Japan

ABSTRACT

This paper reports a new method for generating nonspherical droplets through microchannel (MC) arrays each of which has an appropriately size-controlled step at the inlet and outlet of the channels. Silicon MC array chips consisting of 100–500 channels were successfully used to generate monodisperse discoid oil droplets with sizes down to several micrometers, dispersed in a continuous aqueous phase. Droplet generation via the MC arrays also does not require external shear stress, since the to-be-dispersed oil phase that has passed through the channels spontaneously transforms into oil droplets.

Keywords: Nonspherical droplets, droplet generation, microchannel array, step

1. INTRODUCTION

Monodisperse nonspherical droplets are useful templates for producing monodisperse nonspherical microparticles and microcapsules. They also have useful applications as micromixing and microreacton vessels. Monodisperse nonspherical droplets with sizes of more than 10 μm have been generated using microfluidic devices consisting of interconnected micochannels, e.g. T-shape microchannels and flow focusing geometries [1-3]. Microfluidic devices typically have one channel for the to-be-dispersed phase and require a rapid forced flow of the continuous phase to generate droplets. Our research group introduced microchannel (MC) emulsification for generating monodisperse droplets using MC arrays [4]; however, the droplets generated by MC emulsification have only a spherical shape [4-6]. This paper introduces a novel technique for generating monodisperse nonspherical droplets by simply injecting a to-be-dispersed phase through an MC array into a shallow well filled with a continuous phase.

2. CHIP DESIGN

Figure 1(a) is a schematic of part of an MC array with a step. The well/channel height ratio, h_{well}/h_{ch}, must be precisely controlled to confine the generated droplets in the well. The size of the droplets produced by MC emulsification generally exceeds the channel height by more than three times [4-6]. The previous MC arrays for generating spherical droplets also have deeply etched wells with h_{well}/h_{ch} values of more than ten times.

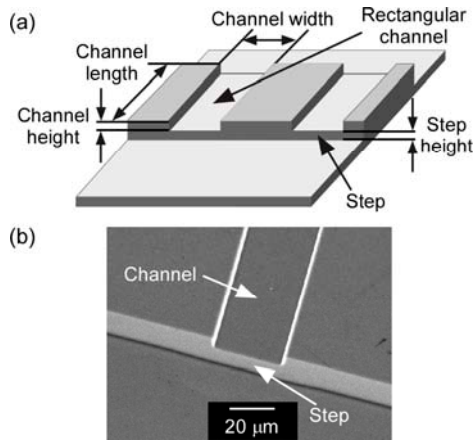

Figure 1. (a) Schematic of part of an MC array with a step. (b) Scanning electron micrograph of a rectangular channel with a step fabricated by two steps of silicon dry etching.

978-0-9798064-0-7/μTAS2007/$20©2007CBMS

We therefore developed new silicon MC arrays where h_{well}/h_{ch} value is two to geometrically confine the droplets generated from the channels (Figure 1(b)).

3. EXPERIMENTAL

We used three MC array chips consisting of uniform channels whose dimensions are presented in Table 1. Silicone oil (KP96-50, Shin-Etsu Chemical Co. Ltd., viscosity η = 48.0 mPa-s at 25°C) was used as the to-be-dispersed phase, and a Milli-Q water solution of sodium dodecyl sulfate (SDS, 1.0 wt%) was used as the continuous phase. A laboratory-scale MC emulsification setup [4] including an MC array chip was used to generate oil-in-water droplets. The to-be-dispersed phase was forced to pass through MC arrays covered by a flat quartz-glass plate, as schematically illustrated in Figure 2.

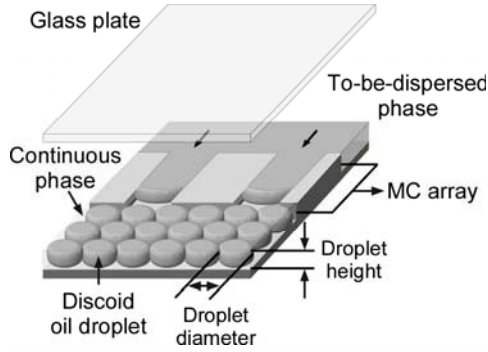

Figure 2. Schematic illustration of the generation of nonspherical oil-in-water droplets via an MC array.

Table 1. Dimensions of MC arrays designed in this research.

No.	Channel width [μm]	Channel length [μm]	Channel height [μm]	Step height [μm]
MCA-A	27.2	199	5.0	4.8
MCA-B	27.2	199	5.0	-
MCA-C	10.2	39.8	1.9	2.7

4. RESULTS AND DISCUSSION

A typical example of oil droplet generation using an MCA-A chip is presented in Figure 3(a). Uniform oil droplets were periodically generated from the channels without applying a forced flow of the continuous phase. Their average diameter, $d_{av,dr}$, of 21.4 μm was significantly larger than their height, h_{dr}, of 9.8 μm. The preceding results demonstrate that the generated oil droplets have a discoid shape with circular interfaces at their top and bottom. Their coefficient of variation, CV [(standard deviation/$d_{av,dr}$)×100], was 1.8%, i.e., monodisperse discoid oil droplets were obtained. In contrast, the oil phase continuously flowed out through MC arrays without a step (MCA-B). As seen in Figure 3(b), monodisperse discoid oil droplets several micrometers in size (7.7 μm in $d_{av,dr}$, 4.6 μm in h_{dr}, and 2.7% in CV) were generated using an MCA-C chip. Although each channel typically generated several to several tens of droplets per second, MC array chips consisting of many channels have potential to generate monodisperse discoid droplets at high production rates.

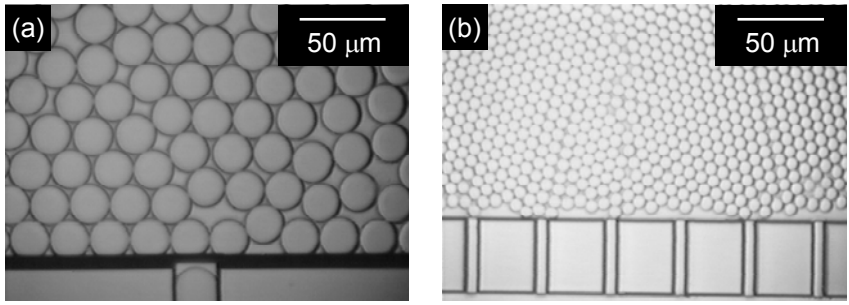

Figure 3. Optical micrographs of the generation of monodisperse discoid oil droplets via MCA-A (a) and MCA-C (b). The pressures applied to the to-be-dispersed phase were 3.1 kPa (a) and 7.1 kPa (b).

5. CONCLUSIONS

Silicon chips consisting of many MCs with a step introduced in this paper were capable of generating monodisperse geometrically confined droplets with a discoid shape. Uniform oil droplets were periodically generated via rectangular MCs with a step without applying a forced flow of the continuous phase in a well. MC arrays with a step of an appropriate size must be used to generate monodisperse nonspherical droplets. Monodisperse discoid droplets several micrometers in size were also generated using an MC array chip.

ACKNOWLEDGEMENTS

This study was supported financially by the Nanotechnology Project of Ministry of Agriculture, Forestry and Fishery of Japan, and by a grant from Ministry of Education, Culture, Sports, Science and Technology (Grant-in-Aid for Young Scientists (B), I.K.).

REFERENCES

[1] Dendukuri, K. Tsoi, T.A. Hatton, and P.S. Doyle, *Controlled synthesis of nonspherical microparticles using microfluidics*, Langmuir, 21, pp. 2113-2116, (2005).

[2] M. Seo, Z. Nie, S. Xu, P.C. Lewis, and E. Kumacheva, *Microfluidics: From dynamic lattice to periodic arrays of polymer disks*, Langmuir, 21, pp. 4773-4775, (2005).

[3] S. Xu, Z. Nie, P.C. Lewis, E. Kumacheva, H.A. Stone, P. Garstecki, D.B. Weibel. I. Gitlin, and G.M. Whiteside, *Generation of monodisperse particles by using microfluidics: Control over size, shapes, and composition*, Agrew. Chem. Int. Ed., 44, pp. 724-728, (2005).

[4] T. Kawakatsu, Y. Kikuchi, and M. Nakajima, *Regular-sized cell creation in microchannel emulsification by visual microprocessing method*, J. Am. Oil Chem. Soc., 74, pp. 317-321, (1997).

[5] S. Sugiura, M. Nakajima, S. Iwamoto, and M. Seki, *Monodispersed droplet formation from microfabricated channel array*, Langmuir, 17, pp. 5562-5566, (2001).

[6] I. Kobayashi, K. Uemura, and M. Nakajima, *Formulation of monodisperse emulsions using submicron-channel arrays*, Colloids Surf. A: Physicochem. Eng. Aspects, 296, pp. 285-289, (2007).

GIANT DEFORMATION AND TIP-STREAMING FROM SHEARED DROPS

Simon Molesin and Charles N. Baroud

LadHyX, Ecole Polytechnique, 91128 Palaiseau cedex, France

ABSTRACT

The presence of surfactant has a strong impact on the deformation of a drop. Creating a strong gradient of surfactant concentration induces giant deformations on a drop until the apparition of a tip singularity. The present study presents a novel experimental approach to obtain detailed statistics and dynamics of drop deformation by using microfluidic chanels. We observe that drops submitted to a strong shear go through a shape transition which is associated with the formation of a singular tip and a strong acceleration.

Keywords: Droplet microfluidics, tip-streaming, transport

1. INTRODUCTION

The velocity of a droplet with respect to the external phase in which is it being transported depends strongly on the details of the microchannels and the presence of surfactants. Moreover, the chemical or thermal exchange between the drop and the external medium depends on the total surface area of the drop, which may go through very large changes if the shape of the drop changes. This also leads to large modifications in the surface concentration of surfactants, and therefore to Marangoni stresses which alter the drop velocity. Below, we address these questions in a well controlled experimental setting.

2. EXPERIMENT

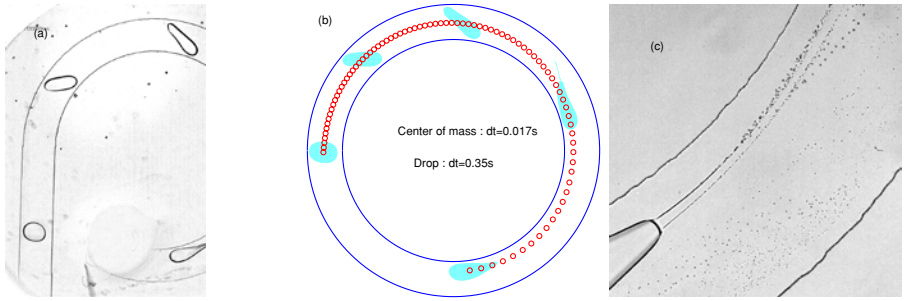

Figure 1: (a) Experimental image and (b) processed evolution of one drop. (c) Experiment image of the rear of a drop after destabilization. Small droplets are about 1 μm.

We demonstrate here that droplets which are transported in the presence of a mean shear can go through giant deformations, which lead to a change in their velocity and of their surface area. In Fig. 1a, we see several drops flowing clockwise in a circular microchannel. The difference in streamline length between the inner and outer radii imposes a shear condition, with the velocity varying by about 25% between the inner and outer walls. Furthermore, we add a small concentration of surfactant (around $0.1\times$ the critical micellar concentration) to the oil. The evolution of individual drops in the experiments may be obtained using image

978-0-9798064-0-7/µTAS2007/$20©2007CBMS

analysis of high-speed sequences. In Fig. 1b, the center of mass and the drop shape are represented at regular time intervals. They show the change in shape and orientation of the drop, as well as its acceleration.

3. TRANSITION

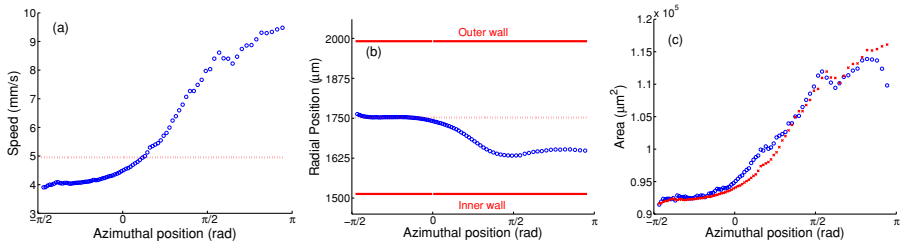

Figure 2: (a) Drop speed. (b) Radial position. (c) Area mesured(o) or computed from speed with Bretherton's law(x). A spectacular increase in velocity is observed at the moment of the destabilization and tip-streaming.

The evolution of the several parameters of a drop demonstrates the existence of a transition :

- First, surface rigidification is observed, due to the deposition of surfactants on the rear of the drop. This leads to the appearance of very well defined angles on the center-oil interface where surfactant accumulates. Drops in this situation flow at a relatively constant velocity, slightly below the velocity of the mean flow (Fig. 2a). During this period, the drop is centered at the center of the channel.

- Next, the high concentration of surfactant leads to the destabilisation of the rear interface through tip-streaming [1], which generates droplets with typical sizes around 1 μm (Fig. 1c). These droplets are very rich in surfactant and therefore act to "melt" the interface by lowering the concentration on the mother drop. Once the tip-streaming begins, the drop accelerates very strongly while moving towards the inner channel wall (Fig. 2a and b).

- Finally, the drop is in a state strongly different to the initial one. It is alignated with the tangent to the chanel. It reaches a velocity of about twice the mean oil velocity.

- The drop acceleration is associated with a thicker film of oil separating the water from the chanel walls. This may be deduced from the increase of the measured surface area in the drop images (Fig. 2c). Here, we show the increase in measured surface area (o) and the prediction from Bretherton's law [2] from the velocity measurements (x).

This typical evolution of a drop reveals a transition, particulary noticeable by the strong acceleration of the drop. The velocity of the drop at the exit of the chanel is about three times the velocity at the entrance.

4. INFLUENCE OF PARAMETERS

Varying the parameter values mainly the changes position at destabilization, all the drop which destabilize having a similar evolution.

In Fig. 3, we show the evolution of drop shapes for a given drop at regular time steps. The drop surface is fixed for all the cases at $82.10^3 \mu m^2 \pm 7\%$. The first column corresponds to a low surfactant concentration (0.05% in mass). For low flow rate (e), the shear is too weak to destabilize the drop. In this case the drop migrates toward the outer wall with a constant velocity. By opposition, for higher flow rate (a and c), drop evolution is the one describe earlier. The drop destabilizes and accelerates aligning itself with the channel. In comparison, the surfactant concentration is ten times higher in the right column so it is more difficult to create a gradient of concentration at the surface and *tip-streaming* appears only for higher flow rate (only b). Moreover the drop acceleration is weak in comparison to the first column. Indeed emission of surfactant by droplets can't eliminate the rigid region at the rear of the drop, so Marangoni stresses continue to slow down the drop. As the drop size is varied, only the position at destabilization will change, with bigger drops destabilizing earlier.

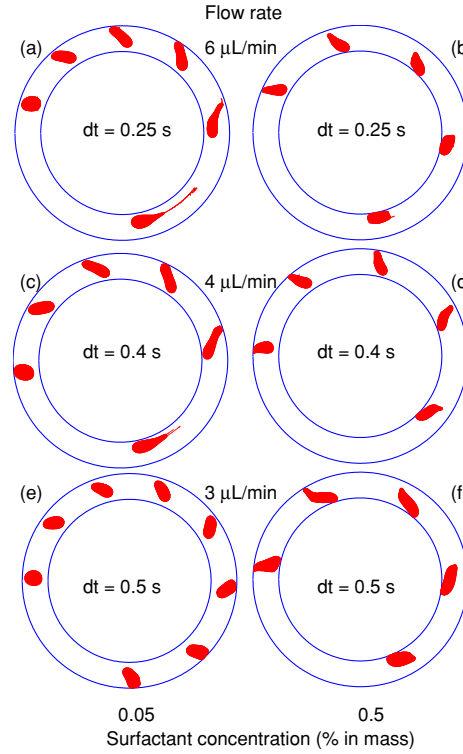

Figure 3: Typical drop shape for several position in the chanel depending on parameters. The drop surface is $82.10^3 \mu m^2 \pm 7\%$. Tip-streaming is observed in (a), (b) and (c).

5. CONCLUSIONS

In addition to the interest in producing sub-micron drops, these results have a strong impact on the use of drops as microreactors, since knowledge of the velocity of the drop is fundamental in order to keep track of the temporal evolution of a reaction. Furthermore, one may use such mechanisms to propel drops, for example in order to sort them or to force their coalescence.

REFERENCES

[1] C.D. Eggleton, T. Tsai and K.J. Stebe. Tip streaming form a drop in the presence of surfactants. *Phys. Rev. Lett.* **87**, 048302, 2001.

[2] H. Wong, C.J. Radke and S. Morris. The motion of long bubbles in polygonal capillaries. Part1. Thin films. *J. Fluid Mech.* **292**, 71-94, 1995.

MANIPULATION OF MONODISPERSE GEL EMULSIONS IN MICROCHANNELS

E. Surenjav, H. Evans, T. Pfohl, C. Priest, S. Herminghaus and R. Seemann

Max-Planck-Institute for Dynamics and Self Organization, Bunsenstraße 10, D-37073, Göttingen, Germany

ABSTRACT

Microfluidics is typically concerned with single phase liquids transported in microchannels. Instead, we explore the possibilities of using a compartmented liquid consisting of an emulsion of water in oil, where the oily phase has a very small volume fraction. This kind of emulsion is called a gel emulsion and is geometrically quite analogous to foam [1]. We study the organization and manipulation of monodisperse gel emulsions flowing along a microfluidic network using a variety of microchannel geometries, droplet sizes and dispersed phase volume fractions. Using this kind of discrete microfluidics we also explore encapsulated protein networks.

Keywords: droplet, manipulation, gel emulsion, channel geometry

1. INTRODUCTION

For a reasonably large volume fraction of the dispersed phase, the monodisperse compartments (droplets) of a gel emulsion assemble into well-defined arrangements while transported along microfluidic channels, cf. Fig 1a. The main issue is the interplay of the internal length scale of the fluid with an external length scale provided by the microfluidic channels. The vision of this work is to exploit the manipulation of emulsion droplets by channel geometry in order to position, sort, exchange, compile and redistribute liquid compartments with different chemical contents. In Figure 1b, a simple Y-piece might either (a) act as a zipper separating or combining two droplet rows, or (b) split the droplets, in the event that the droplet diameter d is at least the size of the main channel in the Y-piece.

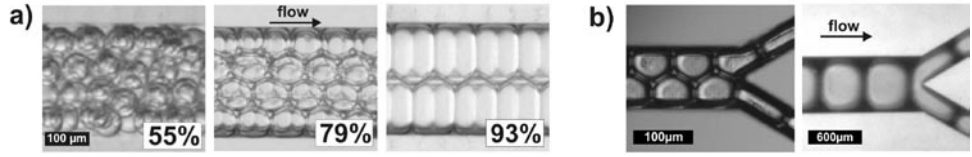

Figure 1 *a) The order in the foam-like arrangement increases as the dispersed phase volume fraction increases from 55% to 93%. b) Y-piece manipulation of droplets. left: Separating or combining a two-row 'zigzag' structure like a zipper (this process is fully reversible with respect to a change in flow direction). right: Splitting of droplets when they arrive in a 'bamboo' arrangement.*

2. THEORY

For a foam-like droplet arrangement, depending on the ratio of droplet size to channel width, either a zigzag or a bamboo arrangement is expected as the stable structure, cf. Fig. 2. In a first approximation, the stable droplet arrangement can be easily calculated using a quasi-two-dimensional model (Hele-Shaw geometry). If each lamella has an excess free energy per unit area of 2γ, where γ is the liquid/liquid interfacial energy in the presence of the surfactant, we can easily express the excess free energy E of each droplet in units of γW where W is the width of the channel, and $E^* := E/\gamma W$. We obtain $E^*_b = 2(1+V^*)$ for the

978-0-9798064-0-7/µTAS2007/$20©2007CBMS

bamboo structure, and $E^*_z = 1+(2+3^{0.5})V^*$ for the zigzag structure, as a function of the scaled '2d-volume' of the cells, $V^* := V/W^2$. The interfaces with the channel walls are assumed to contribute a surface tension of γ. We find that $E^*_b = E^*_z$ if $V^* = 3^{-0.5}$. To summarize, if the droplets are smaller than V^*, then the zigzag structure is stable and the bamboo structure is meta-stable or unstable.

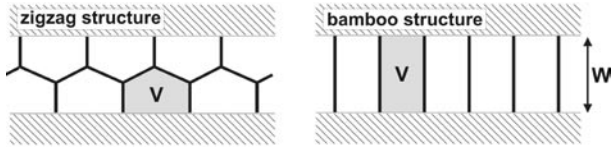

Figure 2 *Two typical structures that are acquired by liquid lamellae in a straight channel due to surface energy minimization. The respective interfacial energies per cell are easily computed and enable predictions of cell volumes that correspond to stable structures.*

3. EXPERIMENTAL

To test the geometrical prediction in a microfluidic device, we dispersed an aqueous phase into an oily phase consisting of Isopar™ M (Exxon Mobile) and 2 wt.% Span 80. The emulsions were produced in situ with volume fractions ranging from 60 to 95 vol.% using step emulsification [2]. Fibrinogen and thrombin (Enzyme Research Laboratory; MobiTec) were diluted in appropriate buffers. The microfluidic devices consist of a channel network in SU-8 photo-resist between two glass wafers. The flow of the fluid phases was controlled using custom made computer controlled syringe pumps.

4. RESULTS AND DISCUSSION

For droplet volumes slightly below the critical droplet '2d-volume' V^*, transformations between a two-row zigzag and a bamboo structure can be induced by an asperity in the channel wall.

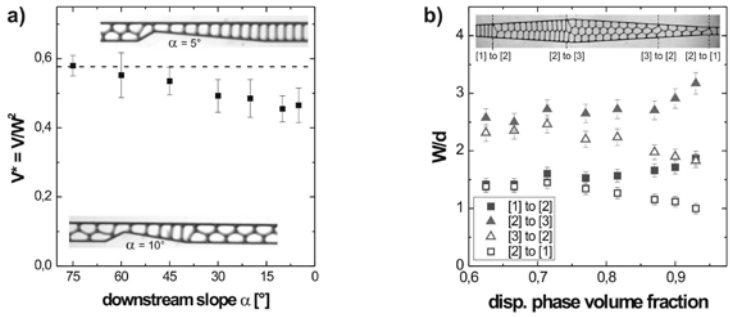

Figure 3 *a) Stability diagram showing the critical scaled droplet volume $V^* = V/W^2$, where either a bamboo [1] or a two-row zigzag [2] structure is found as a function of the downstream slope angle, α, of the asperity. The dashed line denotes the simple geometrical model, $V^* \approx 1/\sqrt{3}$. b) The normalized channel width W/d, where the stationary transitions from [1] to [2] and from [2] to a three-row zigzag [3] structure occur. Inset: Monodisperse gel emulsion flowing through a wedge shaped channel. The dashed lines mark the position of the respective transitions.*

Our experiments confirm the result from the geometrical model when the downstream angle of the asperity, α, is reasonably steep, cf. Fig. 3a. However, the switching behavior is hysteretic and it is possible to retain the emulsion in the metastable bamboo structure if α is small enough that the transition from narrow channel width to initial channel width is very smooth. Besides the exact geometry, the hysteretic behavior also depends on the volume fraction of the dispersed phase [1] as we will demonstrate in the following. In figure 3b the positions within a continuously widening respectively narrowing channel are given where a bamboo arrangement transforms into a two-row zigzag arrangement, and subsequently into a three-row zigzag arrangement flowing along a continuously widening channel. Conversely, the positions where a three-row zigzag transforms back to a two-row arrangement and a two-row zigzag arrangement is returned to a bamboo arrangement by decreasing the channel's width. The hysteresis increases with the volume fraction of the dispersed phase and becomes noticeable above 75%**.** The physical reason for this hysteretic behavior is the finite energy required for topological transitions of the foam network ('T1' process) where two vertices of the foam, *i.e.* points where three adjacent foam lamellae meet, approach each other. The energy required for the T1 process increases for increasing dispersed phase volume fraction.

Active switching between a zigzag structure and a bamboo arrangement may be induced using a ferrofluid (APG 311, Ferrotec) as the continuous phase, cf. figure 4. In an inhomogeneous magnetic field, the ferrofluid tends to flow into regions of high field strength, due to its high magnetic susceptibility. This results in the formation of a liquid plug, which serves as a temporary constriction. The dynamic downstream angle α of about 10° is found in all of our experiments. Thus, similar to the geometrical channel constrictions, the bamboo structure can be driven into the metastable region using ferrofluids.



Figure 4 *Active switching between zigzag and bamboo structures is achieved by applying a magnetic field to an emulsion consisting of a ferrofluid as the continuous phase. The relative magnetic field strength is indicated by the dashed line. The tip of the pole shoe is partly visible at the bottom of the image.*

Discrete microfluidics can also be used to study time-dependent processes, such as the evolution of protein networks. The protein fibrin is used by the vascular system for hemostasis, or the cessation of bleeding via clot formation. Blood clots are necessary to heal wounds; however, clots are detrimental in some cases, such as excessive aggregation induced by foreign therapeutic scaffolds. A better understanding of fibrin networks in the context of material properties and physical behaviors therefore addresses both academic and medical interests. A simplified system, consisting of the proteins fibrinogen and thrombin, is used to form fibrin networks. Fibrinogen molecules (referred to as monomers) bundle and subsequently aggregate in the presence of the enzyme thrombin [3]. Droplets, containing less than 1 nl volume each of thrombin and fibrinogen, are formed within a microdevice. Adjacent droplets are coalesced by an applied electrical pulse of a few volts [4], and the two protein components rapidly mix due to the circulating flow [5].

The dynamic evolution of the protein network is monitored using fluorescence microscopy (fibrinogen monomers are labeled). Figure 5 shows four snapshots in the time evolution of fibrin network development. At the initial time point of coalescence (figure 5a), the partial mixing of the two components gives rise to a swirl pattern. Less than one second later, the fluorescence is evenly dispersed throughout the droplet, which reflects complete mixing (figure 5b). At later time points, fibrin networks are distinguished by the varying sizes of their fluorescent aggregates (figure 5c and 5d).

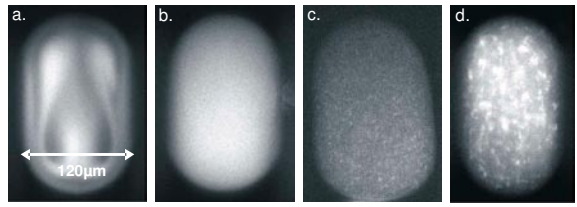

Figure 5 *Time series of fibrin formation from two coalesced droplets containing aqueous solutions of thrombin and fibrinogen; a) mixing pattern after coalescence, b) well mixed droplet, c) beginning of network formation, d) late stage of network formation.*

An immediate consequence of this approach is due to the encapsulation of the network: although the fibrin would clog a conventional microfluidic device instantly, this new approach prevents sticky surface interactions. These results suggest that it is possible to extract kinetic rates and mechanical characteristics of the fibrin networks. Furthermore, this strategy can be used, more generally, to precisely mix small volumes of reactive solutions.

5. CONCLUSIONS

Due to the internal length scale of an emulsion, it assembles into a foam-like topology when flowing through a network of microfluidic channels – provided that the dispersed volume fraction is sufficiently large. The foam-like topology allows for well-defined arrangements when interacting with temporally varying channel geometries. A zigzag structure, for example, can be transformed to a bamboo arrangement. Interestingly, this can significantly impact the outcome from a simple Y-piece. Using ferrofluids as the continuous phase, the switching between structures is controlled externally. In addition, the defined geometries provided by discrete microfluidics enable studies of complex biological phenomena, such as the dynamic evolution and parallel measurement of a dense, encapsulated fibrin network.

ACKNOWLEDGEMENTS

The authors thank Udo Krafft for excellent technical assistance. H. E. acknowledges a fellowship from the Alexander von Humboldt foundation.

REFERENCES

[1] W. Drenckhan, S.J. Cox, G. Delaney, H. Holste, D. Weaire, and N. Kern, *Coll. Surf. A*, **263**, 52 (2005).
[2] C. Priest, S. Herminghaus, and R. Seemann, *Appl. Phys. Lett.,* **88**, 024106 (2006).
[3] J.W. Weisel, *Adv. Prot. Chem.*, **70**, 247 (2005).
[4] C. Priest, S. Herminghaus, and R. Seemann, App. Phys. Lett. **89**, 134101 (2006).
[5] H. Song, J. D. Tice, R. F. Ismagilov, *Angew. Chem. Int. Ed.,* **115**, 791 (2003).

OPTICAL FORCING OF MICRODROPS: FLOWS AND TEMPERATURE FIELD CHARACTERIZATION

M. L. Cordero, E. Verneuil and C. N. Baroud
LadHyX, Ecole Polytechnique, FRANCE

ABSTRACT
A laser focused inside a microchannel was recently used as an optical valve to manipulate the formation of water drops in oil [1]. The heating of the interface induces a hydrodynamic force through the creation of convection rolls in the fluids. Here, we report the measurements of the temperature rise due to laser absorption in a quasi 2D geometry, that we extrapolate to the microdrop geometry. Also, the velocity field created inside the water by the thermal gradient was measured and from it the development time of the force was deduced.

Keywords: Droplet Microfluidics, Optical Forcing

1. INTRODUCTION

Recently, we have presented a new optical tool for the control of microdrop formation [1]. In a flow focusing device (FFD) where water droplets in oil are produced in the presence of surfactant (fig. 1(a)), a laser beam is focused, creating a thermal gradient along the water/oil interface. A thermocapillary flow appears that induces recirculation rolls in the water and in the oil (fig. 1(b)). This external flow produces, through viscous effects, a force that can hold the interface. The velocity of the rolls is believed to be proportional to the maximum temperature increase ΔT. To characterize the force, the temperature increase in the drops is estimated from the temperature profile of a thin water film heated by the laser beam. Further, the rolls are studied by measuring the velocity field inside the water by Particle Image Velocimetry (PIV) and the force development time is deduced from the evolution of the velocity.

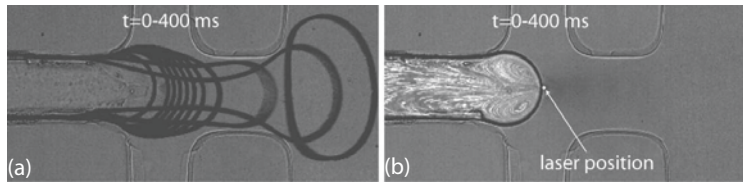

Figure 1: (a) Water drop formation in a FFD. (b) Focusing a laser beam inside the microchannel induces a temperature gradient which creates a force that can hold the interface for up to several seconds.

2. EXPERIMENTAL

The experimental setup (fig. 2) consists of an inverted microscope, with a 10x objective (NA=0.3), used both for imaging and for focusing the laser inside the sample. The focused laser (λ =1480 nm) has a beam waist size $\omega_0 = 5.5$ μm. Epi-fluorescence images of the sample are taken with a fast camera at 500 fps.

The microchannels are fabricated using standard SU-8 lithography and PDMS techniques [2]. Their final height and width are 35 μm and 100 μm respectively.

978-0-9798064-0-7/μTAS2007/$20©2007CBMS

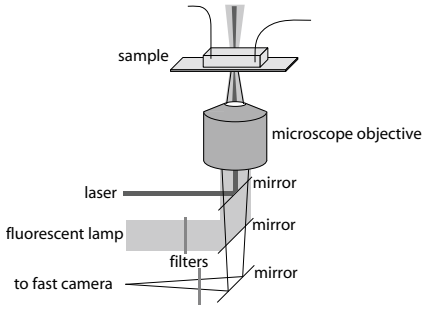

Figure 2: Experimental Setup.

The heating of a water film due to the absorption of the laser beam was measured. For that, an aqueous solution of a temperature sensitive fluorescent dye, Rhodamine B (0.1 mM in TRIS buffer, pH=7.8) is put between two glass slides, separated by a 35 μm thick spacer. After calibration of the fluorescence intensity of the solution with temperature, the temperature profile in the laser heated solution is measured from its fluorescence.

The velocity field of the thermocapillary rolls was measured using PIV by adding colloidal fluorescent beads (0.5 μm FITC labeled) to the water (fig. 1(b)).

3. RESULTS AND DISCUSSION

A steady state temperature profile of the laser heated water film is shown in fig. 3(a) along with a lorentzian curve fit $T = T_0 + \Delta T(1 + (r/\sigma)^2)^{-1}$ [3]. The time required for the temperature at the center, ΔT, and for the width of the hot spot, σ, to reach a steady state are ~ 10 ms and ~ 100 ms (fig. 3(b) and (c)) respectively. For a laser power of 100 mW, the final width of the hot spot is $\sigma \sim 10\mu$m and the maximum temperature increase is $\Delta T \sim 50\ ^o$C.

When the laser is focused inside the microchannels the heating is slightly different, beacuse PDMS has a lower thermal conductivity than glass. These quantitative differences do not affect the qualitative behavior shown above.

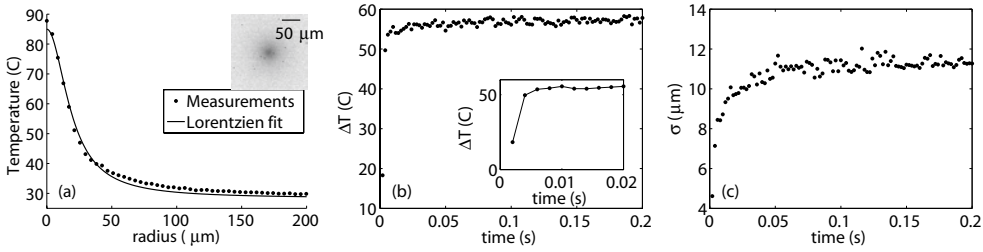

Figure 3: (a) Radial temperature profile. The experimental points are fit by a lorentzian curve. Inset: Fluorescence image of the hot spot. (b) Maximum temperature as a function of time. Inset: Zoom for the first 20 ms. (c) Width of the hot spot, deduced from the lorentzian fit.

An average velocity field inside the water is shown in fig. 4(a). The flow at the interface goes towards the hot spot, indicating an increase of surface tension, contrary to what is expected from the Marangoni effect [4]. This is likely due to the presence of surfactant.

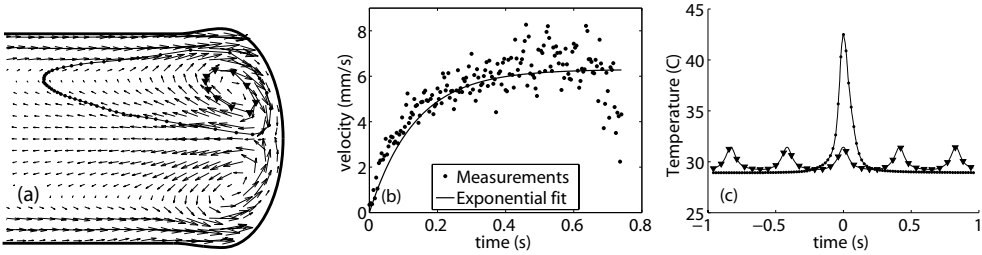

Figure 4: (a) Average velocity field. Two different trajectories are shown. (b) Characteristic velocity as a function of time. (c) Temperature of fluid particles that follows the trajectories shown in (a), assuming as temperature profile inside the water the one shown in fig. 3(a).

A characteristic velocity of the rolls inside the water is deduced from the PIV measurements. The formation time of the rolls is found to be $\tau_{hydro} \sim 100$ ms (fig. 4(b)). Since these rolls are the origin of the hydrodynamic force on the drop, this time corresponds also to the development time of the force.

4. CONCLUSIONS

For lab-on-a-chip applications, the heating may be a major concern, if drops are to be used as reaction chambers for the study of biochemical reactions, for example. However, from the temperature measurements shown here, it is found that the heating is strongly localized. From the Peclet number $Pe = UL/\chi \sim 0.1$, with χ the thermal diffusivity of water, $U \sim v$ and $L \sim \sigma$, we expect that the temperature profile inside the water will be similar to that found in the absence of flow. The temperature experienced by a fluid particle as a function of time can therefore be obtained by combining the velocity field and the temperature measurements as presented in fig. 4(c). Particles remain in the hot zone for around 100 ms, and the maximum temperature increase strongly depends on the trajectory: only the particles very close to the interface experience a temperature increase higher than 15 ^{o}C. Finally, we insist that only a thermal gradient is necessary for the creation of the force. For practical uses, the system can be kept at a low temperature to avoid dammage of the components [5].

REFERENCES

[1] C. N. Baroud, J.-P. Delville, F. Gallaire, and R. Wunenburger. *Phys. Rev. E*, 75(4):046302(5), 2007.

[2] Y. Xia and G. M. Whitesides. *Angew. Chem. Int. Ed.*, 37:550–575, 1998.

[3] S. Duhr and D. Braun. *Phys. Rev. Lett.*, 97(3):038103(4), 2006.

[4] N. O. Young, J. S. Goldstein, and M. J. Block. *J. Fluid Mech.*, 6:350–356, 1959.

[5] R. Zondervan, F. Kulzer, H. Van der Meer, J. A. J. M. Disselhorst, and M. Orrit. *Biophys. J.*, 90:2958–2969, 2006.

POLYMER MICROSPHERE MASS PRODUCTION USING 128-CHANNEL DIGITAL FLUIDIC CHIP

Albert Tsung-Hsi Hsieh[1], Jen-Hao Pan[1], Pablo G. Pinasco[1], Jeff S. Fisher[1], Lung-Hsin Hung[1] and Abraham P. Lee[1,2]

[1]Department of Biomedical Engineering, [2]Department of Mechanical and Aerospace Engineering, University of California, Irvine, 3120 Natural Sciences II, Irvine, CA 92697

ABSTRACT

The conventional microfluidic droplet generation system usually has only one channel for microdroplet generation, so the droplet generation rate is limited. Therefore, it has limitations for industrial applications that require mass production. We developed a device based on Y-junctions with 128-channel microdroplet generation platform by splitting one primary droplet into 128 monodispersed daughter droplets. We also investigated the Y-junction channel with different angels for monodispersed droplet generation and utilized software to simulate the splitting results, and the simulations and experiments agree well with each other.

Keywords: Microdroplet, multi-channel, digital fluidics, monodispersed

1. INTRODUCTION

The general design of microfluidic droplet generation system has only single channel to produce droplets through an orifice one at a time. This design for droplet emulsion processes has severe limitations on the generation rate for mass production. Moreover, in conventional microfluidic droplet generation channels[1,2], it is not easy to generate a given number of same size droplets that have identical chemical or biological conditions. The serially generated and chemically distinct droplets can be replicated through repeatedly splitting channels [3].

2. THEORY

The microdroplet breaking theory was presented [4]. The microdroplet breaking in the fluid is related to the many factors.

$$Ca = \frac{\mu\gamma\, a}{\sigma} \quad Bo = \frac{\Delta\rho g a^2}{\sigma} \quad \lambda = \frac{\upsilon}{\mu} \qquad \textbf{(1)}$$

In equation 1, where $\boldsymbol{\mu}$ and $\boldsymbol{\upsilon}$ are the viscosities of the continuous and dispersed phases, $\boldsymbol{\sigma}$ is the interfacial tension, $\boldsymbol{\Delta\rho}$ is the density contrast between the two phases, $\mathbf{g}$ is the acceleration of gravity, γ is the imposed shear rate, and a is the undeformed drop radius. The fluidic shear force-only droplet splitting usually generates high fluidic resistance in the system. The ninety-degree splitting designs normally result in high resistance and are an obstacle for developing a robust platform which has several consecutive fission bifurcating junctions. Therefore, the goal is to reduce the fluidic resistance in multi-generation droplet generation system and still have sufficient mechanical force to enable microdroplet breaking in microchannels will result in a stable droplet-generation system.

3. EXPERIMENTAL

A 128-channel microdroplet generation platform produces 128 replicated droplets in 45° Y-junction bifurcating channels. The device is made in polydimethylsiloxane (PDMS)

978-0-9798064-0-7/μTAS2007/$20©2007CBMS

material as shown in Figure 1. Three different angles of Y-junction 32-channel microdroplet generators were also fabricated and evaluated. Poly (ethylene glycol)–PEG is a non-toxic and biocompatible drug carrier material [5]. Monodispered PEG microsphere production is critical for drug release and delivery efficiency. The main stream of two merged reagents fluids were pinched by mineral oil and generated microdroplets. The PEG reagents were mixed while droplets traveled in mixing region of device and the reagents are completely mixed in primary droplet and subsequently split into 128 daughter droplets by 7 consecutive fission channels.

4. RESULT AND DISCUSSION

In Figure 2, it is observed that the droplet was not evenly split at the bifurcation point when the divergence angle is 30° (a) and 90° (c), and generated different size daughter droplets. From figure 2 (b), we observed the same size droplet was split at the bifurcation point of 45° channel. Furthermore, the droplet size is monodispersed at the downstream of 32-channel outlet. For the 90° design, the instability may be induced by the high resistance of numerous ninety-degree turns in the system [4, 6-8]. For 30° design, the uneven splitting may be due to the fact that shear force at the 30° bifurcating point is too low to evenly break the droplet, even though the sharp bifurcation point could "cut" the droplet. The droplet splitting has good stability in 45° Y-junction channel. The 45° design not only has shear force induced droplet splitting, but there is also "cutting" of the droplets at the tip of V shape bifurcation point. These two reasons explain why the 45° Y-junction channel can be used as a stable and robust platform for not only 32-channel droplet generation device, but also 128-channel. An empirical photo of Y-junction based 128 microdroplet generation channel is shown in Figure 3. The droplet splitting efficiency is also associated with the droplet length (L) and width (W) ratio (L/W). The L/W ratio associated droplet splitting was evaluated as shown in table 1. The bifurcating angle associated splitting efficiency was also simulated by a multi-physics package (CFD-ACE) to determine an optimal system design as shown in Figure 4. These results agree well with our empirical data as shown in Figure 2. Figure 5 shows the PEG particle formulated using the 128-channel droplet generation platform.

5. CONCLUSIONS

From the experimental result and simulation, we can observe that the channel with 45° bifurcating angle is a stable and robust design for generating monodispersed 128 microdroplets from 7 generations of fission bifurcating junctions. This type of design can be used for polymer microsphere mass production.

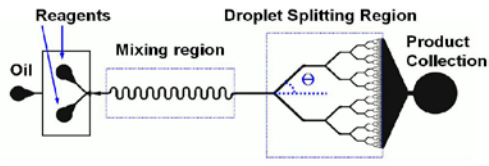

Figure 1: Schematic of Y-junction based 128 multi-split channel system for PEG polymer micro particle formulation.

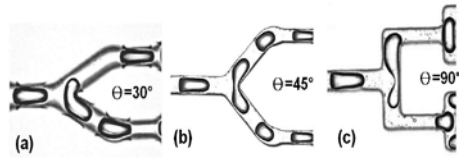

Figure 2. (a)Microdroplet splitting failed in 30-degree bifurcation channel. (b)Microdroplet was evenly split in 45-degree bifurcation channel (c) Micro-droplet splitting failed in 90-degree bifurcation channel

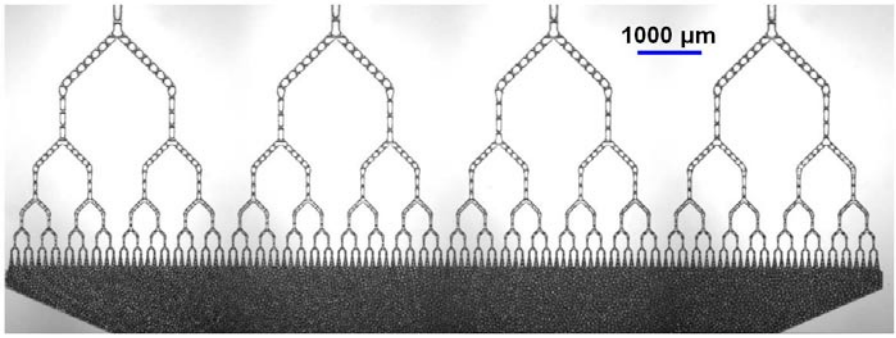

Figure 3. Micrograph of microdroplet splitting, which was successful in 45-degree bifurcation channel of 128 splitting channels. Monodispersed microdroplets in product reservoir have size in 45 µm. Abundant droplets are overlapped.

Table 1. The droplet length (L) and width (W) ratio L/W will affect the droplet splitting results. "F" stands for" failed" monodispsesed droplets generation. "S" stands for "successful splitting" designed for monodispersed droplet generation.

Ratio / Angel	1.6	1.8	2	2.2	2.4	2.6	2.8	3	3.2
30°	F	F	F	F	F	F	F	F	F
45°	F	F	F	F	F	S	S	S	S
90°	F	F	F	F	F	F	F	F	F

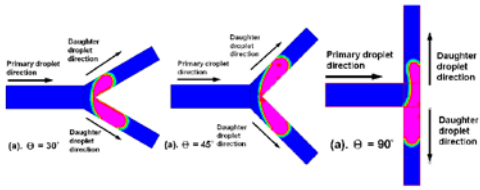

Figure 4. The bifurcating angle associated droplet splitting was also simulated by CFD-ACE. (a) 30- degree, (b) 45- degree (c) 90 degree. The simulation result of 128-channel with 7 generation splitting match our empirical data



Figure 5. PEG particle formulated in microdroplet using 128 multi-split channel system

REFERENCES:

1. Tan, Y.C., et al., *Design of microfluidic channel geometries for the control of droplet volume, chemical concentration, and sorting.* Lab on a Chip, 2004. **4**(4): p. 292-298.

2. Tice, J.D., et al., *Formation of droplets and mixing in multiphase microfluidics at low values of the Reynolds and the capillary numbers.* Langmuir, 2003. **19**(22): p. 9127-9133.

3. Adamson, D.N., et al., *Production of arrays of chemically distinct nanolitre plugs via repeated splitting in microfluidic devices.* Lab on a Chip, 2006. **6**(9): p. 1178-1186.

4.Cristini, V., J. Blawzdziewicz, and M. Loewenberg, *Drop breakup in three-dimensional viscous flows.* Physics of Fluids, 1998. **10**(8): p. 1781-1783.

5. Veronese, F.M. and G. Pasut, *EGylation, successful approach to drug delivery.* Drug Discovery Today, 2005. **10**(21-24): p. 1451-1458.

6. Cristini, V. and Y.C. Tan, *Theory and numerical simulation of droplet dynamics in complex flows - a review.* Lab on a Chip, 2004. **4**(4): p. 257-264.

7. Stone, H.A., *Dynamics of Drop Deformation and Breakup in Viscous Fluids.* Annual Review of Fluid Mechanics, 1994. **26**: p. 65-102.

8. Jousse, F., et al., *Bifurcation of droplet flows within capillaries.* Physical Review E, 2006. **74**(3): p. -.Art. No.036311

SIOC AS A HYDROPHOBIC LAYER FOR ELECTROWETTING ON DIELECTRIC APPLICATIONS

J. Thery[1], M. Borella[2], S. Le Vot[1], D. Jary[1], F. Rivera[1], G. Castellan[1], A.G. Brachet[1], M. Plissonnier[2] and Y. Fouillet[1]

1. Department of Technology for Biology and Health - LETI

2. Department of Technology for NanoMaterials - LITEN

CEA-Leti-Minatec, 17 rue des Martyrs, 38054 Grenoble, France

ABSTRACT

This paper deals with the development of a new hydrophobic technology based on the SiOC layer. Lab-on-a-chip devices using such layers are fabricated and successfully validated. The main advantages and physical properties are discussed.

Keywords: Digital microfluidic, Electrowetting, Super-hydrophobic

1. INTRODUCTION

The electrowetting on dielectric (EWOD) technique can modify the apparent contact angle of a conductive droplet placed on a hydrophobic and dielectric surface deposited on a buried electrode. This phenomenon was explained by Berge [1] and is now used by numerous research laboratories in different fields of application. A critical point in electrowetting technology is the fabrication of the dielectric and hydrophobic layer. The EWOD techniques is generally based on a first dielectric layer (Si3N4 or SiO2), subsequently coated with a hydrophobic layer. Until now, this hydrophobic layer has been made of fluoro-polymers such as Teflon® [2, 3] usually deposited by dipping or spinning procedures. Unfortunately, these technologies are neither conform to the shape of a 3D structured substrate nor reproducible. For Lab-on-a-chip systems, where the hydrophobic layer must be deposited on processed surfaces, with large aspect ratio structures, conformal growth techniques are required. We have developed a new dielectric / hydrophobic coating, for EWOD microfluidic applications that can be deposited by PECVD (Plasma Enhanced Chemical Vapor Deposition). The deposited layer is made of SiOC which is a standard material used as a dielectric layer in CMOS technology. The nature of precursor and the plasma conditions were optimized in order to improve the hydrophobic properties.

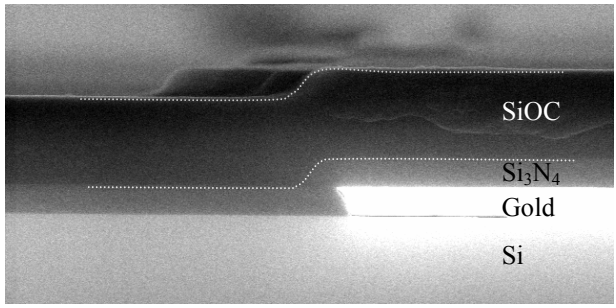

Fig 1: MEB visualisation of the stack composed of: gold electrode 300nm / Si_3N_4 300 nm / SiOC 1000 nm. Conformational property of SiOC layer is observed over the electrode edge (interfaces of the stack are highlighted by dotted lines).

978-0-9798064-0-7/µTAS2007/$20©2007CBMS

2. SIOC CARACTERISITCS AND TECHNOLOGY

The electrical properties of SIOC were measured and compared to Teflon (Fig.2). With a wetting hysteresis of water under air of around 10° and contact angles of 105°, droplets actuation characteristics are closed to those observed with Teflon®. This deposition process is performed at room temperature and is therefore compatible with the use of a polymeric substrate. In addition, it is fully compatible with clean-room requirements and can handle full 200 mm wafers. Another advantage compared with Teflon is that fluorocarbon solvent like FC-70 can be used instead of conventional oil as the ambient medium.

	ε_R *relative dielectric coefficient*	*dielectric strength* 10^8 *V/m*
Teflon	~2	~1.5.
SiOC	2.75	1.5 – 4.7.

(a)

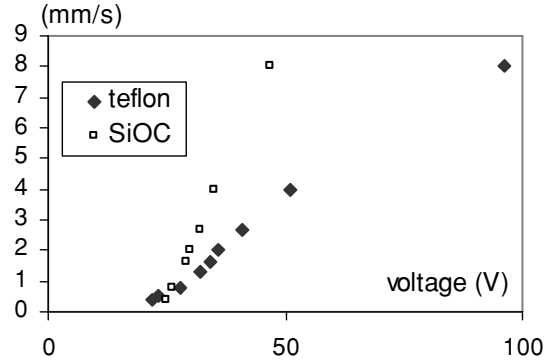

(b)

Fig 2: (a) Comparison of SIOC and Teflon (AF 1600 DuPont ® deposited by spin coating). (b) Droplet velocity versus voltage on open EWOD chip [4] coated with SiOC or Teflon. Droplet volume is 0.8µl of water and ambient medium is oil (viscosity 30mPa.s).

Respective influences of the thickness of SiN and SiOC coating on both actuation tension and dielectric breakdown were studied in order to optimize the technology (Fig 3). Surface degradation may occure when the total applied tension reaches a value leading to the breakdown of the 1000 nm thick SiOC film. The theoretical value of this total tension is given by the dashed line considering a repartition of the total applied tension between SiOC and SiN film. For larger total applied tension, the whole tension is localised in SiN layer. Electrolysis will occur after the breakdown of this layer (full line). The experimental data (squares, crosses, triangles and diamonds) corresponding to electrolysis appearance match well with theoretical curves ; experimental conditions are F=3kHz, droplet of Tris HCl 1mM, T=20°C. One can thus define a working zone where no electrolysis and no surface degradation are observed.

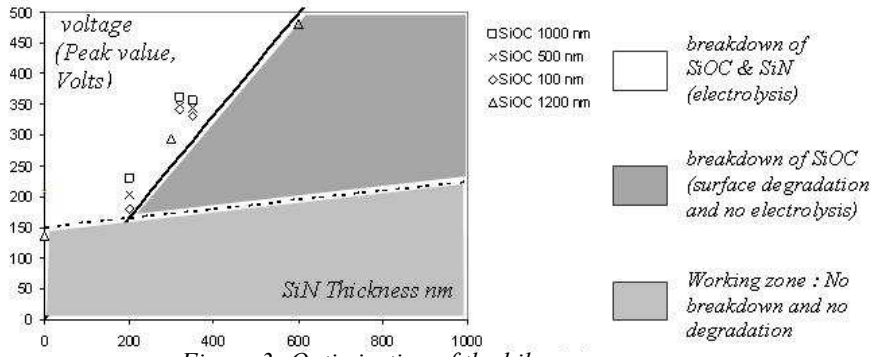

Figure 3: Optimisation of the bilayer.

3. CHIP VALIDATION

The chip is obtained using the following stack: a 300nm thick layer of gold is deposited on an insulating substrate. The gold electrodes are etched and covered with a 300nm thick dielectric layer of silicon nitride. Walls of 100µm high are implemented using an Ordyl dry film resist (Elga) and further coated with a 1000nm layer of SiOC. The walls are also used to isolate different chip zones such as reservoirs or reaction zones, or to limit cross-talks between droplets [5]. Conformational properties of the SiOC layer are essential to avoid droplet wetting on Ordyl walls. This technology was validated by biological experiments : DNA amplification of different biological models (human DNA, bacterial DNA from *E. Coli*, viral DNA from λ phage and others) has been performed by PCR with real time fluorescence detection. It has been shown that the amplification realized in a 64nl droplet takes place with the same specificity and same yield as a 10µl test in tube.

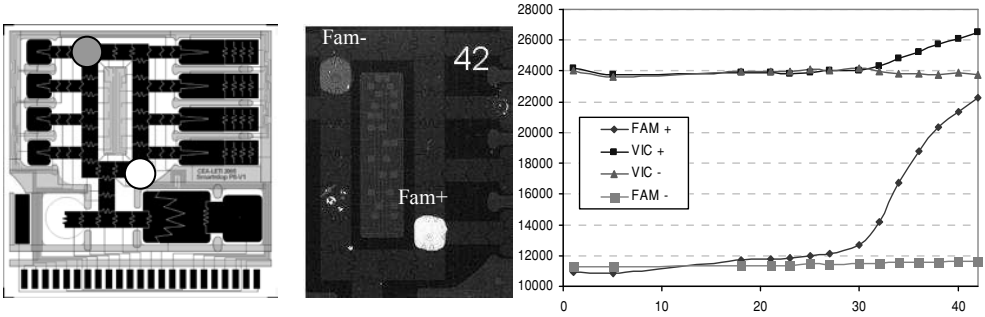

Figure 4:. Genotypage validation. From left to right: EWOD chip layout [5], Real time PCR in 64 nl droplet: in the fluorescent droplet 50 copies of human DNA have been amplified and the other droplet is the negative control. Two colors fluorescence (FAM, VIC) of heterozygote sample and negative control versus cycle number.

5 CONCLUSION

A new hydrophobic coating was developed and validated for Lab–on-a-chip with dielectric and hydrophobic properies equivalent to Teflon. One advantages is the use of standard microelectronics machine giving a very reproducible and homogeneus layer on the whole wafer surface. The conformal layer can be deposited on non planar substrate presenting walls or grooves. Futhermore, the material is bio-compatible with common protocole like PCR. SIOC layer is now our standard process for EWOD technology.

REFERENCES

[1] B. Berge, Electrocapillarity and Wetting of Insulator Films by Water. C.R. Physique, **5**, 577 (2004).

[2] M. G. Pollack, R. B. Fair, and A. D. Shenderov, Electrowetting-based actuation of liquid droplets for microfluidic applications. Applied Physics Letters 77, 1725 (2000).

[3] H. Moon, S. K. Cho, R. L. Garrell, et al., Low voltage electrowetting-on-dielectric Journal of Applied Physics 92, 4080 (2002).

[4] R. Bavière and y. Fouillet, Dynamics of droplet transport induced by electrowetting actuation. Microfluidics and Nanofluidics (2007) accepted.

[5] Y. Fouillet, D. Jary, C. Chabrol, P. Claustre, C. Peponnet., Digital microfluidic design and optimization for lab on a chip systems Microfluidics and Nanofluidics (2007) accepted.

SURFACE INDUCED DROPLET FUSION IN MICROFLUIDIC DEVICES

Luis M. Fidalgo[1], Chris Abell[2] and Wilhelm T. S. Huck[1]

[1]Melville Laboratory for Polymer Synthesis, Department of Chemistry, University of Cambridge, Cambridge, United Kingdom, [2]Department of Chemistry, University of Cambridge, Cambridge, United Kingdom

ABSTRACT

Here we demonstrate a new method for droplet fusion based on a surface energy pattern on the walls of a microfluidic device, that does not require active elements nor accurate synchronization of the droplets.

Keywords: Microdroplets, Droplet Fusion, Surface Patterning

1. INTRODUCTION

Microdroplets formed within microfluidic devices present a unique platform for the miniaturization of chemical and biochemical reactions.[1] The principal benefits lie in the ability to create nanoliter to femtoliter-sized individual reactors in which the contents can be accurately controlled. Microdroplet formation and stability depends on the interfacial energies between the different phases as well as the channel walls of the device. Stable water-in-oil emulsions are readily formed by injecting an aqueous stream into an oil stream within a hydrophobic device;[2, 3] changing the surface energy of the channel may compromise their stability. Droplet fusion is a fundamental tool for the control of microdroplets in microfluidic devices and their use as microreactors, as it allows the precise mixing of reagents at well-defined points in space and time. Thus far, both electric fields and physical contact have been used to induce droplet coalescence.[4, 5] In this paper we describe a new method of droplet fusion based on surface energy patterning inside microfluidic channels that allows the fusion of more than two droplets at a single point.

2. EXPERIMENTAL

To generate the surface energy pattern we used a photografting method developed and optimized by Allbritton et al.[6] In this method, poly (acrylic acid) (PAA) is grafted *via* UV photopolymerization on planar benzophenone-containing poly(dimethyl siloxane) (PDMS) substrates (Fig. 1 a). Selective grafting is achieved by exposing PDMS to UV through a photomask. The grafted PAA pattern is hydrophilic, whereas native PDMS is hydrophobic. These patterned substrates are used to fabricate microfluidic devices by aligning them with moulded PDMS microchannels.[7] To seal the devices, both the channel and the grafted surface are treated with an oxygen plasma and then immediately brought into contact. Figure 1 (b) shows a micrograph of a device where the PAA pattern was selectively stained with toluidine blue. Typical widths of the PAA patterns used are in the 100 µm range. All chemicals were obtained from Sigma–Aldrich. Oil phases used were 30% wt solutions of 1H, 1H, 2H, 2H-perfluoro-1-octanol in Fluorinert FC-77. The black aqueous phase in Figure 2 was black food dye. Aqueous solutions of Fe(NO)3 (0.067 M) and KSCN (0.2 M) were used in Figure 4. Flow rates in Figure 2 were 105 µl/h for the oil phase and 6 µl/h for each aqueous phase. Flow rates in Figure 4 were 300 µl/h for the oil phase and 30 µl/h for the aqueous phase at each flow focusing device.

978-0-9798064-0-7/µTAS2007/$20©2007CBMS

3. RESULTS AND DISCUSSION

Figure 1 (c) shows a schematic for a patterned device with a double T-Junction channel. This geometry allows the formation of alternating droplets of two different aqueous streams by injecting them into a stream of immiscible oil. Figure 2 shows micrographs of such a device in operation. Droplets of distilled water and a dye solution are formed in a continuous fluorous phase. When these droplets flow past the hydrophilic stripe (center of dashed rectangle), they interact with it and are trapped. If more than one droplet is trapped, they are effectively fused and their contents mixed. The trapped droplet is released when the viscous drag force overcomes the surface energy stabilization. The insets in Figure 2 show a time sequence of droplet trapping, fusion and release. As the Figure demonstrates, this method effectively fuses alternating droplets with different contents.

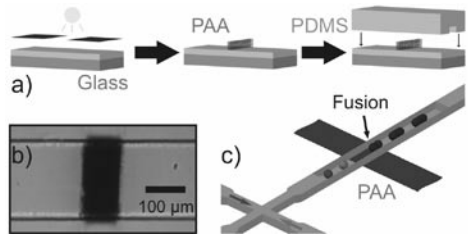

Figure 1 (a) Schematic of surface energy patterned microfluidic device fabrication. Glass supported PDMS substrates previously infiltrated with benzophenone are covered with a solution containing acrylic acid, exposed to UV light and sealed to PDMS moulded microchannels **(b)** Micrograph of a microfluidic channel containing a patterned poly(acrylic acid) structure that was stained with toluidine blue **(c)** Schematic of a PDMS microfluidic device containing a hydrophilic pattern. Droplets of different components are formed at a double T-junction, and when they encounter the hydrophilic pattern they are trapped, fused and effectively mixed.

When considering the process in more detail, we can divide surface induced droplet fusion in two subsequent processes: droplet trapping and droplet detachment. Droplet trapping can be understood as coalescence between the droplets and the pattern, and depends on the same factors as coalescence in bulk. Droplet detachment is essentially similar to droplet formation and is governed by the balance between viscous drag force and interfacial force. In the limit of low Reynolds number, increasing the outer fluid velocity decreases the volume at which the viscous drag overcomes the interfacial tension and causes a droplet to detach.[8] In our case this means that increasing oil speed will induce the detachment of smaller droplets and hence decrease the number of droplets added before droplet detachment. Therefore, controlling the oil speed provides control over the number of droplets fused before a new one is released (Fig. 3). Eventually, increasing the fluid velocity will lead to a time of contact between the droplet and the pattern insufficient for coalescence. The results shown in Figure 3 were obtained by generating droplets at a flow focusing device. This geometry is known to form droplets in a very reliable and controllable manner.[2] For a large number of chemical reactions more than two reagents need to be combined simultaneously. Several components can be incorporated to a droplet at a single fusion step using devices comprising multiple flow focusing devices and surface energy patterns. Figure 4 shows a device where droplets of $Fe(NO_3)_3$, KSCN and water are formed separately before fusion. Upon fusion, Fe^{3+} and SCN^- react forming a coloured complex. The process is similar to the fusion of two droplets and shows dependence on the same variables. Increasing the number of flow focusing devices could potentially provide a tool to combine an unlimited number of components at a single fusion step with very fast mixing.

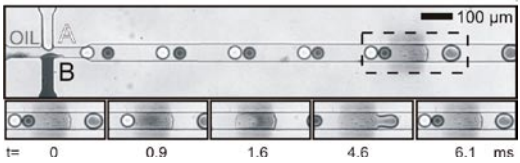

Figure 2 Sequence of surface induced droplet fusion. Droplets of different components approach the hydrophilic pattern (t=0 ms) before they are trapped and fused (t=0.9, 1.6 ms). A new droplet combination of both is released (t=4.6, 6.1 ms)



Figure 4 Incorporation of several components into a droplet *via* a single fusion event. Three different streams of droplets are generated at independent flow focusing devices and combined at the hydrophilic pattern forming droplets containing the three components.

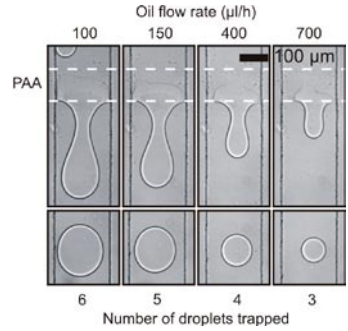

Figure 3 Control of surface induced droplet fusion by variation of fluid velocity. The upper series of micrographs shows the hydrophilic pattern retaining different amounts of water for different oil flow rates. The lower series of micrographs shows the resultant water droplet released for each flow rate.

4. CONCLUSIONS

In summary, we present a new approach for microdroplet control in microfluidic devices. Surface modification can be used to induce fusion and fast mixing of several previously formed droplets. It does not require active elements nor accurate synchronization of droplets, and it is compatible with standard device fabrication techniques. It allows fusion of more than two droplets at a single step and potentially the incorporation of any desired number of components at once.

ACKNOWLEDGEMENTS

This work was supported by the EPSRC and the RCUK Basic Technology Programme.

REFERENCES

[1] Song, H., D.L. Chen, and R.F. Ismagilov, *Reactions in Droplets in Microfluidic Channels.* Angew. Chem. Int. Ed., 2006. **45**: p. 7336-7356.

[2] Anna, S.L., N. Bontoux, and H.A. Stone, *Formation of dispersions using "flow focusing" in microchannels.* Appl. Phys. Lett., 2003. **82**: p. 364-366.

[3] Thorsen, T., et al., *Dynamic Pattern Formation in a Vesicle-Generating Microfluidic Device.* Phys. Rev. Lett., 2001. **86**: p. 4163-4166.

[4] Ahn, K., et al., *Electrocoalescence of drops synchronized by size-dependent flow in microfluidic channels.* Applied Physics Letters, 2006. **88**: p. 264105.

[5] Tan, Y.-C., et al., *Design of microfluidic channel geometries for the control of droplet volume, chemical concentration, and sorting.* Lab Chip, 2004. **4**: p. 292-298.

[6] Wang, Y., et al., *Covalent Micropatterning of Poly(dimethylsiloxane) by Photografting through a Mask.* Anal. Chem., 2005. **77**: p. 7539-7546.

[7] McDonald, J.C., et al., *Fabrication of microfluidic systems in poly(dimethylsiloxane).* Electrophoresis, 2000. **21**: p. 27-40.

[8] Umbanhowar, P.B., V. Prasad, and D.A. Weitz, *Monodisperse Emulsion Generation via Drop Break Off in a Coflowing Stream.* Langmuir, 2000. **16**: p. 347-351.

THERMALLY TRIGGERED MODULATION OF FLOW CHANNEL GEOMETRY AND LAYOUT

Vahid Bazargan and Boris Stoeber
University of British Columbia, CANADA

ABSTRACT

This paper demonstrates new methods to modify the geometry and layout of individual flow channels on a microfluidic chip during operation. Using Pluronic as a thermally responsive polymer in the fluid stream allows controlled and reversible gel formation in the micro channel through controlling the device temperatures to modulate the channel width. In addition, by combining Pluronic besides a saline solution in a T-shape microfluidic channel interdiffusion of the two species leads to a lower gel formation temperature, which is used for automatic formation of a separation wall along the channel axis.

Keywords: Microfluidics, Pluronic, Thermal channel variation.

1. INTRODUCTION

In conventional microfluidic devices, the geometry of flow channels and structures is defined by photolithography and, once built, the channel layout cannot be changed. Here we use controlled uniform heating of the microfluidic chip to achieve strategic gel formation of a Pluronic solution as a thermally responsive fluid (TRF) for temporary channel geometry modification after fabrication. Pluronic solutions solidify reversibly at elevated temperature and form a soft gel. In addition, these materials are shear thinning, leading to higher gel formation temperature in regions of high shear. Previously, Pluronic solutions were used for active microvalves [1] and for passive flow control due to viscous heating [2]. Here we have realized the temporary channel modification in two different ways. In method 1, as shown in Fig.1.a, Pluronic gels at elevated temperatures in the low shear regions of a microfluidic channel (see Fig. 1.c), because of its shear thinning properties, so that temperature variations modulate the channel width. In the second method, a salt from a co-streaming fluid promotes gelation at lower temperature, leading to a wall within the channel at the interface between the fluids.

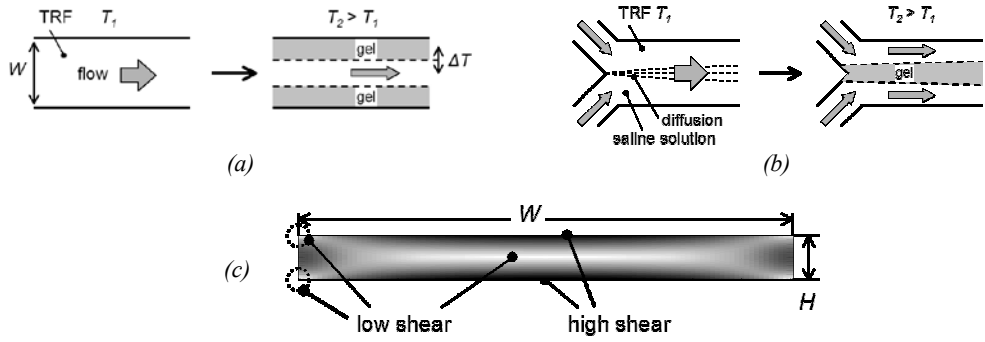

Figure 1: (a) Thermal modification of the channel width, (b) co-streaming saline solution promotes gel at lower temperature at the Pluronic-saline interface, (c) shear rate distribution of a Newtonian fluid in a channel cross section.

978-0-9798064-0-7/μTAS2007/$20©2007CBMS

2. EXPERIMENTAL

The polymer Pluronic F127 (from BASF) is used at a concentration of 15wt% in water as the thermally responsive fluid. Microdevices are fabricated from PDMS (poly dimethyl siloxane) and glass using soft lithography to form microchannels at a height of 10µm and a width of 524 µm. Sodium phosphate with a concentration of 1 mol/L is used as the co-streaming saline flow. The solutions are seeded with fluorescent particles (200 nm) for flow visualization. The flow is driven using a syringe pump. The device temperature is controlled by a Peltier device.

3. RESULTS AND DISCUSSION

The 15 wt% Pluronic solution flows through the channel at a constant flow rate $Q = 3$ µL/min. At temperatures above the gel temperature, gel formation originating from the low-shear regions in the channel corners propagates toward the channel center as shown in the micrograph in Fig. 2a. At $T = 28°C$ the channel cross section is reduced by 50%. Low velocity profile of this solution in the flow channel at $T_1 = 24°C$ and at $T_2 = 28°C$ from micro PIV (particle image velocimetry) measurements is shown in Fig. 2b. At T_2 the flow velocity is only non-zero near the channel center, in the gel free region shown in Fig. 2a. The resulting reduction of the channel cross section can be controlled through temperature.

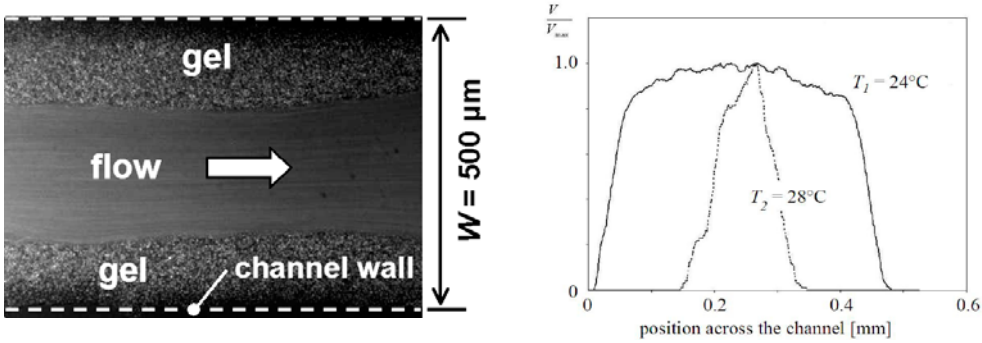

(a) (b)

Figure 2: (a) Thermal gel formation modifies the channel width during device operation, (b) velocity distribution across the channel at $T_1 = 24°C$ and at $T_2 = 28°C$ from MicroPIV measurement.

In the second method addition of sodium phosphate to the Pluronic solution was used to lowers the gelation temperature [3] and to form a gel wall within the flow channel (Fig. 3a). A 15 wt% Pluronic solution and a 1 mol/L sodium phosphate saline solution stream side by side in a channel system at flow rates Q_P and Q_S respectively with $Q_p < Q_S$. The higher viscosity of the Pluronic solution leads to a wide Pluronic stream in the channel next to a narrower saline stream. Pluronic and sodium phosphate diffuse into the respective other stream; this leads to a lower gel formation temperature near the interface, allowing gel formation in this region at 24°C as shown in Fig. 3a.

The flow field from micro PIV in Fig. 3b ($Q_P = 3$µL/h and $Q_S = 30$µL/h) shows an asymmetric velocity distribution within the Pluronic stream with a lower flow velocity near the gel wall. This is due to a viscosity gradient caused by slight diffusion of sodium phosphate into the Pluronic stream. Once formed, the wall can be maintained by keeping

the temperature constant, regardless of the flow rates of the two streams. It is possible to define the location of wall formation in the channel through the viscosities and flow rates of the two streams, while the temperature affects the wall thickness.

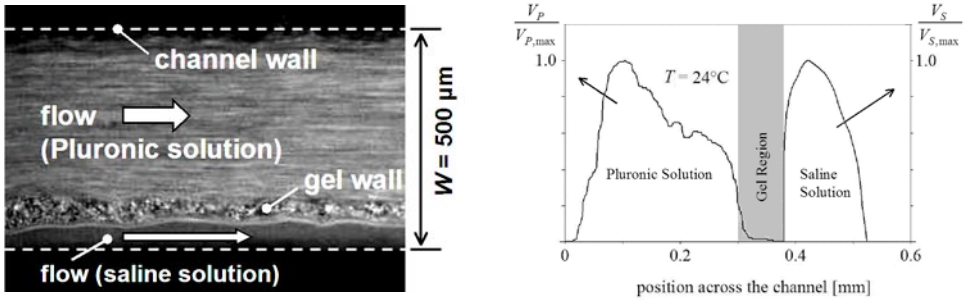

Figure 3: a) At T = 24°C a gel wall forms at the interface between the two fluids within the channel, b) velocity distribution across the flow channel after gel wall formation at 24°C from MicroPIV measurements.

4. CONCLUSIONS

Arbitrary modulation of a microchannel width is achieved so that flow rate and flow velocity can be set independently. This allows arbitrary modulation of the channel width after fabrication without using photolithography. In addition, a wall can be formed within a flow channel separating two co-streaming fluids. This mechanism can be used for automatic formation of a separation wall at constant temperature if the saline concentration is increased. This is an attractive regulation mechanism where under regular conditions cross-stream diffusion is desired such as in the "T-sensor" [4], while diffusion of ionic solvents such as sodium phosphate into a stream containing a biological sample should be limited.

REFERENCES

[1] "Flow Control in Microdevices using Thermally Responsive Triblock Copolymers," B. Stoeber, Z. Yang, D. Liepmann, S. Muller, Journal of Microelectromechanical Systems, 14, 207-213, (2005).

[2] "Passive Flow Control in Microdevices using Thermally Responsive Polymer Solutions," B. Stoeber, C.-M. Hu, D. Liepmann, S. Muller, Physics of Fluids, 18.5, art. no. 053103 (2006).

[3] "Effect of Salts on the Micellization, Clouding, and Solubilization Behavior of Pluronic F127 Solutions," N. Pandit, T. Trygstad, S. Croy, M. Bohorquez, C. Koch, Journal of Colloid and Interface Science, 222 (2), 213-220, (2000).

[4] "Microfluidic Diffusion-Based Separation and Detection", B. H. Weigl, P. Yaeger, Science, 283, 346-347, (1999).

UNIFORM DROPLET GENERATION IN SURFACTANTS/POLYMER/OIL SYSTEMS USING MACRO TO MICRO SCALED CO-FLOW CHANNELS

Manuela R. Duxenneuner[1,2], Peter Fischer[2], Erich J. Windhab[2], and Justin J. Cooper-White[1]

[1]Laboratory of Tissue Engineering and Microfluidics, The University of Queensland, Australia; [2]Laboratory of Food Process Engineering, ETH Zurich, Switzerland

ABSTRACT

This work reports on the drop generation of highly monodisperse water droplets in oil using co-flow and flow-focusing channels of different length scales. The drop formation and breakup dynamics at the capillary tip is analysed thoroughly by using a Phantom high speed camera. Tween®20 surfactants and surfactant/guar gum solutions of different concentrations were used as disperse phase to show the influence of interfacial tension and elasticity forces on the drop formation and breakup event. The experiments were characterized in terms of Weber (We) and Capillary (Ca) number.

Keywords: coflow, droplet formation, surfactants, guar,

1. INTRODUCTION

The production of monodisperse emulsions is highly sought-after in industries required to produce well-structured multiphase systems, as well as for lab-on-the-chip analysis systems[1]. The droplet size and size distribution represent the most important characteristics of designed emulsions. Modern dispersing techniques achieve a polydispersity of the order of 10% (e.g. membrane emulsification) to 1% (e.g. microchannels), with the size being mainly a discrete function of the capillary size and channel geometry[2-5]. In order to produce uniform droplets at the capillary tip, it is important to understand the influence of single parameters and to control them properly.

2. EXPERIMENTAL

Water-like disperse phase was injected into the coflowing continous phase (sunflower oil SFO, Coles Farmland AUS) using coflow glass devices with macro to mini length scale (fig.1A-B), and flow-focusing PDMS-microchannel (fig.1C).

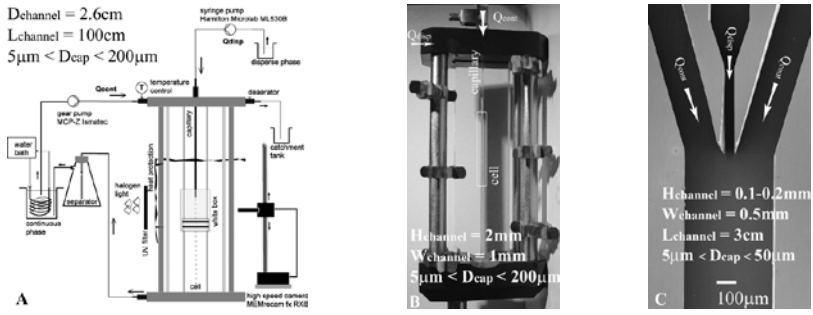

Figure 1. *Two coflow cells of different length scale (**A**: draft of macro setup / **B**: picture of mini glass cell) and a flow focusing microchannel (**C**: PDMS made).*

978-0-9798064-0-7/µTAS2007/$20©2007CBMS

Single process and material parameters could be varied e.g. capillary size (D_{cap}=0.005-1.8mm), cell and capillary material (glass, PDMS, stainless steel), cell dimension (D_{cell}=0.5cm-2.9cm), flow rates (Q_{cont}=0.001-2000ml/min, Q_{disp}=0.0001-1ml/min), and interfacial tension (Γ=4-25mN/m). The dynamic viscosities (η_{cont}=52mPa.s, η_{disp}=1mPa.s) as well as the density of both phases ($\rho_{cont} \approx 0.92 g/cm^3$, $\rho_{disp} \approx 1 g/cm^3$) were kept constant. Tween®20 (polyethylene glycol sorbitan monolaurate) surfactants (c_{TW20}=0.1cmc-100cmc) or surfactant/polymer (JAGUAR HP8; 2-hydroxypropylether guar gum) mixtures (c_{JAG}=0.1- 0.2wt%) were added to the disperse phase. To study the drop generation a Phantom v5 highspeed camera system (30'000fps, 1024x128) was utilized.

4. RESULTS AND DISCUSSION

As illustrated in fig.2A, the drop diameter depends strongly on the concentration of surfactants and also on Q_{cont} in "macro-to-mini" length scale, which agrees with results from literature[2]. However, in microchannel devices the surfactants do not have any influence on drop size and the drop formation event which is also shown in fig.2B and 3.

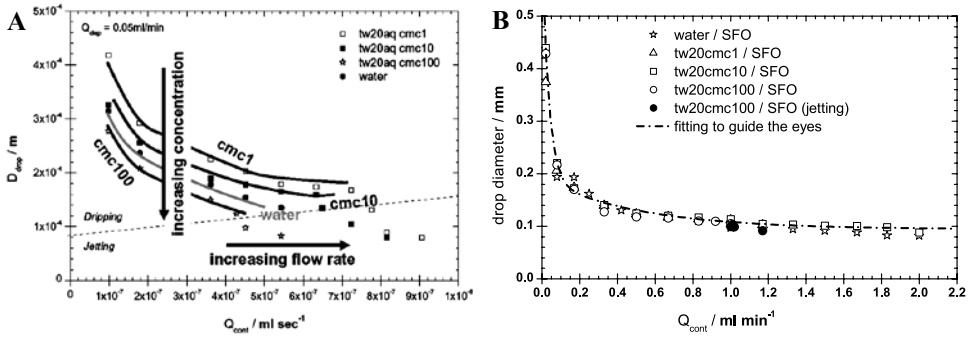

Figure 2. *Dependency of D_{drop} on flow rate of Q_{cont} and concentration of Tween®20 surfactants in macro and mini coflow channels (**A**). Drop diameter versus Q_{cont} for drop formation within microchannel (**B**). All fittings are only to guide the eyes.*

The addition of guar gum to the drop phases increases the elastic effects on the drop creation which is displayed by the enormous thread formation while pinching off (fig.3). With increasing polymer concentration, the length of the thread grows and finally breaks up in several satellite droplets. The size of the droplet also increases with polymer concentration since the drop has more filling time through the thread during pinch-off.

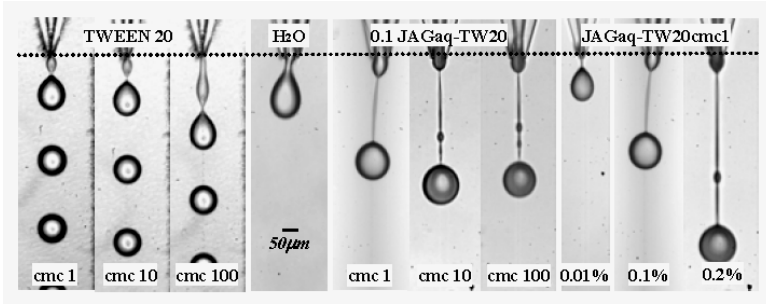

Figure 3. *Drop generation in SFO using microchannel with D_{cap}=0.03mm, Q_{cont}=10ml/h, Q_{disp}=0.1ml/h.*

Fig.4 presents a phase chart of Capillary (Ca= viscous forces / interfacial tension forces) versus Weber number (We= inertia forces / interfacial tension forces) of material and process parameters to illustrate all acting forces on the drop generation at the capillary tip. It was found for "macro-to-mini" scale, that at higher velocity ratios (η_{disp}/η_{cont}) the drag forces imposed by the bulk fluid on the forming droplet dominated interfacial forces. The presence of surfactant had little influence under such flow conditions and the droplets are highly uniform.To the contrary, at lower ratios the interfacial forces strongly effect the drop formation, breakup and satellite droplet formation. The lower the interfacial tension, the greater the number of larger satellite droplets produced. In microchannels, the drop formation is mainly dominated by viscous forces and minimally affected by interfacial tension.

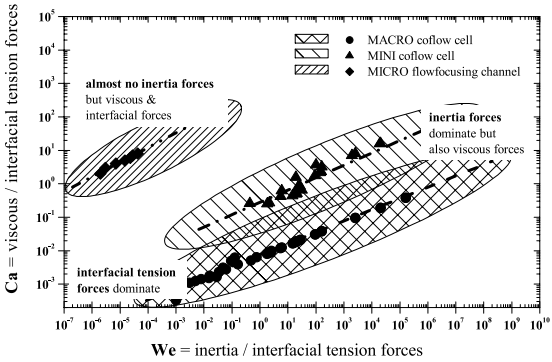

Figure 4. *Phase diagram Capillary, Ca, versus Weber number, We, for all drop breakup setting showing major forces which affect the drop formation.*

5. CONCLUSIONS

We investigated drop formation and pinch-off at the capillary over a large range of length scales systematically, varying different material and process parameters. With the addition of Tween®20 surfactants and guar/surfactants to the disperse phase, differences could be clearly observed. These differences included elongated drop creation and the generation of a thread while pinching off, which is a result of the elastic stresses developed within the fluid. Using the material modification, a diagram of We versus Ca number over a huge range of magnitude, was constructed to illustrate which forces dominate during drop formation. It represents a significant contribution to predicting the flow behavior of drop breakup dynamics in geometrically similar drop dispersing devices.

ACKNOWLEDGEMENTS

This work was mainly setup under DPPICM between University of Queensland and ETH Zurich. It was also financially supported by the ARC Discovery Grants Australia, the fund TH-38/03-3 of the ETH Zurich, and the EU-Project NMP-033339 "Controlled Release".

REFERENCES

[1] G. M. Whitesides, *The origins and the future of microfluidics*, Nature, 442(7101), 368-373, (2006).

[2] C. Cramer, P. Fischer, and E. J. Windhab, *Drop formation in a co-flowing ambient fluid*, Chemical Engineering Science, 59(15), 3045-3058, (2004).

[3] P. B. Umbanhowar, V. Prasad, and D. A. Weitz, *Monodisperse emulsion generation via drop break off in a coflowing stream*, Langmuir, 16(2), 347-351, (2000).

[4] J. Husny and J. J. Cooper-White, *The effect of elasticity on drop creation in T-shaped microchannels*, Journal of Non-Newtonian Fluid Mechanics, 137(1-3), 121-136, (2006).

[5] S. Sugiura, M. Nakajima, and M. Seki, *Prediction of droplet diameter for microchannel emulsification*, Langmuir, 18(10), 3854-3859, (2002).

USING MICROFLUIDIC TECHNOLOGY TO PRODUCE DOUBLE EMULSIONS

Nicolas Pannacci, Thibaut Lockhart, Jérémie Mortreux, Patrick Tabeling, Hervé Willaime

Laboratoire MMN,UMR Gulliver, ESPCI, 10 Rue Vauquelin, 75005 Paris, France

ABSTRACT

We are interested in the morphology of double emulsions in a microfluidic device. The experiments are made in a PDMS microsystem, considering 30 triplets of different fluids. Thanks to classical energetic considerations, we are able to predict the morphologies of the double emulsions. The main conclusion is that the morphologies of the double emulsions created in microfluidic devices are controlled by surface energy.

Keywords : Double emulsions, complete engulfing, janus, morphology

1. INTRODUCTION

Double emulsions (emulsions of two liquids dispersed in a third liquid phase) are widely used in medicine (drug delivery, vaccination,...), cosmetics, food industry etc. Current technologies do not succeed to produce double emulsions under controlled conditions. In this respect, microfluidic technology is extremely promising. Recent studies [1][2] demonstrated the production of double emulsions in glass and PDMS microsystems. Several morphologies (janus, complete engulfment) are currently observed. In this context, it is crucial to have the capability of predicting the structures that are obtained in a given microfluidic device, for a given triplet of fluids. This question is adressed here by considering 30 triplets of fluids, with different surfactants, different materials. In the majority of the cases the morphologies of the double emulsions created in microfluidic devices can be predicted by surface energy considerations.

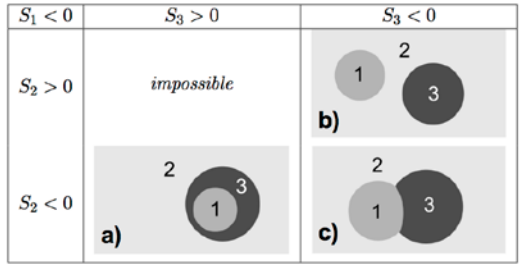

Figure 1. Three possible equilibrium states : a) complete engulfing, b) non-engulfing, c) partial engulfing, depending on spreading coefficients.

2. THEORY

The theory is based on minimizing surfaces energies : according to classical references [3], let us consider interfacial tension γ_{ij} for *i* and *j* fluids and spreading parameters $S_i=\gamma_{jk}-(\gamma_{ij}+\gamma_{ik})$ in case of three *i,j,k* different immiscible fluids. With the convention $\gamma_{12}>\gamma_{23}$, Fig. 1 illustrates the three possible different equilibrium configurations depending on the sets of the *Sij* values : complete engulfing, partial engulfing, no-engulfing.

978-0-9798064-0-7/µTAS2007/$20©2007CBMS

3. EXPERIMENTAL

The systems we used are made in PDMS or NOA (according to a novel technological process [4]) with a double flow focusing geometry (Figure 2). For PDMS systems, the main channel section is 100*100 μm^2 and the walls are hydrophobic or hydrophilic due to oxygen plasma treatment used for the PDMS/PDMS bonding. The double emulsions are obtained either in the dripping or the jetting regime. We measured the interfacial tensions for each fluid interfaces using a ring tensiometer or the pendant drop method. The objects we made are observed after the flow is interrupted.

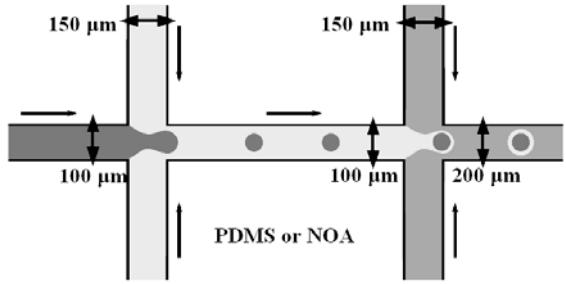

Figure 2. Double flow focusing geometry

4. RESULTS AND DISCUSSION

Fig. 3 is shown a partial engulfing and its comparison to numerical prediction and Fig. 4 shows an example of complete engulfing. Fig. 5 shows typical examples with water, water + SDS (1% w/w), fluorinated oil, silicon oil, colza oil, mineral oil, TPGDA, tetradecane and air. Span 80 is added to some samples of oils. As a whole, we observed consistency between theory and experiment taking into account an uncertainty of 1 mN/m on the measurement of the interfacial tensions. In some cases one can take into acount sharing coefficient between two fluids or the possible spreading of a monolayer in order to explain some discrepancies. It is worth noting that the structures we obtained after stopping the flow are different from those produced just after the nozzle. This indicates that, if one is able to freeze the structures as in Ref [1], one may used microfluidic technology to obtain structures unrealizable with current technologies.

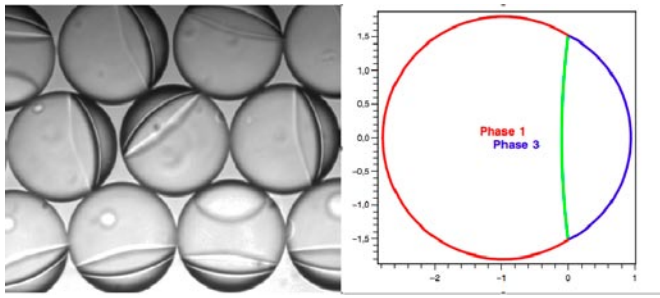

Figure 3. Partial engulfing Silicon oil/Colza oil/Water (left) and predicted morphology.

5. CONCLUSIONS

Microfluidic technology is a powerful tool to accurately control the production of double emulsions and to create new structures.The main conclusion is that surface energy allows to predict the morphologies of double droplets we obtain in a microfluidic device.

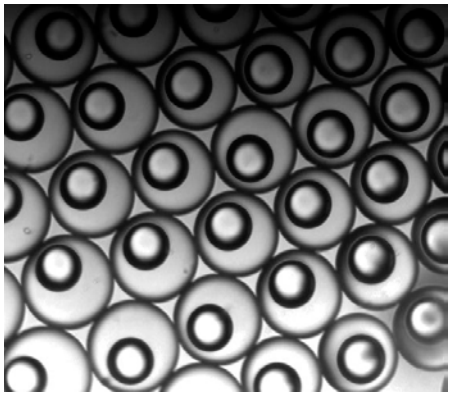

Figure 4. Complete engulfing
Fluorinated oil/Silicon oil/Water + SDS

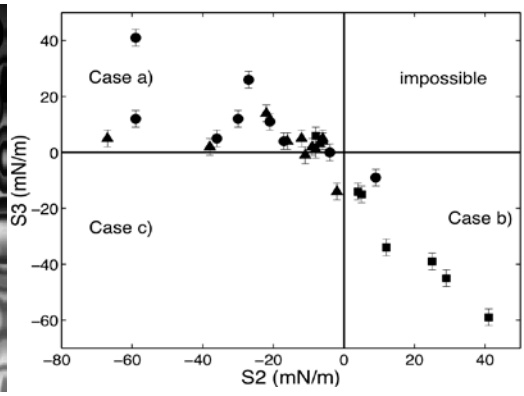

Figure 5. Theory-experiment comparison for 30 fluid triplets (S_1<0). circle: complete engulfing observation; triangle: partial engulfing observation ; square: non engulfing observation

REFERENCES:

[1] Z. Nie, S. Xu, M. Seo, P. Lewis and E. Kumacheva, *Polymer Particles with Various Shapes and Morphologies Produced in Continous Microfluidic Reactors* Journal of American Chimical Society, **127**, 8058-8063 (2005).

[2] V. Barbier, M. Tatoulian, H. Li, F. Arefi-Khonsari, A. Ajdari and P. Tabeling, *Stable Modification of PDMS Surface Properties by Plasma Polymerization: Application to the formation of Double Emulsions in Microfluidic Systems*, Langmuir, **22**, 5230 (2006).

[3] S.Torza and S.G. Mason, *Three-Phase Interactions In Shear and Electrical Fields* J. Colloid Interface Science, **33** (1), 67-83 (1970).

[4] D. Bartolo, G. Degré, P. Nghe and V. Studer, *Stick and flow : fast simple prototyping method for performance microfluidic device*, MicroTAS2007.

ADSORPTION-FREE MICROPARTICLE MANIPULATION USING 3D OPTOELECTRONIC TWEEZERS COMPOSED OF DOUBLE PHOTOCONDUCTIVE LAYERS

Hyundoo Hwang[1], Youngjae Oh[1], Jae-Jun Kim[1], Yong-Je Choi[1], Wonjae Choi[1], Je-Kyun Park[1], Se-Hwan Kim[2] and Jin Jang[2]

[1]Korea Advanced Institute of Science and Technology (KAIST), KOREA and
[2]Kyung Hee University, KOREA

ABSTRACT

We report a three-dimensional optoelectronic tweezers (3D OET) composed of two photoconductive layers for adsorption-free manipulation via three-dimensional trapping and vertical focusing of microparticles. This paper demonstrates that vertical focusing of microbeads via 3D OET prevents non-specific interactions between the particles and surfaces of the device, and provides increased efficiency of particle trapping and manipulation.

Keywords: three-dimensional optoelectronic tweezers (3D OET), lab-on-a-display, dielectrophoresis, optoelectronic tweezers (OET)

1. INTRODUCTION

Optoelectronic tweezers (OET) has become a powerful technology for parallel manipulation of microparticles using light-induced dielectrophoresis (DEP). Recently, two different approaches for driving OET have been reported using a digital micromirror display (DMD)[1] and a liquid crystal display (LCD)[2]. However, non-specific interactions such as hydrophobic and electrostatic interactions between the particles and device surfaces interfere with the effective non-contact particle manipulation using an OET. Nevertheless, the particle-surface interactions are unavoidable if we manipulate the particles in the conventional OET device which uses DEP forces acted on only one direction by negative DEP (nDEP) or positive DEP (pDEP). In order to deal with these problems, we suggest a new OET platform called three-dimensional optoelectronic tweezers (3D OET) based on double photoconductive layers to focus microparticles vertically and trap them with 3D DEP cages, providing perfectly adsorption-free particle manipulation.

2. PRINCIPLE

In the 3D OET device, the liquid layer containing micro-particles is sandwiched between two photoconductive layers differently from the OET device composed of a photoconductive and a ground layer (Figure 1). When an AC bias voltage is applied

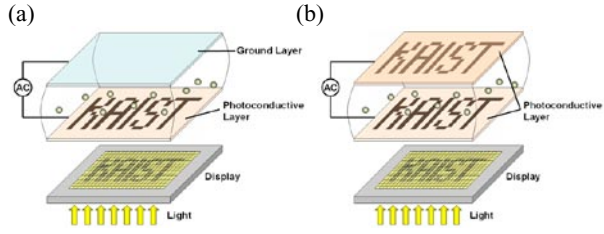

Figure 1. Schematic of (a) OET and (b) 3D OET

978-0-9798064-0-7/μTAS2007/$20©2007CBMS

between two photoconductive layers, the transmitted light beam forms virtual electrodes on the surfaces of the top and the bottom photoconductive layers, resulting in an electric field gradient in the liquid. The virtual electrodes in 3D OET generate a 3D DEP cage to trap the particles and focus them vertically using DEP forces. Consequently, we can manipulate the vertically focused microparticles under the perfectly non-contact and adsorption-free environments.

The electric field distribution in the liquid chamber of 3D OET was simulated and described as compared with that of OET in Figure 2. According to the simulation results, the microparticles which follow nDEP would be moved in the direction from the dark region to the light region. That is, microparticles in 3D OET device would be focused into the middle of the liquid layer and kept apart from the surfaces of device. Consequently, we can manipulate the particles free from the particle-surface interactions using 3D OET devices.

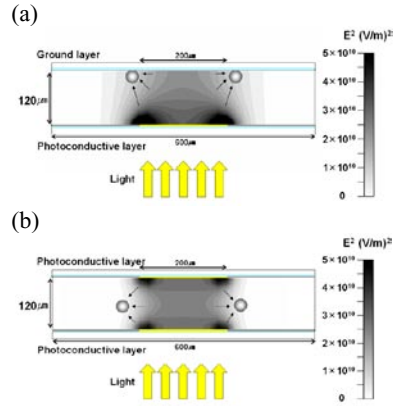

Figure 2. Simulated electric fields in the liquid chamber of (a) OET and (b) 3D OET.

3. EXPERIMENTAL

We used an indium tin oxide (ITO) layer as the transparent and conductive layer for the ground. As shown in Figure 3, the photoconductive layer was comprised of four layers: a 180 nm thick ITO layer, a 50 nm thick n^+ a-Si:H layer, an 800 nm thick intrinsic a-Si:H layer, and a 20 nm thick SiN_x layer. The triple layers of n^+ a-Si:H, intrinsic a-Si:H, and SiN_x were consecutively deposited by plasma enhanced chemical vapor deposition (PECVD) method on the ITO-coated glass substrate in a single chamber reactor.

A 1.3 in monochromatic LCD module was used in this research. It was consisted of 800 × 600 pixel array with 33 µm pixel pitch. The microscopic pictures were taken without any image patterns of LCD, because the optical observation of the beads in the dark region was limited in the 3D OET device.

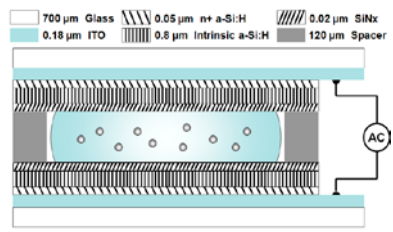

Figure 3. Configuration of 3D OET

4. RESULTS AND DISCUSSION

Microscopic pictures on three different heights – bottom, middle, and top – of the liquid chamber are shown in Figure 4. In the 3D OET device, the polystyrene beads were successfully focused into the middle of the liquid layer by a 3D DEP cage (Figure 4(b)), while they were adsorbed on the surface of the ground layer by electrostatic surface-particle interactions in the OET device (Figure 4(a)). Figure 5 shows the number of moving beads by several LCD images in OET and 3D OET devices under the condition of 20 V bias at 100 kHz. The image appears gradually during 60 seconds, forming letter “I”, “X” and “O”. The number of particles successfully moved by 3D OET was about two times more than that of particles moved by OET. The microscopic photographs of concentrated particles by LCD images forming letter “O” (the inside of dotted lines is dark region) by

using OET and 3D OET devices are shown in Figure 6(a) and 6(b), respectively. The increased particle trapping efficiency of 3D OET is definitely shown. The result of time domain analysis is also described in Figure 7. While the number of moving beads in OET decreases as time goes by, most of the particles in 3D OET device were moved continuously without adsorptions. In the OET device, the adsorbed particles induce strong electrostatic attractive forces and pull other particles around them, interfering with the continuous particle manipulation in a long term process.

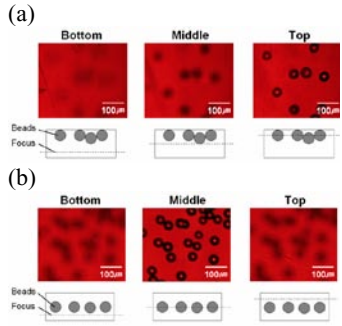

Figure 4. Micro-photographs according to the heights of the liquid layer of (a) OET and (b) 3D OET devices.

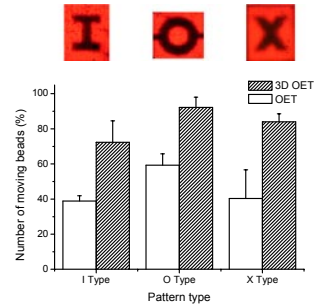

Figure 5. Percentages of moving beads by several LCD images in OET and 3D OET devices.

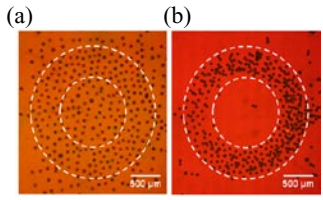

Figure 6. Micro-photographs of microbeads concentrated by (a) OET and (b) 3D OET devices.

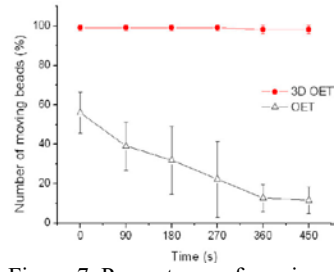

Figure 7. Percentages of moving beads according to the time in OET and 3D OET devices.

5. CONCLUSIONS

In this work, 3D OET, which contains two photoconductive layers as a pair, for 3D trapping and manipulation of microparticles has been developed. We have successfully manipulated the polystyrene beads without attachments using 3D OET on a LCD. The performances of 3D OET were compared with those of OET according to several parameters; LCD images, bead sizes, and manipulation times. The 3D OET shows higher particle trapping efficiency and less particle adsorptions than a typical OET. However, the optical observation of the beads in a dark region was limited when a thick photoconductive layer is used as the upper photoconductive layer.

ACKNOWLEDGEMENT

This research was supported by the Nano/Bio Science & Technology Program (2006-00955) of the Ministry of Science and Technology (MOST).

REFERENCES

[1] P.Y. Chiou, A.T. Ohta and M.C. Wu, *Massively parallel manipulation of single cells and microparticles using optical images*, Nature, 436, pp. 370-372 (2005).

[2] W. Choi, S.-H. Kim, J. Jang and J.-K. Park, *Lab-on-a-display: a new microparticle manipulation platform using a liquid crystal display (LCD)*, Microfluid. Nanofluid., 3, pp. 217-225 (2007).

CONDITIONS FOR CAPILLARY FILLING IN MICROFABRICATED CHANNELS WITH HYDROPHILIC AND HYDROPHOBIC WALLS

Ville Jokinen[1,2] and Sami Franssila[2]

[1] *Protein Chemistry Unit, Institute of Biomedicine, Biomedicum Helsinki, University of Helsinki, Finland*

[2] *Micro and Nanosciences Laboratory, Helsinki University of Technology, Finland*

ABSTRACT

Capillary filling of microchannels with rectangular cross section and both hydrophilic and hydrophobic walls was examined theoretically and experimentally. A method of going through various types of capillary flows and selecting the type that minimizes the total surface free energy is described. The predictions of the method were tested experimentally and some agreement with the measurements is reported, especially at lower contact angles.

Keywords: Capillarity, microfluidics, SU-8

I. INTRODUCTION

Capillarity is a promising technique for fluid transport in the micro- and nanoscale [1]. In channels with circular cross section and uniform surface properties, capillarity is well understood. However, channels that are used in microsystems applications typically have non circular cross sections and often have at least one channel wall that is made from a different material than the other walls. While a lot is known about capillarity in these geometries, a complete picture is still missing. In this paper we discuss the elementary question of when a microfabricated channel fills spontaneously by capillarity from a surface energy minimization point of view. The question is also investigated experimentally on microfabricated SU-8 channels with hydrophilic and hydrophobic walls.

II. THEORY

The geometry under investigation is a microchannel with effectively infinite length and a rectangular cross section shown in Figure 1a. The channel is taken to be in contact with a large liquid reservoir and gravity is neglected. It is also assumed that capillarity is the only driving force. Capillary pressure in such a channel is calculated [1] as:

$$P_{cap} = \gamma \left(\frac{2 \cdot \cos \theta_s}{w} + \frac{\cos \theta_t + \theta_b}{d} \right), \quad (1)$$

where θ_s, θ_t and θ_b are the contact angles of the side, top and bottom walls, w and d are the width and the depth of the channel and γ is the surface energy of the liquid-vapor interface. In the absence of other driving forces, the condition for filling a channel can be taken to be that capillary pressure (1) is positive. This approach contains the assumption that the meniscus in a filling channel spans the entire cross section of the channel.

The principal new idea of this paper is a way of taking capillary flows in sub sections of the channel into account. The analysis is started from the least inclusive flow type, which is film flow on a fully wetting wall, and continued to include increasingly more inclusive flow types until the final consideration is a flow that fills the entire channel. If capillary filling is thermodynamically favorable at any step, that sub section of the channel is considered to be filled to its equilibrium extent in all subsequent steps. In essence, this procedure minimizes the total surface free energy.

978-0-9798064-0-7/μTAS2007/$20©2007CBMS

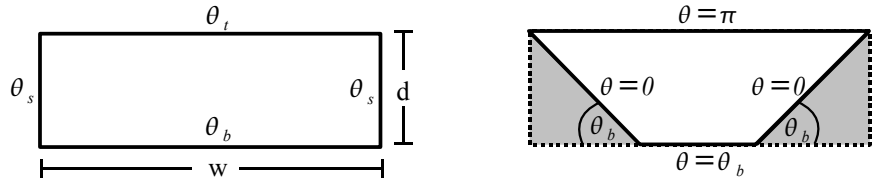

(a) (b)

Figure 1. (a) Geometry of a typical microchannel. (b) Geometry of an imaginary microchannel after the bottom corners have filled to their equilibrium extent.

To illustrate the procedure, consider the geometry of Figure 1a. with $\theta_s = \theta_b = \theta > 0$ and $\theta_t = 180°$. This will also be the geometry that is studied experimentally. All contact angles of this geometry are greater than zero, so film flow on a single wall is not possible. Next least inclusive filling types are those that touch two walls of the channel. Of these, only corner flow in the two identical bottom corners can be thermodynamically favorable in the present geometry. Filling of these corners is favorable if the condition $\theta < 45°$ [2] is satisfied. The corresponding equilibrium shape is a straight meniscus meeting the bottom wall at angle θ_b as shown in Figure 1b.

The final consideration is filling of the whole channel. If filling of the corners is thermodynamically favorable, then according to the method of this paper, the filling of the whole channel is determined by the change in surface energy when the as yet unfilled part of the channel fills (see Figure 1b). The free energy change of this is negative if the condition:

$$w/d < \frac{2 \cdot \sin\theta}{1 - \cos\theta} \tag{2}$$

is satisfied. On the other hand, setting the capillary pressure of (1) as greater than zero and using this to predict the filling gives:

$$w/d < \frac{2 \cdot \cos\theta}{1 - \cos\theta} \tag{3}$$

as the condition for capillary filling of the entire channel.

III. EXPERIMENTAL

We fabricated test channels from epoxy polymer SU-8 [3]. The bottom and side walls of the channels were made from two layers of SU-8 and the channels had no solid lid. Two different depths, 22.2 μm and 9.5 μm, were fabricated and and the widths of the channels ranged from 5 μm to 700 μm. The contact angle modification was achieved through oxygen plasma treatments of various durations. Advancing contact angles were measured by sessile drop method (CAM 200 from KSV instruments) on planar surfaces on both the floor and the side wall layers. The contact angle of the top wall consisting of air is 180º.

Capillary filling experiments were performed within two hours of the contact angle measurements. The test structure was an array of channels connected to a reservoir area. A large droplet of de-ionized water (about 50 μl) was dropped on a reservoir area. Capillary filling of the test channels was then observed under a microscope. Once the movement of the liquid meniscus appeared to stop, the liquid was given at least five minutes to advance further. If after this time the meniscus still had not moved, the situation was judged as a

mechanical equilibrium. The experiment was performed simultaneously with four identical test structures located on different areas of the same wafer to minimize the effect of local variation in either the surface properties or channel geometry.

IV. RESULTS AND DISCUSSION

The main results of the capillary filling experiment are presented in Figure 2. Contact angles of the SU-8 layer that formed the floor and the SU-8 layer that formed the side walls were so similar that a single advancing contact angle was chosen to characterize the channels. The condition (2), derived in this paper, seems to under predict filling of the channels. To some extent this is expected, since hydrostatic- and Laplace pressures of the reservoir droplet were neglected, but the magnitude of these is unlikely to be sufficient to completely explain the deviation. However, quantifying these two is tricky because of the irregular shape of the droplets on top of the reservoir area. The greatest deviation between the predictions of Equations (2) and (3) is at lower contact angles, where it is clear that Equation (3) is overly optimistic about filling of the whole channel. This suggests that in a channel with sharp features and hydrophilic and hydrophobic walls, it is not sufficient to merely compare an empty channel to a completely filled channel.

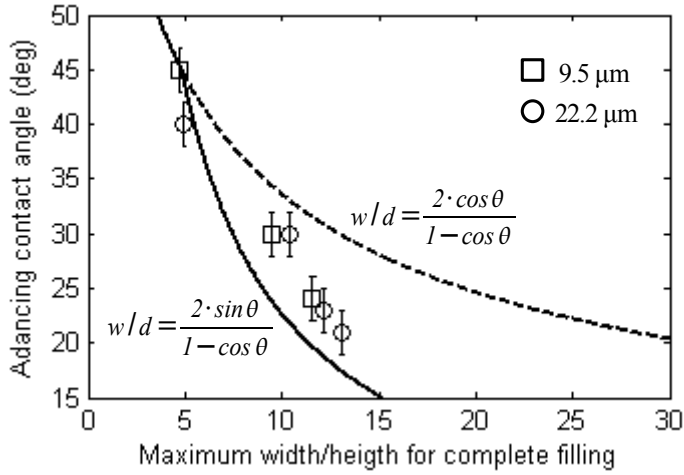

Figure 2. Results of a capillary filling experiment of 9.5 μm and 22.2 μm deep channels. The squares and circles mark the widest channel in each experiment that filled.

ACKNOWLEDGEMENTS

The project was funded by the National Graduate School in Nanoscience (NGS-NANO) and Finnish Agency for Technology and Innovation (TEKES).

REFERENCES

[1] E. Delamarche, D. Juncker and H. Schmid, *Microfluidics for Processing Surfaces and Miniaturizing Biological Assays,* Advanced Materials, 17, pp. 2911-2933, (2005).

[2] P. Concus and R. Finn, *On Capillary Free Surfaces in the Absence of Gravity,* Acta Mathematica, 132, pp. 177-198, (1974).

[3] T. Sikanen, S. Tuomikoski, R. A. Ketola, R. Kostiainen, S. Franssila and T. Kotiaho, *Characterization of SU-8 for electrokinetic microfluidic applications,* Lab on a Chip 5, pp. 888-896, (2005)

CONTROL OF THE PHASE BEHAVIOR OF AQUEOUS SOLUTIONS USING MICROFLUIDICS

Jung-uk Shim[1], Seth Fraden[2]

[1]*Microdroplets Group, University of Cambridge, Cambridge, UK*

[2]*Complex Fluids Group, Brandeis University, Waltham, USA*

ABSTRACT

A microfluidic device denoted the *Phase Chip* has been developed to exploit water permeations through poly(dimethylsiloxane) (PDMS) in order to vary the concentration of aqueous nanoliter volume microdroplets stored in wells. The phase diagram of a polymer/salt mixture is measured employing the Phase Chip. Also, we show that we can induce nucleation and then grow protein crystals in stored protein droplets.

Keyword: microfluidics, PDMS, water permeation, the Phase Chip.

1. INTRODUCTION

This paper reports the development of a microfluidic device, the Phase Chip shown in Figure 1a, which is designed to determine the phase diagram of multi-component fluid mixtures. It is a poly(dimethylsiloxane) (PDMS) device based on the droplet microfluidic technology[1]. One of the Phase Chip's innovations is to exploit surface tension forces to guide each drop to a well, illustrated in Figure 1(c). After the drops are formed, they are confined in a flat flow channel, which has 100μm width and 30μm height. Wells, located to the side of the channel with typical dimensions of 300μm length and 50μm depth, are deeper than the flow channel. A drop in a well can adopt a spherical shape, minimizing its surface area and its surface energy.

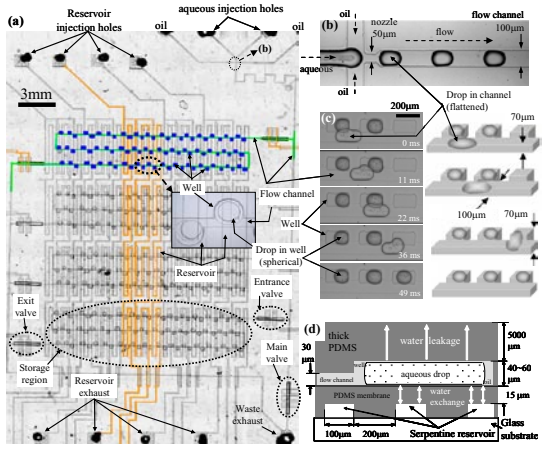

Figure 1: (a) Plan view of the Phase Chip. (b) Drop formation at nozzle. (c) Photographs of surface tension guided storage of aqueous drops into rectangular wells. Drops sequentially fill the wells, with the first drop docking in the first well. (d) Schematic vertical structure of the Phase Chip. Aqueous drops are in wells. In the upper, thick (5 mm) layer, there are flow channels and storage wells. In the lower, thin (40 μm) layer, there is a reservoir, sealed by a 15 μm thick PDMS membrane.

To control water contents of stored drops, the bottom of the wells are constructed from a thin PDMS membrane (15μm thick) that is slightly permeable to water[2], but impermeable to proteins and salts. The other side of the membrane contains a reservoir, through which flows an aqueous salt solution as shown in Figure 1(d). This produces a chemical potential gradient between the solution stored in the well and the reservoir. When a concentrated salt solution is introduced into the reservoir, water permeates from the stored drops through the membrane into the reservoir. Thus drops in wells shrink and drop concentrations increase.

978-0-9798064-0-7/μTAS2007/$20©2007CBMS

If pure water is introduced in the reservoir, water flows from the reservoir to the drop, thereby diluting each component as the drops swell.

2. Control of the Phase behavior of Salt/Polymer mixture in the Phase chip

To demonstrate the performance of the Phase Chip, the phase diagram of a mixture of polymer and salt is measured. For certain compositions, mixtures of poly(ethylene glycol) (PEG) and ammonium sulfate in water will phase separate into two liquid phases. First the Phase Chip generates drops containing mixtures of PEG and salt (ammonium sulfate) whose concentrations vary in a linear fashion as described in [1]. Drops that have varied concentrations of components are stored in wells in sequence as shown in Figure 1(c).

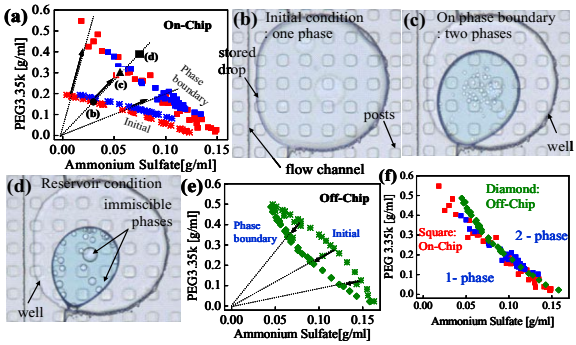

Figure 2 (a) The phase diagram of a mixture of PEG and salt measured on the Phase chip. Asterisks are initial conditions. Squares denote the phase boundary. The mixture is single phase below the boundary and two phases above the boundary. (b),(c),(d) The photographs show the drops while the water is leaving the drop. (e) The plot shows the phase diagram of the mixture measured off the chip. (f) The phase diagrams measured on- and off-chip are plotted together.

We drive the phase transition by removing water from the drops by filling the reservoir with a 6 M NaCl solution. The solute concentrations increase as water leaves. Because only water can permeate through PDMS and the height of the docked drops remains constant, we can determine concentrations by measuring the area of the drop. And, in order to measure the salt concentration in drops, a blue food dye is added into the ammonium sulfate stock solution. After the initial concentration is determined by analyzing the intensity of transmitted light, concentrations of each solute in the drop are subsequently calculated by measuring the area of drops. The images of the drops are viewed and the point at which liquid-liquid phase separation is observed is noted as the phase boundary.

In Figure 2(b) an image of a drop at the beginning of the experiment is shown. This drop has a composition indicated by point (b) in the phase diagram of Figure 2(a). As the drop shrinks concentrations of each solute in the drop increase, but because none of solutes leaves the drop the ratio of solute concentrations remains constant. This constrains the concentrations to increase linearly. In Figure 2(c) the appearance of two liquid phases is first observed. By measuring the area of this drop the concentration of the solutes is determined and noted as point (c) in Figure 2(a). This process is repeated for each initial composition shown in Figure 2(a) to determine a complete phase diagram.

3. Protein Crystallizations in the Phase chip

The strategy for protein crystallizations in the Phase chip is to formulate a combinatorial sequence of protein solutions of different salt and protein concentrations as described in [1] and subsequently store these drops in wells. Next these protein drops are concentrated by introducing a solution high in salt into the reservoir. Such conditions often lead to the creation of many small crystals or protein gels. We regard this material as seeds and subsequently change reservoir conditions by introducing a solution low in salt into the

reservoir. Water permeates from the reservoir into the protein solution and reduces the protein concentrations, which lowers the chemical potential difference ($\Delta\mu$) between the protein in the solution and that in the crystal. This shifts the nucleation barrier causing the smaller nuclei to dissolve and the larger crystals to grow, thereby transforming the many small defective crystals into a few, large high quality crystals [3].

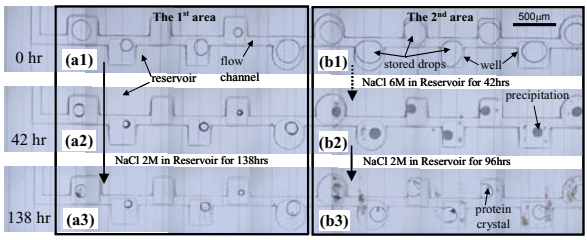

Figure 3: The protein crystallizations with respect to the kinetic path. The each row of photographs was taken at same moment. The 2nd and the 3rd row were taken at 42hours and 138hours later. (a). the area truncated in a left box: After storing protein drops, 2M NaCl solution flows in the reservoir for 42hours. Although the drop condition is in the supersaturation region, drops are clear. After 138hours, one protein crystal out of five drops is found. (b) The area, truncated in a right box, firstly has 6M NaCl solution in the reservoir for 42hours. The protein drops are precipitated since they are in the deep supersaturation region. The reservoir condition is replaced with 2M NaCl solution. The drops become clear, and subsequently the crystallizations occur. All wells in the area have protein crystals.

As shown in Figure 3, protein crystals grow in the wells in various ways. The initial and the final conditions of both reservoirs are the same. The difference is a kinematical path in the phase diagram. The left region stays on the 2M reservoir for 138hours, where the drops are always clear and only one crystal comes out. The right region firstly stays in high supersaturation (6M) for 42hours, where the gelation happens (the black aggregations). After 138 hours since drops are exposed to the less salty reservoir (2M), all seven wells in this photograph are crystallized. We claim that during the precipitation process (6M) many nuclei are born in the protein drop, and, when the protein drop is brought into the region of the shallow supersaturation (2M), the nuclei, which overcome the free energy barrier, grow into crystals. This is a clear evidence of being able to accelerate protein crystallization by controlling concentrations, realized in the microfluidic device.

4. CONCLUSION

We have manufactured a class of microfluidic devices designed to measure the phase diagrams of multi component aqueous systems. As a test of the Phase Chip the phase diagrams of PEG/salt solution were measured. And the chip can be applied to the high throughput screening of protein crystallizations. The Phase Chip, with its ability to reversibly control water content of drops stored in wells, renders varying concentration as convenient as varying temperature.

REFERENCES

[1]. Zheng, B., L.S. Roach, and R.F. Ismagilov, *Screening of protein crystallization conditions on a microfluidic chip using nanoliter-size droplets.* Journal of the American Chemical Society, 2003. **125**(37): p. 11170-11171.

[2]. Watson, J.M. and M.G. Baron, *The behaviour of water in poly(dimethylsiloxane).* Journal of Membrane Science, 1996. **110**(1): p. 47-57.

[3]. Debendetti, P.G., *Metastable Liquids: Concepts and Principles*. 1996: Princeton University Press.

VERTICAL MICROREACTOR WITH FLUID FILTERS CHARACTERIZED BY 3D-CAPILLARY-BUNDLE FOR HIGH-THROUGHPUT IMMUNOASSAY

Yoshiaki Ukita[1] , Toshifumi Asano[1], Kuniyo Fujiwara[1], Katsuhiro Matsui[2], Masahiro Takeo[2], Seiji Negoro[2], Tomohiko Kanie[3], Makoto Katayama[3] and Yuichi Utsumi[1]

[1]Laboratory of Advanced Science and Technology for Industory(LASTI) University of Hyogo, JAPAN and

[2]Graduate School of Engineering University of Hyogo, JAPAN and

[3]SUMITOMO ELECTRIC INDUSTORIES, LTD., JAPAN

ABSTRACT

This paper proposes a vertical microreactor with multifunctional fluid filters which characterized by 3D-capillary-bundle. The high-efficiency micromixing properties of the fluid filter is proved with CFD and enzyme reaction. The ELISA method is demonstrated by using vertical microreactor and the advantages of 3D structure are duscussed.

Keywords: three dimensional structure, deep x-ray lithography, microvalve, micromixer, enzyme-linked immunosorvent assay, high-throughput screening

1. INTRODUCTION

The use of three-dimensional (3D) structure provides many useful and unique characteristics on lab on a chip (LOC). [1-3] Especially the high-efficiency micromixing properties and large-scale integration are essential for advanced high-throughput screening technology (HTS) using LOC. We have been proposed the use of vertical microreactor stack with fluid filters which characterized by 3D-capillaty-bundle. [4,5] This paper shows novel micromixing characterictics of the fluid filters and an application to enzyme linked immunosorvent assay (ELISA) of vertical microreactor stack.

2. VERTICAL MICROREACTOR STACK

Figures 1 shows the schematic diagram of vertical fluid flow operation and vertical microreactor stack for ELISA.The basic concept of liquid manipuration in vertical microreactor is based on digital microfluidics concept. The fluid filters have 3D-capillaty-bundle in its body and liquid pulg can be held on the fluid filters by surface tension and can be pneumatically driven through the capillaries toward next reservoir . It is expected that the efficient micromixing can be acheved with 3D coanda effect during transporta-

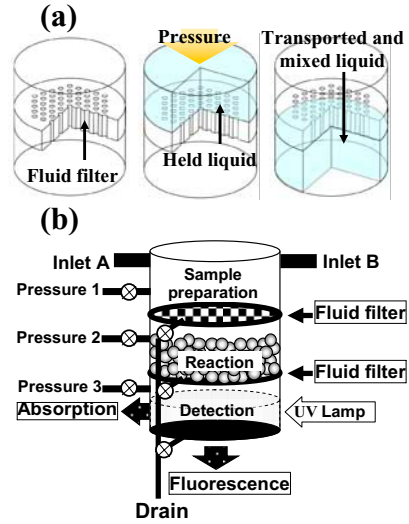

Figures 1 (a) Concept of vertical fluid flow operation (b) Schematic illustration of vertical microreactor stack

978-0-9798064-0-7/μTAS2007/$20©2007CBMS

tion fig. 1(a) [4,5]. As shown in fig. 1(b) the vertical microreactor stack consist of vertically stacked reservoirs for sample preparation, biochemical reaction with antigen immobilized polystyrene beads, spectroscopy, and two fluid filters separating them.

3. FABRICATION OF THE VERTICAL MICROREACTOR AND FLUID FILTERS

Polymethylmethacrylate (PMMA) fluid filters are fabricated with deep X-ray lithography using the large-area LIGA beamline (BL-2) [6], which constructed in NewSUBARU facility in Hyogo JAPAN, is used. Cylindrical PMMA reservoirs with 3 mm and11 mm in diameter and length respectively, are fabricated by high-precision machining [4,5]. The 3D structure of microreactor stack allows to simply insert a pair of optical fibers of portable spectrometer into reservoir for on-chip monitoring. Photographs of vertical microreactor stack and fluid filters are shown in Fig.2.

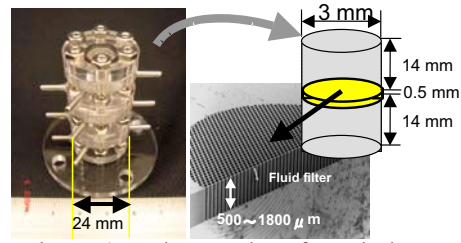

Figure 2 Photographs of vertical microreactor stack and fluid filter

4. EVALUATION OF MIXING PERFORMAMCE OF 3D-CAPILLARY-BUNDLE

In the case of competition ELISA, quarity of mixing directly influence on the quarity of reaction, and inadequate mixing of liquids result in the poor signal to noise ratio (S/N). To predict mixing behavior, the computational fluid dynamics (CFD) using FLUENT software is carried out. To visualize the mixing behavior center of water is colored and it is assumed to be held on the fluid filter as shown in Fig. 3 (a). As the result of simulation, deformation and dilution of the colored water is observed during the transportation fig. 3(b). By repeating liquid transpot, mixing is enhanced as shown in Fig.3(c). We also confirmed that the concentration standard deviation of colored water decreases with mixing progress.

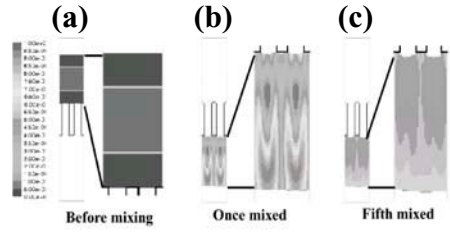

Figure 3 Simulated mixing behavior (a) initial state (b) once mixed (c) fifth mixed

An enzyme reaction is applied to evaluate the mixing effects on chemical reaction. Enzyme (catechol 2,3-dioxygenase) and substrate (catecol) were gently injected onto a fluid filter to avoid mixing due to convection, and concentration of product (2-hydroxymuconate semialdehyde) is measured in real-time via mixing with fluid filter. As shown in fig. 6, in the case of without mixing, the absorbance of the product is saturated at much lower level than mixed case. In contrast to without mixing, once mixing is very effective, and fifth and ninth mixing are slightly faster than once and they are almost same behavior. So it suggest that the regents are completely mixed in fifth mixing while once mixing is very effective.

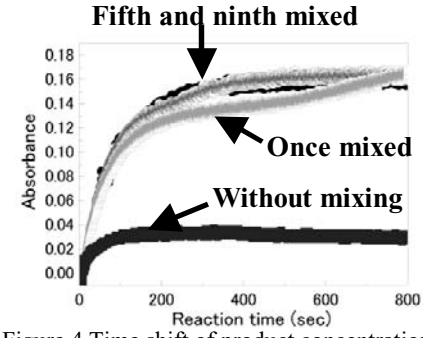

Figure 4 Time shift of product concentration

5. DEMONSTRATION OF AN IMMUNOASSAY

The monoclonal antibodies for endocrine- disrupting chemicals (EDCs), such as nonylphenol and nitrophenol, are immobilized on the surface of the polystyrene beads, and an antigen antibody reaction with an environmental sample is subsequently carried out. The alkylphenol (AP) concentration is estimated from the competition of enzyme-labeled haptens and non-labeled haptens to combine the immobilized antibody on the polystyrene beads as shown in Fig.5(a).

Enzyme linked immuno-solvent assay (ELISA) is demonstrated by using this microreactor. Enzyme-labeled (HRP-AP) and non-labeled (nonylphenol; NP) hapten are immediately mixed and injected onto the fluid filter to be held with anti-NP antibody immobilized polystyrene beads. After the antigen-antibody reaction, beads are filtered to remain and the substrate (3,3',5,5'-tetramethylbenaidine; TMBZ) is injected into the microreactor to induce enzyme reaction. Finally sulfaric acid is mixed with substrate to interrupt the enzyme reaction and get exact signal by using fluid filter. Figure 5(b) shows the obtained inhibition ratio, which defined as ratio of absorbance with and without non-labeled hapten (B/B0). As the figure shows the analytical curve of the non-labeled hapten, or antigen, is successfully taken with range of 1- 1000 ng/ml.

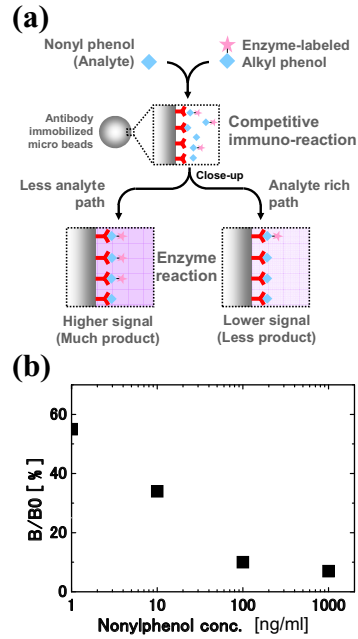

Figure 5 (a) Schematic illustration of competition ELISA method (b) Analytical curve taken from competition ELISA

6. CONCLUSIONS

This paper shows advantages of the vertical microreactor stack with fluid filters. The mixing property of fluid filter was estimated by means of CFD simulation and chemical reaction. The high efficiency mixing performance of the fluid filter is suitable for the competition ELISA especially in the case of mixing of analyte and labeled hapten and enzyme reaction stopping. The successfully taken caribration curve suggests the possibility of application to ELISA of vertical microreactor. From practical point of view, the 3D structure of the vertical microreactor stack is promising way to integrate many microreactors for HTS since it needs no special detection system.

REFERENCES

[1] Y. Kikutani *et al.*, Lab Chip, **2** (2002) 188.
[2] K. Ikuta *et al.*, Proc. MEMS99 (1999) 376.
[3] R. Yang *et al.*, J. Micromech. Microeng., **14**, (2004) 1345.
[4] Y. Utsumi *et al.*, J. Vac. Sci Technol. B, **24**, (2006) 2606.
[5] Y. Ukita *et al.*, Jpn. J. Appl Phys, **45**, (2006) 7203.
[6] Y. Utsumi, T. Kishimoto: J. Vac. Sci. Technol., **23** (2005) 2903.

COUPLED FREE-SOLUTION SEPARATION AND ON-CHIP HYBRIDIZATION OF OLIGONUCLEOTIDES IN A NANOFLUIDIC DEVICE

David E. Huber[1], Marci L. Markel[1], Sumita Pennathur[2], and Kamlesh D. Patel[1]

[1]*Sandia National Laboratories, USA and*
[2]*University of California, Santa Barbara, USA*

ABSTRACT

While the challenges and advantages of micro-scale analysis systems are well known, those of systems incorporating nano-scale features have only recently begun to be recognized. One such advantage is the capability to perform novel separations based upon nano-scale physical phenomena [1]. In this work, we present experimental results demonstrating on-chip oligonucleotide hybridization and free-solution (gel-free) separation of hybridized (ds) DNA from single-stranded (ss) DNA using a fundamentally new separation mechanism inherent to nanofluidic channels.

Keywords: nanofluidics, separations, hybridization, oligonucleotide

1. INTRODUCTION

The most common hybridization assays are DNA microarrays, which use surface-bound probes and require large amount of DNA and long hybridization times. The most common means of separating DNA, for detection and sequencing, is through the use of a sieving matrix. The addition of sieving matrices, however, makes it difficult to interface with upstream hybridization assays or additional downstream manipulations or studies. At Sandia, we are working to develop a coupled free-solution separation and hybridization assay for applications in rapid biodetection and bioanalysis.

2. THEORY

By performing free-solution hybridization assays in nanochannels, we take advantage of both the improved mixing times afforded by the reduced channel size [2] and the separation capabilities of nanochannels, initially demonstrated by Pennathur and Santiago [3]. In a nanochannel, the electrical double layer occupies a significant proportion of the fluid volume, generating transverse electric fields that couple with nonuniform velocity fields to cause a valence-based separation modality [1]. In addition, larger molecules such as DNA also experience steric interactions with the wall, which vary with the length of the DNA and also contribute to the separation mechanism [4]. We take advantage of the conformational difference between single-stranded and double-stranded DNA (e.g., the relative stiffness and persistent lengths) to perform separations in a nanochannel. Here, we present the on-chip hybridization of fluorescently-labeled oligonucleotides and separation of a 20-mer double-stranded DNA from its unhybridized constituents.

978-0-9798064-0-7/μTAS2007/$20©2007CBMS

3. EXPERIMENTAL

Hybridization and separation were performed in fused-silica nanochannels fabricated using conventional MEMS processing techniques [3]. As depicted in Figure 1, the device consisted of a 5-port structure. Ports A and B form a mixing Tee which feeds into a standard offset-T injection structure, with the separation channel extending from the injection region to the buffer waste port. The nominal channel depth is 400 nm and the width is 10 µm. Full-field fluorescence images were captured using a CCD camera (Cascade 128+, Roper Scientific) mounted on an epifluorescent microscope (Nikon TE-2000). Electropherograms were generated by averaging a 100 pixel section of the channel at a distance 22 mm from the injection region. Figures 2a and 2b demonstrate the successful separation of hybridized probe and target DNA from unhybridized probe. Figures 3a and 3b presents electropherograms for on-chip hybridization at two different hybridization times.

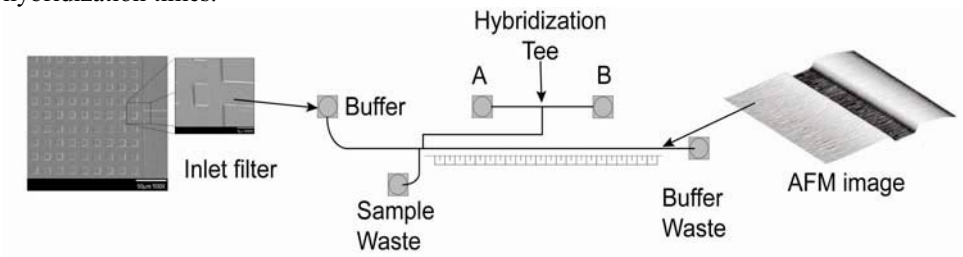

Figure 1. Device schematic and detail images. The schematic illustrates the 5-port device layout, including sample wells (A and B), mixing Tee, offset Tee injector, and separation channel (leading to the buffer waste port and indicated by the tick marks beneath). The left-most image is a scanning electron micrograph of the port region, showing the filter blocks, while the right image is a representative AFM measurement of a channel section.

4. RESULTS AND DISCUSSION

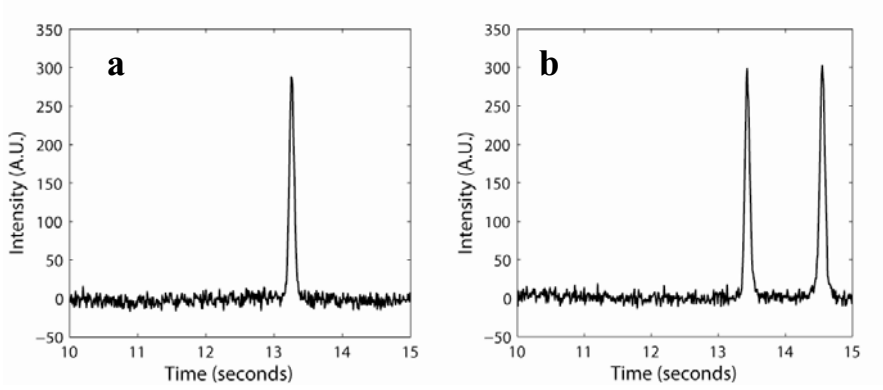

Figure 2a: Electropherogram of single-stranded DNA. The plot shows the resultant peak for a 20 base pair probe oligonucleotide labeled with Alexa Fluor 546. The single stranded DNA was loaded into port A at a concentration of 1 µM in a 10 mM borate buffer. The field strength in the separation channel was 360 V/cm. Figure 2b: Separation of single-stranded and double stranded DNA. The electropherogram shows the separation of

hybridized and unhybridized probe DNA. The separation conditions were identical to figure 2a, with the addition of 1 μM probe and 0.5 μM unlabeled complement in port B.

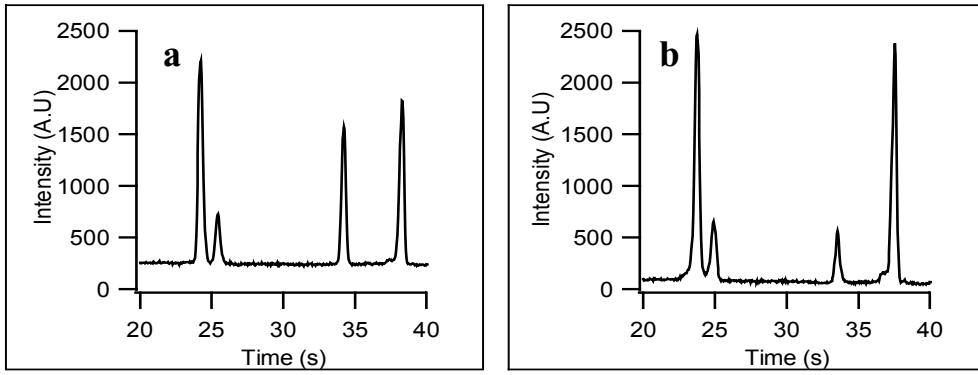

Figure 3a: On-chip hybridization studies. In the electropherograms above, the first pair of peaks are the reference dye markers (Fluorescein and Oregon Green) added to the single strand DNA solutions at Ports A and B, respectively. The second pair of separated peaks show the relative concentration of the unhybridized and hybridized DNA with no additional mixing or hybridization time. Whereas in Figure 3b, the applied field is turned off for 300 s to increase hybridization time in the mixing Tee just prior to injection. A decrease in peak height is observed for the unhybridized ss-DNA peak and an increase in height for the hybridized ds-DNA peak with the longer mixing time, suggesting an improvement in hybridization. The separation conditions for the electropherograms are identical: 10mM Tris, 1mM EDTA background buffer with 1mM NaCl and an applied field strength of 720 V/cm.

5. CONCLUSIONS

We have demonstrated successful on-chip hybridization and oligonucleotide separation with a nanofluidic device using a fundamentally new separation mechanism inherent to nanofluidic channels.

ACKNOWLEDGEMENTS

Sandia is a multiprogram laboratory operated by Sandia Corporation, a Lockheed Martin Company, for the United States Department of Energy's National Nuclear Security Administration under contract DE-AC04-94Al85000.

REFERENCES

[1] S. Pennathur and J.G. Santiago, *Electrokinetic transport in nanochannels. 1. Theory*, Anal. Chem., 77, pp. 6772-6781, (2005).

[2] S. Pennathur et al, *Diffusion-based Free Solution DNA Hybridization and Transport in a Nanofluidic Device*, Proc. of μTAS, 2006, Tokyo Japan, pp. 1079-1081, (2006).

[3] S. Pennathur and J.G. Santiago, *Electrokinetic transport in nanochannels. 2. Experiments*, Anal. Chem., 77, pp. 6782-6789, (2005).

[4] S. Pennathur et al, *Free-solution oligonucleotide separation in nanometer scale fluidic channels*, submitted to Lab on a Chip, (2007).

ELECTROKINETIC AND ATOMIC FORCE MICROSCOPY CHARACTERIZATION OF INTERFACIAL VAPOR VOID PHENOMENA IN HYDROPHOBIC MICROFLUIDIC DEVICES

V. Tandon[1], A.N. Sharma[2], S.K. Bhagavatula[3], and B.J. Kirby[4]

[1]Biomedical Engineering, [2]Applied and Engineering Physics, [3]Electrical Engineering, and [4]Mechanical and Aerospace Engineering, Cornell University, Ithaca, NY

ABSTRACT

Here we characterize electrokinetic actuation in hydrophobic microfluidic channels by combining macroscopic zeta potential measurements with nano-scale atomic force microscopy. The zeta potential measured in PTFE microchannels is shown to have pH and temperature dependence consistent with thermodynamic models. Measurements of the zeta potential in zeonor microchannels after methanol-water solvent exchange captured transient effects which may be indicative of interfacial vapor void formation and dissolution over time.

Keywords: Electrokinetic, Hydrophobic, Zeta Potential, Nanobubble

1. INTRODUCTION

We report measurements and modeling of electrokinetic phenomena in hydrophobic microfluidic devices with attention to the effects of solvent rinses and temperature cycling. As the use of cyclic olefin copolymers (COCs) and Teflon have become more common in microfluidic systems [1,2], the need for theoretical models of device performance has become critical. Modeling issues include interfacial slip, charge formation at interfaces, and generation of interfacial voids. Electrokinetic actuation is ubiquitous in analytical microfluidic devices, since it enables precise generation of flow rates at micro/nano scales. However, microbioanalytical techniques such as electrochromatography and PCR often rely on temperature cycling and/or solvent changes, which lead to uncertainty in electrokinetic actuation owing to changes in chemical kinetics and the generation of interfacial voids.

Our long term goal is to determine the physical origins of uncertainties associated with electrokinetics in hydrophobic microsystems through careful accounting of slip, charge formation, and void formation at interfaces. Here, we use electrokinetics, atomic-force microscopy, and a model-based framework to describe electrokinetics in hydrophobic microdevices.

2. LANGMUIR ADSORPTION MODEL

Since the presence of surface charge on hydrophobic substrates can be postulated to be caused by hydroxyl ion adsorption, we have developed a model for the pH and temperature dependence of electrokinetic performance using Langmuir kinetics (Figure 1), which parameterizes the equilibrium state with a free energy change of adsorption. This model assumes that binding events can be described by a single free energy change, and that there are a finite number of binding sites. The

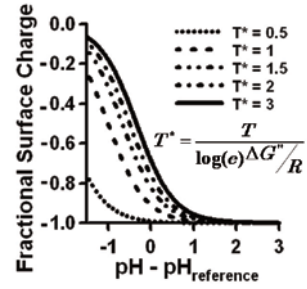

Figure 1. Langmuir adsorption isotherms for hydroxyl ion adsorption calculated from the proposed model.

978-0-9798064-0-7/μTAS2007/$20©2007CBMS

presence of gaseous voids or “nanobubbles” at the interface affects this free energy change and introduces a slip velocity boundary condition, which can increase the apparent electrokinetic potential.

3. RESULTS AND DISCUSSION

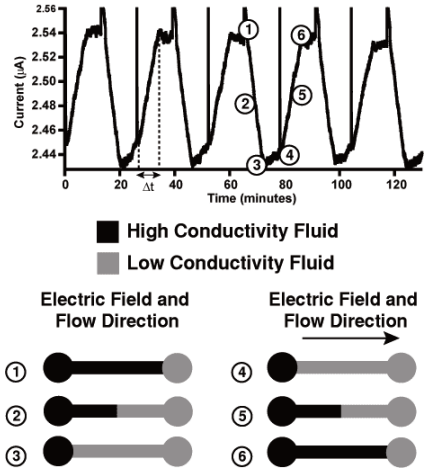

Figure 2. Schematic of a current monitoring experiment.

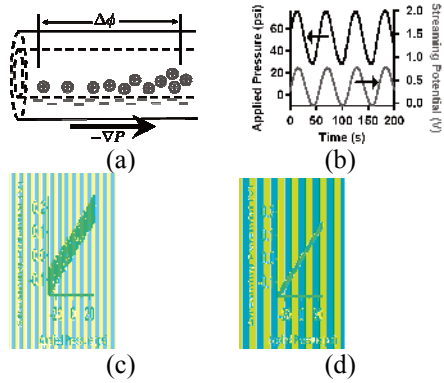

Figure 3. (a) Schematic of a streaming potential experiment. (b) Applied sinusoidal pressure and resulting streaming potential as functions of time. (c) Noise in streaming potential vs. pressure data can lead to ambiguous linear fits. (d) Fourier processing removes the ambiguity.

The electrokinetic performance of Zeonor and Teflon microfluidic channels are measured using automated current monitoring (Figure 2) and phase sensitive streaming potential (Figure 3) experiments. In current monitoring, a microchannel made of the material under study connects two reservoirs filled with solutions of slightly different conductivity. When driven by electroosmosis, fluid from one reservoir displaces the other, leading to a change in resistance in the system. The electroosmotic velocity may be obtained by measuring the time it takes for the current to change from a constant high to a constant low and vice versa. Streaming potential refers to the electrical potential that arises when an applied pressure gradient causes the redistribution of ions in a microchannel. In phase sensitive streaming potential experiments, a sinusoidal driving pressure results in a sinusoidal streaming potential signal, which facilitates noise removal in post processing.

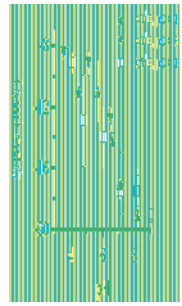

Figure 4. Observed electrokinetic potential, ζ, for PTFE as a function of pH and temperature. Data points are shown as a mean ± standard deviation, and n>20 for all points. All experiments were run with potassium phosphate buffer (pC = -log C, where C is the counterion concentration in M)

Current monitoring results for the electrokinetic potential as a function of pH at room temperature in Teflon

microchannels (Figure 4) show a pH dependence consistent with trends predicted by the Langmuir kinetics model, which gives a standard free energy change adsorption of -23 kJ/mol for the adsorption of hydroxyl ions onto the surface. Results at higher temperature (40 °C) are only qualitatively consistent with the model, as significant deviation from Langmuirian behavior is observed.

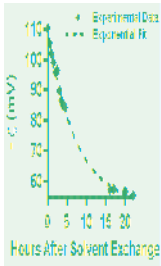

Figure 6. Observed electrokinetic potential for Zeonor as a function of time after methanol-water solvent exchange, indicating a change in surface properties with a characteristic decay time of 7.3 hours. The data is empirically well fit by an exponential function.

We have used phase-sensitive streaming potential experiments to observe transient electrokinetic effects due to methanol solvent rinses in zeonor microchannels (Figure 6). The electrokinetic potential takes several hours (~7.3 hours) to stabilize after introduction of methanol, which indicates that changes in surface properties due to the solvent change have a slow equilibration time. Since methanol affects the solubility of gas in the liquid, this could be indicative of an initial increase in the presence of interfacial vapor voids, which would lead to an initial increase in the apparent electrokinetic flow rate. Experiments by Attard et. al [3] have shown that nanobubbles at the interface have a similarly slow equilibration time, suggesting a possible link between nanobubbles and the electrokinetic performance of hydrophobic microchannels. This is important in PCR, for example, where thermal cycling leads to the generation of vapor voids at the interface, causing transient electrokinetic behavior that decays with slow time scales.

AFM experiments are focused on direct observation of interfacial nanobubbles and their generation/dissolution over time with solvent rinses and temperature cycling. When combined with electrokinetic characterization, ongoing AFM experiments will help define the putative link between nanobubbles and electrokinetic performance. AFM data for dry Zeonor surfaces is shown in Figure 6, which shows roughness features of height 5-10 nm. AFM measurements [3] for hydrophobic surfaces in fluid, on the other hand, show feature heights on the order of 30 nm, indicative of the presence of vapor at the interface.

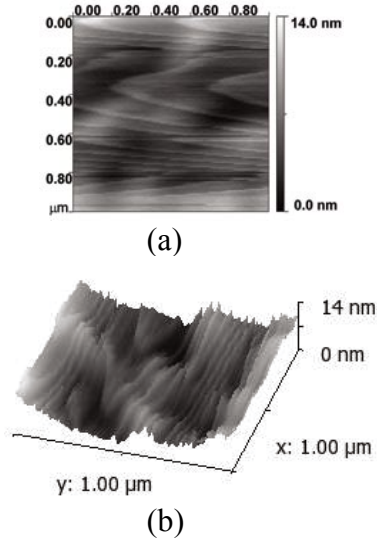

Figure 7. (a) AFM data shown as a height contour map of a 1μm x 1μm area of a Zeonor 1020 polymer surface. (b) 3D view of the same area.

4. REFERENCES

[1] Mela, P et al. *Electrophoresis*. 26(9): 1792–1799, 2005.

[2] Cho, SK et al. *Journal of Microelectromechanical Systems*. 12(1): 70-80. 2003.

[3] Attard, P. et al. *Physics A*. 314: 696-705, 2002.

HIGH SPEED SHEAR-DRIVEN FLOWS THROUGH MICRO-STRUCTURED 1D-NANO-CHANNELS.

Joris Vangelooven[(1)], Wim De Malsche[(1,2)], Kris Pappaert[(1)] , David Clicq[(1)] , Han Gardeniers[(2)] and Gert Desmet[(1)].

[(1)]Department of Chemical Engineering, Vrije Universiteit Brussel

[(2)] Research Program Mesofluidics, MESA+ Institute for Nanotechnology, Enschede

Abstract

A new, potentially interesting flow type for the conduction of rapid chromatographic and macro-molecular nanoscale separations is reported. It combines the pressure-drop-less operation mode of shear-driven flows through 1D nano-channels with the meandering flow paths that are present in ordered arrays of micro- and nano-pillars. In the present contribution, we report on a series of flow resistance and band broadening experiments that have been conducted to characterize the hydrodynamical properties of this new flow type.

Keywords: Nanofluidics, Hydrodynamics, Micro-pillars

Introduction

The past decade has witnessed a gradual shift of the scale at which the separation possibilities of so-called lab-on-a-chip or microfluidic devices are being explored and exploited [1]. This decreasing size of the separation channels and their internal features has given rise to the exploration of very diverse and original separation mechanisms [2,3].

The shear-driven flow principle, originally introduced by Desmet *et al.*[4], has the advantage that it establishes a flow velocity which is independent of the channel dimensions. This is a great advantage over pressure- and electrically driven flows through nano-channels, both being limited by respectively a pressure and a voltage drop. Being essentially limited by the camera recording rate, shear-driven flows of up to 5 cm/s could be demonstrated in channels with a depth of 100 nm [4]. For chromatographic purposes, it would be advantageous to "pack" the previously used open channels with microfabricated pillars to create a larger contact surface and thus increase mass loadability which in turn improves detection limits in these nano-channels.

Experimental Set-up

1D-Nano-scale channels were fabricated by Reactive Ion Etching (RIE), a siliciumenriched-nitride layer which was deposited on a silicon chip, leaving 250 nm high pillars of siliciumenriched-nitride (Fig.1). This etched chip is pressed against a flat glass surface with a pneumatic piston, using the microstructured pillars at the same time as a potential separation agent and as a spacer structure, and thus creating a 250 nm channel between the glass and the etched surface. By moving the glass plate, a shear driven flow is generated through this nano-channel, in which the velocity depends only on the velocity of the moving glass plate (Fig. 2).

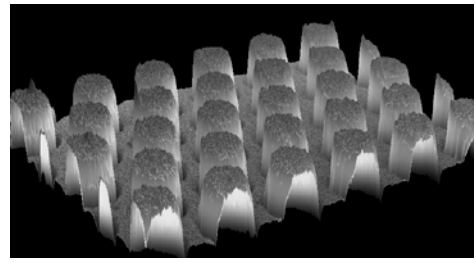

Figure 1: *Wyko image of one of the studied pillar beds. These cylindrical pillars have a diameter of 7 µm and are placed in a equilateral triangular pattern with an external porosity of 0.6 with an inter-pillar distance of about 1.5 µm.*

978-0-9798064-0-7/µTAS2007/$20©2007CBMS

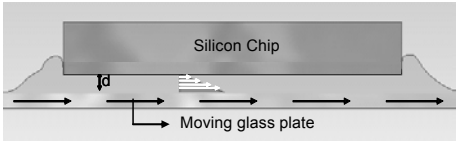

Figure 2: *Schematic profile of the experimental set-up. An etched silicon chip is pressed against a glass surface leaving an open channel with a depth d equal to the height of the etched pillars. Following movement of the glass plate results in a shear-driven flow of the fluid through the channel.*

Results and Discussion

We were able to inject sharply delimited tracer plugs of about 100 µm wide into the micro-machined pillar arrays as can be observed in fig. 3. The difference in light intensity between the light tracer plug and the dark pillars proves a close contact between the pillar tops and the glass plate.

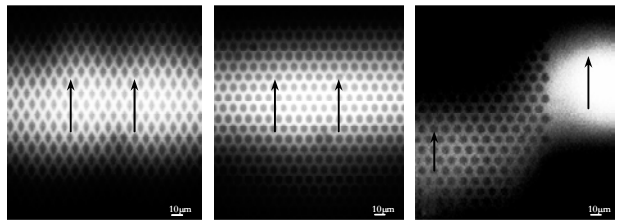

Figure 3: *Images of a sharply delimited tracer plug (rhodamine 6G) moving through the pillar beds (40x magnification).* ***(a)****: diamond shaped pillars ($ø_{lat}$ = 7 µm) in the middle of the pillar bed.* ***(b)****: cylindrical shaped pillars (ø = 7 µm) in the middle of the pillar bed.* ***(c)****: cylindrical shaped pillars (ø = 7µm) on the border of the pillar bed, showing the difference in flow resistance between the pillared region and an open channel. The darkness of the pillars proves a close contact between the pillars and the moving glass plate.*

Fig. 4 shows the migration of an injected band (initially injected width = 100 µm) and its intensity profile in the first two millimeters of one of the arrays. As can be observed, the amount of band broadening in the pillar array is extremely small. Fig. 5a shows the evolution of the mean band position with the product of time and u_{wall} for a range of different velocities. By multiplying time with the moving wall velocity, a correction is made for the different moving wall velocities. As can be noted, the lines from different velocities coincide, proving there is a fixed, linear relation between the mean liquid velocity and the moving wall velocity (the slope of the line), in agreement with the laminar nature of the flow. For a laminar shear-driven flow through an open-tubular channel with a flat-rectangular cross-section (w >> d), a similar relation is found. In the latter case, it can relatively easily be demonstrated theoretically that this relation is given by: $u_{liq} = ½\ u_{wall}$ *(eq.1)*

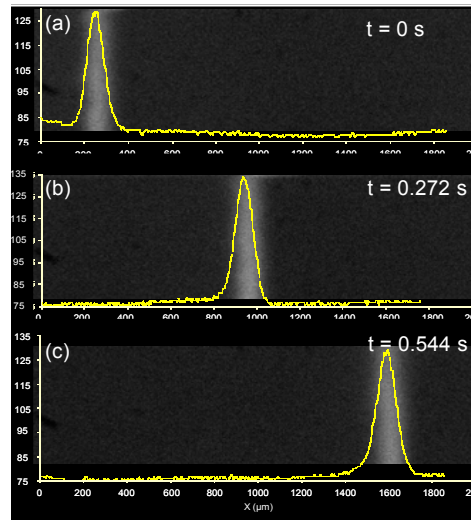

Figure 4: *Movement of a band of a fluorescent tracer plug (Rhodamine 6G) through a pillar bed consisting of cylindrical pillars (ø = 7 µm) at a velocity of 2.5 mm/s.*

In [5] this was confirmed experimentally. As a line of reference, eq. (1) has been added to Fig 5a. Comparing this line with the experimental data points shows that, compared to the open-tubular case, the fluid in the pillar array is slightly retarded.
The factor ½ in eq. (1) corresponds with the ratio of moving (flow generating) surfaces over total surface and can thus be directly explained. It is therefore perfectly understandable that in the pillar array case, where the ratio of moving over total surface is slightly larger than in the open-tubular case, the proportionality constant between u_{liq} and u_{wall} is given by a slightly lower value. Calculating the average slope of the different lines shown in Fig 5, it is found for the considered case of 7 µm cylindrical non-porous pillars and with an external porosity of ε = 0.6 that:

$$u_{liq} = 0.429 \, . \, u_{wall} \qquad \text{(eq. 2)}$$

The value of the proportionality constant agrees very well with the geometrically calculated value of S_{moving}/S_{total}, which is approximately equal to 0.457 for the considered channel.
Apart from the achievable liquid velocity, another important feature of a well functioning separation device is its ability to transport sample species and particles with a minimum of axial intermixing or axial dispersion. Fig 4b shows a Van Deemter plot in which the obtained plate heights, a traditional measure of axial dispersion, are plotted as a function of the peak velocity. Very low plate height values and thus very low dispersion have been measured, with a minimum plate height of 0.23 µm for a peak velocity of 4.2 mm/s. This is more than an order of magnitude smaller than in a packed bed HPLC column.

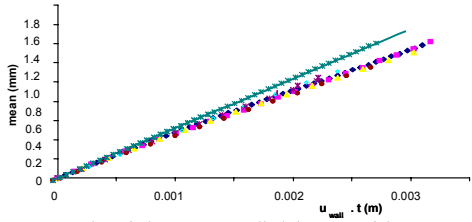

Figure 5: *Plot of the mean travelled distance of the tracer plug vs the product of wall velocity and time. This way the slopes of the lines represent the ratios of liquid velocity over moving wall velocity. The top reference line has a slope of ½, which represents the flow in an open channel. All other lines represent the flows through an array of cilindrical pillars (d=7 µm, height = 250 nm) at different velocities. These ratios are clearly independent of the moving wall velocity as all lines coincide.*

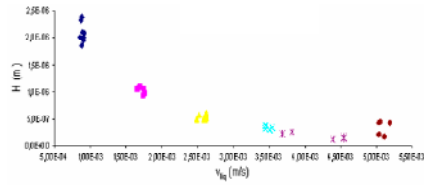

Figure 6: *A Van Deemter curve showing the axial dispersion of a non-retained tracer molecule in a pillar bed (ø = 7 µm) as a function of fluid velocity. A minimal plate heigth of 0.2 µm was obtained. This is more than an order of magnitude smaller than in a packed bed HPLC column.*

Conclusion

Shear-driven flows through arrays of micro-pillars are feasible and show only minimal axial dispersion. This new type of flow opens the door to both vast improvements to chromatographic applications of shear-driven flows and new separation mechanisms to be tested in a shear-driven mode, e.g. using the micro-pillars as a sieving matrix.

Acknowledgements

J.V gratefully acknowledges a research grant from the Institute for Innovation by science and Technology of Flanders (IWT-Vlaanderen)

References:

[1] **Eijkel, J. en van den Berg, A.** (2005). *Microfluid nanofluid* **1**, 249-267.
[2] **Han, J. en Craighead, H. G.** (2000). *Science* **288**, 1026-1029.
[3] **Huang, L.R., Cox, A., Sturm, J.C.** (2004). *Science* **304** (5673), 987-990.
[4] **Desmet, G. and Baron G. V.** (2000). *Analytical Chemistry* **72**, 2160-2165.
[5] **Clicq, D., Vervoort, N., Vounckx, R., Ottevaere, H., Gooijer, C., Ariese, F., Baron, G. V. and Desmet, G.** (2002). *Journal of Chromatography A* **979**, 33-42.

IONIC CURRENTS IN METAL-GATED NANOCHANNELS AND CARBON NANOTUBES

Christine Meyer, Marc Zuiddam, Vishal Merani, Serge Lemay, and Cees Dekker

Delft University of Technology, NETHERLANDS

ABSTRACT

In this paper, we investigate the effects of a non-zero gate current in an ionic transistor. A metal-liquid interface will lead to electrochemical reactions that complicate the interpretation of ionic transistor measurements.

Keywords: nanochannel, nanofluidics, ionic transistor, gate leakage

1. INTRODUCTION

In an ionic transistor one can modulate the ionic current through a fluidic channel by application of a voltage to a side gate. This is possible because, at low salt concentrations, the ionic current in a nanochannel is determined by its surface charge density [1] (see Fig. 1). If this charge density can be changed by an applied gate potential, the ionic current as well as the flow behavior can thus be influenced. A few cases of ionic transistor behavior in nanofluidic channels have been reported [2-4]. Total compensation of the silicon dioxide surface charge at neutral pH has not been shown though. For practical use in lab-on-chip technology, it would be desirable to induce large current changes by applying small gate voltages. One way of achieving this is decreasing the distance between the gate electrode and the fluid. It thus is useful to investigate the effects of direct metal-electrolyte contact on ionic transistor measurements.

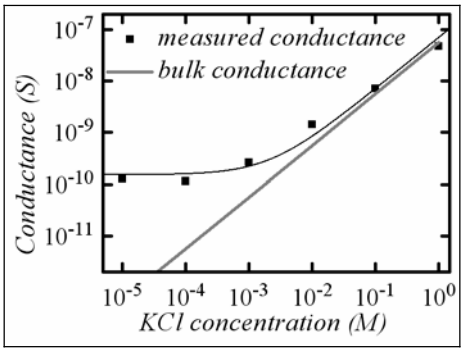

Figure 1. The conductance in a silicon oxide nanochannel (120 nm high, 400 µm wide and 4.5 mm long) saturates at low salt concentrations

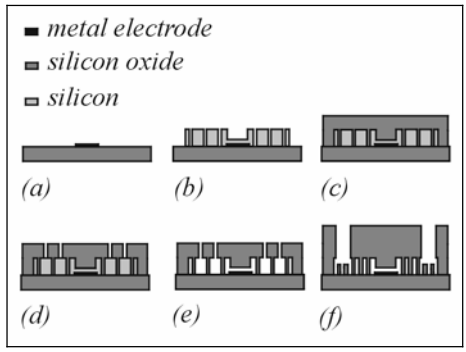

Figure 2. Fabrication scheme. Electrodes (a) and a silicon sacrificial layer (b) are deposited onto a fused silica substrate and overgrown by oxide (c). Through access holes (d) the sacrificial layer is removed (e). Finally the channel is closed and filling points are added (f).

A typical surface charge for a silicon dioxide layer at neutral pH is 50 µC/cm^2 [1]. The capacitance per surface area of a 10 nm silicon dioxide dielectric layer is 0.4 µF/cm^2. This

978-0-9798064-0-7/µTAS2007/$20©2007CBMS

means that an applied voltage of 1 V changes the surface charge by about 1 % only. In contrast, the capacitance of the metal liquid interface for platinum in aqueous solutions is reported to be about 50 $\mu F/cm^2$ [5]. However, electrochemical reactions can then occur at the metal-liquid interface. The effects of the accompanying non-zero gate currents on ionic transistor measurements have so far not been considered.

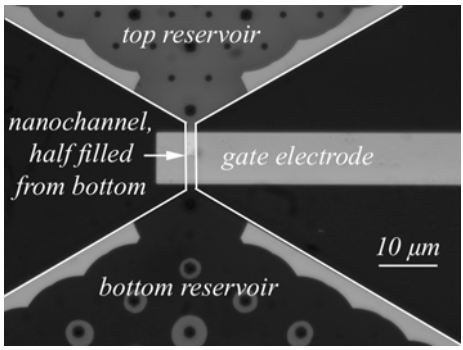

Figure 3. Fabricated channel structure: Two reservoirs are connected by a nanochannel with a local gate electrode. White lines are added to the channel boundary as a guide to the eye. Liquid is filling the nanochannel from the bottom; the height of the whole structure is 120 nm.

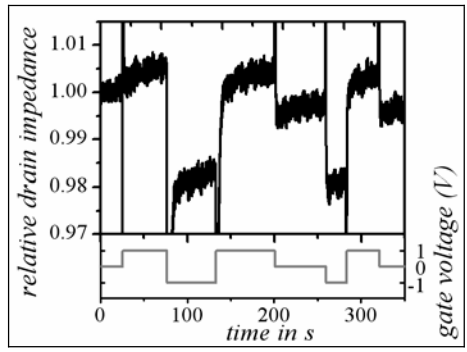

Figure 4. The demodulated current measured in the source-drain circuit shows three different levels for drain-gate voltages of +1V, 0V, or -1V. The gray line indicates the gate voltage levels on the right scale.

2. FABRICATION AND EXPERIMENTS

We fabricated nanofluidic channels using a sacrificial-layer etching process. A fabrication scheme can be found in Fig. 2. The fluidic channel area was built on top of a metal electrode using a sacrificial silicon layer process. After enclosing this layer with silicon oxide, it was etched away selectively, thus creating a hollow path that can be filled with electrolyte. To be able to investigate the effects of gate currents, we put the metal electrode in direct contact with the fluid in the channel. An image of a half-filled fabricated channel including a local electrode is shown in Fig. 3. With the same fabrication scheme, we integrated a single single-wall carbon nanotube as a nanoscopic fluidic channel. Its extraordinarily flat hydrophobic walls promise unique flow properties. We plan to do experiments on fluidic transport through a single nanotube.

For an ionic transistor, we need to measure the gate-dependent source-drain resistance. It is worth noting that it is impossible in this geometry to measure the source, drain and gate resistance independently as there is no electrical contact at their “crossing point” in the middle of the channel. We modulated the source-drain voltage using a lock-in amplifier and measured the demodulated source-drain current at different gate voltages as depicted in Fig. 4. We also measured the drain-gate characteristics as shown in Fig. 5. An equivalent circuit is shown in Fig. 6.

3. EXPERIMENTAL RESULTS AND DISCUSSION

The demodulated source-drain and gate-drain current provide a measure for the ratio of drain resistance to gate resistance, though no absolute values. For a constant gate resistance, changes in the demodulated soure-drain current can still be attributed to the

drain resistance. However, the drain-gate current voltage characteristic shows that the gate resistance does depend on gate voltage (Fig. 4). Though the different levels in demodulated drain current for different gate voltages could be attributed to an ionic transistor effect, we rather ascribe the change (at least the major part of it) to a change in gate resistance. It is often assumed that an applied gate voltage will only have a gating effect. In practice, however, depending on geometry of the device, huge gate currents may flow. In this case both, drain and gate resistance, change with gate voltage due to an ionic-transistor effect and electrochemistry at the gate, respectively. Unfortunately, these two effects cannot be simply disentangled. One way of having a well-controlled measurement of a drain-resistance change in case of non-zero gate currents would be to measure the voltage drop in the drain channel directly, e.g. by introducing two independent electrodes there.

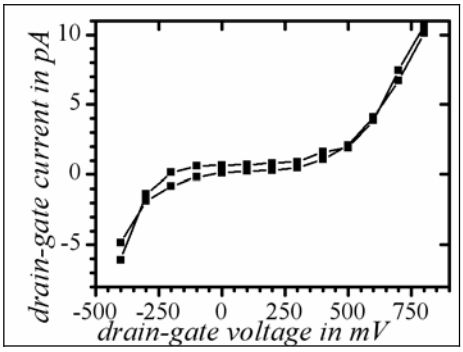

Figure 5. Drain gate characteristic. Current measured between reference electrode in reservoir and nanoelectrode in channel.

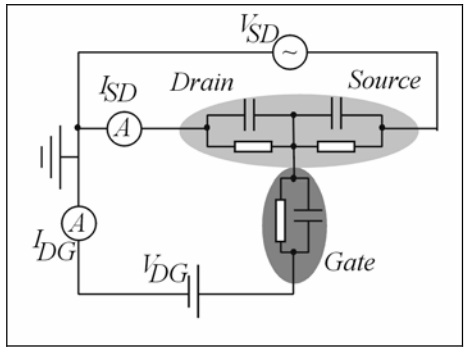

Figure 6. Equivalent circuit of a nanochannel with gate electrode. Light grey: source drain channel, dark grey: gate electrode.

4. CONCLUSIONS

We conclude that a not-well-insulated fluid electrode boundary complicates ionic transistor measurements. Minimization of electrochemical gate currents is important for accurate studies of an ionic transistor.

ACKNOWLEDGEMENTS

We thank NanoNed for funding and J. de Grebber for his help in process development.

REFERENCES

[1] D. Stein, M. Kruithof, and C. Dekker, *Surface-Charge-Governed Ion Transport in Nanofluidic Channels*, Phys. Rev. Lett. **93**, 035901 (2004)

[2] R. B. M. Schasfoort, S. Schlautmann, J. Hendrikse, and A. v. d. Berg, *Field-Effect Flow Control for Microfabricated Fluidic Networks*, Science **286**, 942 (1999)

[3] R. Fan M. Yue, R. Karnik, A. Majumdar, and P. Yang, *Polarity switching and transient responses in single nanotube nanofluidic transistor,* Phys. Rev. Lett. **95**, 086607 (2005)

[4] R. Karnik, R. Fan, M. Yue, D. Li, P. Yang, A. Majumdar, *Electrostatic Control of Ions and Molecules in Nanofluidic Transistors*, Nano Lett. **5**, 943 (2005)

[5] J. P. Carr and N. A. Hampson, *Differential capacitance of the platinum/aqueous-solution interphase,* Electrochim. Acta, **17**, 2117 (1972)

MESOSCOPIC CONCENTRATION FLUCTUATIONS IN A NANOFLUIDIC DEVICE

Marcel A.G. Zevenbergen, Bernhard L. Wolfrum and Serge G. Lemay

Kavli Institute of Nanoscience, Delft University of Technology, Lorentzweg 1, 2628CJ Delft THE NETHERLANDS

ABSTRACT

A direct consequence of downscaling fluidic devices to nanometer dimensions is that the number of molecules being detected or manipulated decreases, ultimately leading to such small numbers of analyte molecules that their discreteness and accompanying statistical fluctuations can no longer be ignored. Here we study these fluctuations both experimentally and theoretically in a nanofluidic cavity capable of detecting ~450 electrochemically active molecules. Due to Brownian motion, the average number of molecules in the device fluctuates, leading to intrinsic fluctuations in the electrochemical signal. We theoretically analyze this diffusive motion and report excellent agreement between the measured and calculated power spectrum densities without fitting parameter.

Keywords: Redox cycling, Brownian motion, Nanofluidics

1. INTRODUCTION

In electrochemical sensing, the presence of an analyte is detected by the transfer of electrons to an electrode immersed in the solution. Usually one or a few electrons per molecule are involved in this reaction, rendering the direct detection of a single molecule virtually impossible. The current per molecule can be greatly enhanced for reversible reactions by placing a second electrode in close proximity. Each diffusing molecule in the region between the two electrodes can then be repeatedly oxidized and reduced, thereby shuttling multiple electrons (figure 1).

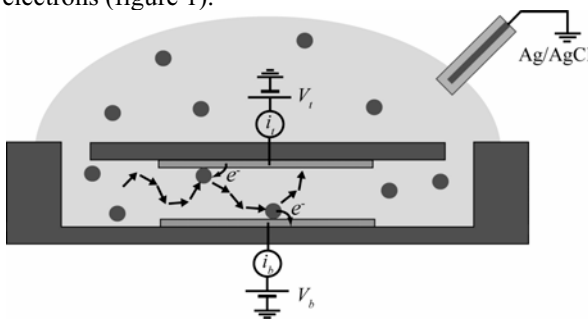

Figure 1. Device concept. Redox-active molecules undergo a random walk in a nanofluidic cavity embedded between two electrodes thereby shuttling multiple electrons between the electrodes. V_b and V_t are the potentials applied with respect to an Ag/AgCl reference electrode to the bottom and top electrode, respectively, while i_b and i_t are the corresponding currents.

2. THEORY

Each molecule traverses the cavity in a typical time $\tau = z^2 / 2D$, where D is the diffusion coefficient, and z the height of the cavity . In each back-and-forth cycle, the molecule

978-0-9798064-0-7/μTAS2007/$20©2007CBMS

shuttles one electron between the electrodes. If on average $\langle N \rangle$ molecules are present in the cavity, the current I_P is then given by

$$I_P = \langle N \rangle e / 2\tau = \langle N \rangle eD / z^2 \tag{1}$$

where -*e* is the electron charge.

The average number of molecules present in the cavity $\langle N \rangle$ fluctuates due to Brownian motion, which leads to fluctuations in the current I_P. The power spectral density exhibits the form for "diffusion noise"; a plateau S_0 for $f \to 0$ and a power law decay with slope -1.5 at higher frequencies. We have derived an analytical expression for S_0 [1]:

$$S_0 = \langle N \rangle \left(\frac{eD}{z^2} \right)^2 \left(\frac{L_A^2}{3D} + 2\frac{L_A L_E}{D} + 2\frac{L_A}{\kappa} \right) \tag{2}$$

Here L_A and L_E are the length of the active area and the entrance channels of the device, respectively (figure 2a). κ is an escape rate describing the probility per unit time of a molecule escaping from the cavity [2]. We evalutate $\kappa = 8.3 \times 10^4$ m/s for this device from finite-element calculations [1].

3. EXPERIMENTAL

The device is shown in figure 2a. The design and fabrication process have been described elsewhere [1, 3] A device's functioning is shown in figures 2b and 2c. Redox cycling permits a ~500X amplification of the signal from molecules in the device. In figure 3a we show that the current I_P scales linearly with the bulk concentration of redox active molecules, as expected. From a linear fit and equation 1 we determined the height of the cavity to be 116 nm. The smallest signal detected corresponds to ~450 molecules present in the channel and each molecule shuttles ~10^4 electrons during the time it is present in the device.

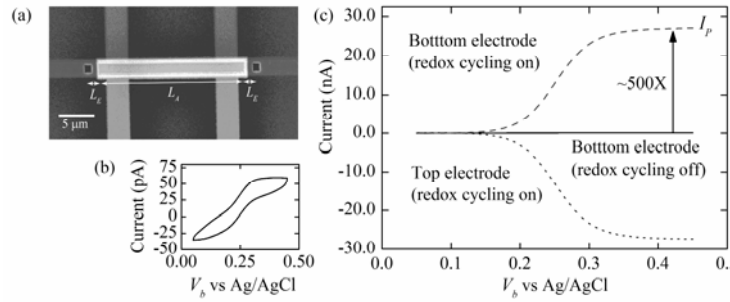

Figure 2. (a) SEM image of a device. L_A = 20 µm and L_E = 1 µm are the length of the active area and the entrances. Wires leading to macroscopic contact pads can be seen at the top and bottom. (b) Cyclic voltammetry performed with the bottom electrode while the top electrode was electrically disconnected (redox cycling off) (c) Cyclic voltammetry when V_t = 0.10V (dashed curve, redox cyclig on). The amplification is approximately 500 times compared to the case of redox cycling off (solid line, same data as in (b)). The dotted curve represents the current through the top electrode. It is a mirror image of the current through the bottom electrode, indicating that nearly 100% of the generated product is cycled.

In figure 3b, fluctuations in the current I_P are shown as time traces. Clearly, the noise amplitude increases with the average number of molecules in the channel. The

corresponding power spectral densities revealing the characteristics for diffusion noise are shown in figure 3c. In figure 3a the height of the plateau S_0 in the spectrum is shown as a function of the bulk concentration redox active molecules c_0. Both S_0 as I_P scale linearly with $c_0 \sim \langle N \rangle$. The signal-to-noise ratio $I_P / \sqrt{S_0}$ scales as $\sqrt{\langle N \rangle}$. Therefore, as $\langle N \rangle$ decreases, the noise becomes increasingly dominant. All the constants in equation 2 are known. Therefore, a direct comparison with the data *without additional fitting parameter* is given by the dashed line in figure 3a showing an excellent agreement.

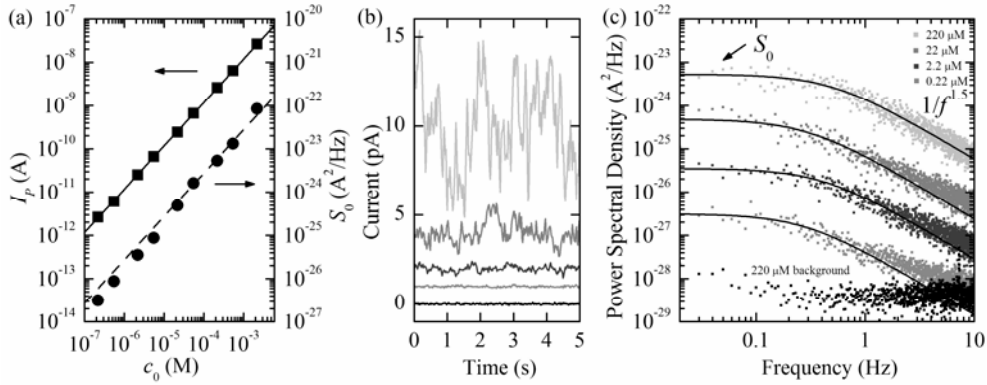

Figure 3. (a) Height of the plateau in the current I_P (squares) and in the power spectral density S_0 (circles) as a function of the bulk concentration redox active molecules. Both show a linear dependence over four orders of magnitude. The solid line is a linear fit to equation 1. The dashed line is calculated according to equation 2 *without fitting parameter*. (b) Current time traces revealing fluctuations due to the fluctuations of the number of molecules in the cavity. The absolute fluctuation level decreases with decreasing number of molecules. Curves have been offset for clarity. (c) Corresponding power spectral densities showing the characteristics of "diffusion noise". Solid lines are a fit to the form expected for diffusion noise.

4. CONCLUSIONS

Redox cycling was implemented in a 116 nm high cavity bounding two parallel plate electrodes, capable of detecting ~450 electrochemical active molecules in the cavity. Each molecule shuttles ~10^4 electrons during the time it is present in the cavity. The good agreement between measurement and calculated spectra indicates that fluctuations in the detected signal result from the independent Brownian motion of the molecules. As the current per molecule increases dramatically with decreasing channel height, we expect that reducing the device dimensions will ultimately lead to single redox molecule detection.

REFERENCES

[1] Marcel A.G. Zevenbergen, Diego Krapf, Marc R. Zuiddam and Serge G. Lemay, *Mesoscopic concentration fluctuations in a fluidic nanocavity detected by redox cycling*, Nano Letters **7**, 384-388 (2007)

[2] S.M. Bezrukov et al., *Particle number fluctuations in a membrane channel*, J. Chem. Phys **113**, 8206-8211 (2000)

[3] Marcel A.G. Zevenbergen, Diego Krapf, Marc R. Zuiddam and Serge G. Lemay, *Giant amplification of redox current in a nanofluidic channel*, Proceedings of the 10th Microtas conference, Tokyo, Japan, 654-656 (2006)

SPONTANEOUS STRETCHING OF DNA IN A TWO-DIMENSIONAL NANOSLIT

Madhavi Krishnan[1], Ingolf Mönch[2] and Petra Schwille[1]

Biophysics Group, Biotechnologisches Zentrum, Technische Universität Dresden, Tatzberg 47-51, 01307 Dresden, Germany[1]. Leibniz Institute for Solid State and Materials Research (IFW) Dresden, Helmholtzstraße 20, 01069 Dresden, Germany[2].

ABSTRACT

DNA molecules in silicon dioxide-glass fluidic nanoslits spontaneously extend at the lateral sidewalls of the slit. The nanoslit geometry however, physically confines polymer molecules to two spatial dimensions; further reduction in configurational entropy resulting in axially stretched molecules arises spontaneously, and appears to be electrostatically mediated. The observations not only shed light on electrostatic interactions of charged soft matter with like-charged confining walls but also offer a new method to stretch DNA in solution.

Keywords: DNA stretching, nanoslits, nanofluidics, confined polyelectrolytes

1. INTRODUCTION

Stretching a DNA molecule in free solution unravels its contour length, normally stored in a random coil, and exposes it to observation by fluorescence microscopy. This has tremendous implications for studies on DNA-protein interactions at the single molecule level, sequence- related analytical operations such as restriction mapping [1, 2].We recently reported a regime of confined macromolecule behavior where a proportion of DNA molecules confined in solution to a two-dimensional fluidic slit – slits several microns in width, but less than 100 nm in depth - spontaneously assumes axially extended states at the lateral edges of the fluidic slit [3]. The molecules thus localized at the edge distribute their mass preferentially along the major axis of the slit rather than sampling both dimensions of the fluidic plane in a two-dimensional random walk. This behavior is intriguing on account of the self-organization inherent in the process: molecules in solution spontaneously seek the lateral edges of the slit, shed their configurational entropy and stretch out in one dimension.

2. EXPERIMENTAL

Devices were fabricated by patterning silicon substrates bearing approximately 1000 nm Silicon dioxide using laser lithography. Silicon dioxide was etched by two different methods: Reactive Ion Etching in CHF_3 plasma using a photoresist mask and wet-etching in HF using 50 nm Cr mask. Wafers were diced so as to expose the extremities of the etched channel regions to the lateral edges of the substrate. Fluidic slits were produced by anodic bonding of patterned substrates to cover glass suitable for microscopy. Devices consisted of several parallel fluidic slits of width 2, 5 and 10 μm.

λ-DNA (Fermentas Life Sciences) was labelled with YOYO-1 (Invitrogen) at a ratio of 1:10 (dye:basepair). A drop of solution containing labeled DNA (10 ng/μl) in TrisHCl at the relevant concentration was placed at the entry to the nanoslits. Solution was drawn into the nanoslits by capillary effect was allowed to flow for at least one minute. The pressure gradient over the length of the slit was eliminated by placing a drop of buffer of the same

978-0-9798064-0-7/μTAS2007/$20©2007CBMS

concentration at the inlets and outlets of the slits. Upon equalizing the pressure at both ends of the slits, DNA molecules confined in the nanoslits showed an abrupt transition from flowing to diffusive behavior. Dynamics of DNA molecules in the nanoslits was studied using fluorescence microscopy on a Zeiss Axiovert inverted fluorescence microscope using a 60X N.A. 1.2 water immersion objective (Carl Zeiss AG) and a Cascade II EMCCD camera (Visitron Systems GmbH) for imaging. Groups of molecules were imaged for about 5 s at 10-20 frames per second. The lower limit on the solution ionic strength in our experiments was established by the 10 mM TrisHCl content of our commercially obtained λ-DNA stock solution.

3. RESULTS AND DISCUSSION

λ-DNA molecules, fluorescently labeled with YOYO-1, were introduced into slit shaped channels of depth ranging from 50 to 350 nm. In slits of depth 200 nm and higher, molecules occupied the footprint of the slit in coiled configurations, as intuitively expected. In slits of depth 100 nm and less, a proportion of molecules was observed to adopt axially extended configurations along the edges of the slit and exhibited thermally induced fluctuations in contour length along the major axis of the slit. The extended length of individual molecules, which we define as the linear projected length along the slit edge over which the polymer mass was distributed, was found to depend strongly on ionic strength of the medium (Figure 1D). The data show that the magnitude of molecular extension does not depend strongly on slit depth below a depth of 100 nm. Our measurements of the average observed extended length of DNA molecules were influenced by random breakage of DNA molecules mainly due to photocleavage and to some extent physical breakage during flow. Smaller fragments were eliminated by visual inspection and only the largest extended molecules under a given set of conditions were used to obtain estimates of the average end-to-end length shown in the Figure 1D. The measurements involved experiments performed in several different devices, and the spread of the distribution of molecular extension at any given salt concentration inherently incorporates small variations associated with device-to-device variability.

5. CONCLUSIONS

Our observations on the spontaneous extension of DNA molecules confined in solution to two dimensions in nanoslits present intriguing evidence of attractive interactions between like charged macroions and high-curvature (edge) regions of confining sidewalls. In slits of depth 100 nm and less, attractive interactions, whose origin is the subject of current investigation, arise between the molecules and high curvature edge-regions of slit. This attractive potential results in virtual quasi one-dimensional nanochannel zones at the slit edges, within whose confines the molecules shed configurational entropy and extend out along the edge.

From a technological standpoint, silicon dioxide-glass nanoslits present a simple system to stretch DNA in solution. Capillary flow transports dozens of DNA molecules simultaneously for stretching into nanoslits enabling high throughput single molecule DNA-protein interaction studies. The ability to stretch DNA in planar fluidic nanoslits could facilitate the direct observation of association and dissociation of proteins on the backbone of DNA, and the formation of induced tertiary structures such as loops, that may not be possible using existing methods.

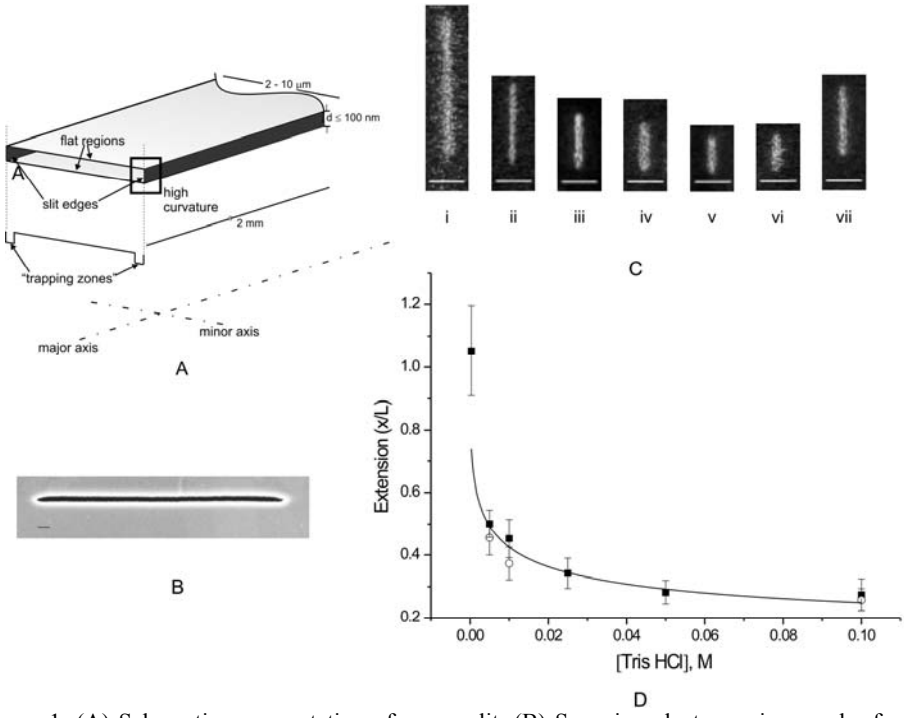

Figure 1. (A) Schematic representation of a nanoslit. (B) Scanning electron micrograph of a 2 μm wide and 50 nm deep slit. Scale bar represents 100 nm. (C) Fluorescence micrographs of representative individual extended molecules in 100 nm deep slits for ionic strengths ranging from 0.35 – 100 mM TrisHCl (i - vi), and in a representative biochemical buffer (Lambda- exonuclease reaction buffer -67 mM Glycine-KOH, 2.5 mM MgCl2, 50 μg/ml BSA) (vii). Scale bars represent 5 μm. (D) Average extended lengths of DNA molecules as a function of ionic strength. Data is displayed for the following conditions: 100 ± 10 nm deep slits (black squares), 50 ± 5 nm deep slits (open circles). Each data points represent averages over 15 – 40 molecules.

In addition, the fact that the information to stretch DNA in solution - a combination of confinement and electrostatics, in this case - is built into the structure of the device, offers an alternative to macroscopic experimental set-ups involving externally applied forces and fields to stretch DNA: a nanostructured coverslip that exploits the fortuitous interplay of physical phenomena that dominate at small length scales.

REFERENCES

[1] R. Riehn, M. C. Lu, Y. M. Wang, S. F. Lim, E. C. Cox, R. H. Austin, *Restriction mapping in nanofluidic devices,* Proc. Natl. Acad. Sci. USA, 102(29), 10012-10016, (2005).

[2] K. Jo, D. M. Dhingra, T. Odijk, J. J. de Pablo, M. D.Graham, R. Runnheim, D. Forrest, D. C. Schwartz, *A single-molecule barcoding system using nanoslits for DNA analysis*, Proc. Natl. Acad. Sci. USA, 104(8), 2673-2678, (2007).

[3] M. Krishnan, I. Monch, P. Schwille, *Spontaneous Stretching of DNA in a Two-Dimensional Nanoslit,* Nano Lett., 7(5), 1270-1275, (2007).

SUB-100NM LITHOGRAPHY WITH NANOSPHERES ARRAYED IN A TEMPLATE

Seungwon Jung[1] and Junghoon Lee[1]

[1]*Department of Mechanical and Aerospace Engineering, Seoul National University, Korea*

ABSTRACT

Nanosphere lithography has been studied as a general fabrication method to produce periodic particle array with nanometer scale features. This paper presents the first sub-100 nm nanosphere lithography (NSL) with an optimized spin coating condition and a nano template structure. The spin coating condition was tuned to obtain the best possible crystal formation. The qualities of the crystal domain, i.e., regularity and coverage, were further improved when a nano-trench structure was used as a template. We demonstrate a sub-100 nm nanohole array over 1 mm^2 area with subsequent fabrication steps.

Keywords: non-optical lithographic method, nanosphere lithography(NSL), nanohole array

1. INTRODUCTION

Nano-scale fabrication based on optical lithography is limited by the diffraction of light. Cost and complexity still prevent the wide use of approaches with shorter wave length to reduce the feature. Among non-optical lithographic methods studied as alternatives in recent days, NSL has been proved useful when a regular pattern on a large area was needed for applications such as optical filters, photonic crystals, and data storage [1-3]. Advantages include low cost, quick process, and the freedom in choosing various materials on diverse substrates.

In the NSL approaches, nanospheres are arrayed with methods such as drop-coating, spin-coating, and Langmuir-Bladgett film. These methods, however, have the possibility of forming multi-layer and multi-domain, resulting in a poor coverage and irregular patterns. No previous methods claim successful results with sub-100 nm features on a reasonably large area. In our approach, we achieved sub-100nm patterning over a large area through the optimization of the spin coating and the use of a mold pattern on the substrate.

2. EXPERIMENTAL

Our strategy is illustrated in Figure 1 that shows nanospheres arranged onto a template. Figure 2(a) shows the fabrication process of our approach. First, the nano template with 100 nm depth and 300 nm gap spacing was fabricated by nano imprint lithography (NIL) (Figure 2(b)). Then polystyrene nanospheres with 100 nm diameter (Duke Scientific Co., USA) were spin coated on the SiO_2 substrate (1mm x 1mm). To optimize the spin coating condition, we investigated the mode of crystal formation related to the spin rate. The initial set of the experiments were carried out without nano template, and then the same approach was tried with the nano template. O_2 plasma (Oxford etcher, 50W, 50mTorr) was treated for

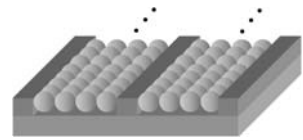

Figure 1. Schematic of template-assisted nanosphere array

978-0-9798064-0-7/μTAS2007/$20©2007CBMS

shrinking the nanospheres. Then chromium was deposited by the E-gun evaporator as a nanohole etching mask. After the nanospheres were removed thorugh a lift-off process with toluene, the nanoholes were etched with a reactive ion etching (RIE).

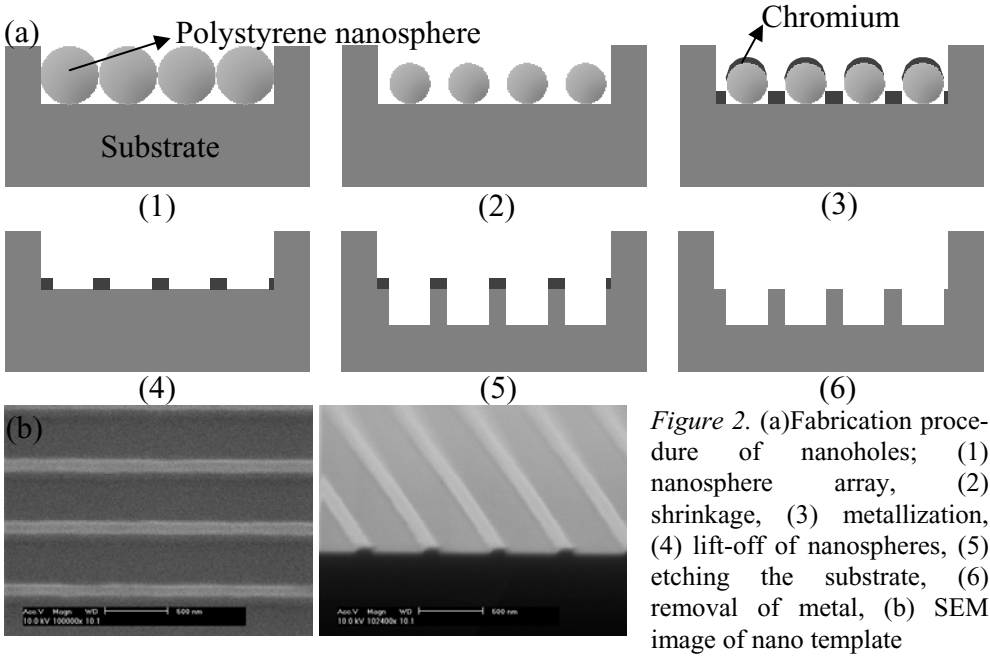

Figure 2. (a)Fabrication procedure of nanoholes; (1) nanosphere array, (2) shrinkage, (3) metallization, (4) lift-off of nanospheres, (5) etching the substrate, (6) removal of metal, (b) SEM image of nano template

3. RESULTS AND DISCUSSION

Figure 3 shows the result of nanospheres array with various spin rates without nano template. It was found that lower spin rate enables the larger single domain. However, Spin rates lower than 200 rpm deteriorated the quality of the array (image not shown).

We introduced the nano template to enforce the periodic arrangement of the nanospheres. The gap size of the nano templates is 300 nm as mentioned above. This dimension is a key factor for arraying nanospheres as the gap size is determined by the following equation

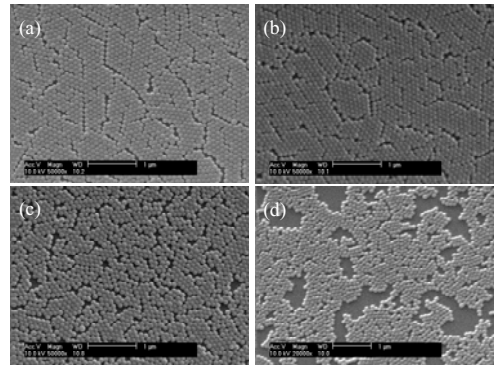

Figure 3. SEM images of nanosphere arrays using only spin coating with (a) 200 rpm, (b) 500 rpm, (c) 800 rpm, (d) 1500 rpm

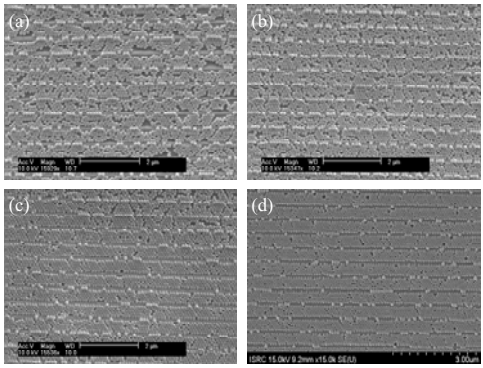

Figure 4. SEM images of Results of Template-assisted spin coating with (a) 1500 rpm, (b) 1200 rpm, (c) 800 rpm, (d) 200 rpm

$$l_g = (\frac{n-1}{\sqrt{3}} + 1)d \times 1.1 \qquad (1)$$

where n is the number of nanosphere row per gap, d the diameter of nanospheres, 1.1 the factor considering size variation [4]. The results in Figure 4 clearly show that the nano template assisted the periodicity of the nanosphere array over the large area.

Figure 5 shows the result of shrinkage by O_2 plasma. The 100 nm nanospheres were shrunk to 70 nm uniformly. After the chromium deposition and the lift-off of nanospheres, we obtained the sub-100nm nanoholes through a reactive ion etching (Figure 6).

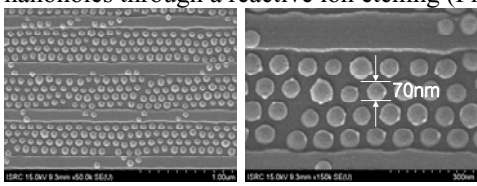

Figure 5. SEM image after O_2 plasma (30% shrinkage)

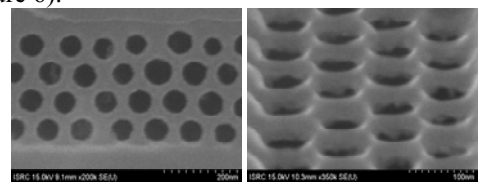

Figure 6. SEM image after chrome deposition, lift-off and etching

5. CONCLUSION

We developed a nanosphere array method on a large area with template-assisted spin coating. Nano template in this method assisted the arrangement of nanospheres on a substrate. The sub-100nm nanohole array was fabricated through the subsequent steps of shrinkage, metallization, lift-off, and RIE etching. This fabrication method will enable many applications that need a periodic nano-array pattern over a large area with a simple process.

6. ACKNOWLEDGEMENT

This work was supported by the Korea Science and Engineering Foundation (KOSEF) grant funded by the Korea government (MOST) (R08-2004-000-10320-0), and the Samsung Advanced Institute of Technology (SAIT).

REFERENCES

[1] K. Kempa et al , "Photonic crystals based on periodic arrays of aligned carbon nanotubes", Nano Letters, 3(1), 13(2003)

[2] A. L. Thangawng, J. Lee , "Fabrication of a micro/nano integrated roughened structure using nanosphere lithography(NSL)", Proceeding of IMECE04, IMECE2004, 62248(2004)

[3] A. J. Haes et al, "Detection of a biomarker for alzheimer's desease from synthetic and clinical samples using a nanoscale optical biosensor", Journal of the American Chemical Society, 127, 2264(2005)

[4] E. Kumacheva et al, "Colloid Crystal Growth on Mesoscopically Patterned Surfaces: Effect of Confinement", Advanced Materials, 14(3), 221(2002)

ARGON AND ACRYLIC ACID PLASMA TREATED ELECTROSPUN NANOFIBER SCAFFOLD

KwangHo Lee[1], GuHan Kwon[2], SuJung Shin[2], JinYoung Lee[2], YongDoo Park[2], ByoungGoo Min[3], and SangHoon Lee[2]

[1] Interdisciplinary Program Bioengineering Major, Seoul National University, KOREA
[2] Dept. of Biomedical Eng., Korea University, KOREA
[3]Dept. of Biomedical Eng., Seoul National University, KOREA

ABSTRACT

In this paper, we report here modification of polyurethane electrospun nanofibers matrices by treating plasma and acrylic acid(AA). To provide the well-defined 3D environments for human mesenchymal stem cells (hMSCs). The hMSCs were seeded on the surface of both treated and untreated nanofiber matrices and the morphological investigation by the actin filament staining assay and the scanning electron microscopy were executed. The proliferation test by WST-1 and Live/Dead assay were carried out to investigate the cell culture environment. We demonstrated the integration of plasma treated PU ENM into the microfluidic chip as ECM for the perfusive cell culture system.

Keywords: Acrylic acid, Nanofber, PDMS, Mesenchymal stem cell, Tissue engineering

1. INTRODUCTION

The electrospun porous nanofiber scaffolds are of particular interest in and regenerative medicine and tissue engineering. The nanofiber scaffolds can be designed to mimic the natural extracellular matrix characteristics and behavior [1]. We have stabilized the electrospun nanofiber scaffolds surface's hydrophilic properties using AA plasma treatment in order to perform suitable for cell adhesion, migration, and culture in PDMS-base microfluidics cell culture chip (Figure 1).

2. EXPERIMENTAL

Due to its excellent biocompatibility, Polyurethane (PU) solution was prepared [2]. We have electrospun prepared PU solution by using the electrospinning apparatus. In order to induce the radicals onto ENM, plasma treatment was carried out under argon (Ar) gas and then a hydrophilic acrylic acid monomer by using the radio frequency glow discharge device. The different characteristics of the untreated and plasma treated scaffolds were evaluated by contact angle and ATR-FTIR. The hMSCs were cultured and the actin filaments were visualized by staining with actin-palloidin for cytoskeletal structures[4].

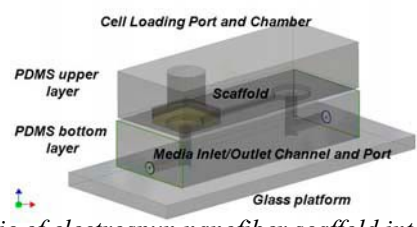

Figure 1. Schematic of electrospun nanofiber scaffold integrated PDMS-based microfluidics cell culture chip

978-0-9798064-0-7/μTAS2007/$20©2007CBMS

3. RESULTS AND DISCUSSION

The smooth and uniform nanofiber scffolds were produced successfully and their SEM image was illustrated in figure 2. Such porous structures play an important role as cell culture matrices with good feature for cell adherence and migration and the perfusion of nutrients or oxygen through such porous scaffols become easier. The appearance of the peaks is due to the hydrogen bonds of the –COOH groups in figure 3. Additionally, the contact angel decreased from 121° for the untreated scaffolds to 14°, which is caused by the hydrophilic –COOH groups in the figure 4. We have dyed the actin filaments staining of hMSCs and illustrated the fluorescent image of dyed cell which were cultured on the untreated and plasma treated nanofiber scaffolds in figure 5. Even cell morphology explained that the hydrophilic scaffolds have the specific advantages in cell adhesion and culture. In the figure 6, SEM showed apparent morphological differences. 10 days after seeding, hMSCs in untreated scaffolds appeared rounded in shape. However, hMSC in plasma treated scaffolds apparently attached to plasma treated scaffolds and penetrated into nanofiber pores.

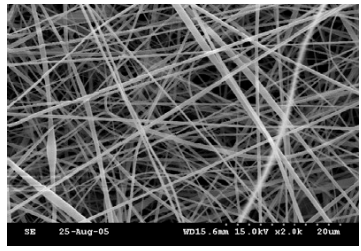

Figure 2. Polyurethane nanofiber fabricated by the electrospinning

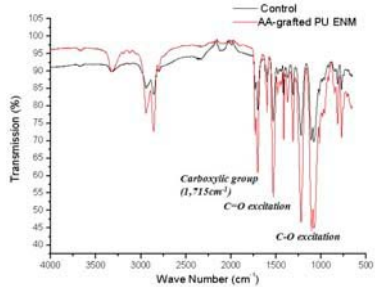

Figure 3. ATR-FTIR spectra of PU electrospun nanofiber and AA -treated PU electrospun nanofiber scaffold

(a) (b)



Figure 4. Water-contact angle and the corresponding shapes of water droplets (a) untreated (b) AA-treated scaffold

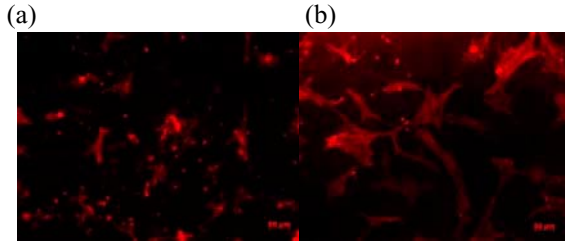

Figure 5. The fluorescent image of dyed cell which were cultured on the control and AA--plasma treatment nanofiber scaffolds (a) untreated, (b) AA-treated scaffold

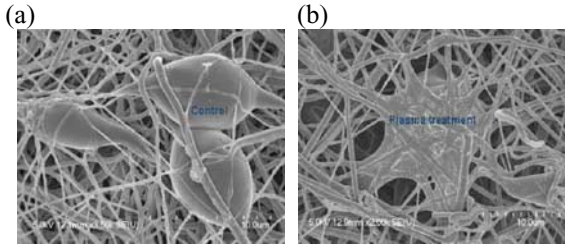

Figure 6. SEM images illustrating the hMSCs topography in nanofiber scaffolds (a) untreated, (b) AA-treated scaffold

4. CONCLUSIONS

In this paper, we demonstrated that hydrophilic scaffolds are important for good cell adhesion and culture in microfluidics chip. The plasma treatment is an excellent method for surface modification without changing the bulk properties of the electrospun nanofiber scaffolds. And the hydrophilicity was easy to cell attachment and spreading in scaffolds. So, we expected that this electrospun nanofiber scaffolds and surface modification using plasma treatment in PDMS-based microfluidics chip.

ACKNOWLEDGEMENTS

This study was supported by a grant of the Korea Health 21 R&D Project, Ministry of Health & Welfare, Republic of
Korea. (0405-ER01-0304-0001)

REFERENCES

[1] D. Han, P. Gouma *Electrospun bioscaffolds that mimic the topology of extracellular matrix* , Nanomedicine, pp.22-37, (2006)

[2] K. H. Lee, D. J. Kim, B. G. Min, and S. H. Lee *Polymeric nanofiber web-based artificial renal microchip,* Biomedical Microdevices, on-line available, (2007).

[3] W. Meng, S. Y. Kim, J. Y. Yuan, J. C. Kim, O. H. Kwon, and I. K. Kang *Electrospun PHBV/collagen composite nanofibrous scaffolds for tissue engineering* W. Meng, J.Biomater. Sci. Polymer, pp.18, (2007)

[4] X.Xin, M. Hussain, J. J. Mao, *Continuing differentiation of human mesenchymal stem cells and induced chondrogenic and osteogenic lineages in electrospun PLGA nanofiber scaffold*, Biomaterials, pp. 28, (2007)

HIGHLY PARALLEL FABRICATION OF MICROFLUIDIC CHIPS FOR LONG DNA MOLECULE SEPARATION

J. Shi[1,2], A.P. Fang[1], L. Malaquin[1], J.L. Viovy[3], A. Pépin[1], D. Decanini[1] and Y. Chen[1,2*]

[1]Laboratoire de Photonique et de Nanostructures, CNRS, 91460 Marcoussis, France
[2]Ecole Normale Supérieure, 24 rue Lhomond, 75005 Paris, France
[3]Laboratoire Physico-chimie Curie (UMR CNRS 168), Institut Curie Section de Recherche, 26 rue d'Ulm, 75230 Paris, France

ABSTRACT

High density nanopillars have been fabricated by soft UV nanoimprint lithography and then been integrated into microfluidic devices for long DNA molecule separation. This method is based on a mix-and-match approach for high throughput manufacturing which should also be suitable for integration of other types of micro and nanostructures. The proof-of-concept experiment has been demonstrated on the separation of λ-DNA and T4-DNA.

Keywords: Nanoimprint, microfluidics, electrophoresis, DNA separation

1. INTRODUCTION

Capillary electrophoresis (CE) is one of the commonly used techniques in molecular biology and genomic studies. In order to gain more efficiency, many efforts have been devoted to the fabrication of microfluidic devices that can be produced cost-effectively. One of the approaches is to integrate high density nanopillar arrays into a microfluidic channel as sieving matrices. While previous works have been mostly based on electron beam lithography [1-3], the development of a high throughput manufacturing method is expected. In this work, we demonstrate a mix-and-match method by combining soft UV nanoimprint (UV-NIL), photolithography and reactive ion etch techniques. As a proof-of-concept, electrophoresis separation of long DNA molecules has been demonstrated.

2. EXPERIMENTAL

Figure 1 shows the soft UV-NIL based nanofabrication process [4]. Here, a 160 μm thick fused silica plate was used to pattern both sieving nano-pillars and working microfluidic channels, which is relevant for high resolution imaging during CE experiments. First, soft UV-NIL is used to pattern nano-pillars. After lift-off of a 40 nm thick Ni film, microfluidic channels are defined on the same substrate by contact optical lithography with alignment. Then, a second lift-off is performed and the fused silica plate is etched by reactive ion etching (RIE) with SF_6 gas. Finally, the Ni etch masks is removed and the patterned structures are closed with a flat cover sheet made of polydimethylsiloxane (PDMS). To image single DNA migration behaviour and to record electropherograms, the fabricated device is placed on the sample stage of an inverted microscope (Axiovert 200 from Zeiss) equipped with a CCD camera and a photomultiplier tube (PMT).

978-0-9798064-0-7/μTAS2007/$20©2007CBMS

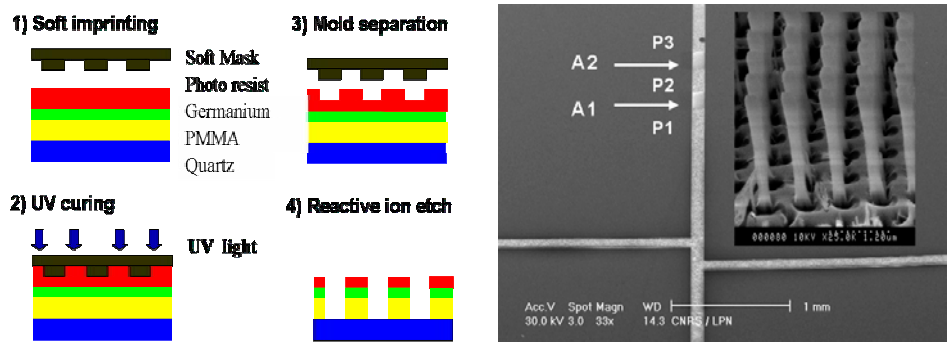

Figure1. (Left) Schematic representation of soft UV-NIL with a tri-layer resists system. (Right) Scanning electronic micrograph of the CE channels and one of the integrated nano-pillar arrays with 300 nm diameter, 800nm period and 3µm height.

3. RESULTS AND DISCUSSIONS

In order to demonstrate the ability of long DNA molecule separation of the fabricated devices, the proof-of-concept experiments have been performed with λ-DNA (48Kbp) and T4 DNA (166Kbp), both labelled with fluorescent dye YOYO-1 with a concentration of 3µg/ml.

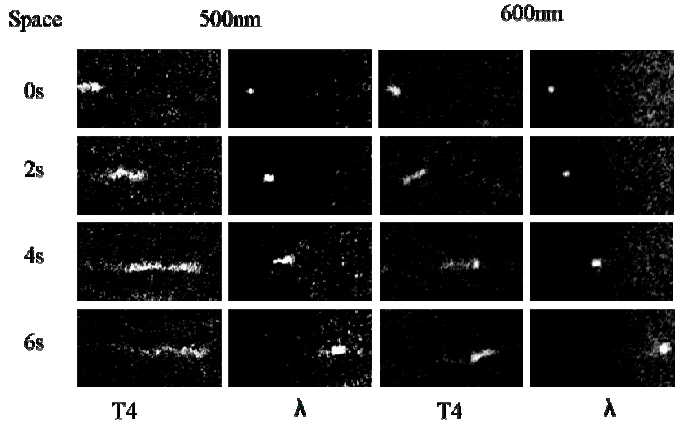

Figure2. Fluorescence images of λ DNA and T4 DNA single molecule migrating through different sized nano-pillar arrays.

After injection into the nanopillar arrays, conformation changes of single DNA molecules were observed (Fig. 2), indicating that both λDNA and T4 DNA molecules are stretched in A1 (with a pore size of 500 nm) but the stretching effect is clearly larger for T4 DNA because of its larger size; in A2 (with a pore size of 600 nm), λ DNA stays in a rather spherical conformation while T4 DNA can still be stretched to a long chain. This can be understood based on the molecular interpretation [5]. Here, the gyration radius of λ DNA and T4 DNA molecules are respectively 520 nm and 970 nm. Because of the size effect, λ DNA could migrate most-likely with a compact conformation in both A1 and A2 arrays, whereas T4 DNA has to be deformed to pass through the nanopillars arrays.

To demonstrate the electrophoresis separation of the two types of DNA, a mixture of DNA and T4 DNA (both at the concentration 50µg/ml) was loaded into the device by applying a DC electric field of 500V/cm. Then, the electropherograms were recorded at different observation points. At the down stream of the two nanopillars arrays, the two types of DNA molecules were well separated within a couple of minutes (Fig. 3). This is qualitatively in agreement with the previous discussions based on molecular interpretations [1]. Finally, we also noted that the separation efficiency of the A1 array is clear less than A2.

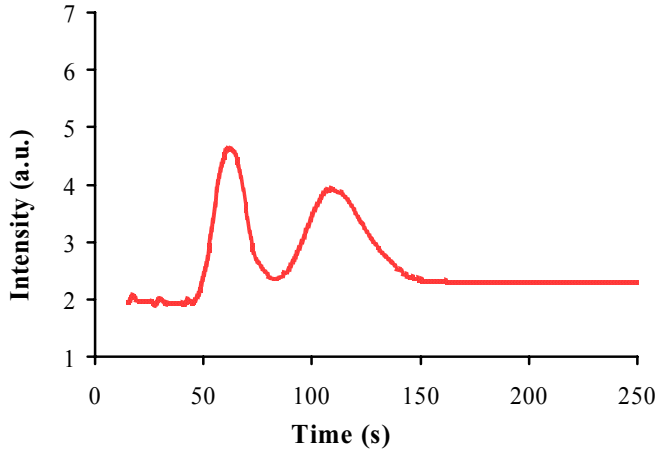

Figure 3. Electropherogram of λ DNA and T4 DNA separation recorded at point P3 with an applied electric field of 500V/cm.

4. CONCLUSION

In conclusion, we have developed a highly parallel and mix-and-match fabrication method than can be applied to the integration of nanopillar arrays into microfluidic devices for long DNA molecule separation. We believe that this method is flexible and versatile also for integration of other types of micro and nanostructures.

ACKNOWLEDGEMENTS

This work was partially supported the European Commission through project contract NMP4-CT-2003-505311 (Nabis) and NMP4-CT-2003-500120(Napa) and the French Ministry of Research-CNRS through project contract ACI Nanosciences-Nanotechnologies (Nanobiolab).

REFERENCES

[1] N. Kaji, Y. Tezuka, Y. Takamura, M. Ueda, T. Nishimoto, H. Nakanishi, Y. Horrike, Y. Baba. Anal. Chem. 76, 15 (2004).
[2] M. Baba, T. Sano, N. Iguchi, K. Iida, T. Sakamoto, and H. Kawaura, Appl. Phys. Lett. 83, 14683 (2003).
[3] T.A. J. Duke, R. H. Austin, E. C. Cox, S. S. Chan. Eletrophoresis 17 (6), 1075 (1996).
[4] J. Shi, C. Peroz, D. Perade, J. Salari, M. Belloti, W.H. Huang, Y. Chen. Microelectron. Eng. 83, 1664 (2006).
[5] J.L. Viovy, Rev. Mod. Phys. 72, 813 (2000).

ISOLATION OF DNA MOLECULE IN MICROCHANNEL AND SINGLE MOLECULE TRAPPING BETWEEN MICROELECTRODES

Momoko Kumemura[1], Dominique Collard[2], Christophe Yamahata[1], Naoyoshi Sakaki[1], Gen Hashiguchi[3], and Hiroyuki Fujita[1]

[1]Institute of Industrial Science, The University of Tokyo, JAPAN,
[2]LIMMS-CNRS/IIS, (UMI 2820), The University of Tokyo, JAPAN, and
[3]Faculty of Engineering, Kagawa University, JAPAN

ABSTRACT

This paper proposes an efficient way to minute isolate and trap single long DNA molecule. The microfluidic device uses Electrophoresis (EP) + microchannel to isolate molecule and dielectrophoresis (DEP) to trap it on fixed electrodes.

Keywords: Single molecule, Isolation, Microchannel, Dielectrophoresis

1. INTRODUCTION

A systematic and automated method is required to bring the single molecular characterization for common users conducting biological and medical analysis. Lab-on-a-chip approach is an appropriate mean as it encompasses accurate molecular level engineering tools with inexpensive production cost owing to bath fabrication. As a first step in that direction, this paper presents a systematic method to isolate and trap λ-DNA segments between microelectrodes in a microchip. Molecule flux in microchannel with EP was evaluated. Then, using this isolation method, we demonstrated that single DNA molecule trapping between aluminum electrodes with DEP [1] in the microchip. The new topics compared with previous paper [2], we investigated and realized the isolation efficiency in microchannel, and we also succeeded stretching and trapping single DNA molecule between electrodes.

2. EXPERIMENTAL

The microchip was consisted of glass plate with evaporated 50 nm thickness aluminum and Poly (dimelylsiloxane) (PDMS) film having microchannel (**Figure 1**). The pattern of electrode was fabricated by conventional photolithography and lift-off process. The gap for tapping DNA molecule was 10 μm. The PDMS film was prepared by molding from a master made in a silicon wafer. The channel sizes were 300 μm wide for the access channel and 2 μm wide for the separation channel. The depth of both channels was 4 μm. Two access holes were made at the access channel for introducing DI water and DNA solution.

The experiment procedure is following (**Figure 2**); Injection of DI water into two access holes. Injection of 2 μL of YOYO-1 fluorescent dyed λ-DNA solution (0.4p mol/L) into one side of access hole. Applying DC voltage (0-4V/4mm) for EP. Observation of DNA molecule movement with a fluorescent microscope. For DNA molecule trapping, we switched from applying DC voltage (for EP) to applying AC voltage (for DEP, 900 k Hz, 1MV/m).

978-0-9798064-0-7/μTAS2007/$20©2007CBMS

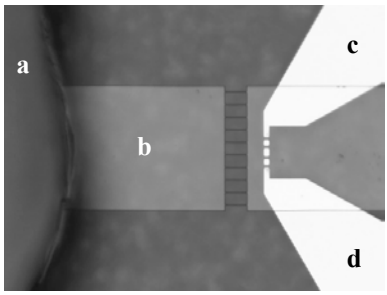

Figure1. Close-up view
on the active part of the microchip
a: access hole, **b**:access channel,
c:electrode forDEP(signal),
d:electrode for DEP (ground)

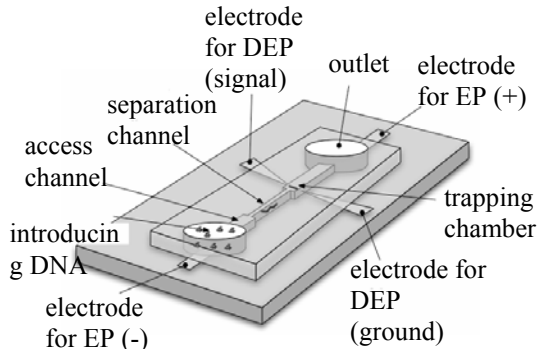

Figure2. Schematic illustration of microchip

3. RESULTS AND DISCUSSION

We optimized isolation condition to achieve successful single molecular trapping. The isolation efficiency can be evaluated by measuring the molecular flux (number of molecules per second) in a separation channel. The molecular flux was modulated at the separation channel. The separation channel provided easily isolated molecular flux, as low as 0.12 s^{-1} at 4V for a 0.2 p mol/L solution (**Figure 3**). Three out of ten separation channels effectively provided DNA molecules between the gap of trapping electrodes; excess number of channels were necessary to ensure good alignment between channel exits and the gap. Molecular flax from these three channels was low enough to ensure a proper trapping of individual molecule. We observed DNA molecule flows in separation channel one by one (**Figure 4**). Due to the abrupt transition between the access and separation channels cross-sections, molecules experience complex motion in this area. The EP electric field attracts the molecules towards the separation channel, while electro osmotic flow (EOF) slows down their progression towards it. The EOF is dragged along by the cations motion in the surface double layer which extends over the Debye length. Scaling laws show that the influence of this flow increases in channel with tiny cross-section as the surface effect becomes more and more significant [3].

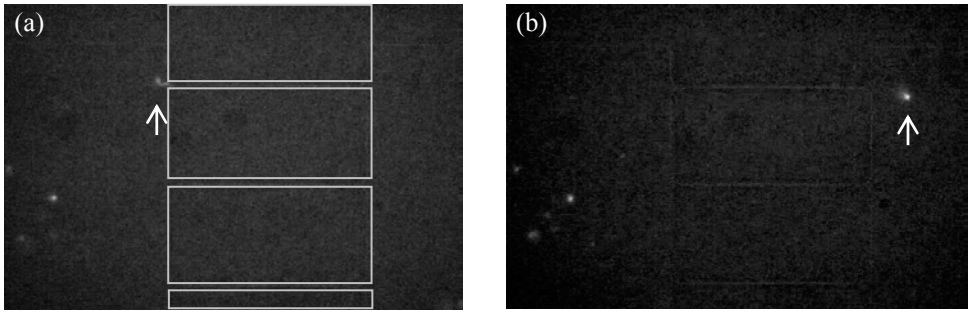

Figure4. Single DNA molecule passing through a separation channel

To successful trapping of a molecule, we employed floating electrode design [4] for trapping electrodes. Owing to this floating electrode, we can avoid liquid circulation, which

is induced by electric field and heating. Following isolation step, we succeeded single DNA molecule trapping between electrodes by applying AC voltage (**Figure 5**).

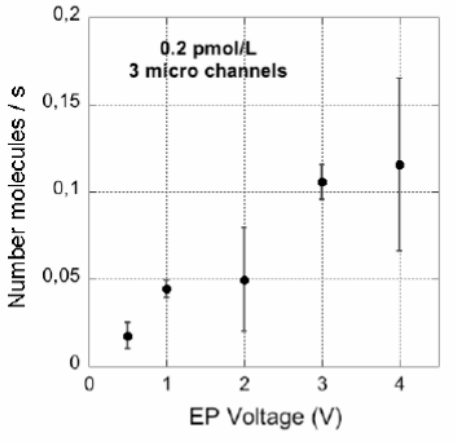

Figure3. Molecule flux in the separation channel versus V_{EP}

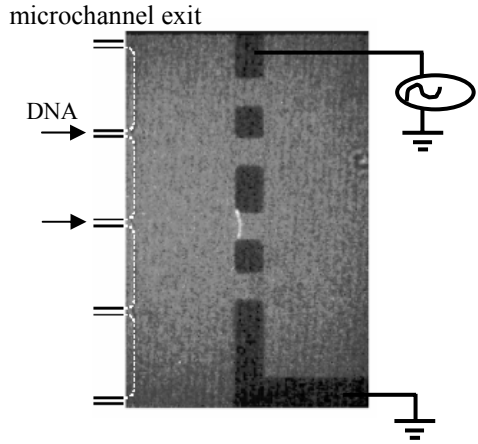

Figure5. Single DNA trapping between electrodes

4. CONCLUSIONS

λ-DNA molecule isolation was performed in microfluidic device, and the single molecule was stretched and trapped between electrodes by dielectrophoresis. This technique could be used to investigate single molecule characterization.

ACKNOWLEDGEMENTS

We acknowledge M. Washizu from the University of Tokyo for providing us with precious advice. This work was supported by JST Grant for Advanced Instrumentation "Development of Handling and Characterization Tools for Nano Objects". The mask preparetion was supported by VLSI Design and Education Center (VDEC), the University of Tokyo in collaboration with ADVANTEST Corporation.

REFERENCES

[1] M. Washizu, *Electrostatic Manipulation of DNA in Microfabricated Structures*, IEEE Trans. Ind. Appl., 26, pp.1165-1172, (1990).

[2] M. Kumemura, K. Tamura, G. Hashiguchi, and H. Fujita, "*DNA molecular isolation in nano channel for single molecule trapping between micro electrodes*", Proc. Micro Total Analysis Systems 2005, Transducer Research Fundation, San Diego, USA, pp.521-523, (2005).

[3] A. T. Conlisk, J. McFerran, Z. Zheng, & D. Hansford, "*Mass Transfer and Flow in Electrically Charged Micro- and Nanochannels*", Anal. Chem. 74, pp.2139-2150, (2002).

[4] M. Washizu, O. Kurosawa, I. Arai, S. Suzuki, & N. Shimamoto, "*Applications of electrostatic stretch-and-positioning of DNA*", Ind. Appl. IEEE Trans., 31, pp.447-456, (1995).

LOCALIZED GENE REGULATION BY A REMOTE OPTICAL SWITCH

Eunice S. Lee, Gang L. Liu, Luke P. Lee

Department of Bioengineering, University of California, Berkeley, CA, USA

ABSTRACT

The ability to control protein expression in cells is of particular significance since effective nucleic acid-based methods are in critical demand for understanding cellular mechanisms, quantitative cell biology, and systems biology. By intracellular introduction gold nanoplasmonic particle (GNPs) carriers of oligonucleotides, selective control of gene release is accomplished by a new nanophotonic remote optical device called Oligonucleotides on a Nanoplasmonic Carrier-based Optical Switch (ONCOS).

Keywords: nanoparticle, gene delivery, photothermal

1. INTRODUCTION

We have created a new biomolecular nanophotonic device called ONCOS to regulate gene and protein expression. With nanoscale spatial resolution, ONCOS can control protein translation for cell biology, systems biology, and therapeutic applications. By intracellular introduction of custom ONCOS nanocarriers, selective control of gene release is accomplished by a remote nanoscale optical switch. Here, antisense oligonucleotides are selectively released on command, and are allowed to bind with target mRNA and thereby inhibit gene expression.

Even though previous methods such as enzymes[1], radio frequencies[2], thermo-responsive polymers[3], and thermal ablation[4] have been demonstrated to release DNA from their carriers, these techniques lack precise spatial and temporal control. Whereas the use of thermal ablation of the carriers maintains the highest degree of spatial and temporal control, the method is strongly correlated with cell death due to the consequential extreme heating effect within cells. However, ONCOS takes advantage of the photothermal effect that is localized at the GNP surface (Fig. 1a), to release genes at a specific melting temperature and interfere with protein translation (Fig 1b).

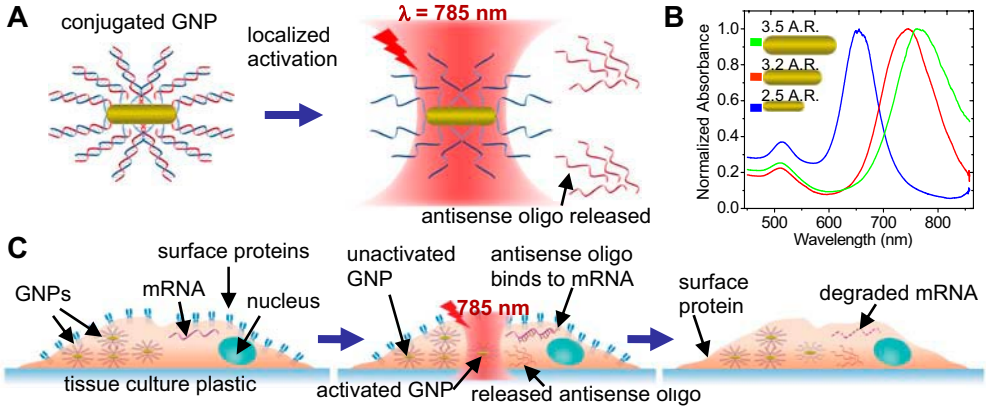

Figure. 1. Concept of ONCOS. (A) photothermal release mechanism. **(B)** Absorbance spectra of tunable nanocarriers based on aspect ratio (A.R.). **(C)** optical switch of protein downregulation within cells.

978-0-9798064-0-7/μTAS2007/$20©2007CBMS

A 2D Femlab simulation in Fig.2 shows that at the surface of the GNP, the temperature starts at the melting temperature of the oligonucleotides and falls off exponentially to 37ºC within 100 nm from the GNP's surface. This demonstrates that the heat generated using ONCOS is highly localized to the GNP's surface and should not propagate significantly throughout the intracellular milieu.

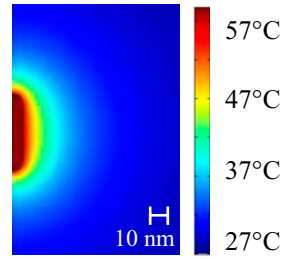

Figure 2.

2. EXPERIMENTAL

Preparation of oligonucleotide-conjugated GNPs - Rod-shaped GNPs with aspect ratio of 3.5 are synthesized using a previously reported seed-mediated growth method[5]. Phosphorothioate oligonucleotides sequences directed against the 5' region of the ERBB2 mRNA molecule on ERBB2 expression are purchased from Integrated DNA Technologies (Coralville, IA). The sense sequence is 3'-GTGAGCACCATGGAG-5'-SH and the antisense sequence is 3' - CTCCATGGTGCTCAC-5'. 100 µl of 100 µM thiolated, sense oligonucleotides is incubated with 2,000 μl of GNPs ($1x10^9$ particles/ml) and 40 μl of phosphate-buffered saline (PBS) on a rocker for 24 hours. To hybridize antisense oligonucleotides to the sense oligonucleotides, 100 μl of 100 μM antisense oligonucleotides is added to the conjugated GNPs solution. This mixture is then heated for 2 minutes at 80˚C and then heated for 15 minutes at 65˚C. The mixture is finally incubated at room temperature on a rocker for 24 hours to ensure maximum hybridization. For use with cell culture, the conjugated GNPs are concentrated to $1x10^{14}$ particles/μL by centrifugation at 5,000 rpm for 30 minutes, removal of the supernatant, and sonnication for 1 minute to resuspend the GNPs.

Cell preparation - The human breast carcinoma line BT474 was purchased from the American Type Culture Collection (Rockville, MD). Cells are cultured in DMEM media supplemented with 10 % heat-inactivated fetal bovine serum and are maintained in a 37˚C incubator with 5 % CO_2 humidified air. Cells are initially seeded in 96-well plates at 20,000 cells/well. The cells are plated for 24 hours prior to treatment with conjugated GNPs.

ERBB2 downregulation using ONCOS - 10 μL of conjugated GNPs ($1x10^{14}$ particles/μL) to each well of the 96-well plate. The cells are incubated for 24 hours at 37°C with the conjugated GNPs. After 24 hours, A 785 nm laser is positioned above a sample and the spot size of the laser is broadened to 5 mm in diameter using a concave lens (25 mm focal length) to illuminate the entire cell sample. The laser is used to illuminate the cells at 2 mW/cm^2 for 2 minutes. When the temperature on the GNPs reaches the melting temperature of the oligonucleotides, the double-strands denature and the antisense strands are released to subsequently interfere with ERRB2 mRNA translation. The cells are then incubated at 37°C for 48 hours. To qualitatively visualize ERRB2 downregulation, the cells are then stained for ERBB2 using mouse anti-ERBB2 (OP15T, Calbiochem) primary antibody (1:100 dilution) for 90 minutes and anti-mouse IgG (F5262-1ML, Sigma-Aldrich) secondary antibody conjugated with (1:128 dilution) FITC dye (488 nm excitation/518 nm emission). To quantitatively analyze ERBB2 inhibition, ONCOS-treated and untreated cells

are stained with PE-labeled antibodies against ERBB2 and their fluorescence is analyzed by flow cytometry.

3. RESULTS

Immunostaining results qualitatively show that untreated cells continue to generate ERRB2 whereas a decrease in fluorescence in ONCOS-treated cells indicates ERRB2 translation has been blocked (Fig. 3). Flow cytometry results quantitatively show that all untreated cells express ERBB2 whereas an 11.7% decrease in ERBB2 levels is detected in the ONCOS-treated cells (Fig. 3).

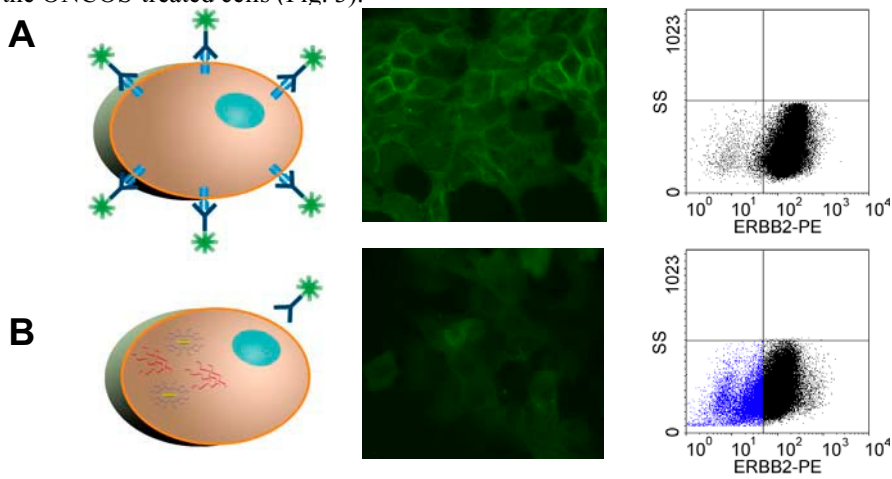

Figure 3. ERRB2 downregulation by ONCOS. Immunostaining and flow cytometry results of **(A)** untreated BT474 cells and **(B)** ONCOS-treated BT474 cells.

4. CONCLUSIONS

In summary, we have designed new biomolecular nanophotonic device called ONCOS which can control gene regulation and protein expression in living cell for applications requiring nanometer-scale targeted release and precise temporal control of release. Using ONCOS, it is possible to gain more control and flexibility in genetics- and systems biology-related studies as well as therapeutic applications.

ACKNOWLEDGEMENTS

The authors thank Megan Dueck, Frank Kim, Yitao Long, Terry Johnson, Blake Simmons, and Ken Patel for their technical insight. The authors also thank the undergraduate student, Shalini Indrakanti, for her assistance with experiments.

REFERENCES

[1] Rosi, N.L., et al. *Science* 312, 1027-1030 (2006)
[2] Hamad-Schifferli, et al. *Nature* 415, 152-155 (2002)
[3] Howard, K.A., et al. *Small* (2006)
[4] Chen, C.C., et al. *J.Am.Chem.Soc.* 128, 3709-3715 (2006)
[5] Gou, L. & Murphy, C.J. *Chem. Mater.* 17, 3668-3672 (2005)

SILICON NANOWIRE ARRAY AS A BIOCHEMICAL SENSOR / NANO-HEATER FOR POTENTIAL APPLICATIONS IN CELLULAR PROTEIN DETECTION

Inkyu Park [1], Zhiyong Li [2], Albert P. Pisano [1], and R. Stanley Williams [2]

[1] *Berkeley Sensor and Actuator Center (BSAC), University of California at Berkeley, USA*

[2] *Quantum Science Research (QSR), Hewlett-Packard Laboratories at Palo Alto, USA*

ABSTRACT

In this paper, we present a biochemical sensor platform based on the silicon nanowire (SiNW) array and its potential applications in cellular protein detection. Here, SiNWs are used both as field effective transducers sensitive to target analyte and as nanoscale heaters for minimally invasive thermal-based cell lysis. This platform would provide a very simple and purely electrical assay of intracellular protein molecules.

Keywords: Silicon nanowire, Protein detection, Cell lysis, Biochemical sensor

1. INTRODUCTION

Silicon nanowire (SiNW)-based biochemical sensors have been intensively developed recently [1-4] due to its great sensitivity, selectivity, and simplicity of the assay via purely electrical measurement without needs of complicated sample labelling process. SiNW has a large surface-to-volume ratio and quasi-1D characteristics, and thus provides high sensitivity. Its surface is surrounded by thin oxide layer with many active hydroxyl (-OH) sites for further surface functionalization via organosilane linkers. This flexible surface functionalization with a variety of receptor molecules facilitates selective detection of target analytes. However, most of the developed SiNW sensors have been used for the biochemical detection of pre-purified and concentrated sample solutions. In this paper, we are presenting our development of silicon nanowire arrays as biochemical sensor and nanoscale heaters for cellular protein detection and cell lysis component (Figure 1). First set of SiNWs (five right SiNWs) are used for cell membrane lysing while the second set of SiNWs (five left SiNWs) are used for the detection of extracted protein molecules.

2. DESIGN, FABRICATION, AND EXPERIMENTATION

SiNWs were fabricated by electron beam lithography followed by reactive ion etching on sililcon on insulator (SOI) substrate with a 50nm thick single crystalline (100) silicon

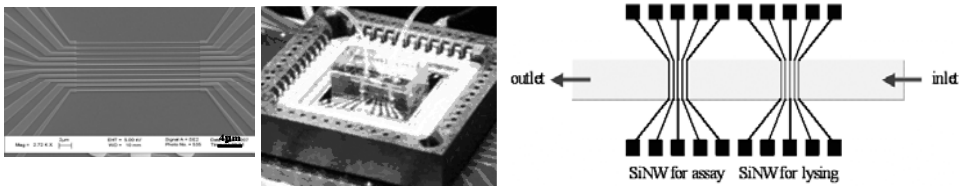

(A) (B) (C)

Figure 1: A) SiNW array fabricated by EBL and RIE of SOI substrate. B) Fabricated SINW sensor device with microfluidic and electronic packaging. C) Schematic of sensor system. First set of SiNWs are used for cell membrane lysing and second set of SiNWs are used for cellular protein detection

978-0-9798064-0-7/μTAS2007/$20©2007CBMS

device layer. After the fabrication of SiNWs, Al contacts were patterned and annealed. Polydimethylsiloxane (PDMS) channels were fabricated and bonded to the SiNW chip. A solution of 3-aminopropyltriethoxysilane (APTES) in ethanol (0.2 volume/volume %) was flown through the PDMS channel at a flow rate of 0.5mL/hr for 0.5 hour for the surface functionalization of SiNW array. For the detection of protein molecules (avidin), the SiNWs were further functionalized with NHS-biotin solution (5mg NHS-biotin in 10mL phosphate buffered saline (PBS) solution) at a flow rate of 0.15mL/hr for 2 hours. For the detection experiment, an AC voltage (100mV amplitude, 10Hz frequency) was supplied and the conductance change was measured by data acquisition board. For the visual verification of localized nanoscale SiNW Joule heating, the SiNW array was coated with thin (50nm) polymer layer (polytetrafluoroethylene; PTFE) and their ablation was imaged by AFM. The thermal lysing of HeLa (Henrietta Lacks) cells by SiNW Joule heating was observed by optical microscopy.

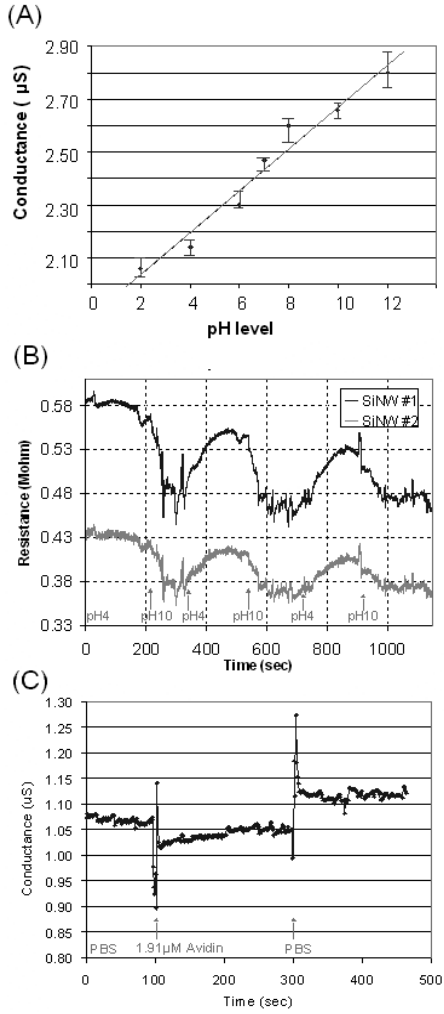

Figure 2: A) pH level detection of solution by SiNW sensor array. B) Detection of pH level of alternating pH buffer solutions. (pH=4 and pH=10) C) Detection of avidin molecules (1.91μM) by SiNW sensor array functionalized with biotin.

3. RESULTS AND DISCUSSION

The result of solution pH level detection is shown in Figure 2(A). The electrical conductance of SiNW increases with increasing pH level. Since the SiNW is doped with boron (B), the mobile charge carriers are holes. In high pH level, the surface of SiNW gets deprotonated by attachment of abundant OH^- ions. Thus, the holes are accumulated at the surface and electrical conductance is increased. Opposite phenomenon occur at low pH levels. Detection with alternating pH buffer solutions (pH=4 and 10) is shown in Figure 2(B). The resistance of SiNW changes by alternating the pH buffer solution (τ ~80 s). The conductance change gradually decreases with more cycles of solution change. This may be due to a mixing of two different buffer solutions in the microfluidic channel and unstable protonation/deprotonation at the SiNW surface. Optimization of surface chemistry and microfluidic transport in the SiNW sensors should be done in order to improve the reproducibility of signals in the pH level detection. The detection of avidin is demonstrated in Figure 2(C). The switching from PBS solution to avidin (1.91μM in PBS) caused a conductance drop by ~50nS (4.6%). Since the avidin molecules (pI=10.5) have positive charge at neutral pH level (pH=7.4 PBS solution),

positive surface charge at the surface of SiNW causes depletion of holes in SiNW and thus reduces the electrical conductance. When the PBS solution was injected again, the conductance was increased again by ~70nS (6.7%). However, the absolute conductance value was continuously drifting. This drift may be due to unstable avidin / biotin binding and thus the detection protocol should be refined.

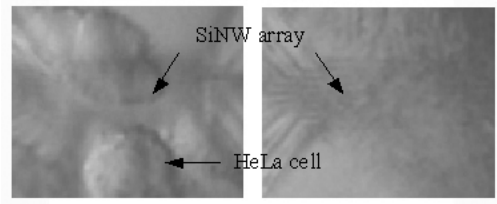

Figure 3: Lysis of HeLa cells by localized heating of SiNWs. A bias of 30V across an array of 100nm wide, 50 nm high, and 20μm long SiNWs induces a nanoscale Joule heating to cause local breakage of enclosed HeLa cells (left) to lysed HeLa cells (right)

SiNW can be used not only as biochemical sensors but also as nanoscale heaters by which the treatment of biological tissues or cells can be carried out. Especially, its highly localized heating can be employed for the thermal cell lysis with minimal damage to the intracellular components such as organelles, cytosols with macromolecules (eg. proteins, RNAs, etc). By numerical thermal simulation of SiNW Joule heating, we found that SiNWs can be easily increased to high temperature (>350 K) by an application of low electrical bias. Furthermore, the temperature increase is very localized by a few 100's nm distance. Therefore, the cell membrane can be easily broken while the intracellular components are not significantly destroyed. The optical microscope image of cell lysis by an application of 30V bias is shown in Figure 3. Here, the breakage of HeLa cell membrane and dispersion of intracellular material is easily observed. The potential benefit of this method is to easily open the cell membrane without affecting intracellular molecules as opposed to conventional thermal lysis method [5].

5. CONCLUSIONS

In this paper, we have developed a SiNW array that can be used for both biochemical sensor and cell lysis component. By combining these two functionalities, it is expected that this sensor platform will provide a very simple and fast analysis of intracellular molecules.

ACKNOWLEDGEMENTS

This project has been funded by Center for Nanoscale Mechatronics and Manufacturing (Grant No. 019997), Republic of Korea and Hewlett-Packard (HP) Laboratories, USA.

REFERENCES

[1] Y. Cui, Q. Wei, H. Park, C.M. Lieber, "Nanowire nanosensors for highly sensitive and selective detection of biological and chemical species", *Science*, **293**, 1289, (2001).
[2] Z.Li, Y. Chen, X. Li, T.I. Kamins, K. Nauka, R.S. Williams, "Sequence-specific label-free DNA sensors based on silicon nanowires", *Nano Lett.*, **4**, 245, (2004).
[3] O.H. Elibol, D. Morisette, D. Akin, J.P. Denton, R. Bashir, "Integrated nanoscale silicon sensors using top-down fabrication", *Appl. Phys. Lett.*, **83**, 4613, (2003).
[4] G. Zheng, F. Patolsky, Y. Cui, W.U. Wang, C.M. Lieber, "Multiplexed electrical detection of cancer markers with nanowire sensor arrays", *Nat. Biotech.*, **23**, 1294, (2005).
[5] A.D. Russell, W.B. Hugo, S.P. Denyer, N.A. Hodges, S. P. Gorman, *Pharmaceutical Microbiology*, Blackwell Publishing, (2004).

SINGLE-MOLECULE LIGATION OF DNA AS A UNIT OPERATION FOR MOLECULAR SURGERY

Rikiya Watanabe[1], Hidehiro Oana[1,2] and Masao Washizu[1,2]

[1]Dept. of Mechanical Engineering, The University of Tokyo, Hongo 7-3-1, Bunkyo-ku, Tokyo 113-8656, Japan [2]JST, CREST

ABSTRACT

We have already demonstrated the cutting of DNA at aimed position, which we named "molecular surgery" [1], where DNA-cutting enzymes are immobilized on a micro particle, which is grasped by optical tweezers and pressed against stretch-and-positioned DNA, so that the cutting reaction occurs at the contact point. This paper for the first time demonstrates its reverse reaction, *i.e.* single molecule ligation, where two cohesive DNA ends are brought into close proximity by physical means under the presense of ligating enzymes, and joined together. The maximum extendable length after ligation is experimentally confirmed to be equal to the sum of the two DNA fragments joined. It is observed that the ligation seldom occurs when too long fragments are used, presumably due to the formation of randomly-coiled conformation which hampers the DNA ends from being well exposed for the interaction with the other fragment.

Keywords: molecular surgery, Ligation, restriction enzyme, single molecule observation

1. INTRODUCTION

Genetic information is recorded on the DNA as the sequences of four kinds of bases, so that the "position" of the base on the DNA strand has an essential meaning; however, conventional solution based biochemistry cannot make a full use of the information about position, in that it handles statistical average of many strands in the solution, and its long-range resolution is limited by the electrophoretic method which is about several hundred bases at present. If we can manipulate DNA in single-molecule level and apply operations, such as cutting, joining, or modifications, on the specific positions on the targeted DNA strand, we will not only have highly efficient gene analysis but also a completely new world of gene manipulations.

In this view, we have been engaged in the development of "Molecular Surgery", where physical means, including microfabrication or laser manipulation, are used to enable an access to targeted position on a targeted DNA, to perform molecular operations. Specifically, we have demonstrated the cutting of DNA at aimed position [1], where DNA-cutting enzymes are immobilized on a micro particle, which is grasped by optical tweezers and pressed against a stretch-and-positioned DNA, so that the cutting reaction occurs at the contact point. Molecular surgery realizes DNA dissection with a molecular structure chemically defined by the enzyme, at the position physically determined by the mechanical manipulation. Cutting of DNA demonstrated there, however, is easier than its reverse reaction, *i.e.* joining, in that it involves only two bodies to be brought into contact, DNA strand stretched and immobilized on a solid surface, and the enzymes also immobilized on a solid particle. But for joining (ligation), three bodies, *i.e.* two free DNA ends fluctuating due to thermal motion, and the ligating enzyme, must be in contact. Thermal fluctuation might cause another difficulty in that DNA ends be embedded inside the random-coil conformation the strand forms.

In this paper, we use i) a solid surface having a DNA fragment with a cohesive end, and ii) a micro particle (hereafter called bead) having a fragment with the complementary end. The bead is laser-manipulated and brought into contact with the DNA on the solid surface under the

978-0-9798064-0-7/μTAS2007/$20©2007CBMS

presence of DNA ligase, to demonstrate the ligation among two targeted DNA fragments. We also discuss the condition for the single-molecule ligation based on the obtained results.

2. METHOD

Our experimental process is depicted in fig.1 a. As it is our purpose to demonstrate one-to-one DNA ligation, we must first have a way to guarantee one DNA on the surface, and another on a bead. This is done by the following procedure. 1) Prepare λ-DNA (48,502kb=16μm in length) having biotin at both ends and fluorescence labeled by Yo-PRO1 for visualization. 2) Coat a glass substrate with avidin, with the density 1.7 molecules/μm^2. Block-coat the remaining free glass surface with BSA to prevent unwanted adsorption. 3) Feed the DNA solution on the surface; The density of avidin is sparse enough that i) only one DNA binds with each avidin spot, and ii) DNA cannot bridge over two spots. 4) Feed avidin-coated beads ($2\mu m^{\phi}$) and let them bind with the free ends of the immobilized DNA. 5) Wash out free molecules in the solution. At this stage, we have DNA strands, isolated from each other at the density of about 0.4 /μm^2, with one end anchored onto the solid surface and having a bead on the other end. Then 6) Feed a restriction enzyme to cut DNA tethering the bead: The bead is released, but a part of DNA is still bound with the avidin on the solid surface, and emits enough fluorescence to be located. 7) Pick up the released microparticle (having a DNA fragment with the cohesive end defined by the restriction enzyme) with the optical tweezers, and place it in the cellar (see fig.1 b). 8) Wash out the restriction enzyme, and feed the ligase. 9) Bring the bead back with the optical tweezers, and made into contact with the DNA fragment on the surface. In order to guarantee the contact of the two fragments, the bead is pushed and rolled against the DNA on the surface. In order to facilitate the process, we used a micro channelas depicted in fig.1 b, which is made by standard PDMS lithography and mounted on the glass surface. It is designed to have a controlled flow velocity with a syringe pump and full replacement of the solution, yet the released particle can be temporarily stored in one of the flow-less cellars. All observations are performed under a fluorescence microscope.

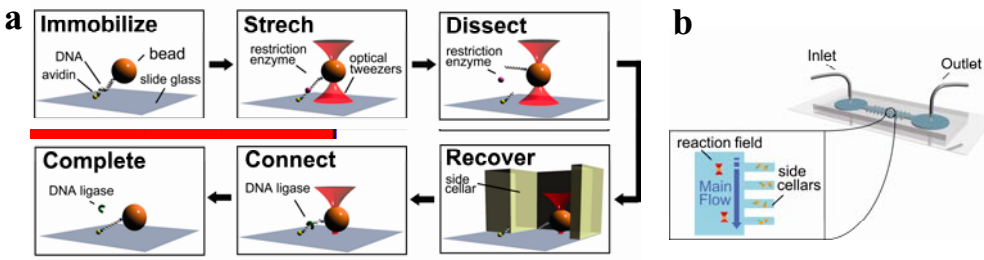

fig. 1. The process of single molecule dissection and ligation

3. RESULTS and DISCUSSION

3-1 The effect of DNA stretching on the dissection with restriction enzymes

An interesting phenomenon was observed during the restriction digestion (procedure 6) above). DNA tethering the bead takes coiled conformation when no stress is applied, while it can be stretched to full length with the use of optical tweezers, so that the functioning of the restriction enzyme can be detected by the release of the bead from the anchoring point. What we found is that the time it takes for the enzyme to work (*i.e.* the time constant of the reaction) depends upon the stretching, quicker when stretched. The phenomenon is observed both with *Xba*I and *Bgl*II (fig.2 a), among which the case of the former is plotted in fig.2 b, taking the time exposed to the enzyme as the abscissa, and cumulative cutting probability as the ordinate. The

concentration of the enzyme used is chosen so that the time constant of cutting is 1 hr in solution, and the observed time constant for non-stretched DNA was observed to be about 1hr. But when stretched, the time constant shortens to about 4 min as shown in the figure. Our interpretation for this is that the DNA becomes more accessible for the enzyme when stretched. This phenomenon can be, and in fact was utilized in the actual experiment, to specify which molecule to cut; among DNA strands immobilized in the microscope view, the one that is stretched by optical tweezers will be the one to be cut, while the others remain intact.

a

Enzyme	Recognition	Restriction map on λ-DNA (bp)
*Xba*I	5'-T C T A G A-3' / 3'-A G A T C T-5'	*1bp = 0.34nm; 24508; 29179
*Bgl*II	5'-A G A T C T-3' / 3'-T C T A G A-5'	415; 22010; 13286; 651; 2392; 60; 9688

b

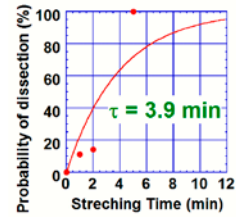

fig. 2. The dissection properties of *Xba*I and *Bgl*II for λ-DNA

3-2 one-to-one ligation of DNA

The tethered bead, after procedure 6) above, is movable around the anchoring point with the radius r = 0.5 μm (L_{max}) which is determined by the length of the tethering λ-DNA (L_{DNA}) (see fig.3 b). With the use of a restriction enzyme *Bgl*II, the DNA is dissected into 7 fragments as depicted in fig.2 a. Assuming full digestion, the DNA fragment remaining on the bead and on the solid surface is either 9688bp (3.3μm) or 415bp (0.14μm). Hence, if the ligation successfully takes place, the length of lilgated DNA will be one of 3.3+3.3, 3.3+0.14, or 0.14+0.14 μm, and the bead will be tethered and movable in the range corresponding to the lengths. An example of the experimental result is shown in fig.3 a, giving r = 0.5μm, corresponding to the ligation of 0.14+0.14 μm. Among 8 times trial, 3 times of successful ligation was observed, and all of them was 0.14+0.14 μm. As a matter of fact, we have done the same experiment with the restriction enzyme *Xba*I that approximately halves λ-DNA, but no ligation occurred. Our interpretation for the phenomenon is that longer fragments take entangled conformation so that the cohesive ends are less likely to be exposed.

a

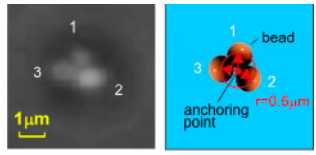

b

$$L_{DNA} = \sqrt{L_{max}^2 + 1} - 1$$

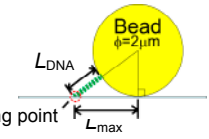

fig. 3. Single-molecule ligation as measured by extension length of DNA.

4. CONCLUSIONS

We have successfully demonstrated the targeted one-to-one DNA ligation with the use of optical tweezers as a means to bring the molecules into physical contact.

REFERENCES

[1] Yamamoto.T, Kurosawa.O, Kabata.H, Shimamoto.N and Washizu.M: "Molecular surgery of DNA based on electrostatic micromanipulation", *IEEE Transaction IA*, Vol.36, No.4 (2000)

TRAPPING OF SINGLE DNA MOLECULES BY MEMS TWEEZERS WITH PULSED DIELECTROPHORESIS

Naoyoshi Sakaki[1], Momoko Kumemura[1], Dominique Collard[2], Gen Hashiguchi[3], and Hiroyuki Fujita[1]

[1]CIRMM/IIS, The University of Tokyo, JAPAN
[2]LIMMS-CNRS/IIS, The University of Tokyo, JAPAN
[3]Faculty of Engineering, Kagawa University, JAPAN

ABSTRACT

This paper proposes a method to trap a single DNA molecule in an aqueous solution by micromachined silicon-based tweezers using pulsed dielectrophoresis (DEP). The tips of the tweezers were dipped into a droplet of a solution containing DNA molecules, and then pulsed DEP was performed in order to avoid the formation of a DNA bundle which was seen in our previous work. We have successfully trapped a single DNA molecule between the tips of the tweezers.

Keywords: DNA, MEMS tweezers, pulsed dielectrophoresis, single molecule

1. INTRODUCTION

Nonuniform electric fields produce forces on dielectric particles and induce displacement of the particles, which phenomenon is known as dielectrophoresis (DEP). Manipulation of biological samples such as living cells by DEP is one of the potential fields, which have been intensively studied recently [1]. High-frequency and high-intensity electric fields generated by microfabricated electrodes can be used to stretch DNA molecules in solution and to immobilize the molecules with their ends onto the edge of the electrodes [2].

In our previous work [3], we developed MEMS-based tweezers (Figure 1) that have two opposed sharp electrodes. By dipping the electrodes of tweezers in DNA solution and applying a high-frequency AC voltage, it was possible to attract and stretch DNA molecules to form a DNA bundle between the electrodes. After the DEP application, we successfully retrieved the bundle from the solution.

Our goal is to trap and manipulate a single DNA molecule with MEMS tweezers, and examine mechanical and electrical properties of that molecule. However, even with a low concentration of DNA solution, it was not possible to trap a single molecule due to a lack of control of the DEP duration. In this study, in order to avoid the formation of DNA bundle, we decreased the duration of DEP to 100 ms or less (pulsed DEP) and successfully trapped a single DNA molecule.

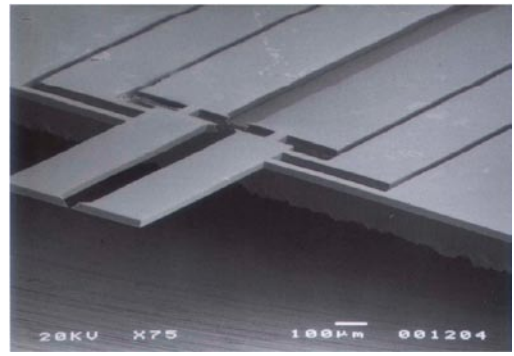

Figure 1. A SEM image of a MEMS tweezers that have a pair of opposed sharp electrodes.

978-0-9798064-0-7/µTAS2007/$20©2007CBMS

2. EXPERIMENTAL

The fabrication process of the MEMS tweezers is based on Silicon-On-Insulator (SOI) technology [3]. The tweezers was fabricated by a combination of KOH anisotropic etching of silicon and local silicon oxidation to form the opposite sharp tips, then the structure of the tweezers was defined by deep reactive ion etching (DRIE). Gold was evaporated on the device as a final step to permit non specific attachment of the trapped DNA on the tweezers tips. The gap between the electrode tips was designed to be 16 μm corresponding to the length of a λ-DNA molecule.

A schematic diagram of the experimental setup is shown in Figure 2. The MEMS tweezers fixed on a printed-circuit board (PCB) were attached to a manipulator. The proper positioning of the tweezers and the operation of DNA trapping were monitored under an inverted fluorescent microscope. A droplet of 2-5 μl containing DNA (1 pM λ-DNA) and a fluorescent dye (10 nM YO-PRO-1) was placed on a cover glass. The tweezers were dipped into the droplet by the manipulator, and then sine AC voltages (0.5-1 MHz, 140-160 V_{p-p}) were applied between the tweezers tips (actually 14-μm gap) during 10000-50000 cycles. To avoid DC voltage, which causes electrophoresis (molecule attraction without stretching), a high pass filter with a cutoff frequency of 1.5 kHz was used. The fluorescent image through an image intensifier was taken by a CCD camera and recorded with a DVD recorder (movies of real time trapping are available).

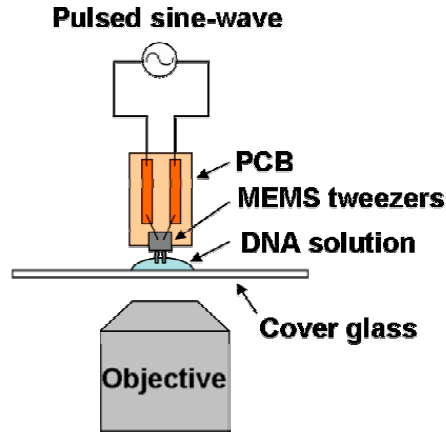

Figure 2. A schematic diagram of experimental setup. The MEMS tweezers were dipped into a droplet of DNA solution by a manipulator, and then pulsed DEP was performed.

3. RESULTS AND DISCUSSION

With pulsed DEP, we successfully trapped a single DNA molecule between the tips of the tweezers (Figure 3). Because of the short duration of the pulsed DEP, several applications of the pulsed DEP were often needed to attract a single molecule, stretch it and fix it between the tips, to finally trap a single DNA molecule.

Due to multiple experiments, DNA molecules can easily stick to one tip or to the other one (without bridging them) as shown by the bright fluorescent area near the tips in Figure 3. Usually, the electro dynamic flow induced by the DEP prevents to trap DNA molecules, but by using pulsed DEP with short duration, the flow has not enough time to develop, making single molecule trapping possible.

We have not yet retrieved a single DNA molecule from a droplet because of its breakage by the surface tension. The strength of the DEP force on DNA molecule depends on the composition of the medium and frequency and intensity of the electric field. Optimization of condition is needed for efficient trapping of single DNA molecules.

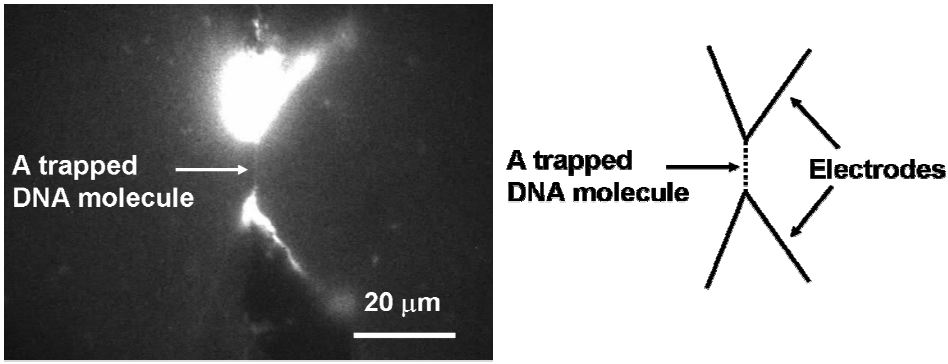

Figure 3. Fluorescent microscope image of a single DNA molecule trapped between the opposite sharp electrodes of a MEMS tweezers (left). Schematic location of the electrodes and the trapped DNA molecule of the upper image (right). The dotted line indicates the trapped DNA molecule. The bright fluorescent regions indicate areas where DNA molecules have adhered to the electrodes. The actual gap of the electrodes is 14 μm.

4. CONCLUSIONS

We have successfully trapped a single DNA molecule in an aqueous solution with micromachined silicon-based tweezers using pulsed DEP. The trapped DNA molecule could not be retrieved because the molecule easily broke during a retrieval operation due to the illumination and surface tension of the droplet.

ACKNOWLEDGEMENTS

We acknowledge M. Washizu from the University of Tokyo for providing us with precious advice. This work was supported by JST Grant for Advanced Instrumentation "Development of Handling and Characterization Tools for Nano Objects".

REFERENCES

[1] M. Frenea, S. P. Faure, B. Le Pioufle, P. Coquet, and H. Fujita, "Positioning living cells on a high-density electrode array by negative dielectrophoresis," Mat. Sci. & Eng. C, 23, 597-603 (2003).

[2] M. Washizu and O. Kurosawa, "Electrostatic manipulation of DNA in microfabricated structures," IEEE Trans. Ind. Appl., 26, 1165-1172 (1990).

[3] G. Hashiguchi, T. Goda, M. Hosogi, K. Hirano, N. Kaji, Y. Baba, K. Kakushima, and H. Fujita, "DNA Manipulation and Retrieval from an Aqueous Solution with Micromachined Nanotweezers," Anal. Chem., 75, 4347-4350 (2003).

NANOCHANNEL CHROMATOGRAPHY - SEPARATIONS BASED ON THE UNEVEN DISTRIBUTIONS OF SPECIES IN NANOCHANNELS

Shaorong Liu, Jianzhen Kang, Shili Wang and Juan Lu

Department of Chemistry & Biochemistry, Texas Tech University, Lubbock, TX 79407, USA

ABSTRACT

Due to the electric double layer overlap, ions are distributed distinctively inside a nanochannel. In a nanochannel with a negatively charged surface, anions are concentrated in the middle while cations are enriched near the channel surface due to the electrostatic repulsive/attractive forces from the surface. As a pressure-driven flow is induced (the solution in the middle will move faster than that close to the wall), the anion will migrate faster than the cation. A chromatographic separation is thus produced. This separation technique is referred to as nanochannel chromatography.

Keywords: Nanochannel, Nanochannel Chromatography, Nanochannel Separation

1. INTRODUCTION

Owing to the electric double layer (EDL) overlap, ions are distributed distinctively inside a nanochannel.[1-5] Using a nanoscale capillary with a negatively charged surface as an example, anions are concentrated in the middle of the channel (see Figure 1a), while cations are enriched near the channel wall (see Figure 1c) due to the electrostatic repulsive/attractive forces between the ions and the charged surface. When a pressure-driven (Poisseuille) flow is induced (see Figures 1b and 1d), the anions will migrate faster than the cations. A chromatographic separation is thus produced. Since the concentration profile (which can be calculated using the Boltzmann equation,[2,5]) of an ion is characteristic of its charge (z), all analytes carrying different charges can be separated under pressure-driven flow conditions. Considering the fact that this kind of separation does not involve the traditional "mobile" and "stationary" phases, and the separations occur in nanochannels, we refer to this separation technique as nanochannel chromatography (NC).

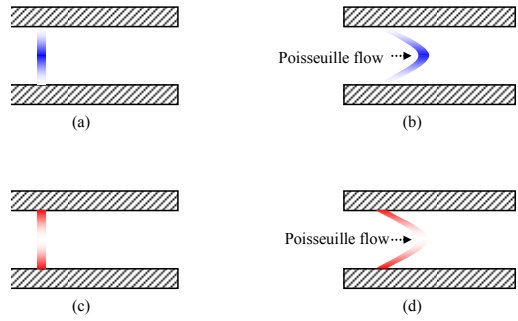

Figure 1. Characteristic migration of ion in nanochannel

2. RESULTS AND DISCUSSION

Figure 2 presents the NC mobilities of ions with different charges (z). The NC mobility of an ion is defined as the ratio of the average velocity of the ion to the average

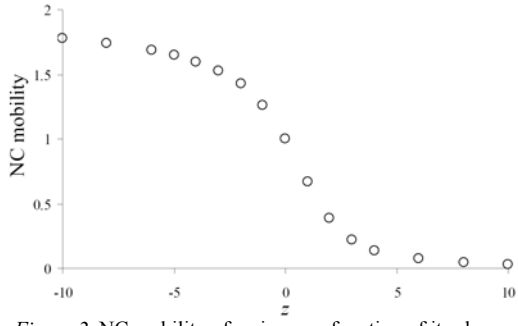

Figure 2. NC mobility of an ion as a function of its charge

978-0-9798064-0-7/μTAS2007/$20©2007CBMS

velocity of the bulk solution. For the simplicity of the presentation, only the data points between z = -10 and z = 10 were displayed. From these data, we can draw four conclusions that are fundamental characteristics (rules) of NC.

1. Coions move faster than neutral species, and neutral compounds migrate faster than counterions. In addition, a higher charged coion moves faster than a lower charged coion, while a higher charged counterion moves slower than a lower charged counterion. Here, coions and counterions are relative to the charge on the surface of the nanocapillary.

2. The NC mobility of an ion is a function of its z value, the channel geometry, flow pattern, and degree of EDL overlap, but independent of the bulk flow rate. This implies that the separation time could be shortened and resolution be improved (due to diminished longitudinal diffusion) by increasing the flow rate of the eluent.

3. The unit-charge resolution ($\Delta R/\Delta z$) decreases with the absolute value of z. For example, separating X^{-1} and X^{-2} is easier than separating X^{-10} and X^{-11}.

4. A condition of ζ (zeta potential) $\neq 0$ is required for NC. If $\zeta = 0$, all substances will be uniformly distributed inside a nanochannel and no NC separations will occur.

To demonstrate the feasibility of NC, we employed a 44-cm-long (effective 39 cm) and 800-nm-radius fused silica capillary (customly-produced by Polymicro Technologies, Phoenix, AZ) as the NC column. After the capillary was cleaned with 1 M NaOH and filled with 100 µM sodium tetraborate solution (eluent), a sample containing 0.5 µM rhodamine B, 0.1 µM fluorescein and 0.2 µM 2′,7′-bis(2-carboxyethyl)-5(6)-carboxyfluorescein (BCECF) in 100 µM sodium tetraborate was injected into the capillary with pressure (80 p.s.i.). The eluent was then pressuized into the capillary, driving the sample forward to carry out the separation. The separated bands were monitored by a laser-induced fluorescence (LIF) detector whose configuration was described previously.[6]

Figure 3 presents three typical separation traces of NC. To our (pleasant) surprise, very high separation efficiencies were obtained. Referring to the inset, the numbers of theoretical plates [$N=5.54x(t/\Delta t_{1/2})^2$, where t is the migration time and $\Delta t_{1/2}$ is peak width at half-maximum] were respectively 38000, 45000 and 31000 for peaks 1-3. Since the effective separation length was 39 cm, the plate height was around or less than 10 µm. These efficiencies were much better than those of open tubular chromatography and comparable to those of capillary electrophoresis. These efficiencies are expected to improve if narrower capillaries and higher eluent flow rates are used.

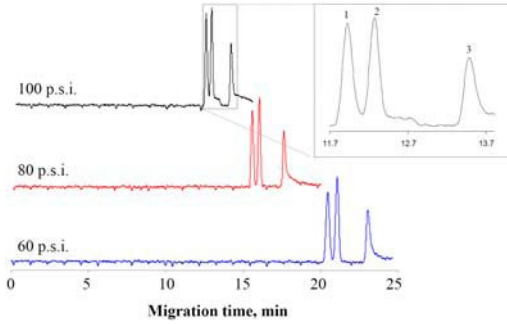

Figure 3. Typical separation traces of NC
Sample injection condition: 80 p.s.i. for 10 seconds; Eluent composition: 100 µM Borax. The pressure values indicated in the figure are separation pressures. Peak identification: 1 – BCECF, 2 – fluorescein and 3 – rhodamine B.

Separations of rhodamine 6G (a cationic fluorescent dye) by NC was also performed. However, the retention time was long (~5-fold of rhodamine B) and the peak was severely tailed, an indication of its adsorption to the wall. Counterion adsorptions will be an inherent issue for NC – low efficiencies for large counterion separations. Nevertheless, this result, combined with the data shown in Figure 3, confirmed NC rule #1.

The three separation traces shown in Figure 3 were obtained by separating the same sample under different pressures or different elution rates, while all other conditions were the same. In all cases, BCECF had a speed of 1.13 times and fluorescein had a speed of 1.10 times that of rhodamine B. The constant relative velocity (NC rule #2) was preserved. The constant-relative-velocity phenomenon has

also been observed recently by Stein *et al*,[7] when they pressure-drove DNA polymers through nanochannels.

From the results presented in Figure 3, resolutions [$R=2x(t_2-t_1)/(w_1+w_2)$, where t_1 and t_2 are the migration times and w_1+w_2 are the peakwidths of compounds 1 and 2] were calculated, as well. The resolution between rhadamine B and fluorescein was ~4.0 and that between fluorescein and BCECF was ~1.2. Because $\Delta z = 2$ in both cases, NC rule #3 was validated.

To confirm NC rule #4, we derivatized the inner surface of a capillary following the protocols described previously.[8,9] The residual zeta potential was estimated to be less than 1 mV based on the electroosmotic mobility data after derivatization.[8] This capillary was then used to separate BCECF, fluorescein and rhodamine B under a pressure of 80 p.s.i. All other conditions were the same as indicated in Figure 3. The three compounds were eluted out unresolved. These results are in agreement with rule #4.

It should be mentioned that, under the influence of a longitudinal electric field, separations of analytes based on their charges have been carried out in nanochannels,[10-13] and the technique was termed Electrokinetic Separations by Ion Valences (EKSIV).[10,11] In EKSIV, NC-type separations occur because ions are unevenly distributed in the nanochannel and the profile of the electroosmotic flow is parabolic. Meanwhile, electrophoretic separations also happen due to the presence of the longitudinal field. Therefore, the separation mechanism of EKSIV is in fact a combination of zone electrophoresis and NC.

One may compare NC with narrow capillary open tubular chromatography (OTC). The setup of these two techniques is indeed similar, but the separation mechanisms are fundamentally different. OTC separations are the result of the differential distributions of analytes between a stationary and a mobile phase, while NC separations are based upon different NC mobilities of analytes in a single phase solution. In OTC, the migration velocity of an analyte is always slower than the eluent. In NC, however, the movement of a coion will be faster than that of the eluent. In addition, NC can produce much greater separation efficiencies (<10 μm plate height) than OTC does.

3. CONCLUSIONS

We have demonstrated the feasibility of a new separation technique – nanochannel chromatography. Outstanding separation efficiencies have been obtained. The efficiencies can be further improved when the capillary size is reduced and the eluent flow rate is enhanced. With the capability of current micro- and nano-fabrication technologies, nanometer-deep channels can be produced on a microchip device using various materials. Because of the elimination of high electric fields for separations, silicon wafers can be used to host the separation channels. This broadens the applications of micro- and nano-fluidic devices tremendously. Because of the small size of the channel, the number of molecules in the detection zone was about a few thousands of fluorescein molecules. With the availability of a single molecule detection technique, the capillary size can be further reduced. We envision that separations and analyses of single molecules in real-world samples (such as single cells) will be performed on NC in the near future.

REFERENCES

1. Burgeen, D.; Nakache, F. R. *J. Phys. Chem*., **1964**, 68, 1084–1091.
2. Hunter, R.J. *Zeta potential in colloid science principles and applications*; Academic Press: London, **1981**.
3. Pu, Q.; Yun, J.; Temkin, H.; Liu, S. *Nano Letters*, **2004**, 4, 1099-1103.
4. Liu, S.; Pu, Q.; Gao,L.; Korzeniewski, C.; Matzke, C. *Nano Letters,* **2005**, 7, 1389-1393.
5. Liu, S.; Pu, Q.; Byun, C. K.; Wang, S. Lu, J.; Xiong, Y. *J. Phys. Chem. C*, accepted. **2007**.
6. Lu, J.J.; Liu, S. *Electrophoresis*, **2006**, 19, 3764-71.
7. Stein, D.; van der Heyden, F.H.J.; Koopmans, W.J.A.; Dekker, C. *Proc. Natl. Acad. Sci. USA,* **2006**, 103, 15853-15858.
8. Gao L.; Liu, S. *Anal. Chem.* **2004**, 76, 7179-7186.
9. Shen, Y.; Xiang, F.; Veenstra, .T. D.; Fung, E. N.; Smith, R. D. *Anal. Chem.* **1999**, *71*, 5348-5353.
10. Pennathur, S.; Santiago, J.G. *Anal. Chem*., **2005**, 77, 6772-6781.
11. Pennathur, S.; Santiago, J.G. *Anal. Chem*., **2005**, 77, 6782-6789.
12. Garcia et al, *Lab on a Chip*, **2005**, 5, 1271-1276.
13. Bluhm et al., *Langmuir* **1999**, 15, 8668-8672.

CONJUGATED FLUORESCENT NANOSOMES FOR A NOVEL LABEL-FREE MICROARRAY CHIPS FOR DNA ANALYSES

Dong June Ahn,[1]* Eun Jin Kim,[1] Doo Ho Yang,[1] Gil Sun Lee,[1] and Jong-Man Kim[2]

[1]Korea University, Korea and
[2]Hanyang University, Korea

ABSTRACT

A rapid label-free method to detect DNA hybridization with high sensitivity and specificity will play a very important role in medical diagnoses by replacing current time-consuming DNA analyses. In this work, we demonstrate that a fluorescent nanosome chip for label-free DNA detection can provide a simple and robust technical platform in this purpose.

Keywords: Fluorescent Polydiacetylene Nanosomes, Label-Free DNA Chips

1. INTRODUCTION

The conjugated polydiacetylene (PDA) nanosomes (or vesicles) have been proved as convenient chemical and biological sensors due to their unique chromatic properties. The polymerized nanosomes have a bichromic property from blue to red upon external interactions including molecular recognition. Employing their unique property, PDA-based sensors have successfully detected influenza virus, Cholera toxin, *Escherichia coli* (*E. coli*), c-myc epitope, oligonucleotides, and lipopolysaccharides [1-2]. However, most experiments have been carried out in aqueous solutions, which requires large amount of nanosomes, probes, and targets, hence it is limited in application to high-throughput assay. To overcome these limitations, a protocol for immobilization and micro-patterning of PDA nanosomes on a solid substrate was developed recently, and a target chemical was successfully detected by fluorescence-level changes in the nanosome microarrays [3-4]. In the present study, we demonstrate label-free detection of DNA hybridization using microarrays based on conjugated PDA nanosomes.

2. EXPERIMENTAL

In order to test the feasibility of using PDA nanosome chip for detecting DNA hybridization, we spotted PDA nanosomes on glass using a conventional microarrayer. Standard experimental protocols for the syntheses of PDA nanosomes and for the fabrication of the corresponding microarrays on glass were decribed in the literature [4].

3. RESULTS AND DISCUSSION

Each spot was formed by spotting ca. 4 nL of the nanosome solution and its diameter was ca. 200 μm. After polymerization, the nanosome microarrays did not show any fluorescence (Figure 1, top). Then the green fluorescence was observed as probe DNAs (NH_2-5'-GTTACCCGTAGGTAG-3') labelled with fluorescein were attached on the surface of the nanosomes, which proves successful binding of the pDNAs. By contrast, red fluorescence was not seen indicating the nanosomes was not disturbed at this step (Figure 1,

978-0-9798064-0-7/μTAS2007/$20©2007CBMS

middle). When the chip surface was exposed to 100 nM of target DNAs (3'-CAATGGGCATCCATC-5'), the red fluorescence emitted from the PDA nanosomes was observed, demonstrating the nanosomes' capability for detecting DNA hybridization (Figure 1, bottom).

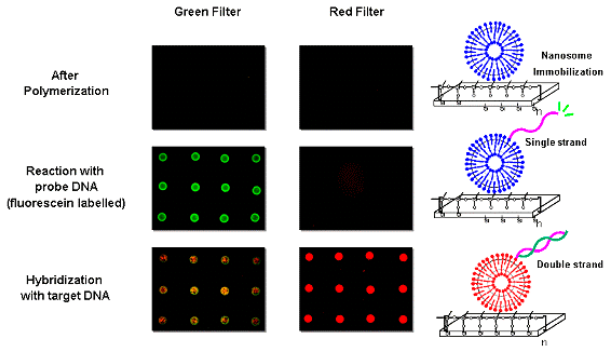

Figure 1: Fluorescence profiles observed as spotted nanosomes were polymerized (top), reacted with probe DNAs (middle), and hybridized with target DNAs (bottom).

In the next stage, we spotted pre-spot solution of nanosome-*p*DNA complex on glass, which was followed by reaction with "non-labelled" target DNAs of which concentration ranged from 100 nM to 1 fM. As shown in Figure 2, we could observe evident self-emitted fluorescence profiles.

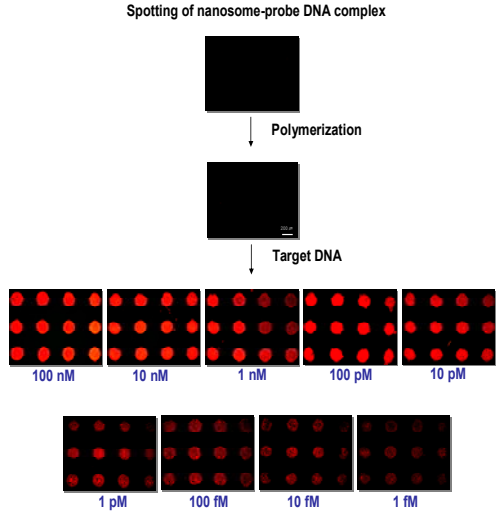

Figure 2. Fluorescence profiles observed after microarrays of PDA nanosome-pDNA complex were exposed at 37 ^{o}C to "non-labelled" target DNAs in concentrations of 100 nM to 1 fM.

Although the system was not optimized yet, the detection limit went down to ca. 10 fM that easily surpasses ca. 600 fM of the current DNA chip technology employing molecular fluorophores such as Cy3 or Cy5 (Figure 3).

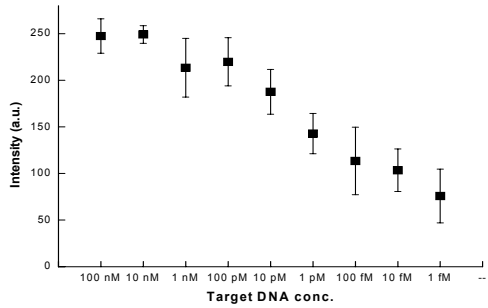

Figure 3. Sensitivity analyses: detection limit is ca. 10 fM that compares to 600 fM when using molecular fluorophores as labels (dotted line).

5. CONCLUSIONS

In conclusion, the PDA nanosomes were demonstrated as a novel and efficient chip material for label-free DNA analyses in the aspect of sensitivity. The proposed system would provide a simple and robust technical platform for a novel DNA applications.

ACKNOWLEDGEMENTS

This work was supported partly by the Ministry of Health, the Korea Science and Engineering Foundation, and the Korea Research Foundation.

REFERENCES

[1] D.H. Charych, J.O. Nagy, W. Spevak, and M.D. Bednarski, "Direct colorimetric detection of a receptor-ligand interaction by a polymerized bilayer assembly," Science, **261**, 585 (1993).

[2] D.H. Charych, Q. Cheng, A. Reichert, G. Kuziemko, M. Stroh, J.O. Nagy, W. Spevak, and R.C. Stevens, "A 'litmus test' for molecular recognition using artificial membranes," Chemistry & Biology, **3**, 113 (1996).

[3] J.-M. Kim, E.-K. Ji, S.-M. Woo, H.-W. Lee, and D.J. Ahn, "Immobilized Polydiacetylene Vesicles on Solid Substrates for Use as Chemosensors," Advanced Materials, **15**, 1118 (2003).

[4] J.-M. Kim, Y.B. Lee, D.H. Yang, J.-S. Lee, G.S. Lee, and D.J. Ahn, "A Polydiacetylene-Based Fluorescent Sensor Chip," Journal of the American Chemical Society, **127**, 17580 (2005).

CHARGED PHOSPHOLIPID POLYMER SURFACES WITH HIGH CELL ADHESION RESISTANCE FOR CELL CHIP

Yan Xu, Tomohiro Konno, Madoka Takai, and Kazuhiko Ishihara

Department of Materials Engineering, School of Engineering, and Center for NanoBio Integration, The University of Tokyo, Japan

ABSTRACT

Protein adsorption-resistant and cell adhesion-resistant surfaces were successfully constructed both on quartz plates and in quratz microchanenls by simple one-step modifications with newly designed and synthesized phospholipid polymers having different charge conditions(surface ζ-potentials varying from –24.2 ± 2.5 mV to 26.1 ± 0.6 mV) for a full functional cell processor chip.

Keywords: Phospholipid polymer, surface modification, antibiofouling, cell processor

1. INTRODUCTION

We have developed an electroosmotic flow (EOF) actuated cell sorter chip[1]. In the chip, the EOF was controlled by voltage(voltage control). Recently, we try to integrate this innovative technique into a newly designed full functional cell processor chip composed of units of cell transport, separation, culture and monitoring to do on-chip cell sensing and drug discoveries. However, the voltage control seems unsatisfactory, hazardous and impossible when a number of flows need to be controlled simultaneously in the chip having complicated channel networks. We have reported that the control of EOF from surface(surface control) holds the possibility to replace voltage control, and has advantages in simultaneously controlling several EOFs[2]. To make EOFs varying in magnitude and direction, surfaces with different (negative, neutral and positive) charge conditions are necessary. Nevertheless, the charged surface may easily disadvantageously induce analyte-wall adsorptions, especially protein adsorption and cell adhesion. To resolve the problem, newly designed charged phospholipid polymers (Figure 1) containing 2-methacryloyloxyethyl phosphorylcholine (MPC)[3] were applied to construct high antibiofouling surfaces for the cell chip.

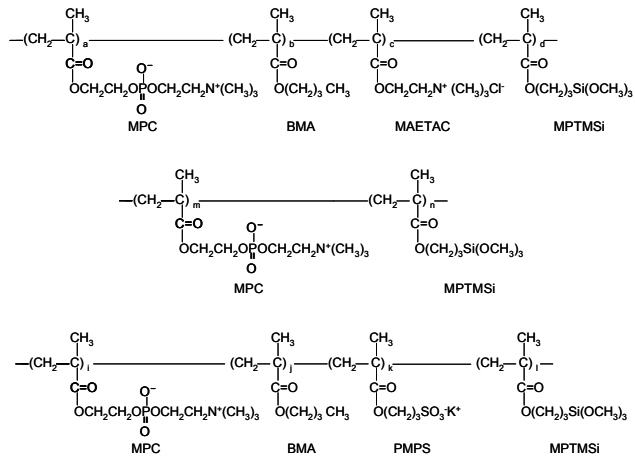

Figure 1. The chemical structures of PMBSSi (upper) and PMSi (middle) and PMBASi (lower).

2. EXPERIMENTAL

Three phospholipid polymers (referred to as

978-0-9798064-0-7/μTAS2007/$20©2007CBMS

PMBSSi, PMSi and PMBASi, shown in Figure 1) were synthesized by conventional radical polymerizations of the corresponding monomers. A dip-coating procedure and a filling method were applied to one-step modify the quartz plate and the microchannel, respectively. The surface ζ-potential was measured by an electrophoretic light-scattering spectrophotometer with a plate cell. The amount of protein adsorption on quartz plates was determined by employing a micro BCA protocol [2]. A mouse fibroblast cell line L929 and a human premyelocytic leukemia cell line (HL-60, RCB0041) were used as model cells to evaluate the cell adhesion on the plate and to monitor the cell delivery in microchannel.

Table 1. Synthesis and Characterization of MPC Polymers.

Abb	Composition in Mole Fraction [MPC/BMA/X/MPTMSi][a]		$Mw^b/10^3$
	in feed	in polymer	
PMBSSi	50/33/ 7 /10	46/32/ 9/ 13	11.8
PMSi	90/ 0/ 0/10	80/ 0/ 0/ 20	9.7
PMBASi	50/20/20/10	48/23/18/11	9.9

[a] X is PMPS in PMBSSi or MAETAC in PMBASi. [b] Mw is weight average molecular weight.

3. RESULTS AND DISCUSSION

Polymers containing MPC units can form nonbiofouling surfaces from a bulk class to micro- and nano-scale [4]. The newly designed phospholipid polymers (Figure 1) contain not only the MPC unit, but also different charged units. The polymers were termed as PMBSSi(anionic), PMSi(neutral) and PMBASi(cationic). After synthesized, their structures and molecular weights were determined by ^{1}H nuclear magnetic resonance (NMR) and gel permeation chromatography (GPC), respectively (Table 1). The modification process is very simple, that is, just one-step coatings with 0.3 %(w/v) polymer alcoholic solutions and then dried under normal atmosphere. The unmodified quartz surface had a ζ-potential of –47.4 ± 0.9 mV at neutral pH. After modified by 0.3 % (w/v) polymer solutions, the ζ-potential was altered to –24.2 ± 2.5 mV, –1.5 ± 1.2 mV and 26.1 ± 0.6 mV in cases of PMBSSi modification, PMSi modification and PMBASi

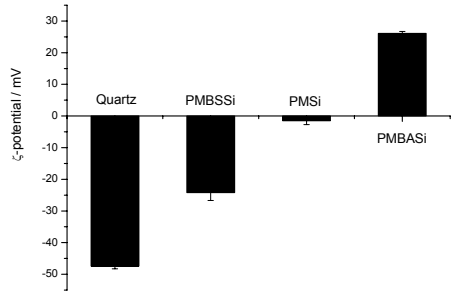

Figure 2. ζ-potentials of the quartz plates modified by 0.3% (w/v) PMBSSi, 0.3% (w/v) PMSi and 0.3% (w/v) PMBASi at neutral pH.

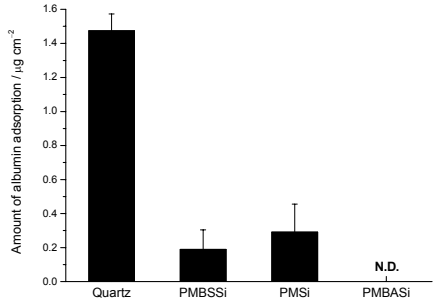

Figure 3. Amounts of BSA absorbed on the quartz plates modified by 0.3% (w/v) PMBSSi, 0.3% (w/v) PMSi and 0.3% (w/v) PMBASi in comparison with those on the unmodified quartz plates.

modification, respectively (Figure 2). In contrast with unmodified quartz which showed heavy protein adsorption, all the modified surfaces showed excellent adsorption resistance against a serials of proteins with different isoelectric point (*pI*). As an instance, Figure 3 revealed the significant difference in the amounts of bovine serum albumin(BSA) adsorbed on the unmodified quartz in comparison with those on the modified quartz surfaces. Mouse fibroblast cell line L929 were used to evaluate the cell adhesion resistance. L929 cells were cultured in dishes together with quartz plates. After cultured one day, L929 adhered to the unmodified quartz surface as to the dish surface, while they did not adhere to all modified quartz surfaces (Figure 4). This suggests that the newly designed MPC polymers in this research have high abilities to resist cell adhesion although they are charged. More importantly, the surface charge provided potential to generate EOF. Figure 5 demonstrates a transport course of HL-60 cells in a quartz microchannel modified by PMBSSi. It is the EOF generated from the PMBSSi surface that drove the microflow in the microchannel.

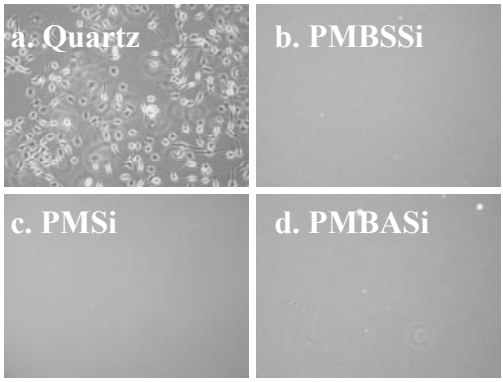

Figure 4. Microscopic images of surfaces on which L929 cells were cultured for one day. a. quartz surface and b. 0.3% (w/v) PMBSSi, c.0.3% (w/v) PMSi, d.0.3% (w/v) PMBASi modified quartz surfaces, respective

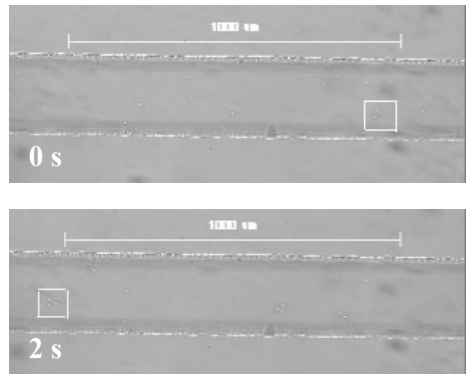

Figure 5. Time course (0 s and 2 s) of HL-60 cells handled in 0.3% (w/v) PMBSSi modified quartz microchannel by EOF. The rectangle shape indicates the positions of a group of HL-60 cells. The white scale bar is 1000 μm.

4. CONCLUSIONS

In conclusion, these charged MPC polymers are advantageous for creating surfaces to suppress the cell adhesion and as well as to generate EOF simultaneously in cell chip.

REFERENCES

[1] M. Takai, H. Onoda, K. Ishihara and Y. Horiike, *Newly designed biocompatible polymers having phospholipid polar group for electro-osmosis pump actuated cell sorter chip*, Proc. MicroTAS 2004, RSC, Cambridge, UK, Vol. 2, pp. 115-117, (2004).

[2] Y. Xu, M. Takai, T. Konno, K. Ishihara, *Microfluidic flow control on charged phospholipid polymer interface*, Lab Chip, 7, pp. 199-206, (2007).

[3] K. Ishihara, T. Ueda, N. Nakabayashi, *Preparation of phospholipid polymers and their properties as polymer hydrogel membranes*, Polym. J., 22, pp. 355-360, (1990).

[4] K. Ishihara, E. Ishikawa, Y. Iwasaki, N. Nakabayashi, *Inhibition of fibroblast cell adhesion on substrate by coating with 2-methacryloyloxyethyl phosphorylcholine polymers*, J. Biomater. Sci. Polym. Edn., 10, pp. 1047-1061, (1999).

DEVELOPMENT OF ENZYME-RELEASE CAPILLARY FOR CAPILLARY-ASSEMBLED MICROCHIP TOWARDS MULTIPLE METABOLITE SENSING

T. G. Henares[1], E. Maekawa[1], F. Mizutani[1], R. Sekizawa[2] and H. Hisamoto[3]

[1]University of Hyogo, JAPAN, [2]Metaboscreen Co. Ltd., Yokohama, JAPAN

[3]Osaka Prefecture University, Osaka, JAPAN

ABSTRACT

A simple sensing conduit for capillary-assembled microchip (CAs-CHIP) integration that is capable of metabolite detection by fluorescence microscopy is developed. This sensing capillary called enzyme-release capillary (ERC) contains enzyme/s that are adsorbed inside the square glass capillary with the aid of polyethylene glycol acting as scaffold. Metabolite solution enters the conduit via capillary force and the enzyme/s are released leading to the detection of a fluorescent biochemical product. Here, the stability of the β-galactosidase immobilized capillary is observed to last for almost a month. Moreover, the co-immobilized glucose oxidase-peroxidase-thiamine system for glucose measurement showed a detection limit of about 30 μM.

Keywords: capillary-assembled microchip, capillary force, metabolite sensing

1. INTRODUCTION

Multiple metabolites sensing in a single microfluidic device is one of the most important direction of a point-of-care microchip, since it offers minimal sample/reagent consumption and short analysis time. However, every metabolite requires different biochemical reaction for detection, thus, presenting difficulty in integration on a single microfluidic device. Recently, our group demonstrated the simple simultaneous detection of different unrelated analytes in a capillary-assembled microchip (CAs-CHIP) integrated with reagent-release capillaries using the "drop-and-sip" fluid handling technique [1]. The avenue for new research is by improving the sensing conduit of the CAs-CHIP that caters to the desired target analyte.

In this study, we developed a new sensing component for the CAs-CHIP called enzyme-release capillary (ERC) wherein the enzyme/s together with the fluorescent probe are non-covalently immobilized inside the square glass capillary. Here, the stability of the ERC is monitored by using β-galactosidase immobilized capillary. Also, the glucose oxidase-peroxidase-thiamine ERC is used to study its response in various glucose concentration.

2. EXPERIMENTAL

The basic model of ERC is shown in Figure 1a, and Figure 1b demonstrates the corresponding biochemical reaction for detection. Using a syringe pump, the ERCs were prepared by co-immobilizing the enzymes/s and fluorescent probe in the four corner of the square glass capillaries with the aid of poly(ethylene) glycol serving as a scaffold. Nanoliter of sample volume enters the ERC via capillary force. All ERC characterizations were done using a fluorescence microscope.

978-0-9798064-0-7/μTAS2007/$20©2007CBMS

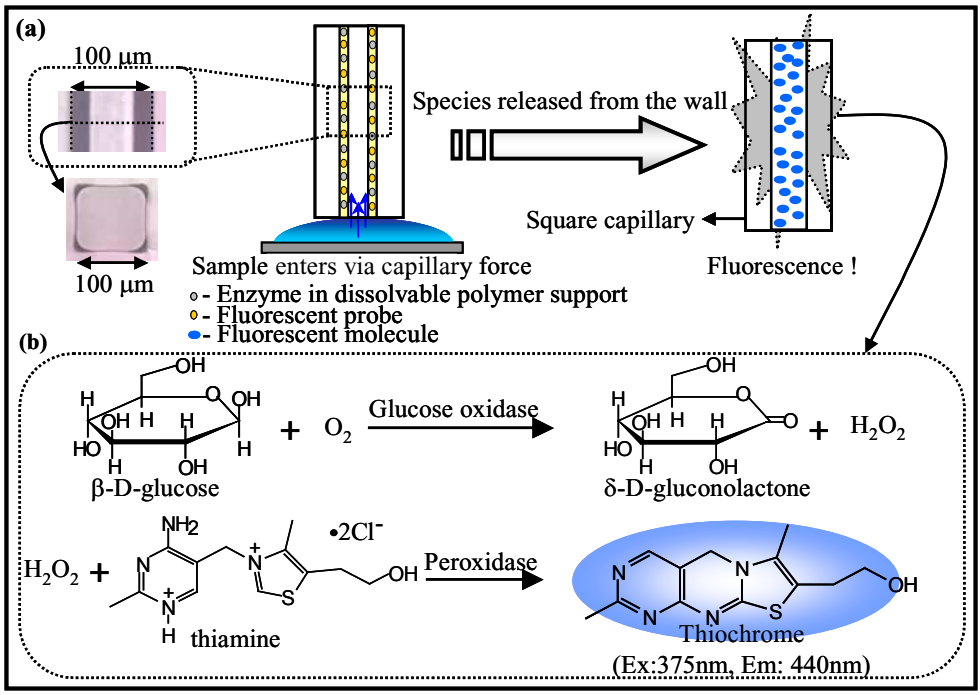

Figure 1. (a) Fundamental concept of enzyme-release capillary (b) Glucose sensing with thiamine as fluorescent probe.

3. RESULTS AND DISCUSSION

The simple integration of various analytical principles in a single microfluidic device is the pillar of the CAs-CHIP system and this includes the development of new sensing component with the square capillary [2-3].

To develop a metabolite sensing capillary, a particular enzyme/s that is specific with a given metabolite must be immobilized inside the square glass capillary. However, enzyme immobilization is delicate to handle since it is prone to denaturisation due to various factors in their biological environment. Thus, the stability of the ERC involving the enzyme/s is an important aspect to consider. The immobilized β-galactosidase inside the square glass capillary reacts with the 0.01mM fluorescein-digalactopyranoside, that is introduced via capillary force, liberating the fluorescein molecule. This study was monitored for almost a month. Figure 2a revealed that a β-galactosidase immobilized capillary is stable for at least a month at 10°C storage. This is a valuable result in terms of the practical use of this sensing capillary. Another important parameter to consider is the metabolite quantitation. Here, the glucose measurement using the co-immobilized glucose oxidase-peroxidase-thiamine system was performed. Sample solutions containing glucose molecules were introduced and production of blue fluorescent thiochrome molecule was monitored. Using the same capillary, the precision of fluorescence response was evaluated and yielded a 6% relative standard deviation (n=15). This sensing capillary demonstrated an excellent response with changes in glucose concentration as depicted in Figure 2b with detection limit of about 30µM.

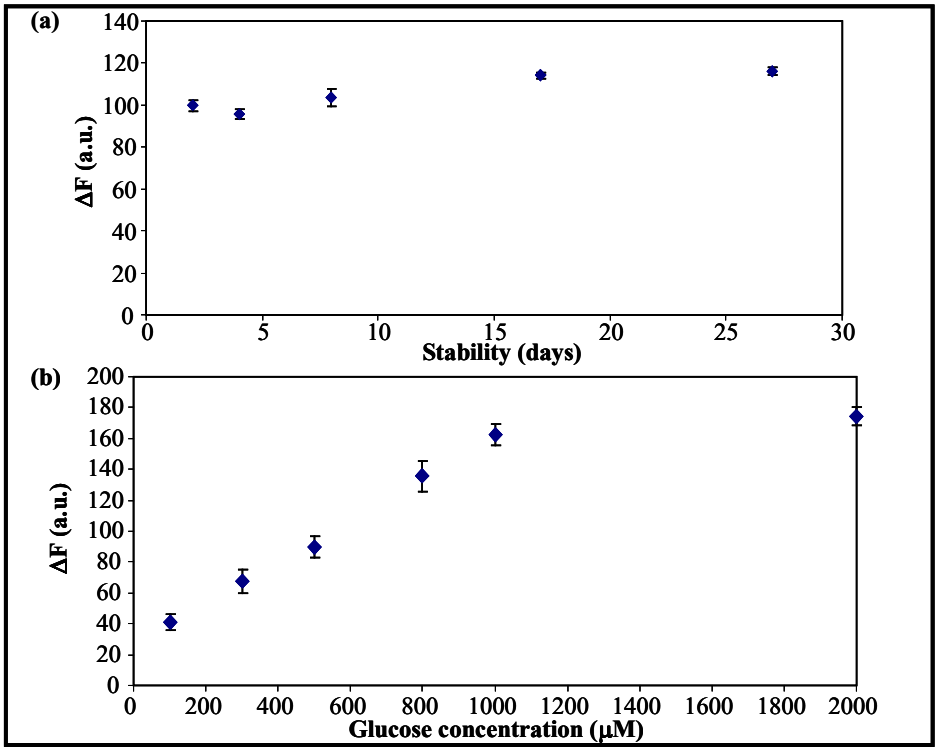

Figure 2. (a) β-galactosidase stability in ERC (b) Response curve of the glucose sensing capillary in different glucose concentration.

4. CONCLUSIONS

The ERC opens a broad spectrum of application by immobilizing not only enzymes but other type of proteins as well like antibodies, antigens, and the likes. This is considered the first demonstration of such sensor and our group is on its way to show its role in a microfluidic device, CAs-CHIP, gearing towards simultaneous, multiple metabolite sensing for clinical diagnostic purposes.

ACKNOWLEDGEMENTS

This research work is partially supported by the New Energy and Industrial Technology Development Organization (NEDO) and the Grant-in-Ais for scientific Research from the Ministry of Education, Culture, Sports, Science and Technology of Japan. T.G.H. also wish to thank the Monbukagakusho of Japan for the scholarship.

REFERENCES

[1] T.G. Henares, M. Takaishi, N. Yoshida, S. Terabe, F. Mizutani, R. Sekizawa, H. Hisamoto, ***Anal. Chem***., 79, 908 (2007).

[2] H. Hisamoto, Y. Nakashima, C. Kitamura, S-i. Funano, M. Yasuoka, K. Kikutani, T. Kitamori, S. Terabe, ***Anal. Chem***., 76, 3222 (2004).

[3] H. Hisamoto, S-i. Funano, S. Terabe, ***Anal. Chem***., 77, 2266 (2005).

DIRECT POLYMERIZATION PATTERNING BASED ON EB LITHOGRAPHY FOR CONTROL OF CELL ADHESIVE ORIENTATION

N. Idota[1], T. Tsukahara[1,2], A. Hibara[1,2], T. Okano[3] and T. Kitamori[1,2]

[1] Core Research for Evolutional Science and Technology (CREST), Japan Science and Technology Agency, [2] Department of Applied Chemistry, School of Engineering, The University of Tokyo, Japan and 3 Institute of Advanced Biomedical Engineering & Science, Tokyo Women's Medical University, Japan

ABSTRACT

In this study, we demonstrated a novel simple preparation process of the patterned polymer-grafted glass surfaces using electron beam (EB) lithography system without any photo-masks. *N*-isopropylacrylamide (NIPAAm) was locally polymerized and directly grafted onto surfaces only by single step of EB lithography. On these surfaces, cells adhered and spread with an orientation in accordance with the stripe pattern direction. When temperature decreased to 25°C, the cultured cells were detached from the surfaces and shrunken along the stripe pattern direction.

Keywords: EB lithographic polymerization, thermoresponsive surface, cell patterning cell adhesive orientation.

1. INTRODUCTION

Microfabrication techniques with surface chemistry have provided the ability to spatially control protein or cell adhesion, and applied to cellular assays such as proliferation differentiation, migration, and apotosis [1]. In many researches using cellular patterning, all analysis process proceeded only on the patterned culture surfaces. If the cells cultured on the patterning surfaces can be harvested with controlling their morphologies, this recovered cells will be useful for biomedical applications such as tissue engineering and microfluidic cellular assay. Okano et al. have developed a functional cell recovery system using poly(*N*-isopropyl- acrylamide) (PNIPAAm)-grafted surfaces [2]. In their system, when culture temperature decreases after cells reach confluency on these surfaces, all cells are harvested as a single continuous cell sheet with intact cell-cell junctions and extra-cellular matrix, which play a desirable role as an adhesive agent in transferring cell sheets onto other substrate surfaces [3]. In the present paper, we develop a single step method of preparing nano- or micropatterned glass surfaces grafted with PNIPAAm using EB lithography system, and the cellular adhesive orientation and detachment behavior from these surfaces are regulated by design of patterned surfaces.

2. EXPERIMENTAL

Silanization reaction of vaporized 3-methacryloxypropyltrimethoxysilane (MPTMS) with the bare slide glass proceeded after oxygen plasma treatment, and hydrophilic poly-(acrylamide) (PAAm) were covalently grafted onto these surfaces by redox polymerization. Next, NIPAAm monomer and conductive polymer solution were sequentially spin-coated on these slide glasses, and EB was locally exposed to these surfaces using EB lithography system [4]. After the exposure, the slide glasses were rinsed with pure water.

978-0-9798064-0-7/μTAS2007/$20©2007CBMS

In cell adhesion and spreading assay, bovine aortic endothelial cells (BAECs) and NIH/3T3 fibroblast cells were seeded to the patterned PNIPAAm-grafted slide glasses at a and cultured at 37°C. After cells proliferate until reaching confluency, culture temperature decrease to 25°C for detachment of these cells from patterned PNIPAAm-grafted surfaces. Cell morphologies at each process were continuously observed and photographed under a phase contrast microscope.

3. RESULTS AND DISCUSSION

For surface characterization of patterned PNIPAAm-grafted surfaces prepared by EB lithographic polymerization, the profiles of the PNIPAAm layers modified onto MPTMS-immobilized surfaces were evaluated by AFM observation (**Fig. 2**). The pattern profiles can be observed, which indicates that only monomer exposed with EB were polymerized and covalently grafted onto the surfaces. In addition, 200nm width of PNIPAAm patterning can be successfully prepared using this technique. Conventionally, the preparation of nano-ordered patterning surfaces must require for the large number of the troublesome fabrication process. In our methods, the nano-patterned polymer-grafted surfaces were successfully prepared only by single step of EB lithography.

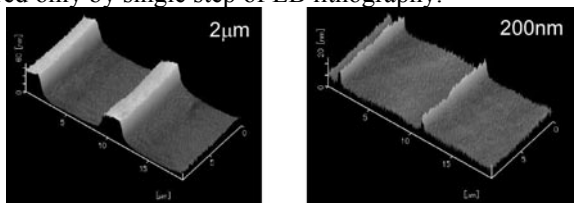

Fig.2 AFM observation of patterned PNIPAAm-grafted surfaces prepared by EB lithographic polymerization. Scan area: 20μm x 10μm.

To investigate the cell adhesion morphologies on the patterned surfaces, the patterned PNIPAAm layers were grafted onto PAAm-grafted glasses by EB lithographic polymerization. The microscopic images of adhesion of BAECs on the patterned PNIPAAm-grafted surfaces are shown in **Fig.3**. While BAECs adhered with random spreading directions on the surfaces uniformly grafted with PNIPAAm (**Fig.3-a**), the adhered cells oriented along the stripe line of the patterned PNIPAAm-grafted surfaces (**Fig.3-b**). The PAAm-grafted surfaces prevent protein adsorption and cellular adhesion, and cells can adhere on the PNIPAAm-grafted surfaces similar to ungrafted culture dishes at 37°C [2]. Thus, cultured cells will selectively spread toward the patterned PNIPAAm-grafted surfaces, which exhibits higher cell adhesion properties, for maintaining stable adhesion states.

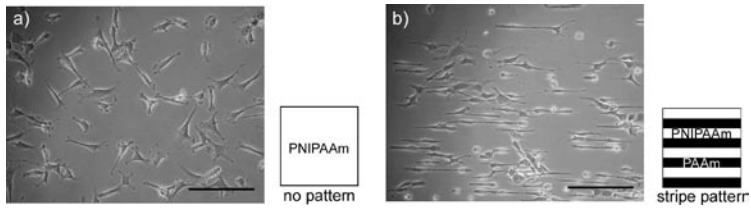

Fig.3 Microscopic observation of BAECs adhered on a) the surfaces uniformly grafted with PNIPAAm and b) the patterned PNIPAAm-grafted surfaces (stripe pattern: 9μm pitch) prepared by EB lithographic polymerization. Scale bar: 200μm.

A decrease in culture temperature releases a cell sheet from thermoresponsive PNIPAAm-grafted surfaces without the enzymatic digestion [3]. Then, the detachment behavior of fibroblast cells cultured on the patterned PNIPAAm-grafted surfaces was observed under phase-contrast microscopy. Fibroblast cells proliferated and reached confluency on both patterned surface with grafted PNIPAAm (**Fig.4-a,b**). When the temperature decreased to 25°C, the patterned cell sheets detached form the uniform PNIPAAm-grafted surfaces with isotropic shrinkage (shrinkage ratio: 68 % for major axis and 64% for minor one, **Fig.4-c**). In contrast, detached cell sheets from the PNIPAAm-grafted surfaces prepared by EB lithographic polymerization were mainly shrunken along the stripe pattern direction (shrinkage ratio: 74% for major axis and 49% for minor one, **Fig.4-d**). After low-temperature treatment, the remaining intact cell–cell junctions and the peripheral bands composed of actin filaments induce to the contractile forces to shrink the whole cell sheets [3]. On the patterned PNIPAAm-grafted surfaces prepared by EB lithographic polymerization, the contractile forces mainly work toward stripe pattern direction, caused by the cells elongated and oriented at 37°C. Therefore, the shrink and folding direction of detached cell sheets by decreasing temperature can be controlled on the PNIPAAm-grafted surfaces with stripe patterning.

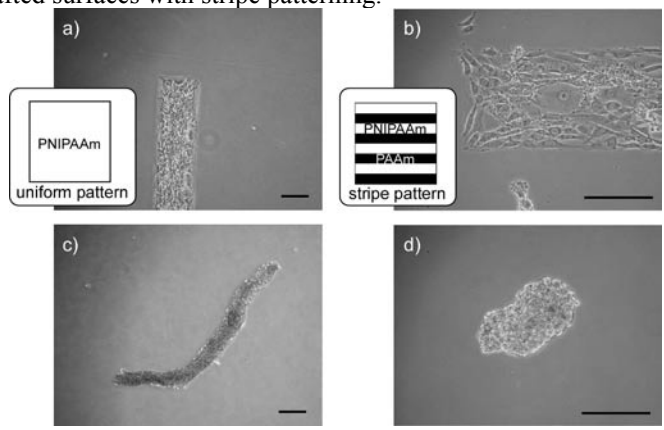

Fig.4 Microscopic observation of fibroblast cells detached from a,c) the surfaces uniformly grafted with PNIPAAm (area: 5000µm x 300µm) and b,d) the patterned PNIPAAm-grafted surfaces (stripe pattern: 3µm pitch, area: 1200µm x 300µm) prepared by EB lithographic polymerization. Incubation temperature: a,b; 37°C, c,d; 25°C. Scale bar: 200µm.

4. CONCLUSIONS

Using EB lithography system, polymerized NIPAAm was directly grafted onto the glass surfaces with nano/micro-stripe patterning. Cultured cells were adhered and oriented along the stripe line of these surfaces at 37°C, and detached with shrinkage along the stripe direction by decreasing temperature. In conclusion, we developed a novel direct patterning technique and cell recovery system with controlled shrinkage direction.

REFERENCES

[1] D. Flaconnet et al., Biomaterials, 27, 3044-3063 (2006).
[2] N. Yamada et al., Makromol. Chem., Rapid Commun., 11, 571-576 (1990).
[3] A. Kushida et al., J. Biomed. Mater. Res., 45, 355-362 (1999).
[4] A. Hibara et al., Anal. Chem., 74, 6170-6176 (2002).

FEATURES OF THERMORESPONSIVE POLYMERS GRAFTED ONTO HYDROPHILIC AND HYDROPHOBIC SURFACES AND APPLICATION OF THE SURFACES FOR RAPID RECOVERY OF THE CELL SHEET

Yoshikatsu Akiyama, Masayuki Yamato, Akihiko Kikuchi and Teruo Okano
Tokyo Women's Medical University, Japan

ABSTRACT

We successfully developed poly(N-isopropylacrylamide) (PIPAAm) grafted culture surfaces exhibiting rapid cell sheet recovery, grafting PIPAAm with nano-ordered thickness onto hydrophilic surfaces. In contrast, PIPAAm grafted onto hydrophobic TCPS surfaces exhibit slow recovery of cell sheet. Water molecules released from hydrophilic basal component allowed for acceleration of hydration of the grafted PIPAAm. Alternatively, ultra thin grafted polymer layer is influenced by properties of basal surfaces.

Keywords: N-Isopropylacrylamide, Ultra Thin Layer, Acrylamide, Cell Sheet

1. INTRODUCTION

We reported that, to PIPAAm grafted TCPS (PIPAAm-TCPS) showing cell attachment and detachmet properties in response to temperature, grafting 20 nm thickness of PIPAAm layer is a key factor. The degree of the chain mobility at the outermost surfaces is dependent on that of restriction of the grafted polymers chains by immobile and hydrophobic basal TCPS surfaces in the vicinity of the interfaces of TCPS (Fig. 1).[1] However, in this case, spontaneous cell sheet detachment from PIPAAm is relatively a slow process, occurring gradually from the sheet periphery toward the interior. Thus, significant incubation time at reduced temperature is required to lift up an intact cell sheet completely. On the other hand, we developed PIPAAm grafted surfaces showing rapid cell detachment properties, incorporating hydrophilic unit such as PEG and CIPAAm into the grafted PIPAAm gel or grafting PIPAAm porous membrane.[2,3] The hydrophilic units releasing water molecules or basal porous membrane permeable to water molecules accelerate hydration of the grafted PIPAAm chains. Based on these results, we hypothesized that PIPAAm chains grafted onto not hydrophobic but hydrophilic polymer layer as basal substrate are more mobile and possibly hold more amount of water molecules than those onto hydrophobic TCPS, and consequently, the basal hydrophilic polymer layer can accelerate hydration of the grafted PIPAAm chains (Fig. 2). Owing to the facilitated hydration of the grafted PIPAAm chains, cultured cells are more rapidly detached from the surface of PIPAAm grafted onto the hydrophilic polymer.

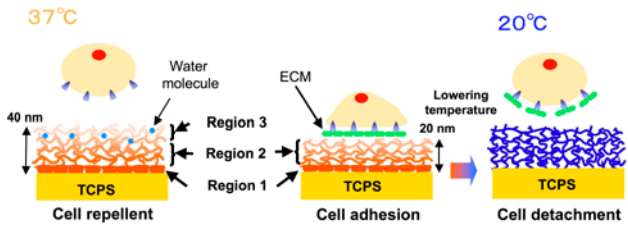

Fig. 1. Influence of PIPAAm-grafted polymer densities on cell-adhesive characteristics. Region 1: highly hydrophobic and aggregated chains, Region 2: restricted hydration and mobility of chains, Region 3: hydrated and mobile chains.

978-0-9798064-0-7/μTAS2007/$20©2007CBMS

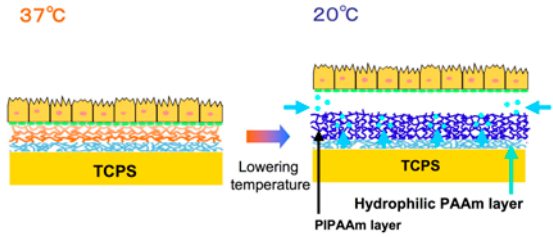

Fig. 2. Illustration of rapid cell sheet recovery form 120PIPAAm-022PAAm-TCPS (amount of the grafted PIPAAm and PAAm = 1.20μg/cm^2 and 0.22μg/cm^2).

2. EXPERIMENTAL

In order to verify this hypothesis, firstly, we prepared PAAm-TCPS as a model hydrophilic basal surface, using electron beam irradiation. As a second step, PIPAAm was grafted onto the hydrophilic PAAm-TCPSs (PIPAAm-PAAm-TCPS). These surfaces were examined by XPS, contact angle measurement and FT-IR / ATR. We also further investigated cell attachment, detachment properties and cells sheet recovery in response to temperature, using PIPAAm-PAAm-TCPSs and, finally, we discussed the phenomenon in terms of molecular motion of the grafted polymers chains and role of the grafted PAAm for the grafted PIPAAm chains.

3. RESULTS AND DISCUSSION

PAAm-TCPS with the grafted PAAm more than 0.33μg/cm^2 showed cell repllent surfaces, and PIPAAm grafted onto such PAAm-TCPS surfaces also exhibited cell repllent surfaces even at 37°C. By contrast, PAAm-TCPS with 0.22μg/cm^2 and 0.30μg/cm^2 were

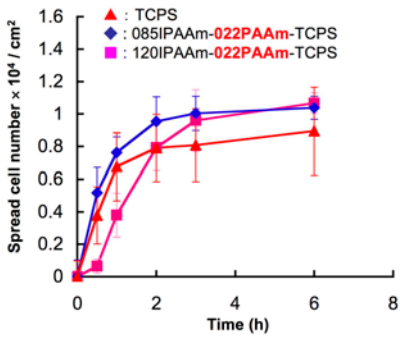

Fig. 3. Spreading behavior of ECs on (a) PIPAAm grafted onto 0.22PAAm-TCPS. TCPS was also investigated for comparison. Data are expressed as the mean with standard error of mean (n=3). ECs were seeded at a density of 1.5 × 10^4 cells/cm^2.

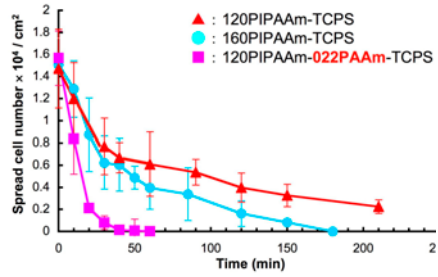

Fig. 4. Cells detachment behavior from surfaces of 120PIPAAm-TCPS, 160PIPAAm-TCPS and 120PIPAAm-022PAAm-TCPS by lowering temperature at 20°C after 24 h culture at 37°C. Data are expressed as the mean with standard error of mean (n=3). Initial seeded cell density : 1.5 × 10^4 cells/cm^2.

cells adhesive surfaces. 022PAAm-TCPS and 030PAAm-TCSP with PIPAAm more than 1.60μg/cm^2 were cell repllent. By sequential graft of optimum amount of PAAm and PIPAAm onto hydrophobic TCPS, we succesfully prepared temperature responsive culture

dish exhibitng more rapid cell detachment properties than 1.60PIPAAm-TCPS (amount of the grafted PIPAAm = 1.60μg/cm^2)) and cell adhesion properties equivalent to TCPS (Fig. 3). By lowering temperature, 1.20PIPAAm-0.22PAAm-TCPS (amount of the grafted PIPAAm and PAAm = 1.20μg/cm^2 and 0.22μg/cm^2) attained more rapid cell detachment and cell sheet recovery than 1.20PIPAAm-TCPS regardless of grafting same amount of PIPAAm (Fig. 4). XPS analysis for 1.20PIPAAm-0.22PAAm-TCPS surfaces indicate that a peak assigned to carbonyl group of PIPAAm (287.9 eV) shifted toward to 288.5 eV assigned to carbonyl groups of PAAm. Namely, PAAm composition is more abundant in the vicinity of TCPS interface. This result demonstrates successful graft of PIPAAm onto PAAm layer.

4. CONCLUSIONS

The small amount of the grafted PAAm as basal composition possibly play a role of providing water molecules with the grafted PIPAAm and accelerating hydration of the grafted PIPAAm. The role of the grafted PAAm facilitating hydration of the grafted PIPAAm is similair to that of hydrophilic unit such as PEG and CIPAAm as described in previous report.[2, 3] And also these results suggest that those of basal surfaces influence properties of the grafted polymers with ultra thin thickness.

REFERENCES

[1] Y. Akiyama *et al,* Langmuir, 20, 5506 (2004). [2] M. Ebara *et al,* Biomacromolecules, 4, 344 (2003). [3] OH. Kwon *et al*, Biomaterials, 24, 1223 (2003)

NONBIOFOULING SURFACES AND MICROPATTERNED BIORECOGNITION LAYER ON POLYMERIC MATERIALS FOR HIGHLY SENSITIVE MICROARRAY BIOSENSORS

James Sibarani, Tomohiro Konno, Madoka Takai, Kazuhiko Ishihara

Department of Material Engineering, School of Engineering and Center for NanoBio Integration, The University of Tokyo

ABSTRACT

Preparation of nonbiofoling surfaces and construction of micropatterned biorecognition layer over nonbiofouling surfaces based on biocompatible poly(2-methacryloyloxyethyl phosphorylcholine(MPC)) brushes were constructed on polymer substrates.

Keywords: photoiniferter, poly(MPC) brushes, micropatterned biorecognition layer

1. INTRODUCTION

To create useful materials for many biotechnology applications, interfaces are required that have both enhanced specific binding and reduced non specific binding. Thus, in application such as biosensors, the tailoring of surface chemistry and the use of micro or nanofabrication technique becomes an important avenue for the production of surface with specific binding properties and minimal background interference especially in microfluidic devices handling very low concentration and small amount of volume of analyte. The aims of this study are to prepare nonbiofouling surface bearing highly biocompatible poly(2-methacryloyloxyethyl phosphorylcholine (MPC)) brushes [1] on polymeric substrates commonly used for microchip devices such as polycarbonate (PC), poly(methylmethacrylate) (PMMA), and poly(dimethyl siloxane) (PDMS) and to construct micropatterned recognition layer on microfluidic system for enhancing high signal/noise (S/N ratio) in biosensors (Fig. 1) using living radical polymerization based on dithiocarbamate as photoiniferter (initiator, transfer, and terminator) [2].

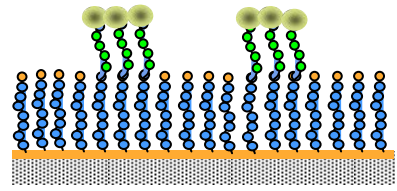

Fig. 1 The ideal construction of micropatterned biorecoginiton layers over the nonbiofouling MPC-brushed type surface. substrate, macrophotoiniferter layer, MPC, PEG-NHS, Biomolecule (protein/cell)

2. EXPERIMENTAL

The macrophotoiniferters comprised of 2-ethylhexyl methacrylate (EHMA) and 4-vinylbenzyl *N,N*-diethyldithiocarbamate (VBDC) (PEV as shown in Fig. 2) were synthesized with variation of VBDC content of 10% - 40% (PEV10, 20, 30, 40). Properly cleaned polymer substrates (PMMA,

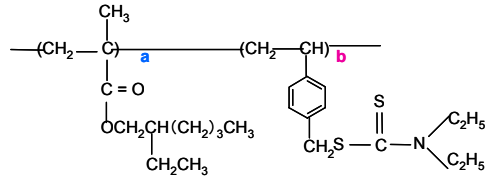

poly(EHMA-co-VBDC) (PEV)

Fig. 2 Chemical Structure of macrophotoiniferter

978-0-9798064-0-7/μTAS2007/$20©2007CBMS

PC, and PDMS) were coated by dipping in 0.25% (by weight) of the macrophotoiniferter solutions in 1,4-dioxane for coating PMMA and PC while chloroform used for coating PDMS. The photoiniferter-coated plates with aqueous solution of 0.3M MPC were irradiated with UV lamp (360 nm) at room temperature. The surface characterization of the poly(MPC)-modified surfaces (represented as PEV-g-MPC) was conducted by water contact angle, X-ray photoelectron spectroscopy (XPS), and atomic force microscope (AFM) observation. Nonspecific protein adsorption resistance of these modified surfaces was investigated by contacting to a mixture of 0.045 g bovine serum albumin (BSA) and 0.030 g human plasma fibrinogen (HPF) in 100 ml PBS solution (pH 7.4) and the total protein adsorption was measured by Micro BCA Method. The micropatterned nonbiofouling surface and biorecognition layers (methacryl-polyethylene glycol conjugated with N-succinimidyl carbonate (Methacryl-PEG-NSC) were constructed by using micromask with 100 μm in size and and evaluated by contacting with FITC- albumin in PBS solution (pH 7.4). The intensity of fluorescence was measure by fluorescence microscope at 490 nm.

3. RESULTS AND DISCUSSION

The density and the length of the poly(MPC) chains were governed via composition of VBDC in the macrophotoiniferter and irradiation time, respectively. The hydrophilicity of the modified surfaces (termed as substrate/ PEV-g-MPC) increased compared to unmodified ones and the surface mobility (M_f) of the modified surfaces significantly increased as well (Fig. 3 and Fig. 4). These are due to the hydrophilic phosphorylcholine group on MPC units which were located on the surfaces. From these results, it can be seen that all polymer substrates used in this experiment can be modified by this simple procedure. The values of phosphorus/carbon (P/C) on the modified surfaces vary on different substrates due to the compatibility of the substrate with the solvent used to dissolve the macrophotoiniferter on the coating process (Fig. 4). The highest value of the P/C of 0.08 for PMMA/PEV20-g-MPC, which is close to the theoretical value of 0.09, indicates that the poly(MPC) was highly oriented on the surfaces. The AFM observation shows that morphology and roughness of the modified surfaces also vary depending on substrate used while the density of the

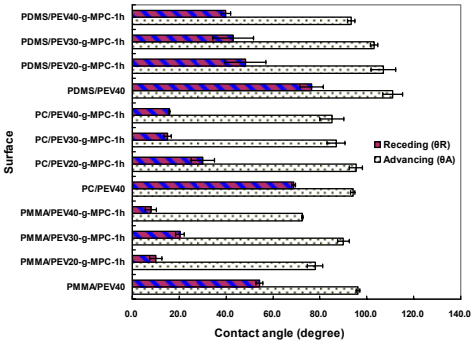

Fig. 3 Dynamic contact angles of poly(MPC)-modified surfaces at different substrates and density of photoiniferter.

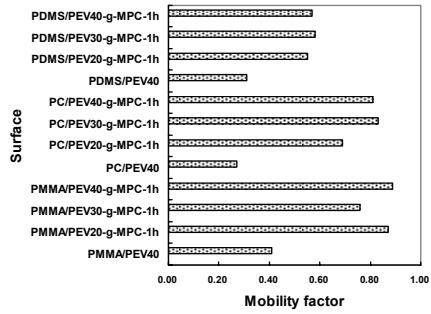

Fig. 4 Mobility factor $\{(\theta_A-\theta_R)/\theta_A\}$ of poly(MPC)-modified surfaces

poly(MPC) chains only slightly effect on the morphology and roughness (Fig. 5) although the roughness of modified PMMA is higher compared to modified PET at the same grafting time and chain density. The nonspecific protein adsorption resistance of these modified surfaces was investigated by contacting to human plasma proteins. The modified surfaces significantly reduce nonspesific protein adsorption although highly roughness surfaces still prone to lead inevitable non specific protein adsorption as reported in the previous study using PET substrate grafted with MPC with the same method [3]. Furthermore, the micropatterned nonbiofouling surface and biorecognition layer could be easily achieved by using photomask with high fidelity as evaluated by contacting with FITC-albumin solution (Fig. 7) while construction of the micropattered biorecognition layer over the biocompatible poly(MPC) brush layer and micropatterning inside the microchannel is still on going.

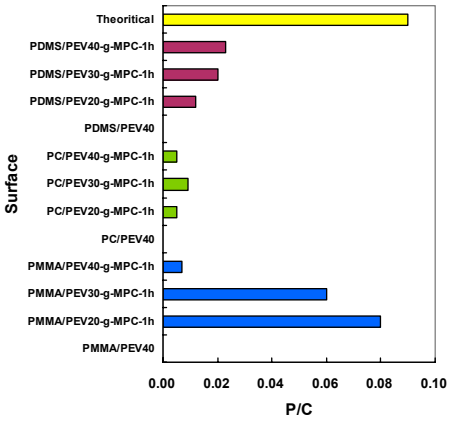

Fig. 5 The value of P/C of modified-surfaces taken from XPS measurement at 90o takeoff angle in

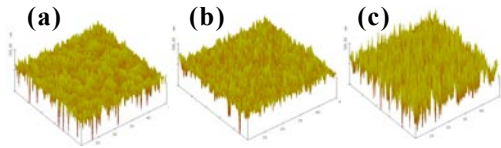

Fig. 6 Surface morphology of modified surfaces on PMMA at different grafting density (PEV20, PEV30, and PEV40 for a, b, and c respectively) with surface roughness of 26.71, 20.48, and 27.59 nm for a, b, c respectively. (50µm x 50 µm in size; z scale= 100 nm)

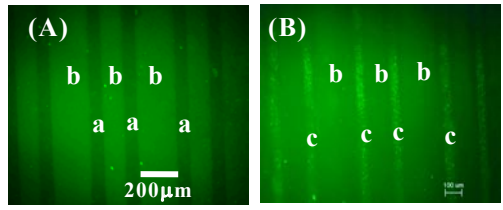

Fig. 7 Evaluation of micropatterned nonbiofouling surface (A) and biorecognition layer (PEG_{350}-NSC) (B) by contacting with FITC-albumin. The dark lines (a) are the poly(MPC)-modified regions while the green lines (b) are the non-modified ones. The bright green lines (c) are the PEG_{350}-NSC regions immobilized with FITC-albumin.

4. CONCLUSION

Living radical polymeriza- tion using photoiniferter is a generic method for preparation of nonbio-fouling surfaces bearing poly(MPC) brushes and for construction of micropatterned nonbiofouling surface and biorecognition layer by using microphotomask.

5. REFERENCES

[1] W. Feng, K. Ishihara, J. L. Brash, *Langmuir*, **21** (13), 5980 (2005)

[2] Y. Nakayama and T. Matsuda, *Macromolecules*, 29, 8622 (1996)

[3] J. Sibarani, T. Konno, M. Takai, K. Ishihara, *Key Engineering Materials*, 342-343, 789 (2007)

PHOSPHOLIPID POLYMER SURFACE SHOWING THEIR BIOCOMPATIBILITY RAPIDLY FROM DRY TO WATER ENVIRONMENT FOR MICROFLUIDIC DEVICES

Koji FUTAMURA, Madoka TAKAI, and Kazuhiko ISHIHARA

Department of Materials Engineering, School of Engineering and Center for NanoBio Integration, The University of Tokyo

ABSTRACT

We developed a new type of phospholipid polymer (poly(2-methacryloyloxyethyl phosphorylcholine (MPC) -*co*-2-vinylnaphthalene: PMvN) forming a phosphorylcholine (PC)-enriched surface even in dry state that directly achieves excellent biocompatibility. Poly(ethylene terephthalate) (PET) could be readily coated with PMvN. Dynamic contact angle measurements revealed that the surface mobility of the PMvN coated PET was extremely low and yet the surface hydrophilicity was remarkably high. When bovine serum albumin (BSA) was in contact with the polymer surface in dry state without any pretreatment, the amount of adsorbed BSA on this polymer coat was effectively reduced. Remarkably, the PC-enriched surface formed by the PMvN directly achieved excellent biocompatibility even when it was applied from dry state. PMvN is a functional coating material to improve the biocompatibility for many microfluidic devices.

Keywords: Phospholipid polymer, Surface mobility, Hydrophilicity, Biocompatibility

1. INTRODUCTION

With the recent development of microfluidic devices, many biological applications such as DNA separation, immunoassay, cell sorting, biosensors, and enzymatic assays have come into great demand. The advantages include lower sample consumption, shorter analysis time, smaller dimensions, disposability, low-cost fabrication, and multiplex functionality. Recently polymeric materials such as poly(ethylene terephthalate) (PET) rather than glass and quartz are preferred for fabrication of the new microchips, due to a low cost and an ease of fabrication. However, protein and cell adhesion onto the polymeric materials are severe compared to glass or quartz based materials. Indeed, the density of blood red cell adhesion on PET is much higher than that occurs in quartz because of large surface hydrophobicity [1]. To solve this problem, we have previously prepared several hydrophilic polymers for the surface modification, based on the use of 2-methacryloyloxyethyl phosphorylcholine (MPC) polymer, the chemical structure of which mimics that of cell membrane bringing about an effective reduction of protein adsorption [2]. For example, poly(MPC-*co*-*n*-butyl methacrylate) (PMB) has extensively been utilized for this purpose with a simple one step dip coating procedure. This coating, however, requires a long time pretreatment to obtain their good biocompatibility. Our previous work has shown that the phosphorylcholine (PC) groups in dried condition are vuried under the hydrophobic polymer chains to decrease the surface free energy [3], causing an restricted rate of steric rearrangement of this polymer.

In the present work, poly(MPC-*co*-2-vinylnaphthalene) (PMvN) was newly synthesized by radical polymerization. The selected comonomer 2-vinylnaphthalene, distinct from MPC unit, possesses a high hydrophobicity and a high glass transition temperature. The expected amphiphilicity based on the monomer combination along with synergistic chain interactions involving naphthalene rings stacking effect may gain a unique control over specific

978-0-9798064-0-7/μTAS2007/$20©2007CBMS

functional group's associative as well as orienting features. The prepared polymer surface was characterized by dynamic contact angle (DCA) measurements for the assessment of surface mobility and the dry state surface hydrophilicity. The protein adsorption onto the polymer surface was also evaluated.

2. EXPERIMENTAL

Fig. 1 shows the chemical structure of PMvN. PMvN was synthesized by a conventional radical polymerization using α, α'-azobisisobutyronitrile as an initiator. A PET plate was cleaned by sonication in ethanol for 30 min. Mixed solvent of ethanol/ water (0.5w%, 20:80 (v/v)) was used as coating solvent in order to make PMvN phase-separated state, because poly(MPC) can be solved in ethanol but poly(2-vinylnaphthalene) cannot be solved. The PET plate coated with PMvN was treated at 40 ˚C for 100 minutes for predrying and then dried in vacuo for overnight. Another PET plate was immersed into an ethanol solution containing 0.5 wt% of PMB. It was slowly dried under ethanol-vapor atmosphere over a day and then in vacuo. DCA (Dynamic Contact Angle Analyzer, Cahn) measurements based on the wilhelmy plate method was carried out to determine the surface mobility of the polymer surfaces and the surface hydrophilicity in dry state. Bovine serum albumin (BSA) was used for protein adsorption evaluation. Non-coating PET, the PET coated with PMvN, and the PET coated with PMB were contacted with 0.45g/dL BSA in PBS (pH 7.4, ion strength = 0.15M) for 60 min at 37 ˚C in dry state without any pretreatment and then rinsed with fresh PBS. The plates were soaked in 1wt% aqueous sodium dodecyl sulfonate solution for 20 min with sonication to desorb the protein adsorbed on them. A protein analysis kit (Micro bicinchoninic acid (BCA) protein assay reagent kit, Pierce, Rockford, IL) was used to determine the concentration of the BSA.

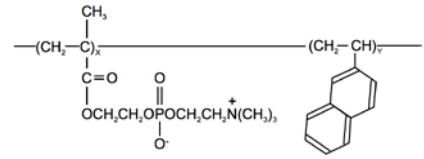

Fig. 1. Chemical structure of PMvN

3. RESULTS AND DISCUSSION

Fig. 2 shows DCA curves of the PMvN- and the PMB coated PET. Table 1 summarizes data of advancing (θ_A) and receding contact angles (θ_R) assessed from Fig. 2. A large hysteresis is evident for the PMB costed PET (Fig. 2), corresponding to a large θ_A and a small θ_R as shown in Table 1. In dry state, the PC groups of PMB may be vuried under the hydrophobic polymer chains decreasing the surface free energy. On the other hand, the PC groups should be exposed to the aqueous environment to reduce the interfacial free enegy. Thus the observed large hystelysis for the PMB may relate to an occurrednce of reorientation of the PC groups (Fig. 3). On the other hand, hystelysis is hardly visible in the PMvN DCA curve yielding small θ_A and θ_R (Table 1). This may be attributable to the ability of the PMvN network to promptly create PC-enriched surface even in dry state along with the restricted surface mobility of the PC groups due to the presence of high glass transition temperature component, namely, 2-vinylnaphthalene (Fig. 4).

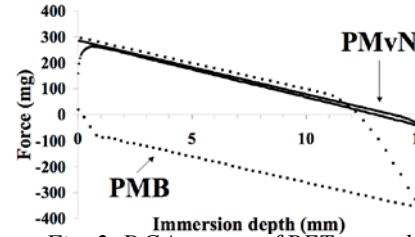

Fig. 2. DCA curves of PET coated with PMvN, PMB

Table 1. Advancing contact angle by water from dry state (PET plate)

Sample	Contact angle (degrees)		M_f[a]
	Advancing	Receding	
PMvN	24	22	0.083
PMB	101	16	0.84
Non-coating	90	60	0.33

[a] Mobility factor

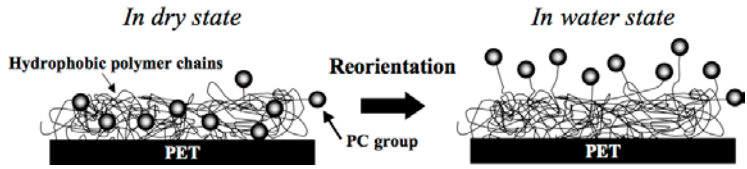

Fig. 3. Reorientation of the PC-group of the MPC polymers from dry state to water state

When BSA was in contact with the polymer surface in dry state without any pretreatment, the amount of adsorbed BSA on the PMvN coated PET was effectively reduced compared to bare- and the PMB coated PETs (Fig. 5). Again, the suppressed protein adsorption onto the PMvN coat could be caused by the formation of PC-enriched surface even under the dried state. Fig. 6 shows images of droplet wept on each type of polymer surface demonstrating superior hydrophilicity of the PMvN coated surface to others.

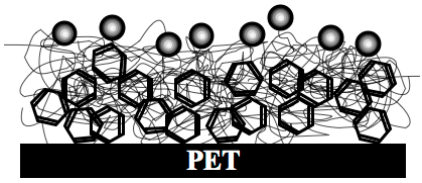

Fig. 4. Expected surface structure of PMvN on the PET surface in dry state

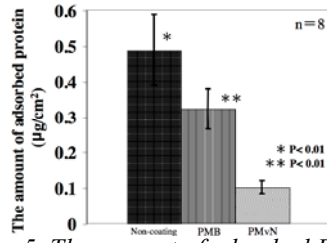

Fig. 5. The amount of adsorbed BSA

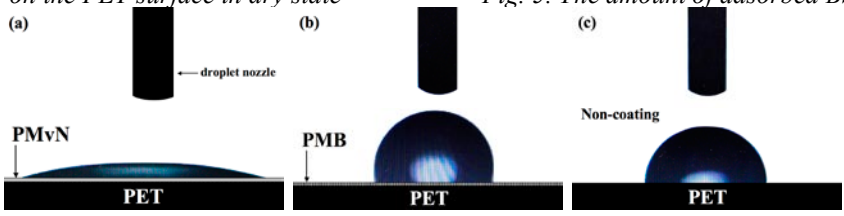

Fig. 6. A droplet wept on the surfaces of PET coated with PMvN (a), PMB (b), original (c)

4. CONCLUSIONS

PMvN is capable of forming a PC-enriched surface even in dried state providing a surface with excellent biocompatibility. The process took place promptly even when it was allowed under dried environment. It was also revealed that other (than PET) relevant polymers such as acrylic resin and polycarbonate surfaces could be readily coated with PMvN. With these features, PMvN represents an attractive option for functional coating material to improve the surface biocompatibility applicable to microfluidic devices in various aspects.

REFERENCES

[1] Y. Horiike *et al*. Lab-on-a-chip, Biochips aiming at advanced medical treatment, eds. R.E. Oosterbroek and A.van den Berg, Elsevier, 335-372 (2003)

[2] J. Sibarani *et al*, "Surface modification on microfluidic devices with 2-methacryloyl oxyethyl phosphorylcholine polymers for reducing unfavorable protein adsorption", Colloids Surf B: Biointerfaces, 54, 88-93 (2007).

[3] A. Yamasaki *et al*, "Surface mobility of polymers having phosphorylcholine groups connected with various bridging units and their protein adsorption-resistance properties", Colloids Surf B: Biointerfaces, 28, 53-62 (2003)

NANOSTRUCTURE ENHANCED SURFACE PLASMON RESONANCE IMAGING DETECTION OF DNA HYBRIDIZATION

L. Malic[1], B. Cui[2], T. Veres[2] and M. Tabrizian[1]
[1]*Biomedical Engineering Department, McGill University, CANADA*
[2]*Industrial Materials Institute, NRC, CANADA*

ABSTRACT

Surface plasmon resonance imaging (SPRi) has been successfully employed in the past decade as a label-free method to detect DNA hybridization. However, the low sensitivity of conventional SPRi limits its use in certain applications. In this paper, we demonstrate that periodic gold nanostructures fabricated on gold surface can enhance the sensitivity of conventional SPRi. Specifically, arrayed gold nanoposts, on gold-coated glass substrate, with optimized 30nm height, 50 nm size and 110 nm period provide five-fold SPR signal amplification compared to the plain 50nm thick gold film used as control.

Keywords: Surface plasmon resonance, nanostructure, detection, DNA hybridization

1. INTRODUCTION

In the last decade, the surface-sensitive optical technique of SPRi has emerged as an attractive alternative to traditional fluorescence-based microarray detection methods for the label-free detection of DNA hybridization. Although SPRi combines many of the desirable characteristics for a DNA hybridization sensor, the sensitivity of conventional SPRi apparatus is limited by small angular shift of the SPR spectrum dip and small fractional reflectivity change. In order to overcome the sensitivity limitation, nanoparticle-based SPR biosensors have drawn tremendous interests in recent years. The exploitation of nanoparticles allows strong optical coupling of incident light to localized surface plasmons (LSPs) [1,2]. In terms of conventional SPR sensor, various interactions between LSPs, propagating SPs, and binding biomaterial in the presence of nanoparticles can lead to different resonance properties, resulting in enhanced sensitivity [3]. It has been empirically shown that colloidal gold nanoparticles attached to thin film of an SPR biosensor exhibit more than 10-fold signal amplification [4]. While the nanoparticles generate pronounced SPR signals, they essentially transform an advantageous label-free sensing technique into a labeled one. On the other hand, noble metal nanostructures residing on SPR-active thin gold film can also be used to amplify the SPR signal. In comparison to colloidal gold nanoparticles, use of periodic gold nanostructures provides the advantage of spatial uniformity and performance reproducibility, while retaining the benefit of SPR label-free detection. Recently conducted theoretical studies have shown that periodic gold nanowires with optimized design provide an order of magnitude sensitivity enhancement [5,6]. Until now, no experimental studies have been reported to confirm these findings. In this paper, we demonstrate experimentally that periodic gold nanostructures can enhance the sensitivity of conventional SPRi. Specifically, arrayed gold nanoposts, on gold-coated glass substrate, with various widths and periodicity are fabricated using electron beam lithography (EBL) and functionalized with thiolated single stranded ss-DNA probe. Scanning-angle SPR imaging apparatus (Genoptics, France) at 800 nm wavelength is used to conduct the SPR kinetic analysis of DNA hybridization with complementary target sequence, and assess the corresponding SPR signal amplification.

978-0-9798064-0-7/μTAS2007/$20©2007CBMS

2. NANSTRUCTURE FABRICATION

Test substrates, having 400x400 μm arrays of differently sized 30 nm high nanoposts with 110 and 200 nm periods are fabricated using EBL on SF-11 glass substrate coated with 20 nm gold film. The nanostructure shape is defined by the shape of the beam, while the exposure dose is adjusted to obtain the structures of different size. Fig.1a shows a sample SEM image of nanoposts of nominally circular shape with 110 nm period having a diameter 50±3.5 nm. AFM characterization shows that the fabricated nanoposts are dome-shaped (Fig.1b), as expected from anisotropic gold evaporation in the narrow PMMA trenches defining the nanostructures. The height and the period of the nanoposts were found to be of excellent uniformity with the 3.73% and 1.21% variation, respectively.

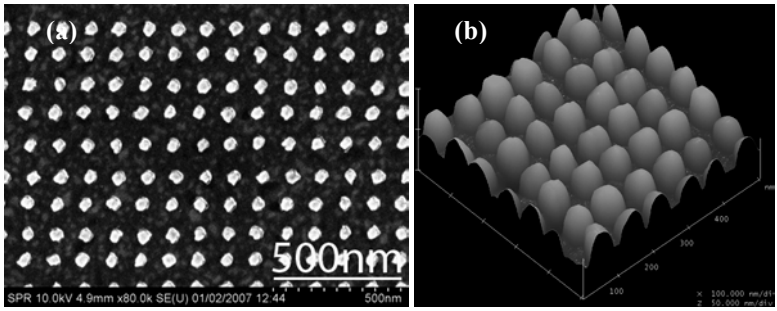

Fig.1 *Sample images of fabricated gold nanoposts (a) SEM image; (b) AFM surface plot*

3. SURFACE FUNCTIONALIZATION

Surface functionalization is carried out using 1μM thiol-modified 20-mer oligonucelotide probe sequence suspended in 1M KH_2PO_4, deposited on piranha-cleaned substrates for 120 min. Following the immobilization, the substrates are treated with 1mM Mercapto-hexanol for 90 min, to render the probes highly accessible to target while preventing unspecific target-binding to the gold surface [7].

4. SPRi DETECTION OF DNA HYBRIDIZATION ON NANOSTRUCURES

All DNA hybridization experiments are carried out using 20-mer oligonucelotide target sequence complementary to the immobilized probe with 250nM concentration suspended in 1M NaCl in TE buffer. Hybridization kinetic curves are monitored using SPRi as follows. Initially, a baseline signal is obtained for the buffer only, followed by hybridization signal during which target is brought in contact with the surface, allowing it to bind to the immobilized probe. Finally, the substrate is washed with the buffer and the difference in the reflected intensity is computed by taking the difference between the initial and final buffer injections. The kinetic curves of the reaction on the nanostructured gold surface are shown in Fig.2. From the curves, it can be seen that the nanoposts with 110 nm period exhibit higher reflectivity change compared to plain gold surface than those with 200 nm period, which perform similar to or inferior to the control. This corresponds to earlier theoretical studies confirming that the smaller spacing between the neighboring structures allows for more pronounced coupling of LSPs and SPPs, resulting in enhanced electromagnetic fields in the presence of the dielectric layer [5]. Although the periodicity of the nanoposts plays the main role in the SPR signal amplification, the sensitivity enhancement can be further fine-tuned by nanostructure size. From Fig.3, nanoposts that have 50 nm diameter and 110 nm period yield highest signal amplification, while the smaller, 30 nm structures, exhibit performance similar to that of control.

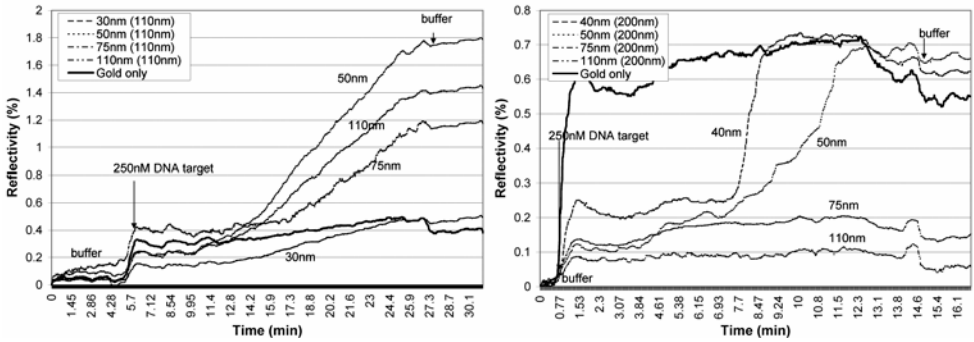

Fig.2 *Kinetic curves of 250nM DNA target hybridization on nanostructured SPR substrate having 110 nm period nanoposts (left) and 200nm period nanoposts (right)*

To enable qualitative assessment of the effect of nanostructure design on SPR signal amplification, the reflectivity sensitivity enhancement factor RSEF is included to describe the ratio of the maximum change in reflected intensity due to DNA hybridization on nanostructured surface, to that of control. Experimentally obtained RSEF for 110 and 200 nm period structures is plotted in Fig.3. Signal amplification is obtained for all the structures having 110 nm period, with 50 nm diameter nanoposts exhibiting maximum amplification equal to five times that of a conventional SPR biosensor surface.

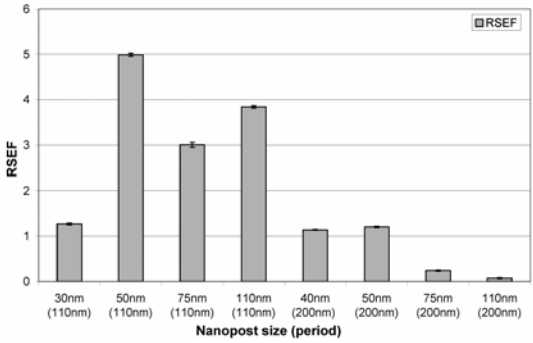

Fig.3 *RSEF for different nanoposts size and period with respect to control*

5. CONCLUSION

In this paper, we have shown that nanostructure-based SPR biosensor yields an enhancement in the sensitivity of a conventional SPRi, by amplifying the SPR signal up to five times for the optimized structures. This work demonstrates a considerable sensitivity improvement in comparison with a conventional SPR biosensor, with potential for future applications in ultrasensitive DNA detection and DNA microarray analysis.

REFERENCES

[1] Endo T. et. al., Science and Technology of Advanced Materials. 2005; **6**:491-500.
[2] Haes AJ. et. al., Analytical and bioanalytical chemistry. 2004; **379**:920-930.
[3] Hutter E, Fendler JH., Advanced Materials. 2004; **16**:1685-1706.
[4] He L. et. al., J Am Chem Soc. 2000; **122**:9071-9077.
[5] Byun KM. et. al., Optics Express. 2005; **13**:3737-3742.
[6] Byun KM. et. al., Sensors and Actuators B. 2006; **117**:401-407.
[7] Peterson AW. et. al., Nucleic Acid Research. 2001; **29**:5163-5168.

TOWARDS SELECTIVE OPTOCHEMICAL GAS SENSING BY LUMINESCENT MARINE DIATOMS

A. Setaro[1], S. Lettieri[1], L. De Stefano[2], P. Maddalena[1]

[1]CRS Coherentia CNR-INFM & Dipartimento di Scienze Fisiche, Università di Napoli Federico II, Via Cintia 80126 Napoli, ITALY and

[2]IMM- Unità di Napoli, CNR, Via P. Castellino 111, 80131, Napoli, ITALY

ABSTRACT

Diatom frustules are nanostructured silica shells that spontaneously arise in every aquatic environment. They strongly emit in the visible range when pumped up by UV radiation and their photoluminescence, in virtue of their high surface-to-volume ratio, is strongly affected by changes of the surrounding atmosphere. Frustules belonging to different families were exposed to various chemical species in order to test their reactivity to different polluting gases. Different species of diatoms were found to exhibit different relative responses and different gas concentration ranges of sensitivity, depending on the morphology and porosity of their frustules. Due to the large variety of dimensions, porosities and surface morphologies available in nature, these materials appear to be promising to improve the selectivity of gas sensing based on photoluminescence optochemical transduction, opening the way to the implementation of an all-optical analogous of the electronic nose.

Keywords: Natural Nano-structured Materials, Chemical Sensing, Photoluminescence, Quenching Mechanisms

1. INTRODUCTION

In the last decades a big effort has been spent in developing new techniques to design complex top-down nanostructures for chemical sensing. A completely different point of view consists in exploiting nanostructures that nature has already realized and optimized during its evolution. Diatoms are microscopic algae constituting the largest part of the phytoplankton living thanks to photosynthetic processes. They are enclosed within a transparent glass shell made of hydrate silica $SiO_2 \cdot n(H_2O)$ that is called *frustule*. In order to ensure maximum exposition to sunlight, the algae's surface possesses a fractal-like structure consisting of regular arrays of chambers whose diameter may range from a few hundred nanometers up to a few microns. The frustules' surface to volume ratio reaches high values making them very sensitive to the surrounding environment. There are thousand different diatoms, each kind possessing its peculiar frustule with its own geometry. Due to their peculiar structures, the large variety of different morphologies and their robustness, a widespread interest about diatoms and their possible application in nanosciences and nanotechnology has been growing. In a recent work [1] it has been shown that the photoluminescence intensity of the *Thalassiosira Rotula Meunier* is affected by the chemical nature of different gases present in the atmosphere, being either quenched or enhanced by electrophilic or nucleophilic gases. As a further step toward the implementation of an optochemical gas sensor based on diatoms frustules, we thus investigated their ability in detecting not only the presence of a chemical species but also its amount and its nature, exploiting the gas-sensitive light emission properties of diatoms' frustules belonging to different families (characterized by different morphologies and

978-0-9798064-0-7/μTAS2007/$20©2007CBMS

specific surfaces), paying attention to the modifications of photoluminescence properties induced by adsorption of nitrogen dioxide, methane and carbon monoxide.

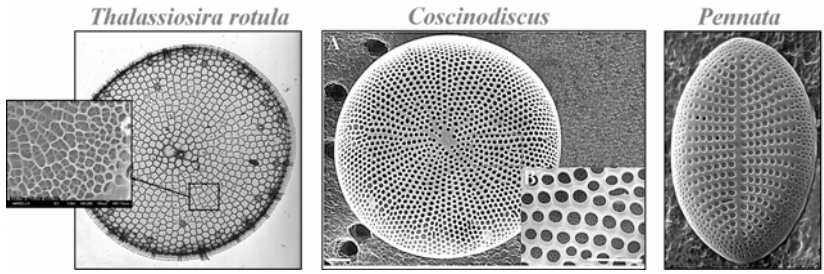

Figure 1.SEM-microscope photographs of the used frustules.

2. EXPERIMENTAL: RESULTS AND DISCUSSION

The diatoms used in the present work are *Thalassiosira Rotula Meunier*, *Coscinodiscus wailesii* (*centric* diatoms, since their skeleton possesses a radially symmetric structure, see figure 1) and *Pennata* (anisotropically shaped, as it can be seen in figure 1); the silica skeletons, dropped on a silicon substrate, were placed on a holder and enclosed inside a test chamber equipped with quartz windows in order to optically access to the sample. A mass flow control system provided calibrated mixing of synthetic air and chemical species inside the chamber, allowing to change the polluting gas (NO_2, CO and CH_4) concentration inside the chamber. PL spectra were obtained by using the UV spectral line of an He-Cd laser (325 nm wavelength) as excitation source. The emitted spectra, once collected, are sent to a spectrometer equipped with a 600 grooves/mm grating blazed at 500 nm and coupled with a Peltier cooled CCD camera.

Silica is an insulator with a band gap of about 9 eV; therefore the observed photoluminescence results as direct excitation from states placed within the band gap. The visible observed photoluminescence is attributed [2] to the excitation of 2.2 eV *a*-SiO_2 self-trapped exciton photoluminescence band. There is no appreciable difference between the observed spectra of the different species, coherently to what already observed in the analogous situation of samples made up from mesoporous silica with pores of different sizes [3]: the peak position and full with at half maximum of the emitted spectra neither showed dependence upon porosity.

PL spectrum is significantly quenched even at very slight amounts of NO_2 in air (few hundred parts over a billlion). In figure 2-a the maxima of the PL spectra (normalized to the maximum value in dry air) *vs*. NO_2 concentration are reported for the three diatoms species. All the considered diatoms strongly react to the gas presence, quenching their photoluminescence, even at the slightest gas concentrations (detecting amounts of about hundred part of NO_2 over a billion part of dry air), confirming diatoms as highly sensitive and reactive candidates for optical gas detecting purposes. As it is moreover possible to see in figure 2-a, different diatoms belonging to different species (and thus offering different specific surfaces to the interaction with the polluting gas), even though made of the same material (amorphous silica), do quench differently their PL spectra: each species possesses its own different sensing characteristics. Although there is no significant difference between the shape of the PL spectra of diatoms belonging to different species, it is possible to recognize that the difference in the frustule morphology strongly affects their reactivity and sensitivity to nitrogen dioxide. In figure 2-b is moreover reported the response of the

Thalassiosira Rotula to the different chemical species, showing how the PL signal reacts differently to different gases: it resembles not only the electrophilic or nucleophilic nature of the chemical species (quenching or enhancing itself) but moreover shows different operational ranges.

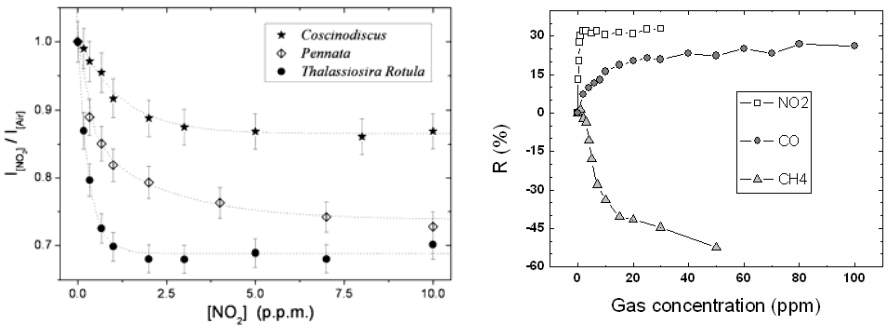

Figure 2. (a) Photoluminescence efficiency quenching for the three different samples as a function of NO_2 concentration and (b) Relative response R vs. gas concentration for the *Thalassiosira* sample (R is defined as $R = (I_{AIR}-I_{GAS})/I_{GAS}$ and is measured in percent units in the graph).

4 CONCLUSIONS

In this work we show our recent results on investigation of gas-sensitive light emission properties of diatoms frustules. We investigated porous frustules having different morphologies and porosities. Very large sensitivity to nitrogen dioxide, carbon monoxide and methane has been observed in all the investigated samples. Nitrogen dioxide and carbon monoxide act as photoluminescence quencher, while methane acts as photoluminescence enhancer. Diatom's optical sensing characteristics, in particular their operational range and sensitivity, do change by changing the species, thus suggesting a critical dependence of such parameters upon the frustule morphology. Since nature provides us thousands of different kind of diatoms, it will be very fruitful to deeper study the interplay between morphology and sensing character. Such wide availability and the consideration that they do not need to be fabricated (they just need to be cleaned up from the organic material), have an high replication rate (their reproduction can occur several times per day) and are very robust (can resist to acid cleaning without damage), make diatoms very appealing for optical gas sensing purposes and promising materials for improving the selectivity of gas sensing based on photoluminescence optochemical transduction.

REFERENCES

[1] L. De Stefano, I. Rendina, M. De Stefano, A. Bismuto, P. Maddalena, *Marine diatoms as optical chemical sensors*, Appl. Phys. Lett. **87**, 233902 (2005)

[2] K. Tanimura, C. Itoh, and N. Itoh. *Transient optical absorption and luminescence induced by band-to-band excitation in amorphous SiO_2*, Journal of Physics C: Solid State Physics, **21**(9), 1869 (1988).

[3] A. Anedda, C.M. Carbonaro, F. Clemente, R. Corpino, and P.C. Ricci. *Low temperature investigation of the blue emission in mesoporous silica*. Materials Science and Engineering: C, **25**(5-8), 631 (2005).

A PHOTOPATTERNABLE SILICONE FOR BIOMEMS APPLICATIONS

Salil P. Desai, Brian M. Taff and Joel Voldman
Massachusetts Institute of Technology, USA

ABSTRACT

Here we show the application of a commercially available photopatternable silicone (PPS) that combines advantages of both PDMS and SU-8 to address a critical need in material building blocks for bioMEMS. Using PPS we have demonstrated the ability to pattern free-standing mechanically isolated elastomeric structures on a silicon substrate, a feat challenging to approach using soft lithography-based fabrication. PPS can be readily integrated in cell-based bioMEMS since it exhibits low-autofluorescence and cells can attach and proliferate on PPS-coated substrates. PPS is compatible with standard microfabrication processes and can be easily aligned to complex featured substrates on a wafer-scale. By leveraging PPS's unique properties we demonstrate the design of a simple dielectrophoresis-based bioMEMS device for patterning mammalian cells.

Keywords: Silicone, bioMEMS, photolithography

1. INTRODUCTION

Polydimethlysiloxane (PDMS) has emerged as one of the most commonly used bioMEMS materials because it displays low autofluorescence, excellent biocompatibility, and can be molded with reasonably high resolution. Because PDMS is formed by relief casting, it can be challenging to create mechanically isolated structures. Further, its flexible nature makes alignment with pre-existing substrate features challenging. SU-8, meanwhile can easily make isolated structural features and can leverage conventional photolithographic alignment for multi-level patterning [1]. However, SU-8 is highly autofluorescent and thus poorly suited for high-contrast fluorescence imaging. Here we show the application of a commercially available photopatternable silicone (WL-5150, Dow Corning Corporation) [2] that combines advantageous features of both PDMS and SU-8 to address a critical need in the microTAS community.

Prior work with photopatternable silicones has involved either custom synthesis [3] and thus was not readily available, or was aimed at bench-top rapid prototyping, and thus had poor resolution (50-75 μm) and incompatibility with conventional lithography [4, 5]. PPS consists of siloxane precursors that form a densely crosslinked elastomer on exposure to UV light. It was originally developed for electronics packaging applications. In this abstract we show its first application for cell-based bioMEMS.

2. METHODS

PPS coatings and free-standing structures were fabricated using standard photolithographic techniques. Briefly, silicon wafers were oxygen plasma-cleaned for 5 minutes. Next, PPS films were spun for 10 seconds at 500 rpm followed by 1500 rpm for 30 seconds. Two-minute prebakes at 120 ºC were performed followed by UV exposure of the samples and subsequent postbake for 3 minutes at 150 ºC. Samples were developed for 6 minutes in mesitylene and finally cure baked at 150 ºC for 2 hours. PDMS thin films

978-0-9798064-0-7/μTAS2007/$20©2007CBMS

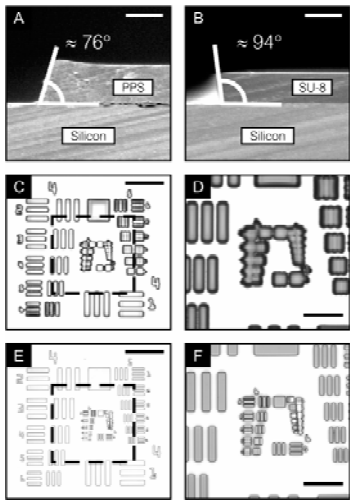

Figure 1: Resolution tests. (A) & (B) show scanning electron micrographs (SEMs) of sidewall angles in a direct comparison between patterns formed using PPS and SU-8. Scale bar 25 μm. (C) and (E) show bright-field microscopy images of the standard USAF 1951 resolution test pattern for the case of PPS and SU-8 respectively. Scale bar 50 μm. (D) examines the outlined region in (C) and (F) surveys the outlined region in (E) in closer detail. Scale bar 25 μm.

were obtained using a similar spin protocol. All SU-8 processing was performed according to established guidelines provided in the associated product datasheets. Standard cell culture techniques were used for growing NIH 3T3, HeLa and BA/F3 cells. Dielectrophoresis (DEP) devices were fabricated on silicon by depositing aluminium and subsequently dry etching to form interdigitated electrodes. Laser-cut silicone gaskets with a coverslip cap functioned as flow channels to sequester cells over the active electrode regions.

3. RESULTS AND DISCUSSION

We obtained PPS in a formulation suitable for creating ~20-μm-thick films that are processed as conventional photoresists. Using traditional contact lithography, we determined that the material patterns with feature resolution down to ~10 μm, and exhibits sidewalls of ~75º (Figure 1). Our primary motivation in using this material was to create low-autofluorescent isolated structures. In Figure 2 we show the creation of free-standing mechanically isolated posts on a silicon substrate, which would be challenging to create using conventional PDMS casting. As an initial demonstration of the biocompatibility of PPS, we grew NIH3T3 and HeLa cells on PPS-coated silicon substrates. As a control, cells were also grown on a standard tissue culture dish. Both cell types proliferated and displayed normal morphology. One of the primary drawbacks of SU-8 for cell-based bioMEMS is its high autofluorescence. Figure 3 shows quantitative measures of fluorescence of PPS as compared to other materials, clearly showing that PPS has fluorescence intensity levels comparable to those of PDMS, whereas SU-8 is highly

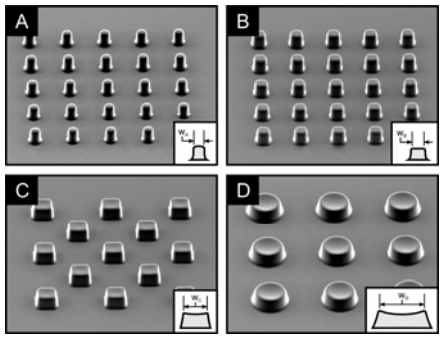

Figure 2: Free-standing PPS microstructures. SEM images of free-standing circular, (A) and (D), and square, (B) and (C), pillars patterned on a silicon substrate. Inset schematics portray the basic cross-sectional geometry of each feature ($w_A \approx 15$ μm, $w_B \approx 20$ μm, $w_C \approx 45$ μm, and $w_D \approx 80$ μm). This type of isolated feature is difficult to realize using conventional soft lithographic fabrication techniques. Based on the SEM images, shapes with smaller footprints show slightly convex tops while features with larger footprints exhibit concave geometries.

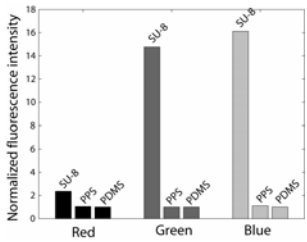

Figure 4: Auto-fluorescence. Quantitative comparison of fluorescence intensities of SU-8, PPS, and PDMS (normalized to PDMS), indicating high auto-fluorescence of SU-8 in green and blue channels.

autofluorescent. Finally, we created devices where PPS is aligned to patterned features. Such structures are difficult to realize using PDMS because of the difficulty in aligning PDMS to substrates and the limited bonding capabilities of PDMS with substrate patterned metals such as gold and aluminium. As a simple test, we created a dielectrophoretic trap where PPS was aligned to interdigitated electrodes. Figure 4 shows that murine BA/F3 cells are levitated and patterned in the regions without PPS, whereas they remain unpatterned in regions covered with PPS.

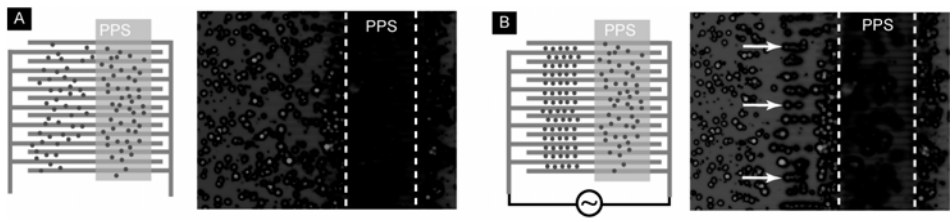

Figure 5: Cell patterning. (A) Schematic of top-down view of bioMEMS device architecture with PPS aligned to interdigitated electrode array where cells (gray circles) are randomly seeded on device. Left panel shows fluorescence image of randomly seeded cells. Cells seeded on PPS (dashed line) appear out-of-focus. (B) On application of 500 kHz waveform, cells are levitated and patterned above the electrodes (indicated by arrows). Scale bar 50 μm.

4. CONCLUSIONS

We believe that PPS's unique properties frame it as an ideal candidate material for integration in many bioMEMS applications. Its combination of low autofluorescence, biocompatibility, alignment capabilities for patterned substrates, and moderately high resolution (~10 μm) position it as a complement to SU-8 and PDMS. The key material properties and integration capabilities explored in this work should present new avenues for exploring elastomeric microstructures for the design and implementation of increasingly complex bioMEMS architectures.

ACKNOWLEDGEMENTS

We thank Herman Meynen for valuable technical discussions and the MIT Microsystems Technology Laboratory staff for assistance with fabrication.

REFERENCES

[1] D. R. Albrecht, *et al.*, Lab on a Chip, **5**, (1), 111-18 (2005).
[2] H. Meynen, *et al.*, Microelectronic Engineering, **76**, 212-218 (2004).
[3] K. M. Choi and J. A. Rogers, JACS, **125**, 4060-4061 (2003).
[4] C. Khoury, G. A. Mensing, and. D. J. Beebe, Lab on a Chip, **2,** 50-55 (2002).
[5] R. Delille, *et al.*, Journal of Microelectromechanical Systems, **15,** 1108-1120 (2006).

APPLICATION OF HIGH RESOLUTION 2D-SPR IMAGER TO LIVING CELL-BASED ALLERGEN SENSING

M. Horii[1, 2], H. Shinohara[1], Y. Iribe[1] and M. Suzuki[1]

[1]*Graduate School of Science and Engineering, University of Toyama, JAPAN and*
[2]*Toyama New Industry Organization, JAPAN*

ABSTRACT

Newly developed two-dimensional surface plasmon resonance (2D-SPR) sensor system can obtain 2D image of refractive index difference on the surface of a gold thin film in 1 μm resolution. Here, we examined to observe the allergenic response of a mast cell model, rat basophilic leukaemia cell (RBL-2H3) by using the 2D-SPR imaging system after pre-sensitization with 0.1 μg/mL anti-dinitrophenyl (DNP) immunoglobulin E (IgE). Response of individual cell was successfully observed upon the stimulation with DNP-modified bovine serum albumin (DNP-BSA) using the 2D-SPR system. Furthermore, multi-channel measurement was performed for sensitized and non-sensitized cells in a polydimethylsiloxane (PDMS) well-array sheet.

Keywords: 2D-SPR, living cell imaging, mast cell response, multi channel sensing

1. INTRODUCTION

SPR sensor has been well used as a high-sensitive biosensor that can detect binding and dissociation of molecules on a gold chip at real-time and without labelling. Recently (one-dimensional) SPR signal changes due to physiological response of some mammalian cells such as RBL-2H3, a mast cell model were reported [1, 2]. Our used instrument, 2D-SPR04A (NTT-AT Corp., Japan) can obtain 2D image of reflection index change of the surface on a gold thin film in about 1 μm resolution [3, 4]. The resolution is enough to observe the image of single cell response. In this paper, the allergic responses of presensitized RBL-2H3 cells were observed by the 2D-SPR imager as increment of reflection intensity of the cell part. The 2D-SPR is further expected to be available for detection of single cell response and multi-channel measurement. In this paper, we examined detection of single cell response and multi-channel measurement for antibody-sensitized and non-sensitized cells in a PDMS well-array sheet by using the 2D-SPR system.

2. EXPERIMENTAL

The 2D-SPR imager (2D-SPR04A, NTT-AT Co. Corp., Japan) possesses a collimator to parallelize incident light, a cooling CCD camera to obtain reflection image and four kinds of lens (1 ×, 2 ×, 4 ×, 7 ×) to enlarge image. Figure 1 shows the measurement scheme with the 2D-SPR04A and comparison of the phase contrast microscopic image and the 2D-SPR image for adherent RBL-2H3 cells on the identical chip. 2D-SPR image is contracted longitudinally.

RBL-2H3 was cultured on a 50 nm gold-coated SF6 chip (18 × 17 mm) with the flexiPERM (Greiner bio-one, Germany) (11 × 7 × 10 mm) in a 5% CO_2, humidified atmosphere at 37 ℃. In the case of multi-channel measurement, PDMS well sheet with 9

978-0-9798064-0-7/μTAS2007/$20©2007CBMS

holes (1 mm in diameter) was put on the chip surface before cell culture. Minimum essential medium (Invitorogen, USA) supplemented with 10% fetal bovine serum was used for cell culture. After 1-6 days in culture, cells were washed with Hanks' balanced salt solution (HBSS) and were pre-sensitized with 0.1 g/mL anti-DNP IgE for 1 hour. Before SPR measurement, cells were washed with HBSS. SPR signal of the cell-cultured chip filled with HBSS was measured at the incident angle reduced by 0.5 from resonance angle. Various concentration of the antigen, DNP-BSA was injected during SPR measurement and the change in reflection intensity was observed.

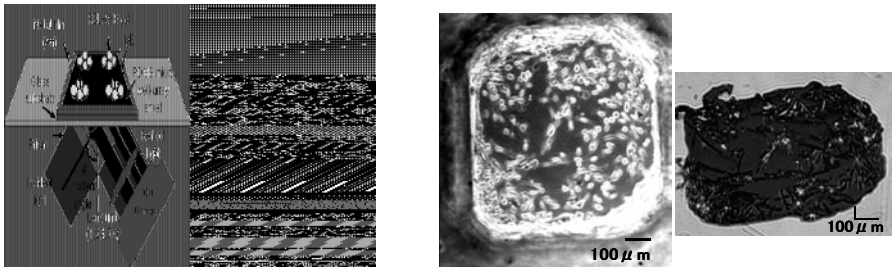

Figure 1. Scheme of the 2D-SPR measurement (left) and comparison of the phase contrast image (middle) and the 2D-SPR image of identical RBL-2H3 cells (right).

3. RESULTS AND DISCUSSION

Responses of RBL-2H3 cell colonies, which were pre-sensitized with 0.1 μg/mL anti-DNP IgE, were observed on the 2D-SPR image at real-time upon 1-100 ng/mL DNP-BSA stimulation (data is not shown). Increment of SPR signal for the antigen concentration increase was correlative to that of secreted β-hexosaminidase which is a marker enzyme contained in the secretion granule of RBL-2H3 (data is not shown). Figure 2 (A) shows 2D-SPR images of sparsely adhered cells (1 day incubation), before and after addition of 0.1 ng/mL antigen DNP-BSA. Figure 2 (B) shows time-courses of reflection intensity of selected individual cells which changed their reflection intensity by antigen addition. The result demonstrated clearly that the 2D-SPR can monitor the difference of the response of individual cell.

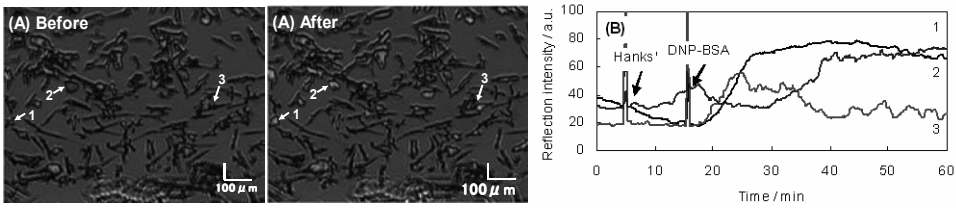

Figure 2. (A) 2D-SPR images for dispersed RBL-2H3 cells before (left) and after (right) antigen addition (final concentration 0.1ng/mL). (B) Antigen-responsive change of reflection intensity in focused cells (cell 1, 2, 3).

Figure 3 shows multi-channel measurement using 1mm-diameter well-array sheet. Cells in upper 2 wells which were pre-sensitized with 0.1 μg/mL anti-DNP IgE, showed clear response to antigen stimulation. In contrast, the cells in lower 2 wells which were not pre-

sensitized showed no change in their reflection intensity. These data demonstrated that 2D-SPR is useful to easily distinguish pre-sensitized cell and non-sensitized cell by difference of their response.

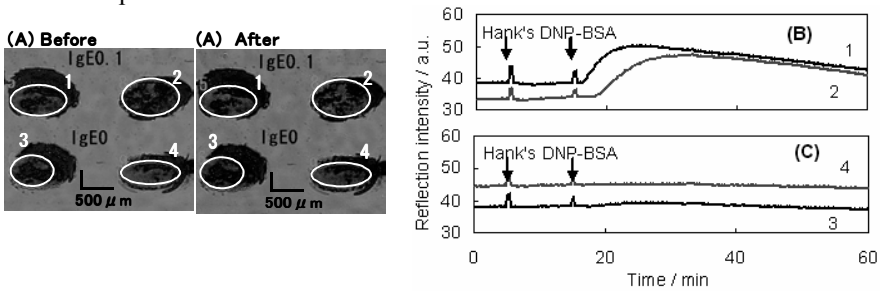

Figure 3. (A) 2D-SPR images (1× lens) for RBL-2H3 cells in 1 mm-diameter wells before (left) and after (right) antigen addition (final concentration 100ng/mL). (B) Changes in reflection intensity of IgE pre-sensitized (IgE 0.1μg/mL) cells (1, 2) and (C) Non-sensitized (IgE 0 μg/mL) cells (3,4).

4. CONCLUSIONS

Our study demonstrated that high resolution 2D-SPR imager was a very powerful tool for simultaneous and individual observation of multi-cell responses. Furthermore, multi-channel measurement for each cell group in a PDMS well-array sheet was available for biosensing of specific antigen as a cell-stimulant. A 2D-SPR imager might be a promising detector for individual cell-based multi-biosensor.

ACKNOWLEDGEMENTS

This study was supported in part by Grant from Toyama Medical-Bio Cluster, Japan.

REFERENCES

[1] M. Hide, T. Tsutsui, H. Sato, T. Nishimura, K. Morimoto, S. Yamamoto and K. Yoshizato, "Real-Time Analysis of Ligand-Induced Cell Surface and Intracellular Reactions of Living Mast Cells Using a Surface Plasmon Resonance-Based Biosensor", Analytical Biochemistry Vol. 302, pp. 28- 37, (2002).

[2] Y. Yanase, H. Suzuki, T. Tsutsui, T. Hiragun, Y. Kameyoshi and M. Hide, "The SPR Signal in Living Cells Reflects Changes Other than The Area of Adhesion and The Formation of Cell Constructions", Biosensors and Bioelectronics Vol.22, pp. 1081-1086, (2007).

[3] T. Tobita, H. Tabei, Y. Iwasaki, O. Niwa, K. Kurihara and K. Suzuki, "Development of 2D-SPR Measuring Instrument and Application to Multi-channel Measurement – Multiple 2D Biochemical Measurement Using SPR", Technical Report of IECE OME 2000-136, 51-56, (2000).

[4] M. Suzuki, S. Hane, T. Ohshima, Y. Iribe and T. Tobita, "Detection of antibodies in 10 μm wells on micro-arrayed cell chips by 2D-SPR affinity imaging", Micro Total Analysis Systems 2006, Vol. 1, pp. 756-758 (2006).

DESIGN AND CHARACTERIZATION OF MACH-ZHENDER INTERFEROMETRIC IMMUNOSENSORS OPERATING AT NEAR INFRARED

Jongin Hong[1] and Tae Song Kim[2]
[1]*Imperial College London, UK and*
[2]*Korea Institute of Science and Technology, KOREA*

ABSTRACT

We demonstrated here on a new approach to determine the antigen-antibody interaction using the Mach-Zehnder interferometer (MZI) based on silicon dielectrics operating at near infrared. The building block, single-mode waveguide of total internal reflection, was precisely designed using a finite element method (FEM) and then we firstly built up the spatial maps of refractive index as a function of waveguide geometries and operating wavelength. We also introduced the calixcrown self-assembled monolayers (SAMs) and silicon oxynitrides to improve the activity of capture proteins and the correct orientation into MZI immunosensors. The C-reactive protein was used for this feasibility study of immunosensors.

Keywords: Mach-Zehnder interferometer, immunosensor, silicon oxynitride

1. INTRODUCTION

For the last decade, the label free immunosensors have been developed to transform efficiently a biological reaction into a measurable signal for biological process, healthcare, drug discovery, medical diagnostics, environmental monitoring, food industry and military defence. Optical transducers offer more attractive characteristics like high sensitivity and immunity to electromagnetic interference. Initiated by the pioneering work of Tiefenthaler and Lukosz [1], an integrated optics that utilizes the evanescent field has developed the compact sensing devices with high sensitivity, fast response and real-time monitoring. Compared to the conventional optical ones, it has opened the possibility of miniaturization, robustness and mass production [2-5]. Recently, we demonstrated the Mach-Zehnder interferometer (MZI) based on silicon dielectrics operating at near infrared [5]. Silicon dielectrics have the excellent optical properties like low absorption losses in the visible and near infrared and the desired characteristics of fibre coupling. Their refractive index can also be easily adjusted over a wide range between 1.46 (SiO_2) and 2.05 (Si_3N_4) using the deposition technique for low cost mass production. In this article, we have performed the feasibility of MZI immunosensors based on silicon oxynitride operating at near infrared. We introduced the guideline to obtain the single mode propagation as a function of waveguide geometries and operating wavelength using FEM. The C-reactive protein that is a very important inflammation biomarker and a major predictor of cardiovascular disease (CVD) was detected with the detection limit of 1 ng/ml or less at near infrared.

2. BASIC PRINCIPLE

The main sensing principle is the integrated optic (IO) sensor effect in an optical waveguide, which was discovered by W. Lukosz and K. Tiefenthaler [1]. The optical waveguide defines as a material medium that confines and guides propagation electromagnetic waves. If the material is surrounded by other materials with lower

978-0-9798064-0-7/μTAS2007/$20©2007CBMS

refractive indices, the incident light is confined and so guided along the waveguide. However, a part of the guided wave penetrates a small distance into the surrounding medium. It is called the evanescent field that decays exponentially with the distance from the waveguide surface. Thus, the IO sensor effect results from the interaction of the evanescent field of the guided wave with the surrounding medium. That is to say, the evanescent field is very sensitive to the change in the refractive index distribution near the waveguide surface.

Interferometric detections are commonly used to convert a phase shift into an intensity variation that is directly measurable. We have chosen a Mach-Zehnder interferometer because of high sensitivity and an internal reference for compensation of thermal drifts and non-specific adsorptions. In the MZI configuration, an optical waveguide is split two arms, sensing and reference ones, and after a certain distance they recombine again. The waveguide is completely covered with the cladding layers and the only sensing zone is exposed to the outer medium in a certain area for the specific binding of antigen to antibody. The guided light in the sensing arm will experience a phase shift compared with tat in the reference arm. Therefore, the interference of lights travelling through two arms causes the intensity modulation at the sensor output.

3. EXPERIMENTAL

The fundamental building block of the MZI is the optical waveguide of total internal reflection. In order to develop the MZI sensor with performance and reproducibility, it should be designed as a single-mode propagation. If the incident light with several modes is propagated via the waveguide, each mode can interact with the change in the outer medium and the fraction of power can be changed by the incident angle on the waveguide. The multi-mode waveguide is not suitable for robust immunosensors and so we introduced a numerical simulation based on a finite element method to find the boundary between cut-off, single-mode and multi-mode regions (Figure 1). The detailed mode analysis can be found in reference 5.

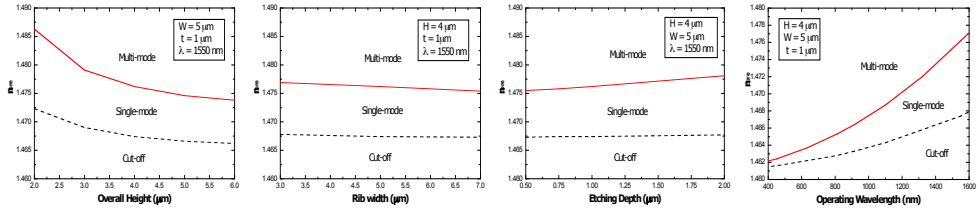

Figure 1. Spatial maps of refractive index as a function of waveguide geometries and operating wavelength

Non-stoichiometric silicon oxynitride as a waveguide core was deposited on the silica substrate by plasma enhanced chemical vapour deposition (PECVD). Its refractive index was controlled by the flow ratio of nitrous oxide gas (N_2O) to silane (2% SiH_4/H_2) gas. Rib waveguides for optical confinement were defined using a photolithographic technique. After depositing the upper cladding of silicon oxide on the patterned layer, a sensing zone was opened using reactive ion etching (RIE). The wafer was cut into an individual chip and then its side used as input and output were polished mechanically for end-fire coupling. The MZI was functionalized to determine the antigen-antibody interaction at the surface. We introduced a novel immobilization method to capture proteins that used a calixcrown

derivative with bi-functional cross linking properties containing aldehyde (-CHO) groups for the formation of a self-assembled monolyer (SAM) on the aminated chips and a crown moiety that provides a molecular recognition site for protein immobilization and then monoclonal anti-CRP was incubated on the SAM. The light was coupled into the waveguide through a single-mode fibre (SMF) and then it was collected by a multi-mode fibre. The intensity was monitored by homemade software and data acquisition hardware. Precise translation stages were used for the accurate alignment of all the components. The feasibility of MZI immunosensors were performed with different concentrations of CRP antigen.

4. RESULTS AND DISCUSSION

The refractive index of silicon oxynitride grown by PECVD can be varied with the growth parameters like flow ratio, deposition temperature and RF power and so the flow ratio was changed to modulate the refractive index while both deposition temperature and RF power were kept constant. Figure 2 shows the variation of the refractive index in silicon oxynitride films as a function of different flow ratios. The refractive index decreased from a value about 1.53 down to 1.46 and then was saturated with the increase in the flow ratio. The high refractive index is due to the incorporation of silicon and nitrogen in the films. The fabrication window for single-mode propagation is also depicted in Fig. 2. Therefore, we could fabricate the MZI interferometer with single-mode propagation by FEM simulation and optical characterization.

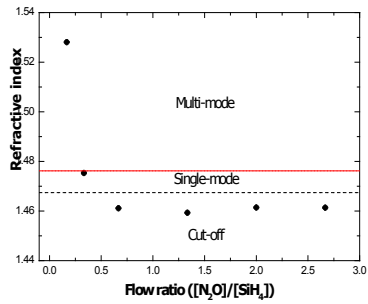

Figure 2. Refractive index of PECVD silicon oxynitride as a function of flow ratio $R=[N_2O]/[SiH_4]$

Figure 3 shows phase shift for the binding of CRP to monoclonal anti-CRP with various concentrations of CRP. The MZI immunosensor retained the ability to detect CRP even at a low concentration of 1 ng/ml. We can emphasize that the binding of antigen to antibody would cause the change in the refractive index and thickness of functional layers at the sensing zone. We also expect that the detection limit would be less than the concentration of 1 ng/ml. Although the systematic biological studies of clinical samples are needed to verify the significance of our immunosensors, we can say that it should be the future candidate of the antigen-antibody reaction with no labelling, high sensitivity, quick speed and free choice of sample matrix and origin operating at near infrared.

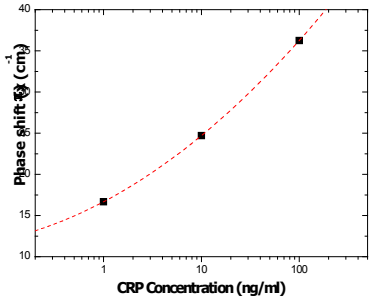

Figure 3. Phase shift as a function of CRP concentration measured at near infrared

5. CONCLUSIONS

To monitor and diagnose diseases, the quantitative detection of biomarker proteins, which is directly relevant to various diseases, is required and so it allows us to precisely diagnose given disease by the detection of appropriate protein. In this article, we have developed the MZI immunosensor based on silicon oxynitride operating at near infrared and the refractive index of the waveguide core was accurately controlled by the flow ratio combined with a finite element method. We have determined the binding of CRP to monoclonal anti-CRP with the detection limit of 1 ng/ml or even less. We firstly introduced calixcrown SAMs to immobilize the monoclonal anti-CRP into the integrated optic immunosensor.

ACKNOWLEDGEMENTS

This work was supported by the Ministry of Science and Technology ("Protein Chip Technology Research Center" and "21C Frontier R&D Program") and the Korea Research Foundation Grant funded by the Korean Government (MOEHRD) (KRF-2006-214-D00056).

REFERENCES

[1] K. Tiefenthaler and W. Lukosz, J. Opt. Soc. Am. B, 6, pp.103 (1989)
[2] Optical Sensors: Industrial Environmental and Diagnostic Applications, ed. R. Narayanaswamy, O.S. Wolfbeis, Springer, 1st edn. (2004)
[3] F. Prieto, B. Sepulveda, A. Calle, A. Llobera, C. Dominguez, A. Abad, A. Montoya and L.M. Lechuga, Nanotechnology, 14, pp.907 (2003)
[4] A. Ymeti, J.S. Kanger, J. Greve, G.A.J. Besselink, P.V. Lambeck, R. Wijn and R.G. Heidman, Biosensors and Bioelectronics 20(7), pp.141 (2005)
[5] J. Hong, J.S. Choi, G. Han, J.K. Kang, C.-M. Kim, T.S. Kim and D.S. Yoon, Analytica Chimica Acta, 573-574, pp.97 (2006)

DEVELOPMENT OF DIFFERENTIAL INTERFERENCE CONTRAST THERMAL LENS MICROSCOPE

H. Shimizu[1], K. Mawatari[2], and T. Kitamori[1,2]

[1] *School of Engineering, The University of Tokyo, JAPAN*

[2] *Kanagawa Academy of Science and Technology, JAPAN*

ABSTRACT

We present a new background-free photothermal spectroscopy based on thermal lens microscope (TLM) to realize single molecule counting. For single molecule counting, approximately 20 times increase of sensitivity is necessary compared with conventional TLMs. For this purpose, a new differential interference contrast thermal lens microscope (DIC-TLM) was developed. The basic principle was verified, and sensitivity was proved to be 5 times higher than conventional TLMs. We believe single molecule counting will be possible with some improvements.

Keywords : Photothermal, differential interference contrast, gold nanoparticle

1. INTRODUCTION

Recently the targets of analytical chemistry have been rapidly miniaturizing from micro to nanospace. This ultimate miniaturization puts several higher demands to detection technologies. Firstly, single molecule counting is required due to the extremely small space. Furthermore, detection of non-fluorescent molecules is also necessary for wide application. From the view point of sensitivity, laser induced fluorescence (LIF) has been commonly used. Although LIF can count single molecules in optimized conditions, LIF is applicable only to fluorescent molecules, and the applications are limited.

To resolve the problems, we have developed a TLM which is based on photothermal phenomena of non-fluorescent molecules. So far, we verified that TLM had sensitivity of single molecule concentration corresponding to 0.4 molecules in 7fL detection volume [1], and succeeded in counting single metallic nanoparticles [2]. However, single molecule counting has not been achieved, and still 20 times higher sensitivity is required. One of the sensitivity limitations comes from high light background. TLM measures the small change of the probe beam intensity in large background, and the sensitive photodetection can not be applied in principle. This basic principle in conventional TLMs causes low dynamic range for realizing single molecules counting.

Here, we focus on reduction of the high background in TLM and reduce it by introduction of differential interference contrast (DIC) to sensitize TLM.

2. PRINCIPLE

The principle of conventional TLM is shown in Figure 1a. Non-fluorescent molecules in microchannel absorb excitation beam and generate heat by non-radiative relaxation, and refractive index gradient is generated by the temperature change of solvent. This is called thermal lens (TL). Then, the probe beam refracts by TL effect, and the intensity of probe beam that passes a pinhole changes. This change is detected as signal, but the magnitude is much smaller than background light intensity (signal-to-background (S/B) ratio ~1/1000), which causes sensitivity limitation in conventional TLM.

978-0-9798064-0-7/μTAS2007/$20©2007CBMS

The principle of DIC-TLM is shown in Figure 1b. Probe beam is split into two beams with perpendicular polarization by an upper DIC prism and mixed again by a lower DIC prism. Excitation beam is not split because its polarization is rotated an angle of 45°. When no particle is in the beam waist, the intensity of transmitted probe beam is zero. If there is a particle, however, it absorbs excitation beam and generates heat, which results in decrease of refractive index of the solution. Then, phase contrast is generated between the two probe beams, and new component is generated after mixing as shown. By detecting this new component through a polarization filter, background-free measurement can be achieved and sensitive photodetection enhances the TLM sensitivity resulting in high dynamic range.

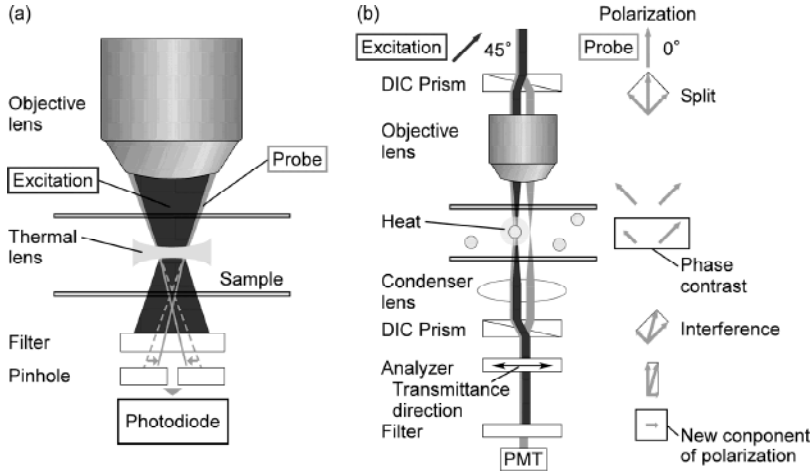

Figure. 1. Principle of (a) conventional TLM (b) DIC-TLM

3. EXPERIMENTAL

The setup of DIC-TLM is shown in Figure 2a. The most important factor is the distance of two probe beams (shear value) because it must be longer than thermal diffusion length to produce high phase contrast. We fabricated new prisms for DIC-TLM which have larger shear value (5μm) than that of commercial prisms for optical microscopy. The shear value was confirmed by a CCD camera.

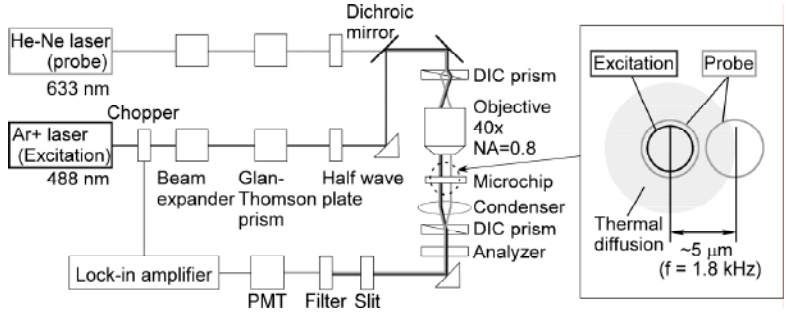

Figure 2. Experimental setup

4. RESULTS AND DISCUSSION

For principle verification, concentrated dye solution (10^{-4}M) was measured as shown in Figure 3. The output from photodetector was directly monitored without a lock-in amplifier. In conventional TLM, the change of the probe intensity was not observed, while clear difference was observed for DIC-TLM due to large S/B. The S/B ratios for conventional TLM and DIC-TLM were 0.0024 and 0.11, respectively. This means that 40 times improvement of S/B ratio was achieved, and the basic principle of background reduction by DIC-TLM was verified.

For performance evaluation, individual gold nanoparticles (5 nm) were counted as model sample. The result is shown in Figure 4. The performance was evaluated by S/N ratio of each pulse signals corresponding to individual particles. In comparison with conventional TLM, the maximum S/N ratio improved from 7 to 35, and 5 times higher sensitivity was achieved.

For single molecule counting, 4 times higher sensitivity is required than the present DIC-TLM. Now, sensitivity and optics optimization is under progress to achieve single molecule counting.

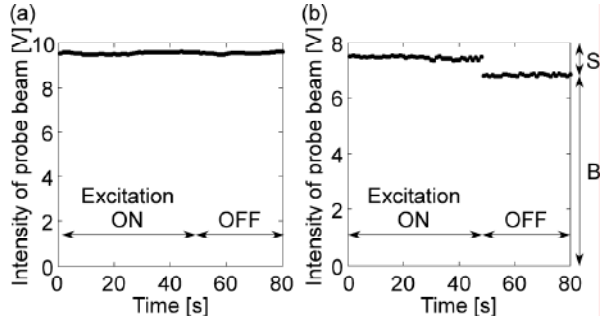

Figure 3. Waveform of probe beam
(a) conventional (b) DIC-TLM

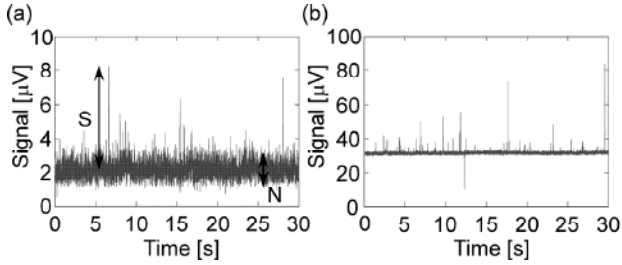

Figure 4. Result of gold nanoparticle (5 nm) counting.
(a) conventional (b) DIC-TLM

5. CONCLUSIONS

We developed DIC-TLM for background reduction. S/B ratio was 40 times improved than that of conventional TLM, and its S/N ratio of counting signals became 5 times larger. Additional 4 times increase of sensitivity is necessary for single molecule counting. We believe that single molecule counting becomes possible by conditions optimization and utilizing sensitive photodetection..

REFERENCES

[1] M. Tokeshi, M. Uchida, A. Hibara, T. Sawada, T. Kitamori: Anal. Chem., **73**, 2112 (2001)
[2] K. Mawatari, T. Kitamori, T. Sawada : Anal. Chem., **70**, 5037 (1998)

IMMERSION REFRACTOMETRY ANALYSIS OF LIVING CELLS IN MICROFLUIDIC CELL CULTURE CHIP

X. Zhang[1], R. Chua[2], P. H. Yap[2], W. Z. Song[1] and A. Q. Liu[1†]

[1]School of Electrical & Electronic Engineering

Nanyang Technological University, Nanyang Avenue, Singapore 639798

[2]Defence Medical & Environmental Research Institute

DSO National Laboratorie, 27 Medical Drive, Singapore 117510

([†]Corresponding author. Tel: +65-6790 4336; Email: eaqliu@ntu.edu.sg)

ABSTRACT

This paper reports a method for measuring the refractive index (RI) of living cells using immersion refractometry integrated with microfluidics. Theoretically, the RI of the cells can be determined to an accuracy of 0.0001. This method features high speed, high accuracy, less damage to cells, ultra integration and real time measurement during long-term cell culture, making it promising for many applications, for example, real-time monitoring of cells.

Keywords: immersion refractometry, living cell, cell culture, lab on a chip

1. INTRODUCTION

The field of cell culture and cell analysis is developing much more sophisticated abilities based on micro-fabrication techniques. But today's research of cell culture chip is majorly about cell morphology and chemistry. This paper demonstrats a method to measure the RI, one of the physical properties of living cells by using immersion refractometry on chip. Compared with previous report for measuring the RI of single cell[1], this method can be used for real-time analysis of the RI of group cells such as monitoring pathological changes of cells [2].

2. WORKING PRINCIPLE

Figure 1 shows the principle of phase contrast microscopy and immersion refractometry of living cells. When the RI of surrounding buffer (n_1) is different from that of the cells (n_2), obvious contrast appears at the cell edge. $n_1 > n_2$ corresponds to a bright image of cells while $n_2 > n_1$ to a dark image. In contrast, no phase difference can be observed in case of $n_1 = n_2$. Typically human eyes can detect a phase shift as small as $\lambda/1000$, hence the least detectable difference in RI will be about $\lambda/1000t \approx 0.0001$[3]. Such method possesses a special advantage of large phase difference across the cell edge. It can be as large as $\lambda/4$ in comparison to the typical $\lambda/20$ in the common bright field microscopy.

978-0-9798064-0-7/μTAS2007/$20©2007CBMS

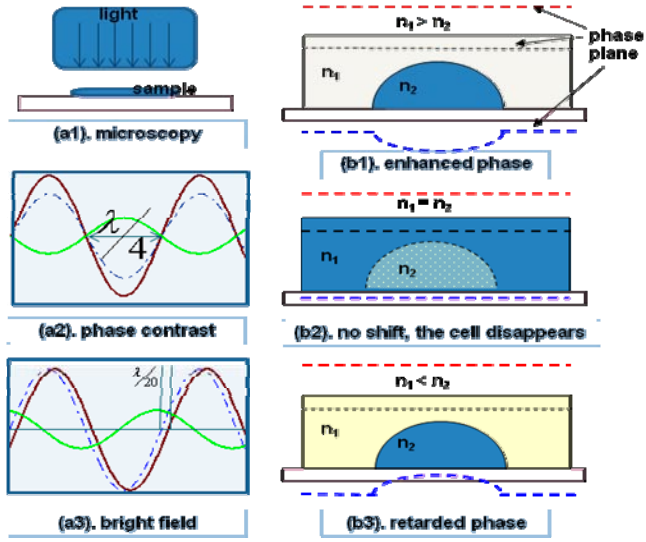

Figure 1. Principles of (a) phase contrast microscopy; (b) immersion refractometry.

3. DEVICE DESCRIPTION

The culture and assays chip is fabricated by laser engraving technology on polymethylmethacrylate (PMMA) as shown in Fig. 2, whcich consists of a cell culturing chambers and a mixing structure. Three layer of PMMA slided were firstly etched and then bonded together by heat-and-press methond. The culturing chamber has a diameter of 600 µm and a volume of 0.56 µl. Optical fiber is introduced into the chamber for real-time measure of medium's RI. During the experiment, Madin-Darby canine kidney (MDCK) cell line was loaded into to the chip and cultured. After the cell formed a confluent monolayer, saturated BSA (bovine serum albumin) aqueous solution and FBS (fetal bovine serum) were loaded to generate a time-scale concentration gradient. Cells' image and the RI of medium is recorded.

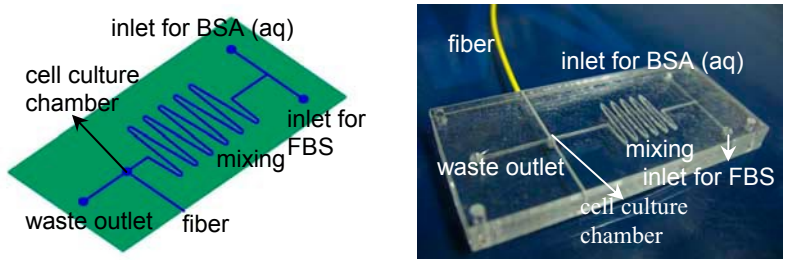

Figure 1. Schematic diagram and the photograph of the microchip for cell culture and virus assays

4. RESULTS AND DISCUSSION

Figure 3 shows three pictures of MDCK cells cultured for three days and immersed in different buffers (a) 39% BSA (aq.), $n_1 = 1.3954 > n_2$; (b) BSA (aq.), $n_1 = n_2 = 1.3877$; (c)

FBS (fetal bovine serum) $n_1 = 1.3593 < n_2$. And the cells' images turn from bright, to invisible and finally to dark.

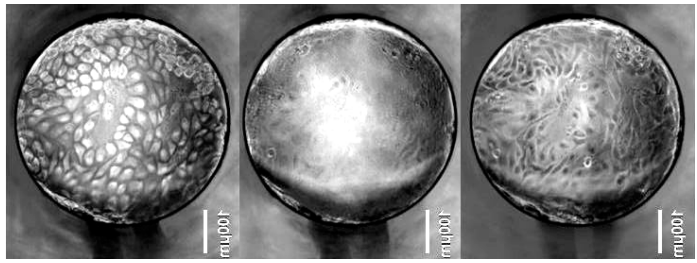

Figure 3. Photograph of MDCK cells in buffers with different RI: (a) $n_1 = 1.3954 > n_2$; (b) $n_1 = n_2 = 1.3877$; (c) $n_1 = 1.3592 < n_2$.

Figure 4 shows the intensity curves of pixels from the mentioned three pictures (1392×1049). The observation region is from No. 940 – 1140 pixel along the *x*-direction central line. The curves from (a) and (c) have peaks and valleys while the curve from (b) is much more even.

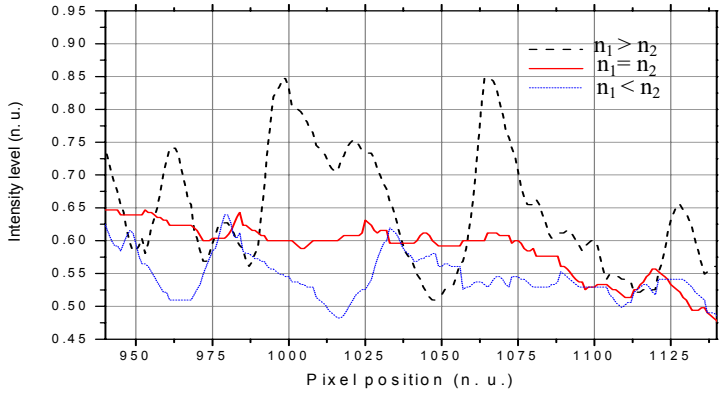

Figure 4. Pixels' intensity in three different phase shift.

5. CONCLUSIONS

In summary, we have shown preliminary results of a microfluidic chip integrated with both cell culture array and time-sale concentration gradient generator to measure the RI of living cells to potentially 0.0001. Further work will focus on real-time monitoring of the cells' refractive index during long-term cell culturing.

REFERENCES

[1] W.Z. Song, et al., *Optical detection of living cells' refractive index using microfluidic chip via modulated buffer,* microTAS, 5-9 November 2006, Tokyo, Japan, pp. 528-530, (2006).

[2] V. Backman, et al., *Detection of preinvasive cancer cells,* vol. 406, pp. 35-36, (2000).

[3] R. Barer, *Refractometry and interferometry of living cell,* J. Opt. Soc. Am., vol. 47(6), pp. 545-556, (1957).

ION-SELECTIVE NANOPLASMONIC OPTICAL SENSOR

Taewook Kang,[†] Yeonho Choi,[†] Dukhyun Choi, Eunice Lee, and Luke P. Lee

Department of Bioengineering, University of California, Berkeley, CA, USA, [†]Both authors contributed equally to this work

ABSTRACT

In this paper, we demonstrate a label-free ion-selective optical sensor for metal ion. This sensing mechanism is based on (1) selective formation of metal-ligand complex on the surface of nanoplasmonic probes and (2) selective plasmonic resonance energy transfer (PRET) between conjugated metal-ligand complex and gold nanoplasmonic probes (GNPs). We used functionalized GNP with ethylenediamine ligands in order to demonstrate high selectivity and sensitivity toward Cu^{2+}. Due to the selective energy transfer from GNP to *d-d* transition of the Cu^{2+} complex, the scattering spectrum of GNP changes quantitatively down to 1 nM of Cu^{2+}. Moreover, this Cu^{2+} nanoplasmonic senor has selectivity over Na^{+}, Ca^{2+}, K^{+}, and Mg^{2+}.

Keywords: Plasmonic Resonance Energy Transfer, Gold Nanoparticle, Rayleigh Scattering, Metal-Ligand Complex

1. INTRODUCTION

The detection and measurements of heavy metal ions present in aquatic streams are of great importance in assessing environmental damage and possible strategies for remediation. Several methods are available for determining heavy metal ions concentration, such as polarography, atomic absorption and inductively coupled plasma spectroscopy. In spite of the fact that some of these techniques are rapid and precise, recent analytical interest has focused on developing optical sensors that can be reused and do not involve the destruction of samples [1]. They also have the advantages of size, cost-effectiveness, simplicity, and portability. Optical sensors developed to date, however, require the use of fluorescently tagged agents or carriers having a selective affinity for the target metal ion of interest. Moreover, fluorescently-tagged methods suffer from low signal-to-noise ratio and limited temporal resolution (observation time) due to photo-bleaching.

Previously, we found that when the electronic transition energy of molecule matched well with the plasmon resonance energy of metallic nanoparticles such as gold or silver, plasmon resonance energy in the metallic nanoparticles was transferred to the attached molecule, which yielded spectral dips in the Rayleigh scattering spectrum of the single nanoparticle (PRET) [2].

Based on the fact that some transition metal ion complexes can show an absorption band around 500 ~ 600 nm because of *d-d* transition, suggesting that metal ion complex can be a plasmon resonance energy receptor in PRET, we reasoned that if the scattering spectrum of gold nanoplasmonic probes (GNPs) functionalized with ion-selective ligands would change quantitatively (sensitivity) and qualitatively (selectivity) at different metal ion concentrations, these conjugated GNPs would act as nanoscale optical probes for the detection of metal ions.

978-0-9798064-0-7/μTAS2007/$20©2007CBMS

2. THEORY

Ligands donate electron density to transition metal ions, permitting overlap between highest occupied molecular orbital (HOMO) of the ligands with the lowest occupied molecular orbital (LUMO) of the metal ions. The energy difference in the d-orbitals has a strong effect in the optical absorbance complexes. In case of $[Cu(TMSen)_2]^{2+}$ (N-[3-(trimethodxysilyl)propyl]ethylenediamine, TMSen), unlike $[Cu(TMSen)]^{2+}$ (650 nm), UV-vis spectrum shows the maximum absorbance at 550 nm. The wavelength shift of *ca.* 100 nm clearly illustrates the ligand field effect.

3. EXPERIMENTAL

A cleaned glass slide was modified with 3-mercaptopropyltrimethoxysilane (MPTMS), and followed by the immobilization of 50 nm spherical GNPs. Freshly prepared GNPs on the glass slide was immersed into 1 mM MPTMS. For the hydrolysis of silane group, the silane-functionalized GNPs were immersed in a 0.1 M HCl for 1h (1). Finally, (1) was incubated with 1mM TMSen for 24 h.

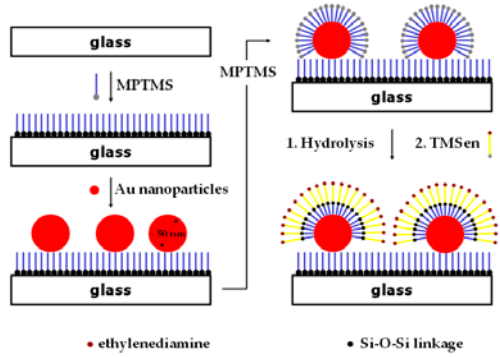

Figure 1. Schematic illustration of the fabrication processes.

4. RESULTS AND DISCUSSION

As a demonstration of ion-selective nanoplasmonic sensor, we have quantified Cu^{2+} because of its environmental and biological importance. We used surface immobilized GNPs with TMSen as probes (see Figure 2) for the selective detection of Cu^{2+}.

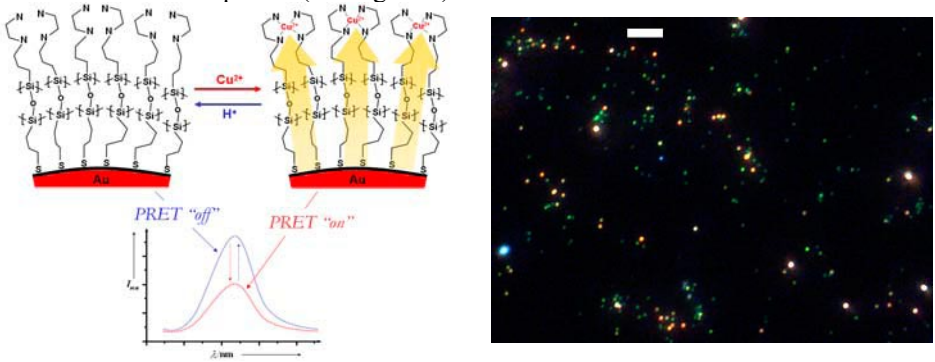

Figure 2. (Left) Top: schematics of the nanoscopic detection of Cu^{2+} based on the plasmonic resonance energy transfer and bottom: corresponding scattering spectra. (Right) Dark-field image of functionalized GNPs on a glass slide (white bar: 10 μm).

We used GNPs 50 nm in diameter in order to ensure a sufficiently intense light-scattering signal. Functionalized GNPs were illuminated with unpolarized white light, and light scattered by individual particles was collected by a darkfield microscope in transmission mode. The immobilized GNPs had the ethylenediamine on the surface, allowing them to form complexes with Cu^{2+}. After the Cu^{2+} solution was introduced to the functionalized GNPs on the glass surface, the scattered intensity of the single GNP immediately decreased within 5 min (Figure 5), depending on the concentrations of Cu^{2+}, allowing us to quantify Cu^{2+}. The detection limit could be as low as 1 nM and the linear regression coefficient in standard curve could be high than 0.995 (semi-logarithmic scale) for a concentration range from 1 nM to 1 mM. The response (differential scattered light intensity) of the TMSen-functionalized GNPs also showed good selectivity for Cu^{2+} over other metal cations such as Ca^{2+}, Mg^{2+}, and K^{+}.

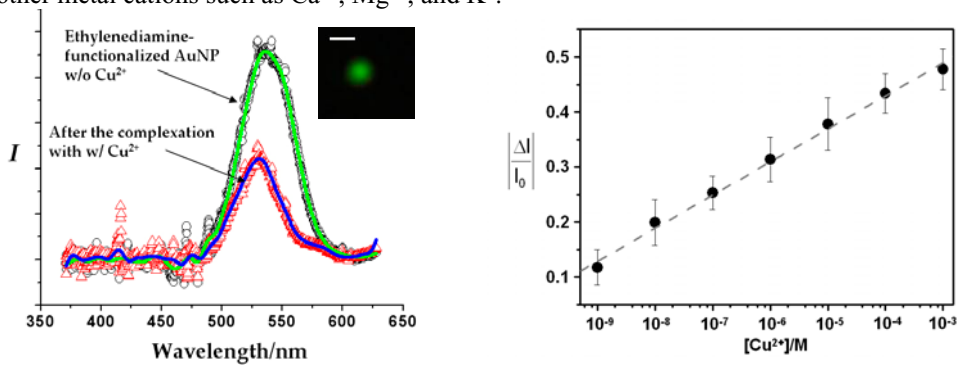

Figure 3. (Left) representative scattering spectra of TMSen-functionalized GNP and after exposure with 100 ppm Cu^{2+}. Inset: single GNP appears green (bar corresponds to 2 μm). (Right) equilibrium differential scattering intensity change at scattering maxima (taken as absolue value) as a function of Cu^{2+} concentrations.

5. CONCLUSIONS

In conclusion, we have described a new approach to selective metal ion sensing by exploiting selective plasmonic resonance energy transfer (PRET) between GNP and conjugated $[Cu(TMSen)_2]^{2+}$ complex. Our label-free ion-selective optical nanoplasmoinc probe prepared by utilizing self-assembly technique demonstrated the capability to detect low concentrations of Cu^{2+} down to 1 nM as well as good selectivity for Cu^{2+}.

ACKNOWLEDGEMENT

This work was supported by a grant (code #: 05K1501-02810) from 'Center for Nanostructured Materials Technology' under '21st Century Frontier R&D Programs' of the Ministry of Science and Technology, Korea.

REFERENCES

[1] M. Bruchez, M. Moronne, P. Gin, S. Weiss, A. P. Alivisatos, Semiconductor nanocrystals as fluorescent biological labels, Science, 281, 2013 (1998).

[2] Y, Long, G. Liu, Y. Choi, T. Kang, L. P. Lee , Nanoscopic Biomolecular Absorption Spectroscopy Enabled by Single Nanoparticle Plasmon Resonance Energy Transfer, Nature Methods, under revision (2007).

ON-CHIP pH AND TEMPERATURE SENSING WITH GEL-TOOL MANIPULATED BY OPTICAL TWEEZERS

Hisataka Maruyama[1] Fumihito Arai[2] and Toshio Fukuda[1]

[1]*Department of Micro-Nano Systems Engineering, Nagoya University, Japan*
[2]*Department of Bioengineering and Robotics, Tohoku University, Japan*

ABSTRACT

A multiple environments measurement with multiple sensing gel-tool in a microchip was developed. The gel-tool was fabricated by connecting gel-microbeads impregnated different indicators. In this paper, Bromothymol blue (BTB) and Bromocresol green (BCG) were used as pH indicators. Rhodamine B was used for temperature measurement. Gel-microbead is made by salting-out of hydrophilic photo-crosslinkable resin (ENT-3400, Kansai Paint) [1]. The gel-microbead is manipulated by optical tweezers and is polymerized by UV-ray. Polymerized gel-microbead adheres to glass and other gel-microbead under an electrolyte solution. Connection of gel-microbeads is operated by only contact. Multiple environments measurement is carried out by detecting the color and fluorescence intensity of each gel-microbead. We succeeded in fabricating multiple sensing gel-tool, measuring pH with wide range, and measuring pH and temperature at desired point of microchip.

Keywords: Measurement, pH, temperature, optical tweezers

1. INTRODUCTION

Local environment measurement in a microchip is important for on-chip cell analysis and chemical synthesis. Several methods such as fluorescent observation, electrochemical sensors and surface modified microsphere by indicators, were developed [2-5]. Fluorescent observation is major approach for on-chip measurement. However, fluorescent methods have problems with absorption, quenching and photo-degradation. Integrated sensor can measure precisely, but measurement area is limited. Surface modified microsphere can measure at the desired location by manipulating the microsphere. However, measurement of several environments are difficult because modification of single microsphere with several indicators decreases sensitivity. In this research, we proposed a multiple sensing gel-tool, which is composed of gel-microbeads impregnated several indicators for multiple measurement of the local environmental condition at the desired position in microchip.

2. MULTIPLE SENSING GEL-TOOL IMPREGNATED SEVERAL INDICATORS

Multiple sensing gel-tool is composed of gel-microbeads and several indicators. Figure 1 shows schematics of the multi sensing gel-tool. The gel-tool is manipulated by optical tweezers at the desired point in microchip. The gel-tool is composed of connected gel-microbeads impregnated different indicators as shown in Figure 1(a) for preventing interference of indicators. When there is no interference between indicators, different indicators can be introduced into same gel-microbead as shown in Figure 1 (b). We can position the gel-tool at desired point of the microchip by optical tweezers. A schematic of fabrication process of the gel-tool is shown in Figure 2. Gel-microbead impregnated by an indicator is generated by stirring the mixture of 0.9 g ENT-3400, 0.3 g indicator solution,

978-0-9798064-0-7/μTAS2007/$20©2007CBMS

and 2.4 g potassium chloride aqueous solution. We used BTB and BCG as pH indicators. Lower critical concentration of the electrolyte for salting-out is 20 wt%. Generated gel-microbeads are polymerized by UV-ray illumination (peak wavelength: 366 nm) and introduced into the microchip. The gel-microbeads are connected by contact gel-microbead to other one as shown in Figure 3. Lower critical concentration of the connection of the gel-microbeads is 11 wt%. pH value is measured by color difference of red of the gel-tool because the colors of BTB and BCG change from yellow to blue according to pH value. RGB information is converted to YCrCb information by equation 1. Temperature is measured from relative fluorescence intensity based on the intensity at 25 °C.

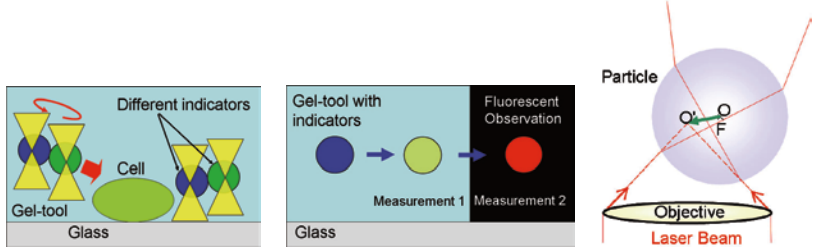

(a) Connection type (b) Coexistance type (c) Optical tweezers

Figure 1. Schematic of multiple sensing gel-tool

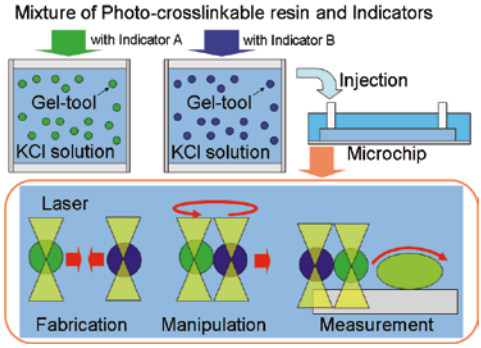

Figure 2. Schematic of fabrication process

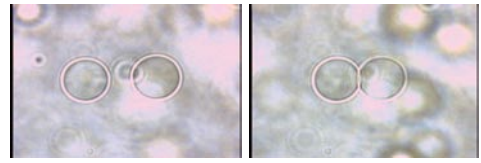

Figure 3. Connection of gel-microbeads

$$Y = 0.299R + 0.587\mathrm{G} + 0.114\mathrm{B}$$
$$Cr = 0.5000R - 0.419G - 0.081B \quad (1)$$
$$Cb = -0.169R - 0.419G + 0.500B$$

3. EXPERIMENTAL

The calibration results are shown in Figure 4. Cr and $F_{Intensity}$ represent color difference of red and relative fluorescence intensity respectively. Measurement range of BTB is from pH 6 to 9 and that of BCG is from pH 4 to 6. We employed Rhodamine B for temperature measurement. Fluorescence intensity of Rhodamine B decreases depending on the temperature increase. There were proportional relations between pH and Cr in BCG and BTB and between $F_{Intensity}$ and temperature. Therefore, pH and temperature are calculated by equations 2, 3, 4. Figure 5 shows the wide pH measurement using the gel-tool impregnated BTB and BCG. This is connection type gel-tool. After fabrication of the gel-tool in pH 9 solution, pH 4 solution was introduced and the color change was detected. Figure 6 shows the temperature and pH measurements by coexistence type gel-tool. BTB and BCG can coexist with Rhodamine B because they are not excited by the wavelength which excites Rhodamine B. Local measurement of several environments was achieved by multiple sensing gel-tool in microchip.

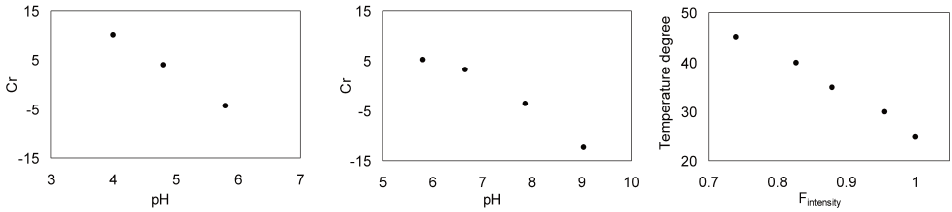

(a) BCG (b) BTB (c) Rhodamine B

Figure 4. Calibration results of pH and temperature

$$pH = -1.7 \times 10^{-1} \times Cr + 7.1 \quad (2)$$

$$pH = -1.3 \times 10^{-1} \times Cr + 6.0 \quad (3)$$

$$Temperature = -1.3 \times 10^{-2} \times F_{Intensity} + 1.3 \quad (4)$$

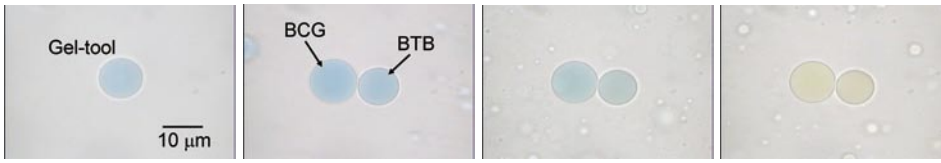

(a) Gel-tool with BTB (b) Connection (pH9) (c) pH 8.1 (d) pH 4.6

Figure 5. Wide range pH measurement by connection type gel-tool

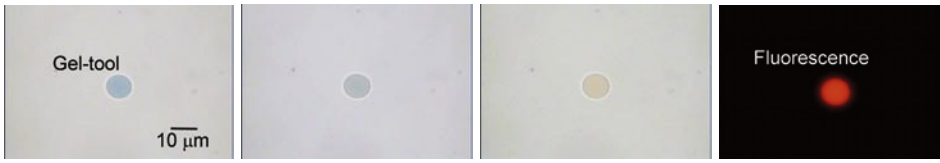

(a) pH 8.9 (b) pH7.7 (c) pH 4.5 (d) Temperature: 25 °C

Figure 6. Temperature and pH measurement by coexistence type gel-tool

5. CONCLUSIONS

We proposed multiple environments measurement using the gel-tool impregnated several indicators, and demonstrated on-chip fabrication of the multiple measurement gel-tool and measurement of the multiple data of different environmental condition. This technique for environmental condition will make great contributions for cell biology.

ACKNOWLEDGEMENTS

This research is supported by The Ministry of Education, Culture, Sports, Science and Technology Grant-in-Aid for Scientific Research (17040017).

REFERENCES

[1] H. Maruyama, F. Arai, T. Fukuda, Proc of μTAS2006, pp. 222-224 (2006).
[2] G. Nishimura, Y. Shiraishi, T Hirai, Chemical Communications, pp. 5313-5315 (2005)
[3] N. Klauke, P. Monaghan, et. al., Lab on a Chip, pp. 788-793 (2006)
[4] K. Shinohara, Y. Sugii, et. al., Meas. Sci. Technolo, pp. 955–960 (2004).
[5] J. K. Cho, L. S. Wong, et. al., Chemical Communications, pp. 1470-1471 (2004)

OPTOFLUIDIC BLOOD CELL SORTING

I.A. Andreev[2], A.C. Riches[2], T. Briscoe[2],
L. Paterson[3], K. Dholakia[2] and M.P. MacDonald[1].
[1]University of Dundee, [2]University of St Andrews and [3]Heriot Watt University, Scotland.

ABSTRACT

Optofluidics is rapidly becoming an established part of the microfluidic toolkit, due in part to the ease with which an optofluidic device can be reconfigured. In this paper we describe how it is possible to sort blood cells by configuring an optically induced potential energy landscape within a microfluidic flow to selectively deflect erythrocytes. When transported within an isotonic buffer, blood cells can be sorted according to their shape. Alternatively, by placing the cells in a hypotonic buffer, erythrocytes can be spherised and sorting can be accomplished according to size.

Keywords: optofluidics, optical manipulation, blood, cell sorting

1. INTRODUCTION

Sorting cells using optical techniques is an established technique in macroscopic devices but remains a fledgling technology in microscopic devices [1]. In our approach to optically enabled micro-TAS[2] the balance between the optical forces acting on a μm-size particle in a patterned optical field, such as those seen in figure 1, in competition with the drag force exerted by a carrier fluid, leads to selective deflection of cells and colloid in a microfluidic flow.

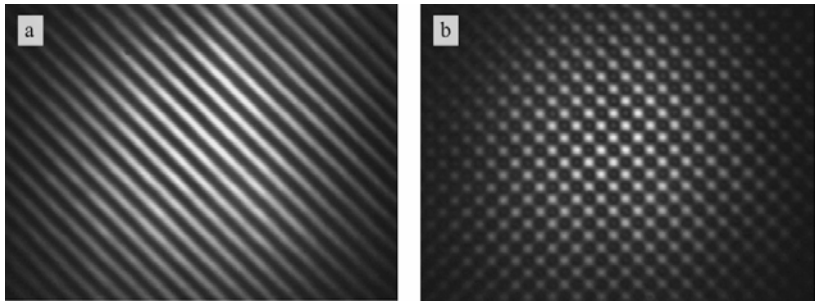

Fig. 1 – Optical patterns of the kind used to sort blood cells. (a) was created by interfering 3 laser beams and (b) with 5 beams. The spacing between the fringes is approximately 5 μm. The spacing and thickness of the fringes and the form of the lattice can be re-configured in real time to sort different types of cell.

Our technique is passive, in that it does not inherently require either the attachment of markers, or any decision making process. Cells and colloid are separated based on size, shape and refractive index. The potential of this passive sorting technology has been demonstrated on colloidal particles with different sizes or refractive indices [2], but its application to the sorting of living cells remains a challenge. One of the reasons for that is that the ensemble statistics of cellular objects must to be taken into account. Spherical colloid, for which optical sorting of this nature has so far been observed in the majority of cases, is characterised by a tight distribution in size, shape and refractive index, without any overlapping of these parameters between different species. In this case the optical force

978-0-9798064-0-7/μTAS2007/$20©2007CBMS

acting on a colloidal particle of one kind is statistically different from the force acting on a particle of a different species; a clear requirement for quantitative passive optical sorting. However, the ensemble statistics of living cells are characterized by natural factors, such as the different age of cells in the ensemble, stage of differentiation, etc. This results in wide distributions in the properties used for passive optical sorting and often these distributions overlap for different species.

2. BLOOD SORTING

However, there are particular living cell systems which could benefit from a passive sorting technique and which have appropriate ensemble statistics. One example is that of red and white blood cells, which have sizes and shapes that are markedly different. Human erythrocytes have a biconcave-disk shape with height in a range 2-3 μm and diameter of about 7 μm under physiological conditions and the volume of fully differentiated red blood cells is tightly distributed in 80-98 femtolitre range. Different types of Leukocytes in blood have a spherical shape and are larger in volume [3].

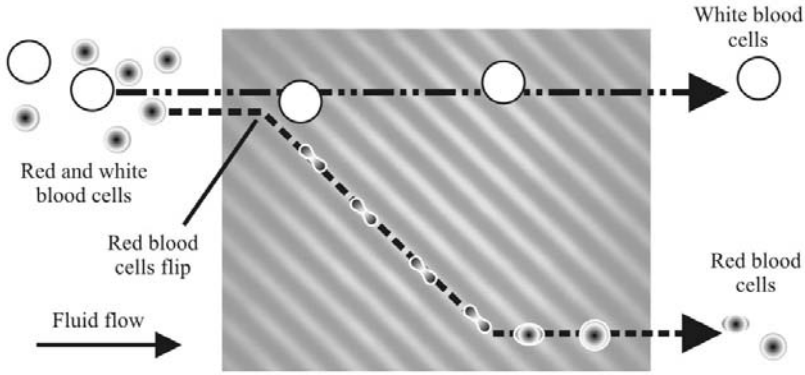

Fig. 2 – Schematic showing the concept by which Red and white blood cells are separated within a microfluidic flow. Erythrocytes flip and align to the optical pattern and are subsequently deflected.

The deflection force felt by a cell when travelling through the optical potential is proportional to the volume over which the interaction between the cell and the light takes place. Hence, cells of different volume and shape can be sorted from one another due to their differing interaction strengths with the optical landscape.

Erythrocytes derived from human blood are deflected within a microfluidic flow and are sorted from different types of leukocytes as they pass through an optical pattern. In the majority of cases the pattern shown in Fig. 1(a) is used. Notably, the majority of erythrocytes flip and align vertically in the optical field [4] and it is this behaviour that is used for sorting; see figures 2 and 3. Currently erythrocytes flip with an efficiency of approximately 95% meaning that, in order to effectively sort red and white blood cells, re-circulation of the analyte is necessary. Re-circulation is a simple step in optofluidics though, as the optical pattern can be turned off, the flow quickly reversed, then flow resumed in the usual direction.

The need for the erythrocytes to flip can be removed by placing them in a hypotonic buffer which changes the shape of erythrocytes from biconcave to a highly monodisperse

collection of spherical cells[5] with a diameter of about 5 μm, as seen in figure 4. By tuning the optical pattern to sort 5 micron particles, the erythrocytes were sorted from a flow whilst the larger lymphocytes were left unaffected.

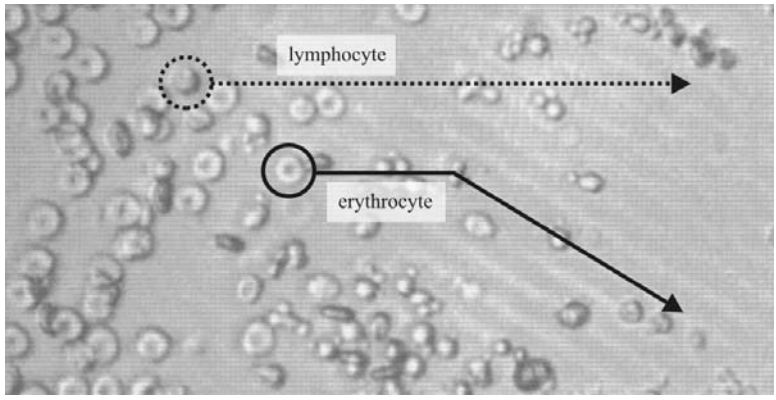

Fig. 3 – Sorting of red blood cells from white blood cells via flipping and deflection of the red blood cells. NB – the ratio of white to red cells has been increased before sorting to allow a clearer demonstration.

3. CONCLUSIONS

The majority of blood separation techniques either involve a pre-treatment step which has the potential to alter the function of the white blood cells which are the usual targets of a sorting procedure or, like centrifugation, which are not suited to scaling down to into a micro-TAS system. We have shown an optofluidic based technique where sorting is possible without any pre-treatment of cells or with the minimally invasive step of controlling the osmolarity of the buffer. This opens up possibilities for on-chip studies of lymphocytes without the risk of affecting the function of the cells.

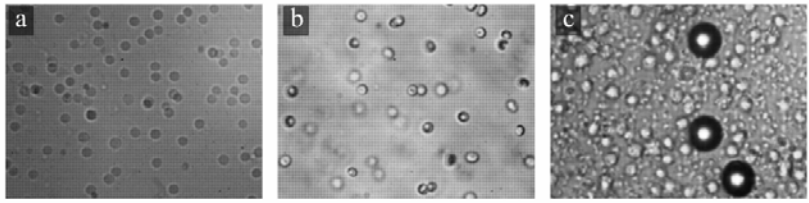

Fig. 4 – Red blood cells in hypotonic buffer with different osmolarity showing how they become spherised: ~135mOsm (a), ~160mOsm (b), leukocytes under physiological conditions (c) with 20 μm polymer spheres

REFERENCES

[1]. Michael Eisenstein. Nature **441**, 1179-1185 (2006)
[2]. MP MacDonald, GC Spalding, K. Dholakia. Nature **426**, 421-424 (2003)
[3]. AV Haffbrand, JE Pettit and PAH Moss. Haematology. 4th edition, Blackwell Science Ltd (2004)
[4]. JV Kruchenok, SB Bushuk, GI Kurilo, NA Nemkovich, AN Rubinov. J Biol Phys **31**, 1 (2005)
[5]. E Evans and YC Fung. Microvasc. Res **4**,335 (1972)

REFRACTIVE INDEX DETECTOR FOR NANOCHANNEL USING ALTERNATIVE DIFFRACTION GRATING NANOCHANNEL

Kazuma Mawatari[1], Kotaro Oda[2], Akihide Hibara[2] and Takehiko Kitamori[1,2]

[1] *Kanagawa Academy of Science and Technology (KAST), Japan*

[2] *The University of Tokyo, Japan*

ABSTRACT

We report a novel refractive index detector for nanochannels utilizing alternative diffraction grating nanochannels. Reference and sample nanochannels were arranged alternatively, and each channels worked as diffraction gratings. By detecting the intensity of the diffracted beams, we could measure the difference of the refractive index between reference and sample channels. The basic principle was verified for the first time, and the performance was evaluated.

Keywords: Nanochannel, Grating, Refractive index detection

1. INTRODUCTION

Recently, integration of fluidics into nano space has been increasingly studied. In addition to higher speed and more efficient chemical process than micro fluidic systems, new physical properties of liquid confined in nano space can be expected. Actually, we found unique liquid properties that water molecules in nanochannels were loosely structured and the proton exchange rate was increased [1]. Nanofluidics are now considered to be promising fields for realizing various unique chemical processes.

As one of the basic technologies for nanofluidics, detection method is a key technology. Especially, universal, label free and in-situ nanochannel detection methods become essential for these researches. Although laser-induced fluorescence method can be used for sensitive nanochannel detection, it needs fluorescent labels which limits analytes to fluorescent molecules. Refractometer is one of the candidates due to the wide applicability. However, the conventional refractometer can not be applied to nanochannels due to the much smaller size of the nanochannels than the light diffraction limit.

For these purposes, we developed a new differential refractometer: alternative diffraction grating nanochannel spectroscopy (ADGNS). We resolved the light diffraction limit by utilizing nanochannel diffraction gratings.

2. EXPERIMENTAL

The basic principle was illustrated in Figure 1. ADGN was composed of two kinds of nanochannels: one for sample (S) solution and the other for reference solution (R). Those nanochannels were aligned alternatively and periodically as a diffraction grating. Probe laser beam was introduced to ADGN, and its sub-order (center of two usual order diffracted beams) diffraction beam intensity was detected. When refractive index difference of both S and R channels is zero, diffracted probe beams from both channels are interfered and completely canceled out at sub-order angle because the phase difference of both beams is just 180°. When substance in the channel S changes, refractive index difference is induced, and the phase difference at sub-order angle deviates from 180°. As a result, the sub-order

978-0-9798064-0-7/μTAS2007/$20©2007CBMS

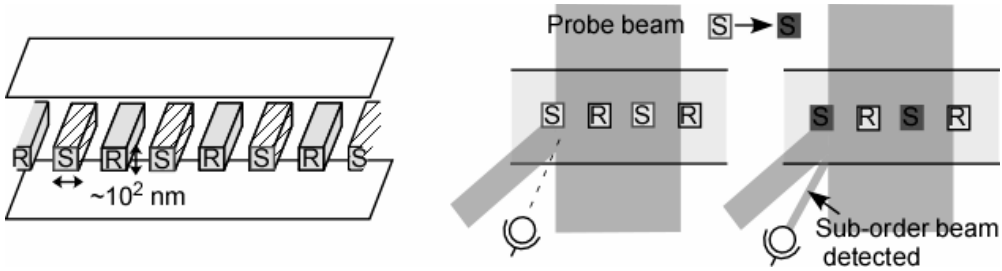

Figure 1 Principle of ADGNS

diffraction patterns emerge. The intensity (I) of the sub-order diffracted beam is expected to be dependent on refractive index difference (Δn) between the channel S and R. Thus, ADGNS works as a differential refractometer.

To verify the principle and performance of ADGNS, we fabricated alternative diffraction grating chip by EB lithography as shown in Figure 2. Inter-digital channel pattern was used to introduce liquids individually to each channels. One loopback of the nanochannel was ascribed as pseudo-one channel. The nanochannel width was 850 nm and depth was 170 nm. Pure hexane and the mixture of hexane and CCl_4 at various mixing ratio were used as reference and sample. He-Ne laser (633 nm) was used as probe beam. The diffracted beam intensity I was measured by a photodiode.

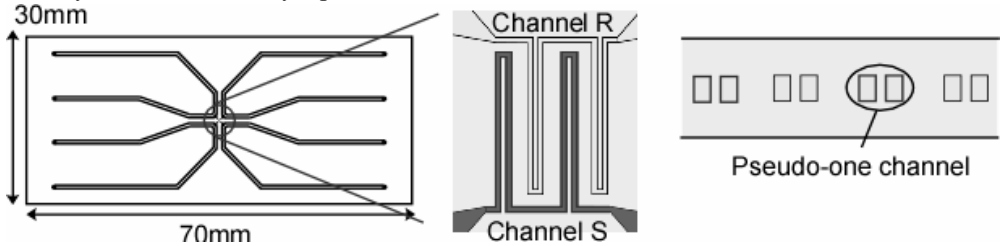

Figure 2 Design of micro/nano chip for ADGNS

3. RESULTS AND DISCUSSION

Firstly, the liquid introduction to each channels by capillary force was verified. For the R and S channels, air and hexane were introduced, respectively. The result is shown in Figure 3. The picture shows the alternative nanochannels are precisely formed without liquid leakage. By hexane introduction, generation of sub-order diffraction grating pattern was also confirmed as shown in Figure 4. The basic principle of differential

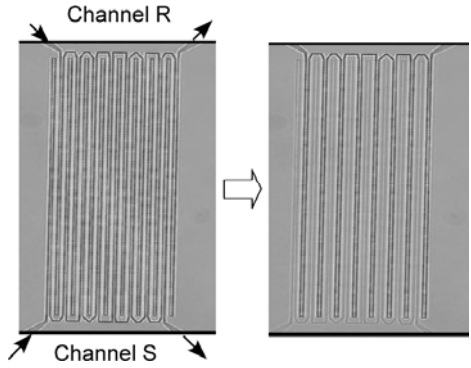

Figure 3 Picture of nanochannels: before hexane introduction (left), after introduction (right)

refractometer was successfully verified.

Finally, we evaluated the basic performance of the ADGNS. For R and S channels, hexane and mixture of hexane and CCl_4 was filled, respectively. By changing mixing ratio of hexane and CCl_4, differential refractive index was changed from 0 to 0.08. The I-Δn plot was shown in Figure.5. The experimental values matched with theoretical curve which was derived from light diffraction theory. The lower detection limit was estimated roughly to be 10^{-3} RIU. This is a first demonstration of refractive index detection in nanochannels, which was quite difficult by conventional refractometry due to the light diffraction limit.

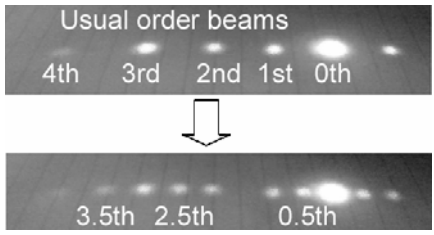

Figure 4 Change of diffraction pattern after hexane introduction to S channel

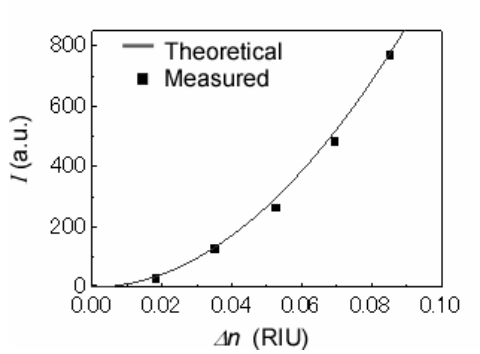

Figure 5 Performance evaluation of ADGNS

4. CONCLUSIONS

We realized a refractometer in nanochannels for the first time. The basic technologies were established, and the principle was successfully verified. This method can be applied to various chemical processes in nanochannels by introducing this grating structure at detection point. Furthermore, this structure has another advantage; it detect Δn between S and R channels. Therefore, the effect of bulky glass substrate to signals can be ignored. This feature is essential for femtosecond time-resolved measurement of liquid dynamics confined in nanochannels by intensive pulse lasers. This work is in progress and also illustrated in the presentation.

REFERENCES

[1] T. Tsukahara, T. Kitamori et. al., "NMR Study of Water Molecules Confined in Extended-Nano Spaces," Angew. Chem. Int. Ed., 46, 1180-1183 (2007).

AN ELECTROCHEMICAL SENSOR INTEGRATED ON FABRIC

G. Marchand[1], M.-L. Cosnier[1], N. David[1], C. Chabrol[1], A. Bourgerette[1], F. Vrillon[1], T. Flaven[1], I. Chartier[2], J. Bablet[2] and N. Dunoyer[2]

1. *Department of Technology for Biology and Health –CEA LETI Minatec*
2. *Department of Technology for NanoMaterials - LITEN*
CEA Grenoble 17 rue des Martyrs, 38054 Grenoble, France

ABSTRACT

The dehydration of emergency disaster personnel can lead to severe physiological consequences being able to go until the death. The follow-up of the sodium ions concentration in the sweat allows to evaluate this dehydration state in real time and to intervene quickly in the event of problem. This paper deals with the development of an electrochemical sensor and its transfer on fabrics. A portable and autonomous mini-potentiostat connected to the sensor is described too.

Keywords: electrochemical sensor, textile, emergency, disaster personnel

1. INTRODUCTION

During interventions on disasters, the emergency personnel are exposed to extreme physical conditions and an important physiological consequence can be the dehydration. Thus, an abnormally high loss of sodium in the sweat can lead to a hyponatremia [1] and this low concentration of sodium in the plasma can next generate a cerebral oedema and its ultimate consequence is the death. Thus, following the sodium concentration in the sweat seems to be an important parameter to ensure the good health of the personnel. However, this application necessitates a portable and not much bulky device in order to not hinder the firefighter. This paper deals with the integration of an electrochemical sensor on fabric and the development of a portable mini-potentiostat.

2. CARACTERISTICS AND TECHNOLOGY

The developed electrochemical sensor consists of host molecule included in a conducting polymer, to perform specific transducer that precisely and selectively measures the sodium concentration. Thus, the complexation of the targeted ion (with positive charges) by the host molecule leads to a modification of the electrochemical response of the conducting polymer. Firstly, we have developed a metallic coating on fabric by Pulverization Vapor Deposition (PVD) to realize structured electrodes (Figure 1).

978-0-9798064-0-7/µTAS2007/$20©2007CBMS

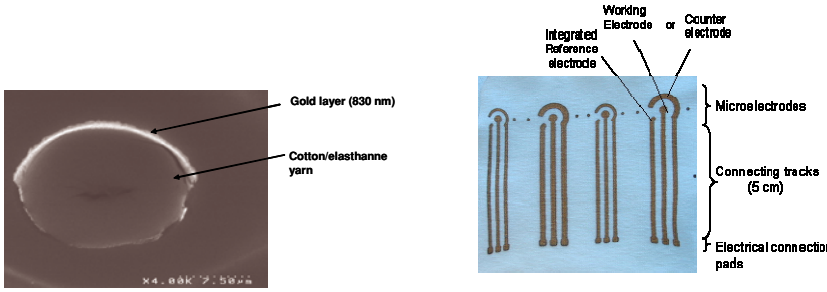

Figure 1. A- SEM of a cotton/elasthanne recovered bya gold layer deposited by PVD; B- Picture of an example of structured electrodes on fabric.

Groups of three electrodes constitute electrochemical cell for measurements. On the working electrode, we have electrodeposited the poly(3,4-ethylenedioxythiophene) (PEDOT) at 1.2V in trapping the 4-tert-butylcalix[4]arenetetraacetic acid tetraethylester (Figure 2).

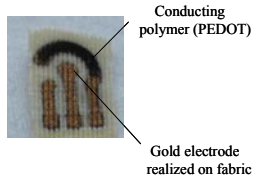

Figure 2. Picture of gold electrodes structured with a conducting polymer coating on working electrode

The electrochemical sensor was connected to a portable mini-potentiostat (Figure 3) via a flexible sheet compatible with a Samtec connector (ZF5). The developed mini-potentiostat is able: i/ to perform successively measurements on several electrochemical cells (the tension at the counter electrode is tuned by the potentiostat to maintain the potential difference between the reference electrode and the working electrode equal to the chosen orders), ii/ to perform cyclic voltammetry with speed between 50mV/s and 200mV/s, and potentials included in a range of ±1V, iii/ to measure currents included in a full scale range of ±30µA to ±1µA, iv/ to concurrently work on two working electrodes (differential function) and v/ to be portable and autonomous.



Figure 3. Picture of mini-potentiostat prototype including all analogical parts connected to an electrochemical sensor with a flexible sheet

3. MEASUREMENT VALIDATION

The detection of Na^+ ions variations by the electrochemical sensor [2,3] on fabric was firstly validated by cyclic voltammetry (Figure 4) with a biochemical sensing fabric connected to a potentiostat on laboratory bench. Model solutions and synthetic sweat have been used to evaluate the sensitivity, the dynamic range and the selectivity. Next, the mini-potentiostat, preliminarily characterized with a simple redox couple in solution ($Fe^{II/III}$), has been connected to the electrochemical sensor and we were validated the detection of Na^+ ions on this device. This promising result permits to envisage future developments on fabrics.

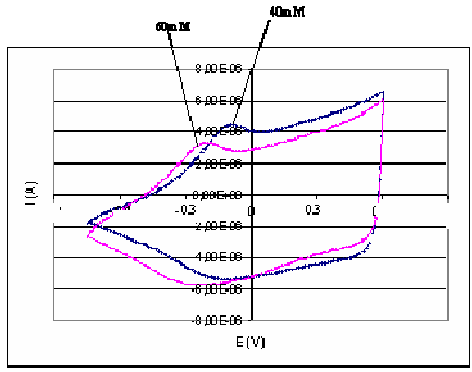

Figure 4. Cyclic voltammogramms obtained PDOT layers with trapped calixarene in NaCl solutions 40 and 60mM.

5 CONCLUSION

An electrochemical sensor, specific of Na^+ ions, was developed and transferred on fabrics. After connexion to a portable and autonomous mini-potentiostat, the sensor was validated with synthetic sweat. In the future evaluation, this equipement will be integrated in firefighters inner garments and tested in real conditions.

REFERENCES

[1] D.P. Davis et al, The Journal of Emergency Medicine, 2001, 21 (1), 47-57.

[2] L.M. Goldenberg, M. R. Bryce and M.C. Petty, J. Mater. Chem., 1999, 9, 1957-1974

[3] N.J.L Guernion, A. Blencowe, W. Hayes, P. Lozano-Sanchez and S. Skaarup, Reactive and Functional Polymers, 2006, 66, 201-218

LOW-NOISE OPERATION OF CHARGE-TRANSFER-TYPE pH SENSOR USING CHARGE ACCUMULATION TECHNIQUE

E. Watanabe[1], T. Hizawa[1], S. Mimura[2], T. Ishida[3], H. Takao[4,5], K. Sawada[1,4,5] and M. Ishida[1,4,5]

[1]Dept. of Electrical and Electronic Eng., Toyohashi University of Technology, Japan,
[2]HORIBA, Ltd., Japan, [3]Orimacky, Ltd., Japan,
[4]Intelligent Sensing System Research Center, Toyohashi University of Technology, Japan,
[5]Core Research for Evolutional Science and Technology (CREST), Japan

ABSTRACT

A pH sensor with high sensitivity and high SNR (signal to noise ratio) characteristics was successfully demonstrated by using a charge-transfer-type pH sensor. It is found that the SNR characteristics are improved by charge accumulation operation. The noise converted pH as input-referred value of a charge-transfer-type pH sensor is 0.0023pH (using 5 accumulation cycles). This is about 2 times lower than that of the Ion Sensitive Field Effect Transistor (IS-FET). Therefore, it is able to realize a high performance pH sensor to use a charge accumulation technique.

Keywords: pH sensor, ISFET, charge transfer technique, accumulation operation, noise characteristics

1. INTRODUCTION

Various types of biosensors have been developed to understand chemical phenomena. A pH sensor is one of the most important devices of biosensors. The conventional solid-state-type pH sensor is the Ion Sensitive Field Effect Transistor (IS-FET) [1]. The ideal maximum sensitivity of the IS-FET is 59mV/pH from the Nernst equation at room temperature (25°C). The resolution of the IS-FET is restricted by the 1/f noise [2]. Thus it is difficult for the IS-FET to measure the infinitesimal variations of the pH value. Previously we have proposed pH sensor based on the principle of a charge coupled device [3]. By a charge accumulation operation of the charge-transfer-type pH sensor, it was confirmed that its pH sensitivity was 1130 mV/pH with 5 charge accumulation cycles [4]. However we have not evaluated noise characteristics of the charge-transfer-type pH sensor on charge accumulation operation.

2. THEORY

A charge-transfer-type pH sensor was fabricated on a 5μm rule CCD/CMOS process. The structure and the operation of this sensor are shown in Fig. 1 and Fig. 2, respectively. This sensor consists of seven elements: an input diode (ID), an input control gate (ICG), an ion sensing region, a transfer gate (TG), a floating diffusion (FD), a reset gate (RES) and a source follower circuit. The sensing region is the thin Si_3N_4 film that acts as an ion-sensitive membrane. A procedure of the operation without accumulation cycle is shown in Fig. 2(a) - (d). To accumulate signal charges, the (a) – (d) cycles are repeated as shown in Fig. 2(e) and (f) [4].

978-0-9798064-0-7/μTAS2007/$20©2007CBMS

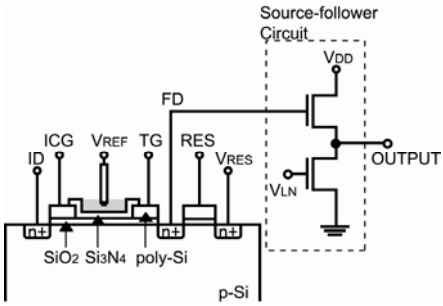

Figure 1. The structure of a charge-transfer-type pH sensor.

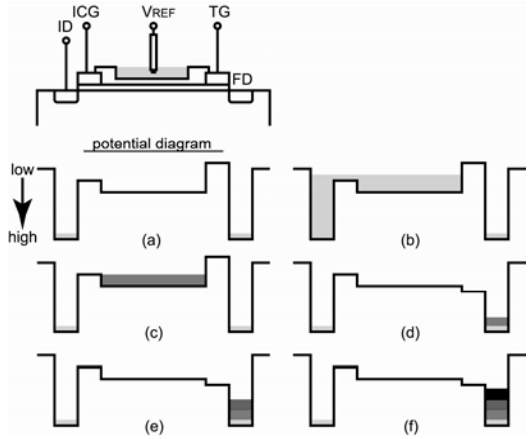

Figure 2. Principle of conversion from pH to charge.

It is expected that SNR (signal to noise rate) of the sensing signals by the accumulation cycle. If the sensing signals S_0 is accumulated n times, the total quantity of the signal S is described as follow:

$$S = nS_0 \tag{1}$$

The total quantity of the noise N is described as follow:

$$N = \sqrt{{N_1}^2 + {N_2}^2 + \cdots + {N_n}^2} \tag{2}$$

Where N_1, N_2, ···, N_n are the noise components of each accumulation stage. If these components are same, above equation is simplified as

$$N = \sqrt{n{N_0}^2} \tag{3}$$

Therefore, the total SNR is given by

$$\frac{S}{N} = \frac{nS_0}{\sqrt{n{N_0}^2}} = \sqrt{n}\,\frac{S_0}{N_0} \tag{4}$$

From Eq. (4), the SNR increase $n^{0.5}$ times if the accumulation cycle is repeated n times.

3. EXPERIMENTAL AND RESULTS

The equivalent circuit of the IS-FET measurement using cell batteries and low noise resistor is shown in Fig. 3. The output signal was taken with 1 kHz sampling rate. The output signal fluctuation of the ISFET is 108μVrms at peak to peak, and the sensitivity of this sensor is 21.1mV/pH. The noise converted pH as input-referred value of the ISFET is 0.0051pH. The output signal and its noise power level of a charge-transfer-type pH sensor are shown in Fig. 4. The sampling rate of the charge-transfer-type pH sensor was varied in 1-5 kHz, which depended on the accumulation cycle. However, the sampling rate was almost same as the measurement of IS-FET. The output signal is proportional to accumulation cycles and the noise power level increases on (the gain of the sensor)$^{1/2}$. Thus, the noise converted pH as input-referred value are reducing that shown in Fig. 5. In 1 accumulation cycle, it is 0.0052pH, which is the same level of the ISFET. The noise is reduced to accumulation cycles and it is 0.0023pH in 5 accumulation cycles.

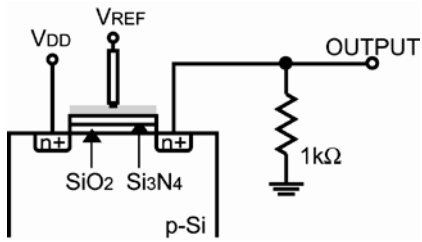

Figure 3. The equivalent circuit of the IS-FET measurement.

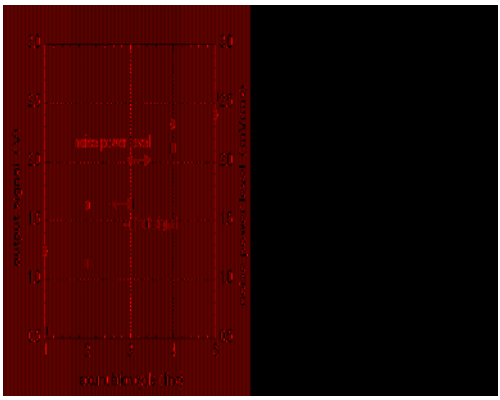

Figure 4. The output signal and the noise power level of a charge- transfer-type pH sensor.

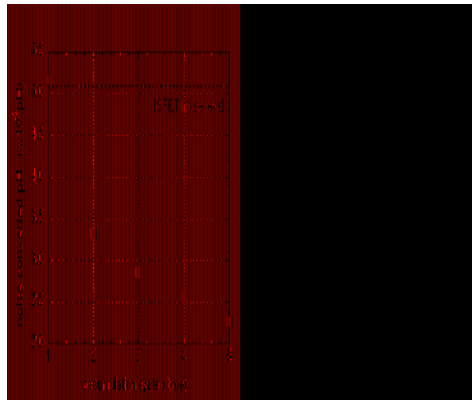

Figure 5. The noise converted pH as input-referred value of a charge-transfer-type pH sensor.

4. CONCLUSIONS

On the proposed charge accumulation operation of a charge-transfer-type pH sensor, it is possible to increase an input signal quantity by the charge accumulation cycle. Moreover, if noise components are random noise, the SNR increases $n^{1/2}$ times, as the signal is integrated n times. Thus, the pH sensor with accumulation operation is expected to improve the SNR.

ACKNOWLEDGEMENTS

This work was partially supported by The 21st Century COE Program (Intelligent Human Sensing", Cooperation of Innovative Technology and Advanced Research in Evolutional Area from the Ministry of Education, Culture, Sports, Science and Technology, Japan (MEXT), and a Grate-in-Aid for Scientific Research (B) (No. 18360170) from MEXT.

REFERENCES

[1] P. Bergveld, IEEE Trans. Biomed. Eng., vol. BME-17, pp.70-71, (1970).
[2] C. G. Jakobson and Y. Nemirovsky, Proc. Electrotechnical Conf. 1998, MELECON 98, 9th Mediterranean, vol. 2, pp. 1456-1460, (1998).
[3] K. Sawada, S. Mimura, K. Tomita, T. Nakanishi, H. Tanabe, M. Ishida and T. Ando, IEEE Trans. Electron Devices, vol. 46, No. 9, pp. 1846-1849, (1999).
[4] T. Hizawa, K. Sawada, H. Takao and M. Ishida, JJAP, vol. 45, No. 12, pp. 9259-9263, (2006).

A FULLY INTEGRATED AND DISPOSABLE POLYMER BIOSENSOR USING MICRO DIAPHRAGM STRUCTURE OF PIEZO-COPOLYMER (PVDF-TrFE)

Soohyun Lee[1,2], Chunyan Li[1], Younmee Chae[2], Jiyoon Kang[2] and Chong H. Ahn[1]

[1]*Microsystems and BioMEMS Laboratory, University of Cincinnati*
Cincinnati, OH, U.S.A
[2]*Korea Institute of Science and Technology*
Seoul, KOREA

ABSTRACT

In this research, a fully integrated and disposable polymer biosensor has been designed, fabricated and characterized for the applications of immunosensor in a lab-on-a-chip platform. For the biosensor, a piezoelectric-based circular micro diaphragm was used to measure the shift of resonance frequency due to on the mass change of target biomolecules immobilized over the diaphragm. PVDF-TrFE was chosen as the piezoelectric material of the diaphragm, which has superiorities to normal PVDF in terms of sensitivity and fabrication process [1]. The fabricated polymer biosensor was integrated with polymer microfluidic channel for an end-user friendly biosensor in a disposable format. In this work, a fully integrated polymer-based piezoelectric biosensor on polymer lab-on-a-chip as a disposable platform is newly reported and shows a promising detection level of 1 ng/ml in peptides and proteins such as prostate specific antigen (PSA).

Keywords: Polymer biosensor, piezo-copolymer (PVDF-TrFE), resonance frequency

1. INTRODUCTION

Recently, there are large demands for the development of label-free detection methods to detect biomolecular because of its simple, rapid and cost-effective detection approach. Corresponding to the demands, this polymer biosensor to measure the shift of resonance frequency based on the mass change of target biomolecular has been investigated in this work. Specially, a micro diaphragm structure was utilized as a sensing component for the level free detection. Since the micro diaphragm structure has higher quality merit factor (Q factor) than micro cantilever structure [2], the micro diaphragm shows higher resolution in determining resonance frequency. Even, in liquid solution, the micro diaphragm structure can have reasonably high Q factor, which can detect target biomolecules in ***in-situ*** status.

2. DESIGN AND FABRICATION

Figure 1 (a) shows total schematic of polymer biosensor using micro diaphragm structure. And successive bio processes are illustrated in Figure 1 (b), (c) and (d). Self Assembly Monolayer (SAM) made by MPA/MUA was exploited to capture the monoclonal PSA (Prostate Specific Antigen) antibody on the sensing surface. The fabrication processes are summarized in Figure 2. The sensor layer is made by spin coating method. PVDF-TrFE powder, one of the piezoelectric copolymer, is dissolved in methylethylketone (MEK). Sensing area and electrodes of Cr/Au were evaporated in vacuum onto both surfaces of PVDF-TrFE layer using shadow mask. As a polarization method, DC poling method was

978-0-9798064-0-7/μTAS2007/$20©2007CBMS

implemented. Following crystallization at 120°C, the sensing layer was poled under electric field of 50 V/㎛ through both side electrodes. Finally, microfluidic layer and sensing layer are bonded by UV epoxy. Figure 3(a) shows the pictures of the polymer biosensors which have different diameter sizes, 0.5, 1, 2 and 3 mm, of sensing area. The experimental setup has been presented in Figure 3(b).

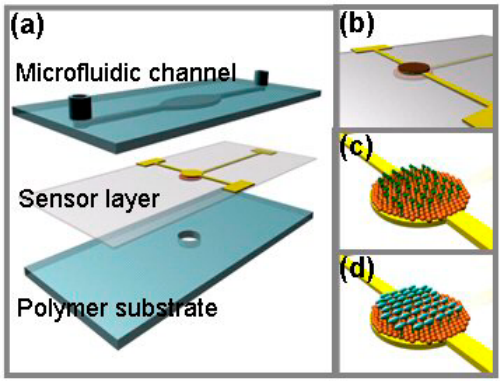

Figure 1. Total illustration of integrated polymer biosensor (a) Design of top layer: microfluidic channel for quantified sample loading (b) (c) and (d) Design of bottom layer and bio processes: micro diaphragm structure made by PVDF-TrFE copolymer

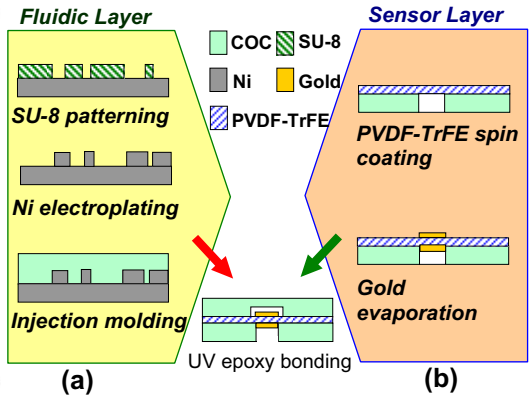

Figure 2. Summary of fabrication processes (a) top layer (b) bottom layer

3. RESULTS AND DISCUSSION

Remnant polarization value of polymer biosensor with different sensing areas was measured to seize the piezoelectric property of sensing layer. As shown in Figure 4, hysteresis loops of polymer biosensors obtained from TF analyzer demonstrated that sensing area has piezoelectric property. And then, each polymer biosensor was measured natural resonant frequency using impedance analyzer (HP 4294A). There are 2 dominant modes of vibration and thickness over the frequency range in Figure 5. Figure 6 clearly shows the change of the resonance frequency based on different concentrations of PSA.

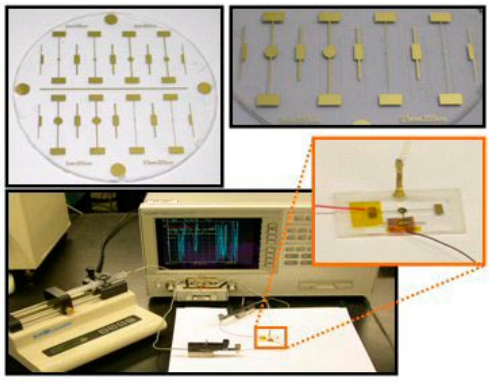

Figure 3. (a) Microphotograph of fully disposable and integrated polymer biosensor (b) Experimental setup

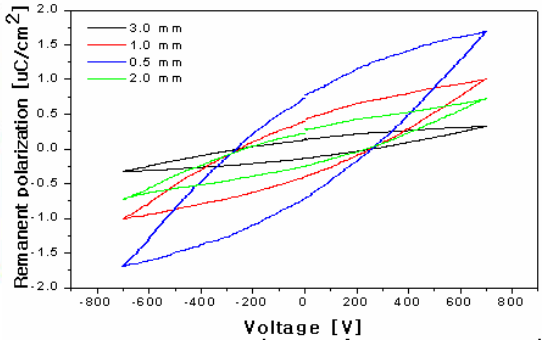

Figure 4. Hysteresis loop of PVDF-TrFE polymer biosensor with different sensing diameters: Applied 700V of triangular wave form

4. CONCLUSIONS

In conclusion, this lab-on-a-chip type of polymer biosensor has been developed and characterized well for label-free bioassay through the integration of piezo sensing layer with microfluidic chip. The resonance frequency of polymer biosensor has been shifted based on the mass change respect to different concentration of PSA. *The detection level of 1 ng/ml for PSA has been successfully achieved in this biosensor. Furthermore, this polymer biosensor has a great potential to measure the binding constants between any antibody and antigen because micro diaphragm structure can have high Q factor even in liquid, it allows* ***in-situ*** *detection over the time.*

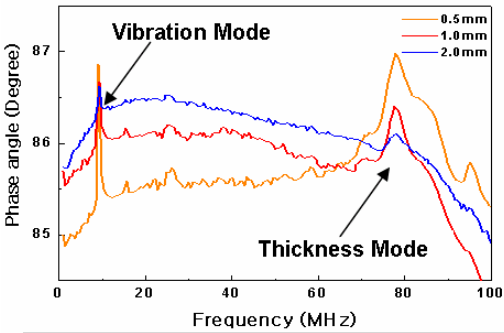

	0.5 mm	1 mm	2 mm
f_1	9.415 MHz	9.175 MHz	9.415 MHz
f_2	78.715 MHz	77.845 MHz	77.725 MHz

Figure 5. Natural resonant frequencies of vibration mode and thickness shear mode for different diameter polymer biosensors

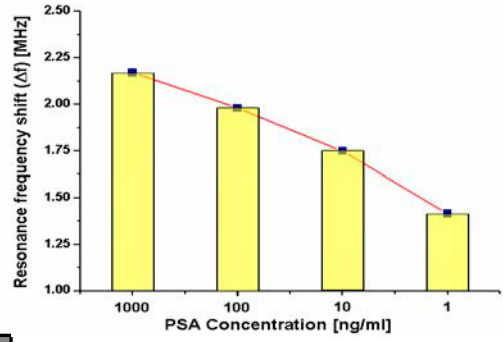

Figure 6. Resonant frequency shift based on the mass change of different PSA concentrations (1000, 100, 10 and 1 ng/ml): In case of PSA antibody concentration, 10 ug/ml was used. The shift of resonance frequencies are 2.17, 1.98, 1.75 and 1.415 MHz based on PSA concentration, respectively.

REFERENCES

[1] R. G. Kepler and R. A. Anderson, "Ferroelectric polymers", ADVANCES IN PHYSICS, **41**, 1-57 (1992)

[2] Zhimin Li *et al,* "Piezopolymer Diaphragm as high performance biosensor platform", Mater. Res. Soc. Symp. Proc. Vol. **889**, W01-09.1 (2006)

[3] Takeo Furukawa, "Piezoelectricity and Pyroelectricity in Polymers", IEEE Transaction on Electrical Insulation, Vol. 24, 375 (1989)

DIFFERENTIAL IMPEDANCE SPECTROSCOPY WITH AN ARRAY OF FIELD-EFFECT TRANSISTORS AS NOVEL BIOSENSOR CONCEPT

Sven Ingebrandt, Yinhua Han, Günter Wrobel, Stefan Eick, Susanne Schäfer, and Andreas Offenhäusser

Forschungszentrum Jülich, Institute of Bio- and Nanosystems, D-52425 Jülich, GERMANY

ABSTRACT

We present an impedimetric biosensors system for the label-free, direct electronic detection of biomolecules and for the observation of the cell-substrate adhesion on an individual cell level. We are utilizing a microarray of non-metallized, silicon field-effect transistors (FET) immersed into an electrolyte solution. With a differential, impedimetric readout, we are able to detect the DNA hybridization, protein binding, and the adhesion of individual cells on the small gate areas of the chips.

Keywords: Field-Effect Transistor, DNA Detection, Biosensor, Cellular Adhesion

1. INTRODUCTION

The impedimetric readout of FETs has already been described [1]. When used in a differential approach, it enables a stable sensor signal, a reliable readout and a possibility for quick screening of a large number of sensor spots [2]. The signals can be generated by either a different binding affinity of target molecules to probe molecules, which were immobilized at the individual sensor spots (e.g. DNA or proteins), or by individual cells which adhered to the open gate structures of the FETs. The main advantage of utilizing field-effect sensors for impedimetric sensing is the possibility to amplify the impedimetric effects utilizing the combination of FET and first operational amplifier (OP).

2. THEORY

The detection of biomolecules utilizing the transfer function of FETs has been explained by impedance changes of the biomolecules in close contact to the transistor gate [1].

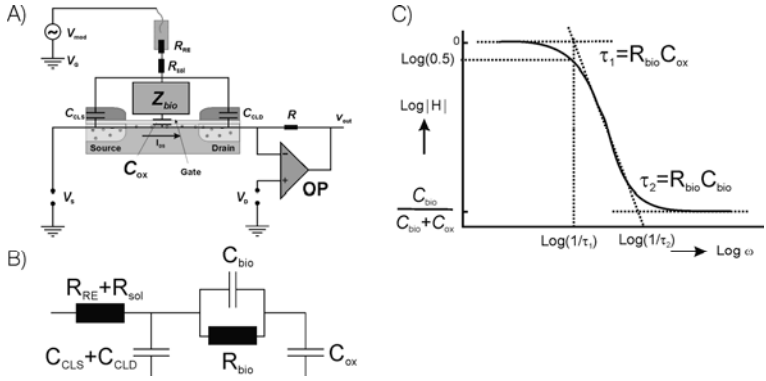

Figure 1. A) Schematics for the impedimetric detection of a bioprobe with a FET device. B) Equivalent electronic circuit and C) theoretical response of the low pass.

978-0-9798064-0-7/μTAS2007/$20©2007CBMS

In general, the transconductance g_m of a transistor is described by:

$$g_m = \frac{\partial I_{DS}}{\partial V_{GS}} \Big|_{V_{DS}=const} = \frac{i_{DS}}{v_{GS}} \quad (1)$$

with i_{DS} and v_{GS} being the 'small-signal' values. The output voltage v_{out} (Fig. 1A) can be calculated by $v_{out} = -Ri_{DS} = -Rg_m v_{GS}$, with R being the feedback resistor of the first OP. If a bioprobe is attached to the gate electrode, the voltage v_{GS} is divided into the voltage drop over the bioprobe and the gate oxide, respectively. This reduces the potential difference between gate and source. Then the transfer function $H(j\omega)$ needs to be introduced:

$$H(j\omega) = \frac{1}{1 + j\omega(R_{RE} + R_{sol})C_{CL}} \cdot Z_{bio} \quad (2)$$

The impedance, which is introduced by the bioprobe Z_{bio}, can in a first approximation be described as a RC element composed of R_{bio} and C_{bio}, with ω being the angular frequency. The input capacitance of the gate oxide is C_{ox} (Fig. 1). The transfer function factor (Eq. 2) can then be used to describe the frequency-dependency of v_{out} with $v_{out} = -Rg_m H(j\omega) v_{GS}$.

3. EXPERIMENTAL

We developed 8- or 16-channel FET chips and a portable amplifier system for our proof-of-principle experiments. The FET chips were designed such that the uncoated readout channels show an identical electrical response in *dc*- as well as in *ac*-mode. The miniaturized amplifier system also contains 16 independent *dc* and *ac* amplifier circuits. In the *ac*-mode, we can either scan the frequency-dependent transconductance of the field-effect devices or operate at a fixed frequency in a time-dependent mode. The temperature of the chip surface can be precisely controlled, which enables binding studies or melting curves of DNA or measurements with living cells. The size of the individual FET gates is smaller than the size of an individual cell.

4. RESULTS AND DISCUSSION

Here we present three possible bioassays with our detection system. We previously demonstrated the high selectivity for DNA detection by identifying point mutations in short DNA samples (Fig. 2) [2].

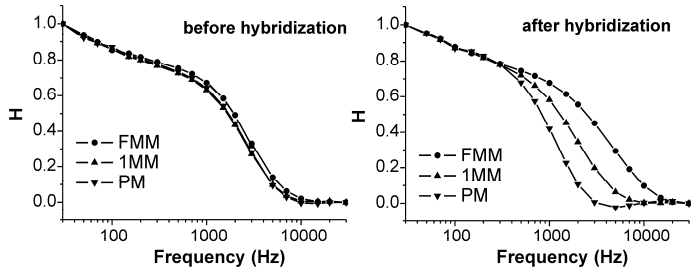

Figure 2. Detection of point mutations with an ISFET array.

Here, the transfer characteristics of three transistor channels are shown, where full-mismatch (FMM), single-mismatch (1MM) and perfect match (PM) DNA sequences were

immobilized. After the hybridization reaction with the target DNA, the sequence-specific responses can be clearly identified. The FET system can also be used for the electronic detection of the binding reaction between biotin and streptavidin (Fig. 3).

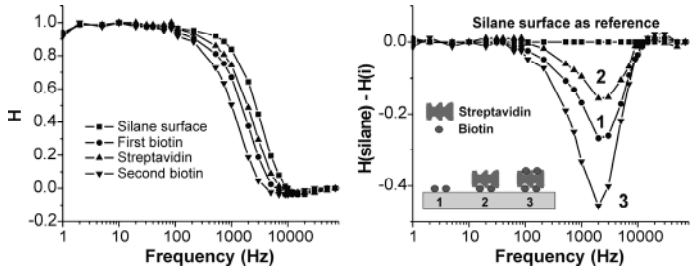

Figure 3. Detection of biotin-streptavidin binding with the FET system.

Our study demonstrates a proof-of-principle concept for impedimetric detection of larger biomolecules. As a third application, the system can be used for the non-invasive, electronic monitoring of the cell-substrate adhesion. We present cellular adhesion measurements of HEK 293 cells on an individual cell level (Fig. 4). The system can additionally be used to probe the viability of individual cells.

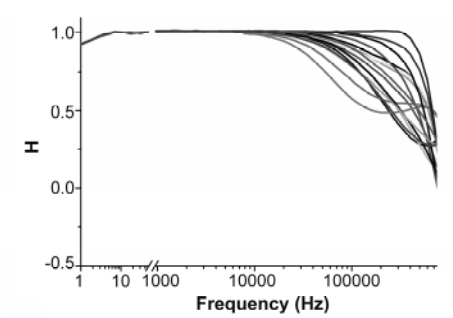

Figure 4. Transfer function measurements of all 16 transistors of one chip, when HEK 293 were attached to the gate structures with a different adhesion strength and sealing.

5. CONCLUSIONS

As a summary our novel biosensing concept utilizing field-effect transistor microarrays is demonstrating a promising performance for many different bioassay applications.

REFERENCES

[1] A.B. Kharitonov, J. Wasserman, E. Katz and I. Willner, *The use of impedance spectroscopy for the characterization of protein-modified ISFET devices: Application of the method for the analysis of biorecognition processes*, J. Phys. Chem. B, 105, pp. 4205-4213, (2001).

[2] S. Ingebrandt, Y. Han, F. Nakamura, A. Poghossian, M. J. Schöning, and A. Offenhäusser, *Label-free detection of single nucleotide polymorphisms utilizing the differential transfer function of field-effect transistors*, Biosens. Bioelectron., 22, pp. 2834–2840, (2007).

DUAL FREQUENCY RESONANCE IMPEDANCE SPECTROSCOPY FLOW CYTOMETRY FOR BLOOD AND TUMOR CELLS

Siyang Zheng and Yu-Chong Tai

Department of Electrical Engineering, California Institute of Technology, U.S.A.

ABSTRACT

In this paper, we successfully demonstrated dual frequency resonance impedance sensing of blood cells and tumor cells in a micro flow cytometry format. Two inductors of different inductance values are connected to two pairs of electrodes closeby to induce resonance and nullify the capacitive components of the system at different resonance frequencies. Leukocytes show different characteristics from erythrocytes. Tumor cells from two different cell lines can also be differentiated from blood cells.

Keywords: resonance, impedance, blood cells, tumor cells

1. INTRODUCTION

As a label-free sensing mechanism, electrical impedance sensing has been used widely for detection and characterization of individual biological cells under either stationary or flow cytometry format [1, 2]. One problem inherited in scaling down impedance sensors from macro to micro domain is the increase of double layer impedance between electrode-electrolyte interfaces. Along with the stray capacitance, they eventually dominate system impedance in a wide frequency range. To increase sensitivity, we proposed a novel approach by connecting an external parallel inductor to induce resonance and nullify the capacitive components at resonant frequency. In this paper, we demonstrate blood and tumor cells sensing at dual frequency with this technique. As the dielectric property of cells is a function of frequency, it's advantageous to sensing at multiple frequencies simultaneously [3].

2. EXPERIMENTAL

The device was fabricated by forming fluidic channel on PDMS, then bonding it to glass wafer with Ti/Pt (100Å/2500Å) patterned electrodes (Fig.1). Two pair of electrodes for sensing at low and high frequency respectively was separated by 100μm, which also measures real time particle velocity inside channel. An inductor of 1mH was connected parallel to the device for sensing at 2.05MHz and inductors with total of 1H inductance were used for sensing at 77kHz. Without inductor connected, the differences among system impedance spectra in air, DI water and electrolyte solution PBS were small meaning the device have a poor sensitivity. Parallel inductors introduced resonance at specific frequencies chosen by the inductance (Fig.2). The higher the inductance, the lower the resonance frequency. The impedance spectra can be modeled (Fig.3) and the sensitivity can be shown to improve by orders of magnitude.

978-0-9798064-0-7/μTAS2007/$20©2007CBMS

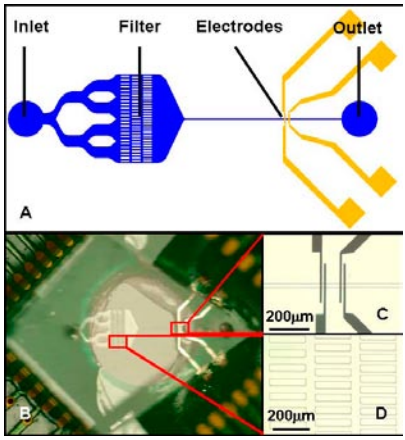

Figure 1. Device design and fabricated device. (A) Fluidic passage including inlet/outlet, filter and channel and with electrodes patterned on bottom. (B) Assembled device. (C) Close-up view of the sensing region. (D) Close-up view of the filter region.

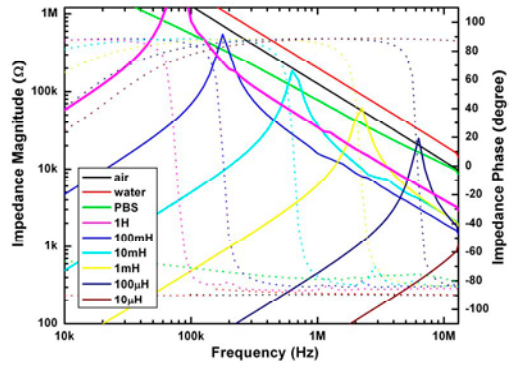

Figure 2. Impedance magnitude (left axis and solid lines) and phase (right axis and dotted lines) spectra of device without inductor connected and filled with air, DI water and electrolyte PBS, as well as device in PBS with inductors of various values connected.

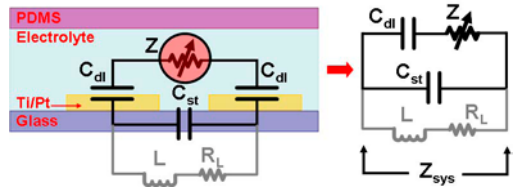

Figure 3. System is modeled electrically by channel impedance Z, double layer capacitance C_{dl}, stray capacitance C_{st} and parallel inductor with inductance L and resistance R_L.

4. RESULTS AND DISCUSSION

The devices were first validated with a mixture of 5μm and 10μm diameter polystyrene beads (Fig.4). Scatter plot of impedance at high frequency verse that of low frequency showed two separated region. For human blood cell testing, two types of samples of blood cells were used. Diluted whole blood mainly shows the characteristic of the red blood cells (RBCs) because of the overwhelming number of RBCs over white blood cells (WBCs). Leukocyte rich plasma (LRP) was prepared with WBC to RBC ratio on the order of 1:1. The difference between scatter plot of diluted blood and LRP shows the characteristics of WBCs. WBCs have higher impedance magnitude for both frequencies than RBCs, but the opacity (the slope of fitted straight line) almost stays the same. Two epithelial tumor cell lines (breast adenocarcinoma MCF7, Φ13.6μm±1.3μm; urinary bladder carcinoma T24, Φ16.43μm±1.16μm) were used as models of tumor cell characterization. Both types of the tumor cells might be circulating tumor cells in bloodstream. Fig.6 shows scatter plots of each cell line without and with added blood. The diluted blood acted as an internal reference and also as a model system for detection circulating tumor cells in blood. Both cell lines have a range of impedance values, but the opacity keeps relatively constant. Also they are distinctive from blood cells, which can be the basis for detection and isolation of circulation tumor cells from bloodstream.

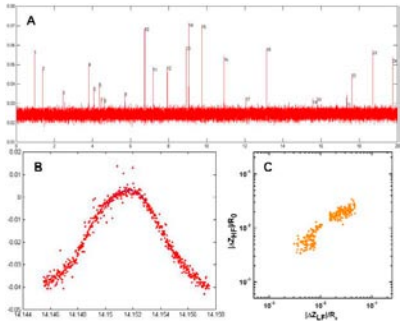

Figure 4. Testing with 5 µm and 10 µm polystyrene beads mixture in 20 µm channel dimension device. (A) Time trace of 20 seconds. (B) Close-up of an individual peak. (C) Scatter plot of impedance magnitude..

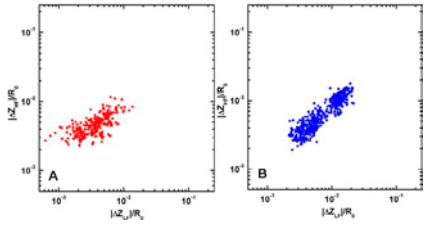

Figure 5. Scatter plots of testing with 200 times diluted human whole blood (A) and 1:1 diluted leukocyte rich plasma (B) in 15µm channel dimension device.

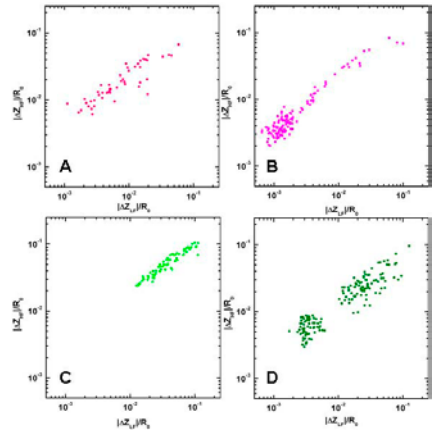

Figure 6. Scatter plots of testing with: (A) breast canner cell line MCF7, (B) MCF7 mixed 1:1 with 1000 times diluted human whole blood, (C) bladder canner cell line T24 and (D) T24 mixed 1:1 with 1000 times diluted human whole blood in 20µm channel dimension devices.

5. CONCLUSIONS

Dual frequency inductor induced resonance impedance spectroscopy is demonstrated for blood cell and tumor cells sensing. Scatter plots can differentiate leukocytes from erythrocytes, as well as solid tumor cells from blood cells.

ACKNOWLEDGEMENTS

The authors would like to thank Henry Lin from University of Southern California, U.S.A. to provide tumor cells for testing. This work was supported by the National Space Biomedical Research Institute (NSBRI) through NASA NCC 9-58.

REFERENCES

[1] S. Gawad, L. Schild, and P. Renaud, "Micromachined impedance spectroscopy flow cytometer for cell analysis and particle sizing," *Lab on a chip*, vol. 1, pp. 76, 2001.

[2] A. Han, L. Yang, and A. B. Frazier, "Quantification of the heterogeneity in breast cancer cell lines using whole-cell impedance spectroscopy," *Clinical Cancer Research*, vol. 13, pp. 139-143, 2007.

[3] K. Cheung, S. Gawad, and P. Renaud, "Impedance spectroscopy flow cytometry: On-chip label-free cell differentiation," *Cytometry Part A*, vol. 65A, pp. 124-132, 2005.

ELECTRICAL DETECTION OF ION CHANNEL ACTIVITY IN AN ARRAY OF SUSPENDED LIPID BILAYERS

Armelle Varnier[1], Thomas Plénat[1], Lamya Ghenim[1], Damien Fajolle[2], Vincent Agache[2], Fabien Sauter[2], François Chatelain[1] and Alexandra Fuchs[1]

[1]Laboratoire Biopuces, DSV, CEA Grenoble, FRANCE and
[2]CEA-LETI, MINATEC, FRANCE

ABSTRACT

We present here an array of individual suspended bilayers integrated on a printed card board, allowing parallel measurement of the activity of embedded ion channels. Solvent-free lipid bilayers are suspended over a two micron diameter aperture processed in a silicon membrane. The aqueous solution reservoirs on each side of the membranes are formed by droplets that can be deposited by any standard dispensing robot. Signal recordings induced by addition of the channel forming peptide Alamethicin in the lipid membrane are shown.

Keywords: Channel, lipid bilayer, patch clamp, silicon

1. INTRODUCTION

In pharmaceutical research, fast and highly sensitive methods for functional drug screening are in demand as an increasing number of membrane proteins, ion channels in particular, are identified as targets for therapeutic agents. Several reports of ion channel recordings using planar substrates have been published [1-3], but novel designs are needed to meet the requirements of high throughput screening (HTS). Silicon wafer process allows for high yield production of microsized pores on silicon nitride membranes. The small size of the aperture is compatible with the formation of a solvent-free lipid bilayer over the pore, by fusion and burst of giant lipid vesicles. Microelectronic fabrication allows easy integration of individual electronic circuits and parallel measurement over an array of individual sites. Surface treatment of the printed card board (PCB) hosting the silicon membranes was designed for the partition of 10 - 20 µl droplets on each site, compatible with liquid deposition by any standard dispensing robot and avoiding the need for individual fluidic channels. We report here the fabrication of solvent-free suspended lipid bilayers over the micropores array and Alamethicin activity recording.

2. EXPERIMENTAL

The fabrication process of silicon nitride/silicon dioxide membranes and the chip packaging was reported at "Transducers 2007" [4]. Figure 1 shows the multisite device and the schematic cross section of a single measuring site.

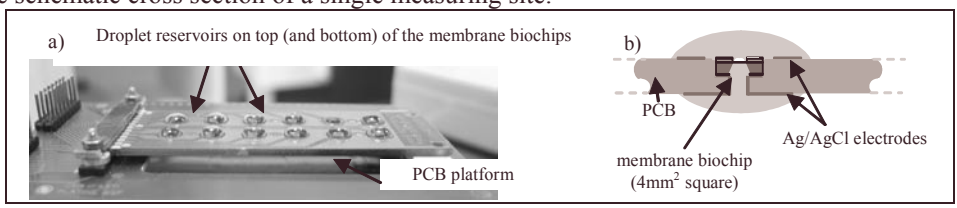

Figure 1. a) PCB into which are inserted the chips [4] b) Cross-section view of a biochip.

978-0-9798064-0-7/µTAS2007/$20©2007CBMS

Silicon nitride membranes were passivated with 2µm of thermal oxide. Chips were treated under oxygen plasma prior to use, charging the layer negatively. The buffer solution contained 5 mM HEPES pH 7.4, 100 mM KCl, 5 mM $CaCl_2$. The measurement of the ionic flux through the aperture was carried with an Axopatch 200B connected to the pins of the PCB.

Negatively charged giant unilamellar vesicles (GUVs) made of asolectin were produced by electroformation and dispensed to the upper droplet-reservoirs over membranes bearing a single pore. Simultaneously, an appropriate voltage bias was applied across the silicon membrane to electrofocus the sucrose-loaded GUVs towards the pore. Concomitantly, impedance measurements were taken to follow vesicle fusion over the pore. After a seal formation was obtained, 1 µl of a freshly made solution of Alamethicin in the same buffer solution with 0.1% ethanol is added to the upper droplet to a final concentration of 20 nM.

3. RESULTS AND DISCUSSION

We found that the resistance increased drastically from a few hundred kOhm to a few GOhm upon addition of the GUVs. Figure 2 shows that the current decreases within a few seconds.

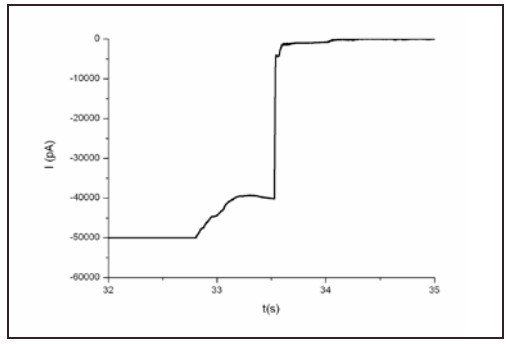

Figure 2. Current versus time for -100 mV applied voltage, showing the seal formation after addition of negatively charged vesicles.

A few minutes after dispensing Alamethicin in the upper droplet, the current increases over a few tens of seconds. Figure 3 shows the ionic current as a function of time induced by addition of the peptide.

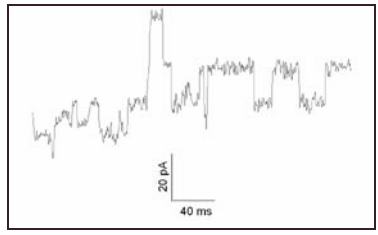

Figure 3. Electrical signal induced by addition of Alamethicin to a final concentration of 20 nM. Current versus time diagram recorded at V=-80mV in 5 mM HEPES pH 7.4, 100 mM KCl and 5 mM $CaCl_2$.

4. CONCLUSIONS

We have shown the functionality of this device with a channel forming peptide. Complex membrane receptors associated to an ion channel can be incorporated in giant unilamellar vesicles and could be used for the functionalization of the device with target proteins of valuable interest for pharmaceutical industries.

ACKNOWLEDGEMENTS

This work is supported by the 6th Framework Programme of the European Commission under the contract NMP4-CT-2005-017114 "RECEPTRONICS".

REFERENCES

[1] "A Chip-Based Biosensor for the Functional Analysis of Single Ion Channels," C. Schmidt, M. Mayer, H. Vogel, Angew. Chem. Int. Ed., **39**, 3137 (2000)

[2] "High-resolution electrophysiology on a chip: Transient dynamics of alamethicin channel formation," M. Sondermann, M. George, N. Fertig, J.C. Behrends, Biochimica Biophysica Acta, **1758**, 545 (2006)

[3] "Silicon chip-based patch-clamp electrodes integrated with PDMS microfluidics," R. Pantoja, J.M. Nagarah, D.M. Starace, N.A. Melosh, R. Blunck, F. Bezanilla, J.R. Heath, Biosens Bioelectron., **20**, 509 (2004)

[4] "Fabrication and packaging of nanoporous membrane chips for label-free ion-channel tranducer based biosensor," V. Agache, F. Sauter, C. Pudda, R. Blanc, C. Chabrol, P. Caillat, T. Plenat, A. Varnier Agasøster, L. Ghenim, A. Fuchs, Transducers (2007)

IMPEDANCE SPECTROSCOPY ON A MICROFABRICATED FLOW CYTOMETER: LABEL-FREE DETECTION OF *BABESIA BOVIS* PARASITES IN BOVINE RED BLOOD CELLS

C. Küttel[1], E. Nascimento[2], N. Demierre[1], T. Silva[2], T. Braschler[1], A.G. Oliva[2] and P. Renaud[1]

[1]Ecole Polytechnique Fédérale de Lausanne, SWITZERLAND, and [2]Universidade Nova de Lisboa, PORTUGAL

ABSTRACT

In this paper we report the detection of *Babesia bovis* infected red blood cells by microchip based impedance spectroscopy. The microfabricated chip with single-sided liquid electrodes allows a simple setup for impedance spectroscopy. With this device we achieved the detection of parasitised red blood cells without staining or time-consuming sample pretreatment.

Keywords: Microfabricated Flow Cytometer, Impedance Spectroscopy, Label-Free, Dielectrophoretic Parasite Detection

1. INTRODUCTION

Impedance spectroscopy is a non-invasive, potentially cheap method for detecting and sorting cellular populations. Further it offers the advantage of easy integration on chip, as only electrodes and microchannels are required for its implementation [1]. In contrast to other well-known detection methods [2] this method does not require any expensive reagents for sample preparation nor does it imply any cell modification by staining.

B. bovis is an intraerythrocytic unicellular parasite infecting bovine red blood cells. It is responsible for great economic losses in cattle industry. The life-cycle of *B. bovis* is very similar to that of *Plasmodium sp.*, the agent of malaria in humans [3].

The changes in cellular impedance have been used for enrichment of malaria-infected erythrocytes by free-flow fractionation using dielectrophoresis [4]. We propose here to use the properties of similar changes in impedance to detect *B. bovis* infected cells, which has to our knowledge not been reported yet.

2. EXPERIMENTAL

We use a differential bipolar measurement setup for the impedance measurement. To reduce the complexity and cost of the chip fabrication, we implemented single-sided electrodes, which can also be used for on-chip dielectrophoresis [5].

The Ti/Pt (20nm/200nm) electrode pairs are fabricated on float-glass wafers by a liftoff procedure and the fluidic channels are defined by lithography of SU-8 (20µm) (Fig. 1A). To close the entire structures a flat PDMS cover containing the predefined access holes for the liquids is reversibly bonded to the chip. Small posts on the electrodes avoid sagging of the PDMS cover and enable with this a larger area of the single-sided liquid electrodes.

The cells are driven through the microchannels by defined overpressures at input and output and the particle stream is focused with sheath flow, where the side inlets allow the focusing of the particle flow from the particle inlet in the middle.

978-0-9798064-0-7/µTAS2007/$20©2007CBMS

An AC electric field is applied between the two electrodes of each electrode pair. To avoid signal-drift we measure and compare the current across two electrode pairs (Fig. 1B), as previously described for top-bottom electrodes [1]. The current between each electrode pair is propotional to the impedance in the channel, which shifts when a cell is passing. The cell's impedance depends on the amount of polarisation and on the frequency of the applied electric field. At low frequencies, the measured impedance gives information about the cell size since the current mainly flows around the particle due to the membrane capacitance. The higher the frequency, the lower the membrane polarisation and the more current flows through the cytoplasm revealing the impedance of the cell interior.
Calibration with microbeads showed a broad frequency range available for measurements (30 kHz - 20 MHz) and a coefficient of variation (CV) comparable to other methods (CV for 6 μm beads: vendor 1 %, this system 2.7 %).

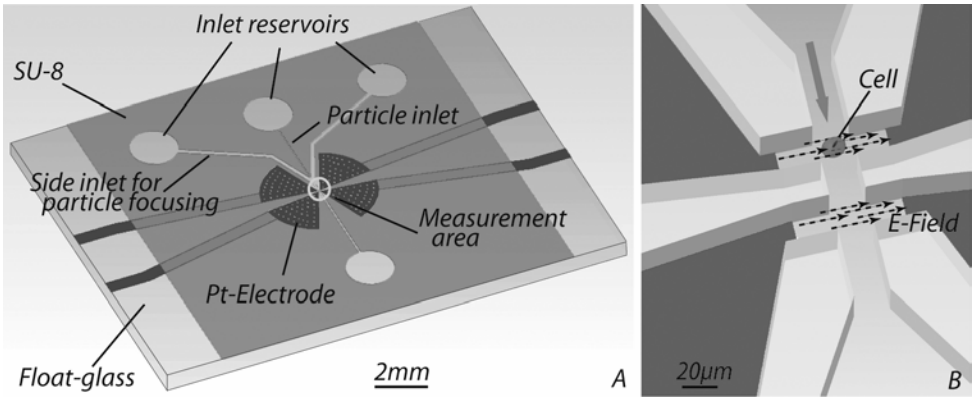

Figure 1. Schematics of the microfluidic device for impedance spectroscopy. The device is shown without PDMS cover. (A) Chip design – the Pt electrodes and the SU-8 layer for definition of the microfluidic channels and liquid reservoirs are structured on a float-glass chip. (B) Illustration of the measurement area - a cell flows along the fluidic channel (arrow) and comes in reach of the electrical field of the first electrode pair. The measured current is compared to the current of the second electrode pair without cell.

3. RESULTS AND DISCUSSION

B. bovis infected samples with different parasitaemias and control samples of uninfected bovine erythrocytes and erythrocyte ghosts synthesized from uninfected bovine erythrocytes were analysed at an optimal frequency of 8.7 MHz. Impedance changes at this frequency indicate a variation of the dielectric properties of the cytoplasm. The resulting scatterplot (Fig. 2) is divided in three areas, parasitised red blood cells (C), uninfected red blood cells (B) and ghost red blood cells (A). The sample containing infected cells shows changes of the signal amplitudes into area C, which do not appear in the uninfected control sample, and an average change in signal phase of 20° can be observed. Erythrocyte ghosts of all three samples, which appear due to membrane rupture or cell ageing, are located in area A. The assignment of areas was verified by additional measurements with a simultaneous optical assay of the *B. bovis* infected samples using fluorescence microscopy.

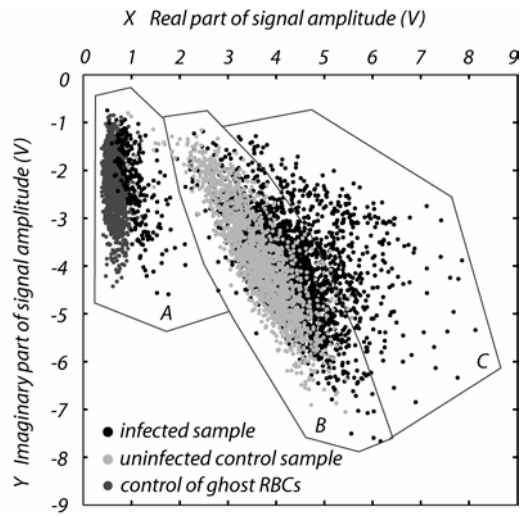

Figure 2. Representative scatterplot of on-chip impedance spectroscopy measurements of the dielectric changes in *Babesia bovis* infected cells at 8.7 MHz. The domains for uninfected RBCs (B), parasitised RBCs (C) and ghost RBCs (A) are marked. The signal amplitudes are split into real (X) and imaginary (Y) parts. The number of cells used was 2700 (infected sample), 1700 (uninfected control sample), and 1500 (control of ghost RBCs) after extraction of invalid signals from the samples.

4. CONCLUSION

The obtained results show that a detection of *B. bovis* infected red blood cells is possible using on-chip impedance spectroscopy. Future work with samples from infected animals can show the sensitivity limitations of such a sensor.

ACKNOWLEDGEMENTS

B. bovis clonal lines M07 and C61411 were kindly provided by Dr. Erik de Vries, Utrecht University, Netherlands. Bovine blood from healthy donors was kindly provided by Dr. Maria Irene Vasques and Dr. João Maria Neto, Estação Zootécnica de Santarém, Portugal. This work was supported by the European Community-funded CellPROM project under the 6th Framework Programme, contract No. NMP4-CT-2004-500039.

REFERENCES

[1] S. Gawad, L. Schild, P. Renaud, *Micromachined impedance spectroscopy flow cytometer for cell analysis and particle sizing*, Lab Chip 1, pp. 76-82, (2001).
[2] R. Böse, W.K. Jorgensen, R.J. Dalgliesh, K.T. Friedhoff, A.J. de Vos, *Current state and future trends in the diagnosis of babesiosis*, Vet. Paras. 57, pp. 61-74, (1995).
[3] B.M. Cooke, N. Mohandas, A.F. Cowman, *Cellular adhesive phenomena in apicomplexan parasites of red blood cells*, Vet. Parasitol. 132, pp. 273-295, (2005).
[4] P. Gascoyne, J. Satayavivad, M. Ruchirawat, *Microfluidic approaches to malaria detection*, Acta Trop. 89, pp. 357-369, (2004).
[5] N. Demierre, T. Braschler, P. Linderholm, U. Seger, H. Van Lintel, P. Renaud, *Characterization and optimization of liquid electrodes for lateral dielectrophoresis*, Lab Chip 7, pp. 355-365, (2007).

CANTILEVER-BASED SENSOR WITH INTEGRATED OPTICAL READ-OUT USING SINGLE MODE WAVEGUIDES

Maria Nordström[1], Dan. A. Zauner[1], Montserrat Calleja[2], Jörg Hübner[1] and Anja Boisen[1]

[1]MIC – Department of Micro and Nanotechnology, Nano DTU, Technical University of Denmark, DTU bldg. 345 east, DK-2800 Kgs. Lyngby, Denmark

[2]Biosensor Group, Institute of Microelectronics of Madrid, IMM-CSIC, Isaac Newton 8 (PTM), 28760 Tres Cantos, Madrid, Spain

ABSTRACT

This work presents the design, fabrication and mechanical characterisation of an integrated optical read-out scheme for cantilever-based biosensors. A cantilever can be used as a biosensor by monitoring its bending caused by the surface stress generated due to chemical reactions occurring on its surface. Here, we present a novel integrated optical read-out scheme based on single-mode waveguides that enables the fabrication of a compact system. The complete system is fabricated in the polymer SU-8. This manuscript shows the principle of operation and the design well as the fabrication of the system and characterisation of the read-out method.

Keywords: Cantilever sensor, SU-8, integrated waveguides

1. INTRODUCTION

Cantilever-based biosensors have evolved as a promising alternative to surface plasmon resonance (SPR) and quartz crystal microbalances (QCM) for biosensing applications such as detection of DDT [1] and protein conformations [2]. The read-out of the cantilever is obtained by monitoring the bending of the cantilever structure, which is a beam of micrometer dimensions clamped at one side and free to move at the other [3]. To increase the sensitivity of the cantilever it is beneficial to fabricate the structure in a polymeric material due to the low Young's modulus of such materials compared with Si or Si_3N_4, conventionally used [4]. However, to obtain a true point-of-care diagnostics device the system should also be portable and therefore we have developed an integrated optical read-out method. Here, the light is guided via single-mode waveguides towards the cantilever and is transmitted through the cantilever structure, that also acts as a waveguide, and exits the system via an output waveguide. Figure 1 shows a schematic drawing of the system. As the cantilever deflects, less light can couple between the cantilever and the output waveguide and the decrease in optical output from the output waveguide is used as the read-out of the degree of cantilever bending.

2. SYSTEM DESIGN & FABRICATION

The complete system is fabricated in the polymer SU-8. SU-8 2005 is used for the core structures of the single-mode waveguides and the cantilever. The modified SU-8, mr-L 6050 [5] is used as cladding material and also comprises the chip body. The chemical modification of the mr-L material is an addition of the plasticizer *propylene carbonate* that reduces the refractive index of the material by 0.004 compared with standard SU-8. This

978-0-9798064-0-7/μTAS2007/$20©2007CBMS

material combination ensures a good modal match with the input and output fibers as well as reduced process challenges due to the low stress properties of the mr-L resist [6]. The cantilever/waveguide layer has a thickness of 4.5 µm to ensure that the waveguides are single-mode in the vertical direction when operated at a wavelength of 1310 nm. The light is guided from the laser source (HP 81552SM) via single-mode fibers of 9 µm diameter to the chip where it is butt-coupled into the single-mode input waveguides. The width of the waveguides is 10 µm to ensure low coupling losses. Between the input waveguide and cantilever there is a 5-µm-wide gap where the light crosses. The light then travels into the cantilever waveguide, which is 75 µm wide and 100 µm long and exits the system via the output waveguide that is tapered down from the cantilever width to 10 µm. The intensity of the output light is detected by a photo-detector (HP 81532A).

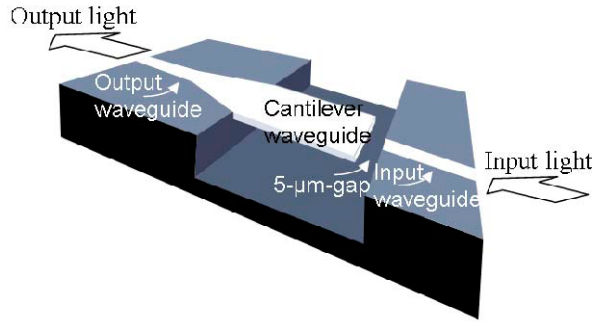

Figure 1. Schematic drawing of the system with the different waveguide regions marked. As the cantilever deflects, less light can couple into the cantilever. This intensity decrease is used as the read-out of the cantilever deflection.

At perfect alignment of the cantilever and the output waveguide, approx. 40 % of the light couples into the cantilever waveguide. As the cantilever deflects, the intensity of the output light decreases with a Gaussian distribution following the single-mode profile of the waveguides. The propagation loss of these waveguides at 1310 nm is 1 dB/cm and the coupling loss is 0.25 dB/facet.

Both SU-8 and mr-L are negative resists that are structured by UV lithography. The chips are structured 'up-side-down' with the cantilever/waveguide layer facing the 4" Si carrier wafer and the lower cladding structured on top. A fluorocarbon coating is used for a dry release [7]. After release, the chips are turned and air is used as top cladding of the waveguides. Figure 2 shows a SEM image of a final chip, zoomed at the cantilever region.

3. READ-OUT CHARACTERISATION

The read-out principle is characterised by mechanically deflecting the cantilever a known distance by a tungsten probe. The probe is mounted in a custom-built set-up where its position can be controlled in all three directions. The vertical displacement of the probe is controlled to a precision of ± 0.25 µm. The read-out in the transmission mode is monitored as the cantilever is deflected a total distance of 9 µm downwards. The output data is shown in figure 3. From the graph it can be seen that a minimum detectable cantilever deflection of 45 nm can be obtained if the system is operated in the most sensitive region with an initial deflection of 3 µm. This value is found by estimating the minimum detectable change in intensity to be 0.01 µW. A 45 nm deflection corresponds to

a differential surface stress of 0.19 N/m for this 100 µm long and 4.5 µm thick cantilever structured in SU-8.

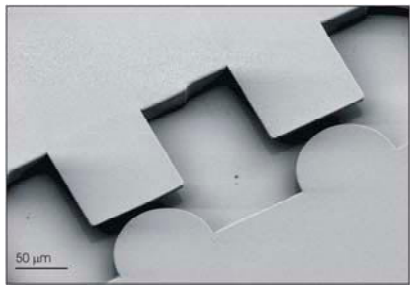

Figure 2. A zoom of two free-hanging cantilevers where air is used as the top cladding and mr-L is structured as the bottom cladding and chip body. These input waveguides have been structured with two lenses. However, these were not used on the characterization chip.

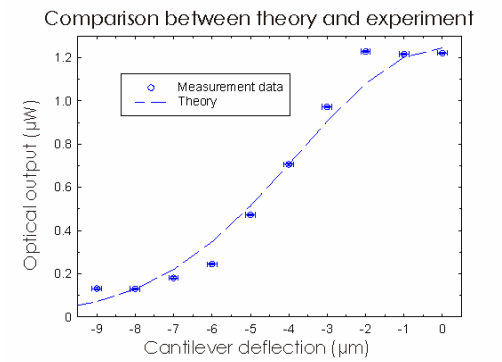

Figure 3. As the cantilever is deflected the output intensity is decreased following a Gaussian distribution corresponding to the mode profile of the single-mode waveguide. A good match between the theoretically calculated data points and the measured data is seen.

4. CONCLUSIONS

The system presented here shows a novel integrated optical read-out scheme for cantilever-based sensors. This read-out method opens up for the fabrication of portable analysis systems since the bulky external optical read-out is not used. The results show that a differential surface stress of 0.19 N/m can be measured with this system but naturally this sensitivity can be further improved by fabricating a longer and thinner cantilever.

REFERENCES

[1] M. Álvarez, A. Calle, J. Tamayo, L.M. Lechuga, A. Abad, A. Montoya, *Development of nanomechanical biosensors for detection of the pesticida DDT*, Biosensors & Bioelectronics **18** (2003) 649-653

[2] R. Mukhopadhyay, V.V. Dumbayev, M. Lorentzen, J. Kjems, P.A. Andreasen, F. Besenbacher, *Cantilever sensors for Nanomechanical detection of specific protein conformations*, Nano Letters **5**(12) (2005) 2385-2388

[3] M. Calleja, J. Tamayo, A. Johansson, P. Rasmussen, L. Lechuga, A. Boisen, *Polymeric cantilever arrays for biosensing applications*, Sensor Letters **1** (2003) 20-24

[4] M. Calleja, J. Tamayo, M. Nordström, A. Boisen, *Low-noise polymeric nanomechanical biosensors*, Applied Physics Letters **88** (2006) 113901

[5] www.microresist.de

[6] M. Nordström, D.A. Zauner, A. Boisen, J. Hübner, *Single-mode waveguides with SU-8 polymer core and cladding for MOEMS applications*, Journal of Lightwave Technology **25**(5) (2007) 1284-1289

[7] D. Haefliger, M. Nordström, P.A. Rasmussen, A. Boisen, *Dry release of all-polymer structures*, Microelectronic Engineering **78-79** (2005) 88-92

DEVELOPMENT OF NOVEL CELL ANALYTICAL SYSTEM BASED ON HIGH SENSITIVE QCM SENSOR

Etsuko WATARAI, Madoka TAKAI, and Kazuhiko ISHIHARA

Department of Materials Engineering, School of Engineering, Center for NanoBio Integration, The University of Tokyo, Japan

ABSTRACT

We developed novel cell analytical system, which can analyze materials-single cell interactions by the quartz crystal microbalance (QCM). The QCM of 35 MHz for controlling measurement area was used and the correlation with a few attachment cells compared with 9 MHz was observed. The phospholipid polymer for controlling cell attachment area was used and the polymer surface resisted cell attachment by 95 % compared with the Au surface. Furthermore, we fabricated microchip which channel was 30 μm in width and separated a single cell. This QCM system combined with microchip was suitable for the single cellular behavior analysis on materials.

Keywords: QCM, phospholipid polymer, materials-cell interactions

1. INTRODUCTION

As a high-resolution mass and viscoelasticity sensor, the quartz crystal microbalance (QCM) has been widely used in biology and biotechnology, increasingly in bioadhesion and biosensors fields. Especially as a measure of analyzing materials-cell interactions, QCM is an effective device for real-time and quantitative monitoring. However, these studies treated large number of cells approximate to confluent state and various effects including cell-cell interactions are confused, so materials-cell interactions cannot be understood. Therefore, it is necessary for accurate analysis of materials-cell interactions to focus on a single cell on the materials and understand reversible and irreversible mechanism of complex network of the cell. So, constructing novel cell analytical system based on high sensitive QCM with controlled electrode like cell array (Fig. 1) is important.

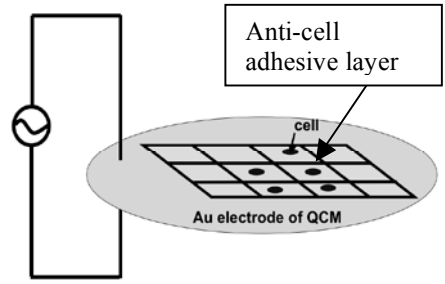

Figure 1. Schematic illustration of QCM with controlled electrode.

2. EXPERIMENTAL

From our previous research, by using 9 MHz quartz, single cellular behavior on different materials could be measured by the QCM using resistance change (ΔD), which is related to the number and geometry of adherent cells(Fig. 2). However, the Δf was independent, it was caused by the difference of the sensitivity of the area on the surface[1], and it was found that the cell attachment and measurement area should be limited when analyzing of single cellular behavior with Δf. So, we solved the problem by using 35 MHz (overtone of 5 MHz) for controlling measurement area, because in the case of overtones, the higher frequency is used, the smaller area is measured, and by using newly synthesized phospholipids polymer; PMSH(Fig. 3) for controlling cell attachment area. The PMSH has

978-0-9798064-0-7/μTAS2007/$20©2007CBMS

thiol group in the side chain which binds covalently to Au electrode of QCM and phospholipids(PC) group which was inspired from the cell membrane structure to inhibit the non-specific cell adhesion[2].

By using QCM of 35 MHz quartz, the cellular behaviours [250,000, 25,000, 2,500 cells/mL × 80 μL (capacity of QCM chamber) L929 cell suspension (medium: Dulbecco's Modified Eagle Medium without serum)] on Au electrode and PMSH at 37℃ for 3 h are summarized from the data of the Δf and the cell geometry was observed by optical microscope.

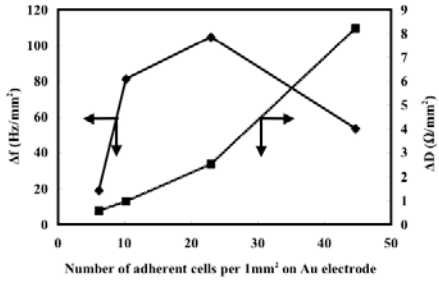

Figure 2. Correlation between Δf, ΔD values and the number of cells attached (using 9 MHz quartz).

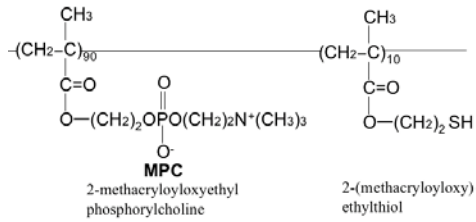

Figure 3. Chemical structure of PMSH.

3. RESULTS AND DISCUSSION

The cellular behaviours and the cell geometry on Au electrode and PMSH monitored by QCM and microscope are shown in Fig. 4, Fig. 5, Fig. 6. It is found that PMSH surface inhibited cell attachment and spreading by 95% of the Δf values comparing with the Au electrode. Even more interesting, cells on PMSH made round shape, while cells on Au adhered and spread steadily with spatulate shape. As shown in Fig. 7, the correlation between Δf of 35 MHz and the number of cells attached on the surface, in comparison to Δf of 9 MHz (Fig.2), suggested that the behavior of a single cell could be measured with QCM of 35 MHz. Furthermore, we fabricated cell separation microchannel chip taking a single cell made of polydimethylsiloxane (PDMS), whose inner face was modified with another phospholipid polymer (PMED) for PDMS[3, 4] (Fig. 8). By using this microcahnnel chip, we could examine interactions between materials and desired number cells by the QCM system with the chip.

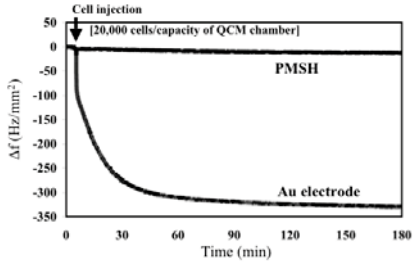

Figure 4. Measurement result of QCM of L929 cellular behavior on Au and on PMSH (using 35 MHz).

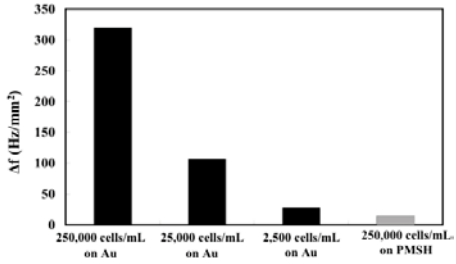

Figure 5. The Δf value of each cell density after 3h.

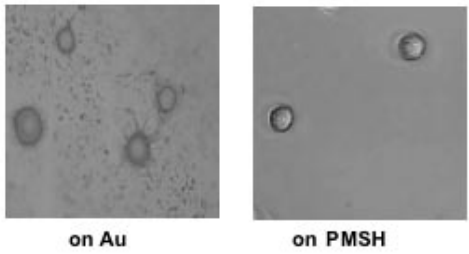

Figure 6. Photographs of L929 cellular behavior in 90 min after injection of cell suspension on Au electrode and on PMSH.

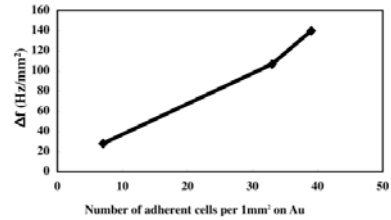

Figure 7. Correlation between Δf values and the number of cells attached (using 35 MHz quartz).

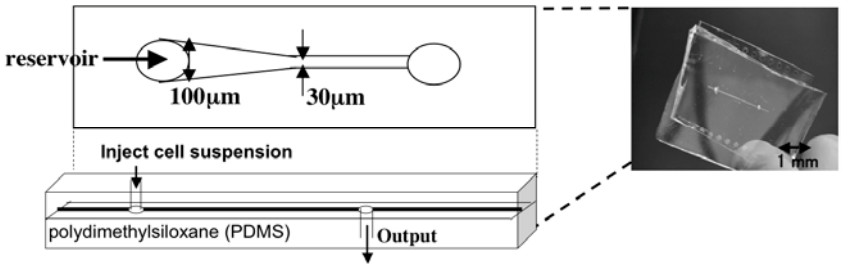

Figure 8. Schematic illustration and photograph of cell separation microchannel chip.

4. CONCLUSIONS

The PMSH resisted cell attachment and QCM of 35 MHz resulted in the correlation with the small number of attachment cells on the surface compared with 9 MHz. From above, it is concluded that the PMSH can be utilized to limit the cell attachment area and high sensitive QCM of 35MHz is suitable for the single cellular behavior for investigating materials-cell interactions. By combination with the single cell separation microchannel chip and the high sensitive QCM having controlled electrode, it is confirmed that various materials-cell interactions can be analyzed quantitatively.

This system provides us to examine materials-cell interactions and design materials for tissue engineering.

REFERENCES

[1] C. Kurosawa et al. “Computational Simulation of Vibration Displacement on Piezoelectric Quartz Crystal Using Finite Element Method”, Proceedings of the 2004 IEEE International Frequency Control Symposium and Exposition, 554-557 (2005. 3).

[2] K. Ishihara et al. “Hemocompatibility of human whole blood on polymers with a phospholipid polar group and its mechanism”, J. Biomed. Mater. Res. , 26, 1543–52 (1992).

[3] J. Sibarani et al. ”Surface modification on microfluidic devices with 2-methacryloyloxyethyl phosphorylcholine polymers for reducing unfavorable protein adsorption”, Coll. and Surf. B: Biointerface, 54(1), 88-93 (2007).

[4] E. Watarai et al. ”Analysis of material-cell interaction by QCM sensor combined with cell separation chip”, Proceedings of UT Symposium on NanoBio Integration, 319-320 (2006. 12).

MICROFLUIDIC IMMUNOCHIP BASED ON ELECTRICAL DETECTION SYSTEM FOR CANCER BIOMARKER

Joon-Ho Maeng[1], Yong-jun Ko[2], Yoomin Ahn[2], Seoung-Hwan Lee[2], Nahm-Gyoo Cho[2] and Seung Yong Hwang[3]

[1]Dept. of Biochemistry, [2]Dept. of Mechanical engineering, [3]Div. of Molecular and Life Science, Hanyang University, Ansan, Korea

(E-mail: syhwang@hanyang.ac.kr)

ABSTRACT

We have developed and characterized a novel microbiochip which can simultaneously detect three cancer biomarkers by using microbeads, gold nanoparticles and silver enhancer. The integrated microbiochip that includes a Pt electrode to measure an electrical signal and a microfilter to fix the microbeads was fabricated. We adopted a filtration method using microbeads to immobilize antibody and an immuno-gold silver staining (IGSS) method to amplify electrical signals. Cancer biomarkers, α-fetoprotein (AFP), carcinoembryonic antigen (CEA) and prostate-specific antigen (PSA), were successfully assayed by a sandwich immunoassay with this system.

Keywords: Microbead, Microfilter, Immuno-gold silver staining, Biomarker

1. INTRODUCTION

Immunoassay is extensively applied for clinical diagnosis because of high specificity and sensitivity. However, the conventional immunoassay is laborious, expensive, and requires prolonged development time. Since large scale detection devices are also needed, immunoassays are difficult to adopt in Point Of Care Testing (POCT). In order to improve these problems, we developed a PDMS-glass microbiochip which can detect an antigen-antibody reaction through electrical signals. Platinum (Pt) electrodes for electrical signal were fabricated onto the glass substrate and a microchannel and pillar-type microfilter was formed in the PDMS layer. The detection of cancer biomarkers (AFP, CEA and PSA) was performed in the microfluidic immunochip to demonstrate that the microbead, microfilter and immuno-gold-silver staining (IGSS) complex could be used for signal amplification. Immuno-gold-silver staining employs a histochemical method called autometallography (AMG) to amplify tiny gold particles. Gold particles in the presence of silver ions and a reducing agent act as a catalysts to reduce silver ions to metallic silver. The silver is then deposited onto the gold and enlarges the particles (30 to 100 nm diameter) [1-3].

2. EXPERIMENTAL

The working concept of bead based immunosensor is shown in Fig. 1. Streptavidin coated microbeads were selected for the solid phase and the microbeads were coated with biotinylated antibody (capture antibody) using the ABC (avidin-biotin coupling) method. The complexes were then introduced to the microbiochip by a syringe pump. They were put on a Pt electrode by the microfilter in the microbiochip. Next, a sample containing biomarkers (AFP, CEA and PSA) was reacted with the beads, and the gold nano-particle

978-0-9798064-0-7/μTAS2007/$20©2007CBMS

conjugated antibody (second antibody) was introduced into the microchannel. Before the silver enhancer was injected, unbound antibody and antigen were removed by washing buffer. To amplify the electrical signal, the silver enhancer was injected to the washed particles. Finally, washing buffer was injected and a silver bridge was formed between the Pt electrodes, provided the sandwich immune-complex was specifically formed. Thus, it is possible for Pt electrodes to be charged with electric current. Electrical resistance was measured with a multimeter.

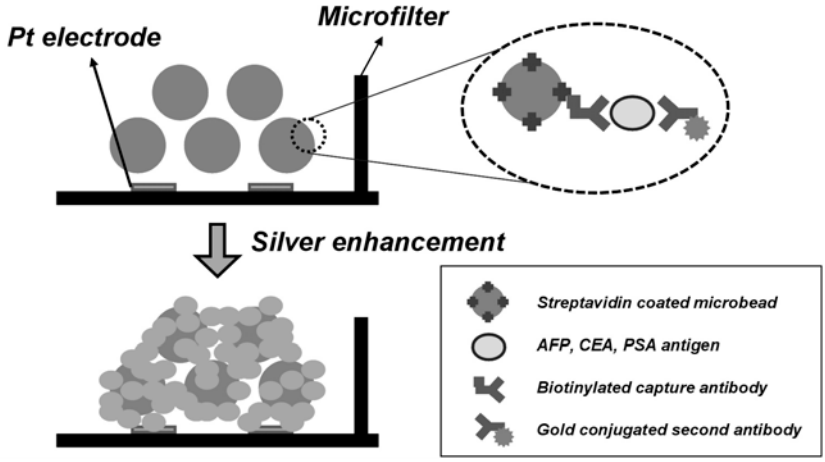

Fig. 1 Schematic of the electrical immunoassay using microbeads to the IGSS.

3. RESULTS AND DISCUSSION

3.1 Microbiochip design and fabrication

The chip is composed of a PDMS layer over a Pyrex glass substrate. A platinum (Pt) microelectrode for electrical signal detection was fabricated on the substrate and microchannel and a pillar-type microfilter was formed in the PDMS layer (Fig. 2, 3).

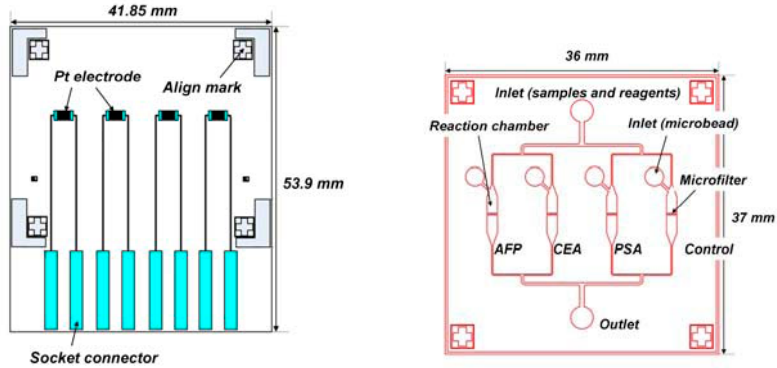

Fig. 2 Layout of microfluidic immunochip. (Left) Pt electrode coated glass chip; (Right) PDMS (inlet, outlet, reaction chamber)

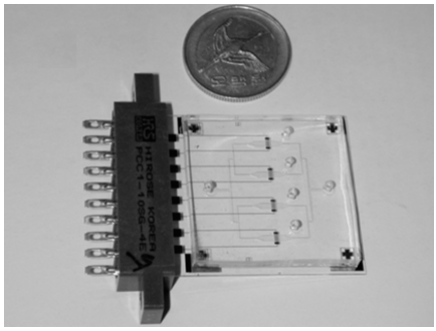

Fig. 3 Photograph of the fabricated microbiochip.

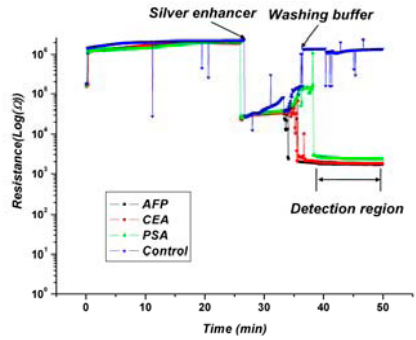

Fig. 4 The electrical signal curve (Time versus Resistance).

3.2 Measurement of electrical signal

Under the optimal condition, we were able to measure an electrical signal with three biomarkers. The signal pattern of resistance corresponding to time is shown in Fig. 4. Resistance, which is measured from the microbead injection to the second antibody was approximately 8~10 MΩ. The resistance is nearly constant during each step. When the silver enhancer was injected for signal amplification, resistance dramatically decreased to about 1~10 kΩ. As the concentration of biomarkers decreased, the resistance gradually increased (Fig. 5). The total assay time including all incubation and detection steps were less than one hour.

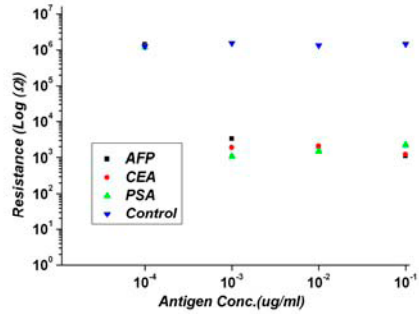

Fig. 5 Antigen concentration dependence of resistance.

4. CONCLUSIONS

The electrical detection of AFP, CEA and PSA was successfully achieved in a microfluidic immunochip, and our immunoassay results are adequate for use in clinical diagnosis. Moreover, this system can be further miniaturized and integrated with microfluidic devices.

ACKNOWLEDGEMENTS

This work was supported by grant No. R01-2003-000-10614-0 from Basic Research Program of the Korea Science & Engineering Foundation.

REFERENCES

[1] Baschong, W., Stierhof, Y.D., Microsc. Res. Tech. 42, 66-79 (1998)
[2] Lackie, P.M., Histochem Cell Biol 106, 9-17 (1996)
[3] Weipoltshammer, K., et al., Histochem Cell Biol 114, 489-495 (2000)

SUPRAMOLECULAR CHEMISTRY IN AN NMR-CHIP

M. Victoria G mez ,[1] David. N. Reinhoudt[1] and Aldrik H. Velders[1]

[1]Supramolecular Chemistry and Technology. Faculty of Science and Technology. MESA + Institute for Nanotechnology. University of Twente. Enschede. NETHERLANDS

ABSTRACT

A microfluidic chip equipped with a planar transceiver nuclear magnetic resonance coil (viz. an NMR-chip) has been designed for the excitation and detection of NMR signals at 9.4 T (400 MHz). The resolution and the sensitivity obtained with the NMR-chip are surprisingly good and open the way for the investigation of complexation studies inside a microchip. In a proof of principle we studied the host-guest interaction of double rosettes and more recently now also β-cyclodextrin (β-CD) with benzoic acid (BA) inside the microfluidic chip.

Keywords: NMR, microfluidic chip, supramolecular chemistry

1. INTRODUCTION

Recently, an NMR-chip has been designed and employed for the kinetic measurements of a condensation reaction using a 60 MHz apparatus [1]. Respect to our previous work we have significantly improved the system which now works at 9.4 T (400 MHz). The higher resolution ($\Delta\upsilon$ = 3Hz, 0.009 ppm) and higher sensitivity obtained with our new design offer the possibility of working with more complicated chemical structures and at much lower concentrations, which opens the window to study supramolecular interactions and complexation inside the NMR-chip with very small quantities of material.

2. THEORY

One particularly approach to enhance NMR sensitivity for small-volume, mass-limited samples uses reduced diameter NMR coils [2]. Miniaturized coils may be used advantageously since the amplitude of the NMR signal is maximized when the size of the RF coil matches that of the sample. Reducing the coil diameter improves the signal to noise ratio (SNR), but also decreases the NMR spectral resolution. Most of the work to date in micro-scale NMR has focused on solenoidal type microcoils due to their higher sensitivity compared to planar microcoils. However, planar microcoils are more easily to integrate in microfabrication processes using photolithography techniques which allow a precisely controlled geometry and an accurate coil sample positioning [3].

3. EXPERIMENTAL

Two Borofloat glass wafers were powder blasted to obtain the channels and throught holes of the chip (figure 1). The powder blasting process gives a round V-shape cross section of the channel. The wafers were direct bonded and annealed at 600 ºC. The wafer stack was thinned down on one side by HF etching to decrease the distance between the coil and the channel to about 80 μm. A copper coil was electroplated on top of the channel. Important chip and coil design parameters have been optimized. A planar coil is defined by number (N), width (w), height (h), separation of the windings (s), inner diameter (2ri) and coil material (figure 2). The microchip design parameters are material, size, geometry,

978-0-9798064-0-7/μTAS2007/$20©2007CBMS

number of microfluidic channels, shape and diameter of the channels, reaction chambers and mixing area. Finite elements simulations (FEMM) [4] can be used to predict which of these parameters provide the B_1 optimization for a better design of the NMR-chip.

The NMR-chip is put on the top of a hollow tube equipped with a specifically designed holder for optimized positioning and handling of the NMR-chip inside the superconducting magnet. Two adjustable capacitors are mounted on the upper part of the probe and electrically connected to the coil for tuning the system to 400 MHz.

Different solutions with the same concentration of β-cyclodextrin (15 mM) in which the concentration of benzoic acid is varied (β-cyclodextrin/ benzoic acid ratio from 3.0 to 0.2) were prepared. Each solution was loaded in the chip using a syringe. All the acquisition parameters were optimized for a reference solution (absence of guest). All the solutions were measured with the same acquisition parameters as the reference one.

4. RESULTS AND DISCUSSION

^{1}H-NMR experiments and titration experiments in H_2O can be performed in our NMR-chip. The non-covalent interaction between benzoic acid and β-cyclodextrin can be followed inside the NMR-chip by the chemical shift variation of H_3-β-cyclodextrin (4.93 ppm) when the concentration of benzoic acid is varied (table 1). The high sensitivity obtained offers the possibility of working at low concentrations and nanomol quantities of material can be detected. The determined association constant values are similar to the ones obtained from a normal reaction scale (48 M^{-1}) illustrating the good performance of our NMR-on-a-chip design.

Table 1. Chemical shift variation in ^{1}H-NMR (H_3-β-cyclodextrin)

Entry	β-CD/ BA	$\Delta\delta_{H3}$
1	1.9	0.03
2	1.1	0.05
3	0.9	0.06
4	0.2	0.08

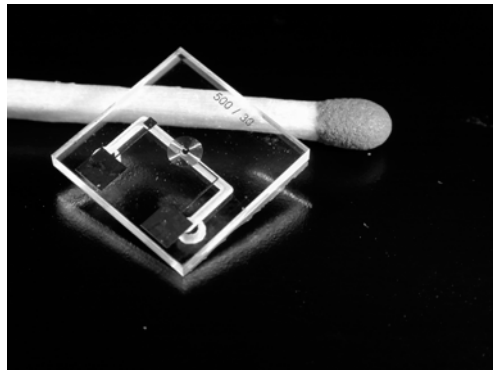

Figure 1. NMR-chip

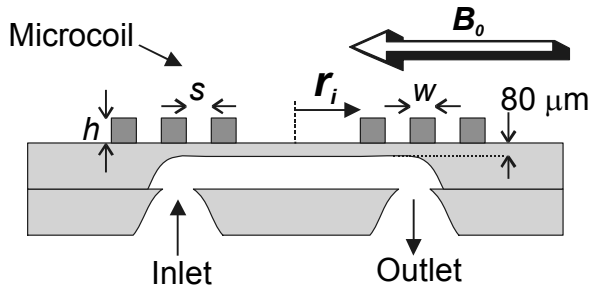

Figure 2. NMR-chip cross-section

5. CONCLUSIONS

A microfluidic chip with an integrated planar NMR microcoil has been developed. Volumes of less than 60 nanoliter can be measured. Promising sensitivity and resolution, in 1D spectra are obtained on nanomol quantities. Proof of principle is giving characterizing nanomol quantities of cyclodextrin and quantifying its interaction with benzoic acid.

ACKNOWLEDGEMENTS

This research was supported by a Marie Curie Intraeuropean Fellowship within the 6th European Community Framework Programme.

REFERENCES

[1] H. Wensink, F. Benito-Lopez, D. C. Hermes, W. Verboom, H. J. G. E. Gardeniers, D. N. Reinhoudt, A. Van den Berg, *Measuring reaction kinetic in a lab-on-a-chip by microcoil NMR*, Lab Chip, **3**, 280, (2005).

[2] D. L. Olson, T. L. Peck, A. G. Webb, R. L. Magin, J. V. Sweedler, *High-resolution Microcoil ^{1}H-NMR for Mass-Limited, Nanoliter-Volume Samples*, Science, **270**, 1967, (1995).

[3] C. Massin, F. Vicent, A. Homsy, K. Ehrmann, G. Boero, P.-A. Besse, A. Daridon, E. Verpoorte, N. F. De Rooij, R. S. Popovic, *Planar microcoil-based microfluidic NMR,* Journal of Magnetic Resonance, **164 (2)**, 242, (2003).

[4] FEMM free software available from http://femm.foster-miller.net

A PHOTOLITHOGRAPHY-BASED SILICON NANOWIRE FABRICATION USING UNDERCUT ETCHING OF (110) SILICON WAFER FOR BIOSENSOR APPLICATIONS

Sung-Sik Yun, Sung-Keun Yoo, Sung Yang, and Jong-Hyun Lee
Department of Mechantronics, GIST, South Korea

ABSTRACT

In this paper, a novel photolithography-based SiNW fabrication using wet etching of (110) silicon wafer is proposed for biosensor applications. The silicon microstrcutre prepared by the conventional photolithograpy can be down scaled to 200 nm in top-width by crystalline and isotropic wet etching. The silicon nanostructure is exposed under the thermal oxidation at 970 °C to electrically isolate the SiNW from the substrate. Finally, the SiNW of 135 nm-width and 1000 μm-length is obtained and evaluated by investigating *I-V* characteristics. The *I-V* characteristics of the SiNWs indicates that the Al-Si interface is ohmic contact.

Keywords: silicon nanowire, photolithography, wet etching, (110) silicon

1. INTRODUCTION

Silicon nanowires (SiNW) have recently shown remarkable potential as highly sensitive biochemical sensor [1]. Particularly, top-down method can easily fabricate SiNWs on the desirable position while bottom-up method needs complicated fabrication process, such as silicon growth and individual alignment with poor accuracy [2]. In the top-down method, SiNWs have conventionally fabricated by an electron beam lithography and silicon etching of the SOI (silicon-on-insulator) wafer. However, an electron beam lithography is a time-consuming process and is not suitable for massive production due to the direct writing of every pattern. On the contrary, photolithography can transfer the whole patterns on a photomask to the substrate enabling the fabrication of very long nanowire structures. As a result, several photolithography-based processes have been recently introduced for massive production of SiNW devices. One is the size reduction lithography using thin sidewall deposition, which needs an additional imprinting process for sensor application [3]. The other one is thermal oxidation of inverted triangular silicon made by crystalline wet etching of (100) silicon wafer [4]. This method also needs to release the fabricated SiNWs and transfer them onto other substrate to isolate every electrical sensing device.

2. FABRICATION

To generate the SiNW using the photolithography irrespective of patterning resolution, we developed two critical process steps, roughness reduction process of line edges by crystalline etching and isotropic etching of (110) silicon (p-type, ρ=3~9 Ωcm) for size reduction as shown in fig. 1(a). The line edges of microscale line pattern fabricated by photolithography normally shows considerable roughness of 150~200 nm. The roughness can be reduced by crystalline etching of (110) silicon when the line patterns are aligned with (111) plane [5]. The line patterns of 2-μm in width were fabricated on the same Si_3N_4 layer aligned parallel to the (111) plane (fig.1(a) B). The TMAH crystalline etching allows the line patterns to have vertical sidewall along the (111) plane (fig.1(a) C), which will be

978-0-9798064-0-7/μTAS2007/$20©2007CBMS

facilitated for the nanowire formation in oxidation process later. Another necessary condition for nanowire fabrication is an accurate measurement of the initial line width and the isotropic etch rate of silicon. The opaque Si_3N_4 layer with no silicon underneath it was partially removed so that the remained Si_3N_4 line pattern clearly indicates the initial width of silicon with only 50-nm error (fig.1(a) D, fig 1(b)). Figure 1(b) shows the SEM images of the line edge before and after partial removal of Si_3N_4 layer. Now the width in microscale of silicon line pattern changes into nanoscale of 200-nm by silicon isotropic etching as shown in fig.1(a) E.

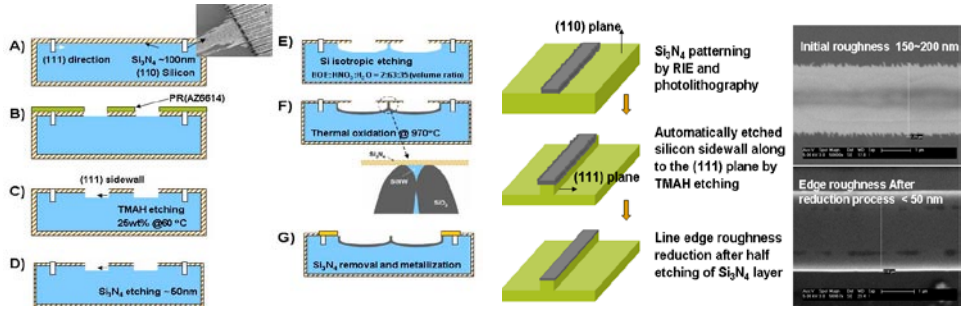

(a) (b)

Figure 1. (a) The fabrication sequence of a silicon nanowire using undercut etching of (110) silicon wafer and oxidation, (b) Half etching of the nitride layer to measure the initial width of the silicon microstructure and the SEM images of the SiNW showing the line edge roughness before and after nitride etching.

Fig.2(a) shows the SEM image of silicon nanostructure fabricated by the previous TMAH etching (25 wt% at 60 °C) and present isotropic etching ($BOE:HNO_3:H_2O$ = 2:63:35) with the etch rate of 100-nm/min. To form the SiNW by further reducing the thickness, the silicon nanostructure was treated by thermal oxidation at 970 °C during 25 min. (fig.1(a) F), where the topside of silicon shows low oxidation rate due to Si_3N_4 layer. Finally, we obtained one SiNW of near to 100-nm in width and over 1000-μm in length, which was electrically isolated from the silicon substrate as shown in fig.2(b).

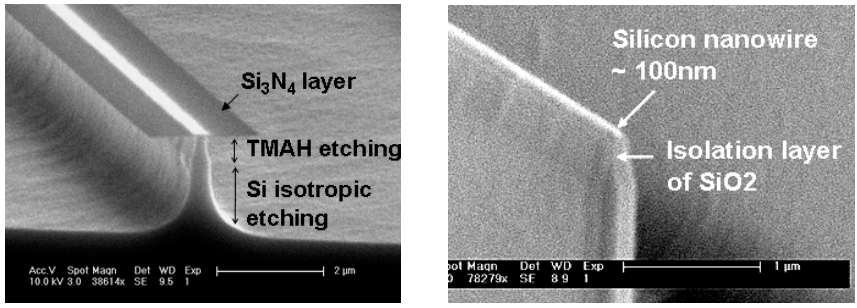

(a) (b)

Figure 2. (a) SEM image of the silicon nanostructure after TMAH crystalline and isotropic etching, (b) silicon nanowire electrically isolated from Si substrate after thermal oxidation process

3. *I-V* CHARACTERISTICS

The fabricated SiNW was evaluated in terms of *I-V* characteristic. In order to make electrical contacts, aluminium (50-μm line and space pattern) was sputtered to electrically separate the initial SiNW into of many 50 μm-long SiNWs, as shown in fig.3(a). The *I-V* characteristics of the SiNWs indicates that the Al-Si interface is ohmic contact, as shown in fig.3(b). The resistance, which includes the resistance of SiNW and contact resistance, increases with average width (W_a), and width variance (W_v) degrades the linearity of *I-V* characteristic, as shown in the inset of fig.3(b).

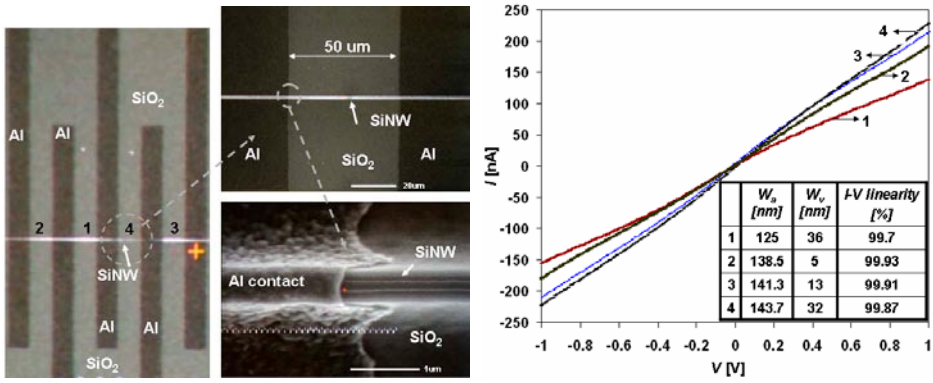

(a) (b)

Figure 3. (a) SEM image of the SiNW electrically contacted by Al electrode. (b) different ohmic characteristics of *I-V* curve in the fabricated SiNWs, respectively.

4. CONCLUSIONS

We propose a novel photolithography-based SiNW fabrication using wet etching of (110) silicon wafer for biosensor applications. The SiNW of 135 nm-width and 1000 μm-length was fabricated. The *I-V* characteristics of the SiNW shows the ohmic contact. The proposed process will be promising fabrication method to massively produce SiNW with low cost for biosensor applications.

ACKNOWLEDGEMENTS

This research has been supported by the Center for Distributed Sensor Network(CDSN) at GIST, Korea

REFERENCES

[1] Eric stern, et al., “Label-free immunodetection with CMOS compatible semiconducting nanowires," Nature letters, 445, 519 (2007).

[2] A.K. Wanekaya, et al., “Nanowire-Based Electrochemical Biosensors,” Electroanalysis 18, 533 (2006).

[3] Y. Choi, et al., “Fabrication of sub 10-nm silicon nanowire arrays by size reduction lithography,” J. Phys. Chem. B, 107, 3340 (2003).

[4] K. Lee, et al., “Fabrication of nanowire device using silicon nanowires transfer method and biosensor applications,” The 8th Korea MEMS conf., 666 (2006).

[5] S-S. Yun, et al., “Fabrication of vertical optical plane using DRIE and KOH crystalline etching of (110) silicon wafer,” Sensors and actuators A 128, 387 (2007).

FABRICATION AND OPERATION OF A MICRO ORIFICE ARRAY CHIP WITH HIGH ELECTROPORATION EFFICIENCY

Murat Gel[1] Osamu Kurosawa[2], Hidehiro Oana[1], Masao Washizu[1]
[1]University of Tokyo, JAPAN, [2]Advantec Co., JAPAN

ABSTRACT

This paper reports microfabrication and operation of a micro orifice array chip for high volume batch electroporation of cells. The chip makes use of electroporation method based on small openings on an insulating layer [1-2], which is used to immobilize cells as well as to obtain electric filed concentration. After explanation of the fabrication method, the PDMS assembly to operate the chip in micro fluidic setup is discussed. Furthermore electroporation efficiency obtained by immobilization of approximately 300 jurkat cells is characterized by delivering DNA binding dye into cells.

Keywords: Electroporation, micro orifice, cell manipulation, micro fabrication

1. INTRODUCTION

Cell membrane surrounds the cytoplasm to regulate transportation of the moving material towards inside and outside of the cell. When external electric field in the order of 1 kV/cm is applied, the voltage across membrane exceeds dielectric strength of the membrane, resulting in formation of pores. These hydrophilic pores are formed typically at the threshold values of 0.5-1V of trans-membrane potential and they allow the surrounding material to diffuse inside of the cell. The process is called electroporation and it is a technique frequently used to introduce materials in to bacteria and cells. As long as the membrane potential doesn't go beyond the threshold value the electroporation is reversible and pores reseal after a given time. However, when irreversible electroporation occurs the pores remain open and destruction of the cell occurs. The conventional bulk electroporation uses aluminium electrodes placed in side of a cuvet with a typical volume 400 µl and 240 V is applied between electrodes. The efficiency of the technique is quite low ending in destruction of high percentage of the cells due to large electric field and thermal heating effects.

Huang and Rubinsky [1] introduced how micro orifice can be used for electroporation on microfabricated devices. The device is formed by bonding two silicon wafers including electrodes involving SU-8 channel layer. The complexity of the fabrication process motivated researchers to find simpler ways of using micro orifice for on-chip electroporation. Recently, Washizu and Kurosawa [2] reported a simple approach based on laser machined polyimide sheet. The approach makes use of 7 micron thick KAPTON film with an array of orifice having diameter of 5 micron. When pulse is applied from both side of the film, the concentration of electric field lines around orifice causes temporary rapture of cell membrane thus allowing external material to diffuse into the cell. However, due to hydrophobic nature of polyimide surface it is difficult to wet inside and surrounding area of the orifice. Furthermore, as the film thickness is similar to size of the cells, after aspiration of cells to orifice, they show tendency to get stuck inside making it difficult to release for post-electroporation treatment.

978-0-9798064-0-7/µTAS2007/$20©2007CBMS

In this work we fabricated micro orifice array on 1.5 micron thick silicon oxide by using microfabrication. This thickness is one order magnitude smaller than the cell size, thus making recovery possible without damage. Furthermore hydrophilic nature of silicon dioxide prevents wetting problems.

2. EXPERIMENTAL

Fabrication of the orifice chip is based on 200um silicon wafer with 1.5um oxide. First oxide layer is patterned by using standard lithography to open holes with size of 2.5 um radius. Then silicon wafer is patterned from back side by using double side aligner and deep reactive ion etcher. Fabrication process can be seen in figure 1.

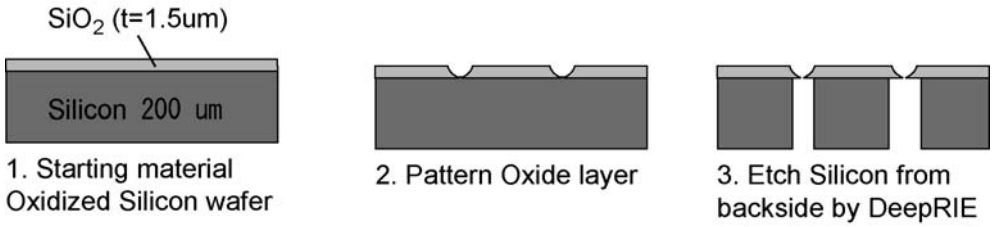

Figure 1. Micro Orifice Chip Fabrication

Figure 2a shows scanning electron microscope image of fabricated device from top. Close view of an orifice shows the diameter of approximately 2.5um on patterned oxide layer. In order to characterize electroporation efficiency a PDMS fluidic assembly is used. Silicon micro orifice chip is embedded in to two PDMS layers with a thickness of 1 mm. By using this technique it becomes possible to integrate chip with PDMS micro fluidics. Punch holes located in upper and lower layer allow liquid flow through the chip to aspiration channel. The voltage applied to both sides of the chip can be controlled by ITO coated glass as top and bottom respectively.

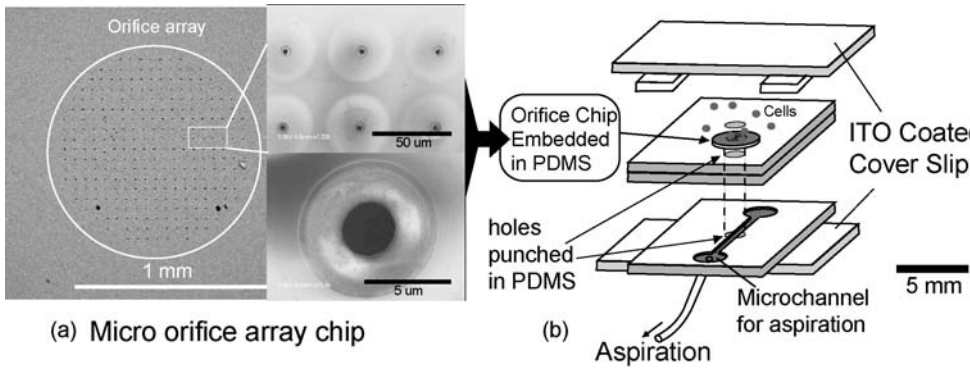

Figure 2. (a)SEM view of orifice chip (b) PDMS assembly to operate orifice chip

3. RESULTS AND DISCUSSION

Jurkat cells immobilized by aspiration can be seen in figure 3a. Aspiration channel pressure of 0.5kPa is enough for the immobilization. Before applying pulse to ITO electrodes 100uM of YO-PRO1 (DNA binding dye) is introduced to the buffer flowing in the aspiration channel. A pulse train of 500 kHz for 30 sec is applied and fluorescent intensity changes in the cells are observed. Figure 3b shows fluorescent image of the immobilized cells. Bright areas are showing the regions where the DNA binding dye is accumulated.

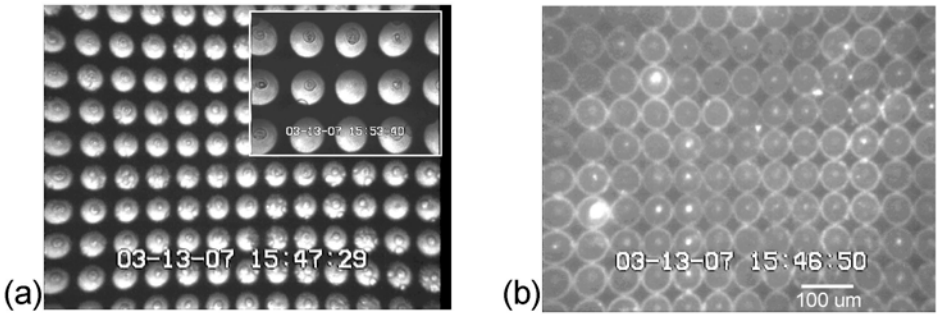

Figure 3. (a) Jurkat cells immobilized on orifice chip. (b) Fluorescent image of chip after electroporation

4. CONCLUSIONS

We demonstrated fabrication and operation of micro orifice array chip with a PDMS assembly which can handle 300 cells at a time. Electroporation results showed more than %90 electroporation efficiency with applied voltage range of less than 5 volts with 500 kHz applied for 30sec.

ACKNOWLEDGEMENTS

VDEC Electron Beam Lithography system for mask fabrication and Deep RIE system is used for device fabrication

REFERENCES

[1] Y. Huang and B. Rubinsky, *Flow-through micro-electroporation chip for high efficiency single-cell genetic manipulation*, Sensors and Actuators A, pp. 205-212 104, 2003.

[2] O. Kurosawa, H. Oana, S. Matsuoka, A. Noma and M. Washizu, *Electroporation through a micro-fabricated orifice and its application to the measurement of cell response to external stimuli*, Meas. Sci. Technol., pp. 3127-3133, 17,2006.

FAST ETCHING OF SACRIFICIAL GALVANIC COUPLED METALS FOR NANOCHANNEL FABRICATION: EXPERIMENTS AND THEORY

W. Sparreboom, J.C.T. Eijkel and A. van den Berg
MESA+ Institute for Nanotechnology, THE NETHERLANDS

ABSTRACT

We demonstrate a 10-fold enhancement of the etch rate of sacrificial metals for nanochannel fabrication by galvanic coupling. This results in an etch time for the here examined nanochannels of 10 hours instead of 9 days without galvanic coupling. An additional feature of our device is that we integrated bare electrodes inside the channel. Furthermore, we offer a theoretical explanation of the observed etch rate based on mass transport.

Keywords: Nanochannel, fabrication, surface-machining, electrodes

1. INTRODUCTION

Sacrificial layer etching offers the possibility of easy integration of nanofluidic channels with electrodes and electronics [1,2]. However, the etching of sacrificial layers is usually slow, which poses a limit on the practical length of the channels [3]. Several methods to circumvent this limit have been described in literature [3,4,5,6]. Of these methods, the use of galvanic coupled metals as a sacrificial layer appears to be most promising for integration with metal electrodes.

The use of galvanic coupled metals (GCMs) in micro/nano fluidic channel fabrication was first described in [6]. However, theory explaining the etch rates is lacking.

In this paper we demonstrate a 10-fold increase in the etch rate of sacrificial metals for nanochannel fabrication. An additional feature of our device is that we integrated bare electrodes inside the channel. Furthermore, we explain the high etch rate by increased diffusion and a chemically induced electric field that assists diffusion in the transport of reaction products.

2. THEORY

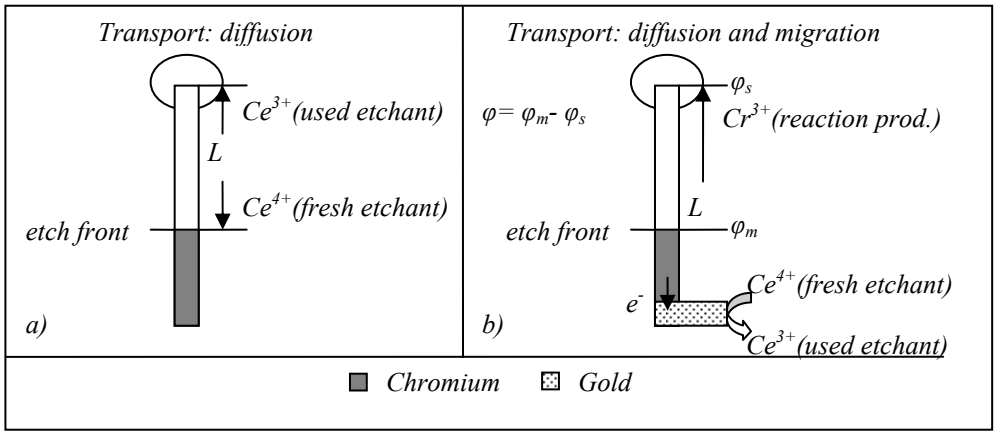

Figure 1: Proposed concepts: a) Single metal sacrificial layer, and b) Galvanic coupled sacrificial layer.

978-0-9798064-0-7/μTAS2007/$20©2007CBMS

Galvanic corrosion is defined as the corrosion that occurs as a result of one metal being in contact with another in a conducting, corrosive environment [7]. Because of the 1-D geometry of the channels it is likely that the etch rate is limited by the transport of reagents and reaction products to and from the etch front.

Proposed concept

To describe this transport, we derived two concepts, one for a single metal sacrificial layer and one for GCMs (see figure 1). In the first case, transport is limited by the diffusion of reagents to and from the etch front. In the second case, transport is limited by diffusion and migration of reaction products from the etch front. The transport in the second case is faster, because there is a larger concentration difference (causing faster diffusion) and an assisting electric field. We derived an equation (1) to describe the etch rate controlled by mass transport based the Nernst-Planck equations. In this case we only consider diffusion and migration.

$$L = \sqrt{2\frac{M_{W,Cr}}{\rho_{Cr}}\left(DC + \frac{\sigma}{zF}\varphi\right)t} \qquad (1)$$

Where L is the etch distance; $M_{W,Cr}$ is the molecular weight of chromium; ρ_{Cr} is the density of chromium; D is the diffusion constant of chromium ions in a nitrate containing electrolyte; C is the concentration of chromium ions at the etch front; σ is the conductivity of the solution inside the nanochannel; z is the ionic valence; F is Faraday's constant; φ is the measured potential of the metal with respect to the solution outside the channel; and t is the elapsed time.

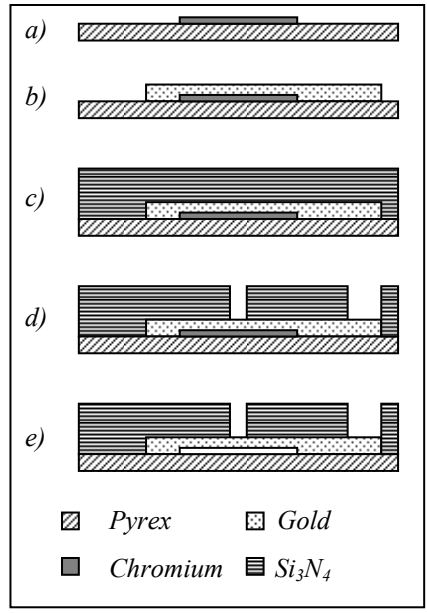

Figure 2. Fabrication process: a) deposition of a sacrificial chromium layer b) deposition of gold electrodes, c) deposition of a 2 µm nitride layer by PECVD, d) ion beam etching of access holes, and e) standard wet chemical etching of the sacrificial chromium layer.

3. EXPERIMENTAL

We have fabricated 4 mm long, 5 µm wide and 50 nm high nanochannels with integrated electrodes. The sacrificial GCM consists of chromium and gold. The gold remains, because it is inert to the etchant, and forms the integrated electrodes. The fabrication process is described in figure 2.

The etching process was observed using an inverted microscope (Leica DM IRM) equipped with a digital camera (Olympus CC-12). During etching the corrosion potential between the chromium/gold couple and the etch solution was measured using a potentiostat (PARSTAT 2263).

4. RESULTS AND DISCUSSION

In figure 3 the theoretical and experimental results are given. The proposed theory appears to be in qualitative agreement with the experiments. However, if the maximum

possible concentration of chromium ions and the measured potential are used, the etch rate is overestimated. This is most likely caused by an overestimation of the concentration of chromium ions at the etch front. A fit to the experimental data has been obtained, using the chromium concentration gradient as a fit parameter. From this fit we calculated that for GCMs the etch rate limited by diffusion is typically 3 times faster than for single metals. The self-induced electric field additionally increases the etch rate by a factor 3.

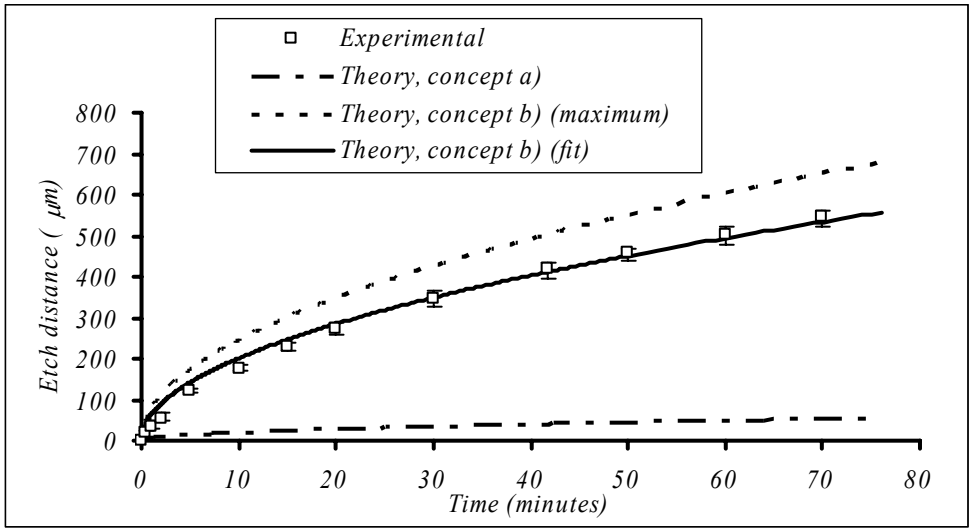

Figure 3. Experimental and theoretical etch distances plotted as a function of time. The induced potential for concept b) is set to the measured value of 0.96 V. The maximum is the theoretical maximum based on the maximum solubility of chromium. The fit is based on a concentration at the etch front of 1 M.

5. CONCLUSION

We used GCMs to successfully fabricate 50 nm high nanochannels with integrated bare electrodes. Furthermore, a theory explaining the high etch rates has been proposed. The results of this theory are in close agreement with the experimental results.

ACKNOWLEDGEMENTS

The authors wish to thank Johan Bomer for assistance in the cleanroom and useful discussions concerning fabrication. Nanoned is gratefully acknowledged for the financial support via a Nanoned grant.

REFERENCES

[1]M.B. Stern, M.W. Geis, 1997. J. Vac. Sc. B 15 (6) pp. 2887.
[2]A. Rasmussen, M. Gaitan, L.E. Locascio, M.E. Zaghloul. 2001. J. MEMS. 10 (2) pp. 286.
[3]N.R.Tas, J.W. Berenschot, P. Mela, H.V. Jansen, M. Elwenspoek, A. van den Berg. 2002. Nano Lett. 2 pp.1031
[4]C.K. Harnett, G.W. Coates, H.G. Craighead. 2001. J. Vac. Sc. B 19 pp.2842.
[5]W. Li, J.O. Tegenfeldt, L.Chen, R.H. Austin, S.Y. Chou, P.A. Kohl, J, Krotine, J.C. Sturm. 2003. Nanotechnology15 pp. 578.
[6]H. Zeng, Z. Wan, A.D. Feinerman. 2006. Nanotechnology 17 pp.3183.
[7]H.P. Hack. 1988. Galvanic Corrosion (Philidelphia, PA: ASTM) pp. 5.

IMPLEMENTATION OF MICROFABRICATED SUTURE-LESS FLEXIBLE PARYLENE TISSUE ANCHORS ON MINIMALLY INVASIVE BIOMEDICAL IMPLANTS

Po-Jui Chen[1], Damien C. Rodger[1,2], Saloomeh Saati[3], Juan Carlos Altamirano[3], Chun-Hui Lin[1], Rajat Agrawal[2,3], Rohit Varma[2,3], Mark S. Humayun[2,3] and Yu-Chong Tai[1]

[1]California Institute of Technology, USA [2]University of Southern California, USA
[3]Doheny Eye Institute, USA

ABSTRACT

This paper presents novel microfabricated biocompatible flexible parylene tissue anchors and their implementation on minimally invasive biomedical implants. Incorporating foldable-arm and rollable-wing designs, these flexible tissue anchors can compliantly change their shapes to achieve minimally invasive needle-based device implantation and robust suture-less implant anchoring. The tissue anchors are monolithically fabricated and integrated with microchannels to realize tube-type glaucoma drainage devices (GDDs) as examples of the technology. Successful *in vitro* and *in vivo* characterization demonstrates the functionality of the tissue anchors and reveals their great potential for bioimplants.

Keywords: Biomedical implant, parylene, tissue anchor

1. INTRODUCTION

The implantation scheme is considered one of the most crucial factors for the successful implementation of bioimplants, especially when targeting delicate organs such as the human eye. For example, surgical and post-operative complications of glaucoma drainage devices (GDDs) leading to device failure and even tissue deterioration have been discussed in the literature [1][2]. The creation of invasive large-area incisions (e.g. scleral flap) and the use of sutures may induce such deleterious consequences as well as increase implantation complexity. Therefore, a needle-based implantation scheme (Fig. 1) can mitigate such problems to achieve minimally invasive implantation. This scheme especially favors transscleral and transendothelial implants in which integrated flexible tissue anchors are an excellent alternative to sutures for final implant fixation.



Figure 1. Minimally invasive needle-based device implantation scheme. The white region represents location of implant with an HDPE hollow ball used for demonstration purposes.

2. DESIGN AND FABRICATION

Fig. 2 shows proposed tissue anchoring structures in foldable-arm and rollable-wing shaped conformations. The foldable anchors consist of parylene or parylene/silicon arms and parylene flexural joints connected to the implant main body, while the rollable wings are

978-0-9798064-0-7/μTAS2007/$20©2007CBMS

realized using a patterned parylene slab. The designed flexible anchors can be compliantly folded or rolled when loading the device into a hypodermic needle. After needle incision and device unloading across the target tissue, the anchors spontaneously stretch back to their original conformation, enabling the implant to be fastened to the tissue after needle retraction. Parylene C (poly-para-xylylene C) is selected as the structural material of the flexible anchors because of its exceptional mechanical properties (Young's modulus ~4 GPa and yield strength ~59 MPa), its pinhole-free conformal deposition, and its biocompatibility (USP Class VI grade and ISO-10993 standard).

The fabrication process of the tube-type GDD integrated with tissue anchors (Fig. 3) is partly adapted from a modified embedded channel process [3]. High-aspect-ratio parylene-refilled deep trenches were created to define foldable arms and guard columns for silicon etching, and square-like channels with large cross-section were constructed using isotropic XeF_2 silicon etching and parylene deposition/patterning. Fig. 4 shows the microfabricated implants embodying approximately 150-µm-wide, 150-µm-high, 4-mm-long artificial conduits and flexible arm/wing parylene anchors on the ends. The wingspan of the stretched anchors was 800 µm, larger than the needle outer diameter and the corresponding incision hole.

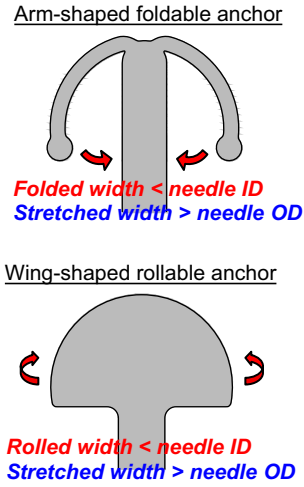

Figure 2. Flexible anchor designs.

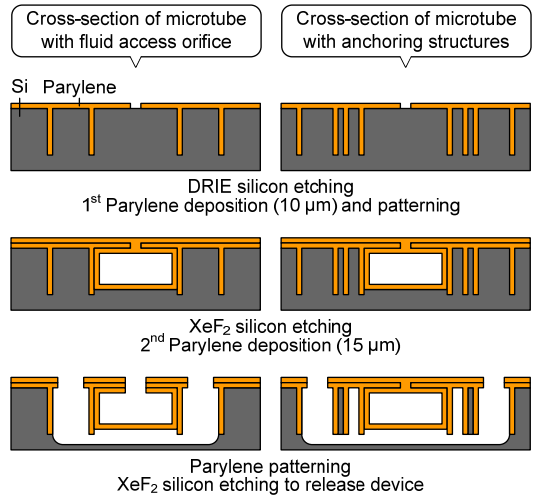

Figure 3. Fabrication process flow with silicon-embedded arms as example of anchoring structures.

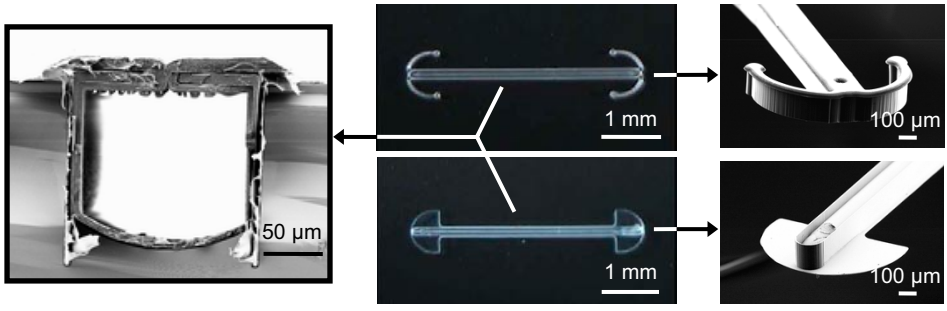

Figure 4. Microfabricated parylene-based implants (middle) with SEM images highlighting artificial conduit cross-section (left) and tissue anchors (right). The foldable arm-shaped anchor is shown top-side up and the rollable wing-shaped anchor is shown bottom-side up.

3. RESULTS AND DISCUSSION

The fabricated devices were first tested *in vitro* to verify their functionality. Pressure/flow rate characterization using water as the testing fluid (Fig. 5) indicates that the tubes have fluidic conductances in the range of 1-10 μL/min/mmHg, comparable to contemporary GDDs [4]. Anchor testing (Fig. 6) confirms all devices were successfully fastened in their predetermined positions across the simulated eyewall after needle incision/retraction, with the arm anchors providing better visualization due to the embedded silicon while the wing anchors were structurally more robust. *In vivo* testing in rabbit eyes was also conducted to evaluate the bioefficacy of the flexible tissue anchors (Fig. 7). Remarkably, the implantation surgery was completed within five minutes due to its suture-less minimally invasive nature. No device dislocation was found more than 30 days after surgery. A pilot study is underway to characterize the chronic behavior of the implant in the intraocular environment.

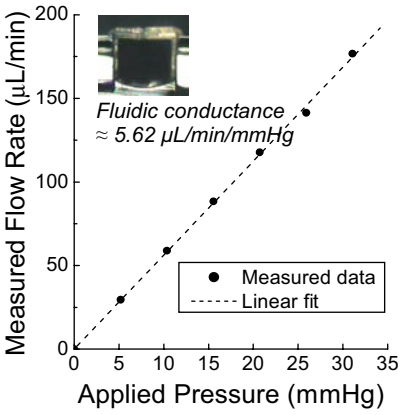

Figure 5. *In vitro* pressure/flow rate characterization.

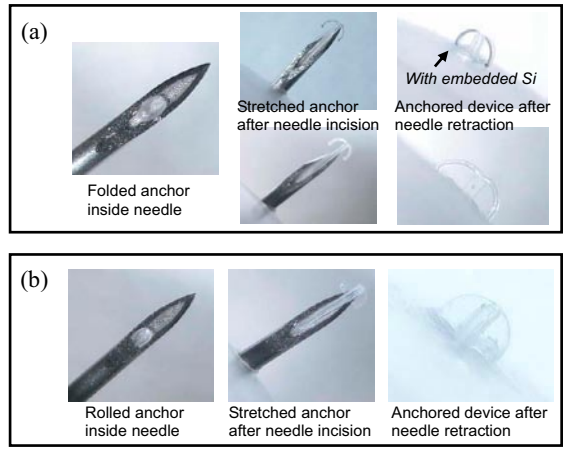

Figure 6. *In vitro* tissue anchor testing: (a) Foldable arm-shaped anchor, (b) Rollable wing-shaped anchor.



Figure 7. *In vivo* animal study of the flexible tissue anchor. Fluorescein angiogram shows no noticeable blood vessel leakage at implantation site.

REFERENCES

[1] C.-H. Hong, D. Zurakowski and R.S. Ayyala, *Survey of Ophthalmology*, **50**, 48 (2005).
[2] K.S. Schwartz, R.K. Lee and S.J. Gedde, *Current Opinion in Ophthalmology*, **17**, 181 (2006).
[3] C.-Y. Shih, W. Li and Y.-C. Tai, presented at *MSB2006*, Amsterdam, Netherlands, Jan. 22-26, 2006.
[4] D.L. Eisenberg *et al.*, *Ophthalmic Surgery and Lasers*, **30**, 662 (1999).

This work was supported in part by the Engineering Research Centers Program of the National Science Foundation under NSF Award Number EEC-0310723 and by Bausch and Lomb.

INVESTIGATION OF INTERSTRUCTURAL COLLAPSE OF PDMS MICROSTRUCTURES

Yi Zhao
The Ohio State University, USA

ABSTRACT

This paper reports structural instability between closely spaced PDMS microstructures, where the characteristic feature sizes are in the order of or less than a few micrometers. The instability criteria were determined using beam theory and experimentally validated using microfabricated PDMS gratings. The dynamic behaviour of the interstructral collapse between the microstructures was obtained using optical microscopy. This work demonstrates a unique tool to quantify the viscoelastic properties of polymeric materials and to investigate the interfacial phenomena at the small scales. This work also provides guidance for the design of polymeric "lab-on-chip" systems to enhance their throughput and efficiency as a whole.

Keywords: Micromechanics, Structural Instability, Polydimethylsiloxane, Microfabrication

1. INTRODUCTION

With the rapid development of Micro Total Analytical Systems (μTAS), polydimethylsiloxane (PDMS) microstructures are increasingly used due to their low elastic modulus, biocompatibility and optical transparency. For example, it has been successfully demonstrated that the PDMS microstructures can measure minute cellular mechanical forces at the small scales. For such applications, microstructures with complex geometries and high aspect ratios are usually needed, which may raise concerns of structure instability [1, 2]. The microstructures either collapse to the ground, or to the neighbouring peer structures, losing the mechanical sensitivities they have been designed for. In this work, we focus on the interstructural collapse in closely spaced PDMS microstructures. The collapsing criteria were estimated using beam theory, and compared to the experimental measurements. Dynamic behaviour of the instable collapse was also reported. This work is expected to help in the development of functional polymer microdevices, and provide useful insight in characterization of material and mechanical properties of polymeric materials at the small scales.

2. MICROFABRICATION

Figure 1 shows the schematic view of the fabrication process of the closed spaced PDMS microstructures. In order to avoid the surface stress that may be induced during the peeling process in conventional replica molding, we formed the master template using thick photoresist AZ 9260. The photoresist was dissolved after the PDMS was cured, leaving intact microstructures with minimal surface stress. The height of the microstructures was adjusted by spin-coating the photoresist of different thicknesses. The PDMS microstructures were immersed into methanol and evaporated. The structure deformation throughout evaporation was recorded using a video camera.

978-0-9798064-0-7/μTAS2007/$20©2007CBMS

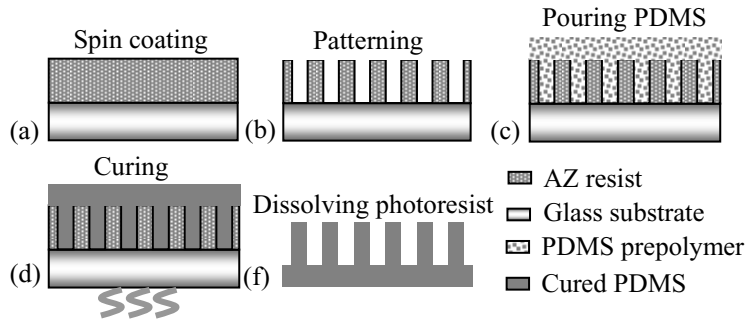

Figure 1. Fabrication process of PDMS microstructures. In order to avoid the surface stress induced during the peeling off, a photoresist layer was patterned as the master template, which was dissolved after the curing process. The height of the PDMS microstructures was determined by the thickness of the photoresist.

3. THEORETICAL ANALYSIS

The collapsing height of the PDMS microstructures was estimated using the beam theory as below. The strain energy stored in the collapsed cantilever pair (Figure 2a) was calculated as:

$$U_E = \frac{6EIa^2}{s^3};\ I = \frac{wt^3}{12}, \tag{1}$$

where E is the Young's modulus, I is the moment of inertia of one structure with respect to x axis. The strain energy stored in the microstructure pair is $U_s = -r_s w(1-s)$, where w is the width, and r_s the surface energy. The collapsing height was determined from the point of minimum total energy:

$$s^* = \left(\frac{3Et^3a^2}{r_s}\right)^{1/4} \tag{2}$$

This theoretical estimation was compared with the experimental measurements (Figure 2b). It is noted the observed collapsing height is smaller than the estimation, which may partially due to the deformable PDMS base substrate, where part of the strain energy are stored.

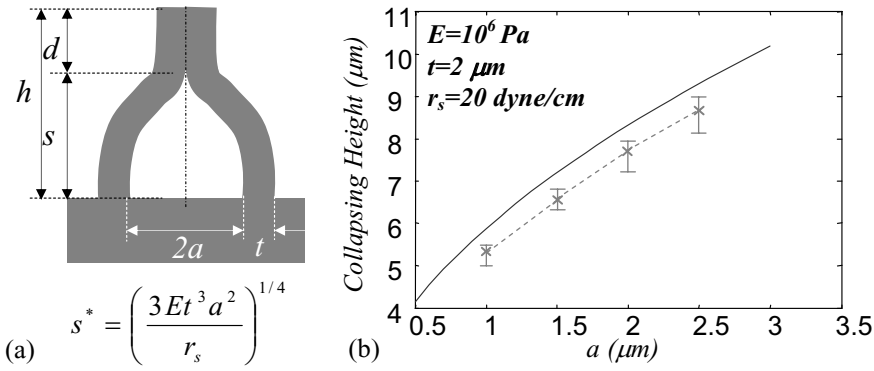

Figure 2. (a) Cross section of a pair of collapsed PDMS microstructures; (b) the theoretical collapsing height (solid line) and the measured height (dashed line).

We also investigate the dynamic instability of single spaced microstructures (2 μm in width and 2 μm in spacing) whose heights are below the threshold. In very short microstructures, the interstructural collapse was not observed (not shown). There is no deformation during the evaporation. In the microstructures with mid aspect ratios, the neighbouring structures collapse to each other during evaporation, rapidly detached and then returned to their original positions, as shown in Figure 3. As the height increased, it took longer for the microstructures to completely detach. When the height exceeded the threshold, the structures kept collapsed after the solution was fully evaporated (not shown). The separation time of microstructure pairs is a function of their spacings and aspect ratios. This time-dependent behaviour is believed due to the viscoelastic properties of the polymeric materials. The in-depth study will be performed to determine the correlation between the dynamic behaviour and the viscoelastic properties.

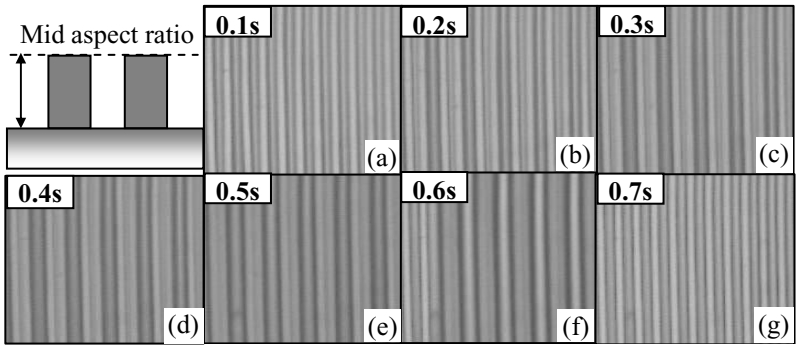

Figure 3. The microstructures with mid aspect ratios collapsed during the evaporation (a)-(e). However, the collapsed ridges quickly separated and returned to the original positions (e)-(g). The height is smaller than the threshold.

5. CONCLUSION

We report herein the interstructural instability in closely spaced PDMS microstructures. The instability criteria were determined using the beam theory and experimentally validated. The dynamic behaviour of PDMS microstructures below the threshold was also reported, which may provide a unique measure of the viscoelastic properties of polymeric materials at the small scales.

ACKNOWLEDGMENTS

This work is partially supported by IMR facility grant from the Institute of Material Research at The Ohio State University. The author would also thank the technical staffs at the Nanotech West Laboratory for their generous support.

REFERENCES

[1] K. J. Hsia, Y. Huang, E. Menard, J.-U. Park, W. Zhou, J. Rogers, and J. M. Fulton, 2005. Collapse of Stamps for Soft Lithography Due to Interfacial Adhesion, Applied Physics Letters, 86 154106.

[2] C.Y. Hui, A. Jagota, Y. Y. Lin and E. J. Kramer, 2002. Constraints on Microcontact Printing Imposed by Stamp Deformation, Langmuir 18: 1394-1407.

MAGNETIC MICROVALVE WITH BIOCOMPATIBLE SURFACES USING ELECTROCHEMICAL DEPOSITION AND PASSIVATION

M. Tijero[1], L. J. Fernández[1], J. M. Ruano-López[1], K. Mayora[1], M. V. Rodríguez[2] and J. Elizalde[1]

[1]MEMS/MST Dept., Ikerlan S.Coop, Mondragón, SPAIN and

[2]Dept. Electronics and Telecomunications, University of Basque Country, SPAIN

ABSTRACT

This paper describes a novel fabrication process based on electrochemical deposition and passivation that allows us the fabrication of magnetic and biocompatible microvalves.These valves were integrated in SU8 microfluidic channels and characterized, showing successful results.

Keywords: microvalve, nickel, titanium, passivation

1. INTRODUCTION

Scientific areas related to health care have promoted miniaturization of biological and chemical processes. That is why a big effort in researching is being developed in microvalves, which are essential components of micro-total-analysis systems (μTAS). In this work we propose a novel microvalve for biomedical applications.

The fabrication process is based on the creation of through holes on silicon wafers by KOH, reaching the titanium/nickel structure which will be used as valve. In order to prevent the attack of the KOH solution to the titanium, an electrochemical etch stop was performed, being the first time this technique is used for such application.

2. EXPERIMENTAL

Figure 1 shows the schematic overview of the proposed microvalved. The nickel based membrane is actuated by a magnet in order to close the fluidic channel.

The fabrication process (see Figure 2) starts with the aligned definition of fluidic inlets and outlets on an oxidized (100) p-type silicon wafer by HF etching. Next the aluminium layer, which will be used as sacrificial material, is sputtered and patterned. Then the titanium/gold seed layer is sputtered, and the photoresist mould for electrochemical deposition of the valve is deposited. The structural layer of 10 μm thick layer is then deposited by electroplating at 30 A/dm^2. Finally silicon anisotropic etching is performed by KOH solution (25% at 80ºC).

High etching rate (85 μm/h) and selectivity with respect to oxide, and low density of hillock defects were obtained [1]. In order to avoid etching of the titanium structural material, electrochemical etch stop is carried out by placing the wafer in sealed holder and applying –1.1 V during KOH etching. This voltage allows the formation of a non-conductive oxide on the titanium surface, which acts as etch stop layer (see Figure 3).

978-0-9798064-0-7/μTAS2007/$20©2007CBMS

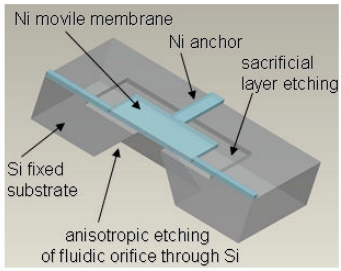

Figure 1. Microvalve schematic

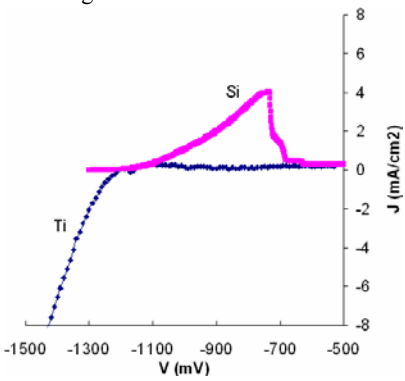

Figure 3. Polarization at -1100mV in KOH passivates Ti by formation of a non-conductive oxide and etches Si

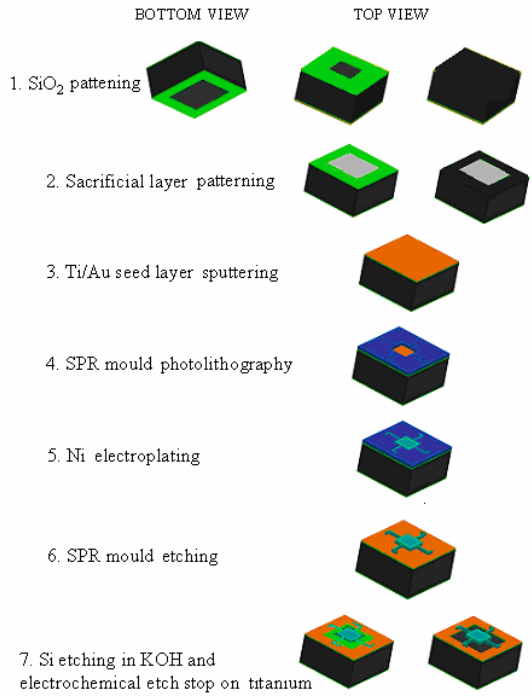

Figure 2. Schematic of the fabrication process

3. RESULTS AND DISCUSSION

These microvalves are suitable for biomedical applications as TiNi alloys and Ti oxides are biocompatible materials. The released microvalve shown in figure 4 reveals a very low stress process. A polymeric reusable packaging was used for the characterization of the valves using NdFeB magnets as actuators. Figure 5 shows the air flow rectification of magnetic microvalve. Low leakage of air in reverse direction is found, while figure 6 shows no leakage of water flow.

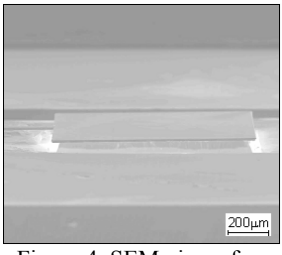

Figure 4. SEM view of no stressed freestanding membrane on Si substrate

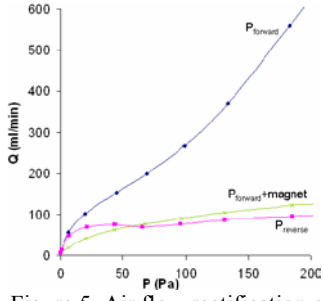

Figure 5. Air flow rectification of externally actuated microvalve

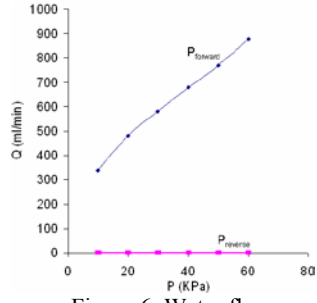

Figure 6. Water flow rectification of passive microvalve

The achieved uniform and reproducible thickness of released membranes improves the results obtained with similar techniques like galvanic etch stop [2]. Furthermore, superior etch selectivity (1:250) and area efficiency (1:1) were achieved with respect to previous works [3]. Unlike other reported works [4], the proposed magnetic microvalve is batch fabricated, where low cost and fast etch of silicon is used instead of dry etching [5]. High thickness of magnetic membranes with no stress and reproducible properties are obtained by electrochemical deposition, in contrast to previously reported membranes [6]. Figure 7 shows these valves integrated in SU8 microfluidic channels.

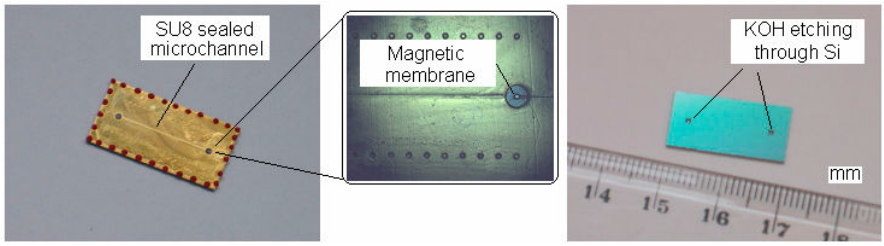

Figure 7. Integration of magnetic microvalve with SU8 sealed microchannel

4. CONCLUSIONS

This fabrication process has a wide range of possibilities to obtain microvalves for biomedical applications as TiNi alloys and Ti oxides are biocompatible materials. This is the first report of a batch-fabrication process to obtain magnetic microvalves suitable for biomedical applications. Moreover integration of these microvalves with microfluidic channels of SU8 was achieved, which opens future development of microfluidic systems.

ACKNOWLEDGEMENTS

This research is sponsored by the basque Government, under the PhD formation program in R+D corporations of basque Country and ETORTEK program.

REFERENCES

[1] S-S. Tan, M.L. Reed, H. Han and R. Boudreau, *Mechanisms of etch hillock formation*, J. Microelectromech. Systems, **5,** no. 1, pp. 66-72, (1996).

[2] E.J. Connolly , P.J. French, X.H. Xia and J.J. Kelly, *Galvanic etch stop for Si in KOH*, J. Micromech. Microeng., **14**, pp. 1215-1219, (2004).

[3] C.M.A. Ashruf, P.J. French, P.M. Sarro, X.H. Xia and J.J. Kelly, *Galvanic etching for sensor fabrication*, J. Micromech. Microeng., **10**, pp. 505-515, (2000).

[4] T. Pan, S.J. McDonald, E.M. Kai and B. Ziaie, *A magnetically driven PDMS micropump with ball check valves*, J. Micromech. Microeng., **15**, pp. 1021-1026, (2005).

[5] J.S. Bintoro and P.J. Hesketh, *An electromagnetic actuated on/off microvalve fabricated on top of a single wafer,* J. Micromech. Microeng., **15**, pp. 1157-1173, (2005).

[6] K. Yanagisawa, H. Kuwano and A. Tago, *Electromagnetically driven microvalve*, Microsystem Technologies, **2**, pp. 22-25, (1995).

RELIABLE BATCH MANUFACTURING OF MINIATURIZED VERTICAL VIAS IN SOFT POLYMER REPLICA MOLDING

Carl Fredrik Carlborg, Tommy Haraldsson,
Göran Stemme and Wouter van der Wijngaart
Microsystem Technology Lab, KTH - Royal Institute of Technology
Stockholm, SWEDEN (e-mail: fredrik.carlborg@ee.kth.se)

ABSTRACT

We introduce and have successfully tested an uncomplicated polydimethylsiloxane (PDMS) compatible method for batch manufacturing vertical microfluidic interconnects via a surface inhibition of cationic photopolymerization. The yield of the maskless method is 100% and it also enhances bond strength with subsequently laminated polymer layers.

Keywords: polymer replica molding, vertical vias, uv-curing, PDMS, microfluidics

1. INTRODUCTION

Previously shown 3D vertical microfluidic interconnect methods in soft polymer replica molding [1,2] suffer from residual membranes in the vias caused by difficulty in squeezing out the prepolymer at the mold interface [3] (Fig. 1 A).

2. PRINCIPLE

Our novel method (Fig. 1 B) provides reliable via formation with perfect yield by locally inhibiting polymerization of a thin layer of the prepolymer. We use an epoxyfunctionalized PDMS prepolymer that UV photopolymerizes rapidly by cationic reactive centers with aryliodonium salt as photoinitiator. The prepolymer is brought in contact with inhibitor locally at the top surface. The strong acid species formed by the aryliodonium salt upon UV irradiation react readily with the inhibitor, consisting of tertiary amines, to form ammonium ions, which are too stable to react further with epoxy groups. This chemistry provides a convenient way to inhibit polymerization at the vias.

3. EXPERIMENTS

The technology was demonstrated and evaluated successfully by fabricating a reliably perforated 50 μm thin membrane in PDMS-like polymer from Epoxy Technolgies (OG133) which already contains an amount of cationic photoinitiator. Additional aryliodonium cationic photoinitator was added to fine tune the polymerization. The process was also successfully tested with epoxy terminated PDMS, mixed with aryliodonium photoinitator (Gelest, Inc). A mold of densely packed pillars, 50 μm high and 40 μm in diameter was dry etched in silicon and passivated with fluoropolymer to facilitate demolding (Fig 2 a). The prepolymer mixture is then cast against the mold (b). A glass cover with spun-on inhibitor layer is then pressed onto the mold (c). UV irradiation forms acid species throughout the monomer solution as a part of the polymer curing process. Near the glass surface these are inactivated by the tertiary amine groups whereas deeper in the bulk polymerization is unaffected (d).

978-0-9798064-0-7/μTAS2007/$20©2007CBMS

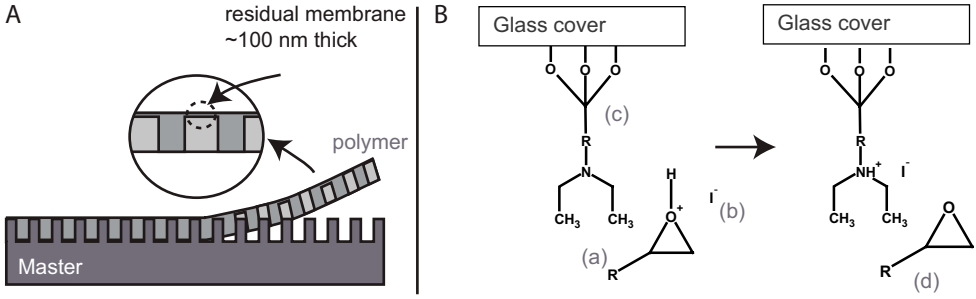

Figure 1. **A)** Reliability problem of previous methods for creating 3D vertical interconnects. The polymer is clamped between the master and a top layer. A residual membrane is left in the vias opening and blocks the interconnects [3]. **B)** During the cationic photopolymerization process, the epoxy terminated monomer forms a reactive cationic intermediary (a) with a stable counterion (b). In the presence of tertiary amines (c) the reactive centers are deactivated by a proton transfer to the amine, leaving the epoxy unreacted (d).

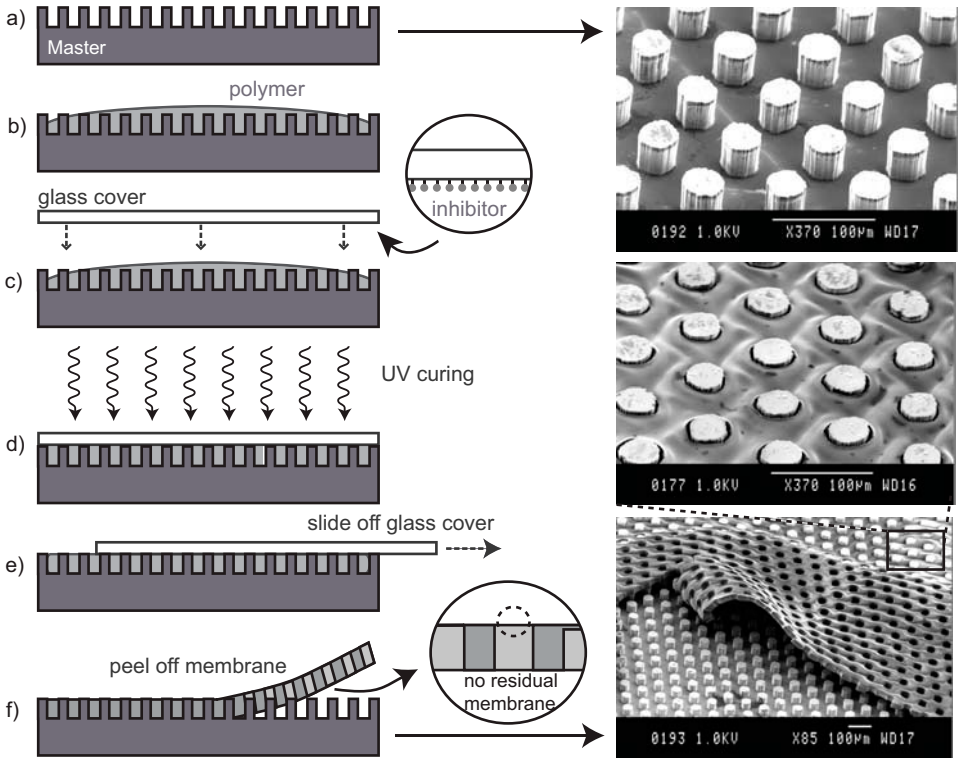

Figure 2. Fabrication procedure for a reliably perforated thin polymer membrane via surface inhibition of cationic photopolymerization. A master of pillars is fabricated in silicon or SU8 (a), the UV-curable PDMS is cast against the master (b) and a glass slide treated with tertiary amine groups is pressed onto the master (c) and exposed to UV light (d). The glass slide is removed (e) and after washing away the thin unpolymerized layer the membrane can be peeled off (f). SEM photos of the master and membrane are shown to the right.

In this manner a thin layer of unpolymerized monomer resides adjacent to the glass surface, allowing removal of the glass slide. After rinsing the unmolded sheet with isopropanol, the pillars protrude through the polymer (e). The sheet can now be readily peeled off from the mold. Examination of the perforated membrane in a SEM showed that 100% of the vertical vias were free from blocking residual membrane (f).

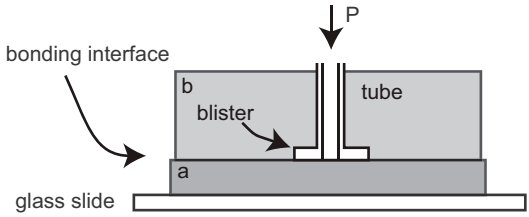

Figure 3. Experimental setup for testing bond strength between two laminated polymer layers (a) and (b) of which the top surface of (a) has been previosly inhibited. The layers are bonded together except for a circular region acting as a blister. The blister is pressurized and the delamination pressure registered.

4. EVALUATION

The depth of the inhibition can be controlled by adjusting the amount of photoinitiator in the prepolymer (Table 1). A profilometer surface scan of the polymer surface showed a thickness variation of less then ±1 μm at the areas where the membrane was not perforated. The inhibition process leaves a layer of partially uncured polymer at the surface facilitating bonding to a subsequent layer. Bond test structures were fabricated by laminating two polymer sheets of which one surface was inhibited during previous polymerization. The bond was UV irradiated for 1 min. In a blister pressure test (Fig. 3) the bond remained intact at pressures up to 7 atmospheres (700 kPa), which was the limit of our setup. When rupturing the structure by mechanically pulling the tube connector, the mechanical failure of the PDMS occurred throughout the bulk of the material and not at the interface, indicating a monolithic bond.

Table 1. The effect of adding aryliodonium photoinitiator to the UV curable polymer OG133 on the film thickness.

Aryliodonium salt in OG133 (mass%)	Depth of inhibited zone (μm)
0 %	15
1%	2
3%	5

5. CONCLUSIONS

In this paper we proposed a novel method for spatially controlling curing of PDMS like polymers, which allows for an uncomplicated, high-yield fabrication of vertical interconnecting channels and a high throughput stacking method for building 3D microfluidic systems by replica molding.

REFERENCES

[1] B. H. Jo, L. M. Van Lerberghe, K. M. Motsegood and D. J. Beebe, J. Microelectromech. Syst., (2000), 9, 76.

[2] J. R. Anderson, D. T. Chiu, R. J. Jackman, O. Cherniavskaya, J. C. McDonald, H. K. Wu, S. H. Whitesides and G. M. Whitesides, Anal. Chem., (2000), 72, 3158.

[3] U. Kloter, H. Schmid, H.Wolf, B. Michel, D. Juncker, 17th IEEE International Conference on. MEMS, 2004, 745- 748

A LATERALLY OPERATING LIQUID ASPIRATION AND DISPENSING UNIT BASED ON AN EXPANDING PDMS COMPOSITE

Björn Samel, Niklas Sandström, Patrick Griss, Göran Stemme
Microsystem Technology Lab, School of Electrical Engineering
KTH - Royal Institute of Technology, SE-10044 Stockholm, Sweden

ABSTRACT

In this work we present the development of an in-plane liquid aspiration and dispensing unit based on a single-use thermally expanding PDMS composite which consists of a PMDS matrix with incorporated expandable microspheres (XB). The approach for controlled on-chip liquid aspiration and release thereafter is facilitated by a novel selective PDMS adhesive bonding technique. Fabricated devices have been tested successfully, are based on the expandable composite and use low-cost materials and wafer-level processes only.

Keywords: microfluidics, disposable, PDMS, bonding

1. INTRODUCTION

Developments in the field of micro total analysis systems (μTAS) [1,2] aim at miniaturization and integration toward systems for applications, such as drug screening, drug delivery, cellular assays, protein analysis, genomic analysis and handheld point-of-care diagnostics. Such systems offer to reduce liquid reagent consumption, increase sensitivity and speed of analysis, but require the integration of various components such as pumps, valves, mixers, etc. Actuation principles and materials with the advantages of low cost, easy integration, high reliability, and compact size are required to promote the development of sophisticated microfluidic systems. Several actuation principles and materials suitable for that purpose have recently been reported [3-5]. Some designs are limited by the need for localization of the active medium at specific positions, which hinders integration and development toward technically mature systems. Our group previously presented single-use pumps and valves for precise displacement of liquids in microfluidic applications [6]. The approach is based on the use of a single-use thermally responsive PDMS composite which consists of expandable microspheres incorporated into a PDMS matrix and facilitates novel approaches for disposable liquid handling platforms [7]. The irreversibly expanding characteristic of this composite actuator has so far limited its application to pumping and valving of liquids. In this paper we instead utilize the possibility of altering the surface topography of an initially unstructured thermally expanding PDMS composite layer to develop a liquid handling concept with added functionality. The concept is used to fabricate devices for controlled laterally operating liquid volume aspiration and release thereafter.

2. PRINCIPLE OF OPERATION

Liquid aspiration and release is achieved by patterning the composite accordingly via integrated heaters to form an enclosed cavity in the system, i.e. inverse volume displacement. The principle of operation is described in Figure 1. The design consists of outer heaters, an inner heater, inlet and outlet valves and a microchannel containing barriers (Figure 1a). The initial state of the device at the channel inlet is normally open whereas the channel outlet is normally closed prior to liquid aspiration. This is achieved via a supplementary barrier in the microchannel outlet as depicted in Figure 1. At the barrier position, the PDMS interface is bonded reversibly to the PCB/PDMS-XB stack alike the area where the cavity is being created during operation. Adequate voltage applied to the outer heaters makes the composite expand, resulting in lifting of the cover-lid and hence creating of a cavity in the system (Figure 1). Addressing the inlet and outlet valve heaters subsequently results in closing and opening the channel inlet and outlet, respectively (Figure 1c). Triggering the inner heater of the device, results in release of the before aspirated liquid volume (Figure 1d).

978-0-9798064-0-7/μTAS2007/$20©2007CBMS

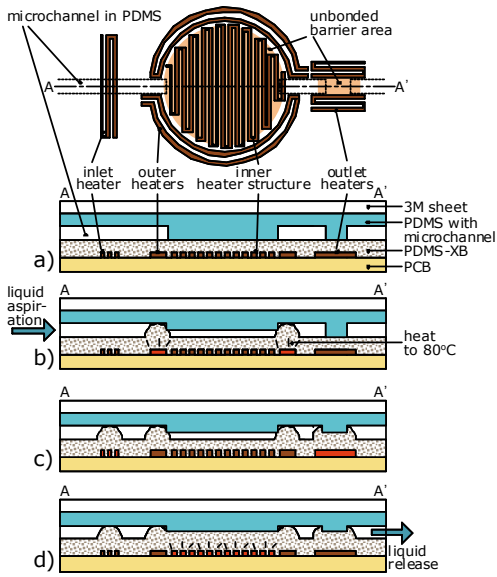

Figure 1: a) Schematic of the working principle showing the layout of the heater structures and microchannel with its barriers as well as the cross-sectional view along the cutting line AA'. b) Upon triggering the outer heaters the PDMS-XB composite expands and as a consequence a cavity is being created which leads to liquid aspiration through the inlet. c) Subsequently triggering the valve heaters leads to closing and opening of inlet and outlet channel, respectively. d) The earlier aspirated liquid is released into the outlet channel upon triggering the inner heater.

3. FABRICATION

The principal fabrication steps are depicted in Figure 2. The microheater patterns are lithographically defined on standard FR4 printed circuit boards (PCB) (Fig. 2a). The composite is obtained as earlier described [6] and spun on the patterned PCB.

To compensate for the low Young's modulus of PDMS a reinforced cover-lid with integrated microchannels is fabricated (Fig. 2b). PDMS is spun onto a master and a sheet of 9742-release-liner (3M) is placed on top followed by a degassing step and heat curing. To bond the cover-lid to the previously fabricated stack of PCB/PDMS-XB a novel selective PDMS adhesive bonding technique is applied. Areas to be bonded permanently are defined via microcontact printing (μCP) of PDMS curing-agent via a replicated PDMS stamp (Fig. 2c).

The fabricated PDMS stamp is pressed on a curing-agent coated substrate to pick up the curing-agent and subsequently placed on the stack of PCB/PDMS-XB (Fig. 2d). The transferred curing-agent represents a patterned intermediate layer for adhesive bonding which fulfills the bonding function at specific regions. Various prototypes are fabricated by changing the dimensions of the PDMS stamps used for μCP.

Finally the lid is aligned and placed on the stack of PCB/PDMS-XB/curing-agent (Fig. 2e). A permanent bond is accomplished at the interface where curing-agent is present (Fig. 2f).

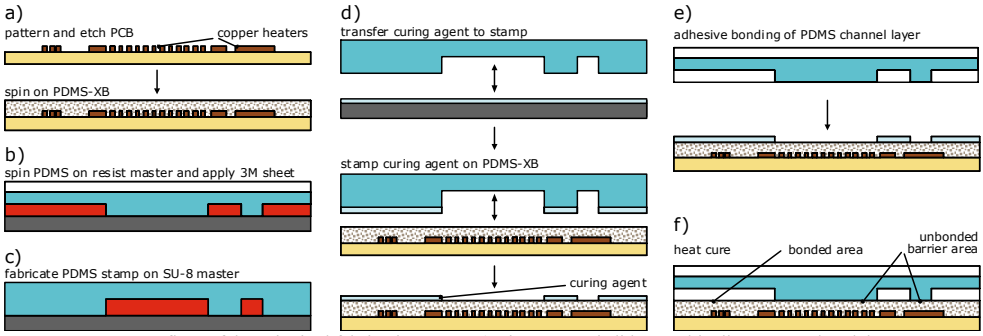

Figure 2: Process flow of the principal fabrication steps: a) First a PCB is lithographically patterned and the PDMS-XB composite subsequently spun on and cured. b) A reinforced cover-lid with replicated microchannels is fabricated by spinning PDMS on a resist mold and adding a 3M-sheet. c) A PDMS stamp for μCP is fabricated by casting PDMS over an SU-8 mold. d) PDMS curing-agent is spun on a substrate and transferred to the previously fabricated stack of PCB/PDMS-XB from (a) via μCP utilizing the stamp. e) The cover-lid with integrated microchannels from (b) is then aligned and placed onto the PCB/PDMS-XB/curing-agent stack from (d). f) Finally the device is heat cured to generate a permanent bond between the layers.

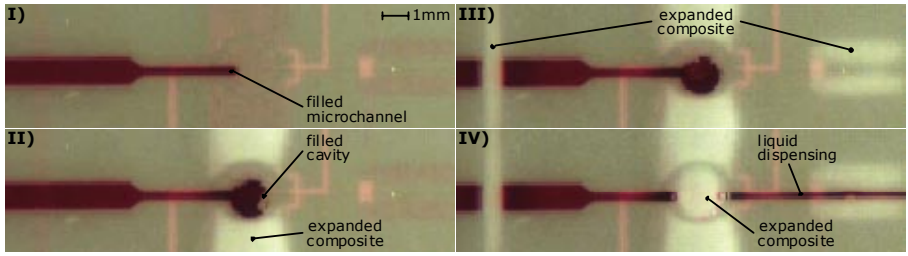

Figure 3: Picture sequence showing the device under operation: I) filled microchannel inlet after sample loading in vacuum; II) triggering the outer heaters leads to liquid aspiration; III) Subsequently triggering all valve heaters closes the channel inlet and opens the channel outlet; IV) Triggering the inner heater results in dispensing of the afore aspirated liquid volume into the microchannel outlet.

4. EXPERIMENTAL

For evaluation purposes the inlet channel is filled under vacuum with glycol and ethanol based colored dye (red) diluted in deionized water. Figure 3 I shows the initial structure after filling prior to device operation. The picture sequence (Figure 3 I-IV) shows active liquid aspiration and release. Applying voltage to the outer heaters results in liquid aspiration through the channel inlet into the created cavity (Figure 3 II). Subsequently triggering the valve heaters leads to closing off the inlet and opening of the outlet, respectively (Figure 3 III). This enables liquid release of the aspirated liquid volume trough the channel outlet by triggering the inner heater (Figure 3 IV). The heaters were driven at an average power of 700 mW for 8 and 4 seconds, respectively. Volume measurements were conducted using the advancing liquid meniscus inside the microchannel as the measure of displaced liquid. Liquid volumes ranging from 28 nl to 476 nl were released from differently sized prototypes after liquid aspiration (Figure 4).

5. CONCLUSIONS

We have shown an active laterally operating liquid aspiration unit based on a single-use thermally expanding PDMS composite for effective liquid aspiration and release. The electrically controllable units do not require external actuation, allow for wafer-level fabrication and use low-cost materials only. The concept potentially enables controlled and cost-effective point-of care diagnostics, disposable biochips and lab-on-a-chip applications.

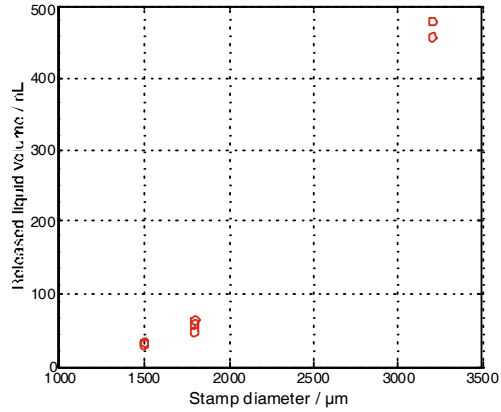

Figure 4: Graph showing the released liquid volume after liquid aspiration for differently sized devices. The stamp diameters used for microcontact printing of curing-agent determines the dimension of the resulting cavity and thus the displaced liquid volume.

ACKNOWLEDGEMENTS

This work is done within the FP6-IST-SABIO project (026554), funded by the European Commission.

REFERENCES:

[1] Harrison, D.J., v.d.Berg, A. (Eds.) MicroTotalAnalysisSystems98, Kluwer Academic Publishers: Dordrecht, 1998
[2] Manz, A., Becker, H., (Eds.), Top. Curr. Chem., 194, Springer-Verlag: Berlin, Germany, 1998
[3] Liu, R.H., Yu, Q. and Beebe, D.J., Journal of Microelectromechanical Systems, 11 (1), 45-53 (2002).
[4] Carlen, E.T., Mastrangelo, C.H., Journal of Microelectromechanical Systems, 2002, 11 (3), pp. 165-173
[5] C-C. Hong, S. Murugesan, S. Kim, G. Beaucage, J-W. Choi and C.H. Ahn, Lab-on-a-Chip 2003, 3, pp. 281 – 286.
[6] Samel, B.; Griss, P. & Stemme, G. *Journal of Microelectromechanical Systems,* 2007*, 16*, 50-57.
[7] Samel, B.; Nock, V.; Russom, A.; Griss, P. & Stemme, G. *Biomedical Microdevices, Springer,* 2007*, 9*, 61-67

A PARTICLE CLASSIFICATION CHIP FOR BOTH AIRBORNE AND LIQUID-SUSPENDED BIOLOGICAL PARTICLES

Yong-Ho Kim, Se-Chul Park, Dong-Ho Park, Il-Hyun Jung, Jungho Hwang, and Yong-Jun Kim

[1]*School of Mechanical Engineering, Yonsei University, South Korea*

ABSTRACT

Two types of a virtual impactor are proposed to classifiy particles suspended with a difference media according to their own inertia. A single-stage virtual impactor was utilized for classifying polystyrene beads of 3 μm and 15 μm suspended with distilled water. Then the virtual impactor was cascaded to three stages, and its characteristics were examined through airborne particles, dioctyl sebacate particles and carbon particles.

Keywords: Particle classification, virtual impactor

1. INTRODUCTION

Particle classification is a crucial process for in environmental monitoring [1] and biochemical analysis [2]. Thus, various particle classifiers have been developed for airborne particles [3, 4] or biochemical substances [5, 6]. In environmental monitoring, particulate matters and hazardous gases are a main concern and they exist in air. However, cells and proteins are an analyzing target in biochemical analysis and they normally are contained in liquid. Up to date, particle classifiers have been separately developed only for each application. Thus the particle classifier presenting here is capable of classifiying both airborne particles and biological substances. In the virtual impactor, large-inertia particles go straight to the minor channel, but small-inertial particles follow the major channel whose turning angle is 90° relative to the injection nozzle (Fig. 1). Thus, we first present a single-stage virtual impactor in order to classiy biological particles according to their size. Then the virtual impactor was cascaded into three-stage and applied to classify airborne particles.

2. DESIGN AND FABRICATION

2.1 Single-stage virtual impactor for biological particle classification

The cut-off diameter is the aerodynamic diameter of a particle that collection efficiency is 50%. It is depends on Stokes number (Stk), Reynolds number (Re), slip correction factor (SCF), velocity, viscosity of working fluid, density of a particle and width of an injection nozzle [7]. Stk is the ratio of particle-stopping-distance at the average air velocity to half of the nozzle width (Eq. (1)). Stk_{50} is adopted as a design rule which is the Stk whose collection efficiency is 50%, it is recommended to use 0.23 for a square channel [8]. For effective collection efficiency, the Reynolds number was determined to 1,000, the SCF was 1. By applying Eq. (1) and (2) to Eq. (3), the width of the injection nozzle was calculated to 156 μm by which the width of the major flow channel was calculated to 234 μm. Material properties of the working fluid followed standard water condition. Fabrication result of the virtual impactor is shown in Fig. 2.

978-0-9798064-0-7/μTAS2007/$20©2007CBMS

$$Stk = \frac{\tau U}{W/2} = \frac{\rho_p d_p^2 U C_c}{9\mu W} \tag{1}$$

$$\mathrm{Re} = \frac{2\rho W U}{\mu} \tag{2}$$

$$U = \frac{q}{Wt} \tag{3}$$

2.2 Cascade virtual impactor for airborne particle classification

The three-stage virtual impactor was designed by determining the width of the injection nozzle in which the Stk, Re and SCF were the major variables (Fig. 3(a)). First, the flow rate was 0.03 ℓ/min for the three minor channels and 0.27 ℓ/min for the major channels in the third stage. The thickness of a channel for the first, second and third stage were 600, 400, and 200 μm, respectively. Second, the Stk was determined to 0.23. The slip-correction factor was 1 for the first and second stage and 2.39 for the third stage. Once Stk_{50} and the SCF have been determined, the width of the injection nozzle can be calculated using Eq. (4). Using the above design procedure, the width of each injection nozzle for the first, second and third stage was determined to be 3700, 1850 and 350 μm when the flow rate of the inlet was 0.36 ℓ/min, respectively. Fabrication results of the cascade virtual impactor is shown in Fig. 3(b).

$$W = \sqrt{\frac{\rho_p d_p^2 q C_c}{9\mu Stk_{50} t}} \tag{4}$$

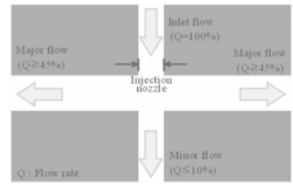

Figure 1. Schematic diagram of the virtual impactor



Figure 2. Fabrication result and assembly of the single-stage virtual impactor

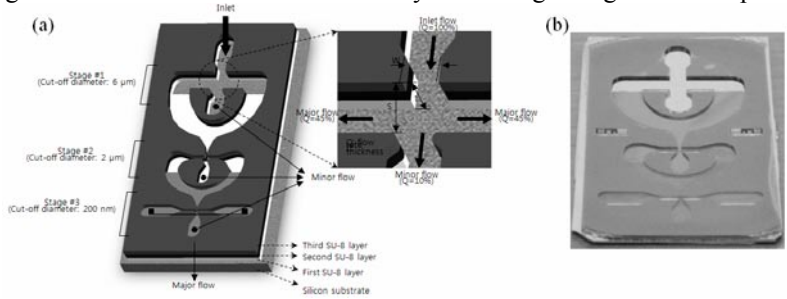

Figure 3. Cartoon of three-stage virtual impactor and fabrication result

3. EXPERIMENTS AND RESULTS

For classification of liquid-suspended particles, 2.7×10^7 for 3 μm and 2.88×10^7 for 15 μm PS bead were suspended with 25 ml DI water. The number of PS beads collected in the major port was counted using the hemocytometer (Table 1). At the major channel, collection efficiency for the 3 μm PS bead was 68%.

For classification of airborne particles, DOS of 100 to 600 nm and carbon particles of 0.6 to 10 μm were used. The flow rate distributor makes 0.27 ℓ/min for the major flow, and 0.03 ℓ/min for the minor flow. Figure 4 shows the performance of virtual impactor. To find out the cut-off diameters, the collection efficiency data was curve-fitted. The measured cut-off diameters were 135 nm, 1.9 μm, and 4.8 μm.

Table 1. PS beads classification result

Measurand	The average number of the PS beads	
	Major flow	*Minor flow*
3 μm PS bead	1.95×10^7	0.23×10^7
15 μm PS bead	1.08×10^7	0.87×10^7

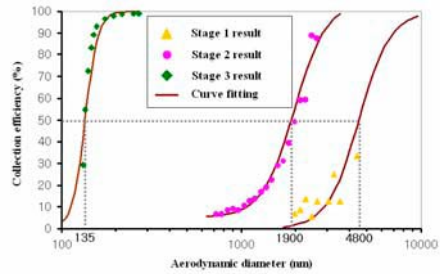

Figure 4. Collection efficiency curve of the each stage and curve fittings

4. CONCLUSIONS

We proposed the design, fabrication and experiment results of the virtual impactor capable of classifying airborne and biological particles by simply changing design parameters. Even though the collection efficiency presented here is not enough, it can be easily enhanced by changing the Stk. Due to versatileness and possibility of high efficiency of the proposed virtual impactor, the particle classifier is expected to used for μTAS.

ACKNOWLEDGEMENTS

This work was supported by the IT R&D program of MIC/IITA. [2005-S-093-02, Implantable system based on biomedical signal processing]

REFERENCES

[1] L. Madler et al., J. Aerosol Sci., 30, pp. 451-465, (1999).
[2] V. Studer et al., Microelect. Eng., 73-74, pp 852-857, (2004)
[3] P.A. Baron and K. Willeke, *Aerosol measurement*, Wiley, pp. 229-260, (2001)
[4] M. Shapiro and V. Galperin, Chem. Eng. Process. 44, 279 (2005).
[5] K.L. Chan et al., Proc. The 20th IEEE EMBS, 6, pp. 2953-2956, (1998).
[6] M. Yamada and M. Seki, Lab on a Chip, 5, pp. 1233-1239, (2005).
[7] C.C. Chen et al., Sens. Actuator B-Chem. 102, pp. 59-66, (2004).
[8] J.S. Haglund and A.R. McFarland, Aerosol Sci. Technol. 38, pp.664-674, (2004).

A STRAIGHT SILICON TUBE AS A MICROFLUIDIC DENSITY SENSOR

M. Najmzadeh[1] , S. Haasl[2] and P. Enoksson[1]
[1]*Chalmers University of Technology, SWEDEN*
[2]*Imego AB, SWEDEN*

ABSTRACT

In this paper, a 2.65 cm long silicon straight tube with a hexagonal cross-section is tested as a microfluidic density sensor. KOH etching and silicon-to-silicon fusion bonding were the major fabrication steps. The first three vibration modes were investigated using laser Doppler vibrometry and each mode was calibrated using different known liquid mixtures. By measuring the resonance frequencies of an unknown-liquid filled tube, its density can be extracted from the calibration curves.

Keywords: Resonating tube, density sensor, MEMS, microfluidic

1. INTRODUCTION

Three micromachined tube-based fluid density sensors have been presented [1-3]. The use of microtubes as a fluid density sensor has the advantage of requiring only a small volume sample (in the order of 10 µL). All the prior tube structures have shown good fluid density sensitivity, which according to theory is proportional to the cross-sectional area ratio of the tube to the fluid, but all of them have corners. Corners can add an additional pressure drop over the structure and can increase the risk of clogging by gas bubbles or micro-particles in the sensor which can decrease the accuracy of the sensor [4].
In this paper, we present a resonating straight tube as a microfluidic density sensor. The resonating element, a 2.65 cm long straight tube, is supported mechanically by a surrounding silicon frame. The sample volume of just 9.3 µL allows the density of a fluid to be continuously monitored with high resolution.

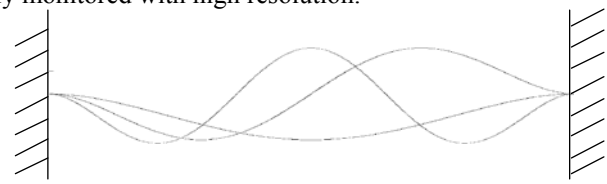

Figure 1: Three vibration modes of a fixed-fixed resonating structure.

2. THEORY

By using an earlier derived formula in [5] and by simplifying all the geometric parameters into one constant C_i, the i-th resonance frequency of a fixed-fixed tube can be calculated by $f_i=C_i\cdot(E/(\rho_t A_t+\rho_f A_f))^{0.5}$, where C_i depends on the tube dimensions and the vibration mode. E is Young's modulus of silicon. ρ_t and ρ_f are the densities of tube and fluid and A_t and A_f are the cross-sectional area of the tube and fluid, respectively. The fluid density sensitivity of a densitometer can be calculated by $S=f_r^{-1}\cdot(\partial f_r/\partial \rho_f)$. Therefore, for a tube structure, $S=-0.5/(\rho_f+\rho_t A_t/A_f)$. The A_t/A_f area ratio for this design is 0.535 yielding a fluid density sensitivity of -223 ppm/kg.m^{-3} for water in theory.

978-0-9798064-0-7/µTAS2007/$20©2007CBMS

3. FABRICATION

The fabrication is illustrated in Figure 2. KOH etching and silicon-to-silicon fusion bonding are the major fabrication steps. The interior and exterior of the tubes were etched by KOH to achieve hexagonal silicon tubes. The wafer was diced to open up the tubes and create 10 mm×28.5 mm sensor structures. For evaluation, the sensor was glued to a fixture using epoxy. The fluid was lead to the silicon tube by stainless steel tubes. The electrodes, which are parallel to the resonating tube, were patterned on an etched recess of a glass slide. The fixture clamps the glass slide close to the vibrating element. The recess depth, and thus the electrode distance, was 6 μm.

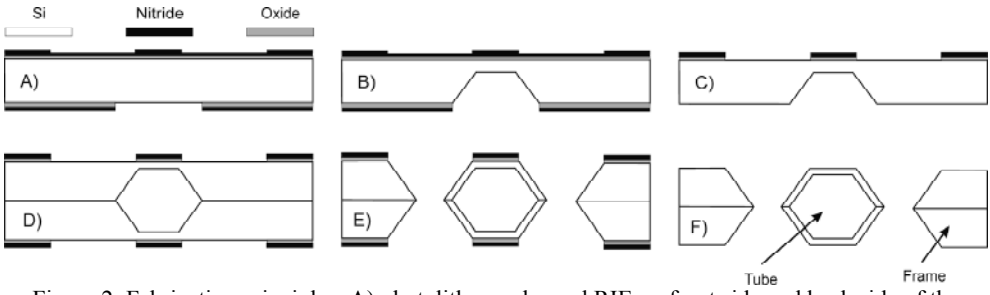

Figure 2: Fabrication principles: A) photolithography and RIE on front side and back side of the wafers; B) KOH etch of two Si wafers to form the inside of the tubes; C) strip nitride and oxide from bond interface; D) Direct wafer bond; E) KOH etch to define the outside of the tubes; F) Mask material strip and dicing.

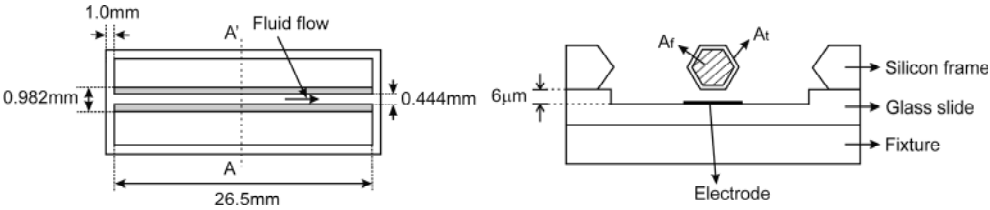

Figure 3: Design dimensions of the silicon sensor (left); Cross-section A-A' of a sensor with the electrodes in its fixture (right).

4. EVALUATION

The density sensor was calibrated in a vacuum chamber under 2×10^{-4} mbar pressure. A laser Doppler vibrometer was used to detect the vibration modes and to measure the resonance frequencies. Air and five different liquid mixtures of 2-propanol/water were used to calibrate the density sensor. The density of each liquid mixture was measured using a volumetric flask and a scale. Then, the resonance frequency of each mode was measured with 1 Hz resolution. Fig. 4 represents the calibration curves using a plot of $1/f_i^2$ vs. ρ_f and passing three regression lines using least square approximation.

5. RESULTS AND DISCUSSION

The sensor has shown a fluid density sensitivity of -256±6 ppm/kg·m^{-3} around the density of water. Possible mask underetch during the fabrication process can describe the difference between the observed and the predicted values. The three vibration modes of a

water-filled tube have shown a Q-value in the range of 50-100 at 2×10^{-4} mbar ambient pressure. The Q-value of the sensor is limited because of structure loss and clamping loss. Using a stiffer glue or encapsulating the sensor can improve the Q-value.

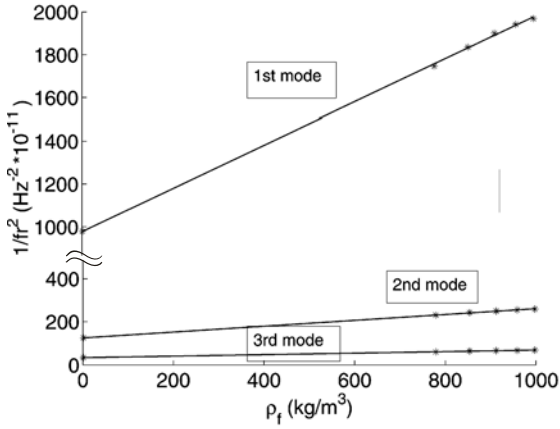

Figure 4: $1/f_r^2$ plot of air-filled tube and five different 2-propanol/water mixtures and the relevant regression lines using least square approximation.

6. CONCLUSIONS

A silicon straight tube was tested and calibrated as a density sensor. This fixed-fixed resonating structure has shown linear calibration curves and good fluid density sensitivity. To eliminate the structure loss and the clamping loss, the sensor should be vacuum encapsulated to achieve to a higher Q-value.

REFERENCES

[1] P. Enoksson, G. Stemme and E. Stemme, "Silicon tube structures for a fluid density sensor", Sensors and Actuators A: Physical, Vol. 54, Issues 1-3, June 1996, Pages 558-562.

[2] D. Sparks, R. Smith, M. Straayer, J. Cripe, R. Schneider, A. Chimbayo, S. Ansari and N. Najafi, "Measurement of density and chemical concentration using a microfluidic chip", Lab Chip, Vo1.3, p.19 (2003).

[3] D. Westberg, O. Paul, G. I. Andersson and H. Baltes, "A CMOS-compatible device for fluid density measurements", Micro Electro Mechanical Systems, 1997, MEMS '97, Proceedings, IEEE, Tenth Annual International Workshop on 26-30 Jan. 1997 Pages: 278 - 283.

[4] D. Sparks, V. Cruz and N. Najafi, "The resonant behavior of silicon tubes under two-phase microfluidic conditions with both microbeads and gas bubbles", Sensors and Actuators A 135, 2007, Pages 827-832.

[5] R. D. Blevins, "Formulas for Natural Frequency and Mode Shape", Van Nostrand Reinhold Company, 1979.

CONTINUOUSLY MICROFLUIDIC CENTRIFUGATION IN SEQUENTIALLY CONNECTED SEMICIRCULAR MICROCHANNELS FOR MICROMETER-SIZED PARTICLE ENRICHMENT

Dongsheng Xu[1,2] Wei Wang[1], Yufeng Jin[1] and Zhihong Li[1]

[1]National Key Laboratory of Micro/Nano Fabrication Technology, Institute of Microelectronics, Peking University, Beijing, 100871, CHINA

[2]Shenzhen Graduate School of Peking University, Shenzhen, 518055, CHINA

ABSTRACT

A continuously microfluidic centrifugation was realized in sequentially connected semicircular microchannels whose radii vary from 50μm to 110μm. It was numerically and experimentally demonstrated that, in the present chip, enrichment of micrometer-sized particles could be realized due to the high quality centrifugal performance.

Keywords: Continuously microfluidic centrifugation, sequentially connected semicircular microchannel, micrometer-sized particle, enrichment

1. INTRODUCTION

Recently, centrifugation is believed to be a promising candidate for the on-chip separation/enrichment. A high quality centrifugation (up to 1.6Mg) was realized in a microcavity by a high-speed lid-driven flow[1], and a single semicircular microchannel with curved radius of 20mm was proposed to separate particles continuously [2]. As the nominal centrifugal acceleration is in inverse proportion to the second power of the curvature radius, the microchannel prepared by the microfabrication technique is able to achieve very large centrifugal acceleration in chip. An Archimedean spiral microchannel with curved radius ranging from 100μm to 2500μm has been developed to realize continuously microfluidic centrifugations in a single chip, and white blood cells can be enriched up to 6 folds from whole blood directly by this centrifugal device [3]. The Archimedean spiral microchannel is a good choice to realize continuously microfluidic centrifugations because of its compact structure, but its curvature radius enlarged rapidly with the developing angle increasing and thereby high centrifugal accelerations can only be obtained near the inlet. In this work, sequentially-connected semicircular microchannels with different radii was developed to overcome this drawback. Numerical simulation and experimental studies were carried out to evaluate the centrifugal performance of the present chip.

2. WORKING PRINCIPLE

Working principle of the present chip is shown in Figure 1(a), and it is the same as that of the microfluidic centrifugation in the Archimedean spiral microchannel. To avoid the rapid-decrement of the centrifugal acceleration with the increased developing angle, sequentially connected semicircular microchannels with gradually increased radii are used here. Fluidic characters in the present chip were studied numerically by Fluent™. Variations of the maximum centrifugal acceleration along the microchannel with different flow rates are shown in Figure 1(b). When the flowrate is about 3.5μl/s, the maximum

978-0-9798064-0-7/μTAS2007/$20©2007CBMS

centrifugal acceleration in the first semicircular microchannel is about 0.37Mg and decreases nearly 48.6% in the third part (0.19Mg) due to the enlarged curvature radius. In an Archimedean spiral microchannel with the same innermost radius of 50μm, for comparison, the nominal centrifugal acceleration will decrease 77.6% when its developing angle varies from π to 3π, according to the numerical results shown in Figure 1(c).

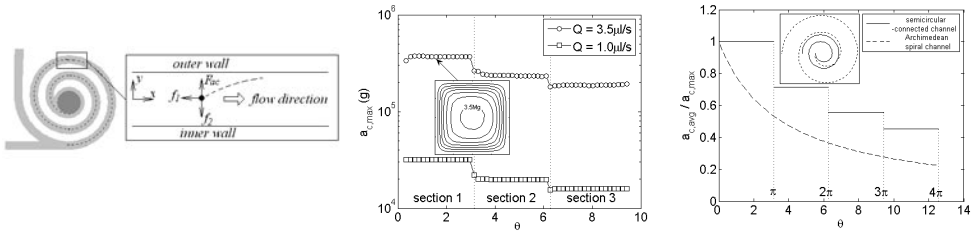

(a) (b) (c)

Figure 1 (a) Working principle of the present chip. (b) Variation of the maximum centrifugal acceleration along the microchannel. (c) Variation of the nominal centrifugal acceleration along different microchannels, and the insert shows the schematic structures of two microchannels

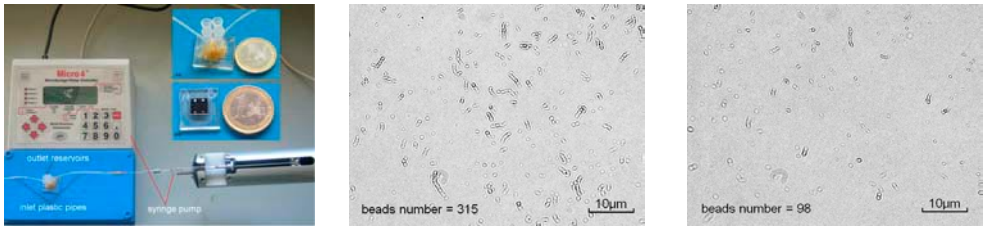

(a) (b) (c)

Figure 2. (a) Photograph of the experimental setup. The insert figures are front and back sides of the (assembled) chip (twin devices in a single chip). And typical photographs of the beads in the experiment with a flow rate of 3.8μl/s, (b)outer outlet, and (c) inner outlet.

3. EXPERIMENTAL

Microfabrication process of the present chip was the same as that reported in the reference [3]. A 2.5mm-thick PMMA plate (20mm×20mm) was bonded to the chip with 301 epoxy (Epoxy Technology Inc., Billerica, MA, USA), on which through holes with diameter of 1.5mm were drilled at the positions of the inlet and outlets. Plastic pipe and pipette tips were glued in these through holes, and were used as the injection tube and outlet reservoirs, respectively. The experimental setup is also shown in Fig. 2(a). A microliter syringe (250μl) controlled by the Micro Syringe Pump Controller Micro4^{TM} (World Precision Instruments, USA) supplied the driven pressure. Magnetic bead (SiO_2, Chemicell，Germany) with diameter of 1μm and density of 2.25g/cm^3 was selected as the experimental particles. The sample fluid with the initial concentration of 50mg/ml was diluted 10,000 times by the deionized water. In ilka experiment, the particle-laden sample was oscillated to be uniform by a vortex agitator (QL-901, Kylin-Bell Lab Instruments Co., Ltd., Haimen, Jiangsu, China), and then injected into chip with a given flow rate by the syringe. Samples in the two outlet reservoirs were collected by pipettes. 1μl of these samples was dropped on a clean slide and the beads inside were adsorbed on the surface by

a magnet just under the slid. A microscope (ECLIPSE 80i, Nikon, Japan) was used to get the photographs of these captured beads, typical results were shown in Figure 2(b) and 2(c), from which the bead number was counted.

4. RESULTS AND DISCUSSION

The slid background was tested in advance, and the present slid shows a reasonable low noise (the number of the spots having a similar diameter as the experimental particle's being smaller than 20). All the experimental results presented here had eliminated the background effects. Variation of the enrichment efficiency, which was defined as the number ratio of the particle in the outer reservoir to that in the inner one, with the flow rate is illustrated in Fig. 3. As predicted, the enrichment efficiency increases gradually when the flow rate varied from 1.5μl/s to 3.8μl/s, and the maximum particle number ratio in the present experiment was 2.5±0.3.

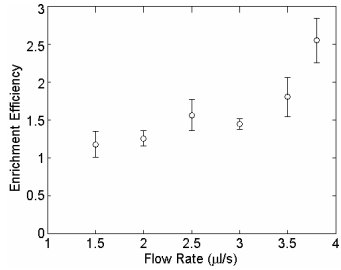

Figure 3. Enrichment efficiency of the present chip with different flow rates, the error bar is calculated with 3 groups experimental data.

5. CONCLUSIONS

Sequentially connected semicircular microchannels were proved to be able to realize a high-quality centrifugation in chip with the centrifugal acceleration up to 0.37Mg, and the centrifugation performance in the present layout decreased much slower than that in the Archimedean spiral microchannel. Enrichment experiment of this chip showed that about 2.5±0.3 fold increment of the 1μm SiO_2 particle number could be achieved by a high flow rate of 3.8μl/s

ACKNOWLEDGEMENTS

The project was financially supported by National Natural Science Foundation of China (Grant No. 60576020 and 60606014).

REFERENCES

[1] J. P. Shelby, D. S. Lim, J. S. Kuo, and D. T. Chiu, Nature 425 pp. 38 (2003).
[2] S. Ookawara, R. Higashi, D. Street, and K. Ogawa, Chem. Eng. J. 101 pp.171 (2004).
[3] W. Wang, Dongsheng Xu, and Zhihong Li, Proc. Micro Total Analysis Systems 2006, Kluwer Academic Publisher, Tokyo, Japam, pp. 543-545, (2006)

ELECTROSPRAY IONIZATION FROM A SILICON EMITTER WITH AN ADJUSTABLE GAP

T. Schönberg[1], P. Ek[2], J. Sjödahl[2], J. Roeraade[2] and C. Vieider[1]

[1]*Dept. of Nanoelectronics, Acreo AB, Sweden and*

[2]*Dept. of Analytical Chemistry, Royal Institute of Technology, Sweden*

ABSTRACT

An improved emitter construction for electrospray ionization mass spectrometry (ESI-MS), where the electrospray is formed from an adjustable gap between two beam-like structures, has been developed, fabricated and tested. The gap is filled with sample solution by capillary forces and electrospray is formed at the sharp tip defined by the intersecting crystal planes of <100> silicon when high voltage is applied. ESI-MS has successfully been performed.

Keywords: adjustable gap, electrospray, ionization, silicon beam.

1. INTRODUCTION

Using MEMS as a fabrication technique for electrospray emitters is a well known concept [1], but to our knowledge all the presented designs are based on spraying orifices with fixed dimensions. An adjustable width of the orifice allows the system to be tuned to obtain an optimized signal for the analyte. The adjustable width also makes it possible to adapt the system to different flow rates.

We have previously demonstrated electrospray ionization from an adjustable gap [2]. The main modification in the present study includes a new emitter design and development of a fabrication process using silicon as base material and MEMS technology. The micromachined structures have a well defined flatness on the surfaces forming the gap walls, which should allow smaller gap widths with uniform distance along the gap. The structures have sharp tips on one side defined by the intersecting crystal planes of <100> silicon and are well suited for mass production with high reproducibility.

2. EXPERIMENTAL

A 525 µm thick silicon wafer is oxidized, deposited with LPCVD nitride and subsequently patterned using a photo resist mask. Deep V-grooves are etched through the wafer on the bottom side using 50% KOH leaving a tilted wall on the front and back side of each structure. An aluminum layer is deposited as mechanical support and etch stop on the bottom side of the wafer. The oxide on the top side is patterned forming the beam and outlining the structure. A photo resist mask is patterned on top of the oxide mask defining the outline of the structures which is then etched down 375 µm by deep reactive ion etch (DRIE). The photo resist is removed and a second DRIE is carried out to form a 1 mm long, 150 µm high and 40 µm wide silicon beam with a very sharp front end used as spraying point and a blunt back end. In addition, the structure is cut out from the rest of the wafer leaving just a small silicon hinge to keep the structure in place. The hinge enables each structure to be gently snapped off from the bulk wafer before use. All layers are removed before a second oxidization creates a hydrophilic surface on the structure. The final structure is 1 mm wide for handling purposes and can be seen in Figure 1a with a close-up of the sharp tip in 1b.

978-0-9798064-0-7/µTAS2007/$20©2007CBMS

Two of the fabricated beam-like structures are individually mounted on translation stages in such a way that the top sides of the beams are facing each other forming a gap guiding the sample solution. The emitter setup is aligned in front of the mass spectrometer inlet as seen in Figure 2. The blunt back end is used as contact point for the sample solution applied from a fused silica capillary connected to a syringe pump. The liquid is spontaneously filling the gap by capillary force and electrospray is formed from the area between the sharp tips when high voltage is applied to the mass spectrometer inlet and the sample solution is grounded.

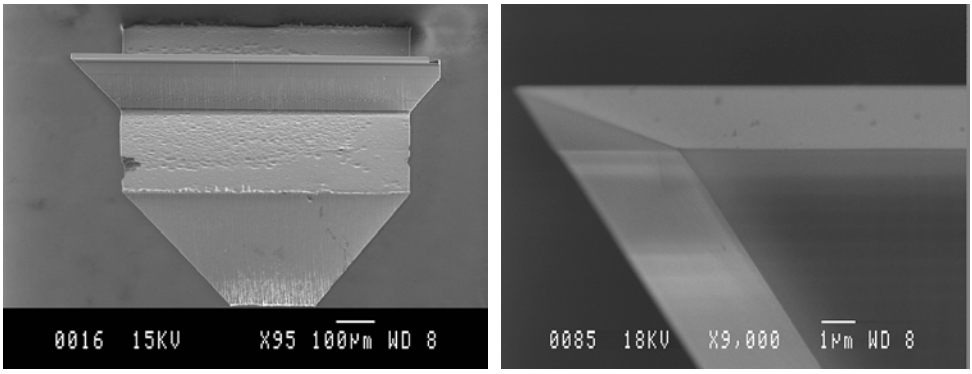

Figure 1. Scanning electron micrograph of (a) a beam-like structure and (b) a close-up showing the tip sharpness at the intersecting crystal planes.

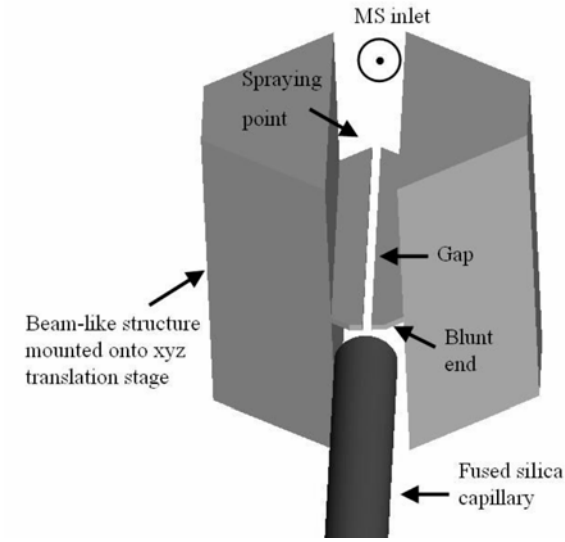

Figure 2. Schematic view of the emitter setup with two beam-like structures facing each other and a capillary dispensing the sample solution to the back end of the gap via a liquid bridge. Electrospray is formed at the spraying point.

3. RESULTS AND DISCUSSION

The structures were mounted in an ESI-MS setup and aligned to be parallel. A sample solution of 10 µM angiotensin I in 50:50 (v/v) acetonitrile/water with 5 mM formic acid was applied from a fused silica capillary connected to a syringe pump. The capillary was placed close to the blunt back end of the gap in such a way that a liquid bridge was formed and the sample solution filled the gap by capillary force. A high voltage was applied to the MS inlet forming a Taylor cone and electrospray at the sharp end of the structures. Mass spectrum can be seen in Figure 3.

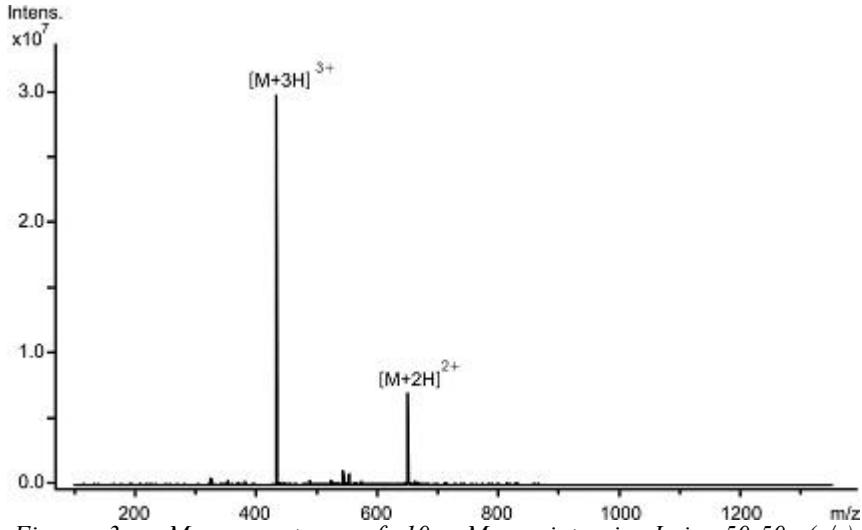

Figure 3. Mass spectrum of 10 µM angiotensin I in 50:50 (v/v) acetonitrile/water with 5 mM formic acid.

4. CONCLUSION

We have demonstrated that our silicon emitter structures can successfully be used for ESI-MS. The choice of beam width and the dynamically adjustable gap width allows the system to be tuned for optimized signal. The adjustable gap width also enables different flow rates.

ACKNOWLEDGEMENTS

We thank the Nanochemistry program, funded by the Swedish Foundation for Strategic Research and the Swedish Science Council for financial support.

REFERENCES

[1] W-C. Sung, H. Makamba and S-H. Chen, *Chip-based microfluidic devices coupled with electrospray ionization-mass spectrometry*, Electrophoresis, vol. 26, pp. 1783-1791, (2005).

[2] P. Ek, J. Sjödahl and J. Roeraade, *Electrospray ionization from a gap with adjustable width*, Rapid Commun. Mass Spectrom., vol. 20, pp. 3176-3182, (2006).

HIGH THROUGHPUT CONTROLLED BACTERIAL TRANSPORT USING GEOMETRICAL FLUIDIC MICROCHANNELS OR 3D MICROFIBERS STRUCTURES

S. Martel and M. Mohammadi

NanoRobotics Laboratory, Department of Computer Engineering, École Polytechnique de Montréal, Montréal, CANADA. (correspondence: sylvain.martel@polymtl.ca)

ABSTRACT

A novel method of transport for samples in aqueous medium is proposed and validated. The method makes use of Magnetotactic Bacteria (MTB) as controlled carriers to transport samples in fluidic channels. Furthermore, we demonstrate that to achieve higher density transport channels, the swimming paths of MTB can be controlled in fluid retained through capillary forces in geometrical fluidic channels or though a thin layer of aqueous solution on microfibers that can be constructed onto various 3D structures. This approach provides an alternative to other transport methods used in microsystems with specific characteristics that can be advantageous to many applications.

Keywords: Magnetotactic Bacteria, Bacteria Transport, Microchannel, Microfiber

1. INTRODUCTION

Transport methods typically used in lab-on-a-chip or in Micro-Total-Analysis Systems (μTAS) such as pumping fluid containing samples to be analyzed using micro-pumps are often relatively bulky and often difficult to integrate in very constrained spaces, and/or require relatively high power to operate. Other popular techniques such as electro-osmosis or dielectrophoresis (DEP) are based on the principle of electrokinetics where relatively high frequencies and voltage amplitudes dependent on dielectric properties are required to induce a force of the samples to be transported. Our proposed method referred to as *bacterial transport* in this paper, minimizes electrical power requirements and can be easily integrated in very small spaces while being independent of dielectric properties. As such, bacterial transport may prove to be suitable for many applications when low electrical power, compactness and/or specificity among micro-objects with similar dielectric properties are required. When coupled with fluid retention through capillary force in various geometrical fluidic microchannels or 3D microfibers structures, high density bacterial transport can be embedded in various microsystems including μTAS.

2. THEORY AND METHOD

Because flagellated bacteria are very effective in low Reynolds number hydrodynamics, the flagella motor embedded in each bacterium can be exploited to provide a propulsion force sufficient to transport samples being attached to the cells. Directional control is achieved by inducing a torque on a chain of nanoparticles called magnetosomes acting like a compass embedded in each MTB. Such directional torque can be provided by a permanent magnet or by using an electrical current. Although MTB can be oriented with directional magnetic field intensities equivalent to the geomagnetic field (0.5 Gauss), higher directional magnetic field intensities in the order of 3 Gauss provide better and highly predictive responses and hence optimal computer-based control by making magnetotaxis the dominant

978-0-9798064-0-7/μTAS2007/$20©2007CBMS

factor over other influencing factors in the motion behavior of the MTB such as chemotaxis and aerotaxis. Here, MTB of type MC-1 cultivated in our laboratory are used for several reasons but particularly beside being a polar bacteria, because of its higher swimming speed (speeds up to 300 µm/s have been recorded by our group) compared to other flagellated bacteria, superior thrust (>4 pN compared to 0.3-0.5 pN for many other bacteria).

A solution that can be used in combination with narrower channels to increase channels density is to exploit capillary retention in angular regions of the microchannels. Simple examples using a square shape microchannel or using two fibers in parallel are shown in Fig. 1. In Fig. 1, a single fluidic microchannel for instance is replaced by four channels by exploiting capillary force and channel geometry. Depending upon different factors such as surface tension and the level of complexity in fabrication of microchannels with more angles along the periphery, a higher density of channels can be realized.

The same approach can be applied between two or more microfibers as depicted in Fig. 1 and even on a single fiber when a thin layer of fluid is retained. In the latter case, we can show that the layer thickness of only a few micrometers is sufficient for the MTB (cell diameter of MC-1 MTB is approximately 2-3 µm) to swim along providing efficient yet very dense transport channels where bacterial transport can be done in two reciprocal directions simultaneously.

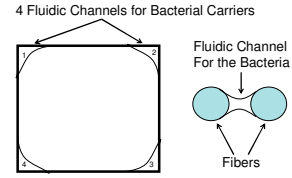

Figure 1. Fluidic channels formed by capillary retention.

Attachments to polymer microbeads or nanoparticles that may be coated with samples being transported are typically done using antibodies developed by our group and specific to the MC-1 bacteria.

3. EXPERIMENTAL RESULTS

As a simple example that proves the concept is the one in [1] where we demonstrated a single MTB pushing a microbead (that could be coated with reactive agents or other samples) following a pre-determined swimming path (see Fig. 2a.

In [2], MC-1 MTB have been controlled to navigate inside microfluidic channels. An example is depicted in Fig. 2b. In this example, all bacteria follow the same channels. If different paths are required, several fluidic channels would be required at the cost of decreasing the channels density unless more advanced microfabrication techniques are used to reduce the width of the channels. Another alternative is depicted in Fig. 2b. A proof of concept showing MC-1 MTB swimming along four fluidic channels formed by capillary retention along the four corners of a simple square microchannel is depicted in Fig. 3. In this example, the average swimming speed of the bacteria measured by dark-field microscopy using analysis of video images was 180µm/s. Experimental results related to Fig. 3 showed that bacteria swim to the left in 50% of the channels with the remaining bacteria swimming to the right. The microchannel depicted in Fig. 3 was made of Pyrex glass. Only a thin layer of water at the corner of the fluidic channel was used by the bacteria to swim in both directions. Here a 10 Gauss DC magnetic field was used during the experiments. Much lower magnetic field intensities could also be used.

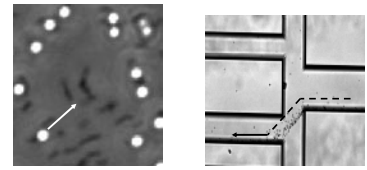

(a) (b)

Figure 2. a. Example of a 3 µm bead being pushed by a single bacterium b.agglomeration of bacteria being navigated in microfluidic channels

More complex paths are also possible. Fig. 4 for instance shows bacteria swimming along right-angle paths. Although relatively complex computer-based control can be used when bacteria are tracked and the directional magnetic field is changed in real-time accordingly, sophisticated travel paths for bacterial carriers along 2D or 3D fluidic structures are possible using fixed permanent magnets. For instance, by increasing the DC magnetic field intensity to above approximately 120 Gauss using stronger permanent magnets or placing the magnets closer to the fluidic structure, the bacteria will automatically reverse their swimming directions when reaching the end of a swimming path, which is not the case when the field intensity is lower. Hence, by integrating permanent magnets providing high low field intensities throughout the fluidic structures and constraining the swimming paths of the bacteria with thin layers of water, complex micro-transport systems requiring no electrical power can be implemented.

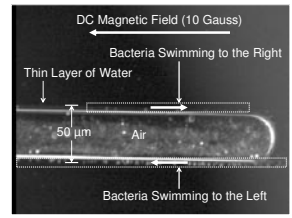

Figure 3. Bacteria swimming along thin layers of water at the corners of a square fluidic channel

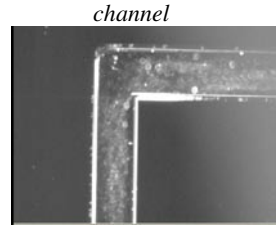

Figure 4. Bacteria swimming along right-angle paths

4. DISCUSSION AND CONCLUSIONS

Our initial experimental results show that MTB can be used as an effective means of transport that is well adapted to the requirements of many applications in microsystems and particularly in µTAS. By exploiting the motility of bacteria, less electrical energy is required leading to further miniaturization while avoiding problems such as Joule heating in small fluid samples. A binding techniques to such bacterial carriers based on antibodies have been implemented successfully. The use of MTB allows us to control its displacement in various ways that can be implemented in computer software. Although this novel approach has many advantages, it also has limitations such as limited operation in higher temperature, constraints related to the type of aqueous medium used, etc. Nonetheless, this approach still may be more appropriate in many applications used in µTAS or at least providing a complementary alternative to other existing transport techniques used in fluidic microchannels.

ACKNOWLEDGEMENTS

The project is supported by the Canada Research Chair (CRC) in Micro/Nanosystem Development, Fabrication and Validation, the National Sciences and Engineering Research Council of Canada (NSERC), the Canada Foundation for Innovation (CFI), and the Government of Québec.

REFERENCES

[1] S. Martel, C. Tremblay, S. Ngakeng, and G. Langlois, "Controlled manipulation and actuation of micro-objects with magnetotactic bacteria," S. Martel, *Applied Physics Letters*, **89**, 233904 (2006).

[2] Z. Lu and S. Martel, "Microfluidic system for assessing the controllability of MC-1 magnetotactic bacteria as carriers in micro-channels," *The Nanotechnology Conference and Trade Show (NSTI) Nanotech*, Boston, MA, USA, May 7-11 (2006).

MICROFLUIDIC DISTRIBUTION SYSTEM FOR HOMOGENEOUS INJECTION THROUGH A NEEDLE MATRIX

Antonin Hoel[1], Lluis Mir[2], Bruno Lepioufle[1] and Marie-Caroline Jullien[1]
[1]SATIE, CNRS, ENS Cachan Antenne de Bretagne, France
[2]Institut Gustave Roussy, CNRS, France

ABSTRACT

We report a microfluidic device able to control the ejection of fluid through a matrix of out-of-plane microneedles. The device comprises a matrix of open dispensing units connected to needles and filled by a common filling system. The ejection of fluid is obtained by the deformation of a membrane inside the dispensing units. A sufficient pressure over the membrane ensures that all dispensing units deliver a fixed volume (their content) irrespective of the hydrodynamic pressure outside the dispensing unit outlet. The geometrical parameters of the device are optimized to avoid as much dead volume as possible, as it was though to handle plasmid DNA solutions which are very expensive. Conception and fabrication of the system as well as experimental results are described in the paper. Our prototype is conceived to inject in a uniform way 10 µl of drug through 100 microneedles distributed over one square centimeter.

Keywords: microfluidic, distribution system, transdermal injection

1. INTRODUCTION

Since a decade of years, microneedle matrixes have been proposed as an innovative tool to enhance transdermal drug delivery [1,2]. However, even if a lot of papers deal with microneedle matrix manufacturing [1-4], just a few papers [3, 4] report how to connect this objects to a liquid injection/extraction process.

The simplest way to inject a liquid through a microneedle matrix is to use a single reservoir that is emptied through the whole matrix. This type of system is presented for example in the work of B. Stoeber [3]. While the liquid should mainly pass through the needles with the lower hydrodynamic resistance, such a system should not permit to control the quantity of drug that is injected through each needle. Indeed, apart from the fact that the needles are hardly exactly identical, the skin is not a homogeneous material leading to different hydrodynamic resistance at needle exit. Therefore emptying a single reservoir through a matrix could lead to an inhomogeneous injection since most of liquid tends to pass through the less resistive pathways. Furthermore, therapeutical DNA solutions are very expensive, and should not be wasted. Manipulating those solutions needs a distribution system wich optimizes the use of the drug by achieving a good distribution over the treated surface and minimize the drug losses during manipulation.

978-0-9798064-0-7/µTAS2007/$20©2007CBMS

2. SYSTEM DESCRIPTION

The system is composed of a matrix of dispensing units (reservoirs) that is covered by a deformable membrane (figure 1). Reservoirs are connected to each other via a microchannel network to allow the filling of the system from a single entry. This allows reducing liquid manipulation to a single shot for the whole system filling (a volume of about 20 µL). A fluidic diode end the filling circuit in order to close it during the drug ejection process. Excluding the entry of the filling circuit, the whole system is enclosed into a box in which the pressure can be controlled in order to actionnate the membrane deformation.

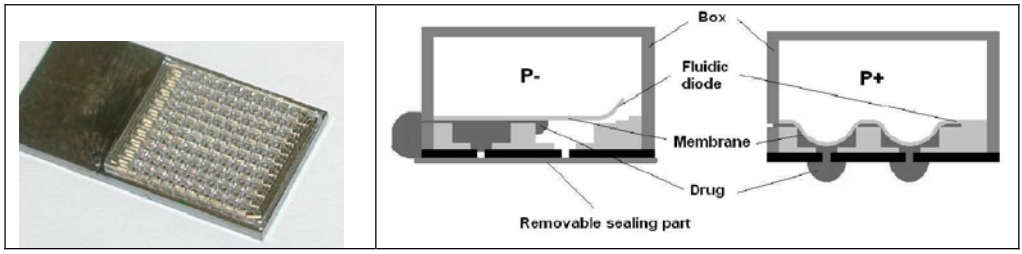

Figure 1 : left) The microfluidic distribution system stuck on a hollowed silicon matrix; right) left (negative pressure), the chamber during the filling process, right (high pressure), liquid is chased out through the needle

3. WORK PRINCIPLE

The filling of the system is obtained by placing a drug drop at the filling circuit entry and applying an under pressure inside the box (figure 1.right). The drug is sucked through the filling circuit, and fill the whole reservoir matrix. To achieve a good filling, the needles should be closed (e.g. sticked into a soft material) and the system walls have to be hydrophobics. With hydrophilic walls, air bubbles remain in each chamber.

The ejection of the drug is obtained by applying an over pressure inside the box. This deforms the membrane toward the reservoir matrix (figure 1.right) and then chase out the liquid from each reservoir through the corresponding needle (figure 2). During injection, the membrane blocks the filling circuit. This leads to the independence of each chamber, that is able to eject only its own liquid content, through its corresponding needle.

The system was characterized and modelized (COMSOL) in order to determine the required membrane thickness and the pressure to apply. The activating pressure was then set to 1bar for a 30µm thick membrane.

4. RESULTS AND DISCUSSION

Our first prototypes were able to achieve an injection of regular ink through 80% of the needles (the other were clogged during fabrication process) with an ejected volume of 120 nl ± 10 nl per needle (figure 2). These results proove that even with great iregularities in resistance towards ejection (clogged needles, different needle diameters...), the system is

able to provide an homogeneous repartition over a microneedle matrix. However, injection test into the skin remains to be done to validate the system.

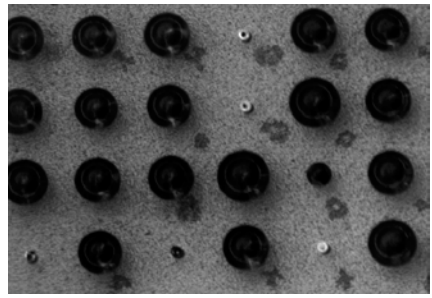

Figure 2 : The ejection of ink trough the needles

Note that electrophoresis tests were done to verify the integrity of DNA molecules after passing through the system. The asseys showed that a 7kbp plasmide DNA did not fractionate in our conditions of use.

5. CONCLUSION

A microfluidic distribution system has been designed, fabricated and tested. We successfully perform the manipulation of small liquid volumes (inital drop of 20 µl) and further inject the liquid through a microneedle matrix with a minimal loss of the drug (about 50% of the used drug). It provides a homogenous injection over the entire matrix and allows controlling the quantity of drug that is injected (120 nl ± 10 nl for each needle, i.e. a total injected volume about 10 µl).

ACKNOWLEDGEMENT

This work was done within the framework of the European project ANGIOSKIN (project number: LSH-2003-512127) and has been patented (European patent n°: 06425292.7 (2006))

REFERENCES

[1] “Microneedles for transdermal drug delivery”, M. R. Prausnitz, Advanced Drug Delivery Reviews, 56, pp. 581–587, 2004
[2] “Side-opened out-of-plane microneedles for microfluidic transdermal liquid transfer”, P. Griss, G. Stemme, Journal of Microelectromechanical Systems, 12 (3), pp. 296- 301, 2003
[3] “Design, fabrication and testing of a mems syringe”, B. Stoeber and D. Liepmann, Solid State Sensor and Actuator Workshop, 2002.
[4] “A novel microneedle array integrated with a pdms biochip for microfluid systems”, S. J. Paik, J. M. Lim, I. Jung, Y. Park, S. Byun, S. Chung, K. Chun, J. Chang, and D. D. Cho, Transducers ’03, 2003.

MONOLITHIC TEFLON MEMBRANE VALVES AND PUMPS FOR HARSH CHEMICAL AND LOW-TEMPERATURE USE

Peter A. Willis[1], Brian D. Hunt[1], Victor E. White[1], Michael Ikeda[1], Michael C. Lee[1], Michael J. Pelletier[2], and Frank J. Grunthaner[1]

[1]*Jet Propulsion Laboratory, California Institute of Technology, Pasadena, CA, USA 91109*
[2]*Pfizer Global Research and Development, Ann Arbor, MI, USA 48105*

ABSTRACT

Pneumatically actuated diaphragm valves and pumps utilizing Teflon membranes as the valving element between etched glass wafers are fabricated and characterized. These devices survive the extreme low-temperature cycling required for spaceflight applications and are amenable to use with a wide variety of solvents.

Keywords: Teflon membrane microvalve, micropump, Teflon AF, laminated membrane

1. INTRODUCTION

General purpose microfluidic systems for exploration and sampling of foreign planetary surfaces must be extremely temperature resistant and chemically/physically robust in order to survive space travel, launch/entry/descent/landing, and ambient conditions on the planet of study. For these considerations, motivated by the well-established chemical and temperature resistance of Teflon, a general purpose Teflon monolithic valve and pump design was developed, using the Grover PDMS monolithic device geometry[1] as the starting point. Membranes incorporated into devices were either spun films of Teflon Amorphous Fluorocarbon (Teflon-AF®), or commercial Teflon/Teflon-AF® films bonded between conformal coatings of Teflon-AF®. The additional perfluoro-2,2-dimethyl-1,3-dioxole (PDD) groups present in Teflon-AF® lower the glass transition temperature of the material, aid in the bonding between fluorocarbons and glass, and increase the solubility of the polymer, enabling spin casting of extremely flat films.[2]

2. EXPERIMENTAL

Devices were fabricated in three-layer stacks, comprised of an upper, fluid-bearing glass "channel" layer, a middle Teflon membrane layer, and a lower pneumatic "manifold" layer for actuation of membranes (Fig. 1). Very flat membranes of pure Teflon-AF® were fabricated by performing repeated spin/cure cycles on a blank glass wafer. A stack comprised of two such wafers with the Teflon-AF® films facing inward was then clamped in an

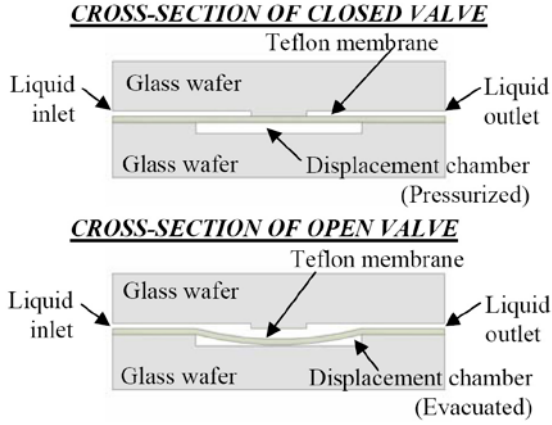

Figure 1. Valve Cross Sections

978-0-9798064-0-7/μTAS2007/$20©2007CBMS

evaculated wafer bonder apparatus and held at 210ºC under 310 kPa mechanical pressure for one hour. Following that, the membrane was released by immersing the stack in HF solution to completely dissolve away the glass. For fabrication of "laminated" membranes, a commercially procured PTFE membrane or a higher melting point Teflon-AF-2400® membrane was placed in the center of this stack prior to application of pressure and heat.

Fluid and gas bearing channels were etched in glass wafers using standand lithography and wet etching techniques. Following that, adhesion promoter (either Cr metal or plasma deposited fluorocarbon) was applied to the wafers. An additional lithography and dry etching step was then performed so as to remove adhesion promoter from the valve seat region of the devices. Following that, membranes were placed between the etched wafers and the device was bonded into a stack as described earlier.

3. RESULTS AND DISCUSSION

Images of microfabricated valves are shown in Fig. 2. These devices survived temperature cycling between -125ºC and +50ºC. A post-processing "embossing" procedure was explored in which a pressure of 84 kPa was applied to the underside of a dry valve manifold while the device temperature was slowly increased. As the valve temperature approached the softening point of the membrane, the air leak rate through the valve dropped sharply and shifting patterns of Newton rings were optically observed in the valve seats. After cooling to room temperature, the single valve sealing characteristics were improved. These observations are consistent with flattening of the membranes against the valve seats. Fig. 3 displays the resulting flow rate through valves fabricated from differing membrane types under an applied inlet water pressure of 3.5 kPa. At left, negative applied manifold pressures open the valves.

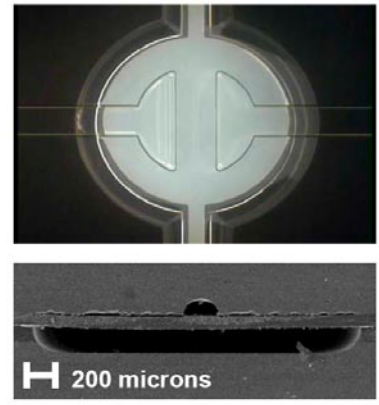

Figure 2. *Top*: Optical micrograph of a single layer Teflon-AF® membrane device. *Bottom*: Scanning electron microscope image of a laminated PTFE device diced through a valve region.

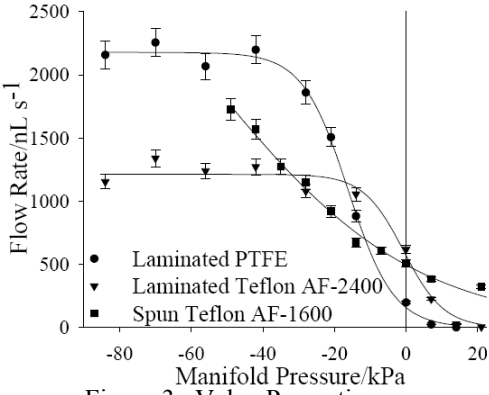

Figure 3. Valve Properties

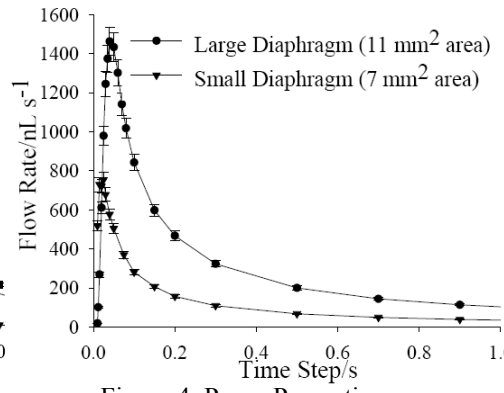

Figure 4. Pump Properties

The embossing process improved the sealing characteristics of all membrane types studied. The Teflon-AF-1600 single layer valves, which we observed to sag the most after fabrication, effectively did not close at all until after embossing. However, even after embossing they were never observed to seal as well as laminated devices. The PTFE laminated devices sagged negligibly in the valve seat region (Fig. 2, bottom) and performed the best without embossing, showing reasonable on-off flow characteristics. However, even these valves were improved after embossing.

Three valves placed in series were used to pump liquid peristaltically. One pump cycle consists of five discrete pumping stages.[1] Valves were opened and closed at -84 kPa and +35 kPa, respectively, to ensure complete actuation. Absolute pumping rate was measured for optimized PTFE diaphragm pumps as a function of time delay between pump stages (Fig. 4). Pump rates as high as 1600 nL/s were observed, which is extremely high relative to rates reported in analogous PDMS devices.[1] Analysis of the maximum volume delivered per stroke in these pumps showed that the membranes did not stretch or deform as much as the analogous PDMS devices (accessing just 13-24% of the manifold displacement volume in comparison to 82% of the volume in the case of PDMS membranes). The overall pumping rate is faster for the Teflon devices due to the extremely fast response of the membrane to applied pressures, as the Young's modulus of elasticity of bulk PTFE is on the order of 10^3 times greater than that of bulk PDMS.[3] This enables a great number of pump cycles per unit time. Indeed, the optimal cycle time for the Teflon pumps is more than an order of magnitude shorter than that for an equivalent PDMS pump.[1]

4. CONCLUSIONS

Monolithic diaphragm valves and pumps utilizing Teflon-based membranes as the actuating element have been successfully fabricated, characterized, and observed to survive extreme cooling cycles required for spaceflight applications (-125ºC to +50ºC). Extremely high pumping rates (1600 nL/s) were achievable in the devices relative to pumping rates for analogous PDMS diaphragm pumps.[1] These robust devices are ideal candidates for biotechnological applications, exhibiting low protein absorption, biocompatibility, and porosity. Another key feature of these devices is their extreme chemical resistance, suggesting general purpose usage in miniaturized "chemical factories" employing organic solvents or strongly caustic/acidic reagents.

ACKNOWLEDGEMENTS

The authors wish to acknowledge the contributions of Rich Mathies's group at UC Berkeley to this work. The research described in this paper was carried out at the Jet Propulsion Laboratory, California Institute of Technology, under a contract with the National Aeronautics and Space Administration.

REFERENCES

[1] W.H. Grover, A.M. Skelley, C.N. Liu, E.T. Lagally, and R.A. Mathies, Sens. Act. B, 89, pp. 315-323 (2000).

[2] P.R. Resnick and W.H. Buck, in *Fluoropolymers 2: Properties*, edited by Hougham et al., Plenum Press, New York, USA, pp. 25-33 (1999).

[3] J.C. Lötters, W. Olthus, P.H. Veltink, and P. Bergveld, J. Micromech. Microeng., 7, pp. 145-147 (1997)

ON-CHIP MICROFLUIDIC GRADIENT GENERATION FOR NANOFLOW LIQUID CHROMATOGRAPHY

Reid Brennen, Hongfeng Yin, & Kevin Killeen
Agilent Technologies, USA

ABSTRACT

We have designed, fabricated, and tested laser-ablated microfluidic chips that generate a liquid composition gradient for nanoflow liquid chromatography (LC). These chips work together in tandem with a microfluidic LC chip to perform high-throughput nanoflow LC/mass spectroscopy (LC/MS). The gradient delay time is decreased from the several minutes when using current LC pumps to only a few seconds by using this gradient generator chip. The gradient generator chip simplifies the nanoflow solvent delivery system and increases robustness, reliability, and ease of use.

Keywords: microfluidics, gradient, mass spectrometry, liquid chromatography

1. INTRODUCTION

NanoLC/MS technology offers high detection sensitivity and is widely applicable in the field of proteomic research and biomarker discovery but the gradient delay time of systems using conventional nanoflow LC pumps is still significant, especially at low flowrates. Other methods for forming nanoflow gradients include pre-formed solvent gradients[1], low to high pressue LC gradient conversion[2], multiple mobile phase reservoirs[3,4], and electorkinetic pump gradients.[5,6] However, these alternatives and conventional gradient pumps have mechanical, chemical, or electrical properties that may work against optimum system use.

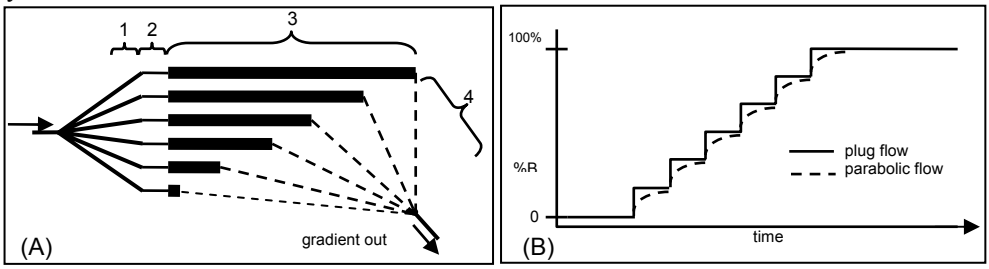

Figure 1. Schematic of the six-stage gradient generation (A) concept and (B) output. Sections: (1) inlet manifold; (2) restrictor; (3) timing channels define each stage's dwell time; (4) outlet manifold. Pressure-driven flow will result in a parabolic velocity profile.

2. CONCEPT & DESIGN

As shown in Fig. 1, the core feature of gradient generation on the microfluidic chip is the *gradient generator* which consists of *n* stages (also called channels) in parallel. In section 2, the restriction channels are small, an effective 5-20 μm diameter and 2 mm length, and a very large flow resistance. The restriction channels therefore define the flow rate through all six stages because the section 3 "timing channels" have large cross-sections (e.g. 200x200 μm) with each channel of different length.

978-0-9798064-0-7/μTAS2007/$20©2007CBMS

The gradient generator structure is initially filled with liquid A and an on-chip reservoir is filled with liquid B, as shown in Fig. 2. Liquid A at high pressure and a controlled, low flow rate is introduced into the reservoir which pushes the liquid B into the gradient generator structure. Since the liquid B takes different amounts of time to travel through each stage (the dwell time), a gradient profile output is created after recombination. Based on the total flow rate and the volume of each stage, the gradient profile with respect to time is determined.

The gradient-generating chip is connected *directly* to the HPLC-Chip containing the LC column such that the delay volume is reduced to a few nano-liters, resulting in a delay time of a few seconds even at the low flow rates which are best for high sensitivity electrospray. The gradient generator chips were fabricated and mounted as described by Yin, et al.[7]

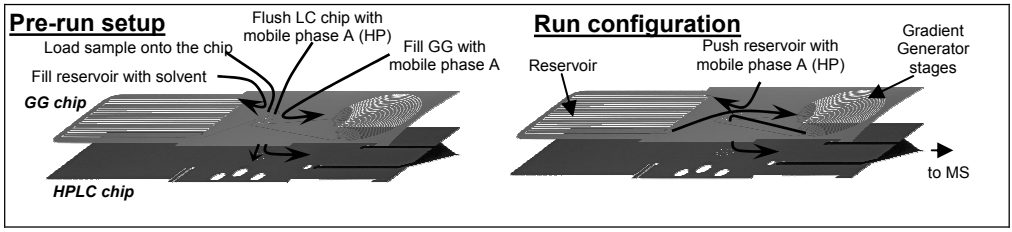

Figure 2. Flow paths for a 20-stage Gradient Generator chip with an HPLC MS chip.

3. RESULTS AND DISCUSSION

The mobile phase gradient profile was monitored by two different tracers, betaine and glucosamine, added to the A and B mobile phases, respectively, which were then pre-loaded into the gradient structure and reservoir. Fig. 3 shows the tracer response for both A and B mobile phases for a flow rate of 200 nanoliters/min.

Nanoflow LC gradient separations of bovine serum albumin digest were performed using an Agilent HPLC MS chip using a gradient formed by either a gradient chip and an Agilent nanopump. The Agilent LC/MSD time-of-flight mass spectrometer resulted in extracted ion currents for 12 selected ions as shown in Fig. 4. The separations were similar but the gradient generator chip system had a duty cycle of 40% compared to 20% for the gradient pump system. Fig. 5 plots, for five replicate runs, the 70 most abundant ions found by MassHunter software and show that peak width and retention time reproducibility are comparable between the gradient chip and a pump-generated gradient.

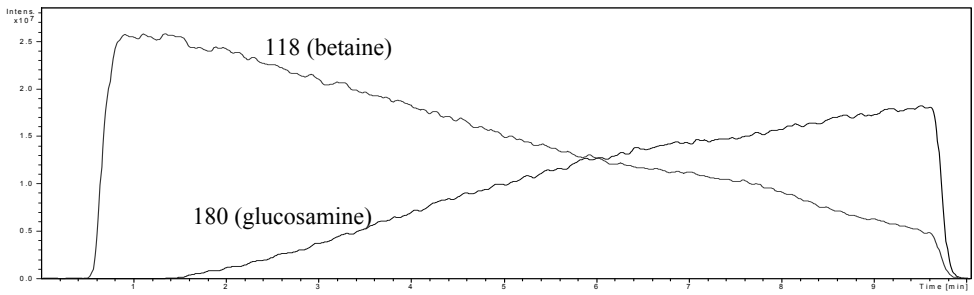

Figure 3. Tracer profiles during LC run represented by EIC of 118 (betaine) and 180 (glucosamine). The nanoPump ran at 200 nl/min during the entire LC run.

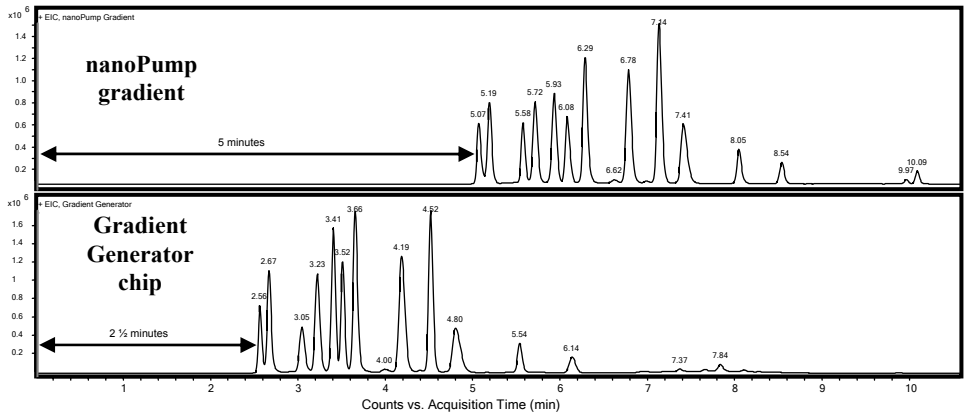

Figure 4. Experimental data comparing the results produced using a standard pump-generated gradient and a gradient generator chip gradient. The data is based on 12 extracted ions.

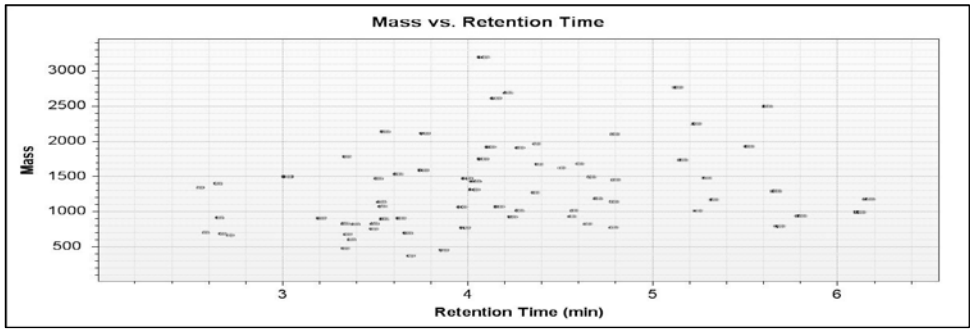

Figure 5. Retention time reproducibility of the 70 most abundant molecular features.

4. CONCLUSIONS

The concept of gradient generation on a chip was implemented and tested both for gradient characterization and for actual sample analyses. Separation of a test mixture of BSA digest was demonstrated with the 20-stage gradient chip and good reproducibility, chromatographic performance, and a stable MS electrospray was achieved with the system.

ACKNOWLEDGEMENTS

The authors extend thanks to Debbie Ritchie of Agilent Technologies for her support on chip fabrication and to Uwe Effelsberg, also of Agilent, for hardware and software support.

REFERENCES

[1] Eschelbach, J.W. and Jorgenson, J.W., Anal. Chem. 2006 78, 1697-1706
[2] Deguchi, K.; Ito, S.; Yoshioka, S.; Ogata, I.;and Takeda, A, Anal. Chem. 2004, 76, 1524-1528
[3] Natsume, T.; Yamauchi, Y.; Nakayama, H.; Shinkawa, T.; Yanagida, M.; Takahashi, N. and Isobe, T., Anal. Chem. 2002, 74, 4725-4733
[4] Capiello, A.; Famiglini, G.; Fiorucci, C.; Mangani, F.; Palma, P.; and Siviero, A., Anal. Chem. 2003, 75, 1173-1179
[5] Figeys, D; and Aebersold, R., Anal. Chem. 1998, 70,3721-3727
[6] Xie, J.; Miao Y.; Shih, J.; He Q.; Liu, J.; Tai, Y. and Lee, T. D., Anal. Chem. 2004, 76, 3756-3763
[7] Yin, H., Killeen, K., Brennen, R., Sobek, D., Werlich, M., van de Goor, T., Anal. Chem. 2005, 77, 527

PERISTALTIC MICRO PUMP ACTUATED BY SINGLE INPUT SIGNAL

Ok Chan Jeong[1,2] and Satoshi Konishi[3]

[1]*Department of Biomedical Engineering, INJE University, KOREA*
[2]*MEMS/NANO Fabrication Center, Busan Techno-Park, KOREA*
[3]*Department of Micro System Technology, Ritsumeikan University, JAPAN*

ABSTRACT

This paper presents the fabrication of the self-generated peristaltic micro pump operated by the single-phase pneumatic force for the practical application. The micro pump consists of the actuator part and the micro channel structure. The actuator part having triple actuators is connected with the single micro channel for the supply of the external compressed air. The peristaltic motion of the cascaded actuators is created by the time-delay effect of the applied pressure from the inlet port. Both the fluidic resistance along the micro channel and the fluidic capacitance of actuator diaphragm results in the sequential deformation of the cascaded actuators. Such a natural phenomenon enables to realize the peristaltic pump by the single-phase input signal. The proposed operational method is verified computationally and experimentally.

Keywords: Cascaded actuator, Peristaltic micro pump, Polydimethylsiloxane

1. INTRODUCTION

The development of the digital micro fluidic system enables the large-scale micro fluidics system and various logical operations on a chip [1-3]. Many useful methods have been reported for the effective control of the complicated pneumatic network such as the multiplexer, de-multiplexer, latch, etc. Other interesting study is about the self-generated peristaltic pump operated by the single-phase input signal [4]. Both the rubber-seal valve and the liquid pumping motion of the general-purpose micro pump were successfully demonstrated.

Our approach in this paper differs from our previous work [4] in the specific design of the actuators for the practical application. The circular shape of the deformable actuator allows to minimize the dead volume of actuators under the relatively lower operational pressure. The linearity of the unidirectional flow rate of the working fluid can be also improved.

2. STRUCTURE AND OPERATIONAL METHOD

Figure 1 shows the computational understanding of the proposed actuators for the self-generated peristaltic micro pump. All actuators are connected with the single micro channel for the supply of the compressed air. The pressure control channel exists between two actuators in order to increase the fluidic resistance of the supplied air pressure. The diameter of the deformable actuator diaphragm is 500 μm. The thickness of the actuator diaphragm is 50 μm. The width and the height of the channel are 50 μm and 10 μm, respectively. If the compressed air is supplied into the inlet port, the magnitude of the applied pressure is reduced along the micro channel structure (a). Thus, the cascaded actuators have different deformations because of the pressure distributions (b). Figure 1 (c) shows the summary of the free-deformation of the cascaded actuators along A-A' and their correspondent pressures.

978-0-9798064-0-7/μTAS2007/$20©2007CBMS

Figure 2 shows the simulation result of the contact analysis of the single actuator. Since the free deformation of the actuator diaphragm as shown in Fig. 1(a) is constrained by a 10-μm-depth of the liquid chamber (a-b), their vertical deformations of the actuator diaphragms are nearly same (c-d). The difference of the generated volumes between act-I and act-III is less than 9 %. Assuming that all actuators have the same value of the fluidic resistance, R (=9.06×10^{12} [Pa s/m^3]) and the capacitance, C (=1.93×10^{-16} [m^3/Pa]), the time constants of the actuators are 0.59 msec for act-I, 1.12 msec for act-II, and 8.83 msec for act-III, respectively. Therefore, the natural peristaltic motion of the cascaded actuators can be created by using the passive and active structure of total pneumatic network.

3. EXPERIMENTAL

Figure 3 shows the fabricated peristaltic micro pump. The two-layer bonded PDMS (Sylgard 184 from Dow Corning) structure is fabricated by using the soft lithography. For the drive-test of the micro pump, the additional PDMS layer is bonded with the micro pump structure.

Figure 4 illustrates captured figures showing the liquid pumping of the self-generated peristaltic pump. A 16 kPa of the square-wave compressed air is supplied into the inlet port while the outlet port opens to the air (b). The operational frequency is 10 Hz and the duty ratio of the square-wave input signal is 50 %. The red-ink as working fluid is used for the visualization of the liquid pumping. The average flow rate of the working fluid is estimated from the movement of the interface between the air and the liquid (c-d). It is about 5.7 nL/min. It is 3.3 times larger than our previous work [4] under 2.5 times lower pressure.

4. CONCLUSIONS

This paper presents the self-generated peristaltic pump actuated by the single input signal. The operational method for the peristaltic micro pump is proposed to minimize the essential control signals with different phases. The increment of the hydraulic resistance along the micro channel structure and the deformation of the flexible PDMS diaphragm result in the different dynamic characteristics of each actuator diaphragm like the peristaltic motion of the cascaded actuators in nature.

As the further study, the micro pump unit will be integrated with the micro finger/hand [6] for the future multi-functional micro surgical tool.

REFERENCES

[1] J. P. Urbanski, W. Thies, C. Rhodes, S. Amarasinghe and T. Thorsen, *Digital Microfluidics using Soft Lithography*, Lab Chip, Vol. 6, pp. 96-104, (2006).

[2] W. H. Grover, R. H. C. Ivester, E. C. Jensen and R. A. Mathies, *Development and Multiplexed Control of Latching Pneumatic Valves using Microfluidic Logical Structures*, Lab Chip, Vol. 6, pp. 623-631, (2006).

[3] T. Thorsen, S. J. Maerkl, S. R. Quake, *Microfluidic Large-Scale Integration*, Science, Vol. 298, pp. 580-584, (2002).

[4] O. C. Jeong and S. Konishi, *Self-generated Peristaltic Motion of Cascaded Diaphragm Actuators for Micro Fluidic Systems*, 20th IEEE MEMS Conf., Kobe, Japan, pp. 135-138, Jan. 2007.

[5] O. C. Jeong and S. Konishi, unpublished.

[6] O. C. Jeong and S. Konishi, *All PDMS Pneumatic Micro Finger with Bidirectional Motion and Its Application*, Journal of MEMS, Vol. 15, No. 4, pp. 896-903, (2006).

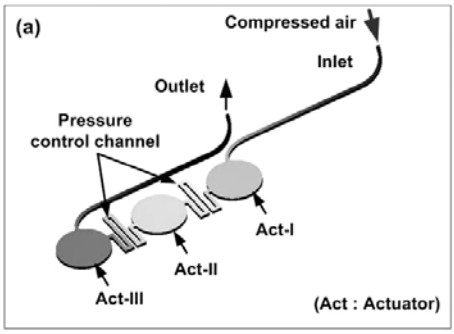

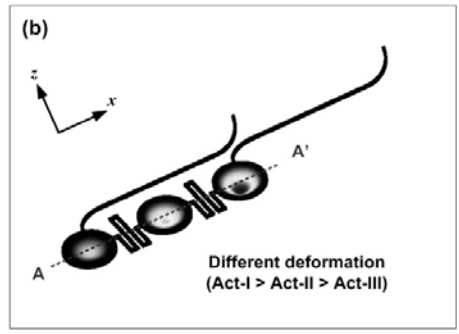

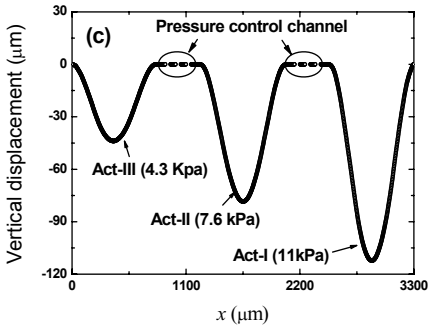

Figure 1. Static deformation of the cascaded actuators induced by a 16 kPa of the compressed air from the inlet port. The solid-fluid analysis method is used to solve the highly nonlinear problem. (FEMLAB from Comsol Inc.) A two-term Mooney-Riviln material model [6] for PDMS diaphragm as a nearly incompressible material and the incompressible Navier-Stoke model for the compressed air are used. (a) pressure distribution, (b) structural deformation of actuator diaphragms, (c) free deformation of the cascaded actuators along A-A'.

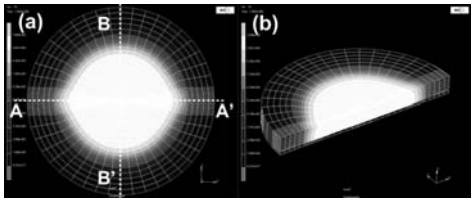

Figure 2. Deformable contact analysis of the actuator for the estimation of the generated volume stroke of the actuator. (Marc-Mentat from MSC software). (a) top view, (b) angled view, (c) node-path plot of AA', (d) one of BB'.

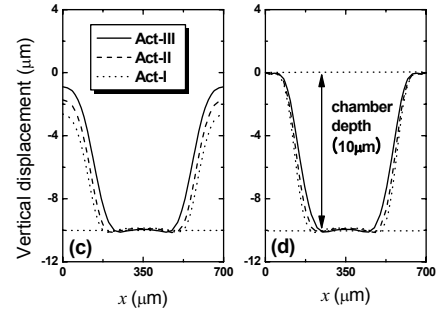

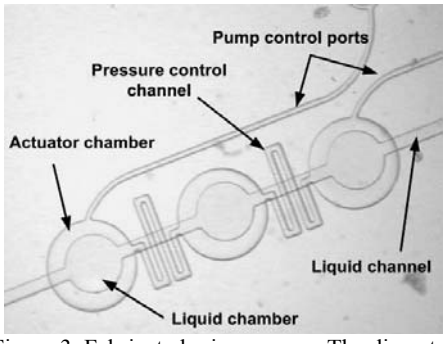

Figure 3. Fabricated micro pump. The diameter of the actuator chamber and the liquid one are 700 μm and 500 μm, respectively.

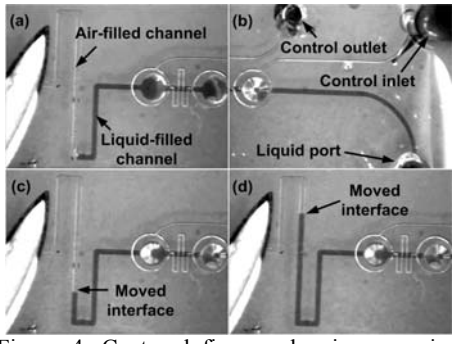

Figure 4. Captured figures showing pumping motions. (a) initial, (b) operational condition. (c-d) moved interface for 12 seconds.

PARTICLE POSITIONING IN MICROCHANNELS USING ULTRASONIC STANDING WAVES REINFORCED WITH RADIATED NEAR AND FAR FIELD PRESSURE WAVES

S.K. Ravula, D.W. Branch, J. Sigman, C. Arrington, P.G. Clem and I. Brener
Sandia National Laboratories, USA

ABSTRACT

This paper describes our continuing work in using ultrasonic standing waves to manipulate particles in microfluidic channels. Here, we present our work in creating microfluidic channels for particle routing and planar piezoelectric PZT transducers for particle focusing. Near field pressure is used to "reinforce" the standing wave node at the center of a glass microfluidic channel and is shown to improve the focusing capabilities. Moreover, the design is compatible with future designs that use multiple piezoelectric transducers for phased three-dimensional particle manipulation in microfluidic channels.

Keywords: ultrasonic standing waves (USW), microchannels, near field, far field

1. INTRODUCTION

Ultrasonic manipulation technologies have matured in the last ten years to allow more sophisticated handling of particles in microsystems. While there have been many studies that use ultrasonic standing waves to move particles reliably in one dimension in microsystems, there have been no devices that use phased ultrasonic radiation fields in combination with ultrasonic standing waves to move particles in microchannels [1-4]. These systems could allow for a greater degree of freedom in movement and higher efficiency focusing within the channels using less complex electrode architectures. In this paper, we present the design, fabrication, and characterization of a new ultrasonic particle positioning system that allows both standing waves and near field radiation fields to be synergistically used to manipulate microparticles in microfluidic channels.

2. THEORY

In the design, we have incorporated micropatterned piezoelectric transducers that could be phased together to achieve three-dimensional focusing within a microchannel. Moreover, the thickness and the surface area of the transducer were chosen to maximize the acoustic efficiency of the standing wave node reinforced with a near field radiation node. Toward this end, we chose PZT transducers with a thickness of 500μm giving an unloaded resonant frequency of 4.41 MHz. For an optimal design the transducer must be relatively insensitive to drive frequency to avoid power losses from external perturbations such as variation in the fabrication process. To support standing waves in the cavity (i.e. water), a cavity height of λ/2 or 170μm is required in the water. The reflector, however, must be λ/4 in the Pyrex or 320μm. To take advantage of near field effects, the transducer dimension must be chosen to be within the near field limit, given by $nf \cong a^2 / \lambda$ for a circular transducer, where a is the transducer radius and λ is the wavelength. In contrast, the far field acoustic radiator acts like a point source which is ideal in beam steering applications.

978-0-9798064-0-7/μTAS2007/$20©2007CBMS

In general, the acoustic pressure field is highly complex for arbitrary transducer geometries and difficult to calculate; however, circular designs have closed-form solutions. In Figure 1, we show the relative acoustic pressure field from a circular transducer for several values of the radius (a) scaled by wavelength, where λ=340μm as a function of the on-axis distance from the transducer. The key design feature requires that $a = 5.245\lambda$ such that a pressure minimum exists at ~85μm or half the cavity height. Though a minima exists when $a = 1.225\lambda$, the resulting transducer area is too small for effective impedance matching. Our result causes the standing wave minimum to overlap with the near field minimum from the transducer pressure field. The radius for this design gives $a = 1.783mm$. The far field boundary would be over 8.9mm from a source with this dimension. The transducer area in this design is ~10^{-5} m^2.

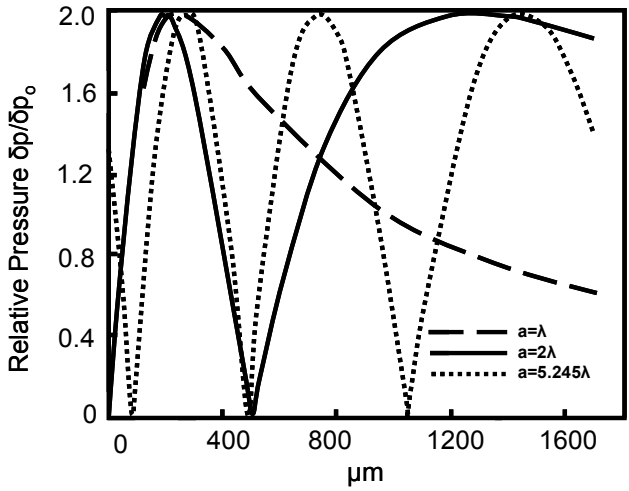

Figure 1. Relative acoustic pressure in the transducer near field.

3. EXPERIMENTAL METHODS

The integrated ultrasonic manipulation system was fabricated using one of two techniques. In the first technique, platinum was deposited on an alumina substrate and then an aerosol PZT was sprayed and heat treated on top. Finally, a top electrode was patterned through a shadow mask using the DC sputterer. In the second scheme, a 1.5in. PZT disc (500μm thick) was patterned with a top electrode metal layer using a liftoff procedure. In both cases, a glass microfluidic channel (Micronit Microfluidics, The Netherlands) was pressure/heat bonded to the transducer substrate. For focusing experiments, 20μm polystyrene beads (Sigma-Aldrich, St. Louis, MO) were injected into the channels with a syringe pump (Harvard Apparatus PHD 2000), and the transducers were driven with an Agilent 33250A function generator.

4. RESULTS AND DISCUSSION

The fabricated systems are shown in Figure 2. The system shown in Figure 2b was modelled using 1-D transmission line theory to determine the frequency properties. The resonant frequency was around 4MHz. In this particular design, the length and width of the transducer determine the location of the near field radiation pressure minimum and the thickness of the transducer determines the standing wave pressure minimum. By choosing either a $\lambda/2$ or $\lambda/4$ thickness cavity we have been able to focus the particles at either the top of the microchannel or the middle. The near field radiation pressure reinforces the standing wave pressure minimum established in the system. By using this technique, we have been

able to obtain tighter z-dimensional focusing (20% reduction in stream broadening) of the particles in each ultrasonic stream. Future designs will include the use of more than two electrodes to steer the particles laterally within the microchannel so that highly focused pressure minima can be established not only in the z dimension within the microchannel but also laterally along its width.

5. CONCLUSIONS

In this paper, we present the use of near field radiation forces to supplement standing wave nodes in microfluidic channels for particle positioning applications. The combination of both of these forces has the potential to allow for finer particle manipulation. Moreover, multiple acoustic radiators can be incorporated into these systems to allow for further control of particles using far field effects.

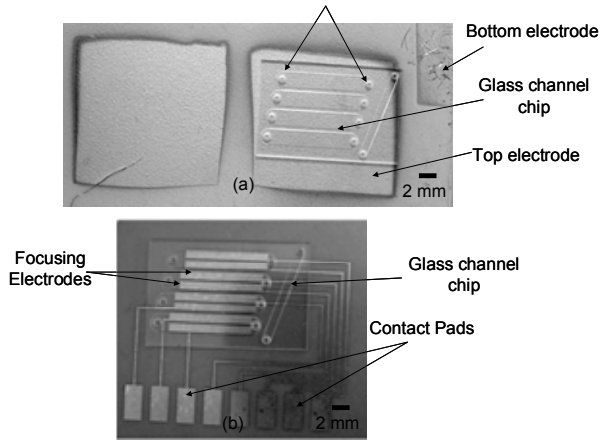

Figure 2. Fabricated patterned PZT approaches for integrated particle positioning system. (a) In this design, aerosol PZT (75µm thick) is used and the top electrode is patterned with a shadow mask in a DC sputterer. (b) In this design, bulk PZT (500µm thick) is used and the top electrode is patterned with photolithography and liftoff. In both cases, a microchannel chip is bonded to the top using SU 8 photoresist.

Sandia is a multiprogram laboratory operated by Sandia Corporation, a Lockheed Martin Company, for the United States Department of Energy under contract DEAC04-94AL 85000.

REFERENCES

[1] A. Haake and J. Dual, "Micro-manipulation of small particles by node position control of an ultrasonic standing wave," *Ultrasonics*, vol. 40, pp. 317-322, 2002.

[2] N. R. Harris, M. Hill, S. Beeby, Y. Shen, N. M. White, J. J. Hawkes, and W. T. Coakley, "A silicon microfluidic ultrasonic separator," *Sensors and Actuators B*, vol. 95, pp. 425-434, 2003.

[3] S. K. Ravula, D. S. Lidke, J. M. Oliver, G. Kaduchak, D. W. Branch, C. D. James, and I. Brener, "A microfluidic platform with microacoustics and dielectrophoresis for high throughput analyses of spatiotemporal signalling in biological cells," presented at Transducers, Lyon, France, 2007.

[4] S. K. Ravula, K. M. Taylor, D. S. Lidke, J. M. Oliver, C. D. James, and I. Brener, "A microfabricated flow cytometry system for optical detection of cellular parameters," presented at Biophysical Society Meeting, Baltimore, MD, 2007.

ALUMINIUM PRINTED CIRCUIT BOARD TECHNOLOGY FOR BIOMEDICAL MICRO-DEVICES

B. Iafelice[1,2], F. Destro[3], D. Manessis[1], D. Gazzola[2], E. Jung[1], L. Böttcher[1], M. Borgatti[3], T. Braun[1], J. Bauer[1], R. Gavioli[3], R. Gambari[3], A. Ostmann[1], R. Guerrieri[2]

[1]Fraunhofer Institute for Reliability and Microintegration (IZM), GERMANY
[2]Advanced Research Center on Electronic Systems (ARCES), Bologna University, ITALY
[3]Department of Biochemistry and Molecular Biology, Ferrara University, ITALY

ABSTRACT

This paper presents an innovative Printed Circuit Board (PCB) technology for biomedical microdevices. The fabrication process combines biocompatible tested materials and pure metal layers to build micro systems that mix active/passive electronics with microfluidics. Its peculiarity with respect to existing technologies is that it uses standard PCB processes, thereby preserving its characteristics as low production cost and large scale development, necessary for disposable applications.

Keywords: PCB, Biomedical microdevice, Microfluidics, Aluminium, Lab on a Chip

1. INTRODUCTION

Several technologies for microfluidics device fabrication and packaging have been proposed to integrate sensing capabilities and electrical interfaces into a single device [1]. All of these approaches require complex steps or expensive facilities, and mostly are useful only for prototyping. Otherwise the demand for low priced disposable has steadily increased due to the large developments in the area of devices miniaturization. However it is extremely expensive to transform one of these technologies in large scale production.

In the last years, PCB technology has reached resolution of tens of micrometers which is enough for many microfluidics applications. As an example in [2-4] micro channels and viaducts are used to integrate liquid in quasi-standard FR4-PCB. The main limitation of these approaches in biomedical applications is the involved materials which biocompatibility is not guaranteed. Recently the range of materials for PCB technologies has been extended by the introduction of new ones, many of these developed for flex circuits and rapidly becoming an industrial standard. This paper describes the development of a cost-effective technology with selected PCB bio-materials and microfluidics features.

2. BIOLOGICAL VALIDATION

The long-short time biocompatibility of a set of materials used in standard and quasi-standard PCB processes (e.g. flex circuits) has been in-vitro studied. The study has been carried out using a lymphoblastoid cell-line (LCL) [5] to determine possible antiproliferative effects. Furthermore, being this cell line extensively used for screening of cytotoxic T-lymphocytes (CTLs) [6], we were able to determine the effects of the materials on a specific biological function, i.e. the CTL-mediated lysis of target cells. The materials-under-test were embedded in standard multiwell plates as shown in Figure 1. Table 1 reports the toxicity induced by the tested materials after long-short time incubation. Different surface treatments modifying the hydrophilicity/hydrophobicity has been also studied.

978-0-9798064-0-7/μTAS2007/$20©2007CBMS

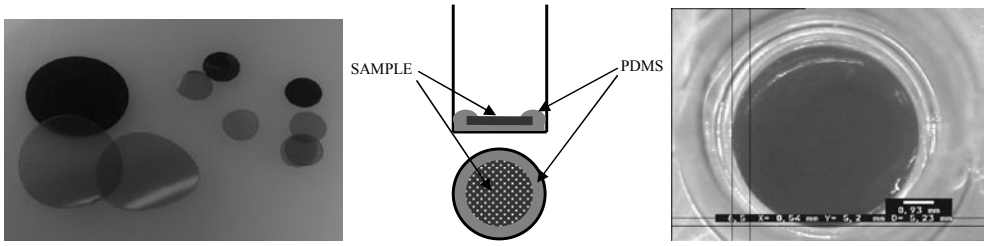

(a) (b) (c)

Figure 1. Materials embedding in standard multiwell plate for biocompatibility tests. The materials are cut by laser in round samples (a) and then embedded in PDMS (Sylgard 184 – DowCorning), used for covering the cut edges to prevent any contamination coming from the support material (b). The dispensing parameters are adjusted measuring the PDMS covering (c).

3. TECHNOLOGY DEVELOPMENT

The key point of this work is to develop an extended PCB technology with the same facilities used in industrial Copper-PCB processes. This technology allows to laminate different metal foils (copper, aluminium, platinum, gold) with several dielectric materials (Polyimide, Polyurethane, Pyralux) – see Figure 2. Wet etching, laser ablation and mechanical drilling are used to structure the electrical circuit and the microfluidics network with a resolution up to ten micrometers and layer thicknesses from few micrometers to millimeters. The compatibility with standard metal covering as nickel, gold and palladium was preserved in order to allow the integration of standard electronics components and copper based connections. Furthermore the surface treatments with Teflon, Parylene-C, Thiols, Certonal, silanes, plasma and corona activations allow the designing of hydrophilic-hydrophobic patters in the PCB-developed microfluidics.

In particular aluminium is a very interesting metal because of its low price, biocompatibility, wide range of foil thicknesses and good electrical conductivity. Additionally few nanometers of its oxide self-passivate the aluminium surface making it stable in wet environments and this thin protective layer can be overcome in electrical measurements by increasing the signal frequency. Following these notes we created an aluminium PCB-process with standard industrial facilities and bio-tested dielectrics.

Table 1. Results of biocompatibility tests

Material	Cytotoxicity	Effects on LCL cell growth	
		continous incubation	*pulse (60 min)*
Metals			
Cu	(1)	x	x
Al	●	■	■
Pd	●	■	■
Au over Ni	●	x	■
Au over Pd	●	x	■
Dielectrics – adhesives			
Polyimide	●	■	■
Pyralux uncured	●	x	■
Pyralux cured	●	■	■
PDMS cured/uncur.	●	■	■
Polyurethane uncur.	●	■	■
Polyurethane cured	●	■	■
Printable Epoxy cur.	●	x	■
Aramid uncured	(1)	x	x
Aramid cured	●	x	■
Surface treatments			
Au over Ni + ODT	●	■	■
Au over Pd + ODT	●	x	■
Pd + ODT	●	■	■
Cu + ODT	●	x	sx
Certonal FC-732	●	■	■
41-90 molding agent	●	■	■

●=not affected; ■=no effects; x=inhibition; sx=slow inhibition; (1)=increase of unspecific lysis; ODT=1-octadecanethiol C_{18}

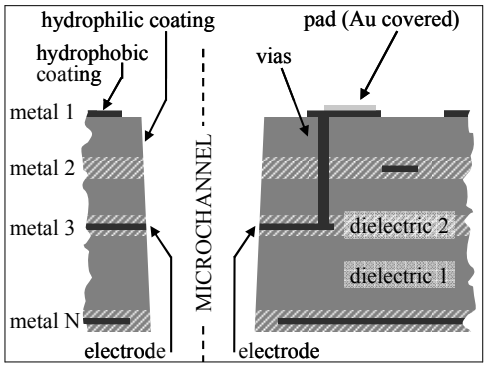

Figure 2. Schematic cross-section of the PCB-stack combining metal and dielectrics in a micro-device with fluidics and electronics integrated.

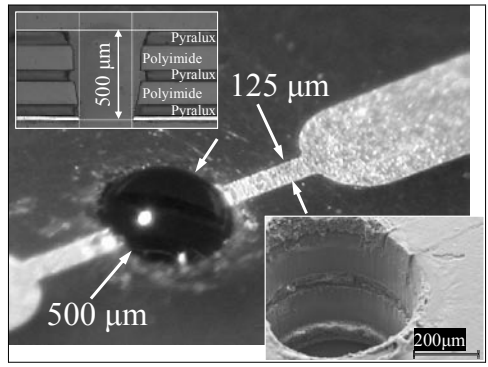

Figure 3. A 500µm well of the meniscus sensor. The inlet pictures show cross-section (top) and SEM image (bottom) of the microwell.

4. TECHNOLOGY DEMONSTRATION

The ability of the Al-PCB technology has been demonstrated by developing an electronic meniscus sensor (Figure 3) [7] with 300µm and 500µm wells. On the top surface an hydrophobic coating with Teflon confines the liquid in the well. The sensor correlates the meniscus height above the microwell and the electrical impedance measurement through the two faced Al electrodes. It can be integrated in microstructured biosensors governing the fluid flow induced by evaporation to drag cells and replicated as many times as required by its parallelism. This microsystem is a unique PCB-stack created in a unique process within microfluidic elements and electronics.

ACKNOWLEDGEMENTS

This work has been developed in the framework of CoChiSe European Project (project reference: 034534).

REFERENCES

[1] D.R. Reyes et al., *Micro Total Analysis Systems. 1. Introduction, Theory, and Technology*, Anal. Chem., 74, pp. 2623, (2002).

[2] A. Wego et al., *Fluidic Microsystems based on printed circuit board technology*, J. Micromech. Microeng., 11, pp. 528, (2001).

[3] J. Schütze et al., *An Integrated Micro Cooling System for Electronic Circuits*, IEEE Transactions on industrial electronics, 48, pp. 281, (2001).

[4] N.T. Nguyen, X. Huang, *Miniature valveless pumps based on printed circuit board technique*, Sensors and Actuators A, 88, pp. 104, (2001).

[5] F. Micheletti et al., *Supra-agonist peptides enhance the reactivation of memory CTL responses*, J. Immunol., 165, pp. 4264, (2000).

[6] A.B. Rickinson and D.J. Moss, *Human cytotoxic T lymphocyte responses to Epstein-Barr virus infection*, Annu. Rev. Immunol., 15, pp. 405, (1997).

[7] D. Gazzola et al., *An integrated electronic meniscus sensor for measurement of evaporative flow*, Transducers Conference, (2007).

ENERGY SCAVENGING FROM TRANSPIRATION: ELECTROSTATIC POWER GENERATION USING EVAPORATION-INDUCED BUBBLE MOTION

R. T. Borno, J. D. Steinmeyer and M. M. Maharbiz
University of Michigan, USA

ABSTRACT

We present the first microfabricated system that can scavenge energy from room temperature evaporation to produce electrical power. Evaporation-induced flows within leaf-like microvasculature networks drive the movement of gas bubbles through capacitor plates, which allow the charge pumping of an on-chip circuit.

Keywords: Energy Scavenging, Microfluidics, Evaporation.

1. INTRODUCTION

This paper presents a system that scavenges energy from evaporation to produce electrical power. We have previously used evaporation gradients to generate mechanical motion in biomimetic surface-tension driven actuators [1]. In this work, evaporation-induced flows within leaf-like microvasculature networks drive the movement of gas bubbles through capacitor plates (Fig. 1). The alternating dielectric of gas and liquid allows the charge pumping of an on-chip circuit (Fig. 1a), from which voltage and current could be measured and used to provide electrical power. This method of power scavenging has unique properties: (1) volumetric power density is high and scales favorably with miniaturization of evaporative feature sizes, (2) devices are robust and easy to fabricate, and (3) any humidity gradient can provide energy.

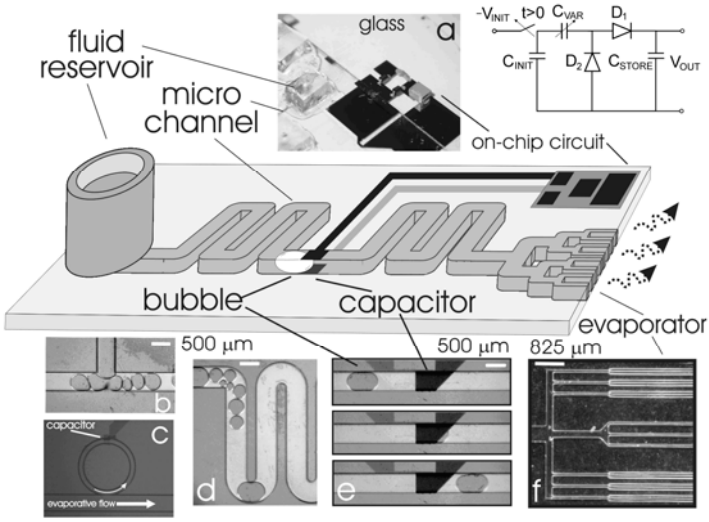

Figure 1. Schematic of device with close-up insets: (a) on-chip surface mount circuit, (b) bubble generator, (c) trapped bead racetrack; flow along main channel induces rotating flow in racetrack, (d) meandering microchannel allows for long bubble train, (e) bubble transiting between capacitor plates (1 s apart), (f) 'Murray's law' evaporator; smallest channels are 75 µm deep x 100 µm wide.

978-0-9798064-0-7/µTAS2007/$20©2007CBMS

The water potential, a ubiquitous potential energy gradient used by nature to extract work, has been almost completely ignored by power-scavenging systems. The large difference in water potential created by microscale leaf pores drives the evaporative processes which plants use to passively transport water. Like plant vasculature, the networks designed here obey Murray's law [2]. Previous devices have used Murray's law to mimic blood vessels [3] and evaporation has been used in ultra-low dosing methods [4].

2. THEORY

Water movement due to evaporation is attributed to a difference in the chemical potential of the water as opposed to an applied pressure [5]. In the devices presented here (Fig. 1), the water potential drop is dominated by the surface tension of the menisci at the pores of the evaporator outlet ($\Psi_{capillary}$) (Fig. 2). Since the contributions to the water potential from atmospheric vapor (Ψ_{atm}) and gravity ($\Psi_{gravity}$) at the reservoir are smaller than that due to surface tension, the net liquid flow is to the evaporator end [5]. The capillary pressure at the outlet prevents the end of the channel from drying out.

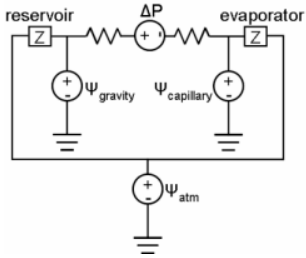

Figure 2. Fluidic circuit of the device. (1) Existence of a non-zero voltage on the capacitor plates generates an electrostatic pressure drop across the bubble interface counter to the fluid flow. (2) Evaporative pressure drop is dominated by the surface tension at the ends of the evaporator.

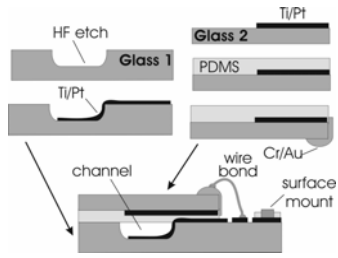

Figure 3. Fabrication process flow using two glass wafers: Channels were etched isotropically for a 50 μm depth on glass (Plan Optik) wafer 1 (left). Capacitor plates were patterned on the bottom of the channels (300 Å Ti/ 1000 Å Pt). Similar Ti/Pt pads were patterned on wafer 2 (right) and the entire wafer was spin-coated with 8.2 μm of Sylgard 184. Holes were drilled into wafer 2 for interconnection. Both wafers were exposed to O_2 plasma (100 W, 150 mT, 1 min), aligned and bonded. Fluidic interconnects were attached. Surface mount components of the circuit were assembled on Ti/Pt pads on wafer 1.

3. EXPERIMENTAL

Devices were fabricated from two glass wafers using the process illustrated in Fig. 3. During testing, gas bubbles were formed at a Y-junction of a gas line and a liquid line filled with fluorophore solution (Fig. 1b). Bubbles imaged and electrical measurements (Figs. 4, 5) were taken during evaporative flow. Evaporation-driven flow rates for bubble-filled devices were measured as a function of bubble length and main channel width (Fig. 6) and commonly ranged from 10–100 nL/min. Obviously, the creation of bubbles introduces energy into the system, but this is not fundamental to the operation of the devices. To demonstrate this, we have built devices with embedded dielectric beads that flow around a racetrack and could perform the same function as bubbles (Fig. 1c).

4. RESULTS AND DISCUSSION

The type of circuit here (Fig. 1a) has been used in vibrational energy scavenging [6].

C_{INIT} is pre-charged at t<0. As a bubble moves through the capacitor, the reduction in C_{VAR} at the water-air interface forces charge through a forward-biased D_1 and into C_{STORE}; D_1 is then reverse biased and prevents backwards charge movement. Each leading bubble edge increases V_{OUT} given sufficiently low dissipative parasitics. In early circuit prototypes, the change in C_{VAR} is large (Fig. 2, 5), but V_{OUT} is dominated by parasitics from the surface-mount components. Current work is focused on improving the circuit performance.

From flow rates, bubble spacing and capacitance changes, it is possible to extrapolate power density as the evaporator pore size is reduced (Fig. 7). A lower scaling limit (1.6 nm) is set by the size of the opening at which the evaporator is at equilibrium with 50% relative humidity where no evaporation occurs [5]. Expected power density for these devices is comparable to vibration scavenging methods, even for low voltages and pessimistic assumptions about ΔC_{VAR} (Fig. 7).

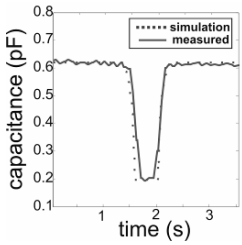

Figure 4. Measured and simulation values of C_{VAR} (at 1 MHz) vs. time as a bubble transits between plates; compare to Fig. 1e.

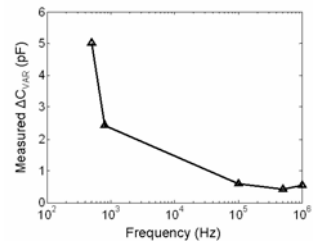

Figure 5. Measured value of the change in C_{VAR} due to a bubble as a function of the operation frequency. The relative permittivity of water varies nonlinearly with frequency [7].

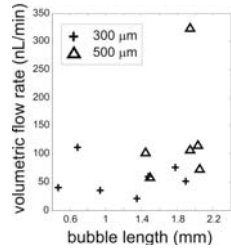

Figure 6. Evaporation driven flow rates in devices with two different channel widths at 25 °C as a function of bubble size.

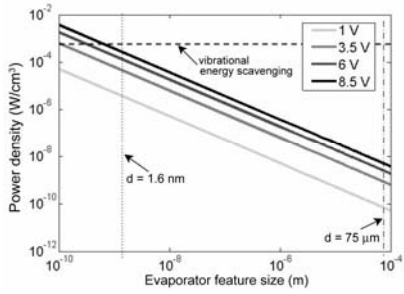

Figure 7. Volumetric power density scaling as a function of evaporator opening for various V_{INIT}. The pore size limit (1.6 nm) and the size of the current devices (75 µm) are shown as vertical lines. The minimum single device volume is $6x10^{-6}$ m^2 x 100 µm thickness (Power ∝ flow rate ∝ pressure ∝ 1/channel diameter). Vibrational energy scavenging has been reported to generate 375 $\mu W/cm^3$ of power [8]. The ΔC_{VAR} used in this calculation is pessimistic as it was measured at 1 MHz (Fig. 5).

REFERENCES

[1] R. T. Borno, et al, *J. Micromech and Microeng*, vol. 16, pp. 2375-2383, 2006.
[2] K. A. McCulloh, et al, *Nature*, vol. 421, pp. 939-942, 2003.
[3] D. Lim, et al, *Lab on a Chip*, vol. 3, pp. 318-323, 2003.
[4] M. A. Burns, et al, *Science*, vol. 282, pp. 484, 1998.
[5] J. C. T. Eijkel and A. v. d. Berg, *Lab on a Chip*, vol. 5, pp. 1202-1209, 2005.
[6] R. Tashiro, et al, *Journal of Artificial Organs*, vol. 5, pp. 239-245, 2002.
[7] D. P. Fernández, et al, *Int'l Journal of Thermophysics*, vol. 16, pp. 929-955, 1995.
[8] S. Roundy, et al, *IEEE Pervasive Computing*, vol. 1, pp. 28-36, 2005.

MICROFABRICATED NEBULIZER CHIPS FOR ATMOSPHERIC PRESSURE PHOTOIONIZATION-MASS SPECTROMETRY

Markus Haapala[1], Jaroslav Pól[1], Tiina Kauppila[1], Laura Luosujärvi[2], Ville Saarela[3], Sami Franssila[3], Raimo A. Ketola[1,4], Tapio Kotiaho[1,2] and Risto Kostiainen[1]

[1]*Division of Pharmaceutical Chemistry, University of Helsinki, Finland*
[2]*Laboratory of Analytical Chemistry, University of Helsinki, Finland*
[3]*Micro and Nanosciences Laboratory, Helsinki University of Technology, Finland*
[4]*Drug Discovery and Development Technology Center, University of Helsinki, Finland*

ABSTRACT

New applications for heated nebulizer microchips using atmospheric pressure photoionization-mass spectrometry (APPI-MS) are presented. The chips vaporize and mix a sample with nebulizer gas and a confined jet of sample vapor is formed by a nozzle and ionized by APPI. The chips are used to combine gas chromatography and capillary liquid chromatography to MS. Furthermore, a new ambient desorption/ionization method, desorption atmospheric pressure photoionization, (DAPPI) is presented. In DAPPI, a heated jet of vaporized solvent and a photoionization lamp are used to desorb and ionize analytes from surfaces.

Keywords: mass spectrometry, microchip, APPI, desorption

1. INTRODUCTION

This paper describes the versatility of microfabricated heated nebulizers as ionization devices for atmospheric pressure photoionization-mass spectrometry (APPI-MS). We introduce two analytical techniques and an entirely new desorption/ionization method, all based on microchip nebulizers. We have previously presented a nebulizer chip made of silicon and glass [1]. The chip has been applied to direct infusion APPI–MS [2], sonic spray ionization [3], and to combine gas chromatography (GC) and capillary liquid chromatography (capLC) with atmospheric pressure chemical ionization-mass spectrometry (APCI-MS).[4, 5] Recently we presented an improved full-glass version of the chip.[6]
Here, microchip APPI (μAPPI) is used as an ion source with GC as well as with capLC for the first time. Previously, GC-APPI-MS and capLC-APPI-MS have been achieved only with conventional macro scale ion sources. As a further proof of the versatility of microchip nebulizers, we present a novel desorption/ionization method for ambient surface analysis, desorption atmospheric pressure photoionization (DAPPI).

2. EXPERIMENTAL

The nebulizer chips consist of a silicon plate and a glass plate (Fig. 1 (A)) or two glass plates (Fig. 1 (B)). The chips include a sample inlet channel, nebulizer gas and dopant inlet, vaporizer channel, nozzle, and platinum heater. The combination of GC-μAPPI-MS (Fig. 1 (C)) consists of a GC, heated transfer capillary, microchip, photoionization lamp, and triple quadrupole MS. CapLC-μAPPI-MS was performed by connecting a column of a capillary LC directly to the heated nebulizer chip through a transfer capillary. With both techniques, nitrogen was used as nebulizer gas for the chip and toluene as dopant.

978-0-9798064-0-7/μTAS2007/$20©2007CBMS

In DAPPI the narrow jet of vaporized solvent (toluene or acetone) and nebulizer gas (nitrogen) from the microchip nebulizer is directed towards a surface (Fig. 1 (D)). The jet desorbs analytes from the surface, which are ionized by 10-eV photons, and collected into an ion trap mass spectrometer.

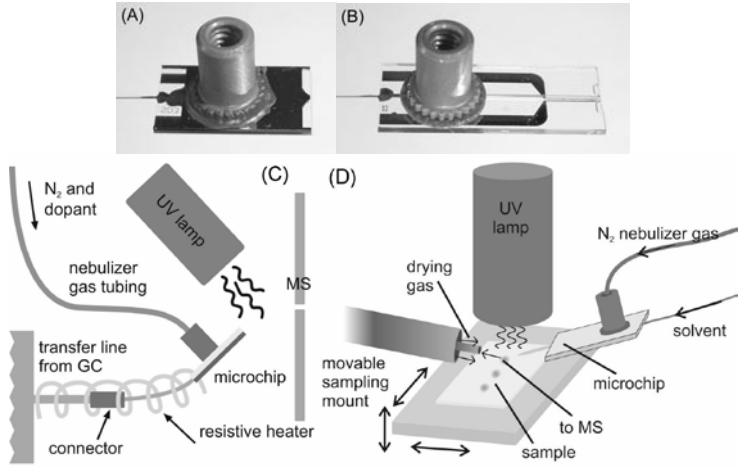

Figure 1. Microchip nebulizers fabricated of (A) silicon and glass and (B) glass only. Schematic views of the (C) GC-μAPPI-MS setup and (D) DAPPI-MS setup.

3. RESULTS AND DISCUSSION

Figure 2 (A) shows chromatograms of an analysis of testosterone and progesterone by capLC-μAPPI-MS. The quantitative performance of the method is good as seen from the analytical parameters in Table 1. Figure 2 (B) shows chromatograms of selected polycyclic aromatic hydrocarbons (PAHs) analyzed by GC-μAPPI-MS with good quantitative characteristics (Table 1).

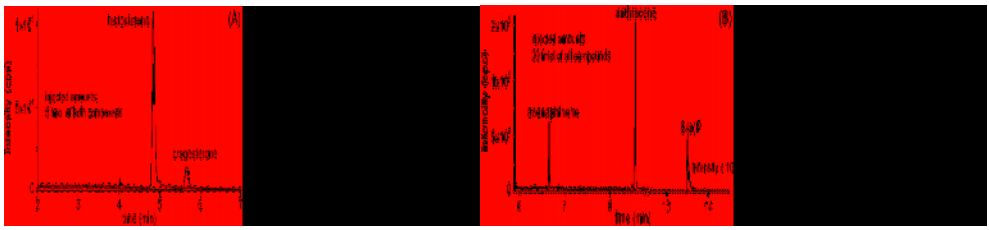

Figure 2. (A) Selected reaction monitoring (SRM) chromatograms of testosterone and progesterone analyzed by capLC-μAPPI-MS. (B) SRM chromatograms of acenaphthene, anthracene, and benzo(a)pyrene analyzed by GC-μAPPI-MS.

Table 1. Analytical performance of GC-μAPPI-MS and capLC-μAPPI-MS methods.

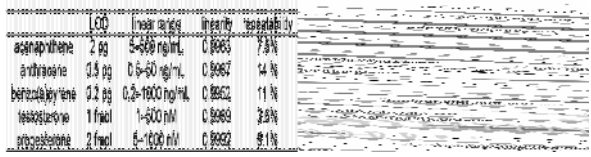

Figure 3 (A) presents a DAPPI-MS spectrum resulting from analysis of four compounds of various polarities on a poly(methylmethacrylate) (PMMA) surface. Figure 3 (B) shows a mass spectrum of an intact Tylenol Cold tablet. The examples prove that DAPPI is capable of ionizing both non polar and polar compounds simultaneously with high efficiency. Since the popular desorption electrospray ionization (DESI) is inefficient in ionization of low polarity compounds such as PAHs, DAPPI significantly widens the range of compounds that can be analyzed with ambient MS techniques. The ionization mechanism of DAPPI is presumably a combination of thermal desorption and gas phase ionization.

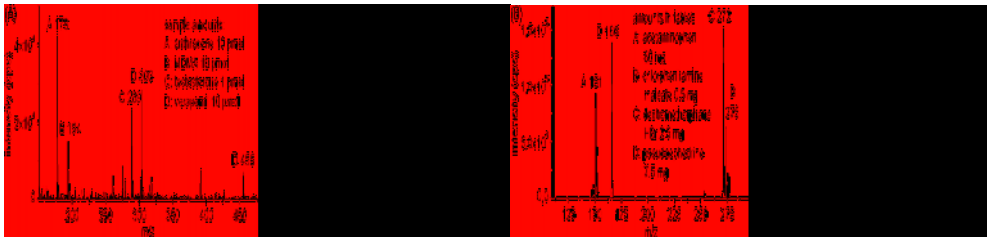

Figure 3. Mass spectra from (A) PMMA surface and (B) surface of a Tylenol Cold tablet measured by DAPPI-MS.

4. CONCLUSIONS

The new methods presented in this paper emphasize the wide applicability of microchip nebulizers. First of all, they can be employed for several ionization techniques. Secondly, they can be connected to both liquid and gas phase separation devices. Moreover, the chips are not limited to certain mass spectrometers as commercial ion sources, but can be used with any MS instrument equipped with an atmospheric pressure ion source.

ACKNOWLEDGMENTS

Financial support from the Graduate School of Chemical Sensors and Microanalytical Systems (CHEMSEM), Academy of Finland, and Finnish Funding Agency for Technology and Innovation (Tekes) is acknowledged.

REFERENCES

[1] P. Östman, S. J. Marttila, T. Kotiaho, S. Franssila and R. Kostiainen, Anal. Chem., **76**, 6659–6664 (2004).

[2] T. J. Kauppila, P. Östman, S. Marttila, R. A. Ketola, T. Kotiaho, S. Franssila and R. Kostiainen, Anal. Chem., **76**, 6797–6801 (2004).

[3] J. Pól, T. J. Kauppila, M. Haapala, V. Saarela, S. Franssila, R. A. Ketola, T. Kotiaho, and R. Kostiainen, Anal. Chem., **79**, 3519–3523 (2007).

[4] P. Östman, L. Luosujärvi, M. Haapala, K. Grigoras, R. A. Ketola, T. Kotiaho, S. Franssila and R. Kostiainen, Anal. Chem., **78**, 3027–3031 (2006).

[5] P. Östman, S. Jäntti, K. Grigoras, V. Saarela, R. A. Ketola, S. Franssila, T. Kotiaho and R. Kostiainen, Lab Chip, **6**, 948–953 (2006).

[6] V. Saarela, M. Haapala, R. Kostiainen, T. Kotiaho and S. Franssila, Lab Chip, **7**, 644–646 (2007).

MANIPULATIONS OF BIO-MOLECULES INSIDE DISCRETE DROPLETS WITH DROPLET CONTROLS BY OPTICAL IMAGING

Ieng Kin Lao[1], Chengkuo Lee[1,2], Hanhua Feng[1]

[1]Bioelectronics Program (BEBM), Institute of Microelectronics, Singapore,
[2]Department of Electrical Engineering, National University of Singapore, Singapore

ABSTRACT

This work reports manipulations of suspended discrete droplets and bio-molecules within the discrete droplets using projected images on a single platform based on optical dielectrophoresis (ODEP) and optical electrowetting-on-dielectric (OEWOD). Cell manipulations inside a droplet, such as moving and trapping, are successfully demonstrated. Cells differentiation based on viability is shown and result is compared with simulation. Using the same device, moving and combination of discrete droplets are performed.

Keywords: Optical dielectrophoresis, Optical electrowetting-on-dielectric, Digital microfluidics, Optofluidics, Virtual electrode, Manipulation of particle in droplet

1. INTRODUCTION

Manipulation of charged particles within discrete droplet based on electrophoretic force on a micro electrowetting-on-dielectric (EWOD) device has been reported recently [1]. Micro electrodes for both electrophoresis and EWOD are patterned on top and bottom device substrates respectively. Applying a projected image to generate virtual electrodes due to localized photoconductivity change has been applied to optical dielectrophoresis (ODEP) [2]. In this work, we report simultaneous manipulations of droplets and bio-molecules within the droplets with projected images utilizing ODEP and optical electrowetting-on-dielectric (OEWOD) on a single platform. Using the projected virtual electrodes for both ODEP and OEWOD provide high flexibility with a simple setup, overcome sample adsorption and the particle limitation of electrode distance compared to previous studies.

2. EXPERIMENTAL

Figure 1 shows an illustration of our device. A droplet containing bio-molecules is suspended in silicone oil between two ITO-glass substrates at 1-mm apart. The bottom substrate is deposited with photo-conductive amorphous silicon (a-Si), passivated with silicon nitride and treated with Sigmacote. The top substrate is the same but without a-Si. Optical images are projected to the bottom substrate. Bio-molecules and droplet movements are recorded from the top substrate. An AC voltage is applied to the two substrates.

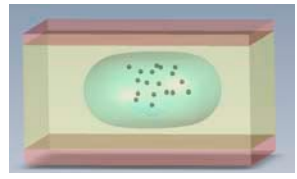

Figure 1. Illustration of our device for ODEP and OEWOD.

978-0-9798064-0-7/μTAS2007/$20©2007CBMS

3. RESULTS AND DISCUSSION

A cross-shape image is projected onto the device generating ODEP for cell trapping. Figure 2 shows snapshots of cells *(Giardia lamblia* with size of 9 μm) moving within a droplet. The cells are randomly distributed in the droplet initially, and eventually concentrate at the illuminated image due to positive dielectrophoresis.

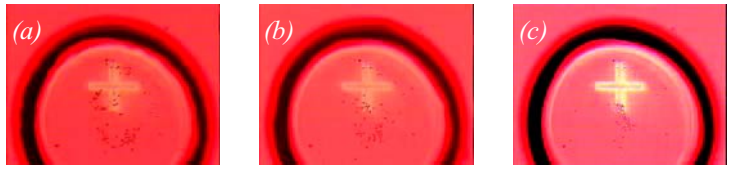

Figure 2. Still images of *Giardia lamblia* cell trapping within a droplet by ODEP.

An image of 13 μm-square-array, which each square works as a virtual electrode, is illuminated on our device to demonstrate the differentiation of viable/non-viable cells in a droplet. Figure 3 shows responses of viable/non-viable yeasts to different AC frequencies. At 1 kHz, non-viable yeasts show no response, whereas viable yeasts move and concentrate to the square edge. At 15 MHz, opposite observations are found, only non-viable cells respond to the image. These results support that ODEP is not affected and the partical distance limitation between two electrodes can be overcomed when operating ODEP in droplets. Figure 4 shows the simulation result (calculated by ANSYS) of gradient of the square of electric field on an illuminated virtual electrode (surrounded by dotted line in Figure 3a). The gradient is lowest at the centre of each square image and highest at the edge. Therefore, cells are trapped at the edge in Figure 3b and 3c due to positive DEP.

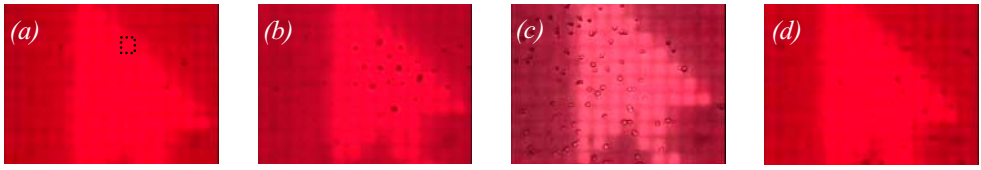

Figure 3. Non-viable and viable yeast cells responses to different AC frequencies with ODEP (a) Non-viable yeasts at 1 kHz, (b) Viable yeasts at 1 kHz, (c) Non-viable yeasts at 15 MHz and (d) Viable yeasts at 15 MHz.

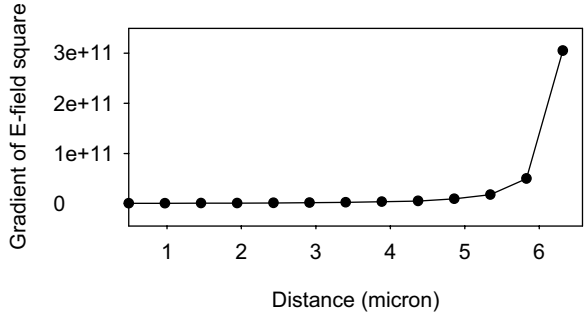

Figure 4. The gradient of the square of electric field strength for a square virtual electrode (surrounded by dotted line in figure 3a). The x-axis of distance origins from the square centre.

Besides bio-molecules manipulation, many biological applications require liquid environment operations, such as washing, mixing and dilution. These can be achieved through transportation, combination and splitting of discrete droplets without additional structures to our device using OEWOD, where virtual electrodes are optically patterned for electrowetting. Figure 5 shows that two droplets can be combined and mixed together. Further, a droplet can be moved to different locations and back to its original location by changing the position of the illuminated image (Figure 6). OEWOD droplet operations can be conducted at any time with simultaneous ODEP bio-molecules manipulations within the droplet on the same device.

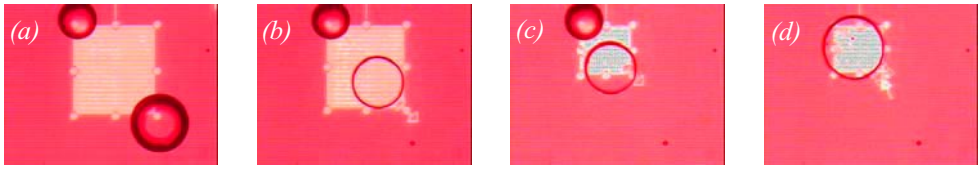

Figure 5. An example of combination of discrete droplets by OEWOD.

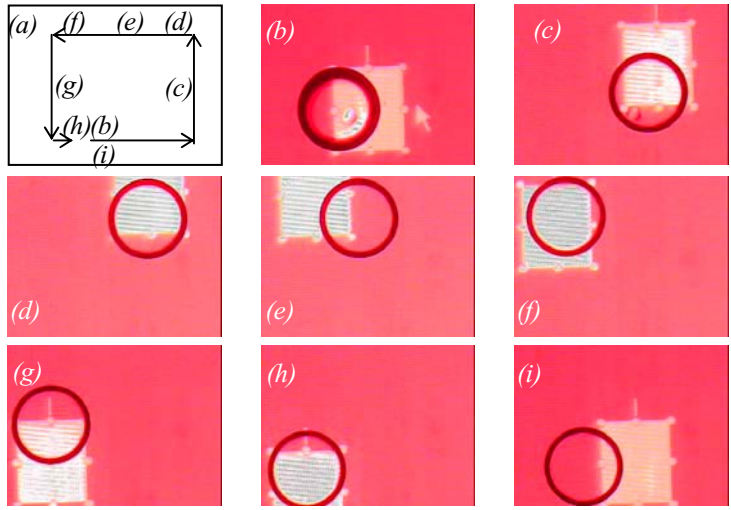

Figure 6. Transportation of a discrete droplet by moving an illuminated image (a) Paths of the illuminated image locations for figures (b) to (i), (b)-(i) Snapshots of the droplet at different locations.

4. CONCLUSIONS

Our strategy using projected virtual electrodes for ODEP and OEWOD provides a promising and flexible approach to manipulate biomolecules within a droplet and also the droplet itself on the same platform. This solves the issues of sample adsorption and partical electrode distance limitation encountered in previous studies.

REFERENCES

[1] S. K. Cho, Y. Zhao, C-J. Kim, “Concentration and binary separation of micro particles for droplet-based digital microfluidics”, Lab on a Chip **7**, 490 (2007).

[2] P. Y. Chiou, A.T. Ohta, M. C. Wu, “Massively parallel manipulation of single cells and microparticles using optical images”, Nature **436**, 370 (2005).

FERROFLUID PATTERN FOR GUIDING MAGNETIC BEADS SELF-ORGANISATION: APPLICATION TO AFFINITY CELL SEPARATION AND ON CHIP CELL CULTURE

Antoine-Emmanuel Saliba[1], Eleni Psichari[1], Laure Saias[1], Nicolas Minc[1], Vincent Studer[2], Jean-Louis Viovy[1]

[1]Institut Curie, 26 rue d'Ulm, 75005 Paris, France, [2]ESPCI, 10 rue Vauquelin, 75005 Paris, France

Contact : jean-louis.viovy@curie.fr

ABSTRACT

This abstract presents the development a microfluidic system for cell sorting and cell culture. Magnetic functionalized beads with antibody against membrane markers are self-assembled in a tridimentional reversible array of columns under an external magnetic field, forming an immunoaffinity separation matrix. We developed an original strategy for matrix formation, using a hexagonal ferrofluid pattern in order to drive the self-assembled of magnetic columns into a pattern that is both optimal for cell migration and more resistant to flow.

Keywords: self- assembly, cell separation, magnetic beads, cell culture

1. INTRODUCTION

Self-organized arrays of magnetic particles were previously used for the separation of long DNA molecules [1]. We already proposed a new strategy based on a template of ferrofluid patterned on the lower surface of a microchannel, guiding the formation of magnetic columns with large spacing, suitable for cell sorting [2]. Here we integrate this technology into a fully automated microfluidic cell sorting and culture device, and propose a quantitative evaluation of its performance with mixed populations of lymphocytes. This technique allows for the positive selection of cells with high yield and purity, the application of elaborate cell identification post-capture protocols, or subsequent on-chip culture of captured cells.

2. EXPERIMENTAL

Hexagonal arrays of 10 µm diameter ferrofluid spots are formed by microcontact printing (Fig 1b,c). A PDMS microchannel including two layer monolithic valves [3] is then sealed on the patterned coverslip (Fig.1a). The flow of reagents is controlled dynamically using a customized MFCS microfluidic controller (www.fluigent.com), involving high pressure outlets for the operation of valves, and low-pressure outlets for the synchronous control of reagents and sample introduction [4]. A suspension of magnetic beads suspension grafted with anti-CD19 antibodies (Ø 4.5µm, Dynal) is injected into the channel and a uniform magnetic field of 30 mT is subsequently applied using a cooled electromagnetic coil. Channel rinsing at a moderate flow rate eliminates residual beads not attached to ferrofluid spots, leading to a regular magnetic array of columns on the ferrofluid pattern without any interstitial filament (Fig.1d). Lymphocytes T cells (LT, Jurkat, CD19-),

978-0-9798064-0-7/µTAS2007/$20©2007CBMS

lymphocytes B cells (LB, Raji, CD19+) or mixtures of both cell types are introduced in the channel (Fig 2a) and distinguished using a green Cell Tracker CMFDA dye (Invitogen). Culture of cells in chemostatic and thermostatic conditions was achieved by constantly perfusing fresh media and maintaining the temperature at 37 °C using Joule heating from the electromagnetic coil. Cells can be monitored during an extensive period of time at a single-cell resolution.

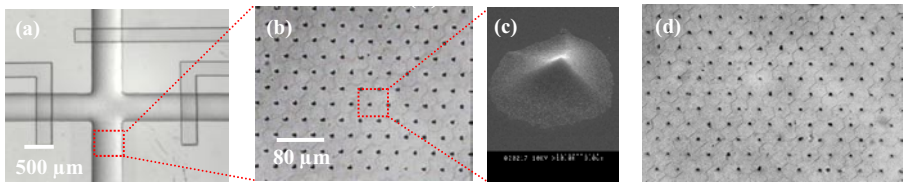

Figure 1: The main cross channel surmounted by valves (a) is patterned by ferrofluid 10 µm diameter dots: The printing stamp is formed by soft-lithography, soaked in an ink-pad obtained by spin-coating ferrofluid on a glass coverslip, and printed on a new glass coverslip finally baked at 150 °C overnight to irreversibly bind the ferrofluid to the glass (b,c). After beads introduction and magnetic field application, beads self-assembled on the pattern (d).

3. RESULTS

Independent experiments Jurkat and Raji cells, respectively, show that Jurkat cells never get bounded to the columns (n=1000, fig2c) whereas Raji cells are captured (n=400, fig2b). Various experiments in which a mixture of both populations was introduced (see Table 1), demonstrated a capture yield of Raji at least 94% and a selectivity among captured cells greater than 96%. The entrapment yield remains constant for flow velocity up to 600 µm/s, beyond which magnetic columns start to detach. The microsystem allows for organizing the cells into high density array up to 1500 cell/mm² and is amenable to rapid and high quality optical characterization of the cells. The trapped cells are suited for further in-situ immunophenotyping (fixation, membrane permeabilisation and labeling) or cell culture (Fig.3).

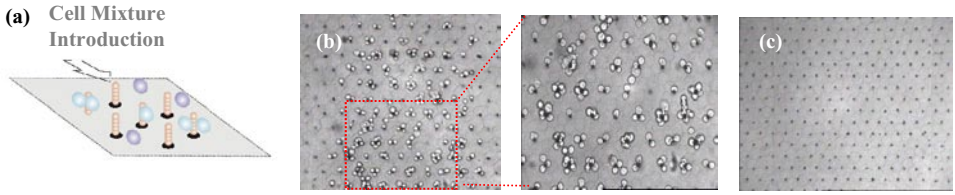

Figure 2: (a) Schematic representation of the cell separation method. Mixture of cells flows in the array of mAb coated beads columns which allow for cell positive selection. An array of anti-CD19 coated magnetic beads is formed and (b) a pure cell population of LB (Raji cell line, n=400) is introduced showing a specific trapping of the cells. (c) Column state is depicted after that 1000 cells are introduced in the channel following by a rinsing step. No cells were bounded on the columns.

Table 1: Results obtained from the separation of a mixture of Raji and Jurkat in an array formed of anti-CD19 coated magnetic beads. A yield is calculated as the ratio between the number of entrapped or eluted cells of a specific population divided by the total number of this cell type entered in the array.

	Input		Column			Effluent		
Number of cells analysed	Fraction of Raji	Fraction of Jurkat	Entrapement yield of Raji	Entrapement yield of Jurkat	Selectivity in Raji	Elution yield of Raji	Elution yield of Jurkat	Purity of Jurkat
242	0.85	0.15	0.95	0	1	0.05	1	0.80
299	0.60	0.40	0.94	0.04	0.97	0.06	0.96	0.91
618	0.33	0.67	0.94	0.02	0.96	0.06	0.98	0.97

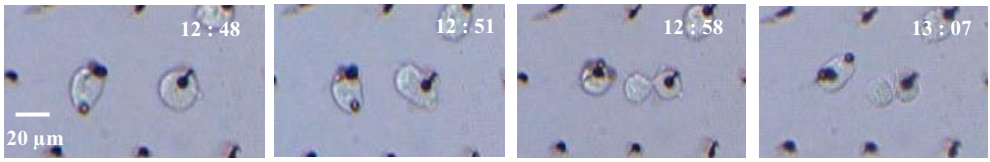

Figure 3: Cell division sequence. Time indicated refer to the time after the beginning of culture in the chip, in hours.

4. CONCLUSION

By combining templated self-assembly of magnetic particles and multiplexed pressure-based flow control, it is possible to separate, phenotype and culture cells in a highly automated way and with high purity. This system may have multiple applications in diagnosis, directed mutagenesis or stem cells research (sorting according to genes expression and further characterization and culture).

REFERENCES

[1] Doyle et al., *Science*, **295**, 2237 (2002)
[2] Psychari et al., *µTAS Proceedings 2005*, 355-357
[3] Unger et al., *Science*, **288**, 113-116 (2000)
[4] Fütterer et al., *Lab Chip*, **4**, 351-356 (2004)

HIGH-THROUGHPUT, CONTINUOUS-FLOW, DIELECTROPHORETIC SCREENING OF *MYCOBACTERIUM SMEGMATIS* IN COHERENTLY PATTERNED, POLYMERIC MICRO-CHANNELS

B.G. Hawkins[1], A. E. Smith[2], and B.J. Kirby[3]

[1]Biomedical Engineering Department, Cornell University, USA, [2]Applied and Engineering Physics Department, Cornell University, USA, [3]Mechanical and Aerospace Engineering Department, Cornell University, USA

Keywords: Insulative dielectrophoresis, Mycobacterium smegmatis, Zeonor

ABSTRACT

We report continuous-flow, dielectrophoretic (DEP) cell manipulation with application to rapid screening of mutated *Mycobacterium smegmatis* populations. Innovative aspects of the device include (i) the use of novel, DC-offset, AC electric fields, (ii) the use of high width to depth aspect ratio constrictions (250:1), and (iii) application to post-mutagenesis screening *M. smegmatis* based on cell membrane characteristics.

1. INTRODUCTION

Mycobacterial infections, such as tuberculosis, are characterized by the formation of encapsulating granulomas. *Mycobacterial* granulomas, i.e., macrophage-encapsulated *Mycobacterium* bacilli surrounded by inflamed tissue, are caused by glycolipids that make up the *Mycobacterium* cell wall. The mechanisms by which *Mycobacterial* cell wall lipids generate this response are not well understood [1]. Determination of these mechanisms requires the development of a library of *Mycobacterium* with mutations in these and other cell wall constituents implicated in the development of *Mycobacteria*'s unique granuloma structure. Unfortunately, current screen-



Figure 1. Microchannels are fabricated in Zeonor polymer with curvilinear constrictions in channel depth, creating the gradients responsible for DEP (nominal channel depth is 100μm).

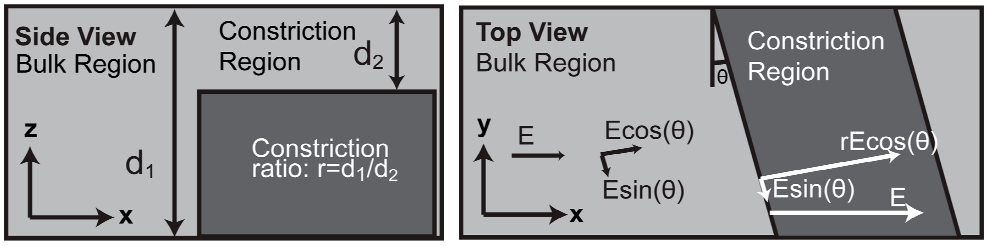

Figure 2. Constrictions in channel depth (bottom) create electric field gradients that drive DEP forces normal to the constriction. Decomposing the electric field into components normal and tangential to the constriction (top – dark region), illuminates the dependence of the normal component on the constriction angle and the constriction ratio (defined in figure). The magnitudes of the resulting gradients that drive DEP are similarly dependent on the constriction ratio and the ridge angle, θ.

978-0-9798064-0-7/μTAS2007/$20©2007CBMS

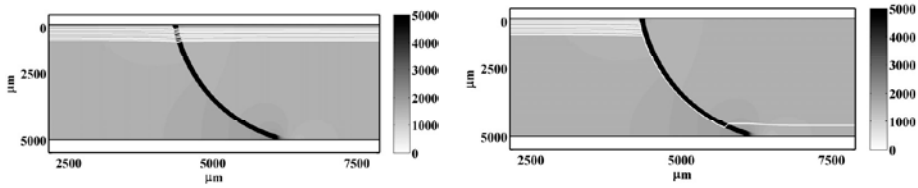

Figure 2. The numeric electric field solutions for a curvilinear constriction in channel depth show predicted particle deflection transverse to the direction of flow as a function of DEP mobility. Low DEP mobility particles (left) pass the constriction in channel depth unaffected, while higher DEP mobility particles (right), are deflected transverse to the direction of flow by tangential electrokinetic effects.

ing techniques for cell membrane mutations in *Mycobacteria* are limited to direct inspection for morphological changes. DEP, however, has been shown to be sensitive to cell membrane characteristics, such as permeability [2], and shows promise for sorting cellular samples based on cell morphotype. DEP based separation in microfluidic devices utilizes minute sample volumes, interrogates individual particles, and requires no affinity coupling.

2. RESULTS AND DISCUSSION

A two stage silicon master fabrication procedure followed by hot embossing of micro-channels in polymer substrates allows for rapid and facile fabrication of devices with high width to depth aspect ratios (250:1). After hot embossing, a chemical bonding procedure is used to enclose the embossed channel in polymer [3]. Regularity of the aspect ratio across the channel was confirmed via profilometry after hot embossing and confocal visualization after enclosing the channel.

A novel device design modulates electric fields in three dimensions using coherently patterned, curvilinear constrictions in the depth of a microfluidic channel (Figure 1). Curved constrictions induce dielectrophoretic trapping normal to the constriction and transport tangent to the ridge, achieving a continuous particle separation transverse to the direction of flow (Figure 2). Linear and non-linear electrokinetic phenomena are independently modulated using a DC offset, AC electric field.

Particle separation takes 5mm of channel length and accomplishes sorting in seconds, after which particles can be transported via linear electrokinetic effects to separate output channels. The small spatial scales and rapid time scales of this sorting technique, coupled with the ability to act on a large number of particles *simultaneously*, yields excep-

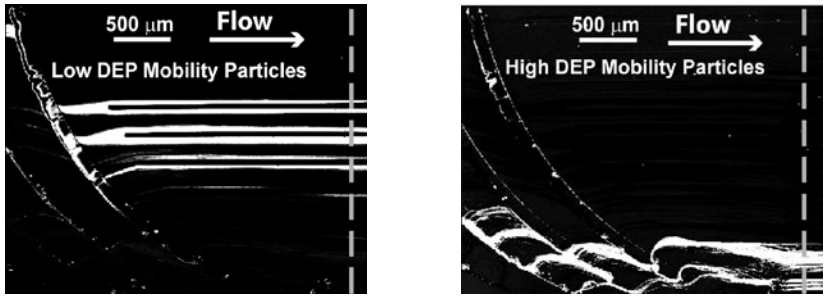

Figure 3. Continuous flow separation of polystyrene microspheres based on DEP mobility from a localized, mixed input stream is shown as a time average of 30 frames. (Images have been separated for clarity).

tionally high throughput compared to other continuous flow particle sorting techniques such as FACS and flow cytometry.

We have demonstrated separation of polystyrene particles with 20% variation in DEP mobility (Figure 3) and continuous control of *M. smegmatis* particle stream position transverse to the direction of flow (Figure 4).

Well-characterized particles exhibit predictable behavior, traveling tangential to a curvilinear constriction in depth until linear electrokinetic mobilities dominate and particles pass the constriction at a point transverse to flow characterized by their particular mobility ratio and the operating conditions of the experiment. *M. smegmatis* show the same transverse deflection observed with microspheres and predicted by our model. Successes in sorting particles based on DEP mobility, dielectrophoretic manipulation of *Mycobacterium*, and validation through a model-based framework positively indicate the potential to use this device for high-throughput screening random mutations in *Mycobacterium*.

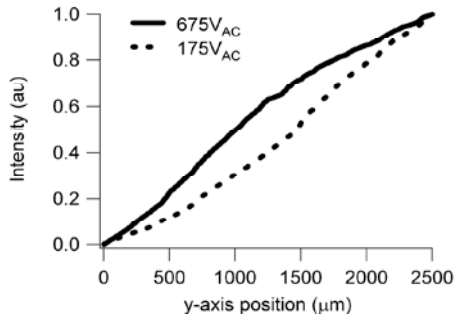

Figure 4. Fluorescently labeled M. smegmatis cells show a variation in output distribution as a function of applied AC electric field. A cumulative distribution function, calculated based on fluorescence intensity at the output (dotted line in Figure 3) quantifies increased deflection transverse to flow.

3. CONCLUSIONS

Using DC-offset, AC electric fields, we demonstrate continuous-flow particle separation and cell manipulation by insulative dielectrophoresis. DEP is induced by 3-dimensional modulation of electric fields via curvilinear, insulating constriction in the depth of a high-aspect ratio channel.

ACKNOWLEDGEMENTS

The authors would like to thank Blake Simmons and Eric Cummings for their contributions to this work.

REFERENCES

[1] Giesel et al, *J. Immun.* 2005, 174:5007-5015
[2] Gascoyne et al, *Electrophoresis* 2002, 23(13):1973-1983
[3] Wallow et al, *Lab on a Chip* 2007, Submitted

STUDYING REPROGRAMMING OF SOMATIC CELLS VIA FUSION WITH EMBRYONIC STEM CELLS: A MASSIVELY PARALLEL DEVICE FOR CELL FUSION

Alison M. Skelley[1,2], Oktay Kirak[3], Rudolf Jaenisch[3], and Joel Voldman[1,2,4]

[1]Research Laboratory of Electronics, MIT, USA
[2]Microsystems Technology Laboratories, MIT, USA
[3]Whitehead Institute, MIT, USA
[4]Electrical Engineering and Computer Science, MIT, USA

ABSTRACT

Controlled fusion between an embryonic stem cell and a somatic cell is an important strategy for cellular reprogramming. We have developed a microfluidic system specifically to address the main limitation of current fusion technologies: the positioning and pairing of cells prior to fusion. We present a PDMS device designed to pair cells prior to fusion. Thousands of properly paired cells are obtainable within a mm-sized area, and the device is compatible with both chemical and electrical fusion. Fusion efficiencies obtained with our device demonstrate a significant improvement over current technologies.

Keywords: Embryonic stem cell, cell fusion, cell reprogramming, hydrodynamic trap

1. INTRODUCTION

Researchers have recently demonstrated that somatic cells can be reprogrammed back to an embryonic, pluripotent state. Several reprogramming methods have been demonstrated in the literature, including nuclear transfer, fusion with an oocyte, and, recently, fusion with an embryonic stem cell [1]. While these advances hold great promise, the reality is that little is known about cellular reprogramming, primarily due to the limitations of current technologies. State-of-the-art protocols use polyethylene glycol (PEG) or electric fields to disrupt the cell membranes and induce fusion, but cannot control the cell pairing. In addition, the cells must remain immobilized in cytotoxic fusion buffer during the delicate fusion process, necessitating a trade-off between successful fusions and viability. As a result, current fusion techniques yield at best ~5% successfully fused somatic and embryonic stem cells in a high background of non- and incorrectly fused cells, necessitating days of culturing and colony picking to isolate the desired fusions, and preventing the use of assays on pooled populations.

2. RESULTS

The PDMS device for cell pairing contains thousands of capture combs accessed by microfluidic channels (Figure 1). Modeled after previously published designs [2], the PDMS combs utilize a novel double-well structure to enable efficient trapping and pairing of two different types of cells. Cells are loaded sequentially, first capturing one cell of type A per comb (Figure 2, step 1). The flow is then reversed, and all cells of type A are shifted simultaneously to larger wells (Figure 2, step 2). This is a fast (<1 second) and massively-parallel recapture that utilizes the laminar flow attainable in the microfluidic system. The second type of cell is then loaded, and the larger wells already containing cell A now also capture one cell of type B (Figure 2, step 3), precisely positioning the two cells next to each other and in tight contact in preparation for the fusion protocol. Efficiencies of >50 % red-green pairs are capable over the entire device, with >70 % efficiencies in the bottom half of the device (Figure 3), a

978-0-9798064-0-7/μTAS2007/$20©2007CBMS

dramatic increase over existing methods.

Initiation of fusion is accomplished by exposing the cells to either a chemical fusion buffer or an electric field. In Figure 4 we show the time course of PEG-induced cell-cell fusion. Opening of pores in the membrane and exchange of cellular contents, demonstrated by the dye within one cell moving into the other cell, takes place over a 20-minute period. An additional advantage of our device is that by physically constraining the cells, additional doses of PEG can be applied to further increase fusion efficiency while still maintaining proper cell contact. Using a 5-minute dose of PEG, the fusion efficiency doubles when second and third doses are applied.

3. CONCLUSIONS

The ability to immobilize and observe thousands of paired cells during fusion while precisely controlling the exposure of the cells to harmful fusion buffers now allows detailed studies of cellular fusion while increasing the number of viable fused cells for further experiments. With this system we now aim to examine the short-timescale dynamics of reprogramming as well as perform gene expression assays on pooled populations.

REFERENCES/ACKNOWLEDGEMENTS

[1] "Nuclear reprogramming of somatic cells after fusion with human embryonic stem cells," C. A. Cowan, J. Atienza, D. A. Melton and K. Eggan, Science, 5739, 1369-1373 (2005).
[2] "Single-cell enzyme concentrations, kinetics, and inhibition analysis using high-density hydrodynamic cell isolation arrays," D. Di Carlo, N. Aghdam and L. P. Lee, Anal. Chem., 14, 4925-4930 (2006).
This work was supported in part by the NIH (EB007278).

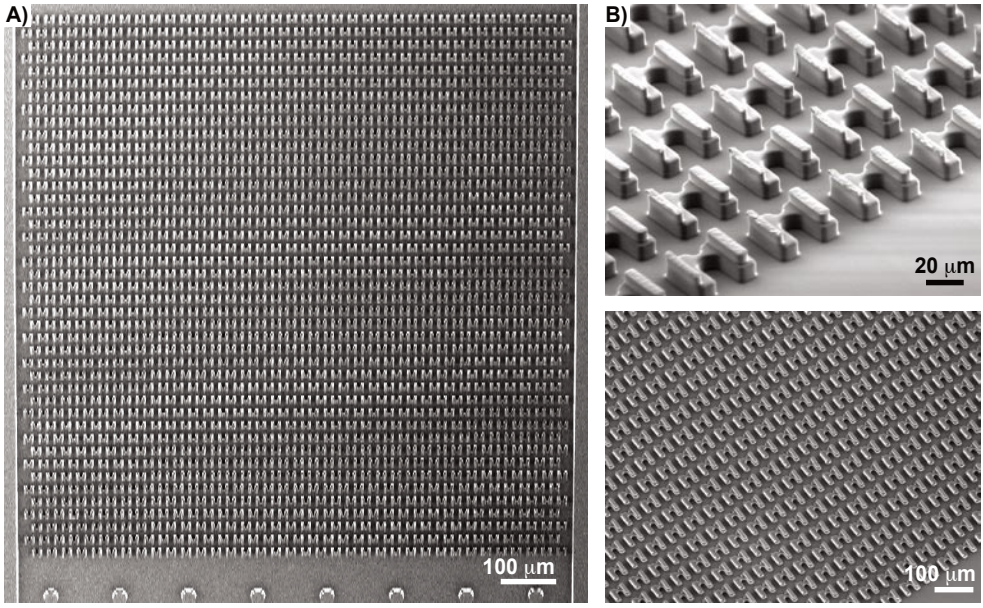

Figure 1. SEM images of the 2-cell capture device. A) Top view showing the 2-mm by 2-mm capture area. B) Close-up SEM photos showing the capture comb and support pillars. The front chamber (top in A) fits 2 cells,while the back chamber (bottom in A) fits one cell.

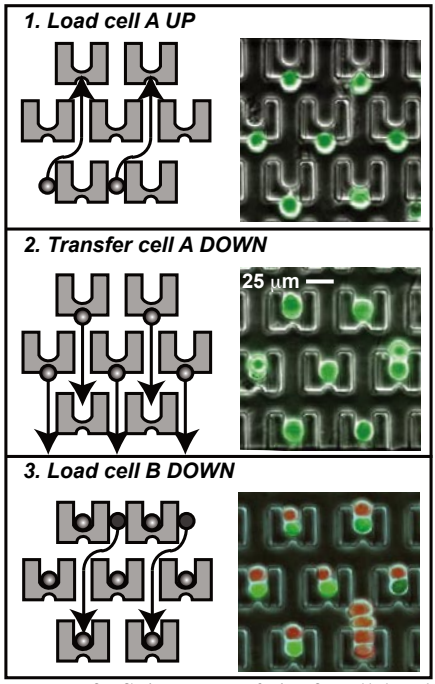

Figure 2. Schematic of the 2-cell loading process.

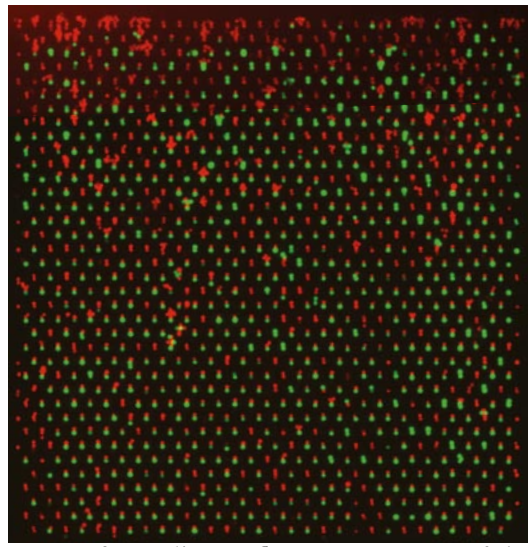

Figure 3. Red/green fluorescent images of the 2-mm by 2-mm capture aray. Green and red 3T3 cells were loaded as described in Figure 2. Efficiencies of >50 % R/G 2-cell capture are possible over the entire device, with >70 % efficiencies in the bottom half of device.

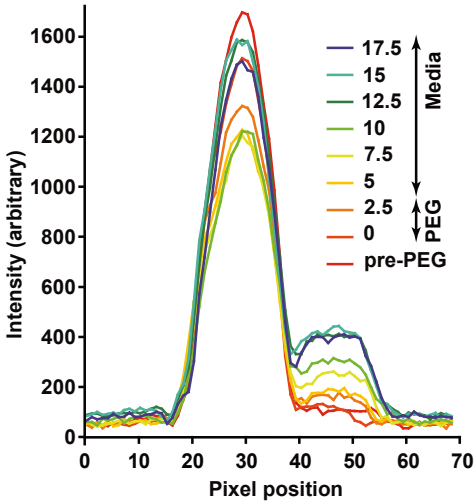

Figure 4. Timecourse for PEG-induced fusion monitored by transfer of dye from one cell to the other. The green fluorescence is initially localized within one cell. After a 3-minute dose of PEG, the green fluorescence is visible within the second cell. The signal stabilizes after ~ 15 minutes.

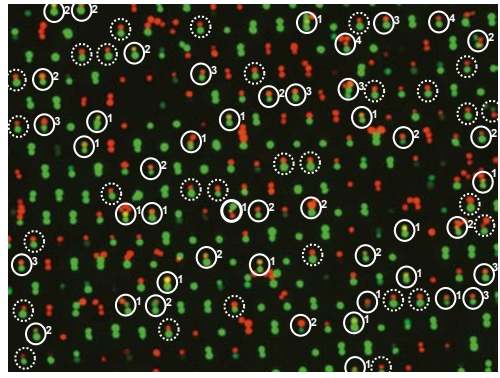

Figure 5. Fusion of 3T3 cells with multiple doses of PEG. Solid circles indicated fused cells along with the dose that initiated fusion (total 35% red/green cells are fused); dashed circles indicate potentially fused cells (57% total confirmed and possible fusions).

CONCENTRATION, LYSIS AND REAL-TIME PCR ON A SU-8 LAB ON A CHIP FOR RAPID DETECTION OF *Salmonella* spp. IN FAECES

M. Agirregabiria[1], D. Verdoy[2], G. Olabarria[2], J. Berganzo[1], J. Berganza[2], L. J. Fernandez[1], M. Pascual de Zulueta[2], K. Mayora[1] P. Aldamiz-Echevarría[2], and J. M. Ruano-López[1]

[1]MEMS/MST Dept., Ikerlan S.Coop, Pº Arizmendiarrieta 2, 20500 Mondragón, SPAIN
[2]Gaiker-IK4, Centro Tecnológico, Ed. 202, 48170 Zamudio, SPAIN

ABSTRACT

This work describes a SU-8 microdevice for the detection of *Salmonella* spp. This device is able to perform (i) the concentration of the target microorganisms from human faecal samples, (ii) their lyse and (iii) the amplification of the extracted DNA by real time-PCR (qPCR). All the steps are carried out in a single 2.5 µl microchamber in 25 minutes. The threshold cycle (C_T) is 15.

Keywords: SU-8, microdevice, qPCR, real human sample.

1. INTRODUCTION

The fabrication of Lab on a Chips in SU-8 by photolithography and bonding is of particular interest due to the use of simple and promising standardised processes. Although PCR devices made of SU-8 have been reported before [1, 2, 3], we present for the first time the realization of sample preparation and q-PCR on a single SU-8 chamber.

2. EXPERIMENTAL

The SU-8 fabrication process was based on the bonding and releasing of photopatterned SU-8 layers [4]. In this way, a 200 µm high, 3 mm wide and 5.4 mm long SU-8 microchamber (2.5 µl) was fabricated on a Pyrex substrate, where a resistive Ti/Pt sensor and two parallel heaters were previously fabricated by sputtering and lift off.

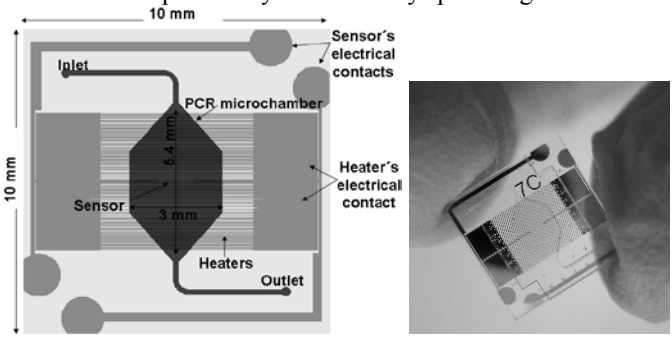

Figure 1. Schematic top view of the 10 x 10 mm PCR device. It consists of a 5.4 x 3 mm rhombus shape microchamber, a resistive Ti/Pt sensor and two parallel heaters.

SU-8 photolithography offered more precise dimensional tolerances and easier electrode integration than replicated PDMS [7, 8]. Besides, in contrast with other SU-8 related works

978-0-9798064-0-7/µTAS2007/$20©2007CBMS

[1, 3], the sealing layer was also developed for the creation of inlets and outlets, simplifying the packaging. The SU-8 chip was easily replaced by opening the capsule (see Figure 2).

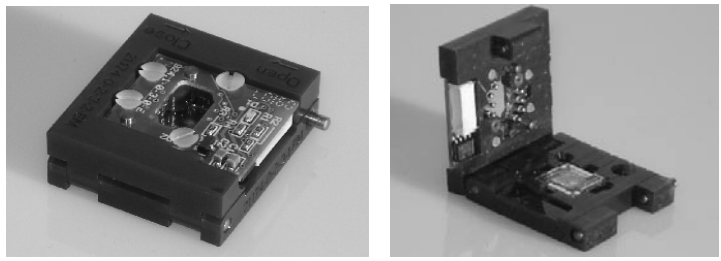

Figure 2. Photographs of the PCR microdevices: closed and opened packaged devices.

The experimental procedure described in Figure 3 was carried out for the characterisation of the devices. Analyzed stool samples were previously diagnosed as salmonellosis by q-PCR at laboratory scale. A swab was then inserted in a stool sample, transferred to sterile buffer and left to release the bacteria. Next, functionalized magnetic beads with Salmonella antibodies were added. The sample was then inserted in the packaged SU-8 microdevice using a syringe. The magnetic field created by magnets placed under and above the chip captured the beads while the liquid was displaced (see Figure 4). Subsequently, PCR mastermix was inserted, the inlet/outlet were sealed, magnets were carried off and lysis and amplification were performed. The initial 10 min-denaturation step at 94ºC was enough for cell thermal lysis.

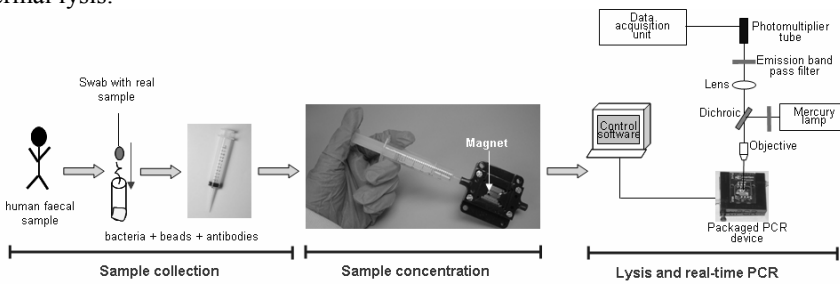

Figure 3. Experimental procedure for sample collection, target microorganism concentration using immunomagnetic beads, cell thermal lysis and real-time PCR for pathogen detection. Once the sample is collected, all the analysis was carried out on a single microchamber.



Figure 4. Picture showing the concentration of magnetic beads obtained when two Neodymium Iron Boron (NdFeB) magnets were used, and a preasure difference of 0.2 bar was applied to the fluid.

3. RESULTS AND DISCUSSION

The whole protocol, including *Salmonella* spp. concentration, DNA extraction and real time amplification was successfully achieved in 25 minutes. Figure 5 shows the Cy5 fluorescence signal observed in real time by the photomultiplier tube through the SU-8 cover. The real time method showed a high specificity and accuracy.

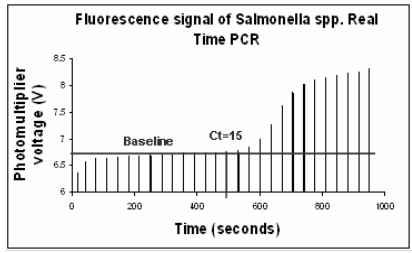

Figure 5. Cy5 fluorescence signal vs time. Fluorogenic specific probes were used. The baseline signal was surpassed in cycle 15 (C_T). The plateau was reached after cycle 22th. The initial denaturing time was 10 min at 94ºC, followed by 30 PCR cycles of 94ºC, 8 s; 62 ºC, 8 s and 72 ºC, 8 s.

4. CONCLUSIONS

This work demonstrates that a simple syringe and an SU-8 microdevice are enough to carry out a complete DNA analysis, from real sample preparation to detection. This technology offers a simple microfabrication and packaging of Lab on a Chips. In addition, several improvements are achieved in comparison with other q-PCR devices based on silicon [4, 6] or PDMS [7, 8]: (i) real human samples are used; (ii) microorganisms concentration, lysis and qPCR are carried out in a single microchamber; (iii) less PCR mixture (2.5 µl) is required; (iv) less time (25 minutes) is needed for the complete analysis and (v) a higher sensitivity (C_T=15) is obtained.

ACKNOWLEDGEMENTS

This project is carried out within the European project OPTOLABCARD and ETORTEK program, sponsored by the Basque Government.
We would like to thank BIOEF for its contribution to this project.

REFERENCES

[1] Haukur Gudnason et al., Proceeding of µTAS 05, 820-822 (2005).
[2] Janette L. M. Schulze et al., Proceeding of µTAS 06, 1423-1425 (2006).
[3] Nan-Chyuan Tsai et al., Biosensors and Bioelectronics, 22, 313-317 (2006)
[4] Maria Agirregabiria et al., Lab Chip, 5, 545-552 (2005)
[5] Jeong-Gun Lee et al., Lab Chip, 6, 886-895 (2006)
[6] Phillip Belgrader et al., Science, 284, 449-450 (1999)
[7] Chih-Hao Wang et al., J. Micromech. Microeng., 17, 367-375 (2007)
[8] Guoqing Hu et al., Analytica Chimica Acta, 557, 146-151 (2006)

ON-CHIP SINGLE MOLECULE ASSAY DEVICE INTEGRATING CELL LYSIS AND PROTEIN EXTRACTION-PURIFICATION-ASSAY COMPONENTS FOR GENETICALLY ENGINEERED PROTEINS

Tetsuya Nakayama[1], Kazuhito Tabata[2], Hiroyuki Noji[2], Ryuji Yokokawa[1,3]

[1]*Ritsumeikan Univ., JAPAN*

[2]*The Institute of Scientific and Industrial Research (ISIR), Osaka Univ., JAPAN*

[3]*CREST, JST, JAPAN*

ABSTRACT

We have developed a single molecule assay device applicable to the evaluation of genetically engineered proteins. Cell lysis, protein extraction, purification, and assay were sequentially performed on a chip. The cell lysis part was evaluated by absorptiometry and proved to retrieve enough proteins for the assay. Target proteins were purified and assayed on a functionalized channel surface. The single molecule assay on the fabricated chip provides compatible results to a bulk-scale assay.

Keywords: Cell lysis, On-chip purification, Single molecule assay, Protein assay

1. INTRODUCTION

Many fractionated components for protein engineering have been developed such as devices for electroporation, cell culture, cell lysis, and protein assay. They, however, are not well integrated because a processed sample from each device is not directly applicable to the next due to differences of sample amount or concentration. Only a report realized processes from cell lysis to fluorescence assay [1], but protein activity was not evaluated quantitatively. Therefore, we propose a novel assay device along with cell lysis and protein purification, which is applicable to the *E. coli*-based gene expression system. The device necessitates only a countable number of proteins thanks to the on-chip single molecule assay.

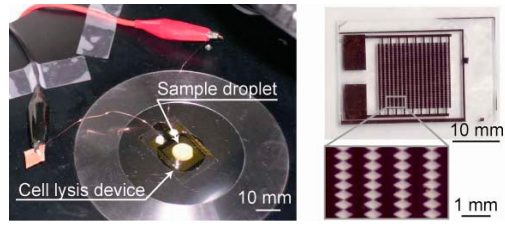

(a) Cr/Au were patterned on a coverslip. Electrode gap and height are 50 μm and 150nm, respectively.

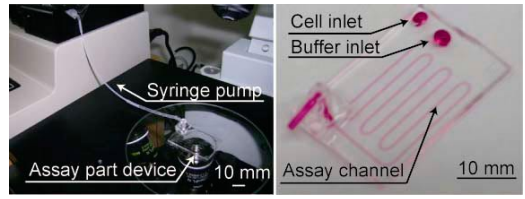

(b) Assay part device consisted of Y-shape microchannel (H: 100 μm, W: assay channel 540 μm, cell inlet channel 60 μm, buffer inlet channel 440 μm) and Ni-NTA coated coverslip.

Figure 1. Devices for cell lysis (a) and extraction-purification-assay (b).

978-0-9798064-0-7/μTAS2007/$20©2007CBMS

2. EXPERIMENTAL

We first fabricated two devices for cell lysis and extraction-purification-assay (Fig. 1) for verification of each component, which were finally integrated for the sequential procedure (Fig. 2). A target protein was F_1-ATPase expressed in *E. coli* known as a rotary molecular motor [2]. Cells were lysed by square pulse voltages applied by triangular electrodes. The amount of extracted protein was measured by absorptiometry.

Crude sample from cell lysis device (applying voltage; 250 V, pulse width; 50 μsec, duty ratio; 0.01%, number of pulses; 1800) without any pretreatment was injected to extraction-purification-assay device for its evaluation. F_1-ATPase molecules are trapped on the channel surface by affinity between Ni-NTA coated on a glass and His-tag expressed in F_1-ATPase. Sequentially, streptavidin-coated beads was injected and immobilized on biontinylated moiety of the protein. The bead rotation was monitored by a microscope after injecting ATP. The total processes from cell lysis to assay were performed in the integrated device by just injecting 4 μl solution containing cells.

3. RESULTS AND DISCUSSION

For cell lysis evaluation, OD_{280} corresponding to protein concentrations are plotted depending on applied voltage and pulse width (Fig. 3). Higher electric field and wider pulse provide efficient cell lysis and protein extraction. Extracted protein concentration is lower than one obtained by bulk-scale ultrasonic lysis, however, it is high enough for the single molecule assay. Extraction-purification-assay part is evaluated by the number of rotating beads density depending on the channel position (Fig. 4). When cells are lysed on a chip, rotating beads density has peak across the channel. Diffusion in a Y-shape microchannel makes sample concentration gradient, and automatically optimizes sample concentration for the assay. This is an advantage over the bulk scale optimization which is usually realized by preparing several samples with discrete concentrations in tubes. The total revolutions of three beads assayed in the integrated device are compared with results obtained by the conventional purification and assay (Fig. 5). It proves the integrated device has possibility to replace the bulk experiments, since the protein activity is comparable each other.

4. CONCLUSIONS

On-chip electrical cell lysis and protein extraction were optimized for *E. coli*-based gene expression system. The extracted target protein was purified and assayed in the chemically modified microchannel. We integrated two devices to one chip and demonstrated the

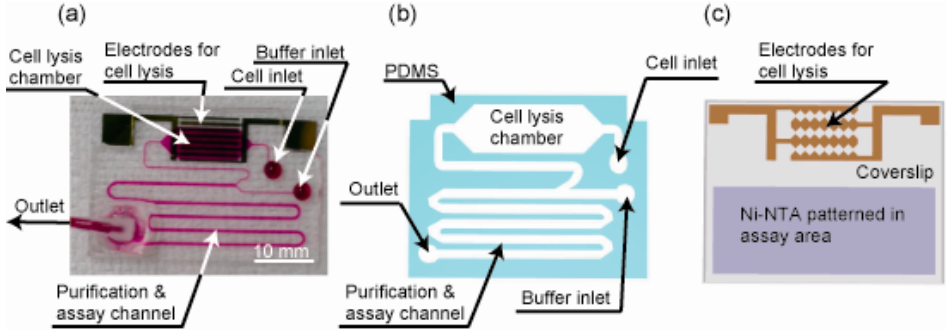

Figure 2. A single molecule assay device integrating cell lysis, protein extraction-purification-assay components. (a) An integrated device. (b) and (c) are schemes of bottom and top layer, respectively.

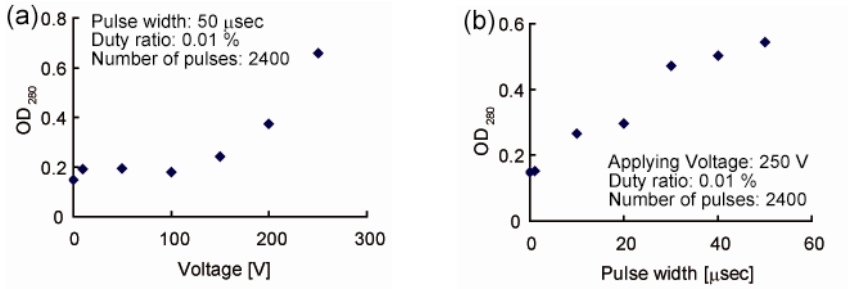

Figure 3. Results of cell lysis: (a) Relationship between absorbance and applied voltages. (b) Relationship between absorbance and applied pulse width.

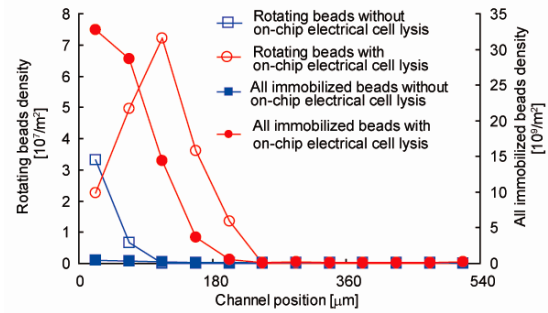

Figure 4. Relationship rotating beads density and all immobilized beads density on coverslip to channel across position: PDMS walls of cell inlet side and buffer inlet side in assay channel were defined 0 μm and 540 μm as channel position, respectively.

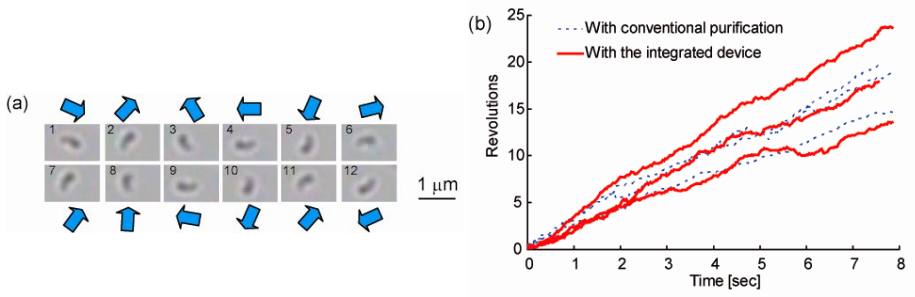

Figure 5. Analysis of rotating beads in an integrated device as shown in (Fig. 2): (a) Observation of a bead rotated by single F1-ATPase molecule in the device (frame rate: 15 Hz). (b) Analysis of rotating beads using F1-ATPase by conventional purification and the integrated device.

sequential single molecule assay from cell lysis to rotation analysis. Results prove the total process time decreased from a few days to one hour without losing protein activities. The presented device can be expanded by integrating other components such as electroporation or cell culture for sequential evaluation of genetically engineered proteins.

REFERENCES

[1] E. A. Schilling *et al.*, *Anal. Chem.,* vol. 74, pp. 1798-804, 2002.
[2] H. Noji *et al.*, *Nature,* vol. 386, pp. 299-302, 1997.

MICROFLUIDIC CHIPS FOR MEMBRANE PROTEIN CRYSTALLIZATION

P.J.A. Kenis, J.D. Tice, S.L. Perry, G.W. Roberts, and S. Talreja
Department of Chemical & Biomolecular Engineering, University of Illinois, USA

ABSTRACT

This paper reports novel microfluidic chips designed to screen for protein crystallization conditions with control over the kinetics of supersaturation. Using preliminary designs, we demonstrated that kinetic control can influence both the size and morphology of crystals of a model membrane protein.

Keywords: microfluidic, kinetic control, protein, crystallization

1. INTRODUCTION

Analysis indicates that nearly 30% of the proteins encoded for in the genomes of *E. coli*, *S. cerevisae*, and *H. sapiens* reside in cellular membranes [1]. Membrane proteins act as mediators for signal, energy, and material transduction into and out of the cell. As such, their malfunction has been implicated in a number of serious diseases including autism, epilepsy, migraines, depression, drug abuse, and cystic fibrosis [2]. However, of the more than 44,000 protein structures deposited in the Protein Databank [3], only 256 are of membrane proteins [4]. Because of the limited quantities resulting from difficulties in expression, extraction, and purification, the development of microscale screening strategies to determine crystallization conditions is critical for further protein structural studies.

In prior work we have demonstrated control of the evaporation rate of solvent from a microliter-sized hanging drop in a small compartment and the resulting kinetic control over crystal nucleation and growth (Figure 1) [5]. The evaporation rate is determined by the cross-sectional area and length of a microfluidic channel connecting the compartment to the surrounding environment. In this study, we used this evaporation-based method to crystallize the model membrane protein bacteriorhodopsin while demonstrating kinetic control over the size of the resulting crystals. We also present work miniaturizing the crystallization platform to reduce sample consumption, increase throughput, and automate crystallization trials. Preliminary microfluidic trials on the nanoliter-scale demonstrated control over both the size and morphology of bacteriorhodopsin crystals.

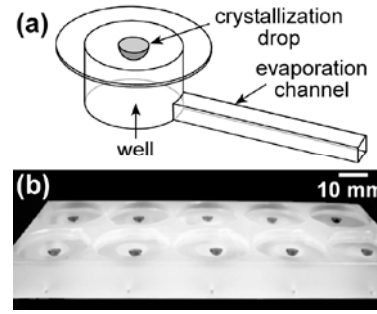

Figure 1: *(a) Schematic of the evaporation-based platform. (b) Optical micrograph of a multi-well evaporative crystallization platform for µL-sized droplets.*

2. EXPERIMENTAL

Using the previously reported platforms [5], crystals were grown from microliter-sized droplets containing bacteriorhodopsin (solubilized in 25 mM NaH_2PO_4 with 1.2 w/v% octyl β-D-glucopyranoside, pH 5.6) at different initial concentrations (C_{P0}). The wells were vented to the outside environment through channels 0.6 mm in diameter and 7 mm long.

978-0-9798064-0-7/µTAS2007/$20©2007CBMS

To miniaturize the evaporation-based crystallization process, we first created a simple microfluidic device consisting of only a microfluidic channel (100 µm wide and 10 µm high) molded in polydimethylsiloxane (PDMS) and sealed to a glass substrate after brief exposure to oxygen plasma. An inlet hole, approximately 0.5 mm in diameter and 5 mm long, was punched with a needle to the channel. We infused a solution of bacteriorhodopsin (8 mg/mL) into the channel. The device was left under ambient conditions, allowing water vapor to diffuse out both through the inlet hole and the bulk of the PDMS, although we believe water is lost more rapidly through the inlet.

We have also completed a more exact microfluidic replication of the original evaporation-based crystallization device. A microfluidic network with integrated valves was used to direct, meter, and dispense discreet quantities of reagents. The network was fabricated in PDMS by multilayer soft lithography [6]. Through holes were fabricated in a separate layer and used to connect the network to an array of wells underneath. To fabricate the through holes, PDMS (5:1 w/w prepolymer/cross-linker) was spun onto a wafer containing an array of posts at 4000 rpm, >30 seconds, such that the posts protruded above the PDMS [7]. To prevent evaporation through the PDMS, the underside of the PDMS assembly was first exposed to oxygen plasma in a reactive ion etcher (300W, 200 mTorr, 20 sccm O_2, 10 min.), and then 20 nm of HfO_2 was deposited via an e-beam evaporator at 0.5 Å/s. Wells and microfluidic channels used to control evaporation were fabricated by molding Norland optical adhesive 73 on a glass slide using a PDMS stamp containing inverse relief structures of the wells and channels. The optical adhesive was exposed to a long wavelength UV light source through the PDMS stamp until almost fully cured. The PDMS components were aligned with the crystallization wells, and then the whole assembly was exposed to the UV light source to complete the fabrication.

3. RESULTS AND DISCUSSION

Using the microliter-scale device reported previously [5], we showed that the rate of supersaturation at the solubility boundary was important in influencing the size of the membrane protein crystals (Figure 2a-c). At a constant evaporation rate and equal volumes, droplets with greater bacteriorhodopsin concentrations crossed the solubility boundary at slower rates of concentration compared to droplets with smaller initial concentrations of protein. This lower rate allowed for the nucleation and growth of fewer, larger crystals.

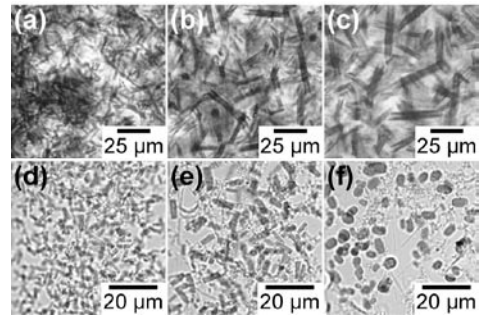

Figure 2: *Optical micrographs of bacteriorhodopsin crystals obtained on microliter-scale (a-c) and nanoliter-scale (d-f) evaporation platforms. (a) C_0 = 2 mg/mL, (b) C_{P0} = 4 mg/mL, (c) C_{P0} = 6 mg/mL at constant rate of evaporation. (d-f) C_{P0} = 8 mg/mL with decreasing rate of evaporation (d) to (f).*

In the single channel microfluidic device, we demonstrated that crystals grown closer to the inlet (higher rate of solvent evaporation) formed small bricks, while further from the inlet, larger crystals of different morphologies were seen (Figure 2d-f).

To interrogate the rate of evaporation more rigorously on the nanoliter-scale, we designed a more sophisticated microfluidic chip that retained the main concepts of the

larger evaporation-based devices (Figure 3). In addition to evaporation wells and channels, it also included microfluidic circuitry to perform the intricate fluid handing needed for crystallization screens. First, reagents were metered into a serpentine channel, where the ratio of the reagents was controlled by a pneumatic valve (Figure 3b-d). The individual chambers were then isolated from the main distribution channels, and reagents were extruded through vias into 30 nL crystallization wells (Figure 3e). A thin HfO_2 film inhibited evaporation through the PDMS components of the device so that the rate of evaporation was controlled by the dimensions of channels that vent the wells to the outside environment.

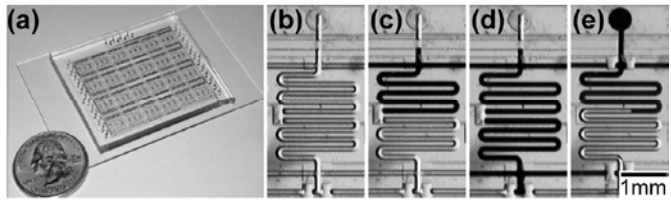

Figure 3: *(a) Photograph of the miniaturized evaporation-based crystallization device. (b-e) Micrographs of metering and dispensing of reagents on-chip to an individual well.*

Currently, the chip is configured to screen one protein solution against 48 different precipitating reagents at a time. For each precipitant, the device formulates three different protein/precipitant concentration ratios, leading to a total of 144 trials per. The device could also be configured so that one protein/precipitant concentration ratio is tested at multiple evaporation rates, etc.

4. CONCLUSIONS

We have shown that kinetic control over crystallization conditions is crucial to determining the size and morphology of membrane protein crystals. We have designed a device that will reduce sample consumption, increase throughput and enable automation while retaining control over kinetics of the crystallization process.

ACKNOWLEDGEMENTS

This work was funded through the NIH Roadmap for Medical Research, Grant R21 GM075930-01. We thank Dr. M. Chiu (Abbott Labs) and Dr. A. Pawate for the bacteriorhodopsin, and Dr. R.B. Gennis for helpful discussions.

REFERENCES

[1] Seddon, A. A., Curnow, P. and Booth, P. J., *Bba-Biomembranes* **2004**, *1666*, 105-117.
[2] Quick, M. and Javitch, J. A., *P Natl Acad Sci USA* **2007**, *104*, 3603-3608.
[3] RCSB Protein Data Bank. http://www.rcsb.org/ (6/19/2007)
[4] Membrane Proteins of Known 3D Structure. http://blanco.biomol.uci.edu/Membrane_Proteins_xtal.html (6/19/2007)
[5] Talreja, S., Kim, D. Y., Mirarefi, A. Y., Zukoski, C. F. and Kenis, P. J. A., *J Appl Crystallogr* **2005**, *38*, 988-995.
[6] Unger, M. A., Chou, H. P., Thorsen, T., Scherer, A. and Quake, S. R., *Science* **2000**, *288*, 113-116.
[7] Kartalov, E. P., Walker, C., Taylor, C. R., Anderson, W. F. and Scherer, A., *P Natl Acad Sci USA* **2006**, *103*, 12280-12284.

A SINGULAR VIEW OF DNA TRANSACTIONS

Gijs J.L. Wuite

Division of Physics and Astronomy, Vrije Universiteit, Amsterdam, THE NETHERLANDS

ABSTRACT

The genetic information of an organism is encoded in the base pair sequence of its DNA. Many specialized proteins are involved in organizing, preserving and processing the vast amounts of information on the DNA. In order to do this swiftly and correctly these proteins have to move quickly and accurately along and/or around the DNA constantly rearranging it. In order to elucidate these processes we perform single-molecule experiments on model systems such as bacterial gene regulators and repair proteins. The data we use to extract forces, energies and mechanochemistry driving these dynamic transactions. The results obtained from these model systems are then generalized and though to be applicable to many DNA-protein interactions.

Keywords: single-molecule techniques, DNA-protein interactions

1. INTRODUCTION

Increasingly more physics is brough into biology in order to attempt to quantitatively describe, underpin, and unify seemingly disparate biological phenomena. To this end the mechanics and dynamics of biological systems is being unraveled using an array of experimental techniques such as Atomic Force Microscopy (AFM), optical tweezers and (single-molecule) fluorescence microscopy. Below I have sketched a few active research topics that we currently pursue.

Homologous recombination - Homologous recombination is essential for maintaining genome integrity. The catalytic core of the recombination reaction is formed by recombinases (for example Rad51) that drive DNA strand exchanges between homologous DNA molecules or chromosomes. Strand exchange by Rad51 initiates through the assembly of an ATP-bound nucleoprotein filament on single-stranded DNA. This filament promotes recognition of homologous sequences in a duplex DNA molecule and catalyzes strand exchange between the invading single-stranded DNA and the homologous duplex DNA. The molecular mechanism by which the recombinase nucleoprotein filament identifies homology and catalyzes strand exchange is a central unsolved puzzle of homologous recombination. To study the mechanistic aspects of homologous recombination we have taken a single-molecule approach in which we combine (single-molecule) fluorescence with optical manipulation of DNA molecules and proteins.

DNA organization – The genomes inside organisms are organized by multitudes of proteins in structures called chromosomes. In order to respond to environmental changes the transcription activity of the genes within the chromosomes are constantly regulated. The physical mechanisms of this dynamic organization are hardly understood. We are currently performing biophysics experiment to elucidate the functioning of the bacterial chromosome (nucleoid) at various levels, starting from single proteins interacting specifically with DNA, to molecular machinery involved in transcription and regulation, all the way up to emerging properties due to arrays of (non-)specific proteins interacting with each other and with multiple DNA strands.

978-0-9798064-0-7/μTAS2007/$20©2007CBMS

3. EXPERIMENTAL

The majority of the experiments has been carried out with the use of an instrument that combines optical trapping with the capability to visualize (single) fluorescent molecules on DNA (Fig. 1a) [1]. We also build a multi-beam optical trap and combined it with advanced fluidics devices (Fig. 1b) [2]. Both instruments are at the very front of what is possible with single-molecule techniques and have some unprecedented ability to follow DNA-protein interactions in real time.

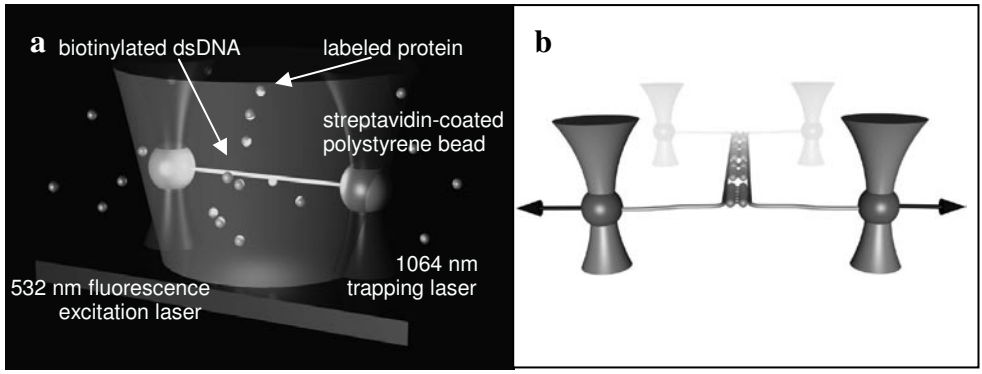

Figure 1. **a.**Combining optical tweezers with single-molecule fluorescence. Image by *van Mameren*. **b.** Using four optical tweezers to manipulate two DNA pieces. Image by *Noom.*

4. RESULTS AND DISCUSSION

Homologous recombination - We have visualized the interactions of fluorescent Rad51 proteins with a single DNA molecule. Fluorescence imaging revealed that Rad51 filament formation on dsDNA initiates from multiple nucleation points. The heterogeneous elastic properties of discontinuous filaments were assessed by combining fluorescence microscopy with force-extension measurements using optical traps. The non-fluorescent zones of DNA-Rad51 constructs showed the well-known stretching behavior of bare DNA. In contrast, the fluorescent, Rad51-coated zones did not overstretch but remained stably bound in a structure that is 45% longer than bare DNA [1].

DNA organization – With the multi-bead optical trap we individually manipulate and probe two DNA molecules. Using this setup we investigate the mechanism and dynamics of physical linkage of DNA duplexes mediated by H-NS. In particular we explore the unzipping of regions bridged by this protein. Unzipping occurs in regular steps reflecting an organization of multimeric H-NS building blocks. Finally, we determine an energy landscape for the interaction between H-NS and DNA following a dynamic force spectroscopy approach. These measurements show that the binding strength of H-NS does not necessarily impede RNA polymerase movement during transcription [2].

REFERENCES

[1] J. van Mameren, M. Modesti, R. Kanaar, C. Wyman, G.J.L. Wuite, E.J.G. Peterman, *Dissecting elastic heterogeneity along DNA molecules coated partly with Rad51 using concurrent fluorescence microscopy and optical tweezers,* Biophys. J., 91(8), (2006)

[2] R.T. Dame, M.C. Noom, G.J.L. Wuite, *Bacterial chromatin organization by H-NS protein unraveled using a dual DNA assay,* Nature, 444, (2006)

FORMATION OF ARRAYED PLANAR LIPID MEMBRANES BY THE ACCUMULATION OF UNIFORM AQUEOUS PLUGS IN A PSEUDO-POROUS MICROCHANNEL

Takahiro Baba, Takeshi Hatsuzawa and Takasi Nisisako
Tokyo Institute of Technology, JAPAN

ABSTRACT

We present a new technique for generating an array of planar lipid membranes (PLMs) in a microfluidic channel. Uniform aqueous plugs were formed in an organic stream containing lipid molecules at a cross junction. Subsequently, downstream of the microchannel, the lipid solution between the aqueous plugs was preferentially removed through hydrophobic pseudo-porous sidewalls. The resulting contact of the aqueous plugs reproducibly formed an array of self-standing PLMs. Fluorescence microscopy was carried out for the detection of Ca^{2+} transport through the PLMs.

Keywords: planar lipid membrane, microfluidics, capillary force, membrane protein

1. INTRODUCTION

Artificial planar lipid bilayers between two aqueous compartments have been widely studied for the electrophysiological analysis of purified membrane proteins [1]. Recently, several lab-on-a-chip devices have been proposed for generating planar lipid bilayers [2–4]. However, very few methods are suitable for the high-throughput screening application, due to difficulties in the independent analysis of each compartment and the rapid formation of a large number of lipid membranes.

Here, we propose a new technique for the formation of arrayed planar lipid membranes (PLMs). In the microchannels, monodisperse aqueous plugs are formed alternately in an organic phase stream (Fig. 1a). Subsequently, the lipid molecules in the organic phase self-assemble at the oil/water interfaces. The organic phase can be preferentially extracted through the hydrophobic pseudo-porous sidewalls of the microchannel, and an array of PLMs is produced by the accumulation of aqueous plugs (Fig. 1b).

2. EXPERIMENTAL

Microchannels with rectangular cross-section were fabricated on a glass substrate by the dry-etching technique. The geometry of the microchannels consisted of a wide main channel (width: 200 μm, depth: 100 μm, Fig. 2a) and narrow subchannels in both sidewalls (width: 20 μm, depth: 100 μm, pitch: 50 μm, Fig. 2b). All the microchannels were modified to be hydrophobic by a siliconizing agent for the formation of aqueous plugs [5] and for the selective withdrawal of the organic phase. Syringe pumps were used for infusing fluids and withdrawing the lipid solution through the subchannels in both sidewalls.

DI water or electrolyte solutions (KCl, $CaCl_2$, etc.) were used for the aqueous phase. For the organic phase, 5 mg dioleoylphosphatidylcholine (DOPC) and ionophores (3 μg gramicidin A (Calbiochem) or 30 μg A23187 (Wako Pure Chemicals)) were dissolved in 1 mL chloroform. A fluorescent Ca^{2+} indicator (F14200, Molecular Probes) was used for detecting Ca^{2+}.

978-0-9798064-0-7/μTAS2007/$20©2007CBMS

3. RESULTS AND DISCUSSION

The formation and the accumulation of uniform aqueous plugs was observed under the specific low capillary number condition (Ca = 10^{-6}–10^{-3}, Figs. 3 and 4a). In order to adequately remove the organic phase between the aqueous plugs, we made the withdrawal flow rate equal the infusion flow rate of the organic phase. After the organic phase was adequately removed, the accumulation of the aqueous plugs produced an array of stable PLMs. When we used two different aqueous phases, we obtained an array of PLMs similar to the structure inside and outside the cell membranes. The area of the PLMs could be controlled by varying withdrawal flow rate (Figs. 3b–d). It was also possible to remove one of the two aqueous phases selectively when they had different interfacial energies (Figs. 3e and f). We could also vary the length of the aqueous compartments by changing infusion flow rates (Fig. 4b).

The accumulation of the aqueous plugs depended on the capillary pressure in the subchannels, as indicated by the following equation:

$$\Delta P \cong 2\gamma \cos\theta \left(\frac{1}{w} + \frac{1}{h} \right) = 1.67\,\text{kPa} \tag{1}$$

where ΔP is the differential pressure; γ = 19.3 mN m^{-1} is the interfacial tension; θ = 30° is the contact angle; w = 20 μm is the width of the subchannels; and h = 100 μm is the height of the subchannels. Since the solid-liquid (*s-l*) interfacial tension of the organic phase in the hydrophobic channel was smaller than that of the aqueous phase, the organic phase could preferentially flow into the pseudo-porous sidewalls.

Finally, we could detect Ca^{2+} transport through A23187 mounted in the PLMs by using the fluorescent Ca^{2+} indicator. We achieved the accumulation of two groups of aqueous plugs made from $CaCl_2$ solution and fluorescent Ca^{2+} indicator solution. When they accumulated, we could observe the emission of fluorescent Ca^{2+} indicator (Fig. 5). We conclude that the PLMs with A23187 were successfully formed by the accumulation of the aqueous plugs.

4. CONCLUSIONS

We have proposed a new microfluidic technique that can generate an array of PLMs. Since a large number of membranes can be reproducibly formed, our method would be applicable to the high-throughput analysis of the functions of membrane proteins in physiological and pharmaceutical studies. The integration of microelectrodes in the microchannel would enable further characterization of the PLMs.

ACKNOWLEDGEMENTS

This work is partially supported by Mizuho Foundation for the Promotion of Sciences.

REFERENCES

[1] B. Hille, *Ion Channels of Excitable Membranes*, Sinauer Associates, Massachusetts, 2001.
[2] H. Suzuki et al., *Langmuir* **22**, pp.1937-1942(2006).
[3] N. Malmstadt et al., *Nano Lett.* **6**, pp.1961-1965(2006).
[4] K. Funakoshi et al., *Anal. Chem.* **78**, pp.8169-8174(2006).
[5] T. Nisisako et al., *Soft Matter* **1**, pp.23-27(2005).

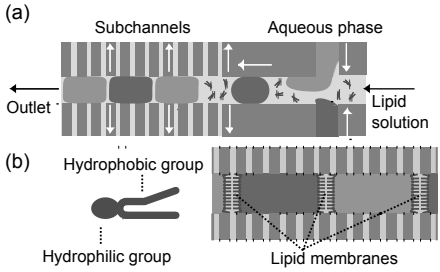

Figure 1. A schematic showing the formation of arrayed planar lipid membranes by the accumulation of uniform aqueous plugs in a microchannel.

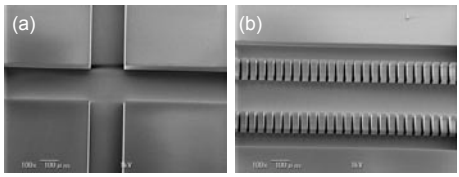

Figure 2. SEM images of (a) a cross-shaped groove and (b) pseudo-porous sidewalls.

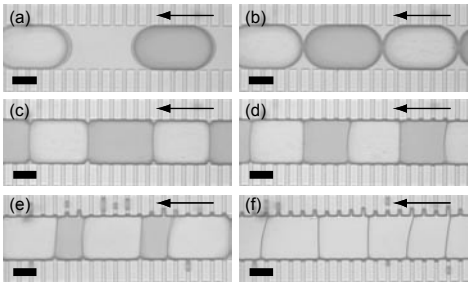

Figure 3. The formation of arrayed PLMs by the selective withdrawal of the organic phase. Aqueous plugs from one of the two inlets are stained by blue ink. The infusion flow rate of the organic phase is 0.2 mL h^{-1}, while the aqueous phase flowing from the two inlets flows at a rate of 0.01 mL h^{-1}. The withdrawal flow rates into the subchannels are (a) 0 mL h^{-1}, (b) 0.2 mL h^{-1}, (c) 0.22 mL h^{-1}, (d) 0.23 mL h^{-1}, (e) 0.25 mL h^{-1}, and (f) 0.28 mL h^{-1}. The scale bars are 100 μm.

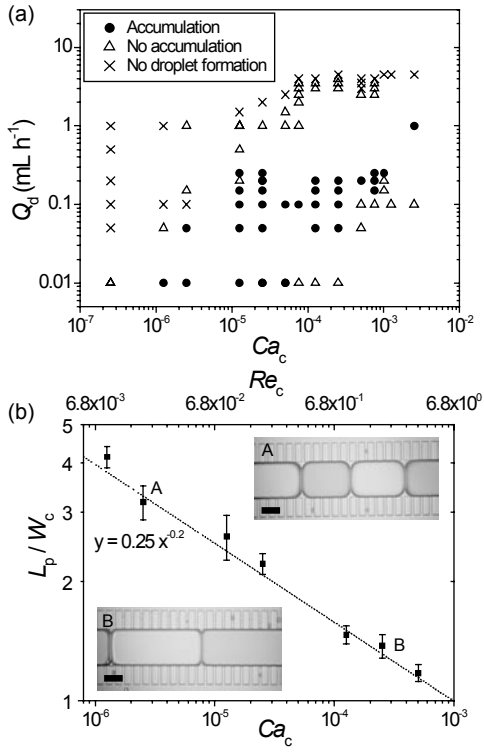

Figure 4. (a) A flow diagram showing where accumulation of aqueous plugs occurs successfully. The X-axis represents the capillary number of the organic stream ($Ca_c = 2\eta_c U_{c,avg} \gamma_{l,l}^{-1}$), where η_c = 0.59 mPa s, $U_{c,avg}$ is the average flow speed. The Y-axis denotes the aqueous phase flow rates (Q_d). (b) Aqueous plug length versus the condition of the organic stream. The plug length (L_p) is scaled by the channel width (W_c, 200 μm). The scale bars are 100 μm.

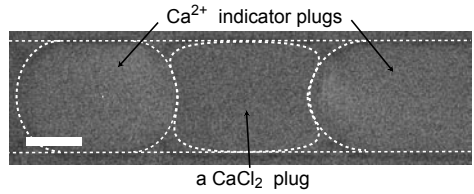

Figure 5. Photomicrograph of the emission of fluorescent Ca^{2+} indicator in the plugs. The scale bar is 100 μm.

SINGLE CELL ENCAPSULATION AND SORTING IN MICRODROPLETS USING PASSIVE HYDRODYNAMIC EFFECTS.

Max Chabert and Jean-Louis Viovy.
Institut Curie. UMR CNRS 168. 75005 Paris. France.

ABSTRACT

We present a method for performing single cell encapsulation in microdroplets and sorting these drops using only passive hydrodynamic effects. Our system combines a cell-triggered Rayleigh-Taylor instability for encapsulation, with droplets shear-induced migration and steric interactions for sorting. We demonstrate encapsulation of 70 to 80% of the injected cells with a 99% resulting droplets purity.

Keywords: cells, encapsulation, microdroplets, flow-focusing.

1. INTRODUCTION

The encapsulation of cells in microdroplets is a powerful tool for automated, high-throughput cell assays. Important applications involve in-vitro directed evolution and screening protocols for drug discovery. Previous attempts to realize microfluidic single cell encapsulation used a complex active process [1], or did not statistically provide the insurance of having only one cell per drop [2]. Here, we present a new strategy to create a population of droplets all containing one and only one cell, using entirely passive hydrodynamics.

2. EXPERIMENTAL

The system and its operating diagram are plotted in figure 1. A concentrated cell suspension (10^8 cells/mL, flow rate Q_c) exits from a central channel and is focused by two asymmetric mineral oil streams (flow rates $Q_{o2} = 0.5Q_{o1}$, viscosity 120 mPa.s). Depending on flow conditions, the resulting jet can either be totally unstable, either break into droplets in the central focusing channel, or remain stable throughout the focusing region. We work in domains in which the jet breaks in the focusing region, and select flow conditions so that the natural diameter Φ_N of droplets in the absence of cells ("negative" droplets) is smaller than the cell diameter Φ_C (figure 1A, domains 2 and 3). The passage of cells in the focusing zone disrupts the neck of the jet and results in the nucleation of a big "positive" drop around each cell (figure 1C, top). The extensional flow in the jet tends to separate closely spaced cells from each other. The difference in size between positive and negative droplets is then used to separate them, due to the asymmetry in the oil flow rates. Because of shear induced migration in the viscous Poiseuille flow of oil, big positive drops are driven closer to the center of the focusing channel than negative ones. In the sorting chamber, this effect is supplemented by enhanced self-diffusivity taking place in concentrated suspensions: droplets interact and are driven into streamlines more widely separated than original ones. In domain 3 of figure 1A, negative drops reach both outlets. In domain 2, no empty drop enters the top outlet, but big positive drops come out "above" small ones, and are pushed towards the top outlet of the chamber (figure 1C bottom) by interaction with negative drops.

978-0-9798064-0-7/μTAS2007/$20©2007CBMS

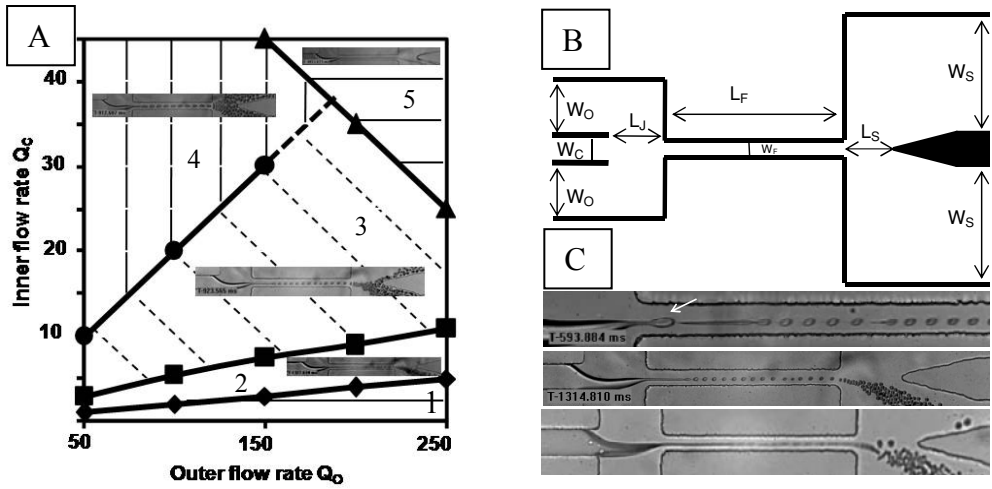

Figure 1. A. Experimental phase diagram for droplet formation in the absence of cells as a function of oil and cell culture medium flow rates Q_{o1} and Q_c. For $Q_{o1} < 50$ µL/h, the device functions in dripping mode (not depicted). Above the (▲) line (domain 5), the cell medium stream is stable across the whole system, and correct sorting of positive droplets is not possible. Domain 1 corresponds to unstable jetting. In the remainder of the diagram, the jet breaks at a stable position in the strait. The lines separating domains 1, 2, 3 and 4 correspond to a fixed droplet diameter: (♦) $\Phi_N = 7$ µm ± 10%; (■) $\Phi_N = 10$ µm ± 10%; (●) $\Phi_N = 17$ µm ± 10%. In domain 2 all negative droplets exit in the bottom channel. B. The system comprises two chambers separated by a focusing channel, and is microfabricated in one step by soft-lithography (uniform height of 30 µm). The first chamber involves a classical flow-focusing geometry, while the second chamber contains a Y-shaped passive droplet sorter. Inferior and superior regions of this picture are denoted as bottom and top in the text. C. Illustration of system operation. Top: perturbation of the focusing neck by a cell. Middle: functioning of the device at $Q_{o1} = 100$ µL/h, $Q_c = 5$ µL/h, with only negative droplets going in the bottom outlet. Bottom: sorting of positive drops at $Q_{o1} = 150$ µL/h, $Q_c = 7$ µL/h.

3. RESULTS.

Statistical results for cell sorting are presented in table 1. By choosing optimal flow conditions (grey line, Table 1), we retrieve around 80 % of the cell-containing droplets with an average cell encapsulation rate of 20 cells/s, less than 1% negative droplets among positive ones and less than 2% multiple cells per drop. Indeed, multiple-cells encapsulation is due to cell-cell adhesion prior to sorting, i.e. to an intrinsic biological property. When non-adhering cells enter the jet in a concentrated manner, they are separated and encapsulated as one single cell per drop. Thus, we were able to encapsulate and sort up to 160 cells per second from a highly-concentrated cell suspension, with a positive drops recovery rate around 72% and no increase in multiple cells encapsulation. The slight decrease in recovery rate is linked to the interaction between closely spaced positive droplets in the post-focusing widening. More generally, the loss of positive droplets is mainly due to the variability in size of cells in a population. The size of positive droplets is proportional to that of the cells they

contain: smaller positive drops are harder to sort correctly because they flow on lower streamlines in the strait.
From the biological point of view, although cell viability still has to be investigated in a more detailed manner, screening with Trypan-Blue demonstrated that the cell membrane is still intact after encapsulation.

Table 1: statistical results for the cell sorting system (Jurkat T-cells, 10^4 cells/µL). Grey line corresponds to an optimal efficiency. Encapsulation of multiple cells per drop is statistical and does not depend on the flow rates used.

Oil flow rate (µL/h)	Cells flow rate (µL/h)	multiple cells per drop (% of the total cell number)	positive drops sorted (%)	Number of cells counted	Empty drops among positive drops (%)
50	3	2.4%	50.0%	172	<1%
50	**3.5**	2.2%	69.4%	187	<1%
50	4	7.4%	70.2%	766	64.9%
100	2	8.8%	36.0%	341	<1%
100	3	2,0%	45.7%	310	<1%
100	4	3.1%	59.7%	256	<1%
100	5	4.6%	61.2%	389	<1%
100	**6**	4.2%	74.0%	802	3.9%
150	3	7.5%	36.7%	106	<1%
150	4	3.6%	49.1%	289	<1%
150	5	2.2%	59.2%	377	<1%
150	6	5.8%	70.5%	530	<1%
150	**7**	1.4%	79.2%	936	<1%
150	8	7.5%	77.4%	1311	5.7%
200	6	4.2%	16,0%	379	<1%
200	7	5.4%	29.4%	286	<1%
200	8	4.9%	38.8%	444	<1%
200	9	7.4%	51.5%	607	<1%

4. CONCLUSIONS

We developed a simple and high-throughput cell encapsulation device with numerous potential applications. The positive droplets can be subsequently coalesced (see e.g. [3]) with other droplets containing reagents of interest, for multi-steps assays. Due to the small volume of the droplets generated, it should be particularly powerful for single-cell molecular biology applications such as PCR [4], where dilution is critical.

ACKNOWLEDGEMENTS

M.C. acknowledges a grant from French DGA. This work was supported by the EU FP6 Nanosciences programme (NABIS project).

REFERENCES

[1] He, M. *et al.* Selective Encapsulation of single cells and subcellular organelles into picoliter- and femtoliter-volume droplets. *Anal. Chem.* **77**, 1539-1544 (2005).
[2] Huebner, A. *et al.*, Quantitative detection of protein expression in single cells using droplets microfluidics. *Chem.comm.* **12**, 1218-1220 (2007).
[3] Chabert, M., Dorfman, K. D. & Viovy, J.-L. Droplet fusion by alternating current (AC) field electrocoalescence in microchannels. *Electrophoresis* **26**, 3706-3715 (2005).
[4] Chabert, M., Dorfman, K. D., deCremoux, P., Roeraade, J. & Viovy, J.-L. Automated Microdroplet Platform for Sample Manipulation and Polymerase Chain Reaction. *Anal. Chem.* **78**, 7722-7728 (2006).

MICROCHIP TITRATION BY UTILIZIGN LAPLACE VALVE

Akihide Hibara[1,2,3] , Mari Nonogi[1] and Takehiko Kitamori[1,2,3]

[1] *Department of Applied Chemistry, The University of Tokyo, JAPAN*

[2] *Kanagawa Academy of Science and Technology, JAPAN*

[3] *Japan Science and Technology Agency, JAPAN*

ABSTRACT

Quantitative sample injection, preparation of titlate droplets and mixing of sample and titlate were integrated into a glass microchip. In these operations, Laplace pressures were controlled by using surface modification. Acid-base titlation in the microchip was demonstrated.

Keywords: surface modification, Laplace pressure, batch process, titlation

1. INTRODUCTION

By utilizing microchannel networks, our group has demonstrated effectiveness of continuous flow chemical processing. When versatile operation method for batch process in microchannels is available, applicability of the microchip operation will be extended very much. In previous report [1], we have demonstrated a gas-liquid flow operation utilizing selective modification of microchannel wall. The hydrophilic / hydrophobic selective modification of single microchannel can be used as a stop valve, which is named as Laplace valve [2]. In this report, a microchip titlation system utilizing Laplace valve is demonstrated.

2. THEORY

Figure 1 shows principle of Laplace valve. When aqueous solution is introduced to a microchannel having hydrophilic surface, the solution is introduced by capillary action. At the boundary of hydrophilic / hydrophobic surfaces, the solution stopped. Even when dynamic pressure is applied to the solution, the interface deforms to generate Laplace pressure, which is balanced with the dynamic pressure. Laplace pressure is described with Young-Laplace equation, and the higher limit of Laplace pressure is governed by advancing contact angle of water on hydrophobic surface [3].

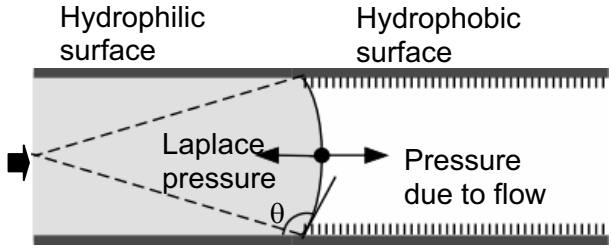

Figure 1. Principle of Laplace valve

978-0-9798064-0-7/μTAS2007/$20©2007CBMS

3. RESULTS AND DISCUSSION

Figure 2 illustrates conception of microchip titlation system. As a measuring pipette in ordinary operation, a sample measuring method is used (Figure 2, upper left). The sample solution is introduced from lower left inlet and fills the microchannel. Excess solution in the U-shape channel is purged to cut the sample solution in the straight part as illustrated in Figure 2. As a bullet, titlant solution measuring part is proposed (Figure 2, upper center). By controlling pressures of titrant solution and air, constant-volume droplets are generated. As a beaker, a chamber which contacts with shallow channel was introduced. After the sample solution is introduced to the chamber by air flow, the solution stops because air flows the shallow channel. By utilizing the same principle, sequential introduction of the titlant droplets.

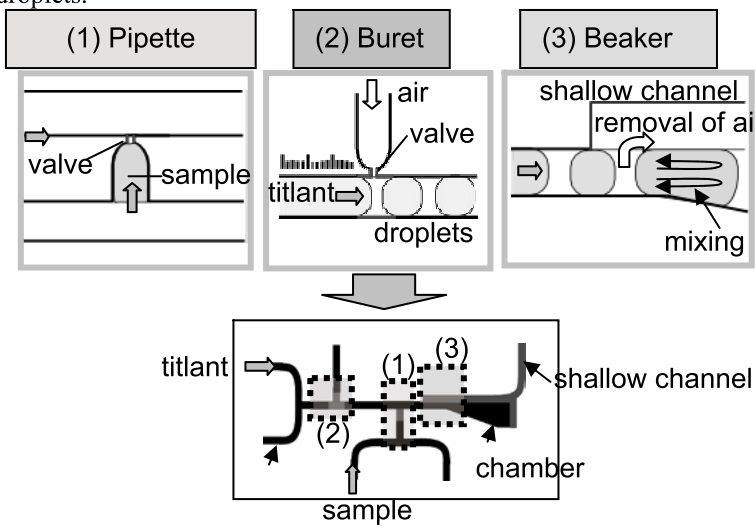

Figure 2 Integration of operations of titlation.

Figure 3a shows repeatability of the pipette part. Sufficient repeatability was confirmed. Figure 3b shows a fluorescent micrograph of the titlant droplets generated by the bullet part. Repetitive and constant-volume droplet formation was confirmed. Figure 3c shows mixing operation at the beaker part. As expected, air flows the shallow channel and the sample and titlant solutions were mixed.

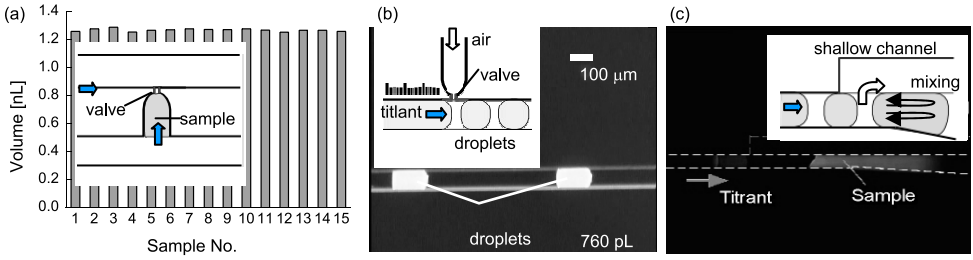

Figure 3 (a) Repeatability of sample injection. (b) Repetitive formation of droplets of titrant. (c) Purge of air between sample and titlant, which corresponds to mixing operation.

Figure 4 shows a result of acid / base titlation of Na_2HPO_4 by HCl. In the bulk experiment, the solutions were mixed in ordinary labware and introduced to the chamber. As shown in the figure, we found good correlation between the microchip and bulk titlations. We would extend this method to chelate and redox titlation.

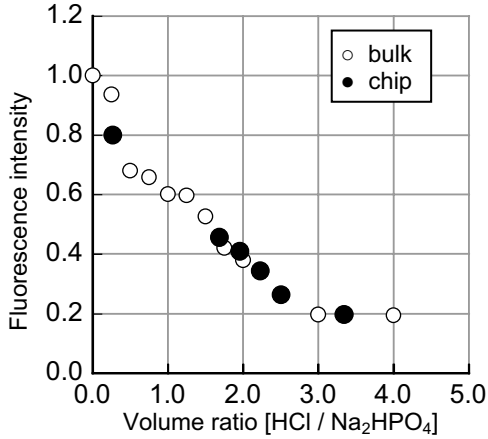

Figure 4 Titlations of Na_2HPO_4 by using orginary labware and by the microchip

REFERENCES

[1] A. Hibara, S. Iwayama, S. Matsuoka, M. Ueno, Y. Kikutani, M. Tokeshi, T. Kitamori, *Surface modification method of microchannels for gas-liquid two phase flow in microchips,* Analytical Chemistry, 76, 943-947 (2005).

[2] G. Takei, M. Nonogi, A. Hibara, T. Kitamori, H.-B. Kim, *Tuning microchannel wettability and fabrication of multiple-step Laplace valves,* Lab on a Chip, 7(5), 596-602 (2007).

[3] A. Aota, A. Hibara, T. Kitamori, *Pressure Balance at the Liquid-Liquid Interface in Micro Counter-Current Flows in Microchips,* Analytical Chemistry, 79(10), 3919-3924 (2007).

MICROFLUIDIC ORGANIZATION OF LIPID TUBULE BIOREACTORS

Jonathan West, Ulrich Marggraf, Andreas Manz, Joachim Franzke and Petra S. Dittrich

ISAS – Institute for Analytical Sciences, Bunsen-Kirchhoff-Str. 11, D-44319 Dortmund, Germany.

ABSTRACT

Micro and nanoscale biological structures have exquisite morphologies and associated functions. As a formative step towards emulating these bioreactors we have developed microfluidic methods for the controlled formation of lipid tubule structures.

Keywords: Microfluidics, lipid tubule, microporous membrane, extrusion

1. INTRODUCTION

Life is highly compartmentalized across length scales spanning organs, tissues, cells and organelles. Miniature cellular compartments with exquisite morphologies are bound by lipid bilayer membranes and at micro and nanometer scales mass and energy transfer phenomena are exploited for a vast array of molecular processing functions. By using microtechnologies we are now in a position to fabricate microscale biomimetic structures, and further harness life's biochemical processing capabilities.

The application of point loads has been used for the forced shape transition of lipid vesicles into nanofluidic conduits and networks [1]. This capability has been used to great advantage to create a new class of life-like conduits for enzyme reactions [2] and electrophoretic transport [3]. These remarkable systems are constructed by directly writing features onto a surface in a serial manner. It would also be desirable to develop a method for the parallel production of microscale as well as nanoscale lipid aquaducts.

Recently, we reported the use of a 200 nm thick silicon nitride membrane with multiple micropores for the controlled extrusion of lipid tubules of extraordinary length (millimeters) with diameters matching the 3.5 μm micropore diameter [4]. To further enable the translation of designs into reproducible lipid structures there is a pressing need to better understand the mechanics of tubule formation. In this paper we describe the use of microfluidic arrangements to explore methods for the controlled formation of micro and nanoscale lipid tubule structures.

2. EXPERIMENTAL

Silicon devices comprising a lipid reservoir above a membrane with micropores (figure 1a and 1b) were fabricated and assembled with a basal poly(dimethylsiloxane) (PDMS) microfluidic channel as previously described [4]. Tubule extrusion was achieved by first wetting the lipid reservoir followed by vacuum actuation of aqueous flows in the microchannel. Alternative embodiments used syringe driven flows for tube swelling and elongation: One system comprised a lipid film sandwiched between a top PDMS plate and a porous polymeric membrane. The membrane was supported above a microfluidic channel

978-0-9798064-0-7/μTAS2007/$20©2007CBMS

in a bottom PDMS plate. The other system comprised a PDMS channel that first diverges, bypassing a lipid reservoir, and then converges into a central channel. A second PDMS layer with a linear microchannel is positioned orthogonal to the lipid reservoir for lipid wetting and joins the central channel for lipid tubule tweezing (figure 2).

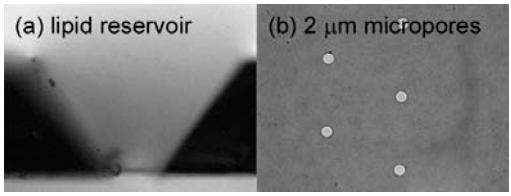

Figure 1. Cross section of the silicon device lipid reservoir (a), and an array of micropores in a Si_3N_4 membrane (b).

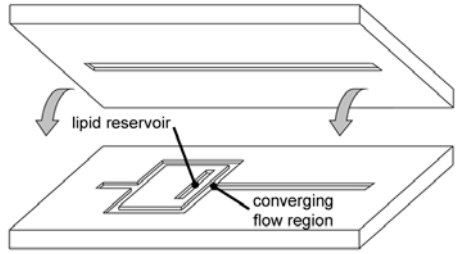

Figure 2. Lipid tubule tweezer schematic.

3. RESULTS AND DISCUSSION

Microtubules formed by vacuum driven extrusion were highly uniform with diameters matching the silicon micropore diameters (1, 2, 3.5 and 5 μm). These tubules are compared with tubules produced from the polymer membrane with a syringe driven flow (figure 3). With the polymer membrane, giant (~10 μm) tubules or bud structures first swell from the pores before elongating with the flow with 1-2 μm diameter tubule stems.



Figure 3. Microtubules extruded through micropores of equivalent diameter using a vacuum driven flow (a). Elongation of these microtubules along the PDMS microchannel (b). Hydrodynamic extrusion of 1-2 μm diameter tubules using a 1:1 aspect ratio porous (θ=10 μm) polycarbonate membrane (c).

The separation of swelling and elongation processes can also be achieved vertically without a membrane. Here giant tubules swell from a lipid reservoir and are slowly transported near the 'no-slip' boundary before encountering secondary flows that support the tubules within the vertical centre of the Poiseuille flow for high velocity extrusion. Using this system we have observed classical elongation of microtubules from bud and giant tubule structures at low velocities (figure 4a). At higher velocities the giant tubule lipid film experiences a velocity jump and is tweezed into a nanoscale tubule (figure 4b). As the velocity is reduced, a shape transition occurs and is followed by elongation of constant micron diameter tubules, with material depletion from the giant tubule (figure 5).

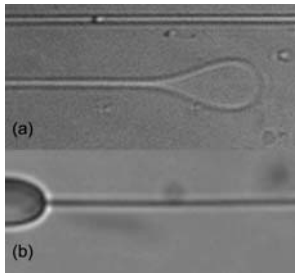

Figure 4. A 10 μm diameter lipid bud exhibiting early elongation with the flow to produce a 3 μm diameter stem (a). High velocity (>2 mm s^{-1}) tweezing of a <1 μm tubule (b).

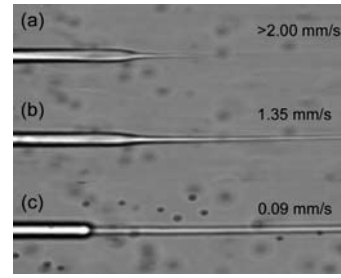

Figure 5. Images taken during velocity relaxation; pulling nanoscale tubules that taper from the main body (a); shape transition (b); and constant 3.5 μm diameter tubules (c).

4. CONCLUSIONS

In conclusion we have used three different microfluidic arrangements for the separation of tubule swelling prior to hydrodynamic extrusion. Collectively these microfluidic systems offer new tubule engineering capabilities and could be used for the creation of organelle and cell mimics with controlled morphologies. This work forms the basis of our ambition to develop methods for the guided organization of self-assembling lipid bioreactor architectures. More sophisticated life-like tubule systems could be studded with membrane proteins or internalized with proteins and used to probe deeper into biochemical processes, and ultimately used to develop novel chemical manipulation schemes.

ACKNOWLDEGMENTS

The authors would like to thank Martin Heule and Philippe Renaud (Microsystems Laboratory, EPFL, Switzerland) for fabrication of the first generation silicon devices. We are also grateful for financial support from the European Community's 6th Framework Programme (*CellPROM*, contract no. NMP4-CT-2004-500039).

REFERENCES

[1] E. Evans, H. Bowman, A. Leung, D. Needham and D. Tirrell, "Biomembrane templates for nanoscale conduits and networks", Science, **273**, 933 (1996).

[2] D. T. Chui, C. F. Wilson, A. Karlsson, A. Danielsson, A. Lundqvist, A. Strömberg, F. Ryttsén, M. Davidson, S. Nordholm, O. Orwar and R. N. Zare, "Manipulating the biochemical nano-environment around single molecules contained within vesicles", Chemical Physics, **247**, 133 (1999).

[3] M. Tokarz, B. Åkerman, J.-F. Joanny, P. Dommersnes and O. Orwar, "Single-file electrophoretic transport and counting of individual DNA molecules in surfactant nanotubes", Proceedings of the National Academy of Sciences USA, **102**, 9127 (2005).

[4] P. S. Dittrich, M. Heule, P. Renaud and A. Manz, "On-chip extrusion of lipid vesicles and tubes through microsized apertures", Lab on a Chip, **6**, 488 (2006).

HIGHLY SENSITIVE MEASUREMENT OF PNA-DNA HYBRIDIZATION USING OXIDE-FREE SILICON NANOWIRE SENSORS

Guo-Jun Zhang, Ajay Agarwal, Kavitha D. Buddharaju, Navab Singh and Zhiqiang Gao

Institute of Microelectronics, 11 Science Park Road, Singapore 117685

ABSTRACT

Complementary metal oxide semiconductor (CMOS)-compatible oxide-free silicon nanowire (SiNW) sensors for detection of single-stranded oligonucleotides are presented. The SiNW sensors without native oxide show higher detection sensitivity compared to other SiNW ones. This work demonstrates how to improve SiNW performance for sensing DNA by altering surface functionalization of SiNW.

Keywords: SiNW, biosensing, surface chemistry, PNA, DNA, hybridization

1. INTRODUCTION

SiNWs have been proven to be highly sensitive and selective sensors for label-free detection of metal ions [1], nucleic acids [2], and proteins [3]. The native silicon oxide coating on the SiNW surface is an effective layer in most cases which can usually be functionalized with bioaffinitive moiety. However, this oxide coating can lower and limit sensor performance because it acts as a dielectric layer and induces trap states at the SiO_2/Si interface. Recently, methyl functionalized SiNWs have been demonstrated that they had improved field effect transistor characteristics [4]. More recently, real-time measurements of DNA hybridization without the native oxide layer exhibited a significantly enhanced sensitivity, over 2 orders of magnitude, in which an electrostatic method was employed for the immobilization of DNA capture probes on the surface of the SiNW, and only DNA-DNA hybridization was tested [5]. In this presentation, a covalent binding protocol is developed to immobilize peptide nucleic acid (PNA) on the CMOS-compatible SiNW surface, and electrical detection is carried out after complementary target DNA is hybridized to the PNA functionalized SiNWs. Since PNA is neutral, PNA-DNA hybridization enables SiNW sensors to improve detection sensitivity greatly. This approach allows for integration of SiNW sensors and benefits SiNW devices for diagnostic applications.

2. EXPERIMENTAL

The integrated SiNW sensors were fabricated by self-limiting oxidation process of silicon beams patterned using conventional photolithography, as described previously [6]. As shown in Scheme 1, a procedure reported elsewhere was used to functionalize hydrogen-passivated SiNWs with 10-*N*-Boc-Amino-dec-1-ene [7] Removal of the *t*-BOC protected group leaves amine moieties on the SiNW surface. To covalently immobilize amine-modified PNA on the SiNWs, a bifunctional linker, glutaraldehyde, was employed to bind its one end to the SiNW amines, and leave the other end to bind the amine-modified PNA. The PNA-functionalized SiNWs were hybridized with various concentrations of target DNAs. Electrical measurements were finally performed by monitoring the resistance change of the SiNWs before and after hybridization.

978-0-9798064-0-7/μTAS2007/$20©2007CBMS

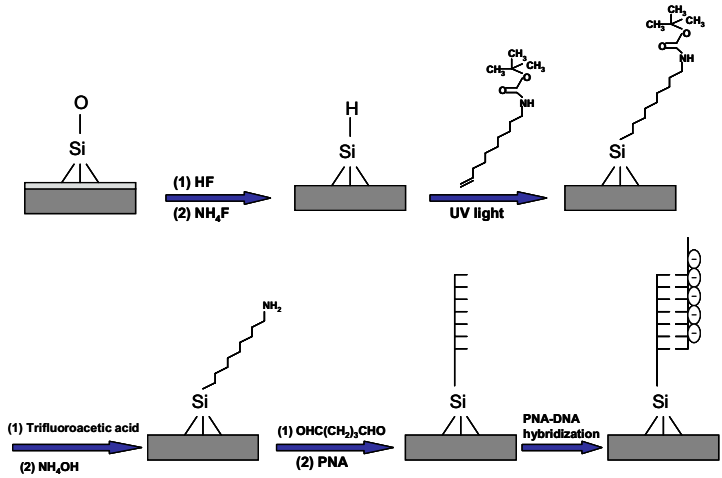

Scheme 1. Schematic illustration of PNA immobilization and PNA-DNA hybridization on SiNW surface.

3. RESULTS AND DISCUSSION

Amine-modified PNA is selectively and covalently attached onto the SiNW surface via photochemical hydrosilation chemistry [7]. Target DNA is introduced to the SiNW via hybridization. To demonstrate the specificity and selectivity, complementary DNA was applied to the SiNWs immobilized with PNA. The SiNWs were then characterized by epi-fluorescence microscope (Figure 1). Strong fluorescent signals on the SiNWs were obtained and the bright arrays of SiNWs were clearly visible. The dark regions outside the SiNW arrays correspond to the oxide surface. This fluorescent imaging indicates that the complementary target DNA was hybridized to the immobilized PNA as expected and confirms the specificity of binding between the target and PNA. Notably, the PNA immobilization and PNA-DNA hybridization are extremely selective and the interactions of PNA-DNA only occur on the SiNWs rather than on the oxide layer.

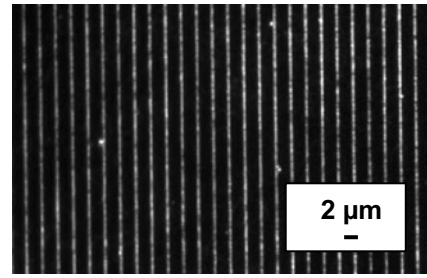

Figure 1. A fluorescent image of Cy 3-labeled complementary DNA hybridized to the immobilized PNA. SiNW array diameter: 30 nm; Pitch: 2 µm.

The selective functionalization of SiNWs is critical to improve sensitivity due to avoidance of binding competition. DNA detection was further performed by monitoring the resistance change of the SiNWs before and after different concentration of the target DNA was hybridized to PNA. As shown in Figure 2, while 1 nM complementary DNA was treated with the PNA functionalized SiNWs, an obvious resistance change (~51%) was observed. Whereas a ~6% resistance change was obtained when 10 fM DNA was employed. Further dilution of DNA concentrations does not result in any change, pointing to a detection limit of our SiNW sensors down to 10 fM, which are 3 orders of magnitude lower than the reported SiNW sensors [5].

The specificity of the SiNW sensors for the detection of target DNA was further evaluated by hybridizing fully complementary, one-base mismatched, and non-

complementary DNAs, respectively, to the PNA-functionalized SiNWs. As above-mentioned, 1 nM fully complementary target DNA can lead to a ~51% resistance change. As seen in Figure 3, if the fully complementary target was replaced by a non-complementary one, neglectable resistance change could be obtained, indicating that no duplex forms between a pair of non-complementary sequences. Furthermore, the SiNW sensors allow obvious discrimination against mismatched sequence. Merely ~8% resistance change was visible while one-base mismatched target was employed. The results suggest that the SiNW sensors are applicable for SNPs detection, allowing perfect discrimination between fully complementary and mismatched sequences.

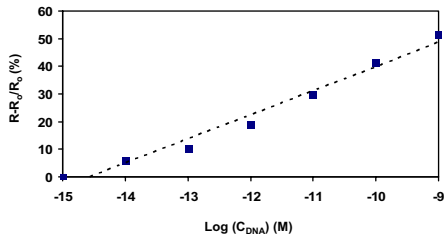

Figure 2. Response of the PNA-functionalized SiNWs to target DNA of different concentrations.

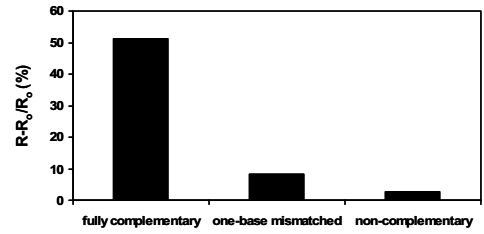

Figure 3. Specificity of the SiNW sensors for the detection of target DNA.

4. CONCLUSIONS

In conclusion, for the first time we present oxide-free SiNW sensors which exhibit a higher sensitivity for the detection of PNA-DNA hybridization compared to other SiNW sensors. The selective functionalization of SiNWs avoids PNA immobilization and PNA-DNA hybridization on the entire surface. The PNA-functionalized SiNWs are therefore more sensitive than the DNA-functionalized ones. In addition, covalent binding enables more PNA to be attached onto the SiNW surface, leading to higher hybridization efficiency. This work investigates DNA sensing behaviors by using the oxide-free SiNWs, and further enables the development of the integrated SiNW sensors.

References

1. G.-J. Zhang, A. Agarwal, K. D. Buddharaju, N. Singh and Z.-Q. Gao, *Highly sensitive sensors for alkali metal ions based on complementary-metal-oxide-semiconductor-compatible silicon nanowires*, Appl. Phys. Lett. 2007, 90, 233903.
2. J.-I. Hahm and C. M. Lieber, *Direct ultrasensitive electrical detection of DNA and DNA sequence variations using nanowire nanosensors*, Nano Lett. 2004, 4, 51.
3. G. Zheng, F. Patolsky, Y. Cui, W. U. Wang and C. M. Lieber, *Multiplexed electrical detection of cancer markers with nanowire sensor arrays*, Nat. Biotechnol. 2005, 23, 1294.
4. H. Haick, P. T. Hurley, A. I. Hochbaum, P. Yang and N. S. Lewis, *Electrical characteristics and chemical stability of non-oxidized, methyl-terminated silicon nanowires*, J. Am. Chem. Soc. 2006, 128, 8990.
5. Y. L. Bunimovich, Y. S. Shin, W.-S. Yeo, M. Amori, G. Kwong and J. R. Heath, *Quantitative real-time measurements of DNA hybridization with alkylated nonoxidized silicon nanowires in electrolyte solution*, J. Am. Chem. Soc. 2006, 128, 16323.
6. Z.-Q. Gao, A. Agarwal, A. D. Trigg, N. Singh, C. Fang, C.-H. Tung, Y. Fan, K. D. Buddharaju, J.-M. Kong, *Silicon nanowire arrays for label-free detection of DNA*, *Anal. Chem*. 2007, 79, 3291.
7. T. Strother, R. J. Hamers and L. M. Smith, *Covalent attachment of oligodeoxyribonucleotides to amine-modified Si (001) surfaces*, Nucl. Acids Res. 2000, **28**, 3535.

PROBING CYTOSKELETON DYNAMICS WITH MULTI-DIRECTIONAL TOPOGRAPHICAL GUIDANCE

Junyu Mai[1,2], Cheng Sun[1], Song Li[2], and Xiang Zhang[1]

[1]NSF Nanoscale Science and Engineering Center, [2]UCSF/UC Berkeley Joint Graduate Group in Bioengineering, University of California, Berkeley, USA

ABSTRACT

We used microfabricated topographical guidance to manipulate the organization of a single cell cytoskeleton, and to probe a cell from multiple directions to study the molecular mechanisms regulating the coordination process of cell migration.

Keywords: cell migration, contact guidance, single cell manipulation, surface topography

1. INTRODUCTION

Cell migration plays a central role in a wide range of biological processes [1]. Conventional methods to study cell migration are often limited to stimulating a cell along a single direction or at a single location [2-8]. Previous research indicates that a cell can sense and react to micrometer or even nanometer scale substrate topography [9,10]. Here we use geometrically patterned topographical features to stimulate a cell from multiple directions, and to study coordination of actin polymerization during cell migration.

2. THEORY

We use a grid patterned topographically structured surface (TopoSurface) to apply stimulations in the form of contact guidance to a cell from multiple directions (Figure 1). We ask how local reactions at different parts of a cell communicate with each other, and how a cell globally regulates these local activities.

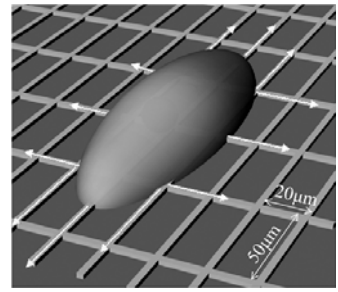

Figure 1. Schematic of applying multi-directional contact guidance to a single cell on TopoSurface.

3. EXPERIMENTAL

Fabrication of TopoSurfaces We fabricated TopoSurfaces from PDMS using standard softlithography techniques [11]. Before cell culture, the TopoSurface was incubated with 20 μg/ml fibronectin.

Cell culture and imaging Primary Bovine Aortic Smooth Muscle cells (BASM) were cultured in DMEM plus 10% Fetal Bovine Serum at 37°C and 5% CO_2. Inhibitors were added to cell suspensions before plating. For fluorescent imaging, cells were fixed and stained with Rhodamine-Phalloidin and DAPI.

Time-lapse fluorescent microscopy Cells were transfected with Green Fluorescent Protein (GFP) plasmid using Lipofectamine 2000 (Invitrogen). Transfected cells were cultured on TopoSurface and maintained at 37°C in CO_2 Independent Media on the fluorescent microscope stage.

978-0-9798064-0-7/μTAS2007/$20©2007CBMS

4. RESULTS AND DISCUSSION

Accurate and flexible cytoskeleton response to non-straight topographical guidance

To test the responsiveness of the cells to non-straight topographical cues, we cultured cells on substrates with concentric ring pattern. Within 2 hours cells aligned along the rings with diameters ranging from 100 μm to 2 mm (Figure 2). Cells could also flexibly reorganize their actin cytoskeleton to follow the zigzagging guiding ridges (Figure 3).

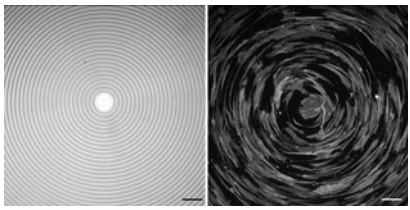

Figure 2. Circular alignment of BASM on concentric ring patterned substrate. Scale bars, 50 μm.

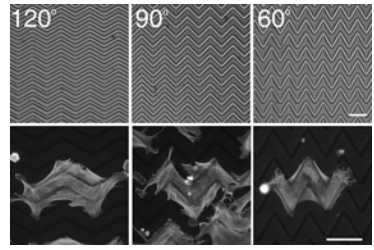

Figure 3. Actin skeleton of a single cell reorganized on zigzagging patterned TopoSurfaces. Scale bars, 20 μm.

Distinct cell alignment pattern under multi-directional guidance on TopoSurfaces

We cultured the cells on grid-patterned surfaces to see how a cell reacts when facing guidance leading to different directions. We fabricated substrates with 20μmx20μm square grids, representing equal guidance in multiple directions, and 20μmx9μm and 20μmx50μm rectangular grids, representing anisotropic guiding cues. On square grids, cells aligned randomly as on a flat surface. On rectangular grids, cells preferred to align in the direction of the longer side of the grid (Figure 4). Time-lapse recording of GFP-transfected BASM showed that during migration, cells protruded along the ridges both at the front and on the side of the cell body. Extensions along side ridges were retracted in about 100 minutes, whereas protrusions along the direction of denser and longer ridges were strengthened, resulting in a persistent polarity and migration direction.

Inhibition of myosin II contractility caused multi-directional protrusions on grid patterned TopoSurface

To investigate how force generation inside the cell is involved in the regulation of actin polymerization, we treated cells with 50μM Blebbistatin, a specific inhibitor of myosin II contractility. Two hours after plating, all cells extended multiple protrusions along the guiding ridges (Figure. 5). They freely turned or branched when reaching a crossing ridge. And the main cell bodies did not have consistent, grid pattern dependent orientations as the untreated cells did. To test the involvement of possible upper stream regulators, we treated cells with 20 μM Y27632, a specific Rho Kinase (ROCK) inhibitor, and 20 μM ML-7, an inhibitor to both Myosin Light Chain Kinase (MLCK) and Zipper Interaction Protein (ZIP) kinase, before plating the cells on grid-patterned substrates. Cells treated with ML-7 showed no impairment in establishing correct orientations on the grid. Cells treated with Y27632 behaved very similarly as those treated with Blebbistatin.

These results demonstrate that when facing attractions from multiple directions, without actomyosin contractility, a cell cannot down-regulate actin polymerization in minor directions. ROCK is the possible upstream regulator involved in the coordination process.

5. CONCLUSIONS

For the study of cytoskeleton dynamics under multi-directional stimulations, a grid patterned TopoSurface can apply visible guidance cues to a cell from different directions without overlapping and allow long-term observations. When used in combination with other molecular manipulation and imaging tools, this platform will reveal more details of the signal transduction network involved in cell migration.

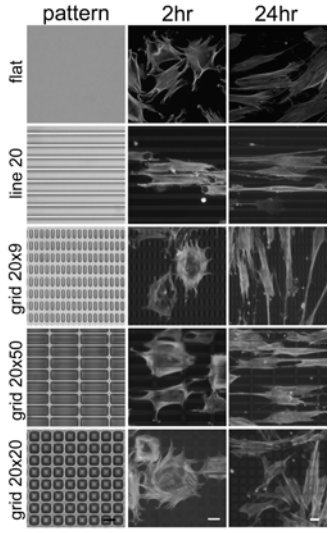

Figure 4. Distinctive cell alignment and migration pattern on different grid-patterned substrates. Scale bar, 20 μm.

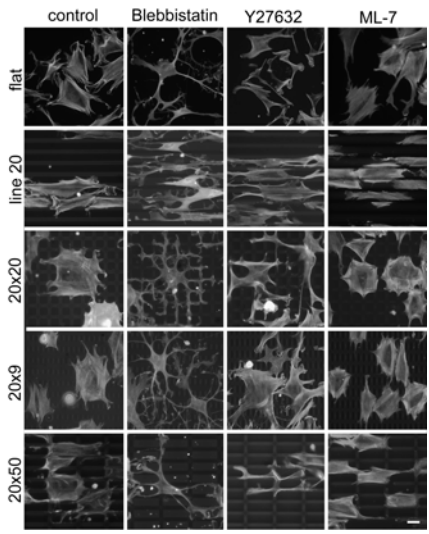

Figure 5. Coordination of actin cytoskeleton on grid surface during cell spreading is inhibited by Blebbistatin and Y27632, but not ML-7. Scale bar, 20 μm.

ACKNOWLEDGEMENTS

This work was supported by the Center for Cell Mimetic Space Exploration and NSF Nanoscale Science and Engineering Center. J. M. is supported by NSF-IGERT Fellowship.

REFERENCES

[1] A. J. Ridley, M. A. Schwartz, K. Burridge et al., Science 302 (5651), 1704 (2003)
[2] P. D. Ponath, J. Wang, H. Heath, Methods Mol. Biol. **138**, 113–20, (2000).
[3] D. Zicha, G. Dunn, G, Jones, *Methods Mol. Biol* **75,** 449–57 (1997)
[4] N. L. Jeon, H. Baskaran, S. K. W. Dertinger et al., Nature Biotechnology 20 (8), 826 (2002).
[5] D. Choquet, D. P. Felsenfeld, and M. P. Sheetz, Cell 88 (1), 39 (1997).
[6] A. R. Bausch, W. Moller, and E. Sackmann, Biophysical Journal 76 (1), 573 (1999).
[7] Y. X. Wang, E. L. Botvinick, Y. H. Zhao et al., Nature 434 (7036), 1040 (2005).
[8] M. Prass, K. Jacobson, A. Mogilner et al., Journal of Cell Biology 174 (6), 767 (2006).
[9] R. G. Flemming, C. J. Murphy, G. A. Abrams et al., Biomaterials 20 (6), 573 (1999)
[10] V. Vogel and M. Sheetz, Nature Reviews Molecular Cell Biology 7 (4), 265 (2006)
[11] G. M. Whitesides, E. Ostuni, S. Takayama et al., Annual Review Of Biomedical Engineering 3, 335 (2001)

MICROFLUIDIC CHIP FOR RELATIVE QUANTIFICATION OF mRNAs BY MLPA

T. Roeser[1], K.S. Drese[1], X. Fuetterer[1], A. Nygren[2], M. Weniger[1], and M. Ritzi[1]

[1]Institut fuer Mikrotechnik Mainz GmbH, GERMANY
[2]MRC-Holland b.v., THE NETHERLANDS

ABSTRACT

The multiplex ligation-dependent probe amplification (MLPA) [1] allows simultaneous amplification of up to 50 DNA sequences in one easy to perform, PCR based reaction. MLPA can discriminate sequences that differ in single nucleotides. It can also be used for relative quantification of up to 50 different mRNAs to detect e.g. cancer markers on the level of expression. This paper reports the adoption, miniaturization, and simplification of the MLPA method for an enhanced, automated performance within a microfluidic device. This device is developed as an integrated module of a new miniaturized system for the isolation and characterization of circulating tumor cells.

Keywords: Microfluidic chip, circulating tumor cells, expression profiling, MLPA

1. INTRODUCTION

Circulating tumor cells (CTC) are tumor cells that invade the bloodstream and cause distant metastases. The detection of occult metastases, e.g. detection of CTCs, could have a substantial clinical impact on the prognosis and optimal disease management of patients with cancer since undetected micrometastases can contribute to the failure of primary treatment. Direct determination of the presence of and changes in the number of residual malignant cells after surgery may be useful for the monitoring of therapy efficiency.

A panel of about 20 mRNA markers for breast cancer has been chosen to allow thorough characterization of the CTCs. The expression levels of these mRNA markers are to be detected via MLPA within a microsystem that will integrate modules for immunomagnetic cell enrichment from peripheral blood, cell isolation and counting, mRNA isolation and amplification (MLPA), and finally the detection of the amplicons. This microsystem should have its use as a time and labor saving, minimally invasive tool for cancer therapy selection and monitoring, and for the detection of recurrent disease.

To allow an enhanced and automated gene expression profiling with MLPA on chip the multistep MLPA concept was adopted, miniaturized and simplified.

2. THEORY

In MLPA a copy of each target sequence is made by hybridization of probe oligonucleotides to the target sequences and subsequent ligation of the hybridized probes. The ligated probes are flanked by identical user-defined sequences that allow simultaneous amplification in a multiplex PCR with only one pair of primers. Therefore not the sample nucleic acids are amplified, but the added probes.

Due to its multistep character the MLPA protocol for expression profiling requires a complex microfluidic design including up to four reaction chambers for (1) reverse

978-0-9798064-0-7/μTAS2007/$20©2007CBMS

transcription (RT) and pre-PCR (if necessary), (2) hybridization, (3) ligation, and (4) MLPA-PCR. Accordingly, in a microsystem up to four heating elements and several reagent reservoirs, valves, metering and mixing structures are needed (Fig. 1) which lead to a complex chip design.

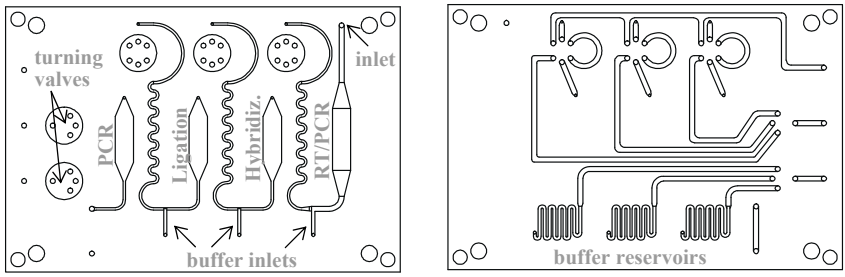

Figure 1. Basic chip design for gene expression profiling via MLPA

Because of the complexity of the microfluidic chip in case of a one-to-one implementation, the standard assay had to be tightened to allow a broad simplification of the microfluidic system. In this context every single MLPA step was checked in order to ease its performance on chip. Correspondingly, two of the four MLPA steps were merged. The reverse transcription reaction and the pre-PCR as well as the ligation and MLPA-PCR, each pair is now performed in one reaction. This reduces the number of reaction chambers and heating elements to the half (Fig. 2). Furthermore the simplified protocol decreases the number of master mixes and reagents that need to be stored, merged and mixed on chip. Probe hybridization occurs during the sample transport from the RT/pre-PCR chamber to the MLPA-PCR chamber. By using two times concentrated probes, hybridization time shall be reduced down to 1h as compared to the recommended 16 h in the standard protocol.

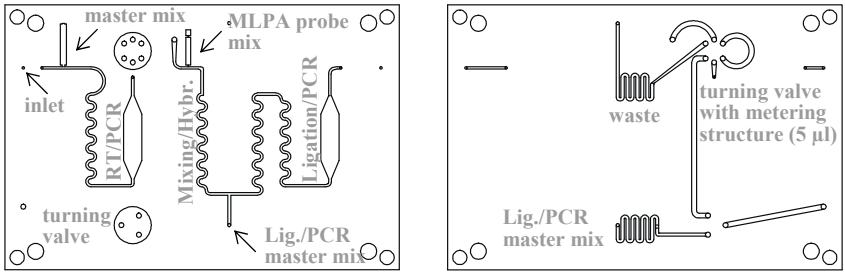

Figure 2. New chip design for the redesigned MLPA protocol

3. EXPERIMENTAL

The feasibility of the proposed MLPA simplification concept had to be proven experimentally. In first instance the merged reactions were tested in the standard macro assay. Thereby a reduction of reaction volumes and a minimization of hybridization time by using two times increased probe concentrations was investigated. To ensure reproducible thermal cycling on chip the temperature profile was recorded within the sample. For this purpose a thermocouple was tightly integrated into the reaction chamber and temperatures logged. In addition, initial hybridization experiments on chip were performed. After

denaturation of the DNA sample in a standard thermocycler, hybridization with probes was realized on chip. The following protocol steps were performed in a standard cycler again.

4. RESULTS AND DISCUSSION

The feasibility of the MLPA simplification concept was successfully demonstrated in macro assay experiments. For the combined RT/pre-PCR reaction as well as the combined ligation/MLPA-reaction the expected MLPA products (Fig. 3) were detected. Furthermore the possibility to reduce reaction volumes without affecting the quality of the overall assay could be proven experimentally (Fig. 3). By using two times concentrated probes the hybridization interval was reduced to 1h.

A reliable and reproducible thermal cycling profile was demonstrated by on chip temperature measurements. Based on the results achieved in the standard macro assay, the MLPA reactions will now be converted to the newly designed microfluidic system. Initial hybridization experiments on chip already showed successful performance. Moreover the RT/pre-PCR chamber will be reused for the following ligation/MLPA-PCR reaction, if possible. As a consequence the presented chip design will be redesigned and considerably simplified anew.

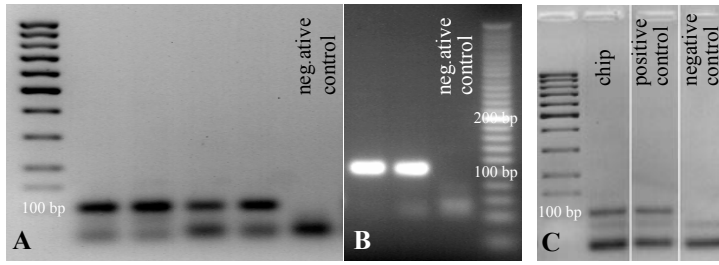

Figure 3. Combined performance of ligation and MLPA-PCR in 40 µl (A) or 20 µl (B); hybridization on chip (C). Probe mix with 5 BRAC1-gene probes, product size is 100 bp.

5. CONCLUSIONS

The complex MLPA standard protocol for relative quantification of mRNAs was successfully adopted for an enhanced and automated performance on a newly developed microfluidic chip. Besides the general benefits of high throughput, reduced costs, size, and assay duration its modular design holds the potential for combination with other modules like cell separation/isolation, cell lysis and mRNA extraction modules or sensor modules for the detection of the MLPA products.

ACKNOWLEDGEMENTS

This paper describes work undertaken in the context of EC IST project 027652 MASCOT. The IST programme is partially funded by the EC. The authors would like to acknowledge the contributions of the consortium participants (http://www.imec.be/mascot).

REFERENCES

[1] J.P. Schouten, C.J. McElgunn, R. Waaijer, D. Zwijnenburg, F. Diepvens and G. Pals, "Relative quantification of 40 nucleic acid sequences by multiplex ligation-dependent probe amplification", Nucleic Acids Research, 30, (12) e57, (2002).

BIOPHYSICAL FLOW CYTOMETRY FOR HEMATOLOGIC DISEASES

Michael J. Rosenbluth[1], Wilbur A. Lam[1,2], and Daniel A. Fletcher[1]

[1]*UC Berkeley Department of Bioengineering and*
UC San Francisco/UC Berkeley Joint Graduate Group in Bioengineering, USA
[2]*UCSF Department of Pediatrics, Division of Pediatric Hematology/Oncology, USA*

ABSTRACT

This paper reports the development of a simple biophysical flow cytometer for quantification of blood cell deformability. Using the cytometer, comprised of a microfluidic PDMS device and image analysis software, we can characterize alterations in blood cell deformability associated with the pathophysiology of hematologic diseases.

Keywords: microfluidics, cell mechanics, leukemia

1. INTRODUCTION

In diseases of the blood, alterations of the mechanical properties of blood cells can significantly impede the progress of blood cells through small capillaries [1]. One example of this is leukostasis, a poorly understood and often fatal condition of acute leukemia in which leukemia cells aggregate in the vasculature, causing respiratory failure and brain hemorrhage [2]. Although leukostasis is known to occur more often in patients with acute myeloid leukemia (AML) than those with acute lymphoid leukemia (ALL) [2], no effective methods currently exist to diagnose or predict leukostasis. Therefore, an assay that assists physicians in identifying patients at risk for leukostasis could significantly improve treatment options and reduce mortality. In addition, a device that also serves as an *in vitro* leukostasis model would provide a much-needed research platform to elucidate the exact mechanisms of this poorly understood complication. The biophysical flow cytometer (*fig 1A-E*) was developed as a first step to serve these purposes.

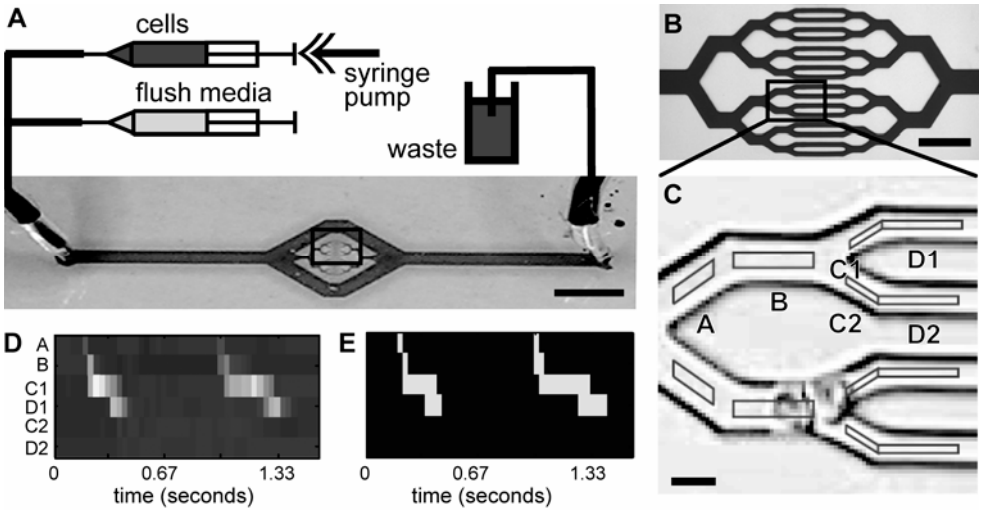

Figure 1. Experimental setup of the biophysical flow cytometer. (A) Cells were flowed into the PDMS device at a constant flow rate. The boxed section can be seen more clearly in (B). (C) Regions of interest (A-D2) were selected to assist in the automated analysis of transit time. (D) Standard

978-0-9798064-0-7/μTAS2007/$20©2007CBMS

deviation (SD) of each ROI in (C) was calculated to determine the presence of a cell. Here, lighter boxes indicate a higher SD. (E) SD was then thresholded to indicate cell presence.

This work builds upon our previous work quantifying leukemia cell deformability with atomic force microscopy [3, 4]. Microchannels have also been used previously to characterize alterations in cell deformability, primarily through measurement of bulk filtration time or pressure [5, 6] rather than single-cell transit time.

2. METHODS

To determine differences in cell transit time, patient samples and leukemia cell lines were flowed into the biophysical flow cytometer. Cells were loaded into a glass syringe and pumped into the PDMS microfluidic channels at 0.6 μL/min and 37° C (*fig 1A*). Two wide channels bypass the capillary network to prevent a change in pressure drop when cells plug the smallest channels (*fig 1B*), which are 8 um wide by 14 um tall by 100 um long. An additional syringe is used to flush the channels clear of cells between experiments. After passing through the device, the cells drain to a waste container. To detect transit time, regions of interest were selected for each of the small channels and the channels leading into them to track the passage of cells (*fig 1C*). The standard deviation (SD) of the pixel intensity was then tracked for each region of interest (ROI) for each frame (*fig 1D*). Then the SD was thresholded to determine the presence of a cell (*fig 1E*). Pertinent data such as transit time and blockage initiation could then be determined. This technique effectively can detect differences in transit time of cells passing into the cytometer (*fig 2*).

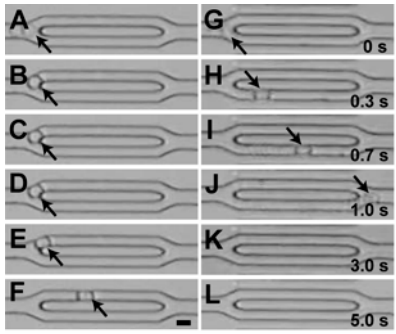

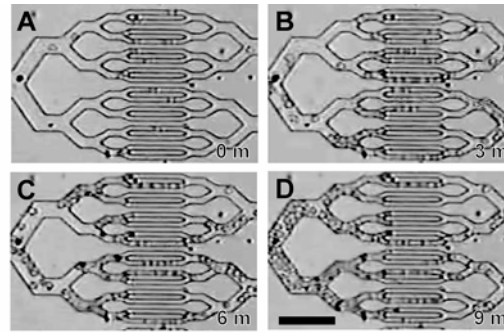

Figure 2 (Left). Visualization of leukemia cell compression into the channels demonstrates differences in cell deformability. Two types of leukemia cells were flowed through the microchannels. On the left (A-F), one HL-60 cell compresses into the capillary channel within 5 seconds. On the right (G-L), a Jurkat cell compresses into the channel within 1 second. Scalebar 10 μm.

Figure 3 (Right). AML cells at high concentration block flow and create aggregation events similar to leukostasis. HL-60 cells were flowed through the microchannels at a concentration of 50,000 cells/μL. Initially the cells flowed through the chanels (A). Within minutes, the cells began backing up from the smallest channels (B,C). After 9 minutes (D), little flow was seen through the channels. Scalebar 100 um.

3. RESULTS AND DISCUSSION

We found that cells from both an AML patient with leukostasis symptoms and from an AML cell line (HL60) took significantly longer to pass into the channels than cells from an ALL patient, an ALL cell line (Jurkat), and normal red blood cells (Mann-Whitney test, $p < .05$, *fig 4a*). AML and HL60 cells were also more likely to initiate a blockage in the channels (Chi-squared test, $p < .05$, *fig 4b*) than ALL cells, Jurkat cells, and normal red

blood cells, consistent with clinical findings. Cell diameter was positively correlated with transit time for the leukemia cells measured, though the correlation was not high (r = 0.41, 0.19, 0.30, 0.23 for AML, HL60, ALL, and Jurkat, respectively), indicating that other factors, such as cell deformability, impact transit time.

Blockage events were amplified when cells were flowed through the biophysical flow cytometer at higher concentrations (*fig 3*). Within three minutes, 50% of the 8 μm channels were blocked by the HL60 cells (*fig 3B*). Within 9 minutes, cells blocked over 90% of the 8 μm channels and backed up into larger channels, effectively creating a leukostasis-like condition (*fig 3D*).

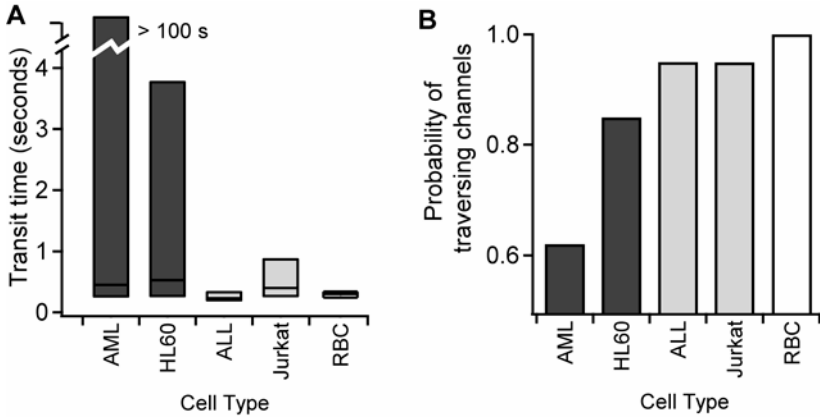

Figure 4. Myeloid leukemia cells take longer to transit into small channels and are more likely to initiate aggregation than lymphoid leukemia cells and healthy blood cells. (A) Both a myeloid leukemia patient sample (AML) and cell line (HL60) took significantly longer to traverse the channels than a lymphoid leukemia patient sample (ALL) and cell line (Jurkat) and healthy red blood cells (Mann-Whitney test, $p < .05$). The box plot ends are the 25th and 75th percentile. (B) Myeloid leukemia cells also were significantly less likely to traverse the channels (and create aggregations) than the lymphoid leukemia cells and red blood cells (Chi-squared test, $p < .05$). These findings are consistent with clinical findings that leukostasis is more common in patients with AML than ALL.

Many hematologic diseases are associated with reduced deformability of blood cells through the vasculature. We have shown that a simple microfluidic device and analysis system is able to determine quantifiable differences in blood cell transit time and that these differences are consistent with clinical outcomes. These tests could be performed in the future as an early indicator for potential complicating factors related to cell deformability, such as during chemotherapy for leukostasis.

REFERENCES

1. Somer, T. and H.J. Meiselman, *Disorders of blood viscosity.* Ann Med, 1993. **25**(1): p. 31-9.
2. Porcu, P., et al., *Hyperleukocytic leukemias and leukostasis: a review of pathophysiology, clinical presentation and management.* Leuk Lymphoma, 2000. **39**(1-2): p. 1-18.
3. Lam, W.A., M.J. Rosenbluth, and D.A. Fletcher, *Chemotherapy exposure increases leukemia cell stiffness.* Blood, 2006.
4. Rosenbluth, M.J., W.A. Lam, and D.A. Fletcher, *Force microscopy of nonadherent cells: a comparison of leukemia cell deformability.* Biophys J, 2006. **90**(8): p. 2994-3003.
5. Inoue, Y., et al., *A neutrophil elastase inhibitor, sivelestat, improves leukocyte deformability in patients with acute lung injury.* J Trauma, 2006. **60**(5): p. 936-43; discussion 943.
6. Shevkoplyas, S.S., et al., *Direct measurement of the impact of impaired erythrocyte deformability on microvascular network perfusion in a microfluidic device.* Lab Chip, 2006. **6**(7): p. 914-20.

MULTIFUNCTIONAL BARCODED PARTICLES FOR HIGH-THROUGHPUT MOLECULAR SCREENING

Daniel C. Pregibon[1], Mehmet Toner[2], and Patrick S. Doyle[1]

[1] Massachusetts Institute of Technology, USA

[2]BioMEMS Resource Center and Center for Engineering in Medicine, Massachusetts General Hospital, and Harvard Medical School, USA

ABSTRACT

We demonstrate a method, based on multifunctional barcoded particles, for the sensitive and accurate multiplexed detection of biomolecules. We discuss means of particle synthesis, sample hybridization, and particle scanning in a flow-through device. Our approach is unique from others in that (1) we can fabricate, encode, and functionalize particles in a single step, (2) the particles are composed of poly(ethylene glycol) hydrogel to increase both sensitivity and specificity, and (3) only a single fluorescent wavelength is required to decode the particles and quantify the corresponding targets [1].

Keywords: nucleic acid hybridization, high-throughput screening, flow lithography

1. INTRODUCTION

The detection of multiple targets in a single sample is important for many applications including medical diagnostics, genotyping, and drug discovery. The current approaches to multiplexing, such as planar arrays (like DNA microarrays) and suspension (particle-based) arrays, require expensive or cumbersome means of encoding, decoding, or functionalizing substrates [2, 3]. Currently, commercially available approaches for multiplexed analysis are cost-prohibitive for high sample throughput, low-cost applications such as bedside diagnostics. Our approach provides an extremely efficient method for particle preparation and requires only single-fluorescence detection, which should dramatically decrease the cost needed for multiplexed analysis.

2. OUR APPROACH

We have developed a system to synthesize and scan particles for highly-multiplexed, sensitive and reproducible detection of biomolecules [Fig. 1]. Using a one-step method based on continuous-flow lithography [4], we synthesize microparticles with multiple functional regions [Fig. 1a]. Each particle bears a fluorescent dot-pattern barcode (capable of providing over a million unique codes) to identify the target(s) it is probing for, and one or more spatially separated regions containing a probe where those targets can bind and be detected via fluorescence. The spatial separation of barcoded and target-capture regions eliminates potential "cross-talk" between encoding and reporter fluorescence, which could jeopardize accurate quantification. The ability to incorporate multiple functionalities in each particle also allows the addition of a negative control region for quality control (not shown here).

Particles from a library can be mixed and incubated in a single sample to simultaneously detect many targets [Fig. 1b]. As a proof-of-concept, we performed multiplexed detection of 20mer DNA oligomers using three batches of barcoded particles, two of which contained a probe specific for one of the oligomers, and the third with no probe to serve as a negative control [Fig. 2]. The detection of targets is not only sensitive but also extremely specific

978-0-9798064-0-7/μTAS2007/$20©2007CBMS

[Fig. 2] due to the porous and bio-inert nature of the hydrogel structure that allows target molecules to diffuse and bind deep into the transparent particle surfaces [Fig. 3]. Using hydrogel particles loaded with only a modest amount of DNA probe, were able to comfortably detect target levels down to 500 attomoles, the lowest value we tested.

In order to facilitate rapid scanning of the particles, we also developed a microfluidic flow-cytometer [Fig. 1c]. In this simple flow-focusing device, images are taken as particles flow by a detection region. The barcodes of each particle are decoded and the corresponding targets quantified. Because the code and target probe-regions are spatially separated on each particle, the scanning system only requires a single fluorescent color, simplifying the detection scheme.

3. CONCLUSION

We have demonstrated specific and sensitive multiplexed analysis of DNA oligomers using barcoded particles capable of highly-multiplexed detection. The particles are synthesized in a single step and can be rapidly scanned in a simple flow-through device using a single fluorescent color, potentially providing a very economical means of multiplexed analysis. Such cheap and high throughput biomolecule analysis may be enabling for applications such as bedside diagnostics, "theranostics," and diagnostics in underdeveloped countries.

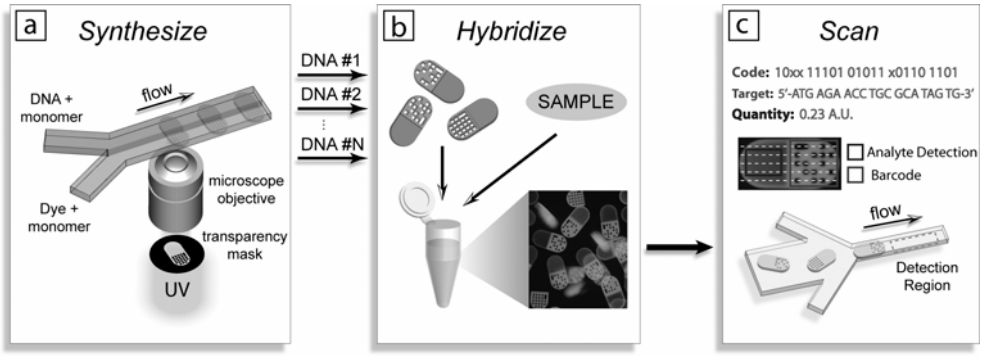

Figure 1: Overall multiplexing scheme showing synthesis of bi-functional, barcoded particles, hybridization of mixed particle populations with a sample, and particle scanning in a flow-through microfluidic device. (a) Particles are synthesized across laminar streams in a microfluidic device using flow-lithography. (b) Mixtures of different batches of particles (with differing probes and dot-pattern barcodes) are incubated with a sample for multiplexed analysis. (c) After hybridization the particles are analyzed in a flow-through device.

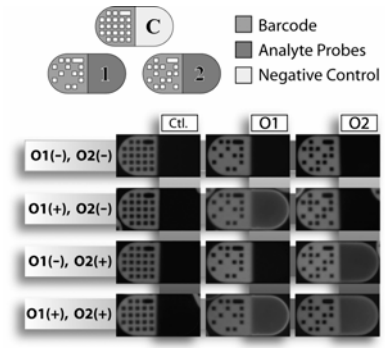

Figure 2: Demonstration of highly specific DNA oligomer detection. Three batches of particles were mixed together (to detect oligomer 1, O1, oligomer 2, O2, or serve as a negative control, Ctl.) and hybridized in a common sample containing one, both, or neither oligomer target. Quantity of target is indicated by level of fluorescence in the probe region (right half) of each particle.

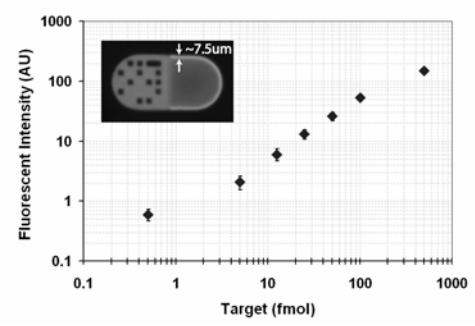

Figure 3: Detection of oligomer target at various target amounts using hydrogel particles. The porous hydrogel surface allows binding of target molecules several microns into the particle surface (shown in inlay), providing sensitive detection (lowest level of 500 attomole easily detected),

REFERENCES

[1] "Multifunctional Encoded Particles for High-Throughput Biomolecule Analysis," Pregibon D.C., Toner M., Doyle P.S., *Science*, **315**, 1393 (2007).

[2] "Barcoding the Microworld," Finkel N.H., Lou X., Wang C., He L., *Analytical Chemistry*, **76**, 352A (2004).

[3] "Encoding Microcarriers: Present and Future Technologies," Braeckmans K., De Smedt S.C., Roelant C., Leblans M., Pauwels R., Demeester J., *Nature Reviews Drug Discovery*, **1**, 447 (2002).

[4] "Continuous Flow Lithography for High-Throughput Microparticle Synthesis," Dendukuri D., Pregibon D.C., Collins J., Hatton T.A., Doyle P.S., *Nature Materials*, **5**, 365 (2006).

BIOLOGICALLY INSPIRED MICROFLUIDIC SPINNING OF SILK FIBERS

David N. Breslauer[1,2], Susan J. Muller[3], and Luke P. Lee[1,2,4]
[1]*Department of Bioengineering, University of California Berkeley, USA*
[2]*Berkeley Sensor and Actuator Center, Berkeley, CA, USA*
[3]*Department of Chemical Engineering, University of California Berkeley, USA*
[4]*Biomolecular Nanotechnology Center, Berkeley, CA, USA*

ABSTRACT

We are developing a biologically inspired microfluidic device for silk fiber formation that mimics the complexity of *in vivo* arachnid silk spinning organs. Current methods of fiber formation involve high temperatures and pressures to extrude polymer fibers, which is prohibitive for many biological applications such as tissue engineering. Spiders, however, are able to produce high strength silk fibers under benign conditions. Examination of the spider silk gland reveals that it is essentially a complex microfluidic system [1]. Through in depth understanding of microscopic hydrodynamics, we are developing a device that mimics the mechanics and chemistry of arachnid silk glands for the precision production of silk fibers at ambient temperatures and pressures.

Keywords: fibers, polymer, biologically inspired, silk

1. INTRODUCTION

Spider silk is an extremely impressive fiber with mechanical properties that well exceed those of man-made fibers. To date, fiber spinning technology has yet to be able to reproduce silk fibers with mechanical properties similar to those produced *in vivo*, nor has it been able to emulate the low energy spinning mechanisms found in the spider. We have designed biomimetic microfluidic channels that emulate the geometry found in the spider silk gland, as well as a microfluidic device for the diffusive introduction of chemical gradients along a flow channel. Our device is designed to produce high strength silk fibers with properties similar to those produced *in vivo*, and with the same minimal energy requirements for fiber production as the spider.

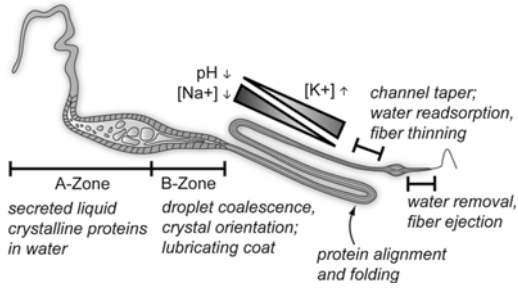

Figure 1. Schematic diagram of the fiber-forming mechanisms in the silk gland.

2. BIOMIMETIC MICROFLUIDIC GEOMETRIES

From computational simulation of the complex flow in the spider silk gland (Fig. 2), we have identified critical fluidic parameters governing the microflow of silk solution to direct

978-0-9798064-0-7/μTAS2007/$20©2007CBMS

Table 1. Flow characteristics in the silk gland.

Strain Rate (⟨ε'⟩)	0.63 /s
Reynold's Number (Re)	$1.4 \cdot 10^{-7}$
Deborah Number (De)	0.25
Elasticity Number (El)	$1.8 \cdot 10^{6}$

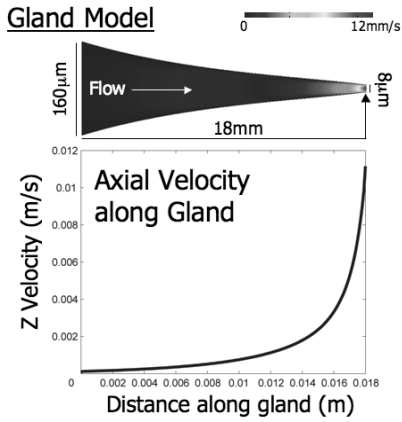

Figure 2. Computational model of flow in the silk gland.

the design of our microfluidic device (Table 1). Notably, the velocity profile along the gland centerline can be fit extremely well to an exponential increasing function, suggesting the gland is an increasing strain rate funnel. The strain rate in the gland is 0.63/s and the characteristic Deborah number is 0.25, indicating a slow elongation of the silk solution along the gland length, and suggesting long channel length is important to minimize the effects of strain hardening. Specifically, the Deborah Number ($De = \lambda/\tau$) is the ratio of the relaxation time of the polymer (λ) to the time scale of the experiment (τ). $De >> 1$ indicates that the polymer is under significant extension. Because $De < 1$ in the silk gland, the polymer is under low stresses before it is drawn into an extremely strong fiber. The Elasticity Number ($El = De/Re$) is the ratio of elastic to inertial forces in the system. A large elasticity number indicates that the flow has a strong elastic (stretching) component and will act in a non-Newtonian manner. The extremely large elasticity number in the silk gland demonstrates the complex characteristics of the flow in the silk gland, and thus the difficulty in designing a comparable microfluidic system. From these parameters, we have designed microfluidic contractions that exert comparable fluidic forces as in the *in vivo* silk gland (Fig. 3.)



Figure 3. Example microfluidic contraction to extrude silk fibers, designed based on the increasing strain rate profile of the arachnid silk gland.

3. CHEMICAL GRADIENTS ALONG A CONSTANT FLOW

In addition to microscale hydrodynamic effects, silk glands have been shown to subject developing fibers to a variety of chemical conditions (pH, K^+, etc.) These chemical baths have been implicated in protein refolding as well as alterations in silk dope viscosity [2]. To implement chemical gradients along the length of the extrusion channel, we have integrated buffer flow channels along our extrusion funnel. These flow channels are separated from the main channel by a 2μm high gap (Fig. 4.) Because the aspect ratio between the gap and the flow

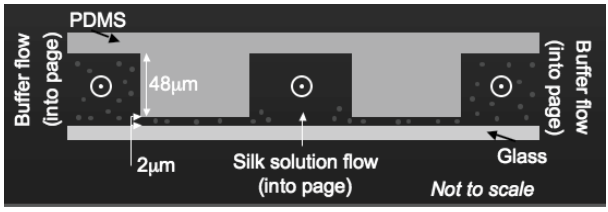

Figure 4. Implementation of buffer diffusion along extrusion channel. Cross-section schematic of high aspect ratio gap for diffusive transport of chemicals.

channels is so large, its hydraulic resistance is orders of magnitude higher. Therefore, transport of chemicals into the extrusion channel will be diffusion, rather than convection dominated, enabling the addition of chemicals into the flowing silk solution without modifying its flow profile. Figure 5a demonstrates the implementation of this methodology with a fluorescent dye (Rhodamine 6G.) The side channels have a constant flow of high concentration fluorescent solution (1mg/mL,) whereas the center channel has a flow of zero concentration. In all channels, flow is constant at 50µm/s. Along the length of the center channel the fluorescence dye concentration increases (Fig. 5b) due to constant flux from the side channels through the 2µm gap. By integrating this gradient generation system with our biomimetic extrusion geometres, we will be able to introduce chemical gradients into the flowing silk solution, just as the spider does in order to polymerize silk protein into fibers.

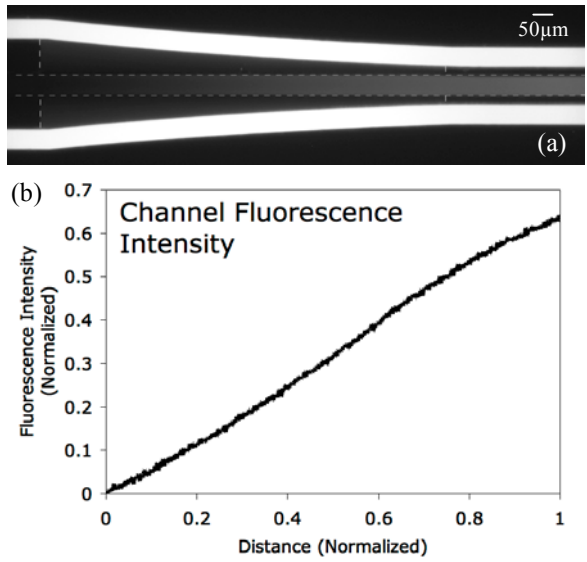

Figure 5. (a) Fluorescence demonstration of device to generate an increasing concentration gradient along a flow. Flow is from left to right. (b) Normalized fluorescence along the channel length.

4. RESULTS AND DISCUSSION

We have demonstrated the creation of microfluidic geometries that mimic the arachnid silk spinning organs. We have also demonstrated the creation of a novel device for the integration of chemical gradients along a constant flow. By further understanding the microscopic hydrodynamics and chemistry of the silk gland, and implementing these mechanisms into our microfluidic system, we anticipate spinning silk fibers with similar mechanical properties as those produced by spiders, and with the same minimal energy requirements.

ACKNOWLEDGEMENTS

The authors would like to acknowledge Terry D. Johnson for assistance with designing the gradient device, NSF, GlaxoSmithKline, and the Berkeley Sensor and Actuator Center for funding. All fabrication was performed in the Berkeley Microfabrication Facility.

REFERENCES

[1] F. Vollrath and D.P. Knight, *Liquid crystalline spinning of spider silk*, Nature, 29;410(6828):541-8, (2001).

[2] C. Wong Po Food, *et al., Role of pH and charge on silk protein assembly in insects and spiders*, Appl Phys A. 82(2):223-33, (2006).

INSTANTANEOUS CARBON-CARBON BOND FORMATION USING A MICROCHANNEL REACTOR WITH A CATALYTIC MEMBRANE

Yasuhiro Uozumi, [†]* Yoichi M. A. Yamada,[†] Tomohiko Beppu,[†] Naoshi Fukuyama,[†] Masaharu Ueno,[‡] Takehiko Kitamori[‡]

[†]*Institute for Molecular Science and CREST*

[‡]*University of Tokyo*

ABSTRACT

Instantaneous catalytic carbon-carbon bond forming reactions were achieved in a microchannel reactor having a polymeric palladium complex membrane. The catalytic membrane was constructed inside the microchannel via self-assembling complexation at the interface between the organic and aqueous phases flowing laminarly, where non-crosslinked polymer-bound phosphine and ammonium tetrachloropalladate dissolved, respectively. Palladium-catalyzed coupling reaction of aryl halides and arylboronic acids was performed using the microchannel reactor to give quantitative yields of biaryls within 4 seconds of retention time in the defined channel region.

Keywords: Palladium, membrane, catalyst, cross-coupling

1. INTRODUCTION

Recently, microreactor systems offering many fundamental as well as practical advantages have been considered as innovative devices for chemical experimentation.[1] Considering that the majority of chemical reactions are carried out by mixing two unique solutions of reactants, it is not surprising that the catalyst-immobilized microreactor for liquid-solid-liquid triphase reaction systems would be an eagerly-awaited device.[2]

2. RESULTS AND DISCUSSION

Polymer deposition at the laminar interface was originally reported by Whiteside et al. for the acid-base reaction of a polymeric sulfonate salt and a polymeric ammonium salt,[3] but, to the best of our knowledge, nothing has appeared so far on the interfacial deposition of transition metal complexes with the view of using them as catalytic membranes (Figure 1). The formation of the palladium complex membrane, poly(acrylamide)-triarylphosphine-palladium (PA-TAP-Pd), [4] was carried out with a microchannel reactor having a channel pattern of 100 μm width, 40 μm depth, 140 mm length, and a Y-junction (Figure 2 (B)). We charged the ethyl acetate solution of PA-TAP (5.0 mM; solution A) and the aqueous solution of $(NH_4)_2PdCl_4$ (1.7 mM; solution B) oppositely into the microchannel at 25 °C for 10 min with a flow rate of 5.0 μl/min. Two-phase parallel laminar flow was formed under the flowing conditions and a polymer membrane was precipitated at the interface between the two parallel flows.[5]

To explore the utility of the microchannel bearing the PA-TAP-Pd membrane in catalytic organic transformations, we preliminarily elected to study the palladium-catalyzed cross-coupling of aryl halides with arylboronic acids (the so-called Suzuki-Miyaura reaction). Representative results are shown in Table 1. We were very pleased to find that the coupling reaction proceeded smoothly in the channel and was completed within only 4 seconds to give a quantitative yield of the desired biaryl

978-0-9798064-0-7/μTAS2007/$20©2007CBMS

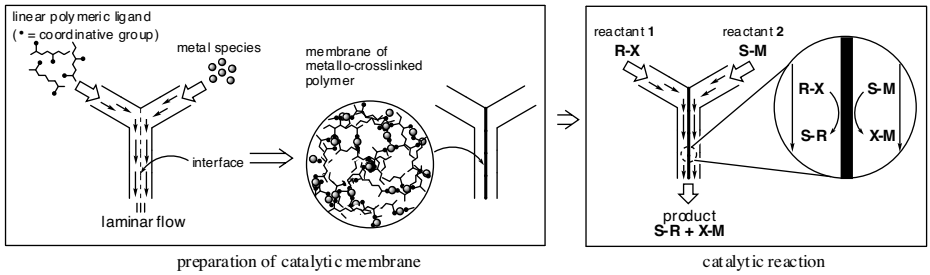

Figure 1. Concept of a Microchannel-Flow Reaction System with a Catalytic Membrane.

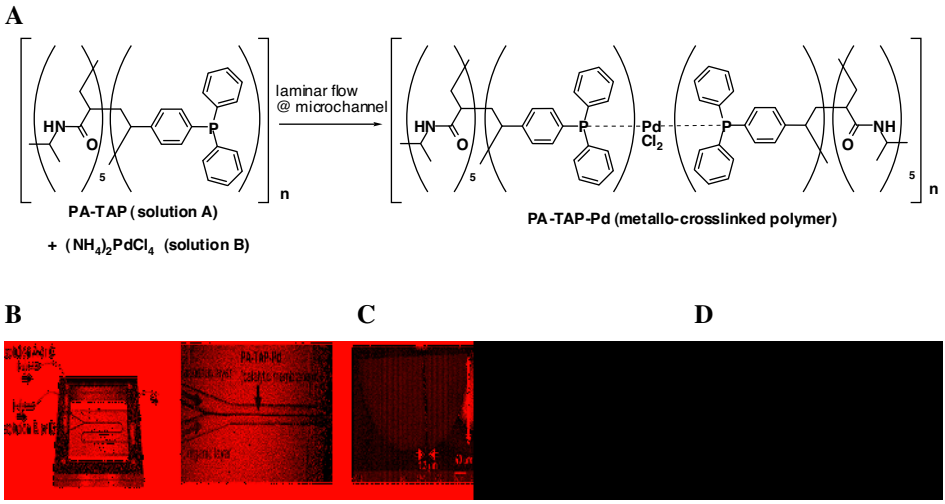

Figure 2. Formation of Catalytic Membrane inside a Microchannel. **A**: Metallo-crosslinking formation of PA-TAP-Pd polymer. **B:** Reaction apparatus. **C:** Microscopic view of the membrane formation (top view). **D:** Microscopic (SEM) view of the membrane inside the channel (cross-section).

product. Thus, a solution of aryl iodide in EtOAc/2-PrOH (6.3 mM; solution C)) and an aqueous solution arylboronic acid with Na_2CO_3 (9.4 mM; solution D) were oppositely introduced into the membrane-divided channels at 50 °C with a flow rate of 2.5 ml/min (for solution C) and 5.0 ml/min (for solution D), respectively, and two parallel laminar layers flowed to pass through the channel in 4 seconds. The resulting organic/aqueous micro stream was collected from the outlet of the channel to afford a quantitative yield of the corresponding biaryls (Table 1) This coupling reaction includes two intermolecular reaction steps, oxidative addition forming the arylpalladium intermediate on the membrane, and (ii) reaction of the arylboronic acid with the resulting arylpalladium intermediate to give the biaryl product, each of which has a unique reaction rate. By using this catalytic membrane-divided microchannel reactor, the fine optimization of the reaction conditions was made possible easily by

changing the concentration of each reactant solution as well as the individual parallel laminar flow rates. Compared to the conventional flask reaction system, this method of performing a catalytic reaction involving multiple intermolecular steps offers a great advantage.

Table 1. Suzuki-Miyaura Coupling using the Microchannel Reactor Having a Catalytic Membrane.[a]



entry	Ar	Ar'	yield (%) of Ar-Ar'
1[b]	C_6H_5	4-$MeOC_6H_4$	99[c]
2		3-MeC_6H_4	96
3		2-MeC_6H_4	99
4	3-$EtOCOC_6H_4$	4-$MeOC_6H_4$	99
5	3-ClC_6H_4		88
6	4-$CF_3C_6H_4$		99[dc]

[a] aryl iodide (6.3 mM in $CH_3CO_2C_2H_5$/*i*-C_3H_7OH (2/5); flow rate: 2.5 mL/min), arylboronic acids (9.4 mM in 18.3 mM aq Na_2CO_3); flow rate: 5.0 mL/min), 50 °C, residence time = 4 sec; [b] aryl iodide (12.5 mM in *i*-C_3H_7OH), arylboronic acids (18.8 mM in 37.5 mM aq Na_2CO_3). [c] TOF = 600 h^{-1} [d] 240 mg/h of the coupling product was isolated by use of 1 microreactor.

REFERENCES AND NOTES

1 For recent reports on flow-reactors bearing immobilized palladium catalysts, see: (a) Jas, G.; Kirschning, A. *Chem. Eur. J.* **2003**, *9*, 5708. (b) Kirschning, A.; Solodenko, W.; Mennecke, K. *Chem. Eur. J.* **2006**, *12*, 5972. (c) Kunz, U.; Schönfeld, H.; Solodenko, W.; Jas, G.; Kirschning, A. *Ind. Eng. Chem. Res.* **2005**, *44*, 8458. (d) Baxendale, I. R.; Griffiths-Jones, C. M.; Ley, S. V.; G. K. Tranmer *Chem. Eur. J.* **2006**, *12*, 4407. (d) Kobayashi, J.; Mori, Y.; Okamoto, K.; Akiyama, R.; Ueno, M.; Kitamori, T.; Kobayashi, S. *Science* **2004**, *304*, 1305.

2 Uozumi, Y.; Yamada, Y. M. A.; Beppu, T.; Fukuyama, N.; Ueno, M.; Kitamori, T. *J. Am. Chem. Soc.* **2006**, *128*, 15994.

3 (a) Kenis, P. J. A.; Ismagilov, R. F.; Whitesides, G. M. *Science* **1999**, *285*, 83. (b) Zhao, B.; Viernes, N. O. L.; Moore, J. S.; Beebe, D. J.; *J. Am. Chem. Soc.* **2002**, *124*, 5284. (c) Hisamoto, H.; Shimizu, Y.; Uchiyama, K.; Tokeshi, M.; Kikutani, Y.; Hibara, A.; Kitamori, T. *Anal. Chem.* **2003**, *75*, 350.

4 Yamada, Y. M. A.; Takeda, K.; Takahashi, H.; Ikegami, S. *Org. Lett.* **2002**, *4,* 3711.

5 The physical properties of the membrane are as follows: thickness = 1.3 μm, height = 40 μm, length = 140 mm, density = 1.3 g/cm^3, palladium loading = 0.37 mmol/g (3.2 mmol/channel).

MANUFACTURING OF MICROPARTICLES WITH CONFIGURABLE SHAPE AND SEQUENCE ANISOTROPY BY FLUIDIC PROCESSING

K.E. Sung[1], S.A.Vanapalli[1], D. Mukhija[1], H.A. McKay[2], J.M. Millunchick[2], M.J. Solomon[1], and M.A. Burns[1,3]

[1]Department of Chemical Engineering, [2]Department of Materials Science and Engineering, [3]Department of Biomedical Engineering, University of Michigan, Ann Arbor, MI, USA

ABSTRACT

We present the continuous manufacturing of particles by fluidic processing using precursor particles that can be conveyed and fused to obtain anisotropic microparticles with unique sequences and shapes. The shape of the anisotropic particles is formed by employing both geometrical confinement and microfluidic control to collect precursor particles into a narrow, terminal channel. The controlled manufacturing technique of microparticles with programmable anisotropy and sequence is important to emergent applications such as chemical sensors, microbarcodes, and optical materials.

Keywords: Anisotropy, Microparticles, Microfluidics, Thermal fusing

1. INTRODUCTION

To date, spherical shaped microparticles are mainly used in microparticle research, and very few techqniques have been developed to synthesize non-spherical anisotropic microparticles. However, the need for anisotropic microparticles with controlled shape and sequence is increased greatly because of applications in self-assembly, drug delivery carrier design and barcoding. Therefore, many different techniques have been developed to synthesize precisely shaped anisotropic particles[1-4]. Microcontact printing is one technique that has been successfully used for fabricating non-spherical particles [1]. Microcontact printing uses non-wetting substrates and molds to confine liquid precursors inside the features of the mold, allowing for the generation of isolated particles. Continuous flow lithography, a second technique, uses microscope-projection photolithography to polymerize mask-defined regions in microchannels containing monomer flows [2]. The use of liquid precursor in these two methods to synthesize particles has the advantage of speed with few shape limitations. However, the technique in limited in the type of materials that can be used, reducing the functionality of the synthesized particles.

2. CONTINUOUS MANUFACTURING OF ANISTROPIC PARTICLES

Precursor particles have been used in our technique to synthesize anisotropic microparticles that may include unique information and functions in each synthesized particles. In our approach (Fig 1), particles are transported by fluid flow into the reaction zone of a microfabricated device where physical fusing occurs. The sequence of particles is maintained by matching the channel to the particle dimensions, and the particles against a constriction using fluid flow. An on-chip resistive heater is fabricated on the backside of the device in order to increase the temperature near the glass transition temperature of the polymer particles for thermal fusing. After thermal fusing is completed, fused chains are collected at the collection chamber by fluidic control.

978-0-9798064-0-7/μTAS2007/$20©2007CBMS

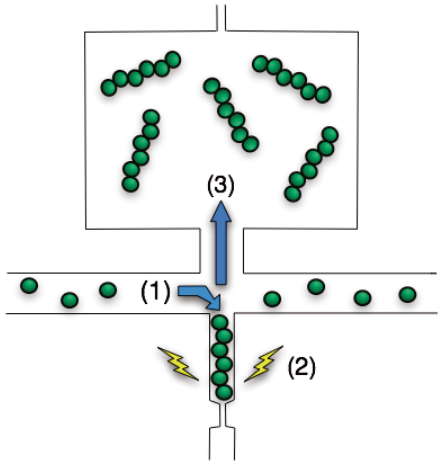

Figure 1. Schematic diagram of the continuous synthesis process: (1) injection of precursor particles, (2) reaction, (3) product collection

3. EXPERIMENTAL

Fluidic channels and metal heater were fabricated on a silicon oxide wafer by standard lithography using deep reactive ion etching for channels and metal lift-off for the heater. Fluid assess holes were drilled on a pyrex glass wafer and anodic bonding was performed to bond the silicon and glass substrates. Two different polystyrene particles (21.21 ± 0.04 μm and 9.91 ± 0.73 μm) were used as precursors. Dimethyl sulfoxide (DMSO) was chosen because of its high boiling temperature (189 °C). Three different states (pressure, neutral, and vacuum) were applied through synringes connected to each fluidic port. Synringes were connected to a set of 2-way and 3-way solenoid valves that were operated by computor control (Labview 7.1). All experiments were imaged with a stereoscope (Olympus SZX-12) and digital camera (Nikon Coolpix 4500). High-resolution images were acquired with 10x and 40x objectives on an upright microscope (Zeiss Axioscope).

4. RESULTS AND DISCUSSION

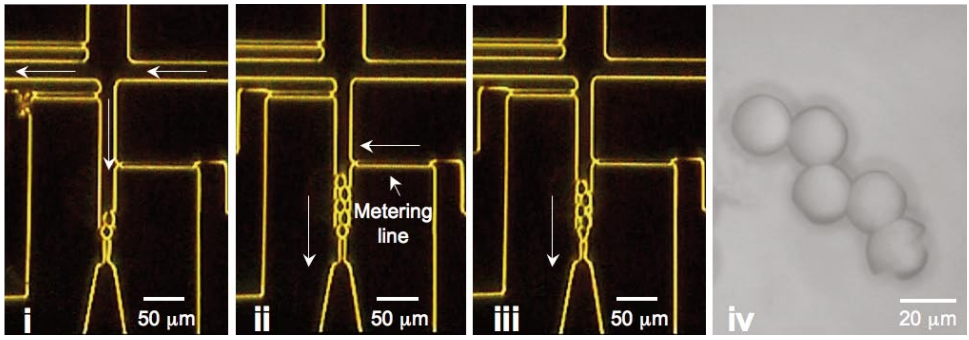

Figure 2. Synthesis cycle for homogeneous five-particle chain : (i) particle injection by pressure control, (ii) measuring of particles by metering line, (iii) thermal fusing at 80 °C, (iv) high resolution image of a fused particle chain. Arrows indicate direction of flow.

Figure 2 shows the steps of a synthesis cycle for a homogeneous linear chain composed of 5 precurosor particles and Figure 2-iv is a high resolution image of a fused particle chain. This particle length is obtained by using the metering line located along the side of the collection channel. Tail imprinting is achieved by applying vaccum during thermal process. This pressure controlled manufacturing is flexible so the particles with different shapes and sequences can be synthesized by changing the design of the collection channel and incorporating metering lines to measure out exact number of particles.

5. CONCLUSIONS

This work presents a new synthesis method for anisotropic particles that incorporates both confinement and microfluidics. This system is very flexible because other reaction methods, such as chemical reaction and UV photopolymerization, or different particle materials can be used with no major changes to the process.

ACKNOWLEDGEMENTS

We acknowledge helpful discussion with S.C. Glotzer and N.A. Kotov. This study was supported by NSF CBET 0507839.

REFERENCES

[1] J. P. Rolland, B. W. Maynor, L.E. Euliss, A.E. Exner, G.M. Denison, J.M. DeSimone, *Direct Fabrication and Harvesting of Monodisperse, Shape-Specific Nanobiomaterials*, Journal of the American Chemical Society, 127, 10096 (2005).

[2] D. Dendukuri, D. C. Pregibon, J. Collins, T. A. Hatton, and P. S. Doyle, *Continuos-flow lithography for high-throughput microparticle synthesis*, Nature Material, 5, 365 (2006).

[3] Y. Xia, Y. Yin, Y. Lu, and J. McLellan, *Template-Assisted Self-Assembly of Spherical Colloids into Complex and Controllable Structures*, Advanced Functional Materials, 2003, 13, 907 (2003)

[4] S. Xu, Z. Nie, M. Seo, P. Lewis, E. Kumacheva, H. A. Stone, P. Garstecki, D. B. Weibel, I. Gitlin, and G. M. Whitesides, *Generation of Monodisperse Particles by Using Microfluidics: Control over Size, Shape, and Composition*, Angew. Chem., 117, 734 (2005)

ACTUATING LAYER-EMBEDDED MICROCANTILEVER FOR HIGHLY SENSITIVE BIOMOLECULE DETECTION

Kyo Seon Hwang, Sang Kyung Kim, and Tae Song Kim
Nano-Bio Research Center, Korea Institute of Science and Technology, KOREA

Keywords: Microcantilever, Diagnosis, Resonant frequency

There has been growing interest of miniaturized mechanical system after the special talk "There's Plenty of Room at the Bottom" by Richard P. Feynman at 1959. Recent works have been shown that the biological and biomedical applications of micro-and nano-technology have become increasingly prevalent and have found sidespread use in a wide variety of applications. As a candidate for biomolecules detection system in the future, a number of researcher keep an eye on cantilever sensor platform.

Research trend of cantilever sensor for the biomolecules detection. A couple of groups have shown the meaningful results based on mechanical properties change of cantilever by measuring the cantilever deflection (i.e. static mode) and resonant frequency change (i.e. dynamic mode) originated from biomolecular interaction on cantilever surface. Majumdar and coworker firstly presented application feasibility of microcantilevers in disease diagnosis. They report in published paper [1] that microcantilevers of different geometries have been used to detect two forms (cPSA and fPSA) of prostate-specific antigen (PSA) over a wide range of concentrations from 0.2 ng/ml to 60 μg/ml in a background of human serum albumin (HSA) at 1 mg/ml. Gerber and coworkers firstly presented biomolecular recognition feasibility through DNA hybridization onto nanomechanical microcantilever surface. They monitored sensing the single-stranded DNA hybridization with two microcantilevers in parallel which was functionalized with a selection of biomolecules[2]. The differential deflection of the cantilevers was found to provide a true molecular recognition signal despite large nonspecific responses of individual cantilevers. Manalis and coworkers newly proposed suspended microchannel resonator to avoid mechanical damping effect of dynamic cantilever in liquid environment [3]. They showed that the problem of damping and viscous drag associated with a resonant beam sensor in fluid can be circumvented by confining the fluid to the inside of the resonant beam while leaving the channel exterior in a gaseous environment, or vacuum. They demonstrated tha their resonator can weigh single nanoparticles, single bacterial cells and sub-monolaters of adsorbed proteins in water with sub-femtogram resolution [4]. Craighead and coworkers have detected the binding of functionalized 1578 base pair long double-stranded DNA [5], to nanomechanical oscillators by measuring the resonant frequency shift due to the added mass of the bound molecules. Dravid and coworkers studied MOSFET-embedded microcantilevers for measuring deflection in biomolecular sensors [6]. They measured deflection, which is on the order of tens of nanometers, by embedding a metal-oxide semiconductor field-effect transistor into the base of the cantilever and recording decreases in drain current with deflections as small as 5 nanometers.

978-0-9798064-0-7/μTAS2007/$20©2007CBMS

High sensitive actuating layer-embedded microcantilever for label-free detection of a variety of biomolecules. Current disease diagnosis depend on fast and specific detection of marker biomolecules. Detection tools with advantages such as, accuracy, high sensitivity, reproducibility, and rapidness, in need are from the medical and biological markets. Here, we present actuating layer-embedded microcantilevers for detecting the marker proteins by measuring a mechanical proterty (i.e. resonant frequency) before and after the specific interaction of biomolecules. Our nanomechanical dynamic microcantilevers were proposed as a new sensing tool that allows early, rapid, and correct detection in clinical range. We fabricated microcantilever with composition of Ta/Pt/PZT/Pt/SiO_2 layer on a SiN_x supporting layer by standard MEMS fabrication process.

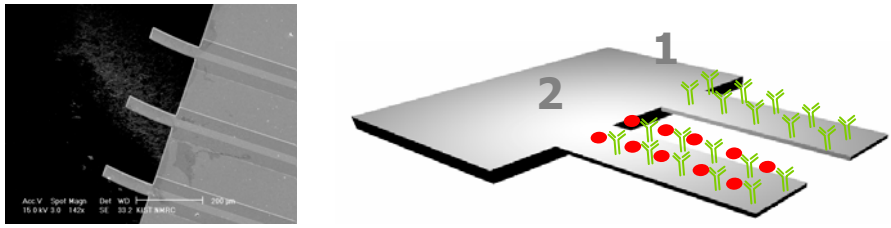

(a) (b)

Figure 1. (a) SEM image of microcantilever assay and (b) schematic diagram of before(#1) and after(#2) the receptor-ligand specific interaction.

New mathematical model was developed by consideration of multi-layered cantilever structure and the relation between surface stress and resonant frequency. Theoretical results from new mathematical model was correspondenced with experimental results that measure the resonant frequency of microfabricated cantilevers and mechanical property change of cantilever in biomolecular interaction [7,8]. This indicated that the resonant frequency shift was dominated by the surface stress in biomolecular interaction. The surface stress generated by biomolecular interaction was calculated in range of mN/m level. The new model enabled more tangible understanding of the protein dynamics in bioassay. Moreover, we could detect and analyze several biomolecules (Postate specific antigen, Myoglobin antigen, C-reactive protein and HCV helicase) related to disease by using our fabricated microcantilever [8-11].

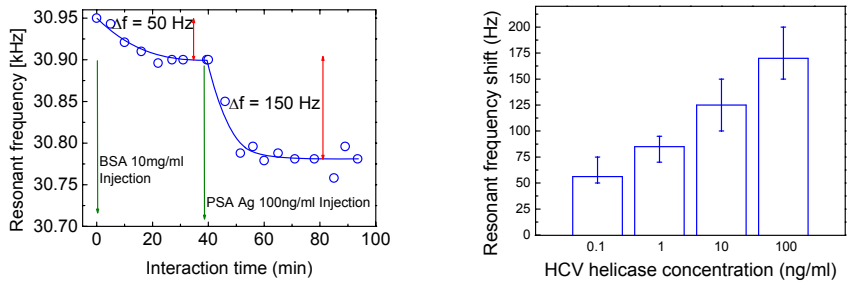

(a) (b)

Figure 2. Self-exciting microcantilever-based biomolecules detection. (a) In-situ PSA detection and (b) HCV helicase detection with use of RNA aptamer as receptor molecule.

Four different biomolecules (proteins) were quantitatively detected by the functionalized microcantilevers. The dynamic range of our microcantilevers was ranging from pg/ml level to ng/ml level. Limit of detection (LOD) was distributed from 10 pg/ml to 1 ng/ml depending on target, which was low enough for applications in clinical diagnosis.

In addition, sensing performance of microcantilevers was enhanced by physical and biochemical methods. We used established washing condition, smaller microcantilever, and sandwich assay using polyclonal antibody with and without nanoparticles for selectivity and sensitivity improvement. The reproducibility was improved from 21.48% (coefficient of variance (CV)) to 15.68% and the sensitivity was enhanced to 1 pg/ml.

The capacity of dynamic microcantilevers is the sensitive, accurate, rapid and label-free detection biomolecules detection and analysis. The self-exciting cantilever sensor will lead to rapid a biochemical analysis tool of biomolecules as well as a disease diagnostic system.

ACKNOWLEDGEMENTS

The authors are grateful for the financial support by Intelligent Microsystem Center sponsored by Korea Ministry of Science and Technology as a part of the 21st century's Frontier R&D Projects (Grant MS-01-133-01) and National Core Research Center for Nanomedical Technology sponsored by KOSEF (Grant R15-2004-024-00000-0).

REFERENCES

[1] G. Wu, R.H. Datar, K.M. Hansen, T. Thundat, R.J. Cote, A. Majumdar, Nature Biotechnology, **19**, pp. 856-860, (2001).

[2] J. Fritz, M. K. Baller, H. P. Lang, H. Rothuizen, P. Vettiger, E. Meyer, H. -J. Guntherodt, C. Gerber, J. K. Gimzewski, Science, **288**, pp. 316-318, (2000).

[3] T.P. Burg, S.R. Manalis, Appl. Phys. Lett., **83**, pp. 2698-2700, (2003).

[4] T.P. Burg, M. Godin, S.M. Knudsen, W. Shen, G. Carlson, J.S. Foster, K. Babcock, S.R. Manalis, Nature, **446**, pp.1066-1070, (2007)

[5] B. Ilic. Y. Yang, K. Aubin. R. Reichenbach, S. Krylov, H.G. Craighead, Nano. Lett., **5**, pp. 925-929, (2005).

[6] G. Shekhawat, S.-H. Tark, V.P. Dravid, Science, **311**, pp. 1592-1595, (2006).

[7] J.H. Lee, T.S. Kim, and K.H. Yoon, Appl. Phys. Lett., **84**, pp. 3187-3189, (2004).

[8] K.S. Hwang, K. Eom, J.H. Lee, D.W. Chun, B.H. Cha, D.S. Yoon, T.S. Kim, J.H. Park, Appl. Phys. Lett., **89**, 173905, (2006)

[9] K.S. Hwang, J.H. Lee, J. Park, D.S. Yoon, J.H. Park, and T.S. Kim, Lab Chip., **4**, pp. 547-552, (2004).

[10] J.H. Lee, K.S. Hwang, J. Park, K.H. Yoon, D.S. Yoon, and T.S. Kim, Biosens. Bioelectron., **20**, pp. 2157-2162, (2005).

[94] J.H. Lee, K.H. Yoon, K.S. Hwang, J. Park, S. Ahn, and T.S. Kim, Biosens. Bioelectron., **20**, pp. 269-275, (2004).

A PARYLENE BASED DOUBLE-CHANNEL MICRO-ELECTROPHORESIS SYSTEM FOR RAPID MUTATION DETECTION

S. Sukas[1], A.E. Erson[2], C. Sert[1], and H. Kulah[3]

[1]Dept. of Mechanical Engineering, [2]Dept. of Biology, [3]Dept. of Electrical and Electronics Eng., Middle East Technical University, Ankara, TURKEY

ABSTRACT

This paper presents the design and implementation of a double-channel micro-electrophoresis system for rapid mutation detection using heteroduplex analysis (HDA) method. The reported system implements two identical parylene channels located side-by-side, and allows HDA to be performed within a short separation length and time.

Keywords: Microchip electrophoresis, mutation detection, heteroduplex analysis.

1. INTRODUCTION

Microchip capillary electrophoresis (CE) systems for DNA separation applications offer many advantages compared to macro scale devices in terms of compact geometry, low cost, ease of use, less labor, and short separation times [1,2]. Due to these advantages, micro CE systems are widely used in several different applications such as mutation detection. Performing HDA for mutation detection in micro scale using the common single channel systems [3] may lack reliability in the absence of a control channel. To solve this problem, micro capillary array electrophoresis (CAE) systems were proposed for HDA in the literature. However, these structures have two main drawbacks: First, most of these CAE systems are just a combination of single channels over a chip area [4]; therefore they require complex detection systems. Second, the remaining approaches utilize turning geometries in the separation channel [5], which cause dispersion, degrading the resolution dramatically. In this paper, we propose a new double channel architecture which solves the aforementioned problems and shortens the total analysis time and separation length.

2. THEORY AND DESIGN

HDA is one of the simplest and most widely used mutation screening methods [6]. The technique is based on electrophoretic conformational separation of dsDNA fragments with perfect sequence complementarities (homoduplex) from the ones with mismatches (heteroduplex). These mismatches cause a distortion in usual conformation of dsDNA molecules when run on high resolution separation matrices (e.g. polyacrylamide). Heteroduplex samples with even *one mismatch* migrate slower compared to homoduplex counterparts. Figure 1 shows the proposed system based on this phenomena, where wild type and potentially mutant samples are injected and separated synchronously on two identical channels under identical conditions. Although it looks like a traditional cross layout, the separation channel is divided by a thin wall to obtain identical side-by-side double channel structure. Also, two more reservoirs are added for doubling the injection channel. There are two sample loading and waste reservoir pairs located symmetrically, where the buffer loading and separation waste reservoirs are kept common. This symmetrical structure guarantees the identical gel polymerization and injection/separation for both of the channels. Another important feature of this design is the application of

978-0-9798064-0-7/μTAS2007/$20©2007CBMS

U-turn injection method. This method was simulated by using CFD-ACE+ and precise injection controllability has been verified.

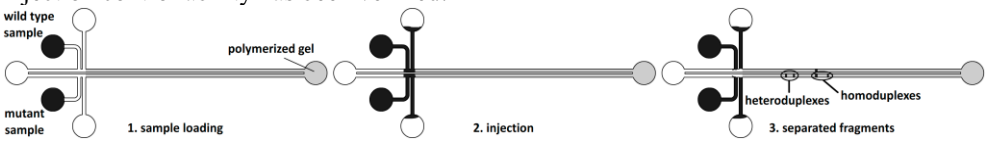

Figure 1. Proposed HDA technique.

3. FABRICATION

Fabrication of the proposed system is very simple and requires only 3 masks [2] as shown in Figure 2. First, a 5μm thick parylene is deposited on Si wafer. Then Ti-Au is sputtered and patterned to form the on-chip electrodes. Next, a 25μm height photoresist (PR) is patterned to define the channels. Then, 20μm thick parylene is deposited, and reservoir openings are etched with RIE. Finally, channels are released by the removal of the sacrificial PR. Parylene-C is used as the channel material due to its conformal deposition, no requirement for surface treatment, transparency, bio-compatibility, and low background fluorescence. Figure 3 shows the fabricated micro-electrophoresis chip for HDA.

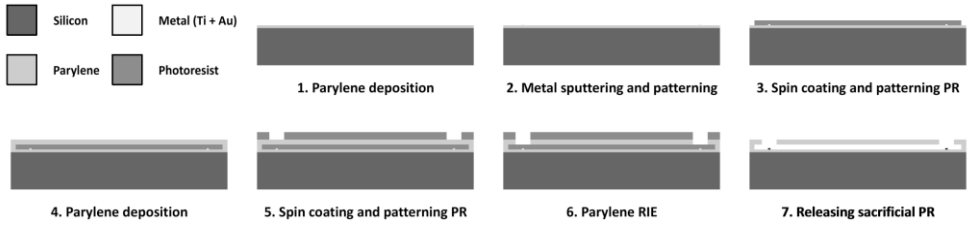

Figure 2. Fabrication process flow.

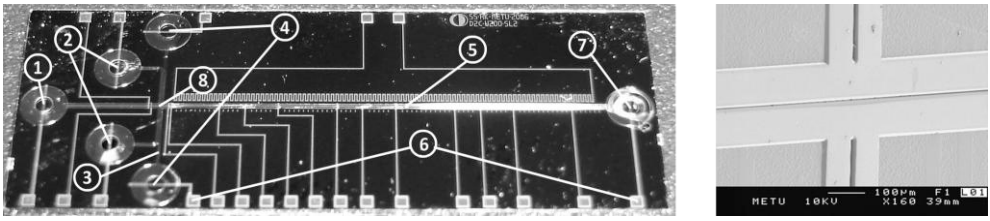

Figure 3. Double channel μ-electrophoresis chip. 1: Buffer loading reservoir, 2: Sample loading reservoirs, 3: Injection channels, 4: Injection waste reservoirs, 5: Separation channel, 6: Electrodes, 7: Separation waste reservoir, 8: Channel crossing (SEM picture).

4. EXPERIMENTAL RESULTS

Electrophoresis was performed with a commercially available heteroduplex control sample (Lonza Biosystems), which contains 350 bp homoduplexes and heteroduplexes. HD control was labeled with a fluorescent dye, YOYO-1 (Invitrogen). UV cross-linked polyacrylamide (ReproGel High Resolution, Amersham) was used as the sieving material. First, channels were filled with acrylamide from the separation waste reservoir. After the UV polymerization of gel in separation channel, the remaining aqueous gel was vacuumed. Then, 0.5X TBE (Tris Borate EDTA) buffer was loaded. Finally, the sample was loaded, and injection and separation were performed. Entire analysis was monitored through fluorescence microscopy (Olympus SZX-12).

Figure 4 shows the application of the U-turn injection method. As the figure shows, it is possible to control the sample amount carried to the junction for separation by adjusting the injection time. One possible disadvantage of this method is the non-compact shape of the generated sample plug. However, this disadvantage is eliminated by using polyacrylamide as the sieving material, since the sample plug compacts itself at the gel interface (Fig. 4 (d)). Figure 5 shows the separated homoduplex and heteroduplex fragments in double channel and single channel chips. Separating the same sample in both channels simultaneously (Fig. 5 (a)) also proves that identical conditions can be provided. These results indicate potential uses of the proposed system for HDA for even single base mismatches, because the separation length is very short compared to the total channel length.

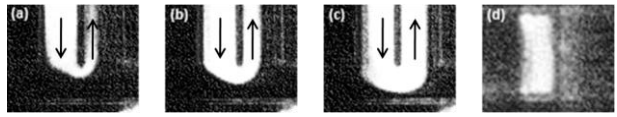

Figure 4. Injected sample amounts for U-Turn injection method after (a) 28s, (b) 33s, (c) 100s, (d) compacted sample at the gel interface.

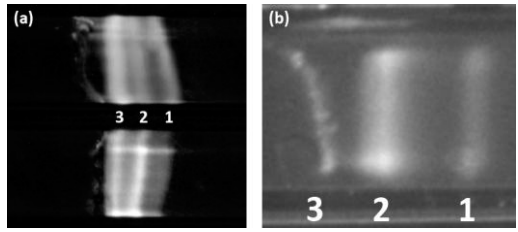

Figure 5. Separation results for (a) double channel, (b) single channel. 1: Homoduplexes, 2: Heteroduplexes, 3: Gel interface. Migration direction is from left to right (E = 25 V/cm). Note that soon after the samples passed through the gel interface, separation of heteroduplexes from homoduplexes were observed.

7. CONCLUSION

A parylene based double-channel micro-electrophoresis system is proposed and successfully applied for HDA. The most important aspect of this system is that under the same conditions, electrophoresis can be performed for both channels simultaneously. This gives the chance of having a control channel, which is very critical for the accuracy and reliability of the results in genetic analyses. In addition to HDA, this system can be applied for a number of applications such as various other mutation detection systems for determining the length of a PCR product with running a ladder in the control channel.

ACKNOWLEDGEMENTS

This work was supported by TUBITAK with grant number 104S605. The authors thank to Mr. Orhan Akar from METU-MET and Mr. Ata Tuna Ciftlik for their contributions.

REFERENCES

[1] V.M. Ugaz et al., *Electrophoresis*, 24, pp 151-157, (2003).
[2] J. Zheng, Ph.D. Dissertation, *The University of Michigan*, (2003).
[3] T. Footz etal., *Genetic Testing*, Vol. 7, No. 4, pp. 283-293, (2003).
[4] Q. Gao, Y. Shi and S. Liu, *F. J. Anal Chem*, 371, pp 137-145, (2001).
[5] N. J. Munro et al., *Clinical Chemistry*, 45, No.11, pp. 1906-1917, (1999).
[6] C.M. Nagamine, K. Chan and Y-F.C. Lau, *Hum. Genet.*, 45, pp 337-339, (1989).

CHIP-BASED MAGNETIC BIOAFFINITY TECHNIQUE ADAPTED FOR QUALITATIVE ANALYSIS OF FOOD ALLERGENS

M. Slovakova[1], B. Jankovicova[1], S. Rosnerova[1], L.Korecka[1], N. Minc[2], J.-L.Viovy[2], L. Hernychova[3], M. Hubalek[3], Z. Bilkova[1]

[1]*Univerzity of Pardubice, CZECH REPUBLIC,* [2]*Institute Curie, FRANCE*
3University of Defense, Hradec Kralove, CZECH REPUBLIC

ABSTRACT

The project presents examples of bioanalysis based on the self-organization of superparamagnetic beads under a magnetic field in a simple well-established microfluidic device. Fixed plugs of magnetic nanoparticles functionalized by protease and specific antibodies inside the channel of device have been utilized for identification of lead vaccine structure of antigen by epitope extraction technique. As a model antigen the food allergen chicken ovalbumin was chosen. The protease reactor developed with necessary optimizations, was loaded into the chip channel and used for limited or total proteolysis. Specific anti-ovalbumin IgG were immobilized by oriented immobilization technique to the carrier with low non-specific sorption. Ovalbumin digests were captured by this specific immunosorbent, washed and eluted under the conventional conditions. Immunogenic peptide was consequently confirmed by MALDI-QTOF mass spectrometry.

Keywords: magnetic carrier, allergen, epitope extraction, microfluidic device

1. INTRODUCTION

There is a continuous push to miniaturize and integrate as many laboratory instrumentation pieces as possible in the quest for a lab-on-chip . Parallel to the boom of microfluidic systems, nanomaterials with paramagnetic properties have become a hot topic in recent research [1,2]. We present examples of bioanalysis based on the self-organization of superparamagnetic beads under a magnetic field in well-established microfluidic device fabricated in polydimethylsiloxane (PDMS) by soft lithography and rapid prototyping. As previously published [3,4], the microanalytical system with plug of bio-active beads profits from a large surface-to-volume ratio and minimal diffusion effect (Fig. 2).

2. THEORY

Within the last few years, coupling techniques as epitope excision or epitope extraction with mass spectrometric peptide mapping have been developed for identification of lead vaccine structure of antigens [5]. The scope of this study was to combine chip-based magnetic enzyme reactors (Fig.1A) enabling decrease the digestion time to seconds with immunoaffinity capturing of specific peptides (Fig.1B). Well-known food allergen ovalbumin (OVA) was digested by a variety of chip-integrated enzyme reactors (trypsin, proteinase K, chymotrypsin) with the aim to prepare fragments maintaining some of the biological properties of the intact molecule. The peptides with immunogenic potential were captured by the carrier with orientedly immobilized anti-OVA IgG. The traditional methodology includes lengthy incubation (hours) and extensive manual steps, the goal was to avoid time-consuming methodology and make analysis as cost-effective as possible.

978-0-9798064-0-7/μTAS2007/$20©2007CBMS

Figure 1. Epitope Extraction Technique:

A – immobilized magnetic enzyme reactor (IMER)
B – immobilized magnetic affinity reactor (IMAR) with captured biospecific peptides.

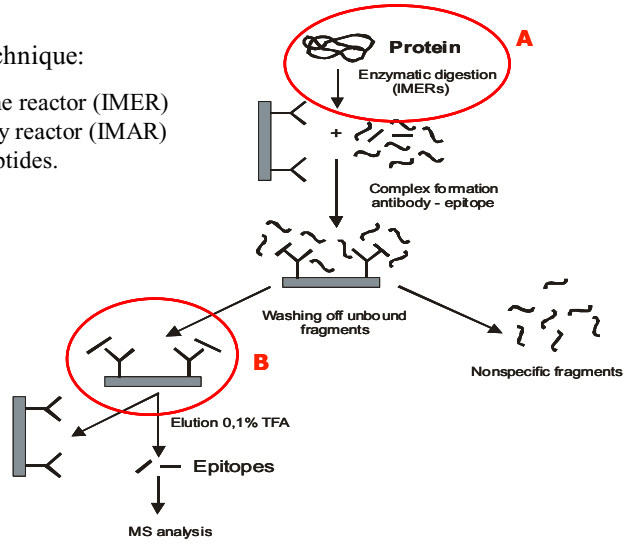

3. EXPERIMENTAL

Proteases as TPCK-trypsin, α-chymotrypsin or proteinase K (Sigma-Aldrich, USA) immobilized on SiMAG-carboxyl, -amino, -PGL (Chemicell, Germany) microspheres, integrated into chip channel and utilized for limited/total proteolysis of food allergen ovalbumin (unfolded by RapidGest™, Waters, UK), E:S molar ratio 1: 1. Immunosorbents for capturing of peptides with immunogenic potential were prepared by immobilization of rabbit polyclonal (Bethyl Laboratories, USA) or mouse monoclonal (Sigma-Aldrich, USA) anti-OVA IgG on SiMAG-hydrazide, -cyanuric (Chemicell, Germany) or Estapor-COOH (Merck, Germany) microspheres. Elution fractions (0.05% TFA, pH 2.5) were analyzed by SDS-PAGE and/or MS. 1μl of matrix (2,5-DHBA in 20% ACN and 0.1% TFA) was spotted after becoming dry of sample. Samples were analyzed by technique MALDI-TOF-MS on Voyager-DE™ STR (Applied Biosystems, USA) using laser intensity about 2500. Peptide sequence was confirmed by tandem MS sequencing on QTOF Ultima API (Waters, UK). The fragmentation pattern of the peptide was compared to theoretical pattern of the studied sequence using PepSeq script in MassLynx 4.0 (Waters, UK).

4. RESULTS AND DISCUSSION

Developed enzymes reactors were utilized for total and/or limited proteolysis of the model food allergen, ovalbumin from hen egg white (Mw (monoisotopic mass): 42722.46, pI: 5.19). Total/limited digests of ovalbumin were applied to magnetic immunoaffinity reactors with monoclonal or polyclonal anti-ovalbumin antibodies. Captured specific peptides were eluted and subsequently identified by MALDI-TOF MS (Fig. 3). Fragmentation of the ion (1016.6615 m/z) by Q-TOF mass spectrometer resulted in spectrum providing the putative sequence KIKVYLPR. This sequence is matched to the peptide position 277-284 with 2 missed cleavagaes of ovalbumin. The main immunogenic structure of ovalbumin molecule was proved.

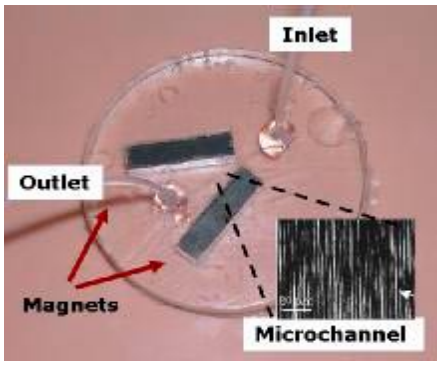

Figure 2. Simple microfluidic device fabricated in PDMS by soft lithography and rapid prototyping (orientation of the magnetic field lines parallel to the flow direction), dimensions: (mm) 20(l) x 0.25(h) x 1(w), VM of capillary – 5 µl).

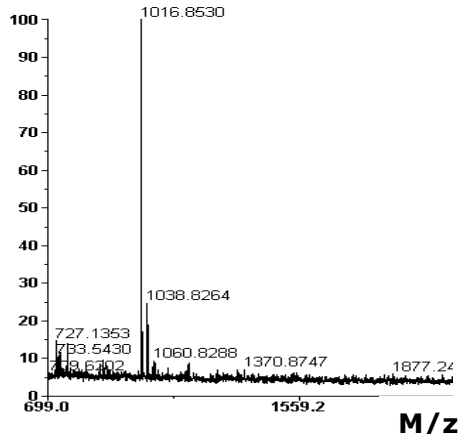

Figure 3. MALDI-TOF analysis of fraction eluted from immunoaffinity carrier (peptide M/z 1016.6615, 2 missed cleavages, position: 277 - 284).

5. CONCLUSIONS

Chip-based epitope extraction technique consisting of 2 steps in off-line, on-line or in-line arrangement can be an excellent basement for high-throughput screening of other food allergens and predicting epitopes with immunogenic potential. The versatility of the new microfluidic device enabling integration of different reaction steps, e.g. peptide mapping technique, epitope extraction technique or immunospecific detection of pathological proteins, peptides was confirmed.

ACKNOWLEDGEMENTS

The authors wish to acknowledge Ministry of Education (MSMT 0021627502) and Czech Science Foundation for financial support (GA203/05/0241, GA203/05/2106). We also thank to Dr. Stulik from University of Defence, Hradec Kralove (CZ) for facilitating of the MS measurements.

REFERENCES

[1] I. Safarik, M.Safarikova, *Magnetic techniques for the isolation and purification of proteins and peptides*, Biomagn. Res. Technol. 2, pp. 7,,(2004).

[2] L. Korecka et al., *Immobilized magnetic enzyme reactors: effective tool for isolation and study of highly heterogeneous glycoproteins*, J. Magn.Magn. Mat. 293, pp. 349, (2005).

[3] Z. Bilkova, et al., *Functionalized magnetic micro- and nanoparticles: optimization and application to µ-chip trypsin digestion*, Electrophoresis 27, pp. 1811, (2006).

[4] M. Slovakova, et al., *Use of self-assembled magnetic beads for protein on-chip digestion*, Lab-on-chip 5, pp. 935, (2005).

[5] E. O. Hochleitner, et al., *Mass Spectrometric Characterization of a Discontinuous Epitope of the HIV-gp120 Recognized by the Human Monoclonal Antibody 1331A,* J. Immunol.164, pp. 4156-4161, (2000).

[6] Z. Bilková et al., *Epitope extraction technique using a proteolytic microreactor combined with FTICR-MS as a tool for screening of potential vaccine lead proteins*, Eur. J. Mass Spectr. 11, pp. 489, (2005).

ELECTROWETTING ON NANOFILAMENT SILICON FOR MATRIX-FREE LASER DESORPTION/IONIZATION MASS SPECTROMETRY

C.W. Tsao[1], P. Kumar[1], J.Liu[1], C.F. Kung[1,2] , C.C. Chang [2] and D.L. DeVoe[1]

[1]Department of Mechanical Engineering, University of Maryland, College Park, MD, USA

[2]Division of Mechanics, Research Center for Applied Science, Academia Sinica, Taipei, Taiwan

ABSTRACT

Matrix-free laser desorption/ionization mass spectrometry (LDI-MS) using nanofilament Si substrates combined with electrowetting is demonstrated for high-sensitivity analysis of small molecules such as low molecular weight peptides. Individual peptides have been measured with a detection limit of 12 amol, and peptide mass fingerprinting is achieved from tryptic digests of BSA with loadings as low as 150 amol.

Keywords: MALDI-MS, Nanofilament, Electrowetting

1. INTRODUCTION

Matrix-assisted laser desorption/ionization (MALDI)-MS, which employs an organic matrix to absorb and transfer UV energy for soft ionization of analyte molecules from a target plate, suffers from excessive matrix background signal below *ca.* 500 m/z and limited sensitivity. A matrix-free approach called desorption/ionization on porous silicon (DIOS)[1] replaces the organic matrix with an electrochemically-etched porous silicon (pSi) substrate which efficiently absorbs UV. The DIOS technology suffers from several limitations. The hydrophobic pore surfaces do not readily wet, resulting in limited surface binding capacity and loss of analyte during sample cleanup. Additionally, the pSi substrates do not allow sample to be constrained to selected regions during deposition. In this paper, we describe LDI-MS measurements using an alternative nanofilament Si substrate fabricated by etching a Si wafer coated with a sub-monolayer of gold in a HF/H_2O_2/EtOH solution.[2] These substrates offer potential benefits for matrix-free LDI-MS due to their open-pore structure. In addition, by employing an electrowetting strategy, sample droplets are anchored to the superhydrophobic surface and allowed to penetrate through the full depth of the nanofilaments, leading to improved LDI-MS sensitivity.

2. RESULTS AND DISCUSSION

The nanofilament chip in Figure 1 was fabricated by coating 3 nm of gold on a 10 cm p-type Si wafer, followed by a 32 s etch in HF/H_2O_2/EtOH (1:1:1 v/v/v). The etched substrate was rinsed with methanol and by blown dry in a gentle stream of N_2. The patterned nanofilament regions shown in Figure 1 were formed using a shadow mask during the Au deposition step. The surfaces were oxidized to form a thin dielectric layer and fluorinated

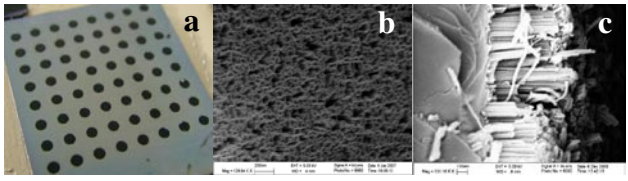

Figure 1. (a) 8x8 array of 1 mm diameter nanofilment targets, (b) SEM image of 10~100nm diameter pores, and (c) view of 20 nm diameter, 500 nm deep nanofiaments.

978-0-9798064-0-7/μTAS2007/$20©2007CBMS

with a silylating reagent to enhance the binding of hydrophobic analyte molecules on the nanofilaments.[3] The fabricated surfaces exhibit superhydrophobic behavior, preventing undesirable spreading of deposited sample droplets. To provide controllable penetration of analyte into the nanofilament pores, an electrowetting voltage is applied to the silicon substrate. Figure 2 shows the reduction in DI water contact angle achieved with increased electrowetting voltage by this approach, using the electrowetting deposition system setup shown in Figure 3.

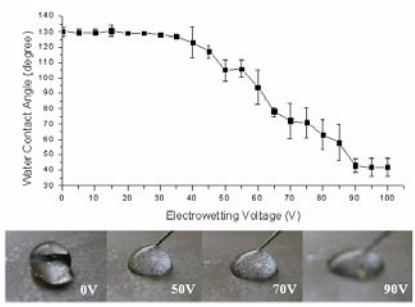

Figure 2. Variation in water contact angle with increasing electrowetting voltage.

A nanofilament chip was bonded on a stainless steel plate and fixed on a 3-axis stage to position the nanofilament substrate. Native oxide on the backside of the chip was removed by buffered oxide etchant to ensure good electrical conductivity. A 100 µm capillary was used to deliver 150 nL droplets of peptide sample to the target, followed by application of the electrowetting bias. After allowing peptides to bind with the nanofilament substrate for 30 s while maintaining the electrowetting bias, the remaining liquid was removed from the surface with a stream of N_2, removing salts and other contaminants in the droplet which would otherwise interfere with LDI-MS detection limits. All electrowetting deposition experiments were performed under an optical goniometer to monitor the droplet contact angle change throughout process.

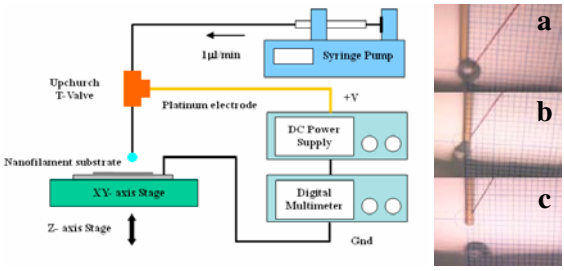

Figure 3. Experimental electrowetting deposition setup (left) and typical deposition process: (a) contact sample with nanofilament substrate (b) electrowetting deposition at 75 V for 30 s, and (c) remove deposition capillary from chip surface.

Sensitivity of LDI-MS from the nanofilament substrates was evaluated using a mixture of 9 model peptides ranging from 800 Da to 3000 Da. Figure 4 shows a comparison of the mass spectra of angiotensin II (m/z:1045.5), bradykinin (m/z:1059.6) and angiotensin I (m/z:1295.7) measured on nanofilament and conventional MALDI-MS targets. The signal intensity (~850 mV) of a 15 fmol peptide mixture on the nanofilament chip is comparable to that of a 125 fmol sample using MALDI-MS, but with 5 times higher signal-to-noise.

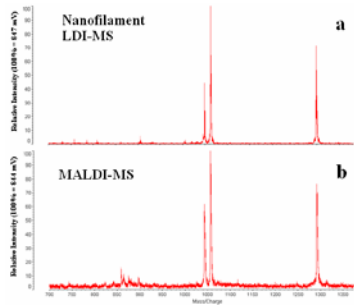

Figure 4. MS spectra of (a) LDI-MS and (b) CHCA MALDI-MS

Performance of the nanofilament substrates was further evaluated using the tryptic digest of bovine serum albumin (BSA). Figure 5 shows the spectra of a 700 fmol sample of BSA digest

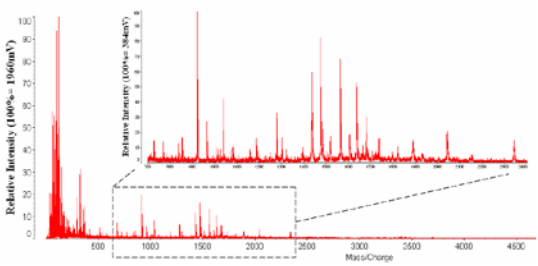

Figure 5. Mass fingerprints of trypsin digested BSA.

analyzed by nanofilament LDI-MS. Peptides with molecular weights between 700 to 2500 Da are readily observed.

Electrowetting provides dynamic control of wetting into the nanofilament pores, enabling more efficient peptide binding on the nanofilament substrate. Using constant laser power during LDI-MS, the signal intensity of a 15 fmol peptide sample increases almost linearly with applied voltage (Figure 6a). However, the noise level is also increased, leading to lower S/N values (Figure 6b). By reducing the laser power to optimize the S/N ratio, the signal intensity drops (Figure 6c) while the S/N value increases with electrowetting voltage (Figure 6d). For the case of 150 amol angiotensin I, (Figure 6e, f) an average S/N ratio of 38 was achieved, suggesting a detection limit of 12 amol for this peptide. Overall, the average S/N can be enhanced by a factor of 4 using the electrowetting approach.

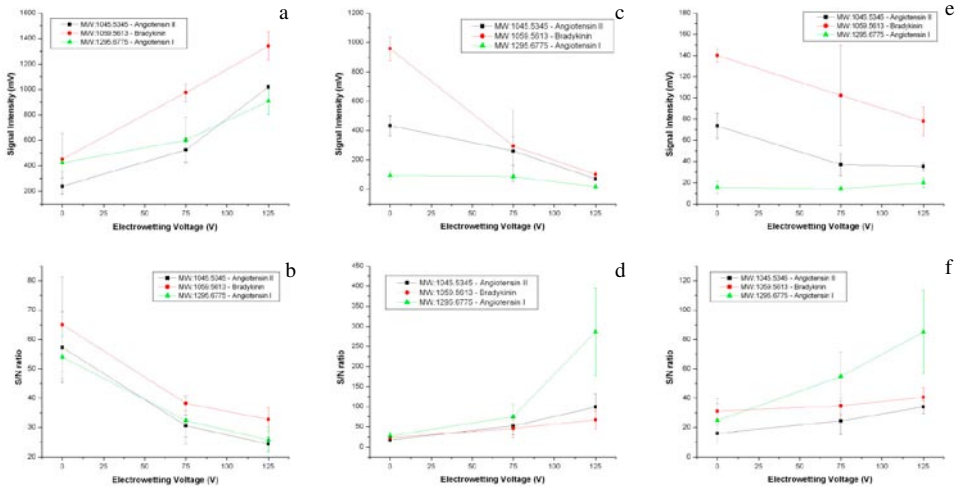

Figure 6. Electrowetting nanofilament LDI-MS analysis. (a,b) Signal intensity and S/N measured for 15 fmol sample of 3 peptides with constant laser power, (c,d) with optimized laser power, and (e,f) with optimized laser power using 150 amol of peptide sample. Error bar shows standard deviation based on three individual measurements.

REFERENCES

[1]. J. Wei, J. M. Buriak and G. Siuzdak, *Nature*, 1999, **399**, 243-246.
[2]. X. Li and P. W. Bohn, *Applied Physics Letters*, 2000, **77**, 2572-2574.
[3]. S. A. Trauger, E. P. Go, Z. X. Shen, J. V. Apon, B. J. Compton, E. S. P. Bouvier, M. G. Finn and G. Siuzdak, *Analytical Chemistry*, 2004, **76**, 4484-4489.

EVALUATION OF MICROFLUDIC DNA EXTRACTION SYSTEM USING A NANOPOROUS ALUMINUM OXIDE MEMBRANE

Jungkyu Kim[1] and Bruce K. Gale[2]

[1]*Department of Bioengineering, University of Utah, USA*

[2]*Department of Mechanical Engineering, University of Utah,USA*

ABSTRACT

A nanoporous membrane was integrated into a microfluidic system designed for extraction of gDNA (genomic DNA) from lysed whole blood. The effectiveness of this system was tested by passing known concentrations of gDNA through nanoporous membranes of varying sizes and measuring the amount of gDNA deposited on the membrane as related to varying salt concentrations. DNA extraction efficiency increased as concentrations of salt increased and nanopore size decreased. It is anticipated that small pore sizes will present clogging problems due to the complex composition of lysed blood. Based on this result, gDNA was extracted from whole blood successfully followed by PCR which was completed successfully without inhibition. With the overall goals of high extraction rates, purification levels and DNA retrieval, it was determined that 200nm sized pores and high salt concentrations yielded the most favorable results.

Keywords: aluminum oxide membrane (AOM), microfluidic, DNA extraction, salt concentration, nanopore effect, lab-on-a-chip.

1. INTRODUCTION

In a micro TAS (Total Analysis System), sample preparation plays an important role in system success. DNA retrieval from biological samples has included methods such as silica, magnetic silica for solid phase extraction, chitosan for ionic interaction and micro/nanopillar sieve separation. [1, 2, 3] Silica bead extraction uses sol-gel-immobilized silica particles in a microchannel for purification of DNA on a microchip SPE device.[3] Chitosan coated microfluidic channels make use of pH-dependent protonation, with pH 5 leaving chitosan protonated for negatively charged DNA interaction and pH 9 leaving chitosan neutral for DNA release. This concept is sufficiently robust to extract DNA from

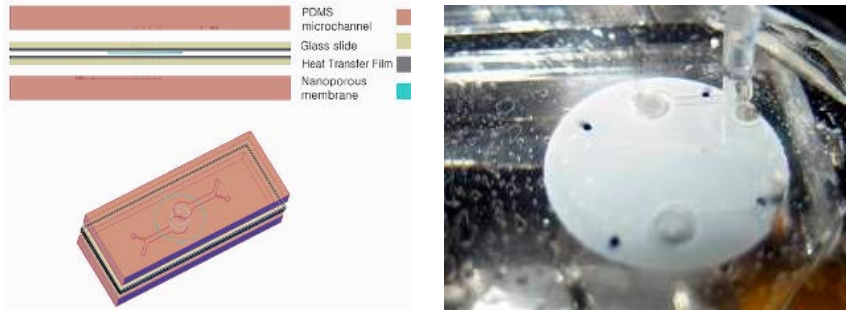

(a) (b)

Figure 1. (a) Fabrication of microfluidic DNA extraction system. (b) Microfluidic DNA extraction system integrated with nanoporous membrane.

978-0-9798064-0-7/μTAS2007/$20©2007CBMS

complex biological systems such as lysed whole blood. [1] Such methods require various reagents, washing steps and have varying levels of effectiveness. Nanoporous membrane gDNA extraction is especially favorable because of its simplicity. [4] In preparation for use in a clinical setting, quantification and qualifying tests will be performed.

2. MATERIALS AND METHOD

The chip that incorporates the nanoporous membrane was fabricated with an SU-8 mold, heat transfer film and glass slides. The nanoporous membrane was embedded and sealed with heat transfer film between glass slides. The microfluic channel was made with PDMS bonded to the top and bottom of the glass. Samples with approximately 500ng of gDNA were passed through using varying salt concentrations. The amount of gDNA in the waste solution was measured using a spectrometer (Nanodrop N-100), therefore suggesting an amount of gDNA left captured on the membrane. Results relating pore size (200nm, 100nm, 20nm) with salt concentration and gDNA capture were obtained by spectrometry. To verify this system, gDNA was extracted using whole blood mixed with lysis buffer and then Real-Time PCR was performed on the gDNA. Initial denaturing at 95°C for 15 seconds followed by 45 cycles of 95°C for 0 seconds, 60°C for 0 seconds, and 74°C for 8 seconds. The temperature transition rate for all steps was 20°C/sec. A 192bp amplicon size of VKORC1 gene was amplified with forward primers and reverse primers. After finishing the PCR step, DNA melt analysis was performed at a rate of 0.3°C/s.

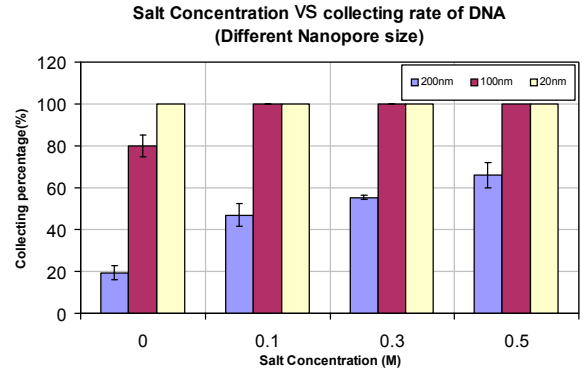

(a)

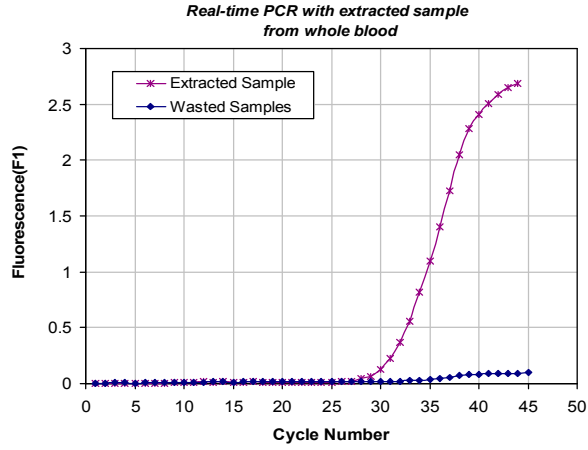

(b)

Figure 2.(a) DNA yield rate depends on salt concentration. As salt concentration increasrd, DNA morphology changes and aggregates more readily.(b) Real-Time PCR amplification with extracted gDNA from blood samples showing PCR compatibility.

3. RESULTS AND DISCUSSION

Membrane pore sizes of 200nm, 100nm and 20nm collected DNA at rates of 20%, 80% and 100% respectively. Implementing a high salt concentration causes gDNA to aggregate, therefore increasing the capture rate. The capture rate for 200nm sized pores increased from 20% to 70 % with this change as shown in Figure 2a. Salt concentration greater than 0.1M caused the majority of the gDNA to be captured in the 100nm pore size membrane. Small pore sizes presented difficulty in maintaining high purity, decreasing the collecting time and avoiding pore blockage due to the complex material found in lysed whole blood. It was determined that 100nm and 200nm sized pores, coupled with the effects of high salt concentration yielded the most favorable results. Downstream PCR is not inhibited by the high salt concentration because the captured gDNA is detached using a separate buffer. To validate the microfludic DNA extraction system, a gDNA elution test was performed with blood samples and then amplified using the eluted samples, see Figure 2b. In a positive control and extracted sample, the amplification of VKORC1 gene was completed successfully without inhibition and melting peaks appeared at 88.5°C, typical of the VKORC1 gene. Nanoporous membrane gDNA extraction methods can help to increase efficiency in lab-on-a-chip applications.

4. CONCLUSION

Nanoporous aluminium oxide membrane was embedded in microfluidic system for extracting gDNA from human blood. Before use the whole blood sample, the membrane-on-a-chip was evaluated with different pore sized membrane and salt concentration. Based on this evaluation, the gDNA was extracted from whole blood sample and VKORC1 gene was amplified with the primer. The extracted gDNA was amplified effectively without PCR inhibition factor. This method is possible to use as the first part of lab-on-a-chip.

ACKNOWLEDGMENTS

The authors acknowledge funding from the State of Utah Center of Excellence program and the University of Utah Synergy program.

REFERENCES

[1] Weidong Cao, Christopher J. Easley, Jerome P. Ferrance, and James P. Landers *Chitosan as a Polymer for pH-Induced DNA Capture in a Totally Aqueous System*, Anal. Chem., **78**, 7222-7228 (2006)

[2] Po Ki Yuen, Larry J. Kricka, Paolo Fortina, Nicholas J. Panaro, Taku Sakazume and Peter Wilding ,*Microchip Module for Blood Sample Preparation and Nucleic Acid Amplification Reactions*, Genome Research, **11**,405-412(2001)

[3] Qirong Wu, Joan M. Bienvenue, Benjamin J. Hassan, Yien C. Kwok, Braden C. Giordano, Pamela M. Norris, James P. Landers and Jerome P. Ferrance ,*Microchip-Based Macroporous Silica Sol-Gel Monolith for Efficient Isolation of DNA from Clinical Samples*, Anal. Chem., **78,** 5704-5710(2006)

[4] Jungkyu Kim, Karl Voelkerding, and Bruce K. Gale, *Patterning of an nanoporous membrane for multi-sample DNA extraction*, Journal of Micromechanics and Microengineering, **16**, 33-39, (2006)

SLANTWISE RADIATIVE HEATING SYSTEM FOR TEMPERATURE GRADIENT CE DETECTION OF DNA MUTATION ON A MICROFLUIDIC CHIP

H.D. Zhang[1], J. Zhou[1], Z.R. Xu[2], J. Song[1], J. Dai[3], J. Fang[1*] and Z.L. Fang[2*]

[1]China Medical University, [2]Northeastern University, [3]Shenyang Jianzhu University, Shenyang, China

ABSTRACT

A simple and robust chip-based temperature gradient capillary electrophoresis (TGCE) system was developed for DNA mutation/single-nucleotide polymorphism (SNP) detection using a radiative heating system. Reproducible, stable and uniform spatial temperature gradients with high resolution were established along the electrophoretic separation channel, for the first time, using a slanting–plate radiative heater. A wide range of DNA mutations were successfully detected under a wide temperature gradient of 10℃ and within a short gradient region of about 3 cm (3.3 ℃cm^{-1} gradient).

Keywords: Temperature gradient capillary electrophoresis, Microfluidic chip, DNA mutation, Single-nucleotide polymorphism (SNP)

1. INTRODUCTION

Temperature gradient capillary electrophoresis (TGCE) is an effective and simpler alternative to DNA sequencing for detecting SNPs and mutations. In TGCE, the DNA fragments consisting of homoduplexes and heteroduplexes are separated according to the difference of their melting temperatures. The heteroduplexes that reach their equilibrium temperatures, Tms, earlier due to mismatch exhibit retarded mobilities in the gel. The most outstanding advantage of TGCE is that it can detect mutations without knowing their exact nature, as long as the Tms of the samples studied are sufficiently close to the applied temperature gradient range. Chip-based TGCE with short separation channels are particularly attractive in offering higher efficiencies, but various heating systems developed thus far show a general lack of robustness and stability [1, 2]. In this work, we developed a simple and robust system for spatial TGCE separations using a slanting–plate radiative heater and glass chips.

2. EXPERIMENTAL

As shown in Figure 1a, a thermostated aluminium heater plate, heated by a semiconductor heating element, was slightly slanted relative to the plane of the glass chip with dimensions of 63 mm × 21 mm at 0.2 º -1.3 º by inserting thin spacers between the plate and chip at one end to produce differences in radiative heating that created the spatial temperature gradient along separation channel. 3% of PVP solution with a final concentration of 1 μM YOYO-1 was prepared in 1×TBE buffer as sieving matrix. 4 point mutant DNA model samples and K-ras gene mutations of 4 colon cancer cell lines were detected. The heteroduplex was formed by mixing, denaturing, and then reannealing.

978-0-9798064-0-7/μTAS2007/$20©2007CBMS

3. RESULTS AND DISCUSSION

Figure 1b shows the temperature distribution along the separation channel from channel crossing to detection point with 1.3 º slanting angle when the heater aluminium plate was thermostated at 85 ℃, temperature gradients of 3.5 ℃cm^{-1} were achieved within a short gradient region of about 3 cm. At different slanting angles tested, uniform thermal gradients required for performing mutation detection were established along the separation channel. Compared with results reported elsewhere [1, 2], a much shorter heating length of only 3.0 cm (4.5 cm separation length) was employed, and found to be sufficient for resolving point mutations of all samples studied.

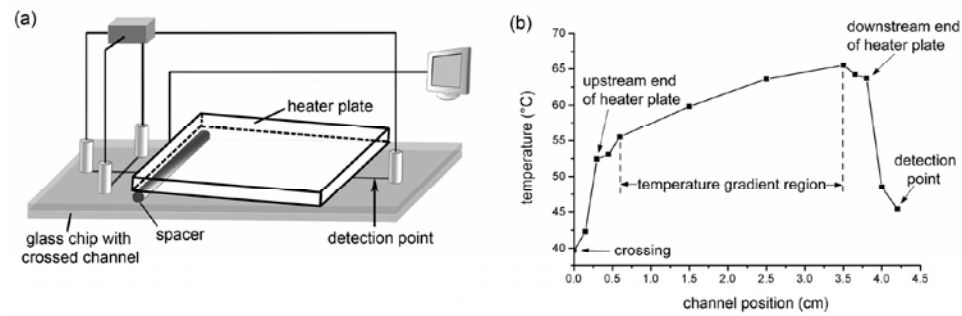

Figure 1. Schematic view of microfluidic system for TGCE analysis. (a) 3D view; and (b) temperature distribution along separation channel with 1.3º slanting angle when heater plate was thermostated at 85 ºC.

On-chip TGCE analyses of 4 point mutant DNA model samples between 144 bp and 258 bp, with a wide range of melting temperatures from 56℃ to 61℃, showed that mutations were successfully detected under a temperature gradient of 5℃ (1.7 ℃cm^{-1} gradient) which was set according to the individual melt maps of the samples (Figure 2).

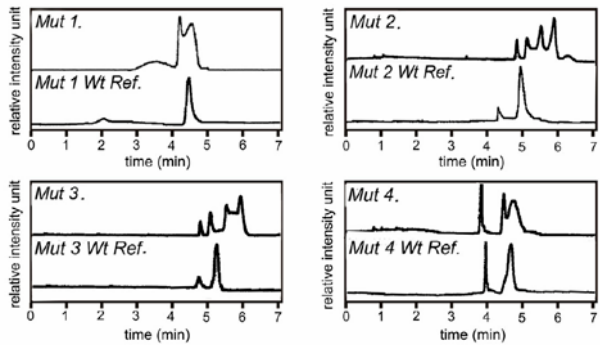

Figure 2. Electropherograms of four known point mutation samples and their wild type references employing 5 ºC temperature gradients (1.7 ºC cm-1) from 58 ºC to 63 ºC for Mut 1, from 53 ºC to 58 ºC for Mut 2 and Mut 3, and from 55 ºC to 60 ºC for Mut 4.

Further studies were performed to demonstrate the broad applicability in detecting unknown mutations without prior knowledge of the actual sequence of mutations. Figure 3 shows that the 4 mutant DNA model samples were successfully detected under a single temperature gradient of 10℃ (3.3 ℃cm^{-1} gradient).

Effectiveness of the system was demonstrated by the detection of K-ras gene mutations in colon cancer cell lines with different mutation status. Electropherograms in Figure 4 showed mutational patterns obtained by this system. Clone A cell sample with heterozygous mutation was resolved into multi-peaks, while both of the homozygous SW480 and wild type CX-1 and HT29 cells showed a single major peak. After mixing the CX-1 cells with SW480, the electropherograms of the heteroduplex and homoduplex displayed significant difference.

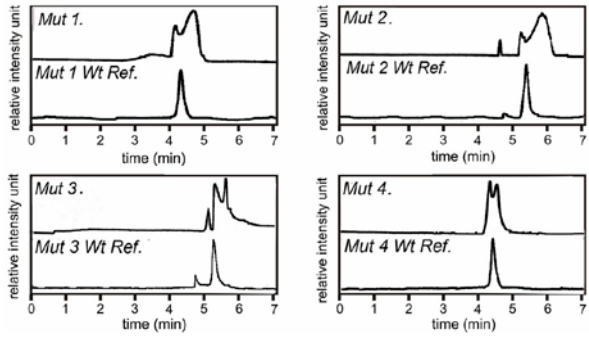

Figure 3. Electropherograms of four known point mutation samples and their wild type references with 10 ºC temperature gradient from 54 ºC to 64 ºC (3.3 ºC cm^{-1}).

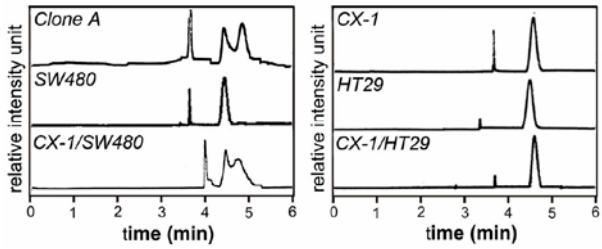

Figure 4. Electropherograms of K-ras gene in 4 colon cancer cell lines with 5 ºC temperature gradient from 55 ºC to 60 ºC (1.7 ºC cm^{-1}).

4. CONCLUSIONS

The spatial TGCE system reported here, using a glass chip and slanting-plate radiative heater, was successfully used to detect a wide range of mutations under a relatively broad temperature gradient with good stability, showing good potentials for clinical applications.

REFERENCES

[1] Q. Gao and E.S. Yeung, “High-throughput detection of unknown mutations by using multiplexed capillary electrophoresis with poly(vinylpyrrolidone) solution”, Anal. Chem. Vol. 72pp. 2499-2506:Jun.

[2] J.S. Buch, C. Kimball, F. Rosenberger, W.E. Highsmith, D.L. DeVoe and C.S. Lee, “DNA mutation detection in a polymer microfluidic network using temperature gradient gel electrophoresis”, Anal. Chem. Vol. 76pp. 874-881:Feb.

VERSATILE ACRYLAMIDE-BASED MICROCHAMBERS FOR SINGLE MOLECULAR BIOLOGICAL ASSAYS AND ANALYSIS

L. Lam[1], S. Sakakihara[1], K. Ishizuka[1], S. Takeuchi[2] and H. Noji[1]

[1]*Institute of Scientific and Industrial Research (ISIR), Osaka University, JAPAN and*
[2]*Center for International Research on MicroMechatronics, University of Tokyo, JAPAN*

ABSTRACT

Here we present the work on the development of a novel acrylamide (AA)-based femtoliter microchamber system to carry out direct observation of biological assays at the single molecule level, with the aim to achieve an improvement in reaction time and efficiency. By exploiting the porous feature of AA, various ways of manipulating biological samples can be realized. In this study, the functionality of the AA-based microchambers is demonstrated by performing the electrostretching of encapsulated DNA fragments in the presence of linear polyacrylamide (LPA) using an alternating field as well as the restriction enzyme digestion on DNA molecules without immobilization.

Keywords: Acrylamide-based, microchamber, electrostretching, digestion

1. INTRODUCTION

Typical bulk methods for biological assays are currently still widely used, however relatively long processing time and procedures are often required for effective analysis. From time to time, the evaluation results also include some degree of inaccuracy and complexity. The advancement in engineering microscale structures over the recent years has allowed many researchers to embark on the challenge of addressing these existing drawbacks by developing various chip-based techniques to down-scale analytical processes.

In our previous studies [1], we have demonstrated that femtoliter microchambers made of poly-dimethylsiloxine (PDMS) have the potentials of measuring biomolecular reactions at the single molecule level without the need for immobilization. Recently, this method was adapted to produce acrylamide (AA)-based microchambers [2]. It has been shown that the porous structure of AA permits the migration of ions and enzymes as well as the penetration of electric field through the gel matrix. By exploiting this aspect, it was possible to control the execution of biological reactions.

In this study, the viability of using this novel AA-based microchamber approach for single molecular biological assays was investigated by performing two independent functions namely DNA fragments analysis by electrostretching [3, 4] and restriction enzyme digestion. Here, we present the relationships between the stretched lengths and stretching conditions, governed by the field strength and frequency of the applied alternating field.

2. MATERIALS

The microchambers were cylindrically structured with a height of approximately 1.5 μm and a diameter of 17.5 μm. 14% acrylamide gel solution was prepared with a mixture of 30%w/v acrylamide solution, containing N, N'-Methylenebis-acrylamide (Wako, Japan), N,N,N',N'-tetramethylethylenediamine (TEMED; Wako, Japan) and ammonium persulfate (APS; Wako, Japan). The solution was then poured on a mold patterned with

978-0-9798064-0-7/μTAS2007/$20©2007CBMS

microchambers and cured at room temperature for 40 mins. *Nhe* I, *Pme* I and *BamH* I were used for the experiments. Each type of restriction enzymes digests λDNA molecules into fragments larger than 5 kbp, suitable for observations under our microscope system.

3. EXPERIMENT

In our experiments, DNA molecules stained with SYBR Gold dye were encapsulated in the AA-based microchambers using a glass needle which pushed the gel against the underlying glass slide (Figure 1). The images of activities in the microchambers were obtained through a fluorescence microscope equipped with a mercury arc-lamp, a 6% ND filter and an image intensifier unit (Hamamatsu Photonics C8600-05, Japan). For electrostretching the encapsulated fragments, 300 nm Titanium microelectrode patterns were printed onto the underlying glass slide and connected to a HP8114 pulse generator (Agilent, USA) for the input of an alternating field (Figure 3b).

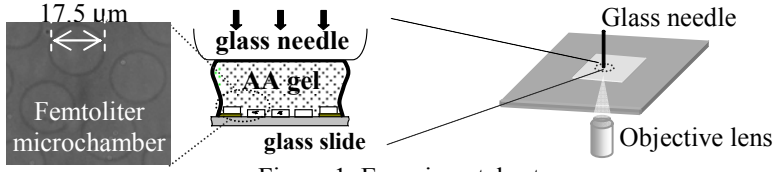

Figure 1. Experimental setup

4. RESULTS AND DISCUSSION

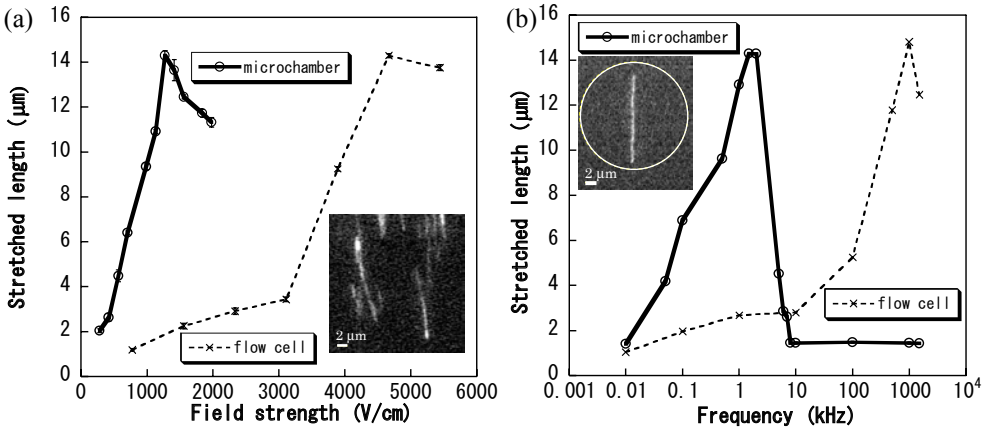

Figure 2. (a)Relationship between stretched length and field strength (inset: image of DNA stretching in flow cell), (b)Relationship between stretched length and frequency (inset: image of DNA stretching in microchamber)

The field strengths and frequencies of the applied alternating field as shown in Figures 2a and 2b respectively, were studied for electrostretching λDNA molecules using a flow cell and the AA-based microchamber. 7% LPA was included in the sample solution to facilitate the stretching process in the microchamber. In the flow cell, full stretching could be observed when subjected to the applied field strength of approximately 4600 V/cm at 1 MHz; comparable to previously reported results [3]. Meanwhile, the optimum stretching conditions for the encapsulated λDNA molecule in the AA-based microchamber were observed at approximately 1200 V/cm, 1.5 kHz. Although the applied field strengths for

both experiments were in the similar range of 10^3 V/cm, the respective frequency values differed significantly by three decades. It was also found that DNA electrostretching in microchamber can be extended to analyze non-linear DNA molecules - plasmids (Figure 3a).

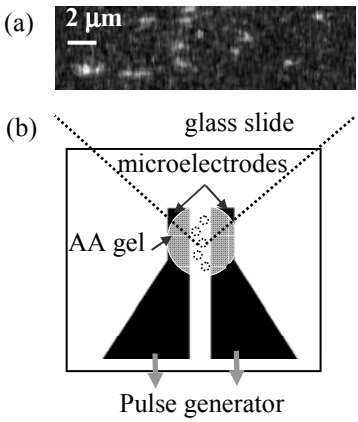

Figure 3. (a)Plasmid stretching, (b)Microelectrodes on glass slide

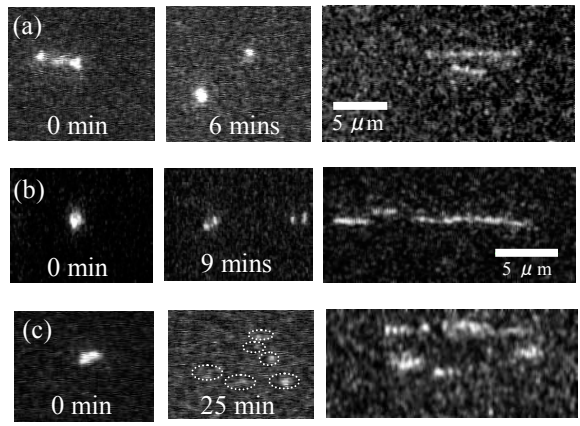

Figure 4. Electrostretching of cleaved fragments resulting from (a)*Nhe* I, (b)*Pme* I, (c)*BamH* I digestion on λDNA

For restriction enzyme assay in a microchamber, magnesium chloride solution was initially applied to the exterior of the AA gel, allowing Mg^{2+} ions to diffuse through the gel matrix to initiate the cleaving action on the encapsulated λDNA molecule (Figure 4). Upon complete digestion, the cleaved fragments were then electrostretched and the lengths were determined by direct measurement and using a conversion factor of 0.28 μm/kbp. DNA size distribution and DNA mapping can be determined by the measured fragment length [5].

5. CONCLUSIONS

Electrostretching of DNA fragments and restriction enzyme assay were performed to demonstrate the versatility of this novel AA-based microchamber system which allowed real-time observation of single-molecular DNA activities. This technique also possesses the prospect as an alternative for use in other biological applications.

REFERENCES

[1] Y. Rondelez G. Tresset, T. Nakashima, Y. Kato-Yamada, H. Fujita, S. Takeuchi, H. Noji, *Highly coupled ATP synthesis by F1-ATPase single molecules*, Nature, 433, pp. 773-777, (2005).

[2] L. Lam, K. Ishizuka, S. Sakakihara, H. Noji, *Restriction enzyme assay in femotoliter microchamber*, Proc. Micro Total Analysis Systems 2006, 2, pp. 1429-1431, (2006).

[3] M. Washizu, O. Kurosawa, *Electrostatic manipulation of DNA in microfabricated structures*, IEEE Trans. on Industry Applications, 26 (6), pp. 1165-1172, (1990).

[4] M. Ueda, *Dynamics of long DNA confined by linear polymers*, Journal of Biochemical and Biophysical Methods, 41, pp. 153-165, (1999).

[5] F.C. Minion, K.J. Jarvill-Taylor, D.E. Billings, E. Tigges, *Membrane-associated nuclease activities in mycoplasmas*, J. Bacteriol., 175 (24), pp. 7842-7847, (1990).

A MICROFLUIDIC AFFINITY APTASENSOR

T.H. Nguyen[1], R. Pei[2], M. Stojanovic[2], D. Landry[2] and Q. Lin[1]

Departments of Mechanical Engineering[1] & Medicine[2], Columbia University, USA

ABSTRACT

We present a prototype biosensor suitable for selective detection of analytes and controlled release of metabolic drug molecules. The device consists of microfabricated PDMS channels on glass with two microchambers (sensing and delivery) filled with ribonucleic acid aptamer responsive media. Using adenosine monophosphate (AMP) as an analyte and drug molecule, we demonstrate detection of trace amounts of AMP as well as controlled delivery of AMP by thermal activation. The system is viable and regeneratable in aqueous medium, providing long-term functionality on a biocompatible platform.

Keywords: Aptamer, aptasensor, drug delivery, point-of-care

1. INTRODUCTION

Modern warfare demands reliable point-of-care (POC) devices. Self-diagnoses and medical treatment under extreme duress is difficult in the field. Hence, POC chips require unambiguous sensing, stable drug delivery, and simplicity. Given such conditions, POC instruments need selective and responsive analyte recognition surfaces.

Biosensors are increasingly important components in POC chips. Antibody- and enzyme-based sensors are most common, but have limitations. Enzyme sensors require auxiliary reagents and/or separation steps [1], while antibody sensors exhibit limited shelf life and labelling degradation. Aptameric sensors based on RNA and DNA can alleviate these problems. They can be engineered for bio-specificity toward possibly any target molecule that binds nucleic acid. In addition, aptamers offer room temperature stability, easy immobilization to surfaces and controlled functionality [2].

Microfuidic POC chips may also administer drugs utilizing a responsive surface. Existing functional surfaces involve hydrophobic and ion-exchange media which lack high selectivity to target molecules [3]. Thus, unwanted impurities are retained with the target drug which degrades device performance. Unlike these former retention mechanisms, the selectivity of aptamers insures controlled retention and delivery of only the desired drug.

There are applications which may benefit from integrating biosensing and drug delivery on a single device. One example is the diagnosis and treatment of shock (hypotension and tissue death from inadequate perfusion) caused by hemorrhage (shock) or infection (septic). Our future goal is a system that manages this condition using a POC chip that detects and administers the hormonal peptide vasopressin [4]. As a model system, we present a prototype aptameric device for trace detection and controlled delivery of a metabolic steroid, adenosine monophosphate (AMP). Aptamer selectivity is tested against non-specific analytes and drug release is performed by heat activation at 36 ^{o}C. Additionally, we demonstrate device reusability by regeneration of the aptamer in an aqueous medium.

2. EXPERIMENTAL METHODS

Biotinylated adenosine triphosphate aptamer (ATP-aptamer) is purified while AMP, cytidine, uridine, and guanosine triphosphate (C/U/G-TP) are synthesized and labeled with thiazole orange. Buffer solution is prepared from Tris-HCl, NaCl, KCl, and $MgCl_2$ in

978-0-9798064-0-7/μTAS2007/$20©2007CBMS

water. Streptavidin coated agarose beads (~65 μm O.D.) provide support surfaces. A fluorescence microscope is employed for detection. Gold resistive heaters and sensors provide integrated thermal control while a syringe pump provides fluidic control.

A typical device is shown in Fig. 1a. Chambers **S** and **D** (8/4 × 0.8 × 0.3 mm) are for sensing and drug delivery, respectively. All solutions (5 μl) are introduced by channels **c1** and **c2** (height × width: 0.04 × 0.05 mm). Microbeads are packed into **S** and **D** via auxiliary side channels. Microfabrication is based on standard techniques (Fig. 1b). PDMS is poured over an SU-8 mold and cured while Cr/Au (15/150 nm) films are patterned on glass slips which are passivated by Si_xN_y. PDMS and glass are bonded after O_2 plasma treatment of the interface. Micro to macro interfaces are then produced with silica capillary tubing.

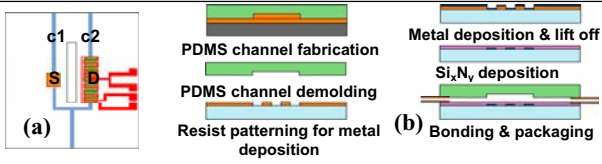

Figure 1. **(a)** Device schematic. **(b)** Chip microfabrication process flow.

The chambers are first rinsed with buffer (10 μl/min, 10 min). All following experimental washes are identical. Bio-ATP-aptamer is incubated (10 μl, 20 min) in chambers **S** and **D**. After a subsequent wash, a 10× objective is focused on a single spot in each chamber. Unless otherwise stated, AMP solution (1 μM) is introduced at 24 ^oC and 10 μl/min into the sensing and delivery chambers followed by a subsequent buffer rinse. This protocol also applies to UTP, CTP and GTP samples.

3. RESULTS

We first investigated the detection limits of the biosensor in our system. AMP is loaded in trace amounts (10^{-4}, 10^{-3}, 10^{-1}, & 1 μM; Fig. 2) into chamber **S**. Below 10^{-4} μM, no measurable signal above the background is detected. Concentrations above 10^{-4} μM however, are detectable for this device (S:N = 3:1). Additionally, this system appears to exhibit a dose responsive relationship (i.e. there is a steep linear increase in fluorescence above 0.1 μM). This may explain the detection threshold seen at the 10^{-4} μM range. Using noise analysis for this system, AMP detection on the order of 10^{-5} μM is possible with improved hardware. This is promising for practical applicability. For example, stable and shock indicating vasopressin levels in serum are 10^{-5} and 10^{-4} μM, respectively [4].

Analyte specificity is another important characteristic of the biosensor. We tested the specificity of ATP-aptamer to AMP by subjecting the sensing surface (with and without aptamer) to non-specific analytes (CTP, UTP, and GTP: 1 μM; Fig. 2b). As expected for an aptamer-free surface, all compounds produce approximately background signal. However, fluorescence is detected specifically for AMP when aptamer is present on the surface. To further emphasize the selectivity of ATP-aptamer to AMP, non-specific samples are introduced into chamber **S** directly following an AMP sample. If affinity is low, then competitive dissociation would decrease the AMP signal. As shown (Fig. 2b-iii), AMP signal is maintained which further emphasises the aptamer selectivity to target analytes.

To investigate controlled release and regenerative properties of the aptamer surface, AMP sample is retained in chamber **D** and exposed to heat (26-60 ^oC; Fig. 3a). At 36 ^oC, fluorescence decrease occurs until background levels are attained (54 ^oC). No signal implies an absence of coupled AMP/ATP-aptamer, meaning release of the drug. Hence,

adequate drug release at low temperature (36 ^{o}C) is possible. Repeatable functionality of the aptamer surface allows reusability, necessary for long-term drug treatment. To demonstrate this function, the chamber is cooled and a second AMP sample is introduced, producing a similar initial signal as the first. Implanted POC devices may require regeneration at higher temperatures (> 37 ^{o}C) which can be addressed for this system by potentially modifying the aptamer's properties.

A desirable characteristic of a drug transport mechanism is that it releases the drug completely in a controlled fashion. To generate an AMP release profile, chamber **D** is heated (36 ^{o}C) and fluorescence decrease is monitored over time (Fig. 3b). The profile suggests that AMP release is initially stalled but subsequently increases steadily until full release after 1 minute. Thus, the desired effect of a steady release profile is achieved. Presently, the kinetics of analyte release for this aptamer is not well understood. Resolving this issue can potentially enable the tuning of AMP release profiles for a given application.

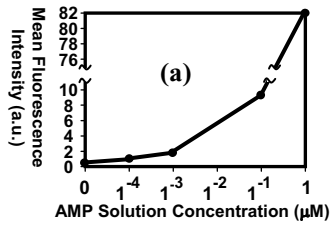

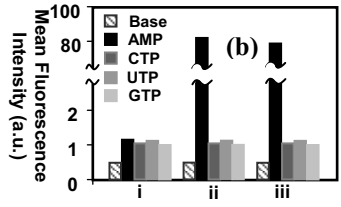

Figure 2. **(a)** Trace detection of AMP. **(b)** Selectivity of (AMP, CTP, UTP, GTP: 1 mM): **i**-non-functional surface; **ii**-functional surface; **iii**-AMP detection against competitive solution.

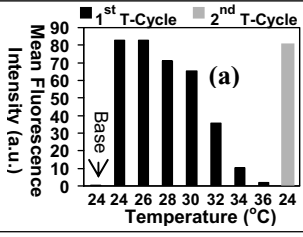

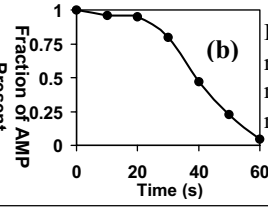

Figure 3. **(a)** Thermal release and regeneration of AMP (1 μM) from the responsive surface. **(b)** Controlled release of 1 μM sample of AMP.

4. CONCLUSIONS

We present an aptameric sensor capable of selective detection of analytes and controlled release of drug molecules. This system offers trace detection and stable delivery of AMP at 36 ^{o}C. In addition to reusability, our device is biocompatible and demonstrates a promising model for a practical shock indicating POC instrument based on vasopressin.

ACKNOWLEDGEMENTS

This research has been funded by the National Science Foundation (Grants # CBET-0693274 & EIA-0324845). We thank Mr. J. Rothsman for synthesis of labeled AMP.

REFERENCES

[1] C. O'Sullivan. "Aptasensors-the future of biosensing?" *Anal Bioanal Chem*, vol. 372, pp. 44-48, 2002.

[2] S. Tombelli et al. "Analytical applications of aptamers." *Biosens Bioelecton*, vol. 20, pp. 2224-2434, 2005.

[3] R. Majors. "New directions for concentration sensitivity…," *LC GC N. Am*, vol 19, pp. 14-25, 2001.

[4] C. Holmes et al. "Physiology of vasopressin…," *Chest*, vol. 120; pp. 989-1002, 2001.

A NEW ON-CHIP PLATFORM FOR RAPID AND EASY-TO-USE IMMUNOASSAY

Mai Ikami[1], Manabu Tokeshi[1,2], Noritada Kaji[1,2] and Yoshinobu Baba[1,2,3,4]

[1]Department of Applied Chemistry, Graduate School of Engineering,
[2]MEXT Innovative Research Center for Preventive Medical Engineering, Nagoya University, JAPAN
[3]Health Technology Research Center, AIST, JAPAN
[4]Institute for Molecular Scinece, JAPAN

ABSTRACT

We describe a new platform for chip-based immunoassay to create the effective reaction sites of immunological reaction between antigen and antibody. The reaction sites were fabricated by the UV photopolymerization of novel PEG-based polymer and the antibody-immobilized polystyrene beads. Our platform has many advantages; (i) rapid analysis (a few minutes), (ii) easy handling (no need pump and valve), (iii) low-cost (disposable), (iv) small volume (1 droplets (0.25μL) of sample and reagents), and (v) high sensitivity.

Keywords: Polystyrene bead, photopolymerization polymer, immunoassay

1. INTRODUCTION

Microfluidic devices offer a powerful platform for the integration of bioassays such as immunoassay. In the past decade, many researchers focused on the integration of immunoassay on a chip [1]. However, these microdevices suffer from the lack of a simple method for handling multiple reagents and require complicated fabrication of chips. Therefore, these are not satisfactory for practical use. To make practical use of on-chip immunoassay, it is necessary to develop a new on-chip platform for rapid, easy-to-use, low-cost, immunoassay. In this paper, we report development of a new on-chip platform for immunoassay to resolve problems as mentioned above.

2. CHIP FABRICATION

For on-chip immunoassay, the most important issue is to create the reaction sites of the reaction between antigen and antibody inside a microchannel. Although the packed bead bed formats for the effective reaction sites were proposed by several groups [2], they used the relatively large size of the beads, e.g., 20-45μm, due to easy liquid handling and low pressure drop. Our idea is to use 1 μmϕ polystyrene beads and a photopolymerization polymer (poly(ethylene glycol) (PEG)-based polymer) for the creation of the effective reaction sites with easy liquid handling. The reaction sites inside the microchannel were fabricated by the UV photopolymerization of novel PEG-based polymer and the antibody-immobilized 1 μmϕ beads (Figure 1). Microchip consisting cyclic olefin copolymer (COC) substrates (30mm×70mm) has simple straight microchannels (W: 1000μm, D: 50μm). The diameter of each reaction sites is 400μm.

3. ASSAY PROCEDURES

Since the reaction sites are located discretely in the microchannel, sample and reagents can easily be delivered by using capillary force. The protocol is shown in Figure 2. First, a

978-0-9798064-0-7/μTAS2007/$20©2007CBMS

drop of sample solution was manually dropped on an inlet by using a pipette and then the microchannel was filled with the sample solution by capillary force. After incubation, unreacted sample was sucked through an outlet. Second, a droplet of washing buffer solution was dropped on the inlet and is sucked through the outlet. Third, a drop of fluorescent-labeled secondary antibody was dropped on the inlet. After incubation, the solution in the microchannel was replaced by phosphate buffer. Finally, fluorescence intensity was detected by using a fluorescence microscope. All of these operations were carried out with capillary force and suction.

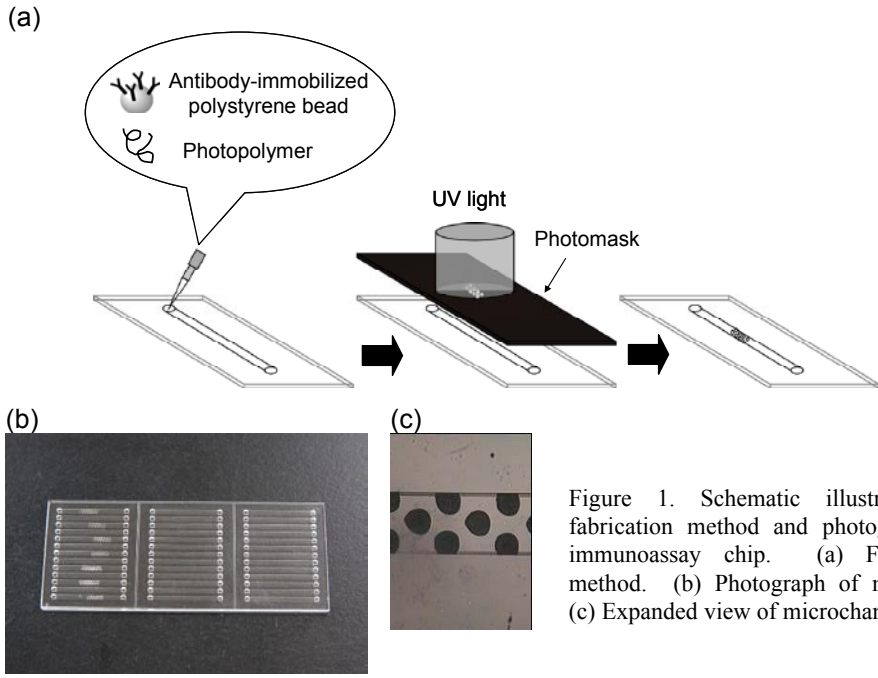

Figure 1. Schematic illustration of fabrication method and photographs of immunoassay chip. (a) Fabrication method. (b) Photograph of microchip. (c) Expanded view of microchannel.

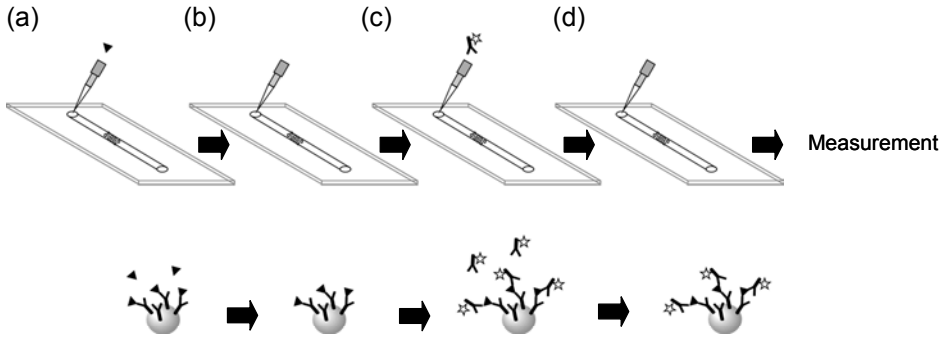

Figure 2. Assay protocol for our immunoassay chip. (a) Sample introduction. (b) Washing. (c) Fluorescent-labeled 2nd antibody introduction. (d) Washing.

4. ASSAY FOR AFP

In order to evaluate our platform, we carried out (sandwich) immunoassay for α-fetoprotein (AFP), which is known as a tumor marker. Figure 3 shows the calibration curves of AFP. In the case of 1-min incubation (total assay time: ca. 3 min), the limit of detection (LOD) was 10 ng/ml. This value is comparable to that of conventional method using a microtiter plate with 4 h of total assay time. The LOD for 3-min incubation was 2 orders lower than that of conventional one.

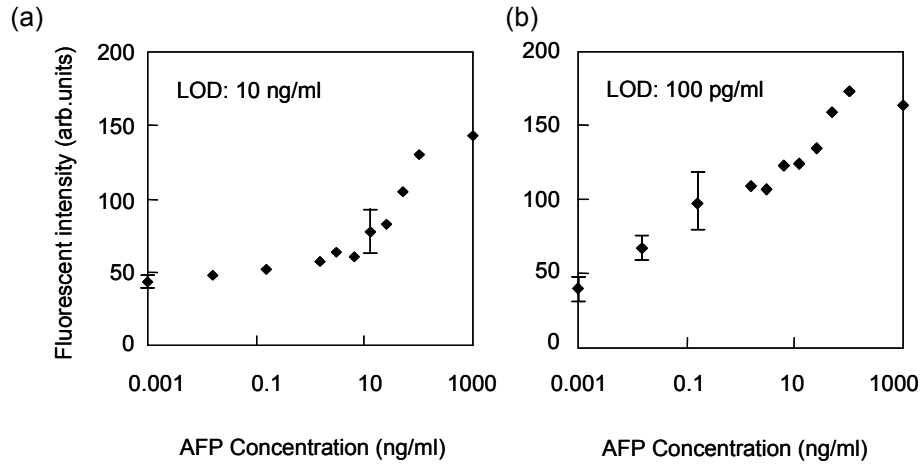

Figure 3. Calibration curves of AFP. (a) Incubation time: 1 min (total assay time: ca. 3 min). (b) Incubation time: 3 min (total assay time: ca. 7 min).

5. CONCLUSIONS

We have successfully developed a new on-chip immunoassay platform which provides rapid, easy-to-use, inexpensive and high sensitivity. We believe that this platform has a great potential for a wide range of practical applications.

ACKNOWLEDGEMENTS

The authors would like to greatful acknowledge Masaya Kakuta for his important contribution at the early stage of this research and Hiroko Takahashi for her technical assistance. This work was supported by JSPS Grant-in-Aid for Scientific Research (B) (17310037).

REFERENCES

[1] L. J. Kricka and D. Wild, *Lab-on-a-Chip, micro-, and nanoscale immunoassay systems*, In: The Immunoassay Handbook. Third Edition (Ed, D. Wild), Chapter 17, 294 (2005).

[2] C. T. Lim and Y. Zhang, *Bead-based microfluidic immunoassay: The next generation*, Biosensensors and Bioelectronics, 22, 1197-1204 (2000).

BIOMEMS FOR OSTEOPROTEOGERIN DETECTION WITH GOLD NANOPARTICLES

Kanika Singh , Hyung Hoon Kim and Kyung Chun Kim
Pusan National University, Busan, 609-735, South Korea

ABSTRACT

This paper reports a novel BioMEMS chip, based on gold nanoparticles, for the detection of Osteoproteogerin (OPG). The biochip is used to evaluate the bone conditioning which is directly related to the diagnosis and prognosis of the Osteoporosis(OP), in an effective manner [1, 2].

Keywords: BioMEMS, Gold Nanoparticles, Microfluidics,Osteoproteogerin

1. INTRODUCTION

There are different conventional methods used for the detection of OPG. One of the methods is ELISA (Enzymatic-Linked Immunoabsorbent Assay), which is, commonly used these days, complex, time consuming and expensive. Other technique used for OPG detection is, RANKL-based-sensor, but it has also drawback of poor reproducibility. A real-time piezoelectric immunosensor has been developed [3], which is regenerable and sensitive, but is not available in micron size. Miniaturization has been pursued to develop a new clinical diagnostic biochip for detection of OPG. Gold nanoparticles (AuNP) [4] are used to provide larger surface area, in combination with the conducting polymer, poly-5,2′:5′,2″-terthiophene-3′-carboxylic acid, polyTTCA which have a significant impact on the performance of immunosensors by enhancing the conductivity and sensitivity of immunosensing for OPG. The present BioMEMS-chip consists of a microfluidic channel integrated with combinatorial 2D micromixing phenomenon (combination of serpentine and chaotic mixing), CSC mixing, and electrochemical detection technique [5], showing improved performance, to enable early detection of OP, for better healthcare.

2. EXPERIMENTAL

Here, poly-dimethyl siloxane (PDMS) microfluidic channel with CSC mixing was successfully fabricated by using the well-known surface micromachining and soft lithography. The numerical simulation models with volume of fluid (VOF) using CFD-Ace, for two phase homogeneous flow model was employed to CSC micromixing of the microchannel. The end channel detection was performed using glassy carbon electrodes (GCE), and modified by growing the polyTTCA layer (TTCA monomer in a 0.1 M TBAP/CH_2Cl_2 1.0mM of solution) by electrochemical polymerization. Then electrochemical deposition of AuNPs were achieved by sweeping the potential between -0.1 V and +1.0 V versus Ag/AgCl in a 0.1 M H_2SO_4 solution containing 1mM $HAuCl_4$ at optimized scan rate of 100 mV s^{-1}. The AuNPs/polyTTCA-modified electrode were treated with EDC immobilized anti-OPG. This antibody was used for the competitive reaction between free antigen OPG and conjugated or labeled OPG with HRP for the active site of the anti-OPG. The H_2O_2 concentration as an enzyme substrate was stabilized. HRP has redox activity, which when reacted with H_2O_2 produces electronic current (see Fig.1).

978-0-9798064-0-7/μTAS2007/$20©2007CBMS

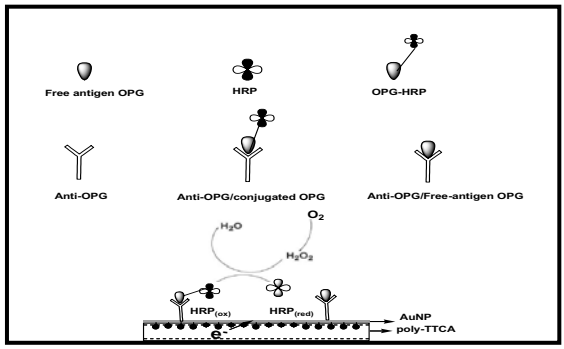

Figure 1. Electrochemical Detection Scheme

3. RESULTS AND DISCUSSION

The current response of H_2O_2 was found to be mainly due to the catalytic effect of HRP which was used as a label to OPG. The enzymatic activity was assessed by amperometric technique. The AuNPs were characterized by SEM images (Fig. 2(a)). The present BioMEMS chip is found to have mixing capabilities of 30-33% in Fig.2(b). The channel depth is 50µm, width is 100µm and length about 20000µm.

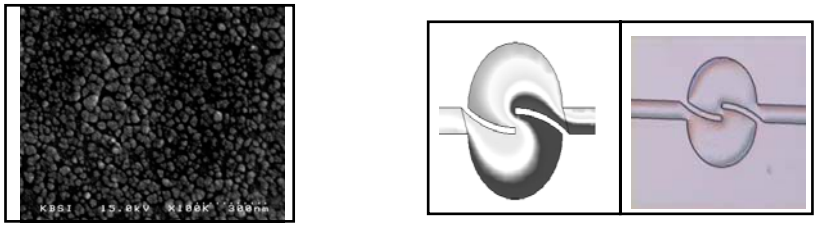

Figure 2. a) SEM image of deposition of AuNPs/polyTTCA/GCE b) CSC Micromixer: Simulation results and fabricated micromixer

The schematic diagram is shown in Fig.3(a) with the design of the bioMEMS chip with experimental set-up (Fig.3(b)) and the measurement system using the potentiostat.

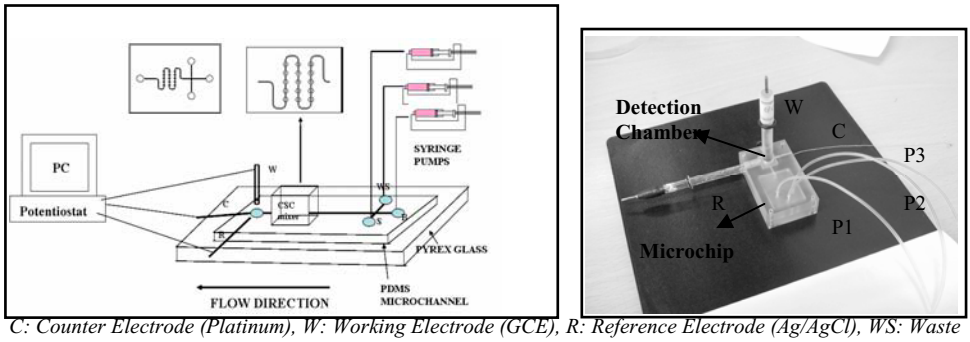

C: Counter Electrode (Platinum), W: Working Electrode (GCE), R: Reference Electrode (Ag/AgCl), WS: Waste Buffer, B: Buffer, S: Sample, P1-3: Pressure tubing, CSC: Combinatorial (serpentine & chaotic) micromixer

Figure3. (a)Schematic and (b)Experimental set-up with BioMEMS chip for detection of OPG

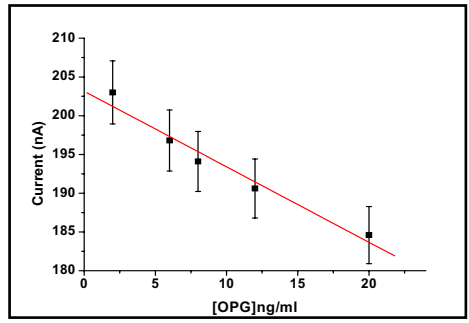

Figure 4. Amperometric response and calibration plot using OPG-HRP/Anti-OPG/AuNPs polytTTCA modified electrode towards different concentration of free OPG

Fig.4 gives the calibration plot of ampereometric current response versus concentration of OPG, decreasing the amount of HRP-OPG labeled antigen on the immobilized anti-OPG. The feasibility study confirms the success of the chip with the measuring range of the BioMEMs chip as 2-20ng/ml, response time ranges from 10-15mins and r^2=-0.986.

4. CONCLUSION

A novel BioMEMs-based chip, by using gold nanoparticles, has been developed for the detection of Osteoproteogerin (OPG). The work is in progress and the chip will be used for clinical trials with serum samples. The present BioMEMS-based chip will have a broader impact on the human society as OPG is identified as a biomarker for different deadly diseases.

ACKNOWLEDGEMENTS

This study has been supported by a grant of the KH 21 (02-DJ3-PG6-EU05-0001),Ministry of Health & Welfare, Korea. One of the authors, Kanika Singh, is thankful to Korea Research Foundation, Korea Government, for the financial support (grant no. KRF-2005-211-D00203) and to IGNOU, New Delhi, to make the investigation possible.

REFERENCES

[1] W.J. Boyle, W.S. Simonet, D.L. Lacey, *Osteoclast differentiation and activation,* Nature 423, pp.337–342, (2003).

[2] K. Singh, S.H Lee and K.C Kim, Review: *Osteoporosis: New Biomedical Engineering Aspects,* J Mech Eng Sci Technol, 20 (12), pp.2265-2283, (2006).

[3] P. Skl´adala, Z.J´ılkov´aa, I.Svobodab and Vladim´ır Kol´aˇrb, *Investigation of osteoprotegerin interactions with ligands and antibodies using piezoelectric biosensors,* Biosens. Bioelectrons. 20**,** pp**.**2027–2034, (2005).

[4] E Katz and I.Willner, *Integrated Nanoparticles-Biomolecule Hybrid Systems: Synthesis, properties, and applications*, Nanobiotechnology, Angew. Chem., 43, pp.6042- 6108, (2004).

[5] F. Darain, Ang-Un Park and Y.B. Shim, *Disposable amperometric immunosensor system for rabbit IgG using a conducting polymer modified screen-printed electrode,* Biosens. Bioelectrons, 18, pp.773-780, (2003).

MICROFLUIDIC ELISA USING MAGNETIC BEADS AND PRESSURE VALVES TO REDUCE ASSAY NOISE

M. Herrmann[1,2], E. Roy[2], M. Tabrizian[1,*] and T. Veres[2,*]

[1]McGill University, CANADA and [2]Industrial Materials Institute, CANADA

ABSTRACT

Usual surface treatments against non-specific adsorption (NSA) such as pre-coating of the channels with serum albumin, exposure to oxygen plasma, poly-ethylene glycol grafting are time-consuming and often suffer from poor stability, high associated cost or complexity. Here, we present a new generation of microfluidic ELISA that addresses the problem of NSA with an innovative design incorporating pressure valves and the precise 2-dimentional control of magnetic bead displacement. With our platform, a standard curve for the quantification of a model antibody was realized in about 30 minutes with a detection limit of 530 fM and good linearity of the signal over 1.5 orders of magnitude.

Keywords: microfluidic ELISA, non-specific adsorption, magnetic beads, PDMS valve

1. INTRODUCTION

The Enzyme-Linked Immuno-Sorbent Assay (ELISA) is common practice for protein quantification in clinical diagnostic, food quality control and environmental applications. The typical 96-well plate ELISA format however is not fit to routine or *on-field* measurements due to the large volumes of expensive reagents needed and time-consuming protocols. Since the emergence of rapid prototyping and microfluidics [1], many research groups have focused their efforts into developing low cost and rapid immunoassays [2; 3]. In microfluidic systems, the non-specific adsorption (NSA) that generates background noise and lowers sensitivity, is amplified due to the high surface-to-volume ratio of the channels. Most common treatments for passivation, such as pre-coating of the channels with serum albumin, exposure to oxygen plasma, poly-ethylene glycol grafting are time-consuming and often suffer from poor stability, high associated cost or complexity [4].

Here, we present an original concept of microfluidic ELISA, featuring dual networks of channels, pressure valves and magnetic bead manipulation, which permits to realize eight parallel ELISA measurements entirely *on-chip* without previous passivation of the microfluidic channels.

2. THEORY

The concept of microfluidic ELISA with dual networks of channels relies on the physical separation of the immune complex formation and the enzymatic reaction phases (*Fig. 1*). A first network of channels (complexation network) is used to achieve the formation of the immune complex, consisting of binding consecutive antibodies and antigens to the surface of the magnetic beads. A second network of channels (reaction network), free of non-specifically adsorbed proteins, is employed to carry on the enzymatic reaction at the surface of the beads. The two networks are independent, linked only by fluidic bridges through which the reactive beads are magnetically transferred. To ensure the complete separation of the networks, bi-layer PDMS pressure valves were incorporated in the design. These valves completely cut off the fluidic circulation between the two networks, preventing contamination, and can be transciently opened to allow the reactive bead transfer to the raction network.

978-0-9798064-0-7/μTAS2007/$20©2007CBMS

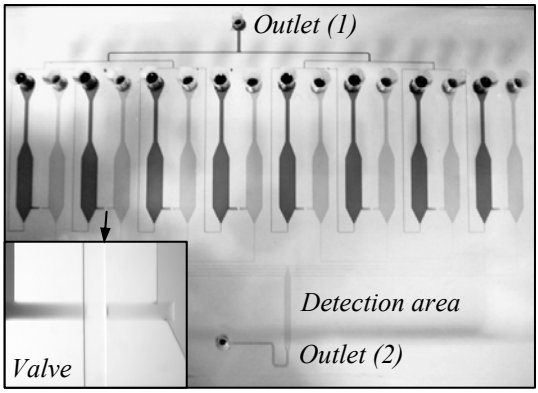

Figure 1: *microfluidic ELISA chip with pressure valves. Dark grey: complexation network (1), light grey: reaction network (2).*

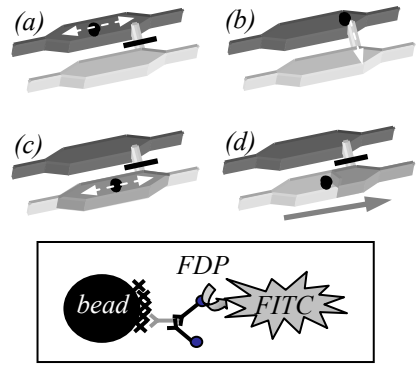

Figure 2: *formation of the immune complex (a), bead transfer (b), signal amplification (c) and detection (d).*

3. EXPERIMENTAL

All features of the masters for the two layers of PDMS (fluidic and valve layers) but the fluidic bridges were fabricated at a 40 μm height by conventional soft-lithography using SU-8 1070 (Microchem, MA). The fluidic bridges were fabricated in AZ 50xt (AZ Electronic Materials, NJ) in order to achieve a semi-circular cross-section after reflow of the positive resist. The two layers of PDMS (Sylgard184, Dow Corning, MI) forming the pressure valves were thermally bonded as previously established by Quake's group [5].

After priming the channels with a Tris-buffer 0.02% Tween-20 (TBS-T), the microfluidic chip is inserted into its support and the connection for the control channel is secured. The streptavidin-coated beads (Dynabeads® M-280 Streptavidin (2.8μm), Invitrogen, ON) are injected into the complexation network and captured inside the complexation chambers by eight individual magnets placed directly under the chip, which ones can be moved with precision in any directions. The solutions of anti-streptavidin antibodies (Rockland Immunochemicals, PA) and Alkaline-Phosphatase coupled antibodies (Anaspec, CA) are successively injected into the complexation network and incubated for 5 minutes each with gentle mixing induced by moving the beads (*Fig. 2a*). Between each step, the channels are rinsed at least once with TBS-T. The valves are transiently opened and the now reactive beads transferred inside the reaction chambers (*Fig. 2b*). A solution of FDP (Anaspec, CA) is injected into the reaction network and incubated for 5 minutes with gentle mixing (*Fig. 2c*). Finally, the reacted FDP solution (processed into FITC) is displaced to the detection area (*Fig. 2d*). A single picture taken on a fluorescent microscope (TE2000-U, Nikon) and analyzed with ImageJ (http://rsb.info.nih.gov/ij/) permits to quantify the obtained fluorescent signal. The total assay time was about 30 minutes. All data were normalized by subtracting the value of the negative control. The detection limit was defined by the concentration at 3 times the standard deviation of the control.

4. RESULTS AND DISCUSSION

In order to validate the concept of dual networks for microfluidic ELISA, a standard curve for the quantification of a model antibody was realized without previous passivation of the channels (*Fig. 3*). As a control experiment, the entire assay was performed *on-chip* in a single network with identical experimental conditions.

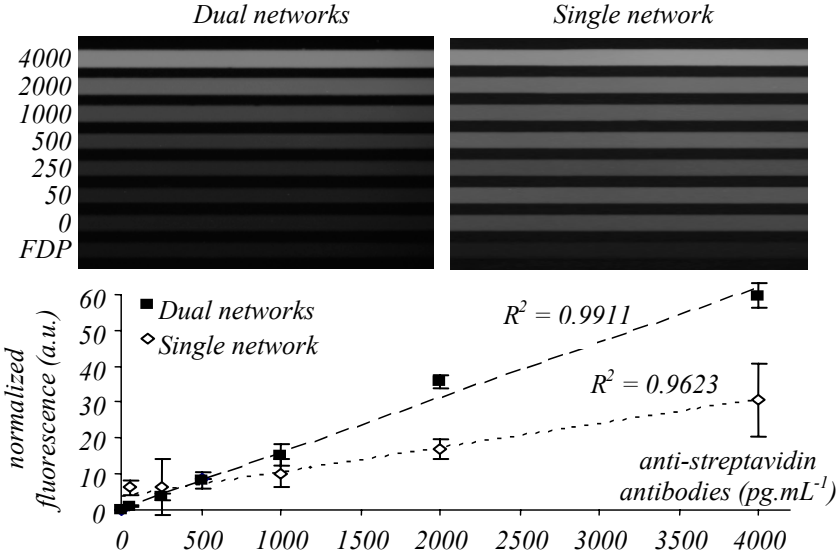

Figure 3: *Comparison of microfluidic ELISA using single or dual networks of channels*

From the fluorescent microscopy images, it is striking that the level of noise caused by NSA on the channel walls is greatly reduced in the dual network system. With the dual network protocol, a detection limit of 80 pg.mL^{-1}, corresponding to a molarity of about 530 fM, and good linearity over 1.5 orders of magnitude were observed for the tested anti-streptavidin antibody. When comparing the assays using either a single or dual networks, both the linearity and the contrast between the signals corresponding to increasing concentrations of anti-streptavidin antibodies are strongly improved in the dual network system.

5. CONCLUSION

Using our new design of microfluidic ELISA with dual neworks of channels, we achieved a standard curve for the sensitive quantification of a model antibody in about 30 minutes without the need for costly, complex and time-consuming pre-treatments. The data obtained are comparable to the performance of the most sensitive microfluidic immunoassays reported to date.

ACKNOLEDGMENTS

This work is supported by a joint grant from the Canadian Institute for Health Research and the National Research Council of Canada, as well as by the Fonds Quebecois de la Recherche de la Nature et des Technologies through the Centre for Biorecognition and Biosensors.

REFERENCES

[1] D.C. Duffy *et al.*, Anal. Chem. Vol. 70pp. 4974-4984:1998.
[2] L.J. Lee *et al.*, Adv. Clin. Chem. Vol. 42pp. 255-295:2006.
[3] M. Herrmann *et al.*, Lab. Chip. Vol. 6pp. 555-560:2006.
[4] H. Makamba *et al.*, Electrophoresis Vol. 24pp. 3607-3619:2003.
[5] M.A. Unger *et al.*, Science Vol. 288pp. 113-116:2000.

MULTI-ARRAY FLOW-FOCUSING DEVICES TO ACCELERATE PRODUCTION OF MICROBUBBLES FOR CONTRAST-ENHANCED ULTRASOUND IMAGING

Kanaka Hettiarachchi[1], Esra Talu[2], Marjorie L. Longo[2], Paul A. Dayton[2], Abraham P. Lee[1]

[1]University of California, Irvine, USA and [2]University of California, Davis, USA

ABSTRACT

The feasibility of creating integrated multiplexed flow-focusing chamber arrays for increasing the production rate of ultrasound contrast agents to an adequate level required for imaging is demonstrated. With eight connected flow-focusing chambers, we are still able to produce 5μm microbubbles. The PDMS-based microfluidic devices feature multiple flow-focusing regions and expanding nozzle geometry with a 7μm orifice width. Higher liquid flow rates are required when using multi-arrays to maintain the same microbubble size as in a single chamber system.

Keywords: Contrast Agents, Microbubbles, Microfluidics, Ultrasound Imaging

1. INTRODUCTION

The production of micron-sized monodisperse lipid shell-based perfluorocarbon gas microbubbles for use as ultrasound contrast agents was recently reported by our group [1]. However, the production rates obtainable with a single flow-focusing chamber would require on the order of 10^3 seconds to produce enough agent for a single animal contrast imaging exam (~10^7 microbubbles).

Simply increasing the gas and liquid flow rates decreases the distance between exiting bubbles, and these contact interactions cause them to coalesce due to the lower shell resistance in a high flow velocity environment as in the expansion chamber (Fig 1a), destroying the desired monodispersity of the bubble population. In addition, DPPC and DSPC lipids exist as liposomal particles in the aqueous continuous phase, and their opening up and spreading as a monolayer at the gas/liquid interface (Fig. 1b) is a dynamic adsorption process [2]. This adsorption process upstream of the orifice is affected at high rates of flow.

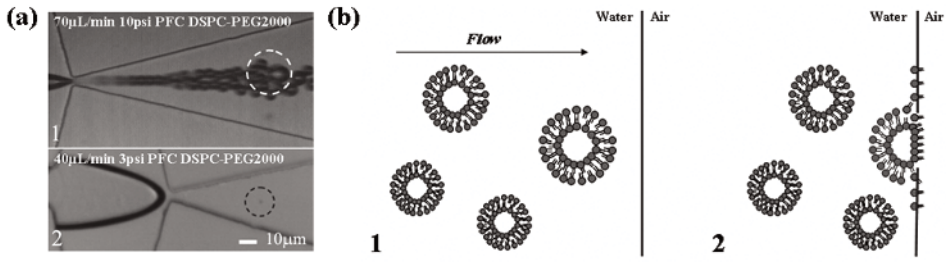

Figure 1. (a) Coalescence of microbubbles and ideal size & stability flow conditions. (b) The dynamic adsorption process of DPPC and DSPC lipids at the gas-liquid interface.

978-0-9798064-0-7/μTAS2007/$20©2007CBMS

2. THEORY

A single microfluidic flow-focusing device is shown in Figure 2a. To increase microbubble production, we investigate two, four, and eight chamber flow-focusing arrays (Fig. 2b). One key feature is that the path lengths from each flow-focusing chamber to the gas and liquid phase inlets are the same. This will ensure monodisperse bubble production in all chambers based on geometry. Incorporating only two controllable inputs (gas and liquid) (Fig. 2c) instead of the normal sixteen for eight independent flow-focusing chambers greatly reduces the complexity of the system, eliminating potential errors due to fluctuations from multiple sources.

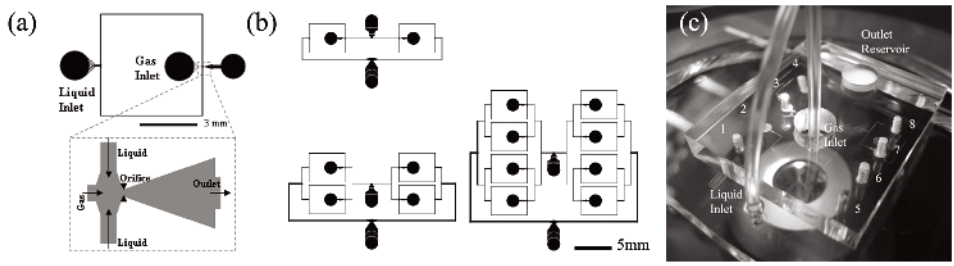

Figure 2. Schematic view of microfluidic devices with (a) single and (b) {2,4,8} flow-focusing chambers respectively. (c) The 2-layer PDMS device has two inlets (gas & liquid) and eight outlet channels that connect to a single open outlet reservoir for bubble collection.

3. EXPERIMENTAL

The devices were fabricated from a SU-8 master with the channels molded in poly(dimethylsiloxane) (PDMS) using standard soft lithography and rapid prototyping techniques. A high resolution 20,000 dpi photomask enabled designs having critical channel widths such as a 7μm orifice and closely spaced filtering channels to prevent clogging due to PDMS debris accumulation.

The PDMS flow-focusing devices were characterized by forcing a central stream of nitrogen gas and two side sheath flows of an aqueous 2% Tween 20 (polyoxyethylene 20 sorbitan monolaurate, Sigma-Aldrich) surfactant mixture through a 7μm orifice, generating microbubbles. The gas is supplied from a pressurized tank via flexible tubing and delivered into the chamber using a micro flow meter. The continuous liquid phase mixture is pumped at a constant flow rate using a digitally controlled syringe pump. A Nikon inverted microscope and high-speed camera is used to capture images and record movies of the microbubbles within devices.

4. RESULTS AND DISCUSSION

With eight connected flow-focusing chambers, we are still able to produce 5μm microbubbles. We observed several channel related effects on bubble size. PDMS is a gas permeable material with a permeability to nitrogen of 245×10^{-10}cm^3(STP)·cm/cm^2·s·cmHg. When using nitrogen, the flow-focusing chambers closest to the gas inlet produced larger microbubbles than the chambers at a greater distance away. The use of the high molecular weight perfluorocarbon gas octafluorocyclobutane (C_4F_8, MW=200) with a lower permeability in PDMS resulted in the production of consistently sized microbubbles in all flow-focusing chambers. The generated size of microbubbles increases exponentially as the array number doubles when using the same liquid flow rate and gas pressure (Fig. 3).

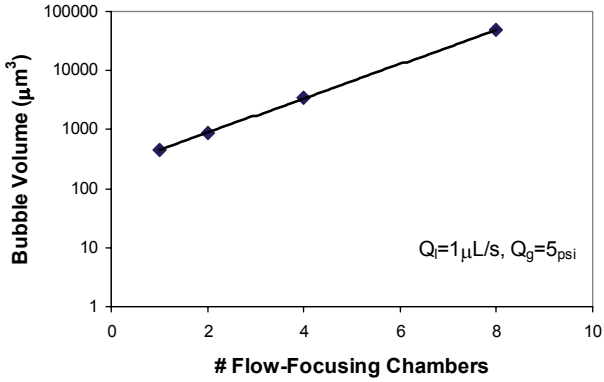

Figure 3. Relationship between the number of flow-focusing chamber arrays and bubble size for a constant gas and liquid flow rate (Tween 20 coated nitrogen microbubbles).

Higher liquid flow rates are therefore required when using multi-arrays to maintain the same microbubble size as in a single chamber system. As microbubble size and production rate are highly prone to downstream pressure conditions, it is crucial that channels remain free of debris and to monitor for surface effects that can vary the liquid flow.

Microfluidic systems are generally inexpensive to manufacture and can be easily automated for performing multiple assays or steps on a single device. PDMS-based microfluidic technology allows us to easily and inexpensively integrate and multiplex several flow-focusing circuits together, resulting in higher throughput and speed in microbubble production.

5. CONCLUSIONS

The limited production of lipid-stabilized microbubbles from a single flow-focusing system is a significant issue to overcome in order to achieve the quantity of microbubbles necessary for ultrasound imaging studies. By adjusting the flow rates accordingly, we have demonstrated the capability to produce a microfluidics system with 8 times the volumetric rate capacity of the single system. Although 8 times is not a large increase, this result demonstrates proof of the ability to multiplex, which will be important for scale-up production of these new contrast agents.

ACKNOWLEDGEMENTS

The authors would like to acknowledge funding from UC Discovery Grant BIO-ELE04-10462 and by the National Institutes of Health through the NIH Roadmap for Medical Research, Grant # 1 R21 EB005325-01.

REFERENCES

[1] K. Hettiarachchi, E. Talu, M. L. Longo, P. A. Dayton, and A. P. Lee, "On-chip generation of microbubbles as a practical technology for manufacturing contrast agents for ultrasonic imaging," Lab Chip, Vol. 7, pp. 463-468 (2007).

[2] X. Wen and E. I. Franses, "Role of Subsurface Particulates on the Dynamic Adsorption of DPPC at the Air/Water Interface," Langmuir, Vol. 17, pp. 3194-3201 (2001).

PROGRESS TOWARD A FLOW-THROUGH MEMBRANE ELISA IN A MICROFLUIDIC FORMAT

Paolo Spicar-Mihalic, Dean Y. Stevens, Paul Yager
University of Washington – Seattle, U.S.A.

ABSTRACT

We report on progress toward development of an inexpensive, disposable point-of-care diagnostic microfluidic system for use in the developing world. It will feature on-card reagent storage, low reagent consumption and a short analysis time based on a microfluidic ELISA. This paper describes a strategy to enable such an assay at subnanomolar analyte levels.

Keywords: ELISA, microfluidic, flow-through, nitrocellulose membrane

1. INTRODUCTION

Due to the demand for new sensitive immunoassays, numerous experimental approaches for using porous substrates have been proposed and investigated [1-2]. Many of them require complex and expensive instrumentation and fabrication processes. We have chosen to base our immunoassay approach on a commercial nitrocellulose (NC) membrane, an inexpensive porous substrate that has a 250-fold greater surface area than solid planar supports of the same dimensions. Although widely used in immunoassays such as dot-blot assays [3], lateral flow immunoassays [4], or analysis in 96-well flow-through format, nitrocellulose is underutilized as a substrate due to the procedures necessary to cut it into desired size and shape for a microfluidic format. We have developed a new protocol to rapidly cut nitrocellulose membranes, and have demonstrated the utility of such membranes using immunoassays for *Plasmodium falciparum* histidine-rich protein II (*Pf*HRPII) using horseradish peroxidase-3,3',5,5' tetramethylbenzidine (HRP-TMB) and gold colloid as detection systems.

2. DESIGN

To prevent nitrocellulose ignition during the process of cutting NC membranes with a CO_2 laser, the membrane was sandwiched between two thin polymer layers. This procedure also protects the membrane from cutting-generated dust and provides a simple mean of clean storage. To miniaturize the assay and minimize reagent consumption, a piezoelectric printing system was used to print sub-nanoliter volumes of protein at micrometer resolution in all three axes onto the substrate [5]. A 4×4 square pattern with a spot-to-spot distance of 900 μm was patterned on the membrane. For rapid troubleshooting of the key parameters of the immunoassay, a small vacuum platform was fabricated that allows simple transport of samples, secondary antibody and amplification reagents through the membranes. The vacuum is controlled by using a system of valves, regulators and a gauge that enables maintaining reproducible experimental conditions.

978-0-9798064-0-7/μTAS2007/$20©2007CBMS

3. EXPERIMENTAL

Two detection methods are being investigated - HRP/TMB with a blue precipitate as the end product [6] and gold nanoparticles as a direct labeling agent. A membrane onto which capture antibody has been printed is placed onto a metal mesh support (40,000 openings per square inch, with a wire diameter of 40 μm) and covered with chemically-resistant silicone rubber. A miniature vacuum regulator controls the flow rate (1.0-2.0 μL/s). This simple system enables fast and reliable single-membrane, multi-spot experiments. Given the fast kinetics of the antigen-antibody reaction, we decided to premix the reagents, lowering the total volume of reagents to only 400 μL and significantly reducing the total assay time. *Pf*HRPII (*MW* 95,000) was assayed in a range from 6.25 ng/mL to 200 ng/mL (0.066 nM - 2.105 nM). Experiments were performed under continuous flow, requiring 6 minutes for the HRP/TMB system and 4 minutes for the gold nanoparticle system. Experimental steps are schematically shown in Figure 1. Gold colloid with a 40 nm diameter was produced by reduction of tetrachloroauric acid with trisodium citrate [7]. Immunogold conjugates were formed by sequential incubation of the colloid with anti-PfHRP2 IgG and BSA, followed by centrifugation and resuspension [8].

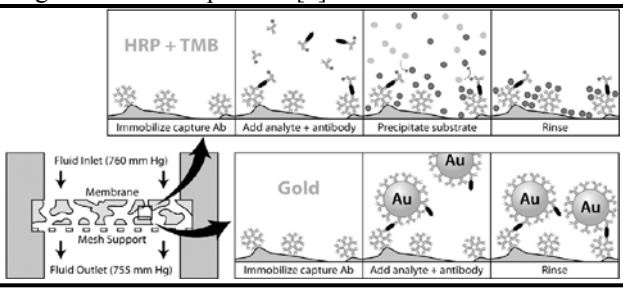

Figure 1. *Schematic representation of the flow-through immunoassay detected using the HRP/TMB amplification system (upper images) and gold colloids (lower images)*

4. RESULTS AND DISCUSSION

Ideally, in a sandwich flow-through immunoassays the intensity of the signal depends on the concentration of antigen (Figure 2). Upon completion of the experiments, membranes were imaged on a flatbed scanner and the intensity was measured using ImageJ software (NIH). The normalized intensity was calculated by using the following formula:

$$NI = \frac{I_B - I_S}{2^{BD}}$$

NI - normalized intensity
I_B - background intensity, green channel
I_S - sample intensity, green channel
BD - bit depth

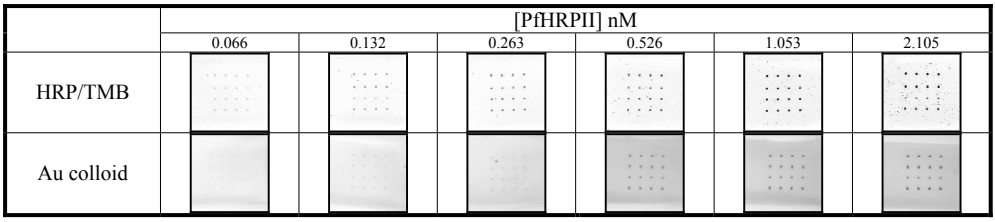

Figure 2. *Scanned images of the developed membranes (top) - comparison between HRP/TMB and Au nanoparticle detection system (bottom).*

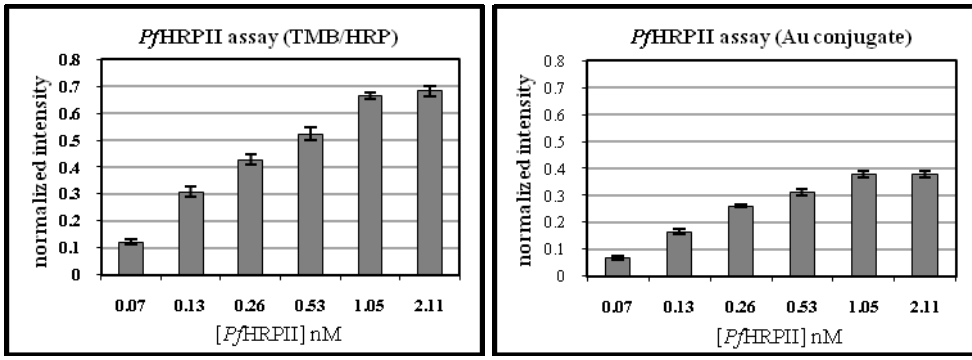

Figure 3. *Dependence of the signal intensity (green channel) on the analyte concentration for the amplified system (left) and unamplified system (right).*

These preliminary experiments indicate that the HRP/TMB system has a lower limit of detection than gold nanoparticles. The slope representing the dose response also differs between the two methods, but both assays achieve signal saturation when the total mass of antigen exceeds 30 ng (0.316 pmol).

ACKNOWLEDGMENTS

The work has been supported by a grant from the Bill & Melinda Gates Foundation**.** The authors would like to Drs. Roger Peck and Cori Barfield for their assistance with gold conjugation as well as Drs. Ken Hawkins and Jennifer Foley for helpful discussions.

REFERENCES

1. McDevitt J. T. et al., *Application of microchip assay for the measurement of C-reactive protein in human saliva.* Lab on a Chip. **5**: p. 261-269, (2005).
2. Krishnan**, R.**, Ghindilis, A.L., Atanasov, P., Wilkins, E., Montoya, J., Koster, F.T., *Fast amperometric immunoassay for hantavirus infection.* Electroanalysis. **8**(12): 1131-1134, (2005).
3. Ziegler, A., Mayo, M. A., Torrance, L., *Synthetic antigen from a peptide library can be an effective positive control in Immunoassays for the detection and identification of two geminiviruses.* Phytopathology. **88**: 1302-1305, (1998).
4. Wilkinson, R., Rowland, D., Ching, W. M., *Development of an improved rapid lateral f low assay for the detection of orientia tsutsugamushi-specific IgG/IgM antibodies.* Ann. N.Y. Acad. Sci. **990**: 386-390, (2003).
5. Hasenbank, M., Edwards, T., Fu, E., Garzon, R., Kosar, F., Mashadi-Hossein, A, Yager, P., *A versatile piezoelectric printing method for multi-analyte detection applications.* Lab. Chip. – submitted
6. Mesulam, M.M., Hegarty, E., Barbas, H., Carson, K.A., Gower, E.C., Knapp, A.G., Moss, M.B., Mufson, E.J., *Additional factors influencing sensitivity in the tetramethyl benzidine method for horseradish peroxidase neurochemistry.* The Journal of Histochemistry and Cytochemistry. **29**(11): p.1255-1259, (1980).
7. Deroe, C., Courtoy, P.J., Baudhuin, P., *A Model of Protein Colloidal Gold Interactions.* Journal of Histochemistry & Cytochemistry. **35**(11): p. 1191-1198, (1987).

RAPID DETECTION OF KINASE TRANSLOCATION AT THE SINGLE CELL LEVEL ON A MICROFLUIDIC CHIP

Jun Wang[1], Ning Bao[1], Leela L. Paris[2], Hsiang-Yu Wang[3], Robert L. Geahlen[2] and Chang Lu[1, 3, 4, 5]

[1]Departments of Agricultural and Biological Engineering, [2]Department of Medicinal Chemistry and Molecular Pharmacology, [3]School of Chemical Engineering, [4]Birck Nanotechnology Center, [5]Bindley Bioscience Center, and Purdue University, USA.

ABSTRACT

Detection of localization of kinases within cells has been largely carried out based on imaging of a low number of cells or subcellular fractionation/Western blotting which provide only the average behaviors of cell populations. Here we demonstrate a new tool, referred to as microfluidic electroporative flow cytometry (EFC), to detect the translocation of an EGFP-tagged tyrosine kinase, Syk, to the plasma membrane in B cells at single cell level. Due to the frequent involvement of kinase translocations in disease processes such as oncogenesis, our approach will have utility for kinase-related drug discovery and tumor diagnosis and staging.

Keywords: translocation, electroporation, flow cytometry, microfluidics, Syk, kinase

1. INTRODUCTION

Translocation of a protein between different subcellular compartments is a common event during signal transduction in living cells. Integrated signaling cascades often lead to the relocalization of protein constituents such as translocations between the cytoplasm and the plasma membrane or nucleus. The protein-tyrosine kinase, Syk, is a prime example of a protein that translocates to the plasma membrane as part of its role in signal transduction.

Determination of the translocation of kinases within cells has been traditionally carried out using methods such as subcellular fractionation/Western blotting or imaging of a few cells. However, when heterogeneous cell populations (e.g., samples derived from primary materials) are studied, it is always beneficial to obtain quantitative information of the entire population at the single cell level to prevent cell subsets from being overlooked. As the present techniques have their own limitations, a new high-throughput technique is introduced here, which we refer to as electroporative flow cytometry (EFC), to observe the translocation of the kinase Syk from the cytoplasm to plasma membrane at the level of the cell population with information gathered from single cells. We found that the amount of SykEGFP left in the cells after electroporation was related to whether or not translocation of Syk to the plasma membrane occurred. Microfluidic EFC was able to detect the translocation of Syk and provide characteristics of the entire cell population in terms of the release of the intracellular kinase. We envision that the same mechanism can be extended to the detection of translocations involving other kinases and cell types.

2. EXPERIMENTAL

Microfluidic EFC devices with varied geometry (Fig. 1*A*) were fabricated based on PDMS using standard soft lithography method [1]. One half of the SykEGFP-DT40-Syk$^-$-Lyn$^-$ cells (10^6 cells/ml) were kept unstimulated, while the other half were stimulated with 50 μg/ml goat anti-chicken immunoglobulin M (IgM) antibody for 1 h at 20 °C. To establish a negative control, both stimulated and unstimulated DT40- Syk$^-$-Lyn$^-$ cells were labeled with a fluorogenic dye, calcein AM.

978-0-9798064-0-7/μTAS2007/$20©2007CBMS

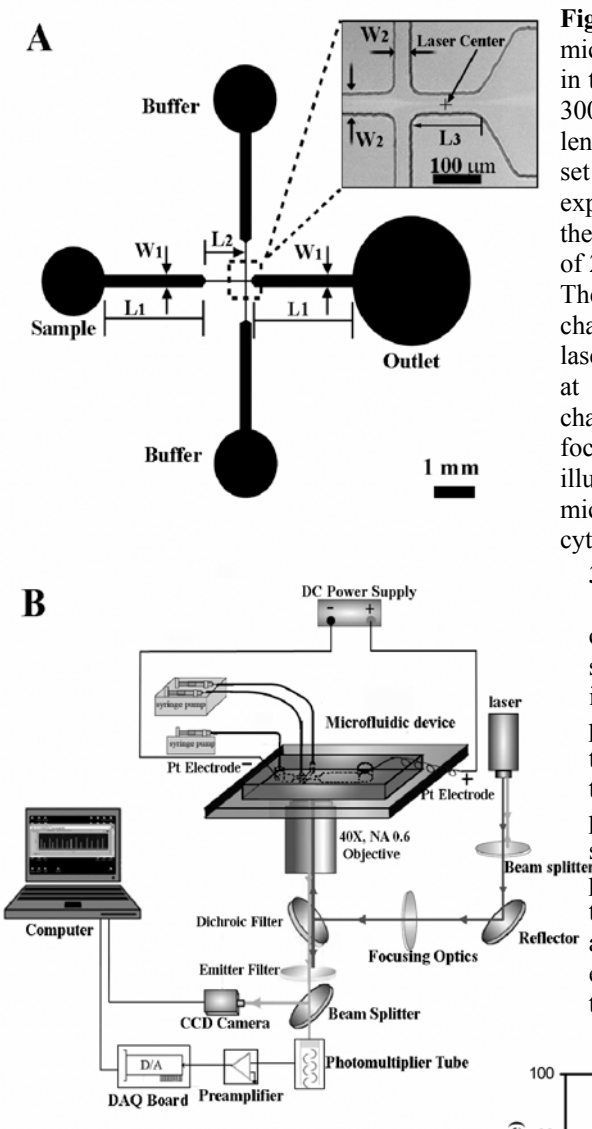

Fig. 1. (*A*) The layout of the microfluidic chip. The width varied in the horizontal channel with W_1 of 300 μm and W_2 of 33 μm. The length of the narrow section L_2 was set as either 1 or 2 mm in different experiments. The other sections in the horizontal channel had a length of 2.5 mm for L_1 and 150 μm for L_3. The depth of the microfluidic channels was uniformly 33 μm. The laser detection point was positioned at the center of the horizontal channel after hydrodynamic focusing. (*B*) A schematic illustration of the setup of the microfluidic electroporative flow cytometry apparatus.

3. RESULTS AND DISCUSSION

Chicken B cell population containing EGFP tagged Syk stimulated with anti-IgM (which induced translocation of Syk to the plasma membrane) had more EGFP tagged Syk remaining in cells after the electroporation than the population which was not stimulated (Fig. 3A and B). We proposed that the binding between the surface receptor and Syk was able to retain the kinase during electroporation when Syk was translocated to plasma membrane.

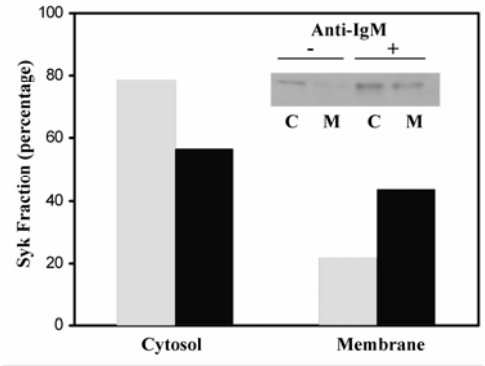

Fig. 2. Western blotting analysis of the SykEGFP fraction in the cytosol and on the membrane with (black) and without (grey) stimulation by anti-IgM Antibody. By measuring the SykEGFP percentages in the cytosol and on the membrane, on average 22% of SykEGFP was translocated to the membrane when the cell was stimulated.

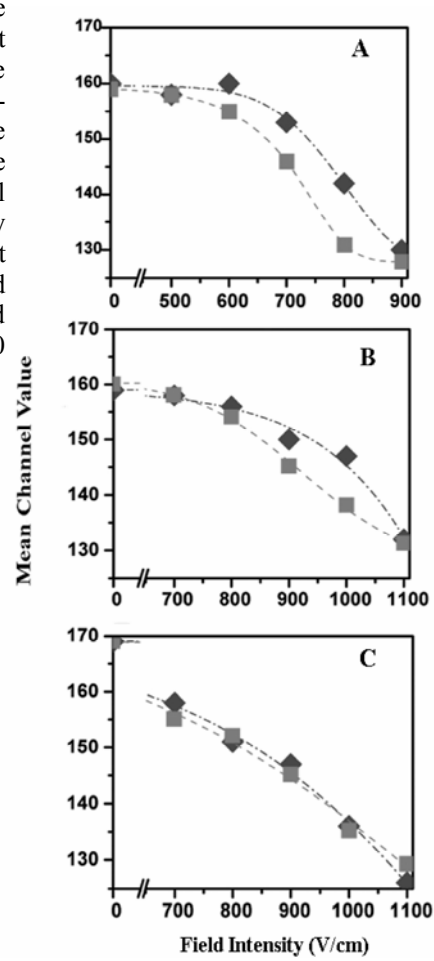

Fig. 3. The variation of the mean fluorescence intensity value of the cell population at different field intensities with (black) and without (grey) the stimulation by anti-IgM Abs. SykEGFP-DT40-Syk$^-$-Lyn$^-$ cells were applied in (*A*) and (*B*), while calcein AM stained DT40-Syk$^-$-Lyn$^-$ cells were used in (*C*). The black dots were generated by cell populations stimulated by anti-IgM and the grey dots were obtained from cell populations without stimulation. The data in (*A*) and (*B*) were obtained with different electroporation durations of 120 and 60 ms, respectively. The duration in (C) was 60 ms.

We did not observe significant difference between the cell population added with anti-IgM and the population without the antibody at any field intensity when the cells were labeled with calcein AM (Fig. 3C). This confirms that the differentiation was closely related to the translocation of SykEGFP. The extent of the differentiation between the stimulated and unstimulated populations reached its maximum at 800 V/cm when the electroporation duration was 120 ms and at 1000 V/cm with 60 ms. It is estimated that the average percentage of EGFP-tagged Syk translocating to the plasma membrane in the cell population was around 16.8%~ 21.2% which is comparable to 22% obtained using subcellular fractionation/Western blotting under similar stimulation conditions (Fig. 2).

4. CONCLULSIONS

By combining electroporation with flow cytometry, we demonstrate microfluidic EFC as a new tool to differentiate cell populations with different activation states based on the subcellular localization of a kinase. Microfluidic EFC offers a simple and robust physical tool for detecting kinase translocation within the scope of the entire cell population. This microfluidics-based technology provides a platform that is well suited for both research and clinical settings and will potentially contribute to drug discovery as well as having utility for both biomarker analysis and patient-stratification.

ACKNOWLEDGEMENTS

We thank Purdue University and grant CA37372 from the National Cancer Institute for the financial support.

REFERENCES

[1] J. Wang and C. Lu, Microfluidic cell fusion under continuous direct current voltage. *Applied Physics Letters* 89, 234102 (2006).

STORAGE AND REACTIVATION OF ENZYMES IN A DISPOSABLE, SELF-CONTAINED LAB-ON-A-CHIP SYSTEM

A. Gulliksen[1, 2], M.M. Mielnik[3], E. Hovig[4], F. Karlsen[1], L. Furuberg[3] and R. Sirevåg[2]

[1] NorChip AS, NORWAY, [2] University of Oslo, NORWAY
[3] SINTEF, NORWAY, [4] The Norwegian Radiumhospital, NORWAY

ABSTRACT

For a point-of-care chip, it is important to have reactants stably stored on-chip. In this study, deposition and drying of a solution of three enzymes have been examined. The time for diffusion/rehydration of fluorescently labelled mouse IgG in the dried enzyme solution was ~10 minutes. Microchips with native cyclic olefin copolymer (COC) surfaces showed large adsorption of mouse IgG, while polyethylene glycol (PEG) coated surfaces showed adequate protein resistance. Successful amplification on chip in 500 nl reaction chambers was obtained for spotted and dried enzymes when mixed with 0.5% PEG 8000.

Keywords: NASBA, mRNA amplification, fluorescence detection, diagnostics

1. INTRODUCTION

In this work, which is part of a project aimed at the development of a self-contained disposable microchip, we have explored an approach for stabilization and storage of three labile enzymes (AMV-RT, RNase H and T7 RNA polymerase) in a single formulation on-chip for the isothermal amplification of mRNA and ssDNA by nucleic acid sequence-based amplification (NASBA) [1]. Similar work has been performed by Weigl and co-workers [2] for air drying and reactivation of PCR mixes in conventional macro scale volumes using 96-well plates. While PCR is only dependent on the activity of one enzyme for amplification, NASBA requires 3 functional enzymes. NASBA has previously been demonstrated on-chip with premixed reagents [3]. The work reported herein evaluates the reactivation of enzymes after drying on-chip. To our knowledge, this is the first time the NASBA enzymes have been successfully dried and reactivated in a microchip. For self-contained systems, both liquid and dried reagents have been proposed as plausible solutions for long-term on-chip storage of reagents [4, 5].

2. EXPERIMENTAL

For the experiments, COC chips were employed Figure 1 (a). The microchips were O_2 plasma activated prior to coating with 0.5% PEG in methanol (Sigma Aldrich Norway AS, Norway). The NASBA reagents were provided in the PreTect HPV-Proofer kit (NorChip AS, Norway). A stabilizing agent, PEG 8000 (Sigma Aldrich Norway AS), was added to the enzyme solution prior to spotting and drying. For the enzyme wall adsorption and the diffusion experiments, fluorescently labelled mouse IgG (Southern Biotech, Birmingham, AL) was used as a model molecule. The microchips were spotted with enzymes, dried in room temperature for up to 2 days before they were sealed with adhesive tape. The amplification reaction was performed by manually mixing the NASBA reagents, including the positive control sample of human papillomavirus (HPV) type 16. The mixture was first incubated at 65˚C for 3 minutes followed by 3 minutes at 41˚C. The microchip containing the dried enzymes was adjusted to 41˚C before 1 µl reaction mixture was applied to each

978-0-9798064-0-7/µTAS2007/$20©2007CBMS

reaction chamber on the microchip. A custom-made instrument recorded the fluorescent signal of the amplification reaction at 41˚C [3].

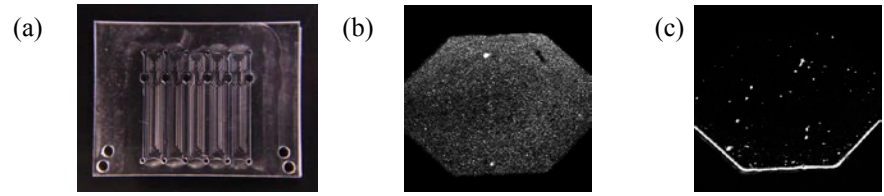

Figure 1. (a) COC microchip fabricated using hot embossing. The outer dimensions of the chip were 43 mm × 32 mm, while the dimensions of the reaction chambers were 1.6 mm × 1.6 mm × 0.2 mm, corresponding to a volume of 500 nl. (b), (c) Adsorption of fluorescently labelled mouse IgG on native COC and PEG coated COC surfaces. (b) The native COC surface was only plasma activated. No amplification could be observed for microchips with native COC surfaces. (c) The PEG coated COC surface showed adequate resistance to the fluorescently labelled IgG. PEG coated surfaces gave successful amplification reactions.

3. RESULTS AND DISCUSSION

Adsorption of enzymes to the microchip surface, as well as the process of rehydration of the dried enzymes in the liquid sample, were investigated experimentally using confocal laser scanning microscopy (CLSM). Both native COC and PEG coated surfaces were incubated with NASBA reaction mixture including fluorescent IgG at 41˚C for 2.5 hours followed by a washing step with water. The native COC surfaces showed large adsorption of IgG, while PEG coated surfaces showed adequate protein resistance, Figure 1 (b) and (c).

For the diffusion measurements, the enzyme solution was mixed with fluorescent IgG prior to spotting and drying. Rehydration and diffusion of the fluorescent IgG species were essentially completed after approximately 10 minutes, see Figure 2.

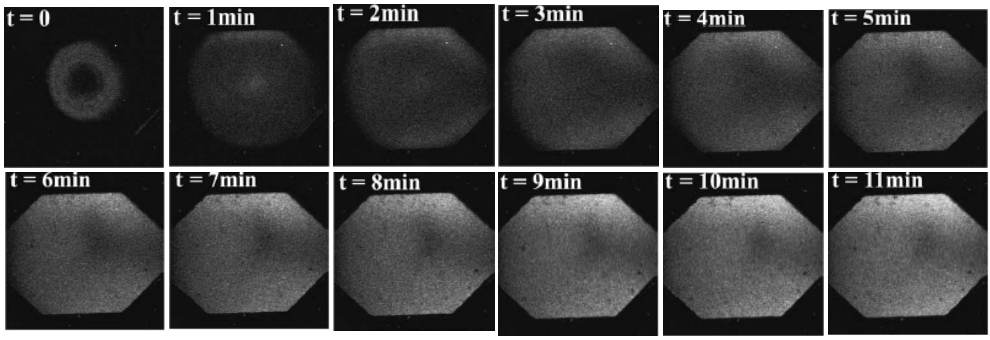

Figure 2. Rehydration of dried enzymes, temporal evolution. The time between frames was 1 minute. The dissolving liquid was a solution of all the NASBA reagents except the enzymes. The dried enzyme spot was inside a 500 nl chamber. All images were taken with the focal plane positioned 150 µm above the bottom wall of the reaction chamber.

The estimated time of diffusion time for a distance of 150 µm was ~3 minutes. The observed longer time required, may indicate that the process was dominated by rehydration and not by diffusion. The fluorescent IgG tracer (150 kDa) modelled the largest enzyme (AMV-RT, 160 kDa).

Figure 3 shows amplification curves of the 500 nl reaction chambers for reactivation of spotted and dried enzymes containing 0.5% PEG 8000. No amplification was observed when PEG 8000 was excluded in the drying procedure. The 10 minutes required for enzyme dissolution was shown to be acceptable.

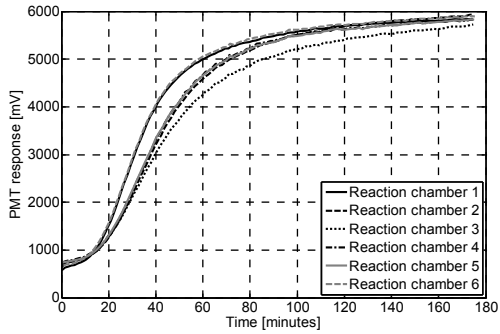

Figure 3. Amplification curves of the six 500 nl reaction chambers run simultaneously on one microchip employing a sample of positive control for HPV type 16 (0.1 μM). The dried enzymes including PEG 8000 were rehydrated after one day at room temperature.

4. CONCLUSIONS

The present work demonstrates on-chip storage of dried enzymes which are reactivated upon rehydration of sample. These results are promising with regard to the development of disposable, self-contained microchips for NASBA.

ACKNOWLEDGEMENTS

This work has been partially financed by an EU-project (MicroActive – Automatic Detection of Disease Related Molecular Cell Activity - IST-NMT-CT-2005-017319). The authors would like to thank Dr. L. Solli (NorChip AS) for valuable discussion about design of the microchips and the results obtained. Thanks to Dr. I-R Johansen and H. Schumann-Olsen (SINTEF) for helping with the custom-made instrument. Thanks to Dr. R. Gransee (IMM, Germany) for manufacturing of the COC chips.

REFERENCES

[1] J. Compton, *Nucleic acid sequence-based amplification*, Nature, 350, 91 (1990)

[2] B. H. Weigl, J. Gerdes, P. Tarr, P. Yager, L. Dillman, R. Peck, S. Ramachandran, M. Lemba, M. Kokoris, M. Nabavi, F. Battrell, D. Hoekstra, E. J. Klein and D. M. Denno, *Fully integrated multiplexed lab-on-a-card assay for enteric pathogens*, Proc. of SPIE, 6112, 1 (2006)

[3] A. Gulliksen, L. Solli, K. S. Drese, O. Sörensen, F. Karlsen, H. Rogne, E. Hovig and R. Sirevåg, *Parallel nanoliter detection of cancer markers using polymer microchips*, Lab Chip, 5, 416 (2005)

[4] E. Garcia, J. R. Kirkham, A. V. Hatch, K. R. Hawkins and P. Yager, *Controlled microfluidic reconstitution of functional protein from an anhydrous storage depot*, Lab Chip, 4, 78 (2004)

[5] V. Linder, S. K. Sia and G. M. Whitesides, *Reagent-loaded cartridges for valveless and automated fluid delivery in microfluidic devices*, Anal Chem, 77, 64 (2005)

COMBINED LAB-ON-A-CHIP AND MICROARRAY APPROACH FOR BIOMOLECULAR INTERACTION SENSING USING SURFACE PLASMON RESONANCE IMAGING

G. Krishnamoorthy, J.B. Beusink, E.T. Carlen, S. Schlautmann, H.L. de Boer, A. van den Berg and R.B.M. Schasfoort

Biochip Group/BIOS, MESA+ Research Institute, The Netherlands.

ABSTRACT

Surface plasmon resonance imaging (SPR) is a well-established label-free detection technique for real-time biomolecular interaction measurements. An integrated Lab-on-a-chip (LOC) sensing system with fluidic control for sample movement to specific locations on the microarray surface in combination with SPR imaging is demonstrated by the measurements of human IgG and anti-IgG interactions from 24 patterned regions.

Keywords: SPR, Biomolecular Interaction, Microarray, Lab-on-a-chip

1. INTRODUCTION

Lab-on-a-chip systems are rapidly becoming vital for the miniaturization of analytical techniques for various applications, such as genomics and proteomics [1]. LOC systems with integrated fluidic transport capability combined with SPR imaging provides a powerful technique to perform label-free multi-analyte interaction measurements in microarray formats [2]. Multi-analyte detection in microarray formats is very important in the field of medical diagnostics and drug discovery. The goal of this article is to develop a multi-analyte immunoassay based on a SPR imaging platform and integrated microfluidics with fluidic transport for sample addressing.

2. PRINCIPLE OF SURFACE PLASMON RESONANCE IMAGING

SPR imaging, a typical system is shown in figure 1a, is based on the excitation of surface plasmons of a thin metal layer (~50 nm), most commonly gold, by excitation with p-polarized light. With the excitation source at a certain angle of incidence the free electron oscillation reaches a maximum and an evanescent field is enhanced at the dielectric-gold

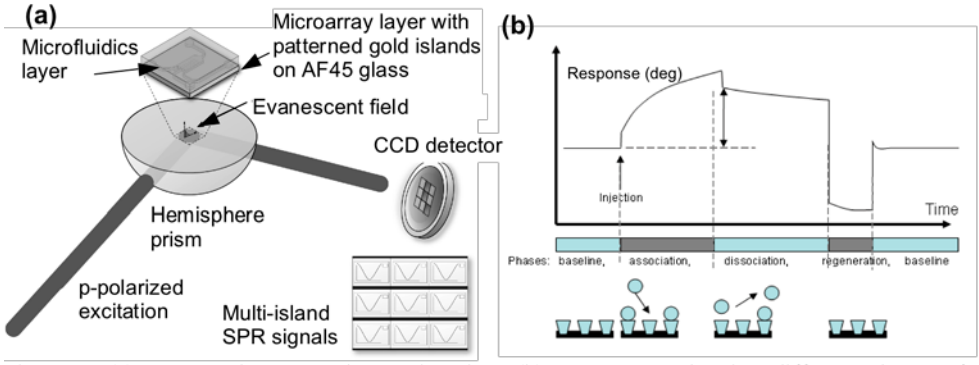

Figure 1. (a) Integrated LOC and SPR imaging; (b) sensorgram showing different phases of biomolecular interaction.

interface. The amount of substance adsorbed at the surface during immobilization and

978-0-9798064-0-7/μTAS2007/$20©2007CBMS

antibody-antigen binding results in a measurable change in the surface plasmon resonance condition. In this case, the change in angle is measured temporally upon binding, shown qualitatively in the sensorgram in figure 1b. The baseline phase establishes a starting point before introducing the target analyte to the prepared surface. The association phase shows an increasing sensor response as the injected target analyte is injected and binds to the immobilized probe on the sensor surface. The dissociation phase results following the injection of a running buffer and non-specifically bound molecules dissociate from the surface. The regeneration phase proceeds with the injection of low pH buffers to remove bound target analytes. Following the regeneration phase the sensor response should return near the starting baseline signal.

3. SYSTEM DESIGN

The sensing system consists of a commercially available surface plasmon resonance imaging system (iSPR, IBIS Technologies, b.v., Hengelo, The Netherlands) integrated with a LOC system with multiple sample inlets and outlets and electrodes for electrokinetic fluidic transport. Figure 1(a) shows a schematic of an integrated system.

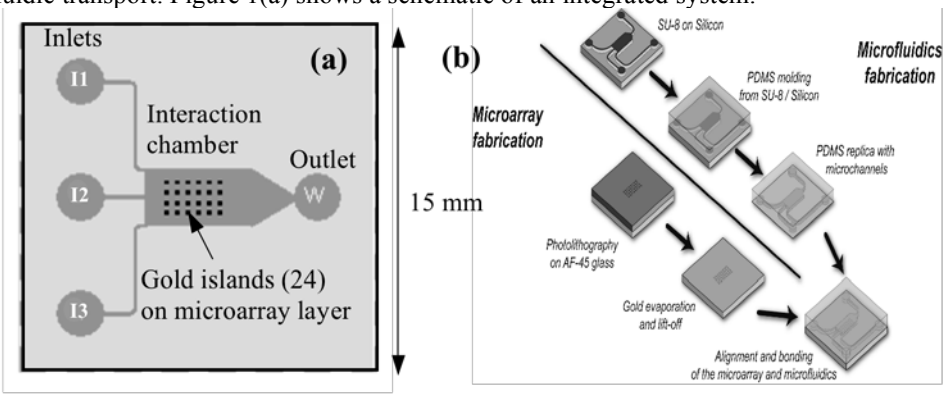

Figure 2. (a) top microfluidic layer with inlets (I1-I3), waste outlet (W), microchannels and interaction chamber. The microarray layer contains the patterned gold islands within the interaction chamber. (b) Two-path microfabrication process diagram used for manufacturing the LOC system. The microarray and microfluidic layers are aligned and bonded together realizing the final composite structure.

The schematic of the LOC system is shown in Figure 2(a). The microfluidic layer consists of an interaction chamber that is interconnected with three inlets I1-I3 for a buffer solution, samples and reagents. The outlet is to remove waste (W) following an analysis operation. The microarray layer consists of gold regions, aligned to the interaction chamber of the microfluidic layer. The gold sensing surface can be a continuous layer or patterned regions as shown in figure 2a. For multi-analyte sensing applications each gold region can consist of a different immobilized probe and necessary experimental controls. Different methods are available for probe immobilization including non-contact protein printing [3] or in-situ immoblization using microfluidic networks [4].

4. MICROFABRICATION

The biochip consists of two layers, as shown figure 2(b). The top layer is made of poly di-methyl siloxane (PDMS) (Sylgard 184, Dow Corning, USA) that contains the channel structures, interaction chamber, inlets and outlet. The SPR gold was deposited on

the bottom layer that consists of AF45 glass refractive index (n=1.52) matched to the hemispherical prism. The microfabrication is performed in two separate processes. The PDMS layer is fabricated using a silicon wafer with patterned SU-8 (MicroChem Corporation, USA) structures to form the microfluidic structures. The lower microarray layer consists of gold islands for SPR imaging formed using a conventional lift-off procedure. The two layers are finally aligned and bonded with the aid of oxygen plasma activated surfaces. In the case that the probe molecules are first immobilized on the gold, then only the top microfluidic layer surface is treated with the oxygen plasma activation step.

5. RESULTS AND DISCUSSION

The microfabricated biochip was placed in a custom fixture with 10 µL cuvettes directly coupled to the inlet ports. The glass microarray layer was then placed in direct contact with the hemispherical prism of the SPR imaging system. Fluidic control is performed using electroosmotic flow with Pt wires immersed in the solution and connected to a high voltage power supply. The applied voltages were controlled with a LabView program. To demonstrate the concept 1mg/mL human IgG probe molecules are loaded into the sample

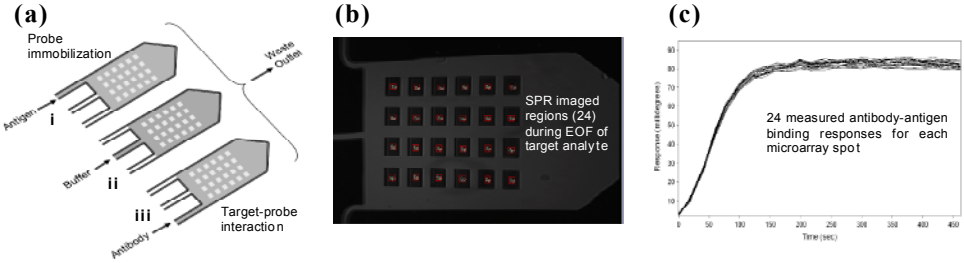

Figure 3. (a) Three step process for i: probe immobilization, ii: surface cleaning with buffer, and iii: antibody-antigen interaction. (b) SPR image of our chip with 24 gold islands; (c) Sensorgram of 24 human IgG and anti-human IgG interactions using EOF.

cuvette. The probes are then transported to the interaction chamber by applying 100 V between inlet port I1 and the exit port W. The antigens are immobilized by direct adsorption onto the gold surfaces. The second inlet reservoir I2 is then filled with PBS buffer (pH 7.2) and transported through the system. The 10 mg/mL anti-human IgG is then loaded into inlet I3 and transported to the immobilized probes electroosmotically with an applied voltage of 50 V. The general procedure is shown in figure 3(a). The real-time biomolecular interaction was measured by SPR imaging, shown in figure 3(b) and (c). We were able to control the flow of anti-IgG over the IgG patterned gold islands in the biochip and detect the binding of anti-IgG to the immobilized IgG on the gold islands with SPR imaging.

ACKNOWLEDGEMENTS

Dutch Technology Foundation STW grants 6635 and 6209

REFERENCES

1. R.B.M. Schasfoort. Expert Rev. Proteomics 1(1), 123–132 (2004).
2. G.A.J. Besselink et al., Electrophoresis, 25, 3705-3711 (2004).
3. Heij, B. de, et al., Anal. Bioanal. Chem. 387, 119-122 (2004).
4. V. Kanda et al. Anal. Chem. 76, 7257-7262 (2004).

HIGHLY PARALLELIZED LIPIDIC BILAYERS ARRAY FOR ION CHANNEL RECORDING

Bruno Le Pioufle[1,3], Hiroaki Suzuki[2], Shoji Takeuchi[1,4]

[1] *LIMMS, CNRS-IIS, The University of Tokyo, Japan*

[2] *Institute of Industrial Science, The University of Tokyo, Japan*

[3] *CNRS-SATIE/BIOMIS, ENS Cachan, France*

[4] *PRESTO, JST, Japan*

ABSTRACT

In this paper we show the feasibility to array high number of miniaturized artificial lipidic bilayer membranes on a chip for the insertion and electrical monitoring of ion channels. For this purpose biochips were microfabricated, including a thin parylene membrane, in which up to 100 micro-apertures were etched, for the parallel formation of lipid bilayers devoted to ion channel monitoring. The miniaturization of lipid bilayers is advantageous for increasing their stability and sealing resistance. We could successfully visualize the simultaneous formation of 25 lipid bilayers, and record the incorporation of α-hemolysin membrane protein on these chips. This result is a step towards miniaturization of highly parallelized membrane protein biochips.

Keywords: Bilayer, ion channel, biochip

1. INTRODUCTION

Potential applications of miniaturized chips for the study and cribling of membrane proteins are huge in the pharmaco-toxicology domain. Indeed, these proteins are key components in cancer and in drug rejection [1, 2]. Moreover, ion channels - a class of membrane proteins responsible of the ion transport across the cell membrane – are involved in many cardiovascular and nervous system diseases [3]. Activity of ion channels can be recorded using either the patch clamping method on cell membrane [4], or using planar artificial lipidic bilayer membrane reconstituted across an aperture opened in a substrate. Flow of ions through the membrane is monitored as an electric current using Ag (Silver) and AgCl (Silver Chloride) electrodes [5]. Microfabrication technology enables us to miniaturize the apertures for bilayer membrane formation, which was shown to increase the stability and sealing resistance [6-8]. We could prove in this paper that a large number of lipid bilayers can be parallely and simultaneously formed on an array of micro-apertures made out of a thin palylene membrane embedded in a plastic chip.

2. FABRICATION

The key part of our biochip is the array of circular micro-apertures devoted to the reconstitution of lipid bilayers. These apertures, whose diameter is 40 μm, are made out of a 20μm thick parylene film deposited by CVD (Chemical Vapor Deposition). Apertures are opened using oxygen plasma etching, through an aluminum mask obtained by means of conventional photolithography. Such patterned parylene film is then sandwiched between CIS chamber and TRANS channel made out of a PMMA (Poly Methyl Metacrylate) plate, as shown on figure 1. Two biochips involving respectively arrays of 25 holes and 100 holes were used in our experiments. We can see on figure 2 the SEM (scanning electron microscopic) view of part of the one hundred apertures array.

978-0-9798064-0-7/μTAS2007/$20©2007CBMS

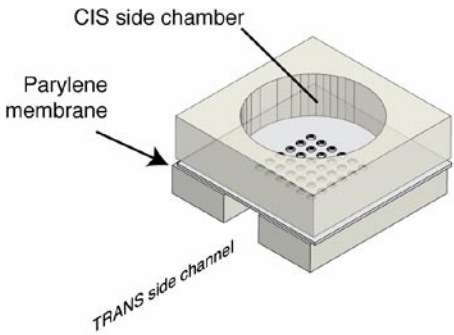

Fig 1: Scheme of the membrane protein chip

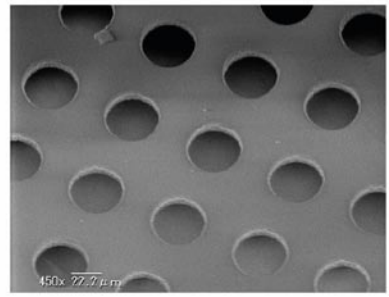

Fig 2: SEM view of the holes in parlylen membrane

3. EXPERIMENTAL

40 µl of buffer (300 mM KCl + 10 mM MOPS at pH=7.0) was first introduced in the CIS chamber. 8 µl of lipid solution (10 mg of DPhPC (Avanti polar lipids, USA) dissolved in 1 ml of n-decane), was then introduced in the TRANS channel, followed by 80 µl of buffer. The ion channel protein was then introduced in the upper chamber (3µl of α-hemolysin (Sigma, USA) at 0.5 mg/ml). The ionic current across the artificial membrane was measured using patch-clamp amplifier (CEZ-2400, Nihon Kohden, Japan) and recorded using a digital data acquisition system (Digidata 1322A and pCLAMP ver. 9, Molecular Devices, USA).

4. RESULTS AND DISCUSSION

We could view on a 25 parallel aperture chip, the simultaneous bilayer formation (see figure 3 where the Plateau-Gibbs border of bilayers [7] can been seen in each aperture).

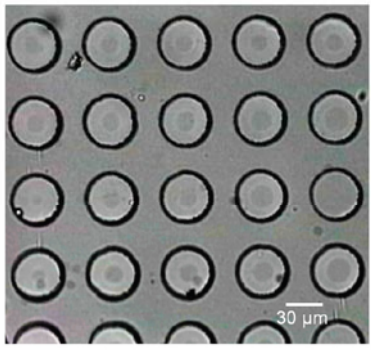

Fig 3: Visualisation of simulaneous 25 layers

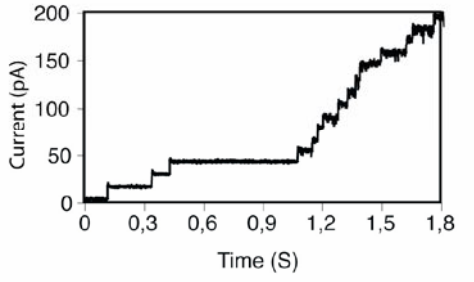

Fig 4: α-hemolysin electrical recording 100 holes chip

All membranes were confirmed to be a bilayer membrane, from the fact that the area of the Plateau-Gibbs border increased simultaneously in all apertures when the membrane potential was applied. Formation of the functional bilayer membrane was further confirmed

by reconstituting α-hemolysin (transmembrane protein which associates 7 domains to form a pore [9]) in the 100 parallel aperture chip. Stepwise increase of membrane current shown in Fig. 4 corresponds to the formation of single α-hemolysin membrane proteins in the set of arrayed artificial bilayers, that explains two things: 1) all one-hundred apertures were closed by a lipidic layer with no short-circuit, 2) bilayers formed in this device is biofunctional (α-hemolysin can only penetrate and be functional in a lipidic bilayer). The high success rate of formation and high stability of the 100 lipid bilayers on this chip are due to the small diameter of apertures, thin thickness of the parylene film, and the use of microfluidic channel to flow the lipids.

5. CONCLUSIONS

Highly parallelized formation of lipid bilayers for the monitoring of ion channels was demonstrated for the first time. The efficiency of the method lay on the miniaturized features of our microfluidic biochip. α-hemolysin membrane protein incorporation in the bilayer array could be electrically monitored at the resolution of a single protein. This result is a step towards new chip generations for the screening on membrane proteins.

ACKNOWLEDGEMENTS

This work was supported by JST PRESTO, MEXT, Japan (Grants-in-Aid for Scientific Research on Priority Areas - innovative nanoscience), and CNRS, France.

REFERENCES

[1]. J. Dancey and E. A. Sausville Issues and progress with protein kinase inhibitors for cancer treatment. *Nature Reviews Drug Discovery* **2**, 296-313 (2003).

[2]. M. M. Gottesman, T. Fojo、 S. E. Bates Multidrug resistance in cancer: role of ATP-dependant transporters. *Nature Reviews Cancer* **2**, 48-58 (2002).

[3]. J. Denyer, J. Worley, B. Cox, G. Allenby、M. Banks HTS approaches to voltage-gated ion channel drug discovery. *Drug Discovery Today* **3**, 323-332 (1998).

[4]. J. Xu, X. Wang, B. Ensign, M. Li, L. Wu, A. Guia and J. Xu Ion-channel assay technologies: quo vadis? *Drug Discovery Today* **6**, 1278-1287 (2001).

[5]. C. Miller Ion channels reconstitution. (Plenum Press, 1986).

[6]. N. Fertig, M. George, M. Klau, C. Meyer, A. Tilke, C. Sobotta, R. H. Blick and J. C. Behrends Microstructured apertures in planar glass substrates for ion channel research. *Receptors Channels* **9**, 29-40 (2003).

[7]. H. Suzuki, K. V. Tabata, H. Noji and S. Takeuchi Highly Reproducible Method of Planar Lipid Bilayer Reconstitution in Polymethyl Methacrylate Microfluidic Chip. *Langmuir* **22**, 1937-1942 (2006).

[8]. M. Mayer, J. K. Kriebel, M. T. Tosteson and G. M. Whitesides Microfabricated teflon membranes for low-noise recordings of ion channels in planar lipid bilayers. *Biophys J* **85**, 2684-2695 (2003).

[9]. L. Song, M. R. Hobaugh, C. Shustak, S. Cheley, H. Bayley and J. E. Gouaux Structure of Staphylococcal alpha -Hemolysin, a Heptameric Transmembrane Pore. *Science* **274**, 1859-1865 (1996).

RAPID HIGH-THROUGHPUT MICROARRAY ANALYSIS – A SHEAR-DRIVEN APPROACH

Kris Pappaert[1], Frederik Detobel[1], Paul Van Hummelen[2] and Gert Desmet[1]

[1] *Vrije Universiteit Brussel IR-CHIS, Brussels, BELGIUM*

[2] *VIB MicroArray Facility, Leuven, BELGIUM*

ABSTRACT

The present work reports on a method where a shear-driven microfluidic system is employed to enhance the sensitivity and analysis time of the DNA-microarray analysis. This unique technique uses an alternative fluidic platform to reduce the analysis time from 16 hours to only 2 hours, whereas the sensitivity reaches a similar value.

Keywords: DNA-microarrays, Shear-driven microfluidics

1. INTRODUCTION

DNA-microarray technology enables researchers to perform high-throughput genomic analysis for various clinical applications [1]. As the importance of this technology increases so does the demand for a better reliability and reproducibility as well as an improved sensitivity and a faster analysis time. The introduction of a certain degree of automation in the microarray protocol (hybridization, washing and drying steps) and the accessibility of different commercial platforms has already brought a significant improvement when it comes to the reproducibility of the microarray experiments [2]. An improvement in sensitivity and a reduction of the analysis time can be attained through miniaturization [3]. During the hybridization process a combination of fluid convection (overcoming target depletion) and low sample volumes (increasing target concentration) are highly beneficial [4]. The current commercially available automated hybridization stations cannot achieve this combination as these systems require large sample volumes (>150µl) to pump around the target solution, hence even reducing the sensitivity of the microarrays.

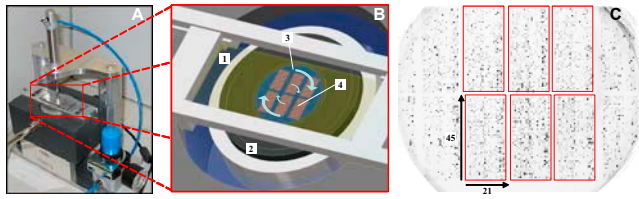

Figure 1. Overview of the shear-driven hybridization system (SDH) for DNA-microarrays (A-C).

Our group is currently developing a DNA-microarray hybridization system [3][4] based on the shear-driven flow principle (fig. 1). As this flow principle is able to generate high velocity fluid flows in micro- and nanochannels without any need for pumping devices, the combination of low sample volumes (less than 5 µl) and a convective sample displacement over the microarray surface can be obtained. With this unique microarray hybridization method considerable gains in sensitivity and/or hybridization time can be anticipated.

978-0-9798064-0-7/µTAS2007/$20©2007CBMS

2. THEORY

From a theoretical point of view the most optimal design for a microarray hybridization system uses a limited amount of sample and combines this with a mixing effect. This combination is feasible using a shear-driven microfluidic system as the typical flow rate is only determined by the velocity of the moving wall element. The axial velocity in a laminar flow between two flat plates displays a perfectly linear profile, going from u=0 near the stationary wall to $u=u_{wall}$ near the moving wall [5]. As the viscous drag effect sustains this so-called shear-driven flow (SDF) at literally each point of the channel axis, the flow is generated without any pressure-drop or pressure build-up. It can be shown [5] that in a channel with a flat rectangular cross-section, a flow with a substantially linear radial velocity profile is established, with the mean fluid velocity (u_m) given by:

$$u_m = \frac{1}{2} u_{wall} \tag{1}$$

wherein u_{wall} is the velocity of the moving wall.

3. EXPERIMENTAL

The system used to perform shear-driven hybridization (SDH) on microarrays (fig. 1) fixes a microarray slide on top of a circular microchamber (typical depth 1-5µm). By rotating the microchamber, the target mixture inside it flows over the probe spots, hence increasing the hybridization rate. Detailed technical aspects of the hybridization system have already been described [4]. The microarray experiments were performed in cooperation with the Microarray Facility Lab (www.microarray.be).

4. RESULTS AND DISCUSSION

This novel hybridization system has enabled us to get some new fundamental insights in the different aspects that influence the hybridization reaction. We have already reported [1,4] on the impact of process parameters like the sample concentration and the size of the microchannel, more recently new insights concerning the fluid velocity and the refreshment rate have been revealed. A fundamental conclusion that resulted from this investigation is that a continuous flow of the target solution has a rather detrimental effect. A continuous fluid flow reduces the final signal intensity significantly even compared to a case without a flow present. The optimal solution is obtained in-between these two cases. An intermediate flow driving principle where the fluid is discontinuously moved was found to be the most ideal system. By alternating between phases that allow the hybridization to occur in a stationary fluid layer and phases where the fluid is moved and consequently also refreshed.

Apart from studying the fundamental aspects, a series of real sample hybridization experiments (fig. 2-3) were performed with the SDH-system. Total RNA samples of mouse heart and spleen tissue were hybridized on high-density mouse microarrays. Time series experiments show that the greatest gain can be obtained during the first two hours of the hybridization. For longer hybridization experiments with the SDH-system (going to overnight periods) the final intensity signal still enhances but not to the same degree as in the first two hours. Numerous repetitive hybridization experiments demonstrate the good reproducibility of the SDH-system (fig. 2A) with typical correlation coefficients of 0.948, 0.918 and0.957. Unique spike-in experiments (fig. 2B), where the differentially expressed

genes are used as spikes, show the maximal obtained sensitivity. Compared to the already existing hybridization systems, like the Lucidea SlidePro (LSP)-system (fig. 3), our system reaches equal sensitivity in a shorter time period.

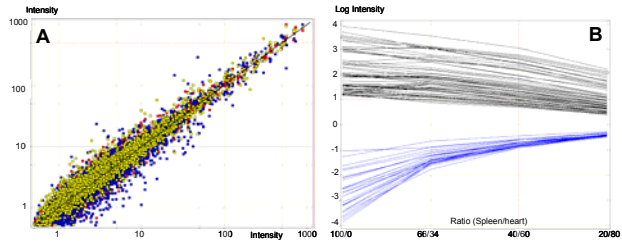

Figure 2. (A) Three repetitive SDH experiments. (B) A spike-in experiment

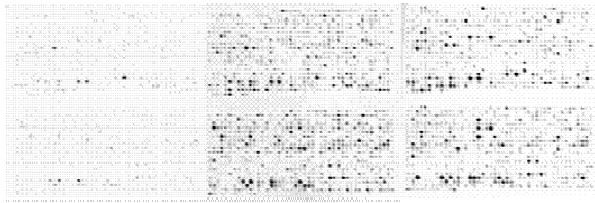

Figure 3. Comparison of a hybridization experiment done with the LSP-system (16h - 5 pmol) (A), the SDH-system (2h - 5 pmol) (B) and the LSP-system (16h - 40 pmol).

5. CONCLUSIONS

By studying real mouse and spleen samples experimental evidence has been gathered to demonstrate that this novel hybridization method is able to speed up the hybridization rate of DNA-microarrays compared to commercial devices while the reproducibility and sensitivity remain equivalent.

ACKNOWLEDGEMENTS

K.P. is Postdoctoral Fellows of the Research Foundation – Flanders (FWO Vlaanderen).

REFERENCES

[1] van't Veer L.J. et al. *Gene expression profiling predicts clinical outcome of breast cancer.* Nature 415 (6871): 530-536 (2002)

[2] Shi L.M. et al. *The MicroArray Quality Control (MAQC) project shows inter- and intraplatform reproducibility of gene expression measurements.* Nature Biotechnology 24 (9): 1151-1161 (2006)

[3] Vanderhoeven J. et al. *Comparison of a pump-around a diffusion-driven, and a shear-driven system for the hybridization of mouse lung and testis total RNA on microarrays.* Electrophoresis 26 (19): 3773-3779 (2005)

[4] Vanderhoeven J. et al. *DNA microarray enhancement using a continuously and discontinuously rotating microchamber.* Analytical Chemistry 77 (14): 4474-4480 (2005)

[5] Desmet G. and Baron G.V. *On the possibility of shear-driven chromatography: a theoretical performance analysis.* Journal of Chromatography A 855: 57-70 (1999).

A DISPOSABLE MAGNETIC PLANAR PERISTALTIC PUMP FOR SELF-CONTAINED LAB-ON-A-CHIP (LOC) CARTRIDGE

Levent Yobas, Lih Feng Cheow, Kum Cheong Tang, and Cheng Yong Teo
Institute of Microelectronics, 11 Science Park Road, S117685, SINGAPORE
Corresponding Author: Leventy@ime.a-star.edu.sg

ABSTRACT

We demonstrate a disposable magnetic *planar* peristaltic pump for LOC applications. The planar feature of the pump allows for its direct integration with a microfluidic chip, producing a compact and low-cost cartridge that does not need any external pump.

Keywords: Magnetic, pump, peristaltic, cartridge

1. INTRODUCTION

Miniaturization of pumps has been an intense field of research in order to attain a truly integrated and portable lab-on-a-chip system [1]. Nevertheless, there remains an inherent limitation with the pump miniaturization as pumping energy drops significantly at least several orders of magnitudes. Meanwhile fluidic resistance increases with viscous forces taking over inertia in smaller channels [2]. Although, fluidic integration is paramount to lab-on-a-chip applications, such feature should be sought without compromising on the pump performance.

A new pump introduced here demonstrates fluidic integration without miniaturization of the pumping mechanism. The peristaltic action that drives the pump is generated by magnetized steel ball which pinches-off an underneath channel while moving under the influence of a rotating magnetic field (Figure 1).

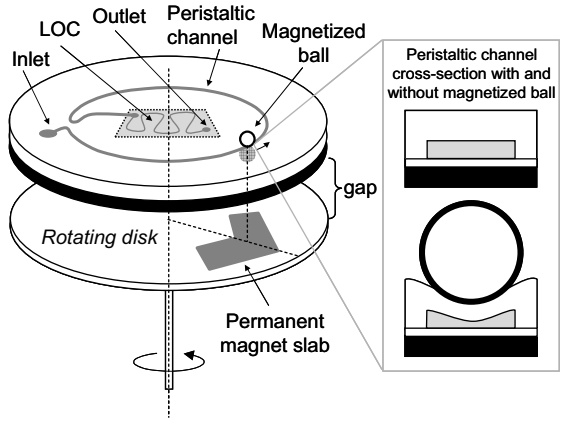

Figure 1. Schematic of the planar peristaltic pump showing working principle.

2. EXPERIMENTAL

A simple prototype of the pump was realized by replica-moulding silicone elastomer polydimethylsiloxane (PDMS). The mould was formed in a 130 μm-thick grinding tape.

978-0-9798064-0-7/μTAS2007/$20©2007CBMS

The tape was first laminated on a polished surface of silicon wafer and then patterned with a negative image of pump layout. The patterning was done via thermal ablation from a CO_2 laser. The laser beam penetrated through the entire tape without leaving any mark on silicon. Unwanted sections of the tape were peeled off to create a relief structure. A thin PDMS sheet was replicated and irreversibly bonded to a plain PDMS sheet via oxygen-plasma surface activation. The pump actuation was realized by an apparatus employing a rare-earth magnet slab from a harddisk drive, 6-mm-diameter steel ball from a ball-bearing, and a DC Motor (Faulhaber) controlling a rotating stage.

3. RESULTS AND DISCUSSION

The pump concept was first tested with a prototype having only a single channel. Figure 2 shows the prototype and measured fluidic characteristics. The critical pump parameters include compliance of the peristaltic membrane and separation between magnet and ball.

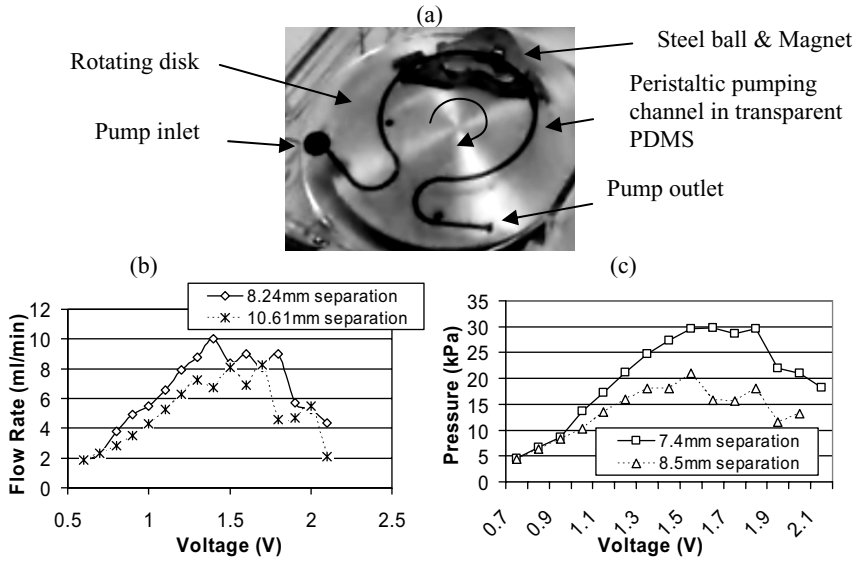

Figure 2. (a) Picture of a pump prototype in PDMS actuated by a single pair of magnet-ball. (b) and (c) Pumping characteristics as a function of applied voltage: flow rate (open-end) and (c) pressure buildup (closed-end). The legends show separation of ball centre from magnet surface. Pumping channel is 2 mm wide and PDMS membrane cap is ~1 mm thick.

To demonstrate pump utility, we built a self-contained LOC cartridge with an integrated fluidic delivery mechanism (Figure 3). A microfluidic chip was directly mounted on cartridge using double-sided adhesive tape. Fluidic was designed for sequential injection of reagents as in heterogeneous immunoassay or nucleic-acid purification. To avoid use of valves, the design was such that all reagents can be sequentially stored and isolated by air plugs along a channel [3]. To prevent air plugs from entering into peristaltic channel, reagents were stored at channel downstream while the channel remaining was primed with inert liquid (water) to pump and push the sample and reagents. Since the sample is not typically available at the time of loading the cartridge, channel segment for the sample was replaced by a detachable tube externally bridging segregated channels. A similar tube was

also used for collection of the assay product. With both tubes inserted, a closed-loop channel in an entirely self-enclosed cartridge was attained, a desired feature for processing contagious samples.

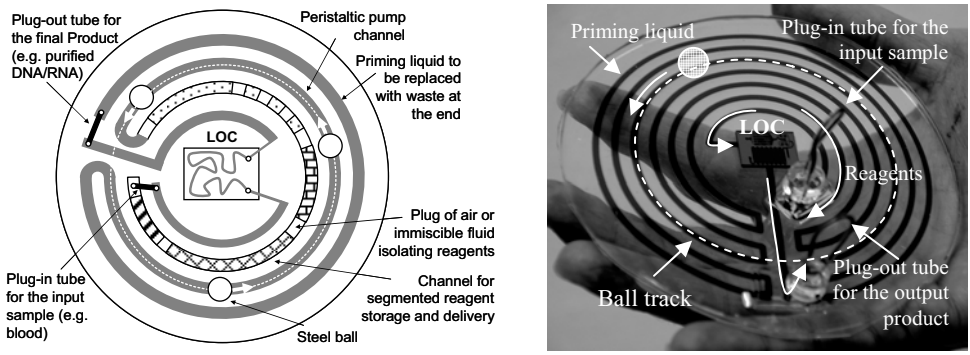

Figure 3. Self-enclosed LOC cartridge with an integrated fluidic delivery mechanism using a planar peristaltic pump: schematic layout and photograph of a PDMS prototype with a silicon-based LOC.

Figure 4 shows flow characteristics of the cartridge and the chip when actuated with two diametrically opposed magnet-ball pairs. Flow rates < 5 µl/min were also observed (e.g. 2.2 µl/min at 100 rpm and 12.5 mm magnet-ball separation).

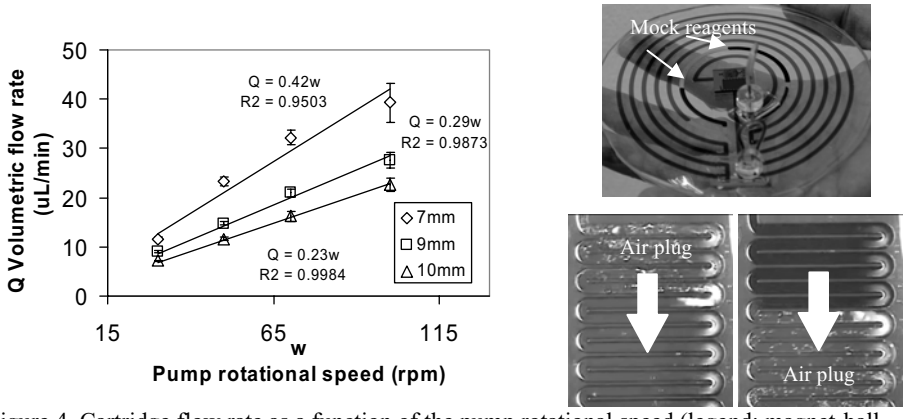

Figure 4. Cartridge flow rate as a function of the pump rotational speed (legend: magnet-ball separation). Pictures: the cartridge loaded with segmented dyes representing reagents and the serpentine microchannel in the silicon LOC while being pumped with each dye segment.

REFERENCES

[1] D.J. Laser, and J. G. Santiago, "A review of micropumps," *J Micromech Microeng*, **14**, R35 (2004).

[2] N.-T. Nguyen, X. Huang, and T.K. Chuan, "MEMS-Micropumps: a review," *J Fluid Eng-T. ASME*, **124**, 384, (2002)

[3] V. Linder, S.K. Sia, and G.M. Whitesides, "Reagent-loaded cartridges for valveless and automated fluid delivery in microfluidic devices," *Anal Chem*, **36**, 3342 (1997).

BIOMAGNETIC BEAD BASED MICROFLUIDIC DEVICE FOR RAPID NAKED EYE FIELD DIAGNOSTICS OF CATTLE PNEUMONIA

J. Gantelius[1], C. Hamsten[2], A. Persson[2], M. Uhlen[2] and H. Andersson-Svahn[1]

[1]Dept. of Nanobiotechnology, School of Biotechnology, Royal Institute of Technology, Stockholm

[2]Dept. of Proteomics, School of Biotechnology, Royal Institute of Technology, Stockholm

ABSTRACT

Infectious mycoplasma-based diseases are a common problem for the agricultural community and there is a great need for rapid point of care (POC) diagnostics. Here we describe a novel portable system that can be used to detect the presence of antibodies specific to 28 different mycoplasm antigens. The presented microfluidic system encloses a printed antigen array that captures antibodies from crude bovine serum. Detection of bound antibodies and signal amplification is performed by enriching micrometer-sized anti-immunoglobuline (IgG) supraparamagnetic beads on the array. Due to the non-transparancy of the magnetic beads, positive microarray spots can be discerned by naked eye observation.

Keywords: antigen microarray, magnetic beads, infection, naked eye detection

1. INTRODUCTION

Infectious mycoplasma-based diseases are recurring problems for farmers and agricultural communities world wide [1]. Entire populations of animals that may have been exposed to the pathogen often needs to be put down due to lack of readily available diagnostics. This results in large economical setbacks as well as unnecessary loss of life. Here, we present a novel integrated portable system for rapid naked eye detection of antibodies in crude bovine serum binding to 28 different bacterial antigens. Visualization is performed using anti- IgG coated superparamagnetic beads, as has been previously described by our group [2,3]. This portable field device has the possibility to quickly verify on site whether an animal has acquired the infectious agent or not.

2. EXPERIMENTAL

To analyze the bovine serum, a microarray of 28 different surface protein antigens from a bacterium known to cause severe pneumonia in cattle was printed on epoxy slides. A PDMS chamber with high aspect ratio designed for microarrays was mounted on the antigen array and fitted with inlet/outlet (fig. 1A). Crude bovine sera previously diagnosed with disease were diluted 100X in Phosphate buffered Saline + 0.1% Tween20 (PBST) and introduced in the flow chamber, followed by a 30 minute incubation. To detect serum antibodies bound to the antigen array, 1 µm superparamagnetic beads coated with anti-IgG were introduced in the chamber, magnetically enriched on the surface followed by magnetic removal of unbound beads (fig 1A-C). A zoom-in on a bead filled spot can be seen in fig. 2. Sera from two disease-carrying individuals were analyzed at least four times each, and results from one individual are presented here.

978-0-9798064-0-7/µTAS2007/$20©2007CBMS

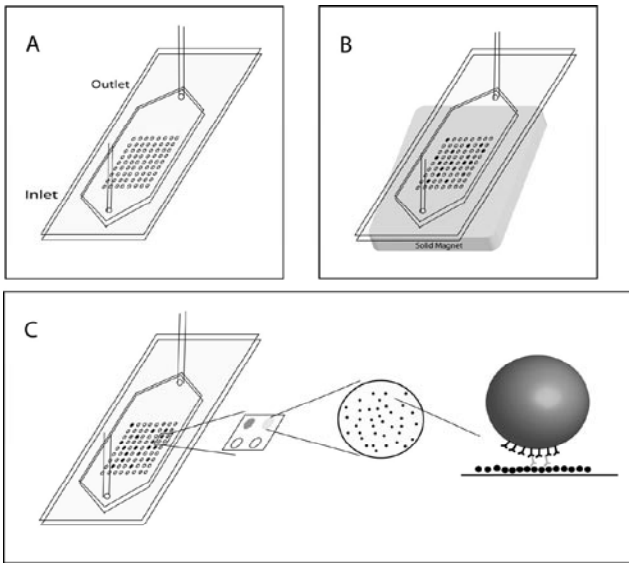

Fig. 1. A high aspect ratio PDMS channel was fitted on top of the antigen array (A). The serum was introduced into the channel by means of a manual syringe pump and incubated on the array. After washing, anti-IgG-coupled beads were introduced in the channel. The beads were enriched magnetically on the array (B), followed by magnetic removal of weakly bound beads. Bead-filled spots could be observed with the naked eye (C).

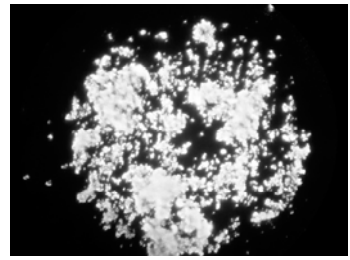

Fig. 2. Zoom in of a bead-covered spot

3. RESULTS AND DISCUSSION

It was expected and found that different individual sera would give different binding patterns on the array, although the presence of antibodies bound to any of the antigen-spots would be indicative of infection. Thus, the presented setup enables the possibility to draw conclusions both from the individual antigen spots and from the binding pattern of the whole array. A conventional assay for analyzing the binding of antibodies to an antigen surface is *via* a secondary fluorescent anti-IgG antibody. Results from the bead assay were comparable to those of the standard setup (fig. 3A&B), 53/56 spots agreeing on the binary yes/no classification of each spot. The standard setup gave rise to slightly higher background and sometimes random areas of high signal which can be seen in figure 2B spot E3-4, F3-4. The bead setup gave less background, but sometimes lower signals in some spots, such as for instance spot G7, H7. More than approximately 20 beads on one spot were visible to the naked eye or a digital camera (fig. 4). Naked eye observations correlated well with those from the scanned image.

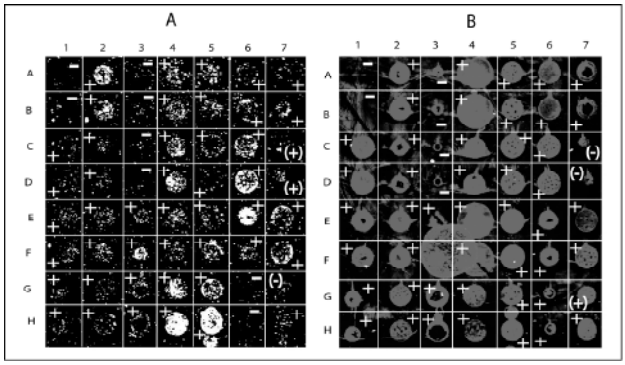

Fig. 3. The antigen array consisting of 28 bacterial antigens printed in doublets (A1=B1, C1=D1 etc.) was incubated with serum diluted 100X in PBST. Parallel detection was subsequently performed using either anti-IgG superparamagnetic beads (A) or fluorescent anti-IgG (B). Positive spots are indicated with + and negative with -. The spots that have ambiguous signals between the bead and the conventional method are given as (+) or (-). The binary signals agree in all spots except C7, D7 and G7.

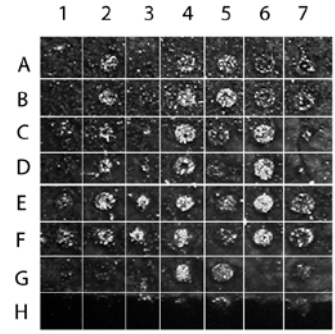

Fig. 4. The bead visualisation allows for naked eye detection on spots that harbour >20 beads. Here the array (ca 0.5*0.5mm) is imaged with a non-professional modern digital camera.

4. CONCLUSIONS

In this work we present a working prototype of a portable microfluidics analysis system for rapid naked eye screening of bovine serum for bacterial infection. Next step is to analyze whole-blood and sera from more individuals in a field environment. We believe that this integrated on-site kit will be very helpful in minimizing the adverse effects of infectious diseases in cattle

ACKNOWLEDGEMENTS

We thank Laurent Barbe for assistance in imaging and for fruitful discussions. Funding from Knut and Alice Wallenberg Foundation and the Royal Academy of Science (KVA) is gratefully acknowledged. Thanks to 'the VINNOVA supported AlbaNova VinnExcellence Centre for Protein Technology'.

REFERENCES

1. "The immunology of the bovine respiratory disease complex" TR. Ames, The Veterinary clinics of North America. Food animal practice, **3**, 13 (1997).
2. "Rapid and sensitive detection of protein biomarkers on reverse phase serum arrays using biomagnetic beads" J. Gantelius, J. Lindberg, M.Uhlen and H. Andersson-Svahn, Submitted to Journal of Immunological Methods
3. "Synthetic Visual DNA – identification of DNA sequence variations by bead trapping," P.L. Ståhl, J. Gantelius, C. Natanaelsson, A. Ahmadian, H. Andersson-Svahn and J. Lundeberg, Submitted to Nucleic Acids Research

CCD CAMERA-BASED OPTICAL READOUT SYSTEM FOR RT-PCR DNA ANLYZER: TOWARD RAPID AND CHEAP DETECTION OF PATHOGENS IN FOOD AND CLINICAL SAMPLES IN NANOGRAMS PER MILILITER CONCENTRATION OF DNA

Rafał Walczak[1,2], Jan A. Dziuban[1,2], Jan Koszur[1], Anders Wolff[3], Dang Duong Bang[3], Minqiang Bu[3]

[1]*Institute of Electron Technology,POLAND, e-mail: rafal.walczak@pwr.wroc.pl*
[2]*Wrocław University of Technology, POLAND*
[3]*Danish Technical University, DENMARK*

ABSTRACT

In this paper the description and first results of test of a miniaturized fluorescence optical readout RT-PCR instrumentation. The unique coupling of CCD-based microdetectors array and expertise software enables detection of DNA in ng/ml range as well as real-time recording and processing of fluorescence signals during PCR.

Keywords: RT-PCR, CCD camera, fluorescence, food pathogens

1. INTRODUCTION

Human illnesses caused by food pathogens (e. g. *Salmonellosis* or *Campylobacter* bacterias) are common and cost-generating problems. Currently, tests are carried out in specialized laboratories by conventional microbiological methods - they are expensive and time-consuming. Therefore, there is a great need for rapid detection of pathogens in food or earl state of bacterial infection in human, carried out outside specialized laboratories by the use of a cheap and mass produced device. The RT-PCR technique utilizing laser induced fluorescence is the most promising alternative method. However, a critical requirement here is the highly sensitive detection of amplified DNA and recording of real-time-dependant fluorescence signals, as well as measuring of DNA melting temperature. Reported in literature [1-3] different methods of on-chip integration of the optical readout systems or miniaturization of the macroscopic solutions do not meet this specifications mainly due theirs sophisticated optical configuration. In this paper we present a cheap, simple and miniature optical readout instrumentation for detection of DNA amplified by RT-PCR technique inside glass/SU8 microreactor, developed for European FP6 OPTOLABCARD project.

2. INSTRUMENTATION

The developed system (Fig. 1) consists of: solid-state laser 636 nm, CCD camera (Sony 1/3”B/W SuperHAD, Japan) working as an array of VIS/NIR microdetectors, 650 nm long-pass interference filter (ThorLabs, USA) and PCR glass/SU8 microreactor chip with on-chip integrated SU8 planar waveguides ended with microlenses, made as the integral part of the PCR microreactor (Fig. 2a). Laser light is guided to PCR by a 100/150 μm glass fiber (OceanOptics, USA), which is coupled with SU8 planar waveguide. CCD camera, distanced a few millimeters perpendicularly to the surface of the microreactor, collects fluorescence images (Fig. 2b). In order to thermocycle the DNA sample, the chip is

978-0-9798064-0-7/μTAS2007/$20©2007CBMS

positioned on a temperature controlled 20x20 mm^2 flat-table (Peltier module) equipped with a K-type thermopile positioned closed to the chip.

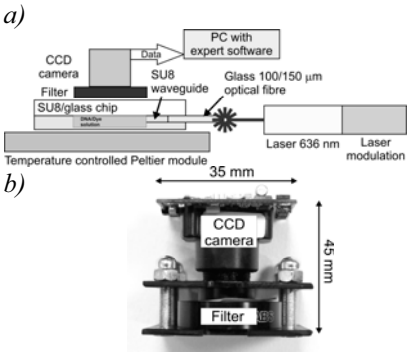

Fig. 1. CCD-based optical readout system: a) scheme, b) camera module with optical filter positioned above RT-PCR chip

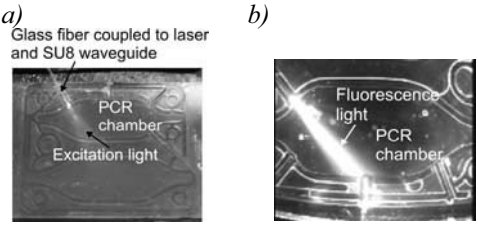

Fig. 2. RT-PCR chip: a) top view of the structure with mounted glass fiber illuminating detection area, b) view of the PCR chamber as collected by CCD camera/filter module – fluorescence light emitted by 2.5 μg/ml salmon sperm DNA is visible as the "light torch"

Signals are transmitted by a video capturing card to PC computer where specialized software visualizes and computes fluorescence images in order to evaluate the desired characteristics and/or tabulated data (Fig. 3). The I/O steering device (USB 6009, National Instruments) and LabViwe-based software are used to control the chip temperature.

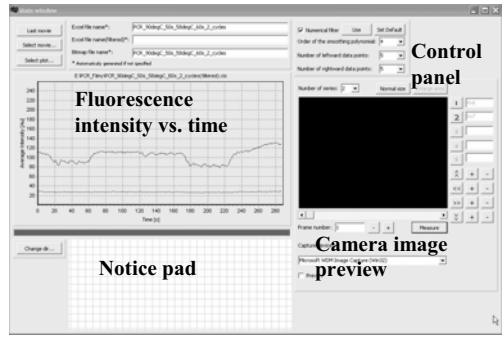

Fig. 3. Graphical user interface of the expert software for the optical readout system

3. EXPERIMENTS AND RESULTS

Testing of the system has been done with use of salmon sperm DNA (Sigma Aldrich, USA) samples with concentrations from 2.5 ng/ml to 2.5 μg/ml and 0.5 μM TO-PRO 3 (BioScience, USA). The chromofore photobleaching effect is minimized because laser light is 1 kHz pulse-modulated and power of the light is below 1 mW. Illumination of the sample is shorter than 25% of total time of single PCR cycle. Intensity of fluorescence of DNA sample is recorded at from two to five detection areas during PCR process. Expert system chooses the best two areas and evaluates finally the desired data. The experimentally confirmed detection limit of the system is about 2 ng/ml of DNA but - to increase the proofness of RT-PCR - the electronically adjusted limit of detection of unknown samples is 10 ng/ml (Fig. 4). The melting curve of salmon sperm DNA/TO-PRO 3 complex has been obtained, melting temperature is about 77,8^{o}C (Fig. 5). The RT-PCR process has been carried out with *Campylobacter* DNA. Fluorescence dependence on PCR thermal cycling of DNA samples (94°C/15 s, 58°C/50 s, 72°C/50 s) (Fig. 6a) as well as fluorescence intensity increasing during PCR are well observed (Fig. 6b). Tha quality of PCR has been confirmed by gel electrophoresisof PCR products (Fig.6b). Full

characterization of the PCR process is done about 5 seconds after collection of images. System works continuously, data can be stored in a computer memory or e-mailed.

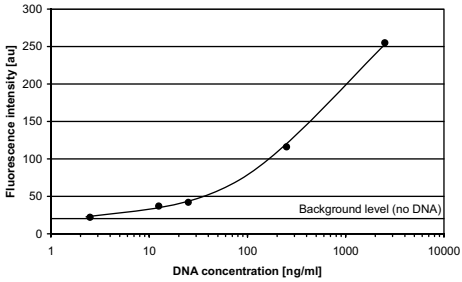

Fig. 4. Fluorescence intensity as function of salmon sperm DNA concentration marked, background signal level (no DNA) is also shown

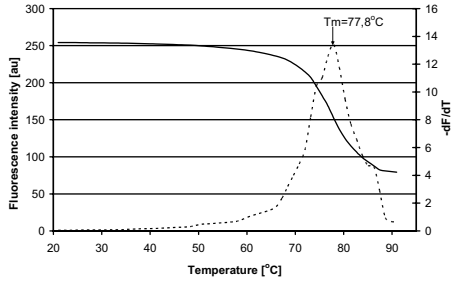

Fig. 5. Melting curves of salmon sperm/TO-PRO 3 sample: fluorescence intensity (solid line) and differential fluorescence (dashed line) as function of temperature

a)

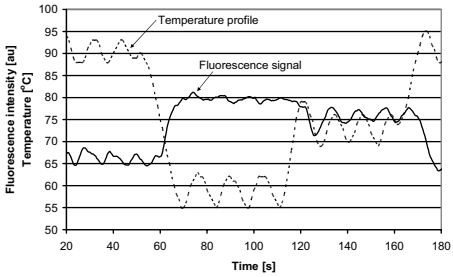

b)

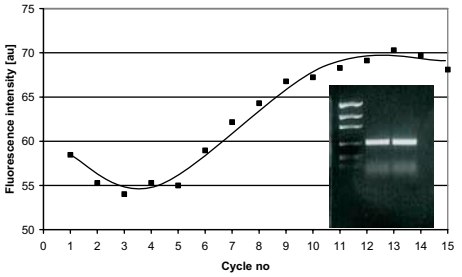

Fig. 6. Campylobacter bacteria RT-PCR/DNA carried out with developed instrumentation: a) fluorescence intensity during a single PCR cycle, b) average fluorescence intensity at annealing PCR cycles as function of cycle number, inside photo shows gel electrophoresis analysis result confirming proper DNA amplification

5. CONCLUSIONS

The developed instrumentation enables carrying out of RT-PCR with novel type of optical readout system with sensitivity in nanograms per milliliter range. Unique combination of cheap optical hardware and expertise software results in low-price and high-sensitivity of the system. It makes the developed instrumentation attractive solution for all types of fluorescence-based tests including cheap, rapid and mass-produced devices.

REFERENCES

[1] M. Hashinoto et al, "Rapid PCR in a continuous flow device", *Lab Chip*, vol. 4, 2004, pp. 638-645, 2004.

[2] P. Neuzil et al, "Disposable real-time microPCR device: lab-on-a-chip at a low cost", *Mol. BioSyst.*, vol. 2, pp. 262-298, 2006.

[3] P. Novak et al, "A palm-sized real-time (RT) PCR", *Proc. of uTAS 2006,* November 5-9, Tokyo, Japan, pp. 332-334, 2006

DIAGNOSIS-ON-A-CHIP: A MICROFLUIDIC PLATFORM FOR CELL CULTURE AND VIRUS ASSAYS

X. Zhang[1], R. Chua[2], P. H. Yap[2] and A. Q. Liu[1†]

[1]School of Electrical & Electronic Engineering

Nanyang Technological University, Nanyang Avenue, Singapore 639798

[2]Defence Medical & Environmental Research Institute

DSO National Laboratories, 27 Medical Drive, Singapore 117510

([†]Corresponding author. Tel: +65-6790 4336; Email: eaqliu@ntu.edu.sg)

ABSTRACT

A high-throughput microfluidic chip for cell culture and immunofluorescence virus assays is presented in this paper. The chip is fabricated by laser engraving technology with the polymer material polymethylmethacrylate (PMMA). Madin-Darby canine kidney (MDCK) cell line has been successfully loaded, cultured and passaged in culturing chambers with 1mm diameter and 1.5 µl volume; and rapid growth of influenza A virus (H3N2) in MDCK cells cultured has been observed and proved by immunoflorescence assay. This kind of cell culture array could offer a platform for virus growth testing for vaccine production and also is promising for early diagnosis and drug screening. in drug screening, bioinformatics, and quantitative cell biology

Keywords: MDCK cells, influenza A, *in situ* observation, lab on a chip

1. INTRODUCTION

The field of cell culture is developing much more sophisticated abilities based on micro-fabrication techniques. Compared with conventional cell culture technology which recruits instruments of large size and manual manipulation, the microfluidic system features high throughput, low cost and portability allows integration with other functions and provides static microscale cultures more similar to *in vivo* microenvironment. Some microfabricated eukaryotic cell culture devices have previously been demonstrated with various kinds of cells. However, little work has been done to simulate virus assays onto chip. In this paper a high throughput chip designed for long-term cell culture and virus growth is presented, combined with real- time optical monitoring.

2. DEVICE DESIGN AND FBRICATION

The culture and assays chip is developed as shown in Fig. 1, whcich consists of two pairs (could be more) of cell culturing chambers. One is connected to a virus inlet while the other has no virus connection for comparison purpose. Culturing medium, antibody and other reagents are loaded through the major inlet into the branch channels designed as a symmetric arc with binary splitting so as to provide equal flow to all the chambers.

978-0-9798064-0-7/µTAS2007/$20©2007CBMS

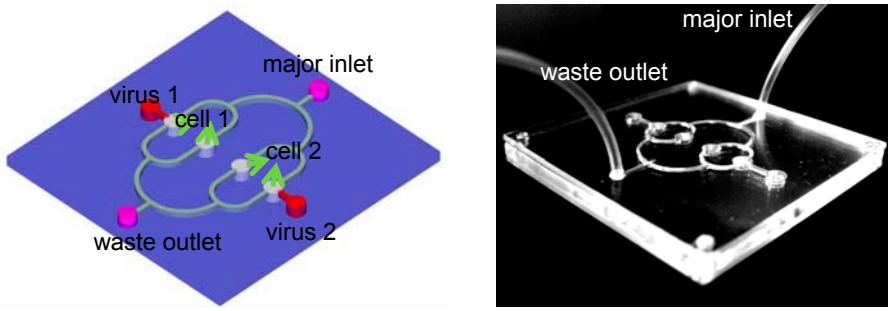

Figure 1. Schematic diagram and the photograph of the microchip for cell culture and virus assays

The array chip is fabricated by a CO_2 laser engraving system on polymethylmethacrylate (PMMA) which, compared with conventional PDMS lithography technology, is cost effective and are especially useful in microfluidic prototyping due to the very short cycle time of production [1]. During the experiment, Madin-Darby canine kidney (MDCK) cell line, which has long been known to successfully support influenza growth [2]. were loaded into to the chip and cultured. After the cell formed a confluent monolayer, influenza A (flu A) virus was introduced and incubated. After obvious lysis was observed, monoclonal flu A antibody-FITC was loaded for the immunofluorescence.

3. RESULTS AND DISCUSSIONS

Figure 2 shows pictures of the *in situ* morphology of MDCK cells cultured in a chamber (diameter 600 µm, volume 0.56 µl). (a) The cells were suspended right after cell loaded; (b) the cells have attached and divided after 24 hr culturing; (c) The cells formed a confluent monolayer after 48 hr culturing and then were inoculated with flu A. The other three pictures were taken: (d) 1hr after inoculation; (e) 24 hr later; (f) 48 hr later, and show the gradually lysed cells. Before the flu A inoculation, the cells are cultured in DMEM (Dulbecco's modified eagle media, invitrogen) with 10% FBS (fetal bovine serum, invitrogen), and DMEM with 1% FBS after that. In these assays MDCK cell line exhibits super reliability to support influenza growth.

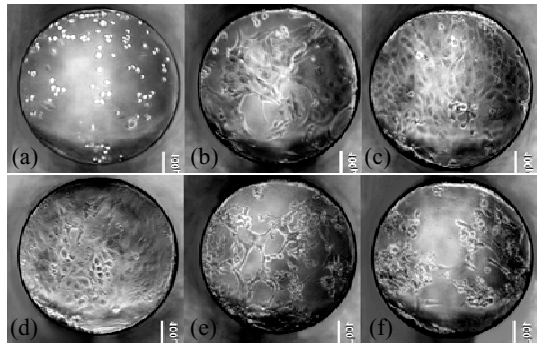

Figure 2. Photograph of MDCK cells. (a) Right after being loaded; (b) cultured for 24 hr; (c) cultured for 48 hr; (d) 1 hr after flu A virus being loaded; (e) 24 hr later; and (f) 48 hr later.

Figure 3 shows the immunoflurescence of MDCK cells. The bright spots are positive cells (infected), and the dark ones are negative (uninfected). This is, to our best knowledge, the first demonstration of virus infection and immunofluorescence assay in micro chip.

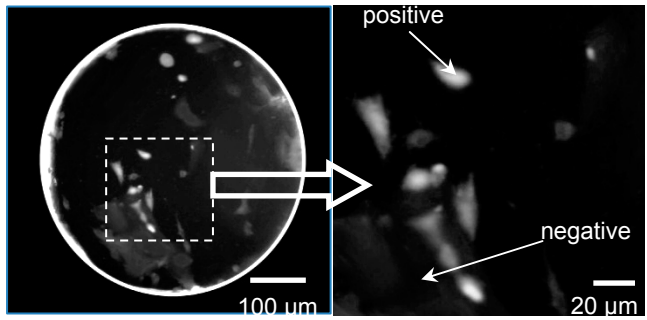

Figure 3. Immunofluorescence of MDCK cells cultured for two days and then inoculated with flu A virus, followed by culturing for another two days.

Multiple parallel experiments such as culture of different cell line and virus infections can be done on the chip with outside optical system for real-time monitoring. This kind of cell culture array could offer a platform for virus growth testing for vaccine production which is determined by how well the virus is able to replicate and how easily the cell line can be maintained [2], it also has potential applications in drug screening, bioinformatics, and quantitative cell biology [3].With all these capabilities, it is possible to realize the diagonosis of disease on a single chip.

4. CONCLUSIONS

In conclusion, a high-throughput microfluidic for long-term cell culture and immunofluorescence virus assays is proposed. Madin-Darby canine kidney (MDCK) cell line has been successfully loaded, cultured and passaged in culturing chambers with 1mm diameter and 1.5 μl volume; and rapid growth of influenza A virus (H3N2) in MDCK cells cultured has been observed and approved by the immunofluorescence assay.

REFERENCES

[1] H. Klank, J. P. Kutter and O. Geschke, *CO_2-laser micromachining and back-end processing for raid production of PMMA-based microfluidic systems,* Lab Chip, vol. 2 , pp. 242-246, (2001).

[2] R. Youil, Q. Su, T. J. Toner, C. Szymkowiak, W. S. Kwan, B. Rubin, L. Petrukhin, I. Kiseleva, A. R. Shaw and D. Distefano, *Comparative study of influenza virus replication in Vero and MDCK cell lines,* J. Virol. Meth., vol. 120, pp. 23-31, (2004).

[3] P. J. Hung, P. J. Lee, P. Sabounchi, R. Lin and L. P. Lee, *Continuous perfusion microfluidic cell culture array for high-throughout cell-based assays,* Biotech. Bioeng., vol. 89(10), pp. 1-8, (2005).

ON-CHIP HIGH-SENSITIVITY FLUORESCENCE DETECTION SYSTEM USING CROSS-POLARIZATION AND ORGANIC THIN FILM DEVICES FOR A DISPOSABLE LAB-ON-A-CHIP

Ansuman Banerjee, Andrea Pais, David Klotzkin and Ian Papautsky
Department of Electrical and Computer Engineering, University of Cincinnati, USA

ABSTRACT

In this paper, we present a high sensitivity, low-cost, portable and disposable lab-on-a-chip (LOC) device with an integrated organic light-emitting diode (OLED) excitation source and organic photodiode (OPD). A novel cross-polarization scheme is used to filter out excitation light from Rhodamine 6G fluorescent dye emission spectrum, enabling a detection limit of 100 nM.

Keywords: On-chip fluorescence detection, OLED, OPD

1. INTRODUCTION

Fluorescence is one of biotechnology's essential analytical and diagnostic methods, and commonly used in LOC systems. It is a simpler and quicker approach than bio/chemiluminsescence. However, the major hindrance in this approach is the leakage of the excitation light into the dye emission spectrum. To date, OLEDs have only been used as integrated excitation source for fluorescence analysis with external detectors (a photomultiplier tube [1] or conventional microscope [2]). OPDs have never been used for fluorescence-based detection, but rather only with chemiluminescent reactions [3]. Here, we demonstrate a simple and inexpensive cross-polarization filter scheme which enables the use of an OLED source and OPD detector for fluorescence detection and to achieved detection limits 100 times lower than previously reported with chemiluminescence [3].

2. EXPERIMENTAL

The prototype system is schematically shown in Figure 1. The microfluidic device was fabricated in polydimethylsiloxane (PDMS) using soft lithography. The chip contained a 4 mm diameter well, capable of holding 1 µL of sample liquid. Input and output microchannels were 55 µm deep and 200 µm wide. A TPD/AlQ thin film OLED was used as an excitation light source. The OLED structure is shown in Figure 2(a). The excitation light was linearly polarized (Edmund Optics NT45-667 polarizing film) and used to illuminate the microfluidic device. An

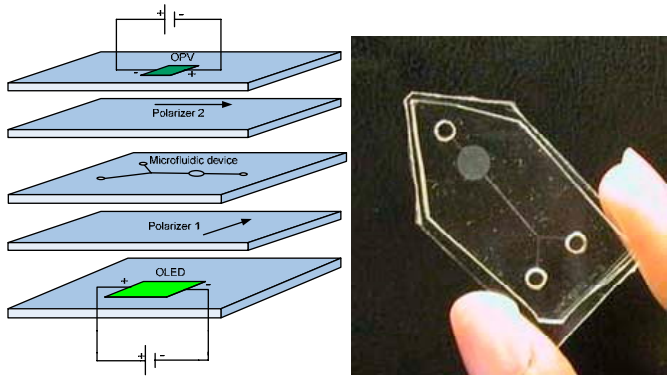

(a) (b)

Figure 1. (a) Integrated organic excitation/detection system concept. (b) PDMS microfluidic device.

978-0-9798064-0-7/µTAS2007/$20©2007CBMS

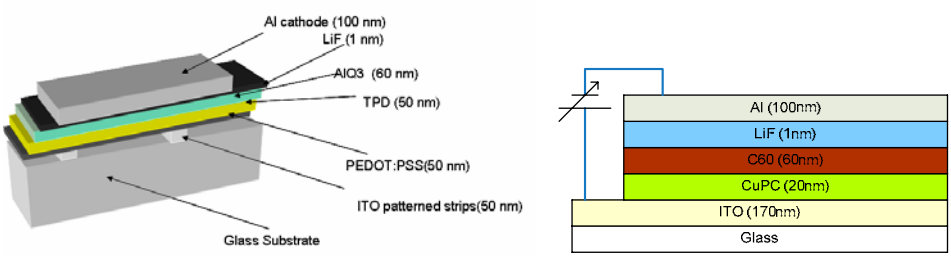

(a) (b)

Figure 2. Schematic of the (a) OLED and (b) OPD layers.

OPD was used as an intensity photodetector. The OPD consisted of a CuPC/C_{60} heterojunction with an indium tin oxide (ITO) anode and aluminum cathode, as depicted in Figure 2(b). The detector was then shielded by a second polarizer, oriented orthogonally to the excitation light, thus reducing the intensity of the excitation light on the detector by as much as 30dB. The fluorescence emission light, which was randomly polarized, was only attenuated by ~3dB. The fluorescence signal from Rhodamine 6G (λ_{em} = 570nm) was measured in a dilution series form 100 nM to 1 mM. A Keithley 2400 Source meter was used to supply bias voltage to OLED and OPD, and measure the OPD photocurrent.

3. RESULTS AND DISCUSSION

The OLED excitation light source exhibited the peak wavelength of 530 nm, which overlaps with the peak excitation of Rhodamine 6G (λ_{ex} = 530 nm). Figure 3 shows the CIE coordinates of the emitted light from the OLED. The maximum luminance of the OLED was 997 cd/m^2.

The OPD exhibited peak responsivity in the 550-650 nm range (Figure 4) at 0 V bias, which is within the Rhodamine 6G spectral emission (555-585nm).

To demonstrate cross-polarization, the degree of isolation from the excitation light source, the polarization angle *vs*. the photocurrent was measured using polarized excitation light as input while rotating the second polarizer from 0° to 360°. Edmund Optics polarizer film used in this work has an extinction ratio of ~2700 at 550 nm [4]. Figure 5 shows the expected sinusoidal dependence of photocurrent on polarizer angle as

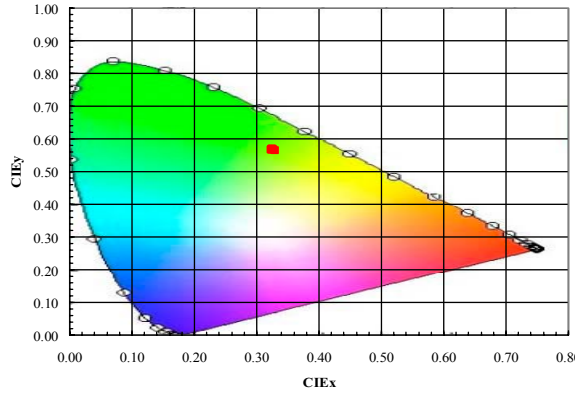

Figure 3. CIE plot for green OLED.

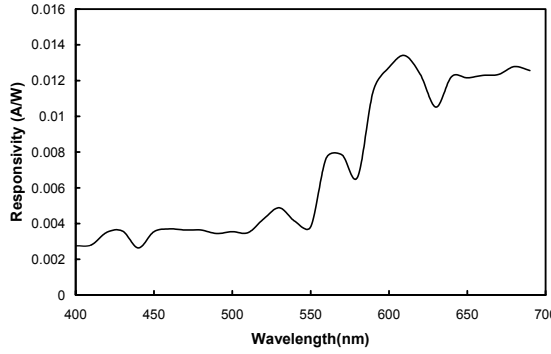

Figure 4. Responsivity curve for the OPD.

the two polarizers go from parallel to orthogonal. The cross polarization scheme reduces the signal intensity by a factor of approximately 25dB.

The fluorescence signal from Rhodamine 6G measured in a dilution series form 100 nM to 1 mM is shown in Figure 6. Ethanol was used to flush the microfluidic channel between experiments and to establish a background signal before each experiment (which was constant at ~5.3nA). The signal to noise ratio varied from ~4.5 at 1 mM to ~1.3 at 100 nM. These results to demonstrate a 100 nM limit of detection for Rhodamine 6G, which is 100 times lower that what was previously reported for microfluidic systems integrated with organic detectors.

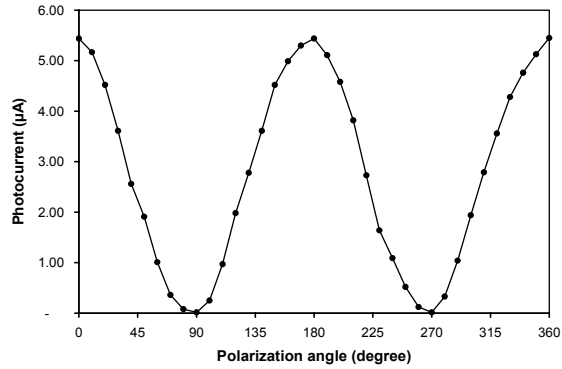

Figure 5. Photocurrent response of the OPD vs polarization angle.

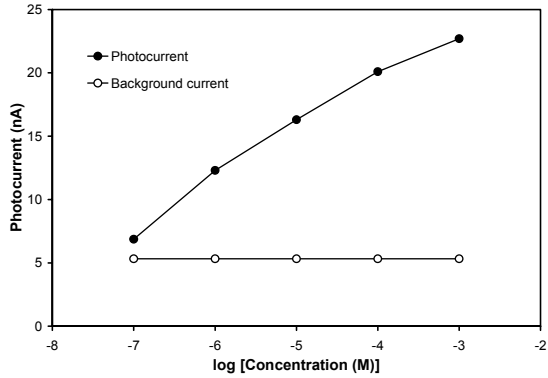

Figure 6. Rhodamine 6G dilution series.

4. CONCLUSIONS

The prototype fluorescence detection system consisting of an OLED source, PDMS chip, and OPD as intensity detector was successfully demonstrated and characterized. The cross-polarization scheme permitted us to overcome the limitations of current systems and to demonstrate a 100 times improvement in the detection limit. The developed approach is ideally suited for integration with disposable LOCs for point-of-care and on-site hand held devices.

ACKNOWLEDGEMENTS

The authors gratefully acknowledge the National Science Foundation (award #0428600) and the UC Institute for Nanoscale Science and Technology for the support of this work.

REFERENCES

[1] B. Yao, *et al.* "A microfluidic device using a green organic light emitting diode as an integrated excitation source", *Lab Chip*, **5**, pp. 1041–1047, (2005).

[2] J. B. Edel, *et al.* "Thin-film polymer light emitting diodes as integrated excitation sources for microscale capillary electrophoresis", *Lab Chip*, **4**, pp. 136– 140, (2004).

[3] O. Hoffmann, *et al.*"Thin-film organic photodiodes as integrated detectors for microscale chemiluminescence assays", *Sensors Actuators B,* **106**, pp. 878–884, (2005).

[4] http://www.edmundoptics.com/

A NEW METHOD FOR CELL CO-CULTURE USING MICRO-MOLDING IN CAPILLARIES TECHNOLOGY: STUDY OF CELL TRANSMIGRATION

Yi-Chi Huang[1], Yi-Hsien Huang[2], Keng-Shiang Huang[1], Li-Wha Wu[2], Yu-Cheng Lin[1]*

[1]Dept. of Engineering Science, [2]Dept. of Institute of Molecular Medicine, National Cheng Kung University, Taiwan

**Email: yuclin@mail.ncku.edu.tw*

ABSTRACT

This study reports a new cell co-culture method using micro-molding in capillaries (MIMIC) technology that was utilized to observe the transmigration conditions of two types of cells with and without under flow shear stress. In the study, endothelial cells (ECs) and smooth muscle cells (SMCs) were used. In addition, the cell concentration is 20000 cells/μL, the shear stress is 2.17 dyne/cm^2, and the isolation distance between two types of cell is 500 μm. Results show that (1) the velocity of SMCs migration was always larger than that of ECs migration before they touched each other, and (2) the velocity of cell migration not under shear stress was bigger than that under shear stress.

Keywords: Cell co-culture, micro-molding in capillaries, flow shear stress

1. INTRODUCTION

The co-culture technique could be utilized to discuss the intercellular communications and the clinical application of tissue engineered constructs. By incorporating the SMCs into a matrix of collagen gel, Ziegler *et al.* demonstrated that ECs which cocultured with SMCs aligned more rapidly with the flow direction than those grown on plastic [1]. More recently, Rainger *et al.* constructed a system by combining a parallel-plate flow chamber and a co-culture module in which ECs and SMCs were grown on opposite sides of a thin porous membrane [2]. MIMIC technique has been applied to microfluidic network for pattern biomolecules and cell culture [3, 4]. To date, no effort has been made to apply the MIMIC technique to do cell co-culture. Therefore, our work is aimed to develop a working co-culture model of ECs and SMCs to observe and analyze the transmigration circumstance.

2. EXPERIMENTAL

The processes of cell co-culture method were as follows Figure 1, a. cleaning PDMS and slide following by combining both them together, b. adding A cells and B cells, both of which will be inhale into the channel by capillary, and c. removing PDMS after cell culture 12 hr, and then observing the results. The device combines microfabrication and surface micropatterning techniques to create a two-compartment cell co-culturing device that can be used in a number of cell co-culture research applications. The device was fabricated by polydimethylsiloxane (PDMS), utilizing soft lithography technology. The PDMS was put on grass substrate, forming two channels. Figure 2 is fabrication process for PDMS. We used SU-8 thick photoresist to form grooves on the glass slide, then PDMS was replicated from the SU-8 mold.

978-0-9798064-0-7/μTAS2007/$20©2007CBMS

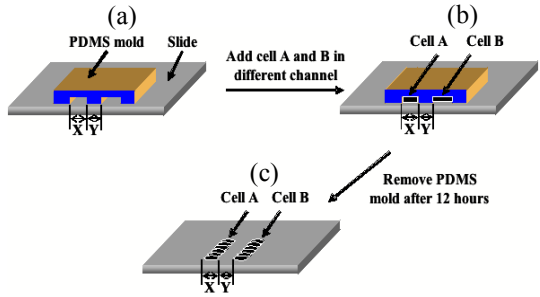

Figure 1. Schematic drawings of the cell co-culture method by MIMIC, where two types of cells were isolated and do cell co-culture by the device.

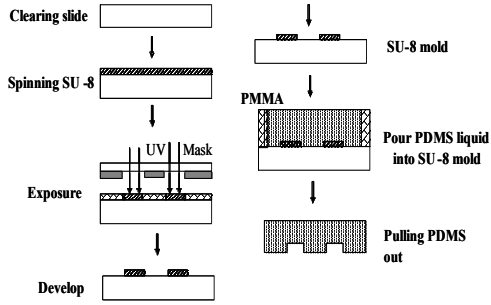

Figure 2. Schematic of fabrication process for PDMS. The fabrication process on left side shows the formation of grooves on the slide using a thick photoresist layer. Right side process is formed by replica molding PDMS from SU-8 mold.

3. RESULTS AND DISCUSSION

The new cell co-culture method was applied ECs and SMCs co-culture under environment of shear stress or not in this study. The 20000 cells/μL of cell concentration was used in the experiment. We used PDMS with the middle block of 500 μm to isolate ECs and SMCs, and then PDMS would be removed after 12 hr, after that they would be utilized under environment of shear stress. The result shown in Figure 3.

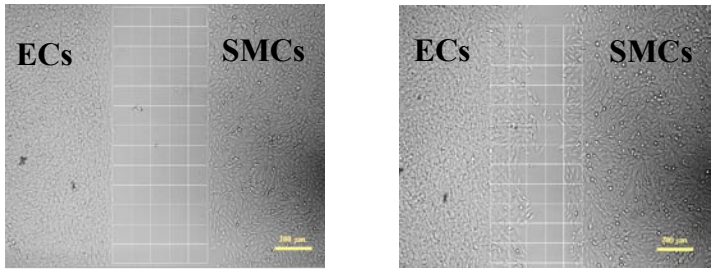

(a) (b)

Figure 3. ECs and SMCs was co-cultured on glass that was not under flow shear stress, after 12 hr for those two types of cells were isolated by 500 m. The figure was taken after PDMS was removed off glass, culture time: (a) 0 hr, (b) 12 hr (Scale bar: 200 μm).

Compareing ECs and SMCs was co-culture under non-flow shear stress with under flow shear stress. The average velocity of ECs and SMCs under non-flow shear stress was 34.23 m/hr. The average velocity of ECs and SMCs under flow shear stress was 24.19 m/hr. The former was 10.04 m/hr more than the later. So flow shear stress can suppress the touch velocity of endothelial cells and smooth muscle cell. The average velocity data were compared in Figure 4. The each experiment was done by three same of experiments.

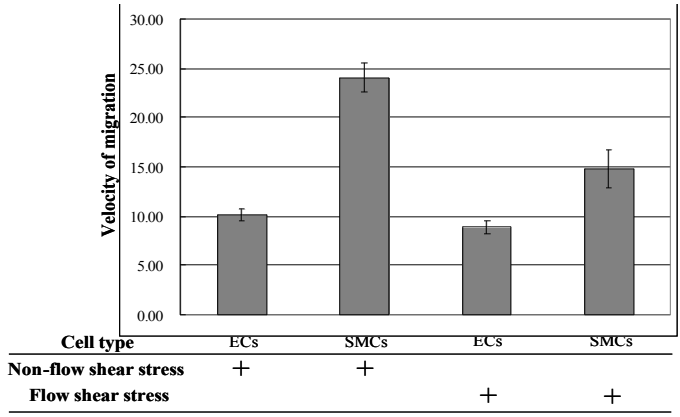

Figure 4. The relationships of migration velocity and cell type under flow shear stress or not.

4. CONCLUSIONS

We have successfully proposed a new cell co-culture method that was utilized to study the transmigration condition of ECs and SMCs. The results show that (1) the velocity of SMCs migration was always larger than that of ECs migration before they touched each other, and (2) the velocity of cell migration not under shear stress was bigger than that under shear stress. The proposed method offers a convenient way to do cell co-culture and a number of biological study applications where cells need to be exposed to well-controlled fluidic environment. This method has advantages of rapid and easy operation, and low cost.

ACKNOWLEDGEMENTS

The authors would like to thank the Center for Micro/Nano Technology Research, National Cheng Kung University, Tainan, for their equipment.

REFERENCES

[1] T. Ziegler, R.W. Alexander and R.M. Nerem, Annals of Biomedical Engineering, Vol. **23**, pp. 216-225, (1995).

[2] G.E. Rainger, P. Stone, C.M. Morland and G.B. Nash, Journal of Immunological Methods, Vol. **255**, pp. 73-82, (2001).

[3] E. Delamarche, A. Bernard, H. Schmid, B. Michel and H. Biebuyck, Science, Vol. **276**, pp. 779-781, (1997).

[4] S.W. Rhee, A.M. Taylor, C.H. Tu, D.H. Cribbs, C.W. Cotman and N.L. Jeon, Lab on a Chip, Vol. **5**, pp. 102-107, (2005).

ANALYSIS OF PRESSURE-DRIVEN AIR BUBBLE ELIMINATION FOR A LARGE-AREA MICROFLUIDIC CELL CULTIVATING DEVICE

Joo H. Kang[1], Yu Chang Kim[1,2], and Je-Kyun Park[1]

[1]*Korea Advanced Institute of Science and Technology (KAIST), KOREA and*
[2]*Korea Institute of Machinery & Materials (KIMM), KOREA*

ABSTRACT

We report an analysis of pressure-driven bubble elimination for a large-area microfluidic cell cultivation device. In this study, we described bubble elimination in a microfluidic employing a gas permeation model and calculated removal efficiency. We also successfully demonstrated human breast cancer cell (MCF-7) cultivation and subcultivation of several rounds in a microfluidic device having the largest area ever reported (1.7 cm^2).

Keywords: Bubble elimination, gas permeability, cell cultivation, MFC-7

1. INTRODUCTION

Elimination of air bubbles in microfluidic devices is a very significant issue because recently described microfluidic devices have become more intricate and are integrated with other functional compartments to be more powerful, offering more chances that bubbles can be trapped in the channels. Although several groups have reported bubble removal methods using vacuum and pressurized conditions [1, 2], it still requires a simple method and a quantitative estimation model of bubble-removal processes.

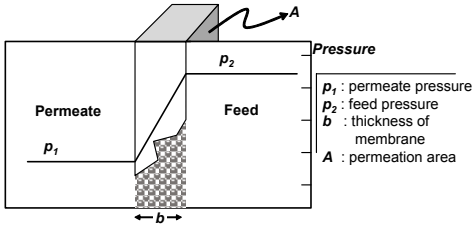

Figure 1. Principle of gas bubble elimination in a PDMS microfluidic device. When pressure difference is generated across the membrane, gas penetrates the membrane according to the condition.

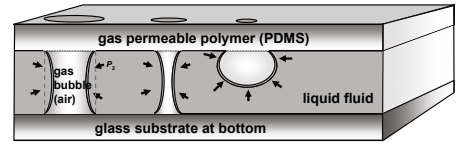

Figure 2. Scheme of disappearance of bubbles trapped in a microfluidic channel.

2. THEORY

When pressure difference is formed in steady-state across the gas permeable membrane (Figure 1), the gas (mostly air) penetrates the membrane depending on permeability (P), pressure gradient (p_2-p_1), penetration area (A), and thickness (b) as defined in equation 1.

$$J_A = -\frac{dV}{dt} = \frac{PA(p_2 - p_1)}{b}\frac{T\ 76}{273\ P_{atm}} \qquad (1)$$

978-0-9798064-0-7/μTAS2007/$20©2007CBMS

where T is the absolute temperature in Kelvin and P_{atm} is the atmospheric pressure in cmHg. Based on equation 1, we derived equation 2 to correlate experimental results of bubble removal with numerical estimation.

$$A(t) = c_1 e^{kt} + c_2 = c_1 e^{\frac{aP(p_1 - p_2)}{hb}\frac{T\,76}{273\,P_{atm}}t} + c_2 \qquad (2)$$

where c_1 and c_2 are appropriate constants, t is time in seconds and a is a correction factor for effective permeation area. As described in Figure 2, the volume of trapped air in microchannel is gradually decreased in simple experimental condition of Figure 3.

3. EXPERIMENTAL

To validate the analysis model of bubble removal, we used experimental setup presented in Figure 3. Two types of PDMS device were used for analysis of bubble elimination and large area cell cultivation, respectively. Removal rate of air bubbles were measured by CCD images of the bubbles surrounded by fluorescent solution (Figure 4). For the large area cell cultivation, we demonstrated perfusion cultivation of MCF-7 in 1.7 cm^2 area (8.5 μL of volume) (Figure 6). When we subcultured the proliferated MCF-7 to detach the cells from the bottom of microchannels, trypsin solution was injected into the microchannel without air-trapping.

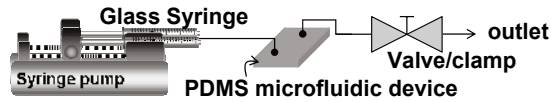

Figure 3. An experimental setup for simply eliminating air bubbles in PDMS chip. While liquid samples are injected to the device, closing valve or clamping off tubes at the outlet ports makes pressure in PDMS chamber accumulated and consequently trapped gas removed.

4. RESULTS AND DISCUSSION

According to equation 2, the trapped bubbles vanishes at a rate of the first order exponential decay, which is confirmed by experimental data (Figure 4) using FITC solution and the measured area of bubbles are plotted in Figure 5. As pressure is accumulated in microchannels, there is neither leakage nor breakup of bonding between PDMS and bottom glass substrate because maximum applied pressure is much less than the bonding strength (74 psi) of PDMS to glass [3].

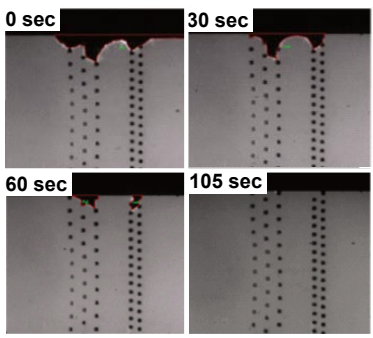

Figure 4. Sequential photographs prove that bubbles of 8.8 nL are removed in about 105 s at the pressure of 11.0 psi. Scale bar is 1.0 mm.

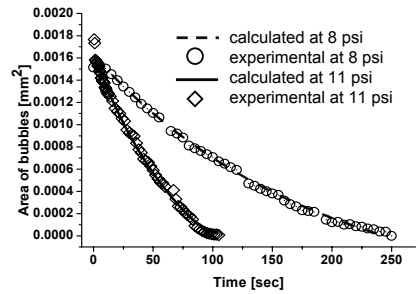

Figure 5. Bubble disappearance data when the microchannel was constantly pressurized, fitting with gas permeation model. The gas volume vanished according to the first order exponential decay.

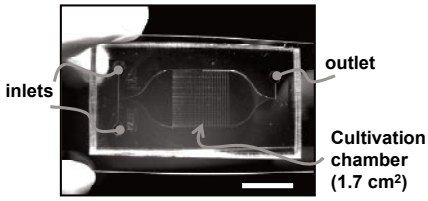

Figure 6. A picture of the cell cultivation device. (area; 1.7 cm^2 and volume; 8.5 μL) Scale bar is 1.0 cm.

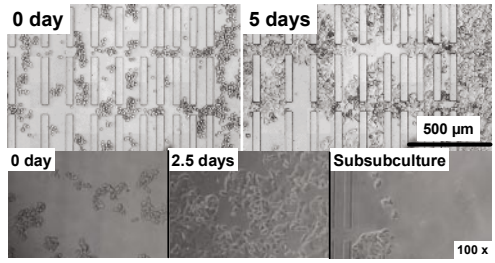

Figure 7. Large area (1.7 cm^2) human breast cancer cell (MCF-7) cultivation for 5 days and subculture of the third round.

As shown in Figure 7, the cells have been cultivated for 5 days and successfully subcultured for several rounds.Viability tests using calcein AM and ethidium homodimer-1 (Figure 8) also support that the large-area microfluidic cell cultivation and subcultivation were successfully carried out without any failures caused by trapped bubbles.

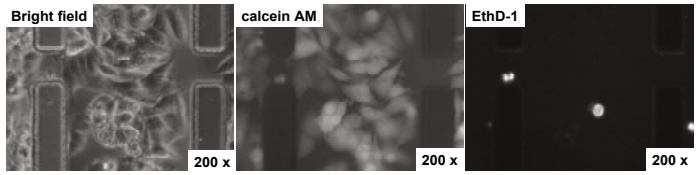

Figure 8. Viability test of cultivated MCF-7 in the microfluidic device for 3 days using calcein AM (live cells)/ ethidium homodimer-1 (dead cells). Images were captured at the same position by switching fluorescence filters.

5. CONCLUSIONS

The prediction of bubble removal rate in microfluidic networks is important not only in intricate or large-area microfluidic manifolds but also in gas-generating devices such as electrolysis and microfluidic fuel cell because we need to know the accurate removal rate of generated or trapped air bubbles to vanish them through the gas permeable microchannel surfaces.

ACKNOWLEDGEMENT

This research was supported by a grant from the CHUNG Moon Soul Center for BioInformation and BioElectronics, KAIST.

REFERENCES

[1] C.-H. Hsu and A. Folch, *Microfluidic devices with tunable micro-topographies*, Appl. Phys. Lett., 86, 023508 (2005).

[2] J. Monahan, A. A. Gewirth and R. G. Nuzzo, *A method for filling complex polymeric microfluidic devices and arrays*, Anal. Chem., 73, 3193 (2001).

[3] S. Bhattacharya, A. Datta, J. M. Berg and S. Gangopadhyay, *Studies on surface wettability of poly(dimethylsiloxane) (PDMS) and glass under oxygen-plasma treatment and correlation with bond strength*, J. Microelectromech. Syst., 14, 590 (2005).

BLOOD PLASMA EXTRACTION FROM A MINUTE AMOUNT OF BLOOD USING DIELECTROPHORESIS

Y. Nakashima and T. Yasuda
Kyushu Institute of Technology, JAPAN

ABSTRACT

This paper presents a microfluidic device that can extract blood plasma from about 10 μl of blood without any external mechanical driving source. The fabricated device consists of a PDMS channel and two electrodes which were designed like a framed rectangle shape and a pin shape. Blood is automatically injected into the microchannel by capillary force and separated into blood cells and blood plasma by dielectrophoresis. Experiments using human blood showed that blood cells were repelled from the pin electrode and trapped in the framed rectangle electrode. Also, blood plasma extraction was affected by magnitude and frequency of applied AC voltage.

Keywords: Blood plasma extraction, Dielectrophoresis, Microfluidic device

1. INTRODUCTION

Our purpose is to fabricate microfluidic devices which can extract blood plasma from a minute amount of blood, and to apply them to a point-of-care medical diagnosis. Generally, external mechanical driving sources such as a centrifugal machine are required for extracting blood plasma from blood. Thus we cannot perform at-home health checkup to detect potential diseases using conventional methods. Development of an easily operated universal microfluidic device for medical diagnosis at home is awaited. Many microfluidic devices for cell separation have been already developed [1-3]. However, these techniques require external mechanical driving sources for extracting blood plasma. In this paper, we present a microfluidic device for separating blood plasma and blood cells by dielectrophoresis. This device can be applied to medical diagnostics technology such as health checkup at home.

2. DESIGN AND FABRICATION

Figure 1 shows the schematic of a blood plasma extraction device. This device consists of two electrodes and a PDMS channel. The left side electrode and right side electrode were designed like a framed rectangle shape and a pin shape, respectively. Figure 1(b, c) shows the blood plasma extraction method. Blood enters the microchannel by capillary force when we drop a blood droplet of 10 μl at the channel inlet. When we apply an AC voltage between two electrodes, blood cells are repelled from the right side electrode and trapped in the left side electrode because inhomogeneous electrical field is generated between the two electrodes (Fig. 1(c)). Consequently, blood plasma is extracted in between the two electrodes. As shown in Fig. 2, the two electrodes were fabricated on the glass plate using vacuum deposition and a lift-off process. The width of each electrode was about 60 μm and the interelectrode distance was about 50 μm.

978-0-9798064-0-7/μTAS2007/$20©2007CBMS

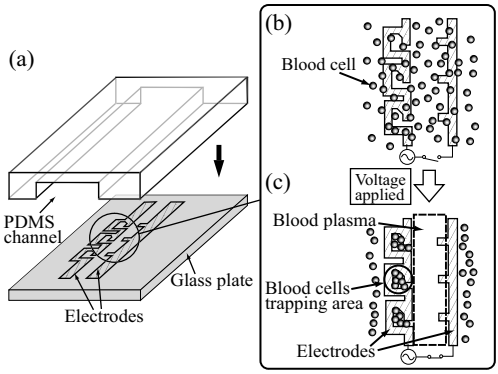

Figure 1. Schematic of a blood plasma extraction device.

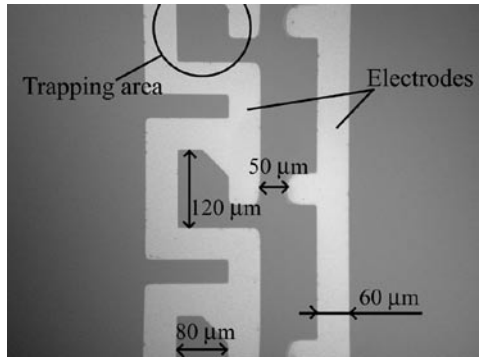

Figure 2. Photograph of the fabricated electrodes on the glass plate.

3. EXPERIMENTAL RESULTS

We carried out blood plasma extraction tests by dielectrophoresis using human blood that was diluted by PBS (phosphate buffer solution) by 10 %. We observed motion of blood cells while AC voltage was applied between the electrodes. Blood plasma extraction, in case of applied AC voltage of 20 $V_{p\text{-}p}$ and 1MHz, is shown in Fig. 3. When we applied AC voltage, blood cells located outside the electrodes were repelled from the electrodes. Also, blood cells on and in between the two electrodes moved toward the weaker electric field direction, i.e. blood cells moved toward the framed rectangle shape electrode. Moreover, blood cells were trapped on the center of the framed rectangle shape electrode, and blood plasma was extracted in between two electrodes.

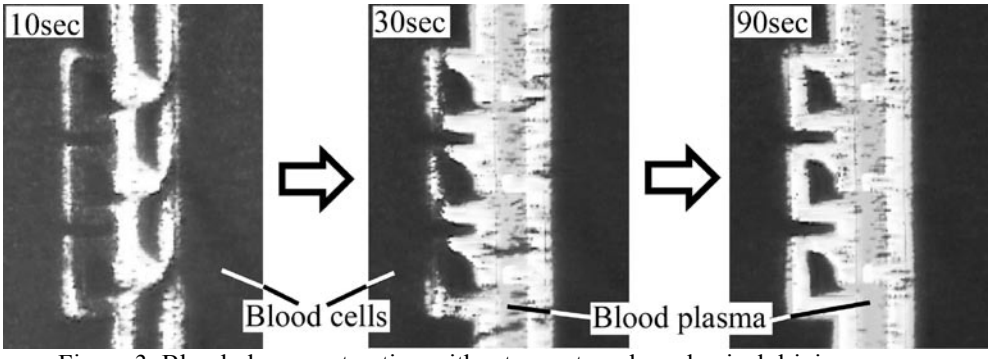

Figure 3. Blood plasma extraction without an external mechanical driving source.

We measured the area of blood plasma that was extracted by dielectrophoresis using three kinds of frequencies (100 kHz, 1 MHz, and 10 MHz) as shown in Fig. 4. As a result, areas of blood plasma became larger in relation to the increase in applied voltage. Also, areas of blood plasma in cases of 100 kHz and 1 MHz were about twice as large as that of 10 MHz. Moreover, to figure out the optimal shape of the electrodes, we tested four patterns as shown in Fig. 5. In case of the 4th pattern of electrodes, it was difficult to extract blood plasma because an enclosure frame was not fabricated in the left side electrode thus blood cells could not be trapped effectively. In all cases, when we applied

AC voltage at 100 kHz, we could remove blood cells most effectively compared to that of 1 MHz and 10 MHz.

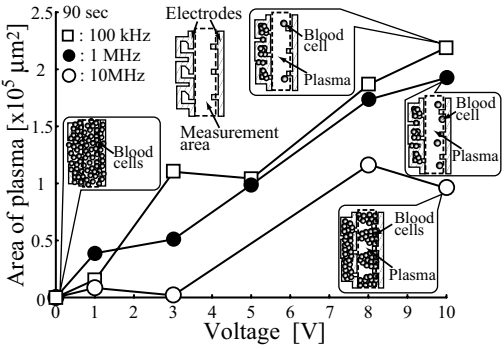

Figure 4. Relationship between applied voltage and area of blood plasma.

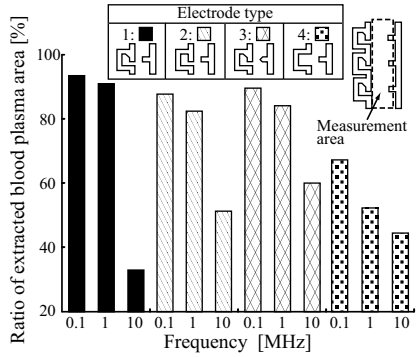

Figure 5. Ratio of extracted blood plasma area to measurement area.

4. CONCLUSIONS

We succeeded in blood plasma extraction from a minute amount of blood without any external mechanical driving source. An electrode having enclosure frame shape is required for separating blood cells and blood plasma, and its efficiency depends on the magnitude and frequency of applied AC voltage. Blood cells and blood plasma will be completely separated by optimizing arrangement, shape, etc. of electrodes of the device.

REFERENCES

[1] Hiroki Ogawa, Masao Nagai, Jun Kikuchi and Yasuhiro Horiike, "Blood Painless Collection System Equipping Detection Functions for Search of Vein," Proc. μTAS, Vol. 1, pp. 741-744, (2003).

[2] Masumi Yamada, Miyuki Matsuda, and Minoru Seki, "Microfluidic device for continuous and hydrodynamic separation of blood cells," Proc. μTAS, Vol. 2, pp. 1052-1054, (2006).

[3] Che-Hsin Lin, Cheng-Yan Lee and Lung-Ming Fu, "Numerical and Experimental investigations into a Novel Cell Sorter utilizing Continuous Effect," Proc. μTAS, Vol. 2, pp. 1091-1093, (2006).

LONG-TERM CYTOTOXIC DRUG ASSAY VIA SINGLE-CELL MICROFLUIDIC ARRAY

Liz Y. Wu, Dino Di Carlo, and Luke P. Lee

Biomolecular Nanotechnology Center, Berkeley Sensor & Actuator Center
Department of Bioengineering, UC Berkeley

ABSTRACT

In this work, we use a single cell trapping array device for cytotoxic drug investigations on a large amount of single cells. The uniform and precise microenvironment for each single cell rigorously controls the drug assay experiment. The dynamic perfusion flow supplies media with/without drug to properly simulate the *in vivo* drug delivery mode. Drug assays for both adherent and non-adherent cell lines were demonstrated in the device. We have evaluated dose conditions of Taxol on HeLa and HL-60 cells. By tracing each single cells before, during and after the drug exposure, we first correlate the lifetime of the cells and their condition when exposing to the drug.

Keywords: Single cell analysis, cell culture, drug assay, microfluidic devices

1. INTRODUCTION

Cellular *in vitro* drug assays are important tests for estimating the performance, toxicity and side effect of new drug candidates. Most current drug assays are based on the average cellular response of large cell populations (i.e. heterogeneous conditions). To observe large quantity of cells under/after drug exposure at a single-cell resolution while providing each cell with equivalent microenvironment provides a more information-rich assay. To facilitate drug assay application, cells must be well cultured in the device and drug concentration and exposure time for each cell must be precisely controlled. Previously, we published a device to trap single cells by a purely hydrodynamic method and provide a good cell culture environment with media perfusion and waste removal [1]. The dynamic perfusion flow supplies media with/without drug to properly simulate the in-vivo drug delivery mode (Figure 1). Drug assays for both adherent and non-adherent cell lines were demonstrated in the device. We have evaluated reproducibility and dose condition of the taxol drug assays done by traditional method on HeLa cells and HL-60 cells [2,3]. The response time of each single cell was recorded and easier operational process and more systematic assay results were presented.

2. EXPERIMENTAL

The single cell trapping array device is fabricated by using PDMS replicate molding. We designed U-shape structures on PDMS side which distances from bottom bonding glass of 2μm to trap the single cells. The traps were arrayed in a 450μm * 1400μm microfluidic chamber. Detailed characterization of the trapping efficiency was reported previously [1]. The device was sterilized carefully prior to use. HeLa/HL-60 cells were suspended from culture dishes at $1*10^6$ cells/ml and loaded into the single cell culture chambers using a sterile syringe. Cells were then cultured with a perfusion of CO_2 Independent Medium (Gibco, Grand Island, NY) supplemented with 10% fetal bovine serum, 4 mM L-glutamine, and 1% penicillin/ streptomycin. Perfusion of 0.8μL/min was controlled with a

978-0-9798064-0-7/μTAS2007/$20©2007CBMS

programmable syringe pump. We integrated a temperature control plate to the stage of the microscope for real time observation of cell's movement, morphology and growth. Images were recorded every 6 minites. To get the drug response of HeLa cells, after 24 hrs from the cell loading, we treated the cells with 10 μM Taxol prepared in the culture media for 2 hours of perfusion. Media without drug was then supplied to the cells for 3 days. From the 3-day movie of the cells after drug treatment, we characterized the timing when each cell entered the mitotic phase arrest. Also, the timing of cells death was recorded. Statistical analysis of the lifetime after each cells entered the mitotic phase was thus completed. The response of HL-60 cells to the drug was also recorded and analyzed.

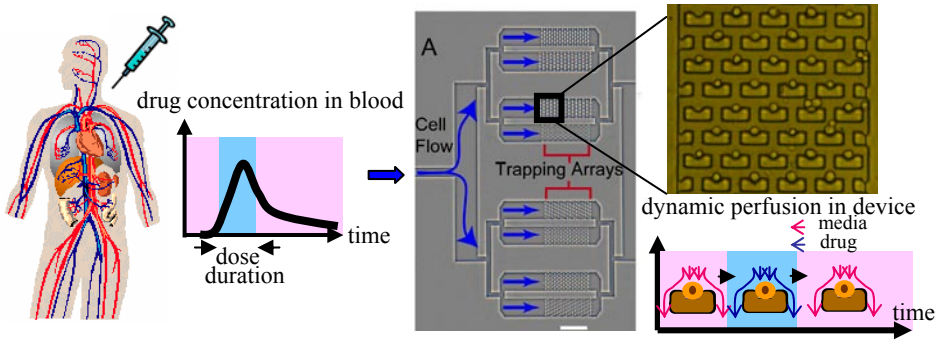

Figure1. The dynamic perfusion flow supplies media with/without drug to properly simulate the *in vivo* drug delivery mode. The uniform and precise microenvironment for each single cell rigorously controls the drug assay experiment.

3. RESULTS AND DISCUSSION

During the 3-day period of observation, more than 95% of the HeLa cells were successfully traced and analyzed (Figure 2). After 24hrs of cell culture under fresh media perfusion, most of the cells adhered and spread near their traps (Figure 2b). HeLa cells detach and round up from the substrate upon entering the mitotic phase right before cell division. After we perfused 10μM of Taxol for 2 hrs and switched back to fresh media, the cells rounded up sequentially as they entering the mitotic phase and became arrested at this stage. In Figure 2c, after 10hrs of drug exposure, some cells were locked in the mitotic phase. The big round cells then died with failure of division.

We recorded the time required for each single cell to enter mitotic arrest and plotted the result in Figure3a. More than 70% of the cells entered mitotic arrest at the beginning 24 hrs after dose. After each cell entered mitotic arrest, they lasted for a short lifetime and then died due to failure of division. We recorded the lifetime of each cells after they entered mitotic arrest. Each cell was in a different condition when first exposed to the Taxol. Some of them were well spread, some were ready to divide with round shape, and some were newborn cells.. We sorted the cells into these three categories and plotted their life time distribution in Figure 3b. The cells which spread well before the drug dose had a longer lifetime than the rounded cells. The new-born cells also had a longer lifetime after entering the mitotic stage. For HL-60 cells, similarly, when the cells were dosed with 0.1μM Taxol for 22 hrs, the cells grew bigger and arrested in mitotic phase but died of failure of division.

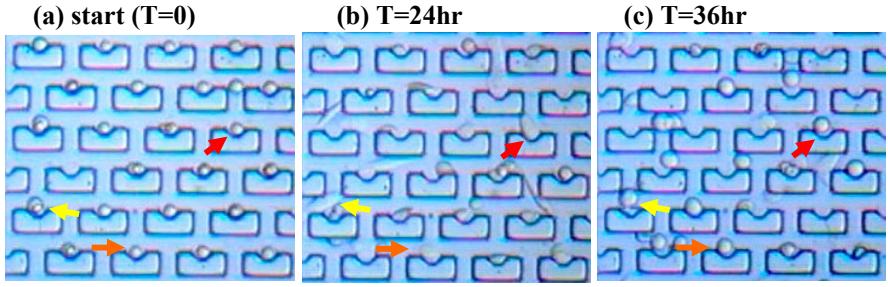

Figure.2 Taxol drug assays on HeLa cells. (a) image taken after cell loading (b) After 24hrs, most of the cells spread near their traps (c) After 10hrs of dose, some cells rounded up as they entering the mitotic phase and being arrested at this status.

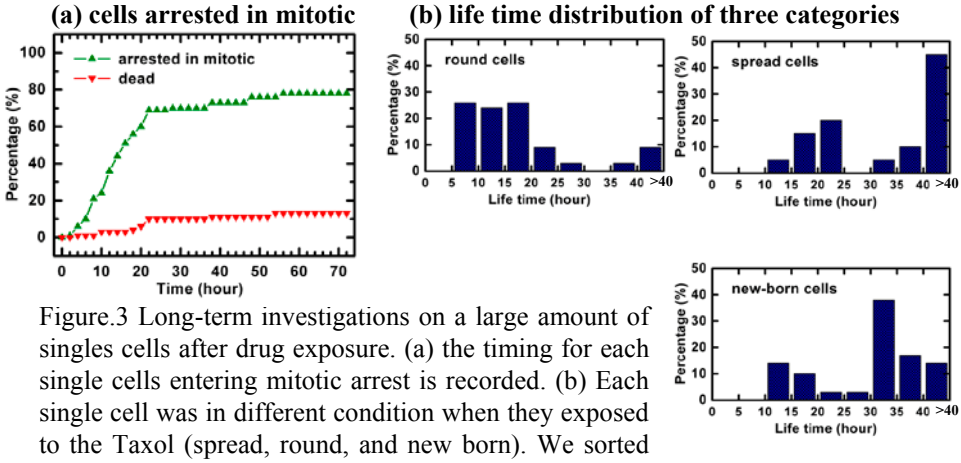

Figure.3 Long-term investigations on a large amount of singles cells after drug exposure. (a) the timing for each single cells entering mitotic arrest is recorded. (b) Each single cell was in different condition when they exposed to the Taxol (spread, round, and new born). We sorted the cells into these three categories and plotted their life time distribution.

4. CONCLUSIONS

The single cell trapping array device successfully provides long-term investigations on a large amount of singles cells after drug exposure. The uniform and precise microenvironment for each single cell rigorously controls the drug assay experiment. By tracing each single cells before, during and after the drug exposure, we first correlate the lifetime of the cells and their condition when exposing to the drug.

ACKNOWLEDGEMENTS

This research was supported by Intel Research Fund, GSK, Taiwan Merit Scholarship TMS-094-2-A-008 (L.W.)

REFERENCES

[1] Di Carlo, D., Aghdam, N. & Lee, L. P. , *Analytical Chemistry*,78, 4925-4930, 2006.
[2] J.Michalakis et al., Cancer Chemother Pharmacol (2005) 56: 615–622
[3] E.K. Rowinsky, R.C. Donehower, R.J. Jones, and R.W. Tucker, Cancer Research, 1988, 48, 4093-4100

CELL CHIP TO MONITOR THE INFLUENCE OF ELECTRIC FIELD ON THE HUMAN MESENDHYMAL STEM CELLS

Gu-Han Kwon* , Kwang Ho Lee, Eun-Joong Lee* and Sang-Hoon Lee***

* Department of Biomedical Engineering, College of Medicine, Korea University ,
**Interdisciplinary Program in Medical and Biological Engineering Major, Seoul National University, Korea

ABSTRACT

A new micro cell chip which can induce stem cells to differentiate into specific body cell types has been designed and fabricated for tissue engineering. This paper presents the fabrication and preliminary test results of a MEMS cell electric stimulator. It provides a new tool of cell electric stimulation, culture and analysis for stem cell research. This study provides the controlling proliferation as well as morphology of human mesenchymal stem cell on the microchip. DC 1V, 5V, 12V, AC 5V, 1 ㎐, 1K ㎐, 1M ㎐ were compared with electric stimulation for their impact on the expansion and morphology of mesenchymal stem cells (MSCs). It provides a new generation of cell culture, stimulation and analysis devices for stem cell research and tissue engineering.

Keywords: Human mesenchymal stem cells(hMSC), Electric stimulation, Cell Proliferation,

1. INTRODUCTION

Human mesenchymal stem cells (hMSCs) are multipotent that can be isolated from adult bone marrow and can be induced in vitro and in vivo into a variety of mesenchymal tissues, including bone, cartilage, tendon and fat and have broad potential applications in the production of bio-organs[1-2]. However, their behavior such as proliferation or differentiation under the electric field was not studied extensively, even though the study on the effect of other stimulation carried out broadly[3].

2. EXPERIMENTAL

The objective of this paper is to scrutinize efficiently the influence of electric field on the human MSCs by using the cell chips having 7 culture chambers. The frontal and lateral schematics of cell chip are shown in Figure 1 and this was fabricated by combining the slide glass having ITO electrode and PDMS platform. The fabrication process is summarized and photograph cell chip in Figure 2 and Figure 3.

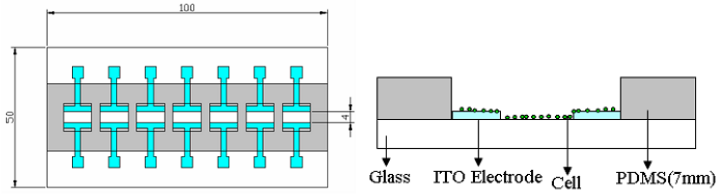

Figure 1. Schematic of electric cell stimulator

978-0-9798064-0-7/μTAS2007/$20©2007CBMS

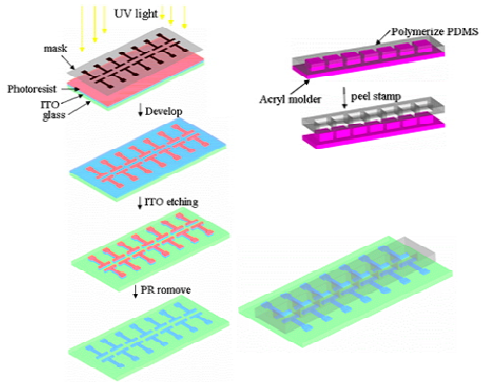



Figure 2. Fabrication Process of Microchip Figure 3. Photograph of the fabricated cell chip.

Our cell chip has some inherent potentials such as the reduction of the necessary quantity in stem cells, the cost reduction in process, and the increase of throughput. In addition, the experiments can be carried out simultaneously under the same culture conditions. ITO glass is transparent enough to monitor cells. For the compatibility of ITO electrode to the hMSCs, we have coated the surface with Gelatin (concentration: 1mg/ml). Human MSCs were cultured in DMEM with 10% (v/v) fetal bovine serum and 1% (v/v) antibiotics containing penicillin and streptomycin in a humidified incubator (5% CO2, 37℃). We have seeded hMSCs ($1x10^4$) from passage two on the 7 culture chambers and harvested them in the CO2 incubator.

3. RESULTS AND DISCUSSION

To investigate the influence of diverse electric fields, we applied 6 kinds of electric fields simultaneously while they were cultured; DC 1V, 5V, 12V, AC 5V, 1Hz, 1K Hz, 1M Hz. After 2 days, we have examined the expansion and the morphology of mesenchymal stem cells (MSCs) through the optical and fluorescent microscope.

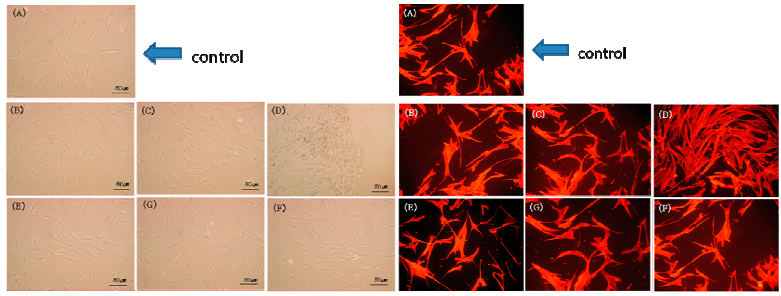

Figure 4. Cellular morphology of MSCs in Electric Stimulation at 48 hours (x200) (A) control, (B) DC 1V, (C) DC 5V, (D) DC 12V (E) AC 5V, 1 Hz, (F) AC 5V, 1K Hz, (G) AC 5V, 1M Hz, Figure 5. Actin filament staning of hMSCs in Electric Stimulation at 48 hours

Figure 4 is optical image and Figure 5 illustrates the micrograph of hMSCs exposed to the electric fields and corresponding actin filament stained image and cells were adhered and

proliferated well except 12V. For the quantitative assay of proliferation, we carried out WST-1 test and the result is shown in Figure 6.

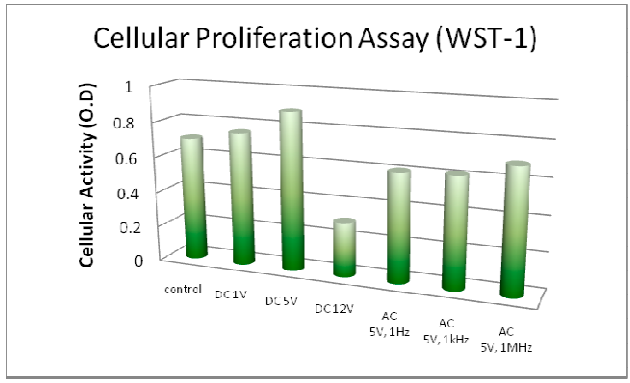

Figure 6. Cellular proliferation assay of hMSC Electric Stimulation at 48 hours

Cells were proliferated well than control cells under the DC 1 and 5 volts electric field, while AC fields did not influenced on the cells. But, when the electric fields are over 10 volts, cells were damaged significantly. For the further study, we will examine the changes of gene profile and immunophenotyping according to the electric field and the effect of diverse electric stimulation to the stemness and differentiation of hMSCs.

4. CONCLUSIONS

Electric micro cell stimulator, which can apply various electric stimulations simultaneously, is developed and tested. We show the possibility that the proliferation and morphology of hMSCs can be changed by electric stimulation. The feasibility of MEMS cell stimulator as a convenient and effective tool for stem cell research and tissue engineering is demonstrated.

ACKNOWLEDGEMENTS

This study was supported by a grant of the Korea Health 21 R&D Project, Ministry of Health and Welfare, Republic of Korea (02-PJ3-PG6-EV10-0001)

REFERENCES

[1] "Multi-organ, Multi-Lineage Engrafment by a Single Bone MarrowDerived Stem Cell." Krause, D.S., et al., Cell, 2001. 105(3):p. 369-77.

[2] "Pluripotency of mesenchymal stem cells derived from adult marrow." Jing, Y., et al., Nature. 202. 418(6893):p. 41-9.

[3] "An Electromagnetic Compressive Force by Cell Exciter Stimulates Chondrogenic Differentiation of Bone Marrow–Derived Mesenchymal Stem Cells" Park S,. Et al., Tissue Engineering, 2006. 12(11):p.3107-16

CULTIVATION OF DIELECTROPHORETICALLY TRAPPED SINGLE CELLS UNDER OPTIMAL ENVIRONMENTAL CONDITIONS

Hendrik Kortmann[1], Lars Mathias Blank[1, 2], and Andreas Schmid[1, 2, *]

[1]ISAS-Institute for Analytical Sciences, Dortmund, Germany,

*[2]Chair of Chemical Biotechnology, University of Dortmund, Germany,**

ABSTRACT

We here describe the development of a single cell bioreactor termed CER (controlled environment bioreactor) that enables in a controlled environment cultivation, analysis, and retrieval of single cells. We used the reproducibility of growth experiments starting from a single *Saccharomyces cerevisiae* as measure of a stressless growth environment. The main features of the microfluidic chip are the temperature control and the contact-free cell trapping using dielectrophoresis. Our aim is to overcome the limitation of cell population research by implementing single cell handling and analysis as a standard biological technique.

Keywords: Single cell analysis, controlled environment bioreactor (CER), dielectrophoresis, temperature control

1. INTRODUCTION

Selection, maintenance, analysis, and retrieval of single cells have great potential in cancer research, biomedical applications, and metabolic engineering. First steps were made by the integration of microsystems and high sensitive analytical methods, offering new insights into cellular processes at the single cell level [1]. Microchamber and microfluidic chips are frequently use as microcultivation devices. The first, however, cannot guarantee constant medium, thus growth environment conditions. In contrast, the latter assures constant medium conditions by a steadily delivered micro flow. The flow through, in addition contains the cell's traces (analytes), which can be exploited by in line or integrated analysis techniques.

2. RESULTS AND DISCUSSION

Our approach integrates the benefits of non-disturbing contact-less cell trapping and analysis in a microfluidic bioreactor. Trapping of cells by negative dielectrophoresis might lead to unfavourable spatial electrical heating [2]. We here, however exploit Joule heating of the dielectrophoretic cage in combination with an extra tailored Peltier system (Fig. 1) for temperature maintenance. The temperature rise due to cage activation as the sum of medium composition, voltage, and frequency, was spatially quantified with Rhodamine B (Fig. 2).

We can control the preferred temperature for yeast incubation (30 °C), knowing the heating effect of the trapping conditions (Fig. 3, inset). Thus we use the heating effect of a dielectrophoretic trap for temperature maintenance and can employ it for temperature perturbation experiments at the millisecond scale.

978-0-9798064-0-7/μTAS2007/$20©2007CBMS

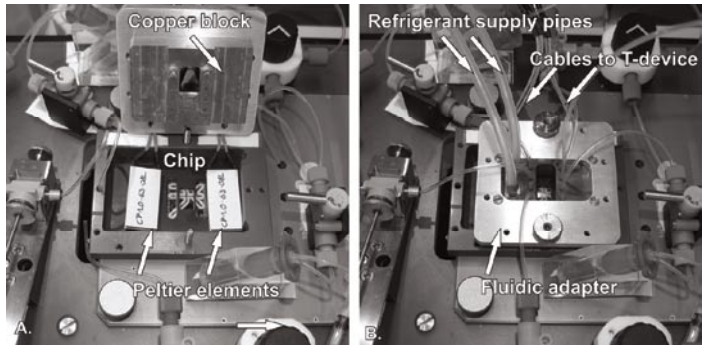

Figure 1: The new temperature control device. A. opened device, B. assembled device. The temperature is measured by an AD590 thermo sensor, which is placed on the bottom side of the chip. The Peltier elements are controlled via a TEDC200C temperature controller.

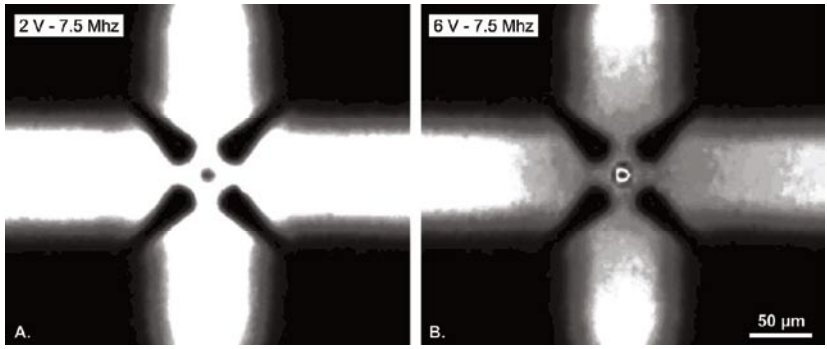

Figure 2: Spatially resolved temperature profiles. The activated electrodes (cage) give rise to Joule heating in dependence of the applied voltage. The false colour images were taken with Rhodamine B.

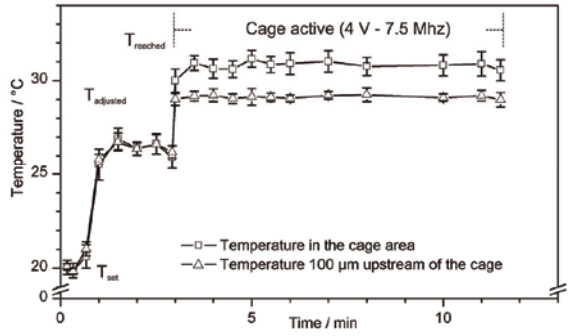

Figure 3: Temperature regulation of the cage area. The figure shows control of 30 °C, after prior chip temperature adjustment to 26 °C using the Peltier elements. Inset: same experiment without prior temperature adjustment.

The excellent growth conditions in the modified microfluidic chip were verified by comparing the specific growth rate and generation time with data from shake flask experiments [3] that were $\mu = 0.42\ h^{-1}$, and $t_D = 1.6$ h (Fig. 4). The cells under study can be retrieved by an automated fractionation collector and further analysed in an automated micro well cultivation system. The high reproducibility of the growth analysis in the automated cultivation device could be validated by population research in a first step (data not shown).

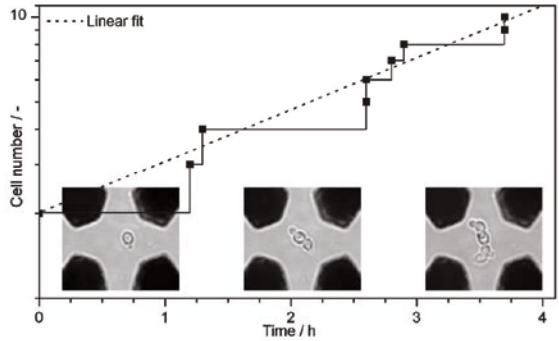

Figure 4: Growth curve of a single *S. cerevisiae*. The diploid yeast cell is growing as pseudohyphae due to nitrogen limiting conditions. The insets present cells at different times during growth.

3. CONCLUSIONS

We established a single cell bioreactor that allows reproducible long-term experiments. The reactor is tuned for the introduction of environmental perturbations at very small time scales. The combination of this single cell reactor setup with cell retrieval and automated growth monitoring at larger scale allows using the analysed single cell as progenitor for a new population. We thereby bridge the gap between single and cell population research.

ACKNOWLEDGEMENTS

The authors would like to acknowledge funding from the ICA-Project (Leibniz Association/PAKT). This project is co financed by the European Union (EFRE) and supported by the Ministry of Innovation, Science, Research, and Technology of North-Rhine Westphalia.

REFERENCES

[1] L. Cai, N. Friedman, and. S. Xie, *Stochastic protein expression in individual cells at the single molecule level,* Nature, **440**(7082), 358 (2006)

[2] T. Mueller, A. Pfen- nig, et. al., *The potential of dielectrophoresis for single-cell experiments*, IEEE Eng Med Biol Mag, **22**(6), 51 (2006).

[3] L. M. Blank, L. Kuepfer, and U. Sauer, *Large-scale ^{13}C-flux analysis reveals mechanistic principles of metabolic network robustness to null mutations in yeast*, Genome Biol., **6**(6):R49 (2005)

** Correspondence to: Andreas.Schmid@bci.uni-dortmund.de*

DEVELOPMENT OF NANOSTRUCTURES FOR CELL ADHESION SURFACE AND BIOLOGICAL ANALYSES OF HUMAN CELLS CULTURED ON THE SURFACE

Yasuyuki Sakamoto, Kiichi Sato, Takehiko Tsukahara, Takehiko Kitamori, Ichiro Matsumoto, Keiko Abe and Etsuro Yoshimura

The University of Tokyo, JAPAN

ABSTRACT

We studied the interaction between cells and their adhesion surface structure. In this study, we fabricated substrates with/without well-defined nanostripes, on which we cultured human cells and compared morphology, motility and gene expression of the cells by time-lapse imaging and DNA microarray analyses. As a result, it was found that morphology, motility and gene expression of the cells differ evidently between the two conditions.

Keywords: cell adhesion, cell motility, gene expression, nanostructure

1. INTRODUCTION

Cell adhesion plays an important role in adherent cells, because it triggers signal transduction, which affects cell growth, proliferation, and differentiation. Many studies on the interactions between cells and adhesion surfaces were reported. For example, we reported sub-cellular stripe patterns (100 - 1,000 nm scale) fabricated on a glass substrate and morphological change of cells cultured on it [1,2]. To elucidate the change, genetic analyses are useful, while more than 10^6 cells are necessary for each DNA microarray analysis. Therefore, a large culture substrate with a nanostructure is required. In this study, we fabricated large cell culture substrates with well-defined nanostructures easily, and then morphology, motility, and gene expression of human cells cultured on the surface were studied by time-lapse imaging and DNA microarray analyses.

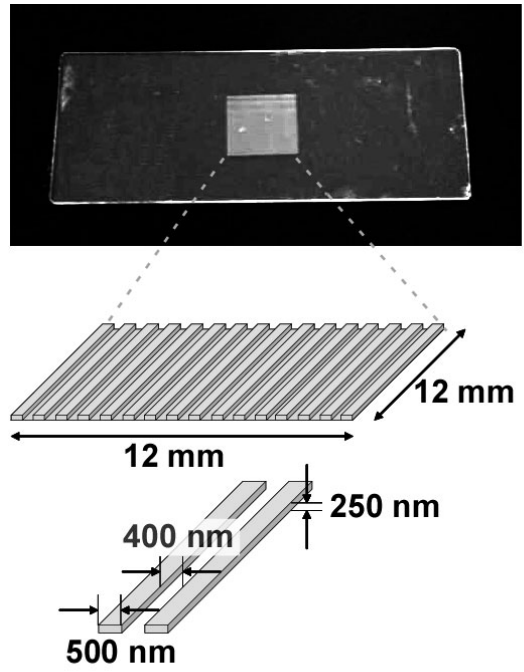

Fig. 1 Glass mold for PDMS culture sheet with nanostripes.

2. EXPERIMENTAL

A glass mold was fabricated by electron beam lithography and dry

978-0-9798064-0-7/μTAS2007/$20©2007CBMS

etching methods and 1.2-cm square of nanostripe structures were obtained (Fig. 1). Poly-dimethylsiloxane (PDMS) prepolymer was casted on the mold and cured at 120˚C for 150 s. Typical dimensions of the obtained nanostripes were 400 nm in width with 900 nm intervals and 200 nm in height (Fig. 2). A cell culture dish was paved with the PDMS replicas. By the simple and rapid method, many culture dishes with the nanostructures can be prepared easily.

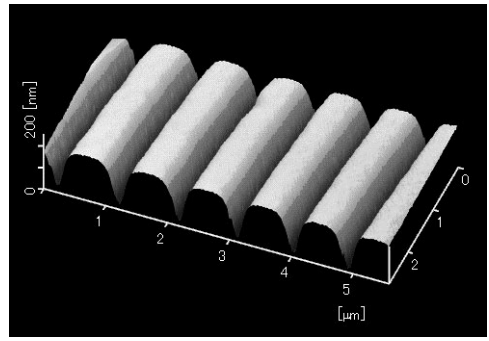

Fig. 2 AFM image of the PDMS culture sheet with nanostripes.

A human stomach cancer cell line, SH-10-TC, cells were cultured on the dish in RPMI-1640 medium supplemented with 10% fetal bovine serum at 37˚C. Cell growth and behavior were monitored with an Olympus inverted microscope and a CCD camera. Actin filament (cytoskeleton) was stained with rhodamine phalloidin, and vinculin (focal adhesion protein) was stained with FITC-labeled antibodies.

Total RNA was extracted from cells cultured on the dish to 70% confluent, and purified by routine procedures. The total RNA was converted to biotinylated cRNA and analyzed with a GeneChip Human Genome Array (Affymetrix) according to the standard protocol. RNA expression in cells cultured on the nanostripes was compared with that in cells on the flat PDMS sheet.

3. RESULTS AND DISCUSSION

Cells were elongated along the nanostripes (Fig. 3). Moreover, we found that most actin filaments were also along the stripes and many vinculin spots were located at the front edge of the cells (Fig. 4). It may mean that the cell is willing to elongate along the nanostripes. In addition, cell motility was remarkably induced on the nanostructure. Cells walked around along the stripe direction.

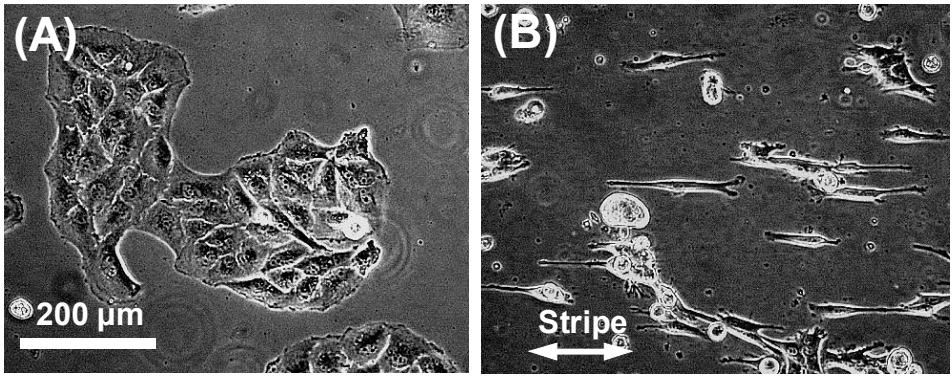

Fig. 3 Phase contrast image of SH-10-TC cells cultured on (A) conventional dish and (B) the nanostripes.

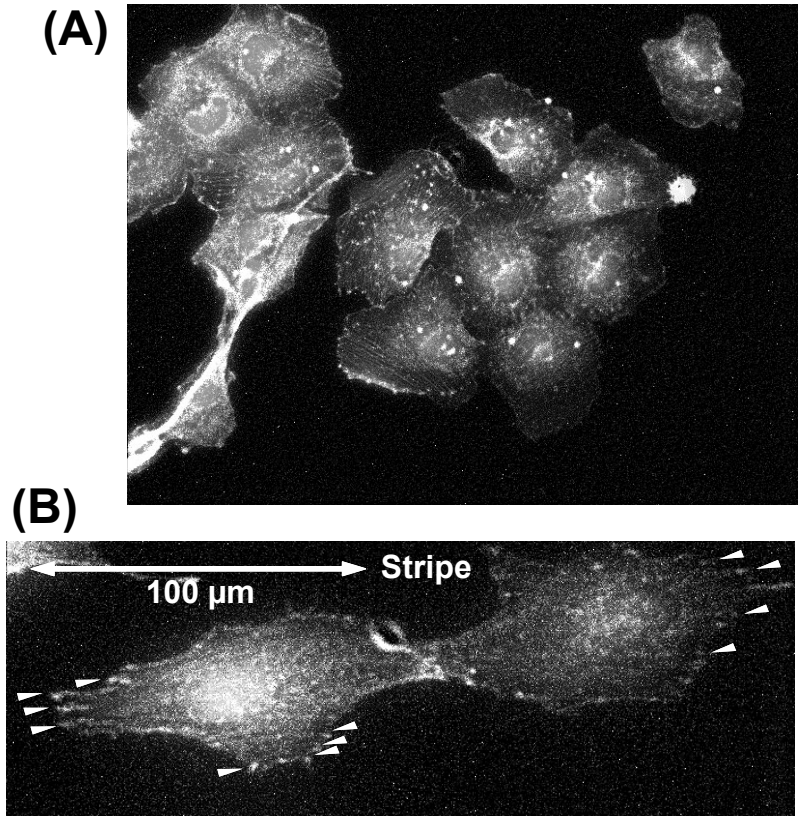

Fig. 4 Fluorescent image of SH-10-TC cells cultured on (A) conventional dish and (B) the nanostripes.

By DNA microarray analyses, many gene-expression changes were found. Especially, expression of genes related to cell adhesion, motility, chemotaxis, and cytoskeleton organization was changed appreciably. For example, most genes in integrin-mediated cell adhesion pathway were significantly upregulated.

4. CONCLUSIONS

It is concluded that the nanostructure enhance the cell motility, which has an orientation with a clear direction, and affects the cell adhesion process from gene expression level.

REFERENCES

[1] M. Goto, K. Sato, T. Tsukahara, T. Konno, K. Ishihara, T. Kitamori, "Micro/Nano-Patterned Surfaces for Control of Cell Adhesion and Cell Functions: Differentiation into Adipocytes", Proc. μ-TAS 2006, 993 (2006)

[2] M. Goto, T. Tsukahara, K. Sato, T. Konno, K. Ishihara, K. Sato, T. Kitamori, "Nanometer-scale Patterned Surfaces for Control of Cell Adhesion", *Anal. Sci*., **23**, 245 (2007)

DIELECTROPHORETIC SEPARATION OF HUMAN SPERMATOZOA FROM EPITHELIAL CELLS

G. Medoro*, E. Brighenti*, A. Fittipaldi*, G. Tresca*, S. Gianni*, G. Perozziello*, M. Timken, M. Buoncristiani**, N. Manaresi***

**Silicon Biosystems S.p.A., ITALY*

*** Department of Justice DNA Lab, (CA) USA*

ABSTRACT

In this paper we report a method to perform a separation of human sperm cells from epithelial cells in a lab-on-a-chip device by means of dielectrophoresis (DEP). The proposed technique represents a useful support to the investigation of sex crimes offering a quick and low cost preparative step for forensic DNA analysis; after the separation the sperm cells can be recovered from the microchip for downstream analysis using standard STR amplification, in order to identify the perpetrator in sexual assault cases.

Keywords: Forensic, Dielectrophoretic cages, Cage-speed separation, Sperm

1. INTRODUCTION

The current practices adopted in forensic laboratories are based on macroscopic sample preparation with test tubes, centrifuges and differential cell lyses [1], which yield a sample which in some cases does not enable DNA identification due to the low number of sperm cells recovered. Another technique is based on the use of cell sorting by flow cytometry [2], with much better yields in DNA quantity and quality; this technique distinguishes sperms from vaginal cells using the properties of cell size and shape, surface phenotype, cytoplasm and ploidy. Unfortunately the sample size requirements and cost are still major hurdles in making it a universal routine test. Recently a method based on ultrasound trapping and laminar flow have been proposed [3] using a microfluidic device; the main drawback of this approach is that epithelial cells must be selectively lysed as with the conventional methods.

2. EXPERIMENTAL

According to the method presented in this paper, sperm cells can be separated from epithelial cells on the basis of their different size exploiting a protocol based on the principle of "cage-speed" separation [4] implemented on a commercial device (SmartSlide™ lab-on-a-chip from Silicon Biosystems).

Sperm cells are entrapped in DEP cages and moved from the original sample into a clean buffer while epithelial cells are moved in the opposite direction (the approach is furthermore robust to the presence in the sample of free DNA; in fact molecules, due to the small size, can not be entrapped by DEP cages and will move randomly around the original position following Brownian motions). Figure 1 shows a flow-diagram and some snapshots from a separation run. Sinusoidal voltages @200kHz are applied to the finger electrodes and Indium Tin Oxide (ITO) lid to create the DEP cages. During slow cage motions (15s/step) electrode and lid voltage amplitudes are 3V and 2V respectively, whereas for fast cage motions (3s/step) 2V electrode and 4V lid amplitudes are applied.

978-0-9798064-0-7/μTAS2007/$20©2007CBMS

The sequence of Right (R), Left (L) and Center-to-Edge (CtE) iterations (each of three electrodes as the cage pitch) is as follows: Rx4-Lx100-Rx10-Lx100-Rx15-Lx100-Rx20-Lx100-Rx30-Lx20-Rx10-Lx10-CtEx55. The total number of steps (toward the right for sperm cells and toward left for epithelial) is redundant with respect to the number of electrodes, so as to be more tolerant to occasional step-losses in either directions for the cell which have to move at that time.

3. EXPERIMENTAL

The separation protocol has been successfully tested using reconstructed biological samples. In brief, epithelial cells are obtained from a mouth swab, and sperm cells from freezed samples. Both type of cells are prepared by washing three times with working buffer (Buffer5B, Silicon Biosystems, Bologna, Italy), with a conductivity of about 280mS/m.

Cells are counted and mixed in a known proportion before injection. Figure 1 (a) shows the chip filled with clean buffer (the chip is loaded by pipetting); (b) the mixed sample (5 µl) is injected from the left side of the chip; it is possible to distinguish some cluster of epithelial and sperm cells aligned inside the dielectrophoretic cages. In (c) it is shown an image of the recovery chamber at the end of the separation protocol where only sperm cells are visible. At the end of the protocol 3.5µl are recovered from the right and sperm and epithelial cells counted. Experiments were run in triple for Sperm/Epithelial ratios (S/E) of 1 and 0,1. For S/E=0,1 the last CtEx55 protocol step was skipped, to prevent contamination although at the expense of a lower yield of sperm (S_{out}/S_{in}).

As shown in Table 1 the enrichment is very good and S/E_{out} always meets the need of having more than 20 sperm per epithelial cells which is about the ratio to obtain a clean genotyping with Capillary Electrophoresis.

4. CONCLUSIONS

With respect to the state of the art, the proposed approach offers several advantages: an improved separation quality, a reduction of the overall cost per analysis (in terms of labor, reagents and disposables) and the capabilities of operating with raw samples, producing an high quality separation with a significant simplification of the procedure.

ACKNOWLEDGEMENTS

The authors wish to thank Tecnobios srl for providing sperm cells for this project.

REFERENCES

[1] AM Giusti et al, "Application of deoxyribonucleic acid (DNA) polymorphism to the analysis of DNA recovered from sperms", J. Forensic Sci, **31**, 409-417 (1986).

[2] W M J Schoell, "Separation of Sperm and Vaginal Cells Based on Ploidy, MHC Class I-, CD45-, and Cytokeratin Expression for Enhancement of DNA Typing After Sexual Assult", Cytometry, **36**, 319-323 (1999).

[3] M. Evander, "Using Acoustic Differential Extraction To Enhance Analysis of Sexual Assault Evidence on a Valveless Glass Microdevice", MICROTAS, 1055-1057 (2006).

[4] G. Medoro et al, "Dielectrophoretic cage-speed separation of bio-particles", Proc. of IEEE Sensors Conference, 76- 79 (2004).

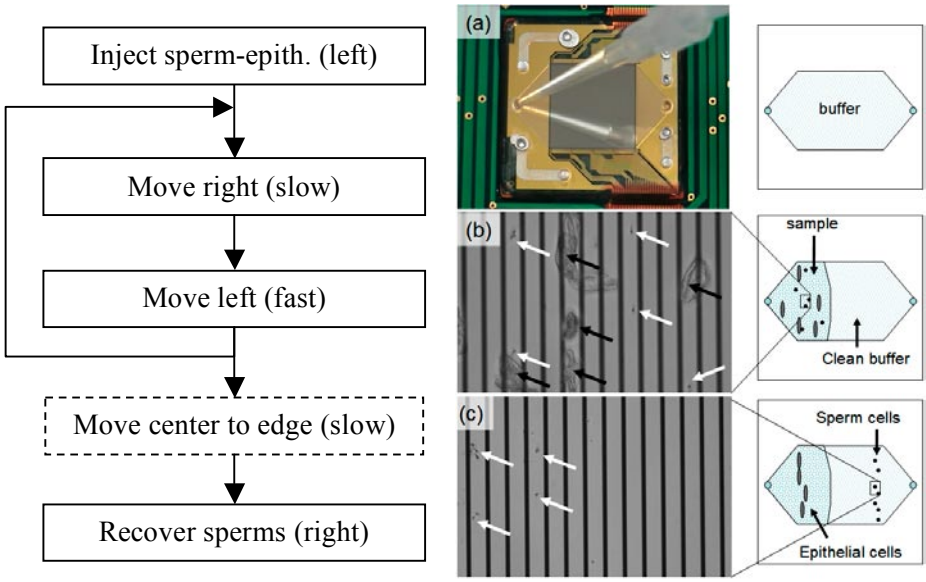

Figure 1: On the left: Flow-diagram of the separation protocol. Upon slow cage motions both fast (epithelial) and slow (sperm) cells move; upon fast cage motions only epithelial cells move. After slow (sperm) cells have crossed the mid point of chip active area, and epithelial cells have been accumulated on the left side of the chip, a final substep of motion of cages from center of chip to active area edges completes the segregation of sperms (toward the right) from epithelial cells (toward the left). On the right: picture of the chip at buffer injection (a), after caging the sperm-epithelial mix (b) and sperm cells on the right before recovery.

Table 1: Summary of experimental results of sperm-epithelial cell separation

		S/E_{out}			Yield		
		avg	*min*	*max*	*avg*	*min*	*max*
S/E_{in}	1,0	62,6	53,3	73,5	80,8%	76,6%	85,3%
	0,1	27,6	20,0	34,3	54,4%	38,4%	70,1%

ELECTROPHORESIS-ASSISTED ELECTROPORATION FOR EFFICIENT INTRACELLULAR SINGLE-CELL DELIVERY

Cristian Ionescu-Zanetti,[1] Andrew Blatz,[1] and Michelle Khine[2]

[1] Fluxion Biosciences, San Francisco, CA, USA *and*

[2] School of Engineering, University of California, Merced, Merced, CA USA

ABSTRACT

We introduce a new strategy to enhance exogenous transport efficiency: electrophoresis delivery of compounds subsequent to single-cell electroporation. Electrophoresis is used to assist loading of otherwise impermeable anionic fluorescent dyes of various molecular weights. We demonstrate delivery rate enhancements of more than an order of magnitude using electrophoresis, compared to diffusion alone, subsequent to electroporation.

Keywords: single-cell electroporation, electrophoresis

1. INTRODUCTION

We previously demonstrated a bench-top single-cell electroporation array system consisting of a control interface, with disposable mating 96-well-based microfluidic chips, that enables cells to each be controlled, monitored and individually electroporated [1, 2]. Our minimally invasive approach, using a feedback control loop which releases the electric field immediately after electroporation, enables improved membrane resealing kinetics for greater percentage cell viability. However, a consequence of the rapid resealing is the limited amount of material that can be delivered into the cell by diffusion. We therefore introduce here a new strategy to improve exogenous transport efficiency: electrophoresis delivery of compounds subsequent to electroporation.

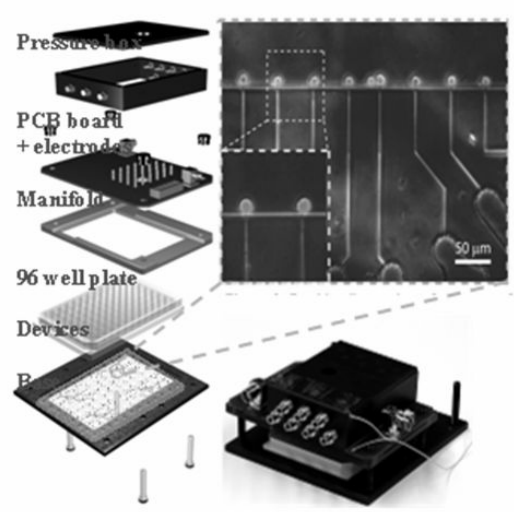

Figure 1. Schematic of electroporation arrays with photo of interface (right) which sits atop an inverted microscope stage. The microfluidic electroporation devices are fixed to the bottom of standard 96 well plates. Inset: overlay of FITC and bright field image of Calcein labelled Hela cells trapped in one well. This is a close up of the lower half (bottom row) of the viewing window.

2. THEORY

Electrophoresis can be used to assist loading by first pre-concentrating exogenous molecules at the cell- channel interface. Then, the electric field is used to drive these molecules into the cell post-electroporation. We demonstrate the feasibility of electroporating an array (n=15) of Hela cells in suspension and inserting otherwise impermeable Calcein (Invitrogen, MW=622) and Oregon Green Dextran 514 (OGD, Invitrogen,

978-0-9798064-0-7/µTAS2007/$20©2007CBMS

MW = 70,000) by electrophoresis. Moreover, in our configuration, extracting the content of one cell per well would thus be feasible by operating in reverse mode. Because the cells in our configuration are each attached to their own capillary, cross contamination between channels can be avoided (Figure 1). This technology can thus be leveraged to extract the contents of single cells and can be eventually combined with fluorescence labelling for high-sensitivity detection [3, 4].

3. EXPERIMENTAL

The bench-top 96-well format microfluidic array for single-cell electroporation is detailed elsewhere [2]. A bottomless 96-well plate is divided into 4 quadrants and each bonded to a disposable microfluidic polydimethylsiloxane (PDMS, Dow Corning) chip with lateral channels which terminate in 3μm wide capillaries for the cell trapping and electric field focusing (Figure 1). Each capillary channel is pneumatically and electrically independently addressable and connects to its own well on a standard size 96 -well plate (bottomless 96 well plates, Nalge Nunc International). Hela (human cervical cancer) cells in suspension are loaded into the device, trapped in its capillary channel by slight transient negative pressure, and the voltage is applied through a modified patch clamp amplifier (the Warner 505B Patch Clamp Amplifier).

The capillary channels are preloaded with the exogenous fluorescent molecules. For the larger molecules, we implement the following protocol to enhance delivery rate: an electric field (0-300mV) that is below the electroporation threshold (0.5-2V) is applied to the cell trapping microchannel after the positioning of a cell pneumatically at the opening. After accumulation of the species of interest for a set period of time (verified by fluorescence intensity), the cell is electroporated by applying a larger amplitude square wave (5-30ms). Subsequent loading into the cell is driven via electrophoresis during the resealing period post-electroporation.

4. RESULTS AND DISCUSSION

Holding the cell at -200mV immediately after electroporation enables Calcein loading into the cell within 3 seconds (Figure 2); by diffusion alone, this required upwards of 16 seconds. Using the protocol, we demonstrate we can even load cells that reseal quickly after the electroporation event. The duration and intensity of the electrophoretic field can be furthermore used to control and concentrate the amount of material inserted, leading to dose control.

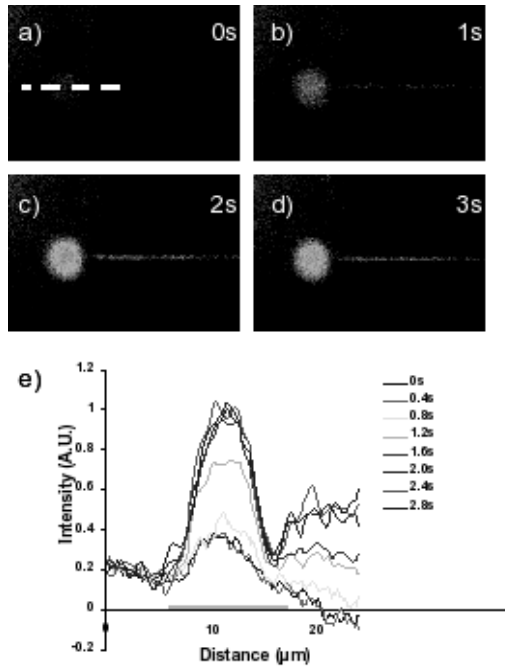

Figure 2.Fast calcein loading. (a-d) Within a 3 sec time span, membrane impermeable Calcein is loaded into the cell using an electrophoretic driving force. (e) The cell intensity measured across a cell section (dotted line in a). Accepte for publication in Biomedical Microdevices.

Moreover, this enables the delivery of even larger molecules (70kD) into the cell on a time scale that could enable the cell to remain viable. Using diffusion loading alone, it took upwards of 30 minutes to load the cell with the large OGD. Conversely, when an electrophoretic field is applied (-100 mV intracellular), we demonstrate routine loading of OGD within 40 s (Figure 3).

5. CONCLUSIONS

In conclusion, we have successfully demonstrated the use of smaller electric fields post-electroporation to load exogenous anionic fluorescent molecules of various sizes into single cells. Variation in field intensity and duration both before and after the electroporation protocol can be used to control the amount of material inserted, or to control the 'dosage'. The difference in load rate between no potential and a -200 mV applied voltage is approximately 40x for large molecules.

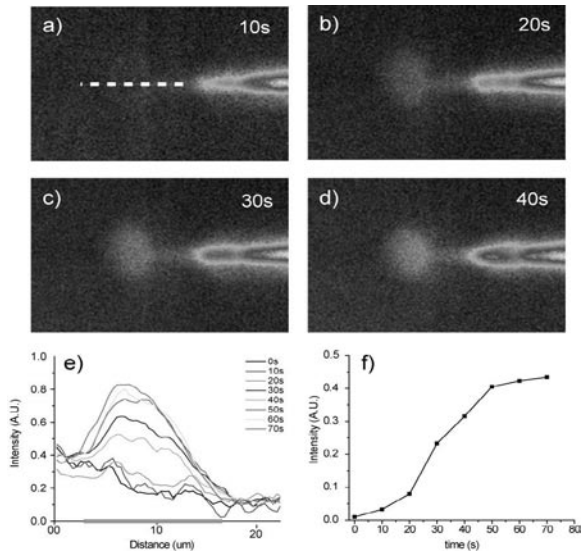

Figure 3. Fast loading of large dextran. (a-d) Within a 1min time span, labeled OGD have been loaded into the cell using a electrophoretic driving force. (e) The cell intensity measured across a cell section (dotted line in a). (f) Integrated cell intensity as a function of time. EP event was measured at the 10s time point. Accepted for publication in Biomedical Microdevices.

ACKNOWLEDGEMENTS

Funding Source: National Institute of Health NIGMS 1 R43 GM075509-01.

REFERENCES

[1] M. Khine, A.Lau, C. Ionescu-Zanetti, J. Seo. L.P. Lee, A single cell electroporation chip, *Lab Chip* , **5**,1,:38-43 (2005).

[2] M. Khine, C. Ionescu-Zanetti, A. Blatz, L.P. Wang, L.P. Lee, Single cell electroporation arrays with real time monitoring and feedback control, *Lab Chip*, **7**,4,457-62 (2007).

[3] S.D. Gilman, A.G. Ewing, Analysis of single cells by capillary electrophoresis with on-column derivatization and laser-induce fluorescence detection, *Anal. Chem*., **67**, 58-64 (1995).

[4] N.R. Munce, J. Li, P.R. Herman, L. Lilge, Microfabricated system for parallel single-cell capillary electrophoresis, *Anal. Chem*., **76**, 4983-4989 (2004).

FIBROBLAST AND CANCER CELL BEHAVIORS IN THREE-DIMENSIONAL SILICON MICROSTRUCTURES

Mehdi Nikkhah[1], Jeannine S. Strobl[2], and Masoud Agah[1]

[1] Virginia Tech MEMS Laboratory, Bradley Department of Electrical and Computer Engineering, [2] Edward Via Virginia College of Osteopathic Medicine
Blacksburg, VA, USA

ABSTRACT

This paper reports the development of three dimensional (3-D) microfabricated silicon cell culture substrates comprised of star and circular microchambers, microfluidic networks, and channels with rough surfaces using a single-mask fabrication process [1]. The aim of creating such microstructures is to provide valuable data regarding growth, spreading, and deformation of normal and cancer cells on different surface topographies and roughness.

Keywords: Silicon microstructure, Three dimensional, Cell culture

1. INTRODUCTION

Microminiaturized cell culture environments offer many potential advantages over plastic multi-well plates and provide alternative ways to simulate a more natural substrate to conduct cell biology research [2]. Others have demonstrated cell culture in micro-environments [3, 4]; however, none have compared different cell types in three-dimensional (3-D) silicon microstructures. Creating 3-D complex micro-environments can establish new experimental tools to study different cellular behavior in healthy, stressed, or disease states. Herein, we report the fabrication of 3-D silicon microstructures to study normal HS68 human fibroblasts and MDA231 human breast cancer cell behaviors on these microstructures.

2. MATERIALS AND METHODS

2.1. Fabrication Process

Figure 1 shows the photo image of the fabricated devices. The fabrication process has been described in our previous work [5]. Also shown are SEM images of four typical cell culture dishes composed of star-/circular-shape microchambers (Figure 1A), microfluidic channels with different widths and depths (Figure 1B, 1C) and channels with a rough bottom (Figure 1D).

2.2. Cell culture

Both normal HS68 human fibroblasts and MDA231 human breast cancer cells were used in this work. Cells were maintained in plastic T-75 cm^2 culture

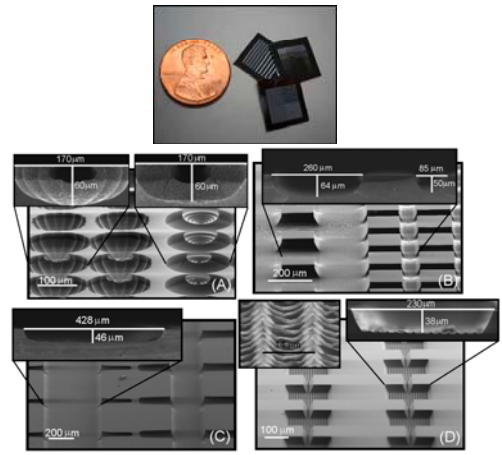

Figure 1: SEM images of four typical cell culture dishes comprising star and circular microchambers (A), microfluidic network (B,C), and channels with rough surfaces (D).

978-0-9798064-0-7/μTAS2007/$20©2007CBMS

flasks in an RPMI culture medium which contained 10% fetal bovine serum (FBS), 1mM sodium pyruvate, and penicillin-streptomycin (100U/ml) where U stands for enzyme activities. Cells were incubated at 37 °C in a 7.5% CO_2 and then were fixed in a 50%-ethanol-3.7% formaldehyde-0.1% crystal violet solution in normal saline for 10 minutes.

2.3. Imaging

All photographic images were taken using a CALTEX VZM-2000 digital-video optical microscope with a maximum magnification of 2000. The optical microcopy was used to visualize the cell shapes and to determine how they spread on the smooth surfaces of silicon substrate. Scanning electron microscopy (SEM) was performed to assess the dependence of cell morphology to the geometry of the microfabricated structures. For SEM imaging, after culture fixation, the samples were critical point dried and sputter-coated with a thin layer of gold palladium.

3. RESULTS AND DISCUSSION

The cells were attached and well-spread on the smooth surfaces of silicon chips about six hours after they were seeded at low-density. Both fibroblast and cancer cells proliferate on silicon surfaces with typical cell growth kinetics on glass slides. Figure 2 demonstrates lag, logarithmic, and plateau phases of fibroblast cells and lag and logarithmic phases of cancer cells. Typically, cancer cells achieve higher cell densities than fibroblast cells and enter a plateau phase of growth after 144 hours of incubation. This figure also shows that the cancer cell logarithmic growth rate exceeds that of the fibroblast cells.

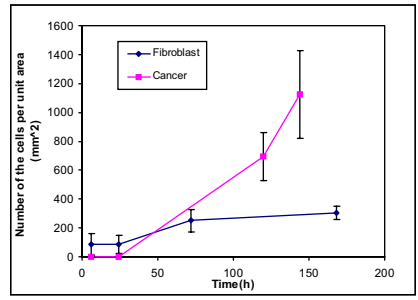

Figure 2: Fibroblast and cancer cell growth as a function of time showing typical cell growth kinetics. Data shown are the mean and standard deviation of the cell #/mm^2.

Figure 3 shows optical microscope images of the HS68 and MDA231 cells on the microfabricated culture substrates. After one week, the cells adapt to the substrate geometry and deform to accommodate the reduced smooth surface areas on the chip.

Growth patterns and cell shape inside the microchambers and channels were characterized using SEM (Figure 4). Fibroblast cells spread and attach to channels with flat sidewalls but stretch in microchambers to avoid curved sidewalls (Figure 4A). Cancer cells, on the other hand, tend to spread and attach on both flat and curved sidewalls (Figure 4B). It is well known that the cells respond differently to the substrate and its stiffness [6]. We propose possible mechanisms which explain such behaviors. First, fibroblast

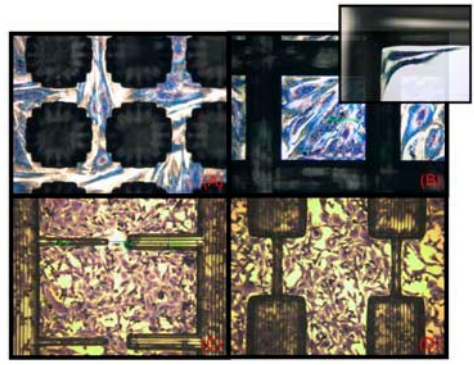

Figure 3: Optical microscope images of fibroblast (A and B) and cancer (C and D) cells cultured on four different substrate geometries for one week.

cells show the preference of growth on flat surfaces and it seems they are less likely to distort their cytoskeleton structure to take the shape of rigid curved sidewall channels. Second reason might be due to high stiffness of these cells in which they do not tend to bend inside the curved sidewall channels and prefer to extend and stretch their structure inside these channels and maintain a more organized cytoskeleton structure. However, cancer cells demonstrate various shapes i.e. rounded or spread on flat and curved sidewall channels. This might be due to metastatic nature of these cells and having no preference in maintaining an organized cytoskeleton structure. We also hypothesize that these cells exhibit a different adhesion model to the substrate compared to fibroblast cells.

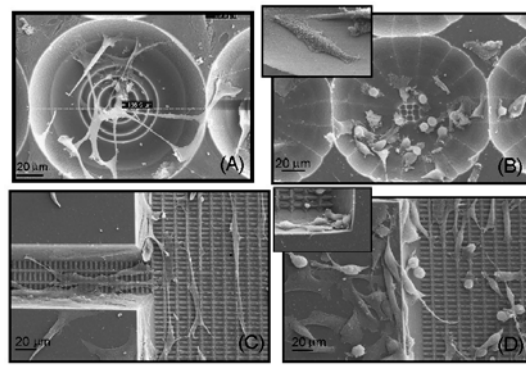

Figure 4: SEM images of HS68 human fibroblasts (A and C) and MDA231 cancer (B and D) cells cultured on different silicon microstructures.

The surface roughness influences fibroblast cell shape; fibroblasts tend to align their cytoskeleton structure and spread along the microgrooves inside the rough channels (Figure 4C). This behavior has been previously observed by others as well [7-9]. Here we mainly focus on cancer cells. The cancer cells, however, are less discriminating on this type of substrate and grow well inside rough channels as well as on flat surfaces (Figure 4D) and show no preferential alignment inside microgrooves. This behavior makes it more evident that these cells do not tend to maintain an organized cytoskeleton structure.

4. CONCLUSIONS

In this work, we reported the fabrication of 3-D silicon microstructures to study the behaviors of normal human fibroblast and breast cancer cells on various microstructures. Our findings demonstrate the potential of 3-D silicon microstructures as reliable platforms for studying various cell behaviors and can lead to new methods in cell separation and anticancer drug testing.

REFERENCES

[1] K. Gantz *et al.*, in Transducers, Lyon, France (2007), pp. 755-8
[2] A. Prokop *et al.*, Biomed. Microdevices **6**, 325-39 (2004).
[3] H. H. Liao *et al.*, Biomaterials **24**, 649-54 (2003).
[4] E. Leclerc *et al.*, Biomed. Microdevices **5**, 109-14 (2003).
[5] M. Nikkhah *et al.*, in IEEE EMBC, Lyon, France, (2007), To be presented
[6] D. E. Discher *et al.*, Science **310**, 1139-43 (2005).
[7] A. S. G. Curtis *et al.*, Crit. Rev. Biocompat. **5**, 343-62 (1990).
[8] E. T. denBraber *et al.*, Biomaterials **17**, 1093-9 (1996).
[9] X. F. Walboomers *et al.*, J. Biomed. Mater. Res. **47**, 204-12 (1999).

GUIDING OF NEURITE OUTGROWTH BY TOPOGRAPHICAL MICROSTRUCTURES AND MICROSIEVES

T. Lehnert [1], M. Wiesli [2], S. Weigel [2], O. Agabi [2,3], M. Gijs [1] and A. Bruinink [2]

[1]Ecole Polytechnique Fédérale de Lausanne (EPFL), Institute of Microelectronics and Microsystems, 1015 Lausanne, Switzerland
[2]Materials-Biology Interactions Lab, EMPA, 9014 St. Gallen, Switzerland
[3]Neuronics AG, Technopark Strasse 1, 8005 Zürich, Switzerland

ABSTRACT

The challenge of this project is to show the feasibility of controlling a robotic arm by extracellular recordings of a number of individual neurons. As a first step, we developed different planar and 3-dimensional sieve-type guiding structures. We could demonstrate that outgrowing neurites of motor neurons align to channel-like topographical structures.

Keywords: neuroprosthesis, neurite guiding, topographical patterns, sieve electrode

1. INTRODUCTION

The development of neuroimplants for the peripheral nerve system, e.g. to bridge a peripheral nerve lesion or to connect a distal nerve stump to an artificial limb, is an emergent field in neurobiology. For this type of biohybrid microdevice, control of neurite outgrowth and guidance by chemical and/or topographical patterns on material surfaces has become an important topic in biomedically oriented material science. In the feasibility study presented in this paper, we investigated the growth properties of neurites upon growing into defined topographical planar structures and 3-dimensional sieve structures. This is a first step towards an *in vitro* platform for modelling parts of the somatic nervous system. This platform will combine motor neurons, sensory neurons and myofibrils on the same chip.

2. TOPOGRAPHICAL MICROCHANNEL STRUCTURES

Planar topographical structures were patterned in spin-coated thin polyimide films on oxidized silicon wafers. A “neurite racetrack” consists of a parallel arrangement of equidistant polyimide lines on the SiO_2 surface (fig. 1). The lines were fabricated by using standard photolithographic and dry etching techniques (Al etch mask, O_2 plasma). Two

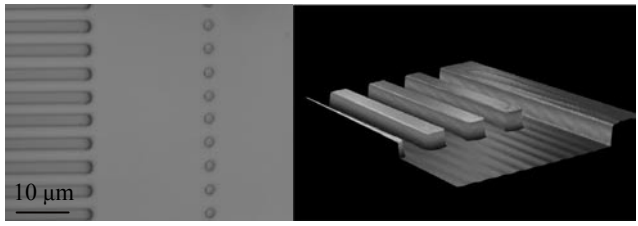

Figure 1. Polyimide lines (top view and 3-d view) on a Si/SiO_2 surface form the topographical pattern of the "neurite racetracks” (5 to 100 µm wide, 1.3 µm or 3.0 µm high). Dots or dot clusters may serve as anchors for cells.

978-0-9798064-0-7/µTAS2007/$20©2007CBMS

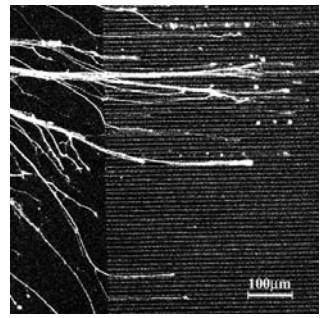

Figure 2. Fluorescent image of neurites growing from reaggregates of spinal cord neurons into a topographical channel array formed by polyimide ridges (5 µm wide and 1.3 µm high, pitch 10 µm). A good alignment of the neurite outgrowth with the surface pattern can be clearly observed.

different ridge heights were investigated (1.3 µm and 3.0 µm), whereas the line width and distance (channel width) were varied over a wide range (from 5 µm to 100 µm). The neurite racetrack has typically a length of 1 mm and connects two planar "reservoirs", i.e. polyimide-free areas on either side of the topographical pattern (1.5 x 1.5 mm^2 each). One receives the neurons, the other one may receive target muscle cells. The entire chip was covered with a 40 nm thick diamond-like carbon (a-C:H) passivation layer. Subsequent poly-D-lysine and laminin coatings are required to provide good neurite adhesion and growth conditions. In this way a chemically uniform surface was obtained [1].

3. GUIDED NEURITE OUTGROWTH ON PLANAR PATTERNS

Reaggregates of spinal cord motor neurons of chicken embryos were used for the neurite outgrowth experiments. The neurons were transfected *in ovo* with plasmids coding for a fluorescent protein. This allowed live observation of neurite outgrowth using a confocal laser scanning microscope (fig. 2). Trajectories of single growth cones were assessed on timelapse movies in a semi-automated way and their behavior was quantitatively analyzed for each structure. We could show that the neurons respond to purely topographical patterns by aligning their neurites parallel to the coated polyimide/SiO_2 ridges. Narrow channels, i.e. 5 µm or 10 µm wide, aligned neurites significantly better along the structure axes than wider ones. The ridge height of only 1.3 to 3.0 µm is too low to form a merely mechanical barrier for the neurites and cannot explain the guidance phenomena. The influence of the ridge height was not significant in the considered range.

4. SIEVE MICROSTRUCTURES

In a second part of this project, we aim at developing an *in vitro* 3-dimensional nerve cell / muscle cell model using a sieve-like structure for guiding neurites to muscle cells (fig. 4a). Polyimide sieves with relatively large hole diameter have been proposed earlier [2]. To be able to record the electrical activity from single cells, the neuroimplant should have microholes designed for outgrowth of individual neurites (Ø ≈ 1 µm). Si/SiO_2 is known to be biocompatible and offers the possibility to integrate on-chip recording and amplification. Sieve structures have been fabricated by deep reactive ion etching with hole diameters in the range of 2 to 5 µm and a microtube length of 20 to 30 µm (fig. 3). The fabrication

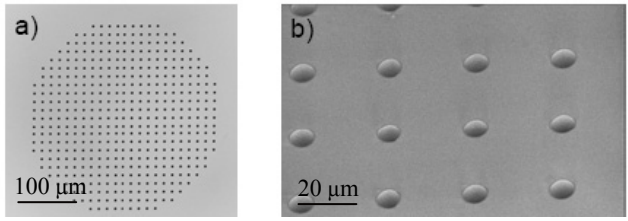

Figure 3. Sieve chip with a Si membrane perforated by an array of microholes (Ø 2 to 5 µm).

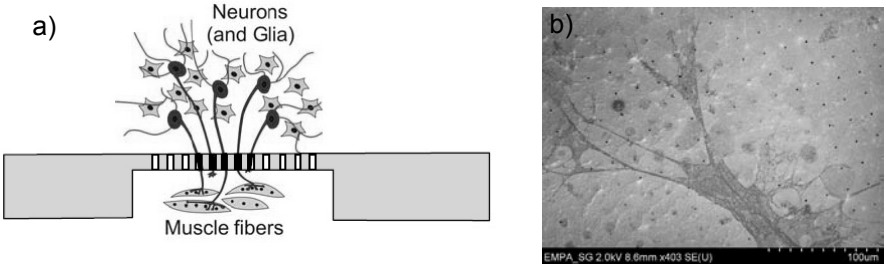

Figure 4. a) Neurons are cultured on one side of the sieve chip. The neurites will connect to muscle cells cultured on the other side of the chip. b) The SEM picture shows cells that have grown through the microhole array.

process is derived from the one of a single-hole patch-clamp chip [3,4]. Initial experiments demonstrate successful cell growth through these microstructures (fig. 4b).

5. CONCLUSION

In the present work we demonstrate that channel-like topographical patterns on a chemically uniform substrate can guide the outgrowth of neurites of motor neurons. The preferential growth direction is parallel to the lines. This effect is most pronouced for ridge distances of 5 to 10 µm. Ridge edges appeared to serve as guidance cues for growth cones rather than simply providing a physical barrier. First experiments with sieve electrodes show that cell growth through microholes is possible.

ACKNOWLEDGEMENTS

We would like to thank Dr. U. Müller (EMPA) for coating part of the chips with a-C:H.

REFERENCES

[1] T. Osterwalder et al., *Proc. 19th Europ. Conf. on Biomaterials*, Sorrento, Italy (2005).
[2] T. Stieglitz et al., *Biosensors and Bioelectronics* **17** (2002) 685-696.
[3] T. Lehnert et al., *Applied Physics Letters*, **81** (2002) 5063-5065.
[4] T. Lehnert et al., *Microfluidics and Nanofluidics* **3** (2007) 109-117.

HYDRODYNAMIC MICROSYSTEMS FOR NON DILUTED BLOOD FRAGMENTATION

E. Sollier[1], H. Rostaing[1], Y. Fouillet[1], J.L. Achard[2] and P. Pouteau[1]

[1]CEA / LETI / Minatec, Department of Technology for Biology and Health,
[2]INPG / LEGI, Laboratory of Geophysical and Industrial Fluid Flows,
Grenoble, FRANCE.

ABSTRACT

In most blood analysis, a hands on multi-step procedure is necessary to separate plasma from bood cells, which includes a centrifugation and a physical separation. As a consequence, results are obtained hours after sampling in dedicated laboratories and can't be integrated in lab-on-chips. To design a performant device for integrated plasma extraction, we recently started some experiments to assess some emerging hydrodynamic techniques in microchannels, such as centrifugation, filtration or cell free layer.

Keywords: Blood fragmentation, cell-free layer, centrifugation, Dean vortices.

1. INTRODUCTION

Diagnostic tests are essentially performed on blood or plasma which is easily accessible and often representative of complex patient pathologic states. Lots of research labs have already investigated blood diagnosis in microsystems however often avoiding the crucial blood fragmentation step. Indeed separating blood cells from plasma, remains one of the last hurdles towards the total integration of blood analysis for diagnostics. For high analytes concentrations for which micro volumes of finger-pricked samples can be used, a major difficulty lies in extracting the plasma with no analyte loss and with no initial dilution of blood. Thus our goal is to perform an efficient point-of-care sample preparation device to quickly, easily and reproducibly extract plasma from whole blood.

Such a separation device would take advantage of some emerging separation techniques based on hydrodynamic effects in micro channels [1]. The separation efficiency of these techniques is estimated here. From an overview of the state-of-the-art, different devices based on micro separation techniques have been designed, micro fabricated with the same wafer process and tested: cross flow filtration, sedimentation, centrifugation, lateral migration are types of the addressed techniques (Figure 1). Only the last two are presented here.

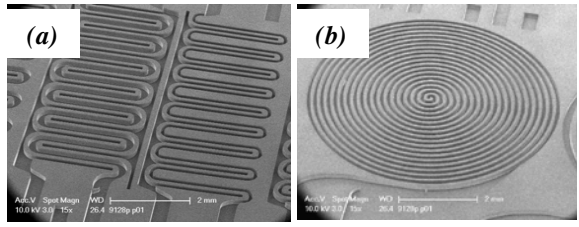

Figure 1. MEB images of some of our extraction devices. (a) Filtration in the double depth etched snail chip. (b) Separation in spiral chip.

978-0-9798064-0-7/µTAS2007/$20©2007CBMS

2. EXPERIMENTAL

Our chips are based on silicon technology with two different etch levels: a deep etch for 200µm main channels and a variable silicon oxide RIE etch for pores of filter. The samples are pumped through the inlet channel by an external syringe pump. To evaluate the efficiency of each design different tests have been performed: firstly with fluorescent beads (ø = 0.5, 1, 3, 5 et 10µm, density = red blood cell density) suspended in plasma, then with pig blood diluted 1/10 in plasma and with whole non diluted blood.

3. RESULTS AND DISCUSSION

In the spiral design, the liquid is injected at the center of the spiral trough a deep etched hole. At the end of the spiral, the liquid is equally separated between its inner (I) and outer (O) outlet (Figure 1.b). Our tests are performed with low concentrated fluorescent beads (5µm) in plasma. Thus, by counting fluorescent beads in each outlet (C_I and C_O) we can estimate bead separation due to hydrodynamics effects (Figure 2).

At low flow rates (< 10 µL/min), the beads are mainly concentrated outside the channel (factor 2). Here is the separation caused by the centrifugation. While flowing through the spiral the beads move towards the external part of the channel due to their higher density. For intermediate flow rates (10-30µL/min), Dean vortices appear tending to mix beads and oppose centrifugation. Thus there is no more separation (C_I=C_O). Dean vortices prevail on centrifugation for higher flow rates (30-300µL/min) and we observe an alternative separation between the inner and the outer part of the channel as the flow rate increases. The optimal separation is at 60µL/min (ratio C_I/C_O>2). Our syringe pump cannot produce higher flow rates than 300µL/min. Our results are similar to those of I. Gregoratto [2].

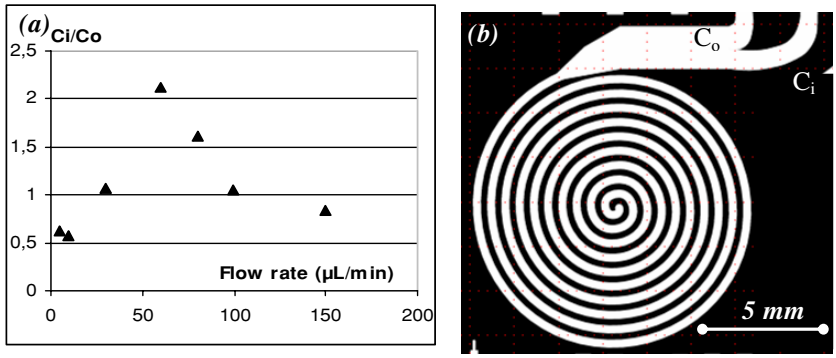

Figure 2. Dean vortices and spiral-designs. (a) Inside/Outside ratio versus injection flowrate. (b) Spiral design. center.

In the chamber design, the sample is injected by the left inlet of 400µm wide (Figure 3). Fluidic chambers are tested with 5µm fluorescent beads and 1/10 plasma diluted pig blood injected at several flow rates (2-500 µL/min). Different physical behaviour are shown. Firstly, at low flow rates, beads repartition is homogenous (Figure 3.a). Then, at 50 µL/min, a boundary layer of some dozens of microns is depleted of beads (Figure 3.b). This phenomena is slightly enhanced by the increasing flow rate, as shown by the Figure 3.c at 200 µL/min. This "cell-free layer", due to Poiseuille flows, is well described in literature [3]

and has a circular profile in square section channels. A surconcentrated layer of beads also appears on the edge of the flow and is enhanced by the flow rate. Similar results (cell-free layer) are observed with 1/10 diluted pig blood even for really low flow rates (2 µL/min, Figure 3.d) due to the rheological specificity of blood (shape and deformability of cells). Experiments with whole blood have just started showing the cell-free layer but also specific difficulties to overcome such as clogging of red cells in filters or higher viscosity of blood for centrifugal designs.

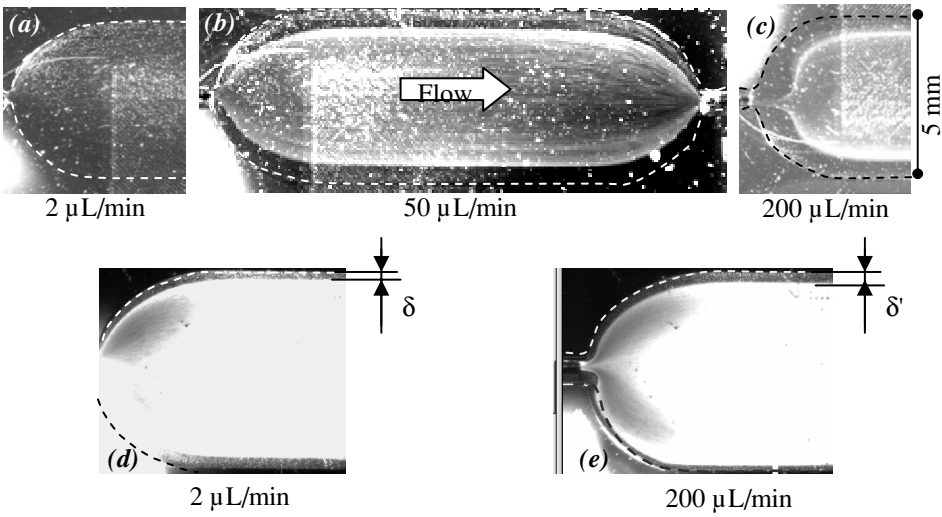

Figure 3. Beads lateral migration and chamber designs. (a) Homogenous migration at 2µL/min. (b) Beads free layer at 50µL/min and (c) at 200µL/min. Cell free layer for 1/10 blood at 2 µL/min (d) and 200 µL/min (e).

4. CONCLUSION

Robust fluidic phenomena have been emphasized in different designs and observed either with beads or blood micro flows. Perspective works concern a better understanding of these blood microfluidic phenomena in order to optimize designs and protocols in particular for whole blood and also to quantify and compare them.

REFERENCES

[1] M. Toner and D. Irimia, *Blood on a chip*, Annu. Rev. Biomed. Eng., 7, 77-103 (2005).

[2] I. Gregoratto, C.J. McNeil and M.W. Reeks, *Micro-devices for rapid continuous separation of suspensions for use in micro-total-analysis-systems*, Proc. of SPIE Vol. 6465, 646503, (2007).

[3] G. Thurston, *Plasma release-cell layering theory for blood flow,* Biorheology, 26, 199-214 (1989).

MICROFLUIDIC CELL ANALYSIS PLATFORM: CELL CULTURE AND ELECTROCHEMICAL LYSIS

J. Tanner Nevill, Ryan Cooper, Megan Dueck, Dino Di Carlo, and Luke P. Lee

UCSF/UCB Joint Graduate Group in Bioengineering, Biomolecular Nanotechnology Center, Berkeley Sensor & Actuator Center, University of California, Berkeley, USA

ABSTRACT

We present an integrated microfluidic platform developed for automated cell culture and lysate analysis. Through the combination of previous technologies developed in our lab - on-chip cell culture and electrochemical lysis - we have designed, fabricated and characterized a platform that cultures cells for extended periods and lyses them on demand without the need for the addition of lysing or washing reagents. We have accomplished the successful culture and lysis of four cell lines: HeLa, MCF7, Jurkat, and CHO. Cells were cultured successfully for greater than five days, and complete on-demand lysis was demonstrated by local electrochemical generation of hydroxide. Lysate was shown to contain both nucleic acids and proteins. Additionally, the biological activity of the lysate was investigated by studying the effects of electrochemical lysis on the enzymatic activity of a model enzyme.

Keywords: microfluidic cell culture, electrochemical cell lysis, cell-based bioassay

1. INTRODUCTION

Cell-based bioassays are commonly performed for many applications including drug discovery, cancer biology research, and synthetic biology. Many of these studies are achieved by culturing cells under varying conditions and then lysing them to examine expression levels of intracellular biomolecules. Performing these tasks using standard plate-based methods can be very time consuming due to reagent additions and wash steps. The development of an integrated microfluidic system to accomplish these tasks automatically would be of great benefit to the scientific community. In addition to time and cost savings, microfluidic devices for cell culture studies better mimic *in vivo* physiological environments with constant perfusion, waste removal, and 3D extracellular matrix structure. To address this need we are developing an integrated microfluidic platform for automated cell analysis.

2. EXPERIMENTAL

Soft lithography using a two layer SU8 mold patterned on a silicon wafer was used to create microfluidic cell culture chambers as shown previously [1]. The cell culture chambers were aligned to platinum electrodes, patterned on a glass substrate, and bonded with an oxygen plasma treatment. The cell chambers were designed to have four fluid-permeable cell holding structures with 11 nl of volume each which equates to roughly 12,500 cells per trap and 50,000 cells per chamber. Each device has six chambers, and each chamber is individually addressable via polymer tubing connections. The lysing electrodes are placed on either side of the trapping region which are also individually addressable.

Filters were added in multiple locations to help keep debris from entering the trapping region, break up cell clumps into individual cells, and flatten out the flow profile. The high resistance region was added to reduce the stress on the regions where the electrodes enter the chambers, as the PDMS does not permanently bond to the metal and is a source of potential leakage. Cell loading was accomplished with a syringe pump connected to the

978-0-9798064-0-7/μTAS2007/$20©2007CBMS

device with polymer tubing, and lysis was performed by applying a DC voltage across the lysing electrodes which are spaced 2.2 mm apart. Both brightfield and fluorescent videos were recorded on an inverted microscope for loading, culturing, and lysing analysis. Cell culture was accomplished by placing a loaded device inside an incubator and slowly perfusing media with a syringe pump. Cell viability was determined by perfusing a live/dead stain through the device at different time points. Lysate content was studied by staining specific components of the cell and observing the stained material upon lysis. HeLa cells transfected to produce intracellular GFP were loaded, lysed, and observed. The genetic material of CHO cells and the membranes were stained, loaded, and lysed. To investigate the viability of biological material in the lysate, a solution of horse radish peroxidase (HRP) was slowly passed through a device at different voltages. The solution was collected and a colorimetric assay using the HRP was performed off chip.

3. RESULTS AND DISCUSSION

Complete cell loading can be accomplished in minutes using high cell densities in the loading solution, but can take longer with dilute cell suspensions. Larger cells, such as HeLa, MCF7 and CHO, are able to completely fill the cell trapping regions, but smaller cells (Jurkat) are unable to fill the trapping region completely because they squeeze beneath the trap and escape. All cell types mentioned were successfully cultured for at least five days with high viability. Cell lysis was accomplished by the generation of hydroxide ions at the cathode upstream of the cell chamber (Fig 2). The hydroxide ions cause cleavage of fatty acid groups in the cellular membrane, resulting in membrane permeabilization and cell lysis. At 2.5V, complete lysis of a full chamber takes less than ten minutes (Fig 4). By observing fluorescently stained cell components, it is clear that intracellular proteins, membrane-bound proteins, and genetic material leave the cell upon lysis and move downstream (Fig 3). In order to ensure that the lysing process does not completely denature proteins in the lysate, the activity of an HRP solution exposed to the lysing process was studied. Figure 5 shows that at high voltages, the enzymatic activity of HRP is greatly compromised. However, at lower voltages there is still significant activity. The threshold for fast and complete cell lysis is shown to be around 2.5V, and the activity of HRP exposed to this voltage is roughly 78%. This suggests that this method of lysis could be used to produce lysate that is largely active for downstream assays.

4. CONCLUSIONS

We demonstrate the functionality of an integrated microfluidic cell analysis platform for culturing and electrochemically lysing cells on demand. The lysate is shown to contain both genetic and proteinaceous material that can be collected downstream. An enzymatic assay was applied to show that it is possible to lyse cells with electrochemically generated hydroxide and can maintain significant bioreactivity for downstream assays.

ACKNOWLEDGEMENTS

Funded by GlaxoSmithKline and an NDSEG Fellowship.

REFERENCES

[1] Philip J. Lee, Paul J. Hung, Vivek M. Rao, and Luke P. Lee, *Nanoliter scale microbioreactor array for quantitative cell biology*, Biotechnology and Bioengineering, 94, pp 5-14, (2005).

[2] Dino Di Carlo, Cristian Ionescu-Zanetti, Yolanda Zhang, Paul Hung and Luke P. Lee, *On-chip cell lysis by local hydroxide generation*, Lab on Chip 5, pp 171-178, (2005).

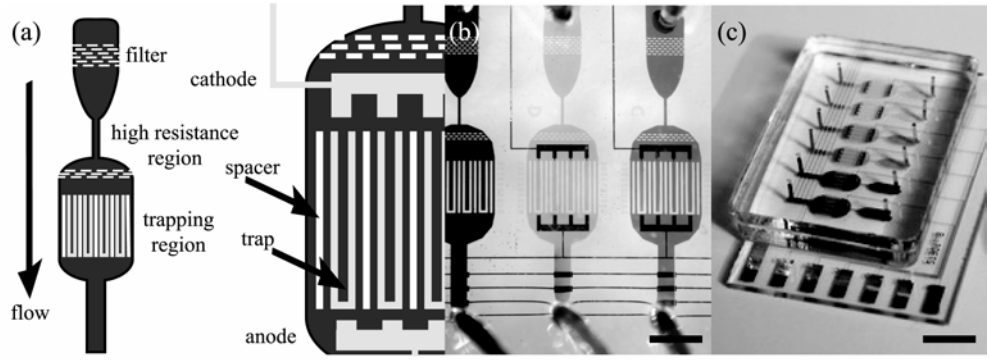

Figure 1. (a) Overview of the trapping and lysing chamber. (b) Image of chambers filled with dye for visualization; scale bar is 2.5 mm. (c) Image of device filled with dye; scale bar is 5 mm.

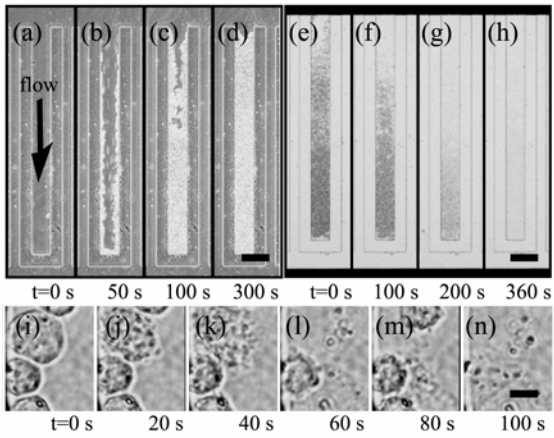

Figure 2. Video images of (a-d) a cell trap loading, (e-h) a loaded cell trap being lysed, and (i-n) a single cell being lysed. Scale bars are 175, 175, and 8 microns, respectively.

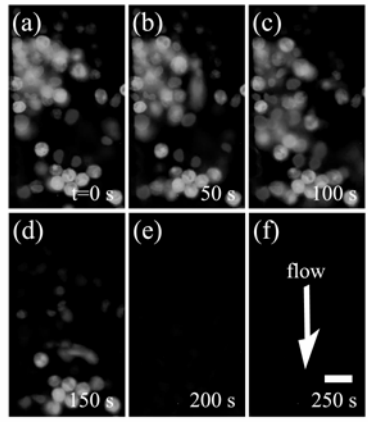

Figure 3. Fluorescent video images of CHO cells with membrane and nuclear stains being lysed; scale bar is 25 microns.

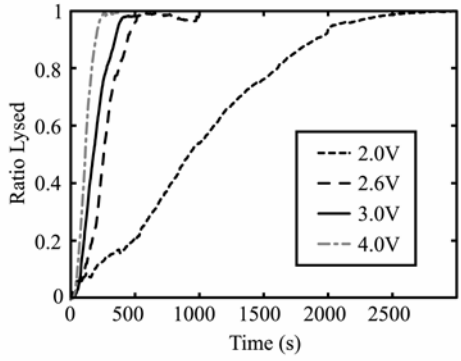

Figure 4. The normalized ratio of trapped cells lysed over time as a function of voltage.

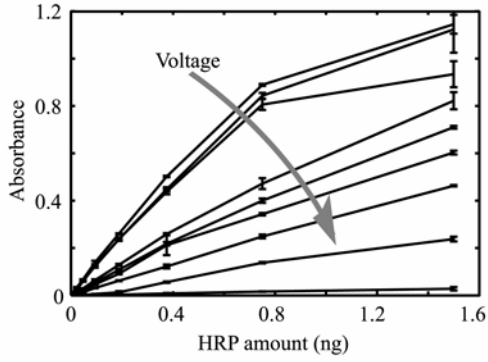

Figure 5. Enzymatic activity of HRP that has been exposed to 0, 1, 1.5, 2, 2.5, 3, 4, 5, and 6 Volts.

LOW COST CYTOMETER BASED ON A DVD PICKUP HEAD

S. Kostner, and M.J. Vellekoop
Vienna University of Technology, Austria

ABSTRACT

Cytometry is a process that allows for measuring characteristics of single biological cells [1]. In this paper we report on a novel cytometric cell detector using a DVD pickup head. The system uses a microfluidic chip with a flow cell that allows for hydrodynamic focusing of the sample flow. The reflected optical signal intensity is influenced by particles that pass the beam and is measured directly in the pickup. Measurement results on a mixture containing erythrocytes and polystyrene particles are presented and the cytometric separation is shown in a two-parameter histogram.

Keywords: Cytometer, Single Cell Detection, Cell Counter, Digital Versatile Disk

1. INTRODUCTION

In optical flow cytometry characteristics of single biological cells are determined as light from a laser beam is scattered by the cells. Depending on the angle of the scattered light, the measured intensities can be related to biological or physical parameters of the cell. Often fluorescent dyes are used for labeling specific cells in a population. A common technique for cell counting is to add counting beads to a cell suspension that has different cytometric output. In a histogram the ratio between cells and counting beads can be used to calculate the density of the cell population. In this paper we present a low cost system that allows for optical detection of cells and particles.

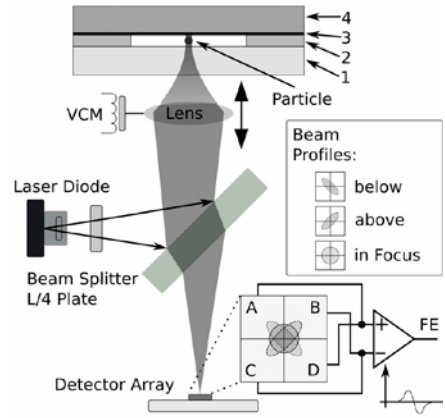

Figure 1: Principle of the cytometer: A laser beam is focused into a microchannel where it interferes with a particle and is reflected back to a detector array. A voice coil motor (VCM) is used to adjust the focus onto the reflective surface (3) utilizing the focus error (FE) signal which originates from the elliptic beam profile. The microfluidic chip consists of 1: transparent glass slide, 2: SU-8 layer, 3: mirror, 4: silicon wafer.

2. EXPERIMENTAL

A laser diode is used to generate an optical beam (650 nm) that passes a beam splitter and is focused to a small spot on a reflective surface inside a microchannel (Fig. 1). The position of the lens can be controlled using a voice coil motor (VCM). After reflection the beam passes the splitter again and propagates towards a four quadrant photodiode array that is used to measure the reflected intensity. An astigmatic distortion causes the beam profile at the detector to be circular only if the beam is reflected at its focal point. If not, the profile

978-0-9798064-0-7/μTAS2007/$20©2007CBMS

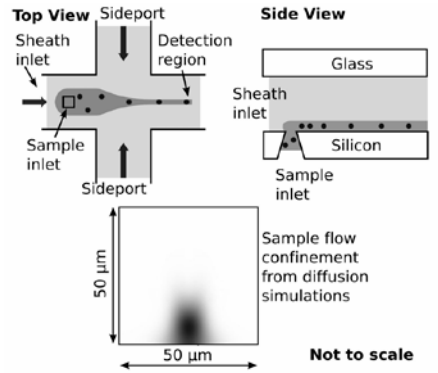

Figure 2: Flow cell for sample injection. Sheath liquid from back and side squeezes the sample closely over the mirror. The sample flow confinement for sample 5µl/min, sheath 40µl/min, and side 60µl/min is given in the cross section of the channel.

back and side squeeze the sample flow to a close distance to the reflective surface using syringe pumps. In FEM studies the optimum flow rates have been determined that result in a sample flow cross section given in Fig. 2.
Fig. 3 shows the fabricated microfluidic chip with channel dimensions of 50 µm x 50 µm at the detection region. It was fabricated using SU-8 wafer bonding technology.

3. RESULTS AND DISCUSSION

The principal operation of the device has been shown with measurements on polystyrene beads in flow and on cells that were adhered on a mirror surface [3]. Now we show for the first time measurements with biological cells (erythrocytes from cattle) in the flow. Fig. 4 shows the sorted sensor responses for a sample population containing both, red blood cells (left) and polystyrene particles (diameter 8 µm, right). Both types can be clearly distinguished by their signal shape. Moreover, a two-parameter histogram (minimum and maximum signal intensity) shows the clear separation between both subpopulations (Fig. 5).

becomes elliptic with the principal axis depending on the sign of the focus error (FE). This allows for generating an electric signal proportional to FE by summing up: A+D-B-C as shown in Fig. 1.

In the experiments the reflected intensity signal changes with each cell or particle that influences the optical path. Due to the high numerical aperture of the beam (NA=0.6) it is important to have control over the position at which the particles hit the beam. Therefore a flow cell (Fig. 2) has been designed that allows for precise positioning of the sample flow in the detection region [2]. Sheath liquid from the

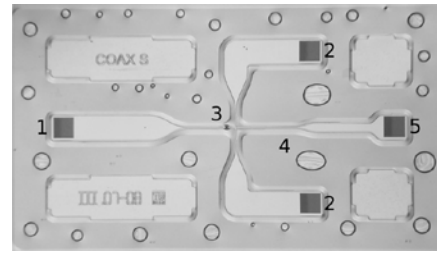

Figure 3: Image of the fabricated device (9 mm x 13 mm). 1: sheath inlet, 2: side inlets, 3: sample inlet, 4: detection region, 5: outlet.

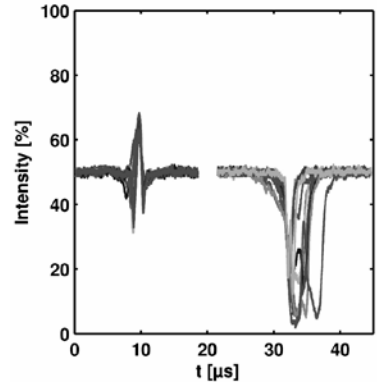

Figure 4: Sensor readings for erythrocytes (left) and polystyrene counting beads (right). The beads cause an intensity drop while erythrocytes cause a signal rise.

4. CONCLUSIONS

We have successfully shown the cytometric separation of erythrocytes from polystyrene counting beads in a two-parameter histogram utilizing a DVD pickup system. Our current research is focused on recognizing different cell types and automation of our experimental setup.

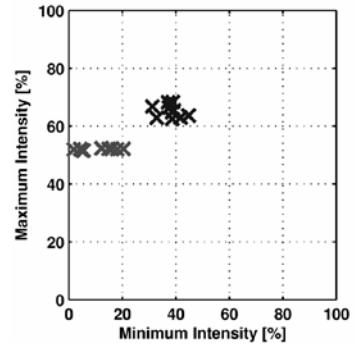

Figure 5: Histogram for the measurements from Fig. 4. The parameters are minimum intensity and maximum intensity of the peaks. The plot shows clearly two sub-populations in the sample.

REFERENCES

[1] H.M. Shapiro, "Practical Flow Cytometry", 4th ed., 2003, Wiley & Sons

[2] J.H. Nieuwenhuis, J. Bastemeijer, P.M. Sarro, and M.J. Vellekoop, "Integrated Flow-Cells for Novel Adjustable Sheath flows", Lab on a Chip, vol. 3, pp.56-61, 2003

[3] S. Kostner, and M.J. Vellekoop, "Detection Of Single Biological Cells Using A DVD Pickup Head", Proceedings of Transducers & Eurosensors 2007, Lyon, France, pp. 2123 - 2126

MICROFABRICATED CONSTRAINTS FOR STUDYING FUNGI FORCE PRODUCTION

Nicolas Minc and Fred Chang
Department of Microbiology, Columbia University,
701W, 168th St, NY, NY 10032 USA

ABSTRACT

Fungi cells are able to generate enormous forces that they use for substrate penetration and host infection [1]. Here, we used the fission yeast *Schizosaccharomyces pombe* to investigate force production at the single cell level. To that aim, single rod-shaped yeast cells are forced to grow in microfabricated round microholes smaller than their final size. When reaching the border of the hole the cells buckle under their own pushing forces. By using different sizes of holes and cells, we show that yeast cells, when constrained, are able to raise their force in order to buckle. The technique further allows for a measure of the unconstrained growing force. In the future we will combine this approach with yeast genetics to understand the molecular mechanism that regulate force production in fungi.

Keywords: Microfabricated constraints, fission yeast, force production, buckling.

1. EXPERIMENTAL

Using standard microlithography, we fabricated round PDMS microholes of different diameters (from 10-30μm) where cells can be grown individually (Fig. 1). Fission yeasts normally grow by tip extension from 7μm to 14 μm. Using mutants that delay in interphase (*cdc22-25*) we can generate longer cells that reach 30-35μm allowing for measurement at different scales.

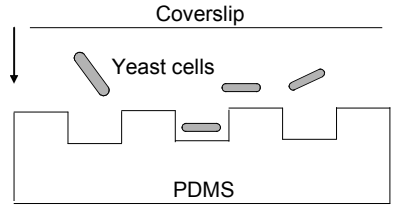

Figure 1. Fission yeast cells are trapped in PDMS microholes and allowed to grow.

2. RESULTS

Relying on robust polarity pathways, fission yeast cells grow exclusively at their tips and depict a rod shape all along their cell cycle [2]. When grown in a microhole with a diameter smaller than their final size, cells buckle under their own mechanical effort, adopting a bent morphology (Fig. 2). Using a measure of the elastic modulus of the cell wall E_{cw}=3.5 MPa obtained by AFM indentation, we can compute the force necessary for buckling as:

$$F_B = \frac{\pi^2 (E_{CW} I)}{L_0^{\,2}},$$

978-0-9798064-0-7/μTAS2007/$20©2007CBMS

where L_0 is the chamber diameter, $I=\pi R^3\sigma$ the area momentum of the cylindrical cell wall shell, with σ the cell wall thickness and R the radius of the cell. For a 30µm cell, this gives a buckling force of approximately 0.15µN whereas a 10µm cell will buckle under a force of 1.25µN. Since we observed buckling events in microholes with diameters ranging from 10-30µm (Fig. 3), it means that cells are able to raise their force production at the tips by at least one order of magnitude.

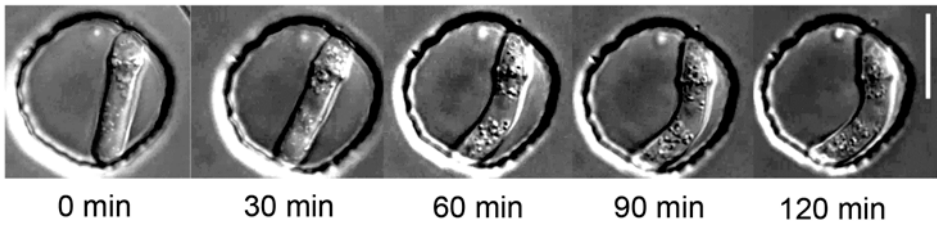

Figure 2. A cdc25-22 fission yeast cell (that normally grows straight) buckles under its own pushing forces when trapped in a microhole. Bar=10µm.

To further analyze these buckling events, we performed time-lapse imaging of single cells growing and buckling in holes with different sizes (Fig 2). By tracking the cell length and the curvature at the same time we could observe that there was a delay, Δt, between the moment the cell was reaching the border of the well and stopping to elongate and the moment it was buckling (Fig. 3).

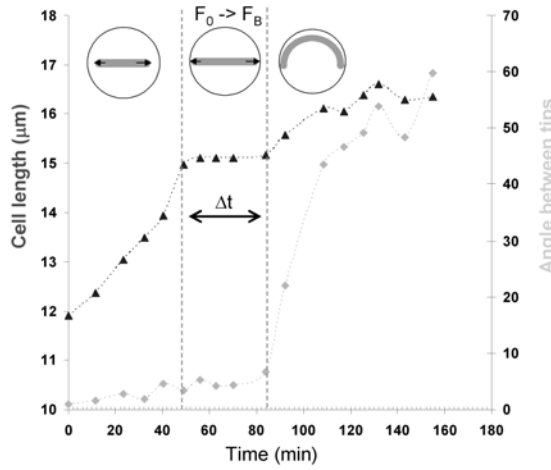

Figure 3. Plot of cell length (left axis) and angle between cell tips (right axis) versus time, for a yeast cell growing and buckling in a 15µm hole. In the left part of the graph (t < 45min), the cell grows with no constraint with a force F_0. In the center (45min < t < 85min), the cell reaches the borders of the microhole, stops elongating, and starts building up some force, eventually reaching the force necessary for buckling, F_B. In the right part (t> 85min) the cell has buckled and continue to elongate in a bent morphology and eventually enters mitosis (t>120min).

If one assumes that the unconstrained growing force F_0 is independent of the cell size, the delay Δt corresponds to the time necessary for the cell to raise its force from F_0 to F_B. We thus measured Δt for cells buckling in holes with different sizes and plotted the corresponding F_B as a function of Δt (fig. 4). The scaling was reasonably linear, allowing for an indirect estimation of the growing force without constraints at the zero-delay limit (fig. 4): $F_0 = 0.08 \pm 0.04$ µN. Furthermore, these data allow for computing the power developed by each cell to raise its force at the tip: $P = 4.0 \pm 2.0$ fW.

The way fungi cells build up such forces at their tip is not well understood. We foresee the use of this method, in conjunction with yeast genetics and fluorescence microscopy, to study the molecular mechanism underlying this process.

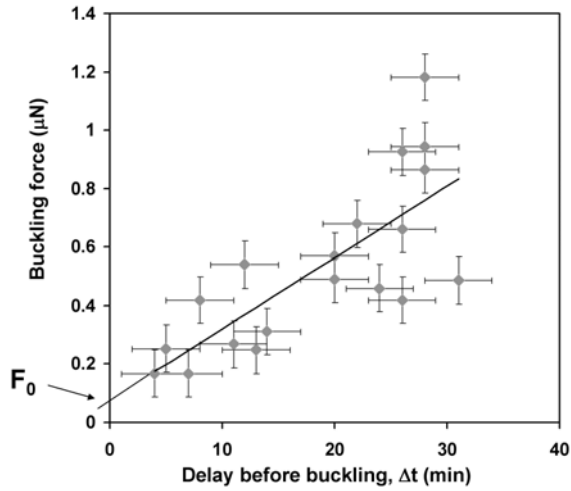

Figure 4. Buckling force as a function of the delay, Δt, necessary to raise the force from F_0 to F_B. The Y-intercept of the linear fit gives an estimate of F_0.

3. CONCLUSION

This paper introduces a simple and inexpensive method that allows for studying force production in fungi at the single cell level. Coupling this method with fluorescence microscopy and yeast genetics will generate a great deal of new data for understanding general cell polarization mechanisms and fungi host invasion.

REFERENCES

[1] "Force exertion in fungal infection", M. Bastemeyer, H Deising and C. Bechinger, Annu. Rev. Biophys. Biomol. Struct., **31,** 321-41 (2002)
[2] "Yeast make their mark", F. Chang and M. Peter, Nat Cell Biol., **4**, 294-9 (2003)

MICROFLUIDIC TENSILE LOADING SYSTEM FOR MEASUREMENT OF MECHANICAL PROPERTIES OF VORTICELLA

Moeto Nagai[1], Momoko Kumemura[1], Naoyoshi Sakaki[1], Hiroshi Asai[2] and Hiroyuki Fujita[1]

[1]CIRMM/IIS, The University of Tokyo, JAPAN

[2]Advanced Research Institute for Science and Engineering, Waseda University, Japan

ABSTRACT

Vorticella is a motile microorganism that has a contracting filament; this filament can be used to drive MEMS in water. We measured the mechanical properties of vorticella by using the flow in a micro-fluidic device. A vorticella could not contract against the fluidic viscous force of 0.34 μN. The vorticella was elongated and was cut at 9.9 μN. The cutting occurred in the filament because one of the vorticella's filament ends was still attached to a coverslip. These experimental results are valuable for using vorticella as a micro-component

Keywords: Vorticella, tensile loading, mechanical property, actuator

1. INTRODUCTION

Vorticella is a motile microorganism that has a contracting filament (Figure 1). Vorticella can contract in 9 msec by spasmoneme; its contracting force was estimated to be above 55.8 nN [1]. Actuation range of its filament is around a few hundred μm. We can control the contraction and elongation of vorticella by adjusting the concentration of calcium ion after surfactant-treatment. Following the treatment, the vorticella is regarded as a sensor-equipped actuator. It can be used as controllable driving sources for microfluidic components e.g. pumps or valves. Although such an application requires good understanding of the mechanical properties of vorticella, they have not been measured well except in the case of glycerin-treated vorticella [2]. We have used flow, up to 7 m/s in microfluidic channels to apply μN forces to living vorticellas. Reduction of the channel dimension from millimeter-scale to micrometer-scale enabled us to produce fast flow easily.

2. EXPERIMENTAL

We designed a microfluidic device that contained a chamber for culturing vorticella and micro-channels for applying a load to vorticella (Figure 2). Two chambers were connected via microfluidic channels. We used a replica molding method to fabricate the microfluidic devices. After fabrication process, entire microfluidic devices were immersed into the cultivation medium and vorticellas were cultured in these chambers. A vorticella grown near a channel was sucked into the channel and loaded with flow.

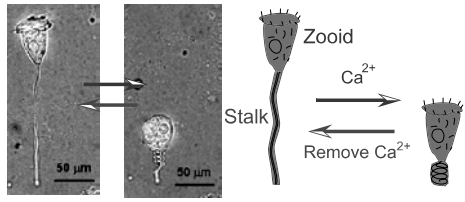

978-0-9798064-0-7/μTAS2007/$20©2007CBMS

Fig. 1. Vorticella contracts and elongates in response to the concentration of calcium ion.

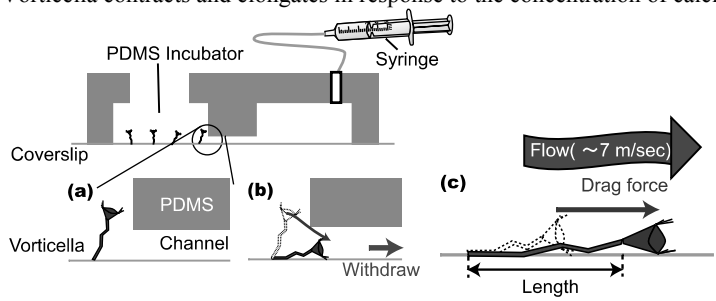

Fig. 2. A schematic of tensile testing system for measurement of mechanical properties of vorticella. (a) A vorticella was cultured near a micro-channel. (b)The vorticella was sucked into the channel. (c) The vorticella was pulled with drag force by withdrawing water through the channel.

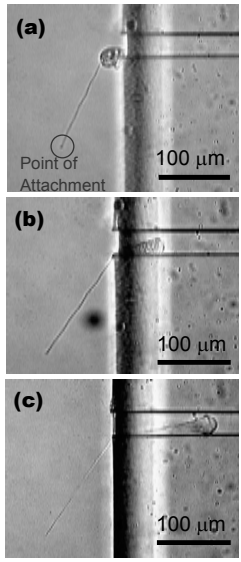

Fig. 3. Vorticella cultured near the microfluidic channel. (a)Unloaded state. (b) 0.34 μN and (c) 9.9 μN were loaded.

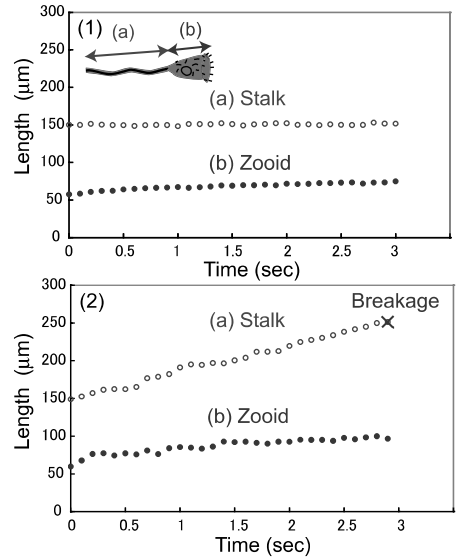

Fig. 4. One of Vorticella's zooid and stalk of length change. (1) 0.34 μN and (2) 9.9 μN were loaded. We define t = 0 as the moment at which vorticella was fully extended to 150 μm.

3. RESULTS & DISCUSSIONS

Figure 3(a) shows a vorticella that grew near a micro-channel and attached to a coverslip. The vorticella's zooid was sucked into the channel and was stretched due to the flow (Figure 3(b),(c)). The back side of the zooid (connected to the stalk) was more elongated than the front side meaning that vorticella was loaded at the thickest part of zooid. The vorticella was stretched and could not contract at flow rate of 500 μl/min. Although stalk length stayed nearly-constant, the zooid elongated from 57 μm to 75 μm (Figure 4(a)). The stalk elongated from 149 μm and was cut at 251 μm about three seconds after loading with flow in micro-channel at 5000 μl/min (Figure 4(b)). The vorticella's zooid elongated even

further from 60 μm to 97 μm, because the vorticella's zooid is composed of a flexible membrane containing liquid. The fixation of the vorticella to the coverslip was strong enough to sustain the load until the stalk was cut.

Drag force was estimated from experimental conditions. Primary parameters appear in Table 1. Reynolds number N_{Re} is given by flow velocity and the diameter of vorticella's zooid, 25 μm. N_{Re} was above 1, meaning inertia force was dominant. Therefore, we applied Bernouli's formula

$$F = C_D \pi r^2 \left(\frac{\rho V^2}{2} \right). \quad (1)$$

Where r and ρ are radius of vorticella's zooid 12.5 μm and density of water 1000 kg·m^{-3}. Assuming the vorticella to be spherical, we can calculate the drag coefficient for the following conditions ($1<N_{Re}<10^4$) as

$$C_D = \left(0.55 + \frac{4.8}{\sqrt{N_{\mathrm{Re}}}} \right)^2. \quad (2)$$

Each flow velocity was estimated from flow rate and cross-sectional area of micro-channels. From Bernouli's formula, we obtained the loaded force, F=9.9 μN at 6.9 m/s and F=0.34 μN at 0.69 m/s. From these analyses, we concluded that the stalk was cut at 9.9 μN and it cannot contract at 0.34 μN.

Table 1. Primary parameters on drag force.

***Flow rate* [μl/min]**	***V* [m/sec]**	**N_{Re}**	**C_D**	***F* [μN]**
5.0 x10^2	0.69	17	2.9	0.34
5.0 x10^3	6.9	1.7 x10^2	0.84	9.9

4. CONCLUSIONS

Mechanical properties of vorticella were measured with the flow in a microfluidic device through flow. Mechanical strength of vorticella's stalk was below 9.9 μN. Vorticella's contraction force was below 0.34 μN. If we presume to load its force to a PDMS cantilever of which length, width, thickness and Young's modulus are 50 μm, 8 μm, 8 μm and 2.5 MPa respectively, 0.34 μN of force will be able to cause a displacement of 5.5 μm at the free end of the cantilever.

ACKNOWLEDGEMENTS

We would like to acknowledge Mr. Mauricio Cordero for critical reading of the manuscript.

REFERENCES

[1] Y. Moriyama et. al., *Biophysical Journal*, Vol. 74, p. 487, (1998).
[2] Y. Moriyama et. al., *Cell Motility and the Cytoskeleton*, Vol. 34, p. 271, (1996).

MICROREACTOR MODEL FOR BIOFILM-ASSOCIATED INFECTION OF MEDICAL IMPLANTS

J.-H. Lee, H. Wang, M. Libera, and W.Y. Lee
Stevens Institute of Technology, USA

ABSTRACT

This paper reports the exploration of microfabricated bioreactors ("microreactors"), as new *in vitro* tools for studying the complexity of biofilm-associated infection of implantable medical devices. We designed, fabricated, and evaluated microreactors in an iterative manner to assess the feasibility of studying interactions between *Staphylococcus epidermidis* and osteoblasts in the presence of surfaces relevant to implantable biomaterials.

Key words: Biofilm, *Staphylococcus epidermidis*, medical implant, infection, osteoblast

1. INTRODUCTION

In many infections, bacteria attach to the surfaces of medical devices or immunocompromised tissues, and subsequently aggregate, proliferate, and colonize into highly cooperative biofilm communities that are encapsulated and protected by exopolysaccharide matrices. Biofilms interact in complex and dynamic manners with device surfaces, host cells, therapeutic interventions, and environmental factors. Thus far, there is no ideal experimental method to study these events under physiologically relevant microenvironments. Conventional approaches include the use of flow cells combined with fluorescence confocal laser scanning microscopy to resolve the effects of flow conditions and mass transport on biofilm physiology. Typically, flow cell reactors [1-2] made of two parallel flat plates with spacers between the plates or of simple glass capillary tubes with limited options over precise flow control, mixing, and geometry. In this study, we explored the use of poly(dimethylsiloxane)-based (PDMS), microfabricated bioreactors ("microreactors"), as new *in vitro* tools, for studying the life cycle behavior of *S. epidermidis* biofilm and the adhesion and spreading behavior of osteoblasts while assessing a culture medium suitable for co-culture of *S. epidermidis* and osteoblasts.

2. MATERIALS AND METHODS

Several types of microreactors were fabricated by conventional molding of PDMS channels on photoresist-patterned silicon. For the shallow (i.e., less than 30 μm) and deep (more than 30 μm) channel depths, SPR-220-7.0 resist and SU8-2025 resists were used, respectively. Most of the molds were fabricated at the Stanford Microfluidic Soft Lithography Foundry. A bacterial strain of biofilm-producing *Staphylococcus epidermidis*, which had been isolated from the surfaces of infected intravenous catheters removed from patients, was obtained from Prof. Jeff Kaplan at the University of Medicine and Dentistry New Jersey. Inoculum was prepared using the procedure described elsewhere [3] with the resulting inoculum concentration of 1×10^9 colony forming units (CFU)/ml, confirmed by plating serial decimal dilutions of the inoculum onto 5% sheep blood agar plates incubated for overnight. Dilutions were made to achieve desired inoculum concentrations used for the microreactor flow experiments in a trypticase soy broth (TSB) medium. MC3T3-E1 mouse preosteoblasts (ATCC CRL-2594) were maintained in alpha minimum essential medium (α-MEM) supplemented with 10% fetal bovine serum and 1% antibiotic at an incubator of 37°C and 5% CO_2. The α-MEM medium was used for microreactor and co-

978-0-9798064-0-7/μTAS2007/$20©2007CBMS

culture experiments after further modifications of α-MEM with Leibovitz L-15 medium under no additional CO_2 provided conditions. [4]

3. REDULTS AND DISCUSSION

Figure 1a shows the life cycle behavior of *S. epidermidis* biofilm cultured inside a 200x30 μm microchannel. An inoculum concentration of 10^7 CFU/ml was used to seed the PDMS microchannel surface with *S. epidermidis*. The planktonic bacteria concentration exiting the microreactor was measured by a conventional plating method. In the first 20 h after inoculation and culturing in the TSB medium, bacteria cells readily colonized the PDMS surface without any detectable bacteria exiting the microreactor. At about 24 hours, bacteria were detected in the exit stream and their concentration increased to a steady state level of 10^7 CFU/ml at about 30 h. Figures 1b and 1c show microscopic images of *S. epidermidis* cells adhered and aggregated on the PDMS surface of a 100x100 μm microchannel after 24 h culture. The adhesion, colonization, and dispersion results corresponded to well-documented characteristic stages of a typical biofilm life cycle.

Unlike the bacterial cells, osteoblast cell adhesion and spreading inside microchannels were strongly influenced by microchannel dimensions. Figure 2a shows the cell density of the osteoblasts adhered on the PDMS surface 1 h after seeding as a function of microchannel width in the 100 to 800 μm range at constant depths of 100 and 200 μm. The data suggested that the cell density decreased significantly with decreasing the microchannel dimensions. With the largest dimensions that we evaluated (i.e., 800x200 μm), the cell density measured from the microreactor approached to that observed at conventional cell culture conditions. Comparison of these observations suggested that *S. epidermidis* bacteria were more active and viable in the smaller microscale environments than osteoblasts.

We developed and optimized a co-culture medium suitable for both *S. epidermidis* and osteoblasts and corresponding procedural protocols initially using Petri-dish methods. Figure 3 shows Petri-dish data after sequential seeding *S. epidermidis* and osteoblasts at *S. epidermidis* to osteoblast cell density ratios of 0.01 and 1.0 and subsequent co-culture for 3 h on PDMS substrates in the modified α-MEM medium with Leibovitz L-15 without using antibiotics. The increased density ratio of *S. epidermidis* reduced the adhesion of the osteoblasts and changed the adhesion behavior of *S. epidermidis* (not visible at the magnification of the micrographs shown).

4. CONCLUSIONS AND FUTURE WORK

These preliminary experiments show the feasibility of studying interactions between *S. epidermidis* and osteoblasts in physiologically relevant fluidic microenvironments with microreactors as new *in vitro* tools. We are now in the process of incorporating the new culture medium and co-culture protocols into a new microreactor, as our exploratory steps towards our long-term motivation for developing more predictable *in vitro* models for infection control through surface modifications of biomedical implants.

REFERENCES

[1] S. A. Rani, et. al, *Antimicrobial Agents and Chemotherapy*, **49**, 728-732 (2005).
[2] V. E. Wagner, et. al, *Biomaterials* **25,** 2247-2263 (2004)
[3] J. B. Kaplan, et. al, *Antimicrobial Agent and Chemotherapy*, **48**, 2633-2636 (2004)
[4] A. Leibovitz, *American Journal of Hygiene*, **78**, 173-180 (1963)

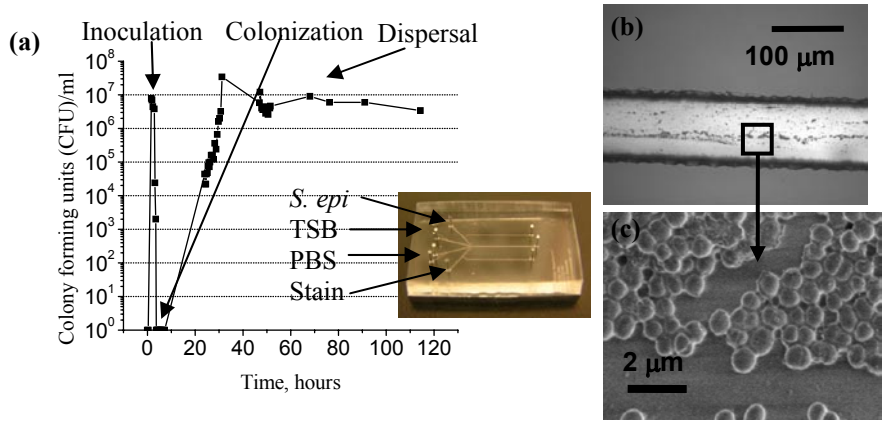

Fig. 1. (a) *S. epidermidis* concentration exiting the PDMS microreactor with 200x30 μm microchannel, as a function of culture time, with 10^7 CFU/ml inoculum concentration and 30 μl/min TSB flow. (b) and (c) optical and SEM images of biofilm formed inside 100x100 μm microchannel with inoculation at 10^9 CFU/ml and 24 h of 10 μl/min TSB flow.

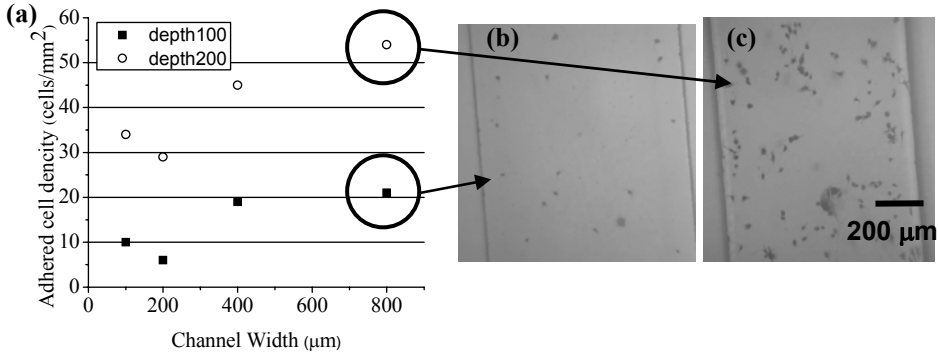

Fig. 2 (a) Adhered osteoblast cell density as a function of microchannel width after 1 h from seeding at two constant microchannel depths. Cell seeding densities for channels of 100 and 200 μm deep were 30 and 60 cells/mm^2 respectively. (b) and (c) optical images.

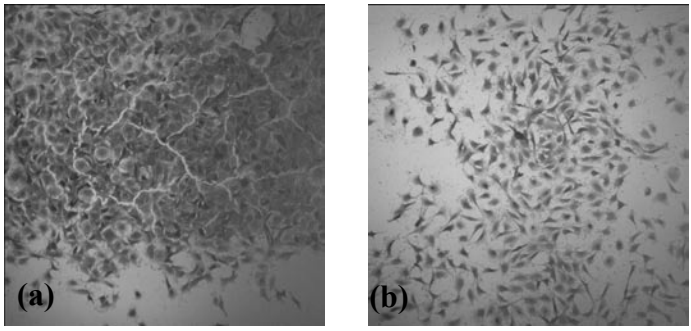

Fig. 3 Osteoblast co-cultured with *S. epidermidis* on PDMS substrates in modified α-MEM with Leibovitz L-15 at *S. epidermidis* to osteoblast cell ratios of:(a) 0.01 and (b) 1.

PARALLEL MICROPIPETTE ASPIRATOR ARRAYS FOR HIGH-THROUGHPUT MECHANICAL CHARACTERIZATION OF BIOLOGICAL CELLS

C. Moraes[1,2], J. Tong[1], X.Y. Liu[1], C.A. Simmons[1,2], and Y. Sun[1,2]

[1]Dept. of Mechanical and Industrial Engineering, [2]Inst. of Biomaterials and Biomedical Engineering, University of Toronto, Canada

ABSTRACT

Existing techniques are not capable of quantifying mechanical parameters of biological cells in statistically significant quantities. Hence, cellular rigidity remains unexplored as a potential marker for identification of cell type and condition. To address this, an array of aspirators has been developed, which permits the aspiration of several cells in parallel. The resulting deformations are recorded, and automated image processing is used to quantify cell deformations. Parallel aspiration of L929 fibroblasts was demonstrated. This technique eliminates the need for skill-dependent micromanipulation, indicating the potential for a 26-fold increase in throughput from traditional, serial micropipette aspiration.

Keywords: mechanical characterization, high throughput, micropipette aspiration

1. INTRODUCTION

Micropipette aspiration is used to determine mechanical response of individual cells to mechanical forces[1]. The data is used to quantify such parameters as cellular stiffness and viscosity, and further to make inferences regarding the internal cellular structure, cell type, and condition.

In this technique, a micromanipulator is used to carefully position a micropipette in contact with a single cell. A known negative pressure is applied, and the cell is partially aspirated into the micropipette. The rigidity of the cell influences the aspiration length and outer radius of the cell. These observations can then be used to determine cellular mechanical parameters (e.g., modulus and viscosity). The use of these parameters for sorting cells based on type has been demonstrated[2], and could potentially be used to isolate specific cell types from a mixed population. For example, individual multipotent progenitor stem cells might be identified and separated from a heterogeneous sample.

Though powerful and versatile, this technique is currently limited by two major drawbacks: (1) micromanipulation requires expertise and extensive operator training; and (2) the serial manipulation process severely limits throughput. These factors prevent the collection of statistically significant quantities of data on a population of cells.

This paper presents the development of a prototype, array-based aspiration device for parallel mechanical characterization of biological cells. An array of aspiration channels (Figure 1(a)(b)) permits parallel aspiration of several cells simultaneously, and is capable of greatly speeding up data collection. Typical rates of mechanically characterization by traditional micropipette aspiration are ~6 cells per hour. Leveraging recent progress in automated aspiration image analysis and measurement[3], these parallel micropipette aspirator arrays can potentially characterize 160 cells per hour, increasing throughput by a factor of 26.

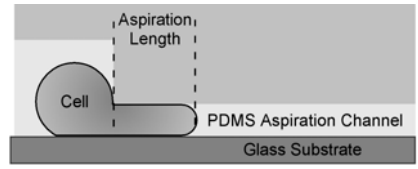

Fig. 1(a): Schematic of a cell undergoing aspiration in a channel

978-0-9798064-0-7/μTAS2007/$20©2007CBMS

2. METHODS

Multilayer SU-8 masters were fabricated on a glass substrate, using standard processes. An unpatterned 2µm thick SU-8 seed layer was used to improve adhesion between the glass and the small features. A network of parallel aspiration channels, 4µm square in cross section, was fabricated. A branching geometry (Figure 1(b)) distributes pressure equally to each channel inlet. A second thick SU-8 layer was then spun, aligned and exposed, to obtain the cell delivery channels. Polydimethylsiloxane (PDMS) constituents were mixed, cast and cured, to create a negative relief structure. The patterned PDMS was then cored and bonded to a glass substrate by corona discharge treatment.

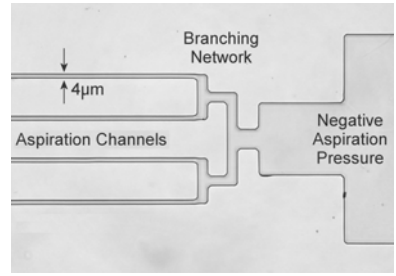

Fig. 1(b): Branching network of 4 aspiration channels in PDMS

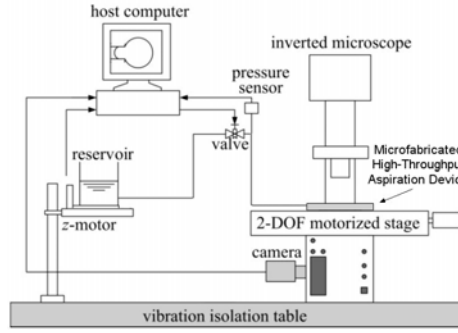

Fig. 1(c): Schematic diagram: parallel micropipette aspiration system.

The devices were placed on a motorized microscope stage. A height-adjustable, reservoir pressure source was used to apply and control aspiration pressure (Figure 1(c)). Device operation was demonstrated using a suspension of L929 mouse fibroblast cells. A dense suspension (~10 million cells/mL) was prepared in supplemented DMEM culture media, and injected into the cell delivery channels. These cells were allowed to settle in close proximity to the aspiration channel inlets. An initial tare pressure (-500Pa) was applied for 60 seconds, to allow the cells to seal against the small channels. Excess cells were flushed out, and aspiration pressures between 0 and -780Pa were applied in five steps. Images were recorded for each cell at equilibrium. Figures 2(a) and (b) show four aspirated cells at 32x and 96x magnifications at an aspiration pressure of -780Pa. Aspiration lengths and outer cell radii measurements at various aspiration pressures were obtained through off-line image processing.

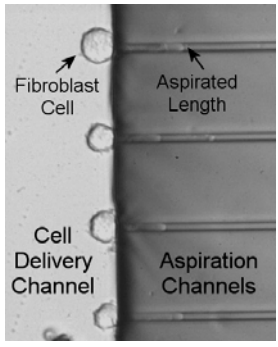

Fig. 2(a): Fibroblasts aspirated at -780Pa

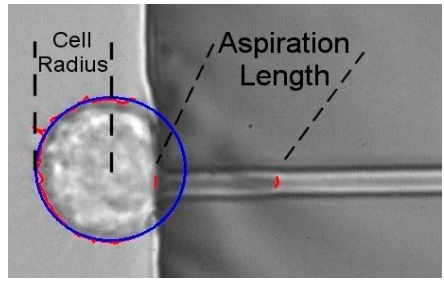

Fig. 2(b): 96x magnification image of a cell aspirated at -780Pa. Automated image processing results are overlaid.

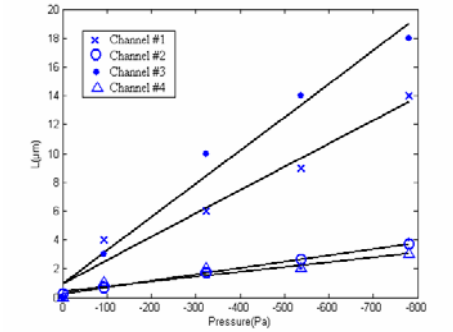

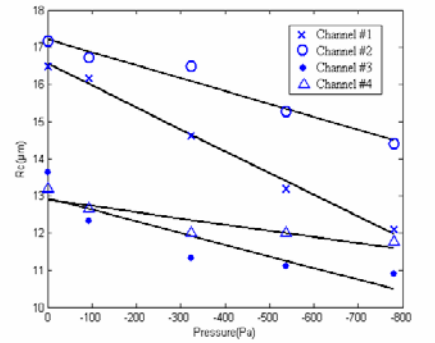

Fig. 3 (a): Aspiration length versus pressure. **(b)**: Cell radius versus pressure.

3. RESULTS AND DISCUSSION

Experimental results for the aspiration lengths and aspirated cell radii for four individual cells at five equilibrated pressures are shown in Fig. 3. The results indicate much variation in the stiffness of a supposedly homogeneous cell population. This result is expected, and emphasizes the need for high-throughput mechanical characterization of cells.

Existing aspiration models cannot be applied in this case, due to the square geometry of the channels. Based on Fig. 3(a), it can be inferred that the cells in channels 2 and 4 are stiffer. Figure 3(b) indicates that the initial cell diameter in channels 3 and 4 are smaller. However, the relative changes in radius do not correspond to the relative changes in aspiration length. This is likely due to non-uniform stresses on the cell membranes because of the square channel cross sections. Further data is being collected to test this hypothesis.

Obtaining a good seal between cell and channel was difficult, and required a high initial tare pressure. A single leaky channel will vary the applied pressures at every other channel. In order to rectify these drawbacks, future designs will elevate aspiration channel inlets to the centerline of the cell. In addition, existing analytical models of micropipette aspiration need to be modified to extract relevant mechanical parameters from experimental data.

4. CONCLUSION

A microfabricated system to mechanically characterize biological cells in a parallel fashion has been demonstrated. This system eliminates the need for a micromanipulation setup and a skilled human operator, making the technique more generally accessible. The system can be scaled up to improve characterization throughput over traditional micropipette aspiration and to obtain statistically significant quantities of data, and thus, enabling the evaluation of mechanical stiffness as a marker for cell type and condition.

REFERENCES

[1] R. M. Hochmuth, "Micropipette aspiration of living cells," *J Biomech,* vol. 33, pp. 15-22, Jan 2000.

[2] J. Guck et al., "Optical deformability as an inherent cell marker for testing malignant transformation and metastatic competence," *Biophys J,* vol. 88, pp. 3689-98, May 2005.

[3] X. Y. Liu, Y. F. Wang, and Y. Sun, "Real-time high-accuracy micropipette aspiration for characterizing mechanical properties of biological cells," *IEEE International Conference on Robotics and Automation (ICRA2007), Rome* 2007.

PRESSURE-DRIVEN MICROVALVE ARRAY FOR CONTROLLING CHEMICAL RELEASE TO CULTURED CELLS

T. Yasuda, T. Yamami, and H. Yano
Kyushu Institute of Technology, Japan

ABSTRACT

A microfluidic device including four pressure-driven microvalves that control the amount of chemicals released through nano-holes to cultured cells was fabricated and tested. Each microvalve consists of hydrophobic and hydrophilic microchannels and is opened and closed by applying pressures from a liquid inlet and from an air inlet, respectively. Conditions of liquid and air inlet pressures required to switch the four microvalves individually were derived through the experiments.

Keywords: microvalve, pressure-driven, hydrophobic, chemical stimulation

1. INTRODUCTION

The authors previously developed a device having a microvalve and a nano-hole array integrated close to each other on a single Si wafer in order to control chemical stimulation to nerve cells [1]. A device presented in this paper permits stimulation control on a wider chamber area using multiple kinds of chemicals. Various pressure-driven microvalve arrays have been already fabricated by other researchers [2,3], but they are difficult to miniaturize enough for localized chemical stimulation to cultured cells because they have mechanically movable parts.

2. DESIGN AND FABRICATION

The device consists of a cell-culture chamber, several microchannels for liquid and air injection, and four nano-hole arrays for release of chemicals included in the liquid (Fig.1). A hydrophobic microvalve using different liquid surface tensions on hydrophobic and hydrophilic channels is constructed at the T-shaped crossing of the microchannel close to each nano-hole array. Liquids injected into the hydrophilic channels stop at the boundary between the hydrophilic and hydrophobic channels. The air that was initially in the hydrophobic channel separates the two liquids. When pressure is applied from the liquid inlet, the liquid will break into the hydrophobic channel and merge with the outlet liquid (Fig.2(a)); this presents the valve open state. If the inlet liquid includes chemicals for cell stimulation, they will diffuse into the outlet liquid and eventually be released from nano-holes. When pressure is applied from the air inlet, the liquid will be separated into two parts again and they will return to original positions (Fig.2(b)); this presents the valve close state.

Four microvalves were arranged as shown in Fig.3, and fabricated using the microfabrication process of a SOI (Silicon on Insulator) wafer. The hydrophilic and hydrophobic surfaces were formed by sputtering SiO_2 and by Au lift-off followed by a hydrophobic SAM (Self-assembled Monolayer), 1-octadecanethiol, formation, respectively (Fig.4). The nano-holes of 0.5 μm in diameter were opened in a SiO_2 membrane by FIB (Focused Ion Beam). The microchannels were covered with a PDMS base.

978-0-9798064-0-7/μTAS2007/$20©2007CBMS

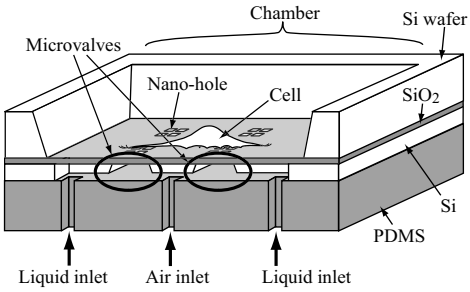

Figure 1. Schematic of a device for chemical stimulation to a cultured cell.

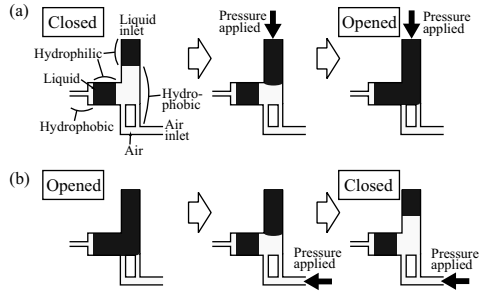

Figure 2. Principle of valve open (a) and close (b).

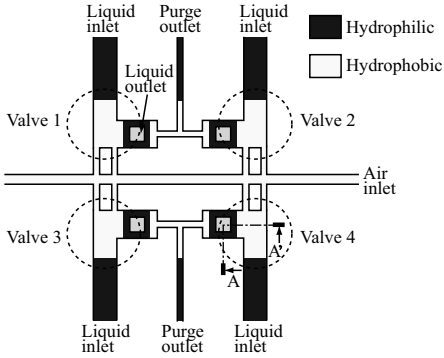

Figure 3. Design of a 2x2 microvalve array.

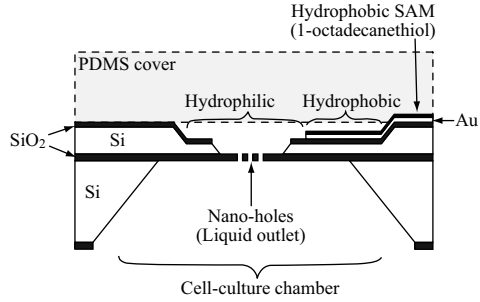

Figure 4. Cross-section of a liquid outlet and its vicinity (A-A' in Fig.3).

3. EXPERIMENTAL

The fabricated device (Fig.5) was tested by applying inlet liquid and air pressures simultaneously controlled by electropneumatic regulators and PC (Fig.6). The valve open/close state was determined by the relative effects of liquid and air inlet pressures as shown in Fig.7. This result gives us a guideline for valve switching procedure. In order to open the valve, keep the valve state, and close the valve, we can fix the air inlet pressure, for example, to 10kPa and apply the liquid inlet pressures of 20kPa (A), 10kPa (B), and 0kPa (C), respectively. Also, the variation of four valves in required pressures, which is indicated as error bars in Fig.7, was small enough to switch the valves individually. Moreover, we carried out a preliminary experiment of chemical release through nano-holes using a fluorescent dye solution as an inlet liquid, and observed the dye release while opening three valves (Fig.8).

4. CONCLUSIONS

The authors demonstrated that the four microvalves integrated on a single microfluidic device can be switched individually by adjusting liquid and air inlet pressures depending on the valve open/close state. In the near future, chemical concentration distribution on the cell-culture chamber will be controlled by switching the valves individually.

ACKNOWLEDGEMENTS

This work was supported by a fund from the Ministry of Education, Culture, Sports, Science and Technology via Grant-in-Aid for Scientific Research (B).

REFERENCES

[1] Y. Nakashima and T. Yasuda, "Cell Growth Control Using Chemical Stimulation Regulated by Microvalve Switching," Proceedings of μTAS2006, pp. 440-442, 2006.

[2] N. Li, C.-H. Hsu, A. Folch, "Parallel Mixing of Photolithographically Defined Nanoliter Volumes Using Elastomeric Microvalve Arrays," Electrophoresis, Vol. 26, pp. 3758-3764, 2005.

[3] W. H. Grover, E. C. Jensen, R. H.C. Ivester, and R. A. Mathies, "Programmable Pneumatic Logical Circuits for Microfluidic Device Control," Proceedings of μTAS2006, pp. 506-508, 2006.

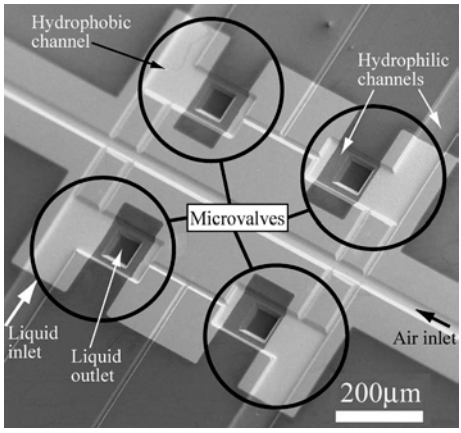

Figure 5. Photograph of the fabricated valve array.

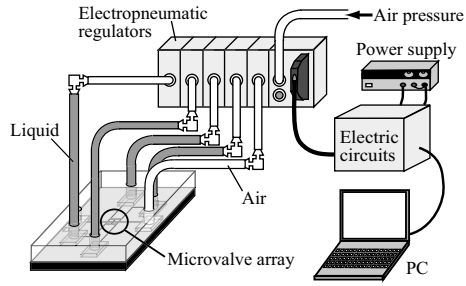

Figure 6. Experimental setup.

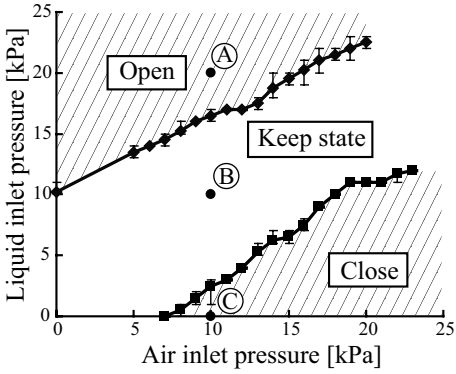

Figure 7. Valve states when liquid and air inlet pressures were applied simultaneously.

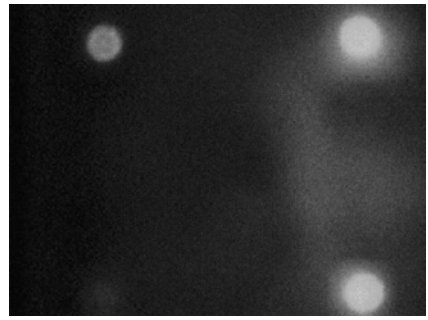

Figure 8. Experimental result of fluorescent dye release from liquid outlets by opening three valves.

RAPID DETECTION OF DRUG EFFLUX FROM SINGLE BACTERIAL CELL ENCLOSED IN FEMTOLITER CHAMBER ARRAY

Ryota Iino[1], Kunihiko Nishino[1], Masayoshi Nakata[1], Eiji Nikaido[1], Yoshimi Matsumoto[1], Shouichi Sakakihara[1], Shoji Takeuchi[2], Akihito Yamaguchi[1], and Hiroyuki Noji[1]

[1]Institute of Scientific and Industrial Research, Osaka University, JAPAN and
[2]Institute of Industrial Science, The University of Tokyo, JAPAN

ABSTRACT

We developed rapid and highly sensitive method assessing drug efflux from a gram negative bacterium, *Escherichia coli* (*E. coli*). By enclosure in femtoliter chamber array [1, 2], very small amount of fluorescent substrate exported from single cells were successfully detected under an optical microscope. Applicability of this method was tested by screening of the genes that encode drug efflux transporters in the *Salmonella enterica* genome.

Keywords: Single cell measurement, Transporter protein, Femtoliter chamber array

1. INTRODUCTION

Multidrug resistance of bacteria is a serious problem in antibiotic treatment of infection. Multidrug resistance often results from expression of efflux transporters located in the cell membrane. Drug efflux activity of bacteria is usually assessed by growth in the presence of drugs. However, conventional method assessing growth is time-consuming and indirect. In this study we developed novel method that can improve these problems.

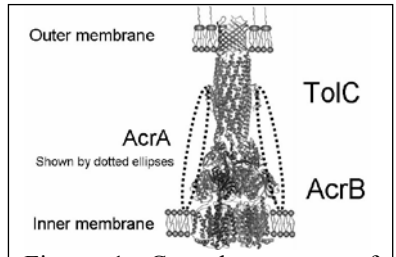

Figure 1. Crystal structure of AcrAB-TolC complex.

As a first target, we selected AcrB. AcrB is a RND family transporter constitutively expressed in the inner membrane of *E. coli*. AcrB exports wide variety of drugs by cooperation with outer membrane channel TolC and adaptor protein AcrA (Figure 1).

2. EXPERIMENTAL

Drug efflux by AcrAB-TolC complex was detected by enclosure of single *E. coli* cells in femtoliter (fL) chamber array made from poly-dimethylsiloxane (PDMS) and coverglass (Figure 2) [1, 2]. Fluorescein-di-β-D-galactopyranoside (FDG) was used as substrate (Figure 3A). FDG has no charge and was permeable to the outer and inner membrane, and diffused into the cell. FDG was hydrolyzed to a fluorescent dye, fluorescein by β-galactosidase in the cytoplasm (Figure 3B). Fluorescein has negative charge and was less permeable to the membranes, and exported from cell

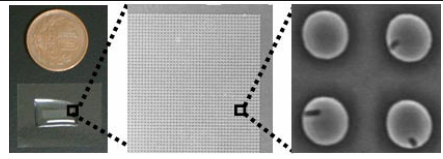

Figure 2. Femtoliter (fL) chamber array. By sandwiching between PDMS sheet with microcavities and coverglass, single cells are enclosed in 50fL chambers (right).

978-0-9798064-0-7/μTAS2007/$20©2007CBMS

mainly by active efflux. The small amount of fluorescein from single cell was accumulated in the fL chamber, and imaged under an optical microscope (Figure 3C).

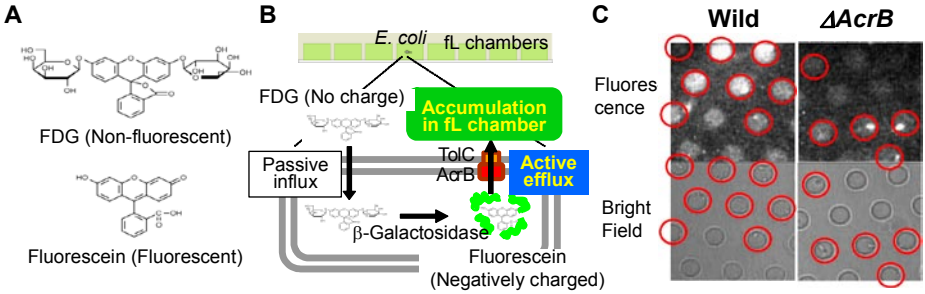

Figure 3. A, Chemical structures of FDG and fluorescein. B, Principle of measurement in fL chamber array. C, Fluorescence (top) and bright field (bottom) images of the fL chambers containing wild type (left) and *ΔAcrB* (right) cells. Images were taken within 10 min after enclosure.

3. RESULTS AND DISCUSSION

When wild type *E. coli* was enclosed in fL chamber array, bright fluorescence not only from the cell but also the chamber was observed within 10 minutes (Figure 3C). In contrast, in many case of mutant cell that is deficient in AcrB (*ΔAcrB*), only cell emitted fluorescence.

Analysis of many cells was carried out by measuring fluorescence intensity of chamber and cell. When fluorescence intensity of chamber containing single cell was plotted against that of the cell, distribution for *ΔAcrB* (crosses in Figure 4) exhibited significant difference from that for wild type (circles). When we set the boundary between "active" and "inactive" at 25AU fluorescence intensity of chamber, 40% (56/139) was classified into "active" in wild-type. In contrast, fraction of "active" in *ΔAcrB* cells decreased to 4% (9/235). One drawback in this method is that significant fraction exhibited very low fluorescence intensity both in chamber and cell (plot around the origin in Figure 4). This fraction may represent the cells with very low expression level of β-galactosidase [3].

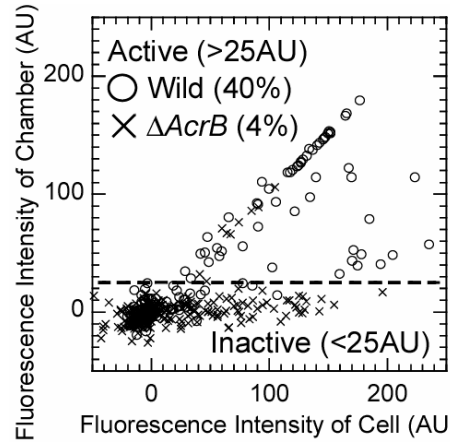

Figure 4. Distribution of fluorescence intensity of cell and chamber. Fluorescence intensity of background (chamber without cell) was subtracted. Dashed line indicates boundary (25AU) between "active" and "inactive". AU, arbitrary unit.

Next, we tried to apply this method to screening of genes that encode efflux transporters. Fragments (4-10 kbp) of the genome of *Salmonella enterica* was cloned into pBR322 plasmid vector. This plasmid library was transformed and expressed in the AcrB deficient

E. coli cells. As first screening, transformed cells were cultured in the presence of several drugs that are toxic to the cell and substrates of the AcrAB-TolC complex. Next, efflux activity of fluorescein was assessed against clones grown.

As shown in Table 1, clones resistant to acriflavine did not recovered efflux of fluorescein (fractions of active were 8-19%). These clones were transformed by *SmvA,* a gene encodes a MSF family transporter that exports acriflavine as well as AcrB. The genes transformed into the clones resistant to novobiocin and methylene blue were *AcrB* or *AcrE* (a relative of *AcrB*). Clones resistant to novobiocin recovered efflux of fluorescein (fractions of active were 28-47%). The result of clones resistant to methylene blue was not simple. Although three clones exhibited high fractions of active (49-64%), that of one clone was low (10%). Now we are investigating the causes of this complex result, such as heterogeneity in the expression level of AcrB among clones that have same genotype.

Table 1. Number of clones that recovered growth, and fraction of efflux active after transformation of gene library from *Salmonella enterica* into AcrB deficient *E. coli*.

Drug (50 μg/ml)	# of clones recovered growth per plate	# of clones assessed efflux of fluorescein	Fraction of efflux active in each clone (%)	Genes transformed
Acriflavine	808	5	19 (16/85)	*SmvA*
			13 (13/99)	*SmvA*
			9 (7/79)	*SmvA*
			9 (9/100)	*SmvA*
			8 (7/91)	*SmvA*
Novobiocin	3	3	28 (29/102)	*AcrB*
			42 (43/103)	*AcrB*
			47 (48/102)	*AcrB*
Methylene blue	10	4	10 (10/99)	*AcrB*
			49 (41/84)	*AcrB*
			60 (62/104)	*AcrB*
			64 (63/99)	*AcrE*

4. CONCLUSIONS

Our method is simple but highly sensitive. Results shown above indicate that efflux active cell can be easily detected at the single cell level. This method can be applied to the screening of genes that encode transporters.

REFERENCES

[1] Y. Rondelez, G. Tresset, K. V. Tabata, H. Arata, H. Fujita, S. Takeuchi, H. Noji, *Microfabricated arrays of femtoliter chambers allow single molecule enzymology*, Nature Biotechnology, 23, 361 (2005).

[2] Y. Rondelez, G. Tresset, T. Nakashima, Y. Kato-Yamada, H. Fujita, S. Takeuchi, H. Noji, *Highly coupled ATP synthesis by F_1-ATPase single molecules*, Nature, 433, 773 (2005).

[3] E. M. Ozbudak, M. Thattai, H. N. Lim, B. I. Shraiman, A. Van Oudenaarden, *Multistability in the lactose utilization network of Escherichia coli*, Nature, 427, 737 (2004).

SKELETAL MYOBLAST PROLIFERATION AND FUSION REGULATED BY MICROELECTRODE ARRAYS

Yi Zhao
The Ohio State University, USA

ABSTRACT

This paper reports the use of microelectrodes arrays to regulate the cell proliferation and fusion in skeletal muscle precursor cells. The microelectrode arrays were fabricated to apply high frequency, low amplitude AC fields to skeletal myoblasts C2C12. Experimental results showed that the cells under AC electric fields express a frequency-dependent myogenisis, as evidenced by the average nuclei number in a single myotube and the morphological profiles of the myotubes. This work provides a novel route to investigate the electromehcanical coupling in skeletal muscle precursor cells and will contribute to the new knowledge base of muscular tissue engineering.

Keywords: Precursor Cell Differentiation, Skeletal Muscle, Tissue Engineering, Microelectrode Arrays

1. INTRODUCTION

Skeletal muscle regenerates by the proliferation of mononuclear myogenic precursor cells that ultimately fuse and become incorporated into multinucleated myotubes, which later mature into myofibres [1]. This process occurs during the embryonic histogenesis of muscle and in postnatal muscle regenerating in response to injury, or in myopathies [2]. With the rapid development of skeletal tissue engineering, there is a pressing need to regulate such proliferation and control the differentiation of skeletal muscle precursor cells into certain phenotypes. To this end, tools are needed to allow a deep understanding of the cell-environment interaction and the electromechanical coupling during myogenesis.

In this work, we report the regulation of C2C12 proliferation and fusion using high frequency, low amplitude AC electric signals using microelectrode arrays. The results show that the cell proliferation and fusion are frequency dependent. Under certain frequencies, the myogenetic rate reaches the maximum and the skeletal myotubes can be rapidly formed within a short period of time. This innovative method of skeletal myogenesis control will help the mechanism understanding of skeletal muscle precursor cells differentiation and benefit muscular tissue engineering.

2. MICROELECTRODE ARRAY

Figure 1 shows the experimental setup. We first fabricated microelectrode arrays on glass substrates using photolithography and lift-off processes. The microelectrode pads were fabricated by sequential patterning of titanium and platinum layers. The total thickness of the two layers is about 100 nm. The substrates were then placed in a 100 culture dish and transferred on the stage of an optical microscope.

978-0-9798064-0-7/μTAS2007/$20©2007CBMS

The AC electric field was applied to stimulate the cells using a function generator. A 50% duty cycle square wave with the voltage amplitude of 0.5 V (Low: -0.25V, High: +0.25V) was used. The stimulation frequencies were 100 kHz, 500 kHz, 1000 kHz and 3000 kHz. The electric field between the microelectrodes were estimated based on the spacings between the oppositing microelectrodes. We also used COMSOL software bundles to estimate the field distribution and field concentration at the tips (not shown).

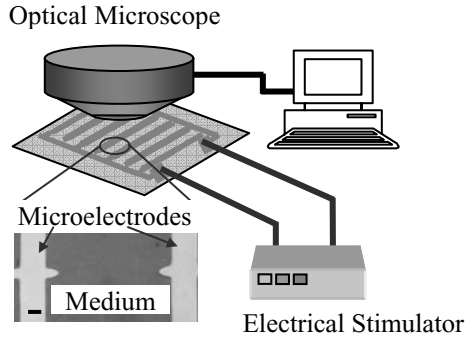

Figure 1. Schematics of the experimental setup. The subfigure shows the optical micrograph of the microelectrodes array. Spacebar indicates 100 μm.

3. CELL CULTURE

C2C12 murine skeletal myoblasts were first cultured in the regular proliferation medium (DMEM, supplemented with 10% fetal bovine serum). After 24 hrs from the start of culture, the cells established attachment with the substrate. Then, the differentiation culture medium containing 2% house serum was used to initiate cell differentiation. The morphologic changes were continuously monitored and the immunofluorescence staining (DAPI) was performed at the end points to visualize the F-actin, myosin heavy chain and the cell nuclei.

4. RESULTS AND DISCUSSION

Electrical stimulation was applied 30 min/day for 4 days. Observation after stimulation showed that the cells under the AC field have frequency-dependent morphologies upon the differentiation (Figure 2). At relatively low frequencies (100 kHz and 500 kHz), the cells proliferated slowly. Only a small percentage of cells were fused at the end of the 4th days. On the contrary, the cells under high-frequency electric stimulation (1000 kHz and 3000 kHz) proliferated at much higher rates and express different levels of cell fusion. The highest myotube intensity was observed under 1000 kHz.

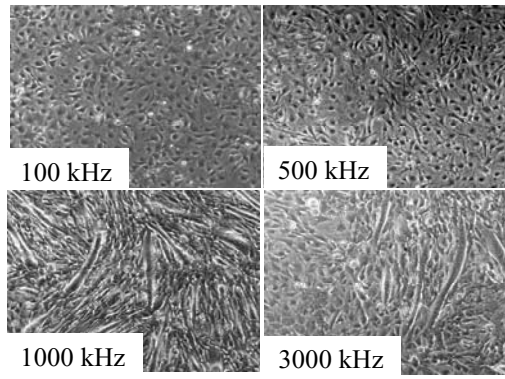

Figure 2: Frequency-dependent proliferation and cell fusion was observed at the end of the 4th day electric stimulation. The highest myotube intensity was observed under 1000 kHz.

The experiment results were confirmed by immunofluorescence staining (Figure 3). It is seen that the fused myotubes have an elongated cell shape, organized actin meshwork, and multiple nuclei. Interestingly, we noted that the aspect ratio of the myotubes (the length ratio between the long axis and the short axis) and the numbers of nuclei strongly depend on the stimulation frequency. As seen from the figure, there are a large number of long myotubes formed under 1000 kHz. Each myotube has 10+ nuclei, and the aspect ratio is above 10. The cells stimulated under 500 kHz, on the other hand, have a relative small number of nuclei (less than 5) and lower aspect ratios (less than 10). Although the mechanism is not yet known, we believe the AC electric signals may affect the cell proliferation and fusion by regulating the transmembrane communication. The mechanism understanding of the AC field regulated cell behaviour is the focus of our further study.

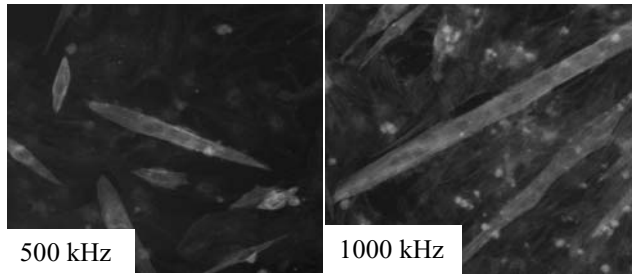

Figure 3. Immunofluorescent staining shows that enhanced cell fusion was obtained using electric stimulation under certain frequencies. The myotubes with multiple nuclei were formed where the F-actin filaments stretch through the entire length of the myotubes. The numbers of nuclei and the morphologic profiles of the myotubes vary with the stimulation frequency.

5. CONCLUSION

This paper reports the use of microelectrode arrays to regulate the cell proliferation and fusion in skeletal precursor cells. The high frequency, low amplitude AC signals were used to regulate the myogenesis. This frequency-dependent cell behaviour has the potential to be a unique tool for the mechanism understanding of the electromechanical coupling in the skeletal myogenesis and contribute to the assembly of artificial skeletal tissues.

ACKNOWLEDGMENTS

This work is partially supported by IMR facility grant from the Institute of Material Research at The Ohio State University. The author would thank the technical staffs at the Nanotech West Laboratory for their generous support. The author would also thank Dr. Sudha Agarwal for the valuable advice.

REFERENCES

[1] R. Lieber, “Skeletal Muscle Structure, Function, & Plasticity: The physiological Basis of Rehabilitation” 2nd Edition, Baltimore, MD, Lippincott Williams & Wilkins, 2002.

[2] J.J. Crisco, P.Jokl and G.T. Heinen, et al., “A Muscle Contusion Injury Model. Biomechanics, Physiology, and Histology”, Am J Sports Med 22 (1994) pp. 702-710.

STUDYING CELL CHEMOTAXIS USING A MICROFLUIDIC CONCENTRATION-GRADIENT GENERATOR

Ajit Thupil[1], Mu-ming Poo[2], and Lydia L. Sohn[3]
Depts. of [1]Materials Science and Engineering, [2]Molecular and Cell Biology, and [3]Mechanical Engineering, University of California, Berkeley, CA USA

ABSTRACT

Microfluidic devices are optimal for studying cell chemotaxis, as they provide rapid diffusion times with low consumption of reagents and the capability to perform parallel experiments on a single chip. We demonstrate a microfluidic device that establishes and maintains a quantifiable concentration-gradient profile within a cell-culture chamber without the need for flow through that chamber. We describe the method we use to prepare our devices. Further, we present modeling and experimental results and plans for future experiments.

Keywords: microfluidics, chemotaxis, concentration-gradient

1. INTRODUCTION

Numerous groups have used microfluidics to investigate chemotaxis in a variety of cell-culture systems [1-5]. Key to all the currently-employed devices is the need for continuous fluid flow through the cell-culture chamber in order to establish and maintain a concentration gradient. While successful, these devices are not generally applicable, as the required fluid flow prevents the study of cells that are either adversely affected by shear flow (i.e. primary neurons) or respond to shear stress through mechanotransduction pathways (i.e. endothelial or epithelial cells). Diao et. al. have recently developed and demonstrated a novel microfluidic device that establishes and maintains a quantifiable concentration-gradient profile within a cell-culture chamber without the need for flow through that chamber. Our device is an adaptation of this design. In this paper, we present both the results of the modeling we performed for device optimization and the experimental results we obtained from culturing primary neurons in our device.

2. EXPERIMENTAL

Fig. 1 is a schematic of our device: a polydimethylsiloxane (PDMS) slab embedded with alternating cell-culture chambers (**A**, **B**, and **C**) and reagent channels (**1**, **2**, **3** and **4**) that are all interconnected via micro-channels. The cell-culture chambers are ~4000 μm x 1000 μm x 100 μm (L x W x H), the reagent channels are ~5000 μm x 500 μm x 100 μm (L x W x H), and the micro-channels are ~300 μm x 4 μm x 2 μm (L x W x H). Soft-lithography techniques are used to mold the PDMS, which is subsequently sealed to a glass substrate. After autoclaving, the entire device is wet with media and cells are injected into the cell-culture chambers. For the experiments presented here, we used embryonic rat hippocampal neurons. After the cells adhere to the glass substrate, different concentrations of small molecules (e.g. pharmaceutical agents and second messengers) or macromolecules (e.g. neurotrophins and other proteins) flow through the reagent channels. The small molecules or macromolecules quickly diffuse through the interconnecting micro-channels, thereby establishing specific and different concentration gradients in the cell-culture chambers.

978-0-9798064-0-7/μTAS2007/$20©2007CBMS

The concentration gradients can be maintained in the cell-culture chambers for a period of days, thus allowing us to investigate, for instance, axonal chemotaxis with our primary neurons.

3. RESULTS

We have simulated the fluid flow and the concentration-gradient profiles in our device using the Navier-
modeling show that the inlet and outlet holes of the cell culture chamber need to be plugged in order to achieve lowest shear stresses. Fig. 2 shows near-zero shear flow in, and a linear concentration-gradient profile in the center portions of, the cell-culture chambers. To confirm the predicted static conditions in the cell-culture chambers, we cultured primary neurons over time in our devices while flowing media (without guidance cues such as brain-derived neurotrophic factor) at a flow rate of 2.5 nL/min through the reagent channels. Fig. 3 shows primary neurons after 8 days in one of our devices: the neurons are healthy and exhibit normal neuronal morphology. To confirm the predicted gradient profile, we flowed a fluorescent cyclic adenosine monophosphate (cAMP) analogue (100 μM, cAMP-Alexa Fluor 488-conjugated, $D \sim 3 \times 10^{-6}$ cm^2/sec) into the reagent channels at a rate of 1.2 μL/min. Fig. 4 shows the resulting concentration-gradient profile after 30 minutes.

Overall, our microfluidic device provides an opportunity to investigate, quantitatively and systematically, cell chemotaxis (i.e. neuronal polarization and axon pathfinding) of shear-sensitive primary neurons. More importantly, our device, as a platform technology, can greatly expand the types of experiments that can be performed in systems involving other shear sensitive cells such as endothelial cells and stem cells.

ACKNOWLEDGEMENTS

This work was partially funded through NIH grant no. 1R21NS058600-01. We would like to thank Hongfeng Gao for providing us with the primary neurons.

REFERENCES

1. J. Diao, L. Young, S. Kim, E.A. Fogarty, S.M. Heilman, P. Zhou, M.L. Shuler, M. Wu, M.P. DeLisa (2005). *A three-channel microfluidic device for generating static linear gradients and its application to the quantitative analysis of bacterial chemotaxis.* Lab Chip. **6**(3): 381-388.
2. Jeon, N. L., H. Baskaran, S. K. W. Dertinger, G. M. Whitesides, L. Van de Water and M. Toner (2002). *Neutrophil chemotaxis in linear and complex gradients of interleukin-8 formed in a microfabricated device.* Nat. Biotechnol. **20**(8): 826-830.
3. Lin, F., C. M. C. Nguyen, S. J. Wang, W. Saadi, S. P. Gross and N. L. Jeon (2004*). Effective neutrophil chemotaxis is strongly influenced by mean IL-8 concentration*. Biochem. Biophys. Res. Commun. **319**(2): 576-581.
4. Wang, S. J., W. Saadi, F. Lin, C. M. C. Nguyen and N. L. Jeon (2004). *Differential effects of EGF gradient profiles on MDA-MB-231 breast cancer cell chemotaxis.* Exp. Cell Res. **300**(1): 180-189.
5. Chung, B. G., L. A. Flanagan, S. W. Rhee, P. H. Schwartz, A. P. Lee, E. S. Monuki and N. L. Jeon (2005). *Human neural stem cell growth and differentiation in a gradient-generating microfluidic device*. Lab on a Chip **5**(4): 401-406.

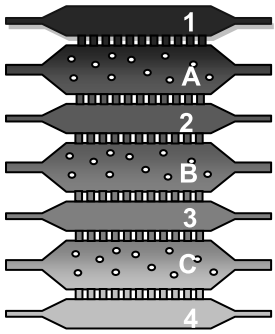

Figure 1: *Schematic of our microfluidic concentration-gradient generator. As shown, the device consists of several alternating chambers that are interconnected via a set of microchannels. A, B, and C correspond to cell-culture chambers and 1, 2, 3 and 4 correspond to reagent channels.*

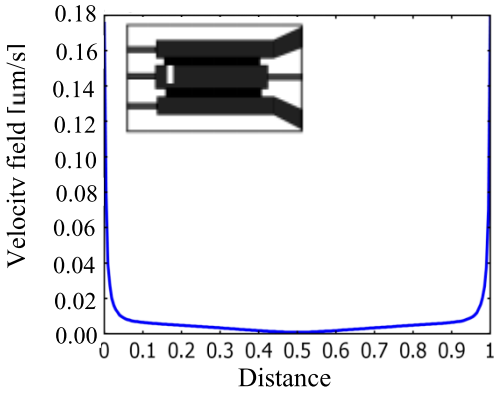

Figure 2a: *Modeled velocity profile within the cell-culture chamber when flowing 1 uL/min of fluid through the surrounding reagent channels. Inset: Dashed line in the device indicates where the velocity profile was taken.*

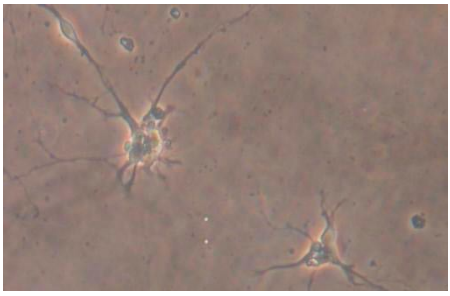

Figure 3: *Optical photograph of primary rat hippocampal neurons cultured neurobasal media for 6 days in the device.*

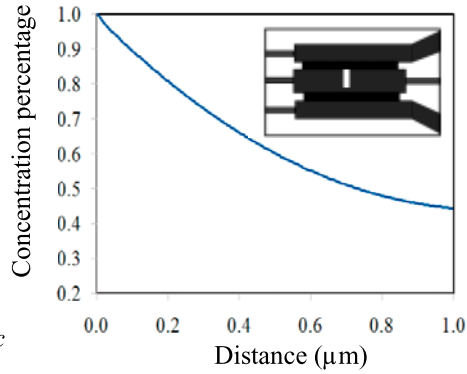

Figure 2b: *Concentration gradient profile in the cell-culture chamber after 30 min, assuming a flow velocity in the reagent channel of 1 uL/min and a diffusion constant, D ~4.3 x 10^{-10} m^2/s. Inset: white dashed line in the device schematic indicates where the gradient profile was taken.*

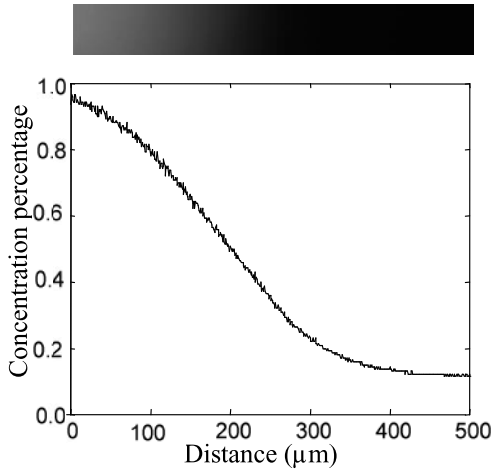

Figure 4: *Measured concentration gradient profile of cAMP-AF at the center of the cell-culture chamber after 30 mins.*

TOWARDS MULTI DIMENSIONAL CHEMICAL MANIPULATION OF LIVING CELLS: CHEMOTAXIS ANALYSIS OF SOCIAL AMOEBAE

C. A. Schumann, P. S. Dittrich, J. Franzke and A. Manz
ISAS – Institute for Analytical Sciences, Dortmund, GERMANY

ABSTRACT

In this study, we designed a two-layer microfluidic chip that facilitates multidimensional chemical treatment of living cells to investigate the chemotaxis of the amoeboid organism *Dictyostelium discoideum*. The chip uses membrane permeability and laminar flow behaviour to generate gradients of the chemoattractant.

Keywords: Chemotaxis, Multi layer, Dictyostelium, Laminar flow

1. INTRODUCTION

Today individual cells can be addressed using microscaled tools with the same dimensions as the cells themselves. In several studies, microfluidic chips have already been successfully employed for cell culturing, handling and analysis [1]. Typically, these chips have a planar topology, thus limiting cell manipulation to two dimensions. In this work, the chips consist of multiple layers connected via a porous membrane. Hence, true three dimensional manipulation of individual cells is facilitated, and different reagents can be supplied to the cell with high spatial and temporal control. In the following study the potential of multilayer chips is explored with an amoeboid organism (*Dictyostelium discoideum*) that moves chemotactically towards a chemoattractant (cAMP).

The full potential of the chip is exploited by introducing laminar flow of different buffers in the upper channel allowing to study the influence of further factors on the chemotactic behaviour while maintaining a control group at the same time. The chip design is readily suitable to investigate protein expression and cell viability using fluorescence spectroscopy.

2. THEORY

The channel design with four merging channels enables the formation of four laminar streams per layer. Different supplies from inlet to inlet create a checkboard array of 16 (4 x 4) spatially defined chemical microenvironments. Using these fields different chemical signals can be addressed to parts of a cell population or even parts of a single cell.



Figure 1. Creation of microenvironments by multi laminar streams in the two levels of the chip, visualized by solutions of Rhodamine B and fluorescein.

978-0-9798064-0-7/μTAS2007/$20©2007CBMS

The chip thereby combines concepts of laminar flow [2] with embedded PC membranes [3] and enables to influence cells through micropatterned porous membranes. Peterman [4] influenced cells through a membrane but in silicon and not in a continuous stream.

3. EXPERIMENTAL

Microchannels for both top and bottom layers are moulded from polydimethylsiloxane (PDMS) by standard soft lithography. To produce a thin bottom layer (~200 µm), a 24 x 40 mm glass plate is aligned onto the PDMS before curing. To produce a thick top layer (7 mm), a frame is positioned on the master into which the PDMS is poured. 1 mm access holes are punched into the top layer and both parts are cleaned with 70% ethanol and DI-water. To facilitate bonding, the dried parts are exposed to an oxygen plasma for 4 min at 1 mbar. A 10 µm thick polycarbonate membrane (PC) with 100 nm pores is cut to size and sandwiched between the PDMS layers at the cross section of the channels. Finally, PEEK tubing is inserted into the chip and connected to a parallel syringe pump system (Cetoni, Korbussen (Germany)).

Characterization of membrane permeability and concentration gradient is achieved using fluorescein solutions (0.1µM to 100µM) in sodium phosphate buffer (pH 9.0). *Dictyostelium discoideum* AX2 is cultured in a semi-synthetic medium under axenic conditions. The culture is maintained at densities between $1 \cdot 10^5$ and $2 \cdot 10^7$ cells per ml, washed and resuspended in low-molarity phosphate buffer (Sørensen buffer) before they are transfered to the chip. Solutions of the chemoattractant cAMP (1 µM to 100 µM) are prepared in phosphate buffer. To study chemotaxis, a suspension of Dictyostelium discoideum in its single cell phase is inserted into the top channel. Adhesion to the polycarbonate membrane is promoted by stopping the flow for 20 min and resuming a flow of 0.5 µl/min. Then, the bottom channel is filled with laminar streams at a flow rate of 5 µl/min, one of which contains the chemoattractant and the cells are observed continuously for one hour.

4. RESULTS AND DISCUSSION

The gradient formed by a substance passing from lower to upper channel was visualized using fluorescein. In addition to the dependence on the concentration of the solution fed into the chip the flow rate in the upper channel determines residence time and availability. Diffusion in z-direction further reduces the concentration in the fluid layer close to the membrane where the cells are located.

Using *Dictyostelium*, the cells in the top channel move towards and aggregate in areas where cAMP concentrations are highest. This behaviour can not be observed uniformly for all cells and may distinguish behavioural heterogeneity in the populaton. Random movement is observed both at high concentrations and without chemoattractant whereas at intermediate concentrations chemotactic movement can be seen. The velocity of movement varies between 1.9 µm/min and 5.2 µm/min, with an average velocity of 3.5 µm/min. A temporal and spatial heterogeneity in the population is revealed via the observation of the cells crawling randomly and orthogonally to the gradient, and even ceasing movement for up to three minutes in addition to their assumed movements.

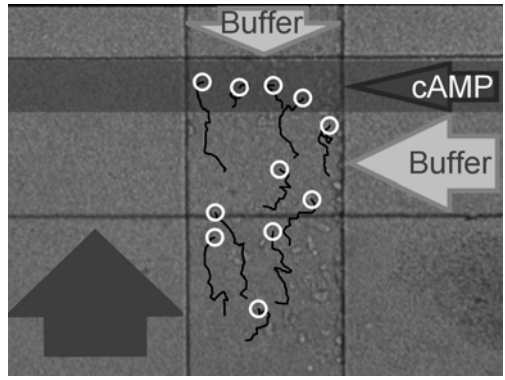

Figure 3. Time-lapse cell tracking during an experiment on chemotaxis with circles highlighting cells at the end of the 23 min assay.

5. CONCLUSIONS

We developed a multi layer chip embedding a porous membrane using soft lithography. The system was characterized using fluorescent dyes and provides multiple chemically distinct concentration distributions. The platform has been used to study *Dictyostelium* chemotaxis. The setup developed provides a very well suited tool to search for answers to many leading biological questions such as cell viability, immuno response and gene expression.

ACKNOWLEDGEMENTS

We thank Stephan Adelt, University of Wuppertal for valuable discussions and for providing *Dictyostelium* samples.

REFERENCES

[1] P.S. Dittrich, K. Tachikawa and A. Manz, *Micro total analysis systems. Latest advancements and trends.* Anal. Chem. 78(12): 3887-908, (2006).

[2] S. Takayama, E. Ostuni, P. LeDuc, K. Naruse, D.E. Ingber and G.M. Whitesides, *Selective Chemical Treatment of Cellular Microdomains Using Multiple Laminar Streams.* Chemistry & Biology 10: 123-130, (2003).

[3] K. Fa, J.J. Tulock, J.V. Sweedler and P.W. Bohn, *Profiling pH gradients across nanocapillary array membranes connecting microfluidic channels.* JACS 127(40): 13928-13933, (2005).

[4] M.C. Peterman, J. Noolandi, M.S. Blumenkranz and H.A. Fishman, *Localized chemical release from an artificial synapse chip.* PNAS 101(27): 9951-9954, (2004).

USING IONIC LIQUID IN PL-SEGMENTED SAMPLING/FLUORESCENT LABELING/CE-LIF ANALYSIS ON A CHIP FOR SINGLE CELL ANALYSIS

Ming Li, Yan Huang and Jong Hoon Hahn

Department of Chemistry, BK School of Molecular Science, Pohang University of Science and Technology, South Korea

ABSTRACT

A simple microfluidic device, which consists of a plate of PDMS containing a poly(diallyldimethylammonium chloride) (PDDAC) coated separation channel and a interfaced silica capillary micropipette inside coated by polyethylenimine (PEI), was developed for on-chip diffusion-free sampling, labeling, and separation for single cell analysis. A sample mixture of flavins was segmented by injection of two water immiscible room temperature ionic liquid (IL) droplets, and successfully separated with 6-fold improvement in sensitivity and 3-fold narrower peak width compared to normal electrokinetic injection. Furthermore, on-chip fluorescence labeling was demonstrated in the IL droplets segmented zone for laser induced fluorescence (LIF) detection of nonfluorescent biomolecules.

Keywords: Diffusion-free sampling, ionic liquid droplets, microchip electrophoresis, on-chip labelling

1. INTRODUCTION

For pL to fL of ultrasmall sample volume analysis, like single cell analysis [1], most of sampling methods including subcellular sampling and cell-release sampling suffer from losing detection sensitivity and separation efficiency due to the rapid analytes diffusion at the preseparation stage on column. The components with very low concentration in a biosamples may not be detectable even by a high sensitivity detection method (such as electrochemical detection, LIF detection) [2]. In this paper, a diffusion-free sampling technique was developed by injection of two water immiscible IL droplets into the micropipette based on its electrocapillarity [3] and electroosmotic flow (EOF), successfully solved the diffusion problem of an ultrasmall volume sample in capillary electrophoresis.

2. THEORY

The motion of IL can be described by Lippmann-Yong's equation (1).

$$\gamma = \gamma_o - cV^2/2 \quad (1)$$

where γ_o is the surface tension when there is no voltage applied across the chip, and c the capacitance per unit area of the electrical double layer for CEW, and V voltage applied. Young's equation can be used to express the Eq(1) in terms of contact angle as Eq(2).

Young's equation can be used to express the Eq(1) in terms of contact angle as equation (2).

$$\cos\theta = \cos\theta_o + cV^2/2\gamma_{LG} \quad (2)$$

978-0-9798064-0-7/μTAS2007/$20©2007CBMS

where θ_o is contact angle when no voltage applied across interfacial layer, γ_{LG} liquid-gas surface tension. Note that cos θ_o and γ_{LG} are considered independent of the applied voltage. Under a reversed EOF by a cationic polymer coating, the motion of IL drop is more easily obtained.

3. EXPERIMENTAL

PDMS microchips are fabricated by photolithography and replica molding method. Capillary micropipette tips of below ten micrometers of inlet inner diameter were prepared by pulling 50 μm i.d. × 180 μm, o.d. fused silica capillary (Polymicro, Phoenix, AZ, USA) using P2000 laser-heated capillary puller (Sutter Instruments, Novato, CA. USA). Two kinds of cationic polymers, PEI (MW750 000) and PDDAC (MW400 000~500 000) solution were dynamically coated onto the inner surface of capillary micropipette tips and PDMS channels, respectively. A PEI coated capillary micropipette tip was interfaced with PDDAC coated PDMS channel to form a chip for single cell analysis. For sample segmentation, [Bmim]NTf_2, analyte, and another [Bmim]NTf_2 were injected sequentially for 2 s, 1s, and 1s under a voltage of 600 V.

4. RESULTS AND DISCUSSION

The concept of diffusion free sampling is showed in Fig. 1. The IL is difficult to be introduced into the native silica capillary at a buffer solution of pH > 4 without IL breaking, because at this pH the capillary is anionically charged and both EOF and electrocapillary flow of IL are coexist and oppositely directed each other. So, to reverse the EOF flow cationic polymers were dynamically coated on the micropipette inner wall and channel. Fig. 2 shows a captured image from a moving IL segmented 1 μM flavin adenine dinucleotide (FAD) and flavin mononucleotide (FMN) mixture (about 30 pL) in the PEI coated silica capillary micropipette tip without breaking. We observed that the IL droplets were broken from its core under an applied separation voltage, when the sample segment travelled up to the PDDAC coated separation channel due to the strong hydrophobic interaction, and through the opened channel sample mixture got separated. Table 1 shows the contact angle of IL droplets on the PEI and PDDAC coated glass plate and PDMS plate. Fig. 3 shows the comparison of electropherograms injected by diffusion free sampling method and general electrokinetic method. The diffusion free sampling method improved the sensitivity and reduced the peak width by a factor of 6.3 and 3.5, respectively. An application of this method on the in-capillary labeling technique is shown in Fig. 4 based on the IL segmentation. A mixture of myoglobin, cytochrome *c* and lysozyme were separated after labeled with 2,4-naphthalenedicarboxaldehyde (NDA) and mercaptoethanol in the IL segmented zone.

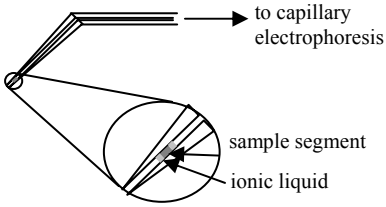

Figure 1. Concept of diffusion-free sampling.

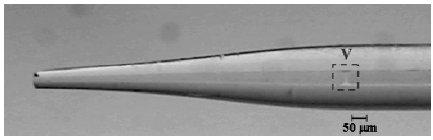

Figure 2. CCD image of segmented flavin sample mixture (use dyed IL).

Table 1. Contact angle of IL droplet on different polymer coated plates

Plate	Contact angle (^{o})
native PDMS	70±1
0.5% PEI-coated slide glass	41±1
0.5% PDDAC-coated PDMS	33±1

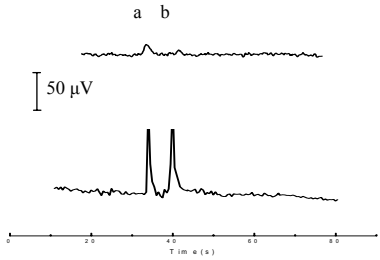

Figure 3. Electropherograms obtained by diffusion-free sampling method and general electrokinetic injection method with same injection time. a, FAD, b, FMN.

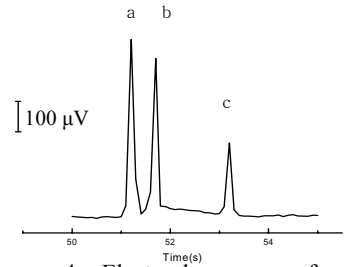

Figure 4. Electropherogram of protein mixture labeled by NDA in IL droplets segmented reactor. a, myoglobin, b, cytochrome *c* , c, lysozyme.

5. CONCLUSIONS

The use of IL phase segmented sampling, labeling and microchip electrophoresis separation was demonstrated for on-line biosample analysis. The present method may have a variety of applications and would be a potential use in practical analysis of extra small volume sample.

REFERENCES

[1] T. M. Olefirowicz, and A. G. Ewing, *Dopamine concentration in the cytoplasmic compartment of single neurons determined by capillary electrophoresis*, J. Neurosc. Meth., 34, pp. 11-15 (1990).

[2] X. Lu, W. H. Huang, Z. L. Wang, and J. K. Cheng, *Recent developments in single-cell analysis*, Anal. Chim. Acta, 510, pp. 127-138 (2004).

[3] B. D. Fitchett, J. B. Rollins, and J. C. Conboy, *Interfacial tension and electrocapillary measurements of the room temperature ionic liquid/aqueous interface*, Langmuir, 21, pp. 12179-12186 (2005).

A MICRO-WELL PERFUSION BIOREACTOR FOR HUMAN EMBRYONIC STEM CELL

Natanel Korin, Avishay Bransky, Uri Dinnar and Shulamit Levenberg
Technion, ISRAEL

ABSTRACT

Human embryonic stem cells (ESC) culture in micro-bioreactors has great potential for biology studies and applications. However, human ESC are highly sensitive to culture conditions. The present work studies experimentally and theoretically the use of micro-wells as shear protectors and demonstrates the co-culture of human ESC with human feeder cells within a microchannel perfusion bioreactor. The experimental results and the theoretical mass and flow transport model outcomes indicate that the use of a micro-well perfusion bioreactor is a suitable method for culturing human ESC in a micro-reactor.

Keywords: Perfusion bioreactor, embryonic stem cell, microwell

1. INTRODUCTION

Embryonic stem cells (ESC) research is a promising field for tissue engineering due to their proliferative capacity and pluripotent abilities. Micro-Bioreactors have great potential for ESC biology studies and applications. Beebe's group has shown the ability to culture an undifferentiated human ESC colony in a microchannel under static conditions [1], with medium exchanged daily. Despite its prospective; this has not been achieved in a microfluidic perfusion bioreactor. We have previously demonstrated the long-term culture of mammalian (HFF-Human Foreskin Fibroblasts) cells in a microchannel (130μm) bioreactor under constant perfusion in a straightforward simple approach [2]. HFF may serve as human feeder cells for growing undifferentiated human ESC colonies. However, human ESC were found to be highly sensitive to flow and culture conditions and did not grow in a co-culture with HFF, under flow rates which were suitable for HFF long-term culture [3]. The present research provides an experimental and theoretical approach to using micro-wells as shear protectors for co-culturing human ESC with HFF feeder cells within a microchannel.

2. EXPERMENTAL

Conventional soft-lithography techniques were used to fabricate PDMS microchannels (130 μm x0.5/1mm wide x20mm long) sealed irreversibly with a PDMS microwell array (ϕ100μmx65μm, various spacing) cover. The microchannel was filled with ethanol for sterilization and bubble removal, coated with a human fibronectin solution and seeded with HFF. After a period of static incubation, the microchannel was connected to a perfusion system comprising: a syringe pump, a permeable tube oxygenator, and a waste container. A perfusion flow rate of 0.01-0.1 ml/hr was used to culture the cells (shear stress<10 mPa). After 24 hours, human ESC were seeded in the microchannel with the HFF cells, incubated in human ESC medium and then connected to the perfusion system. The ability of the microwells to prevent human ESC detachment and maintain their culture was examined.

978-0-9798064-0-7/μTAS2007/$20©2007CBMS

3. THEORETICAL

Mass Transport and fluid mechanics models were used to evaluate the culture conditions within the micro-bioreactor (shear stress, oxygen level, nutrients level etc.). 3D finite element fluid mechanics analysis (Comsol 3.3) was preformed to estimate the maximum shear stress at the bottom of the wells compared to the shear stress at the microchannel surface. A 2D simplified finite elements model which accounts for convective and diffusion mass transport was used to examine the oxygen level within grooves in a bioreactor.

4. RESULTS AND DISCUSSION

Human ESC were successfully co-cultured with HFF as feeder cells in the microwell perfusion bioreactor. Following 24 hours culture of HFF in the micro-reactor (Figure 1a), human ESC were added to the HFF and cultured inside the microwells in the microchannel (Figure 1b,c). The microwells efficiently protected the human ESC from shear stress and allowed their culture under perfusion. While human ESC located outside the micro-wells, on the surface of the channel, were eventually washed out.

Additionally, the fluid mechanics analysis showed that a 30 times reduction of shear is attained under these conditions (Figure 2) and the mass transport model indicated that the cells can be cultured without reaching any hypoxia (Figure 3, oxygen level> 10mmHg).

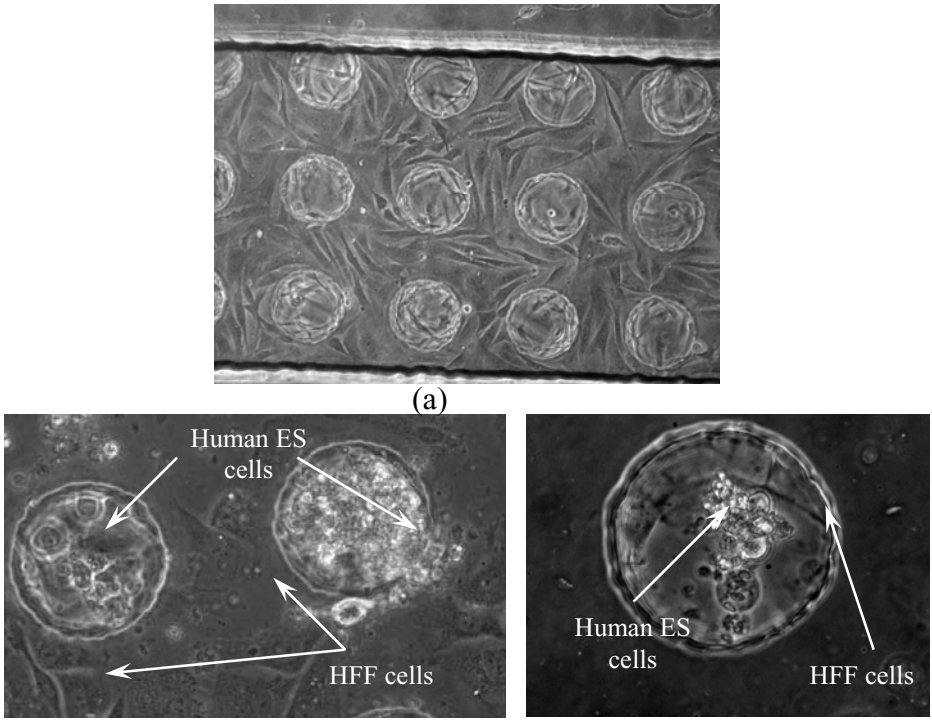

Figure 1. Co-culture of HFF and human ESC in the microwell bioreactor. (a). HFF cultured for 24 hours under perfusion, (b,c). Human ESCs co-cultured in the wells with HFF in the microchannel bioreactor.

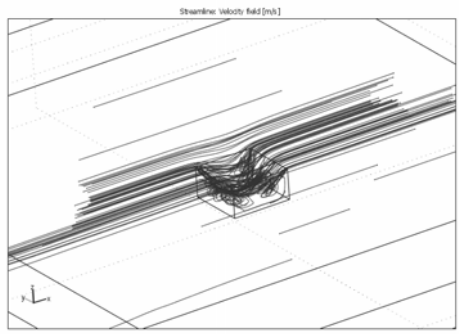

Figure 2. Streamlines of the flow in the microwell (Comsol 3.3- 3D finite element simulations). These simulations indicate a 30 times reduction in shear stress an the bottom of the well compared to the surface of the channel.

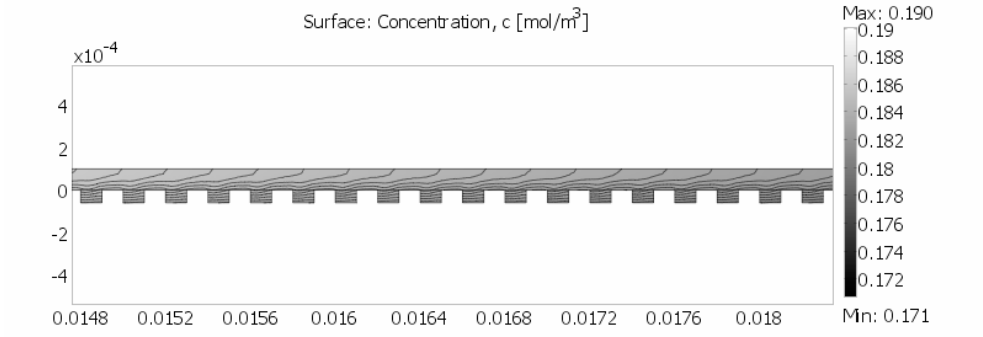

Figure 3. Iso-contours of oxygen level in a groove microchannel bioreactor (flow rate- 0.1 ml/hr) obtained using a convective and diffusion mass transport 2D finite elements model.

5. CONCLUSIONS

The experimental results and the theoretical model presented in this study indicate that the use of a micro-well perfusion bioreactor is a suitable and promising method for culturing human ESC in a micro-reactor.

REFERENCES

[1]. V.V. Abhyankar, G.N. Bittner, J.A. Causey, T.J. Kamp, D.J. Beebe, Embryonic stem cell culture in microfluidics channels, *7th international Conference on Miniaturized Chemical and Biochemical Analysts System* (μTAS 2003),pp. 17-20, (2003).

[2]. N. Korin, A. Bransky, U. Dinnar, S. Levenberg, A Parametric Study of Human Fibroblasts Culture in a Microchannel Bioreactor, *Lab on a Chip*, 7, pp. 611-617, (2007).

[3]. N. Korin, A. Bransky, U. Dinnar, S. Levenberg, The culture of human embryonic stem cells in microchannel perfusion bioreactors, *Proc. SPIE vol. 6416*, Biomedical Applications of Micro- and Nanoengineering III, pp. 64160N, (2006).

ENCAPSULATION OF LIVING CELLS INTO ALGINATE GEL MICROTUBE BY MICROFABRICATED NOZZLE ARRAY

S. Sugiura[1, 2], T. Oda[3], Y. Aoyagi[3], M. Satake[4], N. Ohkohchi[3], and M. Nakajima[1, 3]

[1]*National Food Research Institute, JAPAN,*
[2]*National Institute of Advanced Industrial Science and Technology (AIST), JAPAN*
[3]*University of Tsukuba, JAPAN and*
[4]*National Cancer Center, JAPAN*

ABSTRACT

This paper reports the novel method to encapsulate living cells into an alginate gel microtube with 120 μm diameter using microfabricated nozzle (MN) array. Alginate aqueous solution containing living cells was extruded through a silicon MN (60 μm x 60 μm) into $CaCl_2$ aqueous solution and alginate gel microtube was formed. The encapsulated cells in the microtube with 120 μm diameter grew in the entire tube and formed cylindrical organoid, while the cells encapsulated in that with 670 μm diameter grew only at the periphery of the tube.

Keywords: cell encapsulation, gel fabrication, micro nozzle array

1. INTRODUCTION

Microencapsulation of living cells that have been genetically modified to secrete proteins represents a promising alternative nonviral strategy to gene therapy [1]. For this application, smaller microcapsules offer many advantages, such as better transportation of nutrients and oxygen, smaller volume and better dispersion. Recently several research groups including our group have proposed microfabricated device to prepare size controlled microcapsules [2-5]. We have reported a microfabricated device, MN array [2], and micro-airflow-nozzle [3], to produce 100 to 300 μm alginate gel microcapsules containing living cells. In this study we propose the micrometer-scale tubular gel for cell encapsulation carrier.

2. FABRICATION

Figure 1 illustrates the MN fabricated on the silicon plate. The MNs were fabricated by photolithography and the deep reactive ion-etching (RIE) process on a 4-inch silicon wafer with 400 μm

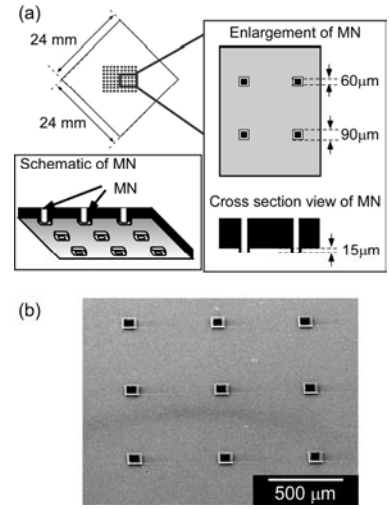

Figure 1: Micro-nozzle (MN) array fabricated on a silicon plate. (a) Schematics of the silicon plate. (b) SEM photograph of the MN array.

978-0-9798064-0-7/μTAS2007/$20©2007CBMS

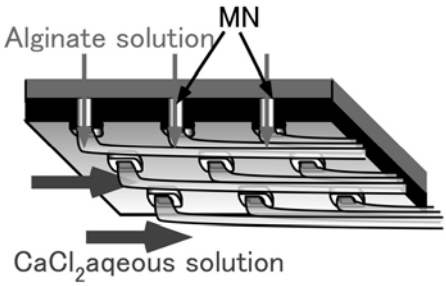

Figure 2. Schematic mechanism of the calcium alginate gel microtube formation through MN.

thickness. The fabrication process was based on the previously reported method [2, 3, 6]. In order to fabricate thoroughly etched thin holes, the silicon wafer were etched from both side of the silicon wafer by the RIE. The fabricated MNs have an inner width of 60 μm, an outer width of 90 μm, and a nozzle height of 15 μm.

3. EXPERIMENTAL

Figure 2 shows the schematic mechanism of the alginate gel microtube formation through MN. Sodium alginate 1.5% aqueous solution was fed into 0.01 mol/L $CaCl_2$ aqueous solution through MN. The formed calcium alginate gel microtubes were recovered and hardened in 0.1 mol/L $CaCl_2$ aqueous solution.

For cell encapusulation into microtube, human kidney 293 cells were transfected with vector encoding green fluorescence protein (GFP) (293/GFP cells), and were encapsulated in alginate microtubes. The harvested cells were suspended in a sodium alginate solution at a final concentration of 1.0 x 10^7 cells/mL, and alginate solution containing cells was fed into 0.01 mol/L $CaCl_2$ aqueous solution through MN. The recovered calcium alginate gel tube containing cells were hardened in 0.1 mol/L $CaCl_2$ aqueous solution and coated with a polyu-L-lysine (PLL) layer as described previously [7]. The PLL coated alginate gel microtubes with two different diameters (120 μm and 670 μm) were cultured for two weeks.

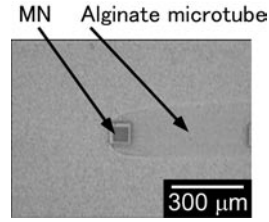

Figure 3. Microscope photograph of calcium alginate microtube formation through MN.

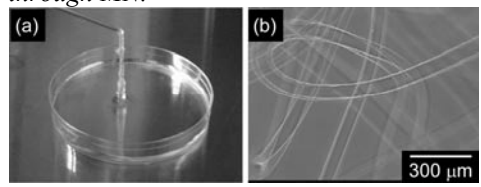

Figure 4. Morphology of the prepared calcium alginate microtubes. (a) Alginate microtube handled with tweezers. (b) Microscope photographs of prepared alginate microtubes.

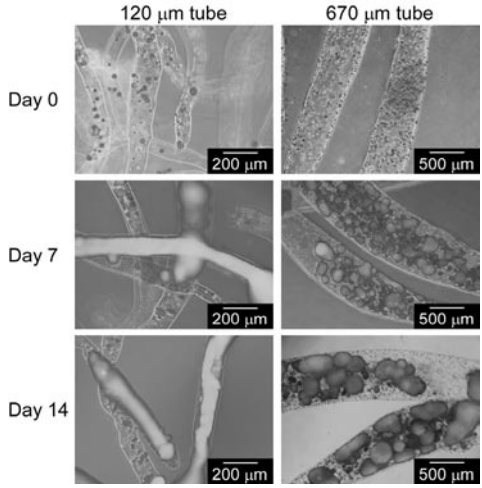

Figure 5 Microscope photographs of alginate microtubes containing 293/GFP cells. Green fluorescence images exhibiting GFP were overlaid on to bright field images.

4. RESULTS AND DISCUSSION

Calcium alginate microtube was prepared with 100 mL/hour flow rate of alginate solution and 1000 mL/hour flow rate 0.01 ml/L $CaCl_2$ solution. The clcium alginate gel microtube were successfully prepareed in the stream of $CaCl_2$ solution as shown in Figure 3. The prepared alginate gel were recovered and hardened in 0.1 mol/L $CaCl_2$ solution, and the resulting calcium anginate gel had 120 μm diameter. The hardened microtubes were enough strong to be handled with tweezers (Figure 4a) and were not aggregated each other in in the 0.1 mol/L CaCl2 solution (Figure 4b).

Calcium alginate microtubes containing living cells were successfully prepared as shown in Figure 5. The prepared calcium alginate microtubes were coated with a poly-L-lysine layer for further cell cultivation. Cell growth in 120 μm diameter microtube was compared with that in 670 μm diameter tube, which had been prepared with 22 gauge syringe needle. The cell proliferation was better in thinner microtubes. The cells encapsulated in 120 μm microtubes can grow in the entire space of the microtubes formed cylindrical organoid within two weeks. In contrast, the cells encapsulated in 670 μm tubes grow only at the periphery of the tube, leaving a great deal of dead space in the tubes. The thiner microtubes provide higher diffusion efficiency and large scaffold surface area compared to thicker microcapsules, which resulted in higher cell growth in thinner microtube.

REFERENCES

[1] T. Joki, M. Machluf, A. Atala, J. H. Zhu, N. T. Seyfried, I. F. Dunn, T. Abe, R. S. Carroll and P. M. Black, "Continuous release of endostatin from microencapsulated engineered cells for tumor therapy," Nat. Biotechnol., **19**, 35 (2001)

[2] S. Sugiura, T. Oda, Y. Izumida, Y. Aoyagi, M. Satake, A. Ochiai, N. Ohkohchi and M. Nakajima, "Size control of calcium alginate beads containing living cells using micro-nozzle array," Biomaterials, **26**, 3327 (2005)

[3] S. Sugiura, T. Oda, Y. Aoyagi, R. Matsuo, T. Enomoto, K. Matsumoto, T. Nakamura, M. Satake, A. Ochiai, N. Ohkohchi and M. Nakajima, "Microencapsulation of Living Cells into 150 Micrometer Microcapsules Using Microfabricated Airflow Nozzle," Biomed. Microdevices, **9**, 91 (2007)

[4] K.S.Huang, T.H. Lai, Y.C. Lin, "Manipulating the generation of Ca-alginate microspheres using microfluidic channels as a carrier of gold nanoparticles," Lab Chip, **6**, 954 (2006)

[5] K. Liu, H.J. Ding, J. Liu, Y. Chen, X.Z. Zhao, "Shape-controlled production of biodegradable calcium alginate gel microparticles using a novel microfluidic device" Langmuir **22**, 9453 (2006)

[6] I. Kobayashi, M. Nakajima, K. Chun, Y. Kikuchi and H. Fukita, "Silicon array of elongated through-holes for monodisperse emulsion droplets," AIChE J., **48**, 1639 (2002)

[7] J.M.Van Raamsdonk and P. L. Chang, "Osmotic pressure test: A simple, quantitative method to assess the mechanical stability of alginate microcapsules." Journal of Biomedical Materials Research **54,**264-271 (2001).

MICROFLUIDIC DEVICE BASED BIODEGRADABLE MICROFIBER SCAFFOLD FABRICATION FOR TISSUE ENGINEERING APPLICATION

Chang Mo Hwang[1,2] and Kyung Sun[1,2] and Sang Hoon Lee[1,2]

[1]Korea Artificial Organ Center, REPUBLIC OF KOREA and

[2]Korea University Medical Center, REPUBLIC OF KOREA

ABSTRACT

In this paper, we developed microfluidic chip-based fiber spinning of poly(lactic-co-glycolic acid). To make the poly glycolic-co-lactic acid(PLGA) micro fiber, the micro-channel based polydimetylsiloxane(PDMS) spinning device was fabricated, PLGA solution in dimethylsulfoxide (DMSO) and aqueous glycerol solution was used for fiber spinning. By controlling the sample and sheath flow condition, fiber could be made with various diameter from about 20um to 220um. PLGA fibers have dense surface morphology with few surface pore, whereas inside the fiber, highly porous structure with interconnected pores.

In cell culture assay for tissue engineering scaffolds, cells were aligned along the fiber axis after 72 hr culture and no evidence of cytotoxic effect induced by the process.

Keywords: PLGA microfiber, phase inversion, PDMS microfluidic chip, tissue engineering scaffold

1. INTRODUCTION

A microfluidic chip based micro fiber fabrication method is established for tissue engineering. This method use phase inversion method for fiber spinning under wet condition. MEMS based biodegradable polymer constructs for cell based engineering have been using photo curing or thermal melting process. Microfluidic chip based hydrogel fiber spinning methods have been reported, but they need crosslinking chemical agent or UV curing process. Proposed method is basically similar to wet spinning in principle, but adopt micro device without UV curing and thermal process. In this study, poly(lactic-co-glycolic acid)(PLGA) fiber is fabricated in fluidic chip. To investigate feasibility for tissue engineering scaffold, human fibroblast cells are cultured and cell viability was investigated.

2. EXPERIMENTAL

Microfluidic device is fabricated with PDMS as shown in Figure 1. Fluid channel is formed with glass tube, and micro spinning part is consisted with micro glass tip and hollow PDMS sheath part. The glass micro tip size is about 50micron and core polymer flows, and sheath part has 750 micron inner diameter. Core solution is 10%(w/v) PLGA dissolved in dimethylsulfoxide(DMSO) and the sheath solution is glycerol 50% aqueous solution. For flow condition, sheath flow rate was set to 1mL/min and the core flow rate was varied from 1ul/min to 50ul/min. Core PLGA solution and the sheath glycerol solution are in contact near the tip region, DMSO solvent moves from core solution to sheath region and PLGA polymer fiber starts solidification process to form fiber. Electric motor based device is used for fiber winding and used for cell culture.

978-0-9798064-0-7/μTAS2007/$20©2007CBMS

For the application of tissue engineering scaffold, L929 human fibroblast cells were seeded on the fiber wound coverslip and incubated with low media height to help cell attachment onto fiber, and media cultured for several days. Cells are fixed, stained and examined with immunofluorescence and scanning electron microscopy.

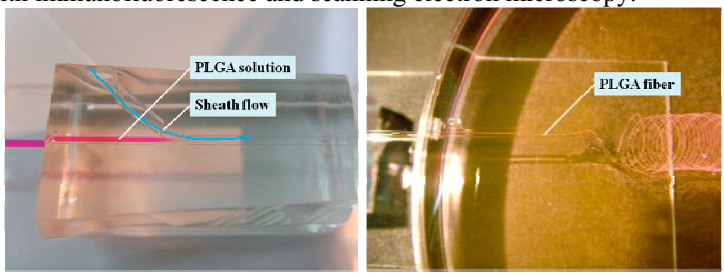

Figure 1. PLGA fiber spinning with microfluidic chip, core PLGA solution is stained with rhodamine-B dye

4. RESULTS AND DISCUSSION

Under proper flow condition, the microfluidic chip showed continuous process of PLGA fiber production. Fiber diameters obtained in this experiment ranged from 20um to 220um, and could be controlled by proper adjustment of core and sheath flow rate[Fig. 2].

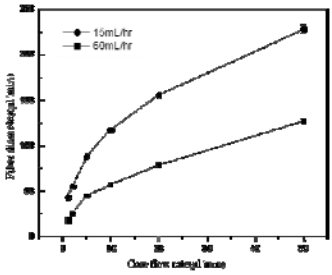

Figure 2. Fiber diameter vs PLGA flow rate of 10% PLGA solution under 15mL/hr and 60mL/hr sheath flow rate

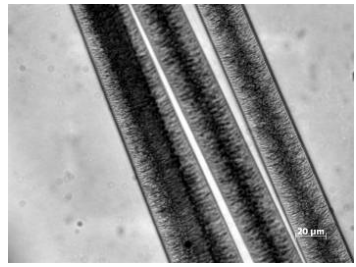

Figure 3. Optical microscopy of PLGA fiber (core flow/sheath flow = 2uL/min : 1,000μL/min)

Under fixed flow condition, fiber size is almost constant and low deviation from mean value. PLGA fibers have axi-symmetric along the longitudinal axis of the fiber, and had somewhat transparent feature in optical microscope observation[Fig. 3]. The fibers' surface have smooth and few pores, but the cross-section shows highly porous structure with radially distributed pore inside of the fiber [Fig. 4]. After 72hrs from cell seeding of L929 fibroblast, cells attached and distributed along the fiber.

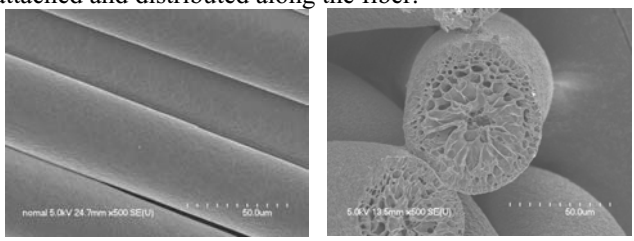

(a) (b)

Figure 4. SEM image of PLGA fiber surface(a) and cross-section

It looks cells proliferate on the fiber without cytotoxic effect. Figure 5 shows actin staining result of cell cultured fiber after 72 hours. The red color-stained actin filaments are arranged along the PLGA fibers, which reflect the cells have preferred orientation to long axis of fibers.

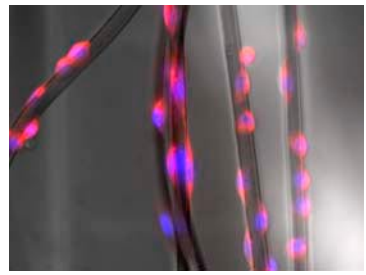

Figure 5. Actin stained L929 fibroblast cells on PLGA fiber (3 day culture)

5. CONCLUSIONS

Using microfluidic chip, simple PLGA manufacturing process is developed. This device can control the fiber size as easy as changing the core and sheath flow condition. Under constant sheath flow rate of 15mL/hr and 60mL/hr and core flow rate 1 to 50uL/min, we obtained various PLGA fiber diameters from 20um to 220um. This chip based fabrication method has the advantages over conventional ones: (1) The fabrication apparatus is simple and chip is small in size and the resulting fiber size can be controlled various diameter with one chip by varying flow conditions. (2) The fabrication process does not requires specific conditions such as high temperature or high pressure and the sensitive biological materials such as proteins can be incorporated. The PLGA fibers showed good structure for cell culture scaffold for tissue engineering application. This micro fluidic chip based fiber making device has many applications in clinical application including tissue engineering and drug delivery.

ACKNOWLEDGEMENTS

This research was supported by a grant(Code # : M103KV010031-07K2201-03110) from Brain Research Center of the 21st Century Frontier Research Program funded by the Ministry of Science and Technology, and the Korea Health 21 R&D Project(A020609), Ministry of Health and Welfare, the Republic of Korea.

REFERENCES

1. “Hydrodynamic microfabrication via "on the fly" photopolymerization of microscale fibers and tubes”, Jeong, W., J. Kim, S. Kim, S. Lee, G. Mensing, and D.J. Beebe Lab On a Chip, 4, 576(2004).
2. “Effect of fiber diameter and orientation on fibroblast morphology and proliferation on electrospun poly(D,L-lactic-co-glycolic acid) meshes” Bashur, C.A., L.A. Dahlgren, and A.S. Goldstein. Biomaterials,27, 5681(2006).
3. “Degradation of electrospun PLGA-chitosan/PVA membranes and their cytocompatibility in vitro”, Duan, B., L. Wu, X. Li, X. Yuan, X. Li, Y. Zhang, and K. Yao, J Biomater Sci Polym Ed, 18, 95(2007).

A MORE EXCELLENT CONSTRUCTION METHOD OF A MULTI FUNCTIONAL ENVELOPE-TYPE NANO DEVICE ON MICRODEVICE FOR GENE THERAPY

Hiroshi Kuramoto[1], Noritada Kaji[3,4], Kentarou Kogure[7], Manabu Tokeshi[3,4], Yasuo Shinohara[2], Hideyoshi Harashima[7] and Yoshinobu Baba[3,4,5,6]

[1] Faculty of Medicine, Kanazawa university
[2]Institute of Genome Research , The University of Tokushima, Japan
[3] Department of Applied Chemistry, Graduate School of Engineering,
[4]MEXT Innovative Research Center for Preventive Medical Engineering, Nagoya University, JAPAN
[5]Health Technology Research Center, AIST, JAPAN
[6]Institute for Molecular Science, JAPAN
[7]Department of pharmaceutical sciences, Hokkaido University, Japan

ABSTRACT

A multifunctional envelope-type nano device (MEND) is an extremely efficient technology for a non-viral gene delivery system. However, the construction processes of the MEND by the existing method are very complicated. Therefore we develop a new method to construct it quickly and easily in the previous work. In this work, we report a new on-chip construction method of the MEND which is much more suitable for the gene therapy.

Keywords: Multifunctional envelope-type nano device (MEND), on-chip construction, non-viral gene delivery system, gene therapy

1. INTRODUCTION

To date, many polymorphisms have been found to be associated with disease. There is no doubt that the information from polymorphisms will be useful tools to decrease the disease risk generally or specifically. So we'll effectively treat any and all of diseases by putting gene therapy into practice. In gene therapy, gene vectors play essential roles of an efficient gene delivery. MEND, a highly-functionalized non-viral vector, is superior to current vectors (Figure.1). But the current construction method of the MEND is time-consuming, labor intensive and tedious task. Microdevice gives us many advantages in terms of reaction time and efficiency; therefore we developed a new construction method of the MEND by using a microdevice.

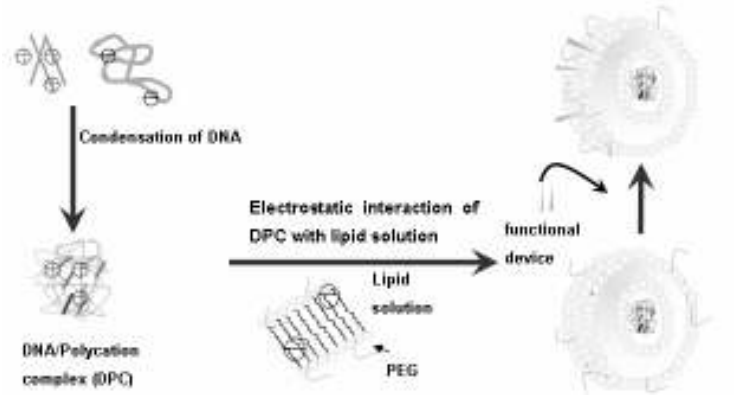

Figure 1: Schematic drawings of the preparation process of MEND

978-0-9798064-0-7/μTAS2007/$20©2007CBMS

2. EXPERIMENTAL

In this study, we examined the two processes of constructing MEND on the microdevice. In the first step, we constructed DNA/poly cation complex (DPC) on the microdevice with three fluid channels . In this process, we applied plasmid DNA into channel A, d.d.water into channel B, poly-L-lysine (PLL) into channel C and DNA was condensed by PLL (Figure2A). The second process was coating process of DPC by lipid solution (Figure 2B). The lipid solution was composed of L-α-Phosphatidylethanolamine, Dicetyl phosphate, 1,2-disetearoyl-sn-glycero-3-phosphoetanolamine-N-[Methoxy(polyethylene glycol)-2000], n-Octyl-β-D-glucopyranoside. We applied lipid solution into channel A and C, DNA condensates into channel B. We examined various flow rate and concentrations of materials to construct them, and then, measured the zeta potential and the diameter of targets by using dynamic light scattering (DLS).

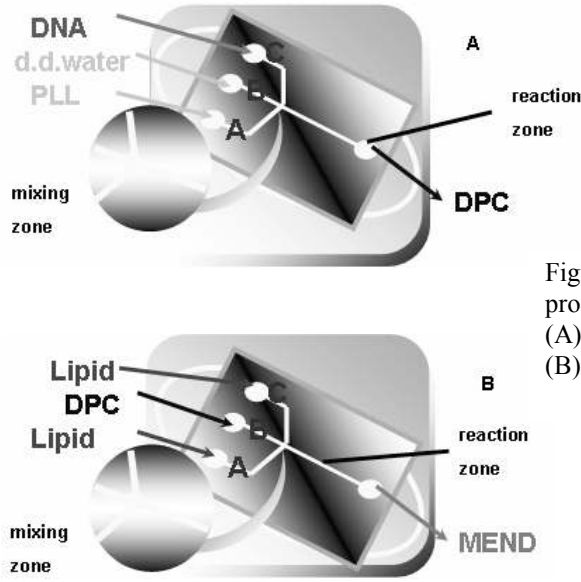

Figure 2. Schematics of the construction process of MEND on a microchip.
(A) DNA condensation process by PLL.
(B) Coating process of DPC by lipid layer

4. RESULTS AND DISCUSSION

The smaller vectors are easily taken up by the nucleus of cells. In the first step, we determined the fittest flow rate (10μl/min) and concentration of materials (DNA:0.01mg/ml, PLL:0.01mg/ml) to construct the minimum DPC (the size of MEND:130nm, Figure 4A, B). The size of DPC transited from 220nm to 130nm. In the second step, we also determined the best parameters to construct the minimum MEND (flow rate: 10μl/min, lipid: 0.05, DPC:1, Figure 5A, B). The size of MEND transited from 180nm to 110nm.We also determined if the yields were higher than the existing methods. We got 4 times yields of MEND as much as the existing method in the specific concentrations of materials.

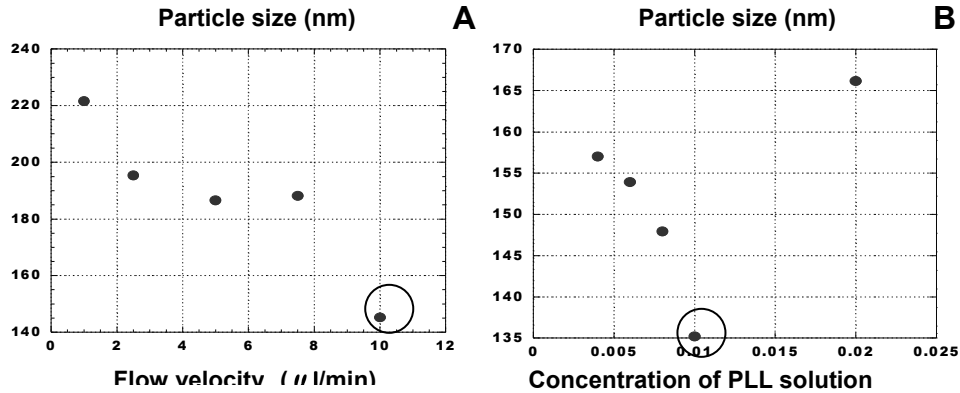

Figure 4. Transition of DPC particle size
(A)Transition dependent of flow rate, (B)transition dependent of concentration of material

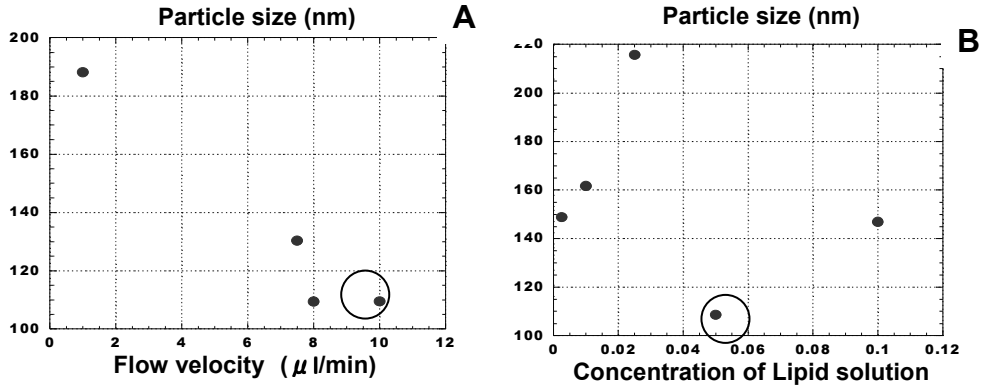

Figure 5. Transition of MEND particle size
(A)Transition dependent of flow rate, (B)transition dependent of concentration of materials

5. CONCLUSIONS

We developed the more suitable on-chip construction method of the MEND for gene therapy. We could also accomplish the yield improvement. The modification of the fluid channels on the microdevice and the change of the solutes and solvents will be one of the keys to improve the efficiency of this device much further. It'll much contribute to the gene therapy.

REFERENCES

[1]. " Construction of multifunctional envelope-type nano device by a SUV*-fusion method," K. Sasaki, K. Kogure, S. Chaki, Y. Kihira, M. Ueno, H. Harashima, *Int. J.Pharm.*, 296, 142-150 (2005).

[2]. "On-chip construction of a multifunctional envelope-type nano device for a non-viral gene delivery system," M. B. Sinclair, M. A. Butler, A. Hiroshi Kuramoto, Noritada Kaji, Kentarou Kogure, Manabu Tokeshi,
Yasuo Shinohara, Hideyoshi Harashima and Yoshinobu Baba, Micro Total Analysis Syatem 2006, 10, 1005-1007 (2006).

ENZYME ASSEMBLY AND CATALYTIC ACTIVITY IN A REUSABLE BIOMEMS PLATFORM FOR METABOLIC ENGINEERING

Xiaolong Luo, Angela T. Lewandowski, Gregory F. Payne, Reza Ghodssi, William E. Bentley and Gary W. Rubloff

University of Maryland, USA

ABSTRACT

We report a reversible, chitosan-mediated biofunctionalization strategy for assembling a biocatalytically-active enzyme in reusable bioMEMS devices as a first step toward an experimental platform for metabolic engineering applications, e.g. drug discovery. We demonstrate (a) the assembly of a Pfs enzyme at a specific electrode address and (b) the efficient catalytic activity of this enzyme in the bioMEMS. Enzymatic activity is robust, remaining over days. In addition, biofunctionalization can be reversed, making the bioMEMS reusable for repeated assembly and catalytic activity.

Keywords: Enzyme assembly, catalytic activity, bioMEMS, chitosan

1. INTRODUCTION

Robust and reproducible enzyme assembly witin microfluidic devices is challenging. We report a reversible, chitosan-mediated biofunctionalization strategy for assembling a biocatalytically-active enzyme in reusable bioMEMS devices. We exploit an integrated device and package design [1] which supports programmable bio-component assembly at selected sites [2]. The aminopolysaccharide chitosan is utilized as the interfacial biofunctionalization material for (1) the chemical signal-guided conjugation of chitosan to a Pfs enzyme through its pro-tag, which is genetically engineered at the C-terminal of Pfs and is activated by tyrosinase for the conjugation, and (2) the electric signal-guided electrodeposition of the Pfs-chitosan conjugate to a selective electrode under negative bias in the microfluidic channel.

2. THEORY

Fig. 1 illustrates our concept that the programmable and reversible assembly of biologically-active components (i.e., enzymes) enables prefabricated MEMS to be repeatedly biofunctionalized for multiple uses. First, the bioMEMS device in Fig. 2 was prefabricated for multiple uses [1]. Second, Pfs is conjugated to the aminopolysacchoride chitosan through a C-terminal pro-tag genetically-engineered into the Pfs enzyme. As illustrated in Fig. 1b, tyrosinase mediates the conversion of tyrosyl residues of Pfs into active o-quinones that conjugate to chitosan and confers stimuli-responsive properties. Third, the Pfs-chitosan conjugate in a slightly acidic solution (pH<6.3) is introduced into a microchannel and electrodeposited onto a selected electrode under negative bias as illustrated in Fig. 1c. With biofunctionalizaton complete, Fig. 1d shows the Pfs-mediated reaction is performed by introducing the substrate S-adenosylhomocysteine (SAH) into the microchannel for conversion into the products S-ribosylhomocysteine (SRH) and adenine. Downstream reaction solutions are collected and analyzed with high-performance-liquid-chromatography (HPLC).

978-0-9798064-0-7/μTAS2007/$20©2007CBMS

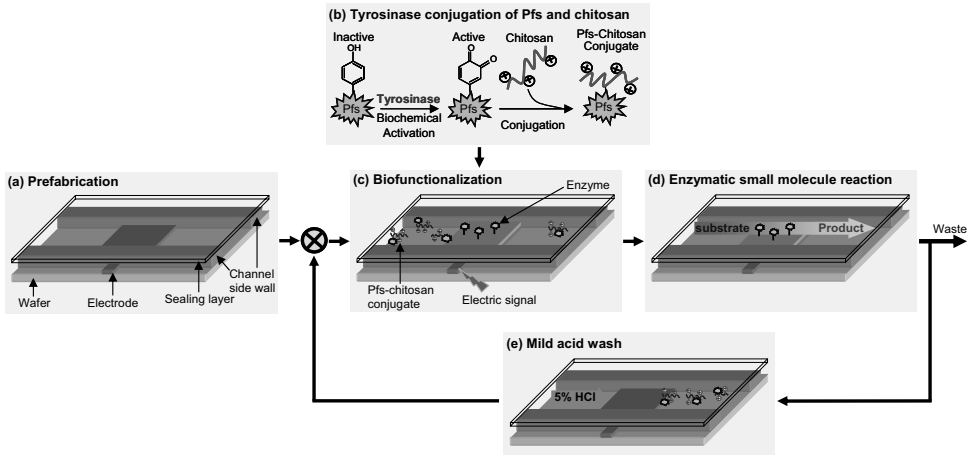

Figure 1. Schematic flow of reversible enzyme assembly and catalytic activity in reusable bioMEMS device. (a) Device prefabrication, (b) enzyme-chitosan conjugation, (c) electrically programmed assembly of Pfs-chitosan conjugate, (d) small-molecule reaction by enzyme catalysis, (e) mild acid wash to remove biofunctionalization and reuse bioMEMS device.

3. EXPERIMENTAL METHODS

The experimental sequence of operations to demonstrate catalytic activity and reversibility of the enzyme and reuse of the bioMEMS device is shown in Fig. 2(c), with tests of catalytic conversion color-coded (steps 6, 9, 15, 17) for comparison with the experimental results in Fig. 3. After demonstrating efficient enzyme activity (Day 2, step 6), the acid wash (Day 2) removed catalytic activity (step 9). Subsequent biofunctionalization with Pfs-chitosan (Day 3) re-established enzymatic activity (step 15) comparable to the original (Day 2, step 6), illustrating enzyme reversibility and bioMEMS

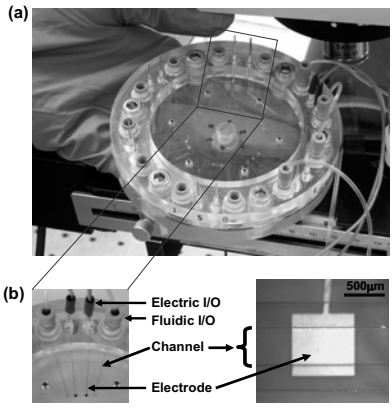

(c)

	Step #	Procedure	Flow rate (µL/min)	Time (min)
Day 1	1	DI water cleaning	50	
	2	BSA	3	120
	3	PBS buffer	3	30
	4	**Pfs-chitosan assembly**	**static**	**4**
	5	PBS buffer	5, 20	30
Day 2	**6**	**Enzymatic reaction (SAH)**	**3, 22**	**600**
	7	HCl wash	22	10
	8	DI water cleaning	50	90
Day 3	**9**	**Enzymatic reaction (SAH)**	**3**	**120**
	10	DI water cleaning	50	60
	11	BSA	5	120
	12	PBS buffer	5	30
	13	**Pfs-chitosan re-assembly**	**static**	**4**
	14	PBS buffer	5, 20	30
Day 4	**15**	**Enzymatic reaction (SAH)**	**3, 22**	**600**
Day 5-7	16	In PBS buffer	static	3 days
Day 8	**17**	**Enzymatic reaction (SAH)**	**3, 22**	**360**
	18	Cleaning	50	

Figure 2. Experimental setup and processedure. (a) Prefabricated bioMEMS device with electrical connections and fluidic inputs/outputs. (b) one microfluidic channel with colored dye flowing and enlarged view of one electrode. (c) Experimental sequence of operations, including enzyme assembly and catalytic activity measurement (steps 1-6), removal of biofunctionalization and measurement (steps 7-9), enzyme re-assembly and measurement (steps 10-15), storage (step 16) and measurement (step 17).

reuse. Storage in PBS buffer at room temperature for 4 days degraded the conversion efficiency slightly (to 35%), demonstrating robustness of the assembled enzyme.

4. RESULTS AND DISCUSSION

This work demonstrates the efficacy of a biological agent – here, the enzyme Pfs – in carrying out a biochemical function it serves in living cells: Pfs converts SAH to SRH and adenine in one step of a multi-step cell-signaling process (autoinducer-2 production), a quorum sensing phenomenon that determines pathogenicity of bacteria. These results are very encouraging for use of bioMEMS as a metabolic engineering platform, e.g. for drug discovery through an efficient screening of potential enzyme inhibitors as antimicrobial drug candidates. They also illustrate the flexibility of the bioMEMS platform in enabling reversible biofunctionalization and device reuse.

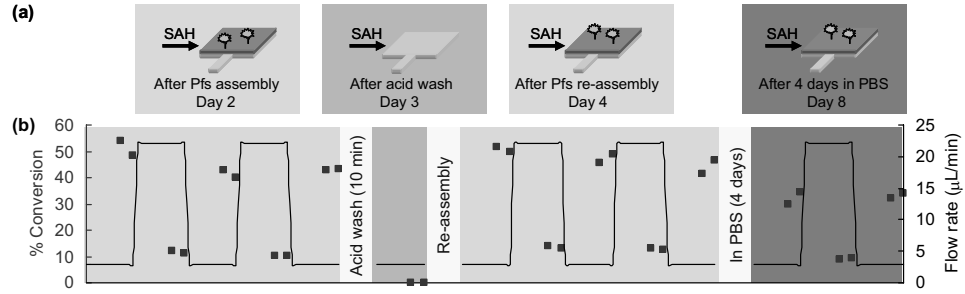

Figure 3: Results of experimental sequence (Table 1) to demonstrate enzyme catalytic activity, its reproducibility after enzyme removal, and its robustness over time. The background colors in each step correspond to the colors in experimental process in Table 1. (a) Schematic flow of enzymatic reaction, (b) % conversion vs. various flow rates.

5. CONCLUSIONS

This work demonstrates a chitosan-mediated biofunctionalization strategy for the assembly of catalytically active enzymes within completely packaged bioMEMS devices. The HPLC results show that assembled enzymes are catalytically active, robust and stable with time, and that our strategy is reversible for multiple uses of our bioMEMS devices.

ACKNOWLEDGEMENTS

This work was supported in part by the Robert W. Deutsch Foundation and NIST.

REFERENCES

1. J. J. Park, T.M. Valentine, R. Ghodssi, and G. W. Rubloff, The 9th International Conference on Miniaturized Chemical and Biochemical Analysis Systems (MicroTAS), Boston, MA, Oct 9-13, 2005.
2. J. J. Park, X. L. Luo, H. M. Yi, T. M. Valentine, G. F. Payne, W. E. Bentley, R. Ghodssi and G. W. Rubloff, *Lab on a Chip*, 2006, 6, 1315-1321.

HYBRID MICROPATTERNS OF CELLS AND CONDUCTING POLYMERS

Matsuhiko Nishizawa, Takashi Kamiya, Soichiro Sekine, Takeaki Kawashima, Hirokazu Kaji and Takashi Abe

Tohoku University, JAPAN

ABSTRACT

We will report a novel technique to make biocompatible, conductive micropatterns on insulating substrates such as glass or polyimide by controlling the lateral growth rate of polypyrrole (PPy) upon electropolymerization at microelectrodes formed on the substrates. We found that pre-modification of the substrate surface with self-assembled monolayer (SAM) of alkylsilane or heparin induces anisotropic (more than 10 times faster) lateral growth of PPy films along the substrate surface. This controllable anisotropic growth of conducting polymers has enabled the following studies, including the formation of hybrid micropatterns of cells and conducting polymers.

Keywords: neurons, conducting polymer, micropatterning, electrode

1. INTRODUCTION

Engineering the interfacial contact between microelectrodes and biological cells is of central importance to the advancement of cell-based bioelectronic devices. Conducting polymers such as polypyrrole (PPy) and poly(3,4-ethylenedioxythiophene) (PEDOT) are excellent candidates for bioelectrode materials owing to their inherent electrical conductivity, controllability of surface biochemical properties, and biocompatibility. In particular, their large surface area due to a fibrous structure increases the interfacial electrical capacity, ensuring noninvasive electrical stimulation of biological cells. On the other hand, recent technical progress in cellular micropatterning has made bioassays possible using cellular networks combined with electrode arrays. Such advanced in-vitro cellular assays also require a high-capacity noninvasive electrode. Many research groups including ours have cultured neuronal cells on a microelectrode array substrate in a manner allowing alignment of the micropatterns of cells to that of electrodes. Smart bio-interfacing with micropatterned conducting polymers will contribute to the realization of these next-generation bioassay chips.

The present work is the combination of two techniques: the electrochemical biolithography [1] and the anispotropic polymer growth [2]. We will present the possible formation of hybrid micropatterns of conducting polymer and living cells on a chip.

2. NONINVASIVE STIMULATION OF CARDIAC MYOCYTES

The PPy film laterally grown around the electrode anchors the whole film and significantly enhances film adhesion. The anchored PPy film was stable even during a long-term cultivation, and serves as an electrode for reproducible, noninvasive, external stimulation of a cultured excitatory cells. For example, the myocytes on the microelectrode substrate were electrically conjugated to form a sheet, and showed synchronized beating upon stimulation (Fig. 1). The threshold charge for effective stimulation of an 0.8 cm^2 sheet of myocytes was systematically evaluated to be around 0.2 μC, as shown in Fig.1(c).

978-0-9798064-0-7/μTAS2007/$20©2007CBMS

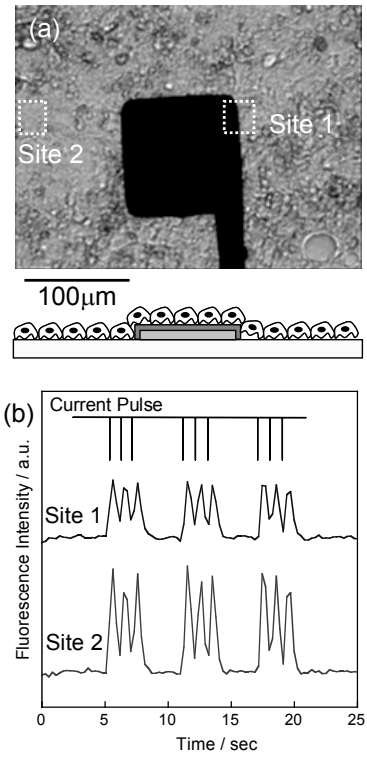

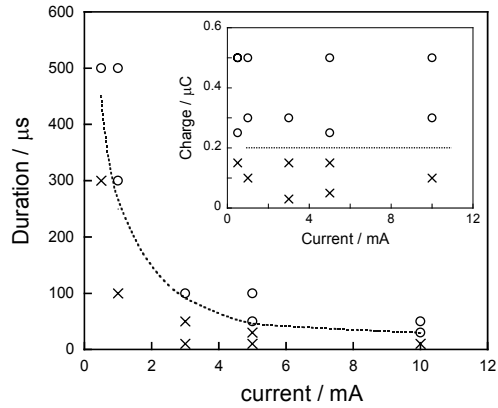

Figure 1. (a) Cardiac myocytes cultured over the polypyrrole-coated Pt microelectrode. The cells were stained with fluo-3 for visualizing cellular responses to electrical stimulation.
(b) Time course of fluorescence intensity changes measured at the sites 1 and 2 in (a). Negative current pulses (interval: 1 s, duration: 100μs, amplitude: 10 mA) were applied.
(c) The plot of excitation (O) and non-excitation (X) of cardiac myocytes in the current-duration format. The dotted blue curve roughly shows the threshold duration for each current amplitude. Inset: the replot in the current-charge format.

3. IN SITU MICROPATTERNING OF CONDUCTING POLYMER

The micropatterns with SAM of alkylsilane or heparin lead to a micropatterns of PPy upon the polymerization (Fig. 2). Importantly, the electropolymerization of PPy can be conducted even during cell cultivation without significant damage to the existing cells (data will be shown in presentation).

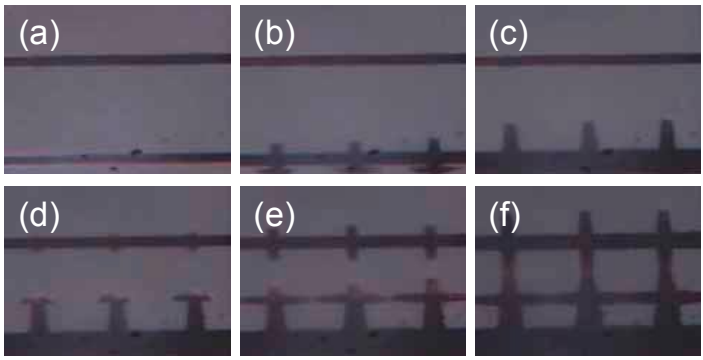

Figure 2. Photographs of the PPy micropattern growing from a twin microband (20μm width) electrodes. The pretreatment with SAM of Octadecylsilane was conducted as to give a checked pattern.

Figure 3 demonstrates the in-situ electrical wiring to cultured cells. A hydrophobic pattern was previously formed around electrode, HeLa cell was put on the pattern, and then polypyrrole was synthesized. We preliminarily studied the toxicity of the pyrrole monomer by culturing HeLa cells in a culture media containing 0.1 M pyrrole. Even after 1 day of cultivation, more than 80 % of HeLa cells were alive and still proliferated, suggesting a comparatively brief exposure to pyrrole solution during polymerization (typically for a few min) would not significantly affect the cellular viability.

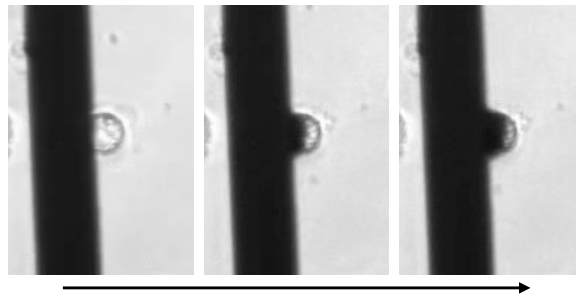

Figure 3. Photographs of the PPy micropattern which is growing with wrapping a HeLa cell

4. ELECTROOCHEMICAL BIOLITHOGRAPHY

The surface modification with heparin can be easily detached by a non-invasive electrochemical biolithography [1], and thus we can draw micropatterns of PPy by using a needle-type microelectrode as a "pen" (Fig. 4). Since this lithography can be applied even during cell cultivation, we can expect the formation of hybrid micropatterns of conducting polymer and living cells.

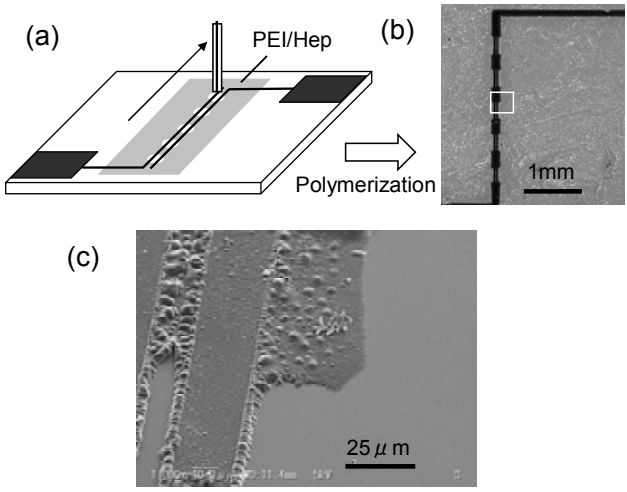

Figure 4. (a) Schematic drawing of the micropatterning of PEI/Hep by electrochemical biolithography. A Pt microelectrode was approached to ca. 50 μm above the substrate surface, and scanned with 0.5 mm steps along the twin-microband electrode, waiting for 10 sec at each step with application of 1.7 V vs. Ag/AgCl in 25 mM KBr buffered solution.
(b) A photograph of the PPy film formed at the microband electrode.
(c) An SEM image of the boxed area of (b).

5. REFERENCES

[1] Electrochemical Biolithography:
J. Am. Chem. Soc., (2004) 126, 15026; *Anal. Chem.*, (2006) 78, 5469; *Langmuir*, (2006) 22, 10784.
[2] Anisotropic Growth of Conducting Polymers:
J. Electrochem. Soc. (1993) 140, 1650; *Biomaterials*, (2007) 28, 1480.

NOVEL HIGHLY-SENSITIVE DETECTION TECHNIQUE OF MONOSACCHARIDES OF GLYCOPROTEINS USING HETEROGENEOUS BUFFER ON MICROCHIP ELECTROPHORESIS

Hideya Nagata[1], Yuichiro Yoshida[1], Tomomi Ishido[1], Yoshinobu Baba[1, 2], Mitsuru Ishikawa[1] and Ken Hirano[1, 3]

[1]Health Technology Research Center, National Institute of Advanced Industrial Science and Technology (AIST), Japan, [2]Graduate School of Engineering, Nagoya University, Japan, [3]PREST, Japan Science and Technology Agency (JST), Japan

ABSTRACT

We report improved detection sensitivity of monosaccharides by a factor of 9 using the heterogeneous buffer. The current attainment is fully compatible with that of conventional capillary electrophoresis (CE) technique. The current technique improved fluorescence intensity using a heterogeneous combination of a sample buffer and a separation buffer, thereby allowing us to develop efficient prospective tools for highly-sensitive detection of monosaccharides.

Keywords: heterogeneous buffer, conformational separation, monosaccharide, pH

1. INTRODUCTION

In the postgenomic era, proteomics is a new goal. There is a large gap in our knowledge connecting the relationship between genotype and phenotype. Connecting the function and significance of sugar chains of glycoproteins plays an important role in bridging this gap. The development of comprehensive analysis of glycoproteins, such as determining the site of modified amino acid in the protein, and structure of the attached carbohydrate chain, is required. We reported conformational separation of monosaccharides labeled with fluorescent dye 2-aminoacrydone (AMAC) on a microchip [1]. However, detection sensitivity of ref. 1 was a little bit inferior to that of typical capillary electrophoresis. In the current work, we report improved detection sensitivity using a heterogeneous combination of a sample buffer and a separation buffer.

2. EXPERIMENTAL

A mixture of monosacharides was separated into each monosaccharide using a plastic microchip and a microchip electrophoresis machine (SV1100 Microchip CE system, Hitachi, Tokyo). An SV1100 machine has a light-emitting diode for excitation at 470 nm and confocal fluorescence detection system for emission around 580 nm. A mixture of AMAC-labeled five neutral monosaccharides, D-glucose (Glc), D-mannose (Man), D-galactose (Gal), L-fucose (Fuc), and D-xylose (Xyl) was dissolved in a sample buffer of 200 mM borate, pH 7.0; and separated using a separation buffer of 2.0 wt% hydroxyethylcellulose (HEC), 200 mM Tris-borate, and 2 mM EDTA, pH 9.3. We call a combination of the above sample buffer and the above separation buffer a "heterogeneous buffer" because electrolyte composition of both buffers is different from each other. On the other hand, we call a combination of a sample buffer, 200 mM borate and a separation buffer, 0.5 wt% methylcellulose, 200 mM borate, pH 8.5 a "homogeneous buffer", because

978-0-9798064-0-7/μTAS2007/$20©2007CBMS

electrolyte composition of both buffers was identical to each other. This homogeneous buffer was used in ref. 1.

3. RESULTS AND DISCUSSION

A mixture of AMAC-labeled five neutral monosaccharides was analyzed by microchip electrophoresis using a heterogeneous buffer (Fig. 1). The mixture was successfully separated on the basis of the difference in stability of the complex between hydroxyl residues of monosaccharides and borate ions (Fig. 1). Thus, we found that the use of a heterogeneous buffer was essential to the successful separtion of AMAC-labeled neutral monosaccharides.

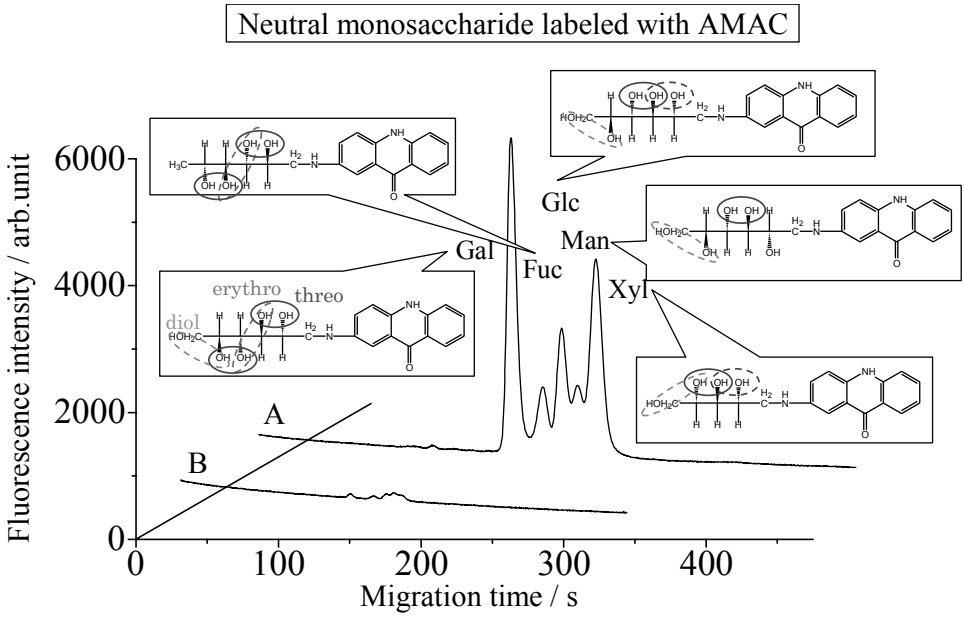

Figure 1. Electropherograms of AMAC-labeled neutral monosaccharides. Conditions: A; heterogeneous buffer, 168 V/cm, B; homogeneous buffer, 168 V/cm.

Highly-sensitive detection of neutral monosaccharides (0.097 μM) was attained at 168 V/cm, which is the maximum voltage of an SV1100 machine. All peak intensities of monosacharides using a heterogeneous buffer were higher than those obtained in ref. 1, in which a homogeneous buffer was used, by a factor of 9 (Fig. 1). The detection limits were increased by a factor of two at least and nine at the best using the current heterogeneous buffer: 0.097 μM for Glc and <0.5 μM for other monosaccharides (Fig. 2). The mechanism of the enhanced fluorescence intensity is unknown at this moment. Because the peaks of electropherograms that we obtained were not sharp, we can rule out a possibility that an on-line concentration enhances fluorescence intensity in the current work. The fluorescence intensity of AMAC, which is a neutral dye, was almost independent of TRIS concentrations and pHs (Fig. 3). Detailed analysis is in under way to understand the mechanism of the enhanced fluorescence intensity.

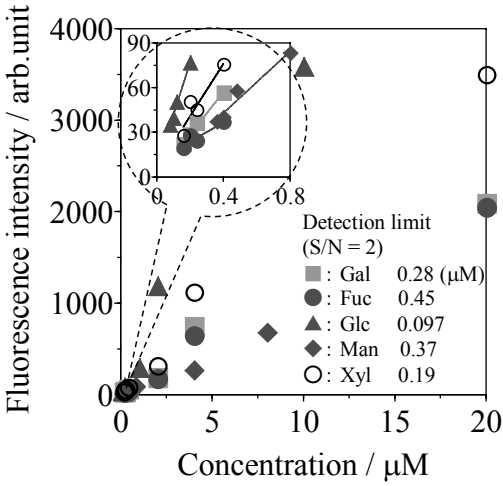

Figure 2. Dependence of fluorescence intensity on concentration of AMAC-labeled neutral monosacchardes.

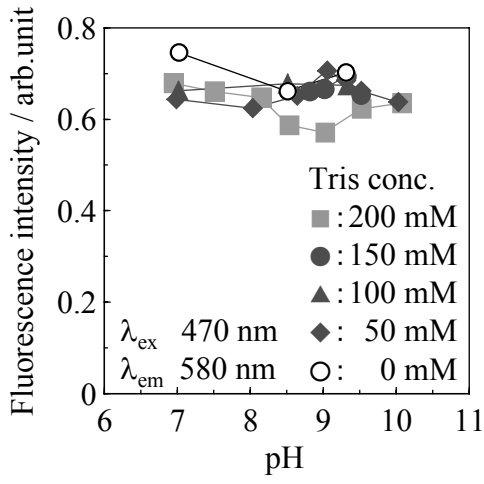

Figure 3. Effect of Tris concentrations and pHs on the fluorescence intensity of neutral monosaccharides. AMAC labeled monosacchaides at a concentration of 28.6 μM were measured using a spectrofluorometer (RF-5300PC, Shimadzu, Kyoto)

4. CONCLUSIONS

We report that the detection sensitivity of monosaccharides was improved by a factor of 9 using a heterogeneous buffer. The current attainment is fully compatible with that of conventional CE technique although the mechanism of the enhanced fluorescence intensity is unknown. The use of a heterogeneous buffer improved fluorescence intensity, thereby allowing us to develop efficient tools for highly-sensitive detection of monosaccharides.

REFERENCES

[1] E. Maeda, K. Hirano, Y. Baba, H. Nagata, M. Tabuchi, *Conformational separation of monosaccharides of glycoproteins labeled with 2-aminoacrydone using microchip electrophoresis*, Electrophoresis, 27, pp. 2002-2010, (2006).

PROGRAMMABLE MAGNETIC CELL SORTER FOR DIFFERENT SIZE USING LOCAL MAGNETIC FIELDS GENERATED BY CONTROLLING CURRENT UNDER EXTERNAL FIELD

Jaehoon Chung, Hyung-Kew Lee, Young-Ji Kim and Euisik Yoon
Department of Electrical and Computer Engineering, University of Minnesota, USA

ABSTRACT

This paper presents a programmable magnetic cell sorter to seperate different-sized cells. The cell sorter consists of a series of seperating units, comprising ferromagnetic nickel lines and current-carrying gold lines. The magnetized nickel lines and the current of gold lines can generate local field and attract the cells coated with magnetic nanoparticles. By changing the current, we could control the local magnetic field, which enables the device to sort the target cell sizes selectively. We successfully demonstrated this scheme by sorting three different sizes (6, 10, and 15 μm in diameter) of magnetic beads under the different current of 21, 37, and 68mA/line to the gold lines in the fabricated microfluidic chip.

Keywords: magnetic nanoparticle, cell sorter, programmable, microfluidic

1. INTRODUCTION

Specimens obtained from patients contain target cells as well as other cells. For effective drug screening, it is desirable to collect only target cells of a specific size with small variation. A macro magnetic sorter can separate target cells; however, the screened cells are not 100% pure and their sizes vary in a wide range. We have developed a microfluidic magnetic cell sorter which enables to separate cells by size which are coated with magnetic-nanoparticles. The principle of operation is based on the phenomenon that magnetic particles move to the minima of magnetic energy [1]. We designed a programmable magnetic cell sorting scheme combining ferromagnetic layers and current-carrying metal lines to precisely control local magnetic fields.

2. WORKING PRINCIPLE

Figure 1 shows the operation principle of the proposed microfluidic magnetic sorter. Each stage consists of two guiding elements: ferromagnetic lines and current-carrying lines. The ferromagnetic lines generate energy minima by concentrating the external magnetic field provided by permanent magnets [2]. The current-carrying lines generate the local energy minima at the edges [3]. By changing the amount of current, we can control the local magnetic force on cells. The operation principle of each stage is as follows. As the injected cells approach the ferromagnetic lines, they are attracted and move to the center of the channel (A → B) as a combination of magnetic and hydrodynamic force. Laminar flow of the microchannel maintains the cells in the center stream (B → C). When the cells reach the current-carrying lines, the local magnetic field attracts the cells and loads them into the microwell (C → D). Cascading of the ferromagnetic and current-carrying lines enables cell sorting in various sizes by programming the current in each stage. The size of the attracted cells depends on the amount of current; as we increase the current, larger cells are attracted.

978-0-9798064-0-7/μTAS2007/$20©2007CBMS

More stages can be added for different currents and the number of stages can be extended to meet the sorting purpose.

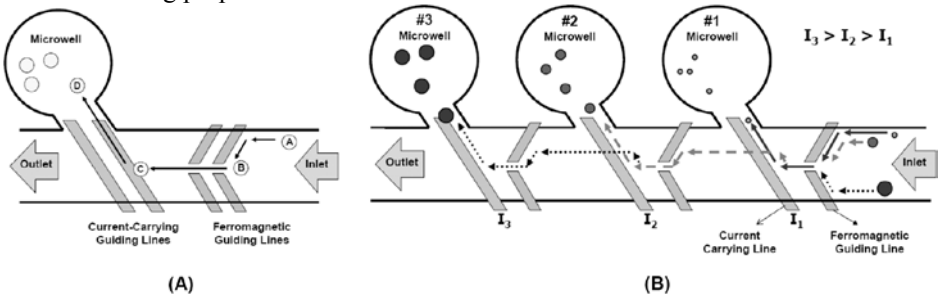

Figure 1. Operation princle of magnetic cell sorting: (A) Single stage, (B) Sorting the magnetic nanoparticle-coated cells of three different sizes by cascading three stages in series.

3. EXPERIMENTAL

To demonstrate the feasibility of the idea, we have fabricated a prototype with three stages by bonding a PDMS microchannel structure to the silicon substrate patterned with nickel ferromagnetic layers and gold current-carrying lines (Figure 2 and 3). We tested our device using three different-size magnetic beads (6, 10, and 15μm in diameter, polymer microbeads coated with magnetite to emulate the cells), which were suspended in DI water with equal concentrations (4×10^5 beads/ml). The suspended magnetic beads were injected using a syringe pump at 0.16μl/min flow rate. To apply the external magnetic field, two permanent magnets were placed in both sides parallel to the microchannel. The experimental setup was shown in Figure 4.

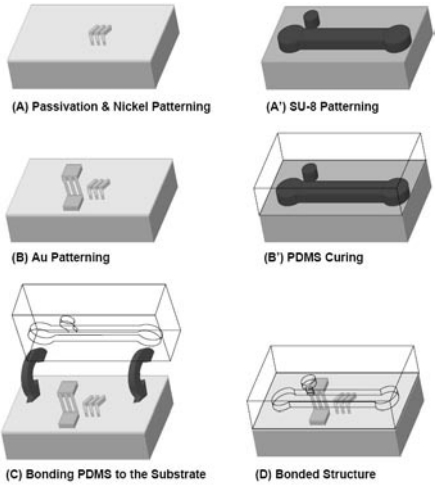

Figure 2. Fabrication Process: (A) and (B) Patterning of nickel ferromagnetic layers and gold current-carrying lines on silicon substrate; (A') and (B') SU-8 Patterning for a master mold and PDMS replica formation; (C) Bonding the PDMS replica to the substrate; and (D) completed structure

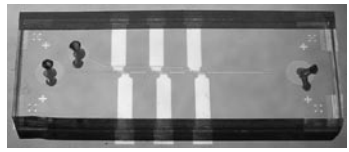

Figure 3. The fabricated microfluidic magnetic cell sorter

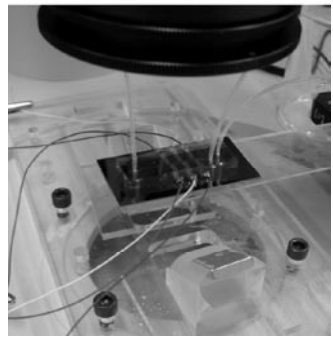

Figure 4. Experimental Setup. Device was monitored during operation by a microscope. The position of devices was controlled by a microstage.

4. RESULTS

Magnetic beads were separated in different sizes and captured in the corresponding microwells by applying different currents (21, 37, and 68mA/line) to each stage. We successfully collected 6μm, 10μm and 15μm beads in microwell #1, microwell #2, and microwell #3, respectively (Figure 5). Around 90% of all the captured beads were collected in the corresponding microwells. The errors were mainly due to unstable flow generated from syringe pump.

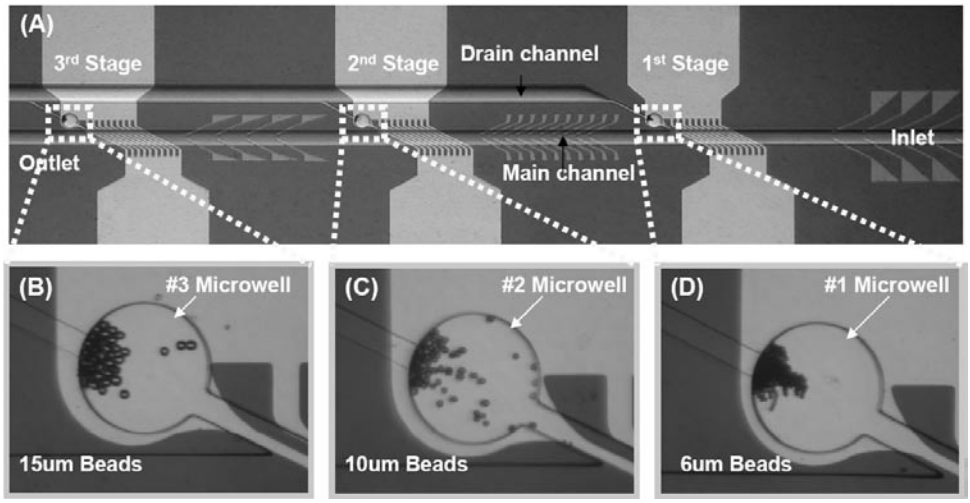

Figure 5. Experimental sorting results: (A) Overall structure of the sorting device, (B) 15μm beads captured in the third microwell, (C) a 10μm bead captured in the second microwell and (D) 6μm beads captured in the first microwell.

5. CONCLUSIONS

Magnetic cell sorter capable of separating different size of cells has been successfully demonstrated. In order to test the device, the solution of 6, 10 and 15 μm magnetic beads in diameter, was injected and the beads were separately collected in the corresponding microwells respectively by adjusting the current in each stage (21mA/line, 37mA/line, and 68mA/line). Around 90% of beads were captured into the target microwell and the error was primarily due to the unstable flow from syringe pump. This sorting device can be programmed by controlling current for different sizes and can be easily extended by adding more stages.

REFERENCES

[1] T. Deng, G. M. Whitesides, M. Radhakrishnan, G. Zabow, M. Prentiss, *Manipulation of magnetic microbeads in suspension using micromagnetic systems fabricated with soft lithography*, Applied Physics Letters, 78, 1775, (2001).

[2] D. W. Inglis, R. Riehn, R. H. Austin, J. C. Sturm, *Continuous microfluidic immunomagnetic cell separation*, Applied Physics Letters, 85, 5093, (2004).

[3] H. Lee, A. M. Purdon, R. M. Westervelt, *Manipulation of biological cells using microelectromagnet matrix*, Applied Physics Letters, 85, 1063, (2004)

TRANSLOCATION OF THE RIBOSOME IN TEMPERATURE-CONTROLLED MICROFLUIDIC CHANNELS

Bin Wang, Jingyi Fei, Ruben L. Gonzalez and Qiao Lin
Columbia University, USA

ABSTRACT

This paper reports on the application of temperature-controlled microfluidic channels for the single-molecule study of the temperature-dependent tRNA-mRNA translocation in the ribosome. Multiple parallel microchannels are formed between a quartz slide and a glass coverslip that is integrated with on-chip heaters and resistive temperature sensors. At precisely controlled temperatures, the fluorescent decay of single dyes is recorded, and the translocation time is analyzed to reveal the temperature-dependent behavior in tRNA-mRNA translocation.

Keywords: temperature-controlled microchannels, single-molecule studies, ribosome, translocation

1. INTRODUCTION

With sensitive kinetic assays enabled by single-molecule fluorescent spectroscopy and microscopy techniques, single-molecule studies of the translocation of the tRNA-mRNA complex within the ribosome, a fundamental step during protein biosynthesis, have drawn much attention lately [1]. In general, ribosomal translocation has a significant dependency on temperature. Such studies, therefore, require fast and accurate well-controlled environment within precise locations. However, conventional temperature control methods are cumbersome and inflexible, and are therefore not suited to single-molecule studies.

Due to its ease in integrating microscale thermal elements, MEMS technology has the potential to enable effective and accurate temperature control in a micro environment tailored to the needs of single-molecule studies. We have previously shown the detection of temperature-dependent photobleaching of single fluorophores in microchannels [2]. Here we present the application of microfluidics to single-molecule studies of the kinetics of mRNA-tRNA translocation within the ribosome at multiple, precisely controlled temperatures. Multiple parallel microchannels are integrated with heaters and temperatures sensors, and embedded within a total internal reflection fluorescence (TIRF) set-up. Analysis of measurement data at varying temperatures reveals a temperature-dependent change in the translocation rate, implying the existence of at least one temperature-dependent step in mRNA-tRNA translocation.

2. EXPERIMENTAL

The microfluidic device consists of parallel microchannels sandwiched between a quartz slide derivatized with biotin-polyethylene glycol and a microfabricated coverslip incorporating temperature-control elements (Fig. 1a). The device is outfitted onto the stage of a TIRF microscope (Fig. 1b). Temperature control is realized through the adjustment of heater load currents in response to a real-time feedback loop using temperature sensors

978-0-9798064-0-7/μTAS2007/$20©2007CBMS

underneath the microfluidic channels (Fig. 1c). Fluorescence is detected by a high numerical aperture objective and recorded by a CCD camera.

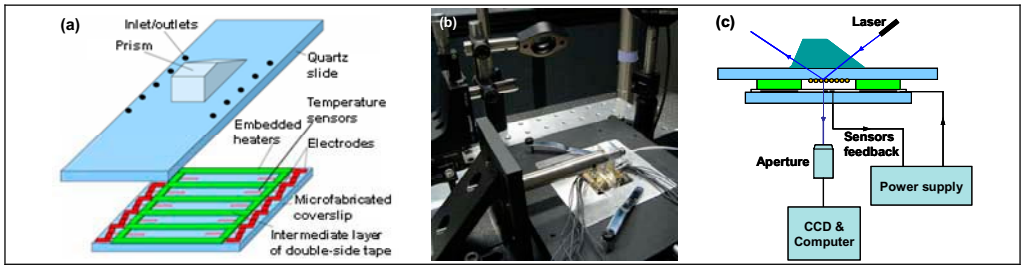

Fig. 1 (a) Device schematic. (b) Outfitted TIRF stage. (c) Temperature control scheme.

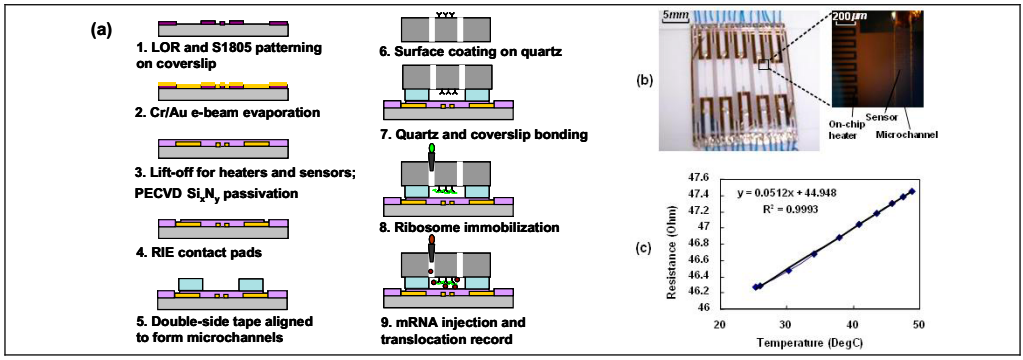

Fig. 2 (a) Fabrication and surface functionalization process. (b) Packaged device with a heater and temperature sensor near an inlet. (c) Characteristics of a typical temperature sensor.

The device is fabricated (Fig. 2a) on a glass coverslip by lift-off to form Cr/Au (5/200 nm) heaters and resistive temperature sensors, which are passivated by PECVD silicon nitride (300 nm). The coverslip is then bonded to a derivatized quartz slide with a spacer layer defining the microchannels (Fig. 2b). From calibration, a typical temperature sensor (Fig. 2c) has a reference resistance of 46.30 Ω with a temperature coefficient of resistivity (TCR) of 1.14×10-3 /˚C and a linear similarity of 99.93%. Accordingly, a temperature measurement resolution of approximately 0.02 ˚C can be achieved.

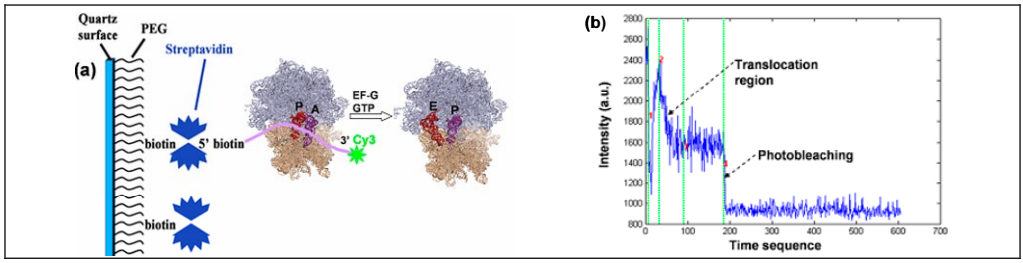

Fig. 3 (a) Surface functionalization scheme and ribosome translocation mechanism. (b) Typical fluorescent decay of a single dye.

Fluorescently-labeled mRNA undergoes a 10%-20% decrease of fluorescence emission intensity upon translocation, providing a direct measure of translocation rates for individual ribosome immobilized onto the microfluidic channel [3]. During experiments, ribosomal complexes containing a 5'-biotinylated/3'-Cy3-labeled mRNA and an initiator tRNA are in

vitro assembled, purified, and subsequently immobilized via biotin-streptavidin-biotin interaction on a derivatized quartz slide (Fig. 3a). Translocation is then initiated by aminoacyl-tRNA, in complex with elongation factor Tu and GTP, and elongation factor G, in complex with GTP [1]. Fig. 3b presents a typical single-molecule fluorescence intensity trace as a function of time.

3. RESULTS AND DISCUSSION

Translocations are measured at controlled temperatures of 22 (room temperature), 25, 31, 34, and 37 ˚C, respectively. The time required for translocation (i.e., translocation lifetime) on a single ribosome is defined as the time for the gradual decrease in fluorescence intensity to plateau. Fig. 4a shows the population histogram of the translocation as a function of time interval after initial exposure to the inducing laser light and its fitting to a sigmoidal distribution, through which the translocation lifetime can be obtained. The population results (Fig. 4b) at different temperature setpoints show a decrease in translocation lifetime (Fig. 4c), or an increase of translocation rate, with temperature. Such single-molecule results are consistent with bulk measurements [3].

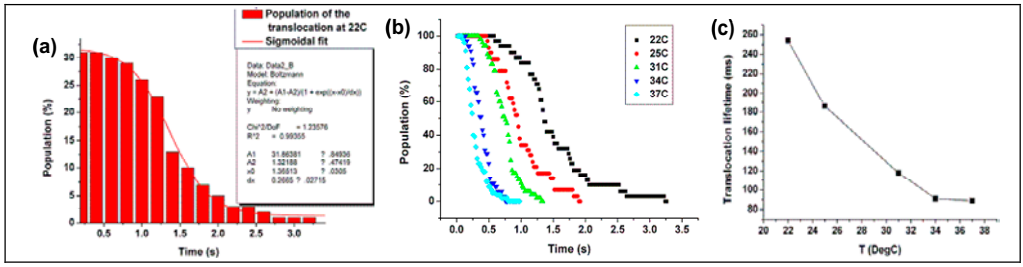

Fig. 4 (a) Population histogram of the translocation as a function of time at 22 ˚C. (b) Population of the translocation and (c) translocation lifetimes at different temperatures.

4. CONCLUSIONS

We have presented the application of microchannels with integrated temperature control to the study of tRNA-mRNA translocation in the ribosome. With on-chip heaters and temperature sensors, translocation at controlled temperatures has been measured, revealing significant temperature-dependent translocation rates. These results demonstrate the capability of this device for temperature-dependent kinetic studies at the single-molecule level with higher accuracy and sensitivity than afforded by conventional technology.

ACKNOWLEDGEMENTS

This work was supported by the National Science Foundation (Grant No. CBET-0639274).

REFERENCES

[1] S. C. Blanchard, et al. *tRNA dynamics on the ribosome during translation*, PNAS, 101, 12893-12898 (2004).

[2] B. Wang, et al. *Single-Molecule Detection in Temperature-controlled Microchannels*, IEEE-NEMS, Bangkok (2007).

[3] S. M. Studer, et al. *Rapid Kinetic Analysis of EF-G-dependent mRNA Translocation in the Ribosome*", J. Mol. Biol., 327, 369-381 (2003).

AN INTEGRATED PROTEIN ANALYSIS CHIP: ON-CHIP COMBINATION OF IMMUNOAFFINITY CHROMATOGRAPHY AND ISOELECTRIC FOCUSING

Kiyohito Shimura and Takehiko Kitamori

Dept. of Applied Chemistry, School of Engineering, The University of Tokyo

ABSTRACT

The integrated protein analysis chip was designed and fabricated. It allows precise identification and quantification of a specific protein by the double criteria of immunochemical reactivity and isoelectric points in a short time and with a small amount of a sample.

Keywords: Protein analysis, immunoaffinity chromatography, isoelectric focusing, isoelectric point

1. INTRODUCTION

Immunoassay is widely used for identification and quantification of a protein in a complex sample matrix. Nonspecific binding and cross-reactivity of the antibodies sometimes compromise the assay results. These problems can be solved by the use of double criteria for identification of protein, e.g., Western blotting, the use of molecular size and immunochemical reactivity. Previously, we suggested the integration of immunoaffinity chromatography (IAC) and isoelectric focusing (IEF) on a chip [1]. In this paper, we report a new chip that enables the direct coupling of IAC and IEF.

2. EXPERIMENTAL

A Tempax glass plate (0.7 x 30 x 70 mm) was etched to make channels of 200-µm wide and 90 µm deep, and bonded to the plate of the same size with holes for chip ports (Fig. 1). A dam structure of a height of 80 µm was made by two-step etching to retain chromatographic packing in the channel. The inner wall of the channel was covalently coated with polydimethylacrylamide to suppress electroosmosis and protein adsorption. The chip was assembled with the holder having eight on-chip connector valves (Fig. 2) [2]. Electrodes were placed outside the valves and connected to the ends of the IEF channel with electrode solutions containing 0.5% hydroxypropylmethylcellulose (Fig. 2 and 3).

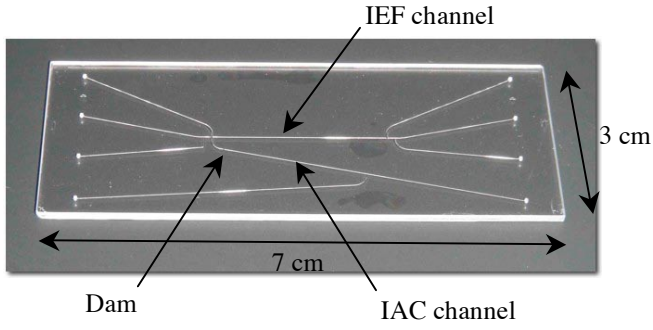

Figure 1. IAC-IEF chip.

978-0-9798064-0-7/µTAS2007/$20©2007CBMS

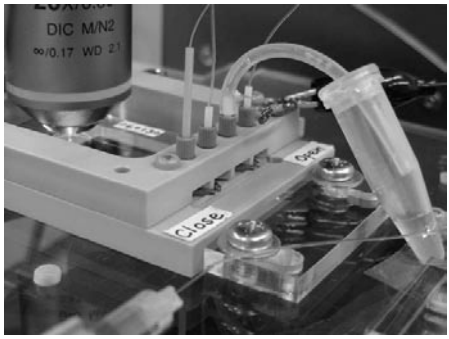

Figure 2. IAC-IEF chip assembly with the holder and the electrode.

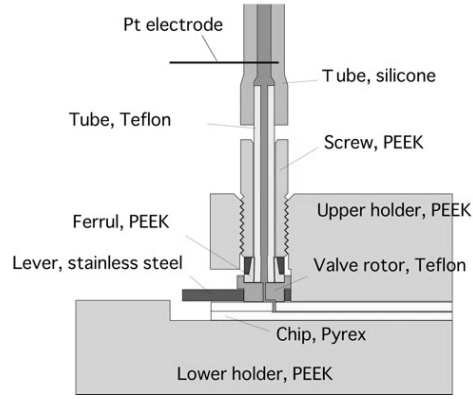

Figure 3. The section of the on-chip connector valve and the electrode.

3. RESULTS AND DISCUSSION

To demonstrate the IEF separation in the chip, the mixture of four tetramethylrhodamine labeled peptide pI markers dissolved in 2.5% (v/v) Pharmalyte 3-10 was introduced in the IEF channel (24 mm long) and focusing was done at 1 kV for 2 min [3]. The IEF channel was scanned with a laser at 532 nm, and fluorescence was detected. Four pI markers were separated with almost linear relationship between the pI values and the distance between the peaks, indicating the formation of the pH gradient expected for the carrier ampholyte used (Fig. 4 and 5).

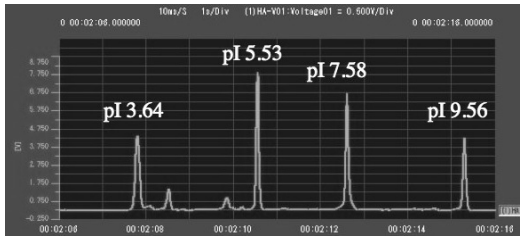

Figure 4. IEF separation of four fluorescence-labeled peptide pI markers at 1 kV for 2 min.

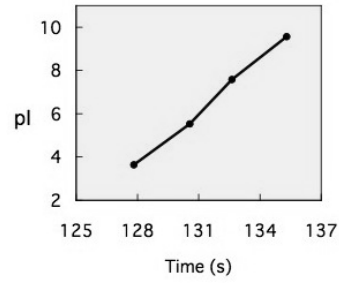

Figure 5. The relationship between pI and scan time at a constant scanning speed.

The column channel was filled with the agarose gel beads on which anti-E tag antibody was immobilized. The recombinant Fab fragment bearing E tag (pentadecapeptide affinity tag) was labeled with tetramethylrhodamine at a specific cysteine residue and purified by IEF in a gel. The labeled Fab fragment (0.1 μM, 0.1 μL) was injected to the chip equilibrated with the Pharmalyte solution from an external injector. The column was washed, and the bound protein was eluted with 6 M urea in the Pharmalyte solution (Fig. 6).

When eluted peak reached to the IEF channel, the column flow was stopped, and the sample in the IEF channel was subjected to IEF separation. The focusing for 2 min revealed one sharp peak for the Fab fragment (Fig. 7), indicating successful operation of IAC in the chip. We are planning applications to samples with more complex sample matrices.

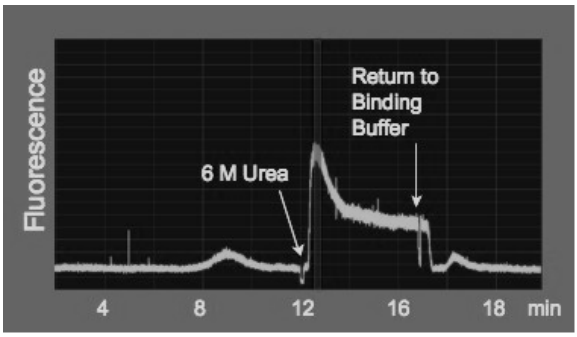

Figure 6. Immunoaffinity chromatography of labeled Fab (10 fmol) on the anti-E tag column. The red-labeled peak fraction was analyzed by IEF.

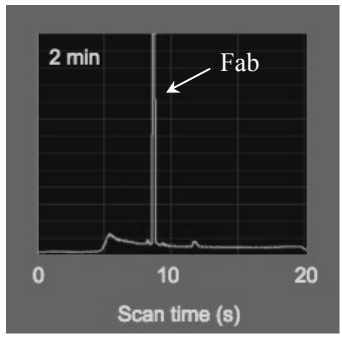

Figure 7. IEF separation of the peak eluted with 6 M urea in Figure 6. Focusing at 1 kV for 2 min.

4. CONCLUSIONS

In many field of biochemical analysis, rapid and accurate immunochemical detection is being required. The integration of immunoaffinity chromatography and isoelectric focusing on a chip is a promising solution for this requirement.

REFERENCES

[1] Y. Koyama, T. Kitamori, and K. Shimura, "A protein analysis chip integrating affinity chromatographic column and isoelectric focusing channel", Proc. Micro Total Analysis Systems 2006, Society for Chemistry and Micro-Nano Systems (CHEMINAS), Tokyo, pp. 939-941 (2006)

[2] K. Shimura, Y. Koyama, K. Sato, and K. Kitamori, "On-chip connector valve for immunoaffinity chromatography in a microfluidic chip", *J. Sep. Sci.* (in press, published online 29 May 2007)

[3] K. Shimura, K. Kamiya, H. Matsumoto, and K. Kasai, "Fluorescence-labeled peptide pI markers for capillary isoelectric focusing", *Anal. Chem.*, **74**, 1046-1053 (2002)

ASYMMETRIC INERTIAL MIGRATION IN CURVILINEAR LAMINAR FLOWS FOR MICRO-SEPARATION

J. Seo, M. H. Lean, and A. Kole
Palo Alto Research Center, USA

ABSTRACT

Membrane-free microseparation by asymmetric 'tubular pinch' effect is studied. Fluid in laminar flow in a curved channel, experience a centrifugal force which perturbs lateral symmetry of particle concentration at the tubular pinch equilibrium. Bifurcated outlets separately collect the particle suspension and process fluid. The spiral continuous filtration relies solely on internal fluidic shear characteristics, eliminating the need for membrane-filters or external force-fields. This device has the potential for high-throughput and low cost for preparative filtration at both macro and micro scales.

Keywords: Microfluidics, particle separation, asymmetric tubular pinch effect, asymmetric inertial migration

1. INTRODUCTION

We present a new separation technology based solely on intrinsic flow characteristics in curvilinear channels. Dispersed particles in a curvilinear channel at low Reynolds numbers make transverse migration and become ordered for micro-separation. The transverse particle migration involves competition between three effects from shear flows: the tubular pinch effect (TP effect) [1], centrifugal force, and Dean's vortex [2-3], resulting in counterintuitive ***'inside'*** particle concentration.

Laminar flows in curved channels involve both centrifugal and perturbed lateral forces in addition to the TP effect, resulting in asymmetric lateral inertial migration (Fig. 1). The centrifugal force on particles competes with three forces from the TP effect. The centrifugal force on a fluid induces the transverse secondary flow or Dean vortex due to fluidic continuum. Particulates entrained within the fluid circulate with the Dean vortex until they loop around to the inner wall. Force balance establishes stable equilibrium positions near the inside fluidic walls depending on the size and mass of particles. Particles at separate equilibrium positions run into different outlets to achieve micro-separation.

2. EXPERIMENTAL

A double spiral microfluidic device demonstrated micro-separation in a curvilinear laminar flow (Fig. 2). The prototype fabrication for building the membrane-less spiral micro-separator employed soft-lithography with Polydimethylsiloxane (PDMS). Each spiral device has 12 turns and channels are designed to be 300 μm wide and 300 μm apart. The mold was prepared by patterning 100 μm thick SU-8 negative photoresist on a 100 mm silicon wafer. The pre-mixture with 10:1 ratio of base and curing agents was poured and

978-0-9798064-0-7/μTAS2007/$20©2007CBMS

cured on the mold. The detached devices were punched to accomodate 0.5 *mm* diameter holes for outside fluidic connections. The devices were then bonded on self-adhesive 500 μm thick silicon sheets.

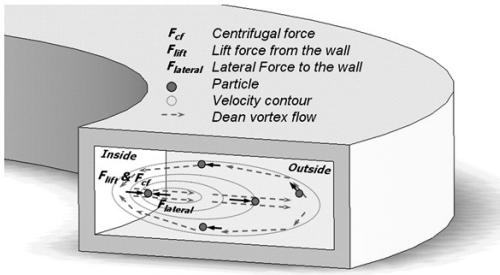

Figure 1. Asymmetry inertial migration.

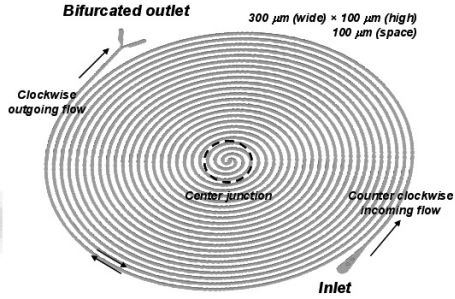

Figure 2. A double-spiral design to maximize separation efficiency.

3. RESULTS AND DISCUSSION

A flow of 10 μm polystyrene beads clearly exhibits inside micro-separation as shown in Fig. 3. A dispersed particle suspension was introduced into an inlet with average flow velocity of 184 mm/s. A clean particle band was developed at outlets. The inside outlet collected concentrated particles while clear water flowed out through the outside outlet.

To confirm the effect of particle size on separation, a mixture of 3, 6, and 10 μm polystyrene beads was flowed though the spiral channel (Fig.2) at 184 mm/s. The collected samples from each outlet were compared by counting the number of particles (Z2™ COULTER COUNTER®, Beckman Coulter, CA, USA). The counting results are shown in Fig. 4. The concentration difference of 10 μm beads between the inside and outside outlet was two orders of magnitudes. No significant concentration difference were observed for 3 μm beads, indicating that higher velocity is needed for increased discrimination.

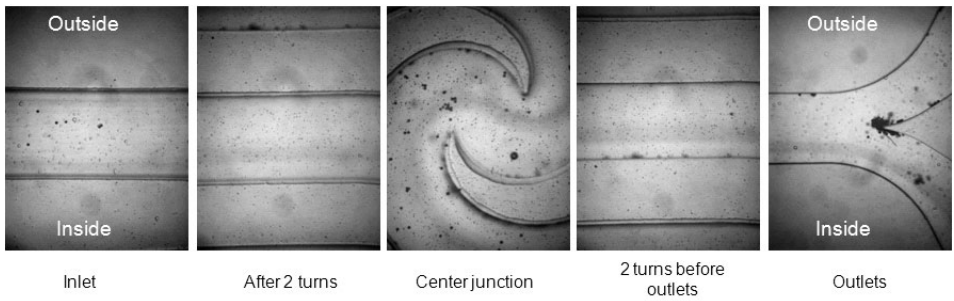

Figure 3. Sequential images along a fluidic path. Dispersed particles at the inlet form into a band near the inside wall at the outlets. (The fluid runs left to right or bottom to top at the mean fluidic velocity of 184 *mm/s*.)

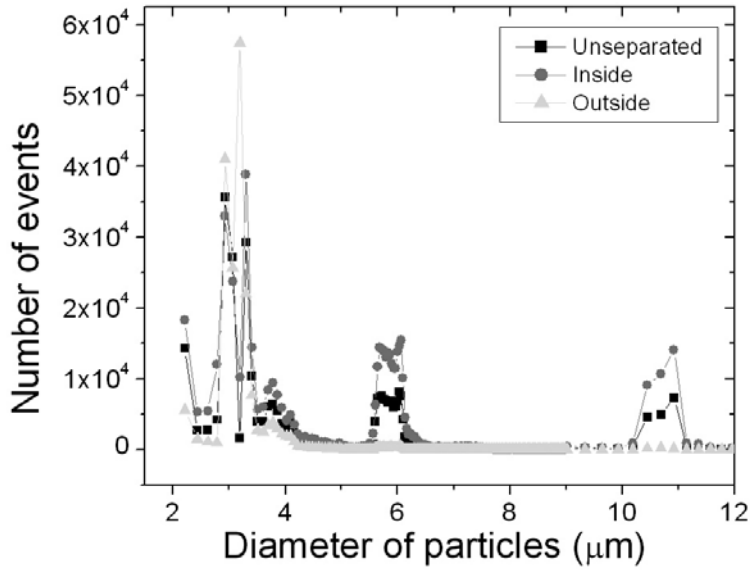

Figure 4. Particle counting results from separations of a mixture of 3, 6, and 10 μm polystyrene beads. The 6 and 10 μm beads show effective separation between the inside and outside collected samples.

4. CONCLUSIONS

In summary, a novel micro-separation technology and device based solely on intrinsic flow characteristics are presented. The intrinsic properties from shear flow in a curvilinear channel effectively separates particles with no physical filter interfaces or external fields involved. The TP effect and Dean's vortex including the centrifugal force causes transverse particle migration across flow stream lines. The efficiency of this process is a function of particle size with the given fluidic parameters, and can be further optimized for any given size range, channel width, and flow rate. Multi-stage separation can also be envisioned to increase efficiency. This spiral micro-separator can be applicable to separate bio-agents such as cells, bacteria, and other pathogens. Simplicity in the spiral micro-separation concepts allows great potential for miniaturization and standalone or in-line integration with other applications.

REFERENCES

[1] G. Segre and A. Silberberg, "Radial Particle Displacements In Poiseuille Flow of Suspensions," Nature 189, pp. 209-210 (1961).

[2] W. R. Dean, "Fluid Motion in a Curved Channel," Proc. R. Soc. London, Ser. A, 121(787), pp. 402-420 (1928).

[3] S. A. Berger, L. Talbot and L. –S. Yao, "Flow in curved pipes," Ann. Rev. Fluid Mech., 15, pp. 461-512 (1983).

CONFINEMENT EFFECT ON THE STRUCTURE OF POLYMER MONOLITHS PHOTOPATTERNED WITHIN MICROCHANNELS

M. He, Y. Zeng and D. J. Harrison
Department of Chemistry, University of Alberta, Canada

ABSTRACT

We report on confinement effects on the structure of polymer monoliths photopatterned within microchannels, as observed by laser scanning confocal microscopy (LSCM) and scanning electronic microscopy (SEM). The extent of deviation from bulk porous structures under confinement strongly depends on the ratio of space to monolith pore size. Significant deviations from bulk porosity are observed for confinement dimension to pore size ratios less than 5. A surface effect on structure evolution indicates that surface tension or wetting play a role. Confinement effects were employed to achieve thick wall coatings in open channels. Understanding confinement effects is critical for designing integrated microfluidic and nanofluidic devices with polymerized monoliths.

Keywords: Confinement, polymer monolith, coatings, porosity

1. INTRODUCTION

Polymer monoliths have been widely used as an attractive alternative to particle packing in column preparation. The most appealing advantage of polymer monoliths for integrated multifunctional microsystems is the relatively simple preparation afforded by photopatterning. Integration of porous polymer monoliths into microfluidic devices has received increasing interest in many applications, such as mixers, reactors, solid-phase extraction, and separation [1]. Here we report that channel dimensions and surface chemistry may affect the porosity and nature of confined monolithic structures. This behavior is similar to that of sol-gel systems which become much more porous under confinement [2, 3]. This similarity occurs even though the polymerization mechanisms are quite different for the two materials. The random porous structure of polymer monoliths tend to deform and open up under tight confinement also, which makes it difficult to predict the structures that will be realized in a microchannel. We systematically investigated factors that affect structure using scanning electronic microscopy (SEM) and laser scanning confocal microscopy (LSCM), and show here that the ratio of channel to monolith pore size plays a strong role in the geometry of the product formed.

2. EXPERIMENTAL

At least 4 channels or capillaries were characterized for each monolith. To complement the SEM observations, LSCM was used to achieve nondestructive three-dimensional (3D) characterization of monolithic structures in glass chips (See Figure 1). A mixture of dimethyl sulfoxide and benzyl alcohol (4:1 v/v, refractive index ~1.5) containing Rhodamine dye was used to match the refractive index of monoliths for deep imaging.

3. RESULTS AND DISCUSSION

Direct visualization by LSCM has better depth resolution, and enables 3D visualization in a nondestructive manner [4], in contrast to SEM, while SEM images provide more graphically clear representation to the eye. A variety of polymer monoliths were prepared

978-0-9798064-0-7/μTAS2007/$20©2007CBMS

by UV-initiated free-radical polymerization in various diameter capillaries. Figure 1 shows the SEM and 3D reconstructed LSCM images of the various monoliths. As the diameter of the capillary decreased, the spatially random porous structure deformed, eventually evolving to an obvious layer attached to the wall of the capillary. The structures created in capillaries and microchannels are comparable. Comparison of SEM and LSCM images shows the same trends, although the LSCM images make it clear that there is some damage to the structure near the surface of the SEM cut. As a result the most representative SEM images were always used for the evaluation. The change in porous structure with capillary size was observed for all the polymer monoliths with different pore sizes that were studied. The structure deformation has onsets at differing confinement dimensions, dependent on the bulk pore size of the material. For both cylindrical and slot (or channel) geometry the smallest dimension of the confined space appears to be the controlling characteristic. A rough rule of thumb established from this study is that bulk-like porosity is observed for a confinement dimension to pore size ratio > 10, and significant deviation is observed for a ratio < 5.

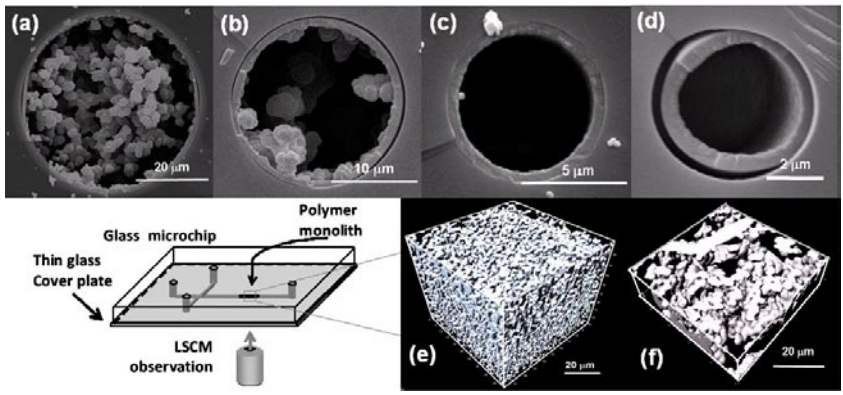

Figure 1. SEM and reconstructed LSCM images of polymerized monoliths formed in silica fused capillaries (a-d) and glass microchannels (e, f) with different diameters and depths. (a), (e) 50 μm, (b), (f) 20 μm, (c) 10 μm, (d) 5 μm. Polymerization condition: 2-hydroxyethyl methacrylate (HEMA) 12 wt%, Ethylene dimethacrylate (EDMA) 28 wt%, toluene 60 wt%, Benzoin 1 wt% of monomer, UV exposure at 312 nm for 16 mins. No treatment on the capillary or channel surface.

The effect of surface chemistry on the structure has also been studied. A hydrophilic polymer monolith deformed more under the influence of a hydrophilic surface at small diameters than it did at a hydrophobic surface. This can be seen from the volume fraction distribution profile in Figure 2. The density distribution shows a large decrease in material just outside the wall region, which reaches the extreme case of a wall coating and hollow interior, as the channel diameter decreases. This effect is more severe when both the surface and polymer are hydrophilic, indicating that surface tension or wetting play a role in structure formation. Our observations suggest a novel coating strategy taking advantage of surface wetting under confinement to create robust, thick wall coatings for applications such as EOF control, surface biocompatibility, and chromatography. Figure 3 shows a microchannel coated by a positively charged thin film of 150 nm used to reverse electroosmotic flow. An electroosmotic mobility of $\sim 2\times10^{-4}$cm^2/Vs was obtained, with a variability of ± 2 % over 15 days of use.

4. CONCLUSIONS

Recognition of the structural evolution of monoliths under confinement is critical for designing integrated microfluidic and nanofluidic devices with monoliths. The fact that a wall coating is obtained when the column is small enough, with an open central region provides a novel method to create coated capillary devices for open tubular chromatography, or for prevention of non-specific adsorption on capillary walls.

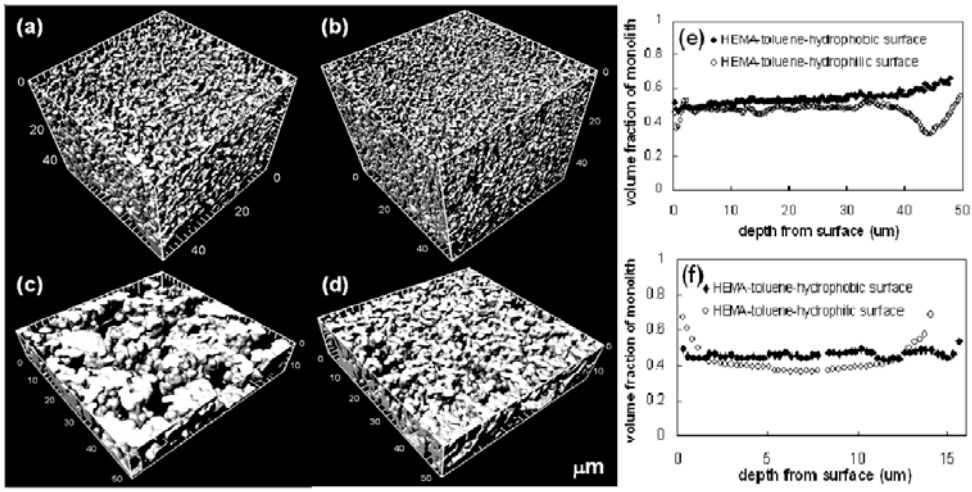

Figure 2. The structure morphology and volume fraction distribution profile of the monoliths in the microchannels with different surface chemistries: (a, c) hydrophilic surface created with 1-[3-(Trimethoxysilyl)propyl] urea and (b, d) hydrophobic surface created with triethoxy(octyl)silane. The monoliths were formed in (a, b) 50 μm and (c, d) 15 μm deep channels using the same polymerization conditions as in Figure 1.

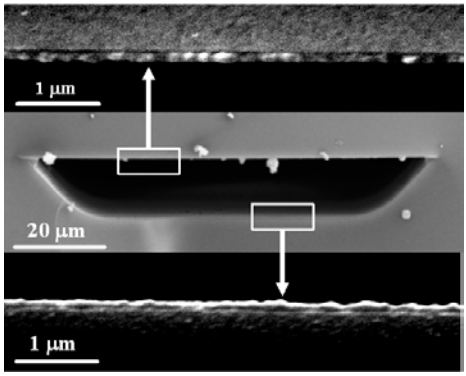

Figure 3. Cross sectional SEM images of the microchannel coated with a positively charged polymer layer. Polymerization conditions: HEMA 2 wt%, EDMA 4 wt%, [2-(methacryloyloxy) ethyl] trimethyl ammonium chloride (META) 4 wt%, toluene 90 wt%, UV exposure at 312 nm for 16 mins. Channel depth is 10 μm and width is 50 μm. The thickness of the polymer layer is about 150 nm.

REFERENCES

[1] F. Svec and J. M. J. Fréchet, Ind. Eng. Chem. Res., 38, 34 (1999).
[2] K. Kanamori, H. Yonezawa, K. Nakanishi, K. Hirao and H. Jinnal, J. Sep. Sci., 27, 874 (2004).
[3] U. Steiner, J. Klein, E. Eiser, A. Budkowski and L. J. Fetters, Science, 258, 1126 (1992).
[4] K. Kanamori, K. Nakanishi, K. Hirao and H. Jinnai, Langmuir, 19, 5581 (2003).

CONTINUOUS SEPARATION OF PROTEINS AND CELLS BY TWO-PHASE ELECTROPHORESIS IN MICROCHANNELS

G. Münchow[1], S. Hardt[2], J. P. Kutter[3] and K. S. Drese[1]

[1]Institut für Mikrotechnik Mainz GmbH, GERMANY,
[2]Leibniz Universität Hannover, GERMANY and
[3]Technical University of Denmark, DENMARK

ABSTRACT

This work reports on transport phenomena of proteins and cells observed in partitioning experiments with a novel setup for continuous-flow aqueous two-phase electrophoresis. After phase boundaries are formed in flow direction inside a microchannel, the system allows a continuous separation of proteins from cells. While proteins, here bovine serum albumin (BSA), overcome the phase boundary and, supported by an electric field, leave the phase they have been dissolved in almost completely, lymphoplastoid cells are retained, thus allowing a continuous separation of proteins from cells.

Keywords: two-phase flow, separation, electrophoresis, cells, proteins

1. INTRODUCTION AND THEORY

Aqueous two-phase systems (ATPSs) are widely used for the purification and isolation of biomolecules [1]. ATPSs are formed by dissolving small amounts of two incompatible polymers, such as polyethylene glycol (PEG) and dextran, or one polymer and a salt above a given concentration. Since both of the phases consist largely of water (80–90% (w/w)) ensuring a high biocompatibility and low interfacial tension, such systems lend themselves for an affinity-based separation of biomolecules. Here, biomolecule partitioning takes place due to different physico-chemical affinities of macromolecular species to the different polymers. These affinities and the transport resistance across the phase boundary depend on the properties of the biomolecule such as isoelectric point, surface hydrophobicity, molecular mass as well as on medium properties as polymer molecular mass, pH, and salt concentrations. By controlling these factors, the selective partitioning and recovery of a target biomolecule can be achieved.

First attempts in protein partitioning in ATPSs supported by an additional electric field have been undertaken in macroscale [2-3] but also in microscale [4] setups. Without an electric field ATPSs in microchannels have been mainly used for cell separation [5]. By contrast, we present a separation of a suspension of lymphoplastoid cells and proteins (bovine serum albumin) utilizing the fact that intact cells adhere to the phase boundary while proteins are able to pass it - both driven by an applied electric field perpendicular to the phase boundary.

3. EXPERIMENTAL

The immiscible aqueous phases are derived from a PEG – dextran system and injected separately into a microchannel (W x D x L: 0.8 x 0.1 x 25 mm), cf. Fig. 1., forming a two-phase flow with a stable boundary. The lower PEG phase contains a mixture of BSA molecules and lymphoplastoid cells. Sometimes gravity affects the partitioning behaviour

978-0-9798064-0-7/μTAS2007/$20©2007CBMS

of cells, but here their migration is perpendicular to the direction of gravity which eliminates its influence. In order to apply an electric field perpendicular to the trilaminar flow while preventing bubble generation by electrolysis inside the channel, the side walls are partially made of agarose gel material which serves as an ion conductor and fluidically decouples the channel from the electrodes. Further details about the microfluidic system used can be found in [4]. The proteins were labeled with fluorescence markers using the Alexa Fluor® 488 protein labeling kit. For cell labeling CFSE dye was used which reacts with the lysine side chains of cellular proteins and emits in a similar wavelength range as the Alexa label. The total flow rates used in the experiments were 0.05 and 0.03 ml/h for the upper and lower PEG phases and 0.008 ml/h for the dextran phase, respectively.

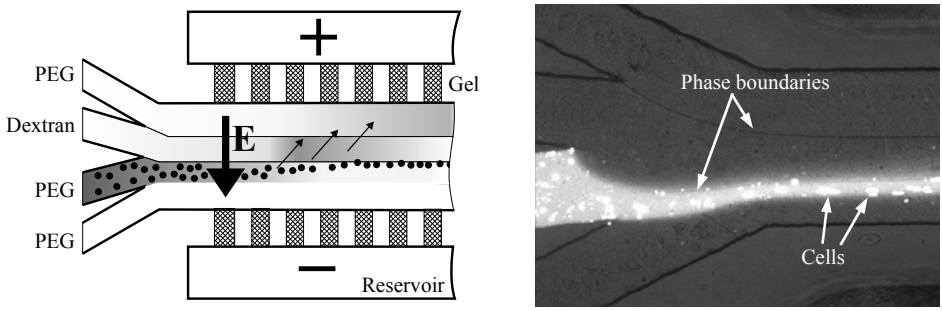

Figure 1. Left: Schematic showing the transport of proteins and cells in a trilaminated two-phase system. Below a critical electric field strength the cells are trapped at the phase boundary. Right: Entrance of the separation channel. Cells (fluorescent dots) and proteins (background fluorescence) are contained in the lower PEG phase.

4. RESULTS AND DISCUSSION

At the entrance of the separation channel both proteins and cells are dissolved in the same PEG phase, cf. Fig. 1. Without an electric field and once the different phases get in contact, diffusion of proteins into the dextran phase is observed. Halfway along the channel the cells are randomly distributed within their preferred PEG phase while the proteins diffuse not only into the neighboring dextran phase but also into the gel matrix.

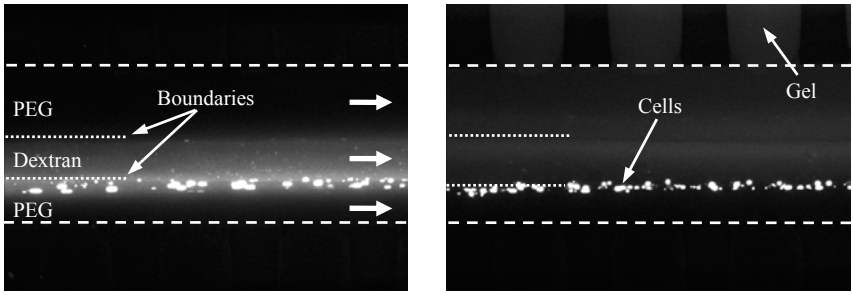

Figure 2. Left: Halfway along the channel at 4 VDC. Proteins have been partially transported into the dextran phase, cells are retained at the phase boundary. Right: End of the channel at 4VDC. Cells have been trapped in their preferred phase and collected at the phase boundary while the proteins have already crossed the intermediate dextran phase and reached the upper PEG phase of the trilaminated flow.

After applying an electric field the proteins start to move into the central dextran phase and finally, near the outlet of the channel, into to upper PEG phase and gel matrix, cf. Fig. 2. By contrast, the cells are retained by the phase boundary and stay in their preferred PEG phase. A further increase of electric field strength would force them to cross the boundary continuing their electrophoretic migration towards the positive electrode, cf. Fig. 3. But below this critical field strength 100% of the cells are found in the PEG phase, lined up at the phase boundary like pearls on a string.

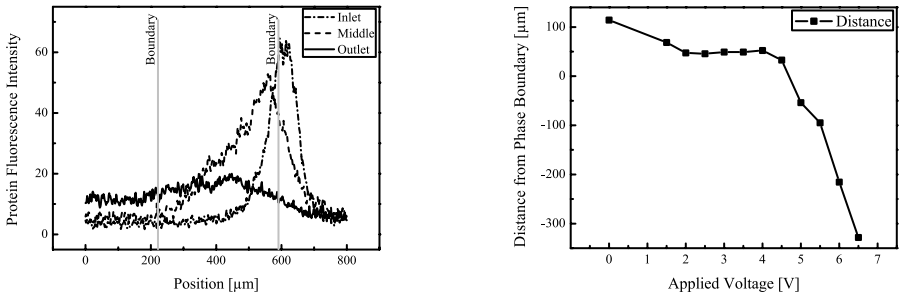

Figure 3. Left: Fluorescence intensity profiles of proteins across the channel near the inlet of the channel, halfway along the channel and near the outlet at 3.5 VDC. Right: Maximum distance of a cell from the phase boundary at different electric field strengths near the outlet. At 4.5 VDC the cells start to penetrate the boundary and resume their electrophoretic motion.

5. CONCLUSIONS

As a preliminary conclusion, it follows that microfluidic systems making use of electrophoretic transport in ATPSs offer a high potential for different kinds of purification and separation processes involving proteins and cells. In the present case, such a system was used for the separation of cells and proteins, exploiting the local accumulation of cells at the phase boundary which is permeable for proteins.

ACKNOWLEDGEMENTS

This work is supported by the German Research Foundation, priority program 1164.

REFERENCES

[1] P. Å. Albertsson, *Partition of cell particles and macromolecules*, 3rd ed., Wiley, New York, USA (1986).

[2] M. L. Levine and M. Bier, *Electrophoretic transport of solutes in aqueous two-phase system*, Electrophoresis, 11, pp. 605-611, (1990).

[3] W. M. Clark, *Electrophoresis-enhanced extractive separation*, Chemtech, 22, pp. 425-429, (1992).

[4] G. Münchow, S. Hardt, J. P. Kutter and K. S. Drese, *Electrophoretic partitioning of proteins in two-phase microflows*, Lab Chip, 7, pp. 98-102, (2007).

[5] M. Yamada, V. Kasim, M. Nakashima, J. Edahiro and M. Seki, *Continuous cell partitioning using an aqueous two-phase flow system in microfluidic devices*, Biotechnol. Bioeng., 88, 489-494, (2004).

CONTINUOUS-FLOW PI-BASED SORTING OF PROTEINS AND PEPTIDES FOR ISOLATION OF BASIC PI RANGE MOLECULES

Yong-Ak Song, Chris Celio and Jongyoon Han

Department of Electrical Engineering and Computer Science / Department of Biological Engineering, Massachusetts Institute of Technology, USA

ABSTRACT

A novel continuous-flow isoelectric point (pI)-based sorting technique has been developed for proteins and peptides in PDMS microfluidic chip. As a free-flow electrophoresis, it can continuously sort the biomolecules at a relatively high flow rate up to 5μL/min. The electrophoretic field required for the separation of biomolecules can be generated either by the diffusion potential or by an external power source in combination with the diffusion potential field. As for applying an external electric field, we have developed a simple patterning technique to generate a nanogap junction between the main sorting channel and the electrode reservoirs. This junction allows an effective integration of the external electric field into the sorting channel. Using the hybrid sorting technique, we could demonstrate a pI-based sorting of proteins and peptides even in basic pH ranges.

Keywords: Separation, Proteins, Peptides, Free-Flow Electrophoresis

1. INTRODUCTION

Free-flow electrophoresis allows a high-throughput fractionation of biomolecules according to the mass-to-charge ratio. Since no carrier ampholytes are required for this sorting process, interference of these small molecules with subsequent sensing steps, such as MS (mass spectrometry), can be eliminated. Exploiting this separation principle, we have developed a continuous-flow sorting scheme to isolate proteins and peptides within predetermined pI range out of complex protein mixtures. While the diffusion potential generated *in-situ* at the liquid junction between two laminar flows can be used [1, 2], we have developed a "hybrid" sorting method by integrating an external field into the sorting process in order to achieve higher sorting efficiency. Such method can be successfully applied in sorting biomolecules in basic pH ranges, which is difficult to achieve with the current isoelectric focusing techniques.

2. EXPERIMENTAL

All experiments were performed in microfluidic channel made of polydimethylsiloxane (PDMS) (Sylgard 184, Dow Corning Inc., Midland, MI). The separation channel was 100-1000 μm wide, 2000 μm long and 10 μm deep. Three IEF markers (Sigma-Aldrich, St. Louis, MO) with pI's of 5.1, 7.2 and 10.3 as well as rhodamine 6G and bodipy dye were used for the experiment.

3. RESULTS AND DISCUSSION

For the fabrication of the sorting device, we coated the glass substrate partially with an ultrahydrophobic solution, Teflon, using the reversibly bonded PDMS microchannels. Then,

978-0-9798064-0-7/μTAS2007/$20©2007CBMS

we plasma bonded the patterned substrate with a PDMS device. Due to the hydrophobicity of Teflon, the submicron thin stripes generate nanogap junctions between the main sorting channel and the side channels connected to the reservoirs, as shown in Figure 1. These junctions allow application of an external electric field up to 400 V/cm without concentration polarization and bubbles.

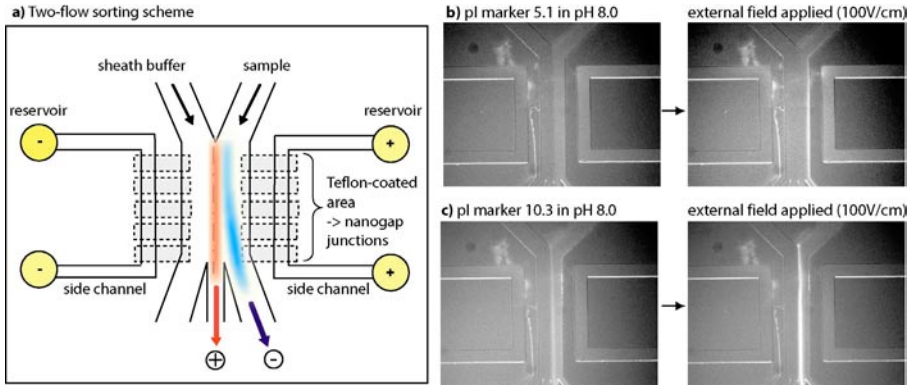

Figure 1. a) Schematic of the two-flow sorting scheme. b) Deflection of negatively (pI 5.1) and c) positively charged (pI 10.3) pI markers in pH 8.0 phosphate buffer solution under an external electric field of 100 V/cm. The negatively charged pI marker 5.1 was deflected towards the anode on the right side when an external field of E=100 V/cm was applied. The positively charged pI marker 10.3 was focused to the liquid junction in the middle of the sorting channel close to the cathode.

In addition to the two-flow sorting, a three-flow sorting with the hydrodynamically focused sample has also been realized, as shown in Figure 2.

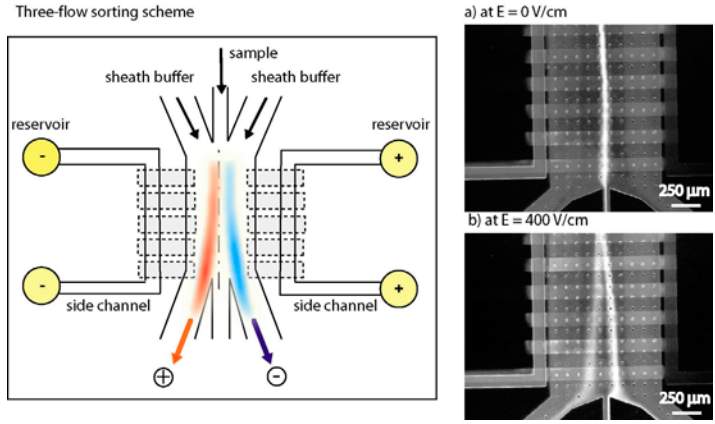

Figure 2. Three-flow active binary sorting of two dyes in pH 8.0 phosphate buffer solution with an external electric field of 400 V/cm. The sample mixture was injected into a 1mm wide sorting channel using hydrodynamic focusing. Once an external field was turned on, the negatively charged bodipy was deflected to the right outlet, while the positively charged rhodamine 6G was deflected to the left outlet.

To demonstrate a pI-based isolation with our sorting technique, we first sorted a mixture of three pI markers 10.3, 7.2 and 5.1 in pH 8.0 buffer solution, as shown in Figure 3a). The collected mixture of pI 5.1 and 7.2 was further sorted out after titration of the sample from pH 8 to pH 6. Through this second sorting step, pI marker 7.2, which falls between pH 6-8, could be successfully isolated from the mixture through the middle outlet (Figure 3b).

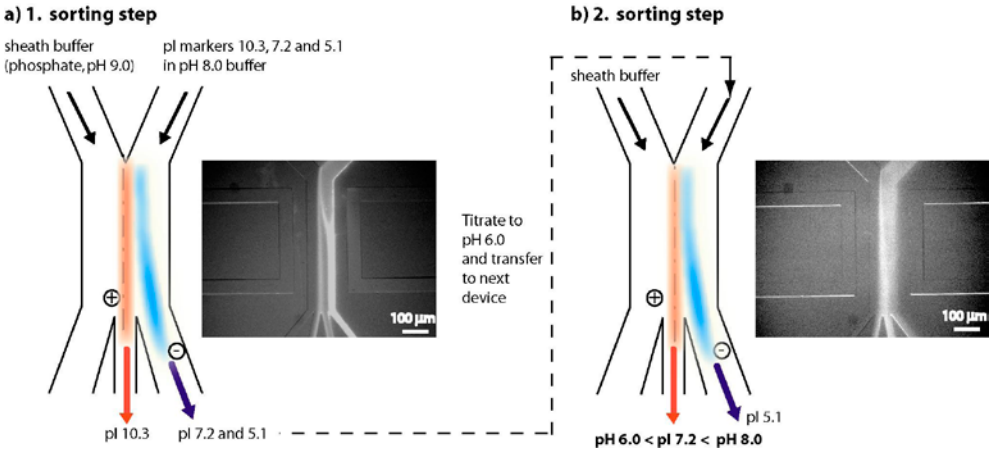

Figure 3. pI-based sorting of three pI markers, pI 5.1, 7.2 and 10.3 in pH 8.0 phosphate buffer with an external electric field of 100 V/cm. a) While the positively charged pI marker10.3 was focused to the liquid junction corresponding to the result of Figure 1c), both the negatively charged pI markers 5.1 and 7.2 were deflected to the anode side and were collected from the right outlet for the second sorting step. b) pI markers 5.1 and 7.2 were further sorted out in the second sorting step.

5. CONCLUSIONS

Using a simple surface patterning technique, we created a nanogap junction to apply external electric field to the sorting channel from the reservoirs. The free-flow sorting technique allows a pI-based binary sorting of the molecules, even in high pH values. By combining two sorting steps with a titration, an isolation of the molecules within a specific pI range set by the buffer pH values before and after titration can be realized. We plan to integrate the pI-based sorting device to MS for the shotgun proteomics.

ACKNOWLEDGEMENTS

This work was partially supported by NSF-CTS division (CTS-0347348) and KIST-IMC of Korea.

REFERENCES

[1] Song, Y.-A. and Han, J. "Continuous pI-based sorting of proteins and peptides in an microfluidic chip using diffusion potential," *Proceedings of the MicroTAS 2005 Symposium,* Boston, MA, Vol. 2, pp. 1025-1027.

[2] Song, Y.-A., Hsu, S., Stevens, A. and Han, J. "Continuous-flow pI-based sorting of proteins and peptides in a microfluidic chip using diffusion potential," *Analytical Chemistry* 78, 3528-3536 (2006).

DEVELOPMENT OF A NOVEL 5 WAY-CROSS MICROCHIP DEVICE FOR EFFECTIVE ON-LINE SAMPLE PRECONCENTRATIONS TOWARD HIGH PERFORMANCE ELECTROPHORETIC ANALYSIS

Kenji Sueyoshi, Fumihiko Kitagawa and Koji Otsuka
Graduate School of Engineering, Kyoto University, JAPAN

ABSTRACT

This paper reports an improvement of on-line sample preconcentration and separation efficiencies in microchip micellar electrokinetic chromatography (MCMEKC) combined with the partial filling (PF) and sweeping techniques on a 5 way-cross microchip. In the PF–sweeping–MCMEKC analysis, a distortion of a concentrated sample zone which reduced the concentration and separation efficiencies was effectively eliminated by using the newly fabricated microchip with a narrower channel. As a result, a 3.5-fold enhancement of the detectability and a 1.2-fold increase in the resolution of rhodamine dyes compared with our previous work were achieved with the fabricated chips.

Keywords: microchip electrophoresis, partial filling technique, sweeping, micellar electrokinetic chromatography

1. INTRODUCTION

In capillary electrophoresis (CE), the partial filling (PF) technique is one of the useful separation modes when running buffer components reduce the detectability, e.g., nonvolatile surfactants in CE–mass spectrometry. In microchip electrophoresis (MCE) with conventional cross-channel chips, however, the PF technique can not be applied because of the limitation in the sample injection. The PF technique requires the simultaneous injection of two solutions, i.e., the sample and separation solutions, but only one sample solution can be introduced into the separation channel on the conventional cross-channel chip. To overcome this limitation, we fabricated the T-cross microchip [1] which enables the injection of two solutions into the separation channel successively, in which the separation of rhodamine dyes was successfully attained with the PF technique. The increase in the peak height due to the sweeping effect was also observed. For further improvement of the detectability, we developed the 5 way-cross microchip, where the sweeping technique was applied to the PF–microchip micellar electrokinetic chromatography (MCMEKC) analysis [2]. In this study, the 5 way-cross chip with a narrower channel was newly fabricated to enhance the concentration and separation efficiencies in PF–sweeping–MCMEKC. Furthermore, effects of the injection volume of the pseudostationary phase (PSP) and the sample (S) plugs on the sensitivity enhancement factor (SEF) and resolution (R_S) were investigated.

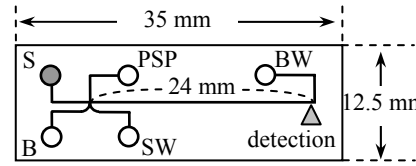

Figure 1: Schematic of the 5 way-cross microchip. B, running buffer; BW, running buffer waste; SW, sample waste reservoirs, respectively.

2. THEORY

In the PF–sweeping–MCMEKC analysis, the PSP is partially filled in front of the S plug (Figure 2b, 2c). When sodium dodecyl sulfate is employed as the PSP and the S contains

978-0-9798064-0-7/μTAS2007/$20©2007CBMS

no PSP, the S zone injected as a long plug should be concentrated by the sweeping effect (Figure 2c and 2d). In the case of faster velocity of the S compared to the PSP, the S can be separated during the migration in the PSP plug and overtake the PSP zone (Figure 2e). After passing through the PSP plug, the separated S zones are detected without any interference of the PSP (Figure 2f).

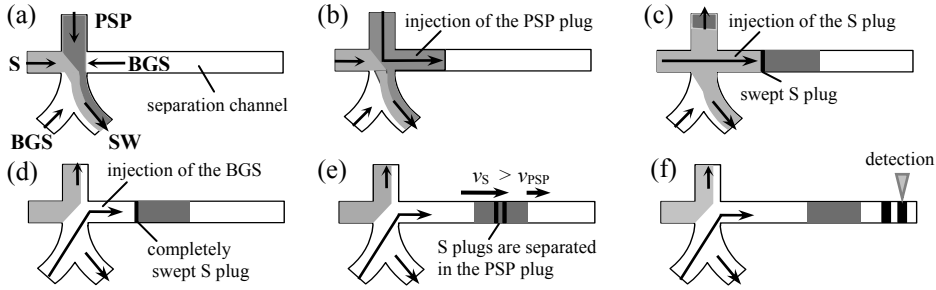

Figure 2. Principle of PF–sweeping–MCMEKC on 5 way-cross chip. (a) Loading, (b) injection of PSP, (c) injection of S, (d) concentration by sweeping, (e) separation of S in partially injected PSP plug, and (f) detection of separated S without any interference of PSP.

3. EXPERIMENTAL

Quartz microchips with a 5 way-cross channel were fabricated by the photolithographic technique. The S and PSP plugs were injected by the gated injection method. The injection times were controlled by the applied voltages. Detection was carried out by the laser-induced fluorescence (LIF) scheme. Rhodamine derivatives, such as sulforhodamine B (SRB) and sulforhodamine 101 (SR101), were used as the test analytes.

4. RESULTS AND DISCUSSION

On the 5 way-cross chip, both the PSP and S solutions could be introduced into the separation channel as the long plugs by the gated injection technique. Good repeatability of the injection volume was attained with the relative standard deviation of 5.1%. The injection volume was increased linearly with increasing the injection time of the PSP ($t_{inj,PSP}$) and the S ($t_{inj,S}$). In the PF–sweeping –MCMEKC analysis on the previous 5 way-cross chip with a broader channel, the concentrated S zone showed an extremely distorted parabolic profile due to the difference in the electroosmotic velocities between the PSP and S zones as shown in Figure 3a, which would reduce the concentration and separation efficiencies. This distortion was effectively eliminated by using the newly fabricated microchip with a narrower channel (Figure 3b) since the broadening of the S zone caused by a laminar flow according to the difference in the electroosmotic velocity between the S and PSP zones was dependent on the channel radius. As a result, the SEF and R_S of rhodamine dyes were improved from 24 to 37 and 2.3 to 2.7, respectively, under the same experimental conditions.

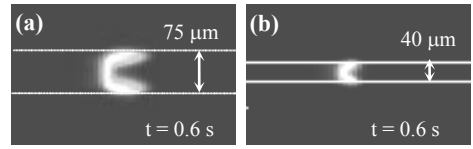

Figure 3. Fluorescence images of the swept S plug at 0.6 s after the injection of the S on (a) previously and (b) newly fabricated 5 way-cross chips.

To evaluate the performance of on-line sample preconcentration in PF–sweeping –MCMEKC, a large volume injection of the S using the 5 way-cross chip was carried out

at the $t_{inj,PSP}$ of 2.0 s. The values of the SEF were increased with increasing $t_{inj,S}$ due to the sweeping effect. At the $t_{inj,S}$ of 6.0 s, the 225-fold enhancement of the detectability for SR101 was achieved (Figure 4b) in comparison with conventional MCMEKC (Figure 4a). At the $t_{inj,S}$ of 8.0 s, the SEF of SR101 was evaluated to be 320, while for SRB it was reduced to be 91 because the overload of SRB reduced the concentration efficiency.

The effect of the injected volume of the PSP plug on R_S was investigated. At $t_{inj,PSP}$ of 1.0 s, i.e., the injected length of 70 μm, the rhodamine derivatives were well separated with R_S of 2.7 as shown in Figure 5a. The R_S value was improved from 2.7 to 5.0 with increasing the $t_{inj,PSP}$ from 1.0 to 5.0 s since longer micellar plug provided a larger phase ratio. The degree of band broadening by the diffusion for the swept S would be larger after overtaking the PSP plug than that in the PSP, so that the peak width was decreased with increasing the length of the PSP plug. As a result, number of theoretical plates of SR101 increased from 21000 to 56000 with the increase in $t_{inj,PSP}$, which provided the larger R_S. At the $t_{inj,PSP}$ of 7.0 s, however, the swept S bands could not overtake the PSP plug, so that they were detected as the extremely sharp peaks.

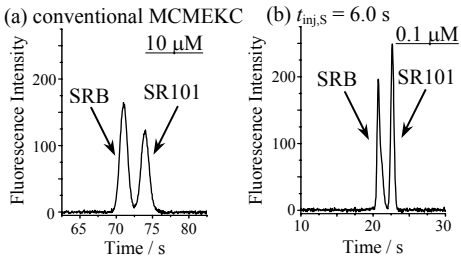

Figure 4. Electropherograms obtained with (a) conventional MCMEKC and (b) PF–sweeping –MCMEKC using the 5 way-cross microchip at $t_{inj,S}$ of 6.0 s. Sample concentration (a) 10 μM and (b) 0.1 μM; $t_{inj,PSP}$, 2.0 s.

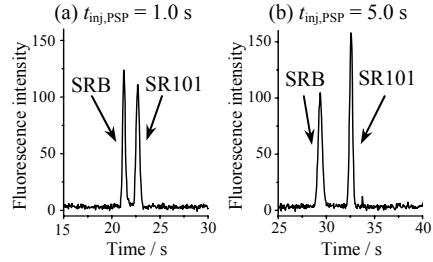

Figure 5. PF–sweeping–MCMEKC separation of rhodamine dyes at $t_{inj,PSP}$ of (a) 1.0 and (b) 5.0 s. $t_{inj,S}$, 2.0 s. Sample concentration, 100 nM.

5. CONCLUSIONS

We have demonstrated the application of the PF and the sweeping techniques to MCMEKC on the 5 way-cross microchip. The distortion of the concentrated S plug was successfully suppressed by using the 5 way-cross chip with the narrower channel, which improved the efficiency of on-line sample preconcentration and the MEKC separation. Under the optimal condition, a 225-fold increase in the SEF and the baseline separation was achieved by PF–sweeping–MCMEKC. The simultaneous application of the PF and sweeping is promising for a high performance MCE analysis.

ACKNOWLEDGEMENTS

The authors thank Dr. H. Nagai, Dr. S. Wakida, Dr. J. Nishii (National Institute of Advanced Industrial Science and Technology, AIST) for their assistance in the fabrication of the quartz microchips.

REFERENCES

1. K. Sueyoshi, et al., Meas. Sci. Technol., 17, pp. 3154-3161 (2006).
2. K. Sueyoshi, et al., Proc. Micro Total Analysis Systems 2006, pp. 374-376 (2006).

FABRICATION AND CHARACTERIZATION OF MULTILAYER POLYMER MICROFLUIDIC SYSTEMS WITH CROSSOVER CHANNELS

H.V. Fuentes, M.G. Larsen, and A.T. Woolley
Department of Chemistry and Biochemistry, Brigham Young University, Provo, Utah, USA

ABSTRACT

We have applied a recently developed phase-changing sacrificial layer microfabrication approach in constructing multilayer polymer microchips. These systems have two separate layers with microfluidics, and a thinner via layer in between. Microchannels can thus be made to cross one over another. We have found the capillary electrophoresis performance in these devices to be comparable to what is obtained in standard designs without crossover channels. Importantly, neither pressure-driven flow nor applied electric fields in the crossover channels have a negative effect on the separation performance. These multilayer microfluidic systems have potential for simplifying multiplexed analyses and end-column labeling.

Keywords: multilevel microfluidics, capillary electrophoresis, polymer microchips, sacrificial layers.

1. INTRODUCTION

Microfluidics is a vibrant research field with a growing number of applications in chemical and biological analysis. However, the two-dimensional nature of planar microchip systems presents challenges for making highly parallel microfluidic arrays or multidimensional separation devices. Some effort has been directed at creating three-dimensional, layered microfluidic manifolds in glass [1] and poly(dimethylsiloxane) (PDMS) [2,3]. Glass devices provided an elegant initial demonstration, but were difficult to construct [1]; on the other hand, PDMS systems were easy to build [2,3], but were made from a material noted for its poor compatibility with many analytes. Therefore, new approaches are needed for the fabrication of complex sample handling manifolds for parallel or multidimensional analysis in protein-compatible materials.

We recently developed a phase-changing sacrificial layer (PCSL) method for the straightforward fabrication of polymer microdevices [4,5]. We have applied the PCSL approach in solvent bonding polymeric substrates to form capillary electrophoresis (CE) microchips [4] and in interfacing ion-permeable hydrogels with microchannels for analyte preconcentration [5] or electric field gradient focusing [6]. The simplicity of this fabrication technique, and the excellent separation performance and robustness of the resulting devices, are key features that make PCSLs a promising tool for the construction of multilayer microchip analysis systems.

2. EXPERIMENTAL

We have applied the PCSL approach in fabricating multilayer polymer microchips. Figure 1 illustrates schematically our design for a fluidic routing manifold with two independent crossing channels; the microchannel array is made from three polymer pieces. The main fluidic layer (having the separation systems) is the bottom substrate (Figure 1C); the middle piece (Figure 1B) provides through-holes that connect channels in the bottom substrate to a bridging channel in the top; and the upper layer (Figure 1A) has a fluidic

978-0-9798064-0-7/μTAS2007/$20©2007CBMS

routing channel that bridges between the through-holes. Thus, in a bonded device (Figure 1D), two independent channels cross paths without fluidic contamination. A PCSL is used to block the channels and through-holes during solvent bonding of the three layers, after which the PCSL is melted and removed, leaving open microcapillaries.

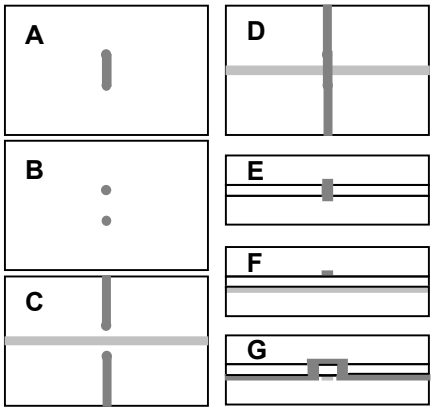

Figure 1. *Three-layer fluidic manifolds. Different shades of gray represent two independent channels. Top view of (A) top, (B) middle, and (C) bottom layers. Channels are imprinted on the bottom of (A) and the top of (C); through-holes in the middle piece interface with channels above and below. (D) Top view of the assembled three-layer device. (E) Cross-sectional view of (D) along a horizontal line bisecting a through-hole. (F) Cross-sectional view of (D) along a horizontal line following the light gray channel. (G) Cross-sectional view of (D) along a vertical line following the dark gray channel.*

3. RESULTS AND DISCUSSION

We have applied this approach in fabricating multilayer microdevices having two CE analyzers, with one crossing over the other (Figure 2). High-performance CE separation of fluorescently labeled amino acids was performed in <15 s in a 3-cm-long channel in these devices (Figure 2-right/top). We have found that pressurized flow in the crossing channel does not affect separation quality, and no analyte leakage is observed between crossing microcapillaries. Importantly, we have also determined that multilayer crossover channels are electrically independent; separation performance in a CE analyzer is not affected by an applied electric field in a crossing channel (Figure 2-right/bottom).

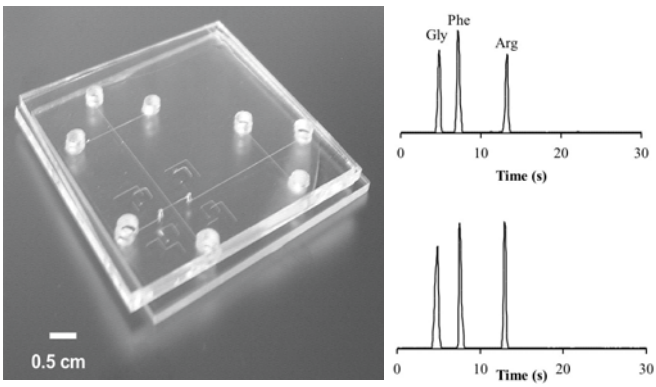

Figure 2. *(left) Photograph of a multilayer polymer microchip with a crossover channel. (right) CE separations in a multilayer microdevice like the one at left. (right/top) Analysis of fluorescently tagged amino acids; (right/bottom) same as right/top, but with 250 V/cm applied in the crossing channel.*

These crossover microfluidic systems have broad potential for application in microchip analyses. For example, Figure 3A illustrates a design for carrying out multiple, independent electrophoretic assays on a sample placed in a single reservoir on-chip, and Figure 3B shows a format for facilitating multiplexed end-column labeling in parallel CE analyses.

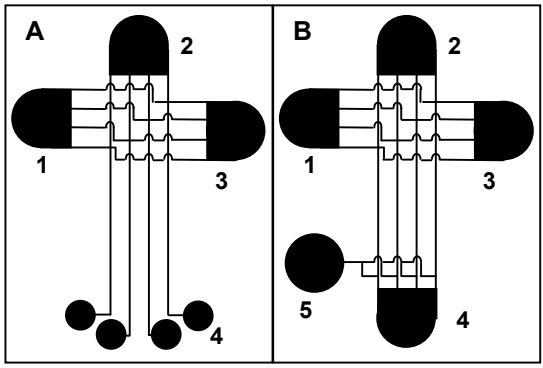

Figure 3. *Device designs with crossover channels for multiplex analysis and labeling. (A) Layout having four discrete separation channels to allow parallel analyses of a sample by different electrophoretic methods. Reservoirs are: 1, sample; 2, buffer; 3, sample waste; and 4, separation waste. (B) Design with crossover channels for end-column labeling in multiplexed microchip CE. Reservoir 5 contains the label.*

4. CONCLUSIONS

We have developed procedures for the construction of multilayered microfluidic systems in polymers. These microdevices provide similar CE performance to typical planar chips, and separation is not perturbed by either flow or an applied potential in crossover channels. PCSL fabrication of multilayer polymer microdevices should help in expanding the range of experiments feasible in microchip systems.

ACKNOWLEDGEMENTS

We gratefully acknowledge the National Institutes of Health (R01 EB006124-01) for funding. Micromachining work was carried out in the Integrated Microelectronics Laboratory at Brigham Young University.

REFERENCES

1. Verpoorte, E.M.J.; van der Schoot, B.H.; Jeanneret, S.; Manz, A.; Widmer, H.M.; de Rooij, N.F. Three-Dimensional Micro Flow Manifolds for Miniaturized Chemical Analysis Systems. *J. Micromech. Microeng.* **4**, 246-256 (1994).
2. Grover, W.H.; Skelley, A.M.; Liu, C.N.; Lagally, E.T.; Mathies, R.A. Monolithic membrane valves and diaphragm pumps for practical large-scale integration into glass microfluidic devices. *Sens. Actuators B* **89**, 315-323 (2003).
3. Liu, J.; Hansen, C.; Quake, S.R. Solving the "world-to-chip" interface problem with a microfluidic matrix. *Anal. Chem.* **75**, 4718-4723 (2003).
4. Kelly, R.T.; Pan, T.; Woolley, A.T. Phase-Changing Sacrificial Materials for Solvent Bonding of High-Performance Polymeric Capillary Electrophoresis Microchips. *Anal. Chem.* **77**, 3536-3541 (2005).
5. Kelly, R.T.; Li, Y.; Woolley, A.T. Phase-Changing Sacrificial Materials for Interfacing Microfluidics with Ion-Permeable Membranes To Create On-Chip Preconcentrators and Electric Field Gradient Focusing Microchips. *Anal. Chem.* **78**, 2565-2570 (2006).
6. Kelly, R.T.; Woolley, A.T. Electric Field Gradient Focusing. *J. Sep. Sci.* **28**, 1985-1993 (2005).

FABRICATION OF POLYMERIC MICROSTRUCTURES TO CAPTURE CHROMOSOMES ON MONOLAYER OF ANTIBODIES

P. J. Shah, J. M. Lange, C. H. Clausen, M. Dimaki, L. B. Jensen, M. H. Jakobsen, O. Geschke and W. Svendsen

MIC – Department of Micro and Nanotechnology
Technical University of Denmark, DK-2800 Kgs. Lyngby, Denmark

ABSTRACT

Our interests lie in capturing single chromosomes to study the effects of translocations in the chromosomes, which may possibly be the cause of various genetic diseases. Various clinical procedures are prevalent to extract chromosomes from cells, but we would like to prepare an integrated lab-on-chip solution to capture cells, lyse them and capture individual chromosomes to analyse them for translocations. This work is directed towards fabricating polymeric constructs which can be used for biolithographic patterning of monolayers of antibodies which have affinity towards chromosomes. These patterned antibodies can be used to immobilise chromosomes at specific sites.

Keywords: Biolithography, Surface Functionalization, Self Assembled Monolayers, Laser fabrication

1. INTRODUCTION

Our work is targeted at fabricating microstructures in various polymers and testing their efficiency to capture chromosomes. Polymer microstructures are fabricated using conventional photolithographic as well as unconventional laser ablation and micromilling fabrication techniques. Self Assembled Monolayers (SAMs) of poly (ethylene glycol) and antibodies are attached to these microstructures using directed self-assembly to chemically activated areas, where the surface is functionalized to create chromosome specific adhesion.

2. FABRICATION

Using conventional fabrication techniques, a negative relief of poly (dimethylsiloxane) (PDMS) microstencils were created by spincoating PDMS precursor on positive relief SU-8 microstructures fabricated by photolithography (Fig.1a). Other polymers like Poly (methyl methacrylate) (PMMA) and Cyclic Olefin Copolymers (COC) were also tested. A Laser Ablation process (Fig. 1b) was used to fabricate masters in PMMA and COC and later was also tested to produce PDMS masters. The laser used for ablation is a $CO2$ laser from Synrad Inc., USA (Fig. 2), with an output power of $50W$ and a wavelength of $10.6\mu m$. A computer-controlled unit is attached to the laser which allows the user to control the path of the beam through the control-software: WINMARK Pro. The galvano-mirrors deflect the beam onto a work area of 110 mm by 110 mm positioned under the lens at the focal length of 189 mm.

978-0-9798064-0-7/μTAS2007/$20©2007CBMS

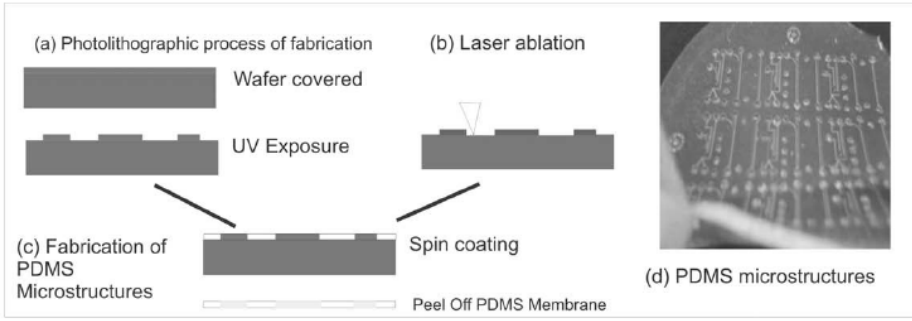

Figure 1: Fabrication of PDMS Microstructures using (a) Photolithography (b) Laser Ablation (c) Spincoating and curing PDMS followed by peel off (d) PDMS microstructures



Figure 2: Setup of Laser Ablation system

3. SURFACE FUNCTIONALIZATION

The substrate surface is created with PEG (poly (ethyleneglycol)) to minimize unspecific binding of chromosomes. The idea is that the surface is locally activated by cyanuric chloride through a polymer mask, and centromere specific antibodies will subsequently bind selectively to these activated spots. Hence leading to capture of chromosomes at sites patterned with antibodies.

4. RESULTS AND DISCUSSION

An extensive investigation was carried out on the effects of surface roughness and the profile of the microstructures fabricated using CO_2 laser ablation along with their effects on deposited SAMs. This was carried out using Dektak and Atomic Force Microscopy (Fig 4).Various surface functionalization techniques were used to work around the problems of PDMS, among others, plasma functionalization and adhesive metal evaporation. As PDMS suffers some degradation in the process of creating SAMs due to solvent absorption, we tried several surface functionalizing techniques and used Titanium (Ti) coated PDMS microstructures.

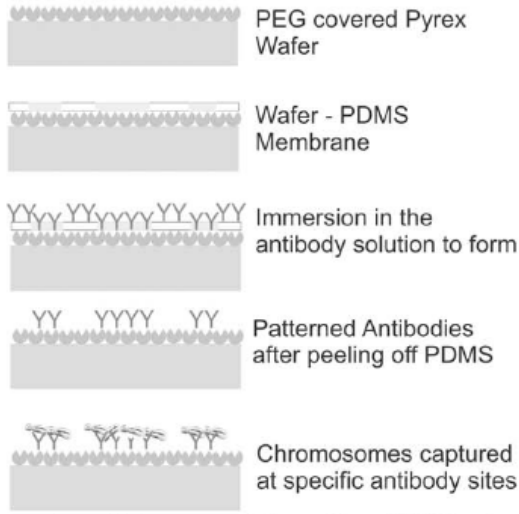

Figure 3: Process of deposition of SAMs of antibodies on PEG surface and capturing chromosomes

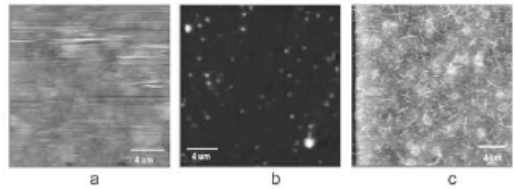

Figure 4: AFM images of laser ablated polymer surfaces (a) PDMS (b) PMMA (c) COC

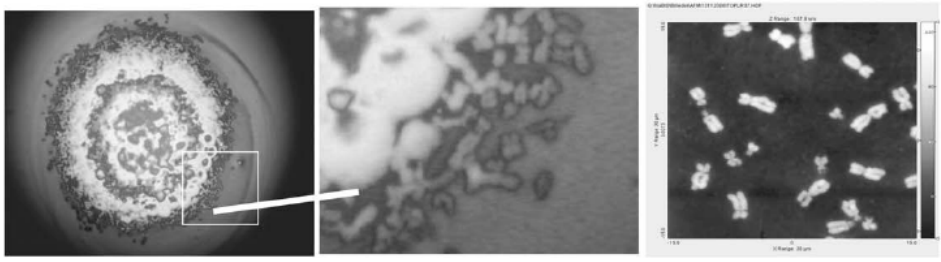

Figure 5: Images of chromosomes adhered to the surface of the substrate

When chromosome suspension is dispensed on the substrate-PDMS complex, the chromosomes adhere to the antibody surfaces (Fig 1,5). In future, we aim to work on a release technique to free chromosomes from binding sites. This will allow us to manipulate and address individual chromosomes. Hence, allowing us to have greater control over capture and release of chromosomes. We envisage that this could play a significant role in detecting translocations and mutations on a single chromosome on a lab on chip system. This will provide a greater efficiency and faster analysis compared to time consuming staining techniques.

FIELD AMPLIFIED CONTINUOUS SAMPLE INJECTION (FACSI): A NEW METHOD FOR RAPID ANALYTE PRECONCENTRATION IN MICROFLUIDIC APPLICATIONS

Matthew S. Munson, Jonathan G. Shackman, Grégoire Danger, and David Ross

National Institute of Standards and Technology, USA

ABSTRACT

We detail development of a new sample preconcentration technique for microfluidic applications: field amplified continuous sample injection (FACSI). Using counterflow, a diffusion-stabilized interface between a lower conductivity sample buffer and a higher conductivity separation buffer is established ***outside*** the microchannel. With application of an electric field, analyte focuses onto the interface and selectively elute into the separation channel. FACSI in combination with temperature gradient focusing (TGF) achieves concentration enhancements proportional to the conductivity ratio (γ) squared. Gradient elution isotachophoresis (GEITP) giving concentration factors of $\approx 10^5$ within two minutes.

Keywords: Sample Stacking, Temperature Gradient Focusing, ITP

1. BACKGROUND

As with conventional field amplified sample stacking (FASS) or field amplified sample injection (FASI), FACSI is implemented by preparing the sample in a lower conductivity buffer than the separation buffer. With FASS and FASI, the conductivity interface is located in the separation channel. Consequently, the interface moves with bulk flow, limiting the concentration enhancement to γ. With FACSI, the conductivity interface is located outside the separation channel, in the sample reservoir (Fig. 1). Because the fluid velocity is much lower in the sample reservoir, the interface is diffusion stabilized and does not move. Analytes are then concentrated onto the interface by a degree significantly greater than γ. The separation buffer flows out of the channel from (left to right in Fig. 1) and forms a hemispherical interface with the sample buffer outside the channel entrance (Fig. 1a and 1b). Under an electric field, the fluorescent analyte ions focus on the discontinuous buffer interface. Variation of the bulk flow rate through the channel by application of controlled pressure (Fig 1c: 5000 Pa, 1d: 1000 Pa) causes the buffer interface and the focused analyte zone to expand or contract.

TGF is a counterflow electrophoretic separation technique that has been demonstrated to provide simultaneous concentration and separation of a wide variety of analytes in microfluidic channels.[1] With an axial temperature gradient and the use of a buffer with a temperature dependent ionic strength, a velocity gradient is developed along the channel length, causing different analytes to migrate to and accumulate or "focus" at different zero-velocity points along the temperature gradient. Because TGF is a counterflow separation, it is ideally suited for use with FACSI for two-stages of analyte enrichment.

To create an isotachophoresis (ITP) interface, a high concentration of a leading electrolyte (LE) is incorporated into the separation buffer located in the pressure controlled buffer reservoir; a terminating electrolyte (TE) with an electrophoretic mobility less than the analyte is included in the sample matrix. When voltage is applied at the sample

978-0-9798064-0-7/μTAS2007/$20©2007CBMS

reservoir, electrophoresis is counteracted by electroosmotic flow and the hydrodynamic flow, pushing LE into the sample reservoir and forming a discontinuous buffer boundary. Analytes and TE are driven by electrophoresis into the ionic interface, forming enriched ITP zones. As the counterflow is lowered through reduction in applied pressure, the interface and accumulated analytes are sequentially introduced onto the capillary, where they can then be detected. To achieve discrimination of fluorescent analytes with similar emission spectra, either discrete non-fluorescent components can be added to the sample matrix,[2] or, in the case of multi-analyte separations, a continuum of spacers can be achieved by introducing ampholyte mixtures.[3, 4]

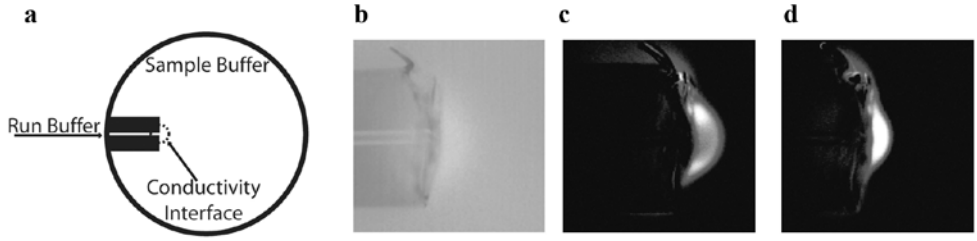

Figure 1: FACSI occurring at a conductivity interface at various bulk flow rates.

2. RESULTS

Characterization of FACSI-TGF was performed by constructing calibration curves of peak height as a function of analyte (OG488) concentration. The separation buffer used for all experiments was 0.5 mol L^{-1} tris-borate (TB), while sample buffers varied from 31 mmol L^{-1} to 1 mol L^{-1} TB. OG488 concentrations varied from 31 pmol L^{-1} to 64 nmol L^{-1}. A temperature gradient of 30 °C mm^{-1} (80 °C to 20 °C) was applied across 2 mm segment of a 30 mm long capillary. A voltage of -3 kV was applied at the sample reservoir (run buffer reservoir grounded) giving an approximate field strength of -1 kV cm^{-1}. During each experiment the pressure was held for 30 s with the voltage applied at a pressure of +250 Pa. The pressure was then reduced to -375 Pa in 5 Pa increments and held for 2 s at each pressure. For conventional CE with FASS or FASI, the concentration enhancement is no greater than γ. In contrast, measurements of fluorescent dye concentration in the channel during FACSI injection (not shown) indicate a concentration enhancement significantly greater than γ. With FACSI-TGF, a best fit to the data indicates that the additional concentration enhancement due to FACSI is equal to γ^2.

The GEITP process can be visualized in Fig. 2. Sample buffer, 0.5 mol L^{-1} TB (pH 8.3), contained 100 nmol L^{-1} each of fluorescein and carboxyfluorescein (FAM) and 1 mol L^{-1} glycine (acting as a spacer). The pressure controlled waste reservoir contained 100 mmol L^{-1} citrate balanced to pH 8.3 with tris. In this instance, citrate acted as the LE and borate as the TE. At high counterflow rates (1800 Pa applied pressure; Fig. 2a) no enrichment was detectable, likely due to the high rate of LE efflux and rapid dispersion. As the counterflow rate was reduced (850 Pa; Fig. 2b), a single concentrated fluorescent spot outside of the capillary was observed. When the flow rate was further reduced (730 Pa; Fig. 2c), FAM was introduced onto the capillary. Note that the use of the spacer excluded fluorescein from entering the capillary until further reduction in counter flow (590 Pa; Fig. 2d).

Resulting peak height in GEITP was demonstrated to be linear with analyte concentration (Fig. 3). The sample buffer was 0.5 mol L^{-1} TB while the separation buffer

was 100 mmol L^{-1} citric acid, pH adjusted to 8.3 with tris. An applied voltage of 3000 V was applied across a 3 cm length of capillary. The applied counterpressure started at -850 Pa and was reduced at a rate of 5 $Pa \cdot s^{-1}$. A resulting electropherogram of 10 pmol L^{-1} FAM are shown in Fig. 3a. A signal to noise ratio of 20 is observed. Calibration was conducted by varying FAM concentration from 10 pmol L^{-1} to 60 pmol L^{-1} (Fig. 3b). Error bars are ± 1 standard deviation (*n=3*). From these results the limit of detection was estimated to be 1.8 pmol L^{-1}. The limit of detection with our experimental apparatus in the absence of sample enrichment was determined experimentally to be 0.27 µmol L^{-1}. Thus the concentration factor observed with GEITP was 1.5×10^5.

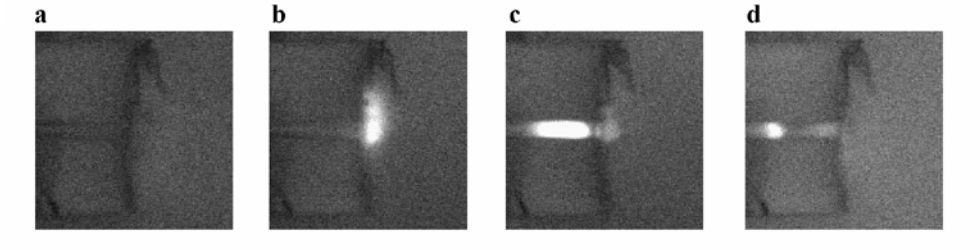

Figure 2: Separation and concentration of two analytes using GEITP

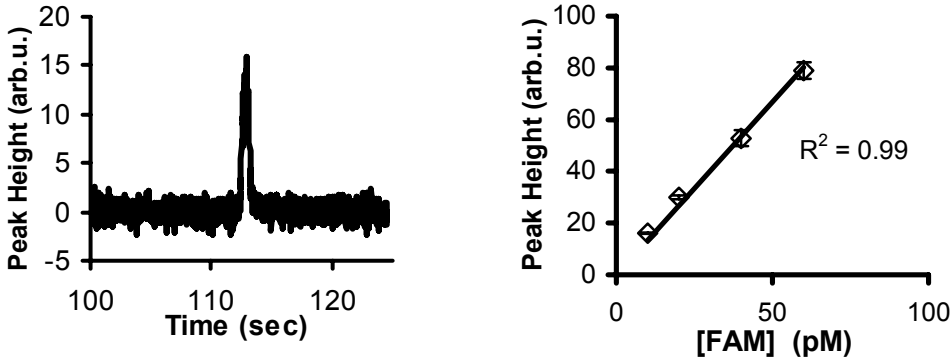

Figure 3: Performance of GEITP with a single analyte.

3. CONCLUSION

The serial combination of focusing techniques allows the reduction in analysis time without sacrificing resolution or limits of detection. Conversely, the limit of detection can be improved without alteration of the resolution or analysis time. Finally, the techniques described maintain one of the fundamental benefits of counterflow gradient separations: matrix exclusion. This allows for the rapid high sensitivity of small molecules from complex sample matrices such as biological and environmental samples.

4. REFERENCES

(1) Ross, D.; Locascio, L. E. *Analytical Chemistry* **2002**, *74*, 2556-2564.
(2) Marak, J., et al. *Journal of Chromatography A* **2003**, *1018*, 233-249.
(3) Chartogne, A., et al. *Journal of Chromatography A* **2002**, *959*, 289-298.
(4) Inano, K., et al. *Annals of Clinical Biochemistry* **2000**, *37*, 708-716.

HIGHER EFFICIENCY AND THROUGHPUT IN PARTICLE SEPARATION WITH 3D C-MEMS DIELECTROPHORESIS

R. Martinez-Duarte[1], H. A. Rouabah[2], N. G. Green[2], M. Madou[1] and H. Morgan[2]

[1]*Mechanical and Aerospace Engineering Department, University of California, Irvine. USA*
[2]*School of Electronics and Computer science, University of Southampton, SO17 1BJ. UK*

ABSTRACT

We report on the use of three dimensional electrode structures, fabricated with C-MEMS (Carbon MicroElectroMechanical Systems) technology, to improve efficiency and throughput in dielectrophoretic particle separation. The electrodes are tested in comparison with normal planar electrodes structures using yeast cells. Initial results on the prototype device demonstrate a two-fold increase in separation efficiency.

Keywords: C-MEMS, Dielectrophoresis, separation, bioparticles

1. INTRODUCTION

Many successful dielectrophoresis (DEP) applications [1] have been demonstrated using planar metal electrodes with a thickness of approximately 100nm. These types of devices all suffer from the fact that the induced DEP force exponentially decreases as distance from the electrodes increases. Therefore many targeted particles could flow over the electrode array without experiencing any force. The premise of using three dimensional electrodes is that dielectrophoretic separation efficiency is improved by reducing the mean distance from the sample to the surface of any electrode.

Three dimensional metal electrodes for dielectrophoresis have been reported recently [2-4]. Dielectrophoresis using planar carbon electrodes has also been reported [5, 6]. The novelty of the work presented in this paper is the use of a simple and relatively inexpensive fabrication technique, C-MEMS [7], to obtain electrochemically stable volumetric carbon electrodes for particle separation in a DEP-controlled active filter. Furthermore, C-MEMS technology allows the fabrication of complex and highly-reproducible three dimensional carbon structures which improve the throughput of DEP devices. We present similar separation devices based on 3D and planar carbon electrodes for comparison and discuss the relative advantages of the two.

2. FABRICATION

SU-8 (MicroChem, US) was used as precursor resist. The substrate material was silicon with a 500nm layer of silicon dioxide grown thermally to act as an electrical insulator. The complete process is shown in Fig. 1 for 5×29 arrays of pads (planar) and posts (3D). SU-8 structures were fabricated in a two-step photolithography sequence (Fig. 1 a, b) and were then carbonized. Figures 1 c and d show the resulting carbon electrodes and connecting leads. Table 1 summarizes the data on heights for the posts. In order to prevent physical obstacles and to protect leads from lifting off, the channel bottom was planarized by a 1.4 µm layer of SU-8 (Fig. 1 e, f). A 500 µm wide, 65 µm high channel was then fabricated using SU-8 (Fig. 1 g, h). Finally, the device was sealed with a glass lid and electrical connections were made.

978-0-9798064-0-7/µTAS2007/$20©2007CBMS

Table 1. Height Dimensions of SU-8 and Carbon structures. All dimensions in µm.

	SU-8 Structures		Carbon Structures		Shrinkage (%)		Electrode Diameter
	Leads	*Electrodes*	*Leads*	*Electrodes*	*Leads*	*Electrodes*	
Planar	9.78	22.62	1.5	5.6	84.6	75.24	20.3
3 - D		130.4		60.5		53.6	

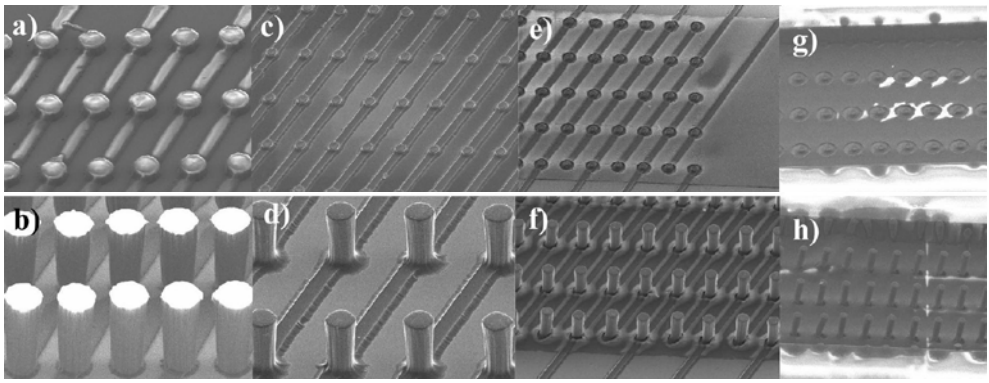

Fig. 1. Sequential (from left to right) SEM pictures of the fabrication process with the planar electrodes above and the 3D electrodes below. Gap between carbon electrodes in the horizontal axis is 45.3 µm and 110.7 µm in the vertical one. See text for details.

3. EXPERIMENTAL

Yeast (S. cerevisiae) was grown overnight in Sabouraud medium (30 g/l) at 30° C and 250 RPM, washed and re-suspended in water with peptone (6 g/l) at a concentration of 5.1×10^7cells/ml. The concentration of non-viable cells was 20%, remaining constant throughout experiments, and was determined using methylene blue (Sigma-Aldrich, US). The sample conductivity was 51 mS/m and a 10 MHz, 10 Vpp sinusoidal signal was applied between the electrodes to perform DEP trapping of viable yeast cells. The numbers of viable and non-viable yeast cells at the output was determined by direct observation for the same signal and increasing flow rate for a fixed sample volume of 50 µl.

4. RESULTS AND DISCUSSION

Fig. 2 shows the retention efficiency as a percentage, calculated as the ratio of the quantity of the targeted particles (viable cells) retained by the filter, to the quantity entering the filter, for different flow rates. As can be seen, the 3D electrodes array act as a better filter, with the retention efficiency higher at all flow rates, achieving a greater enrichment of the non-viable yeast cells. The planar electrode array also demonstrates the expected behavior that the retention efficiency goes down as the flow rate increases. The 3D electrode array, however, demonstrates an initial decrease in efficiency but then has the same efficiency for the higher flow rates measured.

5. CONCLUSIONS

C-MEMS technique offers highly reproducible carbon electrodes for DEP whose fabrication process is relatively simple and non expensive. DEP has successfully been demonstrated using 3D carbon electrodes, demonstrating higher efficiency than planar

electrodes. The difference in filter retention efficiency between the array types increases as flow rate increases, demonstrating the suitability of the 3D electrode arrays for rapid, high efficiency DEP-controlled active particle separation.

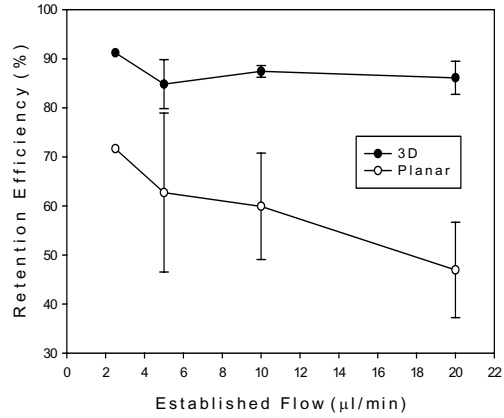

Fig. 2. Retention Efficiency as flow rate increases for both planar and volumetric electrodes. Experiments done at 2.5, 5, 10 and 20 µl/min flow rates. Mean values and Standard Error bars are shown.

ACKNOWLEDGEMENTS

Authors acknowledge the great help received from our colleagues in UC Irvine: R. Gorkin, D. Shah, N. Kim, B. Park, R. Zaouk, G. Turon, J. Siegrist, H. Kido and J. Zoval and R. Rodriguez, M. Jaramillo and A. Juarez from Universitat de Barcelona. Biological samples were kindly provided by Laboratorio de Nanobioingenieria at Parc Cientific de Barcelona. The Authors also thank the INRF manager and technicians for their enormous help.

REFERENCES

[1] P. Gascoyne, J. Vykoukal, *Dielectrophoresis-Based Sample Handling in General-Purpose Programmable Diagnostic Instruments*, Proceedings of the IEEE, **92,** 1, pp. 22-42, (2004).

[2] L. Wang, A. P. Lee, *A Microfabrication Process for Polymer Microchannel with Embedded Vertical Electrodes for Microfluidic Applications,* Proceedings of 2004 ASME: International Mechanical Engineering Congress & RD Expo, Anaheim, California, pp. 439-442, (2004).

[3] J. Voldman, M. Gray, M. Toner, M. Schmidt, *A Microfabrication-based Dynamic Array Cytometer*, Analytical Chemistry, **74,** pp. 3984-3990, (2002).

[4] C. Iliescu, L. Yu, G. Xu, F.E. H. Tay, *A Dielectrophoretic Chip With a 3-D Electric Field Gradient*, Journal of Microelectromechanical Systems, **15,** 6, pp. 1506-1513, (2006).

[5] B.Y. Park, R. Zaouk, M. J. Madou, *Validation of lithography based on the controlled movement of light-emitting particles,* SPIE Microlithography, Emerging Lithographic Technologies VIII, SPIE, Bellingham, WA, pp. 566-578, (2004).

[6] R. Martinez-Duarte, M. Castellarnau, R. Perez, R. Rodriguez, G. Gomila, J. Samitier, M. Madou, *Carbon MEMS (C-MEMS) for Dielectrophoresis Applications*, Proceedings of the California Catalonia Alliance for Miniaturization Science and Engineering Workshop, Micro and Nano-Engineering 2006 Conference, Barcelona, Spain, pp. 1-2, (2006).

[7] C. Wang, G. Jia, L. Taherabadi, M. Madou, *A Novel Method for the Fabrication of High Aspect Ratio C-MEMS Structures*, IEEE Journal of MEMS, **14,** 2, pp. 348-358, (2005).

INTEGRATING INDEPENDENT SILICA MONOLITH ELECTROOSMOTIC PUMPS FOR REAGENT DELIVERY AND SAMPLE PRECONCENTRATION IN A μ-TAS DEVICE

Fu-Qiang Nie, Brett Paull, Mirek Macka

National Centre for Sensor Research and School of Chemical Sciences, Dublin City University, Glasnevin, Dublin 9, IRELAND

ABSTRACT

We present a microfluidic chip-based total analysis system (μ-TAS) for the flow injection analysis (μ-FIA) demonstrated on trace inorganic cation analysis. The μ-TAS integrates two independent monolithic electroosmotic pumps (EOPs) one of which also works as a column for on-chip preconcentration and off-chip photometric/conductometric detectors. An improvement of 100 times in limit of detection (LOD) using the conductometric detector down to 0.01 mmol/L can be achieved.

Keywords: Monolith, electroosmotic pump, preconcentration, μ-TAS

1. INTRODUCTION

Trace ion analysis is important in many areas, including environmental, pharmaceutical and biological. During the past decade, miniaturization of analysis system like μ-TAS has been developed as a crucial analytical approach due to its fast analysis speed and small reagent requirement and rapidly moved to several application areas including inorganic ion analysis [1]. However, some obstacles such as compatibility of detection and its sensitivity have been limiting its further applications. Sample preconcentration is an approach generally leading to lowering LODs but has not been fully utilised in μ-TAS devices.

2. EXPERIMENTAL

Based on our previous work on monolithic EOPs and on-chip μ-FIA using monolithic EOPs [2, 3], the third generation of μ-TAS here is designed using CAD 3D Excalibur software on a 40 × 30 × 2 mm polymethylmethacrylate (PMMA) substrate and fabricated using a computer numerical control milling machine (Figure 1). The monolith fused silica capillary columns used for EOP are embedded in 400 × 400 μm channels micromilled in PMMA bonded with the top plate using a double-sided adhesive polypropylene layer and these columns are sealed with epoxy glue through access holes in the top plate. For on-chip cation-exchange micro-solid phase extraction (μ-SPE) preconcentration, the silica C_{18} monolith column is semi-permanently coated with dioctylsulphosuccinnate (DOSS) [4]. The μ-SPE preconcentration step is followed by elution of the analyte from the EOP-b and injection of the zone of preconcentrated analyte in a μ-FIA stream of reagent. This is visualised in Figure 2 where eluted Ca^{2+} as a test analyte is seen exiting the EOP-b as purple zone as it reacts with *o*-cresolphthalein complexone (*o*-CPC).

4. RESULTS AND DISCUSSION

The novelty of the μ-TAS (Figure 1) rests in the integration of two independent EOPs, one as the reagent μ-FIA pump (EOP-a), and a second (EOP-b) for analyte preconcentration

978-0-9798064-0-7/μTAS2007/$20©2007CBMS

by μ-SPE; both using silica monolithic capillary columns embedded in the chip, and applying light emitting diode (LED) based photometric and capacitively coupled contactless conductometric (C^4D) detections, which are easily coupled with the microfluidic chip through a fused silica capillary. Pumps EOP-a and EOP-b contain 3 parallel pieces and 1 piece of 100 μm i.d. monolith containing fused silica capillary columns, respectively, each 10 mm in length. The advantage of using commercial silica-based monolithic fused silica capillary columns (Caprod, Merck) is in significant simplification of the process of making the μ-TAS chip. The chip is designed so that the μ-FIA reagent is placed in a reagent reservoir propelled indirectly by the EOP-a pumping water. In this way, the composition of the reagent can be independent from the propellant liquid, which is kept constant (water).

The DOSS coating process and column capacity are well controlled and characterized using the C^4D detector through observing a complete breakthrough and a 30 min coating was determined as sufficient from Figure 3. The green LED detector (576 nm) and the C^4D are used in an off-chip-configuration on the fused silica capillary (on-capillary detection) exiting the chip (Figure 1). The advantages are flexibility of the design, as well as approved robustness of on-capillary detection and relatively better sensitivity and S/N ration compared to on-chip photometric and C^4D detection methods.

Ethylenediamine/phthalate eluent (pH=4.5) was chosen due to its elution strength and low conductivity background [5]. An elution time of 60 s (Figure 4) lead to band broadening and a longer analysis time, so 10 s elution was chosen as optimal. Figure 5 shows the μ-TAS with μ-SPE achieving preconcentration factor of approx. 10x judged by the LED-detection peak height. It is estimated that only 20 μL volume of sample and 7 nL eluent volume are consumed. The potential of the approach has been demonstrated by trace analysis of calcium cations achieving LOD of 0.01 mmol/L which is an improvement in LOD by 100 times (Figure 6).

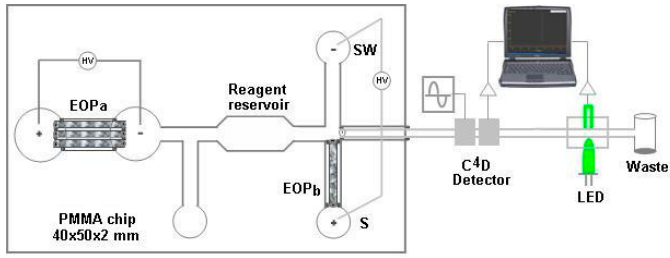

Figure 1. Schematic diagram of the μ-TAS device: EOP_a= injecting pump; EOP_b= dispensing pump; Detector= LED-based optical detector and C^4D.

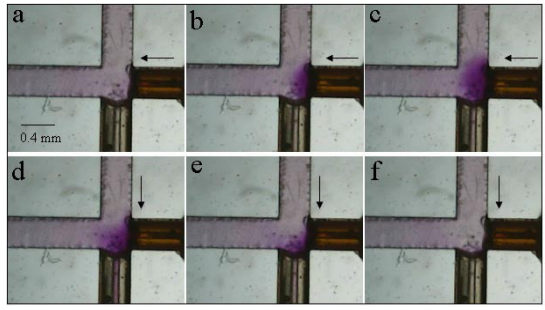

Figure 2. Visible images of the intersection of microfluidic chip during the elution and delivery.

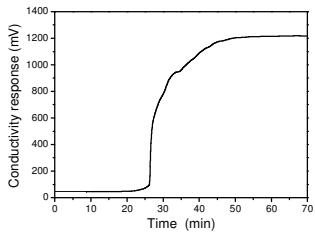

Figure 3. Conductivity response to the DOSS coating as a function of time demonstrating the saturation point.

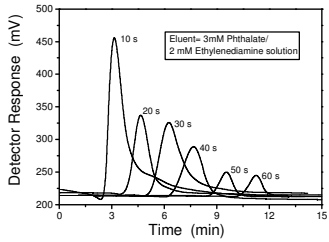

Figure 4. Conductivity signal as a function of elution time.

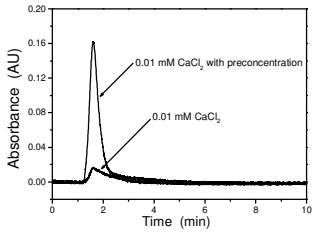

Figure 5. Absorbance (ε_{max}=576 nm) for 0.01 mM Ca^{2+} without and with preconcentration.

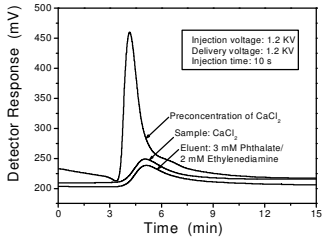

Figure 6. Conductivity signal for 0.01mM Ca^{2+} without and with preconcentration.

5. CONCLUSIONS

The validity of this novel µ-TAS integrating two independent EOPs, on-chip preconcentration and two off-chip detectors on a small microfluidic device has been demonstrated. The improvement of detection limits for calcium down to ca. 10 µmol/L illustrates the potential of on-chip preconcantartion. The flexibility of this µ-TAS approach could contribute to its wider applicability in the area of trace analysis on chip.

ACKNOWLEDGEMENTS

Funding from Science Foundation Ireland (F.Q. Nie) and Marie Curie Excellence Grants award (M. Macka).

REFERENCES

[1] M. Novič and M. Guček, *Ion exchange-based preconcentration for determination of anions by capillary electrophoresis*, J. Chromatogr. A., **868**, 135-139 (2000).

[2] F. Q. Nie, M. Macka, L. Barron, D. Connolly, N. Kent and B. Paull, *Robust monolithic silica based on-chip electro-osmotic micro-pump*, The Analyst, **132**, 417-424 (2007).

[3] F. Q. Nie, M. Macka and B. Paull, *Miniaturisation and integration of sample injecting and dispensing silica monolithic electroosmotic pumps on a microfluidic chip*, Proc. NanoTech 2006, Montreux (2006).

[4] D. Connolly, D. Victory and B. Paull, *Rapid, low pressure, and simultaneous ion chromatography of common inorganic anions and cations on short permanently coated monolithic columns*, Journal of Separation Science, **27**, 912-920 (2004).

[5] P. Hatsis and C. A. Lucy, *Improved sensitivity and characterization of high-speed ion chromatography of inorganic anions*, Analytical Chemistry, **75**, 995-1001 (2003).

MICROFABRICATED PLATFORM WITH MICROPILLARS FOR ELECTROPHORETIC SEPARATIONS

V. Dauriac[1,2], S. Descroix[1], H. Sénéchal[1], Y. Chen [2], M.C. Hennion [1], G. Peltre[1]

[1]Laboratory of Environment and Analytical Chemistry, ESPCI, FRANCE, [2]Laboratory of Microfluidics, Chemical Organization and Nanotechnology, ENS, FRANCE

ABSTRACT

This paper presents a novel microfabricated platform in polydimethylsiloxane (PDMS) to perform electrophoretic separations. This microchip consists in a rectangular zone of PDMS micropillars protruding on a PDMS block. The manufacturing of such microchips has been performed and optimized with a view to integrating a second dimension. The geometry and the dimensions of micropillars have been optimized in order to maintain the liquid solution within the micropillar zone and to get the best protein migration as possible. The feasibility of micropillar platform-based isoelectric focusing (IEF) has been successfully demonstrated by separating a mixture of 7 proteins in less than 10 min with satisfying resolution.

Keywords: PDMS, micropillars, isoelectric focusing, proteins

1. INTRODUCTION

In the field of allergy diagnosis, one needs to perform selective, efficient, sensitive and fast analysis to separate complex protein mixtures. Electrophoretic techniques have been widely used for that purpose, especially isoelectric focusing as first dimension of 2D gel electrophoresis. Nevertheless, gels have limitations in their use in terms of time consumption, sample amount and disposability. The transposition of such techniques to microfluidic format therefore appeared as an alternative and has been studied since several years. Most of the studies have been performed in microchannels [1]. Our method thus differs from previous works in the original design we use. Our microchip consists in a rectangular zone of PDMS micropillars protruding on the PDMS bulk. PDMS has been one of the most actively developed polymer for microfluidics since few years as it reduces the complexity and the cost of prototyping and manufacturing. This study describes the prototyping and the manufacturing of a novel microfabricated micropillar platform in PDMS dedicated to protein separation. The performance of the device has been evaluated by separating 7 proteins and the results have then been compared to those obtained on conventional gels.

2. DEVICE FABRICATION

The PDMS microfluidic device (Figure 1) has been fabricated by soft lithography using protocols described previously [2]. The micropillar area was used to mimic a gel structure and to allow liquid to remain amongst micropillars by capillarity effect (cf. Figure 1.C). The platform is uncovered to keep the ability to perform an immunoblot after the protein separation.

The design of such a device was first optimized. The micropillar area length has been selected depending on the dimensions of the electrophoretic apparatus. As the Phast System (GE Healthcare) electrodes are 4.2 cm away, we decided to set the length of the area at 5 cm. Secondly, we have chosen to set the width of the area at twenty micropillar

978-0-9798064-0-7/µTAS2007/$20©2007CBMS

rows, which is a good compromise between filling aptitude and dimension scale to integrate IEF with another on-chip separation dimension. Micropillar area is 50 µm in height, corresponding to the minimal thickness of agarose gels casting in our laboratory. We have then compared several micropillar dimensions as well as several micropillar geometries and arrangements. Different parameters have been studied: filling aptitude, evaporation process, isopotential lines inside the separation area and separation resolution (data not shown). Finally, we have chosen a micropillar area of 5 cm long and 3.9 mm wide with square micropillars of 100 µm side. The micropillars are triangularly arranged in such a way that the distance between adjacent micropillars is 100 µm and the distance between adjacent rows is 100 µm equally (cf. Figure 1).

3. RESULTS AND DISCUSSION

The feasibility of micropillar platform-based IEF was then successfully demonstrated by separating a mixture of 7 coloured proteins (Table 1). To compare IEF performed with our PDMS microchip to the results obtained on conventional gels, experiments have been performed on polyacrylamide mini-gels 4.2 by 4.2 cm. These mini-gels could already be considered like miniaturized systems compared to the classical 11 by 25 cm IEF gels. Separation parameters, such as electrolyte composition, voltage, time focusing and protein sample loading have been optimized. For gel electrophoresis, IEF was carried out using a pH gradient from 2 to 11 made by 5 % v/v carrier ampholyte in water. 1 µL of proteins was loaded with a sample application comb, during the second step of the electrophoretic process. For micropillar platform electrophoresis, we used the same electrolyte but 30 % v/v glycerol was added. Glycerol has been added considering its benefit in IEF to reduce the electroosmotic flow [3] and in evaporation limitation. Before micropillar platform-IEF, the microchip was put inside a plasma cleaner for 30 s at 300 mTorr. 1 µL (32 µg) of proteins was directly mixed in the electrolyte solution. It could appear like a huge amount of proteins compared to the small dimensions of the device but is necessary due to the absence of detection unit in the Phast System, so that the protein focusing was visually followed by a camera. Focusing was carried out under electric fields up to 500 V/cm for both systems. The focused protein images were then analysed by software GeneTools to achieve an electropherogram. A comparison between the results obtained on conventional mini-gels and on the microchip is shown in Figure 2, A and B respectively. The protein mixture is focused in less than 10 min on the micropillar platform, whereas the focusing on mini-gels is achieved in approximately 20 min, which is already far less than the several hours required for classical gels. Furthermore, the PDMS microchip can be reused several times if attention is paid to post-run cleaning, while gels are disposable. All proteins were clearly distinguished for both systems with correct resolution (ΔpI of 0.25). Band distortion in the microdevice could be explained by side effects due to the geometry of the chip. The plot of pI versus migration distance of focused proteins suggests a more fairly linear pH gradient in the microchip, with a correlation coefficient (R^2) of 0.994 for the linear regression, than in conventional gels ($R^2 = 0.972$).

4. CONCLUSION

In this work, we have shown the potential of a novel microfabricated platform to perform electrophoretic separations. The short analysis time and the low cost of IEF in the microchip make it promising to integrate IEF with another on-chip separation dimension. We are currently working on milk proteins separation and immunoblot detection.

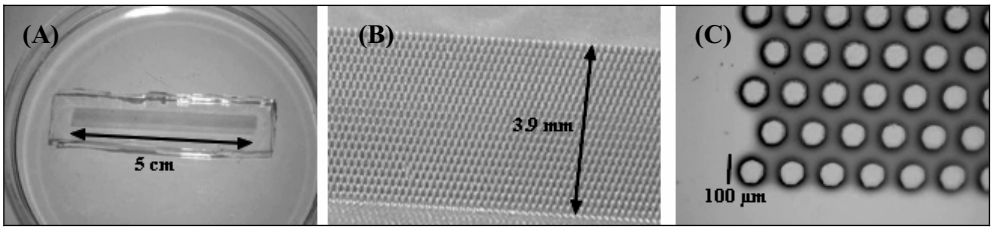

Figure 1. Pictures of the microfabricated platform. The micropillar zone was filled with a coloured solution. **(A)** General view, **(B)** Zoom of the micropillar area. The device shown in this figure is composed of an area (5cm length, 3.9 mm width) of **(C)** round micropillars (100 µm in diameter, 50 µm in height) in triangular arrangement.

Table 1. Coloured proteins, isoelectric point markers (BDH®)

Proteins	pI	Number (on Fig. 2)	Colour
C-Phycocyanin	4.75, 4.85	1	dark blue
Azurin	5.65	2	blue
Trifluoroacetylated Myoglobin Met (porcine)	5.9	3	yellow
Myoglobin Met (porcine)	6.45	4	yellow
Myoglobin Met (equine)	7.3	5	yellow
Myoglobin Met (sperm whale)	8.3	6	yellow
Cytochrome C	10.6	7	red

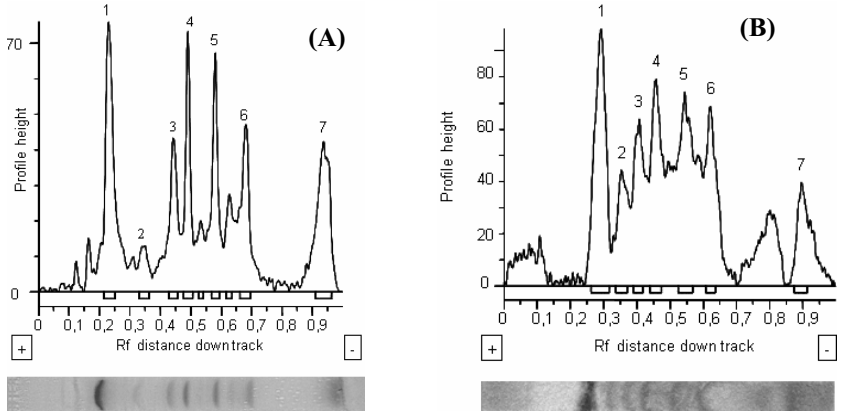

Figure 2. IEF separation of a set of 7 naturally coloured proteins (see Table 1 for protein identification). **(A)** Polyacrylamide mini-gel and **(B)** Micropillar platform. Top: electropherograms obtained by GeneTools software: profile height is not representative of protein abundance but is proportional to its colour intensity. Bottom: **(A)** Part of the mini-gel after focusing and **(B)** photo of focused proteins on our chip.

REFERENCES

[1] Cui, H., Horiuchi, K., Dutta, P., Ivory, C. F., *Anal. Chem.* 2005, *77*, 1303-1309.

[2] Duffy, D. C., McDonald, J. C., Schueller, O. J. A., Whitesides, G. M., *Anal. Chem.* 1998, *70*, 4974-4984.

[3] Busnel, J.-M., Varenne, A., Descroix, S., Peltre, G., Gohon, Y., Gareil, P., *Electrophoresis* 2005, *26*, 3369-3379.

MONOLITHICALLY INTEGRATED ELECTROPHORESIS MICROCHIP WITH ELECTROSPRAY IONIZATION MASS SPECTROMETRIC DETECTION

Santeri Tuomikoski[1], Tiina Sikanen[2], Raimo A. Ketola[2], Risto Kostiainen[2], Tapio Kotiaho[2], Sami Franssila[1]

[1]Helsinki University of Technology, FINLAND and
[2]University of Helsinki, FINLAND

ABSTRACT

In this work we have developed monolithically integrated microchips for analysis of small organic molecules and biomolecules by electrophoretic separation and on-line electrospray ionization mass spectrometric (ESI-MS) detection. The microchips are fabricated fully of SU-8 with simple process using standard photolithography. The microchips show good performance in separation and the ESI-MS detection can be done efficiently due to accurate nozzles microfabricated monolithically at the end of the separation channel.

Keywords: SU-8, Electrophoresis, Electrospray ionization, Mass spectrometry

1. INTRODUCTION

Electrophoresis-ESI-MS is widely used technique with conventional systems, and some attempts have also been made towards chip-based systems [1,2]. However, the separation efficiency of earlier microdevices has not been optimal. Furthermore chip fabrication has required manual processing (like inserting nanospray needles or manual tip polishing) which has made the fabrication process difficult and chip accuracy and analytical reproducibility has been compromised. In this work we report a monolithically integrated electrophoresis ESI-MS microchip with excellent separation performance. The chip is ready for use after microfabrication without assembly or other manual steps.

2. METHODS

The microchips have been fabricated lithographically using epoxy photoresist SU-8, by modifying techniques we have earlier presented for fabrication of separate ESI emitters [3] and electrophoretic channels [4]. The microfluidic network is fully enclosed and released from the substrates as shown in Figure 1. Electrophoresis-ESI chips with wide variety of microchannel configurations and dimensions have been fabricated and tested. All versions have electrophoresis channel with simple cross injector. The formation of ESI is aided with hydrodynamically induced auxiliary liquid flow (Figure 2 (a)), which improves ionization and stability of the ES. All other liquids are driven in channels by electric field without additional pumping. Therefore use of the chips is easy.

3. RESULTS AND DISCUSSION

Lithographic SU-8 processing enables sample introduction unit, separation channel and sharp emitter for ESI to be integrated on a single microchip without dead-volumes. Figure 2 (b) shows a scanning electron micrograph of a sharp ESI emitter of the chip. Fabricational accuracy is in the micrometer range for all layers and therefore accurate tips

978-0-9798064-0-7/μTAS2007/$20©2007CBMS

can be accomplished. Correspondingly stable electrospray is obtained from batch to batch. Ion current stability is typically <5% RSD. Geometries and dimensions of the channels as well as separation conditions have been optimized based on the analytical performance of the chips. With optimized channel configuration a detection limit of 5 amol (100 nM) has been obtained for verapamil using MS/MS detection.

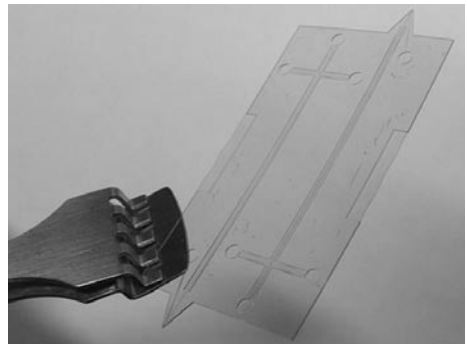

Figure 1: Optical photograph of a released microchip for electrophoresis ESI-MS. The chip is fabricated completely of SU-8 and it has two separation devices next to each other.

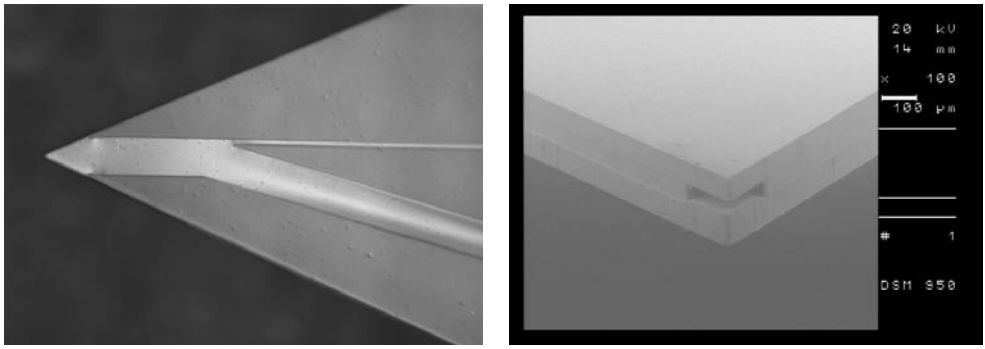

Figure 2. (a) Optical image of the ESI end of a chip. Auxiliary flow joins the separation buffer from one side to improve ESI stability. (b) Scanning electron microscope image of the ESI tip of a microchip. Accuracy of fabrication process enables straightforward fabrication of sharp ESI tips.

Electrophoretic separations with on-line ESI-MS detection have been carried out using small organic molecules and biomolecules. In Figure 4 a separation of three peptides (Substance P (1-11), Angiotensin I and Angiotensin II) is demonstrated in full-scan MS mode. The amounts of peptides injected were 11.3 fmol (each). The peptides were efficiently separated (R_S values 3.3 and 2.0) within 80 s and the number of theoretical plates for the peptides were 40 600-115 900 m^{-1} within a 2-cm separation path. By comparing the separation efficiency of microchip electrophoresis using SU-8 microchannels and fluorescence detection, it can be concluded that introduction of the auxiliary flow does not significantly cause broadening of the analyte zones in our monolithically integrated device. Separation performance of our chips remains very stable from run to run as can be seen from Figure 5 that shows six repeated separations of the peptides using MS/MS detection.

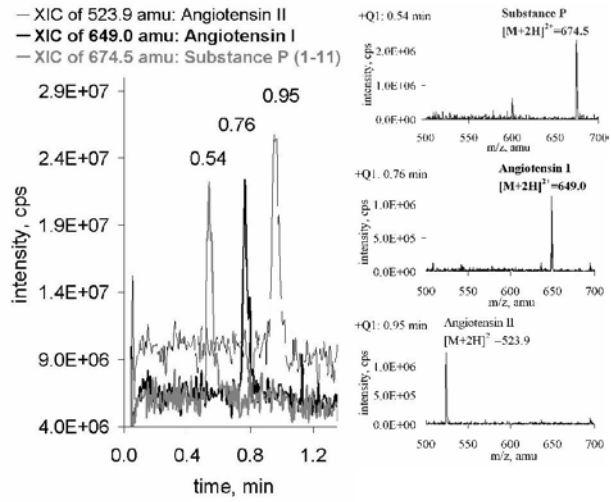

Figure 4: Separation of 3 peptides (Substance P (1-11), Angiotensin I and Angiotensin II). Separation buffer was 20 mM ammonium acetate with 60% methanol and auxiliary flow was methanol-water 80:20 with 1% acetic acid. Applied voltages relative to MS: separation voltage 4.5kV, antileakage voltages 4.0kV and spraying voltage 2.5kV (relative to MS). The detection was performed in full-scan MS mode (500-700 amu).

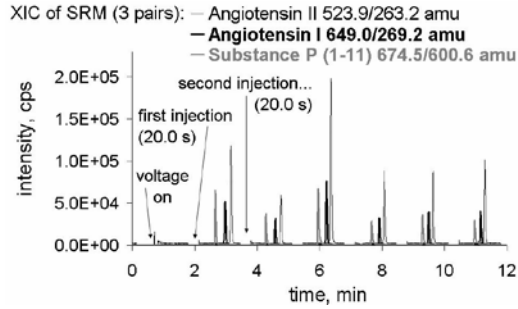

Figure 5: Six repeated injections and separation cycles of a peptide sample. Separation conditions are the same as described in Figure 4. The detection was performed in MS/MS mode using selected reaction monitoring.

CONCLUSIONS

Cheap and easy SU-8 fabrication process together with the excellent separation performance makes our chip suitable for high throughput analysis of biomolecules.

REFERENCES

[1] Li, J., Thibault, P., Bings, N., Skinner, C., Wang, C., Coyler, C., Harrison, J., *Anal. Chem.*, **71**, (1999), 3036-3045.

[2] Foret, F., Kusy, P., *Electrophoresis*, **27**, (2006), 4877-4887.

[3] Tuomikoski, S., Sikanen, T., Ketola, R., Kostiainen, R., Kotiaho, T., Franssila S., *Electrophoresis*, **26**, (2005), 4691-4702.

[4] Sikanen, T., Tuomikoski, S., Ketola, R., Kostiainen, R., Franssila S., Kotiaho, T., *Lab Chip,* **5**, (2005), 888-896

pH GRADIENTS IMMOBILIZED ON-CHIP FOR RAPID ISOELECTRIC FOCUSING

G.J. Sommer[1], A.K. Singh[2], and A.V. Hatch[2]

[1]*Department of Mechanical Engineering, University of Michigan, Ann Arbor, MI USA*
[2]*Biosystems Research Department, Sandia National Laboratories, Livermore, CA USA*

ABSTRACT

We present a method for establishing and then immobilizing well-defined polymer gradients in microchannels. The method is used to create microscale immobilized pH gradients for rapid, on-chip isoelectric focusing of analytes. Focusing is demonstrated across a pH 3.8 – 7.0 gradient using fluorescent p*I* markers and green fluorescent protein.

Keywords: Immobilized pH gradient, isoelectric focusing, polyacrylamide gel electrophoresis

1. INTRODUCTION

Microscale immobilized pH gradients (μIPGs) were created for isoelectric focusing (IEF) applications where analytes are separated at unique locations along a stable pH gradient based on differences in isoelectric point (p*I*) [1,2]. IPG strips have been widely used for macroscale (7-18cm long strips) 2-D gel separations [3], but microfluidic IEF has been limited to mobile solution gradients (e.g., focusing of ampholytes by an electric field). The method presented here enables chip-based IPG fabrication with rapid separation times (< 30 minutes) compared to standard IPG (12-24 hours) due to shorter separation lengths and higher applied electric fields. The μIPG also provides a method to couple IEF to other chip-based techniques for rapid multi-dimensional separations [4].

2. MICROCHIP FABRICATION AND FOCUSING EXPERIMENTS

Polymer gradients were fabricated within existing microchannels using the method shown in Figure 1. First, a thin polyacrylamide membrane is photopolymerized within a central channel (IPG channel) where the polymer gradient will later be formed. The membrane prevents fluid flow through the IPG channel, but allows a gradient to be established by diffusion of monomer into the IPG channel. To create a well-defined gradient of monomer along the IPG channel, different aqueous monomer solutions are then fed continuously, by gravity, through side channels serving as both source and sink of monomer at each end. The monomer solutions contain acrylamide/bisacrylamide, a photoinitiator, and calculated concentrations of acrylamido monomers of varying p*K* to generate the desired pH gradient. The resulting gradient depends on IPG channel length, diffusivity of monomer species, and time allowed for diffusion. Linear gradients of monomer (but not necessarily pH) are established by allowing sufficient time to achieve steady-state concentration profiles. Once the desired gradient of monomer is established, it is immobilized by photopolymerization via UV light.

Formation of a linear polymer gradient was verified visually by introducing AlexaFluor 555 on one side (acrylamide/bisacrylamide on both sides) to form a gradient of fluorophore (not pH in this case). The fluorescence profiles at different times are shown in Figure 1(b).

To evaluate μIPGs, fluorescent p*I* markers and green fluorescent protein (GFP) were introduced and rapidly focused via applied electric fields across the chip. Reservoirs were filled with dilute buffering solutions (lysine/arginine, cathodic; phosphoric acid anodic).

978-0-9798064-0-7/μTAS2007/$20©2007CBMS

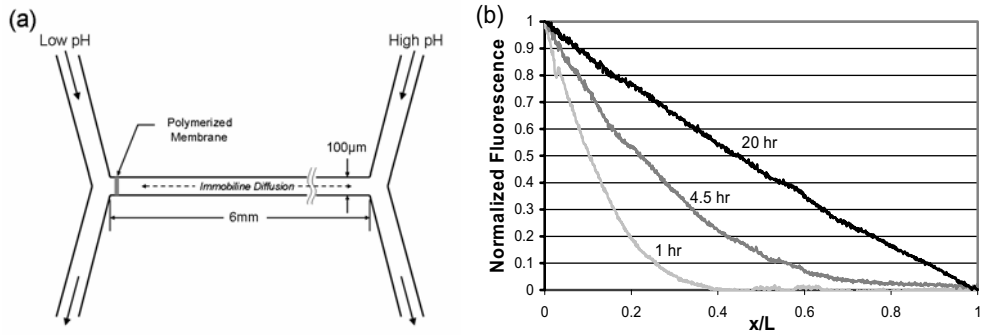

Figure 1. (a) Fabrication of on-chip µIPG. Continuous flow of aqueous acrylamide/acrylamido buffer solutions of low and high pH allows diffusion of immobilines across separation channel. Entire channel is polymerized following equilibration to immobilize pH gradient within gel matrix. (b) Fluorescent intensity profiles of AlexaFluor 555 gradient produced in a 6mm-long, constant pH channel.

3. THEORY

A numerical model was used to design or predict pH gradient profiles by adjusting immobiline concentrations at each end. The model uses the simple transient diffusion equation to predict the time needed for adequate species equilibration, and the following ionization equilibrium equations to predict the pH at any point in the channel:

$$K_{i,acidic} = \frac{[B_i^-][H^+]}{[B_i^0]} \qquad K_{j,basic} = \frac{[B_j^0][H^+]}{[B_j^+]} \qquad K_{water} = [H^+][OH^-] = 10^{-8}\, mol \cdot m^{-3}$$

where K is the equilibrium constant, B^0 denotes a neutral species, and B^- and B^+ denote ionic species.

4. RESULTS

The model was used to determine boundary concentrations of acrylamido monomers needed to generate a linear pH 3.8 - 7.0 µIPG. Upon polymerization the channel was soaked in deionized water and rinsed with cathodic and anodic buffering solutions to remove any unpolymerized monomer. Analytes were electrophoretically fed into the µIPG channel and focused under E-fields ranging from 30 – 500 V/cm over 30 minutes. Figure 2 shows a sample image of fluorescent p*I* marker separation and the resulting pH profile across the channel. Figure 3 shows the focusing of native GFP. The typical primary band (p*I* 5.00) and secondary bands (p*I* 4.88 and p*I* 5.19) for GFP are clearly seen.

5. DISCUSSION AND CONCLUSIONS

The method presented here allows for simple and reliable polymer gradient generation in microchannels. We have immobilized a microscale pH gradient in a polyacrylamide matrix using acrylamido monomers of varying concentration. This technique could greatly enhance microscale IEF which is typically conducted in free flow ampholyte solutions and can suffer from poor stability, resolution and reproducibility. This approach can be used to couple µIPG's to other on-chip mechanisms to enable 2-D separations (e.g. IEF/SDS-PAGE), or used to generate polymer gradients for other µTAS applications.

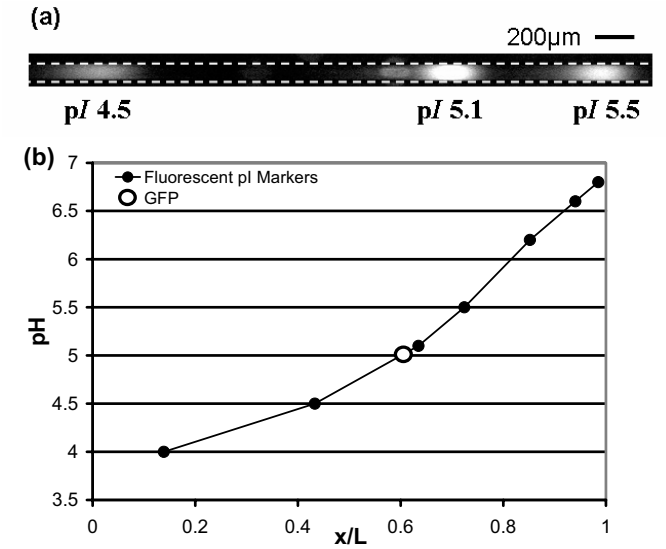

Figure 2. Focusing of fluorescent pI markers (filled circles) and GFP (open circle) in pH 3.8 - 7.0 µIPG. (a) Sample image of focusing results. (b) Resulting pH profile across channel.

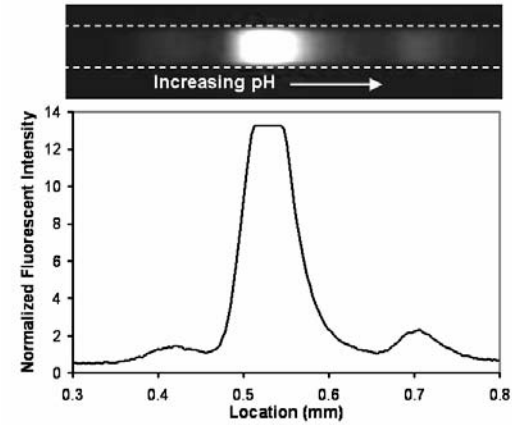

Figure 3. Focusing of 200nM native GFP across pH 3.8-7.0 µIPG. Approximate E-field: 300 V/cm. Results shown following 20 minutes of focusing. The primary band (p*I* 5.00) and secondary bands (p*I* 4.88 and p*I* 5.19) for GFP are clearly seen.

REFERENCES

1. W. Thormann, R.A. Mosher, M. Bier. *Journal of Chromatography A*, **351**, 17-29 (1986).
2. P.G. Righetti. *Electrophoresis*, **27**, 923-938 (2006).
3. B. Bjellqvist, K. Ek, P.G. Righetti, E. Gianazza, A. Gorg, R. Westermeier, W. Postel. *Journal of Biochemical and Biophysical Methods*, **6**, 317-339 (1982).
4. A. Gorg, C. Obermaier, G. Boguth, W. Weiss. *Electrophoresis*, **20**, 712-717 (1999).

VISCOSITY-TUNABLE POLYMER FOR MICROCHIP ELECTROPHORESIS OF DNA

Daisuke Kuroda[1], Noritada Kaji[1, 2], Manabu Tokeshi[1, 2], Yoshinobu Baba[1-4]

[1]Department of Applied Chemistry, Graduate School of Engineering,
[2]MEXT Innovative Research Center for Preventive Medical Engineering,
Nagoya University, JAPAN
[3]Health Technology Research Center, AIST, JAPAN
[4]Institute for Molecular Science, JAPAN

ABSTRACT

A versatile alternative to entangled and random-coiled polymers, Pluronic F127, has been developed for a DNA separation matrix in microchip electrophoresis. This temperature-sensitive and viscosity-tunable polymer provided excellent resolutions over a wide range of DNA sizes based on a different separation mechanism compared with conventional polymers such as cellulose-derivatives.

Keywords: Pluronic F127, Microchip electrophoresis, DNA, Viscosity-tunable polymers

1. INTRODUCTION

Pluronic F127 is a tri-block copolymer consists of poly(ethylene oxide)[E] and poly(propylene oxide)[P] chains with an approximate chemical formula ($E_{100}P_{70}E_{100}$).(Fig. 1)[1] It has a unique feature, "sol-gel transition", depends on temperature. At lower temperatures (≤18°C), it is a hydrated liquid even in a concentration range of about 18-30% and can be easily introduced into microchannels. With elevation of temperature, it changes phase from sol to gel-like state and shows its potential as a DNA sieving matrix. (Fig. 2)

2. EXPERIMENTAL

In this work, 20%(w/w) Pluronic F127 solutions were applied to separation of several sizes of DNA molecules in microchip electrophoresis under temperature control. The powder of Pluronic F127 was dissolved in 1xTBE buffer with 10 μM TO-PRO-3 at refrigerator temperature overnight, and then, Pluronic F127 solution was introduced into commercially available PMMA(polymethylmethacrylate) microchip for DNA separation or home-made PDMS(polydimethysiloxane) microchip for a single DNA observation on ice. Microchip electrophoresis was performed on Hitachi SV1210 microchip instrument or fluorescence microscope under temperature control. Various sizes of DNA ladder were used for DNA

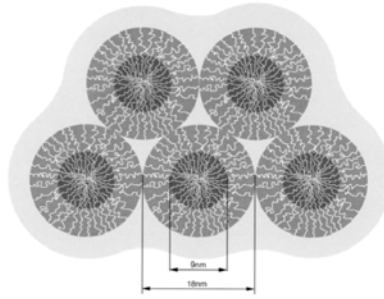

Figure 1. Schematic of Pluronic F127 micelles solution. The darker gray region represents hydrophobic cores of P segments and lighter gray region represents mesh domains of hydrated E chains [1].

978-0-9798064-0-7/μTAS2007/$20©2007CBMS

separation and T4 DNA (165.6 kbp) was used to reveal DNA migration behavior in Pluronic F127 solutions. The viscosity of Pluronic F127 solutions was measured by Viscolite 700, MTL Instruments.

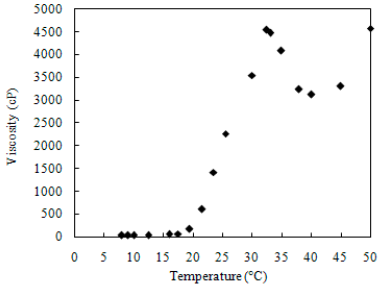

Figure 2. Temperature dependence of viscosity of 20%(w/w) Pluronic F127 solution. Sol-gel transition point is about 23°C.

3. RESULTS AND DISCUSSION

At lower temperatures below 15°C on ice, Pluronic F127 solution could be easily introduced into the microchannel by capillary force since its viscosity was almost comparable to water. As shown in Fig. 3, higher temperature (40°C) gave better separations in the range of 50 to 1,500 bp compared with lower temperature (15°C). It is interesting that gel-like state with higher viscosity at 40°C gave higher migration velocities for all of the separations. This unique property resolved 25 bp ladder well especially the larger portion indicated by dotted rectangle in Fig. 4. Fig. 5 shows the relation between electrophoretic mobility and DNA size in Pluronic F127 and methylcellulose solution. This figure indicated that Pluronic F127 offered a better resolution over a wide range of DNA size than 0.2%(w/v) methylcellulose. Especially in the larger portion of 25 bp ladder, Pluronic F127 solution resolved it better than methylcellulose. This is an opposite tendency compared with conventional polymers like polyacrylamide and methylcellulose. These unique properties promise to separate a wide size range of DNA with a short time. These results indicated that the separation mechanism is fundamentally different from that in crosslinked polymers.

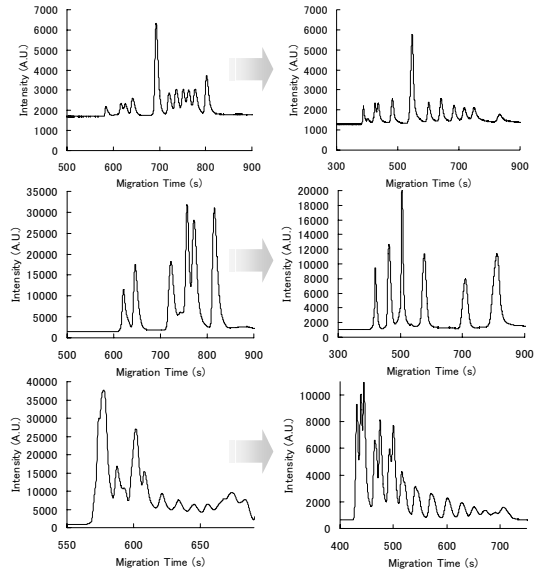

Figure 3. Electropherogram of separation of DNA ladders, 100bp Ladder (upper), PCR-Markers (middle), and 50bp Ladder (lower) at 15°C (left) and 40°C (right) by using 20%(w/w) Pluronic F127 solution.

To reveal the separation mechanism, T4 DNA (165.6 kbp) migration behavior in Pluronic F127 solution was observed at a single molecule level. T4 DNA showed that it migrated interstitial spaces between micelles and hydrated poly(ethylene oxide) strands with squeezing out random-coiled conformations. It was also found that DNA molecules tend to trace the pass of which adjacent molecules passed as shown in Fig. 6. This phenomenon has never observed in conventional gel or polymer systems. So this migration behavior might cause low-reproducibility of the separation using Pluronic F127.

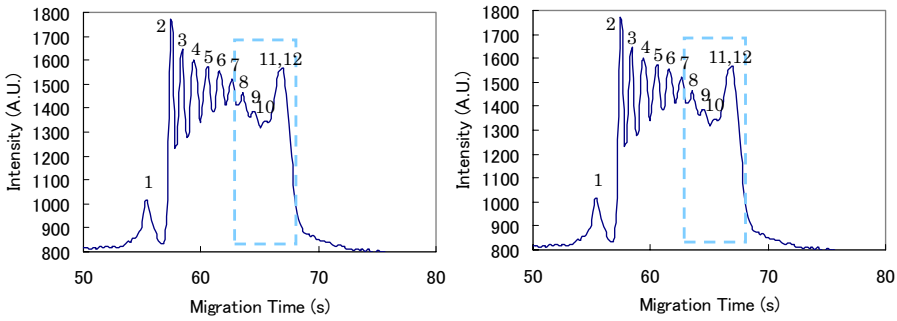

Figure 4. Separation of 25 bp DNA Ladder by 0.2%(W/V) methylcellulose (left) and 20%(V/V) Pluronic F127 solution (right).

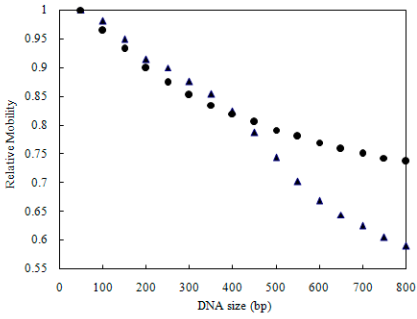

Figure 5. Relative mobility of Pluronic F127(triangle) and Methylcellulose(circle) at 40°C calculated from the result of 50bp DNA Ladder separation.

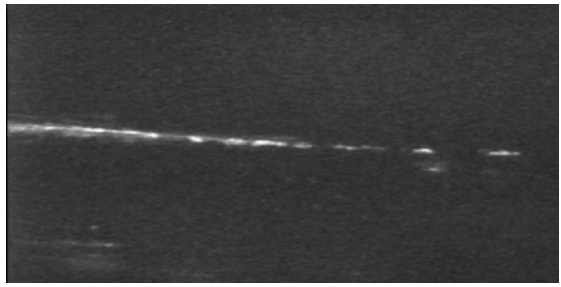

Figure 6. Observed image of DNA electrophoretic migration in 20%(w/w) Pluronic F127 solution at 26℃ in PDMS microchannel. DNA molecules showed tendency to trace the same trajectory that has been explored by preceded DNA molecules.

5. CONCLUSIONS

Viscosity-tunable polymer, Pluronic F127, showed good ability as a DNA separation matrix in microchip electrophoresis. Separation performance over a wide size range of DNA and easy introduction into microchannel is suitable for future microchip-based separation techniques. While further investigations about separation mechanism are still required, the unique property and various advantages of Pluronic F127 over conventional polymers provide opportunities in microchip electrophoresis.

REFERENCES

[1] R. L. Rill, Y. Liu, D. H. Van Winkle, B. R. Locke, *Pluronic copolymer liquid crystals: unique, replaceable media for capillary gel electrophoresis*, *J. Chromatography A*, 817, pp.287-295, (1998).

DEVELOPMENT OF INTEGRATED *IN SITU* ANALYZERS (IISA) FOR OCEANOGRAPHY APPLICATIONS

T. Fukuba[1], A. Miyaji[2], N. Fukuzawa[1], C. Provin[1]
T. Yamamoto[1], L. Glutz[3], T. Okamoto[1] and T. Fujii[1]
[1] *Institute of Industrial Science, The University of Tokyo, Japan*
[2] *Tokyo Institute of Technology, Japan*
[3] *Ecole Polytechnique Federale de Lausanne (EPFL), Switzerland*

ABSTRACT

In this study, PDMS based microfluidic devices were applied to develop "integrated *in situ* analyzers (IISAs)". The IISAs will enable to perform totally automated field survey about microbial gene (IISA-Gene), ATP (IISA-ATP) and manganese ion (Mn^{2+}) concentration (IISA-Mn) in oceanic environments including deep-sea. Development and evaluation of each prototype is presented here.

Keywords: IISA, PCR, ATP, manganese

1. INTRODUCTION

In the field of biological and chemical oceanography, application of functionally integrated and miniaturized *in situ* analysis devices is strongly demanded to perform 3D or 4D data acquisitions. Some research groups had reported about their pioneer works to develop miniaturized *in situ* devices to analyze inorganic nutrients contained in seawater before now (e.g. [1]). However, well-miniaturized devices for biological analysis or heavy metal quantifications are not reported yet in our knowledge. In this study, *in situ* devices for biological and chemical analysis have been developed as "IISA" series and evaluated here.

For all IISA microchips, microchannels are patterned on PDMS material by using conventional SU-8 based process. 6 pairs of heater (Cr) and temperature sensor (Pt) are integrated on a glass substrate (50 mm x 75 mm) for IISA-Gene.

2. IISA-Gene

Gene analysis is one of the most powerful solutions to understand microbial communities in extreme environments because of difficulty in culturing them. PCR based *in situ* gene analysis will reveal their real diversity and specificity without any risks of contamination or degradation during sampling processes. The IISA-Gene has whole functions for gene analysis of microbes (Fig. 1). Microbial cells are chemically lysed with GuSCN based chaotropic reagent and genomic DNA is purified in a glass beads (30-50 μm in dia.)

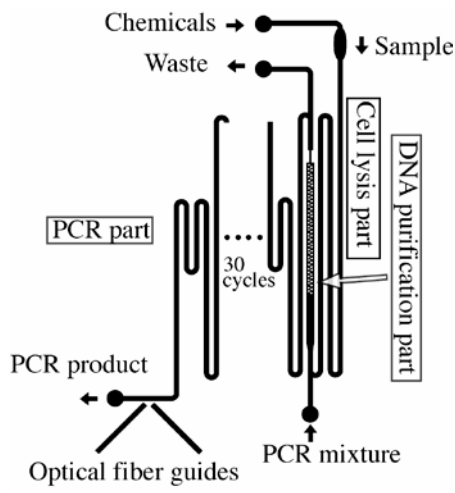

Figure 1. A schematic drawing of the PDMS microchip for IISA-Gene.

978-0-9798064-0-7/μTAS2007/$20©2007CBMS

packed microchannel. The targeted gene is amplified in a flow-through PCR part [2]. Subsequently, fluorescently labeled PCR products are optically detected by using optical glass fibers (225 μm core dia.) embedded in the PDMS chip. The fibers are connected to a LED light source and a photomultiplier tube (PMT). The PDMS microchip is connected with miniature pumps, valves and chemical reservoirs for *in situ* operations. The IISA-Gene was mounted on a remotely operated underwater vehicle (ROV) and operated in deep-sea environments in May 2005 and July 2006 (Fig. 2). In spite of successful operations in a laboratory environment, the preliminary field trials that were targeted to detect bacterial 16S rRNA gene or particulate methane monooxygenase gene didn't provide significant positive signal (data not shown). The reliability and sensitivity are being improved towards the next *in situ* trial.

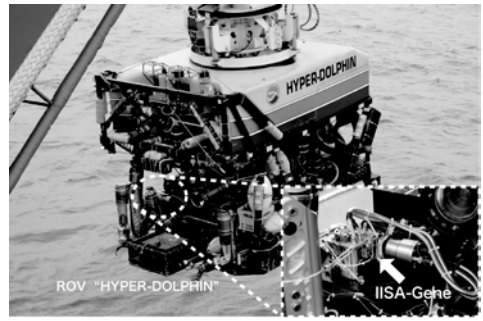

Figure 2. The IISA-Gene mounted on the ROV "HYPER-DOLPHIN".

3. IISA-ATP

Cellular ATP concentration is also important parameter to assess microbial activities and abundances in oceanic environments [3]. Microbial intracellular ATP can be quantified by using the IISA-ATP. In a microchannel of an IISA-ATP prototype chip (Fig. 3), cell lysis is performed subsequently to extracellular ATP elimination. As the final step, ATP is quantified by luciferin-luciferase reaction in a detection coil. CheckLite HS Set (Kikkoman Co., JAPAN) was used for all experiment. The photo intensity is measured by a PMT.

A prototype of IISA-ATP was evaluated in laboratory. The IISA-ATP could quantify 0.1 to 100 nM of ATP (Fig. 4). Two seawater samples were collected in Tokyo bay and supplied to the IISA-ATP without any pretreatments to evaluate its applicability to real field samples. As a result, 0.47 and 3.23 nM of intracellular ATP was detected and these values were consistent with the result from conventional test tube method.

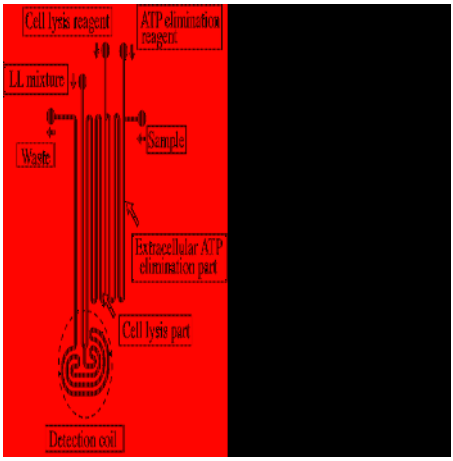

Figure 3. A schematic drawing of the PDMS microchip for IISA-ATP.

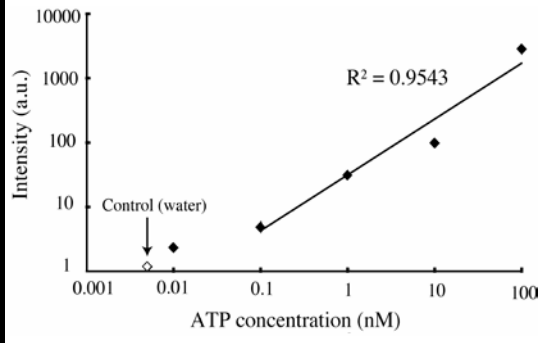

Figure 4. Result of ATP quantification with the IISA-ATP prototype.

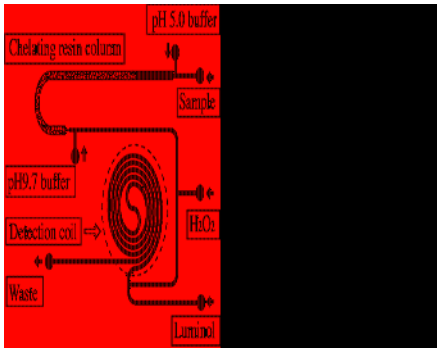

Figure 5. A schematic view of the PDMS microchip for IISA-Mn.

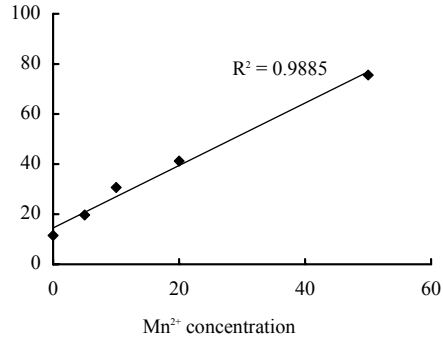

Figure 6. Result of Mn^{2+} quantification under coexistence of 10 μM of Fe^{2+}

4. IISA-Mn

Manganese ion (Mn^{2+}) that is one of the useful markers to find hydrothermal activities in deep-sea environments [4] can be quantified by IISA-Mn with chemiluminescence-based method. After adjusting pH of samples, inhibiting metal ions (e.g. Fe^{2+}) are removed by pass-through a chelating resin column (8-quinolinol modified Fractogel TSK HW-75 (TOSOH Co., JAPAN)) in a microchannel. Finally, Mn^{2+} is quantified by luminol reaction in a spiral shaped detection coil (Fig. 5).

Detection limit of IISA-Mn was evaluated with Mn^{2+} standard solution. As a result, 10 nM of Mn^{2+} was successfully quantified under coexistence of 10 μM of Fe^{2+} (Fig. 6).

ACKNOWLEDGEMENTS

We are grateful to the crew of the R/V Natsushima and operating team of ROV HYPER-DOLPHIN (JAMSTEC) for their helpful assistance during the cruises. This work was supported by grant-in-aid for scientific research (S) and grant-in-aid for young scientists (B) from Japanese Ministry of Education, Culture, Sports, Science, and Technology (MEXT).

REFERENCES

[1] D. Thouron, R. Vuillemin, X. Philippon, A. Lourenço, C. Provost, A. Cruzado and V. Garçon, “An autonomous nutrient analyzer for oceanic long-term *in situ* biogeochemical monitoring”, *Anal. Chem.,* **75**, pp. 2601-2609, (2003).

[2] T. Fukuba, T. Yamamoto, T. Naganuma and T Fujii, “Microfabricated flow-through device for DNA amplification – Towards in situ gene analysis”, *Chem. Eng. J.,* **101**, pp. 151-156, (2004).

[3] D. M. Carl, “Cellular nucleotide measurements and applications in microbial ecology”, *Microbiol. Rev.,* **44**, pp. 739- 796, (1980).

[4] K. Okamura, T. Gamo, H. Obata, E. Nakayama, H. Karatani and Y. Nozaki, “Selective and sensitive determination of trace manganese in sea water by flow through technique using luminol-hydrogen peroxide chemiluminescence detection”, *Anal. Chim. Acta*, **377**, pp. 125-131, (1998).

MICRO PARTICLE SAMPLING ON MICRO-FABRICATED PERFORATED FILTER MEMBRANES

Y. Zhao[1], S. K. Chung[1], U.-C. Yi[2] and S. K. Cho[1]*

[1]Department of Mechanical Engineering and Materials Science, University of Pittsburgh, USA, [2]Core MicroSolutions Inc.

ABSTRACT

This paper describes micro particle sampling on various microfabricated perforated filter membranes using EWOD-actuated droplet sweeping. Three designs of filters with different hole shape, size and opening ratio were microfabricated and tested, demonstrating high sampling efficiencies: over 95% for 8-μm glass bead sampling and over 85% for 8-μm polystyrene bead sampling.

Keywords: Particle Sampling, Micro Filter, Droplet, Electrowetting

1. INTRODUCTION

Recently, we reported that EWOD-actuated moving droplets can efficiently sweep and sample various micro particles on a flat surface [1]. In addition, we presented that this method is also highly effective on perforated filter membranes (Fig. 1) [2]. In this previous work, however, since only one kind of membrane was commercially available, both filter holes and particles tested were limited to the pretty large dimension (~ 100 μm), making the sampling method impractical. Typical airborne target particles range in several microns in size. In this paper, we microfabricated filters of several-μm sized holes and examined them with 8-μm particles, targeting for practical airborne particle sampling.

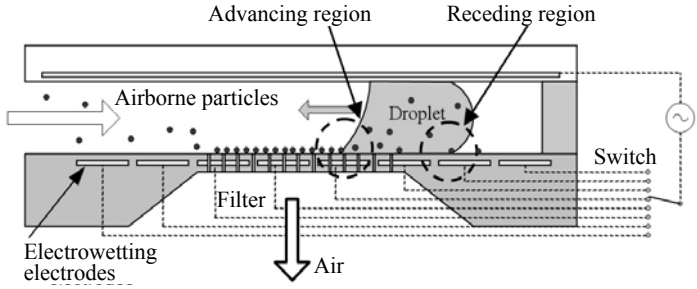

Figure 1. Airborne particle sampler. Particles can be swept and sampled into the droplet driven by electrowetting-on-dielectric (EWOD) principle. The EWOD electrodes placed in the perforated filter membrane are sequentially energized for droplet actuation. The particle sampling occurs in both advancing and receding regions of the droplet.

2. FABRICATION

Figure 2 shows micro fabrication steps (Fig. 2a-d) of the perforated filter membrane embedded with an EWOD electrode array. The filter membrane was made of the low-stress SixNy layer deposited Si wafer. After backside KOH etching, the filter holes on the membrane were opened by RIE etching (Fig. 2a). For a linear array of EWOD electrodes, a gold layer (1000 Å) along with a Cr seed layer (100 Å) was sequentially deposited by an E-beam evaporator and patterned. Finally a parylene layer (1 or 3 μm thick) is conformally

978-0-9798064-0-7/μTAS2007/$20©2007CBMS

coated on the membrane structure, followed by a 100 Å thick teflon layer. Three different kinds of membrane designs were fabricated: Design 1 (rounded rectangle hole of 48 μm × 6 μm, opening area ratio of 5 %); Design 2 (rounded rectangle hole of 24 μm × 6 μm, opening area ratio of 20 %); Design 3 (circular hole of 8-μm dia., opening area ratio of 9 %).

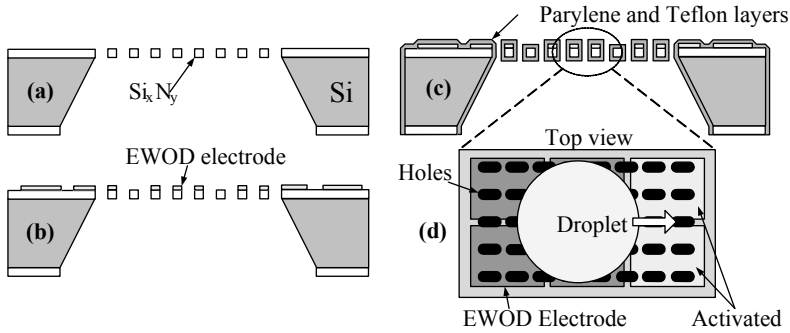

Figure 2. Fabrication of filter membrane embedded with EWOD electrodes: **(a)** The low stress SixNy membrane is fabricated by KOH backside etching. Filter holes are opened by RIE etching. **(b)** A gold layer (1000 Å) along with a Cr seed layer (100 Å) was sequentially deposited on the membrane and patterned. **(c)** A parylene layer (1 or 3 μm thick) is deposited on the membrane followed by a 100 Å thick teflon layer. **(d)** Configuration of droplet on the electrodes.

3. RESULTS AND DISCUSSION

Shown in Fig. 3 are sequential pictures of testing results for design 1 with 8-μm glass beads. First, 8-μm glass beads are uniformly deposited on the membrane (Fig. 3a). An EWOD-actuated droplet moves from right to left along the array of electrodes, simultaneously sweeping and sampling the particles into the droplet (Figs. 3b, c). Particles seldom remain on the path where the droplet has passed. Finally, the sampled particles are suspended inside the droplet (Fig. 3d).

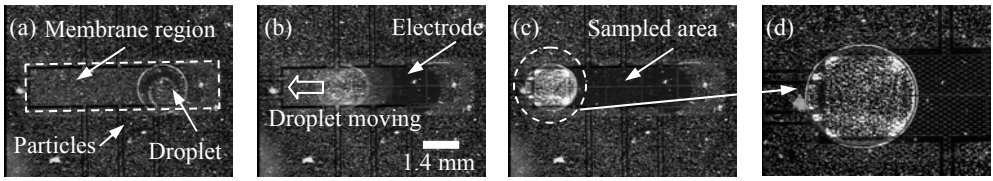

Figure 3. Sequential pictures of glass beads sampling viewed through the transparent top glass plate: **(a)** glass beads (white dots, 8-μm dia.) and a droplet are deposited on the perforated membrane. **(b, c)** the droplet moves left when the EWOD electrodes are sequentially activated to the left. Glass beads are picked up by the moving droplet. After the droplet passes, the membrane surface becomes clean (not frosted) with no bead left behind. **(d)** Collected beads are suspended in the droplet (close-up view).

For each membrane design, two kinds of particles were tested: 8-μm glass beads and 8-μm polystyrene beads. The sampling results of three filter designs are shown in Fig. 4. We can see that almost all of the glass beads are sampled into the droplet in all the three designs whereas some polystyrene beads remain on the droplet path, especially in designs 2 and 3. It seems to be more difficult to sample the polystyrene particles trapped in the holes. Table 1 lists the sampling efficiency for the three designs after counting particles in a number of

membrane sections. Overall the three designs show high sampling efficiencies (over 95% for glass beads and over 86 % for polystyrene beads). In particular, design 1 shows highest efficiencies for the glass as well as polystyrene beads. This may be due to the largest dimension of 48 μm in hole length facilitating sampling of the trapped particles in the hole.

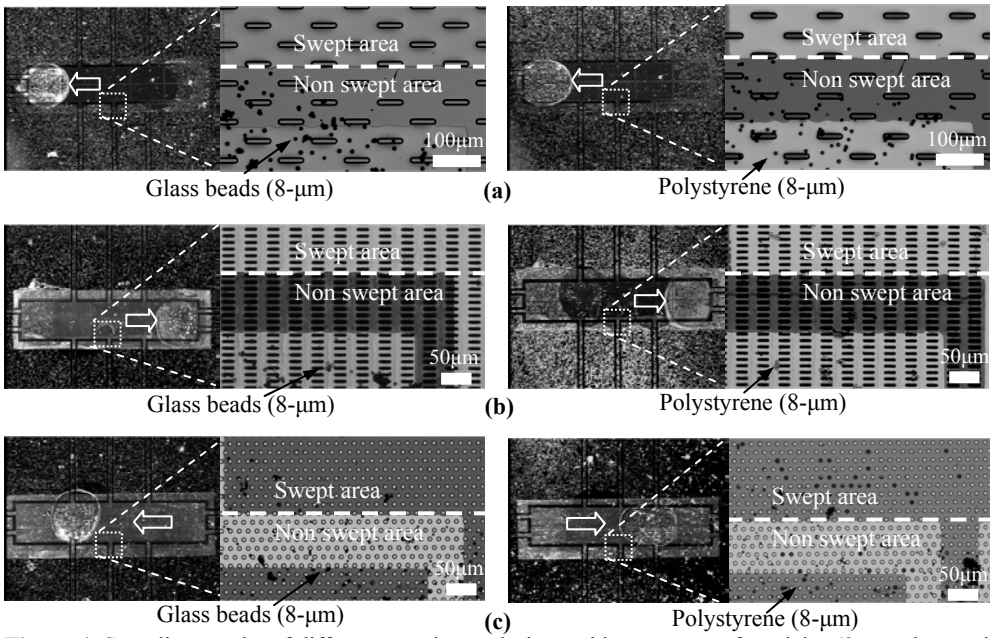

Figure 4. Sampling results of different membrane designs with two types of particles (8 μm glass and polystyrene beads): **(a)** Design 1 (rounded rectangle hole of 48 μm × 6 μm, opening area ratio of 5 %). **(b)** Design 2 (rounded rectangle hole of 24 μm × 6 μm, opening area ratio of 20 %). **(c)** Design 3 (circular hole of 8-μm dia., opening area ratio of 9 %). The upper part of dotted lines denotes droplet-swept region.

Table 1. Sampling efficiency for the three filter designs

Particle	Contact angle with water (degree)	Sampling efficiency (%)		
		Filter 1	Filter 2	Filter 3
Glass	14	99.5	98.7	95.9
Polystyrene	66	93.9	87.2	86.4

4. CONCLUSIONS

The present particle sampling method shows high sampling efficiencies: over 95% for 8-μm glass bead sampling and over 85% for 8-μm polystyrene bead sampling using an extremely small amount of liquid volume (several droplets of about 500 nanoliters each).

REFERENCES

[1] Y. Zhao and S. K. Cho, "Microparticle sampling by electrowetting-actuated droplet sweeping," *Lab Chip*, Vol. 6, pp. 137-144 (2006)
[2] S.-K. Chung, Y. Zhao, and S. K. Cho, "Micro particle sampling on a perforated filter membrane by EWOD-actuated droplet sweeping," μTAS 2006, Tokyo, Japan, pp. 31-33.

MICROFLUIDIC REACTION OPTMISATION USING INTELLIGENT FEEDBACK.

Christopher Rowlands,[1] Richard Winkle,[2] Robert Wootton[1] and Andrew de Mello[2]

[1] *University Chemical Laboratory, Cambridge University, CB2 1EW, UNITED KINGDOM*
and
[2] *Department of Chemistry, Imperial College London, SW7 2AZ, UNITED KINGDOM*

ABSTRACT

A system for the automated optimisation of chemical reactions within microfluidic devices using intelligent feedback is described. Various search algorithms are employed and their utility and performance compared.

Keywords: Synthesis, optimisation, control systems, feedback.

1. INTRODUCTION

Microfluidic synthesis offers many advantages over conventional bulk synthesis; reactions can be performed in a continuous flow configuration, allowing facile online monitoring and high-throughput reaction screening to be performed[1]. These features mean that reaction optimisation can be performed with a tiny fraction of the time, expense and effort usually required. Since reaction optimisation can save a company many millions of pounds[2] in the form of higher yields and fewer byproducts, this capability is of great commercial interest.

The focus of this work is the creation of an entirely automated system for optimising a continuous-flow microfluidic synthesis. The system must be suitable for a wide variety of different reactions, and must be able to find a suitable optimum rapidly and with no other user input.

2. THEORY

A number of algorithms were investigated in order to determine which were best able to cope with real-world synthetic conditions. These algorithms can all be considered to be topological operations on a multidimensional "configuration space" where the axes of this configuration space correspond to the flow rates of the pumps. They are as follows:

Simplex Algorithm – A series of test points are created in configuration space, and a new point to test is created by moving away from the worst point.

Nelder Mead Simplex Algorithm – As above, but the simplex is permitted to change shape to better fit the contours of configuration space.

Pattern Search – a starting point is found and a series of test points are generated in the area most likely to produce a better result. The next starting point is generated by drawing a line from the start point, through the best test point to a final point beyond.

Look / Monte Carlo – points are tested at random in the vicinity of the current 'best' point, and if a better point is found, points are generated around that instead.

Genetic Algorithm – Each flow rate is considered as a gene on an artificial genome, and the configurations producing the best yield are "mated" in order to produce offspring with similar characteristics in the next generation.

978-0-9798064-0-7/μTAS2007/$20©2007CBMS

3. EXPERIMENTAL

Automated Microfluidic Synthesis System

The microfluidic synthesis system consisted of a series of computer-controlled syringe pumps which controlled the flow of reagents into a glass microfluidic reactor. Optical fibers were placed on either side of the exit channel of the reactor. One fiber was coupled to an Ocean Optics HL-2000 tungsten halogen light source (7W output) and the other was coupled into an Ocean Optics USB2000 Vis-NIR spectrometer.

The spectrometer was connected to the same computer as the pumps, and the entire experiment was controlled using a custom-built control program written using Labview 7.1 from National Instruments. The spectrum was analysed by the computer in order to determine the concentration of product by using the Beer-Lambert Law, and the resulting yield was used to determine the next setting to be used by the pumps.

Experimental Results

The reaction that was selected for optimisation was a two-step synthesis of Sudan I:

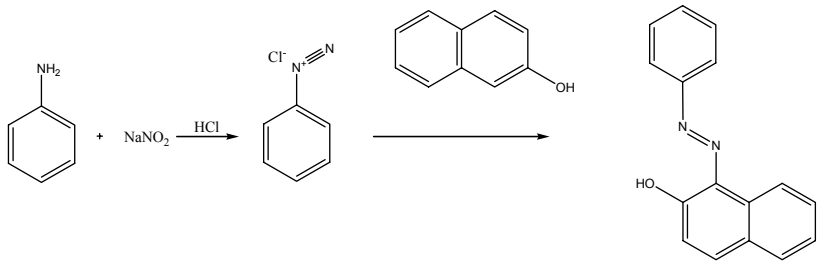

Scheme 1. Synthesis of Sudan 1

A series of different algorithms were tested in order to determine the speed of convergence and the quality of the optimum. The results are shown below; the vertical axis

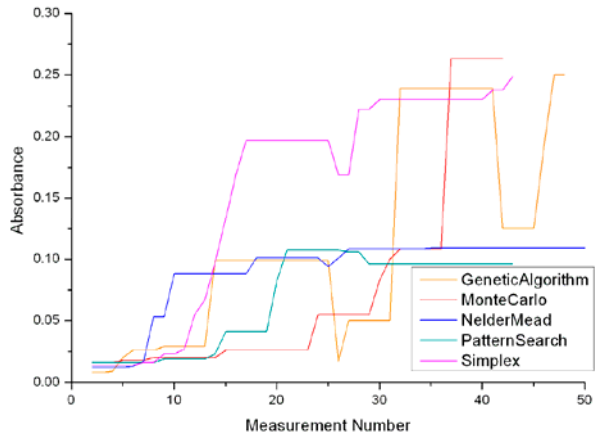

Figure 1. Results of optimisation of Sudan synthesis by various algorithms

measures the highest absorbance measured up until that point by the algorithm and is a direct measure of the concentration of Sudan I produced by those reaction conditions. Downward steps are caused when the reaction conditions are re-evaluated and found to be lower. This function serves to reduce the effect of experimental noise on the measured optimum.

RESULTS AND DISCUSSION

The results of this optimisation were typical of other optimisation runs performed on this synthesis and also reflected the relative performance characteristics on other chemical syntheses. Some common observations on the algorithms are outlined below:

Simplex Algorithm – generally this performed well and was resilient towards experimental fluctuations. Since a major cause of error in the experiment was the system having insufficient time to settle down if the reaction conditions were varied a great deal, the fact that the simplex algorithm only makes incremental changes to the reaction conditions meant that it rarely had to re-evaluate a peak. Convergence time was generally acceptable, and the optima were good.

Look / Monte Carlo – this performed reasonably well over time but its tendency to rapidly change reaction conditions lead to costly errors. Performance fluctuated a great deal, as can be expected.

Genetic Algorithm – this generally outperformed the Look algorithm but suffered from the same tendency to vary the reaction conditions rapidly. Performance was better on more higher-dimensional problems; on simple syntheses with only one or two variables it was often outperformed and no better than the Look Algorithm.

Nelder Mead Simplex Algorithm – performance was good when there was little experimental error, however since the simplex will shrink in certain conditions, occasionally it shrinks for no reason, costing the algorithm a great deal of time, making it's progression slower and consequently lowering the quality of the optimum.

Pattern Search – similar problems affected the pattern search, however, it expands more readily so in general managed to cope better than the Nelder Mead Simplex.

CONCLUSION

This work represents the beginning of a completely automatic system for the optimisation of a chemical reaction, with the potential to revolutionise bulk synthesis of industrial chemicals. A series of different optimisation algorithms have been evaluated and their performances analysed.

Generally the Simplex Algorithm performed the best, finding a good optimum quite rapidly, with good tolerance for random fluctuations and reliably moving towards the theoretical optimum.

REFERENCES

1 - Leung, S.-A.; Winkle, R. F.; Wootton, R. C. R.; de Mello, A. J. *The Analyst* 2005, **130**, 46-51

2 - Harre, M.; Tilstam, U.; Weinmann, H. *Organic Process Research and Development* 1999, **3**, 304-318.

CONTINUOUS GENERATION OF PROTEIN CONTAINING HYDROGEL BEADS USING MICROFLUIDIC DROPLET-MERGING CHANNEL

Eujin Um[1], Dae-Sik Lee[2], Hyeon-Bong Pyo[2] and Je-Kyun Park[1]

[1]Department of Bio and Brain Engineering, Korean Advanced Institute of Science and Technology (KAIST), KOREA and

[2]Electronics and Telecommunications Research Institute (ETRI), KOREA

ABSTRACT

We present a method to encapsulate biomaterials in hydrogel beads using two-phase microdroplet generating and merging system. Poly(dimethylsiloxane) (PDMS) microchannel includes the double-T junction, in which the hydrogel droplets merge with other solutions through the symmetric side branches. This simple design increases the coalescence frequency and the contact time of the solution with hydrogel droplets, and the efficiency of encapsulation in hydrogel droplets is up to 100% at various flow rate conditions. The platform demonstrates gelation of the cell-encapsulated hydrogel and enzyme-substrate reaction with glucose oxidase in hydrogel beads for further application.

Keywords: Microdroplet, hydrogel beads, two-phase flow, biomaterial encapsulation

1. INTRODUCTION

The difficulty in two-phase microdroplet technology arises when there is a need for merging of more than two aqueous solutions, because each liquid is separated by the oil layer. Droplet-based merging has been controlled by means of electrostatics [1] or asymmetry of the channel geometry and flow rate, but integration of the methods for multiple droplet merging is complex to achieve especially in biological applications [2]. Otherwise, all liquids are mixed prior to the injection to the channel. However, various reagents, biomaterials, and hydrogel in sol-state need to be mixed after droplet formation to detect instantaneous reactions or to reduce damage in biological materials.

2. PRINCIPLE

Hydrogel droplets in sol-state are generated from the focusing channel and the second solution for cross-linking of hydrogel is injected alternatively from two sides of the branch in double-T junction (Figure 1). There are two parameters for efficient merging of liquids: the contact time and the coalescence frequency. The former is increased in this device

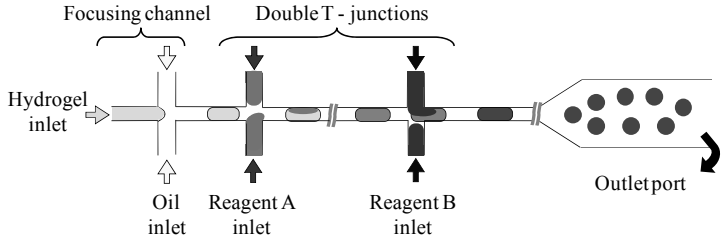

Figure 1. A schematic design of the microfluidic device for hydrogel droplet generation and droplet-based merging with other reagents using double-T junction channels.

978-0-9798064-0-7/μTAS2007/$20©2007CBMS

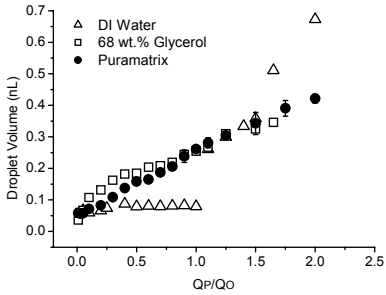

Figure 2. Volume of the hydrogel droplets produced from the focusing channel. Qp/Qo indicates the flow rate ratio of aqueous phase to the oil phase.

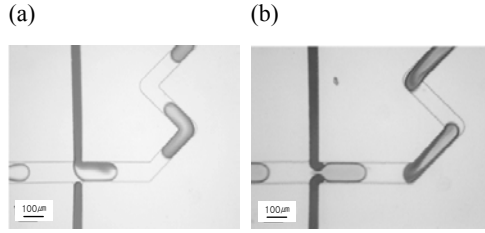

Figure 3. Microscope image of the double-T junction. (a) Droplet merging with red dye at the first double-T junction. (b) Droplet merging with blue dye at the second double-T junction.

because hydrogel droplet passes the junction in long plug-shape. The latter rises when the injection time of the second solution synchronizes with the time hydrogel droplet passes the junction. In the single-T junction, this is realized only in very few flow rate conditions. In the double-T junction, even when one branch is blocked from pressure unstability, the other branch will inject the solution. Therefore the coalescence frequency is high at various flow conditions.

3. EXPERIMENTAL

We used Puramatrix (BD Sciences) and alginate as biocompatible hydrogel materials which start cross-linking under certain salt concentrations. The focusing channel creates various sizes of droplets in microscale (Figure 2). Droplet-based merging of liquids at the double-T junction is demonstrated with water and dye (Figure 3). Series of double T-junctions can be integrated downstream of the channel, and the degree of mixing of solutions is controlled with the serpentine channel shape. To measure droplet merging efficiency, sequential 100 hydrogel droplets were counted and the experiments were repeated three times at each flow rate condition.

4. RESULTS AND DISCUSSION

Since the size of the droplet depends on the flow rate, it is important the droplet merging occur at the various flow rates. Figure 4 shows the result of comparison in merging efficiency at the single and double-T junction with water droplet and dye solution. With the efficiency of more than 80% at the various Qd/Qw (flow rate ratio of dye and water) at the double-T junction, various types of hydrogel beads, partially or fully filled with dye, rod-shaped hydrogel enclosed in dye-droplet, and cell-encapsulated gel beads could be

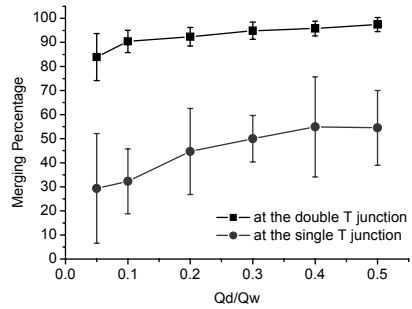

Figure 4. Comparison of droplet-based merging efficiency between the double T-junction and the single T-junction.

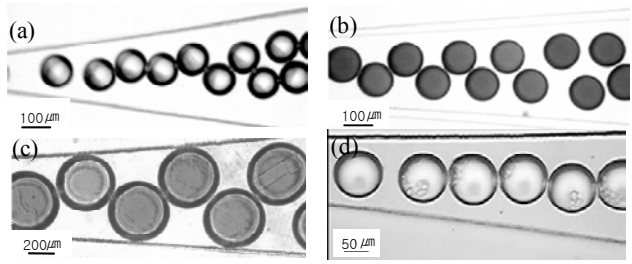

Figure 5. Hydrogel beads at the channel outlet. (a) hydrogel beads half-filled with red dye after the first double-T junction. (b) Purple hydrogel beads thoroughly mixed with red and blue dye after passing two double-T junctions. (c) Rod-shaped hydrogel enclosed in dye-droplets. (d) HepG2-encapsulated hydrogel beads

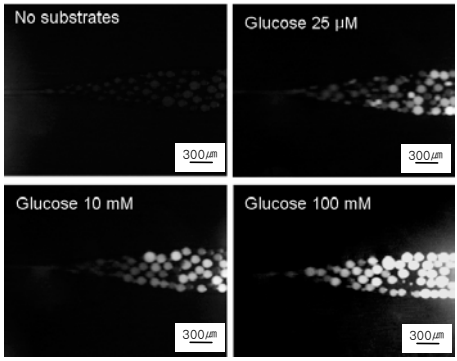

Figure 6. Images of fluorescence intensity from Amplex Red and glucose oxidase encapsulated hydrogel beads after merged with different concentrations of glucose solution.

produced at the outlet (Figure 5). To demonstrate the possible applications of the hydrogel beads and the device, glucose oxidase is encapsulated in hydrogel droplet at the first double T-junction and further mixed with the enzyme substrate, glucose solution, at the second double T-junction. The enzyme-substrate containing hydrogel beads are continuously monitored by the fluorescence intensity of by-products of the reaction (Figure 6).

5. CONCLUSIONS

Here, we propose a simple double-T junction channel to provide up to 100% droplet-based merging at various flow rate, without external forces. The device is suitable for in-situ formation of hydrogel beads encapsulating biological materials. Further application shows the possibility of biological assay applications, such as protein-protein interaction and cell encapsulation.

ACKNOWLEDGEMENT

This work was supported by IT Convergence Technology Research Division, ETRI.

REFERENCES

[1] D. R. Link, E. Grasland-Mongrain, A. Duri, F. Sarrazin, Z. Cheng, G. Cristobal, M. Marquez and D. A. Weitz, *Electric control of droplets in microfluidic devices*, Angew. Chem. Int. Ed., 45, 2556 (2006).

[2] L.-H. Hung, K.M. Choi, W.-Y. Tseng, Y.-C. Tan, K.J. Shea and A.P. Lee, *Alternating droplet generation and controlled dynamic droplet fusion in microfluidic device for CdS nanoparticles synthesis*, Lab Chip, 6, 1 (2006).

ELECTROCHEMICAL MICRO-FLOW-CELL FOR RAPID AND EFFICIENT CONCENTRATION OF [^{18}F]FLUORIDE TO APROTIC SOLVENT FROM [^{18}O]WATER

Ryo Yamahara[1], Hiroaki Nakanishi[1], Katsumasa Sakamoto[1], Hidekazu Saiki[1], Eiichi Ozeki[1], Ren Iwata[2]

[1] Technology Research Laboratory, Shimadzu Corporation, Kyoto 619-0237, Japan
[2] Cyclotron and Radioisotope Center, Tohoku University, Sendai 980-8578, Japan

ABSTRACT

A novel micro-flow-cell which could electrically concentrate [^{18}F]fluoride to organic solvents has been developed for convenient preparation of positron emission tomography (PET) probes. The miniaturized flow-cell enables to reduce an ordinary solvent volume to 1/100 and a period of concentration time. [^{18}F]Fluoride produced in a few ml of [^{18}O]water is concentrated in µl order of an aprotic solvent for successive nucleophilic substitution and purification in a micro-reactor.

Keywords: [^{18}F]fluoride, concentration, micro-flow-cell, electrochemical

1. INTRODUCTION

^{18}F-Labeled compounds are the most widely used radiopharmaceuticals for diagnosis by PET. As a half-life of ^{18}F is about 110 min, shortening a process time is advantageous to efficient preparation. In this paper, a micro-flow-cell which can electrically concentrate [^{18}F]Fluoride to organic solvents is described.

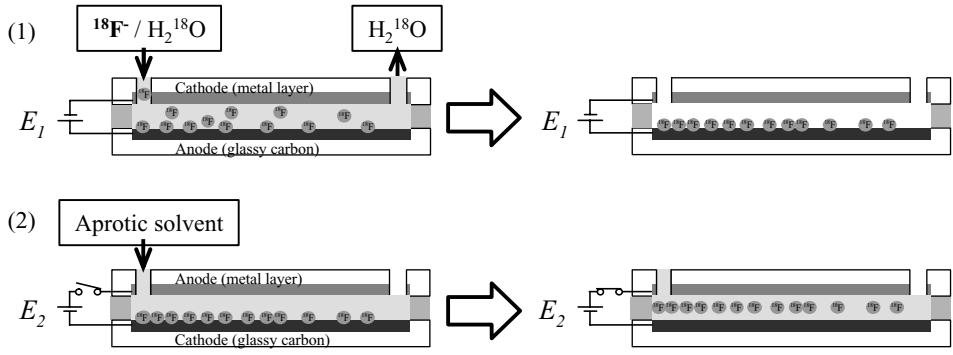

Fig. 1: Principle of concentration of [^{18}F]fluoride. (1): First step: Deposition of [^{18}F]fluoride on GC. (2): Second step: Recovery of [^{18}F]fluoride from GC to aprotic solvent.

978-0-9798064-0-7/µTAS2007/$20©2007CBMS

2. EXPERIMENTAL

The principle of [^{18}F]fluoride concentration is illustrated in Fig. 1. Distance between glassy carbon (GC) and platinum electrodes was 100 µm in this study (cell volume: about 16 µl). First step of concentration process is shown in Fig. 1(1). [^{18}F]Fluoride / [^{18}O]water solution was continuously flowed through a micro channel between the GC and platinum electrodes to which voltage E_1 (1.0–10.0 V) was applied to deposit [^{18}F]fluoride on GC. Second step of the process is shown in Fig. 1(2). An aprotic solvent is filled in the micro channel. Then reverse voltage E_2 (3.5 V) was applied between the electrodes with stopped flow to recover [^{18}F]fluoride from GC. Radioactivity of deposited [^{18}F]fluoride and recovered one were measured by scintillation counter.

3. RESULTS and DISCUSSION

A relationship of deposition yield of [^{18}F]fluoride on GC and applied voltage is shown in Fig. 2. The deposition yield of [^{18}F]fluoride on GC was about 90% with applied voltage of 6.0 V. In previous report, the voltage to deposit about 90% [^{18}F]fluoride was higher than 110 V/cm and a distance of electrodes was 2.7 mm [1]. To avoid electrochemically induced side-reactions such as electrolysis, the reduction of applied voltage for concentration is very effective. Fig. 3 shows dependence of [^{18}F]fluoride deposition yield on flow rate of [^{18}F]fluoride / [^{18}O]water solution. Typically high deposition yield (92.6%) was obtained in

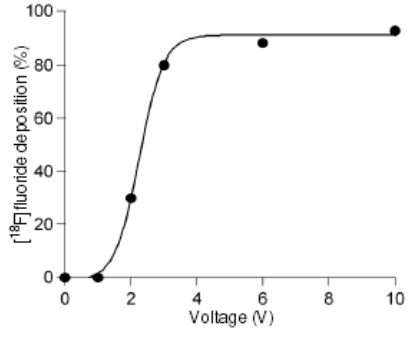

Fig. 2: Voltage (E_1) dependence of [^{18}F]fluoride deposition on GC. [^{18}O]water solution flow = 200 µl/min, [^{18}O]water = 2.0 ml, Temp. = room temp (r. t.).

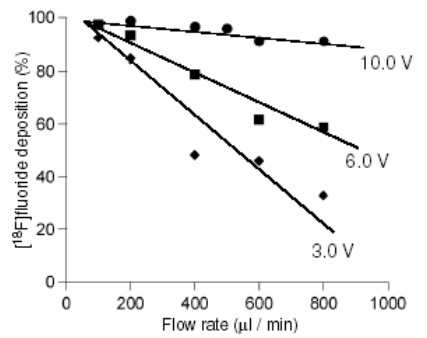

Fig. 3: Flow rate vs. [^{18}F]fluoride deposition on GC with E_1. [^{18}O]water = 2.0 ml, Temp. = r. t.

Table 1: The recovery yields of [^{18}F]fluoride to various solvents from GC.

Solvents	[^{18}F] yield (%)	Temp. (°C)
Water	85.6	r. t.
CH_3CN	0	80
K.222 / CH_3CN*	84.5	80
DMSO	69.4	100
DMF	83.9	100

* K.222 is associative reagent to $^{18}F^-$ ion with ionic interaction and help to transfer the CH_3CN.

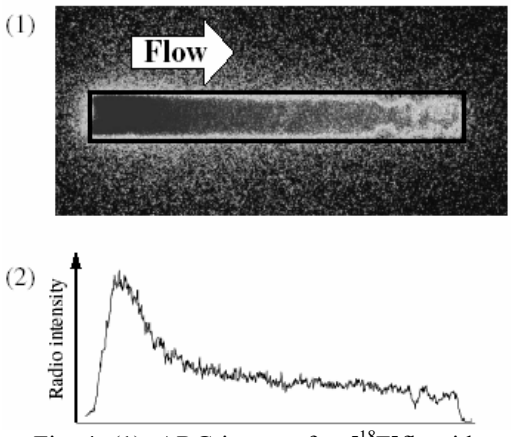

Fig. 4: (1): ARG image after [^{18}F]fluoride deposition. (2): histogram of radio intensity on GC.
[^{18}O]water solution flow rate = 500 µl/min, [^{18}O]water = 2.0 ml, Temp. = r. t., E_1 = 10.0 V.

4 min using a flow rate of 500 µl/min of a 2.0 ml of irradiated target water and applied voltage of 10.0 V. An autoradiographic image (ARG) after [^{18}F]fluoride deposition and a histogram of radio intensity on GC are shown in Fig. 4(1) and (2).

The results of [^{18}F]fluoride recovery yields from GC to several solvents were summarized in Table 1. Asetonitorile (CH_3CN), dimethyl sulfoxide (DMSO) and dimethyl formamide (DMF) were used for aprotic solvents. According to the Table 1, using the [^{18}F]-collective reagent (kryptofix® 222 = K.222), [^{18}F]fluoride recovery yield is 92.6% which is enough yield to synthesis radiopharmaceutical product. The recovered yields to DMSO and DMF which were useful solvents for various organic synthesis were reached 69.4% and 83.9% each other. The volume of [^{18}F]fluoride recovery solutions is decreased to µl order as same volume as the cell channel.

4. CONCLUSION

Electrochemical micro-flow-cell has been developed. Reduction of solnvent volume to 1/100 and a period of concentration time are achieved using the cell. This concentration method of [^{18}F]fluoride is useful for ^{18}F-labeld PET proves synthesis.

REFERENCE

[1] K. Hamacher, Th. Hirschfelder, H. H. Coenen, *Appl. Radiat. Isot.* 2002, 56, 519-523.

IN-SITU MICROFLUIDIC SYNTHESIS OF MATERIALS FOR NONLINEAR OPTICAL DEVICES: CONTROL OF ATOMIC VAPOR POPULATIONS IN MICROCHANNEL WAVEGUIDES

Vishal Tandon[1], Saikat Ghosh[2], Amar R. Bhagwat[2], C. Kyle Renshaw[2], Shireen Goh[2], Alexander L. Gaeta[2], and Brian J. Kirby[3]

[1]Biomedical Engineering, [2]Applied and Engineering Physics, and [3]Mechanical and Aerospace Engineering, Cornell University, Ithaca, NY 14850

ABSTRACT

This paper (a) reports the use of liquid-phase microfluidic materials synthesis to pattern polymers, crystals, and metals in microfluidic systems to create nonlinear devices and (b) reports the performance of nonlinear devices based on atom-photon interactions within silica waveguides. Liquid-phase materials synthesis in microdevices provides unique potential for creation of nonlinear optical materials, control of atomic vapor interactions, and design of magneto-optical devices. Here, we show electromagnetically-induced transparency at levels 10^7-fold below previous results in microchannel waveguides, facilitated by material modification of the silica microchannel. These capabilities give potential for single-photon quantum networks and ultrasensitive chemical detection in microchannels.

Keywords: Waveguide, Materials Synthesis, Nonlinear Optics, Atomic Vapor

1. INTRODUCTION

Electromagnetically-induced transparency (EIT; [1]) renders an optically thick ensemble transparent by initiating a coherent superposition of atomic states via an electromagnetic control field; EIT is thus a canonical example in which the quantum states of light are controlled via atom-photon interactions. However, successful realization must occur in waveguiding microchannels so as to spatially localize the probe and control laser fields (ideally, to single-photon pulses).

Fabricating materials in microchannels for quantum optical applications brings challenges: (a) high-quality air-core waveguide structures are three-dimensional and incompatible with layering of lithographically-patterned material, requiring in-situ materials synthesis in 3-D structures; (b) atomic vapors react with silica, requiring polymeric protection layers; and (c) metallic and crystalline ma-

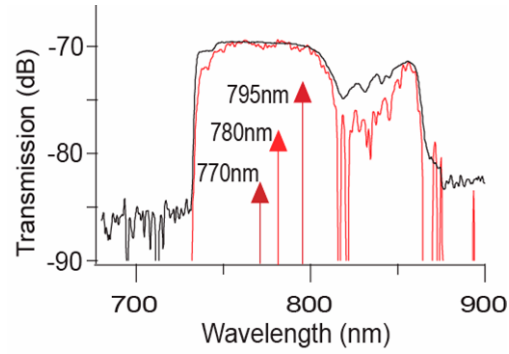

Figure 1. Microchannel waveguide transmission performance before (black) and after (red) liquid-phase deposition of octadecyldimethylmethosysilane to give the surface paraffin-like chemical properties. Photonic bandgap is unaffected by deposition. Probe (795 nm), control (780 nm), and desorbing (770 nm) laser wavelengths are also shown. Waveguide is a 6 μm microchannel surrounded by a honeycomb diffractive waveguide, fabricated by high-temperature drawing.

978-0-9798064-0-7/μTAS2007/$20©2007CBMS

terials are also needed to enable magneto-optical devices and to enable a breadth of nonlinear processes.

2. RESULTS/DISCUSSION

To enable atomic vapor loading in microchannels, paraffin-like chemical moieties are created via liquid-phase functionalization of the silica surface. This modification maintains the essential transmission properties of the microchannel waveguide (Figure 1). While this does not prevent chemisorption of atomic vapors, it does allow user-controlled regeneration of atomic vapor populations with laser-induced atomic desorption (LIAD [2]; Figure 2), in which a blue-shifted 770 nm laser beam is used to desorb the atoms. This allows generation of an enormous optical depth (2000), as shown by transmission as a function of time following a LIAD pulse (Figure 3).

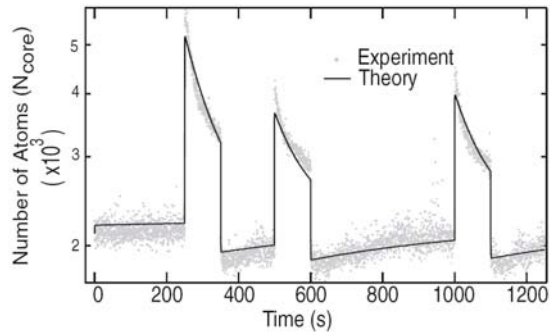

Figure 2. Rubidium atom population (N_{core}) in the microchannel as a function of application of a desorbing laser beam.

Generation of such a large atomic vapor population in a microchannel waveguide allows simultaneously for (a) extreme localization of laser fields and (b) intense nonlinear interaction between atoms and photons. These enable EIT with 10 nW input fields—seven orders of magnitude lower than previously reported in microchannel waveguides [3]. Figure 4 shows transmission with a control field of 3 μW—here, transmission at linecenter of the probe beam is increased by a factor of 10^{500} through application of the control field.

LIAD on polymer-modified silica microchannel waveguides combined with magneto-optical trapping shows the potential for rapid and effective generation of Bose-Einstein condensates. This process is facilitated by material deposition of metallic and crystalline materials within microchannel waveguides. We have deposited silver and silver iodide within microchannels using liquid-phase deposition processes (Figure 5).

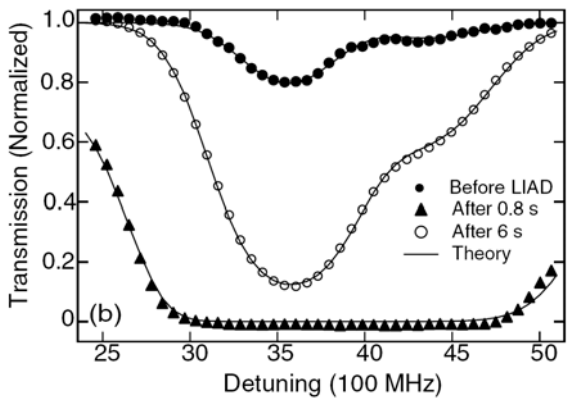

Figure 3. Aborption of laser light at 795 nm shows establishment of large atomic vapor population and large optical depth. Here, spectral measurements are made as a function of time—these measurements are the input to Figure 2.

Overall, we have demonstrated the ability to synthesize polymer, metal, and crystalline materials inside microchannel waveguides and have shown EIT at nanowatt control fields. This work has the potential to enable quantum networks and ultrasensitive chemical detection.

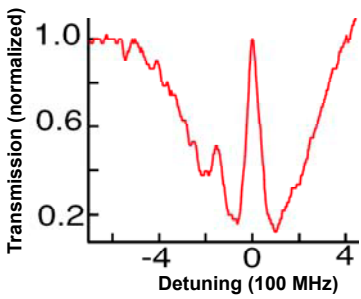

Figure 4. Electromagnetically-induced transparency demonstrated using a Rubidium vapor confined within a silica microchannel waveguide. An atomic ^{87}Rb vapor with an optical depth in excess of 2000 for light transmission at 795 nm (the D_1 line of ^{87}Rb) is rendered optically transparent by the application of a μW control beam at 780 nm. Transparency is indicated by the transmission peak at zero detuning.

REFERENCES

[1] S.E. Harris. Phys Rev Lett 62:1033, 1989.
[2] S.N. Atutov et al, Phys Rev A 60:4693 1999.
[3] Ghosh et al, Phys Rev Lett 94 063902(2005) and Benabid et al, Opt Express 13, 5694 (2005).

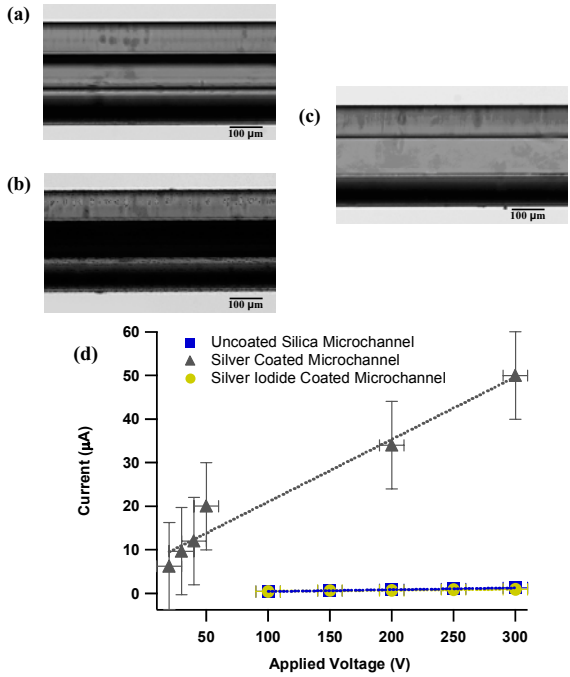

Figure 5. Metal and crystal formation in silica microchannels. (a-c): light microscopy of microchannels showing (a) untreated silica, (b) silver-coated silica, and (c) silver-iodide-coated silica. (d): electrical characterization of metallic and crystalline thin films in silica microchannels (made in series with an electrolyte solution), showing the integrity of the silver wires. Silver conductors patterned around microchannel waveguides give potential for magneto-optic control of atomic vapors.

SIZE CONTROL OF NANO-PORES ON MICROCAPSULE FOR CONTROLLED RELEASE

Dae Geon Won[1], Je Myoung Cha[1], S. H. Yoon[1], Eun Ho Jeong[1], Takahiro Arakawa[2], Shuichi Shoji[2], Kyung Chun Kim[1] and Jeung Sang Go[1]

[1]School of mechanical Eng. Pusan National Univ., 609-735, South Korea
[2]Major in Nano-science and Nano-Engineering, Waseda Univ., 169-8555, Japan

ABSTRACT

Nanoporous polymeric microcapsules were produced in the stable manner for the various concentrations of a block copolymer in an organic solvent. The size of the microcapsules was increased while that of the nano pores were decreased by increasing the concentration. Their hallow characteristics was also visualized. To control the concentration of the block copolymer provides an effective way to control feature sizes, compared with other wises using temperature or stirring rate.

Keywords: polymeric microcapsule, self-assembly, micro droplet, nano pores

1. INTRODUCTION

In the previous work, polymeric microcapsules with uniform size and nano-prous surface was successfully fabricated by supramolecular selfassembly in crossed microchannel (Figure 1) and It was proved that this method is efficient to control the uniform size of polymeric microcapsules[1] and these products by this way can be used as a potential encasulant[2]. In this paper, we try to more efficiently control the size of the polymeric microcapsule by changing the concentration of a block copolymer dissolved in organic solvent. A various concentration of the block copolymer dissolved in organic solvent was used in this research and the result was estimated by SEM image.

For the shell structuration of microcapsule, the block copolymer of PS-b-PMMA was synthesized by atomic transfer radical polymerization [3]. The molecular and poly dispersity index were characterized to be 9837 g/mole and 1.08, respectively by using gel permeation chromatography. To visualize the procedure of microcapsule formation, a cross microchannel was fabricated by bonding a transparent glass anodically. The width and depth of the microchannel were 100 μm each.

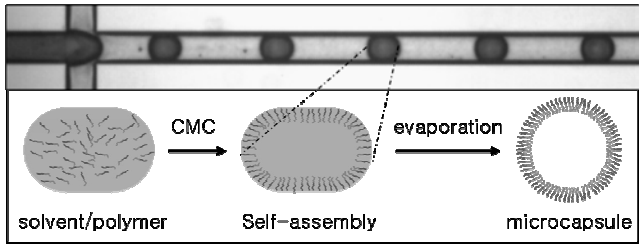

Figure 1. Kernel process of nanoporous microcapsule production using flow-through droplet flow

978-0-9798064-0-7/μTAS2007/$20©2007CBMS

2. MICROCAPULES FORMATION

Table 1. shows the concentration of the PS-b-PMMA copolymer dissolved in CH2Cl2 used in this study to fabricate microcapsule. Each different concentration of organic fluids was introduced into crossed microchannel thorough middle channel with the same flow rate of 5 ul/min. 3%wt PVA aqueous solution was into two side channels with the flow rate of 5um/min. Figure 2 visualizes that the produced droplets had the same diameter of 120 um even for the different concentrations. However, after an hour at which they were drained out and dispersed in the DI water, the size shrinkage of droplets occurred differently. Figure 3 shows rate of droplets produced from the various concentration. When the concentration is lower (until 10mg/ml), the shrinkage rate is lager. But at over 10mg/ml, the shrinkage rates rarely change.

Table 1. Concentration rates of the pre-synthesized amphiphilic block copolymer to DCM

PS-b-PMMA [mg]	5.2	5.1	5.0	25	50	40	60	80	100
CH2Cl2 [ml]	5.0	3.3	2.7	5.0	5.0	2.0	2.0	2.0	2.0
Concentration [mg/ml]	1.04	1.53	1.85	5.0	10.0	20	30	40	50

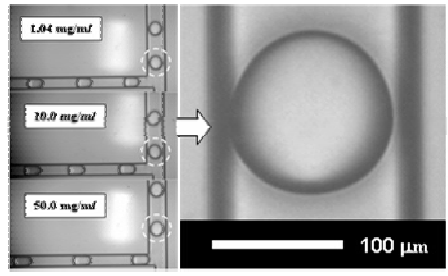

Figure 2. A consistent size of droplets for different polymer concentrations in the ratio of inlet flow rate of 0.025

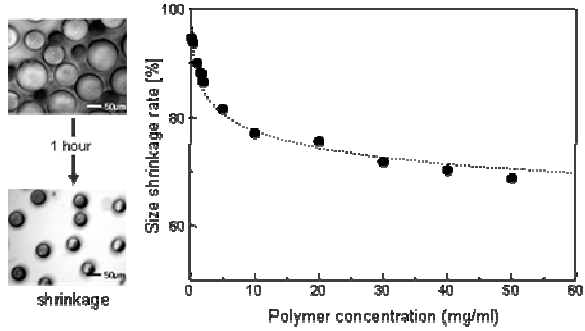

Figure 3. Size shrinkage of droplets obtained from the different polymer concentrations

3. RESULTS AND DISCUSION

The microcapsules were solidified after evaporation. Figure 4 shows SEM images of the polymeric microcapsules fabricated for the different concentrations. It is identical that the size of microcapsules depends on the concentration and there exist the nano-pores on the surface. Also, based on Figure 5(a), it can be concluded that increase in the polymeric concentration results in the larger size of microcapsules, while the size of nano-pores is decreased. Figure 5(b) shows the SEM image of partially broken microcapsules produced at the concentration of 10 mg/ml. The hollow microcapsule was clearly shown and the shell thickness was measured to be about 0.5 um. From the microcapsule size of 26 um, it is expected that the 89 % volume of the entire microcapsule can be used to encapsulate foreign molecules.

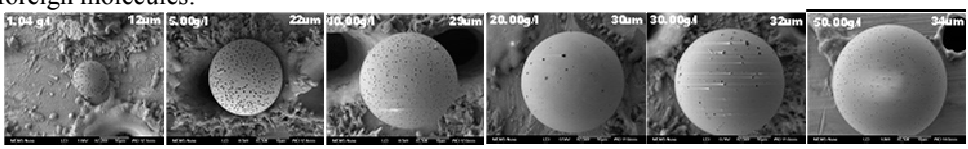

Figure 4. SEM image of microcapsules obtained for the various polymer concentrations.

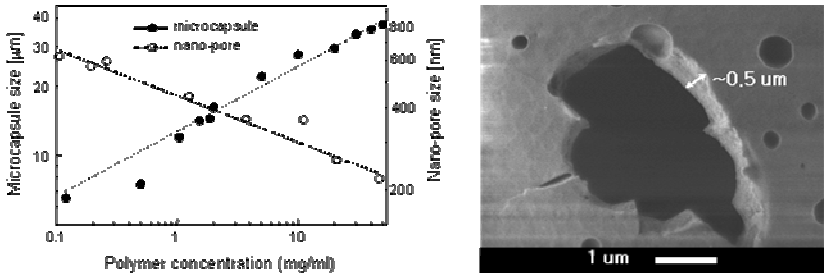

(a) (b)

Figure 5. (a) Size measurement of microcapsule and nano-pores for the different polymer concentrations, (b) Thickness measurement of a microcapsule

4. CONCLUSIONS

The polymeric microcapsules with nano-pores have been successfully produced. In addition, the size of the microcapsules and nano-pores could be controlled by changing the concentration of the PS-b-PMMA copolymer dissolved in organic solvent. For further study, the release performance of microcapsule with the different size of nano-pores will be examined for the various stimuli.

REFERENCES

[1] E. H. Jeong, S. Abraham, T. Arakawa, I. Kim, S. shoji, K. C. Kim, and J. S. Go, *Synthesis of spherical microcapsules with nano-pores and use as a potential encapsulant,* MicroTAS, 1, pp.1002-1005, (2006).

[2] G. Ibarz, L. Dahne, E. Donath and H. Mohwald, *Smart micro- and nanocontainers for strage, transport and release* ,Adv. Mater, 13, pp.1324-1327, (2001).

[3] K. Matyjaszewski, D. A. Shipp, G. P. Mcmutry, S.C. Gaynor and T. PAkula, *Simple and effective one-pot synthesis of (meth)acrylic block copolymers through atom transfer radical polymerization,* J. Polym. Sci. Part A: Polym. Chem., 38, pp.2023 - 2031, (2000).

MICROFABRICATION OF SELF-OSCILLATING GELS FOR GEOMETRICAL CHEMICAL REACTOR NETWORKS

Masanori Ueda
RIKEN (Institute of Physical and Chemical Research), JAPAN

ABSTRACT

We demonstrated wave propagation on microfabricated self-oscillating gel peaces. The propagating manners were restricted by the geometrical conditions of the gel peaces. We try to create "wet computing" on this gel reactor network.

Keywords: BZ reaction, gel, soft matter, wet computing

1. INTRODUCTION

In order to study geometrical effects in chemical reactor networks, microfabrication techniques for soft-matter like gels and polymers were investigated. Micro-scale gel pieces including metal catalyst were fabricated on a glass plate, and isolated with micro gaps each other. The gel pieces work as chemical reactors in appropriate chemical solutions, and the shape of piece or the geometry between many pieces influence the total chemical reaction on the gels.

The self-oscillating polymer investigated in our previous study is depicted in Figure 1[1]. This polymer catalyses a BZ reaction with $Ru(bpy)_3$, and exhibits turbidity oscillation synchronized with the BZ reaction due to the thermally responsive component (NIPAAm: *N*-isopropylacrylamide). In this current study we use microfabricated gel patterns made of this self-oscillating polymer.

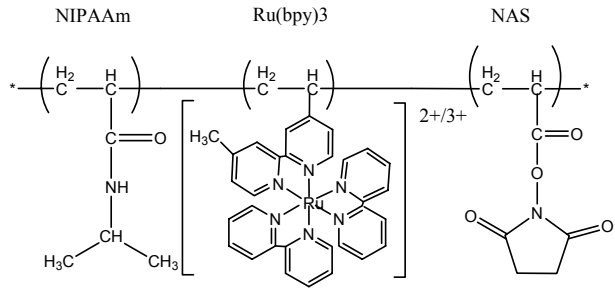

Figure 1. Molecular structure of self-oscillating polymer

BZ reaction is famous oscillatory chemical reaction. $Ru(bpy)_3$ is one of the metal catalysts for BZ reaction, which is localized on gel fibers in our study. Therefore, BZ reaction is limited within the gel, which is much smaller than the outer solution. The reaction is able to be regarded as a non-equilibrium open system. Gel structure prevents the unexpected convection of solutions. Therefore, the gel piece is able to be regarded as

978-0-9798064-0-7/μTAS2007/$20©2007CBMS

one reactor for BZ reaction. By means of photo chemical cross-linking, it is easy to fabricate the gel into any shape onto a glass plate. Using this microfabricated gel, we can study geometrical effects on chemical networks from simplest compelled oscillator to complex labyrinth structures.

2. THEORY

In general, reaction-diffusion system such as a BZ reaction can be expressed by $\partial \mathrm{X} / \partial t = F(\mathrm{X}) + D\Delta \mathrm{X}$. For simplicity, we deal with two-variable system $\mathrm{X} \equiv (u, v)$, where u and v indicate the concentrations of activator and inhibitor investively. The following equations (1a) and (1b) can express the reaction diffusion system in gel peace regions. The v is proportional to $Ru(bpy)_3$, which is fixed on gel fibers. Therefore, equation (1b) has no diffusion term.

$$\partial u / \partial t = F(u, v) + D\Delta u \tag{1a}$$

$$\partial v / \partial t = G(u, v) \tag{1b}$$

In gap regions, the following equation (2) can express the reaction diffusion system because there is no $Ru(bpy)_3$ in this region.

$$\partial u / \partial t = F'(u) + D\Delta u \tag{2}$$

The behaviour of the total system can be affected by the geometry of the boundary condition between gel and gap regions. Although the total behavior is complex, in simple case like two-peace system we can control the propagation of chemical wave by regulating the geometrical conditions of the gel peaces (gap size, shape of gel peace). We expect to create larger well-defined system by combining such simple two-peace system. Finally, we aim to demonstrate a kind of "wet computing" by using the microfabricated geometrical chemical reactor networks.

3. EXPERIMENTAL

Microfabrication process is the following. First, a micro pattern to be investigated was made of SU-8. Second, the pattern was translated to PDMS. The PDMS template was placed onto a glass plate. Pre-gel solution including $Ru(bpy)_3$ and NIPAAm was introduced into the micro-channel between PDMS and the glass plate. Finally, the pre-gel solution was explored from the bottom side by UV light, and the polymer was photo-chemically cross-linked into the designed shape.

The glass plate with gel peaces was dipped in an appropriate BZ solution for several hours. After an induction time for a few hours, spatio-temporal patterns appeared spontaneously. The experimental set up for observation was similar to that used previously. Temperature was controlled at 20 °C, which is below the phase-transition temperature of NIPAAm gel.

4. RESULTS AND DISCUSSION

Figure 2 shows chemical waves restricted on the microfabricated gel. White wave fronts indicate the reduced state of $Ru(bpy)_3$, and other dark places in the oxidized state. "5" indicates the place which is without gel, and the chemical reaction can not occur on the mark. The line size of the "5" is 500 μm, and BZ reaction is not able to transmit the 500μm gap. However, when the gap size becomes smaller, the wave can diffuse across the gap. Furthermore, the direction of wave propagation can be controlled by regulating the shape of the gap.



Figure 2. Chemical waves on microfabricated gel pattern

5. CONCLUSIONS

The direction and frequency of propagation in chemical wave between gel peaces can be controlled by the size and the shape of the gap. Integration of the appropriate gel peace pairs will be able to control the global pattern dynamics of the chemical waves. We call such a system "wet computer".

ACKNOWLEDGEMENTS

This work was supported in part by a Grant for the Next Generation of Nanoscience (RIKEN), and Grants-in-aid for scientific research (No.18651073). We are grateful to Dr. R. Yoshida (The University of Tokyo) for useful discussion and comment on gel fabrication methods.

REFERENCES

[1] M. Ueda, Y. Hara, T. Sakai, R. Yoshida, M. Takai, Y. Ito, *Characterization of a self-oscillating polymer with periodic soluble-insoluble changes,* Journal of Polymer Science Part B: Polymer Physics, Vol. 45, pp1578-1588, (2007).

THE PERFORMANCES OF AN ENZYME-BASED MICROFLUIDIC BIOFUEL CELLS USING VITAMIN K_3-MEDIATED GLUCOSE OXIDATION

M. Togo, A. Takamura, T. Asai, H. Kaji, T. Abe and M. Nishizawa
Department of Bioengineering and Robotics, Graduate School of Engineering,
Tohoku University, Sendai 980-8579, Japan

ABSTRACT

This paper reports performances of an enzyme-based microfluidic biofuel cell under several controlled flow conditions. A reference and counter electrode-containing microfluidic biofuel cell enables to evaluation an individual performance of anode and cathode, separately. By using this system, we studied the optimum design of microfluidic biofuel cell.

Keywords: biofuel cell, enzyme, vitamin K_3, microfluidics

1. INTRODUCTION

Enzyme-based biofuel cells would be formatted into microfluidic systems as power sources for independent power-on-chip and implantable devices because such cells can have a simple structural design (non-compartmentalized) and can operate under mild conditions. Such systems are also useful when evaluating the electrochemical stability or activity of an experimental biofuel cell, because the fuel flow rate, which can affect the cell's performance, can be regulated. We, therefore, constructed a microfluidic-type biofuel cell system containing an Ag|AgCl reference electrode and a Pt counter electrode.

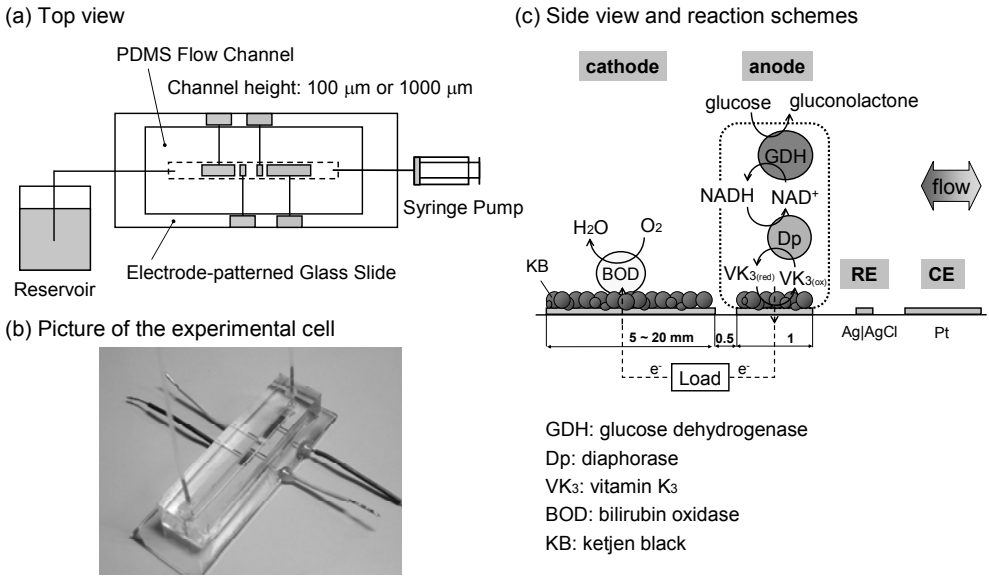

Figure 1. Schematic illustration(a), picture (b) and reaction schemes(c) of microfluidic biofuel cell.

978-0-9798064-0-7/μTAS2007/$20©2007CBMS

2. EXPERIMENTAL

A schematic illustration and a picture of the present microfluidic biofuel cell are shown in Figure 1. Because this experimental system is equipped with an Ag|AgCl reference electrode and a Pt counter electrode in addition to glucose anode and an O_2 cathode, we can evaluate electrochemical reaction of an anode and a cathode separately as well as total cell performance. Figure 1(c) shows reaction scheme of the enzyme-catalyzed glucose oxidation[1, 2] and O_2 reduction at anode and cathode electrodes. By using vitamin K_3 as an electron mediator, our fuel cell becomes harmless for environment.

3. RESULTS AND DISCUSSION

Figure 2 shows the current density of O_2 reduction at enzyme cathodes (poised at 0V vs. Ag|AgCl) as a function of electrode area, studied in 1000 μm and 100 μm height fluidic channels. The O_2 reduction current density decreased with increasing electrode area and with decreasing the channel height probably due to the growth of O_2 depletion zone comparable to the channel height. It is suggested, however, that the "fuel utilization" can be improved in a narrower microchannel. Figure 3 shows the cell and electrode performance with different positioning of electrodes: the upstream cathode (●) and downstream cathode (□). As described above, our microfluidic biofuel cell system contains reference electrode and counter electrode, we can evaluate performance of anode and cathode, separately. At higher current region (> 20 μA), the current of biofuel cell with upstream cathode was higher than that with downstream cathode. The analogy in V-I shapes of the biofuel cell and the anode indicates the anode reaction kinetically limits the total performance of the cell. The upstream cathode reaction eliminated O_2, that slightly oxidize the anode constituents from the vicinity of downstream anode, and improved anode's and total cell's performances.

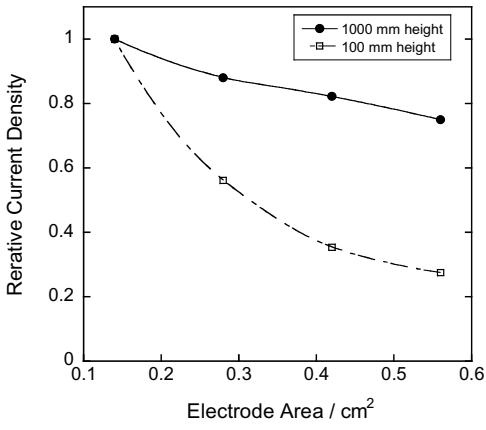

Figure 2. O_2 reduction current density versus electrode area (electrode length) with channel height of 1000 μm or 100 μm. The 0.1 M NaCl containing-phosphate buffer (pH 7) at room temperature was flowed at 10 cm min^{-1}.

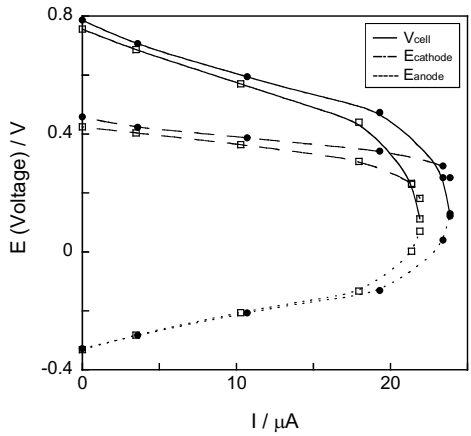

Figure 3. E(V)-I curve of microfluidic biofuel cell, anode and cathode operating under 10 mM glucose 1 mM NAD^+, 0.1 M NaCl containing phosphate buffer (pH 7) at room temperature, with a flow rate of 10 cm min^{-1}. Chennel height: 1000 μm. Upstream cathode (●) and downstream cathode (□).

Figure 4 shows the illustration and the performance of microfluidic biofuel cells constructed by sandwiching a silicone spacer of 100 μm or 1000 μm thickness between two electrode-patterned glass slides. Operation with the 100 μm-height channel (▲) shows smaller cell current and power than those with the 1000 μm-height channel (●) because of depletion of fuel in the narrower flow channel. The maximum cell current (I_{max}) of the 1000 μm-height cell (44 μA) was almost twice of that shown in Figure 3(●) (24 μA), corresponding to the increased electrode area. Although the I_{max} in 100 μm-height channel didn't become double due to the influence of highly developed depletion zone, the volume density of the current and power obtained in a 100 μm height channel was bigger than that in a 1000 μm-height channel (data not shown).

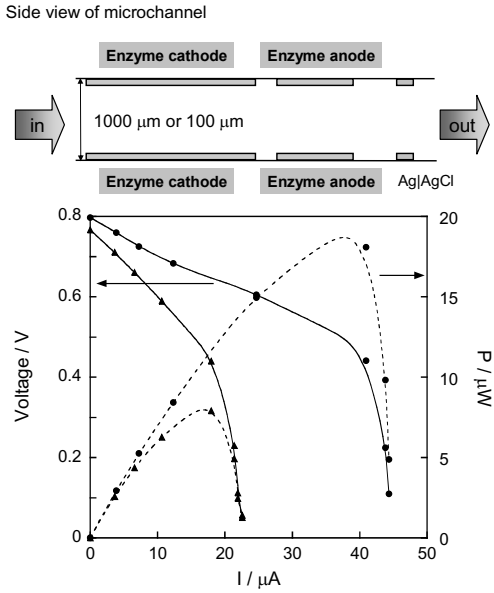

Figure 4. Schematic illustration (top) and performance (bottom) of microfluidic biofuel cell operating under 10 mM glucose, 1 mM NAD^+, 0.1 M NaCl-containing phosphate buffer (pH 7) at room temperature, with a flow rate of 10 cm min^{-1}. Channel height: 100 μm (▲) and 1000 μm (●).

4. CONCLUSIONS

We assembled a microfluidic biofuel cell equipped with reference and counter electrode to evaluate the anode's and cathode's performances individually. It is important to consider depletion zone of fuel and oxidant in order to develop a high performance microfluidic biofuel cell. The depletion zone was easily developed within a microfluidic channel, and thus the prereduction of O_2 by upstream cathode can improve anode performance. Also, the power density and fuel utilization was higher in case narrower channel.

ACKNOWLEDGEMENTS

Author express appreciation to Dr. Kosuge and Dr. Fukasaku (Daiichi Pure Chemicals Co., Ltd.) for synthesis of mediator polymers. This work was partly supported by Health and Labor Sciences Research Grant from the Ministry of Health, Labor and Welfare of Japan. Glucose dehydrogenase was donated from TOYOBO.

REFERENCES

[1] M. Togo, A. Takamura, T. Asai, H. Kaji, M. Nishizawa, Electrochim. Acta, 52 (2007) 4669.

[2] F. Sato, M. Togo, M.K. Islam, T. Matsue, J. Kosuge, N. Fukasaku, S. Kurosawa, M. Nishizawa, Electrochem. Commun., 7 (2005) 643.

RELATIONSHIP BETWEEN FLOWS AND SHAPES OF THE LIQUID-LIQUID INTERFACE IN MICRO COUNTER-CURRENT FLOWS

Arata Aota[1], Akihide Hibara[1,2,3], Yasuhiko Sugii[4] and Takehiko Kitamori[1,2,3]

[1]*Kanagawa Academy of Science and Technology, JAPAN*

[2]*The University of Tokyo, JAPAN*

[3]*Japan Science and Technology, JAPAN*

[4]*Kogakuin University, JAPAN*

ABSTRACT

We investigated shapes of the liquid-liquid interface in micro counter-current flows formed in microchannels. The pressure balance at the liquid-liquid interface was evaluated from the shapes of the liquid-liquid interface. Assuming steady laminar flow, the shape should be an arc. However, the shapes consisting of three arcs were observed. Around the center of the microchannel, Laplace pressure (171-450 Pa) was induced toward the aqueous phase. Contrastively, around the both wall sides, Laplace pressure (81-166 Pa) was induced toward the organic phase. This result suggested the mechanism of the loop-like flows reported previously. Furthermore, the opposite flow direction in each phase just around the liquid-liquid interface, namely a possibility of slip, was suggested.

Keywords: Multiphase flow, Liquid-Liquid Interface, Interfacial tension, Surface modification

1. INTRODUCTION

We have developed parallel micro counter-current flows of immiscible solutions in microchannels [1]. In the micro counter-current flows, the contact line can be pinned at the boundary between the hydrophilic and hydrophobic surfaces along the microchannel, although the flow direction of the aqueous phase is opposite to that of the organic phase. Prevously, we have reported the observation of loop-like flows around the liquid-liquid interface in the micro counter-current flows [2]. However, physical mechanism of the loop-like flow generation is not clarified. Here, we focused on shapes of the liquid-liquid interface. In this paper, relationship between the shape of the liquid-liquid interface and the flow in the micro counter-current flows is reported.

2. THEORY

Main forces in the micro counter-current flows are two kinds of pressures [3]. One is pressure that drives the fluids. When the two fluids have different viscosities, the pressure difference between the two phases ΔP_{Flow} should be a function of the contact length and the flow velocity. The other is Laplace pressure $\Delta P_{\mathrm{Laplace}}$ caused by the interfacial tension between the two phases. The position of the

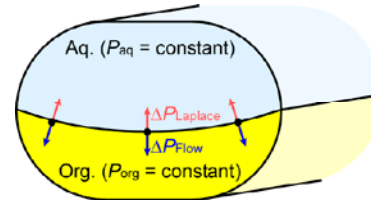

Figure 1. Pressure in each phase assuming steady laminar flow. ΔP_{Flow} and $\Delta P_{\mathrm{Laplace}}$ are constant at all positions. Therefore, the shape of the liquid-liquid interface can be predicted to be an arc.

978-0-9798064-0-7/μTAS2007/$20©2007CBMS

interface is fixed at a certain position in the microchannel by the balance established between the $\Delta P_{Laplace}$ and ΔP_{Flow}. Figure 1 illustrates pressure balance at the liquid-liquid interface. When steady laminar flow is assumed, pressure in each cross section of the two phases (P_{aq} and P_{org}) are constant. Therefore, constant ΔP_{Flow} should be induced at the liquid-liquid interface in the cross section and the shape of the liquid-liquid interface is considered to be an arc of a single circle as illustrated in Figure 1.

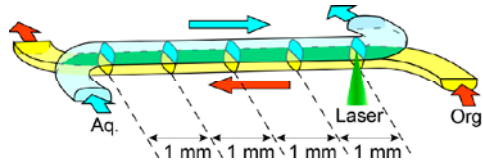

Figure 2. Measurement of the liquid-liquid interface by scanning laser spot. The shapes were measured at five points of 1 mm interval.

3. EXPERIMENTAL

In order to form the micro counter-current flows, the microchannels, which had a width of 300 µm, a depth of 200 µm and a liquid-liquid contact length of 4 mm, were used. The shapes of the liquid-liquid interface were measured by scanning laser spot. The laser was focused at the liquid-liquid interface and the spot was detected by a visual observation. The shapes of the liquid-liquid interface were measured at five points of 1 mm interval as illustrated in Figure 2.

4. RESULTS AND DISCUSSION

Figure 3a shows the coordinate system, where x=0 and y=0 correspond to the confluence at the upstream part of the aqueous phase and the boundary between the hydrophilic andhydrophobic surfaces, respectively. Figure 3b and c show the measured shapes of the liquid-liquid interface when the flow rates of water and toluene were 1.0 and 2.0 µl/min, and each 1.0 µl/min, respectively. The experimental data are fitted by an arc of a single circle. In Figure 3b, the shapes can be fitted by an arc. However, in Figure 3c, the shapes at x=0-3 mm cannot be fitted by a single arc. They have large deformation around the center of the microchannel. They can be fitted by arcs of three circles. Figure 4a shows the $\Delta P_{Laplace}$ predicted from the shape.

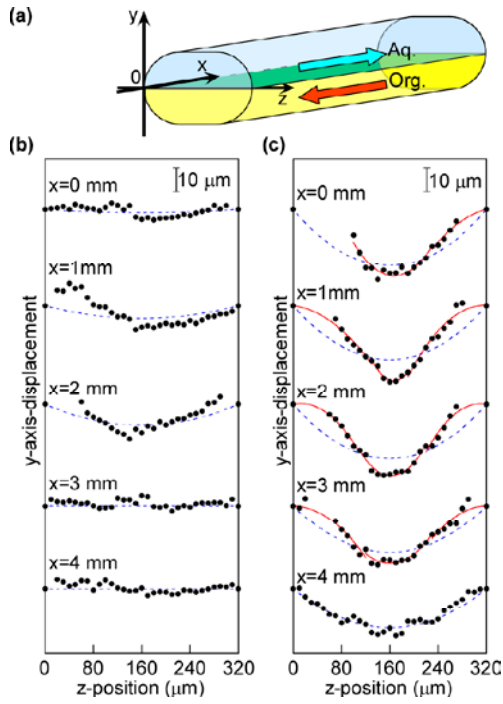

Figure 3. (a) Coordinate system for shape measurement of the liquid-liquid interface. (b) Measured shapes of the liquid-liquid interface in the micro counter-current flows at five positions when the flow rates of the aqueous and organic phases were 1.0 µl/min and 2.0 µl/min, and (c) when the flow rates of the aqueous and organic phases of 1 mm were 1.0 µl/min. Solid circles show the results. Dotted lines and solid lines show fitted curves by a single arc and three arcs, respectively.

$\Delta P_{\text{Laplace}}$ was evaluated to be 171-450 Pa around the center of the microchannel and 81-166 Pa around the wall. In the aqueous phase, the pressure P_{aq} around the center of the microchannel is higher and P_{aq} around the wall is lower, namely water flows from the center of the microchannel to the contact line around the liquid-liquid interface as shown in Figure 4b. However, in the toluene phase, toluene flows from the contact line to the center of the microchannel around the liquid-liquid interface. Considering the mass balance in the microchannel, the flow from the wall to the center of the microchannel should be generated in the aqueous phase as shown in Figure 4c. As same, the flow from the center of the microchannel to the wall should be generated in the organic phase. Considering the flow velocity along the microchannel, this result suggested loop-like flows in the micro counter-current flows. Actually, the loop-like flows were observed previously [2]. The deformation of the liquid-liquid interface may generate secondary flows in the micro counter-current flows of low Reynolds number.

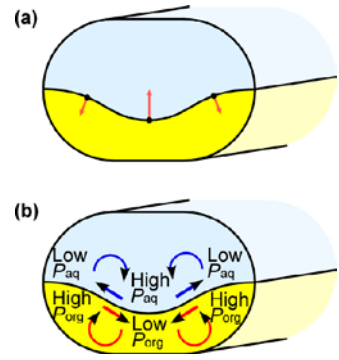

Figure 4. (a) Laplace pressure at the deformed liquid-liquid interface. (b) Pressure distribution and flow directions around the deformed liquid-liquid interface.

Furthermore, the flow directions in each phase just around the liquid-liquid interface were opposite, namely slip may occur at the liquid-liquid interface although the conventional boundary condition is non-slip. As molecular behaviors in the liquid-liquid interface investigated by molecular dynamic simulation [4], rapid changes of the flow velocity in the liquid-liquid interface might be observed as apparent slip on macro scale.

5. CONCLUSIONS

The shapes of the liquid-liquid interface in the micro counter-current flows were measured. The pressure distribution was evaluated from the measured shapes. The loop-like flows were suggested from the pressure distribution. Furthermore, slip at the liquid-liquid interface was suggested.

REFERENCES

[1] A. Aota, M. Nonaka, A. Hibara and T. Kitamori, *Angew. Chem. Int. Ed.*, **46**, 878-880 (2007).
[2] A. Aota, A. Hibara and T. Kitamori, *Proceedings of μTAS 2005*, 118-120 (2005).
[3] A. Aota, A. Hibara and T. Kitamori, *Anal. Chem.*, **79**, 3919-3924 (2007).
[4] J. Koplik and J. Banavar, *Phys. Rev. Lett.*, **96**, 044505 (2006).

"DROP-AND-SIP" FLUID HANDLING TECHNIQUE FOR REAGENT-RELEASE CAPILLARY-BASED CAPILLARY-ASSEMBLED MICROCHIP (CAS-CHIP): MULTIPLE CELL LYSATE SAMPLE DELIVERY AND CASPASE-ACTIVITY SENSING

T. G. Henares[1], F. Mizutani[1], R. Sekizawa[2] and H. Hisamoto[3]

[1]University of Hyogo, JAPAN, [2]Metaboscreen Co. Ltd., Yokohama, JAPAN

[3]Osaka Prefecture University, Osaka, JAPAN

ABSTRACT

The basic concept of "drop-and-sip" fluid delivery on a reagent-release capillary-based capillary-assembled microchip (RRC-based CAs-CHIP) has been published elsewhere [1]. Here, we intend to present significant details on the active and passive microfluidics present in the RRC-based CAs-CHIP. More importantly, this fluid handling technique is implemented on a real sample, HeLa cell lysate, wherein chemotheraphy-induced cell death with a certain drug, doxorubicin, is profiled with ten different protease-sensing capillaries embedded on the CAs-CHIP comparing the enzyme activities in a doxorubicin-treated and untreated cell lysates simultaneously.

Keywords: capillary-assembled microchip, "drop-and-sip", caspase activity

1. INTRODUCTION

Fluid handling and transport inside a micro-total analysis system is an important operation to consider for a successful microchip towards clinical diagnostic and drug-screening applications. Recently, we developed a fluid handling technique called "drop-and-sip" wherein a microliter volume of sample solution is "drop" on the inlet hole and "sip" in another hole producing a sample plug flow in the main microchannel concurrently filling each sensing capillaries with sample solution [1]. However, the details of this technique and real sample application have not been discussed yet.

Here, we present the detailed accounts with regards to the active and passive microfluidics of the "drop-and-sip" fluid handling technique. Also, using this technique, multiple sample introduction and simultaneous sensing of different proteases for cell apoptosis are realized. The analysis of ten different proteases present in the doxorubicin-treated and untreated HeLa cell lysate were analysed simultaneously.

2. EXPERIMENTAL

The RRC-based CAs-CHIP is composed of square glass capillary (o.d. 300μm square, i.d. 100μm square) and the PDMS microchannel (width and depth: 300μm). The basic concept of "drop-and-sip" is shown in Figure 1a. The RRCs were prepared by immobilizing various peptidyl-4-methyl-coumaryl-7-amide (peptidyl-MCA) in the four corners of the square glass capillaries with the aid of poly(ethylene glycol) serving as a scaffold. The chip layout used in this presentation is depicted in Figure 2b, in which a total of 20 RRCs were embedded to simultaneously analyse the treated and untreated cell lysate. All analysis was done using a fluorescence microscope.

978-0-9798064-0-7/μTAS2007/$20©2007CBMS

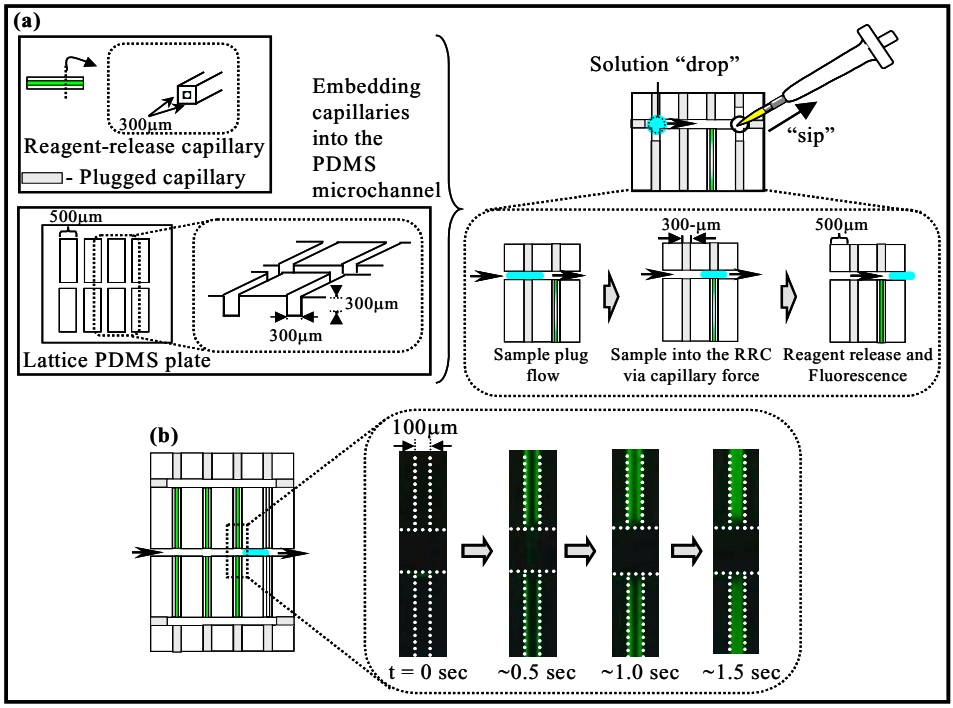

Figure 1. (a) Basic concept of "drop-and-sip" fluid handling technique for RRC-based CAs-CHIP. (b) Actual image of reagent release in the fluorescein-release capillary.

3. RESULTS AND DISCUSSION

In general, the fluid handling and transport is a function of the microchannel design and dimension, and the wettability of the material used for fabrication. In the case of CAs-CHIP [2-3], heterogeneous surfaces (hydrophobic and hydrophilic) are present inside the device as a consequence of square glass capillary (hydrophilic)-PDMS lattice microchannel (hydrophobic) assembly. However, the facile "drop-and-sip" fluid delivery takes advantage of such heterogeneity.

The contact time between the sample plug passing through the main microchannel and the sensing capillaries were video captured using a CCD camera (Figure 1b). The approximated capillary filling time of more than 0.008 second and reagent diffusion time into the main microchannel of less than 10 seconds sets the requirement for the contact time between the sample plug and the sensing capillaries. The use of micropipette was justified by the optimized volume setting of 20 µL, which produced a contact time of 0.7 s for 1 µL sample allowing sufficient capillary filling without leakage of the released reagent into the main microchannel. Sample solution entered the RRCs via capillary force, in which the reagent-release is primarily governed by convective (Peclet number ~ 57,000) and diffusive (due to stop-flow) fluid transport.

To effectively demonstrate its importance, a cancer cell lysate treated and untreated with apoptosis inducer drug, doxorubicin, was used. Figure 2a-2c displayed an interesting outcome in which the untreated cell lysate showed minimal activity relative to the treated sample.

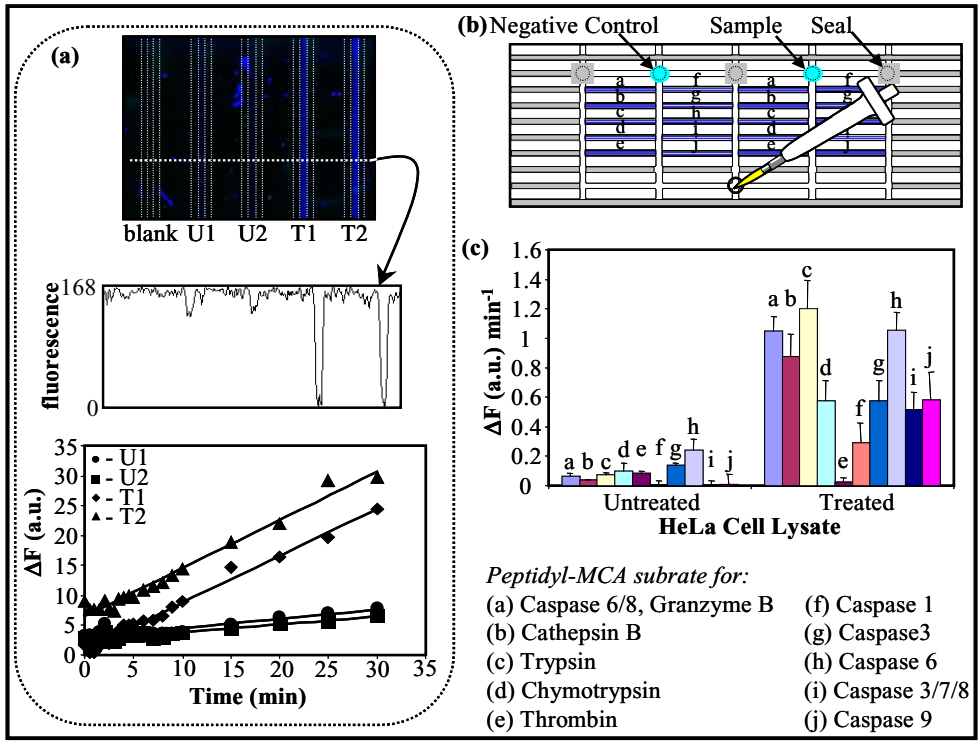

Figure 2. (a) Caspase 3 sensing capillary response to treated (T) and untreated (U) HeLa cell lysate. (b) RRC-based CAs-CHIP for multiple sample and analyte sensing. (c) Protease activity profiles of various RRC inside the CAs-CHIP.

4. CONCLUSIONS

The "drop-and-sip" fluid handling technique in the RRC-based CAs-CHIP prove to be a simple and useful technique for the multiple sample analysis and simultaneous analyte detection. Demonstration of this method to simultaneous real sample analysis opens the avenue towards practical application in the field of clinical diagnostic and drug screening.

ACKNOWLEDGEMENTS

This research work is partially supported by the New Energy and Industrial Technology Development Organization (NEDO) and the Grant-in-Aid for scientific Research from the Ministry of Education, Culture, Sports, Science and Technology of Japan. T.G.H. also wish to thank the Monbukagakusho of Japan for the scholarship.

REFERENCES

[1] T.G. Henares, M. Takaishi, N. Yoshida, S. Terabe, F. Mizutani, R. Sekizawa, H. Hisamoto, ***Anal. Chem***., 79, 908 (2007).

[2] H. Hisamoto, Y. Nakashima, C. Kitamura, S-i. Funano, M. Yasuoka, K. Kikutani, T. Kitamori, S. Terabe, ***Anal. Chem***., 76, 3222 (2004).

[3] H. Hisamoto, S-i. Funano, S. Terabe, ***Anal. Chem***., 77, 2266 (2005).

ELECTROSTATIC PARTICLE-PARTICLE INTERACTIONS IN OPTOELECTRONIC TWEEZERS

Hyundoo Hwang, Jae-Jun Kim, Youngjae Oh, Yong-Je Choi and Je-Kyun Park

Department of Bio and Brain Engineering, Korea Advanced Institute of Science and Technology (KAIST), KOREA

ABSTRACT

This paper reports experimental measurements and numerical simulation of electrostatic attraction and repulsion of microparticles in an optoelectronic tweezers (OET). The electrostatic particle-particle interactions are simulated based on the point-dipole model. Discrete element method was also utilized to track the position, velocity and other parameters of particles in multi-particle system. The experimental measurements of the simulated movements of microparticles are also performed with a lab-on-a-display platform.

Keywords: electrostatic particle-particle interaction, dipole forces, dielectrophoresis, optoelectronic tweezers (OET), lab-on-a-display

1. INTRODUCTION

Optoelectronic tweezers (OET) is a remarkable technology for parallel manipulation of microparticles using dynamic optical images [1]. When an image pattern of a display is projected onto the OET device, a virtual electrode generated forms non-uniform electric fields, inducing dielectrophoresis (DEP). The dielectrophoretic forces result from the induced dipole moments of the dielectric particles, which also cause the electrostatic interactions among them. Since the electrostatic particle-particle interactions influence microparticle manipulation more dominantly in the channel-less system like an OET device than in the other DEP-based microsystems, the dipole interactions should be considered seriously when we use an OET device. Therefore, it is important to understand, estimate and control the electrostatic particle-particle interactions in OET. In this study, we first demonstrate the electrostatic particle-particle interactions in the OET device. Simulation studies for inspection, analysis and expectation of the interactions among polarized particles are also performed.

2. THEORY

The electrostatic forces acting on the polarized particles in an electric field were predicted based on the point-dipole (PD) model [2]. All simulation works are based on the assumption that the electric field direction around a particle is in *z*-direction like that in the OET device. Figure 1 shows the simulated electrostatic forces acting on one particle around the other particle

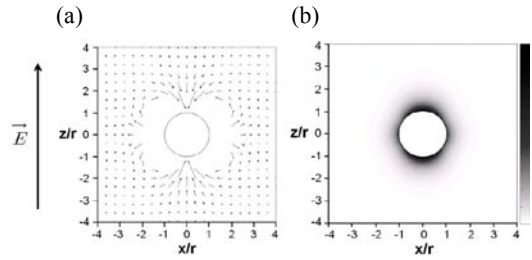

Figure 1. Simulated electrostatic forces acting on a particle around another particle (circle); (a) vectors and (b) normalized magnitudes.

978-0-9798064-0-7/μTAS2007/$20©2007CBMS

whose position is represented by a circle. The distances from the center of the particle are normalized by the radius of the particle. Forces acting on the particles on the line $x = 0$ are always attractive while those on the particles on the line $z = 0$ are always repulsive. Based on this model, we could estimate the movements of microbeads by the dipole interactions in OET device.

3. EXPERIMENTAL

The experimental setup for observation of the electrostatic particle-particle interactions in an OET device is shown in Figure 2. We utilized a lab-on-a-display platform which is a new OET template based on a liquid crystal display (LCD) [3]. We used two illumination of the microscope: one for generation of virtual electrodes on the photoconductive layer of OET device, the other for observation of the electrostatic particle-particle interactions. The movements of microbeads were observed and recorded using an upright microscope with a digital camera. The recorded movies were analyzed by using MATLAB.

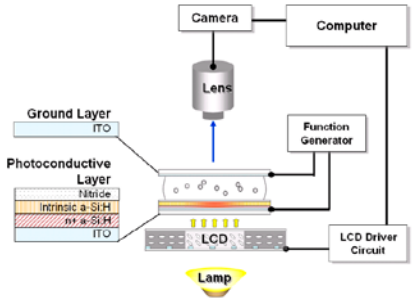

Figure 2. Experimental setup

4. RESULTS AND DISCUSSION

The captured movie of attractive interactions and the simulated trajectories of the 45 μm diameter size polystyrene beads are shown in Figure 3(a) and 3(b), respectively. The attractive interactions occurred when the positions of the beads are close to each other and out of the horizontal. The attractions make the beads form a perl chain in the direction of electric field. The velocities of beads moved by attractive forces were measured according to the projected distances between them (Figure 4). Theoretical values (red, solid line) and the fitted model (black, dotted line) were also represented. The measured values show consistent tendency with the theoretical values.

The repulsive interactions among the beads were also observed and simulated (Figure 5(a) and 5(b)). The microbeads are arranged with their own equilibrium positions resulted from the repulsion among them. Figure 6(a) and 6(b) shows the distribution of center-to-center particle spacings and standard deviation according to the time, respectively. When the beads are at the same level with each other, they are arranged with regular center-to-center particle spacing by repulsions in process of time.

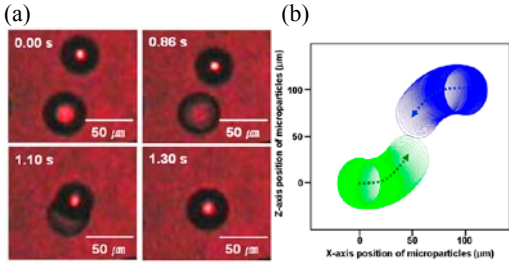

Figure 3. (a) Captured movie and (b) trajectory simulation of electrostatic attractive interactions. They form a chain in the electric field direction.

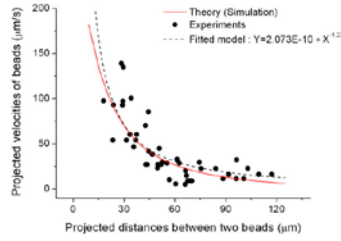

Figure 4. Measured velocities (black, dot) of beads moved by attractive forces according to the projected distances between them.

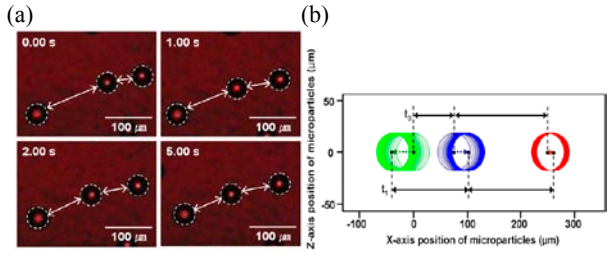

Figure 5. (a) Captured movie and (b) trajectory simulation of electrostatic repulsive interactions.

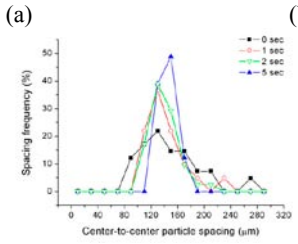

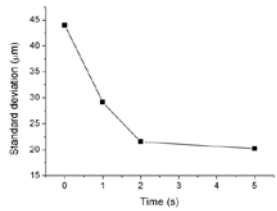

Figure 6. (a) Frequency distribution and (b) its standard deviation of center-to-center particle spacings according to the time.

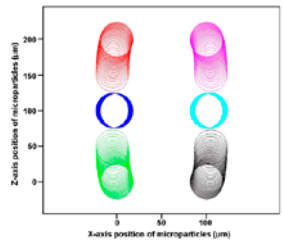

Figure 7. Simulated trajectories of six particles. They form two chains in the electric field direction.

The trajectories of particles by electrostatic particle-particle interactions in multi-particle system could be simulated with a discrete element method (DEM). Figure 7 shows the simulated trajectories of six particles. The particles form two perl chains in the electric field direction and repulse each other in the direction perpendicular to the electric field. These results make sense as compared with the experimental measurements.

5. CONCLUSIONS

In this study, we report experimental measurements and numerical simulation of electrostatic attraction and repulsion of microparticles in lab-on-a-display. The simulation studies explain well the experimentally observed movements of microparticles due to the electrostatic particle-particle interactions in OET.

ACKNOWLEDGEMENT

The microfabrication works for photoconductive layer were performed at the TFT-LCD Research Center, Kyung Hee University (Seoul, Korea).

REFERENCES

[1] P.Y. Chiou, A.T. Ohta and M.C. Wu, *Massively parallel manipulation of single cells and microparticles using optical images*, Nature, 436, pp. 370-372 (2005).

[2] J. Kadaksham, P. Singh and N. Aubry, *Dynamics of electrorheological suspensions subjected to spatially nonuniform electric fields*, J. Fluid. Eng., 126, pp. 170-179 (2004).

[3] W. Choi, S.-H. Kim, J. Jang and J.-K. Park, *Lab-on-a-display: a new microparticle manipulation platform using a liquid crystal display (LCD)*, Microfluid. Nanofluid., 3, pp. 217-225 (2007).

FLOW OF ARTIFICIAL MICROCAPSULES IN MICROCHANNELS: A METHOD FOR MEASURING MEMBRANE ELASTIC PROPERTIES

Eric Leclerc, Yannick Lefebvre, Johann Walter, Florence Edwards-Lévy*, Dominique Barthès-Biesel

CNRS-UMR 6600, Laboratoire de Biomécanique et Génie Biomédical, Compiègne, FRANCE

**CNRS-FRE 2715, Laboratoire de Pharmacotechnie, Reims, FRANCE*

Contact : eric.leclerc@utc.fr

ABSTRACT

The paper presents a method to characterise membrane properties of liquid filled microcapsules. The technique consists of flowing microcapsules into a microchannel of comparable dimensions, observing the deformation as a function of flow rate and deducing the membrane elastic modulus by means of an inverse method based on a numerical model of the flowing capsule. The present results demonstrate that membrane mechanical properties of microcapsules can be evaluated by means of flow experiments in comparable size channels associated to a full mechanical model of the fluid structure interaction that occurs during the deformation process.

Keywords: microcapsules, microfluidic flow, mechanical behaviour, microcirculation

1. INTRODUCTION

Micron size artificial capsules consisting of an internal liquid protected by a thin hyperelastic membrane are used in many applications (biomedical, cosmetics, pharmaceutical industries). One of the membrane functions is to protect the encapsulated substances and control exchanges with the external medium. The membrane mechanical properties thus play an important role in the design of artificial capsules and a key issue of capsule manufacturing is the control of these properties through physico-chemistry. However, the membrane constitutive behaviour is quite difficult to measure owing to the smallness of artificial microcapsules. The objective of this work is to present an original method for the evaluation of some mechanical properties of microcapsule membranes.

2. EXPERIMENTAL WORK

The microcapsules were prepared from ovalbumin through an interfacial cross-linking process using terephthaloyl chloride, in an emulsion system. A variant of an earlier method was used for the present study in order to produce 50±10 μm-sized particles, consisting of a liquid core surrounded by a cross-linked protein membrane [1]. Non-deformed microcapsules are shown in figure 1. The microcapsules were then stored in distilled water. For the experiments, 60 μL of the capsule suspension was mixed with 2 mL of 100% glycerin. The resulting suspension was flowed through two co-axial cylindrical glass capillary tubes (Beckman Coulter, Fullerton, Ca, USA), with external and internal diameters of 1000 and 400 μm for the largest, and of 375 and 75 μm for the smallest. The larger tube allowed the connection to the perfusion system. Both co-axial glass capillaries

978-0-9798064-0-7/μTAS2007/$20©2007CBMS

were embedded in a solidified transparent silicone in order to match optical refractive index at the cylindrical interface. The total flow rate was varied between 0.6 µL/min and 25 µL/min. The capsule deformation and velocity V were measured inside the 75µm pipe as a function of capsule size and flow rate, by means of a high speed video camera mounted on a microscope (Figure 2).

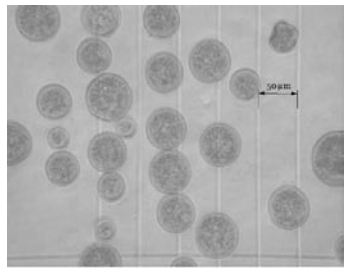

Figure 1: Microcapsules obtained by an interfacial cross-linking process, scale bar is 50 µm.

3. NUMERICAL WORK

An axisymmetric numerical model of an initially spherical capsule with radius a, flowing in a cylindrical tube with radius R has been designed [2]. The capsule is liquid filled and enclosed by a very thin sheet of a hyperelastic material with surface shear modulus G_s and area dilation modulus K_s. A Skalak *et al.* type of constitutive law is assumed for the membrane [2]. We further assume that the capsule is subjected to a positive osmotic pressure difference between the internal and external phases that is characterized by a pre-inflation coefficient α defined by $a=(1+\alpha)a_0$ where a_0 is the unstressed capsule radius. The suspending liquid is Newtonian with viscosity μ and flows with a mean velocity V. For an isolated capsule, the model computes the deformed profile of the capsule for given values of size ratio a/R, pre-inflation α, area dilation to shear moduli ratio K_s/G_s and flow strength measured by the ratio ε of viscous to elastic forces $\varepsilon=\mu V/G_s$.

4. RESULTS AND DISCUSSION

The measured size ratio a/R between the capsule and channel varied between 0.83 and 1.2. Depending on the values of V and a/R, the capsules took parachute or slug shapes (Figure 2), as reported in millimeter-size channels [3]. Assuming that the membrane constitutive law was of the Skalak *et al.* type, with a ratio $K_s/G_s=3$, we compared experimental and numerical deformed profiles for case A corresponding to $a/R=0.92$ (Figure 2) and found for what value of ε they matched. Then, knowing V and μ, we deduced the value of the membrane shear elastic modulus $G_s=0.06$ N/m and of pre-inflation $\alpha=$ 1.5%. Using the same values of α and G_s, we then could reproduce the different deformed profiles of capsules for a range of values of V and a/R, as shown for cases B to D (Figure 2). This indicates that the measured capsules have a membrane that is well modelled by Skalak *et al.* law and that within this hypothesis, values for the membrane elastic moduli can be inferred.

Obviously, this does not guarantee uniqueness of the solution we found. Indeed, it is quite possible that another set of parameters values (or another constitutive law) could give an equally good match.

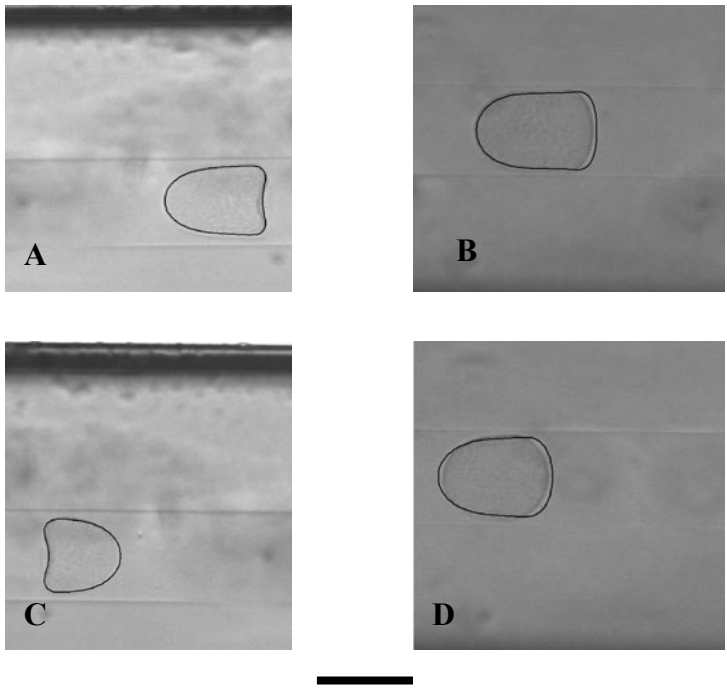

Figure 2: Superimposition of the experimental and numerical (full line) profiles of deformed microcapsules ; (A) a/R = 0.92; V = 3.7 mm/s; (B) a/R = 1.05; V = 2.6 mm/s; (C) a/R = 0.83; V = 3.7 mm/s; (D) a/R = 0.96; V =1.4 mm/s. Scale bar is 75 μm.

5. CONCLUSIONS

The present results demonstrate that membrane mechanical properties of microcapsules can be evaluated by means of flow experiments in comparable size channels associated to a full mechanical model of the fluid structure interaction that occurs during the deformation process. This result is important since it is very difficult to measure directly such properties, in view of the smallness of the capsules.

ACKNOWLEDGEMENTS

The support of Conseil Régional de Picardie and ANR-PNANO is gratefully acknowledged.

REFERENCES

[1] M.C. Andry, F. Edwards-Lévy and M.C. Lévy, *Free amino group content of serum albumin microcapsules III: a study at low pH values*, Int J Pharm, 128, (1996)

[2] Y. Lefebvre and D. Barthès-Biesel, *Motion of a capsule in a cylindrical tube: effect of membrane pre-stress*, J. Fluid Mech., In press (2007)

[3] F. Risso, F. Collé-Paillot, M. Zagzoule, *Experimental investigation of a bioartificial capsule flowing in a narrow tube*, J. Fluid Mech., 547, (2006)

MAGNETICALLY MODIFIED PDMS DEVICES FOR ACTIVE MICROFLUIDIC CONTROL

Yoko Yamanishi[1], Yu-Ching Lin[2] and Fumihito Arai[3]
Tohoku University, JAPAN

ABSTRACT

In this paper we describe novel magnetically driven polymeric microtool for non-intrusive and no contamination experiments on a chip. The composite is formed by suspending magnetite particles in polydimethylsiloxane. In order to obtain precise and complicated pattern of micromagnetic tools, a photolithography techniques has been applied by making good use of thick KMPR-1050 photoresist as sacrifice-mold. The novelties of these tools are 1. fabrication of any 2D shape, 2.softness, 3. no contact actuation, 4. mass production with low cost. These versatile micromagnetic tools can be applied to various functions such as stirrer and valve. The potential impact of this technology includes sample selection and separation, particle loading and immobilization, genetic operation, tracking, mixing and reaction techniques into portable microfluidic labs-on-a-chip, culture systems.

Keywords: magnetically-driven, actuator, microtools, microfluidic control

1. INTRODUCTION

We propose a novel magnetically driven microdevices to allow active control of fluid transport through microfluidic channels. Conventionally magnetic actuation has been produced by metal or metal membrane [1], whereas miniaturized hard magnetic materials have not been used until recently due to the difficulties of micromachining processes. Recently the use of the composite of magnetic powder and PDMS has been applied to local actuation in microchannel with an important feature of easy fabrication. However the control of magnetic membrane on the surface of microchannel constraint the area and direction of movement of actuation in microchannel, whilst there is potential requirement of versatile movement in biochip.

The present work has proposed that a novel on-chip PDMS-based versatile micromagnetic tools by means of photolithography techniques. We use the nanoparticle of iron oxides (Magnetite, Fe_3O_4) in order to mix with PDMS. The novelties of present work are: firstly, the tools can be fabricated to any 2D shape precisely. Secondly, these are soft enough to be harmless to manipulate cells in biochip. Thirdly, the tools can move any direction smoothly in the biochip by surface Teflon coating which suppress any stiction to the PDMS microchannels or cover glass and these are difficult to be rusted by long term immersion in the fluid in the biochip. Fourthly, the tools can be mass produced with low cost and they are disposable.

2. EXPERIMENTAL

Figure 1 shows the fabrication methods to produce micro magnetic tools. The mold to produce micromagnetic tools was fabricated patterning the photoresist layer (KMPR-1050) on a silicon substrate. Then PDMS-magnetite composites have been molded into designed configurations of micromagnetic tools and baked at 80℃ for 20 min in order to cure the composite. Finally the patterned substrate is put in the stripper liquid bath (Remover PG at

978-0-9798064-0-7/μTAS2007/$20©2007CBMS

70℃) (Fig.1 (3)). As the KMPR resist has been dissolved by the stripper liquid, the gap between KMPR resist and PDMS-magnetite composites have been produced. Then the large stir bar collects a number of patterned PDMS-magnetite composites automatically due to their magnetism. This method can be applied to produce small, fine and complicated pattern of micromagnetic tools. In order to prevent any stiction of produced micromagnetic tools to the PDMS biochip, the surface of PDMS was Teflon coated with CF_4 gas by plasma ashing method (Discharge Power:130 W) for 30 minutes.

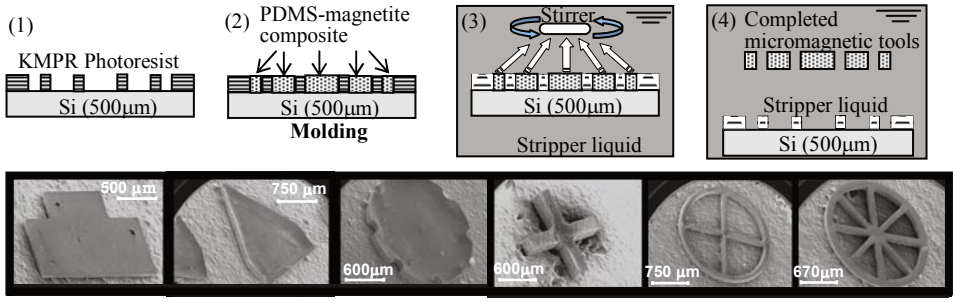

Figure 1. Processes flows and SEM photos of produced micromagnetic tools.

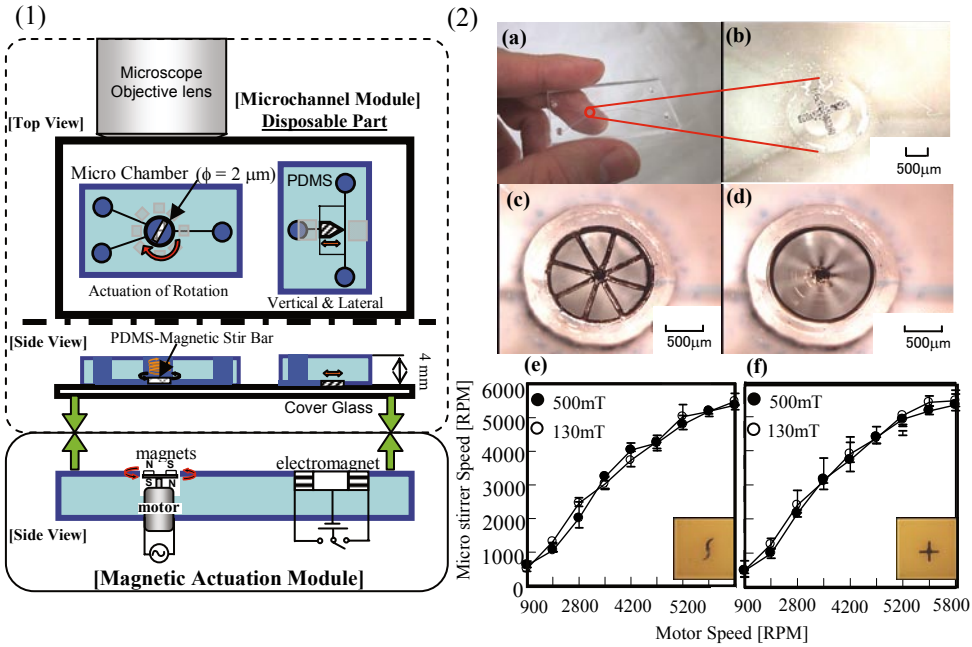

Figure 2. (1):A schematic of independent modules of microchannel and magnetic actuation. (The module of microchannel is disposable).(2): The micro stirrer in microfluidic environment. (a)A photograph of the PDMS double-Y shape biochip.(b), (c)Microscope view of stir bars in biochip (d) Microscopic view of rotating stir bar in biochip. (e),(f)Rotating speed of micro stir bars (e)2-wings and (f)plus shape. The vertical bars indicate the standard error in the mean value ($\sigma/n^{0.5}$).

Figure 2(1) shows schematic of independent modules of microchannel and magnetic actuation. They are combined when the micro tools are actuated and they are disconnected when the module of microchannel is replaced by new one in order to avoid any contamination. Figure 2(2) shows the representative photo of micromagnetic tools of rotating actuation used as micro stirrers. The rotating speed of the stir bars and motor on which the disk shaped ferrite magnets (130 and 500 mT) are attached was 1000-5500 rpm in a micro channel. It was observed that stir bar rotated following the rotation of magnet for most of the cases. The rotating speed did not clearly affected by the differences of shape of the stirrers and magnet forces for the current setting.

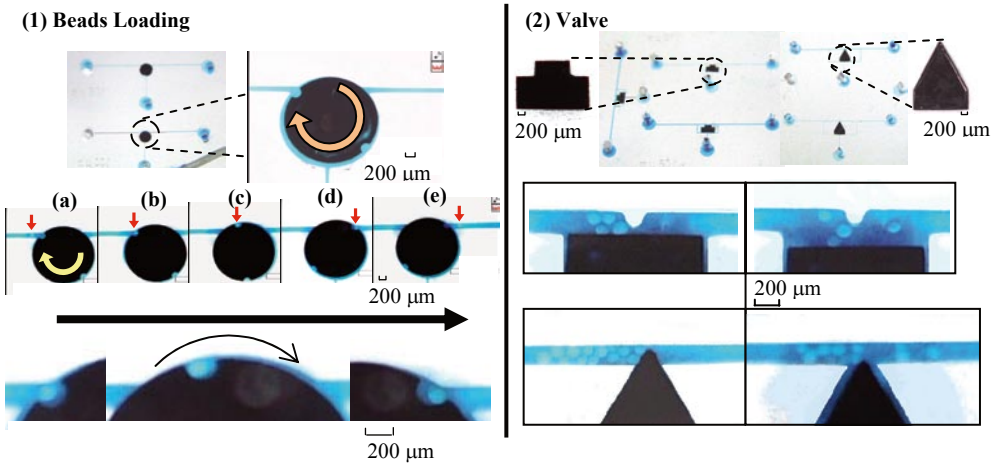

Figure 3. (1): A photo of micromagnetic tool with beads loading function in the biochip and a sequential shots (a)-(e) of loading a single polystyrene bead (100 µm). (2): A photo of micromagnetic tool with valve function in the biochip and magnified photos of operation of valve for beads. The microchannel was dyed by methylene blue.

Figure 3(1) shows beads loading system as one of the examples of the revolving type rotation. For the current study, the polystyrene beads used for the experiment have a size of 100 µm, assuming the size of embryo cell (≈ 100 µm). This step rotation provides accurate one by one beads loading system. The depth clearance between the magnetic tools, PDMS ceiling and cover glass was designed to be less than the size of the beads. Figure 3(2) shows valve systems for two phase flow as one of the examples of the one dimensional actuation of vertical and lateral motion of micromagnetic tool.

ACKNOWLEDGEMENTS

This work has been financially supported by the Research and Development Program for New Bio-industry Initiatives and the ministry of Education, Culture, Sports, Science and Technology Grant-in-Aid for Scientific Research (17040017).

REFERENCES

[1] H. Maruyama.,F. Arai and T. Fukuda, ”On-Chip Microparticle Handling Using Magnetically Driven Microdevice”, µ-TAS2005, pp.1422-1424, 2005.

MODELING ELECTROKINETIC TRANSPORT IN NANOCHANNELS: CLASSICAL POISSON-BOLTZMANN APPROACH MAY NOT BE SO BAD AFTER ALL

Robert H. Nilson and Stewart K. Griffiths
Sandia National Laboratories, California, USA

ABSTRACT

Disparities between atomistic simulations and classical Poisson-Boltzmann calculations of electroosmotic flow speeds often result largely from differences in predicted counterion densities in surface layers, leading to large differences in zeta potentials for a prescribed surface charge density. By use of Density Functional Theory to model the non-continuum atomistic physics of the electric double layer we show that classical Poisson-Boltzmann modeling should yield adequate predictions of ion distributions and mean electroosmotic speeds in many applications, including nanochannels, provided that the no-slip boundary condition and the zeta potential, inferred from measurements in a wide channel, are both applied at the center plane of the fluid monolayer in contact with the surface.

Keywords: nanofluidics, microfluidics, electroosmosis, DFT

1. INTRODUCTION

Previous atomistic modeling studies suggest that classical Poisson-Boltzmann (PB) modeling may substantially overestimate electroosmotic flow speeds in nanoscale channels [1,2]. This is partly because Molecular Dynamics (MD) simulations of electroosmotic flow invariably utilize a prescribed surface charge, inviting comparison with classical PB modeling based on the same surface charge. Further, owing to the non-continuum physics of highly charged surface layers, atomistic models often predict zeta potentials and electroosmotic speeds that differ substantially from PB calculations for the same surface charge. However, despite these differences, we show here that PB and atomistic predictions of mean electroosmotic speed are in relatively good agreement when the zeta potential at the center plane of the first fluid layer is the same for both. We also find that computed zeta potentials are relatively insensitive to channel width, suggesting that values of zeta inferred from measurements in wide channels can be used in PB analyses of nanochannel flows.

2. MATHEMATICAL MODEL

Our modeling approach [2] which uses Density Functional Theory (DFT) to incorporate atomistic physics into continuum-like conservation equations has been previously shown to provide good agreement with MD simulations [2,3,4] but requires far less computer time. The integral equations of DFT are used to describe the mean-field interaction among charged and uncharged species in terms of Lennard-Jones pair potentials, Coulombic forces, short-range electrical interactions, and hard sphere repulsions. Our formulation is similar to that described by Tang et al. [5]. The parametric inputs to DFT are the same as those needed for MD - molecular diameters, interaction energies, and molecular charge. The electric field is determined by solving the Poisson equation using the DFT charge distributions. These charge distributions are also used to compute driving forces for continuum-like analysis of the electroosmotic fluid motion [2].

978-0-9798064-0-7/μTAS2007/$20©2007CBMS

3. DISCUSSION OF RESULTS

Figure 1 illustrates differences between solvent and ion density profiles computed by DFT versus PB for the same surface charge density, $\sigma^*=\sigma d^2/e$. It is seen that DFT predicts a total charge within the first molecular layer that exceeds classical PB. As a result, DFT also yields a lower zeta potential on the no-slip surface, as illustrated in Fig. 2. Further, because the total charge within the fluid must balance the prescribed surface charge, σ^*, it follows that DFT predicts a lower net charge within the central portion of the channel. This reduction in zeta potential and shift of the charge distribution reduces the computed electroosmotic speeds. This is illustrated in Fig. 3 where classical PB results are compared with DFT for a range of prescribed surface charge density.

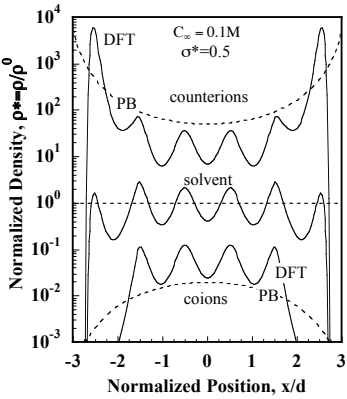

Figure 1. Ion density profiles in a slit having a width of 6 molecular diameters, w/d=6. DFT (solid) and PB (dotted).

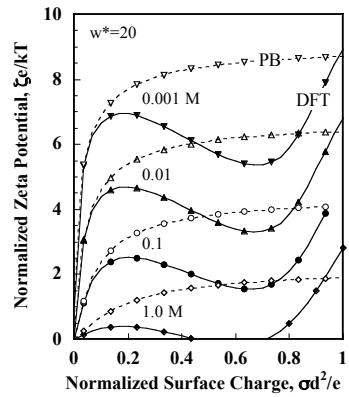

Figure 2. Zeta potential on the no-slip surface located d/2 from fluid/solid interface. DFT (solid) and PB (dotted).

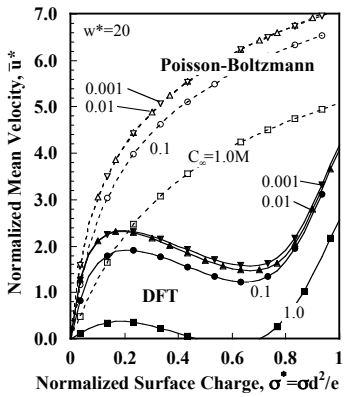

Figure 3. Mean fluid speeds computed by DFT (solid) and classical PB (dotted).

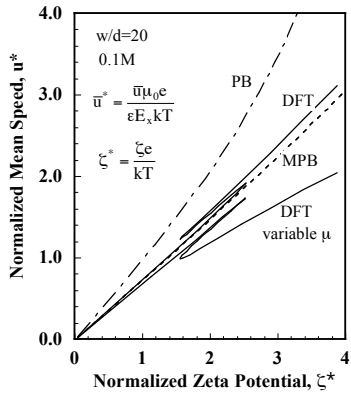

Figure 4. Mean fluid speeds computed by DFT (solid), MPB (dotted), PB(chaindot).

These differences between PB and DFT are substantially reduced if the zeta potential computed by DFT is used as a boundary condition on the no-slip surface for the PB analysis. This approach, referred to here as Modified Poisson-Boltzmann (MPB), is compared to DFT in Fig. 4. Here, the DFT curves fold back on themselves because there are three values of σ^* for some values of $\zeta^* = \zeta e / kT$, as apparent in Fig. 2. The MPB model is in very good agreement with the upper set of DFT results for uniform fluid viscosity. The lower set of DFT calculations include increases in fluid viscosity resulting from increased fluid density in highly charged surface layers, as calculated using a modified Chapman-Enskog model [2]; this too may potentially be incorporated into MPB.

Thus, it appears that errors inherent in classical PB modeling of charged surface layers can be minimized by application of zeta potential rather than surface charge boundary conditions. This has always been the preferred boundary condition for modeling of electroosmotic flow, but it is difficult to apply in MD and it was not obvious that flows having the same ζ^* but differing σ^* would be so comparable. In addition, it is seen in Fig. 5 that, for a given σ^*, ζ^* is nearly independent of channel width down to channels as small as 3 molecular diameters. Thus, zeta potentials routinely measured in wide channels can be applied at much smaller scales. Further, Fig. 6 indicates that the relatively good agreement between MPB and DFT solutions in Fig. 4 does not deteriorate with decreasing channel size. Although these results bode very well for PB modeling of electroosmotic flows in channels of all sizes, including nanochannels, atomistic modeling is still required in other applications, particularly those involving highly concentrated electrolytes and highly charged surfaces, as in desalination and supercapacitor applications.

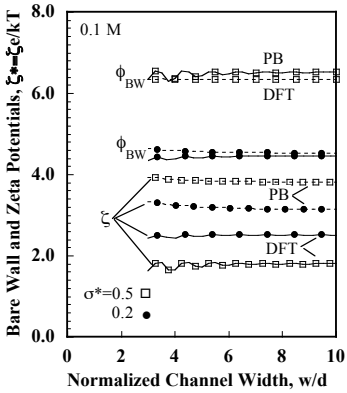

Figure 5. Zeta potential and bare-wall surface potential versus channel width.

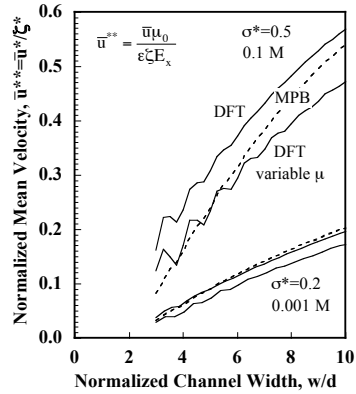

Figure 6. Variation of electroosmotic speed with channel width.

REFERENCES

[1] R. Qiao and N. R. Aluru, J. Chem. Phys. 104 (3) 268, 2003.
[2] R. H. Nilson and S. K. Griffiths, J. Chem. Phys. 125 (16) 164510, 2006.
[3] I. Bitsanis, T. Vanderlick, M. Tirrell, and H. Davis, J. Chem. Phys. 89 (5) 3152, 1988.
[4] T. K. Vanderlick, L. E. Scriven, and H. T. Davis, J. Chem. Phys. 92, 5087, 1990.
[5] Z. Tang, L. Mier-Y-Teran, H. T. Davis, L. Scriven, Molecular Physics 71 (2) 369, 1990

STRUCTURE OF ELECTROOSMOTIC MICROCHANNEL FLOW AFFECTED BY NONUNIFORM WALL ZETA-POTENTIAL

Y. Kazoe, N. Miki and Y. Sato
Keio University, JAPAN

ABSTRACT

The present study experimentally investigated the three-dimensional structure of electroosmotic microchannel flow with nonuniform zeta-potential. The effect of zeta-potential distribution at the wall on electroosmotic flow was evaluated quantitatively by the velocity measurement using spatially averaged time-resolved particle-tracking velocimetry (SAT-PTV). This paper reports the measurement using a straight microchannel comprised of glass and PDMS with the surface chemical modification.

Keywords: Electroosmotic flow, zeta-potential, surface modification, evanescent wave

1. INTRODUCTION

The objective of the present study is to investigate electroosmotic flow affected by the zeta-potential distribution with the heterogeneity of materials and the surface chemical modification. The knowledge obtained from this work will contribute to achieve the precise flow control using electrokinetics.

2. EXPERIMENTAL SETUP

The present study performed the velocity measurement by SAT-PTV [1] using the fluorescent particles. SAT-PTV enables the time-resolved velocity measurement by spatially averaging of the velocity vectors obtained by PTV. Carboxylate-modified fluorescent particles (Molecular Probes) as shown in Table 1 were used as the tracer particles.

Figure 1 illustrates a measurement system comprised of an inverted fluorescent microscope, an optically pumped semiconductor laser (λ = 488 nm), a 60× objective lens (NA = 1.45) and a high speed CMOS camera. In the bulk velocity measurement, the excitation light was provided from the mercury lamp. The measurement depth was calculated to be 1.9 μm [2]. In the near wall velocity measurement, the particles in the vicinity of the wall was excited by the evanescent wave with the penetration depth of 74 nm, which was generated by total internal reflection of the laser beam at glass-solution interface. The electroosmotic velocity vector was obtained by subtracting the particle electrophoretic velocity from the particle velocity [3]. The spatial resolution was 29.3 × 29.3 μm based on the size of reference window. The time resolution was 5 ms, which is equal to the frame rate of CMOS camera.

Table 1. Properties of fluorescent polystyrene particles

Diameter	(μm)	0.5
Density	(g/cm^3)	1.055
Volume concentration	(%)	0.2
Excitation wavelength	(nm)	505
Emission wavelength	(nm)	515
Mobility	(cm^2/Vs)	4.52×10^{-4}

Figure 2 shows a schematic of the straight microchannel comprised of PDMS and borosilicate glass.

978-0-9798064-0-7/μTAS2007/$20©2007CBMS

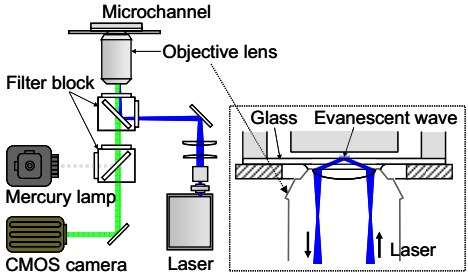

Figure 1. Schematic of the measurement system with the high speed CMOS camera. Mercury lamp and the evanescent wave were used as the light source.

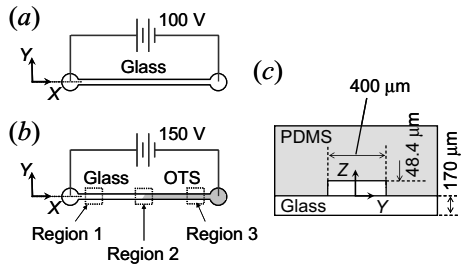

Figure 2. Top views of (a) the pristine and (b) OTS-modified microchannel with the length of 27 mm. (b) Cross-sectional view of the microchannel.

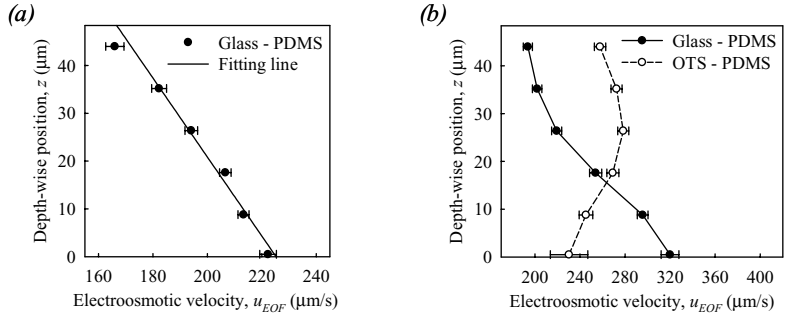

Figure 3. Z-direction profile of spatially and temporally averaged electroosmotic velocity, u_{EOF}, in (a) the pristine and (b) OTS-modified microchannel (Region 1: Glass-PDMS, Region3: OTS-PDMS).

Octadecyltrichlorosilane (OTS) was modified on the glass surface by micro-contact printing [4] as shown in Figure 2(b). The experiments were performed by using the pristine and OTS-modified microchannel. A 5 mM HEPES solution with 0.5 mM NaCl and the tracer particles was injected into the microchannel and the electric field was applied. Measurements were performed in electroosmotic flow in the steady state.

3. RESULTS AND DISCUSSION

Figure 3 shows the profile of electroosmotic velocity in the *Z*-direction at $y = 0$. Because the zeta-potential at top and bottom wall was uniform in the pristine microchannel, electroosmotic flow has the linear velocity profile. From the regression line, the zeta-potential at the glass and PDMS wall was calculated to be −74.9 mV and −55.4 mV, respectively, from the Helmholtz-Smoluchowski equation. On the other hand, electroosmotic flow in the OTS-modified microchannel has the velocity profile as shown in Figure 3(b) because of the effect of surface modification. The zeta-potential at the glass and OTS-modified wall was evaluated to be −70.9 mV and −51.1 mV, respectively, by using the near wall velocity. The flow rate in region 1 and 3 was approximately estimated to be 4.9×10^{-12} m^3/s and 5.0×10^{-12} m^3/s, respectively. These results show that the electroomotic velocity profile was changed by the zeta-potential at the wall to keep the constant flow rate. The results at region 2 in the OTS-modified microchannel were shown in Figure 4 and 5. In

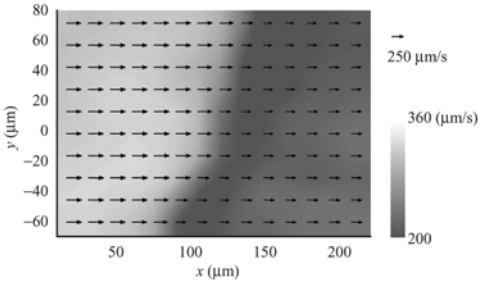

Figure 4. Electroosmotic velocity vector map in the XY-plane in the vicinity of the wall (z = 0). Contour shows the vector magnitudes.

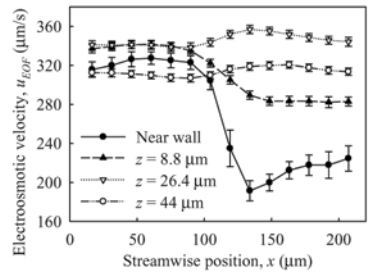

Figure 5. Profiles of streamwise electroosmotic velocity, u_{EOF}, in the X-direction at y = –1.8 μm.

the vicinity of the wall, the electroosmotic velocity was changed with the pattern of surface modification. The gradient of electroosmotic velocity in the *X*-direction becomes smaller with increasing the depth-wise position, *z*, because of the effect of uniform zeta-potential at the PDMS wall. The depth-wise velocity was calculated from the mass conservation law by applying the streamwise and spanwise velocities. As shown in Figure 6, the depth-wise velocity was generated to conserve the difference in the streamwise velocity near the wall with nonuniform zeta-potential.

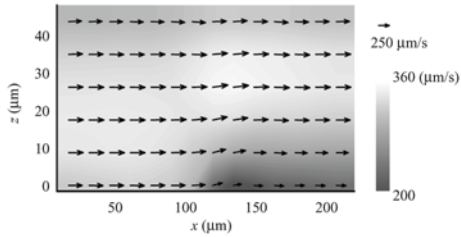

Figure 6. Electroosmotic velocity vector map in the XZ-plane at y = –1.8 μm.

4. CONCLUSIONS

Electroosmotic microchannel flow with nonuniform zeta-potential was investigated by the velocity measurement. It is concluded that the three-dimensional structure of electroosmotic flow was changed by the zeta-potential at the wall to keep the mass conservation. The future work will perform the measurement of electroosmotic flow in the transient state on an application of electric field.

ACKNOWLEDGEMENT

The first author is supported by the 21st COE for "System Design: Paradigm Shift from Intelligence to Life" from the Ministry of Education, Culture, Sports, Science and Technology (MEXT) in Japan. This research is subsidized by the Grant-in-Aid for Young Scientists of MEXT (No. 14702030 and No. 17686017).

REFERENCES

[1] Y. Sato, S. Inaba, K. Hishida and M. Maeda, Exp. Fluids, **35**, pp. 167-177, (2003).
[2] C. D. Meinhart, S. T. Wereley and M. H. B. Gray, Meas. Sci. Technol., **11**, pp. 809-814, (2000).
[3] Y. Sato and K. Hishida, Fluid Dynamics Research, **38**, pp.787-802, (2006).
[4] Y. Jun, D. Le and X.-Y. Zhu, Langmuir, **18**, pp. 3415-3417, (2002).

A MICROFLUIDIC AUTOSAMPLER WITH TRUE TEFLON VALVES: DESIGN AND APPLICATION TO SUSPENDED MICROCHANNEL RESONATOR MASS SENSORS

William H. Grover[1], Yao-Chung Weng[2], and Scott R. Manalis[1,3]

[1]Biological Engineering Division, Massachusetts Institute of Technology, USA
[2]Computational and Systems Biology Initiative, Massachusetts Institute of Technology, USA
[3]Department of Mechanical Engineering, Massachusetts Institute of Technology, USA

ABSTRACT

We present an "autosampler chip," a microfluidic replacement for a conventional autosampler instrument. By actuating on-chip valves, nanoliter-scale volumes can be routed or pumped between any of the on-chip fluid connections. The valves utilize an inexpensive Teflon film that is impervious to virtually all chemicals. We also interface the autosampler chip to a suspended microchannel resonator (SMR) mass sensor. The autosampler chip performs all fluidic operations involved in building a complex multilayer inside the SMR, detecting protein binding, and stripping away the multilayer using "piranha" in preparation for the next measurement. This is one of many applications in which the autosampler chip could replace bulky and costly sample handling hardware.

Keywords: Autosampler, Teflon, valves, suspended microchannel resonator

1. INTRODUCTION

The conventional autosampler instrument is a ubiquitous "front end" in many biological and chemical assays. Benchtop autosamplers and other robotic sample handlers typically include multiple sample vials or microtiter well plates, machinery for choosing samples, pumps for dispensing known amounts of solution, and mechanisms for rinsing their internal volumes. While useful as generic tools for fluid manipulation in many different contexts, autosamplers are too large, expensive, and delicate for many point-of-care and field applications.

We present here a complete microfluidic replacement for a conventional autosampler. For maximum compatibility with a variety of chemical and biological systems, our autosampler chip is fabricated in glass and uses a chemically-inert Teflon valve membrane. These valves are modeled after previously-demonstrated monolithic membrane valves that utilize commercially-available PDMS membranes bonded between etched glass wafers [1]. Since these valve membranes are featureless (not molded as in soft lithography), many off-the-shelf materials can be substituted for PDMS in these valves. Alternative membranes for monolithic membrane valves were first investigated by scientists in the In Situ Instrument Systems Section at the NASA Jet Propulsion Laboratory [2].

2. RESULTS AND DISCUSSION

In this work, a 25 μm thick perfluoroalkoxy (PFA) Teflon membrane (DuPont) is thermally bonded between glass wafers containing etched fluidic and pneumatic features (Figure 1). The valves are normally closed; applying vacuum to an etched displacement chamber in the pneumatic wafer pulls the Teflon membrane away from a discontinuity in the fluid channel and opens the valve (Figure 2). These Teflon monolithic membrane valves control fluid flow as well as their PDMS-based counterparts (Figure 3).

To select from different samples and reagents, the microfluidic autosampler chip shown in Figure 1 includes two fluidic bus channels [3], each containing six bus valves with associated fluid connections. By opening selected bus valves, fluid from any of the six connections can flow to any other connection (Figure 4). In addition, by actuating the valves according to a pumping pattern, the autosampler chip can actively pump or recirculate fluid between any of the connections. Finally, the entire internal volume of the autosampler chip can be automatically rinsed to eliminate cross-contamination between samples. Taken together, these operations replace and expand upon the capabilities of a traditional autosampler.

978-0-9798064-0-7/μTAS2007/$20©2007CBMS

We demonstrate the capabilities of the autosampler chip by interfacing it to a suspended microchannel resonator (SMR) mass sensor [4,5] (Figure 5). When particles or solutions with different densities flow through the vibrating silicon microchannel, the resonance frequency of the channel changes by a measurable amount. In Figure 6, the autosampler chip is used to alternately flow two solutions of different densities through the SMR. The autosampler chip replaces the contents of the SMR in only 300 ms. The autosampler chip is also used to build up and then remove a complex multilayer on the inside surface of the SMR in Figure 7. Frequency changes following polylysine-polyethylene glycol-biotin and neutravidin solutions indicate that binding has occurred inside the SMR, and the return to baseline frequency following delivery of "piranha" to the SMR (concentrated sulfuric acid and hydrogen peroxide) confirms the removal of the multilayer. Preliminary results suggest that the Teflon valves remain unchanged and fully functional following piranha exposure. This is one of many applications in which the microfluidic autosampler could replace bulky and costly upstream fluidic hardware for cheaper and more portable analysis systems.

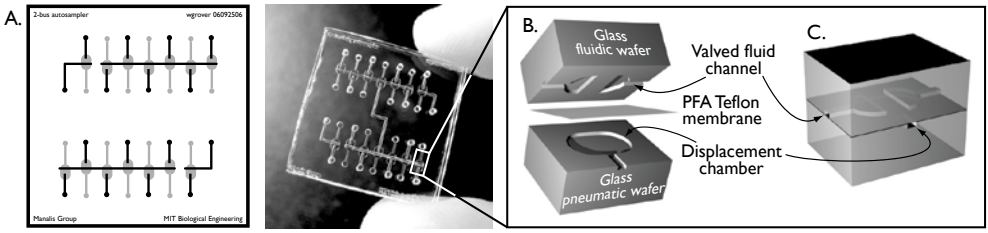

Figure 1. (A) The microfluidic autosampler chip. Black features are etched into the fluidic wafer and gray features are etched into the pneumatic wafer. Exploded (B) and assembled (C) detailed views of a single PFA Teflon valve.

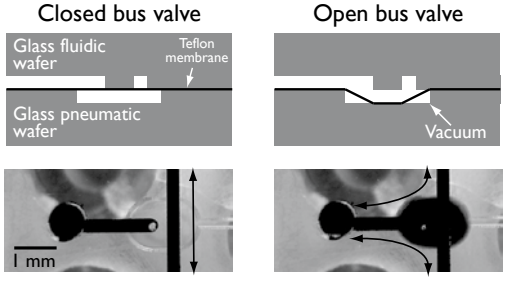

Figure 2. Cross-sectional diagrams and top-view photos of dye in closed and open Teflon bus valves. In the closed valve, fluid is still free to flow through the vertical bus channel. Opening the valve diverts flow through the valve.

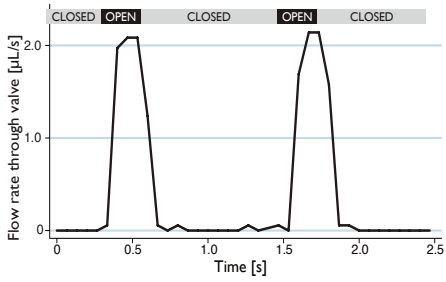

Figure 3. Pressure-driven flow of water through a Teflon monolithic membrane valve held alternately open for 300 ms and closed for 1 s.

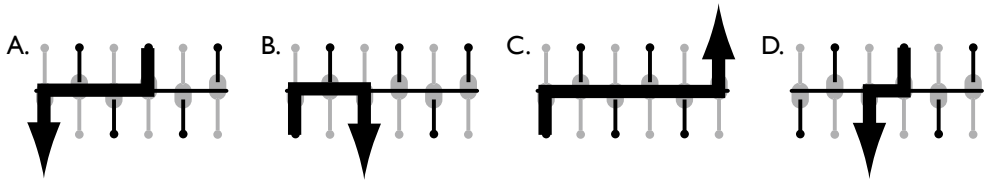

Figure 4. Illustrations of three of the 30 possible paths of fluid flow between the six fluidic connections on one of the two bus channels in the autosampler chip. Operation C rinses the internal fluid volume of the autosampler chip. Flow can be driven by external pressure or actively pumped by the autosampler chip if the valves are actuated in a pumping pattern [1].

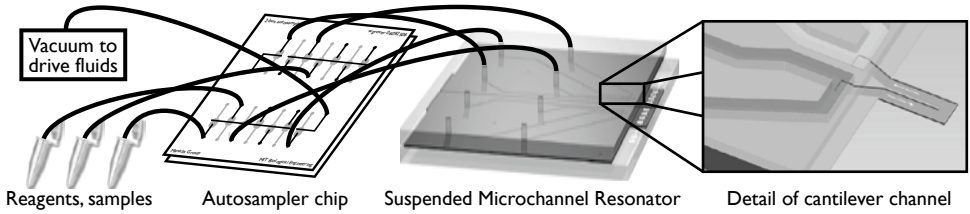

Figure 5. Diagram showing fluidic connections (capillary tubing) between the autosampler chip and the suspended microchannel resonator (SMR) sensor. Using on-chip valves and a single vacuum source, the autosampler chip controls all routing of samples and reagents to and from the cantilever channel.

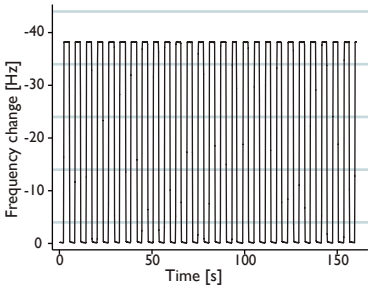

Figure 6. Frequency response of the SMR while the autosampler chip switches rapidly between flowing water (0 Hz relative frequency) and 0.5 x phosphate buffered saline (-38 Hz; mostly 70 mM NaCl) through the SMR. The autosampler chip replaces the 10 pL contents of the cantilever every 3 seconds, requiring only 300 ms per switch.

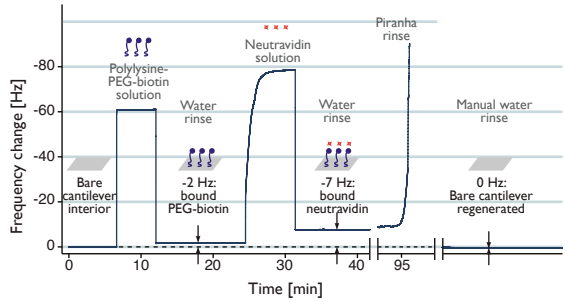

Figure 7. Using the autosampler chip to build and remove a complex polylysine-polyethylene glycol-biotin-neutravidin multilayer on the inside surface of the SMR. The -7 Hz change at 35 minutes confirms binding of polylysine-PEG-biotin and neutravidin to the inside walls of the cantilever channel. The autosampler chip then delivers piranha (concentrated sulfuric acid with hydrogen peroxide) to remove the multilayer. The return to baseline frequency after rinsing confirms that the SMR surface was regenerated. The Teflon valves appear to remain fully functional following piranha exposure.

1. W. H. Grover, A. M. Skelley, C. N. Liu, E. T. Lagally and R. A. Mathies. Monolithic membrane valves and diaphragm pumps for practical large-scale integration into glass microfluidic devices. *Sensors and Actuators B* **89** (3), 2003.

2. Peter A. Willis, In Situ Instrument Systems Section, NASA Jet Propulsion Laboratory, California Institute of Technology, personal communication.

3. W. H. Grover and R. A. Mathies, An integrated microfluidic processor for single nucleotide polymorphism-based DNA computing. *Lab on a Chip* **5**, 2005.

4. T. P. Burg and S. R. Manalis, Suspended microchannel resonators for biomolecular detection. *Applied Physics Letters* **83** (13), 2003.

5. T. P. Burg, M. Godin, S. M. Knudsen, W. Shen, G. Carlson, J. S. Foster, K. Babcock, S. R. Manalis. Weighing of biomolecules, single cells and single nanoparticles in fluid. *Nature* **446**, 2007.

ACTIVE MICROMIXER BASED ON ION DEPLETION AND ENRICHMENT THROUGH POLYELECTROLYTIC FILTERS

H.G. Chun[1], H.C. Kim[2] and T.D. Chung[2]
[1]*University of North Carolina, Chapel Hill, USA and*
[2]*Seoul National University, KOREA*

ABSTRACT

This paper reports a new type of micromixer based on alternative depletion-enrichment in ionic distribution using a pair of positive polyelectrolytic plugs (pPPs). The pPPs were formed by photopolymerizing corresponding diallyldimethyl ammonium chloride (DADMAC) monomer solution. A main microchannel was designed to pass between a pair of pPPs facing to each other. An external AC source has electrical contact with the pPPs via respective 1 M KCl solutions and Ag/AgCl electrodes. Upon an electric bias, anions were exclusively extracted through one of the pPPs to create a local ion-deficient region. Simultaneously, an ion-rich region was developed near the other. As the direction of the charge flow was alternately reversed by applying AC voltage to disturb the fluidic system on the push-pull basis. As a result, the solutions were mixed rapidly in the microchannel without any mechanical moving part or specially machined structure. The mixing efficiency was higher than 90% for aqueous Rhodamine 6G dye and PBS.

Keywords: Mixer, Ion Depletion, Salt Bridge, Polyelectrolytic Plug

1. INTRODUCTION

Han and his coworkers used a nanochannel perpendicular to the microchannel to generate local ion depletion[1,2]. In that study, cations were extracted to produce the ion-depleted region for sample preconcentration but not injected to make ion-enriched microspace. We perceived the similar ion depletion region could be generated much more efficiently by replacing the nanochannel with the pPPs, which were previously reported as an electrocytometer chip[3]. Furthermore, the design could be easily modified to make better for the purpose of mixing. The present work is the first example of active micromixer based on alternating ion depletion-enrichment in the microchannel by employing pPPs instead of the nanochannel. Since the pPPs have far larger cross-section than the nanochannel, extraction of ions is much faster. Moreover, the device in this study can perform both ion extraction and injection, the direction of which can be reversed or oscillated by applying appropriate electric modulation. We confirmed the proof-of-concept and investigate the effects of fluid rate and applied potential to the mixing performance.

2. THEORY

The mixing principle in a microfluidic system using a pair of pPPs is illustrated in Figure 1. Suppose that two solutions flow from left to right in a microchannel in parallel and a pair of pPPs lie in a perpendicular channel to the main stream as shown in Figure 1(a). Figure 1(b) presents what happens when an electric current flows through the pPP pair. Anions come in through the lower pPP while going out through the upper one. It results in ion depleted and enriched regions at the upper and lower parts in the microchannel,

978-0-9798064-0-7/μTAS2007/$20©2007CBMS

respectively. By reversing the direction of electric current, the ion depleted and enriched regions are switched as shown in Figure 1(c). This effect can be greatly amplified by applying an AC voltage that leads to repetitive alternation of the local ion depletion and enrichment, which results in solution mixing.

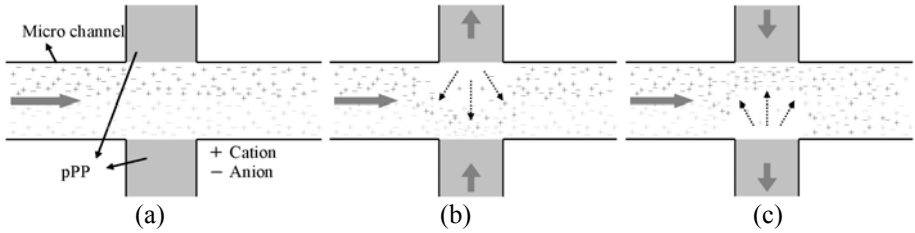

Figure 1. The mixing principle in a microfluidic system using a pair of pPPs

3. EXPERIMENTAL

Figure 2(a) is the picture of pPPs facing to each other, which were fabricated in this study. As expected, the horizontal laminar flow of Rhodamine 6G and phosphate buffered saline was notably disturbed by external field as seen in Figure 2(b) and (c). We could confirm the ion depletion and enrichment near the respective pPP. Upon AC voltage of 4V at 10 Hz, the laminar flow at flow rate of 4 mm s^{-1} was completely mixed at no less downstream from the pPPs than 100 μm.

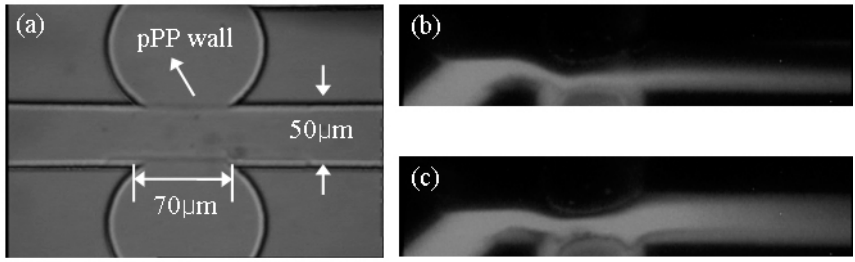

Figure 2. A pair of pPPs facing to each other (a), no field applied (b), and electric field turned on (c)

4. RESULTS AND DISCUSSION

The effects of flow rate and applied potential were investigated to the mixing efficiency, which was summarized in Figure 3. Basically, the proposed pPPs system has exactly the same structure as that for electrocytometer, which we previously reported. Table 1 indicates that the identical unit device can play two different roles depending on the electric current and frequency. Facile ion transport across the pPPs makes the electrical conductance sufficiently high. Therefore a low voltage power supply is enough to operate the proposed micromixer, which can be hardly realized by previously reported electrokinetic mixers. Besides, the structure of the proposed mixer using pPPs is simple and easy to fabricate and handle, as found in the fact that this device involves no active mechanical part.

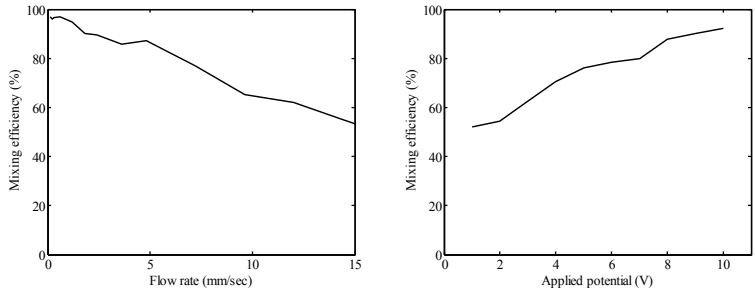

Figure 3. Dependence of mixing efficiency on flow rate(a) and applied potential(b)

5. CONCLUSIONS

All those features suggest the proposed system to be a competitive alternative to the conventional mixers.

Table 1. Polyelectrolytic Plugs for Cytometer vs. Mixer

	Cytometer	Mixer
Current	~10 μA	~200 μA
Frequency	DC (0 Hz)	AC (~10 Hz)
Purpose	Particle Detection	Solution Mixing

ACKNOWLEDGEMENTS

This research was supported by the MIC(Ministry of Information and Communication), Korea, under the ITRC(Information Technology Research Center) support program supervised by the IITA(Institute of Information Technology Advancement) (IITA-2006-(C1090-0602-0002).

REFERENCES

[1] Y. -C. Wang, A. L. Stevens, J. Han, *Million-fold Preconcentration of Proteins and Peptides by Nanofluidic Filter*, Analytcal Chemistry, 77, pp. 4293-4299, (2005).

[2] S. J. Kim, Y. -C. Wang, H. Jang, J. H. Lee, J. Han, *Nonlinear Electrokinetic Flow Pattern near Nanofluidic Channel*, Proc. Micro Total Analysis Systems 2006, Kluwer Academic Publisher , Tokyo, Japan, pp. 522-524, (2006).

[3] H. Chun, T. D. Chung, H. C. Kim, *Cytometry and Velocimetry on a Microfluidic chip Using Polyelectrolytic Salt Bridges*, Analytcal Chemistry, 77, pp. 2490-2495 (2005).

CENTRIFUGAL MICRODEVICE FOR CONTINUOUS AND SIZE-DEPENDENT SEPARATION OF PARTICLES

Satoshi Sunahiro[1], Masumi Yamada[2], Masahiro Yasuda[1], and Minoru Seki[1,3*]

[1]Osaka Prefecture University, 1-1 Gakuen-cho, Naka-ku, Sakai, Osaka 599-8531, JAPAN
[2]Tokyo Women's Medical University, 8-1 Kawada-cho, Shinjuku-ku, Tokyo 162-8666, JAPAN and [3]Chiba University, 1-33 Yayoi-cho, Inage-ku, Chiba 263-8522, JAPAN
mseki@faculty.chiba-u.jp

ABSTRACT

A microfluidic system is presented for continuous particle separation according to size, driven by centrifugal pumping. Previously, we have developed a method for continuous size-separation of particles, named "Pinched-Flow Fractionation (PFF)"[1,2], utilizing a laminar flow profile in a pinched microchannel. In this study, centrifugal pumping was employed to separate particles without using complicated outer/inner pumping devices or schemes. Hydrodynamic resistances of each channel segment were adjusted to specific values for the precise control the inlet and the outlet flow rates, which is prerequisite for accurate particle manipulation. In the experiment, two types of microdevices were designed and fabricated, and polymer particles with diameters of 3~15 μm were successfully separated. This microfluidic system is useful and versatile, due to its accuracy and simplicity in operation.

Keywords: continuous particle separation, centrifugal pumping, microfluidic device

1. INTRODUCTION

Size-dependent separation of particles, including polymer beads, cells, and biomacromolecules, is essential for various research fields and industrial applications. We have previously proposed a concept of 'Pinched Flow Fractionation (PFF)[1,2] (Fig. 1), and successfully separated sub-micron to micron-size particles using pressure-driven flow. In this study, centrifugal force was adopted as the driving force of fluid flows with and without particles, since the control of centrifugal rotation is easily and accurately achieved, which is suitable for microdevice manipulation[3]. In PFF system, the inlet flow rates should be rigidly adjusted to focus the particle positions onto one sidewall in the pinched segment. In order to achieve the perfect focusing of particles, the positions of the inlet ports and the hydrodynamic resistances of the channel segments were precisely designed regarding the channel network as a resistive circuit.

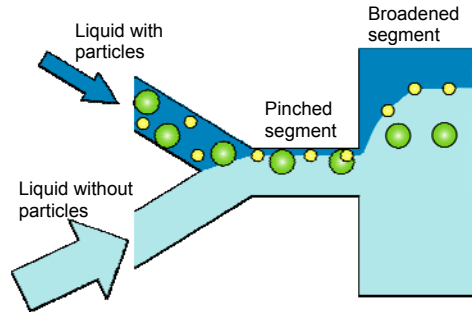

Figure 1. Principle of Pinched Flow Fractionation. In the pinched segment, particles are focused onto one sidewall regardless of size by controlling the flow rates from two inlets. Particles are then separated according to size by the spreading flow profile at the boundary of the pinched and the broadened segments. The region without particles is light-colored.

978-0-9798064-0-7/μTAS2007/$20©2007CBMS

2. EXPERIMENTAL

PDMS microdevices were fabricated using usual replica-molding techniques. First, a microdevice (Microdevice 1) with 12 outlet channels were fabricated as shown in Fig. 2 (a) and Fig. 3, with the pinched-segment width of 20 μm. The ratio of flow rates from Inlets 1 and 2 was calculated to be 1:16.9, and the introduced flow would be equally distributed through 12 outlets. An aqueous suspension containing 5.0 and 15.0 μm particles was dropped into Inlet 1, while distilled water was dropped into Inlet 2. Then the microdevice was rotated at 800 rpm for 30 seconds to separate these particles.

Second, to improve the separation efficiency, a microdevice (Microdevice 2) with asymmetrically-arranged 7 branches (Fig. 2 (b) and Fig. 4) was fabricated. The ratio of outlet flow rates was calculated to be (1.3):(1.9):(2.6):(3.2):(4.3):(62.2):(24.6). The pinched segment width was 20 μm, and the channel depth was 20 μm. Fluorescent polystyrene beads with diameter of 3.0 or 9.9 μm were introduced and separated. After dropping aliquots with and without particles, the microdevice was rotated at 1500 rpm for 150 seconds.

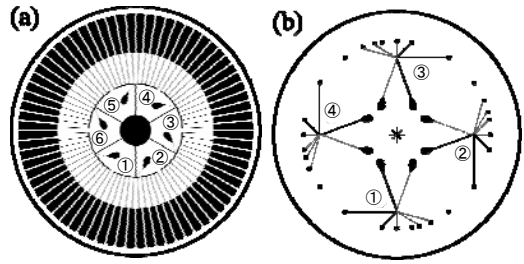

Figure 2. Microdevice designs; (a) Microdevice 1 and (b) Microdevice 2. There are independent six and four channel structures in Microdevices 1 and 2, respectively.

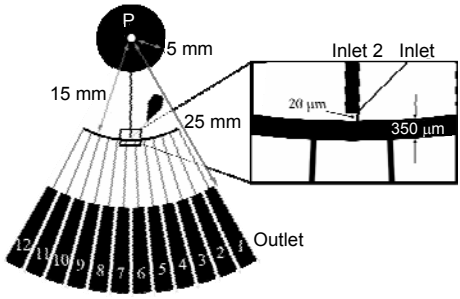

Figure 3. Enlarged diagram of the channel design of Microdevice 1. Point P indicates the center of rotation.

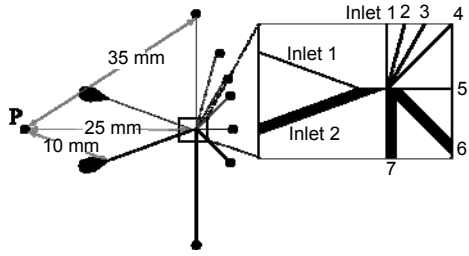

Figure 4. Enlarged diagram of the channel design of Microdevice 2. Point P indicates the center of rotation.

3. RESULTS AND DISCUSSION

Photographs of the separated particles using Microdevice 1 are shown in Fig. 5; these particles (5.0 or 15.0 μm in diameter) were almost perfectly separated, although only two of 12 outlets are mainly used. Also, when Microdevice 2 was employed, the particles (3.0 or 9.9 μm in diameter) were successfully separated (Fig. 6 and Table 1). In this device, 7 outlets were effectively used compared to Microdevice 1, due to the microchannel geometry with nonidentically-designed outlet channels. It was also confirmed that the separation efficiency was comparable to that of the pressure-driven flow scheme (Table 1). These results successfully demonstrated that the presented system is versatile due to the simplicity in operation, without using complicated pumping schemes.

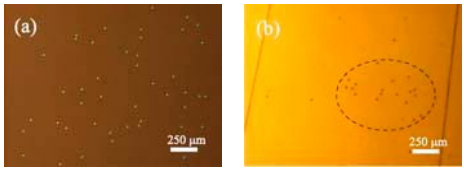

Figure 5. Micrographs showing (a) Outlet 1 and (b) Outlet 2 of Microdevice 1, after rotating at 800 rpm for 30 seconds. 5.0 μm and 15.0 μm particles were almost perfectly separated.

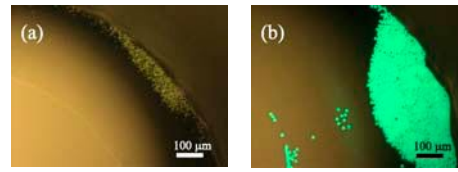

Figure 6. Micrographs showing (a) Outlet 2 and (b) Outlet 4 of Microdevice 2, after rotating at 1500 rpm for 150 seconds. Yellow particles are 3.0 μm in diameter, and blue particles are 9.9 μm in diameter.

Table 1. Ratios of particles recovered from each outlet, when pressure- or centrifugal-pumping scheme was employed using Microdevice 2.

3.0-μm particles		Outlet	9.9-μm particles	
Pressure pumping	Centrifugal pumping	No.	Pressure pumping	Centrifugal pumping
0.090	0.014	1	-	-
0.900	**0.946**	2	-	-
0.010	0.040	3	-	-
-	-	4	**1.00**	**0.940**
-	-	5	-	0.053
-	-	6	-	0.007
-	-	7	-	-

4. CONCLUSIONS

The presented centrifugal-driven system for particle separation will become a useful tool for various applications, such as selection of specific cells from a complicated mixture, and preparation of monodispersed particles.

ACKNOWLEDGEMENTS

This research was supported in part by Grants-in-aid for JSPS fellowship from JSPS and Scientific Research B (16310101) from the Ministry of Education, Science, Sports, and Culture of Japan.

REFERENCES

[1] M. Yamada, M. Nakashima, M. Seki, *"Pinched Flow Fractionation: Continuous Size Separation of Particles Utilizing a Laminar Flow Profile in a Pinched Microchannel,"* Anal. Chem., **76**, 5465 (2004).

[2] J. Takagi, M. Yamada, M. Yasuda, M. Seki, *"Continuous Particle Separation in a Microchannel Having Asymmetrically Arranged Multiple Branches"* Lab Chip, **5**, 778 (2005)

[3] D. C. Duffy, G. J. Kellogg et al., "Microfabricated Centrifugal Microfluidic Systems: Characterization and Multiple Enzymatic Assays," Anal. Chem., **71**, 4669 (1999).

CHAOTIC MIXING IN A HELE-SHAW CELL, WITH APPLICATION TO DNA CHIP HYBRIDIZATION

Florence Raynal[1], Aurélien Beuf[1], Frédéric Plaza[1], Philippe Carrière[1], Michel Cabrera[2], Jean-Pierre Cloarec[2], Vincent Dugas[2,3], Emmanuel Fradier[2], and Éliane Souteyrand[2,3]

[1]LMFA UMR 5509, [2]INL UMR 5270, [1,2]CNRS/Université de Lyon, [3]Rosatech, 69130 Écully, FRANCE.

ABSTRACT

We propose here theoretical, numerical and experimental works aimed to improve DNA micro-arrays hybridization. We show that, thanks to an efficient mixing, we obtain a much more rapid process, with a much better reliability.

Keywords: Mixing, chaos, DNA chip, hybridization

1. INTRODUCTION

A *DNA chip* is composed of an array of biological probes (chains of nucleotides, i.e. *cDNA*) fixed to a solid surface. When the array is exposed to a solution containing single-stranded DNA samples (*targets*), the latter have a tendency to hybridize with the complementary probe on the chip, if present: this phenomenon is called *hybridization*. It is therefore of primary importance to make sure that a given target visits the *whole* surface of the chip in a reasonable time. During static hybridization (or *cover-slip* method), where no fluid flow is applied, only molecular diffusion allows targets to move, and significant variations in the response of the chip are commonly observed, even after overnight hybridization. We propose here to improve the reliability of the results, and speed up the process, thanks to an efficient mixing: the chip is put inside an hybridization chamber of small height, in which a flow is created. Because of the small dimensions of the device, only creeping flows are available. It is now well-known however that even creeping flows can lead to good mixing, thanks to chaotic advection [1]. Here, because of the large aspect ratio of the chamber, the flow is of Hele-Shaw type; in that case, it is quasi bi-dimensional, so that, in order to have chaotic advection, time-periodicity is required.

2. OPTIMIZATION OF MIXING IN THE HELE-SHAW CELL

We proposed two time-periodic protocols of mixing based on chaotic advection, the first one –denoted (S)– using syringes, the second one –denoted (P)– using pumps (figure 1). The governing non dimensional parameter for mixing is α, which represents the volume of fluid displaced during one period T compared to the volume of the chamber (here α=0.18 T). In order to decide which protocol is the most efficient, what is the optimum α and the best geometry, we developed a complete Fluid Mechanics analysis:

- *3D-numerical* Poincaré sections and Lyapunov exponents were computed for *both protocols* with *various values of* α in a *squared* hybridization chamber [2,3].
- A 10:1 model experiment was carried out to confirm numerical results.
- Using a *two-dimensional model*, which allows to change geometry easily thanks to a Schwarz-Christoffel transformation, *a similar analysis* was performed for *different shapes* of the chamber (circular, squared or rectangular), with same total area.

978-0-9798064-0-7/µTAS2007/$20©2007CBMS

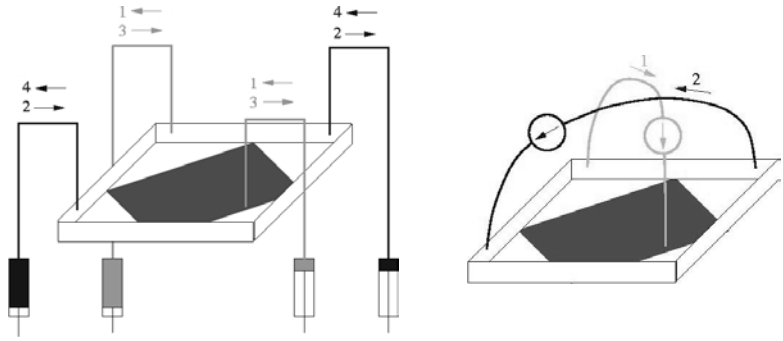

Figure 1. *(a)* Alternating injection scheme for protocol S . Each quarter-period step of the protocol involves two opposite syringes (the grey ones in step 1 and 3, the dark ones in steps 2 and 4), the two other ones being inactive. *(b)* Same for protocol P. Each half-period step of the protocol involves only one pump. One pump always pushes the fluid in the same direction, or else is inactive.

We found in a very wide range of α that the most efficient mixing (homogeneous Poincaré section) was obtained with protocol P, associated with the rectangular geometry. Lyapunov exponents (not shown here) show that this also corresponds to the most rapid mixing. Figure 2 shows some results obtained for α=0.72 (T= 4 s).

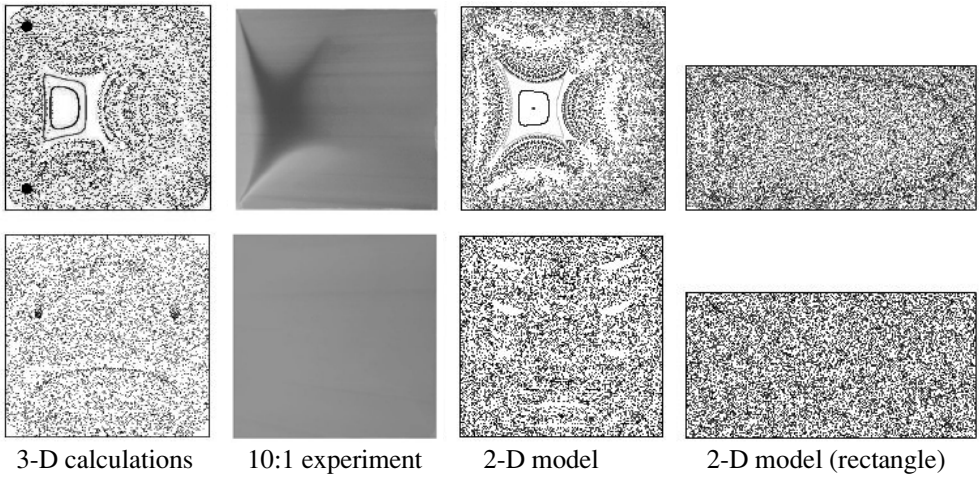

Figure 2. Poincaré sections and experiments for the case α=0.72 (T= 4 s): above, protocol S; below, protocol P.

3. APPLICATION TO CHIP HYBRIDIZATION

Following our theoretical results, the *Rosamix*, an entirely automated prototype of micro-mixer for DNA-chips was manufactured, using pumps and rectangular geometry. Although this device is not integrated on a lab-on-a-chip (the total volume, 500 µl, is ten times more important than for cover-slip method), the results shown for a reference DNA

chip with two types of probes, differing from only one nucleotide (HPA1a and HPA1b, 12 mer), and regularly positioned across its surface are striking (figure 3):

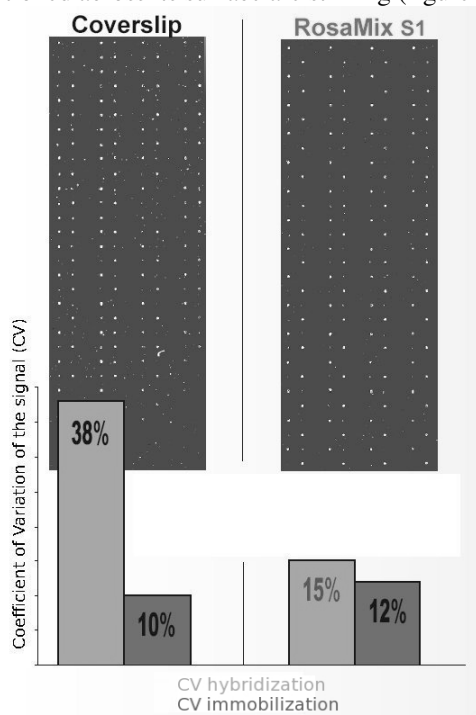

Figure 3. Detection of a Single Nucleotide Polymorphism (SNP) on DNA chip, with cover-slip method or using the Rosamix, with the same quantity of targets (5 pmol) and the same hybridization time (two hours).

With *the same amount of DNA targets* (5 pmol of HPA1 84 mer), after *the same total hybridization time* the Rosamix hybridized chip exhibits a decrease of the coefficient of variation of the hybridization signal better than 2 fold.

4. CONCLUSION

We have shown here that an efficient and rapid mixing could greatly speed-up and improve the reliability of DNA chip technology. We expect miniaturization to further decrease this (already low) total hybridization time.

REFERENCES

[1] H. Aref, *Stirring by chaotic advection,* J. Fluid Mech., 143:1-21, (1984).

[2] F. Raynal, F. Plaza, A. Beuf, Ph. Carrière, É. Souteyrand, J.-R. Martin, J.-P. Cloarec, and M. Cabrera, *Study of a chaotic mixing system for DNA chip hybridization chambers*, Physics of Fluids, 16(9): L63-L66, (2004).

[3] F. Raynal, A. Beuf, F. Plaza, J. Scott, Ph. Carrière, M. Cabrera, J.-P. Cloarec, and É. Souteyrand, *Towards better DNA chip hybridization using chaotic advection,* Physics of Fluids, 19(1): 017112, (2007).

CHARACTERIZATION OF THREE-DIMENSIONAL SERPENTINE MICROMIXERS: EFFECTS OF ROTATION, LAMINATION AND CHAOTIC ADVECTION

Jang Min Park and Tai Hun Kwon

Department of Mechanical Engineering, Pohang University of Science and Technology, Korea

ABSTRACT

The present study comprehensively investigates flow and mixing characteristics of Three-dimensional Serpentine Micromixer (TSM) of three representative types. Even if TSM has been well known to be an attractive design for micromixers due to its relatively simple fabrication, their mixing mechanism is not fully investigated notwithstanding several reports [1-3]. In this regard, the present work attempts to understand the mixing mechanism of TSM thoroughly in terms of three major characteristics, namely rotation, lamination and chaotic advection. In particular, the rotation and lamination are dominated by channel aspect ratio and geometric configurations of TSM, while the chaotic advection significantly depends on Reynolds number (*Re*). Poincaré map and Lyapunov exponents clearly confirm such effects.

Keywords: Serpentine micromixer, rotation, lamination, chaotic advection

1. INTRODUCTION

The TSM is one of the widely accepted micromixers to achieve a rapid mixing in miniaturized analysis systems due to its fabrication-wise design with efficient mixing performances [1-3]. In several reports of the TSM, mixing performances are characterized via well-organized experiments, however, comprehensive explanations of the mixing mechanisms and flow characteristics have not been fully accomplished yet. In this regard, the present study attempt to investigate the flow and mixing characteristics of the TSM in detail based on a numerical analysis.

2. NUMERICAL ANALYSIS

Particularly three representative types of TSM are considered: Serpentine-Type-C (STC, Figure 1(a), [1]); Serpentine-Type-L (STL, Figure 1(b), [2]); Improved Serpentine Laminating Micromixer (ISLM, Figure 1(c), [3]). Numerical investigation is extensively conducted using repetitive units (inside dotted line in Figure 1) which represent overall performances of each micromixer. Finite element analysis enables us to investigate flow characteristics with accuracy, and colored particle tracking method not only visualizes the mixing performance but also provides dynamical system analysis by means of Poincaré map and Lyapunov exponent [4]. Especially in this study, two different channel aspect ratios of 0.2 and unity are considered: as we shall note in the following section, the channel aspect ratio turns out to play an important role in determining the flow and consequently mixing characteristics of the TSM. In addition, inertia effects on the mixing behaviours are observed by considering various flow rates (thus *Re*) for each design.

978-0-9798064-0-7/μTAS2007/$20©2007CBMS

3. RESULT AND DISCUSSION

In Figure 2 and 3, numerical analysis results are introduced in a qualitative manner particularly in terms of: i) the cross-sectional colored particle distribution with interface trajectory of two liquids; and ii) conceptual drawing of the flow characteristics with Poincaré map, for Stokes flow regime. Shown in Figure 4 and 5 are quantitative evaluation of mixing performance in terms of the Lyapunov exponent for several *Re*.

In Stokes flow regime, three-dimensional serpentine geometry turns out to rotate the fluid such that the interface is twisted after the serpentine region (Figure 2, 3). The rotation is mainly due to 'no-slip condition' at the channel wall and 'viscous force': fluid near the channel wall flows along the serpentine wall path and this stream together with a viscous force drives the rotation of fluid. With this in mind, flow characteristics in Stokes flow regime are briefly summarized as follows.

- Channel aspect ratio of 0.2: Weak rotations are observed. STC rotates the interface in an alternating manner with canceling effect (Figure 2(a), (b)); STL rotates the interface in a successive manner resulting in a stretching and twisting of the interface (Figure 2(c), (d)); ISLM also rotates the interface successively like STL, especially additional split/recombination paths (dotted lines in Figure 2(f)) developing lamination (Figure 2(e), (f)).
- Channel aspect ratio of 1: Degree of rotation is remarkably increased to almost 90°, while rotational direction remains the same (Figure 3). Especially for the case of ISLM, increased rotation deteriorates the lamination as described in Figure 3(e), (f).

Effect of chaotic advection is characterized with respect to *Re* with the help of Lyapunov exponent (a stretching measure of fluid elements) which are plotted in Figure 4, 5. One can briefly summarize the results as:

- Generally, effect of chaotic advection increases as *Re* increases.
- Channel aspect ratio of unity shows steeper increasing trends of Lyapunov exponent than that of 0.2.
- In particular, Lyapunov exponents of STL and ISLM with channel aspect ratio of 0.2 are larger than that of STC in low Re regime, mainly due to the previously mentioned twisting and lamination (Figure 4).

Consequently, rotation, lamination and chaotic advection would be the principal characteristics of serpentine-type micromixers which eventually determine the mixing performance.

ACKNOWLEDGEMENTS

The authors would like to thanks the Korean Ministry of Commerce, Industry and Energy for financial support via the Development of Next-Generation New Technology Program.

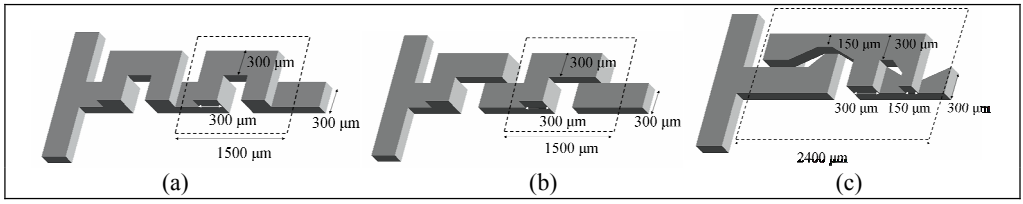

Figure 1. Schematics of (a) STC, (b) STL and (c) ISLM

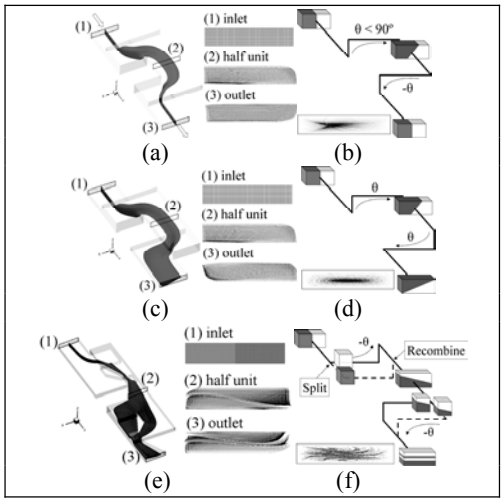

Figure 2. Colored particle tracking result with interface trajectory of (a) STC, (c) STL and (e) ISLM, and conceptual drawing and Poincaré map representing the flow characteristics of (b) STC, (d) STL and (f) ISLM in Stokes flow regime when the channel aspect ratio is 0.2

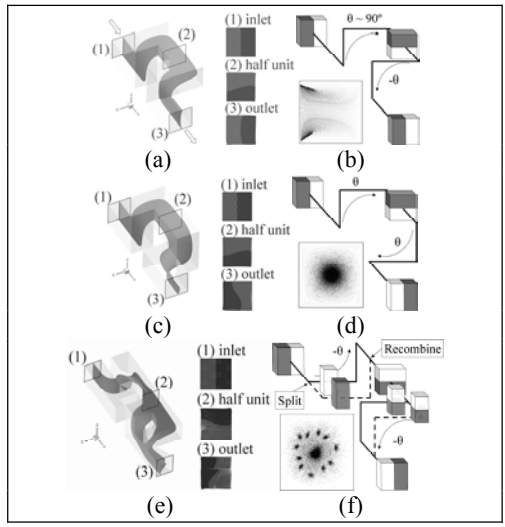

Figure 3. Colored particle tracking result with interface trajectory of (a) STC, (c) STL and (e) ISLM, and conceptual drawing and Poincaré map representing the flow characteristics of (b) STC, (d) STL and (f) ISLM in Stokes flow regime when the channel aspect ratio is 1

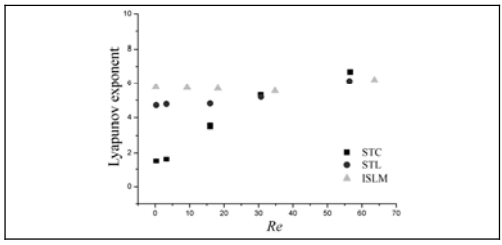

Figure 4. Lyapunov exponent results for several *Re* with channel aspect ratio of 0.2

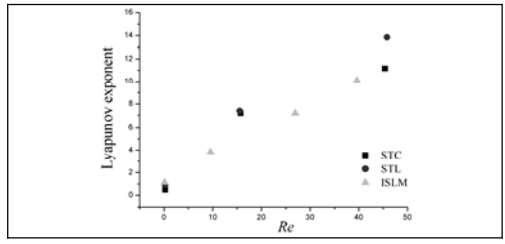

Figure 5. Lyapunov exponent results for several *Re* with channel aspect ratio of 1

REFERENCES

[1] R. H. Liu, M. A. Stremler, K. V. Sharp, M. G. Olsen, J. G. Santiago, R. J. Adrian, H. Aref and D. J. Beebe, *Passive mixing in a three-dimensional serpentine microchannel*, J. Microeletromech. Syst., 9, pp. 190-197, (2000).

[2] R. A. Vijayendran, K. M. Motsegood, D. J. Beebe and D. E. Leckband, *Evaluation of three-dimensional micromixer in a surface-based biosensor*, Langmuir, 19, pp. 1824-1828, (2003).

[3] D. S. Kim, S. H. Lee, T. H. Kwon and C. H. Ahn, *A serpentine laminating micromixer combining splitting/recombination and advection*, Lab on a chip, 5, pp. 739-747, (2005).

[4] T. G. Kang and T. H. Kwon, *Colored particle tracking method for mixing analysis of chaotic micromixers*, J. Micromech. Microeng., 14, pp. 891-899, (2004)

DEVELOPMENT OF PORTABLE POROUS PDMS PUMP FOR MICROFLUDIC LAB-ON-A-CHIP

Kyoung Je Cha[1], Dong Sung Kim[2] and Tai Hun Kwon[1]

[1] Dept. of Mechanical Engineering, POSTECH, KOREA and

[2] School of Mechanical Engineering, Chung-Ang University, KOREA

ABSTRACT

In this paper, we have proposed and demonstrated a novel potable pump for microfluidic lab-on-a-chip using a porous PDMS (polydimethysiloxane) sponge ($1.5 \times 1.5 \times 1 cm^3$). The porous PDMS sponge was fabricated by a sugar leaching technique developed in this study. The porous PDMS sponge was coated by PDMS to be used as a pump for microfluidic lab-on-a-chip. The fabricated porous PDMS pump was successfully utilized in the microfluidic lab-on-a-chip as a pump. The porous PDMS is portable and could be readily employed on top of the inlet portion of various lab-on-a-chips.

Keywords: potable pump, porous PDMS sponge, porous PDMS pump, sugar leaching

1. INTRODUCTION

Pumping fluid is essential to manipulate the flow inside various microfluidic lab-on-a-chips [1]. Macro scale pumps externally installed, for instance a syringe pump, are frequently utilized in a pressure driven flow in microfluidic systems. The syringe pumps, however, are generally limited in use due to its size and high cost [2]. In this regard, various types of micropumps have been developed including mechanical and nonmechanical pumps [1]. But previous micropumps make the systems complex to fabricate and difficult to operate. In this regard, we propose a low cost and portable pump for microfluidic lab-on-a-chip using porous PDMS sponge.

2. DESIGN AND FABRICATION

The operation process of the porous PDMS pump system suggested in this study is illustrated in Figure 1. The basic concept of the pumping mechanism is that pressing porous pump releases working fluid (saline) in the porous PDMS pump (Figure 1(a)), which then pushes medium fluid (e.g., reagent or bio sample) inside the inlet into microchannel and finally to the outlet in a lab-on-a-chip (Figure 1(b)).

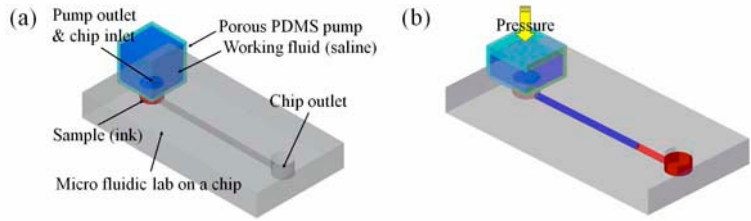

Figure1. Schematic diagram of the operation process of the porous PDMS pump system.

Figure 2 schematically shows the fabrication process of a porous PDMS sponge. Lumps of sugar are piled up in a Petri dish (Figure 2(a)) inside which PDMS prepolymer mixed

978-0-9798064-0-7/μTAS2007/$20©2007CBMS

with thermal curing agent in 10:1 weight ratio is poured (Figure 2(b)). The Petri dish containing PDMS prepolymer is then placed inside a vacuum desiccator. The PDMS prepolymer is infiltrated into the lumps of sugar ($1.5 \times 1.5 \times 1cm^3$) (Figure 2(c)). Curing PDMS prepolymer followed by leaching (dissolving) sugar via water (Figure 2(d)) result in a porous PDMS sponge (Figure 2(e)). Figure 3(a) shows so fabricated PDMS sponge. Shown in Figure 3(b) is the SEM picture of interconnected micropores inside the porous PDMS sponge.

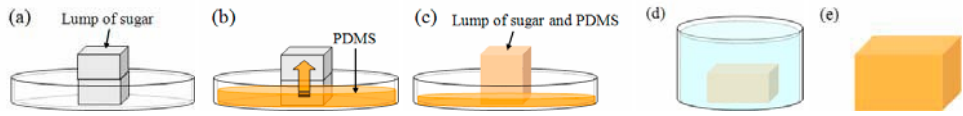

Figure 2. Fabrication process of the porous PDMS sponge:(a) piling up two lumps of sugar in Petri dish, (b) pouring PDMS inside Petri dish, (c) absorbing PDMS by lump of sugar due to capillary force, (d) dissolving lumps of sugar via water and (e) the porous PDMS sponge.

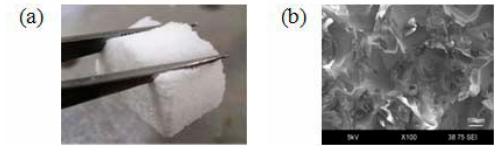

Figure 3. Images of (a) completed porous PDMS sponge and (b) SEM image of cross section of the porous sponge.

3. EXPERIMENTAL

A porous PDMS pump is finally realized by coating the surface of PDMS sponge with a hole being introduced on each of the top and bottom surface. The coating is needed to prevent working fluid from leaking through the side walls (Fig. 4(a)). Backward flow from the channel to the inlet after the pumping action is prevented by the hole on the top. The hole on the bottom is just for the connection with the inlet of microchannels (Fig.4(b)).
The fabricated porous PDMS pump is successfully employed to a lab-on-a-chip with a micromixer, as shown in Fig. 4(c).

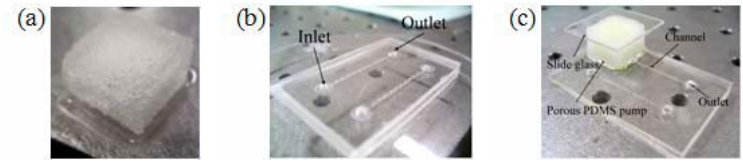

Figure 4. Images of (a) coated porous PDMS sponge (porous PDMS pump), (b) microfluidic lab on a chip [3] and (c) experimental set up for pumping system.

4. RESULT AND DISCUSSION

Performance of PDMS pump could be characterized by the porosity and released working fluid which are indicated in Table 1 and table 2, respectively. Porosity is defined by the ratio of the volume of void-space to the total volume of material. The porosity was calculated from the weight measurements of the pump itself and that with saline infiltrated in it (Table 1). Five PDMS sponges were used in these measurements. The potosity is decreased after PDMS coating to PDMS sponge, but still large enough to be used as a

pump for microfluidic lab-on-a-chip. To chararterize a PDMS pump, we have measured a amount of released working fluid by applying pressure (Table 2). The fabricated porous PDMS pump is successfully employed to a lab-on-a-chip with a micromixer, as shown in Fig. 4(c). Shown in Figure 5 are snap shots of the experimental result of mixing in the lab-on-a-chip via the porous PDMS pump.

Table 1. Measured porosities of five porous PDMS sponges and porous PDMS pumps.

	1	2	3	4	5	Average
PDMS sponge	0.72	0.65	0.69	0.65	0.69	0.68
PDMS pump	0.32	0.32	0.32	0.39	0.38	0.35

Table 2. A mount of released working fluid by pressure with three PDMS pumps

	1	2	3
Working fluid (ml)	0.6	0.56	0.57

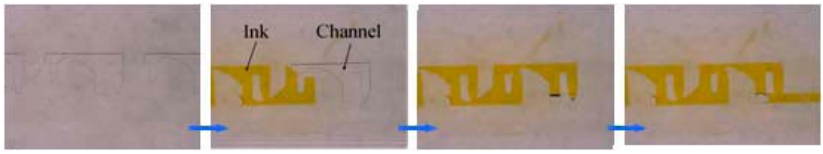

Figure 5. Snap shots of experimental results of the porous PDMS pump.

5. CONCLUSION

In this paper, we have developed a novel potable pump for microfluidic lab-on-a-chip using a porous PDMS (polydimethysiloxane) sponge. The fabricated porous PDMS pump was utilized successfully in the microfluidic lab-on-a-chip as a pump. Furthmore the cheap portable porous PDMS pump could be readily employed to various lab-on-a-chips since the shape and size of the pump depend on lumps of sugar.

ACKNOWLEDGEMENTS

The authors would like to thank Defense Acquisition Program Administration and Agency for Defense Development (UD060049AD) and the Korean Ministry of Commerce, Industry and Energy for financial support via the Development of Next-Generation New Technology Program (Development of Intelligent Robot Technologies for Laboratory Medicine by Applying Biotechnology) (10024719).

REFERENCES

[1] “A review of micropumps,” D.J. Laser and J.G. Santiago, J. Micromech. Microeng, **14**, R34(2006)

[2] “On-chip syringe pumps for picoliter-scale liquid manipulation”, R. Yokokawa, T. Saika, T. Nakayama, H. Fujita and S. Konishi, Lab Chip, **6**, 1062 (2006).

[3] “Design and fabrication of mold insert for injection molding of microfluidic lab-on-a-chip for detection of agglutination” S.H. Choi, D.S. Kim and T.H.Kwon, Transactions of Materials Processing, **15**, 667(2006)

ELECTROKINETIC MIXERS BASED ON STIMULI-RESPONDING SURFACES

G. Paumier [1], J. Sudor [1,2], E. Collé [1], B. Marty [1], A. Bancaud [1], T. Camps [1] and A.M. Gué [1]

[1] LAAS-CNRS, Université de Toulouse, FRANCE
[2] CEA/Léti, Grenoble, FRANCE

ABSTRACT

We report on a novel approach for mixing fluids in microsystems, relying on convective rolls and complex flows caused by on-demand surface charge inhomogeneities. Spatio-temporal control of surface properties is achieved through switchable thermo-sensitive polymers grafted on charged surfaces and activated by integrated addressable microheaters.

Keywords: Poly(N-isopropyl acrylamide), Thermoresponsive, Mixing, Microheaters

1. INTRODUCTION

Mixing solutions in microfluidic systems is a real challenge, mainly because diffusion is slow and flow velocity fluctuations are absent. The large increase of surface-to-volume ratio causes surfaces properties to rule over the bulk ones. At low Reynolds numbers, the lateral mixing of a fluid is purely diffusive and relatively slow compared to the convention of the fluid along the channel. Any mixing faster than diffusion is thus highly desirable in most of microfluidic devices. Various methods have been investigated to break laminar flows, such as passive mixing using particular geometries of channels [1]. Another way to mix fluids is to create active mixing functions, for instance by modifying surfaces charges with an appropriate chemistry. It is now well known that inhomogeneously charged surfaces can generate complex electro-osmotic flows [2]; for instance, patterned surfaces are able to induce steady convective rolls [3], allowing thus active mixing within microchannels. We have recently demonstrated that surface electrokinetic properties can be dynamically controlled through the use of end-grafted, stimuli-responding polymers [4]. Here we go a step further and report on the development of 2D-mixers based on such active polymer layers and arrays of addressable integrated microheaters.

2. THEORY

Recently, we reported on the use of charged surfaces decorated with stimuli-responding polymers (poly(N-isopropyl acrylamide) (PNIPAM)) for a dynamic control of electrokinetic flows in fluidic microsystems [4]. End-grafted brushes built from PNIPAM change their properties upon heating: the brush is hydrophilic and swollen (~10 nm) bellow its critical temperature (~32°C), while it becomes hydrophobic and collapsed (~1 nm) above this temperature. We have demonstrated that with this approach, one can manipulate in a dynamic manner the flow-boundary conditions at the nanometer scale within the electrical double layer and gain a control over the liquid flow on the macroscopic scale. For instance, electrokinetic flows can completely be blocked by the brush in its swollen state, while they can build up unhindered when the brush is collapsed.

978-0-9798064-0-7/μTAS2007/$20©2007CBMS

3. EXPERIMENTAL

To build 2D electro-kinetic mixers with active surfaces, we have developed first a set of polysilicon heater arrays which have been manufactured using standard silicon technologies. Polysilicon non-linear elements having symmetrical thresholds characteristics have been directly integrated in the heating element in order to achieve the individual electrical addressing of each heater [5]. The non-linear elements correspond to P and N zones realized by ionic implantation in a polysilicon thin layer (0.5 µm) (Figure 1) and the symmetrical threshold characteristic corresponds to a NPN (or PNP) structure. The global threshold can be adjusted by changing the doping level and/or by integrating several NPN elementary structures in series. The surface of this array was covered with a thin layer of PECVD silicon oxide (500 nm). The SiO_2 surface generates a negative charge at basic pHs and can also be end-grafted with PNIPAM polymers. Fluidic microchannels were then performed using PDMS soft lithography and reversibly reported onto the silicon devices.

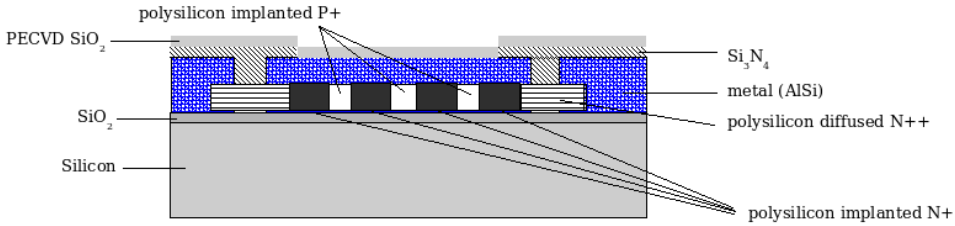

Figure 1. Schematic cross section of an elementary heater cell.

3. RESULTS AND DISCUSSION

The structure of the heating arrays are given in Figure 2.

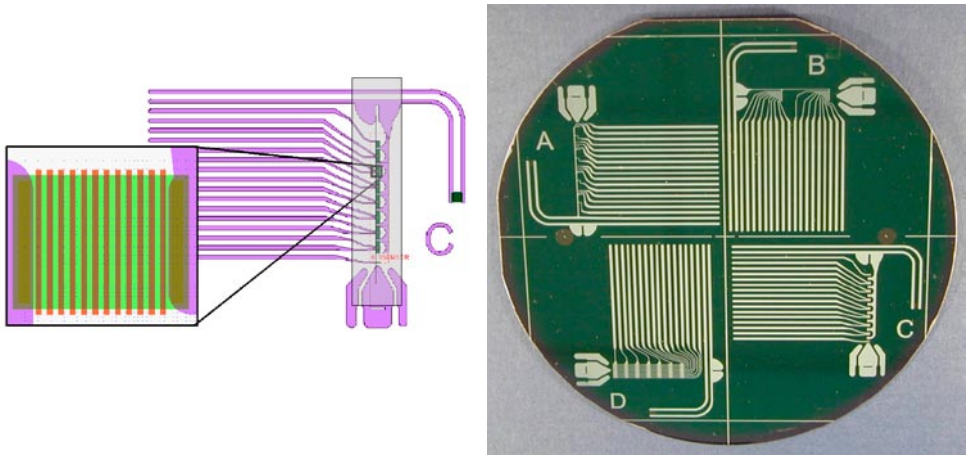

Figure 2. *(left)* Structure of the heaters, one is magnified. The shaded area symbolizes the PDMS part. *(right)* Photo of the whole device (4 sets of heaters).

In order to evaluate the microfluidic performances of this approach, various array designs have been realised and characterized. The 500 µm x 500 µm heaters are composed of 12 alternate 20 µm-wide strips of polysilicon implanted P+ and N+. The 16 independently addressable heaters are separated from 500 µm. PDMS channels (typically 500 µm high x 500 µm wide, 100 µm x 100 µm and 50 µm x 50 µm) are placed over the line of heaters. Mixer is presently under evaluation. We expect to generate with this device rolls and evolving complex flows patterns under certain operation.

5. CONCLUSIONS

We demonstrated we could achieve spatio-temporal control of solid-liquid charged interfaces at the nanometer scale, using thermo-responsive PNIPAM in the aim of manipulating fluids. We have also developed built-in microheaters to integrate localized heat sources directly in our devices, thus allowing precise spatial thermal control. Assembling these technologies together to develop hybrid PNIPAM-based microsystems for biochemical analyses.

REFERENCES

[1] A.D. Strook, S.K.W. Dertinger, A. Adjari, I. Mezic, H.A. Stone and G.M. Whitesides, *Chaotic Mixers for Microchannels*, Science, Vol. 295, pp647-651 (2002).

[2] A. Ajdari, *Electro-osmosis on inhomogeneously charged surfaces*, Phys. Rev. Let., Vol. 75, pp.755-759 (1995).

[3] A.D. Stroock, M. Weck, D.T. Chiu, W.T.S. Huck, P.J.A. Kenis, R.F. Ismagilov and G.M. Whitesides, *Patterning electro-osmotic flow with patterned surface charge*, Phys. Rev. Let., Vol. 84, pp.3314-3317 (2000).

[4] J. Sudor, G. Paumier, F. Vinet, A. Estève and M. Djafari-Rouhani, *Spatio-temporal tuning of stimuli-responding surfaces for dynamic control of electroosmotic flows*, Proc. 10th Int. Conf. on Miniaturized Systems for Chemistry and Life Sciences (µTAS'2006), Tokyo (Japan), 5-11 November 2006, pp.74-76 (2006).

[5] M. Dumonteuil and T. Camps, *Polysilicon microheaters 2D addressed array using symmetrical thresholds elements*, Proc. 7th Int. Workshop on Electronics, Control, Modelling, Measurement and Signals (ECMS'2005), 17-20 May 2005, Toulouse (France) (2005).

OSCILLATING MOBILE BUBBLES FOR MICROFLUIDIC MIXING ENHANCEMENT

Sang Kug Chung and Sung Kwon Cho
Department of Mechanical Engineering and Materials Science,
University of Pittsburgh, USA

ABSTRACT

This paper describes a new highly efficient fluid mixing method in which an oscillating mobile bubble agitates the surrounding fluids. A series of experiments show that fluid stirring by oscillating mobile bubbles significantly reduces time for stirred fluid to reach the end of mixing chamber and thus augments the mixing efficiency..

Keywords: Oscillating Mobile Bubble, Electrowetting-on-Dielectrics (EWOD), Mixing

1. INTRODUCTION

When a gaseous bubble in liquid is excited by an acoustic wave, it oscillates (expands and shrinks) in harmonic with the applied frequency, generating strong vortical flows around the bubble (Fig. 1, known as "acoustic streaming"). Liu *et al.* is one of the first that utilized oscillating bubbles to agitate the surrounding fluid for mixing enhancement [1]. However, their oscillating bubbles were fixed in predefined spots without any mobility, still requiring significant time for flow agitation to propagate from the bubble to the end of the mixing chamber. In this paper, we infuse mobility into oscillating bubbles using the electrowetting-on-dielectric (EWOD) principle [2, 3]. Then, oscillating mobile bubbles are applied to fluid mixing enhancement.

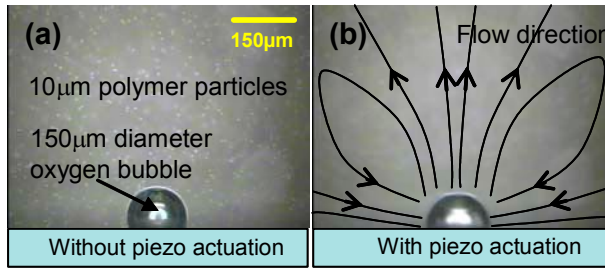

Fig. 1 Acoustic streaming with an oscillating bubble **(a)** before excitation. **(b)** The bubble is excited by an ultrasonic wave (25 kHz) generated by a piezo actuator beneath the bottom substrate. The applied frequency is set at the resonance frequency of the bubble. Strong vortical flows are generated around bubble.

2. EXPERIMENTAL SETUP

Figure 2 shows schematic of testing devices. A bubble can be moved back and forth by sequentially activating a row of EWOD electrodes on the bottom in the mixing chamber ($7.5 \times 4.5 \times 1.5$ mm^3). A disk type piezo-actuator (20-mm diameter) mounted underneath the substrate excites the bubble at the resonance frequency of the bubble (6 kHz), Four different combinations of the two actuations were examined for mixing enhancement: (case 1) no actuation (mixing by diffusion only), (case 2) reciprocating bubble motions by EWOD without acoustic excitation, (case 3) acoustic excitation without EWOD, and (case 4) both EWOD and acoustic excitation. For visualization, 10μm polymer particles were seeded in the fluid.

978-0-9798064-0-7/μTAS2007/$20©2007CBMS

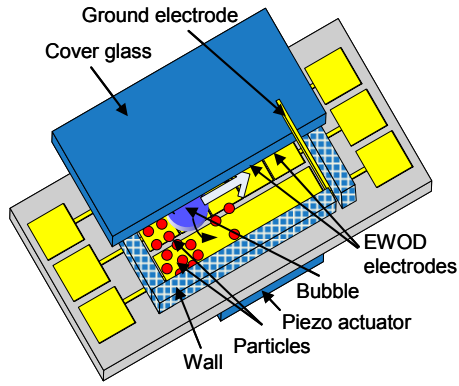

Fig. 2 Schematic of mixing chamber. Note that particles inside the chamber can be mixed by an oscillating mobile bubble simultaneously actuated by EWOD and acoustic wave.

3. EXPERIMENTAL RESULTS

Figure 3 shows sequential images of cases 2 and 4. Initially particles are seeded in the lower side of the mixing chamber. In case 2 (Fig. 3a-d), a bubble is moved up by EWOD and carries some particles. However, most of particles remain where they are and could not reach the upper side of the mixing chamber. However, when an acoustic wave is applied to the mobile bubble, the flow agitation is significantly improved (Fig. 3e-h). The initially gathered particles are widely spread over the entire area of the mixing chamber.

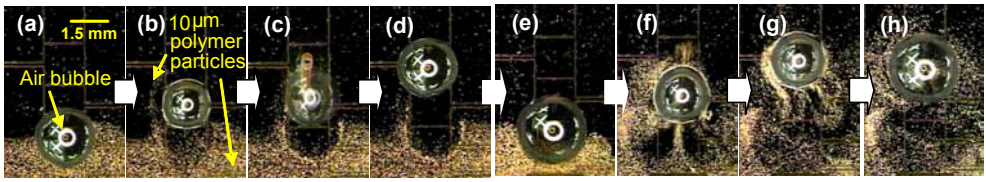

Fig. 3 Sequential pictures of particle mixing **(a-d)** (case 2) a bubble is moved up by EWOD with no acoustic excitation. Particle agitation is not significant.; **(e-h)** (case 4) A bubble is moved up by EWOD and simultaneously oscillated by an acoustic wave. Particles are significantly agitated and spread over the entire area.

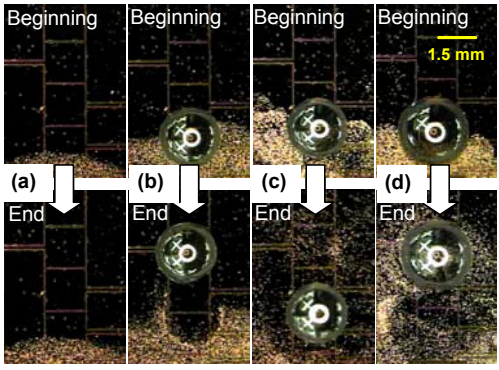

Fig. 4 Comparison of mixing for four cases. Top and bottom images show the initial states and the final states after 2 minutes actuation, respectively. **(a)** mixing by diffusion only (case 1), **(b)** mixing by an EWOD-actuated bubble without acoustic excitation (case 2). **(c)** mixing by an oscillating bubble without EWOD transportation (case 3) **(d)** mixing by an oscillating mobile bubble actuated EWOD and acoustic wave (case 4). In the order from case 1 to case 4, the mixing performance becomes better.

Figure 4 shows the initial and final state images of the four cases with 2 min. actuations. Since the seeded particles are pretty big in size, the diffusion mixing is almost negligible (Fig. 4a). In the order from case 1 to case 4, we can see particles spread more uniformly in the mixing chamber. Case 4 shows the best performance in particle spreading and mixing among the four cases.

4. MIXING EFFCIENCY QUANTIFICATION BY IMAGE ANALYSIS

We quantified the mixing efficiency for the four cases through image analysis, following these steps: color and contrast adjustment (Fig. 5a-c), calculation of the total particle area in six sections (sections A1 through F1) in the mixing chamber (Fig. 5d), calculation of the ratio of the total particle area to the mixing chamber area after excluding the bubble area (Fig. 5e, f).

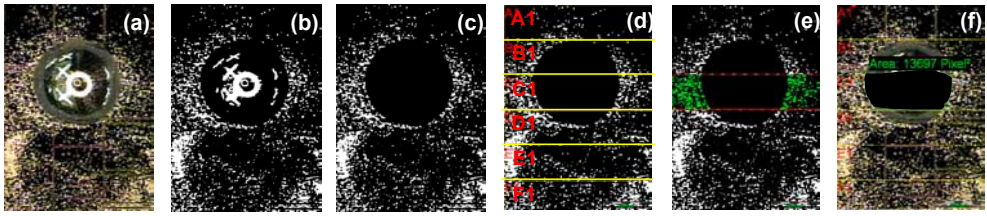

Fig. 5 Image analysis for mixing quantification (case 4) : **(a)** captured image; **(b-c)** adjustment of color and contrast; **(d)** dividing the image into six sections (A1-F1); **(e)** measurement of the particle area and calculation of the ratio of the particle area to the total area; **(f)** subtraction of the bubble area.

5. CONCLUSIONS

Quantified results for cases 2-4 in Fig. 6 show that combined actuation of EWOD and acoustic excitation (case 4) produces the highest mixing among the cases. Furthermore, the highest mixing is also prominent in section A1 in case 4, indicating that the combined actuation is highly effective in carrying fluids the farthest from the one end to another.

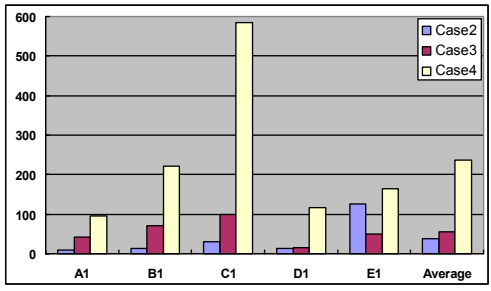

Fig. 6 In each divided section, the ratio of particle occupied area is normalized by the one of case 1, except section F1 due to high particle concentration. Case 4 shows the best mixing performance throughout all the sections.

ACKNOWLEDGEMENTS

The work was supported by the National Science Foundation (NSF ECS-0601470).

REFERENCES

[1] R. H. Liu et al., *Lab Chip*, Vol. 2, pp. 151-157, 2002.
[2] S. K. Chung, Y. Zhao, U.-C. Yi and S. K. Cho., MEMS 2007, Kobe, Japan, pp. 31-34.
[3] Y. Zhao and S. K. Cho, *Lab Chip*, Vol. 7, pp. 273-280, 2007.

RAPID MIXING BY AC ELECTROTHERMAL FLOW

Naoki Sasaki[1†] , Takehiko Kitamori[1,2,3] and Haeng-Boo Kim[1,2,3]

[1] *School of Engineering, The University of Tokyo, JAPAN*

[2] *Kanagawa Academy of Science and Technology, JAPAN*

[3] *CREST, Japan Science and Technology Corporation, JAPAN*

[†] *Present address: RIKEN (The Institute of Physical and Chemical Research), JAPAN*

ABSTRACT

We present rapid mixing of fluids in microchannel by AC electrothermal flow. Mixing was accelerated by the flow with low AC voltage (30 $V_{p\text{-}p}$, 5 MHz) and simple experimental setup, which led to reduced operation time and efficient chemical processing. Rapid fluorescence staining of protein with the mixer was also demonstrated.

Keywords: AC electrothermal flow, micromixer, active mixer, microelectrode

1. INTRODUCTION

Efficient mixing of fluids in microchannel is required for many chemical and biochemical applications. A number of micromixers have been reported for the past decade [1,2]. In the previous paper, we reported rapid mixing utilizing AC electroosmotic flow induced in electrode-integrated microchannel [3]. The mixing could be applied for the salt concentration up to 1 mM [4]. In this paper, we studied mixing by AC electrothermal flow (AC-ETF) [5] to expand the applicable range of the mixer.

2. PRINCIPLE

Applying an AC voltage to the coplanar electrodes induces AC-ETF as a result of electrical stress on fluids [5]. AC-ETF becomes obvious in high salt concentration solution because conductivity gradient in fluids due to Joule heating plays an important role in this phenomenon. Mixing is achieved by arranging the electrodes in parallel to a microchannel and inducing the flow perpendicular to the channel. As shown in Figure 1, efficient mixing of fluids is achieved by the use of meandering electrodes, which can make periodical changes in both direction and velocity of the AC-ETF along the fluid streams and can accelerate mixing.

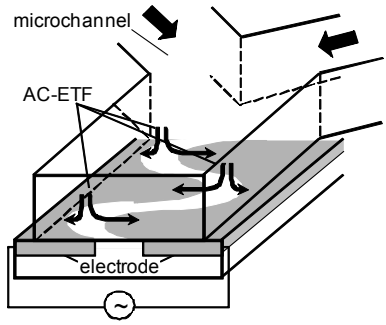

Figure 1. Schematic illustration of microchannel with a pair of coplanar meandering electrodes. The direction of AC-ETF is indicated by arrows.

978-0-9798064-0-7/μTAS2007/$20©2007CBMS

3. EXPERIMENTAL

Aqueous solution of fluorescently-labelled dextran (M.W. ~70,000) and water was used as test solutions. The two solutions were introduced to the mixer with a syringe pump, and AC voltage was applied to the electrodes. Salt concentration of test solutions were adjusted to 0.1 M by KCl. Mixing processes were visualized by a fluorescence microscope equipped with a CCD camera. Mixing index was defined as described previously [3]. Mixing time was calculated from channel length and mean flow velocity of solution. Temperature rise during the mixing was estimated in a separate experiment by the change in fluorescence intensity of dye (Rhodamine B).

4. RESULTS AND DISCUSSION

Figure 2 shows mixing time dependence of mixing index. The results clearly indicated the increase in mixing index, which meant the acceleration of mixing, by the present mixer. The mixing time required for the mixing index of 0.9 (= almost complete mixing) was reduced to ~1/5 compared with diffusional mixing. Mixing index increased with increasing applied voltage as shown in Figure 3, as a result of the increase of AC-ETF. The temperature of the solution during mixing also increased as shown in Figure 3 because of the Joule heating of fluids.

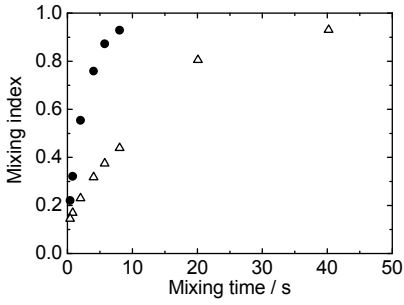

Figure 2. Mixing time dependence of mixing index for the present mixer (filled circle) and diffusional mixing (open triangle). Applied voltage was 30 $V_{p\text{-}p}$, 5 MHz.

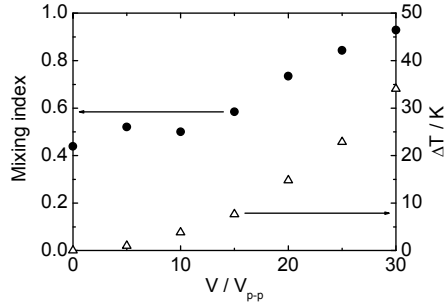

Figure 3. Voltage dependence of mixing index (filled circle) and the maximum of temperature rise during mixing (open triangle).

Rapid mixing and reaction with the mixer was demonstrated by fluorescence staining of human serum albumin (HSA) as shown in Figure 4. Before applying the AC voltage, HSA reacted with the fluorescence reagent, SYPRO Red, around the boundary of the streams because of small diffusion coefficients of HSA (~10^{-7} cm^2 s^{-1}) as shown in Figure 4(a). However, by applying the AC voltage, two streams were rapidly mixed and fluorescence by reaction was observed from whole of the channel (Figure 4(b)). The mixing caused the enhancement of fluorescence intensity and uniform distribution of stained HSA as shown in Figure 4(c).

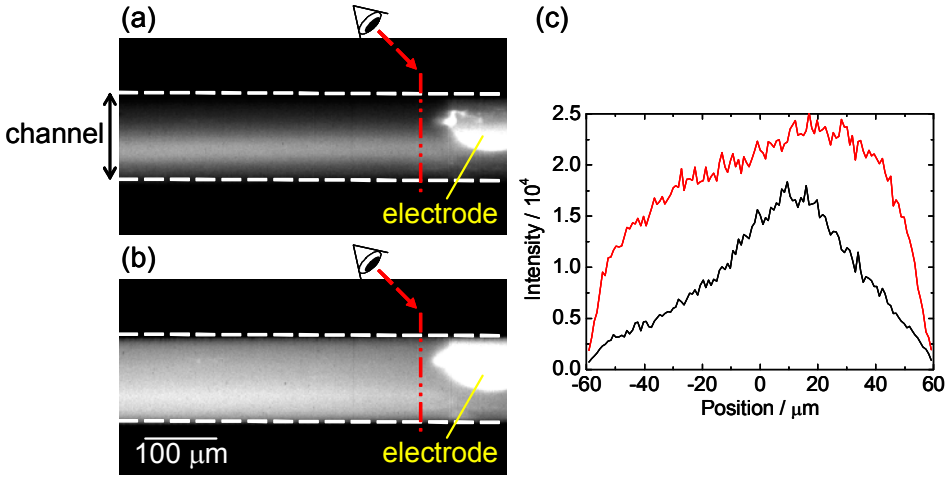

Figure 4. Fluorescence images of human serum albumin stained with SYPRO Red in 0.1 M sodium borate solution (a) without AC-ETF and (b) with AC-ETF. (c) Fluorescence intensity profile along the line shown in Fig. 4(a) (black line) and 4(b) (red line). Mean flow velocity was 0.4 mm s^{-1}. Applied voltage was 30 $V_{p\text{-}p}$, 5 MHz.

5. CONCLUSIONS

We demonstrated mixing of high salt concentration (0.1 M) solution by AC electrothermal flow. Rapid fluorescence staining of DNA with the mixer was also demonstrated. The structure of the mixer is the same as that in our previous study utilizing AC electroosmotic flow [3]: however, the frequency of applied voltage is different. Therefore, the present mixer is applicable to wide range of solution by choosing appropriate frequency and mixing principle. The present mixer can be a powerful tool to realize highly efficient chemical and biomedical analysis in microfluidic devices.

ACKNOWLEDGEMENTS

The authors acknowledge Grants-in-Aid from The Murata Science Foundation for support of part of the research.

REFERENCES

[1] V. Hessel, H. Lowe and F. Schonfeld, *Micromixers - a review on passive and active mixing principles,* Chem. Eng. Sci., 60, 2479-2501 (2005).

[2] N. T. Nguyen and Z. G. Wu, *Micromixers - a review,* J. Micromech. Microeng., 2005, 15, R1-R16.

[3] N. Sasaki, T. Kitamori and H.-B. Kim, *AC electroosmotic micromixer for chemical processing in a microchannel,* Lab Chip, 6, 550-554 (2006).

[4] N. Sasaki, T. Kitamori and H.-B. Kim, *AC electroosmotic micromixer: viscosity and ionic strength dependence of mixing time,* Proc. Micro Total Analysis Systems 2006, Society for Chemistry and Micro-Nano Systems, Tokyo, Japan, 1103-1105 (2006).

[5] A. Ramos, H. Morgan, N. G. Green and A. Castellanos, *Ac electrokinetics: a review of forces in microelectrode structures,* J. Phys. D: Appl. Phys., 31, 2338-2353 (1998).

AN ON-CHIP CONTINUOUS-FLOW SEQUENTIAL TILING MICROMIXER

Yan Xie, Yingying Wang, Farouk Azizi, Li Chen and Carlos H. Mastrangelo
Dept. of Electrical Engineering and Computer Science
Case Western Reseve University, Cleveland, OH, 44106, USA

ABSTRACT

A new type on-chip continuous-flow sequential micromixer has been fabricated with a two level PDMS process. This micromixer works based on rapid flipping of two laminar flows thus forming a checker board tiling flow pattern. This scheme exhibitis the rapid mixing characteristics of flow segmentation mixers but it does not interrupt the flow.

Keywords: Tiling, Sequential Micromixer, Continuous-flow

1. INTRODUCTION

Efficient mixing of samples in microfluidic systems can be achieved via disruption of flow laminarity [1]. For example, laminarity is broken in flow segmentation mixers [2, 3] by the formation of a series of short alternating sample plugs as shown in Fig. 1(a). The short plugs are rapidly mixed by dispersion-enhanced diffusion [4] as they travel down the capillary [1, 2]. Sequential segmentation devices are however rarely used in practical microsystems because the plug formation requires flow interruption which severely disrupts system pressure and instantaneous mass flow balance. In this paper we present a new type of continuous-flow sequential mixer technique based on rapid flipping or tiling of two laminar flows.

2. SEQUENTIAL TILING MICROMIXER STRUCTURE

The sequential tiling micromixer (STM) works by flipping of two laminar flows as shown in Fig. 1(b). This new sequential mixing technique does not interrupt the flow yet it

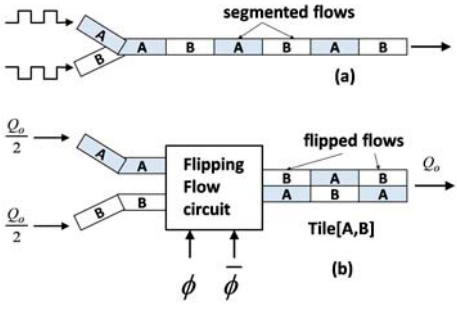

Fig. 1. (a) In segmentation mixing the flow of each component is periodically interrupted. (b) Tiling mixing: continuous flow is flipped periodically forming a checker-like flow pattern Tile[A,B].

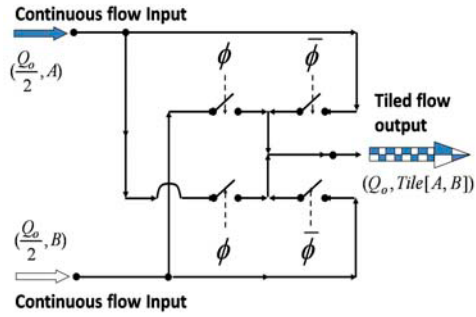

Fig. 2. Schematic of flow-flipping circuit for generation of the tiled flow pattern at the output terminal. The valves are driven by digital clock ϕ.

978-0-9798064-0-7/μTAS2007/$20©2007CBMS

exhibits then same rapid mixing characteristics of the segmentation scheme. Fig. 2 shows a schematic of a sequential tiling micromixer (STM) implemented with a 4-valve flow multiplexer. The multiplexer does not interrupt the input flows but rather re-routes them in a fashion yielding the tiling of the output. Fig. 3 shows a photograph of an on-chip continuous-flow STM in a small ~5 mm^2 area with flow channel around 25x16 μm^2. STM chips were constructed using a double-layer PDMS process [5] with integrated pneumatic valves and through-level via connections. These via connections permit the crossing of separate fluidic lines and the jointing of the two fluidic levels. Rapid tiling of laminar flow can also be realized without using via connections. Fig. 4 shows a photograph of such a microfluidic circuit. In this configuration, instead of using via connections, eight computer controlled on-chip valves were used to implement the sequential tiling of the flow.

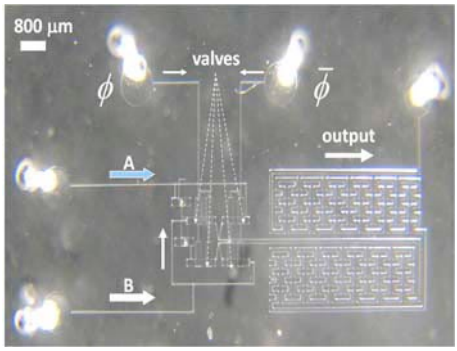

Fig. 3. Photograph of sequential tiling micromixer (STM) circuit implemented with a two-level PDMS process with via connections.

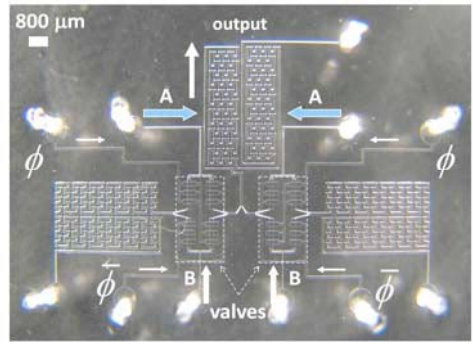

Fig. 4. Photograph of sequential tiling micromixer (STM) circuit implemented with a two-level PDMS process without via connections.

3. EXPERIMENTAL RESULTS

During the experiment, the STMs were driven at different frequencies using equal fluorescein and water flows at 6~15 PSI yielding average output flow velocities varying from about 5 mm/s to 8.5 mm/s. The time dependent intensity of the fluorescence at different locations downstream from the STM output was recorded with an Olympus MVX10 fluorescence microscope and Hamamatsu EM-CCD intensified camera. The flipping action of the STM of Fig. 3 is shown in Figs. 5(a) and (b). In Fig. 5(a) the fluorescein dye is introduced from the bottom and water from the top into the STM exit channel. In Fig. 5(b) the dye and water flows are flipped. Fig. 5(c) shows an photo showing the tiling of the output flow of a STM with fan-out exit channel. The photo clearly shows the reversal of the flow which is characteristic of the tiling pattern. We computed the degree of mixing [6] (DOM) of the STM shown in Fig. 3 from measured fluorescence data versus downstream distance from the STM exit under different pressures as shown in Fig. 6. The maximum apparent DOM was 0.8 corresponding to that measured with uniform concentration flows in our rounded-top flow microchannels. We also calculated the DOM of the STMs shown in Fig. 3 and Fig. 4 at different clock frequencies from the STM exit under different pressure as shown respectively in Figs. 7 and 8.

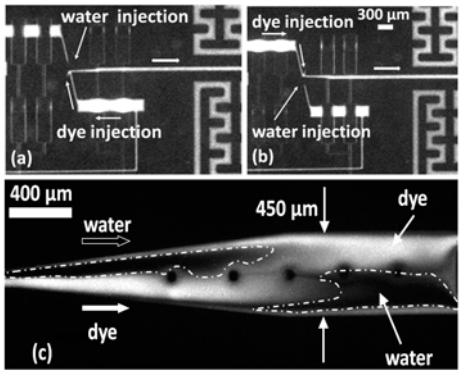

Fig. 5. Tiling of flow pattern. (a) dye introduced from bottom, and (b) dye introduced from top. (c) STM with fan-out exit showing tiling of dye and water flows.

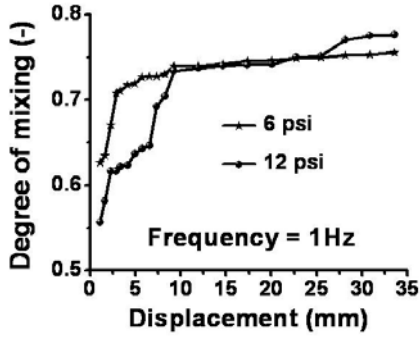

Fig. 6: DOM versus distance from the STM (Fig. 3) output at 1 Hz under different pressure. The maximum DOM is < 1 because the cross-section is rounded.

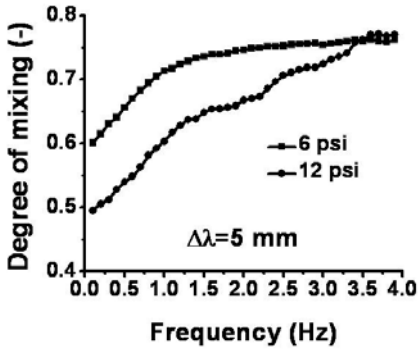

Fig. 7: DOM versus frequency at 5 mm from the outlet (Fig. 3). Flow velocity was ~5 mm/s for 6 psi and 8 mm/s for 12 psi.

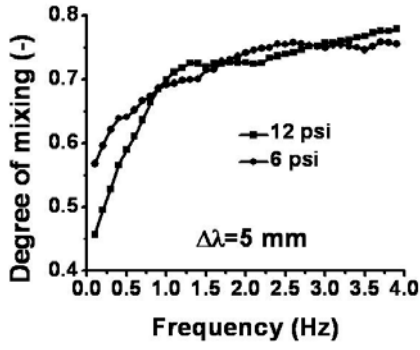

Fig. 8: DOM versus flipping frequency at 5 mm away from the STM outlet (Fig. 4).

REFERENCES.

1. N. T. Nguyen and W. Zhigang, "Micromixers: a review," *J. Micromach. Microeng*, Vol. 15, 2, pp. R1-R16, (2005).
2. I. Glasgow and N. Aubry, "Enhancement of microfluidic mixing using time pulsing," *Lab On A Chip*, Vol. 3, pp. 114-120, (2003).
3. R. A. Truesdell et al, "Direct measurement of mixing quality in a pulsatile flow micromixer," *Experiments in Fluids*, Vol. 39, pp. 819-827, (2005).
4. Probstein, *Physicochemical Hydrodynamics*, Wiley NY, 2003.
5. M. A. Unger, et al, "Monolithic Microfabricated Valves and Pumps by Multilayer Soft Lithography", *Science,* Vol. 288, pp. 113-116, (2000).
6. I. Glasgow, S. Lieber and N. Aubry, "Parameters influencing pulsed flow mixing in microchannels," *Anal. Chem*., Vol. 76, pp. 4825-4832, (2004).

DIAMAGNETIC LEVITATION BASED DIGITAL MICROFLUIDICS

Christian Jeandey[1], Hichem Chetouani[1,2], Vincent Haguet[1], Franąois Chatelain[1], Gilbert Reyne[2]

[1]*Commissariat à l'Energie Atomique (CEA), Grenoble, FRANCE*
[2]*Laboratoire de Génie Electrique de Grenoble, INPG-UJF-CNRS, Saint-Martin-d'Hères, FRANCE*

ABSTRACT

This paper presents a new technology to handle low-volume droplets without any physical contact. This innovative approach of digital microfluidics is based on the diamagnetic trapping of liquids above permanent NdFeB macro- and micro-magnets. Stable levitation and motion of droplets are achieved within punctual and linear magnetic traps.

Keywords: digital microfluidics, levitation, diamagnetism, permanent magnet

1. INTRODUCTION

A new digital-microfluidics technology was developed for handling low-volume droplets: digital microfluidics based on diamagnetic levitation. The possibility to levitate microdroplets in air with appropriately configured permanent magnets was demonstrated recently [1,2]. The main advantage of diamagnetically levitating droplets compared to other digital microfluidics technologies (droplet arraying with a spotter, EWOD, SAW actuation…) is the absence of contact between the droplets and any surface, which consequently allows avoiding any sample contamination or adsorption. Other advantageous features for lab-on-chip devices include stable and passive levitation of various liquids, as well as parallelisation and small size of the permanent magnets.

Here, we show recent results about trapping and motion of microdroplets levitating in air by means of centimeter-scale NdFeB magnets and micro-magnets. The "macro-scale" permanent magnets were used to investigate stable punctual levitation of bead-containing droplets and mixing of droplets. Linear motion of levitating droplets was obtained with micro-magnets produced by sputtering of a very thick NdFeB layer on silicon wafers.

2. TRAPPING AND MIXING OF MICRODROPS

A punctual magnetic trap is produced by a cylindrical NdFeB magnet made by 8 sectors forming a central hole and having radial magnetisation (Fig.1a). The ~1.2 T sectors were surmounted by a ferromagnetic polar ring in order to concentrate the magnetic field at the center of the ring. The magnetic well is created by a radial and vertical magnetic force which counterbalances the gravity and geometrically confines the levitating bodies. As the result, the droplets falling in the magnet area are magnetophoretically repulsed towards the magnetic levitation site located at the limit between the ferromagnetic ring and the top of the magnet sectors.

Figure 1b shows a levitating water droplet containing fluorescent 1µm-wide latex microbeads observed by optical microscopy. First, a water droplet was sprayed towards the magnet and captured in the levitation site. After stabilisation of the droplet levitation,

978-0-9798064-0-7/µTAS2007/$20©2007CBMS

another water droplet containing the latex microbeads was sprayed and coalesced with the first droplet, resulting to a larger droplet with latex microparticles in levitation in air. A constant movement of the latex beads was observed inside the droplet. Fast movement of the beads indicates the presence of a strong agitation within the droplet in the magnetic trap. The rapid agitation in the levitating liquid was maintained during the lifetime of the droplet. We conclude that internal circulation inside the levitating microdrops could be used e.g. as a practical way for rapid mixing between two solvents.

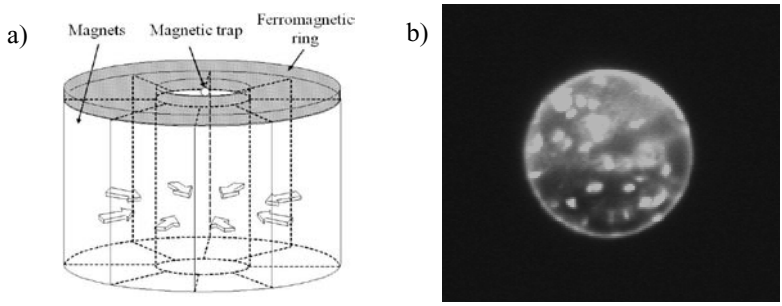

Fig. 1. a) Magnetic trap produced by centimeter-scale magnet sectors and a ferromagnetic polar piece. b) A levitating water droplet containing fluorescent latex microparticles.

An oil droplet encapsulated by a water droplet was levitated on the same device (Fig. 2). The initial droplet was a Brookfield oil droplet (density of 0.914, dynamic viscosity of $5x10^{-3}$ Pa.s and volume magnetic susceptibility of $-9.6x10^{-6}$) levitating at the center of the hole made through the permanent magnet. Small water droplets (dynamic viscosity of $1.002x10^{-3}$ Pa.s and volume magnetic susceptibility of $-9.048x10^{-6}$) were then sprayed towards the water droplet. The thickness of the water layer progressively increased around the oil droplet by fusion of the water microdrops. In absence of perturbations, the resulting droplet remains in stable position. A water droplet surrounded by an oil droplet was also successfully produced. In the latter configuration, evaporation of water was avoided.

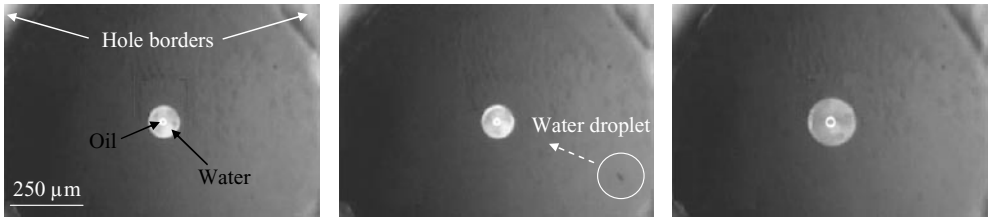

Fig. 2. Water/oil droplet levitating in air in the air gap of a centimeter-scale permanent magnet. The water layer is progressively increased by addition of water droplets.

3. CONTACTLESS GUIDING OF PICOLITER DROPLETS

NdFeB micro-magnets were manufactured to carry out diamagnetic trapping and linear guiding of picoliter droplets. A ~30µm-thick NdFeB magnetic layer [3] was sputtered onto a silicon wafer containing high-aspect-ratio Si pillars and grooves to shape the magnet

microarray. Finally, perpendicular magnetization of the micromagnets was collectively achieved using a ~5 T electromagnet.

Figure 3 presents the capture and the guiding of water droplets in linear magnetic wells produced by NdFeB micromagnets. The capture of a droplet falling in the magnetic trap is shown in Fig. 3a. When located in the linear wells, the droplets can move in levitation between the micromagnets due to air flows along the grooves. The distance between droplets remains almost constant during their displacement. The measured velocity of droplets within the wells is about 400-500 µm/s. Moreover, the vertical position of levitation can be modulated by using an external magnetic field. In Fig. 3b, the external magnetic field was produced by a macroscopic NdFeB magnet placed under the micromagnet chip with the same magnetisation direction. The resulting height of levitating water droplets was lowered (Fig. 3b) compared to the height observed with the same device without the external magnetic field (Fig. 3a).

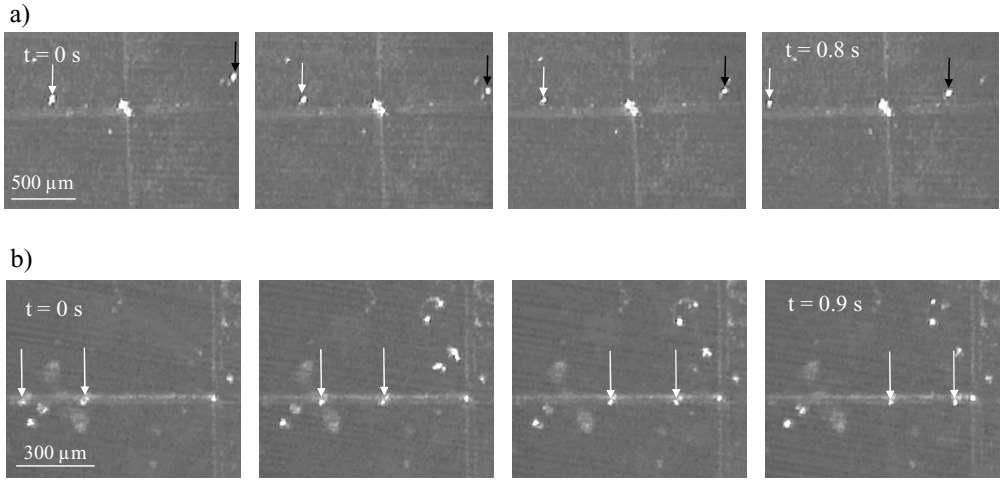

Fig. 3. Levitation and motion of water droplets along linear magnetic grooves. a) The black arrows on the two left images show the capture of a droplet within the linear magnetic well in the air gap. b) The micro-magnets are combined with an external magnetic field produced by a macroscopic magnet. As a result, the levitation height is lower than in a).

REFERENCES

[1] H. Chetouani, C. Jeandey, V. Haguet, H. Rostaing, C. Dieppedale, and G. Reyne, "Diamagnetic levitation with permanent magnets for contactless guiding and trapping of microdroplets and particles in air and liquids", IEEE Trans. Magn., 42(10), 3557 (2006).

[2] V. Haguet, C. Jeandey, H. Chetouani, G. Reyne, and F. Chatelain, "Magnetic levitation of microdroplets in air", Proc. MicroTAS 2006, vol. 1, pp. 110-112, Tokyo, Japan, Nov. 5-9, 2006.

[3] N.M. Dempsey, A. Walther, F. May, D. Givord, K. Khlopkov, and O. Gutfleisch, "High performance hard magnetic NdFeB thick films for integration into micro-electro-mechanical systems", Appl. Phys. Lett., vol. 90, 092509, 2007.

DROP STIRRING FLOW UNDER EWOD AND EHD ACTUATION: A NEW STEP TOWARDS BIOLOGICAL SAMPLE PREPARATION

L. Davoust[1], Y. Fouillet[2], Y. Ishida[2]
[1] *CNRS, LEGI, BP 53, 38041 Grenoble cedex 9, FRANCE*
[2] *CEA-Leti-Minatec, 38041 Grenoble, France*

ABSTRACT

This paper addresses electrically-induced drop mixing. The configuration studied here is typical of electrowetting on dielectrics (EWOD) – based actuation with a drop staying on a hydrophobic dielectric substrate. Application of normal and tangential components of an electric field at and along the interface is found to give rise to an electric surface stress able to pump drop vortices (electrohydrodynamics of Taylor-Melcher type) with a remarkable efficiency.

Keywords: Electrowetting, Electrohydrodynamics, Drop, Mixing

1. INTRODUCTION

Droplets as common carriers for bio-chemical agents have found growing impact in lab-on-a-chips devoted to bio-medical analysis. The basic operations addressed by a droplet-based lab-on-a-chip include generation, motion, coalescence and cutting. ElectroWetting On Dielectrics (EWOD) is a well-known physical mechanism capable of promoting all these digital operations [1, 2, 3]. This paper aims at investigating the abilities of EWOD to perform drop stirring as a new and useful operation.

Purification of biological samples proves to be a process to perform firstly in a digital lab on chip. EWOD could be thought of as the natural physics to use in order to get a fully integrated chain of digital micro-processes including typically centrifugation of a liquid sample. A centrifugation within a drop followed by EWOD-driven cutting could be a good way to purify a liquid sample and to extract target biochemical species. Recent experimental investigations have demonstrated that any EWOD-driven motion of a drop, even if submitted to circular trajectories, is never able to provide the centrifugation level required for purification purposes [4].

2. DROP MIXING AND EHD INTERPRETATION

Quite recently, we have produced a very efficient stirring (velocity~1m/s) within a 1mm-drop submitted to EWOD actuation but staying at rest over isolated electrodes. Different experimental configurations have been studied, especially those which are able to produce stable vortices. A pretty well organised flow is made evident making use of fluorescent DNA strands (figure 2) and hollow glass beads covering drop surface (figures 3, 4). Considering the frequency range of the applied AC voltage (1 KHz, 50V rms), electrohydrodynamics of Taylor-Melcher type (EHD, [5]) is found to be responsible for arising of vortices *via* the tangential component of the jump momentum balance across the drop surface. Considering the Ohmic current is much larger than the displacement current, the only non-vanishing electric charges accumulate to the drop surface provided that the dielectric permittivities of the involved fluids are different (water/air for instance) and that the electric field displays a component normal to the drop surface (Gauss' law, figure 1).

978-0-9798064-0-7/μTAS2007/$20©2007CBMS

At points of the drop surface where a tangential electric component E_ϕ is made available, the resulting azimuthal Coulombic stress is balanced by a viscous stress. In this way, vortices are pumped within the drop. Depending on the way the drop is located with respect to the underlying electrodes, the EHD-driven flow exhibits either two or four vortices (see focusing of bead tracers on the vortices centres where local pressure is the smallest, figures 3, 4).

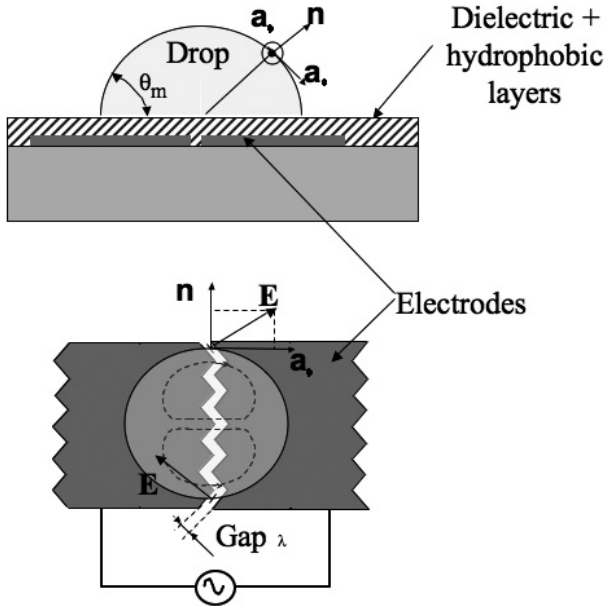

Figure 1: First configuration studied: one water drop staying over stripe electrodes. Side and top views.

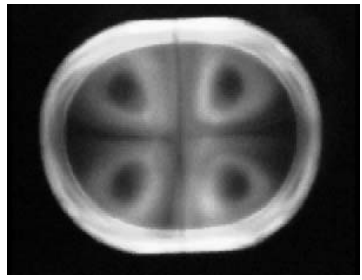

Figure 2: Vortical flow inside the deposited drop as made evident from solubilized labeled DNA strands (see top view in figure 1).

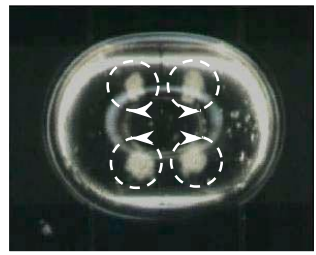

Figure 3: Same vortices made evident from the focusing of hollow glass beads over the drop surface. The water drop is as large as the actuation area.

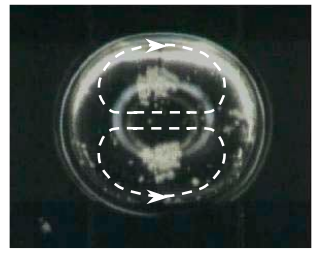

Figure 4. Vortices as made evident from the focusing of hollow glass beads over the drop surface. The drop is smaller than the actuation area (see also attached configuration in figure 1).

A modelling is put forward to predict the EHD-induced flow within a liquid spherical cap. Numerical calculations are performed considering the surface Coulombic stress behaves as a momentum source. The agreement with experimental results is fairly good if a specific constitutive law for the contact line dynamics is introduced [6]. Original geometries of electrodes are suggested in order to enhance drop centrifugation.

REFERENCES:

[1] Y. Fouillet, D. Jary, A.G. Brachet, R. Blervaque, L. Davoust, J.M. Roux, J .L Achard & C. Peponnet, EWOD digital microfluidics for lab on a chip, Proceedings of ASME ICNMM2006, 4th International Conference on Nanochannels, Microchannels and Minichannels, June 19-21, Limerick, Ireland, (2006)

[2] S.K. Cho, S-K. Fan, H. Moon & C-J. Kim, Towards digital microfluidic circuits: creating, transporting, cutting and merging droplets by electrowetting-based actuation, IEEE Conf. MEMS, Las Vegas NV, 32, (2002)

[3] Y. Fouillet & J-L. Achard, Microfluidique discrète et bio-technologies, C.R. Physique, **5**, 577 (2004)

[4] R. Bavière, & Y. Fouillet, Dynamics of droplet transport induced by electrowetting actuation, Microfluidics & Nanofluidics, to appear (2007)

[5] J.R. Melcher & G. I. Taylor, Electrohydrodynamics: a review of the role of interfacial shear stresses, Ann. Rev. Fluid Mech., **1**, 111 (1969)

[6] L. W. Schwartz & R. V. Roy, Theoretical and numerical results for spin coating of viscous liquids, Phys. Fluids, **16**, 569 (2004)

DROPLET GENERATION IN HEAD-ON DEVICES

Lingling Shui, Jan C.T.Eijkel, Albert van den Berg
MESA+ Research Institute, University of Twente, The Netherlands

ABSTRACT

This paper reports droplet generation in head-on devices. Two-phase flow diagrams are presented showing different breakup mechanisms at different flow regions. At low flow rates(10^{-6}<Ca<10^{-5}), droplet size is determined solely by the device geometry and independent of flow rate, which is a new phenomenon not yet reported. Moreover, droplet size is a function of the restriction channel width in the flow-ratio determined flow region.
Keywords: Droplet, two-phase flow, head-on devices

1. INTRODUCTION

Multiphase microfluidics is a rapidly expanding field due to its great range of potential applications. Both droplet-based flow and stratified flow have found applications for chemical and biological tasks[1]. Multiphase microfluidics experiments have mostly been done in T-junction[2] or flow-focusing devices(FFD)[3] made of PDMS. The devices we present in this paper (Figure 1) are different since they are head-on and made of hard material, enabling operation at extremely low and high flow rate (or pressure) which soft material (PDMS) does not allow due to its permeability and deformability. We performed experiments in a broad range of flow rates. Oil in water emulsions formed due to the hydrophilic channel walls. Flow behavior in the capillary number range 10^{-6}<Ca<10^{-1} was characterized, and geometrical effects were investigated.

2. THEORY

The breakup of a fluid phase to generate droplets depends on the forces acting on its interface. In microfluidic devices, the main forces are viscous and interfacial forces, and the ratio of them is given by the capillary number:

$$Ca = \frac{\eta v}{g_c \sigma}, \qquad (1)$$

where η is the viscosity, v is the flow velocity, g_c is a geometrical constant, and σ is the interfacial tension. At low flow rates the interfacial force dominates the breakup of the fluid phase to form droplets. At higher flow rate, the breakup depends on the ratio of viscosity and the flow rates of the two phases. The breakup mechanism is then determined by the competition of these forces, leading to a rich and complex behaviour.

3. EXPERIMENTAL

The detailed structure of the head-on device is shown in Figure 1. The water phase (DI water + 0.01M SDS + 0.01M fluorescein sodium salt) and oil phase (hexadecane) were pumped head-on as shown in the figure. Microchannels and connection holes were fabricated in a silicon wafer which was anodically bonded to a Pyrex wafer and then diced. The chips were fit in a chip holder and connected to gas-tight syringes driven by a syringe pump. The flow was visualized by an inverted microscope and CCD camera.

978-0-9798064-0-7/μTAS2007/$20©2007CBMS

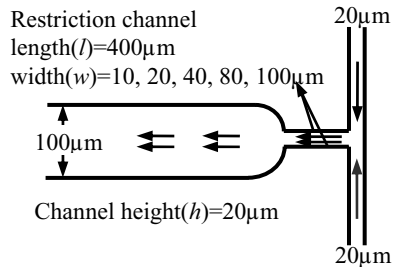

Figure 1. The head-on configuration for two-phase flow.

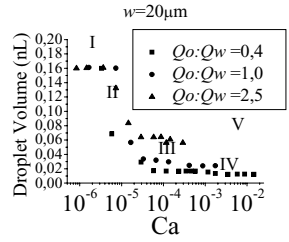

(a)

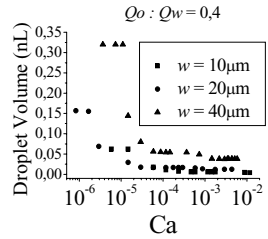

(b)

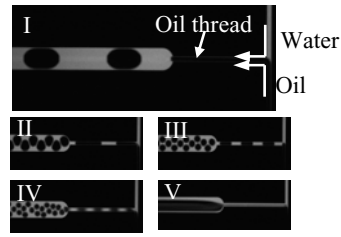

(c)

Figure 2. (a) Droplet volume as a function of Ca at three different oil to water flow ratios (w=20µm, Qo and Qw are the oil and water flow rate, respectively); regions I-V are distinguished (b) droplet volume as a function of Ca at three different restriction channel widths ($Qo:Qw$=0.4), (c) different flow patterns in regions I-V shown in the flow diagrams.

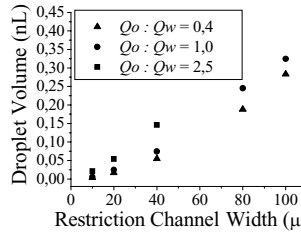

Figure 3. The oil droplet volume in region III as a function of the width of restriction channels.

4. RESULTS AND DISCUSSION

Different flow regions were seen in a very broad flow rate range 10^{-3}~10μL/min, corresponding to $10^{-6}<Ca<10^{-1}$. Figures 2 show the droplet volume generated as a function of Ca at three different flow ratios (Figure 2a) and three different restriction channel widths (Figure 2b), and the flow patterns (Figure 2c). At extremely low flow rate ($10^{-6}<Ca<10^{-5}$), the oil threads did not breakup until they reached the wide channel where the pressure suddenly dropped (region I). The size of restriction channels therefore determined the generated droplet size. Such a geometrically dependent flow region was never reported. Droplet size then decreased with the flow rate (region II) where the thread breakup position was determined by the pressure drop. In region III, the breakup time was inversely proportional to the water supply rate, the generated droplet size was therefore proportional to the oil to water flow ratio (droplet size kept constant at the same flow ratio). With further increased flow rate, shear(viscous force)-dominated droplet breakup occurred (region IV) with the droplet size proportional to the flow rate ratio (but smaller than in the previous region). Finally, flow became stratified at high flow rate (region V) when the breakup time was longer than the equilibration time.

All pressures acting on the oil thread are a function of geometrical parameters. The effect of the restriction channel width was therefore investigated (Figure 3). The droplet volume in region III was seen to increase with the width of the restriction channels.

5. CONCLUSIONS

Oil and water two-phase flow in head-on devices was investigated. Different flow regions could be observed in a broad flow rate range possible by the hard and impermeable material used. A flow region where droplet size was geometrically determined at extremely low flow rates was reported for the first time. Furthermore flow-ratio dependent flow regions were found at different flow rates. All flows became stratified when flow rates increased further. Furthermore, the investigation of the geometrical effect showed that, in the flow-ratio dependent regions, the droplet size was a function of the restriction channel width.

ACKNOWLEDGEMENTS

This research was supported by the Dutch Ministry of Economic Affairs through a Nanoimpuls grant.

REFERENCES

[1] Shui, L., J.C.T. Eijkel, and A. van den Berg, *Multiphase flow in microfluidic systems-control and applications of droplets and interfaces.* Advances in Colloid and Interface Science. In Press.

[2] Garstecki, P., et al., *Formation of droplets and bubbles in a microfluidic T-junction - scaling and mechanism of break-up.* Lab On A Chip, pp. 437-446, (2006).

[3] Anna, S.L., N. Bontoux, and H.A. Stone, *Formation of dispersions using "flow focusing" in microchannels.* Applied Physics Letters, pp. 364-366, (2003).

[4] Garstecki, P., G.M. Whitesides, and H.A. Stone, *Mechanism for flow-rate controlled breakup in confined geometries: A route to monodisperse emulsions.* Physical Review Letters, pp. 1645011-1645014, (2005).

DROPLET-BASED MICROFLUIDICS AT HIGH DISPERSED-PHASE VOLUME FRACTIONS

Craig Priest[1,2], Enkhtuul Surenjav[1], Stephan Herminghaus[1], Ralf Seemann[1]
[1]Max-Planck-Institute for Dynamics and Self-Organization, Germany, and [2]Ian Wark Research Institute, University of South Australia, Australia.

ABSTRACT

We demonstrate droplet generation, manipulation, and targeted electrocoalescence for aqueous droplets at high dispersed-phase volume fractions. We show that monodisperse gel emulsions may be manipulated in an extremely well-defined manner driven by changes in the microchannel geometry, such as a bend.

Keywords: discrete, droplet, translocation, manipulation

INTRODUCTION

Droplet-based microfluidics, or "discrete microfluidics", has attracted attention as an alternative to continuous phase flow [1]. Confinement, transport, and analysis of sample, reagent and/or catalyst in discrete nanolitre compartments provides greater flexibility in microfluidic processing. By addressing individual droplets in real time, complex processing of chemicals (*e.g.* for synthesis and analysis) and bio-matter (*e.g.* cell viability, protein crystallization) can be achieved. Varying reaction conditions, *e.g.* temperature, reagents, and/or catalysts, through sequences of discrete droplets will allow interrogation of phase-space using a single microchip. To achieve this kind of processing, the droplet volume should be adjustable and precisely known, the location of individual droplets must be well-defined and switchable, and coalescence must to be targeted enabling specific pairs or groups of droplets to be combined rapidly on demand [3]. Here we address the influence of microchannel geometry, specifically a bend, on the droplet arrangement.

EXPERIMENTAL

Microchannels were prepared either using photolithography of SU8 photoresist (for channel widths < 200 μm) or by micromachining poly(methylmethacrylate), PMMA, (for channel widths > 200 μm). *Photolithography:* A 50 μm layer of SU8 photoresist was spun onto a glass disk (0.95 mm thick), which was pre-coated with a 5 μm layer of cross-linked SU8 resist. The channels were closed by thermally bonding a second glass disk coated with a 10 μm thick PMMA layer at 180°C in a mechanical press. *Micromachining:* Microchannels and threaded inlets were machined into the surface of PMMA blocks using sub-millimeter drilling tools. The channels were closed using a plate of PMMA. For electrocoalescence, gold electrodes were deposited by metal vapor deposition and insulated using a 10 μm thick PMMA layer. Water-in-oil emulsions were prepared using Millipore water (18 MΩ.cm) with the addition of 2%wt NaCl. Surfactant (2% Span 80) was added to the oily phase (IsoparM) to stabilize the droplets against coalescence. Flow was controlled using computer controlled home-built syringe pumps.

RESULTS AND DISCUSSION

The generation of droplets at high-dispersed phase volume fractions, *i.e.* gel emulsions, can be achieved in a microchannel using a step in the channel's dimensions. Termed "step

978-0-9798064-0-7/μTAS2007/$20©2007CBMS

emulsification", the method satisfies the general requirements of high production frequency, excellent monodispersity, and tunable droplet volume, while allowing for the reduction of the continuous phase down to 4% [2]. As shown in Fig. 1, gel emulsions generated using step emulsification immediately self-organize into an extremely well-organized array of closely packed droplets. The droplet arrangement is determined by the channel dimensions and droplet volume according to surface energy minimization. Shown in Fig. 1 are two common droplet arrangements, "bamboo" and "zig-zag", that may be observed. Each droplet's position is well-defined relative to its neighbors however droplets may be precisely manipulated using subtle changes in channel geometry, shown in Fig. 2.

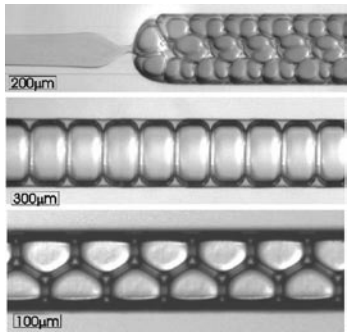

Figure 1 *Generation of high dispersed-phase emulsions by terminating a co-flowing stream at a step in the microchannel (top),"bamboo" packing (middle), and "zig-zag" packing (bottom) in microchannels.*

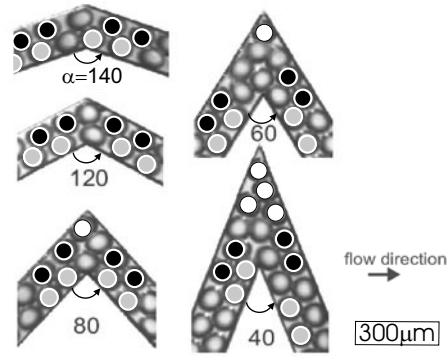

Figure 2 *Translocations through various bend angles. The inner (grey) and outer (black) rows of droplets are labeled to indicate the translocations. Droplets (white) are trapped in the acute bends.*

We prepared microchannels incorporating a sequence of bends of varying bend angle. The bend angle, α, is measured where the two linear channels meet sharply. By following the reorganization through each bend, the translocation of droplets relative to their neighbors could be identified. Our results are summarized in Fig. 2, in which the inner and outer droplets are indicated before and after the bend using grey and black shading, respectively. For the 140° bend, no translocation was observed (the arrangement of the droplets before and after the bend was identical). For the slightly sharper bend at 120°, the inner row of droplets (grey) moved one position ahead of the outer row of droplets (black). For acute angles the number of translocations increased; two positions at 60° and three positions at 40°. For these bend angles droplets were permanently captured in the bend (labeled white in Fig. 2). The more acute the angle, the greater number of captured droplets.

One possible explanation for translocation through a bend might be the different path-length for the inner and outer row of droplets, see Fig. 3. Where the difference between inner and outer row path-lengths, λ, is at least half of the "lattice" spacing, d, one could crudely expect a dislocation in the arrangement leading to a translocation. This geometric condition is met in terms of the bend angle, α, and "lattice" angle, β, when $2/\tan(\alpha/2) \geq \tan(\beta/2)$. Angle β is largely dependent on the droplet and channel dimensions

as well as the volume fraction. Upstream of the bends the "lattice" angle, β, was 80°. Thus, translocation could be expected for bend angles less than 134°, which is consistent with the experiments shown in Fig. 2. However, other effects may also contribute, such as droplet deformation and channel obstruction by captured droplets. For example, according to this geometric consideration, translocation is not expected in Fig. 4, where $\alpha = 90^{o}$ and $\beta = 135^{o}$ but, possibly due to droplet deformation, was observed. This result highlights the need for a more complete understanding of droplet movement in microchannels.

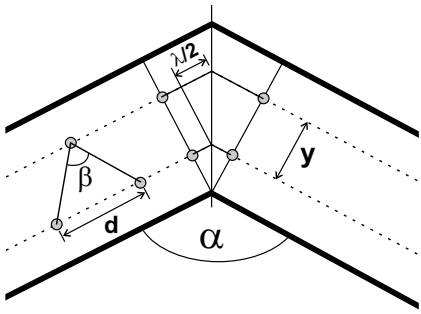

Figure 3 *A schematic of path lengths for the inner and outer rows of droplets (grey dots) around a bend. The path length difference, λ, is indicated along with the spacing of adjacent droplets, d.*

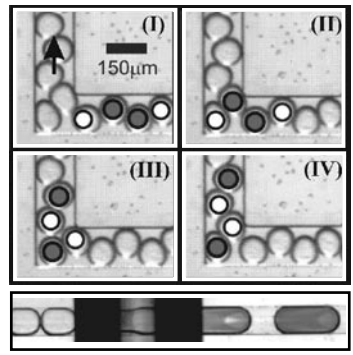

Figure 4 *Bend-induced translocations can be used to bring droplets together (above) for targeted electrocoalescence (below), 1V DC; electrodes are black.*

Translocation of droplets in microchannel bends can be reversed using a subsequent bend or may be used to position droplets relative to one another as shown in the sequence in Fig. 4. Following droplet positioning, reactions may be initiated using electrocoalescence. Electrocoalescence can be induced by applying a low electrical potential, < 5 V, across the thin lamella separating aqueous droplets. The mechanistic details of electrocoalescence have been described elsewhere [3]. The lower image in Fig. 4 shows the initiation of a complexation reaction ($Fe^{3+} + SCN^{-} \rightarrow Fe(SCN)^{2+}$) by electrocoalescence. The formation of the dark red $Fe(SCN)^{2+}$ complex can be observed down stream from the electrodes. This approach is well-suited to studies of mixing and reaction kinetics in droplet-based systems.

CONCLUSIONS

We have explored the processing advantages of using high-dispersed phase emulsions, "gel emulsions", for microfluidic processing. We have demonstrated that monodisperse gel emulsions may be manipulated in an extremely well-defined manner driven by changes in the microchannel geometry, such as a bend. We anticipate that high-volume fraction emulsions will prove useful for microfluidic processing of droplet sequences or arrays.

REFERENCES

[1] H. Song, D.L. Chen, R.F. Ismagilov, *Angew. Chem. Int. Ed.*, **45**, 7336 (2006).
[2] C. Priest, S. Herminghaus, and R. Seemann, *Appl. Phys. Lett.* **88**, 024106 (2006).
[3] C. Priest, S. Herminghaus, and R. Seemann, *Appl. Phys. Lett.* **89**, 134101 (2006).

EXPERIMENTAL ANALYSIS OF LIPOSOME WATER TWO PHASE FLOW IN MICRO CHANNEL FOR LOCALIZING REACTION SYSTEM USING LIPOSOME

Yasumasa Ichikawa*, Tetsuo Kan*, Hiroaki Onoe*, Eiji Iwase*, Kiyoshi Matsumoto* and Isao Shimoyama*

**Graduate School of Information Science and Technology, the University of Tokyo, JAPAN*

ABSTRACT

We demonstrated the control system for local reaction in a micro channel with liposome as solution carrier. The dynamics of two-phase flow of liposome and water in our micro channel systems was observed. In this report, some results of the liposome motion in the diffuser, the inducer and the phase control channel in the systems are shown and discussed.

Keyword : Liposome, Two Phase Flow, Micro Channel Design, Local Reaction Control.

1. INTRODUCTION

A micro TAS (Total Analysis System) generally consists of several components such as inlets, confluence channel, branches and outlets. Since mixing and reaction occur along the channel in conventional micro TASs, it is difficult to precisely control the reacting location.

We are developing a method to overcome this difficulty. We use liposome (Giant vesicle) as a carrier of solution and fabricate a liposome flow control system with a pairing-control unit and a pressure control diffuser. Liposome is used in various fields because it can wrap solutions of various materials. For example, liposome is used as a drug carrier in Drug Deliver Systems (DDS).

Our method has advantages that the reaction area is localized and small, and the solution concentration as well as the reaction pressure is controllable. In this report, we present the concept of this method in detail and evaluate the properties of two-phase flow of liposome and water.

Figure 1 shows a plan of the system with localized reactions. The liposome A (solution A included) and B (solution B included) are introduced from the inlet 1 and 2, respectively. The solution A and B are prepared for the required concentration. The transport of the liposomes is arranged by the pairing-control unit so that they collide and form a pair. The paired liposomes receive large pressure, and their velocity is reduced in the diffuser. The pressure and the liposome velocity are controlled by an angle of the diffuser. If the liposomes receive some treatment such as UV light exposure, mixing/ reaction will occur locally in this area.

Many studies have been done in the field of two-phase flow of liposome and water in the micro channels[1][2]. The details of flow structures have not yet been clarified. We investigated a pairing-control channel, an inducer and a diffuser, which are key components of the channel system in Figure 1, by using visualization method under the microscope.

2. EXPERIMENTAL SETUP

The experimental system consists of a pressure pump, a suction pump, test channels, a motorized focus microscope with high-speed video system as shown in Figure 2.

We have two steps to evaluate the performance of our system. Firstly, we made an experiment in the effect of pressure gradient for a liposome in a simple diffuser 40μm deep and 50μm to 200μm wide.

Secondly, we used the total system as shown in Figure 3. It consists of 2 inlets, a junction, a pairing-control unit, an inducer, a straight channel and a diffuser. The channel

978-0-9798064-0-7/μTAS2007/$20©2007CBMS

depth is 30μm. The pairing-control unit and the straight channel are 50μm wide and 30μm wide, respectively. The inducer and the diffuser are 50μm to 30μm wide and 30μm to 200μm wide, respectively.

3. RESULTS AND DISCUSSION

In order to observe the pressure-rising effect in the diffuser, we use the simple diffuser. A long liposome is squashed in the large hydrostatic pressure gradient as shown in the time-series in Figure 4. Liposomes longer than the characteristic length of the pressure gradient are squashed when coming into the diffuser zone. Therefore, we expect that the paired liposomes receive large compressing force from the pressure gradient in the diffuser zone. This pressure gradient may be estimated from the angle of the diffuser.

Figure 5 and 6 show the flow pattern in the total system with pairing-control unit. The pairing-control unit possesses two parallel rows of rectangular blocks. These blocks partially separate the space inside the channel into three sub-channels, a center sub-channel and two outer sub-channels. Liquid can flow from one sub-channel to another through the gap between the blocks. As shown in time-series, three liposomes, A, B, and C move at different speeds in the flow. Liposome C catches up with liposome B from behind.

Figure 6 shows a time-series of a liposome moving around a obstructed center sub-channel in the pairing-control unit. The liposome flows from the center sub-channel to one outer sub-channel when encountering the obstacle. It returns back to the center sub-channel after passing the obstructed part. This means that a pressure drop domain exists right behind the obstacle.

4. CONCLUDING REMARK

A method for controlling the local reaction in a micro TAS that uses liposomes is discussed. The liposome-water two-phase flow in our microfluidic system is observed.

The experimental result shows that this method is effective for the pairing-control of liposomes. In addition, it also shows that the pressure gradient can be designed by changing the angle of the diffuser in the reaction area.

5. ACKNOWLEDGMENT

This work was supported by the Ministry of Education, Science, Sports and Culture, Grant-in-Aid, 17656084, 2006.

REFERENCE

[1] K. H. de Hasse, et al., Phys. Rev. E, 56, 7132 (1997).
[2] V. Vitkova, M. Mader, and T. Podgorski, Europhys. Lett., 68, 398(2004)

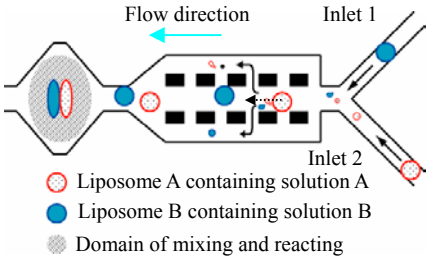

Fig.1 A schematic diagram of local reacting system with liposomes.

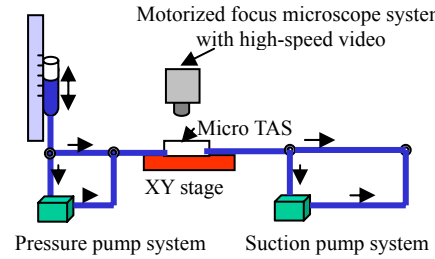

Fig.2 A schematic diagram of an experimental setup.

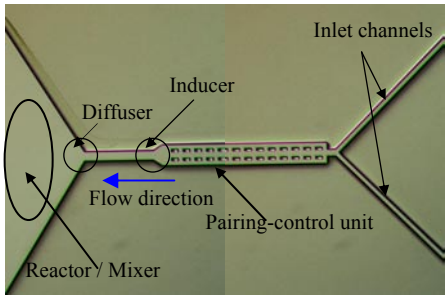

Fig.3 Photographs of fabricated micro channel system with pairing control unit.

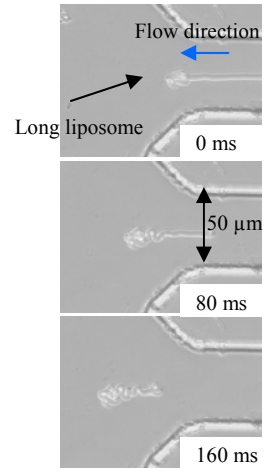

Fig.4 A long liposome squashed due to the large hydrostatic pressure gradient in the diffuser.

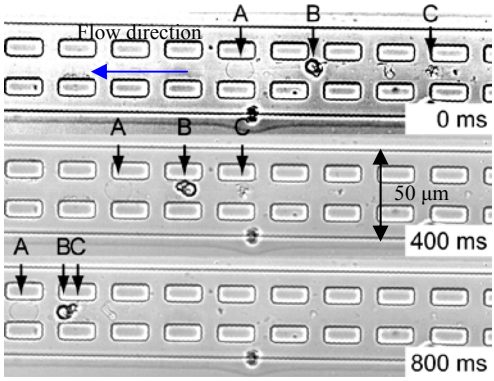

Fig.5 Time-series of Liposomes motion in the pairing channel. The distance between "A" and "B" got smaller, and "C" caught up with the "B".

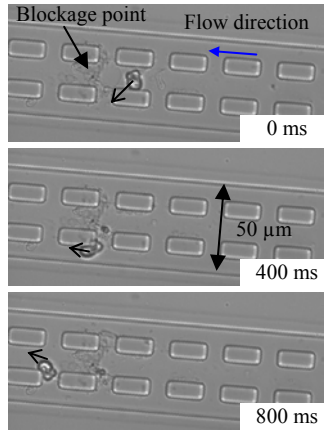

Fig.6 A small liposome motion near a obstructed center sub-channel in the paring control unit.

EXTERNALLY ACTUATED MAGNETIC FLOW REGULATOR FOR DISPOSABLE DRUG INFUSORS

M. Duch[1], J.Casals-Terré[2] , J. A. Plaza[1], J. Esteve[1], R Pérez-Castillejos[1], E. Vallés[3] and E. Gómez[3]

[1]*Centro Nacional Microelectronica, SPAIN and*
[2]*Technical University of Catalonia, Mechanical Engineering Department, SPAIN and*
[3]*University of Barcelona, SPAIN*

ABSTRACT

A magnetic microfluidic valve has been designed, fabricated and tested. Operation relies on the use of a permanent magnet which interacts with an electrodeposited layer of Co-Ni on a V-shaped cantilever beam. The deflection caused by the magnetic forces opens or closes the fluid flow. The microvalve performance has been optimized by means of finite element analysis (FEA). Then, the microvalve has been demonstrated to work as a check valve or flow regulator when being magnetically actuated.

Keywords: Microfluidic, MEMS valve, magneto-static analysis.

1. INTRODUCTION

Portable drug infusors are used to provide a slow infusion into the bloodstream; this allows drug treatments to be given at home. Current state-of-the-art of portable drug infusers are single passive fluidic resistors [1],[2]. In this paper a microfluidic regulator is presented. The main advantages of this system are: portability and no power consumption (permanent magnets) and no interaction of the controlling system with the fluid. These features are suitable to build disposable drug infusers and improve significantly the patient's life quality.

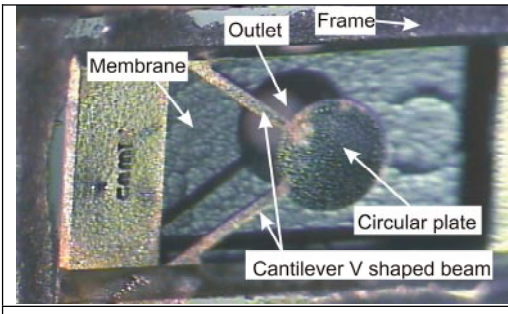

Figure 1. Picture of the chip valve cap.

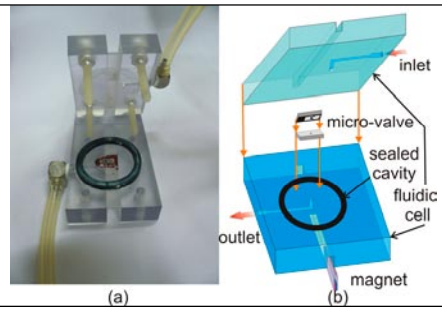

Figure 2. Microvalve and the fluidic cell. (a) experimental set-up. (b) schematics.

The microfluidic regulator has two parts: top V-shaped cantilever beam and the bottom membrane. The top cantilever beam is a V-beam anchored at one end, see figure 1. The V-shaped beam has an electrodeposited Co-Ni layer which causes the top beam deflection in presence of an external magnetic field generated by permanent magnet. Due to the deflection caused by the magnet, the outlet is closed and, the flow path obstructed. An O-ring is placed between both parts of the fluidic cell which causes a sealed cavity. The fluid

978-0-9798064-0-7/μTAS2007/$20©2007CBMS

is forced into the cavity through the inlet, the only way to proceed is through the microvalve which is placed in the path of the fluid, see figure 2.

2. FEA MAGNETIC-STRUCTURAL MODEL

Ansys Multiphysics V.10 finite element analysis software is used to perform a direct magnetic/structural analysis to characterize the motion of the magnetically actuated cantilever beam. The magnetic field model is an infinite 3D model. INFIN47 elements model an infinite extension of the air surrounding the structure. The magnetic load is provided by the NdF-eB235 permanent magnet, meshed using SOLID96 elements. In figure 3 all volumes used to created the 3D model are plotted. The magnetic field distribution obtained from this model is applied as input to the structural model formed by the microvalve itself, meshed using SOLID45 elements. The two analysis advance using an one way iterative coupled field analysis, where physics coupling passes loads across physics field interfaces (in this case the surface of the microvalve). The structure of the microvalve requires displacement constrains once the magnetic load is applied. The frame is completely fixed against all translations and rotations at its nodes. The only forces used in the structural model are Maxwell forces, which are transferred from the magnetic model onto the structural model through the FLAG surfaces.

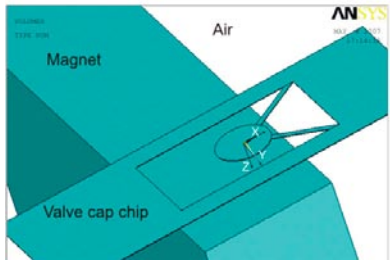

Figure 3.Volumes used in coupled-field structural and magnetic FEA model

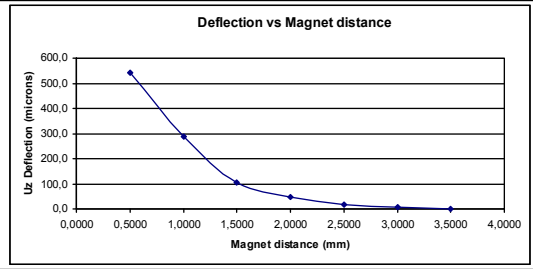

Figure 4. Evolution of the deflection of the tip of the cantilever versus the distance in Z direction of the magnet placed under the microvalve

The magnetic force and the deflection decay are exponential. In figure 4, distances between the magnet and the microvalve higher than 2 mm produces deflection on the tip of the cantilever lower than 50 µm. This is considered not enough to close microvalve. So a reasonable initial distance from magnet to the Co-Ni layer of the cantilever beam was fixed to 1520 µm: 500 µm polycarbonate thickness + 500 µm of the handle wafer (membrane) + 500 µm of adhesive layer + 20 µm distance from the bottom of the wafer to the cantilever.

3. EXPERIMENTAL RESULTS

Several initial prototypes have been micro-machined using a combination of silicon micromachining technologies and electrodeposition of magnetic CoNi alloy, [3]. These initial prototypes have been used to validate the model. Figure 5 shows the pictures of the microvalve taken with the confocal microscope, without magnet and with magnet. The magnet was placed under the valve and left there to do the measurements statically. The deflection difference between the two states is considered the real deflection. In figure 5 the

deflection in the model is 48.7 μm for a distance between the magnet and the microvalve set to 2 mm compared to 59 μm in the confocal microscope. Besides, the complexity of the measurements, the deviation is low enough to consider the model valid to proceed with the analysis. Prototypes of the whole system were tested using N_2 demonstrating the proper functionality of the flow regulator as active controller and as check valve; with pressures up to 50mbar applied to the microvalve, see figure 6.

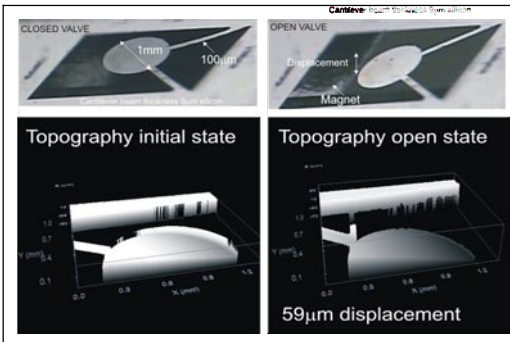

Figure 5. Micro-valve measured displacements (Confocal microscope).

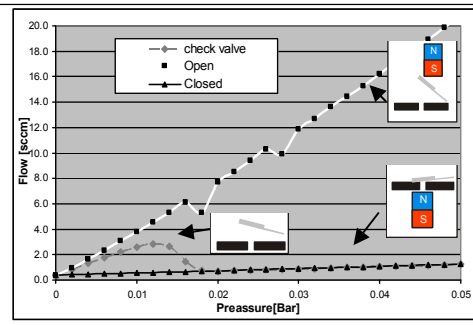

Figure 6. Flow through the fluidic cell with the micro valve in different situations: acting as check-valve, open or closed.

3. CONCLUSIONS

A new microfluidic flow regulator has been proposed, which uses permanent magnet actuation which does not require any type of power input to control the fluid flow. This provides several advantages in MEMS applications, such portability, light weight and low cost. Its performance has been analyzed and its actuation principle shown, along with a study of its main parameters. An FEA model has been developed to analyze the main design parameters; the performance of the model has been validated comparing the results with the measured deflections of a microfabricated valve using confocal microscopy. The microvalve has been successfully integrated into a fluidic cell, demonstrating the feasibility to be used as an active fluid flow regulator and the possibility to be used as a check valve too. This type of actuation does not interfere with the fluid and provides power savings with respect other type of actuation, such as electrostatic or thermal. The use of an array of this type of microvalves could become a novel microflow variable regulator.

REFERENCES

[1] DOSI-FUSER *Portable elastomeric infusor* www. Leventon.es

[2] Department of Health, Bath Institute of Medical Enginering. The Wolfson Centre. "*Market survey: Non-electrically powered disposable infusion devices*". Bath, UK September 2005.

[3] M Duch, J Esteve, E Gomez, R Perez-Castillejos and E Valles. *Electrodeposited Co-Ni alloys for MEMS.* Journal of Micromechanics and microengineering. Vol 12 2002. pp. 400-405.

FAST & HIGH SPATIAL RESOLUTION TRANSPORT OF MAGNETIC CARRIERS FOR MAGNETICALY ASSISTED LAB ON A CHIP

Qasem Ramadan[1*], Jewel Ellyna Widjaja[2], Tang Kum Cheong[1], Wong Yew Fung[2], Balakumar Subramanian[1], Liao Ebin[1], ChenYu[1]and Poenar Daniel[2]

[1]Institute of Microelectronics 11 Science Park Road, Singapore 117685, [2] Nanyang Technological University, Singapore 639798

[*]Contact EMAIL : qasemr@ime.a-star.edu.sg)

ABSTRACT

Reconfigurable magnetic paths were created using on-chip custom designed micro-coils (MCs). By alternatively injecting currents in an array of such MCs, magnetic beads were guided in different movement modes and step sizes.

Keywords: Micro-coils, Magnetic path, magnetic carriers

1. INTRODUCTION

Moving magnetic beads requires to shift local magnetic potential wells by programming the currents injected through an array of MCs.

In this paper 3 different motion modes of magnetic beads generated by 3 different configurations of MCs are descriped. Fig.1 shows schematic presentation of the 3 MC realized and used in our experiments i.e. MC1, MC2 and MC3, respectively. In each array, DC current can be injected selectively in one conductor to generate the magnetic potential well which consequently defines their motion path. The magnetic force on a magnetic particle suspended in a fluid is given by $\vec{F}_m = \frac{1}{2}\frac{V\chi}{\mu_0}\nabla B^2$, where B is the magnetic fiel, *R* the particle radius, χ the magnetic susceptibility of the particle, being directed along the steepest increase of the magnetic field density gradient $\left(\nabla B^2\right)$. Therefore, obtaining large magnetic forces can be realized efficiently in a miniaturized microcoils system.

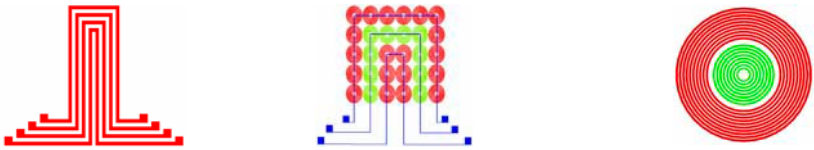

(a) MC1 (b) MC2 (c) MC3

Figure 1: Schematic configurations of the three micro-coil designs

2. EXPERIMENTAL

High aspect ratio trenches (10 μm deep and 3 μm wide) were etched in silicon, passivated with a thin (~1000 Å) oxide layer, filled by Cu electroplating and then surface planarized using Chemical Mechanical Polishing (CMP), respectively. A second passivation SiO_2 film and an Al layer (each ~1 μm thick) were deposited and patterned, the

978-0-9798064-0-7/μTAS2007/$20©2007CBMS

latter forming the bonding pads and leads bridging them with the inner coil ends. A detailed description of the whole fabrication processes is given elsewhere [1].

Experiments to test the magnetic devices for magnetic beads trapping and transporting were conducted using superparamagnetic particles (Estapor® magnetic microspheres) with diameter of 1 μm. The chip was initially mounted on a Printed Circuit Board (PCB) and wire bonded to the PCB with gold wires. DC current conrol was made using a custom made electric switch which allowed selective switching the current into the desired MC. Particle tracking was performed with an optical microscope equipped with a CCD camera which allowed the capture of still pictures and videos for real-time tracking of the particle movement.

3. RESULTS AND DISCUSSION

MC1 consist of 6 independent concentric conductors with each conductor can be operated independently using its own bonding pads. When the current is injected in the most inner conductor, magnetic beads trapped and confined around the conductor with an average capture radius of 20 μm. By switching the current to the next conductor, magnetic beads follow the growing potential well around it and this motion can be repeated in both directions IN/OUT.

MC2 consists of an array of spiral micro-coil arranged in three concentric loops (inner, middle and outer) with each loop consists of several micro-coils connected in series. In the same manner beads trapped in multi-potential wells in the inner loop when the current injected into it and move to the middle and then to the outer ones simultaneously as the current switches alternatively through the loops.

MC3 consists of two concentric spiral micro-coils (inner and outer). By alternative injecting of the current between the inner and outer coils magnetic beads can be transported in radian motion. Fig.2(a) presents the magnetic flux density profile calculated using Finite Element Analysis (FEA) for each conductor. Each individual conductor generates a magnetic force capable to move the beads initially captured by any conductor in the array. Fig. 2b shows frame by frame sequential images of the bead transport from the inner to the outer conductor with step size of 3 μm. The magnetic beads used in our experiments have a saturation mass magnetization of 35 to 40 $A \cdot m^2/kg$ and they saturate at an external magnetic field of 40 kA/m. In the same manner Figs 3 &4 show the results of MC2 and MC3, respectively. Magnetic beads traveled in step sizes of 85 μm and 75 μm for the MC2 an MC3, respectively.

4. CONCLUSIONS

In conclusion, customized designs of current carrying conductors were fabricated and employed for magnetic beads trapping and movement, as required in many bioanalytical applications.

REFERENCES

[1] Qasem Ramadan, Victor Samper, Daniel Poenar and Chen Yu, *Fabrication of three-dimensional magnetic micro-devices with embedded micro-coils for magnetic potential concentration*, J. Microelectromechanical Systems, 15 (3) 624-638, (2006).

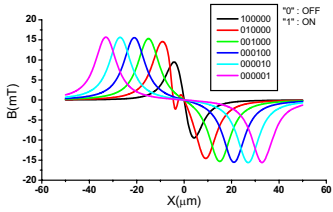

(a)

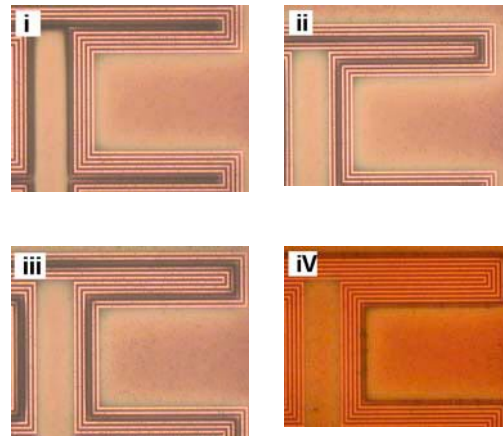

(b)

Figure 2: (a) magnetic flux density profile generated by 6 conductors independently; (b) Shifting magnetic beads between 6 conductors by injecting currents into each conductor alternatively.

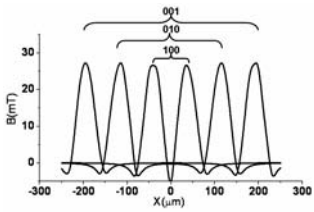

(a)

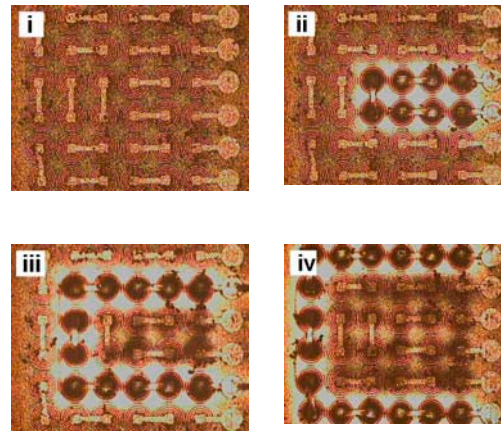

(b)

Figure 3: (a) magnetic flux density profile generated by 3 spiral MCs; (b) Shifting magnetic beads between 3 loop array by injecting currents into each loop alternatively.

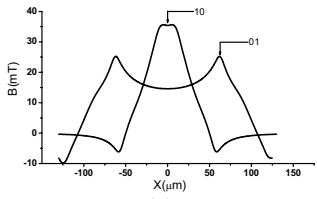

(a)

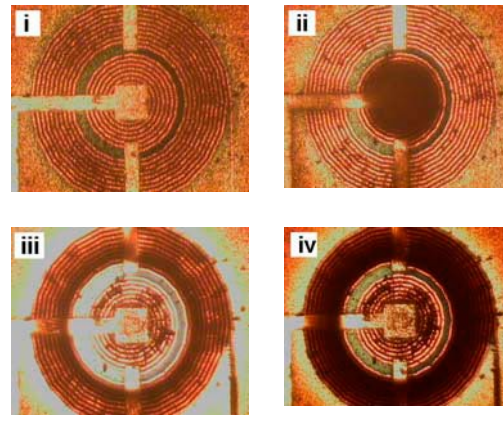

(b)

Figure 4: (a) magnetic flux desnity profile generated by 2 concentric spiral MCs; (b) Shifting magnetic beads between the 2 MCs in radian motion by injecting currents into each MC alternatively.

FLEXIBLE CAPILLARY-BASED SEQUENTIAL INTRODUCTION FOR MULTIPHASE DROPLET MICROFLUIDIC SYSTEMS

Wen-Bin Du, Lei Dong, Qun Fang*

Institute of Microanalytical Systems, Department of Chemistry, Zhejiang University, Hangzhou, China, 310058

ABSTRACT

A novel approach for continuous and precise generation of droplets in the picoliter to nanoliter range was developed. The system was composed of a capillary with a tapered tip, a syringe pump and a slotted-vial array autosampling device. Potential applications of the system in protein crystallization and double emulsion generation are demonstrated.

Keywords: Droplet generation, capillary, protein crystallization, double emulsion, high throughput screening

1. INTRODUCTION

Droplet handling microfluidic device has recently attracted a lot of interests, for its ability of precise mixing and reaction controlling, and great potential in high throughput screening.[1] In most of microfluidic droplet systems, monodisperse droplets were frequently employed. However, on-line generation of droplets with different size and composition still presents a challenge.

Recently, we reported a microfluidic sample introduction approach using a capillary sampling probe and a slotted-vial array sample presenting system, and applied it in microfluidic chip-based flow injection analysis.[2] Based on this work, more recently we developed a simple capillary-based microfluidic analysis system (CBMAS) to perform sequential injection analysis without resorting to complicated microfabrication techniques.[3] In this work, the strategy was applied in continuous and flexible generation of nanoliter droplets for high throughput screening.

2. EXPERIMENTAL

A 5-cm long 150-μm i.d. fused-silica capillary with a 25μm i.d. tapered tip was used as sampling probe and microchannel as shown in Fig.1. Before use, the inner wall of capillary was treated with perfluoro-deyltriethoxysilane to obtain a hydrophobic surface.[4]

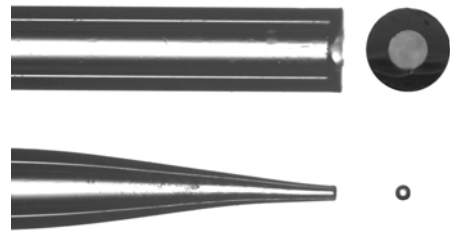

Figure 1. A typical tapered tip (25 μm i.d. and 50μm o.d.) comparing with a flat tip capillary (150 μm i.d., 330 μm o.d.).

The system setup is shown in Fig.2. A syringe pump (Pico plus, Harvard Apprautus) was connected to the capillary for flow-driven. The slotted vials fixed on the autosampler[4] were used to hold oil carrier and aqueous sample and reagent solutions. Automated and continuous droplets generation was performed by rotating the autosampler, allowing the capillary tip to sweep through the liquid filled in the vial, sequentially sipping different

978-0-9798064-0-7/μTAS2007/$20©2007CBMS

liquids into the capillary under driving of the syringe pump. The moving sequence of the autosampler and the pump flow-rate were set and precisely controlled by a home-written LabVIEW (National Instruments, TX) program.

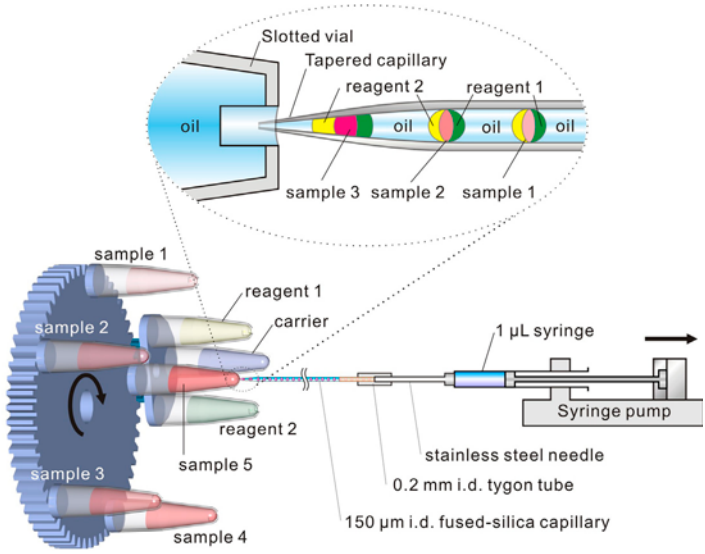

Figure 2. Setup of capillary-based droplet generation system.

3. RESULTS AND DISCUSSION

In this work, the shape of the sampling capillary tip was optimized to reduce the carryover between neighboring vials. The capillary with a tapered tip demonstrated the best performance, which could produce droplets with size much smaller than the inner diameter of the capillary.

In the performance testing experiment, tetradecane with 2% Span 80 was used as carrier and water solutions containing different dyes as droplet phase. Monodisperse droplets of fluorescein solution with a smallest volume of 20 pL were obtained (Fig. 3A). Generation of droplets with different composition and tunable size (20 pL to 1.6 nL) was also achieved according to the setting of program. The result is shown in Fig. 3B-C. The droplets (as shown in Fig.3D) with different composition were produced by infusing red and blue dye solution as well as water to form a 2.5 nLdroplet.

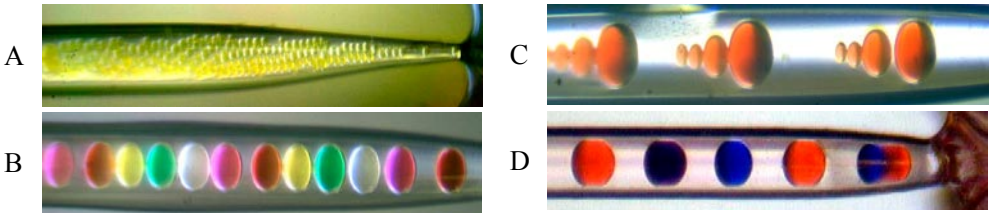

Figure 3. (A) Monodisperse 20 pL droplets; (B) Continuous generation of 1.6 nL droplets with different dyes; (C) Polydisperse droplets with volume of 20, 40, 160 and 1000 pL; (D) 2.5 nL droplets formed by sequentially introducing red dye solution, water and blue dye solution with different combination ratios(1:1.5:0, 0.5:1.5:0.5 and 0:1.5:1).

Protein crystallization experiments were carried out by sequentially introduce precipitants (2.0 mol/L potassium sodium tartrate) and proteins (30 mg/mL Thaumatin)[5] with volume ratio of 1:1 into the capillary to form 1.6 nL droplets. Thaumatin crystals were observed within the droplets after 8 hour incubation (Fig.4). The system was also used in forming double emulsions by adding 1% Tween 20 in the yellow aqueous phase. Double emulsion with a total volume of 1.6 nL was generated as shown in Fig.5.

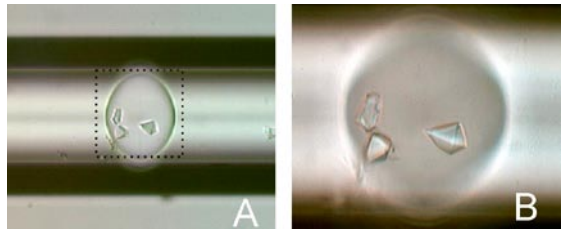

Figure 4. Protein crystallization of Thaumatin in a 1.6 nL droplet.

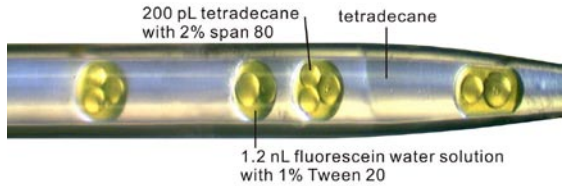

Figure 5. Fusion of double emulsion.

4. CONCLUSIONS

In conclusion, the present capillary-based system demonstrated precise control ability on the size and composition of each droplet, which provided a flexible and versatile tool with low cost for droplet-based high-throughput screening.

ACKNOWLEDGEMENTS

This work was supported by the National Natural Science Foundation of China (Grant 20575059) and Ministry of Education (Grant NCET-05-0511).

REFERENCES

[1] H. Song, D. L. Chen, R. F. Ismagilov, *Angew. Chem. Int. Ed.* **2006**, 45, 7336.
[2] W. B. Du, Q. Fang, Q. H. He, Z. L. Fang, *Anal. Chem.* **2005**, 77(5): 1330-1337.
[3] W. B. Du, Q. Fang, Z. L. Fang, *Anal. Chem.* **2006**, 78, 6404.
[4] Y. Kobayashi, M. Ueno, S. Kobayashi, T. Kitamori, *Proc. Micro Total Analysis Systems 2004*, 97-99.
[5] D. L. Chen, C. J. Gerdts, and R. F. Ismagilov, *J. Am. Chem. Soc.* **2005**, 127, 9672-9673.

FLOW VISUALIZATION OF POLYMER/WATER/SURFACTANT DROPLETS IN OIL USING COFLOW AND FLOW-FOCUSING CHANNELS WITH μPIV TECHNIQUE

Manuela R. Duxenneuner[1,2], Peter Fischer[2], Erich J. Windhab[2], and Justin J. Cooper-White[1]

[1]Laboratory of Tissue Engineering and Microfluidics, The University of Queensland, Australia; [2]Laboratory of Food Process Engineering, ETH Zurich, Switzerland

ABSTRACT

This work presents the study of the flow behaviour during drop formation and breakup at a capillary tip with two different channel (coflow and flow-focusing) and capillary (flat and pointy) designs. Utilizing μPIV and streak imaging by means of fluorescence particles, the flow fields of both aqueous and oil phases were simultaneously visualized. The effect of elasticity on drop formation and breakup has also been explored by various Tween®20 surfactants and surfactant/guar polymer solutions as the disperse phase.

Keywords: μPIV, flow visualization, drop formation, coflow

1. INTRODUCTION

Studies of microdroplet creation in microchannels formed in different geometries (mostly T-channel or flow-focusing) have been the subject of much research for application in pharmaceutical, food, and personal care industries. Most publications focus on pure visualization of the drop creation event with very few focusing on measurements of the flow field characteristics[1-2]. However, to understand and analyse drop formation and breakup dynamics and also in order to design micro-flow devices and droplet based reactors, it is important to measure the dispersed and continuous flow fields in and around a droplet. μPIV and streak imaging are a useful technique to investigate and map the entire flow situation given by the geometry, process conditions, and material parameters[3-6].

2. EXPERIMENTAL SETUP AND METHOD

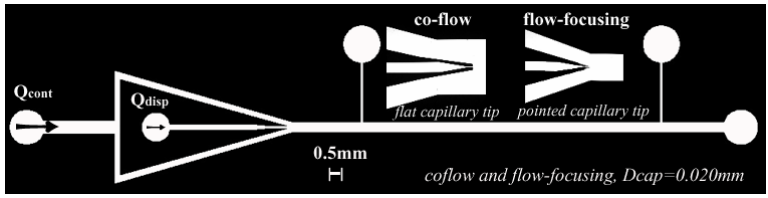

Figure 1. *Flow-focusing and coflow PDMS-microchannel, focused especially on capillary size and geometry (flat and pointed tip).*

A coflow PDMS microchannel and a flow-focusing channel were used in this study as shown in fig.1. The geometries were different mainly in the capillary shape such as a flat tip (thicker capillary wall) and a pointed tip. The size of the capillary outlet, D_{cap}, was in both cases around 0.020mm. The disperse phase, which was either water or water/surfactant/guar gum (2-hydroxypropylether guar gum, HPG) solution (c_{TW20}=1cmc,

978-0-9798064-0-7/μTAS2007/$20©2007CBMS

c_{guar}=0.1-0.2wt%), was injected parallel to the continuous oil phase (sunflower oil SFO, Farmland Coles AUS) at different flow rates ($0.1 \leq Q_{disp} \leq 0.2$ml/h, $0.1 \leq Q_{cont} \leq 50$ml/h) to produce droplets of around D_{drop}=0.01-0.3mm. Fluorescent particles (Duke Science R700, $D_{particle}$=0.3-0.71µm) were seeded into both the oil and water phases allowing the flow inside and outside of different sized droplets during formation and breakup to be visualized and analysed simultaneously by means of a microscope and µPIV laser technique.

3. FLOW FIELD MEASUREMENTS

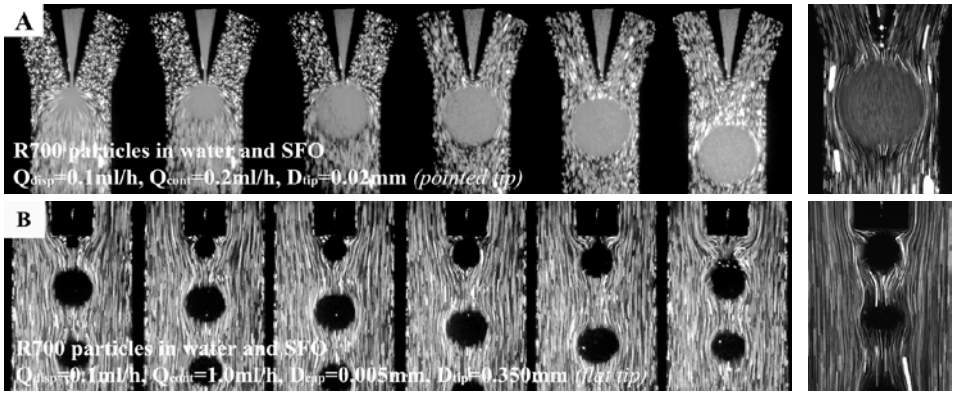

Figure 2. *Flow visualization of drop formation at the (**A**) pointed capillary and (**B**) flat capillary tip utilizing µPIV technique (**left**) and streak imaging (**right**).*

Fig.2 visualizes the flow inside and around the droplet for both geometries of capillary (pointed tip (A) and flat tip (B)). Especially for the outer continuous phase, the stream lines show nicely the differences of drop formation at either capillary. The drops were smoothly formed at the pointed tip (A) with only little blockage of the continuous phase, whereas the flow around the flat capillary tip (B) caused vortices which influences the size final size.

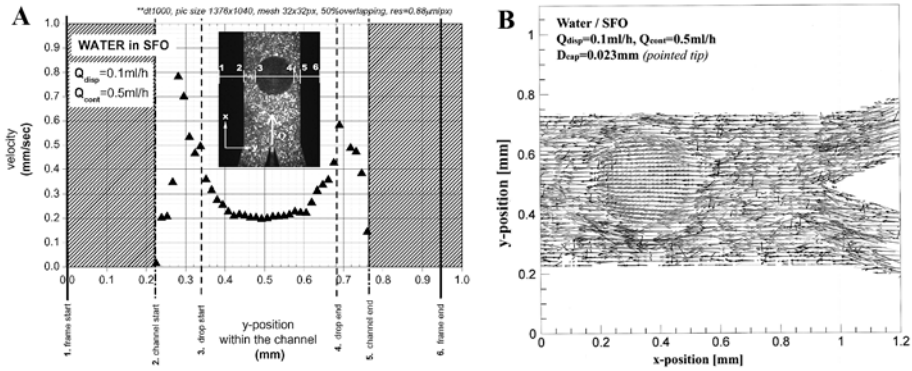

Figure 3. *Example of a velocity profile (**A**) of a water drop flowing in SFO which could be extracted from µPIV measurments (**B**).*

In fig.3 the droplet and continuous phase velocity distributions are quantified during droplet formation, pinch-off, and drop convection along the length of the channel. The velocity

profiles show that fluid recirculation occurs inside the drop only when the drop is in contact with the wall and is blocking the continuous phase passing by. The recirculation can be attributed to wall slip and shearing at the leading edge and backside of the droplet. This is consistent with previous two-phase studies utilizing confocal μPIV[2] or ordinary μPIV[1] for water/glycerol droplets in silicon oil. However, this phenomenon was not observed when the droplet creation event was very fast, resulting in the droplet size being much smaller than the channel depth.

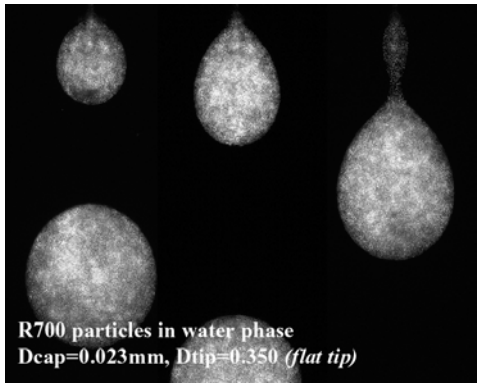

Figure 4. *Flow visualization of a elastic drop formation with guar0.2wt%-TW20cmc1-water in SFO.*

The effect of elasticity on drop formation and breakup has also been explored by using various solutions of surfactant/polymer solutions as the disperse phase (fig.4). At constant flow rate, it was found that with increasing polymer concentration, the elasticity of the fluid increases and therefore the pinch-off distance of the droplet increases. The elongated neck of the drop results in small satellite droplets. The flow field inside the formed thread was stable and illustrated a continuous flow of the solution into the drop until pinching-off.

4. CONCLUSION

We were able to visualize both internal and external flow field by using μPIV with fluorescence particles in the water and oil phase. With the addition of Tween®20 surfactants and guar gum, the effect of elasticity on the drop creation and on the thread formation during breakup could be investigated. The tracing of the fluorescence particle showed the flow of the disperse phase into the droplet while the drop is pinching off.

ACKNOWLEDGEMENTS

This work was mainly setup under DPPICM between University of Queensland and ETH Zurich. It was also financially supported by the ARC discovery grants Australia, the fund TH-38/03-3 of the Swiss Federal Institute of Technology ETH in Zurich, and the EU-Project NMP-033339 “Controlled Release”.

REFERENCES

[1] H. Kinoshita, S. Kaneda, T. Fujii, and M. Oshima, *Three-dimensional measurement and visualization of internal flow of a moving droplet using confocal μPIV*, Lab on a Chip, **7**, 338-346 (2007).

[2] A. Y. Yoon, J. M. Kim, and K. C. Kim, *Both internal and external flow fields measurements in around a micro-droplet formed in a microchannel*, In: 9th International Conference on Miniaturized Systems for Chemistry and Life Science - μTAS 2006, Boston, Massachusetts, USA, 626-628 (2005).

[3] S. T. Wereley and C. D. Meinhart C.D., *Micron resolution particle image velocimetry*, In: Microscale diagnostic technique. Editor: K. Breuer., Springer-Verlag, Berlin, Heidelberg 51-154(2005).

[4] M. Raffel, C, Willert, and J. Kompenhans, *Particle image velocimetry - a practical guide*, Springer-Verlag, Berlin, Heidelberg, New York, Barcelona, Hong Kong, London, Milan, Paris, Tokyo (1998).

[5] L. E. Rodd, T. P. Scott, D. V. Boger, J. J. Cooper-White, and G. H. McKinley, *The inertia-elastic planar entry flow of low-viscosity elastic fluids in micro-fabricated geometries*, Journal of Non-Newtonian Fluid Mechanics, **129**, 1-22, (2005).

MICROFABRICATED DROPLET GENERATOR FOR SINGLE MOLECULE PCR IN TUNABLE, MONODISPERSE EMULSIONS

P. Kumaresan, C.J. Yang, R.G. Blazej and R.A. Mathies

University of California, Berkeley, CA 94720, USA

ABSTRACT

A microfabricated droplet generator that produces uniform, nanoliter-volume emulsion droplets for genomic analysis has been developed and evaluated. A flow focusing nozzle structure is used to form monodisperse droplets of PCR reagent, selectable from 1.0 to over 4.0 nL, in emulsion oil. Droplets are collected in conventional PCR tubes for efficient, high-throughput amplification of target DNA. Controlled, nanoliter-volume emulsions (2.2 +/- 0.25 nL) enable efficient and uniform amplification of long 1 Kb DNA template at single molecule template dilutions, generating attomoles of product per template. The system presented here establishes the usefulness of microfluidics-based engineered emulsions to amplify templates for next generation sequencing technologies as well as single molecule/cell genetic analysis.

Keywords: Single molecule PCR, microemulsion PCR, droplet generation

1. INTRODUCTION

A number of new sequencing technologies rely upon the amplification of single molecules in limited nanoliter volumes to form PCR colonies or polonies. Emulsion PCR is a high-throughput single molecule amplification technique that obviates cumbersome transformation and colony picking processes in genomic analysis. However, current emulsion PCR methods rely on bulk emulsion generation [1], which produces highly polydispersed emulsions, resulting in non-uniform reaction efficiencies, low-yield amplification, and poor amplification of long templates. To solve this problem for our microbead integrated DNA sequencing (MINDS) method [2, 3], we need a technology for the rapid generation of monodisperse emulsions with precisely controlled droplet volumes that efficiently amplify full-length DNA sequencing targets (~ 1 Kb).

2. EXPERIMENTAL

Our microfabricated droplet generator is based on a digital microfluidic system from our group that was used to synthesize nanoparticles in controlled emulsions [4]. In the present work a new microdevice has been developed that produces monodisperse, nanoliter volume droplets of PCR mix in emulsion oil (40 % (w/w) DC 5225C Formulation Aid (Dow Chemical Co., Midland, MI), 30% (w/w) DC 749 Fluid (Dow Chemical Co.), and 30% (w/w) Ar20 Silicone Oil (Sigma)) [1]. Figure 1 presents three different conditions for controlled-size droplet generation in the microdevice, and the corresponding emulsions after collection and 40 cycles of PCR. For a PCR mix flow rate of 0.5 μL/min and emulsion oil flow rates ranging from 1.0 to 4.0 μL/min, droplets remain stable while transitioning from the device into the PCR tube and have a tight volumetric distribution that can be tuned from 1.0 to 4.0 nL by varying the flow rates.

978-0-9798064-0-7/μTAS2007/$20©2007CBMS

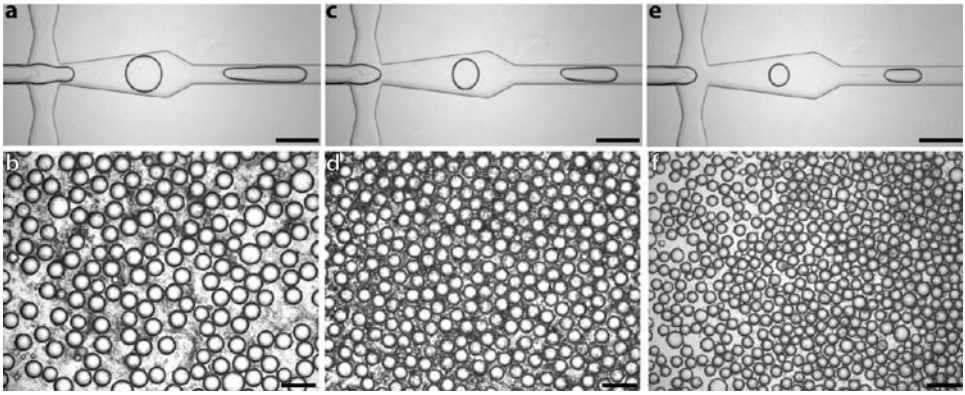

Figure 1. Photographs of droplet generation at three oil flow rates and corresponding emulsions following 40 PCR cycles. (a) PCR mix flow rate (Q_{PCR}) in left channel – 0.5 µL/min, combined emulsion oil flow rate (Q_{oil}) in top and bottom channels – 1.0 µL/min. (b) Droplets from above collected and PCR cycled, average droplet volume – 4.0 nL. (c) Q_{PCR} – 0.5 µL/min, Q_{oil} – 2.0 µL/min. (d) Droplets from above collected and PCR cycled, average droplet volume – 2.2 nL. (e) Q_{PCR} – 0.5 µL/min, Q_{oil} – 4.0 µL/min. (f) Droplets from above collected and PCR cycled, average volume – 1.1 nL. Scale bars – 400 µm.

3. RESULTS AND DISCUSSION

To demonstrate the usefulness of this technique, a 1,008 bp region of the pUC18 genome was amplified from three different stochastic-limit template dilutions in 2.2 nL droplets. Following PCR, droplets and control reactions were purified to remove the oil phase and the extracted amplicons were run on an agarose gel along with a standard to determine DNA product size and quantity (Table 1). Three to five attomoles of product per template molecule is consistently generated for the three different starting average template concentrations of 0.67, 0.067 and 0.0067 molecules/droplet. *These results demonstrate successful amplification of 1 Kb single template DNA molecules in nanoliter volume droplets.* The PCR yield in droplets is 4 to 10 times lower than in respective controls; this is expected due to polymerase adsorption to the oil-aqueous interface in these high surface area to volume ratio droplets.

To efficiently manipulate products amplified from distinct DNA templates in individual droplets, primer functionalized microbeads were next incorporated into droplets at statistically dilute levels so that the PCR progeny are all chemically linked to the beads. We successfully amplified a 545 bp PCR amplicon from the pUC18 genome on single beads encapsulated in individual nL droplets with an average starting template concentration of 85 molecules per bead (Figure 2). The intensely labeled beads demonstrate successful, efficient PCR reaction in bead containing droplets, with 145 attomoles of product being generated on each bead.

Table 1. PCR yield results in microfabricated emulsions

Starting template conc.	**Droplet PCR yield**	**Control PCR yield**
0.67 copy / 2.2 nL droplet	2.7 attomoles / template	28 attomoles / template
0.067	2.8	20
0.0067	5	20

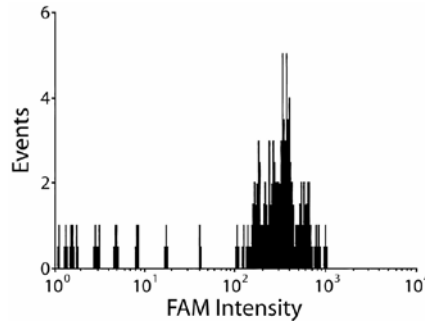

Figure 2. Flow cytometry result of a 545 bp PCR product amplified on beads incorporated in engineered emulsion. X-axis is a log scale representation of fluorescence signal from dye (FAM) labeled PCR product linked to individual beads and y-axis is the corresponding number of beads at each fluorescence intensity value. Droplet size – 2-3 nL, bead size – 25-45 μm, starting pUC18 template concentration – 4.4×10^4 molecules/μL (~ 85 molecules/droplet), bead concentration – 75 beads/μL (0.15 bead/droplet).

4. CONCLUSIONS

We have utilized two-phase microfluidics to generate tunable, monodisperse droplets for efficient emulsion PCR; these droplets provide, for the first time, the ability to perform efficient single molecule amplification of large 1 Kb targets in emulsion droplets. The successful production of full length 1 Kb DNA amplicons at three different stochastic limit concentrations in nanoliter-volume emulsions is a key advance towards preparation of PCR templates for single molecule DNA sequencing. We further show effective PCR amplification on a single bead using our emulsion generation platform, which in turn allows us to manipulate products amplified in individual droplets. PCR yields exceeding 100 attomoles of >500 bp amplicons on each bead establishes the feasibility of this system as a front end to our MINDS process. Future directions will include the production of amplified sequencing templates on a single bead from a single molecule and the direct use of these templates for Sanger extension and sequencing in the ultra-efficient integrated sequencing processors that we have recently developed [2, 3]. The microfabricated emulsion generator presented here also holds great promise as the front end for other new sequencing technologies as well as single cell genetic analysis.

REFERENCES

[1] M. Margulies *et al.*, "Genome sequencing in microfabricated high-density picoliter reactors", Nature, Vol. 437, pp. 376-380, (2005).

[2] R.G. Blazej, P. Kumaresan, R.A. Mathies, "Microfabricated bioprocessor for integrated nanoliter-scale Sanger DNA sequencing", Proc. Natl. Acad. Sci. USA, Vol. 103, pp. 7240-7245, (2006).

[3] R.G. Blazej, P. Kumaresan, S.A. Cronier, R.A. Mathies, "Inline-injection microdevice for attomole-scale Sanger DNA sequencing", Anal. Chem., In press.

[4] E.M. Chan, A.P. Alivosatos, R.A. Mathies, "High-temperature microfluidic synthesis of CdSe nanocrystals in nanoliter droplets", J. Am. Chem. Soc., Vol. 127, pp. 13854-13861, (2005).

OSCILLATORY BUBBLING IN A MICROFLUIDIC T-JUNCTION

S. A. Khan[1,2] and K. F. Jensen[3]

[1]National University of Singapore, [2]Singapore-MIT Alliance, and [3]Massachusetts Institute of Technology, USA

ABSTRACT

In this paper, we study oscillatory bubbling in a microfluidic T-junction. We demonstrate periodic/quasi-periodic oscillations in bubble sizes that can be switched on/off by appropriate design of the gas delivery line. We develop an equivalent electrical circuit model for the system, and discuss important criteria for monodisperse, non-oscillatory bubbling.

Keywords: Segmented flow, bubbles, fluidic circuits, hydraulic inductance

1. INTRODUCTION

Multiphase microfluidic flows have attracted interest in several applications ranging from chemical synthesis to fluidic logic. Syringe pumps are routinely employed to infuse gases and liquids into microfluidic devices. Such pumps operate with motors having stepping rates that depend on syringe diameter and flow rates required. Therefore, periodic pressure signals are obtained, and have been reported previously in the literature [1]. In this work, we highlight the importance of fluid delivery line design in generating stable, monodisperse gas-liquid segmented flows.

2. THEORY

Fluid lines operating in single-phase, pressure-driven laminar flow are directly analogous to linear electrical circuits, and this 'electrical-hydraulic' analogy has been well studied [2]. The expressions for hydraulic resistance (R_H), inductance (L_H) and capacitance (C_H) are given in Equation (1), where μ, ρ, l, r, and κ are the fluid viscosity, fluid density, length, internal radius, and bulk modulus of the fluid line respectively.

$$R_H = \frac{8\mu l}{\pi r^4}; \quad L_H = \frac{\rho l}{\pi r^2} \quad ; \quad C_H = \frac{\pi r^2 l}{\kappa} \tag{1}$$

In the case of flow driven by pressure signals with oscillating components, both the inductance L_H and capacitance C_H are reactive elements that act to oppose (and thereby reduce) the oscillations. The impedances of both these elements are frequency dependent. The resonant frequency of the fluid line is given in Equation (2) below. The hydraulic circuit is primarily inductive below this frequency and is capacitive above it.

$$f_R = \frac{1}{\sqrt{L_H C_H}} \tag{2}$$

3. EXPERIMENTAL

The microfluidic T-junction used in this study is schematically depicted in Figure 1(a), and consisted of PDMS microchannels sealed to a glass substrate. We used a wide diameter gastight syringe as the gas reservoir, and narrow diameter plastic syringes as the liquid reservoirs. Pressure signal frequencies were calculated from the motor-stepping rates

978-0-9798064-0-7/μTAS2007/$20©2007CBMS

provided by the syringe pump manufacturer (Harvard Scientific, USA), and ranged from 0.2-10 Hz in our experiments. Air-ethanol flows were used in all experiments.

4. RESULTS AND DISCUSSION

We demonstrate nearly monodisperse bubbling in Figure 1(b) for two different gas-to-liquid flow ratios. The gas line in these experiments consisted of 0.25-0.5 m of polytetrafluoroethylene (PTFE) tubing (250 μm ID) in series with 0.05 m of narrow diameter polyetheretherketone (PEEK) tubing (65 μm ID) that led into the gas inlet on the chip. Fluid delivery lines composed of flexible tubing in series with a short, rigid tube are a common feature in microfluidic experimentation. Bubble sizes at the T-junction start displaying periodic/quasi-periodic oscillatory behavior when the narrow diameter tube is replaced by a wider diameter PEEK tube of equal length (500 μm ID). Figure 1(c) shows stereomicroscope images of period-2 and period-3 behavior. The graph in Figure 1(d) shows how the amplitude increases and oscillation period decreases with increase in gas volumetric flow rate (Q_G), for a fixed liquid flow rate (Q_L).

An equivalent circuit model of the system, developed in Simulink® (Mathworks Inc., USA), is shown in Figure 1(e). The individual tubes in both fluid delivery lines are R-L-C circuits. The resonant frequency of each line (Equation (2)) is in the kHz range. Since the syringe pumps operate near 1 Hz, the circuit is primarily inductive in nature, and we neglect the capacitance in our model. The presence of narrow diameter tubing in the gas line provides a high L_H, which damps the pressure (and hence Q_G) fluctuations from the pump. High line L_H is an important requirement when pumping gases due to their low density, and therefore low inertia. The increase in oscillation amplitude with Q_G is due to the non-linear, flow-dependent two-phase L_H and R_H downstream of the T-junction. Both these quantities decrease drastically with increase in Q_G [3], leading to increasing oscillation amplitudes. In addition, the T-junction may be interpreted as a signal mixer, where a higher frequency 'carrier' signal from the liquid side is amplitude modulated by a lower frequency 'message' signal from the gas side. Figure 1(f) shows how simple combinations of low and high frequency signals (with frequency ratios similar to those used in our experiments) yield the experimentally observed periodic patterns for the period-2, -3 and -5 cases.

5. CONCLUSIONS

The design of fluid delivery lines is an important requirement in addition to that of the on-chip fluidic circuit(s). High fluidic inductance in the gas line is critical for stable gas-liquid flow networks. The considerations highlighted in our work are generally applicable to systems where flow is generated by periodic signals, and are of importance in designing multiphase fluidic networks with controlled bubbling for chemical synthesis and analysis applications.

REFERENCES

[1] T. Kraus, A. Günther, N. de Mas, M. Schmidt and K. F. Jensen, *Exp. Fluids*, 36, pp. 819-832 (2004)

[2] A. Akers, M. Gassman, and R. Smith, *Hydraulic Power Systems Analysis*, CRC Press (2006)

[3] S. A. Khan, *Microfluidic Synthesis of Colloidal Nanomaterials*, PhD Thesis, Massachusetts Institute of Technology (2006).

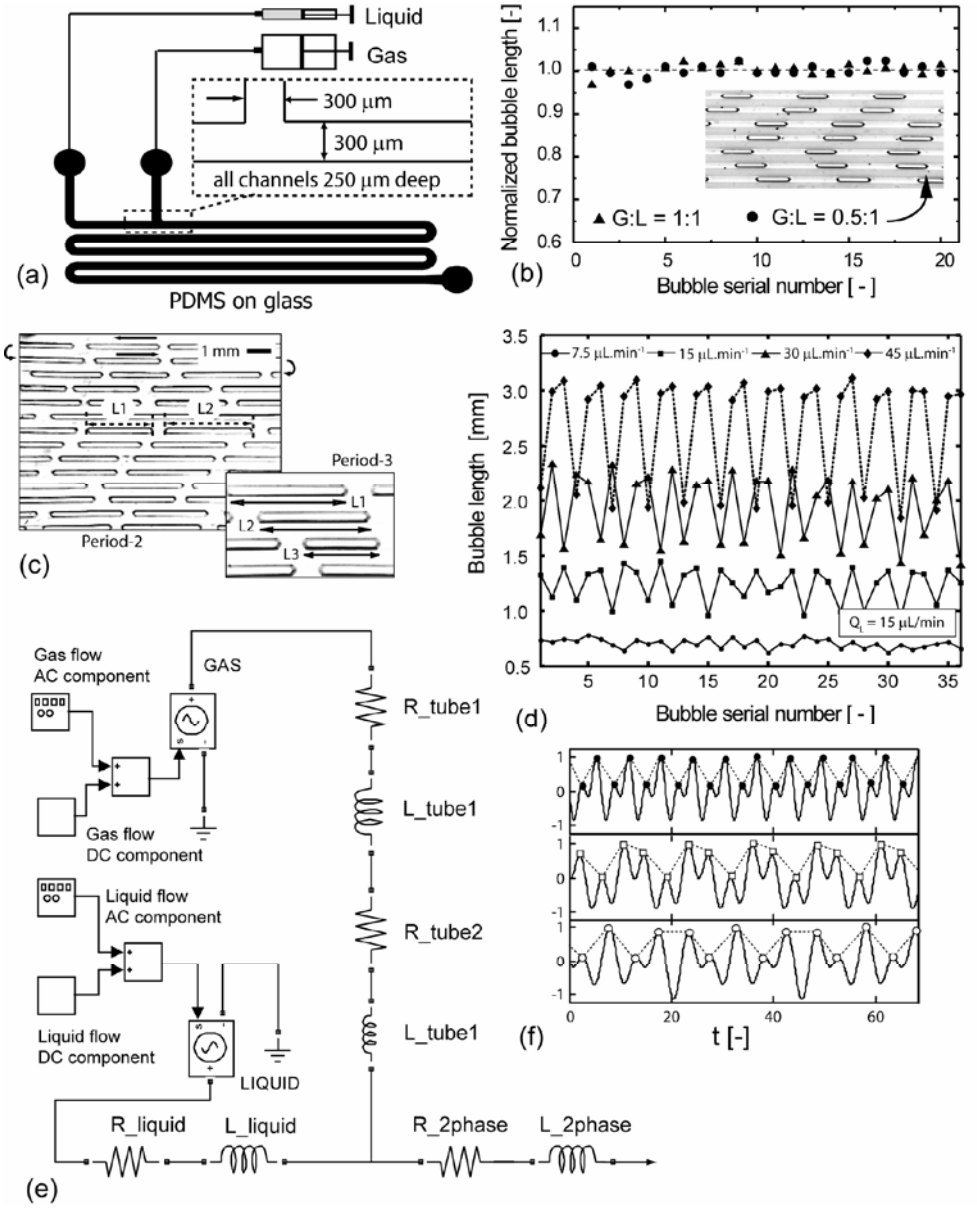

Figure 1: (a) Schematic and details of the experimental setup (b) Graph and photograph (inset) illustrating monodisperse bubbling (c) Stereomicroscope images of period-2 and -3 oscillations in bubble length. (d) The amplitude increases and oscillation period decreases with increasing gas flow rate Q_G, for a fixed liquid flow rate Q_L (e) Equivalent circuit model for the system based on the electro-hydraulic analogy (f) Examples of amplitude modulation that exhibit oscillation patterns similar to those observed experimentally.

TEMPERATURE DEPENDENT PHASE BEHAVIOR OF *N*-CYCLOHEXYL-2-PYRROLIDONE/WATER SYSTEM IN A MICROCHANNEL AND PHASE SEPARATION USING VISCOSITY DIFFERENCE

Yoshikuni Kikutani[1], Hidematsu Ikeda[1]#, Masayuki Harada[2], Yasuhisa Ikeda[2], Manabu Tokeshi[3] and Takehiko Kitamori[4]

[1]*Kanagawa Academy of Science and Technology, Japan,* [2]*Tokyo Institute of Technology, Japan,* [3]*Nagoya University, Japan,* [4]*The University of Tokyo, Japan*

 # Deceased October 20th, 2006

ABSTRACT

Aqueous solution of *N*-cyclohexyl-2-pyrrolidone (NCP), which is known as a selective precipitant for U(VI), changes into two solution phases (NCP-rich and -poor phases) upon heating. Aiming at development of a new actinoid separation method utilizing NCP solutions, we investigated characteristics of NCP solutions. We found that novel phase separation method using microfluidics could be applied to NCP/water system.

Keywords: annular flow, laminar flow, multiphase flow, phase separation, viscosity

1. INTRODUCTION

Separation of actinoids in spent nuclear fuel has been one of the most important subjects in chemical engineering. Uranium and plutonium should be reprocessed. Some rare and valuable isotopes should be collected. It is also necessary to eliminate long-lived radionuclides from radioactive wastes to reduce the amount of high-level radioactive liquid waste. Numerous researchers in the world are trying hard to find a better process.

We recently demonstrated that liquid-liquid extraction of U(VI) from 3M aqueous solution of HNO_3 to 100% tributyl phosphate (TBP), which has been difficult to do in a bulk scale, could be cariied out by using multiphase laminar flow in a microchannel [1]. We thought that when characteristics of micro- and nano-space could be well understood and sutably utilized, innovative actinoid separation methods unmatched by conventional ones would become possible, and we continued investigation of actinoid separation using a microchemical chip.

N-cyclohexyl-2-pyrrolidone (NCP) is a ligand that is expected to be useful in separation of U(VI) from spent nuclear fuel [2]. Unlike TBP which is immiscible with water, NCP is miscible with water at room temperature, and, interestingly, homogeneous NCP/water solution will be separated into NCP-rich and NCP-poor phases upon heating [3]. Novel extraction comprised of efficient complexation reaction step in a homogeneous phase and subsequent phase separation step with an increased temperature might be possible with NCP/water system.

Fig 1. shows the concept of the process integrated in a microchemical chip. Aqueous sample solution and NCP are mixed, and complexation reaction proceeds in a homogeneous phase. After complexation, the solution is heated and changed into NCP-rich and -poor phases. Then the two phases are physically separated and collected. In order to realize those microchemical processes, some novel microfluidic methods has to be developed. In the present work we have investigated microfluidics of NCP/water system.

978-0-9798064-0-7/μTAS2007/$20©2007CBMS

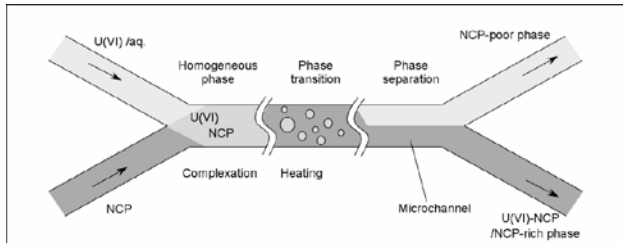

Figure 1. Concept of a novel actinoid separation method using NCP/water in a microchannel.

2. EXPERIMENTAL

NCP solutions were prepared using NCP (Fluka) and ultra pure water. Rhodamine 6G was added to the solutions for discrimination of NCP-rich and –poor phases. Pyrex glass microchips were fabricated using standard wet-etching and thermal bonding methods. A chip holder with transparent ITO-heater was used in monitoring phase change of NCP/water in a microchannel.

3. RESULTS AND DISCUSSION

Fig. 2 shows phase behavior of NCP/water in a microchannel at around 40 - 50 °C, which corresponds to the lower consolute point (LCP) of the solution. When the solution was cooled from temperature above LCP to below LCP, phase boundaries between NCP-rich and NCP-poor phases disappeared. However, distribution of NCP concentration still existed and when the temperature increased again to above LCP, phase boundaries appeared where it had been. Ingredients that diffused during the period when the phase boundary had disappeared were squeezed out from the matrix and formed many small droplets.

Fluorescent image of rhodamine 6G in NCP/water revealed that the phase with the stronger affinity to glass wall corresponded to the NCP-rich phase, in which most of the fluorescent dye dissolved (Fig. 3(a)).

Because both of the phases had similar affinity to channel wall, phase separation using difference of wettability of the two phases [4] was difficult. In order to develop a microextraction system using NCP/water in a microchannel, some other methods to physically separate NCP-rich and NCP-poor phases were desired. We found that chaotic mixture of the two phases could be tuned into an annular flow, where NCP-poor phase with lower viscosity flowed in the center of the channel, by utilizing difference in viscosity of the two phases (Fig. 3(b)).

With a three-pronged microchannel, the annular flow could be roughly separated (Fig. 4).

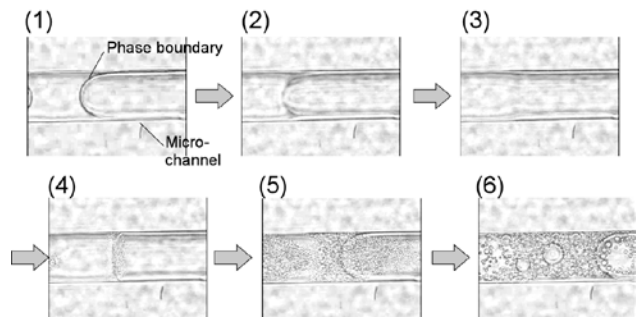

Figure 2: Phase behavior of 30% NCP/water observed in a microchannel (w: 100 μm, d: 40 μm).
Temperature was first decreased from 50 to 40 °C ((1)-(3)) then increased from 40 to 50 °C ((3)-(6))

With the flow control method using viscosity difference, it was also possible to form three-phase annular/laminar flow (NCP-rich, NCP-poor and dodecane phases).

Besides, by using an additional air flow, NCP-poor/NCP-rich two phase annular flow could be changed into side-by-side laminar flow in an asymmetric microchannel with shallow and deep lanes [4] (Fig. 5).

All these fluid control methods were based on the same principle that fluid with low viscosity tends to flow in the center of a microchannel and fluid with high viscosity tends to flow near the channel wall.

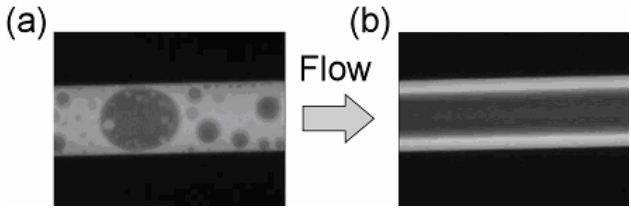

Figure 3: Fluorescent microscopic image of 30% NCP/water doped with 0.2 mM rhodamine 6G in a microchannel. (Temperature: 50 °C.) Bright part corresponds to NCP-rich phase where most of rhodamine 6G dissolved. (a) Under nearly static condition. (b) Under flow condition. (Flow rate: 0.1 μL/min.) NCP-poor phase with the lower viscosity flowed in the center part of the channel and NCP-rich phase with the higher viscosity flowed near the channel wall.

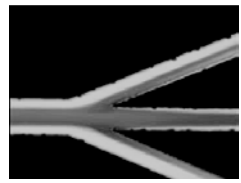

Fig.4: Division of the annular flow of the NCP-rich and NCP-poor phases by a three-pronged microchannel. (Temperature: 70 °C; Flow rate: 100 μL/min.)

5. CONCLUSIONS

New microfluidic methods utilizing viscosity difference has been developed for NCP/water system. NCP has selectivity towards U(IV) and could be used for development of an innovative actinoid separation methods.

ACKNOWLEDGEMENTS

We thank Dr. H. Hotokezaka in Tokyo Institute of Technology for helpful advices. Present study is the result of "Research on Innovative Actinoid Separation Method Using Micro- and Nano-Reaction Spaces" entrusted to Nagoya University by the Ministry of Education, Culture, Sports, Science and Technology of Japan (MEXT)

REFERENCES

[1] H. Hotokezaka et al., Prog. Nucl. Energy, 47, 439 (2005).

[2] N. Koshino et al., Prog. Nucl. Energy, 47, 406 (2005)

[3] A. Lou et al., J. Colloid Interface Sci., 256, 190 (2002).

[4] A. Hibara et al. Anal. Chem., 77, 943 (2005).

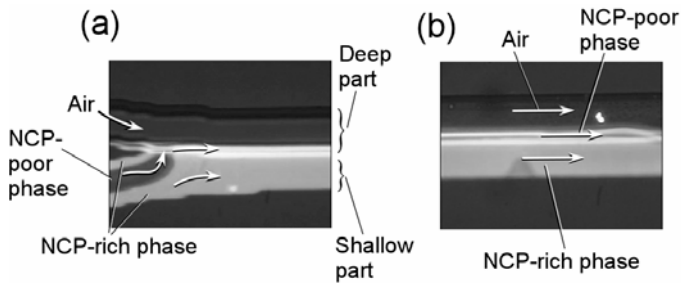

Fig.5: Formation of air/NCP-poor/NCP-rich three-phase flow from NCP-poor/NCP-rich annular flow and air flow.
(a) Microscopic view at the confluence point, and (b) downstream.
(Temperature: 70 °C,
Flow rate of 30 % NCP/aq.: 1 μL/min, air: 1 mL/min.)

A NOVEL $LiNbO_3$ SURFACE ACOUSTIC WAVE PUMP ONTO MICRO CHANNEL WALL

Takuya Sano, Masato Sato, Hiroki Kuwano, and Sumito Nagasawa

Department of Nanomechanics,Graduate School of Engineering, Tohoku University JAPAN

ABSTRACT

This paper describes a novel surface acoustic wave (SAW) micro fluidic pump fabricated on a micro channel wall made of $LiNbO_3$ to reduce fluid friction. The micro-fluidic pump and micro channel were designed, fabricated and integrated as a micro-fluidic system for liquid mixing and reaction. We successfully demonstrated controlled flow rate by varying the input voltage as well as controlled ejection of fluid.

Keywords: Micro Fluidics, Surface Acoustic Wave, MEMS, Pump

1. INTRODUCTION

Since SAW devices are suitable for miniaturization, they have been applied to signal processing devices and communication devices since 1960's. In literatures concerning to SAW applications to liquid, liquid streaming [1], and atomizer [2] were described. In our previous work [3], we proposed a novel surface acoustic wave pump fabricated on a micro channel of AT-cut quartz substrate. In this report, it is shown that a newly developed micro-fluidic device fabricated on a $LiNbO_3$ substrate can control flow rate more widely and continuously.

2. FABRICATION

Figure 1 shows the schematic view of the $LiNbO_3$ micro pump of this paper. It consists of glass and $LiNbO_3$ layers, which provide a micro-fluidic channel and SAW actuating substrate, respectively. Also, device fabrication was carried out in 2 separate processes, as shown in the simplified process chart of Figure 2.

In the $LiNbO_3$ SAW fabrication process, a 200 nm-thick aluminum layer was sputtered and patterned on the 127.86°Y $LiNbO_3$ substrate with the thickness of 350 μm. With the width of 50 μm and the pitch of 100 μm as shown in Figure 3, the Al layer serves as interdigital transducer (IDT) that had the resonant frequency of 19.9 MHz. The process for $LiNbO_3$ part is finished with the half-dicing line incision.

One side of the glass part was patterned and etched to form a fluidic channel and reservoir as shown in Figure 2. The inlet and feed-through holes were made on the other side. These holes were opened with sand blast technique, followed by the bonding between $LiNbO_3$ and glass or quartz with Polyimide. Glass material was chosen to observe fluid characteristics by optical microscope from out side.

Figure 3 shows the fabricated $LiNbO_3$ SAW pump. The Aluminum IDT onto $LiNbO_3$ substrate, the inlet hole, the polyimide bonding region, the feed through hole, and the contact pad can be observed through the glass channel. The channel height fabricated onto the glass substrate was 20 μm. The outlet had 100 μm in width. Figure 4 shows a fabricated micro fluidic system having 5 $LiNbO_3$ SAW pumps and micro channels for mixing and reacting with several liquids.

978-0-9798064-0-7/μTAS2007/$20©2007CBMS

For improving the accuracy of micro-fluidic channel size, we fabricated it with PDMS (Sylgard 184 silicone Elastomer, Dow Corning) instead of Glass. In order to produce the PDMS structure, SU-8 mold are made on silicon wafer using lithography techniques. The PDMS layer was cast from SU-8 master mold. Figure 5 shows the fabricated PDMS micro-fluidic channel. The channel width was 20 μm, height was 30 μm. Before bonding the $LiNbO_3$ substrate and PDMS layer, the surfaces of two layers are treated with oxygen plasma. It was proved that PDMS micro-fluidic channel had a high dimensional accuracy.

3. RESULTS AND DISCUSSION

Figure 6 shows the correlation between the input peak-to-peak voltage of the $LiNbO_3$ SAW pump having the resonant frequency of 19.9 MHz and the flow rate. The flow rate increased as the input voltage was increased from 30 V_{p-p} to 130 V_{p-p}. However, over 130 V_{p-p} the rate decreased. The maximum flow rate was 0.7 μl/min.

To confirm the transportation of a fluid with this device, we performed fluorescence observation of a fluid including fluorescent micro spheres (FluoSpheres, Invitrogen F8823). A diameter of the micro sphere was 1μm. Figure 7 shows that a fluid was ejected by the SAW pump having the resonant frequency of 3.95 MHz. The input peak-to-peak voltage of the $LiNbO_3$ SAW pump was 150V_{p-p}. It was proved that the SAW pump had an ability to eject a small amount of fluid.

4. CONCLUSION

We demonstrated successful operation of the SAW pump having the resonant frequency of 19.9 MHz fabricated on a micro channel wall of $LiNbO_3$ substrate at wide flow rate range up to 0.7 μl/min. The direct observation using a CCD camera showed that a fluid was ejected from the outlet of the micro channel by the $LiNbO_3$ SAW pump.

5. ACKNOWLEDGEMENT

This work was supported in part through the Creative Scientific Research Program (No. 18GS0203) by the Ministry of Education, Science, Culture and Sports (MEXT).

6. REFERENCES

[1] S.Shiokawa, Y.Matsui and T.Moriizumi, J.J.A.P. Vol.28(1989)28-1, pp.126-128

[2] M. Kurosawa, T. Watanabe, A. Futami and T. Higuchi, Sensors and Actuators A, 50, 69 (1995)

[3] Joonhyung Bae, Masato Sato, and Hiroki Kuwano, Digest of Transducers '05, pp.1545-1548 (2005), Soul.

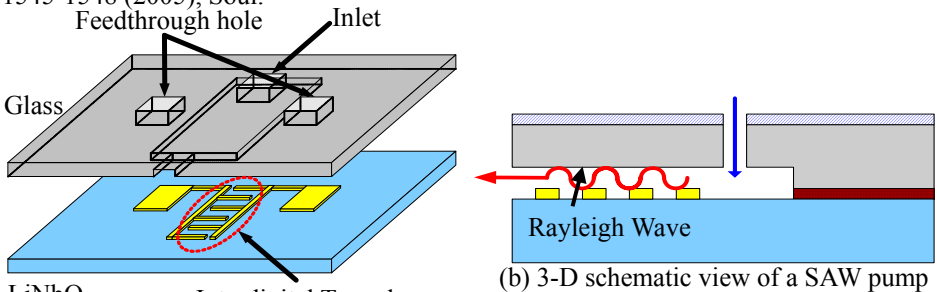

(a) 3-D schematic view of the SAW pump

(b) 3-D schematic view of a SAW pump

Figure 1. Section view of the micro pump.

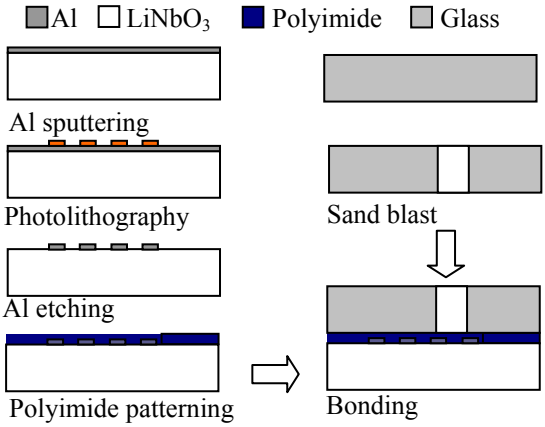

Figure 2. Fabrication process of $LiNbO_3$ SAW pump.

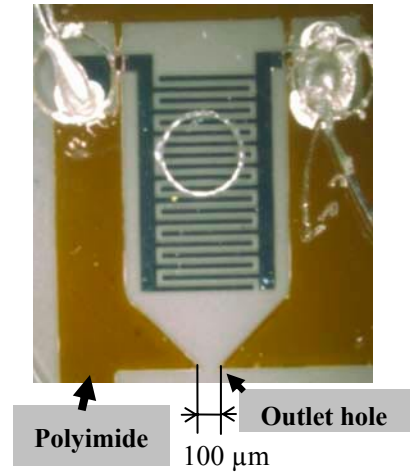

Figure 3. Photograph of the $LiNbO_3$ SAW pump onto a micro channel wall.

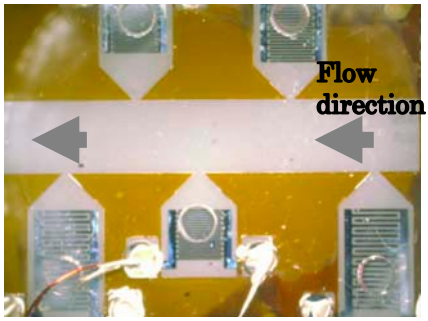

Figure 4. Photograph of a micro fluid system having of 5 SAW pumps and micro channels.

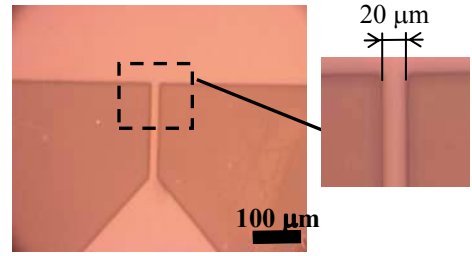

Figure 5. Fabricated PDMS micro-fluidic channel and outlet.

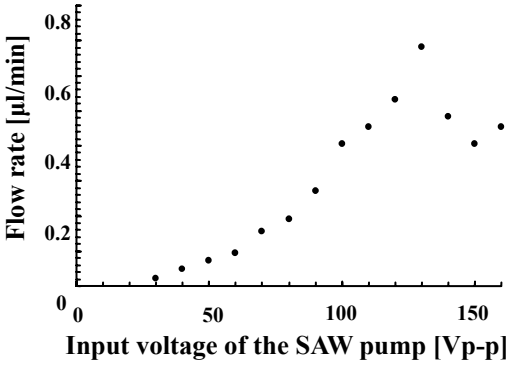

Figure 6. Relationship between the flow rate of $LiNbO_3$ SAW pump and the input voltage.

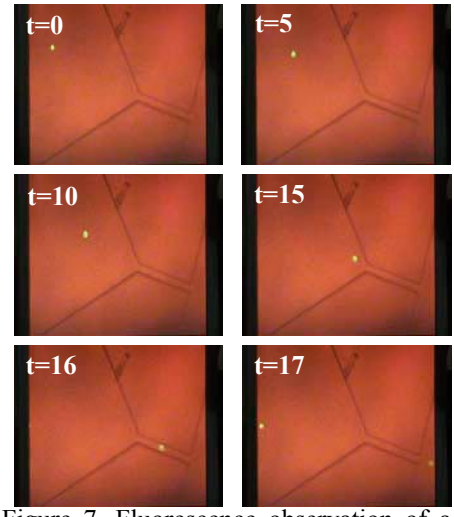

Figure 7. Fluorescence observation of a fluid including fluorescent micro spheres.

FABRICATION OF ALGINATE FIBER USING MICROFLUIDIC DEVICE AND CELL ENCAPSULATION

Su Jung Shin, Kwang Ho Lee, Jin Young Lee and Sang Hoon Lee

Department of Biomedical Engineering, College of Medicine, Korea University

ABSTRACT

In this paper, we demonstrate a new continuous production technique of calcium alginate fibers with the microfluidic platform similar to spider. We have used the poly(dimethylsiloxane) (PDMS) microfluidic device embedded capillary glass pipette as apparatus for fiber generation. As a sample flow, we employed a 2%(w/w) sodium alginate solution and as a sheath flow, a 784mM $CaCl_2$ solution was employed. We evaluated the potential use of alginate fibers as cell carrier by loading human fibroblasts during the 'on the fly' fabrication process. In addition, we evaluate the capability of loading the therapeutic materials onto the alginate fibers by immobilized BSA-FITC in the fibers.

Keywords : Alginate fiber, Microfluidic, Encapsulation, Tissue engineering.

1. INTRODUCTION

One of the emerging microfluidic applications introduced was the 'on the fly' fabrication method of polymeric microstructures (e.g.: fiber, sphere and etc.) has focus due to the diverse applications in the biomedical fields. Such structures can be produced simply and cost effectively by using the microfluidic device. However, it was still difficult to produce biocompatible and biodegradable microstructures. Here, we report the production of calcium alginate fibers by using the microfluidic device. We expect that the produced alginate fibers can be used as a vehicle for cells or therapeutic molecules for the regeneration of damaged tissues or used as 3D-line scaffold to fabricate nerve or muscle fibers.

2. EXPERIMENTAL

Figure 1 illustrates the schematics of the microfiber generation apparatus. The microfluidic device used for fiber production was fabricated by combining the PDMS platform and the pulled borosilicate glass pipette.

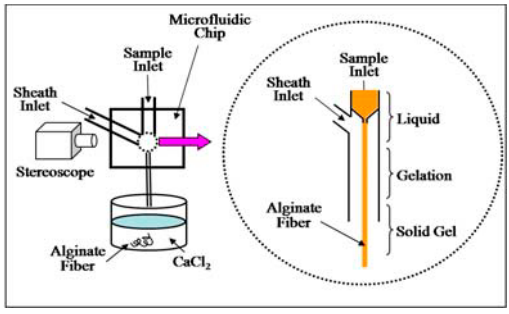

Figure 1. Schematic of microfiber generation apparatus and principle of gelation (dotted circle)

Two fluids, 2% (w/w) sodium alginate solution and 784mM $CaCl_2$ solution, were introduced into the sample and the sheath inlet ports respectively and two syringe pumps

978-0-9798064-0-7/μTAS2007/$20©2007CBMS

were employed for the injection. At the interface of both fluids, the sodium alginate solutions met with the polycation (Ca^{2+}) material and gelation of the cylindrical fibers was achieved by diffusion-controlled ionic cross-linking. All the experiments were carried out under the stereoscope. For the encapsulation of cells, we employed alginate solution including cells and 100mM $CaCl_2$ solution, into the sample and sheath inlets respectively, we created calcium alginate fibers with human fibroblast cells. To demonstrate the capability of loading the therapeutic materials onto the alginate fibers, we immobilized a fluorescently labeled bovine serum albumin (BSA-FITC) in the fibers.

3. RESULTS AND DISCUSSION

Alginate fibers were successfully generated as shown in Figure 2(a) and 2(b-d) shows the colored alginate flow (Rhodamine B) in the outlet pipette. We have measured the diameter of calcium alginate fibers according to the flow rate change of the sample and sheath flow and the results are plotted in Figure 3. As the flow rate increased, spiral curls were formed and their waves increased in density and this curl formation is due to the solidification process of alginate fiber inside the outlet pipette.

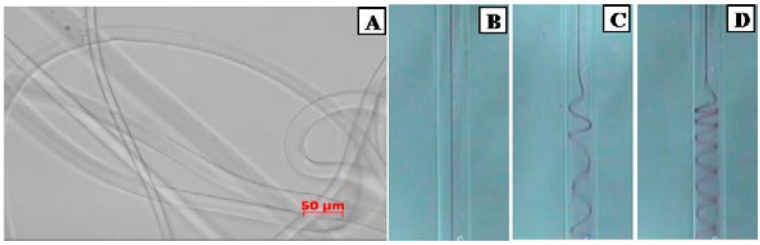

Figure 2. (a) Calcium alginate fibers generated by using microfluidic system, b-d) Formation of spiral curl of alginate solution in the outlet pipette according to the flow changes; (b) Sample flow rate: 1μl/min, (c) Sample flow rate: 3μl/min, (d) Sample flow rate: 5μl/min, Sheath flow was fixed at 20ml/hour

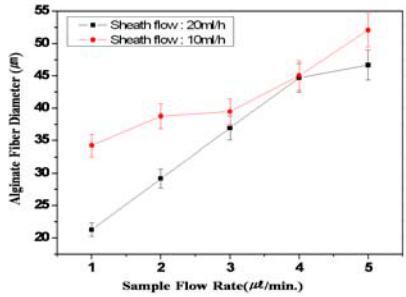

Figure 3. Diameter change of alginate fibers according to the sample and sheath flow rate

We encapsulated human fibroblast cells in the calcium alginate fibers and investigated their morphology and viability. Figure 4(a) illustrates a micrograph of human fibroblast cells (L929)-loaded onto alginate microfibers taken just 1 hour after encapsulation. Figure 4(b) shows the corresponding fluorescent micrograph of the cell tracker and indicates that cells were stabley loaded during the fiber fabrication process. The viability was tested and

the results are illustrated in Figure 5 and over 80% of cells were survied well after one day's culture (Figure 5).

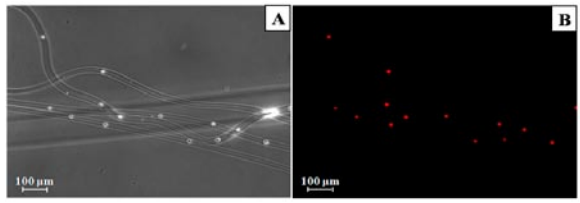

Figure 4. (a) Human fibroblast cell laden calcium alginate fiber, (b) Corresponding fluorescent image of cells which were stained with cell

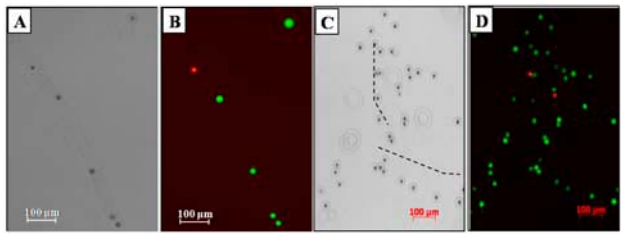

Figure 5. (a) Micrograph of alginate fiber containing fibroblast cells, (b),(d) Corresponding fluorescent image of cells which were stained with Live/Dead assay reagent, (c) Micrograph of cells which were cultured for 24 hours in the fiber (calcium alginate was completely dissolved by the Live/Dead assay reagent)

We have fabricated calcium alginate microfibers containing BSA-FITC to investigate the loading capability of proteins and BSA-FITC was loaded stably and uniformly in the fibers by the 'on the fly' fabrication process.

4. CONCLUSIONS

we have demonstrated that calcium alginate fibers can be produced continuously using microfluidic devices. The produced fibers can be used as a vehicle for cells or therapeutic molecules for the regeneration of damaged tissues or used as 3D-line scaffold to fabricate nerve or muscle fibers. In addition, the alginate fibers, including cells or proteins, can be produced safely and in large quantities by using the microfluidic chip.

ACKNOWLEDGEMENTS

This study was supported by a grant of the Korea Health 21 R&D Project, Ministry of Health and Welfare, Republic of Korea. (0405-ER01-0304-0001)

REFERENCES

[1] "Continuous fabrication of biocatalyst immobilized microparticles using photopolymerization and immiscible liquids in microfluidic systems", W. J. Jeong, J. Y. Kim, J. Choo, E. K. Lee, C. S. Han, D. J. Beebe, G. H. Seong and S. H. Lee, Langmuir, 21, 3738 (2005).

GAS PARTIAL PRESSURES CONTROLLED BETWEEN MICROCHANNELS

Samuel P. Forry[1], Jason G. Kralj[1] and Laurie E. Locascio[1]
[1]National Institute of Standards and Technology, USA

ABSTRACT

The partial pressure of dissolved gas in solution-filled microchannels was controlled by diffusion through the device material from adjacent gas-filled control channels. Equilibrium was rapidly reached, and stable gradients in gas partial pressure were readily generated. Using CO_2, external modulation of pH within stagnant solution-filled channels was demonstrated.

Keywords: gas partial pressure, microfluidic control

1. INTRODUCTION

Poly(dimethylsiloxane) (PDMS) has become a common material for fabricating microfluidic devices [1]. It exhibits, in addition to other interesting properties, high gas permeability [2], which has been demonstrated for water vapor (pervaporation) [3]. Sealed PDMS microdevices placed in controlled-gas environments (e.g. cell culture incubators) allow internal solutions to equilibrate. Gas partial pressures are important for many different solution phase phenomenon (e.g. cell biology, chemical synthesis, and fluorescence quenching). In this work, we utilize the gas permeability of PDMS to facilitate in-plane gas diffusion between microchannels. By rapidly changing the composition of gas-filled channels, the partial pressure of gases dissolved in neighboring solution-filled channels was modulated. Similar strategies have been demonstrated for liquids using porous membranes and other materials [4], but this represents the first use of gas diffusion across a homogeneous device to modulate the gas partial pressure in neighboring channels.

2. EXPERIMENTAL [5]

CO_2 was utilized here as a model gas, though other gases should be amenable to this approach. The CO_2 partial pressure was switched rapidly (in seconds) between 0.035% (ambient) and 5% (cell growth environment). When CO_2 dissolves in aqueous buffers (here, 0.01 mol/L phosphate), it equilibrates with H_2CO_3, allowing indicators of pH to be used to quantify CO_2 partial pressures for known solutions. The indicator carboxynaphthofluorescein (CNF) was used for this investigation, and the ratiometric fluorescence emission intensity was converted to pH as reported previously [6].

3. RESULTS AND DISCUSSION

A simple design was explored with a single gas-filled control line and a several adjacent solution-filled channels (Figure 1). The composition of the gas-filled channel was changed rapidly (seconds) from a partial pressure of 0.035% CO_2 (ambient) to 5% CO_2 by means of a valve located off-chip. The gas partial pressure within the solution-filled channels (phosphate buffer, pH=8.3) quickly equilibrated (minutes) to 5% CO_2 (pH =7.0) at rates that were governed by the mean distance from the control channel (i.e. the distance CO_2 must diffuse).

978-0-9798064-0-7/μTAS2007/$20©2007CBMS

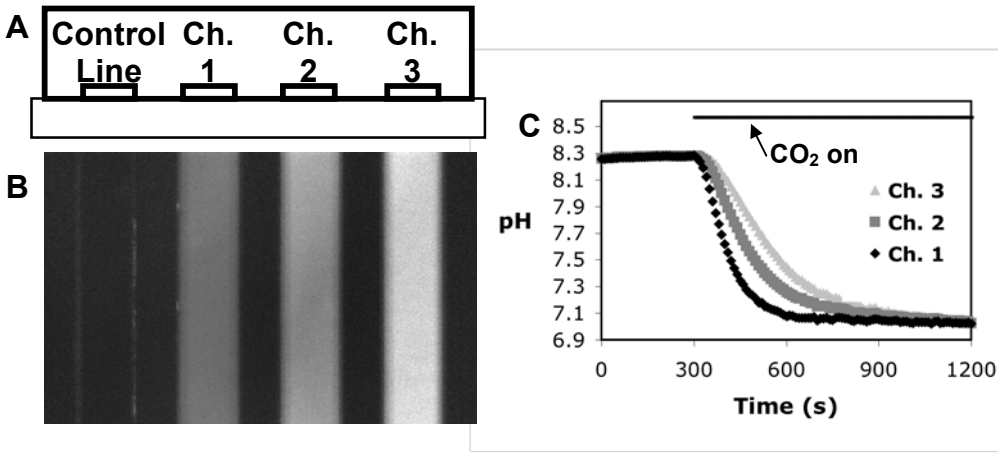

Figure 1. *Gas partial pressure in solution-filled channels is modulated using one in-plane gas-filled control line. (A) The device schematic (not drawn to scale) depicts the gas-filled control line and three adjacent solution-filled channels. (B) The ratiometric fluorescence from CNF at t=450 s shows a substantial difference in CO_2 partial pressure between channels due to differing rates of equilibration. (C) The pH in each channel drops rapidly upon introduction of CO_2 in the control line (at t=300 s) and rapidly equilibrates. The rate of equilibration is governed by the physical separation for each channel (0.4 mm, 0.8 mm and 1.2 mm, for channels 1-3, respectively), In all cases, the separation between all channels was much smaller than the PDMS thickness, minimizing effects from the external environment.*

In a configuration incorporating multiple gas-filled control lines (Figure 2), a stable gradient in CO_2 partial pressure was rapidly generated (minutes) between source and sink control lines (5% CO_2 and 0.035% CO_2, respectively). In this configuration, solution-filled microchannels rapidly reached distinct equilibrium partial pressures as governed by their spatial location relative to the CO_2 gradient. When either the control channel was closed, this gradient rapidly collapsed to either 5% or 0.035 % CO_2.

4. CONCLUSIONS

This research demonstrates the ability to use in-plane gas-filled control channels to modulate the gas partial pressures in solution-filled microchannels across a microfluidic device. Equilibrium within the solution-filled channels was rapidly reached (in minutes), and gradients were readily developed such that gas partial pressures (and for CO2, solution pH) vary spatially between neighboring microchannels. This approach is expected to be useful in enabling incubator-free microfluidic cell culture using conventional culture media.

Shown here only for CO_2, this technique should be applicable for other important gases (i.e. O_2, N_2 and NO).

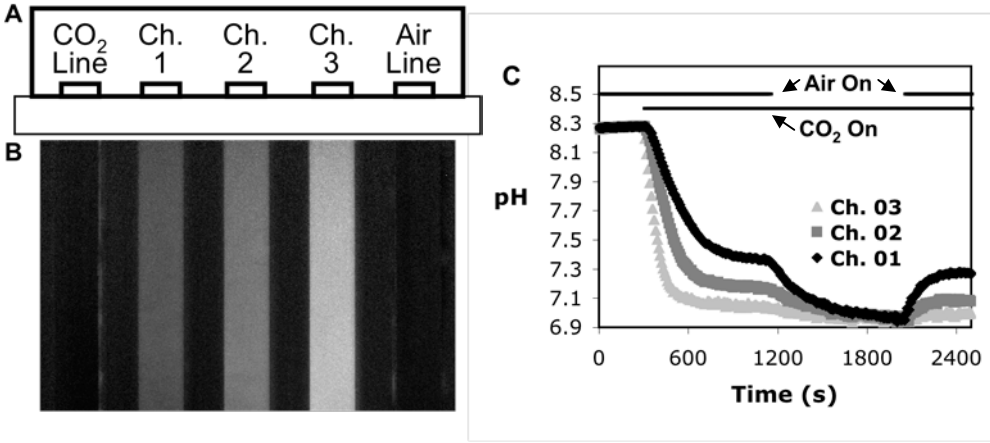

Figure 2. *A stable gradient in CO_2 partial pressure is generated using two control lines. (A) The device schematic (not to scale) indicates the position of three solution-filled channels between the CO_2-filled and air-filled control lines. (B) The ratiometric fluorescence from CNF at t=1000s reveals the generation of a stable gradient in CO_2 partial pressure between the gas-filled control lines. (C) The equilibrium pH of each channel reflects the physical location of that channel within the CO_2 partial pressure gradient. The gradient was generated when both control lines were open (from t=300 s to t=1140 and after t=2050 s). When only one control line was open, the equilibrium CO_2 partial pressure was identical across all channels (before t=300s and t=1140 to t=2050 s).*

REFERENCES

[1] "Fabrication of microfluidic systems in poly(dimethylsiloxane)," J. C. McDonald, et al. Electrophoresis, **21**, 27 (2000).

[2] "Gas sorption and diffusion processes in polymer matrices at high pressures," M. A. Krykin, V. I. Bondar , Y. M. Kukharsky , A. V. Tarasov, Journal of Polymer Science, **35**, 1339 (1998).

[3] "Permeation-induced flows: Consequences for silicone-based microfluidics," E. Verneuil, A. Buguin, P. Silberzan, Europhysics Letters., **68**, 412 (2004).

[4] "Characterization of a membrane-based gradient generator for use in cell-signaling studies," V. V. Abhyankar, M. A. Lokuta, A. Huttenlocher, D. J. Beebe, Lab on a Chip, **6**, 389 (2006).

[5] Certain commercial equipment or materials are identified in this report to specify adequately the experimental procedure. Such identification does not imply recommendation or endorsement by the National Institute of Standards and Technology, nor does it imply that the materials or equipment identified are necessarily the best available for the purpose.

[6] "High-Performance Fiber-Optic pH Microsensors for Practical Physiological Measurements Using a Dual-Emission Sensitive Dye," A. Song, S. Parus, R. Kopelman, Analytical Chemistry, **69**, 863 (1997).

AQUACORE: A GENERAL-PURPOSE ARCHITECTURE FOR PROGRAMMABLE MICROFLUIDICS

Ahmed M. Amin[1], Mithuna Thottethodi[1], T. N. Vijaykumar[1], Steven Wereley[2] and Stephen C. Jacobson[3]

[1]School of Electrical & Computer Engineering, Purdue University, [2]School of Mechanical Engineering, Purdue University , [3]Department of Chemistry, Indiana University

ABSTRACT

Interest in μTAS/LoC systems has grown considerably in recent years. However, the application-specific nature of current μTAS/LoC systems requires a new microfluidic chip to be designed for each type of assay, which incurs significant design effort, turn-around time, and cost, thereby reducing the productivity of μTAS users and slowing widespread use of these devices. To that end, we propose a general-purpose, programmable LoC (PLoC), called AquaCore and demonstrate its use for two simple assays.

Keywords: General-purpose LoC, programmable microfluidics, fluidic instruction set

1. INTRODUCTION

The AquaCore architecture provides a general-purpose design capable of executing a large class of assays, where the actual assay steps are described in a sequence of steps, called "fluidic instructions". In Table 1, we provide a fluidic instruction set, called AquaCore Instruction Set (AIS), which is analogous to an assembly language used for programming computers. Compiler tool-chains can be developed to translate assays specified in easy-to-understand, high-level languages to AIS. Figure 1 illustrates the AquaCore architecture that implements AIS. The "wet" part of AquaCore consists of reservoirs, various fluidic functional units (FFUs) such as mixers and heaters, and a valve-and-channel fabric that can move fluid from any reservoir/FFU to any other FFU/reservoir by actuating the appropriate valves and pumps. The AIS instructions are interpreted by a "dry" microelectronic controller, which actuates the valves, pumps, and FFU controls (e.g., mixer operation and incubator temperatures) to achieve instruction execution.

In contrast to AquaCore's generality, previous work has explored programmability in a limited sense. Recently however, Urbanski et al. [1] replace these limited approaches with the pioneering idea of making LoCs fully programmable. In later work [2] they focus on a new programming language for microfluidics called BioStream, while we focus on the instruction set and architecture.

2. RESULTS AND DISCUSSION

Figure 2(a) and Figure 3(a) show two simple assays: DNA extraction [3] and RT-PCR [4], and Figure 2(b) and Figure 3(b) show their corresponding programs written in AIS. While computers are universal (i.e., they can perform any computation) due to Turing-Completeness of instruction sets and their implementations, fluidics lack such theoretical guarantees. Therefore, we must turn to empirical analysis of the AIS's coverage of real assays from different domains. We show in [5] that our architecture covers assays from genomics, biochemistry, chemical synthesis and immunoassays.

3. CONCLUSIONS

By providing a general-purpose programmable architecture and AIS, we enable μTAS developers to write their custom assays to run on this chip. We believe that the transition from LoCs to PLoCs is a paradigm shift in microfluidics, analogous to that in electronics

978-0-9798064-0-7/μTAS2007/$20©2007CBMS

from calculators to programmable computers. This shift should enable the ubiquitous use of PLoCs and should allow μTAS users to focus on assay design rather than device design, thus boosting productivity.

Table 1. AquaCore Instruction Set (AIS)

Instruction	Description
move *id2, id1, <vol>*	Move the contents of *id1* to *id2*. *id1* & *id2* can be a reservoir, FFU or input/ output port. *vol* is an optional parameter to specify the relative volume to be moved. If no volume is specified, a default is used.
move-abs *id2*, *id1*, *vol*	Similar to move except *vol* is not optional and it specifies absolute volume in nl.
mix *id*, *time*	Mix the contents present in mixer *id* for a duration of *time* seconds.
separate.SIZE *id*, *time*	Separate the contents of the size-based separator *id* into two parts based on their size by passing the contents through an inbuilt filter for a duration of *time* seconds. The two output parts are stored internally in separate pools with unique ids that can be moved later.
separate.CE *id*, *Esep*, *len*, *time*	Using capillary electrophoresis (CE), separate the contents of the separator *id* by waiting for a duration of *time* seconds. The contents pass through a CE column of length *len* under an electric field of *Esep*. If *len* is more than the hardware length, the fluid is automatically cycled for multiple iterations. Separation buffer is moved to the column's buffer port which has a unique id. For gel-based separation, the gel is preloaded into the column's gel port.
separate.AF *id*, *time*	Perform affinity-based separation in separator *id* for a duration of *time* seconds. The two outputs are held in separate pools with unique ids that can be moved out later. The FFU has a special internal pool (with a unique id) to hold the affinity-matrix which is moved there.
incubate *id*, *temp*, *time*	Heat the contents in the heater *id* to a temperature *temp*, incubate the contents at that temperature for a duration of *time* seconds.
input *id2*, *id1* **output** *id2*, *id1*	Input the fluid from the input-port *id1* into the reservoir *id2* Output the fluid stored in the reservoir *id1* to the output port *id2*
coated-plate-setup *id*	Prepare the reaction plate *id* that needs to be coated with specific chemicals/biomolecules. The coating is done by pressure-evaporating the coating compound onto the plate. The compound is dispensed from an input port dedicated to the plate.
sense.OD *id, senseval*	Sense the optical density of the fluid in the optical sensor *id* and copy the sensed value to the dry variable *senseval*. Instruction completion is detected by feedback from the sensor which is typically off-chip.
sense.FL *id, senseval[]*	Continuously sense the fluorescence of the contents of the FFU associated with the fluorescence sensor *id* and periodically copy the sensed value to the dry variable array *senseval*[].
concentrate.EV *id, temp, time*	Concentrate the mixture in heater *id* by evaporating the carrier fluid by holding the mixture at temperature *temp* for duration *time*. Other methods for concentrating (e.g., electrophoresis, dielectrophoresis, precipitation) may be adopted by extending AIS to add other variants of the concentrate instruction.
sort.CELL *id,rate*	Sort cells in sorter *id* using fluorescence activated cell sorting at *rate* in kHz.
dispose *id*	Dispose of the contents of *id* which can be a reservoir or FFU.

REFERENCES

[1] J.P.Urbanski, W.Thies, C.Rhodes, S.Amarasinghe, T.Thorsen, *Lab on a Chip*, **6**(1):96–104, 2006.
[2] W.Thies, J.P.Urbanski, T.Thorsen, S.Amarasinghe, *DNA*, **12** (2006).
[3] J.W.Hong, V.Studer, G.Hang, W.F.Anderson, S.R.Quake, *Nature Biotech.*, **22**(4):435-439, 2004.
[4] L.Warren, D.Bryder, I.L.Weissman, S.R.Quake, PNAS, **103**(47):17807-17812, 2006.
[5] A.M.Amin, M.Thottethodi, T.N.Vijaykumar, S.Wereley, S.C.Jacobson, ISCA 34:254-265, 2007.

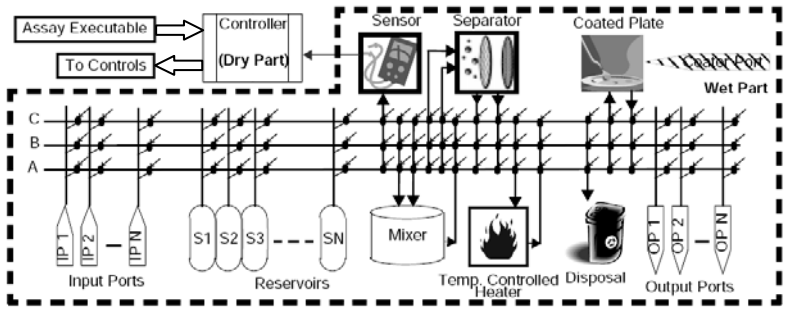

Figure 1. AquaCore Microarchitecture

(a)

1. Load beads into affinity column
2. Load wash and elute buffers
3. Load cell suspension, dilution buffer and lysis buffer
4. Cell lysis: mix the dilution buffer, cell suspension and lysis buffer
5. Move lysate through affinity column
6. Recover purified DNA

(b)

```
DNA-extraction {
input s1, ip1          ; beads
input s2, ip2          ; wash buffer
input s3, ip3          ; elute buffer
input s4, ip4          ; cell suspension
input s5, ip5          ; dilution buffer
input s6, ip6          ; lysis buffer

move separator1.buf, s1
move separator1.wash1, s2
move separator1.wash2, s3

move mixer1, s4
move mixer1, s5
move mixer1, s6
mix mixer1, 240

move separator1, mixer1
separate.AF separator1, 30
dispose separator1.flow-through
output op1, separator1.buf
}
```

Figure 2. DNA extraction
(a) Assay (b) AIS program

(a)

1. Load cells, buffer and sort cells
2. Perform reverse transcription
   a. mix cells and RT buffer
   b. heat to 55ºC for 15 min
   c. heat to 70ºC for 5 min
3. Perform PCR
   a. heat to 95ºC for 3 min (warm up)
   b. repeat for 40 cycles:
      i. heat to 95ºC for 15 s (denature)
      ii. heat to 60ºC for 60 s (annealing)

(b)

```
RT-PCR {
input s1, ip1    ;cell suspension
input s2, ip2    ;RT-PCR buffer
input s3, ip3    ;reverse transcriptase
input s4, ip4    ;DNA polymerase
input s5, ip5    ;gene specific primers & probes

move sorter1.buf, s2
move sorter1, s1
sort.CELL sorter1, 1
move mixer1, s3
move mixer1, s4
move mixer1, s5
move mixer1, sorter1
mix mixer1, 30
move heater1, mixer1
incubate heater1, 55, 900
incubate heater1, 70, 300
incubate heater1, 95, 180
dry-mov r1, 40          ;non-fluidic computer
dry-label loop:         ;instructions
  incubate heater1, 95, 15
  incubate heater1, 60, 60
dry-dec r1              ;non-fluidic computer
dry-bgt loop            ;instructions
}
```

Figure 3. RT-PCR
(a) Assay (b) AIS program

RETENTION, PLATE HEIGHT AND RESOLUTION FOR CHARGED SPECIES TRANSPORT AND SEPARATION IN NANO-SCALE CHANNELS

Stewart K. Griffiths and Robert H. Nilson
Sandia National Laboratories, California, USA

ABSTRACT

Numerical methods are employed to examine the transport and separation of charged species in flow along nano-scale channels having an electric double-layer thickness comparable to the channel size. In such channels, the electric field native to the double-layer produces a transverse species distribution that depends on the species charge. Transverse non-uniformity of flow along the channel thus yields mean axial species speeds that also depend on the charge, enabling species separation. Retention, plate height, and resolution are presented for various conditions relevant to such separations.

Keywords: separation, field-flow, fractionation, charge

1. INTRODUCTION

Field-flow fractionation is a well-established family of methods for separating and identifying particles, macromolecules and molecular analytes [1]. Most such methods employ pressure-driven flow along a channel in conjunction with an applied field that is perpendicular to the direction of fluid motion, resulting in a quasi-steady variation of species concentrations across the channel. The fluid speed in pressure-driven flow likewise varies in the transverse direction, so each species travels along the channel at a mean speed that depends on its transverse species distribution, thus enabling fractionation of a mixture into discrete bands. Here we consider a new variant of electric field-flow fractionation in which the transverse field is provided by the electric field naturally present in the double-layer of a nano-scale tube or channel.

A few preliminary studies have examined mean species speeds in nano-scale channels for electroosmotic [2-5] and pressure-driven flows [5,6]. In this study, we more generally characterize such transport and separation via the classical measures of retention, plate height and resolution. Both pressure-driven and electroosmotic flows are considered.

2. MATHEMATICAL MODEL

The electric potential, ϕ, within a nano-scale channel is governed by

$$\frac{\lambda^{*2}}{y^{*n}}\frac{d}{dy^*}\left(y^{*n}\frac{d\phi^*}{dy^*}\right)=\frac{1}{\zeta^*}\sinh(\zeta^*\phi^*) \qquad \lambda^{*2}=\left(\frac{\lambda}{a}\right)^2=\frac{\varepsilon RT}{2z^2F^2a^2c_0} \tag{1}$$

where $\zeta^*=zF\zeta/RT$, $\phi^*=\phi/\zeta$, $y^*=y/a$, ζ is the zeta potential, a is the tube radius or channel half-height, z is electrolyte ion charge, c_0 is the bulk fluid ion concentration, and $n=0$ or 1 denotes a planar slit-like channel or a cylindrical tube. The species concentrations and average concentration are now given by

$$c_i^*=c_{oi}^*\ e^{-\zeta^*\phi^*z_i^*} \quad \text{such that } c_{oi}^* \text{ yields} \quad \bar{c}_i^*=(n+1)\int_0^1 c_i^*\,y^{*n}dy^*=1 \tag{2}$$

978-0-9798064-0-7/μTAS2007/$20©2007CBMS

and the normalized local and mean species speed are

$$u_i^* = \frac{u_i}{U} = u^* - \frac{\nu_i^* z_i^*}{\gamma \zeta^*} \quad \text{and} \quad \bar{u}_i^* = \frac{\bar{u}_i}{U} = (n+1)\int_0^1 c_i^*\, u_i^*\, y^{*n} dy^* \tag{3}$$

where $U = -\varepsilon\zeta E/\mu$, E is the applied axial electric field, $u^* = 1 - \phi^* - \psi(1-y^{*2})/2(n+1)$ where $\psi = 0$ or $-\infty$ indicates electroosmotic or pressure-drive flow, $\nu_i^* = \nu_i/\nu$ and $z_i^* = z_i/z$ are the ratios of the species mobility and charge to those of the electrolyte ions, and γ is the so-called Levine number [5]. The reduced plate height is then

$$h_i = \frac{H_i}{a} = \frac{\sigma_i^2}{aL} = \frac{2D_i' t_i}{aL} = \frac{2D_i'}{a\,\bar{u}_i} \quad \text{where} \quad D_i' = D_i(1+\alpha_i \mathrm{Pe}_i^2) \tag{4}$$

where α_i is the dispersion coefficient [5], and the normalized resolution can be written as

$$R_{s,i}^* = z\sqrt{\frac{a}{L}} R_{s,i} = \frac{\Delta \bar{u}_i}{4\bar{u}_i} \frac{z}{\sqrt{h_i}} = \frac{1}{4\sqrt{h_i}} \frac{dR_i}{R_i dz_i^*} \tag{5}$$

where L is the channel length, $R_{s,i} = \Delta\bar{u}_i\sqrt{L}/4\bar{u}_i\sqrt{H_i}$ is the resolution and $R_i = \bar{u}_i/\bar{u} = \bar{u}_i^*/\bar{u}^*$ is the retention. These governing equations are solved using a shooting technique to satisfy the boundary conditions $d\phi^*/dy^* = 0$ at $y^* = 0$ and $\phi^* = 1$ at $y^* = 1$.

3. DISCUSSION OF RESULTS

For pressure-driven flows, the mean speeds of charged species exceed the mean fluid speed when the product $z_i^*\zeta^* = z_i\zeta F/RT$ is positive and fall below that of the fluid when this product is negative. This is illustrated in Fig. 1. Further, when all other parameters are fixed, the ratio of the mean species speed to that of the fluid (retention) for pressure-driven flow depends only on the species charge and varies monotonically with this charge, as shown in Fig. 2. Pressure-driven flow thus enables separation based on charge alone.

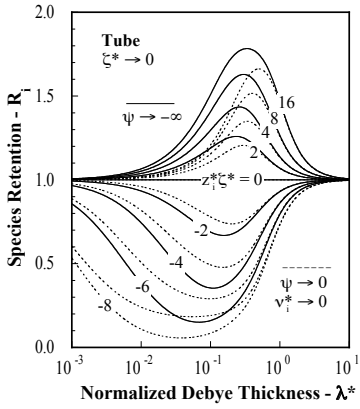

Figure 1. Species retention for pressure-driven (solid) and electroosmotic (dashed) flow. Both flows yield similar retentions when species electrophoretic mobilities are very small, $\nu_i^* \approx 0$.

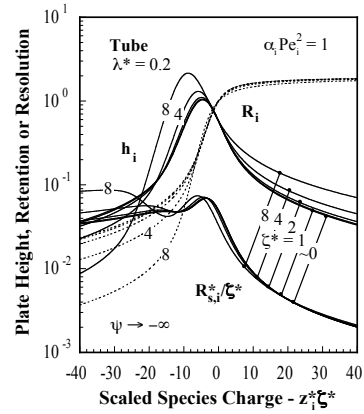

Figure 2. Retention (dashed), reduced plate height and scaled resolution for pressure-driven flow in a tube at optimum conditions given by $\alpha_i \mathrm{Pe}_i^2 = 1$ where $\mathrm{Pe}_i = u_i a/D_i$ is the species Peclet number.

Electroosmotic flows show similar behavior when electrophoretic mobilities are negligible, $\nu_i^* \sim 0$, as in Fig. 1. Generally, however, electroosmotic flows exhibit retentions that decrease with increasing species charge when the charge is large and negative, $z_i^* \zeta^* << 0$, increase with charge for near-neutral species, $z_i^* \zeta^* \approx 0$, and then again decrease as the charge grows large and positive, $z_i^* \zeta^* >> 0$. This is shown in Fig. 3. As a result, electroosmotic flows typically yield identical speeds for several values of the charge, and these speeds depend on both the species charge and electrophoretic mobility. Interpreting peak arrival times for electroosmotic flow is thus highly problematic.

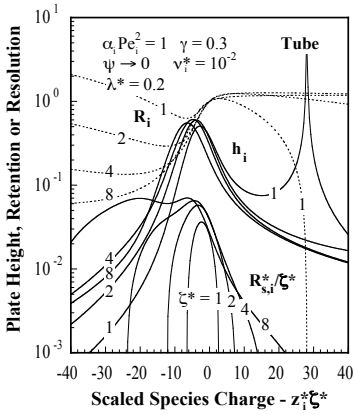

Figure 3. Retention (dashed), reduced plate height and scaled maximum resolution for electroosmotic flow at optimum conditions. Resolution drops abruptly for $z_i^*\zeta^*$ much above or below zero due to sign change in $dR_i/d(z_i^*\zeta^*)$.

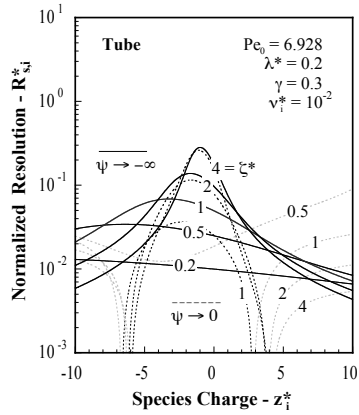

Figure 4. Normalized resolution as a function of normalized charge for electroosmotic (dashed) and pressure-driven flow (solid). High resolution over a wide range of charges can be obtained for pressure-drive flow if ζ^* is small.

As illustrated in Figs. 2 and 3, high resolutions tend to occur for negative values of $z_i^*\zeta^*$ due to higher sensitivity and lower mean species speeds in this regime. Nevertheless, maximum resolution is still obtained at some optimum value of the normalized surface potential and an associated optimum Peclet number. For pressure-driven flows, we find that large zeta potentials yield high resolution over a narrow range of charge; small ζ^* yields lower maximum resolution, but higher resolution over a broad range of species charge. For electroosmotic flows, however, high resolution is always limited to a narrow range of z_i^* regardless of ζ^*. This behavior is depicted in Fig. 4

REFERENCES

[1] J. C. Giddings, *Science*, **260**, 1456-1465 (1993).
[2] S. Pennathur, J. G. Santiago, *Anal. Chem.* **77**, 6772-6789 (2005).
[3] A. L. Garcia, et al., *Lab Chip,* **5**, 1271-1276 (2005).
[4] D. N. Petsev, *J. Chem. Phys.*, **123**, 244907 (2005).
[5] S. K. Griffiths, R. H. Nilson, *Anal. Chem.*, **78**, 8134-8141 (2006).
[6] X. C. Xuan, D. Q. Li, *Electrophoresis*, **28**, 627-634 (2007).

DNA DIAGNOSIS CHIP INTEGRATING PRE-TREATMENT DEVICE AND NANO-GAP-ARRAY FOR INFECTIOUS DISEASE

Shingi Hashioka[1, 2], Kazuya Masu[1] and Yasuhiro Horiike[2]

1. Tokyo Institute of Technology, Japan

2. National Institute for Materials Science, JAPAN

ABSTRACT

This study demonstrates the concept of the simple and rapid diagnosis chips for infectious diseases. A simple and rapid detection of target DNA by purification and hybridization with a pre-treatment device and nano-gap array was performed. T4DNA was immobilized and purified on the micro-pillars in the pre-treatment device. Purified T4DNA was transported to the nano-gap array, fixed with stretching and denatured to single strand. Probe DNA was introduced into the nano-gap array to hybridize the trapped DNA. After probe DNA was introduced, intensive luminescence was observed. These results provide a simple and rapid detection method of the target DNA.

Keywords; DNA diagnosis, pre-treatment device, nano-gap array, probe DNA

1. INTRODUCTION

Infectious diseases such as HIV, viral hepatitis, bird influenza, etc. pose increasingly grave menace to humankind. Virus-caused infectious diseases can be detected by hybridization of the probe DNA with single strand (ss) DNA denatured from double strand (ds) DNA of virus particles in blood. Trap and then extension of ssDNA facilitates this hybridization process. We have developed the one-chip which integrates in series of processes consisting of a virus lysis, a DNA purification, a DNA trapping and subsequent detection. Such detection is advantageous in avoiding the risk of infection of medical staff. Although some studies on DNA trapping using nano-micro-channels were reported [1, 2], they need complicated systems for detection in a chip. We previously reported a simple and rapid detecting method employing hybridization of prove DNA with target DNA trapped by nano-gap array channels [3].

2. EXPERIMENTAL

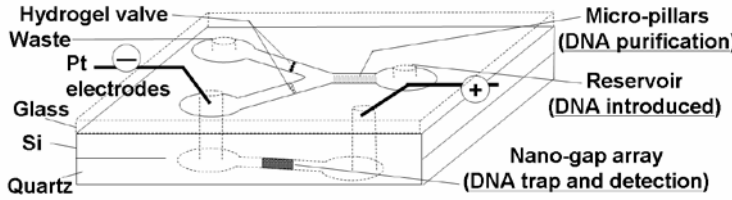

Figure 1. A schematic structure of a chip fabricated.

Fig. 1 shows a schematic structure of a chip fabricated. A purification chip of DNA extracted from lysis of viruses is stacked with a detection chip via a through-hole. Micro-fabricated Si substrate and nano-fabricated quartz one are bonded. Si-side has a pre-treatment device containing micro-pillars for DNA purification and hydrogel valves. A glass plate covers it. Quartz-side has a nano-gap array for DNA trap and detection. Si and

978-0-9798064-0-7/μTAS2007/$20©2007CBMS

quartz substrates were bonded by press with 0.35 MPa with heating to 65 °C after soaked in the H_2SiF_6 solution. Glass cover was anodic bonded.

3. RESULTS AND DISCUSSION

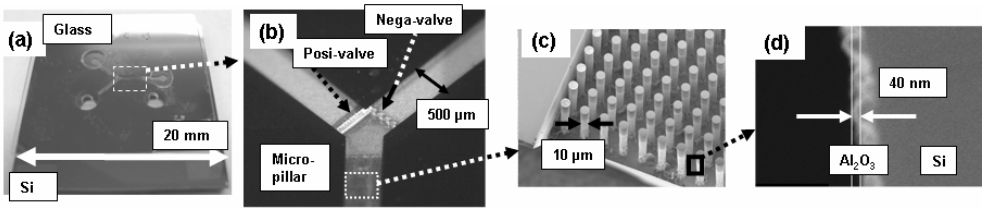

Figure 2. (a) A photograph of DNA pre-treatment device side of the chip (b) Microscopic Photograph of the pre-treatment device (c) SEM image of deeply etched Si micro-pillars (d) Magnified image on sidewall of pillar coated with alumina.

Fig. 2 shows the pre-treatment device chip. To wash DNA, DNA is immobilized on the Si micro-pillars fabricated by Bosch etching, allowing a cleaning solution flow. Alumina is coated on the micro-pillars by an ALD method. Zeta potential of alumina varies from positive in acid to negative values in alkali. Negatively charged DNA is immobilized on the alumina-coated-micro-pillars during purification in acid solution and released during elution in alkaline solution. Two types of pH-sensitive hydrogel-valves [4] were applied to the washing process. A positive-type-valve (posi-valve) is closed in acid by hydrogel-expansion and opened in alkali by shrinkage. A negative-type-valve (nega-valve) is opened in acid and closed in alkali. Washed DNA is transported to the nano-gap-array for the detection.

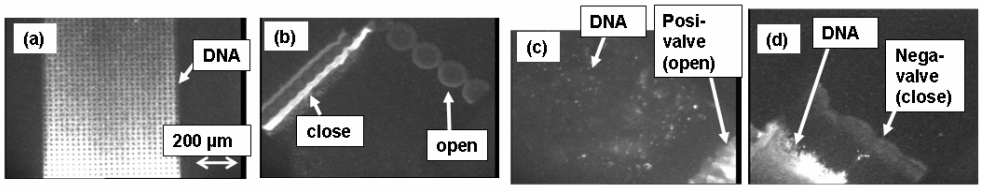

Figure 3. (a) Fluorescence image of pillars after introducing DNA in acid (b) Valves in acid (c) DNA which was eluted by alkali solution and passed through the valve opening (d) DNA blocked by valve

Pre-treatment procedures were performed as shown in Fig. 3. First, T4DNA was introduced into solution with pH=4.7 and the chip were then rotated. Fig. 3(a) shows micro-pillars after the introduction of DNA, and Fig. 3(b) shows the valves at the time. DNA accumulated on the micro-pillars by closing the posi-valve and opening the nega-valve. Next, NaOH (0.02M) was introduced into the channel. As shown in Fig. 3(c), DNA immobilized on the micro-pillars passed through the posi-valve. In the meantime the nega-valve blocked DNA as shown in Fig. 3(d).

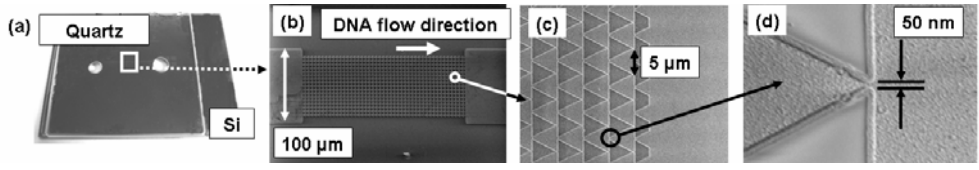

Figure 4. (a) A photograph of nano-gap-array side of the chip (b-d) SEM images of nano-gap-array

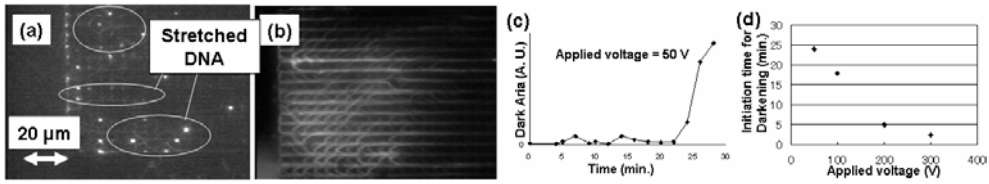

Figure 5. (a) Number of T4DNA trapped by stretching up to a length of 20 μm in nano-gap-array (b) Introduced probe DNA hybridizing the trapped DNA (c) Expansion of Dark Area in the fluorescence image after trapping DNA (d) Initiation time for darkening of DNA against applied voltage

Finally, washed DNA was introduced into the nano-gap-array by electrophoresis. Fig. 4 shows the nano-gap-array, which has 816 triangular channels with minimum width of 50 nm. The depth of the total channel is 140 nm. As shown in Fig. 5(a), DNA dyed by YOYO-1 was trapped in the nano-gap-array and stretched up to a length of 20 μm. We found a marvelous phenomenon that dsDNA denature to ssDNA. Indeed, a probe ssDNA was introduced to the trapping area, thereby hybridizing the trapped ssDNA as shown in Fig. 5(b). This demonstrates just capture of viral DNA. We presumed that this denature was caused by joule heating due to ion current during trapping in nano-gaps. To confirm, we investigated the fluorescence as a function of trapping time as applying voltage of 50V. As shown in Fig. 5(c), the fluorescence started to go out around 23 min. and the dark area expanded. As shown in Fig. 5(d), the initiation time for darkening diminished as applied voltage increased. Measured electric current during the DNA trapping was about 0.03 μA at applied voltage of 50V. It is calculated that DNA solution in micro- and nano-channels is heated by about 90 μJ for 1 min. The heating was assumed to elevate e temperature of the electrolytic solution up to 100 ^{o}C, which was enough temperature to denature dsDNA.

4. CONCLUSIONS

A new DNA diagnostic chip in which integrates procedures from the virus lysis to the detection has been developed based on a finding of denature of dsDNA trapped in the nano-gap array. These results provide a simple and rapid detection method of the target DNA originating from the infection disease.

ACKNOWLEDGEMENTS

This research was partially supported by the Ministry of Education, Science, Sports and Culture, Grant-in-Aid for Young Scientists (B), 18710114, 2006.

REFERENCES

[1] J. Mannion, C. H. Reccius, J. D. Cross and H. G. Craighead, *Conformational analysis of single DNA molecules undergoing entropically induced motion in nanochannels*, Biophys J., **90**, 4538-4545 (2006).

[2] O. Bakajin, T. A. J. Duke, C. F. Chou, S. S. Chan, R. H. Austin and E. C. Cox, *Electrohydrodynamic stretching of DNA in confined environments ,* Phys. Rev. Lett., **80**, 2737-2740 (1998).

[3] S. Hashioka, R. Ogawa, A. Oki, Y. Miyahara and Y. Horiike, *Simple and quick detection of target DNA by Hybridization in Nano Gap Channel Array*, Proc. Micro Total Analysis Systems 2005, pp. 730-732 (2005).

[4] D. J. Beebe, J. S. Moore, J. M. Bauer, Q. Yu, R. H. Liu, C. Devadoss and B-H. Jo, *Functional hydrogel structures for autonomous flow control inside microfluidic channels*, Nature **404**, 588-590 (2002).

FEMTO-LITER TRANSPORT IN 3D NANOCHANNEL MACHINED BY FEMTOSECOND LASER PULSES

Sanghyun Lee[1] and Alan J. Hunt[2]

[1]Mechanical engineering, [2]Biomedical engineering, [2]Center for Ultrafast Optical Science, University of Michigan, Ann Arbor, U.S.A.

ABSTRACT

Femtosecond laser machined nanocapillaries extend the ability to analyze small test volumes down to femtoliters. The nanocapillaries show how quickly nanobubbles in them are compressed and dissolved in water; based on this fast dissolution, several difficult measurements can be effectively performed. Furthermore, recent improvements in subsurface nanocapillary fabrication achieve a new nanocapillary electrophoresis; 600nm separation column having 804um length increases separation speed a lot with reasonable resolution. Increasing the length of capillary further improves the resolution.

Keywords: femtosecond laser machining, femtoliter, nanocapillary, nanobubble

1. INTRODUCTION

Test volumes in microfluidic devices are generally microliter to picoliter; the ability to handle such minute fluid volumes is one of the most significant advantages of microfluidics, because of reduced cost, speed, and accuracy. Recent developments in femtosecond (fs) laser nanomachining constitute a promising way to fabricate submicron scale microfluidic devices [1]-[6], capable of analyzing volumes on the order of femtoliters (fl).

2. EXPERIMENTAL

Fast gas diffusion in nanocapillaries

As the channel diameter is reduced from the micron to the submicron scale, the capillary effect becomes increasingly dominant. Consequently bubbles in nanocapillaries have high internal pressure, which increases the rate that gasses dissolve in the fluid. As shown in fig. 1, when a water droplet covers the entrances of air-filled nanocapillaries (L=24μm, *d*=600nm, vol.=9fl) machined in a glass cover slip, strong capillary force quickly draws water into the capillaries, compressing the air in them into an air plug of L=9μm (V=3.5fl) within 70ms, thus increasing the pressure ~3 folds. Because of the high internal pressure, the bubbles rapidly dissolve in water and completely collapse in about 5 seconds.

The bubble collapse in the nanocapillaries can be divided into two regimes; the first is dominated by compression and the second by diffusion. In the compression regime internal pressure of bubbles can be determined from the volume compression ratio of the air bubbles; thus, the compression ratio of 2.5 gives an estimated internal pressure of bubbles $P_i \approx 260$kPa. Once the internal pressure of the bubbles balances the pressure from capillary action, further collapse of the bubbles occurs as gas dissolves in water and diffuses out of the capillaries.

Nano-capillary electrophoresis

As shown in fig. 2, nanocapillary electrophoresis (nCE) based on the nanoscale separation column machined by fs laser pulses has been successfully fabricated and tested. The most advantageous feature is that the submicron scale separation column allows much higher

978-0-9798064-0-7/μTAS2007/$20©2007CBMS

electric field, which improves separation speed; higher than 10000V/cm e-field is expected to be applicable based on heat transfer analysis and previous CE data [7],[8].

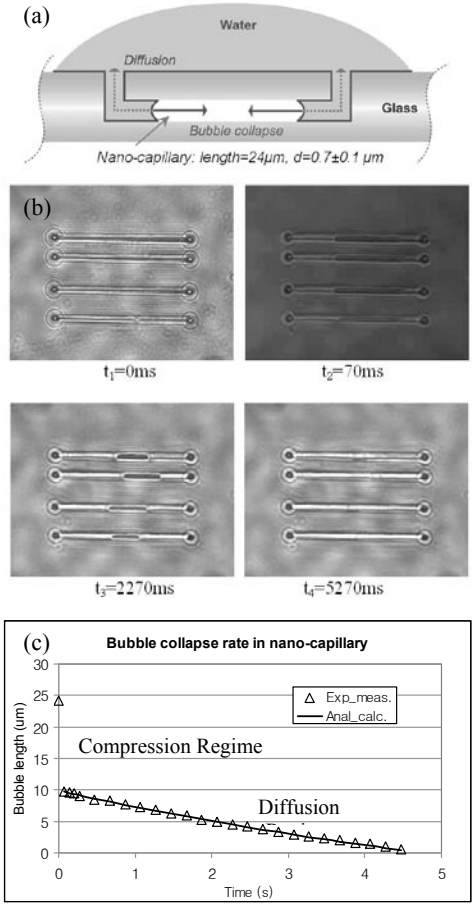

Fig.1. Gas diffusion in nano-capillaries: (a) experimental schematics, (b) microscopic images showing bubble diffusion in nano-capillaries, (c) diffusion analysis in diffusion regime.

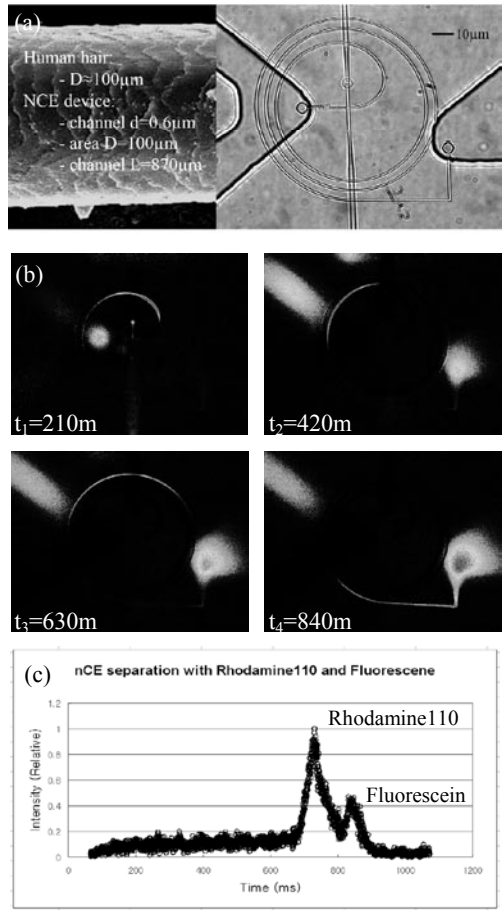

Fig.2. Femtoliter transport in nCE device: (a) actual image of nCE device and size comparison with human hair, (b) 9fl test sample transport in nCE device, (c) electropherogram of nCE separation

Using an e-field of 440V/cm generated by 37V electric potential over 804μm nanochannel (d=700nm) impressive separation performances are achieved; 9fl test sample can be analyzed within 1s. The separation time is about 200ms and the number of theoretical separation plates (N) and height of each plate (H) are 800 and 2μm, respectively.

Based on these results, performance at higher e-fields can be extrapolated; with an e-field of 53kV/cm Rhodamine110 and Fluorescein separate in 0.014ms, and N increases to 85000 with H of 9nm. To apply such a high e-field will require the currently used PDMS header to be replaced with a glass header to prevent e-field leakage between PDMS and glass interface. Also, a rectilineal separation column is in principal a better geometry, though this

would require a linear nano-stage with higher travel range, and would greatly increase the column length.

3. RESULTS AND DISCUSSION

The dynamics of the bubbles can be used to examine several additional parameters: 1) the contact angle in a nanocapillary, which due to optical limitations is very difficult to measure, can be estimated, 2) the relationship between surface charge/zeta-potential and contact angle can be studied, 3) the diffusivity of gas can be easily measured.

The nanocapillary in nCE device can allow higher than 10 times of previous e-field in general CE separation, which improves separation speed a lot. However, due to the limited length of the separation column resolution of the nCE separation is not yet sufficient. In order to further improve resolution, the length of separation column could be increased; however, the separation will take more time. Considering the separation times are already very short, increasing the length of the separation column is a sensible strategy to improve the separation performance; 100 times slowness can perform separation within 1s, which is still much faster than that of general CE.

4. CONCLUSIONS

The femtoliter fluid transports of nanobubbles or a test sample in a nanocapillary, which were very difficult to experimentally examine mainly due to the difficulties of the nanofabrication, can be achieved thanks to recent developments of fs laser nanomachining. In the analysis of nCE separation, the advantages of nanocapillaries for improving separation speed and test sample loading are well shown.

The developed fs laser nanomachining is expected to expedite not only much more studies on the nanoscale fluids behavior but also developments of 3 dimensional nanofluidic devices.

ACKNOWLEDGEMENTS

This work was supported by a grant from IMRA corp. and NIH R21 EB006098-01.

REFERENCES

[1] A.P. Joglekar, *et al*., *Proc. Nat. Acad. Sci.*, 101, 5856-5861 (2004)
[2] J.P. Mcdonald, *et al*., *Appl. Phys. Lett.* 88, 183113 (2006)
[3] K. Ke, E.F. Hasselbrink and A.J. Hunt, *Anal Chem*., 77, 5083-5088 (2005)
[4] S. Lee, *et al*., *Proc. MicroTAS 2005 Conf.*, Boston, 1, 524-526
[5] S. Lee, *et al*., *Proc. MicroTAS 2006 Conf.*, Tokyo, 1, 13-15
[6] S. Lee, J.L. Bull and A.J. Hunt, *Appl. Phys. Lett.* 91, 023111 (2007)
[7] S.C. Jacobson and J.M. Ramsey, *Anal. Chem.*, 70, 3476 (1998)
[8] N.A. Celllar and R.T. Kennedy, *Lab On A Chip*, 6(9), 1205-1212 (2006)

IONIC RECTIFYING EFFECT IN BIPOLAR NANOCHANNELS

Li-Jing Cheng and L. Jay Guo
Department of Eelctrucal Engineering & Computer Science
University of Michigan, Ann Arbor, MI 48109 USA

ABSTRACT

Flow of ions though a nanochannel in some circumstances occurs more readily in one direction than the other. In this paper, we investigate the rectified ionic current through bipolar nanochannels that have asymmetric polarity of surface charge. The channels are 20 nm-thick, 60 μm-long, and are created with different oxide materials. It is found that the rectification of ion current is due to an asymmetric distribution of ions with respect to the junction. The theoretical calculation agrees qualitatively with experiments.

Keywords: Nanofluidics, nanochannel, bipolar nanochannel, ionic rectifying effect

1. INTRODUCTION

In biological cells, some transmembrane ion channels act as diodes or valves allowing current to flow preferentially in one direction. Such a rectifying effect can be implemented on an artificial bipolar nanochannel. The function of a bipolar nanochannel relies on the opposing surface charge distributed asymmetrically along the nanochannels. Similar works have been demonstrated recently by applying modified surface chemistry in nanochannels or nanopores to form a p-i (positive-intrinsic) junction diode nanochannel [1] or a p-n (positive-negative) junction diode [2]. Instead of surface chemistry modification, the devices we present here have one half of the channel made of SiO_2 to provide negative charge in suspension, while the other part, a metal oxide, creates a positively charged surface. The metal oxide can be nickel oxide or aluminum oxide.

Resembling a semiconductor pn-junction diode, the negatively charged SiO_2 nanochannel that enhances cations concentration is a p-type nanochannel whereas the metal oxide serves as an n-type nanochannel. When the device is forward biased, i.e. a positive bias is connected to a p-type nanochannel, the counter-ions from either side are pushed to the junction and drift to the other side. The ion concentration is enriched in the junction. On the contrary, a reverse bias will pull the counter-ions in either nanochannel back to the reservoirs leading to depletion of ions in the junction, resulting in a current drop. Unlike electrons and holes in a semiconductor diode, there is no recombination for cation-anion system. After ions move across the junction, they keep moving to the other ends.

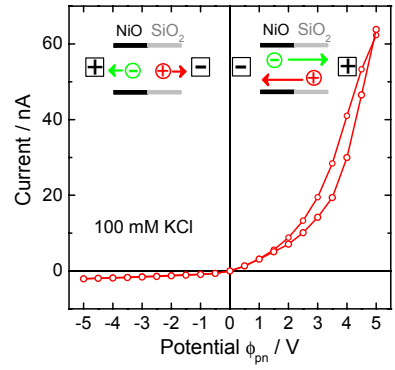

Figure 1. Experimental result of the rectifying I-V characteristics of a bipolar nanochannel.

978-0-9798064-0-7/μTAS2007/$20©2007CBMS

2. EXPERIMENTAL

The bipolar nanochannels were fabricated by conventional microfabrication technology. The thin nickel oxide layers were formed by oxidizing nickel layers in nanochannels after removing a 20 nm thick silicon sacrificial layer. As a result, shown in Figure 2, the nanochannel consists of two channels of different oxide materials connected in series. Determined by the thickness of the sacrificial layer, the channel height is about 20 nm.

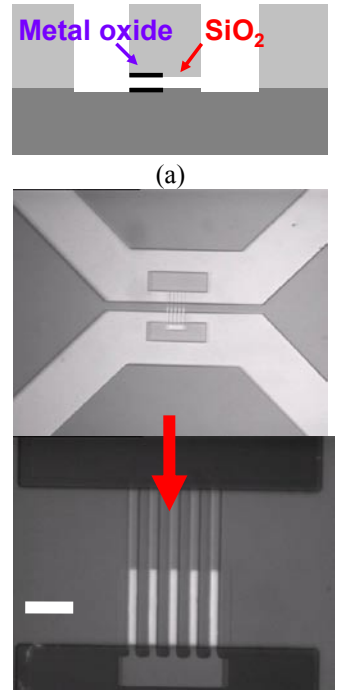

Figure 2. (a) Schematic and (b) optical microscopic image of a bipolar nanochannel. The scale bar represents 20μm

3. RESULTS AND DISCUSSION

The current-potential characteristics of the device in Figure 3 show the rectifying effect especially at the concentration of 0.1 M and 10 mM, (Figure 1). The rectification ratio (RR), as summarized in Fig. 3(c), shows the forward current I_F can be about 30-fold greater than the reverse current I_R. When the concentration is low or as high as 1M, the RRs are suppressed to unity.

To better understand the behavior, the ion profile in the bipolar junction nanochannel is calculated by applying Poisson-Nernst-Planck (PNP) theory. Figure 3 shows the ion distribution along the device at different potentials and various bulk ion concentrations. It is found in experiment that the rectifying effect is not so obvious at low concentrations, such as 0.1 mM, and very high concentrations, 1 M for instance. The calculated results in Figure 3(a) and (c) suggest the phenomenon results from the insufficient difference in ion concentration between forward and reverse bias. At high concentration, the effect is weaker since the Debye length is much

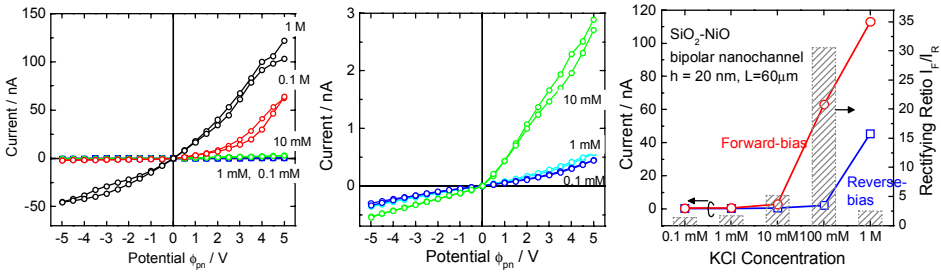

Figure 3. (a) An I-V characteristic of a bipolar nanochannel with bulk ion concentration varies from 10^{-4} to 1 M. (b) Zoom-in view of the curves measured at low ion concentration. (c) Summarized forward, reverse current and rectifying ratio.

shorter than the feature size of the channel, and the screening effect disappears. However, when concentration increases to 10 mM and 100 mM the rectifying effect becomes intensified.

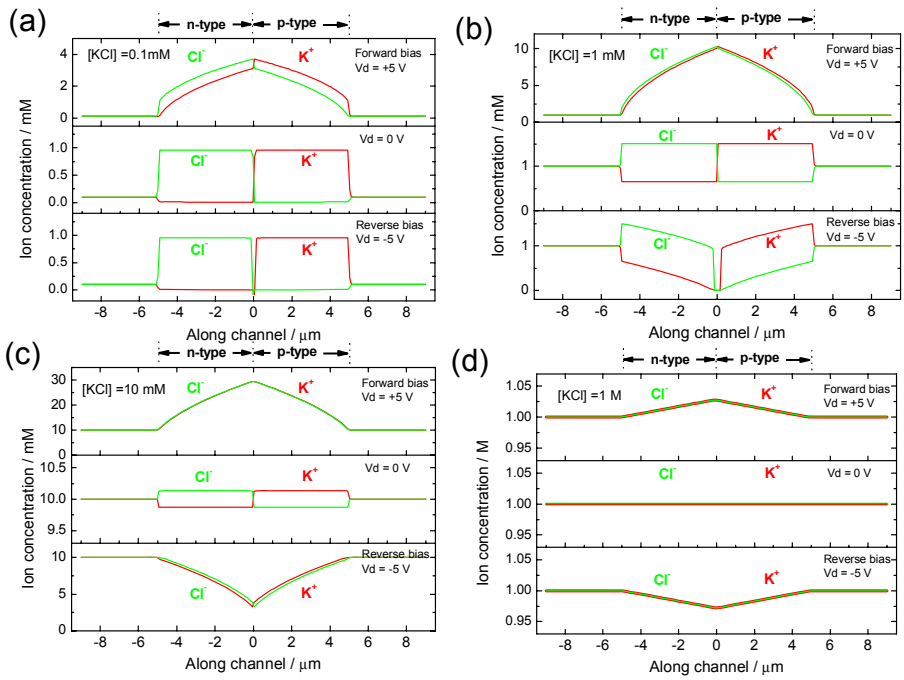

Figure 4. Ion concentration profile of a nanofluidic diode at different biases— (top) forward bias, (middle) no bias and (bottom) reverse bias. Three different ion concentrations are considered—(a) 0.1 mM, (b) 1 mM, (c) 10 mM and (d) 1M.

5. CONCLUSIONS

This paper demonstrates a rectifying effect of ionic current in a bipolar nanochannel. The combination of silicon dioxide and metal oxide patterns allows us to build nanofluidic devices containing various polarities of surface charge via conventional photolithography. The property provides a versatile way to control ion transport which may benefit the application of the devices for chemical delivery.

REFERENCES

[1] Karnik, R. et al., *Rectification of ionic current in a nanofluidic diode*, Nano Letters, **7**, p. 547 (2007).
[2] Vlassiouk, I. et al., *Nanofluidic diode*, Nano Letters, **7**, p. 552 (2007).

NANOFLUIDIC CHANNELS IN SU-8 WITH INTEGRATED FLOOR AND CEILING ELECTRODES

Kevin Paul Nichols[1], Jan Eijkel[2], Han Gardeniers[1]
[1]*Mesoscale Chemical Systems*
[2]*BIOS – The Lab on a Chip Group*
MESA+ Institute for Nanotechnology, University of Twente, The Netherlands

ABSTRACT

This paper reports a method for constructing sacrificially etched 2-D nanofluidic channels using SU-8 as the channel structural material, with integrated floor and ceiling metal electrodes, and an additional metal layer as the sacrificial layer. Channel thickness from 20 nm to 400 nm, widths from 800 nm to 40 μm, and lengths up to 3 mm (without additional etch access windows) have been demonstrated.

Keywords: nanochannel, SU-8, metalized, electrodes, sacrificial etch

1. INTRODUCTION

Sacrificially etched nanochannels have been previously reported [1]. The significance of this method is its use of SU-8 as the channel structural material, providing the following advantages: simpler device fabrication than was previously possible; strong adhesion to certain metal combinations [2]; simple pattering of interconnections due to the photo-definable nature of SU-8 [3]; sufficient etch specificity to prevent channel axial tapering; sufficiently thick channel roofs to prevent bending due to capillarity induced negative pressure, as has previously been problematic [4]; and arbitrary nanochannel geometries due to the conformal nature of SU-8 dispensing. Further, using SU-8 as the channel structural material means that this technique requires neither a bonding step, nor expensive mold masters. For these reasons we expect that this technique can be considered as a superior fabrication technique for certain cases of short 2-D nanochannels. The technique has the added benefit of utilizing more accessible equipment than some, more exotic, approaches; the only equipment necessary is a standard contact aligner and some capability for metallizing substrates. The primary disadvantage of this technique, as is the case with most sacrificial etches, is the long etch time.

2. EXPERIMENTAL

An overview of the fabrication process is presented in Figure 1. In step 1, the top and bottom electrode are defined on a Si substrate, along with the sacrificial layer between the electrodes. Simple electrode geometries with planar channels can be constructed in a single lithography step. More complicated geometries require an additional step to define the electrodes/channel independently. In step 2, a layer of SU-8 is dispensed and patterned to provide fluidic entrance and exit holes, and access to the top and bottom electrodes. In step 3, an additional metal layer is sputtered and patterned to create contact pads and electrical contacts with the top electrode. In step 4, an additional layer of SU-8 is patterned to provide structural support for the device. In step 5, a laminated photoresist is used to mask the contact area of the bottom electrode (as shown, access to the bottom electrode and one of the fluid inlets/outlets are colocated, though this is not necessary). In step 6, the sacrificial layer is removed.

978-0-9798064-0-7/μTAS2007/$20©2007CBMS

Example images of fabricated devices are provided. In Figure 2, images showing typical SU-8 nanochannels, both with and without integrated electrodes, are shown. Figure 3 demonstrates that arbitrary nanochannel designs, in this case pillars, are possible using SU-8. Experiments have demonstrated that the hydrophobic/hydrophilic combination of the SU-8 nanochannel on a Si substrate spontaneously fills with both DI water and Octane. Further, the channels have been demonstrated to be stable for at least two months.

Table 1. Compatibility of structural materials, sacrificial layers, and electrode layers. A "+" symbol indicates inertness in the indicated etch solution. A "-" symbol indicates the material will be dissolved, except for Cu in Au etch, which forms solid CuI. For example, a channel could be constructed in SU-8 using Ta electrodes, and an Au sacrificial layer. [1]"Cr etch" is BASF Selectipur, an ammonium cerium(IV) nitrate based etchant. [2]"Au Etch" is $KI:I_2:DI = 4:1:40$

	SU-8	Pyrex	Cr	Au	Ti	Ti/W	ITO	Pt	Cu	Ta
Cr Etch[1]	+	+	-	+	-	-	-	+	-	+
Au Etch[2]	+	+	+	-	+	+	+	+	-*	+
BHF	+	-	+	+	-	-	-	+	+	-

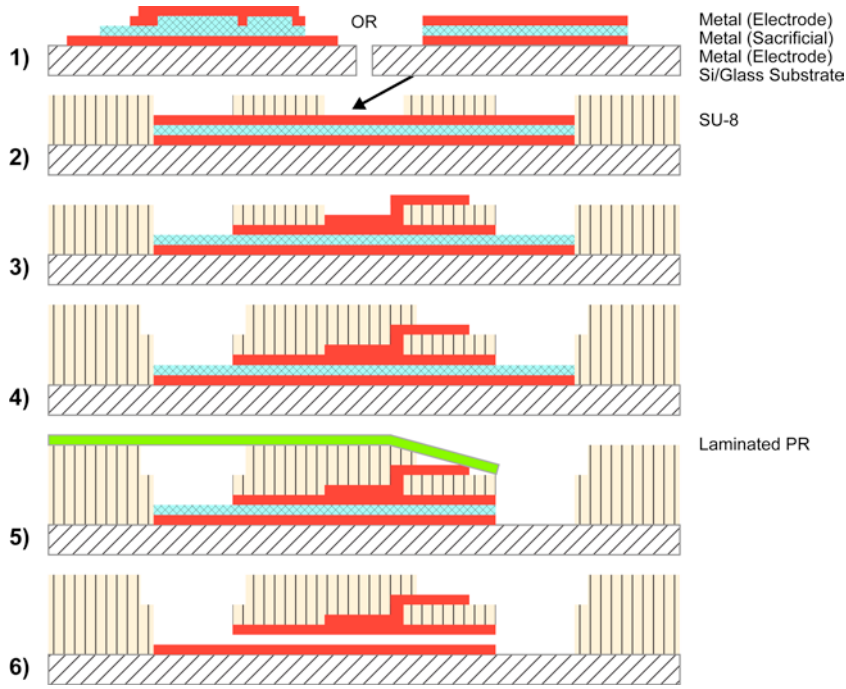

Figure 1 – SU-8 Nanofluidic Channel with Top/Bottom Electrodes Process Flow – 1) Top electrode, bottom electrode and sacrificial layer patterned (multi-step patterning on left, single step patterning on right). 2) SU-8 patterned with fluidic access holes and top electrode access hole. 3) Metal layer sputtered for contact pads and contact with top electrode. 4) Structural SU-8 patterned. 5) Bottom electrode patterned with laminated photoresist mask. 6) Sacrificial layer removed.

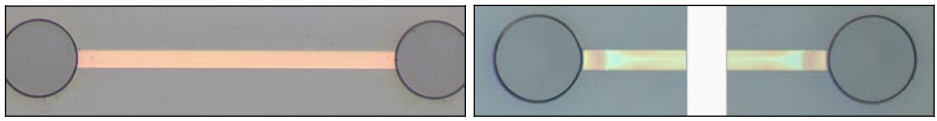

Figure 2 – Two examples of SU-8 nanochannels – The left nanochannel is 100 nm thick, without an integrated electrode. The right nanochannel is 30 nm thick, with two integrated electrodes (only the top electrode is visible as a white vertical strip in the center of the channel). The large black circles are the reservoirs patterned in SU-8. The channel width is 40 μm in both cases.

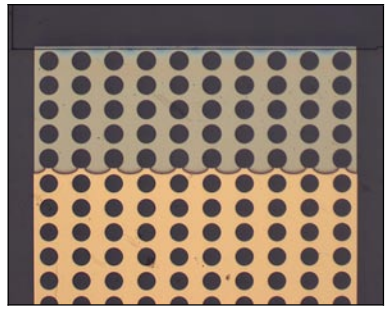

Figure 3 – Arbitrary SU-8 nanochannel patterns – Pillars are shown in 25 nm thick SU-8 nanochannels (partially etched). The conformal nature of SU-8 dispensing permits nanochannels with arbitrary lateral dimensions within the maximum limits permissible to avoid collapse. Also, by performing multi-step sacrificial layer patterning, steps can be created in the nanochannel. The total width is 500 μm.

ACKNOWLEDGEMENTS

This research was financially supported by the Technology Foundation STW, applied science division of NWO and the technology program of the Ministry of Economic Affairs of The Netherlands (project no. 6626).

REFERENCES

[1] D. Mijatovic, J. C. T. Eijkel, and A. Van Den Berg. Technologies for nanofluidic systems: Top-down vs. bottom-up - a review. *Lab on a Chip*, 5(5):492–500, 2005.

[2] M. Nordstrom, A. Johansson, E. S. Nogueron, B. Clausen, M. Calleja, and A. Boisen. Investigation of the bond strength between SU-8 and gold. *Microelectronic Engineering*, 78-79:152–157, 2005.

[3] G. J. Cheng, D. Pirzada, and P. Dutta. Design and fabrication of a hybrid nanofluidic channel. Journal of Microlithography Microfabrication and Microsystems, 4(1):013009, Jan-Mar 2005.

[4] N.R. Tas, P. Mela, T. Kramer, J.W. Berenschot and A. van den Berg. Capillarity induced negative pressure of water plugs in nanochannels. *Nano Letters*. 3:1537-1540, 2003.

NANOFLUIDICS IN HOLLOW NANOWIRES

N. Sköld[1], T. Hernán[1], J. B. Wagner[1], W. Seifert[1], L. Samuelson[1] and J. O. Tegenfeldt[1]

[1] Division of Solid State Physics, The Nanometer Consortium, Lund University, Sweden

ABSTRACT

We present a novel scheme for producing nanotube membranes using freestanding hollow nanowires, with easily controllable dimensions, partially embedded in a polymer film. Electrophoretic transport of T4-phage DNA through the hollow nanowires was demonstrated using epifluorescence microscopy.

Keywords: Nanotube, nanowire, DNA, electrophoresis

1. INTRODUCTION

Synthetic nanotube/nanopore membranes have proven to be important tools for biomolecular manipulation and characterization. Electrophoretic translocation of proteins, DNA and RNA through nanotube/nanopore membranes has enabled both detection and structural analysis of these complex biomolecules [1, 2]. Synthetic nanotube membranes offer several advantages compared to lipid bilayer membranes such as chemical, mechanical, electrical and thermal robustness [3] as well as being easily integratable in a lab-on-a-chip system. The nanotube membranes are generally produced either by track-etching of a polymer film or electrochemical growth of porous aluminum oxide [4], in both cases forming a flat surface membrane. In our approach nanotubes are produced from free standing hollow nanowires, a method that allows for easy control of the nanotube dimensions and position. The hollow nanowires are subsequently partially incorporated into a polymer membrane. As the nanotube tips are left free they can also be used as needles. We believe that this configuration should enable not only biomolecular detection but also injection into living cells in a similar fashion as arrays of hollow microcapillaries [5] but with minimal damage to the cells as the needle diameter is only a few hundred nanometers. It has been shown that cells can be perforated by hundreds of nanowires without any deterioration in viability [6].

2. HOLLOW NANOWIRES IN A POLYMER MEMBRANE

Free standing hollow nanowires can be produced by converting epitaxially grown core-shell nanowires into nanotubes by selective etching of the core [7, 8]. Nanowires are grown on (111)B substrates in two ways. Either gold assisted from size selected gold particles deposited on the substrate where the particle size determines the nanowire diameter or by selective-area growth where the diameter is controlled by the size of openings in a passivating mask on the substrate. In both cases the position of the nanowires can be controlled by positioning the gold particles or mask openings respectively using either electron beam or nanoimprint lithography. By changing the growth conditions the growth mode switches from axial to radial growth and a shell can be epitaxially grown around the nanowire.

We have grown GaAs-AlInP core-shell nanowires by metal-organic vapor phase epitaxy on GaAs (111)B substrates. Prior to growth the substrates were mechanically dimpled from

978-0-9798064-0-7/μTAS2007/$20©2007CBMS

the back side, leaving only 50 μm to the substrate surface. This was done in order to facilitate the back side connection to the membrane at a later stage. Size selected gold aerosols were then deposited on the substrate front side to be used as seeds for nanowire growth. The GaAs core was grown at a low temperature, 450°C, where kinetic limitations suppress radial growth. An $Al_{0.5}In_{0.5}P$ shell, lattice matched to the GaAs core, was grown at a higher temperature, 610°C, where the kinetic limitations are overcome [9]. The core-shell nanowires were subsequently partially embedded in a benzocyclobutene (BCB) film, the Au particles were mechanically removed to access the core which was selectively etched out (NH_4OH:H_2O_2 aqueous solution) and 3-5 μm long tubes with an inner diameter of 100 nm and an outer diameter of 250 nm were produced [10]. Figure 1 a and b shows transmission electron microscope (TEM) images of two tubes in side view and top view respectively. Finally a 100 μm diameter BCB membrane with suspended nanotubes was freed by etching out the remaining part of the substrate in the bottom of the backside dimple (H_2SO_4:H_2O_2 aqueous solution). Figure 1 c shows a scanning electron microscope (SEM) image of the membrane cross section before the substrate has been removed.

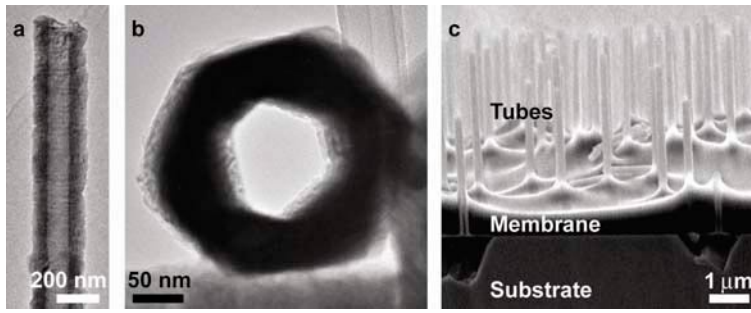

Figure 1. (a) and (b) TEM images of AlInP nanotubes in side view and top view respectively. (c) SEM cross section image of the nanotubes supported by a BCB membrane.

3. ELECTROPHORETIC TRANSPORT IN HOLLOW NANOWIRES

We here demonstrate electrophoretic transport of DNA through the hollow nanowires using T4-phage DNA (170 kbp) in a tris-borate-EDTA (TBE) buffer solution. The DNA was stained with TOTO-1 intercalating dye and applied on the back side of the membrane; the front side was monitored with an epifluorescence microscope connected to an electron-multiplying CCD camera.

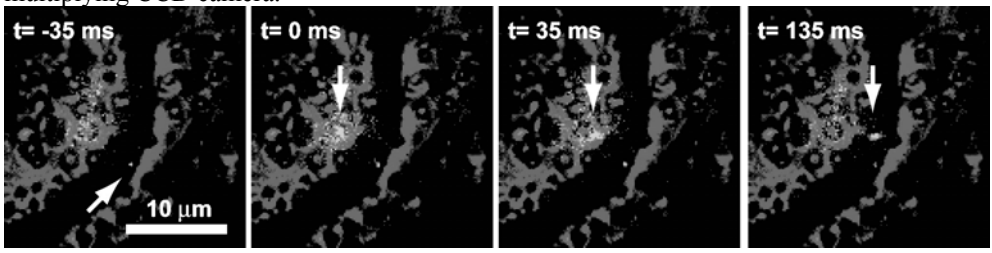

Figure 2. Time series of images illustrating DNA emerging from a nanotube. The nanotubes can be seen as dark circles in the membrane. A DNA strand emerging from a tube at t=0 is marked with vertical arrows in frame 2-4, an immobile DNA strand is marked with a 45° arrow in frame 1.

With a bias of 5 V applied across the membrane, DNA emerged from the tips of the hollow nanowires. Figure 2 shows a time series of images spanning over 170 ms. Each image is a

superposition of a white light image of the membrane (with the tubes seen as dark circles as an effect of diffraction) and the fluorescence image. At t=0 a DNA strand emerges from a nanotube and diffuses away (indicated by vertical arrows in frame 2-4). In some cases the DNA clogs the tube and never leaves (see the immobile DNA strand indicated by a 45° arrow in frame 1) illustrating the importance of optimizing the surface chemistry on the inside walls of the nanotubes.

4. SUMMARY AND OUTLOOK

We have produced freestanding hollow nanowires from GaAs-AlInP core-shell nanowires by selective etching. The hollow nanowires were partially embedded in a polymer film in order to form a nanotube membrane and electrophoretic transport of T4 DNA was demonstrated using epifluorescence microscopy. We believe that this work paves the way for using nanoneedles for injection and aspiration of material to and from single cells.

ACKNOWLEDGEMENTS

This work was carried out within the Nanometer Structure Consortium and was supported by the Swedish Foundation for Strategic Research (SSF) and the Swedish Research Council (VR). We thank Waldemar Hällström, Christelle Prinz, Martin Kanje, Magnus Jonsson and Jason Beech for valuable discussions.

REFERENCES

[1] A.J. Storm *et al., Fast DNA translocation through a solid-state nanopore.* Nano Lett. **5,** 1193-1197 (2005)

[2] Z. Siwy *et al., Protein biosensors based on biofunctionalized conical gold nanotubes.* J. Am. Chem Soc. **127**, 5000-5001 (2005)

[3] J.L. Li *et al.*, *DNA molecules and configurations in a solid-state nanopore microscope.* Nature Mater. **2,** 611-615 (2003)

[4] L.A. Baker *et al.*, *Biomaterials and biotechnologies based on nanotube membranes.* Crit. Rev. Solid State Mat. Sci. **30,** 183-205 (2005)

[5] K. Chun *et al.*, *Fabrication of array of hollow microcapillaries used for injection of genetic materials into animal/plant cells*. Jpn. J. Appl. Phys. Part 2 **38**, 279-281 (1999)

[6] W. Hällström *et al., Gallium Phosphide Nanowires as a Substrate for Cultured Neurons*. To be published in Nano Lett.

[7] J. Noborisaka *et al., Fabrication and characterization of freestanding GaAs/AlGaAs core-shell nanowires and AlGaAs nanotubes by using selective-area metalorganic vapor phase epitaxy.* Appl. Phys. Lett. **87**, 093109 (2005)

[8] R. Fan *et al.*, *Fabrication of silica nanotube arrays from vertical silicon nanowire templates.* J. Am. Chem Soc. **125,** 5254-5255 (2003)

[9] N. Sköld *et al.*, *Phase segregation in AlInP shells on GaAs nanowires.* Nano Lett. **6,** 2743-2747 (2006)

[10] N. Sköld, details to be published elsewhere.

PARTICLE IMAGE ANALYSIS: A NEW TOOL FOR THE EXPLORATION OF NANOFLUIDIC FLOWS

C.I. Bouzigues and P. Tabeling

Groupe Microfluidique MEMs et Nanostructures
UMR Gulliver 7083 CNRS ESPCI, 10 rue Vauquelin 75005 Paris, France

ABSTRACT

In this paper, we expose the developpment of a new method for local characterization of nanoflows based on imaging of nanoparticles by Total Internal Reflection Fluorescence (TIRF). We reconstructed concentration and speed profiles with unprecedent accuracy by the use of this method. This has allowed the measurement of the slip length and of the Debye length in a water flow above a glass surface. Our new tool is thus a powerful method for the investigation of the nanofluidic world and open new perspectives for the fundamental understanding of nanoflows and for the further design of nanofluidic devices.

KEYWORDS : Nanofluidics, Nanovelocimetry, Slip length

1. INTRODUCTION

Nanofluidics is often presented as the future of microfluidics[i]; its development, though, requires considerable progress in instrumentation: at the moment, the available methods for characterizing flows in nanochannels are global measurements (pressure[ii] and voltage[iii]), or nanovelocimetry[iv]. The present work expands particle-based measurements to the extreme vicinity of a wall.

We used 20 nm diameter nanoparticles and evanescent wave to analyze flow properties at distances between 20 and 200 nm from a wall. We succeeded for the first time to perform resolved velocity measurements within this range of scale. We moreover measured diffusion constants and concentration profiles of the nanoparticles and carried out direct estimation of the Debye length. We then determined – by two independent methods – local slip lengths with unprecedented accuracy. The present work opens novel perspectives for analyzing nanoflows in general, and more specifically nanoflows driven in nanofluidic devices.

2. EXPERIMENTAL

In the experimental work we carried out, flows of water are driven along 10 µm x 100 µm microchannels, formed between glass and PDMS. The fluid contains monodisperse (within 5%) 20 nm fluorescent charged particles and is illuminated by an objective created evanescent wave. Under these conditions, illumination power is decreasing exponentially with the distance to the surface, with a penetration length of ~ 100 nm, resulting in the detection of tracers closer than ~ 300 nm of the surface (Figure 1) and allowing a direct reading of particle heights through their fluorescence intensity.

978-0-9798064-0-7/µTAS2007/$20©2007CBMS

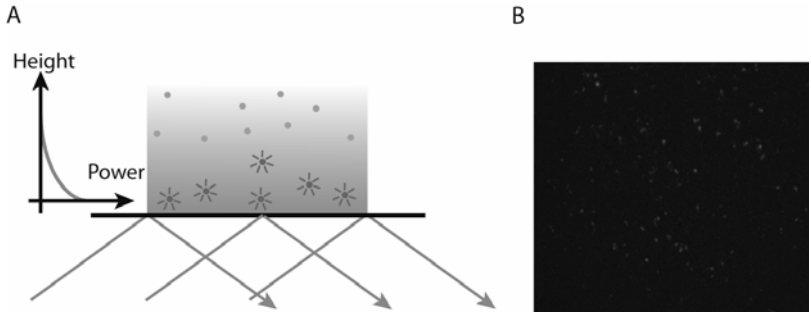

Figure 1. A) *Schematic view of TIRF illumination. The illumination decreases exponentially with the distance to the surface: $I=I_0exp(-z/L)$. Under our experimental conditions L~100 nm.* ***B)*** *Typical recorded image (Objective 100X NA =1.46, acquisition rate = 50 ms, the field of view is 40 x 40 µm)*

3. RESULTS AND DISCUSSION

The concentration profile determination at different salt concentrations reveals a depletion in tracers close to the surface, whose decay length measurement is an *in situ* determination of the Debye length (Figure 2).

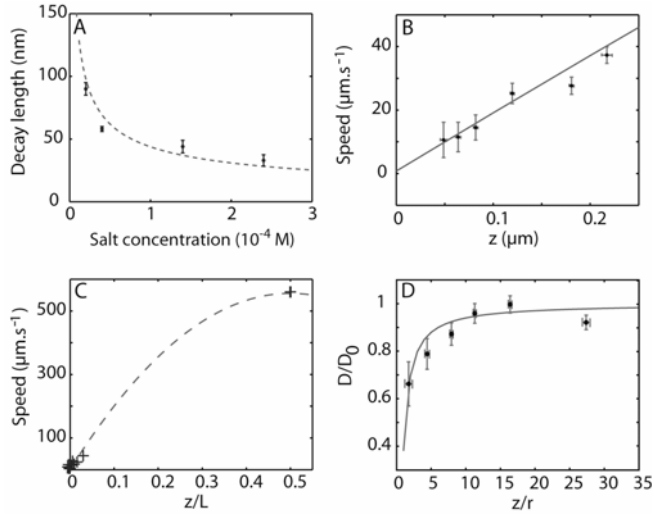

Figure 2. A) *Decay length of the concentration of tracers over the surface (blue dots) as a function of salt concentration compared to the theoretically expected Debye length (grey dashed line).* ***B)*** *Speed profile in the first 250 nm above the surface. Measured speed are black dots and the parabolic fit of the data is the grey plain line (v_{max} =560 µm.s^{-1} and b= 3 nm).* ***C)*** *Speed profile in the whole channel (black crosses) with the corresponding fit (grey dashed line).* ***D)*** *Diffusion coefficient profile (black dots) compared to the first order hydrodynamic model (grey line) for diffusion coefficient variations close of a wall.*

We measured through a 3D-single particle tracking algorithm the speed of the tracers in different planes with a resolution of ~ 20 nm along the direction perpendicular to the surface. The velocity of a tracer is a balance between Brownian diffusion and directed motion due to the flow. The distribution of velocities of thousands particles of the same plane thus provides the speed of the flow and the tracer diffusion coefficient.

We reconstructed flow speed and particle diffusion coefficient profiles over 200 nm with 20 nm accuracy. The speed profile in pure water over a glass surface was correctly approximated by a Poiseuille law with no significant slip length (10 nm>b>-4 nm), and the diffusion coefficient variations were those expected for a purely hydrodynamic coupling between the particle and an hydrophilic wall (5 nm>b>-7 nm) (Figure 2). Our method thus provides two independent methods for the slip length determination, and the measurement consistency highlights its robustness. These results are in agreement with previously established measurements of slip length[v], but provide to our knowledge its first direct estimation on a single velocity profile.

4. CONCLUSION

These experimental developments enable the determination of previously inaccessible quantities such as the velocity profiles over nanostructured surfaces, or within a Debye layer. We provide a powerful tool to investigate liquid-solid interfaces at the nanometer scale, which should be central either in fundamental topics, by testing the standard electro-osmosis theory within the double electrical layer for example, or for the future design of intelligent surface used in nanofluidic devices.

ACKNOWDLEGEMENTS

This work was supported by CNRS, Ville de Paris and the Agence Nationale pour la Recherche Nanodrive program.

---

[i] What does nanofluidics have to offer? R. Mukhopadhyay , Anal. Chem., **78**, 7379 (2006)

[ii] Pressure-driven flow control system for nanofluidic chemical process. E. Tamaki , A. Hibara, H.B. Kim, M. Tokeshi, and T. Kitamori, J. Chromatogr. A., **2**, 256 (2006)

[iii] Electrokinetic pumping and detection of low-volume flows in nanochannels. P. Mela, N.R. Tas, E.J. Berenschot, J. van Nieuwkasteele J, and A. van den Berg, Electrophoresis, **25**, 3687 (2004)

[iv] Near-surface velocimetry using evanescent wave illumination, S. Jin, P. Huang, J. Park, J.Y. Yoo, and K.S. Breuer, Experiments in Fluids, **37**, 825 (2004)

[v] Probing the nanohydrodynamics at liquid-solid interfaces using thermal motion, L. Joly, C. Ybert, and L. Bocquet, PRL, 96(4):046101 (2006)

MODELING THE ELECTROKINETICS OF NANOPARTICLES FOR CONTROLLED ASSEMBLY

Michael D. Vahey[1], Robert J. Barsotti[1], Ryan Wartena[1], Yet-Ming Chiang[1], Francesco Stellacci[1] and Joel Voldman[1]

[1]Massachusetts Institute of Technology, USA

ABSTRACT

We present a predictive framework for the controlled assembly of nanoparticles onto the surface of small (15 - 150 nm) electrode gaps using the dielectrophoretic (DEP) force. By combining Brownian dynamics (BD) simulations with continuum descriptions for the spatial distributions of nanoparticles, we arrive at a concise analytic description for the number of particles assembled as a function of the applied voltage, nanoparticle properties, and geometric parameters, such as the size of the electrode gap. Our model is predictive and successfully describes the presence of a voltage threshold, below which no assembly is observed.

Keywords: nanoparticles, dielectrophoresis, Brownian dynamics simulation

1. INTRODUCTION

Nanoparticles assembled on a surface have enormous potential for applications ranging from low-power electronic devices to chemical and biological sensors. One technique for creating these assemblies uses the dielectrophoretic (DEP) force created by nanometer- to millimeter-scale electrodes to direct particles to or within the electrode gap [1]. Current methods of nanoparticle assembly are predominantly based upon empirically determined parameters. Realizing the full potential of these devices, however, requires the ability to quantitatively understand and thus control both the number and location of the assembled particles, a prospect made more difficult by the combined stochastic and deterministic character of particle dynamics at the nanoscale. Here we present a framework for modeling the assembly of particles which can be customized for an arbitrary range of geometries, particles, and operating conditions, taking into account both linear (i.e. electrophoresis) and nonlinear (i.e. dielectrophoresis, induced charge electrophoresis) electrokinetic phenomena.

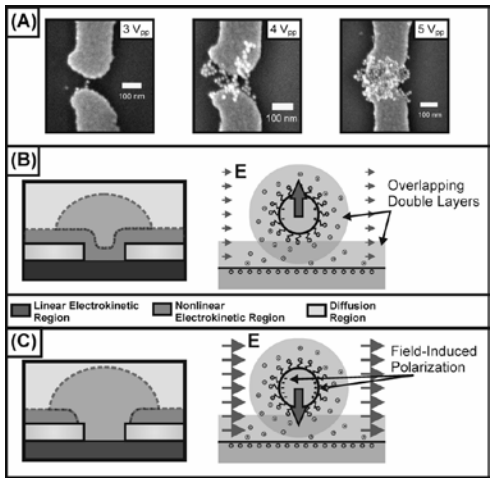

Figure 1. (A) SEM images illustrating the nonlinear relationship between applied voltage and the number of assembled particles. (B) and (C) Assembly as a competition between thermal motion (diffusion) and both linear and non-linear electrokinetic phenomena.

978-0-9798064-0-7/μTAS2007/$20©2007CBMS

2. THEORY

Nanoparticles subject to both external forces and thermal fluctuations undergo a biased random walk. The stochastic nature of the resulting dynamics presents researchers with two primary approaches to modeling assembly; Brownian dynamics (BD) simulations and continuum models. BD simulations correctly account for the stochastic nature of particle movement, but are computationally expensive. Alternatively, continuum models offer a computationally convenient framework for treating the average behavior of large ensembles of particles, but are deterministic and thus do not recapitulate the true dynamics of assembly.

Instead, we have combined both approaches, using a few BD simulations to determine the boundary conditions for a fast, intuitive continuum model. The basis for the continuum model is the concept of a Region of Influence (ROI), inside of which deterministic forces dominate (e.g. DEP and electrostatic), and outside of which thermal fluctuations, as manifested by diffusion, dominate (Figure 1). We use BD simulation to determine the size and shape of the ROI, accounting for its evolution as particles are assembled (Figure 2), and then define the surface of this region as an absorbing boundary in the diffusion equation. We then solve this simple partial differential equation numerically using the exact boundary, or obtain an analytic solution by approximating the boundary using spherical harmonics.

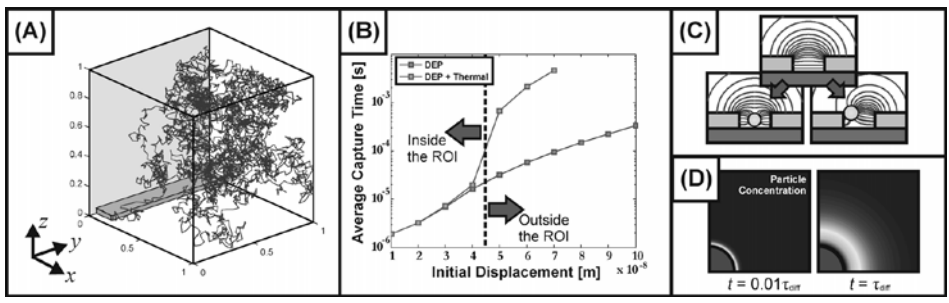

Figure 2. From Brownian dynamics to a continuum model. (A) Brownian dynamics simulations give the trajectory of single nanoparticles subject to both thermal and deterministic forces, revealing a sharp transition (B) in mean capture time for particles initialized outside the ROI. (C) Accounting for distortion of the electric field and ROI by assembled particles allows us to model the self-limiting aspect of assembly. (D) Analytic solution obtained by treating the ROI as a hemisphere.

3. EXPERIMENTAL

To test the predictions of the model, we use electrode gaps fabricated using either electron-beam lithography or localized melting of a 100-nm-wide constriction in a 300-nm-wide wire [2]. This produces electrode gaps ranging from 15 – 150 nm. By placing a droplet of the nanoparticle suspension over the electrode gap and actuating the electrodes, we have access to a large range of experimental parameters, including the amplitude, frequency, and duration of the applied electric field, particle concentration, and solvent properties. Post-assembly SEMs of the electrode gaps allow us to count the number of particles assembled for a given experimental condition.

4. RESULTS AND DISCUSSION

We have used our model to suggest a number of testable predictions for the scaling of nanoparticle assembly with both physical and operating conditions. Experimental observation of assembly as a function of voltage agrees quantitatively with the proposed model (Figure 3). Importantly, this agreement requires the introduction of unexpected nanoscale phenomena; for instance, the presence of a voltage threshold for assembly can be explained by including electrostatic repulsion between the negatively charged substrate and citrate stabilized gold nanoparticles [3]. The range of this model's applicability - both with respect to experimentally accessible degrees of freedom as well as the ease with which it can be extended to other types of particles and electrode geometries - suggest that controlled assembly of a few to hundreds of particles may be possible to within the limits of Poisson statistics.

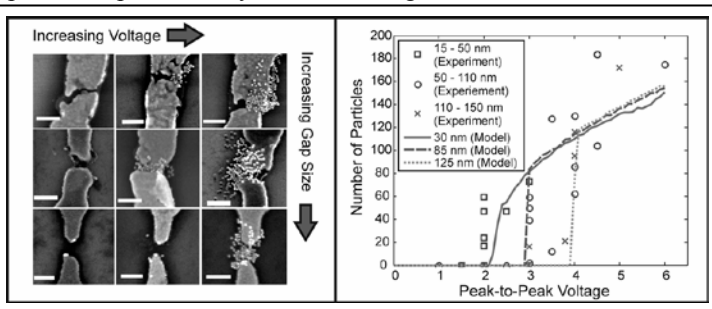

Figure 3. Experimental and modeled assembly of nanoparticles as a function of applied voltage at 1MHz for a durations of 120s. A threshold voltage, below which no particles are assembled, is observed and increases with the size of the electrode gap. Scale bars = 200 nm.

5. CONCLUSIONS

We have developed a predictive description of nanoparticle assembly combining BD simulations and continuum modelling. This model quantitatively predicts particle dynamics, including such emergent behaviour as a threshold voltage for assembly. Future work will focus on extending the applicability of the model and testing its predictions over a broader range of experimental conditions.

ACKNOWLEDGEMENTS

Support from the Singapore-MIT Alliance, the MARCO Interconnect Focus Center, the Department of Defense NDSEG fellowship, the CSBi/Merck graduate fellowship, and the IC Postdoctoral Fellowship is gratefully acknowledged.

REFERENCES

[1] K.D. Hermanson et al., *Dielectrophoretic assembly of electrically microwires from nanoparticle suspensions*, Science **294**, pp. 1082-1086 (2001)

[2] G.K. Ramachandran et al., *Nanometer gaps in gold wires are formed by thermal migration*, Nanotechnology **16**, pp. 1294-1299 (2005)

[3] R.J. Barsotti et al., *Assembly of metal nanoparticles into nanogaps*, Small **3**, pp. 488-499 (2007)

DNA DAMAGE ANALYSIS IN MICROFLUIDIC CHIPS

Yuki Tanaka[1], Henrik Johansson[1], Chatarina Larsson[1], Jonas Jarvius[1], Takehiko Kitamori[2], Mats Nilsson[1]

[1]Uppsala University, SWEDEN

[2]The University of Tokyo, JAPAN

ABSTRACT

This paper reports mitochondrial DNA damage analysis in single cells using a microfluidic platform. DNA damage and single-nucleotide polymorphisms (SNPs) in individual mitochondrial DNA molecules were analyzed using padlock probes, made visible by rolling-circle amplification of the circularized padlock probes. By combining microfluidcs with padlock probes, individual cells have been manipulated and investigated with single-molecule sensitivity.

Keywords: single cell, in situ, single molecule,

1. INTRODUCTION

Mitochondria have been implicated in processes like aging, diabetes and neurodegeneration. The effects of mitochondrial mutations remain unclear, and an important question is how mutations influence mitochondrial phenotypes such as mobility and maintenance. In this research, we applied microfluidics to investigate genotype-DNA damage correlations in mitochondrial biology. The microfluidic format also gives us the possibility to subject a fraction of the cells on the device to specific treatment and to observe the response.

2. KEY TECHNIQUES

Padlock probes [1] are oligonucleotides of about 70-140 nucleotides become circularized by DNA ligation only in the presence of an appropriate DNA (Figure 1). They show highly specific detection of target sequences and single nucleotide varitation can be distinguished through target dependent ligation of the probe ends.

The rolling circle amplification (RCA) [2] is used for increasing the sensitivity of detection of circularised probes. Target-primed RCA of in situ-circularized padlock probes have been applied for *in situ* study of individual mitochondrial DNA molecules [3], enabling analysis of the distribution of mitochondrial genomes within cells.

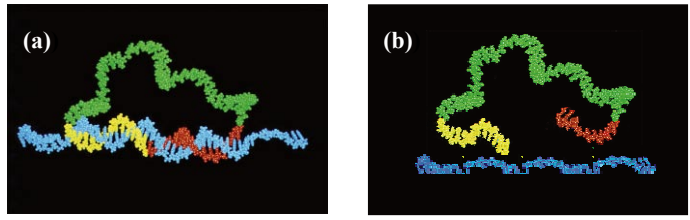

Figure 1. Padlock probe and DNA
(a)circularized on appropriate DNA (b)mismatch in target DNA

978-0-9798064-0-7/μTAS2007/$20©2007CBMS

3. EXPERIMENTAL

The microfluidic device was made of thermoplastics by injection molding and bonded with a PDMS lid [4]. This microfluidic platform is suitable for mass production and has valuable features such as biocompatibility, optical transparency over a wide range, as well as low-cost and disposability. The microchip used for cell experiments is shown in Figure 2. The nine inlets at the left and the one at the right were used for reagents and the middle inlet was used for cells introduction. By applying precise control of the laminar flow we can achieve multilayer flow for selective exposure of cells to reagents. We cultured cells in this microchip and then formed laminar flow with genotoxic agent mitomycin C from the four bottom inlets of those at the left. After 2 hours of exposure, non-damaged mitochondrial DNA were detected with padlock probes and RCA (Figure 3). Cell nuclei are shown in blue, mitochondria are shown in green by MitoTracker dye and normal mitochondrial DNA shown in red by padlock probes and RCA. Damaged mitochondria DNA were not detected. MitoTracker dye was applied to visualize mitochondrial physical structure. This figure shows that mitochondrial DNA damaged by mitomycin while mitochondria themselves were not destroyed. The feasibility of mitochondrial DNA damage analysis using laminar flow has been shown successfully.

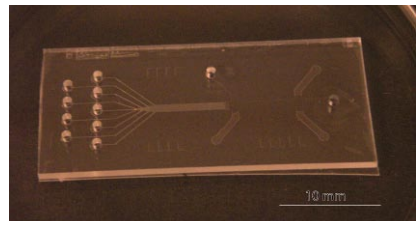

Figure 2. Microchip

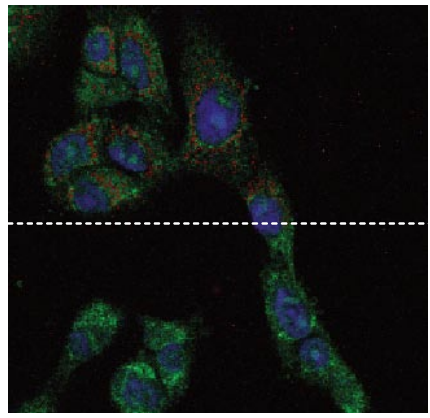

Figure 3. cells after 2 hours partial (bottom half) exposure to mitomycin C. -Color image can be found on the CD-

4. RESULTS AND DISCUSSION

We have also demonstrated the use of padlock probes for damage analysis and single nucleotide genotyping of individual mitochondrial DNA molecules in the microfluidic format. This genotyping method can be applied to study sequence variation in the mitochondrial genome, enabling analysis of the distribution of mitochondrial genomes within cells. The heteroplasmic cell line G55.1.1, having two genotypes of mitochondria that differed in one base pair (A3243G point mutation) was cultured in microfluidic chip. Then mitomycin C (MMC) was applied to the half part of the microchannel for 1 hour followed by mitochondrial

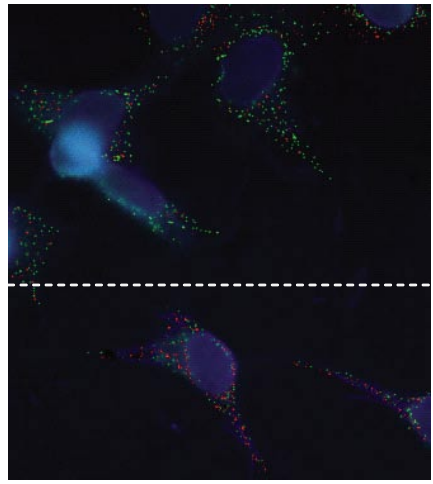

Figure 4. Image of *in situ* genotyping and damage analysis of mitochondrial DNA -Color image can be found on the CD-

genotyping. Individual mitochondrial DNA molecules are visualized as discrete fluorescence labeled rolling-circle amplification products (seen as bright dots) and their genotype could be determined from the color. Figure 4 shows difference of wild-type/mutant mitochondria distribution between the top half and the bottom half. MMC was applied to the bottom half. Signals from the mutant mitochondrial DNA shown in green and the wild type DNA shown in red and the DAPI-stained cell nuclei are shown in blue. Average signal counts in single cells are shown in Table 1. The population ratios of wild-type DNA to mutant DNA are 0.64 in an untreated area and 2.2 in a MMC treated area. This result suggests that damage registance of DNA can be affected by mutation.

Table 1. Average signal counts in single cells

	Wild type	Mutant
Untreated	78	121
MMC treated	63	29

5. CONCLUSIONS

DNA damage analysis and genotyping of single mitochondrial DNA in single cells have been demonstrated in microfluidic device. Combination of laminar flows and *in situ*-reacted padlock probes may open new lines of studies of mitochondrial DNA.

ACKNOWLEDGEMENTS

The authors would like to thank Strategic Japanese-Swedish Cooperative Program on "Multidisciplinary Bio" co-funded by JST, VINNOVA and SSF.

REFERENCES

[1] Nilsson et al. (1994) *Science*, **265**, 2085; Nilsson et al. (1997) *Nat. Genet.*, **16**, 252; Nilsson et al. (2000) *Nat. Biotech.*, **18**, 791; Hardenbol et al. (2003) *Nat. Biotech.*, **21**, 673,

[2] Banér et al. (1998) *Nucleic Acids Res.*, **26**, 5073; Dahl et al. (2004) *PNAS*, **101**, 4548

[3] C. Larsson, J. Koch, A. Nygren, G. Janssen, A.K. Raap, U. Landegren and M. Nilsson, *Nat. Meth.* **1**, 227-232 (2004).

[4] J. Melin, H. Johansson, O. Söderberg, F. Nikolajeff, U. Landegren, M. Nilsson and J. Jarvius, *Anal. Chem.* **77**, 7122-7130 (2005).

DNA NANOFILTRATION AT HIGH ELECTRIC FIELDS

Nabil Laachi,[1] Carmelo Declet,[2] Christina Matson,[3] and Kevin D. Dorfman[1]

[1]Chem Eng Mat Sci, University of Minnesota -- Twin Cities, USA

[2]Chem Eng, University of Puerto Rico -- Mayaguez Campus, PUERTO RICO

[3]Biol Eng, Mississippi State University, USA

ABSTRACT

We present a theoretical study of the electrophoresis of DNA through a periodic array of narrow slits and deep wells (a nanofilter). We focus on the transport of short DNA under strong fields, showing that longer molecules travel faster due to a new mechanism "torque-assisted escape". This new prediction can lead to enhanced nanofluidic separations of DNA.

Keywords: DNA Electrophoresis, non-equilibrium transport, nanofilters, nanofluidics.

1. INTRODUCTION

Nanofilters emerged recently as a promising class of nanofabricated devices for separating short DNA (< 1000 bp) and denatured proteins [1,2]. The device is fabricated by reactive ion etching on a silicon wafer to produce a series of narrow slits alternating with deep wells that trap the migrating molecules [3]. In early experiments [1] on rod-like short DNA, the smaller molecules were found to migrate more quickly than their larger counterparts due to an Ogston sieving-like mechanism [2]. Also, it has been shown that the separation breaks down around 100 V/cm, where all the molecules migrate in a band compressed regime, emerging from the device at the same time [1].

2. THEORY

Although very useful, the previous results are only valid as long as the electric field is low enough (relative to molecular diffusion) to permit sufficient time for the molecules to relax inside the well. In the present paper, we aim to show that the range of useful electric fields can be extended to high values (~ 1000 V/cm). In this regime, the device should operate in a band-inverted manner, with the longer DNA eluting first by a new dynamic mechanism that we call “torque assisted escape” [4]. We focus below on the migration and separation of short DNA in a nanofilter with the geometry described in Fig. 1(a).

The apparent loss of resolution observed experimentally at $E_{av} \sim 100$ V/cm does not result from the absence of trapping. Rather, during their convection-dominated transport across the well, short rigid-like DNA change their orientations by rotational diffusion and must arrive with a favorable orientation in order to enter the slit. This translates to a critical electric field E_{av}^{*}, above which the molecules hardly reorient during the migration and do not become trapped. A simple scaling argument based on the maximum entry angle and the rotational diffusion of the molecule leads to an estimate of $E_{av}^{*} \sim 50,000$ V/cm [4], which exceeds any practical electric field achievable in separation experiments. As a consequence, even beyond 100 V/cm, rotational diffusion will impart some variations in the orientation at the slit entrance, leading to an effective trapping of the DNA.

978-0-9798064-0-7/μTAS2007/$20©2007CBMS

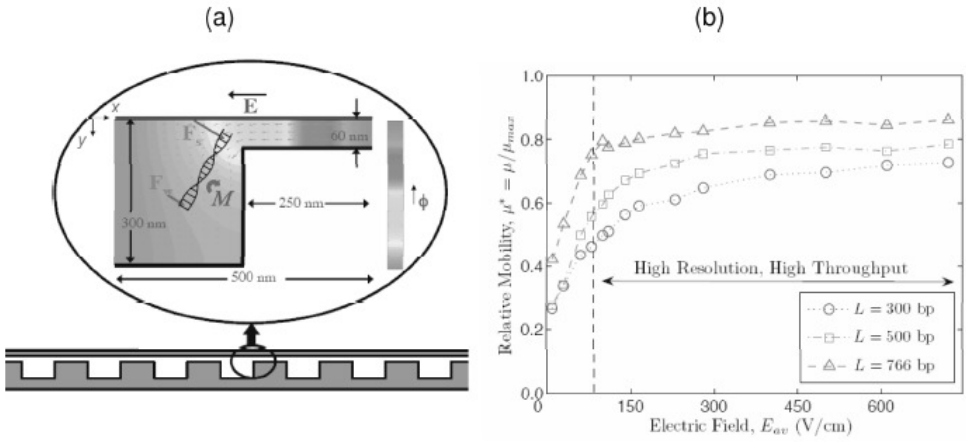

FIG.1: (a) *Schematic of a periodic nanofilter with length scales from [1]. The colors and the arrows indicate the electric potential and the inhomogeneous field lines. The torque acting on a molecule (not to scale) is indicated.* (b) *Mobilities from simulations of different length DNA in the nanofilter.*

To escape and enter the slit, DNA must "undo" rotational diffusion. Two physical processes govern the escape: continual rotational diffusion and the electric field-induced torque that originates from the non-uniformity of the electric field. The relative importance of these two mechanisms can be assessed via the rotational Peclet number, ratio of the characteristic times of rotation by diffusion and torque respectively. We can then write [4]

$$\mathrm{Pe}_r \equiv \frac{\tau_d}{\tau_e} = \left(\frac{1-\delta}{1+\delta}\right)\left(\frac{\hat{q}E_{av}L^2}{k_BT}\right),$$

where δ is the slit to the well depth ratio, L is the length of the molecule, $\hat{q}$ is the effective charge per unit length and k_BT is the Boltzmann factor. For low values of Pe_r, rotational diffusion dominates the torque in the escape process. In this limit, inasmuch as the transport is governed by random motion, we would not expect a sharp separation of the molecules. As the rotational Peclet number passes through values of O(1) we would expect a transition from rotational diffusion to "torque-assisted escape". As the latter mechanism favors long molecules (the torque scales like L^2 [4]), a band inverted regime is predicted where longer molecules will now emerge first. This indicates that separation of short DNA molecules in nanofilters can still be achieved in high fields (due to torque assisted-escape).

Using the experimental values of $\delta = 1/5$, $\hat{q} = 7\times10^{-12}$ J/V m [2], the above equation yields $\mathrm{Pe}_r = E_{av}N^2\times10^{-8}$, where N is the number of base pairs and E_{av} is in V/cm. For a moderate size of $N = 300$ bp, the loss of resolution observed around 100 V/cm occurs when $\mathrm{Pe}_r \sim 0.1$, close to the predicted value for the cross-over to torque-assisted escape.

3. NUMERICAL RESULTS

We compared the results predicted above with Brownian dynamics simulation data on the DNA migration through a series of 2D unit cells. The short DNA is modeled as a rigid dumbbell that consists of two charged beads connected by an inextensible tether. The

motion of the dumbbell is governed by the balance of the forces acting on each bead: (i) an electric force; (ii) the action of the solvent in terms of a drag force and a fluctuating Brownian force; and (iii) a constraining force to maintain the beads at a constant distance. The resulting stochastic differential equations are numerically integrated using the midpoint algorithm, and position updates that put a bead inside the walls are rejected while the time-counter is incremented.

The mobility from the simulation, made dimensionless with the maximum mobility in the nanofilter, is plotted in Fig. 1(b) as a function of the applied field for three DNA molecules of different size. The mobility increases monotonically with the electric field for all molecules until it reaches its limiting value $\mu_{\max}$ imposed by the nanofilter geometry at values of $E_{av} \gg 700$ V/cm, in good agreement with the critical value. Also, the plots indicate a band compression regime between the two shortest DNA at fields $E_{av} < 100$ V/cm, which is again in good agreement with the loss of resolution value observed experimentally [1]. The largest molecule is predicted to move faster as a result of the not so small $\mathrm{Pe}_r \sim 0.6$, indicating that the torque is commensurate with rotational diffusion at 100 V/cm. In general, our model does not predict a single region where all of the DNA would move at the same speeds since the transition into torque-assisted escape regime depends on the molecular weight. Most importantly, the simulation suggests that a band inversion regime follows the band compression one, as expected from the scaling arguments. The transition occurs at $E_{av} \sim 100$ V/cm where all the DNA have passed $\mathrm{Pe}_r \sim 0.1$, indicating that torque-assisted escape is responsible for such behavior.

4. CONCLUSION

In summary, the scaling arguments and simulation results presented above show that nanofilters need not necessarily operate near equilibrium to separate short rigid DNA. The loss of resolution experimentally observed is probably not the upper limit of operation of the device. Rather, we showed that strong electric fields can also lead to a separation with a band inversion; longer molecules elute first due to torque-assisted esacpe. The experimental validation of our results can prove useful for enhancing the separation speed and thus the performance of the promising new class of separation devices.

C.D. and C.M. acknowledge the support of the UMN Bioinformatics Summer Institute. This work was carried out in part using computing resources at the University of Minnesota Supercomputing Institute. We are grateful to Prof. Satish Kumar and Nazish Hoda for useful discussions on Brownian dynamics.

---

[1] J. Fu, P. Mao and J. Han, *Nanofilter array chip for fast gel-free biomolecule separation*, Appl. Phys. Lett. **87**, 263902 (2005).

[2] J. Fu, J. Yoo and J. Han, *Molecular sieving in periodic free-energy landscapes created by patterned nanofilter arrays,* Phys. Rev. Lett. **97**, 018103 (2006).

[3] J. Han and H. G. Craighead, *Separation of long DNA molecules in a microfabricated entropic trap array,* Science **288**, 1026 (2000).

[4] N. Laachi, C. Declet, C. Matson and K. D. Dorfman, *Nonequilibrium transport of rigid macromolecules in periodically constricted geometries,* Phys. Rev. Lett. **98**, 098106 (2007).

ISOLATION OF SINGLE CHROMOSOMAL DNA MOLECULE UNDER MICROSCOPE USING OPTICALLY-DRIVEN MICRO-BOBBINS

K. Terao[1], H. Oana[2] and M. Washizu[2]
[1]Kyoto University, JAPAN
[2]The University of Tokyo, JAPAN

ABSTRACT

This paper presents a novel method for the handling of single chromosomal DNA molecule under a fluorescence microscope. In order to isolate and manipulate single DNA molecule, we developed bobbin-like microstructure, which were fabricated with SU-8 photo resist and grasped by focused laser beams. A targeted yeast chromosomal DNA molecule in solution was wound between the optically-driven bobbins, transferred to desired locations, and released from the bobbins. This handling technique allows us to isolate single giant DNA molecules without breaking, leading to the genomic studies based on the observation of single DNA molecules.

Keywords: Chromosomal DNA, Optical Tweezers, SU-8, Molecular Manipulation

1. INTRODUCTION

The handling of single DNA molecule is a key technique in genomic studies based on the observation of single DNA molecule, such as optical mapping [1] and DNA-protein interaction assays [2]. One requirement for such molecular analysis is to isolate and manipulate fragile chromosomal DNA, ranging from mm to cm in eukaryotes, without breaking. For this purpose, we developed bobbin-like microstructures (micro-bobbins).

2. EXPERIMENTAL

The shape and the dimensions of a micro-bobbin are shown in Figure 1, which is to be grasped by optical tweezers and revolved to wind DNA around them. It has the dimension of 10 μm in height and c.a. 5 μm x 4 μm in cross-section, having a narrow waist at the center. The structures are fabricated by standard SU-8 lithography, scraped off from the substrate and suspended in water.

The driving system is shown in Figure 2. The liquid chamber is mounted on an inverted microscope, and the laser beams are focused by the objective lens and fed from the bottom. Due to the beam profile of a focused laser, an elongated object is oriented with its longest axis parallel to the beam [3]. Hence a bobbin trapped by the beam spontaneously orients itself and stands perpendicular to the chamber bottom. The optical system has two independent laser beams, split from a Yb fiber laser (1066 nm, 1.5 W), one fixed, and the other steered by a scanning mirror. Both beams are focused onto the plane of the observation by the objective lens.

Figure 3 shows how the micro-bobbins are used. First, we draw chromosomal DNA out of cells using electroosmotic flow in the liquid chamber, where the DNA fiber extends a few microns above the bottom [4]. The bobbin's dimension is chosen so that it can accept laterally extended DNA fibers into its waist when it stands in the laser beam. Then micro-bobbins are fed, and arbitrary two of them are picked up by each laser beam. We bring the

978-0-9798064-0-7/μTAS2007/$20©2007CBMS

bobbins into contact with a targeted DNA fiber, and then move one of them around the other, with the revolution radius of c.a. 20μm and the speed of 0.1 – 1 Hz. By doing so, the DNA strand is wound between two bobbins and the tension during the winding guides the strands into the waists. Once wound, the DNA becomes less susceptible to the hydrodynamic breakage, and can be transferred to desired locations. By reversing the rotation, the wound DNA is released to an extended form. This technique may also be used for the isolation of the targeted DNA molecule from the others.

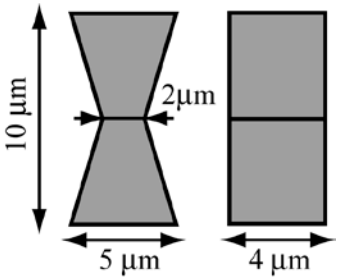

Figure 1. Micro- bobbin. Shape and dimensions.

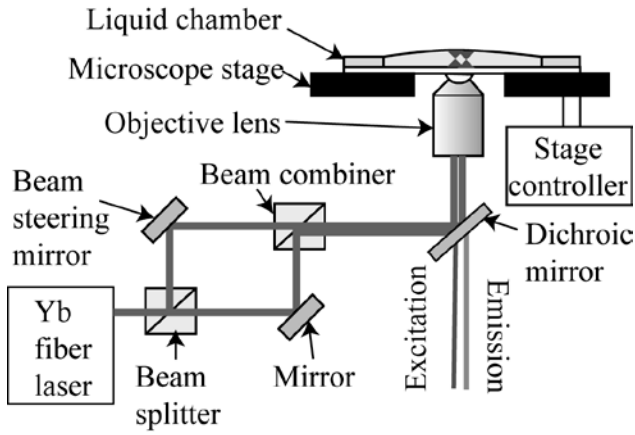

Figure 2. The experimental setup. A laser beam is split into two, one fixed and the other movable around the fixed by the steering mirror.

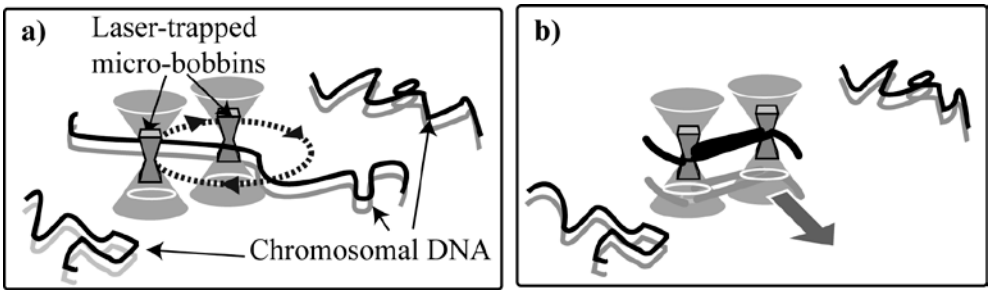

Figure 3. Isolation of a targeted DNA molecule in solution. a) A targeted DNA molecule (middle) is wound between the bobbins by their revolving motion. b) The wound DNA is transferred with the bobbins.

3. RESULTS AND DISCUSSION

Figures 4 and 5 show the snapshots of winding and unwinding. The winding speed in this experiment was about 50 μm/sec, and complete winding of the fission yeast chromosomal DNA was achieved. In unwinding process (Figure 5), the microscope stage was moved in synchronization with the unwinding to avoid entanglement of the released fiber. The DNA molecule was unwound completely and released from the micro-bobbins.

4. CONCLUSIONS

We have demonstrated manipulation of single chromosomal DNA molecule, using optically-driven microstructures. A targeted DNA molecule was wound between a pair of micro-bobbins. The release of the wound DNA molecule was achieved by unwinding of the DNA fiber. This technique allows isolation of single DNA molecule under a microscope without DNA breakage, leading to the observation of single chromosomal DNA molecules for genomic studies

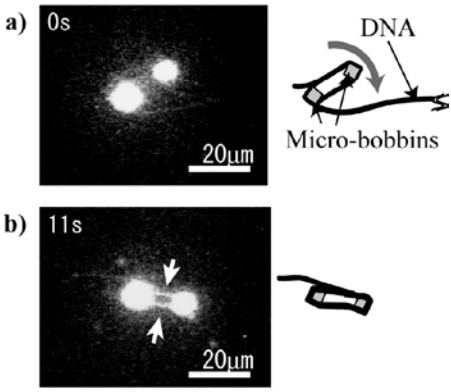

Figure 4. Winding of fission yeast chromosomal DNA, fluorescence images (left) and schematics (right). a) DNA fiber is being wound. b) Winding completed. DNA between two bobbins is observed as the brighter fluorescence bridging over the bobbins (arrows).

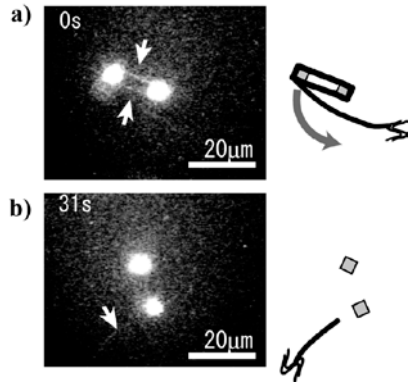

Figure 5. Unwinding of the DNA, fluorescence images (left) and schematics (right). a) Unwinding in progress. The DNA fiber between the bobbins (arrows) is released. b) Unwinding completed. The end came off (arrow).

ACKNOWLEDGEMENTS

This work was supported by Industrial Technology Research Grant Program from the New Energy and Technology Development Organization (NEDO). Photography masks were fabricated using EB lithography apparatus of VLSI Design and Education Center (VDEC), The University of Tokyo.

REFERENCES

[1] J. Herrick, and A. Bensimon, "Imaging of single DNA molecule: Application to high-resolution genomic studies", Chromosome Research **7**, pp. 409-423 (1999).

[2] T. Ha, "Single-molecule fluorescence methods for the study of nucleic acids", Current Opinion in Structural Biology **11**, pp. 287-292 (2001).

[3] R.C. Gauthier, M. Ashman, and C.P. Grover, "Experimental conformation of the optical-trapping properties of cylindrical objects", Applied Optics **38**, pp. 4861-4869 (1999).

[4] K. Terao, H. Kabata, H. Oana, and M. Washizu, "Complete extension of chromosomal DNA and its manipulation using optically-driven micro-fabricated hooks", Proc. μTAS2005 **1**, pp. 715-717 (2005).

MOLECULAR CROWDING EFFECT ON ENZYMATIC REACTION IN A fL-MICROCHAMBER TO MIMIC CROWDED INTRACELLULAR ENVIRONMENT

H. Murahara[1], N. Kaji[1,2], M. Tokeshi[1,2], Y. Baba[1-4]

[1]Department of Applied Chemistry, Graduate School of Engineering, [2]MEXT Innovative Research Center for Preventive Medical Engineering, Nagoya University,[3]Health Technology Research Center, AIST, [4]Institute for Molecular Science, JAPAN

ABSTRACT

In this work, we investigated how the size of reaction space would affect enzyme activities to understand intracellular enzyme kinetics. Two approaches were used to create pseudo-intracellular environments: a high concentration of polymers in bulk state and microfabricated chambers. Both approaches were carefully compared and we found that an enzyme activity was inhibited in 7.2 fL chamber by molecular crowding effect as in the case of highly concentrated polymer solution.

Keywords: single enzyme, molecular crowding, fL-chamber

1. INTRODUCTION

Biomolecules evolved to function within living cell occupy a significant fraction (20-40%) of the cellular volume (Fig.1). In these days, it is clarified that the structure and stability of biomolecules are changed under pseudo-intracellular environments. Therefore, the intracellular enzyme kinetics might be different from bulk phase because of molecular crowding condition which makes minute spaces by an excluded volume effect [1]. In this work, we studied how enzyme activities are inhibited by limiting the reaction space.

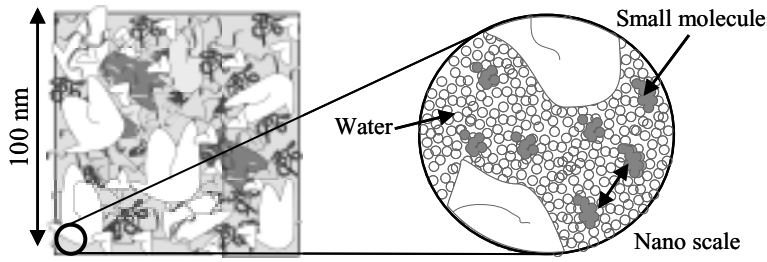

Figure 1. Schematic of the intracellular environment

2. EXPERIMENTAL

We applied two approaches : The first method is to add high concentration of several polymers to buffers (Fig.2a). BSA, Polyethylene Glycol 8000, 20000 and Ethylene Glycol were used as crowding agents to mimic the intracellular environment. The other method is to scale down the reaction volume of single enzyme from pL to fL (Fig.2b). A droplet containing the reacting enzymes was sandwiched by a cover glass and the PDMS device which have several sizes of chambers (pL to fL) to analyze a single-enzyme activity in a

978-0-9798064-0-7/μTAS2007/$20©2007CBMS

microspace [2]. We chose fluorescein-di-β-D-galactopyranoside (FDG) hydrolysis by β-galactosidase (β-Gal) as a model enzyme reaction and evaluated the enzyme activity by fluorescence intensity and compared enzymes activities using the above approaches.

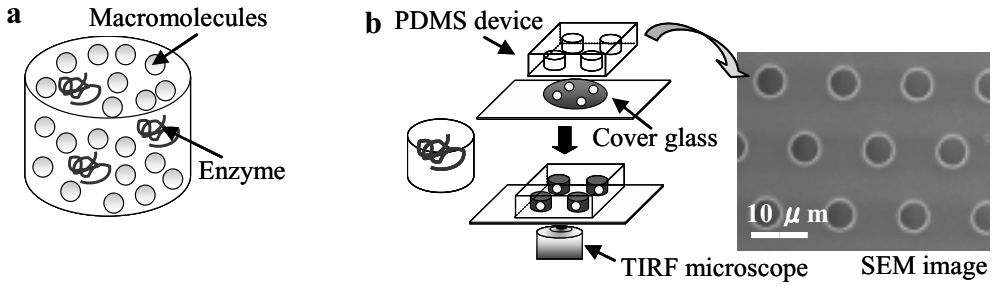

Figure 2. Schematic of pseudo-intracellular environments

3. RESULTS AND DISCUSSION

In the first approach, we obtained the results that, as the concentration of crowding agents increase, the Michaelis-Menten constant (K_M) increased (Fig.3a) but the turnover rate (*k*cat) initially increased, and then decreased (Fig.3b). Both crowding condition in Polyetylene Glycol and BSA have these trends. These results suggested that not particular interactions between the enzymes and crowding agents but the crowding condition affected the kinetic parameters of the enzyme reaction.

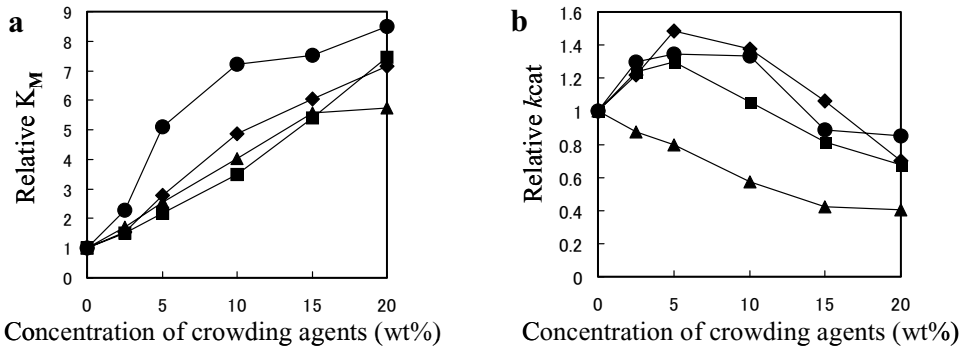

Figure 3. Kinetic parameters of β-Gal in the crowding condition in the presence of BSA (●), Ethylene Glycol (▲), Polyethylene Glycol (MW=8000 (■),20000 (◆))
These parameters were calculated relatively based on the parameters of bulk phase.

Next we tried to investigate the enzyme activity at a single molecule level in microspace to confirm whether the molecular crowding effect is occurred in a microspace where molecular diffusion is strictly inhibited. The single enzyme activity in chambers were calculated from the histograms of increase of fluorescence intensity in 60s (Fig. 4). We fitted the peaks of single enzyme Gaussian distributions and characterized the average as the single enzyme activities. As a result, the enzyme activities in 600 fL and 60 fL chambers showed similar values, but the activity in 7.2 fL chamber was lower (Fig.5). The single enzyme assay gave the unique data of the relationship between a single enzyme activity and

the reaction space and suggested the possibility that the small space like the 7.2 fL raise the molecular crowding effect as well as in the case of highly concentrated polymer solution.

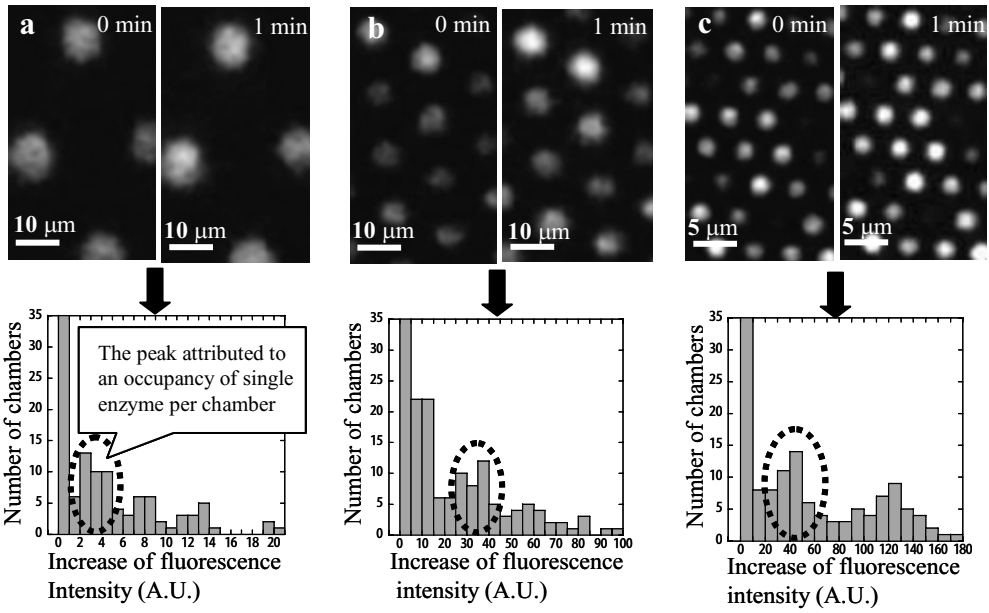

Figure 4. Detection of the activity of the single enzyme. (a), (b), (c) Fluorescence images of the enzymatic activity in 600 fL, 60 fL, 7.2 fL chamber.

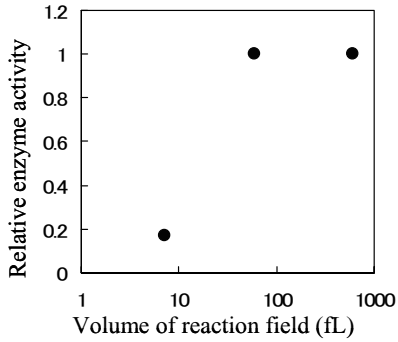

Figure 5. Relationship between the enzyme activity and the reaction space. The enzyme activities were calculated relatively based on the activity in 600 fL chamber.

4. CONCLUSSION

We succeeded to analyze the effect of molecular crowding at a single-enzyme level. Development of a single-enzyme reaction in a microspace is expected to provide a way for precise understanding of biochemical reactions in intracellular environments.

REFERENCES

[1] Goodsell, DS. *Trends Biochem Sci*. Jun; 16 (6): 203-6 (1991)
[2] Rondelez, Y. et al. *Nature Biotechnology*. 23, 3 (2005)

NANOFLUIDIC PRECONCENTRATION OF BIOMOLECULE ANALYTES USING MICROTUBULES

T. Kim[1] and E. Meyhofer[1,2]

[1]*Mechanical Engineering of The University of Michigan, Ann Arbor, MI, USA,*
[2]*Biomedical Engineering of The University of Michigan, Ann Arbor, MI, USA*

ABSTRACT

We successfully developed an innovative biomolecule separation and concentration device by integrating microtubules, one of cytoskeletal filaments, with nanofluidic technology. We functionalized microtubules to obtain numerous, nanoscopic binding sites for specific target molecules and used electrokinetic separation methods to transport the microtubules with bound target molecules in the opposite direction to non-target molecules. Subsequently, since a nanofluidic sieving structure was optimized to completely filter the microtubules[1], we increased the concentration of specific target molecules up to six orders of magnitudes from complex mixtures ranging from 100 pM to 10 fM within 3 hours.

Keyword: Nanofluidics, preconcentration, microtubules

1. INTRODUCTION

It is of significant importance to develop micro-/nano-fluidic techniques enabling sensitive detection, selective separation, and high-throughput concentration of proteins and biomarkers for the advancement of proteomic research and early disease diagnosis[1, 2]. In this work, we demonstrate a novel device that uses functionalized microtubules to selectively capture specific target molecules from complex protein/biomolecule analytes and then separates the microtubules with bound target molecules from other non-target molecules by an electric potential (Fig. 1(A)–(B)). To implement these mechanisms, we designed and fabricated a nanofluidic device that consists of two microchannels (analyte and buffer, Fig. 1(C)) to load analytes and buffer solutions, and a flat nanochannel to electrokinetically connect these adjacent microchannels as seen in Fig. 1 (D).

2. EXPERIMENTAL

First of all, we verified the feasibility of the device by demonstrating that microtubules are concentrated by the nanochannel/concentrator and simultaneously non-target molecules (e.g., FITC-labeled BSA) are removed from the concentrator. As shown in Fig. 2, we loaded a mixture of FITC-labeled BSA and TMR-labeled microtubules into the analyte channel and a buffer solution containing no fluorescein into the buffer channel. In the absence of an electric potential (Fig. 2(A), t=0 s), the analyte channel contains large amount of FITC-labeled BSA. However, as soon as 400V (DC) is applied between the microchannels, FITC-labeled BSA is transported towards the cathode by EOF and approximately 40 sec later, most of the BSA molecules are removed from the microtubule concentrator (Images (A)–(D)). On the other hand, TMR-labeled microtubules continue to head towards the anode but cannot penetrate the nanochannel, resulting in the concentration of the microtubules (Images (E)–(G)). These experimental results prove that the nanochannel successfully acts as a microtubule concentrator and EOF separates non-target molecules from the concentrated microtubules.

978-0-9798064-0-7/μTAS2007/$20©2007CBMS

3. RESULTS AND DISCUSSION

We tested the application of the device to the separation and concentration of BSA molecules that are electrokinetically transported toward the cathode as demonstrated in Fig. 2. For this experiment, microtubules were conjugated with a BSA antibody system via EGS (Ethylene glycol disuccinate di(N-succinimidyl) ester, Sigma Aldrich) as illustration in Fig. 3. These functionalized microtubules were pre-mixed with FITC-labeled BSA and then loaded into the analyte channel. Initially, it is impossible to detect the fluorescence signal from FITC-labeled BSA but, in the presence of an electrical potential (400 V), the signal gradually increases, implying the concentration of BSA. This is because the electrophoretic mobility of the functionalized microtubules still dominates the net mobility of the BSA-bound microtubules. Of course, without the functionalized microtubules, no signal was detected at the concentrator in the control experiment. We note that other target proteins can be also separated and concentrated by replacing the BSA antibody system with other antibody system because microtubules are easily functionalized to concentrate other proteins via the protocol we developed.

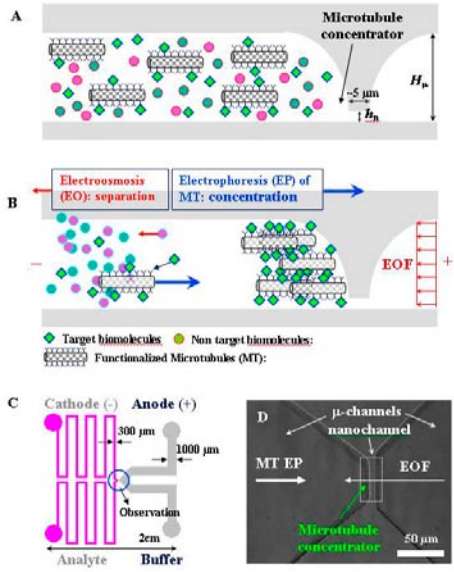

Fig. 1 The basic mechanisms of the device. (A) A mixture of analytes containing specific target molecules, non-target molecules, and functionalized microtubules is loaded into the microchannel at the left side of the nanochannel whereas the right channel is filled with a buffer solution. At this step functionalized microtubules bind specific target molecules. (B) Since the electrophoresis (EP) of non-target molecules is governed by the electroosmosis (EO) of a BRB80 buffer solution in a glass substrate[3], they are electrokinetically separated from the target molecule-bound-microtubules towards the cathode. On the other hand, since the electrophoresis of microtubules dominates EO, the microtubules are transported towards the anode, even though target molecules are bound to the surface of them[4]. Subsequently, the target molecule-bound-microtubules are concentrated by the nanochannel structure, enabling the concomitant concentration of target proteins. This is because the nanochannel is designed to physically prevent the microtubules from penetrating it but to allow ionic current and electroosmotic flow (EOF) to pass through. (C) Shows the micro-/nano-channel network of the device. (D) Shows the detailed top view of the analyte and buffer microchannel and indicates where a nanochannel is fabricated and where microtubules are concentrated.

4. CONCLUSIONS

The sensitivity and the concentration factor of the device are comparable or better compared to other state-of-an-art techniques. However, since the device simultaneously carries out separation and concentration, which are typically performed in order, we can significantly reduce analysis time and efforts and the concentrated, identified target molecules would be useful for post-analysis. Furthermore, biocompatible microtubules can

be differently functionalized to preconcentrate other target molecules and the combination with nanofluidic technology will promise the advancement of μTAS systems.

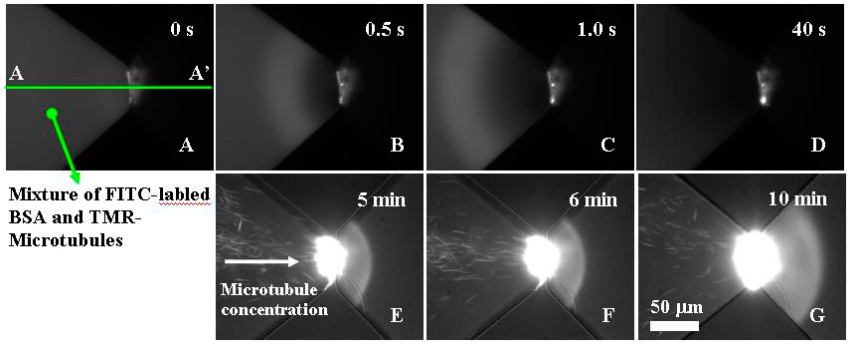

Fig. 2 A mixture of FITC-labeled BSA and TMR-labeled microtubules is injected into the analyte channel whereas a buffer solution is loaded into the buffer channel. (A)–(D) were recorded at blue excitation light to see the mobility of FITC-labeled BSA. When 400V (DC) is applied, FITC-labeled BSA is expelled from the microtubule concentrator by EOF. On the other hand, (E)–(G) were recorded at green excitation light to see the movement of TMR-labeled microtubules. Most of the microtubules are concentrated by the nanochannel and the fluorescence signals at the microtubule concentrator continuously increase.

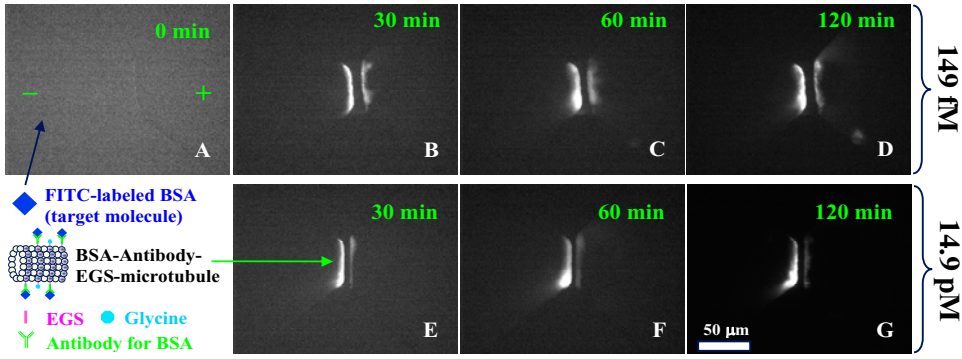

Fig. 3 The qualitative results of the concentration of FITC-labeled BSA analyte with the antibody-functionalized microtubules. The fluorescence intensity signals gradually increase and the concentration area continues to expand with time. This is entirely due to the electrokinetic transport of the functionalized microtubules, implying that BSA can be selectively separated from the analytes and highly concentrated by the nanochannel.

REFERENCES

1. Wang, Y.C., Stevens, A.L. & Han, J.Y. Million-fold preconcentration of proteins and peptides by nanofluidic filter. Analytical Chemistry 77, 4293-4299 (2005).
2. Nam, J.M., Thaxton, C.S. & Mirkin, C.A. Nanoparticle-based bio-bar codes for the ultrasensitive detection of proteins. Science 301, 1884-1886 (2003).
3. Kirby, B.J. & Hasselbrink, E.F. Zeta potential of microfluidic substrates: 1. Theory, experimental techniques, and effects on separations. Electrophoresis 25, 187-202 (2004).
4. Kim, T., Kao, M.-T., Hasselbrink, E.F. & Meyhöfer, E. Active Alignment of Microtubules with Electric Fields. Nano Letters 7, 211-217 (2007).

REAL-TIME, LABEL-FREE PLASMONIC BIOSENSING USING PERIODIC NANOHOLE ARRAYS

Antoine Lesuffleur[1], Adam McFarland[2], Hyungsoon Im[1], Nathan C. Lindquist[1], Christy L. Haynes[2] and Sang-Hyun Oh[1]

[1]Laboratory of Nanostructures and Biosensing, Department of Electrical and Computer Engineering, [2]Department of Chemistry University of Minnesota, Minneapolis, MN, U.S.A.

ABSTRACT

Recent discovery of the extraordinary optical transmission effect provides novel options for surface plasmon resonance biosensing. Here we report the use of a periodic array of nanoscale apertures as a real-time, label-free biosensor. By changing the shape of the nanohole, it is demonstrated that localized surface plasmon resonance can be enhanced, which improves the detection sensitivity for small biomolecules.

Keywords: Nanophotonics, surface plasmon resonance (SPR), label-free biosensing, nanohole array.

1. INTRODUCTION

The capability to analyze complex biomolecular interactions in a quantitative a high-troughput manner is the prerequisite to many important applications in medical diagnostics, systems biology and drug discovery. Surface plasmon resonance (SPR) provides an attractive path towards such quantitative biomolecular analysis wherein the local increase in the refractive index due to molecular binding near a metal-dielectric interface can be optically monitored in a real-time, label-free mode. In this work, a novel SPR sensing methodology is demonstrated, in which the resonant light transmission through a periodic nanohole array is sharply modulated by the adsorption of molecules.

2. THEORY

A decade ago, it was demonstrated that an array of nanohole in a metallic film can present an extraordinary optical transmission (EOT) mediated by surface plasmon resonances for particular wavelength of the incidence light [1]. The resonance wavelengths, where the transmission maxima occur, can be calculated using

$$\lambda_{resonance}(i,j) = \frac{P}{\sqrt{i^2 + j^2}} \sqrt{\frac{\varepsilon_d \varepsilon_m}{\varepsilon_d + \varepsilon_m}} \qquad (1)$$

where P is the periodicity of the array, the integers (i, j) are diffractive orders, and ε_m and ε_d are the dielectric functions of the metal and dielectric, respectively. Adsorption of molecules or molecular interactions at the gold surface change the ε_d value and thus the resonance wavelength, as illustrated in figure 1a.

3. EXPERIMENTAL

Nanohole arrays were fabricated with focused ion beam milling (FEI dual-beam) of 100-nm-thick gold film deposited on standard glass slides. Figure 1b shows a sample array with a 600nm-periodicity and a double-hole shape consisting in two circular holes overlapping to

978-0-9798064-0-7/μTAS2007/$20©2007CBMS

produce apexes at the center. The shape of the nanoholes can strongly influence the transmission properties. Compared to simple circular holes, double-holes allow more intense, sharper and polarization-dependent transmission peaks through the strong localization of the electric field and surface plasmon energy at the apexes. Optical transmission measurements were performed using a microsocope and an Ocean Optics USB4000 spectrometer. A 50× microscope objective was used to focus the incident light on the arrays. For measurements using liquid samples, a flow cell with a height of 150 μm was put on the gold surface.

4. RESULTS AND DISCUSSION

Figure 2a presents the initial transmission spectrum recorded from an array of double-hole with a 600 nm-periodicity without any adsorbed layer. The peak at 650 nm is the resonance we analyzed to study the presence of molecules at the gold surface.

Figure 2b presents the resonance wavelength versus the refractive index at the gold surface of our sensor immersed in different liquids. Our double-hole sensor shows ~600 nm shift per refractive index units (RIU), which is better than the sensitivity measured from a simple circular hole array (333 nm/RIU) [2]. The nanoscale double-hole apertures allow a high confinement of the surface plasmons permitting this higher sensitivity. Figure 3 shows the real-time reponse of the nanohole sensor to the binding on the gold surface of 0.2% bovin serum albumin (BSA) in phosphate-buffer saline solution in a flow-cell (150μm high). The transmission spectrum was measured each 15 seconds over the course of one hour. The total shift due to BSA adsorption was 3.5 nm after 1000 seconds when the response nearly saturates to be compared to the 7 nm shift obtained with a conventional SPR biosensor [3]. This demonstrates the potential of nanohole arrays in a transmission optical setup to perform real time label-free sensing of protein interactions. Although the raw sensitivity of our device is lower than conventional SPR sensors, our nanohole sensor presents a number of advantages, since the transmission geometry for optical detection allows a compact device and the possibility to design portable surface plasmon sensors. Furthermore, the footprint of one array can be as small as 20 μm^2, allowing for a high packing density.

5. CONCLUSIONS

In conclusion, we have demonstrated real-time, label-free sensing of biomolecular adsorption using periodic nanohole arrays. Also, we optimized the shape of the nanohole to maximize detection sensitivity. The ultra-small footprint (20 μm^2) of the nanohole array and the ease of exciting plasmons, which doesn't require a bulky prism, make this device an ideal probing component for future micro total analysis systems.

REFERENCES

[1] T.W. Ebbesen, H.J. Lezec, H.F. Ghaemi, T. Thio and P.A. Wolff, Nature 391, pp. 667-669, (1998).

[2] A.G. Brolo, R. Gordon, B. Leathem and K.L. Kavanagh, Langmuir 20, pp. 4813-4815, (2004).

[3] L.S. Jung, C.T. Campbell, T.M. Chinowsky, M.N. Mar and S.S. Yee, Langmuir 14, pp. 5636-5648, (1998).

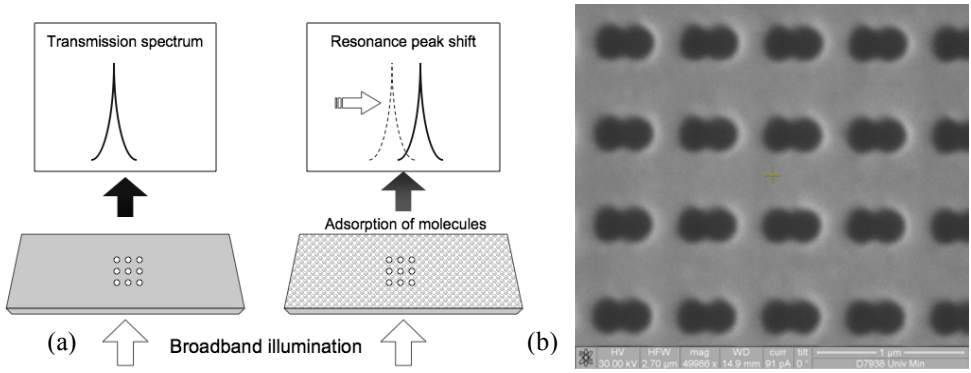

Figure 1. a) Illustration of nanohole biosensing principle b) SEM image of a double-hole array

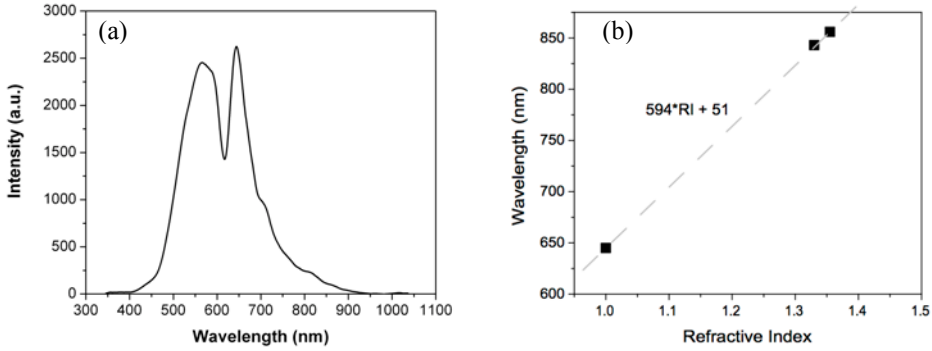

Figure 2. a) Spectrum of the nanohole array and b) resonance wavelength versus refractive index for the sample in acetone (n = 1.36), water (n = 1.33), and air (n = 1).

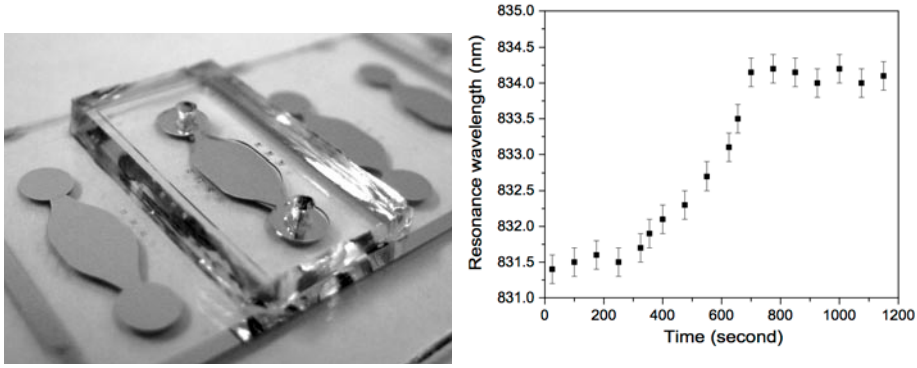

Figure 3. Picture of the device (left) and real time sensing during adsorption of bovin serum albumin (BSA) on the nanostructured gold surface (right).

STATISTICAL MODELS FOR BIOMOLECULAR SHUTTLES GLIDING IN MICROFABRICATED OPEN CHANNELS

C.-T. Lin[1,2], E. Meyhofer[2], K. Kurabayashi[2]

[1]*National Taiwan University, Taipei, Taiwan, R.O.C.(present affiliation)*

[2]*University of Michigan, Ann Arbor, USA*

ABSTRACT

Molecular cargo transport using ATP-fueled motor proteins in a microfluidic system is intriguing for lab-on-a-chip applications as it operates in a self-contained setting with no external power sources. The use of microfabricated channel patterns is common to control the gliding behavior of microtubule molecular shuttles in a microfluidic environment. Here, we establish a theory that accounts for the process of controlling the gliding direction of these molecular shuttles and experimentally validate our theoretical predictions.

Keywords: biomolecular motors, statistical model, microfluidic channel

1. INTRODUCTION

Nature has evolved biomolecular motor proteins as active nanoscale transporters in cells[1]. Integration of motor proteins in a microfluidic network allows a novel on-chip molecular cargo transport system. A common approach to achieve such a biomolecular motor-based microfluidic transport system employs microtubules, one of cytoskeletal components, gliding on a kinesin-coated glass surface as molecular shuttles carrying cargos. Because of their compact size, high chemomechanical energy transduction efficiency, and robust movement *in vitro*[2], kinesins are one of the most promising motor protein species to construct ATP-fueled manmade microdevices[3].

Among several strategies to control the direction of motion of microtubules in an on-chip environment, physical confinement within a lithographically patterned microchannel in the presence of ATP molecules is an intriguing method from an application standpoint. This makes it possible to achieve a fully autonomous, self-contained microfluidic molecular transport system, eliminating the need for external power sources[4]. In this setting, it is critical to design a microfluidic guiding channel that effectively controls the movement of microtubule shuttles to achieve the desired transport performance. However, there is no in-depth theory or model accounting for the physical interaction between kinesin-driven microtubules and microfabricated channels[5]. This limits our ability to design biomolecular motor-based microfluidic transport systems under optimal conditions. Here, we present statistical models to well predict the behavior of microtubules guided by microfabricated structures and experimentally validate them. The established models allow the systematic design of such systems on the basis of detailed understandings of the physics governing the microtubule guiding process.

2. THEORETICAL MODELING

In this work, we modeled the behavior of microtubules when they land from a physiological buffer solution onto an open channel surface and are subsequently guided by a channel sidewall after colliding with the channel sidewall. Our first model predicts the

978-0-9798064-0-7/μTAS2007/$20©2007CBMS

probability of successful landing at a given channel site from a solid angle. The solid angle is determined by the physical constraints as shown in Fig. 1(A). When the incident angle at which microtubules collide with a channel sidewall is small, they are successfully redirected along the channel. Otherwise, they are bent up and lifted away from the kinesin-coated surface. Accounting for bending energy, we developed a statistical mechanics model to predict the success rate of guiding microtubules at a given incident collision angle θ_r as shown in Fig. 1(B).

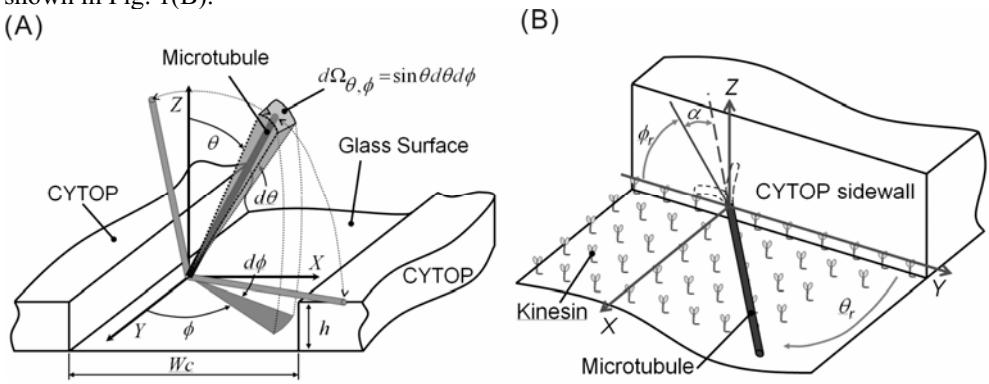

Figure 1. (A) Model for microtubule landing process. For a channel of width W_c, the solid angle can be determined by the geometrical constraints that a sidewall height h and the microtubule length L impose. Microtubules landing into the channel is limited to the light gray angles . Microtubule landing outside this angular range will be blocked by the channel sidewalls as diffusion to the kinesin-coated bottom surface is blocked. (B) Model for guiding and lifting processes of microtubules colliding with channel sidewalls. For simplicity, it is assumed that kinesins are uniformly distributed on the glass surface and do not exist on the sidewall of CYTOP. As the incident angle θ_r becomes larger, a larger amount of bending energy is required for the microtubule to continue to glide with its tip latched onto the adjacent kinesin on the y-axis.

3. EXPERIMENTAL RESULT

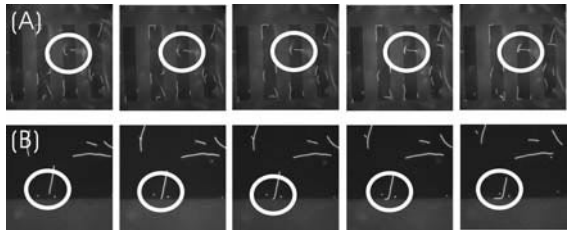

Figure 2. Sequential optical images of a microtubule gliding assay using microfabricated channels. (A) microtubule landing and movement in 20 m-wide channel (within the circle) (B) microtubule guided due to channel collision (within the circle). The sidewall region can be identified as a lighter region due to a moderate auto-fluorescence of the channel material. The microtubule glides on a kinesin-coated glass surface (the dark region) and collides with the kinesin-free channel sidewall.

Moreover, we carried out a series of microtubule gliding assays using microfabricated channels as shown in Fig 2. and observed both the microtuble landing and guiding events at

varying channel width W and incident angles. The average microtubule length L was measured for each experiment and used to normalize the channel width W and sidewall height h. Epifluorescence microscopy with a 40x oil immersion objective lens was used to record each collision event. A successful guiding process was verified by ensuring that the microtubule remained in focus during their gliding motion parallel to the channel sidewall. Fig. 3 compares our theoretical predictions and experimental results. The comparison indicates good agreement between our theory and experiments and validates our models.

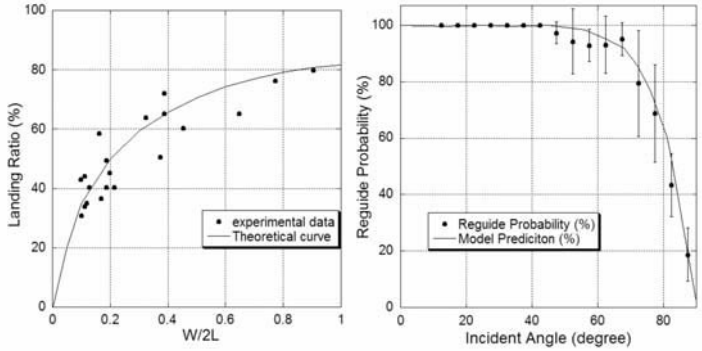

Figure 3. Comparison between theoretical prediction and experimental results. The left picture shows the landing behavior of microtubules in an open microchannel at varying channel width. The right picture shows the success rate of microtubules guided by a microchannel sidewall as a function of incident collision angle.

4. CONCLUSIONS

We have developed statistical models to describe the interaction between microfabricated channels and gliding microtubules. The results of the gliding experiment agree with our theoretical predictions. In the present work, both the statistical mechanics models and the experimental results give us insights into the *in vitro* microtubule gliding behavior in the presence of a microchannel wall. This work provides design guidelines to engineer microtubule-based molecular shuttle transport paths on a microfluidic system.

REFERENCES

[1] Manfred Schliwa, *Molecular Motors,* Wiley-VCH, March 21, 2003
[2] J. Howard, "The movement of kinesin along microtubules", *Annu Rev Physiol*, 58, 703-729, 1996.
[3] L. Limberis, and R.J. Stewart, "Toward kinesin-powered microdevices", *Nanotechnology* 11, 47-51, 2000.
[4] C.-T. Lin, M.-T. Kao, K. Kurabayashi, and E. Meyhofer, "Efficient Designs for Powering Microscale Devices with Nanoscale Biomolecular Motors", *Small*, 2, p281-287, 2006
[5] J. Clemmens, H. Hess, R. Lipscomb, Y. Hanein, K.F. Bohringer, C.M. Matzke, G.D. Bachand, B.C. Bunker, and V. Vogel, "Mechanisms of Microtubule Guiding on Microfabricated Kinesin-Coated Surfaces: Chemical and Topographic Surface Patterns", *Langmuir*, 19, 10968-10974, 2003.

TOWARDS ULTRA-FAST PARALLEL DNA ANALYSIS: SUB-WAVELENGTH METALLIC NANOPORE ARRAYS FOR HIGH-THROUGHPUT SINGLE MOLECULE SPECTROSCOPY

Guillaume A.T. Chansin[1], Rafael Mulero[3], Jongin Hong[1], Min Jun Kim[3], Andrew J. deMello[2] and Joshua B. Edel[1,2]

[1]Institute of Biomedical Engineering, Imperial College London, UK
[2]Department of Chemistry, Imperial College London, UK
[3]Department of Mechanical Engineering & Mechanics, Drexel University, USA

ABSTRACT

We present a novel approach for optically detecting DNA translocation events through an array of solid state nanopores, with the potential to allow for parallelised spectroscopy for high-throughput single molecule DNA analysis.

Keywords: nanopore, translocation, zero-mode waveguide, fluorescence spectroscopy

1. INTRODUCTION

The creation of nanochannels or nanopores in thin membranes has attracted much interest due to the ability to isolate and sense single DNA molecules while they translocate through the highly confined channels [1]. Short translocation lengths make decontamination of the nanopores facile whilst maintaining effective spatial confinement for single molecule detection. Nanopores have already been fabricated in silicon dioxide [2] and silicon nitride [3] membranes and thus in principle may be integrated into monolithic analysis systems. Although the detection of translocation events can be performed electrically by measuring the ionic current [4], we propose to optically probe fluorescently labelled DNA molecules translocating through 50-300 nm wide pores within a thin aluminium/silicon nitride membrane. Such apertures in a metallic layer act as both nanofluidic channels and zero-mode waveguides (ZMW). Since the aperture diameter is much smaller than the excitation wavelength, an evanescent field is produced limiting the excitation regime to a highly localised area [5].

2. EXPERIMENTAL DETAILS

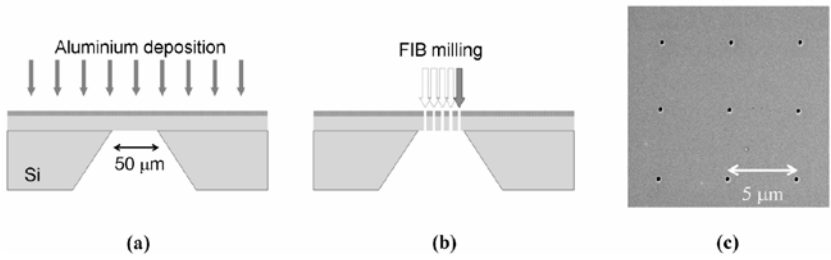

Figure 1. Device fabrication: (a) KOH etching followed by aluminium deposition; (b) Milling of channels by focused ion beam; (c) SEM image of 0.3 μm wide channels.

978-0-9798064-0-7/μTAS2007/$20©2007CBMS

Figure 1 illustrates the basic process for device fabrication. A free standing 200 nm thick silicon nitride membrane is fabricated by standard photolithography and KOH wet etching. The membrane is then deposited with a 100 nm thick aluminium layer. Subsequently, holes are milled sequentially using a focused ion beam (FIB). Figure 1c shows typical results after milling 0.3 μm wide pores in the membrane, giving an aspect ratio close to unity.

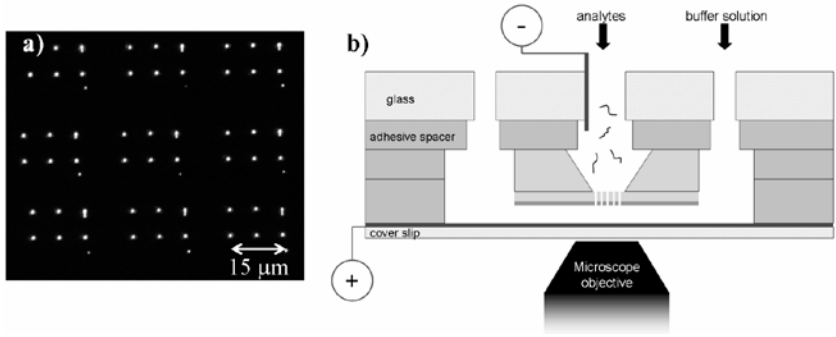

Figure 2. a) Optical image of a membrane: the aluminium layer is opaque to visible light. b) A schematic of the experimental setup for translocation detection.

Double stranded lambda-DNA molecules were labelled with YOYO-1 (Molecular Probes) at a ratio of five base pairs per dye molecule and the solution was then diluted to yield a concentration of 10 pM. Before injecting the analyte solution, the nanopore device was treated with oxygen plasma to ensure the inner surface of the channels is hydrophilic in nature. DNA detection was performed with a custom-built confocal microscope with imaging capabilities. Figure 2 shows the experimental setup. In this approach, the excitation light from a mercury lamp is focused onto the membrane surface and the fluorescence signal is collected by the same objective. The signal is then directed to an emCCD camera. A glass cover slip coated with indium tin oxide (ITO) is used as an electrode to apply a voltage across the buffer solution.

3. RESULTS AND DISCUSSION

Translocations of DNA molecules through the array of pores can be observed in real-time. Figure 3 shows a typical translocation event under an applied voltage of 2.0 V.

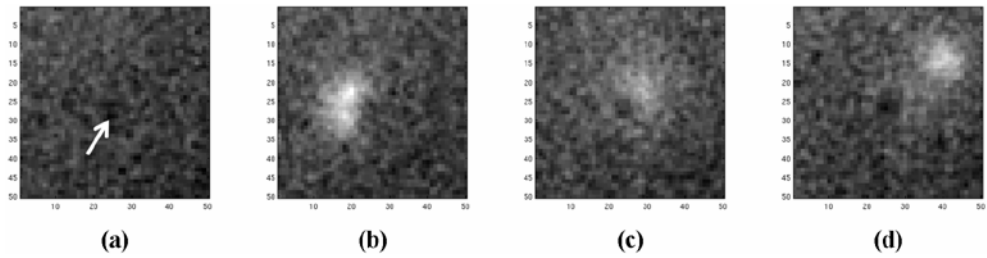

Figure 3. A single DNA molecule translocation imaged at t=0 (a), t=0.11 s (b), t=0.28 s (c) and t=0.50 s (d). Each pixel is 81 nm wide. The arrow points to the center of the pore.

By recording a sequence and selecting the areas of interest on the frames, it is possible to obtain a spectrograph for each of the pores, as shown in Figure 4.

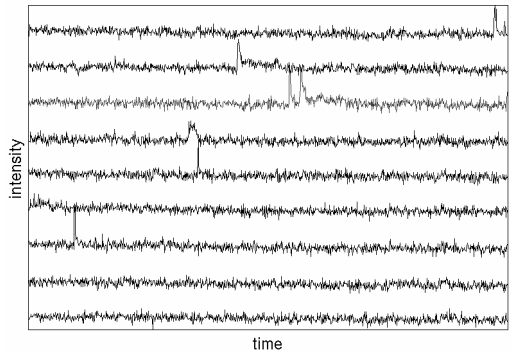

Figure 4. Signal intensities from nine different pores acquired simultaneously under an applied voltage of 4.5 V. The total acquisition time is 20 s. The signals have been shifted vertically for convenience. Each peak corresponds to a translocation.

It is found that the behaviour of the molecules within the channels greatly depends on the hydrophilic state of the surface. Because the oxygen plasma treatment has only a transitional effect, the nanopores start to lose the hydrophilic state after one or two hours.

4. CONCLUSION AND FUTURE WORK

These studies demonstrate that it is possible to obtain a high spatial resolution DNA analysis whilst independently controlling the applied voltage that drives the molecules into nanopore. Another feature of this approach is the possibility of parallelising the analysis of the molecules by probing an entire array of nanopores under uniform illumination. Operations such as fragment sizing of DNA molecules are potentially achievable on timescales significantly shorter than with single pore devices. We expect this work to have a high impact on the biomedical community and to open new routes to faster, parallel biomolecular analysis.

ACKNOWLEDGEMENT

Financial support from The Royal Society is acknowledged.

REFERENCES

1. J. J. Kasianowicz, E. Brandin, D. Branton et al., *Proc. Natl. Acad. Sci. U. S. A.* **93** (24), 13770 (1996).
2. A. J. Storm, J. H. Chen, H. W. Zandbergen et al., *Phys. Rev. E* **71** (5) (2005).
3. J. Li, D. Stein, C. McMullan et al., *Nature* **412** (6843), 166 (2001).
4. J. L. Li, M. Gershow, D. Stein et al., *Nat. Mater.* **2** (9), 611 (2003).
5. M. J. Levene, J. Korlach, S. W. Turner et al., *Science* **299** (5607), 682 (2003).

NMR RELAXATION STUDIES ON THE PROTON TRANSFER DYNAMICS OF WATER CONFINED IN EXTENDED-NANO SPACES ON A CHIP

Takehiko Tsukahara[1,2], Akihide Hibara[1,3], and Takehiko Kitamori[1,2,3]

[1] Department of Applied Chemistry, School of Engineering, The University of Tokyo, JAPAN,
[2] CREST, Japan Science and Technology Agency, JAPAN, and
[3] Kanagawa Academy of Science and Technology, JAPAN

ABSTRACT

We investigated size-confinement effects for proton transfer dynamics of water confined in Extended-Nano Spaces on a chip by utilizing NMR relaxation methods. The results showed that proton transfer rate of water in 120 nm space was about 20 times faster than that in bulk space.

Keywords: NMR Relaxation, Proton transfer, Extended-Nano space, Water

1. INTRODUCTION

Our focus has been centered on the well-defined 10^1 – 10^2 nm-scale channels on a microchip (called Extended-Nano Spaces), since they promise to become an experimental tool for characterizing the complicated collective properties of liquid phase molecules. Previously, we investigated capillarity and time-resolved fluorescent measurements of water confined in such spaces. The results showed that the confined water has a higher viscosity and a lower dielectric constant than that of bulk water [1]. Furthermore, previous NMR chemical shift and relaxation studies showed that translation and proton mobility of water are modulated by size-confinement in the scale size of 40 to 800 nm. From these results, we hypothesized that a proton transfer phase differing from bulk and adsorbed phases, in which water molecules are loosely coupled within 100 nm from the surface, exists in extended-nano spaces [2, 3]. However, the size-confinement effects for the proton transfer dynamics of water in extended-nano spaces are still not clear. Herein, we employ various NMR relaxation rate measurements, which are ^{1}H-NMR spin-lattice relaxation rate ($1/T_1$) spin-spin relaxation rate ($1/T_2$), and rotating-frame spin-lattice relaxation rate ($1/T_{1\rho}$), to clarify slow dynamic modes characterized by proton transfer rates of water molecules in extended-nano spaces.

2. EXPERIMENTAL

The extended-nano spaces (R: 120 nm – 1,500 nm) were fabricated on the synthetic quartz glass by electron beam lithography and plasma etching for high-resolution NMR measurements as shown in Figure 1. The fabricated plase is thermally laminated with cover plate in a vaccume furnance at 1080°C. The ^1H-$1/T_1$, -$1/T_2$, and -$T_{1\rho}$ values of water were measured with the inversion recovery pulse sequence, $(\pi)_x$ - τ - $(\pi/2)_x$, Carr-Purcell Meiboom-Gill pulse sequence, $(\pi/2)_x$ - τ - $((\pi)_x$ - 2τ - $(\pi)_x)_n$, and spin-locking pulse sequence, $(\pi/2)_x$ – $B(\tau)_y$, respectively.

978-0-9798064-0-7/μTAS2007/$20©2007CBMS

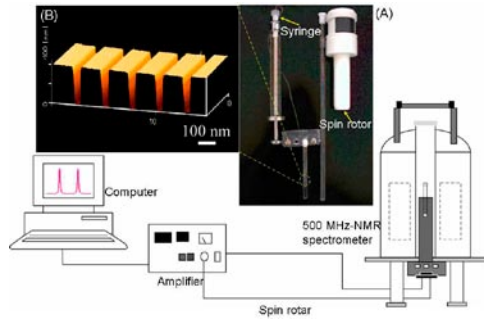

Figure 1: (A) Schematic diagram of NMR setup for the measurements of liquids in 120 – 1,500 nm Extended-Nano Spaces. (B) AFM image of Extended-Nano Spaces on a NMR cell.

3. RESULTS AND DISCUSSION

In general, changes of ^1H-$1/T_1$ values are governed by higher frequency components of motions, and the ^1H-$1/T_2$ and ^1H-$1/T_{1\rho}$ values can provide insight into lower frequency components. Figure 2 shows the plots of ^1H-$1/T_1$, -$1/T_2$, and -$1/T_{1\rho}$ values of water against R. Although all values increased drastically with decreasing in R, in the scale size of 1,500 to around 200 nm, the size dependence of ^1H-T_1 was smaller than that of ^1H-$1/T_2$, -$1/T_{1\rho}$. At below 200 nm, we observed the differences between the $1/T_2$ and $1/T_{1\rho}$ values. These results indicate that molecular motions with slower correlation time, *i.e.*, proton chemical exchange, are mainly influenced by size-confinement, because the order of $1/T_1 << 1/T_{1\rho} \leq 1/T_2$ often appears in compounds with slower components such as macromolecules.

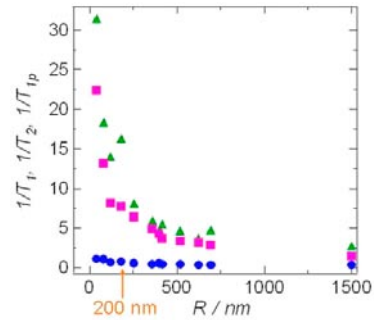

Figure 2. The size-dependences of ^{1}H-$1/T_1$ (●), -$1/T_2$ (▲), -$1/T_{1\rho}$ (■) values for water in the range of 120 to 1500 nm at 500MHz and 20 °C.

To determine the proton exchange correlation time (τ_e), we measured the *rf* field amplitude (B_1) dependence of $1/T_{1\rho}$ values based on changes of NMR signal intensity against spin-locking times, because the $1/T_{1\rho}$ values depend on frequency in spin rotating frame ($\omega_1 = \gamma B_1$). The results were shown in Figure 3. We found that the $1/T_{1\rho}$ values increased with decreasing in B_1, and that the B_1 dependence was enhanced by size-confinement. The τ_e values were obtained according to Eq. (1);

$$\frac{1}{T_{1\rho}} \propto \frac{1}{T_1} + \frac{A\tau_e}{1+4\omega_1^2\tau_e^2} \qquad (1)$$

We found that the τ_e value are reduced by size-confinement as listed in Table 1. The τ_e value of 1.4×10^{-5} sec for a 120 nm space reduced by a about factor of 1/20 from a 5,000 nm. The obtained τ_e value was close to 0.8×10^{-5} sec for pore surface water [4]. Moreover, the coefficient A values, in which a measure of the strength of the proton-proton dipolar interaction, increased considerably with decresing in space sizes These phenomena indicate that the slower component of water motions is modulated in nanospaces, and that

the proton transfer rate of water can be led to an increase more than one order of magnitude compared with bulk water.

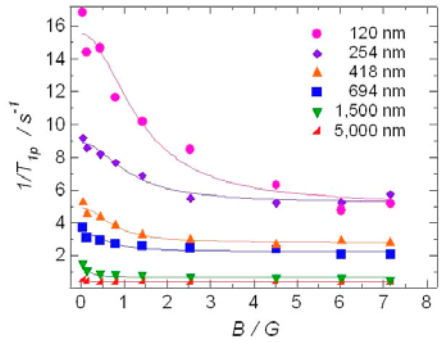

Figure 3.Proton spin-lattice relaxation rates in the rotating frame ($1/T_{1\rho}$) as functions of the rf field amplitude (B_1) at water confined in various extended-nano spaces. The solid lines are the fitted curve to Eq. (1).

Table 1. Results of the analysis of $1/T_{1\rho}$ data using Eq. (1).

R / nm	A / $10^4 s^{-2}$	τ_e / $10^{-5}s$
120	75.7±16.7	1.4±0.3
256	21.8± 4.2	1.7±0.4
418	8.7± 1.5	2.5±0.3
694	4.3± 1.6	2.8±0.1
1,500	0.7± 0.2	11.4±4.4
5,000	0.1± 0.1	21.9±7.2

4. CONCLUSIONS

We examined the ^1H-$1/T_1$, -$1/T_2$, and -$1/T_{1\rho}$ values of water confined in 120 – 5,000 nm spaces, found that the order of $1/T_1 << 1/T_{1\rho} \leq 1/T_2$ appears in nanospaces below 200 nm. Moreover, from B_1 dependence of $1/T_{1\rho}$ results, the proton transfer rate of water in the extended-nano spaces was found to be enhanced by a factor of more than ten from bulk water. These results should be evidence for previous proposal model [2], in which water motions in confining geometries are controlled by the weighted average of three phases such as bulk phase, adsorbed one, and proton transfer one.

REFERENCES

[1] A. Hibara, T. Saito, H.B. Kim, M.Tokeshi, T. Ooi, M. Nakao, and T. Kitamori, *Anal. Chem*., **74**, 6170 (2002).
[2] T. Tsukahara, A. Hibara, Y. Ikeda, and T. Kitmaori, *Angew. Chem. Int. Ed*., **46**, 1180 (2007).
[3] T. Tsukahara, W. Mizutani, A. Hibara, and T. Kitmaori, *Proc. μTAS 2006*, vol.1, 546 (2006).
[4] R. Holly, H. Peemoller, C. Choi, and M.M. Pintar, *J. Chem. Phys*, **108**, 4183 (1998).

MOLDED NANOWELL ELECTRODES FOR SITE-SELECTIVE SINGLE LIPOSOME ARRAYS

Pilnam Kim[1], Bong Kuk Lee [2], Hea Yeon Lee [2], Tomoji Kawai [2] and Kahp Y. Suh [1]

[1] Seoul National University, KOREA
[2] Osaka University, JAPAN

ABSTRACT

In this study, a molded nanowell electrode is introduced as an engineered biosensing platform to electrochemically detect biological reactions on the level of single lipid vesicle or liposome. The liposomes were functionalized with multiple surface moieties for bio-specific recognition (biotin), anchoring on gold electrode (thiol), and mediation of electron transfer in an electrolyte (ferrocyanide). Such functional liposomes were selectively captured within high-density nanowell arrays comprising of a polyethylene glycol (PEG) copolymer on gold electrode. The PEG nanowells enabled docking of single liposomes per unit nanowell while significantly reducing nonspecific adsorption, resulting in distinctively separated single liposome arrays. When this molded nanowell electrode was used to measure streptavidin-biotin interactions on the surface of the captured liposome, the electron transfer was efficiently blocked such that the electrochemical responses were significantly enhanced as compared to bare electrodes (~220 times increase in sensitivity).

Keywords: electrochemical biosensor, PEG, nanowell, nano-molding, sensitivity

1. INTRODUCTION

Recently, biosensors of nanoscale dimensions have attracted wide attention for sensitive, multi-targeting, and labeling-free biomolecular detection. Various affinity-binding-assisted analytical tools have been developed based on nanowires[1], nanotubes, or microcantilevers. The widespread use of these tools, however, has been limited by random configuration of binding molecules and the formation of protein-protein cluster on a solid surface, resulting in a loss or masking of binding sites.[2]

Functional lipid vesicles (FLVs) or liposomes are attractive supramolecular assemblies that could overcome the above-mentioned shortcomings of the lipid membranes for the detection of biomolecule with high sensitivity, but without competition or cluster formation. Therefore, Nanoscale arrays of FLVs are potentially useful when employed in electrochemical studies and applications.[3] To achieve a NW-based electrochemical biosensor with FLVs, three of the key directions are to address how to (i) capture FLVs at predefined locations without nonspecific binding, (ii) make the captured FLVs stable and functional, and (iii) quantitatively interpret signals from affinity binding.

2. EXPERIMENTAL

The NWs were fabricated on gold electrode using dewetting-assisted nanomolding with a polyethylene glycol (PEG) copolymer.(Fig.1) The molded nanowell (NW) electrode is introduced as an engineered biosensing platform to electrochemically detect biological reactions for individual vesicles or liposomes. The liposomes were functionalized with

978-0-9798064-0-7/μTAS2007/$20©2007CBMS

multiple surface moieties for bio-specific recognition (biotin), anchoring on gold electrode (thiol), and mediation of electron transfer in an electrolyte (ferrocyanide).

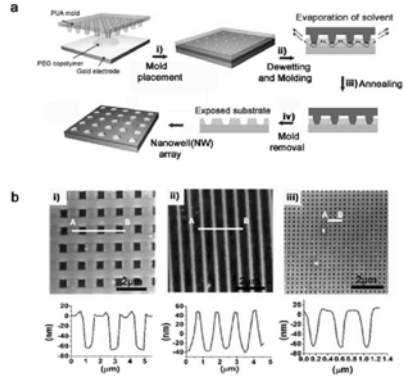

Figure 1. a. A schematic illustration for the fabrication of PEG nanowells with exposure of the substrate. b. Planar and cross-sectional AFM images for three PEG

Such functional liposomes were selectively captured within high-density NW arrays comprising of a polyethylene glycol (PEG) copolymer (diameter of 70 nm, ~750,000 wells per unit electrode area of 500 x 500 μm2) on gold electrode. The PEG NWs enabled docking of single liposomes per unit NW while significantly reducing nonspecific adsorption, resulting in distinctively separated single liposome arrays (Fig. 2)

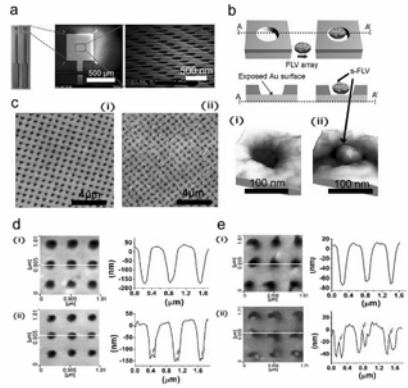

Figure 2a: Optical and SEM images for the 500 × 500 μm^2 rectangular gold electrode. The electrode contained PEG NWs of a cylinder-shape with 150nm diameter at top and 70nm diameter at bottom. b, A schematic illustration for the docking of single-FLVs onto gold An empty. c, AFM images for a large-area view d-e, AFM images showing two NW arrays with 200nm and 70nm height,. Note: (i) before and (ii) after deposition of liposomes

3. RESULTS AND DISCUSSION

To claim that NW electrode can act as a restrictive surface for bioassays, the binding event should block the electron transfer to NW electrode (so called shielding effect). Figure 3a illustrates the streptavidin-biotin interactions using biotinylated FLVs containing thiol, ferrocence and PEG moieties inside NW. With this NW electrode, the

electrochemical responses were significantly enhanced for binding interactions of streptavidin-biotin on the surface of FLVs (~220 times increase in sensitivity as compared to bare electrode) and the
electron transfer was efficiently blocked by the captured liposome. It is envisioned that the above-mentioned features could make the molded NW electrode presented here especially useful for various immunoassays or devices involving biological detections.

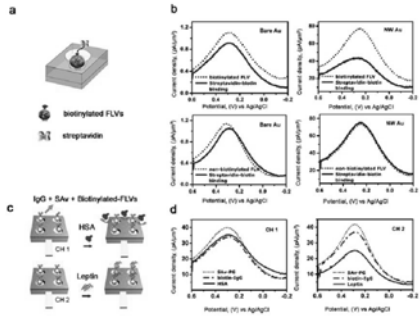

Figure 3. a: A schematic illustration of the binding event between streptavidin and the captured biotinylated FLVs on NW electrode. b: SWV measurements of current density before and after addition of streptavidin. c. A detection scheme of leptin using two channel electrodes (CH1: negative control, CH2: positive control). d, SWV measurements of current density after addition of the biotinylated anti-leptin (biotin-IgG) and HSA (CH 1) or leptin (CH 2). All the SWV data were obtained at a scan rate of 200 mV/s.

4. CONCLUSIONS

Using this nanowell electrode, the electrochemical responses were significantly enhanced for binding interactions of streptavidin-biotin on the surface of FLVs (~220 times increase in sensitivity as compared to bare electrode) and the electron transfer was efficiently blocked by the captured liposome. It is envisioned that the above-mentioned features could make the molded nanowell electrode presented here especially useful for various immunoassays or devices involving biological detections.

ACKNOWLEDGEMENT

This work was supported by the Micro Thermal System Research Center of Seoul National University, the Seoul R&BD Program (Seoul Research and Business Development Program).

REFERENCES

[1] Y. Cui, Q. Q. Wei, H. K. Park, and C. M. Lieber , *Nanowire nanosensors for highly sensitive and selective detection of biological and chemical species*, Science, **293**, 1289 (2001).

[2] E. M. Phizicky and S. Fields, *Protein-Protein Interactions - Methods for Detection and Analysis*, Microbiological Reviews, **59**, 94 (1995)

[3] C. H. Yu, A. N. Parikh, and J. T. Groves , *Direct patterning of membrane-derivatized colloids using in-situ UV-ozone photolithography*, Advanced Materials, **17**, 1477 (2005)

BIOMOLECULE IMMOBILIZATION ON AU SURFACES WITHIN A SEALED PDMS MICROSYSTEM

Armando Tovar, Abraham P. Lee
University of California Irvine, USA

ABSTRACT

A novel process has been developed to immobilize biomolecules on a patterned Au surface on glass while activating and maintaining the glass surface for an irreversible poly(dimethylsiloxane) (PDMS) bond. This protein immobilization capability has been demonstrated to form specific patterns on Au surfaces with nanometer spatial resolution within a PDMS microfluidic system. This novel process has applications that extend to proteomics, immunoassays, biowarfare detection, and DNA and cell manipulation.

Keywords: proteomics, immunoassay, protein, surface modification

1. INTRODUCTION

Current PDMS microfluidic applications extending to proteomics and immunoassays require an irreversible PDMS and substrate seal for biomolecule protection and precise flow control. Standard PDMS microfluidic fabrication processes require that both the glass (substrate) and PDMS be placed within O_2 plasma for a specified amount of time to form an irreversible seal [1]. If the proteins were immobilized on the Au surface prior to being subjected to O_2 plasma then they will be destroyed once O_2 plasma is applied to the surface. However, protein immobilization after air plasma is almost impossible due to the hydrophilic behaviour of the Au surface following the exposure. The Au surface becomes hydrophilic due to a temporary charge caused by the O_2 plasma. This standard bonding process makes protein or biomolecule immobilization within a PDMS microfluidic system very difficult to accomplish when using glass as the main substrate. Through the development of a microfluidic electroimmunoassay, we have developed a process to immobilize biomolecules on a patterned Au surface on glass while activating and maintaining the glass surface for an irreversible PDMS bond.

2. EXPERIMENTAL

The device is fabricated on a glass substrate with Ti/Au surface electrodes with the microfluidic system being formed with PDMS. Using E-beam deposition, 100nm of Au is deposited on a 20nm Ti adhesion layer. The metal layer is then coated with 10µm of Shipley 1827 photoresist. The photoresist is patterned and used as a mask for metal etching. The Au and Ti is etched using the chemicals Transene Gold Etchant GE-8148 and Transene Ti Etchant TFT. Upon completion of the metal etching, the resist is removed using an acetone bath and methanol rinse. Immediately following the removal of the photoresist, chemical treatment of the device is performed to allow PDMS and protein binding. The device is first placed into a 2% HF bath for approximately 10 sec., then rinsed with DI water for 1min, and finally dried using a N_2 stream. The device is then placed back into an acetone bath for 1 min. and rinsed off with methanol for 15 sec. The part is dried using a N_2 stream and placed in a N_2 filled container to keep the Au surface active for protein immobilization and the glass surface active for PDMS bonding. The N_2

978-0-9798064-0-7/µTAS2007/$20©2007CBMS

environment is essential in order to keep both surfaces active as the device is transported for protein immobilization.

The choice of protein immobilization utilizes the Langmuir-Blodgett technique which allows for a hydrophobic-hydrophobic bond between the surface and protein. The phenomenon occurs once the protein medium is placed in air causing the hydrophobic ends of the proteins to realign themselves. The protein medium is then placed in contact with the hydrophobic surface leaving behind a layer of proteins. The protein spotting is performed using a molecular printing system from BioForce Nanosciences called the Nano eNabler. Figure 4 shows the process in which the Nano eNabler Surface Printing Tip (SPT) deposits the proteins on the Au electrodes. Once protein deposition occurs on the Au surface, the PDMS microfluidic system is then irreversibly bonded to the glass. The PDMS is activated for bonding by placing it in O_2 plasma for 1.5min. prior to contact with the glass substrate [1]. To ensure PDMS bonding and protein immobilization, the device is kept in a N_2 environment throughout the protein deposition process. The humidity in the Nano eNabler system is controlled to reach levels no greater than 15% throughout the process.

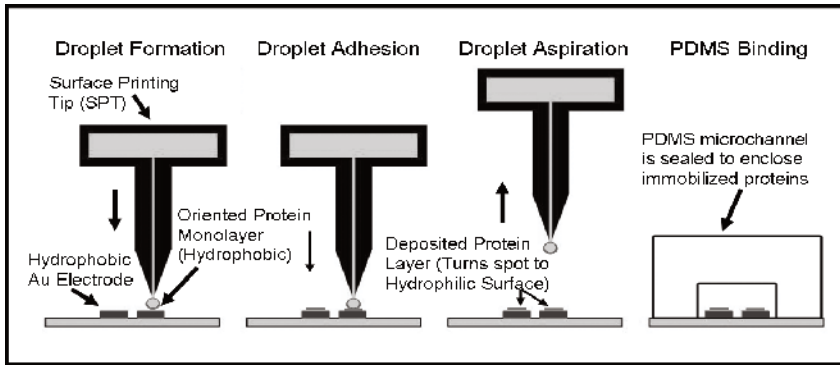

Figure 1. Protein immobilization with PDMS irreversible bonding

The proteins used to develop this process were 3 'specific proteins' (H3L, D8L, D13L) belonging to the Vaccinia family and 2 'non-specific proteins' (2237, 3319) belonging to the Burkholderia Pseudomallei family. VIG was used as the anti-H3L antibodies for the experiments [2]. Fluorescently tagged Cy3-conjugated goat antihuman IgA plus IgG and IgM secondary antibodies were used to confirm antigen/antibody binding within the microchannel using fluorescent detection [2]. The fluorescent detection was achieved using a Perkin-Elmer microarray scanner at 5μm resolution.

3. RESULTS AND DISCUSSION

Figure 2 shows protein immobilization on a Au surface with protein spots approximately 1-2mm in diameter. VIG was used as the primary antibody to determine viability and reactivity of each protein. The fluorescence signifies proteins that bonded with the primary (VIG) and secondary (Cy-3) antibodies within the microchannel. The three 'specific' proteins exhibited fluorescence while the two 'non-specific' proteins did not exhibit fluorescence signifying that the proteins remained viable after PDMS bonding.

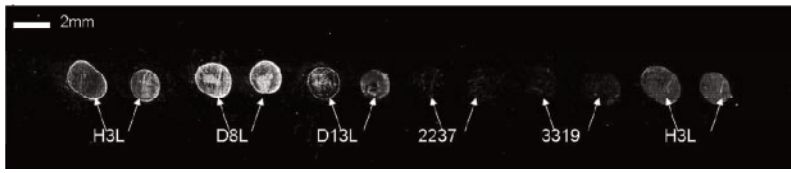

Figure 2: Protein Array on Au surface

Further demonstrations show protein immobilization on Au surfaces as small as 5μm in diameter utilizing the Nano eNabler printing system. Different protein arrays printed with this system can be seen Figure 3. A protein array in the shape of a 'smiley-face' on a Au surface sealed within a PDMS microfluidic system can be seen in Figure 3A. The proteins used were 'H3L' and were deposited with spot sizes approximately 20μm in diameter with spot to spot distances ranging from 10μm to 40μm.

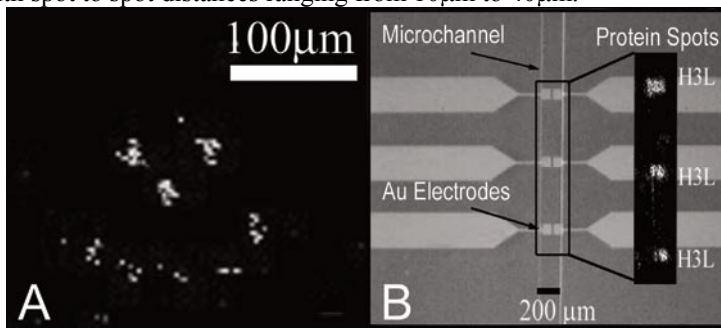

Figure 3. A) H3L protein array - 'Smiley-face' B) H3L proteins on Au electrodes

Figure 3B shows active proteins immobilized on Au electrodes with dimensions of 100μm x 100μm within a sealed PDMS microfluidic channel. All experiments were performed with reagents delivered through the sealed PDMS microfluidic system.

4. CONCLUSIONS

A novel process to immobilize biomolecules on a patterned Au surface on glass while activating and maintaining the glass surface for an irreversible PDMS bond has been developed. Using the Nano eNabler molecular printing system, specific protein patterns have been demonstrated on Au surfaces with precise control and repeatability.

ACKNOWLEDGEMENTS

The authors would like to thank Dr. Philip Felgner at University of California, Irvine for his technical assistance.

REFERENCES

[1] McDonald J C *et al, Fabrication of Microfluidic Systems in Poly(dimethylsiloxane).* 2000 *Electrophoresis* **21** 27–4

[2] D. Huw Davies, Megan M. McCausland, Conrad Valdez, Devan Huynh, et al., *Vaccinia Virus H3L Envelope Protein Is a Major Target of Neutralizing Antibodies in Humans and Elicits Protection against Lethal Challenge in Mice.* Journal of Virology, Sept. 2005. Pg. 11724-11733

NOVEL METHOD FOR CHEMICAL MODIFICATION AND PATTERNING OF THE SU-8 PHOTORESIST

Gabriela Blagoi, Stephan Keller, Anja Boisen and Mogens Havsteen Jakobsen
MIC Department of Micro and Nanotechnology Technical University of Denmark

ABSTRACT
In this paper we describe a new photochemical method to tailor and pattern the surface of SU-8 negative photoresist. Antraquinone (AQ) derivatives were used to chemically modify and pattern SU-8 surfaces. Using AQ derivatives with electophilic moieties (AQ-E), we could chemo-selectively change the wetting behaviour of SU-8. The resolution limit of the AQ photopatterning method was 20 μm when using an uncollimated light source. AQ modification followed by a reaction with amino groups of Alexa-647 cadaverine and a Biotin-amino derivative proved possible modification and patterning of polymeric cantilevers and other MEMS based sensors with biomolecules.

Keywords: SU-8, polymer functionalization, photopatterning

1. INTRODUCTION
The ability to customize surface properties of polymers is a powerful tool to make the surfaces biologically compatible and to enable biomolecular interactions. The combination of chemical surface modifications and patterning techniques enables arrays of miniaturized biosensors to be constructed on polymeric materials [1]. Other applications include patterning of individual cells, proteins, DNA and various biomolecules down to micron resolution [2].
Traditionally, biomolecules are attached to polymer surfaces by passive adsorption based on hydrophobic interactions [3]. These interactions are undefined, unstable, and non-directed causing partial loss of adsorbed biomolecule function. The preservation of the molecular structure and function is crucial when these biomolecules act as a recognition element for an analyte. These drawbacks can be overcome by covalent attachment of molecules to the polymer surface.
We have developed a novel possible cleanroom compatible method to tailor the surface properties of SU-8 negative photoresist. The epoxy based photoresist SU-8 is a valuable material for fabrication of MEMS, rapid prototyping and integration of sensors in a microfluidic system [4, 5]. Therefore, it is of great interest to find new methods for SU-8 surface functionalization especially for bio-analytical applications. SU-8 photoresist was chemically modified and micro-patterned using UV light and antraquinone (AQ) photolinkers [6, 7]. This surface functionalization method can facilitate the use of SU-8 as a structural component in biomedical and lab-on a-chip micro-devices.

2. EXPERIMENTAL
SU-8 samples were prepared by spin-coating of SU-8 2002 on Si wafers (5000 rpm/s, 30 s, 1μm thickness).The excess solvent was evaporated by a soft bake for 10 min at 60 ºC and 10 min at 90 ºC. The SU-8 was exposed to UV light with a dose of 450 mJ/cm^2 and post-baked for 10 min at 60 ºC and 10 min at 90 ºC. The wafers were developed 4 min in PGMEA and then rinsed with isopropanol.
All photochemical reactions were carried out in glassware. Two types of antraquinone derivatives were used: one with an amino group (AQ-NH_2, figure 1a) and with one with an

978-0-9798064-0-7/μTAS2007/$20©2007CBMS

electrophilic group (AQ-E, figure 1b) [6,7]. For the photopatterning and the chemoselectivity experiments, the SU-8 samples were incubated with solutions of 100 µg/ml AQ-NH_2 or 1µg/ml AQ-E aqueous solutions and irradiated with light intensity of 30 mW/cm^2 for 30 minutes in a homemade photoreactor equipped with lamps emitting in UV-A and VIS range. Solutions of 10mM of octadecythiol (thiol with CH_3 end), hexanedithiol (thiol with SH end), mercaptoethanesulfonic acid (thiol with SO_3H end) were incubated for 2 hours with the AQ-E modified SU-8 at a pH=7.4. Also, AQ-E modified SU-8 was reacted with 10 mM ethanolamine (amine with OH end), pH=9.6 for 2 hours. The reaction between the AQ-E modified surface and thiol/amino groups of the above reagents was followed by contact angle measurements using de-ionized water under ambient conditions. The kinetics and the concentration dependence of the reaction between AQ linkers and SU-8 surface were followed by the contact angle as well. For patterning, a Pyrex wafer coated with gold was used as a patterning mask. Following the AQ-E modification, SU-8 patterned surfaces were incubated with 10µg/ml Alexa Fluor 647- cadaverine solution pH= 9.6 for 2 hours. The samples were washed with PBS buffer supplemented with 0.05% Tween 20 (v/v), MilliQ water and dried. When 25 µg/ml Biotin-NH_2 (Biotinyl-3,6-dioxaoctanediamine) was reacted with the AQ-E patterns on SU-8, a blocking step with 1% bovine serum albumin (pH=9.6) was performed before incubating with 10 µg/ml Cy3 Streptavidin (pH=7.4). A fluorescence CCD scanner (5µm resolution) was used to visualize the fluorescence patterns.

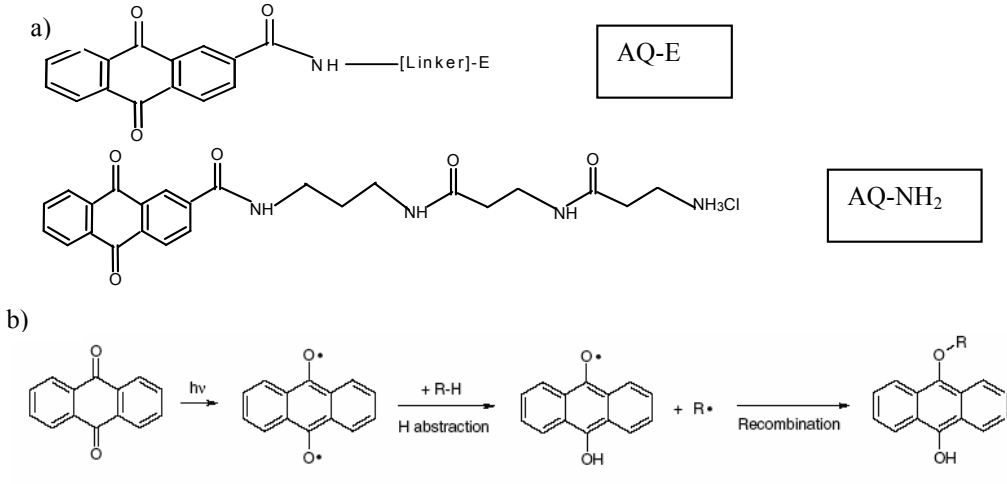

Figure 1. a) Antraquinone (AQ) molecules used in this study and b) Reaction mechanism of antraquinone derivatives (AQ) with the SU-8 (R-H) polymer surface after exposure to UV light.

3. RESULTS AND DISCUSSION

Figure 1b) shows the simplified reaction mechanism between the antraquinone molecule and the SU-8 surface (R-H). Overall, the AQ molecule attaches via O atom to the polymer substrate (RH), forming a new ether bond. This method is very versatile and it can be used to chemically modify and pattern SU-8 surfaces that are fully processed in comparison with the method published by Wang Y et al., method that relies on the residual photoacid generator of the SU-8 polymer [8].

The dependence of surface graft density on UV photografting, UV exposure time and AQ photolinker concentration were investigated. A reaction time of 30 minutes proved sufficient to fully modify the SU-8 surface with both AQ-NH_2 and AQ-E. In figure 2a) is presented the influence of the concentration AQ-NH_2 photolinker on the contact angle of the SU-8 surface. It can be seen that for the 100 µg/ml AQ-NH_2 the saturation of the surface is achieved, the contact angle of fully processed SU-8 decreasing from 80° to 70°. Increasing the concentration of the AQ-NH_2 probably more than an AQ monolayer is formed; the contact angle of the modified surface increases close to the unmodified SU-8 surface.

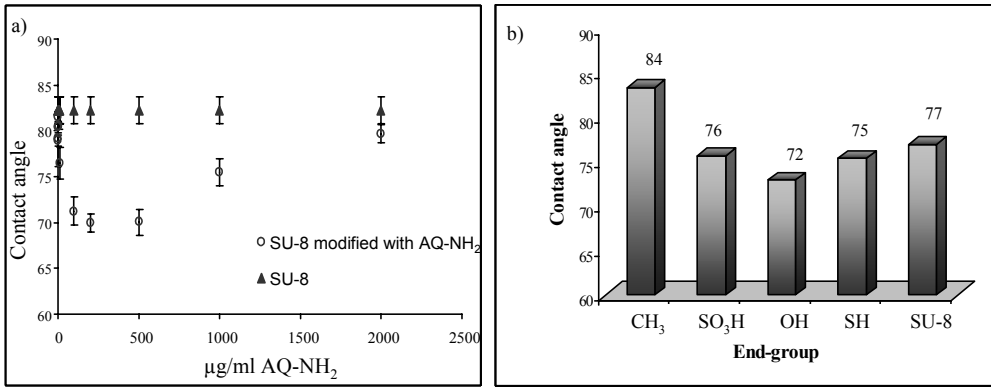

Figure 2. a) Influence of the AQ-NH_2 concentration on the contact angle of the SU-8 surface. b) Tailoring chemoselectively the SU-8 surface hydrophobicity after using an AQ-E photolinker.

For the AQ-E photolinker, 1µg/ml aqueous solution was sufficient to achieve the saturation of the SU-8 surface. For the patterning and chemoselectivity experiments we have worked with the photolinkers' concentrations that gave the optimal surface coverage measured in the highest contact angle changes. When the SU-8 surface was modified with an AQ-E photolinkers chemoselectivity was achieved. As can be seen in figure 3b) the contact angle of the SU-8 surface was varied from 86° when a hydrophobic thiol was used (with CH_3 end group) to 72° when ethanolamine was employed (amine with OH end group). Contact angles of 76° and 75° where obtained when thiols with SO_3H and respectively SH end groups were used. Chemoselectivity was achieved by tuning the pH of the reaction, at pH 7 the thiol groups of react preferentially the modified AQ-E modified surface and at pH 9.6 the amino group is more reactive [7].

Structures with a variety of sizes and shapes can be patterned onto planar or micro-structured SU-8 surfaces using AQ-E photolinkers. Figure 3 illustrates Alexa Fluor-647 cadaverine patterned cantilever shapes and patterns with Biotin-NH_2 and Cy3-Streptavidin. The resolution limit using our homemade reactor is 20 µm. The results were obtained when AQ-NH2 was used in combination with 10% of glutaraldehyde.

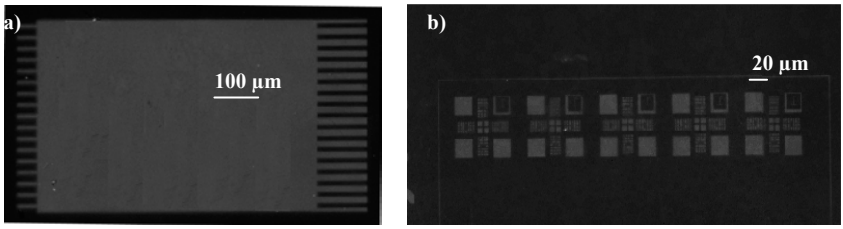

Figure 3. Chemical patterns on SU-8: a) Alexa Fluor 647- cadaverine patterned cantilever shapes (200 µm x20µm), b) Biotin-NH_2 patterned on AQ-E modified SU-8 stained with Cy3- Streptavidin. The surface was blocked with 1% BSA before incubation with Cy3Streptavidin.

4. CONCLUSIONS

We have developed a versatile photochemical method to tailor the surface properties of fully processed SU-8 negative photoresist using AQ photolinkers. Chemoselectivity was achieved when AQ derivatives with electrophilic moieties were used. The *X-Y* spatial resolution of AQ micropatterned SU-8 surfaces was 20 µm when an uncollimated source was used. This surface functionalization method will facilitate the use of SU-8 as a structural component in biomedical and lab-on a-chip microdevices.

ACKNOWLEDGEMENTS

The authors would like to thank the Danish Research Council for Production and Technology for supporting this work.

REFERENCES

[1]. Atkinson, G. M.; Ounaies, Z. *Polymer microsystems: materials and fabrication*. MEMS Handbook ,2nd Edition, 2 9/1-9/39, (2006).

[2]. Schubert, W.; Friedenberger, M.; Bode, M. *Molecular networks in morphologically intact cells and tissue-challenge for biology and drug development.*Methods and Principles in Medicinal Chemistry, 28, 173-183, (2006).

[3]. Grob, P.; Baumann, S.; Ackermann,M.; Suter,M. *A system for stable indirect immobilization of multimeric recombinant proteins*. Immunotechnology,4(2),155-163, (1998).

[4]. Nordstrom, M.; Calleja, M.; Boisen A. *Polymeric micro-channel-based functionalisation system for micro-cantilevers*. Ultramicroscopy, 105(1-4), 281-286, (2005).

[5]. Ribeiro, J.C., G. Minas, P. Turmezei, R.F. Wolffenbuttel, and J.H. Correia, *A SU-8 fluidic microsystem for biological fluids analysis*. Sens. Act. A, 123-24, 77-81, (2005).

[6]. Koch, T. Jacobsen, N.; Fensholdt, J.; Boas, U.; Fenger, M.; Jakobsen, M. H. *Photochemical Immobilization of Anthraquinone Conjugated Oligonucleotides and PCR Amplicons on Solid Surfaces*. Bioconjugate Chemistry , 11(4), (2000).

[7]. Mogens, H. J.; Koch, T. US Patent 6, 033,784

[8]. Wang, Y.; Bachman, M.; Sims, C.E., Li, G.P.; Allbritton, N.L. *Simple Photografting Method to Chemically Modify and Micropattern the Surface of SU - 8 Photoresist*, Langmuir. 22(6), 2719-2725, 2006.

SELECTIVE SURFACE MODIFICATION FOR MICROARRAY ANALYSIS BY PHOTOCHEMICAL GRAFTING OF BIOCOMPATIBLE PHOSPHOLIPID POLYMER

Madoka Takai , Tatsuro Goda and Kazuhiko Ishihara
Department of Materials Engineering, Center for NanoBio Integration, The University of Tokyo, JAPAN

ABSTRACT

2-methacryloyloxyethyl phosphorylcholine (MPC) was graft polymerized from the polydimethylsiloxane (PDMS) substrate using UV irradiation and benzophenone as a photoinitiator. The ellipsometry analysis revealed that the graft layer thickness was constant after the irradiation of 1 min under the monomer concentration of 0.25 M. AFM, XPS measurements and water contact angles indicated increasing the chain density of grafted poly(MPC) which leaded to decrease the amount of absorbed protein on the surface. The phogochemical grafting method of biocompatible phospholipid polymer is suited for the selective surface modifition for microarray analysis.

Keywords: Selective surface modification, photochemical grafting, biocompatible polymer, microarray analysis

1. INTRODUCTION

Recently, fabrication of micro-, nano-patterning of biomolecules based on biocompatible polymer is a significant research for nanobiotechnology field. Therefore we have studied photo-patterned surface by use of biocompatible 2-methacryloyloxyethyl phosphorylcholine(MPC) polymer showing excellent antibiofouling properties that resist protein adsorption and cell adhesion[1, 2]. In this paper, selective surface modification by photochemical grafting of MPC polymer on polydimethylsiloxane(PDMS) surface is reported. The fabrication process of photochemical grafting using benzophenone (BP) as a photoinitiator is very simple and becomes widely-used technique in micro-TAS field [3]. The MPC polymer surface is expected to decrease biomoelcules adsorption and biomolecules can bind only on the PDMS surface and it will be achieved highly-sensitive microarray biosensor.

2. EXPERIMENTAL

PDMS sheet was immersed in acetone solution containing 1wt% BP for 1 min and dried in dark-vacuum condition. The BP coated PDMS was placed in the degassed MPC aqueous solution (0.25 mol/L) and set with patterned glass mask. The photoinduced graft polymerization was conducted using a 500 W of ultra-high pressure mercury lamp for 0-60 min without a filter. After that, the membrane was rinsed in water and ethanol, and dried in vacuo. The ATR-FTIR detected the absorbance of R-COO-R' group (1735 cm-1) in poly(MPC). Fluid tapping AFM images in water on the surface modified PDMS provided PMPC chains and RMS roughness using the NanoScope IIIa. The thickness of graft layer was determined using an ellipsometer under dry at 25 ºC. The total amount of adsorpbed protein was analyzed from protein analysis kit (Micro BCA™ protein assay reagent kit)

978-0-9798064-0-7/μTAS2007/$20©2007CBMS

after detachment of adsorped protein by SDS. 4.5 mg/mL of bovine serum albumin (Mw = 6.7×10^4) in a phosphate buffered saline (PBS) was used as a model protein.

3. RESULTS AND DISCUSSION

The elements of nitrogen and phosphorus on the poly(MPC)-grafted surface (Table 1), and the entity of ester bonding confrirmed by ATR-FITR provide the existence of poly(MPC) on PDMS. Figure 2 is relations between the UV irradiation time and graft layer thickness, and water contact angle, respectively. The graft layer thickness was constant around 40 nm from 1 to 10 min of UV irradiation time. The poly(MPC)-grafted surface showed a good hydrophilicity even though UV irradiation time was only 1min. Considering the AFM images in wet condition (Figure 3), the morphology of graft polymer chain in initial stage was mushroomed structure with low RMS roughness and the productions of chain aggregates were observed with time. The brush-like structure with high polymer density was formed at 20 min UV irradiation time, which was also determined by compositional ratios of poly(MPC) to PDMS calculated by the C1s peak area of XPS spectra.

Table 1 Elemental compositions from XPS analysis.

Code	C	O	N	P	Si
PDMS	46.1	30.8	0.0	0.0	23.1
Poly(MPC) grafted PDMS(10min)	43.5	36.9	1.9	1.7	16

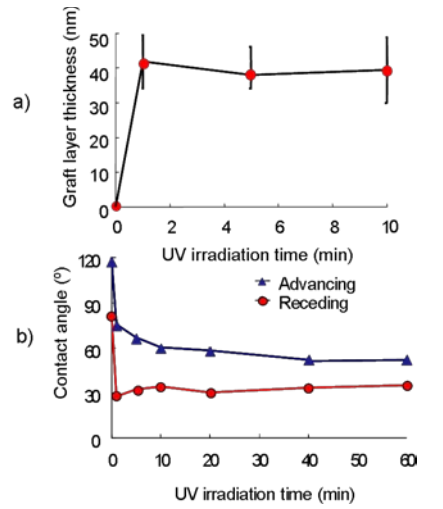

Figure 2 Relations of graft layer thickness a) and water contact angle b) as a function of UV irradiation time.

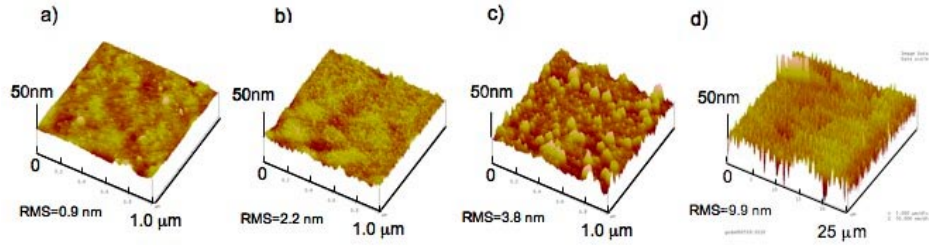

Figure 3 Tapping mode AFM topographical images of PDMS a), poly(MPC) grafted surface on PDMS; 1 min b), 10min c), 20min d) of UV irradiation time.

The amount of adsorbed albumin indicates albumin adsorption behavior on the modified surface is dependent of the UV irradiation time, therefore brush-like structure with high polymer density is much effective for the protein adsorption resistance (Figure 4). By using the optimized UV irradiation condition of 20min, the patterning of poly(MPC) on PDMS was successfully conducted, and the optical microscope images of poly(MPC)-grafted surface were displayed in Figure 5. Finally, we confirmed the cell adhesion, the

poly(MPC)-grafted surface at the incubation day 3 clearly resisted the L929 mouse fibroblast cell adhesions while naked PDMS surface reached confluent.

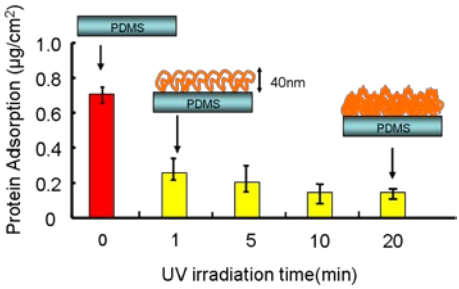

Figure 4. Amount of albumin adsorption on PDMS and Poly(MPC) with various UV irradiation times.

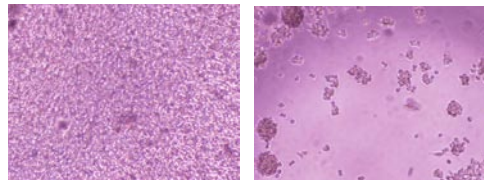

Figure 6. Phase microscope images (x4) of the fibroblast cell attachments after incubation of 3 days on the original PDMS (left) and the poly(MPC)-grafted PDMS for 10 min irradiation (right).

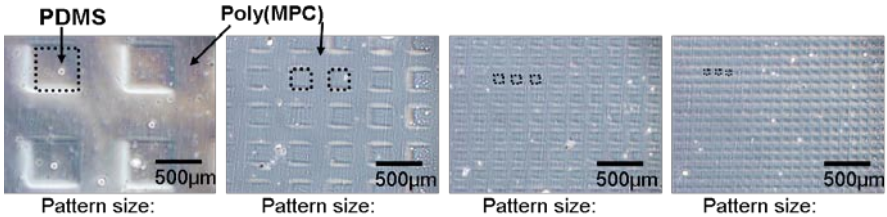

Figure 5 Optical microscope images of patterned poly(MPC) grafted surfaces on PDMS with different pattern size from 500 μm to50 μm.

4. CONCLUSIONS

The poly(MPC)-grafted surface constructed from brush-like structure with high polymer density shows good protein and cell adhesion resistance and it is confirmed that the simple selective modification by photochemical grafting of MPC polymer is a key technology as for highly sensitive biosensor array such as a DNA, protein and cell analysis because noise can be effectively reduced due to a nature of MPC polymer.

ACKNOWLEDGEMENTS

This study was partly supported by Grant-in-Aid for Scientific Research(B) 16310084 from Japan Society for the Promotion of Science.

REFERENCES

[1]. J. Yamaguchi, J. Watanabe, M. Takai, and K. Ishihara, *Phospholipid polymer hydrogel formed by photodimerization of cinnamoyl groups in the polymer side chain*, J. Appl. Polym. Sci., 104, 44-50 (2007).

[2]. T. Konno, H. Hasyda, K. Ishihara, and Y. Ito, *Photo-immobilization of phospholipid polymer for surface modification,* Biomaterials, 26, 1381-1388(2005).

[3]. T. B. Stachowiak, F. Svec, and J.M.J. Frechet, *Hydrophilic, protein-resistant surface modification of polymer monoliths via photografting for multifunctional microfluidic devices*, Proceedings of μ-TAS 2006, 228-230(2006).

SURFACE DERIVATIZATION OF POLY(DIMETHYLSYLOXANE) BY CHEMISORPTION OF FUNCTIONAL COPOLYMERS

M. Chiari, M. Cretich, F. Damin, G. Di Carlo, C. Oldani

Istituto di Chimica del Riconoscimento Molecolare (ICRM), C.N.R., Milano, Italy

ABSTRACT

A robust and rapid method for functionalizing poly(dimethylsyloxane) (PDMS) allowing covalent binding of biomolecules is reported. The coating is based on the adsorption of copoly-DMA-NAS-MAPS, a ter-copolymer based on (N,N-dimethylacrylamide (DMA), N-acryloyloxysuccinimide (NAS) and 3-(trimethoxysilyl)propyl-methacrylate (MAPS). The polymer self-adsorbs onto the PDMS very rapidly, without the need of any surface pre-treatment. PDMS slides coated by copoly-DMA-NAS-MAPS have been tested in bacterial genotyping for the detection of food pathogens inside a microflow cell developed for microarray experiments.

Keywords: PDMS, microarrays, coating

1. INTRODUCTION

Poly(dimethylsiloxane) (PDMS) has become one of the most widely used materials in microfluidics. The inertness of PDMS due to the unreactive and hydrophobic nature of its surface, consisting of a $[–OSi(CH_3)_2–]_n$ backbone, makes it difficult to functionalize this material. PDMS is commonly oxidized by oxygen plasma, corona discharges and ultraviolet/ozone (UVO) to confer an hydrophilic character to its surface. However, the majority of the proposed methods rely on treatments often not available in biochemistry laboratories. In this work we demonstrate that a terpolymer made of *N,N*-dimethylacrylamide (DMA, 97% of moles), N,N-acryloyloxysuccinimide (NAS, 2%), and 3-(trimethoxysilyl)propyl methacrylate (MAPS, 1%) synthesized by a free radical copolymerization process, self adsorbs onto the PDMS surface very quickly, and generates a functional coating for the immobilization of protein and DNA. A PDMS support arrayed with oligonucleotide probes, is embedded in a microfluidic flow cell for the detection of food pathogens consisting of a network of chambers and channels.

2. EXPERIMENTAL

A thin film was generated on a PDMS surface by dip-coating in a diluted aqueous solution of copoly(DMA-NAS-MAPS) (Figure 1-a) according to a procedure previously devised for glass slides (1). The binding capacity of the coating was characterized by spotting an amino-modified, Cy3 labelled 23 mer oligonucleotide (concentration ranging from 0.1 to 10 uM), whose fluorescence was acquired before and after washing. Fluorescent PCR fragments of bacterial 16S rDNA gene were produced by amplification of Genomic DNA from *Staphylococcus aureus subsp. Aureus* (ATCC® 700699D) and from *Listeria monocytogenes* (ATCC® 19115D). The amplicons were denatured at 95°C and hybridized with oligonucleotide probes arrayed on the surface of a coated PDMS substarte. The hybridization was performed at 50°C inside a microflow cell (Figure 2) in 800 seconds under an intermittent flow of 2ul/sec.

978-0-9798064-0-7/μTAS2007/$20©2007CBMS

3. RESULTS AND DISCUSSION

PDMS slides coated by copoly-DMA-NAS-MAPS were tested for their ability to covalently bind biomolecules using an amino-modified oligonucleotide fluorescently labelled with Cy3. The oligonucleotide was spotted on the slides; after an overnight binding step, the attachment efficiency was determined by scanning the slides for fluorescence before and after the washing step. The results are summarized in Figure 1 (b). Notably, fluorescent oligonucleotides without the amino modification do not bind to the polymer coated PDMS. Moreover, no attachment was obtained when the functional groups on the surface were blocked with ethanolamine. This demonstrates that the oligonucleotide binding is mediated by the active esters (NAS) on the surface.

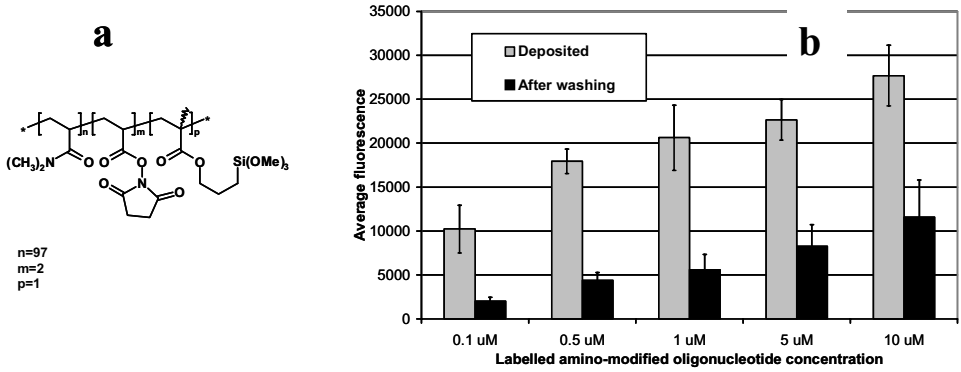

Figure 1: (a) structure of copolyDMA-NAS-MAPS. (b) Attachment density of different concentrations of a labelled amino modified oligonucleotide onto coated PDMS slides .

Rapid and sensitive detection of the presence of pathogenic microorganisms in water or food is important for ensuring environmental quality and public health safety The DNA microarray technology powered by microfluidics meets the demand of rapid and parallel detection of many pathogens in a single experiment; PDMS is the material of choice when cheap and robust lab on chip devices are needed. For these reasons, a pathogen identification microarray was developed on polymer coated PDMS integrated into a microflow chamber made by an etched PDMS slide. The schemes of the microflow system and of the PDMS hybridization chamber are reported in Figure 2.
16S rDNA gene from *Staphylococcus aureus* and from *Listeria monocytogenes* was amplified using fluorescent primers and hybridized onto the copolyDMA-NAS-MAPS coated PDMS oligonucleotide array using a flow of 2uL/sec for 800 sec. As an example, the results of the genotyping of *S aureus* are reported in Figure 3(c).
The use of the microfluidic chamber dramatically reduced the hybridization time and allowed an automatization of the necessary experimental steps.

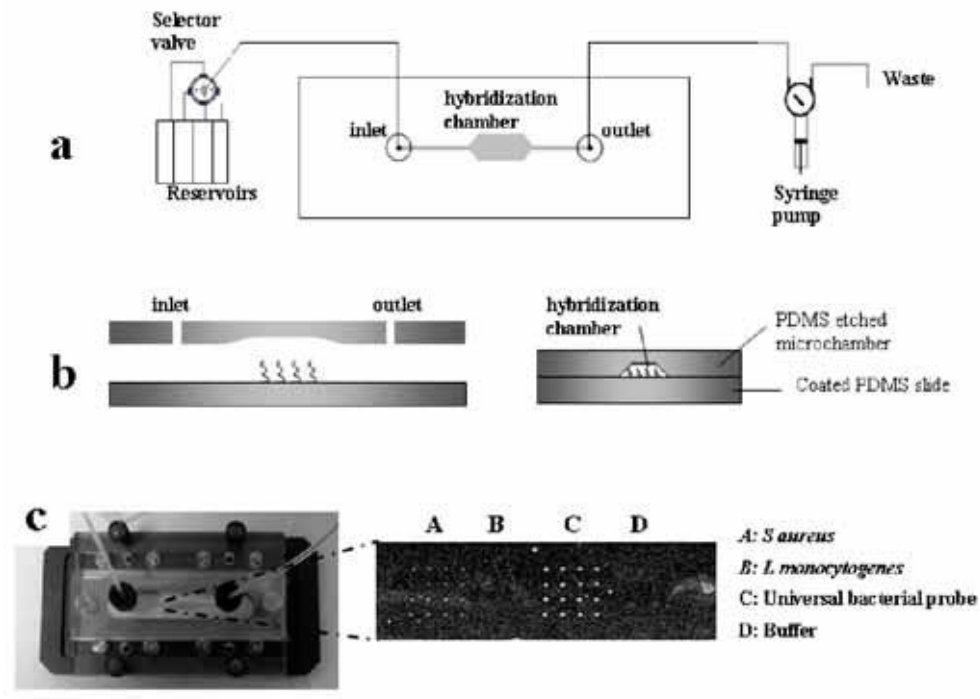

Figure 2:(a) scheme of the microflow system for microarrays. (b) scheme of the hybridization PDMS chamber: probes were immobilized on a coated PDMS slide which was subsequently assembled with a PDMS etched microchamber and clamped inside a microflow chip with fluidic connections (c). Results of hybridization with a PCR sample of *S aureus* are reported.

4. CONCLUSIONS

An easy and robust coating method for functionalizing PDMS surface based on the adsorption of copoly(DMA-NAS-MAPS) is presented. The coating allows the immobilization of biomolecules on PDMS without any surface pre-treatments. The coated PDMS slides have been integrated into a microfluidic system for pathogen detection based on oligonucleotide array.

ACKNOWLEDGEMENTS

Supported by European Commission: TRACEBACK (Integrated System for a Reliable Traceability of Food Supply Chains) Contract Nº FP6-2005-FOOD-036300

REFERENCES

[1] Pirri G, Damin F, Chiari M, Bontempi E, Depero LE. Characterization of a polymeric adsorbed coating for DNA microarray glass slides. *Anal Chem*. 2004 76(5):1352-8

[2] Jin LQ, Li JW, Wang SQ, Chao FH, Wang XW, Yuan ZQ. Detection and identification of intestinal pathogenic bacteria by hybridization to oligonucleotide microarrays. *World J Gastroenterol*. 2005 11(48):7615-9

SURFACE MODIFICATION OF PDMS BY UV LIGHT IRRADIATION

Seisuke Kano*, Sohei Matsumoto*, Tadatake Sato*, and Naoki Ichikawa*

**National Institute of Science and Technology (AIST), JAPAN*

ABSTRACT

Illumination using UV lamplight and UV laser modified a PDMS surface. Using the UV lamp for 15 h irradiation, the surface was maintained at a 60 deg water contact angle 9 days later. Using the UV laser, the surface became more hydrophobic than that of the as-received PDMS until 5 days after treatment.

Keywords: surface modification, PDMS, UV light, wettability

1. INTRODUCTION

Polydimethyl siloxane, PDMS, is an important material for disposable μTAS devices, but its surface is formed as hydrophobic. Therefore, some liquids flow too smoothly. Many researchers have used electro-discharge, plasma irradiation, UV light irradiation, several chemical treatments, and so on to improve the surface properties to control wettability [1]. The hydrophilic mechanism of PDMS surface is reportedly attributable to formation of Si-O with a glassy structure [2]. The problem of these treatments was that the hydrophilic effect disappeared quickly, e.g. after several hours. Laser irradiation using infrared and ultraviolet wavelengths reportedly improves wettability [3, 4]. In those cases, the surface was rendered hydrophobic compared to as-received PDMS. This paper describes wettability modification using UV laser and UV lamp irradiation.

2. EXPERIMENTAL

The PDMS was spin-coated on the 35 × 50 mm^2 slide glass. The coated PDMS film on the glass was heated at 70°C for one hour and cooled in ambient atmospheric conditions. Part of the PDMS film was irradiated using UV lamp light for several minutes at 110 mm distance from the lamp which power of 400 W and wavelengths of 200–600 nm. Part of the irradiating lamp light of PDMS was covered with a Pyrex filter, which cut off wavelengths of less than 300 nm. The others were irradiated using pulsed lasers at 355 and 266 nm in wavelength for several scans. Both laser types were tuned to 1.2 J/cm^2 and scanned to 16 × 20 mm^2 areas several times. After UV light irradiation, the PDMS film surface was observed using a contact-angle tester with distilled water, physiological NaCl solution, citric acid buffer solution (pH 2.2). Bondings near the surface were observed by an FT-IR spectroscope.

3. RESULTS AND DISCUSSION

The UV-lamp-treated surface became glassy with increased irradiation time. This result agreed with reported results. A quite different point is the recovery term of wettability. The results of contact angles of distilled water immediately after UV light irradiation are shown in Figs. 1 and 2. For UV lamp treatment, the contact angle decreased with increasing irradiation time. The lowest contact angle was recorded from 15 h treatment and showed 35 deg, which was quite a low value compared to that of the untreated surface: 115 deg. This surface wettability for distilled water rebounded over time, as depicted in Fig. 1; nevertheless,

978-0-9798064-0-7/μTAS2007/$20©2007CBMS

this effect persisted for more than 60 days later, with a greater than 60 deg contact angle for distilled water.

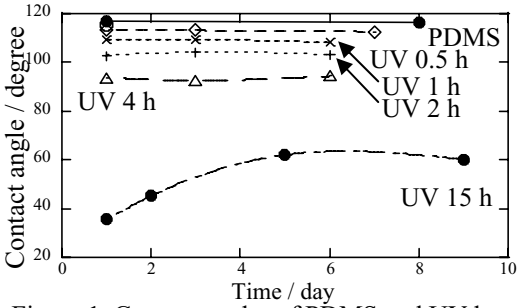

Figure 1. Contact angles of PDMS and UV lamp irradiation for selected times.

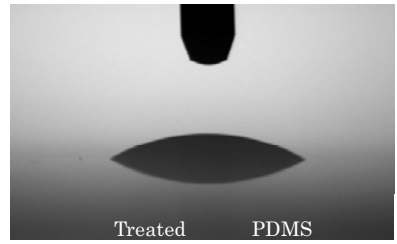

Figure 2. Droplet observation on the UV lamp treated PDMS surface. Irradiation time is 15 h. The distilled water was dropped just after treatment.

On the other hand, the surface treated with pulsed laser irradiation for several scans showed a higher contact angle of ca. 135 deg for distilled water than that of the untreated surface. Results of contact angles and droplets are shown respectively in Table 1 and Fig. 3. Pulsed-laser irradiated surfaces displayed craters and powder-like spots, as shown in Fig. 4.

Table 1. Contact angles of 355 nm and 266 nm wavelength pulsed laser irradiation on the PDMS surface for several scan times.

	355nm 7scan	266nm 200scan	266nm 100scan	266nm 50scan	266nm 20scan
1st day	130.7	130	117.1	113	115.7
2nd day	133.6				
5th day		124.5	125.1	114	115
8th day	132.2				

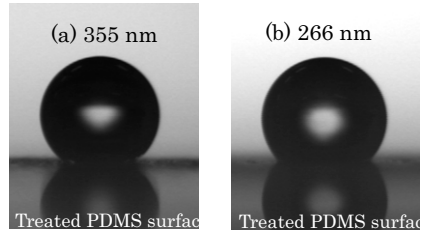

Figure 3. Droplets observed on the UV-laser-treated PDMS surface at 355 nm (a) and 266 nm (b). The distilled water was dropped just after treatment.

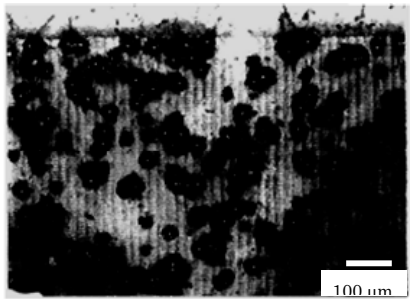

Figure 4. Optical microscopic observation of 355 nm pulsed-laser-irradiated PDMS. The upper part shows non-treated PDMS.

Table 2. Contact angles of UV lamp irradiation for 15 h, 355 nm and 266 nm pulsed laser irradiation on PDMS surface for distilled water, NaCl solution, and citric acid buffer solution. The angles were measured 60 days after treatment.

	UV lamp 15 h	355 nm 7 scans	266 nm 200 scans
Distilled water	75.6	129.3	134.5
NaCl solution	76.3	130.5	134.5
Citric acid buffer	55.8	90.2	96.8

In these cases, the treated surface wettability almost saturated at 60 days. For that reason, the wettability of these treated surfaces was compared for different solutions. Table 2

lists the results. For the citric acid buffer, the contact angles were lower than those of other liquids. However, the trend for the surface treatment was quite similar.

The reason for these surface characteristics after UV light treatment is apparent from the FT-IR spectrum results depicted in Fig. 5. The UV-lamp-irradiated surface shows a typical peak shift at 1110 cm^{-1} of Vas (Si-O-Si) absorption. Comparing the spectrum of PDMS with both UV laser irradiated surface spectra, the absorption peaks at around 850 cm^{-1} of v (Si-C) and at 1200–1400 cm^{-1} of δs (CH_3) are shifted to a higher wavenumber. The PDMS surface that was covered by the Pyrex filter, which absorbed light of less than 300 nm, showed hydrophobicity, similarly to the untreated PDMS surface. However, the UV laser irradiation without the Pyrex filter exhibited hydrophilicity. These results indicate that the surface wettability of PDMS is controllable using both UV lamp and UV laser irradiation with different wavelengths.

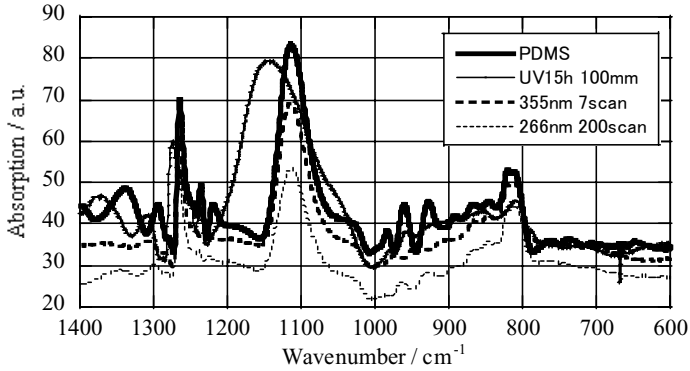

Figure 5. FT-IR spectra of the as-received PDMS, 15 h UV irradiated, 355 nm pulsed laser irradiated, and 266 nm pulsed laser irradiated.

4. CONCLUSIONS

The PDMS surface wettability was changed temporarily, but for a long term of over one week. The surface was made either hydrophilic or hydrophobic using the UV lamp light or UV laser irradiation. Furthermore, FT-IR spectroscopy results indicate that long-term UV lamp light irradiation affects Si-O-Si bonding and UV laser irradiation affects C-H and Si-C bonding. These results indicate that the surface wettability of PDMS is controllable using both UV lamp and UV laser irradiation.

REFERENCES

[1] H. Makamba, J. H. Kim, K. Lim, N. Park, J. H. Hahn, Surface modification of poly (dimethyl siloxane) microchannels, Electrophoresis, **24**, 3607 (2003).

[2] Y. Berdichevsky, J. Khandurina, A. Guttman, Y.-H. Lo, UV/ozone modification of poly (dimethyl siloxane) microfluidic channels, Sensors and Actuators B, **97**, 102 (2004).

[3] M. T. Khorasani, H. Mirzadeh, Z. Kermani, Wettability of porous polydimethyl siloxane surface: morphology study, Applied Surface Science, **242**, 339 (2005).

[4] V.-M. Graubner, O. Nuyken, T. Lippert, A. Wokaun, S. Lazare, L. Servant, Local chemical transformations in poly (dimethyl siloxane) by irradiation with 248 and 266 nm, Applied Surface Science, **252**, 4781 (2006).

THE EFFECT OF THE CONCENTRATION ON OIL DROPLET IN HYDROPHOBIC RECOVERY PDMS MICROCHANNEL

Su Kyoung Chae[1,2], Chang Ha Lee[2], and Ji Yoon Kang[1]

[1] Nano Bio Center, Korea Institute of Science Technology, Korea,
[2]Dept. of Chemical Engineering, Yonsei University, Korea

ABSTRACT

A novel method has been presented for preparing oil droplet with ionic concentration using a hydrophobic recovery PDMS chip after plasma treatment. Oil droplet with calcium chloride in ethanol using hydrophobic recovery PDMS micro channel was successfully formed.

Keywords: Droplet, PDMS recovery, immiscible liquids, Microfluidic

1. INTRODUCTION

The hydrophilic/hydrophobic property of material for a droplet-generating device is important, because the wetting of the channel surface determines the type of dispersion that can be prepared. PDMS (polydimethylsiloxane) are widely used in various areas as diverse as μTAS, lab-on-chip devices since their water-repellent surface is necessary for aqueous drop preparation [1]. On the other hand, the hydrophilic surface of oxidized PDMS with plasma treatment is suitable for organic droplets. The surface properties of PDMS can be changed by various techniques, for example by exposing it to UV light or oxygen plasma treatment.

However, despite its advantages, the use of PDMS is limited because of the poor control of its surface properties that is currently achieved. Moreover, in practice, surfaces with specific properties are often needed (biospecific, hydrophilic, charged, etc.). The control of surface properties is thus essential for an appreciably wide range of applications.

Liquids of the same or similar surface tension exhibit stable laminar flow inside PDMS microchannels. Owing to the different viscosities, densities, and interfacial free energies between liquids, the flow behavior of immiscible liquids was observed to be different from liquids of the same or similar nature.

However, oil or organic liquids such as ethanol are not confined to either the hydrophilic or hydrophobic regions. The lack of confinement is consistent with the fact that the advancing contact angles of these liquid in air on both hydrophilic and hydrophobic regions are smaller than 90°.[2] The important in microfluidics is the wetting properties of liquids on the substrate. Because of wetting implies the existence of three interfaces between two fluids and a solid surface. The whole system will minimize its energy by adopting the optimal configuration. At that time, the formation of spherical shape drop is presented in microchannel.

However, synthesis of droplets with two immiscible liquids such as oil and ethanol of similar surface tension is difficult. Namely, the question is that two liquid phase has similar affinity toward the PDMS surface property. Therefore, we supposed that other force except surface tension such as ion charge interaction could be onto PDMS surface.

In this work, we studied the effect of ion concentration in flowing similar surface tension liquids (oil and etOH) applied toward hydrophobic recovery PDMS surface to oil droplet

978-0-9798064-0-7/μTAS2007/$20©2007CBMS

formation. The effect of the ion charge on hydrophobic recovery surface was evaluated by contact angle measurements.

2. EXPERIMENTAL

Microfluidic channels were fabricated by pouring polydimethoxysilane (PDMS, Sylgard 184, Dow Corning) on a silicon wafer containing positive-relief channels patterned in SU-8 photoresist. The prepolymer mixture was poured 1 mm thick into 4" polystyrene Petri dished, degassed again in the vacuum desiccators, and cured on a hotplate for 30 min at 80 ℃. Following curing, flat PDMS wafers were peeled from the dishes and cut. The channel design and dimension are shown in Figure 1. Contact angles were measured on static 20 $\mu\ell$ drops using a contact angle measurement system. At least five measurements at different locations on a substrate were taken for each of the data points.

3. RESULTS AND DISCUSSION

The chip based on PDMS was stored at room temperature for 7 days after plasma bonding. The wetting angle of the surface was measured by sessile drop contact angle (Figure2). The mineral oil contact angles measured on the surface of the PDMS specimens prepared in this work were 5±3°. Then, 7 days of exposure to air increased the contact angles measured on the prepared PDMS surfaces (table1). The treatment of the PDMS surface with RF plasma induces polar functional groups (-OH), primarily silanol (SiOH) groups [3], on the PDMS surface. However, the hydrophilic surfaces of oxidized PDMS are not stable with time after exposure. Even if the plasma-treated surface never fully regains its initial hydrophobicity, 'hydrophobic recovery' will gradually occur. However, recently, the research revealed that the presence of OH groups remained when the plasma-treated PDMS specimens were stored at room temperature for up to one week [3].

With $CaCl_2$ in ethanol as the continuous phase and oil as the dispersed phase, oil droplet can be generated at a cross junction in hydrophobic recovery PDMS microchannel. Oil droplet is controlled in PDMS-based microchannel with interfacial force between OH group of surface and ion concentration in flowing ethanol. The behavior of flowing liquid by using the imposed shear from each micro channel in PDMS chip is shown in Figure 3. Oil had a good affinity toward surface in PDMS microchannel and instead etOH droplet was observed in channel. The other side, while calcium chloride added to etOH of continuous phase, oil droplet was formed by shear force with etOH containing calcium ion in PDMS microchannel (Figure 4). The contact angle value with various concentrations increase gradually because interaction between ion charge in etOH and OH groups on the PDMS surface. Also, according to ion concentration increase, steady region due to capillary instability sheared change. Therefore, oil droplet without surfactant could be formed and we believe that these oil droplets could be useful to chemical reaction and material preparation.

4. CONCLUSIONS

We could observe that ethanol with calsium ion as continoues phase formed oil droplet in hydrophobic recovery PDMS microchannel. Because of –OH terminal group on surface of recovery PDMS may be interact ion in ethanol.

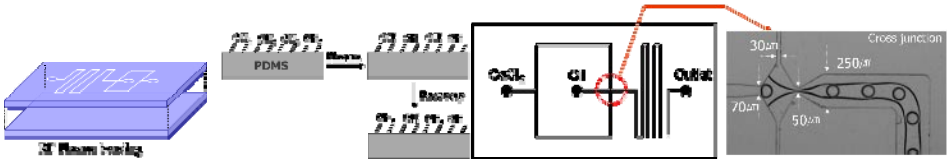

Figure 1.Schematic diagram showing (a) the oxidation and recovery of plasma-treated PDMS (b) the microchannel design for droplet synthesis

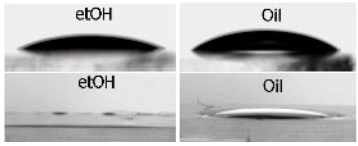

Contact angle(°)	Before plasma	After plasma
Mineral oil	42	~5
etOH	19	-

Figure 2.Contact angles of liquid on the surface of before/after treatment PDMS: (a) before plasma treatment (b) after plasma treatment for 15s

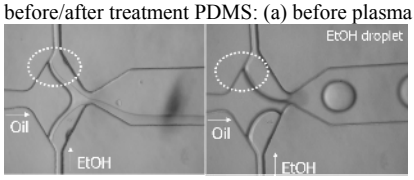

Figure 3. Behavior of flowing liquid (etOH, oil) by using the imposed shear from each side in plasma treated PDMS micro channel: The chip was storage for 5 days in air.

Table1. Contact angle of PDMS, plasma treated PDMS and hydrophobic recovery

	Before treatment	After treatment	Recovery
Mineral oil	55	27	49
0mM $CaCl_2$/etOH	66	-	58
10mM $CaCl_2$/etOH	63	-	46
25mM $CaCl_2$/etOH	46	-	40
50mM $CaCl_2$/etOH	45	-	34
100mM $CaCl_2$/etOH	42	-	34

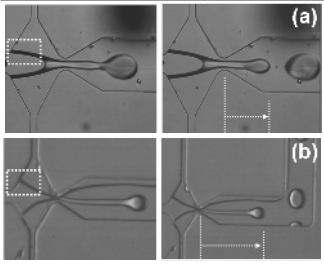

Figure 4. Effect of the ion charge addition to the continuous phase (etOH) on the stability of droplets (a) 100mM $CaCl_2$/etOH (b) 25mM $CaCl_2$/etOH

REFERENCES

1. Alvaro Mata, Aaron J. Fleischman, and Shuvo Roy, *Characterization of Polydimethylsiloxane (PDMS) Properties for Biomedical Micro/ Nano systems*, Biomedical Microdevices 7, 281, (2005)

2. Bin Zhao, Neil O. L. Viernes, Jeffrey S. Moore, and David J. Beebe, *Control and Applications of Immiscible Liquids in Microchannels*, J. AM. CHEM. SOC. 124, 5285, (2002)

3. I-Jane Chen and Erno¨ Lindner, *The Stability of Radio-Frequency Plasma-Treated Polydimethylsiloxane Surfaces*, Langmuir,; 23(6), 3118, (2007)

SUPERHYDROPHOBIC SURFACES: FROM IRREVERSIBLE TO REVERSIBLE ELECTROWETTING

N. Verplanck[1], Y. Coffinier[2], K. Madjour[1], J.C. Camart[1], R. Blossey[2], R. Boukherroub[2] and V. Thomy[1]

[1]Institut d'Electronique, de Microélectronique et de Nanotechnologie (IEMN) - UMR 8520
[2]Institut de Recherche Interdisciplinaire (IRI) - FRE 2963, France

Abstract

This paper reports on the reversible electrowetting of conductive liquid droplets in air on different superhydrophobic surfaces based on silicon nanowires (SiNWs) [1]. The silicon nanowires were grown on Si/SiO_2 substrates using the vapor−liquid−solid (VLS) mechanism, electrically insulated using 300 nm of SiO_2, and hydrophobized by coating with a fluoropolymer C_4F_8. The resulting surfaces displayed liquid contact angle θ around 160° for a saline solution (100 mM KCl) in air with almost no hysteresis.

Key Words: Electrowetting, superhydrophobic, silicon nanowires

1. INTRODUCTION

In the literature, several groups [2-4] have examined the possibility to use superhydrophobic surfaces for electrowetting on dielectric (EWOD) and found an irreversible electrowetting behavior in air. The observed irreversible wetting behavior was assigned to the transition from the Cassie-Baxter regime (hysteresis ~ 10°) to a Wenzel regime (hysteresis ~ 100°) when the liquid fills the nanostructures [5]. In all previous reports, the surfaces investigated consisted on well-defined periodic array of nanopillars. In the present work, a very heterogeneous surface composed of silicon nanowires coated with a fluoropolymer C_4F_8 was used.

2. EXPERIMENTAL

The SiNWs were first grown on Si substrate, electrically insulated with 300 nm of SiO_2, using the vapor-liquid-solid (VLS) mechanism. First, a thin film of gold (4 nm thick) was evaporated on the substrate and then exposed to silane gas at a pressure of 0.1 T or 0.4 T (Q = 40 sccm) at 500°C [1]. According to time and pressure of growth, we realized eight surfaces where the nanowires length varied from 1µm (10 min, 0.1 T) to 30 µm (60 min, 0.4 T) as shown in Table 1.

Table 1: parameters for growth of silicon nanowires (Q = 40sccm, T = 500°C)

#	Time (min)	Pressure (T)	Length (µm)
1	10	0,1	1
2	10	0,4	1
3	20	0,1	2.5
4	20	0,4	15
5	40	0,1	8
6	40	0,4	35
7	60	0,1	7
8	60	0,4	30

978-0-9798064-0-7/µTAS2007/$20©2007CBMS

Figure 1a shows a scanning electron microscopy (SEM) image of SiNWs grown at 0.1 T for 10 min. It consists of low density of SiNWs around 1 µm in length. High density of SiNWs with an average diameter in the range of 20-150 nm and 30µm in length were obtained at 0.4 T for 60 min, leading to a non-uniform structured surface (Figure 1b). To achieve surface superhydrophobicity, the SiNWs were coated with a fluoropolymer C_4F_8 (60 nm thick), deposited using a plasma technique.

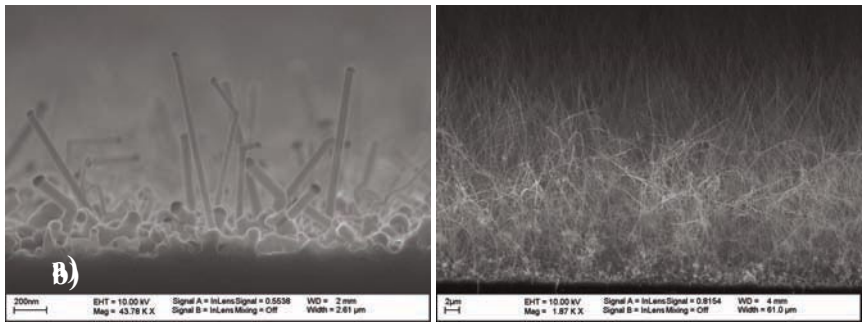

Figure 1: SEM images of SiNWs with gold nanoparticle on top: a) process 1, b) process 8.

3. RESULTS AND DISCUSSION

The resulting surfaces displayed liquid contact angle θ^* around 160° for a saline solution (100 mM KCl) with almost no hysteresis, indicating that the droplet is in a Cassie configuration.

Electrowetting was performed on all surfaces, but a reversible behavior was only observed for the surface prepared according to process #8 (Figure 1b). Applied voltage leads to non-reversible wetting on all other surfaces (droplet trapped in a Wenzel configuration). On surface #8, electrowetting induced a maximum reversible decrease of the contact angle of 23° to reach 137° (150 V_{RMS} at 1 kHz – Figure 2a). Turning off the voltage leads to a complete relaxation of the droplet (Figure 2b) [1]. This effect is ascribed to the high heterogeneity of the surface and trapped air under the droplet preventing to reach Wenzel configuration.

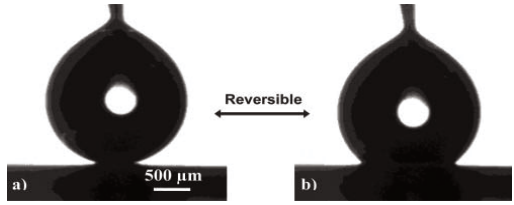

Figure 2: Reversible electrowetting of a saline water droplet (5µL, 100mM KCl) in air environment: a) θ=160° @ 0V, b) θ=137° @ 150V_{RMS}.

Figure 3 shows part of the 1000 wetting/relaxation cycles performed over 18 min. The reversible contact angle change was estimated to be inferior to 40 ms for each cycle and is comparable to those obtained on smooth surfaces.

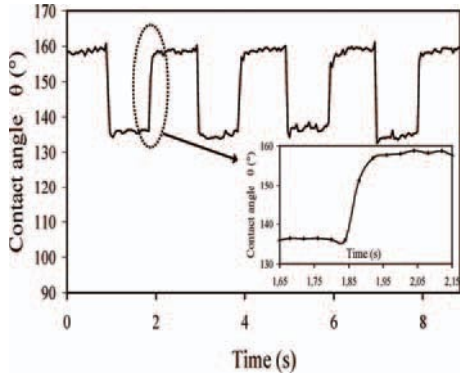

Figure 3: Contact angle vs time for a saline solution droplet (100 mM KCl) in air with successive sequences of 0 V and 150 V_{RMS} proving the repeatable reversibility of the electrowetting on the surface #8. The inset shows the velocity of the relaxation (~ 40ms).

4. CONCLUSIONS

We have shown that reversible electrowetting is possible on superhydrophobic surfaces that display specific geometrical criteria as predicted by Bico [6]. Due to small hysteresis, we assume that small voltages could be efficient for droplet displacement. We have previously demonstrated the possibility to use such surfaces as EWOD ground electrodes with hydrophobic electrodes for matrix-free mass-spectrometry analysis (DIOS analysis) [7]. The next step is the integration of the superhydrophobic electrodes inside a microfluidic microsystem, allowing low voltage actuation of a biological analyte and DIOS analysis.

ACKNOWLEDGEMENTS

We thank for their technical support Mrs. Patricia Lefebvre (nanowires growth) and Mr. Christophe Boyaval (SEM imaging). The European Union, the Centre National de la Recherche Scientifique (CNRS) and the Nord Pas de Calais region are gratefully acknowledged for financial support.

REFERENCES

[1] N. Verplanck, Y. Coffinier, E. Galopin, J.C. Camart, V. Thomy, and R. Boukherroub, "Reversible electrowetting on superhydrophobic silicon nanowires", Nano Lett. **3,** 813 (2007).

[2] T. N. Krupenkin, J. A. Taylor, T. M. Schneider, and S. Yang, "From rolling ball to complete wetting: the dynamic tuning of liquids on nanostructured surfaces," Langmuir **20**, 3824 (2004).

[3] "Electrowetting on superhydrophobic SU-8 patterned surfaces", D. L. Herbertson et al., Sensors and Actuators A, **130-131**, 189 (2006).

[4] M.S. Dhindsa et al., "Reversible electrowetting of vertically aligned superhydrophobic carbon nanofibers", Langmuir **22**, 9030 (2006).

[5] A. Lafuma, and D. Quéré, "Superhydrophobic states", Nature Mater., **2**, 457 (2003).

[6] J. Bico, "Mécanismes d'imprégnation: Surfaces textures, Bigouttes, Poreux", Thesis, Université Paris VI (2000).

[7] N. Verplanck et al., "Nanostructured surface as EWOD counter electrode for matrix-free mass spectrometry analysis", The 10th International Conference on Miniaturized Systems for Chemistry and Life Sciences (μTAS Tokyo), 771 (2006).

ULTRAHYDROPHOBIC PROPERTIES OF POROUS SILICON FOR SURFACE BASED BIOANALYSIS

A. Ressine[1], P. Augustsson[1], G. Marko-Varga[2], T.Laurell[1]
[1]*Dept. Of Electrical Measurements, Lund University, Sweden*
[2]*Dept. of Analytical Chemistry, Sweden*

ABSTRACT

Previously we reported the extreme water repellency of randomly organized macro-/nanoporous silicon surfaces [1]. The texturized silicon with hierarchical porous structure in micrometer and nanometer scale was shown to exhibit the superhydrophobic behaviour. Contact angles as high as 176º can be easily achieved with further fluoroalkylsilane modification of the porous surfaces. Porous silicon technology is compatible with the silicon patterning techniques allowing easy integration of the ultrahydrophobic properties into microfluidic and lab-on-a-chip devices for a new generation of surface based bioanalysis. In this paper we report the fabrication of ultrahydrophobic porous silicon channels and ultrahydrophobic nanovial arrays. Also the MALDI-TOF MS (matrix assisted laser desorption/ionization time-of-flight mass-spectrometry) target anchor chip composed of the hydrophilic anchor points for sample deposition surrounded by the ultrahydrophobic porous area is reported. Such anchor chip allowed the deposition of large sample volumes providing the strategy to improve MALDI-TOF MS sensitivity.

Keywords: Superhydrophobic, microfluidics, porous silicon, water repellency, MALDI-TOF MS

1. INTRODUCTION

As commonly accepted, the necessary condition to achieve the extreme water repellency on solids is the surface roughness at the different scale length (hierarchical texture). The superhydrophobic porous silicon layers were prepared by electrochemical etching of bulk crystalline silicon wafers as described before [2]. Subsequent surface modification with fluoroalkylsilane coupling agent can further improve non-wetting and stabilize the surface. Contac angles as high as 176° were achieved on macro-/nanoporous silicon and ultrahydrophobicity was maintained for many months without degradation [3].

2. RESULTS AND DISCUSSION

We have now utilized these ultrahydrophobic states to develop a new silicon chip integrated with anchor points for MALDI-TOF MS analysis. The concept of an anchor point chip for MALDI preparation is derived from the possibility to deposit large sample volumes still having a good on-target spot confinement, i.e. a small drying area. In order to explore this concept in a potential high density microscale format we created circular anchor points with a diameter of 500 μm by proton beam irradiation of silicon, fig. 1. The processing details of the direct proton beam writing on silicon are briefly the following: proton irradiated areas do not porosify in a conventional porous silicon anodisation process, due to the altered conductive properties in the damaged crystal structure, and thus a direct write patterning of porous and non-porous areas on a silicon chip can be accomplished. After proton beam irradiation the chip was porosified to create a hierarchical porous layer surrounding the proton bean irradiated spots, followed by fluoroalkylsilane surface modification.

978-0-9798064-0-7/μTAS2007/$20©2007CBMS

Using the same porous silicon fabrication protocol we made the array of ultrahydrophobic nanovials for liquid handling, fig. 2. Noteworthy, the nanovial chips possessed ultrahydrophobic behaviour also when the cell culturing media was applied as a liquid, demonstrating potential for cell storing.

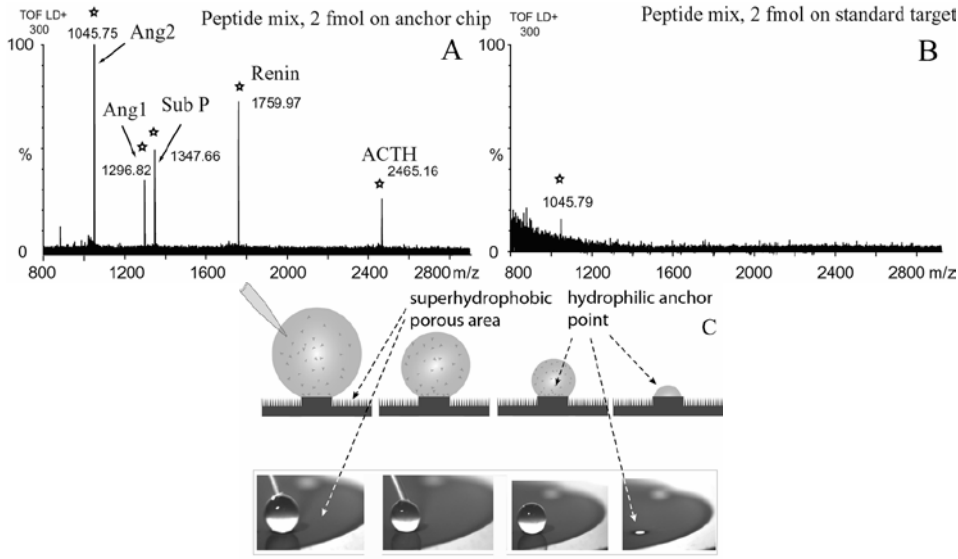

Figure 1. Enrichment by evaporation on superhydrophobic anchor MALDI-TOF MS target chip. A) The resulting MALDI spectra of 5μl of sample mixed with matrix deposited on hydrophilic anchor point. Anchor points of the silicon MALDI target chip with the diameter of 500 μm were surrounded by a non-wetting macro-/nanoporous area. After deposition of 2 fmol of peptide mixture (Ang1, Ang2, Sub.P, Renine, ACTH) in a 5 μl volume droplet diameter around 1 mm the sample/matrix mixture was confined and crystallized only at the anchor point area. Insert shows the sequence of images with drying sample. B) Control experiment: MALDI spectra of the same amount of sample deposited on a standard target (2 μl). C) The principle of enrichment by evaporation on anchor point of MALDI target chip.

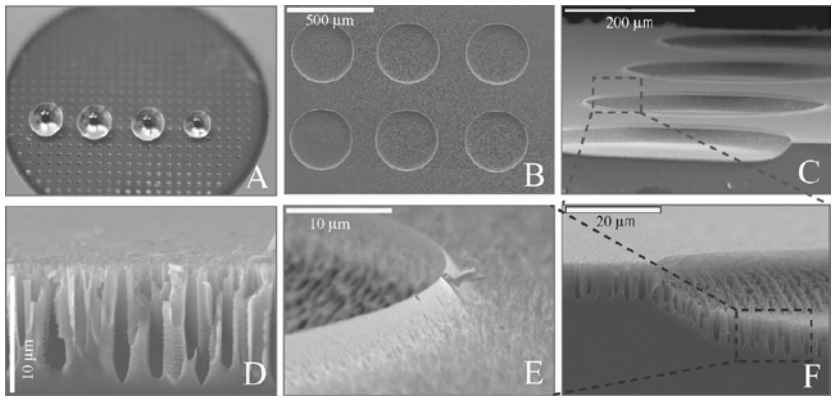

Figure 2. The array of porosified ultrahydrophobic vials of 450 μm diameter for liquid handling. A) Water droplets of 5 mm diameter deposited on the vial array. Contact angle on surface was 176º. B)-F) SEM top view and series of cross-sections of the vial array realising porous structure.

Microfluidic device with ultrahydrophobic porous silicon channels (fig. 3) was fabricated by anisotropic etching of (110) orientation wafer. The porous walls of the channel exhibit hierarchical porous structure (micropores with characteristic sizes around 1 μm combined with side nanoporous structure with the characteristic pore size in the range of 5-10 nm). The comparison of the water flow profiles in porous ultrahydrophobic channels and non-modified (hydrophilic) Si channels are given in fig. 3D and 3E. Ultrahydrophobic surfaces are known to exhibit reduced viscous drag due to "slip" associated with a layer of air trapped at the liquid-solid interface. It is expected that this slip will lead to reduced turbulent skin-friction drag in external flows at higher Reynolds numbers in both the laminar and turbulent regimes.

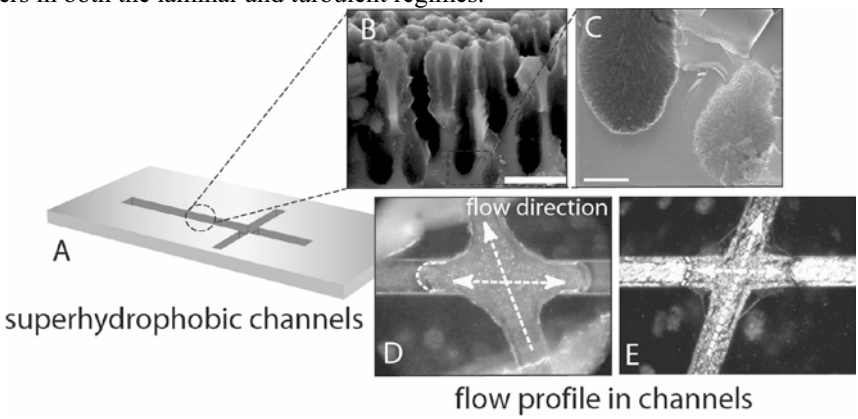

Figure 3. Ultrahydrophobic porous silicon microfluidic device. A) Schematic representation of the microfluidic chip. B) Hierarchical porous structure of the ultrahydrophobic channels: micropores with the characteristic sizes of approx.1 μm are combined with nanoporous structure with characteristic pore sizes of 5-10 nm (image scale bar is 4 μm). C) Close-up of the nanoporous structure over the macropore wall (scale bar is 500 nm). D) Water flow profile in ultrahydrophobic channels (the liquid front is indicated with the red mark and the flow direction with yellow mark). E) Flow profile in non-modified silicon channels.

REFERENCES

[1] A. Ressine, D. Finnskog, D. et al. *Superhydrophobic and hydrophilic states on porous silicon for bioapplications*, Proceedings of μTAS 2005 vol 1, pp.256-258, (2005).

[2] A. Ressine, S. Ekstrom, G. Marko-Varga and T. Laurell *Macro-/nanoporous silicon as a support for high-performance protein microarrays*, Anal.Chem. 75, pp.6968-6974, (2003).

[3] A. Ressine, G. Marko-Varga, T. Laurell *Porous silicon protein microarray technology and ultra-/superhydrophobic states for improved bioanalytical readout*, Biotechnology Annual Review, 13 (2007), *in print.*

A NOVEL MICRO-FLUIDIC WHOLE CELL BIOSENSOR FOR WATER TOXICITY ANALYSIS USING BIOLUMINESCENCE DETECTION

Hadar Ben-Yoav[1], Svyatoslav Yorish[1], Tal Elad[2], Sefi Vernick[1], Shimshon Belkin[2] and Yosi Shacham-Diamand[1]

[1]*Department of Electrical Engineering and Physical Electronics, Tel Aviv University, ISRAEL and*

[2]*Institute of Life Sciences, The Hebrew University of Jerusalem, ISRAEL*

ABSTRACT

A novel micro-fluidic whole cell biosensor for toxicity analysis based on bioluminescence detection was developed. The optical part of the biochip was modelled and simulated to optimize the total light collection efficiency and the system response. The optimization elucidated some of the optical aspects of the biochip. A study evaluating the bioluminescence reaction kinetics was performed and revealed the interdependence between the detected bioluminescence and the physical parameters of the introduced toxin.

Keywords: Whole-cell biosensor, Water toxicity, Bioluminescence, Stray light analysis

1. INTRODUCTION

Bioluminescent microbes are used as sensors for acute toxicity in water [1]. Genetically engineered *E. coli* (Strain DPD2794 carrying a *recA::luxCDABE* fusion) emit light once they are exposed to toxic materials. The microbes are integrated onto bio chips and in this paper we describe the basic chip integration and the optimization of the optical systems using ray tracing algorithms simulated by the ASAP^{TM} software [2].

2. THEORY

Ray tracing methods were used to model the light collection efficiency by the solid state optical detector. The collection efficiency is defined as:

$$\eta_o = \frac{N_c}{N_e} \tag{1}$$

when N_c represents the total number of collected photons and N_e represents the total number of emitted photons. The total number of emitted photons by the *E. coli* is a function of their interaction with the toxic materials. We model their emission as a uniformly distributed light emitting media. Since we have about 10^7-10^8 microbes per cm^3 we assume a uniform nondirectional emission uniformly distributed over 4π radians for every volume unit. We also assume a constant absorption length, α, due to intrinsic absorption by the microbes. We did not take internal scattering into consideration since we assume that it did not change neither the light intensity nor its spatial distribution. Finally we assume ray reflectance and transmittance specified by Fresnel's equations;

978-0-9798064-0-7/μTAS2007/$20©2007CBMS

$$\text{Reflectance (R)} = \left(\frac{n_1 - n_2}{n_1 + n_2} \right)^2 \quad (2)$$

$$\text{Transmittance (T)} = 1 - R = \frac{4 n_1 n_2}{(n_1 + n_2)^2} \quad (3)$$

2. EXPERIMENTAL

The working system for this study was accordingly established by a solid state platform (Figure 1A) and a micro-fluidic biochip (Figure 1B). The measuring platform was designed and manufactured using Computer Aided Design software (CAD). The biochip was made on a Polyvinilidene Fluoride (PVDF) substrate and the bacteria were localized in a fixation agar. The bacteria were genetically engineered to respond to toxic chemicals by activating cascade of biochemical mechanisms, which lead to emission of light. The emitted bioluminescence is detected by a photo-diode array placed on a moving platform that can bring the photo-detector above the luminescent bio-material. The small dimensions of the photo-diodes allow reducing noise generated by the system while the closer the photo-diodes can be put above the micro-reaction chambers the better light collection efficiency will be.

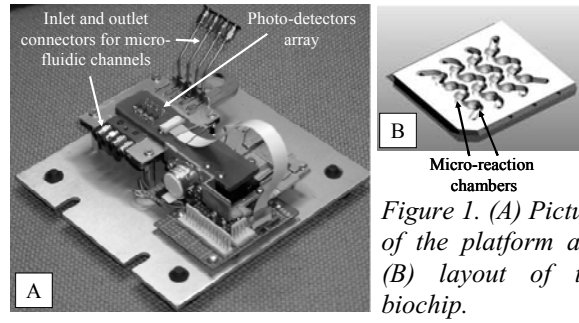

Figure 1. (A) Picture of the platform and (B) layout of the biochip.

3. RESULTS AND DISCUSSION

A bioluminescence distributed in a micro-fluidic biochip was optimized. A 3D optical model of the biochip was constructed (Figure 2). The modelling was done using the optical Advanced Systems Analysis Program (ASAP™, Breault Research Organization, Inc.) program. The model assumes: (a) the geometry of a micro-reaction chamber in the micro-fluidic biochip, (b) incoherent bioluminescence emitted from a shaped fixation agar contains bacteria and (c) physical parameters of light absorption and material's refractive indexes of the biochip.

The biochip optical model was tested with the optical program. The bioluminescence rays distribution in the micro-fluidic biosensor is shown in Figure 3. The program simulated 1000 rays emitted from the bioluminescent

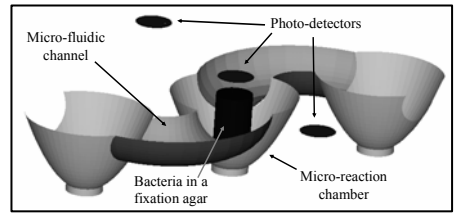

Figure 2. 3D model of the micro-fluidic biochip

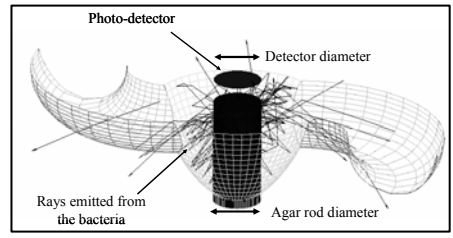

Figure 3. Rays distribution in the biochip

bacteria. The ray's energy lost due to light absorption as a function of the optical path was calculated and light detection optimization was simulated by a variety of optical aspects; detection efficiency and detection yield.

The effect of detector radius and fixation agar rod radius on the detection yield and detection efficiency was investigated. The detection efficiency and yield in response to different detector radiuses is shown in Figure 4. A positive correlation was resulted between the detection yield and the detector radius. Although the total fixed number of $3.5 \cdot 10^5$ bacteria in the system, an optimal detector radius range was observed between the 200 and 700μm detector radius values.

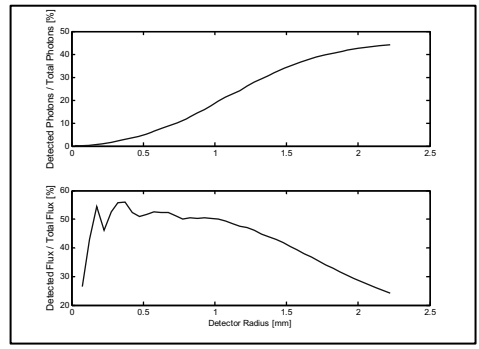

Figure 4. Simulation results for the detection efficiency as a function of the detector radius. Total number of bacteria was fixed on $3.5 \cdot 10^5$ *bacteria. Upper graph represents the detection yield and the lower graph represents the detection efficiency.*

The impact of shifting different fixation agar rod radiuses on the detection efficiency and yield is shown in Figure 5. A decrease with the detection yield as a function of the fixation agar rod radius was observed. Although the higher values of the detection yield resulted for smaller rod agar radiuses, the total number of bacteria in this region was negligible, therefore the total amount of photons was limited. The optimal fixation agar radius range was detected between the 800 and 1100μm agar rod radius values.

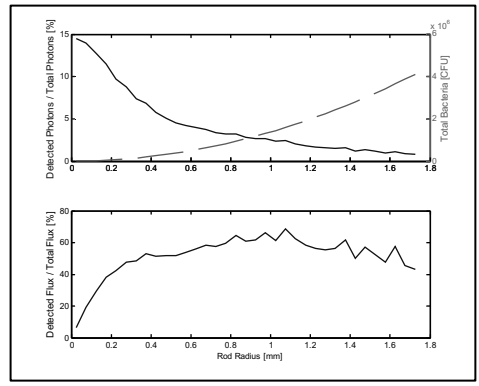

Figure 5. Simulation results for the detection efficiency as a function of the fixation agar rod radius. Upper graph represents the detection yield (left y-axis, filled line) and total number of bacteria (right y-axis, striped line); the lower graph represents the detection efficiency.

The effect of input concentration of analyte molecules on the bioluminescence enzymatic reaction kinetics was experimented when the analyte was introduced to the bacteria, localized in the biochip, in either static or dynamic flow conditions. The bioluminescent reaction of a series of analyte input concentrations under static stream conditions is shown in Figure 6A. Bioluminescence values resulting from the impact of introducing 0-10ppm nalidixic acid (NA) to the bacteria clearly indicated a positive effect for higher NA inputs. The impact of shifting from static conditions to dynamic flow conditions was compared in the presence and the absence of NA (Figure 6B). The data

obtained indicate that for same input of NA, dynamic flow conditions exhibited higher bioluminescence intensity.

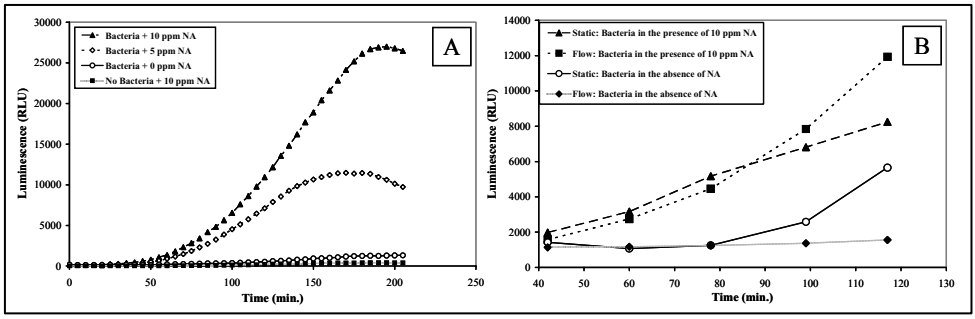

Figure 6. Experimental results for the bioluminescence reaction kinetics. (A) Bioluminescent reaction of a series of NA input concentrations under static conditions; (B) Comparison of the bioluminescent reaction in the presence and the absence of NA under static and dynamic flow conditions.

A 3D optical model of a bioluminescence emitting bacteria localized in a biochip providing an optimization methodology for the detection of light was developed. The model provided a convenient tool for a comprehensive analysis of the stray light in the biochip by simulating several optical aspects with an optical program. The optical aspects were optimized in response to disparate system modifications; detector dimensions and fixation agar dimensions. The data obtained from the experimental results revealed the dependence between the bioluminescence detected and the analyte input concentrations. Furthermore, it clearly appeared that introducing the analyte to the bacteria under dynamic flow conditions resulted in higher bioluminescent signal over a specific time period.

4. CONCLUSIONS

This paper presents a 3D modelling to optimize light detection in a novel micro-fluidic whole cell bioluminescent biosensor. The model was tested with optical software by simulating the bioluminescence emitted in the biosensor. The light detection was simulated by a variety of optical aspects; detection efficiency and detection yield and were optimized in response to a series of detector radius and fixation agar rod radius values. A preliminary study evaluating the bioluminescence reaction kinetics revealed dependence with toxin concentrations and the way the toxin was introduced to the bacteria. This study paves the way to improve both signal and optical parameters of a photo-sensing based biosensors and optical lab-on-a-chip devices for a rapid and sensitive analysis to discriminate between different toxin concentrations in the environment.

REFERENCES

[1] A. Rabner, S. Belkin, R. Rozen, and Y. Shacham, "Whole cell luminescence biosensor based lab-on-chip integrated system for water toxicity analysis", Proc. SPIE. Vol. 6112pp. 33-42:Jan.

[2] http://www.breault.com/

DEVELOPMENT OF PORTABLE SURFACE PLASMON RESONANCE SENSOR WITH MULTI DETECTION POINTS

Hizuru Nakajima[1], Akihide Hemmi[2], Koji Furui[1], Nobuaki Soh[1], Koji Nakano[1], Yasukazu Asano[3], Katsumi Uchiyama[3], Noriaki Kaneki[4] and Toshihiko Imato[1]

[1] *Department of Applied Chemistry, Graduate School of Engineering, Kyushu University, JAPAN*

[2] *Mebius Advanced Technology Ltd., JAPAN*

[3] *Faculty of Urban Environmental Sciences, Tokyo Metropolitan University, JAPAN*

[4] *Computer Science and Systems Engineering, Muroran Institute of Technology, JAPAN*

ABSTRACT

We have developed a new portable surface plasmon resonance (SPR) sensor with multi detection points, which consists a single LED and a linear CCD. The size and weight of this sensor are 170 mm (W) x 110 mm (D) x 150 mm (H) and 1.5 kg, respectively. The sensitivity of the SPR sensor is comparable to that of a conventional SPR sensor. A novel strategy for patterning antibodies inside a microchannel of the SPR sensor chip has also been developed for multi immunoassays.

Key word: Surface plasmon resonance, Photochemical patterning, On-site analysis

1. INTRODUCTION

An analytical method using surface plasmon resonance (SPR) is one of the most powerful methods for evaluating biomolecular interactions without labeling in real-time. Conventional SPR sensors, however, were not suitable for on-site analysis because of the size, weight and cost of the instruments. To overcome these drawbacks, we have developed a palm-sized SPR sensor with dual detection points [1, 2]. Recently, an SPR sensor with multi detection points is desired for field analysis, where many samples and many kinds of target compounds should be determined. We have developed a new portable SPR sensor with multi detection points. A novel strategy for patterning antibodies inside a microchannel of the SPR sensor chip has also been developed for multi immunoassays.

2. EXPERIMENTAL

Figure 1 shows the SPR sensor developed in this study. The size and weight of the sensor were 170 mm (W) x 110 mm (D) x 150 mm (H) and 1.5 kg, respectively. Figure 2 shows the optical system of the sensor. The optical system consisted of a single LED (770 nm), a collimator lens, two cylindrical lenses, a round prism, a polarizer, a pair of collection spherical lenses and a linear CCD (2048 pixels).

978-0-9798064-0-7/μTAS2007/$20©2007CBMS



Figure 1. *Portable SPR sensor developed in this study.*

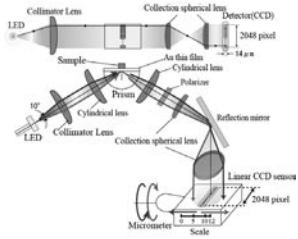

Figure 2. *Optical arrangement of the SPR sensor.*

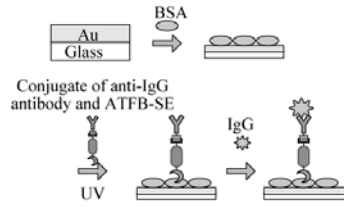

Figure 3. *Schematic diagram of the photochemical patterning process.*

The basic performance of the SPR sensor was investigated using a sensor chip with a microchannel (1 mm x 10 mm x 20 μm). Anti-IgG antibody was patterned inside the microchannel using a photoreactive crosslinker, 4-azido-2,3,5,6-tetrafluorobenzoic acid succinimidyl ester (ATFB-SE) as previously reported [3]. Figure 3 shows the photochemical patterning process. First, BSA was adsorbed on the surface of gold thin layer in the microchannel. The microchannel was then filled with a solution containing a conjugate of anti-IgG antibody and ATFB-SE. Then, the specific position of the microchannel was irradiated with UV light for 30 min. Finally, IgG reacted with the anti-IgG antibody immobilized inside the microchannel. All reactions were monitored by the SPR sensor in real-time.

3. RESULTS AND DISCUSSION

3-1. Evaluation of the basic performance of the portable multi channel SPR sensor

Figure 4 shows the relationship between the light intensity and the scale of the micrometer when water was flowed into the sensor chip. Since the scale of the micrometer corresponded to the angle of the reflected light, the obtained curves were identical to a conventional SPR curve. The lower scale of the micrometer corresponded to the SPR signal at lower resonance angle for the conventional SPR sensor. When sucrose solutions were introduced into the sensor chip, the curves shifted to the higher scale of the micrometer. Thus, the change in the light intensity would be expected to be larger when the scale of the micrometer is set at 4.0~4.5.

Figure 5 shows the SPR responses and calibration curves of the sucrose solutions. The calibration

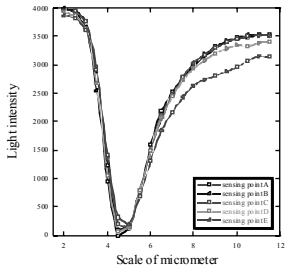

Figure 4. *Relationship between light intensity and scale of micrometer.*

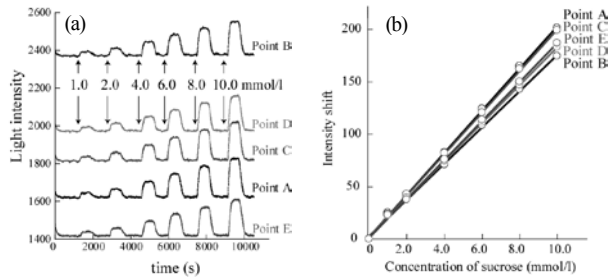

Figure 5. *SPR responses (a) and calibration curves (b) of sucrose.*

curves of the sucrose solutions were linear over the range of 1~10 mM with a correlation coefficient of 0.999 and relative standard deviations of 0.17~0.77 %. The detection limit (S/N=3) was 0.12~0.17 mM, i.e., 6.8~9.2 x 10^{-6} RIU. The sensitivity of this SPR sensor was almost the same as that of the conventional SPR sensor based on the angle shift measurement.

3-2. Photochemical patterning of IgG inside a microchannel

After irradiation of UV light, intensity shift of 111.2 was observed on the irradiated point, while intensity shift on non-irradiated point was only 0.5. Figure 6 shows the calibration curves of IgG obtained on the irradiated point and non-irradiated point. The intensity shift on the irradiated point increased with increase in the concentration of IgG, while that on non-irradiated point was constant at any concentration. These result indicate that the anti-IgG antibody was patterned on the microchannel by UV irradiation. A binding constant of IgG with the anti-IgG antibodies calculated from Langmuir adsorption equation was found to be 1.4 x 10^{6} M^{-1}. This indicates that the irradiation of UV light has little impact on the activity of the anti-IgG antibody.

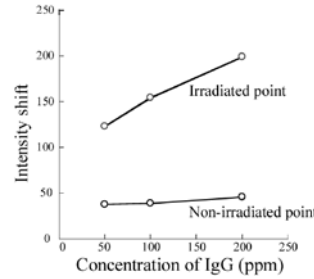

Figure 6. *Calibration curves of IgG.*

4. ACKNOWLEDGEMENTS

This research was partly supported by a Grant-in-Aid for Scientific Research from Japan Society for the Promotion of Science, Japan Science and Technology Agency, Kurita Water and Environment Foundation, Kato Memorial Bioscience Foundation, Shimadzu Science Foundation, The Japan Science Society, Tateisi Science and Technology Foundation, Nippon Sheet Glass Foundation for Materials Science and Engineering, and Kyushu-Yamaguchi High-Tech Enterprise Development Foundation.

5. REFERENCES

1. A. Hemmi, T. Imato, Y. Aoki, M. Sato, N. Soh, Y. Asano, C. Akasaka, S. Ohkubo, N. Kaneki, K. Shimada, "Development of palm-sized differential plasmon resonance meter based on concept of Sprode," *Sens. Actuators B*, **108**, 893-898 (2005).
2. H. Nakajima, Y. Harada, Y. Asano, T. Nakagama, K. Uchiyama, T. Imato, N. Soh, A. Hemmi, "A palm-sized surface plasmon resonance sensor with microchip flow cell," *Talanta*, **70**, 419-425 (2006).
3. H. Nakajima, S. Ishino, H. Masuda, T. Nakagama, T. Shimosaka, K. Uchiyama, "Photochemical Immobilization of Protein on the Inner Wall of Microchannel and Its Application in a Glucose Sensor", *Anal. Chim. Acta*, **562**, 103-109 (2006).

INTEGRATED MICRORING-WAVEGUIDE RESONATOR BIOSENSOR ARRAYS

I. Brener, J.B. Wright, K. Westlake, D.W. Branch, K.M. Taylor, M.J. Shaw, and G.A. Vawter

Sandia National Laboratories, USA

ABSTRACT:

We have successfully designed and fabricated third generation waveguide-based sensor arrays that can operate as high density immunoassay sensors for detection of proteins and other biomolecules in solution. Each die (1.8 cm x 1.5 cm) contain up to 16 sensors and is fully integratable with microfluidic channels. A readout circuit based on a servo-locked laser provides exquisite sensitivity down to 20pg-cm^{-2}.

Keywords: Microring resonator, lab on a chip, microfluidics

1 INTRODUCTION:

High Q evanescently coupled microring resonators have been demonstrated as acutely sensitive biosensors for molecules in solution with sensitivities as low as $1.8x10^{-5}$ Refractive Index Units (RIU) [1]. Using a novel self referencing array (Fig 1.), we have successfully fabricated a waveguide based sensor that achieves sensitivities as low as $1.5x10^{-7}$ RIU.

2 METHOD:

Each sensor in the array is based on an evanescent microring waveguide resonator with high Q (~$2x10^5$, see Fig. 2) that is produced using our low-loss high-Δn process in a standard CMOS production facility [2]. The region above each resonator is etched to 7 μm from the surface and chemically functionalized with an epoxide based organosilane to permit attachment of antibodies. Upon binding, the desired antigen causes a small change in the refractive index of the layer resulting in a shift in the resonance. Each sensor has two rings; one is selectively functionalized while the other ring acts as a reference. By exposing both to the solution to be measured, temperature fluctuations from the solution are removed by subtracting the reference from the functionalized output in the readout.

The silicon chips are pig-tailed to optical fiber arrays for robustness and bonded to glass microfluidic lids fabricated using a combination of wet etching and powder blasting (Micronit Inc.).

Our work provides considerable improvement upon previous published work [1-4] not only in the integration aspects, but also in the newly designed sensitive readout optoelectronic circuitry using telecommunication distributed feedback lasers (DFB) operating at 1550 nm and proportional-integration (PI) servo loops. A schematic diagram is shown in Fig. 3: we use a servo-loop to lock the laser wavelength to the sensor resonance using a PI controller and current feedback. Minute changes in the sensor resonance wavelength are thus tracked by the servo loop and read through the error signal. The die containing the microring resonators are temperature stabilized using a copper block and a thermoelectric (TE) element to ~0.003 °C (5 MHz of resonator frequency stability).

978-0-9798064-0-7/μTAS2007/$20©2007CBMS

Sensitivity calibrations were first carried out by using the natural change in the waveguide effective index (n_{eff}) with temperature. This was performed by carefully varying the temperature of the chip and recording the servo output and the resonance wavelength shifts (1.8 GHz/°C). Small changes in the resonance wavelength ($\Delta\lambda$) are related to changes in n_{eff} by:

$$\Delta n_{eff} = \frac{\lambda \Delta \lambda}{\pi r FSR} \quad (1)$$

where FSR is the free-spectral range and r is the ring radius. Using our measured parameters and the noise floor of our servo readout system we obtained a sensitivity of $\Delta n_{eff} = 4.27 \times 10^{-8}$ for $\Delta\lambda = 38.9$ fm ($\Delta f = 5$ MHz).

3 RESULTS:

We measured the detection limit of the microring biosensor by exposing the surface to varying concentrations of bovine serum albumin (BSA). Phosphate buffered saline 1X (PBS) pH 7.4 was applied for 20 min to achieve equilibration using a flow rate of 100 µl/min. Fig. 4 shows the lowest limit of detection when 5 ng/ml of BSA was injected into the microring sensor.

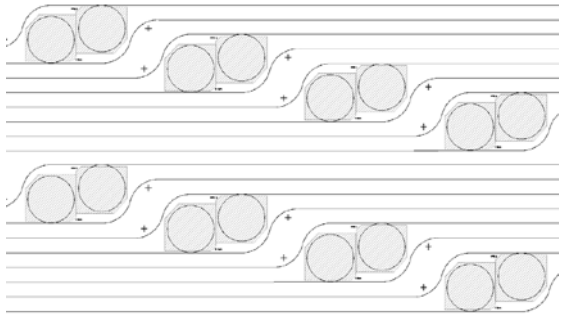

Figure 1. Layout of the microring resonator chip array. Each pair corresponds to one sensor, providing self referencing.

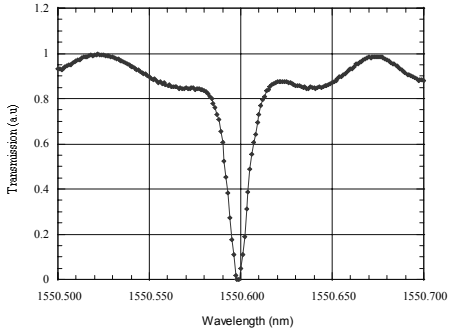

Figure 2. Wavelength scan of a microring resonator with a Q = 240,000. The Ring diameter was 400 µm and the waveguide cross-section was 1.2 µm x 0.2 µm.

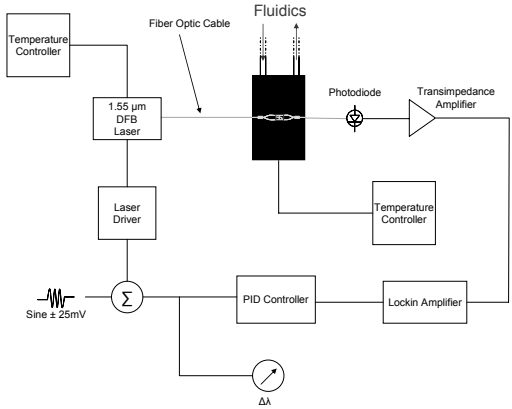

Figure 3. Servo-locked controller acquisition system with temperature stabilization.

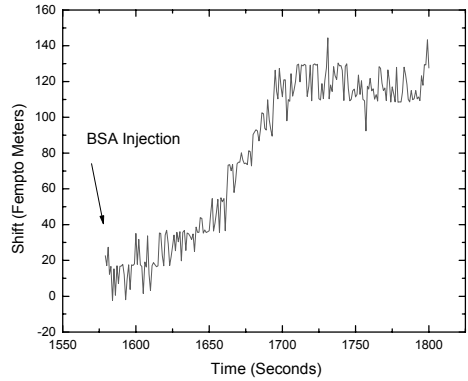

Figure 4. Sensor output after exposure to 5 ng/ml of BSA.

REFERENCES:

[1] "Optical sensing of biomolecules using microring resonators", A. Yalcin, K. C. Popat, J. C. Aldridge, T. A. Desai*, et al.*, *IEEE Journal Of Selected Topics In Quantum Electronics*, **12**, 148, 2006.

[2] "Characterization of Si3N4/SiO2 planar lightwave circuits and ring resonators," G. A. V. Junpeng Guo, Michael J. Shaw, G. Ronald Hadley, Peter Esherick, Anisha Jain, Charles R. Alford, Charles T. Sullivan, presented at Proc. SPIE, 2004.

[3] "High-Q microring resonator for biochemical sensors," G. A. V. Junpeng Guo; Michael J. Shaw, G. R. Hadley, Peter Esherick, Charles T. Sullivan, presented at Proc. SPIE, 2005.

[4] "Protein detection by optical shift of a resonant microcavity", F. Vollmer, D. Braun, A. Libchaber, M. Khoshsima*, et al.*, *Applied Physics Letters*, **80**, 4057, 2002.

MICRODROPLET INTERFEROMETRY FOR LOCAL PRESSURE MONITORING IN MICROFLUIDIC CHIPS

Y. F. Yu[1] , P. H. Yap[2] and A. Q. Liu[1]

[1] School of Electrical & Electronic Engineering
Nanyang Technological University, Singapore
[2]Defence Medical & Environmental Research Institute
DSO National Laboratories, Singapore
([†]Corresponding author. Tel: +65-6790 4336; Fax: +65-6793 3318; Email: aqliu@ntu.edu.sg)

ABSTRACT

This paper presents a sensitive microdroplet interferometry to monitor the local pressure in microfluidic chips. Its work principle is based on the shift of fringes to detect the small variation of a droplet profile under different environmental pressures. An accuracy of 0.01% has been obtained. Compared with other methods, this method features high accuracy, simple design, inexpensive fabrication and little effect on microfluidic system, making it promising for many applications.

Keywords: Microdroplet, interferometry, local pressure, fringe

1. INTRODUCTION

Recently, integration of traditional experiments into micro chips is well known as lab on a chip. In such a microfluidic system, chemical reaction, bioengineering and micro-total analysis system (μTAS) can be carried out easily. Pressure sensor is an important part in microfluidic chips for fluidic control, and is also useful for many other pressure-sensitive experiments on chips. An pressure sensor named microdroplet interferometry is presented in this paper. It's based on the shift of fringes, which is sensitive to the droplet profile [1], to detect the small pressure change of gas around the droplet. Compared with other local pressure sensor for microfluidic chips, such as deformable diffraction grating [2] and small cube comprised of silicone diaphragm [3], it has simpler design, cheaper fabrication and higher accuracy.

2. WORKING PRINCIPLE

The design of chip has a chamber and a pressure sensor (Fig. 1a). Inlet and outlet are used to load and unload samples. The cross-section of the chamber and the sensor shows that the sensor is filled with air and connected to the chamber by a micro channel (Fig. 1b). The liquid-air interface in the channel will have a shift when the pressure is changed. The collinated laser light comes down from the condenser lens, and is partially reflected by the droplet (Fig. 1c). The reflected light interferes with the direct light. When the pressure of air in the sensor becomes higher, the curvature of liquid-air interface of microdroplet decreases and then the angle of incidence (or reflection) becomes larger, which will enlarge the radius of fringes. The change of fringes can be used to detect the pressure in the sensor, which is corresponding to the pressure in the chamber.

For a small droplet, thermodynamic equilibrium is described by Young-Dupre equation,

$$\gamma_{SG} - \gamma_{SL} - \gamma \cos\theta = 0 \quad (1)$$

978-0-9798064-0-7/μTAS2007/$20©2007CBMS

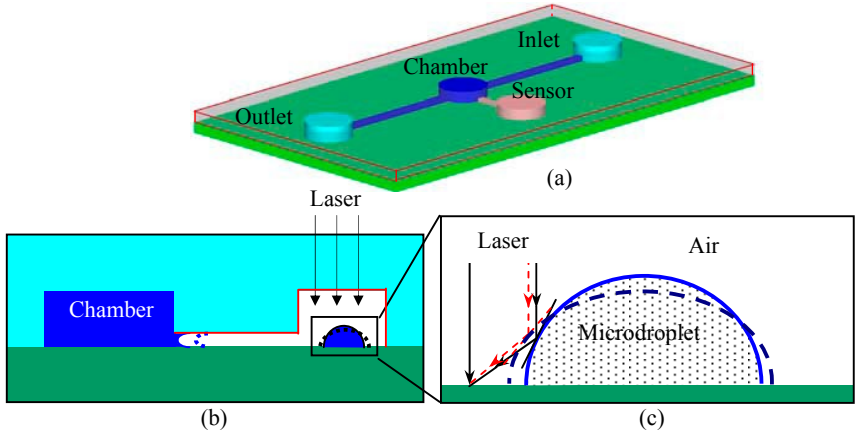

Figure 1. The schematic of a micro fluidic device (a) the whole chip with a chamber and a pressure sensor; (b) the cross-section of a chamber and a sensor; (c) the principle of interferometry.

where free energy per unit area of the interfaces between solid and gas is γ_{SG}, between solid and liquid is γ_{SL}, between liquid and gas is γ and θ is contact angle. There is a certain pressure difference between gas and liquid (Fig. 1c) and is determined as,

$$P_l - P_g = 2\gamma\kappa \qquad \Rightarrow \qquad P_l = P_g + 2\gamma\kappa \tag{2}$$

where κ is the curvature of interface between liquid and gas, and γ is also called surface tension. Due to small size, the gravity is negligible, and therefore the microdroplet can be considered as a spherical cap. When the pressure of gas P_g is increased, the curvature of interface κ becomes smaller and smaller and thus the pressure of liquid P_l rises up.

3. EXPERIMENTAL RESULTS AND DISCUSSION

The chip is fabricated by bonding three patterned PMMA layers using thermal bonding method. The thickness of each layer is 1 mm. The micro droplets in the sensor are formed through heating (80 ℃) and cooling (20 ℃) circles when it is sealed by pure water. The diameters of these droplets depend on the highest temperature, the lowest temperature, the cooling speed, the number of repetitive times and the surface property in the sensor. These diameters are usually in the range from several micrometers to 50 μm. The liquid-sealed structure keeps the sensor under a stable humidity, which prevents the evaporation of micro droplets. In experiences, we leave aside the sensor with newly formed droplets for twenty hours before it is used.

The fringes around a micro droplet are recorded by a high sensitivity camera on microscope when the sensor is illuminated by a laser beam (wavelength 524 nm, Fig. 2a). There are 7 to 8 obvious fringes around the droplet when the microscope is focused on the bottom of the droplet. Hydrostatic pressure is applied on the chamber and adjusted by the heights of water columns in the inlet and outlet. With the increase of the applied pressure, the fringes shift outward (Fig. 2b), but the amounts are not the same for different fringes. In order to increase the accuracy, average shift of the fringes is calculated in fringe area. In Fig. 2b, the fringe area

corresponds to the range of radius from 25 to 35 μm. By this way, an accuracy of 0.01% can be obtained.

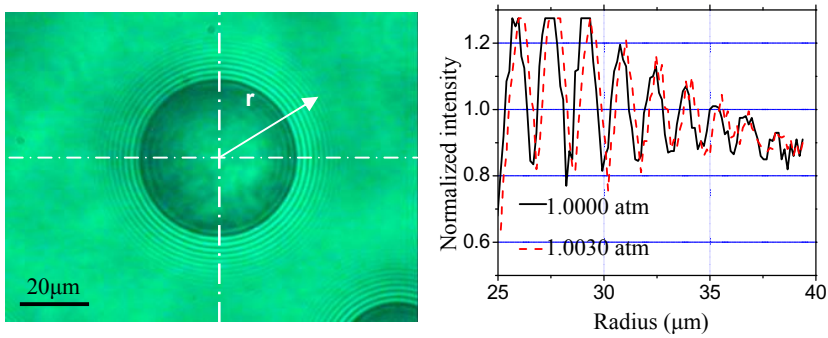

(a) (b)

Figure 2. (a) the fringes around a micro droplet; (b) the shifts of fringes under different applied pressures.

A series of pressures are applied to get experimental data, as shown in Fig. 3 for two sizes of droplets. The solid line and the dashed line are fitted by polynomial interpolation method. It can be read from Fig. 3 that droplets with different diameters have different pressure-shift curves. After the characterization, these curves can be used for local pressure detection in microfluidic chips.

4. CONCLUSION

In summary, a sensitive micro-droplet interferometry is developed to measure local pressure in microfluidic chips. It bears the advantages of high accuracy (0.01%), inexpensive fabrication and little effect on microfluidic system. It is also possible to produce new types of optical micro droplet pressure sensor independently for some traditional applications.

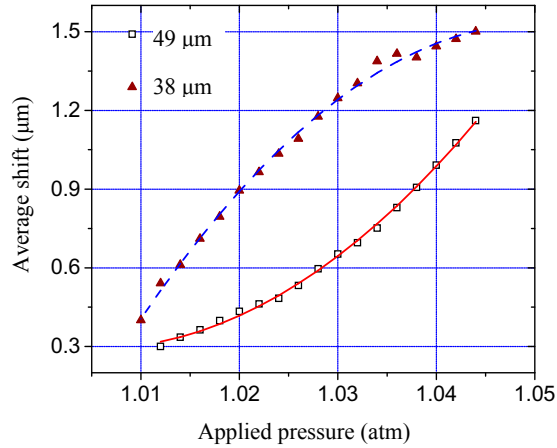

Figure 3. Pressure-shift curves with different diameters of the droplets.

REFERENCES

[1] D. R Secker, P. H. Kaye, R. S. Greenaway, E. Hirst, D. L. Bartley, and G. Videen, *Real-time observation of the change in light scattering from droplets with increasing deformity*, Opt. Exp., Vol. 8, pp.290 (2001).

[2] Y. Sekimori, and T. Kitamori, *Micro fluidic devices in 1 mm cube shape for flow control in a micro chemical chip*, μTAS2006, pp. 1124 (2006).

[3] K. Hosokawa, K. Hanada, and R. Maeda, *A polydimethylsiloxane (PDMS) deformable diffraction grating for monitoring of local pressure in microfluidic devices,* J. M. M., Vol. 12, pp. 1 (2002).

MONITORING MIXING DYNAMICS CONFINED WITHIN AQUEOUS MICRODROPLETS WITH 5 μs RESOLUTION

M. Srisa-Art[1], A. J. deMello[1] and J. B. Edel[1,2]
[1]*Department of Chemistry and* [2]*Institute of Biomedical Engineering*
Imperial College London, UK
Emails: a.demello@imperial.ac.uk, joshua.edel@imperial.ac.uk

ABSTRACT
In this paper, we describe the use of spatially-resolved fluorescence lifetime imaging (FLIM) to reconstruct mixing patterns within microdroplets with a 5 μs resolution.

Keywords: droplets, mixing, fluorescence lifetime, FLIM

1. INTRODUCTION

Water-in-oil microdroplets within fluidic channels have the potential to serve as isolated reaction compartments for monitoring real-time dynamics with high efficiency and repeatability. Droplets can be generated at frequencies in excess of 1 kHz. Although mixing within such microdroplets is normally enhanced by chaotic advection the mixing pattern from droplet to droplet is almost identical and reproducible in form. In this paper, we demonstrate that fluorescence lifetime imaging can be used to reconstruct mixing patterns within a droplet with a time resolution of 5 μs.

2. EXPERIMENTAL

Detection setup: A custom built confocal fluorescence detection system for droplet detection is schematically shown in **Figure 1a**.

Lifetime measurements: A PDMS fluidic chip (containing 50 μm wide and 50 μm deep channels) [1], consisting of 2 aqueous inlets, one oil inlet and a winding section was used for all experiments To create a microdroplet system, an oil phase, a 10:1 (v/v) mixture of perfluorodecalin and 1*H*,1*H*,2*H*,2*H*-perfluorooctanol, and aqueous solutions were continuously pumped at a constant flow rate of 2.0 μl min^{-1} (for each phase), resulting in the total flow rate of 4.0 μl min^{-1} (26.67 mm s^{-1}). The first aqueous inlet consisted of 20.0 μM fluorescein 5-isothiocyanate (FITC) (in pH 9.0 buffer) delivered at a flow rate of 0.75 μl min^{-1}. A 2.0 M potassium iodide (KI) solution (in pH 9.0 buffer) was pumped into the second aqueous inlet at a flow rate of 1.25 μl min^{-1}. A schematic of the microfluidic device topology is illustrated in **Figure 1b.** The KI acts as a fluorescence quencher [2] which decreases the fluorescence lifetime of the dye molecule when fully mixed. We use this attribute to map out mixing within single aqueous microdroplets. FLIM data were recorded at the first loop of the winding channel, which is 253.7 μm downstream of the droplet forming region. The detection probe volume was set at a channel depth of 25 μm and was scanned every 1 μm across the 50 μm wide channel in order to reconstruct the mixing pattern for the whole droplet.

978-0-9798064-0-7/μTAS2007/$20©2007CBMS

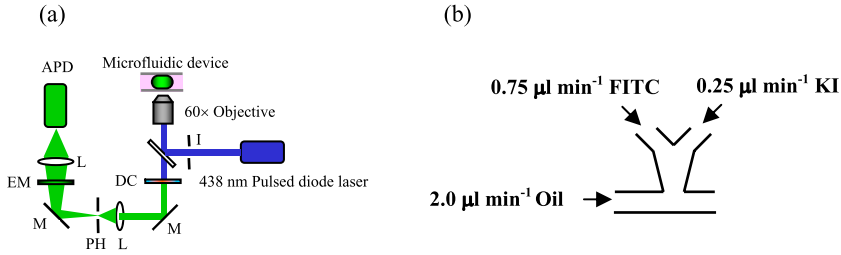

Fig. 1. (a) A home built confocal microscope used for fluorescence lifetime measurements: APD-avalanche photodiode detector, DC-dichroic mirror, EM–emission filter, I-iris, L-lens, M-mirror and PH-pin hole. (b) Schematic of a microfluidic device setup for lifetime measurements.

3. RESULTS AND DISCUSSION

An example of the variation in signal intensity as a function of time is shown in **Figure 2a**. These trajectories were obtained at a position 25 µm deep and 10 µm from the edge of the channel wall. Each peak represents an aqueous droplet transiting the 350 nm wide diffraction limited detection probe volume. In **Figure 2b** the fluorescence lifetime determined using a customized maximum likelihood estimator algorithm is shown for each burst. The algorithm itself is typically used in single molecule lifetime spectroscopy as demonstrated by Edel et al [3]. Each point in this plot represents a fluorescence lifetime measured with a maximum of 20 photons. Using our acquisition electronics, this corresponds to an acquisition time of 5 µs per point. In turn, this corresponds to approximately 600 points per droplet in 1 dimension. A high resolution interpretation of the lifetime trajectory is shown in **Figure 3**. This was obtained by averaging the lifetime of 300 droplets at each and every point. The short lifetimes of ~1.6 ns within the droplets confirm a quenched location and hence complete mixing has taken place at that particular point. A lifetime of 3.7 ns correlates to a perfectly unmixed state. Using this information we show that a droplet can be reconstructed based on fluorescence lifetimes with 5 µs resolution, as shown in **Figure 4**.

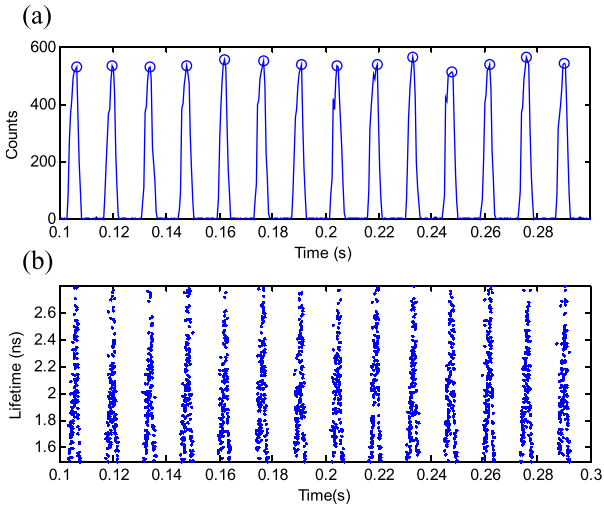

Fig. 2. (a) Intensity trajectory of individual aqueous droplets transiting the detection probe volume. (b) Fluorescence lifetime trajectory of the same droplets.

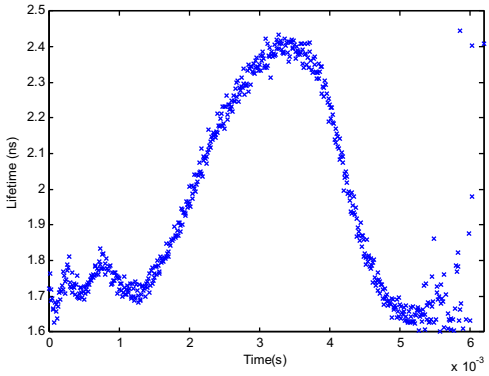

Fig. 3. High resolution lifetime trajectory obtained with 20 photons per point (5 µs). Left most point is the beginning of the droplet transiting the detection probe volume. Right most point is the tail of the droplet.

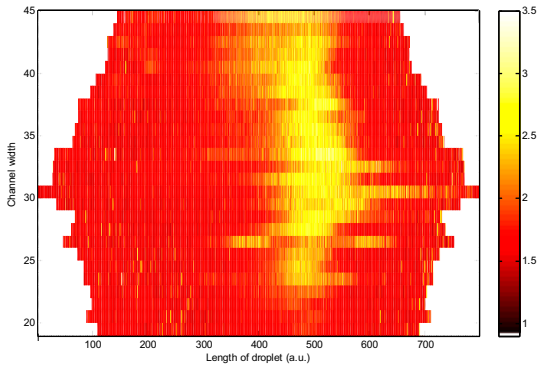

Fig. 4. 2D map of reconstructed droplet at the first loop. The droplets at this point are nearly fully mixed as confirmed by the fluorescence lifetime.

4. CONCLUSIONS AND OUTLOOK

FLIM was successfully used to reconstruct mixing patterns inside droplets with a resolution of 5 µs. Being able to monitor mixing dynamic with such high time resolution will prove to be valuable for monitoring high-speed reaction dynamics and kinetics.

ACKNOWLEDGEMENTS

M. S-A acknowledges the Royal Thai Government for provision of a scholarship. The work was partially supported by the RCUK funded Microdroplets Basic Technology Project

REFERENCES

[1] Huebner, A.; Srisa-Art, M.; Holt, D.; Abell, C.; Hollfelder, F.; deMello, A.J.; Edel, J.B. *Chem Comm.* **2007**, 1218-1220.
[2] Bessoth, F.G.; deMello, A.J.; Manz, A. *Anal. Commun.* **1999**, *36*, 213-215.
[3] Edel, J.B.; Meller, A. *Journal of* Physical *Chemistry B* **2007**, *111*, 2986-2990.

OPTICAL GRATING COUPLER BIOCHEMICAL SENSORS WITH ON-CHIP REFERENCE

Nasser Darwish[1], Eva Baldrich[2], F.Javier Del Campo[2], Mauricio Moreno[1], Francesc Xavier Muñoz[2], Roser Mas[2] and Josep Samitier[1]

[1] Departament d'Electrònica, Facultat de Física, Universitat de Barcelona, SPAIN
[2] Instituto de Microelectrónica de Barcelona, CNM-CSIC, Barcelona, SPAIN

ABSTRACT

We present the development of a grating coupler biosensor in a double pad configuration, with no moving parts. The sensor chips were also designed with a partial-window scheme allowing on-chip reference. Following antibody functionalisation, the immunosensor was successfully used to detect *E. coli*.

Keywords: evanescent field, bacteria detection, on-chip reference, chemical passivation.

1. INTRODUCTION

The wavelength of the visible light (around 0.5μm) makes it ideal to study phenomenons of biological interest. Optical evanescent field techniques are a promising alternative for the detection of a wide range of analytes [1, 2, 3]. In such systems, chemical changes on the sensor surface alter the wave number of the confined radiation (either electromagnetic or plasmonic), which can be optically analyzed later. For specific antigen-antibody reaction, our system requires no labels, and allows detection with minimal sample.

2. THEORY

A grating coupler is an optical waveguide with gratings etched in specific areas [1,3,6]. A film layer, with higher refractive index than its vicinity, confines light because of total internal reflection (TIR), with propagation speed characterized by the effective refractive index n_{eff}. This parameter is extremely sensitive to the waveguide structure and vicinity composition, because of the evanescent field effect. Gratings permit a light beam to couple into the waveguide if the Bragg condition is verified for some angle θ_c:

$$n_{eff} = n_{ext}\sin(\theta_c) + m\frac{\lambda}{\Lambda} \qquad (1)$$

where λ is the wavelength, Λ the grating period, and m the diffraction order.

3. EXPERIMENTAL

A first TE mode is coupled into a planar Si_3N_4 monomode waveguide (from a laser diode, λ = 635nm) at a fixed angle (first order, m = 1), through an isolated grating. The propagating light is then out-coupled at a second pad, exposed to the analyte. Some grating areas are covered by SiO_2 performing *chemical passivation* (fig.1), ie. making the area insensitive to the external medium [5]. The light is out-coupled with two different angles, one for the liquid and the other for the SiO_2 (working as reference). This is an on-chip reference scheme where we measure distances between spots instead of angles.

978-0-9798064-0-7/μTAS2007/$20©2007CBMS

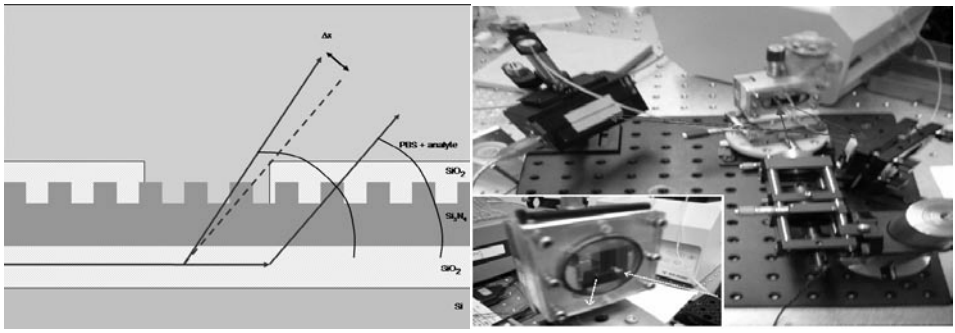

Figure 1. Operation principle of the on-chip reference scheme (left) and developed set-up (right).

A Si_3N_4 waveguiding layer was deposited by LPCVD technique over the thermally oxided surface of the wafer, gratings were etched by e-beam lithography and the sensing windows were photolithographically defined on another oxide layer deposited by PECVD [5]. The light in-coupling (at a totally covered grating) does not depend on the sensed medium composition, so the instrument (fig. 1) needs no moving parts.

The peaks are monitored at a 512x1 CMOS array from HAMMAMATSU, governed by a low-cost microcontroller (PIC 18F452) from MICROCHIP. Images are then transferred to a PC computer (RS232 protocol) and then processed in real time.

4. RESULTS AND DISCUSSION

For water and ethanol (refractive index of 1.33 and 1.36) we found a 100 pixel shift (not shown), so sensitivities around 3e-4 RIU are to be expected. Longer optical paths (easy to get by using mirrors) and the detector substitution (now L_{pix} = 10μm) will allow values around 1e-5 RIU. With a ±10pixel noise alcohols are easily distinguished, but while monitoring bacteria deposition, the signal change for concentrations from 1e3 to 1e6 bacteria / ml, are partially immersed into the noise itself (fig.2).

If we move the detector away to amplify peak separations we will loose sensing range, as CMOS arrays are not infinitely large. For an specific application this won't be a problem. Anyway, if the noise is not removed, the same (but amplified) figure is obtained.
The wavelength of laser diodes (the source of our system) varies with temperature. For a similar source, between 23ºC and 25ºC we found 1nm wavelength shift, changing the coupling angle from 10.15deg. to 10.25deg. Using $\Delta_{pix} = (\sin \vartheta_2 - \sin \vartheta_1) * d / L_{pix}$ we get a 40 pixel shift. Our 10 pixel noise level can then be explained for this more stable source.
The system was used to detect *E. coli* by functionalising a chip with antibodies, followed by blocking with BSA as to prevent unspecific adsorption. Specificity was assessed on a chip treated with only BSA but no antibody. Signal changes in response to different bacterial concentrations were only recorded for the functionalised chip.

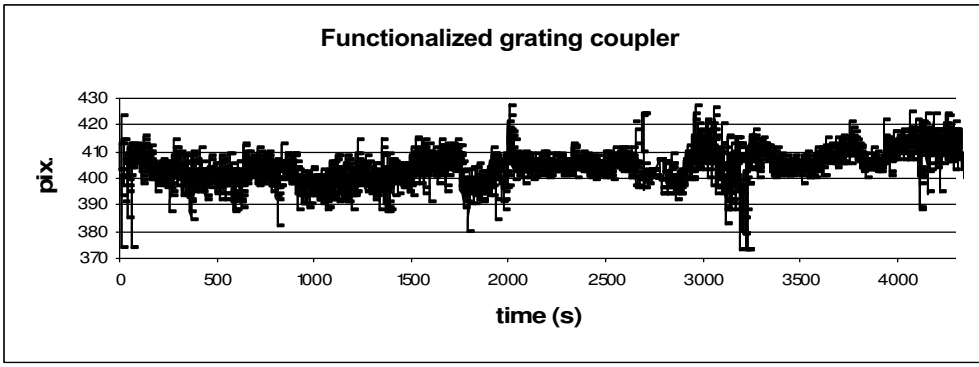

Figure 2. *E Coli* deposition from the injection of 1e3 to 5e4 bacteria / ml. The specific response of the functinoalised chip contrast with the constant signal (around 405pix.) of the blocked one.

5. CONCLUSIONS

The ability of our on-chip referenced sensors to monitor biological interactions was shown, with the added advantage of not needing moving parts. Accurate measures of bacteria surface concentrations depend strongly on the precise control of the sample and also the laser diode's temperature. Small bubbles observed after some injections and surface rearrangements will probably should also be taken into account. Once the noise is reduced it is easy to increase the sensitivity by limiting the sensing range to the application of interest.

ACKNOWLEDGEMENTS

This work was possible thanks to the founding and support of the CICYT projects nr. DPI2003-08060-C03-03 and TEC 2006-1309-C03-03, and the MC2ACCESS program, European contract nr026029, under the FP6 "Research Infrastructures Action" program.

REFERENCES

[1] K. Tiefenthaler and W. Lukosz, "Sensitivity of grating couplers as integrated-optical chemical sensors", J. Opt. Soc. Am. B, Vol. 6, No 2, Feb. 1989.

[2] J. Homola, J. Ctyroký, M. Skalský, J. Hradilová, P. Kolárová, "A surface plasmon resonance based integrated optical sensor" , Sensors and Actuators B 38-39 (1997) 268-290

[3] R.Gush, J.M. Cronin, W.J. Stewart, C.H. Maule, J. Molloy, N.J. Goddard, "The Resonant Mirror: A Novel Optical Biosensor for Direct Sensing of Biomolecular Interactions", Biosensors & Bioelectronics Vol. 8 (1993) pp. 347-353.

[4] R.E.Kunz, J. Dübendorfer & R. H. Morf, "Finite grating depth effects for integrated optical sensors with high sensitivity", Biosensors & Bioelectronics, Vol. 11, No 6/7 (1996), pp 653-667.

[5] N. Darwish, L. Diéguez, M. Moreno, F. Muñoz, R. Mas, J. Mas, J. Samitier, B. Nilsson, G. Petersson, " Second order effects of aspect ratio variations in high sensitivity grating couplers", Journal of Microelectronic Engineering, April 2007.

[6] J.J Ramsden, "Optical Biosensors", Journal of Molecular Recognition, Vol. 10, pp109–120 (1997).

OPTICAL MULTIPLEXING OF MULTIPLE FLUORESCENCE SENSORS FOR COMPACT LAB-ON-A-CHIP SYSTEMS

K. S. Lee[1] H. L. T. Lee[1] R. J. Ram[1]

[1]*Massachusetts Institute of Technology, USA*

ABSTRACT

Frequency domain multiplexing combined with optical waveguides provides a low cost and efficient approach to optical detection in arrayed microfluidic chips by eliminating detection components and improving acquisition time. A waveguide test chip fabricated in PDMS demonstrates 4:1 multiplexing in the readout by utilizing multilayer waveguides.

Keywords: Multiplexing, Optical Detection, Waveguides, Fluorescence Sensor

1. INTRODUCTION

Many biochip systems require optical detection at discrete locations, such as flow cytometers, PCR chips, and bioreactors [1, 2, 3]. Although only requiring point detection, these systems usually have high bandwidth requirements, necessary for high-throughput cell sorters or quantitative fluorescence lifetime detection. To provide sensors for truly portable lab-on-a-chip systems, optical detection must be made compact and cheap, utilizing non-imaging optics such as waveguides and reducing off-chip components such as photodetectors and photomultiplier tubes. Many different approaches to waveguide fabrication have been demonstrated for integration with microfluidic systems [1, 4]. In addition, frequency division multiplexing (FDM) has been explored as a method to reduce component costs and increase speed for multichannel fluorescence microscopes [5]. We present a new detection approach combining waveguides with frequency multiplexed fluorescence detection as a low cost and scalable approach for accurate detection of multiple fluorescence signals located within a single chip.

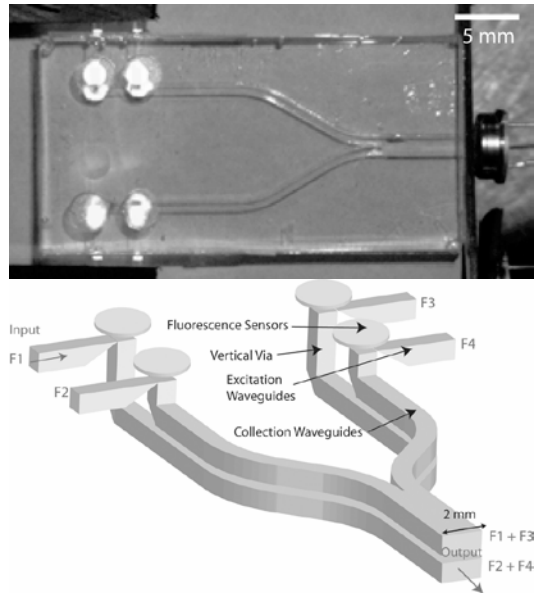

Figure 1. Image and schematic of the waveguide chip. Fluorescence sensors in the fluidic chip are positioned to interface to the detection sites of the waveguide.

2. DESIGN AND FABRICATION

The test chip fabricated is shown in Figure 1. Four individually modulated excitation waveguides are connected to vertical collection waveguides at the

978-0-9798064-0-7/μTAS2007/$20©2007CBMS

optical sensor locations. The collected light is then reflected in plane and combined through a power combiner resulting in all four fluorescence signals converging at a single photodetector. Waveguides with 1x1 mm^2 cross-sectional areas are fabricated using CNC machining of polycarbonate and vapor polishing, followed by cold injection molding of PDMS into the polycarbonate masters [3]. The waveguide bends of each PDMS layer are coated with 200 nm silver mirrors and the layers are plasma bonded. The resulting hollow channels are filled with NOA71 (Norland Products) and cured under UV illumination. Fabricated 1 mm^2 waveguides measure a propagation loss of 0.1 dB/cm.

3. EXPERIMENTAL

The performance of the system is demonstrated by monitoring the oxidation of sulfite – this reaction consumes oxygen and generates an acidic product [6]. The fluidic test chip above the waveguides consists of a reaction chamber, a waste chamber, and a series of peristaltic mixing tubes to provide oxygen for an oxidation reaction. Two detection sites within the reaction chamber contain a pH sensitive (Presens) fluorophor with an excitation modulated at 44 kHz and an oxygen sensitive dye (PtOEP [7]) modulated at 5.08 kHz. In addition to signals from the pH and oxygen sensors, two waveguide ports are used to monitor the fluorescence from CdSe nanoparticles (or quantum dots), also modulated at frequencies close to the chemical sensor modulation frequencies.

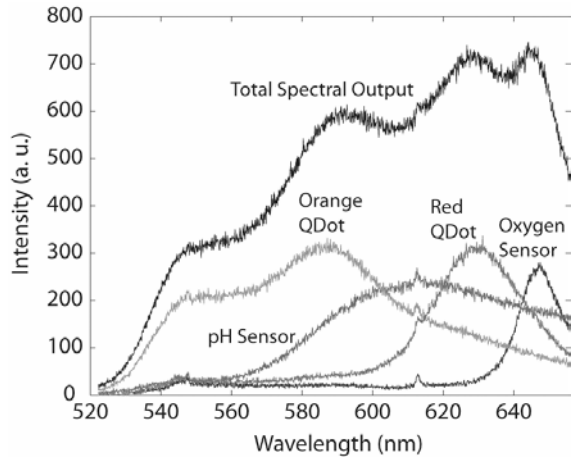

Figure 2. Emission spectra of the waveguide output incident on the photodetector. Oxygen and pH are still distinguishable with frequency multiplexing under large spectral interference.

4. RESULTS

As shown in Figure 2, the overlapping spectra of the fluorescent sensors make simultaneous measurements difficult in wavelength domain. However, with excitations modulated at different frequencies as shown in Figure 3, all four signals are clearly distinguishable from one another. FDM is able to extract data from the sensors

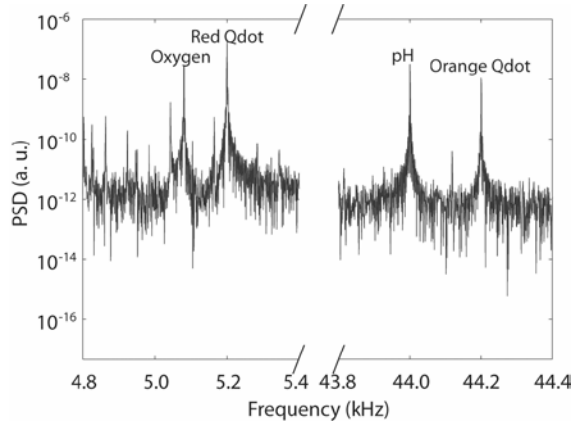

Figure 3. Power spectral density of the output photodetector clearly indicating the modulation frequencies of each fluorophor.

despite the large overlap in emission between different fluorophors. As seen in Figure 4, the oxidation of sulfite consumes the available oxygen and steadily reduces the pH in the chamber. This reaction proceeds until the sulfite begins to deplete, indicated by the gradual rise in oxygen concentration.

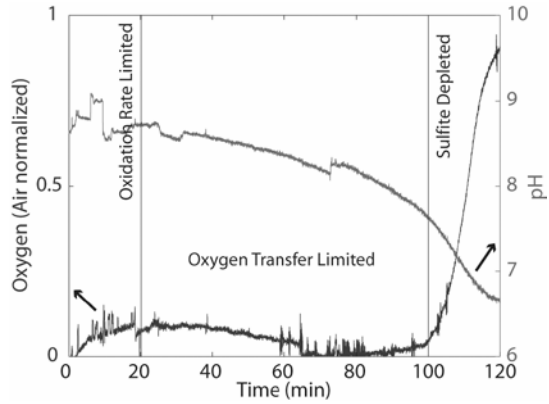

Figure 4. Measured oxygen and pH of a Sodium Sulfite oxidation reaction using the integrated waveguide FDM sensor.

5. CONCLUSIONS

Frequency division multiplexing combined with optical waveguides provides an approach for addressing simultaneous detection in microfluidic arrays. In this work we have demonstrated a 4x multiplexed fluorescence detector capable of both intensity based and lifetime based fluorescence detection.

ACKNOWLEDGEMENTS

We would like to thank the National Science Foundation Center for Material Science and Engineering for their support.

REFERENCES

[1] C. H. Lin, G. B. Lee, G. L. Chang, “Micro flow cytometers integrated with buried SU-8/SOG optical waveguides,” Sensors Actuators A, **130,** 165–70 (2003).

[2] J. Khandurina, T. E. McKnight, S. C. Jacobson, L. C. Waters, R. S. Foote, J. M. Ramsey, “Integrated System for Rapid PCR-Based DNA Analysis in Microfluidic Devices," Anal. Chem., **72**, 2995-3000 (2000).

[3] H. L. T. Lee, P. Boccazzi, R. J. Ram, A. J. Sinskey, “Microbioreactor arrays with integrated mixers and fluid injectors for high-throughput experimentation with pH and dissolved oxygen control,” Lab Chip, **6**, 1229-1235 (2006).

[4] D. A. Chang-Yen, B. K. Gale, “An integrated optical oxygen sensor fabricated using rapid-prototyping techniques”, Lab Chip, **3**, 297-301, (2003).

[5] F. Wu, X. Zhang, J. Y. Cheung, K. Shi, Z. Liu, C. Luo, S. Yin, P. Ruffin, “Frequency Division Multiplexed Multichannel High-Speed Fluorescence Confocal Microscope,” Biophys. J., **91**, 2290-2296 (2006)

[6] R. Hermann, N, Walther, U. Maier, J. Buchs, “Optical Method for the Determination of the Oxygen-Transfer Capacity of Small Bioreactors Based on Sulfite Oxidation,” Biotechnology and Bioengineering, **74**, 355-363 (2005)

[7] C. O’Donovan, J. Hynes, D. Yashunski, D. B. Papkovsky, “Phosphorescent oxygen-sensitive materials for biological applications,” J. Mater. Chem., **15**, 2946-2951 (2005)

SURFACE ENHANCED RAMAN SPECTROSCOPY ON CHIP

Jorg Hubner[1], Thomas Anhøj[2], Sarah Pedersen[1], Dan A.Zauner[3], Anders M. Jorgensen[4], Gabriella Blagoi[1] and Ole Hansen[1]

[1]MIC - Department of Micro and Nanotechnology, Technical University of Denmark NanoDTU,Bldg. 345 east, Dk-2800 Lyngby,

[2]currently with SERSTECH AB, P.O. Box439, SE 201, Malmoe, Sweden

[3]currently with Ignis Photonyx, Blokken 84, 3460 Birkerød, Denmark

[4]currently with AllSun, Brundtlandparken 2, 6520 Toftlund, Denmark

ABSTRACT

In this paper we report low resolution surface enhanced Raman spectra (SERS) conducted with a chip based spectrometer. The flat field spectrometer presented here is fabricated in SU-8 on silicon, showing a resolution of around 3 nm and a free spectral range of around 100 nm. The output facet is projected onto a CCD element and visualized by a computer. To enhance the otherwise rather weak Raman signal, a nanosurface is prepared and a sample solutions is impregnated on this surface. The surface enhanced Raman signal is picked up using a Raman probe and coupled into the spectrometer via an optical fiber. The obtained spectra show that chip based spectrometer together with the SERS active surface can be used as Raman sensor.

Keywords: Integrated spectrometer, Raman spectroscopy, Raman sensor, SERS

1. INTRODUCTION

Lab-on-chip and other minituarized chemical sensor systems are characterized by their sensitivity, selectivity and complexity which in turn is related to cost, ease of use, shelflife time etc. In a number of these systems it would be advantageous to replace sensing based on chemical reactions with spectroscopic investigation of the analyte.

Several spectroscopic methods are routinely used to analyse unknown substances. Some of these methods are inherently difficult to fully miniaturize (e.g. FTIR, mass spectroscopy). Raman spectrometers have the potential to be miniaturized although the obtained signals are very weak. In the 70'ies it was discovered that molecules adsorbed at a nanostructured silver or gold surface exhibited a Raman signal that was enhanced by many orders of magnitude.

In the following we report on promising first results obtained by miniaturizing a Raman spectroscopy system including a chip sized spectrometer and a nanostructured gold surface and prove the principle of a fully integrated Raman sensor unit.

2. EXPERIMENTAL

Integrated spectrometers are designed after principles described in [1] and fabricated using a carefully optimized SU-8 process [2]. They consist of an input waveguide and a concave grating where the dimensions of every grating facet are calculated using a special algorithm so that the output foci for the different wavelengths form a straight line. This allows direct attachment of a CCD sensing element. Figure 1 shows an artists impression of

978-0-9798064-0-7/μTAS2007/$20©2007CBMS

the spectrometer that illustrates the basic principle. The SU-8 layer forming the optical and fluidic circuitry is 40 µm thick and the chip is sealed by a glass lid. Details about the spectrometer are presented in [3].
Figure 1 to the right shows a photograph of the spectrometer chip. Figure 2 (left) shows the setup where the output facet of the spectrometer is projected onto a CCD. Filters are used to clearly visualize the free spectral range.

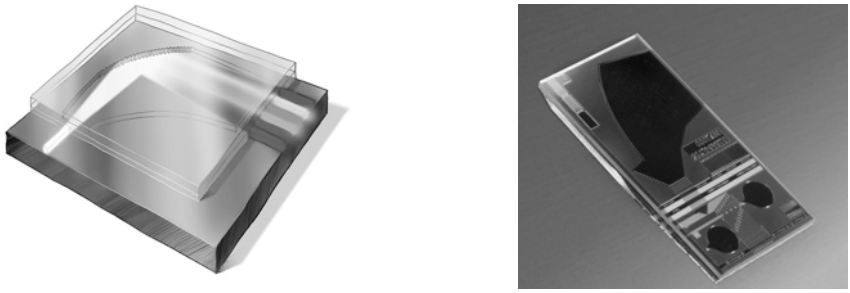

Figure 1. Left: Artist's impression of the chip based spectrometer, showing the principle, including the concave reflection grating and glass lid. Right: Photograph of the spectrometer chip. As the spectrometer is also applicable to spectral analysis of absorbance and/or fluorescence, a micro fluidic circuitry is co-integrated with the spectrometer and waveguide circuitry.

Later versions foresee the integration of the nanostructured surface. The results reported here are obtained by using the SERS signal from a nanosurface on a separate chip as depicted in Figure 2 (left). The output facet of the spectrometer is projected onto a CCD. Filters are used to clearly visualize the free spectral range.

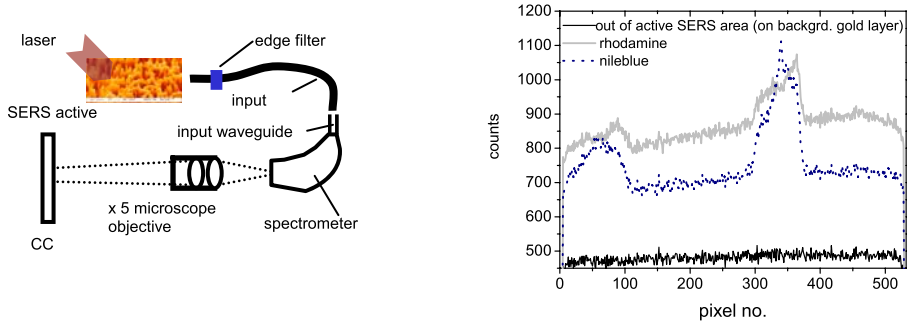

Figure 2: Left: Setup for recording Raman spectra. Bandpass filters can be inserted between the microscope objective and the CCD element. Right: SERS spectra of Nileblue (dark grey) and Rhodamin (light grey). The graph shows the complete facet of the spectrometer imaged on the CCD element. The bump in the graph to the left is caused by different diffraction order which is slightly defocused. These spectra were recorded with a spectrometer working in 7th order with a linear dispersion of 10 µm/nm and an integration time of 1s.

The SERS surface was prepared by a process adapted from [4] where a aquaeous suspension of gold nanoparticles and polystyrene beads was deposited on a gold surface. The suspension was dried and the polystyrene beads were removed using methane dichloride.
The Raman signal is collected using (at this stage) a commercial Raman probe (Avantes) and coupled into the spectrometer using an optical fibre.

3. RESULTS AND DISCUSSION

The SERS surface was impregnated with a droplet (10 µl, 100 µM) of Rhodamin 6G and Nileblue respectively and illuminated by a laser (785nm, around 5W/cm^2).
Figure 2 (right) shows a surface enhanced Raman spectrum of Nileblue and Rhodamin 6G respectively. Although not many spectral details are resolved , it is clearly seen that the two dies have distinct spectral characteristics.
This is, to the author's knowledge, the first demonstration of a Raman spectrum on a chip-spectrometer that can be readily integrated in lab on a chip systems.

5. CONCLUSIONS

We have shown Raman spectra recorded with a chip based spectrometer. The two substances show clearly distinguishable spectral characteristics. This proves that Raman spectroscopy has the potential to become a valuable analytical method in lab-on-chip and related miniaturized sensor systems.

ACKNOWLEDGEMENTS

The authors would like to thank the Danish Research Council for Production and Technology for supporting this work.

REFERENCES

[1] K. A. McGreer. "Theory of concave gratings based on a recursive definition of facet positions", Applied Optics, 35(30) p. 5904-5910, 1996.

[2] Thomas A. Anhoj, Anders M. Jorgensen, Dan A. Zauner, Jörg Hübner, "Optimization of SU-8 processing for integrated optics", Proceedings of SPIE, 6112, 611209. 2006.

[3] Dan A. Zauner, Anders M. Jorgensen, Thomas A. Anhoj, and Jörg Hübner" Concave reflective SU-8 photoresist gratings for flat-field integrated spectrometers", Applied Optics, 45(23) p. 5877-5880, 2006.

[4] D.M. Kuncicky, S.D. Christesen and O.D. Velev, "Role of the Micro- and Nanostructure in the Performance of Surface-Enhanced Raman Scattering Substrates Assembled from Gold Nanoparticles", Applied Spectroscopy, vol.58 no. 4 2005, p.401-409

DEVELOPMENT OF A CEREBROVASCULAR MIMIC USING ON-CHIP VALVES, HYDRODYNAMIC FOCUSING, AND INTEGRATED MICROELECTRODES

R. Scott Martin, Michelle W. Li, Matthew K. Hulvey, Laura C. Mecker, and Michael J. Moehlenbrock

Department of Chemistry, Saint Louis University, St. Louis, MO, USA

ABSTRACT

This paper describes the use of microchip technology to create a three-dimensional cerebrovascular mimic. Microchip-based valves have been developed to rapidly monitor changes in processes occurring on chip. In addition, microchip electrophoresis and amperometric detection have been coupled to the valving system to enable the detection of neurotransmitters released from neuronal cells. A three-dimensional system that incorporates carbon microelectrodes in separate fluidic layers has also been developed and characterized.

Keywords: Microchip electrophoresis, on-chip valving, amperometric detection

1. INTRODUCTION

Current *in vitro* mimics of the blood brain barrier (BBB) involve the use of bovine brain microendothelial cells that are placed in simple diffusion chambers [1]. This is not a realistic mimic, as the BBB has a circulatory portion where blood is constantly flowing as well as a central nervous system portion that contains glia and neuronal cells. Furthermore, detection of analytes in such systems is typically off-line, resulting in a loss of chemical and pharmacodynamic information. Our goal is to make a more realistic mimic that is three-dimensional in nature, incorporates blood flow and a neuronal mimic, and integrates electrochemical-based analysis.

2. EXPERIMENTAL

All poly(dimethylsiloxane) (PDMS) microchips were fabricated with standard lithography procedures [2]. The procedure used to fabricate microchips with integrated valves is based on a previous report [3] except the valving layer is made thick (3.5 mm) through use of a mold. With this approach, fluids can be introduced with conventional tubing and a reversible seal between the flow layer and a PDMS slab is possible. Carbon microelectrodes were fabricated with a micromolding procedure [4]. For studies involving 3-dimensionsal fluid flow, 2 straight flow channels are separated by a polycarbonate membrane [5] using a reversible seal, which is made possible by the individual layers being made of 20:1 and 5:1 PDMS:curing agent, respectively. Microchip-based flow analysis involving the use of an off-chip injection of catechol is similar to previously described studies [4].

3. RESULTS/DISCUSSION

Initially, separate parts of the mimic have been developed. This includes the development of a central nervous system mimic by incorporating PC 12 cells in microchannels [6] and coupling the resulting cell reactor to microchip electrophoresis with amperometric detection. This involves the development of on-chip valving methods to rapidly sample from a continuous flow stream [3], where in the long-term neurochemicals

978-0-9798064-0-7/μTAS2007/$20©2007CBMS

released from the cells are injected into the electrophoresis portion of the device. More recently, valves for on-chip injection of cell stimulant have been implemented. Importantly, these valving chips are amenable to a reversible seal so that cells can be immobilized by previous methods described from our lab [6]. Studies have shown that the valves interfacing the continuous flow cell reactor to an electrophoresis separation channel (Figure 1A) can be actuated every 300 ms, leading to rapid sampling of on-chip changes in concentration. This was demonstrated with the on-chip derivatization of glycine with naphthalene-2,3-dicarboxaldehyde/cyanide, which was used to simulate the release of neurotransmitters from neuronal cells. In addition, these PDMS-based devices have recently been integrated with amperometric detection to enable detection of neurotransmitters. The detection portion of the device involves a palladium decoupler to shunt the separation voltage as well as carbon-based dual microelectrodes that are on the order of 1.0 micron in height (Figure 1B).

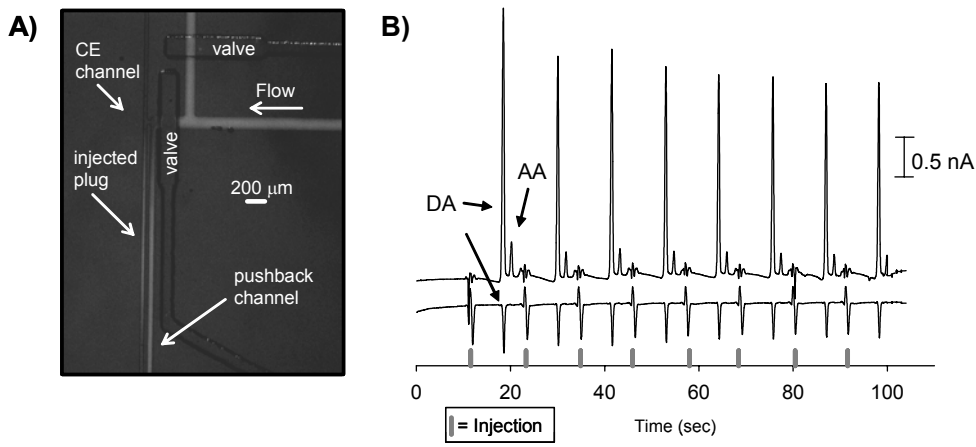

Figure 1. A) PDMS-based valves used to couple a continuous flow stream to electrophoresis; B) Continuous injections and subsequent electrophoresis-based separation and dual electrode detection of dopamine (DA) and ascorbic acid (AA).

The circulatory system portion of the mimic involves the use of microchip-based hydrodynamic focusing to both mechanically deform erythrocytes and quantify the ATP that is released in response to this deformation [7]. Finally, to realize a fully functional BBB mimic that involves flow streams for both the blood and neuronal portion, fabrication of a three-dimensional device where two fluidic layers are separated by a polycarbonate membrane has been achieved. The fabrication method that has been developed incorporates microelectrodes in the separate fluidic layers to selectivity detect the flux of electrochemically active species (such as NO) across the membrane.

Figure 3 shows the continuous injection and simultaneous amperometric detection of catechol in the separate layers. In this experiment, discrete injections of catechol are injected into one flow layer while a buffer flow stream of the same linear velocity is pumped in the separate layer. A portion of the catechol plug diffuses into the separate flow stream and is detected. Importantly, this is the first demonstration of simultaneous amperometric detection in separate fluidic layers. In addition, these electrodes can be modified to be selective for NO.

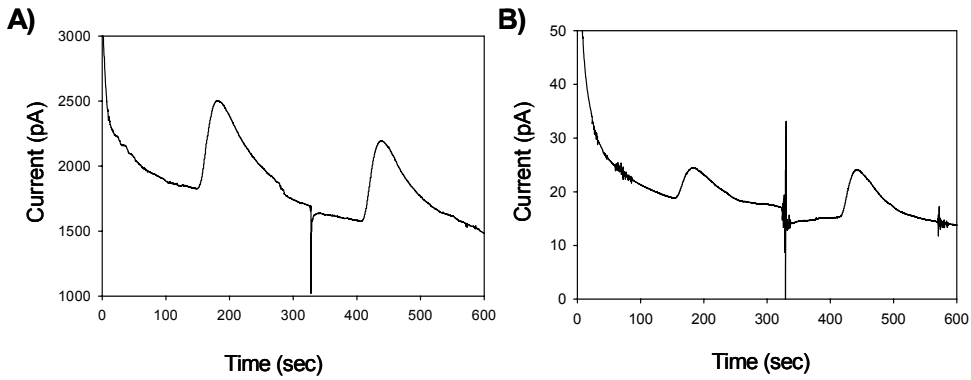

Figure 2. Simultaneous amperometric detection of 2 catechol plugs (500 nL) in a 3-dimenionsal fluidic device on either side of a polycarbonate membrane A) injection layer; B) flow layer on opposite side of the membrane.

4. CONCLUSIONS

Separate portions of a three dimensional cerebrovascular mimic have been described. In addition to the creation of a BBB mimic, new findings in on-chip cell culture, on-chip valving, electrophoresis-based separations, and on-chip amperometric detection have resulted. Future work will detail further integration of these processes to create a cerebrovascular mimic that can be used for pharmaceutical development or to investigate the onset of diseases associated with breakdown of the BBB.

ACKNOWLEDGEMENTS

This work was supported by the NIH (R15NS048103 and R01EB004164).

REFERENCES

[1] M. Gumbleton and K.L. Audus, *J. of Pharm. Sci*. **2001**, *90*, 1681-1698.
[2] R.S. Martin, A.J. Gawron, S.M. Lunte, and C.S. Henry, *Anal. Chem.*, **2000**, *72*, 3196-3202.
[3] M.W. Li, B.H. Huynh, M.K. Hulvey, S.M. Lunte and R.S. Martin, *Anal. Chem*., **2006**, *78*, 1042-1051.
[4] M.L. Kovarik, N.J. Torrence, D.M. Spence, and R.S. Martin, *Analyst*, **2004**, *129*, 400-405.
[5] T.C. Kuo, D.M. Cannon, Y. Chen, J.J. Tulock, M.A. Shannon, J.V. Sweedler, P.W. Bohn, *Anal. Chem.*, **2003**; *75*, 1861-1867.
[6] M.W. Li, D.M. Spence, and R.S. Martin, *Electroanalysis*, **2005**, *17*, 1171-1180.
[7] M.J. Moehlenbrock, A.K. Price, and R.S. Martin, *Analyst*, **2006**, *131*, 930-937.

NOVEL DUAL-CHANNEL AMPEROMETRIC IN-CHANNEL DETECTION IN MICROCHIP CAPILLARY ELECTROPHORESIS

Chuanpin Chen[1] and Jong Hoon Hahn[1,2*]

[1]School of Environmental Science and Engineering, [2]Department of Chemistry, BK School of Molecular Science, Pohang University of Science and Technology, San 31 Hyoja-dong, Pohang 790-784, South Korea

ABSTRACT

In this work, a novel dual-channel capillary electrophoresis (CE) amperometric in-channel electrochemical detection (ECD) system has been developed to eliminate the effect of separation voltage to EC detector. A working electrode (WE) and a reference electrode (RE) are placed at the same position of a separation and a reference channel near its outlet. In this system, the band broadening effects and potential shifts have been removed.

Keywords: Capillary electrophoresis, dual-channel, in-channel electrochemical detection, microchip

1. INTRODUCTION

In CE-ECD system, especially amperometric detection system, the interference from applied voltage for CE operation is the major obstacle. There are three approaches reported to avoid this interference including end-channel, in-channel and off-channel detection methods. [1] In-channel CE-ECD system can offer the solution without band broadening when the EC detector is isolated from the separation voltage. Normally, CE is carried out in a single separation channel and it generates high noise and potential shift during in-channel CE-ECD process. [1] In this report, an interference-free amperometric in-channel ECD in microchip CE has been developed by a dual-channel configuration.

2. EXPERIMENTAL

A gold working electrode (WE) and a reference electrode (RE) are fabricated on a glass plate by thermal evaporation and the micropattern is made by photolithographic technique in a clean room environment. The microchannel for CE is made on poly (dimethylsiloxane) (PDMS) microchip by replica molding technology. As shown in Figure 1, the separation channel is used for sample separation while the reference channel used for auxiliary. The separation and reference channels have the same length of 3 cm. Lengths of all other channels are shown in proportion to those of the two channels. All channels have the same cross section of 50 μm width and 20 μm depth, except the sample waste channel that is double in width. The PDMS microchip with this dual-channel network is bonded with electrode substrate while the two electrodes are positioned about 200 μm prior to the outlets of channels as WE and RE respectively. And then the bonded microchip is utilized for in-channel CE-ECD. In this design, Gold WE and RE are placed across two identical channels to eliminate the interference of separation voltage and a Pt counter electrode is mounted in the waste reservoir to complete a three-electrode electrochemical system.

978-0-9798064-0-7/μTAS2007/$20©2007CBMS

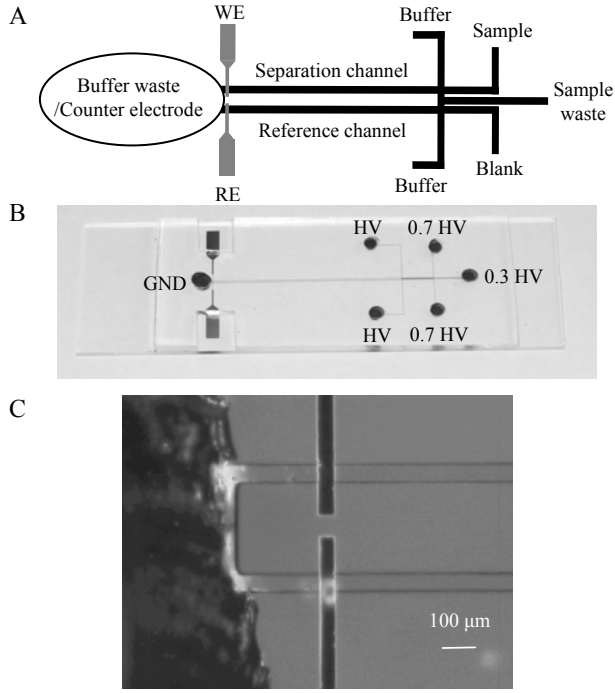

Figure 1 (A) Schematic of the microchannel network in the dual-channel CE microchip with an in-channel EC detector. (B) Photograph of the microchip. Channels are filled with red ink for visualization. (C) CCD image of Au electrodes mounted in the outlets of dual-channels.

4. RESULTS AND DISCUSSION

Figure 2 compares the noise in three electropherograms of dopamine (DA), which have been obtained from different EC detector configurations: single in-channel (A), dual in-channel (B) and head-to-head RE and WE in-channel (C) configurations. Serious drift and high-frequency fluctuations are inevitable in the electropherogram of the single-channel configuration, but that of the double-channel one is essentially free of noise. Note that the base line of Fig. 2B is almost noise free even at low nA region (see the magnified trace). It might be suggested quite possibly that the same effect of noise reduction could be achieved if the two electrodes are positioned head-to-head in the same channel. We have fabricated such a microchip with a 20 μm gap between the heads of WE and RE, and checked noise generated during CE separations. Fig. 2C shows the electropherogram of 5 mM DA, which has been obtained using a microchip with the head-to-head configuration. The serious drift in the electropherogram of the single in-channel, sequential configuration (Fig. 2A) is now removed almost completely, but the high frequency fluctuations still remain noticeable. The noise in the baseline of the electropherogram is much higher than that in Fig. 2B, and thus it is concluded that our dual-channel strategy provides the best performance among different in-channel configurations. Compared with the end-channel detection on the same CE conditions reported previously, [2] a 10-fold increase in the detection sensitivity has been achieved.

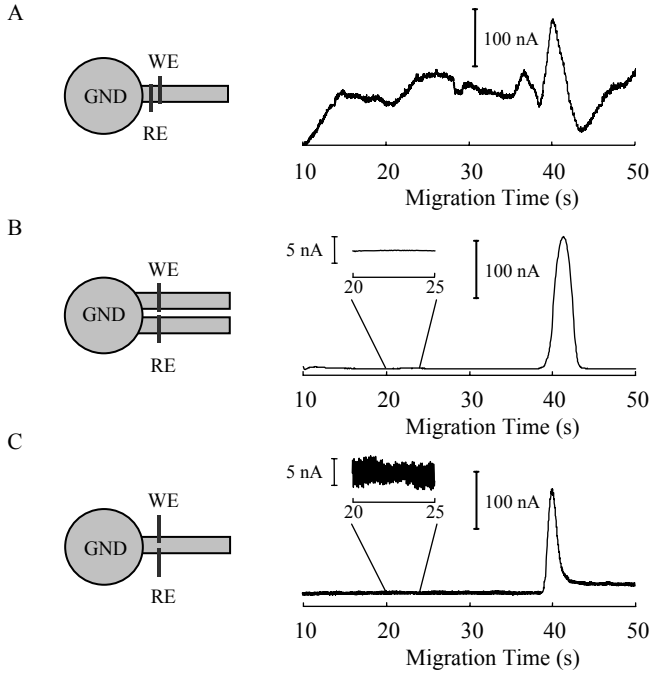

Figure 2. Electropherograms of dopamine in different WE-RE configurations. (A) In-channel configuration. The distance of the forward (upstream) side of WE from the buffer waste reservoir is 200 μm, that of the backward side of RE is 100 μm, and the gap between the two electrodes is 50 μm. Applied voltage between the two electrodes (E) is 3.0 V. (B) Dual-channel configuration. The distances of the forward sides of WE and RE from the buffer waste reservoir are the same: 200 μm. E = 0.7 V. (C) Head-to-head in-channel configuration of WE and RE; the distance of WE and RE is 20 μm; E = 0.7 V. DA of 5 mM is injected for 1 s and run with 20 mM boric acid buffer (pH 9.5). The electric potential of 250 V/cm is applied to each separation channel. A part of the baseline of the electropherogram is magnified down to a low nA scale.

5. CONCLUSIONS

Through this work, a dual-channel method has been proved to have high performance to avoid the interference from the applied voltage for CE operation. The serious drift and high frequency fluctuations have been eliminated from the baselines of electropherograms.

REFERENCES

[1] W. R. Vandaveer IV, S. A. Pasas, R. S. Martin, S. M. Lunte, *Recent developments in amperometric detection for microchip capillary electrophoresis*, Electrophoresis, 23, 3667-3677, (2002).

[2] Y. Park, C. Chen, K. Lim, N. Park., J. H. Kim, J. H. Hahn, *Metal thin-film micropatterns transfer on PDMS and its application to capillary electrophoresis - electrochemical detection on PDMS microchip*, Proc. MicroTAS 2003, 623-626, (2003).

NEW HIGH DENSITY 3D MEAS ASSOCIATED WITH AN INTEGRATED ELECTRONICS ACQUISITION SYSTEM (BioMEA^{TM})

L. Rousseau[1] , V. Perrais[1], G. Charvet[2], R. Guillemaud[2], G. Lissorgues[1], P. Meyrand[3], B.Yvert[3]

[1]Groupe ESIEE, 2 boulevard Blaise Pascal – 93162 - Noisy le Grand cedex, FRANCE
[2]CEA LETI MINATEC, 17 rue des Martyrs – 38054 - Grenoble cedex 9, FRANCE
[3]CNIC UMR5228 CNRS & Univ Bordeaux1 &2, Av. des Facultés, 33402 TALENCE, FRANCE

ABSTRACT

3D Micro Electrode Arrays (MEAs) provide an elegant way to probe the neuronal activity distributed over large populations of neurons either in vitro or in vivo and offer the possibility to deliver appropriate electrical stimulations to neuronal networks. This paper presents both a new etching process to build 3D MEAs with a small electrode pitch, and a compact integrated electronics for recording and stimulation of neuronal networks. This system, named BioMEA^{TM}, has been tested on a whole embryonic mouse spinal cord preparation.

Keywords: Micro Electrode Arrays, 3D silicone probes, Neurons

1. INTRODUCTION

One of the challenges of the current century will be to better understand the functioning of neural networks at the multi-cellular level. Indeed, while neuroscience has recently progressed in the knowledge of large neuronal systems at a macroscopic level with the development of functional imaging techniques (Functional MRI, PET, SPECT, EEG and MEG), these approaches do not hint on the dynamics of neural ensembles at the level of cellular interactions. In this context, Micro Electrode Arrays (MEAs) allow the recording of neuronal activity, and 3D-shaped microelectrodes have been introduced to achieve better contacts with the neural tissue for in vitro applications [1,2]. Classically, the isotropic etching is used to process 3D electrodes, which prevents the fabrication of dense 3D electrode arrays with high aspect ratios (electrode height / electrode pitch ≤ 0.5) [3]. For this reason, we have developed a new technology to build micro needles, using Deep Reactive Ion Etching (DRIE) of a silicon substrate. A specific integrated electronic chip has also been developed in order to allow both recording and stimulation on up to 64 channels simultaneously. Then a complete 256 channels acquisition system including 4 of these ASICs has been developed (BioMEA) and tested on whole embryonic mouse spinal cords.

2. FABRICATION

2.1 MEA

3D microelectrodes offer the opportunity to penetrate the neural tissue so as to be closer to neurons. Figure 1 illustrates the classical steps to make the 3D MEAs using isotropic etching of a glass substrate [2]. However, this process prevents the fabrication of dense 3D electrode arrays with high aspect ratios due to wet etching. To manufacture denser MEAs, a novel process has been developed using DRIE of a silicon substrate. This process achieves high aspect ratios by repetitive alternation of etching and insulation steps [4]. To

978-0-9798064-0-7/µTAS2007/$20©2007CBMS

manufacture micro needles with the DRIE process, it is essential that isotropic and anisotropic steps are alternated to adjust the profile of the micro needle. For instance, with a protective base of 80 µm of diameter, it is possible to obtain a micro needle of 80 µm of height.

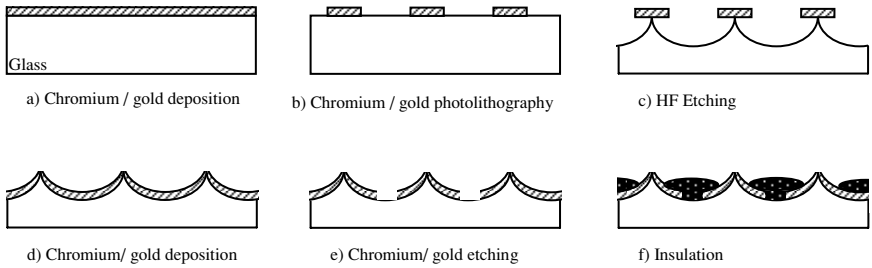

Figure 1. Classical 3D MEAs Process

Using this DRIE-based technology it was possible to manufacture various electrode shapes with a small electrode pitch (Figure 2). Because transparent 3D MEAs are required for visual observations, a silicon wafer can be anodic-bonded to a glass substrate before silicon etching, provided that the silicon wafer is thicker than the desired height of the electrodes.

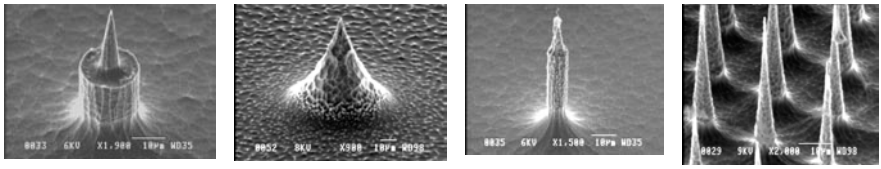

Figure 2. Different shapes of silicon micro electrodes manufactured by DRIE

2.2 INTEGRATED ELECTRONIC

To obtain a compact electronic acquisition system, a 64 channels ASIC (Analogic Specific Integrated Circuit) has been designed to replace classical discrete amplification channels. A low noise preamplifier and an amplifier with an automatic controlled gain are included. This ASIC also allows the stimulation on each channel and offers the possibility to send 8 different patterns to any set of electrodes (fed by 8 external in/out signals for the whole ASIC). The patterns are selectable by a multiplexer. For each channel, a voltage-to-current converter generates uniform current stimulation (max +/- 400 µA peak).

3. RESULTS AND DISCUSSION

The BioMEA system comprises a high density electrode array (256 3D micro-electrodes) interconnected to four dedicated 64 channels ASICs (amplification, analog multiplexing and current stimulation) running in parallel. Specific acquisition boards and user interface have been developed to manage the ASICs and to record all the acquisition channels (figure 3). This system has been tested on whole embryonic mouse spinal cords at embryonic stage E14.5. The neural tube was opened dorsally and laid on the MEA. Spontaneous activity in the medulla characterized by local field potentials (LFP) recurring every 1-3 minutes could be recorded. Those LFPs are recorded by the microelectrodes and amplified by the electronic system (Figure 4) [5]. With this whole acquisition system, it is possible to obtain

a spatio temporal mapping of the spontaneous LFPs over the array (maps built by surface spline interpolation).

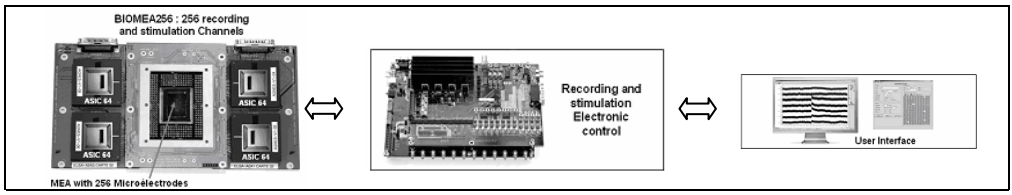

Figure 3. The BioMEA™ system setup

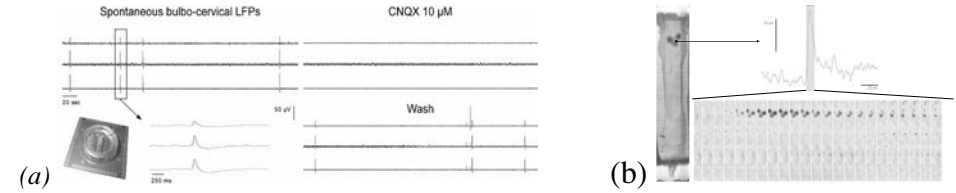

Figure 4. (a) LFP recording, (b) Spatio temporal Mouse spinal cord activation

4. CONCLUSION

In this project we have demonstrated the possibility to use a DRIE process to fabricate dense 3D MEAs. This technique offers the possibility to adjust the profile of the micro-needles and to obtain small electrode pitches. Currently a 1024-electrode MEA with 50 µm pitch and 80 µm electrode height was built. Noise levels as low as +/- 7µV were obtained for platinum electrodes, equivalent to the commercial MEAs with comparable electrode sizes. Transparent MEAs were achieved by bounding of a silicon and a glass wafers. Moreover a compact electronic system has been developed allowing to record and to stimulate on each of 256 channels simultaneously, providing 8 programmable external stimulation patterns. Finally, the data acquired with this system are compatible with the CED Spike2 software, which can be used for further data analysis.

ACKNOWLEDGMENT

This work is supported by The French Ministry of Technology (ACI and NEUROCOM RMNT Project), the Région Aquitaine, the Fyssen and FRM foundations, and the ANR.

REFERENCES

[1] Y.Hanein et al., "Towards MEMS Probes for intracellular Recording".
[2] Heuschkel MO et al., "A three-dimensional multi-electrode array for multi-site stimulation and recording in acute brain slices", J Neurosci Methods 114:135-148, 2002.
[3] N Wilke et al., "Fabrication and characterisation of microneedle electrode arrays using wet etch technologies", EMN 2004.
[4] F.Marty et al., "Advanced silicon etching techniques based on deep reactive ion etching (DRIE) for silicon harms and 3D micro- and nano-structures", EMN 2004.
[5] G.Charvet et al., "BioMEA : A 256-channel MEA system with integrated electronics", Society for Neuroscience Abstract, 694.19, 2006.

EXAMINING CYTOTOXIC EFFECTS ON SINGLE CELLS USING AN IMPEDANCE SPECTROSCOPIC PLATFORM

Daniele Malleo*, J Tanner Nevill†, Dino Di Carlo†, Luke P. Lee†, Hywel Morgan*

**School of Electronics and Computer Science, University of Southampton, UK*
†Department of Bioengineering, University of California at Berkeley

ABSTRACT

We present a microfluidic device for performing impedance spectroscopic analyses of the steady-state and time-transient response of single cells exposed to cytotoxic agents and drug compounds. This platform is capable of long-term label-free assays. Sample preparation steps normally associated with fluorescence analysis (fixing, staining and washing) are avoided. We analysed the transient impedance from single cells to study the kinetics of cell response to Streptolysin-O (SLO) on mammalian cells. The toxin was found to cause a gradual decrease in the impedance, which corresponded to an increase in membrane conductivity. Increasing concentrations of toxins caused a higher rate of change seen as an overall decrease in the impedance.

Keywords: Single Cell Analysis, Label Free Method, Impedance Spectroscopy

1. INTRODUCTION

Impedance spectroscopy is a label-free method of analysis which has the potential to allow quantitative measurements of cell characteristics, for example changes in properties of the membrane, cytoskeleton or nucleus elicited by chemical compounds. Dielectrophoresis is used for the manipulation and sorting of particles in micro-chips. The forces responsible for these phenomena are linked to the intrinsic dielectric properties of the biological particles. However, impedance analysis of cells in micro-systems is not yet part of the μTAS and lab-on-chip toolkit.

The platform described in this paper combines the advantages offered by impedance analysis [1], as used in micro-flow cytometry, with the ability to capture and monitor large numbers of single cells on a single device, so that long-term transient and steady state analysis can be performed. Cells are captured using the arrayed hydrodynamic single cell principle developed by Di Carlo *et al* [2]. The cells are held between two microelectrodes which are used to measure the impedance signal. The system enables the analysis of multiple single cells, allowing the detection of rare events and the identification of unique events. Temporal averaging is avoided because single cells are individually probed, individual responses and fast kinetic events can be recorded.

2. THEORY

The impedance signal from a cell sitting on or between electrodes is modulated by a number of factors, including the area of the cell in contact with the substrate and polarization processes. For a cell immersed in a high conductivity suspending buffer, measurements of the complex permittivity in the frequency range from 10 kHz and 10 MHz can be used to characterise the properties of the cell membrane. At lower frequencies the impedance is dominated by the high capacitance of the membrane. As the frequency increases the permittivity drops due to the short-circuiting of the membrane by the field.

978-0-9798064-0-7/μTAS2007/$20©2007CBMS

The impedance spectrum over the frequency range of 10 kHz to 1 MHz is therefore dominated by the cell membrane capacitance, but is also influenced by the cell membrane conductivity. This in turn is determined by the number and size of transmembrane channels. Calculations made using the single-shell model [3] show that the overall conductivity of the system is most sensitive to membrane conductivity. SLO is a toxic, cytolytic, and immunogenic protein, which represents the prototype of toxins that damage membranes through generation of large transmembrane channels, thus increasing membrane conductivity . Typical values for the membrane conductivity of a viable cell are 10^{-9}S/m, the graphs (figure 1) shows that this has to increase to the order of 10^{-5}S/m (or ~10^{4} SLO pores) to lead to measurable changes.

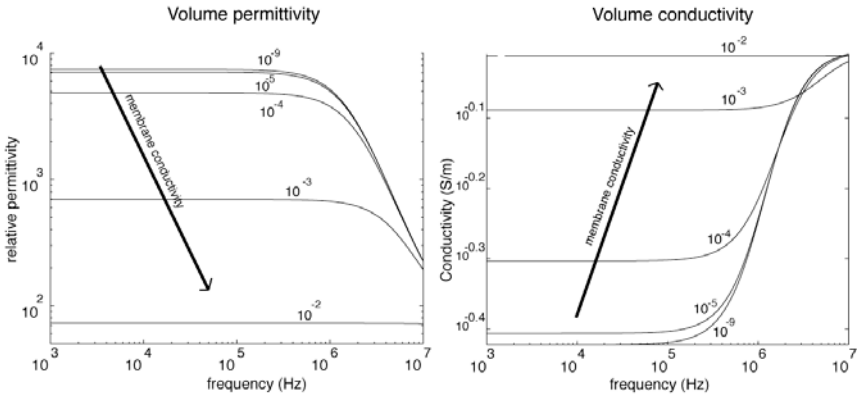

Figure 1. Plots of the permittivity and conductivity calculated using Maxwell's mixture theory for a cell modelled as a single-shell particle. The plot was obtained for a volume of 20x20x20 μm, with a homogenous electric field and a 10 μm diameter cell, immersed in PBS. Membrane conductivity changes from 10^{-9}S/m to 10^{-2}S/m.

2. EXPERIMENTAL SYSTEM

The chip is shown in cross section in figure 2 and contains an array of microelectrodes, two for each cell (for differential measurement) together with an hydrodynamic trap that confines the cell to the measurement region [2, 3]. The excitation frequency is applied through the top ITO (Indium Tin Oxide) electrode and the signal from each of the single cell electrodes is processed by an impedance analyzer connected via a multiplexer. MATLAB scripts control the multiplexing front-end, the impedance analyzer, and post-process the acquired data.

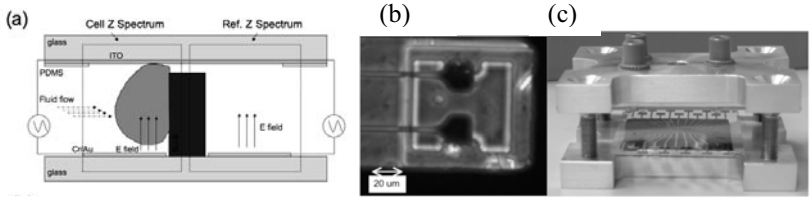

Figure 2 (a) Cross section of the device showing the two microelectrodes on either side of the hydrodynamic obstruction which traps the cell. Fluid flows in from the left. A single cell sits above one electrode, the other is used for differential measurement. The signal is

applied through the top ITO electrode. (b) Photograph of a HeLa cell trapped in the device (c) The assembled device showing the fluid inlet ports on top.

3. EXPERIMENTAL

The device was loaded with HeLa cells suspended in PBS and the impedance continuously monitored from all the electrodes. 1ml of SLO toxin activated by 100mM DTT (DL-Dithiothreitol) was introduced into the device at concentrations ranging from 100 U/ml (0.09 μg/ml) to 10 kU/ml (9 μg/ml)[1] to elicit changes in trapped single cells. As a control, the response to the introduction of 100mM DTT was also measured.

4. RESULTS

Figure 3 shows a time-evolution of the differential impedance (measured at 1kHz) for single HeLa cell after introduction of SLO. The control data demonstrates that the impedance of the cell remains constant with time. Exposure to 100 U SLO leads to a gradual decrease in the impedance, this change increases with increasing level of toxin as expected from the pore forming properties.

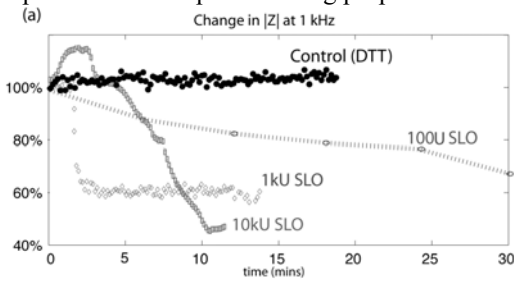

Figure 3. Transient differential impedance response (measured at f =1kHz) from a single HeLa cell trapped in the device. Increasing levels of SLO produce a bigger change in impedance compared with the control (DTT).

5. CONCLUSIONS

We have fabricated a device which successfully combines the advantages offered by impedance-based flow cytometry (ie label-free, electrical-based analysis) with the ability to capture multiple single cells and perform long-term transient and steady state analysis. We have shown that we can measure changes in membrane conductivity elicited by a pore-forming toxin, SLO.

REFERENCES

1. “Single cell dielectric spectroscopy”, Morgan H. et al, J. Phys. D: Appl. Phys. 40, 61–70 (2007)
2. “Single-cell enzyme concentrations, kinetics, and inhibition analysis using high-density hydrodynamic cell isolation arrays”, Di Carlo D., N. Aghdam, and L. P. Lee. Anal. Chem. 78:14, 4925-4930 (2006)
3. H. P. Schwan, in Advances in Biological and Medical Physics, edited by J. H. Lawrence and C. A. Tobias (Academic Press, New York, 1957), Vol. 5, p. 147
4. “Single Cell Differential Impedance Spectroscopy Analysis Using High Density Hydrodynamic Cell Trapping Arrays”, D. Malleo et al., Proceedings of Micro Total Analysis Systems 2006, pp.1292-1294

[1] A unit (U) is defined as causing 50% lysis of a 2% red blood cell suspension in phosphate buffered saline, pH 7.4, after incubation at 37 °C for 30 min.

HIGH SPEED MULTI-FREQUENCY IMPEDANCE ANALYSIS OF SINGLE BIOLOGICAL PARTICLE USING MAXIMUM LENGTH SEQUENCES

T. Sun[1], D. Holmes[1], S. Gawad[2], N. G. Green[1] and H. Morgan[1]

[1]*Nanoscale Systems Integration Group, School of Electronics and Computer Science, University of Southampton, UK*

[2]*Ayanda Biosystems, PSE Parc Scientifique, Building C, EPFL, CH-1015 Lausanne, Switzerland*

ABSTRACT

We describe a novel impedance spectroscopy technique for analysis of single biological particle in a microfluidic cytometer, using Maximum Length Sequences (MLS). The method enables multi-frequency impedance measurements to be performed in a short time period (ms). The impedance spectra of red blood cells and mixed beads of two sizes is measured. A complete spectrum is obtained with an upper frequency limit of 500 kHz, and contains 512 evenly distributed discrete frequency points, measured approximately every ms.

Keywords: Single Cell, Impedance Spectroscopy, Maximum Length Sequence, Microfluidic Cytometer

1. INTRODUCTION

Single cell impedance (dielectric) spectroscopy can now be perfomed using a microfluidic cytometer [1,2]. The method allows biological particles to be analysed one by one at high speed, and offers label-free identification. In previous work, the impedance cytometers analysed particles using single frequency excitation. Microelectrodes are energized by an AC single frequency voltage, and the impedance of a particle is determined from the current response of the system. However, a drawback of this technique is that the number of frequencies that can be measured is severly limited because each discrete frequency that is applied to the system requires demodulation with a lock-in amplifier [2]. To overcome this problem, we have developed a novel technique which uses Maximum Length Sequence (MLS) to characterize the complete transfer-function of the system and thereby extract the frequency-dependent impedance information of single particle.

2. THEORY

MLS is a Pseudo Random Binary Sequence (PRBS) and has a white noise-like power spectrum with the energy uniformly spread over a wide frequency range, enabling multi-frequency measurements to be made in a single measurement. It is generated by an *n*-stage digital shift register with feedback coefficient control, conforming to the linear recurrence. With a given initial state of the shift-registers (figure 1(a)), a specific MLS can be generated. In practical measurement, the 1 and 0 states are often mapped onto −1 and +1 levels respectively, producing a bipolar sequence symmetrical about zero (figure 1 (b)).The bandwidth of the spectrum obtained using the MLS technique is limited by two parameters: the order of MLS, n, and the sampling rate, f_s . The lowest frequency, $f_{\min}$ is determined by

978-0-9798064-0-7/μTAS2007/$20©2007CBMS

the order of the MLS and the sampling rate (equation (1a)). The highest frequency, f_{max}, (equation (1b)) is half the sampling rate:

$$f_{\min} = \frac{f_s}{2^n} \quad (1a)$$

$$f_{\max} = \frac{f_s}{2} \quad (1b)$$

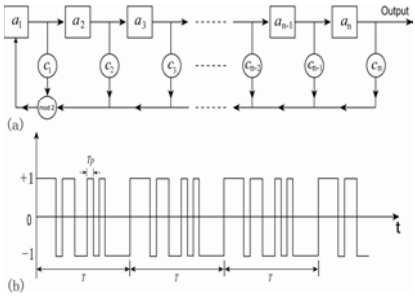

Figure 1. (a) Right shift registers for the generation of MLS (b) A typical bipolar MLS.

Therefore, the number of discrete measurement frequencies is 2^{n-1} . The data are collected in one sequence period. For example, if f_s=1 MHz and the MLS signal is 10th order (n=10), a full data set of 512 frequency points evenly distributed between 976.56 Hz and 500 kHz can be collected in approximately 1 ms.

3. EXPERIMENTAL

Figure 2 shows the principle of the measurement system. Cells flow through a microfluidic channel (left to right) which contains a pair of microelectrodes. The impedance is measured using a differential circuit. Further details can be found in ref [1, 2]. The MLS signal is applied to the top pair of electrodes. When a cell passes through the detection volume, the electric field distribution changes; the difference between the electric current passing through the detection and reference volume is measured to provide the impedance of the cell. The MLS measurement system is shown in figure 2 (b). The digital MLS signal is generated by customed software, programmed in MATLAB™ (Mathworks, Inc., USA). After D/A conversion, the bipolar MLS signal is applied to the cytometer, and after low pass filtering (LPF), the response of the system in the time domain is sampled into digital form by an A/D converter. A Fast M-sequence Transform (FMT) converts the sampled response into the Impulse Response (IR) of the system. Finally a Fast Fourier Transform (FFT) of the IR gives the transfer-function of the system in the frequency domain, from which the impedance of the cell is extracted. The system was evaluated by measuring polystyrene beads of two sizes, 5.49 and 7.18 µm diameter (Bangs Laboratories Inc. USA) and also human red blood cells (RBCs). We used 10th order MLS with a sampling rate of 1 MHz.

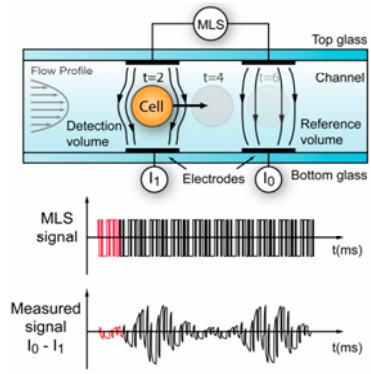

Figure 2 (a) Diagram of the impedance spectroscopy system used for single cell analysis.

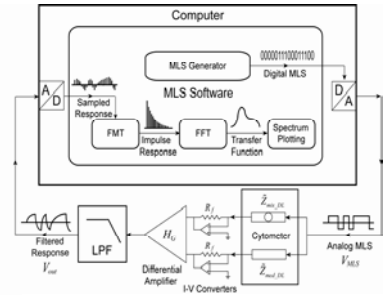

Figure 2 (b) Structure of MLS measurement system

4. RESULTS AND DISCUSSION

Figure 3 (a) shows the real part of the transfer-function of the system when single beads are measured. Only one of the 512 different frequencies (488.28 kHz) is shown. The differences in the amplitude of the signals are indicative of the different sizes of beads. Each pair of peaks (one positive and one negative) is the data from a single bead passing through the measurement area. To validate the MLS, the experimenta data was compared with a PSpice circuit simulation. An equivalent circuit model for a single bead in suspension was used for the simulation [3]. The MLS data was also compared with data from single frequency measurements. The results from all the three methods show good agreement, (figure 3 (b)).

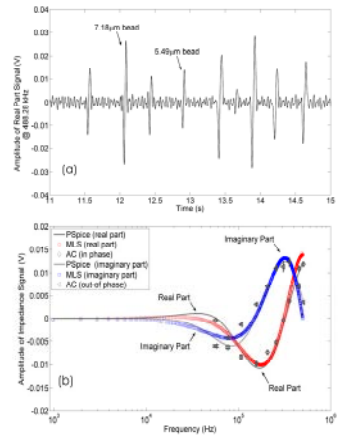

Figure 3 (a) Data showing signals from single beads (b) Comparison between simulation and measurements for 5.49 µm beads.

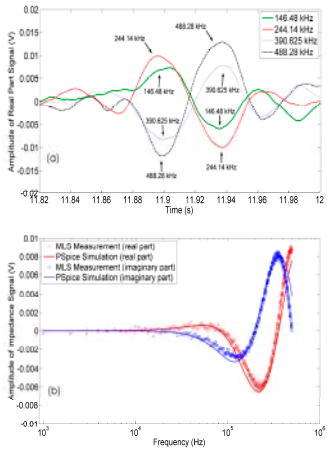

Figure 4(a) Captured single RBC, data shown at four frequencies (b) Impedance spectra valiation of RBC.

Figure 4 (a) shows the data for a captured single RBC flowing through measurement area. The data is the real part of the transfer-function plotted for four discrete frequencies (from 512 total frequencies): 146.48 kHz, 244.14 kHz, 390.625 kHz and 488.28 kHz. Figure 4 (b) compares the impedance obtained from the MLS measurements with PSpice simulations for a single RBC, showing good agreement between the simulation and measurement.

Up to 500 kHz, the impedance spectra of beads and RBCs exhibit similar behaviour, since within this frequenc rage, the electrical double layer effect dominates the measured spectra.

5. CONCLUSION

Future experiments will be focused on impedance measurements for extending the bandwidth of the measured spectrum to radio-frequency range for characterizing the internal properties of biological cells and the improvement of the signal-to-noise ratio (SNR) of the system.

ACKNOWLEDGEMENTS

The work is partly funded by Life Science Initiative, University of Southampton, UK.

REFERENCES

[1] H. Morgan et al., J. Phys. D: Appl. Phys., Vol. 40, pp. 61-70, 2007.
[2] S. Gawad et al., Lab Chip, Vol. 4, pp. 241-251, 2004.
[3] T. Sun et al., Lab Chip, Vol.7, pp. 1034-1040, 2007.

PHYSARUM POLYCEPHALUM ON A CHIP

Ferran D. Revilla, Klaus-Peter Zauner and Hywel Morgan
School of Electronics and Computer Science, University of Southampton
Southampton SO17 1BJ, UNITED KINGDOM

ABSTRACT

A micro-chip has been developed to electrically interface with the true slime mold *Physarum polycephalum*. This device uses micro-fluidic techniques to provide the conditions to sustain the slime mold and also to enable chemical stimulation. Impedance spectroscopy is used to monitor the contractile activity of the organism.

Keywords: Physarum, impedance, bio-sensor, micro-fluidic

1. INTRODUCTION

The plasmodium of the true slime mold *P. polycephalum* (Fig.1) is a giant multinucleated cell that can grow to the size of several square meters. The organism lacks a nervous system, but acts as single integrated entity. Given its large size, intracellular communication is a non trivial task. In *P. polycephalum* communication is achieved by metabolic oscillations which generate rhythmic contractile activity powering vigorous protoplasmic streaming within the cell. These rhythmic contractions play a key role in the growth and migration of the cell. *P. polycephalum* is known to be sensitive to light, temperature, humidity, acceleration and a wide range of chemicals including glucose, NaCl, KCl and others [1, 2]. Stimuli from the environment modulate the oscillations of the cell. Although the mechanism driving the change in oscillation patterns is not well understood, interfacing with the contractile oscillations has recently been used for crude robot control [3].

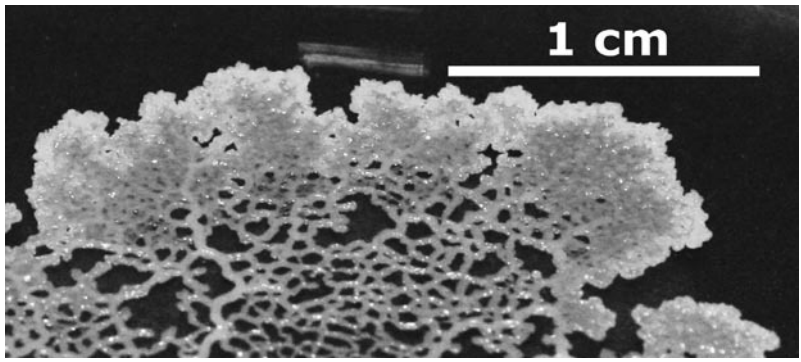

Figure 1 Photograph of P. polycephalum growing on agar.

We have developed a chip that is capable of measuring the rhythmic behaviour of the organisms using electrical impedance. The chip also has microfluidics to control the chemical micro-environment of the plasmodium. This serves to keep the plasmodium alive within the chip for several days, and also provides a means to chemically stimulate the organism.

978-0-9798064-0-7/μTAS2007/$20©2007CBMS

2. EXPERIMENTAL

The device monitors the contractile activity of *P. polycephalum* by measuring the electrical impedance. Sets of electrodes are patterned on a conventional 0.5 mm thick printed circuit board (PCB). Many different electrodes are patterned along a channel to enable simultaneous monitoring of electrical impedance of the slime mold at different locations. Fig. 2 shows a schematic diagram of this micro-device, together with the device assembled on the connection board. The plasmodium grows in a set of wells (1.5 mm diameter) and along channels (0.25 mm wide) cut through the printed circuit board, as shown in Fig 2A.

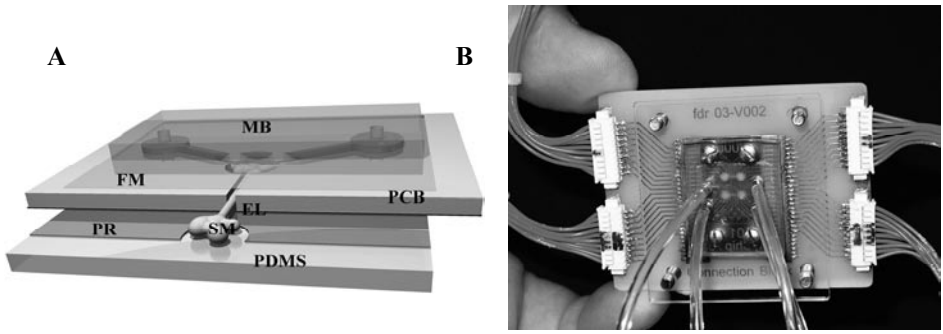

Figure 2. A. Schematic view of the micro-device. The slime mold (SM) is enclosed in a micro-channel cut in printed circuit board (PCB). The channel is covered on one side with a gas-permeable layer of PDMS and on the other side with a non-pore filtration membrane (FM) through which fluid is supplied from a microfluidic block (MB). Electrodes (EL) are etched in the copper side of the PCB and sealed with photoresist (PR). B. Photograph of the micro-device (20x25 mm) assembled on the printed circuit board connection block.

The organism is enclosed by a thin layer of poly-dimethyl-siloxane (PDMS) on the copper side of the PCB and by a polycarbonate filtration membrane (nucleopore Track-Etch 111103, Whatman, Brentford) on the other side. A micro-fluidic system, manufactured from PDMS, is clamped to the top of the filtration membrane to provide both a suitable environment to sustain the slime mold, and localized stimulation with chemical compounds.

3. RESULTS AND DISCUSSION

The normal method of monitoring *P. polycephalum* oscillations is by measuring the optical density (OD) of the organism [1, 2]. To correlate the impedance date, the OD was measured simultaneously with electrical impedance measurements (see Fig. 3(a)). Oscillations of the *Physarum* were measured at different frequencies, and a circuit model developed, which indicates that the impedance change is dominated by thickness variations in the slime surrounding the organism.

The chips were used to monitor the response of *P. polycephalum* to organic compounds, such as phenol. When the plasmodium was exposed to phenol (a mixture of 0.0068% w/v halogenated phenols and 0.0018% w/v phenol) for a continuous period of 35 min, both the frequency and amplitude of the oscillations were reduced for some time (15 minutes). However, after 30 minutes the oscillation reverted to the steady state (see Fig. 3(b)).

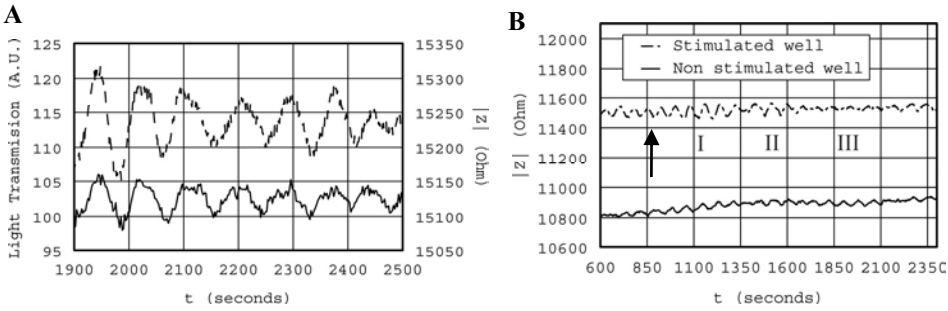

Figure 3. A. Time trace of the electrical impedance between two electrodes (continuous curve) and of the optical density (dashed curve) for an oscillating plasmodium. B. Change in electrical impedance in response to phenol. The arrow indicates the time when the plasmodium is exposed to the stimulus. I, delay before the response occurs. II, decrease in oscillation frequency. III, drop in oscillation amplitude.

4. CONCLUSIONS

A micro-device has been developed for long term monitoring of the behaviour of the true slime mold *P. polycephalum.* The oscillations of the organisms can be used to monitor exposure to organic compounds such as phenol. The results demonstrate a potential application as whole-cell chemical-sensor.

ACKNOWLEDGEMENTS

The authors want to thank Life Sciences Interfaces Initiative in the University of Southampton for funding the scholarship that made this work possible.

REFERENCES

[1] T. Nakagaki, H. Yamada, T. Ueda, *Modulation of cellular rhythm and photoavoidance by oscillatory irradiation in the physarum plasmodium*, Biophysical Chemistry Vol. 82 (1999) pp. 23-28.

[2] Koster, S., Kraus, T., Takamatsu, A., Fujii, T., Verpoorte, E., and de Rooij, N., *Localised Stimulation of Slime Mould Using Microfluidic Devices*, Proceedings of the 8th International Conference on Miniaturized Chemical and Biochemical Analysis Systems (MicroTAS 2004), Vol. 1, Malmo, Sweden (2004) pp.75-77.

[3] Tsuda, S., Zauner, K.-P. and Gunji, Y. P. (2006) *Robot Control: From Silicon Circuitry to Cells*, in Ijspeert, A. J., Masuzawa, T. and Kusumoto, S., Eds. Biologically Inspired Approaches to Advanced Information Technology, Second International Workshop, BioADIT 2006, Osaka, Japan, January 26-27, 2006, Proceedings, pp. 20-32. Springer.

DETECTION OF BACTERIAL CELLS BASED ON MICRO-CHANNEL GATING

Mehdi Javanmard[1, 2], AmirAli H. Talasaz[1, 2], Mohsen Nemat-Gorgani[2], Fabian Pease[1], Mostafa Ronaghi[2] and Ronald W. Davis[2]

1 Electrical Engineering Department, Stanford, CA 94305

2 Stanford Genome Technology Center, Stanford, CA 94305

ABSTRACT

In this communication, we describe a novel methodology for single bacterial detection based on micro-channel gating and involving the use of microelectrodes in a micro-channel for detection of target cell capture. The sensors designed have been shown to be capable of electrical detection of the target cells at the single cell level.

Keywords: Bacterial Detection, Electrical Detection, Label-free detection

1. INTRODUCTION

Current microbiological techniques used for detection of pathogens involve expensive and time consuming methods such as culture enrichment and plating techniques, which can take several days [1]. Described below is a rapid and inexpensive technique which can be used to detect single bacterial cells electrically (label-free format) in real-time. We have successfully demonstrated real-time detection of target cells by measuring instantaneous changes in ionic impedance.

2. THEORY

The cross section of the biosensor used in this study is presented in Fig. 1. Electrodes are labeled A, B, and C for reference. A third gold electrode, B, is included in the active area of the channel, allowing for immobilization of antibodies with an affinity to bind to target bacterial cells in the active area of the sensor. Gold electrodes are very suitable for surface chemistry modifications, like deposition of surface assembled monolayers, which can optimize antibody immobilization. A sample suspicious of bacterial cell contamination is injected into the micro-channel. If the sample contains the targeted bacteria, the cells will attach to the electrodes, partially clogging the channel thus resulting in ionic resistance increase. By monitoring the impedance across micro-electrodes A and C, it is possible to detect the channel gating caused by bacterial cell attachment inside the channel. By choosing channel and electrode geometries close to the cell size, the sensitivity of the device can be increased down to single cell detection.

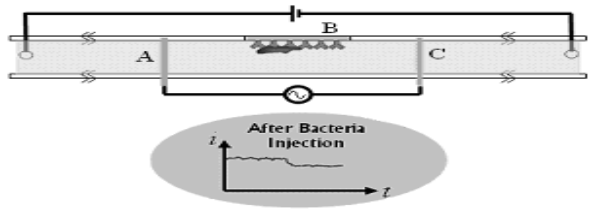

Figure1. Cross Section schematic of gated micro-channel with electrodes labeled A, B, and C. The targ bacteria bind to the antibodies which are immobilized on the gold electrode. (*Bottom plot*) Prediction of current after injection of bacteria.

978-0-9798064-0-7/μTAS2007/$20©2007CBMS

3. EXPERIMENTAL

Presented in Fig. 2a is a schematic design of the micro-fluidic biochip used, consisting of a set of microelectrodes on a glass substrate and a channel right above, embedded in PDMS (fabricated by the Stanford Microfluidics Foundry). The electrodes were constructed onto glass using sputtering and then lift-off (Fig. 2b).

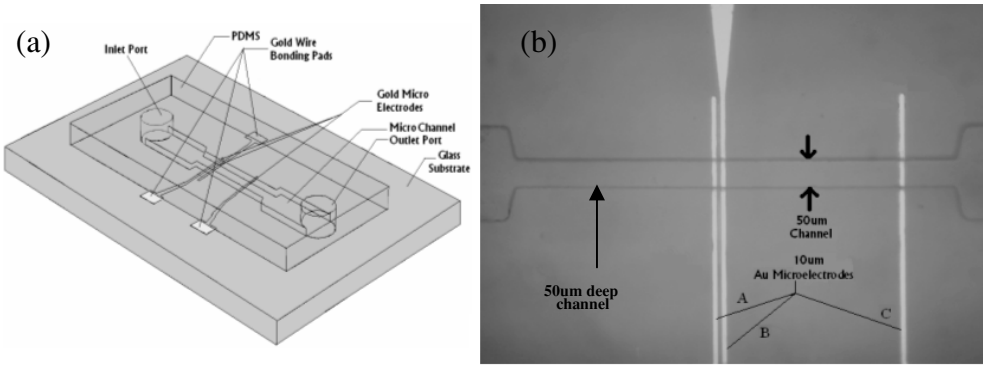

Figure 2. (a) Schematic of microfluidic chip used in this study. (b) Optical micrograph of top view of fabricated device with electrodes labeled A, B, and C. Electrode B was not used in this study.

In this study, yeast cells were used instead of bacterial cells, due to their similarity in size and dielectric properties, and Concanavalin A (ConA), a glycoprotein with affinity for yeast, in place of antibodies in order to obtain preliminary results and demonstrate the success of the technology. Immobilization of ConA on the electrodes was carried out by physical adsorption. ConA solution was injected and incubated into the channel for 15 minutes, then activated by the injection of Mn^{2+}, Mg^{2+}, and Ca^{2+} ions. A 200mM KCl solution in 10mM Hepes buffer with a pH of 6.8 containing yeast was injected into the channel at a flow rate of 100nl/min. The electrical impedance was measured over time between electrodes A and C at a frequency of 29.8 kHz. At this frequency the solution resistance dominates the impedance. The channels were also monitored using optical microscopy simultaneously as electrical impedance was measured.

4. RESULTS AND DISCUSSION

Experiments were performed on various channel sizes. Figure 3a shows yeast cells being captured by the receptors on the electrode surface in the 50um deep channel. Results in figure 3b show an instantaneous increase in electrical impedance as a small number of cells bind to the surface of the electrodes, demonstrating real time detection of cell capture.

Experiments were also performed with a 10um deep channel. In this particular experiment, no receptors were immobilized onto the electrodes, so all capture was a result of non-specific binding. Figure 4a and 4b shows cells being captured on the electrodes and clogging the channels. As shown in figure 4c, the impedance ramps up at a relatively steady rate as result of cell accumulation and drops instantaneously as a result of cells unbinding from the surface and the channel being cleared up. The unbinding of cells results from an increase in the fluid pressure.

For channel sizes comparable to the diameter of yeast (5um), nonspecific binding and channel clogging have been shown to be problematic. Larger channels are more practical for implementation, since they are sensitive enough to electrically detect the presence of a

small number of cells, while at the same time minimizing channel clogging and nonspecific binding.

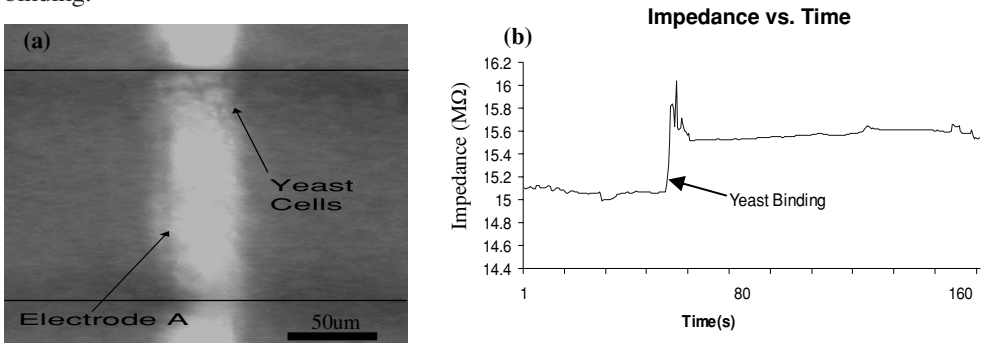

Figure 3. (a) Optical micrograph of gold electrode A after yeast binding has occurred. Electrodes B and C not shown. (*b*) Impedance vs. time. Impedance jump at t = 55s due to yeast binding.

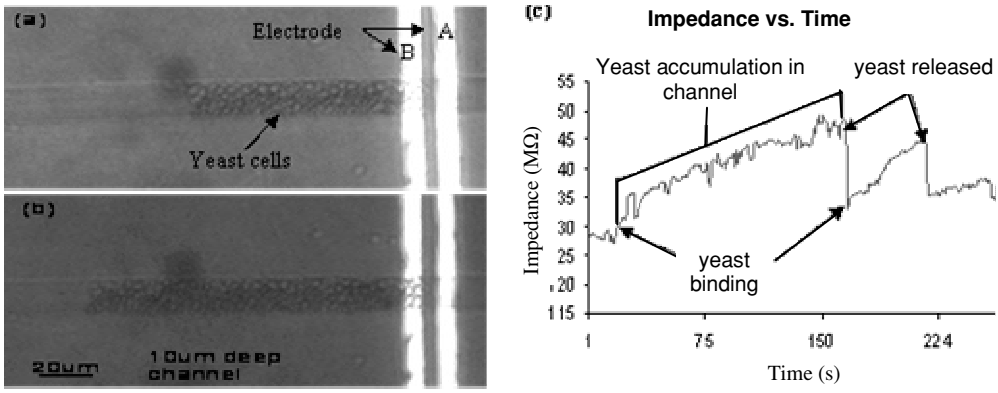

Figure 4. (a) Optical micrograph of yeast cells accumulating in channel at t = 75seconds. (b) at t = 130s. Electrode C is to the left and is not shown in this figure. (c) Plot of impedance over time. Impedance increases steadily as cell's accumulate in channel. Release of cells results in impedance drop at t = 160s. The same cycle is repeated until t = 220. No cells across electrodes after t = 220s.

5. CONCLUSION

A label-free electrical detection platform for bacterial cells based on microchannel gating was developed. We have shown that this technology is capable of electrically detecting the presence of a very small number of target cells. We believe that, with proper optimization and modification, this type of sensor can be used to detect many different types of pathogens and potentially even cancer cells in blood.

ACKNOWLEDGEMENTS

The authors thank Jessica Melin and the Stanford Microfluidics Foundry for their invaluable help in fabricating the microfluidic chips used in this study.

REFERENCES

[1] "FSIS Method for the isolation and identification of listeria monocytogenes from processed meat and poultry products," U.S. Dept of Agriculture, Food Safety and Inspection Service, Laboratory Communication no. 57, 1989.

MEASUREMENT OF BINDING FORCE BETWEEN A RECEPTOR-COATED PIEZORESISTIVE CANTILEVER AND A LIGAND-COATED SURFACE FOR PROTEIN CONCENTRATION SENSOR

Kenta Kuwana, Kiyoshi Matsumoto, Isao Shimoyama

Graduate School of Information Science and Technology, the University of Tokyo, JAPAN

ABSTRACT

We propose a method for measuring concentration of protein. In this method, the concentration is estimated from binding force between two surfaces modified with the protein and the ligand that specifically binds to the protein. The binding force is measured with a piezoresistive cantilever whose surface is modified with the protein. We measured the binding force between an avidin-coated cantilever and a biotin-coated surface.

Keyword : Label-Free, Specific Binding, Force Measurement, Protein Sensor.

1. INTRODUCTION

In the increasing demand for measurement of proteins *in situ*, label-free cantilever-type protein sensors have been studied[1][2]. In these sensors, the cantilever deflection caused by adsorption of the protein onto the cantilever surface is measured. However, to measure this deflection, which is usually small, a complex AFM-like optical system is needed. We propose a measurement method using no optical systems. In our method, binding force between two surfaces is measured with our high sensitive piezoresistive cantilever[3]. Our system favors miniaturization since it needs no optical systems. Furthermore, the deflection will be controlled by designing the cantilever.

2. THEORY

Figure 1 shows our method for measuring protein concentration. The cantilever surface is coated with the target protein. The substrate surface is coated with the ligand of the target protein. A bond is formed when the two surfaces contact. The bond involves multiple binding couples of the target protein and the ligand. Measurements are performed inside sample solutions. When the sample solution contains the target protein, parts of the binding sites of the ligand on the substrate is blocked. The percentage of the blocked binding sites depends on the concentration of the dissolved target protein. Since blocked binding sites are unable to form binding couples, the binding force changes accordingly to the concentration. We measure this binding force. From the change of the binding force, we estimate the concentration of the target protein.

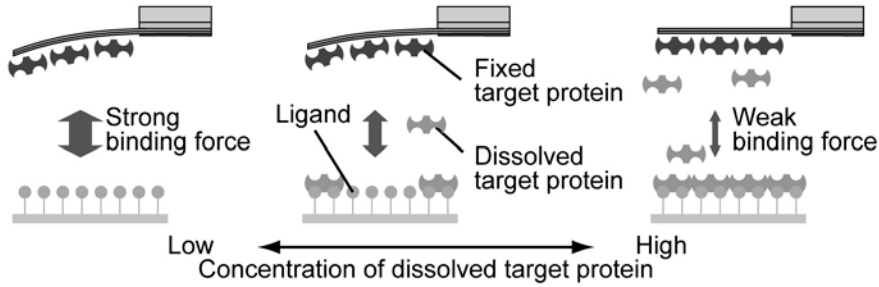

Figure 1. Principle of measuring protein concentration.

978-0-9798064-0-7/μTAS2007/$20©2007CBMS

3. MEASUREMENT OF THE CHANGE OF BINDING FORCE

To obtain the relationship between concentration and binding force, we measured the binding force between a bead coated with target protein and a biotin-coated substrate. Avidin was used as the target protein and biotin was used as its ligand. The binding force was measured with a piezoresistive cantilever in two solutions of pH 7.8 HEPES buffer, one contains dissolved avidin and the other one contains no avidin. The avidin-coated bead bound to the biotin-coated substrate with the specific bindings. We pushed this bead with the cantilever and measured the force at the moment when the bead was detached from the substrate (Figure 2). Figure 3 (a-b) shows the result of the binding force measurement. The averages of binding force of 30 beads in each solution were 2.9 nN and 1.6 nN, respectively (Figure 3 (c)).

4. MEASUREMENT OF THE BINDING FORCE IN OUR METHOD

To measure directly the binding force between an avidin-coated piezoresistive cantilever and a biotin-coated substrate, we used a cantilever with an avidin-coated pad. The pad size was $10\times10\ \mu m^2$ (Figure 4 (a)). The specifications of the cantilever are shown in Figure 4 (b). Figure 5 (a) shows the experimental setup for measuring the binding force between the two surfaces. The cantilever was initially brought to contact with the cantilever, which results in the forming of a bond between the cantilever and the substrate.

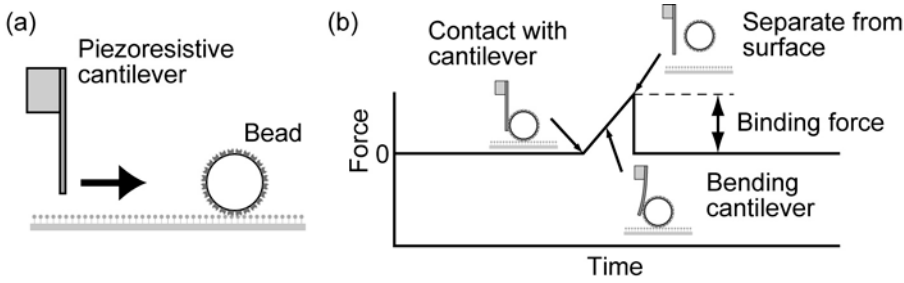

Figure 2. (a) Schematic image of preliminary experiment.
(b) Time response of the piezoresistive cantilever during the measurement.

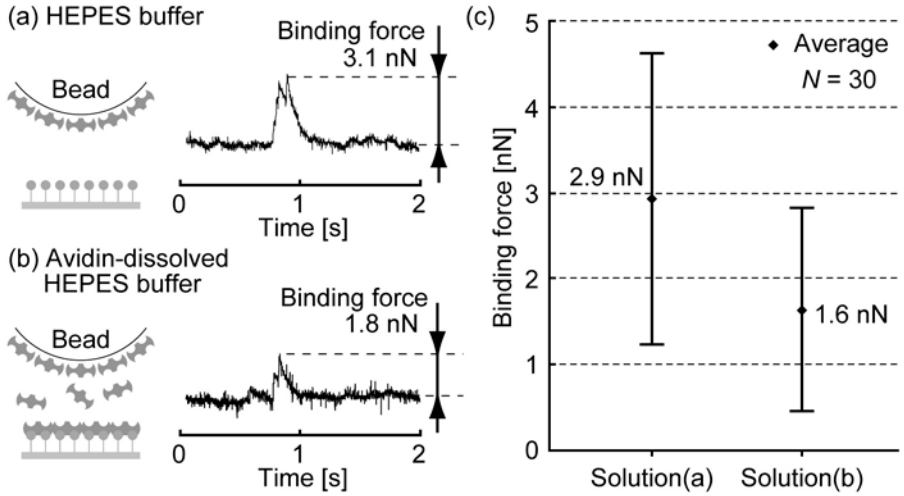

Figure 3. (a) Binding force in pH 7.8 HEPES buffer (Solution (a)).
(b) Binding force in Avidin-dissolved pH 7.8 HEPES buffer (Solution (b)).
(c) Average of the binding force in Solution (a-b)

We then tried to detach the cantilever from the substrate by pulling the cantilever away from the substrate. We measured the force at the moment when the substrate was detached from the cantilever (Figure 5 (b)). The measurement of binding force in solution was accomplished with this system. We measured the binding force between the cantilever and the substrate 30 times. The average of the binding force was about 1 nN and the standard deviation was about 0.13 nN (Figure 6).

5. CONCLUSION

In the first measurement**,** we measured the binding force between an avidin-coated bead and a biotin-coated substrate in solution. The change of this binding force caused by dissolving avidin in the solution was observed. In the second measurement, we directly measured the binding force between an avidin-coated cantilever and a biotin-coated substrate. Combining these results, we suppose that our method is capable of measuring protein concentration. This method can be similarly applied to concentration measurements of other specific binding protein pairs, such as antibody-antigen pairs.

Reference

[1] A.M. Moulin *et al.*, Ultramicroscopy, Vol. 82, pp. 23-31, 2000.
[2] Cagri A. Savran *et al.*, Analytical Chemistry, Vol. 76, pp. 3194-3198, 2004.
[3] M. Gel *et al.*, J. Micromech. Microeng., Vol. 14, pp. 423-428, 2004.

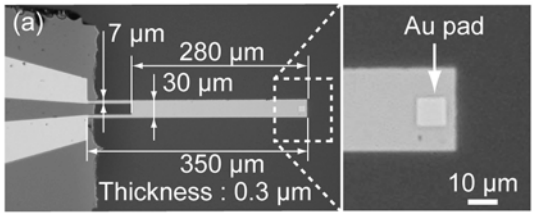

(b) Cantilever specifications

Spring constant	1.0 nN·μm^{-1}
Resistance	9.6 kΩ
Displacement sensitivity	1.5 × 10^{-4} μm^{-1}
Force sensitivity	2.8 × 10^{-4} nN^{-1}

Figure 4. (a) Photograph of the cantilever. (b) Cantilever specifications.

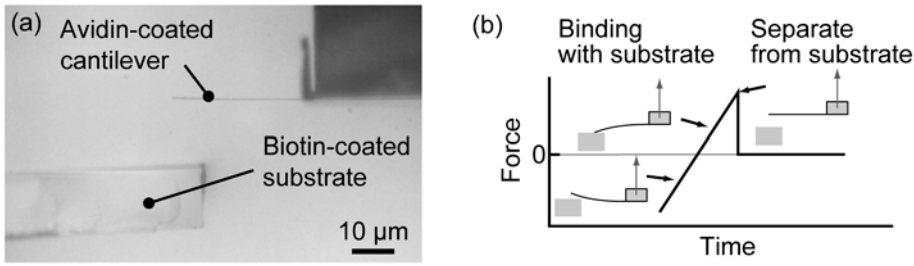

Figure 5. (a) Photograph of the measurement setup.
(b) Time response of the cantilever during the measurement.

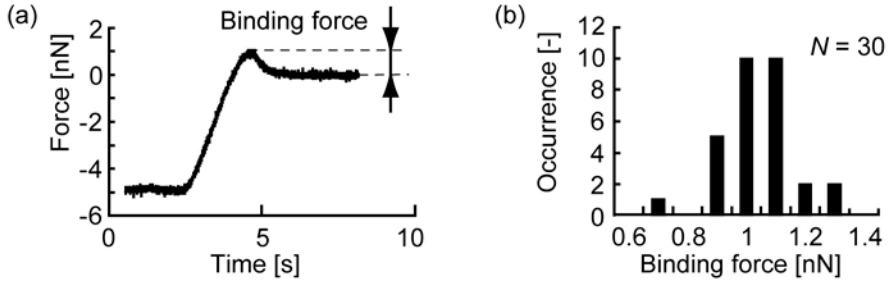

Figure 6. (a) Binding force between the avidin-coated cantilever and the biotin-coated substrate.
(b) Distribution of the binding force.

SITE-SELECTIVE DEPOSITION OF SILVER NANO PARTICLES FOR SURFACE ENHANCED RAMAN SCATTERING

Katsuhito Kurooka[1], Koji Deguchi[1] and Norihisa Miki[12]
[1]*Department of Mechanical Engineering, Keio University, JAPAN*
[2]*Kanagawa Academy of Science and Technology, JAPAN*

ABSTRACT

Surface Enhanced Raman Scattering (SERS) is one of the most promising detection technologies for ultra sensitive detection of virus, proteins, environmental chemicals, etc. On-site and effective application of SERS requests development of micro total analysis systems containing SERS sites and capable of sample handling. This paper reports site-selective deposition of silver nano particles utilizing self-assembled monolayers (SAMs), and a μTAS device for SERS containing locally manufactured SERS sites. All the SERS sites successfully exhibited enhanced Raman signals.

Keywords: Surface Enhanced Raman Scattering(SERS), Self Assembly, Nano Particle, Biosensor

1. INTRODUCTION

Fabrication of SERS sites composed of metal nano particles to enhance the surface electromagnetic field is the key to high-sensitive SERS detection. We reported highly reproducible and low-cost deposition of SERS sites utilizing modified silver mirror reaction [1]. In order to fabricate a high performance μTAS device, we need site-selective deposition processes of silver nano particles. The objective of this study is to manufacture the local SERS sites for a μTAS device by employing SAMs. SAMs capable of changing the surface property have been widely utilized for microfabrication; they were used as a mask for plasma etching [2] and applied to local deposition of ceramic thin films [3]. Micro-contact printing (μCP) is one of the most widely used techniques for patterning SAMs [4]. We fabricated a SAMs-patterned substrate by μCP as preparation for silver mirror reaction processes, and demonstrated a μTAS device with locally manufactured SERS sites.

2. EXPERIMENTAL

Figure 1 illustrates the proposed patterning processes of silver nano particles on a glass substrate. We used octadecyltrichlorosilane (OTS), which chemically adsorbs onto glass as SAM. OTS was patterned by μCP as shown in Figure 1(a). A poly(dimethylsiloxane) (PDMS) stamp was dipped in an anhydrous toluene solution with 1% OTS for 5 minutes and soft-contacted onto the substrate. The substrate was subsequently heated at 120°C for 5 minutes to enhance OTS adsorption. The OTS-patterned substrate was immersed in the silver nano particle solution (silver nitrate solution + ammonia water + dispersants) as soon as hydrazine, a reducing agent, was added to the solution. The silver nano particles only deposit onto the area where OTS was not adsorbed, as depicted in Figure 1(c). Quality of the selective deposition of silver nano particles depends on the μCP processes. Figure 2 describes the SEM images of the glass substrates with silver nano particles at different

978-0-9798064-0-7/μTAS2007/$20©2007CBMS

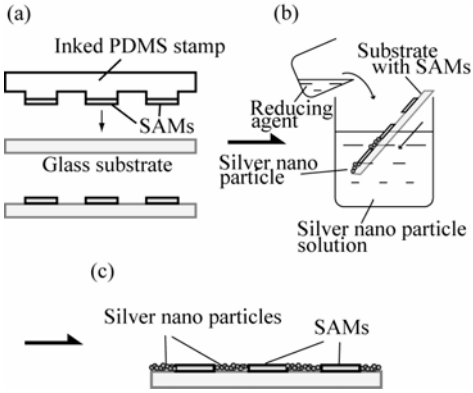

Figure 1. Fabrication processes of the SERS-sites-patterned substrate.

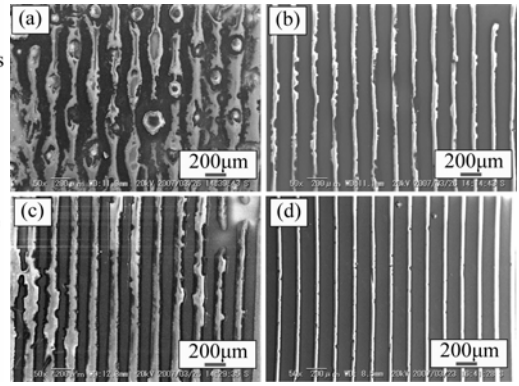

Figure 2. The SEM images of the glass substrates with silver nano-particles at different dipping time and heat treatment time.

Table 1. Optimum conditions of the μCP processes.

	Condition
Rinse	O_2 Plasma Ashing : 5sec.
Stamp Dipping	Solvent : Anhydrous Toluene Conc. : 1% OTS Time : 5min.
OTS Printing	Time : 5sec.
Rinse	Anhydrous Toluene Dried by N_2 gas
Heat Treatment	Temp. : 120 degrees C Time : 5min.

Under N_2 atmosphere

dipping time of the PDMS into the OTS-contained solution and heat treatment time after the soft contact: (a) 30sec, 0min (b) 5min, 0min (c) 30sec, 5min (d) 5min, 5min. The dark and bright regions represent the deposited silver nano particles and the exposed glass, respectively. Superior site-selective deposition was achieved by the dipping for 5 minutes and heat treatment for 5 minutes, which is denoted in Table 1.

3. RESULTS AND DISCUSSION

We placed a droplet of water containing Rhodamine 6G (R6G) on the substrate. When a R6G molecule happens to be at a hotspot, where the surface electromagnetic field is drastically enhanced, a bright point with strong fluorescence appears in a fluorescent image. Figure 3 depicts the fluorescent image of the substrate, where the bright points appear only over the deposited silver nano particles.

We fabricated a μTAS device containing local SERS sites, as shown in Figure 4, by bonding a PDMS structure onto the glass substrate. Since PDMS cannot bond to the OTS-covered glass surface, we removed OTS by oxygen plasma treatment for 0.5 seconds. This process was confirmed not to deteriorate the SERS sites experimentally as shown in Figure 5. Figure 6 depicts SERS signals of 10mM/l R6G from each SERS site of the fabricated μTAS device, indicating all the SERS sites are SERS-active.

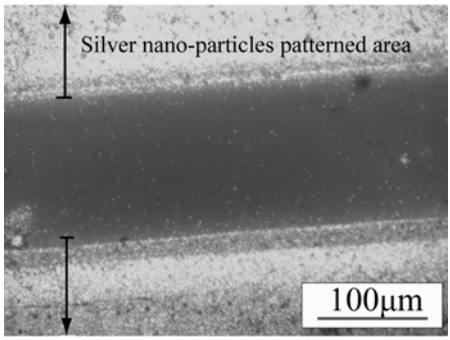

Figure 3. Fluorescent image of the substrate with a R6G-contained droplet.

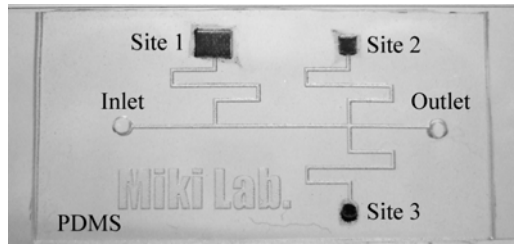

Figure 4. A photo of the fabricated micro-TAS device. Fabrication processes are as follows; Produce the SERS sites-patterned substrate by the processes shown in Figure 1. Remove the SAMs on the substrate by oxygen plasma for 0.5seconds. Bond the molded PDMS whose surface is activated by oxygen plasma.

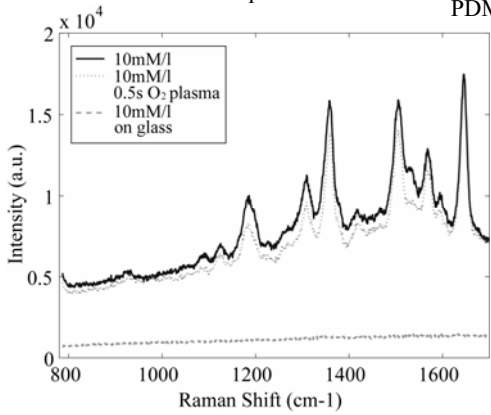

Figure 5. Raman signals of 10mM/l R6G from the SERS sites without and after oxygen plasma treatment for 0.5sec and a glass substrate.

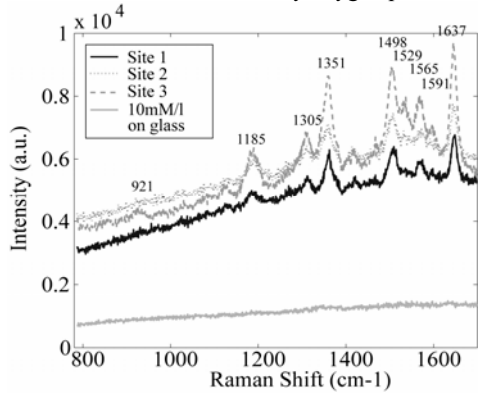

Figure 6. Raman signals of 10mM/l R6G from from each SERS site of the micto-TAS device shown in Figure 4.

4. CONCLUSIONS

We proposed the manufacturing processes of local SERS sites and the μTAS device for SERS utilizing thereof. The active SERS sites were successfully manufactured in the μTAS device. The processes proposed herein are readily applicable to manufacture μTAS for SERS with functions of sample injection and preparation for ultra sensitive and on-site detection.

ACKNOWLEDGEMENTS

This research was supported by Asahi Glass Foundation and Research and Development of Nanodevices for Practical Utilization of Nanotechnology Program by New Energy and Industrial Technology Development Organization (NEDO).

REFERENCES

[1] K. Kurooka and N. Miki, Proceedings of μTAS2006, vol.2, pp.1268-1270, (2006).
[2] H. Sugimura et al., Electrochimica Acta, vol.47, pp.103-107, (2001).
[3] Y. Masuda et al., Journal of Ceramic Society of Japan, vol.112, S1495-S1505, (2004).
[4] A. Kumar, H.A. Biebuyck, and G.M. Whitesides, Langmuir, **10**, 1498-1511, (1994).

SUSPENDED MICROCHANNEL RESONATORS WITH INTEGRATED ELECTRONIC READOUT FOR BIOMOLECULAR AND SINGLE CELL ANALYSIS

R. Chunara[1], T.P. Burg[2], K. Payer[3], P. Dextras[2], S.R. Manalis[2]

[1]Harvard-MIT Division of Health Sciences and Technology, USA
[2]Department of Biological Engineering, MIT, USA
[3]Microsystems Technology Laboratories, MIT, USA

1. ABSTRACT

We describe the fabrication and electrical testing of Suspended Microchannel Resonators (SMRs) with integrated piezoresistive readout. The SMR incorporates fluidic channels inside a resonant cantilever thereby eliminating viscous damping from the solution. Previously, this concept has been used to measure mass in fluid with a resolution of 1 femtogram (1 Hz bandwidth) [1]. Piezoresistive readout eliminates the need for external optics, and we anticipate that the integrated device can be used in a variety of biomolecular and cell-based assays for point-of-use applications.

Keywords: piezoresistor, cantilever, biosensor

2. INTRODUCTION

Suspended microchannel resonators with integrated readout can measure the mass density of solutions with high precision [2,3,4]. We have recently designed SMRs with low intrinsic mass and a very high quality factor [4]. This has enabled the weighing of biomolecules and single cells with a million-fold higher sensitivity than the quartz crystal microbalance [1,5]. So far, the frequency measurement of our device has relied on measuring the deflection of a laser beam that is focused onto the tip of the resonator. The optics used in our lab do not scale favorably for large arrays and are not suitable for point-of-use applications.

3. DESIGN AND FABRICATION

The resonators are vacuum packaged on the wafer scale and integrated with glass microfluidics to provide the fluidic control necessary for biological measurements ([1], Figure 1a). Piezoresistors can be implemented by standard silicon micromachining [6] and are highly robust. For our SMR biosensors, there are two design constraints that must be addressed when piezoresistors are incorporated: i) The doping profile is constrained by the depth of the cantilever lid (3μm) and should be shallow for high sensitivity. The resistor must not penetrate the 0.5μm oxide layer which is between and electrically isolates fluid inside the cantilever from the silicon surface. ii) Power dissipation must be controlled as heating the cantilever may denature or damage biological substrates inside.

We have fabricated SMR piezoresistors with n-type phosphorous dopants at the surface of the cantilever along the <110> direction. Ion implantation is used to achieve a peak dopant concentration of $10^{18}/cm^3$ in a p-type silicon substrate characterized by a resistivity of 10-20 Ωcm. The resistor implant junction depth is 1.6μm. Limiting the resistor to the bottom portion of the cantilever beam (Figure 1b) increases the average stress within the implanted area. A glass layer is anodically bonded to the silicon surface to create a high

978-0-9798064-0-7/μTAS2007/$20©2007CBMS

vacuum chamber. Instead of bonding over metal traces which may compromise the seal, highly doped conductive traces connect the resistor to metal bond pads on the chip edge.

4. RESULTS AND FUTURE

Readout of the resistance change is amplified through a Wheatstone bridge (Figure 2). Potentiometers are incorporated in order to balance the amplifier as well as compensate for capacitive coupling of the electrostatic drive signal. Figure 3 shows the frequency response which corresponds to superposition of the signal from the resistor and the drive signal feed-through. Measurements of resistance change as the entire device is heated in a convection oven suggest that a reasonable bias voltage of 1V on the bridge will result in biocompatible temperatures of less than 40°C. We are currently optimizing the readout signal and developing a variety of biomolecular and cell-based assays for point-of-use applications.

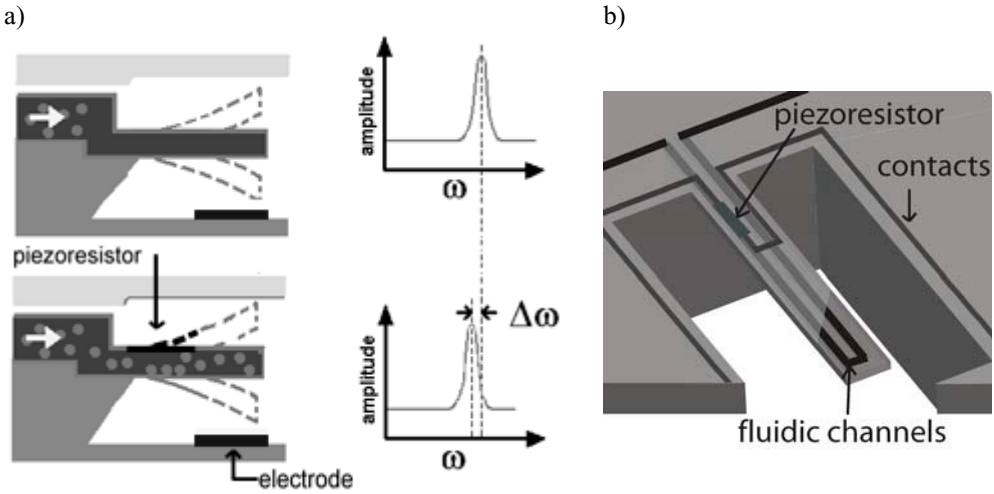

Figure 1: a) Resonant frequency of the SMR shifts upon entrance of biomolecules in the channel. The drive signal is electrostatically applied via an electrode. 1b) 3D-representation of the cantilever. Silicon at the tip is cut away to show the fluidic channels.

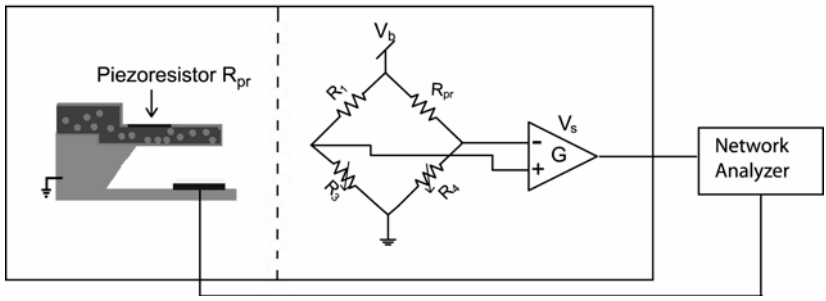

Figure 2: Measurement setup for AC drive of the cantilever and readout from the piezoresistor. The drive signal contains 50VDC and 200mVAC components.

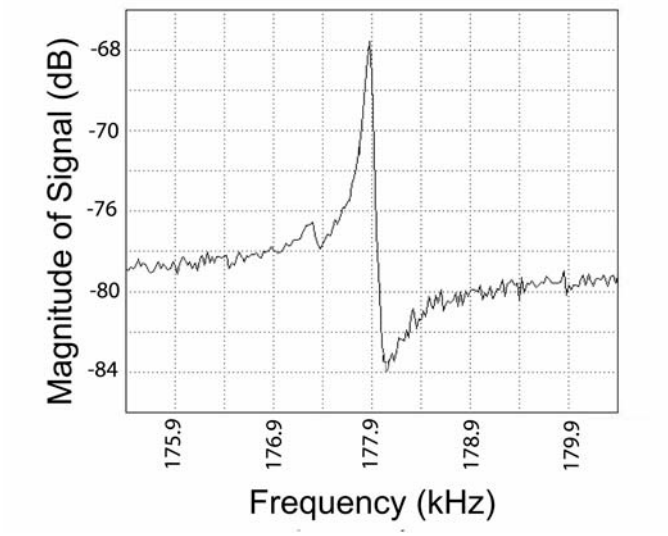

Figure 3: Output spectrum: superposition of the resonant signal from the cantilever and capacitive coupling of the drive signal.

REFERENCES

[1] T.P. Burg, M. Godin, S.M. Knudsen, W. Shen, G. Carlson, J.S. Foster, K. Babcock, S.R. Manalis, "Weighing of biomolecules, single cells and single nanoparticles in fluid", Nature 446 (2007).
[2] D. Westberg, O. Paul, G.I. Andersson, H. Baltes, "A CMOS-compatible device for fluid density measurements fabricated by sacrificial aluminium etching" Sens. Act. A 73 (1999).
[3] P.Enoksson, G.Stemme, E.Stemme, "Fluid density sensor based on resonance vibration," Sens. Act. A, 47 (1995).
[4] D. Sparks, R. Smith, R. Schneider, J. Cripe, S. Massoud-Ansari, A. Chimbayo, N. Najafi,"A variable temperature, resonant density sensor made using an improved chip-level vacuum package" Sens. Act. A 107 (2003).
[5] S. J. Martin, V. E. Granstaff, G.C. Frye, "Characterization of a Quartz Crystal Microbalance with Simultaneous Mass and Liquid Loading", Anal. Chem. 63 (1991).
[6] M. Tortonese, H. Yamada, R. C. Barret, C. F. Quate: Proc. 2nd Int. Conf. on Solid-State Sensors and Actuators (Transducers'91) (1991).

VESICLE LIBRARIES – TOOLS FOR DIELECTROPHORESIS METROLOGY

Salil P. Desai, Michael D. Vahey and Joel Voldman
Massachusetts Institute of Technology, USA

ABSTRACT

We demonstrate the use of phospholipid vesicle electroformation techniques [1] to develop a new class of metrology tools for systems leveraging dielectrophoresis (DEP) to manipulate, pattern, and sort micron-scale particles. These cell-sized phospholipid vesicles, commonly called giant unilamellar vesicles or GUVs, possess specifically engineered electrical properties and thus exhibit identifiable dielectrophoretic responses in microfabricated systems.

Keywords: Vesicles, dielectrophoresis, libraries

1. INTRODUCTION

Dielectrophoresis (DEP) has emerged as an important tool for the manipulation of bioparticles ranging from submicron to the tens of microns in size. Despite the wide biological applicability of microfabricated systems for DEP, the particles available for their characterization serve as poor models for living cells. For example, polystyrene microspheres commercially available in several sizes and surface functionalizations (e.g. carboxyl groups) are the most widely used test particles for characterizing DEP systems. While functionalized microspheres (FMs) can be further engineered with phospholipids in an effort to mimic biological membranes [2] their density, rigidity, conductivity and permittivity are generally quite different from those of biological cells.

As an alternative to FMs, we explore the use of phospholipid vesicles as test particles for DEP. The close parallels between the physical structure of these synthetic particles and live cells make them ideally suited as substitutes for studying the electromechanical response of cells to external electric fields. Importantly, these cell-sized GUVs are straightforward to synthesize and can be customized to exhibit a range of fluorescence and electrical properties by modulating the composition of their aqueous interior and lipid bilayer membrane.

2. THEORY

Electroformation of GUVs has been studied extensively for over 20 years. Notably, because this technique offers flexibility in the choice and composition of both polar and non-polar phases, it is possible to simultaneously control the fluorescence and electrical properties of both the aqueous core and membrane of the vesicles. For example, electroformation enables the encapsulation of electrolytes spanning several orders of magnitude of physiologically relevant electrical conductivities. The impermeability of lipid bilayers to charged species allows these vesicles to retain their electrical properties when resuspended in osmotically balanced solutions of differing conductivity. Incorporating water-soluble fluorescent molecules inside the vesicles visually encodes their electrical conductivity, making the creation and use of large libraries tractable. Finally, conjugating polymeric molecules to the phospholipids comprising the membrane and adding

978-0-9798064-0-7/μTAS2007/$20©2007CBMS

hydrophobic fluorescent markers to the lipid film prior to electroformation lends control over the specific capacitance of the membrane and offers an additional means of visually encoding information (Figure 1).

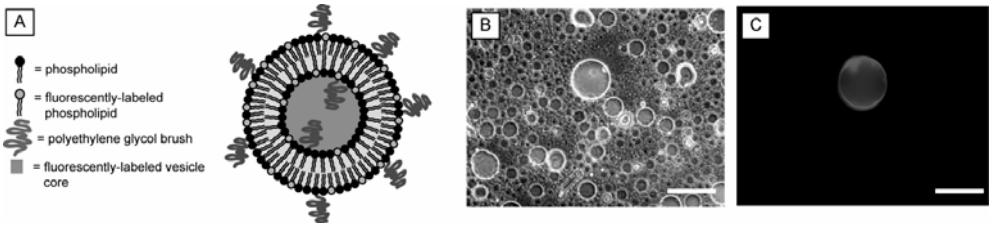

Figure 1: Vesicle libraries (A) Schematic (not drawn to scale) of the concept of a vesicle library where we have independent control over the properties of the vesicle membrane and aqueous core. Fluorescence microscopy images of electroformed vesicles containing fluorescent dyes in the aqueous core (B) and phospholipid membrane (C). Scale bar 50 μm.

3. EXPERIMENTAL

We characterize the electrical properties of the GUVs by performing cross-over frequency (COF) measurements on the vesicles using interdigitated electrode (IDE) arrays. By determing the frequency and medium conductivity at which the DEP force vanishes, we compare the properties of our vesicles with the predictions of widely used models for the electrical properties of layered particles. We perform these measurements on vesicles with different sizes, internal conductivities, and membrane composition to infer from the existing models the effective thickness of the lipid membrane.

4. RESULTS AND DISCUSSION

To demonstrate the capabilities of vesicle-based metrology we construct vesicles encapsulating different conductivity solutions. Figure 2 shows electroformed vesicles labeled with red and green fluorescent dyes randomly oriented on an IDE array. Application of a 1 MHz waveform results in the more polarizable green vesicles undergoing positive DEP and the less polarizable red vesicles undergoing negative DEP.

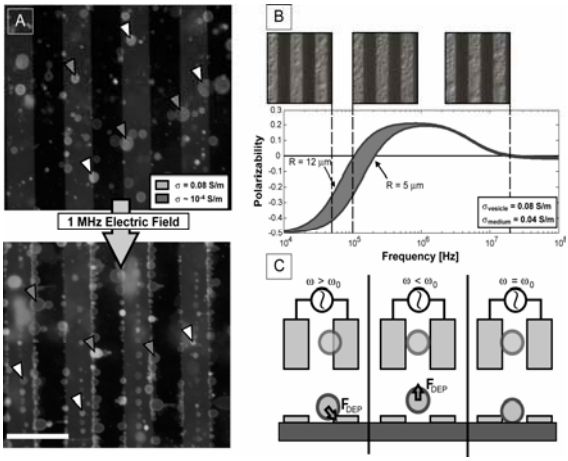

Figure 2: Vesicle measurements. (A) Fluorescence microscopy images of vesicles on IDEs before and after applying a 1 MHz electric field, showing a distinct DEP response of the red (white arrowhead) and green (grey arrowhead) vesicles. (B), (C), We sweep the frequency, ω, observing a single vesicle as it is pulled to and pushed from the electrode edge (C). We narrow the range of frequencies swept until we have converged on the cross-over frequency, ω_0, where the vesicle no longer responds to the electric field. Size and internal conductivity of the vesicle are recorded to generate the spectrum shown in (B). Scale bar 50μm.

Electroformed vesicles with functionalized phospholipids containing PEG brushes attached to their hydrophilic head group along with a fluorescent marker allowed us to test our ability to modulate membrane capacitance (Figure 3). Fluorescence imaging of the electroformed vesicles confirmed that the PEG-functionalized lipids had organized in the vesicle membrane. Interestingly, while COF measurements of non-PEG-functionalized lipid vesicles suggested a membrane thickness of ~5 nm, in agreement with the expected size of a unilamellar lipid bilayer (Figure 3B, black), PEG-coated vesicles exhibited substantially lower effective membrane capacitance, consistent with increased membrane thickness.

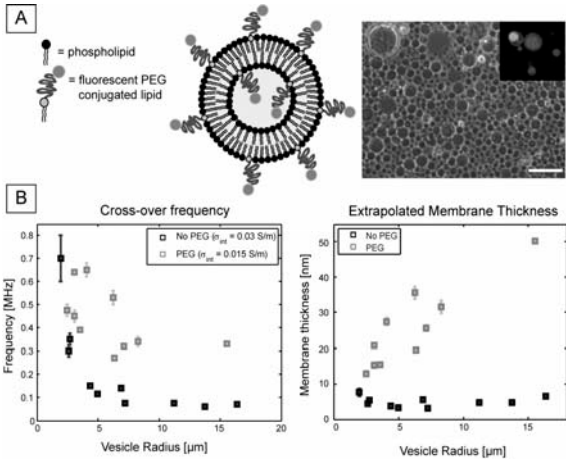

Figure 3: Modulating membrane thickness. (A) Schematic of PEG-modified vesicle (not drawn to scale) and phase microscopy images of electro-formed PEG-vesicles (inset shows fluorescence image of vesicles, confirming PEG-modification). Scale bar 50 µm. (B) Plot of cross-over frequency vs vesicle radius and plot of estimated effective membrane thickness. Vesicles formed in the absence of PEG show a uniform membrane thickness of ~5 nm, as expected for a single lipid bilayer, PEG-coated vesicles exhibit an increased effective membrane thickness that varies with vesicle radius.

5. CONCLUSIONS

We have demonstrated the feasibility of using GUVs as metrology tools for DEP by modulating the conductivity of the aqueous core, the capacitance of the membrane, and the fluorescent signature of both polar and non-polar phases. This, together with post filtration and electrical characterization of the vesicles, allows the creation of combinatorial vesicle libraries and provides a valuable tool in the design and characterization of DEP-based biological microsystems.

REFERENCES

[1] M. I Angelova and D. S. Dimitrov, *Liposome Electroformation*, Faraday Discuss. Chem. Soc., **81**, 303-312 (1986).

[2] J. Vykoukal, D. M. Vykoukal, S. Sharma, F. F. Becker, and P. R. C. Gascoyne, *Dielectrically Addressable Microspheres Engineered Using Self-Assembled Monolayers*, Langmuir, **19**, 2425-2433 (2003).

[3] P. Taylor, C. Xu, P. D. I. Fletcher, and V. N. Paunov, *Fabrication of 2D Arrays of Giant Liposomes on Solid substrates by Microcontact Printing*, Physical Chemistry Chemical Physics, **5**, 4918-4922 (2003).

BIOLOGICAL MEASUREMENTS OF C. ELEGANS TOUCH SENSITIVITY WITH MICROFABRICATED FORCE SENSORS

Joseph C. Doll[1], Nahid Harjee[2], Nathan Klejwa[2], Ronald Kwon[1], Sarah M. Coulthard[1], Miriam B. Goodman[3], and Beth L. Pruitt[1]

[1]*Department of Mechanical Engineering, Stanford University, Stanford, CA, USA*
[2]*Department of Electrical Engineering, Stanford University, Stanford, CA, USA*
[3]*Department of Molecular and Cellular Physiology, Stanford University, Stanford, CA, USA*

ABSTRACT

This paper presents biological measurements performed with a microfabricated force-post fabricated from SU-8 and metal on quartz wafers. The transparent device is used to measure the touch sensitivity of nematodes (*Caenorhabditis elegans*) during normal locomotion. We measure forces in the 0.5μN - 10μN range for wild type and *mec-6*, a touch insensitive mutant, and observe a measurable difference between the two strains.

Keywords: C. elegans, Force Sensor, Mechanotransduction, Locomotion

1. INTRODUCTION

The sensation of touch guides complex organism behavior such as obstacle avoidance and locomotion. Many organisms have highly specialized touch cells that are responsible for the rapid transduction of force into electrochemical signals. Several touch receptor neurons located in *C. elegans* are responsible for the avoidance light touch. Ionic currents in response to touch have been measured [1], however the range of force that mediates a response in normal behavior is not known and the relevance of the applied forces to normal animal behavior has not been quantitatively verified.

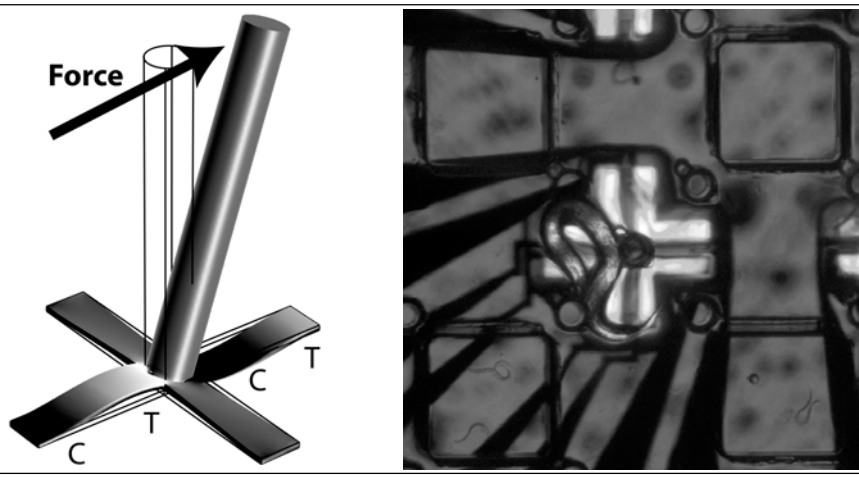

Figure 1. A finite element simulation of force post deflection illustrating the tensile and compressive stresses in the cantilever beams (left) and low magnification image of C. elegans interacting with force post (right).

978-0-9798064-0-7/μTAS2007/$20©2007CBMS

Microfabricated devices have been used in the past to study the forces generated and sensed by small organisms. Previous efforts in studying microscale cell and organism locomotion have utilized both optical and electronic transduction mechanisms. Polydimethylsiloxane (PDMS) has been molded into pillars and visually tracked during deflection to study cell motility [2].

This paper reports new biomechanical measurements using a microfabricated force post system wth direct electronic readout [3]. The device consists of four fixed-guided cantilever arms with a vertical pillar rising from the central junction. Forces applied at the tip of the pillar induce strains in the cantilevers that are sense by metal strain gauges. Differential resistivity measurements are taken along the two in-plane axes aimultaneously to calculate the force.

2. THEORY

The ratio of output voltage to force applied at the pillar tip can be approximated from the bridge bias voltage V_{in}, amplifier gain A, straing gauge Poisson ratio υ, pillar height h, cantilever arm Young's modulus E, width w, and thickness t:

$$\frac{V_{out}}{F} \cong \frac{3V_{in}A(1+2\nu)h}{4Ewt^2}. \quad (1)$$

3. EXPERIMENTAL

Briefly, the device was fabricated from SU-8 photoresist and gold strain gauges on a quartz wafer. Fabrication details and device characterization have been reported in detail previously [3]. Devices with 300μm x 65μm cantilever beams and 300μm tall force posts were used for all measurements.

For measurements, the strain gauges along each axis were connected in a balanced Wheatstone bridge with two-stage amplification for a total of 10,000X gain (TI INA103 and AD622). Calibration was performed with a piezoresistive silicon cantilever. A calibrated force was applied to the pillar tip and the cantilever and force sensor outputs were recorded. A force sensitivity of 0.376 V/μN was measured at a bias voltage of 1V. An optically transparent cover was placed over the sample to shield air currents and data was typically recorded over a period of less than 60 seconds.

C. elegans cultures were prepared on standard growth plates seeded with OP50 and raised at room temperature for several days to obtain adults. Worms were then replated on a clean agar plates and a small piece of agar was cut out and placed on a glass slide. The slide was inverted and attached to the end of a three-axis micromanipulator to position the worms over the force sensors for measurements. Two strains of worm were studied, wild type and *mec-6* (u247), a strain with a defect in the touch sensitive ion channel complex that leads to vastly reduced touch sensitivity [4].

4. RESULTS AND DISCUSSION

The mean contact force for wild type and *mec-6* was 2.5 and 4.7 μN, respectively. A typical force-time plot and histogram of measured forces is shown in Figure 2. The contact force applied by the worms to the pillar during locomotion was typically less than 10 μN. Interactions varied from brief nose touches followed by immediately backing up to wrapping around the post for several seconds. The latter interaction was more common and

the worms appeared to prefer the tight spaces afforded by the posts and spacer blocks rather than shying away from them.

It is likely that the structure of the environment affects locomotion in *C. elegans* and other organisms. The small difference between wild type and touch insensitive mutants suggests that the measured forces are more indicative of locomotion forces than touch sensitivity thresholds.

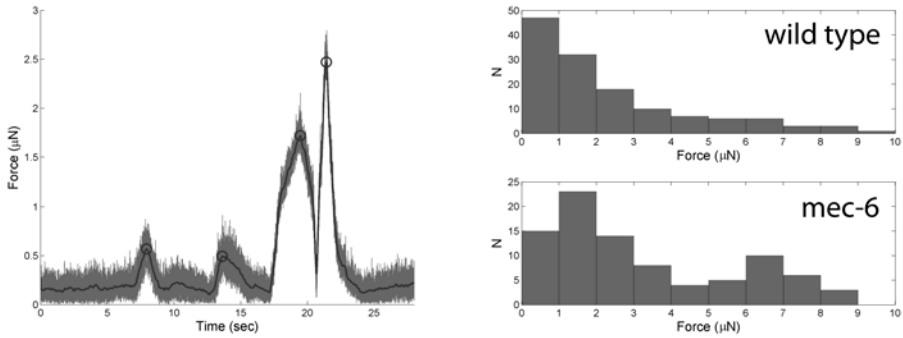

Figure 2. Typical measurement of force over time (left). In post-processing, the force measurements from the x- and y-axes are summed to obtain the total force. The total force is smoothed and the peak forces are identified. These peaks are then plotted in a histogram (right) for wild-type and *mec-6* strains.

5. CONCLUSIONS

We have measured the nose and body touch sensitivity of C. elegans during natural locomotion with a microfabricated force sensors made from SU-8 and metal strain gauges.

ACKNOWLEDGEMENTS

Fabrication work was performed in part at the Stanford Nanofabrication Facility (a member of the National Nanotechnology Infrastructure Network) supported by the NSF under Grant ECS-9731293, its lab members, and the industrial members of the Stanford Center for Integrated Systems. This work was supported by the NSF CAREER Award ECS-0449400. The authors thank S.J. Park for device calibration assistance and J. Cueva for the *mec-6* strain.

REFERENCES

[1] R. O'Hagan, M. Chalfie, M. B. Goodman, *The MEC-4 DEG/ENaC channel of Caenorhabditis elegans touch receptor neurons transduces mechanical signals* Nat Neurosci, 8, 43-50 (2005).

[2] J. L. Tan, J. Tien, D. M. Pirone, D. S. Gray, K. Bhadriraju, C. S. Chen, *Cells lying on a bed of microneedles: an approach to isolate mechanical force* Proc Natl Acad Sci U S A, 100, 1484-1489 (2003).

[3] N. Klejwa, N. Harjee, R. Kwon, S. M. Coulthard, B. L. Pruitt, *Transparent SU-8 Three-Axis Micro Strain Gauge Force Sensing Pillar Arrays for Biological Applications* Proceedings of Transducers 2007, In Press,

[4] G. Gu, G. A. Caldwell, M. Chalfie, *Genetic interactions affecting touch sensitivity in Caenorhabditis elegans* PNAS, 93, 6577-6582 (1996).

FABRICATION AND PHYSICS OF HOURGLASS-SHAPED MICROAPERTURE BY LASER DRILLING TECHNIQUE

Chang-Yu Chen[1], Kuan-Ting Liu[1], De-Shien Jong[2], and Andrew M. Wo[1]
[1]*Institute of Applied Mechanics, National Taiwan University, Taipei, TAIWAN*
[2]*Department of Animal Science and Technology, National Taiwan University, Taipei, TAIWAN*

ABSTRACT

A unique fabrication method to create an hourglass-shaped microaperture was demonstrated. We exploited a simple process of reflow of melted glass by CO_2 laser drilling technique to implement the process. The fabricated aperture revealed smooth, circular, and debris-free nature with controllable diameter by different laser pulse parameters. The physics leading to such formation was also illuminated by computation. Results showed the hourglass feature is clearly evident verifying the simulation captures the dominant physics of glass reflow. The approach is conceivably practical in microsystems and microfluidics for patch-clamp study, droplet handling, or single cell investigation.

Keywords: Hourglass, laser drilling, microaperture, patch-clamp

1. INTRODUCTION

Microfabricated aperture for cellular electrophysiological applications has been demonstrated the usefulness in several approaches. Recent works indicated smooth contact area and freshly-activated glass surface will enhance the seal quality in patch-clamp study. Sordel et al.[1] presented an hourglass SiO_2 coated aperture to increase the chip performance. Lehnert et al.[2] proposed a glass reflow technique to create a funnel shaped aperture with similar surface properties of fire-polished glass pipette. However, complicated fabrication process was generally required.

This work presents a fast and easy method to fabricate an hourglass-shaped aperture for use as patch-clamp by laser drilling technique on glass material, and the physics leading to such formation is illuminated. Conventional laser drilling results in a through hole with the inner wall feature essentially straight wall. Ultra fast laser pulses – capable of generating high aspect ratio holes without heating much of the substrate[3] – are carefully tuned and resulted in three-dimensional contour in the hole inner wall geometry. Here we exploited the heating characteristics of glass and its associated reflow of material during the drilling process to obtain the unique hole aperture. The authors believe this is the first record of using laser to generate an aperture with hourglass-shaped inner contour on glass.

2. EXPERIMENTAL

A 25W CO_2 laser with 10.6μm wavelength was used to implement the process. Figure 1 shows the schematic illustration of laser drilling process. The high density energy melts and vaporizes material for removal. To obtain the unique aperture, a series of microsecond pulses were applied, with the total laser energy designed to just penetrate the 150μm

978-0-9798064-0-7/μTAS2007/$20©2007CBMS

borosilicate glass. The reflow and solidification processes of melted glass occurred spontaneously on the opposite side of the laser entrance surface.

Numerical simulation reveals the physics of the reflow process. Navier-Stokes equation (Comsol Multiphysics Inc.) was coupled with level set method, widely used to trace the evolution of interface[4]. Melted glass and air were treated as two flowing fluid with zero level set defines the interface. Solidification phenomenon was not treated for simplicity, and justified on the basis that solidification would essentially affect only the time rate of the process and not the feature itself. Surface tension was considered and gravity was not important.

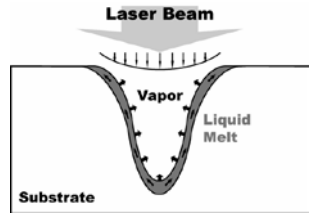

Figure 1. Schematic illustration of laser drilling process. Substrates are vaporized and melted due to high intensity, Gaussian distributed laser beam (TEM_{00}).

3. RESULTS AND DISCUSSION

Figure 2A shows a micrograph of cross-section of a typical hourglass-shaped aperture. SEM image showed smooth, debris-free surface as seen in the isometric view (Fig. 2B), while the top view image revealed circular and crack-free aperture (Fig. 2C). Uniformly fabricated micro-aperture array with diameter of around 10μm is also demonstrated (Fig. 2D). Flatness of glass and laser drilling stability should be carefully considered when fabricating array configurations.

Frequency, duration, and number of laser pulses determine the total energy for drilling process. Figure 3 shows the side view micrographs with increasing aperture diameter. The aperture size is predominantly governed by the energy intensity and density of laser emission.

Figure 4 shows the simulated reflow process at different time steps, which indicated the simulation replicated the hourglass feature observed in surprising detail. The computation was commenced just after the laser penetrated the glass. Melted glass at the rear of the surface gradually reflowed to form the hourglass-shaped feature. Results showed that at 600μs time step, the hourglass feature is clearly evident verifying the simulation captures the dominant physics of glass reflow.

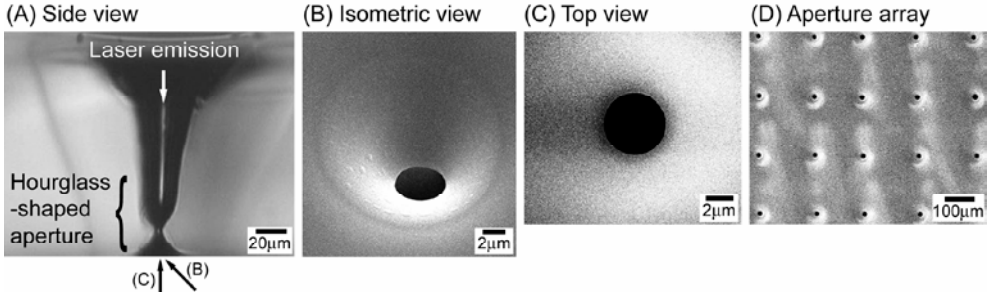

Figure 2. Micrographs and SEM images of the laser drilled aperture. (A) Side view image of the typical hourglass-shaped aperture. The smallest dimension located at the neck of the hourglass shape, ranged from 1~20μm or even larger. (B, C) Isometric and top view of SEM images taken from the rear surface showed the smooth, circular, and debris-free nature of the aperture. (D) Uniformly fabricated micro-aperture array with diameter of around 10μm.

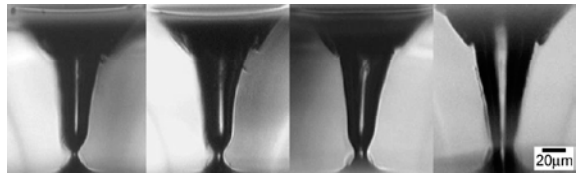

Figure 3. Side view micrographs of the laser drilled aperture with increasing aperture diameter. Frequency, duration, and number of laser pulses determine the total energy for drilling process and resulted in distinct geometry.

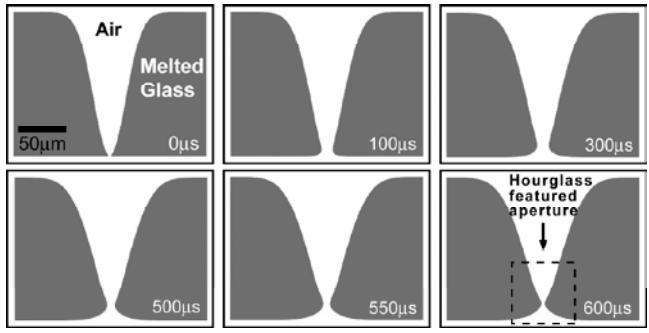

Figure 4. Numerical simulation of the reflow processes of melted glass at different time steps. Melted glass and air were treated as two flowing fluid and Navier-Stokes equation was coupled with level set method to trace the interface. The computation was commenced just after the laser penetrated the glass. Melted glass at the rear of the surface gradually reflowed to form the hourglass-shaped feature. Time steps designated here are merely reference values since the solidifying process is not considered in this computation.

4. CONCLUSIONS

The fabrication method described herein successfully utilizes the melting glass process during laser drilling to create unique-shaped aperture. Numerical calculation confirmed the physics of the phenomenon. The approach is conceivably practical in microsystems and microfluidics for patch-clamp study, droplet handling, or single cell investigation.

ACKNOWLEDGEMENTS

This work was supported by the National Science Council (Grant No. 95-2221-E-002-339), Taiwan.

REFERENCES

[1] T. Sordel, S. Garnier-Raveaud, F. Sauter, C. Pudda, F. Marcel, M. De Waard, C. Arnoult, M. Vivaudou, F. Chatelain, and N. Picollet-D'hahan, "Hourglass SiO2 coating increases the performance of planar patch-clamp," *Journal of Biotechnology*, vol. 125, pp. 142-154, 2006.

[2] T. Lehnert, D. M. T. Nguyen, L. Baldi, and M. A. M. Gijs, "Glass reflow on 3-dimensional micro-apertures for electrophysiological measurements on-chip," *Microfluidics and Nanofluidics*, vol. 3, pp. 109-117, 2007.

[3] L. Shah, J. Tawney, M. Richardson, and K. Richardson, "Femtosecond laser deep hole drilling of silicate glasses in air," *Applied Surface Science*, vol. 183, pp. 151-164, 2001.

[4] J. A. Sethian, *Level set methods and fast marching methods : evolving*, 2nd ed. Cambridge: Cambridge University Press, 1999.

FABRICATION OF A MICROFLUIDIC BEAD ARRAY SENSOR BY PHOTOPOLYMERIZATION AND LAMINATION

S. Begolo[1], T. Carofiglio[2], G. Mistura[1], M. Natali[3]
[1] *Department of Physics, University of Padova,Italy*
[2] *Department of Chemical Sciences and ITM-CNR, University of Padova,Italy*
[3] *ICIS-CNR Padova, Italy*

A novel low-cost polymer microfabrication process is described based on a combination of photopolymerization and lamination. The process allows efficient fabrication of microfluidic chips having complex multilayer geometries. As an application, a colorimetric bead array sensor is fabricated and tested, using commercial Tentagel resin beads which have been functionalised by us with different pH and metal-ion sensitive azo-dyes.

Keywords: sensor arrays, lamination, photopolymerization, multilayer fabrication

1. INTRODUCTION

The integration of sensors into microfluidic chips is a topic of great importance. Bead sensors operating by optical transduction are very interesting in this respect and have recently been used to build an electronic tongue by arranging an array of differently functionalised beads in a micromachined silicon chip [1]. However for mass production of disposable chips polymers are preferred. Many fabrication methods exist to build polymeric microfluidic chips. Nevertheless those allowing efficient fabrication of complex 3D channel geometries - required e.g. for a bead array sensor of the type reported in ref.[1] - are still relatively scarce. Here we propose a new fabrication method based on a combination of lamination and liquid photopolymerization of a thiolene adhesive. Our method is inspired by previous work reported in ref. [2,3] but contrary to these authors we do not require any sacrificial materials, e.g. wax, to build overhanging structures. Compared with processes involving lamination of photolithographically patterned SU8 resist [4] our method allows greater thickness of the layers, requires no clean/yellow/dark room facilities and yields chips resistant to a wider range of organic solvents.

2. EXPERIMENTAL

A schematic layout of the sensor chip is shown in Fig.1a. The chip consists in a multilayer flow cell incorporating an array of sensor beads trapped in well defined locations. The beads are commercial Tentagel resin beads (300 μm diameter) that were functionalised by us with different azo-dyes according to a procedure described previously [5]. To fabricate the chip we use a thiolene based optical adhesive NOA61 from Norland Products. The first layer of the chip is built by squeezing liquid adhesive between two microscope glass slides, separated by 200 μm thick spacers. The bottom slide was previously coated with an octadecyltriclorosilane anti-stick layer and the top pre-drilled with fluid inlet/outlet holes. The adhesive is partially photopolymerized across a transparency mask using a Spectronics SB100 UV flood lamp kept at a distance of 70 cm (exposure time 8 min). The transparency mask was printed on photographic film using a 4000 dpi imagesetter (Q&B Grafiche, Mestrino, Italy). After disassembling the stack, unpolymerized adhesive is rinsed with a 1:1 ethanol/acetone mixture. The pattern is further UV cured to improve its stability and adhesion to the glass slide. The second layer of the

978-0-9798064-0-7/μTAS2007/$20©2007CBMS

chip is fabricated similarly but using a polyester film as a flexible temporary support and a spacer thickness 25 μm. (UV exposure 5 min). After rinsing the precured second layer it is manually laminated to the first layer. The stack is cured to completion by 30 min UV exposure at a distance of 30 cm from the lamp and the polyester backing sheet is then peeled away. The third layer is patterned on a thin microscope cover glass. (spacer thickness 100μm, UV exposure 6min). Sensor beads functionalised with various azo-dyes [6] are manually introduced into the cavities of the array and the chip is sealed by laminating the third layer on top of the other two. Good sealing is achieved at room temperature after 12 hours. PVC tubes are fixed to the chip using epoxy glue. pH measurements are perfomed by flowing a buffer solution (composed of CH_3COONa 0.04 M, H_3BO_3 0.04 M, NaH_2PO_4 0.04 M, Na_2SO_4 0.1 M, adding HCl 3M and NaOH 2M to adjust pH) through the chip using a peristaltic pump (Gilson MINIPULS 3) at a flow rate of 1-2 mL/min and monitoring the color of the beads using a commercial scanner (Epson).

4. RESULTS AND DISCUSSION

A photograph of a fabricated 6x6 bead array chip is shown in Fig.1b while a scanning electron microscope (SEM) image of an exploded cross-section of the chip is shown in Fig.1c. To further demonstrate the 3D capability and the range of sizes accessible we fabricated different multilayer "wood-pile" structures. Some of them are shown in Fig.3. Layer thicknesses ranging from few tens of microns up to several mm and lateral sizes down to 100μm were obtained. To reliably transfer the adhesive from the polyester sheet to the substrate, the adhesion force to the substrate must be greater than to the polyester sheet. This is guaranteed if the substrate is already coated with a cured NOA layer and if the ratio of contact area of the pattern with the substrate and the polymer sheet is not too small. In the case of the wood-pile structures in Fig.2 this ratio is about 1/2. In Fig.4 are shown results of pH measurements performed on the bead sensor array. The colors of the beads in the recorded RGB bitmap images were analized and coded in the CIE- "Lab" color space.

5. CONCLUSIONS

We demonstrated a new polymer microfabrication method well suited to obtain complex multilayer structures useful in microfluidics. As an application, a colorimetric bead array sensor array for pH measurements was fabricated and tested.

REFRENCES

[1] Y.S. Sohn, A. Goodey, E.V. Anslyn, J.T.McDevitt, J.B.Shear, D.P. Neikirk, Biosensors and Bioelectronics, **21,** 303 (2005).
[2] G.Mensing, T.Pearce, and D.Beebe, Journal of Laboratory Automation, **10**, 24 (2005).
[3] J.B. Hutchison, K.T.Haraldsson, B.T.Good, R.P. Sebra, N.Luo, K.S.Anseth, and C. N. Bowman, Lab Chip, **4**, 658 (2004)
[4] M. Agirregabiria, F.J. Blanco, J. Berganzo, M.T. Arroyo, A. Mayora, and J.M. Ruano-López, Lab Chip, **4**, 658 (2004)
[5] L.Brigo, T.Carofiglio, C. Fregonese, F. Meneguzzi, G. Mistura, M.Natali, U.Tonellato, Proceedings IMCS 11 Brescia (Italy), 16-19 july 2006
[6] #1: 2-((4-(2-hydroxyethylsulfonyl)-phenyl)diazenyl)-4-methoxyphenol, #2: 2-((4-(2-hydroxyethylsulfonyl)phenyl)diazenyl)-3,6-dimethylphenol, #3: 4-((4-(2-hydroxyethyl-sulfonyl)phenyl)diazenyl)-2,6-dimethylphenol, #4: 4-((4-(2-hydroxyethylsulfonyl)-phenyl)-diazenyl)naphthalen-1-ol, #5: 5-((4-(2-hydroxyethylsulfonyl)phenyl)diazenyl)quinolin-8-ol. Numbers #1 to #5 correspond to bead numbers in Fig.4. Bead #0 is unfunctionalized.

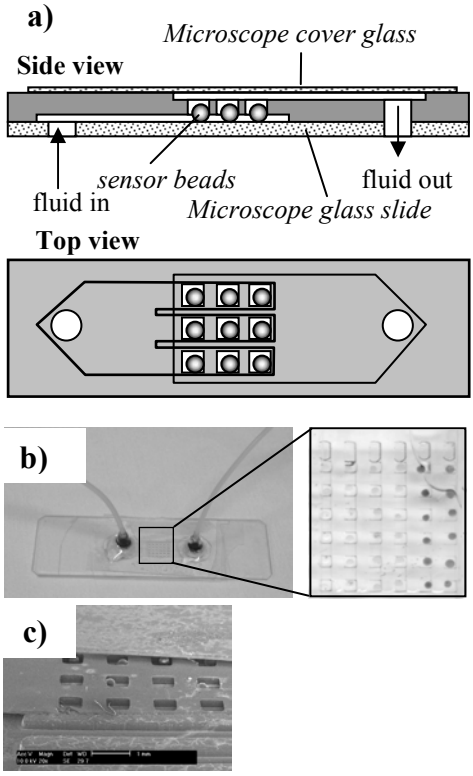

Figure 1. a) schematic layout of the sensor chip, b) photograph of a fabricated 6x6 bead array chip, c) SEM image of an exploded cross-section of a chip,

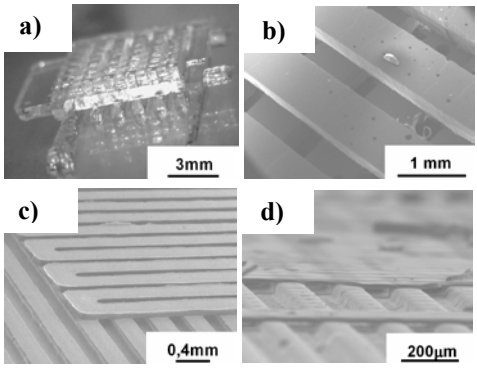

Figure 3. multilayer structures fabricated to illustrate the range of dimensions accessible and the 3D capability of the fabrication method used: a) optical microscope image, b)-d) SEM images.

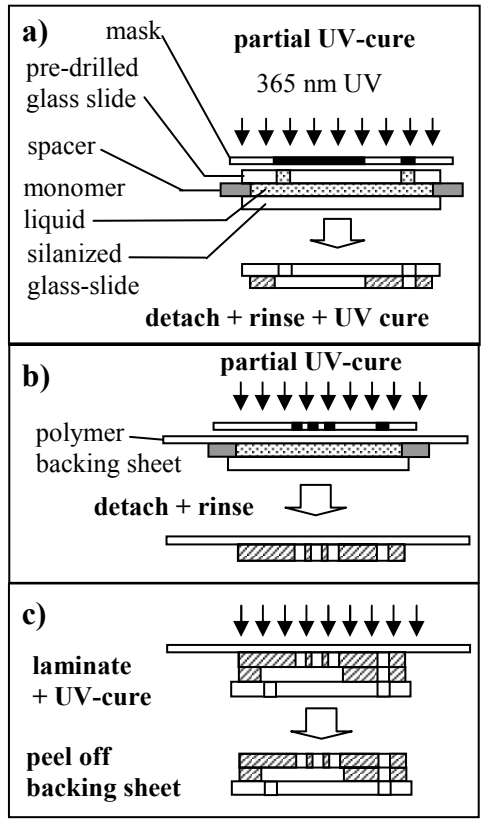

Figure 2. schematic of fabrication process,

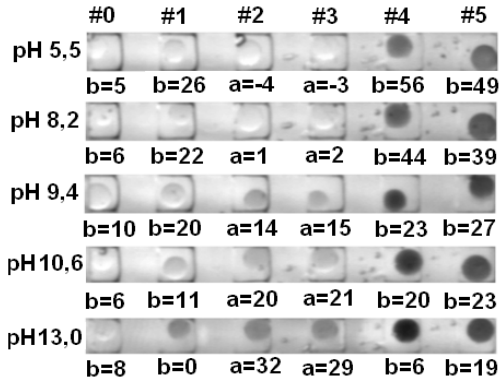

Figure 4. greyscale images of a single line of the sensor array at different pH. The chemical structure of the dyes grafted to the beads is described in [6]. For each bead only the CIE-"Lab" color parameter "a","b" that varies most with pH is reported.

FABRICATION OF HIGH ASPECT RATIO STRUCTURES IN MICROFLUIDIC CHANNEL USING OPTOFLUIDIC MASKLESS LITHOGRAPHY

Su Eun Chung[1], Wook Park[1], Hyunsung Park[2], Kyoungsik Yu[3], Namkyoo Park[2], and Sunghoon Kwon[1]

[1]School of Electrical Engineering and Inter-university Semiconductor Research Center (ISRC), Seoul National University, SOUTH KOREA

[2]School of Electrical Engineering, Seoul National University, SOUTH KOREA, and

[3]Korea Electrical Engineering and Science Research Institute, SOUTH KOREA

ABSTRACT

We demonstrate the fabrication of long polymeric microwires in microfluidic channels using optofluidic maskless lithography. By continuously exposing a time-varying ultraviolet exposure pattern on a photocurable resin flowing in the microfluidic channel, long polymeric microwire structures, whose sizes are much bigger than the exposure field of view, can be fabricated.

Keywords: Optofluidics, Photopolymerization, Maskless lithography, Microwires

1. INTRODUCTION

Continuous-flow lithography [1] can fabricate various types of free-floating polymeric microstructures by selectively polymerizing photocurable resin solutions flowing in microfluidic channels using fixed photomasks. However, the sizes of the fabricated microstructures have been limited by the exposure field of view, and there also exists a tradeoff relationship between the spatial resolution and the total field of view of the lithography systems. Recently, we have demonstrated optofluidic maskless lithography by combining the continuous-flow microfluidic lithography technique and maskless lithography with a daynamic MEMS spatial light modulator [2]. In this paper, we present a lithographic analogy of line scanning display to solve the size limitation problem by extending the concept of optofluidic maskless lithography.

2. DESIGN AND FABRICATION

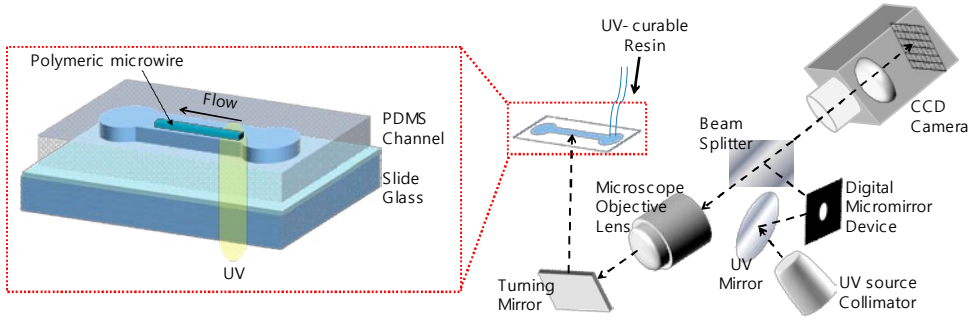

Figure 1. Fabrication of polymeric microwires using an optofluidic maskless lithography technique. The inset shows the details of the microfluidic channel.

978-0-9798064-0-7/μTAS2007/$20©2007CBMS

The experimental setup for the fabrication of polymeric microwires is shown in Figure 1. Computer-generated images are continuously transferred to a two-dimensional programmable spatial light modulator (Digital Micromirror Device from Texas Instruments), which controls the spatial pattern of the ultraviolet (UV) beam exposure on the microfluidic channel. If we keep exposing at one spot while the photocurable resin material (polyethylene glycol (258) diacrylate (PEG-DA) and 5 wt % photoinitiator) flows in the channel as illustrated in Figure 1, the cured spot is extended as a polymeric wire due to the pressure-driven fluid flow of the photocurable oligomer solution. The total length of the microwire grows linearly with the exposure time and the flow speed, and is not limited by the exposure field of view.

3. EXPERIMENTS AND RESULTS

Figure 2 (a) and (b) show two straight polymer lines created by exposing circular UV beams at a fixed location near the center of the microfluidic channel. The line width can be controlled by changing the radius of the UV exposure. Figure 2 (c) and (d) demonstrate curved polymeric microwires. The spatial light modulator is updated at a rate of 10 Hz, and one period of the sinusoidal curve corresponds to 100 exposures for 10 seconds. A circular pattern moves up and down, and its center position follows a sinusoidal curve as a function of time. High aspect ratio microstructures, which are much longer than the exposure field of view, can be fabricated by taking advantage of the fluidic motion in the microfluidic channel.

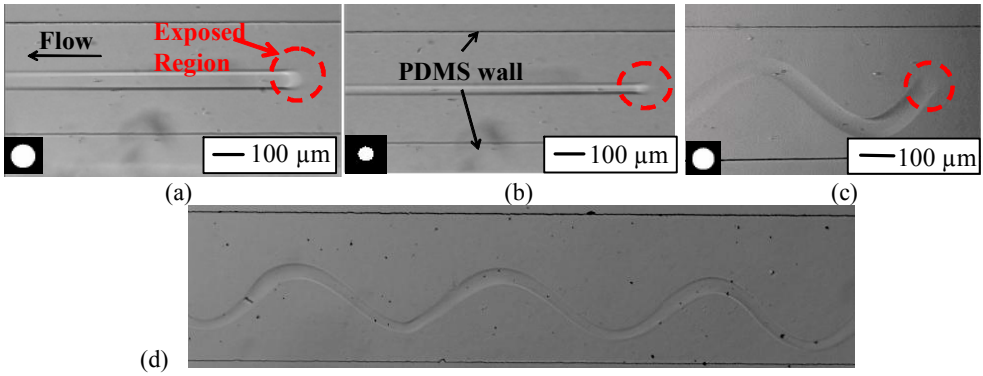

Figure 2. Polymeric wire lines photopolymerized in a microfluidic channel. The straight lines are created by exposing a circular UV beam at a fixed location with approximately (a) 40 µm and (b) 20 µm radius. (c) Sinusoidally-curved polymeric mcrowire in the microfluidic channel. A circular exposure pattern moves up and down within the exposure area at a rate of 10 Hz, and its center position oscillates sinusoidally as a function of time. (d) Curved polymer wire imaged by a differential interference contrast microscope at lower magnification. The exposure circle radius is 25 µm in this case.

It is also possible to use multiple exposure spots oscillating up and down to form interwined microwire structures as shown in Figure 3 (a) and (b). By changing the relative offsets between two exposure spots, we can control the relative position between the two twisted polymeric microwires. The shape and width of the microwires can also be

easily controlled by changing the center position and size of the exposure pattern as a function of time, respectively. Figure 3 (c) shows an example of a polymeric microwire with varying width, which was fabricated by exposing five different bar-shaped patterns. Each bar pattern has different length as shown in Figure 3 (c), and is updated cyclically in order per 0.1 second exposure time, taking advantage of the real-time pattern controllability of optofluidic maskless lithography with a high-speed spatial light modulator.

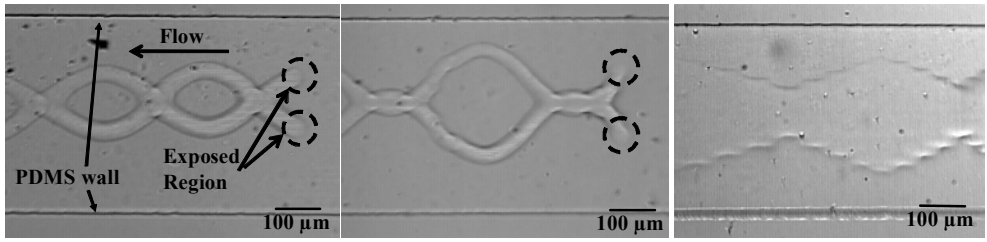

(a) (b) (c)

Figure 3. (a) Twisted polymeric wires fabricated by changing the positions of two circular UV exposure patterns sinusoidally with an amplitude of ~100 μm. Two patterns are out of phase without any vertical offset, and oscillate at the same rate of 0.1 Hz. (b) An offset is added between two circular patterns, and the relative position between two curved microwires is changed. (c) A microscope image of the fabricated microstructure with varying width. Five bar-shaped patterns with different lengths are exposed cyclically in order. The flow rate gets slower during the experiment, and, therefore, the width of the fabricated bar becomes smaller accordingly. The exposure time is maintained at 0.1 seccond.

4. CONCLUSIONS

We have demonstrated the fabrication of long polymeric structures whose sizes are not limited by the lithographic field of view. Unlike conventional lithography techniques based on fixed photomasks, the fabricated polymeric microwires can be arbitrarily long. We envision this technique would enable fabrication of various optofluidic waveguide structures for photonic and optofluidic applicaitons.

ACKNOWLEDGEMENTS

This research is supported by the NANO Systems Institute-National Core Research Center (NSI-NCRC) program of Korea Science and Engineering Foundation (KOSEF), Korea.

REFERENCES

[1] D. Dendukuri, D. C. Pregibon, J. Collins, T. A. Hatton, and P. S. Doyle, "Continuous-flow lithography for high-throughput microparticle synthesis," Nat. Mater. **5**(5), 365-369 (2006).

[2] S.E. Chung, W. Park, H. Park, K. Yu, N. Park, and S. Kwon, "Optofluidic maskless lithography system," Paper 3EA1.P, *Transducers 2007*.

NOVEL BONDING TECHNIQUE USING HYDROPHILIC SU-8

Yu-Tzu Chen and Denz Lee*

Institute of Aeronautics and Astronautics, National Cheng Kung University, Taiwan, ROC.

ABSTRACT

This paper presents a novel bonding technique for fabricating microfluidic devices with surfactant-added SU-8 (hydrophilic SU-8) as structure. The technique is based on an adhesive wafer bonding process. The hydrophilic SU-8 plays the roles of adhesive layer as well as structural layer. Due to its special feature, the layer can be directly bonded to various substrates (glass, silicon or poly(dimethylsiloxane)) after oxygen plasma treatment. The present bonding technique does not need another SU-8 adhesive layer for bonding. Neither is an expensive bonding system needed. The technique is fast, convenient, secure and inexpensive with standard photolithography.

Keywords: bonding, hydrophilic, SU-8

1. INTRODUCTION

Bonding has been an important process in the fabrication of microfluidic devices. Recently, adhesive bonding has drawn certain attention. The main advantages include low bonding temperature, low sensitivity to surface roughness, compatibility with the existing fabrication processes and ability to join various substrate materials. High bonding strength can be achieved in simple, robust, low cost processes. In common practices [1-3], most adhesive bonding techniques need elevated temperature and pressure in certain equipments, or need fabricated SU-8 layers on both top and bottom substrates to be bonded by crosslinking reaction. It requires more complex and time-consuming processes. In the present study, we propose a new method to fabricate a sealed microchannel differs from previous works in the specific material of surfactant-added SU-8.

2. EXPERIMENTAL

We use the hydrophilic SU-8 photoresist which is a mixture of photodefinable epoxy SU-8 and trisiloxane alkoxylate surfactant (Silwet*618, GE)($[(CH_3)_3SiO]_2CH_3Si(CH_2)_3O(CH_2CH_2O)_8CH_3$) as the adhesive layer as well as the structural material. Fabrication procedure is shown in Figure 1. The microstructure

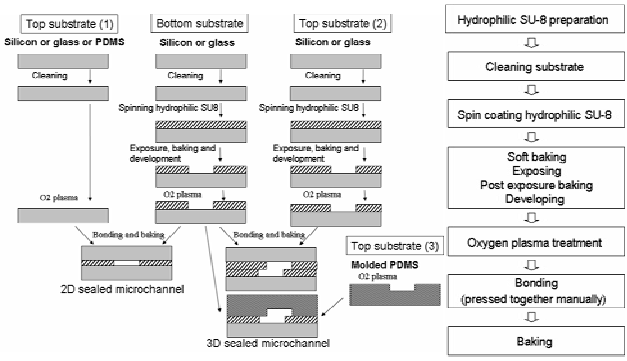

Figure 1. Diagram of the fabrication process.

978-0-9798064-0-7/μTAS2007/$20©2007CBMS

was formed by standard photolithographic process and it enabled direct bonding with another substrate (with or without another SU-8 layer) after oxygen plasma treatment. The performance of the materials were verified by using the Raman spectroscopy to analyze the possible changes on chemical structure, measuring contact angle to characterize hydrophilicity, and several tests to confirm the bonding ability. The bonding quality can be evaluation by scanning electron microscopy (SEM), tensile strength measurements and hydrodynamic tests.

3. RESULTS AND DISCUSSION

Hydrophilic SU-8 mixture is the key materials in the present study, and its features need to be further characterized. Therefore, we first conducted the Raman spectroscopy test. From the comparison of Raman tests, we supposed that the oxyethylene groups (-OCH_2CH_2-) of migrating surfactant provided better hydrophilicity in surfactant-added SU-8 film. Upon oxygen plasma treatment, the surfactant molecules were cleaved forming hydroxyl groups and further enhanced the hydrophilicity of the surface. We suggested that the hydrophilicity and bonding ability were enhanced by both oxyethylene groups and hydroxyl groups. Second, we have measured the contact angle on the glass coated with pure base SU-8 layer (0%) and with surfactant-added SU-8 layer (10% without and with oxygen treatment), the results are shown in Figure 2. The water droplet spreads slowly on the pure SU-8 layer, yet quickly on the surfactant-added SU-8 layer. The results indicate that we have changed the hydrophilicity of SU-8 by adding certain surfactant (hydrophilic SU-8).

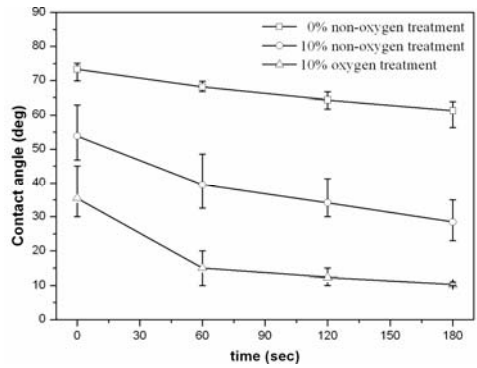

Figure 2. Changes of contact angle of the working liquid on the glass coated with pure base SU-8 layer (square) and with surfactant-added SU-8 layer (10%) without (circle) and with (triangle) oxygen treatment.

To further study the performance which can be expected of this bonding method, we have conducted several bonding tests, the results are listed in Table 1. From Tests No 1-3 and Figure 3, it is seen that the hydrophilic SU-8 we employed possessed bonding ability and could define structure satisfactorily (the concentration of surfactant should be less than 30%). From Tests No 4-5, it can be seen that various structure thickness and adhesive material provide satisfactory bonding quality. From the results of Tests No 6-8 and Figure 4, the hydrophilic SU-8 bonding technique also has good compatibility in the integration with other substrates (glass, Si, PDMS). By utilizing multiple layers of hydrophilic SU-8, we were able to bond two patterned substrates to create 3D channel structure (Test No 9). The strength of the bonding was about 2–14 kg cm^{-2} which is adequate for microfluidic

operation. The hydrodynamic tests demonstrated that the bonding could tightly seal the microstructure.

Table 1. Typical examples and evaluation results of the bonding test.

Test No	Material	Surfactant concentration (%)	Structured thickness (μm)	Substrate	O2 plasma treatment	Cure-bake	Bond strength (kg cm^{-2})	Unbonded area (%)
1	SU-8-25	0	40	glass-glass	v	100°C/20 min	—	>99
2	SU-8-25	10	40	glass-glass	v	100°C/20 min	6	<5
3	SU-8-25	40	40	glass-glass	—	—	—	—
4	SU-8-25	10	5	glass-glass	v	100°C/20 min	6	<5
5	SU-8-50	10	40	glass-glass	v	100°C/20 min	6	20
6	SU-8-25	10	40	glass-PDMS	v	100°C/20 min	>2	30
7	SU-8-25	10	40	Si-glass	v	100°C/20 min	10	<5
8	SU-8-25	10	40	Si-PDMS	v	100°C/20 min	>2	30
9[b]	SU-8-25	10	15	glass-glass	v	100°C/20 min	14	10

[a] The spread, spin, pre-bake, exposure, post-bake and develop conditions are shown in table 1.
[b] Polymer coating on both substrate surface.

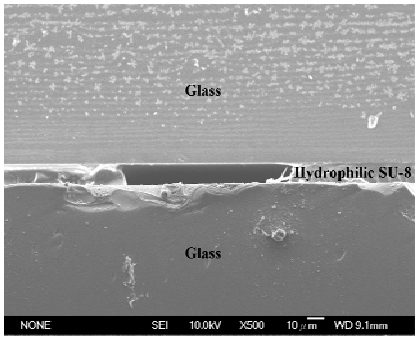

Figure 3. Cross section SEM photograph of the embedded microchannel between glass substrates.

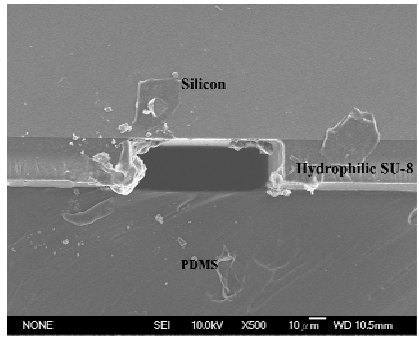

Figure 4. SEM photograph of the bonding interface between Si and PDMS substrates.

4. CONCLUSIONS

A novel bonding technique using hydrophilic SU-8 as the adhesive layer and the structural material as well has been proposed and demonstrated in this study. The hydrophilicity, the feasibility to define structures, the ability to bond and the compatibility with other substrates were verified experimentally. The results lead to a preliminary conclusion that the modification of SU-8 by surfactant can yield satisfactory characteristic for bonding and other applications.

ACKNOWLEDGEMENTS

This study was partially sponsored by the National Science Council of Taiwan under the project NSC 94-2213-E-006-002.

REFERENCES

[1] C. T. Pang et al., *A low-temperature wafer bonding technique using patternable materials*, J. Micromech. Microeng., 12, 611–615, (2002).
[2] R. J. Jackman et al., *Microfluidic systems with on-line UV detection fabricated in photodefinable epoxy*, J. Micromech. Microeng., 11, 263–269. (2001).
[3] J. Carlier et al., *Integrated microfluidics based on multi-layered SU-8 for mass spectrometry analysis*, J. Micromech. Microeng., 14, 619–624, (2004).

ULTRA-THIN AND CONDUCTIVE MEMBRANES FOR NANOMECHNICAL TRANSDUCERS

Tae June Kang, Misun Cha, Jaeha Shin, Yong Hyup Kim, and Junghoon Lee

School of Mechanical and Aerospace Engineering, Seoul National University, Korea

ABSTRACT

We introduce new multilayered nanocomposite membranes with a thickness of 25 nm freely suspended over large square openings with the side dimensions of 50-500 μm. The nanomembranes are electrically conductive due to the single-wall carbon nanotube (SWNT) interlayers, showing a very low electrical percolation threshold with the critical exponent value of 1.4±0.21. The present free-standing, ultra-thin nanomembranes have potentials for transducers with an extraordinary sensitivity and a dynamic range.

Keywords: nanocomposite, membrane, carbon nanotube, polyelectrolyte

1. INTRODUCTION

Measuring extremely small deflections with sensitive membranes is one of the most versatile approaches for pressure, acoustic, chemical and biomolecular sensing [1]. However, the conventional TD (top-down) technologies have limitations for the control of the thickness and process compatibility in order to achieve extreme sensitivity and multifunctionality with the membrane-type transducer. Multilayer films based on the bottom-up technologies have been extensively studied because they allow the fabrication of multifunctional molecular assemblies of tailored architectures. Moreover, the thickness of films can be easily controlled with a molecular precision [2]. We report a MEMS – compatible fabrication of freestanding nanomembranes with the integration of the TD and BU (bottom-up) technologies. Furthermore, a capacitive device was fabricated and tested for demonstrating the transducer configuration and characterizing the sensitivity and the resolution as a nanomechanical transducer.

2. EXPERIMENTAL

In the present study, we use one of the build-up methods, the alternating layer-by-layer assembly of polyelectrolytes with opposite charge, established to prepare ultra-thin and highly ordered polymer films [3, 4]. Nanocomposite membranes were designed as multilayer molecular composites made of the combination of polymeric monolayers (poly(allylamine hydrochloride)(PAH), poly(sodium4-styrenesulfonate)(PSS)) and SWNTs interlayer sandwiched between polyelectrolyte multilayers for electrical conductivity of nanomembranes. SWNT networks formed by spin-coating show very low electrical percolation threshold with a critical exponent value of 1.4.

We have developed a MEMS–compatible fabrication process for nanocomposite membranes with a thickness of 25 nm and freely suspended over large square openings with the side dimension of 50-500 μm. This process includes the integration of the TD and BU approaches for reliable and robust fabrication. To utilize the nanomembranes for a transducer, the components of a sensor including metal contact, spacer and electrodes are

978-0-9798064-0-7/μTAS2007/$20©2007CBMS

fabricated by using a conventional MEMS process. The fabrication scheme of membrane-based sensors is shown in Figure 1.

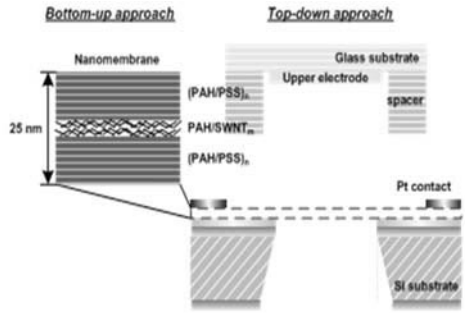

Figure 1. Fabrication scheme of membrane-based capacitive sensors

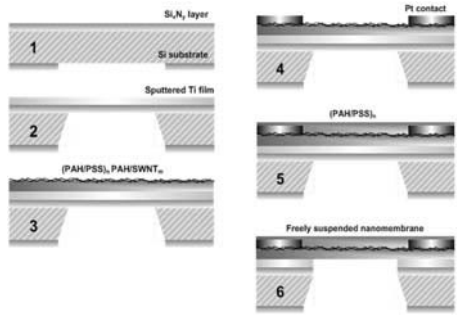

Figure 2. Schematic of the fabrication process

The fabrication process of the free-standing nanomembranes is described in Fig. 2. The process starts with low-stress LPCVD (low pressure chemical vapor deposition) silicon nitride deposition onto the cleaned (100)-silicon substrate (Fig. 2.1), followed by patterning the backside etch holes. The titanium film is sputter deposited after the backside bulk-etching (Fig. 2.2). The bottom-side of polymeric multilayer is deposited, and the SWNT networks are formed by using spin-coating method (see Fig. 2.3). To provide a metal contact, the platinum electrodes are sputter deposited by using a shadow mask to exclude a side-effect of the photo-lithographical technique such photoresist residue (see Fig. 2.4), and then, the upper-side of polymeric multilayer is deposited (see Fig. 2.5). To release the nanomembranes completely from the substrate, silicon nitride is removed by reactive ion etching, and the titanium film is wet-etched by dilute hydrofluoric acid (see Fig. 2.6).

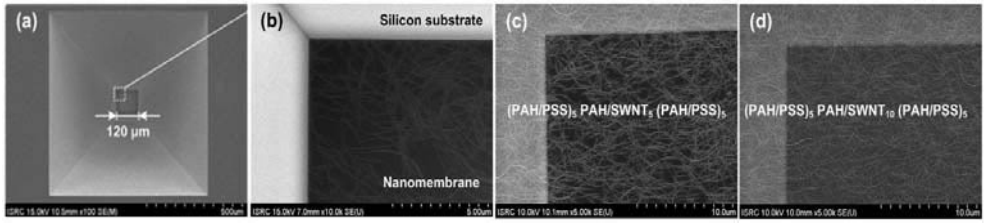

Figure 3. SEM images of released nanomembrane; backside views of (a) and (b), topside views of (c) and (d)

The SEM images of Figure 3 show the backside view of the suspended nanomembrane and the density control of SWNT interlayers. The central layer of SWNT networks sandwiched between the polyelectrolyte multilayers are clearly shown due to the low reflective index (1.63) of utilized polymeric materials.

3. RESULTS AND DISCUSSION

The thickness of the nanomembranes were precisely controlled in the range of single to hundreds nanometer by adjusting the number of polymer bilayers. The upper inset of Figure 4 shows a scanning electron microscopy (SEM) image of the scratched area where the thickness is measured. Figure 4 clearly demonstrates that the thickness of nanomembranes increases linearly with respect to the number of PAH-PSS bilayers.

The controlled volumes of water were used to measure the capacitance change due to the hydraulic pressure. We estimated the maximum deflection of the nanomembrane and the sensitivity of sensors by using the measured values and the shell mechanics (Fig.5). The maximum deflection estimated was 82.0 nm. The capacitive sensitivity of the sensors with respect to the hydraulic pressure was 80.0 aF/Pa which is comparable with the most other pressure sensors even though our device was not optimally configured for pressure sensing [5, 6].

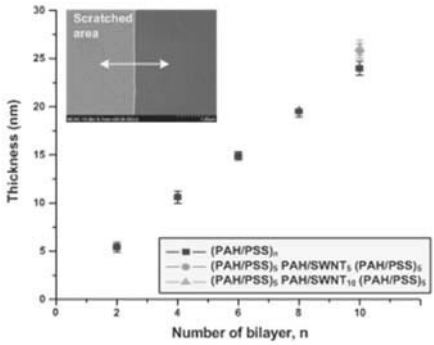

Figure 4. Thickness variation of nanomembranes with the various numbers of polymer bilayers and SWNT layers

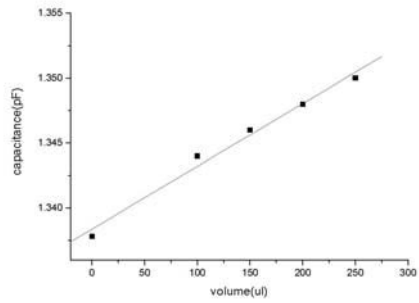

Figure 5. Capacitance variation with the hydraulic pressure change diameter of capillary covering the membrane was 5 mm

4. CONCLUSIONS

We fabricated nanomembranes with a thickness of 25 nm freely suspended over large (hundred micrometres) openings. They were fabricated with molecular precision by spin-assisted layer-by-layer assembly and the MEMS-compatible processing steps. Nanocomposite membranes were composed of multilayered molecular composites combined with polymeric monolayers and SWNT interlayer. The capacitive sensor with nanocomposite membranes was demonstrated and characterized. The present free-standing and ultra-thin nanomembranes can serve as components for a variety of highly sensitive sensors. We are currently developing a transducer with the nanomembrane for an extremely sensitive detection of molecular binding events on the surface.

ACKNOWLEDGMENT

This research has been supported by the Intelligent Microsystem Center (IMC; http://www.microsystem.re.kr) of the 21st century's Frontier R&D Projects sponsored by the Korea Ministry of Commerce, Industry and Energy, and funded by the Micro Thermal System Research Center (ERC) (R11-2001-095-03001-0).

REFERENCES

[1] R. Rodriguez, J. Chung, K. Lee, J. Lee, Bio/chemical Sensing by Thin Membrane Trasducers ASME International Mechanical Engineering Congress and Exposition, Anaheim, California, (2004).
[2] Gero Decher, Science, 277,1232,(1997).
[3] P. Bertrand, et al, Macromol. Rapid Comm., 21, 319, (2000).
[4] J. Cho, K. Char, J. Hong, K. Lee, Adv. Mater. 13, 1076, (2001).
[5] Y. Zhang, S. Massoud-Ansari, G. Meng, W. Kim, Nader Najafi, IEEE, 166, (2001).
[6] S. Chang, M. G. Allen, J. Micromech. Microeng., 14, 612, 2004

A HIGH-PERFORMANCE BONDING TECHNIQUE FOR HOMOGENEOUS POLYMERIC MICROFLUIDIC DEVICES

S.H. Ng, R.T. Tjeung and Z.F. Wang
Singapore Institute of Manufacturing Technology, SINGAPORE

ABSTRACT

We introduce a novel, high yield solvent bonding technique for creating polymeric microfluidic devices with minimal defects in the microchannels. The method is able to achieve high strength sealing with a clear, void-free bonding interface. Without introducing a foreign adhesive material, the bonding interface is homogeneous. Bonding can be achieved typically in 5 to 10 minutes with close to 100% yield. Samples have been successfully tested up to 6 bar (gauge) of internal pressure in the microchannel.

Keywords: bonding, solvent, microfluidics, polymer

1. INTRODUCTION

One of the critical steps in the fabrication of polymeric microfluidic devices is the bonding process. With conventional thermal bonding process, the microstructures deform easily, clogging the microchannels because of the high temperatures and pressures required for bonding to occur. When using adhesives, there is a risk of contamination and bio-/chemical- incompatibility. In addition, the material across the bonding interface will not be homogeneous introducing difficulties in optical detection. The thermal mismatch can cause delamination during elevated temperature operations such as polymerase chain reactions. Hence, a bonding technique for the creation of homogeneous polymeric microfluidic devices is required for some applications.

We found out in earlier tests that the problem with conventional solvent bonding was the deformation of the microchannel by the solvent remaining in it. Shah et al. [1] also reported that a drop of acetone left in their polymethyl methacrylate based microchannel for longer than 2–3 seconds would deform the microchannel. Kelly et al. [2] used melted paraffin wax as a sacrificial material to fill up the microchannels before solvent bonding. But the paraffin wax had to be removed later by an elaborate procedure.

2. EXPERIMENTAL

In our approach, the solvent starts dissolving the polymer only at elevated temperatures. This is critical because the bonding process can then be triggered through thermal control, allowing flexibility and time for the alignment of substrates. The technique involves first flooding of the bonding interface with a solvent to ensure that no air bubbles get trapped. The two pieces of polymer substrates are then aligned and placed onto the bonding fixture as seen in Fig. 1(a). The bonding fixture consists of a top and a bottom platen with sliding guide posts. Matching holes for the microfluidic device inlet/outlet are also created in the bottom platen. The two inlet/outlet of the bottom platen are connected to an external suction pump and a fluid (water, air, or oil) supply. The entire fixture is placed onto a hotplate with a dead weight (5 kg) on the top platen. As the heating begins, the fluid is drawn into the microchannel by the suction pump, displacing the solvent that is already in there. At a critical elevated temperature (70 to 80 °C at the bottom platen), the solvent

978-0-9798064-0-7/μTAS2007/$20©2007CBMS

starts dissolving the polymer at the bonding interface that is outside the microchannel and eventually achieves the bonding.

Polymethyl methacrylate (PMMA) substrates with dimensions 12.7 mm × 25.4 mm × 1.5 mm are utilized for the experiments. A 15 mm long microchannel (85 µm deep and 150 µm wide) is created on the surface of the PMMA sample by excimer laser (see Fig. 1(b)). Two 1 mm diameter holes are drilled on both ends of the microchannel. Another piece of blank PMMA is bonded to this structured substrate to create the sealed microchannels. Bonding is carried out by the displacement of the isopropanol (IPA) solvent in the microchannel with different fluids including: 1) air, 2) water, and 3) hydraulic oil. Five samples are used for each bonding scheme. Bonded samples are subjected to a bubble emission test [3] to estimate the pressure at which leakage starts to occur.

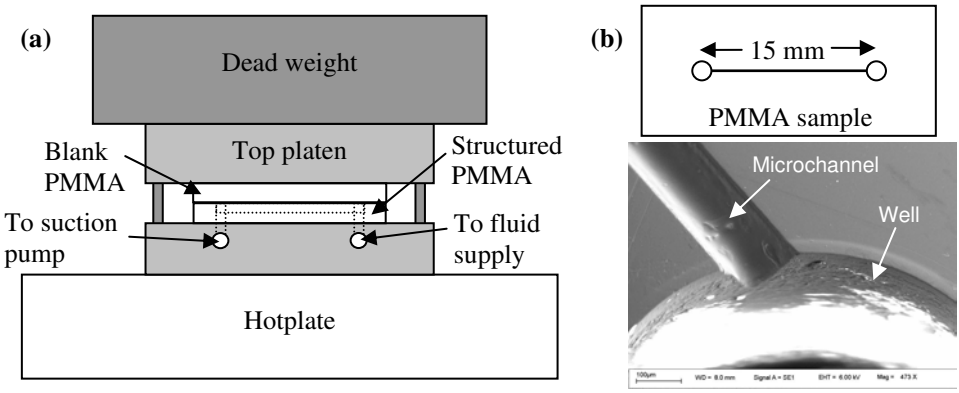

Figure 1. Bonding experimental setup (a), PMMA sample (b).

3. RESULTS AND DISCUSSION

The results were summarised in Table 1. The three schemes were compared to earlier work [3] where the pumping of fluid for IPA displacement was not employed (i.e. IPA remained in the microchannel throughout the bonding process). In the case where IPA remained in the microchannel during the process, strong bonding could be achieved. However, yield was low due to the frequent blockage of microchannels as a result of IPA dissolving the microchannel. Where the IPA was removed from the microchannel by suction (replaced by air), bonding was difficult to achieve for a range of suction pressure (150 to 600 mmHg below ambient measured at the pump). The suction pressure in the microchannel combined with capillary effects could be drawing IPA from the bonding interface into the evacuated microchannel. The starvation of IPA in the bonding interface then resulted in minimal bonding. The significant difference could be seen when water or oil was used where optically clear and strong bonding interfaces were obtained. Almost 100% yield was achieve in both cases (water and oil displacement). No significant difference was seen in samples bonded by both schemes. The samples bonded by the water and oil displacement schemes were filled with silver epoxy to examine the bonding interface just outside the microchannel. Figure 2 showed the top and cross sectional view of the microchannel. From the top view, the side of the microchannel was maintained straight but was not perfectly sharp, having a typical roughness of 5 to 12 µm.

Table 1. Bonding results for pumping different fluids through the microchannels.

No suction	Air	Water	Oil
Bonded	No Bond	Bonded	Bonded
Pass 6 bar pressure limit test	---	Pass 6 bar pressure limit test	Pass 6 bar pressure limit test
~ 50% yield, due to blockage	---	~ 100% yield	~ 100% yield

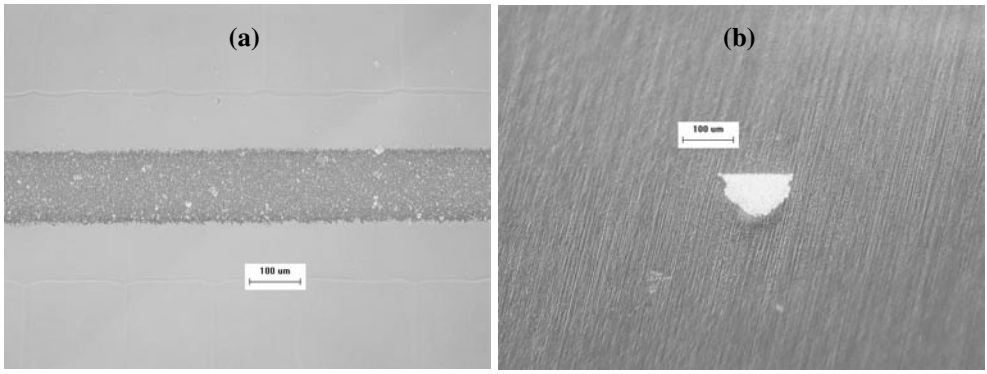

Figure 2. Bonded microchannel filled with silver epoxy: (a) top view, (b) cross sectional view.

4. CONCLUSIONS

The technique presented is suitable for microfluidic applications where an optically clear, homogenous and strong bonding interface is required. Results shows that an almost 100% yield can be achieved for the test vehicle with bonding time as short as 5 to 10 minutes. Multiple layers of polymer substrates can be bonded simultaneously with this technique for the creation of a three-dimensional network of interconnected microchannels.

ACKNOWLEDGEMENT

This research is funded by the Agency for Science, Technology and Research (A*STAR), Singapore.

REFERENCES

[1] J. J. Shah, J. Geist, L. E. Locascio, M. Gaitan, M. V. Rao, and W. N. Vreeland, *Capillarity induced solvent-actuated bonding of polymeric microfluidic devices*, Analytical Chemistry, 78, pp. 3348, (2006).

[2] R. T. Kelly, T. Pan, and A. T. Woolley, *Phase-changing sacrificial materials for solvent bonding of high-performance polymeric capillary electrophoresis microchips*, Analytical Chemistry, 77, pp. 3536, (2005).

[3] S. H. Ng, R. T. Tjeung, Z. F. Wang, A. C. W. Lu, I. Rodriguez, and N. F. de Rooij, *Formation of embedded microstructures by thermal activated solvent bonding*, Proc. Design, Test, Integration and Packaging of MEMS / MOEMS, 1, pp. 173, (2007).

A MICROFLUIDIC DEVICE FOR PRECISE PIPETTING

Chun-Wei Huang, Song-Bin Huang and Gwo-Bin Lee

Department of Engineering Science, National Cheng Kung University, Tainan, Taiwan

ABSTRACT

This paper presents a new microfluidic device capable of precise sampling and variable-volume pipetting. The pneumatic valves were designed to control the volumes of the dispensation channel with specific ratios such as 1×, 5× and 30×. By means of proper combinations of the ratios, variable-volume liquid can be easily dispensed with a volume ranging from 1× to 100×. This microdevice made of polydimethylsiloxane (PDMS) using soft lithography techniques can be easily integrated with other microfluidic devices for further micro-total-analysis-system applications.

Keywords: MEMS, microfluidics, micropipette, precise pipetting

1. INTRODUCTION

Precise pipetting of biological samples and reagents is crucial in biochemical analysis applications, especially in the micro and sub-micro-liter range. Precise pipetting usually involves well-controlled and precise aspirating/dispensing of a fixed volume of liquids/airs. Therefore, it is challenging for micro mechanic pumps to perform the precise pipetting. In order to carry out precise dispensing of a fix amount of samples, microfluidic chips usually use a pipetting device, which may complicate the fabrication and operation process [1]. Thus, this paper presents a new microfluidic device capable of not only precise sampling, but also variable-volume pipetting. It consists of a dispensation microchannel with multiple widths and several pneumatic microvalves. Liquids in the sample reservoir can be extracted to the microchannels pneumatically and then dispensed to the collection reservoir. By means of proper combinations of the ratios, variable-volume liquids can be precisely dispensed with a volume ranging from 1× to 100×.

2. DESIGN AND FABRICATION

A schematic diagram of the device is shown in Fig. 1. It consists of a dispensation microchannel with multiple widths and several pneumatic microvalves. The widths of microchannel were designed with the dimensions of 500, 800 and 1500 μm, respectively. The pneumatic valves were used to control the volumes of the channel with specific ratios such as 1×, 5× and 30×. Liquids in the sample reservoir can be extracted to the microchannels pneumatically and then dispensed to the collection reservoir. Table 1 shows the valve actions in terms of specific ratios of the dispensed volume. By means of proper combinations of the ratios, variable-volume liquids can be precisely dispensed with a volume ranging from 1× to 100×. In the study, the depth of the microchannel is 100 μm so that the volumes of various ratios are 0.06, 0.3 and 1.8 μl, respectively. Moreover, in order to avoid the bubble formation while the liquid was loaded into the channel, especially at the end of the loading process, an "escaping channel" was designed to allow the gas exhausting by stopping the liquid at the escaping side channel due to the hydrophobic effect [2]. The schematic diagram of the "escaping channel" is shown in Fig. 1. The micropipette was fabricated using a SU-8 template and a PDMS casting process. Figure 2 shows a

978-0-9798064-0-7/μTAS2007/$20©2007CBMS

photograph of the micro pipetting device. The dimensions of the chip are measured to be 30 mm × 25 mm, respectively.

3. RESULTS AND DISCUSSION

Figure 3(a) shows a series of photographs for dispensing samples with various specific ratios. The desired volumes of liquids can be generated by combining various specific ratios. Figure 3(b) shows a CCD image of the hydrophobic effect. From the image we can clearly see that the liquid was successfully stopped in the narrow side of the escaping channel due to the hydrophobic effect. The performance of the micropipette was compared with a traditional pipette. Ten pieces of Eppendorf tubes were numbered and weighted. Then the ink was aspirated and injected into the specific Eppendorf tubes individually with various volumes. This process was also performed by using the micropipette. Figure 4 shows the results for the experiment. It can be clearly seen that the micropipette can dispense liquids precisely. The slope of the regressive line is almost the same as a theoretical line. Moreover, a titration experiment was performed to verify the accuracy of the micropipette. Sodium hydroxide (NaOH) was used to titrate benzoic acid (C_6H_5COOH). The concentration and pH value of the sodium hydroxide are 0.04 Mol/L and 12.5 and 0.025 Mol/L and 2.9 for the benzoic acid. 30-μl benzoic acid was stored into an Eppendorf first and 3-μl sodium hydroxide was then aspirated and injected into the Eppendorf tube by using the micropipette. After mixing, the pH value of the mixture was measured. The processes were repeated until approaching the equivalent point while the volume of sodium hydroxide was reduced to 0.3 μl. All of the processes were also performed by using a commercial pipette. Figure 5 shows the titration curve indicating that the performance of the micropipette is almost the same as the one from the commercial pipette. The maximum deviation between these curves is about 0.3. The test results of these two experiments show that the developed micropipette is promising for further micro-total-analysis-system applications.

4. CONCLUSIONS

In summary, the developed microfluidic device consisting of a dispensation microchannel with multiple widths and several pneumatic microvalves was capable of dispensing liquids precisely. By means of proper combinations of the ratios, variable-volume liquids can be precisely dispensed with a volume ranging from 1× to 100×. The experimental results showed the performance of the micropipette is comparable with the commercial ones. The developed microdevice is applicable for drug dosing or other biomedical applications.

ACKNOWLEDGEMENTS

The authors would like to thank financial support from the National Science Council in Taiwan.

REFERENCES

[1] N. Szita, R. Sutter, J. Dual and R. A. Buser, *A micropipetter with integrated sensors*, Sensors and Actuators A, 89, pp.112-118 (2001).

[2] T. Fujii, *PDMS-based microfluidic devices for biomedical application*, Microelectro. Eng. 61-62, pp.907-914(2002).

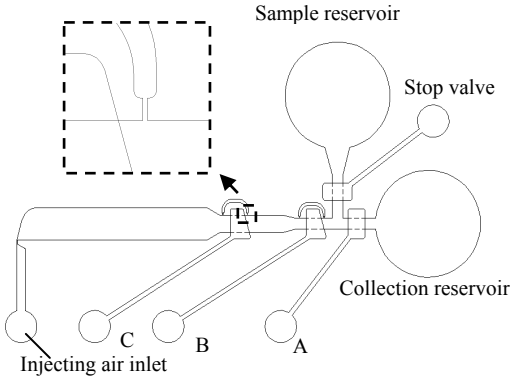

Figure 1 Schematic illustration of a microfluidic device for precise pipetting. It consists of a dispensation microchannel with multiple widths and several pneumatic microvalves.

Table 1 Specific volume ratios vs. valve actions

Ratio	Controlled valves			Dispensed volume
	A	B	C	(μl)
1×	X	X		0.06
5×	X		X	0.3
30×	X			1.8

Note: "X" indicates the valves activated.

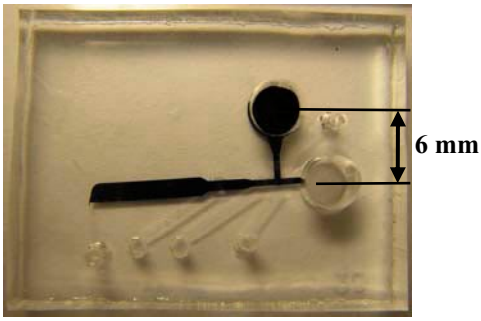

Figure 2 A photograph of the microfluidic chip for precise pipetting.

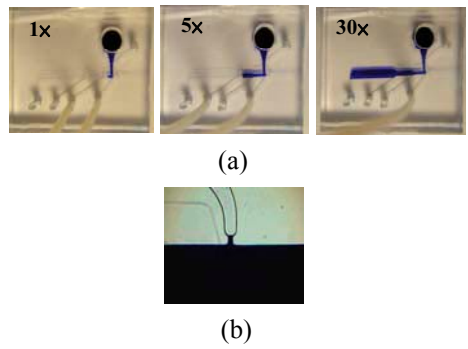

Figure 3 (a) A series of photographs for dispensed samples with various specific ratios. (b) A CCD image of the hydrophobic effect. The liquid is successfully stopped in the narrow side of the escaping channel.

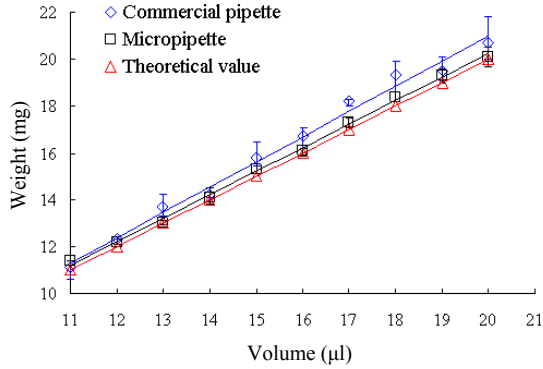

Figure 4 Test results of the dispensed samples showing that the micropipette can dispense samples precisely.

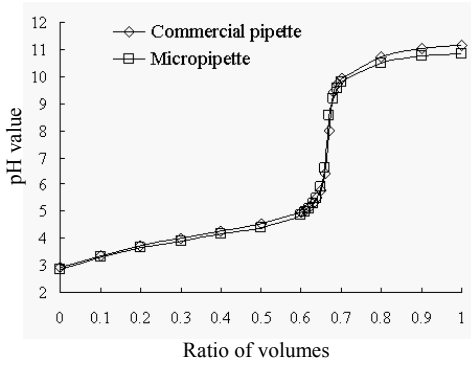

Figure 5 Test results of the titration experiment. The titration curve of the micropipette is consistent with the one from a commercial pipette.

A MICROFLUIDIC SWITCHBOARD

Himanshu J. Sant[1], Tammy Ho[1] and Bruce Gale[2]

[1]Department of Bioengineering and [2]Department of Mechanical Engineering
Utah State Center of Excellence for Biomedical Microfluidics, University of Utah

ABSTRACT

The Microfluidic Switchboard is an array of microvalves and microchannels which create a large scale microfluidic platform that will automate macroscale, bench-top laboratory protocols and package them in low cost, portable lab-on-a-chip systems that can be used for clinical diagnostics, environmental monitoring, pharmaceutical drug discovery and chemical synthesis. This paper describes characterization of actuators for such valves and preliminary design and fabrication of scalable microvalves built entirely on printed circuit board (PCB) material.

Keywords: Microvalves, actuators, phase-change material, PCB

1. INTRODUCTION

The current industrial approach to addressing large scale fluidic manipulation is done using enormous robotic workstations that are bulky, expensive and labor-intensive. There are few reports to create microfluidic multiplexing using pneumatics[1] and binary tree logic[2] for such applications. Several devices have been created to control fluid flow on the microscale but these are also cumbersome or involve complex fabrication procedures[3]. The fluidics themselves are compact and able to perform a variety of procedures, but the fluidic valves are actuated using air pressure, which means even more valves. The system of 'valves controlling valves' not only means more valves, but an entire air routing system consisting of control channels, valves and a pressure source. It should also be noted that the ability to produce large number of fluidic manipulations by these devices resides in the valve and the control channel layout and often requires a complete change in design for even a small change in a particular fluidic manipulation protocol.

The Microfluidic Switchboard completely eliminates external air routing system by containing less-expensive valves that seal the fluidic channel equally well and actuated with only an electric current. The scalability of these valve units makes it possible to design robust microfluidic devices so that the ultimate complexity and applications of highly dense functional valve elements is nearly endless. The complete package will consist of a small, disposable card with only electrical connections for fluidic control and sample inputs.

2. EXPERIMENTAL

Essentially, this design is a multilayer microfluidic system made of one layer containing fluidic microchannels, a silicone membrane layer, and an actuation layer containing an expanding phase-change-material as shown in Figure 1. The melting of a paraffin wax phase-change material is induced using a joule heating-based in-situ heater and not an external thin film[4] or optics[5] based heating mechanism.

The In-situ heater is a composite of paraffin wax and graphite, and requires only electrically conductive traces as the interface. Resistive heating due to the passing of electrical current through graphite powder dispersed in paraffin wax results in melting and

978-0-9798064-0-7/μTAS2007/$20©2007CBMS

expansion of the wax which in turn expands the thin silicone membrane to induce actuation.

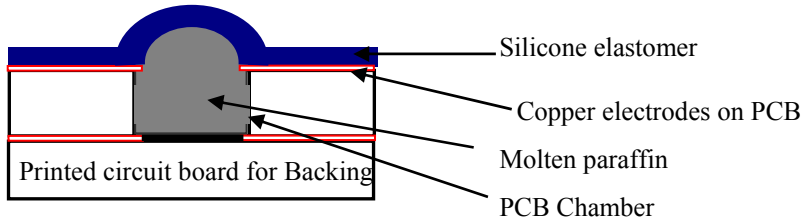

Figure 1 Architecture of the phase-change material based actuator

Valves are created by integrating these actuators with microfluidic channels. Microchannels are created using a thin polymeric liner with press-cure adhesive on both sides. Xurography is used to create the microfluidic channels[6].

3. RESULTS AND DISCUSSION

The actuation of the valve membrane is done in less than a second at only 0.2 W per valve for ~ 300 μm actuation heights as shown in Figure 2.

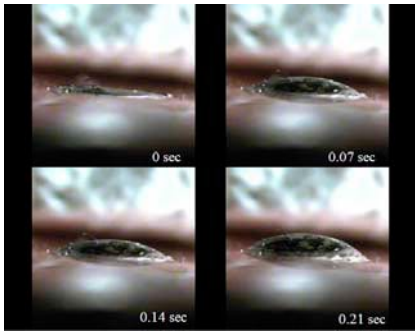

Figure 2. Actuation of the membrane

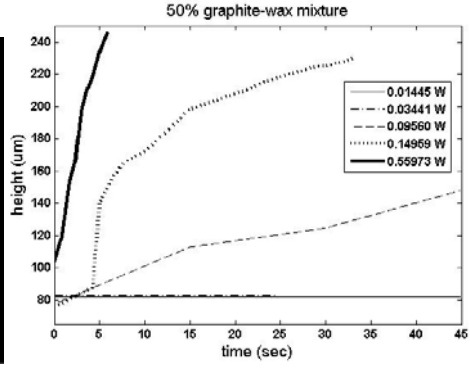

Figure 3. A plot of dot height vs. power and/or actuation time

The use of in-situ heater allows for efficient power usage and very fast actuation. The uniformly dispersed electrically conductive matrix provides a large surface area for heating, which provides for better performance when compared to other reported methods[4]. Figure 3 shows the typical actuation plots for a 50 % graphite-wax mixture. It can clearly be seen that actuation of 200 μm can be achived very fast and it should also be noted that the typical microchannels are much thinner (close to 100 μm) and such channels would require much less power and actuation times.

To demonstrate the scalability of these actuators, a medium scale array of 64 individually addressable actuators is built using PCB as substrate as shown in Figure 4. An electronic circuit with the power programming has been developed that can address each actuator individually to maintain certain height of the membrane.

The raising and lowering of the actuator membrane was used to block or open the fluidic channel respectively. Complete blocking of fluid flowing in a pressure-driven channel (with one syringe pushing fluid at the inlet and another drawing fluid at the outlet) was

observed when the valves were activated. Arrow in Figure 5 shows the valve area at 0 S. After the valve activation, as the time progresses vacuum is created just after the valve area indicating the stoppage of the flow downstream of the valve.

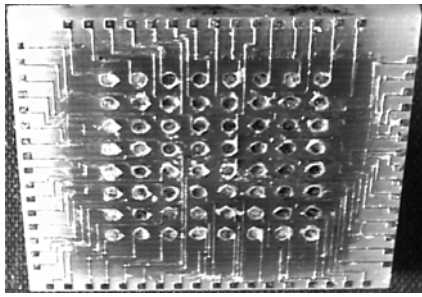

Figure 4. Array of actuators on PCB to be integrated with PDMS microchannels

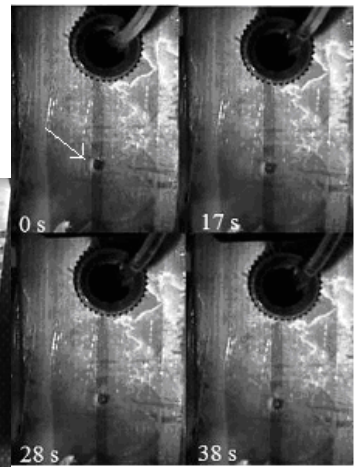

Figure 5. Integration of the actuator with the fluidic channel.

4. CONCLUSIONS

A novel actuation mechanism that can be integrated to microfluidic circuit has been demonstrated and characterized. The performance of this actuator is found to exceed similar devices and is easily integrated with fluidics to create microvalves. Preliminary testing of the microvalve using this technology is encouraging. PDMS fluidic circuitry is being integrated with the 64 actuator system for more complex on-chip analyte manipulation. Array of such valves can be used to perform complex fluidic manipulations of picoliter volume without any outside control inputs other than an electrical connection.

ACKNOWLEDGEMENTS

Partial funding was provided by Utah State Center of Excellence grant.

REFERENCES

1. T. Thorsen *et al*, *Microfluidic Large-Scale Integration*, Science, 298, 580 (2002)
2. W. Grover *et al*, *Development and multiplexed control of latching pneumatic valves using microfluidic logical structures*, Lab Chip, 6, 623 (2006)
3. K. Shaikh *et al*, *A Modular Microfluidic Architecture for Integrated Biochemical Analysis,* PNAS, 102, 9745 (2005)
4. B. Samel *et al*, *A Thermally Responsive PDMS Composite and Its Microfluidic Applications,* JMEMS, 16, 50 (2007)
5. J. Park *et al, Multifunctional microvalves control by optical illumination on nanoheaters* and its application in centrifugal microfluidic devices, Lab Chip, 2007, 7, 557–564
6. D. Bartholomeusz *et al, Xurography: Rapid Prototyping of Microstructures Using a Cutting Plotter* JMEMS, 14, 1364 (2005)

FABRICATION OF SUSPENDED ELECTROOSMOTIC MICROCHANNELS FROM SACRIFICIAL POLYMER FIBERS

Scott M. Berry[1], Thomas J. Roussel[1,2], Scott D. Cambron[1,2], Robert W. Cohn[3], and Robert S. Keynton[1,2,3]

Departments of Mechanical Engineering[1], Bioengineering[2], and the ElectroOptics Research Institute and Nanotechnology Center[3]; University of Louisville, Louisville, KY, USA

ABSTRACT

Suspended microchannels have been created by utilizing sacrificial polymer fibers fabricated from solvated polymer solution with a novel direct-write technique. Characterization of this fiber drawing process has demonstrated correlation between solution concentration and fiber diameter, thereby proving a mechanism for controlling microchannel inner diameter. These hydrophilic microchannels, with diameters ranging from 4 to 100 μm, were loaded with buffer solution and electroosmotic flow was induced.

Keywords: Microfluidics, Polymer Fibers, Electroosmotic Flow, Direct-Write

1. INTRODUCTION

The ability to fabricate three-dimensional microfluidic networks has enabled the design of complex devices in the fields of MEMS and μTAS as channels are no longer constrained within a single plane. Commonly, 3D devices are constructed by layering planar monoliths of polymer with imbedded microchannels to form contiguous fluid pathways [1, 2]. Recently, electrospinning has been employed to produce polymer fibers used as sacrificial structures in the production of nanochannels [3]. Although useful, this electrospinning technique does not permit precise positioning of these fibers. We propose an additional fabrication method which facilitates the construction of 3D suspended microchannels by utilizing precisely-positioned polymer fibers as sacrificial scaffolds. These fibers are fabricated using a direct-write technique recently developed by our group for precision fabrication of 3D suspended micro- and nanoscale polymer fibers by drawing solvated polymer solution with a micromanipulator-controlled, solution-filled syringe (Fig. 1) [4].

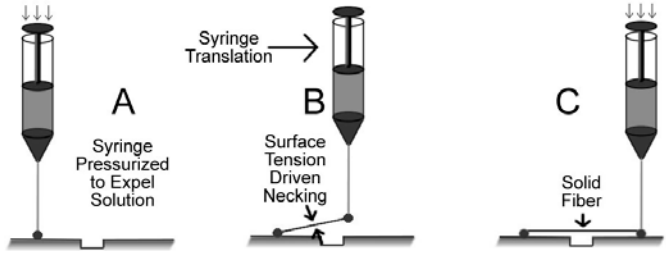

Figure 1 – Direct-write fiber fabrication. a) Syringe pressurized to expel polymer solution into contact with substrate. b) Syringe moved to desired endpoint (1.25 nm resolution). c) Syringe pressurized to expel solution and create second attachment point for fiber.

2. EXPERIMENTAL

The diameters of the fibers produced by the direct-write method (Fig. 1) must first be characterized since fiber diameter ultimately determines the inner diameter of the

978-0-9798064-0-7/μTAS2007/$20©2007CBMS

subsequent microchannel. As such, solutions of 996 kDa poly(methyl methacrylate) (PMMA) dissolved in chlorobenzene were prepared with concentrations ranging from 22% to 26% (by wt.). These solutions were then loaded into the direct-write apparatus (Fig. 1) and drawn into fibers with lengths ranging from 2 mm to 20 mm. Fiber diameter was quantified using a scanning electron microscope (SEM) to measure each fiber in three locations (50 μm from each end and at the middle of fiber).

PMMA fibers produced with the direct-write technique were coated and dissolved to fabricate the suspended microchannels (Fig. 2). First, fibers were coated with a thin (25 nm) layer of borosilicate glass (BSG) via RF sputtering to establish a hydrophilic inner channel wall. Sputtering was performed at low power (140 W) in three layers to prevent excessive heating and mitigate thermal stresses arising from dissimilar thermal expansion of the PMMA and BSG. Next, a 10 μm-thick coating of Parylene was deposited via vapor-phase deposition to enhance the structural integrity of the channel. Access holes were drilled using a micromilling machine and the PMMA was removed via dissolution in acetone and critical point drying in liquid CO_2 to yield hollow, suspended structures.

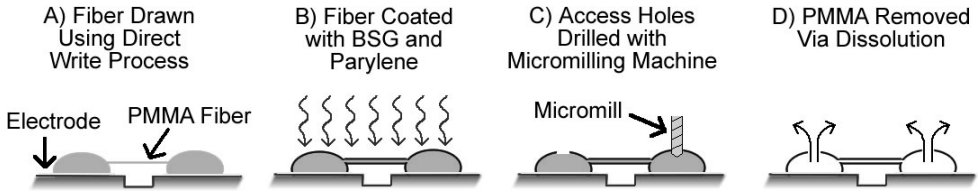

Figure 2 – Fabrication of microchannel from PMMA fiber.

An applied electric field of 25 V/cm was utilized to induce electroosmotic flow (EOF) in microchannels suspended between electrodes on either side of a trench. These channels were filled with phosphate buffer solution (10 mM, pH 6.1) and seeded with 1 μm-diameter fluorescent tracer particles (Duke Scientific). Particle imaging velocimetry (PIV) was employed to quantify the motion of this solution by capturing two fluorescent images in rapid sequence (ΔT = 60 ms) and using the change in tracer particle position to elucidate a vector map of the EOF field with a resolution of ~2 μm.

3. RESULTS AND DISCUSSION

The direct-write method was successfully utilized to draw PMMA fibers and diameter was found to increase with both increasing solution concentration ($P<0.005$) and decreasing length ($P<0.05$). The ability to modulate fiber diameter through variance of the solution concentration provides a mechanism by which fiber diameter can be controlled. SEM imaging of the fibers indicated a smooth surface morphology and an average diameter standard deviation along the length of an individual fiber that was 40% of the mean diameter.

Suspended microchannels were fabricated with inner diameters ranging from 4 μm to 100 μm (Fig. 3). Electroosmotic flow was successfully induced upon application of an electric field between the two electrodes positioned on either side of the microchannel. This flow was visualized and quantified with PIV, and it was demonstrated that flow proceeded toward the negative electrode and flow direction could be controlled by switching the electric field polarity (Fig. 4).

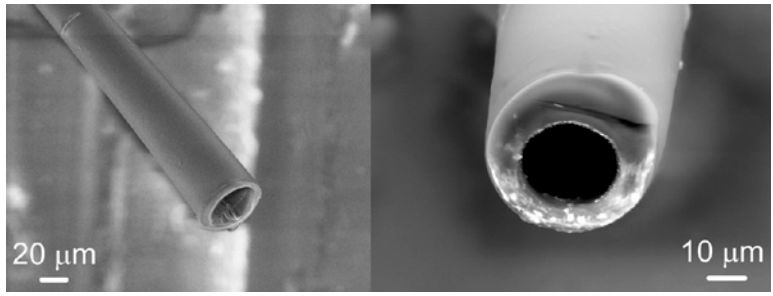

Figure 3 - SEM images of microchannels cleaved in liquid nitrogen.

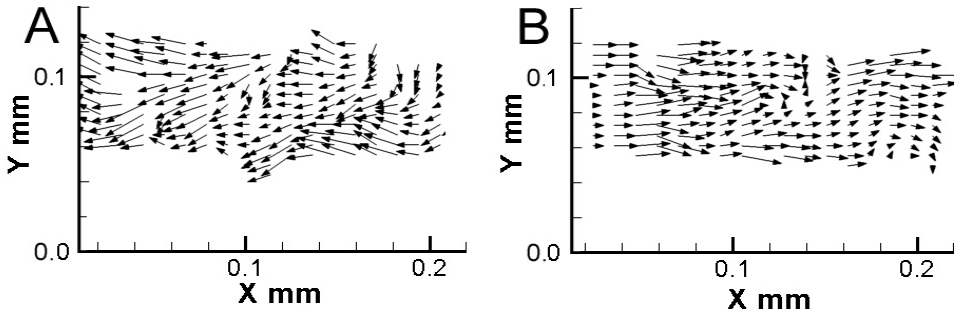

Figure 4 – PIV imaging of EOF induced by a) -25 V/cm electric field (negative electrode at left) and b) +25 V/cm electric field (negative electrode at right).

4. CONCLUSIONS

The proposed technique for microchannel fabrication enables the development of more advanced EOF devices by eliminating restrictions imposed by current 3D microfluidic fabrication technology. The inner diameter of these hydrophilic microchannels can be controlled through variance of the solution concentration. Also, the channels are freely suspended and can be fabricated on substrates with 3D features, allowing the *in situ* fabrication of inter-connecting channels as well as interfacing with existing MEMS components.

ACKNOWLEDGEMENTS

This investigation was funded by National Science Foundation NIRT Program (ECS-0506941), NSF PFI Program (EEC-0438604), and National Aeronautics and Space Administration cooperative agreement (NCC5-571).

REFERNECES

1. Anderson, J.R., Chiu, D. T., Jackman, R. J., Cherniavskaya, O., McDonald, J. C., Wu, H., Whitesides, S. H., Whitesides, G. M., Analytical Chemistry, 72, p. 3158-3164, 2000.
2. Jo, B.H., Van Lerberghe, L. M., Motsegood, K. M., Beebe, D. J., Journal of MEMS, 9(1), p. 76-81, 2000.
3. Verbridge, S.S., Edel, J. B., Stavis, S. M., Moran-Mirabal, J. M., Allen, S. D., Coates, G., Craighead, H. G., Journal of Applied Physics, 97, p. 124317, 2005.
4. Berry, S.M., Harfenist, S. A., Cohn, R. W., Keynton, R. S., Journal of Micromechanics and Microengineering, 16, p. 1825–1832, 2006.

MICROFLUIDIC DISK SAMPLER FOR BIOLOGICAL DETECTION

Wei-Cheng Tian[1], Yu Zhao[1], Shashi Thutupalli[2], Atanu Phukan[2], Christopher Keimel[1], Oliver Boomhower[1], Michael Burrell[1], Li Zhu[1]

[1]GE Global Research Center, Niskayuna, NY 12309, USA

[2]John F Welch Technology Center, Bangalore Karnataka, 560066, INDIA

ABSTRACT

A high throughput, portable biosensor has been designed, fabricated, and tested. The device consists of a disk with rings of pillars that separate antibody coated capturing beads by size. Two different size beads have been separated at up to 100% separation efficiency for one bead size, and 80% for another. Laser RAMAN spectroscopy is used to detect the presence of pathogens bound by Surface Enhanced Raman Spectroscopy (SERS) particles.

Keywords: Microfluidic disk, pathogen/bio detection, MEMS Technologies, Surface Enhanced Raman Spectroscopy (SERS)

1. INTRODUCTION

Detection of biological agents or pathogens in a fluid sample involves three main steps, (a) Sample collection (filtration, rinse and pre-concentration), (b) Sample preparation (lysis, extraction, separation, and amplification) and (c) Sample analysis (labeling, selective binding/recognition, and detection). All of these steps are equally important for effective detections of pathogens. Many separation techniques exist in literature for separating pathogens, such as gravity enabled techniques, electrophoresis, dielectrophoresis, optical-based techniques, etc. A variety of separation methods were benchmarked and a tradeoff matrix was used to determine that the microbead-based disk sampler device is the design most suitable for the multiplexed bioassay in our application.

2. DESIGN AND FABRICATION

We propose a method of separating pathogens using high-aspect-ratio micro-pillars patterned on a planar disk. Unlike other microfluidic disks for bio-assays [1-2], our design uses the entire disk surface to facilitate flow instead of confining flow within channels. This allows efficient filtration of large sample volumes, and concentration of the bead-captured pathogens into a confined area. Further, distinct from conventional pillar based filtration devices [3], our design enables both spatial and spectral multiplexing for high sensitivity detection. Devices were fabricated using glass/silicon or polycarbonate.

Our goal is to capture pathogens on beads via antibody-antigen interaction and then separate these bead-pathogen complexes based on their size in a microfluidic disk. Surface Enhanced Raman Spectroscopy (SERS) labels targeted for specific pathogens are flowed through the disk which bind to pathogen-bead complexes. Finally, the detection is achieved through Raman laser spectroscopy. The combination of spatial separation and spectral multiplexing may enable analysis of up to 20 different pathogens in a single sample.

978-0-9798064-0-7/μTAS2007/$20©2007CBMS

Numerical modeling was performed to optimize the pillar shape and dimensions for separations (Fig. 1). The simulation results were later validated against experimental data and show good correlation (Fig. 2). The first device design consists of two concentric rings of pillars with a pillar spacing of 50um for the inner ring, and 25um for the outer ring. Pillar height was determined to be 100um with an aspect-ratio of 4:1.

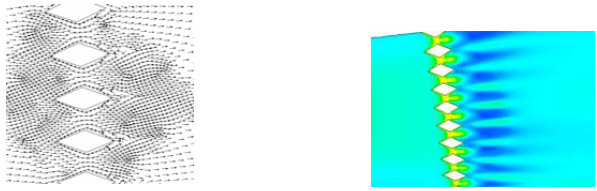

Figure 1. Flow profile (left) and velocity distribution (right) around diamond shape pillar structures (Top view)

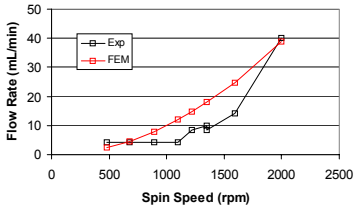

Figure 2. CFD flow model validation

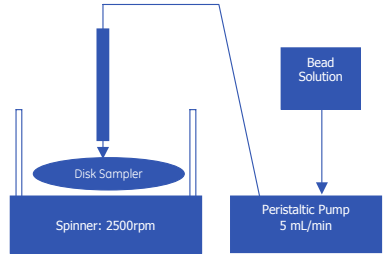

Figure 3. Microfluidic disk sampler operation & test set up

3. EXPERIMENTAL

To test the ability of the inner and outer rings on disks to capture the beads, two sizes of beads 87um and 41um were used. The disk sampler operational and experimental setup is shown in Fig. 3. The typical results of beads distribution at the pillar rings are shown in Figures 4 & 5.

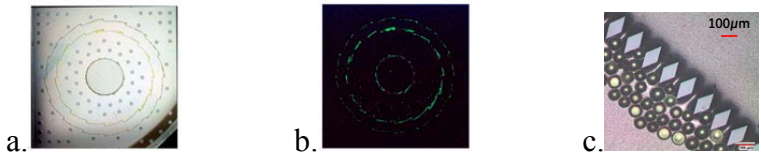

Figure 4. Photos of Design 1 (a) optical photography and (b) fluorescence microscope (c) close up with beads (Large bead diameter 87um and small bead diameter 41um)

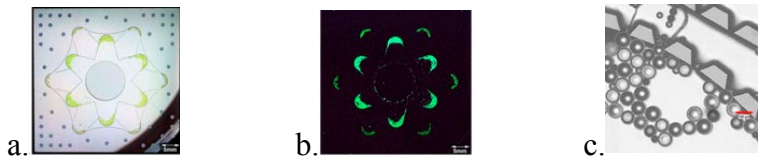

Figure 5. Photos of Design 2 (a) optical photography and (b) fluorescence microscope (c) close up with beads (Large bead diameter 87um and small bead diameter 41um)

4. RESULTS AND DISCUSSION

The performance of the disk sampler is measured by the separation efficiency (SE), the percentage of correct beads for a ring and total number of beads in that ring counted using optical microscopy and image analysis software. For Design 1, the SE of the outer ring remained at 100% while SE of inner ring is ~56% due to clogging. Design 2 aimed to minimize clogging and to confine beads in more localized regions for detection. For the 8700 total beads scenario, the SE of inner ring for design two reached 75% (Fig. 6).

In a separate experiment, the beads were labeled with SERS-active nanoparticle tags. The SERS tags were constructed with QSH (2-quinoline thiol) as a reporter molecule. The confined beads on the disk were probed with a focused laser, and the resultant Raman signal was measured. A strong signal from the attached Raman tags is observed (Fig. 7) and this demonstrates the capability of combining spatial selection with spectroscopic detection.

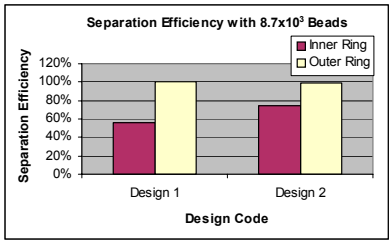

Figure 6. Separation efficiency of two designs

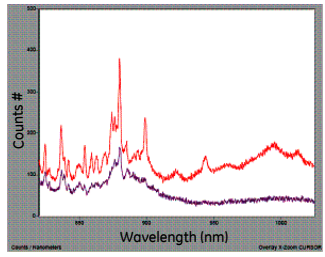

Figure 7. RAMAN spectra of SERS particles on microbeads captured by disk sampler using QSH (2-quinoline thiol) as detection molecule

5. CONCLUSIONS

A disk sampler for biological detection has been designed, fabricated, and tested successfully. Future work will focus on improve the multiplexing by increasing the range of bead sizes for separation and refining bio-assays and detection.

ACKNOWLEDGEMENTS

This work was supported by the GE research funding. The authors thank all the team members, from Micro & Nano Structures Organization, Material Analysis & Chemical Sciences Organizations, and Energy and Propulsion Technologies Organization, who have contributed to the success of this program.

REFERENCES

[1] M. J. Madou, l. J. Lee, S. Daunert, S. Lai, and C.-H. Shih, “Design and Fabrication of CD Like Microfluidic Platforms for Diagnostics: Microfluidic Functions”, Biomedical Microdevices 3:3, pp. 245-254, (2001).

[2] J. V. Zoval and Marc J. Madou, “Centrifuge-based Fluidic Platforms”, Proceedings of the IEEE, 92, no. 1, pp. 140-153, (2004).

[3] R. Carlson, C. Gabel, S. Chan, and R. Austin, “Self-Sorting of White Blood Cells In a Lattice,” Phys. Rev. Lett. 79, pp. 2149–2152, (1997).

MONOLITHIC MULTILEVEL MICROFLUIDIC NETWORKS WITH INTEGRATED MEMBRANE: APPLICATIONS FOR ON-CHIP CELL CO-CULUTRE AND FABRICATION OF BIOMIMETIC CULTURE CHAMBER

M. C. Liu and Y. C. Tai
California Institute of Technology, USA

ABSTRACT

A novel method for monolithically fabricating a multilevel microfluidic structure with an integrated membrane, which allows mass transport between the different levels of microfluidic networks, is presented. Using biocompatible parylene C (poly(chloro-p-xylylene)) as the structural material, a two-level microfluidic device was fabricated. Two applications were demonstrated: 1) the construction of a biomimetic microfluidic culture chamber with uniform microenvironment and 2) the fabrication of microchambers for cell co-culture. The surface micromachining technique simplifies the process for incorporating membranes into microfluidic networks and favorably avoids multilayer bonding.

Keywords: Parylene, Cell Culture, Three-Dimensional Microfluidics, Membrane

1. INTRODUCTION

In recent years, the use of membrane in microfluidics has increased, and the versatile functionalities of the membranes have been demonstrated in various devices for sample preparation, chemical reactors or cellular studies [1]. Many works have been done to incorporate membranes into microfluidics, and a simple and reliable method for integrating the membrane structure is highly desirable. In our previous work, we have demonstrated the use of surface micromachining technology to monolithically fabricate three-dimensional (3-D) microfluidic networks [2]. Here, we expand this technology to create an integrated membrane at the interface of the microfluidic channels. Surface micromachining enables chips to be conveniently batch-fabricated and the integrated method avoids sealing problems when incorporating membrane into devices. In addition, integration with 3-D microfluidic networks expands the complexity of applications for membrane devices. The application of our fabrication technology to cell-related studies was demonstrated.

2. DESIGN

Our device comprises two-level microfluidic networks and a membrane structure that is positioned in between the two microfluidic channels (Fig. 1). Each microfluidic level has its own inlet and outlet ports for sample introduction. Parylene C is chosen as the structural material because of its compatibility with surface micromachining processes, which enable 3-D microfluidic networks to be fabricated monolithically. Other advantageous properties of parylene C include its biocompatibility, optical transparency and chemical inertness. The device is built on a glass substrate for ease of observation by microscopy.

978-0-9798064-0-7/μTAS2007/$20©2007CBMS

3. EXPERIMENTAL

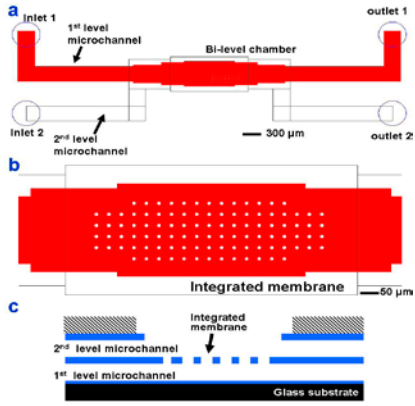

Figure 1. Design layout of device. (a) Top view. (b) Bi-level chamber with integrated membrane in between the two fluidic levels. (c) Cross-section.

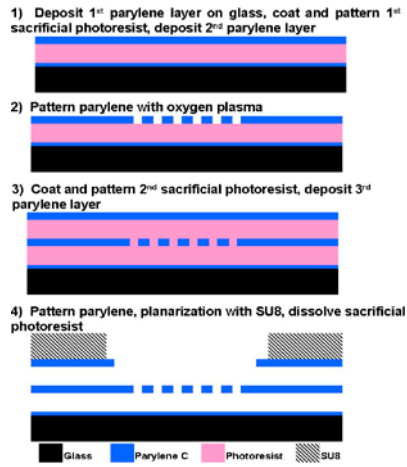

Figure 2. Process flow

The fabrication process is shown in Fig. 2. A first sacrificial photoresist (15 µm) was defined on parylene-coated glass substrate for the 1st-level channels. A second layer of parylene (10 µm) was deposited and parylene was patterned using oxygen plasma to fabricate pores in the membrane. By modifying the mask of this pattering step, membranes with different pore sizes can be created, and membranes with 10-, 20-, and 40-µm pores were made. A second sacrificial photoresist (30µm) was defined for the 2nd-level channels. A third layer parylene was deposited and patterned, followed by chip planarization with SU8 (100 µm). The chips were soaked in IPA to dissolve the sacrificial photoresist, and the remaining hollow parylene structures become the fluidic networks (Fig. 3a and 3b). To package the device, a piece of PDMS with punched holes was aligned under the chip and they were clamped together by two pieces of acrylic. Tubes were plugged into the holes of the PDMS and on-chip experiments were observed with a microscope (Fig 3c and 3d).

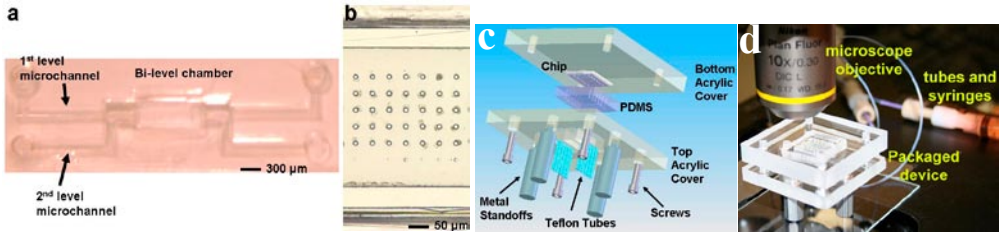

Figure 3. (a) Fabricated device. (b) Integrated membrane with 10 µm pores. (c) Device packaging (d) Testing setup

4. RESULTS AND DISCUSSION

One application of this fabrication method is for fabricating a culture chamber that mimics the *in vivo* tissue environment, where transport of molecules to the cells occurs by interstitial flow (Fig. 4a). With a two-level microfluidic configuration, our cell-culture chamber is separated from the fluid delivery channel, and shear stress, which can be detrimental to many types of cells, is minimized [3]. A FEMLAB simulation shows that the flow velocity gradient inside the culture chamber is minimal (Fig. 4c). With this

configuration, culture media components delivered into the chamber during perfusion can achieve a uniform distribution. The membrane structure allows mass transport of solutions between the two levels of fluidic channels (Fig. 4d). The device can also be used for cell co-culture. Different cells can be loaded into different levels of chamber, and the membrane allows communication between the two levels (Fig. 5). More levels of channels can be constructed to simulate complex *in vivo* microstructures.

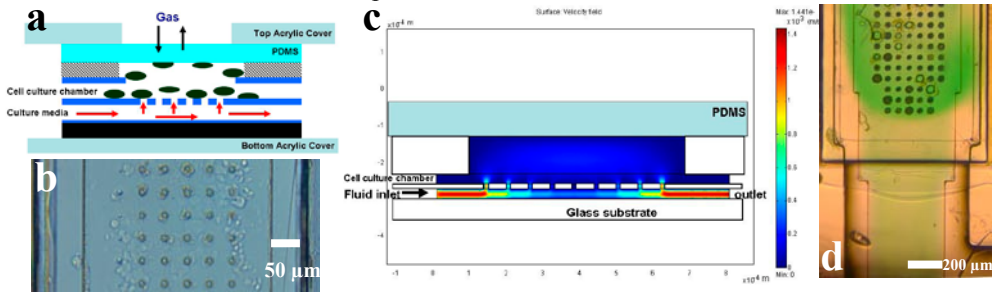

Figure 4. Bi-level cell-culture chamber. (a) Device operation. (b) Cells inside the 2nd level chamber. (c) Fluid velocity simulation. (d) Green solution injected into the 1st level channel can enter the 2nd level channel through the membrane.

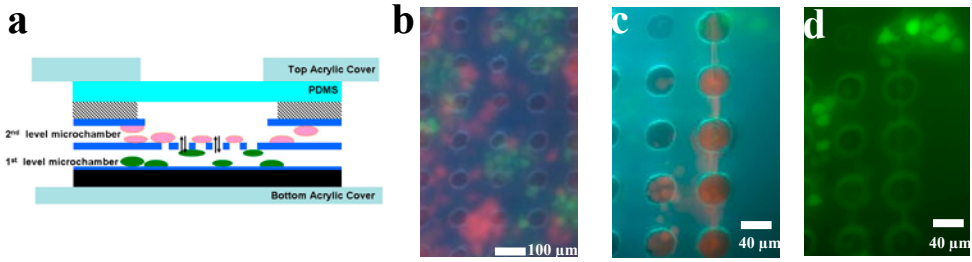

Figure 5. (a) On-chip cell co-culture. (b) Different cells were loaded into the different levels of channels. (c) Cells fluorescing orange are underneath the membrane. (d) Cells fluorescing green are on top of the membrane.

5. CONCLUSIONS

A novel method of fabricating monolithic 3-D microfluidic devices with an integrated parylene membrane has been successfully demonstrated. Our fabrication method enables devices to be conveniently fabricated at the wafer scale, and our device can be integrated with other microfluidic components to build complete lab-on-a-chip systems.

REFERENCES

[1] J. de Jong, R. G. H. Lammertink and M. Wessling, "Membranes and microfluidics: a review", Lab on a Chip, vol. 6, pp. 1125-1139, 2006.

[2] M. C. Liu, D. Ho, and Y. C. Tai, "Monolithic 3-D microfluidic device for cell assay with an integrated combinatorial mixer", Proc. The 14th International Conference on Solid-State Sensors, Actuators and Microsystems (Transducers '07), Lyon, France, vol. 1, pp. 787-790, 2007.

[3] J. Park, F. Berthiaume, M. Toner, M. L. Yarmush, and A. W. Tilles, "Microfabricated grooved substrates as platforms for bioartificial liver reactors", Biotechnology and Bioengineering, vol. 90, pp. 632-644, 2005.

NATURE-INSPIRED ACTIVE MICRO-FLUIDIC MIXING USING ARTIFICIAL CILIA

Jaap M.J. den Toonder[1,2], Femke Bos[1,2], Dirk J. Broer[1,2], Murray Gillies[1], Judith de Goede[1], Titie Mol[1], Mireille Reijme[1], Wim Talen[1], Hans Wilderbeek[1], Viny Khatavkar[2], Patrick Anderson[2]

[1]*Philips Research Laboratories, THE NETHERLANDS*

[2]*Eindhoven University of Technology, THE NETHERLANDS*

ABSTRACT

Creating good mixing flows in lab-on-chip systems poses a special challenge, due to the impossibility to generate turbulence. We propose a novel concept for active mixing, that is inspired by nature, namely micro-organisms that swim through a liquid by beating microscopic hairs, cilia, covering their surface. We have fabricated artificial cilia, based on electro-statically actuated polymer structures, and have integrated these in a micro-fluidic channel. Flow visualization experiments show that our cilia can generate very efficient mixing. Since the artificial cilia can be actively controlled using an electrical signal, they have exciting applications in micro-fluidic devices.

Keywords: Active mixing, polymer actuators, artificial cilia, micro-fluidics

1. INTRODUCTION

Biochemical analyses of body fluids such as saliva, urine and blood give important information about health and disease. An important trend in this field is the transition of centralized lab analysis to cartridge-based near-patient testing using biosensors. These devices contain a micro-fluidic channel system in which the fluids must be manipulated. Often, fast mixing is desired, which is problematic in these small systems since the Reynolds number is generally small so that the flow can never be turbulent. To obtain efficient mixing, special strategies must therefore be used, and many researchers have proposed solutions such as passive groove-type mixers [1]. In this paper we introduce and demonstrate a novel method of active micro-fluidic mixing, using polymer micro-actuators, "artificial cilia", inspired by nature, integrated in a micro-channel.

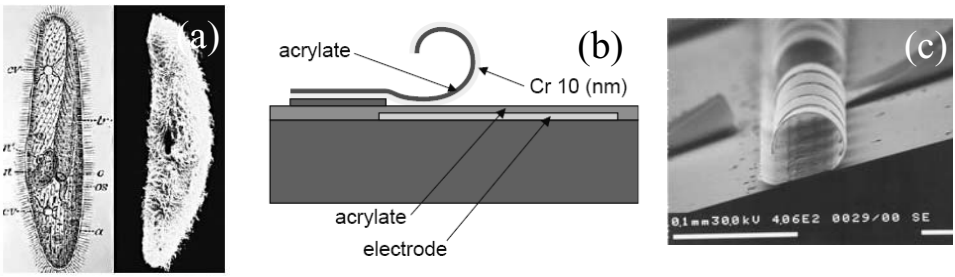

Figure 1: (a) Paramecium: a micro-organism that makes use of beating cilia on its surface for propulsion; (b) sketch and (c) electron micrograph of our artificial cilium with length 100 μm.

978-0-9798064-0-7/μTAS2007/$20©2007CBMS

2. EXPERIMENTAL

Micro-organisms such as Paramecium use tiny beating micro-hairs, “cilia”, with which their surface is covered, to propel themselves through a liquid (see figure 1 (a)). Cilia have a typical length of 10 μm and diameter of 0.1 μm. Inspired by this, we have developed “artificial cilia”: polymer composite micro-actuators responding to an applied electrical field. The typical structure is that of a curled micro-beam consisting of a double-layer of a thin polymer film with a thickness of 1 μm, and a thin conductive chromium (Cr) layer with a thickness of 20 nm. Figure 1 (c) shows a Scanning Electron Microscopy (SEM) image of actual structures made, having a length of 100 μm and a width of 20 μm. As depicted in the schematic in figure 1 (b), the glass substrate is covered with an electrode, and a dielectric layer with a thickness of 1 μm. The micro-actuators are made using existing micro-systems technology processing. The radius of curvature of the micro-actuators is controlled by tuning the mechanical stress in the polymer and Cr films by adjusting the deposition conditions and the relative thickness of both films. By applying a voltage difference between the electrode and the chromium film, the micro-beam is attracted towards the surface and rolls out. After switching off the voltage, it returns to its original shape by elastic recovery. By switching on and off the voltage at a certain frequency, the artificial cilia will make a beating motion.

To test the concept of mixing by the artificial cilia, we have designed and fabricated a Y-shaped mixing channel (cf. figure 2). The artificial cilia are manufactured on a glass plate. A poly-dimethylsiloxane (PDMS) cap, containing the Y-shaped channel structure, is mounted on top of the glass plate. The two inlets are connected to syringe pumps. The bottom channel wall is thus covered with artificial cilia, arranged in sixteen segments of 1 by 1 mm, containing various cilia lay-outs, typically in an A-B-A-B-… sequence. The main flow is driven by the syringe pumps, whereas the movement of the artificial cilia induces a transverse flow.

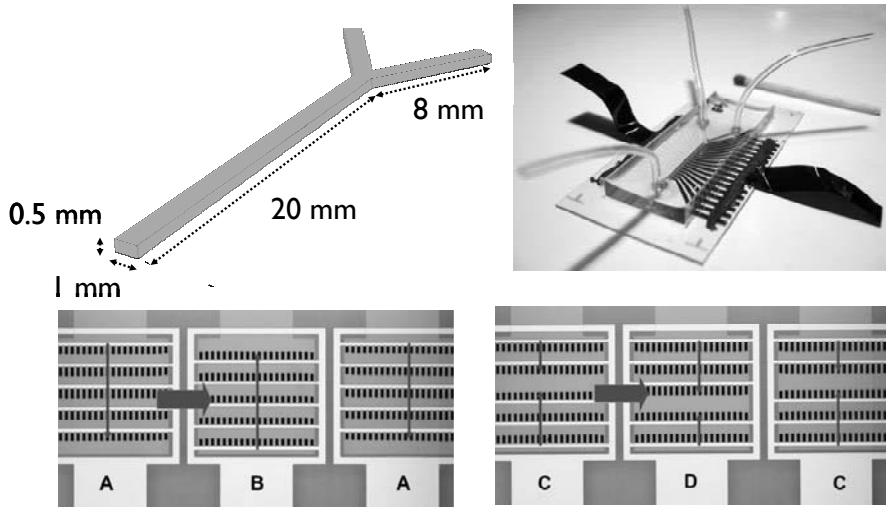

Figure 3: Our artificial cilia mixing Y-channel device. The artificial cilia are fabricated on a glass plate. The cover containing the channel is made of PDMS. Artificial cilia are present on the bottom of the channel, and are arranged in square segments each having their own cilia configuration. Two examples are shown. The main flow is driven by a pump; the moving cilia create transverse flows.

4. RESULTS AND DISCUSSION

In previous work, we showed that the actuated artificial cilia can induce substantial flow velocities [2]. To study the mixing effectiveness, we have carried out flow visualization experiments using silicone oil (viscosity 1 mPa·s), see figure 3. The fluid entering through the two inlets was colored with a red and a blue dye, respectively. The main flow speed was 2 mm/s. At time t=3.56 s the artificial cilia were switched on with a frequency of 50 Hz. A meandering flow pattern immediately occurred, and within 1.5 s, the fluid was homogeneously mixed. This is much more efficient and faster than with known passive mixing configurations, such as the herringbone mixer [1]. In addition, in our approach the effect can be switched on or off on demand.

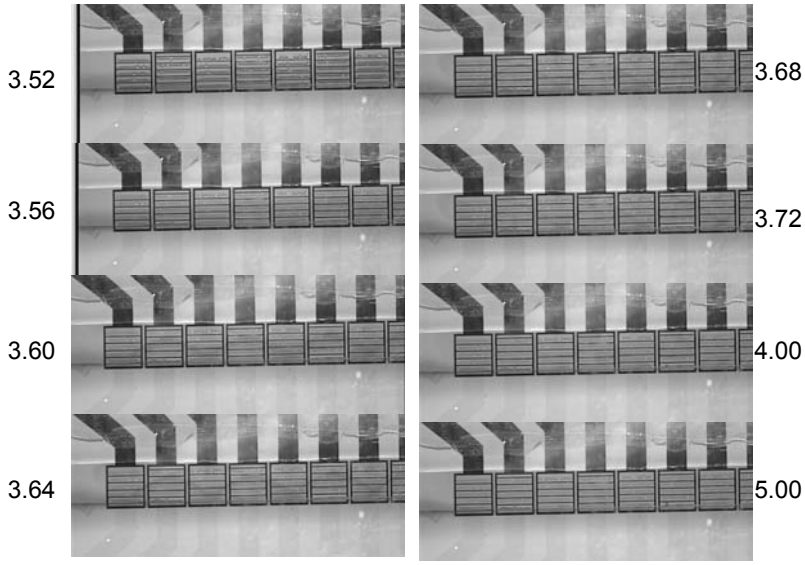

Figure 3: Snapshots from a mixing visualization test using dyed silicone oils (viscosity 1 mPa·s). The externally driven main mean velocity (from left to right) is 2 mm/s. At time t=3.56 s the artificial cilia are switched on with a frequency of 50 Hz. A meandering flow pattern immediately occurs, and within 1.5 s, the fluid is homogeneously mixed.

5. CONCLUSIONS

Our artificial cilia integrated in micro-fluidic channels can generate very efficient mixing flows. The mixing is more efficient and faster than with known passive mixing configurations, such as the herringbone mixer [1]. In addition, an advantage of our approach is that the effect can be switched on or off on demand, at locations of choice.

REFERENCES

[1] "Chaotic mixer for microchannels," A.D. Stroock, S K.W. Dertinger, A. Ajdari, I. Mezic, H.A. Stone, and G.M. Whitesides, Science 295, 647-651, 2002.

[2] "Nature-inspired micro-fluidic manipulation using artificial cilia," J.M.J. den Toonder, D. J. Broer, M. Gillies, J. de Goede, G.N. Mol, W. Talen, and J.T.A. Wilderbeek, microTAS 2006, Tokyo.

SOFT MICROFLOW SENSORS

R. Attia[1], D. Pregibon[2], P. Doyle[2], J.L. Viovy[1], D. Bartolo[3].

[1] Institut Curie, France[2] MIT, USA and

[3] Laboratoire PMMH, ESPC, France

ABSTRACT

We propose a new method for the construction of flow sensors integrated in PDMS microfluidic devices. This new approach takes advantage of flow lithography to construct soft and mobile polymeric structures. We show that the deformation of microsprings or the rotation of microwheels can be used to provide a very sensitive measurement of local flow rate in microcircuits.

Keywords: soft sensor, integrated microflow meter, photopolymerization

1. INTRODUCTION

So far, the search for highly integrated functions in microfluidics chips has been mostly restricted to flow controllers such as mixers, valves, pumps or droplet emitter. The integration of detection functions remains a challenging task for the design of functional lab on a chip devices. Even the simple measurement of the liquid flows rate is an old challenge in microfluidics. The reason for this is that flow measurement requires the presence of mobile or deformable components in the channels. The fabrication of such flow sensitive structures cannot be achieved with the simple lithographic methods well suited for fast prototyping and low cost production methods. Among the numerous strategies that have been proposed to overcome these limitations, a popular indirect approach uses heat transfer by measuring the asymmetry of temperature profile near a heating element [1,2]. The high thermal diffusivity in liquids, however, limits the dynamic range of these methods which have a poor sensitivity for low flow. In addition, it requires prior knowledge of the fluid's heat capacity. Other methods, based on PIV or electrochemistry, require the presence of tracers in the fluid [3,4], which is not wanted in many applications. Overall, in spite of a growing number of locally measured flow velocities, microfluidics is still in need of methods for flow measurement that would be tracerless, sensitive to low flow velocities, and with a high dynamic range.

Here we present a novel family of flowsensors based on the deformation or movement of soft mobile microstructures built *in situ* in PDMS chips.

2. FABRICATION

To include flow responsive elements in a PDMS microcircuit, a photocurable prepolymer is loaded in the 55 µm height channels together with a photosensitive initiator, as shown in Fig. 1a. Soft polymeric structures of mask-defined shapes were formed by exposing the photosensitive liquid to controlled pulses of ultraviolet light through the microscope objective.

In a typical experiment (40x objective), the features on the mask are reduced 16 times, allowing for accurate photolithography from inexpensive masks. Microscope observation allows accurate alignment with the pre-existing microchannel structures such as PDMS pillars or channels walls. The permeability of the silicon elastomer to oxygen is put at work to ensure the mobility of the photopolymerized structures. Indeed, the oxygen molecules

978-0-9798064-0-7/µTAS2007/$20©2007CBMS

inhibit polymerization close to the PMDS surfaces yielding free-standing plastic structures. Four different soft elements free to rotate around PDMS axel are shown in Figures 1-3. To ensure the compatibility of this method with biological applications we have chosen PEG-diacrylate as a liquid prepolymer. This guarantees DNA and protein repellence, and thus compatibility with most bioassays.

3. RESULTS

The first family of sensors tested (see e.g. Fig 1) relies on elastic deformation of springs under viscous flow. The spring length, measured optically, is plotted as a function of flow velocity in Fig 2. This calibration curve is then used to measure the local velocity of fluids driven by any kind of pumping (pressure, electro-osmosis, peristaltic pumping…). We emphasize that the shape of the spring can be tuned in order to impart the structure with suitable length versus velocity behaviour. Here, we designed a spring with nonlinear deformation for increased dynamic range. It covers 2 orders of magnitude with a spring of uniform thickness, but we expect it can be extended to 4 orders of magnitude with a modified design.

For some applications, it would be suitable to have an absolute measurement of flow velocity without a priori knowledge on the fluid's physical nor chemical properties. This could be achieved using rotating wheel devices, as shown e.g. in Fig.3. In contrast with spring systems, whose deformations depend on the fluid viscosity, the rotation velocity of the wheels should be independent of viscosity and be linear in flow rate (in the viscous regime). So far, we observed wheel rotation, but could not achieve this linear regime, due to imperfections in the microfabrication. To overcome this limitation, we are developing improved devices designed with high resolution masks and narrow band UV filters.

4. CONCLUSION

In summary, we present a new family of microfluidic flow sensors. The two physical principles underlying sensing, elastic deformation and rotation of a wheel are straightforward, but the power of in-situ photopolymerization to prepare complex objects offers virtually unbound possibilities for adapting the reactive microstructures to diverse specifications.

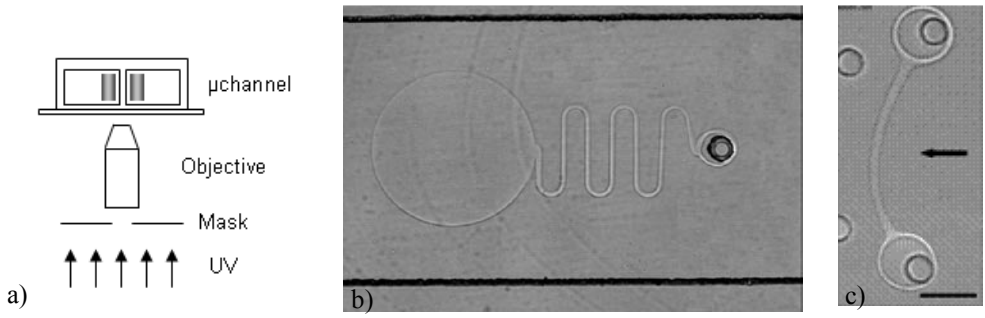

Figure1. a) schematic depicting the set up used in the experiment ; b)Soft spring and its "buoy" in a 500 μm large microchannel. Scale bar 100 μm; c) Elastic string binding under a flow, indicated by the arrow. Scale bar 100 μm

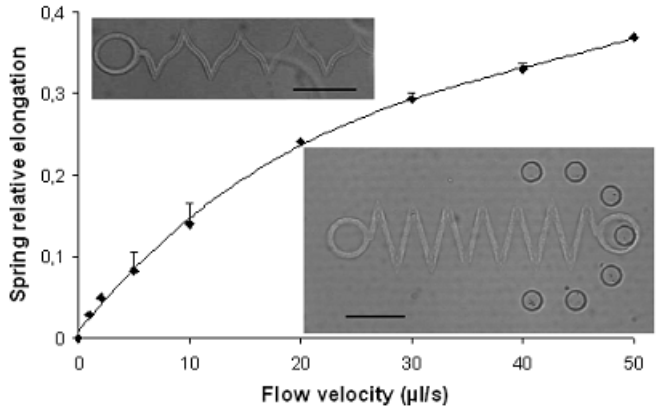

Figure 2. Elongation/flow velocity curve. The bottom spring is in its initial state. Nonlinear deformation of the spring, responsible for the nonlinear characteristics, is shown in the top insert (flow 50 µl/s, scale bar 100µm)

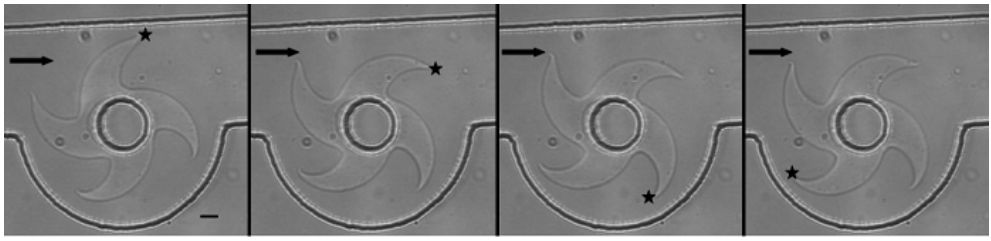

Figure 3. Stack of images of a 180 µm diameter wheel rotating in a 10 µl/s flow. Flow direction is indicated by the arrow. Scale bar 10µm.

REFERENCES

[1] "Thermal flow sensor for liquids and gases based on combinations of two Principles", M. Ashauer , H. Glosch, F. Hedrich, N. Hey, H. Sandmaier, and W. Lang, Sensors and Actuators, **73**, 7 **(**1999)

[2] "MEMS Flow sensors for nano-Fluidic applications," Shuyun Wu, Qiao Lin, Yin Yuen, and Yu-Chong Tai, Sensors and Actuators A, **89**, 152 (2001)

[3] "Velocity Measurement of Particles Flowing in a Microfluidic Chip Using Shah Convolution Fourier Transform Detection", Y. C. Kwok, N. T. Jeffery, and A. Manz, Analitical Chemistry, **73**, 1748 (2001)

[4] "Using electrochemical coupling between parallel microbands for in situ monitoring of flow rates in microfluidic channels," C. Amatore, M. Belotti, Y. Chen, E. Roy, C. Sella and L. Thouin, Journal of Electroanalytical Chemistry, **573**, 333 (2004)

[5] "Continuous-flow lithography for high-throughput microparticle synthesis," D. Dendukuri, D. C. Pregibon, J. Collins, T. A. Hatton, P. S. Doyle , Nature Materials, **5**, 365 (2006)

STARTUBE: A NOVEL TUBE DESIGN FOR BUBBLE TOLERANT INTERCONNECTION IN FLUIDIC SYSTEMS

T. Metz[1], W. Streule[1], R. Zengerle[1] and P. Koltay[1]

[1]Laboratory for MEMS Applications, Department of Microsystems Engineering (IMTEK), University of Freiburg, Germany

ABSTRACT

For the first time we present a new tubing geometry for the bubble tolerant interconnection of fluidic systems. The tube has a star shaped profile, forcing bubbles into its centre by capillary forces. The StarTube is save from being clogged by bubbles as liquid can bypass in the side channels of the tube. The mobility of bubbles is increased decisively as their contact line perpendicular to the movement direction is minimized. A model established for the prediction of bubble configuration shows that the simplest design which leads to a centred bubble requires six grooves and contact angles of $\theta < 20°$.

Keywords: Bubble, Tube, Pipe, Star, Capillary, StarTube

1. INTRODUCTION

Gas bubbles in fluidic connections induce resistance due to contact line effects, with pressure losses in the order of the capillary pressure [1]. The losses accumulate for multiple bubbles. Conventional connections transport bubbles with the flow to positions where they can disturb the operation. Sometimes so called "bubble traps" are used to isolate bubbles and to enable liquid to pass. The presented StarTube is a unique solution enabling trapping of bubbles as well as increasing bubble mobility in the flow.

2. WORKING PRINCIPLE

The star-shaped profile of the StarTube is built up from a circular pattern of rectangles (Fig. 1a.). Gas bubbles are forced into the centre of the tube by capillary forces (Fig. 2a). A centred bubble enables the liquid to bypass in the outer channels formed by the fingers of the profile. The reduced contact line perpendicular to the flow direction maximises bubble mobility. An obstacle across the centre of the tube can hold back bubbles (Fig. 7). This realizes an efficient bubble trap.

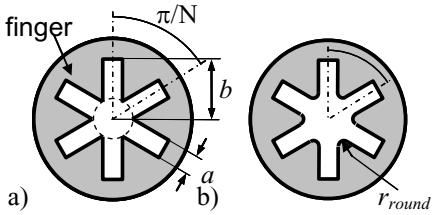

Fig. 1: Cross section of the StarTube: N rectangles forming the grooves and a cavity in the centre. The situation for rounded edges is shown in (b).

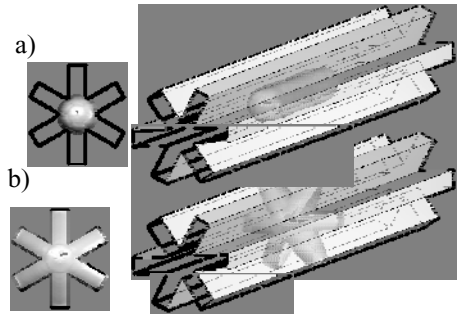

Fig. 2: Simulations of bubbles in a StarTube (N=6, b/a=3). Depending on contact angle and geometry a bubble either adopts a (a) centred ($\theta = 0°$) or (b) clogged ($\theta = 50°$) configuration.

978-0-9798064-0-7/μTAS2007/$20©2007CBMS

2. THEORY

The configuration a bubble attains in a StarTube - centred (Fig. 2a) or clogging the whole cross section (Fig. 2b) depends on the details of the geometry and the contact angle θ. Conditions for centred bubbles can be determined by considering the capillary pressure p_{cap} which is constant all over the surface of the bubble. In the centred position p_{cap} must be lower then the maximum capillary pressure p_s the side channels can exert (Fig. 3). The surfaces of a long bubble in the side channels can be regarded as cylindrical. The maximum pressure p_s it can produce is given by the contact angle and the channel width a, as

$$p_{side} = \sigma \frac{1}{r_s} = \sigma \frac{2\cos\theta}{a}, \qquad (1)$$

where r_s is radius of the cylindrical surface in a side channel. On the other hand, the capillary pressure of the bubble p_{cap} is defined by the bubbles caps. A centred bubble in the StarTube has wall contacts only along the edges and the capillary pressure is given by [2]

$$p_{cap} = \sigma \frac{S}{A}. \qquad (2)$$

S denotes the circumference and A the area of the cross section of the bubble. In the limit of the maximum capillary pressure, the cross section is given by a series of N arcs with radius r_s (Fig. 3). Thus p_{cap} can be evaluated as a function of N and q for this case and compared to p_{side}. If p_{cap} is smaller than p_{side} the bubble is centred. This leads to a condition for centred bubbles, relating the number of fingers and the contact angle of a StarTube:

$$N > \pi \left(\arctan\left(\frac{2\cos^2\theta}{\pi - 2\theta + 2\cos\theta\sin\theta} \right) \right)^{-1}. \qquad (3)$$

Eq. 3 must be fulfilled in order to obtain centred bubbles in a StarTube. The solid line in Fig. 4 represents the case when both sides of Eq. 3 are equal. Only StarTubes with parameters above the curve lead to centred bubbles. It can be seen that these require more at least six fingers. Computational Fluid Dynamics (CFD) Simulations and experiments confirm the model (Fig 4). Simulations were performed with a volume of fluid method, that accounts for surface tension and contact angles (ESI-CFD ACE+ [3]).

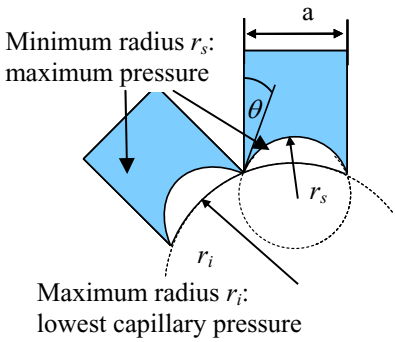

Fig. 3: Part of the cross section of a StarTube. The bubble surface forms arcs in the cross section. Contact angle at the edges can vary what leads to varying arc radii's.

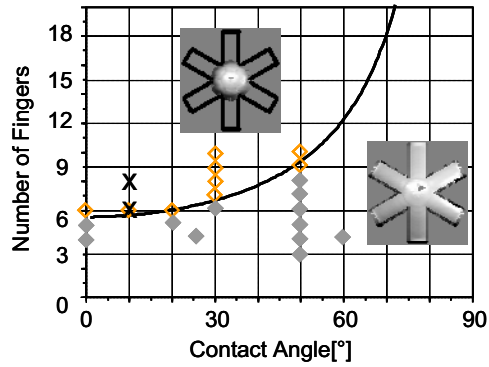

Fig. 4: Necessary number of fingers for functional StarTube. Performed simulations and Experiments are marked: ◇ centred bubble; ◆ clogging bubble; x fabricated tubes (centred bubbles).

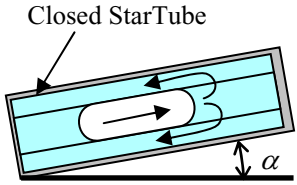

Fig. 5: Experimental setup of buoyancy

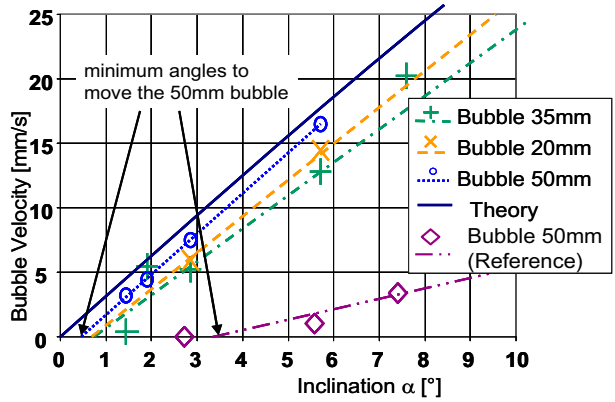

Fig. 6: Observed and theoretical predicted velocities of bubbles moving in inclined StarTube. (a=1100 µm; b=2.5 mm; N=8; r_{round}~250 µm)

3. EXPERIMENTS

StarTubes were fabricated in PDMS, one with six side channels (a=500 µm, b=2.5 mm, N=6, r_{round}~250 µm) and one with eight (a=1100 µm, b=2.5 mm, N=8, r_{round}~250 µm). They were made hydrophilic by HMDSO plasma deposition, leading to a contact angle θ<10°. Bubbles brought into the tubes were centred as predicted. The increased mobility of gas bubbles in the StarTube has been proven by buoyancy experiments as sketched in Fig. 5. In comparison to a circular PDMS tube. The minimum necessary inclination angle to move a bubble is about eight times smaller in the StarTube than in the conventional tube (Fig. 6).

Fig. 7 shows a bubble trap realized by introducing a small blade across the centre of a StarTube.

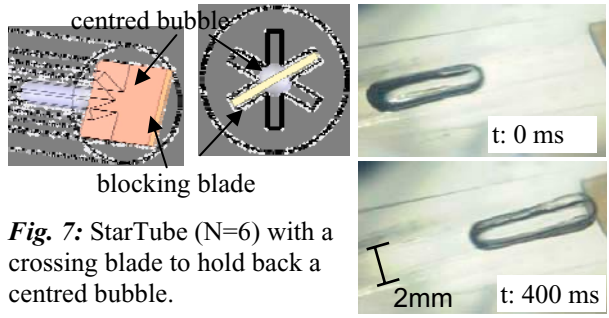

Fig. 7: StarTube (N=6) with a crossing blade to hold back a centred bubble.

5. CONCLUSION

The increased bubble mobility in the StarTube was successfully proven and a theoretical assessment was presented which enables the design of such tubes. The StarTube has a great potential of application in µTAS, it can be used within systems and for connection by external tubing, to form bubble traps and to avoid clogging.

ACKNOWLEDGEMENTS

This work was funded by the German Science Foundation (DFG) under project ZE 527/3.

REFERENCES

[1] H. Wong, C. J. Radke, and S. Morris, "The Motion of Long Bubbles in Polygonal Capillaries .2. Drag, Fluid Pressure and Fluid-Flow" *J. o. Fluid Mechanics*, 1995

[2] D. Langbein, Capillary surfaces : shape, stability, dynamics, in particular under weightlessness, Book, Springer, 2002.

[3] ESI-CFD,CFD-ACE+ Modules Manual, Huntsville, 2006

STICK AND FLOW: FAST SIMPLE PROTOTYPING METHOD FOR PERFORMANCE MICROFLUIDIC DEVICE

Denis Bartolo[1], Guillaume Degré[2], Phillipe Nghe[2] and Vincent Studer[3]

[1] PMMH - ESPCI - CNRS UMR7636 - P6 - P7, France.

[2]UMR Gulliver CNRS UMR7083 - ESPCI, France.

[3]Laboratoire de Neurobiologie - CNRS UMR7637- ESPCI, France.

ABSTRACT

We show in this paper how to produce high performance plastic microfluidic devices by stacking micropatterned stickers. We take advantage of soft UV imprint [1] techniques to tailor the mechanical properties, the surface chemistry and the geometry of the patterned stickers. We emphasize that the method presented below does not require expensive facilities or equipment and allows for replicating complex microfluidics devices in few minutes. The resulting micro-devices combine high spatial resolution, compatibility with organic solvents and mechanical resistance. They open the way to complex fluids and organic liquids microfluidics.

Keywords: Soft Imprint, Fast Prototyping, Microfluidic component

1. INTRODUCTION

Elastomer materials are considered today as excellent options for microfluidic device fabrication [2]. Microfluidic devices made of PDMS by replica molding are now part of the standard instrumental toolbox of many research laboratories. PDMS combines numerous outstanding physical and chemical properties. Nevertheless, some of these properties strongly limit the range of application of PDMS devices. The permanent modification of the chemical properties of PDMS surfaces remains a challenge. This narrows the range of possible formulations in multiphase flows. Furthermore, the low elastic modulus of PDMS limits the working pressure below ~1bar. This prevents a controled transport of viscous fluids and in turn make rheological measurement almost impossible in PDMS devices. To circumvent these important limitations we propose here a fast prototyping method to make high performance plastic microfluidic devices by stacking micropatterned stickers.

2. FABRICATION METHOD

The stickers are patterned using a soft imprint approach, Figure 1. A drop of photocurable polymer is deposited on a flat or patterned PDMS substrate. A second structured PDMS stamp is gently pressed onto the substrate. The resulting sandwich is photopolymerized to form the desired microchannels network. Since the photopolymerization is inhibited by oxygen molecules, the permeability to gas of PDMS ensures that an ultra thin layer of liquid remains uncured [3]. Hence the two PDMS stamps can be removed and replaced by a glass or plastic slide one after the other. A second illumination seals the microfluidics device. An important point is that using low viscosity monomers, the removal of the residual layer does not require any further etching process. Such stencils like stickers enable the realization of complex multilevel devices.

978-0-9798064-0-7/μTAS2007/$20©2007CBMS

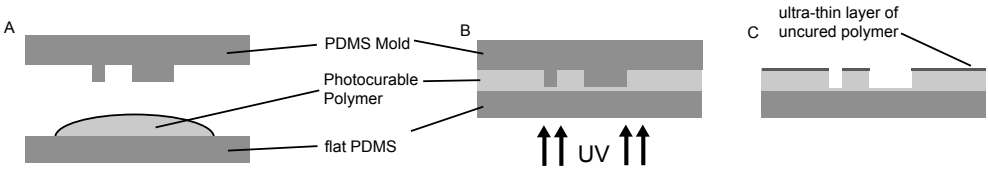

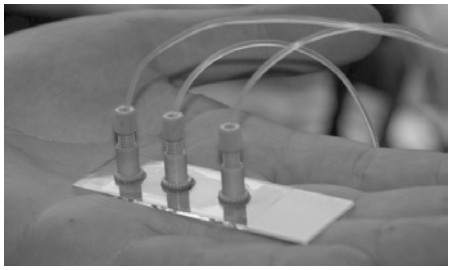

Figure 1. Top: Sketch of the fabrication of the patterned stickers. A and B: the polymer is photocured between a PDMS mold and a flat PDMS sheet or a glass slide. C: The PDMS mold is removed to obtain a microfluidic sticker. Left: Example of a Stick and flow device with upchurch nanoport connections.

We now present two different application of this "*stick and flow*" method:

3. RESULTS

The low elastic modulus of PDMS strongly limits the range of pressure that can be applied without deforming the channels and in turn the range of viscosity of the transported fluids. Even for low pressure changes, the geometry of the channels can be significantly altered. Fig. 2 shows that the *stick and flow* device made of thiolene based resin [4] can bear an applied pressure more than 15 times higher than the same channel made of PDMS without undergoing any measurable deformation. This strong mechanical resistance makes the *stick and flow* method particularly appealing for material science applications. Its application to complex fluid rheology is demonstrated in [5].

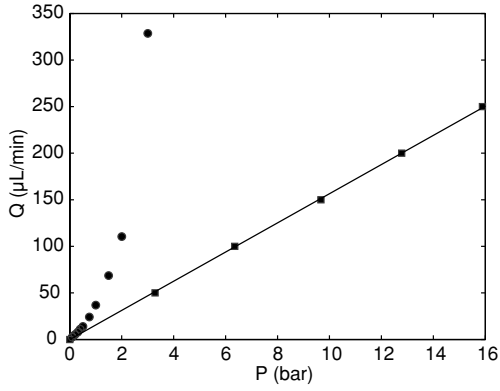

Figure 2: Pressure difference plotted versus the imposed flow rate in a stick and flow (square) and PDMS (circle) microchannels. The deviation to the Darcy law (straight line) at low pressure is due to the deformation of the channel geometry in the PDMS device (Pure water in a straight channel, dimensions: 5cm x *250µm* x *18µm).*

The wide range of different photocuring polymers usable to fabricate microfluidic stickers allows for the fine tuning of the wetting properties of the channels walls. This is of special importance for digital microfluidics [6]. For instance, this offers the opportunity to make either hydrophobic or hydrophilic channels without having to deal with tedious surface modifications. We have made two flow focusing drop emitter devices, one in a hydrophilic

material [4], and the other in a hydrophobic polymer (Trimethylolpropane triacrylate). The first one is used to generate a direct hexadecane in water emulsion whereas the second allows for the production of an inverse water in hexadecane emulsion. We show on Fig. 3 two magnified view of the output channels.

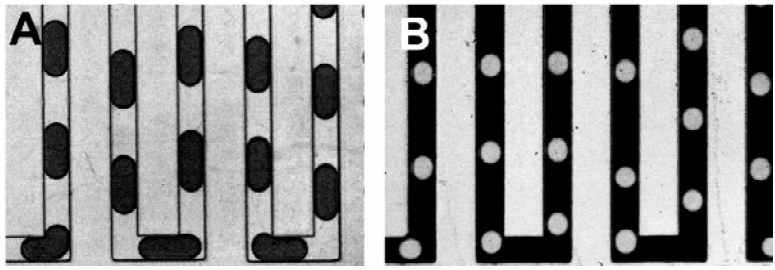

Figure 3. A: Hexadecane in water (colored with Orange G dye) droplets produced with stick and flow flow-focusing channels made of NOA 81. B: Droplet of water (colored with Orange G dye) in hexadecane in the same device geometry but made out of a hydrophobic material (Trimethylolpropane triacrylate). Channels width: 200 µm.

4. CONCLUSION

We have briefly presented a fast and simple prototyping method for performance microfluidic devices. This *stick and flow* method overcome several limitations associated with the very popular PDMS fluidic chips. Another interesting property of microfluidic stickers is that they can be attached in a wet environment. An interesting application of this property is demonstrated in [7].

REFERENCES

[1] L. Jay Guo, *Nanoimprint Lithography: Methods and Material Requirements*, Advanced Materials 19, 495 (2007).

[2] G. M. Whitesides, The *origins and the future of microfluidics* , Nature, 442, 27 (2006).

[3] D. Dendukuri, D. C. Pregibon, J. Collins, T. A. Hatton, and P. S. Doyle, *Continuous Flow Lithography for High-Throughput Microparticle Synthesis*, Nature Materials, **5**, 365 (2006).

[4] Norland Optical Adhesive, NOA81.

[5] G. Degré, et.al., *Microfluidic Characterization of Surfactant Solutions*, Proceedings of MicroTas 2007.

[6] R. Dreyfus, H. Willaime and P. Tabeling, *Ordered and Disordered Patterns in Two-Phase Flows in Microchannels*, Phys. Rev. Lett, 90, 144505 (2003)

[7] M. Morel, D. Bartolo, M. Dahan and V. Studer, *Microfluidic Stickers for Quantitative Studies of Cultured Cells*, Proceedings of MicroTas 2007.

ACTIVE POLYMERIC MICRONEEDLE ARRAY DRIVEN BY THERMOPNEUMATIC ACTUATOR FOR MICROFLUIDIC INTERFACE

Jae-Yong An, Sung-Sik Yun, Il-Han Hwang, Sung-Keun Yoo, Myung-Gon Kim, Sung Yang and Jong-Hyun Lee

Department of Mechatronics,
Gwangju Institute of Science and Technology (GIST), South Korea

ABSTRACT

A novel microstructure for efficient control of microneedle arrays is proposed for the applications of drug delivery. Conventional researches have been focused on the fabrication of fixed microneedles and the interface with microfluidic chip. However, the proposed active microneedle array can be actuated by thermopneumatic force so that the needle array and body skin can be protected from needle broke down and skin damage due to external shock during no operation. The movement of the microneedles reaches up to 413 μm at an input voltage of 50V, which implies that the displacement is large enough to deliver drugs into the skin surface (epidermis). An 40mN of actuation force was experimentally achieved when the initial gap between the needle tip and the skin was 50 μm.

Keywords: Microneedle, Active, Thermopneumatic, Polymer, Actuator

1. INTRODUCTION

As an microelectromechanical system (MEMS) is being applied in many areas of biology and biomedical engineering, there has been growing interest in bio tools for drug delivery, sample preparation and sensing of biomolecules [1-3]. Especially the research on drug delivery has been focused on transdermal delivery with non-invasive method [4-5] and minimally invasive method [6] using microneedles. In order to find the requirements of microneedle for drug delivery, it is necessary to consider the skin structure including epidermis. The outer layer of epidermis is composed of dead cell called the stratum corneum, outermost layer of skin. The stratum corneum acts as a main barrier of drug delivery. The thickness of the epidermis is about 50-100μm, which contains no blood vessels and nerves [7]. Typically the target depth of the microneedle is below the epidermis because the drugs delivered to the dermis can be effectively absorbed in the body.

This paper presents an active microneedle that can be actuated when it is necessary to use. The microneedle proposed in this report is driven by a thermopneumatic actuator. The performance of the system including displacement and actuation force of the microneedle will be experimentally investigated.

2. PRINCIPLE OF ACTIVE MICRONEEDLE

Figure 1 shows a cross-sectional view and a working principle of the proposed thermopneumatic actuator for active microneedle array. When the heater (Ti/Pt) raises the temperature of the air inside of the chamber, the flexible PDMS (Sylgard 184, Dow corning, Midland ,USA) structure with a microchannel is deflected upward due to the volume expansion. Accordingly, the needle supported by channel also moves upward to penetrate the body skin.

The active microneedle array is composed of four layers. Firstly, the protection layer is used to keep the microneedle arrays from undesirable external shock while no operation.

978-0-9798064-0-7/μTAS2007/$20©2007CBMS

Secondly, needle layer consists of SU-8 (Microchem Corp., Newton, MA, USA) microneedles and a flexible PDMS substrate. Utilizing the flexibility of PDMS, the needle layer can easily move upward or downward. Thirdly, the fluidic channel layer has two functions. One is to transport drugs to the microneedle. The other is to transfer the actuation power to the microneedle. Finally, the chamber layer includes a cavity filled with air or working fluid to generate thermopneumatic force. On the glass substrate, both the heater and the temperature sensor are fabricated. The heater is used to raise the temperature of the air or working fluid. The temperature sensor is used to monitor the temperature variation in the thermopneumatic chamber. Assembling the aforementioned four layers on the glass substrate, the proposed active microneedle array with a thermopneumatic actuator can be prepared.

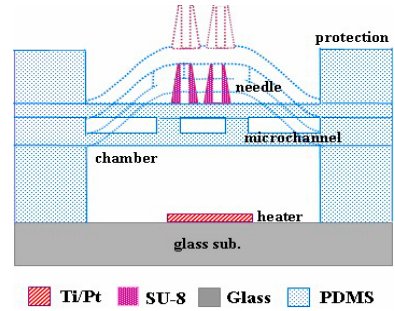

Figure 1. Schematic view of the active microneedle array.

3. FABRICATION

Figure 2 shows a detailed process for the fabrication of microneedle array. The needles are made of SU-8 featuring a high strength and good biocompatibility. In the fabrication of the microneedle array, the SU-8 was exposed from backside of the glass substrate to implement a tapered microneedle. A protection layer, a microfluidic channel and a chamber layer are fabricated using conventional PDMS replica molding technique [8]. As well known, PDMS is so flexible that the membranes can easily deform according to the volume change of the cavity. Figure 3 shows a photograph of the device equipped with four microneedles.

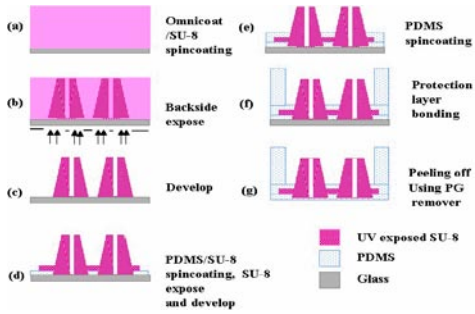

Figure 2. Schematic drawing of the fabrication process of the microneedle array.

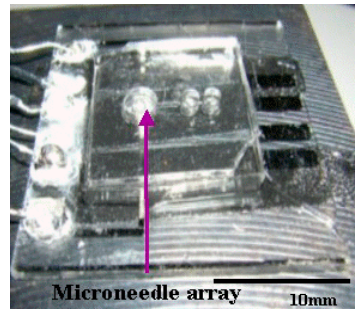

Figure 3. A photograph of the fabricated active microneedle array.

4. RESULTS AND DISCUSSION

Figure 4 shows the measured displacement of the needle array and the temperature variation near the heater region with respect to the input voltages. The displacement of the fabricated microneedles reached up to 413 μm with the input power of 1.89 W at the input voltage of 50 V. This implies that the displacement is large enough to deliver drugs through the skin surface (epidermis). The temperature sensor was calibrated using a conventional RTD (resistance temperature detector) with the four-point method. The temperature near the heater region was also measured with respect to the input voltages during operation. The increment of the temperature near the heater was about 170℃ at the input voltage of 50 V. It is possible to estimate the temperature of the microfluidic channel by conducting numerical analysis, although it is out of scope of this research.

The force gauge (AFG 2.5 N, Mecmesin, Slinfold, United Kingdom) was used to measure the actuation force with initial gaps of 50 μm, 100 μm and 150 μm between the needle and the force gauge tips as shown in Figure 5. It was found that the smaller initial gap is more efficient to generate the larger actuation force than the one obtained from the larger initial gap (100 μm, 150μm).

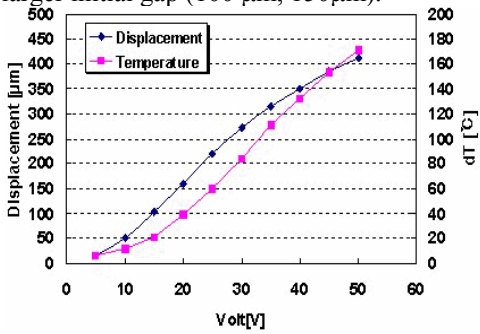

Figure 4. Measured displacement of the micro needle array and temperature variation with respect to the input voltage.

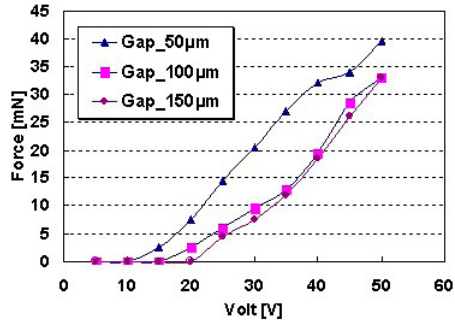

Figure 5. Actuation forces of the fabricated microneedle array (number of needles: 4, inner dia.: 100 μm, out dia.: 130 μm and bottom dia.: 230 μm).

5. CONCLUSIONS

As a feasibility study for the applications of drug delivery, a novel concept for efficient control of microneedle arrays was successfully demonstrated. It was found that the displacement of the fabricated microneedles reached up to 413 μm at the input voltage of 50 V, generating a 40 mN of the actuation force when the initial gap between the needle and the force gauge tips was 50 μm. As a further study, the fabricated microneedle will be tested with animal skin. This new type of actuated microneedle array is anticipated to be useful for drug delivery and sampling body liquid since it is able to perform either in periodic or in continuous treatment or in monitoring of physiological systems.

ACKNOWLEDGEMENTS

This work was supported by the Center for Distributed Sensor Network (CDSN) at GIST, Korea.

REFERENCES

[1] S. Henry, et al., *Micromachined needles for the transdermal delivery of drugs*, Proc. IEEE Micro Electro Mechanical Systems, pp.494-498, (1998).
[2] Y. Huang, et al., *MEMS-based sample preparation for molecular diagnostics*, Anal Bioanal Chem 372, pp. 49-65, (2002).
[3] N. H. Chiem, et al., *Microchip systems for immunoassay: an integrated immunoreactor with electrophoretic separation for serum theophylline determination*, Clin. Chem 44, pp, 591-598, (1998).
[4] Snyder, et al., *Application of the cymbal transducer towards noninvasive transdermal insulin delivery*, Journal of Materials Science -Frontiers of Research in Ferroelectricity - Special Issue , (2005).
[5] Lee, et al., *Noninvasive ultrasonic transdermal insulin delivery in rabbits using the light weight cymbal Array*, Diabetes Technology & Therapeutics, Volume 6 / Issue 6, December, (2004).
[6] K. S. Kim, et al., *A tapered hollow metallic microneedle array using backside exposure of SU-8*, J. Micromech. Microeng. 14, pp.597-603, (2004).
[7] R. Schmidt, et al., *Human physiology*, 2nd edition, Springer-Verlag, New York, pp.501-505, (1989).
[8] G. M. Whitesides, et al., *Soft lithography in biology and biochemistry*, Annual Review of Biomedical Engineering, vol. 3, pp. 335-373, (2001).

FABRICATION OF 3D MICROCHANNELS ON CYLINDRICAL SURFACES BY SINGLE MOLD PROCESS

S. Matsumoto and N. Ichikawa

National Institute of Advanced Industrial Science and Technology (AIST), Japan

ABSTRACT

A new method to construct 3D (three-dimensional) micro channel structures is presented. 3D structures were realized by multi-turn lamination of a polymer film around a cylindrical shaft. Channel patterns were formed on the film by a single mold process. This method provides new packaging options suitable for integration with portable analysis devices and medical devices such as endoscopes. For demonstration of the feasibility, a static micro mixer was fabricated using this approach.

Keywords: 3D micro channels, cylindrical surfaces, mold process, alignment

1. INTRODUCTION

Various fabrication methods of 3D micro channels have been proposed, in order to realize micro chemical chips with functional elements such as mixers and valves. While PDMS (Poly-dimethylsiloxane) multi-layer structures [1] are commonly used for this purpose, their fabrication involves multiple mold processes corresponding to the individual layers, which leads to problems of increasing complexity. Additionally, the packagings of those devices are limited to flat shapes, because they are formed on plane substrates in principle, while curved surfaces with small radius are often suitable for integration with portable analysis devices and medical devices such as endoscopes.

In this work, we propose a new method to construct micro channels with 3D structures on cylindrical surfaces, using flexible films with patterns formed by a single mold process. The basic concept and the design considerations are described in the following sections, through the fabrication of a static micro mixer as an example device. Although we used PDMS as the flexible film, the method is applicable for other polymer materials depending on requirements.

2. DESIGN AND FABRICATION

In our approach, a single polymer film on which channel patterns for successive layers were sequentially arranged was laminated around a cylindrical shaft, with each turn corresponding to a layer. Fig. 1 shows a schematic drawing of the construction of a 3D static mixer realized by three turns of a PDMS film laminated around an acrylic shaft which also provides fluidic interfaces.

The basic dimensions of the example device are given in Fig. 2. The diameter of the shaft was 5mm and the nominal thickness of the PDMS film was 100 μm. Patterns for outer layers should have shapes stretched in the circumference direction, compared to inner layers due to the increase of the base diameter. In order to make the through holes and to define the film thickness, the mold needs at least two

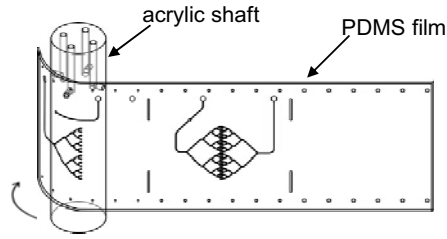

Figure 1. Concept of cylindrical 3D static micro mixer device.

978-0-9798064-0-7/μTAS2007/$20©2007CBMS

levels of height. The two-layer photolithography process of SU-8 3035 was employed to make the two height levels. Fig. 3 shows the fabrication process flow of the PDMS film. The bottom and top layers of SU-8 had the thickness of about 70 μm and 30 μm, respectively. After developing SU-8, a 4 μm thick parylene layer was coated to protect the structures and to ease the mold release. Fig. 4 is the photograph of SU-8 molds realized on a 4 inch silicon wafer. As shown in Fig. 3d, a 100 μm thick PET (Polyethylene terephthalate) film was used as the support layer when casting PDMS. A hot press equipment was used for curing PDMS applying a load of 60 kgf on the wafer under 90°C. Fig. 5 shows the processes of assembly with acrylic shaft and packaging. Alignment against the fluidic interface opening on the cylindrical surface, and that against the preceding layer can be done with microscopic observation from the PET film side. Although the degree of freedom for the latter is restricted, fine adjustment utilizing the flexibility of the film is applicable. Finally the whole structure was covered by a thermal shrink tube, for preventing the leak and for the protection.

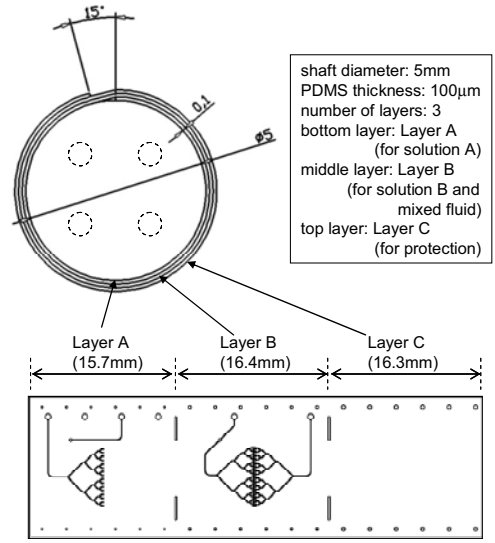

Figure 2. Structure and dimensions of the cylindrical 3D static micro mixer device with three layers. The length of Layer C is rather short because it does not include the region of ~15° margin.

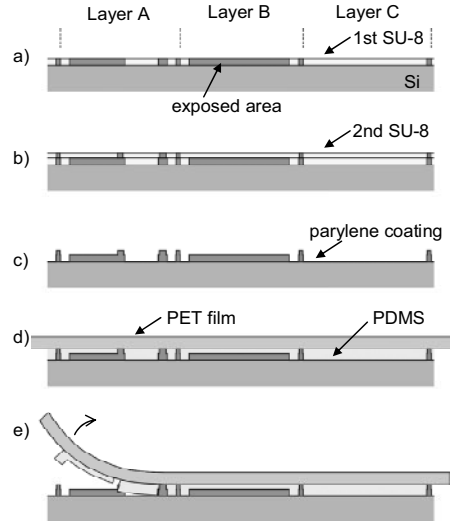

Figure 3. Fabrication process of PDMS film; a) bottom SU-8 patterning. b) top SU-8 patterning, c) parylene deposition on SU-8 mold, d) casting and curing of PDMS with PET support film, e) releasing from the mold.

3. RESULTS AND DISCUSSION

Fig. 6a shows the fabricated 3D static micro mixer device. Because we used a transparent thermal shrink tube, the channel patterns and internal fluid flows were visible. The device was firstly inspected for the accuracy of the pattern alignment. Fig. 6b shows the close-up view of the mixing part, where the accuracy of the alignment was critical to realize the junctions between channels on upper and lower levels. The width of the channels was 60 μm and the diameter of the circular part of the junctions in the upper level was 160 μm. In Fig. 6b, it was demonstrated that the 3D junctions between the channels in the lower level

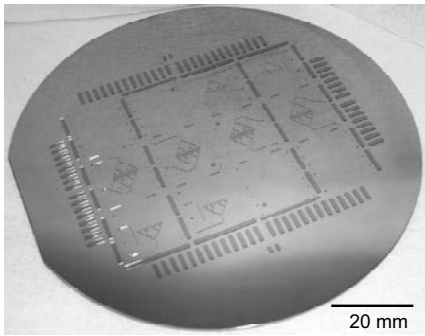

Figure 4. SU-8 molds for four devices patterned on 4 inch wafer.

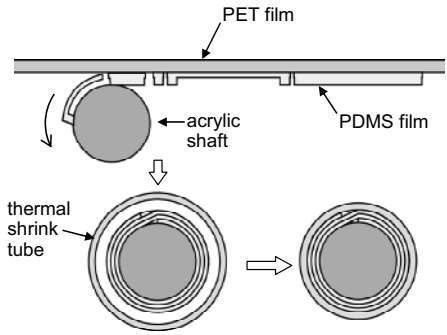

Figure 5. Assembly and packaging of the prototype device.

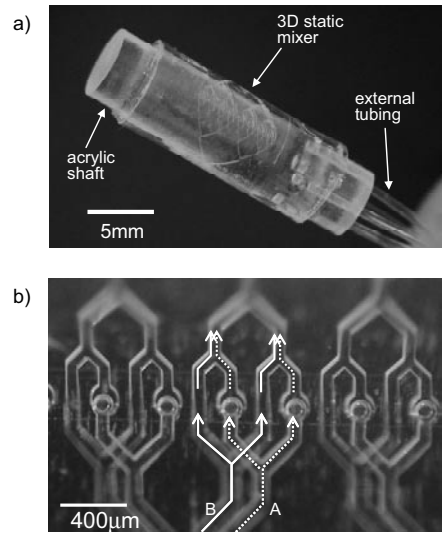

Figure 6. Fabricated 3D static micro mixer device. a) Finished device with mixer channel patterns on curved surface. The diameter and the length of the acrylic shaft are 5mm and 20mm, respectively. b) Close-up view of the mixing junctions. The channel A is in the bottom layer and B in the upper layer. The diameter of the circular part of the junction (Layer B) is 160 μm.

(layer A) and the upper level (layer B) were successfully created and the alignment precision was acceptable. The improvement of the alignment precision depends on the development of appropriate tools for this process. The device was then examined for the situations of actual use. The conductance of the channels and the mixing function were both confirmed using low flow rate DI water. When increasing the pressure, leak was observed in the interface between the PDMS film and the acrylic shaft surface. This is to be resolved by either improving the bonding or using a tighter thermal shrink tube.

4. CONCLUSIONS

A new method for 3D micro channel fabrication on cylindrical surfaces based on a single mold process of flexible film was proposed. It was demonstrated that a 3D static micro mixer was successfully fabricated applying the proposed method. This result makes a new form of micro chemical devices with various potential applications possible.

REFERENCES

[1] B.-H. Jo, L. M. Van Lerberghe, K. M. Motsegood, and D. J. Beebe, *Three-Dimensional Micro-Channel Fabrication in Polydimethylsiloxane (PDMS) Elastomer,*, Journal of Microelectromechanical Systems, 9, pp.76-81, (2000).

STACKED STRUCTURE OF PMMA MICROCHANNELS FOR DNA SEPARATION FABRICATED BY DEEP X-RAY LITHOGRAPHY AND FUSION BONDING

Yuichi Utsumi[1], Tomohiro Ikeda[2], Megumi Minamitani[2], Kazuo Suwa[2]

[1] Laboratory of Advanced Science and Technology for Industry, University of Hyogo, JAPAN and [2] Fujipream. LTD., JAPAN

ABSTRACT

We proposed and fabricated a integrated structure of microchannels consists of three different functional PMMA layers for post-genome analysis, gene diagnosis, and screenings of useful materials for pharmaceutical. This integrated structure with 96 microchip capillary electrophoresis units in one chip is characterized as the simple structure with low cost and new aspects of the serial unit bio-chemical operation from DNA amplification to their analysis using microchip capillary electrophoresis.

Keywords: DNA analysis, Electrophoresis, PCR, Deep x-ray lithography

1. INTRODUCTION

The importance of the micro fluidics for DNA analysis systems have been widely recognized. Moreover it is very important to develop the high throughput DNA amplify technology and succeeding separation technology using electrophoresis in one chip to decode the genome in a short period for identifying gene functions and achieving the custom, order-made medical cares. We developed and evaluated the stacked structure of polymethylmethacrylate (PMMA) micro fluid channels consists of PCR well, DNA separation channel, and heat exchanger water channel using deep x-ray lithography [1], molding and fusion bonding techniques by nanoimprint equipment.

2. DESIGN OF THE STACKED STRUCTURE OF PMMA MICROCHANNELS

The design of the integrated structure with 96 microchip capillary electrophoresis units in one chip was performed using computational fluid dynamics, heat transmission, and electrophoresis simulation. As for the design of the microchip capillary electro phoresis (MCE), the separation resolution of DNA was intended to improve using the micro channel with variable width along with the corner of the channel [2]. We simulated the diffusion of the sample plug during electrophoresis using "FLUENT". As shown in Fig. 1 a), a sample plug diffuses in accordance with the electrophoresis flow. For micro channel with its width was narrowed down along with the corner, the diffusion of the sample plug

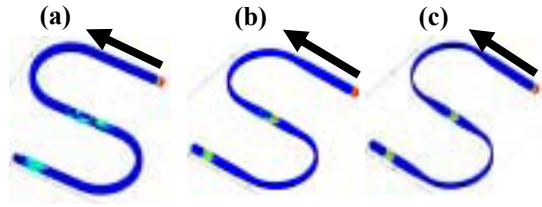

Figire 1 Sample plug diffusion along with the electrophoresis flow. Depth of the channel was 80 μm.
(a) The width of the channel was constant value of 80 μm.
(b) The width of the channel was reduced to 40μm at the corner.
(c) The width of the channel was reduced to 20μm at the corner.

978-0-9798064-0-7/μTAS2007/$20©2007CBMS

was considerably suppressed as shown in Fig. 1 b) and c). The design configuration and SEM image of fabricated structure of micro channels are shown in Fig. 2 (a) and (b). The size of each micro channel
for DNA analysis is 9 x 9 mm square.

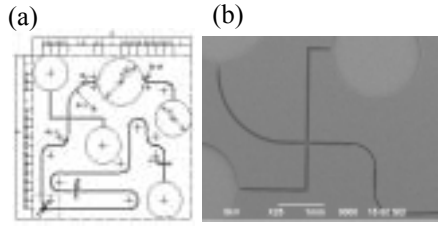

Figure 2 (a) ; The design configuration and (b) : SEM image of replicated structure of micro channels by nano-imprint technique. The diameter of the thermal cycler cell for PCR is 2.75 mm, corresponding to the volume of 1 to 2

3. FABRICATION OF THE THE STACKED STRUCTURE

The three layers of sample reservoir, capillary electrophoresis for DNA, and heat exchanger water channel for PCR thermal cycles were bonded without adhesive agent by fusion bonding at atmospheric pressure. The diameter of the thermal cycle cell for PCR is 2.75 mm corresponding to the volume of 1 to 2 pl. Figure 3 shows the outside view of the stacked structure of PMMA micro fluid channels. The stacked structure contains 96 DNA analysis micro channels, and a heat exchanger water channel. The size is 128 x 88mm square and 7 mm depth. Capillary electrophoresis was performed on a fluorescence microscopic apparatus equipped with a 488nm argon ion laser-induced fluorescence detection.

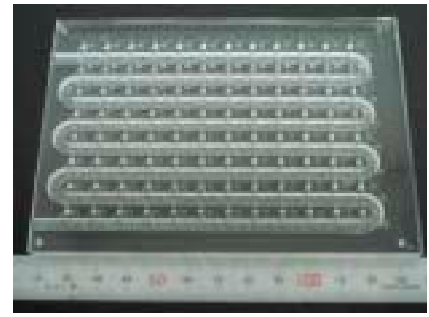

Figure 3. Outside view of the stacked structure of PMMA micro fluid channels. The structure contains 96 MCE channels.

4. EVALUATION OF DNA SEPARATION CHARACTERISTICS

Detection of DNA was carried out by measuring fluorescent at 534nm. A standard DNA stepladder marker (Bio-rad, USA) was used consisting 100 DNA fragments ranging from 100 to 1000bp in exactly 100-bp increments. The running buffer was 1/10 diluted solution of 10×TBE from Wako and 0.01% GelStar Nucleic Acid Gel Stains were used for a fluorescence detection of DNA. The length of the separation channel was 10.5mm and electrophoretic separation were performed at 0.75 kV. Figure 4 shows the electropherograms for separation and detection of 100 DNA fragments by MCE-chemiluminescence. As shown in the figure, DNA fragments ranging from 100 to 1000-bp was clearly separated within 190 sec using this integrated structure of micro fluid channels.

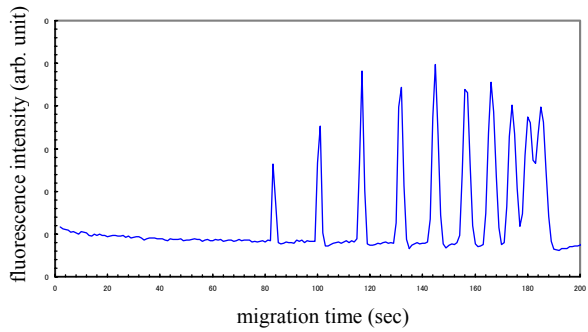

Figure 4 Electropherograms for separation and detection of 100 DNA fragments by MCE chemiluminescence.

5. EVALUATION OF ON CHIP PCR

We also evaluated the PCR property fabricated in the integrated structure of PMMA micro channels using PCR amplification kit "TAKARA EX Tag". The template was λDNA and the length of the target DNA was 714 bp. The holding time on PCR cycle were set 20 second at 92 and 55 ℃ and 60 second at 72 ℃. The total heat cycle of the steps were 25 times loaded by the use of the heat exchanger consists from heat medium channel as showed in Fig. 3. The reproducibility of the heat cycle was measured using thermocouple as shown in Fig. 5. The time set at one heat cycle for DNA amplification is 300 s. Figure 6 shows the peak signal from the 533 nm fluorescence of the amplified DNA, which suggest the possobility of the on-chip PCR at 96 wells using proposed heat exchanger in a DNA analysis MCE unit shown in Fig.3.

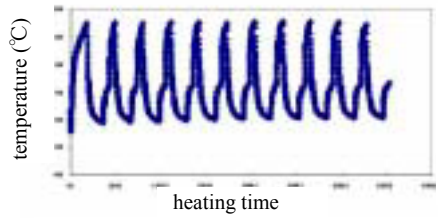

Figure 5 The measured heat cycles loaded by the use of the heat exchanger.

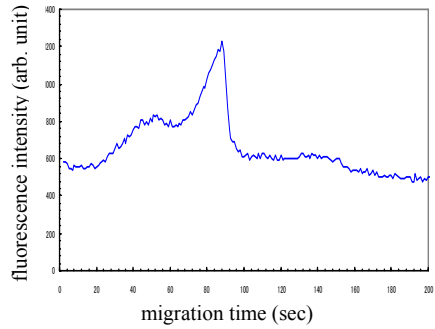

Figure 6 The peak signal from the 533 nm fluorescence of the amplified DNA

6. CONCLUSIONS

The proposed stacked structure of microchannels consists of three different functional PMMA layers is characterized as the simple structure with low cost and new aspects of the serial unit bio-chemical operation from DNA amplification to their analysis using microchip capillary electrophoresis (MCE). To improve DNA separation resolution, micro channel with narrow width at the corner was adapted based on theory proposed by C.T. Culbertson and B.M.Pagel et.al. The DNA fragments ranging from 100 to 1000-bp was clearly separated within 190 sec using this integrated structure of micro fluid channels. We also evaluated the PCR property fabricated in the integrated structure of PMMA micro channels using PCR amplification kit "TAKARA EX Tag". It was demonstrated that the proposed integrated structure of microchannels result in a good performance of the on-chip DNA amplification and separation in a small MCE unit area of 9 mm x 9 mm.

REFERENCES

[1] Y. Utsumi, et.al., J of Vac. Sci. and Technol. B, 2903, (2005)

[2] B. M. Paegel, et.al., Anal. Chem., 72, 3030, (2000).

ON-CHIP ANTIOXIDANT CAPACITY SCREENING USING INTEGRATED LOW-COST ORGANIC PHOTODIODES

Xuhua Wang[1,3], Maliwan Amatatongchai[2,4] , Duangjai Nacapricha[5] , Oliver Hofmann[3], John C. deMello[2,3], Andrew J. deMello[2,3] and Donal D. C. Bradley[1,3]

[1]Department of Physics and [2]Department of Chemistry, Imperial College London, London, SW7 2AZ, United Kingdom

[3]Molecular Vision Ltd, BioIncubator Unit, Imperial College London, London, SW7 2BP, United Kingdom

[4]Department of Chemistry, Faculty of Science, Ubonrajathanee University, Ubonratchthani, Thailand

[5]Department of Chemistry, Faculty of Science, Mahidol University, Bangkok, Thailand

ABSTRACT

We report an on-chip peroxyoxalate chemiluminescence (PO-CL) assay for antioxidant capacity determination with optical detection based on our highly compact and sensitive integrated detectors made from solution processed thin-film organic photodiodes (OPDs). We compared the performance of our OPDs for on-chip antioxidant capacity screening with that of commercial photomultiplier tubes (PMTs). The results show excellent consistency between the two detection methods.

Keywords: chemiluminescence, organic photodiodes, antioxidants, microfluidic chips

1. INTRODUCTION

The emerging organic/polymer photodetector technology offers new prospects for on-chip detection because it is low-cost, highly compact and easily integrated on a variety of substrates including plastics. We demonstrate application of solution processed thin film organic photodetectors to the antioxidant capacity determination of three herbs via a peroxyoxalate chemiluminescence assay performed on a moulded poly(dimethylsiloxane) (PDMS) microfluidic chip. In order to validate our approach, we compared the results with measurements obtained using conventional PMT based detection. While the results show excellent consistency between the two methods in terms of sensitivity of detecting low antioxidant levels, the OPDs offer a highly compact, low-cost and integrated on-chip solution.

2. EXPERIMENTAL

All chemicals were analytical grade and used without further purification. PO-CL reagents were extracted from Omniglow lightsticks. The active ingredients were bis(2-carbopentyloxy-3,5,6-trichlorophenyl)oxalate (CCPO), 9,10-bis(phenylethylnyl)-anthracene (green dye), sodium salicylate (catalyst) and hydrogen peroxide (oxidant). Solution A (PO-CL reagent/dye/catalyst) and solution B (hydrogen peroxide) obtained from the extraction were employed in all experiments. A mixture of ethyl acetate and acetonitrile in a volume ratio of 3:7 was used as solvent system for the preparation of antioxidant standards of α-tocopherol (vitamin E), β-carotene (vitamin A) and quercetin.

The schematic layout of the integrated microfluidic device is shown in Figure 1A. The details of the microfluidic chip fabrication are described in reference [1]. The OPDs were fabricated with blends of regioregular poly(3-hexylthiophene) (P3HT) and (6,6)-phenyl C_{61} butyric-acid methyl-ester (PCBM) by a solution-processing thin-film method [2]. The responsivity of the P3HT/PCBM organic photodiodes and the emission spectrum resulting from the CL reaction are shown in Figure 1B. The transient response for the 1 mm^2 OPDs in terms of rise and fall times are ~0.51 μS and ~0.66 μS, respectively, corresponding to a bandwidth of ~500 kHz [3].

The employed method for the determination of hydrogen peroxide scavenging activity of natural and polyphenolic antioxidants is based on an indirect peroxyoxalate chemiluminescence (PO-CL) assay [4].

978-0-9798064-0-7/μTAS2007/$20©2007CBMS

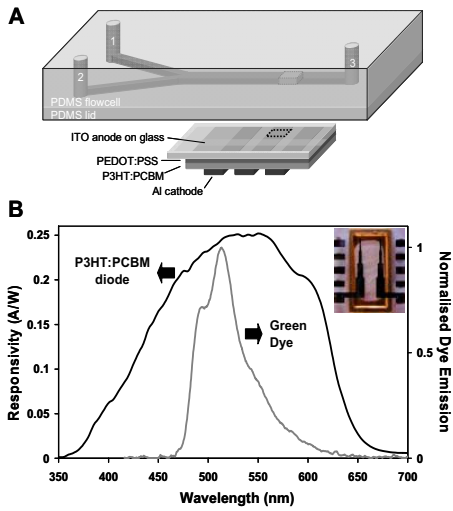

Figure 1. (A) Schematic of the experimental set-up. (B) Responsivity of organic P3HT:PCBM photodetector and its overlap with the CL emission.

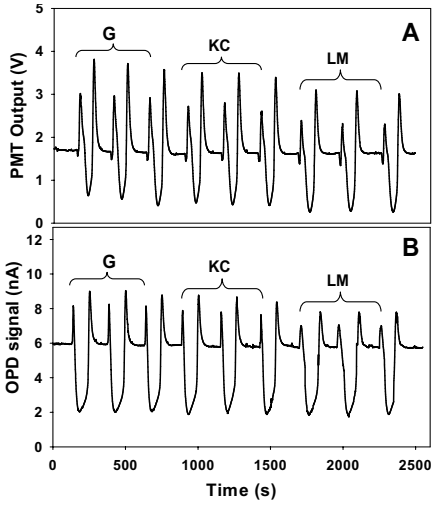

Figure 2. Examples of signal profiles obtained after triplicate injections of antioxidant plugs with (A) PMT detection and (B) OPD detection. G: Alpinia *galanga, KC: Kaempferia galanga, LM: Cymbopogon citratus.*

Three herbs were selected as samples for the total antioxidant capacity assay: Alpinia galanga (Galagal), Kaempferia galanga (Krachai) and Cymbopogon citratus (Lemongrass). The extraction scheme was adapted from the method reported by Parejo et al. [5]. The final extract of the Ethyl Acetate fraction (EAF) for each herb was measured for total antioxidant capacity using the microfluidic method with PMT and OPD based detection.

3. RESULTS AND DISCUSSION

The antioxidant assay was performed in a simple 2-inlet microchip with an in-line Rheodyne injection valve (50 µL injection loop) connected to the hydrogen peroxide inlet. An integrated system with an organic photodetector was developed and its performance was compared with a conventional PMT detection system. While α-tocopherol (vitamin E), β-carotene (vitamin A) and quercetin served as model antioxidants for system evaluation, the method was subsequently applied to the total antioxidant capacity (TAC) determination of herbal extracts.

The comparative performance of our miniaturised OPD detection system relative to conventional PMT detection was investigated through the evaluation of antioxidant standards for hydrogen peroxide scavenging capacity. The results are summarized in Table 1. Both detection systems provided excellent consistency (relative standard deviation (RSD) is < 2%) for 50 µL injections (n=3) of 10 µM β-carotene, 10 µM α-tocopherol and 50 µM quercetin. Furthermore, micromolar limits of detection (defined here as the concentration of antioxidant required to obtain a reduction in CL signal equal to 3 times the standard deviation of the background level) were obtained for all antioxidants. The antioxidant capacities to quench hydrogen peroxide were calculated from the calibration equation [4]. For both detection methods β-carotene was found to be the most efficient hydrogen peroxide

scavenger followed by α-tocopherol and quercetin, respectively.

Table 1
Summary of the analytical features of the microchip assay for TAC evaluation based on PMT and OPD detection.

Figure of merit		[a]Precision (RSD), n=3	[b]Limit of detection (μM)	[c]SA_{HP} ($X\ 10^{-3}\ \mu M^{-1}$)
PMT	β-carotene	0.72	1.92	3.27
	α-tocopherol	0.46	9.92	2.36
	quercetin	1.53	48.08	0.31
OPD	β-carotene	0.86	1.87	3.63
	α-tocopherol	0.41	9.40	2.96
	quercetin	1.60	47.60	0.59

Three herbal extracts were used as samples to evaluate the microchip-based TAC determination method. The ethyl acetate fraction (EAF) of the sample extracts was diluted 10-fold in ethyl acetate prior to injection. Figure 2 shows the comparison of signal profiles obtained from PMT and OPD detection of triplicate injections of herb samples Alpinia galanga (G), Kaempferia galanga (KC) and Cymbopogon citratus (LM) into the microfluidic system. The results show excellent consistency between the two detection methods. The results thus demonstrate that our OPD based detection method is sufficiently accurate and sensitive for TAC determination.

4. CONCLUSIONS

For the first time, we have demonstrated that an integrated microscale CL assay can be implemented in a quantitative low-cost format. Detection is based on a PO-CL reaction using cheap and commercially available reagents. In conjunction with molded PDMS microfluidic chips and organic photodetectors this offers an attractive route towards the fabrication of portable low-cost quantitative diagnostic tests, which incorporate the microfluidic circuit and detector in a single monolithic device.

ACKNOWLEDGEMENTS

The authors acknowledge support from the UK Biotechnology and Biological Sciences Research Council through its Small Business Research Initiative (grant 147/SBRI 19689), and are grateful to Merck UK Chemicals for the provision of P3HT and to LG Philips for provision of substrates. The authors are also grateful to Dr Sung Joon Bae and Dr Paul Stavrinou for useful discussions.

M.A. and D.N. acknowledge financial supports from the Thailand Research Fund and the Center for Innovation in Chemistry: Postgraduate Education and Research Program in Chemistry (PERCH-CIC), Commission on Higher Education, Ministry of Education.

REFERENCES

1. X. Wang, O. Hofmann, J. Huang, E.M. Barrett, R. Das, A.J. deMello, J.C. deMello, D.D.C. Bradley, Biomems and Nanotechnology II: Proc.of SPIE **6036**, 106-109 (2006).
2. X. Wang, O. Hofmann, R. Das, E.M. Barrett, A.J. deMello, J.C. deMello, D.D.C. Bradley, Lab Chip, **7**, 58 - 63 (2007).
3. E.M. Barrett, X. Wang, P.N. Stavrinou, D.D.C. Bradley, to be submitted to IOP journal.
4. A. Arnous, C.P. Petrakis, D.P. Makris, P. Kafalas, J. Pharm. and Toxi. Methods **48**, 171-177 (2002).
5. I. Parejo, F. Viladomat, J. Bastida, R-R Alfredo, N. Flerlage, J. Burillo, C. Codina J. Agri. and Food Chem., **50**, 6882-6890 (2002).

AN INTEGRATED CALORIMETRIC BIOSENSOR AND ITS CHARCTERIZATION

Seung-Il Yoon[1], Mi-Hwa Lim[2], Jeon-Soo Shin[2], and Yong-Jun Kim[1]

[1]*School of Mechanical Engineering, Yonsei University, Republic of Korea*

[2] *Department of Microbiology, Yonsei University College of Medicine, Republic of Korea*

ABSTRACT

A new micromachined microcalorimeter with a split-flow microchannel structure is being reported, and the proposed biosensor is characterized through measuring reaction heat of biotin-streptavidin and detecting Neisseria meningitidis. The split-flow microchannel scheme constantly keeps the output of the microcalorimeter near zero level when there is no biochemical reaction, which eliminates the need of an active element such as a heater. Thermal components for the microcalorimeter have been fabricated on a high thermal resistivity layer to improve the sensitivity of the device.

Keywords: Microcalorimeter, biotin-streptavidin, Neisseria meningitidis, split-flow microchannel

1. INTRODUCTION

Most of conventional microcalorimeter related researches have been carried out in view points of high sensitivity and thermal calibration. For higher sensitivity, it is important to maximize the temperature differences between hot and cold junctions. Thus, there have been various efforts to minimize parasitic heat transfer to a substrate for maximizing the temperature differences [1]. However, hot junctions of the previous microcalorimeter still contact with a high-thermal-loss substrate, thin silicon diaphragm.

In a view point of thermal calibration, microcalorimeters can be classified into two, active and passive. Even though a passive type is simple to fabricate [2], most of microcalorimeter has adopted an active heating element, which can make the temperatures of both junctions same by heating [3]. However the additional heating structure makes fabrication and measurement process more complex.

This work demonstrates an accurate passive microcalorimeter. To improve sensitivity, high thermal resistivity layer, SU-8, was used between the substrate and thermal components. For accurate measurement, the split-flow microchannel was introduced. By using the proposed sensor, a reaction heat of biotin and streptavidin pairs was measured, and *Neisseria meningitidis* was detected.

2. PRINCIPLE AND FABRICATION

The split-flow microchannel structure is introduced to eliminate a calibration process by adopting reference chambers over cold junctions. Fig. 1 shows conceptual and cross-sectional view of the proposed device. A fluidic stream containing target biomolecules splits into the reaction and reference chambers through the split-flow microchannel. The temperature of this fluidic stream itself makes the temperatures of hot and cold junctions at equal level, and offsets external noises in both chambers, which results in near zero output voltages. Then, another fluidic stream with capture biomolecules is applied to the reaction chamber on hot junctions, only. Applied capture biomolecules produces a reaction heat

978-0-9798064-0-7/μTAS2007/$20©2007CBMS

with target biomolecules, which makes the temperature differences between hot and cold junctions. Finally, the voltage is measured as a result of biochemical reaction heat in the reaction chamber. (Fig. 2).

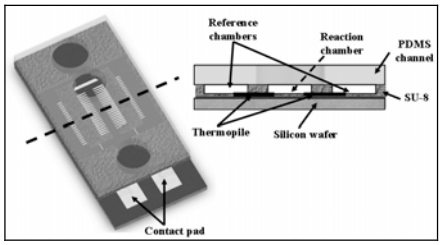

Figure 1. Conceptual and cross-sectional view of the microcalorimeter

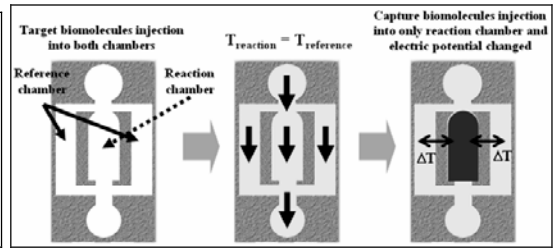

Figure 2. Measurement process

3. EXPERIMENT AND RESULT

In order to verify characteristics of the fabricated microcalorimeter, heats generated from biotin-streptavidin reaction were measured (Fig. 3). In order to verify characteristics of the fabricated microcalorimeter, generated heats due to biotin - streptavidin reaction were measured by using the sensor. At first, 3 μl of biotin was injected into both chambers with a concentration of 3.4 mg/ml. Then, 3μl of streptavidin with various streptavidin concentrations of 0.01, 0.1, 0.25, 0.5 and 1.0 mg/ml was applied into the reaction chamber only. Finally, output signal changes due to biochemical reaction between biotin-streptavidin pairs were recorded by the voltagemeter (Semiconductor Characterization System 4200, Keithley). In results, output voltages of the microcalorimeter were measured to be from 48.5 μV to 499 μV.

At same time, biological reaction of *N. meningitidis* group B (NMGB) and a specific monoclonal antibody to its capsular polysaccharide [4] was detected. At first, 3 μl of NMGB was injected into both chambers with various amounts of 1.0×10^1, 1.0×10^2, 1.0×10^3, 1.0×10^4, 1.0×10^5 and 1.0×10^6 Colony Forming Unit (CFU). Then, 3μl of HmenB3 whose concentration was 100 μg/ml was applied into the reaction chamber only. Finally, output signal changes due to biochemical reaction between NMGB and HmenB3 were recorded by the voltagemeter.

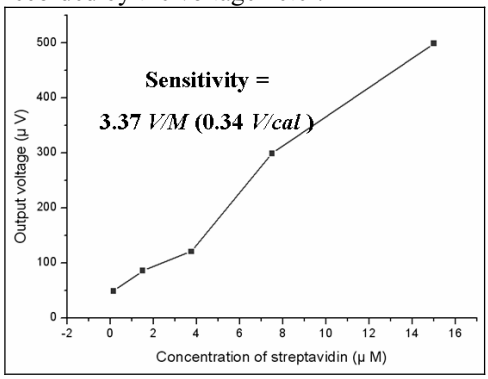

Figure 3. Output voltages according to concentrations of streptavidin

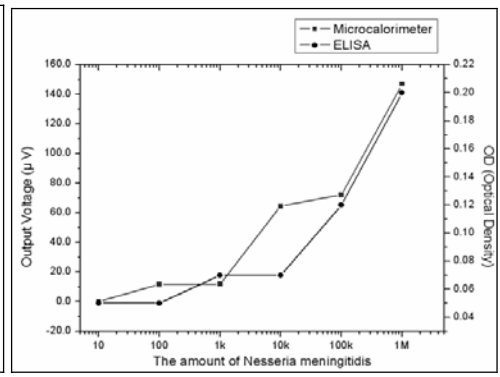

Figure 4. Comparison of results by the microcalorimeter and ELISA

For verifying the results, exactly same number of NMGB was reacted with HmenB3 and optical density was measured by ELISA(enzyme-linked immunosorbent assay). In the ELISA result, optical density increases as the amount of NMGB reacted with HmenB3 increases. As seen in Fig. 4, relatively similar pattern of results can be observed.

4. CONCLUSION

A novel split-flow microcalorimeter was designed and fabricated using polymer-based micromachining. Even though the proposed microcalorimeter is a passive type in which any heating structure does not integrated, the output signal maintained to be a nearly zero level by using the split-flow microchannel when there is no biochemical reaction. At the same time, the split-flow microchannel reduced a measurement time by removing calibration steps. The thermal sensing component has been fabricated on a high thermal resistivity layer to improve the sensitivity. The split-flow microcalorimeter was characterized by measuring reaction heat of biotin-streptavidin pairs. The proposed microcalorimeter could detect 10^{-5}℃ at least, and its sensitivity was 0.34 volt/cal. After its characterization, *N. meningitidis* was detected. Measured reaction heats of *N. meningitidis* and its antibody were 1.26×10^{-6} to 9.22×10^{-5} calories. The measurement results were compared to the commercially available system. The proposed microcalorimeter has the simple structure and measurement process. The microcalorimeter is also compatible with most polymer-based microfluidic components, which can be applied to various fields such as a Lab-on-a-chip.

ACKNOWLEDGEMENTS

This work was supportred by Seoul Research and Business Development Program(10816), a grant from National Core Research Center (NCRC) of Yonsei University and Special Basic R&D Project

REFERENCES

[1] Werner Winter and Gunther W. H. Hohne, *Chip-calorimeter for small samples*, Thermochimica Acta, 403, pp. 43-53, (2003)

[2] Francisco E. Torres et al*., Enthalpy arrays*, PNAS, 10126, pp. 9517-9522 (2004)

[3] D. Voisard et al., *Quantitative calorimetric investigation of fed-batch cultures of Bacillus sphaericus 1593M*, Thermochimica Acta, 394, pp. 99–111 (2002)

[4] J.S. Shin et al., *Monoclonal Antibodies Specific for Neisseria meningitidis Group B Polysaccharide and Their Peptide MimotopesInfect*, Immun, 69, pp.3335-3342 (2001)

INTEGRATING WHOLE TRANSCRIPTOME ASSAYS ON A LAB-ON-A-CHIP: A KEY APPROACH TOWARDS SINGLE CELL GENE PROFILING

N.Bontoux[1,2], L. Dauphinot[1], T. Vitalis[1], V. Studer[1], Y. Chen [2], J. Rossier[1], M-C. Potier[1]

[1]Laboratoire de Neurobiologie, ESPCI, FRANCE

[2]Laboratoire de Photonique et de Nanostructures, CNRS, FRANCE

ABSTRACT

In this paper, we present a novel microfluidic approach for whole transcriptome amplification of single cells. It involves performing all steps, from the capture of a single cell to the reverse-transcription (RT) reaction, in a PDMS lab-on-a-chip. We show that this approach enables 74% of the transcriptome to be profiled at the single cell level whereas this is usually less than 4% when reactions are performed in µL volumes.

Keywords: single cell, PDMS, transcriptome, gene expression, lab-on-a-chip

1.INTRODUCTION

Analysis of all the genes that are expressed in a single cell at a given time and under given physiological or pathological conditions, i.e. of a cell's transcriptome, constitutes a major challenge in understanding the complexity of living organisms. Such analyses will indeed help unravelling cellular regulatory networks and differentiation mechanisms. It is also of significant interest for diagnosis as an efficient means of identifying new therapeutic targets.

In our previous work [1, 2], we had demonstrated that all the steps, i.e. single cell capture and lysis, reverse transcription (RT) and single gene PCR amplification, could be performed at the single-cell-scale using PDMS devices. More recently, Marcus *et al.* [3] have proposed a highly integrated device for the quantitative analysis of the expression of a few genes. Their technology however cannot be used for whole transcriptome assays. Here we report an integrated microchip for cell capture, lysis, RT and PCR.

2.EXPERIMENTAL

Our lab-on-a-chips were made out of PDMS using multi-layer soft-lithography [4]. Each chip consisted in two rotary mixers [5], i.e. two rings where mixing was achieved by peristaltic pumping. The smallest ring had a volume of 8 nL and was used for cell lysis and reverse-transcription; the largest 40 nL ring was used for PCR. Fluidic and control channels, respectively in black and gray on figure 1a., were 15 µm wide. Microfluidic valves were pressure actuated and temperature was controlled using a flat-bed thermocycler.

The on-chip integration of our biological protocol [5] was first validated using mouse brain RNA. We then assessed the sensitivity of our lab-on-a-chip on single cells. Cells were dissected out of the Caudal Ganglionic Eminence (CGE, a region of the neocortex) of 14-days-old mouse embryos and dissociated in PBS. They were peristaltically pumped from the "cells in" entry port using valves 1, 2 and 3 and single cells were trapped between valves 4,5,6 and 7 (fig. 1). Using the other valves, reagents for cell lysis and RT were

978-0-9798064-0-7/µTAS2007/$20©2007CBMS

injected from the "RT mix in" port and the 8-nL rotary mixer was filled up with reagents. The content of the ring was then mixed peristaltically and cell lysis and RT were performed at 37°C. After RT, the ring content was flushed and cDNAs were either collected out of the device and globally amplified in µL volumes or transferred with PCR reagents in a 40-nL PCR ring for single gene amplification.

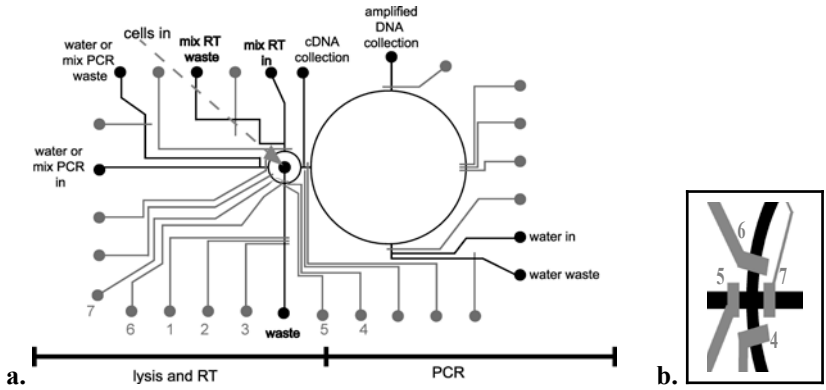

Figure 1: Schematic of the two-layers PDMS device used for on-chip cell lysis, reverse-transcription and single-gene PCR. ***a.*** *Global view of the device.* ***b.*** *Close-up view of the cell trapping region of the device.*

To assess the sensitivity of our method for single cell profiling, gene expression profiles were determined using pangenomic microarrays. The profiles obtained using our device were compared to those obtained when reactions were performed on the same quantity but in µL volumes (in microcentrifuge tubes) and to those obtained using standard profiling methods involving micrograms quantities of RNA.

3.RESULTS AND DISUCUSSION

Although single gene PCR was efficient in PDMS device, global amplification of all cDNAs turned out to be more efficient when conducted in µL volumes rather than on-chip, i.e. in nL volumes. We thus conducted all global PCR amplification in µL volumes, in microcentrifuge tubes.

When performing the RT reaction on-chip in nL volumes and amplifying all cDNAs in µL volumes, we demonstrated that small RNA quantities were amplified with accuracy and efficiency. More specifically, more than 12000 genes were detected reproducibly after amplification when RT was performed on 10 pg in the 8 nL rotary mixer (fig. 2c) whereas only 719 genes could be detected reproducibly when RT was conducted on the same quantity but in a 10 µL volume (fig. 2b). Moreover, integrating RT on chip resulted in an outstanding sensitivity (fig. 2). Indeed, 74% of the genes identified using 15 µg of RNA (fig. 2a,d) were detected at the single-cell level using our microfluidic approach whereas less than 4% were detected with the protocole in a tube (fig. 2d).

On-chip integration of single-cell capture, cell lysis and reverse-transcription also proved successful and specific. Fig. 3 shows that the size and the intensity of the reverse transcribed and amplified RNAs are higher when cell lysis and reverse transcription are done in the microfluidic device as compared to a tube. About 5000 genes were successfully

profiled per cell using our microfluidic device. This is the number of genes expected to be expressed in a given cell at a given time.

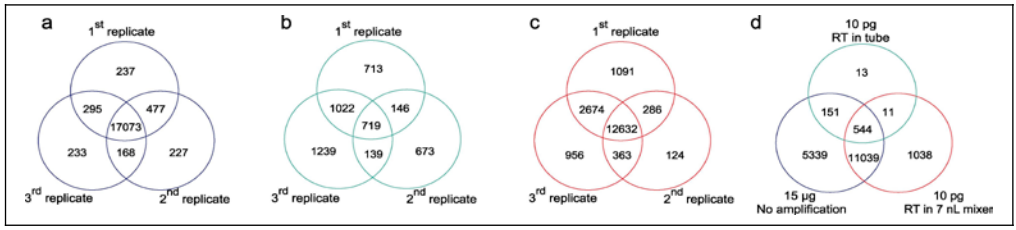

*Figure 2: Venn diagrams illustrating the obtained gene expression profiles in three replicate experiments, when 15 µg of total RNA were reverse-transcribed (**a**) or when 10 pg of total RNA were reverse-transcribed and amplified in µL volumes (**b**) or using our microfluidic approach (**c**). (**d**) Comparison of the expression profiles obtained on microgram amounts of RNA (left) or at the single-cell level, using either the conventional (top circle) or the microfluidic protocol (right circle).*

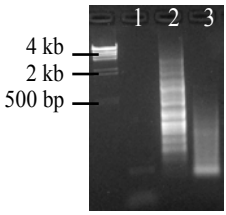

Figure 3 : Electrophoretic assessment of reverse transcribed and amplified RNAs obtained from a single mouse embryonic neuron.
1: PCR negative control
2: cell capture, lysis and RT performed on chip
3: cell capture, lysis and RT performed in a tube, in µL volumes

4. CONCLUSION

To our knowledge, this is the first report of an integrated lab-on-a-chip for single cell whole transcriptome assays. We believe that it constitutes a technological breakthrough. Indeed, it will both ease the manipulation and at the same time substantially increase the resolution of single cell profiling. Such a tool should prove very useful in many fields of biology, where cell heterogeneity is a key paradigm, and also in diagnosis.

ACKNOWLEDGEMENTS

N.Bontoux thanks the Direction Générale de l'Armement and the NAPA project community for their financial support.

REFERENCES

[1] N. Bontoux *et al.*, Proceedings of µTAS 2006 Conference 1, p 7-9 (2006)
[2] N. Bontoux *et al.*, Proceedings of µTAS 2005 Conference 2, p1516-1518 (2005)
[3] J.S. Marcus, W.F. Anderson , S.R. Quake, Anal. Chem. **78** (2006)
[4] M.A. Unger *et al.*, Science **288** (2000)
[5] H.P. Chou, M.A. Unger, S.R. Quake, Biomedical Microdevices **3**, 323-330 (2001).
[6] L. Petalidis *et al.,* Nucleic Acids Res. **31** (2003)

CELL CHARACTERIZATION USING PROTEIN-FUNCTIONALIZED PORES

Andrea Carbonaro[1], Lucy Godley[2] and Lydia L. Sohn[1]

[1]Mechanical Engineering Department, University of California, Berkeley, CA USA

[2]Section of Hematology/Oncology, Department of Medicine, The University of Chicago, Chicago, IL USA[2]

ABSTRACT

Cell characterization based on cell-surface markers is a critical element in clinical diagnosis, therapeutic monitoring, and basic biomedical research. Here, we demonstrate a highly-sensitive and label-free method that identifies the presence of particular cell-surface markers by measuring the electrical current changes across a protein-functionalized pore through which individual cells flow. The specific interactions between the particular cell-surface markers and the functionalized proteins retard the cell, such that the cell traverses through the pore more slowly than if the pore were not functionalized or were functionalized with non-specific proteins.

Keywords: artificial pore, electronic sensing, cell-surface marker, protein-protein interaction

1. INTRODUCTION

Cell characterization through the identification of membrane components expressed at the cell surface is an essential element for basic biomedical research and also for clinical applications. Current technologies (e.g. flow cytometry, fluorescent microscopy, or cell-affinity chromatography) lack information about individual cells and require exogenous labeling and/or advanced sample preparation, which necessitate additional reagents and time. Here, we present a highly-sensitive, accurate, and label-free method for characterizing individual cells based on cell-surface markers, which employs an on-chip artificial pore, resistive-pulse sensing, and surface chemistry. This approach identifies cell-surface markers based on interactions with the functionalized pore.

2. THEORY

Cell-surface marker characterization is performed in a protein-functionalized artificial pore using resistive-pulse sensing. As each cell enters the pore, it partially blocks the flow of current, leading to a transient increase, or pulse, in the pore's electrical resistance. Sensing the resistive pulse is accomplished by performing a four-point measurement of the electrical current through the pore using metal electrodes. While pulse magnitude is related to the cell size ($\delta I/I \sim V_{particle}/V_{pore}$) [2], the resistive-pulse width indicates the transit time, τ, a cell takes to pass through a pore. A cell's transit time through a functionalized pore (τ_2 or τ_3) is greater than that through an unfunctionalized or "blank" pore (τ_1), due to interactions between the cell-surface marker of interest and the functionalized pore surface. If the interaction is non-specific, then $\tau_2 \geq \tau_1$ (center in Fig. 1). If the interaction is specific, then $\tau_3 >> \tau_1$ (right in Fig. 1) [1].

978-0-9798064-0-7/μTAS2007/$20©2007CBMS

3. EXPERIMENTAL

Our method is based on an on-chip artificial pore that is connected to two reservoirs and a set of filters. The device is fabricated using standard soft-lithography and molding techniques: photolithography was first used to pattern a master of the pore, the filters, and reservoirs [3]. Next, the master was cast in a polydimethylsiloxane (PDMS) slab that was subsequently sealed to a glass slide with previously patterned Pt electrodes (Fig. 2A). Before thermally bonding the PDMS to the glass slide, the region between the electrodes is coated with amino-silane groups using a solution of aminopropyltriethoxysilane (APTES) in anhydrous toluene (10% w/w) at room temperature that is applied via micro-contact printing. Then, a micropipette is used to deliver ~50 μL of a 5 mM solution of N-5-Azido-nitrobenzoyloxysuccinimide (ANB-NOS) to the area between the electrodes. Proteins are then injected into the pore and allowed to incubate for 3-4 hours. For the covalent binding of proteins with the ANB-NOS treated glass substrate, the device is placed directly under a UV-light source (Ushio 350DS) for 3 min. This activates the photoreactive groups of ANB-NOS. Excess proteins are then flushed through the device with buffer solution (1× PBS at 25 °C) (Fig. 2B) [4]

4. RESULTS AND DISCUSSION

In Fig. 3 we show our ability to detect CD34 receptors expressed on the surface of murine erythroleukemia (MEL) cells when the pores were functionalized with 1500 μg/mL of antibody. A suspension of 10^5 cells/mL MEL cells was injected at a non-pulsatile pressure (~10 kPa) into 1) a blank pore; 2) a pore functionalized with rat IgG2a isotype control antibody; and 3) a pore functionalized with anti-CD34 monoclonal antibody. MEL cells were significantly retarded when passing through a pore functionalized with anti-CD34 antibody. MEL cells took 4.41 ms longer to travel across the pore when the pore was functionalized anti-CD34 antibody as compared to the case when the pore was unfunctionalized or functionalized with isotype-control antibodies.

As another application to our method, we screened for CD71, a specific receptor found on the surface of human hematopoietic stem cells 7 days into differentiation [5]. [Erythropoietin is used to induce differentiation with these cells.] Fig. 4 shows the transit-time distributions obtained when a population of cells (10^5 cells/mL) was injected into pores functionalized with mouse IgG1, k isotype control and anti-human CD71. In both experiments, the concentration of antibodies was the same (200 μg/mL). Because CD71 is present on the surface of hematopoietic stem cells only during particular phases differentiation, these preliminary data show that our method could be employed to study stem cell differentiation.

5. CONCLUSIONS

The method described here is broadly applicable to experimental or clinical situations in which there is a crucial need to characterize cell-surface components. Interrogation is possible for any cell-membrane component as long as there is a reagent with which it can interact (e.g. detection of particular sugars at the cell surface through binding to functionalized lectins). Because cells are analyzed individually and without the need of an exogenous label, this method could be used to diagnose and monitor disease. As well, this method could be used to separate and recover cells for further propagation, thus enabling studies of cell populations that occur in very small numbers, such as stem-cell populations.

ACKNOWLEDGEMENTS

The authors thank H. Huang for helpful discussions regarding data analysis, J. Crispino for providing the MEL cells, A. Wickrema for providing the stem cells and A. Fischer for her help with the cell culture. This work was partially supported by NIEHS and NSF.

REFERENCES

[1] A. Carbonaro, L. Godley, and L. L. Sohn, submitted, (2007).
[2] Saleh, O.A. and L.L. Sohn, Rev. Sci. Instr., 72(12): p. 4449, (2001).
[3] Y. N. Xia and G. M. Whitesides, Angew. Chem.-Int. Edit., 37, p. 551, (1998).
[4] S. Karrasch, et al., Biophys. J., 65, p. 2437, (1993).
[5] H.K.A. Mikkola et al., Nature, 421, p. 547, (2003).

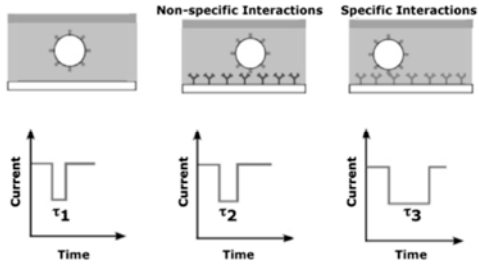

Figure 1. Method description. As each cell passes through the pore, a current pulse is generated. Pulse width indicates cell transit time, τ. Specific interactions between cell-surface markers and a functionalized pore retard the cell [1].

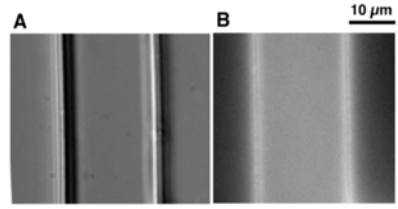

Figure 2. Pore functionalization. A, Optical image of an artificial pore filled with 1× PBS; B, Epifluorescent image of a pore functionalized with 1500 μg/mL of FITC-conjugated anti-CD34 antibody.

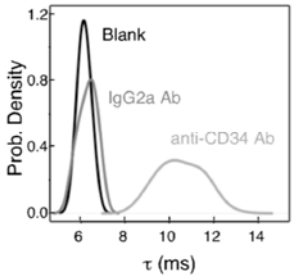

Figure 3. Detection of CD34 receptors on murine erythroleukemia (MEL) cells. Transit-time distributions of MEL cells flowing through a blank pore and a pore functionalized with either IgG2a (non-specific antibody) or anti-CD34 antibody (specific antibody). The shift in transit time is observed only when specific protein-protein interactions occur [1].

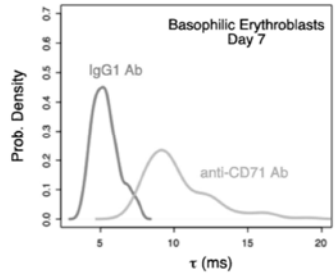

Figure 4. Detection of CD71 receptors on human hematopoietic stem cells. Cells were injected at a pressure of ~8.5 kPa into 800 μm-long × 25 μm-wide × 25 μm-high pore. Transit time distributions of human stem cells flowing through a pore functionalized with either IgG1 (non-specific antibody) or anti-human CD71 antibody (specific antibody).

MULTI-CELL SORTING ON MICRO FLUIDIC CHIPS USING OPTICAL GRADIENT FORCE

Hideya Nagata[1], Yuichiro Yoshida[1], Tomomi Ishido[1], Hidenori Nagai[2], Yoshio Tanaka[1], Shin-ichi Wakida[2], Yoshinobu Baba[1, 3], Mitsuru Ishikawa[1] and Ken Hirano[1, 4]

[1]Health Technology Research Center, National Institute of Advanced Industrial Science and Technology (AIST), Japan, [2]Human Stress Signal Research Center, National Institute of Advanced Industrial Science and Technology (AIST), Japan, [3]Graduate School of Engineering, Nagoya University, Japan, [4]PRESTO, Japan Science and Technology Agency (JST), Japan

ABSTRACT

We have developed a chip-based multi-cell sorter using optical gradient force to recover dielectric microparticles, such as living cells and polymer beads. Unlike other existing optical trapping techniques, our technique allows us to recover dielectric microparticles at an irradiated place by a laser beam, in which optical gradient force is generated. This force resists hydrodynamic force in such a way that flowing microparticles in a channel are deflected from a mainstream to a collection well with a horizontally-directed laser beams.

Keywords: multi-cell sorting, optical gradient force, dielectric microparticle, condensation effect

1. INTRODUCTION

Cell sorters have widely been used to recover desired cells from basic researches, such as abnormal cytology, regenerative medicine, and drug development, to clinical examinations. Typical fluorescence-activated cell sorters (FACS), although they are capable of efficient and high-throughput separations, are not easily miniaturized because of their separation mechanism and complex hardwares. Also, FACS might damage living cells, and was not able to recover simultaneously more than three kinds of cells. Dielectric particles are moved to the focal area of a laser beam though their dielectric properties (Fig. 1) [1]. To miniaturize hardware and to recover gently more than four kinds of cells, we have developed a multi-cell sorter based on optical gradient force technique and microfluidic chip technology. In this article, we demonstrate multi-sorting method of recovering cells and polystyrene beads using an optical gradient force on a chip.

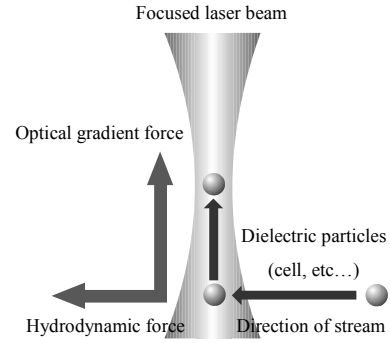

Figure 1. Schematic of a cell sorter using laser gradient force. Using this gradient force, target particles in a channel can be recovered by a change in their moving direction against hydrodynamic force by irradiation of a laser beam [1].

978-0-9798064-0-7/μTAS2007/$20©2007CBMS

2. EXPERIMENTAL

We used two types of optical sorting chips. One had two collection wells (70 μm × 35 μm in square and 25 μm in depth for each well) for recovery of two kinds of microparticles [1]. The other had five collection wells (70 μm × 35 μm in square and 30 μm in depth for each well) for recovery of five kinds of microparticles. Our experiments were carried out using an inverted fluorescence microscope (IX71, Olympus, Tokyo), which was modified to be combined with a horizontal laser manipulation system. Flowing microparticles in a channel were irradiated with a horizontally-directed laser beam passed through an objective lens (Fig. 2). A 100-μm-thick wall between a channel and outside of the chip was essential to focusing a CW Nd:YAG laser beam (1064 nm) at the bottom of a collection well because of the limited working distance of an objective lens (UPlanApo; 40×/0.85, Olympus, Tokyo). Fluorescent polystyrene beads of 2-6 μm in diameter, two types of *E. coli* expressing GFP or DsRed proteins, and yeasts (*S. cerevisiae*) were flowed into an optical sorting chip using three electro-osmotic pumps (RP3, Nano Fusion Technologies, Inc., Tokyo).

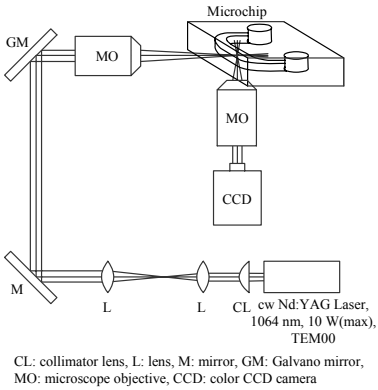

Figure 2. Schematic of a chip-based multi-cell sorter using optical gradient force. A laser beam is scanned using a galvano mirror to sort individual particles into each collection well.

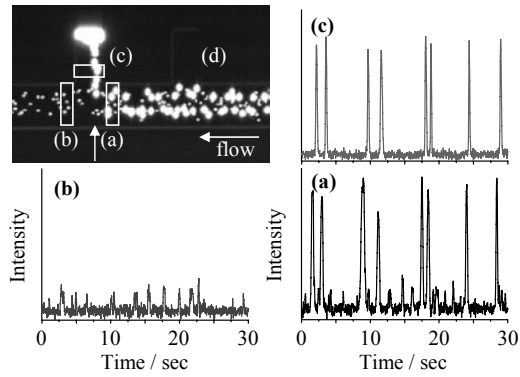

Figure 3. Image of 4.5-μm fluorescent polystyrene beads recovered from a mixture of 4.5-μm and 1-μm beads at a target collection well (c) with a focused laser beam (300 mW). As a negative control, a laser beam was not focused into a collection well (d). No beads were recovered in this well.

3. RESULTS AND DISCUSSION

Figure 3 shows the recovery of beads using an optical gradient force. Because an optical gradient force depends on a particle volume, 1-μm beads were passed through a CW laser beam (Fig. 3(b)); on the other hand, 4.5-μm beads were moved into a target collection well where a laser beam was focused (Fig. 3(c)). Thus, this method of sorting on the basis of their physical size and relative permittivity of particles can sort non-fluorescent particles.

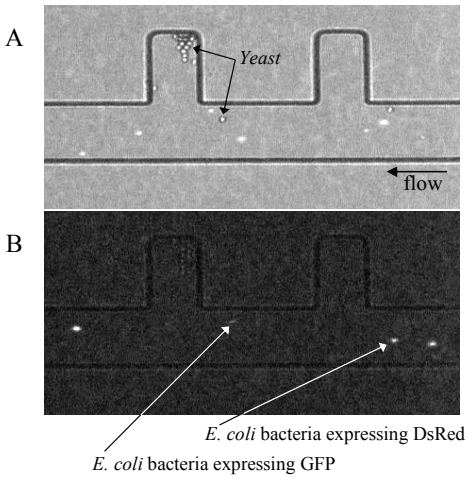

Figure 4. Images of yeasts selectively recovered from a mixture of yeasts and *E. coli* expressing GFP or DsRed proteins at a target collection well by an on-off switching of a laser.

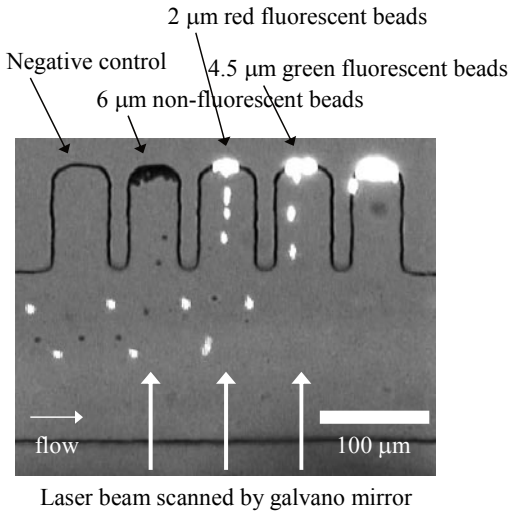

Figure 5. Image of multi-sorting of particles by a laser scanning using a galvano mirror system.

Figure 4 shows images of yeast selectively recovered from a mixture of yeast and two types of *E. coli* by an on-off switching of a laser. The fluorescent cells are *E. coli* expressing GFP or DsRed proteins; non-fluorescent cells are yeast. Yeast was recovered into a target collection well (Fig. 4A), although no *E. coli* was recovered (Fig 4B) by an on-off switching of a laser. A survival rate of yeast recovered by the laser beam is 91%, which was evaluated with colony counts. Figure 5 shows a result of multi-sorting of beads. Thus, we succeeded in sorting each bead into individual target collection wells from a mixture of three kinds of beads.

4. CONCLUSIONS

We have developed a multi-cell sorter on a chip which is able to recover gently cells and to sort each bead into each targeting collection well from a mixture of three kinds of beads. Our multi-cell sorter promises to recover more than three kinds of cells on conventional cell sorters. In the next step of our development, possibilities to recover gently more than four kinds of cells will be considered.

REFERENCES

[1] K. Hirano, Y. Baba, *Optical recovery of particles on a chip toward cell sorting and bead-bed detection*, Proc. Micro Total Analysis Systems 2002, Kluuwer Academic Publisher, Dordrecht, The Netherlands, pp. 272–274, (2002).

PARTICLE SHADOW TRACKING – COMBINING MAGNETIC PARTICLE MANIPULATION WITH *IN-SITU* OPTICAL DETECTION IN A CMOS MICROSYSTEM

U. Lehmann[1)], M. Sergio[2)], S. Pietrocola[1)], C. Niclass[2)], E. Charbon[2)] and M.A.M. Gijs[1)]

[1] *Institute of Microelectronics and Microsystems*
[2] *School of Computer and Communication Sciences,*
Ecole Polytechnique Fédérale de Lausanne (EPFL)
Lausanne, SWITZERLAND

ABSTRACT

We present a hybrid CMOS based microsystem where magnetic actuation of microparticles is combined with integrated optical detection via Single Photon Avalanche Diodes (SPADs). The system's configuration permits the manipulation and detection of single magnetic particles having diameters of 1, 3 and 5 μm. We are able to show a size sensitivity of the particle detection, with a clear distinction between different particle diameters.

Keywords: Magnetic particles, CMOS, optical detection, Single Photon Avalanche Diode

1. INTRODUCTION

Miniaturized magnetic manipulation of microparticles or cells has been gaining interest and applicability within recent years [1, 2]. A promising option is the combination of CMOS and microfluidics in hybrid systems [3], since they offer high flexibility. The system presented here, uses a CMOS chip for magnetic actuation and simultaneous optical detection. The magnetic actuation is achieved by sequential displacement of the magnetic field maximum generated by the currents in a double layer of overlapping square coils. The center of each coil is instrumented with a Single Photon Avalanche Diode (SPAD) which serves as optical sensor [4]. A glass capillary placed on top of the chip holds the magnetic microparticles suspended in an aqueous solution.

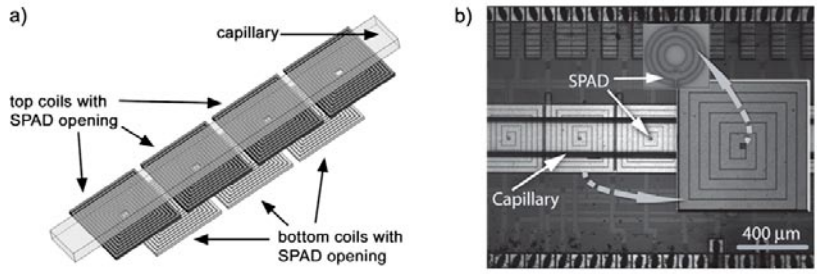

Figure 1. Representation of the CMOS system: a) Schematic explosion view showing the position of the square coils and the capillary, b) Photomicrograph of the hybrid CMOS system, with a coil and a center SPAD in detail.

978-0-9798064-0-7/μTAS2007/$20©2007CBMS

2. OPTICAL DETECTION

When an object, e.g. a magnetic particle, passes over the coil center and thus the sensor it causes a temporary occlusion of the optical path, as depicted in Fig. 2. As a result the photon flux decreases and hence the photon count at the detector site. The photon count reduction is a complex function of the detector's sensitive area, the refraction indexes in the overlaying optical stack, and diffractive effects at and around the surface of the particle. Standard optics tools can predict photon count loss with reasonable precision.

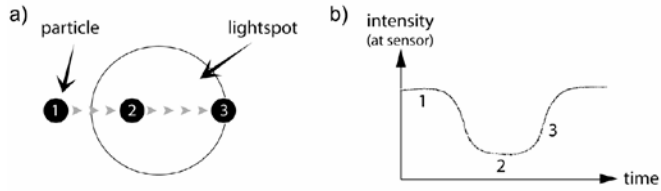

Figure 2. Illustration of the principle of the on-chip optical detection: a) Schematic passage of the particle over the illuminated SPAD, b) Stylized light intensity profile at the SPAD during the passage of a particle

The sensitive surface of the SPAD is a disc with a diameter of 8.4 μm, and its general structure is schematically depicted in Fig. 3a. The SPAD's p-n junction is reverse-biased above breakdown, which causes the optical gain to become virtually infinite. In this regime, the detector is said to operate in Geiger mode, thereby enabling single photon detection. The probability that an impinging photon results in a digital pulse, the photon detection probability (PDP), is plotted in Fig. 3b as a function of excess bias voltage and wavelength. The noise in the dark, or dark count rate, is the main limiting factor to the dynamic range.

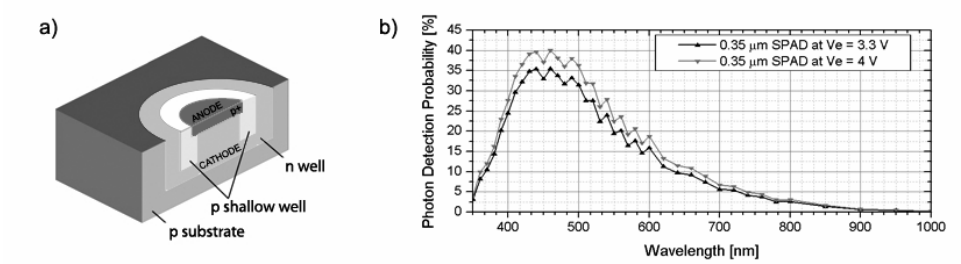

Figure 3. Schematics of the Single Photon Avalanche Diode (SPAD): a) 3D structure of the element, b) Measurement of the Photon Detection Probability (PDP) depending on the wavelength of the impinging field and the excess bias voltage

3. EXPERIMENTS AND RESULTS

In order to test the magnetic performance of our system, we introduced fluorescent magnetic particles of 5 μm diameter (COMPEL magnetic particles, BangsLabs) into the glass capillary. Fig. 4 shows a sequence of images taken during the transport of a group these particles from one coils center to the next. We see that the dispersed particles concentrate around the center of the attractive coil. The particle velocity is about 5 μm/s which is well in agreement with the forces calculated theoretically. The parallel measurement of the SPAD signal shows the expected decrease in photon count, once the particles gather over the coil's center.

For further experiments we strongly diluted the magnetic particle solution in order to obtain freely moving single particles. Figure 5a shows a single particle of 1 μm diameter sitting over a SPAD, where it induced a drop in photon count. Using single particles of 1, 3 and 5 μm in different experiments, we recorded the SPAD signals during particle transit.

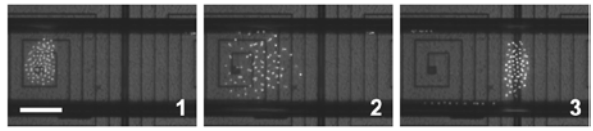

Figure 4. Photographs of a sequence of particle transport. The images of the fluorescent magnetic particles (∅ 5 μm) are overlaid with a photograph of the CMOS chip. The duration of the sequence is 20 s. (Dimension bar: 100 μm)

A comparison of the normalized photon counts, as depicted in Figure 5b, demonstrates the systems capability to distinguish between the different particle sizes with the photon count decreasing for increasing particle diameters, as predicted by theory [5]. Experiments performed using fluorescent light and fluorescent magnetic particles gave identical results indicating that the measured signal is exclusively a consequence of light occlusion.

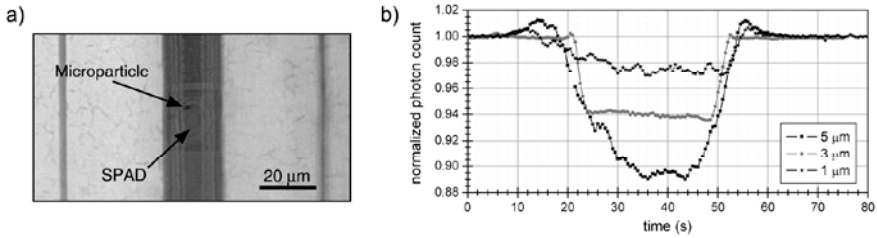

Figure 5. Optical observation and measurements: a) Photograph of a single 1 μm magnetic microparticle partially occluding a SPAD (50x objective), b) Normalized photon count of a bottom SPAD for single particles of 1, 3 and 5 μm diameter.

4. CONCLUSION

Our experiments demonstrate the capability of our hybrid CMOS microfluidic system to manipulate and detect single magnetic particles of 1 to 5 μm diameter. With the ability of the integrated optical detection to distinguish between the different particles sizes, a wide range of applications in miniaturized bioanalytical systems can be envisioned.

REFERENCES:

[1] M. A. M. Gijs, *Magnetic bead handling on-chip: new opportunities for analytical applications*, Microfluidics and Nanofluidics, **1**, pp. 22, (2004).

[2] U. Lehmann, C. Vandevyver, V. K. Parashar, and M. A. M. Gijs, *Droplet-based DNA purification in a magnetic lab-on-a-chip*, Angewandte Chemie-International Edition, **45**, pp. 3062, (2006).

[3] H. Lee, Y. Liu, D. Ham, and R. M. Werstervelt, *Integrated cell manipulation system - CMOS/microfluidic hybrid*, Lab on a Chip, **7**, pp. 331, (2007).

[4] C. Niclass, M. Sergio, and E. Charbon, *A single photon avalanche diode array fabricated in 0.35-μm CMOS and based on an event-driven readout for TCSPC experiments*, Proc. SPIE 6372, pp. 63720S, (2006).

[5] Z. Sandor, *Estimations of orbital parameters of exoplanets from transit photometry by using dynamical constraints*, Celestial Mechanics & Dynamical Astronomy, **95**(1-4), pp. 273, (2006).

ELECTROKINETIC SERS SIGNAL AMPLIFICATION FOR LABEL-FREE BIOMOLECULAR DETECTION

Hansang Cho, Yitao Long, Brian Lee, and Luke P. Lee

Biomolecular Nanotechnology Center, Berkeley Sensor and Actuator Center
Department of Bioengineering, University of California, Berkeley, CA 94720 USA

ABSTRACT

We have accomplished the effective signal amplification of surface enhanced Raman scattering (SERS) by electrokinetics-based sample enrichments. This signal amplification provides a rapid and simple solution for label-free and sensitive biomolecular detection with limited amount of samples. Biomolecules can be concentrated onto SERS-active surface by applying an electric field. The SERS detection limits of adenine reduced 8 orders of magnitude (from 1 μM to 10 fM) within 5 minutes using an electrical field of 0.6 *V*/cm. The integrated microfluidic SERS with electrokinetics-based sample preconcentration method can be further utilized for label-free genomic, proteomic, forensic, diagnostic, water, and environmental monitoring applications.

Keyword: Preconcentration, Electrokinetics, Label-Free, Surface Enhanced Raman Scattering

1. INTRODUCTION

SERS spectroscopy offers the advantage of label-free detection of biomolecules and a number of SERS substrates have been developed by many other groups [1]. The sensitivity of SERS signal is strongly affected by SERS-active substrates; however, the critical problem with SERS substrate is the technology to create a uniform substrate with high sensitivity. Efficient SERS active substrates are needed for the practical detection of low abundance species. The ability to quickly concentrate these molecules directly onto the SERS substrate would greatly enhance the limits of detection, and offer an excellent tool for fast label-free detection [2, 3]. Here we present a new innovative integrated microfluidic SERS and the electrokinetic sample enhancement on demand, which results in a significant amplification of signal.

2. BASIC PRINCIPLE

The basic design concept is based on integrated SERS and electrokinetics-based sample enrichments as shown in Fig. 1. The electrokinetic force moves charged molecules to an Au electrode. The gold-covered electrode has patterned nanostructures that generate plasmon coupling inside the nano-scale gaps to enhance the Raman signal. The SERS signal is further amplified in proportion to the number of adsorbed molecules attracted by electrokinetic preconcentration.

3. EXPERIMENTAL

The SERS substrate is fabricated with oxygen gas etching at the rate of 3 $cm^3 \cdot min^{-1}$ for 30 seconds and Au deposition of 40 nm in thickness [4]. Varying concentrations of adenine with 50 mM Na_2HPO_4 in DI water (600 μL adjusted to pH of 7.4 with H_3PO_4) was measured with SERS while also applying a DC potential of 0.6 *V* to a wire (positive electrode) and the Au surface (negative electrode) in a distance of 1 cm.

978-0-9798064-0-7/μTAS2007/$20©2007CBMS

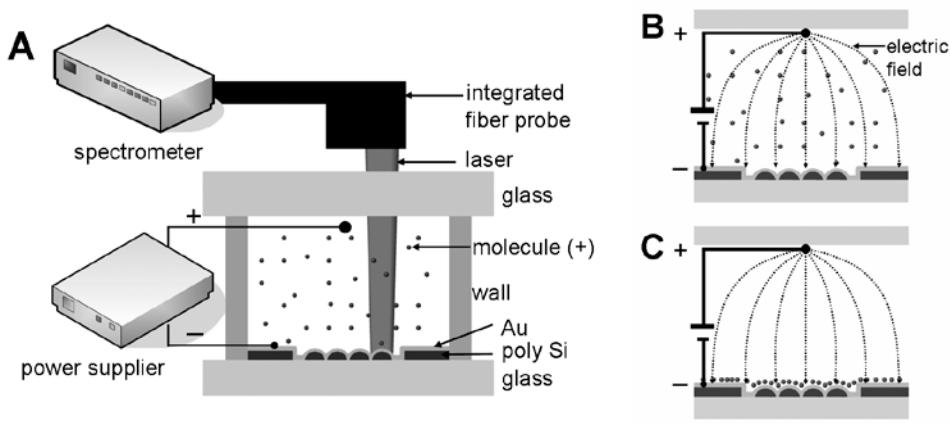

Figure 1. Schematic diagram for the SERS signal amplification with electrokinetics-based preconcentration. (A) SERS signal is measured while applying electrokinetic potential to a SERS substrate. Inset shows SEM image of nanostructure and a scale bar is 200 nm. (B) Positively charged biomolecules are attracted onto a negatively-charged Au electrode, a SERS-active substrate having nanostructures. (C) The molecules are preconcentrated on the substrate, which results in amplification of the SERS signal.

4. RESULTS AND DISCUSSION

Figure 2 compares the amplified SERS spectra at varying time and Fig. 3 compared normalized signal at 735 cm^{-1} at varying time and concentrations. The base lines of the spectra were removed for comparison. The signal at 735 cm^{-1} was normalized based on the intensity at the limit of detection of 1 μM without preconcentration.

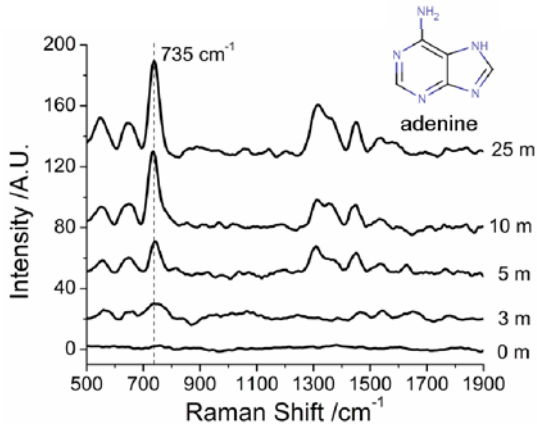

Figure 2. SERS Signal amplification of adenine by electrokinetic preconcentration. SERS signal of adenine at 10 nM was amplified enough to detect within 5 minutes and reached saturation after 10 minutes under the potential at 0.6 *V*/cm. The SERS spectra were measured with a 785 nm excitation laser of $9x10^4$ $W \cdot cm^{-2}$ and an integration time of 10 s.

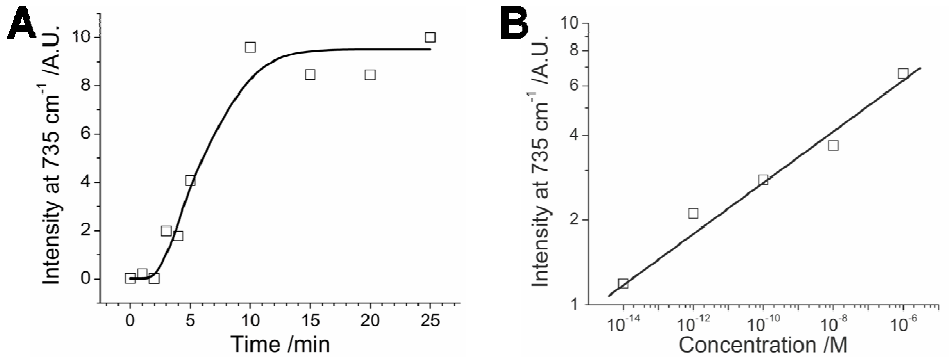

Figure 3. Signal amplification of SERS (A) Normalized signal (at the Raman shift of 735 cm^{-1}) of adenine at 10 nM with time. (B) Normalized SERS signal of adenine at varying concentration was compared after 5 minutes of preconcentration under 0.6 *V*/cm. The electrokinetics-based preconcentration method improved detection limit down to 10 fM. The SERS spectra were measured with a 785 nm excitation laser of $9x10^4$ $W \cdot cm^{-2}$ and an integration time of 10 s.

5. CONCLUSIONS

Using the electrokinetics-based sample enrichments method, we have accomplished the SERS signal amplification of adenine by a factor of 8 within 5 minutes so far. This rapid, simple, and effective sample enrichment improved the detection limits of SERS spectroscopy from 1 μM to 1 fM. This method can be further optimized for the integrated microfluidic SERS with label-free single molecular level detection sensitivity. The integrated microfluidic SERS can be applied for label-free biomolecular analysis, diagnostic, and water monitoring.

ACKNOWLEDGEMENTS

This work was supported by Intel Corp. and the Korea Research Foundation Grant funded by the Korea government (MOEHRD)" (KRF-2005-215-D00411).

REFERENCES

[1] M. Fleischmann, P.J. Hendra, and A.J. McQuillan, *Raman spectra of pyridine adsorbed at a silver electrode.* Chemical Physics Letters, 1974. **26**(2): pp. 163-166.

[2] A.J.d. Mello, and N. Beard, *Dealing with 'real' samples: sample pre-treatment in microfluidic systems.* Lab on a Chip, 2003. **3**(1): pp. 11N-20N.

[3] M. Wang, et al., *An optofluidic device for surface enhanced Raman spectroscopy.* Lab on a Chip, 2007. **7**(5): pp. 630-632.

[4] G.L. Liu and L.P. Lee, *Nanowell surface enhanced Raman scattering arrays fabricated by soft-lithography for label-free biomolecular detections in integrated microfluidics.* Applied Physics Letters, 2005. **87**(7): pp. 074101-074103.

INORGANIC AND ORGANIC ANALYSIS BY A MICRO MASS SPECTROMETER

Eric Wapelhorst, Jan-Peter Hauschild and Jörg Müller

HamburgUniversity of Technology, Germany

ABSTRACT

A mass producible planar integrated micro mass spectrometer (PIMMS) with all essential components integrated on one chip is presented. The function principle is based on electron impact ionization and a Synchronous Ion Shield (SIS) separator. The concept and layout of this PIMMS is optimized for cost efficient micro fabrication using standard MEMS processes.

Keywords: Micro Mass Spectrometer, MEMS Technology

1. INTRODUCTION

Mass spectrometers are the most powerful instruments for chemical analysis of organic and inorganic components. Presently available instruments are still too bulky and expensive for many field applications and monitoring systems. The presented planar integrated micro mass spectrometer (PIMMS) has the size of 5x10mm² and, due to its small dimensions can be operated at a pressure of 1Pa, which can be obtained by a one stage pumping system or a micro pump [1].

2. FUNCTION PRINCIPLE

The PIMMS, shown as a 2-dimensional drawing in Figure 1, generates ions by electron impact ionization: A microwave plasma electron source [2] provides the necessary electron beam (1 A/cm²) for ionizing the sample gas [3]. This electron beam impinges on the sample gas in the ionization chamber. The generated ions are extracted from the ionization chamber and accelerated to an adjustable kinetic energy of 30-200eV. Ion optics [4,5] focus the ions to a beam that enters the mass separator.

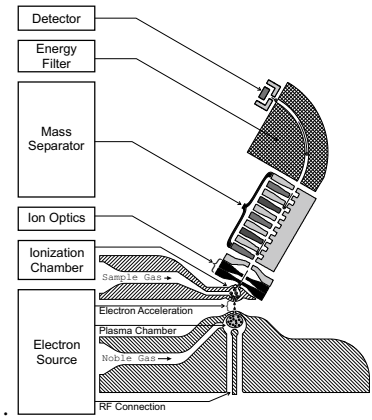

Figure 1. Schematic of the MMS

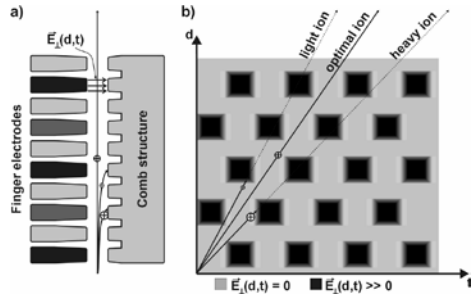

Figure 2. Function principle of the sSnchronous Ion Shield mass filter: (a) mass separator with an injected ion and (b) path-time-field diagram showing E in the center of the ion channel with respect to time t

978-0-9798064-0-7/µTAS2007/$20©2007CBMS

The special structure of the SIS separator (see Figure 2a) allows to build up a traveling electrical field in the ion channel, which is alternately zero or perpendicular to the ions' traveling direction. The field is formed by two 180° phase shifted square wave (SW) signals, variable in frequency, and connected to every second electrode. Figure 2b shows the path-time-field diagram of the electrical field perpendicular to the travelling direction of the ions in the center of the ion channel with respect to time. An ion, denoted as optimal ion in Figure 2b, is able to pass the separator, if it travels in the shielded, field free area (light grey area) through the separator, i.e. the ion's velocity must be equal to the velocity of the traveling field. All other ions are deflected by the electrical field perpendicular to the traveling direction (dark grey areas). By changing the frequency of the SW signals a mass interval can be scanned. A frequency interval of 10 to 35 MHz corresponds to a mass range of 100 to 10 amu, respectively.
To avoid the influence of distributed start energy of the ions an energy filter performed as a 90° sector ist placed between SIS mass filter and detector.

3. FABRICATION

The fabrication of the PIMMS is based on standard MEMS processes. All critical structures of the system are fabricated by a wafer based anisotropic deep silicon etching [6]. Each side of the 300 µm thick silicon structures is bonded to a borosilicate substrate with metal structures for contacting the electrodes. Figure 3 shows the complete PIMMS chip with the SIS separator. An SEM Image of the critical structures fabricated into silicon is shown in Figure 4. The sidewalls of the structures are coated with platinum to increase the long-term stability of the device. This coating prevents reactions between the silicon sidewalls of the structures with reactive ions.

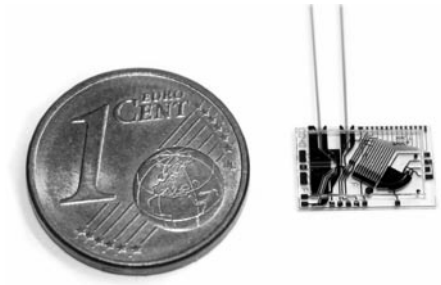

Figure 3. PIMMS chip with Synchronous Ion Shield separator

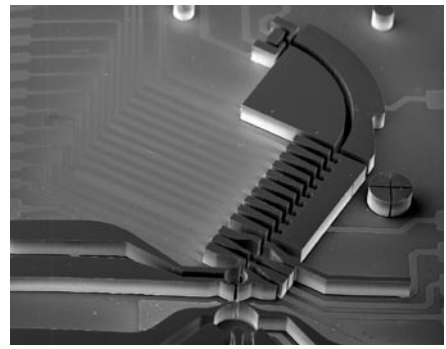

Figure 4. SEM Image of the PIMMS with Synchronous Ion Shield separator

4. RESULTS

To determine the resolution of the PIMMS a spectrum of two gas compositions containing neon, argon and carbon dioxide was measured (Figure 5). The spectrum shows two separate peaks at mass 40 and 44, so that the resolution of the SIS Separator is in the range of one amu for masses <100amu. Figure 6 shows a mass spectrum of lab air, neon and argon. Both spectra show the complete molecules as well as their fragments (C+, O+, CO+, N+, O+). These mass spectra are scanned with a SW signal frequency of 10-35 MHz at an

ion energy of 30 eV. To dissolve higher masses between 100 and 500 amu e.g. for organic substances the ion energy has to be increased to ensure a similar resolution.

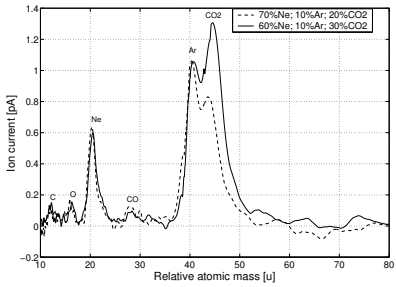

Figure 5. Micro Mass Spectrum of CO2, Ar and Ne obtained from PIMMS including fragments of C, O and CO

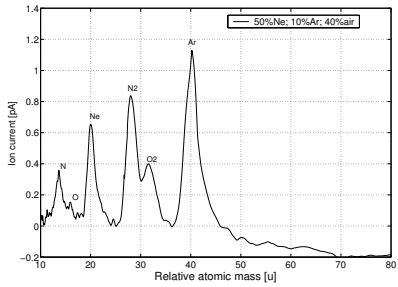

Figure 6. Micro Mass Spectrum of lab air, Ar and Ne

5. CONCLUSION

The entire system is very cost-efficient due to its small size and its mass producibility based on a simple photo mask for all critical structures. The vacuum and power requirements for the PIMMS are relaxed compared to those of state of the art mass spectrometers. A miniaturized mass spectrometer is predestinated for mobile measurements, portable applications as well as continuous process monitoring of inorganic and organic substances.

ACKNOWLEDGEMENTS

This work is funded by Deutsche Forschungs Gemeischaft (DFG).

REFERENCES

[1] M. Doms, J. Müller, “A Micromachined Vapor Jet Pump”, in Sensors and Actuators A 119 ,pp. 462–467, (2005).

[2] J.-P. Hauschild, E. Wapelhorst, J. Müller “A Fully Integrated Plasma Electron Source for Micro Mass Spectrometers”,µTAS, Boston, Massachusetts, USA, (2005).

[3] J. H. Gross, "Mass Spectrometry", Springer, Heidelberg, (2004).

[4] I. G. Brown, The Physics and Technology of Ion Sources. Wiley-VCH, 2. ed., (2004).

[5] H. Zhang, Ion Sources. Tokyo: Springer, (1999).

[6] A.A. Ayon, R. Braff, C.C. Lin, H.H. Sawin, M.A. Schmidt, “Characterization of a Time Multiplexed Inductively Coupled Plasma Etcher,” in Journal of the Electrochemical Society, vol. 146, pp. 339–349, (1999).

2-CHAMBER ATOMIC FORCE MICROSCOPE: TOWARDS A STRUCTURE/FUNCTION ANALYSIS OF MEMBRANE PROTEINS

Simon Scheuring

Institut Curie, UMR168-CNRS, 26 Rue d'Ulm, 75248 Paris Cedex 05, FRANCE

ABSTRACT

Only in the membrane can the native supramolecular assemblies, i.e. nanometric machines constituted of several membrane proteins working together, be observed. These supramolecular assemblies function in signal and energy transduction with impressiv efficiency. We report the supramolecular assembly of membrane proteins in junctional microdomains in eye lens membranes. In order to asses structure/function relations for membrae proteins, we have developed a 2-chamber AFM setup that allows non-supported membranes to be probed. The setup allows the induction of ion-, pH-, and solute-gradients, and the application of physical stress to a membrane, during structural investigation.

Keywords: Atomic force micropscopy, Membrane protein, Membrane structure

1. INTRODUCTION

Biological membranes are two-dimensional layers that define the physical border of cells or confine compartments within cells. Biological membranes are crowded with membrane proteins that fulfil divers crucial functions. About one third of all genes in organisms code for, and the majority of drugs target membrane proteins. We present high resolution topographs of native supramolecular membrane protein assemblies. Furthermore, we have developed an atomic force microscopy setup that allows non-supported membranes, which separate two aqueous chambers, and individual membrane proteins within them to be studied. The setup allows the induction of ion-, pH-, and solute-gradients, and the application of physical stress to a membrane, during structural investigation. Non-supported membrane patches could be imaged at sufficient resolution to delineate a 15Å wide protein pore, and their elastic and yield moduli probed. Using the 2-chamber-AFM setup, for the first time, lateral forces between membrane proteins relevant to protein assembly could be determined.

2. RESULTS

2.1. JUNCTIONAL MICRODOMAINS IN THE EYE LENS MEMBRANE

Gap junctions formed by connexons and thin junctions formed by lens-specific aquaporin-0 (AQP0) mediate the tight packing of fiber cells that is required for lens transparency. While gap junctions conduct water, ions and metabolites between cells, the main function of junctional AQP0 appears to lie in cell adhesion.

High-resolution atomic force microscopy (AFM) revealed the supramolecular organization of these proteins in native lens core membranes, where AQP0 forms two-dimensional arrays that are surrounded by densely packed gap junction channels [1]. These junctional microdomains simultaneously provide adhesion and communication between fiber cells. The AFM topographs also revealed that the extracellular loops of AQP0 in junctional microdomains adopt a conformation that closely resembles that seen in the structure of junctional AQP0, in which the water pore is thought to be closed. Finally, time-lapse AFM

978-0-9798064-0-7/μTAS2007/$20©2007CBMS

imaging provided insights into AQP0 array formation. This first high-resolution view of a multi-component eukaryotic membrane shows how membrane proteins self-assemble in function related microdomains.

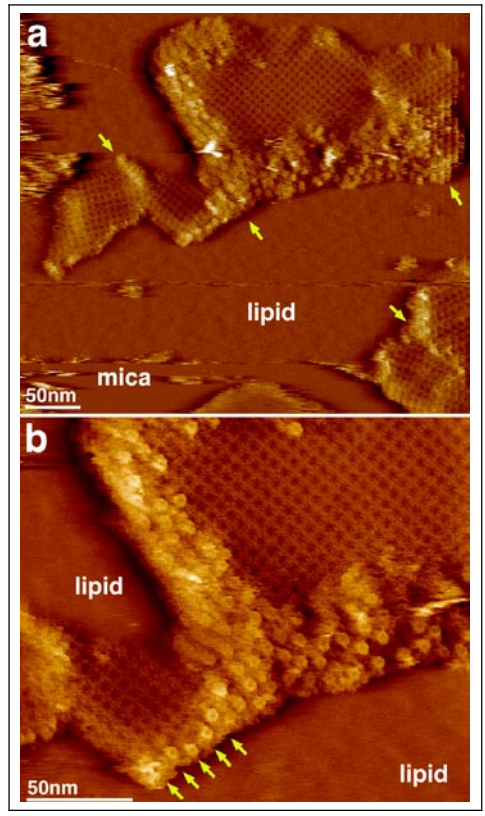

Figure 1. : Junctional microdomains within planar lipid bilayers. (A) Topograph of aquaporin 0 (AQP0) arrays surrounded and separated (arrows) by densely packed connexon patches. (B) A higher magnification topograph that shows the characteristic flower shape of the connexons. The arrows indicate a row of connexons terminating an AQP0 array.

2.1. 2-CHAMBER AFM

Biological membranes are impermeable to ions, protons, and solutes. Nature has evolved specific membrane proteins that create or use membrane gradients of ions and/or molecules for metabolic purposes. Structural and functional analyses of membrane proteins were so far un-coupled, partially because membranes needed to be supported to be observed. We have developed a system that allows observing membrane proteins in membranes that can be functionally stimulated [2]. Ion channels implicated in many of life's processes use specific ion gradients, some open and close to external stimuli, i.e. other ions or solutes. Transporters use ion gradients to actively co- or counter-transport metabolites across the membrane. The same is true for amino acid and neurotransmitter transporters. Last but not least the ATP-synthetase the membrane protein that creates the cellular energy in all living organisms uses a pH- or ion- gradient to form ATP. This incomplete list of membrane proteins excitable through induction of membrane gradients

illustrates the wide application range of the 2-chamber AFM setup, that can however be extended to other applications. Mechano-sensitive channels may be stimulated in non-supported membranes by applying forces during imaging, that will vertically indent and hence laterally augment membrane surface and pressure.

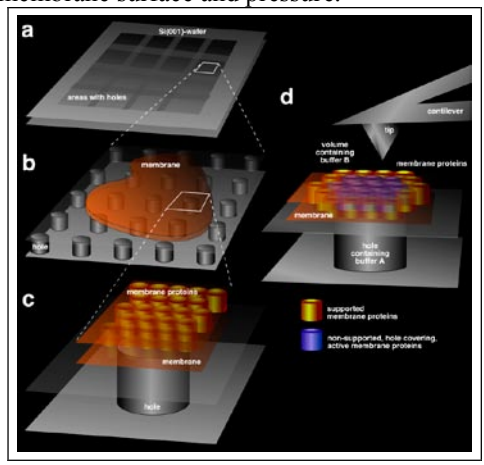

Figure 2: Schematic representation of the 2-chamber AFM setup. a) The Si(001) surface contains square fields of graved holes. b) Membrane with size larger than the hole periodicity will cover at least one hole. c) Many membrane proteins, in reality with size about one order of magnitude smaller than the hole diameter, within the membrane cover the hole. d) during the whole preparation procedure, the surface and the sample are immerged in buffer solution. After adsorption of the membranes to the holey surface, the buffer can be exchanged during the experiment, allowing the induction of membrane gradients over the membrane and consequently activate proteins. Furthermore, the AFM tip can be used to apply physical stress to the hole-covering membrane

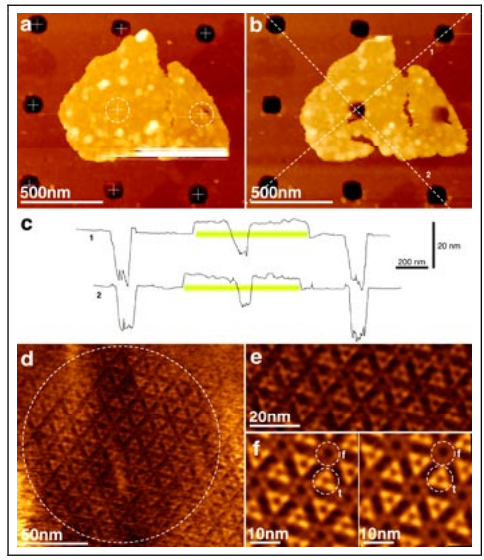

Fig. 3) Medium magnification topographs recorded a) before and b) after the membrane piercing experiment. c) Section analysis along the white lines in b). The non-supported membrane area covering the central hole initially undistinguishable in flatness from the rest of the membrane was pierced during the experiment. Both section analysis (profiles 1 and 2) documented an indentation far deeper than the Si surface (yellow bars). d) High-resolution topograph of the outer S-layer surface before piercing (outline: hole position with ~200 nm diameter) e) Fourier filtered image of d). Inset: average topography of outer surface of supported S-layer. f) Average (left) and symmetrized average (right) topographs. Outlines in f delineate the structural pores of ~15 Å in diameter.

4. DISCUSSION

Over holey surfaces, we can place extracted native membranes, reconstituted membranes, 2D-crystals but also mechanically detached cytoplasmic membranes, for 2-chamber AFM analysis. Further developments in nano-fluidics that will develop more functional supports, and in AFM towards faster and more sensitive image acquisition, will strengthen the presented approach in the near future.

ACKNOWLEDGEMENTS

SS thanks Rui Pedro Goncalves and Nikolay Buzhynskyy, the Institut Curie and INSERM Avenir.

REFERENCES

[1] Nikolay Buzhynskyy, Richard Hite, Thomas Walz, and Simon Scheuring, *The supramolecular architecture of junctional microdomains in native lens membranes*, EMBO Reports, 2007, 8 (1): 51-55.

[2] Rui Pedro Gonçalves, Guillaume Agnus, Pierre Sens, Christine Houssin, Bernard Bartenlian, and Simon Scheuring, *2-Chamber-AFM: Probing Membrane Proteins Separating Two Aqueous Compartments*, Nature Methods, 2006, 3 (12): 1007-1012.

MICROFLUIDIC SCREENING OF APTAMER LIBRARIES

Xinhui Lou[1], Lisan Viel[2], Jiangrong Qian[2], Eric T. Lagally[1], Jeffery B. H-Tok[3], Theodore M. Tarasow[3], Alan J. Heeger[1], and H.T. Soh[1,2]

[1]Department of Materials, [2]Department of Mechanical Engineering
University of California-Santa Barbara,USA
[3]Division of Chemistry and Materials, Lawrence Livermore National Laboratory, USA

ABSTRACT

Aptamers are functional binding molecules composed of RNA or DNA which are selected *in vitro* from combinatorial nucleic acid libraries. The process of selection is termed Systematic Evolution of Ligands by EXponential enrichment (SELEX). Conventional SELEX technologies often require intensive manual labor and multiple rounds. In this work, we present the first Microfluidic-SELEX (M-SELEX) system that is capable of isolating high affinity aptamer binders (K_D ~ low nM) in a single round, using a microfluidic separation device with exceptionally high partition efficiency.

Keywords: SELEX, microfluidics, aptamers, Botulinum Neurotoxin

1. INTRODUCTION

Aptamers are functional binding molecules composed of RNA or DNA which are selected from combinatorial nucleic acid libraries by *in vitro* selection [1, 2]. Unlike traditional reagents (e.g. antibodies) which are protein based, aptamers provide a significant advantages as biosensors in that they can be chemically synthesized, undergo reversible denaturation, and thus, are stable for long term storage. Aptamers have been shown to be effective binders for almost any molecular target including small molecules, peptides, proteins and inorganic materials [3]. Systematic Evolution of Ligands by EXponential enrichment (SELEX) is the leading method to generate aptamers binders; in this process, a large, random population of aptamer molecules (~ 10^{14} to 10^{15}) is synthetically generated, where each candidate molecule adopts a unique three-dimensional conformation. Then, they are successively screened, and amplified (by PCR) for its ability to bind to the target molecule. Finally, the nucleic acid sequences of the molecules with highest affinities are identified through cloning and sequencing. One major drawback of the current SELEX technology stems from the fact that it requires intensive manual labor (typically 8-15 rounds of selection requiring many weeks) that often results in inadequate affinity, specificity, and reproducibility. To address this bottleneck, we present the first Microfluidic-SELEX (M-SELEX) system that is capable of isolating high affinity aptamer binders for protein target in a single round of selection.

2. EXPERIMENTAL AND RESULTS

We report the successful isolation of DNA aptamers directed toward our protein target, Botulinum Neurotoxin Light Chain, type A (BoNT/A rLc), in a single round of selection. The overview of the M-SELEX assay is provided in Fig 1. A single round of SELEX was performed, where the entire library was screened within 30 minutes in the CMACS device. First, we design and synthesize the aptamer library consisting of approximately ~10^{14}

978-0-9798064-0-7/μTAS2007/$20©2007CBMS

members, each molecule containing a 60 random base region flanked by 20-base primer regions for PCR.

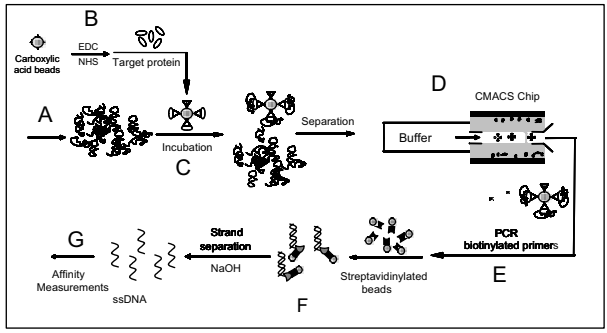

Figure 1. The Microfluidic-SELEX process. *A) Synthesize initial library. B) The target proteins are covalently conjugated to the magnetic beads through carbodiimide coupling. C) The magnetic beads with target protein are incubated with the aptamers library. D) The mixture is separated in the CMACS chip. The aptamer bound to the target proteins on the beads are collected. E) The protein-bound aptamers are PCR amplified using biotinylated reverse primers. F) Single stranded DNA aptamers are generated from doubled stranded PCR amplicons G) The binding kinetics of the resulting aptamers are measured.*

The target protein is immobilized onto a commercial Dynalbeads® M-270 Carboxylic Acid magnetic bead through carbodiimide coupling. The number of bound BoNT/A rLc is measured to be $1.9\pm0.5 \times 10^4$ per bead. We verify that the enzymatic activity of the protein is preserved after the conjugation step using the SNAPtide Assay (List Biological Laboratories, Campbell, CA) to ensure that the aptamers are selected towards the active conformation of the target protein (Fig 2). The linear fluorescence intensity increase over time for the BoNT/A rLc coated beads assay clearly demonstrates that the enzyme activity of the BoNT/A Lc was preserved while negligible fluorescence increase is shown on the bare beads.

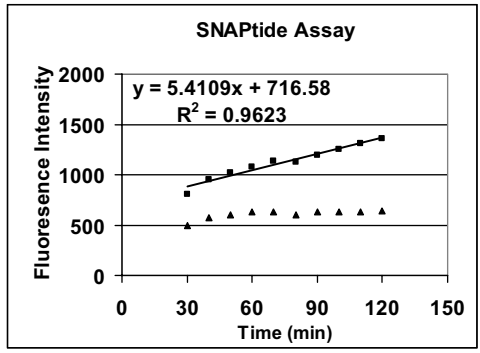

Figure 2. The activity test of BoNT immobilized on the beads measured via molecular beacons*. The activity of the target protein is measured with the SNAPtide assay (List Biological Laboratories, Campbell, CA). The linear fluorescence intensity increase over time clearly demonstrates that the enzyme activity of the BoNT is preserved (■). Fluorescence measurements are performed in 96-well black microplate using TECAN*

microplate reader. Excitation wavelength is 490nm and emission is 523nm. The bare, magnetic beads without the target protein shows negligible activity(▲).

Next, the bead-conjugated target proteins were incubated with the aptamer library and the sample mixture was separated in the Continuous-Flow Magnetic Activated Cell Sorter (CMACS) device [4] previously reported from our group (Fig 3). The flow rates of sample and buffer streams were 1mL/hr and 5mL/hr, respectively, and the eluted samples from both product and waste channels were collected.

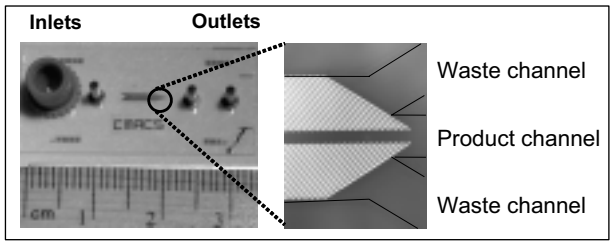

Figure 3: The CMACS Device [4]. *The device has 2 inlets (sample / buffer) and two outlets (product / waste), and measures 35mm by 20mm. The magnetic field gradient generators select the aptamers attached to the target proteins (immobilized on the magnetic beads) into the product channel, where as unbound, free aptamers are directed into the waste channel (inset).*

After the separation step, we generated the fluorescence labelled single stranded DNA for the affinity measurements [5]. The average dissociation constant K_D of the selected DNA library was 33±8 nM assuming Langmuir (1:1) binding.

3. CONCLUSIONS

In this work, we present the first Microfluidic-SELEX (M-SELEX) system capable of isolating high affinity aptamers in a single round, using a microfluidic separation device with exceptionally high partition efficiency that is significantly more efficient than current, macro-scale methods. Further development of such systems may greatly reduce the necessary resources in time, reagents, and manual labor to generate high performance molecular recognition elements.

ACKNOWLEDGEMENTS

We thank the financial support from the ARO Institute for Collaborative Biotechnologies (DAAD1903D004) and LLNL UC-DRD (594100-69758). We thank Prof. Patrick Daugherty, Dr. Yimin Zhu and his group for the use of the TECAN microplate reader and for their kind assistance. Microfabrication was carried out in the Nanofabrication Facility at UC Santa Barbara.

REFERENCES:

[1] A. D. Ellington, J. W. Szostak, Nature, 346, 818-22 (1990).
[2] C.Tuerk, L.Gold, Science, 249, 505-510 (1990).
[3] C. B. Gopinath, 387, 171–182 (2007).
[4] S-H Oh, A.K. Singh, P. S. Bessette, S. A. Kenrick, J. J. Rice, J. Qian, P.S. Daugherty, H.T. Soh, Micro Total Analysis Systems Conference, (2006).
[5] R.Stoltenburg, C. Reinemann, B. Strehlitz, Anal. Bioanal. Chem. 383, 83-91(2005).

INTEGRATED AFFINITY CAPTURE, PURIFICATION AND CAPILLARY ELECTROPHORESIS MICRODEVICE FOR QUANTITATIVE DOUBLE-STRANDED DNA ANALYSIS

Nicholas M. Toriello[1], Chung N. Liu[2], Numrin Thaitrong[3] and Richard A. Mathies[1,3]

[1]UCSF/UC Berkeley Joint Graduate Group in Bioengineering; [2]Department of Chemical Engineering; [3]Department of Chemistry, University of California, Berkeley, CA 94720.

ABSTRACT

A novel injection method is developed that utilizes a thermally switchable oligonucleotide affinity capture gel to mediate the concentration, purification and injection of double-stranded DNA for quantitative microchip capillary electrophoresis analysis.

Keywords: integrated sample preparation, capillary array electrophoresis, genetic analysis, microvalves

1. INTRODUCTION

As microfluidic systems evolve from simple one-step separation devices into fully-integrated platforms capable of performing sample amplification, processing and analysis, the focus in microfluidics is shifting to the challenging tasks of minimizing sample/reactor volumes and efficient integration of multiple processes. The polymerase chain reaction (PCR) coupled with microchip-based capillary electrophoretic (CE) separation systems provides rapid amplification and high-resolution analysis. However, the reproducibility, efficiency and quantitative capabilities of microchip CE are compromised because of difficulties in the direct sample injection from a high-salt solution using the ubiquitous cross-injector structure. It is thus desirable to improve microchip-based CE and especially the injection process to enable quantitatively purifying, concentrating, injecting and separating double-stranded DNA (dsDNA) derived from integrated nanoliter microchip PCR chambers.

2. EXPERIMENTAL

Thermally switchable oligonucleotide mediated affinity capture has previously been employed for purifying and concentrating single-stranded DNA (ssDNA) for sequencing analysis.[1,2] Here we extend this technique to the analysis of dsDNA by exploiting helix invasion capture.[3] Moreover, by appropriate integration of the affinity capture matrix with the separation channel we are able to efficiently purify, concentrate and inject dsDNA for quantitative CE analysis.

The 4-layer glass-PDMS-glass-glass microdevice (Figure 1a) consists of a three-valve pump for metering nanoliter volumes of analyte, etched chambers for affinity capture, and CE separation channels for size-based separation. Metered nL-amounts of analyte are pumped into a hold chamber and then electrophoresed into the capture chamber for affinity capture (Figure 1b-c). After hybridizing to the capture probe, the products are thermally released for CE separation (Figure 1d).

978-0-9798064-0-7/μTAS2007/$20©2007CBMS

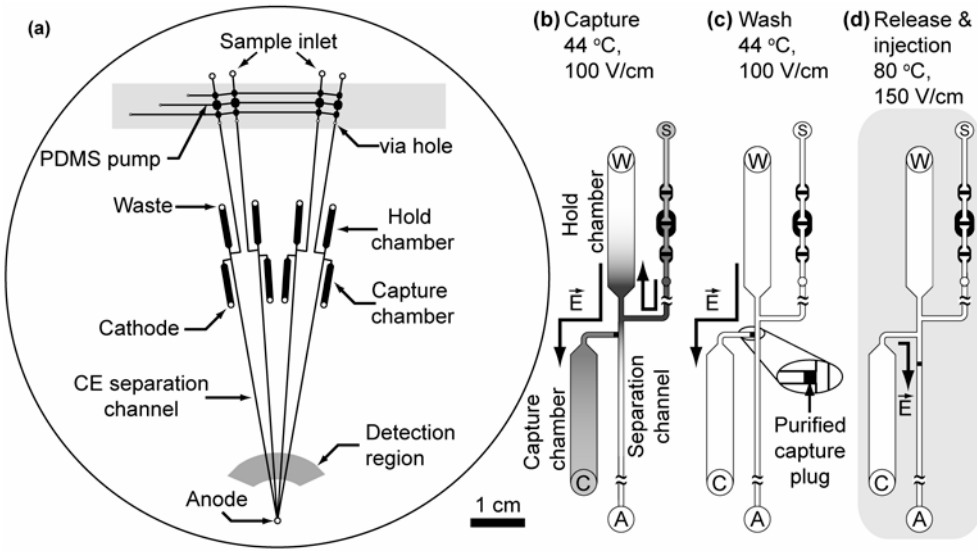

Figure 1. Layout and operation of integrated 4-channel capture, purification and CE separation microdevice. (a) The 4-layer glass-PDMS microdevice consists of a 3 valve PDMS pump for metering nanoliter volumes of analyte, etched hold and capture chambers for affinity capture and 5 cm CE separation channels. A 6% LPA affinity capture matrix copolymerized with a 20 μM capture oligonucleotide is loaded into the capture chamber. Separation matrix is loaded from the anode (A) past the capture chamber to the hold chamber entrance. (b) Analyte is loaded into the sample reservoir (S) and 10 nL are moved into the hold chamber with each pump cycle. Analyte is electrophoretically driven through the capture matrix by applying a constant 100 V/cm field between the waste (W) and cathode (C) reservoirs and complementary fragments are immobilized at the entrance of the capture chamber creating an purified sample plug, followed by electrophoretic washing (c). (d) The temperature of the device is raised to 80 ºC to thermally release the DNA fragments and the sample is separated with a field of 150 V/cm between the cathode and the anode.

3. RESULTS AND DISCUSSION

Figure 2 presents electropherograms of FAM-labeled ssDNA and dsDNA products affinity captured, purified and separated with this injection technique. The capture process exhibits optimal efficiency at 44 ^{o}C with a 100 V/cm loading field and a 20 μM affinity capture probe (T_M = 57.7ºC). A 20-base ssDNA (Figure 2a) and dsDNA (Figure 2b) oligonucleotide are captured with similar efficiency. Also, a 237-bp ds PCR amplicon with complementarity to the capture probe 81-bases from its 5'-terminus is reproducibly captured via helix invasion (Figure 2c). Simultaneous capture and injection of amplicons from *E. coli* K12 and *M13mp18* with a mixture of two different capture probes demonstrates the feasibility of multiplex target capture (Figure 2d). This technique provides a >100x increase in signal intensity over the traditional cross injector (Figure 2e) because all material loaded onto the column is captured and injected. A LOD of 1 pM or ~150,000 fluorescent molecules is determined by injecting various concentrations of FAM-labeled dsDNA (20mer) in a 250-nL volume. By integrating the oligo matrix directly with the CE separation channel, the target fragments are quantitatively captured and injected after thermal release for unbiased and efficient analysis.

4. CONCLUSIONS

The integrated capture/injection method presented here provides 100% recovery of dsDNA amplicons from nL and larger volumes. Thus the loaded sample volume is no longer determined by the geometry of the traditional cross-injector. This capability will facilitate the integration of nL-volume PCR reactions with quantitative CE analysis of products. By combining this injection process with our RT-PCR microsystem [4] and our single-cell capture techniques [5] it should be possible to perform quantitative gene expression profiling and genetic analysis from individual cells.

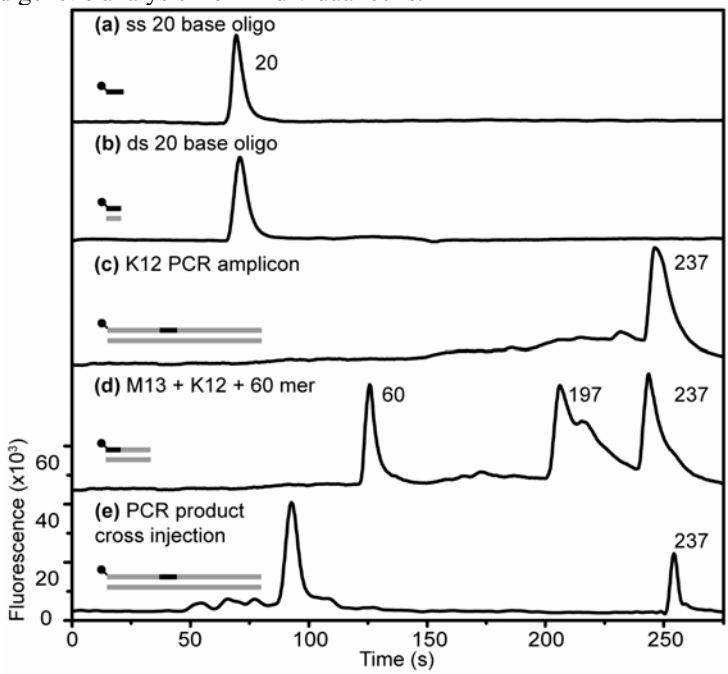

Figure 2. Electropherograms from FAM-labeled DNA fragments captured with a 20 base (20 μM) oligonucleotide capture probe. Purified fragments are thermally released at 80 ºC and electrophoretically separated at 150 V/cm. A depiction of each captured DNA fragment is also shown with the location of the 5' FAM label (black dot) and the complementary sequence (black). (a) A 500 pM ssDNA 20mer complementary to the 20 base capture probe. (b) A 500 pM dsDNA 20mer complementary to the capture probe. (c) A 237 bp double-stranded PCR amplicon generated from *E. coli* K12 cells with complementarity 81 bp from the 5' terminus. (d) A 1:1:1 mixture of a 500 pM dsDNA 60mer, *E. coli* K12 and M13 PCR amplicons. (e) A cross-injection with the same 237 bp ds PCR amplicon results in a very intense unreacted primer peak at 90 s and a product peak that is 1/30 in area.

REFERENCES:

[1] Paegel, B. M.; Yeung, S. H. I.; Mathies, R. A. *Anal. Chem.* 2002, *74*, 5092-5098.
[2] Blazej, R. G.; Kumaresan, P.; Mathies, R. A. *Proc. Natl. Acad. Sci. U. S. A.* 2006, *103*, 7240-7245.
[3] Toriello, N. M.; Liu, C. N.; Blazej, R. G.; Thaitrong, N.; Mathies, R. A. Submitted.
[4] Toriello, N. M.; Liu, C. N.; Mathies, R. A. *Anal. Chem.* 2006, *78*, 7997-8003.
[5] Toriello, N. M.; Douglas, E. S.; Mathies, R. A. *Anal. Chem.* 2005, *77*, 6935-6941.

HIGH-THROUGHPUT PROTEOMIC SAMPLE PRECONCENTRATION IN PDMS MICROFLUIDIC CHIP USING SURFACE-PATTERNED ION-SELECTIVE MEMBRANE

Jeong Hoon Lee, Yong-Ak Song, Sung Jae Kim and Jongyoon Han

Department of Electrical Engineering and Computer Science/Department of Biological Engineering, Massachusetts Institute of Technology, USA

ABSTRACT

We report a novel method of fabricating a high-throughput protein preconcentrator in PDMS microfluidic chip format. Using microstamping or microflow patterning of ion-selective resin, we can build a submicron thick ion-selective membrane on the glass substrate. By simply plasma bonding a PDMS device on top of the thin membrane, we can rapidly prototype a PDMS preconcentrator without complicated microfabrication processes. The PDMS preconcentrator shows a highly efficient preconcentration with a factor as high as ~10^4 in 5 min. Our fabrication method even allows building a massively parallel array of preconcentrators to increase the concentrated sample volume, which facilitates the integration of preconcentrator into various detectors.

Keywords: Preconcentration, Protein, Ion-selective membrane, Microcontact printing

1. INTRODUCTION

Any ion-selective materials (such as Nafion®), as well as nanochannels, can be used for generating ion concentration polarization to build a protein preconcentrator[1,2]. However, assembly and integration of such materials into microfluidic systems pose a challenge. As a simple solution for this, we print a submicron-thick ion-selective material on a glass substrate and bond it to the PDMS microfluidic chip. This PDMS preconcentrator, the fabrication of which only requires an extremely simple membrane formation through two microchannels via printing method, can achieve similar protein preconcentration performance as previously reported with the nanofluidic preconcentration system from our group [3]. Moreover, the fabrication method allows to extend the number of the preconcentrators to a multi-array for high-throughput proteomic sample preconcentration.

2. EXPERIMENTAL

The layout and operation schemes of a PDMS protein concentration chip with surface-patterned Nafion membrane are shown in Fig. 1. It shows the operation of preconcentration consisting of 1) depletion layer formation due to the concentration polarization and 2) preconcentration step using tangential flow to electrokinetically trap the molecules in front of the depletion region. As for the fabrication, we use a Nafion perfluorinated resin solution and pattern a thin planar Nafion film on a standard glass substrate via microcontact printing or micropatterning in capillaries, as shown in Fig. 2. After patterning the ion-selective film in a stripe pattern, it is cured at 90°C and integrated into the PDMS microchannel by standard plasma bonding. Using thsese methods, we acquired a thin membrane with a thickness up to ~200 nm can be achieved consistently.

978-0-9798064-0-7/μTAS2007/$20©2007CBMS

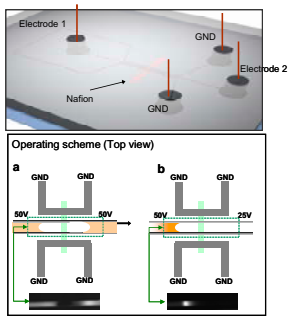

Figure 1. Schematics of PDMS precconcentrator with surface-patterned Nafion membrane on the glass substrate and its operation. The middle channel is loaded with sample and the side channels are filled with buffer solutions. For preconcentration, a potential difference applied across the middle and the side channels in combination with electrokinectic flow.

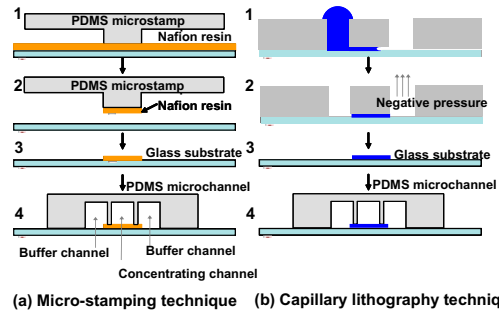

Figure 2. Fabrication of PDMS preconcentration device via surface-patterned ion-selective membrane using (a) micro-stamping technique and (b) micropatterning in capillaries.

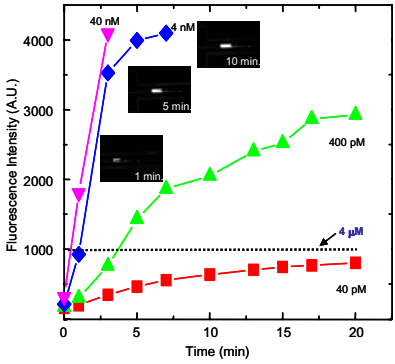

Figure 3. Preconcentration of β-phycoerythrin protein versus electrokinetic trapping time. This result shows that we can achieve a preconcentration factor of ~10^4 in 5 min. Fluorescence images of 4nM protein shown next to the graph indicate an increase of the concentrated plug in size and concentration with trapping time.

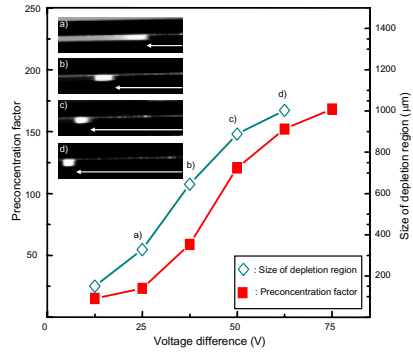

Figure 4. Preconcentration factor and size of the depletion region as a function of voltage difference across the middle channel.

3. RESULTS AND DISCUSSION

To calculate the preconcentration factor, we measured the fluorescence intensity of collected B-phycoerythrin (β-PE) protein as well as that of the standard sample solution (4 μM). By utilizing electrokinetic trapping in PDMS preconcentrator, we achieved a concentration volume of β-PE as high as 200 pL (Fig. 3). This is 350 folds larger than that from our previous report [3], with a concentration factor as high as ~10^4 in 5 min. This result demonstrates a high efficiency of our PDMS preconcentrator. The preconcentration factor and the size of the depletion region show a correlation to each other, as shown in Figure 4, and both increase with higher voltage difference across the depletion region.

Since the patterning technique enables a great flexibility in depositing membranes anywhere on the glass substrate, a massively parallel array of preconcentrators can also be built, as the device array containing 16 single preconcentrators in Fig. 5(a) demonstrates. With this array-type device, the preconcentrated sample volume can be increased according to the number of the single preconcentrators. The entire preconcentrated sample is collected from the middle outlet either manually using pipette tip or it can be sent directly to a mass spectrometer (MS) via electrospray or droplet pumping. We demonstrated the feasibility of an integration of a preconcentrator to mass spectrometer by electrospray from an open channel, as shown in Fig. 5(b).

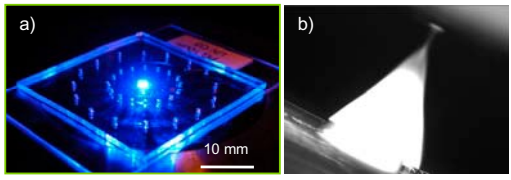

Figure 5. a) Array-type device of 16 single preconcentrators and b) electrospray to MALDI plate

4. CONCLUSIONS

We developed high-throughput proteomic sample preconcentrator uisng PDMS microfluidic chip using surface-patterned ion-selective film membrane. This PDMS preconcentrator could be coupled online with any biosensing modules such as mass spectrometer in order to detect low-abundance proteins and peptides. In addition, the PDMS microfluidic format of this device allows the integration of preconcentrator with many different BioMEMS platform, including cellular BioMEMS devices.

ACKNOWLEDGEMENTS

This work was supported by the NIH Grant (NIBIB, EB005743). J. Han was partially supported by NSF CAREER (CTS- 0347348) program.

REFERENCES

[1] Astorga-Wells, J., Swerdlow, H., “Fluidic preconcentrator device for capillary electrophoresis of proteins”, *Analytical Chemistry* 75, 5207-5212 (2003)

[2] Joensson, M., Lindberg, U., “Bead immobilization in a planar polymer microfluidic electrocapture device”, *MicroTAS 2006*, pp. 606-608

[3] Wang, Y.-C., Stevens, A. & Han, J. "Million-fold preconcentration of proteins and peptides by nanofluidic filter," *Analytical Chemistry* 77, 4293-4299 (2005).

DNA MOVEMENT IN SUB-20 NM NANOSLITS

Georgette Salieb-Beugelaar[1], Juliane Teapal[1], Jan van Nieuwkasteele[1], Daniël Wijnperlé[1], Jonas O. Tegenfeldt[2], Jan C.T. Eijkel[1], Albert van den Berg[1].

[1]BIOS / Lab-on-a-Chip Group, Mesa+ Institute for Nanotechnology, University of Twente, P.O. Box 217, 7500 AE Enschede, The Netherlands and

[2]Division of Solid State Physics, Lund University, PO Box 118, SE-22100 Lund, Sweden

ABSTRACT

The movement of XbaI digested λ-DNA in 20 nanometer and λ-DNA in 12 nanometer high slits was investigated. We found that DNA moved intermittently and following preferential pathways, indicating an important influence of surface roughness. From these intermittent movements two different mobilities were calculated, the total averaged mobilities and averaged mobilities between the intermittent sticking events. The friction coefficient per unit length was calculated from the latter mobilities. A three order of magnitude increase was found for the 12 nm slits compared to the theoretical value. The mobility furthermore differs less than one order of magnitude between 20 nm and 12 nm slits, and the influence of varying the ionic strength of the buffer was not significant. This work is the first time DNA movement in such shallow constrictions is investigated.

Keywords: DNA, intermittent movement, nanoslits

1. INTRODUCTION AND THEORY

This work describes the investigation of the mobility of extremely confined DNA as a function of confinement and ionic strength. To roughly estimate the friction experienced by the DNA, the measured mobilities were used to calculate the friction coefficient per unit length according to [1].

$$\xi = \lambda E / v \qquad (\lambda = \text{charge per unit length} = 1.1\ e_0 / \text{nm}) \qquad (1)$$

The theoretical value for the friction coefficient per unit length was derived from a model of a moving cylinder of width w in a slit of height h [2].

$$\xi = 2\pi\eta / \ln(4h/\pi w) \qquad (h = \text{height nanoslit, } w = \text{width DNA}) \qquad (2)$$

With increasing ionic strength, the screening (Debye) length decreases. This will result in a decrease of the effective width of DNA and an increase of the effective slit height and thus a decrease of the friction coefficient ξ. The dynamics of DNA has been studied before but in a different way and in channels or slits of other dimensions [3, 4].

2. EXPERIMENTAL

Figure 1 schematically presents the Fused Silica chip used. Between two microchannels an array of 100 nanoslits is situated (width 3 μm, length 500 μm) with 12 nm or 20 nm height depending on the etching time with diluted HF. Devices were fusion bonded at 1100°C. Surface roughness was 1 nm rms as measured with AFM. Buffer was introduced through the microchannels and voltage applied over the nanoslits array. An optical setup

978-0-9798064-0-7/μTAS2007/$20©2007CBMS

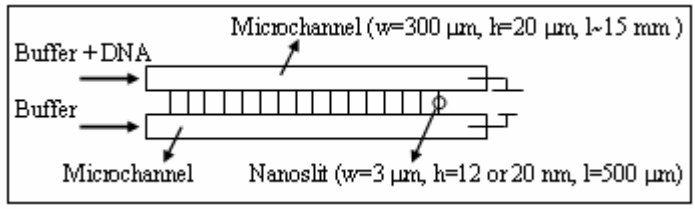

Figure 1. Schematic presentation of the device.

for fluorescence was used with a CCD camera to detect the emitted light. XbaI digested λ-DNA of length 9 μm and λ-DNA of length 18 μm was labeled with YOYO-1 (ratio one dye per 10 basepairs), β-Mercaptoethanol was used against bleaching and polyvinylpyrrolidone (PVP) to prevent surface adsorption and electro-osmotic flow. In 20 nm high slits an electrical field of 4.10^5 V/m was applied and in the 12 nm high slits 2.10^5 V/m.

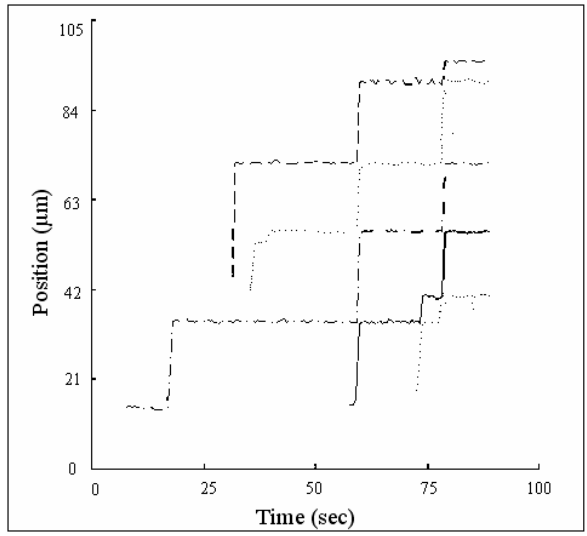

Figure 2. Stop and go movements of undigested λ-DNA (18 μm) in a 12 nm high nanoslit. (1xTBE, 2.5%PVP and 3% β-mercaptoethanol, 2.10^5 V/m). Each DNA molecule is represented as a line. Note that the DNA molecules stop (stick) at the same positions on the channel length axis, followed by movements with comparable slope.

3. RESULTS AND DISCUSSION

Single DNA molecules were traced in time inside the slits. The DNA was seen to move following preferential pathways, suggesting a possible influence of surface roughness. The movements of DNA through the nanoslits furthermore were intermittent as presented in figure 2. The time-averaged total mobilities for both 12 nm and 20 nm high slits are presented in figure 3A and 3B. In fig. 3A XbaI–digested λ-DNA and in 3B whole λ-DNA is used. Clearly no significant influence of the ionic strength on the mobility could be found due to the large standard deviation of the data which we attribute to the influence of local surface roughness introducing a large difference between data measured in different slits. The averaged mobilities in both 12 nm and 20 nm differ less than one order of magnitude.

For the the 12 nm slits, the theoretical friction coefficient is 2.0 mPa·s. If the mobility was determined only from the moving phases in the 12 nm high slits, a friction coefficient of 2.2 Pa·s was calculated with the DNA sticking for 90% of the time. Possible explanations for the large discrepancy of three orders of magnitude are direct surface / DNA friction, an increased water viscosity close to the wall due to molecular ordering, an increased viscosity of the solution adjacent to the wall due to the presence of wall-adsorbed PVP and an influence of electrical double layer repulsion.

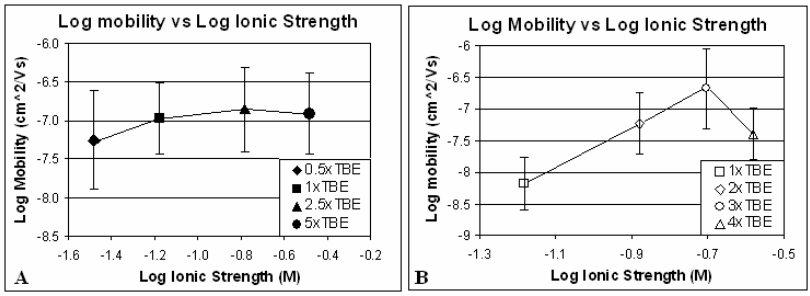

Figure 3. The averaged mobility of λ-DNA. (A) Mobility of XbaI digested λ-DNA in 20 nm high slits (2.5%PVP and 0.2% β-mercaptoethanol and 0.4 MV/m). (B) Mobility of λ-DNA in 12 nm high slits (2.5%PVP and 3% β-mercaptoethanol and 2.10^5 V/m).

4. CONCLUSIONS

This study shows that DNA proceeds through 12 nm and 20 nm slits much slower than predicted from simple theory. Intermittent movements of the DNA and the occurrence of preferential pathways through the slits indicate an influence of surface roughness. No significant influence of the ionic strength on the mobility could be found within our measurement error. The average mobility without intermittence of movement was used to calculate the experimental friction coefficient per unit length of DNA inside a 12 nm slit. The experimental value showed a dramatic increase when compared to the theoretical value. Presently, work is going on to extending the dataset and to decrease the experimental error.

ACKNOWLEDGEMENTS

This work is funded by NanoNed and Nano2Life (European Network of Excellence in the field of nanobiotechnology, FP6).

REFERENCES

[1] J.T. Mannion, C.H. Reccius, J.D. Cross and H.G. Craighead. Biophysical Journal 90, 4538 (2006).

[2] O.B. Bakajin, T.A.J. Duke, C.F. Chou, S.S. Chan, R.H. Austin and E.C. Cox. Physical Review Letters 80, volume 12, 2737 (1998).

[3] J.O. Tegenfeldt, C. Prinz, H.Cao, S. Chou, W.W. Reisner, R. Riehn, Y.M. Wang, E.C. Cox, J.C. Sturm, P. Silberzan and R.H. Austin. Proceedings of the National Academy of Sciences of the United States of America 101, 10979 (2004).

[4] W. Reisner, K.J. Morton, R. Riehn, Y.M. Wang, Z. Yu, M. Rosen, J.C. Sturm, S.Y. Chou, E. Frey and R.H. Austin. Physical Review Letters 94, 196101-1 (2005).

NOVEL DEVICE FOR ELECTROPHORETIC FOCUSING AND SEPARATION AT A MICROCHANNEL-NANOCHANNEL INTERFACE

Thomas A. Zangle, Ali Mani and Juan G. Santiago
Stanford University, USA

ABSTRACT

Recent work suggests that the physics of nanochannels present unique opportunities for sample preconcentration and analysis [1-4]. This paper presents a novel device for simultaneous sample pre-concentration (via electrophoretic focusing) and separation which leverages the physics of a microchannel-nanochannel interface and is supported by a new model and experimental results.

Keywords: Nanochannel, nanofluidics, separation, focusing

1. INTRODUCTION

Counter ions (cations for negatively charged walls) in nanochannels with heights of the same order as the electrical double layer (EDL) thickness carry most of the local ionic current. When an electric field is applied, this ion flux imbalance increases the concentration of both cations and anions on the cathodic side of the nanochannel and decreases the ionic strength on the anodic side. This phenomenon is called concentration polarization (CP) or the exclusion-enrichment effect [1, 2]. There has been significant research activity on the physics of CP [5, 6] and microchannel-nanochannel interfaces [1-3]. However, there are few basic studies of CP coupled with bulk electroosmotic flow (EOF), and, prior to the current work, no models predicting the existence of "focusing zones" caused by this EOF/CP coupling.

In this paper, we present an analytical model of CP which considers the effect of bulk flow and multiple ion species and which predicts focusing of analyte ions. CP establishes significant conductivity gradients which generate local gradients in electric field and analyte drift velocity.

2. THEORY

As shown in Figure 1, focusing occurs where bulk velocity locally balances electrophoretic drift. To derive a set of focusing criteria, we consider two important nondimensional groupings, $\bar{v}^*$, electrophoretic velocity divided by the Helmholtz-Smoluchowski EOF velocity and q^*, the wall/shear plane charge divided by the number of diffuse ions in the nanochannel. q^* determines the degree of ion flux imbalance. The relative strength of q^* and $\bar{v}^*$ define the strength of the field gradients in the enrichment region. Our model provides a focusing criterion that can be simplified to two inequalities for the simple case of small values of λ_D/h, and constant and uniform values of zeta potential, wall charge, and nanochannel centreline concentration. Under these assumptions, a (fluorescent) analyte with a nondimensional mobility v_f^* in a three ion system will focus provided that

$$\frac{v_r}{v_r + q^*} < v_f^* < \frac{v_r\left(1 + q^*\bar{v}^*\right)}{v_r + q^*} \tag{1}$$

978-0-9798064-0-7/μTAS2007/$20©2007CBMS

With $\bar{v}^*$ and v_r defined as:

$$\bar{v}^* = \frac{2v^+v^-\left|z^-/z^+\right|}{v^+ + v^-\left|z^-/z^+\right|} \cdot \frac{z^+F\mu}{\varepsilon|\zeta|} \tag{2}$$

$$v_r = 0.5 + 0.5 \cdot v^-/v^+\left|z^-/z^+\right| \tag{3}$$

In equation 1, $v_f^* = -\mu v_f F|z|/\varepsilon\zeta$, $q^* = -\sigma_{wall}/Fhc$, σ_{wall} is wall charge, F is Faraday's constant, h is nanochannel height, c is concentration of background ions, μ is viscosity, z is ion valence, v is electrophoretic mobility, ε is permittivity and ζ is zeta potential. Figure 2 shows a phase diagram which illustrates when focusing is predicted as a function of these parameters.

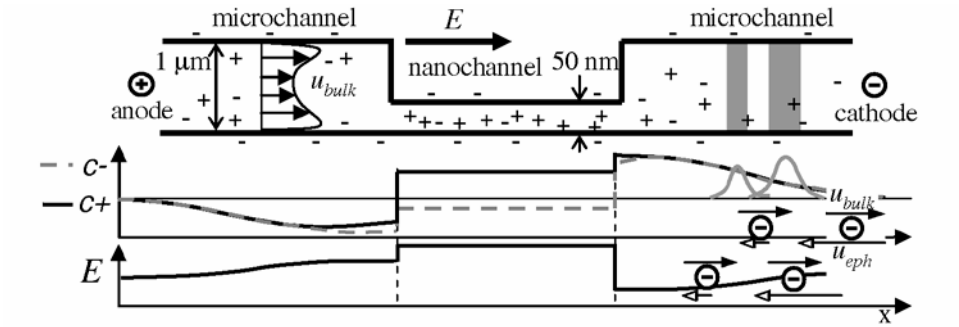

Figure 1. Schematic of analyte focusing mechanism. The area-averaged velocity of water, u_{bulk}, is constant in the microchannel to satisfy mass conservation. CP causes a depletion in background electrolyte (BGE) ionic strength ($c^+ + c^-$) on the anode side and an increase on the cathode side. Local electric field, E, is inversely proportional to local ionic strength, therefore, CP establishes a decreasing electric field in the enrichment region. Analyte anions on the cathode side have an electrophoretic drift velocity (u_{eph}) which is largest furthest from the intersection. A negative ion entering from the cathode well is driven by electrophoresis until it arrives at its mobility-dependent focal point where u_{bulk} equals u_{eph}. Thus, analyte ions with distinct mobilities focus and separate into distinct sample bands. Resolution is determined by both the difference in mobility and the dispersion rate due to a non-uniform bulk velocity (caused by internal pressure gradients).

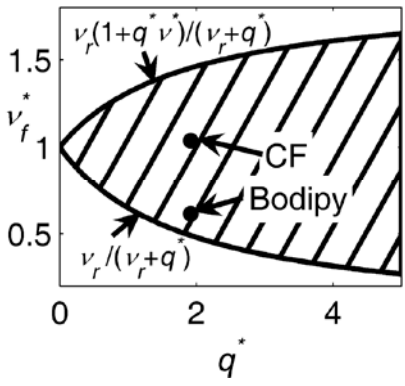

Figure 2. Phase plot of $v_f^* = -\mu vF|z|/\varepsilon\zeta$ (nondimensional mobility of fluorescent analyte) versus $q^* = -\sigma_{wall}/Fh_1c_1$ (nondimensional wall charge). The focusing region for the experiment in Figure 3 (with background electrolyte $\bar{v}^*$ = 1.0, v_r = 1.8) is hatched. q^* and v_f^* for Bodipy and carboxy-Fluorescein (CF) in this experiment are highlighted. Focusing is expected (and shown in Fig. 3) because these points lie within the hatched region.

3. EXPERIMENTAL RESULTS

Our devices consists of a symmetric, in-series arrangement of a nanochannel between two microchannels. We have fabricated and tested fused silica microchannel-nanochannel devices with 50 and 100 nm deep nanochannels and a variety of analyte and background electrolyte combinations. Figure 3 shows one experiment where we focus and separate Bodipy and carboxy-Fluorescein using conditions for which our model predicts focusing (see Figure 2).

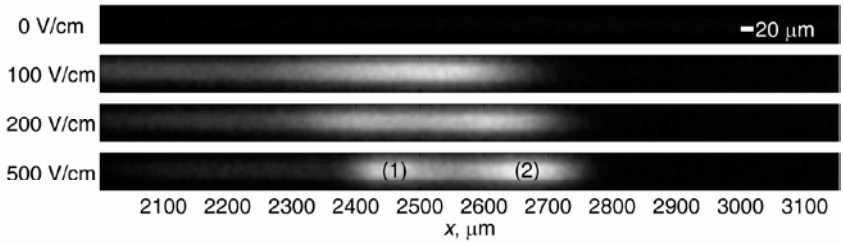

Figure 3. Scalar image of stacked analyte peaks for nominal applied fields of 0, 100, 200, and 500 V/cm. Before voltage was applied, both wells and the entire channel were filled with 0.5 mM-Tris, 0.25 mM HCl, 50 μM Bodipy and 50 μM carboxy-Fluorescein. As predicted by the model, CP quickly (within 50 s) establishes a focusing region on the cathode side of the system. For this combination of background and analyte ions, two focusing points are formed and we observe focusing of carboxy-Fluorescein (1) and Bodipy (2) within 100 s. As the CP-induced gradients in ionic strength develop, the sample bands observably migrate at roughly 10% of the expected electrophoretic drift velocity (2 μm/s drift relative to the lab frame). The microchannel was 1 μm deep and the nanochannel depth was 50 nm. Images were captured with a 10X, NA = 0.4 objective in the cathode-side microchannel focusing region 2 mm from the nanochannel intersection (x origin is at the micro-to-nanochannel junction). Channels were 20 μm wide and dry etched in fused silica. Images were smoothed with a σ = 1.3 μm Gaussian filter.

4. DISCUSSION

We have demonstrated simultaneous separation and focusing with ~100X increase in concentration in less than 100 s. We are using our CP/EOF models to optimize the device for electrophoretic separations and focusing. This mechanism is attractive because it creates focused, nearly-stationary, sample peaks in a microchannel, so that sensitive detection with significant line-of-sight integration is achievable.

ACKNOWLEDGMENTS

This work was sponsored by National Institutes of Health (Contract No. N01-HV-28183) and an NSF PECASE Award (J.G.S., award number NSF CTS0239080). T.A.Z. is supported by a Regina Casper Stanford Graduate Fellowship.

REFERENCES

[1] Plecis, A.; Schoch, R. B.; Renaud, P. *Nano Letters* **2005**, *5*, 1147-1155.
[2] Pu, Q.; Yun, J.; Temkin, H.; Liu, S. *Nano Letters* **2004**, *4*, 1099-1103.
[3] Wang, Y.-C.; Stevens, A. L.; Han, J. *Analytical chemistry* **2005**, *77*, 4293-4299.
[4] Pennathur, S.; Santiago, J. G. *Analytical chemistry* **2005**, *77*, 6772-6781.
[5] Leinweber, F. C.; Tallarek, U. *Langmuir* **2004**, *20*, 11637-11648.
[6] Mishchuk, N. A. *Colloids and surfaces. A, Physicochemical and engineering aspects* **1995**, *95*, 119-131.

DNA SEPARATION BY SQUARE PATTERNED NANOPILLAR CHIPS

T. Yasui[1], N. Kaji[1,2], R. Ogawa[3], S. Hashioka[3], M. Tokeshi[1,2], Y. Horiike[3] and Y. Baba[1,2,4,5]

[1]Department of Applied Chemistry, Graduate School of Engineering, [2]MEXT Innovative Research Center for Preventive Medical Engineering, Nagoya University, JAPAN
[3]National Institute for Materials Science, JAPAN
[4]Health Technology Research Center, AIST, JAPAN
[5]Institute for Molecular Science, JAPAN

ABSTRACT

In this paper, the mechanism of DNA separation by different array-pattern nanopillar chips and the effect of nanopillar spacing were carefully studied. We revealed that array-pattern of nanopillars and nanopillar spacing dominates the separation mode, and furthermore, the square patterned nanopillar chips could achieve a high-resolution and high-speed separation.

Keywords: nanopillar chip, electrophoresis, array dependence, spacing dependence

1. INTRODUCTION

We have demonstrated that nanopillar array structures have ability to separate DNA molecules [1]. Recently, Han *et al.* reported an anisotropic sieving structure consisting of a two-dimensional periodic nanofluidic filter array for separation of DNA and proteins [2]. These nanostructure-based separation techniques hold a great promise to accelerate genomics and proteomics research. Owing to development of nanotechnology, free layout nanostructures are currently available. These nanostructures realize unexpected separations that could not be achieved by natural or synthetic polymers.

2. EXPERIMENTAL

In this work, we fabricated two types of nanopillar array pattern, tilted and square array pattern (Figure 1). Nanopillars were patterned on quartz substrate with a depth of 4 μm using a combination of electron beam lithography and photolithography. The detail fabrication method was shown in [1]. We designed the nanopillar array region as shown in Figure 2 to separate the DNA fragments.

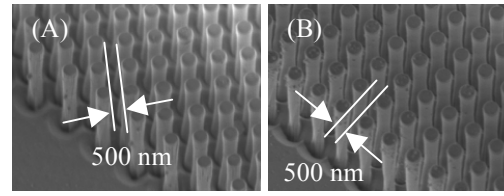

Figure 1. Nanopillars of (A) tilted and (B) square array pattern. Both spacing and diameter of nanopillars are 500 nm.

For fluorescence observation, 1,2,5, and 48 kbp were all stained with the bis-intercalating fluorescence dye YOYO-1. The dye-to-basepair ratio of the final working solution was ~1:15 and the final DNA concentrations were 20-50 ng/μL for DNA separation and ~10 ng/mL for a single DNA molecule observation. The buffer which is consist of 267 mM Tris-borate and 6 mM EDTA (3×TBE) with 10 mM DTT as an antiphotobleaching agent was used. DNA separation and a single DNA molecule observation were done on an inverted microscope which was equipped with a 10×/0.45 NA and a 100×/1.40 NA oil immersion objective lens. DNA bands and motions of an individual DNA molecule were

978-0-9798064-0-7/μTAS2007/$20©2007CBMS

captured by a CCD camera, recorded on a DV tape and then analyzed later by an image-processing software.

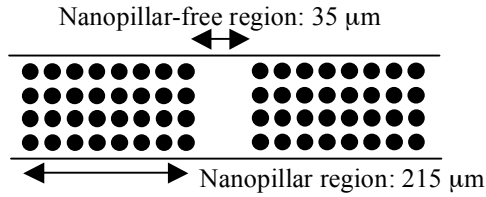

Total number of pillar region: 20
Length of total pillar region: 4.3 mm

Figure 2. Layout of nanopillar array regions.

3. RESULTS AND DISCUSSION

In our previous report, we demonstrated that DNA could be separated by square patterned nanopillar chips based on the difference of gyration radius [3]. The separation mechanism and several parameters affecting the resolving power have been carefully studied, and as a result, we revealed that the DNA migration order in tilted array patterned nanopillar chips was inverted in square array. As shown in Figure 3, in square patterned nanopillar chip with 500 nm spacing, 48 kbp DNA migrated faster than 1 kbp DNA and clearly separated, and moreover, DNA was separated at shorter distance and faster time than in tilted patterned nanopillar chip with 500 nm spacing. This result indicated that the separation mechanism could be easily controlled just by changing array pattern of nanopillars. Single molecule imaging of T4 DNA migration also suggested that DNA molecules took different migration behavior in these array patterns (Figure 4). In tilted patterned nanopillar chip, DNA migrated with hooking the nanopillars and it looks that DNA molecule had molecular sieving. By contrast, in square patterned nanopillar chip, DNA migrated without hooking the nanopillars and went straightforward between nanopillars. The difference of DNA migration behavior might cause the inversion of DNA migration order.

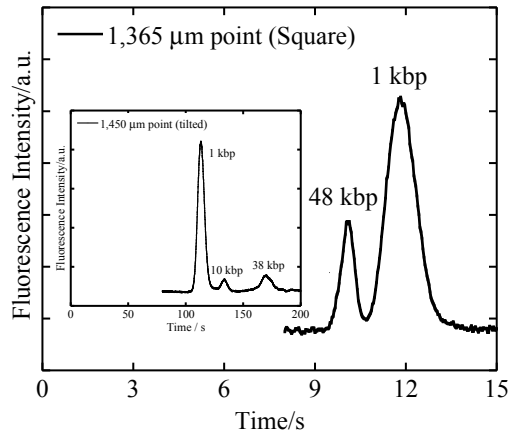

Figure 3. Separation of 1 and 48 kbp DNA by square patterned nanopillar chip with 500 nm spacing. For the sake of comparison, separation of 1, 10, and 38 kbp DNA by tilted patterned nanopillar chip was shown in the inserted electorpherogram [1].

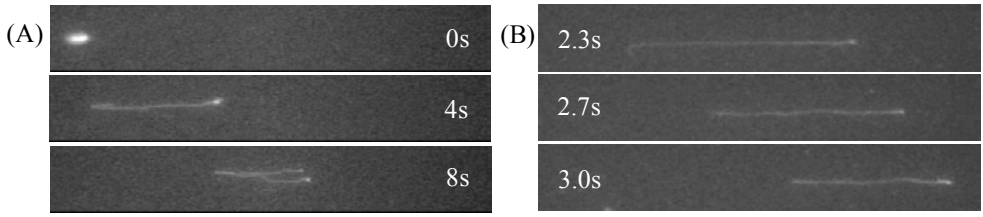

Figure 4. Fluorescence images of a T4 DNA (165.6 kbp) migration in (A) tilted and (B) square patterned nanopillar chip with 500 nm. spacing.

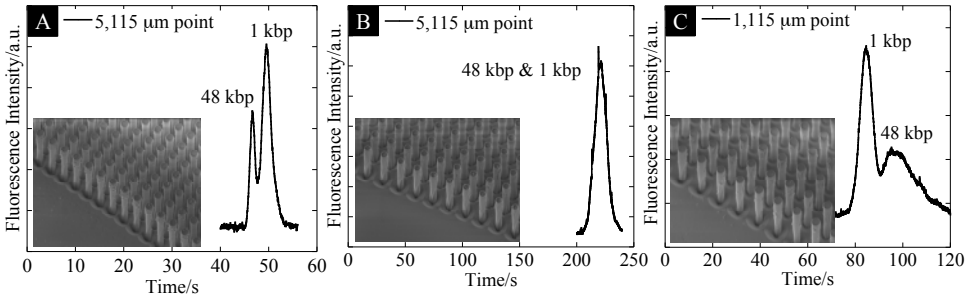

Figure 5. Dependence of nanopillar spacing on DNA separation in square patterned nanopillar chips. (A) 500 nm (B) 700 nm (C) 1,000 nm spacing.

In order to investigate the influence of nanopillar spacing of square patterned nanopillar chips on resolving power, we fabricated 500 nm diameter nanopillars with different spacing, 500 nm, 700 nm, and 1,000 nm. As shown in Figure 5, there was a critical point to dotermine separation mode around 700 nm spacing for 1 and 48 kbp DNA separations.

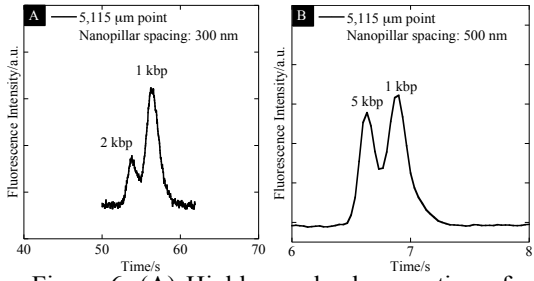

Figure 6. (A) Highly-resolved separation of 1 and 2 kbp DNA by square patterned nanopillar chip with 300 nm spacing. (B) High speed separation of 1 and 5 kbp DNA by square patterned nanopillar chip with 500 nm spacing.

After optimization of the separation conditions by square patterned nanopillar chips, a highly-resolved and a high speed separation was achieved successfully. The mixture of 1 and 2 kbp was separated by the 300 nm-spacing nanopillar chips within 1 min (Figure 6A). The 500 nm-spacing nanopillar chips could separate the mixture of 1 and 5 kbp within only 7 sec (Figure 6B).

4. CONCLUSIONS

We performed DNA separation by square patterned nanopillar chips and revealed that the separation results were array pattern and nanopillar spacing dependent. DNA migration order could be easily shifted by changing array pattern and nanopillar spacing. In addition, the square array pattern nanopillar enabled highly-resolved and high speed DNA separation. These results strongly suggest that the nanopillar chips have a great potential as a novel sieving matrix.

REFERENCES

[1] N.Kaji, et.al., Anal.Chem., 76(1)(2004), pp.15-22
[2] J.Fu, et.al., Nature Nanotechnol. 2(2007), pp.121-128
[3] R.Ogawa, et.al., μTAS 2006, pp.404-406

MICROFLUIDIC TOOLS FOR INVESTIGATING KINETICS AND THERMODYNAMICS OF CRYSTALLIZATION PROCESSES

Philippe Laval, Jacques Leng, Mathieu Joanicot, and Jean-Baptiste Salmon

LOF, UMR 5258 CNRS-Rhodia-Bordeaux 1

178 av. Schweitzer, 33608 Pessac, FRANCE

ABSTRACT

We developed microfluidic tools for acquisition of thermodynamic/kinetic data concerning crystallization. These devices allow to create hundreds of droplets, playing the role of microreactors, and to control their temperature. These chips have been applied to crystallization studies for measuring kinetics of nucleation and solubility. We can induce by cooling a large number of independent crystallizations of the solute present in the small volumes of the droplets, and also follow the crystals dissolution as the temperature is increased. Because of the nanoliter-sized droplets, the crystallization mechanisms are mononuclear and we can investigate nucleation close to homogeneous conditions and reach high supersaturations.

Keywords: crystallization, polymorph, nucleation, droplets

1. INTRODUCTION

Nucleation kinetics plays a fundamental role in crystallization processes. It is responsible for the final properties of the crystals: size, size distribution, habits... The control of nucleation kinetics is thus a challenge for many scientific fields (proteomics, chemical engineering…). Moreover, these topics are facing more complex systems concerning crystallization, depending on multiple parameters. Therefore their complete investigations take time and require significant amounts of products. In this context, microfluidic tools, and more precisely high-throughput strategies, may meet a great success. Recently, the development of microvalves has made possible the production of highly integrated systems which can be used to address individually hundreds of reaction chambers [1]. These devices are well adapted to carry out high-throughput screening of phase diagrams, particularly in the case of protein crystallization investigation. However, their fabrication are still complicated. Another possible strategy is the use of droplets playing the role of nanoliter-sized reaction compartments. These droplets can be produced in specific microfluidic geometries, and their volume and chemical composition can be fixed in a controlled way. In addition, they also allow a rapid mixing of the different compounds, prevent from any cross contamination, and can be stored in microchannels [2].

In this context and using droplet-based microfluidics, we have developed original tools to access kinetic and thermodynamic data concerning crystallization processes, and more precisely: the nucleation rate and the solubility. The first setup allows us to measure continously the nucleation kinetics after a fast temperature quench. The use of droplets allows us to access conditions close to homogeneous nucleation. The second chip allows one to perform rapid screening of solubility diagrams, by creating a two-dimensional array of droplets with both a temperature and a concentration gradient.

978-0-9798064-0-7/μTAS2007/$20©2007CBMS

2. NUCLEATION RATE MEASUREMENTS

One classical method to estimate the nucleation rate J (number of nuclei formed / s m^3) consists in the determination of the induction time t_i which is the time elapsing between the creation of the supersaturation S (e.g. obtained after a temperature quench) and the first appearance of crystals. However, it is difficult to determine J from such measurements since it depends on the sensitivity of the detection and since the growth kinetics of the crystals has to be known. Moreover, in this kind of experiments carried out in macroscopic volumes, impurities play a significant role, and a rapid temperature quench is difficult to achieve. The most reliable way to measure crystal nucleation kinetics is the droplets method [3]. The principle is to divide a volume of solution in a large number of small independent reactors, for example droplets in an inert oil. In this case, one may observe homogeneous nucleation if the number of droplets is larger than the number of impurities initially present in the solution. After a supersaturation S is reached, one measures the fraction of droplets which contain a crystal as a function of time. When the droplets volume V is small enough, the nucleation time is large compared to the growth time, and so only mononuclear nucleation occurs [4]. In that case, nucleation being a stochastic process, the probability P that a droplet contains a crystal evolves as $P(t) = 1-\exp(-JVt)$ when the solution is instantaneously supersaturated at t=0 [4]. With this method, the simple observation of a large number of drops enables one to reach an accurate statistics on P and so to determine the nucleation rate J.

Figure 1 (left) displays out setup which is a microfluidic format of the droplet method. Monodisperse droplets (about 100 nL) are formed at the junction between an oil stream and an aqueous one that contain a solute. These droplets are formed at a temperature T_1 above the solubity temperature to avoid crystallization. These microreactors are flowing continuously in the microdevice at a rate of 1-5 droplets/s and velocities of a few mm/s. After a long microchannel, where the droplets encounter a temperature quench, they enter a long serpentine at a temperature T_2 below the solubility: nucleation may occur. The fraction of droplets that contain a crystal is easily measured as a function of time, since the various part of the serpentine correspond to different residence times of the drops. With this device, one can estimate J as a function of the temperature T_2 with only a few hundreds of droplets. More results concerning these measurements can be found in [5].

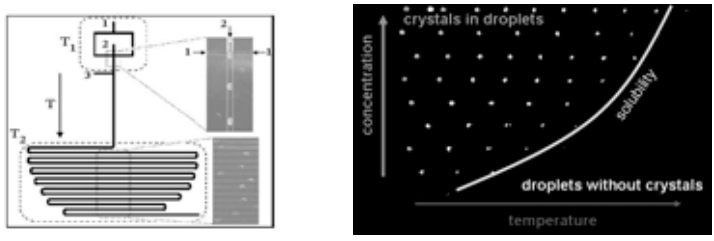

Figure 1. Left: Design of the microdevice. Oil and aqueous phases are injected respectively in inlets 1 and 2. Oil is injected in inlet 3 to increase the droplet velocity. The top-right image shows the formation of the droplets that contain the solute. The two dashed areas are temperature controlled at T_1 and T_2. Right: Microfluidic chip allowing us to store hundreds of drops and to create both a concentration and a temperature gradient. Crystals in the droplets appear as bright pixels. Solubility curves can be measured directly on this chip

with a small amount of solution (200 drops of 100 nL, <250 µL consumed during an experiment).

3. SOLUBILITY MEASUREMENTS

We have also engineered a microfluidic chip that allow a direct and quantitative reading of two-dimensional diagrams (see Fig. 1, right). Hundreds of about 100 nL droplets of different chemical compositions can be stored in parallel microchannels, and a temperature gradient applied along these channels enables us to obtain a two dimensional array of droplets of different concentrations and temperatures. For solubility diagram screening, droplets containing a given solute are first stored with a gradual variation of concentration. Then, crystallization in the droplets is induced by cooling, and finally, the application of an adequat temperature gradient dissolves crystals in droplets whose temperature is higher than their solubility temperature. As a result, we directly read the limit between droplets with and without crystals as shown on Fig. 1, right. which gives the solubility temperatures of the solution at the different concentrations. Thanks to an automated filling procedure using pinch valves, we have demonstrated on a model system (adipic acid in water), that we could easily and directly access to ten simultaneous measurements of the solubility curve on a large temperature range, in less than 1 hr, and with only 250 µL of solution (more details can be found in [6]).

4. CONCLUSIONS

In this work we have demonstrated the possibilities offered by microfluidics to obtain rapidly and with a small amount of solution, kinetic and thermodynamic information concerning the crystallization of a solute. These possibilities come from the use of droplets and the control of temperature. These small drops allow us to follow a large number of *independent* crystallization events, that all come from *mononuclear* nucleation mechanisms. These points are crucial to measure solubility of metastable polymorphic forms, but also to measure nucleation rate.

REFERENCES

1. B.T.C. Lau, C.A. Baitz, X.P. Dong, and C.L. Hansen, A Complete Microfluidic Screening Platform for Rational Protein Crystallization, J. Am. Chem. Soc. **129**, 454 (2007)
2. H. Song, D.L. Chen, and R.F. Ismagilov, Reactions in droplets in microfluidic channels, Angew.Chem.Int.Ed Engl. **45**, 7336 (2006)
3. D. Turnbull, Kinetics of solidification of supercooled liquid mercury droplets, J. Chem. Phys. **20**, 411 (1952)
4. A.C. Zettlemoyer, Nucleation, Marcel Dekker, New York (1969)
5. P. Laval, J.-B. Salmon, and M. Joanicot, A microfluidic device for investigating crystal nucleation kinetics, J. Crystal Growth **303**, 622 (2007)
6. P. Laval, N. Lisai, J.-B. Salmon, and M. Joanicot, A microfluidic device based on droplet storage for screening solubility diagrams, Lab Chip **7**, 829 (2007)

PHASE SEPARATION OF SEGMENTED FLOW BY THE PHOTOCATALYTIC WETTABILITY PATTERNING AND TUNING OF MICROCHANNEL SURFACE

Go Takei[a] , Arata Aota[a], Akihide Hibara[a,b,c], Takehiko Kitamori[a,b,c] and Haeng-Boo Kim[a,b,c]

[a] *School of Engineering, The University of Tokyo, Japan*
[b] *Kanagawa Academy of Science and Technology, Japan*
[c] *CREST, Japan Science and Technology Agency, Japan*

ABSTRACT

We have developed photocatalytic patterning and tuning method of channel surface wettability using titania nanoparticles for microfluid control. Here, we present phase separation of segmented flow by using superhydrophobic/hydrophilic patterned surfaces prepared by the method. The phase separation mechanism, based on pressure balance among hydraulic pressures and Laplace pressure, is discussed.

Keywords: Superhydrophobic and hydrophilic patterning, conversion of segmented flow to parallel flow, Laplace pressure

1. INTRODUCTION

According to the concept of continuous flow chemical processing (CFCP), we have developed various kinds of microfluidic systems by combining plural elementary microunit operations (MUOs) [1]. To construct the systems, utilizing a parallel multiphase flow was attractive because of the unique characteristics being large specific interface area and simple phase separation. Besides the parallel multiphase flow, microfluidic systems based on a segmented flow (plug or slug flow) also have been reported. Many studies including multiphase organic synthesis and micro- or nanoparticle synthesis have been reported [2-4]. If the phase separation becomes possible, the segmented-flow based microfluidic processes can be connected to the subsequent processes such as purification process, and thus be applicable to CFCP as MUO. In previous papers, we reported photocatalytic patterning and tuning method of surface wettability in a microchannel in the range from superhydrophobic to superhydrophilic under controlled photoirradiation [5, 6]. In this paper, we present phase separation of the segmented flow utilizing the surface wettability patterned microchannel and discuss the separation conditions.

2. PRINCIPLE

It is well known that wettability of a surface being nanometer-sized roughness is enhanced; a hydrophobic or hydrophilic surface becomes more hydrophobic or hydrophilic, respectively. First, microchannel surface is coated with titania nanoparticles, which makes the surface superhydrophilic. Subsequent hydrophobic treatment with octadecyltrichlorosilane (ODS) makes the surface superhydrophobic. Since the titania acts as photocatalyst for oxidative decomposition of organic molecules, UV irradiation induces decomposition of ODS to regenerate superhydophilic surface. By using an appropriate photomask, we can pattern superhydrophobic/hydrophilic surfaces in the microchannel.

978-0-9798064-0-7/μTAS2007/$20©2007CBMS

3. EXPERIMENTAL

A microchannel chip was fabricated by ordinary photolithography-wet etching and thermal bonding of Pyrex glass substrates [1]. The channel design is shown in Figure 1. By introducing titania nanoparticle (P-25, Degussa) suspension into the channel, a titania nanoparticle modified microchannel (TMC) was prepared [6]. To modify the TMC with ODS, toluene solution of ODS was used. Then, the superhydrophobic/hydrophilic patterned surfaces were obtained by UV irradiation of the ODS modified TMC through a photomask as shown in Figure 1.

4. RESULTS AND DISCUSSION

Water and toluene were introduced into the microchannel to demonstrate the series of fluid manipulations for phase separation of the segmented flow. As shown in Figure 2, plug formation, conversion of to parallel two-phase flow and phase separation were successfully carried out by using the superhydrophilic/hydrophobic patterned channel as can be seen in pictures (A) to (C) in Figure 2, respectively. It should be emphasized that toluene or water stream was formed only on the superhydrophobic or superhydrophobic surface, respectively, in the conversion part (B). Such complete conversion of the segmented flow to the parallel two-phase flow allowed us the complete phase separation in the separation part (C).

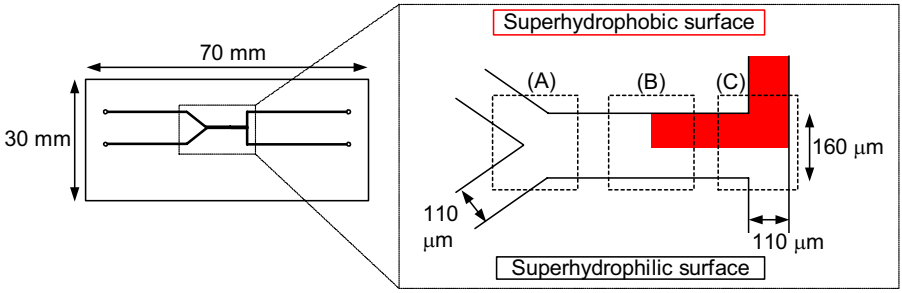

Figure 1. A microchannel pattern design and superhydrophobic-superhydrophobic pattern; (A) plug formation part, (B) conversion part of plug flow to parallel two-phase flow, and (C) phase separation part.

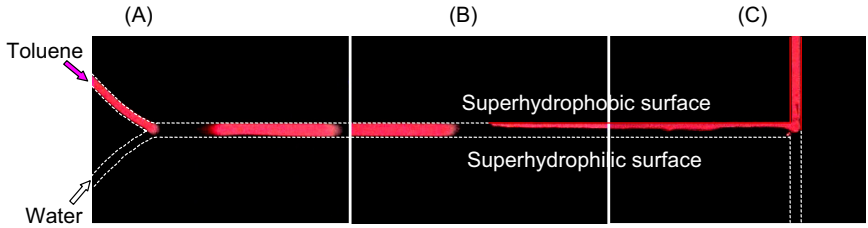

Figure 2. Fluorescence images; the flow rate of toluene (dyed with Nile Red) and water were 1.0 and 0.75 μL min^{-1}, respectively. In the plug formation part (A), toluene plugs in an aqueous carrier flow were observed. In the conversion part (B), the segmented flow was successfully converted to parallel two-phase flow by the superhydrophobic/hydrophilic patterned surface. In the phase separation part (C), the parallel two-phase flow was completely separated.

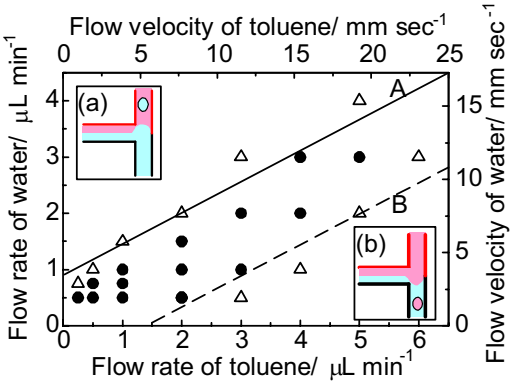

Figure 3. Conditions of flow rates for the phase separation. Closed circles indicate successful phase separation. Open triangles indicate that leakages were observed as shown in (a) and (b). Solid line (A) or broken line (B) shows theoretical upper or lower limit of flow rate of water, which corresponds to Figure 4(b) or (c), respectively.

To determine conditions of flow rates for the successful phase separation, the phase separation part was monitored with changing both flow rates of water and toluene. The results are summarized in Figure 3. The successful phase separation was observed under the conditions indicated by closed circles in Figure 3. At conditions indicated by open triangles, solution leakages were observed as shown in Figure 3(a) or (b).

To discuss the conditions for the phase separation, we considered pressures working at the liquid-liquid interface at the phase separation part; hydraulic pressure of aqueous phase (P^{Aq}) and organic phase (P^{Or}), and Laplace pressure (P_{LP}) as shown in Figure 4. For the stable interface formation and phase separation, it is necessary to balance the pressure difference between the two phases ($\Delta P = | P^{Aq} - P^{Or} |$) with P_{LP}. The predicted upper or lower limit of flow rate of water was shown in Figure 3, which agreed with the experimental results.

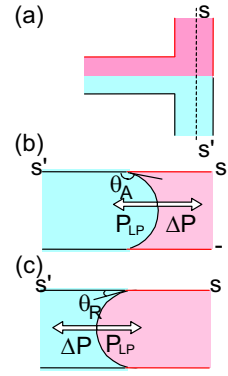

Figure 4. Schematic illustration of the phase separation part (a). Pressure balance and meniscus shape at the interface at $P^{Aq} > P^{Or}$ (b) and at $P^{Aq} < P^{Or}$ (c). The interface is kept as long as $\Delta P < P_{LP}$.

By using the present method, the phase separation of the segmented flow becomes possible and thus is applicable to CFCP as MUO.

REFERENCES

[1] M. Tokeshi, et al. *Anal. Chem*., 2002, **74**, 1565.
[2] H. Song, et al. *Angew. Chem. Int. Ed.,* 2006, **45**, 7336.
[3] M. Ueno, et al. *Chem. Commun.* 2003, 936.
[4] S. A. Khan, et al. *Angew. Chem. Int. Ed.,* 2005, **44**, 724.
[5] G. Takei et al. *Proc. MicroTAS 2006*, 245.
[6] G. Takei, et al. *Lab Chip*, 2007, **7**, 596.

SYNCHRONIZATION IN MICROFLUIDIC CIRCUITS

Manu Prakash and Neil Gershenfeld

Centre for Bits and Atoms, MIT, USA

ABSTRACT

In [1] we introduced Bubble logic, a new digital logic family implemented in two-phase microfluidics capable of universal computation. Bubble logic brings the logic, control and actuation of drops and bubbles on-chip, so bits can simultaneously represent and manipulate materials and information. For error correction in microfluidic circuits we introduced a novel ladder network geometry via passive synchronization. In this paper we quantify both experimentally and theoretically the performance of this timing restoration device. The presented passive synchronization scheme provides a simple, scalable error correction mechanism for multiphase digital microfluidic systems, with applications in microfluidic logic [1], droplet coalescence [2] and large-scale integrated microfluidics.

Keywords: Microfluidic computing, bubble logic, passive synchronization

1. INTRODUCTION

Current microfluidic technologies have a potential to revolutionize analytical chemistry and biology, but still rely on a lab full of external plumbing, valves and computers to operate. Very large-scale integrated (VLSI) microfluidics requires scalable, on-chip control mechanisms for complex routing, storage and processing of reactants on a chip [3]. To this end, we introduced a digital Boolean logic family; Bubble Logic [1], which provides a modular process control mechanism for multi-phase microfluidic systems. Bubble logic uses non-linear hydrodynamic interactions between bubbles flowing in microfluidic geometries to perform complex control operations for e.g. routing, storage, counting etc. without any external macro-scale elements like solenoids. For large-scale error-free operation of bubble logic, timing errors between arrival of different bubbles need to be corrected. Numerous authors have also reported the need for droplets to arrive in a synchronous manner [2] for reliable on-chip droplet coalescence. Here we present experimental data and a lumped element non-linear resistor network model of our device, which passively synchronizes bubbles travelling in microfluidic channels with no external control.

2. MICROFLUIDIC LADDER NETWORK SYNCHRONIZER (LNS)

Design of a LNS (Figure 1(A)) consists of two planar microfluidic channels (width=w_2) with two inlet ports marked 1 and 2 and two outlet ports marked 3 and 4, interconnected by a number of higher resistance flow channels (length L, width = w_3). Bubbles travel from left to right in the device with a constant inlet flow of continuous phase. The operating principle behind LNS is hydrodynamic coupling of flow in the two inlet channels. A single bubble entering the LNS is slowed down (Figure 2(A)) as it travels from left to right. This is due to increase in fluidic resistance of the horizontal channel due to presence of a bubble and existence of an alternate low resistance path for the fluid around the bubble. When two bubbles enter the geometry with a time delay (τ), a net flow from the channel with leading

978-0-9798064-0-7/μTAS2007/$20©2007CBMS

bubble to the one with lagging bubble, creates a relative velocity gradient synchronizing the two bubbles. Since LNS requires no active or moving components, the device can be fabricated using a wide variety of materials like glass, silicon etc.

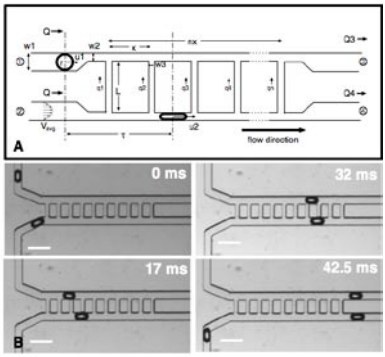

Figure 1. (A) Schematic of synchronization geometry. Bubbles are introduced into the channels at a constant frequency from left to right using a flow-focusing bubble generator operating at a constant flow-rate. (B) Passive synchronization of bubbles in top and bottom channels (width=100μm) in a PDMS device with interconnected channels (n=10, width=50 μm) operating at a constant flow rate of Q_w=0.5 μ l/sec. Timing restoration of 10 ms is achieved in ~40 ms. Scale bar 100 μm.

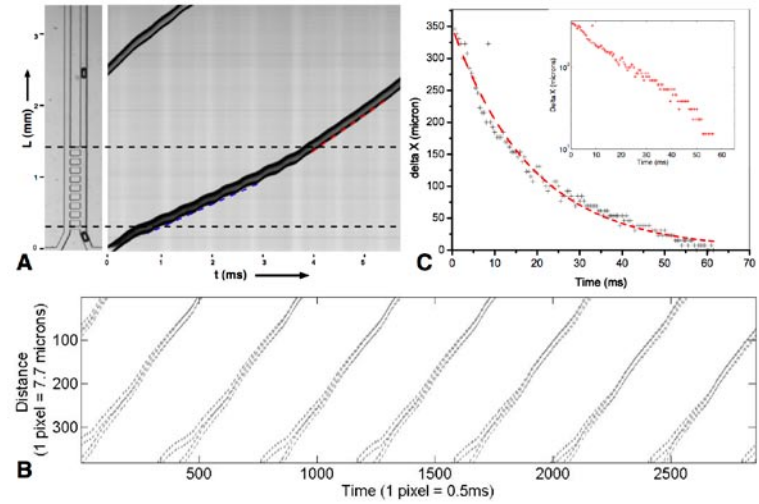

Figure 2. (A) Time series of a single bubble passing through a ladder network. The bubble slows down as it enters the interconnected segment. (B) Dynamics of continuous synchronization at 5Hz. (C) Plot of experimental data of distance between the two bubbles verses time with an exponential fit. Inset depicts a log –linear plot of decreasing distance with time.

3. RESULTS AND DISCUSSION

The operation of the device is depicted in a time series of micro-graphs in figure 1(B), obtained by high speed imaging. Figure 2 and 3 show synchronization dynamics of bubbles in a LNS device. Figure 2(A) shows a time trace obtained by high speed imaging (Phantom v4, 1000 fps) of a single nitrogen bubble in water (2% Tween 20 wt.) travelling

through the LNS geometry. The slope of the trajectory (bubble velocity) is constant in the three zones marked by dashed lines. The bubble velocity is reduced as it traverses the inter-connected channels. Periodic oscillations in bubble velocity are evident due to discrete resistive elements present in device. The device can operate in a continuous fashion, as shown in Figure 2(B) with LNS operating at ~5Hz. Figure 2(C) shows a plot of horizontal distance between the two bubbles reducing with time, with an exponential fit to the data (dashed line). Figure 3 (A) shows a resistor network model of the device. Spice simulations of the geometry depict variation of relative velocity of bubble in upper channel with respect to lower channel for all possible states of the device (M,N).

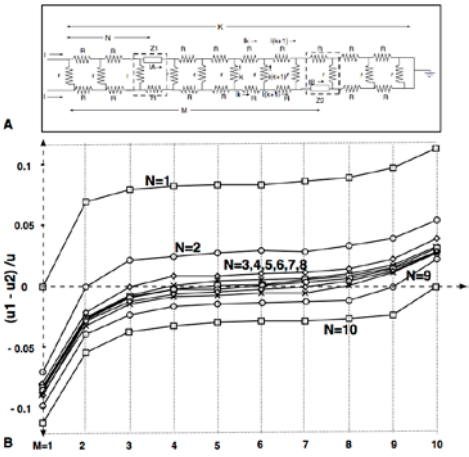

Figure 3. (A) Resistor network model of a synchronizer implemented with time varying non-linear resistors. The state of the system can be completely defined by three independent parameters; u (inlet fluid velocity), N and M (location of bubble in upper and lower channel). (B) Spice simulation of the resistor network model for all possible states of the LNS (Z1=Z2=50R). As is evident; relative velocity of bubble in upper channel (at N) with respect to velocity of bubble in lower channel (at M) is positive for M > N and negative for M < N; resulting in synchronization.

In conclusion, we have presented a novel microfluidic device for completely passive synchronization of bubbles in microfluidic networks. The scheme can also be used to synchronize droplets in microfluidic networks for coalescence and error-correction in microfluidic logic.

ACKNOWLEDGEMENTS

This work was supported by the MIT Center for Bits and Atoms (NSF grant CCR-0122419).

REFERENCES

[1] M. Prakash and N. Gershenfeld, Microfluidic Bubble Logic, Science, **315**, 5813, pp. 832 - 835 (2007).

[2] K. Ahn, J. Agresti, H. Chong, M. Marquez, and D.A. Weitz, Electrocoalescence of drops synchronized by size-dependent flow in microfluidic channels, Applied Physics Letters, **88**, 264105 (2006).

[3] M. Joanicot, A. Ajdari, Droplet control for microfluidics, Science, **309**, 5736 pp. 887-888 (2005).

AUTOMATED AND INTEGRATED MICRO SYSTEM FOR HIGH RESOLUTION IMAGING AND HIGH-THROUGHPUT SORTING OF *C. ELEGANS*

Kwanghun Chung[1], Matthew Crane[2], and Hang Lu[1,2]

[1]School of Chemical and Biomolecular Engineering, [2]Interdisciplinary Bioengineering Program, Georgia Institute of Technology, Atlanta, GA, USA

ABSTRACT

We report an automated and integrated microsystems for high-resolution imaging and high-throughput sorting of *Caenorhabditis elegans* (*C. elegans*). Microfluidic devices are developed to manipulate worms and brief cooling on-chip is used to immobilize the worms without anesthetics. High-resolution images of worms in the devices with a 100X objective are obtained and show the resolution of subcellular structures, comparable to conventional microscopy. We successfully sorted transgenic worms based on their expression patterns of fluorescence proteins with integrated Matlab algorithms that fully automate the sorting process.

Keywords: *C. elegans*, imaging, sorting, automation, high-throughput

1. INTRODUCTION

C. elegans, a free-living soil nematode, is an excellent model system for studying the genetics of development, synaptogenesis, and neuronal basis of behavior [1]. It offers unique opportunities to conduct fundamental biological studies due to the transparency of the organism combined with the availability of many molecular and genetic tools and RNA interference strategies to knock-down gene functions [2]. Because of these distinctive characteristics of *C. elegans*, *in vivo* microscopy has been extensively used for phenotypical characterizations, visual screens [6], and genome-wide promoter activity analysis [3]. Despite the long history of microscopy, the current procedure still requires the worms to be immobilized by anesthetics, which can disrupt neuronal signaling and induce undesirable physiological changes [4]. In addition, the manual handling not only significantly limits the experimental throughput, but also increases noise in the experiments due to sample-to-sample variation in handling. Here, we present a high-throughput automated microsystem for high-resolution imaging and sorting of worms without the use of anesthetics.

2. RESULTS AND DISCUSSION

We have developed a high-throughput automated system for high-resolution imaging and sorting of worms without the use of anesthetics. As a part of this system we have developed a microfluidic device that routes, traps, and immobilizes live animals (Fig 1). The device consists of a two-layer PDMS microfluidic chip bonded onto a glass coverslip. Samples are manipulated in the bottom PDMS layer which is adjacent to the glass coverslip. The top PDMS layer contains channels for actuating push-down valves [6] and circulating cooling fluid. The novel push-down valve structure enables the sample to be brought into close proximity with the cover glass, thereby minimizing changes in the

978-0-9798064-0-7/μTAS2007/$20©2007CBMS

refractive index of the materials along the optical path, which is critical to achieve high-resolution and high-magnification imaging using standard microscopes.

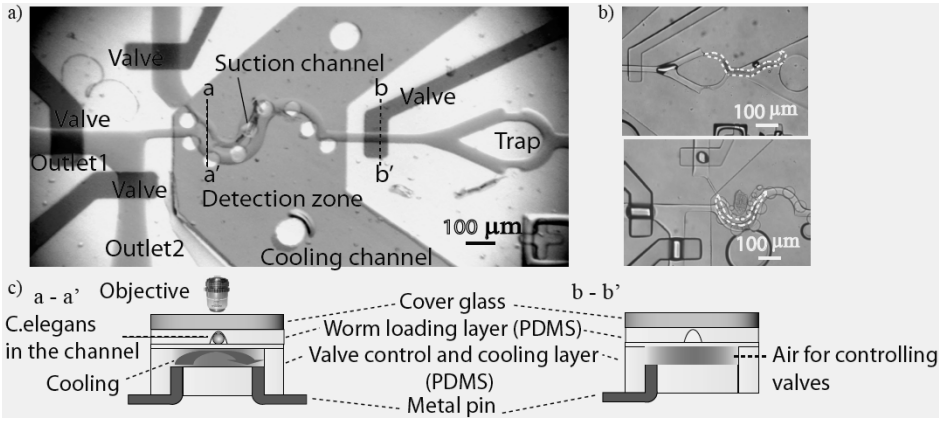

Figure 1. a) Optical micrograph of the device. b) a stopped and unloaded worm at the trap (top) and a positioned worm at the detection zone (bottom). c) schematics of cross-sectional view of a-a' and b-b'.

In order to prevent multiple worms from entering the detection zone, we designed a self-regulated loading scheme taking advantage of pressure drops created by a loaded worm. A worm that passes the trap is guided into the detection zone by the side suction channels. These side channels insure that a worm is positioned identically each time to minimize the time requirement for adjusting the microscope stage to locate the sample finely in the field of view. Once the worm is positioned in the detection zone, the four valves surrounding the detection zone are closed to isolate the detection zone from the rest of the device. This isolation eliminates any flow fluctuation caused by deformability of PDMS device in the detection zone. The nematode's small thermal mass allows it to be cooled and stopped in less than one second. Z-stack images of the worm are subsequently obtained and processed in order to sort the worm. As a result, the time required for sorting is less than 2 seconds; therefore undesirable effects of cooling and photobleaching are negligible. We have developed integrated Matlab algorithms that fully automate the processes outlined above and allow for high-throughput experiments.

To demonstrate the capability of this system as a high-resolution imaging tool we obtained Z-stack images of green fluorescent protein (GFP)-expressing neurons of a stopped worm with a 100X oil objective (Fig 2). Those images show the resolution of single axons/dendrites, comparable to that of current standard optical microscopy.

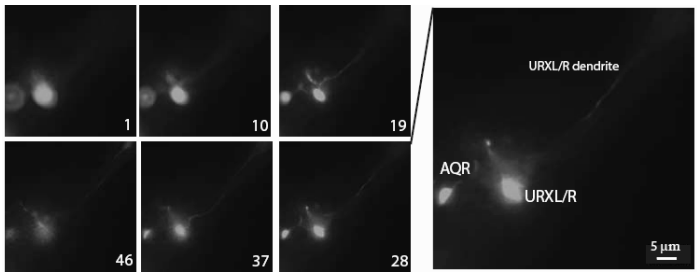

Figure 2. Images of GFP –expressing neurons in *C. elegans* taken in the device using cooling and without anesthetic (100x NA-1.4 objective).

Figure 3 shows an experiment where wild-type animals (without GFP) are sorted out from transgenic animals expressing GFP. We also demonstrate the high-throughput system by sorting worms with stochastic-expression of GFP in the sensory neuron AQR, separating those with bright GFP from those with little or no GFP in AQR (Fig 4). We achieved 80% correct sorting efficiency, and demonstrated that the worms are completely viable after sorting.

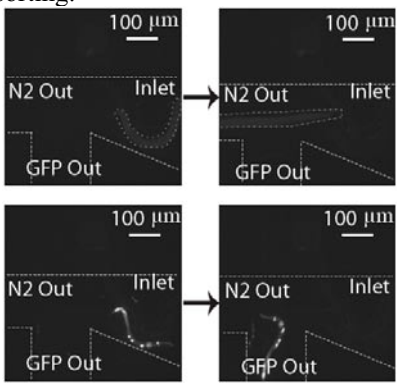

Figure 3. Automated on-chip sorting of transgenic GFP worms from a mixture with non-GFP tagged wild-type worms. 100% of GFP tagged worms were removed.

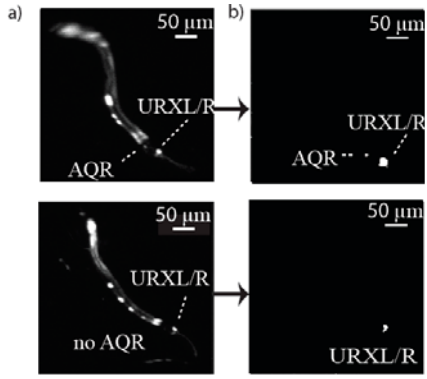

Figure 4. Automated on-chip sorting of transgenic worms with stochastic-expression of GFP a) Raw image used for image processing b) Processed image showing the 1 or 2 neurons of interest to guide the sorting.

3. CONCLUSIONS

We have developed a microsystem for high-resolution imaging and high-throughput sorting of *C. elegans*. This automated system will greatly facilitate numerous studies within worms and other small model systems which require high-throughput image processing and screening.

ACKNOWLEDGEMENTS

The authors acknowledge funding support from NIH-NIBIB, NIH-NINDS, and NSF.

REFERENCES

[1] Donald L. R., et al. C.elegans II, CSHL Press, (1997)

[2] John K. Kim, et al. Functional genomic analysis of RNA interference in C. elegans. Science, 308, 1164, (2005)

[3] Denis Dupuy, et al. Genome-scale analysis of in vivo spatiotemporal promoter activity in Caenorhabditis elegans, Nature biotechnology, 25, 663, (2007)

[4] Rubin, D., et al. Distribution of Glut1 in detergent-resistant membranes (DRMs) and non-DRM domains: effect of treatment with azide. American Journal of Physiology-Cell Physiology, 285, C377, (2003)

[5] Thorsen T., et al. Microfluidic large scale integration. Science, 298, 580, (2002)

[6] Jin, Y. Synaptogenesis (December 23, 2005), *WormBook*, ed. The *C. elegans* Research Community, WormBook.

EUKARYOTIC FLAGELLA AS MOTILE TOOLS FOR MICROFLUIDIC DEVICES

Hajime Nakamura[1], Kaori Kuribayashi[1], Hiroaki Onoe[1] and Shoji Takeuchi[1,2]

[1]CIRMM, Institute of Industrial Science, The University of Tokyo, JAPAN
[2]PRESTO, JST, JAPAN

ABSTRACT

This paper describes a method of producing a rotating flagella array. Flagella of unicellular algae *Chlamydomonas* were released from the cell body, and selectively fixed on the glass substrate where methacryloyloxyethylphosphorylcholine (MPC)–polymer was patterned in order to prevent non-specific binding. They were then reactivated and rotated like micro motors when ATP was added. Using this experimental set-up, we monitored single flagellum continuously on site and changed its rotating speed by controlling the concentration of Ca^{2+}. We believe that rotating flagella can be utilized as actuators for various microfluidic devices.

Keywords : Flagella, MPC-polymer, Micro array, Biomolecular motor

1. INTRODUCTION

Biological molecular motors have several advantages over artificial motors, including efficient energy conversion and the potential for self-assembly. There are numerous studies in developing micro bio-hybrid systems [1, 2]. In this experiment, we used flagella of *Chlamydomonas* as a motile tool; they can be separated from their body and rotate by reactivating with ATP (adenosine triphosphate) [3]. In addition, it is possible to control the rotating speed of flagella by varying Ca^{2+} concentration. Here, we report the method of fixing flagella on a substrate and controlling rotating speed by changing buffer as a fundamental step towards various mechanical functions in microfluidic devices, such as pump and mixer [4].

2. MATERIALS AND METHODS

The concept of the flagella array is shown in Fig. 1. The roots of the flagella of *Chlamydomonas* tend to adsorb to glass, but it can be prevented by coating the glass with MPC-polymer. Therefore, by patterning the surface of MPC-polymer, we can immobilize the flagella on selected regions. These flagella rotate like micro rotary motors in ATP buffer solution.

In this work, we at first cultivated *Chlamydomonas* in a liquid medium for 3 or 4 days. Then, we isolated their flagella by adding dibucaine-HCl, and collected by ultra-centrifugation [3].

A parylene lift-off process was used for the patterning of the MPC-polymer [5,6]. 2 μm parylene was deposited on a glass substrate after spin-coating the MPC-polymer on the glass substrate (Fig. 2 a). The parylene and MPC-polymer layers were then removed by O_2 plasma, and glass regions were selectively exposed; we used photoresist and aluminum as a mask of the dry etching (Fig. 2 b, c). The parylene film was then peeled off from the substrate (Fig. 2 d). We formed circular patterns of which diameters were varied from 5 μm to 20 μm. A polydimethylsiloxane (PDMS) micro fluidic channel was placed on the

978-0-9798064-0-7/μTAS2007/$20©2007CBMS

substrate and then the solution of flagella and ATP was introduced into the channel by sucking with a microsyringe with a syringepump (Fig. 2 e). We observed the motion of the flagella with a dark-field microscope (Fig. 2 f).

3. RESULTS AND DISCUSSION

We investigated the adsorption properties of flagella to a bare glass and a surface treated glass with MPC-polymer or bovine serum albumin (BSA). Fig. 3 is the result of the experiments, showing that flagella have higher affinity to bare glass than to MPC-polymer or BSA; about 80 % of flagella did not adsorb to the substrate covered with MPC-polymer. This figure also illustrated that the adsorption property of flagella with MPC-polymer was hardly affected by the spin-coating speed, while that with BSA was highly affected.

Fig. 4 (a) is a photo of the array of rotating flagella. We observed few flagella on the MPC-polmer region, and most of all the flagella adsorbed to the glass regions. Fig. 4 (b) shows the sequential photos of the single rotating flagellum. The rotational speed of the flagellum ranged from 0.5 rps to 3.0 rps. Fig. 5 shows the ratio of rotating flagella to all flagella attached on the glass regions of the MPC-polymer coated substrate. We found that the ratio depends on the size of the glass regions. As the diameter of the pattern became smaller, the ratio was increased (it reached 73 %, when the diameter was 5 μm).

We found that the motion of the flagella could be controlled by changing the surrounding buffer. Fig. 6 shows the changes of the rotational speed of flagella by changing the Ca^{2+} concentration. When the concentration was increased from 10 nM to 100 nM, the average speed decreased to around 40 % of the original speed.

4. CONCLUSIONS

In this work, we have succeeded in fixing and rotating flagella in a array by selectively exposing glass regions on MPC-polymer coated substrate. The rotational speed of the flagella could be changed by the Ca^{2+} concentration in the surrounding buffer. Just like biomolecular motors such as kinesin and microtubules [7], we believe the flagella prepared with this method have also a potential as biohybrid motors working in micro-systems.

ACKNOWLEDGEMENTS

The authors thank Ritsu Kamiya and Susumu Aoyama (Grad. School of Science, The University of Tokyo) for providing the cells, *Chlamydomonas*, with useful technical advice.

REFERENCES

[1] Y. Hiratsuka *et al.*, PNAS, 103, 37, 13618-13623, (2006).
[2] D. B. Weibel *et al.*, PNAS, 102, 34, 11963-11967, (2005).
[3] S. Aoyama *et al.,* Biophysical J., 89, 3261-3268, (2005).
[4] N. Darnton *et al.*, Biophysical J., 86, 1863-1870, (2004).
[5] S. Takeuchi *et al.*, MEMS2004,pp. 208-210, (2004).
[6] B. Ilic *et al.*, Biomedical Microdevices, 2, 4, 317-322, (2000).
[7] R. Yokokawa *et al.*, J. of Microelectromechanical Systems, 13, 4, 612-619, (2004).

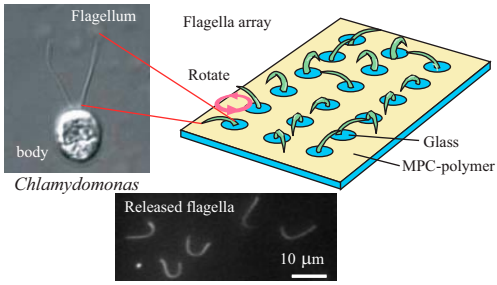

Figure 1. Concept of a rotating flagella array

Flagella (length: 10 μm) of *Chlamydomonas* are isolated from their bodies and fixed to a glass substrate where MPC-polymer is patterned. When in ATP buffer, they rotate as micro motors.

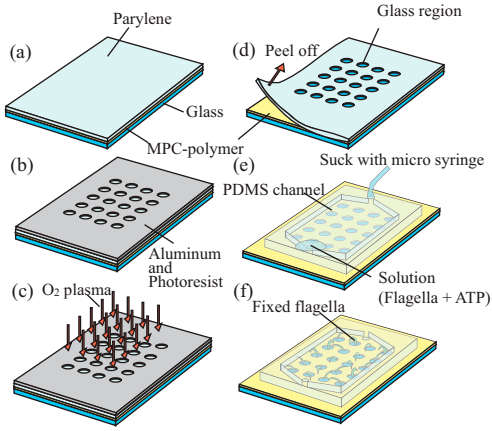

Figure 2. Fabrication process of the array

(a) Parylene film was deposited on a glass substrate after spin-coating MPC-polymer. (b), (c) Parylene and MPC-polymer layers were removed using O_2 plasma. (d) After peeling off the Parylene film, the array of the glass regions on the MPC-polymer coated substrate was then formed. (e) Solution of flagella and ATP (1 mM) was infused into the microfluidic channel (1.2 mm × 10 mm × 0.07 mm). (f) Flagella were fixed and rotated on only the glass regions.

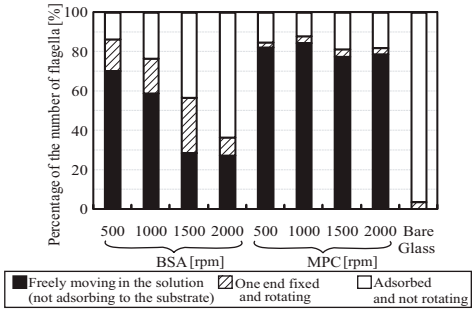

Figure 3. Adsorption properties of the rotating flagella to glass, MPC-polymer and BSA coated glass

The number of rotating flagella adsorbed on the surface of MPC-polymer or BSA coated/non-coated glass is shown. The coating speed was varied between 500 - 2000 rpm. The number of samples was between 141-260 at each data.

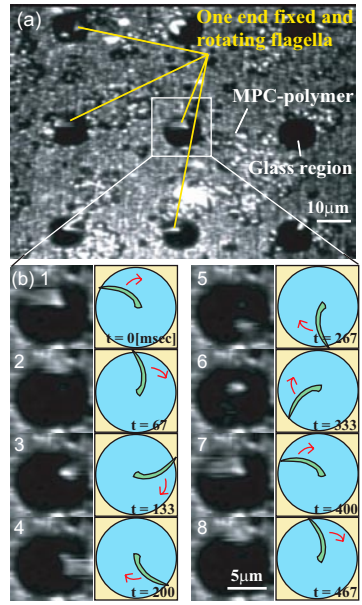

Figure 4. Photos of selectively fixed flagella

(a) Several fixed flagella on the array of glass-exposed regions. (b) Sequential images of an anchored flagellum.

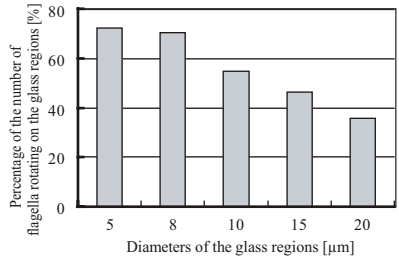

Figure 5. The ratio of rotating flagella to all adsorbed flagella on the glass regions

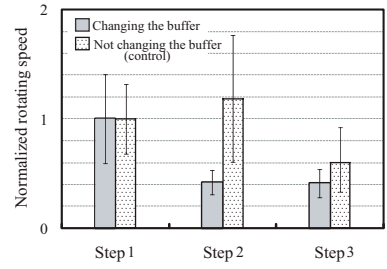

Figure 6. Changes of rotational speed of the flagella

Step 1: 3 minutes after the solution containing flagella; ATP and 10 nM Ca^{2+} buffer was infused. Step 2: About 12 minutes after step 1; The Ca^{2+} buffer was changed to a higher concentration (100 nM) in the microfluidic channel. Step 3: About 30 minutes after step 1; the buffer of 10 nM Ca^{2+} was infused again. The rotational speed was normalized by the speed of step 1. At each step, we also measure the speed of the flagella without changing buffer as the control data.

ELECTROACTIVE MICROFLUIDIC DEVICES FOR CONTROL OF INSECT CYBORG NEUROMUSCULAR SYSTEMS

Aram Chung[1], Donn Kim[2], Likun Chen[1], Roman Akhmechet[1], Bernardo Cordovez[1] and David Erickson[1]

[1]*Sibley School of Mechanical and Aerospace Engineering, Cornell University, Ithaca, NY*
[2]*School of Electrical and Computer Engineering, Cornell University, Ithaca, NY*
ac467@cornell.edu (A. Chung), de54@cornell.edu (D. Erickson)

Keywords: Insect Cyborg Sentinels, Drug Delivery, Electrokinetics, Electroactive Microwells

ABSTRACT

This work describes the development of an electroactive microwell based chemical/drug delivery system and its pupae stage implantation within *Manduca Sexta* Moths. This forms one of the critical components in our development of "Insect Cyborg Sentinels" which aim to fuse nanodevice technology with living systems. The goal of this system is to provide "on-command" chemically induced immobilization and subsequent reanimation of the otherwise autonomous cyborg. In this talk we will present the results of our adult survivability data for late and early pupae stage microdevice insertion experiments, our initial toxin injection experiments, and a comprehensive numerical/experimental study of our electroactive drug delivery system.



Figure 1. Live Insect Cyborg with Electroactive Microfluidic Device

1. INTRODUCTION

Modern microsystems technology has enabled the development of a large number of biomedical devices which allow us to monitor biological systems and biomolecular events with extreme precision. While such technology is proving extremely successful, rarely has the extension been made to exerting active control over a living system. In this work we present our initial results on the development of implanted microfluidic devices which enable such control over flying insects, namely *Manduca Sexta* Moths. One potential application of such a hybrid-insect system is in the development of microscale air vehicles,

978-0-9798064-0-7/μTAS2007/$20©2007CBMS

which exploit the highly evolved aerodynamics of insects with recent advances in microdevice engineering. An overview illustrating the system integration is presented in Figure 1.

2. EXPERIMENTAL RESULTS

As shown in Figure 2, the microdevice platform is partially implanted within the insect at the dorsal thorax of the pupae. To find the optimal location (which minimizes its physiological footprint, maximizes survivability, and favorably disperses the toxin), both the platform size and implantation location were varied. Figure 1 shows the results of a successful emergence of an insect with fully developed wings.

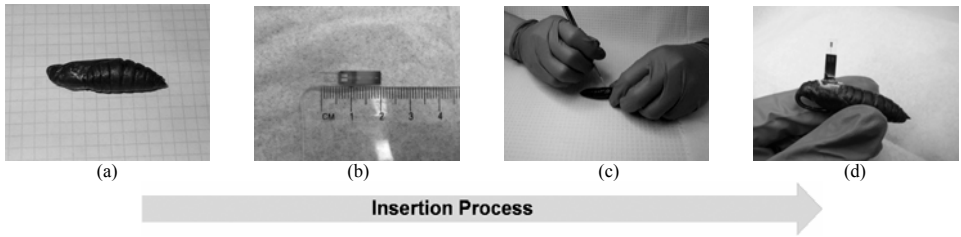

Figure 2. Insertion Experiment Process
(a) Manduca Sexta Moth pupae (b) Microfluidic Chip
(c) Implantation of microchip (d) Two days after insertion

Figure 3 illustrates an abbreviated version of the steps involved in our injection experiments used to determine the dosage effects on the degree and length of insect paralysis. For example injection of 5μL of a 5.839M solution of L-Glutamic acid potassium salt monohydrate, which comprises one of the major components of spider venom, into the thorax, the insect was immobilized for approximately 5hrs, after which the insect regained its pre-injection activity level.

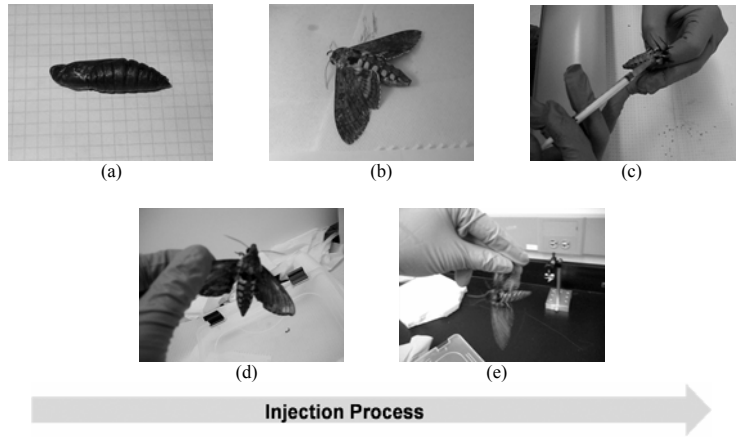

Figure 3. Immobilization Experiment Process
(a) Manduca Sexta Moth pupae (b) Live Manduca Sexta Moth adult (after 3 weeks)
(c) Injecting 5μL of a 5.839M solution of L-Glutamic acid potassium salt monohydrate
(d) Paralyzed after 1minute (e) Revived insect after 5hours of paralysis

The electroactive microwell drug delivery system developed here is based on the fusion of previous implantable drug delivery technologies [1] with our recently developed electrokinetically active microwells [2]. Briefly, the drug is stored within a well, etched into a silicon substrate (similar to illustrated in Figure 1b) which is sealed from the exterior using a thin gold membrane on PDMS (Polydimethylsiloxane). When a dosage command is issued, a voltage is applied to electrochemically dissolve the gold membrane [3], exposing the toxin. Unlike previous approaches, which rely on diffusive transport of the drug, we incorporate an electrokinetic injector whereby a potential field is applied between the top and bottom of the well and the drug is electroosmotically rejected from the well. A detailed, finite element based, model of the local fluid and transport dynamics involved in the drug ejection procedure will be presented along with our initial experimental results (see Figure 4). As will be demonstrated this approach reduces the drug injection time from approximately 30 minutes for diffusive transport to less than 1S.

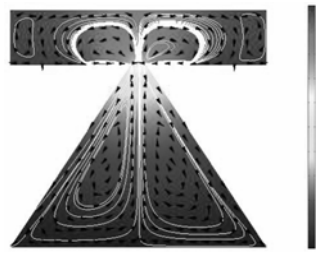

Figure 4. Finite Element Model of Electroactive Toxin Delivery System
Computed fluid and electrical field lines during rejection of chemicals from the electroactive microwell

3. CONCLUSION

In this work we have presented the development of an electroactive microwell drug/chemical delivery device which is implanted in the pupae developmental stage of a moth and used to exert chemical control over the level of neuromuscular activity. Implantation and dosage experiments along with a detailed microfluidic transport analysis will be presented.

4. ACKNOWLEDGEMENTS

This work was supported by the Defense Advanced Research Project Agency through the Boyce Thompson Institute for Plant Research.

5. REFERENCES

[1] J. Santini, M. Cima, and R. Langer, *A controlled-release microchip*, Nature, 397, pp. 335-338, (1999).

[2] B. Cordovez, D. Psaltis, and D. Erickson, *Trapping and storage of particles in electroactive microwells*, Applied Physics Letter, 90, pp. 024102, (2007).

[3] R. Frankenthal, and D. Siconol, *The anodic corrosion of gold in concentrated chloride solutions*, Journal of Electrochemical Society, 129, pp. 1192-1196, (1982).

CONTINUOUS PARTICLE CLASSIFICATION IN MICROFLUIDIC SYSTEMS

Minoru Seki

Chiba University, 1-33 Yayoi-cho, Inage-ku, Chiba 263-8522, JAPAN

mseki@faculty.chiba-u.jp

ABSTRACT

A size-dependent particle separation (classification) is one of the most important procedures in biochemical, environmental, or medical analyses and their applications. However, the smaller particle size or the smaller size difference makes the particle classification difficult. The Lab-on-a-Chip concept have encouraged the miniaturization of various separation or selection methods for small particles, including polymer beads, cells, and macromolecules. Microfluidic devices have a potential to facilitate rapid and precise particle manipulation, due to accurately fabricated structures close to particle sizes, in micrometer or sub-micrometer dimensions.

We have, therefore, proposed a new scheme for particle sorting, "Pinched Flow Fractionation (PFF)", and that for separating and concentrating particles, "Hydrodynamic Filtration (HDF)", utilizing microfluidic devices. By using these methods, the various types of microspheres such as polymer beads, biological cells, droplets or macromolecules have been continuously separated. These microfluidic separation systems will be useful due to its simplicity and accuracy.

Keywords: microfluidic devices, continuous particle separation, pinched flow fractionation, hydrodynamic filtration

1. INTRODUCTION

Particle classification according to their physical or chemical properties is one of the essential techniques in the fields of biological research and medical care. A number of studies have been hitherto reported concerning separation of particles using microfluidic devices. However, it cannot be said that versatile and useful microfluidic systems for particle sorting have been fully established.

2. PINCHED FLOW FRACTIONATION (PFF)

We have proposed a concept of 'Pinched Flow Fractionation (PFF)[1] , and successfully separated various types of sub-micron to micron-size spheres including polymer beads, cells, droplets and macromolecules. The concept of this separation method is shown in Fig.1. In this method, particles can be separated according to their diameters simply by introducing liquid flows with and without particles into a microchannel. Therefore, no outer field controls are needed. Also, in PFF method, separated particles can be continuously collected using multiple branch channels connected to the pinched segment.

However, all branch channels are not effectively used when multiple branch channels are uniformly arranged, since the liquid flow in the pinched segment is equally distributed to multiple branch channels. To overcome this disadvantage, "asymmetric pinched flow fractionation (AsPFF)[2]" has been proposed. The microfluidic device for AsPFF has a drain channel, and a large portion of the liquid flow goes through the drain channel. Liquid flow

978-0-9798064-0-7/μTAS2007/$20©2007CBMS

containing particles is then efficiently distributed to other branch channels. Therefore, almost all branch channels can be effectively used for particle collection.

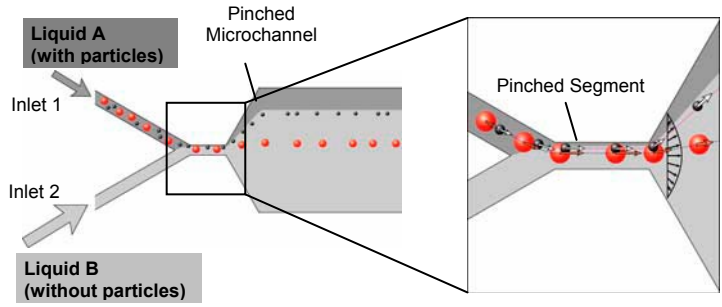

Figure 1. Principle of Pinched Flow Fractionation. In the pinched segment, particles can be aligned onto one sidewall by controlling the flow rates from two inlets. Particles are then separated according to their sizes by the spreading flow profile at the boundary of the pinched and the broadened segments.

In these methods, the effluent positions of particles are determined by the microchannel structure designed and fabricated beforehand. Therefore, we proposed "tunable pinched flow fractionation (tunable PFF)[3]," in which the effluent positions of the particles can be precisely tuned by controlling the flow rates distributed to each outlet using microvalves.

3. HYDRODYNAMIC FILTRATION (HDF)

We have proposed another scheme for continuous separation of particles utilizing laminar flow profiles in a microchannel network with multiple branch channels, named Hydrodynamic Filtration (HDF)[4], in which both concentration and classification of particles can be performed at the same time, by simply introducing a liquid containing a particle mixture. In this method, the hydrodynamics of laminar flow is also utilized in a microchannel having multiple branch points and side channels, not necessitating any outer field controls. In addition, not the cross-sectional size of the microchannel, but the flow profile inside the channel determines the size limit of the concentrated/classified particles. Therefore, a problem of channel clogging, which is similar to the mesh clogging or membrane fouling in the case of existing filtration methods, can be avoided.

The principle of hydrodynamic filtration is shown in Fig. 2. When the relative flow rates distributed into side channels at a branch point are sufficiently low (Fig. 2 (a)), only a small portion of the liquid near the sidewalls is withdrawn from the main stream. In this flow state, particles whose diameter is larger than a specific value would never go through the side channels, even if they are flowing near the sidewalls in the main channel, and even if the particle size is smaller than the cross sectional size of the side channel. In addition, after passing through the branch point, particles are slightly concentrated. On the other hand, when the flow rates distributed into the side channels are increased as shown in Fig. 2 (b) , particles near the sidewalls go through the side channels. Particle concentration and classification can be achieved by combining these flow states, as shown in Fig. 2 (c). By repeating the flow state so as that the introduced particles would never go through the side channels, a large portion of the introduced liquid can be removed from the main stream after passing through the multiple branch points, resulting in the particle concentration and alignment onto the sidewalls. Then by increasing the relative flow rates into other side

channels (selection channels) stepwise, aligned particles are collected independently according to size. This operation dramatically increases particle concentration in the selection channels, since only a small portion of the liquid flow near the sidewalls, which is dense with particles, is collected.

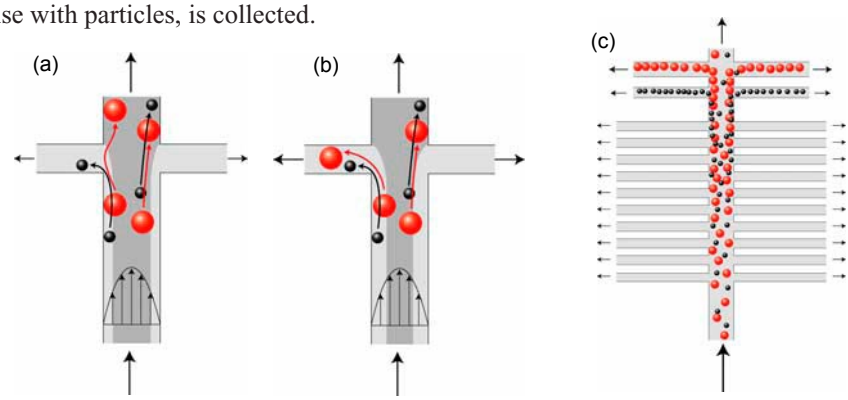

Figure 2. Principle of hydrodynamic filtration. Schematic diagrams showing particle behavior at a branch point; the relative flow rates distributed into side channels are (a) low and (b) high. (c) Schematic diagram showing particle concentration and classification in a microchannel having multiple branch points and side channels.

However, the inevitable contamination of small particles into the concentrated large-particle fraction decreases the separation efficiency. To overcome the disadvantages of the previous scheme, we proposed an improved HDF scheme[5] for particle separation, employing flow splitting and recombining. That is, by repeating liquid flow removal from the main channel, and recombining into the downstream, particles are perfectly alignment onto one sidewall in the main channel. Then, particles can be separated according to size, by increasing the relative flow rates into the outlet channels. Using this modified HDF method, different kinds of microspheres were classified and concentrated.

4. CONCLUSIONS

The presented schemes are advantageous since various types of particles can be separated and precisely classified in a continuous manner, only by introducing suspension into a simple microstructure without any outer devices, and the separation efficiency is not dependent on the total flow rate but the geometrical flow distribution.

ACKNOWLEDGEMENTS

I wish to thank Dr. Masumi Yamada of Tokyo Women's Medical University and other students of my laboratory of The University of Tokyo, Osaka Prefecture University and Chiba University.

REFERENCES

[1] M. Yamada, M. Nakashima, M. Seki, *Anal. Chem*., **76**, 5465 (2004).
[2] J. Takagi, M. Yamada, M. Yasuda, M. Seki, *Lab Chip*, **5**, 778 (2005)
[3] M. Yamada, Y. Sai, M. Seki, *J. Chromatogr. A*, **1127**, 214 (2006)
[4] M. Yamada, M. Seki, *Lab. Chip*., **5**, 1233 (2005)
[5] M. Yamada, M. Seki, *Anal. Chem*., 78, 1357 (2006)

AUTOMATION OF NUCLEIC ACID EXTRACTION BY A CORIOLIS-FORCE ACTUATED DROPLET ROUTER

S. Haeberle[1], S. Pausch[1], R. Burger[1], S. Lutz[1], F. von Stetten[1,2], R. Zengerle[1,2], and J. Ducrée[1]

[1]*HSG-IMIT, Institute for Micromachining and Information Technology, Germany*
[2]*Laboratory for MEMS Applications, Department of Microsystems Engineering (IMTEK), University of Freiburg, Germany*

ABSTRACT

We present an automated nucleic acid extraction protocol by a simple frequency and dispensing protocol of a microfluidic rotor. The key enabling steps are the centrifugally induced generation of droplets which are routed by the Coriolis pseudo force either to the waste or to the eluate reservoir. At centrifugally driven flow rates below 2 µL/s through a packed column of 11 mg silica particles, up to 0.7 µg of purified DNA (recovery ratio of 16%) is collected in an onboard reservoir or – to smoothly interface with common lab environments – in a standard Eppendorf tube ("Eppi") attached to a "flying bucket" rotor.

Keywords: centrifugal microfluidics, droplet formation, routing, DNA extraction

1. INTRODUCTION

Nucleic acid analysis has gained increasing importance for in vitro diagnostics within the last years. The integrated extraction of DNA from e.g. whole blood samples is an essential step towards the implementation of an automated nucleic acid analysis. The process is usually implemented by the reversible adsorption of the DNA molecules to a silica solid phase (the so called "Boom chemistry" [1]). Within this work we use silica microparticles of approximately 110 µm diameter as solid phase and restrain the flow rates to meet the time frame of an optimal physicochemical binding. The applied droplet switch [2] enables the routing of small liquid flows by means of the Coriolis pseudo force.

2. FUNCTIONAL PRINCIPLE

Figure 1 shows the microfluidic channel network comprising an extraction chamber where silica particles are retained by a geometric aggregation step. The extraction buffers

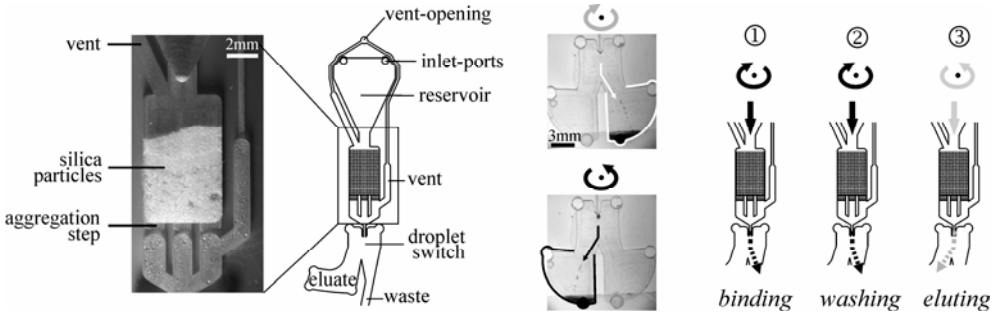

***Figure 1**. Design of the microfluidic structure for centrifugal DNA-extraction. Silica particles are aggregated in front of a geometrical aggregation step at the radial end of the extraction chamber. The droplet switch after the extraction chamber enables the switching between two downstream flow paths as depicted in the middle. The complete process sequence for DNA extraction of binding, washing and eluting is shown on the right.*

978-0-9798064-0-7/µTAS2007/$20©2007CBMS

are filled via the inlet-ports into the reservoir. After the centrifugal flow has passed the stationary phase, the liquid disintegrates and proceeds to the hydrophobic orifice [2]. The issued droplets are deflected against the direction of motion into the waste (clockwise) or eluate reservoir (counter-clockwise), depending on the sense of rotation imposed by the spinning protocol. The silica particles can efficiently be dried by centrifugation prior the elution step, thus ensuring a high purity of the extracted DNA.

The automated protocol consists of three basic steps: the binding of the DNA to the silica particles ①, the subsequent washing in order to remove any unwanted impurity ② and the final eluting to gain the purified DNA ③ (Fig. 1, right). The clockwise sense of rotation for the first two steps routes the binding and washing solutions into the waste reservoir. Within the last flow-through, the sense of rotation is altered and the purified DNA ends up in the eluate reservoir while preventing cross-contamination.

3. EXPERIMENTAL RESULTS

The experimental performance is qualified by the extraction of nucleic acid solutions from calf thymus [3] on silica particles taken from a commercial buffer kit [4]. The particles are filled into the extraction chamber via the inlet reservoir and subsequently compacted by centrifugation. The flow rate through the silica particle aggregation has been measured and is displayed in Fig. 2. The flow rate scales with the square of the rotational frequency as expected from the centrifugal hydrodynamic theory. Flow rates remain below 2 µL/s for frequencies of rotation not exceeding 15 Hz. This is the working range for the flow-rate critical steps during the extraction protocol, namely the binding and eluting step.

The complete DNA extraction protocol comprises the initial binding, three washing and the final elution step. The amount of DNA within the sample and the eluate is measured by a fluorescence labeling kit (*Invitrogen*, *Quant-iT*). Figure 3 identifies a working range between 0.5 µg and 4 µg wherein the mass of DNA in the eluate increases with the amount of DNA in the input sample. The working range corresponds to a volume of whole blood between 16.7 and 133.3 µL (amount of DNA in whole blood: ~ 30 µg/mL).

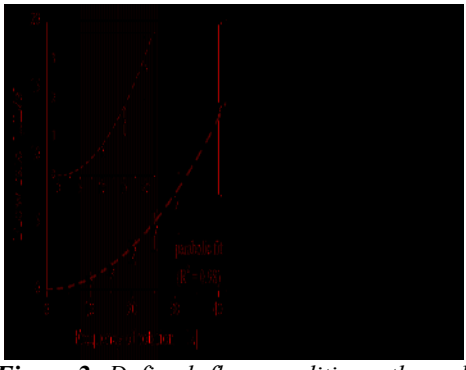

Figure 2. *Defined flow-conditions through the solid-phase (silica particle aggregation). The ratio of diffusion time and transit time can easily be adjusted by the frequency of rotation. The binding and eluting step of the DNA extraction are done below 15Hz.*

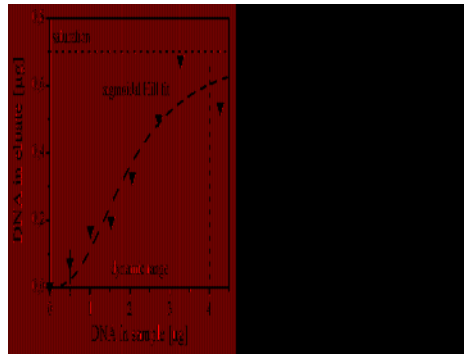

Figure 3. *Results of the integrated DNA extraction on the rotating disk. The amount of DNA in the eluate increases with the amount of DNA in the sample. The maximum amount of extracted DNA within the first eluate is 0.7 µg, corresponding to a recovery ratio of 16 % in the dynamic range.*

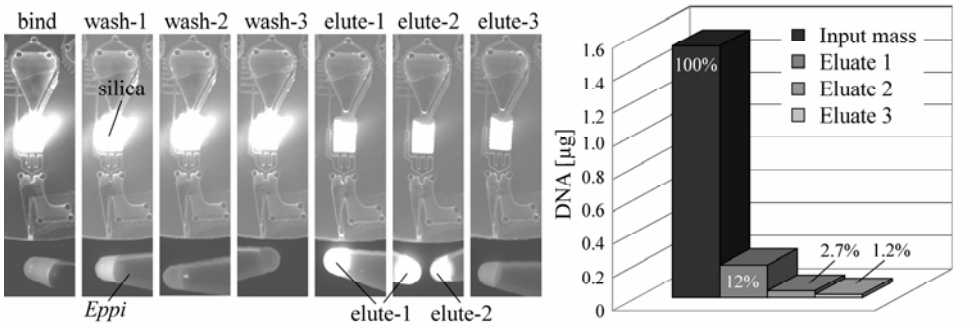

Figure 4. *Left: To investigate the extraction performance, the process is visualized by fluorescent labelling of the DNA molecules in the sample. A fluorescent image is captured after each extraction step: the binding, the three washing and the three elution steps. Besides the microfluidic extraction structure, also the flow of elute into a standard Eppendorf tube ("Eppi") is included in the picture. Right: measured total mass of DNA in the sample and recovery of DNA in each of the three elution steps.*

The experimental data represents a fit to a sigmoidal curve to account for the saturation of the extraction system at 0.7 µg. The recovery ratio, i.e. ratio between input and output DNA, respectively, amounts to 16 % within the dynamic range.

In Figure 4, the fluorescently labeled DNA is tracked at different stages of the extraction procedure in order to qualify the extraction process. Therefore, all liquids are switched into the waste outlet and transferred into a standard laboratory tube ("*Eppi*") for inspection. The small traces of DNA which are initially bound to the channel walls are removed by the first washing step and no measurable amount of DNA is present in the second and third washing solution (liquid within the *Eppi* tubes placed below the microfluidic structure in the fluorescent images). The overwhelming fraction of DNA is eluted by the first and second elution step. Even after the third elution, there is still some DNA bound to the stationary phase. Thus, for a further improvement of the recovery ratio, the elution step should be optimized (see measured amount of DNA in the three eluates in Fig. 4, right).

4. CONCLUSION AND OUTLOOK

The here presented, centrifugal microfluidic technology bears great potential to replace costly, state-of-the art equipment for the integration and automation of nucleic acid extraction procedures. Future work will focus on improvements of the extraction recovery ratio as well as the extension of the process chain by upstream cell lysis and downstream amplification (PCR).

REFERENCE

[1] R. Boom, C. J. A. Sol, M. M. M. Salimans, C. L. Jansen, P. M. E. Wertheim van Dillen, J. van der Noordaa, "Rapid and Simple Method for Purification of Nucleic-Acids", *J. Clin. Microbiol.*, **28**, 495-503, 1990.

[2] S. Haeberle, L. Naegele, R. Zengerle, J. Ducrée, "A Digital Centrifugal Droplet-Switch for Routing of Liquids", *Proc. µTAS 2006*, 570-573, 2006.

[3] *Calf Thymus DNA*, product no. D-1501, *Sigma Aldrich Co.*, Germany, www.sigmaaldrich.com, accessed 2007.

[4] *NucleoBond® CB 500 blood kit*, *Macherey-Nagel GmbH & Co KG*, Germany, www.macherey-nagel.com, accessed 2007.

MICROCHIP-BASED SOLID-PHASE EXTRAXTION AND ENZYMATIC DIGESTION ON POROUS POLYMER MONOLITH FOR DIRECT ELECTROSPRAY MASS SPECTROMETRY

Yujuan Hua, Zhen Wang and D. Jed Harrison
Department of Chemistry, University of Alberta, Canada

ABSTRACT

This work reports the integration of on-chip solid-phase extraction (SPE) and enzymatic digestion using *in-situ* polymerized monoliths, coupled with electrospray ionization-mass spectrometry (ESI-MS). Challenges associated with coating channels for electroosmotic flow (EOF) control, introducing charge to monoliths, and controlling porosity to allow controlled flow in a complex manifold of 36 channels were resolved.

Keywords: Monolith, cationic coating, protein, mass spectrometry

1. INTRODUCTION

The expansion of proteomics demands rapid, sensitive and automated analysis methods. Chip-based microfluidic systems coupled to mass spectrometry (MS) are an attractive approach to meet these needs [1]. Microchip systems enable the integration of multiple sample handling steps. SPE, a widely-used sample preconcentration technique, could be accomplished by coating, packing, or *in-situ* polymerization of polymer monoliths [2]. Monoliths offer many advantages: frit-free construction, good control of porosity and surface chemistry, and high adsorption capacity. More importantly, UV-initiated polymerization enables the formation of monoliths within different regions of a multichannel device simultaneously. Although EOF offers well-known advantages over pressure-driven flow in microfluidic devices, the poor reproducibility due to variability in EOF must be addressed for protein applications. Here a microchip was modified with a cationic coating and integrated with a monolithic bed for protein analysis using ESI-MS.

2. EXPERIMENTAL

Porous polymer monoliths were prepared in microchannel by photoinitiated polymerization of butyl methacrylate (BMA) and ethylene dimethacrylate (EDMA) in porogenic solvents. To retain the monolith in place, a bed with several posts was designed in the device. The microchannel surface was coated with a polyamine coating, polyE-323, for protein analysis. PolyE-323 was prepared according to a previous report (Figure 1) [3].

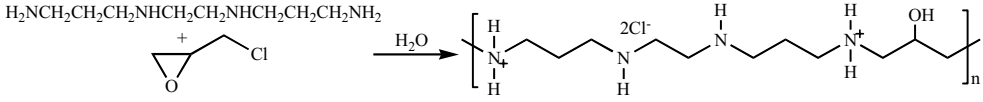

Figure 1. Synthesis and structure of PolyE-323

3. RESULTS AND DISCUSSION

Different monomer compositions and reaction conditions were tested to obtain ideal monoliths for SPE, which should have low flow resistance and high loading capacity. Figure 2 shows a monolith prepared in a bed (20 μm deep, 140 μm wide and 1 mm long,

978-0-9798064-0-7/μTAS2007/$20©2007CBMS

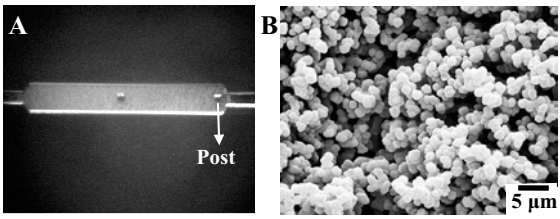

with 30 µm × 30 µm posts) and its porous structure. These images show that the monolith has sharp edges and uniform structure.

Figure 2. (A) Image of a monolith prepared in bed; (B) SEM image of the monolith

Monoliths were also prepared in a 36-channel fractionator developed in our previous work (Figure 3A) [4]. However, the incorporation of neutral monoliths significantly increased the EOF-based flow resistance, and thus the sheath flow effect used in the main channel to control leakage into the fractionation channels did not work well. This was resolved using negatively-charged 2-acryl-amido-2-methyl-1-propanesulfonic acid in the polymerization mixture and fabricating deeper beds to enlarge the cross-section (Figure 3B). Figure 3C shows fluorescence images of flow switching from the 14th to the 18th channel, the sheath flow keeps the BSA stream tightly focused. Figure 3D shows the sorption of protein on the 5th monolithic bed, without leakage into other beds. These experiments indicated the success of the approach.

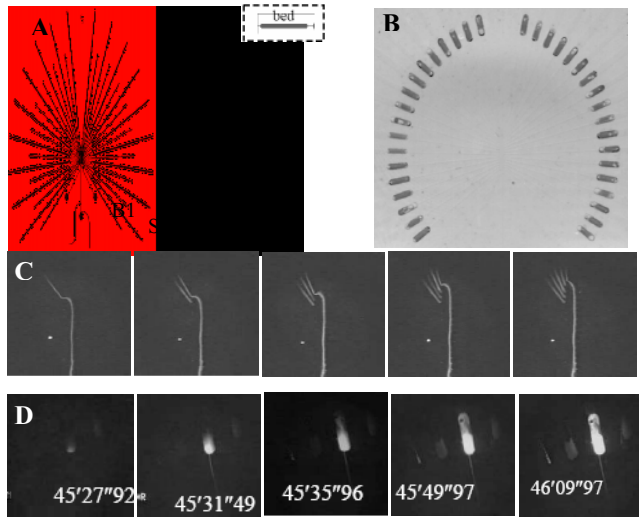

Figure 3. (A) Chip layout of the 36-channel fractionator, S: sample reservoir, B_1 and B_2: Sheath buffer reservoirs; (B) Image of monoliths formed in larger beds in cover plate; (C) Images show the automatic switching of BSA stream from the 14th to the 18th channel; (D) BSA was loaded and adsorbed onto the 5th bed without leakage into other beds.

Four cationic coatings were tested to generate anodal EOF towards the ESI-MS interface and reduce protein adsorption: successive multiple ionic-polymer layer (SMIL) Polybrene (PB)-Dextran Sulfate (DS)-PB coating [5], double-chained surfactant coating [6], a commercial available coating, UltraTrol™ from Target Discovery and a polyamine coating, PolyE-323. These four coatings all show good stability and reproducibility (Table 1), but only PolyE-323 has satisfactorily met the criteria for ESI-MS: high enough anodal EOF to sustain a stable electro-spray in a sheathless ESI interface; high stability with no bleeding from the surface into the MS; strong tolerance to the use of organic modifier.

Table 1. Reproducibility of EOF for cationic coatings

RSD	run-to-run	day-to-day	chip-to-chip
SMIL coating	0.6%	1.1%	1.8%
Surfactant coating	0.7%	2.0%	2.0%
UltraTrol™	3.5%	5.8%	4.1%
PolyE-323	1.5%	3.0%	2.8%

The monolith charge was adjusted to be compatible with the coated channels by adding [2-(methacryloyloxy)ethyl]trimethylammonium chloride. The SPE performance was evaluated with laser-induced fluorescence detection by studying elution peaks for various sample concentrations at fixed preconcentration time. It gave a linear response between peak areas and peak height versus concentrations across the range studied (Figure 4).

A microchip modified with PolyE-323 was then integrated with the monolithic bed and interfaced to ESI-MS. Figure 5 illustrates the elution and mass spectrum of peptide fragments of cytochrome *c* after SPE and tryptic digestion. A total of 17 peaks were assigned to peptide fragments of cytochrome *c*, representing sequence coverage of 87%.

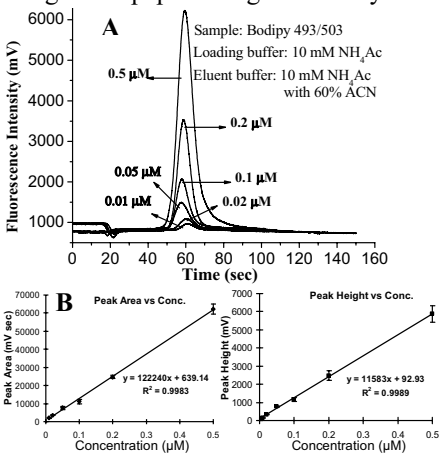

Figure 4. (A) Elution sequences with increasing concentrations; (B) Peak areas and peak heights versus concentrations.

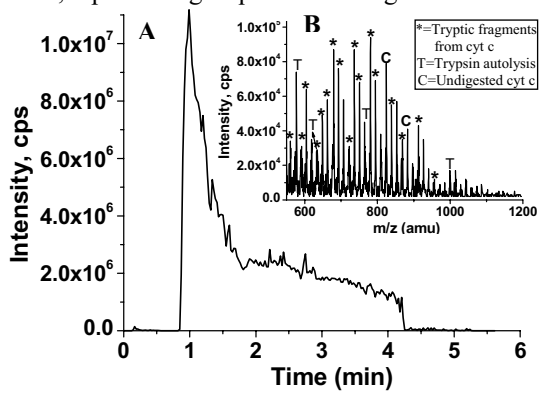

Figure 5. (A) Total ion current trace; (B) Mass spectrum of tryptic fragments of cytochrome c. (Loading: 124 µg/ml Cyt c in 5 mM formic acid (FA); Digestion: 0.31 mg/ml trypsin in 10 mM NH_4HCO_3; Elution: 75% MeOH / 5 mM FA.)

4. CONCLUSIONS

A microchip is successfully integrated with a monolithic bed for on-chip SPE and tryptic digestion and coupled to ESI-MS. Monoliths proved to be good candidates for SPE preconcentration. The simple coating procedure, together with the stable, robust EOF, makes PolyE-323 an attractive coating for use in bioanalytical CE-ESI-MS. This study lays the groundwork for the development of multiplex microfluidic systems for protein analysis.

ACKNOWLEDGEMENTS

We thank the Natural Sciences and Engineering Research Council of Canada (NSERC) for funding and the Killam Trust for its support.

REFERENCES

[1] Sung, W. C.; Makamba, H.; Chen, S. H. *Electrophoresis* **2005**, *26*, 1783-1791.
[2] Yu, C.; Davey, M. H.; Svec, F.; Fréchet, J. M. J. *Anal. Chem.* **2001**, *73*, 5088-5096.
[3] Hardenborg E, Zuberovic A, Ullsten S, Soderberg L, Heldin E, Markides KE. *J. Chromatogr. A* **2003**, *1003,* 217-221.
[4] Wang, Z.; Harrison, D. J. *Proc. µTAS 2006*, Tokyo, JAPAN, p. 1447-1449.
[5] Katayama, H.; Ishihama, Y.; Asakawa, N. *Anal. Chem.* **1998**, *70*, 5272-5277.
[6] Yassine, M. M.; Lucy, C. A. *Anal. Chem.* **2005**, *77*, 620-625.

FAST AND HIGH EFFICIENT MICROFLUIDIC PCR BY MICROWAVE DIELECTRIC HEATING

Pierre-Alain Auroux, Darwin R. Reyes, Jayna J. Shah, Michael Gaitan
NIST, Semiconductor Electronics Division, Gaithersburg, MD 20899, USA

ABSTRACT

We report 100% yield and 40% reaction-time reduction for on-chip DNA amplification using microwave dielectric heating. A passivation protocol has also been developed to suppress the inhibition of PCR in PMMA chips used with a temperature sensor. We finally compare the reaction time of the on-chip microwave PCR amplification and the one of a conventional thermocycler.

Keywords: thermocycling, microwave dielectric heating, PCR, DNA

1. INTRODUCTION

The need for faster methods for DNA amplification developed in this work is motivated by the call for new technologies for reducing the growing backlog of criminal cases that require forensic DNA identification, and by the requirements of new tools and methods for high throughput medical analysis. In addition, the sharp temperature transitions that can be achieved using microwave dielectric heating could improve the specificity of the amplified products. In this paper we report DNA amplification with high efficiency by microwave dielectric heating.

2. EXPERIMENTAL AND DISCUSSION

The experimental set-up for on-chip microwave temperature cycling that is used in this work has been previously described and characterized [1]. Briefly, an x-band waveguide (see Figure 1) is used to deliver microwave energy to the plastic (PMMA) chip by inserting it into a slot machined on the waveguide. Since the plastic chip has a relatively low propension to absorb microwaves compared to water, the power/heat is predominantly delivered directly to the fluid. Temperature feed-back is achieved using a type-T thermocouple. It is inserted into the sample and connected to a computer programmed to modulate the power of the

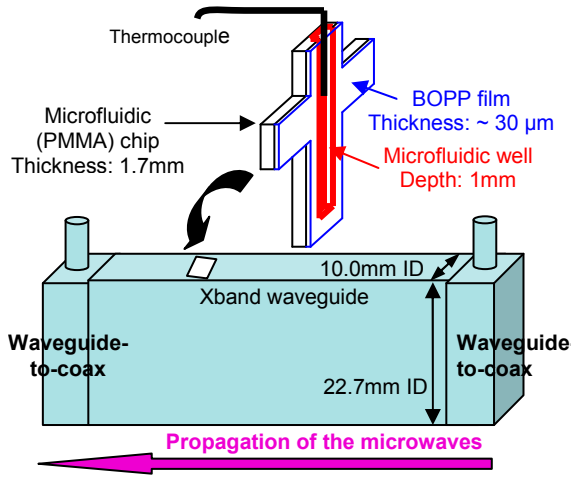

Figure 1. A rectangular x-band waveguide was used to heat the microfluidic device. A slot machined into one of the walls of the waveguide allowed the introduction of the microchip inside the microwave instrument. An amplifier was coupled to the waveguide, enabling the delivery of up to 50W of power over the 8-12GHz frequency bandwidth of the waveguide.

978-0-9798064-0-7/µTAS2007/$20©2007CBMS

Table 1. Test of different additives to prevent inhibition of the DNA amplification by the type-T thermocouple. All samples are compared to a positive control with neither additive present, nor copper. A solution of 3.5% w/v of PVP leads the highest PCR yield.

Additive	Conc. (% w/v)	PCR yield with additive (%)	PCR yield with additive and Cu (%)
BSA	2000 (µg/mL)	93	0
	3000 (µg/mL)	73	8
Sulfobetaine	0.7	0	0
	0.9	6	0
Spermine	1	18	0
	0.05	92	17
PVP (MW:1,300,000)	2.5	92	51
	3.5	78	62
PEG (MW: 8,000)	0.75	85	43
	1.1	73	14

microwave generator according to an operator-determined set of specifications. As the presence of a metal has been previously reported to inhibit PCR [2], we tested several additives to prevent this occurence (see Table 1). We observed that a 3.5% w/v solution of polyvinylpyrrolidone (PVP) (MW: 1,300,000g/mol) displayed the highest PCR yield. A PCR amplification targeting the Rab 1B gene present in R28 rat cells (forward primer: gcatcattgtggtgtatgacg ; reverse primer: tggcgtagcgatctatttcc) was used to characterize the performance of the method.

The thermocycling program consisted of 3 steps repeated 40 times (see Figure 2):
- denaturation (95°C, 20 s)
- annealing (63°C, 60 s)
- extension (72°C, 40 s).

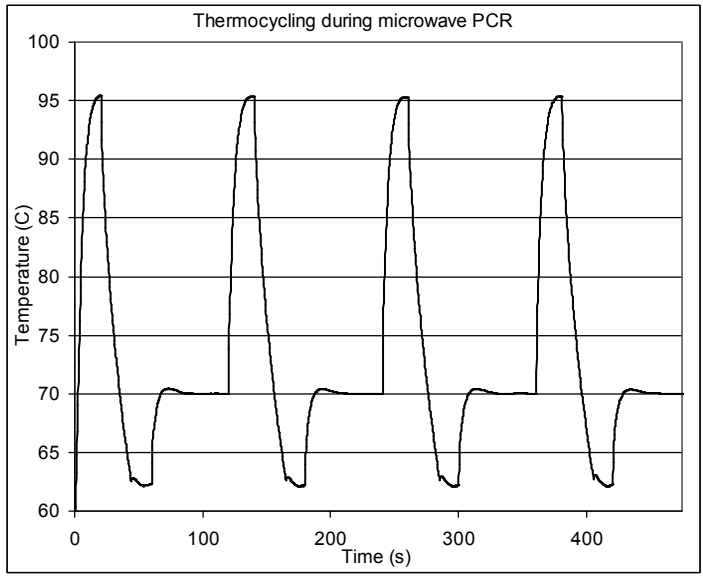

Figure 2. Temperature profile during thermocycling.

The amplified products were pure (single band) and specific to the targeted gene (correct number of bases), as demonstrated by gel electrophoresis (see Figure 3). In addition, the reaction yields were equivalent to the yield of the control reaction (see Table 2). Finally on-chip microwave-heated PCR was performed in 80 minutes, while the macro-scale amplification lasted 130 minutes. The reaction time is therefore reduced by 40%.

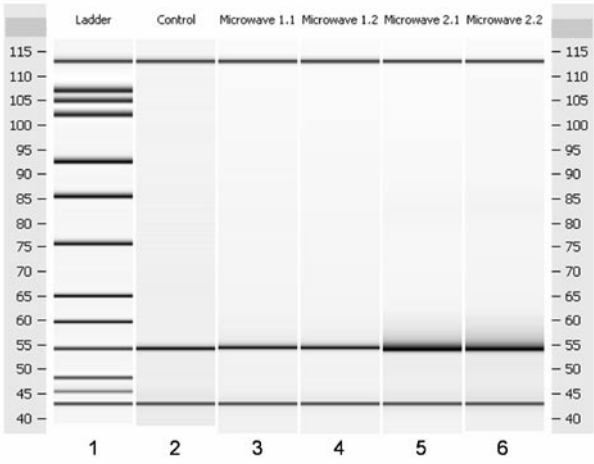

Figure 3. Analysis of the products of on-chip PCR amplification. Lane 1: ladder; lane 2: control; lane 3-4: duplicates sample 1; lane 5-6: duplicates sample 2. The samples amplified by microwave heating are pure and display band intensities similar to the one of the control.

Table 2. PCR yield for on-chip PCR for two sets of amplification. For each sample the analysis is performed in duplicates.

	Size [bp]	Conc. [ng/µL]	Molarity [nmol/L]	Area [A.U.]
Control	101	7.71	115.7	30.6
Microwave 1.1	102	7.95	117.6	76.1
Microwave 1.2	102	7.9	117.1	79.4
Microwave 2.1	100	24.62	373.3	160
Microwave 2.2	100	25.23	382	166.7

3. CONCLUSION

In conclusion, we report efficient and rapid on-chip amplification of DNA using microwave dielectric heating. Although the system could undergo supplementary optimization, our results demonstrate excellent performance compared to protocols using a commercially available thermocycler. The additional integration on the same chip of cell lysis and DNA analysis will further enhance this state-of-the-art PCR chip.

ACKNOWLEDGEMENT

The work is sponsored by the National Institute of Justice, Office of Science and Technology. Financial support for J.J.S. was provided by NIST under Grant #60NANB4D1131.

REFERENCES

[1] Auroux et al., MicroTAS 2006, p1465
[2] Taylor et al., J. Biomed. Microdev. I, 1998, p65

MILI-SECONDS ANALYSIS OF GREEN FLUORESCENT PROTEIN GFP IN fL CONTAINER HEATED BY MICRO FABRICATED THERMALDEVICE

Hideyuki F. Arata[1] Frederic Gillot[2] and Hiroyuki Fujita[1]

[1]CIRMM, IIS, the University of Tokyo, JAPAN and [2]LIMMS-CNRS/IIS, FRANCE/JAPAN

ABSTRACT

Real-time observation of biomolecular behavior focusing on high speed temperature response is a challenging endeavor. We used our own integrated micro thermaldevice composed of a 2µm wide micro platinum heater co-located with a thin film Pt-Cr thermocouple with a 2.5 µm*2.5 µm hot junction to manage a fast temperature switching and control. Green fluorescent proteins (GFPs) were contained in a 15 fL PDMS micro container to prevent from diffusing into the solution. We also theoretically estimated the time for the micro container to reach the thermal equilibrium, which was much faster than the GFP denaturing time length. Consequently, response time of GFP denaturing was measured for the first time to be 20 ms.

Keywords: GFP, temperature response, micro heater, PDMS container

1. INTRODUCTION

GFP is commonly used as reporter protein in biological experiments [1]. It loses its fluorescence when denatured by temperature higher than 343 K, pH extremes or guanidinium chloride. It recovers its fluorescence partially only when renatured [2]. Precise thermal stability of GFP has been studied in bulk experiments, however, these measurements could only be carried out in the time scale of several minutes. Observing protein denaturing in short time scale is necessary for further research, for example, on folding properties of those proteins.

To realize such measurements, we developed a micro thermaldevice which can switch the temperature rapidly under the microscope [3]. This ended up with a successful measurement of GFP denaturing in ms timescale.

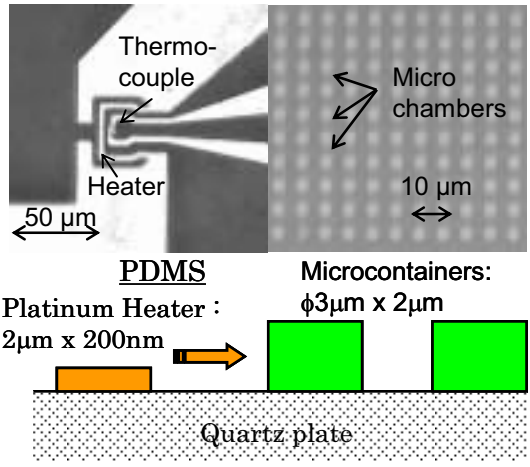

Figure 1: A micro patterned PDMS sheet (right) was mounted on a micro thermaldevice fabricated on a quartz plate (left) to form micro containers. Biomaterials in micro containers were heated up by collocated thermaldevice (bottom).

978-0-9798064-0-7/µTAS2007/$20©2007CBMS

2. MICRO THERMALDEVICE

The micro thermaldevice consists of a micro platinum heater co-located with a platinum-chromium thin film thermo-couple (TFTC) micro fabricated on a quartz wafer (Fig. 1). The TFTC has a mili-seconds response time, which enables us to measure the local temperature at fast response speed. The heater section is 2 m in width x 200 nm in thickness, which allows fast temperature switching. A micro fabricated PDMS sheet was mounted on a thermaldevice to form micro containers. We used FEA (FemLab 3.1) to simulate the temperature inhomogeneity in the micro container when it is heated by the micro thermaldevice (Fig. 2). Simulations showed that after 0.25 ms, the temperature can be considered as enough homogenous in the microcontainer. A delay between sensor output and temperature rise was also negligible.

3. EXPERIMENTAL

GFP sustained in TE buffer at 3.7 nM was contained in 15 fL PDMS micro containers, which contains about 30~40 GFP molecules, located on the micro thermaldevice. The whole sample was put under an inverted microscope IX71 (Olympus) and GFPs were excited by a mercury lamp via filters, ND12 and U-MNIBA3 (Olympus). Limiting the power of excitation light, bleaching of fluorescence is negligible in few seconds in which the experiment was completed. Micro containers show fluorescent intensity when GFP is active (Fig. 3, left). Video images were captured by a high speed camera Cascade II: 512 (EMCCD technology) operated at 7 ms / frame and fluorescent intensity was analyzed by the software (METAMORF).

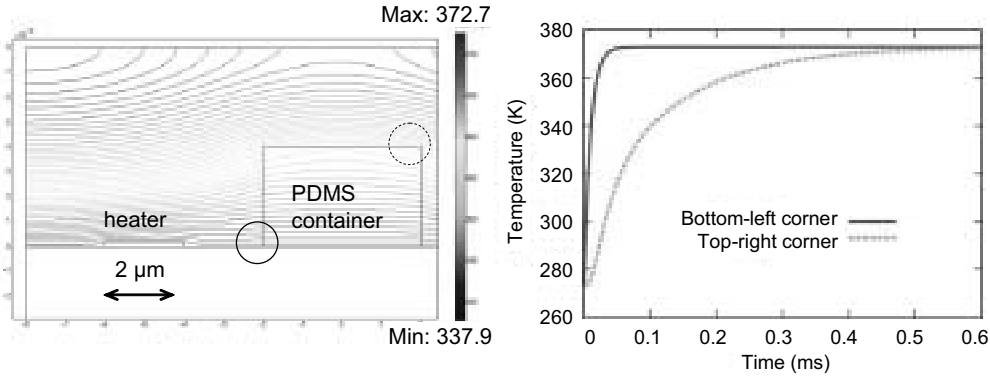

Figure 2. Temperature inhomogeneity during the heating simulated by FEA (FemLab 3.1). The left picture represents the device geometry used for the simulation and the result at step 20 ms. The right graph represents the temperature at bottom-left corner (continuous line) as well as the top-right corner (dotted line) of a microcontainer. When the former reaches 373K, which is the highest temperature for bio experiments, the delay for the latter to reach the same temperature was estimated to be ~0.6 ms. This delay is negligible in our experiments.

4. RESULTS AND DISCUSSIONS

When a heat shock was added by the micro thermaldevice, the intensity of a GFP contained micro container decreased to the value of background noise (Fig. 3 right). This intensity reduction completed within 20 ms. This delay might correspond to the response time of GFP denaturing. This result strongly suggest that response time of conformational change of GFP molecule by denaturing is 20 ms. The background intensity also shows fluorescent light of 20% of that of micro containers before the heat shock. This is probably by a fluorescence of leaked buffer with GFP.

5. CONCLUSIONS

Real-time observation of GFP protein denaturing was achieved thanks to the micro thermaldevice which realizes temperature switching in ms time scale under the microscope. To our best knowledge, it is the first time that a protein denaturing in this time scale was measured. Further study may give a break through of the research area in protein folding-unfolding properties. This method may be extended to other biomaterials such as DNA or other proteins. We believe that this approach gives an access to protein studies in short time scale and acts as a powerful tool in general biology.

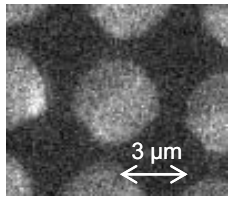

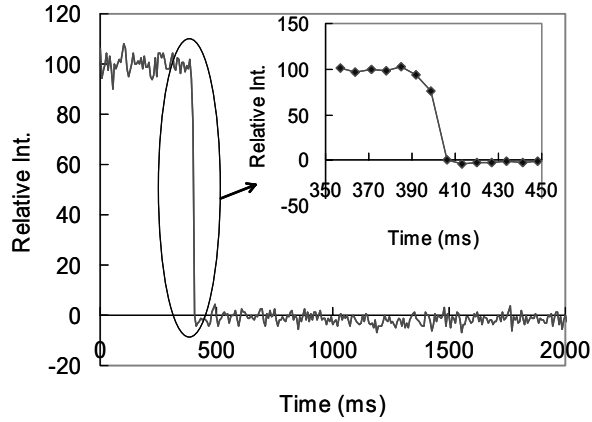

Figure 3. Microscopic view of GFP contained micro containers (top). Time course of fluorescent intensity of a micro container. The intensity decreased to the value of background noise as adding heat shock by the micro thermal device (right).

ACKNOWLEDGEMENTS

We thank Dr. Takahiko Nojima for useful biological discussions. This work was supported by the Japan Society of Promotion of Science (JSPS).

REFERENCES

[1] S. H. Bokman and William W. Ward, "Renaturation of Aequorea Green-Fluorescent Protein", Biochem. Biophys. Res. Com. Vol. 101, No.4, 1981, pp. 1372

[2] M. A. Surpin, and W. W. Ward, 1989, Photochem. Photobiol. 49, 65.

[3] F. Gillot, H. F. Arata, F. O. Morin, D. Collard and H. Fujita, “Micro heater with Pt-Cr thin film thermo-couple for high speed biological measurements”, Proc. of Transducers 2007, Lyon, pp. 21

PROTEOMICS-ON-A-CHIP FOR BIOMARKER DISCOVERY

Richard B.M. Schasfoort, Dietrich Kohlheyer, Stefan Schlautmann, Jan Eijkel and Albert van den Berg,
Biochip Group/BIOS, MESA+ Research Institute, The Netherlands.

ABSTRACT

In proteomics research still two-dimensional gel electrophoresis (2D-GE) is currently used for biomarker discovery. We applied free flow electrophoresis (FFE) separation technology combined with biomolecular interaction sensing using Surface Plasmon Resonance (SPR) imaging in an integrated proteomics-on-a-chip device as a proof of concept for biomarker discovery.

Keywords: Surface Plasmon Resonance imaging, Free Flow Electrophoresis, Proteomics, Label free detection

1. INTRODUCTION

Nowadays a dramatic shift in emphasis from mRNA profiling to proteomics occurs. Although 2D-GE is labor-intensive, slow, and prone to contamination, it is the highest resolution technique for the moment and is still the work-horse in proteomics research. In this paper we show features and benefits of a so-called "proteomics-on-a-chip" device for biomarker discovery based on electrophoresis principle and SPR phenomenon (see Fig. 1). An ideal technology should display the relevant biomarkers or specific binding partners from a cell extract. We developed a patented strategy to discover, categorize and identify potential biomarkers based on Free Flow Electrophoresis (FFE) and SPR imaging.

2. DEVICE DESIGN AND WORKING PRINCIPLE

Surface Plasmon Resonance (SPR) biosensors enable today's research to explore the kinetics of multiple biomolecular interactions (Fig. 1). In the Surface Plasmon Resonance imaging instrument for Biomolecular Interaction Sensing (iSPR-IBIS) from IBIS Technologies BV (Hengelo, NL) a scanning mirror is applied for detecting the so-called SPR-dips of many spots simultaneously. A microscopic view of the SPR reflection of the chip can be observed instantly and up to 500 biomolecular interactions can be

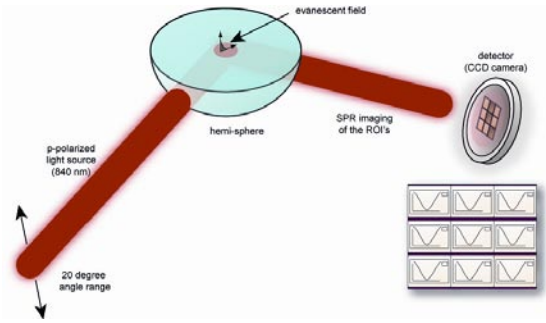

Fig.1. Schematic scanning SPR imaging setup; Biomolecular interactions at up to 500 "Regions of Interests" can be selected by the user and is being detected by a CCD camera.

978-0-9798064-0-7/μTAS2007/$20©2007CBMS

followed in real-time and without using labels.

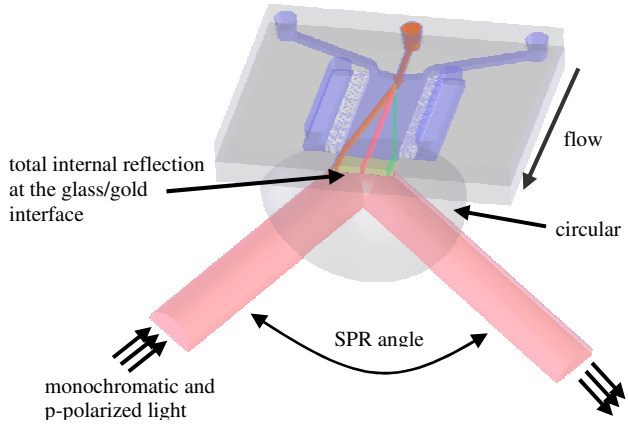

Fig.2 Principle of the "proteomics-on-a-chip" device. Protein sample is separated in the free flow electrophoreses section and guided over gold patches to be detected by Surface Plasmon Resonance imaging.

FFE is a continuous separation method, resulting in bands along a separation area and thus providing a continuous supply of separated components (see Fig. 2). Our approach is to sort and detect specific proteins and antibodies present in human blood serum which provide diagnostic information about e.g. autoimmune diseases. Instead of detection of fluorescent labeled components we use Surface Plasmon Resonance imaging which opens label-free and real-time detection of biomolecular interactions of FFE separated components.

3. MICROFABRICATION

A new FFE chip (see Fig. 3) has been fabricated, which contains a gold surface for SPR measurements. The IBIS instrument in scanning operation should detect the shift of the SPR-dips caused by biomolecular interactions in a special section of the free flow electrophoresis chip

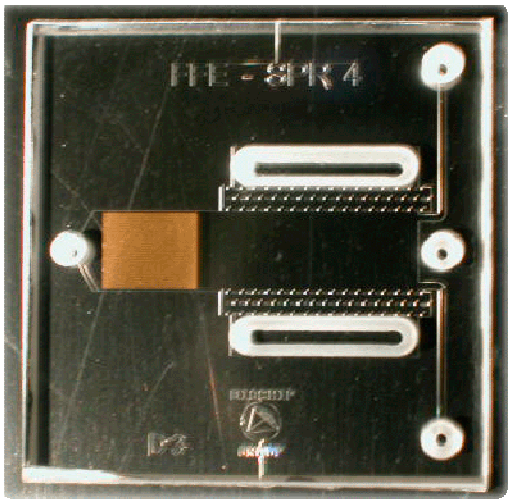

A separated sample can be flown over the SPR gold patches and biomolecular interactions can be detected in real-time. A so-called dynamic blotting technique can be applied and biospecific interactions can be observed in real time and without using labels. The new approach should lead to biomarker discovery of specific diseases.

Fig. 3. FFE-SPR chip (20mm x 20mm) (left) At the right an image showing the SPR gold region inside the FFE chip

4. RESULTS AND DISCUSSION

The FFE-SPR chip was placed inside an IBIS SPR instrument and first preliminary results could be obtained as shown in Fig. 4. The photograph shows the gold region inside the chip with a centered sample stream. The surrounding water is in resonance, while the centered sample (Isopropanol) is out of resonance.

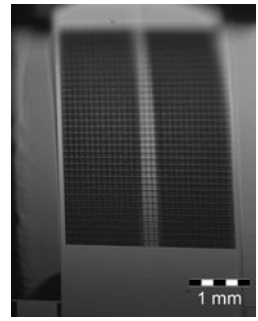

Fig.4 SPR image of the gold section of the IEF chip

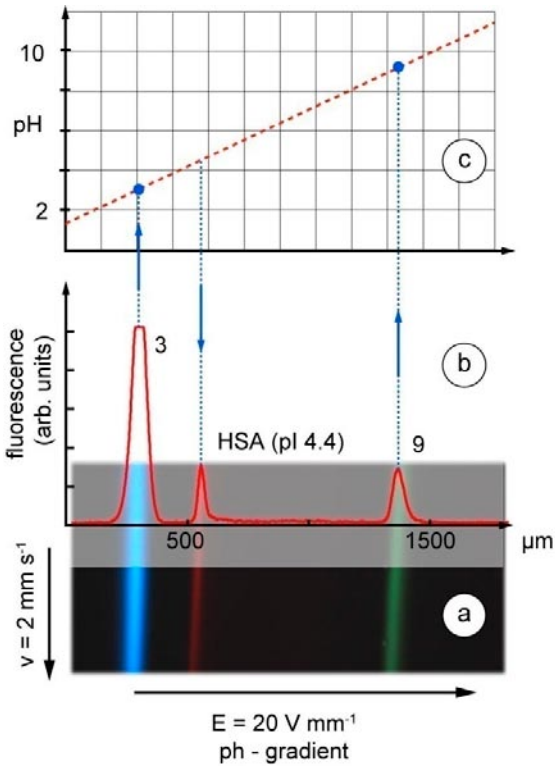

An improved free-flow isoelectric focusing chip (FFEIEF) has been tested by Dietrich Kohlheyer with a set of fluorescent isoelectric focusing markers. For the first time, high resolution results could be obtained in such a microfluidic FFE device.

Fig. 5 FFIEF of two fluorescent IEF markers 3 and 9 and the protein HSA: The focusing of the low molecular weight standards results in wider bands compared to HSA. HSA focused at the pH value 4.4. Concentrations were: 330 µg ml^{-1} HSA, 80 µg ml^{-1} of IEF marker 3 und 9. The focusing residence time was 2.5 s.

5. CONCLUSIONS

It is definitely a trend that the integration of lab on a chip devices and SPR imaging instruments will further be developed for new applications in life sciences. Broadening the options of parallelization and assay implementation, including sample treatment on-a-chip as shown here by the FFE principle, would certainly contribute to the increase of the field of applications.

REFERENCES

[1] R.B.M. Schasfoort. Expert Rev. Proteomics 1(1), 123–132 (2004).
[2] D. Kohlheyer et al. , Lab on a Chip, 2006, 6, 374 – 380
[3] G.A.J. Besselink et. al., Electrophoresis, 25 2004

RNA EXTRACTION ON A CHIP BY COMBINED THERMO-ELECTRIC LYSIS AND ELECTROPHORETIC PURIFICATION

Paul Vulto[1], Christoph Klaunick[1], Manfred Weidmann[2], Peter Zahn[1], Gregory Dame[1], Gerald A. Urban[1]

[1] Laboratory for Sensors, Department of Microsystems Engineering (IMTEK), Albert-Ludwigs-Universität Freiburg, GERMANY

[2] Institute for Virology, University of Göttingen, GERMANY

ABSTRACT

This paper reports a new method for the extraction of RNA from bacteria. The method is based on the combination of AC thermo-electric lysis and electrophoretic purification. The presented approach benefits maximally from the advantages offered by Lab-on-a-Chip technology and has no macro-biological equivalent.

Keywords: RNA, electrophoretic purification, thermo-electric lysis, phaseguides

1. INTRODUCTION

RNA is an important target material for genetic diagnosis of diseases, since it is available in high-copy numbers per cell [1] and is present in both viruses and bacteria. A large problem for working with RNA is its relative instability due to RNase enzymes that are present in the environment as well as in the sample material itself. Common extraction methods include phenol-chloroform extraction and silica columns for purifying nucleic acids from interfering substances. These methods are labor-intensive and time-consuming. The integration of such methods on a chip has been often reported for DNA [2], but rarely for RNA [3].

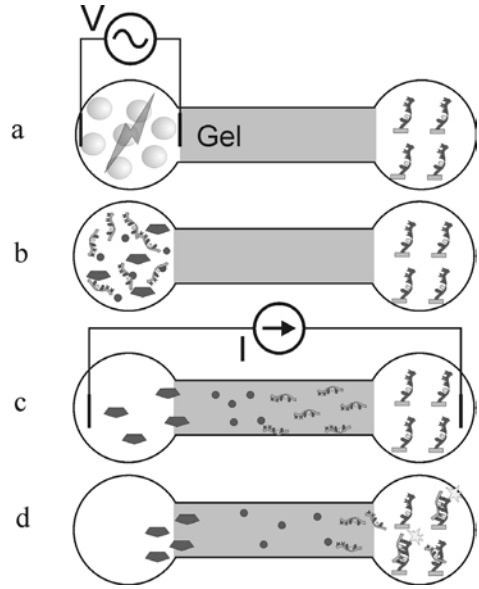

Figure 1. Sketch of the RNA extraction principle. Cells are thermo-electrically lysed (a, b). Small RNA is separated in the gel (c). In the collection chamber the RNA can hybridize (d) or be recovered for further analysis.

2. PRINCIPLE

Our extraction procedure couples an AC thermo-electric lysis step with a direct separation step. The lysis is based on boiling the sample by Joule electric heating. For high frequencies and low buffer conductivity, the current density is highest inside the cells, so that they are heated from within. In order to minimize RNA degradation by RNase, lysate substances are separated by electrophoresis directly after cell lysis. Since RNA has a high electrophoretic mobility it can be eluted from the gel in a

978-0-9798064-0-7/μTAS2007/$20©2007CBMS

purified form and used for further analysis, for instance on a biosensor platform (see figure 1).

3. EXPERIMENTAL

Chips are fabricated using direct wafer bonding of the permanent dry film resist ORDYL SY300 [4]. Silicon-nitrite passivated palladium electrodes are patterned using conventional lift-off followed by reactive ion etching of the nitrite. Ordyl is laminated and exposed in a two-mask process. The first layer (29µm thickness) serves for creating phaseguides for a controlled liquid handling [5]. The subsequent three layers (87µm thickness) are meant for the microfluidic channels. A second Pyrex wafer with drilled acces holes is bonded on top under pressure and heat. Contact pads are diced free by dicing the chip half through, before final dicing of the wafer.

The chip is loaded with a 5% urea-polyacrylamide gel in 0.5x Tris-Borate EDTA buffer (TBE). Escherichia Coli is used as a demonstration species. Transfer-messenger RNA (tmRNA) of around 400 nucleotides [1] is used as a target material. The cells (overnight culture) are boiled at 30 kHz with a current of around 3 mA. Electrophoresis is run at a constant current of 40 µA, for 20 min. The eluted RNA is quantified using quantitative real-time PCR. A plasmid dilution series is thereby used as a reference. The results are compared with a commercial RNA extraction kit from Ambion (RiboPure) with DNase Step (TurboDNA-free).

4. MICROFLUIDIC CHIP

The fabricated chip is shown in figure 2. It consists of a square microfluidic chamber with two open electrodes for electrophoresis and one silicon-nitrite passivated electrode for thermo-electric lysis. The electrode configuration is shown in figure 3. The chip can be selectively filled with gel and buffer due to the presence of phaseguides. These phaseguides change the capillary forces in the chip, so that the liquid-air interface can be spatially guided [5]. The square gel in the center of the chip (see figure 4) can be achieved with simple pipette injection. Any type of gel can therefore be used. Bubble-free elements on top of the electrodes ensure that gas bubbles due to water electrolysis are driven out of the chip.

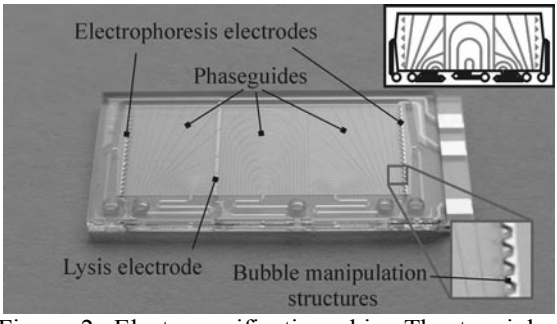

Figure 2. Electro-purification chip. The top inlay shows a simplified layout. Black lines show the microfluidic channels, gray lines depict the phaseguides. The bottom inlay shows a magnification of triangular structures on the electrodes that are used to drive bubbles out.

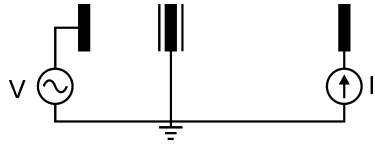

Figure 3. Electric actuation scheme. The central electrode is passivated in order to not disturb the DC electric field. The DC cathode is also used for AC actuation.

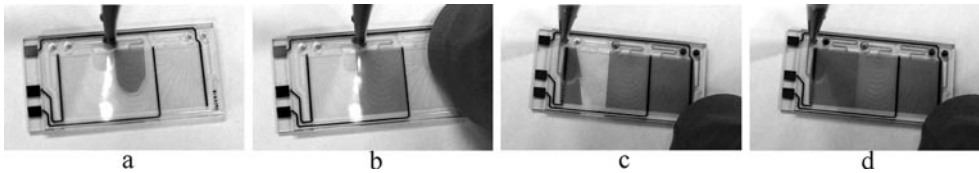

Figure 4. Filling of the chip with gel (a, b) and sample (c, d) using phaseguides. After gel cross-linking, two sample chambers are created that can be filled with buffer and sample.

5. RNA EXTRACTION FROM E.COLI

Figure 5 shows the measured tmRNA copy numbers for cells that have been boiled externally, boiled on-a-chip and not boiled at all, after 20 minutes electrophoresis. Also shown is the result for a commercial Ambion kit after DNase digestion. The chip shows a similar RNA yield as for the Ambion kit and even less DNA contamination. The combined lysis and extraction is fully automatic and lasts about 25 minutes, which is four times faster then commercial extraction kits.

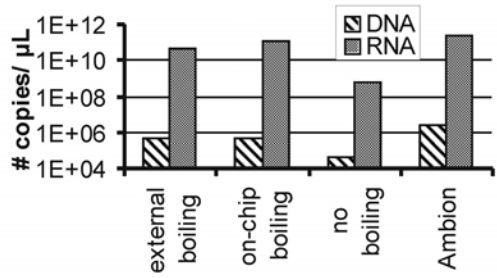

Figure 5. Amount of tmRNA copies measured with quantitative real-time PCR after 20 minutes of electrophoresis.

6. CONCLUSIONS

A microfluidic chip has been developed that is capable of automatic RNA extraction from bacterial cells. The chip employs thermo-electric lysis followed by electrophoretic purification. The chip is competitive with commercial extraction kits in terms of speed and yield.

ACKNOWLEDGEMENTS

This work has been financed by the European Union in the framework of SLIC EU-FP6-513771. Authors would like to thank Dr. Barry Glynn from the National University of Ireland, Galway, for provision of plasmids

REFERENCES

[1] W. Schönhuber, G. Le Bourhis, J. Tremblay, R. Amann, S. Kulakauskas, Utilization of tmRNA sequences for bacterial identification, BMC Microbiology, pp. 1-20 (2001)

[2] P.-A. Auroux, Y. Koc, A. deMello, A. Manz, P. J. R. Day, Miniaturised nucleic acid analysis, L a b C h i p , 2 0 0 4 , 4 , pp. 5 3 4 – 5 4 6

[3] L. Yobas, H.-M Ji et al., Micro-extraction of viral ribonucleic acid (RNA), Proc. of MicroTAS 2006, vol. 1, pp. 317-318

[4] P. Vulto, N. Glade et al., Microfluidic channel fabrication in dry film resist for production and prototyping of hybrid chips, Lab Chip, 5, pp. 158-162 (2005)

[5] P. Vulto, G. Medoro et al., Selective sample recovery of DEP-separated cells and particles by phaseguide-controlled laminar flow, J. Micromech. Microeng., 16, pp.1847-1853, (2006)

AUTOMATED HEMATOCRIT MEASUREMENT AND PATIENT DATA LABELING BY A COMMERCIAL DVD-WRITER WITH A LOW-COST OPTICAL ADD-ON

L. Riegger[1], J. Steigert[1], S. Lutz[1], W. Streule[1], R. Zengerle[1,2], and J. Ducrée[2]

[1]*Laboratory for MEMS Applications, Department of Microsystems Engineering (IMTEK), University of Freiburg, Germany*

[2]*HSG-IMIT, Institute for Micromachining and Information Technology, Germany*

ABSTRACT

This contribution derives an actuation, detection and labeling unit for a recently presented centrifugal hematocrit (*Hct*) test [1] based on an „off-the-shelf" Lightscribe™ DVD-writer and corresponding disk media. While centrifugation is enabled by the DVD-drive, the Lightscribe™ technology allows to directly store individual patient data and the obtained diagnostic results in a human-readable format on the Lightscribe™ surface of the processed disk. To implement an automated, absorption-based readout of the hematocrit after centrifugation, we added a low-cost green power LED and a PIN-photodiode to the commercial writer. Using the device, fully automated *Hct* measurements and labeling have been conducted on untreated whole blood at a very good reproducibility (CV = 2.9 %) and a high linearity (R^2= 0.995) within 3 minutes, only!

Keywords: ***DVD-writer, low-cost optics, hematocrit, LightScribe™, centrifugal microfluidics***

1. INTRODUCTION

For the screening of blood in centralized laboratories, small sample volumes as well as a high degree of parallelization and automation to limit the number of critical manual handling steps is of great importance. These demands can be met by so-called "lab-on-a-chip" technologies [2] which seek to enable full process integration, reduced consumption of sample and reagents as well as short times-to-result and ease of handling. Among the various lab-on-a-chip concepts, "lab-on-a-disk" [3,4] systems exploit centrifugal forces for flow control, metering, accelerated sedimentation of particles in biological suspensions and mixing in order to run fully process integrated assays.

In our lab-on-a-disk approach, we modify a conventional DVD-writer which acts as a cost-efficient centrifuge with low-cost optics to enable the automated, absorption-based determination of one of the most relevant parameters in medical diagnostics and routine blood screening - the hematocrit. Further, by utilizing the Lightscribe™-technology, the obtained patient data can be stored next the sample for displaying and archiving of the diagnostic results.

2. PRINCIPLE AND OPTICAL CONCEPT

The concept is based on the high differential absorption (ΔA ~ 2) of a cellular pellet of RBCs with respect to the plasma at the designated probe wavelength (λ_{peak} = 535 nm) (Fig. 1-A). Assuming full absorption by the cellular pellet, the *Hct* of the blood sample can hence be determined from the intensity of the transmitted light in a predefined area as recorded by the onboard photodiode (Fig. 1-B).

978-0-9798064-0-7/μTAS2007/$20©2007CBMS

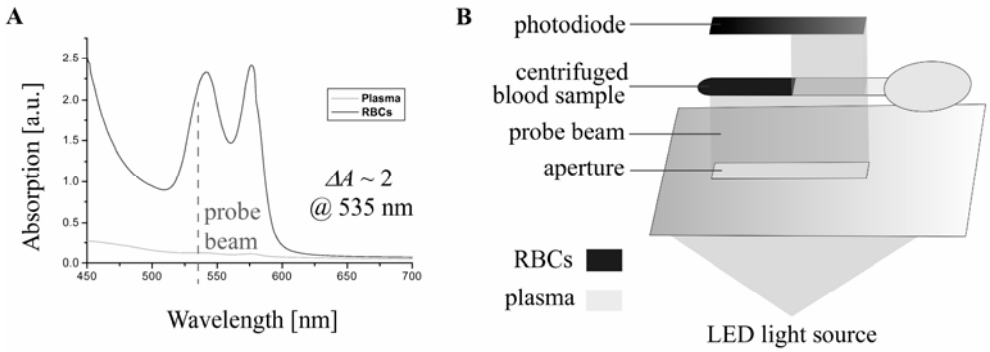

Figure 1. *(A) Light absorption of packed RBCs in contrast to blood plasma. ΔA ~ 2 at a wavelength of 535 nm essentially implies that the probe beam is transmitted by the blood plasma and almost completely absorbed by the RBCs. (B) Optical concept for the hematocrit determination. The emitted light of a green power LED propagates through an aperture to define the spot size. The impinging light is partially absorbed by a centrifuged blood sample. The light intensity captured by a photodiode is thus inversely proportional to the Hct value.*

3. HYBRID DISK FABRICATION AND MODIFICATION OF THE DVD-WRITER

First, the hematocrit structure constituted by an inlet, an overflow channel with a hydrophobic barrier for metering and a capillary for sedimentation is micromachined in a polycarbonate disk (Fig. 2-A). Next, the reflective coating is removed from the outer part of a conventional Lightscribe^{TM}-CD to permit the transmission of the probe beam. The two disks (Fig. 2-B) are finally bonded by an adhesive layer.

The standard Lightscribe^{TM}-writer (Fig. 2-C) comprises a milled aperture, a green power-LED, a low-cost PIN-photodiode with an amplification circuit and a USB-oscilloscope for data logging (not shown). The oscilloscope could be easily substituted by a digital signal processor (DSP) in a product development.

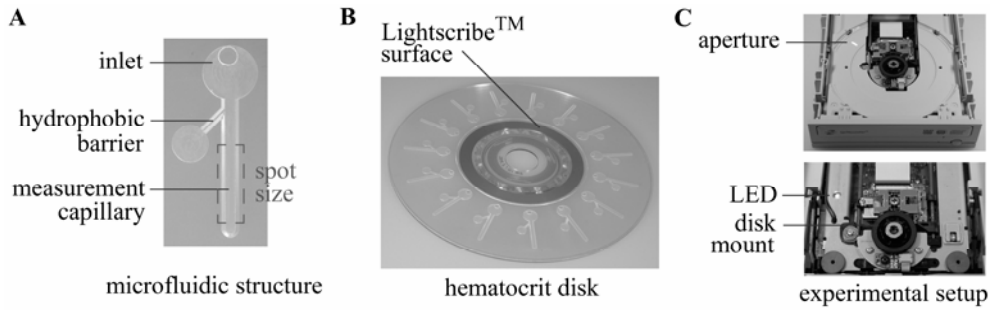

Figure 2. *(A) The channel structure features an inlet, a hydrophobic barrier for metering and a measurement capillary (l = 13 mm, h = 300 µm, w = 1 mm) for sedimentation. The spot size of the light beam defines the working range of the Hct determination. (B) The microfluidic disk is bonded to a conventional Lightscribe^{TM}-CDROM with a partially removed reflective surface. (C) The experimental setup comprises a standard DVD-writer with a milled aperture, a green power LED, a low-cost PIN-photodiode with an amplification circuit and a USB-oscilloscope for data logging (not shown).*

4. EXPERIMENTAL PROCESSING, RESULTS AND PATIENT DATA LABELING

After an unmetered sample of whole blood (V > 5 µL) is introduced *via* the inlets, the disk is inserted into the DVD-drive. While reading the inner data track, the disk spins to precisely meter the blood sample and subsequently sediment the RBCs (t = 2 min) [1]. The photodiode signal of the transmitted light is measured at ν = 50 Hz to determine the *Hct* by comparing the values of the measurement capillaries with the calibration curve (Fig. 3-A). The method displays a very good reproducibility (CV = 2.9 %) and a high linearity (R^2 = 0.995). Finally, after flipping the disk, the Lightscribe™ surface is permanently labeled with the *Hct* values and the patient data next to the respective blood sample (Fig. 3-B).

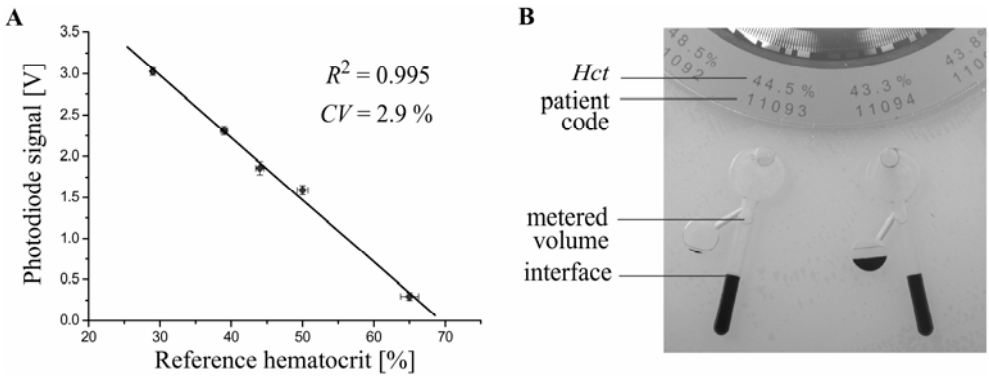

Figure 3. *(A) Calibration curve for the hematocrit determination. The measurements feature a very good reproducibility (CV = 2.9 %) and a high linearity (R^2 = 0.995) over the entire physiological range. (B) Hct value and patient code labelling by the Lightscribe™-technology. The results are permanently written next to the respective blood samples into the disk surface.*

5. CONCLUSION

We introduced a novel, absorption-based hematocrit test on an unmetered amount of whole blood drawn from the finger tip which is carried out on a device derived from a commercial DVD-writer. The processing device features low-cost components (< 100 $), only, while the disposable microfluidic substrate can easily be fabricated by standard polymer microfabrication. The possibility to write permanent, human-readable information next to the blood sample onto the Lightscribe™ surface of individual disks offers promising options for point-of-care settings as well as quality control measures in centralized labs.

REFERENCES

[1] L. Riegger *et al*., Single-step centrifugal hematocrit determination on a 10$ processing device, Biomedical Microdevices, publ. online, DOI 10.1007/s10544-007-9091-1.

[2] R. Oosterbroek and A. van den Berg, Lab-on-a-Chip: Miniaturized systems for biochemical analysis and synthesis, Elsevier Science, Amsterdam, Netherland, 2003.

[3] M. Madou and G. Kellogg, LabCD: A centrifuge-based platform for diagnostics, Proceedings of SPIE, SPIE publisher, San Jose, 3259, pp 80–93, 1998.

[4] Jens Ducrée, Stefan Haeberle, Sascha Lutz, Sarah Pausch, Felix von Stetten, Roland Zengerle. The centrifugal microfluidic Bio-Disk platform. Journal of Micromechanics & Microengineering, 2007. Status: in press.

DETECTION OF EMERGING ZOONOTIC INFECTION IN MICE BY HIGH SENSITIVE MULTIPLEXED MICROFLUIDIC IMMUNOASSAY SYSTEM

F. Ike[1], A. Kajita[1], H. Aoki[2], H. Kase[2], T. Nagamune[3], S. Morikawa[4], A. Yoshiki[1], Y. Obata[1] and Y. Yamagata[1]

[1]RIKEN, JAPAN, [2]Fuence Co. Ltd., JAPAN, [3]University of Tokyo, JAPAN and [4]National Institute of Infectious Diseases, JAPAN

ABSTRACT

Zoonotic virus infection in wild-derived mice was analyzed by using a high sensitive multiplexed microfluidic immunoassay chip system. Purified and/or recombinant virus antigens were deposited on Indium Tin Oxide coated glasses by electrospray deposition method. Polydimethylsiloxane microchannels were overlaid on the glasses. Only few micro litters of diluted mouse sera were applied in the microchannel and antibody titer was detected by image processing of chemiluminescence reaction using enzyme conjugated second antibody and substrates. Results showed highly enough sensitivity was achieved to identify the virus positive sera. This system is useful to monitor such infections in small laboratory animals by limited blood bleeding without euthanasia.

Keywords: Lymphocytic Choriomeningitis Virus, Zoonotic Infection, Microfluidic Chip, Immunoassay

1. INTRODUCTION

Lymphocytic choriomeningitis virus (LCMV) is a prototypic arenaviridae single stranded RNA virus and known as one of emerging zoonotic pathogens widely spread in wild rodents especially in mice. If human is infected, healthy adults generally show moderate influenza like symptoms, but immunocompromised patients or pregnant women became critically ill. In fact, it is reported that organ recipients from a donor infected with LCMV from a pet hamster died in United States of America in 2005 [1]. LCMV monitoring is important for animal caretakers and researchers to prevent this zoonotic infection from rodents at experimental animal facilities.

RIKEN BioResource Center (BRC) received LCMV infected mice from France in 2004 and the infection was revealed by immunofluorescence assay (IFA). The virus was isolated from infected mice, genomic NP region RNA was sequenced and analyzed [2]. As usually observed on RNA virus, high frequent synonymous substitution occurred, which means amino acid sequence is conserved and could be detected by serologically. Because IFA method depends on human eyes and experiences to identify the positive infection, we began to establish a new LCMV serological diagnosis method as an alternative to IFA method using small amounts of diluted sera.

2. THEORY

In order to analyze limited volume of sera taken from the LCMV infected mice, novel MideaChip (Fuence Co., Ltd.) multiplexed microfluidic immunoassay system [3] was utilized. This method consumes only three micro litters of diluted serum. Antigens are deposited on Indium Tin Oxide coated glasses in stripe shape by electrospray deposition method (Fig.1(a)). Polydimethylsiloxane (PDMS) microchannels are overlaid on the glasses

978-0-9798064-0-7/μTAS2007/$20©2007CBMS

(Fig.1(b)). Because microchannels are orthogonalized to the antigen stripe, small areas of intersection points are prepared for antigen antibody reaction space. Diluted sera are applied from the inlet and the fluid is washed out to the outlet (Fig.1(c)). Antigen antibody complexes formed are visualized by chemiluminescence reaction after adding enzyme conjugated second antibody and substrates. Images are recorded using CCD camera device and captured data are converted to figures by image processing.

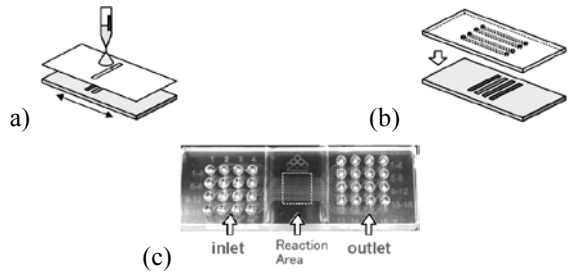

Fig. 1 Configuration of microfluidic microchannel chip, MideaChip.
(a) LCMV antigen was spotted by electro spray deposition method.
(b) PDMS microfluidic channel is put on the spotted glass.
(c) Photograph of the MideaChip (spotted glass and polydimethylsiloxane microfluidic channel) (Reaction area approx. 8x8mm)

3. EXPERIMENTAL

The recombinant antigen [4] was extracted from expressing Sf9 cell homogenates by high-pressure technique and spotted on PDMS microfluidic chips. To compare the antigenicity, the semi-purified antigen from LCMV Armstrong strain infected Vero E6 cells was also used. Sera were applied to MideaChip, microfluidic channels were washed and the bound antibodies were detected by chemiluminescence.

IFA was carried out using slide glasses overlaid with acetone fixed LCMV infected cells.

4. RESULTS AND DISCUSSION

The sera taken from the LCMV infected mice showed strong signals as shown in Fig.2, but some sera showed "hardly detectable" signals (indicated as +/– in Fig.3 column (B)).

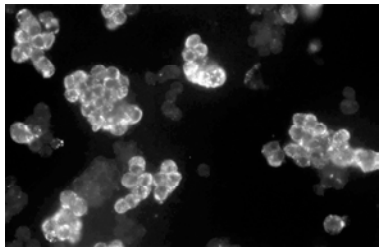

Fig.2. IFA picture of LCMV infected Vero E6 cells.
About 50% of LCMV infected cells were combined with healthy cells. Green fluorescence (LCMV infected cells detected by LCMV infected mouse serum and fluorescence isothiocyanate conjugated second antibody) and red fluorescence (all of cells stained by evans blue dye) were merged. Bright whitish cells are LCMV positive in this picture.

MideaChip system using semi-purified LCMV antigen could detect those sera which were "hardly detectable" by IFA (Fig.3 column (C)). However, MideaChip using semi-

purified LCMV antigen did not detect some IFA positive sera. MideaChip system using recombinant LCMV NP antigen showed more identical results taken from IFA (Fig.3 column (D)). Although there still exists contradictory results between IFA method and MideaChip method, these results clearly indicate sera taken from LCMV infected mice can be detected by MideaChip using both recombinant LCMV NP antigen and semi-purified antigen. The contradictory results might be induced from the differences of antigenic determinants of used antigens. Further analysis on this point is necessary.

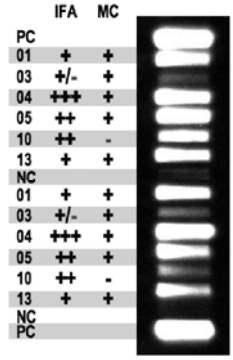

Fig.3 Chemiluminescence image of detected anti-LCMV sera.
IFA-positive sera taken from LCMV infected mice were applied to recombinant LCMV NP antigen spotted MideaChip. Column (A) shows serum number. PC: positive control (anti-LCMV monoclonal antibody). NC: negative control (normal mouse serum). All sera were diluted to 1/40 by phosphate buffered saline. Column (B) shows results of IFA. Symbol + means positive. Symbol +/– means "hardly detectable". Number of symbol + means intensity of positive fluorescence. Column (C) shows results of MideaChip using semi-purified LCMV antigen. Symbol + means positive (strong signal upper than threshold). Symbol – means negative (weak signal lower than threshold). Column (D) shows chemiluminescence image of MideaChip using recombinant LCMV NP antigen.

5. CONCLUSIONS

The MideaChip microfluidic microchannel chip system provides objective and high-sensitive LCMV serodiagnosis. The fact that MideaChip system uses only three micro litters of diluted serum makes this method very humane because we can collect small volume of blood from the same mouse several times without giving excess stress to them.

ACKNOWLEDGEMENTS

This work was supported by the Strategic Programs for Research and Development of RIKEN.

REFERENCES

[1] S.A. Fischer *et al*.: N Engl J Med. 2006, **354:**2235-2249.
[2] F. Ike *et al*.: Comp Med. 2007, **57:**272-281.
[3] Y. Yamagata *et al*.: Micro Total Analysis Systems 2005, pp.650-653
[4] Y. Matsuura *et al*.: J Gen Virol. 1987, **68:**1233-1250.

HIGH PERFORMANCE PENICILLIN SENSOR USING CHARGE TRANSFER TECHNIQUE

Seung-Ro Lee[1], Kazuaki Sawada[2, 3], Hidekuni Takao[2, 3] and Makoto Ishida[2, 3]

[1]*Dept. of Electrical and Electronic Eng, Toyohashi University of Technology, Japan,*
[2]*Intelligent Sensing System Research Center, Toyohashi University of Technology, Japan,*
[3]*Core Research for Evolution Science and Technology (CREST), Japan*

ABSTRACT

A high performances penicillin sensor using charge transfer technique is proposed and demonstrated experimentally. Penicillin sensor of two types, ion sensitive field effect transistor (ISFET) and charge transfer technique penicillin sensor (CTTPS) type were fabricated and comparative sensitivity analysis for each of those were carried out. In the proposed CTTPS, which is accumulation method H^+ ion perception system, the quality of output signal with "signal integration cycles" is high. The fabricated CTTPS possesses a high span penicillin sensitivity of about 47.852mV/mM in the linear concentration range from 0 to 25mM penicillin solution, a low detection limit of about 0.01mM, an upper detection limit of about 200mM.

Keywords: Penicillin sensor, Charge Transfer Technique, Charge Transfer Technique Penicillin Sensor (CTTPS), Ion Sensitive Field Effect Transistor (ISFET)

1. INTRODUCTION

Previously charge transfer type pH sensor based on charge coupled device (CCD) technique was proposed by our group [1, 2]. Furthermore, the charge transfer technique glucose sensor (CTTGS) was applied for diabetes sensors [3]. The ISFET type penicillin sensor is widely used [4]. In this work charge transfer technique penicillin sensor (CTTPS) with high performances is proposed and demonstrated experimentally. Consequently, penicillin sensor of two types, ISFET and CTTPS type were fabricated and comparative sensitivity analysis for each of those were carried out.

2. THEORY

The proposed CTTPS is constructed by immobilizing the enzyme penicillinase onto the ion-sensitive membrane (Si_3N_4) of pH-CCD. The operation principle of the penicillin biosensor can be described as follows [4]: The CTTPS detects variations in the H^+ ion concentration resulting from the catalysed hydrolysis of penicillin by the enzyme penicillinase, corresponding to the following reaction.

$$\text{Penicillin} + H_2O \xrightarrow{penicillinase} \text{penicilloic acid} + H^+$$

The CTTPS is based on the pH-CCD principle. The CTTPS measurement principle is shown schematically in Fig 1. The depth of the potential well in the semiconductor is varied by detecting the change of H^+ ions produced by the penicilloic acid near the sensing region. The CTTPS changes the depth of the potential well to charge quantity by charge transfer technique (fill and spill technique). The charge accumulation operation is continued for five "signal integration cycles" by the amount of penicillin in the sample solution. Thus, the span and sensitivity are increased.

978-0-9798064-0-7/μTAS2007/$20©2007CBMS

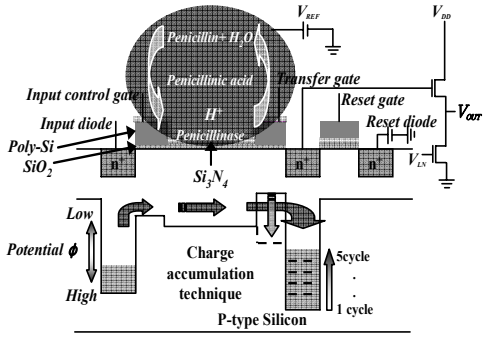

Figure 1. Schematic of the CTTPS measurement principle.

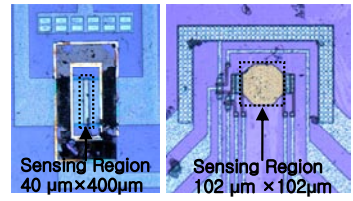

(a) ISFET (b) CTTPS

Figure 2: (a) Photographs of the ISFET type penicillin sensor. (b) Photographs of the proposed charge transfer type penicillin sensor (CTTPS).

3. EXPERIMENTAL

The ISFET penicillin sensors with a Si_3N_4 gate (40μm×400μm; 16000 μm^2) were fabricated. The photograph of the ISFET penicillin sensor is shown in Fig 2(a). The pH sensitivity of the ISFET penicillin sensor is about 45mV/pH in the range of 2-10pH. The fabricated ISFET penicillin sensor has a sensitivity of about 6.56mV/mM in the linear concentration range from 0 to 12.5mM penicillin solution (pH7.0), as shown in Fig 3 and Fig 5. This sensitivity and resolution are insufficient for clinical application. There is also a problem of accuracy in the measurement.

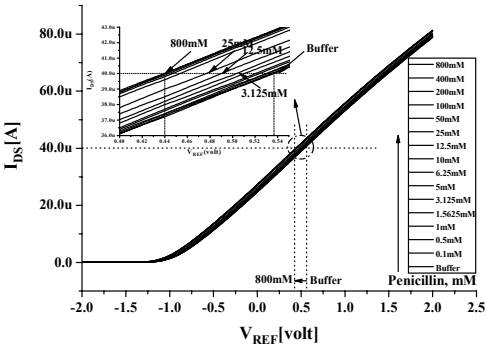

Figure 3. Characteristics of the ISFET type penicillin sensor using solutions, with penicillin concentration from buffer to 800mM.

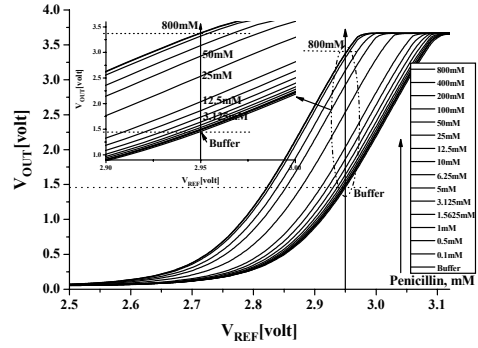

Figure 4. Characteristics of the proposed charge transfer type penicillin sensor (CTTPS) using solutions, with penicillin concentration from buffer to 800mM.

The CTTPS consists of a penicillin-sensitive Si_3N_4/SiO_2/silicon structure on which a layer of the enzyme penicillinase is immobilized. The thicknesses of the gate oxide (SiO_2) and penicillin sensing membrane (Si_3N_4) are 65 and 100 nm, respectively. Si_3N_4 was deposited by thermal low-pressure chemical vapor deposition (LPCVD). The reason why Si_3N_4 was used for the ion-sensing membrane is that it is easy to integrate with the CMOS process. The Photograph of the CTTPS penicillin sensor is shown in Fig 2(b). The sizes of the sensing region and floating diffusion area are 10580 and 795 μm^2 respectively.

4. RESULTS AND DISCUSSION

In the proposed CTTPS, which is accumulation method H^+ ion perception system, the quality of output signal with "signal integration cycles" is high. The fabricated CTTPS possesses a high span penicillin sensitivity of about 47.852mV/mM in the linear concentration range from 0 to 25mM penicillin solution, a low detection limit of about 0.01mM, and an upper detection limit of about 200mM as shown Fig 4 and Fig 5. The CTTPS is better than ISFET penicillin sensor in span, sensitivity and the linear range. The detailed specifications of the penicillin biosensor are summarized in Table 1.

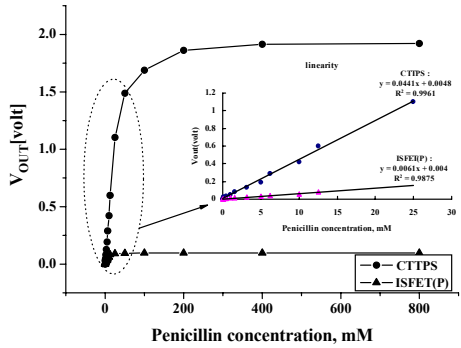

Figure 5. Linearity of ISFET & CTTPS penicillin sensor

Table 1. Specifications of the penicillin sensor

Penicillin sensor	ISFET(P)	CTTPS
Lower detection limit (mM)	0.1	0.01
Upper detection limit (mM)	100	200
Span (volt)	0.096	1.8609
Linear range (mM)	0-12.5	0-25
Sensitivity (mV/mM)	6.56	47.852
Linearity, R^2	0.9875	0.9961
Response time (min)	0.5-3	0.5-3

5. CONCLUSIONS

The CTTPS excels in performance over widely used ISFET penicillin sensor. The CTTPS has the sensitivity which is 7 times higher. Measurement result values fit to linear equation $y=0.0441x+0.0048$ and $R^2=0.9961$. The CTTPS is therefore suitable technology in biotechnological processes as well as in food control.

REFERENCES

[1] "Novel CCD-based pH Imaging sensor," K. Sawada, S. Mimura, K. Tomita, T. Nakanishi, H. Tanabe, M. Ishida IEEE Trans. ED, vol.46, NO.9, pp.1846-1849, (1999)
[2] "Highly sensitive ion sensors using charge transfer technique," K. Sawada, T. Shimada, T. Ohshina, H. Takao, M. Ishida, Sensors and Actuators B, 98, 69-72, (2004)
[3] "High performance blood glucose sensor using charge transfer technique," Seung-ro Lee, T. Hizawa, K. Sawada, H. Takao, M. Ishida, Transducer'07 vol.1, 855-858, (2007)
[4] "Multi-parameter detection of (bio-)chemical and physical quantities using an identical transducer principle," A. Poghossian, J.W. Schultze, M.J. Schoning, Sensors and Actuators B, 91, 83-91, (2003)

MICROCHIP FLOWCYTOMETER USING FLUORESCENT SILICA NANOPARTICLES FOR HIV SCREENING

H. Yun[1], J.K. Min[1], W.G. Lee[1], H. Bang[1], J. Park[2], C. Chung[2], J.K. Chang[2] and D.C. Han[1]

[1]School of Mechanical & Aerospace Engineering and Institute of Advanced Machinery & Design, Seoul National University, South Korea

[2]NanoenTek, Inc., South Korea

ABSTRACT

The development of inexpensive small flow cytometers is recognized as an important goal for many applications. Even though hydrodynamic focusing used in conventional flow cytometers is highly effective in positioning particles, the use of sheath fluid increases assay cost and reduces instrument utilization in field and for autonomous remote operations. This work presents a novel solution by integrating an expansion channel and an asymmetric nozzle into a microchip flow cytometer that enables sample particle focusing to the center of a flow stream without the need for sheath flows. To miniaturize the optical system, two-parameter detection with a single detector using fluorescence dye-doped silica nanoparticles (SiNPs) has been developed and demonstrated using this microchip for HIV screening, one of the killer applications in flow cytometry.

Keywords: Flowcytometry, Silica nanoparticles, Microchip, HIV screening

1. INTRODUCTION

Although CD4+ T-cells are an important target in HIV detection, major problems still exist in diagnosing and monitoring HIV in third world countries and regions with few established medical facilities. As a result, there is a great need for low cost portable diagnostic devices that can count CD4+ T-cells. In general, CD4+ T-cells below 200cells/μL make it necessary to initiate antiretroviral treatment in adults (over 13 years old). However, lymphocyte subsets (including CD4 counts) of infants and young children are higher than those of adults. This fact shows that in children, the percentage of CD4+ T-cells of blood subsets is a more reliable indicator of HIV infection than absolute counts. To quantify the percentage of CD4+ T-cells, two fluorescent dyes with different emission wavelength are typically used, which in general require one laser and two photo multiplier tubes (PMTs). Since there exist many peripheral modules in such method, however, it is difficult to miniaturize the device. In this study, we developed a novel method to control the intensity of fluorescent dye-doped SiNPs. Our experimental result shows that FITC-doped SiNPs conjugated with CD4 antibody is 10 times brighter than FITC-conjugated CD45 antibody. This difference in intensity of these two conjugated complexes enabled us to measure two parameters with only a single PMT and a laser.

2. THEORY

In light of the current methods for two-parameter detection, we should use two fluorescent dyes with two different wavelengths. So it becomes possible to count two cell populations at the same time by labeling the blue florescent dye to one sample, and the red one to another. In the proposed method, the different intensity of two dye complexes was utilized to count two samples at the same time by labeling normal florescence dye to one,

978-0-9798064-0-7/μTAS2007/$20©2007CBMS

and much brighter fluorescent dye to the other. FITC-doped SiNPs is 10 times brighter than FITC molecules, and HIV screening becomes possible with a single detector.

3. EXPERIMENTAL

Fluorescence intensity between FITC-conjugated CD4 antibody and FITC-SiNPs conjugated CD4 antibody is compared using a fluorometer (BioTek, USA). By surface treatment with N-hydroxysulfosuccinimide (Sulfo-NHS) and 1-Ethyl-3-[3-dimethylamino -propyl] carbodiimide (EDC), a polymethyl methacrylate (PMMA) plate with carboxyl groups becomes contacted to the amine group. First, 10mM of Sulfo-NHS is mixed with 200 mM of EDC at one-to-one ration. Then two separate drops of the mixed solution are placed on a PMMA-poly(dimethylsiloxane) wall plate and left at room temperature (RT) for 20 min. The plate is washed with PBS (1X, pH 7.4). FITC-SiNPs-conjugated CD4 is loaded into one chamber, and FITC-conjugated CD4 into another. Then, these are left at 37℃ for 2 hours. During this process, dyes are doped on the well plate as a monolayer. In 2 hours, the intensity of each area was measured using a fluorometer after washing with PBS several times. For a flowcytometry analysis, we prepared two blood samples. Briefly, white blood cell (WBC) is separated and prepared into 500-μL whole blood. And 10 mL of red blood cell (RBC) lysis solution is added to it and then mixed by gently shaking. After the incubation at RT for 10 min and the centrifugation at 1500 rpm for 5 min, its supernatant is removed and 5 mL of PBS is added. With the additional centrifugation at 1500 rpm for 5 min, the pellet is resuspended in 300 μL of PBS. The 20 μL of monoclonal anti-human CD45 FITC and 20 μL of CD4 FITC-SiNPs are added to 100 μL of the WBC solution. After the incubation at 4°C for 30 min, the centrifugation at 1500 rpm for 5 min, and washing with 1 mL of PBS, its supernatant is removed and the remnant pellet is resuspended in 300 μL PBS.

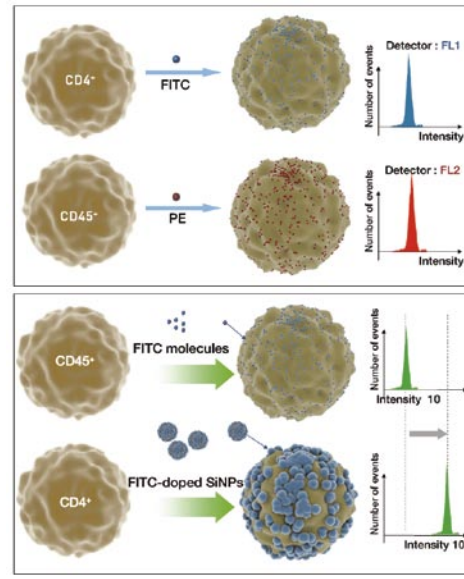

Figure 1. Conventinal method (top) and Proposed method (bottom)

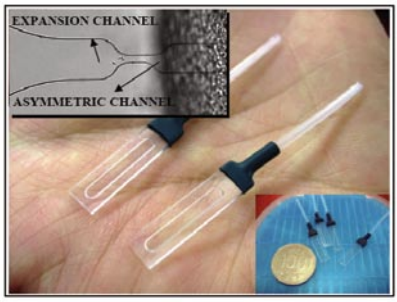

Figure 2. Microchannel patterns were etched on a 4"quartz wafer by 20μm in depth using photo lithography. On another quartz wafer, through holes were punched by sand blasting. These two wafers were bonded by thermo-compression to close each other. Finally, the bonded wafer was diced into 60 microchips, which have an expansion outlet [1] and an asymmetric entry [2]. The expansion channel was designed to prevent stagnation zones. All design parameters were optimized to detect CD molecule of white blood cells (~10 μm diameter in average).

4. RESULTS AND DISCUSSION

When FITC-SiNPs-conjugated CD4 and FITC -conjugated CD4 antibodies occupy the same size on the well plate, the intensity difference between them is obtained as seen in Fig. 3. These results indicate that FITC-SiNPs-conjugated CD4 is 10 times brighter than FITC-conjugated CD4. The total number of WBC can be calculated by detecting the samples labelled with FITC-conjugated CD45. And CD4+T-cells with FITC-SiNPs-conjugated CD4. The number of each samples were calculated from our microchip flowcytometer (see Fig.4).

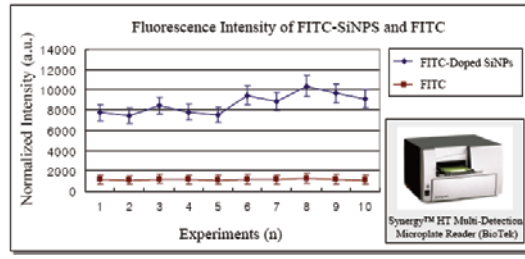

Figure 3. Intensity measurement of the intensity of FITC-conjugated CD4 and FITC-SiNPs using fluorometer.

5. CONCLUSIONS

In this study, we proposed a novel method for sheathless microchip flowcytometers using fluorescent nanoparticles for on-chip HIV screening. This microchip has two strong advantages in a geometric modification and optimization as follows: i) it needs no sheath for particle focusing, and ii) increases detection sensitivity at a high particle-analysis rate. We also tried to show the feasibility of on-chip HIV screening, discriminating the difference between the brightness of CD4 and CD45 simultaneously. As a result, this method made it easier to detect multiple parameters with simple optics where the intensity of fluorescent dye-doped silica nanoparticles could be controlled. Furthermore, it is expected that these findings would contribute to the miniaturization of the next generation of the flowcytometers.

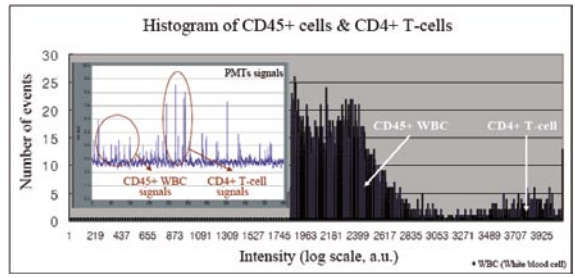

Figure 4. Results from our sheathless microchip flow cytometer. CD4+T-cell and CD45+ cell were counted successfully using only a single detector. And the right panel indicates the histogram obtained from our microchip flowcytometer. Note all data were obtained from a data acquisition board.

ACKNOWLEDGEMENTS

This research has been supported by the Intelligent Microsystem Center (IMC; http://www.microsystem.re.kr), which carries out one of the 21st century's Frontier R&D Projects sponsored by the Korea Ministry Of Commerce, Industry and Energy

REFERENCES

[1] Hyunwoo Bang, Hoyoung Yun, Won Gu Lee, Dong-Chul Han *et al*., "Expansion channel for microchip flow cytometers," *Lab Chip*, 6, 1381–1383, 2006

[2] Junha Park, Seok Chung, Hoyoung Yun, Dong-Chul Han *et al*., "Asymmetric nozzle structure for particles converging into a highly confined region," *Curr. Appl. Phys.*, 6, 992-995, 2006.

MICROFLUIDIC ELISA SYSTEM FOR THE DIAGNOSIS OF HEPATITIS B USING MICROWELLS MADE OF ANODIC ALUMINUM OXIDE

Kwang Suk Yang[1], Hye Jin Kim[2], Jeong Keun Ahn[2] and Do Hyun Kim[1]

[1]Department of Chemical and Biomolecular Engineering and
Center for Ultramicrochemical Process Systems,
Korea Advanced Institute of Science and Technology, South Korea
[2]Department of Microbiology, Chungnam National University, South Korea

ABSTRACT

An efficient microfluidic system for diagnosing disease marker molecules is reported. This system is constructed with the anodic aluminum oxide (AAO) as a porous substrate, which provides havens for target proteins and their antibodies from shear force of flow. AAO is embedded on microfluidic channels, where hepatitis B virus (HBV) antibody is immobilized in the surface-modified AAO pores. The performance using porous AAO in a PDMS microfluidic device is comparable to that of conventional ELISA system for the detection of hepatitis B surface antigen (HBsAg).

Keywords: anodic aluminum oxide, ELISA, immunoassay, hepatitis B virus

1. INTRODUCTION

Microfluidic systems in immunodiagnosis offer many practical advantages over classical technology such as fast detection and quantification of a small amount of target proteins from biological fluids. ELISA (enzyme-linked immunosorbent assay) is one of the widely used immunodiagnostic method with high selectivity and sensitivity. However, conventional ELISA systems are not adequate for high-throughput experiments due to the slow reaction time caused by long molecular diffusion distance. To overcome this limitation, we have investigated an effective microfluidic system using porous substrate such as meso-porous silica, glass membrane, and anodic aluminum oxide (AAO).

In this report, anodic aluminum oxide with highly ordered, uniform, and straight nanopore array is prepared by published method [1] and integrated with poly(dimethylsiloxane) (PDMS) and glass microchannel structure for ELISA to detect hepatitis B surface antigen (HBsAg).

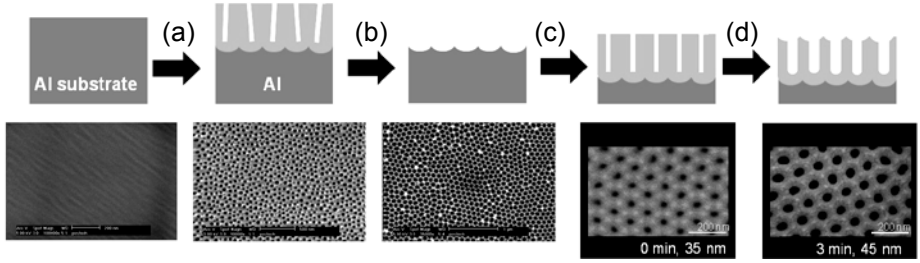

Figure 1. Two step anodizing process. (a) Inter-pore distance definition (0.3M oxalic acid, 40V, 15°C). (b) Hexagonal pore-array formation (0.6M H_3PO_4, 0.2M CrO_3, 60°C). (c) Pore depth control (0.3M oxalic acid, 40V, 15°C). (d) Pore diameter control (0.1M H_3PO_4, 60°C).

978-0-9798064-0-7/μTAS2007/$20©2007CBMS

2. EXPERIMENTAL

AAO is prepared by two-step anodization process as shown in Figure 1. Vacuum-evaporated aluminum thin film on the glass substrate is anodized to obtain AAO nanopore structure. By variation of electrolyte composition, applied voltage and time, pore sizes and depth are tuned to accommodate target proteins.

For the easy fabrication and effective immobilization of primary antibody, surface of AAO is activated by calcination at 400 °C following sol-gel SiO_2 spin-coating [2]. PDMS microfluidic device, fabricated by conventional photolithography process and replica molding technique, is equipped with ports for two controls and three samples which are connected to washing buffer inlet. A schematic of AAO/PDMS microchip are shown in Figure 2.

For the immobilization of hepatitis B virus (HBV) antibody, γ-aminopropyl triethoxysilane and glutaraldehyde as an anchoring bridge are reacted on SiO_2-modified AAO nanopores as shown in Figure 3.

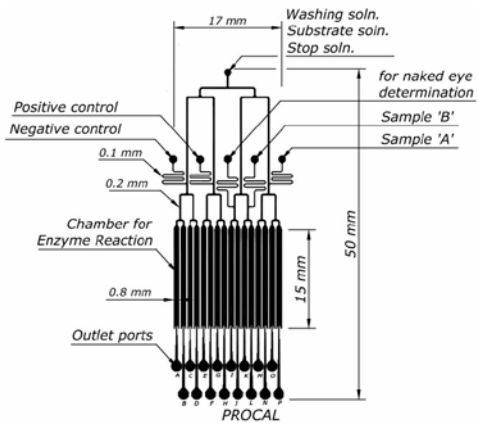

Figure 2. The schematic layout of the immuno-diagnosis device on the glass slide (25 x 75mm).

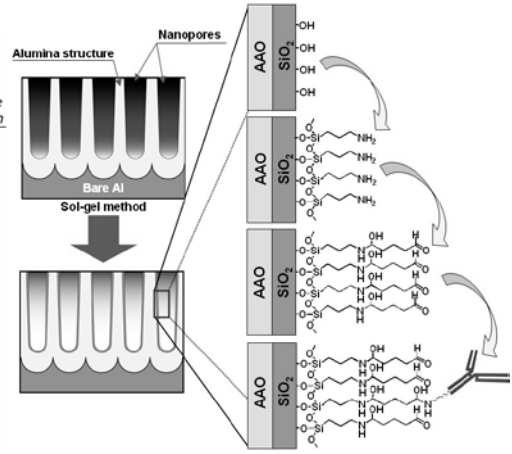

Figure 3. Surface modification process of SiO_2-AAO nanopores. (a) Immobilization of γ-aminopropyltriethoxysilane as an anchor. (b) Introduction of glutaraldehyde as a linker. (c) Reaction with anti-HBs (primary antibody).

A specimen for assay is prepared by arbitrary dilution of HBsAg positive control. Positive control, negative control and a specimen are fed into the AAO/PDMS device under constant temperature of 35°C through appropriate ports at the rate of 15 μL/min for 2 minutes using syringe pumps. Then, the channels are washed with buffer at the rate of 30 μL/min. Sheep anti-HBs/horse radish peroxidase (HRP) conjugate solution is injected and washed in the same manner. For the assay, TMB (tetramethyl benzidine) solution as a substrate for horse radish peroxidase is introduced slowly and reacted for 10 minutes. Conversion of TMB causes the color to change from transparent to blue. The enzyme reaction is quenched by sulfuric acid solution. The schematic procedure is illustrated in Figure 4A.

3. RESULTS AND DISCUSSION

ELISA using porous AAO in PDMS microfluidic device is compared with conventional

ELISA for the detection of HBsAg. Colorimetric assay in Figure 4B shows that absorbance (f′) corresponding to ~60% of (e′) in our device is comparable to (c′) corresponding to ~80% of (b′) in conventional ELISA. Total analysis time including test sample loading, reaction and washing is about 15 minutes based on overall feeding rate (15 μL/min). However, it takes over 130 minutes in conventional ELISA test. With short vertical dimension (25 μm) and wide surface area, this device provides a rapid immune interaction owing to short mass transport distance between AAO surface and reaction chamber.

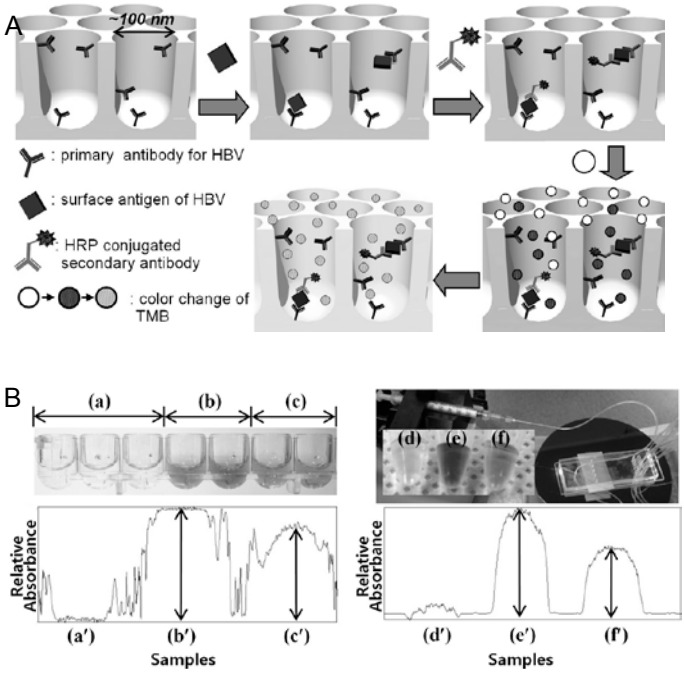

Figure 4. The schematic procedure (A) and results (B) of immunoassay. (a), (b), (c) are obtained from commercial ELISA system. (d), (e) and (f) are obtained from our system. (a), (d) are for negative controls without antigen. (b), (e) are for positive controls with 10 mg/mL of antigen. (c), (f) are for a specimen to be assayed. Sample volume is 100 μL for (a), (b), (c), and 25 μL for (d), (e), (f).

4. CONCLUSIONS

Porous anodic aluminum oxide (AAO) has been successfully integrated into PDMS microfluidic system for the application of ELISA. Whole test time and chemical consumptions are less with our system compared to the conventional ELISA system. This system is expected to be applied to clinical high-throughput diagnosis system for bio-marker proteins.

ACKNOLEDGEMENTS

This work was supported by the Basic Research Program (grant No: R01-2004-000-10681-0) of the KOSEF and the Center for Ultramicrochemical Process Systems sponsored by Korea Ministry of Science and Technology.

REFERENCES

[1] H. Masuda, K. Fukuda, Science, **268**, 1466-1468 (1995).

[2] S. B. Lee, D. T. Mitchell, L. Trofin, T. K. Nevanen, H. Soederlund, C. R. Martin, Science, **296**, 2198-2200 (2002).

MULTIPLEXED ANALYSIS USING NANO-BAR CODES

H. Morgan[1]. S. Banu[1,2], S.W. Birtwell[2], G.R. Broder[3], G. S. Galitonov[2], D.C. Neylon[3], R. T. Ranasinghe, J. K. She[3], N. Zheludev[2] and P. L. Roach[3].

[1] School of Electronics and Computer, [2] Optoelectronics Research Centre, and
[3] School of Chemistry, University of Southampton, Southampton SO17 1BJ, U.K.

ABSTRACT

A new encoding and analysis technology for multiplexed assays has been developed using micron-sized diffractive elements. The barcodes are manufactured using photolithography and nano-imprinting from SU-8. Micron sized particles, imprinted with several superimposed diffraction gratings, can encode many millions of unique codes. Fast detection of single nucleotide differences in a DNA sequence and a four-way multiplexed immunoassay are demonstrated. The diffractively encoded particles are suitable for multistep chemistry. The extremely large encoding capacity of this technology enables the creation of vast libraries of unique particles.

Keywords: Multiplexed analysis, Nano-imprinting, Bar-coding, SU8.

1. INTRODUCTION

Multiplexed assays, where large numbers of different molecular interactions are analysed simultaneously, have many applications in biotechnology. Bead-based assays offer a number of advantages over microarrays, but require a robust method for manufacturing and identifying individual encoded beads, and for high-throughput analysis, the code must be read quickly and reliably. A number of encoding strategies have been demonstrated including nano-scale metallic barcodes, quantum dot-encoded beads, and differently shaped micromachined particles. We have developed a new and robust encoding system based on the manufacture of large numbers of different micro-particles that incorporate diffraction gratings as identifiers. This method allows rapid non-invasive, non-contact reading of extremely large numbers of different codes. The technique is based on making nano-structured micron-sized particles. When excited by a laser beam the particle diffracts light in a way that is determined by the spacing of the diffraction pattern. The codes are "read" by detecting the spatial distribution of light diffracted by the tag [1]. A single grating diffracts the incident light into a unique diffraction pattern. In the simplest implementation, information is encoded in the pitch of the grating, a. When the grating is illuminated with light at wavelength λ, a series of diffracted beams is created at angles θ, according to the equation $a \sin\theta = m\lambda$, where m is the order of the diffracted beam. Measurement of the first order ($m = \pm 1$) diffracted beam position (with respect to the zero order) gives direct information about the pitch a. The encoding capacity of single diffraction gratings is clearly limited, but superimposing different diffraction gratings onto a single particle greatly increases the encoding capacity – Figure 1a. In order to simultaneously read the diffraction pattern (i.e. the code) and particle fluorescence a custom-made optical system was developed - figure 1b. This reads the diffraction pattern and calculates the code (Fourier transform) at high speed (less than 1ms). The system reads static codes or codes flowing in a microfluidic channel.

978-0-9798064-0-7/μTAS2007/$20©2007CBMS

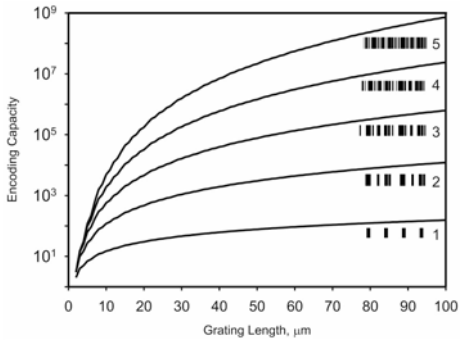

Figure 1(a). Encoding capacity as a function of particle length for different levels of superimposed gratings.

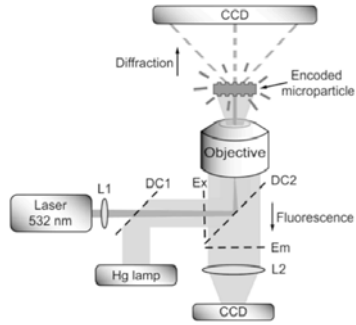

Figure 1(b). Experimental system used for reading the "code" and simultaneously analysing fluorescence-based assays.

2 RESULTS

(i) Fabrication

Large numbers of microparticles are fabricated from a SU8 using conventional photolithography [2] and nano-imprinting techniques. The SU8 is spun onto Al coated Si wafers and patterned into blocks 10 x 30μm. A nano-imprint master was made from Si and used to emboss the SU8. Particles were released by sacrificial etching of the Al layer. An example of a nano-imprinted SU8 surface is shown in Figure 2. This is a two times superimposed diffraction grating giving two first order beams. An example of diffraction patterns from a two-times superimposed nano-imprinted SU-8 grating is also shown in figure 2. The sequence shows how changing one of the grating pitch (keeping the other constant) leads to a change in the position of one of the two first order spots, i.e. changing the code.

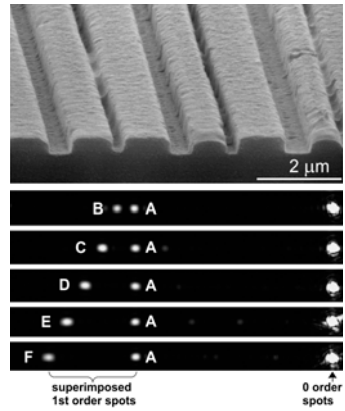

Figure 2. Top: SEM of nano-imprinted SU8 with a two times superimposed diffraction grating. Bottom shows the image from this diffraction grating.

(ii) Multiplexed assay

The coded particles were used in two different classes of multiplexed biomolecular assays. Particles were functionalised either with protein A or Avidin. For hybridisation experiments, biotin-terminated oligonucleotides were synthesised and linked to the particles via the surface-bound avidin – figure 3(a). A multiplexed DNA hybridisation assay was performed using sequences corresponding to a polymorphic locus (N1303K (27)) in the gene encoding the cystic fibrosis transmembrane conductance regulator (CFTR) protein. Two sets of encoded particles were functionalised with avidin and used to capture biotinylated probe oligonucleotides. Wild type sequence P2 was bound to one particle type and the mutant sequence, P1, differing by a single nucleotide, to a different code. Figure 3(b) shows a microscope image and fluorescence image of the two particles type showing that perfectly matched sequence fluoresces but the mismatched sequence does not.

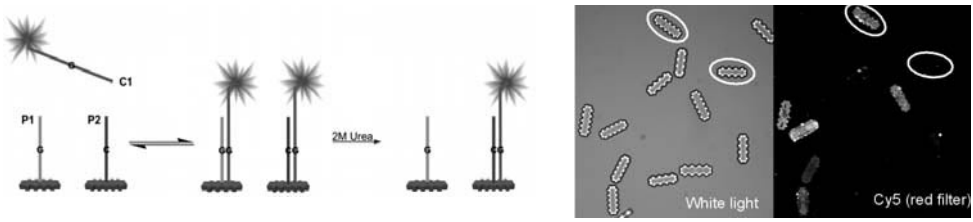

Figure 3a. left. Schematic diagram of a multiplexed assay for detecting two different oligonucleotides. (b) right. Fluorescent images of a hybridisation assay for two different oligomers, one a perfect match and the other with a single base mismatch. Both probes have been fluorescently labelled, but only the matching strand has been hybridised.

To demonstrate the applicability of the technology to immunodiagnostic a multiplexed immunoassay was performed for the detection of immunoglobulin G (IgGs). Two sets of encoded particles were functionalised with two different IgGs using protein A. The particles were incubated with complementary antibodies as shown schematically in figure 3a. The fluorescence images (figure 3b) show the selective binding of the differentially labelled detection antibodies to the correct encoded particle.

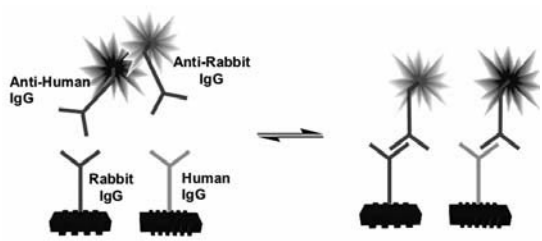

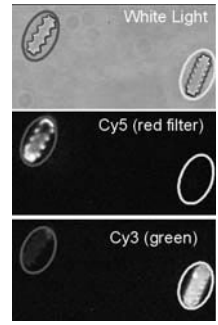

Figure 3a, above. Schematic diagram of a multiplexed assays for detecting two different antibodies immobilised on different codes. (b). right, fluorescence images showing binding of antibodies.

3 CONCLUSIONS

We have demonstrated a new encoding technology using nano-imprinted on micron-sized diffraction gratings. The particles are fabricated from SU8, onto which proteins or oligonucleotides can be immobilised by a number of chemical routes [3]. We are developing microfluidic systems to enable high speed analysis of the microparticles in flow.

4. ACKNOWLEDGEMENTS

This work was funded by the Basic Technology Research Program of the UK Research Councils.

5. REFERENCES

[1] Galitonov, G.S., Birtwell, S.W., Zheludev, N.I. & Morgan, H. Opt. Express 14, 1382-1387 (2006).
[2] Gabriel C, Banu S., Martins H., Ranasinghe R., Cameron C., Morgan H and Roach P.L. J. Comb. Chem., 462 - 472 (2007).
[3] Banu S, Birtwell S, Galitonov G, Chen YF, Zheludev N and Morgan H. J. Micromechanics and Microeng. in the press (2007).

NONSPECIFIC ADSORPTION MINIMIZED NANOMECHANICAL IMMUNOASSAY FOR APPLICATION TO ASSAY USING THE REAL SAMPLE

Kyo Seon Hwang[1,2], Sang-Myung Lee[1], Byung Hak Cha[1], Sang Kyung Kim[1], Jung Ho Park[2], and Tae Song Kim[1]

[1]Nano-Bio Research Center,Korea Institute of Science and Technology, KOREA and
[2]Department of Electronics and Computer Engineering, Korea university, KOREA

ABSTRACT

We report an application feasibility of the dynamic microcantilever to detect the specific protein in human serum. The mechanical response (i.e. resonant frequency) change of functionalized dynamic microcantilever generated by biomolecular interactions allows one to detect the biomolecules of small amount without labeling process. We implemented the label-free detection of PSA in human serum like sample (protein mixture sample). The range of detected PSA was 1 and 10 ng/ml in clinical concentration range. It is suggest that the dynamic microcantilever enables one to apply the sensitive label-free detection of disease marker proteins in a real human sample.

Keywords: Microcantilever, PSA, Clinical range, Real sample

1. INTRODUCTION

A considerable number of researches have been developed nano- or micro-mechanical biomolecules detection system for the diagnosis, monitoring, and evaluation of complex diseases such as cancer, as well as for the basic study [1]. Because nonspecific adsorption has severe influence upon specific biomolecules detection in a variety of protein mixture, the effort to minimize this effect is kept on increasing. Especially, miniaturized mechanical sensor is vulnerable to nonspecific adsorption compare to other detection technologies such as, optical and electrical detection method. Nonspecific binding often triggers unexpected mechanical parameter and affects output signal distortion. This paper reports that nanomechanical dynamic cantilevers are applicable to the label-free detection of specific protein in real blood through the optimized nonspecific adsorption removing process and mixture protein sample with abundant nonspecific proteins.

2. EXPERIMENTAL

Actuating layer-embeded cantilevers were fabricated by micromachining process and its resonant frequency were measured by monitoring the phase angle of impedance with impedance analyzer as shown in Fig. 1. To prove nonspecific adsorption-minimized condition, biologically passivated cantilevers were immersed in Cy5 labeled-BSA diluted solution (Fig. 2(a)). We achieved effective nonspecific adsorption minimized condition (washing for over 15 min.) by controlling the washing time of an orbital shaker as shown in Fig. 2(b). With the established condition, we measured coefficient of variance (CV(%)) for comparison with previous result. Finally, for confirmation of application feasibility of cantilever-based nanomechanical immunoassay was verified using mixed samples. We observed resonant frequency shift of monoclonal anti-PSA immobilized cantilevers after

978-0-9798064-0-7/μTAS2007/$20©2007CBMS

reaction with a variety of protein mixed sample (mixture of PSA, troponin I, CRP antigen and BSA). Two kind of samples were used and their results were compared. The pure sample had only PSA antigen and the mixed sample had PSA (1, 10 ng/ml), troponin I (100ng/ml), CRP antigen (100 ng/ml) and BSA (10 μg/ml). Nonspecfic proteins (troponin I antigen, CRP antigen and BSA) were labeled with Cy 5 dye for cross-validation after assay using nanomechanical cantilever.

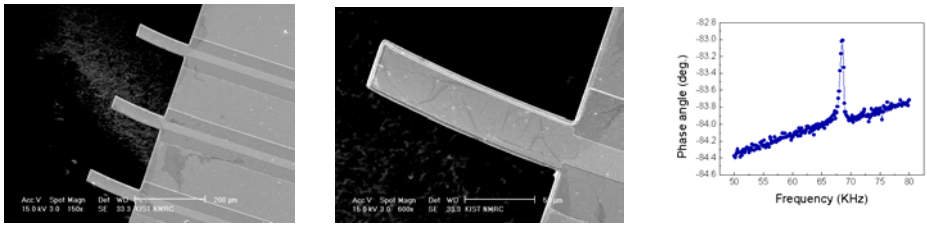

(a) (b) (c)

Figure 1. SEM photographs of microfabricated (a) cantilever array, (b) unit cantilever, and electro-mechanical response signal for measuring the resonant frequency of our nanomechanical cantilever with dimension of 50 μm ×150 μm by using impedance analyzer.

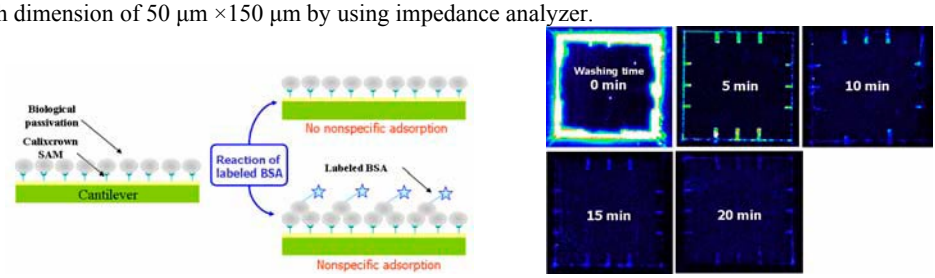

(a) (b)

Figure 2. Effective condition control to minimize the nonspecific protein adsorptions. (a) Schematic diagram and (b) fluorescent images in several washing time conditions. Optimized condition for minimization of nonspecific adsorption was washing for over 15 minutes at 300 rpm using an orbital shaker.

3. RESULTS AND DISCUSSION

We investigated feasibility of nanomechanical immunoassay using human serum like sample (mixed protein). To minimize the non-specific adsorption of proteins, effective condition were established by washing time control of orbital shaker (Fig. 2). According to the established washing condition, we measured coefficient of variance (CV (%)) value for comparison to assay results with conventional washing step. Fig. 3 shows the resonant frequency variance in bioassays of PSA 1ng/ml in case of conventional (Fig. 3 (b)) and newly proposed washing method (Fig. 3 (c)). This result indicates that the variance was decreased from 21.48% to 15.68% by reducing the nonspecific adsorption. Finally, we performed microcantilever-based immunoassay with use of protein mixture sample based on the non-specific adsorption minimized results by assay condition control. The microcantilevers were functionalized by anti-PSA immobilization on the Calixcrown self-assembled monolayer and biological passivation with bovine serum albumin. Fig. 4(b) shows the results of mechanical response change before and after reactions on anti-PSA immobilized cantilevers. This means thath non-specific interaction from the mixed sample

did not contaminate the interaction of target protein with the probe. The small deviation of two cases (assay with pure and mixed sample) seemed due to the competitive interaction in case of assay using mixed sample. Moreover, fluorescent image shows there is no adsorption of Cy 5 labeled nonspecific protein on cantilever surface (Right panel of Fig. 4(b)). These results suggest that our nanomechanical cantilever is very suitable tool for specific protein detection in mixed protein sample like real human blood.

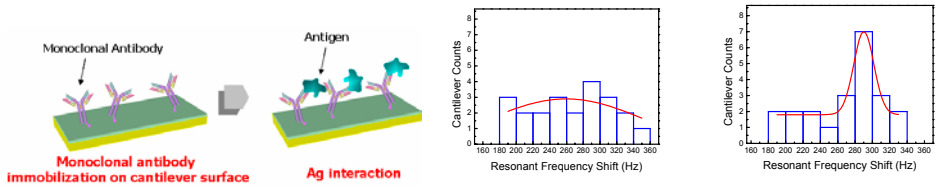

(a) (b) (c)

Figure 3. With established washing condition, coefficient of variance (CV) was measured. (a) immobilization and reaction step, resonant frequency variance in case of (b) conventional and (c) newly proposed washing method.

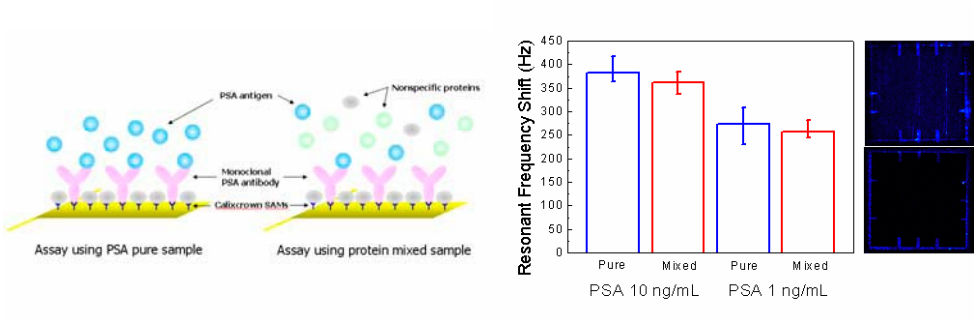

(a) (b)

Figure 4. Bioassay results of PSA using pure and mixed sample (a) schematics and (b) resonant frequency shift as a function of target protein concentration.

4. CONCLUSIONS

We demonstrated the label-free PSA detection in clinical range using the human serum like sample. Our results show that the dynamic microcantilever is one ot the most promising candidate for the sensitive label-free detection of specific proteins in the real human sample.

ACKNOWLEDGEMENTS

The authors are grateful for the financial support by Intelligent Microsystem Center sponsored by Korea Ministry of Science and Technology as a part of the 21st century's Frontier R&D Projects (Grant MS-01-133-01) and National Core Research Center for Nanomedical Technology sponsored by KOSEF (Grant R15-2004-024-00000-0).

REFERENCES

1. G. Wu, R.H. Datar, K.M. Hansen, T. Thundat, R.J. Cote, A. Majumdar, *Bioassay of prostate-specific antigen (PSA) using microcantilevers*, Nature Biotechnology, **19**, pp. 856-860, (2001).

PARALLEL MULTI-REAGENT STREAMS FOR A BIOASSAY ON SINGLE MAGNETIC PARTICLES IN CONTINUOUS FLOW

Sally Peyman, Alexander Iles and Nicole Pamme
University of Hull, Cottingham Road, Hull, HU6 7RX, UK

ABSTRACT

We demonstrate a method for bioanalysis on the surface of single magnetic particles in continuous flow. By generating multi-reagent streams inside a flow cell and deflecting bio-activated magnetic particles through the streams using free-flow magnetophoresis, all steps of a bioanalysis reaction can take place in continuous flow in one device, greatly reducing process time and allowing for analysis on a particle by particle basis.

Keywords: Microparticles, magnetophoresis, bioanalysis, continuous flow.

1. INTRODUCTION

Magnetic microparticles are being used increasingly as solid supports for analytical systems because of their high surface to volume ratio and their ease of manipulation using external magnets. The surfaces of these microparticles can be derivatised to exhibit a range of biological and chemical functionalities. In microfluidic applications, particles are commonly used in a 'trap and release' mechanism [1, 2] by which particles form a 'plug' inside a microchannel and different reagents are flushed over the surface of the particles consecutively (figure 1a). Once the assay has been performed, particles are released by removing the magnetic field. Despite advantages such as decreased reaction times and decreased reagent volumes commonly associated with miniaturisation, this method is essentially still a batch process and is relatively time consuming.

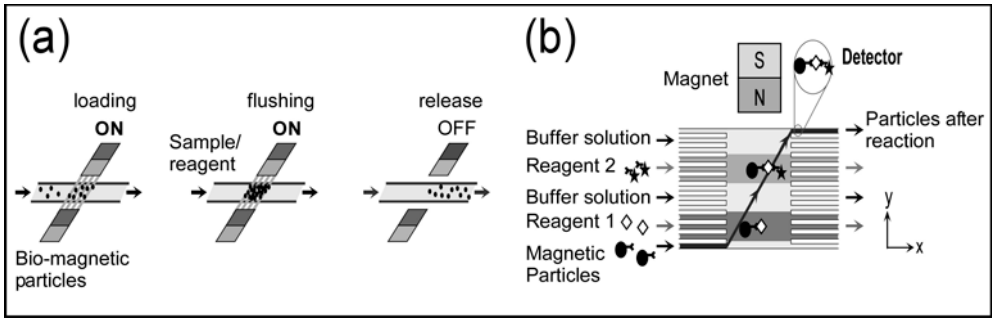

Figure 1.(a) Most bioreactions in microfluidic channels so far have involved the loading, flushing and release of magnetic particles. Particles are trapped in a magnetic field and reagents consecutively flushed over their surface [1]. (b) We propose a continuous flow, all-in-one device in which single functionalized magnetic particles are dragged through multiple reagent streams using free-flow magnetophoresis.

978-0-9798064-0-7/μTAS2007/$20©2007CBMS

Here we introduce a new concept for particle based bioreactions. Parallel reagent streams are generated across a flow cell; due to laminar flow regimes there is minimal mixing between the reagent streams. Magnetic particles can be introduced at one side of the flow cell and a magnetic field can be applied perpendicular to the direction of flow. Particles following the laminar flow in the x-direction will experience a magnetic force in the y-direction and will be deflected, a process referred to as free-flow magnetophoresis.[3, 4] Thus, the particles are pulled through the different flow streams and biochemical reactions can take place on their surface. This allows for continuous, fast analysis where washing and reaction steps are combined in one device (figure 1b).

2. EXPERIMENTAL

The microfluidic chip design is shown in figure 2a, consisting of four branched inlets (one particle inlet and three buffer inlets) with a rectangular reaction chamber 6 mm long and 3 mm wide and a single branched outlet. The chip was fabricated in glass (figure 2b) and etched to a depth of 20 μm. The magnetic field was generated across the reaction chamber using a permanent NdFeB magnet (4 x 5 x 4 mm^3) placed on top of the chip, to the side of the chamber. A suspension of streptavidin coated magnetic particles (2.8 μm, Dynabeads, Invtirogen), buffers and fluorescently labelled (FITC) biotin (Molecular Probes) were introduced to the chip using a four port Harvard syringe pump (Harvard Applications, USA).

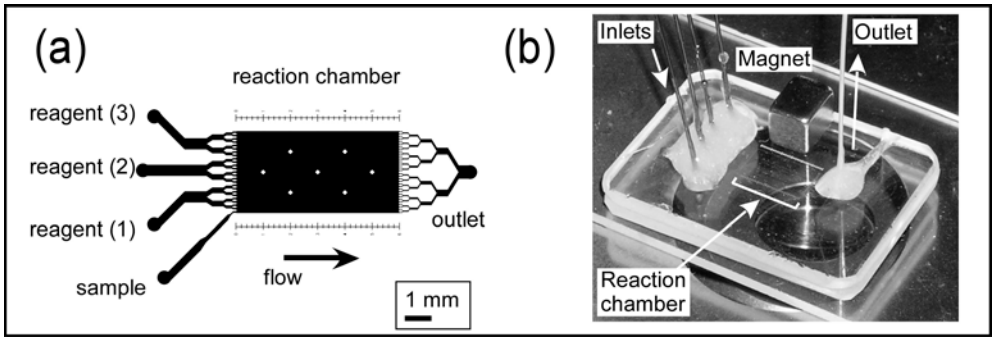

Figure 2. (a) Schematic of the chip design featuring one particle inlet, three buffer/reagent inlets and a branched outlet (b) A Photograph of the chip with NdFeB magnet and capillary tubing interface to a syringe pump.

3. RESULTS AND DISCUSSION

For proof of principle, a streptavidin – biotin assay was performed in the flow cell. The streptavidin coated magnetic particles were deflected through (1) a stream of buffer, (2) a stream of fluorescently labelled biotin, and (3) another buffer stream. As particles were deflected through the biotin-FITC stream, biotin became bound to the streptavidin on the particle surface. Therefore the particles were observed to fluoresce, as they passed through the biotin stream and they continued to fluoresce upon leaving the biotin stream (figure 3).

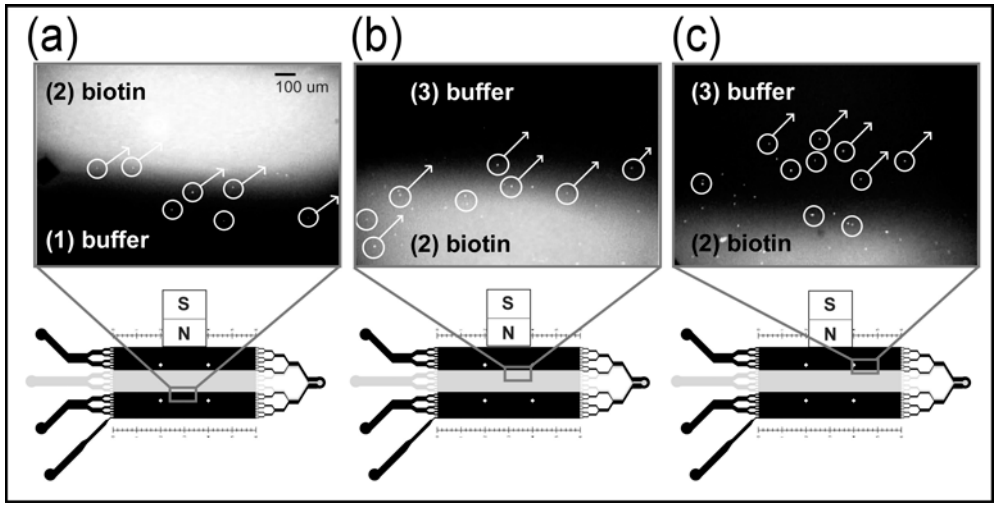

Figure 3. Streptavidin coated particles (a) before entering biotin-FITC stream, (b) passing through the biotin stream and (c) leaving the stream.

4. CONCLUSIONS

Combining multi-reagent streams and free-flow magnetophoresis on chip creates a new dynamic system in which all steps of an analysis can take place in one device in continuous flow. This greatly reduces process time by removing the need for tedious procedures associated with batch processes and allows for analysis on a particle by particle basis. The device could be further developed by increasing the number of reagent streams and by incorporating analyte isolation and pre-treatment steps. The streptavidin – biotin reaction described here was a first example, by varying the surface chemistry of the particles the system would be applicable to many different bioanalytical reactions such as immunoassays, DNA analysis and cell manipulation.

ACKNOWLEDGEMENTS

The author would like to thank the EPSRC for providing funding for the research.

REFERENCES

[1] N. Pamme. '*Magnetism and Microfluidics.*' Lab on a Chip, 6, 24 (2006).

[2] A. M. Gijs. *'Magnetic bead handling on-chip: New opportunities for analytical applications.'* Microfluidics and Nanofluidics, 1, 40, 22 (2004).

[3] N.Pamme, A. Manz. '*On chip free-flow magnetophoresis: Continuous flow separation of magnetic particles and agglomerates.*' Analytical Chemistry, 76, 7250 (2004).

[4] N. Pamme, C. Wilhelm. '*Continuous sorting of magnetic cells via on-chip free-flow magnetophoresis.*' Lab on a Chip, 6, 974 (2006).

RELIABLE CONTINUOUS-FLOW PCR FROM POLYMERASE KITS AND ON-CHIP CELL EXTRACTED DNA

Holger Becker, Richard Klemm and Claudia Gärtner
microfluidic ChipShop GmbH, Jena, Germany

ABSTRACT

This paper describes a complete system for chip-based continuous flow polymerase chain reaction (PCR) comprising several chip types, a control unit as well as recipes to conduct PCR from plasmids and cells with this system.

Keywords: PCR, polymer chip, continuous flow

1. INTRODUCTION

Although continuous-flow PCR has been shown for some time [1,2], it has not been such a widespread and commercial success as expected. Reasons for this can be found on the one hand in the lack of any readily available chip-based PCR system, which makes work on this subject always an engineering job. Secondly, commercial thermocycling systems and recipes have been long optimized and have shown to work reliably. We therefore have focussed our work to present a complete system which allows researchers to transfer the results obtained from conventional systems quickly to a chip-based PCR system.

2. THE CONTINUOUS-FLOW PCR SYSTEM: CHIP AND INSTRUMENT

Two chip-types, one with 15 cyles (i.e. channel meanders) and one with 41 cycles used for continuous-flow PCR can be seen in Fig. 1. They are made out of polycarbonate (PC), were manufactured by injection molding [3], and have the size of a microscopy slide. The channel dimensions are 500 µm width, 100 µm depth with an overall channel length of 818 mm for the 15 cycle chip. A third type contains 35 cycles. Additionally, a chip for shuttling the sample back and forth across the temperature zones was developed which allows the number of thermal cycles to be freely chosen. At the in- and output of the channel, connectors with an inner diameter 1 mm for the connection of tubing are integrated in the chip [4], allowing for easy interfacing.

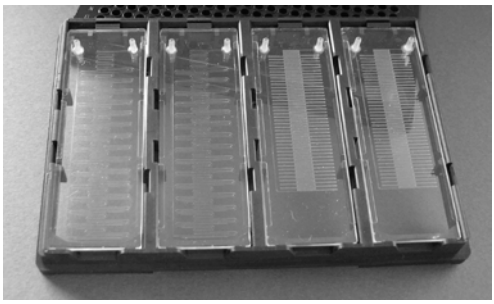

Fig. 1: PCR chips with 15 (left) and 41 (right) cycles in a wellplate-format holder.



Fig. 2: PCR instrument (thermal control unit).

978-0-9798064-0-7/µTAS2007/$20©2007CBMS

The thermal control unit (Fig 2) allows the simultaneous use of two PCR chips. Each chip is placed on three aluminium blocks which can be independently temperature controlled to ±1°C. Fixation of the chips is realized using a plastic microscopy slide holder. The chamber can be closed to minimize heat loss.

3. EXPERIMENTAL RESULTS

In order to obtain consistent results, the PC chip surfaces were coated with a blocking agent. We used bovine serum albumine (BSA) and plyethylene glycole (PEG). Figure 3 shows a concentration ramp between 0 and 1.5% PEG 8000 in a 10 µl sample volume. The results, an optimum in PCR yield at 0.75% PEG are consistent with literature results [5,6].

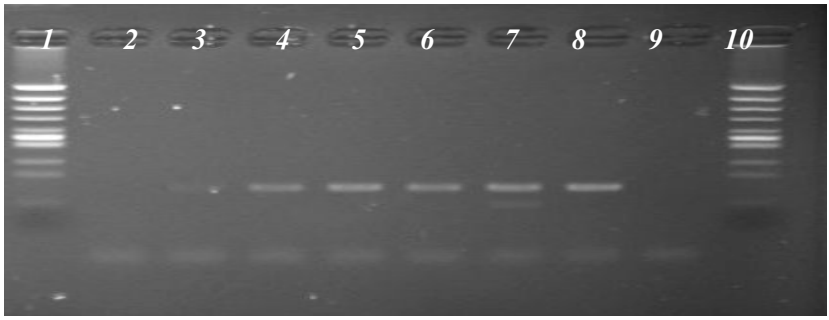

Fig. 3: Lanes 1 and 10 marker, lane 2 and 9 negative control, lane 3 0% PEG, lane 4 0.25%, lane 5 0.5%, lane 6 0.75%, lane 7 1%, lane 8 1.5%

Figure 4 shows the calibration of the system monitoring a 120 bp fragment using 9 DNA concentrations varying between 0.001 ng/µl and 0.2 ng/µl in a 10µl volume. At 0.1 ng/µl concentration, cycle times as low as 6.4 s/cycle could be recorded, resulting in an overall process time of 2.3 minutes for a 15 cycle chip. For this concentration, a PCR yield of 0.55 could be achieved, with yield improving to 0.62 for lower concentrations.

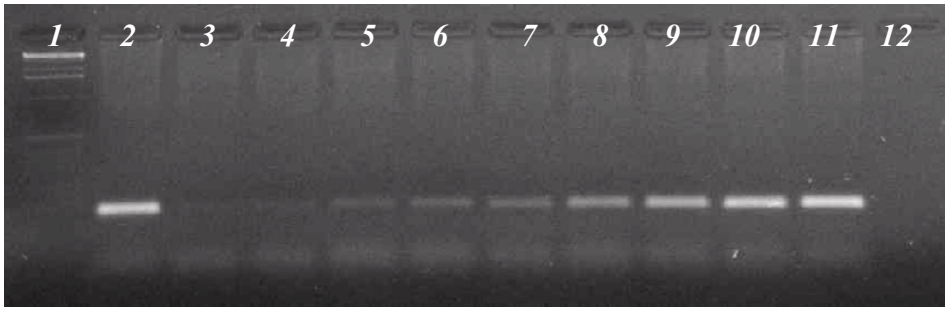

Fig 4: Lane 1: 6 µl Marker (GIBCO 1kb ladder), Lane 2: desktop cycler with 0,1 ng/µl DNA, Lane 3: sample with 0,001 ng/µl DNA, Lane 4: 0,0025 ng/µl DNA, Lane 5: 0,005 ng/µl DNA, Lane 6: 0,0075 ng/µl DNA, Lane 7: 0,01 ng/µl DNA, Lane 8: 0,025 ng/µl DNA, Lane 9: 0,05 ng/µl DNA, Lane 10: 0,1 ng/µl DNA, Lane 11: 0,2 ng/µl DNA**.**

Figure 5 shows a comparison of PCR results from different commercial polymerase kits with a conventional thermocycler at comparable fluorescence intensities for the products.

PCR running times for the chip were 14 minutes for 30 cycles compared to 59 minutes for the benchtop instrument.

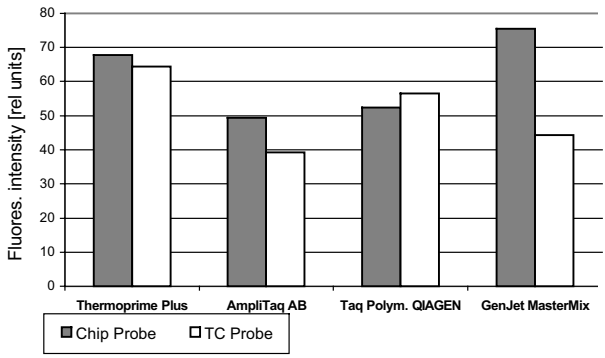

Fig. 5: Comparison Chip-PCR vs. benchtop cycler

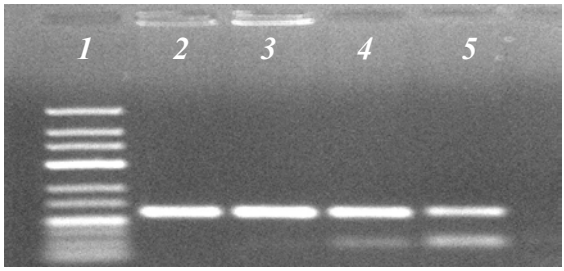

Fig. 6: PCR from E.coli (lanes 2 and 3) and SiHa cells (lanes 4 and 5), marker lane 1, DNA 120 bp GAPDH.

Figure 6 shows results for a 120 bp glyceraldehyde-3-phosphate dehydrogenase (GAPDH) DNA fragment extracted from E.coli and human SiHa cells. In this experiment, the PCR solution passed the chip twice, i.e. the PCR was performed with 30 cycles. Cell concentration was 10^7 and 10^8 cells/µl in case of the E.coli and 300 and 150 cells/µl for the SiHa cells respectively. The saturated signal from the E.coli cells indicates the potential to go to significantly lower cell concentrations in further experiments. Cells were thermally lysed, current experiments work with an improved chip design containing reservoirs and microchannels for on-chip chemical lysis of the cells.

4. CONCLUSIONS

We have presented a complete chip-based continuous-flow PCR system comprising a set of different chips, a thermal control unit and protocols to run the system with plasmid as well as cell-extracted DNA.

REFERENCES

[1] Köhler, J. M.; Dillner, U.; Mokansky, A.; Poser, S.; Schulz, T.. Proc. 2nd Int. Conf. Microreaction Technology, New Orleans, LA, 1998, 241 – 247. German Patent DE000004435107, 30.09.1994 .
[2] Kopp, M. U.; De Mello, A. J.; Manz, A., Science, 1998, 1046 – 1048.
[3] Becker, H., Locascio, L.E., Talanta 56 (2), 2002, 267-287.
[4] Gärtner, C., Becker, H., Anton, B., Rötting, O., Proc. "Microfluidics, BioMEMS, and Medical Microsystems II", San Jose, SPIE Vol. 5345, 2003, 159-162.
[5] Yang, J. et al., Lab Chip, 2002, 2, 179 – 187.
[6] Panaro NJ. et al., Biomed. Microdevices, 6(1), 2004, 75-80.

3D MICROFLUIDIC CHIP FOR MEMBRANE PROTEIN ANALYSIS

Hiroaki Suzuki[1] and Shoji Takeuchi[1,2]

[1]Institute of Industrial Science, The University of Tokyo, Japan and
[2]PRESTO, JST, Japan

ABSTRACT

We have developed a 3D microfluidic chip for membrane protein analysis, in which artificial planar lipid bilayers are formed for screening of ion channel proteins. The chip was made by stereolithography, enabling the integration of built-in 3D channel system for protein injection. It allowed gentle introduction of solution, minimizing mechanical perturbation on the lipid membrane. Integrated channels were also used for metering the injection volume. This device will provide the low-cost and user-friendly platform for membrane protein analysis.

Keywords: Stereolithography, Planar Lipid Bilayer, Membrane Protein

1. INTRODUCTION

In many biochemical assays, *in situ* injection or exchange of solution at an exact amount is required. In such cases, gentle injection is often necessary to minimize mechanical force to avoid alteration in the experimental condition. For example, in motor protein assay under a microscopy, shear force generated by injection stream may affect the motion of proteins [1]. Another example is the bilayer lipid membrane (BLM) experiment, in which the proteoliposomes are added into the bath solution to incorporate proteins into the pre-formed planar bilayer [2,3]. Since the bilayer membrane is extremely fragile (being 5-10 nm in thickness), direct injection by conventional pipetting causes large mechanical shock that may break the membrane. Use of microfludic channel for sample introduction should realize the gentle fluidic manipulation, but fabrication of complicated channel network is laborious and time-consuming. Here we employed the stereolithography system to fabricate 3D microfulidic chip for our lipid bilayer experiments.

2. DESIGN AND PROCEDURE

We fabricated a 3D microfluidic chip by stereolithography (Perfactory®, EnvisionTech, Germany). In this system, 3D CAD model data is translated into a physical model made of photo-curable resin (R11, a resin mainly consists of methacrylate, EnvitionTech, Germany), allowing one-step fabrication of complicated fluidic channel networks. The smallest pixel size of solidification in x(y) and z direction is 16 μm and 25 μm, respectively. The fabricated device (Fig. 1) has six upper chambers (4 mm in both diameter and depth), two straight bottom channels, and 80 μm aperture at the bottom of each upper chamber. Planar lipid bilayers were formed by firstly filling the upper chambers with buffer, and then sequentially introducing lipid solution (10 mg phosphatidylcoline in 1 ml n-decane) and buffer into the bottom channels [3]. A lipid bilayer was formed across the aperture successfully (Fig. 2a). Unfortunately, diameter and height of apertures were not uniform with the present resolution of our stereolithography (the absolute error in fabricated size was up to 30 μm), resulting in poor reproducibility in bilayer formation.

978-0-9798064-0-7/μTAS2007/$20©2007CBMS

Recently, we found that the lipid membrane formed in smaller apertures (20-50 μm in diameter) opened in a thin Parylene film (10-20 μm in thickness) is highly reproducible and stable [4]. Thus, we also fabricated a hybrid device which has apertures opened in Parylene sheet (Fig. 2b), by glueing perforated Parylene sheet between the 3D microfluidic chips equipped with sample injection channels (design not shown).

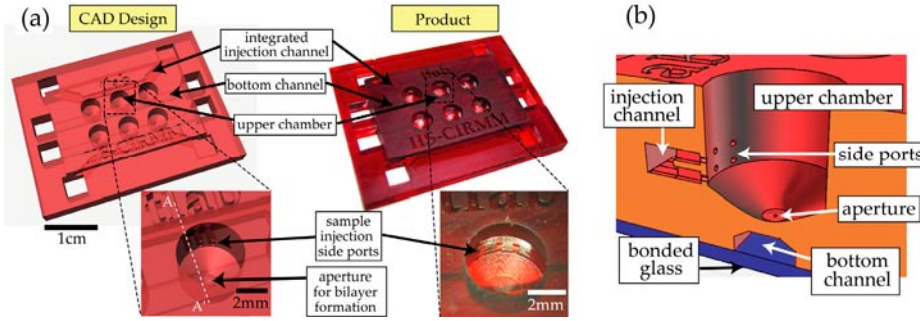

Figure 1 (a) CAD design and product for lipid bilayer chip fabricated by stereolithography. (b) Cross section along the line A-A'. Built-in injection channel leads sample solution into the main chamber.

3. RESULTS

3.1 Injection of Protein Solution: In our previous devices [3], which was made of PMMA plastic, proteins and reagents were directly added to the upper chamber by a pipette. Thus, the planar bilayer broke occasionally due to the mechanical shock. Here the built-in injection channel was connected to the main chamber through side ports (Fig. 1b). As demonstration, fluorescent solution (1mM calcein) was introduced into the side channel. It gently flowed into the upper chamber and the concentration became uniform within 10 seconds (Fig. 3). In the Parylene hybrid device, solution containing pore-forming peptide (gramicidin, Sigma-Aldrich Co.) was introduced into the injection channel after forming a lipid bilayer. Approximately after 30 minutes, ion channel current across the membrane that corresponds to the opening and closing of gramicidin channel was observed by electric measurement (Fig. 2c). To realize stable bilayer formation in the all-stereolithography device, it is necessary to further improve the spatial resolution in stereolithography process.

3.2 Metering of Injection Volume: We also utilized the injection channel for metering of small sample volume (Fig. 4) [5]. Before forming bilayers, protein solution was introduced into the injection channel, also filling the side channels completely. Next, main volume in the injection channel was flushed by an air stream, remaining small metered volume in side channels (0.4 μL in total). Then oil was introduced to prevent backward flow. Finally, metered solution diffused into the main chamber when it was filled by buffer. We confirmed the metered volume was consistent with theoretical amount by measuring fluorescent concentration in the main chamber using a fluorospectrometer.

4. CONCLUSIONS

In our device, all procedures, including lipid bilayer formation, sample metering, and injection, were performed by simple manual pipetting, and did not require any laborious pumping devices. We believe it is important to develop simple and user-friendly chip technology to establish standard membrane protein assay platform in biology laboratories.

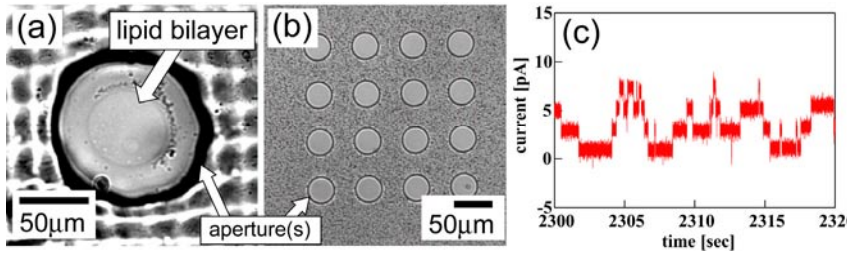

Figure 2 (a) Planar lipid bilayer formed over an aperture in the all stereolithography device. (b) Well-defined apertures (ϕ= 30 µm) opened in a Parylene film. (c) Channel current measured in a Parylene hybrid device at 100 mV voltage clamp.

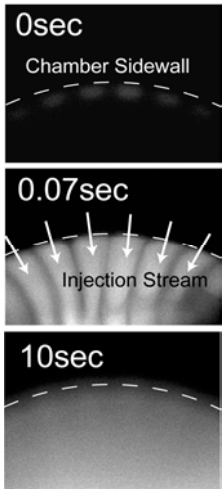

Figure 3. Demonstration of sample injection. After filling the main chamber with buffer, calcein solution was introduced into the injection channel. It spontaneously flowed into the main chamber.

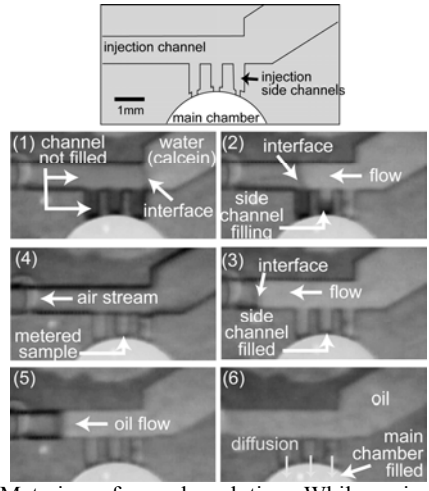

Figure 4. Metering of sample solution. While main chamber is empty, sample solution (calcein) is first introduced into the injection channel (1-3). Side channels were filled completely. After the injection channel is flushed (4) and filled with oil (5), small volume (0.4µL) of sample solution remains in the side channel. When the upper chamber was filled with buffer, metered sample diffused into the upper chamber (6). Images inside the device were visualized by transmitted light.

REFERENCES:

[1] (a) R. Yokokawa et al., "Hybrid nanotransport system by Biomolecular Linear Motors," *J. Microelectromechanical Systems*, **13(4)**, 497 (2004). (b) Y. Hirono-Hara et al., "Pause and Rotation of F_1-ATPase during catalysis," *Proc. Nat. Acad. Sci.*, **98(24)**, 13649 (2001).

[2] C. Miller Ed., "Ion Channel Reconstitution," Plenum Press (1986).

[3] (a) H. Suzuki et al., "Simultaneous reconstitution of multiple planar lipid bilayers," *µTAS 2005*, 1300, (2005). (b) H. Suzuki et al., "Highly reproducible method for planar lipid bilayer reconstituted using a micro fluidic chip," *Langmuir*, **22**, 1937 (2006). (c) H. Suzuki et al., "Electrophysiological recordings of single ion channels in planar lipid bilayers using a polymethyl methacrylate microfluidic chip," *Biosens. Bioelect.*, 22(6), 1111 (2007).

[4] B. L. Pioufle et al., "Highly parallelized lipid bilayers array for ion channel recording," *µTAS* 2007.

[5] (a) M. Yamada and M. Seki, "Nanoliter-sized liquid dispenser array for multiple biochemical analysis in microfluidic device," *Anal. Chem.*, 76, 895 (2004). (b) E. Shigematsu et al., "Development of functional micro dispenser array for producing multiple reaction conditions," *Proc. µTAS*, 1542 (2005).

CELLULAR STUDIES VIA DIELECTROPHORESIS-BASED CELLULAR MICROARRAY CHIP

L.C. Hsiung[1], C.L. Chiu[2], C.H. Yang[1], A.M. Wo*[1], H. Lee[2], D.S. Jong[3], C.H. Chiu[3], J.Y. Cheng[4], M.C. Ho[5], C.Y. Hsu[2] and M.C. Hsu[3]

[1]Institute of Applied Mechanics, [2]Department of Life Science, [3]Department of Animal Science and Technology, National Taiwan University, Taipei, Taiwan

[4]Research Center for Applied Sciences, Academia Sinica, Taipei, Taiwan

[5]Department of Surgery, National Taiwan University Hospital, Taipei, Taiwan

ABSTRACT

This paper reports a dielectrophoresis (DEP)-based cellular microarray platform with embedded concentration gradient generator for cellular studies. Positive DEP was applied to pattern cells on collagen-coated substrate. Results show the approach requires fewer cells, compared to conventional approaches, to be patterned in microarray within minutes and with good uniformity. Further, the embedded concentration gradient generator provides concentrations with high repeatability. High cell viability is obtained after 24 hours incubation. The cellular microarray would allow batch testing with different drug/reagent concentrations in a single chip for high-throughput cellular studies.

Keywords: Celluar microarray, dielectrophoresis, concentration gradient

1. INTRODUCTION

Dielectrophoresis-based chips have been widely used for cell manipulations. Taff and Voldman [1] used DEP-based trap to sort single cells. Ho et al. [2] demonstrated a biomimetic patterning of dual types of cell via DEP. Moreover, Albrecht et al. [3] constructed three-dimensional chondrocyte clusters using a DEP-based chip to discover the cluster size effect on cellular biosynthesis. In contrast, this paper presents a DEP-based cellular microarray chip with embedded concentration gradient generator for high-throughput cellular studies (Fig.1).

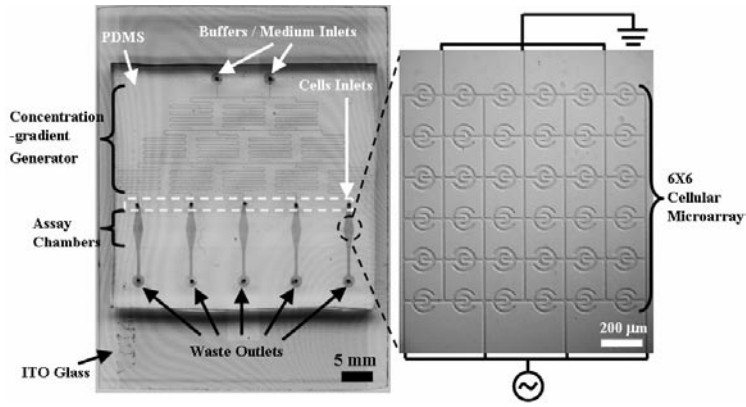

Figure 1. The dielectrophoretic (DEP)-based cellular microarray chip with embedded concentration gradient generator.

978-0-9798064-0-7/µTAS2007/$20©2007CBMS

2. EXPERIMENTAL

The chip microfabrication was as follow. Photoresist was micropatterned on an ITO film (Fig. 2a), and the film was micromachined using argon plasma etching (Fig. 2b). Photoresist was then stripped off in acetone (Fig. 2c). Again, photoresist was used in order to micropattern collagen later (Fig. 2d). Oxygen plasma was applied to bond the PDMS concentration gradient generator to the micromachined ITO glass (Fig. 2e). Holes were punched in the generator as inlets and outlets. After DI water flush, the chip was incubated in collagen I (10 μg/mL, 37°C, 1hour) (Fig. 2f). Photoresist was removed by ultrasonic agitation in ethanol, may reduce the possible denaturation of collagen comparing to acetone, for 10 minutes (Fig. 2g). The chip was flushed in DI water followed by nitrogen dry.

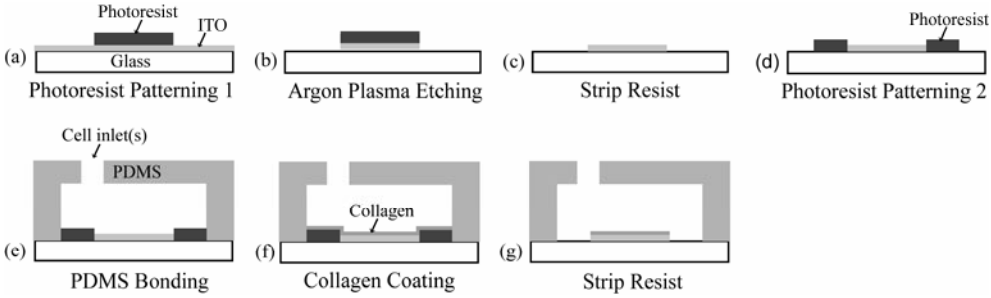

Figure 2. The microfabrication process.

The process for DEP cell patterning (DCP) [2-3] was as follow. First, the DCP buffer (10 mM HEPES, 55 mM D-glucose, 221 mM Sucrose, 1% penicillin/streptomycin; pH 7.0, 300 Osm, 228 μS/cm) was meticulously prepared to ensure long-term cell viability. Cells (HepG2, a hepatocellular carcinoma cell line) suspended in the buffer were successively injected into the chambers. Then AC signal (5 Vpp, 5 MHz) was applied to the electrodes to pattern cells. After the flow of the cell suspension became steady, Ca^{2+}-containing buffer (1.8 mM $CaCl_2$, 420 μS/cm) was injected to sweep away the off-electrode cells, and to promote cell adhesion on the micropatterned collagen. When the sweeping flow became steady, the AC signal was removed. After cells adhered to the collagen, the buffers were replaced with Dulbecco's modified Eagle's medium with 10% fetal bovine serum and 1% penicillin/streptomycin. The chip with the patterned cells was then incubated at 37°C.

3. RESULTS AND DISCUSSION

Results show: (1) the embedded concentration gradient generator provided concentrations with high repeatability which may ensure accurate drug/reagent concentrations (Fig. 3), (2) by DCP, HepG2 were patterned within minutes with good uniformity (Fig. 4a), while hours would be required for microarrayer approaches, (3) most HepG2 were stained positively with calcein AM (the fluorescent stain for live cells) after 24 hours incubation (Fig. 4b) (for some drug screenings, 24 hours is sufficient [4]). The high cell viability demonstrates the biocompatibility of the chip for high-throughput cellular studies.

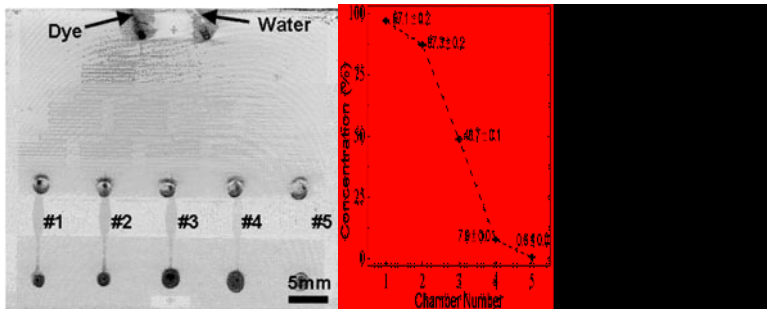

Figure 3. The PDMS concentration gradient generator. Left: Top-view of the generator. Two streams entered from the top, through the channels and the chambers, and exited the five outlets. Right: Measured concentration results showed concentrations at the outlets with high repeatability (data were mean ± standard deviation, n=3).

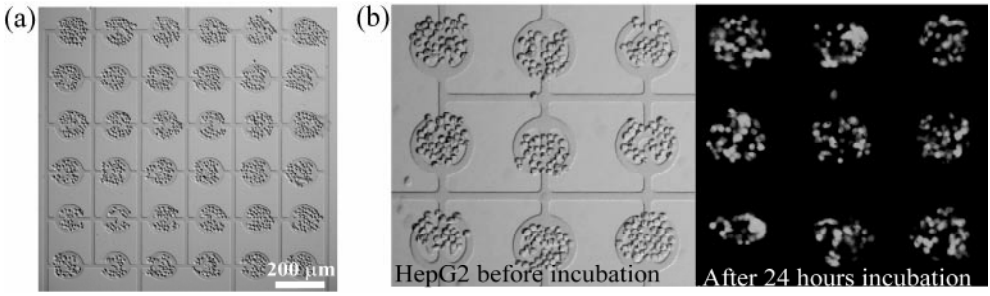

Figure 4. The cellular microarray. (a) By using DEP cell patterning (DCP), HepG2 were patterned as cellular microarray within minutes with good uniformity (cell seeding density was 5 million cells/ml; the applied voltage for DCP was 5 Vpp, 5 MHz). (b) The cell viability of HepG2 at 24 hours. After 24 hours incubation, most HepG2 were stained positively with calcein AM (the fluorescent stain for live cells).

4. CONCLUSIONS

The paper reports a DEP-based cellular microarray chip with embedded concentration gradient generator for high-throughput cellular studies. Results suggest the cellular microarray would allow not only a batch testing with different drug/reagent concentrations in a single chip, but also an *in vitro* assessment to determine efficacy of a particular chemotherapeutic treatment.

REFERENCES

[1] B. M. Taff, J. Voldman, *A scalable addressable positive-dielectrophoretic cell-sorting array*, Analytical Chemistry, Vol. 77, pp. 7976-7983, (2005).

[2] C. T. Ho, et al., *Rapid heterogeneous liver-cell on-chip patterning via the enhanced field-induced dielectrophoresis trap*, Lab on a Chip, Vol. 6, pp. 724-734, (2006).

[3] D. R. Albrecht, et al., *Probing the role of multicellular organization in three-dimensional microenvironments*, Nature Methods, Vol. 3, 369-375, (2006).

[4] L. Barraud, et al., *Increase of doxorubicin sensitive by doxorubicin-loading into nanoparticles for hepatocellular carcinoma cells in vitro and in vivo*, Journal of Hepatology, Vol. 42, 736, (2005).

HIGH-THROUGHPUT MICROFLUIDIC MICROARRAY HYBRIDIZATIONS CARRIED OUT IN SPIRAL CHANNELS ON A COMPACT DISC

Hong Chen[a], Paul C. H. Li[a]*, Hua-Zhong Yu[a], M. Parameswaran[b], Nathan Yoganathan[c]

*a. Department of Chemistry, b. School of Engineering, Simon Fraser University, Burnaby, BC, Canada; c. Med BioGene Inc., Vancouver, BC, Canada, *paulli@sfu.ca*

ABSTRACT

A high throughput microfluidic microarray assay (MMA) was developed through a two-step assembly process. First, a CD-like glass wafer was sealed with a PDMS chip with clockwise spiral channels to print probe lines onto the glass CD surface. Second, the glass wafer was sealed with another PDMS chip with anticlockwise spiral channels to allow the sample to hybridize with the printed probe lines. Using the MMA, 384 assays have been performed on CD at one time, using only 1-μL of each of the 96 samples. Here the hybridizations have been successfully achieved by using both complementary oligonucleotides and cRNA samples.

Keyword: Microfluidic microarray, multi-sample nucleic acid hybridization, spiral microchannel, dynamic DNA/RNA hybridization

1. INTRODUCTION

Currently, microarray chips are widely used for surface-based reactions, notably DNA hybridizations. But in the use of microarray chips, only one sample can be applied on a microarray slide at one time. A microfluidic microarray (MMA) method has been reported, in which DNA hybridizations of 96 samples were performed to 96 probes simultaneously on one CD-like glass wafer [1, 2]. So, the MMA offers the multi-sample advantage, especially when only a limited number of probes is needed, as in some biotechnological applications. In this paper, the next-generation MMA was reported in which 384 x 384 DNA/RNA hybridizations (96 samples in 4-replicate) were achieved simultaneously on 384 probes (96 distinct probes in 4-replicate).

2. EXPERIMENTAL

The MMA system consists of 2 polydimethylsiloxane (PDMS) channel plates, and a third piece of aldehyde-functionalized 4" glass wafer served as the microarray substrate. The 2 channel plates both have 384 spiral channels, of 50 μm width and 25 μm depth, with one in

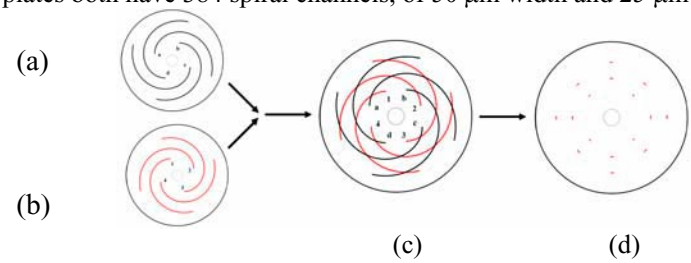

Fig. 1. The double-spiral MMA method. (a) four of 384 spiral channels (clockwise sense), (b) four of 384 spiral channels (anti-clockwise sense), c) anti-clockwise spiral channels aligned with clockwise spiral probe lines, (d) 16 spots of the 384×384 microarray.

978-0-9798064-0-7/μTAS2007/$20©2007CBMS

anticlockwise-sense (Fig. 1). Hence, this new MMA system is called the double-spiral form, as distinct from the radial-spiral one in previous reports [1, 2]. First, aminated DNA probes were introduced into the inlet reservoirs near the centre of plate 1, with the reservoirs arranged in groups of 8 for easy liquid dispensing (Fig. 2). The liquids



(a) (b)

Fig. 2. Images of the PDMS spiral channel plate (anticlockwise) containing 384 channels. (a) before filling blue food dye, (b) after filling blue food dye into 4 groups of a total of 16 spiral channels. The inset shows the entry of the dye from one inlet reservoir into 4 spiral channels in the anticlockwise sense.

flowed from one reservoir into 4 spiral channels to near the perimeter using centrifugal pumping. After chemical reduction, the probes were immobilized onto the surface of aldehyde glass wafer. The channel plate 1 was peeled off, and the glass wafer was assembled with channel plate 2, in which the sample solutions flowed through the second set of spiral channels, intersected and hybridized with the immobilized probe lines.

3. RESULTS AND DISCUSSION

384×384 hybridizations were achieved in a glass wafer (Fig 3). The group of 16 fluorescent patches is the hybridization results of 4 adjacent spiral channels to the 4 adjacent spiral probe lines. We use a set of 10 aminated oligonucleotide probes (ALN1 to

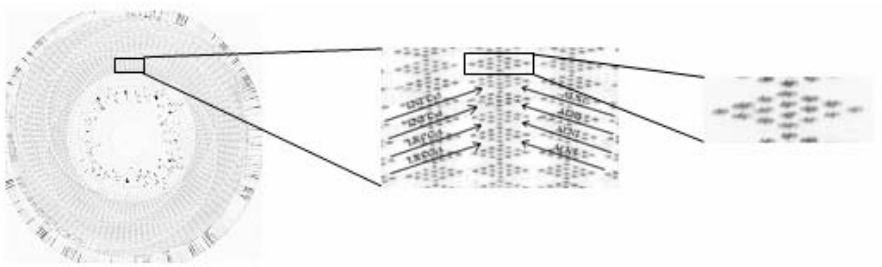

Fig. 3. The 384×384 hybridizations performed on a 4-inch glass CD. Two aminated oligo DNA (ALN1 and ALN5) were used as probes, and their complementary oligo DNA labeled with Cy5 (LN1'Cy5 and LN5'Cy5) were used as samples.

ALN10), e.g. the sequence of ALN1 is amine-CTGTATTGAGTTGTATCGTGTGGTGTA TTT and that of ALN5 is amine-GTTGTGGCCAAGTACAAATTATGGTATCTA. Different concentrations of complementary DNA (Cy5-labeled, in 1×SSC+0.15% SDS) were hybridized with the immobilized ALN (1-10) probes, showing the intensity of the hybridization spots (Fig 4a). Different concentrations of complementary RNA (biotinylated,

in 6×SSC+0.15% SDS) were also tested. Hybridizations were detected by the reaction with Cy5-labeled streptavidin. Different concentrations of cRNA prepared from tissue samples, and biotin-labeled, were also tested (Fig 4b), showing the capability of the MMA in testing actual tissue sample RNAs.

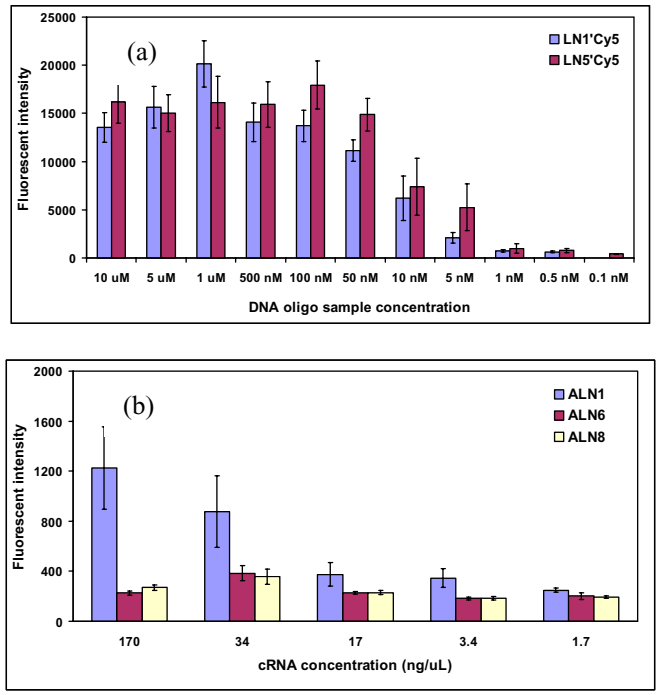

Fig. 4. Fluorescent signals of nucleic acid hybridization to oligonucleotide probe lines printed on the MMA (a) versus different concentrations of LN1'Cy5 and LN5'Cy5 (50 μM of ALN1 and ALN5). (a) versus different concentrations of biotinylated cRNA (100 μM of ALN1, ALN6 and ALN8).

5. CONCLUSIONS

A high throughput MMA method has been presented for DNA/RNA hybridizations. The advantages offered by the intersection approach, such as flexibility in probe lines construction, multi-sample capability, and fast hybridization rate, have been demonstrated because of the ease in liquid delivery offered by centrifugal pumping. The MMA method provided a useful tool to accelerate microarray analysis.

ACKNOWLEDGEMENTS

The authors gratefully acknowledge the financial support from the Idea-to-Innovation Program of NSERC of Canada, Lin Wang and Wa Lok Chou for their assistance.

REFERENCES

[1] X. Y. Peng, et al. MicroTAS'05, 2005, 823-825.
[2] X.Y. Peng, et al. Sens. Actuators B, 2007, in press.

MICRO XEROGRAPHY USING SURFACE ACOUSTIC WAVE ATOMIZER AND ELECTROSTATIC DEPOSITION

Jungmyoung Ju[1], Yutaka Yamagata[2,*], Toshiro Higuchi[1], Kozo Inoue[3] and Hitoshi Ohmori[2]

[1]The University of Tokyo, 7-3-1 Hongo Bunkyo-ku, Tokyo, Japan
[2]Materials Fabrication Laboratory, RIKEN (The Institute of Physical and Chemical Research), 2-1 Hirosawa Wako-shi, Saitama, Japan
[3]Fuence Co., Ltd., 1-11-2, 703 Hiroo Shibuya-ku, Tokyo, Japan
** yamagata@postman.riken.go.jp*

ABSTRACT

This paper represent a new dry direct patterning method, which process is composed of two steps: The first is patterning of the electric charges on the substrate using a corona discharge; The second is deposition of the dried nano-particles on the target place using a surface acoustic wave atomizer and electrostatic deposition (SAW-ED) method. A distinctive merit of proposed method is that it is possible to deposit on the non-conductive substrate, such as glass, plastic or PDMS, which are widely used in the fields of micro total analysis systems.

Keywords: Nano particle, Corona discharge, Surface Acoustic Wave (SAW) Atomizer, Electrostatic deposition

1. INTRODUCTION

In the fields of protein chips, biosensors and other deposition applications, dry patterning methods, such as electrospray deposition (ESD) [1] and surface acoustic wave and electrostatic deposition (SAW-ED) [2] showed good performances in terms of patterning resolution, uniformity and so on. The reason of the high resolution is that these methods are based on the deposition of dry nano particles with electrostatic force. Thus, compared with other wet deposition methods, non uniform deposition caused by coffee-stain effects [3] does not occur.

However, these methods require conductive substrates, such as Indium Tin Oxide (ITO) or metal films for the generation of attracting force between charged particles and conductive substrate. In addition, in the ESD method, basically it is hard to spray highly conductive solutions such as buffer solution for protein. Thus, these dry direct processes are limited by the conductivity of samples or target substrates. To cope with these problems, SAW-ED combined with corona discharge is newly proposed and tested.

2. OPERATION PRINCIPLE

Concepts of proposed method are as follows. First, positive charges are patterned on the non-conductive substrate using a stencil mask. After that, this pre-charged substrate is transferred to the SAW-ED process. In the SAW-ED process, a liquid sample is charged by high voltage and atomized by surface acoustic wave (SAW) atomizer as shown in figure 1 and 2. Then, atomized droplets are quickly dried up to nano-sized particles. Finally, negative-charged nano particles are deposited selectively on the pre-charged areas.

978-0-9798064-0-7/μTAS2007/$20©2007CBMS

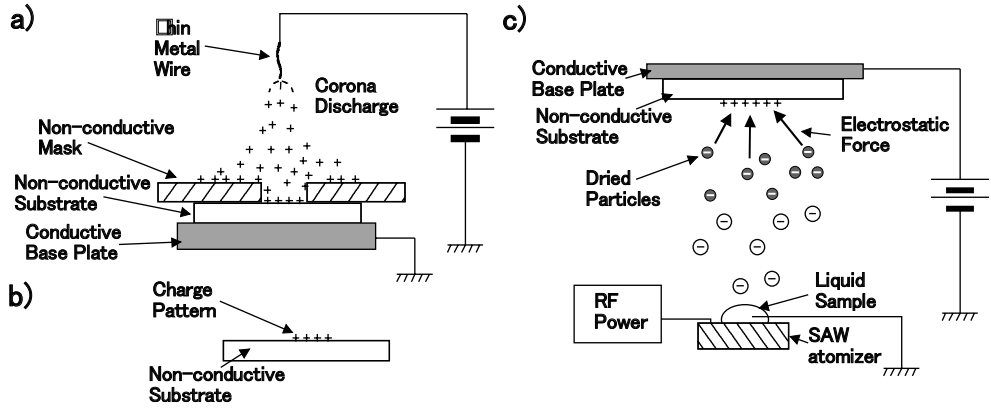

Figure 1 mechanism of proposed method, a) charge pattern generation by corona discharge (high voltage: 4.5 kV, distance: 3 cm, b) substrate with charge pattern, c) SAW-ED (high voltage: 5 kV, distance; 15 cm)

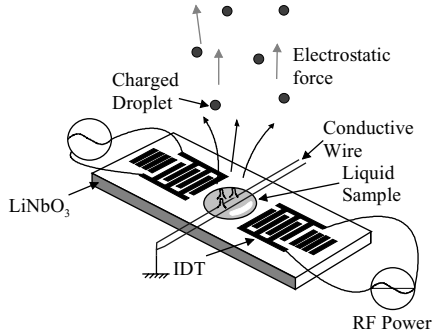

Figure 2 Experimental setup of SAW atomizer (10 MHz)

2. EXPERIMENTAL

To generate charge pattern by corona discharge, a high voltage of 4.5 kV was applied between thin metal wire and conductive base plate in a distance of 3-4 cm. Then, 5 µl of 5 mg/ml Bovine Serum Albumin (BSA) solution was deposited on the charge-patterned substrate by SAW-ED process. The SAW atomizer was made on a 128° Y-cut X-propagation $LiNbO_3$ and is operated at approximately 10 MHz [4]. A high voltage of 5 kV is applied between conductive base plate and thin conductive wires placed just above the atomizer. The distance between atomizer and conductive base plate is approximately 15 cm. Corona discharge is applied for 10 minutes and atomization time was 20 seconds.

4. RESULTS

Figure 3 shows an example of microarray formation by using BSA and toner from laser printer. Patterns ranged from 100 to 300 µm in diameter, are successfully deposited on the non-conductive substrate. Figure 4 shows a micro-channel used as a deposition substrate, which is made from polycarbonate. Figure 5 show images of patterned BSA particles on the micro channel. Approximately 200 µm width lines are deposited successfully.

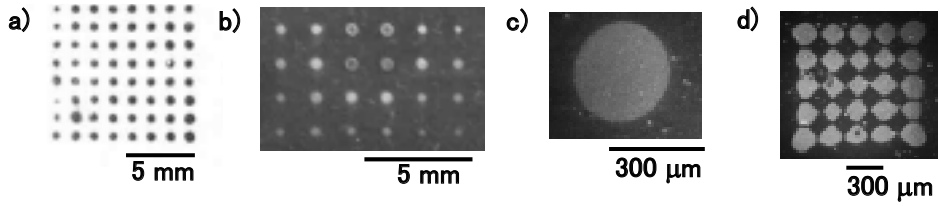

Figure 3 Micro arrays on the polyethylene film, a) toner image, b) protein array, c) protein layer, d) protein array (a, b, c: glass mask, d: SU-8 mask, aperture diameter 300 and 100 μm respectively, Toner patterned by immersion, BSA by SAW-ED.)

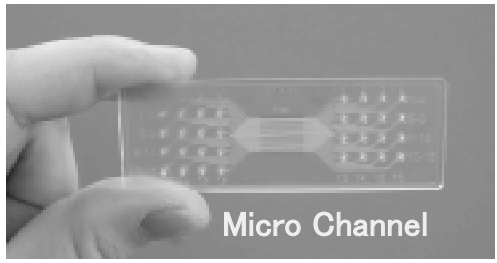

Figure 4 Micro-channel used as deposition substrate (material: polycarbonate)

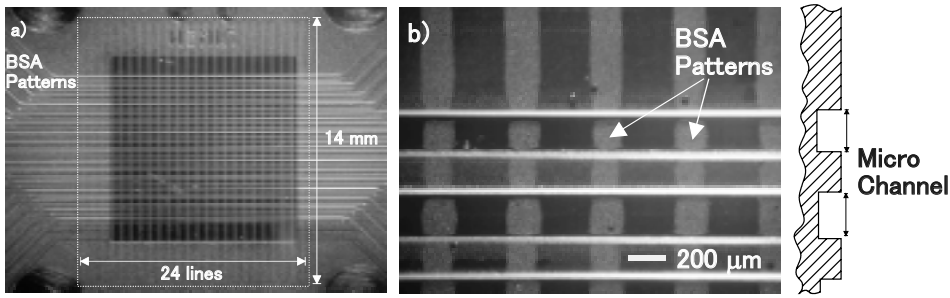

Figure 5 Patterned BSA on the micro channel made from polycarbonate (a) entire images of the deposited lines, (b) enlarged picture

5. CONCLUSION

For the purpose of dry-direct patterning on the non-conductive substrate, new method combined with corona discharge and SAW-ED is proposed and tested. Based on the experimental results, proposed new methods may be useful in surface treatment or immobilization of bioactive spots inside micro channel or on substrates.

REFERENCES

[1] V. N. Morozov, T. Y. Morozova, Anal. Chem. 71, pp 1413-1420 (1999)
[2] J. W. Kim, Y. Yamagata, M. Takasaki, B. H. Lee, H. Ohmori, T. Higuchi, Sensors and Actuators B 107, pp 535-545 (2005)
[3] R. D. Deegan, O. Bakajin, T. F. Dupont, G. Huber, S. R. Nagel, T. A. Witten, Nature, Vol. 389, October (1997)
[4] J. Ju, Y. Yamagata, T. Higuchi, K. Inoue, H. Ohmori, Transducer`07, Vol. 1, pp. 1279-1282 (2007)

MICROFLUIDIC STAND-ALONE DEVICE FOR THE CALIBRATION OF BRAIN-IMPLANTABLE BIOSENSOR MICROPROBES

Olivier Frey[1], Floris H. Falke[2], Peter D. van der Wal[1], Nico F. de Rooij[1] and Milena Koudelka-Hep[1]

[1]*Institute of Microtechnology, University of Neuchâtel, Switzerland*
[2]*University of Twente, The Netherlands*

ABSTRACT

A cartridge-based stand-alone device for three-point calibration and determination of the response time of microprobe-type biosensors is presented. The disposable cartridge consists of an electrochemical microcell – where the needle-shaped microprobe is reversibly inserted – connected to a microfluidic system comprising reservoirs with preloaded samples and integrated pneumatic pumps. Rapid and controlled concentration changes (<1 s) are achieved by consecutive shuttling of the samples into the microcell. Due to the optimized design of the integrated pumps, actuation can be performed simply by using a finger and thus allowing free-standing operation independent of laboratory equipment.

Keywords: biosensor, integrated micropump, fluidic handling, PDMS

1. INTRODUCTION

There is large interest in the in-vivo monitoring of concentration changes of neurotransmitters in real-time for understanding the functioning of the brain. However pre and post implantation calibration of the microprobe-type biosensor are prerequisite steps to ensure reliable in-vivo recordings [1]. Figure 1 shows a SEM picture of the developed silicon microprobe comprising two recessed platinum electrodes (50x150 μm^2, one coated with a membrane) to monitor extra-cellular concentrations of the neurotransmitter choline in brain tissue. The functional principle of the biosensor is the amperometric detection of peroxide [1] using the enzyme choline oxidase immobilized on the platinum surface (right electrode).

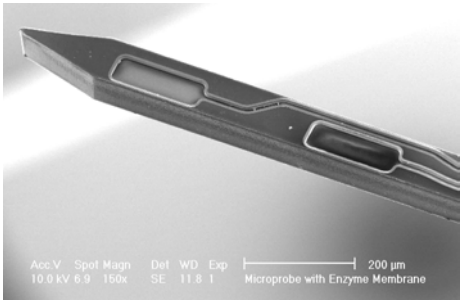

Figure 1. Tip of the 3 mm long microprobe (100x100 μm^2 cross section) with two integrated electrodes (recessed by 10 µm). The right one is covered by the enzymatic membrane.

We present a microfluidic device providing rapid and controlled concentration changes for the calibration and determination of the response time of the biosensor before and after in-vivo use. It is replacing the conventional electrochemical cells, which have the disadvantage of slow concentration transitions due to required mixing of their large volumes (up to 50 ml). The idea is using a microfluidic approach in a disposable polymer

978-0-9798064-0-7/µTAS2007/$20©2007CBMS

cartridge: Preloaded neurotransmitter samples of defined concentration are consecutively shuttled into an electrochemical microcell, into which the microprobe is temporary inserted.

2. DESIGN AND FABRICATION

The schematic layout of the microfluidic cartridge is presented in Figure 2. It consists of a small network of channels (100-400 µm wide, 200 µm high) with microchambers of optimized diameters used as integrated pneumatic pumps. They are actuated by a full deflection of the covering elastic membrane by a pin (insert, Figure 2). Both segments 1 and 2 incorporate a pump (a) for preloading the neurotransmitter solutions of defined concentrations c_1 and c_2 into the meandered reservoirs (<3 µl) and a shuttling pump (b) for the fast and controlled moving of the sample plugs into the microcell, in which the microprobe is placed. A combined reference/counter electrode can be installed separately 7 mm downstream or at the inlet of the cartridge.

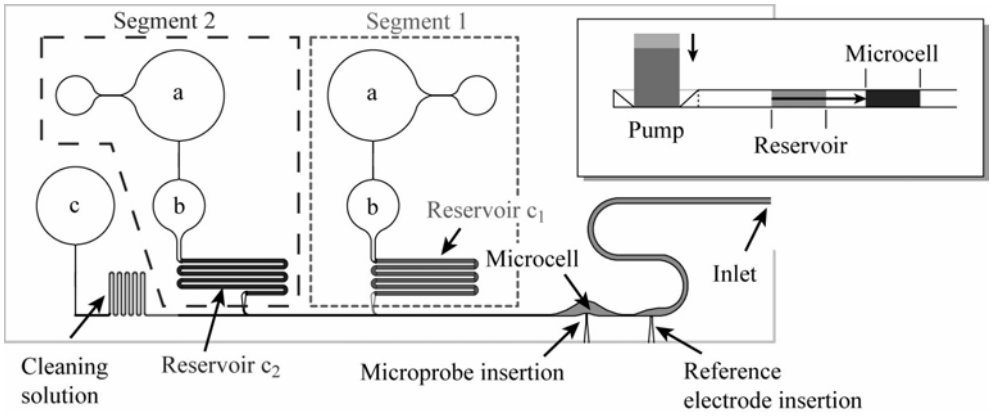

Figure 2. Schematic layout of the PDMS cartridge: Two reservoirs are prefilled using pumps (a) with solutions of defined concentrations c_1 and c_2. They can be shuttled consecutively into the cell using pumps (b) by a full deflection of the covering membrane (insert). Pump (c) allows emptying and refilling the cell with buffer solution.

The assembled system is shown in Figure 3. The strategy of multiple pumps with a two-state-mode offers the possibility to displace liquid volumes very accurately without the necessity to precisely control the deflection of the membrane. Together with the capability of the external actuation, the pumping can be performed by a guided pin simply pressed by using a finger.

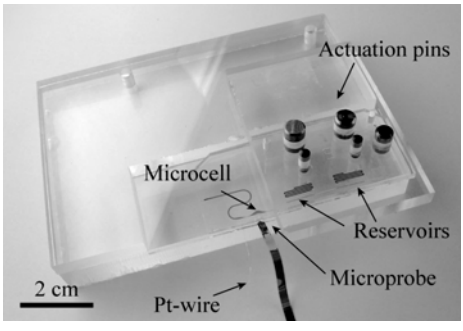

Figure 3. Stand-alone device with preloaded PDMS cartridge and the inserted microprobe and Pt-wire (pseudo-reference electrode). The pins are used for the external actuation of the integrated pneumatic pumps.

The disposable cartridges are fabricated by casting of poly(dimethylsiloxane) (PDMS) in a patterned SU-8 mold and bonding the PDMS layer onto a glass slide to seal the channels and pumping chambers after oxygen-plasma activation. The microprobe is inserted from the side into the microcell through a 60 µm thick membrane using a guiding structure (Fig. 4). The flexible PDMS ensures a good seal after insertion and leakage is prevented during operation and removal of the probe.

3. RESULTS

After insertion of the microprobe each liquid sample is displaced into the microcell – and back to the reservoir after release – in a very fast and reproducible way (<1 s). This allows the determination of the response time and sensitivity of the sensor as illustrated in Figure 5: The three-point calibration curve is defined by the zero level and the current increases of first a 4 µM followed by a 12 µM choline solution injection. Since the liquid is stagnant once in the microcell no convection-induced noise perturbs the measurement.

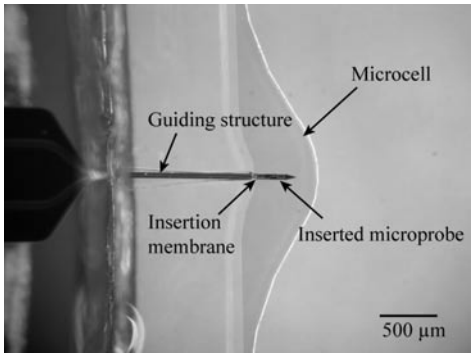

Figure 4. Inserted microprobe in the cell. The guiding structure allows precise positioning. A 60 µm membrane prevents leakage (no liquid is entering the insertion channel).

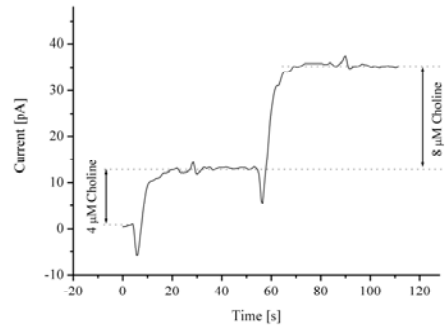

Figure 5. Response curve (raw data) of the biosensor towards 0, 4 and 12 µM choline solutions. The response time (95%) is 10 s.

4. CONCLUSION

The overall concept allows the realization of a hand-held calibration device which is very simple to operate, independent of any laboratory equipment and therefore suitable for transportation and on-site use. Moreover, multiple microprobes can be calibrated with one device since the preloaded samples are shuttled between the microcell and their reservoirs. The design can also be expanded by additional segments for other liquids or additional cells for parallel testing of several probes or combs.

ACKNOWLEDGEMENTS

The authors gratefully acknowledge the COMLAB staff at the joint microfabrication facility of IMT and CSEM. This work is supported by the European integrated project NeuroProbes (www.neuroprobes.org), EU IP IST-027017.

REFERENCES

[1] G. S. Wilson, R. Gifford, *Biosensors for real-time in-vivo measurements*, Biosensors & Bioelectronics, 20(12), 2388-2403 (2005).

NANOSTRUCTURED PHOSPHOLIPID BIOINTERFACE FOR IMMUNOASSAY MICROCHIP INTEGRATED WITH PLASMA SEPARATION MEMBRANE

Kazuki Nishizawa, Tomohiro Konno, Madoka Takai and Kazuhiko Ishihara

Department of Materials Engineering, School of Engineering and Center for Nanobio Integration, The University of Tokyo, JAPAN

ABSTRACT

We developed both non-biofouling plasma separation membrane and solid phase of high sensitive immunoassay for the pre-treatment-free one-chip immunoassay device. The nanofiber for plasma separation membrane and nanosphere for the solid phase of the immunoassay were made by electrospray deposition (ESD) with 2-methacryloyloxyethyl phosphorylcholine (MPC) based polymer which shows a high resistivity to protein adsorption. The MPC polymer modified poly(vinyl alcohol) nanofiber membrane reduced the adsorption of the blood cells after immersing the whole blood. Immunoassay in the microchip using nanosphere shaped bioconjugatable MPC polymer was carried out and the chemiluminescence intensity corresponding to the concentration of analyte was observed.

Keywords: elctrospray, immunoassay, nanofiber, MPC polymer

1. INTRODUCTION

Recently, miniaturized biosensors for microdiagnostic devices have been designed to allow bedside monitoring of chemicals and biomolecules. Fig. 1 shows the image of pre-treatment-free one-chip immunoassay device integrated with plasma separation. In the micro scale environment, the high surface area/volume ratio magnifies the influence of nonspecific binding of an analyte to the surface, arising high background or noise level. To develop highly sensitive immunoassay in the microchip, reduction of nonspecific protein binding and enhance the specific signal from the analyte should be achieved. In the case of plasma separation membrane, nonspecific protein binding to the membrane lowers the reliability of the assay. In this study, 2-methacryloyloxyethyl phosphorylcholine (MPC) which shows a high resistivity to protein adsorption [1] was used for both plasma separation membrane and immunoassay solid phase. A nanofiber for the plasma separation membrane and a nanosphere for the solid phase of immunoassay were made by ESD method. Nanostructure can be changed from sphere to fiber by controlling the impressed voltage and concentration of polymer solution.

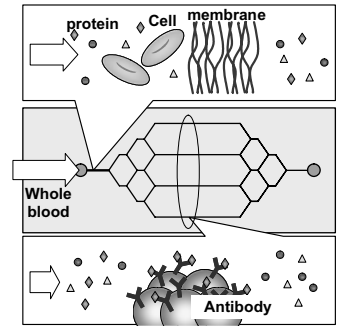

Figure 1. Schematic image of pre-treatment-free one-chip immunoassay device.

2. EXPERIMENTAL

For filtration of plasma from whole blood, poly(vinyl alcohol) (PVA) nanofiber was made by ESD, and the surface modification of PVA nanofiber was carried out using

978-0-9798064-0-7/μTAS2007/$20©2007CBMS

phospholipids polymer (PMBV, Fig. 2). The PMBV have MPC units and phenylboronic acid moiety which can cross-link with hydroxyl group in the PVA [2]. The PVA nanofiber was made by ESD from PVA 15 % water solution with impressed voltage was 15 kV. Then, the PVA nanofiber was immersed in the PMBV 1 % ethanol solution for 24 h. To confirm the adsorption of the blood cells, the PVA nanofiber coated by PMBV was immersed in the whole blood for 1 h at 37 ºC.

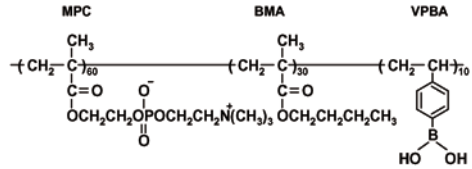

Figure 2. Chemical structure of poly[MPC-co-n-butyl methacrylate(BMA)-co-p-vinylphenylboronic acid(VPBA)] (PMBV).

For the highly sensitive heterogeneous immunoassay in the microchip, nanostructured biointerface was also developed. Our group already reported the nanosphere shaped immunoassay surface made by ESD using bioconjugated phospholipids polymer, PMBN (Fig. 3) [3]. The PMBN has the active ester groups which can conjugate the antibodies via dioxyethylene chain to enhance the antigen-antibody reaction efficiency. We applied nanosphere shaped PMBN surface to the microchannel and immunoassay was carried out. To make a nanostructure using ESD, the voltage has to be impressed between the polymer solution and the microchip. Therefore, we make a patterned Au surface by sputtering on the glass plate and 5 wt% PMBN ethanol solution was sprayed by ESD at 20 kV (Fig. 4). Then, the antibodies were immobilized on the PMBN and immunoassay was carried out on the microchip (Fig. 5). The sandwich type immunoassay was carried using thyroid stimulating hormone (TSH) as an antigen, horseradish peroxidase as a labeled enzyme and luminol as a substrate. These reagents were injected and the flow rate was 5 μL/min. Then, the chemiluminescence intensity was measured using photon counter.

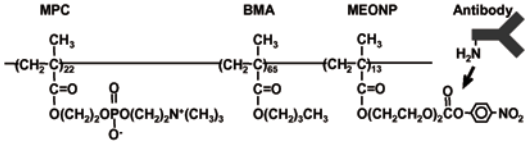

Figure 3: Chemical structure of poly[MPC-co-n-BMA-co p-nitrophenyloxycarbonyl diethylene glycol methacrylate (MEONP)] (PMBN).

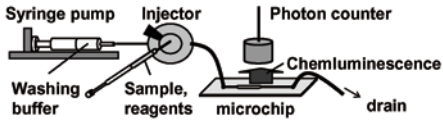

Figure 5. Schematic representation of microchip immunoassay system.

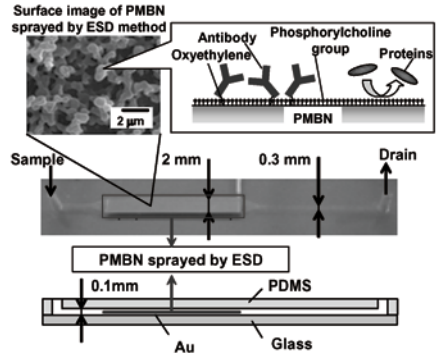

Figure 4. Photograph of microchip and SEM image of PMBN surface sprayed by ESD.

3. RESULTS AND DISCUSSION

The PVA nanofiber which diameter was about 100-300 nm was made by ESD. The PVA nanofiber is easily dissolve in water just after sprayed by ESD, but the PVA nanofiber immersed in the PMBV solution was remained the nanostructure in water (Fig. 6). This water insolubility was due to the cross-linking between phenylboronic acid moiety in the

PMBV and hydroxyl group in the PVA. From the XPS result of the PVA nanofiber coated by PMBV, it was confirmed that the MPC unit was successfully introduced on the PVA nanofiber. When the PMBV modified PVA nanofiber was contacted with whole blood, the adsorption of the blood cells on the surface was restrained.

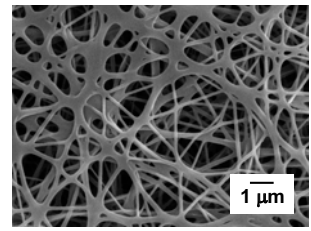

Figure 6. SEM image of PVA nanofiber coated by PMBV.

The immunoassay on the microchip was carried out using nanosphere shaped PMBN surface made by ESD. The chemiluminescence intensity corresponding to the concentration of analyte was observed (Fig. 7). And the standard curve showed a good linearity (Fig. 8). The PMBN surface sprayed by ESD showed high specific signal because of a large number of conjugated antibodies by increasing surface area. And the background level was low because MPC units reduce nonspecific protein adsorption in the microchip. Furthermore, the assay time on the microchip was shortened to 30 min from 4 h.

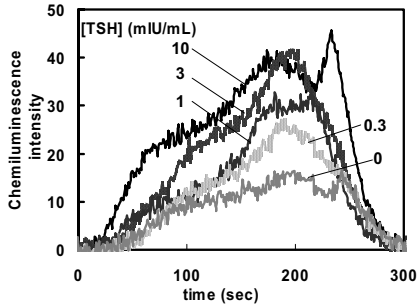

Figure 7. Detection of TSH from chemiluminescence intensity in the microchannel using the PMBN coated by ESD.

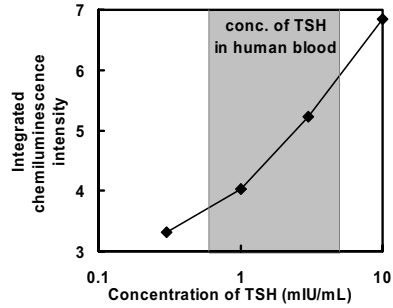

Figure 8. Standard curve of TSH form the integrated chemiluminescence intensity in the microchannel using the PMBN coated by ESD.

4. CONCLUSIONS

The PMBV modified PVA nanofiber membrane reduced the adsorption of the blood cells after immersing the whole blood. Immunoassay in the microchip using nanosphere shaped PMBN was carried out and the good linearity of standard curve was obtained. Combination of the PMBV coated PVA nanofiber for the plasma separation and nanosphere shaped PMBN surface for the high sensitive immunoassay will realize the highly reliable microdiagnostic devices.

REFERENCES

[1] K. Ishihara, Y. Iwasaki, "Why Do Phospholipid Polymers Reduce Protein Adsorption?", J. Biomed. Mater. Res., 39, 323-330, (1998).

[2] T. Konno, K. Ishihara, "Temporal and spatially controllable cell encapsulation using a water-soluble phospholipid polymer with phenylboronic acid moiety" Biomaterials, 28, 1770-1777, (2007).

[3] K. Nishizawa, M. Takai, K. Ishihara, "Electrosprayed Phospholipid Polymer Surface for Enhanced Sensitive ELISA Chip" Proc. μTAS 2006, 1, 335-337, (2006).

NATURAL CONVECTION DRIVEN HANDHELD PCR SYSTEM USING A DISPOSABLE POLYMER CHIP

K.H. Chung, Y.H. Choi, C.H. Jun, D. Lee, H.B. Pyo, M.Y. Jung and S.H. Park

Electronics and Telecommunications Research Institute, South Korea

ABSTRACT

A novel, handheld, self-flow-cycling PCR system, which gives advances in PCR time and the system miniaturization, is presented. Reagents are naturally convected by buoyancy force and continuously circulate in a triangular-shaped closed loop through three temperature zones for PCR amplification. PCR is conducted by dropping a PCR reagent onto a planner polymer chip and inserting it into a heated metal slot. It takes about 10 minutes for the successful amplification of human genomic DNA. The entire PCR system is compact and light because it requires no flow control part like a pump and includes a miniaturized temperature controller.

Keywords: PCR, Buoyancy, Handheld, Convection

1. INTRODUCTION

Miniaturization of PCR devices has been one of the key issues for POCT, and various miniaturized PCR chips have been developed [1-2]. However, the entire PCR system, which includes flow and temperature control units, has not been fully miniaturized for handheld purpose. Self-actuation of reagent using buoyancy-driven flow can be a suitable solution for the system miniaturization [3]. We present a new kind of compact natural convection driven PCR system utilizing a disposable polymer chip.

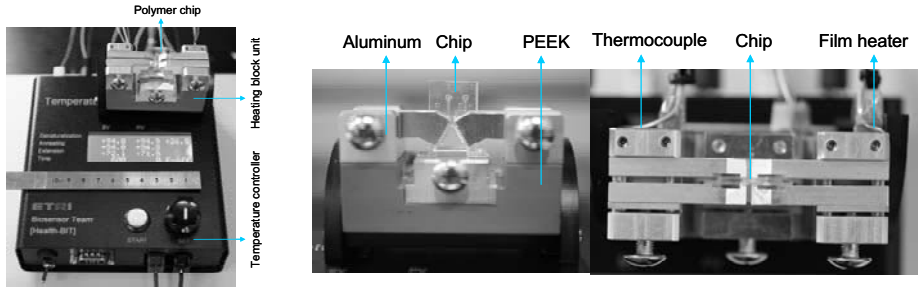

(a) (b)

Figure 2. The present PCR system. (a) Overall view, (b) Heating block unit

2. EXPERIMENTAL, RESULTS AND DISCUSSION

An overall view of the present PCR system is shown in Figure 1 (a). It consists of a polymer chip, a heating block unit and a temperature controller. A polymer chip is inserted into the heating block unit (see, Figure 1(b)), which consists of three separated zones of different temperatures. For thermal isolation, three block zones are mounted on trenched PEEK block and contact with the loop in the chip only at the extruded flat portions of heating blocks. For temperature uniformity inside the block zones, front/rear blocks are thermally contacted each other. Three temperature sensors and three film heaters are

978-0-9798064-0-7/μTAS2007/$20©2007CBMS

attached to the heating block unit, and they are connected to a miniaturized temperature controller. The temperature controller is constructed to maintain the temperature of three zones of heating block unit. It includes LCD display, time controller, RS-232C interface and microprocessor. The entire PCR system is compact and light(~0.6kg) because it requires no flow control part like a pump and includes a miniaturized temperature controller.

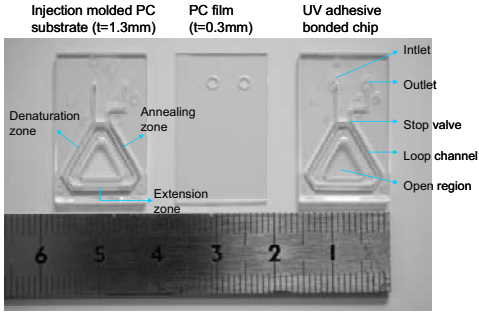

Figure 2. Fabrication of polymer chip

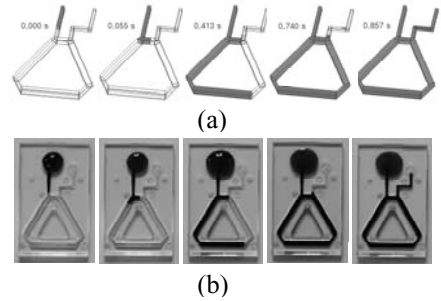

Figure 3. Filling sequence of sample. (a) numerical results using CFD-ACE+, (b) experimental results

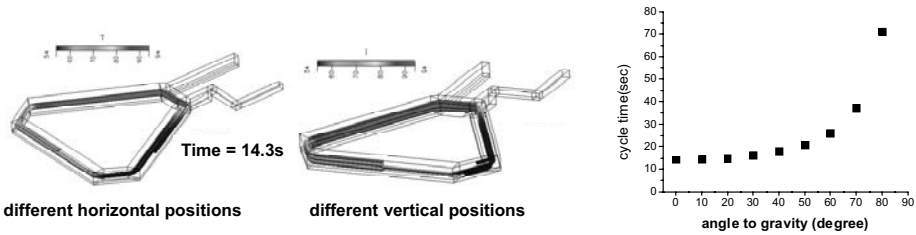

(a) (b)

Figure 4. Exemplary numerical simulations on (a) flow path and temperature fields, (b)cycle time variation with chip orientation to gravity

The temperature differences between three zones generate convection along the closed loop of the polymer chip. One circulation of reagent through the loop comprises one PCR cycling. The fabrication of the polymer chip is shown in Figure 2. PC(Polycarbonate) substrate is fabricated by injection molding and bonded with a PC film using UV adhesive. Figure 3 shows the experimental and numerical results on the filling sequence of reagent into the loop. To fill the loop without bubble formation, a capillary stop valve is formed inside the loop utilizing the capillary stopping/merging phenomenon [4]. The PCR reagent can be filled inside the entire loop without any bubble in a few seconds.

For the exact and reliable PCR cycling, the loop was designed carefully using numerical simulations and theory on buoyant convection. Figure 4 illustrates some numerical simulation results on the flow and thermal characteristics. The PCR cycling time can be modulated by changing the vertical orientation and the geometry of the chip. Numerical results indicates that it takes about 7 minutes for 30 cycles' PCR for the designed chip. The total PCR time can be changed by a constructed angle regulator of the heating block unit.

As shown in Figure 4 (b), the cycle time increases as the orientation of the polymer chip goes away from the gravitational direction.

Figure 5 demonstrates a PCR result for human BRCA-1 gene, which is known as a SNP(Single Nucleotide Polymorphism) of breast cancer. The result which is comparable to that by convectional PCR machine is obtained only in 10 minutes by the present system. The results indicates that the PCR intensity is already saturated at 10 minutes. We found the minimum PCR time can be less than 5 minutes from additional experiments. The PCR time was depenent on the length of genes, templates and PCR temperature conditions.

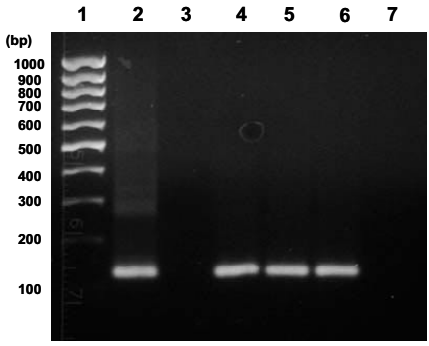

Figure 5. PCR products using human BRCA-1 gene(127bp) as a template.(94°C, 54°C and 72°C for denaturation, annealing and extension) Lane 1 : size maker, lane 2 : reaction by conventional PCR machine (71min.), lane 3 : a conventional machine without template(71min.), lane 4 : reaction by present PCR system (40min.), lane 5 : present PCR system (20min.), lane 6 : present PCR system (10min.), lane 7 : present PCR system without template(20min.)

3. CONCLUSIONS

The presnt PCR system gives remarkable advances in PCR time and the system miniaturization. Natural convection generates continuous circulation of PCR reagent along a triangular-shaped closed loop in the polymer chip. PCR is simply conducted by inserting the polymer chip into a heated metal slot. It takes less than 10 minutes for the successful amplification of human genomic DNA. The entire PCR system is compact and light (~0.6 kg), thus it is useful for handheld POCT of DNA analysis.

ACKNOWLEDGEMENTS

This work was supported by the IT R&D program of MIC/IITA. [2006-S007-01, Ubiquitous Health Monitoring Module and System Development]

REFERENCES

[1] M.G. Roper, C.J. Easley, and J.P. Landers, "Advances in polymerase chain reaction on microfluidic chips", Analytical Chemistry, Vol. 77, 3887, (2005).

[2] C. Zhang, J. Xu, W. Ma, and W. Zheng, “PCR microfluidic devices for DNA amplification”, Biotechnology Advances, Vol. 24, 243, (2006).

[3] M. Krishnan, N. Agrawal, M.A. Burns, and V.M. Ugaz, “Reactions and fluidics in miniaturized natural convection systems”, Analytical Chemistry, Vol. 76, 6254, (2004)

[4] K.H. Chung, J.W. Hong, D. Lee, H.C. Yoon, “Microfluidic chip accomplishing self-fluid replacement using only capillary force and its bioanalytical application”, Analytica Chimica Acta, Vol.585, 1, (2007)

POLYMER-BASED THERAPEUTIC DRUG MONITORING CHIP WITH PERIODIC GOLDNANO-STRUCTURE FOR LOCALIZED SURFACE PLASMON RESONANCE SENSING

Yoshinori Akagi[1*], Kazuki Yamamoto [2], Tutomu Yotsuya [3], Akito Ishida [4], Toshio Mori [5], Hiroaki Kawata [6], Yoshihiko Hirai [6] and Minoru Seki [6,7]

[1]Sekisui Chemical Co., JAPAN, [2]Sekisui Integrated Research Co., JAPAN
[3]Technology Research Institute of Osaka Prefecture, JAPAN
[4]Kyoto Prefecture University, JAPAN, [5]Nara Medical University, JAPAN
[6]Osaka Prefecture University, JAPAN, [7]Chiba University, JAPAN

ABSTRACT

We have demonstrated the therapeutic drug monitoring (TDM) system for the measurement of anticancer drugs. This was achieved by developing a novel light-control micro-pump system, a novel resin and a localized surface plasmon resonance (LSPR) sensor. The novel micro-pump system could be driven by the light-induced gas generation with the sequentially-controlled 40 independent lights. The 3D-micorfluidic device was made up of the novel resin with micro holes and microchannels. The LSPR sensor was fabricated using a nanoimprint lithographic (NIL) technique applied to a Ni mold both with nano- and micro-scale structures, which enabled a highly-sensitive detection of anticancer drugs.

Keywords: Polymer-based 3D-microfluidic device, Light-control micro-pump system, LSPR,

1. INTRODUCTION

TDM can be efficiently employed for the medical treatments of various types of cancers, depressions, asthma and so on. In general, TDM of those patients is performed trough blood concentration measurement by chromatography (GC or HPLC). However, these methods are time and labor consuming, that results in the insufficient feedbacks of measurement data to their therapeutic schedules. In this study, we have developed a polymer-based TDM chip for the measurement of drugs in blood by integrating a novel light-control micro-pump system, a novel resin for the fabrication of 3D-microfluidic device and a periodic nano-structure coated with Au for LSPR sensor.

2. THEORY

The characteristic of TDM system is a wide-range on measurement for immunological assay. This system requires multiple and multi-step batch-operations, which was realized by developing a light-control micro-pump system and a dilution unit composed of microfluidic channels. This dilution unit involves only a microchannel network with multiple passive valves, i.e., a microchannel with a narrow pinched region [1]. A sensing of TDM system is based on LSPR, which provides an affinity-based detection of biomolecules and a high sensitivity based on a noble metal nano-scale structures fabricated using NIL [2]. NIL enabled high productivity of our TDM chip contained nano-scale structures.

3. EXPERIMENTAL

We have developed a novel resin (S-LEAF 50; Sekisui Chemical Co. Ltd, Japan) for a stacked microfluidic-device. This resin has a nature of a negative photo-resist and can be formed in a thin sheet, which is suitable for a rapid micro structure formation by photolithographic process.

The TDM chip composed of 4 units, i.e., a micro-pump array unit, a plasma separator unit, a dilution unit and a 3D-microfluidic unit for liquid handling, which enables a parallel anti-cancer drug assays based on a LSPR-induced fluorescence sensor as shown in Figure 1(b). The 3D-microfluidic channel

978-0-9798064-0-7/μTAS2007/$20©2007CBMS

network was made up by stacking 3 layers; A-, B- and C-layer. A-layer was made of PMMA fabricated by NIL using a Ni-mold with a micro- and nano-integrated structure. The dimension of the nano-structure was determined by the simulation of the finite difference time domain method. B- and C-layers were made of the novel resin fabricated by a usual photolithographic technique. The dilution unit was fabricated on the novel resin by the similar way based on a photolithography. The flow image in 3D-microfluidic device was shown in Figure 2(b)

In order to study the LSPR sensor, the effects of the LSPR on the limit and the range of detection were measured by fluorescence-based immunological assay (Figure 5(a)).

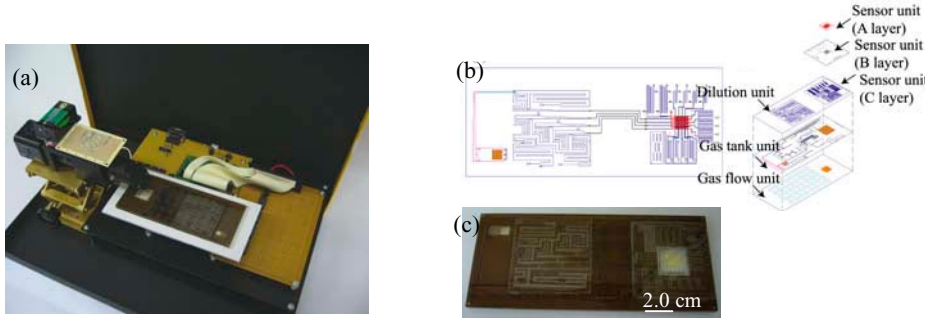

Figure 1 Therapeutic Drug Monitoring (TDM) system. (a): the total TDM system, (b) : schematic image of the TDM chip, and (c); a TDM polymer microchip.

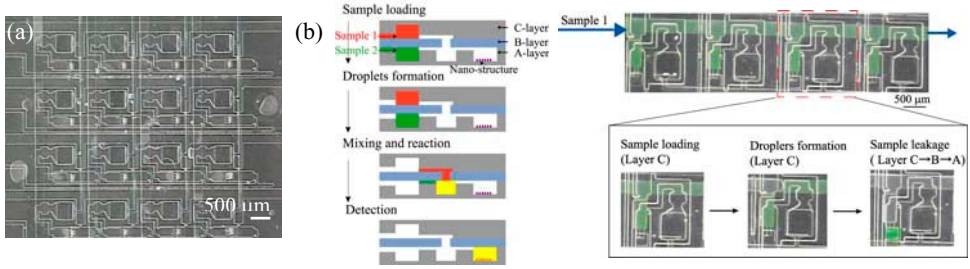

Figure 2 Microfluidic channel network and liquid operation. (a): 3D-microfluidic channel network, (b): principle of liquid operation, and (c) controlled liquid image.

4. RESULTS AND DISCUSSION

The outlook of the developed TDM system was shown in Figure 1(a). At first, the ability of the dilution property of the system was tested from 1/10 to 1/1000. These operations were performed 3 times of the basic process with the sample loadings, the droplet formations, dispensing and mixings. Each process was automatically performed by the light-control micro-pump system. The dilution of a fluorescein solution was performed to dilute from 1/10 to 1/1000 by this micro-pump system. These fluorescence signals detected by a CCD camera were decreased according to the corresponding concentrations. The stacked 3D-microfluidic channel network is demonstrated in Figure 2(a). The liquid operation was performed to flow the solutions containing fluorescein or Texas-Red. These solutions were successfully dispensed simultaneously for 4 channels and the two of these solutions were mixed in a micro-chamber on this 3D-device (Figure 2(c)).

The LSPR sensor chip was observed by a CCD camera and the scanning electron microscope (SEM) as shown in Figure 3. This sensor showed its structural color between red and green, which based on a periodic Au nano-cylindrical structure with a diameter of 240 nm and a pitch of 360 nm. A fluorescence image was obtained by the LSPR sensor with Texas-Red as shown in Figure 4(a) and (b). The limit of

detection in our system was 1.1 x 10^{-6} M of Texas-Red on the LSPR sensor with nano-structures (Figure (c). On Au flat substrate, however, the Texas-Red was not detected from 1.0 to 24 x 10^{-6}M in our detection system. The lower limits of detection were decreased at least about 24-times compared with Au flat structure. For an immunological assay, the standard detection curve of the sensor for an anti-cancer drug, 5-FU, was obtained and demonstrated the ability to quantitative measurement of 5-FU from 3.8 x 10^{-5} M to 3.8 x 10^{-3} M on this LSPR sensor (Figure 5(b)).

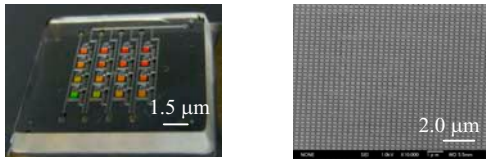

Figure 3 Image of LSPR sensor. A CCD camera image (Left) and a SEM image of nano-structure (Right).

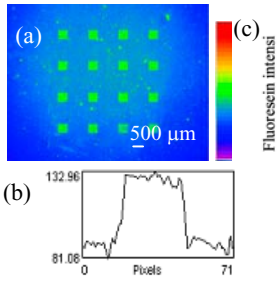

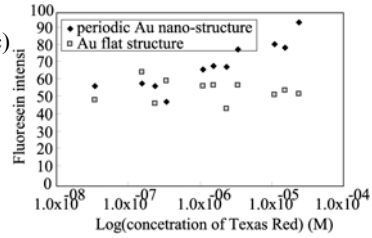

Figure 4 Fluorescent image by the LSPR sensor. (a) LSPR sensor signal modified with Texas-Red fluorescence, and (b) its intensity profile. (c) Effect of nano-structure on the fluorescent intensity.

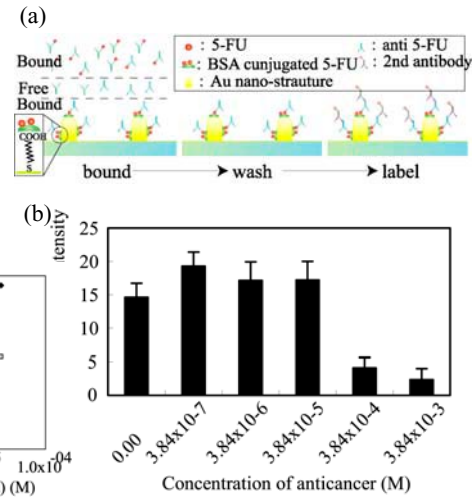

Figure 5 Immunological assay on a LSPR sensor. (a): principle and (b): standard curve for 5-FU.

5. CONCLUSIONS

We have successfully demonstrated the fabrication of the TDM chip both with the 3D-micorfluidic structure and the periodic Au nano-structure which could increase the fluorescent signals.

ACKNOWLEDGEMENTS

We thank Y. Takagi, Y. Masada, A. Sakai, S. Hattori, Y. Wada, M. Ooishi and H. Omura, Sekisui Chemical Co., LTD. for their technical and administrative supports, and K. Kitamura and M. Fukuoka at Taiyo Manufacturing Co., Ltd. for the Ni mold preparation, and the Japanese Ministry of Economy, Trade and Industry-KANSAI for financial support of this work.

REFERENCES

[1] M. Yamada and M. Seki, *Nanoliter-Sized Liquid Dispenser Array for Multiple Biochemical Analysis in Microfluidic Devices*, Anal. Chem., 76, 895-899 (2004).

[2] Y. Hirai *et al.*, *Fine Pattern Imprint Lithography Using Dimpled Mold*, J. Photopolymer Sci. Technol., 13, 435-440 (2000).

[3] D.A. Stuart *et al.*, *Biological Applications of Localized Surface Plasmonic Phenomena,* IEE Proc. Nanobiotechnol., 152, 13-32 (2005).

RAPID PEN-SIDE DIAGNOSTICS USING IMMUNOELECTROPHORETIC ASSAYS

David S. Reichmuth, Serena Wang, Daniel J. Throckmorton, Wayne Einfeld and Anup K. Singh
Sandia National Laboratories, Livermore, CA. 94550, USA

ABSTRACT
This paper presents a novel microdevice for the detection of viruses using a single, fluorescently-labeled antibody, with the intended application the screening of livestock at the animal pen (or "pen-side"). The device uses a nanoporous polyacrylamide structure in an etched glass microfluidic chip to concentrate analytes. Viruses can be detected at the polyacrylamide/channel interface or during a subsequent open channel electrophoretic separation. Swine influenza was used as a model pathogen and presence of the virus was detected in <5 minutes using <50 μl of sample. The fluorescent signal recorded was proportional to the amount of virus in the sample, showing the potential for quantitative measurement of viral particle number.
Keywords: virus, immunoassay, polyacrylamide gel

1. INTRODUCTION
Intentional (agroterrorism) and unintentional spread of veterinary pathogens pose a great threat to the economy, and to public health in the case of zoonotic diseases. As is evident from the foot-and-mouth disease (FMD) outbreak in the UK in 2001, which led to the slaughter of 4 million animals and an approximate $40 billion in lost revenue, early detection and intervention during an outbreak can reduce economic impact and public hysteria. Existing methods to screen farm animals are slow and can require extensive sample handling, complicating the goal of early detection. Hence, there is an urgent need for inexpensive, portable devices that can be used for rapid on-site screening of farm animals for infectious diseases. This device would determine disease status at the animal pen, allowing "pen-side" diagnostics.

We are developing a portable on-site diagnostic system for rapid screening of large populations of livestock, including sheep, pigs, cattle and potentially birds. The device utilizes antibody-based identification of viruses and is targeted at viral markers in saliva or blood. Our current research is focused on a microchip-based non-denaturing electrophoretic immunoassay using photo-patterned gel structures for concentrating and detecting viral particles. We have previously demonstrated the ability to use laser-based photopolymerization to create polymer structures in microfluidic chips(1-4). This work describes a new configuration that allows simultaneous concentration and discrimination of antibody and antibody-virus complex. The electrophoretic immunoassay format is amenable to creating a handheld device with high throughput and sensitivity while giving rapid results.

2. EXPERIMENTAL RESULTS AND DISCUSSION
We have detected swine influenza A H1N1 virus using a rapid (less than 1 minute) electrophoretic concentration with fluorescent detection using labeled anti-virus antibodies (Figure 1). A nanoporous plug is created using a laser to polymerize polyacrylamide in a small section (80 μm wide x 30 μm deep x 180 long μm) of a glass microchip (Figure 2). This plug has pores wide enough to allow antibodies to

978-0-9798064-0-7/μTAS2007/$20©2007CBMS

pass through but virus particles are excluded. During the loading phase, sample is electrophoretically driven to plug region. In the second phase, the sample is cleared from the plug and is sent to waste. In figure 2, a mixture of fluorescently-labeled antibodies can be seen concentrating at the edge of the gel plug. The final fluorescence intensity at the interface is proportional to the concentration of viral particles present (Figure 3). We used bovine enterovirus (BEV) as a negative control. We observed no difference between BEV/antibody and antibody alone, indicating that cross-reactivity is minimal. The overall cycle time is less than 5 minutes and the assay requires <50 μl of sample.

Currently, the concentration of virus is determined from the intensity of fluorescence at the gel plug region. We are investigating the integration of open-channel separations with the concentration device and are also determining the effects of the sample matrix on detection limits. This device will fill an urgent need for portable devices for screening cattle and birds and help contain the spread of disease to other animals and people.

3. CONCLUSIONS

This device shows promise for the rapid and portable detection of viruses for livestock screening applications. Future work will include testing at a USDA laboratory for detection of high-consequence animal pathogens.

REFERENCES

1. D. S. Reichmuth, T. J. Shepodd, B. J. Kirby, *Anal Chem* **76**, 5063-8 (Sep 1, 2004).
2. S. Song, A. K. Singh, T. J. Shepodd, B. J. Kirby, *Anal Chem* **76**, 2367-73 (Apr 15, 2004).
3. A. V. Hatch, A. E. Herr, D. J. Throckmorton, J. S. Brennan, A. K. Singh, *Anal Chem* **78**, 4976-84 (Jul 15, 2006).
4. A. E. Herr *et al.*, *Proc Natl Acad Sci U S A* (Mar 20, 2007).

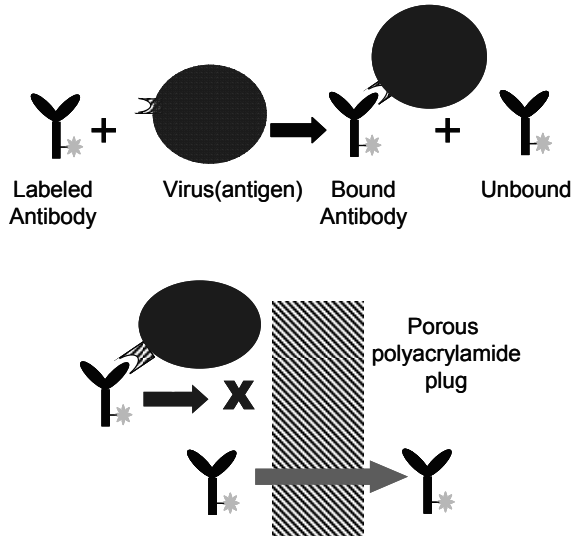

Figure 1: AlexaFluor 488-labeled antibody binds to the surface proteins of the influenza virus. The viral particles are too big to enter the polyacrylamide plug, while the unbound antibodies pass through the plug and do not concentrate. Concentration of the antibody-virus complex causes a detectable increase in fluorescence.

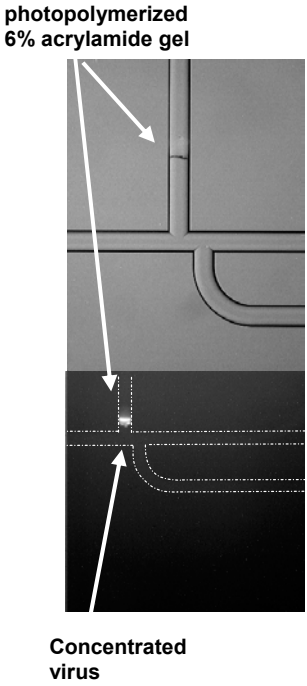

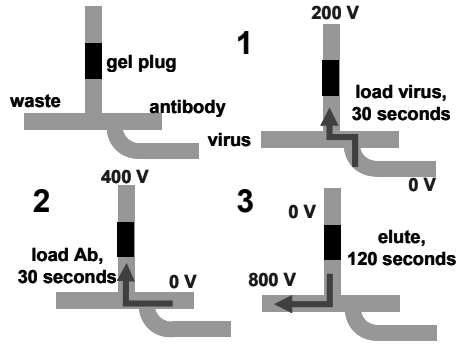

Figure 2: (top left) A 6% polyacrylamide plug is formed in a glass microchip by projecting a shaped UV laser beam onto the acrylamide-containing channel. (bottom left) Viral particles are detected by using epifluorenence microscopy. The virus-labeled antibody complex can be seen concentrated at the plug. (right) The virus and antibody are moved to plug region by electrophoresis. The virus and antibody can be mixed before loading or on chip as shown here.

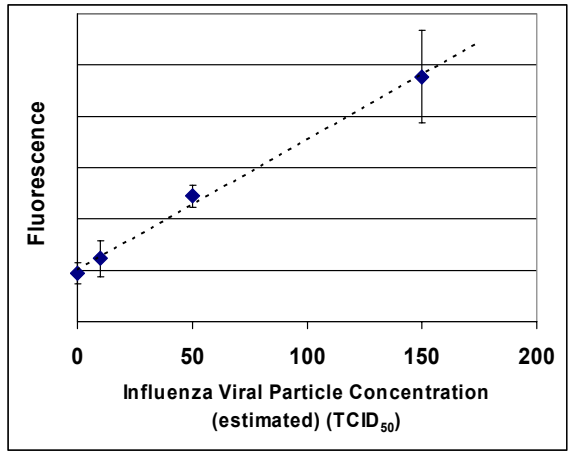

Figure 3: Detection of influenza virus. The fluorescence at the membrane is proportional to the amount of virus present in the sample. TCID50 (Tissue culture infectious dose) is a measure of viral concentration based on the infectivity of the virus. We report an estimated value because chemically inactivated virus was used in this assay, precluding the direct measurement of infectivity. Bovine enterovirus and anti-influenza antibody was used as a negative control and gave the same fluorescence as antibody alone.

THE STUDY OF OSMOTIC VALVE FOR THE INSULIN THERAPY OF DIABETES

Toshiaki Nagakura[1], Kengo Nukada[2], Akira Yamada[2], Masashi Ikeuchi[3], Koji Ikuta[3]

[1]Dept. of Biomedical Engineering, Osaka Electro-Communication University, Japan
[2]Cardiovascular Physiology Okayama University Graduate School of Medicine, Dentistry and Pharmaceutical Sciences, Japan
[3]Dept. of Micro System Engineering, Nagaoya University, Japan

ABSTRACT

There is diabetes mellitus more than 15million people, and this disease cause various serious complication. Diabetes mellitus therapy is insulin therapy, but quantity of insulin is decided by iatric experience. So it has danger of hypoglycemia attack. As for it is expected for insulin therapy to be done by measuring blood sugar level, but there is not still practical method. We developed that insulin valve system driven by osmotic change (blood sugar level change). This system actuation was confirmed by preliminary experiment, we studied system element for optimizing diabetes mellitus therapy.

Keywords: Osmotic pressure, Osmotic valve, Diabetes mellitus, Insulin

1. INTRODUCTION

In 2006, according to the World Health Organization, at least 171 million people worldwide suffer from diabetes mellitus. Type 2 diabetes mellitus accounts for the great majority of cases of diabetes. Diabetes mellitus is not the disease that merely blood sugar level raises but a disease to cause severe complications. And the diabetes causes a serious circulatory disease such as myocardial infarction, cerebral infarction and chronic renal failure. The major complications are neuropathy, retinopathy and nephropathy. The retinopathy lead to blindness, and the nephropathy lead to chronic renal failure and dialysis therapy. Therefore diabetes mellitus increases both medical cost and serious damage of patients.

The usual therapy for diabetes mellitus is insulin therapy. However, dosage of insulin is decided by experience of medical doctor. And it is reported that progress of complications become slow progress by intensive blood sugar level control [1]. But it is needed for patients enough intelligence and patience in this intensive therapy. This therapy sometimes cause extremely harmful hypoglycemic attack. Thus a device of blood sugar level control is needed. The artificial pancreas, which provides insulin by measuring blood sugar level, has been developed. Even this portable artificial pancreas is not used in practical therapy.

2. THEORY

We have studied for the micro valve for insulin therapy. This micro valve is filled with a solution, covered with a semi-permeable membrane. This semi-permeable membrane changes the inside volume of solution according to the concentration of an outside solution. This volume change is not required energy supply and the regulation system. We applied this valve to an insulin delivery system worked by the changing of blood sugar. This principle is shown in Figure 1. We confirmed that the function of osmotic valve by preliminary experiment of implanted at subcutis of rat.

978-0-9798064-0-7/μTAS2007/$20©2007CBMS

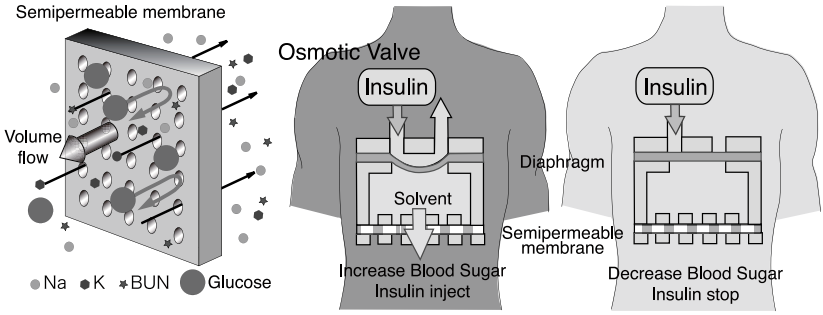

Figure 1: The principle osmotic valve. The molecule of glucose is larger than that of Na, K, BUN. The osmotic valve works during high concentration (blood sugar high)

3. EXPERIMENTAL

This osmotic valve is made by 3D micro stereo-lithography that is irradiated by ultraviolet laser at photosensitive resin [2]. The fabrication process is shown in Figure 2. Our osmotic valve implanted in subcutis of rat could deliver insulin according to the change of blood sugar concentration. This osmotic valve has various advantages in down sizing, such as driving speed, the efficiency of osmotic valve. In the medical devices, the smaller size is the less invasive. We report that the optimization of an osmotic valve to keep adequate blood sugar level in rat that was reported at Transducers 2003 [3].

We tried to improve the fabrication and material of permeable membrane. And also tried to investigate the character of permeable membrane. We made the permeable membrane from the cellulose that was used as a medical material. We tried whether it is possible to make the permeable membrane with chitosan that is also used as a medical material.

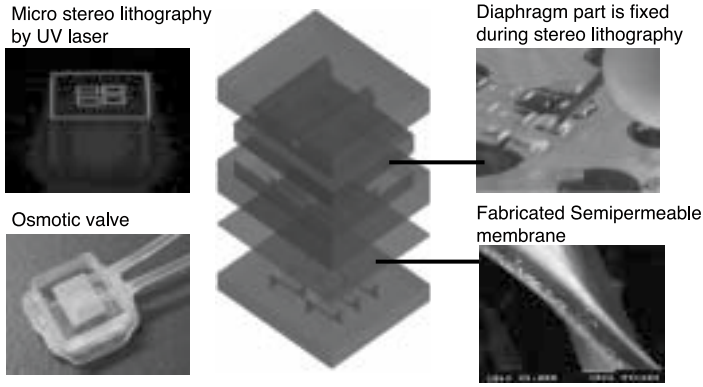

Figure 2. The structure of osmotic valve made by 3D micro stereo-lithography that is irradiated by ultraviolet laser at photosensitive resin.

4. RESULTS AND DISCUSSION

The membrane made by chitosan was better than cellulose as a permeable membrane and the function of osmotic valve made by chitosan was better than that of cellulose, shown in Figure 3. Furthermore, we found that the difference depending upon fabrication, shown in Figure 4.

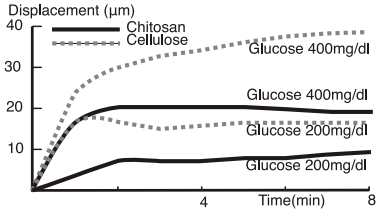

	Chitosan	Cellulose
Thickness [μm]	24.0	20.0
Filtration coefficient [m/sec Pa]	1.1×10^{-12}	4.3×10^{-12}
Permeability ratio [m/sec]	5.5×10^{-7}	5.6×10^{-6}
Displacement [μm] (at 200mg/dl)	10	17
Displacement [μm] (at 400mg/dl)	20	36

Figure 3. The difference of function of osmotic valve between chitosan and cellulose.

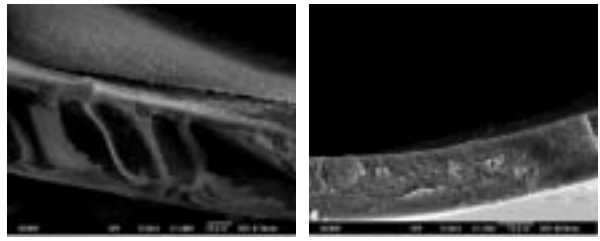

Figure 4. The structure of cellulose membrane was different by the fabrication. The new method made smooth and fine single layer membrane. (SEM; The edge of cellulose membrane)

5. CONCLUSIONS

We tried to investigate that system element for optimized diabetes mellitus therapy. It was confirmed that it could be used as permeable membrane of osmotic valve by chitosan with biocompatibility. In addition, we proved that character of permeable membrane changed by not only material but also a manufacture method of permeable membrane. We will study optimization of another element of the osmotic valve for diabetes mellitus therapy.

ACKNOWLEDGMENTS

The present study was partially funded by the 1997 Ministry of Education Scientific Research Grant (0978081), Suzuken Memorial foundation Award 1998, Nakatani Electronic Measuring Technology Association of Japan 1999, Research for the Future Program of Japan Society for the Promotion of Science under the Project "Integrated Fields, Information on Life Systems, Development of Artificial Cellular Device" (1996-2001), Research Grant Japan Science and Technology Agency (JST) Novel Measuring and Analytical Technology Contributions to the Elucidation and Application of Life Phenomena “New Principle Measurement Tools using Optical-driven Nano Machine” (2004-)

REFERENCES

[1] UK Prospective Diabetes Study (UKPDS) Group, Intensive blood-glucose control with sulphonylureas or insulin compared with conventional treatment and risk of complications in patients with type 2 diabetes (UKPDS 33). LANCET; 352(9131): 837, 1998.

[2] K. Ikuta, S. Maruo, Y. Fukaya and T. Fujisawa, New micro stereo lithography for freely movable 3D structure -Super IH process with submicron resolution-, Proceedings of the IEEE International Workshop on Micro Electro Mechanical Systems (MEMS98), 290-295, 1998.

[3] T. Nagakura, S. Maruo, K. Ikuta, THE STUDY OF MICRO BLOOD SUGAR CONTROL DEVICE WITHOUT ENERGY SUPPLY FOR DIABETES THERAPY, Transducers' 03, The12th International Conference on Solid-State Sensors Actuators and Microsystems Technical Digest, Volume 2/2, p.1209-1212, 2003

A MICROFLUIDIC CHIP FOR VISUALIZATION OF SINGLE MOLECULE INTERACTIONS *IN SITU*

Henrik Johansson, Malin Jarvius, Yuki Tanaka, Mats Nilsson, Jonas Jarvius and Ulf Landegren.

Dept. of Genetics & Pathology, Uppsala University, The Rudbeck laboratory, Uppsala, Sweden

ABSTRACT

This paper reports single molecule analysis on single cells in a microfluidic platform. Individual protein-protein interactions were detected and visualized using rolling circle amplification initiated by proximity probe recognition. The assay was carried out in an injection-molded microfluidic chip.

Keywords: single cell analysis, amplified single molecule, proximity ligation

1. INTRODUCTION

The proximity ligation in situ assay (P-LISA) [1] is used for localized detection of individual target proteins or interacting sets of proteins. The method brings dual-recognition specificity to *in situ* detection of proteins and it permits detection of interacting proteins. In P-LISA, binding of pairs of detection reagents to the same target protein, or to interacting pairs of target proteins, juxtaposes DNA oligonucleotides attached to the affinity reagents. Subsequent ligation and amplification via rolling circle amplification gives rise to a localized product, which is detected using fluorescence labeled oligonucleotides (figure 2). The interaction between the two transcription factors c-Myc and Max was interrogated in the microchip (Figure 3) using P-LISA.

In order to investigate the benefits of using a microfluidic setup we desgined a flow-cell for this purpose. The main goals where to shorten the assay time, improve reproducibility and reduce the hands-on time

2. EXPERIMENTAL

A thermoplastic chip was employed as a platform for cell culturing and P-LISA analysis. The chips were fabricated by compact disc injection molding and then diced out using a milling machine. The chips were coated with silica using sputtering to create a surface compatible with PDMS-glass bonding. To close the structures we used a 250 µm thick membrane of PDMS. The membrane was oxidized using a Corona surface treater and then brought in contact with the sputtered silica on the plastic chip [2]. The platform is biocompatible, optically transparent over a broad spectral range, and it is inexpensive making it suitable for single-use applications. Figure 1 shows the microchip for cell experiments.

To eliminate all hands-on time during each run a java-based software was developed to control one script-operated pump and a 6-port valve. Using this system the six different

978-0-9798064-0-7/µTAS2007/$20©2007CBMS

reagent mixes needed could be prepared in advance and programmed for injection at given time points. An easy-to-use interface between the tube connector and the chip was developed that can sustain a leak tight connection over time.

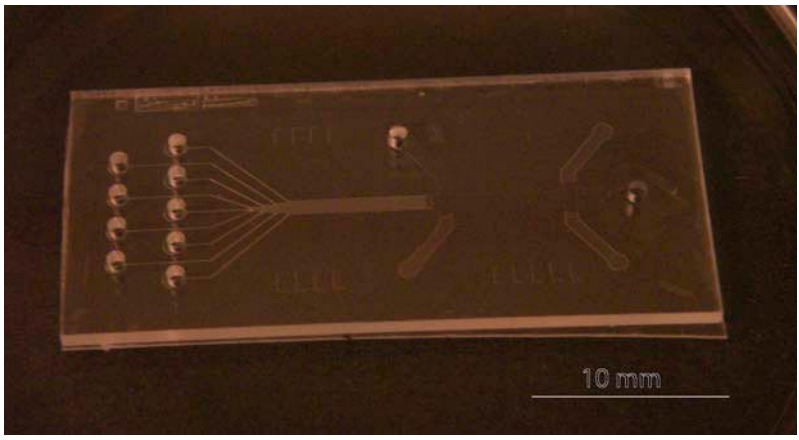

Figure 1. Microchip for cell culture and single molecule analysis.

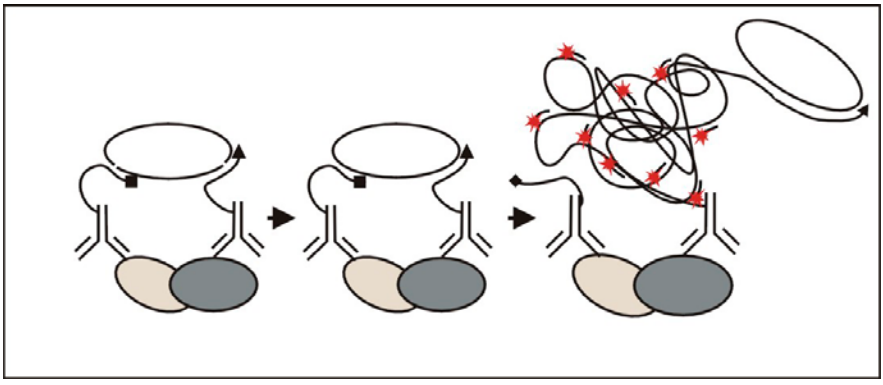

Figure 2. Schematic picture of the Proximity ligation *in situ* assay.

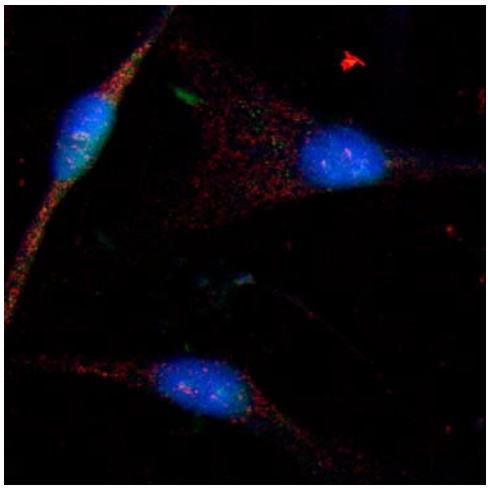

Figure 3. Image of c-Myc/Max staining of the human fibroblasts using proximity ligation in situ performed in microchip. The c-Myc/Max interactions (red dots, Alexa 555), nuclei (blue, DAPI) and actin filaments (green, FITC).

REFERENCES

[1] Direct observation of individual endogenous protein complexes in situ by proximity ligation. Soderberg O, Gullberg M, Jarvius M, Ridderstrale K, Leuchowius KJ, Jarvius J, Wester K, Hydbring P, Bahram F, Larsson LG, Landegren U. *Nat Methods* 12, 995-1000 (2006)

[2] Thermoplastic Microfluidic Platform for Single-Molecule Detection, Cell Culture, and Actuation. Melin, J., Johansson, H., Söderberg, O., Nikolajeff, F., Landegren, U., Nilsson, M. & Jarvius, J. *Anal. Chem.* 77, 7122-7130 (2005).

A MICROFLUIDIC CHIP STUDYING THE EFFECT OF SOLUBLE FACTORS ASSOCIATED WITH THE MODES OF MEDIUM SUPPLY AND PERFORMING CELL ASSAYS

Zeta Tak For Yu[12], Ken-ichiro Kamei[23], Chengyi Jenny Shu[4], Caius G. Radu[3], Owen N. Witte[345] and Hsian-Rong Tseng[23]

[1]Department of Mechanical and Aerospace Engineering, [2]Crump Institute for Molecular Imaging, [3]Department of Molecular and Medical Pharmacology, [4]Department of Microbiology, Immunology, and Molecular Genetics, [5]The Howard Hughes Medical Institute, University of California, Los Angeles, USA

ABSTRACT

This paper presents a micro-device to study how medium flow affects cell growth associated with soluble factors in culture medium. A design with medium reservoirs has been included to rescue cells from the problem of soluble factor and material compatibility. Moreover, two different cell assays, apoptosis assay and genetic manipulation, were demonstrated using the same micro-device.

Keywords: Cell culture, cell assay, soluble factor, medium supply

1. INTRODUCTION

In recent years, several groups have developed microfluidic chips for cell culture and functional assays. Although medium flow effect on cell growth was demonstrated, most of the understanding was based on mechanical or physical standpoint [1-5] that do not completely depict the real biological problem. This paper presents an in depth study, novel design and solution to cell growth associated with the problem of soluble factors in culture medium adsorbed onto system surface. Moreover, different cell assays were demonstrated using the same device.

2. EXPERIMENTAL

A two-layer PDMS microfluidic chip composed of six rectangle-shaped cell culture chambers was developed. The microchip integrated with micro-valves and micro-pumps was fabricated through typical soft-lithography technique, Figure 1. Two different modes of medium supply, i.e., circulatory and direct feeding to cells, were implemented through embedded circle-shaped medium reservoirs and externally connected medium tubings. The nutrient and some soluble factors in the medium coming from the external tubing were depleted through surface adsorption using typical Tygon® lab tubing. The chip was surface-coated with fibronectin to facilitate cell adhesion before cell loading.

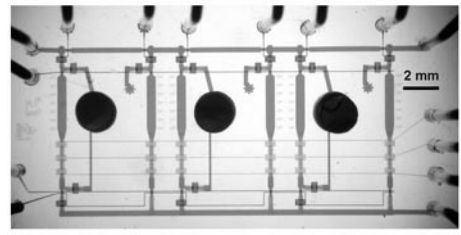

Figure 1: Schematic of the microchip for the study of medium supply.

978-0-9798064-0-7/μTAS2007/$20©2007CBMS

3. RESULTS AND DISCUSSION

NIH 3T3 cells were loaded onto the surfaces of the cell culture chambers, Figure 2 (a). Normal growth and excellent viability were observed in the chamber attached to the medium re-circulation reservoir, (b). However, poor cell growth and abnormal morphology were observed in the chamber directly fed with fresh medium, (c). The difference in viability is believed due to the loss of bio-molecules onto the Tygon® tubing. Because when Tygon® tubing was replaced with Teflon® tubing, normal cell proliferation was observed. Moreover, the use of circulation module saves the cell from material compatibility.

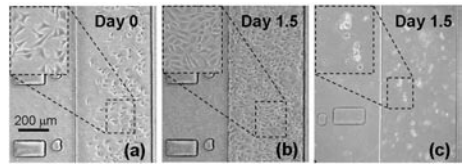

Figure 2. Proliferation of NIH 3T3 cells in the microchip.

Three cell types were cultured using two different medium supply modes (i.e., circulation and direct feeding). The pictures (Figure 3) were taken after 3 days in culture. (a) NIH 3T3, (c) HeLa and (e) B16 using the medium re-circulation approach; (b) NIH 3T3, (d) HeLa and (f) B16 using the continuous feeding with fresh medium approach. Cells cultured in chambers attached to the medium recirculation reservoir show very good viability. PI/AO fluorescence stainings were performed in situ in chambers in which NIH 3T3 cells were cultured for 3 days, Figure 4. AO-staining, Figure 4 (b), indicated that the majority of the cells were viable. PI-staining, Figure 4 (c), showed only a small percentage of dead cells. The results proved that the importance of accumulating and circulating cell secretion is vital to cell survival in general.

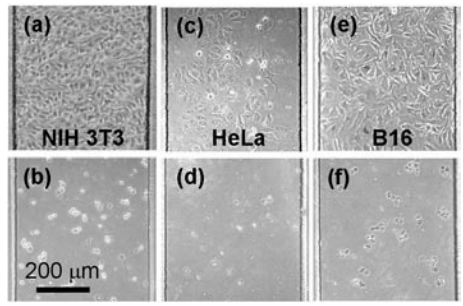

Figure 3. Effect of medium supply to three different cell lines.

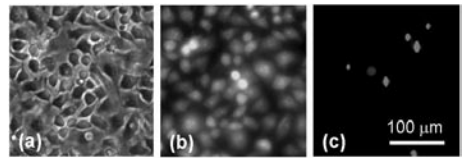

Figure 4. Cell viability test by PI/AO fluorescence staining.

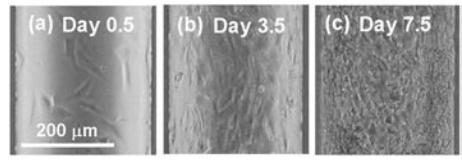

Figure 5. NIH 3T3 cell proliferation in the microchip for 8 days.

With the circulation of medium, different cell lines grew well inside microchips. Representative time-lapse images of NIH 3T3 cells cultured for 8 days in the microchip were shown in Figure 5. Proliferation of the three cell types was quantified by monitoring the numbers of cells inside the cell culture chambers over time, Figure 6.

The microchip capable of culturing cell was used to perform different cell assays. Cell apoptosis was induced inside the microchip (Figure 7). Panels (a-c) show bright field image, Annexin V and MitoTracker Red stainings of B16 cells with staurosporine treatment. In another assay, on-chip genetic manipulation inside cells in the microchip was illustrated (Figure 8). Panels (a-b) show bright field image and fluorescent image of EGFP expression by TPA-induced NIH 3T3 cells.

4. CONCLUSIONS

Circulation of medium is proved to be essential to constitute an appropriate nutrient supply in a microfluidic chip to perform relevant and valid cell experiments to avoid loss of soluble factor due to material adsorption. The microfluidic chip developed can be further used to study unique biological problems, e.g., study and screen the endocrine, autocrine and paracrine characteristics of various cell types; model the difference of the flow network and effect on cells secreting soluble factors.

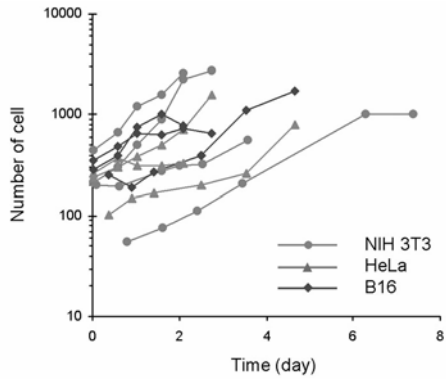

Figure 6. The proliferation of chip-cultured NIH 3T3, HeLa and B16 cells.

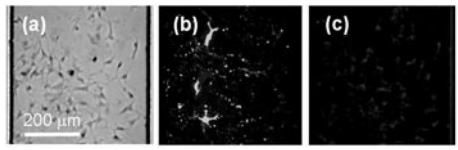

Figure 7. Detection of staurosporine-induced apoptosis of B16 cells cultured in the microchip.

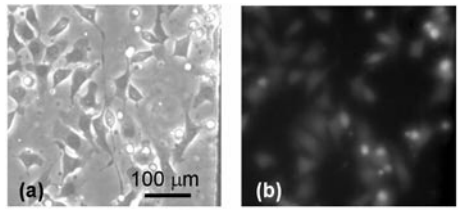

Figure 8. On-chip transcriptional activation in NIH 3T3 cells transfected with an EGFP reporter construct.

ACKNOWLEDGEMENTS

This research was supported by the NIH NanoSystems Biology Cancer Center, the DOE-UCLA Institute of Molecular Medicine and the NIH-UCLA Center for In Vivo Imaging in Cancer Biology and Siemens Medical Solutions USA Inc. We thank Stephanie M. Shelly, Dan Rohle, Shirley Quan and Mireille Riedinger for technical support. ONW is an Investigator of the Howard Hughes Medical Institute. CGR was supported by a Developmental Project Award (ICMIC, NIH/NCI grant # CA08630). C.J.S. was supported by a National Institutes of Health (NIH) Research Training in Pharmacological Sciences training grant PHS T32 CM008652.

REFERENCES

[1] P.J. Hung, P.J. Lee, P. Sabounchi, R. Lin and L.P. Lee, *Continuous perfusion microfluidic cell culture array for high-throughput cell-based assays*, Biotechnol. Bioeng., **89**, pp. 1-8, (2005).

[2] N. Futai, W. Gu, J.W. Song and S. Takayama, *Handheld recirculation system and customized media for microfluidic cell culture*, Lab Chip, **6**, pp. 149-154 (2006).

[3] L. Kim, M.D. Vahey, H.Y. Lee and J. Voldman, *Microfluidic arrays for logarithmically perfused embryonic stem cell culture*, Lab Chip, **6**, pp. 394-406 (2006).

[4] H. Yu, C.M. Alexander and D.J. Beebe, *Understanding microchannel culture: parameters involved in soluble factor signalling*, Lab Chip, **7**, pp. 726-730, (2007).

[5] N. Korin, A. Bransky, U. Dinnar and S. Levenberg, *A parametric study of human fibroblasts culture in a microchannel bioreactor*, Lab Chip, **7**, pp. 611-617, (2007).

A NOVEL MULTIFUNCTIONAL PROCESSOR FOR BIO-PARTICLES

Ching-Te Kuo[1] and Cheng-Hsien Liu[1, 2]

[1]Department of Power Mechanical Engineering, National Tsing Hua University, Hsinchu, Taiwan 300, ROC and

[2]Microelectromechanical Systems Institute, National Tsing Hua University, Hsinchu, Taiwan 300, ROC

ABSTRACT

This paper describes a new multifunctional processor for bio-particles manipulation and biomedical analysis. The processor exploits AC electrokinetics for concentrating, trapping and transporting bio-particles, such as cells and molecules. It has the similar size order to bio-objects and is non-contact approach to bio-particles. Through our proposed asymmetrically modulated method and proper arranged electrodes, we could not only manipulate bio-particles more precisely but also minimize the risk of electrolytic bubble generation.

Keywords: Processor, manipulation, AC electrokinetics, electrolytic bubble

1. INTRODUCTION

Miniaturization of fluidic processes holds great potential for biomedical analysis and it dramatically reduces the amount of sample and reagent required, resulting in substantial savings in both time and cost. Traditional methods for bio-process only include a single function, such as concentrating [1], or it integrates a complicated electrode structure [2]. In this research, we focus on the development of a multifunctional bio-particels processor *via* the asymmetric surface modulation. The asymmetric surface modulation could enhance the desired tangential electric field and spatial electric-field gradient to drive and snare micro-objects. The surface modulation could help to decrease the electrolytic bubble generation. Combining with the positive DEP [3] and AC EOF [4], we could achieve three-modes manipulations including concentrating, trapping and transporting modes. The experimental results successfully demonstrate the concept of our proposed multifunctional bio-particles processor. With our proposed designs, this processor leads more feasibility to approach Lab-on-a-chip.

2. THE CHIP DESIGN AND OPERATIONAL MODES OF MULTIFUNCTIONAL BIO-PARTICLES PROCESSOR

The term AC electrokinetics refers to the movement of particles or fluid via AC electric fields, such as dielectrophoresis (DEP) [3] and AC electro-osmosis flow (AC EOF) [4]. We use these two phenomena to manipulate bio-particles in the micro scale. Figure 1 illustrates the concept of our proposed design. The device consist two concentric electrodes, called "bio-process cell array" [Figure 1(a)]. The cross section of one unit cell is shown in Figure 1(b). Figure 2 is the schematic diagram of the operational modes. These diagrams illustrate the mechanism of AC EOF and DEP trapping due to the modulation of both the asymmetric electrode size and dielectric layer. The plus/minus signs on the electrodes represent the positive/negative potential on the individual electrode. The plus/minus signs at the surfaces

978-0-9798064-0-7/μTAS2007/$20©2007CBMS

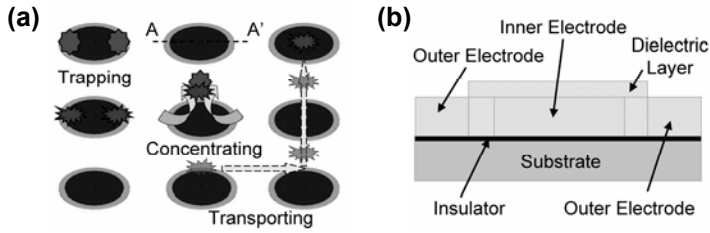

Figure 1. The illustration and chip design for the multifunctional bio-particles processor. (a) Bio-process cell arrays. (b) The cross section A-A' view from (a).

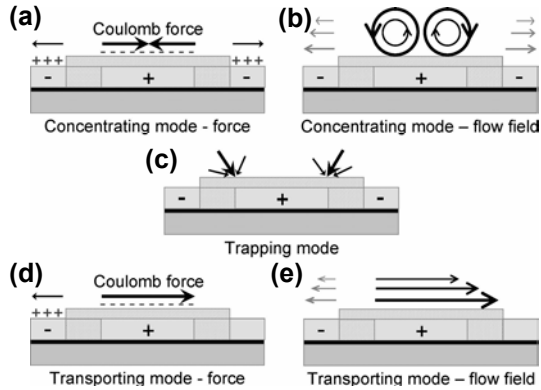

Figure 2. Operational modes for the bio-processor. (a) and (b) are the concentrating mode. (c) is the trapping mode. (d) and (e) are the transporting mode.

of both electrodes and dielectric layers represent the positive/negative ions induced in the electric double layer. The mechanism has three modes: Mode 1- concentrating mode [Figure 2(a)-(b)], Mode 2- trapping mode [Figure 2(c)] and Mode 3- transporting mode [Figure 2(d)-(e)]. The interaction between the induced charges and the tangential electric filed causes a uni-directional net fluid flow (transporting mode) [Figure 2(e)], circular vortex flow (concentrating mode) [Figure 2(b)]. Positive DEP is utilized in trapping mode [Figure 2(c)].

3. RESULTS AND DISCUSSION

Figure 3 shows the simulated and experimental results for the three-modes manipulations. Figure 3(a) and (d) are the CFD-ACE+ simulation results for proof of the manipulation principle. Figure 3(a) shows both the direction of fluid flow and the magnitude of electric field in concentrating principle. Figure 3(d) shows the uni-directional transporting principle. Figure 3 (b)-(c) and (e)-(f) are sequential pictures of concentrating, trapping and transporting modes. After the potential was applied, the randomly distributed particles were then flowing to the inner electrode (concentrating mode) [Figure 3(b)]. Finally, we applied the proper potential, the positive DEP trapped the particles in the edge of inner electrode (trapping mode) [Figure 3(c)]. Figure 3(e) and (f) show the transporting mode, after the proper potential arrangement was applied. The applied potential was 10 Vpp at 4.5 MHz for concentrating and transporting modes, and the DEP trapping was

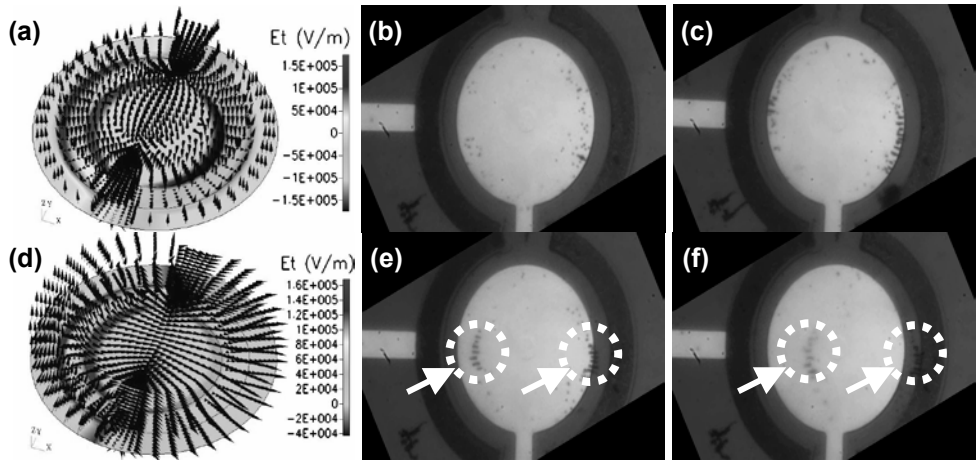

Figure 3. Numerical simulations and experimental results for the three-modes manipulations of the bio-particles processor. (a) and (b) show the simulated and experimental results of the concentrating mode, respectively. (c) shows the trapping mode. (d)-(f) show the simulated and experimental results of the transporting mode, respectively.

achieved in the potential of 10 Vpp at 8 kHz. The particle was 1 μm diameter Latex bead in NaH_2PO_4 buffer solution.

4. CONCLUSIONS

This work reports a novel multifunctional bio-processor device. The functions of concentrating, trapping and transporting modes are demonstrated in this work. More further studies on the functions of the whole processor for bio-applications are in progress in our group. This proposed multi-functional micro-objects processor could be applied to micro-objects manipulation and bio-medical investigation.

ACKNOWLEDGEMENTS

This research was supported by the National Science Council under grant NSC-93-2218-E-007-021 and the Nano-technology Research Program of University System of Taiwan, R.O.C.

REFERENCES

[1] P. K. Wong, C. Y. Chen, T. H. Wang and C. M. Ho, An AC Electroosmosis Processor for Biomolecules, *in Proc. Int. Conf. on Solid-State Sensors and Actuators (Transducer'03)*, 2003.

[2] K. H. Chu and C. H. Liu, A novel multifunction bio-particles manipulation device by AC electrokinectis, *in Proc. Int. Conf on Solid-State Sensors and Actuators (Transducer'07)*, 2007.

[3] N. G. Green, A. Ramos and H. Morgan, AC Electrokinetics: A Survey of Sub-Micrometer particle dynamics, *J. Phys. D: Appl. Phys.*, 2000, **33**, 632-641.

[4] N. G. Green, A. Ramos, A. Gonzalez and H. Morgan, Fluid Flow Induced by Nonuniform AC Electric Fields in Electrolytes on Microelectrodes, *Physical Review E*, 2000, **61**(5), 4011-4018.

MONITORING PROTEIN PHOSPHORYLATION DURING IMMUNE SIGNALING USING INTEGRATED MICROFLUIDIC FLOW CYTOMETRY

Nimisha Srivastava, James S. Brennan, Steven S. Branda, Anup K. Singh and Amy E. Herr

Sandia National Laboratories, Livermore, CA 94550

ABSTRACT

Human response to pathogen invasion relies on signaling in and between sentry cells of the innate immune system, namely macrophage cells. The timing and degree of intracellular signaling events – including protein phosphorylation – are crucial to effective host defense against pathogenic insult. To achieve the temporal fidelity needed for predictive network analyses – resolution sorely lacking from conventional bioanalytical methods – we have developed a microfluidic device that integrates flow cytometry with sophisticated upstream cell-preparation. We report on studies of macrophage cell viability and signaling protein phosphorylation for the case of host insult with a Gram-negative bacteria surrogate using our versatile tool.

Keywords: Sample preparation, flow cytometry, cell signaling, innate immunity

1. INTRODUCTION

Macrophage cells (derived from monocytes, a type of white blood cell) respond to bacteria and other insults through surface receptors called Toll-Like Receptors (TLRs). Specifically, TLR4 receptors identify lipopolysaccharide (LPS) present on Gram-negative bacteria (e.g., *Francisella tularensis, Yersinia pestis*), triggering an intracellular signaling cascade that instructs the cell to mount an innate immune response. The response often encompasses secretion of cytokines and other inflammation effectors [1]. An automated microfluidic device that *integrates* refined cell handling steps with flow cytometry (FC) provides a compelling tool for monitoring time-dependent response of the TLR4 pathway.

FC is a powerful tool that enables detection of surface and intracellular proteins with single cell resolution for statistically significant population [2]. While conventional FC is extremely high throughput (~1000 cells/min), the various cell handling steps involved in preparing cells for FC detection are time consuming and labor intensive. Multiple cell handling steps (e.g., LPS dosage, dilution, mixing, addition of reagents for fixation, permeabilization and fluorescent labeling, as well as selective washing) are amenable to microfluidic-based automation. The approach presented is optimized to monitor and quantitate intracellular and surface events key to the TLR4 signaling pathway. These measurements are essential for refined predictive modeling of the TLR4 signaling network.

2. MATERIALS AND METHODS

To integrate the multiple cell preparation steps required for FC, pressure-driven flow – continuous, stopped, and pulsatile – is employed in devices similar to that shown in Fig. 1A. Functionalities necessary for the cell-preparation steps include: spiral mixers (Fig. 1B), size exclusion filters for exchange of reagents, incubation chambers (~1000 cells per chamber) for host cell (RAW264.7) challenge with LPS (Fig. 1C), and surface and intracellular fluorescent staining with immunoreagents. Subsequent to preparation, cells are analyzed

978-0-9798064-0-7/μTAS2007/$20©2007CBMS

using two-color FC in the same device (Fig. 1D). Fused silica microfluidic chips were designed in-house and fabricated by Caliper Life Sciences (Hopkinton, MA). The glass microchannels are grafted with PEG to prevent adhesion of activated macrophages to the walls of the channel. The movement of fluids within the device is pneumatically controlled using electronic pressure controllers (Parker Life Sciences, Hollis NH). A plastic manifold fabricated in-house interfaces the on-chip wells with external pressure controllers.

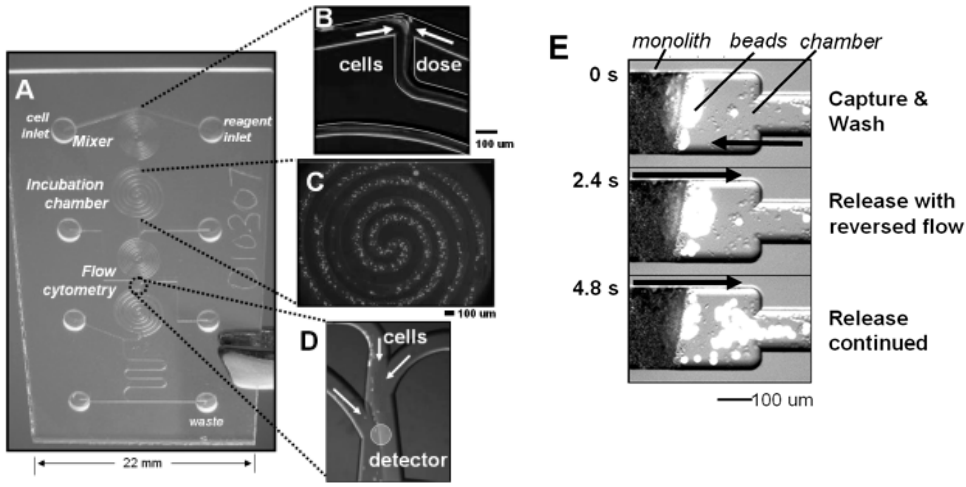

Figure 1: Integrated Cell Assay Microchip: The device contains (B) mixers, (C) incubators, (D) flow cytometric detection capability, and (E) passive monolithic valves. The device contains 8 reservoirs used for loading cells and other reagents as well as for removal of waste streams. The operation of the device in (A) is from top to bottom. The movement of fluid in the device is pneumatically controlled using external pressure (0-5 psig) controllers.

The small channel cross-section (120 µm x 30 µm) and long lengths (~50 mm) of the mixers enable rapid molecular diffusive mixing (~15 s) of challenge (e.g., *E. coli* LPS) with macrophage cells (Fig. 1B). Further, the device contains two chambers, each with a capacity of ~1000 cells (Fig. 1C). The chambers are used to fix the phosphorylated state of the cells in time, permeabilize the plasma membrane, and selectively label phosphorylated proteins with a fluorescently tagged phospho-specific antibody. The device contains a region (Fig. 1D) where cells are focused hydrodynamically for FC (fluorescence, scatter) [3].

In addition to the functionality described and depicted in Fig. 1A-D, flow cytometer based cellular assays require the introduction, routing, and selective exchange of aqueous reagents. Therefore, key components in the microfluidic device are *in situ* photopolymerized porous filters (Fig. 1E) that act as size-exclusion filters – allowing bulk pressure-driven fluid to flow through, while retaining cells in specific locations on the chip. The porous polymer filters were fabricated using *in-situ* phase separation photo-polymerization [4]. The formulation, consisting of butyl methacrylate (monomer), crosslinker, polar solvents and a photoinitiator (AIBN) was optimized to a 4 µm pore size for efficient cell collection and reagent exchange.

3. RESULTS AND DISCUSSION

Monolith enabled *static cytometry* assays were implemented to assess the number (%) of viable cells as a function of different LPS dosages (Fig. 2A). Macrophage cells (10^6cells/mL) were exposed to 32 µg/mL *E. coli* LPS (Sigma, MO) for different durations (1 and 6 hrs). The stimulated cells were briefly incubated on-chip with a fluorescence-based cell viability assay (Molecular Probes, CA). Excess fluorophore was washed away with buffer through the monolithic filter – cells were retained and the population distribution between live and dead cells was determined. The on-chip assay revealed 30% of the cells had compromised cell plasma membranes after a 6 hr exposure to 32 µg/mL LPS, double the compromised number of cells compared to a 1 hr stimulation (Fig. 2B).

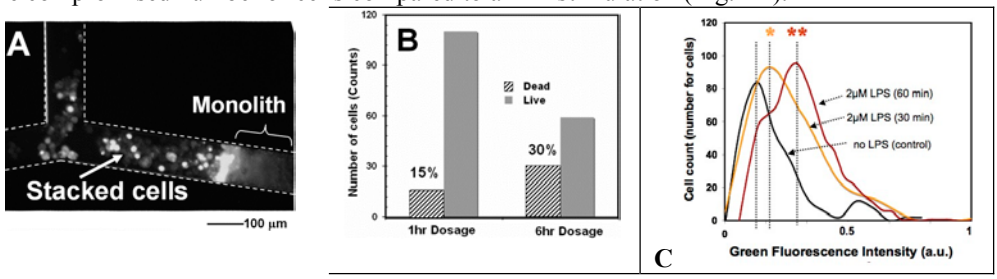

Figure 2. **Static and Flow Cytometry**: (A) Static cytometry using the porous polymer monolith. Compromised cells appear bright (in grayscale rendering of two-color image), while viable cells appear dim. (B) Population distribution of viable cells after varying insult duration. (C) Intracellular FC of ERK. Increased levels of ERK-P are detected at 30 & 60 after insult with 2.4 µM *E. coli* LPS.

To monitor TLR4 signaling, we have employ on-chip FC assays for analyzing the phosphorylation events of ERK (ERK-P), a key intracellular protein in the MyD88 pathway of the TLR4 response. FC is necessary to efficiently measure large populations of cells. Approximately 10^6 macrophage cells were challenged with 1 µM *E. coli* LPS. On-chip FC, validated with conventional FC (BD FACScan), shows significant increases in ERK-P at 30 & 60 min post-LPS exposure (Fig. 2C). Initial results from the on-chip FC system report a similar trend, with the compelling advantage of using only 10 µL of fluid – 0.1% of that required for conventional FC. Enhanced microfluidic transport enables faster fixation, permeabilization and antibody staining and washing. The total time for the cellular assays was reduced by an order of magnitude (few minutes compared to hours). Present studies focus on monitoring of ERK/ERK-P and p38/p38-P at finer time points (< 30 min).

4. SUMMARY

We describe a method that integrates and automates cell preparation and assays for monitoring the TLR4 signaling pathway. Batch processing of cell cultures composed of 10^3 cells in volumes of 100 nL are processed efficiently. Preliminary flow cytometry results suggest our method provides a robust, rapid means to make protein content measurements. While developed to monitor TLR4, the methodology is applicable to cellular signaling.

5. REFERENCES

[1] S. Akira and K. Takeda, *Nat Rev Immunol,* 4, 499-511 (2004).
[2] K. Sachs *et al*, *Science*, 308, 523-529 (2005).
[3] N. Srivastava *et al*, *Proceedings of Transducers, in press.*
[4] S. M. Ngola *et al*, *Anal Chem*, 73, 849-856 (2001).

ARRANGEMENT OF CELLS WITHIN SEMI-CLOSED SPACE WITH MICROELECTRODE-BASED TECHNIQUE

Masahiko Hashimoto, Soichiro Sekine, Takeaki Kawashima, Hirokazu Kaji and Matsuhiko Nishizawa

Department of Bioengineering and Robotics, Graduate School of Engineering, Tohoku University, Sendai 980-8579, Japan

ABSTRACT

This paper reports strategies for the site-specific immobilization of cells within three-dimensional structures, which are based on a newly developed surface patterning technique, electrochemical bio-lithography. The technique uses a microelectrode to electrochemically generate oxidizing agent that causes local detachment of the anti-biofouling molecules from a substrate surface. Subsequent adsorption of cell-adhesive protein on the newly exposed surface induces local attachment. We combine this technique with dielectrophoresis (DEP) to rapidly collect cells on the cell-adhesive region created in a microfluidic chip. Also, the combination of the electrochemical bio-lithography with layer-by-layer deposition enabled the formation of patterned co-culthres inside elastic tubing structures.

Keywords: Cell patterning, co-cultivation, electrochemical method, dielectrophoresis

1. INTRODUCTION

Controlled immobilization of cells within a semi-closed space is an important step for cell-based assays. We have previously reported a method to create a patterned surface within a microchannel by electrochemical means, "electrochemical bio-lithography", which enables site-specific immobilization of proteins after the device is fully assembled [1]. Here, we report a strategy of the rapid cell arrangement within the semi-closed microfluidic channel by combining electrochemical bio-lithography with negative DEP [2]. Negative DEP was used to collect cells on the cell adhesive region which was previously created by the electrochemical bio-lithography. Also, we present a method to pattern two cell types inside ready-made silicone rubber tubing by the microelectrode-based technique and electrostatic deposition [3].

2. RAPID CELL ARRANGEMENT WITHIN MICROCHANNEL

We prepared a microfluidic device with a Pt microelectrode array at the upper wall of the channel (Figure. 1). The Pt electrodes are 20 μm in width and are separated by 50 μm (Figure. 1b). The channel is 300 μm in width and 50 μm in depth. After a 0.1 M phosphate buffer saline (PBS) containing 25 mM KBr (pH 7.4) was introduced into the microchannel which was pre-coated with heparin, a potential pulse of 1.7 V vs. Ag/AgCl was applied to one of the electrodes for 0.5 sec to generate hypobromous acid (HBrO) that quickly removes the heparin, exposing protein-adhesive surface. Subsequently, a solution of fibronectin (30 μm mL^{-1}), cell-adhesive protein, was introduced into the channel and incubated for 10 min, followed by a wash with PBS. Figure. 1c shows Cy3-labeled fibronectin selectively adsorbed onto the bottom wall of channel. After the channel was filled with a suspension of HeLa cells (1 x 10^6 cells mL^{-1}) in GIT medium (13 mS cm^{-1}) containing 50 μg mL^{-1} penicillin and 50 μg mL^{-1} streptomycin, negative DEP (at 10 Vpp and 1 MHz) was used to concentrate HeLa cells on the pre-patterned cell-adhesive region.

978-0-9798064-0-7/μTAS2007/$20©2007CBMS

As shown in Figure 1d, cells quickly moved in the direction of weak electric fields to form a line pattern on the bottom wall within 30 sec. Cells adhered only to the fibronectin-coated bottom wall after DEP remained in operation for another 10 min. Sequential application of the electrochemical bio-lithography and negative DEP enabled rapid arrangement of cells within microchannel, and would be beneficial for simplification of cell-based diagnostic assays.

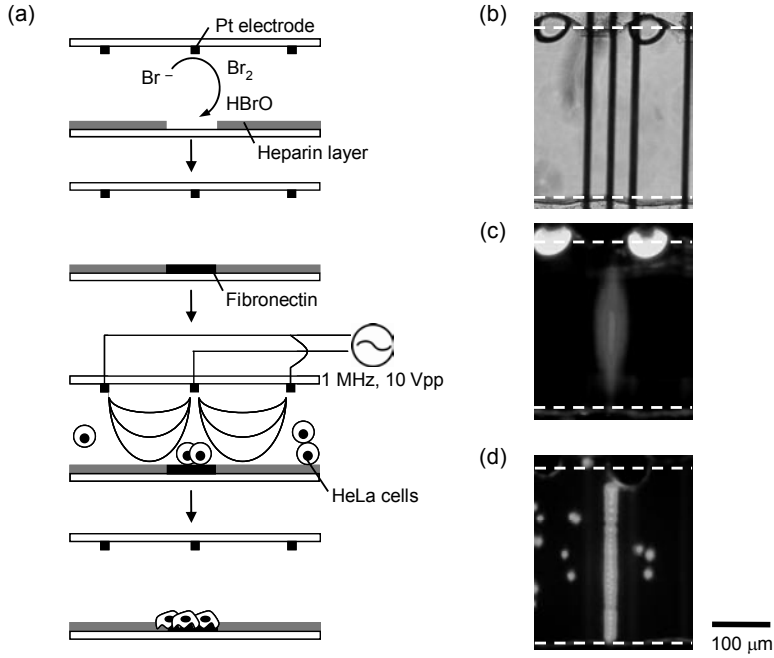

Figure 1. (a) Schematic representation of the cellular patterning within the microchannel by sequentially applying electrochemical bio-lithography and negative DEP. (b) Microelectrode array fabricated at the upper wall of the channel. (c) Fluorescence micrograph of the site-specifically immobilized Cy3-labeled fibronectin. (d) Fluorescence micrograph of concentrated HeLa cells (stained with CellTracker Green) with DEP.

3. PATTERNED CO-CULTURES INSIDE SILINCONE TUBING

Figure 2a shows the scheme for patterning cells inside elastic tubing (inside and outside diameters, 2 and 3 mm, respectively). After the inner surface of the tubing was coated with an anti-biofouling heparin layer, the tip of a Pt needle microelectrode was inserted vertically through the tubing wall to a depth of about 1 mm. The needle shape of the electrode and the elastic of the silicone ensured that the electrode could be inserted without breaking the tubular structure. Subsequently, a Pt needle microelectrode was used to locally generate the HBrO and form a cell-adhesive region on the inner surface of tubing precoated with heparin. After the needle electrode was gently pulled out, a solution of fibronectin was flowed through the tubing, and then a suspension of NIH-3T3 cells was introduced and cultured (Figure. 2b). At this stage of the process, the inner surface of the tubing except for the cell adhesion region is covered with heparin. To alter the anti-biofouling property of the heparin surface to allow adhesion of the second cell type, poly-L-lysine (PLL) and fibronectin were in turn added to the tubing. To avoid any cytotoxic

effect of PLL on the pre-patterned cells, the PLL treatment was carried out at a low concentration (40 μg mL^{-1}) and for a short exposure time (20 min). Subsequently, HepG2 hepatocyte cells was incubated for 30 min in the tubing, followed by a wash with fresh medium to remove non-adherent cells. Although some HepG2 cells attached within the location of the NIH-3T3 cells as seen in Figure. 2c, this could be effectively eliminated by allowing the first cell type a longer initial culture period to enable its population to increase in density and spread. The controlled co-culture inside the elastic tubing should be of value for cell-cell interaction studies following application of chemical or mechanical stimuli and for tissue engineering-based bioreactors.

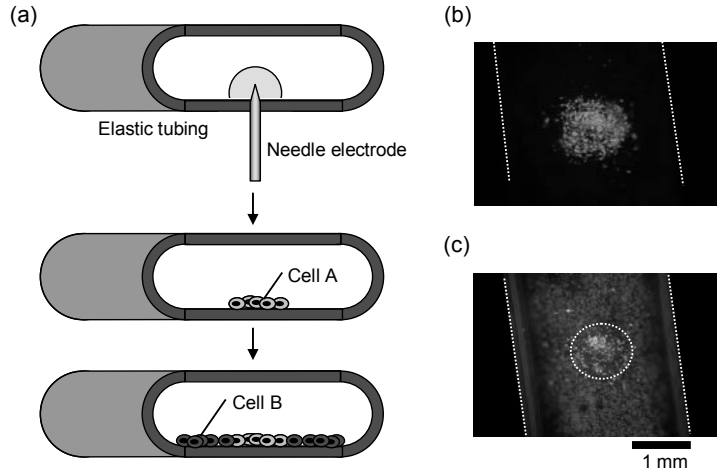

Figure 2. (a) Strategy for patterning cells inside elastic tubing structure. (b, c) Patterned co-cultures of NIH-3T3 fibroblasts (stained with CellTracker Green) and HepG2 hepatocytes (stained with CellTracker Orange) inside the tubing structure. NIH-3T3 cells were initially seeded on the cell adhesion region generated by the needle electrode (b). After the surrounding region was switched from cell-repellent to cell-adhesive by PLL and fibronectin deposition, HepG2 cells were seeded (c).

ACKNOWLEDGEMENTS

This study was supported by Industrial Technology Research Grant Program in 05 from NEDO of Japan, and by a Grant-in-Aid for Scientific Research B (No. 17310080) from the Ministry of Education, Science and Culture, Japan. M.H. acknowledges support from a research fellowship of the Japan Society for the Promotion of Science.

REFERENCES

[1] H. Kaji, M. Hashimoto and M. Nishizawa, *On-Demand Patterning of Protein Matrixes Inside a Microfluidic Device*, Anal. Chem., **78**, 5469 (2006).

[2] M. Suzuki, T. Yasukawa, H. Shiku and T. Matsue, *Negative Dielectrophoretic Patterning with Colloidal Particles and Encapsulation into a Hydrogel*, Langmuir, **23**, 4088 (2006).

[3] H. Kaji, S. Sekine, M. Hashimoto, T. Kawashima and M. Nishizawa, *Stepwise Formation of Patterned Cell Co-Cultures in Silicone Tubing*, Biotechnol. Bioeng., in press (2007).

CELL CULTURE MICROCHAMBER ARRAY WITH INDEPENDENT PERFUSION CHANNEL FOR PARALLEL DRUG TOXICITY ASSAY

S. Sugiura, J. Edahiro, K. Kikuchi, K. Sumaru, and T. Kanamori
National Institute of Advanced Industrial Science and Technology (AIST), JAPAN

ABSTRACT

This paper reports a pressure driven perfusion cell culture chip for parallel drug toxicity assay. The device is equipped with 8 x 5 array of cell culture microchambers with independent perfusion microchannels. We adopted single external pressure source to drive the eight different culture media. The microchip enables a parallel cell viability assay in differently conditioned culture medium.

Keywords: cell culture, perfusion culture, microchamber array, drug toxicity assay

1. INTRODUCTION

In order to realize the high-throughput cell based assay on microchip, integrated cell culture microchamber arrays were reported previously [1, 2]. In this study we report a perfusion culture microchamber array chip for cell toxicity assay of differently conditioned colture media. Our device is different from the previously reported devices at the point that each microchamber has the independent perfusion channel, and that the differently conditioned media are perfused by single pressure source. Microchamber array with independent perfusion channel avoids cross contamination between differently conditioned microchambers. Liquid operation by single pressure source enables to transfer differently conditioned media simultaneously and realizes simple connection interface with macro scale devices.

2. DEVICE DESIGHN

Figure 1 shows the schematic structure of the microchip. Culture media containing eight different ingredients were supplied from medium inlet port. Microchannel network connects to independent perfusion culture channels to transfer the culture media

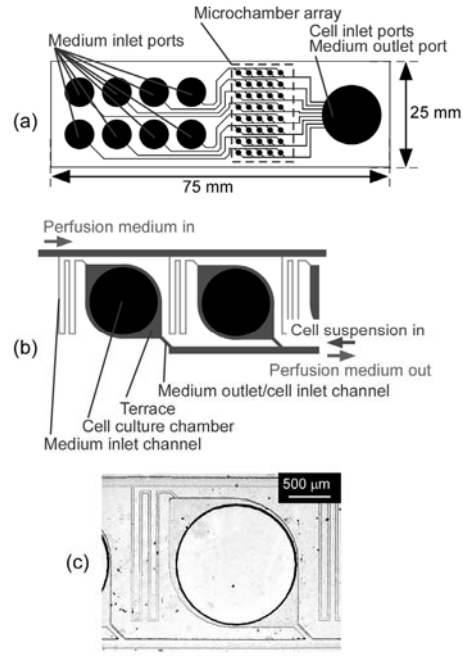

Figure 1: Schematics of perfusion culture microchamber array chip. (a) Microchannel network design. (b) Structure of each microchamber. Black colored chamber is 200 μm depth, dark grey colored channel is 50 μm depth, and light grey colored channel is 5 μm depth. (c) Microscope photograph of the microchamber.

978-0-9798064-0-7/μTAS2007/$20©2007CBMS

into microchambers. Medium outlet port works as cell inlet port. Cells are simultaneously introduced into each microchamber from this port. Each microchamber is composed of narrow fluid resistance channel with 5 μm depth, terrace structure with 50 μm depth, cell culture chamber with 200 μm depth and medium outlet channel with 50 μm depth. These structural dimensions were designed to realize (i) pressure driven long term culture, (ii) simultaneous introduction of determined volume of cell suspension, (iii) easy removal of bubble, (iv) high Peclet Number to avoid cross contamination between each microchamber, and (v) low shear stress in culture chamber.

3. EXPERIMENTAL

PDMS microchip with different depth channels was fabricated by multilayer photolisography using SU-8 photoresist [1].

4. RESULT AND DISCUSSION

Eight different culture media are introduced into medium inlet ports by utilizing single pressure source (Figure 2). Eight different culture conditions were easily formed in 8 x 5 microchamber array. The microchannel network was designed to have high Peclet Number (>20) in medium outlet channel. It lead no cross contamination between different culture condition.

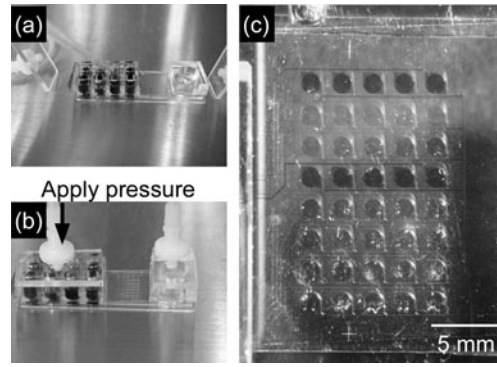

Figure 2. Liquid operation using pressure driven perfusion culture microchip. (a) Aqueous solutions containing eight different dyes were applied into inlet port. (b) Solutions were transferred by the external pressure source. (c) Microscope photograph of the microchamber array. The eight dye solutions were introduced into microchamber array without cross contamination.

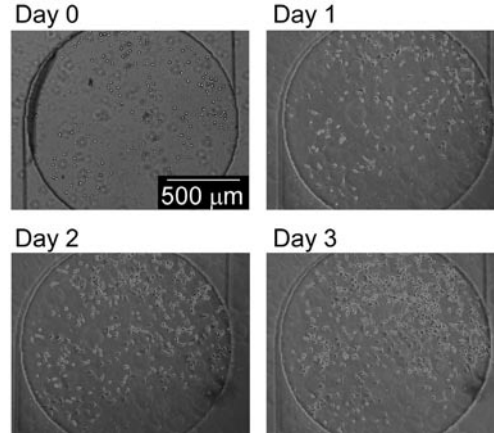

Figure 3. Growth of HeLa cells in microchamber.

HeLa cells from cervical cancer were cultured in microchamber array. Cell suspension with 2.7 x 10^5 cell/mL was seeded from cell inlet port. By applying appropriate pressure to cell inlet port, the determined volume of the cell suspension was introduced into each microchamber. During this step, the medium inlet channels work as hydrophobic passive valves. Introduction of determined amount of the medium enable the homogeneous cell introduction in to each chambers. The number of introduced cells had good agreement with the Poisson distribution.

The seeded cells were cultured in microchamber for 3 days. HeLa cells attached to PDMS surface and grew during 3 day culture indicating that the microchip with oxygen permeable PDMS wall and pressure driven perfusion culture system is applicable to cell growth assay (Figure 3).

Parallel cytotoxicity assay of multiple anticancer drugs was carried out using microchamber array. HeLa cells were seed into microchamber array. After 24 hours cultivation, the culture media containing 8 different anticancer drugs were perfused by single pressure source. After 48 hours cultivation, the living cells were stained with calcein-AM. The number of cells after cultivation was quantified by image analysis from the pictures obtained with fluorescence microscope (Figure 4). We think that the pressure driven perfusion culture system will be a promising platform for further integrated device combined with microfluidic components, such as gradient mixers and microvalves.

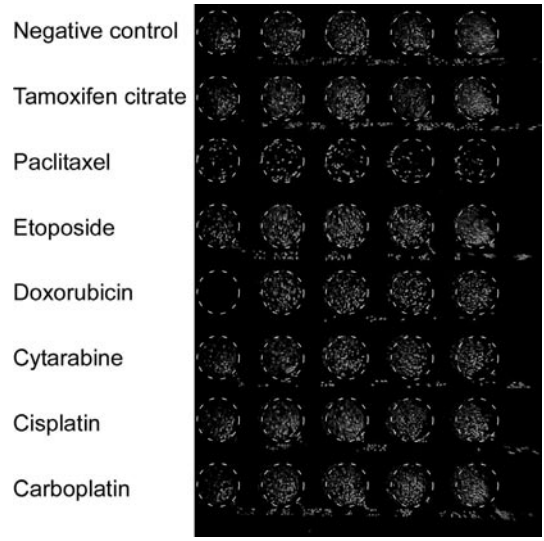

Figure 4. Fluorometric cell growth assay for drug toxicity analysis. Fluorescent microscope image were taken after cultivation in differently conditioned medium.

ACKNOWLEDGEMENTS

A part of this work was conducted in AIST Nano-Processing Facility.

REFERENCES

[1] P. J. Hung, P. J. Lee, P. Sabounchi, N. Aghdam, R. Lin, L. P. Lee, "A Novel High Aspect Ratio Microfluidic Design to Provide a Stable and Uniform Microenvironment for Cell Growth in a High Throughput Mammalian Cell Culture Array," Lab Chip, **5**, 44 (2005).

[2] K. R. King, S. Wang, D. Irimia, A. Jayaraman, M. Toner, M. L. Yarmush, "A High-Throughput Microfluidic Real-Time Gene Expression Living Cell Array," Lab Chip, **7**, 77 (2007).

CHEMOTAXIS-DRIVEN SEPARATION OF MOTILE SPERM BY LONGITUDINAL CHEMICAL CONCENTRATION GRADIENT IN MICROCHIP

Yong-jun Ko[1], Byung-Chul Lee[2], Joon-Ho Maeng[2], Seung-Yong Hwang[3], Yoomin Ahn[4]

[1]Department of Mechanical engineering, Graduate School, Hanyang University, KOREA
[2]Department of Biochemistry, Graduate School, Hanyang University, KOREA
[3]Division of Molecular and Life Science, Hanyang University, KOREA and
[4]Department of Mechanical engineering, Hanyang University, KOREA

ABSTRACT

In this study, we present a new microchip which can separate motile sperm by chemotaxis resulting from longitudinal chemical concerntration gradient in microchannel. In the fluorescent experiment, we verified that good linear concentration gradient was generated in the microchannel without the fluid control device. We performed the experiment of mouse sperm separation by chemotaxis with acetylcoline, chemoattractant, diluted in ratio of 1, 1/2, 1/4, 1/8, 1/16, 1/32, 1/64 and control (DI water) in microchip. As a result, we could separated progressive motile sperm in the specific concentration range of chemoattractant and the optimal concentration range to induce chemotaxis was 0.625~2.5 mg/ml.

Keywords: Chemotaxis, motile sperm, longitudinal chemical concentration gradient, microchip

1. INTRODUCTION

For external fertilization, it is very important to select motile sperm. For selection of a good motile sperm, researches on microchip can separate motile sperm have been recently published [1-3]. Especially, chemotaxis is used as separation method of motile sperm in microbiochip. It is very important factor to generate a chemical concentration gradient in microchannel to use chemotaxis. The recently published papers about the cell separation by chemotaxis used a lateral chemical concentration gradient caused by laminar flow and diffusion of the fluid in microchannel [2,3]. This method requires fluid control devices such as syringe pump and valve, large volume consumption and a lot of processing time. Furthermore, flow of fluid can disturbs separation by own movement of cell.

To overcome these disadvantages, We generated a longitudinal concentration gradient by the diffusion of the fluid without the control of the fluid and fluid control devices and separated the motile sperm according to the optimal concentration rage of chemoattractant with easily simple process and short separation time.

2. EXPERIMENTAL

The schematic of the proposed microchip is shown in Fig.1 (a). The microchip was designed to create linearly good chemical gradient due to diffusion and find the optimal condition of attractant dilution ratio and conduct an experiment about several attractants for

978-0-9798064-0-7/μTAS2007/$20©2007CBMS

chemotaxis at the same time in order to reduce the experimental error. The image of fabricated sperm separation chip is shown in Fig.1(b).

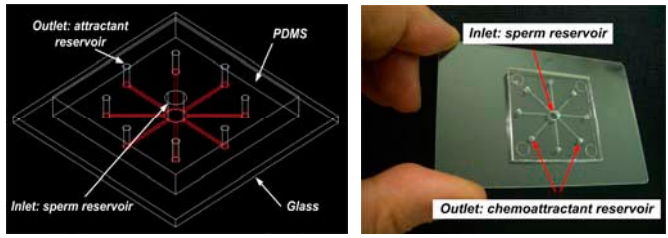

(a) (b)

Figure1. (a) Schematic of microchip for sperm separation 500 ㎛ wide, 10 mm long and 100 ㎛ high in microchannel, 2 mm diameter each outlet and 4 mm diameter inlet (b) Photograph of fabricated microchip

For sperm separation using chemotaxis, we used mouse sperm instead of human sperm and selected acetylcoline as chemoattractant of mouse sperm. We introduced human tubal fluid (HTF), buffer solution into microchip and attractants diluted in ratio of 1, 1/4, 1/8, 1/16, 1/32 and 1/64 including control (DI water) were dropped in each outlet by 2 ㎕ volume with micropippet. After 5min, 5 ㎕ sperm solution was also dropped into inlet. After 10 min when sperm reached to outlet by chemotaxis, we counted sperms in each outlet by using microscopy.

3. RESULTS AND DISCUSSION

As shown in Fig.2, the chemical gradient was linearly kept in microchannel at 5 min after 2 ㎕ PI (propidium iodide) was dropped in each outlet with micropippet. However, after 30 min, the linear chemical gradient was broken because of diffusion of chemical and the wane of fluorescent intensity. Therefore, we verified that it took 5 minutes to complete the linearity of chemical gradient in microchannel of the proposed chip.

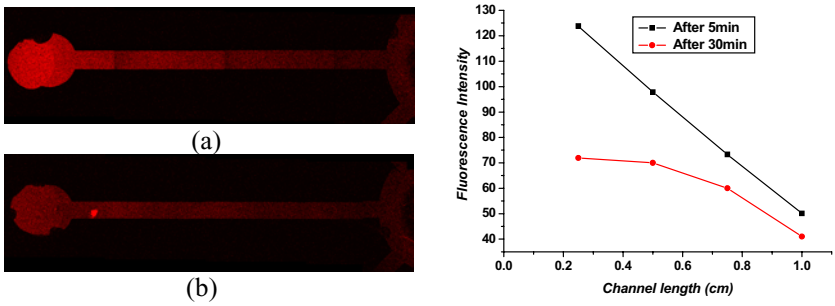

(a)

(b)

(c)

Figure 2. Result of concentration gradient according to channel length (a) after 5 minutes, (b) after 30 minutes when 2 ㎕ propidium iodide was dropped into outlet, (c) fluorescence intensity according to channel length

From the result of separation experiment by chemotaxis shown in Fig.3, we found that the percentage of separated sperm in outlets where 1/8, 1/16 and 1/32 diluted acetylcoline solution was dropped was relatively higher than any other outlets. This result indicates that movement of sperms by chemotaxis is more vigorous in specific concentration range.



(a)

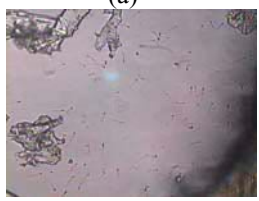

(b)

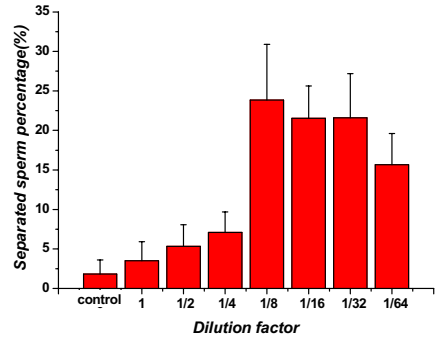

(c)

Figure 3. Separated sperm by the proposed microchip (a) control (b) outlet of 1/8 diluted acetylcholine solution (c) separated sperm percentage according to dilution factor

5. CONCLUSIONS

we could find optimal concentration range of attractant and separated progressive motile sperm by chemotaxis at the same time. In Figure 3, many sperm were isolated at wells where were dropped with 1/8, 1/16, 1/32 diluted solution. Therefore, optimal concentration range to induce chemotaxis was 0.625~2.5 mg/ml. we separated motile sperm by the proposed microchip with small volume (spem solution: 5 $\mu\ell$, attractant: 2 $\mu\ell$ in each outlet) and short time (total separation time: 15 min). Our microchip could have potential application to motile and mature sperm selection for intracellular sperm injection (ICSI).

ACKNOWLEDGEMENTS

"This work was supported by the Korea Research Foundation Grant funded by the Korea Government (MOEHRD, Basic Research Promotion Fund) (KRF-2006-311-D00326)."

REFERENCES

[1] Brenda S. Cho, Timothy G. Schuster, Xiaoyue Zhu, David Chang, Gray D. Smith, and Shuichi Takayama, *Passively driven integrated microfluidic system for separation of motile sperm*, Anal. Chem. Vol. 75, No. 7, pp.1671-1675, April, (2003).

[2] Sachiko Koyama, Dragos Amarie, Helena A. Soini, Milos V. Novotny, and Stephen C. Jacobson, *Chemotaxis assay of mouse sperm on microfluidic devices*, Anal. Chem., Vol. 78, No. 10, May, (2006).

[3] Francis Lin, and Eugene C. Butcher, *T cell chemotaxis in a simple microfludic device*, Lab Chip, Vol.6,pp.1462-1469, (2006)

DIELECTROPHORETIC CELL MANIPULATION ENABLED BY PARASITIC TRAP CANCELLATION

M. Urdaneta, E. Smela
Department of Mechanical Engineering, University of Maryland, Maryland, USA

ABSTRACT

In this work we present the loading of cells into SU8 cages using dielectrophoresis (DEP). Simply attracting cells into the cages using positive DEP is impossible because of parasitic traps that are a result of electric field distortions produced by the cage. By implementing multiple frequencies on multiple electrodes simultaneously, one can cancel the parasitic traps. Using this technique, areas on the substrate in which dielectrophoresis takes place may now include features that would otherwise interfere with the manipulations. Numerical and experimental results are presented.

Keywords: Multiple frequency dielectrophoresis, cell cage, cell loading.

1. INTRODUCTION

This paper describes the loading of cells into cages using multiple frequency dielectrophoresis (MFDEP) [1]. Such cages can be used to restrict the motion of motile cells, such as neurons, in long-term single cell studies [2-6]. Current options for loading cells inside cages are placing the cells by hand [4], using optical tweezers [5], and suctioning cells into place [7]. DEP has also been used to position cells, at speeds comparable to those of suction methods and with the control and positioning accuracy of laser tweezers. DEP has thus far been used to keep cells suspended at a particular position using negative DEP [8] or fixed on a flat sensing substrate using positive DEP [9]. However, it has not been used to attract cells into a physical cage. This is difficult because the cage itself distorts the electric field used to attract the cells: since DEP forces depend on electric field gradients, the distortion results in "parasitic traps", or regions to which cells are undesirably attracted, at the entrance rim of the cage, where cells remain stuck. In this work we address the problem of parasitic traps by actively cancelling them using MFDEP [1]. The method works without modifying the cage geometry or material. This is important because it allows the cage to have the characteristics needed by the application.

The same method could be used in other cases. It could be used, for example, to manipulate cells or nanoparticles around (conducting or insulating) device features. Without this method, parasitic traps severely limit the features that can be present in the vicinity of the DEP manipulation.

2. METHODS

The cell cage and DEP electrodes used to load the cells are illustrated in Figure 1. This device controls the cells in 3D using fluid flow and MFDEP. Cells are brought near the cage by fluid flow. As the cells flow above the cage, positive (attractive) DEP forces produced by an electrode inside the cage attract them into it. However, the SU8 cage (which has a different dielectric constant and conductivity than the medium) distorts the electric fields, resulting in large field gradients at the cage entrance rim. Since the frequency at the electrode produces positive DEP, the gradients at the rim and ceiling electrode edges attract and trap the cells as they approach the electrode inside the vial.

978-0-9798064-0-7/μTAS2007/$20©2007CBMS

We could redesign the cage shape or change the material to give smaller field distortions and smaller parasitic traps, but in many cases the choice of materials and shapes are restricted by device fabrication or function. Instead we found a way to greatly reduce parasitic traps without modifying the cage. Using MFDEP, cells can be attracted into the cage while also being repelled from the cage edges. By exciting electrodes at the location of the parasitic traps (at the entrance rim of the cage) at a frequency that produces negative (repulsive) DEP forces, the particles are pushed away from the trap location.

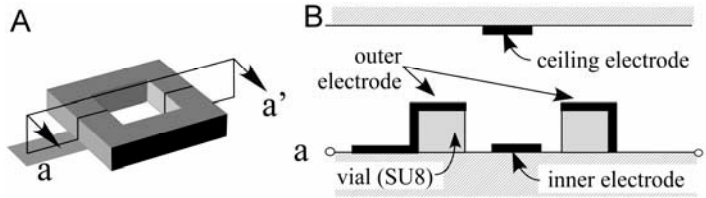

Figure 1. A) Illustration of a cell cage. B) Cross-section of the cage showing the three electrodes.

The negative DEP signal must be large enough with respect to the positive DEP signal to cancel the parasitic traps, but not so large that it prevents cells from going into the vial. Appropriate electrode voltages were found using numerical models. Femlab 3.1 (Comsol) was used to find the DEP forces around the vial using a fixed inner electrode voltage while the outer electrode voltage changed. As the outer electrode voltage increased, force vectors near the cage entrance rim switched from pointing towards the rim (parasitic trap present) to pointing away from the rim (parasitic trap cancelled). The outer electrode voltage used in the experiments is just high enough for it to cancel the parasitic traps. The same ground electrode can be used by both the inner and outer electrode, and this ground electrode was placed on the ceiling of the microfluidic chamber (though it could have also been placed on the chamber floor [1]). To check if cells would still go into the vial if they were being carried by a fluid flow, we modeled the cell trajectories under simultaneous fluid drag and DEP forces using a Matlab 7 (Mathworks) routine, balancing the two forces. Since the flow velocity distribution is needed to obtain the drag forces, we modeled the flow (pressure-driven) near the vial, also using Femlab 3.1.

3. RESULTS AND DISCUSSION

Figure 2A,B show particle tracing simulation results for cell-loading devices without parasitic trap cancellation. In Figure 2A, only part of the ceiling is grounded, whereas in B the whole ceiling is grounded. In both cases, most of the particles that approach the vial are trapped either at the vial entrance or at the ground electrode edges. This shows that parasitic trap cancellation is necessary. Figure 2C shows simulation results with a negative DEP (nDEP) electrode around the rim: most particles go into the vial, although some are still trapped at the rim because 100% cancellation is not possible with this geometry. Note that particles are not just repelled from the edges of the vial, but that they are also pushed away from the ground electrode. This occurs because the ground electrode is closer to the nDEP electrode, making nDEP the dominant signal at that location. The end result is that many more particles go into the vial. Even more particles would be loaded if, upstream from the vial, they were focused to the middle of the channel (not shown) [1].

To demonstrate the technique experimentally, we fabricated a system consisting of a 4x3 array of 12 cages in a microfluidic chamber with microchannels coming in and out. We loaded non-viable yeast into cages at flow speeds of up to 300 μm/s. Hundreds of cells

were loaded into the cages (Figure 2D) in a matter of seconds. When the electrodes were not excited, cells flowed past the vials without going in. Therefore, the number of cells in each vial can be controlled by turning the electrodes on or off.

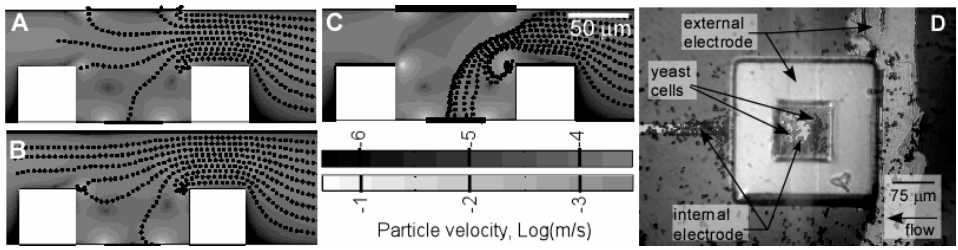

Figure 2. Simulation of particle loading without (A,B) and with (C) parasitic trap cancellation. (D) Non-viable yeast cells loaded into an SU8 cage using MFDEP to cancel the parasitic traps. The inner electrode was excited at f_1=5 kHz (10 V_{RMS}) and the outer electrode at f_2=5 MHz (8 V_{RMS}).

4. CONCLUSIONS

In this work, cells were manipulated using DEP in the presence of field-distorting structures using active parasitic trap cancellation. Broadly speaking, any structure will distort the electric field because its electric properties (conductivity and permittivity) are different from that of the medium. Therefore this method is, to our knowledge, the only way to enable the use of DEP in microfabricated environments with complex topographies and diverse materials, typical of lab-on-a-chip technologies. With trap cancellation, the combination of integration capability, accuracy, ease of control, and loading speed make DEP an excellent loading method.

ACKNOWLEDGEMENTS

We would like to acknowledge the Laboratory of Physical Sciences for their funding.

REFERENCES

[1] Urdaneta, M. and Smela, E., *Multiple frequency dielectrophoresis,* Electrophoresis, 18, (2007).

[2] Merz, M. and Fromherz, P., *Polyester microstructures for topographical control of outgrowth and synapse formation of snail neurons,* Advanced Materials, 14(2), 141, (2002).

[3] Reeves, N.*, et al.*, *Integrated MEMS structures and CMOS circuits for bioelectronic interface with single cells*, IEEE ISCAS, 3, 673 (2004).

[4] Tooker, A.*, et al.*, *Biocompatible parylene neurocages,* IEEE Engineering in Medicine and Biology Magazine, 24(6), 30, (2005).

[5] Tooker, A.*, et al.*, *Parylene neurocages for electrical stimulation on silicon and glass substrates*, IEEE EMBS Annual Intl. Conf., 4322 (2006).

[6] Claverol-Tinture, E., Cabestany, J., and Rosell, X., *Multisite recording of extracellular potentials produced by microchannel-confined neurons in-vitro,* IEEE Trans. on Biom. Eng., 54(2), 331, (2007).

[7] Ionescu-Zanetti, C.*, et al.*, *Mammalian electrophysiology on a microfluidic platform,* P. Nat'l Acad. Sci. USA, 102(26), 9112 (2005).

[8] Voldman, J.*, et al.*, *Design and analysis of extruded quadrupolar dielectrophoretic traps,* Journal of Electrostatics, 57(1), 69, (2003).

[9] Prasad, S.*, et al.*, *Neurons as sensors: individual and cascaded chemical sensing,* Biosensors and Bioelectronics, 19 1599, (2004).

ON-CHIP EVALUATION OF EFFECT OF DRUG-INDUCED APOPTOSIS ON ELECTROPHORETIC MOBILITY OF HEK CELLS

Takanori Akagi[1,2] and Takanori Ichiki[1,2]

[1]*School of Engineering, The University of Tokyo, 2-11-16 Yayoi, Bunkyo-ku 113-8656, Japan*

[2]*Center for Nano-Bio Integration, The University of Tokyo, 7-3-1 Hongo, Bunkyo-ku 113-8656, Japan*

akagi@sogo.t.u-tokyo.ac.jp

ABSTRACT

Cell electrophoretic mobility (EPM) variation owing to apoptosis induced by irinotecan hydrochloride (CPT-11) was evaluated by on-chip cell electrophoresis. Firstly, we investigated the effects of treatment with CPT-11 for 48 h on the viability, DNA content, EPM, and amount of sialic acid of human embryonic kidney (HEK) cells. Apoptosis induced by the treatment with CPT-11 was confirmed. The EPM distribution of the cells was found to shift to the positive-charge side with increasing CPT-11 concentration. Secondly, we investigated the variations in the viability, distribution of phospholipids in the membrane, EPM, and amount of sialic acid of the cells as CPT-11-induced apoptosis progressed at an IC_{90} of 689 μM after treatment with CPT-11. EPM distribution tends to shift to the positive-charge side as apoptosis progressed. Since the amount of sialic acid in the cells decreased as apoptosis progressed, it is considered that the EPM distribution of the cells shifted to the positive-charge side as apoptosis progressed owing to the variation in the amount of sialic acid. These results suggest the possible application of a high-accuracy on-chip cell EPM measurement system for evaluating the variation in the cell surface state owing to the CPT-11-induced apoptosis. This methodology is expected to be useful in the future high-throughput screening (HTS) of antitumor drugs.

Keywords: Apoptosis, Electrophoretic mobility (EPM), Cell electrophoresis

1. INTRODUCTION

Apoptosis, a genetically controlled form of cell death, is one of the fundamental processes by which cells maintain a normally state in organisms. Recent discoveries have shown that apoptosis is the key issue in intractable diseases such as cancer, Alzheimer's disease, and amyothrophic lateral sclerosis. Hence, apoptosis evaluation is necessary for the future high-throughput screening (HTS) of drugs for these diseases. Conventionally, methodologies using biochemical and optical techniques with the use of reagents are used to discover anticancer drugs. Unfortunately, these methodologies still have problems such as fluorescence correction and photobleaching. Therefore, a nonlabeling method of identify apoptotic cells is required to improve the reliability of apoptosis evaluation. Cell electrophoresis is a representative methodology used to evaluate cell surface charge. Cell electrophoretic mobility (EPM), determined by performing electrophoresis experiments, is an important physical property and is almost proportional to cell surface charge. Recently, we have successfully measured cell EPM using microcapillary electrophoresis (μCE) chips to evaluate the different states of cells such as cell cycle and cell damage states [1,2]. This method is advantageous for on-chip analysis since it requires no special pretreatment. In this study, we measured EPM variation as irinotecan hydrochloride (CPT-11)-induced apoptosis progress and discuss the validity of this methodology.

2. EXPERIMENTAL METHOD

Human embryonic kidney (HEK) cells were maintained in a SFM II medium (GIBCO) supplemented with 4 mM glutamax (GIBCO) in a humidified atmosphere of 95% air and 5% CO_2 at 37°C. After treating the cells with CPT-11 in accordance with the schedule shown in Figs. 1(a) and 2(a), we examined the effects of CPT-11 on the viability, DNA content, distribution of

978-0-9798064-0-7/μTAS2007/$20©2007CBMS

phospholipids in the membrane, EPM, and amount of sialic acid of the cells. To measure the viability of the cells, the cells were visually inspected using microscopy after trypan blue treatment. To measure DNA content and the distribution of phospholipids in the membrane, the cells were stained with propidium iodide (PI) and FITC-annexin V, respectively. Subsequently, their fluorescence intensities were determining the using a flow cytometer (BD LSR II). To measure cell EPM, cell electrophoresis using a poly(dimethylsiloxane) (PDMS) μCE chip were carried out as a procedure described previously [1,2]. Note, however, that electric field strength was set at 20 V/cm. To measure the amount of sialic acid in the cells, sialic acids were released by acid hydrolysis. Subsequently, the free sialic acids were analyzed by reverse-phase HPLC after labeling them with 1,2- diamino-4,5-methyleneoxybenzene (DMB).

3. RESULTS AND DISCUSSION

Firstly, we investigated the effects of treatment with CPT-11 for 48 h on the viability, DNA content, EPM, and amount of sialic acid of HEK cells (Fig. 1). To investigate the effect of CPT-11 on the viability of the cells, the total number of living cells was counted. As shown in Fig. 1(b), the number of living cells gradually decreased with increasing CPT-11 concentration. The IC_{50} and IC_{90} of the cells treated with CPT-11 were 44.2 and 689 μM, respectively. To investigate the effect of CPT-11 on the cell cycle, the DNA content of the cells was measured using a flow cytometer. The DNA content distribution of the cells was synchronized in the S-phase for CPT-11 effect determination (Fig. 1(c)). The result indicats that the cells died by apoptosis, and not by necrosis, another form of cell death. We subsequently measured the cell EPM using on-chip cell electrophoresis to investigate the effect of CPT-11 on surface charge. Figure 1(d) shows that the EPM after treatment with CPT-11 tends to shift to the positive-charge side with increasing CPT-11 concentration. Additionally, the amount of sialic acid in the cells was measured by HPLC since sialic acid localizes on the cell surface and its carboxyl group has a negative charge in PBS (pH 7.4). The amount of sialic acid in the cells decreased with increasing CPT-11 concentration (Fig. 1(e)). Thus, it is considered that the variation in the cell EPM after treatment with CPT-11 is due to the variation in the amount of sialic acid.

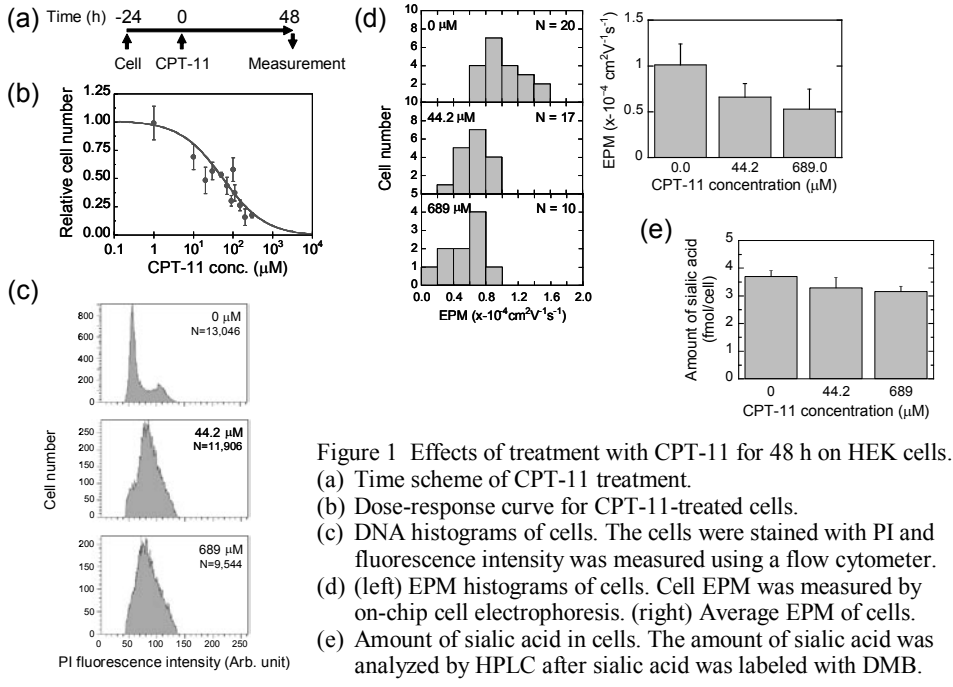

Figure 1 Effects of treatment with CPT-11 for 48 h on HEK cells.
(a) Time scheme of CPT-11 treatment.
(b) Dose-response curve for CPT-11-treated cells.
(c) DNA histograms of cells. The cells were stained with PI and fluorescence intensity was measured using a flow cytometer.
(d) (left) EPM histograms of cells. Cell EPM was measured by on-chip cell electrophoresis. (right) Average EPM of cells.
(e) Amount of sialic acid in cells. The amount of sialic acid was analyzed by HPLC after sialic acid was labeled with DMB.

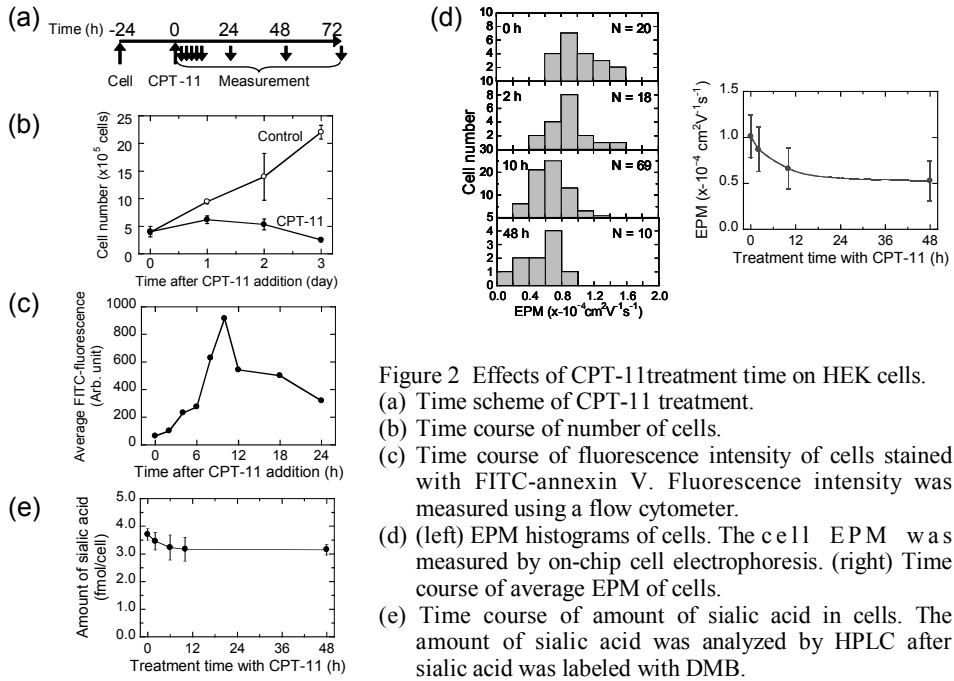

Figure 2 Effects of CPT-11treatment time on HEK cells.
(a) Time scheme of CPT-11 treatment.
(b) Time course of number of cells.
(c) Time course of fluorescence intensity of cells stained with FITC-annexin V. Fluorescence intensity was measured using a flow cytometer.
(d) (left) EPM histograms of cells. The cell EPM was measured by on-chip cell electrophoresis. (right) Time course of average EPM of cells.
(e) Time course of amount of sialic acid in cells. The amount of sialic acid was analyzed by HPLC after sialic acid was labeled with DMB.

Secondly, we investigated the variations in the viability, distribution of phospholipids in the membrane, EPM, and amount of sialic acid of the cells as CPT-11-induced apoptosis progressed at an IC_{90} of 689 μM after treatment with CPT-11 (Fig. 2). To investigate the time course of cell proliferation, the total number of living cells was counted 1, 2 and 3 days after CPT-11 treatment. As shown in Fig. 2(b), the proliferation rate of the cells after CPT-11 addition was found to differ from that after PBS addition. To investigate the distribution of phospholipids in the cell membrane, the binding of FITC-annexin V to the cells was analyzed using a flow cytometer. The degree of the binding of FITC-annexin V to the cells was found to increase with CPT-11 treatment time (Fig. 2(c)). This result indicates that apoptosis progresses after the initiation of CPT-11 treatment. Subsequently, we investigated the EPM variation as apoptosis progressed. As shown in Fig. 2(d), the EPM tends to shift to lower values with CPT-11 treatment time. Furthermore, to investigate why the cell EPM varied as apoptosis progressed, the amount of sialic acid in the cells was measured by HPLC. The amount of sialic acid in the cells gradually decreased with CPT-11 treatment time. (Fig. 2 (e)). Thus, it is considered that the cell EPM variation as CPT-11-induced apoptosis progressed is due to the variation in the amount of sialic acid.

4. CONCLUSIONS

In this study, we demonstrate the possible application of the on-chip cell EPM measurement system for evaluating the variation in the cell surface state owing to CPT-11-induced apoptosis. This methodology is expected to be useful in clinical and pharmaceutical applications such as the future HTS of antitumor drugs.

REFERENCES

[1] T. Akagi, M. Suzuki and T. Ichiki, Jpn. J. Appl. Phys. **45** pp. L1106-L1109, (2006).
[2] T. Akagi, M. Suzuki, T. Sato and T. Ichiki, Jpn. J. Appl. Phys. submitted.

ENDOTHELIAL CELL PHENOTYPE ON GELATIN MICROPATTERNS COMPARED TO THAT IN MICROCHANNELS

Patty P.M.F.A. Mulder[1], Sander Koster[1], Grietje Molema[2], Elisabeth Verpoorte[1]

[1]*University of Groningen, The Netherlands*
[2]*University Medical Center Groningen, The Netherlands*

ABSTRACT

Our long-term interest is to develop new techniques for adherent cell-based drug screening by using microtechnologies to create *in vivo*-like microenvironments. This paper explores the influence of surface properties on the morphology of adherent cells in the presence or absence of a microchannel.

Keywords: Micropattern, Cell Morphology, Endothelial Cells, Polydimethylsiloxane

1. INTRODUCTION

Endothelial cells play an important role in chronic inflammatory diseases and cancer. They are a target for therapeutic intervention [1]. High-speed drug screening using adherent cells in microengineered environments is made possible by lab-on-a-chip technology. We have successfully demonstrated the cultivation of human endothelial cells in microchannels. These cells have a stretched phenotype with alignment along the walls, while cells in 96-well plates have a cobblestone appearance. Cell cultivation in microchannels was performed under static conditions with the exception of twice-daily medium refreshment [2]. It appears, then, that microchannel geometry and/or short-term low-shear flows may significantly influence cell morphology. To address both issues, we have investigated the effect of well-defined patterned environments under static conditions on endothelial cell phenotype.

2. EXPERIMENTAL

To create well-defined patterns, a PDMS chip with straight channels was used as a stencil [2]. This chip was placed on a glass plate and 1% gelatin was added to the channels and crosslinked with 0.5% glutaraldehyde. After several washing steps with medium, the stencil was removed, resulting in gelatin strips on the glass surface. For cultivation of cells in microchannels, the whole glass surface was coated with gelatin and crosslinked. The PDMS chip was then placed on the gelatin-coated glass plate. One mL of medium containing cells was added to each micropattern. A different number of cells (25,000, 50,000, or 75,000) was deposited on each micropattern for the determination of surface influence on cell shape. 45,000 cells were used for the glass/PDMS microchannels. As in the microchannels, the unattached cells were removed after a 1-hour incubation at 37°C under 5% CO_2-95% air, and the micropatterns were covered with medium. The cells were observed under a microscope (Zeiss, Axiovert 25) after 2, 19 and 26 hours of incubation.

3. RESULTS AND DISCUSSION

Aligned and elongated cells were observed along the edges of the gelatin patterns for all cell amounts (Figure 1). Cells were more randomly oriented and less elongated in the middle of the strips. However, cell alignment along the length of the strips becomes more

978-0-9798064-0-7/μTAS2007/$20©2007CBMS

pronounced at higher cell surface densities (up to confluency). This behavior is also observed in microchannels. When cells are seeded onto larger patterns (Figure 2), cells also align themselves along the edge and elongate, even though cells show no distinct orientation away from the edge. Another phenomenon occurs at very low cell concentrations (Figure 1.1a). The cells appear to prefer to attach at the edges of the micropattern under these conditions. When cell numbers are increased, they also settle in other regions (Figure 1.2a and 1.3a).

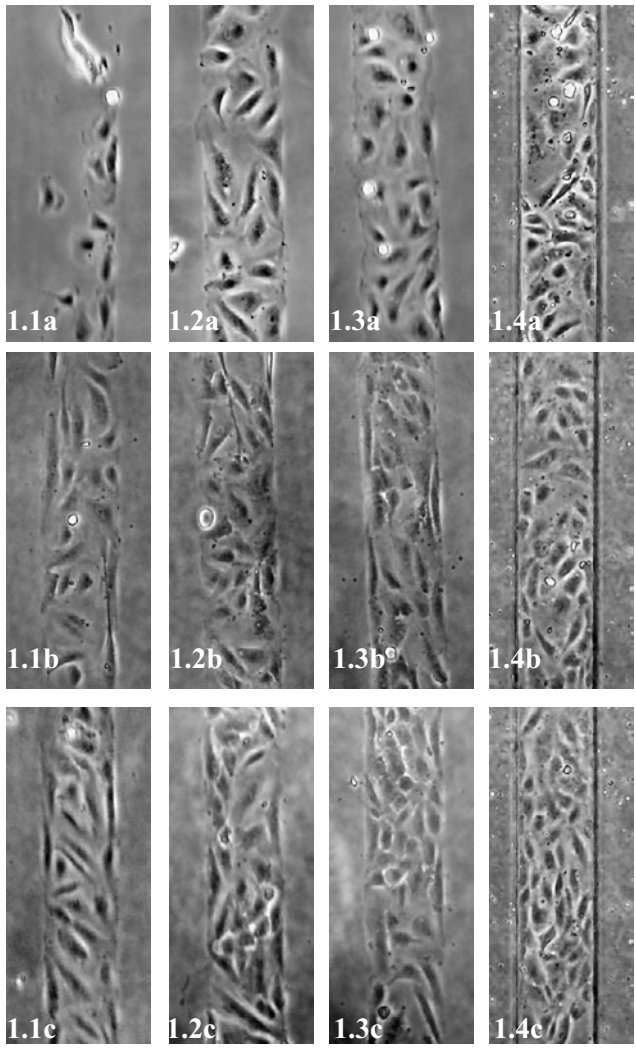

Figure 1. 25,000, 50,000, or 75,000 cells seeded on gelatin patterns (1.1-1.3) or 45,000 cells seeded in micro-channels (1.4) after cultivation for (a) 2 h (b)9 h (c) 26 h.

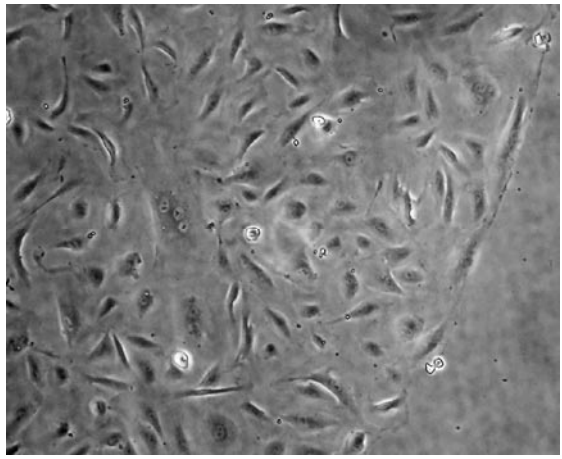

Figure 2. 50,000 cells seeded on a circular gelatin pattern and observed after 26 h.

4. CONCLUSIONS

Based on the similarity in morphologies of cells cultivated in microchannels and on gelatin strips, it can be concluded that microchannel geometry, in particular surface shape, does influence cell shape under static conditions. In the future we want to establish the link between phenotype, gene expression and drug response, in order to make screening tests more informative.

ACKNOWLEDGEMENTS

We thank H. Moorlag for the isolation of endothelial cells. This work was supported by the University of Groningen.

REFERENCES

[1] J. M. Kuldo, K. I. Ogawara, N. Werner, S. A. Asgeirsdottir, J. A. A. M. Kamps, R. J. Kok, and G. Molema, "Molecular pathways of endothelial cell activation for (targeted) pharmacological intervention of chroninc inflammatory diseases", *Cur. Vasc. Pharmacol.*, **3**, 11 (2005).

[2] P.P.M.F.A. Mulder, H.J. van der Linden, S. Koster, G. Molema, and E.M.J. Verpoorte, "Characterization of Human Umbilical Vein Endothelial Cells (HUVEC) cultivated in microfluidic channels", Proc. Micro Total Analysis Systems 2005, Transducers Research Foundation, San Diego, U.S.A., 1383-1385 (2005).

FABRICATION OF A DISPOSABLE ELECTROSONIC MICROARRAY IN THIOLENE AND PERFORMANCE CHARACTERIZATION FOR BIOMOLECULE DELIVERY

J.M. Meacham[1], V. Zarnitsyn[2], M. Varady[2], J. Atencia[1], L. Locascio[1], F.L. Degertekin[2] and A.G. Fedorov[2]

[1]National Institute of Standards and Technology and [2]Georgia Institute of Technology, USA

ABSTRACT

We present the fabrication and performance characterization of a thiolene-based electrosonic ejector microarray for biomolecule delivery. The piezoelectrically-actuated device utilizes resonant operation and acoustic wave focusing by horn structures to create a localized microenvironment, which enables precise control of the bioeffects experienced by treated cells. The simple fabrication process not only yields a microarray that is essentially disposable, but it also allows for greater flexibility in the design of the wave focusing horns.

Keywords: Cell Treatment, Biomolecule Delivery, Electrosonic Atomizer

1. INTRODUCTION

Controlled transport of biomolecules into or out of cells is critical to drug design and delivery, and also in many molecular biology and genetic modification protocols. We describe an electrosonic microarray [1], which has the potential to become an enabling technology platform for biomolecule (DNA/RNA, drug and imaging agents) delivery with control on the scale of an individual cell. Specifically, the work reported here focuses on fabrication and performance characterization of a "disposable" thiolene-based microarray.

2. CONCEPT, FABRICATION AND ASSEMBLY

Figure 1A,B shows a schematic of the electrosonic microarray [1], in which a sample chamber is placed between a nozzle array and a piezoelectric transducer. The sample chamber is loaded with a buffer solution, a suspension of cells and the biomolecule(s) that one desires to deliver into the cells. Horn structures focus the acoustic waves generated when the piezoelectric transducer is driven at one of the resonant frequencies of the fluid-filled chamber [2]. The resulting pressure gradient near the aperture of each nozzle serves

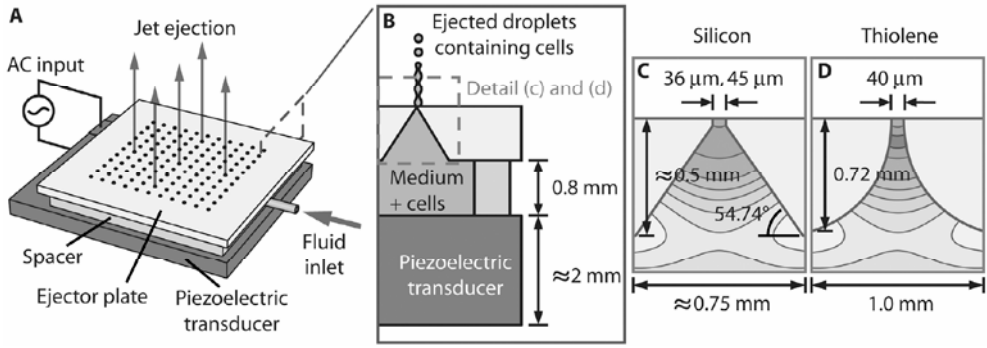

Figure 1. Electrosonic microarray schematic: A) sandwich assembly and operation, B) device cross section, and C,D) details of the nozzle geometry including pressure contours.

978-0-9798064-0-7/µTAS2007/$20©2007CBMS

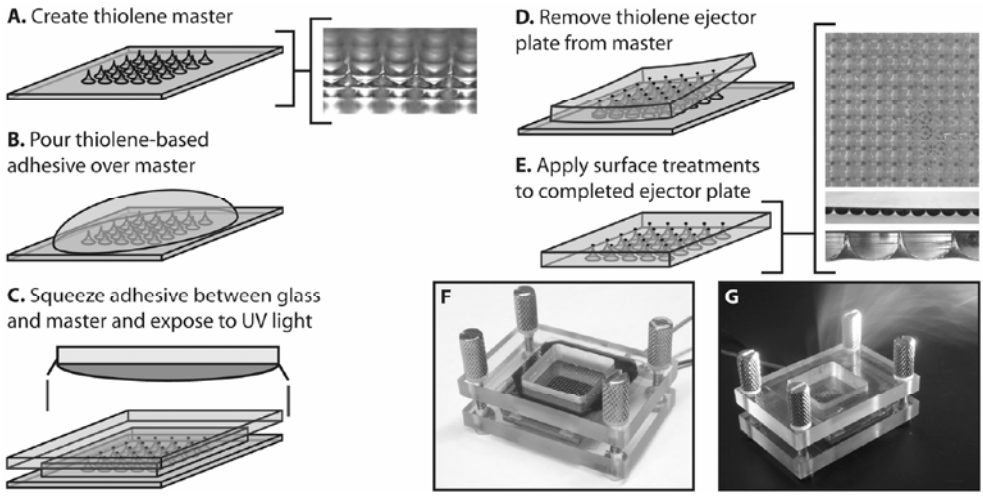

Figure 2. Fabrication and assembly: A–E) fabrication of a thiolene microarray including images of the master and array, and F,G) device assembled for cell treatment experiments.

two purposes: (1) it applies a mechanical force of independently controlled magnitude (via the piezoelectric transducer input voltage) and duration (via the frequency of operation) to the cell membrane, leading to poration and uptake of biomolecules or cell lysis and release of intracellular content; and (2) it allows processed cells to be ejected as a jet or droplet stream [3] for further processing downstream, enabling integration of lab-on-a-chip experiments.

Two microarrays have been characterized for biomolecule delivery (see Fig. 1C,D): (1) a previously reported array of pyramidal horns anisotropically wet etched into [100]-oriented silicon [2,4] and (2) a "disposable" array made by casting over a thiolene master. The fabrication process for the thiolene microarray is shown in Fig. 2A–E. First a master is created using a hierarchical grayscale lithography process, which consists of repetition of individual horns each generated by patterning concentric circles with different grayscale tonalities. This technique allows for modulation of the three-dimensional (3D) topography of the surface conferring a degree of flexibility on the design of the horns that is not possible to achieve by other methods (i.e., the profile of the realized nozzle cross section shown in Fig. 2A, which resembles an exponential horn, was easily achieved with good repeatability). The microarray itself is made by casting thiolenes over the master followed by exposure to UV light (see Fig. 2A–E). The microarray/piezoelectric transducer sandwich structure is assembled between two pieces of polycarbonate during the cell treatment experiments (see Fig. 2F,G).

3. EXPERIMENTAL

Uptake studies have been performed on human malignant glioma cells (line LN443) using the silicon electrosonic microarray [4]. Two orifice sizes (36 μm and 45 μm diameter) were investigated (see Fig. 1C). The small fluorescent (green emission) calcein molecule, which is cell impermeable and highly hydrophilic, was used to evaluate uptake over a range of operating conditions (e.g., frequency and peak-to-peak voltage, V_{pp}, applied to the piezoelectric transducer). Following treatment by silicon and thiolene arrays, nonviable cells were distinguished from viable cells by monitoring fluorescence (red emission) due to staining of nuclear material in cells with ruptured cell membranes by propidium iodide (PI).

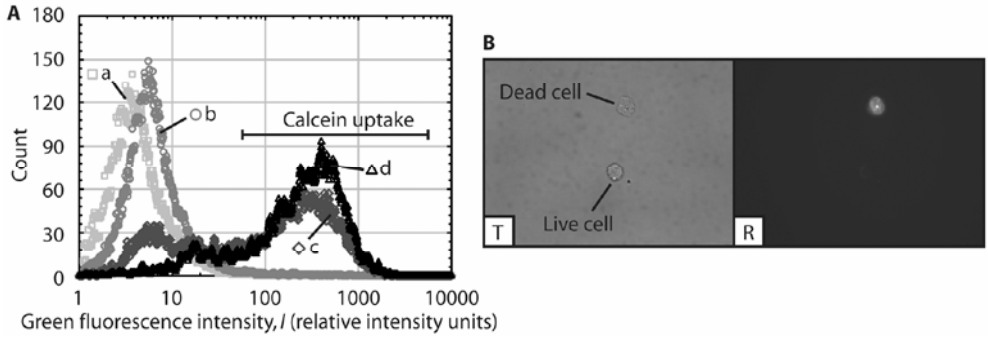

Figure 3. Performance characterization: A) uptake results after treatment by a silicon microarray with 45 μm diameter orifices (□ – calcein-free control, ○ – cells soaked in calcein but not processed, ◇ – cells treated with 156 V_{pp} input and △ – cells treated with 390 V_{pp} input) and B) viability results after treatment by a thiolene microarray (T – transparent illumination and R – red fluorescence).

4. RESULTS AND DISCUSSION

Orifice diameter and input voltage were found to play an important role in cell viability and calcein uptake [4]. Significant cytotoxicity was observed after cell ejection through 37 μm diameter orifices of a silicon microarray while ≈80% of cells survived treatment by 45 μm orifices. For viable cells, uptake increased from 65% to 85% with an increase in voltage amplitude from 156 V_{pp} to 390 V_{pp} (see Fig. 3A). Representative results from a cell viability experiment after treatment by the thiolene microarray are shown in Fig. 3B. The red channel of the fluorescence image indicates that the membrane of one of the two cells has ruptured. Based on a complete analysis of microscopy data, ≈55% of cells remained viable after treatment by this device, consistent with results for the silicon microarrays.

5. CONCLUSIONS

The proof-of-concept experiments reported here demonstrate successful use of an electrosonic ejector microarray for biomolecule delivery. Further, the operating parameters, which are readily realized by this device, span an entire spectrum of conditions that lead to different desired biophysical effects, ranging from cell lysis to poration and drug delivery with a high degree of efficacy [5].

REFERENCES

[1] A.G. Fedorov and F.L. Degertekin, "Electrosonic cell manipulation device and methods of use thereof," *U.S. Patent App.* 11/277,662 (2006).

[2] J.M. Meacham, C. Ejimofor, S. Kumar, F.L. Degertekin and A.G. Fedorov, "Micromachined ultrasonic droplet generator based on a liquid horn structure," *Rev Sci Instrum* **75**, pp. 1347–1352 (2004).

[3] J.M. Meacham, M. Varady, F.L. Degertekin and A.G. Fedorov, "Droplet formation and ejection from a micromachined ultrasonic droplet generator: visualization and scaling," *Phys Fluids* **17**, pp. 100605–100613 (2005).

[4] V. Zarnitsyn, J.M. Meacham, M. Varady, C. Hao, F.L. Degertekin and A.G. Fedorov, "Electrosonic ejector microarray for drug and gene delivery," submitted to *Biomed Microdevices* (2007).

[5] M. Lokhandwalla and B. Sturtevant, "Mechanical haemolysis in shock wave lithotripsy (SWL): I. Analysis of cell deformation due to SWL flow-fields," *Phys Med Biol* **46**, pp. 413–437 (2001).

HIGH THROUGHPUT AND HIGH EFFICIENCY ELECTROPORATION CHIP WITH POLYELECTROLYTE CURRENT PATHS

Jae Hyun Kim[1, 2], Zee Hwan Kim[2], Tae Song Kim[1] and Sang Kyung Kim[1]

[1]Nano Bio Research Center, Korea Institute of Science and Technology, KOREA and [2]Department of chemistry, Korea University, KOREA

ABSTRACT

Electroporation is a technique with which DNA molecules can be delivered into cells. We present a low voltage (10V~20V) DC electroporation for safe and efficient gene transfection by micro-electroporator containing polyelectrolyte salt bridge. Electric field and pulse duration on a cell was precisely controlled and most of adverse effects were not observed such as heating, bubble generation and chemical contamination. Electropermeation of suspension and adherent cells was accomplished with the electroporation chip. GFP plasmid was delivered and expressed successfully.

Keywords: electroporation, micro-electroporation chip, gene transfection, polyelectrolyte hydrogel

1. INTRODUCTION

Gene transfection has an important meaning in biotechnology. One of the gene transfection methods, electroporation is commonly used to introduce molecules such as DNAs into cells due to its essential advantages that can be applicable to any type cells.

With established glass chip and its results [1], we have developed PDMS electroporation chip with modified channel design. This PDMS chip has advantages such as, technically simple process, disposable usage, and reduced chip-to-chip variation, and high throughput (10^5cells/min).

2. EXPERIMENTAL

Our electroporation chips were fabricated by lithographic methods. Its operating principle in an electroporation microchip is illustrated in Figure 1(a). Figure 2 includes the fabricated electroporation chip. The height of channels is 75 μm and the width of mid-channel is 30 μm at the central narrow region. The hydrogel plug are 500 μm wide at the widest and 30 μm wide at the interface to the mid channel. Hydrogel plug was composed of 65% Monomer (diallyldimethyl ammonium chloride), 2% Photoinitiator (2-hydroxy-4'-(2-hydroxymethyl)-2-methylpropiophenone), 5% Crosslinker (N, N'-methylenebisacrylamide) and 500 mM KCl. The electrode (AgCl wire) was inserted to the 3M KCL solution in the chip. DC voltage was applied to the microfluidic channel instead of electrical pulses. Induced voltage ranging from 7 to 20V was provided by power supply (Figure 1(b)). The cell suspension was injected to the inlet of the channel from a syringe pump. For electroproation tests, density of cells was fixed to 1×10^7 cells/mL. For DNA transfection and expression, PEGFP-C2 plasmid was added to the media at a concentration of 0.1μg/μL.

978-0-9798064-0-7/μTAS2007/$20©2007CBMS

To observe the fluorescence from the expressed GFP, excitation radiation was at 488nm and the emission was observed at 527nm.

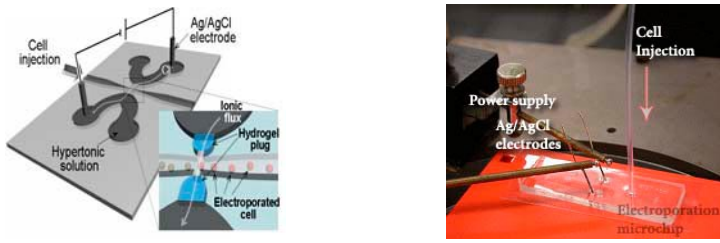

(a) (b)

Figure 1. (a) Schematics of the electroporation microchip (b) Experimental set up for cell electroporation.



(a) (b)

Figure 2. (a) Micro-electroporation device and (b) details of the hydrogel plug; For the precise photolithography defining hydrogel plug, a thin glass slide (100 μm), as the upper plate of the chip, is bonded to the PDMS chip with oxygen plasma.

3. RESULTS AND DISCUSSION

Electropermeation of K562 human chronic leukemia cells and Hepg2 human hepatocellular carcinoma cells were accomplished in the microchip (figure 1(b)) under various potential and flow rates. PI (propidium iodide) was used to visualize the electropermeated cells since it intercalates into nucleic acids in the cells and emits red fluorescence. We could observe the electropermeation from 5V and the electroporation efficiency increased up to 60 % with viability of 80 % as shown in Figure 3(a).

Strong electric field might damage cell membrane, so the viability was decreased gradually with input voltage. Figure 3(b) shows viability and efficiency as a function of cell velocity. It indicates that when the cell velocity is increased, the viability is increased up to 95 % with attenuated efficiency. GFP plasmid was transfected to K562 cells with 12V. The GFP has been used as a marker of gene expression and protein targeting in intact cells and organisms. Most of the cells spread out fluorescence from the expression of green fluorescence protein (Figure 4(a)).

In contrast to suspension cells (K562), adherent cells (Hepg2) generally utilize positively charged transfection agent and they are notorious for the low transfection efficiency. However, the fluorescence of PI was detected from over 90% of treated cells when an electric field was applied in the same range as K562. Hepg2 cells were transfected with DNA plasmid and expression of the protein was demonstrated with fluorescence images

too (Figure 4(b)). With these experimental results, we achieved high transfection efficiency for various cells in our micro-electroporation chip.

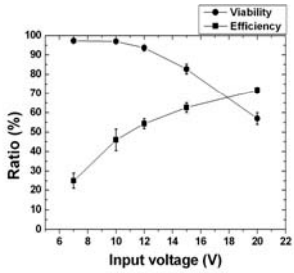

(a)

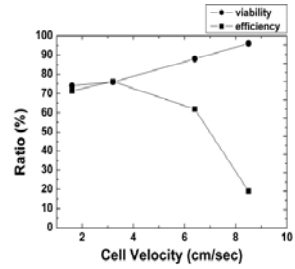

(b)

Figure 3. (a) electroporation efficiency and viability vs. input voltage and (b) electroporation efficiency and viability vs. cell velocity

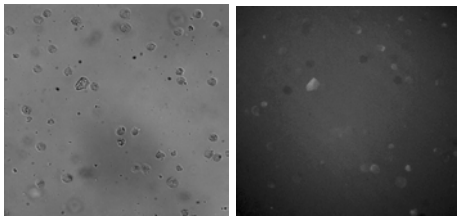

(a)

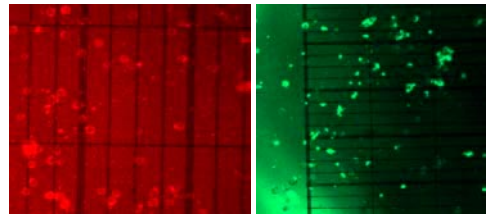

(b)

Figure 4. Images of successfully electroporated K562 cells, Hepg2 cells with GFP. (a) An image from a general optical microscope and fluorescence image with K562. (b) PI was delivered with the electroporation chip. GFP plasmid was transfected and expressed successfully in Hepg2.

4. CONCLUSIONS

We demonstrated the high transfection efficiency using the various cells. Our results show that the microchip is one of the most remarkable candidate for gene transfection. Moreover, we can use the microchannel device as a powerful tool for versatile chemical delivery in high throughput screening systems.

REFERENCES

[1] S. K. Kim, J. H. Kim, K. P. Kim, T. D. Chung, *Low voltage DC electroporation chip with polyelectrolyte salt bridge*, 20th IEEE MEMS conference 2007, Kobe, Japan, pp. 465- 468, (2007).

[2] S. K. Kim, H. J. Lim, T. D. Chung, H. C. Kim, *A miniaturized electrochemical system with a novel polyelectrolyte reference electrode and its application to thin layer electroanalysis* , Sensors and Actuators B, 115, pp. 212- 219, (2006).

MECHANICAL CELL LYSIS USING PDMS MEMBRANE DEFLECTION IN A MICROFLUIDIC DEVICE

Yu Chang Kim[1,2], Wonjae Choi[1], Yun Wook Hwang[2], Sang-Jin Park[2] and Je-Kyun Park[1]

[1]Korea Advanced Institute of Science and Technology (KAIST), KOREA
[2]Korea Institute of Machinery & Materials (KIMM), KOREA

ABSTRACT

The lysis procedure is important for sample preparation and the subsequent assay to be performed. In this study, we present a simple microfluidic device for mammalian cell lysis using poly(dimethylsiloxane) (PDMS) membrane deflection between two microchannels. As a demonstration of the feasibility of this microfluidic device, the lysis of MCF7 cells was achieved by the compressive force through the deflection of the PDMS membrane. The lysis speed was also measured with high-speed camera (135±37 ms, n=30) and the release of cytoplasmic dye (calcein AM) was confirmed via fluorescence analysis.

Keywords: Cell lysis, PDMS membrane deflection, microfluidic device, MCF-7

1. INTRODUCTION

Since the lysis methods can affect the analysis target, i.e. the cellular contents such as DNA, RNA, protein, the choice of cell lysis protocol is important for sample preparation and the subsequent assay to be performed. Conventional microfluidic devices for mechanical lysis utilize shear and frictional forces induced by subjecting cells to enter the microchannel with filter structure [1]. However, mechanical cell lysis with pressure-driven flow cannot be used to lyse adherent cells directly. Here we propose a new mechanical cell lysis method for adherent cells without trypsinizing through the deflected membrane between two microchannels. This mechanical cell lysis also allows rapid recovery of intracellular contents without introducing lytic agents [2] and applying electric field [3].

2. EXPERIMENTAL

Figure 1 and 2a illustrate the cross-sectional view of the microfluidic device. The device consists of three layers: control layer, flow layer, and PDMS membrane (15 μm). The PDMS membrane between two microchannels is deflected by applying pressure to the control channel. This deflected PDMS membrane presses and lyses the cells inside flow channel directly above a certain extent of the pressure. The membrane is also designed to

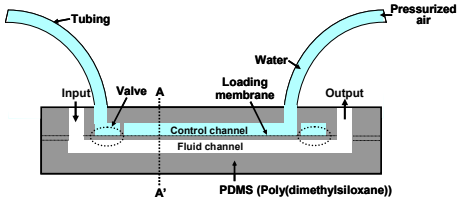

Figure 1. Cross-sectional view of the microfluidic device.

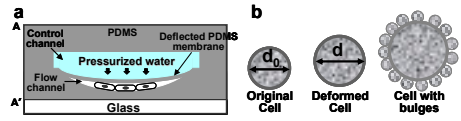

Figure 2. (a) Side view of the deflection of the PDMS membrane between two microchannels for cell lysis. (b) Morphological changes during cell lysis under the compressive force.

978-0-9798064-0-7/μTAS2007/$20©2007CBMS

close a fluid channel or confine the cells in the microchannel. The step of the cell lysis is as follows: cell deformation, bulges formation on lipid membrane, and cell membrane rupture (Figure 2b). For this study, we used MCF7 human breast cancer cells (mammary gland epithelial cell) as a model cell. As shown in Figure 3, the membrane deflection (height at apex) under pressure control was measured from the optical side-view image using an image analysis software in order to characterize membrane deflections (n=6). The measurements were carried out in another device only having one layer and 15 μm-thick membrane.

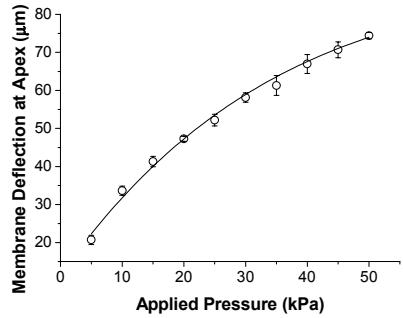

Figure 3. Measurements of membrane deflection at apex for 15 μm-thick membrane. The deflection height was measured from the optical side-view image using an image analysis software (n=6).

3. RESULTS AND DISCUSSION

To monitor mechanical cell lysis, adherent MCF7 cells were compressed at an elevated pressure ranging from 0 to 29.6 kPa for loading membrane (Figure 4). Like engineering materials, cells deform when physical forces are exerted on them. With applied pressure, the membrane deflection increased and small bulges appeared at the cell membrane. Further deflection resulted in an increase of the size and number of the bulges followed by cell bursting. Based on the pressure control of the microchannel with a regulator, we can squeeze biological contents out at the appropriate deflection of the membrane. It was also possible to rapidly lyse the adherent cells by momentarily opening an on/off valve in the external regulated pressure line for lysis (Figure 5). A high-speed camera was used to record images of the lysis event. The lysis was assumed to be carried out within 135±37 ms for MCF7 cells (n=30). Since signal-cascade

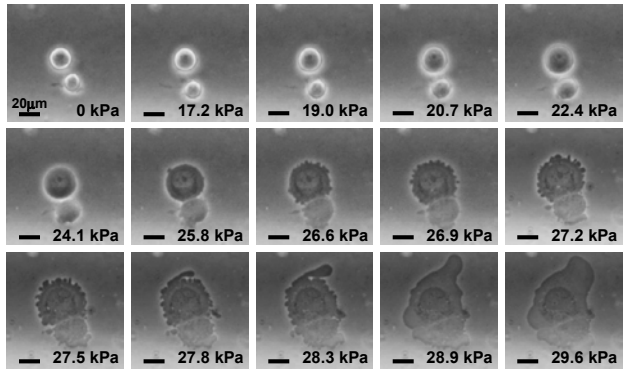

Figure 4. The radial expansion, bulge formation and rupture of cell membrane according to the elevated pressure. Scale bars are 20 μm

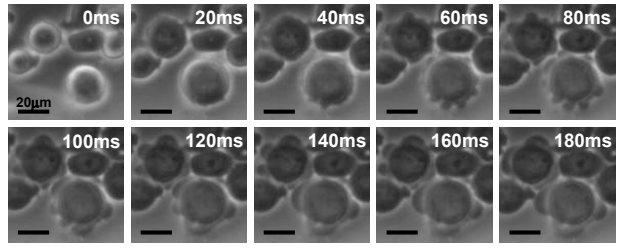

Figure 5. Images of the cell lysis event captured using a high-speed camera. The cells were lysed by momentary deflection of PDMS membrane through the opening of an on/off valve in the control line regulated at 35 kPa. All scale bars are 20 μm

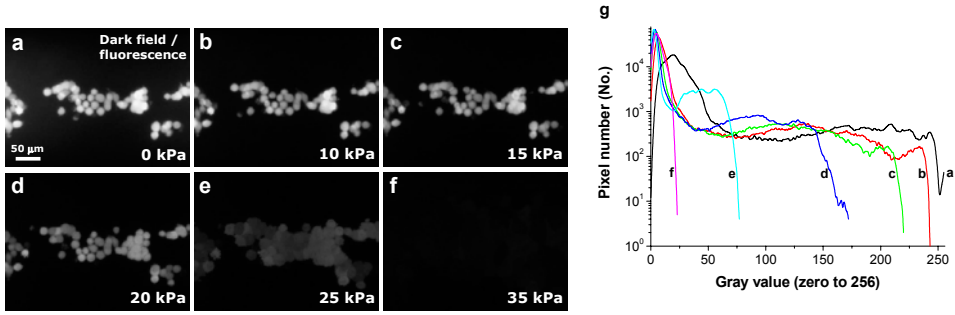

Figure 6. (a)~(f) Series of fluorescent images showing MCF7 cells lysis under compressive force. These images contain information on the leakage of cytoplasmic dye (calcein) during lysis. (g) The distribution of pixel number of each gray value in the fluorescent images (a~f).

events can rapidly change the concentration of cellular contents, the cells should be quickly lysed for the accuracy of the analytical results. Accordingly, this mechanical lysis method provided the best results.

To detect cell burst and leak of cytoplasmic contents in the MCF7 cells, fluorescence measurement was also performed by loading calcein AM (Figure 6). The hydrolyzed dye (calcein) is both cell membrane impermeant and fluorescent. Since the cell membrane was compromised by the compressive force, the calcein was supposed to diffuse out of the cell reducing the fluorescence signal. The pixel number of gray value (near to 0) is increased with compressive force. The left-hand shifting of maximum gray value (near to 256) means that the larger compressive force is applied, the more the cellular membrane got damaged.

4. CONCLUSIONS

In this work, it was confirmed that just subjecting cells to compressive force induced by membrane deflection was enough to rupture the membrane of mammalian cell. This method could be applied to develop the integrated microfluidic devices for sample pretreatment and cell-based assays.

ACKNOWLEDGEMENTS

This work was supported by the Nano/Bio Science & Technology Program (2006-00955) of the Ministry of Science and Technology (MOST).

REFERENCES

[1] D. D. Carlo, K. H. Jeong and L. P. Lee, *Reagentless mechanical cell lysis by nanoscale barbs in microchannels for sample preparation*, Lab Chip, Vol. 3, pp. 287-291, (2003).

[2] E. A. Schilling, A. E. Kamholz and P. Yager, *Cell lysis and protein extraction in a microfluidic device with detection by a fluorogenic enzyme assay*, Anal. Chem., Vol. 74, pp. 1798-1804, (2002).

[3] H. Y. Wang, A. K. Bhunia and C. Lu, *A microfluidic flow-through device for high throughput electrical lysis of bacterial cells based on continuous dc voltage*, Biosens. Bioelectron., Vol. 22, pp. 582-588, (2006).

STIMULATION OF MAMMALIAN CELLS USING MICRO-BEAD IMPACT IN MICRO-BIOREACTOR

Tae-Jin Kim[1], Su-Jin Kim[2], and Hyo-Il Jung[1]

[1]School of Mechanical Engineering, Yonsei University, Republic of Korea and
[2]Nanomedical National Core Research Center, Yonsei University, Republic of Korea

ABSTRACT

We have conducted a new method in cell stimulation by utilizing micro-beads. HeLa cells were cultured in PDMS (Polydimethylsiloxane) microfluidic device and were stimulated using micro-beads with a mean diameter of 2μm and 11μm. The rate of proliferation of cells was compared for devices which circulated the cell culture medium either with or without micro-beads for a specific time interval. Two types of devices have been used for cell stimulation: a straight channel for two dimensional stimulation and a multi-layered channel for three dimensional stimulation (Figure 1).

Keywords: HeLa cell, Cell stimulation, Microfluidic channel, Multi-layered device

1. INTRODUCTION

Experiments such as cell stimulation requires sufficient amount of labor and equipment as conventional cell culturing methods require bulky incubators, large amount of cell culturing related reagents, and space. Thus, miniaturization has become the main concern for laboratories with limited space and resources in order to perform experiments such as cell stimulation. Cell stimulation under microfluidic condition is an efficient method to study as the microfluidic environment utilizes only a small portion of space and requires minimal amount of cells and reagents. A number of researches focus on the development of microfluidic culture devices in order to observe cell differentiation and proliferation using different methods of stimulation including fluidic shear stress [1], pneumatic pressure [2], microfluidic motion [3], etc.

2. THEORY

Various experiments have been actively conducted regarding to cell stimulation. However, most experiments stimulate cells with an indirect approach. Our microfluidic device is designed to physically stimulate cells using micro-beads. The micro-beads suspended in the cell culture media give additional pressure to the cell membrane other than fluid shear force. As most cell stimulation researches rely on indirect mechanical methods, our system may be assessed as a novel device based on micro-beads' impact upon cells. We expect that our microfluidic channel will facilitate the study of effects relating to mechanical stress on cells.

3. EXPERIMENTAL

Two types of cell culturing chamber have been fabricated, where the cell chamber dimensions are: height = 100μm, width = 1mm, length = 6mm for the single channel device, and height = 100μm, inner diameter = 3mm, outer diameter = 1cm for the multi-layered device. PDMS channels were exposed under corona discharge to render the channel hydrophilic. HeLa cells were seeded in the microfluidic chamber with a cell population of

978-0-9798064-0-7/μTAS2007/$20©2007CBMS

10^6 cell/ml and were cultured for 4 days; fresh culture media were supplied every day. Both types of cell culture chambers were then stimulated with polymer micro-beads with a mean diameter of 2μm and 11μm with a flow rate of 7μl/min (for single channel device) and 15μl/min (for multi-layered device) every 12-hour for a total of 60 hours. The concentration was $2.9x10^6$ for 11μm micro-beads and $2.33x10^7$ for 2μm micro-beads. Fresh media were flowed into the control chamber for 15 minutes, while culture media with micro-beads were flowed into the experimental chamber for 10 minutes followed by 5 minutes of fresh media in order to remove remaining micro-beads. Cell population in the control and experimental chamber was observed and compared at a 12 hour interval.

4. RESULTS AND DISCUSSION

Figure 2(a) and (b) shows the cultured HeLa cells with micro-bead stimulation in single channel device and multi-layered PDMS device, respectively. The micro-beads within the microfluidic chamber showed a slight deflection during the flow as the micro-bead passed near the adhered HeLa cells. It can be seen that the micro-beads directly stimulated the outer cell membrane through this motion. Comparison of Hela cells under different micro-bead stimulation is shown in Figure 3. Hela cells in the experimental chamber with 2μm bead stimulation showed a slightly higher proliferation rate than the control chamber, while the experimental chamber with 11μm bead stimulation resulted in a sufficiently higher proliferation rate than the first two chambers (Figure 3).

5. CONCLUSIONS

A new method of stimulating cells has been introduced using two types of PDMS devices. The straight chamber device was used to induce one directional stimulation, while the multi-layered device was designed to stimulate Hela cells in a 3-dimensional direction. The proliferation rate of Hela cells stimulated by 11μm bead was the highest, while the control chamber and the experimental chamber with 2μm bead stimulation showed similar rates. Thus, it can be suggested that micro-beads may physically stimulate cells to affect its proliferation rate.

ACKNOWLEDGEMENTS

This work was supported by ICBIN of Seoul R&BD program (Grant no. 10816) and National Core Research Center (NCRC) for Nanomedical Technology of the Korea Science & Engineering Foundation (Grant no. R15-2004-024-01001-0).

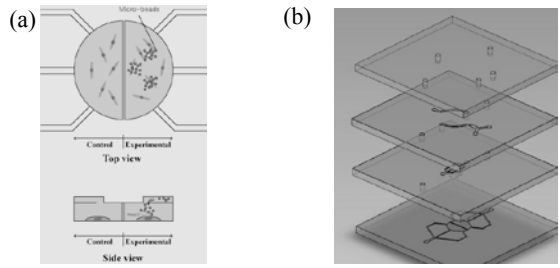

Figure 1(a) Schematic diagram of micro-bead stimulation, (b) exploded view of multi-layered cell culturing device.

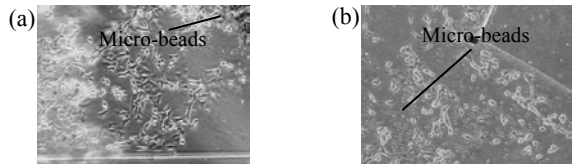

Figure 2 Micro-bead stimulation in (a) single channel device, and (b) multi-layered device.

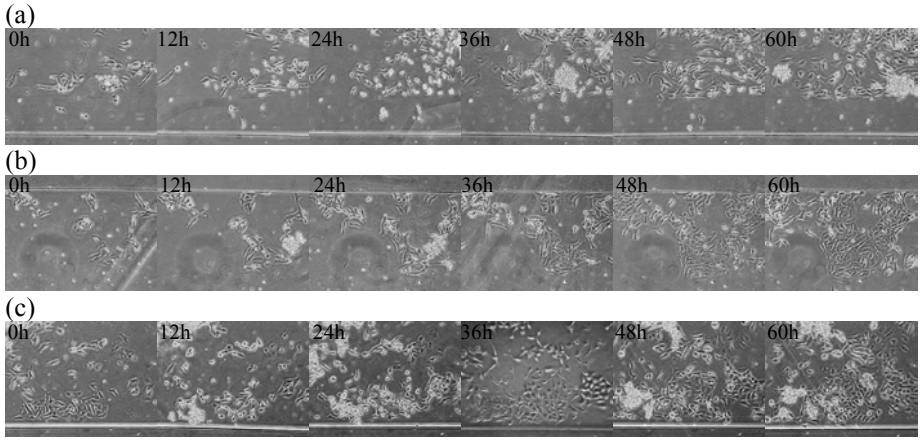

Figure 3 represents HeLa cells in single channel (a) control device, (b) experimental device with 2μm bead stimulation, and (c) experimental device with 11μm bead stimulation.

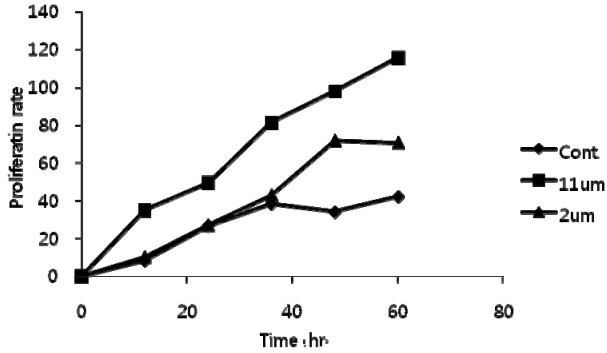

Figure 3 Comparison of proliferation rate of Hela cells under different bead stimulation.

REFERENCES

[1] T. D. Brown, *Techniques for Mechanical Stimulation of Cells In Vitro: a Review*, Journal of Biomechanics, **33**, 3 (2000).

[2] W.Y. Sim, S.W. Park, S.S. Yang, S.H. Park, and B.H. Min, *A Pneumatic Micro Cell Stimulator for the Differentiation of Human Mesenchymal Stem Cells (hMSCs)*, MicroTAS, **10**, 1543 (2006).

[3] D.P. Pioletti, J. Muller, L.R. Rakotomanana, J. Corbeil, and E. Wild, *Effect of Micromechanical Stimulations on Osteoblasts: Development of a Device Stimulating the Mechanical Situation at the Bone-implant Interface*, Journal of Biomechanics, **36**, 131 (2003).

MULTIPHASE FLOW MANIPULATION FOR CONTINUOUS REFRACTIVE INDEX ANALYSIS OF SINGLE LIVING CELL

L. K. Chin[1], A. Q. Liu[1†], C. S. Lim[2] and P. H. Yap[3]

[1]*School of Electrical & Electronic Engineering,*
[2]*School of Chemical & Biomedical Engineering*
Nanyang Technological University, Singapore
[3]*DSO National Laboratories, Singapore*
([†]Corresponding author. Tel: +65-6790-4336; Fax: +65-6793-3318; Email: eaqliu@ntu.edu.sg)

ABSTRACT

This paper reports an integrated microfluidic system for single cell's refractive index measurement. In this system, a serial multiphase flow manipulation is proposed. Comparison to previous methods developed to measure the cell's refractive index in a microfluidic chip, it ensures that each cell is trapped inside a buffer plug and individually passes through the detection area. This method also avoids cell's wastage and measurement failure due to several cells gathered in the detection area. Results show that measured MDCK cells have an average effective refractive index of 1.383 ± 0.001.

Keywords: Multiphase flow, cell analysis, fiber Bragg grating, refractometry

1. INTRODUCTION

In biomedical field, the cell's refractive index (RI) is is found to be associated with certain diseases such as Thalassemia in haematology and cancer diagnosis in oncology. Different optical methods [1-2] have been employed to measure a single cell's RI in a microfluidic chip, where a continuous microfluidic flow is used. However, such microfluidic flow creates difficulties in single cell separation, isolation and trapping. Therefore, to tackle all these problems, a low-capillary multiphase flow [3] is employed for single cell isolation. In this case, prior to the formation of multiphase flow, single cell separation is ensured by hydrodynamic focusing. Furthermore, as buffer modulation method is used for the measurement of cell's RI, smaller buffer plug is mixed with the cell plug in the measurement area.

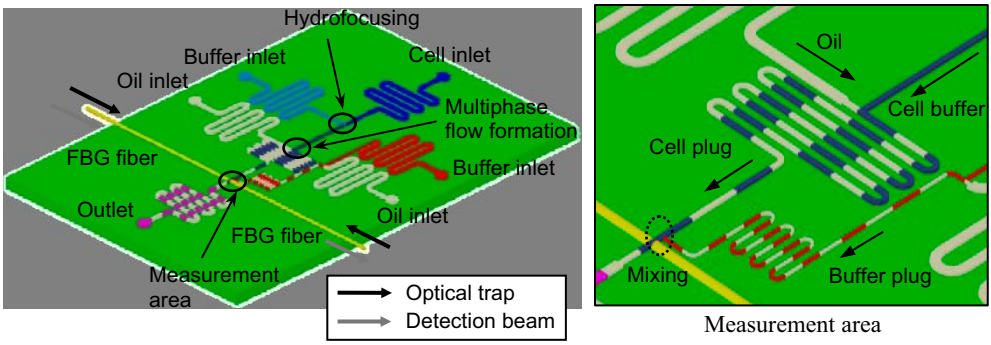

(a) (b)

Figure 1. (a) Multiphase flow system for cell manipulation. (b) Mixing in measurement area.

978-0-9798064-0-7/μTAS2007/$20©2007CBMS

2. WORKING PRINCIPLE

Initially, the injected cells are separated after passing through the hydrofocusing region so that each cell individually reaches the multiphase flow formation region, as shown in Fig. 1a. Then, each cell is trapped within a buffer plug (standard PBS solution) separated by olive oil. Both flows have very slow flow rates in order to obtain a low capillary number ($Ca < 0.1$), so that the plug formation is based only on the channel's geometry and the flow rate ratio. In the detection region, the width of the channel is reduced to extend the length of the plug by 2.5 times. Such arrangement will facilitate the mixing and measuring processes, as shown in Fig. 1b.

The measurement of cell's effective RI is based on the fiber Bragg grating resonant cavity, in which the wavelength shift in the output spectrum is associated with the optical path length within the cavity, i.e. RI and associated physical length. By trapping a single cell within the cavity and changing the surrounding buffer, the cell's effective RI (n_c) and effective thickness (l_c) can be determined by:

$$l_c = (\Delta\lambda_1 - \Delta\lambda_2)/[k(n_2 - n_1)] \quad (1)$$

and

$$n_c = \left(\Delta\lambda_1 / kl_c\right) + n_1 = \left(\Delta\lambda_2 / kl_c\right) + n_2 \quad (2)$$

where n_1 and n_2 are the RI of buffer 1 and buffer 2, respectively, $\Delta\lambda_1$ and $\Delta\lambda_2$ are the wavelength shifts compared between the absence/presence of cell in the cavity with buffer 1 and buffer 2, respectively and k is the peak shift constant.

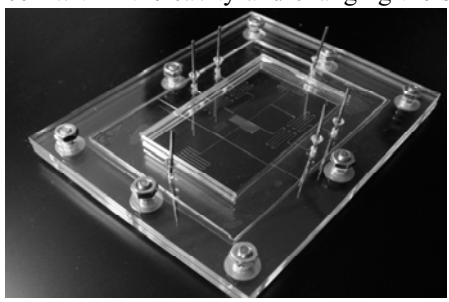

Figure 2. Fabricated PDMS chip.

3. DEVICE DESCRIPTION

The chip is fabricated by PDMS soft lithography. The structures are molded from the SU8 master and then the PDMS slab is bonded on a coverslip by plasma bonding. A pair of FBG fibers with Bragg wavelength of 1258 nm is aligned and forms a cavity for cell trapping by optical traps (high-power laser) as well as for cell measurement (SLED light source) based on the detected output spectra measured by Optical Spectrum Analyzer.

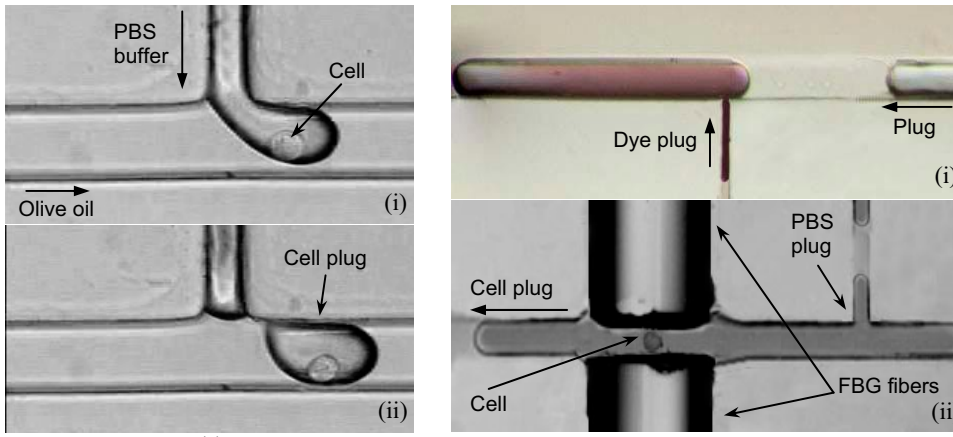

Figure 3. (a) Cell plug formation: (i) t = 0 s, (ii) t = 1 s. (b) Flow mixing: (i) mixing with dye, (ii) mixing of buffer plug with cell plug for cell measurement.

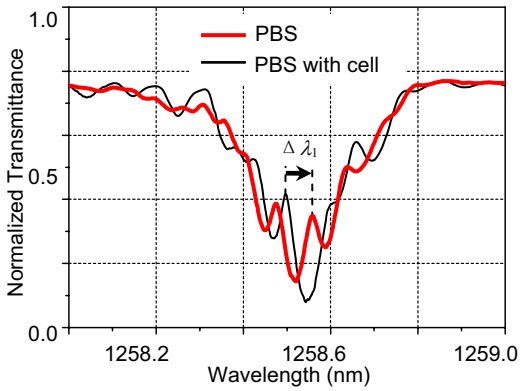

Figure 4. Measured spectra of PBS solution without/with cell.

4. RESULTS AND DISCUSSION

The chip is calibrated with NaCl solution of different concentration to obtain the peak shift constant, k, and it is determined to be 1.56×10^{-4}. After that, Madin-Darby Canine Kidney (MDCK) cell is used for the measurement. Fig. 3a shows the formation of cell plug after the cell is separated by hydrofocusing. A single MDCK cell is successfully trapped within a buffer plug (n_1) with a length of 120 µm. To monitor the mixing process, a dye plug is mixed with a buffer plug as shown in Fig. 3b(i). Recirculating flow generated within the buffer plug has enhanced the mixing process [3]. Fig. 3b(ii) illustrates the MDCK cell trapped within the fiber cavity for RI measurement while a PBS (higher concentration) plug is mixed with the cell plug (n_2) to perform buffer modulation. The output spectra without/with cell before mixing are shown in Fig. 4. The corresponding peak is shifted by 0.0072 nm ($\Delta\lambda_1$). Similarly, the wavelength shift can be obtained after mixing, i.e. 0.0059 nm ($\Delta\lambda_2$). Subsequently, the MDCK cell's effective RI and effective thickness can be determined as shown in Table 1. It shows that MDCK cell has an average effective RI of 1.383 and an average effective thickness of 16.5 µm.

Table 1. Measurement results of cell's effective RI and effective thickness

	Cell 1	Cell 2	Cell 3	Cell 4	Average
n_1	1.355	1.355	1.356	1.355	-
n_2	1.360	1.359	1.359	1.357	-
$\Delta\lambda_1$ (nm)	0.072	0.072	0.072	0.067	-
$\Delta\lambda_2$ (nm)	0.059	0.062	0.064	0.062	-
Cell's effective RI	1.383	1.384	1.383	1.382	**1.383**
Cell's effective thickness (µm)	16.7	16.0	17.1	16.0	**16.5**

5. CONCLUSIONS

In conclusion, an integrated single cell's RI measurement system has been developed. Serial multiphase flow control is employed to enhance the robustness of the system and reduce cell's wastage in the chip. The measurement results show that MDCK cell has an average effective RI of 1.383 ± 0.001. Furthermore, measured cell can be exported for further diagnosis while single cell in plug can be ensured.

REFERENCES

[1] L. K. Chin, A. Q. Liu, C. S. Lim, P. H. Yap, J. H. Ng, J. Z. Hao and S. Takahashi, *Single living cell refractometry using FBG-based resonant cavity*, Proc. Transducers '07, Lyon, France, pp. 851-854, (2007).

[2] W. Z. Song, C. S. Lim, A. Q. Liu and P. H. Yap, *Differential Mach-Zehnder interferometer for simultaneously determining size and refractive index of living cells*, Proc. Transducers '07, Lyon, France, pp. 2159-2162, (2007).

[3] J. D. Tice, H. Song, A. D. Lyon and R. F. Ismagilov, *Formation of droplets and mixing in multiphase microfluidics at low values of the Reynolds and the Capillary numbers*, Langmuir, Vol. 19, pp. 9127-9133, (2003).

NANOFILTER FOR EFFECIENT BACTERIA TRAPPING AND DETECTION

L. Zhu[1,2], X. L. Peh[1], C. Y. Teo[1], H. M. Ji[1], H. H. Feng[1], W.-T. Liu[1]
[1] Institute of Microelectronics, Singapore, [2] National Institutes of Health, Bethesda, MD

ABSTRACT
This paper reports efficient trapping and rapid detection of bacteria cells using microfluidic nanofilters. The novel design of the nanofilter arrangement greatly reduced the flow resistance and clog-sensitivity of the nanofilter device. In combination with in-chip immunofluorescent assay procedures, we successfully demonstrated the trapping and detection of *Escherichia coli* (*E. coli*) at a concentration as low as ~10^4 CFU/mL.

KEYWORDS: Lab-on-a-chip; microfluidic device; by-pass; flow resistance; bacteria

1. INTRODUCTION

Microfilters with gaps > 1 μm have been demonstrated to trap white blood cells[1], protozoa cells[2] and *E. coli* cells[3]. Individual *E. coli* cells were observed to penetrate the 1 μm gaps[3] due to its relatively small size (rod like with ~ 1 μm in diameter) and the high deformability of the cells. Efficient trapping of such small cells require filter gaps at nanometer scale, which, however, lead to substantially high pressure built up before the nanofilter and further squeeze the cells to pass through the gaps or eventually break the cells. Unique multi-layered composite filter structures have thus been designed with by-passes, which reduce the flow resistance >30 times[4]. In this paper we further optimize the filter design for the trapping of bacterial cells ~ 1 μm in size and demonstrated a detection sensitivity of *Escherichia coli* (*E. coli*) cells at ~10^4 CFU/mL.

2. FILTER DESIGN

A dual-layered composite filter structure is illustrated in Fig 1, where each layer comprises of micro-pillars with different gap sizes, which can be classified into fine and coarse filters. The fine filters have small gaps to trap target particles, while the coarse filters have much larger gaps to serve as by-passes to reduce flow resistance. However, these by-passes also provide possible paths (route R3) for the particles to escape through the filter. The loss of target particles could be minimized by the optimization of arrangement of fine filters and coarse filters, as well as the specially designed rain-drop shape pillars (inset of Fig. 1), the tapered tip of which help trap additional particles when they collide due to interception, inertial, or Brownian effects. A microfluidic device with a dual-layered by-pass nanofilter is schematically shown in Fig. 2.

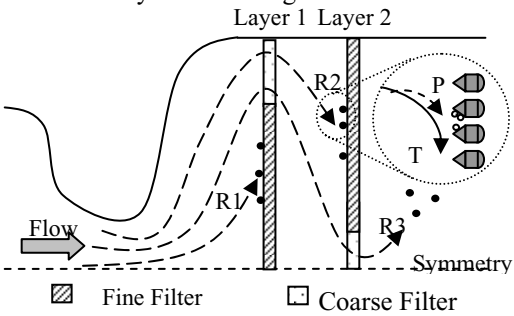

Figure 1: Concept of the multi-layered by-pass filter. Particles following route R1 and R2 are trapped at Layer 1 and 2, respectively. Particles following route R1 escape through by-

978-0-9798064-0-7/μTAS2007/$20©2007CBMS

passes. Inset shows the tangential fluid streamline T at fine filter, and the flowing route P of particle due to impaction.

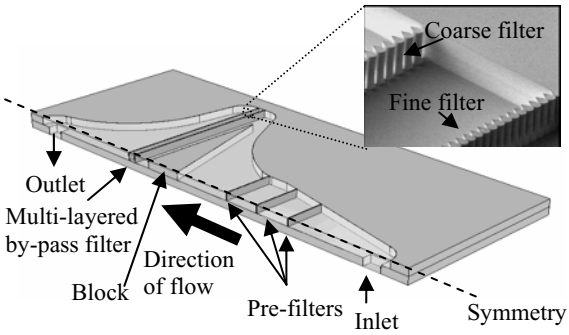

Figure 2. 3D model of the microfluidic by-pass filter device (not-to-scale half-symmetry). Inset shows the SEM photo of the pillars of "raindrop" shape

3. RESULTS AND DIRECTIONS

Pressure test (Fig. 3) shows that the pressure drop over the by-pass filter (fine filter gap size 1 µm) stabilized at 29.4 and 2.1 kPa as the flow rate was kept at 5 and 1 µL/min, respectively, >30 times lower than that obtained with a microfilter of same gap size but without by-passes[5].

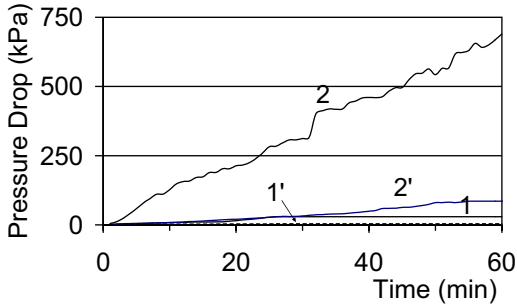

Figure 3. Measurements of pressure drop with by-pass microfilter after injecting filtered PBS solutions at 5 µL/min (curve 1), 1 µL/min (curve 1') and with microfilter without by-passes at 5 µL/min (curve 2), 1 µL/min (curve 2').

The filter efficacy with 0.2 µm fine filter gaps was further tested with 1 µm fluorescent beads. Trapping efficiencies of ~30% were obtained with 50-500 beads, which could be underestimated due to the overlaid beads before the filter (Fig. 4a, b) that were counted as one bead from the top view under microscope. Trapping of *E. coli* cells was successfully carried out followed by fluorescence labeling with fluorophore conjugated antibodies against the target cells. Fluorescence signal could be obtained after injecting at least 10^4 cells (Fig. 4c, d). The whole process could be completed within 30 min, 5-6 times faster than using antibody coated magnetic beads, although the limit of detection is 10 time higher than that method (10^3 cells)[6]. To our knowledge, this is the first paper reporting the use of nanofilters for rapid and sensitive bacteria detection.

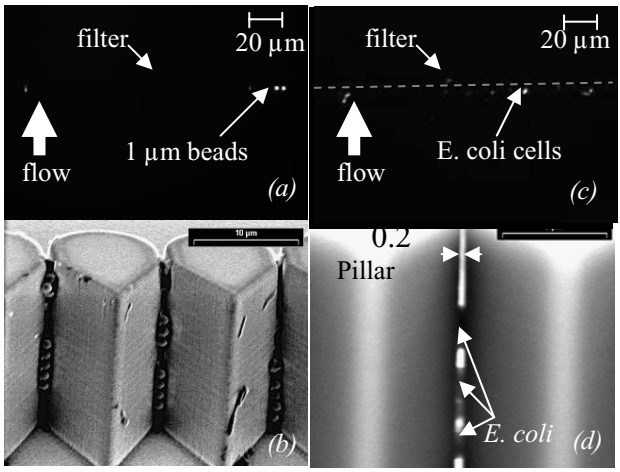

Figure 4. Fluorescence and SEM photos showing the trapping of 1 µm polystyrene beads (a, b) and E. coli cells (c, d) before the by-pass filter, respectively.

4. CONCLUSIONS:

This study observed that the use of by-pass microfilters and the "raindrop" shape pillars could effectively relieve the pressure built-up before the microfilter and reduced the clog-sensitivity of the microfilter. Evaluation of the microfilters was carried out with *E. coli* (~1 µm in size) and 1 µm beads. The relatively poor detection sensitivity obtained with bacterial cells was mainly due to the poor labeling efficiency of the labeling strategy used. Further work to enhance the trapping and detection of bacterial cells is on-going.

REFERENCES:

1. P. Wilding, L. J. Kricka, J. Cheng, G. Hvichia, M. A. Shoffner and P. Fortina, " Integrated cell isolation and polymerase chain reaction analysis using silicon microfilter chambers," Anal. Biochem. 257, 95 (1998).
2. L. Zhu, Q. Zhang, H. Feng, S. Ang, F. S. Chau and W. T. Liu, "Filter-based Microfluidic device as a Platform for Immunofluorescent Assay of Microbial Cells," Lab. Chip, 4, 337 (2004)
3. B. He, L. Tan, F. Regnier, "Microfabricated filters for microfluidic analytical systems" Anal. Chem. 71, 1464 (1999)
4. L. Zhu, X. L. Peh, H. M. Ji, C. Y. Teo, B. R. Chew, H. H. Feng, and W. T. Liu, "Microfilters with Ultra Low Flow Resistance and Clog-Sensitivity for Microfluidic Analytical Systems", Lab. Chip, in submisstion
5. "Cell lose in intergrated microfluidic device" L. Zhu, L. X. Peh, H. M. Ji, C. Y. Teo, H. H. Feng, W.-T. Liu, Biomed. Microdevices, 2007, in press
6. "Self-Contained, Fully Integrated Biochip for Sample Preparation, Polymerase Chain Reaction Amplification, and DNA Microarray Detection," R. H. Liu, J. Yang, R. Lenigk, J. Bonanno and P. Grodzinski, Anal. Chem., 76, 1824 (2004)

NON-CONTACT MEASUREMENT OF YOUNG'S MODULUS OF SINGLE LIVING CELL USING HYDROSTATIC PRESSURE IN A MICROCHAMBER

L. A. G Lin[1] ,Y. F. Yu[2] , A. Q. Liu[2†] and P. H. Yap[3]

[1] School of Chemical & Biomedical Engineering

[2] School of Electrical & Electronic Engineering

Nanyang Technological University, Singapore

[3] DSO National Laboratories, Singapore

([†]Tel: +65-6790-4336; Fax: +65-6793-3318; Email: eaqliu@ntu.edu.sg)

ABSTRACT

This paper introduces a biochip which contains a microchamber for measuring the mechanical properties of cells without physically touching them. Unlike previous methods, dissipative forces such as friction are avoidable increasing the accuracy of our measurements. This can be used for cancer detection at an early stage based on the fact that cancerous cells are more elastic than normal cells as well as for studying the effects of hydrostatic pressure on the biochemical pathways in the cell.

Keywords: Biochip, light scattering theory, living cell, Young's modulus

1. INTRODUCTION

Ever since the first attempt to study the mechanical properties of biological membranes in the 1930s using sea urchin eggs [1], the field of cell mechanics gained increasing focus of interest due to the importance of studying the mechanical interaction of the cell with its surroundings and how this can ultimately lead to diagnosis between normal and infected or cancerous cells. Currently, the more popular methods used to measure the cell's mechanical properties include micropipette aspiration studies, compression studies using atomic force microscopy, glass microneedles and cell poker [2]. Limitations of these methods are that only one cell can be measured at a time, only sections of a cell are being used for measurement and deviations arise at different sections where the measurements are made such as in the close proximity of the nucleus and other bulky organelles. This paper introduces a simple and precise method for generating uniform force around the cell and allows for measurement of many cells simultaneously, hence increasing the accuracy of the measurements.

2. MEASUREMENT PRINCIPLES

The strain could be measured via principles of light scattering. When a monochromatic laser source of wavelength 524 nm passes through a cell, scattering fringes are formed and their position is directly dependent on the instantaneous geometrical shape of the cell. Hence, any changes caused by compression on the cell could

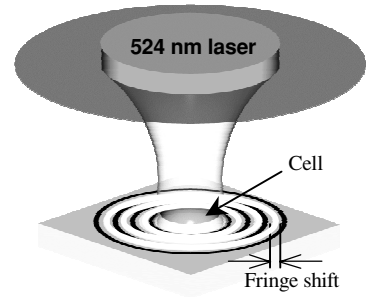

Figure 1. Principle of the optical detection

978-0-9798064-0-7/μTAS2007/$20©2007CBMS

be measured by observing the fringe shift as illustrated in figure 1. The Young's modulus can be calculated via the equations derived from the constitutive Hooke's law and tensor analysis:

$$E = \frac{-P}{tr\varepsilon_{ij}}(1-2\nu) \tag{1}$$

$$\varepsilon_{ij} = \frac{1}{2}\begin{pmatrix} x_1^2 - 1 & 0 \\ 0 & x_2^2 - 1 \end{pmatrix} \tag{2}$$

Where E is the Young's Modulus, P is the pressure exerted, ε_{ij} is the strain tensor, tr refers to the trace function from matrix algebra, ν is the Poisson's ratio and x_1 and x_2 are the ratio between the instantaneous radius and the initial radius of the horizontal and vertical components of the cell respectively.

The biochip's design is illustrated in figure 2 and consists of three parts, the microfluidic structure, a sample chamber and a pressure generator. The microfluidic structure is used for the input of the cells together with their culture medium and oil into the sample chamber. The purpose of the oil is to prevent the cell culture medium to mix with the water generating the pressure. The sample chamber is where the cell is contained and where optical measurement is made. The pressure is generated using hydrostatic pressure via a pressure column which is placed at the inlet and outlet after the cells and the oil are loaded into the sample chamber. As the pressure can be varied in intervals as small as 0.0001 atm, the exact stress the cell is subjected to can be determined to a high accuracy and also more data points can be generated. The device is made up of PMMA annealed to a glass substrate coated with MgF_2 so as to allow clear and distinct scattering fringes.

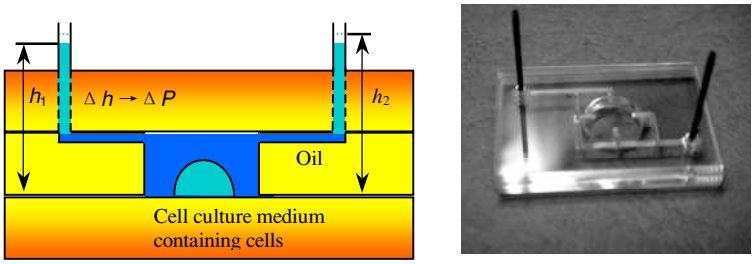

Figure 2. Schematics and photograph of the biochip

3. EXPERIMENTAL RESULTS AND DISCUSSIONS

The cells were loaded to the microchamber. Experiments were done on MDCK(Madin Darby Canine kidney cell) with the size of 15-20 μm and the zebrafish embryo choroid of size 856 μm. The pressure was varied at intervals of 100 Pa. Micrographs as seen in figure 3 were taken for every 10 minute intervals when equilibrium had been established with each pressure variations and the shift in the fringes processed to determine the extent of compression and hence the strain of the cells. The results obtained were plotted as seen in figure 4.

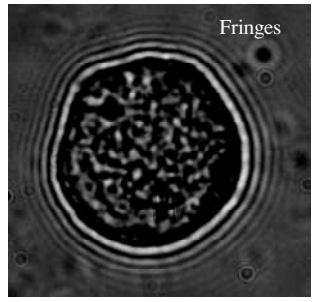

Figure 3. Photomicrograph of a MDCK cell with its fringes

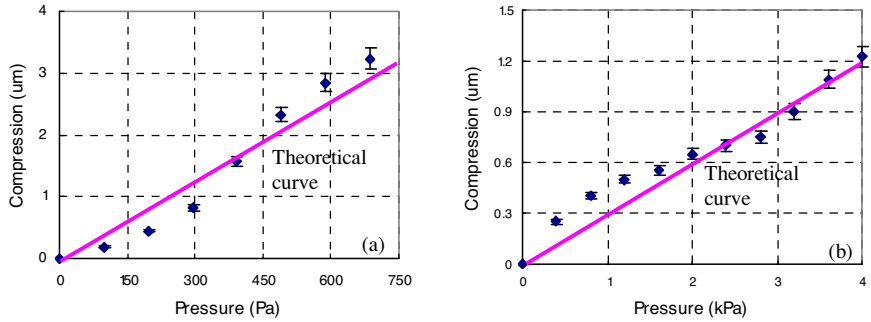

Figure 4. Experimental and theoretical compression vs pressure plot for (a) MDCK cell line; and (b) Zebrafish embryo chorion for 100 samples each

The Poisson's ratio can be estimated by a DICM height measurement method [3] and is found to be around 0.48 for the Zebrafish Embryo and 0.45 for the MDCK cells. Assuming a linear correlation between the pressure and the strain for simplicity, the Young's modulus of the MDCK is calculated to be around 6.2 – 0.031 kPa compared with earlier calculated results of 6.2 – 1.2 kPa [4] and that of the Choroid is calculated to be 1.32 – 0.013 MPa which correlates well with previously published results of 0.98 ~ 1.51 MPa [5].

4. CONCLUSIONS

This paper introduced a method capable of measuring the mechanical properties of many living cells simultaneously. As the cells are not destroyed during the process, they could be reused for other purposes, which is extremely useful for valuable cell types. Moreover, in the absence of detrimental forces, it increases the accuracy and reliability of the measurements.

ACKNOWLEDGEMENT

The author, Lin, is grateful for the Undergraduate Research Programme(URECA) in Nanyang Technological University for supporting his research as well as the A*STAR Graduate Academy for sponsoring his undergraduate education.

REFERENCES

[1] K.S. Cole, *Surface forces of the Arbacia egg*, Journal of Cellular and comparative physiology, The Wistar Institute Press, Hoboken, North America, pp. 1-9, (1932)

[2] P. Janmey and C. Schmidt, *Experimental measurements of intracellular mechanics*, Cytoskeletal mechanics, Cambridge University Press, New York, North America, pp. 18-49, (2006)

[3] D.J. Lin et al, *Step-height measurement by means of a dual frequency interferometric confocal microscope*, Applied Optics,Optical Society of America , Washington, North America, pp. 1472-1479, (2004)

[4] S. Steltenkemp et al, *Membrane thickness of animal cells challenged by osmotic stress*, Small Journal, John Wiley and Sons, Weinheim, Germany, pp.1016-1020, (2006)

[5] D.H. Kim et al, Mechanical property characterization of the zebrafish embryo chorion, Proceedings of IEEE Engineering in medicine and biology society, IEEE , New Jersey, USA, pp.5091-5095, (2004)

OBSERVATIONS OF SPERM CELL BEHAVIOR IN A MICROFLUIDIC IN-VITRO FERTILIZATION DEVICE

M. d. C. Lopez-Garcia[1], R. L. Monson[1], K. Haubert[2], and D. J. Beebe[1]

[1]University of Wisconsin – Madison, U.S.A.[2] Vitae LLC, U.S.A.

ABSTRACT

Microfluidics has shown promise as a platform for assisted reproduction. To assess this potential, we studied the flow characteristics in a device, how sperm interacted with it, and how sperm-oocyte attachment occurs. There is a threshold fluid velocity where sperm transition from traveling with the fluid to a regime in which the sperm can move independently. It was notable that a number of sperm stayed in the inlet well. Also of interest was the tendency for sperm to travel along surfaces. These observations provide insight for optimization for future device designs.

Keywords: sperm cell, sperm motility, microfluidics, IVF

1. INTRODUCTION

Incorporating microfluidic technology in the field of In-Vitro Fertilization (IVF) has become an interest to engineers and reproduction scientists in the last decade. Some in vitro production (IVP) steps that have been demonstrated in microfluidics are sperm sorting, cumulus removal of zygotes, zona pellucida removal of embryos, and oocyte penetration by sperm cell, [1] among others. Attempts to carry out IVF in microfluidic devices have yielded encouraging results [2] [3]. However, the mechanisms that take place in this process are not clear. In our study, we focus on the behavior of sperm in microchannels and the sperm interaction with geometry and flow. Understanding the interactions between sperm, flow and geometry provides the basis for engineers to exploit these interactions when designing devices.

To answer these questions, the following steps were taken: a) baseline flow of the fluid in the channel was studied b) baseline flow information was combined with sperm flow information to understand sperm-device interactions; c) sperm attachment to the oocyte was determined with respect to the baseline flow. During each of the previous steps, the effect of the device geometry on sperm behavior was observed. Having an incubated microscope stage that maintained the ideal environment for fertilization facilitated these observations. Bovine sperm was used for all of these experiments.

2. EXPERIMENTAL

Polydimethylsiloxane (PDMS) devices were made using standard techniques, taken from [4]. Two device geometries were used. They both had a microchannel that was 250 μm tall by 1000 μm wide, and a constriction region that consisted of a wall that came down from the top of the channel leaving an opening of 20 μm above the bottom of the channel (Figure 1a). One device has a constriction that widens into an oval shape (Figure 1b) and the other device has a straight channel constriction (Figure 1c). This constriction area provides a "parking spot" for the oocyte but allows media and sperm to flow past it.

The devices were equilibrated to incubation conditions after which 200 μL of fertilization medium was added at the inlet of the device. Gentle suction was applied to draw the medium into the inlet through the channel. After adding the medium, the device

978-0-9798064-0-7/μTAS2007/$20©2007CBMS

was placed back into the incubator to allow medium to reach an equilibrium static level across the entire device

All of the imaging was done with an IX70 Olympus inverted microscope. UV lighting (555 nm) was used to image the fluorescent beads. A small incubation box with a glass bottom was placed upon the microscope stage. This incubation box allowed for extended observation of the sperm in a cell-friendly environment. Image analyses for flow profiles were carried out with two different software packages. Imaris Bitmap software was used to obtain flow velocities using particle tracking whereas DaVis LaVision PIV software was used to obtain flow profiles.

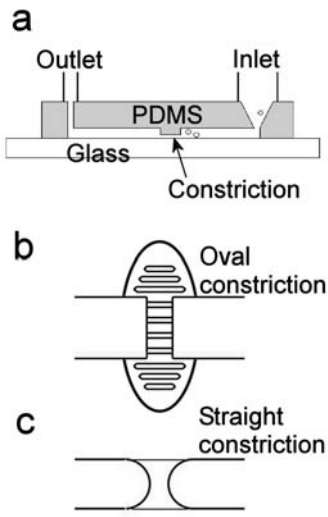

Figure 1. a) Side view of the device b) top view close-up of the oval constriction c) top view close-up of the straight constriction

Base Flow Studies

In the base flow studies, the device was originally filled with medium containing fluorescent beads. Once the device was in the incubated stage, an additional 200 μL of fluorescent beaded media was added at the inlet flow. The baseline flow was studied by recording movies of the flow in the channel. The displacement and the time between frames lead to flow information such as direction and velocity magnitude.

Sperm/Flow Interactions

In this case, a 200 μL aliquot of the sperm sample (in place of the additional beaded medium) was added to the inlet. Movies were then recorded.

Sperm and oocyte studies

The oocytes were inserted into the device first and then the sperm sample aliquot was added. Movies were then recorded.

3. RESULTS AND DISCUSSION

Previous experiments have shown flow behavior in a microchannel of similar size and indicate velocities are laminar [5]. In the present study, the results concurred with previous work reported in the literature, and a laminar flow profile was corroborated (data not shown). In addition, the study of the flow profile over time showed an exponential decrease in velocity (data not shown) with the flow velocity reaching zero approximately 30 minutes after fluid addition. The data that was obtained correlates closely with a mathematical model for flow decay for gravity driven flow in a channel with an open reservoir in each end.

Initially, the sperm swam in the same direction of the fluid flow instead of being dragged by it. This behavior was observed for the first four minutes (roughly 17 μm/s) to ten minutes (roughly 5 μm/s). Once the flow velocity decreased the sperm were seen swimming in directions different than that of the flow (Figure 2).

The sperm/flow interaction can be divided into two regimes. In the first regime, the sperm swim with the flow, or are impulsed. The word "impulsed" may be defined as a combination of "pushed" and "swimming ahead of the stream". In this regime the sperm may not be able to swim

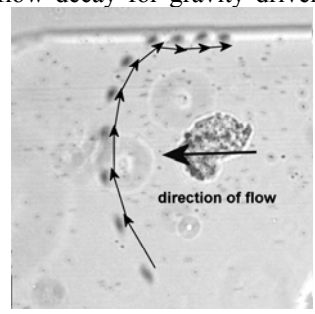

Figure 2. Sperm cell gaining control of direction.

in other directions because the force of the flow may be too great for the sperm to cross streamlines in the laminar fluid flow. In the second regime, the sperm overcome the force of the flow and begin to swim in directions independent from the flow direction. The transition from the first to second regime took place within the first ~10 minutes, which corresponds to a point in the flow profile with respect to time where there is slow flow that has not quite reached zero. Also, this second regime is where we observed that the sperm can begin to interact with the oocyte.

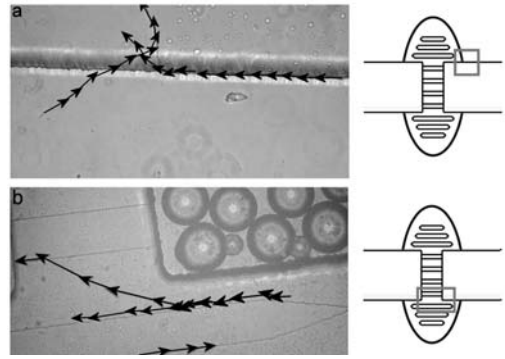

Figure 2. Sperm swimming by contours.

The geometry of the device also played an important part in the sperm behavior within the channel. For example, it was observed that in the inlet area of the device, there was a high sperm concentration. The sperm that were viewed in this area had the characteristic of swimming in circles, which is an indication of poorly functioning sperm. This observation leads us to think that the inlet area may serve as a cut-off for defective sperm. Another case in which the geometry seems to play a key role in sperm behavior is the observation of sperm swimming by surfaces (Figure 3). Knowledge of this tendency could be useful because with today's technology we can control geometry on the microscale and may be able to direct sperm to oocytes by designing devices with guides that lead sperm to desired locations. This finding has applications not only in fertilization, but in sorting and in other in-vitro production steps for IVF sperm preparation.

4. CONCLUSIONS

The observations in this study show that microfluidic devices can be a powerful tool in IVF. The observations presented could help with the design of the improved IVF devices with which we can control when sperm attach to oocytes in the presence of flow, manipulate where sperm go by contour design, and can control the concentration and quality of the sperm that surround the oocyte with special geometrical features and flow.

AKNOWLEDGEMENTS

This research was funded by IEDR, USDA-SBIR, GERS, and JPFP-NASA. We also thank Dr. M. B. Wheeler, Dr. T. Shedd, Dr. W. Crone, and Bitplane Scientific Solutions.

REFERENCES

[1] D. J. Beebe, et al., Microfluidic Technology for Assisted Reproduction, Theriogenology, pp. 125-135, (2002)

[2] R. S. Suh, et al., IVF within microfluidic channels requires lower total number and lower concentrations of sperm, Human Reproduction, pp. 477-483, (2006)

[3] L. J. Kricka and P. Wilding, Micromachining: A new direction for clinical analyzers, Pure and Appl. Chem., pp. 1831-1836, (1996)

[4] S. G. Clark, et al., Reduction of polyspermic penetration using biomimetic microfluidic technology during in vitro fertilization, Lab on a Chip, pp. 1229-1232, (2005)

[5] J. P. Brody, et al., Biotechnology at low Reynolds Numbers, Biophysical Journal, pp. 3430-3441, (1996)

PARALLEL BIOPARTICLE SORTING WITH TGP SOLUTION IN 3-DIMENTIONAL MICROFLOW SYSTEM

Hirokazu Sugino[1], Yuki Nara[2], Yoshitaka Shirasaki[2], Takahiro Arakawa[2], Shuichi Shoji[2] and Takashi Funatsu[1]

[1]Graduate School of Pharmaceutical Sciences, The University of Tokyo, JAPAN
[2]Graduate School of Science and Engineering, Waseda University, JAPAN

ABSTRACT

This paper reports a fluorescence-activated bioparticle sorting system with parallel architecture. We have developed a 4 or 8 channel parallel sorting system using thermoreversible gelation polymer (TGP) to control flow. A sorting time of 10 ms in each channel and a sorting rate of 16 particles/s were achieved. Using this system, we sorted fluorescent microbeads and *Escherichia coli* (*E.coli*) cells expressing fluorescent proteins.

Keywords: microfluidics, parallel sorting, sol-gel transition, PDMS

1. INTRODUCTION

Fluorescence-activated on-chip bioparticle sorting is an attractive method to enrich a specific organelle for proteomic analysis. However, it takes a long time for the sorter to collect a sufficient amounts of organells for the subsequent analysis. Although a high speed sorter with a sorting time of 5 ms has been realized [1], it is not available for organelle sorting to identify its components. Our strategy to save the time for collection is to integrate sorters into a single chip. A pararell bioparticle sorter with a switching time of 10 ms was achieved without substantially increasing the complexity of the sorting system.

2. DEVICE AND SORTING ARGORITHM

We have previously developed a parallel sorting device using soft lithography with polydimetylsiloxane (PDMS) [2]. The device has a multilayer structure with two inlets and two outlets (Fig.1). The structure makes it possible to form laminar flows in each parallel channel by introducing solutions from sample and carrier inlets.

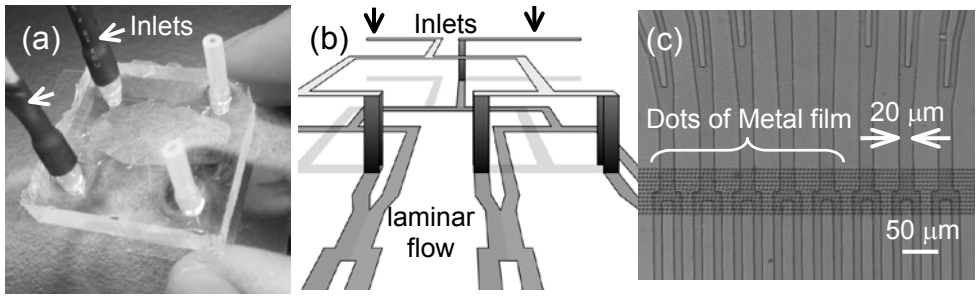

Figure 1. (a) A photograph of PDMS device. (b) Schematic of 3-dimensional channels. (c) Bright field image of PDMS channel. A metal film absorbs infrared laser beam and functions as a heater.

978-0-9798064-0-7/μTAS2007/$20©2007CBMS

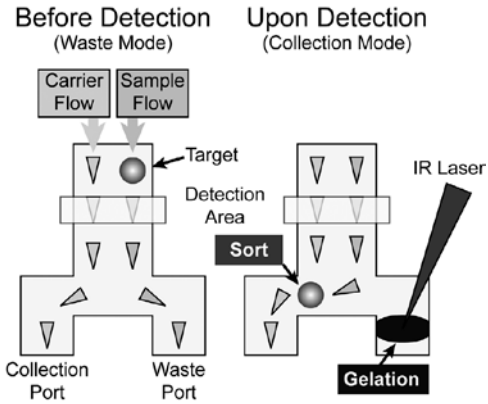

Figure 2. Principle of sorting method. Without detection of fluorescence signals, sample flows into a waste port because of the laminar flow. Upon detection of a signal, the waste port is heated by laser beam to switch the flow into a collection port.

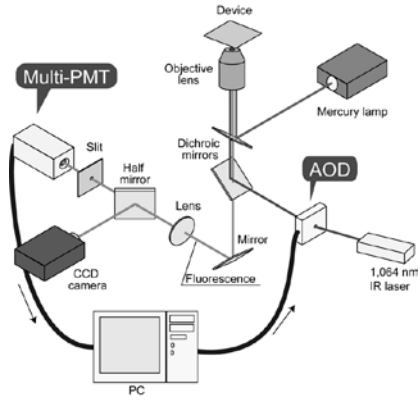

Figure 3. Schematic diagram of the parallel sorting apparatus. Multi-PMT consists of 16 independent PMTs which measure fluorescence intensities of individual channels. AOD deflects the laser beam to the channel where a fluorescence signal is detected.

Flow switching of the sorter depends on the sol-gel transformation of thermoreversible gelation polymer (TGP) solutions [1,3]. Figure 2 shows the principle of a separation method based on TGP. At waste mode, a sample solution containing fluorescent specimen and TGP flows into a waste channel because of the laminar flow of the sample and carrier solutions. Upon detection of the fluorescence signal from the target particle, a gel of TGP is formed at the entrance of the waste channel by heating with an infrared laser and the target particle flows into the collection channel.

3. OPTICAL SETUP

Figure 3 shows the optical setup to detect fluorescence signals and to irradiate each channel with the laser beam. To control every parallel channel, we used a 16 channel multi-photomultiplier tube (PMT) and an acousto-optic deflector (AOD). The signals from multi-PMT were processed by computer software and the position of the laser beam irradiation was determined by an AOD controlled by the software to collect target particles automatically.

4. RESULTS AND DISCUSSION

Figure 4 shows fluorescence images of fluorescent microbeads separation using 4 parallel sorters. In the waste mode, the carrier flow prevents the influx of beads into the left collection channels (Fig. 4-a).

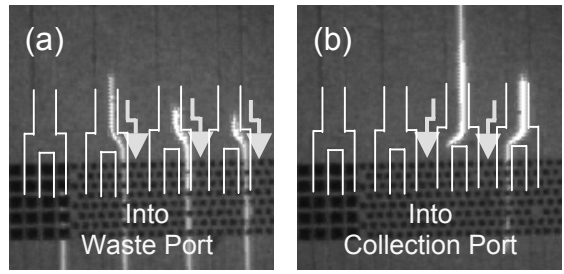

Figure 4. Fluorescence images of microbeads sorting. (a)Waste mode:no opperation of the flow. (b)Collection mode:detect and sort target particles by an infrared laser.

In the collection mode, microbeads are detected and sorted to collection channels by heating the entrance of the waste channel with an infrared laser (Fig. 4-b). The switching time was determined to be 10 ms from the time required for the laser beam irradiation. The flow switching speed of each parallel channel was similar to that of a reported high-speed single sorter system [1]. A sorting rate of 16 particles/s was achieved. We next examined the recovery ratio of microbeads detected at various flow rates (Fig. 5). The results indicate that the recovery ratio increases as the flow rate increases; suggesting that more accurate sorting will be achieved at a higher flow rate. Using this parallel sorting system, we successfully sorted *E.coli* cells expressing fluorescent proteins.

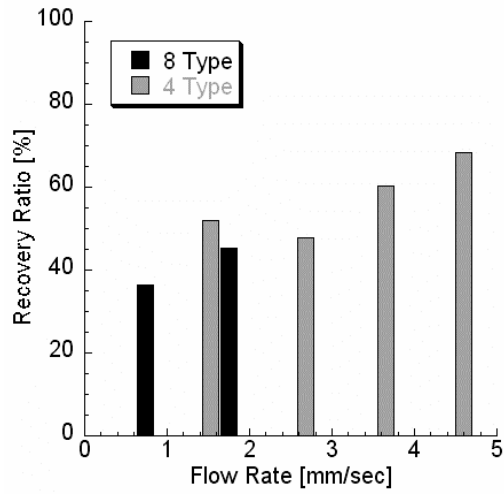

Figure 5. Recovery ratio as a function of flow rate.

5. CONCLUSIONS

We developed a parallel sorting system to realize efficient sorting. A sorting time of 10 ms in each channel and a sorting rate of 16 particles/s were achieved. The *E.coli* cell sorting indicates that this sorting system can be applied to separate organelles like mitochondria. Tests of particle separation at higher flow rates and with 16 channels are currently underway.

ACKNOWLEDGEMENTS

This study was supported by SENTAN, JST and a Grant-in-Aid for SCOE "ASMew" from the Ministry of Education, Cuture, Sports Science & Technology of Japan.

REFERENCES

[1] T. Arakawa et al, "Accurate and High Speed Particles and Biomolecules Sorting Microsystem using 3-Dimensinal Sheath Flow," Micro Total Analysis Systems 2006, 512-514 (2006).

[2] Y. Nara et al, "High Through-put Parallel Biomolecules Sorting Microsystem with Three Dimensional PDMS Stack," Transducers 2007, in press (2007).

[3] Y. Shirasaki et al, "On-chip Cell Sorting System Using Thermoreversible Gelation Polymer," IEEE J. Sel. Top. Quantum Electron, 13 pp.223-227 (2007).

RAPID AND SIMPLE UV-DIRECTED MICROPATTERNING OF PROTEINS

Manuel Théry[1], Ammar Azioune[2], Jenny Fink[2], Raphael Dupont[1], Matthieu Piel[2], Franąois Chatelain[1]

[1] CEA, Grenoble, France, [2] Institut Curie, Paris, France

ABSTRACT

The micropatterning of proteins in biology is a powerful tool to study and manipulate intracellular organization and multicellular assembly. The original microcontact printing technique although very efficient has several drawbacks which prevent its use in routine biological protocols or industrial fabrication processes. We present a new method based on UV crosslinking of adhesion proteins with benzophenone to easily and rapidly produce highly reproducible micropatterns without the use of microfabricated elastomeric stamp [1].

Keyword : UV light, benzophenone, fibronectin, micro-patterns, adherent cells.

1. INTRODUCTION

Micro-patterning is a widely used method to transfer protein to a substrate and pattern them with micrometer resolution [2]. This technique allows the control of the spatial distribution of cell adhesion proteins on the surface and thereby gives access to the manipulation of cell adhesion geometry. It recently proved an inspiring technique for several questions in cell biology. Confinement of single cells allowed us to describe the physical laws governing cell architecture [3], cell internal organization and polarity [4], and cell division axis [5].

The original micropatterning technique, the micro-contact printing of protein, has several drawbacks: it is time consuming; the transfer efficiency is often inhomogeneous and poorly reproducible; stamped surfaces need to be flat and accessible for the stamp; the stamp has to be manipulated manually.

Alternative techniques based on UV directed light micropatterning have been described. They rely on the ability of UV light either to oxidize surface coating and thus destroy their anti-fouling properties or activate photosensitive linkers to graft molecules on the surface. These methods usually require the development of sophisticated chemistry. However new photo-sensitizers such as benzophenone have been modified to become soluble in aqueous solution. Benzophenone, for example, can be linked to poly-ethylene glycols (PEG) coated glass and thereby allows subsequent protein grafting upon UV activation in a one-step procedure [6].

2. EXPERIMENTAL

We took advantage of the cell repulsive property of PEG and describe here a new technique to produce micropatterns of adhesion proteins for cell attachment on glass coverslip based on this UV grafting strategy. It allows the rapid production of highly reproducible patterns without the need of a stamp or any contact with the surface.

Figure 1 shows the procedure. First, a glass slide was activated with an oxygen plasma treatment and then coated by immersion in a Poly-L-Lysine-PEG (PLL-PEG) solution [7]. The PLL-PEG is a copolymer. Several PEG chains are grafted on a PLL backbone. The poly-L-Lysine backbone is charged and binds to the oxidized glass coverslip through

978-0-9798064-0-7/μTAS2007/$20©2007CBMS

electrostatic interactions. The PEG side-chains constitute a cell repulsive layer on the glass slide surface.

Second, a droplet of fibronectin and benzophenone solution in PBS was deposited on a photomask. The droplet was covered by the PLL-PEG coated glass slide. The glass slide was exposed to UV light (365nm) through the photomask. The glass slide displayed an intense and homogeneous grafting of fibronectin only in the UV-exposed regions.

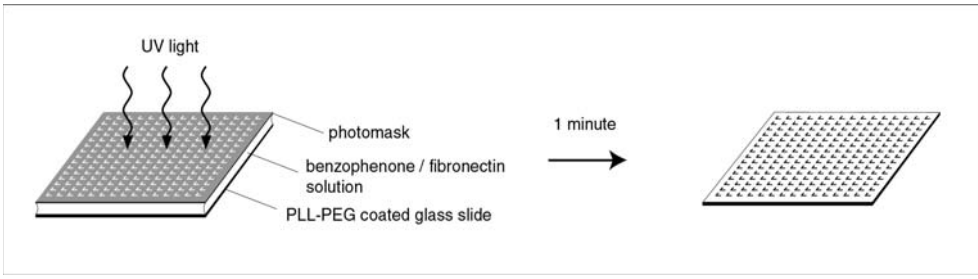

Figure 1. Patterning method. The PLL-PEG coated glass slide is illuminated with UV light through a photomask. Benzophenone initiates the grafting of fibronectin in the exposed regions.

RPE1 cells (Retinal Pigment Epithelial human cell line) were trypsinised, centrifugated, resuspended in the culture medium and platted on the patterned coverslip.

3. RESULTS AND DISCUSSION

Figure 2 shows how cells were nicely constrained in the fibronectin patterns. Large and regular cell arrays were produced by this technique and observed in a time-course experiment. Individual cells (Figure 2A) or larger cell populations (Figure 2B) were perfectly constrained for at least 24h. The same cell type on microcontact printed patterns either spread out of the pattern or rip off the patterned proteins and detach from the slide after 24h [1].

The main advantage of this technique compared to microcontact printing is that the patterns are made in a very rapid (around 30 minutes in total) and simple way. Patterned motifs are also much more efficient and reproducible. Since it doesn't require the use of the stamp and the printing step, this UV based method could easily be automatized for industrial production. However the water soluble form of the benzophenone is still a specialized, and therefore expensive, product that has to be synthesized by Sigma Aldrich upon specific request. The use of 185nm wavelength to produce micropatterns on polystyrene without any photosensitizer [8] is an interesting alternative to this limitation. But Petri dishes in polystyrene don't have good optical property and therefore are not compatible with most of biological imaging protocols. It would be valuable to adapt this patterning strategy on glass coverslip.

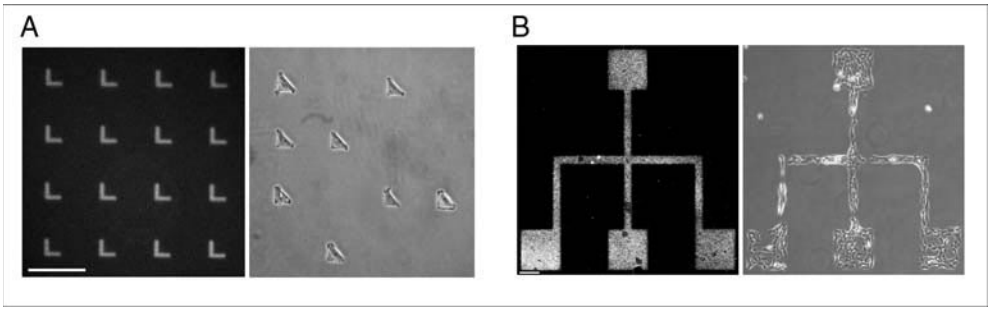

Figure 2. Micro-patterns for individual cells (A) or for cell population (B). In each case, fibronectin-Cy3 is visualized in fluorescence (left) and cells are visualized in phase contrast (right).Scale bar is 100µm.

4. CONCLUSIONS

We showed that micropatterns for individual cells or for multiple cell assembly can be performed by grafting fibronectin with UV light on PEG coated glass slide. This protocol is based on commercially available products and thus could be reproduced in any biology lab without any specialized know-how in micro-fabrication.

Our new technique has promising perspectives since it doesn't require a direct contact with the surface to be patterned, contrary to the classical micro-contact printing technique. The light we used, at 365nm, is in the near UV field and thus could be easily combined with classical optical elements such as microscopes objectives. Future development could also be envisaged in 3D micropatterning.

REFERENCES

1. Fink, J., et al., *Comparative study and improvement of current cell micro-patterning techniques.* Lab Chip, 2007. **7**(6): p. 672-80.
2. Ruiz, S.A. and C.S. Chen, *Microcontact printing: A tool to pattern.* Soft Matter, 2007. **3**(2): p. 168-177.
3. Thery, M., et al., *Cell distribution of stress fibres in response to the geometry of the adhesive environment.* Cell Motil Cytoskeleton, 2006. **63**(6): p. 341-55.
4. Théry, M., et al., *Anisotropy of cell adhesive microenvironment governs cell internal organization and orientation of polarity.* Proc Natl Acad Sci U S A, 2006. **103**(52): p. 19771-6.
5. Thery, M., et al., *The extracellular matrix guides the orientation of the cell division axis.* Nat Cell Biol, 2005. **7**(10): p. 947-53.
6. Balakirev, M.Y., et al., *Photochemical patterning of biological molecules inside a glass capillary.* Anal Chem, 2005. **77**(17): p. 5474-9.
7. Csucs, G., et al., *Microcontact printing of novel co-polymers in combination with proteins for cell-biological applications.* Biomaterials, 2003. **24**(10): p. 1713-20.
8. Welle, A., et al., *Photo-chemically patterned polymer surfaces for controlled PC-12 adhesion and neurite guidance.* J Neurosci Methods, 2005. **142**(2): p. 243-50.

CA^{2+} SIGNAL IS CONTROLLED BY RECEPTOR-MEDIATED ACTIVATION OF G-PROTEINS PATHWAY IN *TETRAHYMENA PYRIFORMIS* DURING CHEMOTAXIS

Seong-Won Nam and Sungsu Park
Division of Nano Science, Ewha Womans University, Seoul, 120-750, Korea

ABSTRACT

In this study, the dynamic transition of Ca^{2+} signaling in *Tetrahymena pyriformis* triggered by chemical cues was optically measured in a microfluidic device, which can generate a chemoeffector gradient with pneumatically actuating a connecting microvalve between the ciliate chamber and chemical chambers. The ciliated protozoan *Tetrahymena pyriformis* is a eukaryotic unicellular model organism, to simplify the study about the relation of motility and Ca^{2+} signaling. The intracellular Ca^{2+} level is predominantly controlled by PI3K and PLC via receptors, whereas the motility correlated stronger with PLC activity. Thus, it can be concluded, the intracellular Ca^{2+} level is regulated by controlling Ca^{2+} influx via receptors, while the chemotactic receptors are controlled by PI3K and PLC.

These results demonstrate that the microfluidic system is useful applied not only for the study of ciliate chemotaxis but also for a better understanding of the intracellular Ca^{2+} signaling and signal transduction mechanism on their receptors.

Keywords: Microfluidic device, ciliate, chemotaxis, Ca^{2+} signaling

1. INTRODUCTION

The directional sensing and migration, as in chemotaxis, is a most conserved mechanism of a cell and is critical in immunity, angiogenesis, wound healing, embryogenesis and neuronal patterning. To study chemotaxis, several methods have been tested like as Boyden chamber [1], multi-chamber capillary [2] and micropipette [3]. we reported a microfluidic device for ciliates chemotaxis previously [4]. *Tetrahymena pyriformis* is a 50 μm long, unicellular, ciliated freshwater protozoan. Because of their high motility, ciliates can respond more quickly to outside stimuli than any other organism and has been used for biological sensors. In this study, the dynamic transition of Ca^{2+} signaling in ciliates triggered by chemical cues was optically measured in a microfluidic device which can generate a chemoeffector gradient with pneumatically actuating a connecting microvalve between the ciliate chamber and chemical chambers. With this device, more exact and detailed analyses of Ca^{2+} signaling was made, which had not been possible with conventional methods using a pipette. The intensity of Fluo-4, a fluorescent calcium indicator, in a ciliate under a linear gradient of an attractant was measured by a laser scan microscopy, to study the dynamic changes of intracellular Ca^{2+} concentration and distribution.

978-0-9798064-0-7/μTAS2007/$20©2007CBMS

2. EXPERIMENTAL

The microfluidic device consists of two PDMS (polydimethylsiloxane, Dow-Corning, Cortland, NY, USA) layers (Fig. 1). The top, thick layer was prepared with a ratio of 1:10 (curing agent: PDMS), whereas the bottom thin layer is 1:30. The switching of the valves was controlled by LabVIEW program (National Instruments Co.). Measurement of cytosolic Ca^{2+} with Fluo-4 was performed using Laser scanning microscope (Model; LSM510, version 4. Carl Zeiss Inc., Jena, Germany), while 3 thousand Images were obtained with 0.5 sec. intervals. After 11 min. and 43 min. valves were opened and attractant was diffused from two surrounding chambers in the middle chamber.

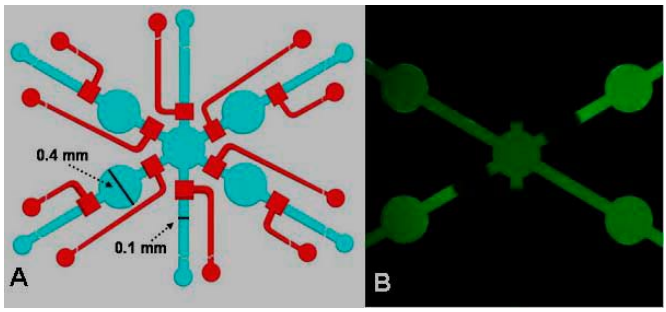

Fig. 1. Microfluidic device. (A) Design of device. (B) Diffusion control by fluorescent sensor.

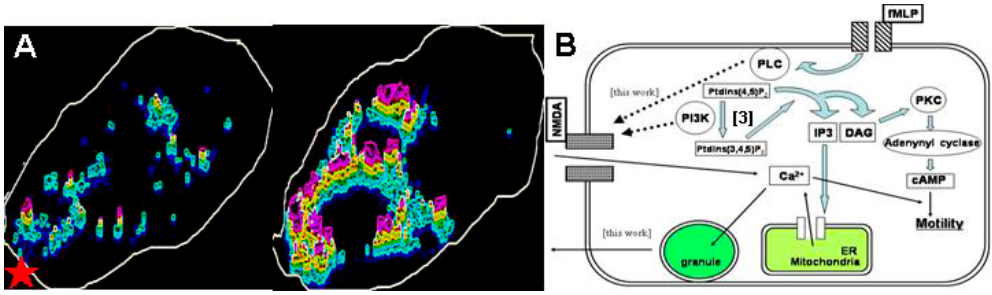

Fig.2. Ca^{2+} signalling during chemotaxis. (A) Images of Ca^{2+} signal after NMDA stimulation. The star indicates the diffusion starting points of NMDA. (B) The putative model of Ca^{2+} controlling in *Tetrahymena pyriformis*.

3. RESULTS AND DISCUSSION

To investigate motility of *Tetrahymena pyriformis* during chemotaxis, NMDA and fMLP were used for chemoattractant. PLC blocker, U-73122 impeded the motility of ciliates, when NMDA and fMLP were used as attractants than ciliates to attractants alone. After diffusing of NMDA an increasing of Ca^{2+} signal was observed and the distribution of cytosolic Ca^{2+} signal was chased the direction of stimulation (Fig. 2A). When PLC was blocked by 40 μM U-73122, the Ca^{2+} signal was increased to 2.5 fold compared to starting Ca^{2+} level and Inhibition of PI3K by 250 nM Wortmannin evoked Ca^{2+} signal to 4.7 fold to

starting level. When NMDA receptor was inhibited by APPA or MK-801, the Ca^{2+} signal remained under starting signal intensity, even though PI3K has been blocked by 250 nM Wortmannin. Therefore it can be concluded, the intracellular Ca^{2+} level is predominantly controlled by PI3K and PLC via NMDA-receptors, whereas the motility correlated stronger with PLC activity (Fig. 2B).

4. CONCLUSIONS

In this study, we presented a new microfluidic device which enable to analyze the chemotactic behavior and intracellular Ca^{2+} signaling mechanism precisely in a chip. Using this system the Ca^{2+} signaling could be observed during chemotaxis without any disruption and thus the new Ca^{2+} controlling role of PLC and PI3K in *Tetrahymena pyriformis* could be recognized.

ACKNOWLEDGEMENTS

This research was equally supported by the Nano/Bioscience & Technology Program (M10536090002-05N3609-00210) of the Ministry of Science and Technology (MOST), the SRC program of the Korea Science and Engineering Foundation (KOSEF) through the Center for Intelligent Nano-Bio Materials at Ewha Womans University (Grant R11-2005-008-02003-0), and the Korean Research Foundation Grant (MOEHRD, Basic Research Promotion Fund) (KRF-2006- 005-J04002).

REFERENCES

[1] Boyden S.V. (1962). The chemotactic effect of mixtures of antibody and antigen on poly-morphonuclear leukocytes. J. Exp. Med. 115, 453-466.

[2] Kohidai L., Kovacs P., Csaba G. (1996). Chemotaxis of the unicellular green alga *Dunaliella salina* and the ciliated *Tetrahymena pyriformis*-effects of glycine, lysine, and alanine, and their oligopeptides. Biosci. Rep., 16, 467-476.

[3] Parent C.A., Devreotes P.N. (1999). A cells sense of direction. Science 284, 765-770.

[4] Nam S.W., Noort D.V., Yang Y., Park S. (2007). A biological sensor platform using a pneumatic-valve controlled microfluidic device containing *Tetrahymena pyriformis*. Lab Chip, 7, 638–640.

SIMULTANEOUS MANIPULATION AND DETECTION OF SINGLE CELLS USING MAGNETIC SENSORS

C. Liu[1,2,*], W. Laureyn[1] and L. Lagae[1]

[1]*Interuniversity Microelectronics Center (IMEC), Belgium and*

[2]*Department of Electrical Engineering (ESAT), Katholieke Universiteit Leuven, Belgium*

ABSTRACT

We present a device for the detection of cells labeled with magnetic particles while the cell-particle complex is being actuated by a traveling magnetic field. The simultaneous actuation and detection was achieved by sending an alternating current to metallic magneto-resistive sensors. In addition to the magnetic force, we also applied a negative dielectrophoretic force in order to control the distance between the device and the cell-particle complex, which will otherwise adhere to each other as the result of the weak electrostatic force and attractive magnetic force component. The device opens the possibility for precise and automatic manipulations of cells in μTAS.

Keywords: cell handling, magnetic particle, magnetic sensor, magnetophoresis

1. INTRODUCTION

Serving both as analyte carriers [1] and signal reporters [2], magnetic particles are very promising for μTAS applications. Sample handling with magnetic particles in prior art is largely focused on the capture [3] and transport [4] of myriad particles in a relatively large scale without sensing. In contrast, we propose a device that exploits both two functions of magnetic particles for the simultaneous manipulation and detection of single cells.

2. THEORY

The device was constructed from magneto-resistive spin valve (SV) sensors. Spin valve sensors are widely used in hard disk read heads. They are made of thin metal films containing two magnetic layers isolated by a non-magnetic layer. The presence of an in-plane external magnetic field changes the magnetization of one of the two magnetic layers with respect to the other, and consequently the resistance (magneto-resistance) of the sensor. In this work, two sets of parallel SV sensors are connected in tandem to form two meandering conductors A and B (Figure 1). When the two conductors are fed with a DC current (I_{DC}) alternately and periodically, a traveling magnetic field is generated allowing to transport magnetizable objects bi-directionally, i.e. magnetophoresis (Figure 2). Meanwhile, the stray magnetic field of the magnetized particle is transduced by the sensor as the output voltage. In this way, the transport and detection functions are performed simultaneously.

3. EXPERIMENTAL AND RESULTS

Cell detection was first demonstrated by measuring the stray magnetic field of a single Molt-4 cell labeled with Dynabead® CD45 magnetic particles when the cell-particle complex was attracted to one of the sensors in the MEM cell culture medium (Figure 3).

* E-mail: chengxun.liu@imec.be

978-0-9798064-0-7/μTAS2007/$20©2007CBMS

However, neither the cell-particle complex nor single particles could be transported by the magnetophoresis in the traveling magnetic field in the MEM medium. Instead they adhered to the device. We believe this was caused by the net attractive force which is the sum of the DLVO force and magnetic force component in the out-of-plane direction [5-7].

To circumvent the adherence problem, we added a dielectrophoretic (DEP) force by superimposing an AC voltage (V_{AC}) across the two conductors to induce a negative DEP, in addition to the traveling magnetic field induced by I_{DC} (Figure 2 & 4) [7]. As a result, the negative DEP force balances the magnetic force component in the out-of-plane direction, resulting in a levitation of the cell-particle complex and free particles during the transport. The magnetic and DEP forces can be adjusted independently by tuning the amplitude of I_{DC} and V_{AC}. In the second experiment a single cell bound with three Dynabead® CD45 particles was successfully transported by the device with a controllable out-of-plane position (Figure 5). The transport velocity increases as a function of I_{DC} and V_{AC} (data not shown). Currently we are engineering the device so that the SV sensing current can be appropriately applied while the DEP field is on.

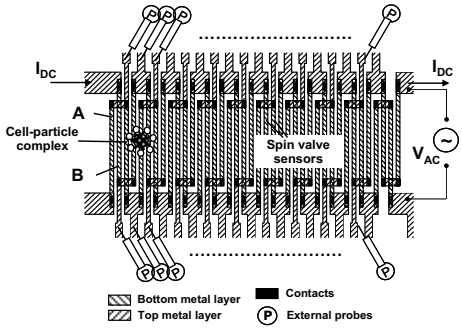

Figure 1. Schematic of the simultaneous transport and detection of magnetically labeled cells. The device consists of two metal layers: a spin valve sensor layer at the bottom and a Au connection layer on top, separated by 200 nm Si_3N_4 with some contacts open to make electrical connection of the two conductors (A and B).

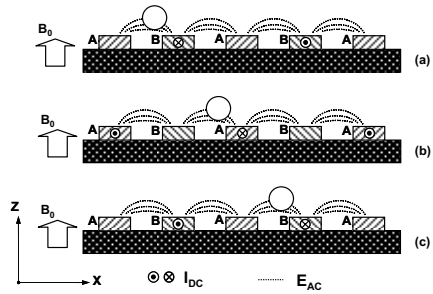

Figure 2. The principle of the continuous transport of a magnetically labeled cell by the traveling magnetic field. A homogeneous magnetic field B_0 is applied to bias the particle magnetization in the out-of-plane direction. The dielectrophoretic field is applied simultaneously to levitate the cell and particles.

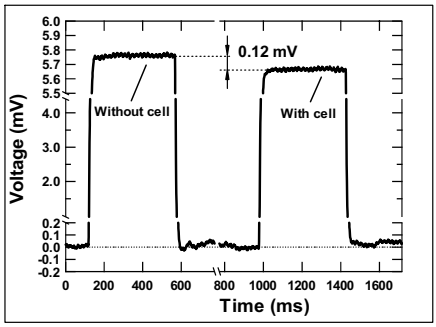

Figure 3. The magneto-resistive signal measured when a single Molt-4 cell bound with three Dynabead® CD45 particles is brought to a spin valve sensor. A DC current I_{DC} =10 mA gives a 0.12 mV difference in the output voltage with and without the presence of the cell-bead complex.

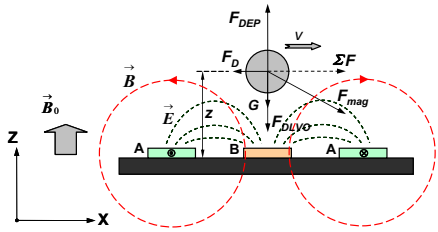

Figure 4. All forces exerted to a magnetic particle for a combined magnetophoresis and dielectrophoresis. F_{mag}: magnetic force; F_D: fluidic drag force; F_{DLVO}: Derjaguin-Landau-Verwey-Overbeek force; F_{DEP}: dielectrophoretic force; G: gravity.

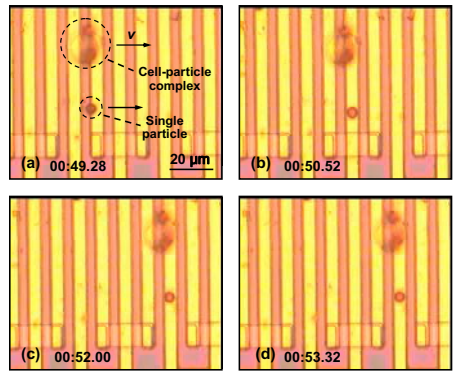

Figure 5. Transport of a single Molt-4 cell labeled with Dynabead CD45 particles by a traveling magnetic field and a simultaneous DEP field. I_{DC} = 10 mA, V_{AC} = 5 V at 1 MHz, B_0 = 1.6 mT. Here the SV sensors in the first experiment (Figure 3) were replaced by thick Au conductors without any insulation to maximize the electric field strength.

5. CONCLUSIONS

In conclusion, single cells can be detected by SV sensors, and be manipulated by the combined magnetophoresis and dielectrophoresis. We believe that the sensor signal given by the magnetically labeled cells can be used not only for the cell detection/counting but also as a feedback signal to allow a better transport control, or a separation of different types of magnetically labeled bio-analytes. We expect the technique to be suitable for accurate control and detection of rare cells, and potential technique for cell sorting in µTAS.

ACKNOWLEDGEMENTS

This paper describes the work undertaken in the context of EC IST project 027652 MASCOT. The authors would like to acknowledge fruitful discussions with the consortium participants.

REFERENCES

[1] V.L. Furdui and D.J. Harrison, Lab Chip 4, 614 (2004).
[2] D.L. Graham, H.A. Ferreira, P.P. Freitas, Trends Biotechnol. 22, 455 (2004).
[3] E. Mirowski, J. Moreland, S.E. Russek, M.J. Donahue, Appl. Phys. Lett. 84, 1786 (2004).
[4] T. Deng, G.M. Whitesides, M. Radhakrishanan, G. Zabow and M. Prentiss, Appl. Phys. Lett. 78, 1775 (2001).
[5] R. Wirix-speetjens, W. Fyen, K. Xu, J. De Boeck and G. Borghs, IEEE T. Magn. 41, 4128 (2005).
[6] C. Liu, L. Lagae, R. Wirix-Speetjens and G. Borghs, J. Appl. Phys. 101, 024913 (2007).
[7] C. Liu, L. Lagae and G. Borghs, Appl. Phys. Lett. 90, 184109 (2007).

STUDY OF ATP-RELEASE FROM ACOUSTICALLY LEVITATED ERYTHROCYTES

Mikael Evander[1], Karolina Mileros[1], Carl Högberg[2], David Erlinge[2], Monica Almqvist[1], Thomas Laurell[1] and Johan Nilsson[1]

[1]Department of Electrical Measurements, Lund University, Lund, Sweden
[2]Department of Cardiology, Lund University, Lund, Sweden

ABSTRACT

Erythrocytes (red blood cells) are known to produce large amounts of Adenosine Triphosphate (ATP). It has recently become clear that the ATP-release is part of a mechanism controlling the dilation of the body's blood vessels. The study of the erythrocyte's behaviour is complicated by the fact that they respond easily to any physical contact. In this paper we propose a new method for studying the dynamics of the ATP-release by combining non-contact acoustic trapping in a microfluidic chip with a chemiluminiscent assay. Sensitivity levels down to 10 pM were achievable and the ATP-release from a cluster of levitated live erythrocytes was recorded.

Keywords: Acoustic trapping, Erythrocytes, ATP, Chemiluminiscence

1. INTRODUCTION

Erythrocytes (red blood cells) have been shown to release Adenosine Triphosphate (ATP) when exposed to low oxygene levels and physical deformation. The ATP triggers the blood vessel endothelium cells to produce nitric oxide (NO). The NO causes the vascular muscle cells to relaxe, creating a dilated blood vessel. By using this mechanism the erythrocytes can control the dilation of the blood vessel, making small capillaries larger and increase the oxygene transfer to regions with low oxygene levels [1,2].

The study of ATP-release from erythrocytes is problematic since any physical deformation, e.g. stirring, pipetting etc, triggers a release of ATP. Probing the erythrocytes for different temperatures can be accomplished but testing for other enviromental properties that might trigger an ATP-release, such as pH, has been proven difficult. By non-contact levitation of the erythrocytes on a microchip, a fluidic network allows for multiple assays to be performed in a convenient format.

2. EXPERIMENTAL

Acoustic trapping has been used earlier for handling of cells and has also been introduced in microfluidic systems for cell-based bioassays (3). The aim of this work is to show that acoustic trapping can be used as a platform for controlled handling of erythrocytes and that the release of ATP from a small population of cells can be detected. The ATP-release from erythrocytes was studied using a chemiluminiscent assay while keeping the erythrocytes acoustically levitated in a standing wave generated in a microfluidic channel. A mixture of luciferin and luciferase was infused and the amount of light emitted from the chemiluminiscent reaction was detected by a photomultiplier tube (PMT) and used as a direct measure of the amount of ATP.

The cell leviation was performed using a 10 MHz transducer (900 μm x 900 μm) mounted in a microfluidic channel (Figure 1 and 2). The channel width was 1 mm and the height was 67 μm, corresponding to a channel resonance of 11 MHz, which was the

978-0-9798064-0-7/μTAS2007/$20©2007CBMS

frequency used in the experiments. During the cell trapping experiments the center transducer was used while perfusing the luciferine/luciferase-mixture from one of the side-inlets.

The total channel volume above the transducer was approximately 57 nl but the erythocytes were trapped in a layer in the center of the channel equivalent to an erythrocyte volume of around 5 nl. The device used was presented at µTAS 2005 and 2006, and is described in further detail in [3].

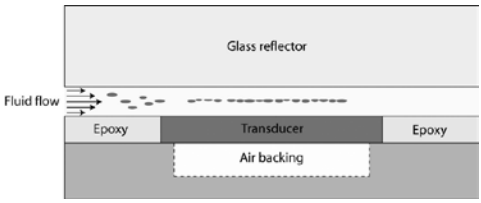

***Figure 1**: An ultrasonic transducer is cast in epoxy with an air backing, directing the ultrasound into the fluidic channel. The standing wave set up in the fluidic channel creates a pressure minima that levitates erythrocytes.*

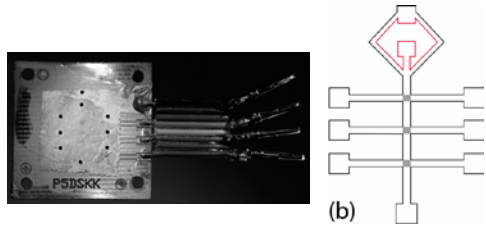

***Figure 2**: Left: Transducer chip with three integrated transducers. Right: The channel structure with inlets on top and three orthogonal side channels. The center transducer was used in the experiments.*

3. RESULTS AND DISCUSSION

ATP-levels down to 10 pM were shown to be detectable during a calibration. ATP and luciferin/luciferase were mixed on-chip and the changes in light intensity were recorded, see figure 3.

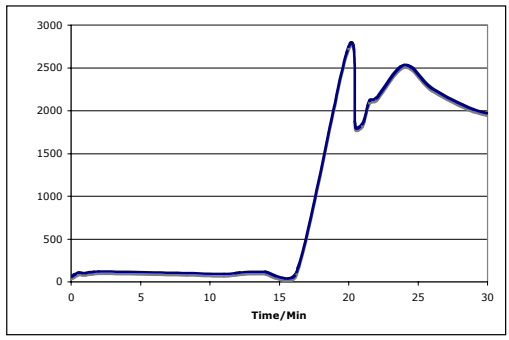

***Figure 3**: PMT response when 10 pM ATP was infused in the chip together with the luciferin/luciferase mixture. The time delay before the response was due to the fluid volume in the connecting tubing of the device.*

To study the ATP-release from the erythrocytes, live cells were supplied to the chip and trapped. A luciferin/luciferase mixture was then introduced and the PMT response was recorded, see Figure 4. Compared to the calibration, the ATP-release would correspond to a concentration of around 2.5 pM. However, during the calibration the chemiluminiscent

reaction was taking place in the entire channel while the erythrocytes only produce ATP at a thin layer in the center of the channel. The actual concentration of ATP released from the erythrocytes is therefore very likely much higher.

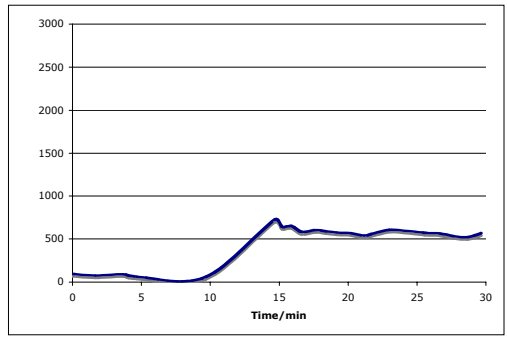

***Figure 4**: PMT response when trapped erythrocytes were perfused with the luciferin/luciferase mixture. The delay in response was due to the tubes connecting the syringe pump to the device.*

4. CONCLUSIONS

The results show that acoustic trapping in microfluidic channels can be used for studies on live erythrocytes and that the sensitivity in the set-up is sufficient to detect the released ATP. The results also indicate that the limit of detection is at least en order magnitude lower than the levels used in the experiments, i.e down to 1 pM.

REFERENCES

[1] D. Erlinge, *Extracellular ATP: a central player in the regulation of vascular smooth muscle phenotype*, Am. J. Physiol. Cell Physiol., 2004, **287**(2): p. C260-C262.

[2] A. Price, R. S. Martin and D. M. Spence, *Monitoring erythrocytes in a microchip channel that narrows uniformly: Towards an improved microfluidic-based mimic of the microcirculation,* J. Chrom. A, 2006, **1111**(2): p. 220-227

[3] M. Evander, L. Johansson, T. Lilliehorn, J. Piskur, M. Lindvall, S. Johansson, M. Almqvist, T. Laurell and J. Nilsson, *Noninvasive Acoustic Cell Trapping in a Microfluidic Perfusion System for Online Bioassays*, Anal. Chem., 2007, **79**(7), pp. 2984-2991

VERY HIGH YIELD ELECTRO CELL-FUSION BASED ON FIELD CONSTRICTION AT A MICROORIFICE

Kinya Tsuda[1], Murat Gel[1], Hidehiro Oana[1,2], Boonchai Techaumnat[3], Hidetoshi Kotera[2,4] and Masao Washizu[1,2]

[1]Dept. of Mechanical Eng., The University of Tokyo, Japan, [2]JST, CREST, Japan
[3]Dept. of Electrical Eng., Chulalongkorn University, Thailand
[4]Dept. of Mechanical Eng., Kyoto University, Japan

ABSTRACT

This paper proposes and experimentally demonstrates a novel method of high yield cell-fusion using a microorifice. Two cells are dielectrophoretically made into contact at the orifice whose diameter is approximately equal to that of cells, and a r.f. modulated pulse is applied. Because of the highly constricted field pattern created by the orifice, the induced cell membrane takes maximum at the contact point, and virtually zero outside the orifice, so that the membrane breakdown occurs nowhere but at the contact point. The method resulted in more than 90% fusion yield.

Keywords: Cell-fusion, dielectrophoresis, microorifice, field-constriction

1. INTRODUCTION

Electro cell-fusion is a method to create a hybrid among two types of cells by electrically "welding" the cell membranes. However, in conventional electro cell-fusion, the fusion yield is known to be as low as 0.1%. There are trials to apply microfluidic structures for cell-fusion, but most efforts are directed towards creating 1:1 hybrid, and there seems to have been no work to essentially improve the fusion yield.

In this paper, we use a microstructure to tailor the field pattern to localize the cell membrane breakdown at the contact point of two cells, so that the fusion takes place in reproducible and reliable manner. As shown in fig.1, a microorifice is opened on an insulator plate, and the electrodes are placed on both sides. Two cells are brought into contact in the orifice using dielectrophoresis (DEP), and a pulse voltage is applied. The field lines, being unable to penetrate the insulator, create a field constriction at the orifice, meaning that the cell membrane voltage becomes maximal at the contact point. Fig,2 is a result of the membrane voltage analysis assuming an axial symmetry [1] showing that ~95% of the applied voltage goes to the membrane at the contact point, and virtually zero elsewhere, so that the membrane breakdown exclusively occurs at the contact point. Due to highly constricted field, the method is essentially insensitive to the size or shape of the cells, or the position of the electrodes.

978-0-9798064-0-7/μTAS2007/$20©2007CBMS

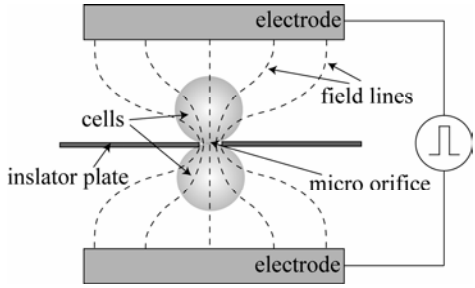

Figure 1. Principle of the cell-fusion based on a field constriction at a microorifice. The field constriction is utilized both for bringing cells into contact at the orifice, and localizing membrane breakdown at the contact point.

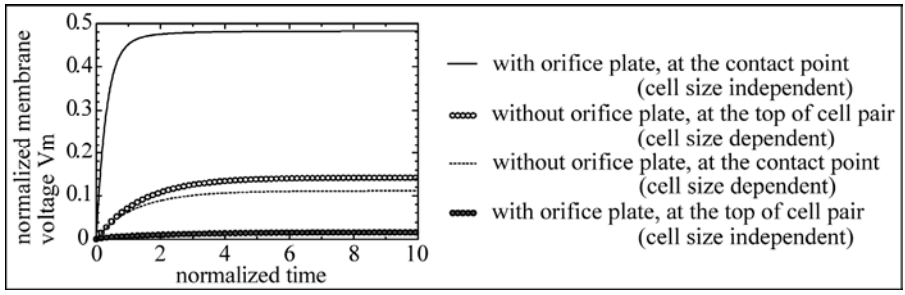

Figure 2. Calculated time course of the membrane voltage V_m for an equal-sized cell pair.Without the orifice plate, V_m is cell-size dependent, and is maximal at the top of the cellpair. With the orifice plate, most voltage is concentrated on the membrane at the orifice(solid line), and virtually zero at other locations (solid circle).

2. EXPERIMENTAL

An experimental demonstration of the principle is done by using a microchamber shown in figure 3. The chamber, 15μm depth, is fabricated with a standard SU-8 lithography and PDMS molding. The orifice is rectangular with the height 15μm and the width 10μm, but still creates an adequate field constriction at the contact point.

Jurkat cells (human T cell lymphoblast-like cell line, 5-15μm$^{\phi}$) are fed into the channel, and are brought into contact at the orifice by DEP with 5MHz 20V_p continuous voltage. Then, 12-20V_p 10ms pulse is applied to initiate the fusion. The pulse waveform is modulated at 20kHz to prevent secondary breakdown of the membrane [2].

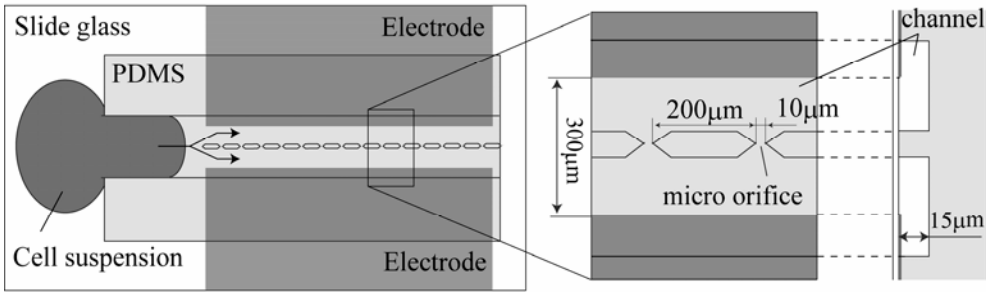

Figure 3. Structure of the device.

3. RESULTS AND DISCUSSION

Figure 4 shows one of the results. Two cells, c.a. 10 and 15μ^{ϕ}, are drawn into the orifice and made into contact by DEP (2), and the r.f. modulated pulse is applied (3). The cells fuse (4) and are taken out from the orifice and isolated by a gentle flow (6).

In all experiment with Jurkat cells and also with plant protoplasts, cell fusion took place so far as the cells can be positioned in the orifice, and the membrane breakdown other than at the contact point is hardly observed. Also, in the cases where more than two cells forming a chain at the orifice, it is the cell pair in the orifice that fuses, and the others has nothing to do with the fusion (like the 3rd cell seen below the cell pair in fig.4). These observations demonstrate the effectiveness of the constricted field design for cell fusion.

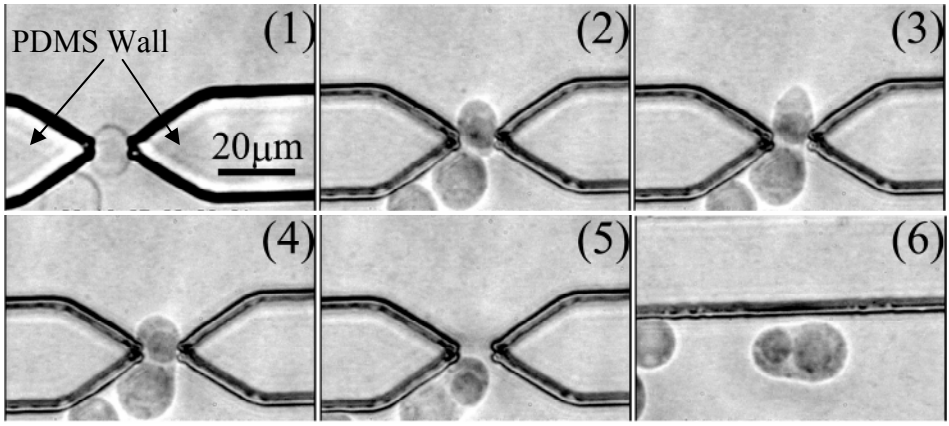

Figure 4. Snap shots of cell-fusion in the constricted field at the orifice

4. CONCLUSIONS

A novel method of high-yield electro cell-fusion based on a field constriction is proposed and demonstrated. The application of the method, being inherently high-yield, is not limited for creating hybrid cells, but also for mixing cytoplasm among cells, to transplant growth, differentiation or cell initialization factors, or organella such as mitochondria, to be used for epigenetic studies, regenerative medicine or plant biotechnology.

ACKNOWLEDGEMENTS

VDEC (VLSI Design and Education Center) Electron Beam Lithography System was used for making devices.

REFERENCES

[1] Boonchai Techaumnat and Masao Washizu, *Analysis of the effects of an orifice plate on the membrane potential in electroporation and electrofusion of cells*, J. Phys. D: Appl. Phys. 40 1831–1837 (2007)

[2] Osamu Kurosawa, Hidehiro Oana, Hidetoshi Kotera and Masao Washizu, *High-yield electroporation using RF modulated field constriction*, μ-TAS 2006, p.458-460 (2006)

NANOPOROUS TITANIA FILMS FOR THE PROMOTION OF STEM CELL PROLIFERATION

Alexander Iles[1], Hossein Hosseinkhani[2], Mohsen Hosseinkhani[3] and Henrik Lindstrom[2]

[1]University of Hull, Dept. of Chemistry, Cottingham Rd., Hull, HU6 7RX, UK.
[2]ICYS, National Institute of Materials Science, Tsukuba, Ibaraki, JAPAN.
[3]Kyoto University Hospital, Dept. of Cardiovascular Medicine, Kyoto, JAPAN, currently at: Harvard-MIT Division of Health Sciences and Technology, MA, USA.

ABSTRACT

We describe the use of nanoporous titania films for the production of robust and highly biocompatible substrates for the study of stem cells in microfluidic devices.

Keywords: stem cells, titania coatings, nanomaterials, biocompatibility.

1. INTRODUCTION

Microfluidic devices are ideal platforms for the study of stem cell proliferation and differentiation.[1] However, chip substrate materials tend to be relatively incompatible with biological systems. This is usually overcome by the use of relatively fragile surface coatings. Care must be taken so that they are not damaged during the course of an experiment. In addition to this, such coatings cannot be sterilised and reused. Recently, we demonstrated a simple technique for depositing a robust and highly porous film of titania nanoparticles on the inside walls of microphotoreactors.[2] Titania is well known for its biocompatibility.[3] Hence, we evaluated the viability of using titania films as biocompatible supports for the proliferation of stem cells in microfluidic devices.

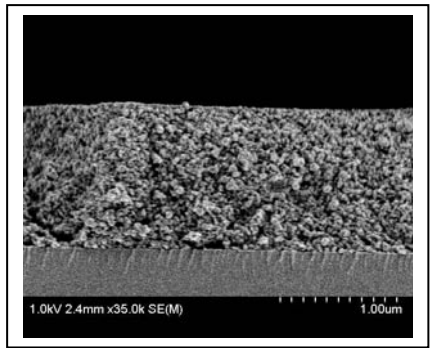

Figure 1**.** Cross sectional SEM picture of a nanoporous film of anatase titania deposited onto glass.

2. EXPERIMENTAL

Titania coated substrates were prepared by treating glass slides with 2M sodium hydroxide before dip coating in colloidal anatase TiO_2 suspension and then baking at 400º C for 6 hours. This produced a highly nanoporous film approximately 1 micron thick (Figure 1). Collagen coated substrates were produced by dropping collagen solution onto

978-0-9798064-0-7/μTAS2007/$20©2007CBMS

glass slides and leaving to dry for one hour. Mesenchymal stem cells (MSC) were isolated from the femurs of 3-week-old male Wistar rats. The bone marrow was flushed out using Dulbecco's modified Eagle's minimal essential medium (DMEM) supplemented with 15 % fetal calf serum (FCS) and 50 U/ml penicillin and streptomycin. The cell suspensions were placed into flasks and cultured at 37 ºC in a 95 % air : 5 % CO_2 atmosphere. MSC were seeded on the substrates at a density of 1×10^6 cells/ml and incubated until a cellular monolayer was formed at 37 °C in a 95 % air : 5 % CO_2 atmosphere. As controls, culture media containing MSC (1×10^6 cells/ml) were seeded on polystyrene tissue culture plates and plain glass slides. Proliferation rates and cell morphologies were observed using optical microscopy.

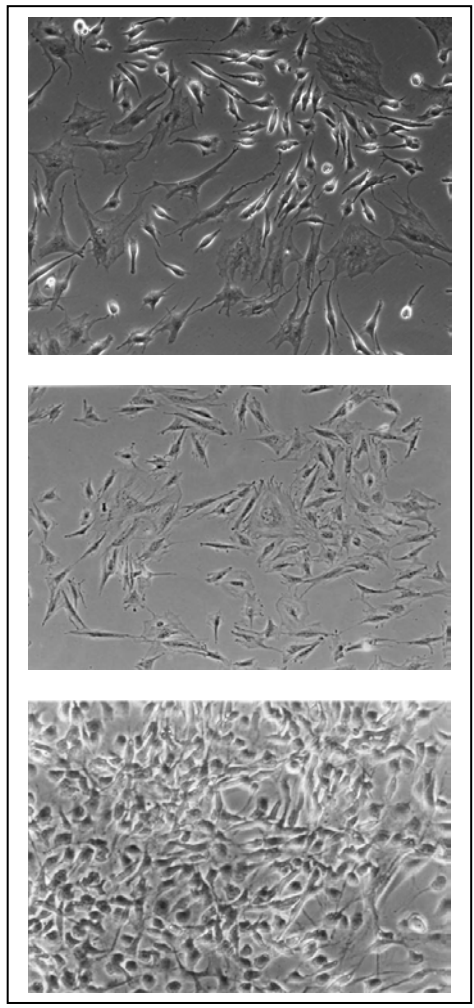

Figure 2. Bone marrow stem cells seven days after subculture on: (top) an uncoated glass slide, (middle) an uncoated polystyrene tissue culture dish, (bottom) on a glass slide coated with nano-porous titania.

4. RESULTS AND DISCUSSION

As can be observed from Figure 2, after seven days, far greater stem cell proliferation occurred on the titania coated substrates than on uncoated culture plates or on glass slides. These experiments were repeated several times and the mean proliferation rates and standard deviations for growth on bare glass, collagen coated glass and titania coated glass are plotted in Figure 3. As can be seen, there is a greater initial adhesion of cells to the titania coated substrates in addition to the higher overall proliferation rate. Furthermore, these titania films are robust and can be sterilised and re-used as required.

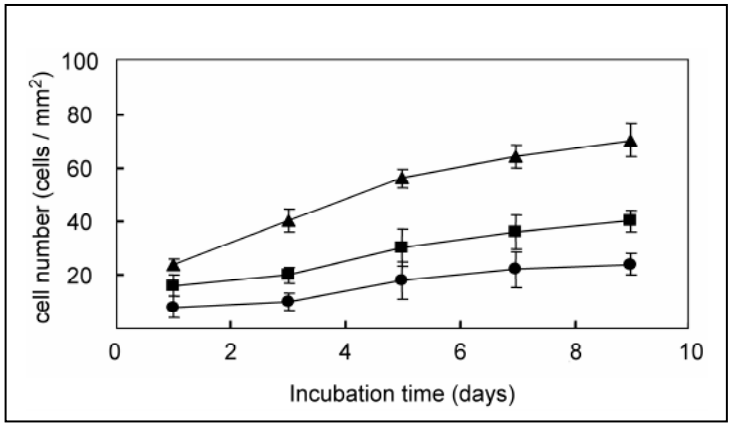

Figure 3. Time course of MSC growth on glass slides coated with: TiO_2 (▲), collagen type I (■), and without any substance (●).

5. CONCLUSIONS

Nanoporous titania films form ideal surfaces for the culturing of stem cells. These films are likely to find widespread use in on-chip studies of stem cells since they can be deposited onto the glass substrates used in PDMS microdevices, or coated onto the channel walls of glass microstructures.

ACKNOWLEDGEMENTS

This work was partially supported by the Japanese Ministry for Education, Culture, Sports, Science and Technology (MEXT).

REFERENCES

[1] B. G. Chung, et al., *Human Neural Stem Cell Growth and Differentiation in a Gradient-Generating Microfluidic Device*. Lab on a Chip, 5, pp 401-406. (2005).

[2] H. Lindstrom, R. Wootton and A. Iles, *High Surface Area Titania Photocatalytic Microreactors*, Journal of the AIChE, 53, pp 695-702, (2007).

[3] P. A. Ramires, et al., *The Influence of Titania/Hydroxyapatite Composite Coatings on In-vitro Osteoblast Behaviour*. Biomaterials, 12, pp 1467-1474. (2001).

THE UTILITY OF INTERSTITIAL, MICROFLUIDIC PERFUSION IN EXTENDED CULTURING OF THICK ORGANOTYPIC BRAIN SLICES

Jelena Vukasinovic, Komal Rambani, Steve M. Potter and Ari Glezer
Georgia Institute of Technology, USA

ABSTRACT

Emerging trends in tissue engineering to scale-up the densities of three-dimensional (3-D) cultures *in vitro* demand efficient perfusion platforms to satisfy cellular requirements in nutrient and gas availability. Commercial devices predominantly rely on diffusive rather than convective interstitial mass transport to augment cellular viability. Their use remains confined to a particular setting with little design flexibility. To address these demands, we disclose a simple design, fabrication and fluidic validation of an autoclavable perfusion platform that allows modifications to suit specific applications challenges. We demonstrate its utility in extended culturing of 700μm thick organotypic brain slices *in vitro*.

Keywords: microfluidics, perfusion, thick brain slices, organotypic cultures

1. INTRODUCTION

Although high-density 3-D cultures better approximate native tissues than cultures grown in monolayers, their extended viability remains poor without efficient perfusion. Our recent findings [1] show that intercellular convection of the nutrient medium through 500-700μm thick neuronal and neural-astrocytic constructs satisfies the metabolic needs of cells plated at 10,000 cells/mm^3, resulting in a uniform >90% viability at 2 DIV. The objective of the present work is to use laminar convection perfusion for long-term support of thicker, physiologically more faithful, *in vitro* preparations [2]. Such preparations decay rapidly, often well before relevant studies have been completed. Although gradual, tissue rundown still causes irreversible damage that is difficult to assess to validate the data being collected.

2. PERFUSION PLATFORM DESIGN AND FABRICATION

Slices were cultured in membrane-aerated perfusion platforms (Figure 1a) with separate bubble traps placed in infusion line to equilibrate the injected medium and remove bubbles.

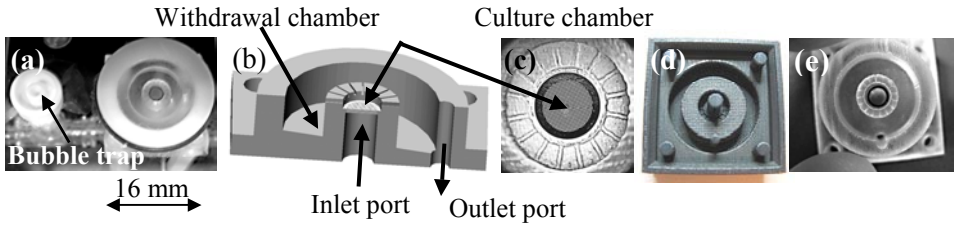

Figure 1. Membrane aerated perfusion platform with an in-line bubble trap (a). Perfusion chamber (b). Culture chamber (c). Extruded mold (d). PDMS replica (e).

Optically clear, membrane aerator [3] encapsulates the device and functions as an aseptic moisture guard. By doing so, a sufficient amount of gas is provided from the top as is from

978-0-9798064-0-7/μTAS2007/$20©2007CBMS

the bottom via injected medium. The perfusion chamber (Figure 1b) consists of an inner culture chamber; an outer withdrawal chamber; inlet and outlet ports. Chambers are connected by microchannels starting mid-height through the culture chamber. Forced convection ensures steady nutrient injection into the culture chamber via inlet port and equilibrated withdrawal of depleted medium and catabolites from the withdrawal chamber through the outlet port. The culture chamber (Figure 1c) contains a micronozzle perfusion substrate attached to its bottom to deliver the medium and peripheral microchannels through which used medium exits the culture chamber. A solid object printer was used to extrude 3-D templates for the replica molding of perfusion chambers in PDMS (Figure 1(d-e)). Commercial gold grids were subsequently sealed to the bottom of the culture chambers.

3. EXPERIMENTAL METHODS

A complex, 3-D flow within the chamber induced by continuous infusion of nutrients and withdrawal of perfusate was verified using microscale particle image velocimetry [4] in a darkfield fluorescent arrangement with 500nm fluorescent tracers suspended in the fluid. Brains were harvested from Thyl-EYFP mice (11-16 postnatal day) and sliced to match the interior of the culture chambers. Laminin coating ensured proper tissue adhesion up to the optimal rate of 20μL/hr as was confirmed at the end of perfusion experiments [2].

4. RESULTS AND DISCUSSION

Velocity fields were measured at several elevations from the bottom of a liquid-filled culture chamber in planes that are parallel to the perfusion substrate (Figure 2a) At a flow

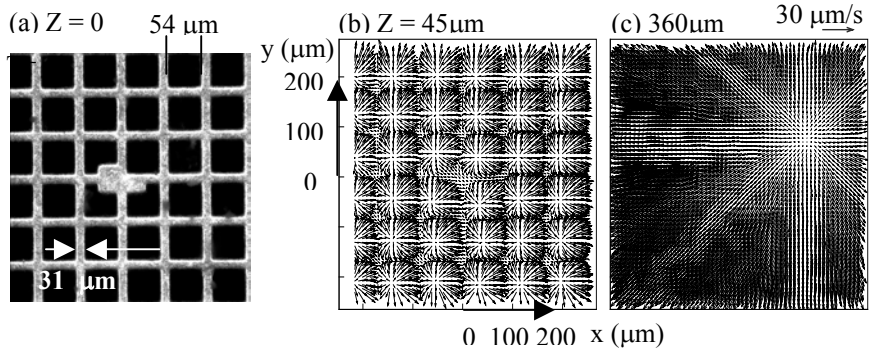

Figure 2. Flow validation. Measurement domain (a). Spreading microjets (b). 3-D convection towards the peripheral microchannels at higher elevations (c).

rate of 5μL/min (~40 exchanges/hr), close to perfusion source, measurements reveal the radial spreading of discrete microjets normal to their axes (Figure 2b). Jets emanating from the nozzles decelerate along their axes due to interactions with the lower momentum fluid within the chamber. Further downstream, laterally broadening jets interact with each other, lose coherence and merge. Starting mid-height through the chamber, peripheral withdrawal of perfusate creates significant 3-D convection that vectors merging jet outflows towards the exit microchannels (Figure 2c). Owing to microjet discharge, interactions and merging, and, fluid withdrawal, mixing within the chamber intensifies as all these motions are effectively convectively induced through the fluid shear. Forced convection interstitial perfusion reproducibly extended the viability of initially 700μm thick organotypic brain

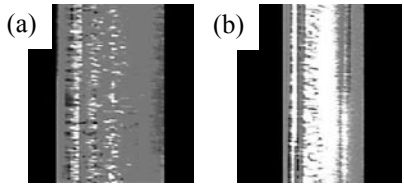

Figure 3. Thickness projection of a perfused (a) and unperfused slice (b).

slices. While in standard protocols tissue thins down rapidly to just a few layers [5], with perfusion thickness was around 600μm, viability >80%, and morphology preserved as *in vivo* at 5 DIV [2]. A live/dead assay confirms that in perfused slices moderate cell death remains confined to certain layers (Figure 3a). Unperfused slices exhibit extensive decay spreading from the interior of the tissue (bright region in Figure 3b) where nutrients and oxygen are lacking most. Even in brain slice chambers of Zbicz [6] or Haas type [7], the interstitial mass transport remains limited by diffusion and/or capillary action, so that the nutrient concentration in the tissue interior never reaches equilibrium with that of the surrounding medium. At sufficiently high rates, forced interstitial convection seemingly provides high nutrient concentration through the full thickness of the tissue to meet its metabolic demands. Available exchange rates exceed those of commercial products by a few orders of magnitude, thereby enabling extended culturing of thicker tissue preparations and successful completion of reproducible studies with a profound impact beyond the field of neurobiology.

5. CONCLUSIONS

A novel microfluidic perfusion method and platform are disclosed. They enable extended culturing of thick preparations that better approximate tissues *in vivo*. Convective perfusion offers rapid exchange rates, active flow control, higher accuracy and repeatability of performed analyses with fine manipulation of the cellular microenvironment. It also introduces scaling capabilities that can be extended to other geometries and applications.

ACKNOWLEDGEMENTS

This work is supported by the NIH 1 R01 EB00786.

REFERENCES

[1] D.K Cullen, J. Vukasinovic, A. Glezer and M.C.LaPlaca, *Microfluidic engineered high cell density three-dimensional neural cultures*, J. Neural Eng. **4**, 159-172 (2007).

[2] K. Rambani, J. Vukasinovic, A. Glezer and S.M. Potter, M*aintaining viable thick cortical slices by perfusion of nutrient medium*, The Society for Neuroscience Annual Meeting, Atlanta, GA (2006).

[3] S.M. Potter and T.B. DeMarse, *A new approach to neural cell culture for long-term studies*, J. Neurosci. Meth. **110**, 17-24 (2001).

[4] J.G. Santiago, S.T. Wereley, C.D. Meinhart, D.J. Beebe and R.J. Adrian, *Particle image velocimetry system for microfluidics*, Exp. Fluids **25**, 316-319 (1998).

[5] L. Stoppini, P.A. Buchs and D.A. Muller, *Simple method for organotypic cultures of nervous tissue*, J. Neurosci. Meth. **37**, 173–182 (1991).

[6] K.L. Zbicz and F.F.Wright, *Transient voltage and calcium-dependent outward currents in hippocampal CA3 pyramidal neurons*, J. Neurophysiol. **53**, 1038-1058 (1985).

[7] H.L. Haas, B. Schaerer and M.A. Vosmansky, *A simple perfusion chamber for the study of nervous tissue slices in vitro*, J. Neurosci. Meth.**1**, 323-325 (1979).

DEVELOPMENT OF A MICRO TOTAL BIOASSAY SYSTEM FOR ANTICANCER AGENT; ASSAY OF INTESTINAL ABSORPTION, HEPATIC METABOLISM, AND ANTICANCER ACTIVITY

Kiichi Sato, Yasuyuki Asano and Etsuro Yoshimura
The University of Tokyo, Japan

ABSTRACT

A micro total bioassay system for an oral anticancer agent was developed, which consists of intestine, liver, and target cancer parts. By using the system, overall characters of an anticancer agent, i.e. intestinal absorption, hepatic metabolism, and anticancer activity, could be assayed with simple operation.

Keywords: anticancer activity, bioassay, intestinal absorption, hepatic metabolism.

1. INTRODUCTION

A bioassay using cultured cells is one of the most important analytical methods in a search for new drugs, a safety evaluation of foods and chemical compounds, and basic biochemical studies. We have reported integration of several bioassay systems into a microchip to realize reduction of assay time, cell and reagent consumption, and troublesome manual operations [1-3]. In the conventional and microchip-based bioassays reported so far, however, only one bioactivity can be assayed. Although oral drugs show their effects only after intestinal absorption (Fig. 1), there is no bioassay system to test both bioavailability and drug activity simultaneously. In this study, a micro total bioassay system for an oral anticancer agent was developed, and overall activity of an anticancer agent, i.e. intestinal absorption, hepatic metabolism, and anticancer activity, can be assayed with simple operation.

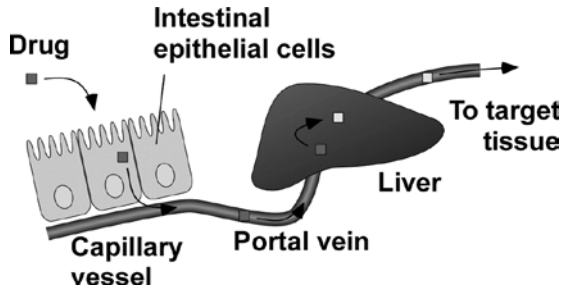

Fig. 1 Pathway of oral prodrugs to the target.

2. EXPERIMENTAL

The microchip was composed of a slide glass and two PDMS sheets, which had microchannels made by soft lithography using SU-8. Collagen-coated membrane filter was laminated between PDMS sheets for separation of two channels (Fig. 2).

Human intestinal model cell line, Caco-2, cells were cultured on the membrane. Human hepatocellular carcinoma, Hep-G2, cells were cultured on the microcarrier beads (Fig. 3), and then packed in the microchannel. Human breast carcinoma, MDA-MB-453, cells were cultured on the fibronectin-coated glass surface of the microchannel as target cells. An anticancer agent for breast cancer, cyclophosphamide (CPA), which is known as an oral

978-0-9798064-0-7/μTAS2007/$20©2007CBMS

prodrug, was used as a model drug. CPA shows its anticancer activity after intestinal absorption and activation at liver.

The system was controlled with microsyringe pumps. Anticancer activity was calculated from survive rate of target cells by fluorescent imaging with calcein-AM or cell activity measurement using resazurin. Lucifer yellow (LY) was used as a

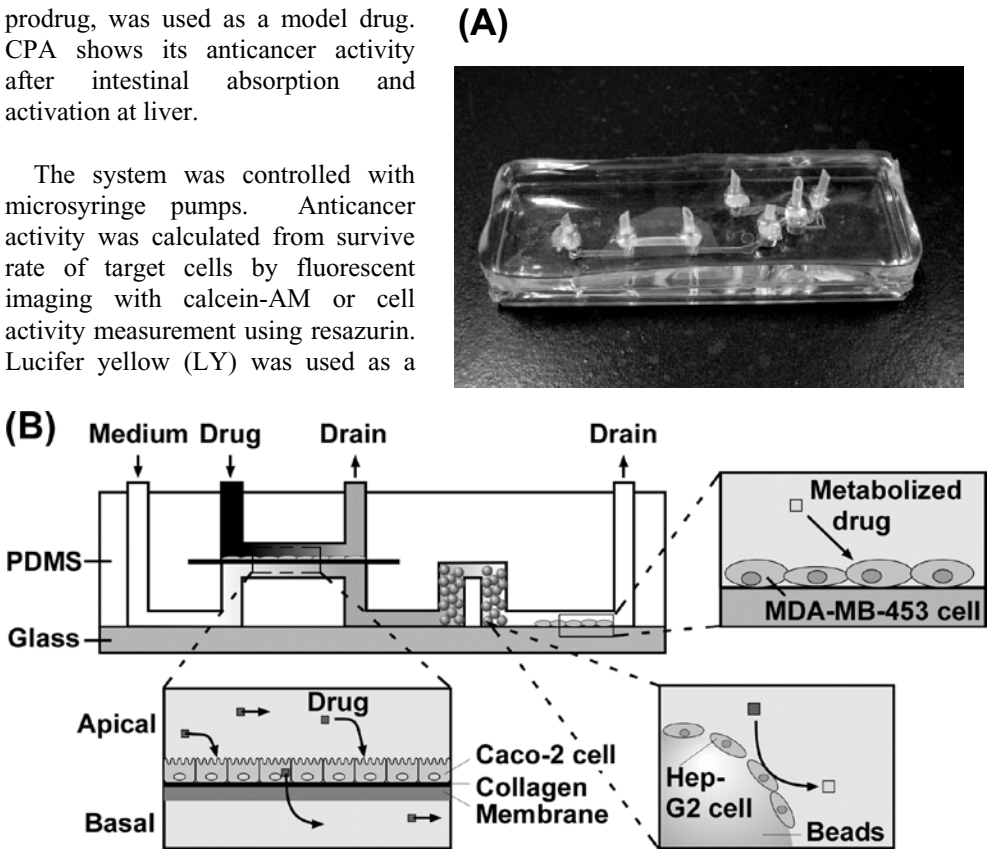

Fig. 2 (A) Photograph and (B) cross sectional illustration of micro total bioassay microchip consisting of intestine, liver, and target cells.

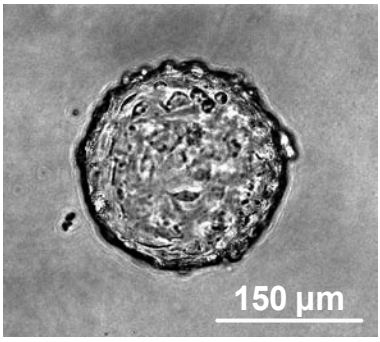

Fig. 3 Hep-G2 cells cultured on a Cytodex bead.

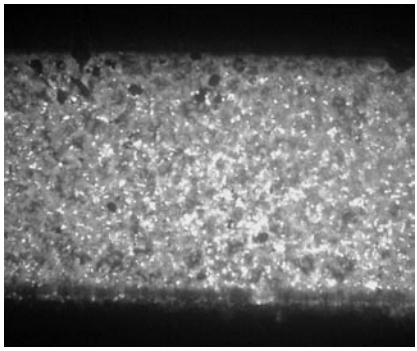

Fig. 4 Caco-2 cells cultured on the membrane in a microchannel for 3 days and stained with calcein-AM.

non-permeable model compound in intestinal absorption experiments.

3. RESULTS AND DISCUSSION

After 3-day culture, Caco-2 cells successfully formed confluent cell sheet on the membrane (Fig. 4). The permeability coefficients of CPA and LY calculated in the microintestinal absorption experiments showed that the microintestine had good barrier function and molecular selectivity (Fig.5).

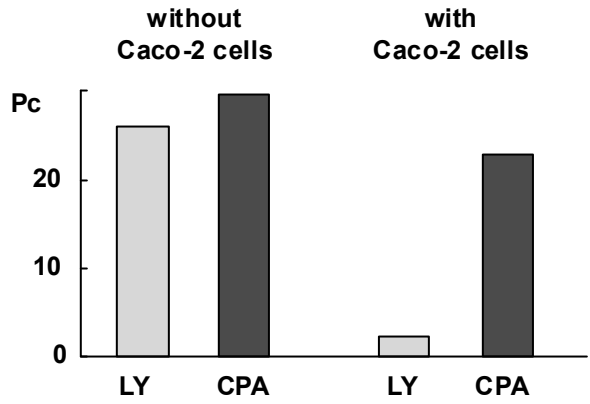

Fig. 5 Permeability coefficients obtained by micro intestine.

All processes of the micro total bioassay system were done by introduction of a mixture of CPA and LY. While the difference in LY permeability between with/without Caco-2 cells was very large, the survive rates of target cells were independent of the presence of Caco-2 cells. The result successfully showed that CPA had high intestine permeability. In the presence of Hep-G2 cells, the survive rates were decreased. It proved the activation of CPA by Hep-G2 cells.

4. CONCLUSIONS

A micro total bioassay system for an oral anticancer agent was developed, which consists of intestine, liver, and target cancer parts. The system realized reduction of assay time and cell consumption. We concluded that the developed system had an ability to evaluate the overall characters of oral anticancer prodrugs without manual operations.

ACKNOWLEDGEMENTS

This work was partially supported by Center for NanoBio Integration, The University of Tokyo.

REFERENCES

[1] “Microbioassay System for an Anti-Cancer Agent Test using Animal Cells on a Microfluidic Gradient Mixer” S. Fujii, M. Uematsu, S. Yabuki, M. Abo, E. Yoshimura, K. Sato, *Anal. Sci*. **22**, 87 (2006).

[2] “Microbioassay System for Antiallergic Drug Screening using Suspension Cells Retaining in a Poly(dimethylsiloxane) Microfluidic Device” T. Tokuyama, S. Fujii, K. Sato, M. Abo, A. Okubo, *Anal. Chem*. **77**, 3309 (2005).

[3] “Development of a Microchip-based Bioassay System using Cultured Cells” M. Goto, K. Sato, A. Murakami, M. Tokeshi, T. Kitamori, *Anal. Chem*. **77**, 2125 (2005).

Syn&Sort – A CHIP BASED TOOL FOR COMBINATORIAL SYNTHESIS AND BIOLOGICAL SCREENING

A. Schober[2)]*, M. Gebinoga[2)], A. Albrecht[1)], T. Lübeck[1)], T. Henkel[3)], P. Hoffmann[3)], U. Klenz[3)], G. Schlingloff[5)], T. Frank[4)], A. Groß[1)]

[1)] Technische Universität Ilmenau, Institute for Micro- and Nanotechnologies, Gustav-Kirchhoff-Str. 7, 98693 Ilmenau, Germany, [2)] Center for Innovation Competence MakroNano®, Institute for Micro- and Nanotechnologies, Technical University of Ilmenau, Gustaf-Kirchhoff-Straße 7, 98693 Ilmenau, Germany, [3)] Institute of Physical High Technology, Helmholtzweg 4, 07745 Jena, Germany, [4)] Little Things Factory (LTF), Ehrenbergstraße 1, 98693 Ilmenau, Germany,
[5)] Nanomics Technologies GmbH, Sturmheide 38, 98693 Ilmenau, Germany.

ABSTRACT

We present a new method and process for combinatorial solid phase library synthesis. This method called "Syn&Sort" combines the advantages of miniaturized parallel synthesis with those of the directed sorting technique. Solid phase support chips were made of glass with an embedded magnetic core coated with functionalized polymer resin. These chips were arrayed by a magnetic clip board technique on slide carriers. The directed sorting step principle was realized combining two encoding principles: spatially resolved encoding was used for slide carriers, bearing 60 solid phase chips and individual barcode-marker encoding for each slide carrier. The single chips were rearranged using a robotic system. The principle was proved preparing a pentameric peptide library.

Keywords: combinatorial chemistry, miniaturized solid phase synthesis, directed sorting, magnetic glass carriers

1. INTRODUCTION

The patented Syn&Sort approach represents a novel, powerful strategy for the chip based synthesis of combinatorial sample libraries [1]. Collections of magnetic chips, each equipped with a resin thin film are organized on magnetic slide carriers and applied for the chemical reactions. After each synthesis step the chips may be reorganized between the different slide carriers (figure 1). Sample tracking is implemented based on the sorting protocol of the single magnetic chips and the chemical procedures applied. Thus, the history of the synthesized substance is known for each chip. The resin functionalized chips consist of glas chips, equipped with an embedded magnetic core and coated with a 20 µm PEGA-resin thin film. The loading capacity for amino- and carboxylic- groups can be adjusted between 0.01 and 1.0 mmol/g. Both resins provide interfaces for coupling of appropriate linkers. Up to 50 nmol may be synthesized on a single chip.

2. METHOD

With Syn&Sort a new approach in the filed of solid phase chemistry take place and combines the advantageous of the classical split and mix synthesis with massive parallel synthesis possibilities connected through a directed sorting step (figure 2) [2]. The Syn&Sort equipment is compatible to standard laboratory equipment (reaction bottles, MTP, etc.) and can be utilized not only for synthesis but also for screening applications e.g. the application to surface controlled binding assays, the production of biosensors or as a

978-0-9798064-0-7/µTAS2007/$20©2007CBMS

documentary and logistic system for all type of assays and compounds. The magnetic forces keeping the single chips attached save to the slide carriers were optimized to withstand at least strong fluidic forces (figure 3).

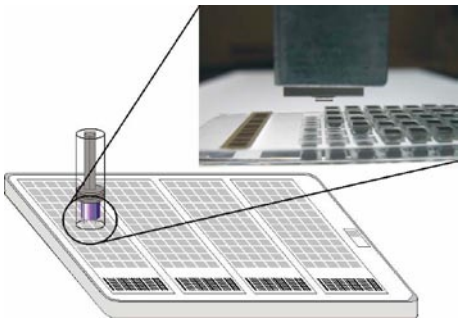

Figure 1: Sketch of a Microtiterplate (MTP) carrier bearing the slide carriers with the magnetic pen to move single magnetic glass chips. Magnification: Photograph of the magnetic pen gripper above a slide-carrier (some chips were removed to see the chip carrier wells)

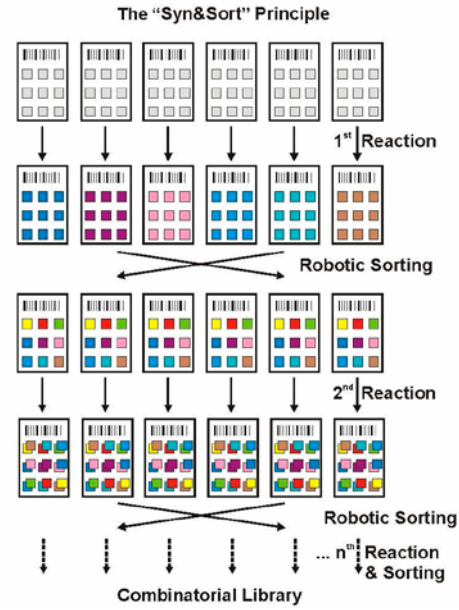

Figure 2: Principle of the "Syn&Sort" technology using a combinatorial directed sorting strategy.

The robotic Syn&Sort platform enables the synthesis of several hundred to several thousand substances and fits to a workbench desktop. The actual platform design, enable the processing of four MTP carriers bearing four 60 chips carrying slide carriers (figure 4). Altogether 960 chips, can be processed in this setup. The described method is particularly suited for the synthesis of several hundreds up to a few thousands of substances. This may be of great value for the synthesis of focused libraries.

3. EXPERIMENTS

A focused peptide library designed for the synthesis of pentameric peptides was prepared using a common Fmoc synthesis strategy (figure 5). The library was designed around a Vancomycin binding motif [3]. Before cleavage the chips were singled out into standard 96 well MTP (figure 4). After cleavage procedure and solvent evaporation the desired peptides were analysed by LC-MS (exemplary result: figure 6). Synthesis was realized at a medium scale of about 50 – 100 nmol/chip. Starting from peptide chemistry the next steps will be the synthesis of diversity oriented libraries and the application to non peptide organic chemistry [4].

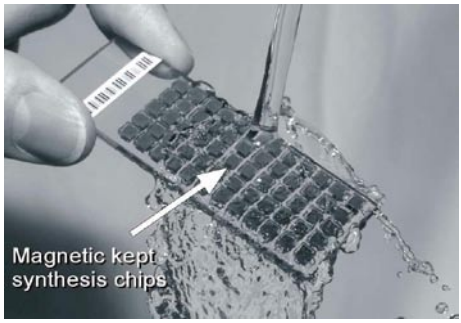

Figure 3: Test of the magnetic fixation. Even the pressure of a water jet will not release the fixed magnetic chips.

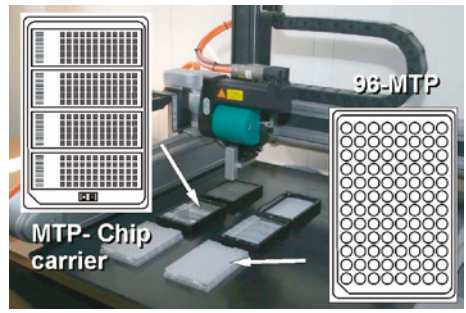

Figure 4: Sorting robot equipped with the magnetic gripper. Directed sorting of single chips between the slide carriers mounted onto the MTP-carriers can be done following the combinatorial strategy. 96-Well MTP were used to single out chips for cleavage.

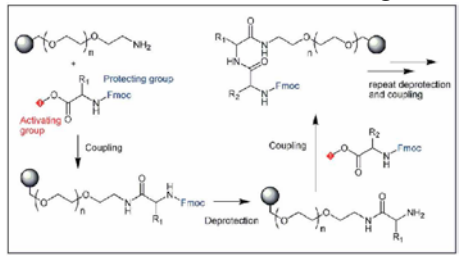

Figure 5: Reaction sequence for the preparation of a combinatorial peptide library using the Fmoc strategy

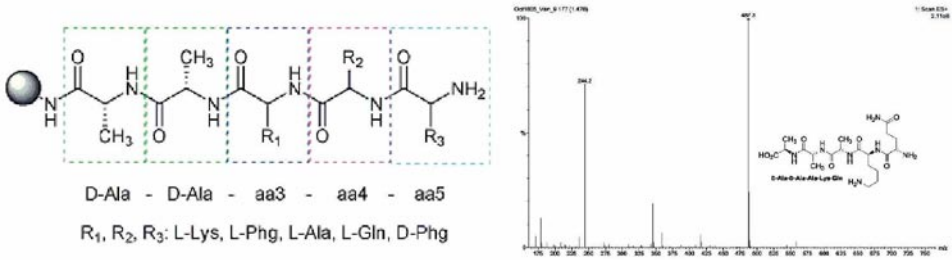

Figure 6: Received peptide library. Exemplary mass spectra of one library member. The MS-spectra shows the desired peptide. In accordance to the peptide composition with glutamine and lysine residues we found aside of the single charged ions also the double charged ions ($M^+ = 487$; $MH^{2+} = 244$).

[1] US2004063150, EP1337846

[2] Gebinoga, M.; Groß, G. A.; Albrecht, A.; Lübeck, T.; Henkel, T.; Hoffmann, P.; Klemm, U.; Schlingloff, G.; Frank, T.; Schober, A., *"Syn & Sort": A Chip based Tool for Combinatorial Synthesis and biological Screening* QSAR & Combinatorial Science (Special Issue: Array Synthesis), 25, (11), 1063 - 1068 (2006)

[3] Loll, P. J.; Axelsen, P. H., *The structural biology of molecular recognition by vancomycin*. Annual Review of Biophysics and Biomolecular Structure, 29, 265-289. (2000)

[4] Groß, G. A.; Wurziger, H.; Schlingloff, G.; Schober, A., *Microreactor array assembly, designed for diversity oriented synthesis using a multiple core structure library on solid support*. QSAR & Combinatorial Science (Special Issue: Array Synthesis), 25, (11), 1055 - 1062 (2006)

A MICROFLUIDIC BIOSENSOR INTEGRATING SELF-ASSEMBLED PEPTIDE MONOLAYERS FOR THE DETECTION OF BOTULINUM NEUROTOXIN

Megan L. Frisk[1,2], William H. Tepp[3], Eric A. Johnson[3], and David J. Beebe[1]

[1]Department of Biomedical Engineering, [2]Department of Chemistry, and
[3]Food Research Institute, University of Wisconsin-Madison, U.S.A.

ABSTRACT

A robust and highly sensitive method for detecting the most poisonous toxin known – botulinum neurotoxin type A (BoNT/A) – has been realized by fusing microfluidics and surface chemistry. Microfluidic channels were interfaced with gold surfaces, which had been functionalized with a fluorescent peptide sequence mimicking the BoNT/A *in vivo* substrate; the peptide thus served as a recognizable element within the channel, conferring specificity. Introduction of 6 μL of a BoNT/A-contaminated fluid to the sensing channel resulted in cleavage of the peptide substrate and release of fluorophore into solution for evaporative concentration and fluorescence detection.

Keywords: biosensor, self-assembled monolayers, toxin

1. INTRODUCTION

Toxins derived from the bacteria *Clostridium botulinum* are of unsurpassed potency, wherein less than 70 μg can be fatal to an adult human [1]. One such toxin, BoNT/A, is a protease responsible for blocking the release of neurotransmitters in the synaptic gap, leading to flaccid paralysis and, in severe cases, death. Deliberate or accidental contamination of food or drink with microbial toxins like BoNT/A is not only a form of bioterrorism, but also a "global public health problem" [2]. Existing approved means of BoNT/A detection – the mouse bioassay and ELISA – are impractical with respect to the goal of on-site detection and analysis due to lengthy protocols and expensive, delicate reagents, respectively. As such, adequate preparation for imminent use of BoNT/A as a bioweapon warrants the development of reliable *microfluidic devices that autonomously perform biochemical sensing* for on-site BoNT/A detection in, for example, milk or orange juice. Toward this end, we have devised a microfluidic platform that incorporates surface chemistry for sensing BoNT/A enzymatic activity in solution.

2. EXPERIMENTAL

Gold (Au) surfaces were patterned as individual 6 mm^2 "pads" onto which polydimethylsiloxane (PDMS) microfluidic channels were placed *(Figure 1)*. Au pads were first functionalized with a 24mer peptidic BoNT/A substrate that was derived from the cleavage site of the toxin's natural synaptic substrate – the SNAP-25 protein [3]. The SNAP peptide was synthesized in-house to contain fluorescein (flu) at one terminus and a Au-reactive cysteine at the other terminus. *Figure 2* illustrates the conjugation chemistry employed for forming self-assembled SNAP peptide monolayers (SAMs) on Au pads. Mixed monolayers consisting of 1-10% aminoalkanethiol as well as the heterobifunctional linker sulfosuccinimidyl-4-(*N*-maleimidomethyl)cyclohexane-1-carboxylate (sSMCC) facilitated attachment of the SNAP peptide.

To assess biosensing capabilities, each microchannel was filled with a positive control, a negative control, or live BoNT/A. After a 3-6 hour incubation period, released

978-0-9798064-0-7/μTAS2007/$20©2007CBMS

fluorophore was concentrated at the outlet port by placing a large (>15 µL) droplet at the inlet (*Figure 1*) and allowing evaporation from the outlet for 20-30 minutes [4]. Concentrated fluorophore was detected at the outlet using fluorescence microscopy. SAM reactivity was also monitored using fluorescent surface scanning.

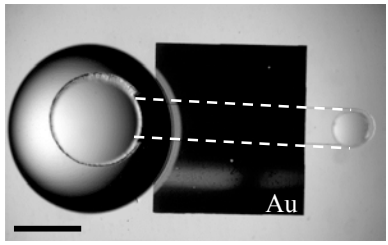

Figure 1. Microfluidic channel (outlined: 750 µm wide, 250 µm tall) overlaying a Au pad. Sample is introduced through larger inlet port (left, 1.75 mm); evaporative concentration takes place at smaller outlet port (right, 750 µm) by placing a large droplet of water at inlet. *Scale bar = 1 mm*.

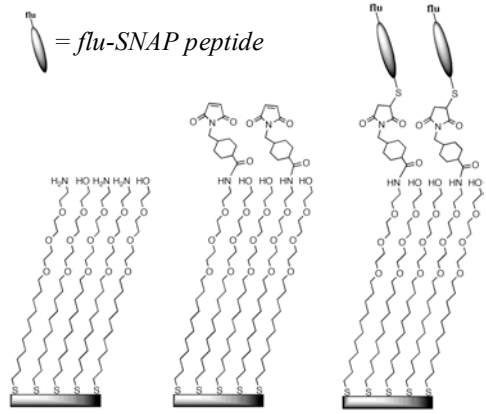

Figure 2. Self-assembled peptide monolayer formation. sSMCC links aminoalkanethiol on Au to fluorescent peptide.

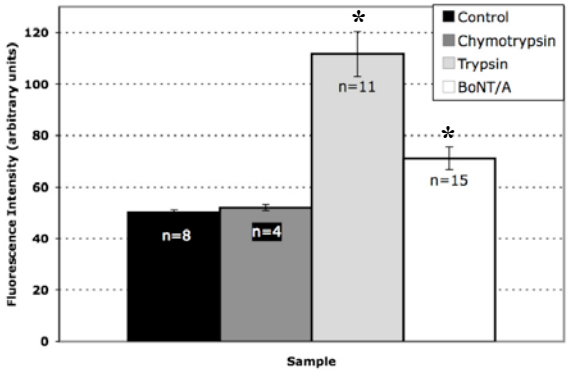

Figure 3. Average fluorescence intensities (*$p < 0.005$, with reference to control).

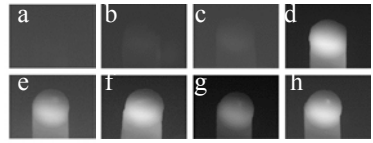

Figure 4. Outlet port fluorescent images of cleaved peptide. (a-c) negative controls: buffer -DTT, buffer +DTT, and 10 nM chymotrypsin; (d) positive control: 10 nM trypsin; (e-h) BoNT/A + 1 mM DTT: 100 nM, 10 nM, 1 nM, and 100 pM, resp.

3. RESULTS AND DISCUSSION

Results indicate that we can detect BoNT/A at picomolar concentrations in < 10 µL of fluid, with fluorescence intensities for the toxin significant against a series of controls (*Figure 3*). Three negative controls (buffer +/- 1 mM DTT and 10 nM α-chymotrypsin) as well as a positive control (10 nM trypsin) are respectively displayed in *Figures 4a-d*. The outlet fluorescence from 100 nM down to 100 pM of BoNT/A are shown in *Figures 4e-h*. Surface scans showing a decrease in surface fluorescence from the cleavage of SAM peptides corroborated solution fluorescence data (not shown).

Because this microfluidic assay capitalizes on the enzymatic activity of the toxin, we experience a natural signal enhancement presumably through catalytic turnover of the

enzyme predict negligible false positives due to high specificity of BoNT/A for its SNAP peptide substrate [5]. Additional fluorescence signal concentration occurs through the well-known microfluidic phenomenon – rapid evaporation. Sensing within a microfluidic device affords the possibility of high throughput screening (HTS) for this potential bioweapon by scaling up the number of SAM-interfaced microchannels. Further applications include sensing other enzymatic toxins such as tetanus toxin or the other six BoNT serotypes and/or screening for inhibitors of toxin activity, all without the use of complex instrumentation, expensive reagents, or animal models.

4. CONCLUSION

We have developed a functional BoNT/A sensor that takes advantage of the toxin's natural enzyme activity and rivals the sensitivity and timeliness of current means of detection by utilizing a peptidic variation of the BoNT/A synaptic protein substrate. The peptide SAMs are currently being optimized within microfluidic channels for HTS capabilities and sensing other biological agents.

ACKNOWLEDGMENTS

MLF would like to acknowledge the UW Biotech Peptide Synthesis Facility, Sudheer Sridharamurthy (UW Electrical Engineering) for help with Au patterning, and Matthew Lockett (UW Chemistry) for development of a SAM protocol. This work is funded by the Department of Homeland Security's National Center for Food Protection and Defense.

REFERENCES

[1] Arnon, S. S., "Botulinum Neurotoxin as a Biological Weapon: Medical and Public Health Management", *JAMA* **2001,** 285, (8), 1059-1070.

[2] Johnson, E. A., Bacterial Pathogens and Toxins in Foodborne Disease. In *Food Safety: Contaminants and Toxins*, D'Mello, J. P. F., Ed. CAB International: 2003; pp 25-45.

[3] Schmidt, J. J.; Bostian, K. a., "Proteolysis of synthetic peptides by type A botulinum neurotoxin", *Journal of Protein Chemistry* **1995,** 14, (8), 703-708.

[4] Walker, G. M., Beebe, D.J., "An evaporation-based microfluidic sample concentration method", *Lab Chip* **2002,** 2, 57-61.

[5] Simpson, L. L., "Identification of the Major Steps in Botulinum Toxin Action", *Annu. Rev. Pharmacol. Toxicol.* **2004,** 44, 167-193.

A MICROFLUIDIC DISPENSING SYSTEM FOR SCREENING PROTEIN CRYSTALLIZATION CONDITIONS

Xuechang Zhou and Bo Zheng

Department of Chemistry, The Chinese University of Hong Kong, Shatin, Hong Kong

ABSTRACT

This study describes a microfluidic liquid dispensing system for screening protein crystallization conditions at the nanoliter scale. In this system, nanoliter reagents with different chemical compositions were infused into the microwells through the reversibly sealed PDMS microchannels. By removing the microchannel patch, arrays of reagent droplets confined in the microwells were obtained. Reactions and screening were conducted by binding two such arrays of reagent droplets. We illustrated the applications of this method by performing sparse-matrix screening of crystallization conditions of several water soluble proteins. Crystals of one unknown protein were harvested from the microwells and subjected to X-ray diffraction study.

Keywords: Microfluidic, liquid dispensing, microwell, protein crystallization

1. INTRODUCTION

Protein crystallization is the bottleneck in determining the tertiary protein structures. Recently, poly (dimethylsiloxane) (PDMS) based microfluidic systems have achieved great success in protein crystallization with the advantages of low sample consumption and high-throughput [1, 2]. However, these systems have some limitations, such as complicated fabrication and operation of the microfluidic device, loss of reagents by evaporation, and expensive equipments for the flow or pressure control. To address the issues and lower the barrier of use, we developed a nanoliter liquid dispensing method for dispensing protein and precipitant reagents into two arrays of microwells, followed by mixing of two such arrays of reagent droplets (Figure 1).

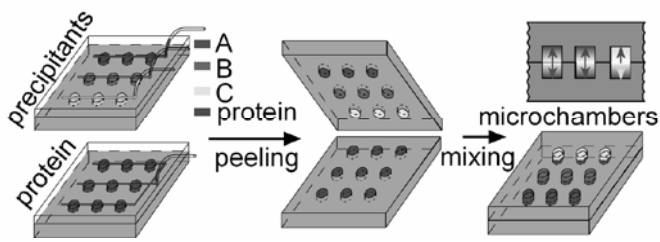

Figure 1. Schematic illustration of the screening of protein crystallization conditions in microwell array.

2. EXPERIMENTAL

PDMS microwell (400 μm in diameter, 150 μm in height) and microchannel (50 μm width × 10 μm height) patches (3 mm thickness) were fabricated using soft lithography [3]. The two patches were reversibly bound together and then placed in a vacuum chamber for 10 min of degassing at 6 kPa. Afterwards, a segment of Teflon tubing pre-loaded with a liquid was inserted into the inlet of the microchannel to start the dispensing in atmosphere. The microchannel patch was removed in the presence of silicone oil after the completion of the dispensing. Arrays of droplets of the protein and commercial precipitant reagents were

978-0-9798064-0-7/μTAS2007/$20©2007CBMS

fabricated. The sparse-matrix screening was performed by binding two such arrays of reagents. The resulting crystallization microchip was incubated in a paraffin oil bath. Microwells fabricated on glass substrate were also successful tested in this method, which allowed long-term incubation.

3. RESULTS AND DISCUSSION

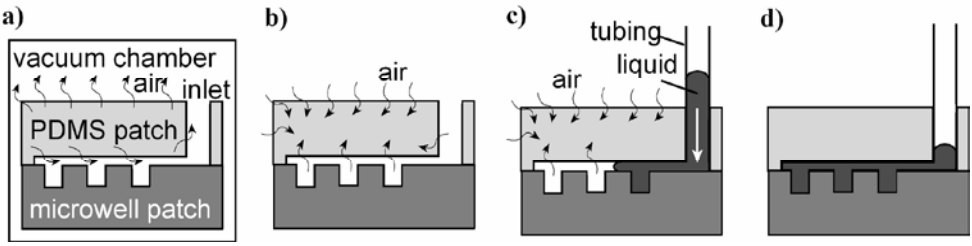

Figure 2. Schematic illustration of the liquid delivery through the degassed PDMS: (a) the degassing of PDMS; (b) the redissolution of air into PDMS; (c) the aspiration of a liquid; (d) the completion of the liquid dispensing.

A pressure difference was generated from the degassed PDMS microchannel patch, which served as an internal vacuum pumping source to aspirate the target liquid into microwells through the microchannel (Figure 2) [4]. The efficiency of this pumping source was evaluated by characterizing the dependence of the filling time t_{total} into an array of microwells on four factors (Figure 3). It took around 10 ~ 15 minutes to degas the PDMS patch (Figure 3a), and the aspiration power was maintained for more than 30 minutes in atmosphere (Figure 3b). Regents with different wettabilities and viscosities were successfully tested, such as glycerol aqueous solution (80%, viscosity 45 mPas). Microwells fabricated in both PDMS (Figure 4a and 4b) and glass (Figure 4c) were compatible with this dispensing method. After the entire empty place was filled up by the reagents, the PDMS microchannel patch was peeled off in the presence of silicone oil, resulting in arrays of reagent droplets confined in the microwells (Figure 4d, 4e and 4f).

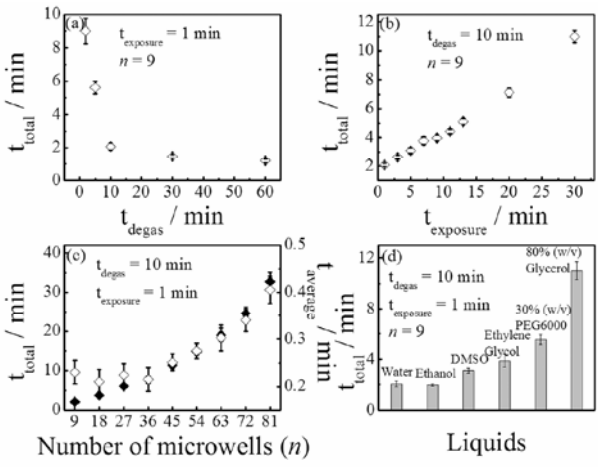

Figure 3. (a) Plot of t_{total} versus t_{degas}. (b) Plot of t_{total} versus $t_{exposure}$. (c) Plot of t_{total} (⬥) and $t_{average}$ (◇) versus the number of microwells (*n*). (d) Plot of t_{total} of different liquids. t_{total}, t_{degas} and $t_{exposure}$ represent the time needed for filling an array of microwells, the duration of the degassing process in the vacuum chamber and the duration when the PDMS microchannel was exposed to atmosphere before the inlet was blocked by the liquid, respectively.

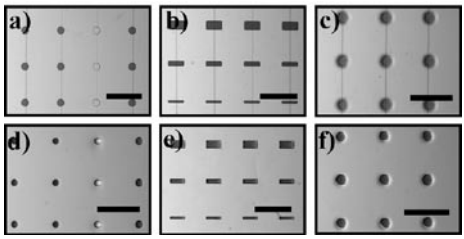

Figure 4. Micrographs of the microwell array filled with aqueous solutions before (a, b, c) and after (d, e, f) peeling off the PDMS microchannel patch. (a, b, d and e) were PDMS microwells, (c and f) were glass microwells. Scale bars: 2 mm.

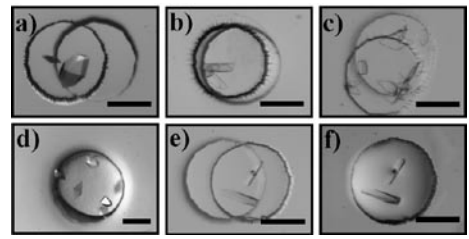

Figure 5. Polarized light micrographs of the protein crystals: (a) lysozyme, (b) horseradish peroxidase, and (c) xylanase in the PDMS microwells; (d) thaumatin in the glass microwell; (e and f) HP0753. Scale bars: 200 μm.

To illustrate the application of this microfluidic system, a sparse-matrix screening of crystallization conditions of several water soluble proteins was conducted by mixing the droplets pre-fabricated in two separate microwell patches (Figure 1). Less than 4 μL of protein solution was consumed for 150 screening trials. Protein crystals were obtained at the optimal conditions (Figure 5a ~ d). Long-term incubation (up to 2 months) of the crystallizing reagent was achieved by employing glass microwells (Figure 5d). An unknown protein HP0753 was also successfully crystallized by using the screening method in microwells (Figure 5e). The crystals of HP0753 with sufficient size were further harvested from the reversibly bound microwells (Figure 5f). X-ray diffraction pattern of the crystals with a resolution of 3.1 angstroms was obtained.

4. CONCLUSIONS

A microfluidic liquid dispensing system has been developed by utilizing the gas permeability of PDMS elastomer. Sparse-matrix screening of conditions of protein crystallization was successfully performed in PDMS and glass microwells by using this dispensing system.

ACKNOWLEDGEMENTS

This work was supported by the Chinese University of Hong Kong and the Research Grants Council of Hong Kong. We thank S. W. N. Au, K. B. Wong and W. J. Li for their help.

REFERENCES

[1] C. L. Hansen, E. Skordalakes, J. M. Berger, S. R. Quake, *Proc. Natl. Acad. Sci. U. S. A.* **2002**, *99*, 16531.
[2] B. Zheng, L. S. Roach, R. F. Ismagilov, *J. Am. Chem. Soc.* **2003**, *125*, 11170.
[3] D. C. Duffy, J. C. McDonald, O. J. A. Schueller, G. M. Whitesides, *Anal. Chem.* **1998**, *70*, 4974.
[4] K. Hosokawa, K. Sato, N. Ichikawa, M. Maeda, *Lab Chip* **2004**, *4*, 181.

MICROFLUIDIC INTERFACED FOR LOCALIZED RELEASE OF NO INTO DEVELOPING RAT DORSAL ROOT GANGLIA

G. Lavella[1†] and P. Padmanabhan[2†], B. Wu[3], M. E. Meyerhoff[3], and M. M. Maharbiz[2]

[1]Department of Electrical Engineering, [2]Applied Physics Program, Department of Biomedical Engineering, and [3]Department of Chemistry, University of Michigan, USA

[†]Both Authors contributed equally

ABSTRACT

We present a microfluidic device capable of generating micro-scale gradients of nitric oxide (NO) in cell cultures. NO release is achieved through the proton mediated reaction of a water-soluble low molecular weight poly(ethylenimine) (LMW PEI) NO donor and a pH buffer solution. Reactions, and subsequent NO release into the cell culture, occur at lithographically patterned laminar flow interfaces made of poly(dimethylsiloxane) (PDMS). The NO flux can be controlled during culture by regulating the flow rate. The device is capable of producing highly localized and physiologically relevant nitric oxide flux rates and is employed to study the role of nitric oxide on the development of neural morphology in the dorsal root ganglia (DRG).

KEYWORDS: Nitric Oxide, Neurons, Dosing, Microfluidics

1. INTRODUCTION

NO is a naturally occurring free radical compound of increasing medical significance. In nerve cells, it has been implicated in neuroprotective roles and growth cone advance [1]. In addition, NO has several vital roles in cardiovascular and pulmonary systems [2]. For these reasons, there has been exceptional growth in nitric oxide research over the past decade. In order to facilitate this effort, several NO dosing devices have been developed and characterized [3]. Of these methods, devices that utilize bulk gaseous NO sources and polymeric membranes have, to date, been the most successful for long term dosing applications [3]. However, current devices are still ill-suited for integration into micro total analysis systems and for performing localized dosing. Our work is focused on the development of NO dosing devices for cell cultures to study the role that localized NO gradients play in the development of neural morphology and gene expression in the dorsal root ganglia.

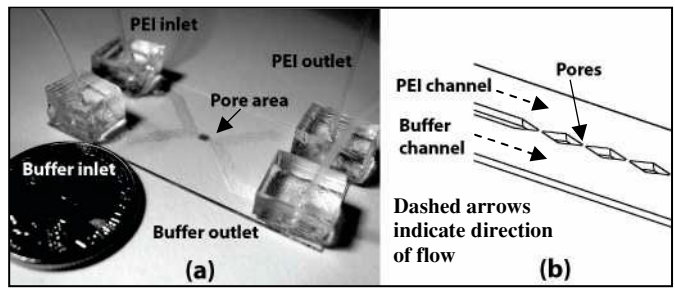

Fig. 1 (a) Image of chip with inlet and outlet port connections and (b) schematic of the pore area. NO generation takes place at each pore due to protonation of the PEI where the buffer and PEI contact.

2. THEORY

The merging of laminar flows has previously been used to control the location and rate of chemical reactions in microfluidic devices [4]. We employ a similar technique, where the flows from two microchannels are merged at pore areas to create an interface between

978-0-9798064-0-7/μTAS2007/$20©2007CBMS

aqueous LMW PEI NO donor [5] and aqueous phosphate buffer (Fig. 1). NO is generated at the interface through a first order protonation of the PEI [5] and diffuses up through the PDMS membrane and into the cell culture. The PDMS membrane serves as a barrier between the cell culture and the reactants, and as a surface for cell adhesion (Fig 2). Different NO micro-scale gradients can be achieved using various micropore layouts. Since NO release from the reaction is both proton mediated and dependent on the diffusivity of the reactants, the rate and magnitude of NO release depends on the pH of the buffer solution, the length of the boundary between the two laminar flows, and the concentration of LMW PEI. In operation, pH gradients and LMW PEI concentration gradients develop around the pore areas. The NO flux rate for a specified volume can be computed directly from the LMW PEI concentration and pH.

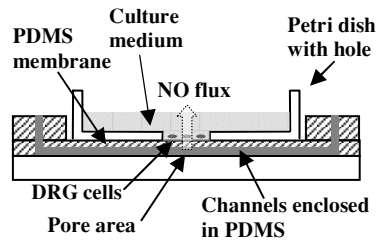

Fig. 2 Schematic of chip cross-section with DRG cell culture. The setup is being used for DRG experiments.

3. EXPERIMENTAL METHODS

The chip was fabricated using lithographic patterning of photoresist (AZ 9260) to form PDMS microchannels on glass. Measures of the total NO released from the chip were made using a Sievers-280 chemiluminescence-based nitric oxide analyzer (CL NOA, Boulder, CO). The analyzer was calibrated using an internal two-point calibration consisting of zero gas and a 45 ppm NO(g) standard. The flow rate was set to 200 mL/min into the analyzer with a cell pressure of 5.4 Torr and an oxygen pressure of 6.0 psi. The nitric oxide released from the chip surface was continuously swept from the headspace of the sample vessel, and purged with a nitrogen sweep gas into the CL NOA. Quantitative NO interrogation experiments were carried out using a 200 mM phosphate buffer (24-25ºC at pH 3) in one channel and a 10 mM LMW PEI and NaOH solution (pH 12) in the other. To eliminate the effects of inter-channel mixing due to flow rate offsets between the channels 0.2 ml/hr flow rates were maintained in both channels using dedicated single syringe infusion pumps (Cole-Parmer).

In order to determine the pH-NO output dependence of the PEI material itself, solutions of PEI at a set pH (pH 5, 6, 7, 8, and 9) were prepared. As soon as the preparation was complete, the solution was injected into a glass vial connected to the nitric oxide analyzer and the NO output was measured over time. All NOA measurements were made using the same protocol described above.

Additionally, experiments to study the morphological effects of NO on dorsal root ganglia from post-natal (P-10) rats are being conducted. A schematic of the full DRG test chip is provided in Fig. 2. P-10 DRGs are explanted onto the PDMS surfaces that are coated with poly-D-lysine (PDL) to improve cell adhesion. After incubation, the chips are placed into an inverted microscopy setup with an environmental control chamber to maintain a temperature of 37°C and a 5% CO_2 level. The reactant flow rate is then established in each chip, and time lapse images of the DRGs are captured over several hours.

4. RESULTS AND DISCUSSION

Fig. 3 shows the pH dependence of the NO donor. Note that the volumetric NO flux rate varies with time (an initial spike followed by an exponential decay as the NO donor

becomes expended); continuous flow of the NO donor and pH buffer streams can be used to 'pin' the flux rate because the unreacted donor concentration is maintained constant at the

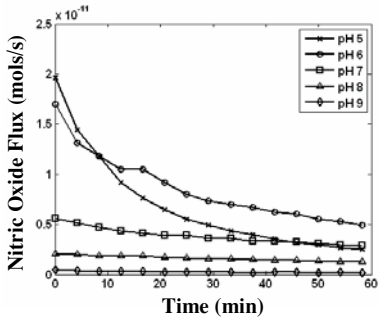

Fig. 3 pH dependence of PEI compound. Lower pH solutions correspond to a higher initial spike in the NO output followed by an exponential decay in the output due to quenching of the NO donor. All data was obtained between 24-26°C with a 1 mg/ml solution (PEI MW 700).

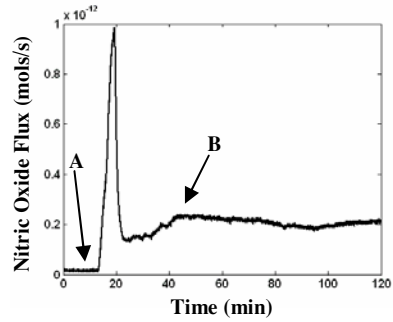

Fig. 4 Nitric oxide flux (mols/s) from cumulative chip surface vs. time (min). Note the flows were started at point A and after a spike in NO, resulting from the initial mixing in the channels a steady state was achieved at point B.

pore. Fig. 4 shows the transient and steady state NO flux rate of the chip during operation. The steady state regime corresponds to the 'pinning' effect which follows an initial transient period in the NO flux rate due to uneven filling of the chip. The results indicate that a stable flux rate of NO for an extended period of time is achievable; a vital requirement for neuronal experimentation.

Fig. 5 shows a DRG that was successfully explanted onto a chip, demonstrating the capability for proper adhesion and growth on the PDMS membrane. In this experiment, NO was not dosed during the incubation or experimental period. DRGs are currently being explanted onto chips, in accordance with the schematic in Fig. 2, and the effects of various NO dosing schedules on the neural morphology are being evaluated.

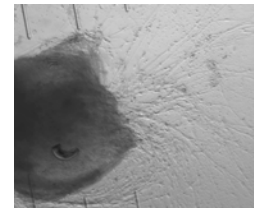

Fig. 5 Explanted DRG with neurite outgrowth on PDMS membrane of chip.

REFERENCES

[1] T. Thippeswamy, R. Morris, *Roles of Nitric Oxide in Dorsal Root Ganglion Neurons*, Ann. N.Y. Acad. Sci. 962: pp. 103–110 (2002).

[2] T. Noboru, A. Kazuhide, O. Tomio, *Interaction of endothelial nitric oxide and angiotensin in the circulation,* Pharmacological Reviews Vol. 59 (1), pp. 54-87 (2007)

[3] Chen Wang and William M. Deen, *Nitric Oxide Delivery System for Cell Culture Studies*, Annals of Biomedical Engineering, Vol. 31, pp. 65–79, (2003)

[4] P.A. Kenis, R. F. Ismagilov, G. M. Whitesides, *Microfabrication Inside Capillaries Using Multiphase Laminar Flow Patterning*, Science, Vol. 285, No. 5424, pp. 83-85, (1999)

[5] Z. Zhou, G. M. Annich, Y. Wu, and M. E. Meyerhoff, *Water-Soluble Poly(ethylenimine)-Based Nitric Oxide Donors: Preparation, Characterization, and Potential Application in Hemodialysis*, Biomacromolecules, Vol. 7, pp. 2565-2574, (2006)

SINGLE MOLECULE ANALYSIS OF CONDENSED DNA: MEASUREMENT OF CONDENSATION SPEED AND SINGLE MOLECULE SIZE USING LASER TRAPPING

Tomomi Ishido[1], Hideya Nagata[1], Yoshio Tanaka[1], Mitsuru Ishikawa[1], and Ken Hirano [1,2]

[1] Health Technology Research Center, National Institute of Advanced Industrial Science and Technology (AIST), JAPAN,

[2] PRESTO, Japan Science and Technology Agency, JAPAN

ABSTRACT

This paper reports an analysis and application of single molecular level for DNA condensation. We were measured firstly a condensation speed of single DNA molecules by polymer and salt induced (psi, φ) condensation system inside microfuidic channel. Furthermore, a direct sizing of single DNA molecules using laser trapping was shown here as an application of condensed DNA molecules.

Keywords: DNA condensation, single molecule, laser trapping, molecular sizing

1. INTRODUCTION

Novel manipulation technique of single DNA molecules is important for further a single genomic DNA analysis on a chip [1]. Laser trapping technique is the most widely recognized as single DNA manipulation technique using bead-binding method, whereas a random-coiled DNA molecule cannot be trapped [2-3]. Using condensation, native huge sized DNA molecule can be manipulate directly to prevent fragmentation of it in free solution [4]. However, basic information for manipulation of condensed DNA molecules, how speed during condensation and how much size of trapped single DNA molecule, are not reported. We show here measurement of condensation speed at single molecular observation in real-time and direct sizing of trapped single condensed DNA molecules using laser trapping.

2. EXPERIMENTAL

(1)Measurement of condensation speed

Lambda phage DNA (48. 5kbp) was used in the present study. For measuring condensation speed, one end of single DNA molecule was fixed on channel surface of PDMS chip by avidin-biotin bound[1]. DNA was stained with DAPI as a fluorescent dye. A condensation was started to exchange solution inside channel (25μm deep, 5mm wide, 5cm long) to condensing agents, [PEG]=60mg/mL and [MgCl2]=30mM.

(2)Direct sizing by laser trapping

Lambda DNA (48. 5kbp), T4 DNA (166kbp), and two genome DNA of *S. cerevisiae* (285kbp, 365kbp) were used in the present study. A condensation condition is same as above. A Nd:YAG laser (1064 nm, CW) was used for laser trapping.

978-0-9798064-0-7/μTAS2007/$20©2007CBMS

3. RESULTS AND DISCUSSION

(1)Measurement of condensation speed

An observation in real-time of the φ condensation in a channel of PDMS chip, is shown in figure 1(a). Time course of condensation for calculating the speed is shown in figure 1(b). The condensed DNAs were categorized two groups, simply condensed DNAs(group A in Fig.1b) and surface interacted DNAs(group B in Fig.1b). It is revealed that the condensation speed of group A is 123. 4kbp/sec which is higher than protein one such as histon which is need for 1-2 hours for genome. This highspeed condensation is benefit to prepare huge sized genomic DNA in condensed state. This high-speed condensation is benefit to prepare huge sized genomic DNA in condensed state for single molecule analysis.

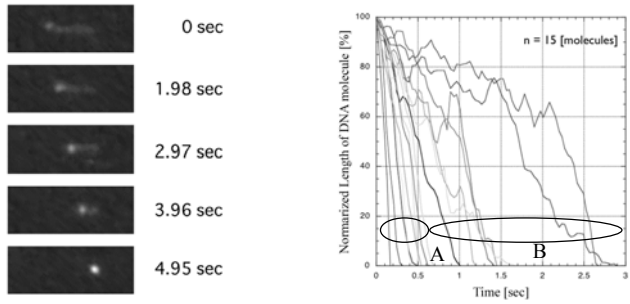

(a) (b)

Figure 1. Real-time observation during condensation of a single DNA molecule (a). Time course of length alteration of DNA molecules during condensation. Length of DNA molecules were normalized (b).

(2)Direct sizing by laser trapping

Figure 2 shows direct laser trapping on condensed DNA molecule. A trapping laser can move in circle shape. When the velocity exceeded a critical value during acceleration, the trapped DNA molecule was released from the laser trapping. It is revealed that this critical velocity proportional to molecular weight of DNA, shown in figure 3a. Using figure 3b as calibration curve, 285kbp DNA molecules was measured critical velocity so then molecular weight was defined at 281±40kbp. We show the new direct sizing method of condensed DNA molecules during laser manipulation. This method has potential as new high-speed sizing method compare with conventional electrophoresis one which is spend for 24-36 hours to analyze genomic DNA.

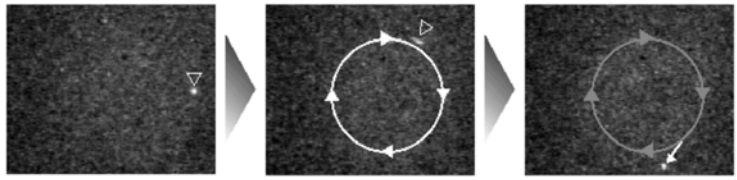

(a) (b) (c)

Figure 2. Measurement of critical velocity of trapped single DNA molecule. (a) trapping of globular DNA(open arrow head), (b) rotation of DNA, (c) releasing from laser focus.

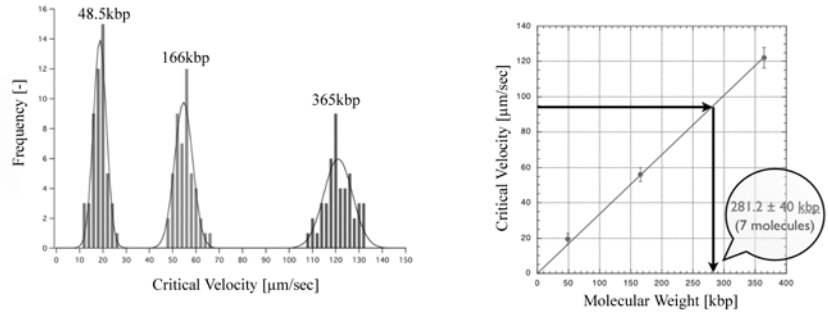

(a) (b)

Figure 3. (a)Histogram of critical velocity of various DNA size measure by laser trapping. (b)Calibration curve obtained from figure 5, for direct single DNA molecule sizing using laser trapping.

4. CONCLUSIONS

We found using direct observation of single DNA molecules that PEG-Mg condensation system occur high speed condensation compared with protein condensation. This high speed condensation is benefit to prepare huge sized genomic DNA in condensed state for manipulation of single DNA molecules. Although a PEG-Mg condensation is reversible reaction, so then we now try measuring decollapse speed of condensed DNA molecules.

We also show the new direct sizing method of condensed DNA molecules, described above, during laser manipulation. This method has potential as new high-speed sizing method compare with conventional electrophoresis one which is spend for 24-36 hours to analyze genomic DNA.

ACKNOWLEDGEMENTS

This work was partly supported by PRESTO from JST for analysis of DNA condensation speed, and Grant-in-Aid for Scientific Research from the Japan Society for the Promotion of Science (No. (C)17560241) for direct sizing of single DNA molecules using laser trapping.

REFERENCES

[1] K. Hirano, et al., *Molecular Processing of a sigle DNA inside Channels for Genome Analysis*, Proc. Micro Total Analysis Systems 2000, Kluwer Academic Publisher, Dordrecht, The Netherlands, pp. 439-442 (2000).

[2] K. Hirano, et al., *Micromanipulation of a sigle DNA Molecule using Laser Assembling of Microparticles*, Proc. Micro Total Analysis Systems 2000, Kluwer Academic Publisher, Dordrecht, The Netherlands, pp. 89-90 (2001).

[3] K. Hirano, et al., *Manipulation of single coiled DNA molecules by laser clustering of microparticles*, Appl. Phys. Lett., **80**, 515-517 (2002).

[4] Y. Matsuzawa, K. Hirano, et al., Laser trapping of an individual DNA molecule folded using various condensing agents, J. Am. Chem. Soc., **121**, 11581-11582 (1999).

800 FOLD SIGNAL ENHANCEMENTS BY TRANSIENT ISOTACHOPHORESIS FOR IMMUNOASSAY OF HSA ON STANDARD CROSS CHANNEL MICROCHIPS

M.R. Mohamadi[1, 5], L. Mahmoudian[1], N. Kaji[1, 2], M. Tokeshi[1, 2] and Y. Baba[1-4]

[1]Department of Applied Chemistry, Graduate School of Engineering, [2]MEXT Innovative Research Center for Preventive Medical Engineering, Nagoya University, [3]Health Technology Research Center, AIST, Takamatsu, [4]Institute for Molecular Science, Okazaki, [5]Nagoya University Venture Business Laboratory, JAPAN

ABSTRACT

A fully automated preconcentration and stacking method based on transient isotachophoresis (ITP) on a standard cross channel microchip made of poly (methylmethacrylate) PMMA has been reported. Previously reported ITP has been either on a special chip design or required a hydrodynamic pressure for sample injection and a pause in the electrophoresis process which caused low reproducibility in analysis. In this work sample injection, preconcentration and separation are done continuously and are controlled solely by a sequential voltage switching program. The ITP followed by non-denaturing gel electrophoresis was applied for immunoassay of HSA.

Keywords: Isotachophoresis, Immunoassay, Microchip Electrophoresis, PMMA

1. INTRODUCTION

Application of microchip electrophoresis-based immunoassay (MCEIA) for protein samples has provided many advantageous such as lower sample consumption, simpler procedure and shorter analysis time. However normal free solution electrophoresis did not fulfil the required resolution and reproducibility for separation of large protein sample from its immunocomplexes. Therefore nondenaturing gel electrophoresis in linear polymers has been tried as an alternative to the free solution electrophoresis [1]. Although nondenaturing gel electrophoresis has provide better resolution and reproducibility for separation of protein sample form its immunocomplex, the problem of peak broadening especially for the large size immunocomplex is still challenging. To overcome this challenge we have developed a new method based on ITP on conventional cross channel microchips [2]. In this method the peak for immunocomplex is preconcentrated and stacked between a terminating and leading electrolyte. The feasibility of the newly developed method for competitive and direct immunoassay of human serum albumin has been studied.

2. EXPERIMENTAL

A plastic microchip made of PMMA, (i-chip 3 DNA, Hitachi Co., Tokyo Japan) was used. The channel cross section was 100 μm (width) by 30 μm (depth), and effective separation length was set at 30 mm. The distances from the intersection of microchannels to the buffer reservoir (BR), buffer waste reservoir (BW), the sample reservoir (SR) and sample waste reservoir (SW) were 5.7, 37.5, 5.2 and 5.2 mm, respectively. An inverted fluorescence microscope, Axivert 135TV, equipped with a 10 /0.3 NA objective lens (both from Carl Zeiss, Tokyo, Japan) illuminated by a 100-W mercury arc lamp (Carl Zeiss) was used. A HVS448 3000V, (LabSmith, Livermore, CA), power supply which was controlled

978-0-9798064-0-7/μTAS2007/$20©2007CBMS

by a PC has been used for MCE. A CCD camera, (EB-CCD, Hamamatsu Photonics, Hamamatsu, Japan), was used to capture the separation process. The captured photos were analyzed by image processing software (Cosmos32, Library Inc., Tokyo, Japan).
For the sample preconcentration the BW, SW, and all the microchannels were filled with 0.5% methylcellulose in the leading buffer (LE). The BR was filled with the same concentration of methylcellulose as used in the microchannels prepared in the terminating buffer (TE). The LE buffer in ITP experiments was Tris 20 mM included 5 mM NaCl and pH was adjusted by HCl (pH= 8.3). The TE in all ITP experiments was 192 mM Gly, Tris 25 mM, (pH= 8.3). All the polymer solutions included 0.01% Tween-20 to decrease protein adsorption. The sample was loaded into the SR. The sample was electrokinetically injected by applying +450 V at the SW for 45 s; all the other reservoirs were kept grounded during the injection. During the separation, the SW and SR were set at +350 V, the BR was grounded, and BW was set at +1450 V (Figure 1).
The immunoassays were done off-chip in the same buffer (Tris-HCl 20 mM, pH= 8.3 including 0.01% of Tween-20). For the direct quantitation of labeled HSA, a constant concentration of mAb Anti-HSA (20 nM) was added to serial dilutions of Alexa Fluor-647 labeled HSA (Alexa-HSA) and the mixtures for direct immunoassay were incubated for 1h at room temperature while shielded from light. For the competitive immunoassay of unlabeled HSA, a constant concentration of Alexa-HSA was added to serial dilutions of un-labeled HSA sample. A constant concentration of mAb Anti-HSA was added to the all competitive solutions. Samples were mixed and incubated at room temperature for at least 20 min while shielded from light. Different concentrations of labeled HSA (500, 250, 125, 62.5 ng/ml) and different molar ratios (16, 8, 4, 2, 1) of mAb to HSA was used.

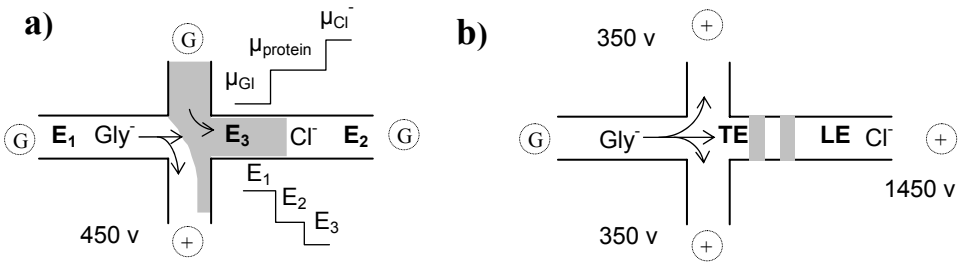

Figure 1. Schematic of the preconcentration (a) followed by ITP (b) in the separation channel. E1, E2 and E3 show the electric field strength in TE, sample and LE zone respectively.

3. RESULTS AND DISCUSSION

The principle of the method is described in figure 1. The sample was electrokinetically injected and arrived at the intersection of the channels. A few seconds (~3 s) later the terminating electrolyte (TE) zone which included low mobility ion (Gly-) arrived from the buffer reservoir at the intersection of the channels. The negatively charged sample plug was forced into the separation channel by a repulsion force from low mobility co-ion (Gly-) which, during the rest of the sample injection led to the accumulation of the sample at the beginning of the separation channel (Fig. 1-a). After 45 s when the injection step was switched to the separation step (Fig. 1-b), the TE zone moved toward the separation channel and swept the sample plug into the separation channel. Due to the low mobility of

Gly- compared to the protein sample a short time lag happened and during this lag, the sample continuously entered the separation channel and a big sample plug was formed. At the beginning of the separation step the sample plug which was captured between TE and leading electrolyte (LE) zone was stacked because of the transient ITP effect.

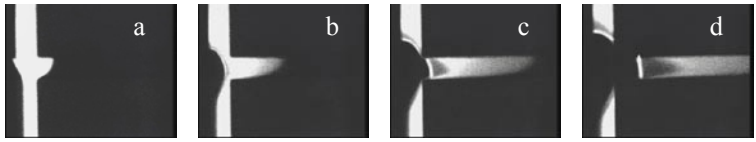

Figure 2. Fluorescent images of the intersections of microchannels, image a shows the sample flow after arrival of the high ionic zone to the intersection of the microchannels. Image b shows the injected sample after switching the voltage to the separation step. Image c and d show the transient ITP. The sample was immunoassay mixture of FITC-HSA 2.5 µg/ml and mAb-anti HSA 5 µg/ml.

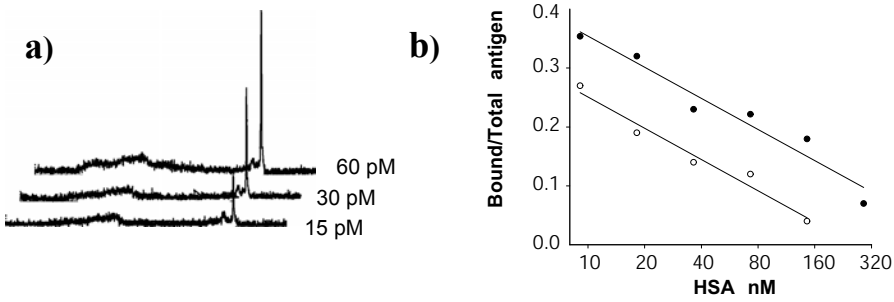

Figure 3. Part a shows the peaks for immunocomplex of Alexa-Labled HSA sample. Part b shows two standard curves for quantitation of unlabeled HSA in a competitive immunoassay by ITP. A known concentration of mAb anti-HSA (5 µg/ml) and Alexa-HSA of concentration of 250ng/ml (●) and 125 ng/ml (○) were added to varying concentration of unlabeled HSA.

Figure 2 shows a series of images from sample injection and the ITP afterward. During the preconcentration, the immunocomplex and HSA were stacked (Fig. 2-c, d). The two sample zones were further resolved by size-based separation in the methylcellulose solution. The direct immunoassay of labled HSA is shown in figure 3-a. The highly stacked peak for the immunocomplex compare to the broadened peak in normal microchip electrophoresis led to several hundreds (~800) signal enhancement (Fig. 3-a). Efficiency and application of the method to competitive immunoassay of an unlabeled HSA is shown in figure 3-b.

4. CONCLUSIONS

In conclusion a novel transient ITP on a conventional cross channel PMMA microchip was introduced. The method was applied to direct immunoassay of mAb anti-HSA and competitive immunoassay of an unlabeled HSA. The preconcentration enhanced the signal for the peak of the immunocomplex by 800-fold.

REFERENCES

[1] Mohamadi, M.R.; Mahmoudian, L; Kaji, N.; Tokeshi, M.; Baba, Y. Electrophoresis 2007, 28, 830-836.

[2] Mohamadi, M.R.; Kaji, N.; Tokeshi, M.; Baba, Y. Anal Chem 2007, 79, 3667-3672.

APPLICATION OF CYCLOOLEFIN POLYMER CHIP DIRECTLY INTEGRATED WITH AN ELECTRONANOSPRAY TIP TO ELECTROPHORETIC SEPARATION AND MASS SPECTROMETRIC DETECTION

Fumihiko Kitagawa[1], Takafumi Suzuki[2], Hidetoshi Shinohara[2], Jun Mizuno[2], Shuichi Shoji[2] and Koji Otsuka[1]

[1]Graduate School of Engineering, Kyoto University, JAPAN and
[2]Major in Nano-Science and Nano-Engineering, Waseda University, JAPAN

ABSTRACT

This paper reports a fabrication of cycloolefin polymer (COP) chip directly integrated with an electrospray ionization (ESI) emitter tip for a microchip electrophoretic (MCE) separation and mass spectrometric (MS) detection on the basis of the hot embossing, low temperature direct bonding, micromachining techniques and direct metallization onto the COP surface. By applying the fabricated COP chip to the MCE–ESI-MS analysis, a successful separation and detection of caffeine and amino acids was attained without any mechanical pump, nebulizing gas and sheath liquid.

Keywords: microchip electrophoresis, electrospray ionization, mass spectrometry, cycloolefin polymer

1. INTRODUCTION

The application of mass spectrometry (MS) to microchip electrophoresis (MCE) as a detection scheme should be promising for the highly selective analysis especially for biogenic compounds. In MCE–MS, electrospray ionization (ESI) is regarded as the most suitable ionization method since an electrode for ESI can be also used for applying the separation voltage. In previous reports, glass or quartz microchips were mainly used for MCE–ESI-MS but they are generally expensive. To overcome this problem, polymer chip devices have been developed. Among several polymers, cycloolefin polymer (COP) has been recently employed as a substrate for MCE and/or MS chips since this material has superior characteristics such as high chemical durability, easy metallization for the electrode, and low impurity content. In our previous study, furthermore, COP was used as the base plate of the chip for the MCE analysis for blood components [1]. As a typical result, serum proteins were detected as a broader and weaker peak on conventional quartz chips due to serious adsorption, whereas on the COP chips a partial peak separation was obtained with ~200-fold increase in the peak height. On the other hand, Kameoka et al. reported that the MCE–ESI-MS analysis on COP chip but their device consists of a conventional ESI emitter using nebulizer gas and liquid. The introduction of sheath liquid stabilized the ESI spray but reduced the detection sensitivity due to sample dilution [2]. In this study, by utilizing the superior processing characteristics of COP, COP microchip directly integrated with an ESI nanospray tip for the MCE–MS analysis without any mechanical pump and nebulizing sources. Since the direct integration of the ESI tip

978-0-9798064-0-7/μTAS2007/$20©2007CBMS

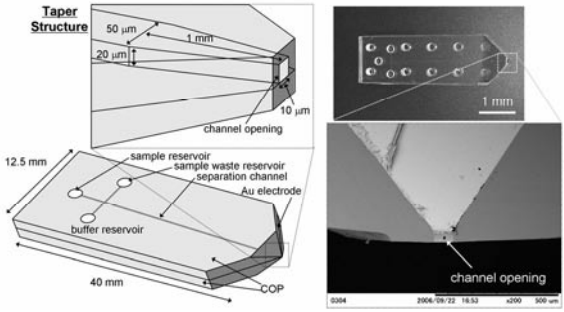

Figure 1. Schematics and photographs of the fabricated COP microchip for the MCE–ESI-MS analysis.

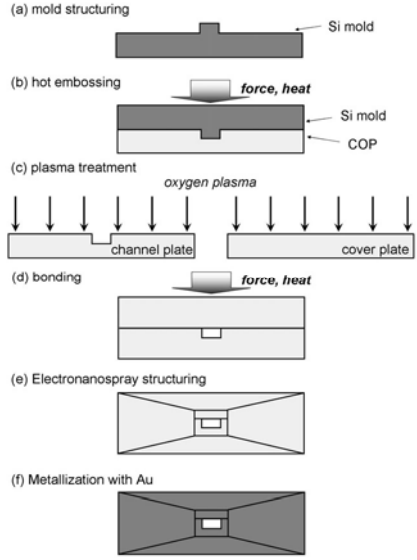

Figure 2. Fabrication process of the COP microchip.

structure onto the exit of a separation channel enables neglected dead volume at the interface, efficient ESI and sensitive detection of sample components is expected.

2. EXPERIMENTAL

As shown in Figure 1, the fabricated device consists of a separation channel and spray tip structure. Dimensions of the channel were 50 μm in width and 20 μm in depth and 30 mm in length. The width of the outlet channel is tapered from 50 μm to 10 μm to enhance the ESI efficiency. The fabrication process was shown in Figure 2. The COP substrate was hot-embossed by using a silicon mold with a conventional cross-type channel configuration under press strength of 1400 N at 165 °C for 4 min. To perform direct bonding with a cover plate at low temperature, the COP substrate was treated with O_2 plasma prior to bonding. Then, bonding was conducted under the contact force of 1000 N at 120 °C for 5 min. After bonding, the ESI tip structure was machined directly with a lathe equipment to form its tip angle of 30 or 60° at the opening of the separation channel end. Finally, a gold electrode to keep the electric contact for ESI was deposited around the electronanospray tip by the EB evaporation. By using the fabricated device, the MCE separation and MS detection were performed with a 5-channel type high voltage supplier and on an LCMS-2010A quadrupole mass-spectrometer (Shimadzu, Japan), respectively.

3. RESULTS AND DISCUSSION

The fabricated chips were evaluated by microscopic observation of the electrospray. To reduce the size of droplets formed at the spray tip, the surface of the Au electrode was modified with mercaptooctadecane prior to ESI. When the voltages of 2.8 and 1.8 kV were applied to the inlet (V_{inlet}) and the ESI (V_{ESI}) electrodes, respectively, and the grounded target electrode (aluminium plate) was spaced a few millimetres from the tip of the ESI

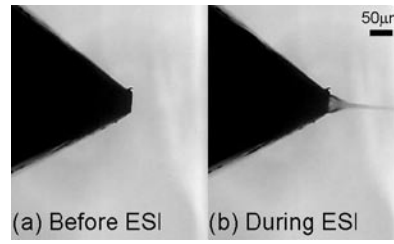

Figure 3. Electrospray formed at the tip of the ESI emitter.

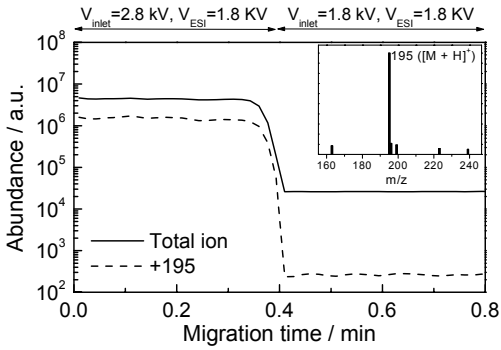

Figure 4. Total and selective ion currents for constant infusion of caffeine obtained with the EOF pumping. Inset shows the MS spectrum at the migration time of 0.11 min.

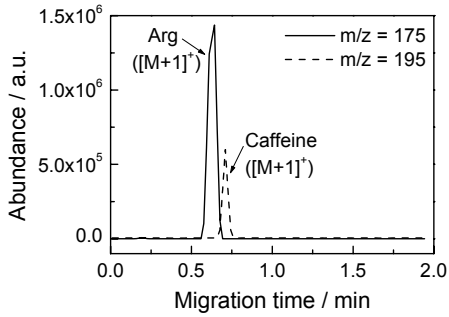

Figure 5. MCE separation of caffeine and arginine.

nanospray, the formation of the Taylor cone and the electrospray were observed at the channel exit as shown in Figure 3. Effect of the tip angle of the nanospray on the ESI efficiency was also investigated. At the angle of 60° shown in Figure 3, an intermittent spray was formed with its repetition rate of ~3 Hz at the ESI tip, while at 30° continuous and stable ESI was obtained. This improvement of ESI by employing the sharper nanospray would be due to effective focusing of the electric field at the tip.

In an infusion analysis of caffeine with the electroosmotic flow (EOF) on the COP microchip with the tip angle of 30°, an MS spectrum with the parent mass number of 195, which accords with that of the protonated caffeine, was successfully obtained in the positive mode as shown in Figure 4. Stable baseline was also observed with its fluctuation of 7.2% in relative standard deviation. Furthermore, the MCE separation and ESI-MS detection of caffeine and arginine (Arg) was also successfully achieved with resolution of 1.0 as shown in Figure 5. Therefore, these results demonstrated that the fabricated COP chip integrated with the electronanospray tip can be employed as the MCE–ESI-MS analysis device.

5. CONCLUSIONS

COP microchips for the MCE–ESI-MS analysis were fabricated by the O_2 plasma/low temperature bonding and EB evaporation techniques. Stable and successive ESI was successfully obtained on the electronanospray with its tip angle of 30°. The MCE–ESI-MS analysis on the fabricated COP chips brought a sufficient separation and successful MS identification of standard samples.

ACKNOWLEDGEMENTS

The authors thank Dr. Akihiro Arai (Shimadzu) for his assistance in ESI-MS measurements.

REFERENCES

[1] F. Kitagawa, T. Tsuneka, Y. Akimoto, J. Mizuno, S. Shoji and K. Otsuka, *Proc. Micro Total Analysis Systems 2005*, pp. 331–333, (2005).

[2] J. Kameoka, H. G. Craighead, H. Zhang, and J. Henion, *Analytical Chemistry*, **73**, 1935 (2001).

DESIGN AND OPTIMIZATION OF FRACTION COLLECTOR FOR CAPILLARY ELECTROPHORESIS

Dawid R. Zalewski[1], Stefan Schlautmann[2], Richard B.M. Schasfoort[2] and Han J.G.E. Gardeniers[1]

[1]Mesoscale Chemical Systems Group (MCS), [2] BIOS Lab-on-a-Chip Group
MESA+ Institute for Nanotechnology, University of Twente, P.O. Box 217,
7500 AE, Enschede, THE NETHERLANDS

ABSTRACT

A microfabricated device capable of collecting multiple components from a mixture separated by capillary electrophoresis (CE) is described. The device operates automatically and consists of three electrokinetically controlled sections: CE part, fractions distributor and storage channels. The platform allows the selection of specific peaks in an electropherogram, and collection of the chosen peak fraction in a vial where it is stored for further work-up. A theoretical model of operation and constraints of the system are given. Experimental results confirm reliability and time stability of the system.

Keywords: CE, fractionation, capillary electrophoresis, sample collection

1. INTRODUCTION

Selective extraction of fractions from a separated multianalyte sample is a recognized technique in biological analysis [1-2]. Microscale fully automated devices are rare [3] due to the difficulties arising from the nature of electrokinetic flow control and lack of tools for integration of mechanical parts into fluidic networks. The microchip shown in Fig. 1 is capable of fast, automatic fractionation of a multianalyte sample. Following the separation, the selected sample fractions are stored in the individually addressable collection chambers. Timing of the fractionation is triggered by the output signal of a conductivity detector, which is integrated in the chip, at the end of the CE separation channel. The fluid flow in the device is controlled electrokinetically, requiring no mechanical parts.

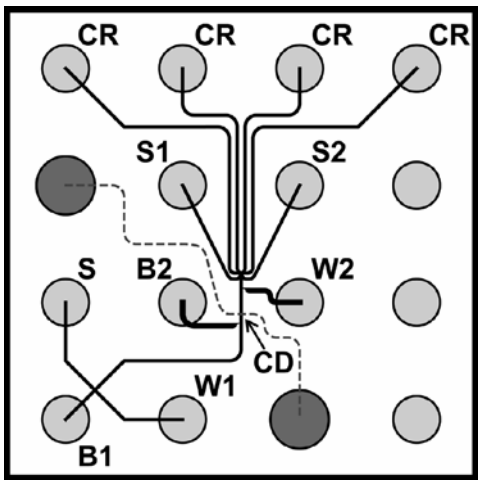

Figure 1. Layout of the chip

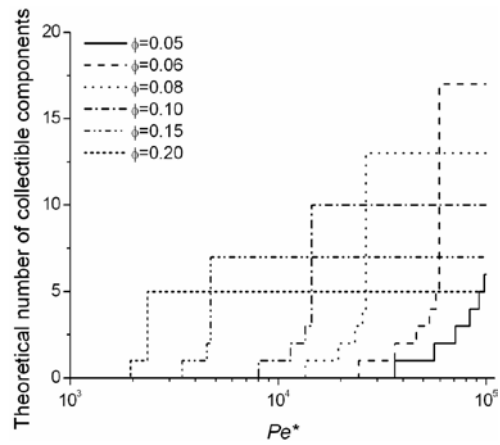

Figure 2. Graph of calculated theoretical number of collectible components.

978-0-9798064-0-7/μTAS2007/$20©2007CBMS

2. THEORY

An analytical model of the operation following methodology principles presented in [4] was derived. Given a sample composition and knowing the fractions of interest the collection intervals and the positions of the fractions can be estimated, allowing more precise manipulation. Based on the analytical model the minimum collectibility criterion (Eq. 1, 2) was defined.

$$\frac{\varphi}{1-(i-1)\cdot\varphi}\cdot\Lambda(\vartheta)\cdot\sqrt{\frac{Pe^*}{\chi Pe^*+2\zeta(i)}}>\gamma \qquad (1)$$

$$\begin{cases}\Lambda(\vartheta)=\dfrac{\sqrt{3+\vartheta}}{1+\sqrt{\vartheta}}\\ \vartheta=\dfrac{6\zeta(i)}{\chi Pe*}\end{cases} \qquad (2)$$

The dimensionless parameters used in the equations are: φ - difference of the components mobilities related to the greatest mobility, Pe* - Péclet number related to the separation path length and χ - a number characterizing the initial dispersion related to separation path length. The $\zeta(i)$ is a complex function describing the relation between the collection time of the first and i-th fraction. In Fig. 2 the result of calculation of the theoretical number of collectible components for boxcar injection profile ($\chi=((33\cdot10^{-6})/2\cdot10^{-2})^2$) are shown.

3. EXPERIMENTAL

The separation starts with an injection of a sample by applying voltages to sample reservoir (S) and waste (W1). Next the voltages are switched to establish a separation field by applying electric potential between B1 and W2. The collection procedure is triggered by the conductivity signal. When a fraction passes the detector electrodes, the potentials are reconfigured; separation is withheld and migration of a sample is forced between B2 and one of the collection channels (CR). Additionally a sheath flow from S1 and S2 is switched on to assist the collection by electrokinetic focusing. After collection of a fraction the separation is resumed and the whole sequence is repeated until all samples are processed. Experiments were performed with a buffer solution of 5mM Hepes, ph 8.0, 0.1% Tween 20. Sample mixture contained 1mg/mL of Rhodamine B and Rhodamine 6G.

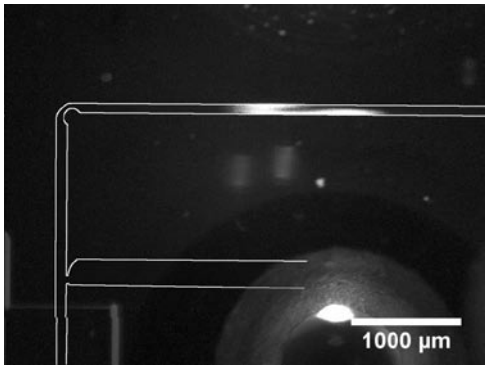

Figure 3. Fluorescence photograph of separation in progress.

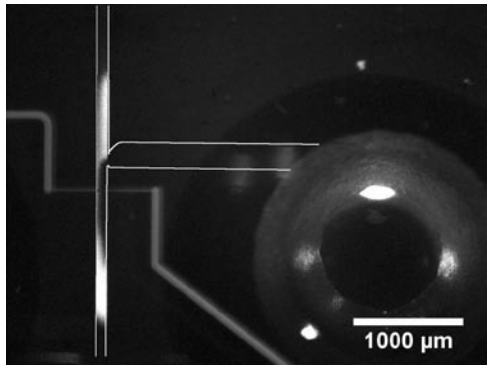

Figure 4. Fluorescence photograph of spatial separation of the components. Picture taken 200ms after starting the collection procedure.

4. RESULTS AND DISCUSSION

Fluorescence intensity profiles taken during the separation of the sample mixture (Fig. 3), followed by detection and collection of the first component (Fig. 4) show good reliability of the automated procedure, which allows spatial separation of overlapping fractions (Fig. 5). Two series of separations run with a 15 minutes interval prove long-term time stability of the system and very good reproducibility of the collection in one series (Fig. 6). Electrokinetic focusing used during the collection prevents cross-contamination (Fig. 7, 8). The demonstrated method provides an efficient and reliable way for automated fractionation.

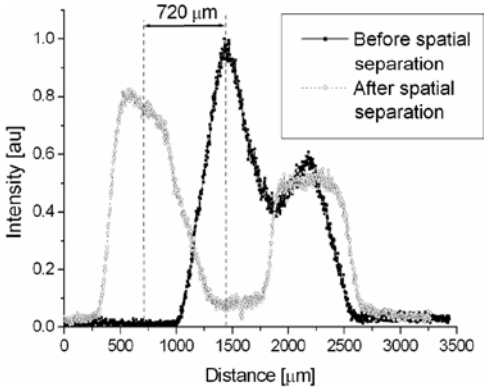

Figure 5. Fluorescence intensity profiles calculated from Fig 3 and 4. A spatial separation of 720 μm was achieved in first 200 ms of collection.

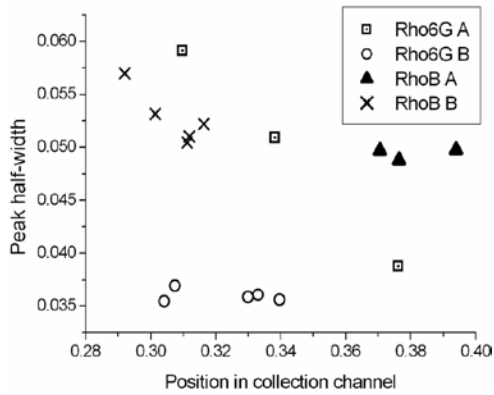

Figure 6. Accuracy and repeatability of fractions parking in collection channels in two experiments (A and B). Values relative to the total length of the collection channel.

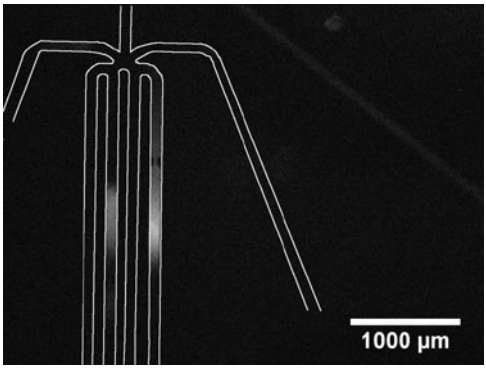

Figure 7. Fluorescence photograph of collected Rhodamine B and Rhodamine 6G.

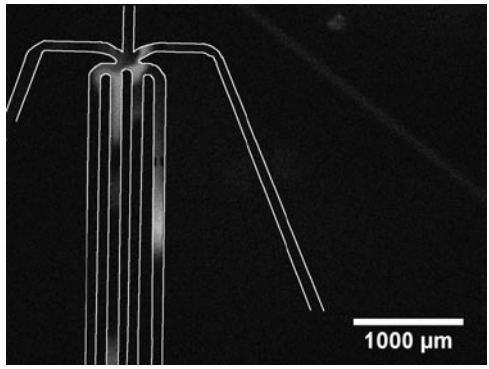

Figure 8. Fluorescence photograph of collection of Rhodamine B in progress with electrokinetic focusing switched off.

REFERENCES

[1] C. S. Effenhauser, A. Manz and H. M. Widmer, Anal. Chem., 67, 2284-2287.
[2] J. Khandurina, T. Chovan and A. Guttman, Anal. Chem., 74, 1737-1740.
[3] J. J. Tulock, M. A. Shannon, P. W. Bohn and J. V. Sweedler, Anal. Chem., 76, 6419-6425.
[4] R. Bharadwaj, J. G. Santiago and B. Mohammadi, Electrophoresis, 23, 2729-2744.

ELECTROKINETIC BIO-MOLECULES PRE-CONCENTRATION AND SEPARATION BY MWCNTS FILTER IN NANOFLUIDIC CHANNEL

Ren-Guei Wu[1], Yi-Shiuan Wu[1], and, Chung-Shi Yang[1,2], Fangang Tseng[1*]

[1] Department of Engineering and System Science, [2] National Health Research Institutes, National Tsing Hua University, Hsinchu, Taiwan (R.O.C.)

ABSTRACT

This paper presents a study of electrokinetic transport in a nanofluidic chip that allow for separation and preconcentration of the molecular mixtures into a well-aligned multi-wall carbon nano tubes (MWCNTs) array of nanochannels. The MWCNTs array was used as an induced surface charge filter to attract the opposite charged molecules on the wall surface by van der Waals and electrostatic force. The surface charge intensity of MWCNTs is inversely proportional to the channel wall thickness and proportional the dielectric constant of itself with an external electric-field. 1 mM FITC fluorescein and Rhodamine 6G dye mixtures during the electrokinetic trapping process for inducing the surface charges of MWCNTs filter, could be easily to separate by the electric property of dyes in a MCNTs filter nanochannel. For bio-molecules preconcentration process, the concentration capability of 0.5 μM FITC-labeling IgG as high as 10000 folds have been demonstrated.

Keywords: Preconcentration and Separation, Carbon Nanotubes Filter, Nanofluidic

1. INTRODUCTION

Most microchip-based separation techniques often analyze only a small fraction of available samples, which could limit the overall detection sensitivity, especially for the detection of low-concentration species in the sample. Several strategies are currently available to provide sample preconcentration in liquids [1-2]. Many of these techniques were originally developed for capillary electrophoresis (CE) and require special buffer arrangements, reagents, or both. Overall, the demonstrated concentration factors for the existing preconcentration schemes in the microchips are limited to 1000-5000 folds, and their coupling with integrated microsystems is difficult due to various operational constraints, such as reagent and material requirements. To solve these problems, we have developed a microfluidic sample separation and preconcentration system based on electrokinetic trapping [3-4] and further to control a reversible surface charges MCNTs nano-filter by the induced electric filed in a chip.

2. EXPERIMENTAL

The design and operation principle are shown in Fig. 1. The system includes a thermal growth MCNTs array which was transferred to the surface of a spinning-PDMS/glass substrate and a PECVD SiO_2 defined nano-channel (width: 50 μm; hight: 500 nm) on the pyrex wafer carrying the electrodes. By the exchange of induced surface charge of MWCNTs filter, the negative charge dye (FITC) and positive charge dye (Rhodamine 6G) could be separate on the MCNTs-filter and channel wall, respectively. SEM photograph shows the MCNTs-filter, electrodes layout and nano-channel geometry and depth, in Fig. 2. On glass substrate, Pt electrodes, coated with 500 nm Si_3N_4 passivitation layer, were

978-0-9798064-0-7/μTAS2007/$20©2007CBMS

employed to induce the surface charge of MCNTs-filter by applied an external electric field. The fabrication process of MCNTs filter nanofluidic Chip was shown in Fig. 3, after cured the MCNTs/PDMS complex, we use the ultrasonic to separate the MCNTs out of the Si substrate. In order to pumping flow by electrokinetic-dynamic force and chip bounding, the MCNTs-PDMS/glass substrate was treated with H_2O surface plasma to be hydrophilic.

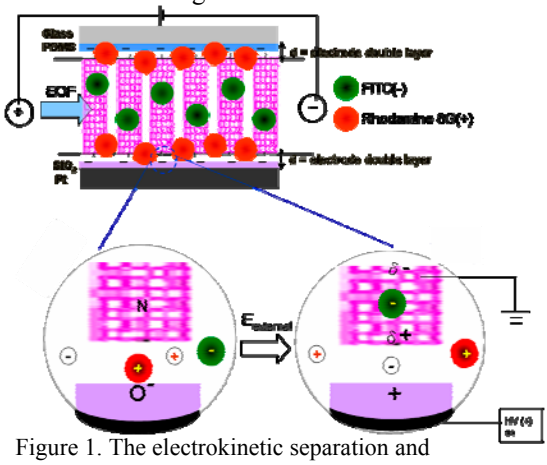

Figure 1. The electrokinetic separation and preconcentration mechanism of MCNTs-filter.

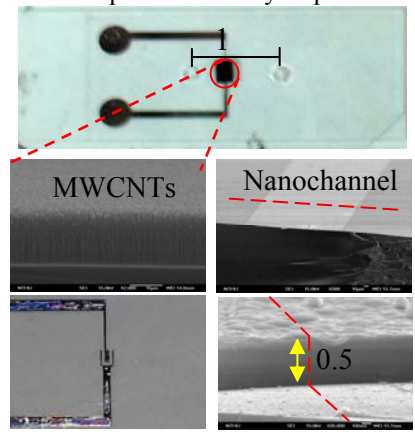

Figure 2. SEM photograph of well-aligned MCNTs-filter and nanochannel.

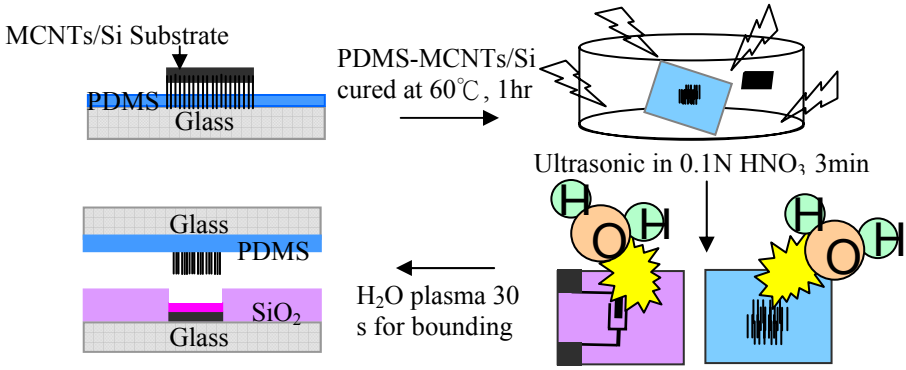

Figure 3. The fabrication process of MCNTs filter nanofluidic-Chip.

3. RESULTS AND DISCUSSION

The Fig. 4 shows the selectivity ability for two mixture dyes, firstly, to loading the FITC and Rhodamine 6G mixtures in to the nano-channel by electroosmotic flow (EOF), then to applied the induced voltage (0 to ±50V) for 3-5 minutes, to washing the non-trapping dyes by raising the electric field to enhance the flow rate of EOF. It can be clear to see that the FITC-green dye was trapped on the MCNTs-fliter and the Rhodamine-red dye was taken out off the nano channel. The preconcentration process of FITC labeling IgG on MCNTs-fliter was shown in Fig. 5. After electrokinetic trapping for several minutes, the fluorescence density of dye becomes more and more greatly bright with the time variation. Fig. 6. shows the concentration capability of FITC labeling IgG could be improved ca. 12000 folds. The linear calibration curve (the linear range is 0.01, 0.05, 0.1, 0.5, 1, 5, 10, 50 mM) was showed in the illustration of figure 6.

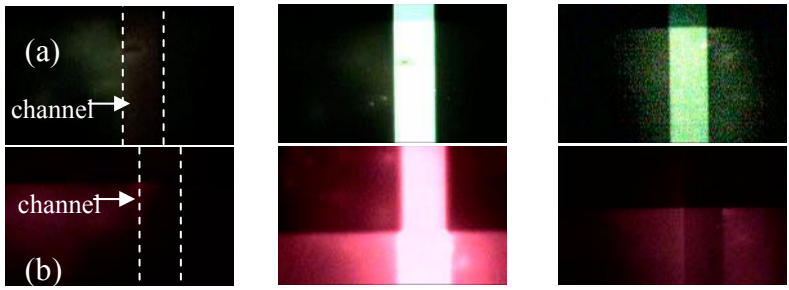

Step 1, sample loading Step 2, electrokinetic trapping Step 3, sample separation

Figure 4. The process of separation for two mixture dyes, (a) FITC, negative charge (b) Rhodamine 6G dye, positive.

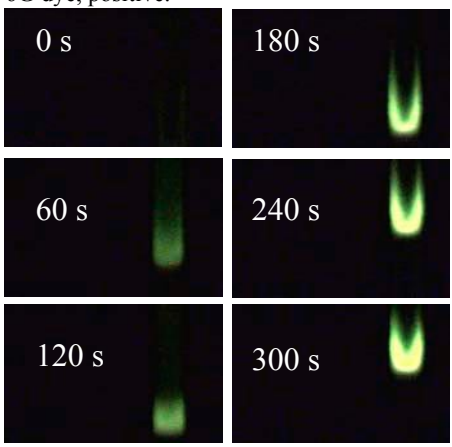

Figure 5. The pre-concentration process of FITC labing IgG on MCNTs filter.

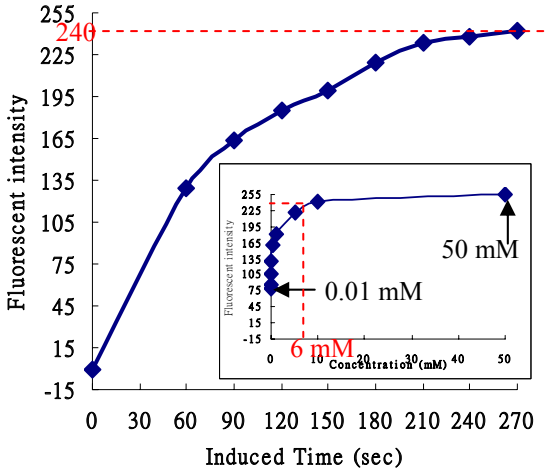

Figure 6. The concentration capability of FITC -labing IgG by MCNTs-filters.

4. CONCLUSIONS

We demonstrate that pre-concentration and separation of fluorescein mixtures in nano channel can be performed by MCNTs-filters. Sample pre-concentration capability up to 10^4 fold has been successfully demonstrated by 0.5μM FITC dye. Further optimization of this system has a potential to improve the sample concentration of bio-molecules for detection.

ACKNOWLEDGEMENTS

This study was partially sponsored by the National Science Council of Taiwan under the project NSC 95-2221-E-007-144.

REFERENCES

[1] Ring-Ling Chien, *Stacking phenomena in electromigration: From basic principles to practical procedures,* Electrophoresis 2003, *24,* 486–497.

[2] Robert S. Foote, Julia Khandurina, et., *Preconcentration of Proteins on Microfluidic Devices Using Porous Silica Membranes*, Anal Chem. 2005, 77, 57-63.

[3] Anthony L. Garcia, Linnea K. Ista, et., *Electrokinetic molecular separation in nanoscale fluidic channels,* Lab on a Chip. 2005, 5, 1271-1276.

[4] Wang, Y. C., Stevens, A. L., Han, J., *Million-fold Preconcentration of Proteins and Peptides by Nanofluidic Filter*, Anal. Chem. 2005, 77, 4293-4299.

FAST SHEAR-DRIVEN OLIGONUCLEOTIDE SEPARATION IN 1D-NANOCHANNELS

Frederik Detobel[1], Veronika Fekete[1], Wim De Malsche[2], Han Gardeniers[2] and Gert Desmet[1]

[1]*Vrije Universiteit Brussel, Belgium*
[2]*University of Twente, The Netherlands*

ABSTRACT

The present study focuses on the implementation of the ion-pair reversed-phase chromatographic separation technique in 1D-nanochannels with the aim of separating single stranded oligonucleotides. Using the shear-driven flow principle, an isocratic separation of 25 en 100 bases long DNA strands could be accomplished in less than 1 s in a 350 nm channel.

Keywords: DNA separation, nanochannel, ion-pair reversed-phase chromatography, isocratic elution

1. INTRODUCTION

Recently, the use of nanochannels gained a lot of attention in DNA analysis, as these channels enable the use of particular nanometer scale phenomena in order to separate the macromolecules. Fu *et al.*, for example, developed a nanofilter array chip which allows the continuous separation of proteins and short DNA molecules, based on the creation of an entropic energy barrier (Ogston sieving) [1]. Petersen *et al.* separated 100 and 1000 bp long DNA strands by electrohydrodynamic chromatography using an electroosmotic flow with double layer overlap and achieved a reversed separation using channels smaller than the molecule size [2]. Also Pennathur *et al.* were able to separate 1 to 100 bp oligonucleotides by electrophoresis in a 100 nm channel in less than 120 s [3]. Here, we report on the first shear-driven separation of single stranded oligonucleotides in channels with a depth of 350 nm by ion-pair reversed phase liquid chromatography (IP-RP-LC).

2. THEORY

IP-RP-LC is a method commonly used in HPLC to separate DNA based on size [4]. In the present study, we introduced the IP-RP-LC separation technique for the first time into 1D-nanochannels. The use of nanochannels strongly reduces the required sample amount compared to HPLC and accelerates the interaction of the macromolecules with the stationary phase due to a reduction of the transverse diffusive path. Hence, combining high flow rates with the small channel dimensions enables a fast separation of the macromolecules.

The generation of high flow rates in nanochannels is however a challenging task. Pressure-driven and electososmotic driven systems are not able to generate the required flow rates, respectively due to the creation of a high pressure drop and to a double layer overlap. The shear-driven flow principle on the other hand, is able to create high fluid flow rates in micro- and nanochannels, independent of the channel size [5]. In this system, a relative movement of two opposite channel walls creates a fluid displacement based on viscous drag forces and the average fluid velocity equals half the wall speed (figure 1a).

978-0-9798064-0-7/μTAS2007/$20©2007CBMS

3. EXPERIMENTAL

A mixture of 25 and 100 bases long FITC-labeled oligonucleotides was injected into a C18-coated silicon nanochannel (350 nm) using an in-house build shear-driven chromatographic system (figure 1b). The separation of these strands by IP-RP-LC was investigated by means of isocratic elution. Triethylammonium acetate (TEAA) was used as the ion-pairing agent and the mobile phase consisted of an organic solvent (methanol), dissolved in 0.2M TEAA. The optimal methanol concentration for separation was determined experimentally.

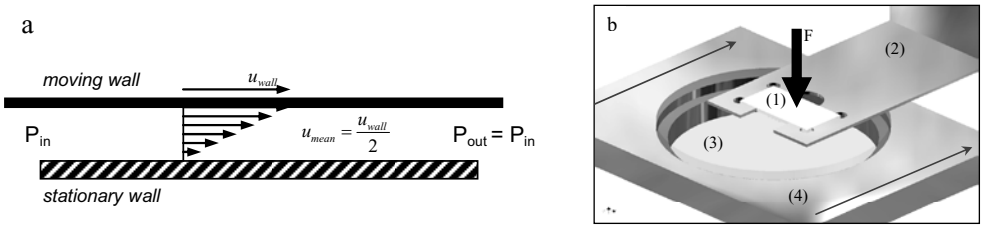

Figure 1. **(a)** Principle of the shear-driven flow in micro- and nanochannels. **(b)** Schematic overview of the assembled shear-driven system: (1) silicon substrate with an etched 1D-nanochannel, (2) immobilized holder of the silicon substrate, (3) fused silica moving wall, transparent to enable molecule detection using an inverted microscope, (4) holder of the moving wall, connected to a motorized translation stage (not shown).

4. RESULTS AND DISCUSSION

As shown in figure 2a, the separation of 25 and 100 bases long oligonucleotides could be accomplished in less than 1 second by means of isocratic elution, consuming only 3.33 fmol of the nucleic acid. The detected peaks were identified by injecting the mixture components separately and comparing their retention time (figure 2b). As expected, the 25b oligonucleotides moved through the nanochannel at the mobile phase velocity (i.e. were non-retaining), while the 100b strands were partially retained.

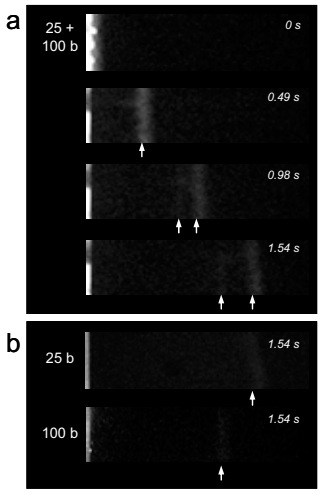

Figure 2. CCD-camera images: **(a)** the separation of oligonucleotides in a 350 nm deep channel. A mixture of 84 µM 25b and 52 µM 100b oligonucleotides in 0.2 M TEAA was injected into the channel. A solution of 10% MeOH in 0.2 M TEAA was subsequently dragged through the channel at an average velocity of 1 mm/s (moving wall displacement at 2 mm/s). The complete separation was accomplished within 1 s. **(b)** Separate injection of 25 and 100 b oligonucleotides.

In the process of isocratic oligonucleotide separations, the organic solvent concentration is very critical. If the organic solvent concentration is too high, the molecules are not retained and no separation can be accomplished (figure 3a). If the concentration is however too low, all mixture components will absorb on the stationary phase (figure 3b). As the interaction of the nucleic acids with the stationary phase increases according to the number of bases in the sequence, the optimal organic solvent concentration for separation also depends on the length of the nucleic acids. Hence, only few strands can be separated by means of isocratic elution and, although the presented results illustrate the possibility of IP-RP-LC-based isocratic separation of oligonucleotides in nanochannels, the separation of more complex mixtures of nucleic acids will require the use of gradient elution. The generation of an on-chip concentration gradient is now under investigation.

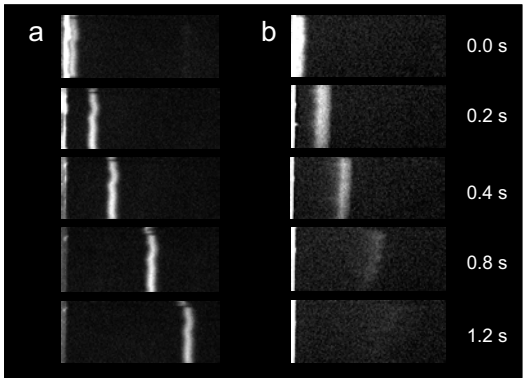

Figure 3. CCD images of the isocratic elution of a 25-100b oligonucleotide mixture at 15% MeOH **(a)** and 5% MeOH **(b)** in 0.2 M TEAA.

5. CONCLUSIONS

Using a combination of the shear-driven system and the IP-RP-LC technique, we demonstrated the isocratic separation of 25 and 100 bases long oligonucleotides in a 350 nm silicon channel. The implementation of an organic solvent concentration gradient during elution will however be required to establish more complex separations.

ACKNOWLEDGEMENTS

F.D. gratefully acknowledges a research grant from the Research Foundation - Flanders (FWO Vlaanderen).

REFERENCES

[1] Jianping Fu, Pan Mao and Jongyoon Han (2005). Nanofilter array chip for fast gel-free biomolecule separation. *Applied Physics Letters* **87**, 263902

[2] N. J. Petersen, J. P. Alarie, S. C. Jacobson, and J. M. Ramsey (2003). Polyelectrolyte transport in nanoconfined channels. *7th International Conference on Miniaturized Chemical and Biochemical Analysis Systems*, October 5-9, Squaw Valley, California USA, 701

[3] Sumita Pennathur, Fabio Baldessari, Mike Kattah, Paul J. Utz and Juan G. Santiago (2006). Electrophoresis in nanochannels. *Proceedings of FEDSM2006, ASME Joint U.S. - European Fluids Engineering Summer Meeting,* July 17-20, Miami, Florida USA.

[4] Douglas T. Gjerde, Christopher P. Hanna and David Hornby (2002). *DNA Chromatography*. Wiley-VCH, Weinheim, Germany, 228pp

[5] Desmet G. & Baron G. V. (1999). On the possibility of shear-driven chromatography: a theoretical performance analysis. Journal of *Chromatography A* **855**, 57-70.

IMPROVED ULTRASONIC MICRO ARRAY SEPARATION USING FAR FIELD ULTRASONIC EXCITATION

Andreas Nilsson, Tomas Jansson and Thomas Laurell
Department of Electrical Measurements, Lund University, SWEDEN

ABSTRACT

This paper reports improved separation efficiency of an ultrasonic standing wave separator microchannel array by means of ultrasonic far field excitation. By putting an aluminium spacer between the transducer and the channel array, the acoustic power transmission region is moved into the ultrasonic far field decreasing the local intensity variations which is induced in close vicinity to the transducer. This generates a more stable acoustic separation, which enables better separation performance and higher separation efficiency.

Keywords: ultrasound, separation, microfluidics, far field

1. INTRODUCTION

Ultrasonic standing wave separation can be used to manipulate and separate cells and particles in microfluidic silicon channels and has previously been reported in projects including plasmapheresis, where the micro separator has been used to generate clean blood plasma [1] and blood wash, where contaminated whole blood was cleaned from lipid particles [2].

2. PRINCIPLE

The ultrasonic transducer used as the acoustic source is placed underneath the separation channel and the separation structure is designed such that it is only in the direction perpendicular to the incident wave propagation that a standing wave criterion is met. The mechanism responsible for this propagation mode conversion is not fully elucidated. We hypothesize that there is a conversion of wave modes in the sharp corners of the fluid channel, such that a longitudinal wave travelling upwards in the silicon wafer looses part of its energy to a shear wave in these areas. As the channel depth is much smaller than the wavelength of the shear wave in silicon, the shear wave will essentially make the vertical walls of the channel act as a piston and sustain the resonance in the flow channel that drives the particle separation.

Increased throughput is desired, since the flow capacity of a single micro separation channel is only about 100 µl/min. This is solved by making an array of parallel channels in a bifurcation structure. The advantage is that all channels can be actuated with the same piezo ceramic transducer, since the actuation is done underneath the channel. However, the drawback with the parallel channel structure is that all channels do not separate with the same efficiency, fig 1. Our new findings show that the reason for this behaviour can be traced to the nature of the ultrasonic near field of the transducer. In the near field, large local variations in the acoustic pressure distribution occur, providing an uneven acoustic power input to the separation chip, fig 2. This causes some separation channels to separate excellent and other to perform poorly. By introducing an acoustic coupling layer, an aluminium spacer, the separation chip is positioned away from the uneven near field, in the

978-0-9798064-0-7/µTAS2007/$20©2007CBMS

more stable far field, fig 3, where the glass bonded micro channel array separator is shown on top of the aluminium spacer. In the far field, the local minima and maxima have smoothened into a more even pressure distribution, as shown in the simulation of acoustic pressure in figure 4.

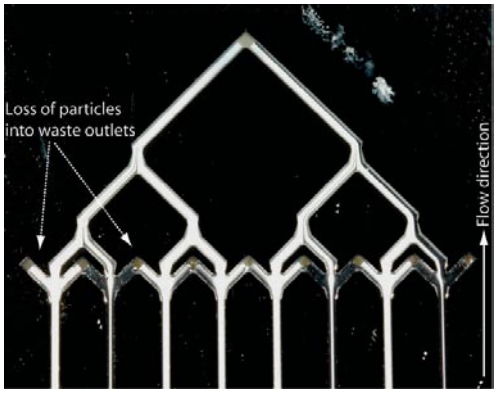

Figure 1. An eight channel parallel structure with inhomogeneous separation caused by the distortion of the acoustic field in the near field. Note the loss of particles into the waste outlets due to poor separation.

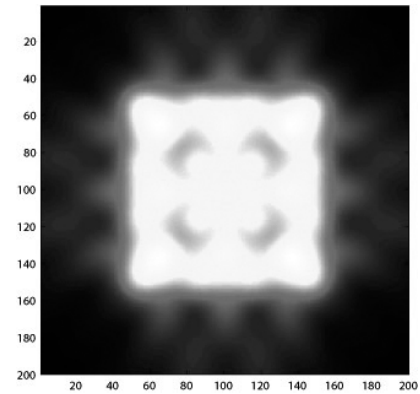

Figure 2. Simulation of the sound profile of an 11 mm square piezo electric transducer 0.5 mm from the surface. Large changes in the local pressure distribution in the near field are shown. Simulations are done using Field II [3].

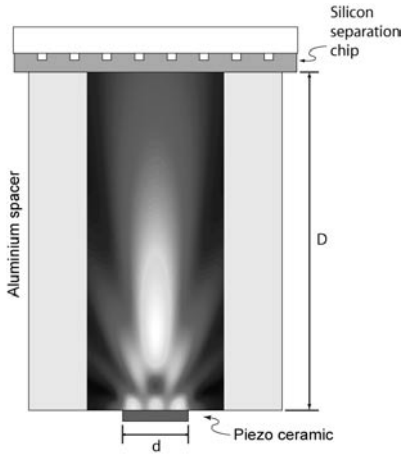

Figure 3. Side view schematic of the separator and the aluminium spacer. Also showing a simulation of the acoustic field in the spacer at a distance D of 50mm from the piezo ceramic surface, that is far out in the far field. Note that this is a free field simulation, neglecting boundary effects of the aluminium spacer.

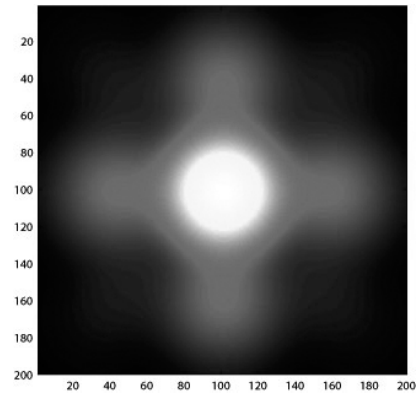

Figure 4. Simulation of the sound profile of an 11mm square piezo electric transducer 15 mm from the piezo surface. Out in the far field the sound profile is more uniform and the acoustic pressure is more evenly distributed over the separation chip. Simulations are done using Field II [3].

3. RESULTS & DISCUSSION

Separation efficiency as a function of the distance between the transducer and the separation channel array were monitored and optically recorded. Separated samples were collected using a fixed loop volume connected to the chip outlet and analysed with a Coulter Counter. The separation ratio was calculated as the enriched fraction divided by the waste + the enriched fractions. As seen in figure 5, separation efficiency vs. aluminium spacer length show that after the near field range has been passed, separation efficiency is much more stable at a high level, >95%, than in the near field case. The high separation rates also indicate that all separation channels are now separating satisfactory as seen in figure 6. Although inhomogeneous particle focusing in the different channels can still be noted a vast improvement is obtained when compared to the corresponding near field situation, Fig. 1.

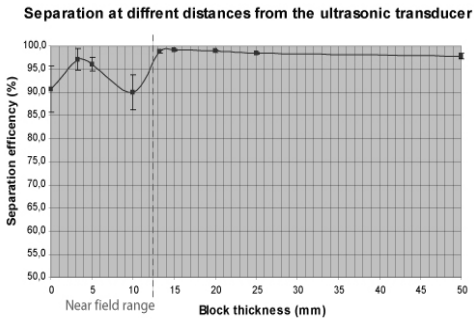

Figure 5. Separation plotted as a function of the distance between the separation channel and the acoustic transducer. It is clear that the separation is much more stable and higher after the near field range has been passed.

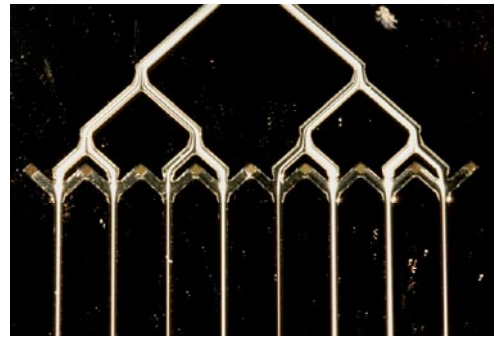

Figure 6. An eight channel parallel structure driven in the ultrasonic far field. The uniform sound profile results in a more homogeneous acoustic separation with no loss of particles into the waste outlets.

It would have been possible to achieve higher separation rates in the near field but at the cost of a lower flow rate and higher acoustic losses. In the near field, a flow rate of merely 0.1 ml/min could be managed if a ~95% separation ratio should be maintained. In the far field, a flow rate five times higher (0.5 ml/min) could be held at the same separation conditions.

REFERENCES

1. Nilsson, A., F. Petersson, and T. Laurell. *Whole blood plasmapheresis using acoustic separation chips*. in *Micro Total Analysis Systems 2006*. 2006. Tokyo, Japan: Society for Chemical and Micro-Nano Systems (CHEMINAS). Volume 1, 314-316
2. Petersson, F., et al., *Separation of lipids from blood utilizing ultrasonic standing waves in microfluidic channels.* The Analyst, 2004. 129 (10): p. 938-943.
3. Jensen, J.A.: Field: A Program for Simulating Ultrasound Systems, Paper presented at the 10th Nordic-Baltic Conference on Biomedical Imaging Published in Medical & Biological Engineering & Computing, pp. 351-353, Volume 34, Supplement 1, Part 1, 1996

INTEGRATED POSITIVE AND NEGATIVE CELL SEPARATION ON AN ON-CHIP MAGNETIC CELL SORTING SYSTEM

Matt Estes[1], Jaephil Do[2], and Chong Ahn[1,2]
Microsystems and BioMEMS Lab
[1]Department of Biomedical Engineering
[2]Department of Electrical and Computer Engineering
University of Cincinnati, Cincinnati, Ohio, 45221 USA

ABSTRACT

This paper presents a new cell sorter that makes use of serial highly selective positive and negative magnetic separation with multiple rounds of on-chip mixing to sequentially incorporate magnetic labels and perform sorting. This system is a low cost, polymer, disposable, modular design that can be integrated with other cell-handling processes.

Keywords: cell separation, magnetic cell sorting, integrated positive and negative cell sorter

1. INTRODUCTION

This paper reports the fabrication and characterization of an innovative on-chip magnetic cell sorting system for multiple surface markers making use of both positive and negative selection. A block diagram of the system is given in Figure 1. The cell sorting system is composed of two micromixers and two magnetic separation chambers, which can be integrated on a chip. This approach as an integrated platform has become desirable as biological researchers map surface proteins to increasingly specific cell subpopulations. No longer is mixing and separation on chip for a single biomarker the pinnacle of micro cell separation science [1]. Additionally, it has been found that transfer between systems for multiple rounds of cell separation results in significant cell loss [2]. Thus the ability to do multiple rounds of separation in a single micro total analysis system (μTAS) device is very desired.

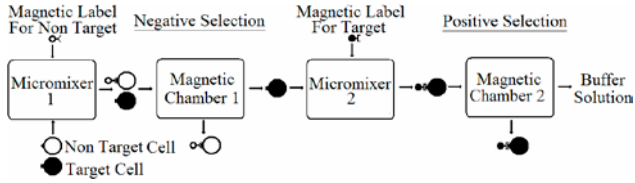

Figure 1. Block diagram of magnetic cell sorting system.

2. DESIGN

The system integrates an existing micromixer device with a paramagnetic array separation device [3,4] as described in Figure 2. The Tesla mixer design was selected because it is a single layer device that circumvents the problems associated with bead loss due to sedimentation at low flow rates in multilayer devices [1], and it has reported adequate mixing at low flow rates. The paramagnetic array based separator was chosen due to its high retention rate and ability to provide a wide dispersion of captured beads, facilitating subsequent quantization of capture rates.

978-0-9798064-0-7/μTAS2007/$20©2007CBMS

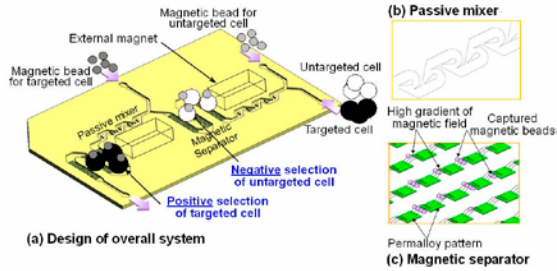

Figure 2. Schematic illustration of serial on-chip magnetic cell sorting system: (a) overall system design, (b) adopted passive mixer, and (c) magnetic separator

3. FABRICATION

The system, as illustrated in Figure 2, was fabricated using two cyclic olefin copolymer (COC) wafers, the first to provide the microfluidic channel and a second to house the paramagnetic array [6]. The fabrication procedure is outlined in Figure 3 and the completed device is shown in Figure 4. The channel height was 130µm and the width was 500µm. The elements of the array themselves were 50µm x 20µm x 1µm in size and they were excited by external NdFeB magnets at a strength of 0.4Tesla.

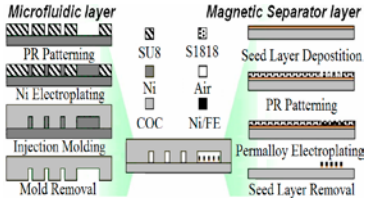

Figure 3. Summary of fabrication procedure

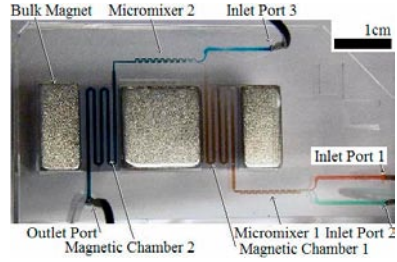

Figure 4. Photograph of the fabricated device

4. EXPERIMENTAL RESULTS AND DISCUSSION

The experimental procedure was carried out as follows using cell substitutes and a variety of flow rates. A mixed cell substitute solution was pumped into the device via Inlet Port 1, seen in Figure 4, and an anti-mouse IgG solution was added via Inlet Port 2. These two solutions were mixed via Micromixer 1 and the mouse IgG substitutes were immobilized in Magnetic Chamber 1. Concurrently anti-streptavidin magnetic beads were added via Inlet Port 3, incorporated via Micromixer 2, and the entire solution then passed through Magnetic Chamber 2 where biotin cell substitutes were positively selected and immobilized by the paramagnetic array.

The immobilized cell substitutes were measured with the aid of fluorescent intensity as seen in Figure 5, and the data for the consecutive negative and positive separations are presented in Figures 6. As can be seen the rate of cell capture increases with higher flow rates, presumably due to better mixing, up to a maximum of roughly 50µl/min. Past that point the rate of capture decreases as the flow rate continues to increase, likely as a result of there being less time allowed for bonding to take place between complementary biological complexes. Further detailed separation results as a function of bead or cell types, flow rates, physical geometry, and magnetic fields are under investigation.

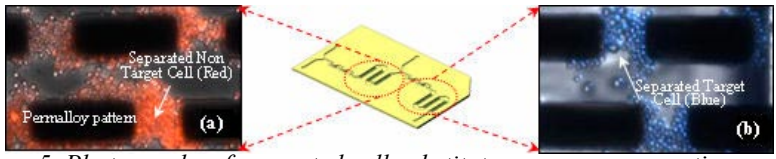

Figure 5. Photographs of separated cell substitutes on a paramagnetic array in: (a) Magnetic Chamber 1 and (b) Magnetic Chamber 2

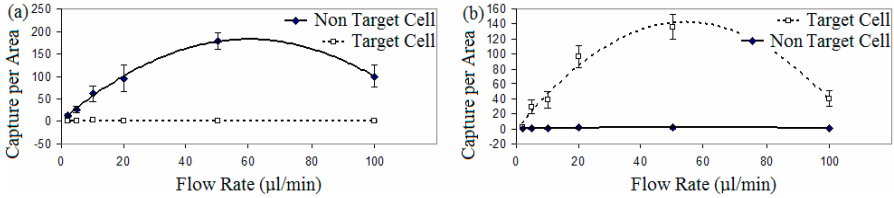

Figure 6. Characterization result with respect to flow rate of: (a) Negative Selection in Magnetic Chamber 1 and (b) Positive Selection in Magnetic Chamber 2

5. CONCLUSION

In this work, for the first time to our knowledge, an on-chip magnetic cell sorting system for multiple surface markers making use of both positive and negative selection has been successfully developed and characterized. The flow rate has been optimized to provide the highest possible yield and selectivity. A functional on-chip cell sorter with the capability of multiple rounds of separation can be envisaged using the on-chip magnetic cell sorting device developed in this work.

ACKNOWLEDGEMENTS

This work was partially supported from the National Institute of Environmental Health Sciences (NIEHS, R01 ES015446) in the National Institute of Health (NIH).

REFERENCES:

[1.] W.H. Tan, Y. Suzuki, N. Kasagi, N. Shikazono, K. Furukawa, T. Ushida, "A lamination micro mixer for µ-immunomagnetic cell sorter," JSME Int. J., Ser. C, **48**:4, pp. 425-435 (2005).

[2.] G.A. Martin Henao, M. Picon, B. Amill, S. Querol, C. Ferra, A. Granena, J. Garcia, "Combined positive and negative selection of allogeneic peripheral blood progenitor cells (PBPC) by use of immunomagnetic methods," Bone Marrow Transplantation, **27**, pp. 683-687 (2001).

[3.] C.C. Hong, J.W. Choi, C.H. Ahn "A novel in-plane passive microfluidic mixer with modified Tesla structures," Lab Chip, **4**, pp. 109-113 (2004).

[4.] J. Do, M. J. Rust and C.H. Ahn, "Electroplated Permalloy Microarrays Embedded Into Polymer Substrate for Disposable Lab-on-a-Chips," Abstracts of the 50th Annual Conference on Magnetism and Magnetic Materials, San Jose, USA, Oct. 30-Nov. 3, pp. 306 (2005).

[5.] H. Suzuki, N. Kasagi, C.M. Ho, "Chaotic Mixing of Magnetic Beads in Micro Cell Separator," Proc. 3rd Int. Symp. Turbulence and Shear Flow Phenomena, Sendai, Japan, June 24-27, pp. 817-822, (2003).

[6] D.S. Kim, S.H. Lee, C.H. Ahn, J.Y. Lee, and T.H. Kwon, "Disposable Integrated Microfluidic Biochip for Blood Typing by Plastic Microinjection Molding," Lab Chip, **6**, pp. 794-802 (2006).

ISOELECTRIC FOCUSING IN A MICRO CHAMBER ARRAY

Ryo Ishibashi, Takehiko Kitamori and Kiyohito Shimura
School of Engineering, The University of Tokyo, JAPAN

ABSTRACT

We have developed a chip-based protein fractionation device, in which two-step isoelectric focusing results in the development of a pH gradient in a square array of hundred chambers (140 nL each). Test samples were fractionated into each chamber, in a total focusing time of less than 30 min.

Keywords: Isoelectric focusing, electrophoresis, protein purification, protein separation

1. INTRODUCTION

Isoelectric focusing (IEF) separates proteins and peptides in a pH gradient according to their isoelectric points (pI), the pH values at which their net charges become zero. The importance of IEF in protein separation has been well established in two-dimensional gel electrophoresis, and now it is in the spotlight in the field of micro TAS by virtue of its high resolving power even at a small scale. IEF is useful for preparative purposes as well, such as purification of proteins and prefractionation of proteomic samples. In this paper, we present a novel chip-IEF device, which can fractionate samples into a hundred chambers, using a new concept of the 'two-step orthogonal IEF'.

2. PRINCIPLE

The concept of the two-step orthogonal IEF is shown in Figure 1. The first IEF results in a parallel separation in ten channels encompassing the entire pH range of the carrier ampholyte used. After the first IEF, the channels are once closed, and re-opened to form channels in the orthogonal direction to the first. The second IEF develops pH gradients within each pH range, roughly a tenth of the first IEF, enabling separation at ten times higher resolution than that achieved in the first IEF. At the end of the second IEF, the entire pH gradient emerges through the array of hundred chambers.

3. EXPERIMENTAL

Two Tempax glass plates (0.7 mm thick) were etched to form identical square arrays of a hundred circular indentations (1 mm i. d., 100 μm deep) (Fig. 2). The two plates are superposed without bonding, facing each other with the etched side. Another glass plate with an opening was bonded to the etched bottom plate to form electrode vessels. The space produced by the indentations between the two plates (14 μL) can be closed to form a hundred isolated chambers or opened to form an array of ten channels for IEF by sliding each other (Fig. 3). The channels can be switched orthogonally. Figure 4 shows the picture of the fabricated micro chamber array chip.

978-0-9798064-0-7/μTAS2007/$20©2007CBMS

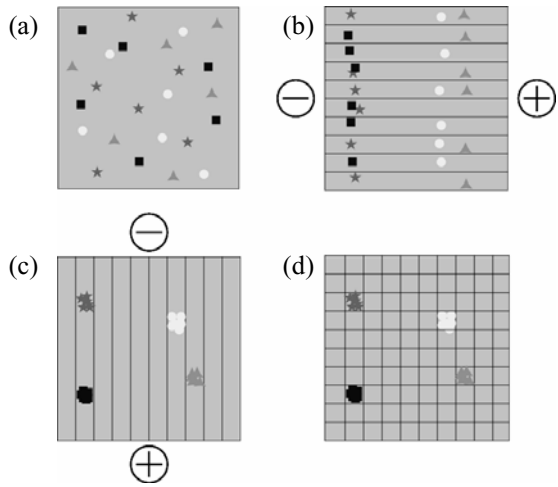

Figure 1. The concept of the two-step orthogonal IEF.
(a) Loading of a protein mixture in the chamber array. Differently shaped dots represent different proteins. (b) The first IEF separation. (c) Change of channel direction and the second IEF separation. (d) Isolation of each chamber.

The chip was coated with polydimethylacrylamide to suppress electroosmosis [1]. Rhodamine-labeled peptide pI markers [2] at 0.4 μM were used as test samples. Platinum plates (10 x 12 x 0.3 mm) were used as the electrodes. The chip was placed on a water cooled (15°C) UV-transparent box, and was illuminated with a UV lamp from the bottom, and the fluorescence was observed from the top. The voltage of 100 V was applied for focusing.

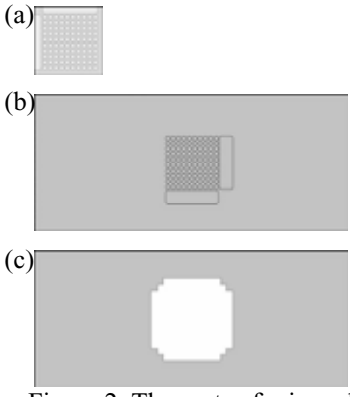

Figure 2. The parts of micro chamber array IEF chip.
(a) Top plate. The bottom surface was etched. (b) Bottom plate. The upper surface was etched. (c) Frame for electrode vessels. The bottom plate and the frame were bonded.

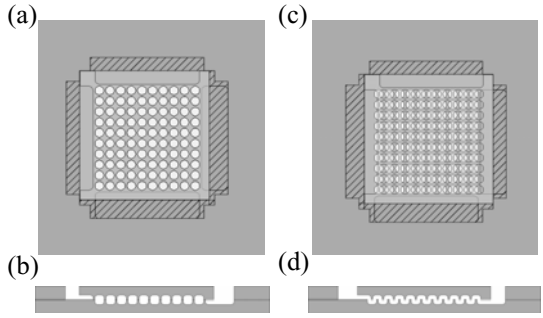

Figure 3. Formation of closed chambers and opened channels by sliding the top plate.
(a), (b) Top view and the cross section of the closed chambers. (c), (d) Top view and the cross section of the opened channels. The hatched area was used for electrode vessels.

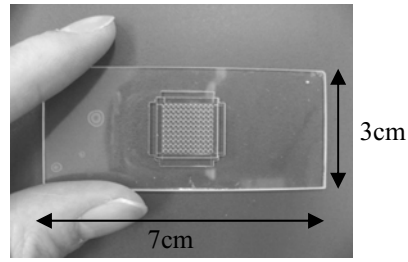

Figure 4. Assembly of the micro chamber array chip.

4. RESULTS AND DISCUSSION

The chip was loaded with a carrier ampholyte solution (pH 3-10, Pharmalyte) containing two peptide pI markers. In the first-step IEF, markers were focused in the ten channels for 8 min at ~70 V cm^{-1} (Fig. 5(a)). Ideally, each marker should align side by side, but some irregularity was observed. In the second-step IEF, each pH zones were further focused for 15 min in the orthogonal direction (Fig. 5(b)). Each of the two markers was recovered in one or two chambers in the array, proving the concept of the two-step orthogonal IEF.

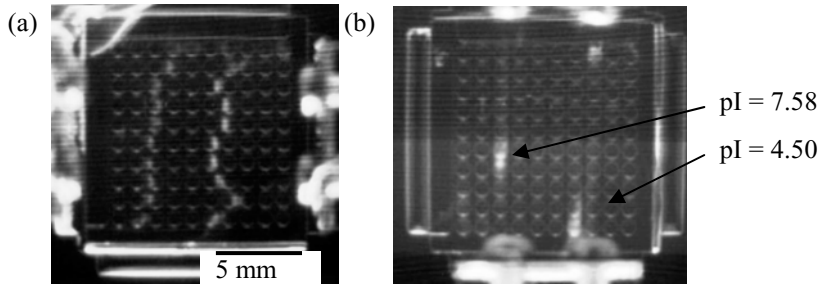

Figure 5. Separation of two pI markers (pI = 4.50 and 7.58) by the micro chamber array IEF chip. (a) First step separation. Left, cathode; right, anode. (b) Second step IEF. Top, cathode; bottom, anode.

5. CONCLUSIONS

We demonstrated the separation of fluorescence labelled peptides with the chip-based protein fractionation device based on the new concept of the two-step orthogonal IEF. The concept of the orthogonal IEF would be useful to develop new IEF apparatuses for protein separation and purification at a micro scale with a low voltage and a short separation time, facilitating biochemical applications of proteins and proteomic analysis.

REFERENCES

[1] H. Wan, M. Ohman, L. G. Blomberg, J. Chromatography A, **924**, 59 (2001)
[2] K. Shimura, K. Kamiya, H. Matsumoto, and K. Kasai, Anal. Chem., **74**, 1046 (2002)

MICROFLUIDIC ZONE REFINING FOR SAMPLE CONCENTRATION

Richard P. Welle and Brian S. Hardy
The Aerospace Corporation, USA

ABSTRACT

This paper reports a new method for separating and concentrating microfluidic samples using repeated freeze-thaw cycles. The technique starts as a microfluidic implementation of zone refining, but the lack of convective currents and the laminar flow typical of microfluidic devices make possible several enhancements on traditional macroscopic zone refining. Devices have been fabricated and tested to demonstrate linear zone refining, flow-through zone refining, and flow-through zone leveling.

Keywords: Zone Refining, Peltier, Concentration, Purification

1. INTRODUCTION

Zone refining is a subset of the broader field of zone melting, which is a well-established class of tools for manipulating impurities in macroscopic samples using solid-liquid and liquid-solid phase transitions [1]. The techniques are based on preferential inclusion or exclusion of solutes or particulates during crystallization of a solvent. In most cases, solutes are more soluble in liquid solvents than in solid solvents, in which case a partial liquid-to-solid phase transition of a solvent/solute system will tend to produce samples in which the solute is selectively concentrated in the remaining liquid phase. For example, slowly freezing salt water will produce a number of crystals of relatively pure water-ice separated by regions of brine. This description, however, illustrates the difficulty of implementing the technique. Once the sample is frozen, it is nearly impossible to separate the regions of relatively high and low concentrations of the solute because they are thoroughly interlocked. On the macroscopic scale, this problem is avoided by inducing circulation in the fluid (to reduce both thermal and concentration gradients), and by restricting the advance of the ice front to very slow rates (1 mm per hour, or less). Alternatively, in macroscopic zone refining, a melt zone is moved repeatedly through a solid sample, always in the same direction, generally causing solutes to move toward one end of the sample. Multiple passes serve to increase the degree of separation accomplished with the technique.

2. MICROFLUIDIC ZONE MELTING

In microfluidics, the small size allows for more precise temperature control and more rapid temperature changes. In addition, the small size typical of microfluidic devices effectively eliminates thermal convection currents and turbulent mixing. As such, one method of freeze concentration potentially useful in microfluidics (but not in macroscopic devices) is to cycle the size of an ice block around a gradually increasing mean. With each freeze cycle, freeze exclusion will push solute away from the central ice block. During the melt cycle, some of the solute will travel back toward the ice block by diffusion, but the cycle time can be short compared to typical diffusion time scales, so the net transport is away from the ice. This suggests a simple concentration device, in which a sample is contained in a flow channel adjacent to a cooling unit that can be operated so as to oscillate the temperature and cause the ice to grow as illustrated in figure 1. After growing the ice block the full length of the channel, most of the solute will be concentrated in the far end of the channel. More useful yet may be a flow-through zone refining system, as illustrated

978-0-9798064-0-7/μTAS2007/$20©2007CBMS

schematically in figure 2. In this device, fluid enters through the inlet at the left. In the triangular region, the sample is maintained mostly in the solid phase, with one or more melt zones (created by linear resistive heaters) moving across the sample from bottom to top. The motion of the phase boundaries causes any solutes or particles present in the system to move toward the top edge. (Solutes having a higher solubility in the solid phase than in the liquid phase will move in the opposite direction.) The output is divided into two or more channels, such that different outlet channels carry liquids with higher or lower solute concentrations. Any solute present is selectively moved toward the upper of the two outlets, while relatively pure solvent flows to the lower outlet. This is a flow-through device in that the inlet flow is continuous, and there is a net transport of material from left to right through the liquid portions of the sample. The relative concentration of the solute in the two outlets can be controlled by adjusting the flow rate and zone cycling rate.

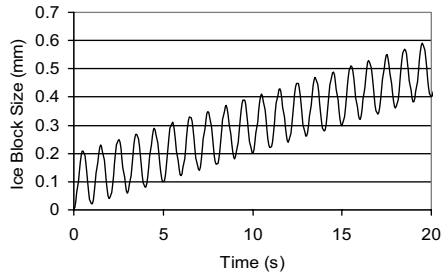

Figure 1. Ice block size oscillating around a gradually increasing mean.

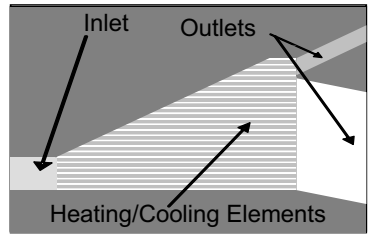

Figure 2. Schematic diagram of a microfluidic flow-through zone refining device.

A closely related technique, know as zone leveling, is useful for mixing. In microfluidic devices, mixing is problematic because almost all fluid flow is laminar. This problem can be overcome in some cases using a device similar to that shown in figure 2 except that there would be two inlets, and a single outlet. In operation, two fluids entering through the two inlets would pass through the section of zone transport. The zones, instead of moving repeatedly in one direction across the device, would move alternately from top to bottom and from bottom to top. This method re-distributes any solutes present in either of the two inlet streams across the full outlet stream.

3. EXPERIMENTAL RESULTS AND DISCUSSION

Figure 3 shows three frames from a video of a microfluidic channel containing red dye dissolved in water and undergoing the gradually increasing freeze-melt cycle illustrated in figure 1. The flow channel is about 25 microns deep and 700 microns wide, and is adjacent to a linear thermoelectric junction designed for creating a Peltier valve [2]. In a linear junction, there is a thermal gradient between the hot and cold junctions that is in the plane of the image. Thus, the coldest spot is at the center of the image. When power is first applied, the center cools enough to form a thin region of ice. Because of supercooling [3],

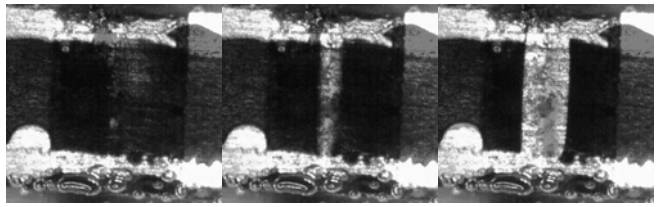

Figure 3. Photos of a 300-micron-wide dye-free zone created by cyclically freezing and thawing a sample of red dye in water in a 700-micron-wide microfluidic channel.

the initial ice block forms very rapidly, trapping some of the solute (red dye). Once a seed crystal is present, it is possible to alternately shrink and grow the ice around a gradually increasing mean. For this experiment, the cycle period was about one second, with an amplitude (measured as the change in ice plug size) of about 100 microns. After about 20 cycles, a region about 300 microns wide showed a substantially reduced dye concentration, while the fluid immediately adjacent to the ice front showed an enhanced dye concentration. The net ice growth rate was thus about 1 mm/min, or two orders of magnitude faster than growth rates possible in macrofluidic devices.

A flow-through zone refining system has the potential for much higher throughput than a linear device. We have built such a device by fabricating a shallow (25 microns deep) but wide fluid channel over the surface of a commercial thermoelectric module. The thermoelectric module is used to freeze a sample of water containing a solute. The wall of the channel also incorporates a set of 96 parallel thin-film electrical resistive heaters (spaced on 275 micron centers). The heaters can be operated independently, allowing them to be switched on or off to control the phase of the water in the channel immediately adjacent to each of the heaters. By switching the heaters sequentially, a liquid zone is made to cross the channel. A portion of the device is shown in the photograph in figure 4. In the image, the horizontal lines are the linear heaters, and the fluid channel is bounded on a diagonal from the lower left to the upper right. The dark filaments near the center of the image are places where concentrated dye leaked into the interface between the flow channel and the heater module. The zone of enhanced dye concentration near the upper right was obtained after about 10 melt zones have moved through the system. The zones are 1 mm wide, and move at 70 microns/s (250 mm/hr).

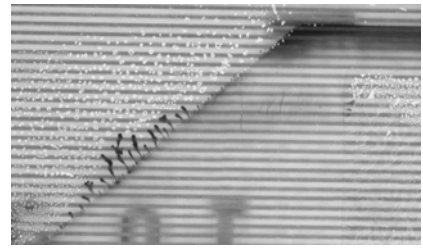

Figure 4. Photograph of a microfluidic flow-through zone refining device.

4. CONCLUSIONS

Because of the lack of thermal convection currents, and the predominance of laminar flow, zone melting and zone refining appear to be tools ideally suited for microfluidic applications. We have developed concepts for a number of microfluidic devices incorporating zone melting techniques, to accomplish both separations and mixing. We have demonstrated a simple linear sample concentration device, and flow-through zone refining and zone leveling devices.

ACKNOWLEDGEMENTS

This work was supported under The Aerospace Corporation's Independent Research and Development Program.

REFERENCES

[1] W. G. Pfann, *Zone Melting*, John Wiley & Sons, New York, 1966.

[2] R. P. Welle and B. S. Hardy, "Fabrication and Characterization of Fast-Acting Peltier-Actuated Microvalves," *Proceedings of MicroTAS 2005*, Boston.

[3] R. P. Welle, C. Chrystal, and B. S. Hardy, "Standoff Pressures and Thermal Characterization of the Peltier-Actuated Microvalve," *Proceedings of the Twenty Fifth International Conference on Thermoelectrics,* IEEE, Vienna, 2006.

MODE TRANSITION & ITS MECHANISM OF RNA/DNA TRAP BY ELECTRIC AND HYDRAULIC FORCE FIELD IN MICROFLUIDIC TAPER SHAPE CHANNEL

Yuzuru Takamura[1], Wako Nagasaka[1], Kunimitsu Ueno[1], Yuichi Tomizawa[1], and Eiichi Tamiya[1,2]

[1]Japan Advanced Institute of Science and Technology (JAIST), JAPAN

[2]Osaka University, JAPAN

ABSTRACT

The accumulation of flowing DNA is observed near the narrowest part of taper shape microfluidic channel when both hydro pressure and electric field are applied in the opposite direction. The position and the shape of the accumulated DNA are changed with increasing the electric force and decreasing the hydro pressure, showing mode transition. To discuss the mechanism, three forces act on DNA, i.e. dc dielectric force, hydro drag force, Lorentz force, are estimated in the channel, and numerical simulation is also performed. It is revealed that the dielectric force is 10^{-4} times smaller than the other forces and the mode transition is described by the change of the balancing position of Lorentz force and hydraulic force.

Keywords: Biomolecule manipulation, DNA/RNA extraction, purification.

1. INTRODUCTION

Extraction and purification of DNA/RNA from cells on chip is an important issue for practical DNA-based micro total analysis systems. We have reported that the DNA is selectively trapped and accumulated at the narrowest position of taper shape channel when electric force and hydro drag force are applied simultaneously in opposite direction[1]. Using this technique, DNA, RNA, Protein, organelles can be trapped, concentrated, and extracted in mixed solution[2]. However, the trap mechanism, is still not clear.

In this paper, we investigated trapping feature of DNA at various conditions, especially from the view point of the mode transition of the accumulating shape and its position of trapped DNA. Then to describe the mechanism, the three forces act on a trapping DNA such as; dc dielectrophoretic (DEP) force, hydro drag force, and Lorentz force, were directly measured in the channel. Based on these values, we discuss about the mode transition and the trap mechanism with numerical simulation method .

2. EXPERIMENTAL

The micro channel was made of polydimethylsiloxane (PDMS) using a conventional photolithograph technique with SU-8 thick resist. The channel was totally 30 mm long, 100 μm wide, 10 μm deep, and at the center of the channel, a narrow part of 10 μm wide was designed as shown in figure 1. A solution of T4 DNA stained by YOYO1 in 0.5 Tris borate EDTA buffer was introduced into the channel. The hydro drag force and the electric force were applied to the solution at the same time in mutually reverse directions by a syringe and dc power supply, respectively. By these force fields, DNA was to be trapped near the narrow position. The motion of each DNA molecule was observed by a fluorescence

978-0-9798064-0-7/μTAS2007/$20©2007CBMS

microscope with high sensitive CCD camera, and was stored in PC as digital data. The electric field, and the flow velocity of the solution were numerically calculated using COMSOL Multiphysics software. The Lorentz force for DNA was calculated from the electric field and charge density of DNA molecule. Hydro drag force was calculated from the solution velocity and experimental value of Lorentz force at a condition when DNA was stopped by balancing the hydro drag force and Lorentz force. DEP force for DNA strongly depends on the solution concentration. We estimated DC DEP force at typical trap condition (DC 20 V, 5 hPa) from frequency dependence of AC DEP force at 2 kVpp, 0.1-100 kHz by extending the value to frequency = 0. The AC DEP force is experimentally measured in our channel by counter hydro drag force to push away DNA against given AC DEP force.

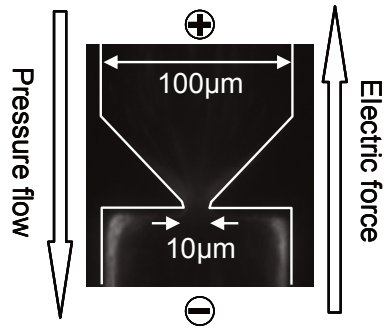

Figure 1. Shape and size of narrowest part of taper shape channel for DNA/RNA trap.

3. RESULTS AND DISCUSSION

Typical photograph of trapped DNA were shown in figures 2. At applied voltage =20V, the DNA molecules are trapped near the side wall. With increase voltage up to 35V, it makes a mode transition of changing its shape and position from side to center. Increasing voltage more to 40V, the shape was elongated along with flow. The condition for the mode transition was investigated at various pressure and voltage. Figure 3 shows the condition map of each trap pattern. From these results, the trap pattern is approximately depend on the ratio of pressure and voltage, i.e. the same ratio shows the same pattern. To discuss the mechanisms of the trap and the mode transition, we estimated three forces act on DNA, i.e. dc dielectric force, hydro drag force, Lorentz force. As result, the DEP force is 10^{-4} times smaller than the other Lorentz force and hydro drag force, and negligible in our trap. By actual motion of the trapped DNA, our trap seems to be caused by the dynamic motion of trap molecule around the balanced position of the two forces, dc electric force and hydro drag force. If this hypothesis is true, the trap position should be located near the area where the two forces are balanced, and the balanced position should move as changing the ratio of

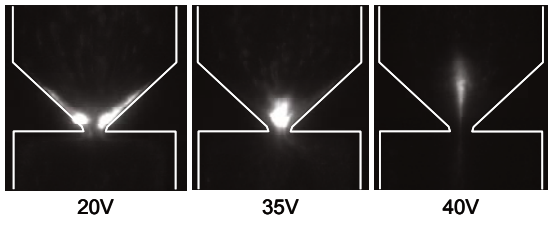

Figure 2. Typical photograph of trap DNA. It shows mode transition with increasing applied voltage.

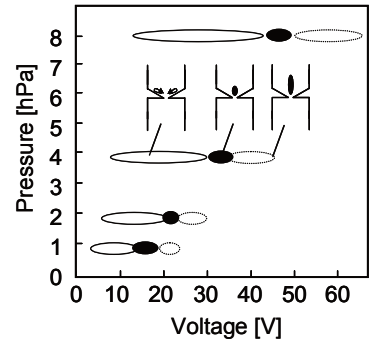

Figure 3. Condition map for each trap pattern.

the two forces. Figures 4 show the typical results of numerical simulation for the total force act on each DNA molecule; left, center, and right figures represent at high pressure / low voltage, middle pressure / middle voltage, and low pressure / high voltage conditions, respectively. The gray area shows the position where the hydro drag force and electric force is nearly balanced. These areas are well correspond with the trap positions in figures 2. The mode transition is clearly described by the change of the balanced position. Chou et al. [3] reported DNA trap by insulated DEP (iDEP) with taper shape channel. In our case, DEP is negligibly small and hydro drag force and Lorentz force seems to play main role for trap mechanism.

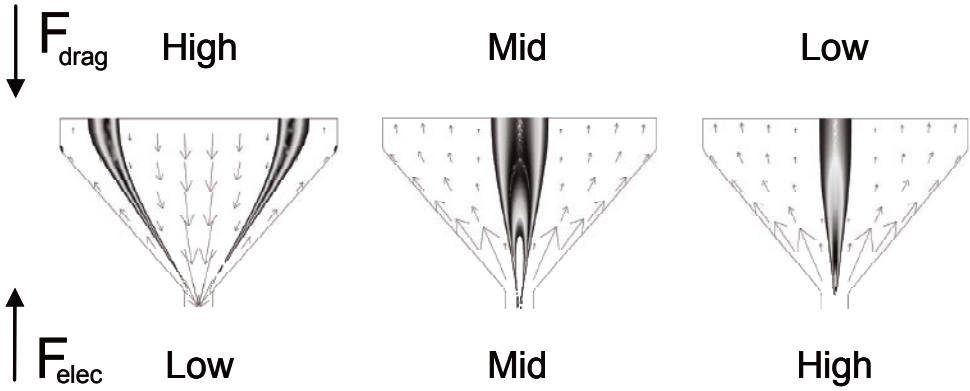

Figure 4. Numerical simulation of the total force act on each DNA molecule. Gray area shows the position where the hydro drag force and electric force is nearly balanced.

4. CONCLUSIONS

The position and shape of trapped DNA by hydro drag force and electric force in taper shape channel was investigated at various condition. The position and the shape changed as a function of the ratio of the electric force and the hydro drag force, and also those were well correspond with the balancing position and the shape of the electric force and the hydro drag force calculated by numerical simulation. On the other hand, three forces act on DNA, i.e. dc dielectric force, hydro drag force, Lorentz force, were estimated in the channel with typical trap condition. It is revealed that the dielectric force is 10^{-4} times smaller than the other forces, and hydro drag force and Lorentz force were major forces in this trap.

REFERENCES

[1] Y. Takamura et al., *DNA trap-and-release element employing electric and hydro drag force fields for on-chip pre-treatment*, Proc. Micro Total Analysis Systems 2002, Nara, Kluwer Academic Publisher, The Netherlands, *1*, pp. 317-319, (2002).

[2] Y. Tomizawa et al., *Biomelecule and organelle trap using electric and hydrodrag force fields in taper shaped micro channel*, Proc. Micro Total Analysis Systems 2006, Tokyo, Japan Academic Association Inc. for Copyright Clearance, Tokyo, *1*, pp. 900-902, (2006).

[3] Chia-Fu Chou, et al., *Electrodeless Dielectrophoresis of Single- and Double-Stranded DNA*, Biophys. J., *83*, pp. 2170-2179, (2002).

NOVEL ONLINE CONCENTRATION OF DNA TO SHORTEN MICROCHANNEL LENGTH USING HETEROGENEOUS BUFFER COMBINATIONS ON MICROCHIP ELECTROPHORESIS

Hideya Nagata[1], Yuichiro Yoshida[1], Tomomi Ishido[1], Mitsuru Ishikawa[1] and Ken Hirano[1, 2]

[1]Health Technology Research Center, National Institute of Advanced Industrial Science and Technology (AIST), Japan, [2]PRESTO, Japan Science and Technology Agency (JST), Japan

ABSTRACT

We have developed a novel high-resolution separation technique of DNA using online concentration based on a heterogeneous combination of a sample buffer and a separation buffer. This technique allows the length of microchannels to be shorter than that of current ones by a factor of 3. This achievement will make it possible to fabricate compact diagnosis devices.

Keywords: DNA, online concentration, heterogeneous buffer combinations, taurine

1. INTRODUCTION

Microchip electrophoresis (MCE) is one of the most successful miniaturized analysis systems, thereby allowing minimal sample and reagent consumption, short analysis time, and automation of manual routine work. Hand-held diagnosis devices have highly been required to obtain experimental data as fast as possible for point-of-care testing use. To meet this requirement, we have developed an online concentration technique of DNA using a heterogeneous combination of a sample buffer and a separation buffer on MCE devices.

2. EXPERIMENTAL

DNA separation was carried out on a MCE device (SV1100, Hitachi, Tokyo). Images of DNA separation were photographed using an inverted fluorescence microscope (Eclipse TE2000-U, Nikon, Tokyo) equipped with a 4×objective lens, a highly-sesitive EB-CCD camera (C7190, Hamamatsu photonics, Hamamatsu), and an optical filter set (G-2A: for excitation around 510-560 nm; for emission longer than 690 nm, Nikon, Tokyo). A Tris-acetate-EDTA (TAE) buffer and a Tris-taurine-EDTA (TTE) buffer were prepared. A TAE buffer was composed of 40 mM Tris-acetate and 1 mM EDTA, pH 8.5. A TTE buffer was composed of 89 mM Tris, 29 mM taurine and 0.1 mM EDTA, pH 9.1. Separation matrices were prepared by dissolving various amounts of hydroxyethyl cellulose (HEC) in a TAE buffer. Concentrations of the final HEC solutions were 1–4 wt% of HEC. Ethidium bromide (EtBr) was mixed into 1–4 wt% HEC solutions. The final concentration of EtBr was 0.5 ng/μL. Unless otherwise noted, these HEC solutions were used as separation matrices. The samples used were 100-bp DNA ladders (Bio-Rad Laboratories, Tokyo) or 10-bp DNA ladders (Invitrogen, Tokyo), and tested on a microchip (i-chip 3 DNA, Hitachi Chemical, Tokyo). A solution of DNA was prepared by dissolving DNA in a TAE buffer or a TTE buffer. In the current paper, we call a combination of a HEC solution in a TAE buffer and a DNA solution in a TAE buffer a “homogeneous buffer combination” because

978-0-9798064-0-7/μTAS2007/$20©2007CBMS

of the common use of TAE. In contrast, we call a combination of a HEC solution using a TAE buffer and a DNA solution using a TTE buffer a "heterogeneous buffer combination" because of the combination of TAE and TTE.

3. RESULTS AND DISCUSSION

A DNA sample was concentrated and sharp bands appeared using a heterogeneous buffer combination (Fig. 1B), while a DNA sample was not concentrated using a homogeneous buffer combination (Fig. 1A). We optimized separation conditions by varying concentration of a HEC solution. Figure 2 shows dependence of resolution on HEC concentration and on DNA size. A 2% HEC solution was found to be the most suitable concentration for high-resolution separation of DNA (Fig. 2B). Moreover, this solution was easily introduced into the microchannels on a chip because of its low viscosity. Resolution of DNA smaller than 600 bp was improved 17–41% in a heterogeneous buffer combination than in homogeneous buffer combinations (Fig. 2A). Theoretical plate numbers using a heterogeneous buffer combination were 40–108% higher than those obtained by the use of a homogeneous buffer combination (Fig. 3A), because DNA samples were highly concentrated.

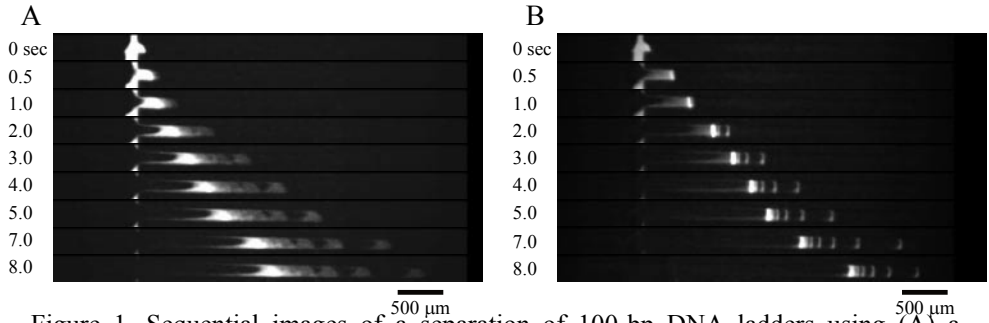

Figure 1. Sequential images of a separation of 100-bp DNA ladders using (A) a homogeneous buffer combination and (B) a heterogeneous buffer combination. PMMA microchips were used with a simple crosschannel, 100 μm in width and 30 μm in depth. The distance from the channel intersection to the sample, sample waste, buffer, and buffer waste wells was 5.25, 5.25, 5.75, and 37.5 mm, respectively. The effective separation channel length was 30 mm.

The use of a high concentration of glycerol (>5%) in a sample buffer of DNA causes band broadening for DNA larger than 300 bp [1]. The current heterogeneous buffer combination overcame the problem of band broadening in the sample with a high glycerol concentration (Fig. 4). Also, baseline separations of 10-bp DNA ladders were attained within 150 s on a separation length of 30 mm using the current heterogeneous buffer combination (Fig. 5). Furthermore, dependence of resolution of DNA fragments on separation length of a channel was obtained (figure not shown.) A length of 10 mm was found to be the most suitable length for high-resolution and highly-sensitive separation of DNA. Thus, a possible channel length will be shortened from 3 cm to 1 cm using the current heterogeneous buffer combination.

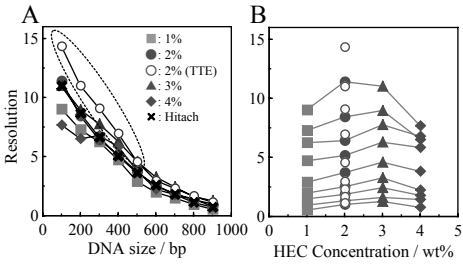

Figure 2. Dependence of resolution of 100-bp DNA ladders on (A) DNA size and (B) HEC concentration. (○) 2% (TTE) a heterogeneous buffer combination; (×) Hitachi i-chip kit: 0.7% hydroxylpropyl methylcellulose (HPMC), pH 9 (Hitachi Chemical, Tokyo). Other conditions were tested in a homogeneous buffer combination.

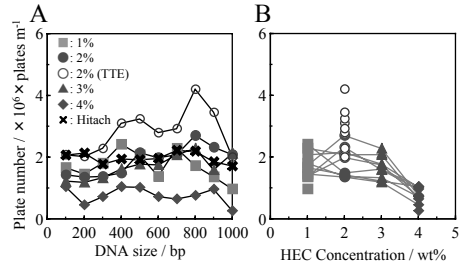

Figure 3. Dependence of plate number on (A) DNA size and (B) HEC concentration.

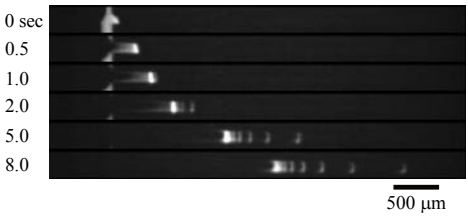

Figure 4. Sequential images of a separation of 100-bp DNA ladders in a sample solution which contained a 5% glycerol using a heterogeneous buffer combination.

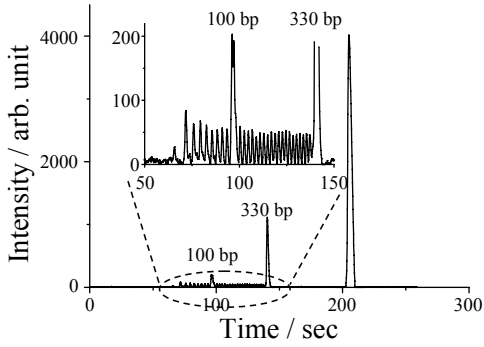

Figure 5. Microchip electropherograms of 10-bp DNA ladders using a heterogeneous buffer combination.

4. CONCLUSIONS

We have developed a novel high-resolution separation technique of DNA using an online concentration technique based on a heterogeneous buffer combination. This technique allows the length of microchannels to be shorter than that of current ones by a factor of 3. This achievement will make it possible to fabricate compact diagnosis devices.

REFERENCES

[1] J. Sambrook, E.F. Fritsch and T. Maniatis, 1992 Molecular Cloning: A. Laboratory Manual. Second edition. pp. 12.108, Cold Spring Harbor Laboratory Press,Cold Spring Harbor, NY.

ON-CHIP LIQUID CHROMATOGRAPHY - ATMOSPHERIC PRESSURE IONIZATION - MASS SPECTROMETRY

Ville Saarela[1], Markus Haapala[2], Jaroslav Pól[2], Nisse Kalkkinen[3], Marko Hukka[3], Kai Kolari[4], Raimo A. Ketola[2], Risto Kostiainen[2], Tapio Kotiaho[2,5] and Sami Franssila[1]

[1] Micro and Nanosciences Laboratory, Helsinki University of Technology, Finland
[2] Division of Pharmaceutical Chemistry, University of Helsinki, Finland
[3] Institute of Biotechnology, University of Helsinki, Finland
[4] VTT Technical Research Centre of Finland, Espoo, Finland
[5] Laboratory of Analytical Chemistry, University of Helsinki, Finland

ABSTRACT

We introduce a liquid chromatography (LC) chip which consists of an anodically bonded silicon-glass wafer stack with a particle column packed against a high aspect ratio plasma etched micro pillar frit. The design of the microchip enables both fluorescence detection through the transparent glass cover and mass spectrometric (MS) detection via attached capillary.

Keywords: Liquid Chromatography, Mass Spectrometry, Micro Column, Frit

I. INTRODUCTION

Liquid chromatography (LC) is a common separation method that has also been applied in microchip devices [1].

Our group has worked on miniaturized devices for mass spectrometry. We have presented a nebulizer chip that enable coupling of small liquid (0.1–10 µL/min) or gas phase flows with mass spectrometry (MS) [2, 3]. Depending on configuration the nebulizer chips can be used for either atmospheric pressure chemical ionization (APCI) [4], atmospheric pressure photoionization (APPI) [5] or sonic spray ionization (SSI) [6]. So far we have used the nebulizer chip with capillary LC, but we are working towards integrating the separation step with the nebulizer chip. In this paper, the design and fabrication process of an LC chip is presented with the first experimental results of chip-LC–chip-APCI–MS.

II. EXPERIMENTAL

The layout is shown in Figure 1. The fabrication of the LC chip is as follows: thermal oxidation of a silicon wafer, lithography and oxide etching, DRIE of silicon using the Bosch process, oxide removal, and anodic bonding to a glass wafer. The width of the column is 200 µm, and the etched depth is 170 µm in order to enable insertion of 150 µm (o.d.) capillaries directly into the channel.

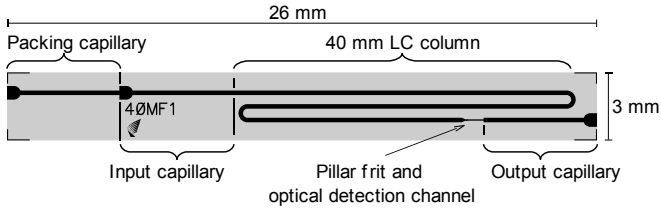

Figure 1. Layout of an LC chip with meander channel.

978-0-9798064-0-7/µTAS2007/$20©2007CBMS

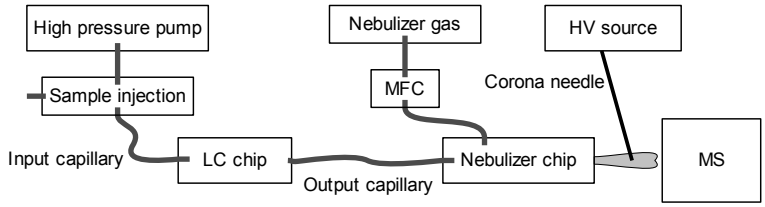

Figure 2. Schematic of the LC-APCI-MS measurement set-up.

To pack the LC column with particles, a slurry is prepared in a vial by mixing the particles with ethanol/acetone mixture (50/50). The slurry is loaded to the chip by applying up to 100 bar pressure to the vial which is connected to the chip with a fused silica capillary. After the channel is filled with the particles, it is rinsed with pure solvent and dried with nitrogen. The capillary used for packing is removed by snapping a part of the chip away, and a portion of the particles is removed from the channel to allow insertion and gluing of a clean input capillary. Output capillary is used to connect the LC chip with the nebulizer chip. A schematic measurement set-up is shown in Figure 2.

After packing of the channel the separation capability was tested with a sample containing corticosterone and 5α-pregnan-3β-ol-20-one. The injection and pumping was done with an Agilent 1100 series capillary LC injector and pumps. Concentrations of the analytes were 10 µM and injection volume was 1 µL. Mobile phase flow rate was 3 µL/min and a gradient elution with water and acetonitrile was performed.

III. RESULTS AND DISCUSSION

A SEM image of the pillar frit is in Figure 3 (a). The column was successfully packed using either 5 µm or 2.5 µm fused silica C18 particles. Figure 3 (b) shows an example of a packed channel. LC-APCI-MS results are shown in Figure 4. The quality of the separation remains to be improved. Issues to attend to include dead volumes at interconnections, optimal packing process and surface modification of the channel walls. Integrating the LC column and the nebulizer part on a single chip should minimize post-column band broadening. Pre-column dead volume at sample inlet can be overcome by focusing the sample at the beginning of the LC column by employing suitable gradient elution.

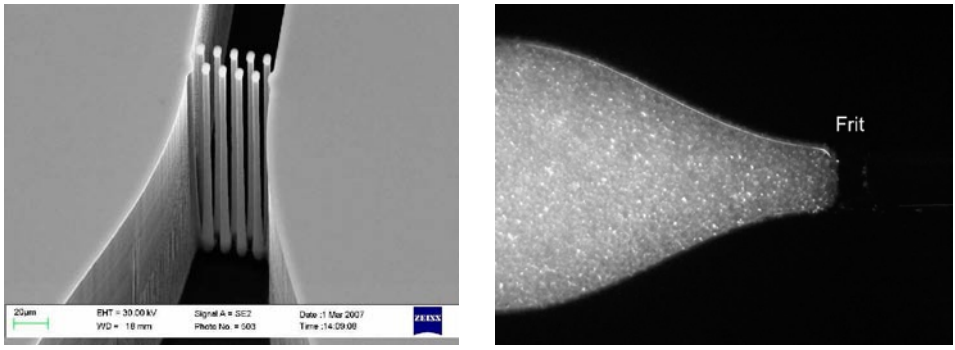

(a) *(b)*

Figure 3. Tilted angle SEM view of the micro pillar frit (a) and a picture of the LC channel packed with a 5 µm particles (b). The channel width narrows down from 200 µm to 50 µm before the micro pillar frit.. The nominal pillar width and the gap between pillars is 5 µm.

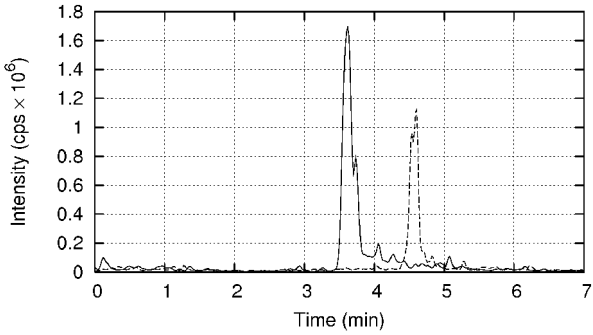

Figure 5. Extracted ion chromatograms of corticosterone (solid line) and 5α-pregnan-3β-ol-20-one (dashed line) measured with LC-APCI-MS.

IV. CONCLUSIONS

After successful demonstration of the LC-on-chip we will integrate a nebulizer on the same chip to enable easy MS interfacing and minimizing dead volumes. The fabrication processes of the LC and the nebulizer [2] chips are very similar, which enables easy integration. Challenges of the integration include mixing of the liquid flow with nebulizer gas, as well as thermal management between the LC part and the heated nebulizer part.

ACKNOWLEDGEMENTS

The project has received funding from the Chemical Sensors and Microanalytical Systems graduate school (CHEMSEM), Academy of Finland and Finnish Funding Agency for Technology and Innovation (Tekes).

REFERENCES

[1] R. E. Majors, *Anatomy of an LC Column: From the Beginning to Modern Day*, LCGC North America, 24 (**Aug 1**), 742–753 (2006).

[2] S. Franssila, S. Marttila, K. Kolari, P. Östman, T. Kotiaho, R. Kostiainen, R. Lehtiniemi, C.-M. Fager and J. Manninen, *A Microfabricated Nebulizer for Liquid Vaporization in Chemical Analysis*, J. Microelectromech. Syst., **15**, 1251–1259 (2006).

[3] V. Saarela, M. Haapala, R. Kostiainen, T. Kotiaho, and S. Franssila, *Glass microfabricated nebulizer chip for mass spectrometry*, Lab Chip, **7**, 644–646 (2007).

[4] P. Östman, S. Jäntti, K. Grigoras, V. Saarela, R. A. Ketola, S. Franssila, T. Kotiaho and R. Kostiainen, *Capillary liquid chromatography–microchip atmospheric pressure chemical ionization–mass spectrometry*, Lab Chip, **6**, 948–953 (2006) .

[5] M. Haapala, L. Luosujärvi, V. Saarela, T. Kotiaho, R. Ketola, S. Franssila, and R. Kostiainen, *A Microchip for Combining Gas Chromatography or Capillary Liquid Chromatography with Atmospheric Pressure Photoionization-Mass Spectrometry*, Anal. Chem, **79**, 4994–4999 (2007).

[6] J. Pól, T. J. Kauppila, M. Haapala, V. Saarela, S. Franssila, R. A. Ketola, T. Kotiaho, and R. Kostiainen, *Microchip Sonic Spray Ionization*, Anal. Chem., **79**, 3519–3523 (2007).

PARTICLE SEPARATION VIA ADJUSTABLE VELOCITY PROFILE GENERATED BY EOF AND PRESSURE DRIVEN FLOW

Y. F. Yu[1], P. H. Yap[2] and A. Q. Liu[1]

[1] School of Electrical & Electronic Engineering
Nanyang Technological University, Singapore
[2]Defence Medical & Environmental Research Institute
DSO National Laboratories, Singapore
([†]Corresponding author. Tel: +65-6790 4336; Fax: +65-6793 3318; Email: eaqliu@ntu.edu.sg)

ABSTRACT

This paper presents an experimental investigation of the effect of velocity profile on the particle separation. Electroosmosis flow (EOF) and pressure driven flow are combined to adjust the velocity profile arbitrarily. Compared with the previous studies on the interface position, this paper finds out that the velocity profile contributes more significantly to the separation performance. In addition, the experimental results show that the velocity profile with higher velocity gradient has better separation performance. The whole design features simple manipulation, high stability and high separation performance, making it promising for particle separation applications.

Keywords: Particle separation, EOF, velocity gradient, separation performance

1. INTRODUCTION

Particle separation is a useful and indispensable technique in the field of drug production, clinical diagnosis, environmental assay and biomarcomolecule analysis. Recently, there are many continuous separation techniques developed in microfuidic devices, such as pinched flow fractionation, continue dielectrophoresis, hydrodynamic chromatography, laser manipulation and acoustic separation. In this paper, the flow fractionation method is used, which is a relatively simple and high throughput technique [1,2]. Different sizes of

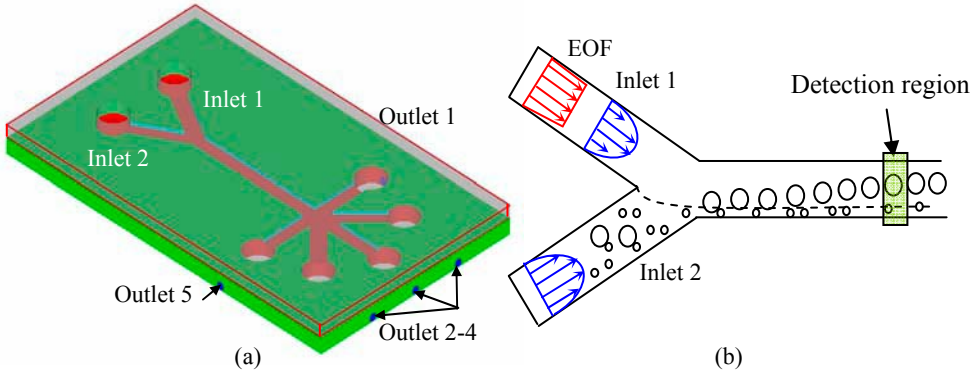

Figure 1. The schematic of (a) micro fluidic separation chip with multi-branches and (b) electroosmotic flow for controlling the separation performance.

978-0-9798064-0-7/μTAS2007/$20©2007CBMS

Particles are separated at a Y-sturcture due to velocity gradient field. The separation performance is affected by the velocity profile, which is adjusted by electroosmosis flow (EOF) [3].

2. WORKING PRINCIPLES

The schematic of the microfluidic separation chip is shown in Fig. 1a. It consists of two inlets and multibranches of outlets, all are arranged in symmetry. A special design is that all the outlets are lead out from the side rather than from the top. Therefore, the outlets are always under the same pressure regardless the difference of liquid volume. Both inlets have pressure driven flow but the pressure driven flow is combined with EOF in inlet 1 (Fig. 1b).

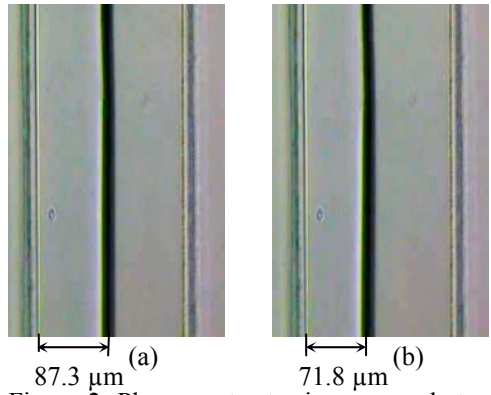

Figure 2. Phase contrast microscope photos under different applied voltages. (a) 290 V; (b) 390 V.

The velocity profile in the horizontal channel is adjusted by the applied voltage and the chemical properties of fluid. When the pressure driven flow and EOF have the same order of magnitude, the tenability of the velocity profile become obviously.

Particles with different sizes in stable velocity field bear different magnitudes of forces, which is related to the velocity gradient and the particle's diameter. In our experiments, particles are suspended in a liquid, so that the effect of gravity is negligible. Under the same velocity gradient, large particles move faster than small particles (Fig. 1b).

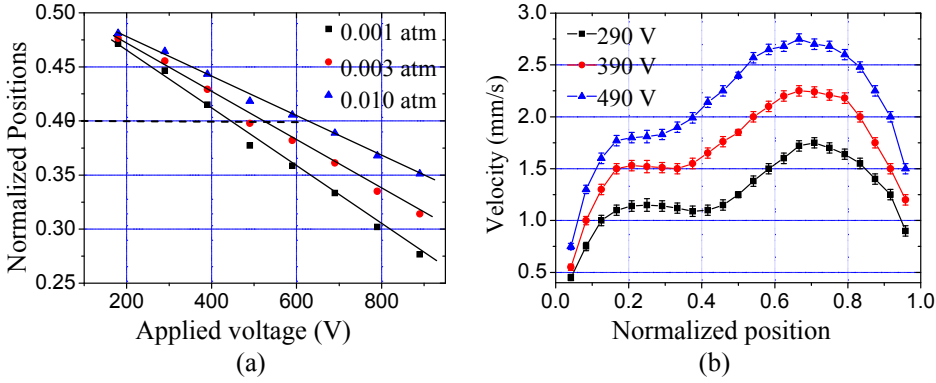

Figure 3. (a)The relationship between interface position and applied voltage; (b) The combined velocity profile under different applied voltage.

3. EXPERIMENTS AND RESULTS

The chip is fabricated using the soft-lithography with polydimethysiloxane (PDMS). Glass slide is used as the substrate and surface plasma treatment is used for bonding. The aqueous NaCl solution (0.001 mol) injected into inlet 1 is driven by pressure and EOF. Polystyrene particles with the size of 2 μm and 5 μm are injected into inlet 2 with the aqueous glycerol

(10%). The same hydrostatic pressures are applied on both inlets.Voltage difference is applied between inlet 1 and outlet 1. Inlet 2 and other outlets are suspended. The positions of interfaces between these two liquids are measured through the phase contrast microscope images (Fig. 2). A drastic intensity change at the interface because of the little difference of refractive index between the two liquids. In addition, the velocity profiles are monitored by the micro Particle Image Velocimetery (μPIV).

When the applied voltage is increased from 290 to 390 V, the distance between the interface and the left wall is decreased from 87.3 to 71.8 μm (Fig. 2). A linear relationship between the interface's position and the applied voltage under the constant hydrostatic pressure is observed (Fig. 3a). In order to fix the interface at the same position, the applied voltage is increased when the applied pressure is increased. The combined velocity profile is modified by applied voltage (Fig. 3b).

Figure 4 presents the separation performance of the chip, i. e. the normalized positions of the particles at the dectection region. The particle number is counted under microscope at the detection region as shown in Fig. 1b. Fig. 4a and 4b shows the distribution of the two particles (2-μm & 5-μm) along the normalized position without and with EOF, respectively. Without applying EOF, the particles have a larger distribution along the normalized position and the separation between the two particles are not distinct and some of them are overlapped. However, when the EOF is applied, both particles have narrower distribution and are also well separated.

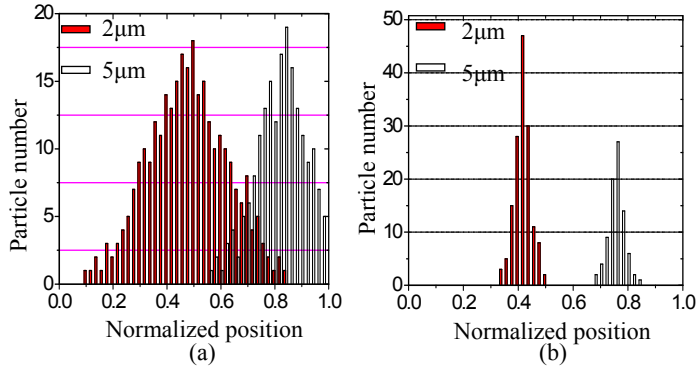

Figure 4. The separation performance. (a) without EOF; (b) with EOF (900 V).

4. CONCLUSIONS

In conclusion, the combination of EOF and pressure driven flow changes the velocity profile in flow fractionation, which can afford high effectiveness in the separation performance. This technique provides a simple, flexible and versatile way of particle sorting.

REFERENCES

[1] M. Yamada, M. Nakashima and M. Seki, Pinched flow fractionation: continuous size separation of particles utilizing a laminar flow profile in a pinched microchannel, Anal. Chem. vol. 76, pp. 5465-5471, (2004).
[2] J. Takagi, M.Yamada, M. Yasuda and M. Seki, Continuous particle separation in a microchannel having asymmetrically arranged multiple branches, Lab Chip., vol. 5, pp. 778-784, (2005).
[3] C. Wang, Y. Gao, N. T. Nguyen, T. N. Wong, C. Yang and K. T. Ooi, Interface control of pressure-driven two-fluid flow in microchannels using Electroosmosis, J. Micromech. Microeng., vol 15, pp. 2289-2297, (2005).

A MINIATURE CENTRIFUGAL CHROMATOGRAPHIC DEVICE FOR THE PRE-CONCENTRATION AND DETERMINATION OF LEAD IN AQUEOUS SAMPLES

Josiane P. Lafleur and Eric D. Salin
McGill University, CANADA

ABSTRACT

Solid Phase Extraction (SPE) columns were implemented on centrifugal microfluidic devices where the analyte was sampled directly by Laser Ablation (LA) Inductively Coupled Plasma-Mass Spectrometry (ICP-MS). The direct analysis of lead-8-hydroxyquinoline complexes adsorbed onto C_{18}-bonded silica gel is demonstrated.

Keywords: Centrifugal chromatography, laser ablation, water analysis

1. INTRODUCTION

Since the concept of micro-Total Analysis System (μTAS) was introduced, the separation of inorganic ions on microfluidic devices has received little attention. Most of the published work in this area involves isotachophoresis (ITP) or ITP hyphenated with capillary zone electrophoresis (ITP-CZE) [1]. When analyte concentrations are very low, such as in drinking or seawater, it is often necessary to pre-concentrate the samples. Seawater also poses additional problems, as its saline composition can be a source of matrix and spectral interference. SPE can be used to overcome these problems.

2. THEORY

SPE is a widely use technique for pre-concentration of trace metals and matrix removal. In this technique, metal chelates are adsorbed on top of a chromatographic bed. The interfering species can then be washed away before elution of the analytes with a small volume of organic solvent. Our technique differs by eliminating the final eluting step. An ultra-violet laser is used to vaporize the thin film covering the miniature SPE column and is then used to directly sample the analytes. Laser sampling of the material directly on the column has several advantages: higher pre-concentration factors, reduced analysis time and minimized analyte losses.

3. EXPERIMENTAL

The device illustrated in Figure 1 was based on a prototype developed recently for the separation of colored dyes [2]. It was built using a combination of thin film lamination [3] and xurography [4]. Reservoirs were created using conventional Computerized Numerically Controlled (CNC) milling of polycarbonate discs (120mm diameter). The channels and vent lines were cut in 100μm adhesive film with a cutting plotter. A 75μm polycarbonate film was used to cover the top of the columns.

The extraction procedure is illustrated in Figure 2. The packing material (5 μm mean particle size) was introduced in the columns as a methanol slurry. The packed bed was consolidated by applying centrifugal force with a 90V DC motor with manual speed control. The packing was conditioned with 5μl of methanol and then washed with 5μl of

978-0-9798064-0-7/μTAS2007/$20©2007CBMS

acidified methanol (1% w/w concentrated HCl in methanol) to remove contaminants. The column was then conditioned for the introduction of the aqueous sample by adding 5µl of water (18MΩ) adjusted to pH 9 with ammonium hydroxide. 8-hydroxyquinoline was added in excess to the lead standard (10 µg g^{-1} Pb) and water blank before adjusting their pH to 9

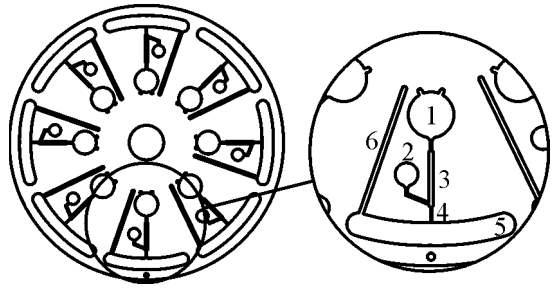

Figure 1. Device layout. All reservoirs are 1.3 mm deep; channels are 0.1 mm deep and 0.5 mm wide, except for the restriction, which is 0.25 mm wide. The column and the vent lines are 1 mm wide. Detailed view: (1) Sample/mobile phase reservoir, (2) packing reservoir, (3) packed micro-column, (4) column restriction, (5) waste reseroir, and (6) vent.

with ammonium hydroxide. The samples were then percolated through the column at 2000 rpm (20-100 µl for the lead standards, 100 µl for the blank). The columns were stored in a dessicator prior to LA-ICP-MS analysis. The laser ablation system (LSX-200, CETAC technologies, Omaha, NE) operating parameters were optimised for the analysis of chromatographic material. The vaporized samples were carried by an argon stream to an ICP-MS system (Perkin-Elmer SCIEX Elan 6000) at a flow rate of 1 L min^{-1}.

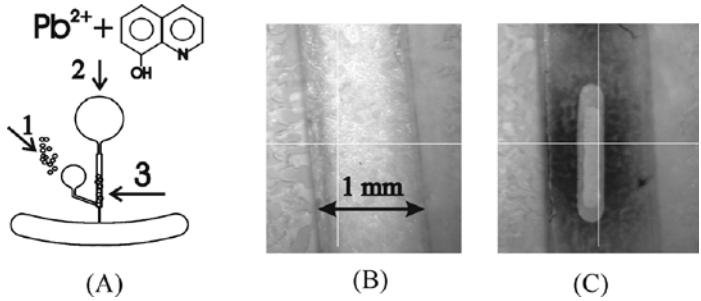

Figure 2. (A) Solid phase extraction procedure. (1) Column packing (2) Adsorption of the chelated sample. (3) Direct laser ablation of the sample. (B) A packed channel (C) The same channel after ablation of the polycarbonate window to expose the packing.

4. RESULTS AND DISCUSSION

As shown in Figure 3, the laser could be used to selectively vaporize the thin film covering the column and the chromatographic bed. Preliminary results show that a linear calibration curve can be obtained, with precision ranging from 31-42% and a limit of detection (3 sigma) of 3 ng. Therefore, only 900 µl is required to quantify Pb in drinking

water at natural levels. Precision and accuracy could be improved by using the silicon present in the stationary phase as an internal standard to account for variations in laser energy, but better column quality and reproducibility is required for this.

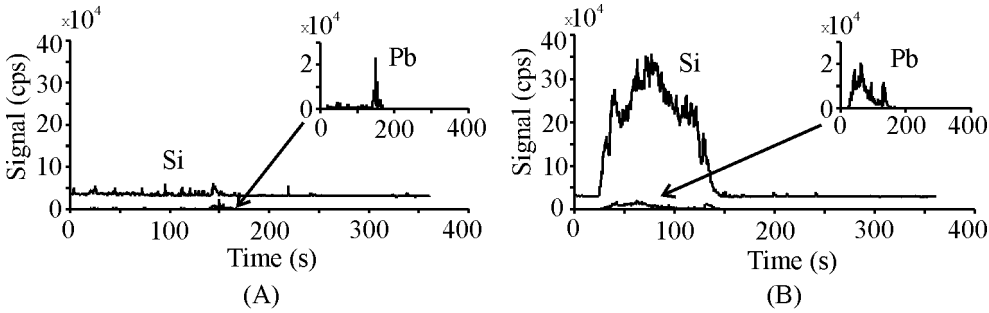

Figure 3. LA-ICP-MS spectra. (A) Only the polycarbonate window is vaporized. (B) During the second ablation scan, the chromatographic material is vaporized.

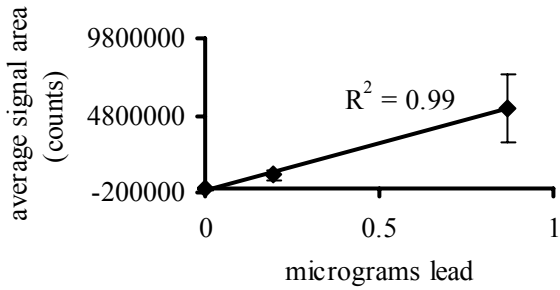

Figure 4. Determination of Lead-8-Hydroxyquinolate adsorbed on C18-bonded silica microcolumns by LA-ICP-MS

5. CONCLUSIONS

It was demonstrated that LA-ICP-MS can be used to retrieve analytes trapped on miniature centrifugal chromatographs without elution of the sample. This technique can be used as a rapid screening technique for the monitoring of contaminated waters.

ACKNOWLEDGEMENTS

We wish to thank Prof. Marc Madou and Dr. Horacio Kido from the University of California at Irvine. Author JPL gratefully acknowledges scholarship support by the Natural Science and Engineering Council of Canada (NSERC).

REFERENCES

[1] Evenhuis, C.J., et al. *Electrophoresis*, 2004. **25**, 3602-3624.
[2] Penrose, A., et al. *Analyst*, 2004. **129**, 704-9.
[3] Weigl, B.H., et al. *Biomedical Microdevices*, 2001. **3**, 267-274.
[4] Bartholomeusz, D. et al. *J. of Microelectromechanical Systems*, 2005, **14**, 1364-1374.

SPECTRAL SEPARATIONS OF CHEMICAL SIGNALS WITH FOURIER MICROFLUIDICS

Yan Xie, Yingying Wang, Li Chen and Carlos H. Mastrangelo
Dept. of Electrical Engineering and Computer Science
Case Western Reseve University, Cleveland, OH, 44106, USA

ABSTRACT

Tapped delay line (TDL) filters based on Fourier microfluidics have been fabricated and tested for the first time. The TDLs are capable of separating dynamic chemical signals through differences in their frequency-domain spectral characteristics. TDL filters are constructed using series/parallel connection of microfluidic delay lines. The transfer function for a three-tap microfluidic feedforward filter has been measured showing two frequency notches at of 0.3 Hz and 0.8 Hz. This work thus demonstrates the wave-like behavior of chemical signals propagating through microfluidic chips.

Keywords: Fourier Microfluidics, Dynamic Fluidic Signals, Tapped Delay Line Filters

1. INTRODUCTION

Chemical analysis techniques such as electrophoresis and LC realize separation based on differential migration or absorption/desorption, but these techniques are essentially used for the analysis of finite, discrete and time invariant samples. In this paper we demonstrate for the first time separation of dynamic chemical signals based not on their chemical nature but their frequency-domain characteristics. To demonstrate such concept we have fabricated a microfluidic TDL filter [1], and we measured its transfer function as described below.

2. THEORY OF FOURIER MICROFLUIDICS

Chemical signals are represented with spatial and time dependent concentrations of an analyte $C(x,t)$ which flows through a microfluidic network with average velocity V from input to output. In this paper we synthesize test signals using the generator shown in Fig. 1 consisting of four valves driven by digital clock signals ϕ and $\overline{\phi}$. The generator maintains a constant flow of analyte (fluorescein 1g/mL) or solvent (H_2O) at excitation frequency ω thus introducing a periodic pulse train into the network. Inside the network, $C(x,t)$ approximately obeys the lumped one-dimensional convection-diffusion equation

$$D \cdot \frac{\partial^2 C}{\partial x^2} - V \cdot \frac{\partial C}{\partial x} = \frac{\partial C}{\partial t} \tag{1}$$

Where D is the effective diffusion constant (Taylor-dispersion adjusted [2]). As this signal propagates, it experiences both delay and dispersion. Since the input signal $C_{in}(x,t)$ is periodic we represent it as phasor $C(j\omega, x)$; hence the time derivative term in Eq. (1) is readily replaced with $j\omega \cdot C$. Solving the resulting ODE with suitable boundary conditions one obtains the transfer function (T.F.) of the microfluidic network

$$T(j\omega, x) = C_{out}(j\omega, x) / C_{in}(j\omega, x) = \exp[\left(V - \sqrt{V^2 + 4j\omega D}\right) \cdot x / 2D] \tag{2}$$

978-0-9798064-0-7/μTAS2007/$20©2007CBMS

where x is the distance measured from the network inlet (its length). For short channels, th e T.F. amplitude decay is negligible, and the T.F. reduces to

$$T(j\omega,x) \approx \exp[-j(\omega \cdot x/V)] = \exp(-j\theta) \quad , \quad \theta = \omega \cdot x/V = \omega \cdot T \tag{3}$$

corresponding to a simple phase delay θ proportional to the signal transit time $T = x/V$. TDL filters are realized with series/parallel connections of these delay elements as shown in Fig. 2 resulting in multiple chemical waveforms mixed at converging nodes constructively or destructively. The TDL filter has the transfer function

$$T_{TDL}(j\omega) = \sum_{i=0}^{N} A_i \cdot e^{-j\theta_i} \tag{4}$$

with coefficients A_i and x_i that can be tailored to display different spectral characteristics.

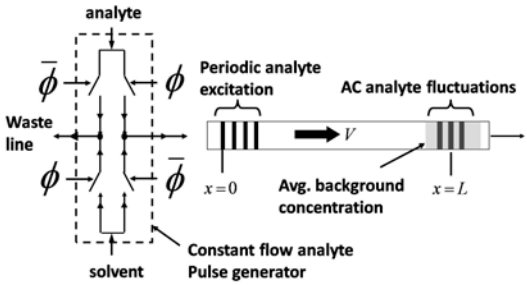

Fig. 1. Microfluidic circuit for generation of periodic analyte excitation into a channel. Analyte waveforms are delayed and dispersed at the channel output.

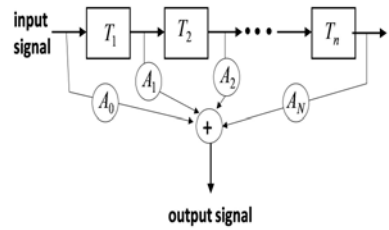

Fig. 2. Schematic of a TDL filter. Each delay element consists of a microfluidic channel with characteristic delay T_i.

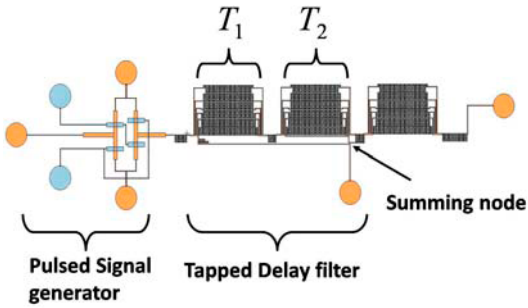

Fig. 3. Physical layout of two stage TDL filter with signal generator implementing a feed forward comb filter.

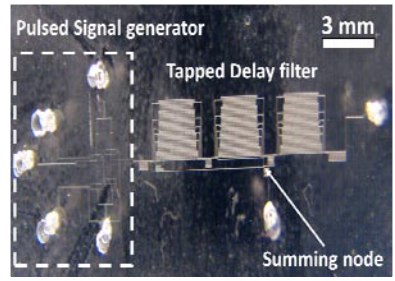

Fig. 4. PDMS tapped delay filter chip

Fig. 3 shows the layout of a two stage TDL network implementing a feed forward comb filter and signal generator. Fig. 4 shows a photograph of the chip constructed using a double-layer PDMS process [3, 4].

3. EXPERIMENTAL RESULTS

Fig. 5 shows the transfer function of an individual microchannel measured with the setup of Fig. 1. Fluorescein was used as an indicator of analyte concentration. The frequency dependent intensity of the fluorescence at different locations down the channel was

recorded with an Olympus MVX10 fluorescence microscope and Hamamatsu EM-CCD intensified camera. The corresponding T.F. approximately matches that of Eq. (2). Next we tested the TDL with the same excitation scheme. Figs. 6 and 7 show the propagation of fluorescein waves through the TDL filter. The measured TDL T.F. shown in Fig. 8 clearly shows two notches at frequencies of 0.3 Hz and 0.8 Hz. Other TDL filters with low, high, and bandpass characteristics can also be realized with different series/parallel element combinations.

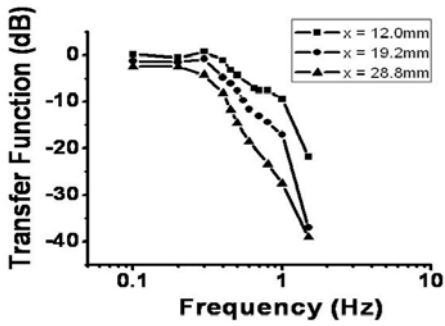

Fig. 5. Observed transfer function of simple channel. At low frequencies the channel behaves as a delay line with $T_d=L/V$.

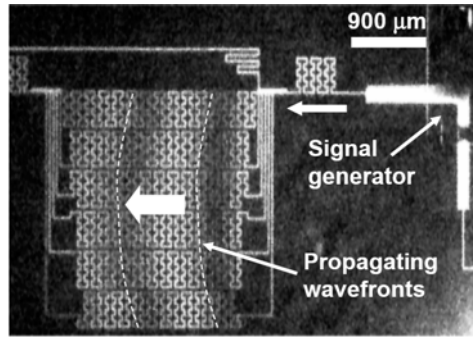

Fig. 6: Propagation of fluorescein wavefronts through a TDL. The arrow indicates the flow direction.

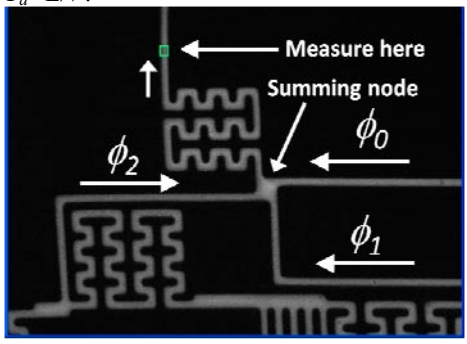

Fig. 7: Propagation of fluorescein wavefronts through a TDL. The arrow indicates the flow direction.

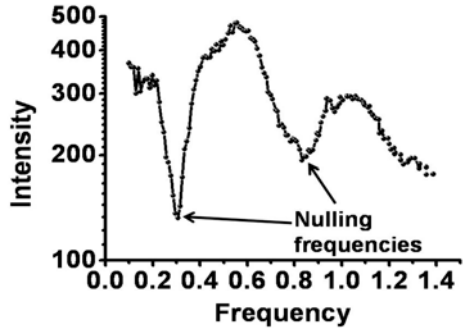

Fig. 8: Transfer function of the TDL filter output.

References.

1. V. Oppenheim et al, *Signals and Systems*, Prentice Hall, NY, 1996.
2. Probstein, *Physicochemical Hydrodynamics*, Wiley NY, 2003.
3. T. Thorsen, S. J. Maerkl, and S. R. Quake, "Microfluidic large-scale integration," *Science*, Vol. 298, pp. 580-584, (2002).
4. M. A. Unger, H. P. Chou, T. Thorsen, A. Acherer and S. R. Quake, "Monolithic Microfabricated Valves and Pumps by Multilayer Soft Lithography", *Science*, Vol. 288, pp. 113-116, (2000)

TWO-DIMENSIONAL PROTEIN SEPARATION IN A PLASTIC DEVICE WITH A MICROVALVE ARRAY

Z. Hugh Fan[1,2], Champak Das[1], Jiyou Zhang[1]

[1]Department of Mechanical and Aerospace Engineering, [2]Department of Biomedical Engineering, PO Box 116250, Gainesville, FL, 32611, USA. Email: hfan@ufl.edu

ABSTRACT

Two-dimensional (2D) protein separation is demonstrated in a plastic microfluidic device by integrating isoelectric focusing (IEF) in 1 channel and polyacrylamide gel electrophoresis (PAGE) in 29 parallel channels that are orthogonal to the IEF channel. An array of microfluidic valves is developed for introducing different separation media into two dimensions and for transferring proteins from the first to the second dimension. Fabrication of valves is achieved by *in situ*, photo-initiated gel polymerization. The total separation time is less than 10 minutes, which is favorable when compared to 1-2 days for conventional 2D slab gel electrophoresis.

Keywords: Two-dimensional separation, microvalves, electrophoresis, proteins

1. INTRODUCTION

Among the approaches being developed for proteomics, two-dimensional gel electrophoresis (2DGE) is an essential tool [1]. 2DGE consists of isoelectric focusing (IEF) as the first dimension and polyacrylamide gel electrophoresis (PAGE) as the second dimension. One major advantage of 2DGE is its enormous separation resolution, whereas its key limitations include poor reproducibility and time-consuming procedure. This work is carried out to address the limitations.

2. EXPERIMENTAL

Cyclic olefin copolymer (Topas) is used to fabricate 2D separation devices using compression molding. **Figure 1** shows the device design; it consists of one horizontal channel (AB) for IEF and 29 vertical channels (CD) for PAGE. The size of the device is 1" x 3", about the size of a microscope slide. All channels are 110 µm wide and 40 µm deep. The distance between channels (center-to-center) is 360 µm. An exploded view of a part of the device is shown in the middle of Figure 1. On the right is the interface between IEF and PAGE, illustrating proteins in each pI band being transferred from the first to the second dimension and then separated. The

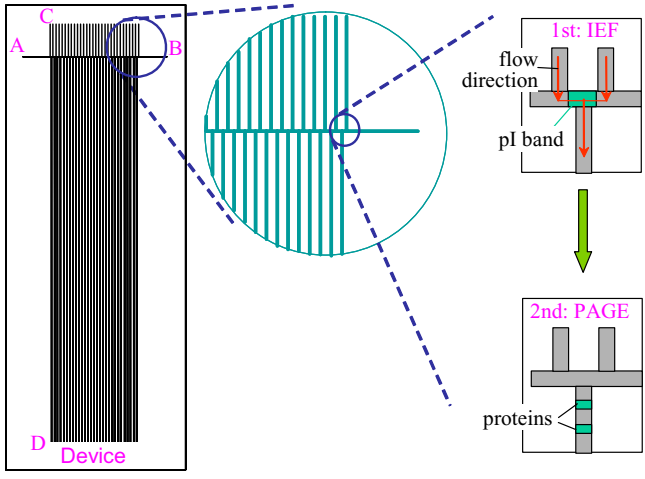

***Figure 1**. Design of a microfluidic device for 2DGE.*

978-0-9798064-0-7/µTAS2007/$20©2007CBMS

arrows indicate the flow direction.

Acrylamide monomer, 1-hydroxycyclohexylphenylketone (HCPK), proteins are purchased from Sigma-Aldrich (St. Louis, MO) while carrier ampholytes are from Bio-Rad Laboratories (Hercules, CA). The detection is carried out using a laser-induced fluorescence, whole-channel imaging system [2].

3. RESULTS AND DISCUSSION

The device in Figure 1 is different from those using two orthogonal separation channels, in which capillary electrophoresis (CE) is coupled with either micellar electrokinetic chromatography [3, 4] or IEF [5]. The key difference is the use of multiple channels, rather than a single channel, for the second dimension to match the separation capacity of the slab in 2DGE. This work is also different from the existing work on miniaturized 2DGE [6, 7]. The key advances are twofold: (1) an array of microfluidic valves allows the seamless introduction of two different separation media; and (2) a fluidic network with densely-packed channels enables the appropriate transfer of proteins from the first to the second dimension.

The valve array is created by *in situ* gel polymerization. To make gel valves at a precise location, acrylamide monomer solution containing HCPK is first filled in all channels. HCPK is a photosensitive agent to initiate gel polymerization, replacing chemical initiators. After the AB channel of the device in Figure 1 is covered by a mask, photopolymerization is conducted by exposure to UV light. The solution in the exposed region (CD channels) polymerizes to form gel, whereas the solution in the AB channel is blocked by the mask and do not polymerize. **Figure 2** shows the gel valve array. These gels function as "closed" valves when an IEF separation medium is introduced into the AB channel without flowing into the CD channels. After IEF, they function as "open" valves when an electric field is applied to the CD channels. The focused proteins can be transferred from the first into the second dimension, because proteins can be electrokinetically injected through gels.

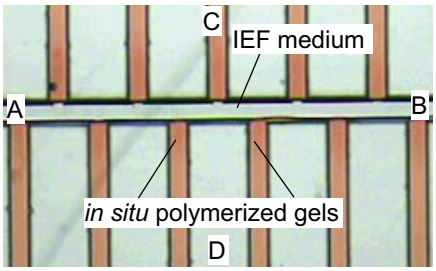

Figure 2. *Micrograph of the valve array. Polymerized gels are dyed for easy visualization.*

In the presence of microvalves, IEF separation of proteins is implemented in the device as shown in **Figure 3**. The pH gradient is established using carrier ampholytes with a pH gradient of 3-10. It should be noted that the IEF analysis time is typically in 2–5 minutes, much shorter than hours needed in the traditional IEF strip format. Three fluorescently-labeled proteins, bovine serum albumin (BSA, pI = 4.6, MW = 66 KDa), ovalbumin (4.6, 44 KDa), and parvalbumin (4.0, 12 KDa), are used in this experiments. BSA and ovalbumin have the similar isoelectric point (pI), thus focused in the same pI segment. However, both of them are separated from parvalbumin. The broad peak of parvalbumin is due to heterogeneity in labeling, which is confirmed by IEF of the individual protein.

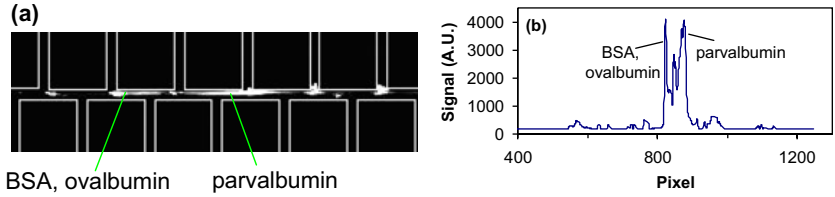

Figure 3. *(a) IEF of fluorescently-labeled BSA, ovalbumin, and parvalbumin in the device. Lines are added to show the channel locations. (b) The corresponding electropherogram of (a). Peaks of proteins are indicated. Each pixel in x axis approximately corresponds to 20 µm.*

BSA and ovalbumin can be separated in the second dimension as shown in **Figure 4**, in which we also used carbonic anhydrase (5.9, 31 KDa) and hemoglobin (6.8, 65 KDa). Electropherograms in all vertical CD channels (#1 to 29) are illustrated together to form the 2D map. The channel number is related to pI while migration time corresponds to the molecular size. The total analysis time is less than 10 minutes. The result suggests that 2DGE can be implemented in a plastic device with a microvalve array.

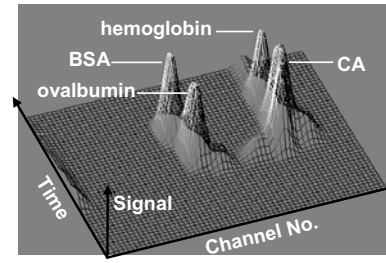

Figure 4. *2D map of BSA, ovalbumin, hemoglobin and carbonic anhydrase (CA) obtained in the 2D electrophoresis device.*

4. CONCLUSION

We demonstrated the integration of IEF and multi-channel PAGE in a plastic microfluidic device. The key element that enables 2D electrophoresis in the device is an array of microfluidic valves, which is created by in situ, photo-initiated gel polymerization. The gel valves allow the introduction of different separation media into two dimensions and the transfer of proteins from the first to the second dimension.

ACKNOWLEDGEMENT

This work is supported in part by the grants (48461-LS, 52924-LS-II) from Army Research Office and the startup fund from the University of Florida.

REFERENCES

1. Service, R. F. *Science* **2001**, *294*, 2074-2077.
2. Das, C.; Xia, Z.; Stoyanov, A.; Fan, Z. H. *Instrumentation Science and Technology* **2005**, *33*, 379-389.
3. Rocklin, R. D.; Ramsey, R. S.; Ramsey, J. M. *Anal. Chem.* **2000**, *72*, 5244-5249.
4. Shadpour, H.; Soper, S. A. *Anal Chem* **2006**, *78*, 3519-3527.
5. Herr, A. E.; Molho, J. I.; Drouvalakis, K. A.; Mikkelsen, J. C.; Utz, P. J.; Santiago, J. G.; Kenny, T. W. *Anal. Chem.* **2003**, *75*, 1180-1187.
6. Chen, X. X.; Wu, H. K.; Mao, C. D.; Whitesides, G. M. *Anal. Chem.* **2002**, *74*, 1772-1778.
7. Li, Y.; Buch, J. S.; Rosenberger, F.; DeVoe, D. L.; Lee, C. S. *Anal. Chem.* **2004**, *76*, 742-748.

ULTRA-TRACE MICRO GAS ANALYSIS SYSTEM OF AMMONIA IN CLEANROOM

Kenji Uchiyama[1], Mari Sasaki[1], Yuko Kihira[1], Katsumi Kuriyama[1], Yoshikuni Kikutani[2], Kazuma Mawatari[2] and Takehiko Kitamori[3]

[1]Institute of Microchemical Technology, JAPAN,
[2]Kanagawa Academy of Science and Technology (KAST), JAPAN
[3]The University of Tokyo, JAPAN

ABSTRACT

We designed a microchip-based gas analysis system to realize ultrasensitive (0.1ppb) and continuous (1 measurement/15 min) detection of ammonia gas in a cleanroom for semiconductor process control. The detection processes consisted of stable gas/liquid laminar flow formation, gas/liquid adsorption and concentration, colorimetric reaction, and TLM (thermal lens microscope) detection for the non-fluorescent molecules. All these processes were integrated into microchips. The detection limit of ~0.05 ppb in 15 min analysis time was realized, and the basic performance was verified.

Keywords: Thermal lens microscope, laminar flow, multi-phase flow, ammonia gas

1. INTRODUCTION

Modern semiconductor industry demands ultra-clean environment in which not only particles but also chemicals should be removed from cleanroom air at a certain level. Ammonia is a basic gas that can form salt with acidic gases, and the salts deposited on a photomask turn into haze and deteriorates quality of photo-patterning. Ammonia can also affect reactivity of some photoresist. In the next decade, control of ammonia concentration in 0.1 ppb level will be required. For this purpose, a portable and continuous monitoring system with 0.1 ppb sensitivity is highly required. However, conventional methods do not meet these demands. Previously, we reported a basic method for sensitive gas (formaldehyde) analysis on a microchip with gas/liquid laminar flow and TLM detection [1]. In this work, we further developed these methods for practical application (ammonia detection) in semiconductor industry.

2. EXPERIMENTS AND RESULTS

Figure 1 shows a concept of the gas analysis system. The system comprised of a gas pump, a liquid pump, a microchip stable gas/liquid laminar flow formation, gas/liquid adsorption and concentration, colorimetric reaction, and TLM detection. Sample gas was introduced by a double-head diaphragm pump to the deep lane of the asymmetric microchannel. Extractant (pure water) was introduced to the shallow lane of the asymmetric microchannel. Ammonia in the gas phase was absorbed in the extractant in the aid of large specific interfacial area between the two phases. After gas absorption, two reagents of indophenol method were added to the extractant and colorimetric reaction took place in the reaction channel. Absorption at 633 nm was measured by a TLM detector downstream.

978-0-9798064-0-7/μTAS2007/$20©2007CBMS

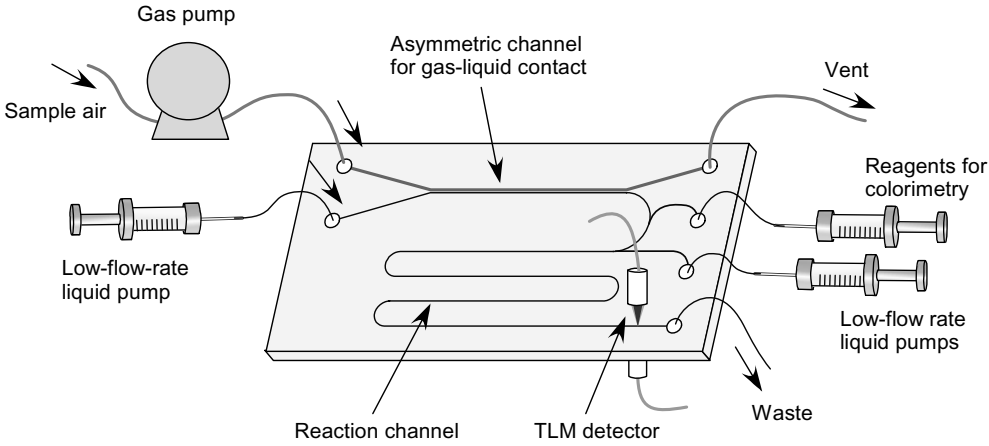

Figure 1. Schematic illustration of analysis system for trace ammonia in air.

Figure 2 shows a structure of a microchannel for gas/liquid laminar flow formation, gas/liquid adsorption and concentration. For sensitive detection, gas/liquid concentration factor is very important. For this purpose, large ratio in Vgas/Vliq (V: volume flow rate) is critical. However, the large difference of V leads to unstable gas/liquid laminar flow. Here, we utilized a Laplace force to stabilize gas/liquid interface and realized large Laplace force with guide structure in microchannel. As a result, Vgas/Vliq of 20000 (Vgas: 400 μL/min, Vliq: 0.02 μL/min) was achieved. In this condition, 17 times concentration with 5 min contact time for gas/liquid was realized (Table 1).

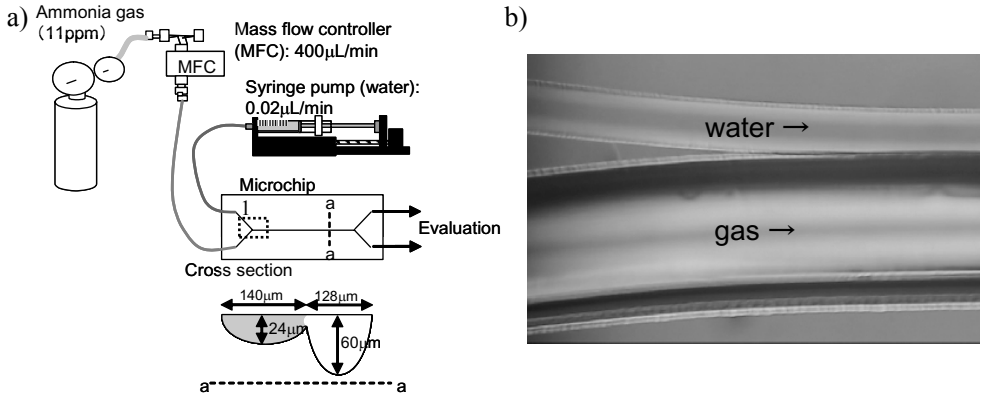

Figure 2. (a) Illustration of gas/liquid absorption and concentration part highlighting (1)Y-junction and a-a' cross section. Guide structure was fabricated to stabilize gas/liquid interface with large flow rate difference. (b) Gas/liquid laminar flow formation was observed at Y-junction.

Table 1. Performance of gas/liquid concentration

V_{gas} (μL/min)	V_{liq} (μL/min)	Extraction (%)	Concentration (times)
400	0.02	89	17

Figure 3 shows a microchip for colorimetric reaction (indophenol method) and TLM detection. Two step colorimetric reaction (10 min) and TLM detection (633 nm excitation) was conducted. From the calibration curve, lower limit of detection (LOD) of approximately 1ppb ammonium solution was calculated. By considering these results (17 times gas/liquid concentration in 5 min and 1ppb ammonium detection in 10 min), 0.05 ppb ammonia gas can be detected within 15 min, and requirements for this system is almost met.

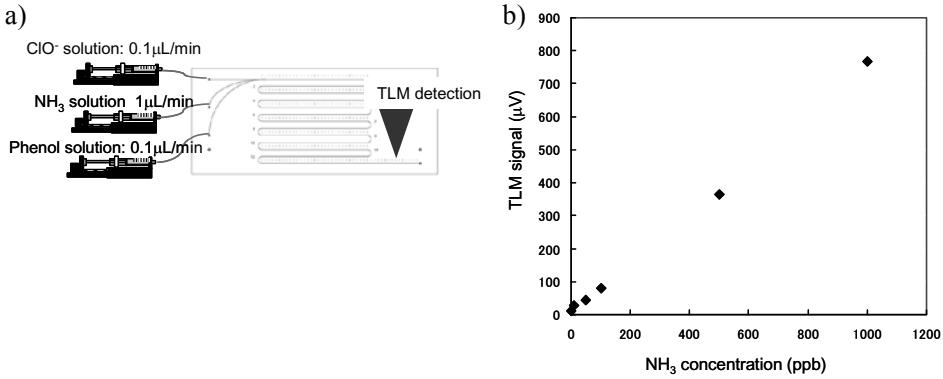

Figure 3. (a) Exprimental setup of determination of ammonia colorized by indophenol method and detected by TLM. (b) Calibration curve of aqueous standard solutions of ammonia.

3. CONCLUSIONS

Our method can be powerful tool for on-site sensitive and fast gas analysis. Now we are optimizing the conditions and integrating these all process into a single microchip. Also, we are making a stable gas pump with low ammonia adsorption and designing a prototype system.

ACKNOWLEDGEMENTS

This research is partly supported by the Ministry of Economy, Trade and Industry.

REFERENCES

[1] M. Tokeshi, et al., *Gas-Liquid Phase Micro Unit Operations Using Two-phase Flow and Its Applications for Chemical Process*, Proc. Micro Total Analysis Systems 2004, Kluwer Academic Publisher, Dordrecht, The Netherlands, pp. 246-248, (2004).

BIOPOLYMER COATED PARTICLE FORMATION UTILISING A MICROFLUIDIC DEVICE AND MULTIPHASE FLOW

Elisabeth Rondeau[1] and Justin Cooper-White[1]

[1]*Australian Institute for Bioengineering and Nanotechnology, University of Queensland , QLD4072, AUSTRALIA*

ABSTRACT

This paper reports the development of a novel and scalable continuous microfluidic-based method for the preparation of coated cross-linked biopolymer microcapsules and microparticles, with a size range of 1 to 100 μm, on a single PDMS (polydimethylsiloxane)-based device. The deposition of a nanometre-thick layer of a second polymer system has successfully been integrated into this one-step process. This new approach has been utilised to produce microparticles of alginate, chitosan, PEO (polyethylene oxide)-based and PLA (polylactide)-based block copolymers.

Keywords: microfluidics, multiphase flow, droplet formation, coated particle

1. INTRODUCTION

Nanometre- and micrometer-sized polymer particles and capsules are widely used as delivery vehicles for a whole host of targeted molecules in food, pharmaceutical, and personal care applications. Microfluidic-based systems promise to give access to new particle morphologies and on-demand structured templates. However, compositional flexibility is still required to enhance the uptake of these devices into industrially scalable formats. We have successfully investigated the production of coated particles generated in a single-step process, building up a simple design based on our original device design. After the formation of reactive polymeric droplets, the hardening of these drops occurs solely within the microfluidic device. We have investigated the influence of the device, flow parameters and polymer solution properties on the droplet generation, as well as the cross-linking reaction, to determine the optimum preparation conditions which afford control over the resulting size and morphology of the produced biopolymer particles. The deposition of a second and of a third polymer layer has also been successfully integrated into this one-step process.

2. THEORY

2.1. Droplet formation

The effects of viscosity and surface tension on break-up dynamics and subsequent formation of drops have been thoroughly investigated[1]. In this work, droplets were initially generated by shearing a stream of the dispersed phase with the flow of the continuous phase via a flow-focusing geometry. The resulting size of the droplets is mainly governed by the properties of the polymer solution and the flow rates of the continuous and droplet phases.

2.2. Cross-linking reaction

The formation of chemically cross-linked microgels in the device was obtained via a photo-curing or via a redox-initiated reaction.

978-0-9798064-0-7/μTAS2007/$20©2007CBMS

The reaction kinetics were independently investigated and reaction times were adjusted to residence times of the polymeric droplets.

3. EXPERIMENTAL

3.1. Materials

Di-acrylated (DA) poly(ethylene oxide)-poly(propylene oxide)-poly(ethylene oxide) triblock copolymers (Pluronic F-127, $EO_{100}PO_{70}EO_{100}$ and Pluronic F-68, $EO_{80}PO_{30}EO_{80}$) were synthesized and analyzed as previously described[2]. The cross-linking reaction was initiated using two alternative cross-linker systems: Vazo®56 and UV-light or ammonium persulfate (APS) and N,N,N',N'-tetramethylene-diamine (TEMED). The coating phases consist of PLA-based block copolymer and monomer (N-vinylpyrrolidone) solutions. The solutions were prepared in deionised water or in dimethyl carbonate (DMC).

3.2 Particle preparation in microfluidic reactors

The channel network used in the present work consists of three functional parts: a sheath-flow junction (1), where droplets are formed, a serpentine channel (2), in which the droplets harden and flow-focusing devices (3) for the subsequent deposition of polymer layers. A schematic of the microchannel pattern is presented in Figure 1. The device design allows reactive mixtures to be processed upstream of the microdroplet creation site.

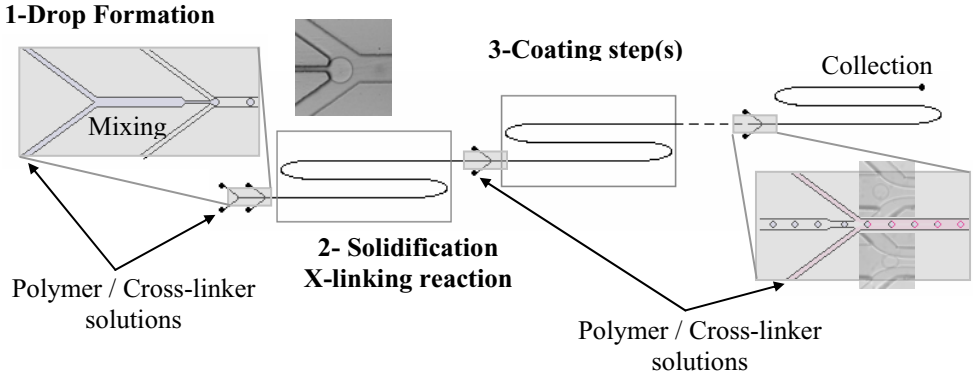

Figure 1. Diagram illustrating the continuous process for the coated particle production.

4. RESULTS AND DISCUSSION

4.1. Droplet formation

Droplets of DA pluronic solutions of varying concentration could be generated in microfluidic flow-focusing devices and we could also confirm that for a given solution with a certain viscosity, the droplet size and the break-up frequency are dependent on the flow rates of the dispersed and the continuous phases.

4.2. Subsequent cross-linking of the pluronic droplets

Different initiation methods for the cross-linking reaction gave rise to different internal morphologies with the produced particles. The same fabrication scheme was shown to allow for the production of dissimilar particles with varying shape, size, composition, porosity or internal structure (see Figure 2 and 3).

(a) 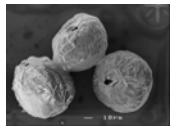 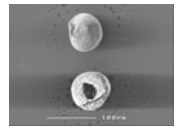 (b) 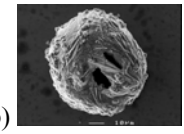

Figure 2.SEM images of DA F-68 (a) and DA F-127 (b) cross-linked microcapsules produced on-chip via a photo-initiated reaction. The particle size is approximately 60 to 80 μm.

(a) 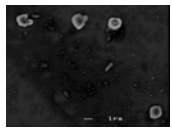 (b) 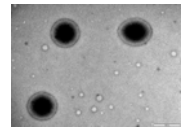 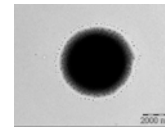

Figure 3. (a) SEM images of DA F-127 cross-linked microparticles produced on-chip via a redox-initiated reaction. The particle size is approximately 1 μm. (b) TEM images of DA F-127 cross-linked microparticles produced via the same process. The particle size is approximately 1 and 5 μm.

4.3. Multi-layer particles

The same device allowed for the preparation of diverse multi-layered particles when processing the deposition of a polymer layer after the particle cross-linking.

(a) 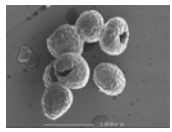 (b) 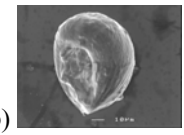

Figure 4. SEM images of (a) DA F-68 cross-linked microparticles coated with PLA-PEO-PLA and (b) DA F-127 cross-linked microparticles coated with polyvinylpyrrolidone.

5. CONCLUSIONS

This technique has proven to allow templating of complex-structured, and also multi-layered, particles. Moreover, this novel method is highly flexible and can be applied to a wide range of biologically derived or synthetic polymers. Part of this work is focused on amphiphilic tri-block copolymers. The interplay between hydrophilic/hydrophobic domains gives rise to unique nano-structured environments within each particle, which can be customised to create an ideal chemical environment to solubilise materials (such as peptides and other drugs) that are otherwise very difficult to incorporate into simple solvents or traditional drug delivery vehicles.

ACKNOWLEDGEMENTS

This work was supported by funds from the Australian Research Council Discovery Projects scheme and from the Australian Research Council Linkage Projects scheme.

REFERENCES

[1] T. Nisisako, T. Torii, T. Higuchi, *Droplet formation in a microchannel network,* Lab Chip*,* 2, (1), pp. 24-26, (2002).

[2] F. Cellesi, N. Tirelli, J. A. Hubbell, *Materials for Cell Encapsulation via a New Tandem Approach Combining Reverse Thermal Gelation and Covalent Crosslinking,* Macromol. Chem. Phys.*,* 203, (10/11), pp. 1466-1472, (2002).

FABRICATION OF NOVEL INORGANIC POLYMER DERIVED MICROCHANNELS FOR MICROREACTOR APPLICATIONS

Tae-Ho Yoon, Lan-Young Hong, Sang-Hee Park, Kyung-Ik Min, Sung-Joon Park and Dong-Pyo Kim

School of Biological Engineering & Applied Chemistry, Chungnam National University, KOREA

ABSTRACT

We report the successful fabrication of inorganic polymer derived microchannels with high organic solvent resistance, optical transparency and biocompatibility via an economic micromolding process, followed by UV and post thermal curing steps. The commercial polyvinylsilazane and allyhydropolycarbosilane mixed with photo and thermal initiators were used to fabricate microchannels. When animal cells were inoculated on the inorganic polymer, better adhesion was shown than that of glass surface. Inorganic polymer microreactro showed comparable performance in photo catalytic decomposition of organic compound and organic synthesis against to commercial glass microreactor.

Keywords: inorganic polymer, biocompatibility, photo-catalytic microreaction

1. INTRODUCTION

Microfluidic systems have highly concerned due to the unique features such as short molecular diffusion distance, excellent heat transfer and large surface-to-volume ratio [1]. In particular, microreaction at lab-on-a chip system has been successfully used in analytical chemistry and bio applications such as biochips. In these applications, the devices have been generally fabricated by glass and metal through etching process, or polymers such as PDMS and PMMA by soft lithography techniques. Althought the etching process to glass and metal with high mechanical strength and chemical resistance has been well-established, the requirement of high cost equipment is disadvantageous. Alternatively, polymers with excellent processibility and replicability are mainly used for aqueous based applications due to the low material stability against organic solvents and the elevated temperatures. Therefore, it must be strongly demanded to develop the novel materials based microfluidics with better mechanical stability by facile fabrication process for versatile applications, including microchemistry under various circumstances.

2. EXPERIMENTAL

To fabricate a inorganic microchip and microreactor, we applied two kind of preceramic precursor, polyvinylsilazane(VL 20®, Kion Corp., USA) and allyhydropolycarbo-silane(Starfire SMP-10, Starfire Co. USA) using spincoating and imprinting lithography with PDMS mold as shown Fig. 1[2]. Fig. 2 shows images of fabricated microreactors by imprinting lithography. To evaluate biocompatibility of inorganic polymer, animal cells (CHO-K1, *Cricetulus griseus*) was incubated on the surface of inorganic polymer. 4-chrolophenol with different concentration was used as a model organic compound to test comparative perpormance of microreactors, which are glass reactor(IMT, Japan) and inorganic polymer microreactor fabricated with SMP-10 with TiO_2 paricles(Degussa P25,

978-0-9798064-0-7/μTAS2007/$20©2007CBMS

USA) as a slurry under 365nm wavelength of UV lamp. Alternatively, 4-(4-bromophenyl)-3-ethoxy-2-oxo-but-3-enenitrile was synthesised with ethylcyanoacetate and piperazine in THF and 4-bromobenzaldehyde in THF as a reactants.

3. RESULTS AND DISCUSSION

Fabrication and characterization of inorganic polymer

The cured inorganic polymers under UV and heating with initiators showed good optical transparency with 85% of UV-B transmittance compare with glass, and solvent resistance against several organic solvents such as alcohol and THF[3]. To evaluate biocompatibility of cured ingoranic polymer, animal cells (CHO-K1) was spreaded on the glass and cured inorganic polymer. After 12 hrs incubations in neutrient buffer, unfixed cells were cleaned with saline buffer. As shown in Fig. 3, more animal cells survived on the cured Kion surface than that of glass. That means cured Kion provides better circumstance for animal cell than glass surface.

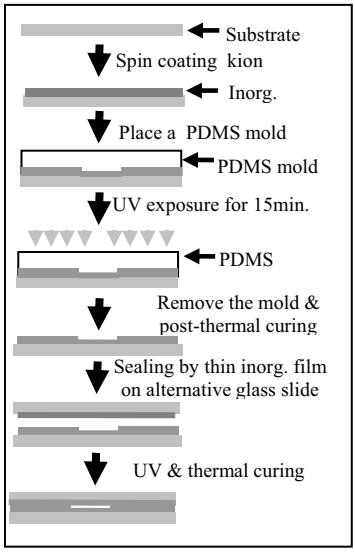

Figure 1. Flow chart diagram for fabrication of sealed inorganic polymer microreactor.

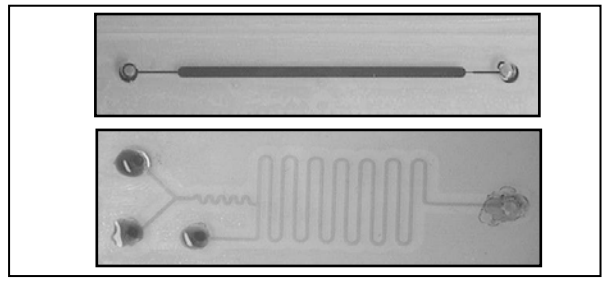

Figure 2. Pictures of fabricated microchannel with inorganic polymer.

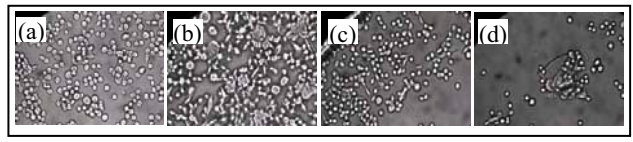

Figure 3. Microscopy images of live animal cells (a) after 12 hrs incubation on inorganic polymer (b) glass, (c) after washout on inorganic polymer and (d) glass.

Application for photo-catalytic reaction and organic synthesis

The performance of the cured inorganic polymer based microreactors(100um width, 40um depth and 80mm length, Figure 4(b) and (c) were investigated in a comparative manner to glass-based microreactor by choosing two model reactions; a TiO_2 photocatalyzed reaction and a Knoevenagel condensation reaction in organic mediums. Firstly, for the degradation of 4-chlorophenol (4CP) in water by UV irradiation with TiO_2(Degussa P25, USA) photocatalyst, 0.1~6.0mM of 4CP solutions were driven into the microchannels at various flow rates by a syringe pump. Figure 5 presents conversion ratio of SMP upto 90% degradation of 4CP compound at flow rate 5uL/min, which is nearly identical performance with the glass microreactor. However, the batch reaction showed only low conversion ratio ca. 10%. Secondly, Knoevenagel condensation reaction as an

alternative model reaction was made for the synthesis of 4-(4-bromophenyl)-3-ethoxy-2-oxo-but-3-enenitrile in THF solvent. In this case, 55~63% of conversion yields were obtained, depending on the flow rates and the used solvents.

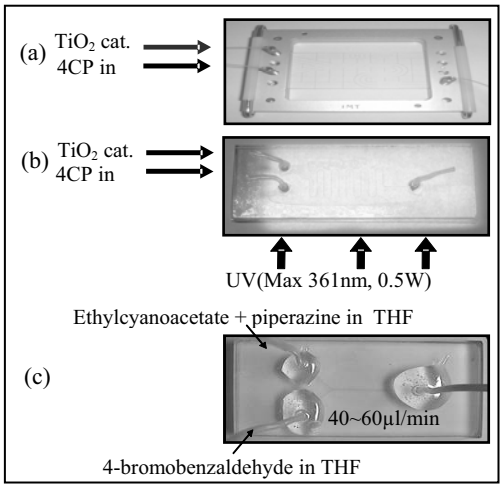

Figure 4. Experimental configurations of microreactor; (a) and (b): commercial glass reactor and inorganic polymer for photo-reaction, and (c): Inorganic polymer reactor for synthesis of 4-(4-bromophenyl)-3-ethoxy-2-oxo-but-3-enenitrile.

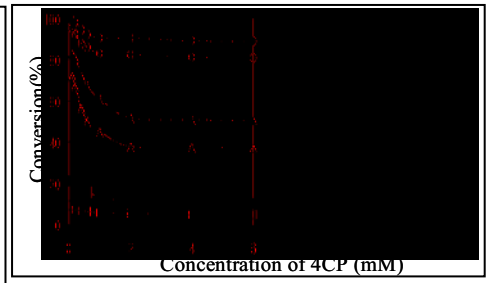

Figure 5. Comparison of conversion rates of glass reactor, SMP polymer reactor and batch reactor at different feed flow rate; ●: 5uL/min at glass reactor, ○ : 5uL/min at SMP polymer, : ▲ 15uL/min at glass reactor, △ : 15uL/min at SMP polymer, ■ : 5uL/min equiv. 80sec at batch, □ :15uL/min equiv. 27sec batch.

Table. 1. Comparision of conversion between SMP microreactor and batch reactor.

Flow rate	Retention time	Conversion
40(㎕/min)	4.32(sec.)	63.47(%)
60(㎕/min)	2.88(sec.)	55.29(%)
Batch	600(sec.)	55.00(%)

4. CONCLUSIONS

In conclusion, it is for the first time, to my best knowledge, that the polymer-based microreactors fabricated via a cheap and simple technique demonstrated the reliable microchemical performance in organic solvents with no swelling problem even for a long period of exposure, which is very promising for developing an integrated microfluidics by taking advantage of available microstructuring techniques of the polymers.

ACKNOWLEDGEMENTS

This work was financially supported by the 2004 National Research Lab (NRL) Project [M10400000320-06J0000-32010] administered by the Korean Ministry of Science and Technology (MOST).

REFERENCES

[1] Y. Matsushita, S. Kumata, K. Wakabayashi, K. Sakeda, and T. Ichimura, Photo-catalytic reduction in microreactor, *Chem. Lett*., pp. 410-411, (2006).

[2] T.H. Yoon, H.J. Lee, J. Yan, and D.P. Kim, Fabrication of SiC-based ceramic microstructures from preceramic polymers with sacrificial templates and lithographic techniques, *J. Cer. Soc. Japan*, pp.473-479, (2006).

[3] A. Asthana, Y. Asthana, I. K. Sung, and D. P. Kim, Novel transparent poly(silazane) derived solvent-resistant, bio-compatible microchannels and substrates: application in microsystem technology, *Lab Chip*, pp.1200-1204, (2006)

PRODUCTION OF DOUBLE EMULSIONS ON ONE CHIP BY MODIFYING SURFACE PROPERTIES

Shinya Tamaki, Satoshi Wada, Hidenori Tsuchiya, Muhammad Imran Al-Haq and Toru Torii

The University of Tokyo, Japan

ABSTRACT

This paper reports the novel technique for producing double emulsions on a single glass chip by controlling wetting property of the microchannel surface with octadecyltrichlorsilane (OTS) coating and ultraviolet (UV) irradiation. The droplet sizes and the numbers of inner droplets could be varied flexibly by changing the flow rates. A prospect of high-volume production is being proposed.

Keywords: Water-in-Oil-in-Water (W/O/W) emulsions, monodisperse, wetting property, microchannel

1. INTRODUCTION

Double emulsions have many applications in the fields of medicine, biology, chemistry, cosmetics, food products, *etc.*, and methods such as mixing, membrane emulsification, *etc.*, are being commercially used; however, it is difficult to control the size and the number of the inner droplets. Our group has previously reported the generation of monodisperse double emulsions with a combination of T-shaped glass microchannels [1, 2], and made it possible to design precise volumes and desired number of droplets. However, in that method, the process required complicated trials, so a simpler method was required for numbering-up of microchannels. Here, we present an alternative method to modify the glass microchannel surface: OTS was used for hydrophobizing the glass surface and then the UV irradiation was used for setting it back to hydrophilic. This technique was applied to generate Water-in-Oil-in-Water (W/O/W) emulsions.

2. EXPERIMENTAL

Figure 1 shows the schematic illustration of the microchannels for generating double emulsion. Inner droplets were to be formed at the first junction part and the outer droplets at the second one. A glass surface is originally hydrophilic. However, W/O emulsions are produced in a hydrophobic junction, and O/W emulsions in a hydrophilic junction. The first formation part, therefore, has to be hydrophobic for producing W/O/W emulsions. Hydrophobic surface was fabricated by introducing OTS solution in a microchannel, and was made hydrophilic again by applying UV light irradiation only on the second formation part by using a mask.

3. RESULTS AND DISCUSSION

We conducted two basic preparatory studies: (1) OTS effect on the glass surface, and (2) UV irradiation effect on it; and an actual study (3) surface modification technique to the microchannel to generate double emulsions.

978-0-9798064-0-7/μTAS2007/$20©2007CBMS

(1) OTS effect on a glass surface: The study showed that hydrophobic surface could immediately be produced by using OTS. Contact angles of aqueous droplets were of more than 100 degrees (Fig. 2). Monodisperse W/O droplets were successfully formed in the T-shaped glass microchannel modified by OTS coating. Figure 3 shows a graph between mean diameter and flow rate of continuous phase.
(2) UV irradiation effect: Figure 4 shows that hydrophilic surface was attained when UV was irradiated for a longer time (7 min), and monodisperse O/W droplets were formed in the T-shaped microchannel (Fig. 5).
(3) Double emulsion formation in one glass chip: W/O/W emulsions were successfully formed on the single glass chip (Fig. 6), and both outer and inner droplets had narrow diameter distributions with coefficient of variation (CV) less than 4% (Fig. 7).

4. CONCLUSION

We made possible to form monodisperse W/O/W emulsions on a single-glass chip by modifying the microchannel surface by using OTS coating and UV irradiation. In future, this technique is expected to enable us to have a mass-production of monodisperse double emulsions.

ACKNOWLEDGEMENT

This work was supported by grants-in-aid for Scientific Research (18310091) by Ministry of Education, Culture, Sports, Science and Technology.

REFERENCES:

[1] S. Okushima, T. Nisisako, T. Torii, and T. Higuchi, *Controlled Production of Monodisperse Double Emulsions by Two-Step Droplet Breakup in Microfluidic Devices*, Langmuir, 20, pp. 9905-9908, (2004).

[2] T. Nisisako, S. Okushima and T. Torii, *Controlled Formulation of Monodispserse Double Emulsions in a Multiple-phase Microfluidic System*, Soft Matter, 1, pp. 23-27, (2005).

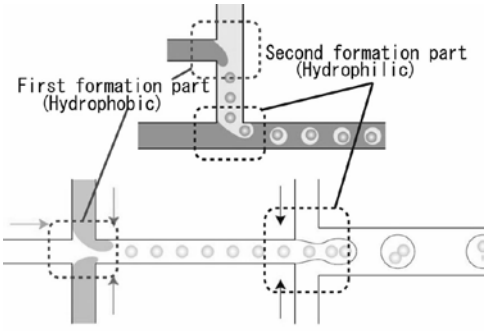

Figure 1. Schematic illustration of microchannels for producing double emulsions (the upper one is T-shape type. The lower one is cross-shape type and can include inner droplets of two kinds of materials).

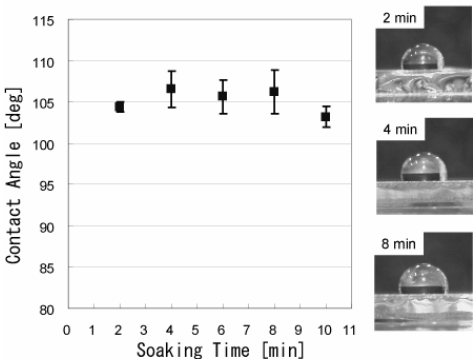

Figure 2. Relationships between OTS soaking time and contact angle of aqueous droplets on the glass surface

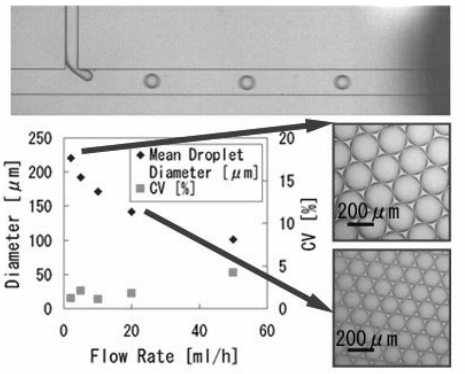

Figure 3. Formation of W/O emulsions in the glass microchannel with OTS modification

UV irradiation time [min]	0	1	3	5	7	10
Contact angle [deg]	93.7	88.6	86.4	81.8	54.5	29.6

Figure 4. Relationships between UV irradiation time and contact angle of aqueous droplets on the glass surface

Dispersion Phase (ml/h)	Continuous Phase (ml/h)	Droplet Diameter	
		Average (μm)	CV
0.02	10.0	115.4	4.5 %
0.4	10.0	133.3	3.3 %
0.8	10.0	141.4	2.8 %
1.0	10.0	148.0	2.5 %
1.0	20.0	95.6	7.1 %
1.0	50.0	62.9	6.6 %

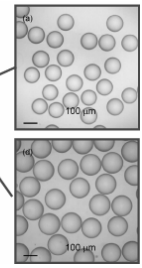

Figure 5. Variation in oil-droplet diameters with the change of continuous and dispersed phase flow rate

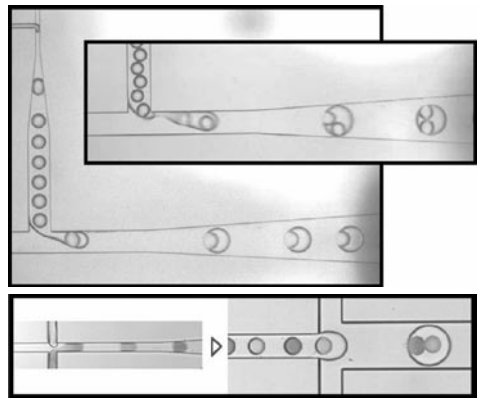

Figure 6. Formation of W/O/W emulsions

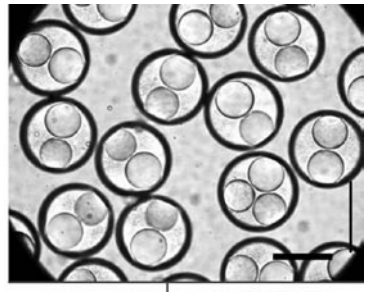

	Droplet Diameter	
	Average (μm)	CV
Outer Droplet	131.5	2.5 %
Inner Droplet (Red)	61.6	3.5 %
Inner Droplet (Blue)	56.5	3.8 %

Figure 7. Photograph of produced double emulsions (Table shows the measurements of both outer and inner droplets diameters)

PHOTOSYNTHESIS OF HIGH-VALUE ADDED COMPOUNDS IN A MICROREACTION SYSTEM

Yoshihisa Matsushita[1], Akiko Murata[2], Toshiaki Murata[3], Hideki Tanibata[4], Tadashi Suzuki[1], and Teijiro Ichimura[1]

[1] Tokyo Institute of Technology, JAPAN
[2] Dainippon Screen MFG. Co., Ltd., JAPAN
[3] Mitsui Zosen Plant Engineering Inc., JAPAN
[4] Mitsui Engineering & Shipbuilding Co., Ltd., JAPAN

ABSTRACT

A microreaction system for photosynthesis was developed and the processes of asymmetric photoreactions, photocatalytic *N*-alkylation of amines, and photocatalytic reduction of carbon dioxide were examined. These model reactions proceeded quite rapidly with considerably large efficiencies as compared to those in batch reaction system. Photocatalytic reduction of carbon dioxide in aqueous solution was examined by using several sort of metal co-catalyst loaded on the photocatalytic TiO_2 surface. It was found that methanol can be obtained as the main product by 6-electron reduction process in the photocatalytic microreaction system.

Keywords: Photoreaction, Asymmetric Reaction, Photocatalyst, Carbon Dioxide

1. INTRODUCTION

Although microreaction systems are successfully applied to a wide range of applications of chemistry, there are only a small number of reports on the application of microreactors to photochemical reactions. One can expect microreactors to exhibit some distinct properties for photoreactions, such as higher spatial illumination homogeneity and better light penetration through the entire reactor depth in comparison to large-scale reactors. In addition to this, if we apply microreactors for photocatalytic reactions, its high interfacial surface area may be an advantage over the conventional large-scale reactors. Therefore, we have been examining photochemical reaction processes in microreactors [1-5]. In this report, we will describe our results on photosynthesis of high-value added compounds in microreactors.

2. EXPERIMENTAL

Photoreaction was carried out in microreactors made of quartz or Tempax (Schott AG) plates and a thin film of self-welding fluorinated polymer which has a microchannel of 500-2000 μm in width, 20-500 μm in depth, and 50-120 mm in length. The microchannel was cut out from the polymer film by laser ablation. The thin film was placed between the two plates and heated under pressure to make a sandwich type leak-free structure. Typical experimental setup is schematically shown in Fig. 1. The bottom wall (one of the plates) of the microchannel was coated with a photocatalytic TiO_2 layer by using sol-gel process for photocatalytic reactions. Particles of metal co-catalysts were loaded on the TiO_2 layer of the microreactor by using a photodeposition method.

It has been widely accepted that the illuminated specific surface area of photocatalyst within a reactor is the most important design parameter of photocatalytic reactors. The

978-0-9798064-0-7/μTAS2007/$20©2007CBMS

illuminated specific surface areas per unit of liquid of the microreactor with a microchannel of 25 μm in depth was calculated to be 5.4 x 10^4 m^2/m^3 without taking into account of roughness of the photocatalyst surface. Thus the microreactors with immobilized photocatalyst have much larger values of illuminated specific surface area of photocatalyst than typical conventional batch reactors.

To show the advantages of the miniaturized reaction vessel, a light source of minimal space and lower photon cost is suitable for the microreaction system. Thus we employed UV light emitting diodes (UV-LEDs, 255, 265, 280, 310, 330 and 365 nm) for the excitation light source. Sample solution was fed into the microreactor with a syringe pump with a flow rate between 2 μl/min to 200 μl/min and irradiated with the UV-LEDs. Reaction products were analyzed by gas chromatograph (SHIMAZU GC-14B or GC-2014).

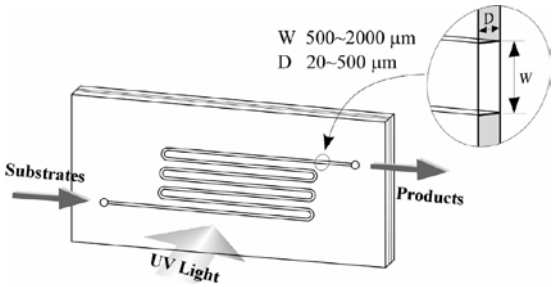

Figure 1. Schematic view of typical experimental setup.

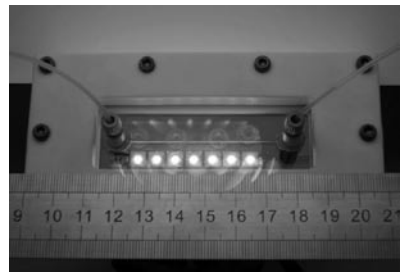

Figure 2. Photograph of a microreactor and UV-LEDs.

3. RESULTS AND DISCUSSION

It was revealed that the efficiency and selectivity of some asymmetric photocycloaddition reactions are greatly enhanced in comparison to the reaction in conventional batch reactors. The photonic efficiency of diastereo-differentiating addition of methanol to limonene in the microreaction system was more than 10 times larger than that obtained in a batch cell [3]. The result was probably brought by the distinct properties of microreactors on photoreactions, high spatial illumination homogeneity and excellent light penetration throughout the reactor. Moreover, in the micro-flow system, the residence time of the substrate is very short and the reaction vessel does not retain the reaction products. These features may prevent sequential side reactions and increase the yield of the photoreaction.

We have developed a photocatalytic microreaction system by immobilizing a photocatalytic TiO_2 layer on inner walls of microfabricated channels. In contrast to the results in a batch reactor, we successfully observed *N*-alkylation of aromatic amines to take place by using the microreactor with immobilized Pt-free TiO_2 as well as Pt loaded TiO_2[4]. *N*-alkylation of benzylamine in ethanol proceeded within only 5 seconds to yield 64 % of *N*-ethylbenzylamine and within 10 seconds to yield 32 % of *N,N*-diethylbenzylamine in a photocatalytic microreactor of 25 μm in depth (Fig. 3).

Photocatalytic reduction of CO_2 was also examined by using several sort of metal co-catalyst loaded on the TiO_2 surface. Though it has been known that CO_2 in aqueous solution can be photocatalytically reduced, only very low reaction yields were reported by using large-scale batch reaction systems. The reaction proceeded very quickly to form methanol as the main reaction product with considerably large efficiencies in our

microreaction system. Among the co-catalysts examined in this study, Pt has shown the highest photocatalytic activity (Table 1).

Table 1. Photocatalytic reduction of CO_2. Distilled water saturated with CO_2 was introduced into a microchannel of 25 μm in depth and then irradiated by 365 nm UV-LEDs (36 mW/cm^{-2}) for 150 seconds.

Photocatalyst	Yield of methanol (mM)
TiO_2/Pt	2.4
TiO_2/Pd	1.4
TiO_2/Rh	2.2
TiO_2/Ag	1.6
TiO_2	0.09

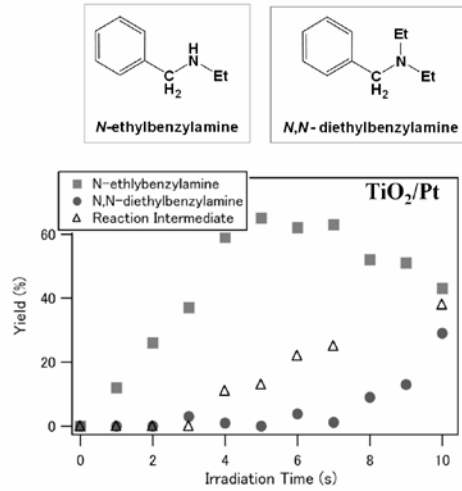

Figure 3. *N*-alkylation of benzylamine in a photocatalytic microreactor excited with 365-nm UV-LEDs.

4. CONCLUSIONS

A microreaction system optimized for asymmetric photoreactions and photocatalytic reactions was developed and the processes of asymmetric photocycloaddition, photocatalytic *N*-alkylation of amines, and photocatalytic reduction of CO_2 were examined. It was revealed that the selectivity and efficiency of the photoreactions can be enhanced by using the unique features of microreactors, for instance spatial illumination homogeneity, large surface-to-volume ratio, and precise control of flow and irradiation conditions.

ACKNOWLEDGEMENTS

This work was supported by a Grant-in-Aid for Scientific Research (No. 16550134) from the Ministry of Education, Culture, Sports and Technology of Japan, and the New Energy and Industrial Technology Development Organization (NEDO), Project of Development of Microspace and Nanospace Reaction Environment Technology for Functional Materials.

REFERENCES

[1] Y. Matsushita, S. Kumada, K. Wakabayashi, K. Sakeda, and T. Ichimura, *"Photocatalytic reduction in microreactors",* Chem. Lett., 35, pp. 410-411 (2006).

[2] Y. Matsushita, N. Ohba, S. Kumada, K. Sakeda, T. Suzuki, and T. Ichimura, "*Photocatalytic reactions in microreactors",* Chem. Eng. J, in press.

[3] K. Sakeda, K. Wakabayashi, Y. Matsushita, T. Ichimura, T. Suzuki, T. Wada and Y. Inoue, "*Asymmetric photosensitized addition of methanol to (R)-(+)-(Z)-limonene in a microreactor",* J. Photochem. Photobiol. A:Chemistry, in press.

[4] Y. Matsushita, N. Ohba, S. Kumada, T. Suzuki, T. Ichimura, "*Photocatalytic N-alkylation of benzylamine in microreactors",* Catal. Commun, in press.

[5] Y. Matsushita, T. Ichimura, N. Ohba, S. Kumada, K. Sakeda, T. Suzuki, H. Tanibata, and T. Murata, "*Recent progress on photoreactions in microreactors",* Pure Appl. Chem., in press.

SPATIALLY RESOLVED MICROFLUIDIC SOLVENT ETCHING OF BICOMPONENT EXTRUSION NANOFIBERS

S. Lok[1], J. P. Hinestroza,[2] B. J. Kirby[3]

[1]Electrical and Computer Engineering, [2]Fiber Science and Apparel Design, [3]Mechanical and Aerospace Engineering, Cornell University, Ithaca, NY 14853

ABSTRACT

We use microfluidic flow patterning to solvent-etch sacrificial polymers from bicomponent extrusion fibers, exposing microscale lengths of isolated nanofiber for mechanical three-point bending tests using AFM tip probes. These isolated nanofibers have been shown to exhibit high elastic modulus, and show potential for novel textiles. The chemically gentle and specific nature of solvent patterning compares favorably with laser techniques, and the simplicity of the device makes it more practical and cost-effective than e-beam or ion-beam patterning techniques.

Keywords: nanofiber, flow focusing, bicomponent extrusion, solvent etching

1. INTRODUCTION

In this work we use microfluidic flow patterning to solvent-etch sacrificial polymers from bicomponent extrusion fibers, exposing microscale lengths of isolated nanofiber for mechanical three-point bending tests using AFM tip probes.

Bicomponent extrusion of polymer fibers embedded in sacrificial material [1] offers a unique opportunity to create mechanically strong nanofibers. Through customizable spin-packs, separate polymer streams are directed through customized distribution plates, forming a conjugated stream. This stream directly exits via a spinneret hole and allows for the production of bicomponent fibers with up to 1200 nanoscale domains (Figure 1). When the dimensions of these nanoscale domains are in the order of tens of nanometers, several unusual flow phenomena occur, including domain encapsulation, domain coalescence, domain dimensional instabilities, differential crystallization kinetics, and induced superdrawing. Recent results using atomic-force acoustic microscopy [2] have shown that elastic moduli of the nanofibers can vary by up to a factor of 100 within a single bicomponent fiber. It is hypothesized that variations in stiffness are caused by differential crystallization kinetics and induced superdrawing by the velocity profile during the extrusion process.

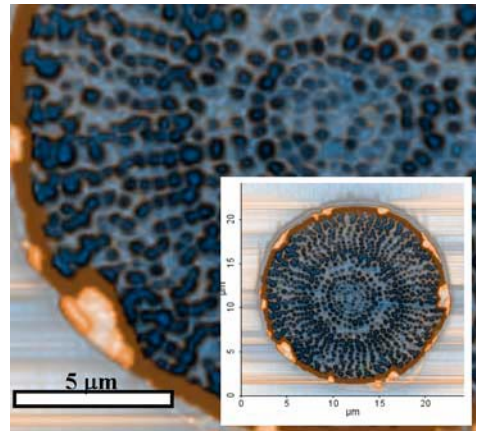

Figure 1. AFM cross-sectional image of a bicomponent fiber containing 1120 nanodomains. The nanoscale domains are made of polyester and the sacrificial material is polyethylene. Domain coalescence and domain dimensional instabilities increase in the radial direction. Fiber strengths are highest near the center.

978-0-9798064-0-7/µTAS2007/$20©2007CBMS

2. MATERIALS AND METHODS

Glass microdevices were purchased from Caliper Life Sciences. Flow was controlled using syringe pumps (Figure 2) and routed to the microdevice with stainless steel tubing and microfluidic fixtures (LabSmith). Etching solvent was visualized with fluorescein and fluorescence with an inverted microscope. Fiber etching was visualized with light scattering.

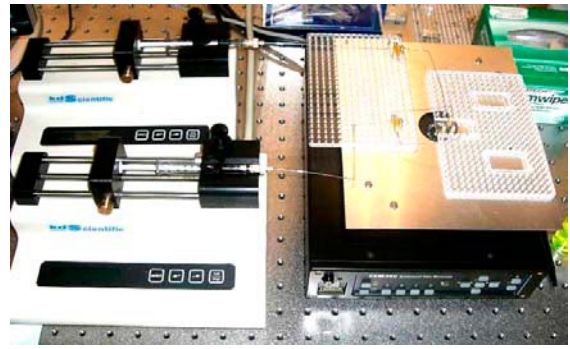

Figure 2. Experimental setup for processing nanofibers.

3. RESULTS/DISCUSSION

Nanofibers are exposed by using a microfluidic flow patterning technique to expose the fiber to a spatially-resolved solvent flow. Laminar flow patterning techniques are combined with equivalent circuit analysis to predict junction pressures and allow control of flow rate ratios of etching solvents and sheath flows. Nanofibers encased within microfluidic devices are exposed to a steady flow of solvent for 1-90 minutes; visual evidence of polymer etching is achieved after only a few minutes, but removal of sacrificial material through a 20 micron diameter fiber typically takes over one hour. The resulting exposed nanofibers (Figure 3) are ideally suited for mechanical testing via three-point bending with AFM tips, owing to the short fiber length and mechanically secure housing. Nylon-66 nanofibers in a sacrificial poly(vinyl alcohol) matrix were subject to a etching solvent flow (0.1 mM pH 9) focused by two methanol sheath flows. Imaging of dye-visualized flow and fiber etching via light scattering (Figure 4) show the capability of this technique to etch nanofibers in a spatially resolved manner. The flow patterning shows ability to resolve the solvent to micron-scale dimensions (Figure 5). The chemically gentle and specific

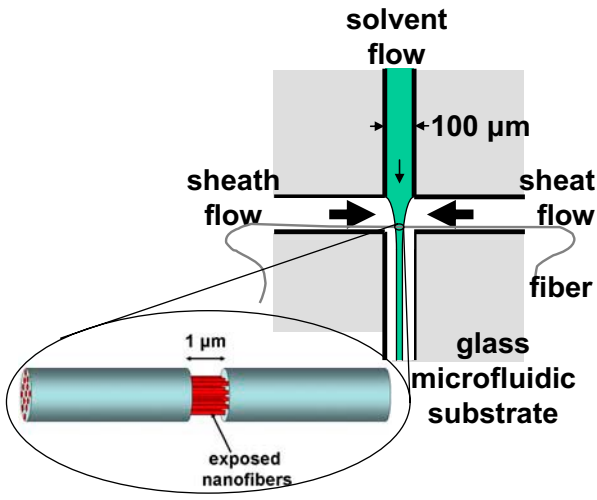

Figure 3. Schematic of microfluidic flow patterning used to solvent-etch fibers. Sheath flow is methanol. Solvent flow is 0.1 mM phosphate buffer, pH=9. Fiber is composed of nylon-66 nanofibers in sacrificial poly(vinyl alcohol) matrix.

nature of solvent patterning compares favorably with laser techniques, and the simplicity of the device makes it more practical and cost-effective than e-beam or ion-beam patterning techniques.

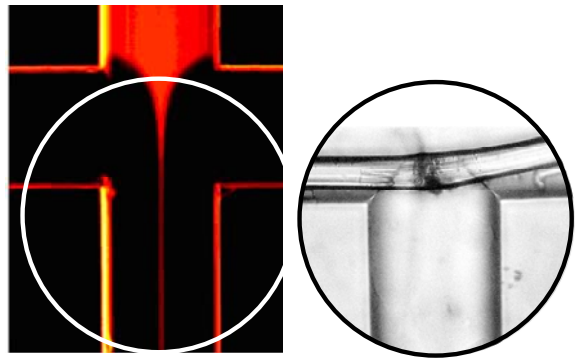

Figure 4. Fiber etching visualized using dye visualization (left) and transmitted light (right). Upon etching the sacrificial layer, the scattering off of the individual nanofibers is increased, leading to a darker appearance.

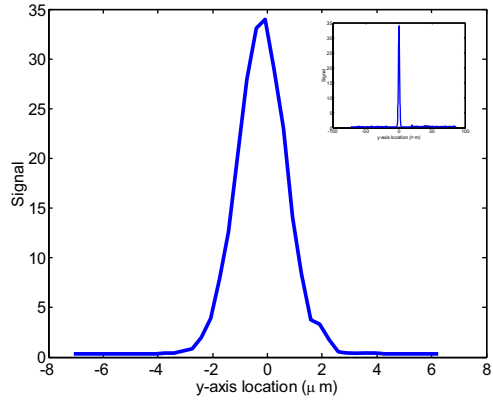

Figure 5. Spatial resolution of etching solvent is on the order of 3 microns, as seen in the blowup of the region around the solvent flow (inset: signal distribution across field of view).

REFERENCES

[1] Kikutani, T., Radhakrishnan, J., Arikawa, S., Takaku, A., Okui, N., Jin, X., Niwa, F., Kudo, Y., Highspeed melt spinning of bicomponent fibers: mechanism of fiber structure development in poly(ethylene terephthalate)/polypropylene system, J. Appl. Polym. Sci., 62, 1913-1924, 1996.

[2] U. Rabe, V. Scherer, S. Hirsekorn, and W. Arnold, "Nanomechanical surface characterization by atomic force acoustic microscopy", J. Vac. Sci. Technol. B 15(4), 1506-1511, 1997.

FUEL AND MEDIA FLEXIBLE AIR-BREATHING LAMINAR FLOW FUEL CELLS

R.S. Jayashree[1], W.-P. Zhou[1], M. Mitchell[1], S.K. Yoon[2], and P.J.A. Kenis[1,2]

[1]Department of Chemical & Biomolecular Engineering and [2]Department of Mechanical Science and Engineering, University of Illinois at Urbana-Champaign, USA.

ABSTRACT

This paper reports on air-breathing laminar flow fuel cells (LFFCs) that are fueled with formic acid, methanol, ethanol, hydrazine, or sodium borohydride. Previously we reported the design and fabrication of air-breathing direct formic acid LFFCs [1]; here, we both demonstrate the ability to use a variety of fuels and electrolytes within the same fuel cell design and provide design rules for the optimization of the performance of these direct liquid LFFCs.

Keywords: membraneless, fuel cell, laminar flow, microfluidics

1. INTRODUCTION

Rising demand for power necessitates the development of high energy density power sources for various applications. Fuel cells exhibit high energy density, and polymer electrolyte membrane fuel cells (PEMFCs), which typically use a Nafion membrane to separate the anode and cathode, are the most widely studied type of fuel cell for portable power sources. There are two major disadvantages of using a Nafion membrane: liquid fuels such as methanol and formic acid can pass through the Nafion membrane, and water is dragged along with the protons from the anode to the cathode side. Laminar flow fuel cells (LFFCs) utilize the property of laminar flow to separate the anode and the cathode streams without the need of a membrane (Figure 1), thereby minimizing water management issues that arise in PEMFCs [2]. Similarly, fuel crossover due to diffusional mixing of the anode and cathode streams can be minimized by appropriately tuning the flow rates and cell dimensions. A variety of liquid fuels are being investigated as direct fuels for fuel cells because many liquid fuels exhibit higher energy densities than gaseous hydrogen. Here, we report the performance of LFFCs fueled with formic acid, methanol, ethanol, hydrazine, and sodium borohydride.

2. EXPERIMENTAL

The anodes were prepared by painting catalyst inks on graphite plates, with different anode catalysts being used for different fuels. The anode catalyst loading was 10 mg/cm^2 of Pt for hydrazine and sodium borohydride, 10 mg/cm^2 of Pt/Ru for ethanol and methanol, and 10 mg/cm^2 of Pd for formic acid. Nafion was used as the binder, and its loading on the anode was 1.5 mg/cm^2. The cathodes were prepared by painting catalyst ink on gas diffusion electrodes. The cathode loading was 2 mg/cm^2 of Pt and 0.1 mg/cm^2 of Nafion binder. An LFFC (depicted in Fig. 1) was assembled by placing a sheet of PMMA with a machined microfludic channel onto a graphite anode with holes drilled for the fuel and electrolyte inlets and the outlet. Then the cathode was mounted on the PMMA sheet with the catalyst side face down, and a graphite plate with a machined window was positioned on the cathode and used as a current collector. The anode stream was composed of the desired concentration of fuel in either 0.5 M H_2SO_4 or 1 M KOH, and the cathode stream was composed of 0.5 M H_2SO_4 or

978-0-9798064-0-7/μTAS2007/$20©2007CBMS

1 M KOH. In all experiments, the flow rates of the anode and the cathode streams were 0.3 ml/min and the anode-to-cathode distance was 2 mm.

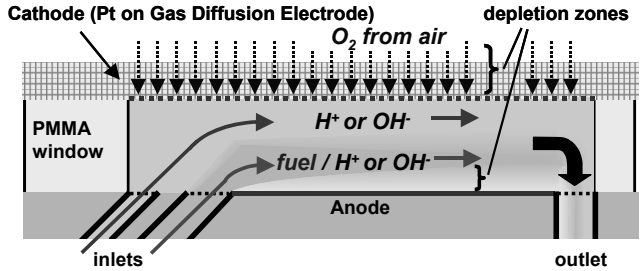

Figure 1. Schematic of an air-breathing LFFC. The anode catalyst is composed of Pt, Pd, or Pt/Ru nanoparticles, depending on the fuel used (adopted from ref. [1]).

3. RESULTS AND DISCUSSION

We have developed laminar flow fuel cells that lack a Nafion membrane. By removing the membrane, we can use different fuels and electrolyte media within the same fuel cell by simply changing the anode catalyst. We have studied the performance of methanol and ethanol LFFCs in both acidic and alkaline media since the kinetics of the oxidation of methanol and ethanol are both superior in alkaline media than in acidic media. Figure 2 depicts the polarization and power density curves for this LFFC in acidic media fueled by formic acid, methanol, ethanol, and hydrazine, with observed peak power densities of 26.0, 11.8, 1.90, and 36.1 mW/cm^2, respectively. The kinetics of the oxidation of formic acid and hydrazine are more facile than the oxidation of methanol or ethanol because oxidation of methanol or ethanol leads to the formation of intermediates such as CO that poison the catalyst surface.

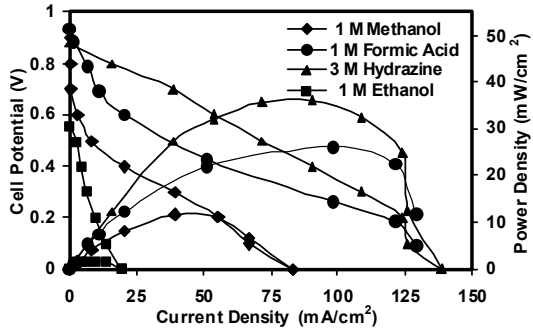

Figure 2. Polarization and power density curves for LFFCs fueled with methanol, ethanol, formic acid, and hydrazine in acidic media (0.5 M H_2SO_4).

Furthermore, we demonstrated the ability to vary the electrolyte media by studying the performance of methanol, ethanol, and sodium borohydride LFFCs in alkaline media, with observed peak power densities of 17, 7.6, and 101 mW/cm^2, respectively (Figure 3). The ability to use alkaline media instead of acidic media is advantageous as evidenced by the improved performance for the oxidation of methanol and ethanol [3,4]. The presence of adsorbed OH species on the catalyst surface in alkaline media enables easy oxidation of intermediates such as CO on the catalyst surface, thereby enhancing the rate of methanol or

ethanol oxidation. The superior performance of sodium borohydride fuel cells is due to the faster kinetics of oxidation of sodium borohydride than of other fuels.

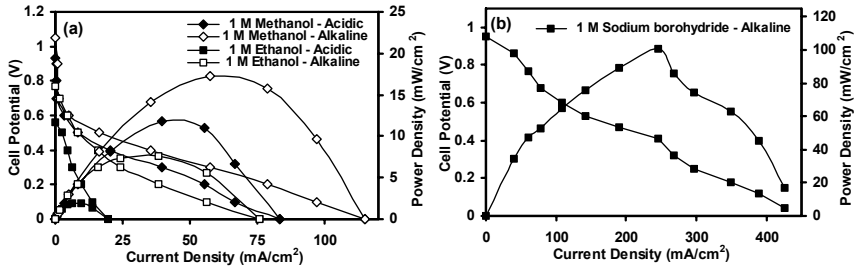

Figure 3. Polarization and power density curves for (a) methanol and ethanol in both acidic and alkaline media, and (b) sodium borohydride in alkaline media.

We also looked to maximize the performance of this LFFC by independently varying parameters such as the total flow rate, the ratio of the anode and cathode flow rates, the electrode-to-electrode distance, and the concentration of oxygen on the cathode side. Reducing the electrode-to-electrode distance and increasing the flow rates of the anode and cathode streams result in higher power densities as a result of improved mass transport to the electrodes. Another measure of fuel cell performance is the fuel utilization. Higher flow rates of the anode and cathode streams yield higher peak power densities, but also result in lower fuel utilization. By using a 1:20 flow ratio of the anode and cathode streams we achieved as high as 40% fuel utilization per pass. We also have adapted the design of the LFFC to handle gaseous fuels, and have observed peak power densities of 115 and 68 mW/cm^2 in acidic and alkaline media, respectively, using hydrogen as the fuel. This fuel cell design is particularly suitable as a tool for cathode optimization, one of the major bottlenecks in fuel cell development and commercialization.

4. CONCLUSIONS

In this work, we present the fuel and media flexibility of laminar flow fuel cells, and we discuss the performance of LFFCs with different fuels such as formic acid, methanol, ethanol, hydrazine, and sodium borohydride. The present LFFC design, with hydrogen flow on the cathode side, can be used as an anode optimization tool. We also discuss the design rules to improve fuel utilization and fuel cell performance for such a fuel cell design.

ACKNOWLEDGEMENTS

Financial support from NSF, ARO, UIUC, and DOE is gratefully acknowledged. The authors thank Fikile Brushett for helpful discussions.

REFERENCES

[1] R.S. Jayashree, L. Gancs, E.R. Choban, A. Primak, D. Natarajan, L.J. Markoski and P.J.A. Kenis, *J. Amer. Chem. Soc.*, 2005, **127**, 16758.
[2] S. Litster and G. McLean, *J. Power Sources*, 2004, **130**, 61.
[3] R.S. Jayashree, D. Egas, J.S. Spendelow, D. Natarajan, L.J. Markoski and P.J.A. Kenis, *Electrochem. Solid-State Lett.*, 2006, **9**, A252
[4] J.S. Spendelow, J.D. Goodpaster, P.J.A. Kenis and A. Wieckowski, *Langmuir*, 2006, **22**, 10457.

MICROREACTORS FOR REACTION KINETICS MONITORING ON A CHIP – FROM SINGLE LINE TO MULTICHANNEL QUENCH-FLOW DEVICE

Wojciech P. Bula[1], David N. Reinhoudt[2], Willem Verboom[2] and Han J.G.E. Gardeniers[1]

[1]Mesoscale Chemical Systems Group (MCS)
[2]Supramolecular Chemistry and Technology Group (SMCT)
MESA+ Institute for Nanotechnology, University of Twente, Enschede, THE NETHERLANDS

ABSTRACT

Two types of silicon-glass microreactors have been designed, fabricated and tested. The conventional single-line microreactor with implemented quenching ability and a microfluidic network where chemical reactions can be performed in 4 parallel lines have been utilized to investigate the kinetics of Knoevenagel condensation reaction in microscale. The system was tested experimentally and showed good reproducibility in the microfluidic and chemical domain.

Keywords: parallel microreactor, kinetic studies, Knoevenagel condensation, rate enhancements, quenching-on-a-chip

1. INTRODUCTION

Nowadays, microfluidic systems offer a number of advantages for the field of chemistry [1]. The fact that reactions can be performed in complex microchannel networks with volumes of nanoliters allows for high-throughput evaluation of (combinatorial) reaction conditions with minute amounts of ingredients of limited availability [2, 3].

In this paper we demonstrate that parallel silicon-glass microreactors allow the accurate investigation of the kinetics of a reaction at different reaction times. A single-line microreactor where chemical reactions can be initiated and quenched on the chip (Figure 1a) and its scaled-up implementation – a microfluidic network that allows the investigation of the reaction at four different reaction times simultaneously (Figure 1b) - is described. The design of both microreactors allows further integration with analytical instrumentation as NMR [4], MS [5].

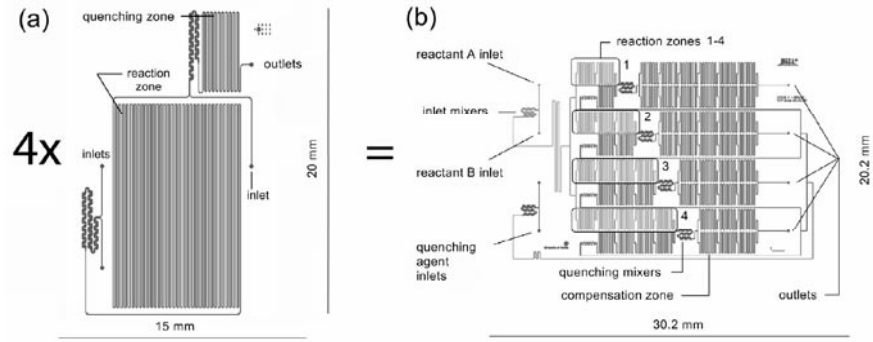

Figure 1. Schematic representation of 1-line (left) and 4-line (right) quench-flow microreactor

978-0-9798064-0-7/μTAS2007/$20©2007CBMS

2. MICROREACTOR LAYOUT

The design of multichannel reactor is such that the total hydraulic resistances and the volumes of each reaction loop are equal, which allows flow parallelization and minimization of the experimental effort and costs (e.g. using a minimal number of pumps). Parallel organic reactions can be initiated, controlled, and chemically quenched on the chip for each reaction line independently. An experiment comprises mixing of reactants and catalyst in an inlet mixer, after which the active mixture is split and passed into 4 different reaction lines. The reaction time for each line is defined as the period between the process initialization in the inlet mixer and the reaction termination in the quenching mixers connected to each line (Figure 1b).

3. MICROREACTOR FABRICATION AND FLOW PARALLELIZATION TESTS

The silicon-glass reactor was fabricated by standard cleanroom processing (Figure 2a). Channel dimensions are 50 µm x 50 µm (width x depth). The shortest reaction coil is built of 2 segments (6.64 cm each), the longest one of 5 segments. The total microreactor volume is 16 µL, of which 2.2 µL is the original reaction mixture in 4 coils.

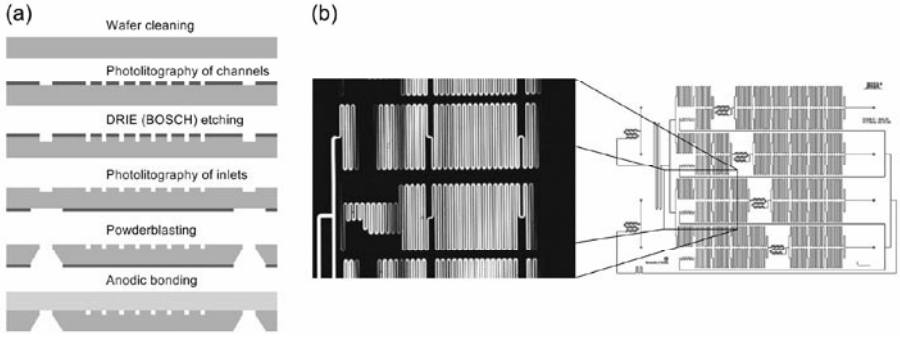

Figure 2. (a) Process scheme for the fabrication of the microreactor. (b) Transport of fluorescent tracers in parallel reaction loops

Flow parallelization tests were performed by observing the transport of fluorescent plugs through parallel channels (Figure 2b). Measured differences between the flows in complementary channels were smaller than 4% for the tested flow rate range (0.1-2 µL/min).

4. KINETIC STUDIES

The microreactor was used to perform parallel Knoevenagel condensation reactions of equimolar (20 mM) solutions of p-methoxybenzaldehyde (1) and malononitrile (2) in acetonitrile in the presence of 1,8-diazabicyclo-(5.4.0)undec-7-ene (DBU) as catalyst (3) and trifluoroacetic acid (TFA) as quenching agent. The temperature of the microreactor was controlled by a thermoelectric module. Temperature variation on the glass surface of the chip was less than 0.1 K. The quenched reaction products were analyzed by UV-Vis absorbance measurements. Reaction rate constants were determined from the experimental data (Figure 3) according to a reversible second-order kinetics model (Table 1).

A remarkable result is that the conversion values and the reaction rates found for the chip experiments are substantially higher than those obtained in lab-scale batch experiments. We attribute the nature of this phenomenon to the mass transport limitations in the lab scale experiments, that are absent in the microreactors.

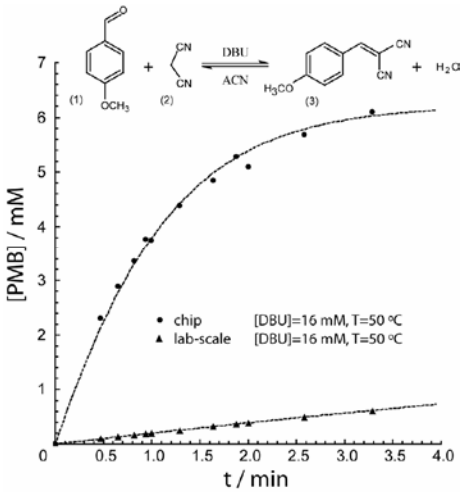

Table 1. Fitted reaction parameters

	k_f [1)] [$M^{-1}min^{-1}$]	k_r [2)] [$M^{-1}min^{-1}$]	C_{PMBe} [3)] [mM]
chip	13.1	28.7	6.1
lab-scale	0.5	4.6	1.9

[1)] k_f – forward reaction constant,
[2)] k_r – reverse reaction constant,
[3)] C_{PMBe} – concentration of product at equilibrium

Figure 3. Scheme of the condensation reaction of 4-methoxybenzaldehyde and propanedinitrile and product formation for chip and batch experiments ([DBU]=16 mM, T=50 ºC). Dashed line – theoretical conversion according to the model.

5. CONCLUSIONS

The microfluidic platform was realized to study organic reactions at microscale in the continuous flow regime. The silicon-glass microreactors allow the accurate investigation of the kinetics of a reaction in microscale with small amounts of reactants. The presented design of multiline quench-flow microreactor overcomes the common problem concerning the difference in pressure drop of a parallel channels having different length. The reaction is performed under identical conditions in all lines but varying residence time. The system showed good reproducibility and precision of kinetic studies in parallel. Higher rate constants were found for the reaction in the chip (compared to the batch experiments). The absence of the mass transport limitations in microscale compared to batch conditions increases the precision of kinetic studies.

ACKNOWLEDGEMENTS

We acknowledge financial support from the Netherlands Organisation for Scientific Research and Advanced Chemical Technologies for Sustainability (NWO-ACTS).

REFERENCES

[1] K. Jähnisch, V. Hessel, H. Löwe, M. Baerns, *Angew. Chem. Int. Ed.* 2004, *43*, 406
[2] H. Song, D.L. Chen, R.F. Ismagilov, *Angew. Chem. Int. Ed.* 2006, *45*, 7336
[3] C.L. Hansen, S. Classen, J.M. Berger, S.R. Quake, *J. Am. Chem. Soc*. 2006, 128, 3142
[4] H. Wensink, F. Benito-Lopez, D.C. Hermes, W. Verboom, J.G.E. Gardeniers, D.N. Reinhoudt, A. van den Berg, *Lab Chip* 2005, 5, 280
[5] M. Brivio, R.H. Fokkens, W. Verboom, D.N. Reinhoudt, N.R. Tas, M.H. Goedbloed, A. van den Berg, *Anal. Chem*. 2002, *74*, 3972; M. Brivio, N. Tas, M.H. Goedbloed, H.J.G.E. Gardeniers, W. Verboom, A. van den Berg, D.N. Reinhoudt, *Lab Chip*, 2005, *5*, 378

A NOVEL COAXIAL SHEATH FLOW DEVICE FOR SAMPLE FOCUSING

G. Hairer, G.S. Pärr, P. Svasek, A. Jachimowicz, and M.J. Vellekoop
Vienna University of Technology, AUSTRIA

ABSTRACT

In this paper we present a novel coaxial sheath flow device where the sheath flow surrounds the sample flow at all sides. This micro fabricated device consists of a simple design and the dimensions of the channel have been chosen such that sample flow diameters of a few microns are feasible in a relatively large channel of 25 x 40 µm². This focusing technique prevents channel clogging and undesired sample adsorption on the channel walls. In this contribution we studied the sample flow profile using laser scanning confocal measurement method. The achieved sample flow dimensions of 1.5 x 12 µm² of the focusing section are verified with 3D simulations.

Keywords: microfluidics, hydrodynamic focusing, coaxial sheath flow

1. INTRODUCTION

The measurement of particles in solution (e.g. beads, cells or molecules) in a MEMS device for analytical purposes makes it necessary to deal with detailed aspects in microfluidics. Especially when it comes to single particle detection or manipulation it is inevitable to use focusing techniques. In literature hydrodynamic focusing techniques with coaxial sheath flow are illustrated in [1], [2], [3], and [4]. These devices are either complex to fabricate or do not have the flexibility in sample adaption inside the channel. Additionally all devices have channel sizes in the range of several hundred micrometers. The use of sheath flow allows focusing a sample flow with high accuracy, which was shown in non coaxial sheath flows [5]. In this contribution we investigate the creation of a very small diameter sample flow in a coaxial sheath flow setup. The dimensions of the channels and fluid inlets have been chosen such that sample flow diameters of a few microns are feasible in a relatively large channel of 25 x 40 µm². This focusing technique prevents channel clogging and undesired sample adsorption on the channel walls. This fabricated coaxial sheath flow device allows single particle detection or manipulation in the range of a few micrometers.

2. DEVICE DESCRIPTION

In Figure 1 a photograph of the fabricated chip is depicted. The chip consists of a silicon-glass sandwich with SU-8 in between. The access holes through silicon (360 µm thick) are anisotropically etched with a KOH water solution. The dimensions of the access holes at the channel side are 330 x 330 µm² (sheath inlet, side ports and outlet), 25 x 25 µm² (sample inlet), and 25 x 50 µm² (lifting inlet). The channel widths at the channel crossing area are 25 µm. The 40 µm thick SU-8 resist define the channel geometry and the channel height. Finally, a 200 µm thick glass cover slide is bonded irreversibly via SU-8 to the silicon. The chip fabrication is carried out with wafers of 100 mm in diameter.

In Figure 2 the principle of the coaxial sheath flow device is shown. The sample liquid is vertically injected into the channel, where a sheath liquid is flowing. After a first focusing

978-0-9798064-0-7/µTAS2007/$20©2007CBMS

section the sample liquid is lifted up by adding sheath liquid through the lifting inlet and a coaxial flow is formed. The side ports additionally focus the sample liquid. The influence on the shape, size and position of the sample flow can be controlled by the relative flow rates of the sheath inlets to the sample inlet.

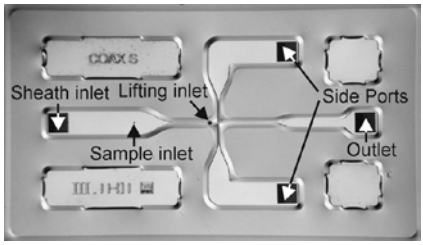

Figure 1. Photograph of the fabricated coaxial sheath flow device (chip dimensions 4 x 7 mm²).

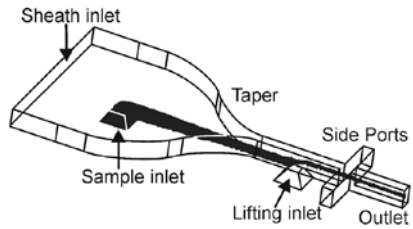

Figure 2. Schematic of the coaxial sheath flow cell.

3. EXPERIMENTAL

For experiments the coaxial sheath flow device is fixed on a custom made holder where silicone tubes are integrated for fluidic connections to syringes. A custom molded silicone gasket is put between the holder and the fluidic chip to achieve a tight connection. The syringe pumps (kdScientific model 200 series) define the flow rates at the different inlets. A diluted fluorescent dye (acridine orange) is used for the sample flow and the sheath flow consists of deionized water. To get information on the real sample flow profile and size we constituted measurements with a confocal laser scanning microscope (Confocal C1 TE300, Nikon).

4. RESULTS AND DISCUSSION

Figure 3 shows the sample flow at the region where the sample flow is lifted up and afterwards gets horizontally focused (top and side view). The images present the emitted green color of the fluorescent dye. The flow rates at the inlet ports are held at 15 µl/min (sheath inlet), 0.5 µl/min (sample inlet), 12.5 µl/min (lifting inlet), and 40 µl/min (side ports). The sample flow is lifted up to the middle of the channel and afterwards gets focused by the side ports. At the focusing region dynamic effects appear to the sample flow and before squeezing the sample flow broadens up. Figure 4 depicts the real sample flow profile at the region A, B, and C (see Figure 3). After lifting the sample flow its profile gets a bit broader and lower. After the side port focusing the height of the profile stays the same. The sample flow dimensions seen in picture C are 1.5 µm horizontally and 12 µm vertically. There is still potential to reduce the vertical dimension by reducing the sample flow height or fabricating the channel height with the same channel width. To verify the results of the measured sample profiles a 3D simulation with Comsol Multiphysics is carried out. The simulation results at the region A, B, and C of Figure 3 are shown in Figure 5. These results are in good agreement with the measured ones in Figure 4.

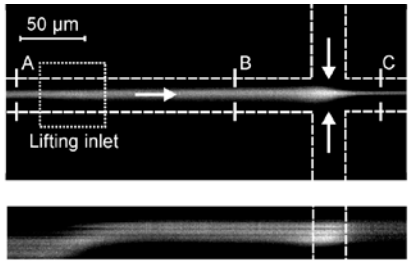

Figure 3. Measurement results with the confocal microscope. Top: Plan view of the section with lifting inlet and side ports. (The edges of the channels are outlined with a dashed line and the lifting inlet in silicon is outlined with a dotted line. The arrows indicate the flow direction). Bottom: Side view of the channel. The flow rates at the inlet ports are held at 15 µl/min (sheath inlet), 0.5 µl/min (sample inlet), 12.5 µl/min (lifting inlet), and 40 µl/min (side ports).

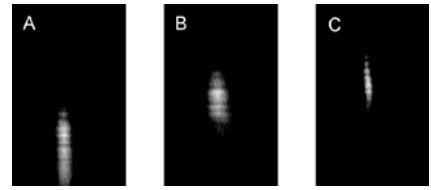

Figure 4. Confocal measurements inside the channel; the pictures reveal the sample flow profiles at the positions A, B, and C (Figure 3).

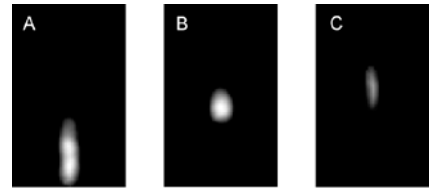

Figure 5. Simulation results of the coaxial sheath flow device; the pictures reveal the sample flow profiles at the positions A, B, and C (Figure 3).

5. CONCLUSIONS

In this contribution we demonstrate a novel coaxial sheath flow device for sample focusing. The sample flow is characterized using confocal measurements and a 3D simulation. The shown sample flow dimensions after the side ports belong to 1.5 µm x 12 µm, where the vertical dimension of the sample flow profile can be still reduced. The simulation results are in good agreement with the measured ones. This coaxial sheath flow device is suitable for focusing and alignment of asymmetric cells to carry out single cell detection.

REFERENCES

[1] N. Sundararajan, M.S. Pio, L.P. Lee, and A.A. Berlin, *Three-Dimensional Hydrodynamic Focusing in Polydimethylsiloxane (PDMS) Microchannels*, J. of Microelectromechanical Systems, Vol. 13, pp. 559-567, (2004).

[2] R. Yang, D.L. Feeback, and W. Wang, *Microfabrication and test of a three-dimensional polymer hydro-focusing unit for flow cytometry applications*, Sensors and Actuators A, Vol. 118, pp. 259-267, (2005).

[3] A. Wolff, I.R. Perch-Nielsen, U.D. Larsen, P. Friis, G. Goranovic, C.R. Poulsen, J.P. Kutter, and P. Telleman, *Integrating advanced functionality in a microfabricated high-throughput fluorescent-activated cell sorter*, Lab Chip, Vol. 3, pp. 22-27, (2003).

[4] C. Simonnet, and A. Groisman, *Two-dimensional hydrodynamic focusing in a simple microfluidic device*, Applied Physics Letters, Vol. 87, 114104, (2005).

[5] G. Hairer, and M.J. Vellekoop, *Experiments on hydrodynamic focusing of non coaxial sheath flows*, IEEE Sensors 2006, Daego, p. 431, (2006).

ELECTROMECHANICAL ANALYSIS OF AC ELECTROWETTING OF A DROPLET

J. S. Hong[1], S. H. Ko[2], K. H. Kang[2], and I. S. Kang[1]

[1]Department of Chemical Engineering, [2]Department of Mechanical Engineering , Pohang University of Science and Technology, South Korea

ABSTRACT

The electrowetting shows some distinctive features when AC electric field is applied instead of DC field including the delay of contact-angle saturation. To excavate those phenomena yet to be explained, we investigated the fundamental nature of AC EWOD (electrowetting on dielectrics), numerically and experimentally. The numerical results showed a good agreement with experimental results.

Keywords: Electrowetting, alternating current, contact angle saturation

1. INTRODUCTION

The electrowetting phenomenon persists even when an AC signal is applied because the electrical wetting tension is proportional to square of applied voltage. Interestingly, if an AC signal is applied instead of DC signal, it shows several distinctive features. Especially, the contact-angle saturation is delayed in AC case [1]. To excavate those intriguing phenomena, we analyze the conventional EWOD system numerically and experimentally. Based on the numerical results, we attempted to explain the cause of delay of the contact-angle saturation, in conjunction with the delay of the dielectric breakdown [2].

2. THEORY

We analyze the electric field around a sessile droplet placed on an insulator-covered electrode as shown in Figure 1.

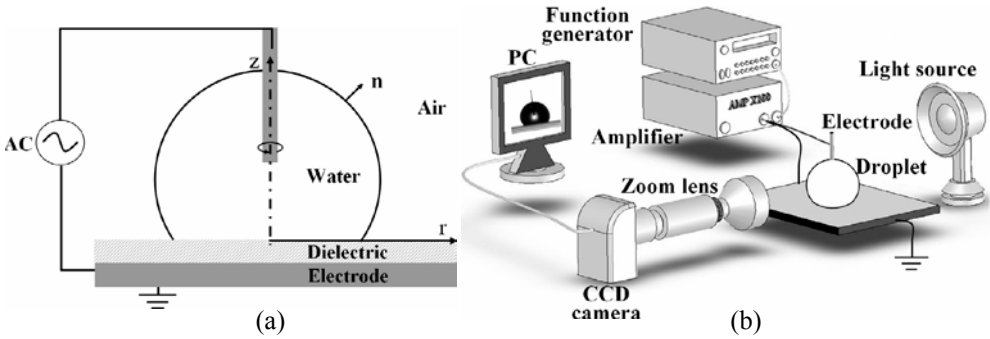

(a) (b)

Figure 1. (a) Domain; (b) Experimental set-up

Under the quasi-static assumption, the governing equation for complex electric potential can be written as following, which is just the charge conservation equation,

$$\nabla^2 \varphi = \nabla^2 (\varphi_r + j\varphi_i) = 0 \quad . \tag{1}$$

978-0-9798064-0-7/μTAS2007/$20©2007CBMS

Equation (1) is solved numerically with proper boundary conditions and then the electric potential and electric field is obtained and used to compute a time-averaged wetting tension by integrating the radial Maxwell stress. Computed wetting tension is compared with experimentally obtained wetting tension.

3. EXPERIMENTAL

The experimental set-up is similar to those of the conventional EWOD systems (Figure 1b). A deionized water droplet (5μl) is placed on a planar insulator-covered electrode. A stainless-steel wire (80μm diameter) is inserted to the droplet as a working electrode. A stainless steel plate is used as the counter electrode. On the electrode surface, the Parylene-C layer (5μm) is deposited as an insulating layer. On top of that, the Teflon AF1600® layer (100nm) is spin-coated. The images of droplet taken by using CCD camera are analyzed to obtain the apparent contact angles at various input frequencies (1 kHz ~ 128 kHz). The measured contact angle values are converted to the wetting tension for comparison with the numerical results.

4. RESULTS AND DISCUSSIONS

Figure 2 demonstrates frequency dependence of droplet shape for 143 V. As shown, the contact angle increases significantly with increasing frequency over 1 kHz.

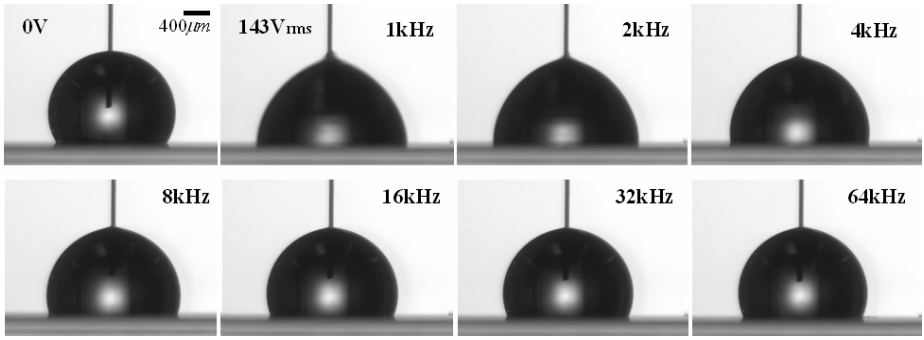

Figure 2. Frequency dependence of the shape of droplet.

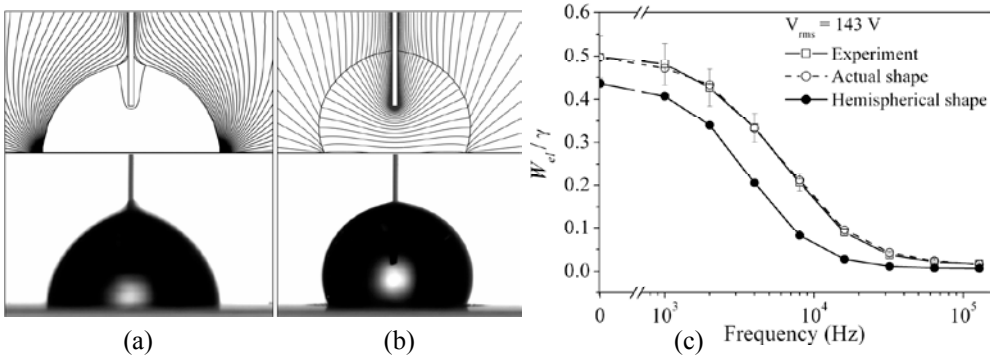

Figure 3. Root-mean-square (rms) potential distribution with corresponding images: (a) f = 1 kHz; (b) f = 128 kHz. (ΔV= 4.77 V) and (c) normalized wetting tension. (γ = 0.072 N/m)

The numerical results show a fairly good agreement with the experimental data. (Figure 3(c)) Figures 3(a) and 3(b) show the potential distributions at low and high frequencies, respectively. At a frequency higher than the Maxwell-Wagner frequency [3], the electric field near the triple contact line (TCL) is much smaller than that at the low frequency (Figure 4(a)). Dielectric breakdown can be delayed due to this reason. Figure 4(b) shows that the input voltage should be increased to maintain the wetting tension constant with compensating the reduction due to the frequency effect. Interestingly, the rms electric-field strength at the TCL (E_{TCL}) decreases even though the applied voltage is increased. Therefore, the high frequency electric field induces a greater change of contact angle when the maximum electric-field strength at the TCL is the same.

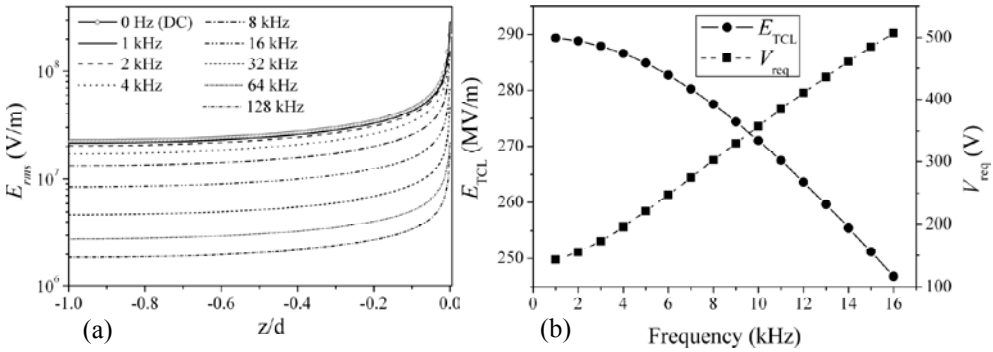

Figure 4. (a) Electric-field strength (E_{rms}) across the dielectric layer. (z = 0 means TCL); (b) Frequency dependence of the localized electric field at TCL (E_{TCL}, circles) and the necessary voltage (V_{req}, squares) to keep the wetting tension constant. (d = 5μm).

5. CONCLUSIONS

We successfully implemented the AC conduction model to analyze the AC electrowetting phenomena. From the numerical results, the maximum electric-field strength is reduced even though the voltage is increased to keep the wetting tension constant. Considering that the dielectric breakdown of the insulating layer is highly related with the contact-angle saturation phenomenon, the present results may explain the reason why contact angle saturation is occurred at higher voltage and smaller angle in AC EWOD, compared to DC case.

ACKNOWLEDGEMENTS

This work was funded by Center for Ultramicrochemical Process Systems sponsored by KOSEF. This work was also supported by the grant R01-2001-00410 from KOSEF and the grant by BK21 program of Ministry of Education of Korea.

REFERENCES

[1] C. Quilliet, B. Berge, *Current Opinion in Colloid & Interface Science* **2001**, 6, 34-39.
[2] A.G. Papathanasiou, A.G. Boudouvis, *Applied Physics Letters* **2005**, *86*.
[3] T. B. Jones, K. L. Wang, D. J. Yao, *Langmuir* **2004**, *20*, 2813-2818.

MICROFLUIDIC CHARACTERIZATION OF SURFACTANT SOLUTIONS

Guillaume Degré and Philippe Nghe

Groupe "Microfluidique, MEMS et Nanostructures",
UMR Gulliver CNRS-ESPCI 7083, France

ABSTRACT

This paper reports a way to study the rheology of a wormlike micelles solution by PIV measurements inside of a microchannel. We observe the presence of shear-banding in this fluid and achieve a local determination of the stress versus shear rate relation thanks to the high aspect ratio geometry of our microchannel. We observe the developement of an instability in this flow.

Keywords: PIV, wormlike micelles, non-linear rheology, shear-banding

1. INTRODUCTION

Surfactant solutions play an important role in oil, food or cosmetic industries; in most cases, their rheological properties need to be documented before they can be used. It is known that, depending on salt and surfactant concentrations, such fluids can form many different type of microscopic structures that have a complex mechanical behavior under shear. For example, wormlike micelles the semi-dilute regime show a dramatic loss of viscosity when a critical shear rate is attained, leading to inhomogeneous velocity profiles. Despite many attempts, this phenomenon is still not understood and the classical rheology obtained by global measurements leads to ambiguous interpretation, even more if instabilities or slippage appear. Here we show that microfluidic technology offers advantages compared to traditional approaches for studying the rheology of such systems.

2. EXPERIMENTAL

Microchannels are made of a photopolymer that bonds strongly to glass and are fabricated with a high resolution soft imprint technique [1]. We build high aspect ratio channels (with a 70 μm by 1 mm section) that are 5 cm long and sustain a 5 bars pressure without deformation or leakage.

We drive semi-dilute CTAB and sodium nitrate aqueous solutions reaching velocities up to 1 mm/s. For such systems, viscosity ranges between 1 and 10000 cp. By the addition of 500 nm fluorescent particles to the solution and PIV measurments (Fig. 1), we can reconstruct the velocity profile along the smallest dimension of the channel (Fig. 2), the 100X objective being mounted on a piezzo electric device that controls its position in the height. At a given height, the velocity is calculated by cross-correlating two snapshots separated by 20 milliseconds via a CCD camera. This operation is repeated 100 times at each height which yields a mean value and a variance for the velocity.

978-0-9798064-0-7/μTAS2007/$20©2007CBMS

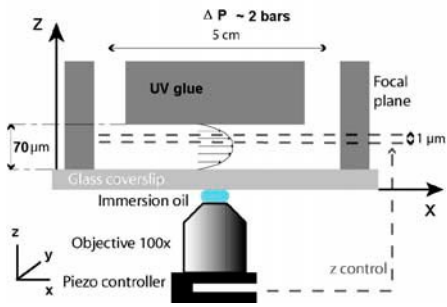

Figure 1. Schematic view of the experimental set-up. A 70 µm x 1 mm x 5 cm microchannel made of a UV cured glue is sealed with a glass coverslip. The 500 nm fluorescent beads positions are recorded from the bottom of the channel through an inverted microscope with a CCD camera.

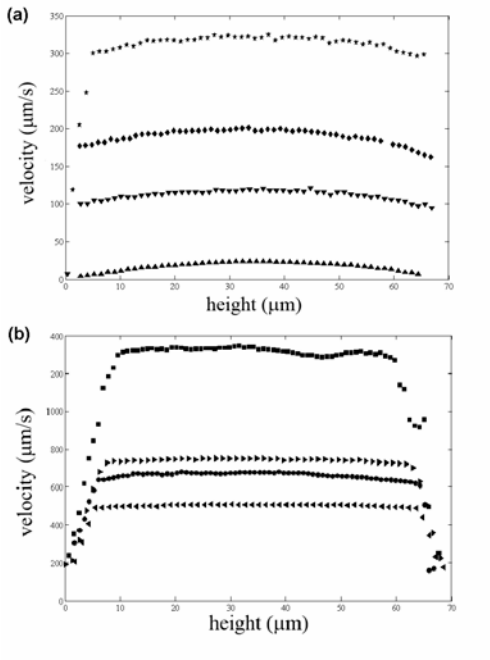

Figure 2. Velocity profiles measured in a CTAB (0.3%) and NaNO3 (0.3%) solution, in a 70 µm x 1mm cross-section channel with inreasing pressures ; (a) parabolic profile and apparition of the second phase bands (b) fully developped shear-banding behavior at higher pressures.

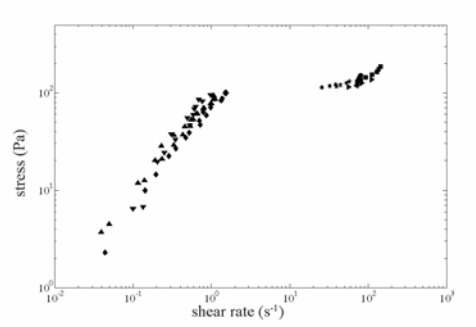

Figure 3. Stress vs. Shear rate curve obtained from local calculations from the velocity profiles of figure 2.

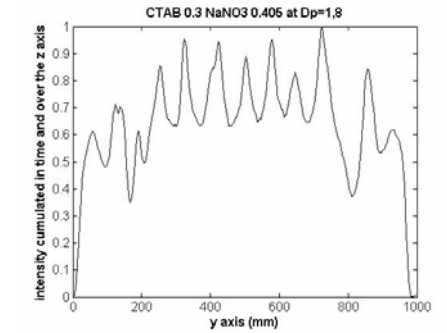

Figure 4. Fluorescence intensity modulations (normalized to the maximum) along the y axis recorded close to the end of the channel for different driving pressures. These modulation reveal the destabilization of the flow.

3. RESULTS AND DISCUSSION

As the pressure driving the flow is increased, the velocity profiles reveal first a newtonian phase, then apparition of a dramatically lower viscosity second phase at the walls (Fig. 2) : this is the so-called shear banding regime.

According to a method already validated on non-newtonian polymer solutions [2], we obtain the rheology of the fluid by a local calculation of the stress and shear rate from the velocity profiles, the result being independant of the slippage at the walls. The point is to verify that the flow is invariant along the vorticity direction on a large zone around the middle line of the channel, hypothesis which is verified at a few hundred millimeters from the channel inlet. This local rheology is in agreement with the global measurements made in a Couette rheometer (Fig. 3).

Instabilities known to occur in Couette cells for this type of systems [3] appear in the downstream direction of the flow. A destabilization of the interface between the two phases in the shear-banding regime is visible in our velocity profiles. By seeding the solution with bigger 3 microns diameter beads that are excluded from the lower viscosity phase, we observe in the case of a stationnary instability, a clear modulation of the tracers density cumulated over the height and shown versus the position in the vorticity direction in Figure 4. The amplitude of this modulation increases downstream.

The advantages of microfluidic technology here lies in the volume reduction, rapidity of the measurements, and full control of the flow.

4. CONCLUSIONS

In conclusion, the association of a new soft imprint technology in a UV-curable optical glue and a PIV set-up offers the opportunity to use microfluidic as a new context for the study of highly viscous complex fluids. We achieve local velocimetry and rheological measurements and take the full benefit of this context to observe and characterize more complex spatio-temporal behavior of shear-banding fluids.

REFERENCES

[1] Bartolo, D, Degré, G, Nghe, P, Studer, V, *Stick and flow: fast simple prototyping method for performance microfluidic device*, Proc. Micro Total Analysis Systems 2007.

[2] Degré, G, Joseph, P, et al., *Rheology of complex fluids by particle image velocimetry in microchannels*, Applied Physics Letters 89 (2): - JUL 10

[3] Lerouge, S, Argentina, M, Decruppe, J P, *Interface instability in shear-banding flow.* Phys Rev Lett 96 (8): 088301 Mar 2006

MOTION OF PARTICLES UNDER NON-UNIFORM AC FIELDS IN A MICROCHANNEL: ANALYSIS OF THE CONTRIBUTION OF AC ELECTROKINETIC FORCES

J.J. Capurro, J. Oh, and H. Noh

Lab-on-a-Chip and BioMEMS Laboratory, Drexel University, Philadelphia, USA

ABSTRACT

When particles are under a non-uniform AC electric field in a microchannel, they are subject to many forces such as dielectrophoresis (DEP), ac electroosmosis (AC-EO), electrothermal effect (ETE), gravity, Brownian diffusion, and particle-particle (dipole-dipole) interaction. This paper describes the qualitative and quantitative analyses of the contribution of the electrokinetic forces to the motion of particles under non-uniform AC electric fields.

Keywords: Dielectrophoresis, ac electroosmosis, electrothermal effect

1. INTRODUCTION

DEP is a particle motion due to the relative polarization between the particle and the surrounding medium in a non-uniform electric field. AC-EO arises from the migration of induced ions on the electrode surfaces due to the tangential component of the electric field [1]. ETE is a motion of fluid generated by non-uniform Joule heating, which affects the temperature-dependent properties (electrical permittivity and conductivity) of the medium and thus creates electrical force in the medium. These three electrokinetic forces have very distinct characteristics. In brief, DEP is a selective force that depends on particle type and size while AC-EO and ETE are electrohydrodynamic effects and are not dependent on particles. AC-EO and ETE have a larger spatial coverage due to the long-range flow pattern than DEP, which has nearly no effect on the particles at a distance from the electrode. Although many researchers have used AC electrokinetic effects in microfluidic and lab-on-a-chip devices [2-4], our knowledge about how each electrokinetic effect contributes to the final particle motion is still fragmental. The goal of this study is to elucidate the contribution of three major electrokinetic effects to the particle motion and to provide general design rules for AC electrokinetic devices.

2. THEORY

Dielectrophoresis: DEP is the movement of particles in non-uniform electric fields due to the relative polarization between particles and medium. The time-averaged DEP force is expressed as [1]:

$$< \vec{F}_{DEP} >= \pi \varepsilon_m r^3 \,\mathrm{Re}[\frac{\varepsilon_p^* - \varepsilon_m^*}{\varepsilon_p^* + 2\varepsilon_m^*}] \nabla \left|\vec{E}\right|^2 \qquad (1)$$

$$\varepsilon^* = \varepsilon - j\frac{\sigma}{\omega}$$

r = particle radius, ε = permittivity,
σ = conductivity, ω = angular frequency

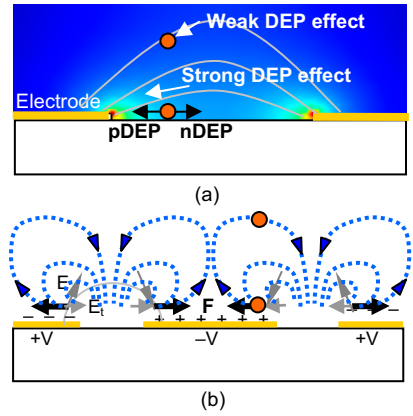

Figure 1: (a) Electric field distribution in a micro-channel with planar electrodes and DEP effects on particles, (b) schematic conceptual diagram of AC-EO. ETE generates a similar fluid motion in a microchannel.

978-0-9798064-0-7/μTAS2007/$20©2007CBMS

AC Electroosmosis: When an electric field is applied to planar electrodes on a substrate, counter ions are collected on the electrodes forming electrical double layers. Since there is a tangential component (E_t) of electric field, the charges in the double layer between the surface and the electrolyte experience a force and move to the center of the electrode. Even in an ac field, the motion of the double layer charges remains unchanged. Such movement of the double layer charges pulls the fluid along and generates a fluid flow. The time-averaged electroosmotic velocity and force for parallel planar electrode system are expressed as [1]:

$$\langle v \rangle = \frac{1}{2}\mathrm{Re}\left[\frac{E_t^* \cdot \Delta\sigma_o}{\kappa\eta}\right] = \frac{1}{8}\frac{\varepsilon_m V_o^2 \Omega^2}{\eta x(1+\Omega^2)^2} \quad \Omega = \omega\frac{\varepsilon_m}{\sigma_m}\frac{\pi}{2}x\kappa \quad F_{EO} = 6\pi\eta r v = \frac{3}{4}\frac{\pi r \varepsilon_m V_o^2 \Omega^2}{x(1+\Omega^2)^2} \qquad (2)$$

Vo = applied voltage, x = distance from the origin, κ-1 = Debye length, σ_o = surface charge density, η = viscosity

Electrothermal effect: The power generated by electric field can result in temperature rise in microchannel. Since the electric field is non-uniform in the microchannel with planar electrodes, the power density is also non-uniform and thus produces local temperature gradient. This temperature gradient causes changes in permittivity and conductivity of the medium and as a result electrothermal force arises. The time-averaged electrothermal force is expressed as [1]:

$$\vec{F}_{ET} = -\frac{1}{2}\left[\left(\frac{\nabla\sigma}{\sigma} - \frac{\nabla\varepsilon}{\varepsilon}\right)\cdot\vec{E}\frac{\varepsilon\vec{E}}{1+(\omega\tau)^2} + \frac{1}{2}\left|\vec{E}\right|^2\nabla\varepsilon\right] \qquad k\nabla^2 T + \sigma\left|\vec{E}\right|^2 = 0 \qquad (3)$$

ε = permittivity, σ = conductivity, ω = angular frequency, τ = charge relaxation time

3. EXPERIMENTAL

Two electrode designs (parallel interdigitated and castellated designs) were used in this study. Cr/Au electrodes were patterned on glass substrates using lift-off technique. Microchannels were made in PDMS layers by replica molding. Polystyrene microbeads (0.2 and 2 μm in diameter) were suspended in water and the solution conductivity was controlled by adding KCl. Particle motion was observed and video-taped with a digital camera attached to a microscope as varying the frequency and amplitude of the applied voltage. DEP force was calculated through electric field and Clausius-Mossotti factor simulation. AC-EO and ETE were approximated using theoretical formula available in reference [1]. Also, numerical simulation studies were performed using Comsol AC/DC module for quantitative analyses of the particle motion.

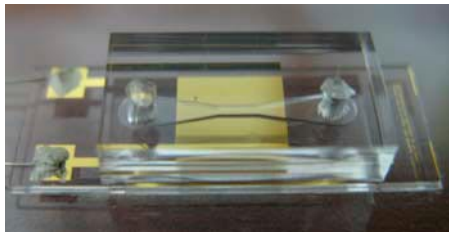

Figure 2: Microfabricated device for AC electro-kinetics study. The device consists of a glass substrate with Cr/Au electrodes and a PDMS microchannel.

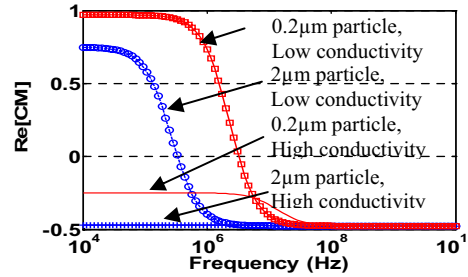

Figure 3: Real part of Clausius-Mossotti factor for two different particle sizes and two different solution conductivities. If Re[CM] is positive, the particle experience positive DEP.

4. RESULTS AND DISCUSSION

When the solution conductivity is low (0.0002 S/m), AC-EO became dominant at low frequencies (< 30 kHz) and particles were aligned in the center of the electrodes. As frequency increased, AC-EO decreased exponentially and positive DEP became dominant. As a result, particles moved from the center to edge of the electrode and formed chains due to dipole-dipole interaction. At higher frequencies (> 600 kHz), particles were all levitated because of negative DEP. When the solution conductivity was high (0.05 S/m), particle behavior was completely different. At low frequencies, most particles were rotating above the electrode edges due to AC-EO. A stronger attraction between particles was observed and particles were aggregated. The rotational motion stopped at higher frequencies (>100kHz), resulting in linear patterns of particles followed by levitation due to negative DEP. These qualitative analysis were verified with quantitative numerical simulations (data not included).

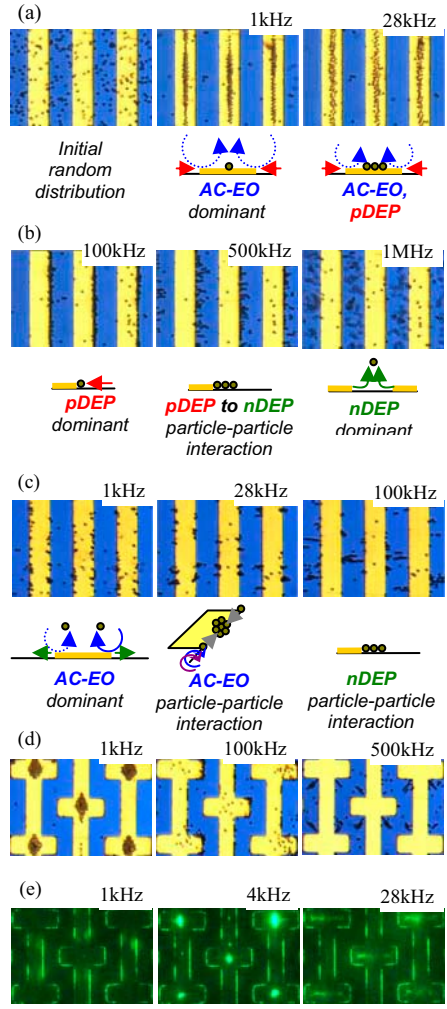

Figure 4: Particle motion as a function of the frequency of the applied voltage and the solution conductivity. (a)(b) 2 µm particle, low conductivity (σ_p=0.0002S/m), (c) 2 µm particle, high conductivity (σ_p=0.05S/m), (d) 2 µm particle, castellated electrode, (e) 0.2 µm particle, castellated electrode.

5. CONCLUSIONS

The contribution of three major electrokinetic forces (DEP, AC-EO, and ETE) to the particle motion under non-uniform AC electric field in a microchannel was qualitatively and quantitatively analyzed using analytical modeling, numerical simulation, and experimental studies. Solution conductivity, the amplitude and frequency of the applied voltage were found to be important parameters that determine the behavior of the particles. This work may provide general design rules for AC electrokinetic devices.

REFERENCES

[1] Ramos, A., Morgan, H., Green, N. G., and Castellanos, A. "Ac electrokinetics: a review of forces in microelectrode structures" *J. Phys. D: Appl. Phys.* 31 (1998) 2338-2353

[2] Hughes, M.P., *Nanoelectromechanics in engineering and biology*, CRC Press, (2002)

[3] Washizu, M., Suzuki, S., Kurosawa, O., Nishizaka, T., and Shinohara, T. "Molecular dielectrophoresis of biopolymers" *IEEE Trans. Ind. Appl.*, 30, (1994) 835

[4] Wong, P. K., Chen, C-Y., Wang, T-H., and Ho, C-M., "Electrokinetic bioprocessor for concentrating cells and molecules"*Analytical Chemistry*, (2004)

SHEATHLESS PARTICLE FOCUSING BASED ON HYDROPHORESIS AND ITS APPLICATION TO BLOOD PLASMA SEPARATION

Sungyoung Choi and Je-Kyun Park

Department of Bio and Brain Engineering, Korea Advanced Institute of Science and Technology (KAIST), KOREA

ABSTRACT

We propose a microfluidic device for sheathless focusing of microbeads and blood cells based on a hydrophoretic platform comprising a V-shaped obstacle array (VOA). The VOA generates lateral pressure gradients in which the pressure has a minimum value at the center of a channel. Therefore, particles passing through the VOA are focused to the center of the channel in the direction of the high-pressure field to the lower field.

Keywords: Hydrophoresis, blood plasma, particle focusing, microfluidics

1. INTRODUCTION

In microchip, techniques to focus particles in a fluid stream have several applications such as cell sorting, media exchange, and particle concentration or removal. For the applications, several microfluidic methods have been demonstrated their capability to focus particles without sheath flows, using dielectrophoresis (DEP), ultrasound standing wave, and splitting-recombining channels. However, DEP often has limitations in biological applications because of buffer incompatibility [1]. For splitting-recombining channels, their complex channel network makes them difficult to integrate with downstream analysis and to multiply the network on a single chip for increasing throughput [2].

2. FOCUSING PRINCIPLE

Hydrophoresis is the first proposed concept to explain the horizontal deflection of particles around slanted obstacles [3]. Our focusing method utilizes a V-shaped obstacle array (VOA; Figure 1) as a source of hydrophoresis, which eliminates the necessity of external potential fields and makes it possible to focus particles in a simple single channel. The VOA is consisted of a series of micro-obstacles in the shape of the letter V. The V-shaped obstacles are alternately formed on the top and bottom of a channel. The difference of a fluidic resistance between the top- or bottom-, and side-area of the obstacle generates lateral pressure gradients, which drive transverse flows. The value of the lateral pressure field is minimum at the center of the channel. Particles passing the V-shaped obstacles are converged to the center of the channel along the pressure gradients.

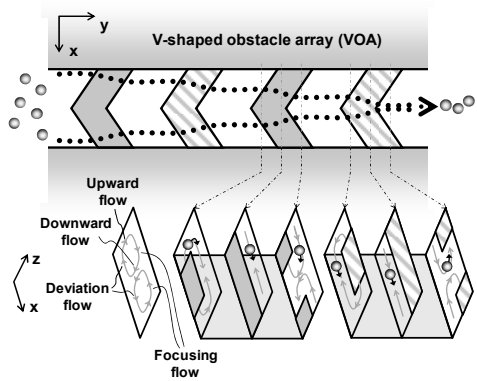

Figure 1. Hydrophoretic particle focusing. Shaded- and lined-areas denote lower and upper obstacles, respectively.

978-0-9798064-0-7/μTAS2007/$20©2007CBMS

3. EXPERIMENTAL

The microfluidic device for hydrophoretic focusing was fabricated with PDMS using a soft lithography process. Plain polystyrene beads of 8, 10, 11, and 15 μm diameters (Sigma-Aldrich Co., MO) were used for the demonstration of hydrophoretic focusing. As a model particle with a concave disk shape, rat blood was drawn with EDTA as anticoagulant.

4. RESULTS AND DISCUSSION

Using the microfluidic device with 19.1 μm-height VOA, we observed that particles passing the VOA travel through the perpendicular direction to the fluid flow (Figure 2). The focusing of the particles to the center occurred right at the top- and bottom-area of the VOA. In the simulated pressure field strength of Figure 3, the overall field strength in the middle of the channel along the x-axis was lower than that of any other areas. Therefore, the velocity vectors were converged into the middle of the x-axis.

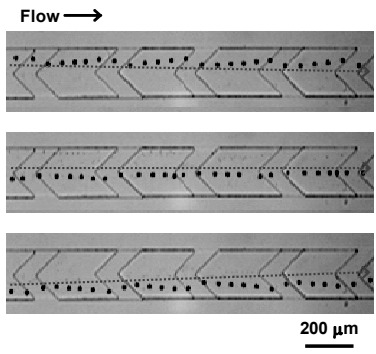

Figure 2. Optical micrographs showing the trajectories of 15 μm beads passing 19.1 μm-height VOA. The beads were injected at a flow rate of 0.3 μL min^{-1}. After the focusing was completed, they stayed in their focused position (the middle of the figures).

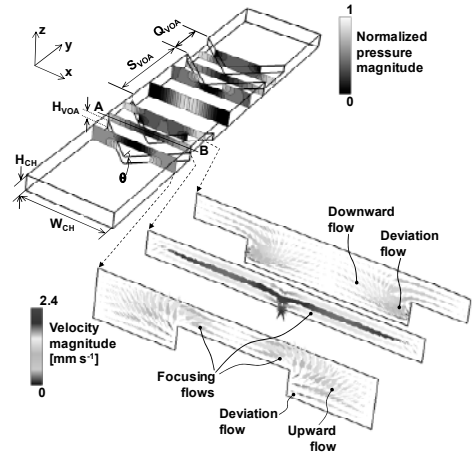

Figure 3. Cross-sectional plots of pressure distributions and magnified plots of velocity vectors.

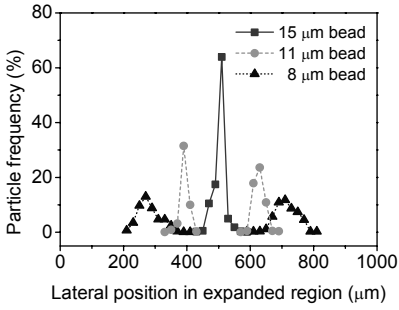

Figure 4. Focusing patterns of 8, 11, and 15 μm beads in the microfluidic device with 19.1 μm-height VOA. The applied flow rate was 2 μL min^{-1}.

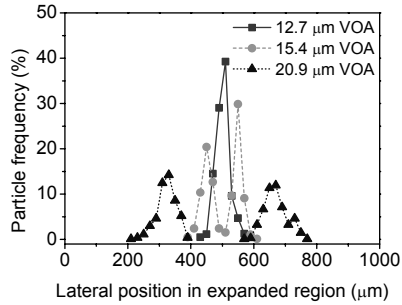

Figure 5. Measured focusing profiles of 10 μm beads in the device with obstacle heights of 12.7, 15.4, and 20.9 μm.

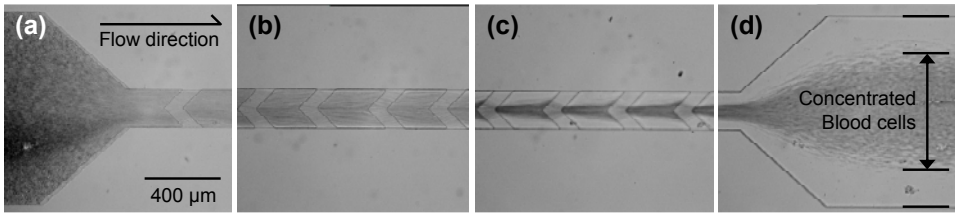

Figure 6. Blood plasma separation. Optical micrographs in an inlet (a), channel regions 1260 μm (b) and 8060 μm (c) apart from the inlet, and an outlet (d). The blood cells were injected into the microfluidic device with 7.2 μm-height VOA at a flow rate of 4 μL min^{-1}.

The dependence of hydrophoretic focusing on the particle diameter was characterized with polystyrene beads of 8, 11, and 15 μm diameters. Figure 4 shows the separated focusing patterns due to the hydrophoretic separation phenomenon [3]. Since the hydrophoretic movement depends on the alignment effect by the VOA, we achieved the complete focusing pattern of 10 μm by lowering the gap height of the VOA (Figure 5).

For the application to blood plasma separation, we injected 1:4 diluted rat bloods into the microfluidic device with 7.2 μm-height VOA. After passing the VOA of 7.2 μm height, most of red blood cells (RBCs) went through the channel within the lateral range from 200 to 800 μm (Figure 6). Under this condition, we can extract ~ 40% of diluted blood volume as plasma.

5. CONCLUSIONS

We have demonstrated a new microfluidic device for hydrophoretic focusing which utilizes transverse pressure gradients generated by the VOA. In our device, the focusing pattern was modulated by varying the gap height of the VOA. By lowering the gap height of the VOA, we can achieve the focusing range of 4.4% CV for 10 μm-sized beads. The microfluidic device is easy to fabricate and does not require complex channel networks. This easiness can facilitate the connection with other microfluidic devices for particle sorting or detection.

ACKNOWLEDGEMENTS

This work was supported by Chung Moon Soul Center for BioInformation and BioElectronics, KAIST. The microfabrication work was performed at the Digital Nanolocomotion Center.

REFERENCES

[1] C. Yu, J. Vykoukal, D. M. Vykoukal, J. A. Schwartz, L. Shi, P. R. C. Gascoyne, *A three-dimensional dielectrophoretic particle focusing channel for microcytometry application*, J. Microelectromech. Syst., Vol. 14, pp. 480-487, (2005).

[2] R. Aoki, M. Yamada, M. Yasuda, M. Seki, *Microfluidic particle alignment for flow cytometric applications utilizing hydrodynamic filtration*, Proc. Micro Total Analysis Systems 2006, Tokyo, Japan, Vol. 1, pp. 515-518, (2006).

[3] S. Choi, J.-K. Park, *Continuous hydrophoretic separation and sizing of microparticles using slanted obstacles in a microchannel*, Lab Chip, Vol. 7, 890- 897, (2007).

THE MECHANICS OF DEFORMABLE FLUIDIC DIODES: IMPLICATIONS FOR DESIGN AND PERFORMANCE

Daniel C. Leslie[1], Christopher J. Easley[2], James P. Landers[1], Marcel Utz and Matthew R. Begley[3]

[1]Department of Chemistry, University of Virginia, USA, [2]Molecular Physiology and Biophysics, Vanderbilt University, USA and [1]Deparment of Mechanical Engineering, University of Virginia, USA

ABSTRACT

This paper describes the physics controlling the performance of deformable fluidic diodes and outlines the theoretical framework needed for *a priori* feature design in terms of specific performance criteria. This framework enables chip designers to identify promising combinations of channel architecture, materials and surface treatements that produce fluidic diodes with specified properties. The framework also allows one to assses the promise and challenges of developing effective diodes quantitatively in terms of common microfabrication techniques and explicit performance criteria demanded by diagnostic microchips.

Keywords: Microfluidic diodes, frequency-specific networks, debonding

1. INTRODUCTION

The diode is a critical element for flow rectification not only because it ensures one-directional flow, but also because it dramatically changes cyclic (periodic) behavior and is inherently non-linear. For example, a fluidic diode can be used to truncate the reversing flow a three-valve peristaltic pump; combined with a fluidic capacitor, stepwise volume transfer from a diode can be smoothed to deliver constant velocity flow [1]. Moreover, under controlled flow-rate conditions, fluidic diodes can be used to control the time release of a fluid from one channel to another [1]. FIG. 1 illustrates two fundamental diode concepts that can be modified to produce a variety of configurations whose underlying function is essentially the same. The "flap diode" (FIG. 1a) described by Quake, *et al.* consists of a small PDMS flap that rests against a microfabricated step [2]. At a critical pressure difference (i.e. p_1-p_2), the flap debonds from the ledge and permits flow. FIG. 1a can also be interepreted as one-half of a check-valve (with the addition of a mirror-image down the vertical axis): in the absence of a step, such a valve opens when the adjoining flaps debond from one another.

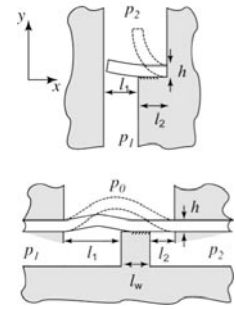

FIG. 1: Side views of the "plate"diode (bot) [1] and "flap" diode (top) [2].

For the plate diode shown in FIG. 1b [2], the PDMS plate debonds from the wier and permits flow into the adjoining channel. This occurs at a critical pressure difference between the fluidic channel and the top of the film: this implies that the plate diode configuration is inherently a fluidic *transistor*, in that flow through the diode can modulated via pressure in a different channel.

978-0-9798064-0-7/μTAS2007/$20©2007CBMS

2. DIODE BREAKTHROUGH

The performance of a both designs in FIG. 1 is governed by the competition between elastic energy stored in the film and the interfacial adhesion energy that controls debonding. For either diode design, the 'breakthrough' event is essentially a film delamination problem, which can be modeled using well-established interface mechanics frameworks [3]. The key concept is that the film will debond when the energy that is released during crack advance (defined by the 'energy release rate') is equal to a critical value, i.e. the interfacial adhesion energy. In this attemp to identify key scaling relationships and establish the range of possible diode performance, we neglect the complexities associated with 'mixed-mode' interface failure, such that the problem is completely described in terms of the energy release rate and the adhesion energy. (That is, we choose to ignore the influence of the mixture of tensile (mode 1) and shear (mode 2) stresses at the debonding interface.)

For pressure-controlled flow, the energy available to drive debonding can be written in generic form (assuming plate-like deformation, [3]) as:

$$G = \frac{c(\Delta p)^2 l^4}{Eh^3} \tag{1}$$

where E is the elastic modulus of the deformable film, c is a constant prefactor that depends on the specific geometry, h is the film thicknes and Δp is the difference in pressure on either side of the film. That is, Δp is the net pressure acting on the film in the direction that will lead to debonding. For the flap diode, $\Delta p=p_1-p_2$ since the relevant pressures are the upstream and downstream pressures, respectively. For the plate diode, $\Delta p=p_1-p_o$, where p_o is the pressure acting on the film outside the channel. The length l refers to the deformable span over which the relevant pressure acts.

The stability of the debonding interface is then determined by comparing this energy (per unit area) with the interfacial adhesion energy that controls debonding, denoted as Γ_i. The break-through pressure of the diode is thus given by:

$$\Delta p_{cr} = \sqrt{\frac{\Gamma_i E h^3}{c_p l^4}} \tag{2}$$

This relationship implies that once debonding at the edge of a pressurized channel is initiated, it will continue without arrest (under constant channel pressure), since the effective span increases as the film debonds [3]. This result defines not only the pressure difference (on adjacent sides of the flap diode, or alternate sides of the plate diode), but also the pressure that will open the diode in the reverse direction: thus, for the plate diode, the ratio of channel pressures that permit opening is given by: $\Delta p_{1\text{-}2}/\Delta p_{2\text{-}1} = (l_2/l_1)^2$.

3. FLOW THROUGH THE PLATE DIODE

Once the diode opens, the flow rate depends on the nature of the fluid/solid interaction. Most microfluidic applications involve purely laminar flow: the entrance lengths are on the order of a micron. Assuming a linear pressure drop through the length of the diode, the flow rate is given by:

$$q = \frac{Wd^3 F(d/W)(p_1 - p_2)}{12\eta l_H} \tag{3}$$

where d is the slot height (i.e. the channel height) and l_H is the distance along the slot overwhich the pressure drop occurs. It is reasonable to expect that the length of the weir, l_w, provides a minimum bound, while the total length of the diode ($L=l_1+l_2+l_w$), provides a maximum bound. For simplicity's sake, we take $l_H=l_w$. Elemenatry plate mechanics yields (for a linear pressure variation):

$$d = \frac{(l_1 + l_w)^2 l_2^2}{10Eh^3 L}\left[(2L + l_2)p_1 + (3L - l_2)p_2\right] \qquad (2)$$

The combination of eqn. (4) and eqn. (3) defines the post-release operation, by describing flow-rate/pressure relationship interms of the geometric variables (W, h, l_1, l_2, l_w) and physical parameters (E, η, Γ_i).

Taking eqns. (3) and (4) together, a univeral map of the flow through the diode can be constructed as a function of pressures, as shown in FIG. 2. In region A, neither the upstream nor downstream pressures are sufficient to activate flow. In region B, only the upstream conditions can release the diode and forward flow occurs. Similarly, in region C, only the downstream conditions can release the diode and backwards flow occurs. In region D, the diode can be released by either either of the upstream or downstream conditions: the direction of flow is dictated by the greater of the two pressures. The most interesting region is E, wherein only the upstream conditions can release the diode, yet backwards flow ensues. This implies that the diode can be used to "pull" fluid into a fluidic network once a critical pressure inside the network has been reached. This may have powerful applications, such as the slowing or outright quenching of a chemical reaction via dilution.

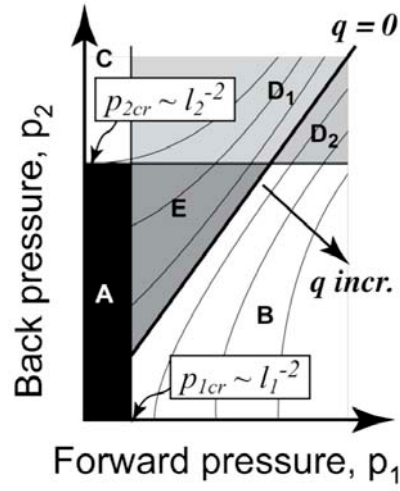

FIG. 2: Regimes of behavior for the "plate" fluidic diode.

4. CONCLUSIONS

Combining the established concepts of solid, fluid and fracture mechanics, it is possible to make quantitative predictions of the behavior of microfluidic diodes based on deformable features. Since the relevant equations can be solved analytically, scaling laws can be extracted that are highly useful in guiding the choice of diode geometry, therefore enabling rational design of devices that are tailored to specific performance goals.

REFERENCES

[1] C.J. Easly, J.M. Karlinsey, D.C. Leslie, M.R. Begley and J.P. Landers, Proc. of the Micro-TAS Conf., Vol. 2, 1065-1068 (2006).

[2] M.I. Adams, M. I. Johnston, A.R. Scherer and S.P.Quake, J. Micro. and Microeng., **15**, 1517-1521 (2007).

[3] M.R. Begley and J.M. Monahan, 3rd Edition CRC Handbook of Microcapillary Electrophoresis, Edited by J.P. Landers, CRC Press, New York, (2007).

VALVES FOR AUTONOMOUS MICROFLUIDIC CAPILLARY SYSTEMS

M. Zimmermann[1,2], P. Hunziker[1], E. Delamarche[2]
[1] *University Hospital Basel, Petersgraben 4, CH-4031 Basel, Switzerland*
[2] *IBM Research GmbH, Zürich Research Laboratory, Säumerstrasse 4, CH-8803 Rüschlikon, Switzerland*
(ymz@zurich.ibm.com)

ABSTRACT

This paper reports a method for adding valves to autonomous microfluidic capillary systems (CSs). The valves have no moving parts and can seamlessly be integrated into capillary systems. These valves enable triggering, timing, or metering of liquids using capillary forces.

Keywords: valves, passive, wettable

1. INTRODUCTION

Autonomous capillary systems employ capillary forces to move liquids inside wettable microchannels and microstructures and they are sealed with an elastomeric sealing cover, which can be used as a substrate for ultraminiaturised immunoassays. [1, 2] The valves shown here are easy to integrate in CSs and rely on a sudden change of the contact angle of a liquid moving in CSs. [3, 4] Such valves have the same wettable surface as the other parts of the CSs.

2. EXPERIMENTAL

The valves are microfabricated in Si, coated with sputtered Au, and derivatised with a (polyethylene glycol)-thiol. The contact angle of water was measured using the sessile drop method and determined to be 40°. The valves were sealed with polydimethylsiloxane prior filling with colored water.

3. PRINCIPLE

Figure 1 shows the concept of valves for autonomous CSs. A liquid wets the microchannel walls having a constant contact angle and fills the microchannel from left to right due to capillary forces. The capillary force and thus the velocity of the liquid filling

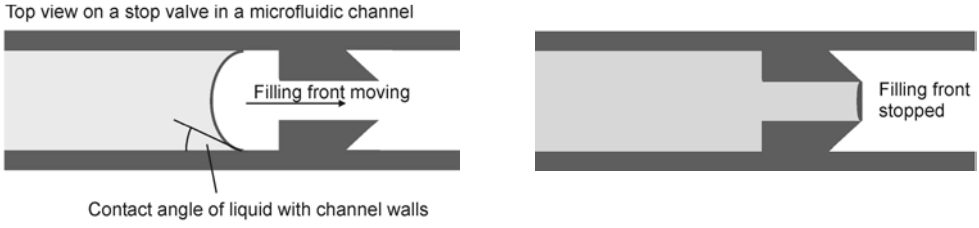

Figure 1. Concept of valves for autonomous CSs. Sudden changes in the geometry of wettable microstructures can pin a liquid filling a microchannel.

978-0-9798064-0-7/μTAS2007/$20©2007CBMS

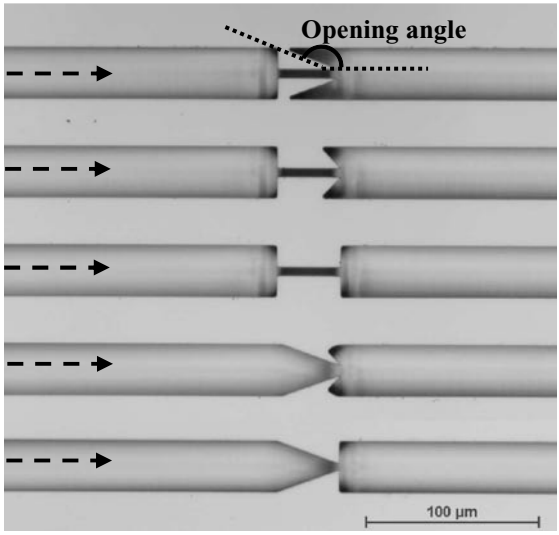

Figure 2. Optical micrograph of stop valves in 30-µm-wide microchannels. The smallest restriction of the valves is 4 or 6-µm wide. At the end of these restrictions, different opening angles induce a sudden change of the contact angles of a liquid filling front.

front depends on the contact angle of the liquid with the walls of the microchannels. The filling front of a liquid moving into such a CS can be stopped by a sudden change of the contact angle. This change can be determined by valves having geometrically structured micro-channel walls, which suddenly expand the microchannel width. At such structures, the meniscus at the filling front looses its curvature and the capillary force drops to zero. Thus the filling front stops when it reaches a valve having an opening angle of ≥ 90° – contact angle.

4. RESULTS AND DISCUSSION

In Figure 2, microfabricated "stop valves" having various opening angles ≥ 90° are shown. Such valves can stop liquids such as water and biological buffers for a few seconds.

Two stop valves can be combined with one outlet microchannel to form a trigger valve. A liquid waiting in the microchannel of a trigger valve can pass to the outlet microchannel when a liquid arrives in the second stop valve. The scanning electron image in Figure 3 shows a trigger valve. These valves are meant to be used with a sealing cover. The edges of the valve, and the bottom edges in particular, are well defined, which is important to prevent leakage of liquid. Figure 4 shows four trigger valves, each having green-colored water in the right inlet channel up to the stopping structure (see arrows in Fig. 4). In these valves, liquid can be retained at least for 15 min, which leads to the possibility of implementing timing functions in CSs.

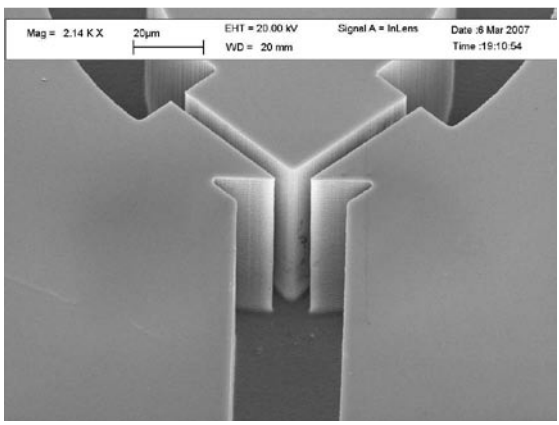

Figure 3. Scanning electron image of a trigger valve etched 60 µm deep in Si.

The trigger valve in Figure 5 acts as a "microfluidic timer": liquid entering this valve follows two paths. The bottom path is longer and has flow resistance to slow the liquid. The liquid can pass the valve only when the liquid in both paths arrives at the valve.

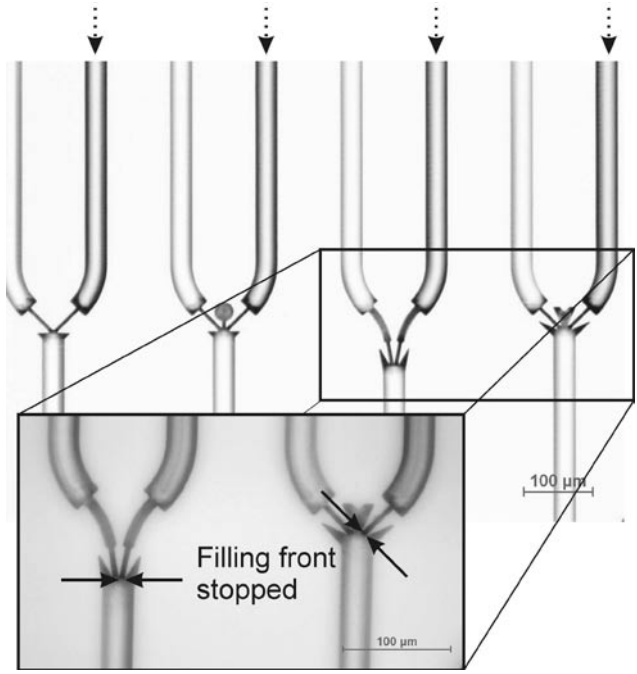

Figure 4. Optical micrograph of trigger valves. The right channel of each trigger valve is filled with green-coloured water. The inset shows a zoom of two trigger valves. The filling front is indicated by the arrows.

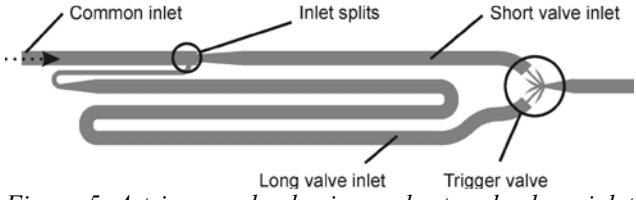

Figure 5. A trigger valve having a short and a long inlet channel can be used as a timer for autonomous CSs.

4. CONCLUSIONS

The results presented here show that autonomous CSs can be expanded with new valving functions. The valves can easily be integrated in the fabrication of autonomous CSs without requiring additional processing steps and can thus be combined with complex and powerful CSs having multiple microchannels and capillary pumps.

REFERENCES:

[1] D. Juncker et al. Autonomous microfluidic capillary system, Anal. Chem. **74**, 6139–6144, (2002).
[2] M. Zimmermann et al. Capillary pumps for autonomous capillary systems, Lab Chip **7**, 119–125, (2007).
[3] P. F. Man et al. Microfabricated Capillary-driven stop valve and sample injector, In Proceedings of IEEE MEMS, 45–50, (1998).
[4] A. Gliere et al. Modeling and fabrication of capillary stop valves for planar microfluidic systems, Sens. Act. A **130–131**, 601–608, (2006).

WORM-LIKE SURFACTANT SOLUTIONS, FLOW INDUCED GELATION AND EFFECTIVE SLIP IN MICROCHANNELS

Lucy E. Rodd and Justin J. Cooper-White
The Australian Institute of Bioengineering and Nanotechnology (AIBN), The University of Queensland, AUSTRALIA

ABSTRACT

The unique rheological properties of worm-like surfactant solutions lead to a *flow-induced* phase transition from a "liquid-like" to "gel-like" phase when the fluid is subjected to shearing and extensional flows in microdevices. We investigate the complex flow behaviour that occurs upstream of a 4:1 planar contraction. Even during slow flows ($Re <$ 0.009), we observe the formation of an extended micellar network, resulting in shear bands, large elastic vortices and extended upstream jetting consisting of an inviscid core bounded by stagnant fluid. Such systems provide great potential for generating shear-free transport zones even in straight channels within microfluidic devices.

Keywords: Non-Newtonian, shear-banding, slip, jetting

1. INTRODUCTION AND BACKGROUND

Worm-like micellar solutions are a unique class of non-Newtonian fluid, in which surfactant molecules (in the presence of strongly binding counterions) self-assemble into micellar structures. Possible configurations include spherical, rod-like and extended worm-like micelles as the surfactant concentration is increased from 1 to 10 cmc. The formation of worm-like structures ($l \sim$ O(10 μm) [1]) results in bulk dynamical properties that are reminiscent of polymer solutions. However, micellar systems are in a state of constant thermodynamic equilibrium, such that chains are continuously breaking and reforming; polymer chains have a fixed length. This results in a fluid microstructure (and therefore bulk properties) that may change significantly according to the imposed flow conditions.

When subject to flow, the dynamical properties of micellar chains and their network give rise to complex flow phenomena that are unprecendented by ordinary polymer solutions. One such phenomenon is the formation of "shear-induced structures" (or "flow-induced gelation") at a critical shear rate and is characterized by an increase in viscosity [2]. This has been observed in *macro-scale* geometries, but only in *pure shearing flows* in which the smallest lengthscale of the geometry was on the order of millimeters [2]. In the present work, we explore the effect of both shearing and extensional flow on the behaviour of semi-dilute micellar solutions flowing through a microfluidic geometry containing a constriction.

2. DIMENSIONLESS GROUPS

The flow of viscoelastic fluids may be characterized in terms of the Reynolds number, *Re* and the Weissenberg number, *Wi*. The Reynolds number is defined by $Re = \rho \bar{V}_{up} D_h \big/ \eta(\dot{\gamma}_{ave,up})$ in which ρ is the fluid density, $\bar{V}_{up}$ is the average upstream

978-0-9798064-0-7/μTAS2007/$20©2007CBMS

velocity, D_h is the upstream hydraulic diameter and $\eta(\dot{\gamma}_{ave,up})$ is the shear-rate-dependent viscosity of the fluid. The Weissenberg number characterizes the relative magnitude of the relaxation timescale of the fluid, λ_M to the timescale of the flow in the constriction, $t_{flow} \sim 1/\dot{\gamma}_{ave,down}$ and is given by $Wi = \lambda_M \dot{\gamma}_{ave,down}$.

2. EXPERIMENTAL

Flow experiments were performed using polydimethylsiloxane (PDMS) microfabricated geometries consisting of a straight rectangular section (200 μm width, 55 μm uniform depth) containing an abrupt planar 4:1:4 contraction-expansion. A series of aqueous solutions consisting of 1 – 10 mM cetyl trimethyl ammonium bromide and equal molar quantities of sodium salicylate (CTAB-NaSal) were subject to a range of pressure-driven flow conditions (0.001 ml/hr < Q < 0.1 ml/hr, 60 < Wi < 1200), in which the effects of inertia are negligible (10^{-4} < Re < 0.009). The kinematic response of the fluid was characterized upstream of the contraction geometry using fluorescent streak imaging and micro-particle image velocimetry. During steady flows, vector fields were quantified using an ensemble average of 25 image pairs.

3. RESULTS AND DISCUSSION

The high elasticity and shear-rate-dependent viscosities of these fluids lead to the appearance of similar flow regimes previously seen for dilute high molecular weight polymer solutions [3] with, however, some significant differences. These flow regimes are illustrated in Figs. 1 and 2 and include Newtonian-like (only observed for very weak flows), steady vortex growth (Fig. 1) and unstable flow (Fig 2). During vortex growth, vortices may grow sufficiently far upstream of the contraction to form a nearly inviscid core of fluid that is bounded by a layer of slow-moving fluid near the walls of the geometry.

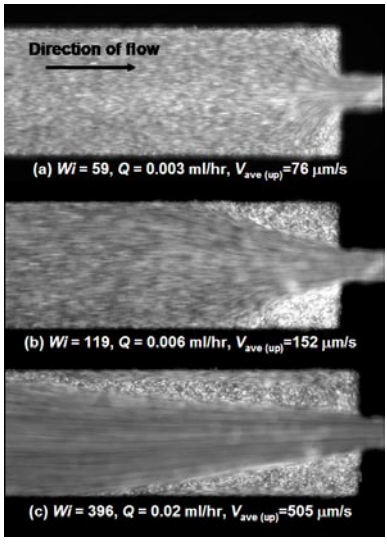

Fig. 1: Fluorescent streak images of steady flow during (a) Newtonian-like (b) symmetric vortex growth and (c) vortex growth regimes.

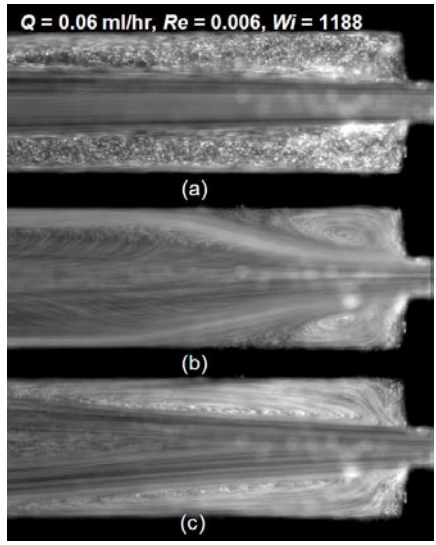

Fig 2. Streak images of time-dependent flow following the onset of an elastic instability; (a) – (c) represent three consecutive time points.

Measurements of the upstream kinematics (Figs. 3 and 4) were used to confirm the presence of a "shear-banding" phenomenon previously observed in shearing flows of similar worm-like surfactant systems. This may be identified as an abrupt change in shear rate towards the centre of the channel, and is illustrated in the lateral velocity profiles in Fig. 4 at various positions upstream of the contraction. Shear-banding also occurs close to the contraction ($x = 0$) where the flow is almost purely extensional and utilizes the adjacent stagnant fluid as the ideal slip interface.

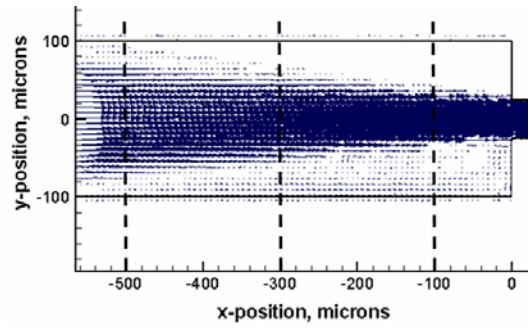

Fig 3. PIV vector field for flow upstream of the 4:1 planar contraction; $Wi = 317$, $Re = 0.0016$

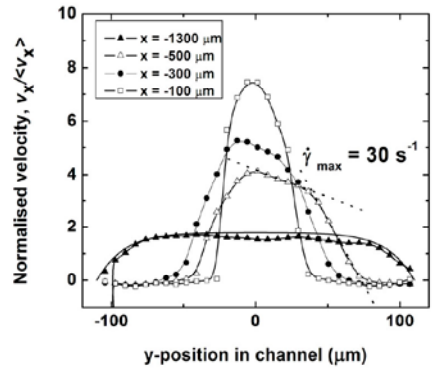

Fig 4. Shear banding illustrated in the evolution of the lateral velocity profile; $Wi = 317$, $Re = 0.0016$.

The maximum value of the shear rate (found nearest the channel edge) was found to correspond closely with the critical conditions for the onset of gelation for this fluid, particularly in the vortex growth regime and at positions upstream where the flow first begins to converge ($x \cong -500$ μm in Fig 3). This suggests that the highly extensional nature of the fluid may be first triggered by the onset of a shear-induced gelation.

4. CONCLUSIONS

This work illustrates the potential for inducing phase transitions in an otherwise homogenous fluid without the use of temperature or radiation. The formation of discrete shear bands (even in very slow channel flows) may be used to generate zones in which the shear rate is uniform and close to zero (Fig 2 a). This could be used to facilitate the safe transport of shear-sensitive biological particulates at relatively fast transport rates.

ACKNOWLEDGEMENTS

We would like to thank the Australian Research Council for their support through the ARC Discovery Scheme.

REFERENCES

[1] T. Clausen *et al.* 1992, J. Phys. Chem. **96**:474-484.
[2] H. Hu *et al.* Sep/Oct 1998, J. Rheol. **42**(5):1185-1208.
[3] L. Rodd *et al.* 2005, J. Non-Newt. Fluid Mech., **129**:1-22.

A PIEZOELECTRIC ACTIVE MICROCHANNEL FOR FLUID TRANSPORT IN μTAS

Takaaki Suzuki[1], Isaku Kanno[1], Junya Ogawa[1], Kensuke Kanda[2] and Hidetoshi Kotera[1]

[1]*Kyoto University, JAPAN and*

[2]*Advanced Software Technology and Mechatronics Research Institute in Kyoto, JAPAN*

ABSTRACT

This paper reports an innovative fluid transport system for intricately-integrated systems on a small chip. In the proposed system, microchannels to connect functional components on a silicon chip have a moving wall of a piezoelectric thin film directly deposited by sputtering on the outside of the microchannels. Since the active microchannel without valves and diffuser was assembled with two-dimensional configuration by simple fabrication process, the transport system can be immediately applied to μTAS without occupied area.

Keywords: Piezoelectric, microchannel, micropump, SOI

1. INTRODUCTION

For many microfluidic systems, it is necessary or highly desirable that the package size of the micropump is comparable to the volume of fluid to be pumped [1]. A mechanical micropump with external/integrated actuators is commonly used for transporting different kinds of fluid with relatively high flow rate [2]. However, the biggest drawback of the external actuators is their large size, which restricts the size of the whole micropump [3]. On the other hand, the most common integrated actuators, such as electrostatic, thermopneumatic and electromagnetic actuators, need the high electric voltage or the large electric current. Regarding these demerits, we propose a piezoelectric thin film actuator for the integrated mechanical micropump. The proposed microfluidic transport system can be driven by low electric voltage, and integrated with intricate network design by direct deposition to the outside of the microchannel.

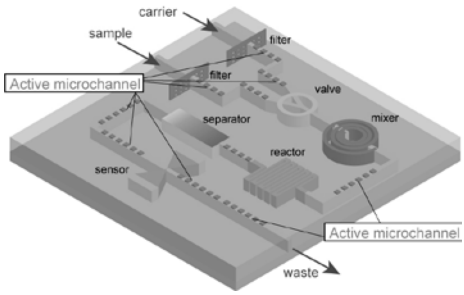

Figure 1. Schematic of piezoelectric active microchannels to connect functional components and transport a fluid on a silicon chip

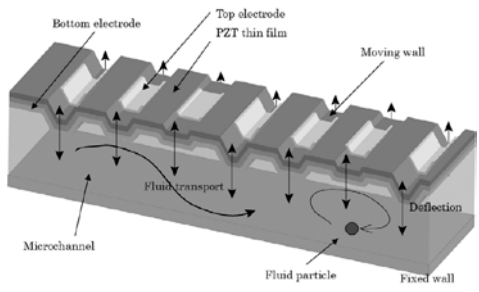

Figure 2. Principle of active microchannel with piezoelectric moving wall

978-0-9798064-0-7/μTAS2007/$20©2007CBMS

2. FLUID TRANSPORT

The proposed system is composed of a microchannel to connect the functional components and a piezoelectric moving wall as shown in Fig.1. Traveling wave was induced on the surface of the piezoelectric moving wall by applying sinusoidal voltages to each patterned top electrode with the different phase [3], and the motion of the microchannel transports the fluid as shown in Fig.2.

3. FABRICATION PROCESS

The piezoelectric thin film layer was directly deposited on the outside of a thin Silicon wall by RF-magnetron sputtering [4], and actuated as a unimorph structure. The Silicon microchannel with thin top wall was fabricated from SOI wafer by using the DRIE. Photographs of the fabricated active microchannel are shown in Fig.3. In the fabricated prototype, four active microchannels with the width of 200μm were arranged on silicon chip with 2-cm-square. However the length of the active microchannel is practically depends on the distance of the functional components, tentative length is about 4mm, which composed of 9 electrodes with 120μm at intervals of 200μm.

4. PUMPING PERFORMANCE

The displacement of the active microchannel measured by a laser Doppler vibrometer in Fig.4 is similar to numerical one obtained by FEM analysis as shown in Fig.5. The three-dimensional velocity profile in the active microchannel measured by a microPIV system [5] is shown in Fig.6. The velocity near the piezoelectric moving wall is faster than the velocity near the rigid wall. The mean flow velocity is about 650μm/s at the applied voltage of 1MHz and 20Vp-p. Since the retention of the tracer particles was observed at specific mode of the applied voltage, the proposed system can be applicable to a mixing device as well as the microfluidic transport.

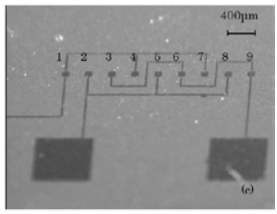

(a) Top electrodes

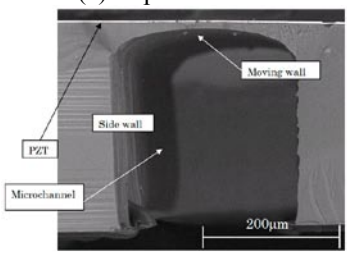

(b) Cross-sectional view of microchannel

Figure 3. Photographs of fabricated active microchannels

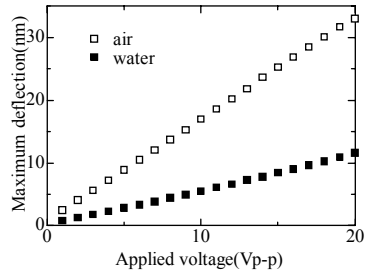

Figure 4. Displacement of active microchannel measured by laser Doppler vibrometer

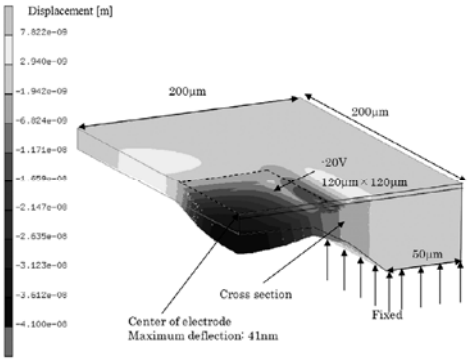

Figure 5. Numerical displacement of active microchannel by FEM analysis (applied voltage: $20V_{p\text{-}p}$)

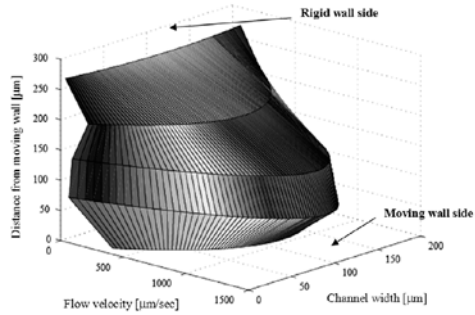

Figure 6. Three-dimensional velocity profile in active microchannel measured by a microPIV with a confocal scanning unit (applied voltage: 1MHz, $20V_{p\text{-}p}$)

5. CONCLUSIONS

In this paper, we propose an innovative fluid transport system for intricately-integrated systems on a small chip. Since the active microchannel was assembled with two-dimensional configuration by simple fabrication process, the transport system can be immediately applied to μTAS without occupied area. The mean flow velocity generated by the fabricated device is about 650μm/s at the applied voltage of 1MHz and 20Vp-p.

ACKNOWLEDGEMENTS

This study is a part of Kyoto City Collaboration of Regional Entities for the Advancement of Technological Excellence of JST on the basis of research results supported in part by Center of Excellence for Research and Education on Complex Functional Mechanical Systems (COE) of MEXT, Japan.

REFERENCES

[1] D. J. Laser and J. G. Santiago, *A review of micropumps*, Journal of Micromechanics and Microengineering, Vol.14, pp.R35-R64, (2004).

[2] N. T. Nguyen, X. Y. Huang and T. K. Chuan, *MEMS-micropumps: A review*, Journal of Fluids Engineering-Transactions of the ASME, Vol.124, pp.384-392, (2002).

[3] T. Suzuki, H. Hata, H. Shintaku, I. Kanno, S. Kawano and H. Kotera, *Visualization and optimization for fluid flow of traveling wave micropump using microPIV and numerical simulation*," Proc. Micro Total Analysis Systems 2005, pp.1108-1110, (2005).

[4] I. Kanno, H. Kotera and K. Wasa, *Measurement of transverse piezoelectric properties of PZT thin films*, Sensors and Actuators A, Vol.107, pp.68-74, (2003).

[5] T. Suzuki, H. Hata, H. Shintaku, I. Kanno, S. Kawano and H. Kotera, *Fast pulsatile flow involved net continuous flow generated by a traveling wave micropump*, Proc. Micro Total Analysis Systems 2006, pp.131-133, (2006).

DISPOSABLE DIFFUSER-VALVE MICROPUMP EXTERNALLY ACTUATED BY PRECISION LINEAR MOTOR

W. Rhie and T. Higuchi
Department of Precision Engineering, School of Engineering, University of Tokyo, JAPAN

ABSTRACT

In this paper, we present a new type of disposable diffuser-valve micro pump which has a novel design and was fabricated from flexible capillary tubing and micro pipettes. Exploiting capillary tubing and micropipettes, low cost fabrication was achieved and thus it is also disposable. The complete process of fabrication was performed in a few minutes without conventional MEMS technology or PDMS molding. The pump is externally actuated by direct contact using a linear motor. Adopting dual anti-phase chamber, pulsation was significantly reduced compared with single chamber actuation.

Keywords: micropump, diffuser valve, tubing, linear motor

1. INTRODUCTION

Miniaturization and integration of the microfluidic devices should be the general challenges in this field. However, micropumps are one of the most difficult elements to be integrated since they do not usually generate enough pressures or do have pulsations as well as they raise unit cost hardly to be disposable. Based on these problems, we suggest "Mass μTAS" that actuates multiple microfluidic devices or micro total analysis systems (μTAS) simultaneously by external actuation on the stage. And as part of the Mass μTAS, we present a disposable micropump which is externally actuated by the linear motor.

Since the idea of diffuser-valve pump was first proposed by Van De Pol in 1989 [1], various designs of diffuser-valve pumps have been reported [2-4]. However, most of them have an oscillating diaphragm which has drawbacks of small amplitude and resonance. Moreover, actuators were usually bonded to the diaphragms, which are not suitable for either reuse or throwaway. In this paper, breaking with convention of planar lithography or PDMS molding, tubing itself performs roles of pump chambers, channels and connectors. Using external actuation, large amplitudes (50~200 μm) and relatively low frequencies (10~100 Hz) became applicable easily.

2. THEORY

While the pump chambers are actuated by linear motor, diffuser and nozzle serve for directing liquids as illustrated in Figure 1. Diffuser allows more flow than nozzle does when the same pressure was applied. Employing dual chamber to reduce pulsations was reported by Ollson et al. in 1995 [2]. Our method differs in that one actuator oscillates both two chambers simultaneously in anti-phase.

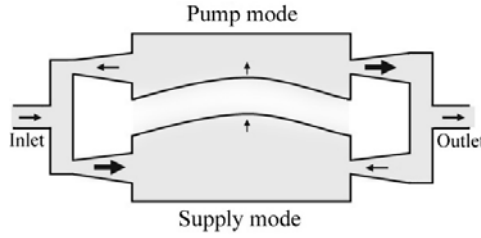

Figure 1. Working principle of the diffuser-valve micro pump

978-0-9798064-0-7/μTAS2007/$20©2007CBMS

3. EXPERIMENTAL

A schematic and a photograph of assembled pump are shown in Figure 2. 4-degree-tapered glass micropipettes having an inner diameter (ID) of 250 μm at the narrow end, 700 μm at the wide end and an outer diameter (OD) of 1 mm are inserted in a elastic heat-shrink tubing (ID shrinks from 1.6 mm to 0.6 mm). Then, two narrow ends of the inlet side micropipettes are connected to thinner heat-shrink tubing (ID shrinks from 0.55 mm to 0.45 mm) and sealed by another heat-shrink tubing (ID shrinks down to zero). The outlet side is connected and sealed in the same manner.

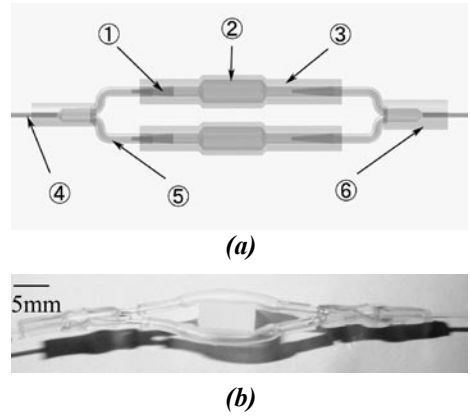

Figure 2. ***(a)*** *Schematic top view of assembled pump ① tapered glass micropipette ② pump chamber (heat shrink tubing, before shrink) ③ heat shrink tubing (after shrink) ④ inlet (PFA tubing) ⑤ heat shrink fluorine resin tubing ⑥ heat shrink tubing (ID shrinks down to zero)* ***(b)*** *Photograph of assembled diffuser-valve pump*

Figure 3 shows the experimental setup for flow rate tests. A rod to actuate the pump chambers was installed on the linear motor oscillating as a sine curve. The pump was placed between two stoppers, and the pump chambers were both half squashed by the rod of 4 mm width. This enables anti-phase actuation with one actuator. The outlet was connected to the inlet of the high-speed flow sensor. The outlet flow from the sensor was measured by electronic scale again in case of sensor errors.

Detailed experimental conditions are as follows. DI water was used for the tests. The length of the inlet and outlet tubing was 15 cm and 25 cm respectively. And they both have 0.5 mm ID and 0.7 mm OD. Pressure difference between the inlet and the outlet was set to zero. The amplitudes input were 100, 150 and 200 μm. The driving frequencies were 10~70 Hz.

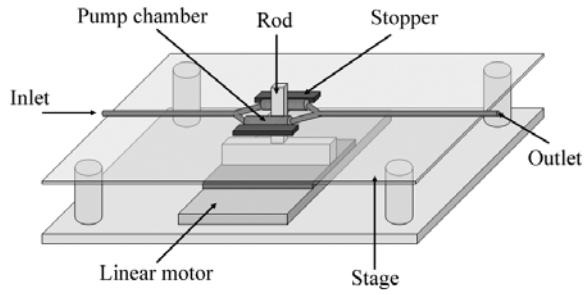

Figure 3. Experimental setup of linear motor (Σ-trac-μ series SGTMM, YASKAWA) and diffuser-valve pump for flow rate test

4. RESULTS AND DISCUSSION

The pumping rate as functions of frequency and amplitude is shown in Figure 4. The water started to be pumped from approximately 30 Hz. It depended on the amplitudes the linear motor made. Figure 5 indicates how the pulsations were reduced by adopting dual chamber. Figure 6 shows the sample results which were measured by flow sensor for 10 seconds each.

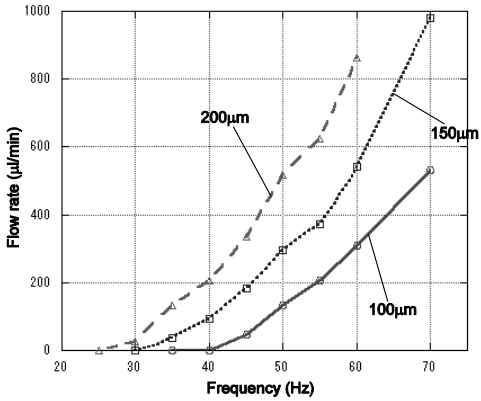

Figure 4. Flow rate of water for different amplitudes and frequencies measured from the weight by electronic scale

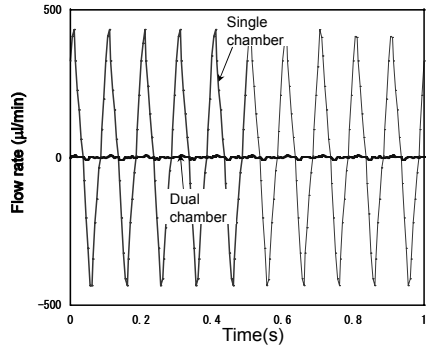

Figure 5. Comparison of pulsations between single chamber and dual chamber for 10 Hz, 100μm-amplitude measured by liquid mass flow meter (ASL-1430-16, SENSIRION)

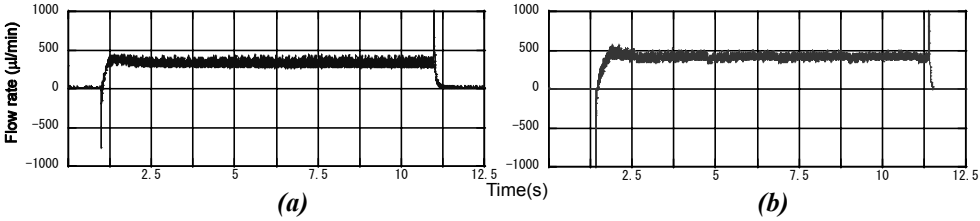

Figure 6. Flow rate of water measured for 10 seconds by liquid mass flow meter (ASL-1430-16) ***(a)*** *45Hz, displacement of ±150μm* ***(b)*** *65Hz, displacement of ±100μm*

5. CONCLUSIONS

We have proposed the concept of "Mass μTAS" which achieve mass parallel processing for laboratory experiments simply by laying out microfluidic chips on the linear motor stage. The diffuser-valve pump based on this concept was designed, fabricated and tested as a first step. Our future work includes developments of other microfluidic devices as well as further miniaturization and optimization.

REFERENCES

[1] F.C.M. Van de Pol, Ph.D Thesis, *A pump based on micro-engineering techniques*, University of Twente, 1989.

[2] A. Olsson, G. Stemme and Erik Stemme, *A valve-less planar fluid pump with two pump chambers*, Sensors and Actuators A, **46-47**, pp. 549-556, 1995.

[3] Jr-Hung Tsai, Liwei Lin, *A thermal bubble actuated micro nozzle-diffuser pump*, Journal of Microelectromechanical Systems, **11**, pp. 665-671, 2002.

[4] C. Yamahata, F. Lacharme, M.A.M. Gijs, *Glass valveless micropump using electromagnetic actuation*, Microelectronic Engineering, **78-79**, pp. 132-127, 2005.

ELECTROCHEMICAL MICROFLUIDIC PUMPS BASED ON SUPER ABSORBING POLYMERS

J. Nestler[1], A. Morschhauser[1], K. Hiller[1], S. Bigot[2], J. Auerswald[3], J. Gavillet[4], T. Otto[5], T. Gessner[1,5]

[1]Chemnitz University of Technology, Center for Microtechnologies (ZfM), GERMANY
[2]Cardiff University, Manufacturing Engineering Center (MEC), UK
[3]CSEM Alpnach, SWITZERLAND, [4]CEA Liten, Grenoble, FRANCE
[5]Fraunhofer IZM, Chemnitz Branch, Dept. Multi Device Integration, GERMANY

ABSTRACT

Electrochemical micropumps based on the electrolysis of water have been fabricated, characterized and tested together with an injection moulded microfluidic polymer chip. In contrast to conventional electrolytical micropumps, a hydrogel based on poly (acrylic acid) sodium salt is used as electrolyte instead of a liquid.

Keywords: micropump, hydrogel, electrolysis, polymer, lab-on-chip

1. INTRODUCTION

For a Lab-on-Chip (LoC) platform for Point-of-Care (PoC) use the controlled transport of liquids like the sample and chemicals like washing buffers is essential. Thus, on-chip microfluidic actuators are desired, which are small in size, inexpensive, easy to integrate but on the other hand able to generate large displacements. Despite of being easy to integrate, the electrochemical generation of gas bubbles by electrolysis fulfils these requirements [1]. However, the integration of a liquid (e.g. water) can be critical for mass fabrication and may also cause problems concerning long-term stability.

A hydrogel based on a poly (acrylic acid) sodium salt (PAAS) was therefore investigated for its applicability as electrolyte, which combines the electrolytic and gas generating properties of water based electrolytes with a good processibility by screen printing or stencil printing due to its gelish properties. It is available at very low cost and non-toxic. The following figure illustrates the working principle of the gel pump.

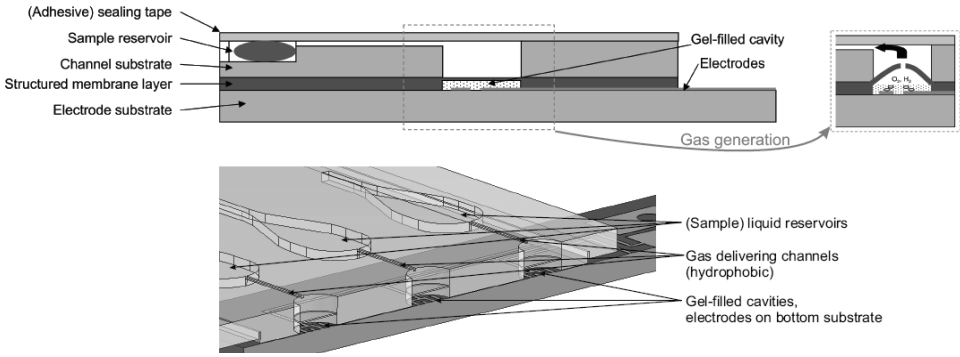

Figure 1. Principle of hydrogel based electrolysis pumps. A thin gel layer is stored on top of electrodes and covered by a thin, pierced membrane. Applying a voltage at the electrodes leads to an electrolytical generation of oxygen and hydrogen gas. The gas enters a gas delivering channel and applies a direct pressure to a liquid plug stored in a reservoir

978-0-9798064-0-7/μTAS2007/$20©2007CBMS

2. THEORY

The electrolysis of water is the dissociation of water molecules into oxygen and hydrogen gas by means of an electric voltage. The reaction is give by:

$$\textit{Anode:} \quad 2H_2O \rightarrow 4H^+ + 4e^- + O_2\,(\text{gas})$$

$$\textit{Cathode:} \quad 2H_2O + 2e^- \rightarrow 2OH^- + H_2\,(\text{gas})$$

The generated gas volume is directly proportional to the transferred charges.

Crosslinked PAAS is a so-called super absorbing polymer which is able to dramatically swell in water. The swollen state is referred to as a hydrogel, which mainly consists of up to 99 wt% of water, but has a very high viscosity. When PAAS is brought in contact with water, the weakly bonded sodium is split off, leaving negatively charged polymer chains and movable sodium ions:

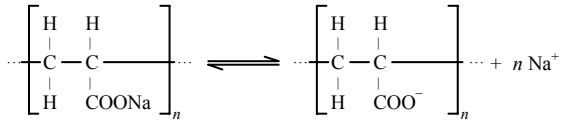

Using this effect, PAAS not only "thickens" the water, but also increases its ion content, which leads to a higher conductivity and thus allows lower voltages for a certain current.

3. EXPERIMENTAL

For pressure tests, electrodes have been deposited and structured on 4 inch polymer (TOPAS 5013) wafers. A frame of 100..200µm high SU8 has been subsequently formed around the electrodes. After dicing, the separated chips were mounted on a PCB board for electrical contactation. The SU8 cavities (3x3mm²) were filled with PAAS gel (1wt% BASF Luquasorb 1010 with 99wt% deionized water) immediately before starting the measurements. For measuring the generated gas over time, a pressure sensor was mounted on the top of the chips. A constant current was then driven though the gel and pressure, voltage and current were recorded over time

For pumping tests, a setup as shown in Fig. 1 was used. Three electrodes were fabricated on one substrate. The electrodes were covered with PAAS gel and a (pierced) and structured PDMS membrane ("membrane layer" in Fig. 1). An injection moulded microfluidic channel system was sealed with adhesive tape on the top and clamped onto the electrodes/gel/PDMS part as depicted in the lower picture of Fig. 1. The reservoirs were then filled with inked water using a syringe and immediately sealed.

4. RESULTS

Using the *pressure test* setup described above, quantitative results of generated pressures over time have been obtained (Fig. 2). However, the volume of the generated gas is usually of greater interest for lab on chip systems. Thus, assuming ideal gas law ($p_1 \cdot V_1 = p_2 \cdot V_2$), the theoretically produced gas volume at atmospheric pressure can been calculated. For the current measurement setup, a pressure of 200mbar equals to a generated gas volume of about 15µl at atmospheric pressure.

These calculated gas volume leads to theoretical flow rates of 11.3µl/min at 1.5mA and 2.3µl/min for a current of 0.29mA. Due to the linear relationship between charge and the generated gas volume, pressures or flow rates can be easily adjusted by changing the driving current.

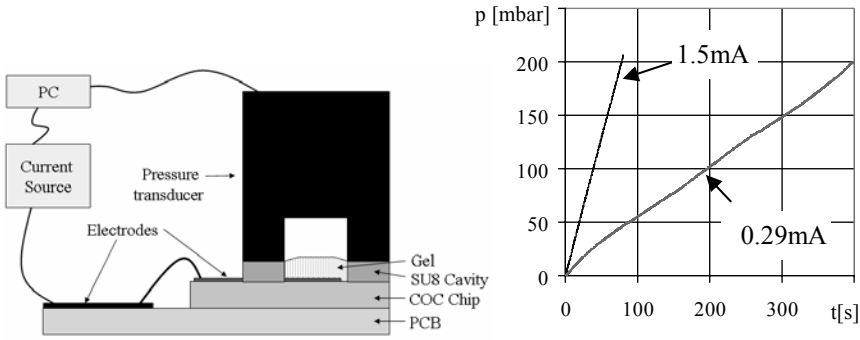

Figure 2. Generated pressures at certain driving currents over time (left: test setup, right: measurement results).

Pumping tests have been performed to illustrate the emptying of reservoirs in a lab-on-chip system. Fig. 3 shows the emptying of the first of three reservoirs.

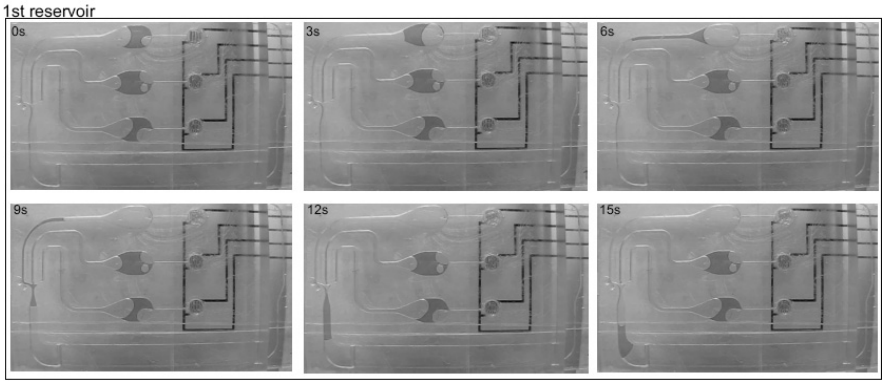

Figure 3. Emptying of a reservoir in a polymer LoC system.

5. CONCLUSIONS

Electrolysis gel actuators have been successfully characterized concerning generated gas pressure/volume over time. They have been tested to empty reservoirs in microfluidic systems, as well as to pump fluids through microfluidic channels. Next steps will target long term stability investigations and the development of gel-sealing technologies.

ACKNOWLEDGEMENTS

This work has been founded by the European Commission under contract number 016768 and is part of the research project SEMOFS (Surface Enhanced Micro Optical Fluidic Systems, www.semofs.com). The authors would like to thank the whole SEMOFS consortium for their fruitful cooperation.

REFERENCES

[1] C.R. Neagu et al. An electrochemical microactuator: principle and first results, J. Micromechanical Syst. 5 (1), pp 2-9, (1996).

MICRO OPTICAL STIRRER FOR MIXING IN MICROCHANNEL FLOW

T. Moriya and Y. Sato
Keio University, JAPAN

ABSTRACT

A novel optical technique for stirring or mixing microscopic objects in a microchannel flow was developed by utilizing laser radiation pressure. The author's group proposed a new technique to manipulate the particles clusters by installing cylindrical lenses in a light pass and by moving mirrors. The laser radiation pressure was distributed elliptically in the solution, thus the number of manipulated particles was increased. The cylindrical lenses were rotated by controlling motors, therefore the elliptic areas of laser radiation pressure were rotated like as a windmill. This study focuses on investigations of performance of "micro optical stirrer".

Keywords: Optical tweezers, laser radiation pressure, mixing, submicron particles

1. INTRODUCTION

A micro optical stirrer was proposed to mix or stir submicron particles in a microchannel flow without complex fabrication. The laser radiation pressure was distributed elliptically in a buffer solution by installing cylindrical lenses and by moving mirrors. The cylindrical lenses were rotated, thus the non-intrusive mixing in microfluidic devices is realized. This study focuses on investigations of performance of the micro optical stirrer that will be available in biological and medical engineering.

2. EXPERIMENTAL SETUP

Optical tweezers have been widely used to trap or manipulate cells or particles in an aqueous solution, which is based on the reflection and refraction of a laser light that enters from the solution to a transparent object (Figure 1(*a*))[1][2]. Due to a limited area of focal point, only a few objects are trapped by the optical tweezers. The authors' group proposed a new technique to manipulate the particle clusters by installing cylindrical lenses in a light path (Figure 1(*b*), CL1 and CL2 in Figure 2) and by moving mirrors (M1 and M2 in Figure 2) [3]. Owing to this slight modification, the laser radiation pressure was distributed elliptically in the solution, thus the number of manipulated particles was increased. In the present study, the cylindrical lenses were rotated by controlling motors, therefore the elliptic areas of laser radiation pressure were rotated like as a windmill (Figure 1(*c*)). Schematic of micro optical stirrer system is illustrated in Figure 2. Two cylindrical lenses, CL1 and CL2, were rotated at 90 degrees/second and two mirrors, M1 and M2, were moved by stepping motors. Figure 3 depicts the time evolution of the laser radiation pressure

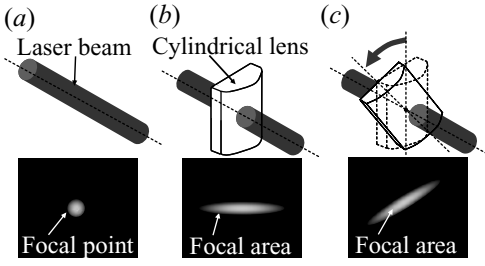

Figure 1. Schematic of (a) the focal point, (b) the elliptic focal area by using a cylindrical lens and (c) the rotated focal area by rotating a cylindrical lens.

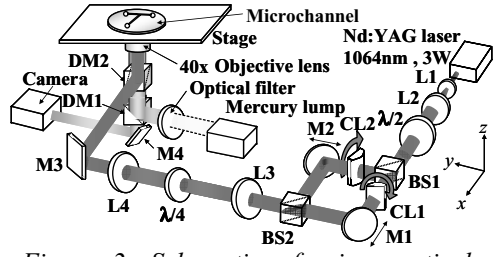

Figure 2. Schematic of micro optical stirrer system.

978-0-9798064-0-7/μTAS2007/$20©2007CBMS

distribution. These images were obtained by projecting the laser power distribution onto a special glass (YAGLASS by Sumita Optical Glass, Inc.) and captured by a CCD camera. It is obvious from Figure 3 that the area of laser radiation pressure was rotated at a constant angular velocity.

3. EVALUATION OF FORCE

The force acting on particles by the micro optical stirrer is investigated. Fluorescent particles B listed in table 1 in a buffer solution (n = 1.30) were selected. The fluorescence of the particles is captured by a high-speed CMOS camera. The force was evaluated by the balance between the force by laser radiation pressure and the Stokes's drag force that was calculated by particle tracking velocimetry (PTV). Then the Stokes's drag force is derived by

$$F = -3\pi\mu d_p u_R \quad (1)$$

where F is the Stokes's drag force, μ is a viscosity, d_p is diameter of particles and u_R is the relative velocity between particles and buffer solution. The force acting on particles is calculated by using equation (1).

The micro optical stirrer was applied to a flow in a T-shaped microchannel as shown in Figure 4. Two stirrers were generated at y = 100 μm and 120 μm in downstream by using the beam splitter in the light path (BS1 and BS2 in Figure 2). Two types of fluorescent particles were selected and are listed in Table 1. 1 μm particles were injected into the inlet A, while 2 μm particles into the inlet B. The bulk velocity was set to be 33.5 μm/s. A ratio of number of particles at y = 200 μm in downstream was measured to validate the mixing performance of the stirrer.

4. RESULTS AND DISCUSSION

The force acting on 2 μm particles by laser radiation pressure was evaluated and one of the results is shown in Figure 5. Figure 5 shows that group of particles by the stirrer is

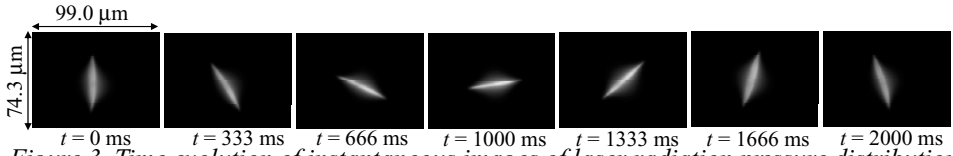

Figure 3. Time evolution of instantaneous images of laser radiation pressure distribution.

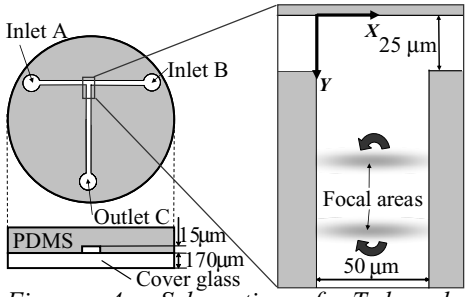

Figure 4. Schematic of T-shaped microchannel and focal areas.

Table 1. Properties of fluorescent particles

	Particle A	Particle B
Material	polystyrene	polystyrene
Excitation wave length	540 nm	505 nm
Emission wave length	560 nm	515 nm
Diameter	1 μm	2 μm
Refractive index	1.59	1.59

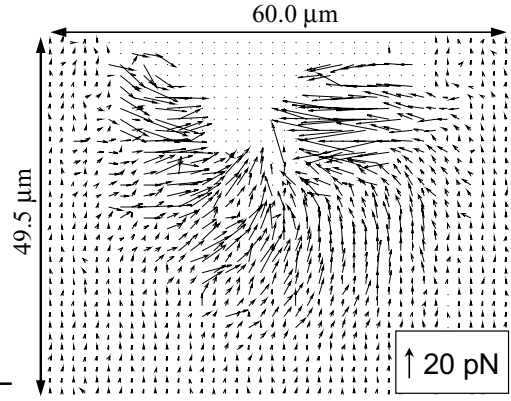

Figure 5. Vector map of force acting on 2 μm particles by the micro optical stirrer.

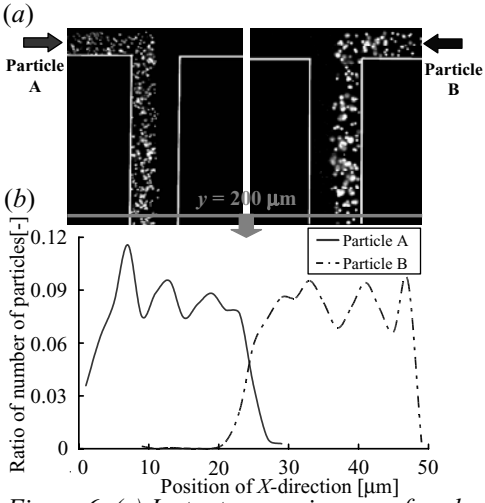

Figure 6. (a) Instantaneous images of each flowing particle by exchanging dichroic mirror and (b) ratio of number of particles at y = 200 μm without the micro optical stirrer.

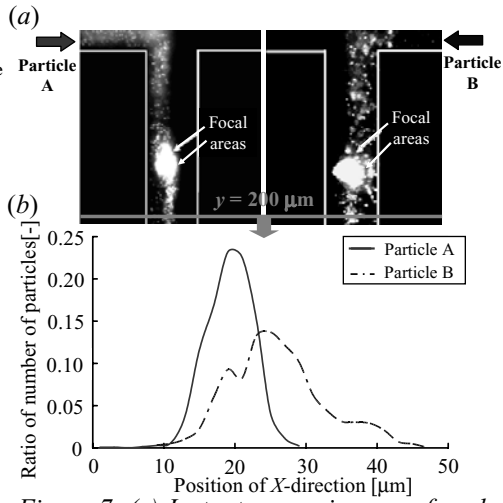

Figure 7. (a) Instantaneous images of each flowing particles by exchanging dichroic mirror and (b) ratio of number of particles at y = 200 μm with the micro optical stirrer.

forced toward to center of focal area rotation. The stirrer was applied in mixing field as shown in Figure 4. Without the micro optical stirrer, instantaneous images of flowing particles and ratio of number of particles are shown in Figure 6. Figure 6 (*a*) and Figure 7 (*a*) are captured by exchanging the dichroic mirror (DM1 in Figure 2). The particles were no longer mixed in downstream. When the micro optical stirrer was applied, the particles were mixed in downstream. This is confirmed by Figure 7 that indicates the number of particles has a peak value at the channel centerline. It is noted that the non-intrusive mixing is realized by the present system.

5. CONCLUSIONS

A technique of mixing group of particles in microchannel flow using laser radiation pressure is developed. The mixing performance of micro optical stirrer is investigated by particle tracking velocimetry. The non-intrusive mixing is realized by the present system and the application to stirring cells is currently underway.

ACKNOWLEDGEMENT

This work is subsidized by Collaborative Development of Innovative Seeds, Potentially verification stage by Japan Science and Technology Agency.

REFERENCES

[1] A. Ashkin, *Applications of Laser Radiation Pressure*, Science, **210**, pp. 1081-1088, (1980).

[2] A. Ashkin, J. M. Dziedzic, J. E. Bjorkholm and S. Chu, *Observation of single-beam gradient force optical trap for dielectric particles*, OPTICAL LETTERS, **1**, pp. 288-290, (1986).

[3] T. Moriya, K. Saiki and Y. Sato, *Continuous particle manipulation in microchannel using laser radiation pressure*, Micro Total Analysis Systems 2006, **1**, pp. 906-908, (2006).

PATTERNING OF BACTERIAL CELLS USING ELECTRO-HYDRODYNAMIC PRINTING

J. H. Kim[1], S. J. Kim[2], H. S. Kim[1], J. S. Park[1] and H. I. Jung[1,2]

[1]*Yonsei University, KOREA*

[2]*Nanomedical National Core Research Center for Nanomedical Technology, KOREA*

ABSTRACT

A new method for patterning the bacterial cells using electro-hydrodynamic(EHD) printing is proposed in this paper. E. *coli* cells in deionized water and EG(ethylene glycol) solution are printed to construct bacterial colony pattern using EHD device. The pattern width is about 150μm and the bacterial cells patterned are found undamaged.

Keywords: EHD(Electro-Hydrodynamic), Bacterial Cell, Patterning, Microfluidics

1.INTRODUCTION

The field of cellular and tissue engineering is widening with the development of microfabrication techniques. Especially, micropatterning and spatial rearrangement of cells have been used in both tissue and cellular engineering to manipulate and position a variety of cell types onto culture plates and scaffolds [1]. Electro-hydrodynamic (EHD) printing method is a new method to pattern cells in micrometer scale. This method can be highly applicable to various samples such as organic, inorganic, metallic, and high viscosity materials[2]. It can make patterns directly and instantly.

2. EXPERIMENTAL

Electro-hydrodynamic(EHD) printing equipment consists of two electrodes, syringe pump, power supplier, moving stage, and controller as shown in figure 1. Two electrodes (negative and positive) induce electrokinetic force by electric field which causes molecules ionized. When dielectric liquid is fully ionized at the tip of syringe needle, the ionic particles or materials will jet through a minute electric field. A syringe pump (KDS-210, KD scientific, USA) supplies liquid flow to the needle. The needle(MNT-28G-13, KGN, Taiwan) is made of stainless steel and has inner diameter of 150 μm and outer diameter of 350 μm. It was charged by the positive electric potential. The coupled ground electrode was placed on the X- and Y- directional moving part. The distance from the needle to the substrate and from the ground needle to the substrate is 1 mm. Power supplier (KSC, Korea) which can supply voltage up to 30 kV was connected with these two electrodes. Moving stage was modified and based on the commercial linear motor (DCT, Korea) which is controlled by a personal computer and controller.

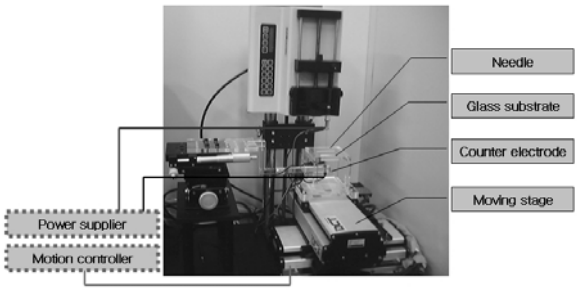

Figure 1. Experimental – setup for printing

978-0-9798064-0-7/μTAS2007/$20©2007CBMS

Membrane filters(Milipore, USA) on the glass cover slips (Marienfeld, Germany) were used as non-conductive, hydrophobic and bio-compatible material substrates.

E. *coli* cells (ATCC 47013, Korea Culture Center Of Microorganism) which has antibiotic resistance were cultured in nutrient broth(BD, USA). E. *coli* cells were separated from this broth medium and suspended by autoclaved deionized water. EG(ethylene glycol) is added to this suspension with various concentrations. To confirm the cell viability of the printing solution, the dye SYTO9 was used. Figure 2 shows cell aggregation in the highly concentrated EG solutions

Table 1. Properties of the printing solutions with bacterial cells

	pure DW	0vol%	20vol%	40vol%	60vol%	80vol%	100vol%	pure EG
viscosity (mPa s)	0.87	1.09	1.52	2.50	4.62	6.68	15.1	20.5
conductivity (uS/mm)	21.7	89.3	70.4	50.6	32.4	23.9	10.6	0.1

3. RESULTS AND DISCUSSION

The width of the patterns were varied dependent upon concentrations of EG. When the concentration of EG increases, the viscosity increases. However the conductivity decreases. This condition is good for stable cone-jet mode to deposit the clear pattern of the bacterial cells. But the higher concentration of EG caused the cell aggregation(figure 2). The optimal condition of the EG concentration was determined as 40vol%, because it makes very fine patterns of viable cells. Figure 3 shows the printed pattern of these solution. Figure 4 shows the ratio of the designed pattern length to the imprinted pattern length which were analysed from the result of the figure 3.

From this optimal condition, we deposited the complex bacterial colony pattern(Figure 5).

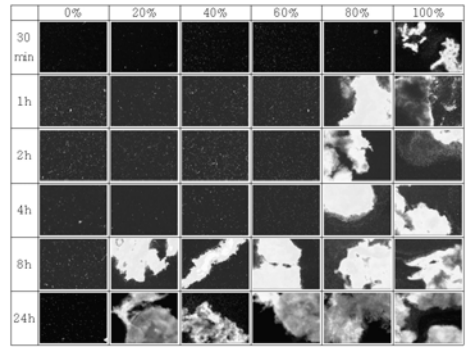

Figure 2. Images observed by microscope of E. *coli* cells intercalating dye SYTO9 in printing solutions of varying ethylene glycol concentrations. This test was done before printing the solutions

4. CONCLUSIONS

High-throughput cellular patterning method using electrohydrodynamic(EHD) printing are designed and experimented. System optimization and theoretical analysis process for the specific purpose were performed. The bacterial cell patterning using membrane filter substrate and EHD printing method is archived and direct cell patterning under 150 μm of width is demonstrated. This method has a potential for the fabrication of biosensors for bacterial cells and can be used to pharmaceutical drug screening and toxicity test.

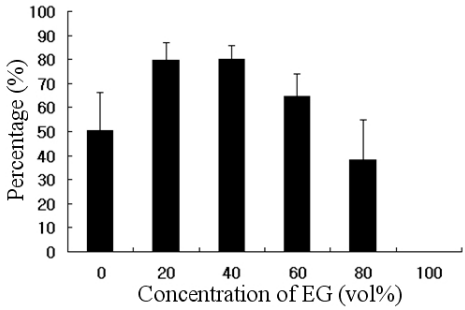

Figure 3. Average percentage of imprinted lines with respect to the total designed lines

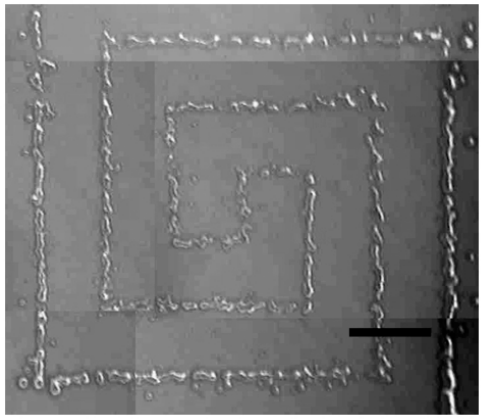

Figure 5. Image of the patterned complex bacterial cell colony in the 40vol% of EG concentration. Black bar indicates 2 mm

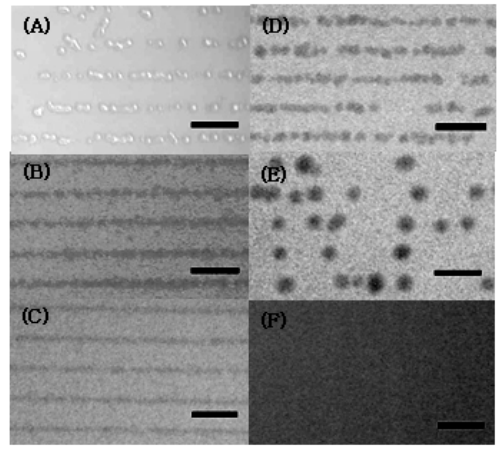

Figure 4. Patterns of droplets with various conditions of EG concentration; (A) 0vol%, (B) 20vol%, (C) 40vol%, (D) 60vol%, (E) 80vol%, (F)100vol%, Black bars indicate 2 mm.

ACKNOWLEDGEMENTS

This work was supported by the Korea Research Foundation Grant (KRF-2006-331-D00040) funded by the Korean Government (MOEHRD), ICBIN of Seoul R&BD program (Grant no. 10816) and National Core Research Center (NCRC) for Nanomedical Technology of the Korea Science & Engineering Foundation (Grant no. R15-2004-024-01001-0).

REFERENCES

[1] H.S. Kim, D.Y. Lee, J.H. Park, J.H. Kim, J.H. Hwang and H.I. Jung, *Optimization of electorhydrodynamic writing technique to print collagen*, Experimental Techniques, in press (2007)

[2] S.N. Jayasinghe, M.J. Edrisinghe, and T.D. wilde, *A novel ceramic printing technique based on electrostatic atomization of a suspension*, Master Res Inno, Vol.6, pp.92 -95, (2002)

SAMPLE METERING AND PARALLEL LIQUID PLUG ACTUATION FOR MULTIPLE BIOCHEMICAL ASSAYS

M. M. Mielnik[1], J. Voitel[1], L. A. Solli[2] and L. Furuberg[1]

[1]SINTEF, Dept. of Microsystems and Nanotechnology, Oslo, NORWAY

[2]NorChip AS, Klokkarstua, NORWAY

ABSTRACT

We demonstrate a passive microfluidic system for simple and efficient metering, handling and control of parallel nanoliter samples on-chip. The system consist of two chips; one for sample loading, splitting and metering (based on capillary forces only), and another for sample plug movement in parallel reaction channels. The latter is based on a set of capillary valves and one single external pressure source only. The strength of the capillary valves determines the logic movement of the parallel sample droplets on-chip, permitting robust system control. In general, the presented system is applicable to a variety of multi-step reaction protocols with a large number of parallel channels.

Keywords: microfluidics, capillary valve, lab-on-a-chip, sample control

1. INTRODUCTION

Passive fluidic manipulation is a promising approach in Lab-on-a-Chip (LOC) systems due to the inherent mechanical simplicity of the resulting device, rendering it well suited for mass production with a minimum of (costly) assembly needs. Such manipulation has been previously explored by e.g. [1], [2], and [3].

Here, we present a passive system designed for on-chip amplification of mRNA and ssDNA by Nucleic Acid Sequence-Based Amplification (NASBA, see [4]), in our case requiring two separate isothermal steps and mixing with two different dried reagents stored on-chip. We demonstrate a passive system providing efficient multi-step control of liquid samples in several separate, parallel microchannels. Specifically, simultaneous fluidic control of seven parallel channel systems is demonstrated, permitting the analysis of a single sample for e.g. seven different markers.

3. EXPERIMENTAL

The experiments were performed using two types of test chips, one for metering (fig.1a) and another for control of sample plug movement in parallel channels (fig.1b). The chips were manufactured in Cyclic Olefin Copolymer (COC) by micromilling (features >100µm) and laser ablation (features of 100µm and below). Because native COC is hydrophobic, the chips were coated with 0.5% polyethylene glycol (PEG) in methanol (Sigma Aldrich). The contact angle of DI water on PEG surface was approx. 30º. The valve structures consisted of a tapered part and a narrow restriction channel, see fig. 2. Teflon fluorpolymer (AF1600, DuPont) was spotted using PipeJet spotting system (BioFluidix) onto the tapered part of the valve, filling the narrow valve structures by capillary action. The contact angle of DI water on Teflon surface was measured to be approx. 110º. After coating and spotting, the chips were sealed with adhesive tape.

Both DI water and pre-mixed NASBA reagents with sample were used as working liquids to verify the chip functionality.

978-0-9798064-0-7/µTAS2007/$20©2007CBMS

The parallel sample plug movement chip (fig.1b.) was mounted in an aluminium frame with fluidic interconnects, and coupled to a syringe pump (PHD2000, Harvard Apparatus) which was used to apply suction to the common chip outlet, withdrawing air from the system at a rate of 10 µl/min. A pressure sensor (TP3100 001A 0P from MEMSCAP) was used for monitoring the pressure in the common tube connection to the parallel channels (see fig. 1b).

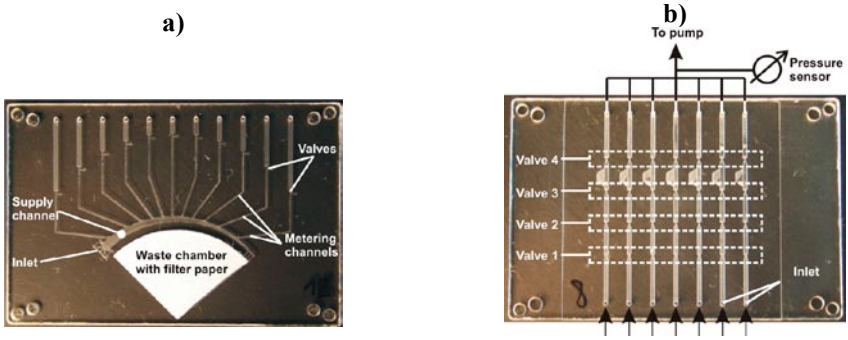

Figure 1: **a)** Sample metering chip. The sample is introduced at the inlet, filling up the supply channel (depth 200µm) and the eleven individual metering channels (75µm×300µm, volume 335nl) up to the hydrophobic capillary valves. Excess sample is drawn into the waste chamber, which contains an absorbing filter paper. **b)** Parallel reaction/actuation chip. The capillary valves increase in strength in the downstream direction, with valve widths of 380µm, 150µm, 75µm and 33µm. The depth of all channels is 200µm. The width of the parallel channels is 800µm.

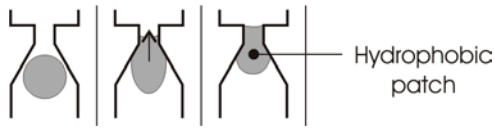

Figure 2: Capillary valve geometry. Hydrophobization was achieved by spotting a droplet of Teflon in the tapered part of the valve, filling the narrow restriction by capillary forces.

4. RESULTS AND DISCUSSION

The metering chip (fig.1a) was tested using different sample volumes at the inlet. It was found that the smallest sample volume permitting proper chip operation was 17µl. For this and larger volumes, the sample was drawn into the supply channel, filled all metering channels up to the position of the capillary valves, while excess sample was absorbed into the waste chamber. During the accompanying drainage of the supply channel, the liquid contained in the parallel metering channels was pinched off at the inlets, leaving a precisely metered sample plug of 335nl in each metering channel. The whole process required approximately 2 minutes from sample insertion till completed absorption of waste. Smaller sample volumes resulted in incomplete filling of metering channels, or incomplete drainage of the supply channel to waste. When the waste chamber was ventilated to the atmosphere, a smaller sample volume (15µl) could be applied at the chip inlet.

The parallel plug control chips (fig.1b) consisted of 7 parallel channels, each containing 4 hydrophobic valves of increasing strength. During operation, sample plugs introduced at the inlets all passed valve 1 before any plug passed valve 2, etc., such that all plugs resided at the same downstream position in the channels. In this manner, parallel, multi-step motion of the sample plugs was achieved.

A typical pressure trace of the movement of seven parallel plugs through the system is shown in fig.3a. For each valve, seven pressure minima can be observed, indicating the passing of a liquid plug through its respective valve. Figure 3b shows average burst pressure data collected from 5 chips. The solid line is the plot of the Young-Laplace equation representing the burst pressure required to overcome a capillary burst valve, see [5]. As can be seen from the figure, the valve performance is well predicted by the theoretical approximation.

a) **b)**

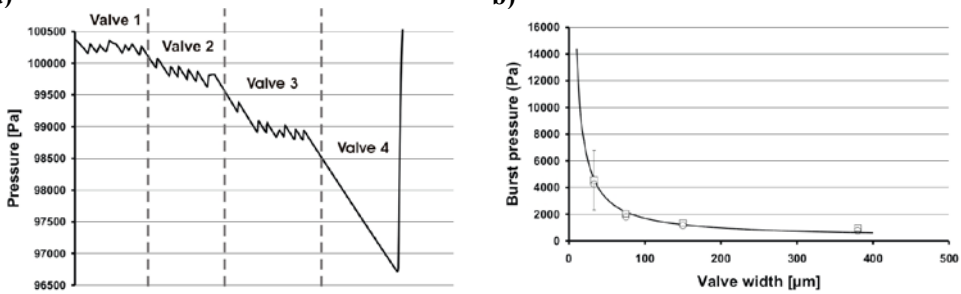

Figure 5: **a)** Pressure trace of seven parallel plugs moving through the parallel actuation chip. At the fourth valve, the first plug to break the valve effectively ventilates the system, and hence the pressure in the system returns to atmospheric conditions. **b)** Pressure characteristics of the capillary valves. Symbols: □ DI water; ○ reagents; solid line represents the analytical values for water.

5. CONCLUSIONS

A passive system capable of robust, parallel sample control on-chip using a single external pressure source has been demonstrated. The system relies on capillary valves of varying strength. The presented method is applicable to a variety of multi-step reaction protocols and can be extended to a large number of parallel channels.

ACKNOWLEDGEMENTS

The present work is partially funded by the MicroActive project, European Commission, contract IST-NMP-CT-2005-0173319, and partially by the Research Council of Norway.

REFERENCES

[1] K. Handique, D.T. Burke, C.H. Mastrangelo, M.A. Burns, *Nanoliter Liquid Metering in Microchannels using Hydrophobic Patterns,* Anal. Chem. 72 (17), pp. 4100-4109 (2000).

[2] C.H. Ahn, J-W. Choi, G. Beaucage, J.H. Nevin, J-B. Lee, A. Puntambekar, J.Y.Lee, *Disposable Smart Lab on a Chip for Point-of-Care Clinical Diagnostics,* Proc. IEEE 92 (1), pp. 154-173 (2004).

[3] S-H. Lee, C-S. Lee, B-G. Kim, Y-K. Kim, *Quantitatively controlled nanoliter liquid manipulation using hydrophobic valving and control of surface wettability,* J. Micromech. Microeng. 13, pp. 89-97 (2003).

[4] J. Compton, *Nucleic-acid sequence-based amplification*, Nature 350 (6313), pp. 91-92 (1991).

[5] H. Cho, H.Y. Kim, J.Y. Kang, T.S. Kim, *How the capillary burst microvalve works*, J. Colloid and Interface Science 306, pp. 379-385 (2007).

TOWARDS A COMPREHENSIVE CENTRIFUGAL PROCESS INTEGRATION BY ROTATIONALLY INDUCED LYOPHILISATE DISSOLUTION AND CELL LYSIS

S. Lutz[1], P. Lang[1], B. Faltin[2], S. Haeberle[1], F. von Stetten[2], R. Zengerle[1,2], and J. Ducrée[1]

[1]HSG-IMIT, Institute for Micromachining and Information Technology, Germany
[2]Laboratory for MEMS Applications, Department of Microsystems Engineering (IMTEK), University of Freiburg, Germany

ABSTRACT

This manuscript shows how the rotational „shake mode“ which has previously been used for mixing of liquids [1] can be adopted for implementing two key steps in typical point-of-care applications, the efficient dissolution of lyophilized beads and cell lysis. The process time is reduced by optimizing the aspect-ratio of an on-disk chamber containing an overall volume of 50 µl. The two upstream processes supplement our existing portfolio of unit operations [2].

Keywords: Centrifugal Microfluidics, Dissolution, Lyophilisate, Blood Lysis

1. INTRODUCTION

One of the key success factors for lab-on-a-chip technologies is linked to the ability to fully integrate and automate complex lab protocols on a single substrate which is loaded by a sample and then inserted into a reusable device. To this end, the protocols of protein or nucleic acid assays have to be translated into a sequence of fluidic unit operations. One of the most key unit operations for assay development is mixing which influences assay steps like incubation, dissolution or sample preparation as shown in Figure 1A. In this work we focus on the optimization of microfluidic mixing processes in centrifugal platforms to enhance the efficiency of typical assay steps: the dissolution of lyophilizate and cell lysis.

2. FUNCTIONAL PRINCIPLE

Our modular setup consists of a microstructured disk (Fig. 1B) which is spun by a frequency programmable rotary motor. During our shake-mode protocol (frequency amplitude: 32 Hz, rotational acceleration: 8 Hz/s, hold time: 0.4 s), steep acceleration ramps imposed by the frequent reversal of the sense of rotation induce inertial mixing in a disk-based chamber [1]. Due to the interplay of viscous shear-stress meditated by the surface and the inertial volume force, the mixing efficiency is tightly linked to the aspect ratio and overall volume of the mixing chamber.

978-0-9798064-0-7/µTAS2007/$20©2007CBMS

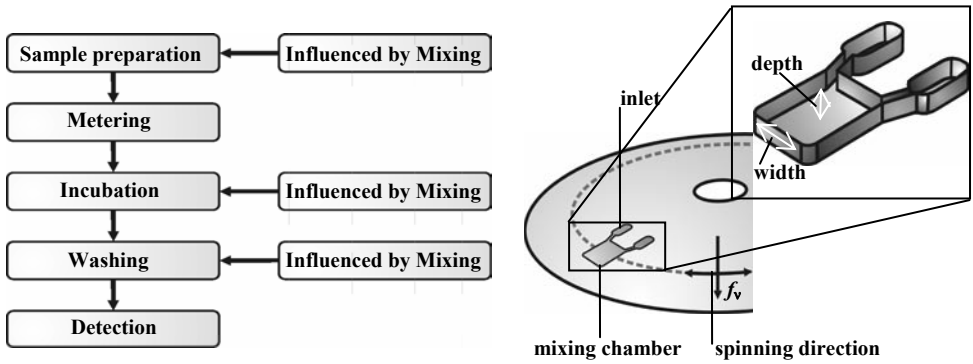

Fig. 1A) Typical unit operations for diagnostic assays and their dependence on mixing. ***B)*** A microstructured COC-disk containing the mixing chamber is used for our experiments. The chamber features a reagent volume of 50 µL at varying aspect ratios.

3. EXPERIMENTS

In Figure 2, the time to dissolve dry reagents by shake mode is experimentally characterized at aspect ratios between 0.04 and 0.5. In all experiments, the chamber volume is kept constant at 50 µl, an amount commonly used in many biological assays. The process time is evaluated by observing the dissolution of 5 mg of the red colored salt potassium ferricyanide in DI-water.

The best performance is achieved at aspect ratios between 0.1 and 0.29 where the shake-mode enhanced dissolution time is cut down by more than 70% with respect to mere diffusion at rest. The presence of silica beads in the mixing chamber does not further enhance the dissolution process (Fig. 3). We assume that their high density (3 g mL^{-1}) pins the beads to an „inefficient domain“ on the outer perimeter of the mixing chamber.

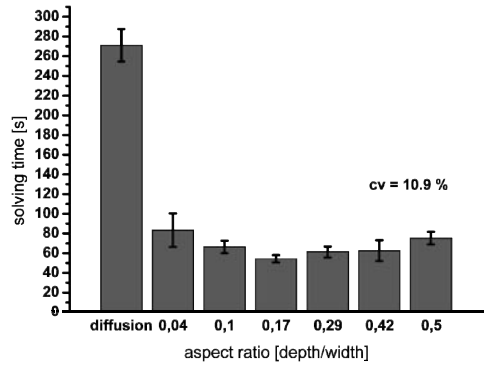

Fig. 2 Correlation between the dissolution time of potassium ferricyanide in 50µL of DI water in mixing chambers with varying aspect ratios.

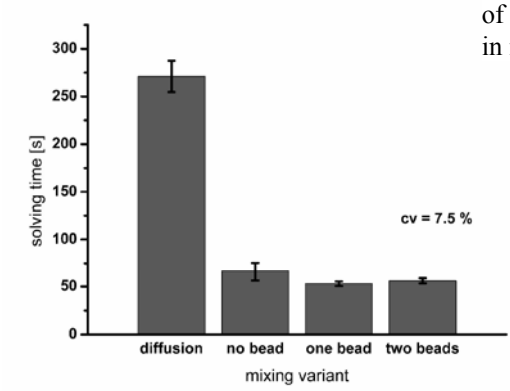

Fig. 3 The influence of silica beads in the mixing chamber on the dissolution time for potassium ferricyanide

We next investigated the dissolution of a single 10.6-mg bead containing the lyophilizate of a PCR master mix (with-

out primers, manufacturer: GE Healthcare) in a chamber displaying an aspect ratio of 0.29. A minimum dissolution time of 250 s, representing a 4-fold acceleration with respect to mere diffusive dissolution, is obtained without silica beads or obstacles for pinning the bead in the center of the chamber (Fig. 4).

Lysis of blood cells in a mixing chamber is demonstrated in Figure 3C. Mixing of lysis buffer and 50 µl of human whole blood is performed with a shake-mode protocol. Nearly 100 % of the blood cells are lysed within 20 s, in a chamber displaying a depth of 1 mm. Cell lysis without shake mode takes about 90 s. The centrifugal force transfers the lysate via a siphon directly into an Eppendorf tube inserted into a „flying bucket“ rotor (Fig. 5).

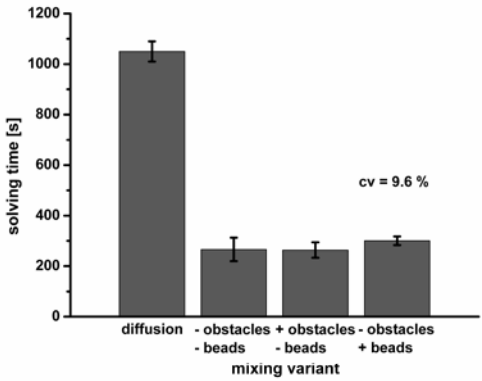

Fig. 4 Dissolution time for 10.6 mg “ready-to-go” PCR lyophilizate beads in 50 µL DI-water. The dissolution time is reduced by a factor of four compared to mere diffusion by using the shake-mode. Obstacles or beads in the mixing chamber show no significant influence on the speed of the dissolution process.

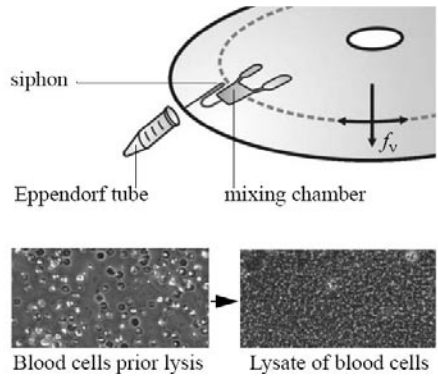

Fig. 5 Lysis of blood cells by shake-mode mixing of lysis buffer with human blood. The siphon keeps blood and buffer in the chamber during spinning of the disk. Adding 20 µL of buffer and spinning forwards the buffer containing the lysed cells into an Eppendorf tube mounted on a flying-bucket holder.

5. CONCLUSION

We identified the aspect ratio of the mixing chamber as the key impact parameters for using the rotational shake-mode to decisively enhance the efficiency of important unit operations on our centrifugal microfluidic platform: the dissolution of dry, lyophilized reagents and cell lysis. Adding these capabilities to our existing portfolio of unit operations [2] will allow to implement more complex protocols while cutting down the time-to-results and minimizing the costs of the disposable.

REFERENCES

[1] M. Grumann, A. Geipel, L. Riegger, R. Zengerle, and J. Ducrée. Batch-mode mixing with magnetic beads on centrifugal microfluidic platforms. Lab Chip, 5(5):560, 2005.

[2] Jens Ducrée, Stefan Haeberle, Sascha Lutz, Sarah Pausch, Felix von Stetten, and Roland Zengerle. The centrifugal microfluidic Bio-Disk platform. Journal of Micromechanics & Microengineering, 2007. status: in press.

ULTRASONIC MIXING IN POLYMER MICROFLUIDICS

Martin Bengtsson, Monica Brivio and Anders Wolff
Dept. of Micro and Nanotechnology (MIC), Technical University of Denmark,
DK 2800, Kongens Lyngby, Denmark

ABSTRACT

Ultrasonic mixing is a convenient method to increase the reaction speed in micro systems of silicon or glass. On polymer devices however this is a rare method due to the high acoustic absorption of most polymers. This paper describes the investigation of the acoustical properties of various polymer materials, with the ultimate goal of developing a micro fluidic system with ultrasonic mixing.

Keywords: Ultrasound, Mixing, Polymers

1. INTRODUCTION

The SMART-BioMEMS project aims at developing an on-chip fully-integrated micro system for DNA analysis. The project combines various functional modules on one disposable polymer chip [1]. Since several of these reactions are very time consuming, mixing though acoustic streaming is proposed in order to decrease the reaction time. The setup used consists of separate piezoelectric ceramics, one for each reaction chamber, coupled to the polymer chip, Fig.1.

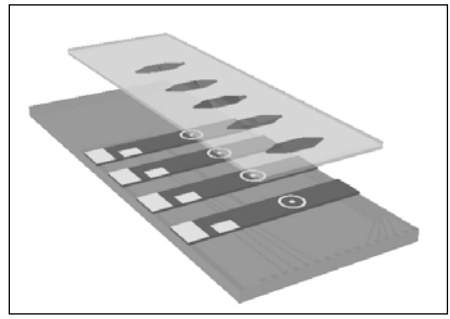

Figure 1. Conceptual drawing of the system. A polymer disposable chip comprises several reaction chambers. Each reaction chamber has a separate a piezoelectric actuator, for mixing.

Acoustic streaming is a well known effect whereby an acoustic field causes a net fluid flow, Fig.2. The concept provide in channel mixing without any moving parts or additional dead volumes. Several recent publications have shown the feasibility of using this phenomenon for micro mixing [2]. For polymer micro fluidic devices however, the concept of acoustic mixing is rare [3]. The acoustic properties of polymers present a number of challenges compared to silicon and glass devices: The higher damping limits the frequency range applicable and the acoustic impedance is close to water why in system resonances are weaker. This paper describes the investigations of using acoustic streaming as a mixing method for the polymer micro fluidic system.

978-0-9798064-0-7/μTAS2007/$20©2007CBMS

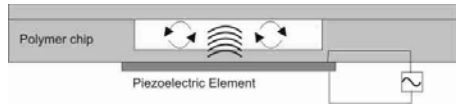

Figure 2. Schematic drawing of the acoustic mixing setup. The acoustic field creates a net flow in the middle of the chamber, the counter flow on the edges causes a vortex flow that provide an efficient mixing.

2. EXPERIMENTAL

For the experiments piezoelectric ceramics (pz26, Ferroperm, Denmark) were used. The acoustic parameters of various polymers were investigated, as well as several materials for coupling the acoustic signal from the piezoelectric ceramic to the chip. The acoustic transmission was measured with a setup with two piezoelements, one transmitter and one receiver. The acoustic damping was then derived from transmission measurements on polymer samples of various thicknesses. Temperature increase due to absorption of acoustic energy was measured on an insulated polymer chip while exposed to acoustic actuation over time, for different actuating voltages at the resonance frequency of the piezoelement. For the mixing experiments the piezoelement was coupled to the polymer chip with ultrasonic gel, and the frequency varied while the flow was visualized with particles in the flow.

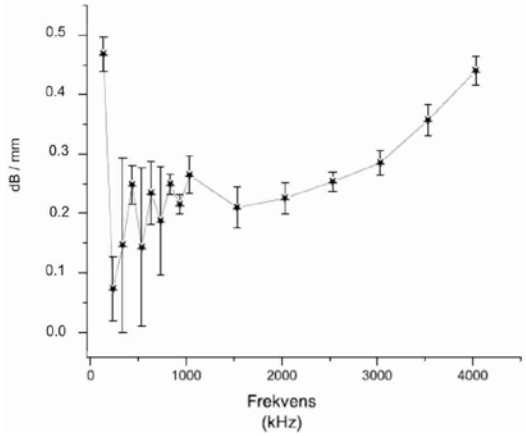

Figure 3. Acoustic damping factor of polycarbonate for frequencies between 100 kHz to 4 MHz

3. RESULTS AND DISCUSSION

The calculated damping factors, Fig.3, shows a rapidly increasing absorption coefficient for frequencies above 2MHz For frequencies above 4 MHz the attenuation losses are doubled. The high absorption of acoustic energy in the polymer also causes concern as the absorbed energy will be converted to heat which may inhibit the analysis on chip and in extreme cases even getting the temperature close to the glass transition temperature of the polymer.

The result of the temperature measurements, Fig.4, illustrates that; the increasing of temperature because of the piezoelectric actuator is dependent on the time of the active mixing, the amplitude of the applied voltage and how close the using frequency is to the resonance frequency. Since processes with biological compounds involved is extremely sensitive to temperature changes, biological compounds also degenerates rapidly at higher temperatures, the temperature increase may totally alter the performance of the system.
It was shown that for applied voltages lower than $40V_{pp}$, there are no immediate causes for concern about too high temperature increasing.

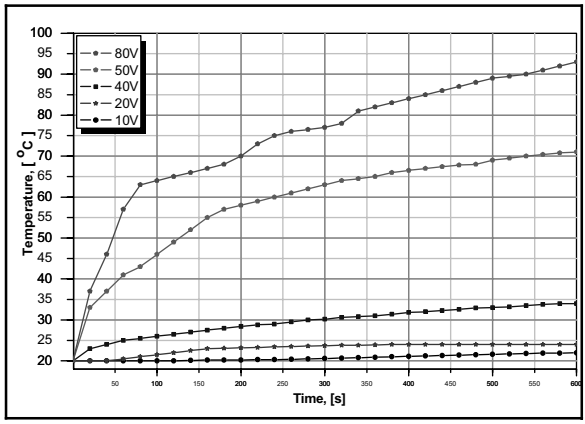

Figure 4. 10 minutes temperature measurement on a 0.75 mm Topas chip with piezoelectric actuation at the resonance frequency 529 KHz. Applied voltages of 10, 20, 40, 50 and 80 volt peak to peak.

It is shown it is possible to generate an acoustic flow in the polymer chip. Various flow patterns has been observed: large vortices covering the entire chamber, smaller vortices less than a millimeter in diameter, flow only in the vertical direction as well as totally chaotic, rapidly changing flow patterns. Very high flow velocities have been observed, up to millimeters per second. The mixing conditions are highly dependent on the signal coupling conditions and the presence of air in the chamber.

REFERENCES

1. "A simple and efficient method for on-chip storage of reagents: Towards lab-on-a-chip systems for point-of-care genetic diagnostics", M Brivio, Y Li, B G Kjeldsen, J L Reimers, M Bu, D D Bang and A Wolff, *Proceedings μTAS 2007*.
2. "Microfluidic Mixer and Transporter Based on PZT Self-Focusing Acoustic Transducers", H Yu, J W Kwon and E S Kim JMMS, 4, p1015, (2006)
3. "A polymer-based microfluidic mixing system driven by vortex micropumps", J H M Lam, R H W Lam; F L Kin, W W Y Chow, W J Li, Fifth World Congress on Intelligent Control and Automation, 2004. Vol.6 p5619-5623 (2004).

USING ASYMMETRIC VOLTAGE SOURCES IN ELECTRO-HYDRODYNAMIC MICROMIXERS

Laurent De Vroey[1], Damien Grenier[2] and Marie-Caroline Jullien[2]

[1] *Université Catholique de Louvain, BELGIUM*

[2] *SATIE, CNRS, ENS Cachan Antenne de Bretagne, Université Européenne de Bretagne, FRANCE*

ABSTRACT

We report an electro-hydrodynamic micromixer, which takes advantage of a non-symmetric power supply. By mean of a transversal non-symmetric electrode patern, and using an electrical offset, charged beads explore the full width of the channel. This mixer can be used both in stop-flow configuration as well as flowing conditions. The experimental set-up is presented, and a theoretical approach is proposed.

Keywords: mixing, non-symmetric power supply, micro-beads

1. INTRODUCTION

In microfluidic, flows are laminar due to low Reynolds numbers (<1). The motion in directions transversal to the main flow, e.g. for mixing applications, is mainly obtained by natural diffusion, which may require long times or long channel lengths. Several micromixers have been proposed to handle with this problematic. The most efficient ones generate chaotic like flows by either modifying the channel geometry [1] or by external perturbation of the flow [2].

Compared to passive or mecanically-driven micromixers, those based on an electro-hydrodynamic actuation are generally easier to produce. However, it can be necessary to use a sequence for the power supply [3] or to use surface treatment [4]. The micro-mixer presented in this paper is based on some principles developed in [5] and takes advantage of electrically-charged micro-beads present in the bulk solution. The use of asymmetric voltage sources enables simple systems and power supply.

2. EXPERIMENTAL

The system is composed of a 2-inlet channel bonded on a serrated electrode pattern (figure 1, left). The channel is manufactured with PDMS molding and the electrodes by chemical etching of a metallized glass wafer (200nm gold on 10nm nickel/chrome).

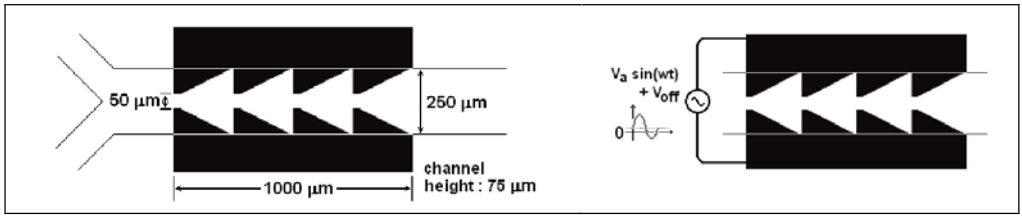

Figure 1. Schematic view of the channel and serrated electrodes (left) ; non-symmetric supply of the electrodes (right)

978-0-9798064-0-7/µTAS2007/$20©2007CBMS

The solution is a mixture of 50% glycerol and 50 % water, with 30mg/l NaCl and slightly negatively charged fluorescent beads of 500nm. Conductivity is 57µS/cm and viscosity 6cP. AC voltage ($w/2\pi$=100Hz, amplitude V_a=8V) is used together with a small offset voltage (V_{off} = 100 to 200mV), leading to an asymmetric power supply (figure 1, right).

Using symmetric voltage sources results in small rolls near the edges of the electrodes, as described in the litterature [7]. With an asymmetric voltage source, non-symmetric streams are observed, forming larger rolls occupying the entire width of the channel (figure 2, left). The sense of rotation of the rolls changes with the sign of V_{off}. The advantage of a serrated electrode pattern lies both in an additionnal velocity component along the channel axis, as well as the possibility for each bead to explore all width, compared to parallel electrodes (figure 2, right) in wich beads explore only channel cross-section.

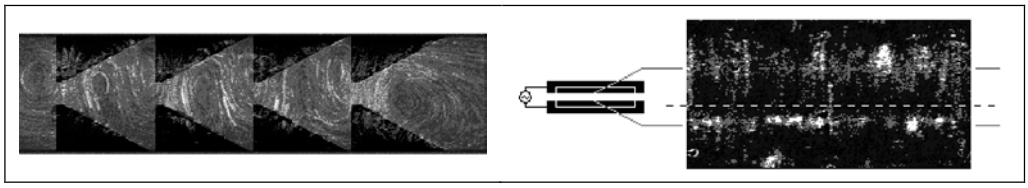

Figure 2. View of the rolls induced by a non-symmetric power supply, in stop-flow condition for serrated (left) and parallel (right) electrodes

On figure 3 the results obtained with an externally-induced flow and asymmetric power supply are shown. Solutions with and without beads are introduced in the channel through separate inlets, giving a global maximum speed of 25µm/s. Mixing appears quite fast, as the streamlines extend to the upper part of the channel in about 500µm. This picture shows the wide potential applications for functionalized beads that have to be mixed with an analyte.

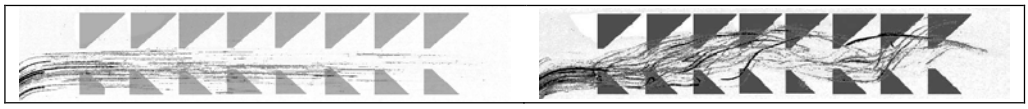

Figure 3 : View of the streamlines without (left) and with (right) asymmetric voltage supply ; convection is clearly visible when the electrodes are supplied

3. THEORY

The DC component in the power supply is responsible for an additional force on electrically charged beads, with a constant value in time. This leads to an additional movement, mainly in the direction of the DC electric field.

In a first linear approach, velocity at the electrodes is described by the Helmholtz-Smoluchowski formula :

$$\vec{v} = 0.5\frac{\varepsilon}{\eta}\,\text{real}\left\{V_{dl,AC}\ \text{conj}\left(\vec{E}_{AC}\right)\right\} \qquad (1)$$

where $\vec{v}$ is the velocity of the fluid, ε is the permittivity of the solution, η its dynamic viscosity, $V_{dl,AC}$ the AC potential drop in the double layer and $\vec{E}_{AC}$ the electric field tangential to the electrode just outside the double layer.

Each bead is subjected to an electrical force, equal to $q_{e,bead}\ \vec{E}_{DC}$, where $q_{e,bead}$ is the electric charge of one bead (10^{-14} .. 10^{-13} meq), and to friction.

Considering the shape of the electrodes and the electrical model of the double layer (see e.g. [6]), it can be shown that $V_{dl,AC}$, $\vec{E}_{AC}$ and $\vec{E}_{DC}$ are more importants in the areas where the electrodes are closer one to another. The global velocity is thus essentially function of what happens in those areas (figure 4).

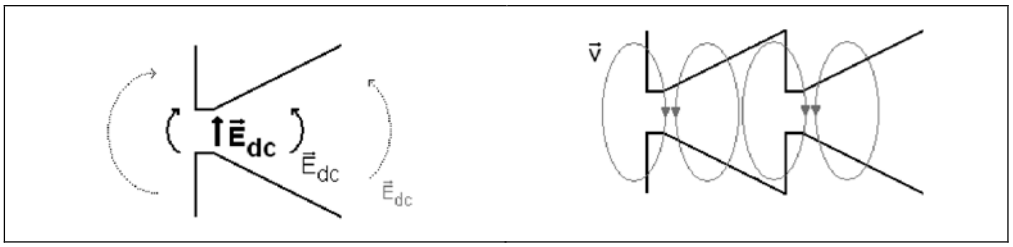

Figure 4. Theoretical principles of the movement with non-symmetric voltage supply : DC electric field (left) and global velocity streamlines (right)

4. CONCLUSIONS AND INSIGHTS

The system described here allows for easy fluid motion, with simple geometries and power supply. A more detailed theoretical study is on the run, taking into account non-linearities (e.g. variable ε and η) and saturation, which are significant in practice.

The experimental results are promising for integrated applications, due to simplicity. Perspectives are in mixing applications, mostly in applications where covalent coupling is suited (e.g. with proteins), for detection purpose for example. For larger beads concentration we expect (insight) that due to viscosity, this movement can be transferred to the whole solution, leading to a global mixer (liquid + beads).

REFERENCES

[1] H.P. Chou, M.A. Unger, S.R. Quake, *A Microfabricated Rotary Pump*, Biomedical Microdevices 3:4, 323 (2001).

[2] A. Dodge, A. Hountondji, M.C. Jullien, P. Tabelling, *Spatiotemporal resonances in a microfluidic system*, Phys. Rev. E 72, 056312 (2005).

[3] J. Ottino, *The kinematics of mixing : stretching, chaos, and transport*, Cambridge University Press (1989).

[4] D. Erickson, L. Dongqing, *Influence of surface heterogeneity on electrokinetically driven microfluidic mixing*, Langmuir 18-5, 1883 (2002).

[5] V. Studer, A. Pépin, Y. Chen, A. Ajdari, *Fabrication of microfluidic devices for AC electrokinetic fluid pumping*, Microelectronic Engineering, 61-62, 915 (2002).

[6] N. Green, A. Ramos, A. Gonzalez, H. Morgan, A. Castellanos, *Fluid flow induced by nonuniform ac electric fields in electrolytes on microelectrodes. I. Experimental measurements*, Phys. Rev. E 61, 4011 (2000)

A MICROFLUIDIC PLATFORM FOR IMPLEMENTING MOLECULAR LOGIC GATE WITH FLUORESCENT CHEMOSENSORS

Songzi Kou, Seong-Won Nam, Juyoung Yoon, and Sungsu Park
Division of Nano Science, Ewha Womans University, Seoul 120-750, Korea.

ABSTRACT

In this research, we report a micropump-actuated microfluidic device based on pneumatically-controlled valves implement molecular logic gates of fluorescent chemosensors which shows different intensities responding to different pH and ion conditions. The polydimethylsiloxane (PDMS) microfluidic device was fabricated by multilayer soft lithography. Logic mixing is achieved in a circulating loop by a pneumatic rotary micropump connected to a computer running LABVIEW program. The loop diameter is 1.6 mm and the channel dimensions are 100 μm wide by 10 μm high. This microfluidic system provides fixed-volume control and five chambers for two-factor logic gate conditioned mixing and efficient chemistry reactions on chip to obtain molecular logic gate of these fluorescent chemosensors. As results, INH and NOR two-input logic gates were attained after logic mixing on chip following changes in the intensity of fluorescent chemosensors. An integrated OR logic gate was achieved with two chemosensors which can behave separately XOR and AND logic gates. We also applied transferrin, a copper-binding protein, to copper chemosensor logic mixing and implemented a biological NOT(INH) logic gate.
These results show that molecular logic gates which have been known to work only in solution can be implemented in an electronically controlled microfluidic device. This also suggests that our molecular logic gate platform will be further utilized in developing a wet microprocessor in the future.

Keywords: Microfluidics, Molecular logic gate, chemosensor, transferrin

1. INTRODUCTION

Microfluidic systems are increasingly used in fields of analytical chemistry and biomedical sciences. Elastomeric pneumatic microvalves and pumps[1] enable to much more precisely conduct control processes at a micrometer scale such as directing the liquid flow by opening and closing channels or even performing relatively complex processes-biological analysis [2] and detection [3], using microfluidic operations. With the characteristic and electrically controllable valve system the microfluidics is envisioned to have significant application potential in computation [4]. Recent work on microfluidic logic gates is an operating microfluidic system as electronic logic circuits and constructed a variety of logic gates, including OR and NAND from redox compounds [5]. Here we demonstrated a microvalve and micropump-actuated microfluidic system taking advantage of fluorescent chemosensors which can implement molecular logic gates by detecting the intensity changes responding to inputs (pH, metal ions).

978-0-9798064-0-7/μTAS2007/$20©2007CBMS

2. EXPERIMENTAL

The microfluidic device was fabricated using multi-layer soft lithography with PDMS, which consists of two layers (Fig. 1). The top, thick layer was prepared with a ratio of 1:10 (curing agent: PDMS), whereas the bottom thin layer is 1:30. Chemosensors used here, SW208 can show strong fluorescence in neutral pH, but SW239 shows strong fluorescence at low pH. Two FITC filter set (Ex 510-560,DM 575,BA 590; Ex 450-459,DM 505,BA 520;) were used and the image was recorded by using a peltier cooled CCD camera (SPOT INSIGHT^{TM} ,MI, USA).

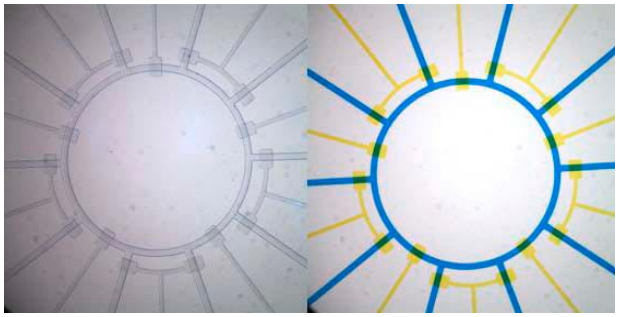

Fig.1. Layout of the microfluidic chip.

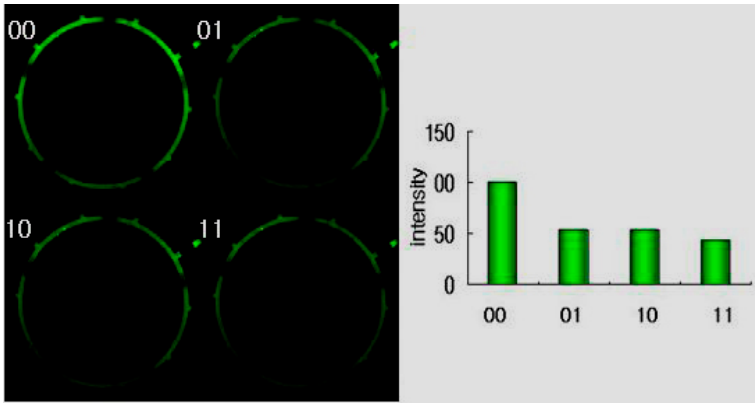

Fig.2. An example of NOR logic gate using 10 μM SW209.

3. RESULTS AND DISCUSSION

The fluidic layer includes five couples of inlet and outlet channels (100 μm wide,10 μm deep) and a central circulating loop (3.2 mm diameter) ,and the overall size of the microfluidic device is 22.62 mm long and 22.2 mm wide (Fig.1). Fluorescent chemosensor was first loaded on chip by opening valve 0,2,4,6,8 and 1 and after the sensor filled the loop valve 0,2,4,6 and 8 were closed and the special pH conditioning solutions (pH=2 buffer, pH=12 buffer) or metal ion solution (Cu^{2+}) were loaded from other inlets selectively. For example, valve 3 and 7 were opened for loading pH=2 buffer and pH=12 buffer. Then, after closing valve 1,3,7 and opening valve 0,2,4,6,8, these three different liquids are mixed

thoroughly by operating valve 0,2,4,6,8 peristaltically on the loop to circulate the fluid inside the reactor, completely mixing the solutions after several minutes. The fluorescent chemosensor during mixing was observed under a fluorescence microscope. Using this device and chemosensors the diverse logics like INH, OR, NOR and inverted INH were presented successfully (Fig. 2).

4. CONCLUSIONS

The results show that molecular logic gates which were known to work only in solution can be implemented in an electronically-controlled microfluidic device. The results hints that our molecular logic gate platform will be further utilized in developing a wet microprocessor in the future.

ACKNOWLEDGEMENTS

This research was equally supported by the Nano/Bioscience & Technology Program (M10536090002-05N3609-00210) of the Ministry of Science and Technology (MOST), the SRC program of the Korea Science and Engineering Foundation (KOSEF) through the Center for Intelligent Nano-Bio Materials at Ewha Womans University (Grant R11-2005-008-02003-0), and the Korean Research Foundation Grant (MOEHRD, Basic Research Promotion Fund) (KRF-2006- 005-J04002).

REFERENCES

[1] M. A. Unger, H.-P. Chou, T. Thorsen, A. Scherer, S. R. Quake, Monolithic microfabricated valves and pumps by multilayer soft lithography. Science 2000, 288, 113.

[2] J. W. Hong, V. Studer, G. Hang, W. F. Anderson, S. R. Quake, A nanoliter-scale nucleic acid processor with parallel architecture. Nature Biotechnology 2004, 22, 435.

[3] F. K. Balagadde, L. You, C. L. Hansen, F. H. Arnold, S. R. Quake, Long-term monitoring of bacteria undergoing programmed population control in a microchemostat. Science 2005, 309, 137.

[4] D. T. Chiu, E. Pezzoli, H. Wu, A.D. Stroock, and G. M. Whitesides, Using three-dimensional microfluidic networks for solving computationally hard problems. PNAS 2001, 98, 2961.

[5] W. Zhan and R. M. Crooks, Microelectrochemical logic circuits. J. AM. CHEM. SOC. 2003, 125, 9934.

CONTINUOUS-FLOW LAYER-BY-LAYER ENCAPSULATION WITH POLYELECTROLYTES THROUGH A MICROFLUIDIC DEVICE

Kai-Qi Peng[1,2], Wee-Liat Ong[1], Levent Yobas[1] and Dieter Trau[2]

[1]*Institute of Microelectronics, 11 Science Park Road, S117685, SINGAPORE and*
[2]*Division of Bioengineering, National University of Singapore, SINGAPORE*

ABSTRACT

A continuous-flow layer-by-layer (LbL) polyelectrolyte encapsulation of colloids in a microfluidic device for the formation of polyelectrolyte multi-layered (PEM) capsules is demonstrated. The device removes non-deposited polyelectrolytes from the coated colloidal droplets *in-situ* via Zweifach-Fung effect. Higher flow rates are found to improve both capsule recovery and excess polyelectrolyte removal. The collected single-layer and double-layer capsules are found to be more stable than purely oil-in-water droplets.

Keywords: Layer-by-layer, polyelectrolyte encapsulation, droplets, continuous-flow

1. INTRODUCTION

This paper introduces a continuous-flow layer-by-layer (LbL) polyelectrolyte encapsulation of colloids in a microfluidic device for the formation of polyelectrolyte multi-layered (PEM) capsules. In LbL polyelectrolyte encapsulation, polycationic- and polyanionic-electrolytes are alternately deposited onto charged templates, for instance colloids, to form PEM capsules (Figure 1) [1, 2]. The resulting micro- and nano-sized capsules can be useful in many diverse fields, for example as potential drug delivery vehicles [3] – [5]. By now, in μTAS, PEM films are predominantly used as channel surface modifiers rather than encapsulants. Here, we demonstrate PEM oil capsules in an oil/water colloidal system by integrating a continuous-flow LbL encapsulation design with a flow-focusing region in a microfluidic device.

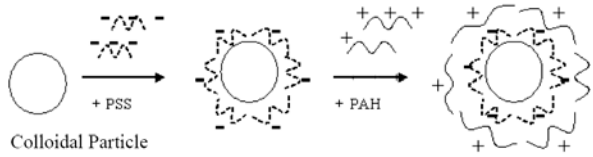

Figure 1. Schematic of the layer-by-layer deposition of polyelectrolytes onto a colloid/droplet

2. THEORY

In LbL encapsulation, washing steps in between polyelectrolyte depositions are critical. Conventionally, this is a time consuming discontinuous process involving multiple cycles of wash, centrifuge, and redisperse. The concept of continuous-flow LbL encapsulation integrates all these cycles in a microfluidic device as described in Figure 2. The device utilizes Zweifach-Fung effect to remove non-deposited polyelectrolytes from colloidal droplets [6]. Unwanted solution is skimmed by smaller bifurcation channels while colloidal droplets remain on course in main channel which has a much smaller fluidic resistance.

978-0-9798064-0-7/μTAS2007/$20©2007CBMS

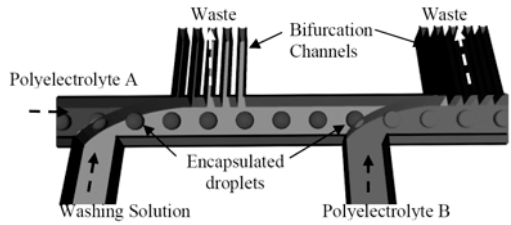

Figure 2. A microfluidic section for continuous-flow layer-by-layer encapsulation. Excess polyelectrolytes are washed away through the bifurcation channels while droplets are retained for further encapsulation. This section can be repeated for deposition of more layers.

3. EXPERIMENTAL

Figure 3 shows our device replicated in poly(dimethylsiloxane) (PDMS) using a lithographically-patterned SU-8 template. The device consists of a flow-focusing region and three subsequent bifurcation regions, with all ~100 μm deep microchannels. The device was oxygen-plasma treated (70 W, 300 s) before use and solutions were pumped into the device from dedicated syringe pumps. These solutions involved Poly(sodium 4-styrenesulfonate) (PSS) and Poly(allylamine hydrochloride) (PAH) both 1 mg/mL dissolved in 0.5 M NaCl, 10 X Phosphate-buffered saline solution. PAH was further labelled with fluorescein isothiocyanate (FITC) (PAH:PAH/FITC 9:1 monomer ratio). Mineral oil was used as the colloidal phase.

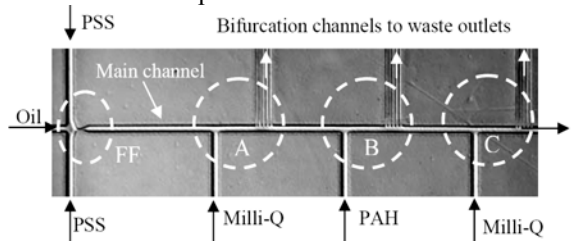

Figure 3. Overall view of the device layout for generation of capsules with maximum two layers of polyelectrolyte (FF: flow-focusing region where oil droplets get dispersed in continuous phase; A, B, and C: junctions where continuous-phase gets replaced with new buffer input).

4. RESULTS AND DISCUSSION

Figure 4 shows high-speed microscopy images of the droplet generation and encapsulation in the device. Monodispersed oil droplets were directly formed in negatively-charged PSS solution as the carrier fluid at the flow-focusing region (FF). The PSS solution was then skimmed at bifurcation junction A and the PSS-encapsulated oil droplets were re-suspended in water (Milli-Q). At bifurcation junction B, the water was similarly skimmed and replaced by positively-charged PAH solution carrying the negatively charged oil droplets to the junction C where they were re-suspended in water for collection at the outlet.

For single-layer PSS capsules, the device efficiency in terms of capsule recovery and excess polyelectrolyte removal with respect to the water flow rate at junction A is listed in Table 1. Higher flow rates improved both capsule recovery and excess polyelectrolyte removal. On the other hand, incomplete polyelectrolyte removal caused slight deposition inside the channel walls. Nevertheless, the encapsulation process could still proceed for more than 4 hours.

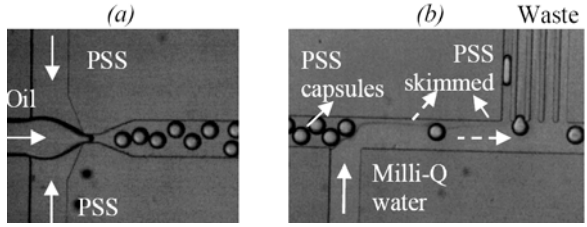

Figure 4. (a) Flow-focusing region where monodispersed oil droplets get generated in PSS solution at flow rates of PSS:oil:PSS = 1.7:0.83:1.7 µl/min (b) Junction A where PSS solution gets replaced with Milli-Q water at input flow rates of A:B:C =16.7:25:25 µl/min

Table 1. Device efficiency for recovering single-layer PSS-encapsulated droplets and removal of excess PSS at junction A

Flow rate of Milli-Q water into A	% Recovery	% Removal
33.3µl/min	82	91
16.7µl/min	76	85

Figure 5 shows images of the collected single-layer PSS and double-layer PSS/PAH capsules. The capsules were stable at the time of collection and 10 min after collection. Unlike, oil-in-water droplets without any encapsulation were unstable and could not be collected. Our study demonstrates that continuous-flow LbL encapsulation with polyelectrolytes in microfluidics is feasible.

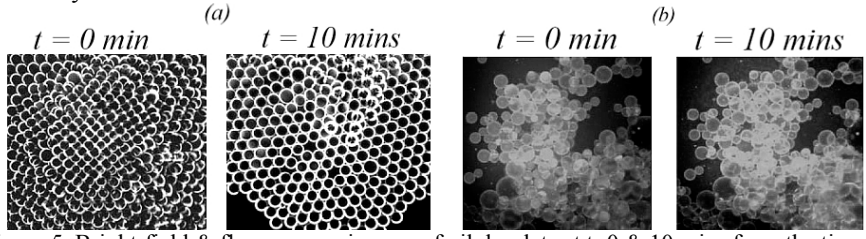

Figure 5. Bright-field & fluorescence images of oil droplets at t=0 & 10 mins from the time of collection: (a) single-layer PSS & (b) double-layer PSS/PAH encapsulated droplets.

REFERENCES

[1] G. Decher, J.D. Hong, and J. Schmitt, "Buildup of ultrathin multilayer films by a self assembly process," *J. Thin Solid Films*, 210, 831 (1992)

[2] F. Caruso, R.A. Caruso, and H. Mohwald, "Nanoengineering of inorganic and hybrid hollow spheres by colloidal templating," *Science*, 282, 1111 (1998)

[3] D. Trau, W. Yang, M. Lehmann, F. Caruso, N.T. Yu, and R. Renneberg, "Nanoencapsulated Microcrystalline Particles for Superamplified Bioassays," *Analytical Chemistry*, 74 (21),5480 (2002)

[4] F. Caruso, D. Trau, H. Möhwald, and R. Renneberg, "Enzyme Encapsulation in Layer-by-Layer Engineered Multilayer Capsules," *Langmuir*, 16(4), 1485 (2000)

[5] A.P.R. Johnston, C. Cortz, A.S. Angelatos, and F. Caruso, "Layer-by-layer engineered capsules and their application," *Curr Opin Colloid In*, 11, 203 (2006)

[6] Y.C. Fung, "Stochastic Flow in Capillary Blood Vessels," *Microvasc. Res*, 5, 34 (1973)

DESIGN PARAMETERS FOR 1XN MICRODROPLET SWITCH

Jeffrey S. Fisher[1], Tim S. Kuo[1], Jason Poulos[1] and Abraham P. Lee[1, 2]
[1]*Department of Biomedical Engineering,* [2]*Dept of Mechanical and Aerospace Engineering, University of California, Irvine, USA*

Keywords: droplets, sorting, switch, sheath flow

ABSTRACT

The sorting of monodisperse oil-water emulsions into *N* number of separate outlet channels is demonstrated. The mechanism of switching is based on asymmetric flow rates of two sheath flows. Design parameters such as channel geometry and fluid properties are explored to determine their effect on the ability to switch droplets.

1. INTRODUCTION

Monodisperse droplet emulsions are increasingly utilized in micro-Total-Analysis-Systems (μTAS) as discrete reaction vessels for chemical and biological analyses. This paper presents an analysis of the design parameters that allow droplets to be switched between *N* outlet channels using asymmetric sheath flow. Similar designs for the switching of bulk fluid [1] or rigid particles [2] do not take into consideration the requirements unique to two-phase (typically water and oil) systems and, therefore, cannot be applied to these systems.

Asymmetric sheath flow possesses a number of advantages for switching in microfluidic platforms. First, no additional equipment is required other than the type of pump already being used to drive the original system. Second, switching control can be achieved with a single microfluidic flow layer, unlike switches using a second layer of control valves. Third, two control lines (the two opposite sheath flows) can serve to distribute analytes to an arbitrarily large number (*N*) of output channels. This is in contrast to two-layer systems that require a minimum of *log N* control lines [3].

2. THEORY

Figure 1 demonstrates a sheath-flow switch. The sample flow is squeezed between two sheath flows, and the ratio between their flow rates determines which outlet the sample flow exits from. For systems in which the sample flow is a single phase (carrying molecules, beads, or cells), very little refinement to this basic design is needed for successful switching. However, sheath-flow switching is not easily obtained in droplet systems because of the effects of viscous flows and shear forces. Unaccounted for, these forces will rip the droplet apart or pull it opposite the direction of desired switching.

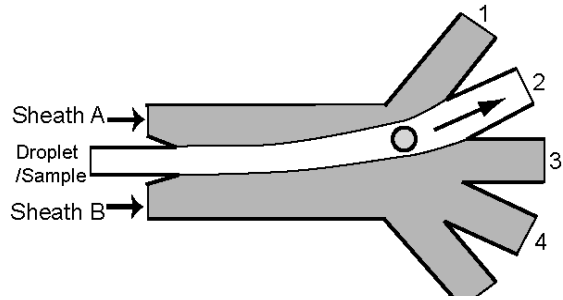

Figure 1. Sheath-flow switch. Flow from channels A and B guide the sample flow into the desired output channel. The ratio of flow rates in this example is approximately 1:1:3 (A:Sample:B).

978-0-9798064-0-7/μTAS2007/$20©2007CBMS

In a typical two-phase system, droplets are generated upstream of the switching junction, using a shearing mechanism [4]. The oil used to create the droplets (i.e. generation oil) is not necessarily the same type of oil as that used for the switching (i.e. sheath oil)

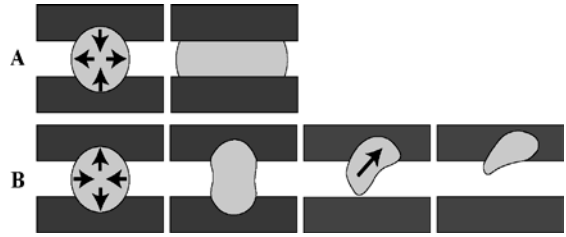

Figure 2. Imbalanced interfacial tensions. In A, the greater interfacial tension between the sheath flow and droplet squeeze the droplet into the generation flow, while in B, the opposite condition results in the droplet being expelled from the generation flow.

If the droplets are small enough, the flow of the generation oil can form a buffer around the droplet that prevents it from contacting the sheath flows (like the droplet shown in figure 1). However, this is not always practical in such systems because it can only be achieved for certain ratios of water to oil in the generation flow rate. The purpose of this work is to develop a mechanism for switching that is independent of the details of the droplet generation. Therefore, to maintain the generality of the method, the conditions when the droplet encounters the sheath flow must also be examined.

When the diameter of the droplet is larger than the width of the generation oil flow, it will contact the sheath flows. With T_{dg} defined as the interfacial tension between the droplet and the generation oil, and T_{ds} as the interfacial tension between the droplet and the sheath oil, the ratio of T_{dg} to T_{ds} will determine what happens to the droplet at the switching junction. If the interfacial tensions are equal (T_{dg}: T_{ds} = 1), then the droplet will expand into the sheath flow but should remain centered in the generation flow. If the interfacial tension of the sheath flow is greater (T_{dg}: T_{ds} < 1), then the droplet will be deformed into a plug shape, completely contained within the generation flow (figure 2a). Finally, if the interfacial tension of the generation flow is greater (T_{dg}: T_{ds} > 1), the droplet will be squeezed out of the generation flow (figure 2b).

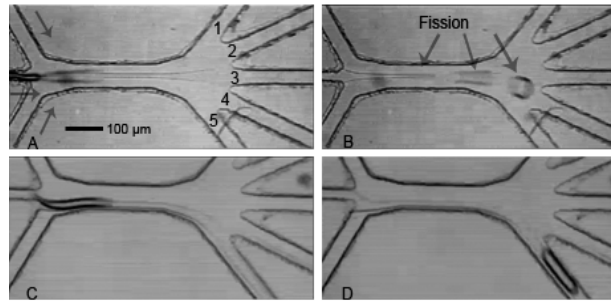

Figure 3: Droplet Fission. Undesired droplet fission (a & b) occurs with oleic acid as the sheath flow and mineral oil as the droplet generation flow. Successful switching can be achieved by interchanging the oils (c & d).

3. EXPERIMENTAL

All experiments were conducted in PDMS microfluidic systems fabricated using standard methods. Channel heights ranged between 35-50 microns. Monodisperse emulsions were formed with a flow focusing design [4] upstream of the switching junction. All droplets were deionized water, and mineral oil (interfacial tension with water, 45 dynes/cm) or oleic acid (15 dynes/cm) were used for the generation and sheath flows.

4. RESULTS AND DISCUSSION

Successful switching of droplets requires: 1) that the integrity of the droplet is maintained, and 2) that the droplets follow the streamlines of the generation flow.

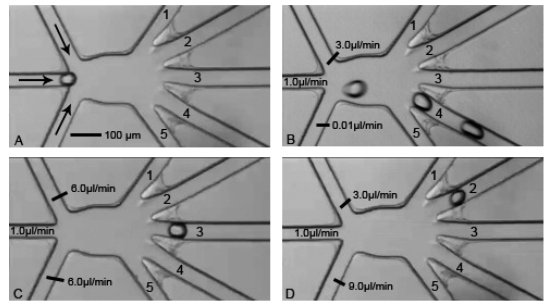

Figure 4. Successful droplet switching.

If the droplet can expand into the sheath flows, it will be exposed to the stress caused by those flows. Figure 3 shows that these stresses can be great enough to break the droplet apart. Using oleic acid to generate droplets and mineral oil as the sheath flows, the droplet expands upon reaching the switching junction (figure 3a) and is ripped apart before it can reach the outlet (figure 3b). However, if the oils are interchanged, such that the droplets are generated using mineral oil, and oleic acid is used as the sheath flows, the droplet will be compressed as was shown in figure 2a. Even though the diameter of the droplet is much larger than the width of the generation flow, it is not allowed to expand into the sheath flows (figure 3c) and, therefore, reaches the desired outlet intact (figure 3d).

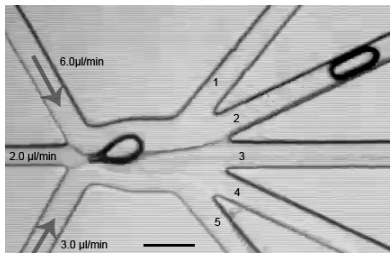

Figure 5: Effects of shear stress and imbalanced surface tension. Shear stress of the oleic acid sheath flow pulls the droplet from the mineral oil generation flow. The flows are balanced to switch droplets into channel 4, but the shear flow pulls the droplet into channel 2.

Shear stresses on the droplet can be reduced by designing the switching junction so as to minimize the shear rate of the flow. Figure 4 shows such a design. The junction has been made wider (top to bottom) to reduce the shear rate and shorter (left to right) both to reduce the time in the junction and to minimize hydrodynamic focusing. Using the same oil for both the generation and sheath flows, this design was able to direct droplets into all the outlet channels. However, even with this improved junction geometry, care must be taken to avoid using a combination of oils that results in the situation shown in figures 2b and 5: a greater T_{ds} forces the droplet out of the generation flow and into the top sheath flow, which carries it astray.

REFERENCES:

[1] "Micromachined pre-focused 1 x n flow switches for continuous sample injection," G.-B. Lee, C.-I. Hung, B.-J. Ke, G.-R. Huang, and B.-H. Hwei, Journal of Micromechanics and Microengineering, 11(5): 567–573, 2001.

[2] "Development of individual cell sorting system for intercellular reaction analysis," S. Otsuka, M. Kanai, M Hayashi, H Nakanishi, S. Shoji, Proc. Micro Total Analysis Systems 2004, **1**, 30 (2004).

[3] "Microfluidic large-scale integration," T. Thorsen, S. Maerkl, and S. Quake. SCIENCE, 298(5593):580–584 (2002)

[4] "Monodispersed microfluidic droplet generation by shear focusing microfluidic device," Y. C. Tan, V. Cristini, and A. P. Lee, *SENSORS AND ACTUATORS B-CHEMICAL*, 114(1):350–356, Mar 2006.

DISCRETE MICROFLUIDICS: PRODUCTION OF SILICA PARTICLES WITH EMULSIONS

Venkatachalam Chokkalingam[1], Craig Priest[1], Michael Krämer[2], Wilhelm F. Maier[2], Stephan Herminghaus[1] and Ralf Seemann[1]

[1]Max Planck Institute for Dynamics and Self-Organization, Goettingen, Germany.
[2]Technical Chemistry, Saarland University, Saarbrücken, Germany

ABSTRACT

Instead of microfluidic processing using single phase liquids in microchannel networks, we explore droplet-based, discrete microfluidics to compartment liquids inside microchannels. By combining individual droplets, we can induce reactions that are neither possible in single phase microfluidics nor in droplet based microfluidics if the chemicals are mixed prior to dispersing the droplets, as shown here for the production of silica particles.

Keywords: emulsions, chemical reactions, silica particles, sol gel.

1. INTRODUCTION

Microfluidic flow in microchannels typically occurs at low Reynolds numbers, such that the flow is purely laminar (the threshold for turbulence is $Re \approx 200$). As a consequence, fast mixing of two substances is difficult, requiring specially designed microfluidic channels to facilitate 'quasi chaotic mixing' [1,2]. Hence, there has been considerable development towards the use of isolated droplets suspended in an immiscible continuous phase [3,4]. The main advantage considered in this context is the twisty flow pattern emerging within the droplets when they are moved through the channel system. Here, mixing of two components is achieved within each droplet separately, and is found to proceed quite efficiently [4].

Another advantage of this approach is that each droplet may carry chemically different contents and be used to perform chemical reactions in a combinatorial way. For *in situ* generation of droplets with various chemical composition droplets are continuously dispersed from merging streams of various components with temporarily varying volumetric flow ratio [5]. Processing reactive fluids, which might precipitate or solidify at the channel walls like fibrin networks or silica particles is hardly possible. In the present study we explore the possibility to produce silica particles using sol-gel chemistry by dispersing reactive compounds in individual droplets and starting the reaction by merging the individual droplets. Since the sol-gel process can be fine tuned to produce mixed oxides with tailored porosity and pore size [6], the production of such uniform spheres is of potential interest for a broad range of applications in heterogenous catalysis.

2. DEVICE FABRICATION

The precondition for droplet based microfluidics is the *in-situ* production of monodisperse droplets. One technique that meets all basic requirements on droplet monodispersity and production frequency is the step-emulsification [7] as we will discuss below. A step-emulsification device can be produced in a single photolithographic exposure step using the geometry sketched in Fig.1a. Microfluidic devices were fabricated

978-0-9798064-0-7/μTAS2007/$20©2007CBMS

in SU8 photoresist on glass substrates and sealed by thermally bonding a PMMA coated glass cover slip to the SU8 structure. Holes were drilled into the glass substrate and connected with Nanoports™ (UpChurch). Flow rates were adjusted using custom made computer controlled syringe pumps.

3. DROPLET PRODUCTION

Emulsification using this device may proceed *via* different mechanisms cf. Fig. 1b. If the flow rate of the dispersed phase, Q_d, is small as compared to the flow rate of the continuous phase, Q_c, respectively the total flow rate $Q_t = Q_d + Q_c$ emulsification occurs at the T-junction where the dispersed phase is injected [8]. For large relative flow rates Q_d/Q_t, the two liquids flow in parallel along the shallow channel segment, and a Rayleigh-Plateau type jet instability occurs beyond the step [9].

For intermediate Q_d/Q_t a third mechanism, called step emulsification [7], has been described. It offers an adjustable droplet production frequency from several tenths up to several hundred droplets per second, while maintaining excellent monodispersity (coefficient of variance < 1.5%). The production frequency can be varied without affecting the droplet size by changing the flow rates of the dispersed and the continuous phase such that the relative flow rates Q_d/Q_t and Q_c/Q_t stay unaffected. The main characteristic is that step emulsification is directly induced by the abrupt change in aspect ratio, where the narrow channel merges into the wide channel. The physical reason for this transition is that the flow profile is effectively two-dimensional in the narrow channel, but is three-dimensional in the wide channel. Since there is no jet instability in two dimensions, the flow is stable up to the step, where it abruptly breaks up. This minimizes the impact of fluctuations, yielding rather well-controlled results.

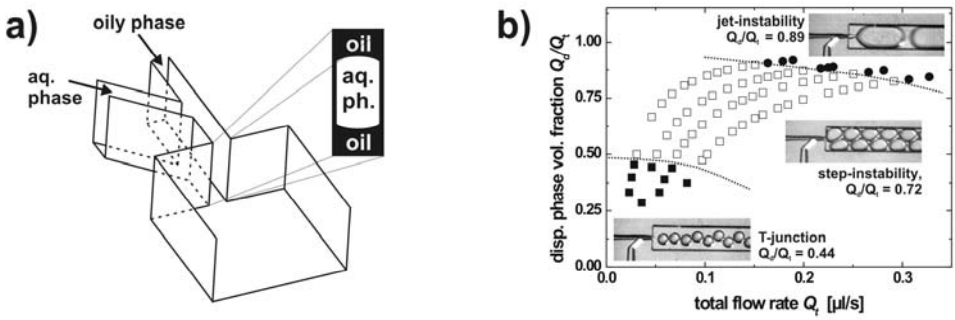

Figure 1. *(a) Sketch of step emulsification device produced in SU8 resin. (b) The Diagram shows the different mechanisms for drop production: T-junction, step- and jet-instability. The dashed lines are guides to the eye and denote the boundaries between the different production mechanism.* We used Millipore™ water as the dispersed phase and a low viscosity organic liquid (ISOPAR™ M, Exxon Mobil) with 2 wt% Span 80 as the continuous phase.

4. CHEMICAL REACTIONS

The application of step-emulsification allowed to dispense an acidified solution of tetramethoxysilane (TMOS) in a mixture of methanol and water (A) as well as an ammonia

solution based on the same solvent (B) into droplets using two separate production units. To stabilize the droplets containing the methanol/water mixture we used a perfluorinated oil (perfluordecalin $C_{10}F_{18}$, ABCR) with 20 wt% of perfluorinated surfactant (pentadecafluoro-1-octanol, $C_8H_3F_{15}O$, ABCR) that is neither miscible with water nor with methanol. The production rate of the two independent production units was triggered with the help of photoelectric barriers. To be able to detect individual droplets the active window of the diode was reduced to about 100 µm. A typical signal is shown in Fig. 2: The intensity of the transmitted light varies with droplets passing by. Thus the flow rates at the respective production unit can be adjusted on-line while monitoring the production rate.

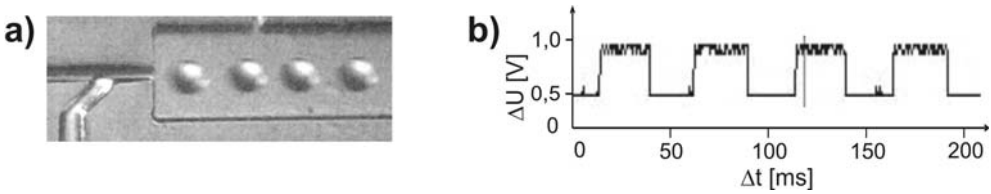

Figure 2. (*a) Optical micrograph of a single coflow production unit. (b)Typical intensity signal as detected by the photoelectric barrier when droplets pass by.*

As shown in Fig. 3a, the individual droplets (A) and (B) are combined into pairs of droplets by a Y-junction. These pairs of droplets are coalesced either by targeted electrocoalescence [10] or by a geometrical constriction as shown in Fig. 3b. Here, we take advantage of the poor stability of the emulsion droplets in the continuous perfluorinated phase: Due to the Laplace pressure inside the droplets an additional pressure is needed to deform the droplet in order to pass the constriction. Thus the flow velocity of the first droplet arriving at the constriction is reduced and the second droplet is pushed towards the first droplet. This small impulse is sufficient to destabilize to coalesce the droplets. Down stream mixing proceeds very efficiently by inducing a twisty flow pattern in a back fold channel geometry [3].

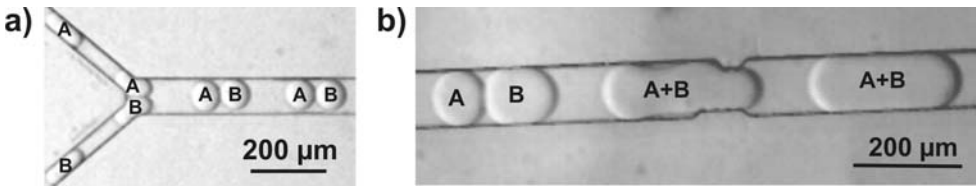

Figure 3. *(a)The different droplets A and B are combined into a single channel using a Y-junction. (b) Sets of droplets can be coalesced by a geometrical constriction.*

5. SILICA PARTICLES

When the droplets are mixed, the condensation of the pre-hydrolysed silicon-precursors immediately starts, resulting in a fast gelation which proceeds within a few seconds. The sol-gel recipe applied has been optimized to provide the desired rapid gelation behaviour. To allow the gel to form, the droplets are delayed in an appropriate network of channels. The resulting gel droplets are not adhesive to each other and stay separated when subsequently collected outside the microfluidic device. The collected droplets of about 80 µm diameter are dried at room temperature for about 48 hours, cf. Fig. 4. During that

process the size of the droplets is reduced to a mean diameter of about 21 µm forming silica particles. Additional heat treatment at 350°C for two days was performed to remove the remaining organic compounds. During that process the average particle size is further reduced to about 15 µm.

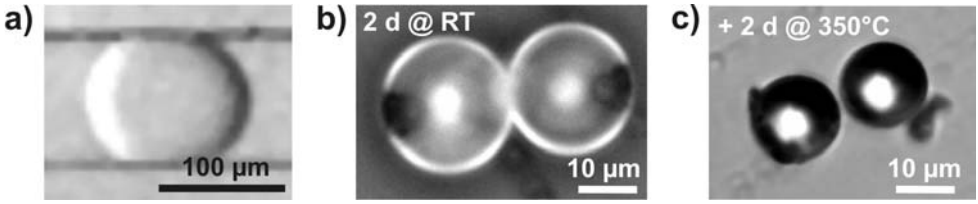

Figure 4. *(a) Large droplet resulting from coalesced droplets (A) and (B). As long as the gel contains significant amounts of water and methanol the droplet is soft and deformable. (b) Silica particles after removing the solvents from the droplets by drying for two days at room temperature. The volume of the droplets is reduced by more than a factor of 100. (c) Silica particles after removal of the organic residue after the final heat treatment at 350°C for two days.*

5. Conclusion

When chemical reactions are induced by combining and mixing of individual droplets with different chemical compounds, the content of the merged 'reaction container' does not contact the microchannel wall. Thus, chemical reactions are possible, which would otherwise clog single phase micofluidic devices as well as droplet based microfluidic devices, where the reactants are mixed prior to droplet formation. Using this approach we demonstrated droplet based production of monodisperse silica particles using sol-gel chemistry. We anticipate that discrete microfluidics is well suited for applications in heterogeneous catalysis and combinatorial chemistry of complex systems.

ACKNOWLEDGEMENTS

The authors thank U. Krafft and W. Keiderling for help with technical problems.

REFERENCES

[1] A. D. Stroock et al., Science, **295**, 647 (2002)
[2] T. H. Solomon, I. Mezic, Nature, **425**, 376 (2003);
[3] Z. B. Stone, and H. A. Stone, Phys. Fluids, **17**, 063103 (2005); F. Sarrazin et al., *AIChE*, **52**, 4061 (2006).
[4] H. Song, J. D. Tice, R. F. Ismagilov, Angew. Chem. Int. Ed., **115**, 791 (2003); H. Song, D. L. Chen, and R. F. Ismagilov, Angew. Chem. Int. Ed., **45**, 7336 (2006).
[5] J. M. Köhler et al., Chem. Eng. J., **101**, 201 (2002); B. Zheng, L. S. Roach, and R. F. Ismagilov, J. Am. Chem. Soc., **125**, 11170 (2003)
[6] G. Frenzer, W.F. Maier, Ann. Rev. Mater. Res. 36, 281-331 (2006).
[7] C. Priest, S. Herminghaus, and R. Seemann, Appl. Phys. Lett. **88**, 024106 (2006).
[8] T. Thorsen, R. W. Roberts, F. H. Arnold, and S. R. Quake, Phys. Rev. Lett. **86**, 4163 (2001).
[9] S. L. Anna, N. Bontoux, and H. A. Stone, Appl. Phys. Lett. **82**, 364 (2003).
[10] C. Priest, S. Herminghaus, and R. Seemann, App. Phys. Lett. **89**, 134101 (2006).

ELECTROHYDRODYNAMICALLY CONTROLLED GENERATION OF A SINGLE OR MULTIPLE DROPS IN THE MICROFLOW OF AQUEOUS TWO-PHASE SYSTEM

Young Hoon Choi, Young Soo Song and Do Hyun Kim
Department of Chemical and Biomolecular Engineering and Center for Ultramicrochemical Process Systems,
Korea Advanced Institute of Science and Technology, South Korea

ABSTRACT

We report a novel method for active generation of drops in an aqueous two-phase system (ATPS). A small volume of fluid of one phase is separated from its laminar stream to be dispersed in the other phase by the perturbation of the liquid-liquid interface which is induced by electrohydrodynamic force. The number of drops generated is controlled by the change in the magnitude and duration of d.c. electric pulse.

Keywords: Aqueous two-phase system (ATPS), electrohydrodynamics, drop

1. INTRODUCTION

Drops have a wide range of potential applications in analytical and industrial systems as reaction vessels that can confine and carry specific volume of liquid with high surface-to-volume ratio, providing advantages such as enhanced mixing by recirculation in the drop. In addition to the hydrodynamic techniques, such as emulsification of one liquid by shear at T-junction and flow focusing, a novel method of generating drops by electrical force has been developed. The immiscible aqueous two-phase system (ATPS) is usually formed by dissolving two incompatible polymers or one polymer and an appropriate salt, or a cationic surfactant and a salt in water, and auto-splitting into two equilibrium phases with a clear and stable interface. We report a methodology for active generation of aqueous drops from ATPS liquid-liquid laminar flow by the application of electric field.

2. THEORY

Not yet available is a complete theory to explain the electrohydrodynamic phenomena in an ATPS where the concentration of ionic species is high and the electrical properties of the fluids are discontinuous across the phase interface. Still it is noticeable that the origin of the charge for viscous organic and inorganic compounds lies in the acid-base equilibrium of the solution [1].

3. EXPERIMENTAL

Figure 1 shows the schematic of the experimental setup of a current microfluidic chip which consists of fluidic channels made of PDMS by soft lithography and a cover of microscope slide glass. Two immiscible aqueous phases are prepared by dissolving tetrabutylammonium bromide (TBAB) and ammonium sulfate (AS) in de-ionized water with the concentration of 17.1(%, w/w) and 29.4(%, w/w), respectively. After phase separation with uneven distribution of ionic and nonionic species [2], the two phases, TBAB-rich phase and AS-rich phase, are individually introduced at the inlets of the microdevice by two syringe pumps. Electric voltage is applied between the electrodes

978-0-9798064-0-7/μTAS2007/$20©2007CBMS

located at the outlet reservoirs as pulsed signal controlled by switching on and off with LabView® software. Video images (15 frames per second) are recorded by a digital camera connected to a microscope and captured images are analyzed with Premiere 6.0® software.

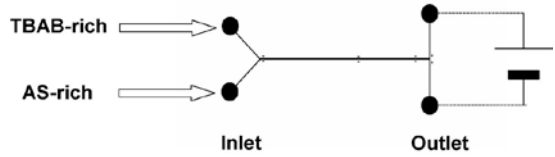

Figure 1. Schematic diagram of experimental setting. The width of channels is 200μm for main and T-branched channels and 100μm for Y-branched channels.

4. RESULTS AND DISCUSSION

Initially both phases occupy about half of the channel width. But from the T-junction one branched channel is totally occupied by TBAB-rich phase and the other branched channel by TBAB-rich phase and AS-rich phase together, as shown in the first image of Figure 2. The AS-rich phase, usually dispersed phase in the bulk scale, is surrounded by continuous TBAB-rich phase. When d.c. voltage is applied, the interface at the center of the branched channel is deformed and attracted to the positive electrode direction where only TBAB-rich phase is flowing out. After the electric pulse signal is switched off, the interface returns into its original shape. Single drop generation by d.c. electric pulse of 20V for 200ms is shown in Figure 2.

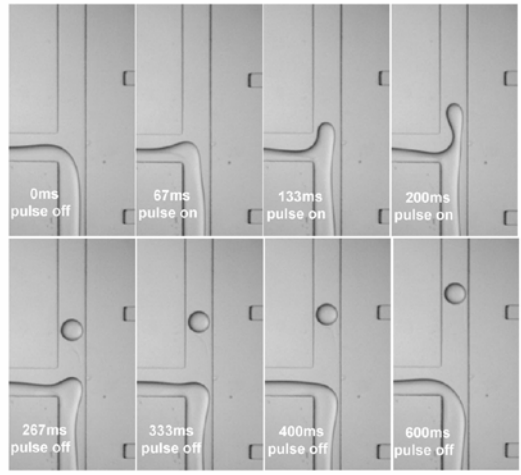

Figure 2. Single drop generation by a 20V, 200ms d.c. electric pulse.

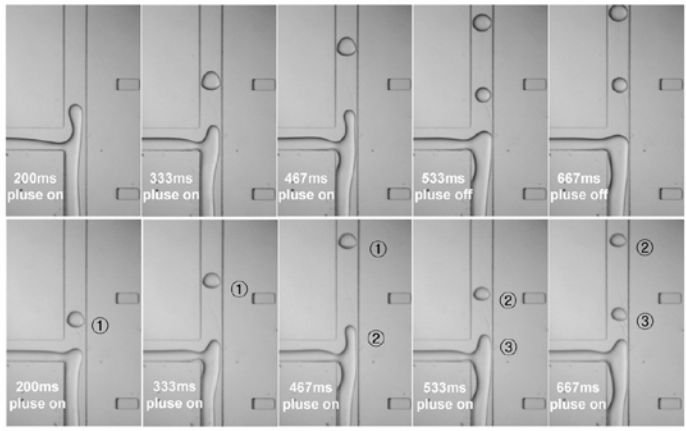

Figure 3. Generation of multiple drops. Two drops are generated by a 20V, 500ms pulse (above). Three drops are generated by a 20V, 800ms pulse (below).

The deformation of the interface at the T-junction leads to the generation of a single AS-rich phase drop and the drop moves together with TBAB-rich phase. Longer and higher voltage electric pulse results in the generation of multiple drops with different volume of each drop as shown in Figure 3. During switching-on of the electric pulse, the drops have bell-shapes and are attracted to the positive electrode in a way similar to electrophoretic motion, while the spherical drops flow freely with continuous phase after switching off. The number of drops generated is controlled by the change in the magnitude and duration of a d.c. electric pulse as shown in Figure 4(a). The minimum voltage required to generate a single drop is smaller when the pH of AS-rich phase is higher, as shown in Figure 4(b), which suggests that the deformation of the interface and generation of drops are due to the accumulation of sulfate ions, which play an important role in determining electrohydrodynamic force. AS, a weak acid, is more easily ionized at higher pH and the concentration of sulfate ion is greater at higher pH. Thus, more negative charge is accumulated on the unit area of the interface and less voltage is required to form an AS-rich phase drop at higher pH.

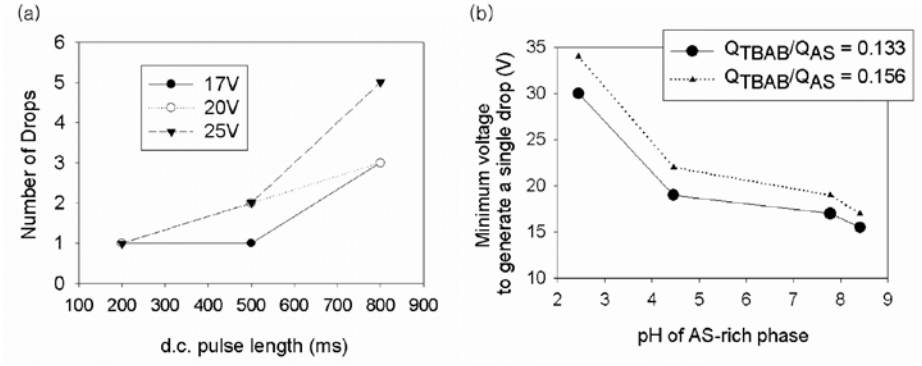

Figure 4. (a) Number of drops generated by d.c. pulse. (b) Minimum voltage to generate a single drop as a function of pH.

5. CONCLUSIONS

We report the generation of a single drop or multiple drops in aqueous two-phase microflow by applying a d.c. electric pulse. The number of drops is easily controlled with the change in the duration and magnitude of electric pulse. The novelty of this method is 'flow-to-dispersion' generation of drops. That is, we can actively generate drops from the laminar flows wherever separation of a part of sample liquid from its continuous flow is desired for specific analysis of molecules, rather than passively generating drops by geometry of microfluidic device.

ACKNOWLEDGEMENTS

This work was supported by the Basic Research Program of the Korea Science and Engineering Foundation (grant number: R01-2004-000-10681-0) and Center for Ultramicrochemical Process Systems sponsored by Ministry of Science and Technology.

REFERENCES

[1] R.F. Probstein, *Physicochemical Hydrodynamics*, Butterworths, New York, pp.190-223 (1989).

[2] Y. Akama, M. Ito, S. Tanaka, *Talanta,* **53(3)**, 645-650 (2000).

HIGH-PERFORMANCE PRODUCTION OF MONODISPERSE EMULSIONS USING MICROFABRICATED ASYMMETRIC THROUGH-HOLE ARRAY

I. Kobayashi[1], G. T. Vladisavljević[2], K. Uemura[1] and M. Nakajima[1,3]

[1]National Food Research Institute, Japan, [2]Loughborough University, UK and [3]University of Tsukuba, Japan

ABSTRACT

This paper reports high-performance production of monodisperse emulsions using numerous asymmetric through holes microfabricated on a silicon chip. Monodisperse oil-in-water (O/W) emulsions with droplet sizes of approximately 30 μm were stably produced via asymmetric through holes at high droplet generation rates up to several hundreds of thousands per second. This paper also reports three-dimensional simulation of emulsion droplet generation via an asymmetric through hole using a computational fluid dynamics (CFD) method. The calculation results showed an excellent agreement with the experimental results and provided a better understanding of the droplet generation process.

Keywords: Asymmetric through holes, droplet generation, CFD, microchannel emulsification

1. INTRODUCTION

A microchannel (MC) emulsification method, introduced by Kawakatsu et al. [1] in the late 1990s, is capable of producing monodisperse emulsions via MC arrays with a slit-like terrace. Microfluidic emulsification methods for generating monodisperse emulsion droplets using e.g. T-junction devices [2] and flow focusing devices [3,4] have been introduced, beginning in the early 2000s, whereas the microfluidic devices usually consisting of a single MC for a to-be-dispersed phase have very low droplet productivity. We recently developed a new MC emulsification device consisting of numerous microfabricated asymmetric through holes for large-scale production of monodisperse emulsion droplets [5]. However, the droplet productivity of monodisperse emulsions via an asymmetric through-hole array has not yet been investigated. Here we present the production of monodisperse emulsions using a microfabricated asymmetric through-hole array device at high droplet production rates. We also simulated emulsion droplet generation via an asymmetric through hole using a CFD method.

2. EXPERIMENTAL

Figure 1(a) is a schematic of a silicon chip consisting of 11,558 asymmetric through holes, microfabricated via three steps of silicon dry etching. Each asymmetric through hole in a WMS2-2 chip (Figure 1(b)) consisted of a slot (10 × 70-μm size and 30-μm depth) and a circular channel (10-μm diameter and 120-μm depth). Refined soybean oil was used as the to-be-dispersed phase, and Milli-Q water solutions containing sodium dodecyl sulfate (SDS) or polyoxyethylene (20) sorbitan monolaurate (Tween20) were used as the continuous phase. Emulsification experiments were conducted by injecting the to-be-dispersed phase via asymmetric through holes into the upper continuous phase region.

978-0-9798064-0-7/μTAS2007/$20©2007CBMS

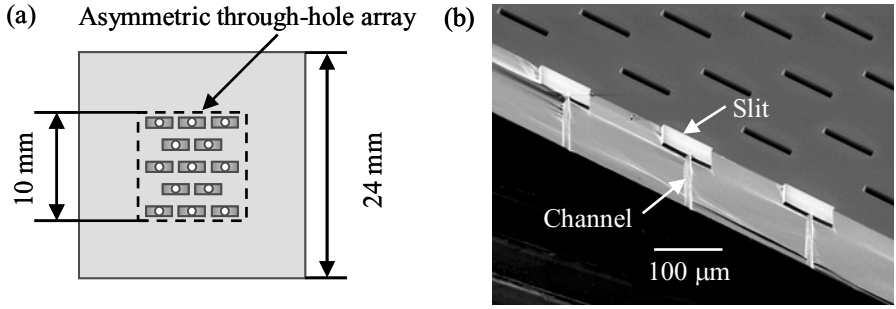

Figure 1. (a) Schematic top view of a silicon chip consisting of a microfabricated asymmetric through-hole array. (b) Scanning electron micrograph of asymmetric through holes microfabricated in a WMS2-2 chip.

A CFD code (CFD-ACE+ version 2004) with a finite volume method was used to calculate the generation of soybean oil-in-water droplets via an asymmetric through hole presented in Figure 3. All the walls in the computational domain were set to be not wetted by the to-be-dispersed phase.

3. RESULTS AND DISCUSSION

As presented in Figure 2, a monodisperse O/W emulsion with an average droplet diameter, d_{av}, of 32.0 μm was stably produced using the WMS2-2 chip at a high flow rate of the to-be-dispersed phase, Q_d, of 10.0 mL/h, which is equal to a droplet production rate of approximately 2.4×10^5 s^{-1}. This Q_d value was higher than those for our previous MC array devices by at least two orders of magnitude.

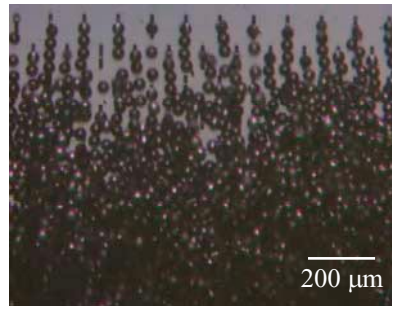

Figure 2. Typical micrograph of the production of a monodisperse emulsion composed of a soybean oil-in-water of 1.0 wt% SDS system via asymmetric through holes (WMS2-2).

A typical example of the results obtained from CFD calculations (Figure 3) demonstrates that an O/W emulsion droplet is stably generated via an asymmetric through hole without applying a forced cross-flow of the continuous phase. Below the critical to-be-dispersed phase velocity inside a channel, U_d, the resultant droplet diameter slightly increased with increasing U_d, and the droplet generation rate linearly increased with increasing U_d. The CFD results for the resultant droplet diameter and droplet generation rate agreed quantitatively with the results obtained from emulsification experiments using a soybean oil-in-water of 2.0 wt% Tween20 system and a WMS1-3 chip (slit: 10×70-μm size and 30-μm depth, channel: 10-μm diameter and 70-μm depth).

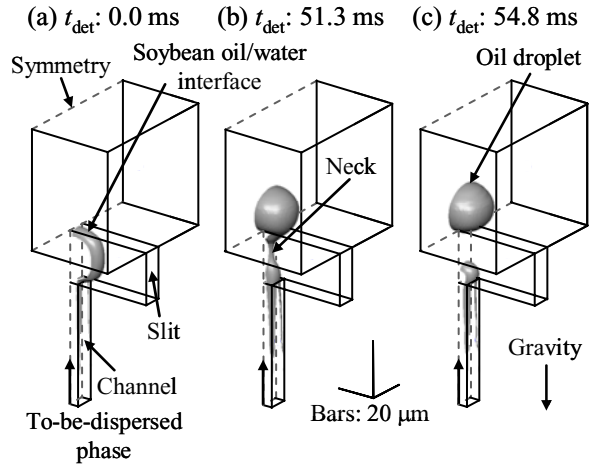

Figure 3. Oil droplet generation via an asymmetric through-hole with a 10 μm-diameter channel obtained from CFD calculation using the Volume of Fluid (VOF) method. U_d was 1.0 mm/s. t_{det} is the droplet detachment time.

4. CONCLUSIONS

We have demonstrated that a microfabricated device consisting of numerous asymmetric through holes enables producing monodisperse emulsions at very high droplet production rates. The generation of uniform emulsion droplets via an asymmetric through hole was simulated excellently using CFD. The numerical CFD results reported in this paper agreed quantitatively with the experimental results. We will scale up microfabricated asymmetric through-hole array devices to achieve the production of monodisperse emulsions at practical droplet production scales.

ACKNOWLEDGEMENT

This study was supported financially by the Nanotechnology Project of Ministry of Agriculture, Forestry and Fishery of Japan.

REFERENCES

[1] T. Kawakatsu, Y. Kikuchi, M. Nakajima, *Regular-sized cell creation in microchannel emulsification by visual microprocessing method*, J. Am. Oil Chem. Soc., 74, pp. 317-321, (1997).

[2] T. Thorsen, R.W. Roberts, F.H. Arnold, S.R. Quake, *Dynamic pattern formation in a vesicle-generating microfluidic device*, Phys. Rev. Lett., 86, pp. 4163-4166, (2001).

[3] S.L. Anna, N. Bontoux, H.A. Stone, *Formation of dispersions using "flow focusing" in microchannels*, Appl. Phys. Lett., 82, pp. 364-366, (2003).

[4] L. Yobas, S. Martens, W.L. Ong, and N. Ranganathan, *High-performance flow-focusing geometry for spontaneous generation of monodispersed emulsions*, Lab Chip, 6, pp. 1073-1079, (2006).

[5] I. Kobayashi, S. Mukataka, M. Nakajima, *Novel asymmetric through-hole array microfabricated on a silicon plate for formulating monodisperse emulsions*, Langmuir, 21, pp. 7629-7932, (2005).

HIGH THROUGHPUT DROPLET-BASED DNA ASSAYS USING FLUORESCENCE RESONANCE ENERGY TRANSFER

M. Srisa-Art[1], E.C. Dyson[1], A. J. deMello[1] and J. B. Edel[1,2]
[1]*Department of Chemistry and* [2]*Institute of Biomedical Engineering*
Imperial College London, UK
E-mails: a.demello@imperial.ac.uk, joshua.edel@imperial.ac.uk

ABSTRACT

Herein, we present a droplet-based microfluidic device integrated with a confocal fluorescence detection system which is used to perform high-throughput binding DNA assays relying on fluorescence resonance energy transfer (FRET). The exploitation of confocal detection allows for online characterisation of individual droplets and their contents in terms of their size, formation frequency, fluorescence intensity and population.

Keywords: droplets, high throughput analysis, binding assay, FRET

1. INTRODUCTION

Droplet-based microfluidic systems have been utilised to address a variety of problems in the chemical and biological sciences [1]. Droplets can be controllably produced at rates in excess of 1KHz onwards with each droplet acting as an isolated reactor. In theory, this means that tens of thousands of individual reactions or assays can be processed in very short time scales. Accordingly, highly efficient detection plays a crucial role in extracting and utilising the vast amounts of information produced in such systems. To this end, we report herein, a confocal fluorescence detection system integrated with droplet-based microfluidic devices to perform high-throughput DNA binding assays based on FRET. Through the integration of high-sensitivity confocal spectroscopy, we demonstrate that high-speed picoliotre-sized droplets in continuous flow can be characterised online and analyte inside such droplets can be accurately and precisely quantified. The virtue of droplet systems in terms of compartmentalisation, negligible reagent dispersion and rapid mixing via chaotic advection is advantageous to laminar flow for studying biological screening and assays.

2. EXPERIMENTAL

Detection setup: A custom built confocal fluorescence detection system for droplet detection is schematically shown in Figure 1a. **Binding assays:** PDMS microfluidic devices, having 50 μm wide, 50 μm deep and ~44 cm long channels, were used. By attaching a FRET donor (Alexa Fluor 488) to streptavidin and labelling a FRET acceptor (Alexa Fluor 647) onto one DNA strand hybridised to a biotylinated complimentary strand, donor and acceptor molecules were brought into close proximity due to streptavidin-biotin binding, resulting in FRET (Figure 1b). To create a microdroplet system, donor-labelled streptavidin and acceptor-labelled hybridised DNA solutions were introduced separately through the aqueous inlets of a microfluidic device to meet a stream of an immiscible oil (continuous) phase, a 10:1 (v/v) mixture of perfluorodecalin and 1*H*,1*H*,2*H*,2*H*-perfluorooctanol, at a T-junction. The concentration of streptavidin was fixed at a desired value whereas the concentration of DNA was ramped by continuous and precise control of input flow rates to assess binding. The flow rates of the oil phase and aqueous solutions

978-0-9798064-0-7/μTAS2007/$20©2007CBMS

were kept constant at 1.5 µl min^{-1}, resulting in a total flow rate of 3.0 µl min^{-1} (20 mm s^{-1}). A schematic of the microfluidic device topology and a sample image of formed droplets are illustrated in Figures 1c and 1d. A buffer stream was delivered into the middle aqueous inlet to prevent reagents from coming into contact prior to droplet formation and to allow for online dilution. Thus, mixing and binding of streptavidin and DNA only occurred inside the droplets. Online fluorescence detection was conducted at ~42 cm or ~20 s (the total channel length is ~44 cm) downstream from the droplet-forming region. Two fluorescence signals, from the donor and acceptor, were recorded simultaneously using separate avalanche photodiode detectors (APDs).

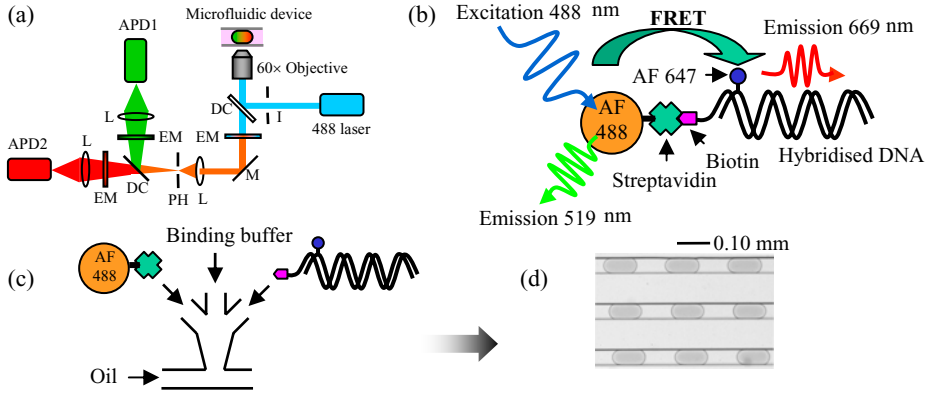

Figure 1. (a) A home built confocal microscope used for droplet detection: APD-avalanche photodiode detector, DC-dichroic mirror, EM–emission filter, I-iris, L-lens, M-mirror and PH-pinhole. (b) FRET process using Alexa Fluor 488 and Alexa Fluor 647 as a donor and an acceptor, respectively. (c) Schematic of microfluidic device used for FRET biological assays. (d) Example image of droplet generated using the microfluidic system.

Binding kinetics: Streptavidin-biotin binding kinetics were also investigated via FRET. Streptavidin and DNA concentrations were fixed at 22.0 and 60.0 nM, respectively, resulting in a binding ratio of 2.73, defined as the ratio between DNA and streptavidin concentrations. Droplet detection was performed by probing the microfluidic channel at different points to extract the binding kinetics.

3. RESULTS AND DISCUSSION

FRET binding assays: An example of a FRET burst scan from the confocal system is shown in Figure 2a. Importantly, the donor and acceptor signals were coincident and only ~1.2% crosstalk (leakage of donor emission into the acceptor channel) of this FRET pair was observed. This indicates that the majority of the signal associated with the acceptor is due to FRET. A plot of binding ratio as a function of the 'red' burst height and fit using the Hill-Waud model [2] are depicted in Figure 2b. Red fluorescence bursts increased with the binding ratio due to a result of greater energy transfer with a higher number of acceptors linked to the donor. Comparison of data measured at different streptavidin concentrations demonstrates that the higher the streptavidin concentration, the higher the energy transfer (due to the increased number of donors to transfer energy). It was observed that all binding curves plateau at binding ratios of ~2.0, indicating that only 2 biotin binding sites on streptavidin were successfully filled.

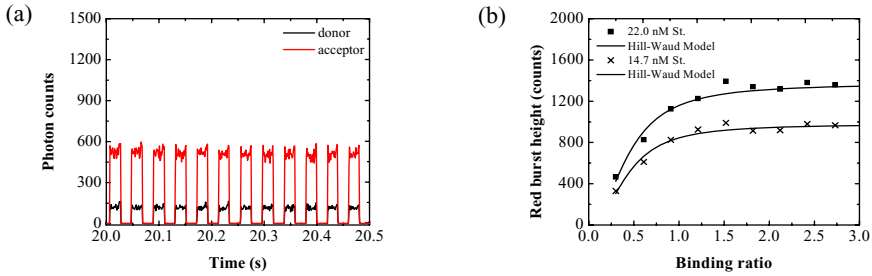

Figure 2. (a) A 500 μs fluorescence burst scan. Data was recorded using a 50 μs resolution. (b) Binding curves.

Figure 3a shows plots of FRET efficiency calculated from the ratio of acceptor fluorescence intensity to the summation of acceptor and donor fluorescence intensities. It can be seen that the FRET efficiency of this system is ~0.75.

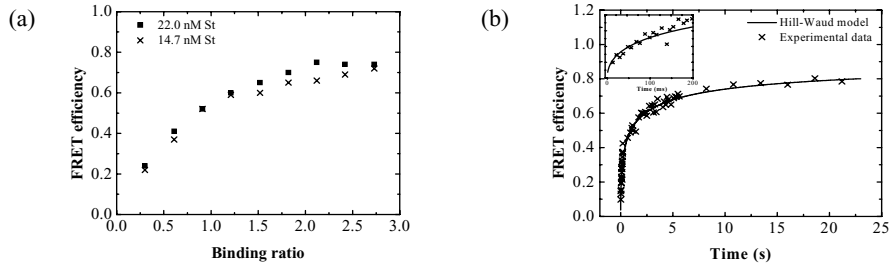

Figure 3. (a) Plots of FRET efficiency as a function of binding ratio. (b) Streptavidin-biotin binding kinetic plot.

FRET binding kinetics: Figure 3b illustrates a streptavidin-biotin binding map plotted using FRET efficiency against time. An inset over 200 ms shows high resolution kinetic measurements on a millisecond timescale. The FRET efficiency drastically increases at the beginning of the curve and remains stable after ~5.0 s. This implies that complete binding of our analytes occurs in a 5 s time frame.

4. CONCLUSIONS

Droplet-based microfluidics integrated with confocal microscopy was successfully exploited to perform high-throughput streptavidin-biotin binding assays. The binding ratio between streptavidin and biotin was found to be ~2.0 with the binding kinetics of ~5.0 s. High FRET efficiency of ~0.75 was obtained from this system. Using this new approach, high-throughput analysis or screening is a highly promising direction for future research.

ACKNOWLEDGEMENTS

M. S-A acknowledges the Royal Thai Government for provision of a scholarship. The work was partially supported by the RCUK funded Microdroplets Basic Technology Project.

REFERENCES

[1] Song, H.; Chen, D.L.; Ismagilov, R.F. *Angew. Chem. Int. Ed*. **2006,** *45*, 73367356.
[2] Moran-Mirabal, J. M.; Edel, J. B.; Mayer, G. D.; Throck, D.; Singh, A. K.; Craighead, H. G. *Biophys. J.* **2005**, *89*, 296-305.

LIQUID-LIQUID-PHASE ELECTROSPRAY IN MICROCHANNELS

Sander Koster[1,2], Volkert de Bot[1], Elisabeth Verpoorte[1]
[1]*University of Groningen, The Netherlands*
[2]*Present address: TNO Kwaliteit van Leven, Zeist, The Netherlands*

ABSTRACT

This contribution describes the operation of a liquid-liquid electrospray (L-L electrospray) device in a microfluidic format. The small droplets generated have a high surface-to-volume ratio that will find use in, for example, fast and efficient extraction processes, currently being investigated in our lab. Such devices are attractive, as they can be coupled to conventional analytical chemistry instrumentation.

Keywords: Liquid-Liquid-Phase Electrospray, Water-Octanol, 2-Phase Flow, Electrospray

1. INTRODUCTION

Electrospray has found widespread use in several industrial applications such as the synthesis of monodisperse micron- and nano-sized particles [1]. In analytical chemistry, electrospray is used to ionise (bio)molecules for mass spectrometric analysis [2]. In all of these applications, a liquid is atomised into a gas in a high electrical field by applying a potential between a capillary, through which a liquid is pumped, and a counter electrode. In his 1964 paper on electrospray, Taylor briefly described the spraying of water into transformer oil [3]. The technique has only been explored for the production of emulsions [4]. This contribution describes the operation of a liquid-liquid electrospray (L-L electrospray) device in a microfluidic format.

2. EXPERIMENTAL

The spray is generated at a nozzle-like geometry, and flow rates are controlled. Our system thus mimics the conventional sprayers used in L-G electrospray, enabling the comparison of experimental results with L-G electrospray theory. The chip had three inlets and one outlet, as can be seen in the upper left frame of Figure 1. Inlet 1 was used to introduce the aqueous phase to be electrosprayed, a 50/50 H_2O/methanol + 0.1% formic acid mixture. Inlets 2 and 3 were used to introduce the non-aqueous phase, 1-octanol. A water /methanol/formic acid mixture was chosen, as this is a very common mixture used for L-G electrospray applications in analytical chemistry. The channel for the aqueous phase was tapered at the point where it converged with channels 2 and 3 to a width of ~40 μm, to mimic an electrospray needle/nozzle.

3. RESULTS AND DISCUSSION

When a voltage of a few kV is applied between the in- and outlet of the chip, electrospray of the aqueous phase in the low-conducting octanol is observed. Octanol and aqueous-phase flow rates applied to the inlet channel are a prerequisite for electrospray. The electrospray-generated-droplets move to the outlet in the octanol flow, which stabilises the spray. Figure 1 presents 6 frames showing the onset of electrospray when the potential is gradually increased from 0 to 5 kV in about 20 seconds. The formation of large droplets is clearly observed in the absence of a potential. Control of droplet size is obtained by

978-0-9798064-0-7/μTAS2007/$20©2007CBMS

varying the octanol flow rate. The appearance of the sprayer at 1-3 kV is instable. From 4 kV onwards, the spray becomes stable. The electrospray-generated droplets are positively charged. A diverging cloud of droplets, due to the diverging electrical field near the sprayer and Coulombic repulsions, is typically observed, similar to conventional L-G electrospray. Figure 2 presents the voltage-current characteristics of the spraying process. The potential at which a stable Taylor cone is observed is from 2.5 kV when increasing the potential, whereas a stable spray can still be observed at 1.5 to 2 kV when decreasing the potential. Hysteresis effects in the current as seen in liquid-gas electrospray are not observed here [5].

4. OUTLOOK

We envision using this chip on-line with L-G ESI for mass spectrometric analysis where compounds form the aqueous phase are selectively extracted towards the octanol phase, see Figure 3. Thereafter, both phases need to be separated prior to spraying the octanol phase. Moreover, the chip can be coupled to analytical instrumentation such as liquid chromatography that is operated under constant flow conditions.

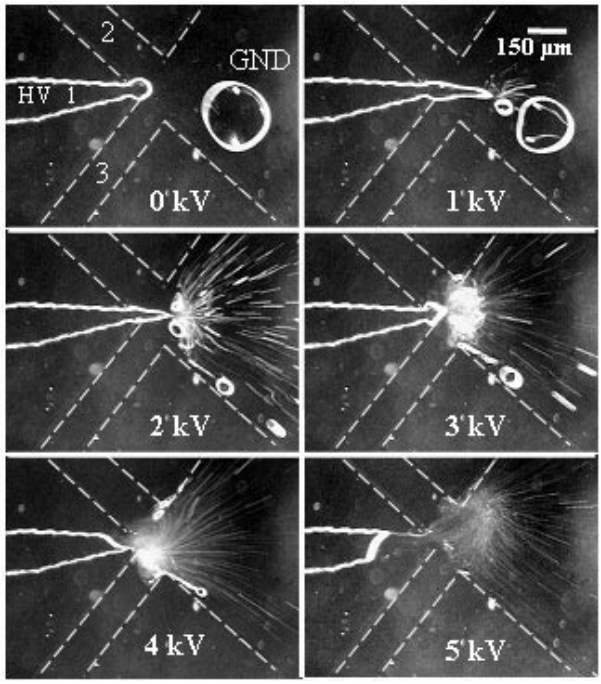

Figure 1. Formation of the Taylor cone in L-L electrospray when potential is increased from 0 to 5 kV. The flow rate for octanol is 2 µL/min from channels 2 and 3, and 0.07 µL/min for the aqueous phase from channel 1.

ACKNOWLEDGEMENTS

We would like to thank Jan Marijnissen (Delft University of Technology) and Andries Bruins (University of Groningen) for useful discussions.

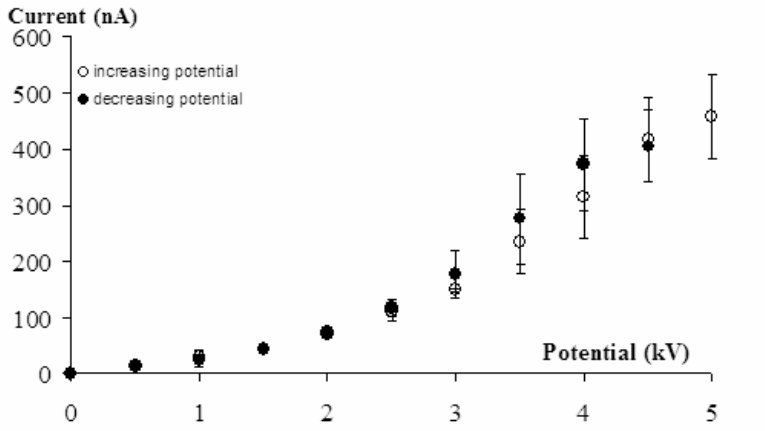

Figure 2. Measured current I (nA) as a function of increasing and decreasing potential (kV). The open circles indicate a potential increasing from 0 to 5 kV. The closed circles represent the current measured when the potential was decreased from 5 to 0 kV.

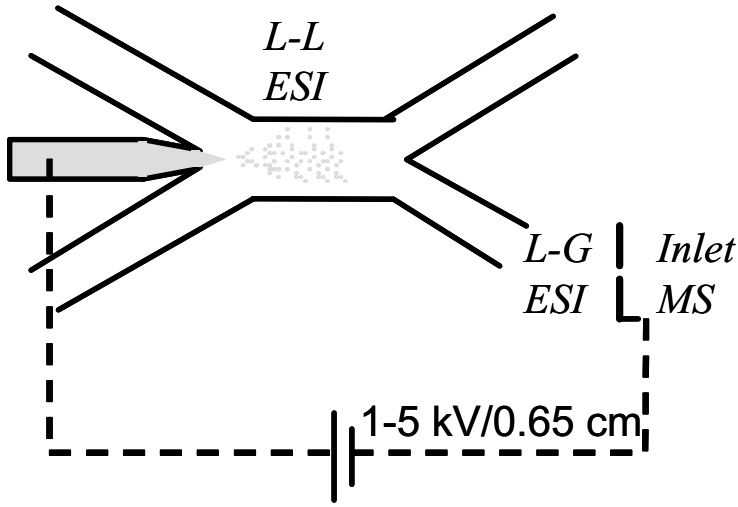

Figure 3. Envisioned chip where analytes are extracted and electrosprayed for mass spectrometric analysis.

REFERENCES

[1] J. van Erven, R. Moerman and J. C. M. Marijnissen, *Aerosol Sci. Technol.*, 2005, 39, 941-946.
[2] M. Yamashita and J. B. Fenn, *J. Phys. Chem.*, 1984, 88, 4451-4459.
[3] G. Taylor, *Proc. Roy. Soc. London A*, 1964, 280, 383-397.
[4] A. Watanabe, K. Higashitsuji and K. Nishizawa, *J. Colloid Interface Sci.*, 1978, 64, 278-289.
[5] D. P. H. Smith, *IEEE Trans. Ind. Appl.*, 1986, 1A-22, 527-535.

MICROFLUIDIC LOGIC GATES AND TIMERS

Michael W. Toepke, Vinay V. Abhyankar, Jay W. Warrick, and David J. Beebe

Department of Biomedical Engineering, University of Wisconsin – Madison, USA

ABSTRACT

We present a passive method of creating microfluidic logic gates and timers based on surface tension forces that does not require extra fabrication steps or specialized equipment. A standard pipette is the only equipment needed to use the new technology. These functionalities demonstrate an important step in implementing autonomous control in microfluidic platforms and increase the accessibility of microfluidics to non-experts.

Keywords: Logic gates, timer, digital, microfluidic

1. INTRODUCTION

Incorporation of actively controlled functionalities into microfluidics often leads to more complex fabrication and the need for ancillary equipment, whereas passive and autonomous microfluidic components can help to reduce the need for additional equipment. Liquid-based logic devices offer the potential to implement autonomous control in microfluidic systems. While various technologies have been used to create microfluidic logic gates, many of these approaches use electronic components that are more complex than the devices themselves. We have developed an alternative approach to creating fluidic logic gates that use a consistent input/output (droplet/droplet), allows for visual signal transduction (droplet/no droplet), and needs only a pipette to implement. The method is based on a previously reported passive pumping technique that uses the pressure differential between surfaces with different radii of curvature[1].

2. EXPERIMENTAL

SU8 masters molds were made using standard soft lithography procedures and devices were cast using polydimethylsiloxane (Sylgard 184, Dow Corning).

3. RESULTS AND DISCUSSION

In passive pumping, liquid droplets with a small radius of curvature are driven to droplets with a larger radius of curvature due to surface tension-based forces. We define a digital input/output using the presence of a droplet to represent 1 and the absence of a droplet to represent 0. An inverter can be created using a microfluidic channel with two ports, as shown in Figure 1. A droplet is placed on one of the ports, which serves as the output. If no droplet placed on the input port (input of 0), the output is 1. If a larger droplet is placed on the inlet, the output droplet will be pumped away, giving an output of 0. A NOR gate is formed by adding a second input port to the inverter structure, as shown in Figure 1c&d.

For the AND gate, we use an output port with a radius larger than that of the input port. The curvature of the meniscus in the outlet port is large enough to drive fluid flow to the outlet from the inlet, provided a sufficiently small input droplet is used. The resulting fluid flow displaces the air/liquid interface from within the port to above the port to form a droplet. A functional AND gate is shown in Figure 1 e-g. The design can be used as an OR gate by simply changing the size or number of droplets that are used to define an input of 1.

978-0-9798064-0-7/μTAS2007/$20©2007CBMS

A NAND gate can be constructed by arranging two channels near one another. The main channel contains three ports for the two inputs and the output. The output port is primed with a droplet prior to placing any input droplets and a second channel is placed in close proximity to the output droplet. If only one input droplet is placed, the output droplet will grow in size but will not overlap with the inlets of the second channel. However, if there are droplets placed on both inputs, the output droplet will grow large enough to overlap with the inlet of the second channel. The output droplet will then be pumped away through the secondary channel, leaving an output of 0. The NAND gate can be operated as a NOR gate by increasing the size of the priming output droplet or the input droplet. A sequence of images showing a functioning NAND gate is shown in Figure 2.

An XNOR gate is formed by modifying the secondary channel of the NAND/NOR design to have a high fluidic resistance. A single input droplet is sufficient to create fluid contact between the two channels and will lead to the outlet droplet being pumped away, though a slower rate than in the case of the NAND gate. The addition of a second input droplet can then be used to increase the output droplet volume such that it is larger than the sink, provided that the output droplet grows much faster than the sink droplet. Thus, the output droplet remains only if the inputs are 0/0 or 1/1. Figure 3 shows the operation of the XNOR gate. The main channel is 250 µm tall while the secondary channel is only 40 µm tall, providing significantly higher fluidic resistance. The gate is set by placing a 1.2 µl droplet on the output port and a 2.5 µl droplet on the sink. Input droplets with a volume of 0.9 µl were used to operate the gate. The input ports to the secondary channel are shorter than on the NAND gate in order to maintain a droplet shape after the output overlaps with the secondary channel ports.

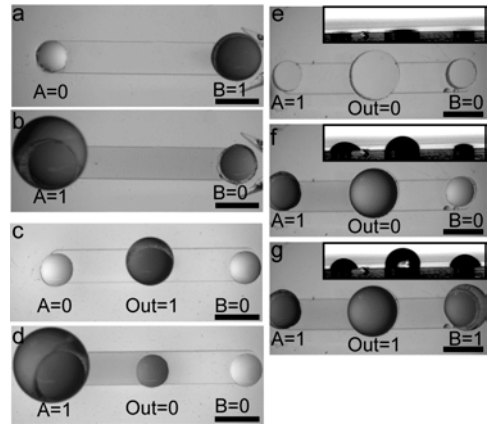

Figure 1. Microfluidic inverter with input port A and output B, shown for inputs of (a) 0 and (b) 1. NOR gate with two input ports (A & B) and an output, shown for inputs of (c) 0/0 and (d) 1/0. The AND gate contains two small ports for inputs A & B and a larger port for the output, shown for inputs of (e) 0/0, (f) 1/0, and (g) 1/1. (bar = 1 mm).

Passive timers can be formed using a two-channel design. A high fluidic resistance channel significantly reduces the flow rate achieve with passive pumping, causing a time delay. The exit of the timer channel is placed close to the entrance of the main channel that is to be treated. The outlet droplet of the timing channel grows as fluid is pumped through the high-resistance channel, eventually growing large enough to overlap the inlet port of the main channel and flow through to the main channel sink droplet. A representative timer can be seen in Figure 4 a-c. Multi-inlet designs can be used to achieve variable fluidic resistance, leading to a programmable timer. Multiple timers can be used to carry out a series of treatments on an individual channel. Figure 4 d-f shows a device with two programmable timer channels. The timer on the left was set for a long time by placing the input droplet on the port furthest away from the sink droplet; the timer on the right was set for a short time by placing the droplet on the port nearest the main channel. Figure 4d

shows the device just after placing the input droplets. Figure 4e shows the device after the short timer on the right has dosed the main channel. Figure 4f shows the device after the main channel has been dosed from the long timer on the left.

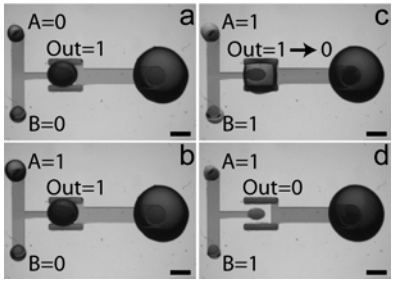

Figure 2. Microfluidic NAND gate. (a) 0/0 input and output of 1. (b) 1/0 input and output of 1. (c) 1/1 input transitioning to 0 output. (d) 1/1 input with final output of 0. (bar = 1 mm).

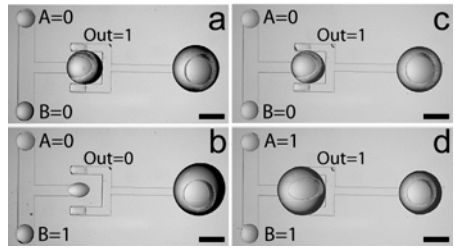

Figure 3. Microfluidic XNOR gate. (a) 0/0 input and output of 1. (b) 1/0 input and output 0. (c) The same conditions as in (a). (d) 1/1 input and output of 1. Channel edges are outlined for clarity. (bar = 1 mm).

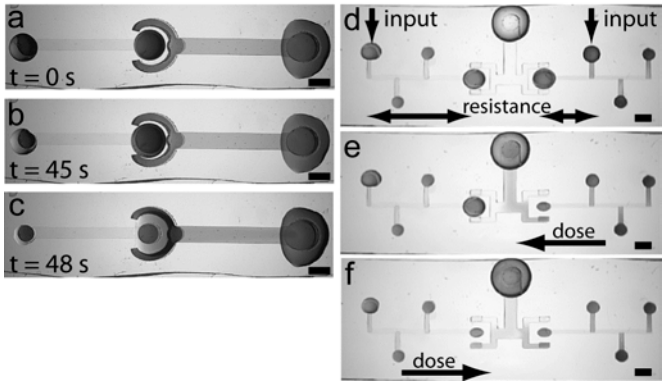

Figure 4. (a-c) A single microfluidic timer. Dual, programmable timer device after (d) setting timers, (e) dosing the main channel with the short timer on the right, and (f) dosing the main channel with the long timer on the left.

4. CONCLUSIONS

This work demonstrates a new method for implementing fluidic logic and temporal control in microfluidic devices using passive pumping. The method provides an easy way to integrate functionalities into microfluidic devices without adding complexity to the fabrication process and limits the dependence on external equipment. The methods can be implemented in a high throughput manner with the use of ubiquitous multi-channel pipettes and robotic dispensers, facilitating use in cell biology research and screening applications.

ACKNOWLEDGEMENTS

We thank Keil Regehr for helpful discussions and the Army Breast Cancer Research Program (W81XWH-04-1-0572) & National Institutes of Health (K25 CA104162).

REFERENCES

[1] Walker, G. M. & Beebe, D. J. (2002) *Lab Chip* **2,** 131-134.

MICROFLUIDIC QUANTITATIVE EXTRACTION IN DROPLETS

Pascaline Mary[1], Vincent Studer[2], Patrick Tabeling[1]
[1]Laboratory of Microfluidics, Gulliver, ESPCI, France and
[2]Laboratory of Biology, ESPCI, France

ABSTRACT

This paper reports a microfluidic method for fast extraction within droplets. We analyze influence of different parameters on extraction (depths of channels, viscosities, materials) within droplets formed in hydrofocusing and we show extraction processes within droplets in a miniaturized system are orders of magnitude faster than in conventional liquid-liquid extractions. We provide interpretation of mass transfers with a parallelism with transport theories through interfaces in the presence of internal recirculations.

Keywords: Extraction, purification, digital microfluidics, droplets, emulsions

1. INTRODUCTION

The miniaturization of liquid-liquid extraction, especially in droplets, is gaining more importance in small scale reactions due to short diffusion lengths for mass transfers and large specific area. In a conventional extraction method with a separatory funnel small droplets are generated with large interface area but the process of shaking last for a long time. Moreover models of transfers result from rough approximations with very limited validity. We concentrated here of droplets extraction in microfluidic systems allowing downsizing reactions and detection scale. Concerning microfluidic droplet-based extraction [1], there is a lack of data and a poor understanding of the physics that drives the mass exchanges between the external and dispersed phases. In this contribution we provided the first set of data with their interpretation.

2. EXPERIMENTAL

Our experimental setup consists of polydimethylsiloxane microchannels fabricated using soft lithography techniques. The experiments we conducted are sketched in figure 1. Droplets are formed in hydrofocusing and T geometry. Channels width w is 205 μm and their height h is in the range 30-95 μm. Droplets are composed by water or water/glycerol mixtures buffered by phosphate buffer saline (PBS, pH=7.2) with octan-1-ol as the external phase. The materials transfered across the droplet interfaces are fluorescein or rhodamine B. Sharing coefficients Kow, defined by the ratio at equilibrium of concentration of fluorophore in octanol to the concentration of fluorophore in aqueous phase, measured are 0.01 and 55 respectively. The tracer was initially introduced either into the dispersed phase (we then refer to purification) or into the external phase (we then also refer to extraction).

978-0-9798064-0-7/μTAS2007/$20©2007CBMS

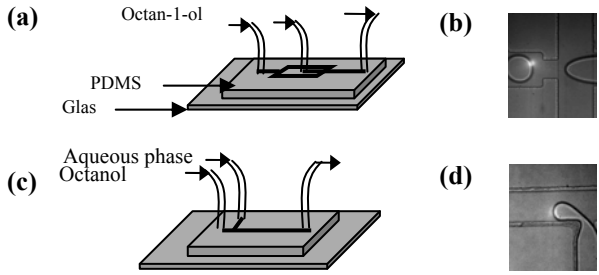

Figure 1. Schematic view of the microfluidic chip. (a) hydrofocosusing device. (b) corresponding optical microscopy image of constriction. (c) T-geometry device. (d) corresponding optical microscopy image of constriction.

Fluids were placed in plastic syringes tubes at the atmospheric pressure and each syringe needle was connected with the microchip. The experimental setup was based on UV-induced fluorescence microscopy. Intensity measurements were performed using a sensitive CCD camera mounted on the microscope.

3. RESULTS AND DISCUSSION

First we concentrated on the process of extraction of fluoresceine from octanol to water droplets in straight channels. Generated droplets have a radius in the range 160-195 µm. To estimate the variation of extraction amount, average fluorescence intensity within droplets at constant interval in microchannel was measured by moving a microscope stage. Figure 2 shows temporal evolution of normalized intensity; intensity was first gradually increased with time before saturating.

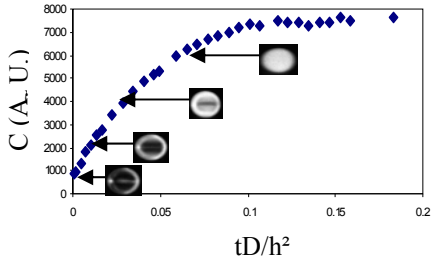

Figure 2. Typical concentration of fluorescein within the droplets as a function of time: h = 70µm.

Using different experimental conditions (depths, viscosities by varying the ratio of glycerol/water mixtures), we also found that the law governing the process towards equilibrium is algebraic: figure 3 shows a loglog plot of normalized intensity vs. time indicating that the intensity of fluorescein increases as the square root of time for a wide range of experimental conditions. We found that the duration of the process, τ_{final}, defined as the time to reach saturation has the same order of magnitude than h^2/D, where D is the diffusion coefficient of fluorophore in water, indicating that transversal diffusion is the limiting process. The interpretation of kinetic of mass transfers refers to a theory concerning transport of tracers through rectangular interfaces in the presence of internal

circulations [2]. According to these theories, in a first step, recirculations within the droplets rapidly homogenize the concentration along the streamlines in a characteristic time $t^* = (h^2/D)Pe^{-2/3}$ which varies between and in our experiments, and, in a second step, diffusion completes the process.

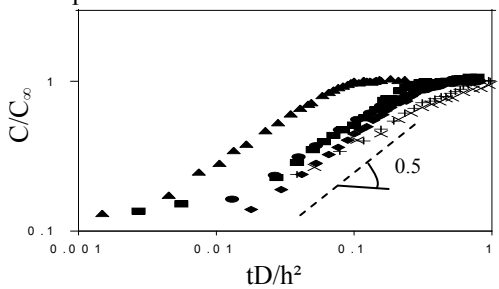

Figure 3. Concentration of droplets vs. time: flow focusing geometry ■ glycerol 30wt%/water mixture, h = 70µm, ▲ glycerol 60wt%/water mixture, h = 70µm, x pure water h=30µm, + pure water h = 40 µm, ● pure water h= 70µm. (C_∞ is the droplet concentration at late times); T geometry, ♦ pure water h= 76 µm.

This leads to power law behaviour of the evolution towards equilibrium. This theory suggested a universal rescaling of $\mathbf{C/C_\infty}$ in function of t/t*. Figure 4 shows good agreement between the experimental and predicted variation in I/I0 with increasing t/t*.

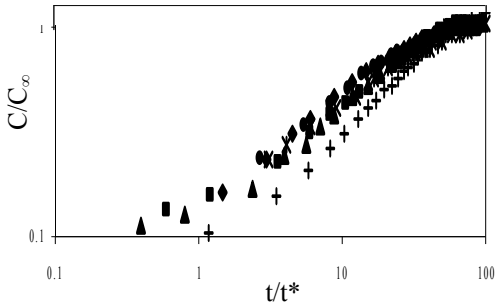

Figure 4. Curves representing normalized concentration vs. time rescaled by the characteristic time of mixing along streamline.

4. CONCLUSIONS

In the present work, the extraction processes we analysed are orders of magnitude faster than in nonminiaturized techniques. This is encouraging for the development of fast extraction microfluidics units that use vastly smaller amounts of organic solvent, provide superior extraction efficiencies, permit the on-line coupling to analytical measurement techniques, and allow easier automation and higher extraction throughput.

REFERENCES

[1] Tokeshi, M.; Minagawa, T.; Kitamori, T. Anal. Chem. 2000, 72, 1711.
[2] Young, W.; Pumir, A; Pomeau, Y. Phys Fluids A 1989, 1, 462.

PIXELATION OF PLANAR BIOCHEMICAL SAMPLES: A NOVEL CONCEPT FOR MICROFLUIDIC IMAGING

K. Tachikawa, P.S. Dittrich, J. Franzke and A. Manz
ISAS – Institute for Analytical Sciences, Dortmund, Germany

ABSTRACT

We propose and experimentally demonstrate a novel concept to spatially resolve the chemical composition of complex biochemical samples by pixelation within a micro total analysis systems (microTAS) platform. The device we have developed images samples of interest by discretising targeted areas into voxals suspended in a two-phase microflow. This microfluidic pixelation method is a technique suitable for obtaining specimens' non-averaged data with reduced arduous preparation steps to recognise their heterogeneity.

Keywords: droplet manipulation, imaging, pixelation, bio-cell characterisation

1. INTRODUCTION

The MicroTAS concept is widely utilised as one of the common forefront aids to applications in natural and life sciences [1]. The analytical challenge currently faced, however, is the inability to specifically identify and distinguish the diverse properties and characteristics of biochemical systems, e.g., tissues and membranes. This is especially so, given an increasing demand to understand heterogeneity in suspended cell populations or tissue at the single cell levels [2]. Moreover, analytical instrumental techniques are often slow and time-consuming in processing the data and incapable of retaining spatial information. Our droplet-based microfluidics approach [3] alleviates these problems by simultaneously injecting arrayed droplets into a linear channel for serial analytical processing, for independent post-treatment and analysis. Subsequent read-out is executed by fluorescence detection techniques or any suitable analytical device, e.g. MS. Reassembly by preserving the initial positions of the pixels finally enables the creation of an image at high resolution (Figure 1).

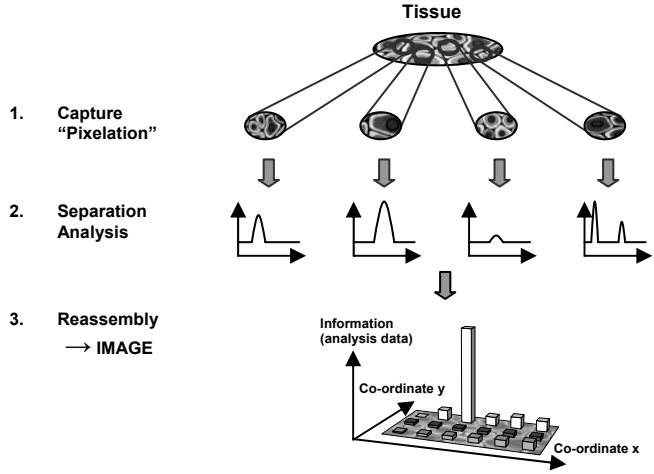

Figure 1. A conceptual flow diagram depicting the method of sample pixelation.

978-0-9798064-0-7/μTAS2007/$20©2007CBMS

2. EXPERIMENTAL

The mould for poly(dimethylsiloxane) (PDMS) and the poly(methyl methacrylate) (PMMA) slides have been produced in-house by the mechanical workshop. The simple and flexible microchip comprises three layers (Figure 2), where each layer contributes a specific role. A 1 mm thick PMMA slide with microarrayed perforations is used to "pixelise" or capture analyte from the surface of a material with soft consistency (Figure 2B). Individual samples trapped in the perforations are mechanically forced out, in piston fashion by micropillar manifolds (270 µm diameter), which insert into the countering holes (Figure 2A and 3A). A PDMS layer embedding a 300 µm wide and deep serpentine microchannel, aligned with the perforations, permits concurrent collection and delivery of ordered droplets to the detection window (Figure 2C). This construction allows easy implementation with a conventional inverted microscope, and arduous array preparation steps are avoided.

3. RESULTS AND DISCUSSION

For a proof of principle, the functioning of the device is tested for various types of samples. Aqueous suspensions of fluorescent beads, densely grown colonies of erythrosine B labelled colon cancer cells, yeast cells and recombinant yeast expressing the Green Fluorescent Protein (GFP) were used. Preliminary studies have proven that upon insertion of micropillars into the perforations, 12 consecutive voxals with an average volume of ca. 60 nL are injected into the microchannel, and transported within mineral oil delivered at the constant flow rate of 20 nL/s. It is also shown that 300µm diameter droplets conserve the same spacing as the perforations (800µm), without diffusion or coalescence in the channel (Figure 3B and C). The consecutive droplets formed are detected in sequence, displaying its ability to maintain spatial orientation.

4. CONCLUSIONS

Precise analyses of the composition of biological and biochemical samples provide a siginificant key towards understanding fundamentals of life building blocks. We have demonstrated a novel concept to spatially resolve the chemical composition of complex biochemical samples by pixelation within a microTAS platform. Further miniaturisation and improved reproducibility for sample injection are currently underway as the device holds ample potential for sample preparation and integration to other separation and detection systems. The method could facilitate the analysis of numerous (sub)cellular biological mechanisms and processes viably, such as simultaneous immunochemical analyses and tests for diagnostic markers in clinical tissue specimens.

REFERENCES

[1] "Micro Total Analysis Systems. Latest Advancements and Trends", P. S. Dittrich, K. Tachikawa, A. Manz, Anal. Chem, **78**, 3887 (2006).

[2] "Microfluidics device for single cell gene expression analysis in *Saccharomyces cerevisiae*", J. Ryley, O. M. Pereira-Smith, Yeast, **23**, 1065 (2006).

[3] "Reactions in droplets in microfluidic channels", H. Song, D. L. Chen, R. F. Ismagilov, Angew. Chem. Int. Ed., **45**, 7336 (2006).

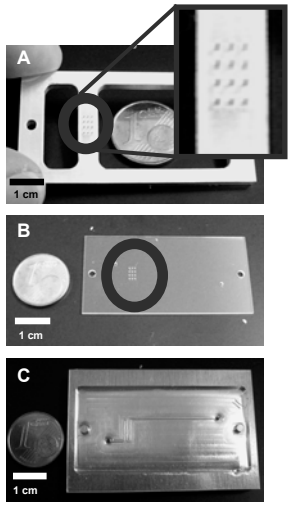

Figure 2. Exploded view of the microdevice. (A) Micropillar manifold made of metal. Pistons for parallel sample injection are shown as the inset picture. (B) Perforations from PMMA cast used to pixelate analyte (circled in grey). (C) Serpentine shaped microchannel cast from PDMS.

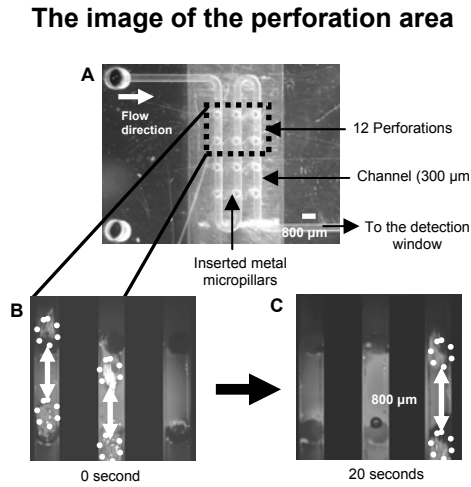

Figure 3. (A) Image of the perforation area design. (B) and (C) show pixelated fluorescent beads transported within the flow of a hydrophobe carrier fluid for subsequent analysis with the retention of droplet inter-spacing (800 µm) at 0 and 20 seconds, respectively. Diffusion or coalescence of droplets could be avoided in the channel. Images have been masked for clarity.

PROGRAMMABLE FLOW-THROUGH REAL-TIME PCR USING DIGITAL MICROFLUIDICS

Philip Y. Paik[1], Dwayne J. Allen[1], Allen E. Eckhardt[1], Vamsee K. Pamula[1], and Michael G. Pollack[1]

[1]*Advanced Liquid Logic, Inc. Research Triangle Park, NC*

ABSTRACT

A digital microfluidic system for rapid, programmable flow-through PCR is presented. Thermocycling is achieved by transporting a microliter-sized droplet between fixed temperature zones within a chip. Equivalent performance to a conventional bench-top thermocycler was demonstrated using a model assay system. Optimization of the chip system for speed has resulted in cycle times as short as 7.5s, enabling 40 cycles of real-time PCR to be successfully performed in 5 minutes.

Keywords: Digital microfluidics, PCR, flow-through, electrowetting

1. INTRODUCTION

In recent years much of the interest in microfluidic devices for PCR has shifted towards "flow-through" systems in which thermocycling is performed by transporting the sample through constant temperature zones within a chip. Compared to stationary formats, flow-through systems offer potentially faster thermocycling, higher sample throughput, simpler operation and better integration with other microfluidic operations [1]. However, existing flow-through approaches lack flexibility with respect to the ability to modify the thermal program during a run, between runs or between samples within a run. We present here experimental real-time PCR results for a flow-through approach based on digital microfluidics [2] which enables fully programmable thermal programs along with the possibility of executing multiple thermal programs simultaneously on a single chip.

2. EXPERIMENTAL

The experimental apparatus consists of a fixture which provides a Peltier heater underneath one end of the chip and a heat sink at the other end of the chip (Figure 1). The Peltier heater provides a constant temperature of 94 ºC within the portion of the chip directly above the heater and the temperature at each adjacent electrode position was

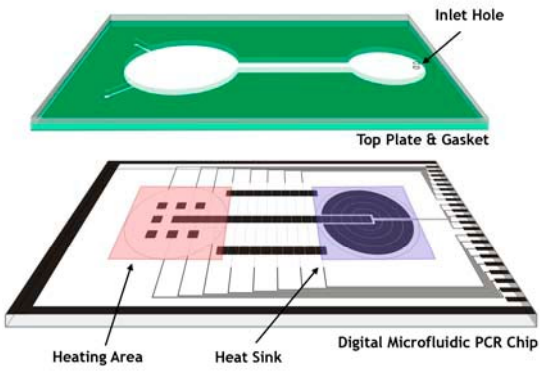

Figure 1: Schematic of the digital microfluidic PCR chip and top plate. The width of each electrode is 1.5 mm and the spacing between the top and bottom plates is 375 µm. Droplets are dispensed by pipetting a fixed volume (1 µL) into the inlet hole with the aid of electrowetting. The surrounding space is filled with hexadecane or silicone oil.

978-0-9798064-0-7/µTAS2007/$20©2007CBMS

determined using a thermocouple. Following this initial characterization, specific positions along the length of the array could be reliably mapped to particular temperatures (Figure 2). The apparatus was mounted on a fluorescence microscope focused on an electrode in the "extension" region to allow fluorescence measurement at the end of each cycle.

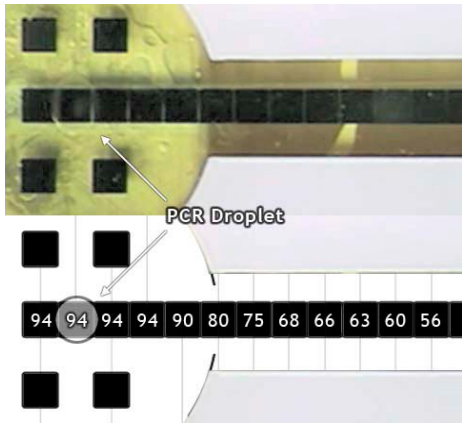

Figure 2: Top-view of the electrode array showing the relative location and position of the Peltier heater and PCR droplet (top) and thermal map of the electrode array (bottom).

3. RESULTS AND DISCUSSION

As a model system for testing the performance of PCR on chip, a 273 bp fragment of the *Candida albicans* 18S ribosomal RNA gene was amplified. The PCR mix consisted of BioRad iQ SYBR Green Supermix, primers and varying concentrations of *Candida* genomic DNA. Additionally, 10 pg of human genomic DNA was spiked into each 1 µL sample to test the robustness of the reaction. The thermal program used on the chip was initially the same as the commercial BioRad instrument: 15 s @ 94°C followed by 30 s @ 60°C. The real-time results on-chip compared favorably with the commercial system for each concentration of DNA tested (Figure 3). The results were validated by gel electrophoresis of the droplets collected at the end of each real-time experiment.

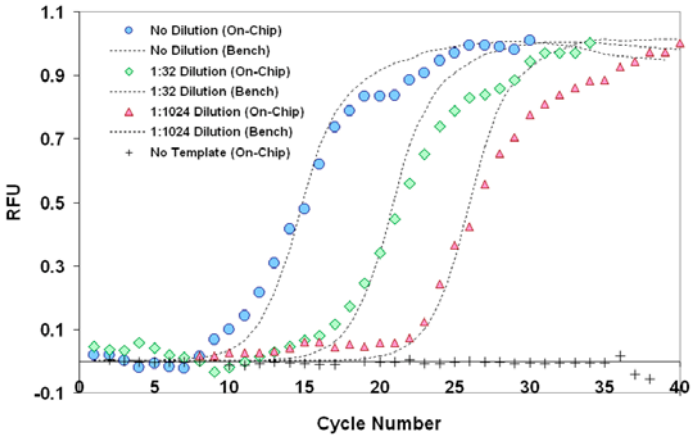

Figure 3: Comparison of real-time PCR results for the chip-based system and a commercial benchtop thermocycler (BioRad iQ5) for varying concentrations of starting DNA.

The time required for the sample droplet to transit between any two electrode positions in Figure 2 is less than 1 second which allows much faster thermal programs to be performed on-chip than can be performed on the commercial system. An optimization was performed using the chip system in which both the denaturation and annealing/extension times were systematically reduced in order to determine the minimum analysis time. A different primer set producing an 80-bp amplicon of the same gene was used in these

experiments, but the primer length remained constant so that specificity was not lost in the transition.

The results shown in Figure 4 indicate that the fastest successful condition for amplification of the 80-bp target from a genomic template was 1.5s @ 94°C and 4s @ 60°C. Combined with 2s total transport time, this results in 7.5s per cycle with 40 cycles of PCR performed in 5 minutes.

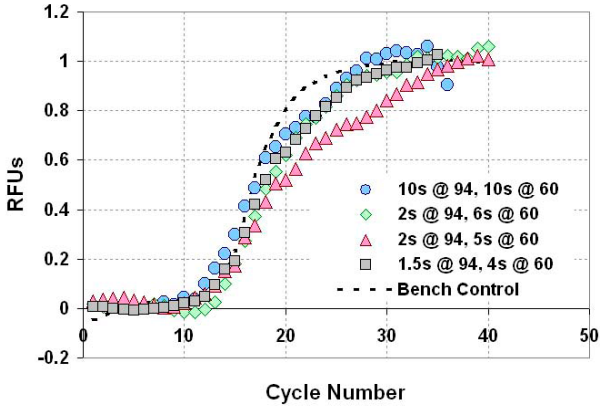

Figure 4: Real-time curves for optimization of time held at both the denaturing and annealing/extension temperature. The target amplicon was 80-bp in length, allowing for a shorter extension period compared to the 273-bp amplicon.

5. CONCLUSIONS

A digital microfluidic system for rapid, programmable flow-through PCR has been demonstrated. The use of a continuous thermal gradient mapped to specific electrode positions allows rapid and programmable thermal programs to be implemented. The speed and flexibility provided by this approach combined with its advantages of low-cost and portability make it an ideal platform for the development of medical diagnostic products.

ACKNOWLEDGEMENTS

This work was supported in part by the National Institutes of Health.

REFERENCES

[1] "Flow-through polymerase chain reactions in chip thermocyclers," I. Schneegas and J.M. Kohler, *Reviews in Molecular Biotechnology*, 82, 101 (2001).

[2] "Electrowetting-based actuation of droplets for integrated microfluidics," M.G. Pollack, A.D. Shenderov and R.B. Fair, *Lab on a Chip*, 2, 96 (2002).

[3] "Investigation of electrowetting-based microfluidics for real-time PCR applications," M.G. Pollack, P.Y. Paik, A.D. Shenderov, V.K. Pamula, F.S. Dietrich and R.B. Fair, *MicroTAS 2003*.

[4] "Design and validation of a complex generic fluidic microprocessor based on EWOD droplet for biological applications," Y. Fouillet, D. Jary, A.G. Brachet, C. Chabrol, J. Boutet, P. Clementz, D. Lauro, R. Charles and C. Peponnet, *MicroTAS 2005*.

[5] "Integrated polymerase chain reaction chips utilizing digital microfluidics," Y.H. Chang, G.B. Lee, F.C. Huang, Y.Y. Chen, and J.L. Lin, *Biomedical Microdevices*, 8, 215 (2006).

THERMAL CONTROL OF DROPLET SIZE IN MICROCHANNELS

Nam-Trung Nguyen[1], Teck-Hui Ting[1], Yitt-Fat Yap[1], Teck-Neng Wong[1], John Chee-Kiong Chai[1]

Wee-Liat Ong[2], Junlong Zhou[1,2], Say-Hwa Tan[1,2], Levent Yobas[2]

[1] *School of Mechanical and Aerospace Engineering, Nanyang Technological University, SINGAPORE*

[2] *Institute of Microelectronics, SINGAPORE*

ABSTRACT

This paper reports an effective method for controlling droplet size in microchannels. The droplet formation process can be controlled precisely using integrated heater and temperature sensor. With a relatively low temperature range from 25°C to 45°C, droplet diameter can be adjusted up to 2.24 times of its original size. That means a droplet volume up to five times of the original value can be adjusted. The low temperature range makes sure that this concept is applicable for droplets containing biological samples.

Keywords: microdroplet, active droplet control, droplet-based microfluidics, LOC

1. INTRODUCTION

Droplet formation is important for many processes in food and pharmaceutical industries. With the emerging field of digital microfluidics or droplet-based microfluidics, controlling the droplet formation process is an important task in designing a droplet-based microfluidic platform. A T-junction or a cross junction can work as microdispensers, where precise aqueous liquid volumes can be dispensed in another immiscible liquid for further processing. This passive formation process depends much on liquid properties such as density, viscosity, interfacial tension, and the flow rates of the aqueous flow and the immiscible carrier flow. Recently, Suryo and Basaran reported numerical results of droplet formation based on thermally induced surface tension gradients [1]. Link et al. reported a method of electric control of droplets in a continuous-flow platform [2]. Recently, our group has shown the use of temperature to control the splitting and switching behavior of microdroplets at a T-junction bifurcation [3].

2. THEORY

In this paper, we report a method for active control of the droplet formation process using integrated temperature sensor and heater. Fixing all geometrical parameters as well as the flow rates, the control over droplet size is accomplished with precise control of the temperature at the location where the formation occurs. We used a cross-junction configuration for the droplet formation exeriments. This design was previously used for passive droplet formation. By approximately balancing the Laplace pressure with the shear force, the diameter of the formed droplet can be predicted as:

$$D = \sigma / \eta\dot{\gamma} \qquad (1)$$

978-0-9798064-0-7/μTAS2007/$20©2007CBMS

where D is the droplet diameter, σ is the interfacial tension between the two immiscible faces, η is the dynamic viscosity of the continuous phase, and $\dot{\gamma}$ is the shear rate. The shear rate is estimated as $\dot{\gamma} = u / W$, where u is the average velocity at the gap between the channel wall and the droplet and W is the width of this orifice. It's safe to assume that the shear rate is constant, if the flow rates and all geometrical parameters are kept constant. Thus, the droplet diameter is proportional to the ratio between the interfacial tension and the dynamic viscosity $D \sim \sigma / \dot{\gamma}$. To investigate the temperature dependence of the three variables in this relation, the droplet diameter, the viscosity and the surface tension are normalized by their corresponding values at a reference temperature such as the room temperature of T_0 = 25ºC: $D^* = D / D_0$, $\sigma^*(T) = \sigma(T) / \sigma_0$, $\eta^*(T) = \eta(T) / \eta_0$. Thus, the dimensionless temperature dependence of the droplet diameter can be described as:

$$D^*(\Delta T) = \sigma^*(\Delta T) / \eta^*(\Delta T) \qquad (2)$$

where $\Delta T = T - T_0$ is the temperature difference.

3. EXPERIMENTAL

We used a cross-junction device for the droplet formation experiments, Fig. 1. This design was previously used for passive droplet formation [4]. The device was made of PDMS and glass. The microheater and temperature sensor were made of platinum sputtered on glass. The glass wafer was coated with a thin PDMS layer before being bonded to the PDMS part. By this way, all four walls of the microchannel have the same surface properties. The orifice size at the junction is 60 μm. Temperature sensor was calibrated so that the resistance values can be used for in-situ temperature measurement. In the experiments, DI water with 0.05 % w/w fluorescence dye (Sigma F6377) was used as the aqueous phase, while mineral oil (Sigma M5904) with 2% w/w span 80 (Sigma S6760). Figure 2 shows the temperature dependence of the viscosity and the interfacial tension. Droplet formation processes with flow rate ratios of 100:40:100 μL/hr and 100:50:100 μL/hr were characterized at different junction temperatures. The optical system consists of an inverted microscope (Model ECLISPE TE2000-S) with a set of epi-flourescent attachments. An sensitive interline transfer CCD camera (HiSense MKII) was used for recording the droplet images. Figures 3 shows the typical recorded images of the droplet at 25 °C and 45 °C. Figure 4 shows the normalized droplet diameters as functions of temperature. The droplet diameter are normalized by their nominal values at 25°C. The results show clearly the possibility of using integrated microheater and temperature sensor for controlling droplet size. In the full paper, we will present detailed physical insights of this effect with analytical and numerical results.

4. CONCLUSIONS

In conclusions, we reported the fabrication and test of a microfluidic device for thermally mediated control of the droplet formation in a microchannel. The results show the possibility of using integrated microheater and temperature sensor for controlling droplet size during its formation. Generally, the droplet diameter is proportional to the ratio between the interfacial tension and the dynamic viscosity.

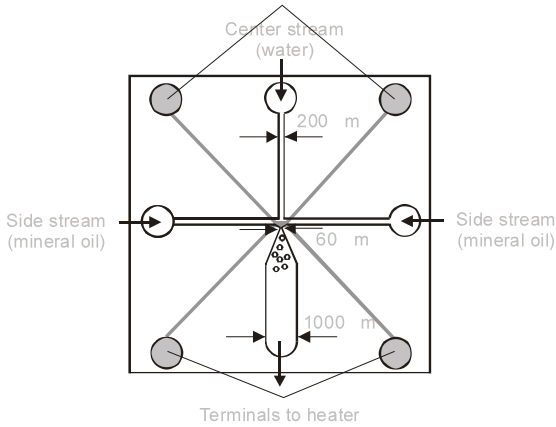

Figure 1. Schematic of the microfluidic chip for investigation of thermal control of droplet size in microchannels.

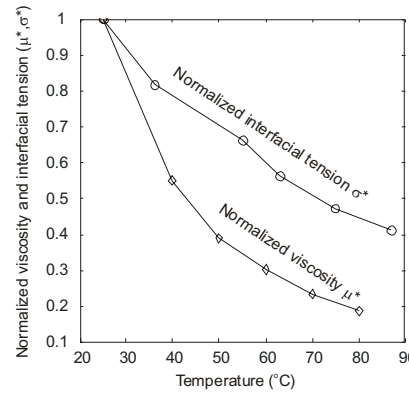

Figure 2. Normalized viscosity and interfacial tension of the carrier fluid as function of temperature.

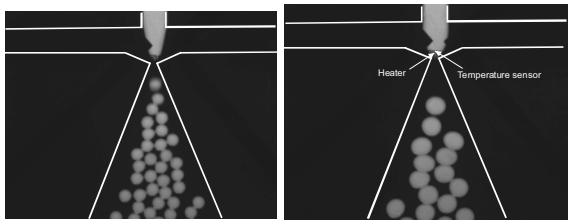

Figure 3. (a) Droplet formation at 25°C, (b) Droplet formation at 45°C.

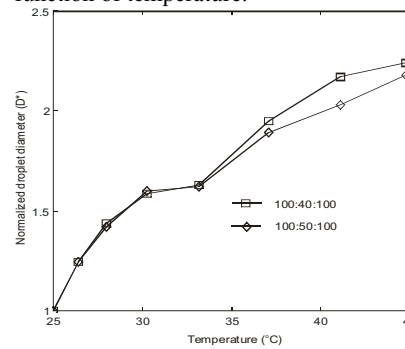

Figure 4. Normalized droplet diameters as functions of temperature.

ACKNOWLEDGEMENTS

The authors would like to thank the Agency of Science, Technology and Research, Singapore (A*Star, SERC grant No. 0521010108, \Droplet-based micro/nanofluidics") for its financial support.

REFERENCES

[1] R. Suryo and O. A. Basaran, *Dripping of a Liquid from a Tube in the Absence of Gravity*, Phys. Rev. Lett. 96, 034504 (2006).

[2] Link et al., *Electric Control of Droplets in Microfluidic Devices*, Angew. Chem., Int. Ed. 45, 2556 (2006).

[3] T. H. Ting, Y. F. Yap, N. T. Nguyen, T. N. Wong, J. C. K. Chai, L. Yobas, *Thermally mediated breakup of drops in microchannels*, App. Phys. Let., 89, 234101 (1996)

[4] L. Yobas, S. Martens, W.-L. Ong, N. Ranganathan, *High-performance flow-focusing geometry for spontaneous generation of monodispersed droplets*, Lab Chip, 6, 1073 (2006)

DYNAMICS MEASUREMENT OF STRUCTURAL CHANGE OF HELICAL POLYMER USING THERMAL LENS MICROSCOPY AND MICROFLUIDIC TECHNIQUE

Keiko Osato[1], Manabu Tokeshi[1,2,3], Noritada Kaji[1,2], Ryu Anraku[4], Takahiro Asai[4], Akihiko Hattori[4], Kazuma Mawatri[3], Takehiko Kitamori[3,5], Eiji Yashima[6] and Yoshinobu Baba[1,2,7,8]

[1]Department of Applied Chemistry, Nagoya University, JAPAN
[2]MEXT Innovative Research Center for Preventive Medical Engineering, Nagoya University, JAPAN
[3]Micro Chemistry Group, Kanagawa Academy of Sience & Technology, JAPAN
[4]Nippon Sheet Glass Co., Ltd., Japan
[5]Department of Applied Chemistry, The University of Tokyo, JAPAN
[6]Department of Molecular Design & Engineering, Nagoya University, JAPAN
[7]Health Technology Research Center, AIST, JAPAN
[8]Institute for Molecular Scinece, JAPAN

ABSTRACT

In this paper, we report a new on-chip system for dynamics measurement of structural change of polymer. This experimental system consists of a thermal lens microscope (TLM) and a microchip. Using this system, we demonstrated that it can measure dynamically molecular structural change in a microchannel by time-resoled measurement

Keywords: Structural change, thermal lens microscope, time-resolved measurement

1. INTRODUCTION

Microchip devices have recently attracted a large amount of interest in various fields such as analytical, biological and medical science. Advantages features of the microfluidic devices are mostly seen as reduced amounts of reagent and sample consumption and waste, high-speed and effective reaction and analysis. Microfluidic devices have an essential feature for flow other than these features. By using the flow in microchannels, it makes possible time-resolved measurement. However, only few reports have been done on time-resolved measurement using microfluidic devices [1,2]. In this paper, we report a new on-chip system, which consists of a thermal lens microscope (TLM) and a microchip, for dynamics measurement of structural change of polymer.

2. EXPERIMENTAL AND PRINCIPLE

In this experiment, polyacetylene derivative (PAD) which possesses the β-cyclodextrin (β-CyD) residue in the side chain was used as a helical polymer [3] (Figure 1). This polymer showed a unique helicity inversion accompanied by color change responding to the external stimulus such as solvent change. Figure 2 shows the dependence of circular dichroism (CD) and absorption spectra on the concentration of dimethyl sulfoxide (DMSO) in the macro-scale experiment. Pyrex microchip used here was parchased from the Institute of Microchemical Technology (Kanagawa, Japan). The Y-shaped microchannel, which

978-0-9798064-0-7/μTAS2007/$20©2007CBMS

was fabricated by using standard photolithographic wet-etching techniques. had a width of 100 µm and a depth of 40µm. This result showed that the helicity and absorbance of PAD changed in the presence of an increasing amount of water. The TLM which can detect small absorbance was used for the measurement. The polymer solution and water were introduced through the two inlets of the microchannel by a syringe pump at constant flow rate. To measure dynamics of structural change of helical polymer, the measurements were carried out by scanning the TLM detection point (p_0~p_x) along the microchannel (Figure 3). From the relation between flow velocity and the detection points, we realized time-resolved absorption measurements. In order to compare between experimental result and numerical simulation, Fluent software was used for its computational fluid dynamic (CFD) analysis.

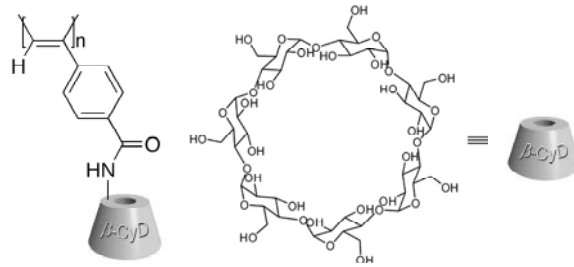

Figure 1. Structure of helical polymer

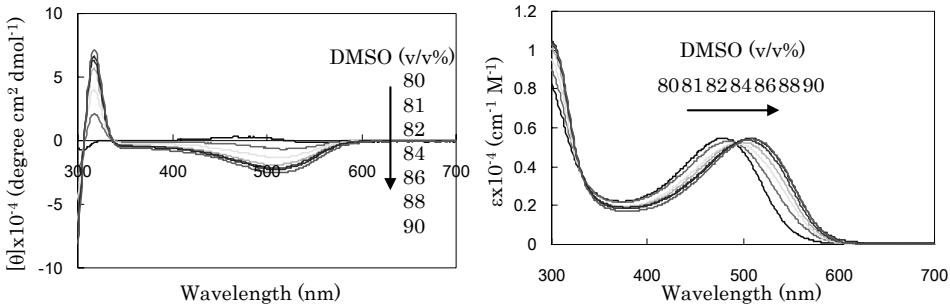

Figure 2. (a) Circular dichroism spectra and (b) Absorption spectra of PDA

3. RESULTS AND DISCUSSION

Figure 4 shows the dependence of the TLM signal on the detection point (= time) obtained by the experimental and simulation results. The TLM signal intensity was decreased with the microchannel length. Both results agree well within experimental error. By analyzing these results, we found that the structural change of PAD occurred within 0.21 s. The system developed here is also very useful for dynamics measurement of structural change of helical polymer such as DNA.

4. CONCLUSIONS

We have carried out time-resolved measurement of structural change of PAD using the thermal lens microscopy and microchip techniques. Time-resolved measurement using the microchip flow technique provides a convinent tool for obtaining chemical information about microsecond to millisecond transient states.

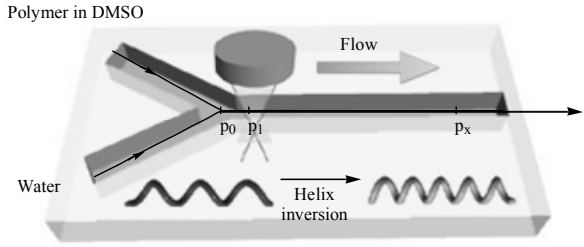

Figure 3. Schematic illustration of the experimental set up.

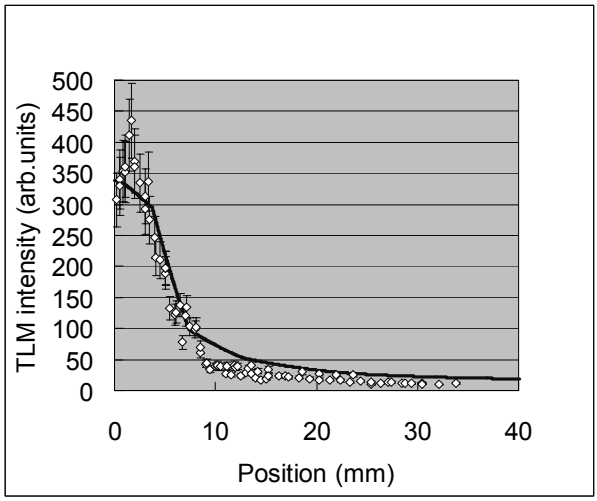

Figure 4. Dependence of the TLM signal on the detection point (= time) obtained by the experimental and simulation results. The diffusion coefficient of DMSO was obtained from Ref. 4.

REFERENCES

[1] D. Pan and R. A. Mathies, *Chromophore structure in lumirhodopsin and metarhodopsin I by time-resolved resonance Raman microchip spectroscopy*, Biochemistry, 40, 7929 (2001).

[2] D. Pan and R. A. Mathies, *Time-resolved resonance Raman analysis of chromophore structural changes in the formation and decay of rhodopsin's BSI intermediate*, J.Am.Chem.Soc., 124, 4857 (2002).

[3] E. Yashima, K. Maeda, and O. Sato, *Switching of a macromolecular helicity for visual distribution of molecular recognition events*, J. Am. Chem. Soc., 123, 8159 (2001).

[4] S. Chowdhuri, A. Chandra, *Tracer diffusion of ionic and hydrophobic solutes in water-dimethyl sulfoxide mixtures: Effects of varying composition*, J.Chem.Phys., 119, 4360 (2003).

GUIDED SELF-ASSEMBLY OF MICROLATCHES USING RAILED MICROFLUIDICS AND OPTOFLUIDIC MASKLESS LITHOGRAPHY

Boyoung Kim[1], Su Eun Chung[1], Hyunsung Park[2], Wook Park[1], Kyoungsik Yu[3], and Sunghoon Kwon[1]

[1]*School of Electrical Engineering and Inter-university Semiconductor Research Center (ISRC), Seoul National University, SOUTH KOREA*

[2]*School of Electrical Engineering, Seoul National University, SOUTH KOREA, and*

[3]*Korea Electrical Engineering and Science Research Institute, SOUTH KOREA*

ABSTRACT

We demonstrate guided self-assembly of various polymeric microstructures with railed microfluidic channels and optofluidic maskless lithography. Using microlatch structures designed to effectively couple complementary polymeric components, we present rail-guided transportation, capturing, and caging of free-floating microparticles inside the microfluidic devices.

Keywords: Microfluidics, Photopolymerization, Maskless lithography, Self-assembly

1. INTRODUCTION

Fluidic self-assembly has been demonstrated for various applications such as RFID assembly [1] and spherical bead packing for biosensors [2]. This type of fluidic assembly mainly relies upon the fluidic force to drive the assembly process, which lacks the accurate controllability on the transportation and carriage of microstructures in the microfluidic environments. For more sophisticated assembly procedures, controlling the position and trace of each component involved in the assembly process is of great importance. Recently, we have developed a railed microfluidics as a mechanically guided transportation method for in-situ photopolymerized microstructures in the microfluidic devices [3]. In this paper, we experimentally demonstrate guided assembly of multiple polymeric microstructures using the rail-based microfluidic system and mechanical latching mechanism.

2. DESIGN AND FABRICATION

The schematic of the experimental setup is shown in Figure 1 (a). A two-layer microfluidic channel with a groove structure, which functions as a guide rail track inside the microfluidic channel, is prepared using standard photolithography and polydimethylsiloxane (PDMS) molding as described in [4]. The channel height and groove depth are 30 μm and 20 μm, respectively. When the ultraviolet (UV) light is exposed on the railed microfluidic channel using maskless lithography [3], the photocurable resin material (polyethylene glycol (258) diacrylate and 5 wt % photoinitiator) inside the microfluidic channel is solidified, and the cross-sectional shape of the synthesized polymeric microstructure approximately follows that of the microfluidic channel, forming a two-layer ridge (fin) structure. Figure 1 (a) describes a simple situation when a circular UV pattern is exposed on the railed microfluidic channel. The ridge region mechanically binds the whole polymerized microstructure on the rail, and guides its movement along the

978-0-9798064-0-7/μTAS2007/$20©2007CBMS

rail like a train on a monorail. Figure 1 (b) shows a design example of a microlatch, which is composed of spring flexures, and male and female latching beams. The spring flexures for female latch beams are designed to be flexible and to deflect easily when a male latching hook of the other microlatch structure pushes its female counterpart. Once microlatch structures are linked, however, it is difficult to separate them because of the hook-shaped latching mechanism as shown in Figure 1 (c).

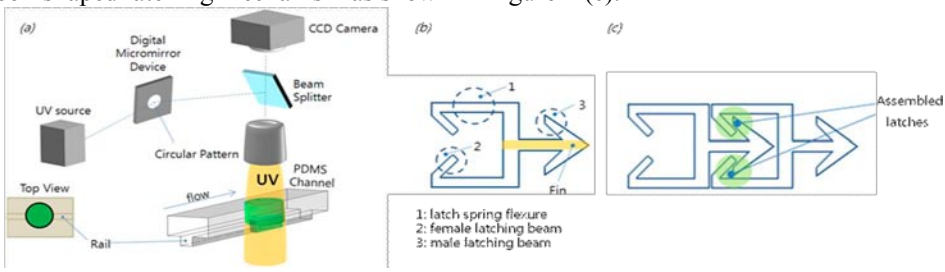

Figure 1. (a) Schematic diagram of the experimental setup for real-time synthesis of photopolymerized microstructures and their rail-guided assembly in the microfluidic channel. The photocurable resin material flows in a PDMS microfluidic channel with a groove structure ('rail'), and gets crosslinked by the patterned UV exposure. The fin (ridge) structure is formed on the photopolymerized microstructure following the cross-sectional shape of the railed channel. (b) An example of the exposure pattern for a microlatch. (c) Two assembled microlatches.

3. EXPERIMENTS AND RESULTS

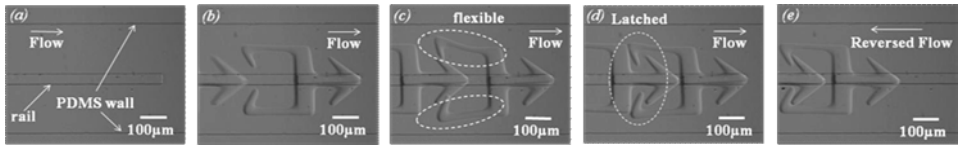

Figure 2. Time-sequential microscope images of a guided assembly process using the rail microfluidics. (a) A two-layer microfluidic channel with a guiding rail structure. (b) Photopolymerized microlatches are generated by patterned UV exposures, and flow downstream along the rail. One microlatch is stuck at the end of the rail. The ridge structures are visible along the rail. (c) The next microlatch arrives, and gets assembled to the first structure by the flow force. The fluid pressure is temporarily increased to facilitate the assembly process. The elastic bends of spring flexures are observed. (d) Two microlatch structures are fully engaged. (e) The microstructures remain engaged even when the flow direction is revered, and flow together as assembled.

Figure 2 shows the rail-guided assembly process near the end of the guiding rail. Multiple microlatch structures are generated using the UV exposure pattern of Figure 1 (b). While the first microlatch is immobilized at the end of the rail due to the ridge structure and the fluid force, the second microlatch arrives and gets connected to the first one. Even after the flow direction is reversed, the assembled microlatches remain engaged, and move backward together (Figure 2 (e)).

Figure 3 shows an application example of the rail-guided assembly technique to collect, cage, and carry microparticles in microfluidic devices. A micropocket structure at the end of the rail can capture and collect free-floating microparticles flowing downstream, and an additional lid structure with matching latches can be assembled later as demonstrated in

Figure 3. Again, the assembled microcage structure remains engaged regardless of the flow direction, and thus can carry the captured microparticles along the rail.

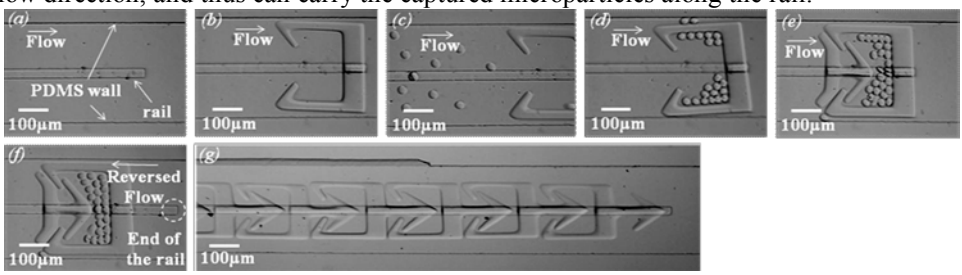

Figure 3. Micropocket assembly using a microlatch mechanism and rail-guided self-assembly technique. (a) A two-layer microfluidic channel with a guiding rail structure. (b) A micropocket structure is synthesized using photopolymerization and maskless lithography, and reaches the end of the rail. (c) Free-floating microparticles are also generated, and follow the flow field in the microfluidic channel. (d) Microparticles are collected in the micropocket. (e) An additional polymeric lid structure is synthesized, and subsequently assembled to the micropocket using the hook-shaped latching machanism. (f) The assembled microcage structure remains engaged even when the flow direction is revered, and can carry the captured microparticles. (g) A chain of microlatches.

5. CONCLUSIONS

We have developed a guided self-assembly technique using the railed microfluidic devices. We envision that this technique could be easily applied to various biological assay and/or microfluidic assembly. Especially, microcages with captured microparticles (such as immobilized cells [5]) can move between different liquid and microfluidic environments, enabling an agile way of exchanging cellular culture environments in an integrated μTAS platform.

ACKNOWLEDGEMENTS

This research is funded by the NANO Systems Institute-National Core Research Center (NSI-NCRC) program of Korea Science and Engineering Foundation (KOSEF), Korea

REFERENCES

[1] H. J. J. Yeh and J. S. Smith, "Fluidic self-assembly for the integration of GaAs light-emitting diodes on Si substrates," *IEEE Photon. Technol. Lett.* **6**(6), 706-708 (1994).

[2] J. C. Hulteen and R. P. Van Duyne, "Nanosphere lithography: A materials general fabrication process for periodic particle array surfaces," *J. Vac. Sci. Technol. A-Vac. Surf. Films* **13**(3), 1553-1558 (1995).

[3] S.E. Chung, W. Park, H. Park, K. Yu, N. Park, S. Kwon, "Optofluidic maskless lithography system," Paper 3EA1.P, *Transducers 2007*.

[4] S.E. Chung, W. Park, H. Park, K. Yu, N. Park, S. Kwon, "A railed microfluidic channel for manipulation of finned microtrains," accepted for presentation, *μTAS2007*.

[5] H. Maruyama, F. Arai, T. Fukuda, and T. Katsuragi, "Immobilization of individual cells by local photo-polymerization on a chip," *Analyst* **130**(3), 304-310 (2005).

MULTIPLE CORE-SHEATH LIQUID TRANSFER USING MATRIX ARRANGEMENT OF 3D SHEATH FLOWS

Hironobu Sato[1, 2], Yutaka Sasamoto[1], Tetsushi Sekiguchi[1], Takayuki Homma[1] and Shuichi Shoji[1]

[1]*Major in Nano-science and Nano-engineering, Waseda University*

[2]*Research Fellow of the Japan Society for the Promotion of Science*

ABSTRACT

Multiple core-sheath liquid transfer for continuous fiber synthesis was realized using matrix arrangement of 3D sheath flows. Each sample could be focused less than 30μm in diameter. The matrix array of the sample flow was achieved by the combination of horizontal and vertical configuration of the separated sheath flows. In this work, 4-sample sheath flows were achieved successfully. This method will be applicable to fabricate multi-component nano/microfibers and tubes.

Keywords: 3D sheath flow, Hydrodynamic position control, Multi-component fibers

1. INTRODUCTION

Continuous micro/nanoscale fibers are useful material for biomedical applications [1-2]. To realize functional fibers, the composite fiber is effective since physical/chemical properties of the composed materials are combined. The multiple core-sheath liquid transfer is indispensable in achieving multi-component nano/microfibers. Fig.1 shows a schematic diagram of the multiple core-sheath liquid transfer. To form matrix arrangement in the cross-section of the channel, horizontal and vertical configuration of the 3D sheath flow should be achieved. In this work, we utilize slanted microgrooves, which were used in chaotic micromixers [3-5], to control the sample flow position to achieve 3D sheath flow.

2. HYDRODYNAMIC POSITION CONTROL OF THE SAMPLE FLOW

Fig.2 shows a concept of the hydrodynamic position control of the sample flow. V-shaped microgrooves are formed on the top wall while slanted microgrooves are symmetrically formed on the side walls of the microchannel. The sample was introduced into the 3D symmetric grooved region (flow shift area) from top center of the microchannel. Since liquid in the channel flows along the microgrooves on the walls, two opposite rotating-flow were induced by the 3D symmetrical microgrooves. Considering the cross-sectional stream in the microchannel, downward stream is generated at the center of the microchannel. The

978-0-9798064-0-7/μTAS2007/$20©2007CBMS

sample flow position is shifted to center by using this downward stream. As a result, the sample flow was completely surrounded by the carrier flow and the 3D sheath flow was achieved.

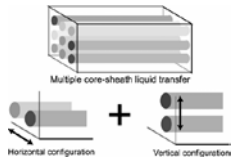

Fig.1 Schematic drawing of the multiple

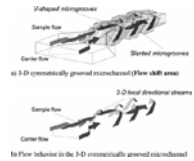

Fig.2 Concept of hydrodynamic position

3. FABRICATION

The flow shift area was fabricated by soft-lithography of the PDMS using a 3D SU-8 structure as a mold. Fig.3 shows the fabrication process of the 3D mold structure. SU-8 was spincoated on the Cr patterned glass substrate and UV was exposed to form microchannel (Fig.3(a)). In order to fabricate symmetric side wall slanted microgrooves, UV was irradiated from the backside of the inclined glass substrate (Fig.3(b)). After spincoating of SU-8 second layer (Fig.3(c)), UV was exposed to form V-shaped microgrooves on the top of the microchannel (Fig.3(d)). Finally, SU-8 was developed and 3D mold structure was obtained (Fig.3(e)).

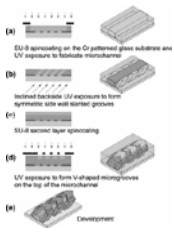

Fig.3 Fabrication process of the 3D mold

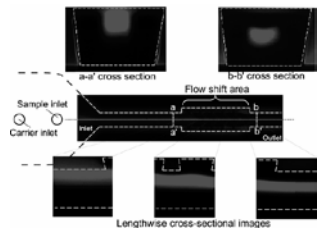

Fig.4 Sample flow behavior in the flow shift area

4. EXPERIMENTAL AND RESULTS

Sample was 3% PVA water solution containing Rhodamine B. Carrier was PVA water solution without fluorescent dye. The flow rate of the sample and currier were 1μL/min and 20μL/min, respectively. Fig.4 shows the sample flow behavior in the flow shift area. It was clearly observed that the sample flow was shifted to the center of the microchannel and 3D

sheath flow was realized. Since the inlet structure of the flow shift area is very simple, in-plane multi-sample sheath flow devices were easily fabricated.

o achieve horizontal configuration of the separated 3D sheath flow, the flow shift areas were connected in parallel. At the Y-junction, separated 2-sample 3D sheath flow of FITC and Rhodamine B was clearly observed (Fig.5). To achieve vertical configuration, cascade connection of the flow shift areas were performed. At the exit of the latter flow shift area, vertically aligned 2-sample sheath flow was obtained (Fig.6). In order to realize 4-sample matrix arrangement, the parallel and cascade connection were combined as shown in Fig.7. As a result, separated 4-sample liquid transfer was realized. The multiple core-sheath liquid transfer can be applied to fabricate multi-component nano/microfibers without complicated co-axis syringes.

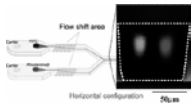

Fig.5 Parallel connection of the flow shift

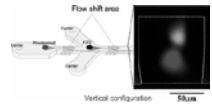

Fig.6 Cascade connection of the flow

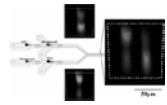

Fig.7 Four-sample matrix arrangement liquid transfer

ACKNOWLEDGEMENTS

This work was partly supported by the Japan Ministry of Education, Culture, Sports, Science and Technology Grant-in-Aid for SCOE (ASMeW) Research of Waseda University and Scientific Basic Research (A) No. A07113700, CREST: Japan Science and Technology Agency and Research Fellowships of the Japan Society for the Promotion of Science for Young Scientists.

REFERENCES

[1] Y.Dzenis, Science, 304, p1917 (2004)

[2] W.Jeong, et al., Lab Chip, 4, p576 (2004)

[3] A.D. Stroock, et al.,Science, 295, p647 (2002)

[4] H.Sato, et al., Sens. Actuators A, 128, p183 (2006)

A NANOFLUIDIC-BASED ENZYMATIC REACTION ON A CHIP

Takehiko Tsukahara[1,2], Eiichiro Tamaki[1], Akihide Hibara[1,3], and Takehiko Kitamori[1,2,3]

[1] *Department of Applied Chemistry, School of Engineering, The University of Tokyo, JAPAN*
[2] *CREST, Japan Science and Technology Agency, JAPAN, and*
[3] *Kanagawa Academy of Science and Technology, JAPAN*

ABSTRACT

We report enzymatic reaction inside extended-nano spaces (10^1 - 10^2 nm) on a chip by using pressure-driven nanofludic control system. We examined the kinetic parameters of enzyme in the extended-nano spaces. The results showed that a first-order rate constant (k_{cat}) for a nanospace was increased by a factor of about two compared with bulk and micro spaces. This is first observation of nanofluidic-based enzymatic reactions.

Keywords: nanofluidics, enzymatic reaction, pressure-driven, extended-nano space

1. INTRODUCTION

Micro-nano chemical systems on a chip are expected as promising tools for a variety of applications in chemical analyses. By utilizing microfluidics characteristics, the acceleration of synthetic and enzymatic reactions has been demonstrated in microchannels in comparison with batch reactions [1]. Recently, we have expected that the 10^1 - 10^2 nm-scaled extended-nano space is an attractive space size for realizing further integration of chemical systems, and developed liquid introduction and mixing methods in extended-nano spaces using pressure-driven flow [2]. On the other hand, on the way of this development, we have found unique properties such as higher viscosity, lower dielectric constant, and higher proton mobility of water confined in extended-nano spaces based on several spectroscopic results [3, 4]. Such unique properties would affect chemical reactions in extended-nano spaces. However, little information is available about size-confinement effects of important chemical reactions. Here, we construct novel pressure-driven flow control system for realizing nanofluidic-based enzymatic reaction, and clarify the kinetic parameters of enzyme in extended-nano spaces.

2. EXPERIMENTAL

Figure 1 shows schematic diagram of pressure-driven nanofluidic control system. A Y-shaped nanochannel was connected to microchannels, and solutions were introduced by controlling of pressure controller. We demonstrated mixing of two different solutions, which are fluorescein derivative 2-Me-4-OMe tokyogreen (abbreviated as TG) aqueous solution (5×10^{-5} M) and buffer solution, as shown in Figure 2. When the fluorescence intensity of TG in nanochannel A and B was compared each other, the TG in nanochannel B showed half intensity rather than that in nanochannel A. Furthermore, stable flow in nanochannel could be kept in the pressure range of 0.005 to 0.3 MPa. These results indicate that it is possible to offer the residence time of 0.1 to 10.0 sec based on the mixing with equal quantity of solutions in the nanochannels.

978-0-9798064-0-7/μTAS2007/$20©2007CBMS

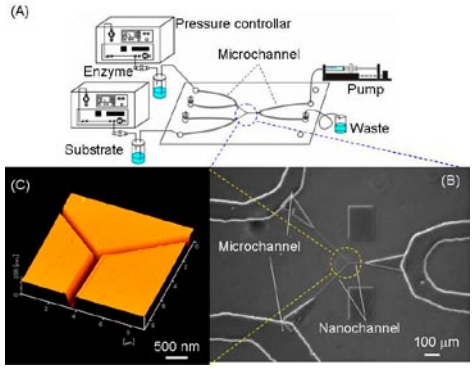

Figure 1: (A) Schematic diagram of pressure-driven nano fluidic control system (B) Photograph of the micro and nanochannels (C) AFM image of Y-shaped nanochannel

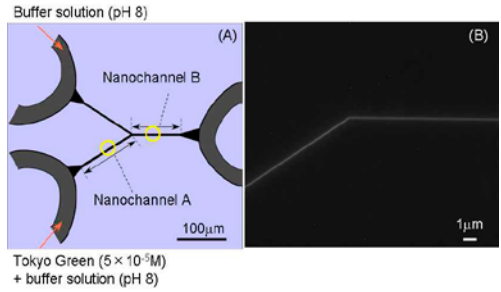

Figure 2. (A) Scheme for mixing with equal quantity by using nanofluidic control system (Nanochanel A= width;400nm, depth;250nm, Nanochannel B= width;600nm, depth;250nm) (B) Fluorescence micrograph of mixing solutions.

3. RESULTS AND DISCUSSION

As an enzymatic reaction system, the hydrolysis reaction by β-galactosidase was selected (See Figure 3). The reaction products had a strong fluorescence at 511 nm. Figure 4 shows the time courses of the fluorescence increase in a Y-shaped nanochannel. Since the slope is related with the initial rate of the enzyme reaction, V_0, the V_0 values for various concentrations of the substrate in the 5 – 130 μM were examined. The kinetic parameters of the enzyme in a nanochannel were evaluated according to the Michaelis-Menten equation (1);

$$\frac{1}{V_0} = \frac{K_m}{V_{\max}} \frac{1}{[S]} + \frac{1}{V_{\max}} \qquad (1)$$

which relates V_0, to the concentration of substrate, [S], a maximum rate, V_{max}, and Michaelis constant, K_m. Obtaining values for K_m, V_{max}, and a first-order rate constant ($k_{cat} = V_{max}$/total enzyme concentration) for cuvvete, microfluidics, and nanofluidics methods were summarized in Table 1. In particular, the values of K_m and k_{cat} of 279.05 μM and 0.0044 sec^{-1} for a nanofluidics increased more than 2 - 5 times from the results of cuvvete and microfluidics. These results indicate that dissociation rate of enzyme in nanospaces did not agreement with those in conventional methods. It seems to that such changes of kinetic parameters can be related with specific properties of liquids confined in extended-nano spaces.

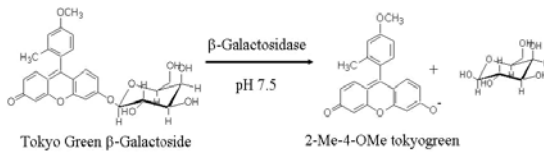

Figure 3. Hydrolysis reaction by β-Galactosidase

4. CONCLUSIONS

We constructed a novel pressure-driven nanofluidics control system, and presented the kinetic parameters of enzymatic reaction such as K_m, V_{max}, and k_{cat} of in a cuvvete, a microchannel, and a nanochannel. From these results, we found that the rate constant of reactions for a nanospace increases by a factor of about two rather than bulk and micro spaces. Accordingly, we can conclude that the rate of chemical reactions leads to large enhancements by size-confinement.

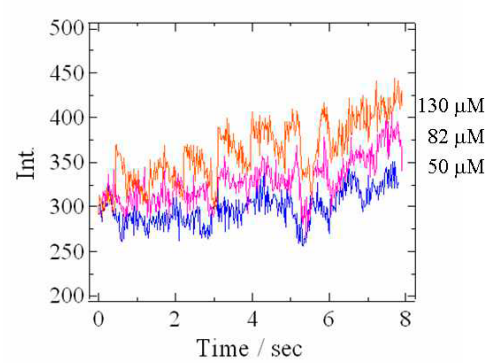

Figure 4. Fluorescence signal of TG produced by hydrolysis of TG-β-gal (50 – 130μM) with β-gal (0.005Unit) at pH = 8.

Table 1. Michaelis-Menten Kinetic Parameters obtained by Cuvette-Based, Microfluidic-Based, and Nanofluidic-Based Measurements (pH = 8).

	Cuvette	*Microfluidics*	*Nanofluidic*
K_m (μM)	44.35	42.96	279.05
V_{max} (nM s^{-1})	13.55	13.69	21.92
k_{cat} (s^{-1})	0.0029	0.0027	0.0044

REFERENCES

[1] Acceleration of an Enzymatic Reaction in a Microchip, Y. Tanaka, M.N. Slyadnev, K.Sato, M.Tokeshi, H-B. Kim, and T. Kitamori, Anal. Sci., **17**, 809 (2001).

[2] Pressure-driven flow control system for nanofluidic chemical process, Journal of Chromatogr. A, **1137**, 256 (2006).

[3] Nanochannels on a fused-silica microchip and liquid properties investigation by time-resolved fluorescent measurements, A. Hibara, T. Saito, H.B. Kim, M.Tokeshi, T. Ooi, M. Nakao, and T. Kitamori, Anal. Chem., **74**, 6170 (2002).

[4] NMR Study of Water Molecules Confined in Extended-Nano Spaces, T. Tsukahara, A. Hibara, Y. Ikeda, and T. Kitmaori, Angew. Chem. Int. Ed., **46**, 1180 (2007).

ASYMMETRIC IONIC CONDUCTANCE IN NANOCHANNELS

Li-Jing Cheng and L. Jay Guo

Department of Eelctrucal Engineering & Computer Science
University of Michigan, Ann Arbor, MI 48109 USA

ABSTRACT

We investigate the rectified ionic current through 4 nm and 20 nm thick homogeneous SiO_2 nanochannels placed between two ionic solutions of different concentrations. The asymmetric behavior is found to result from the dissimilar ion concentration profiles building up at different polarities of applied biases (Fig. 1). The accumulation and depletion of both cations and anions inside the nanochannels contributes to the asymmetric I-V characteristics. The theoretical calculation by using PNP theory qualitatively explains the phenomenon.

Keywords: Nanofluidics, nanochannel

1. INTRODUCTION

Transport of ions through nanofluidic channels has been widely studied due to their capability of handling attoliter-scale samples resulting in less need of reagents, precise quantity control and efficient processes. Quantity improvement aside, nanochannels with proper channel size and bath concentration offer selectivity to charged ions and molecules. The charge selectivity derives from the fact that when the feature size of nanochannel is comparable to or smaller than the Debye length, λ_D, the concentration of the counter-ions in nanochannels can be enhanced while that of co-ions diminished due to the electrostatic interaction between ions and charged channel walls [1]. In this regime, the electric-double layers (EDL) overlap and the ion conductance through the nanochannel is determined by the surface charge instead of the bulk ion concentration in reservoirs. Nanochannels serving as chemical delivery devices are usually placed between two bath ionic solutions with different concentrations. Flow of ions though the nanochannel in such circumstances was observed to pass more readily in one direction than the other. In this paper, we experimentally and theoretically study the asymmetric ionic flux in 4 nm and 20 nm thick nanofluidic channels between ionic solutions of unequal concentrations.

2. EXPERIMENTAL

The experiments were performed in 4 nm and 20 nm thick homogeneous, planar SiO_2 nanochannels fabricated on glass substrates by conventional microfabrication technology (Fig. 2). The 20 nm thick nanochannel structures were created by using XeF_2 gas to remove a 20 nm thick sputtered amorphous silicon sacrificial pattern embedded in a PECVD SiO_2 layer. The thickness of the nanochannel can be narrowed down even more by wet-etching a 20nm thick e-beam evaporated Cr sacrificial

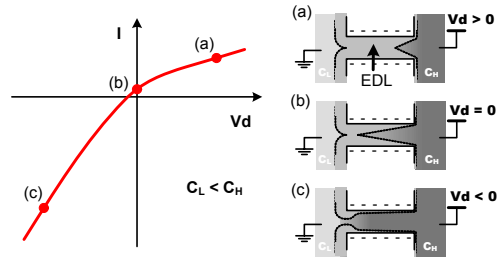

Figure 1. Rectifying effect in a nanochannel with concentration gradient.

978-0-9798064-0-7/μTAS2007/$20©2007CBMS

layer. After DI water rinsing, soaking and drying, the 20 nm-thick, 2.5 μm-wide and 60 μm-long nanochannels collapsed, driven by capillary force. Since the Cr layer has a relatively rough surface, the pinched nanochannels were not completely sealed leaving some gap between two oxide surfaces. The channel heights of the two devices were measured to be 4 nm and 18.7 nm by characterizing the ionic conductance of nanochannels at various KCl concentraions and fitting with a theoretical equation [2] (Fig. 3). For the measurement of asymmetric solutions, a grounded reservoir, C_L, was loaded with a fixed, low concentration of 10^{-4} M KCl solution, while the other side, C_H, connected to Vd was filled with various concentrations, ranging from 10^{-4} M to 1 M.

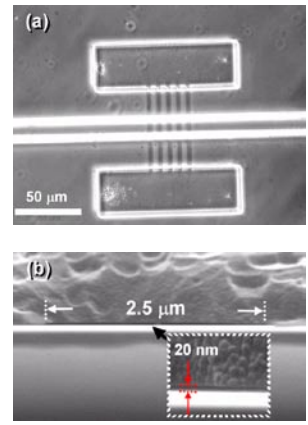

Figure 2. (a) Phase-contrast microscopic image of the device top-view. (b) Cross-section SEM image of a nanochannel.

3. RESULTS AND DISCUSSION

When the nanochannel was connected between two KCl solutions of different concentrations, three conductance regimes were observed: symmetric regime, rectifying regime and weakened rectifying regime. The I-V characteristics corresponding to different C_H with C_L = 10^{-4} M are plotted in Figure 4(a)(c). Their on-currents, off-currents and the rectifying factors or I_{on}/I_{off} are summarized in Figure 4(b)(d). In the symmetric regime, when C_H is lower than 10^{-2} M (for 4-nm channels) or 10^{-3} M (for 20-nm channels), both I_{on} and I_{off} are almost identical and the polarity of bias has no effect on it. Although the bath concentration is asymmetric, the current level is almost consistent with the results collected with symmetric concentration. In the second regime, the rectifying effect becomes most significant at a medium concentration (C_H = 0.1M). As shown in Figure 4(b), the I_{on}/I_{off} is about 3.5. The current level increased at either bias polarity when the C_H ion concentration went to 1M. The weaker asymmetric I-V characteristics is designated the third regime.

The asymmetric ion conduction behavior is qualitatively investigated by calculating their ion distribution profile using 2-dimensional Poisson-Nernst-Planck (PNP) and continuity equations. As shown in Figure 5, at low concentration, C_H = 1mM (λ_D~10nm), the EDL overlaps in the entire channel, the polarity of biases do not change the ion concentration profile too much yielding a symmetric I-V curve. At medium concentration (C_H = 10 to 100 mM), when C_H is positively biased, both cations and anions are depleted. As a result, EDL-overlap extends in nanochannel and hence lowers the ionic conductance. On the contrary, a negative bias at C_H allows the accumulation of both cations and anions yielding higher conductance and

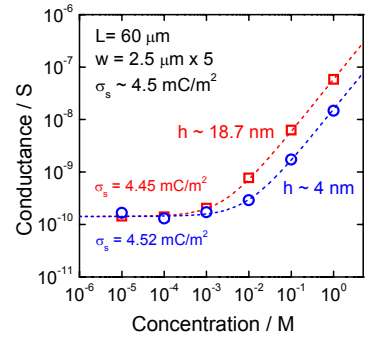

Figure 3. Measured ionic conductance of two nanochannels with various KCl concentrations. The channel heights are estimated to be 4 nm and 18.7 nm by theoretical calculation [2] (dash lines).

therefore greater ionic flux. The on-off current ratios acquired from these two nanochannels share a similar trend except that the 4-nm channels can maintain symmetric behavior at 10 mM while the 20-nm channels cannot. This is simply because its Debye length (λ_D ~ 3nm) is still larger than half of the channel size leading to a complete EDL overlap. When the concentration, C_H, is 1M, the amount of ions is large enough to shield the surface charges in nanochannel. Almost no EDL overlap occurs throughout the entire channel except the very left end. As can be seen in Figure 5(d), the concentrations of both types of ions are almost identical producing a large, constant ion gradient along the channel. Biases of different polarities have little influence on ion distribution; therefore, the asymmetric characteristic is not observable.

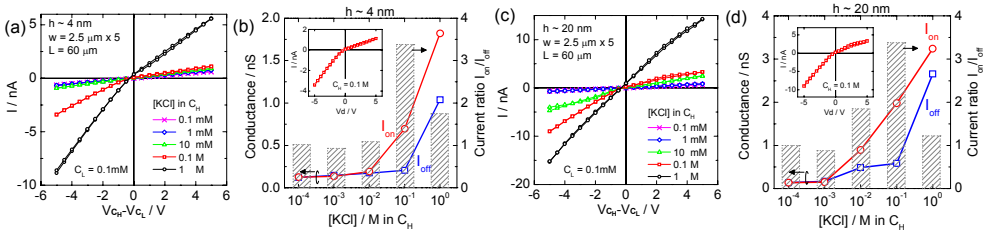

Figure 4. The measured I-V characteristics (a), (c) and summarized conductance (b), (d) of 4 nm and 20 nm thick nanochannels under asymmetric concentrations. C_L was fixed to 10^{-4} M while C_H varied from 10^{-4} to 1 M.

5. CONCLUSIONS

In conclusion, the asymmetric I-V characteristics result from the alteration of ion distributions in nanochannels when different polarities of biases are applied. On the basis of the calculated ion profiles, we attribute the phenomenon to the accumulation or depletion of both cations and anions in nanochannels. The study provides a better understanding of ion transport through nanochannels.

REFERENCES

[1] Stein, D.; Kruithof, M.; Dekker, C. Physical Review Letters**,** 93, p. 4, (2004).

[2] $G = 2\,\mu_K\,\sigma_s\,w/L + 10^3\,q\,(\mu_K+\mu_{Cl})\,c_B\,N_A\,w\,h/L$, with known ion mobilities μ_K and μ_C as well as geometries width, w ,and length, L. c_B and N_A are bath concentration and Avogadro number, respectively.

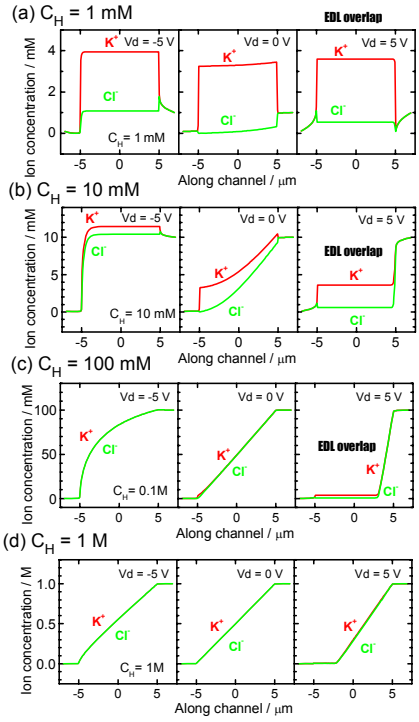

Figure 5. Calculated ion distribution along a 20 nm thick, 10 μm long nanochannel with various C_H and different biases.

DIRECT VISUALIZATION OF DNA IN NANOCHANNELS

Walter W. Reisner[1,2], Jason P. Beech[1], Niels B. Larsen[2], Henrik Flyvbjerg[2], Anders Kristensen[2], and Jonas O. Tegenfeldt[1]

[1]*Lund University, SWEDEN*

[2]*Technical University of Denmark, DENMARK*

ABSTRACT

We have investigated the degree of stretching of DNA in sub-micron channels as a function of ionic strength of the buffer. We found an up to three-fold enhancement of the stretching as the buffer ionic strength is decreased from 200mM to 2mM. This allows us to use larger channels for any desired degree of stretching, facilitating fabrication and usage significantly. To model our results we use a deGennes theory with an effective width of the DNA that takes into account the screening of the electrostatic interaction between distant segments along the DNA.

Keywords: nanofluidics, DNA, polymer physics

1. INTRODUCTION

DNA spontaneously assumes an extended configuration when confined on the scale of a persistence length (~50nm) in a cylindrical channel [1, 2]. This has made it possible to directly visualize single DNA molecules for *e.g.* length measurements [1], observation of DNA-protein interactions [3] and genomic mapping [4]. In contrast to conventional techniques for stretching of DNA on surfaces[5], stretched DNA molecules in nanochannels are not attached to the surface and are allowed to fluctuate thermally, which in turn opens up for higher precision in length measurements by averaging images of single molecules as they map out configuration space over time[1]. Since the stretching is mediated by the confinement alone, it does not rely on applying external forces, thereby resulting in highly uniform stretching. Finally, the device can be operated in a continuous manner integrated in a Lab on a Chip platform for *e.g.* analysis of genetic material from selected single cells. For this technique to be truly useful, it is important to understand how the stretching is influenced by buffer conditions, something that may vary considerably between different types of experiments.

2. THEORY

In moderate confinement, for channels with diameters less than the radius of gyration, yet larger than the persistence length, excluded volume effects lead to the stretching of the DNA[6, 7] resulting in an end-to-end distance, r, given by *eq.* (1) based on a model developed by deGennes together with an expression for the excluded volume by Onsager[8]. Here L is the contour length, p (~50nm for dsDNA) is the persistence length, w is the width of the DNA and D is the diameter of the channel.

$$r \sim L\left[\frac{pw}{D^2}\right]^{1/3} \tag{1}$$

The persistence length, due to short-range electrostatic interactions, varies slightly with ionic strength roughly doubling at 1mM from 50nm at high ionic strengths [9]. On the other

978-0-9798064-0-7/μTAS2007/$20©2007CBMS

hand it is known from *e.g.* knot forming probabilities [10] that the effective width, due to electrostatic repulsion between distant segments, of the DNA is a strong function of ionic strength of the buffer increasing an order of magnitude from 2nm at 1M to 20nm at 10mM.

3. EXPERIMENTAL

The devices (*Figure 1*) are made in fused silica using reactive ion etching, with nanochannels (widths 50nm - 200nm) defined by electron beam lithography, integrated with microchannels defined by UV-lithography. To enable the use of short-working-distance objectives, the channels are sealed with thin slides (~ 150μm) of fused silica by fusion bonding. The devices are mounted in a chuck for both pressure driven flow and electrokinetic flow. The chuck is mounted in an inverted epifluorescence microscope with a mercury lamp light source, a 100x NA1.40 oil immersion objective (Nikon) and an iXon EMCCD camera (Andor). dsDNA λ-phage is stained by YOYO1 at a concentration of 1 dye per 5 base pairs. Working buffers are 5xTBE (0.45M tris-base, 0.45M boric acid, 1mM EDTA) and NaCl in 0.05xTBE. TBE is not a fully dissociated system. To calculate the ionic strengths of the TBE dilutions we have used known pK values to solve the chemical equilibria for each component. To suppress photobleaching we use 3% β-mercaptoethanol and an oxygen scavenging system based on glucose oxidase, catalase and β-D-glucose.

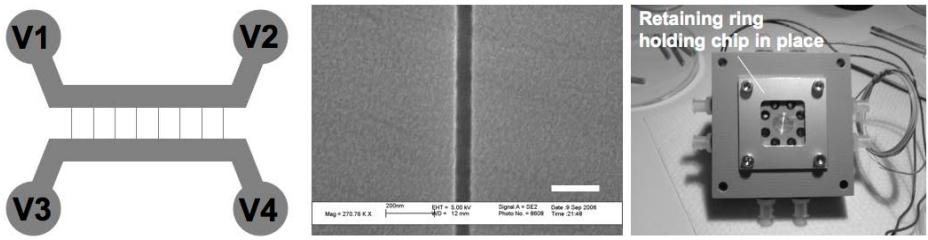

Figure 1. *Device setup. (LEFT) The device with two microchannels are joined by the nanochannels for fast and efficient sample transport. The DNA is introduced in two steps: first into the microchannels (-V1&+V2) and then into the nanochannels (-V1&+V3). (CENTER) 60nm wide nanochannel. Scale bar 200nm. (RIGHT) Device chuck.*

4. RESULTS AND DISCUSSION

We found that by varying the buffer concentration from 5xTBE to 0.05xTBE, the concomitant increase in effective width results in a three-fold improvement in stretching for channels with D=200nm (*Figure 2*). The increase is almost as dramatic in the 100nm channels but almost absent in the 50nm channels which is not surprising since the excluded volume plays a decreasing role as the channel size decreases below the persistence length[2]. The NaCl data is consistent with the TBE data for the 200nm which supports our estimates of the ionic strengths. Our data fits well to *eq.* (1) for the 100nm and the 200nm channels using known persistence lengths and effective widths as a function of ionic strength. However, the model breaks down for the lowest ionic strength in the 50nm channels which is expected since the persistence length exceeds the channel size in that case.

Three main conclusions can be drawn from our work. (1) Diluting the buffer may dramatically enhance the stretching, which in turn is expected to improve imaging conditions of the DNA through less fluctuations[1, 2]. (2) With a successfully verified model for the dependence of the stretching on ionic strength we can better understand and

adapt to experiments taking place under varying buffer conditions as required by the relevant biochemistry. (3) By decreasing the salt concentration from 0.5x TBE to 0.05x TBE we can use 100nm channels instead of 50nm channels or we can use 200nm channels instead of 100nm channels and maintain the degree of stretching that was achieved for 0.5x TBE, facilitating both fabrication and the actual experimental work since it allows us to transport the DNA through pressure driven flow, thereby avoiding any EO-suppressing additives that might otherwise unduly influence the measurements.

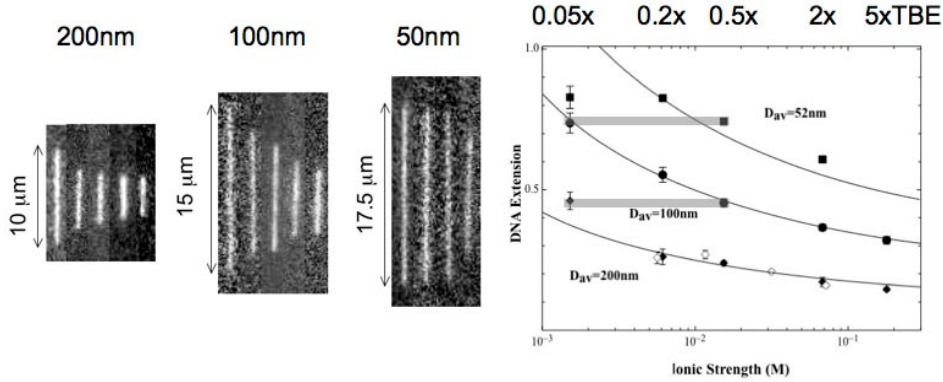

Figure 2. *(LEFT) λ phage DNA in decreasing (from left) buffer concentrations starting at 0.05xTBE (200nm and 100nm) and 0.2xTBE (50nm). (RIGHT) DNA extension as a function of ionic strength for TBE (filled dots) and NaCl (open dots). The solid lines represent single-parameter fits to the data with known persistence lengths and effective widths.*

ACKNOWLEDGEMENTS

Work funded by the *Danish Research Council for Technology and Production Science* (grant No. 274-05-0375) and by the *Swedish Research Council* (grant No 2002-5972).

REFERENCES

1. Tegenfeldt, J.O., et al., *The dynamics of genomic-length DNA molecules in 100-nm channels*. PNAS, 2004. **101**(30): p. 10979-10983.
2. Reisner, W., et al., *Statics and dynamics of single DNA molecules confined in nanochannels.* Physical Review Letters, 2005. **94**(19).
3. Wang, Y.M., et al., *Single-molecule studies of repressor-DNA interactions show long-range interactions.* PNAS, 2005. **102**(28): p. 9796-9801.
4. Riehn, R., et al., *Restriction mapping in nanofluidic devices* PNAS 2005 **102**(29) 10012
5. Cai, W., et al., *High-resolution restriction maps of bacterial artificial chromosomes constructed by optical mapping.* PNAS, 1998. **95**(7): p. 3390-3395.
6. Brochard-Wyart, F., *Dynamics of confined polymer chains.* The Journal of Chemical Physics, 1977. **67**(1): p. 52-56.
7. de Gennes, P.G., *Scaling Concepts in Polymer Physics*. 1979, Cornell University Press.
8. Onsager, L., The effects of shape on the interaction of colloidal particles. Annals of the New York Academy of Sciences, 1949. **51**(4): p. 627-659.
9. Baumann, C.G., et al., *Ionic effects on the elasticity of single DNA molecules.* PNAS, 1997. **94**(12): p. 6185-6190.
10. Rybenkov, V.V., et al., Probability of DNA knotting and the effective diameter of the DNA double helix. PNAS, 1993. **90**(11): p. 5307-5311.

ELECTRO-PRECONCENTRATION OF BIOMOLECULES IN NANOFLUIDICS: CONCENTRATION GRADIENT FOCUSING AT LOW AND HIGH IONIC STRENGTHS

A. Plecis, P. Svarnas and Y. Chen
LPN-CNRS, France

ABSTRACT

The electrical preconcentration of negatively charged molecules using a nanochannel-based system was quantitatively investigated. The dynamic behaviour of the preconcentration with time showed up to be more sophisticated than thought from previous observations [1]. This was attributed to the formation of an ionic concentration gradient at the nanochannel entrance responsible for the focusing of biomolecules. For the first time, preconcentrations of negatively charged molecules were achieved in nanochannels with high ionic strength buffers on the basis of this ionic concentration gradient focusing hypothesis. The present results contribute to the understanding of preconcentration mechanisms in nanofluidics and introduce new opportunities for separation applications involving highly salted biological buffers.

Keywords: Nanochannels, preconcentration, anodic bonding, ionic gradient focusing.

1. INTRODUCTION

The charge-selectivity of nanochannels offers great promises for biomolecules sorting in microTAS. Previous works demonstrated that charge selectivity is maximised in nanochannels when Electrical Double Layer Overlap (EDLO) takes place at low ionic strengths [2]. Han *et. al*. combined this permselectivity with an external electric field in order to preconcentrate negatively charged proteins [3]. Foote *et. al.* integrated a nanoporous membrane in their separation devices and preconcentrated a biological sample before the separation [4]. Beyond these applicative proofs, more quantitative studies are necessary in order to understand the preconcentration rates in these systems. In this work, the spatio-temporal evolution of the electro-preconcentration process around a nanopore was experimentally demonstrated and a new preconcentration regime at high ionic strengths was obtained.

2. PRINCIPLE

A diagram of the experimental system is shown in Figure 1.A. Two microchannels forming the two arms of an “H” configuration were used to flush the solutions in the preconcentration area at the entrance and the exit of a nanochannel. After filling the microchannels with a fluorescein solution, the flow was stopped and an electric field between the reservoirs and through the nanochannel was applied. Depending on the nanochannel charge selectivity, a preconcentration effect appeared at its entrance (Figure 1.B).

The fluorescence spatial profile in the preconcentration area was recorded and quantitatively analysed to better understand the transport phenomena of charged biomolecules across nanochannels.

978-0-9798064-0-7/μTAS2007/$20©2007CBMS

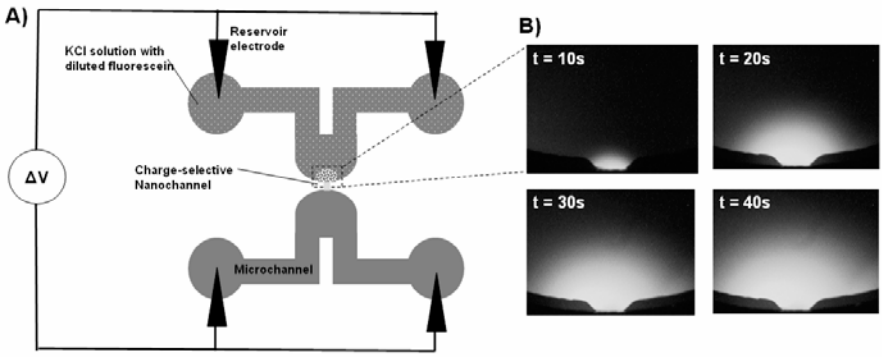

Figure 1. Experimental setup. A) The "H" configuration of the device enables quick renewing of solutions on both sides of the nanochannel for a systematic study of the preconcentration phenomenon with various ionic concentrations. B) An example of preconcentration at the nanochannel entrance as a function of the time.

3. EXPERIMENTAL

The experimental device was fabricated by conventional patterning and anodic bonding techniques (figure 2). Microchannels 3 µm in height were chemically etched in the bottom Pyrex substrate using an HF-HCl solution and a 300 nm thick PECVD Polysilicon layer as a mask. Channel patterns were dry etched in the polysilicon mask using a standard photolithographic step (AZ5214) prior to a SF6 Reactive Ion Etching. After the mask removal, a second layer of amorphous Silicon (70 nm in height) was deposited and used both as anodic bonding layer and spacer for nanochannel fabrication [5]. KCl solutions from 10 µM up to 1M were used as supporting buffers. Fluorescein at 100 pM was used as the dianionic preconcentrated molecule. A CCD camera was interfaced and triggered under Matlab™ environment for image acquisition and data processing.

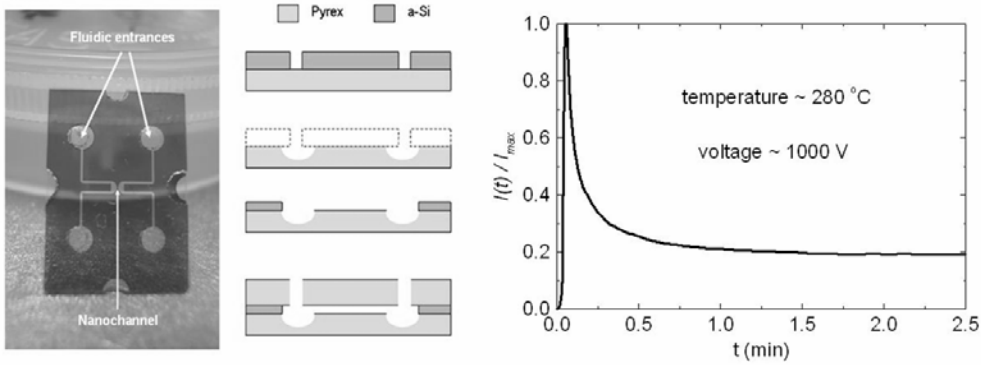

Figure 2. Microfluidic device used for preconcentration studies. On the left, an image of the device and the main fabrication steps are presented. Amorphous Silicon (a-Si) was used both as a masking layer (300 nm) for HF etching of the microchannels and spacer (70 nm in height) in the anodic bonding step. The 70 nm in height nanopore was created between the microchannels where there was no a-Si. On the right, typical evolution of the anodic bonding current up to the saturation phase.

4. RESULTS

Using a 10 µM KCl buffer, a strong preconcentration close to nanochannel entrance was observed (Figure 3.A). However, a spatial shift of the maximum preconcentration *vs.* the time was also found as shown in the same figure. The dynamic of this preconcentration front is quite complex and can be modified by changing the ionic strength of the buffer at nanochannel exit (results not shown here).

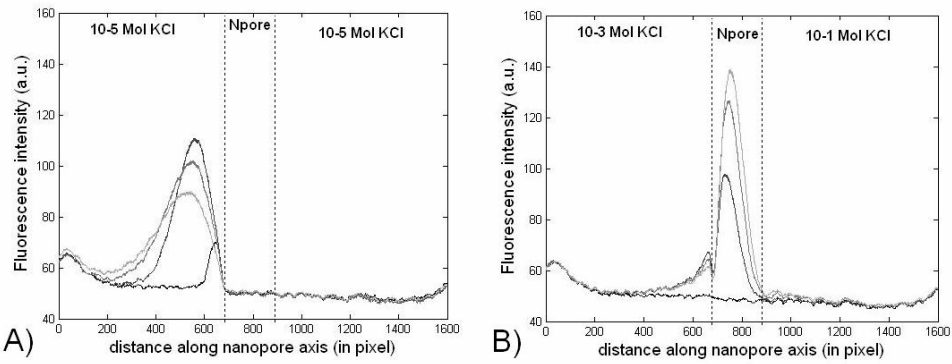

Figure 3. A) Fluorescence intensity profile as a function of the distance along the nanochannel axis for a 10 µM KCl buffer. The curves were plotted each 10 s (lighter for later times). The displacement of the intensity maximum with the time originates from a change in the ionic composition close to the nanopore entrance. B) Fluorescence intensity profile during a preconcentration at high ionic strength. The buffers are 1 mM KCl before the nanochannels and 100 mM KCl on the other side. The intensity recorded into the nanochannel (50 nm deep) indicates a very high preconcentration rate.

The influence of the ionic strength difference on both sides of the nanochannel was further investigated. We could identify different couples of highly salted buffers for which the fluorescein preconcentration was enhanced directly into the nanochannel (figure 4). The preconcentration rate was higher in this regime than at low ionic strengths, which seems to be an important breakthrough for applications in concentrated biological buffers.

REFERENCES

[1] A. Plecis, R.B. Schoch, P. Renaud, *On-chip separation and concentration processes based on the use of charge selective nanochannels*, Ninth International Conference on Miniaturized Systems for Chemistry and Life Siences, Micro Total Analysis Systems, Boston, Massachusetts, USA, October 9-13, 1038-1041 (2005).

[2] A. Plecis, R.B. Schoch, P. Renaud, *Ionic transport phenomena in nanofluidics: Experimental and theoretical study of the exclusion-enrichment effect on a chip*, Nano Letters 5 (6) 1147-1155 (2005).

[3] Y.C. Wang, A.L. Stevens, J.Y. Han, *Million-fold preconcentration of proteins and peptides by nanofluidic filter*, Analytical Chemistry 77 (14) 4293-4299 (2005).

[4] R.S. Foote, J. Khandurina, S.C. Jacobson, J.M. Ramsey, *Preconcentration of proteins on microfluidic devices using porous silica membranes*, Analytical Chemistry 77 (1) 57-63 (2005).

[5] A. Datta, S. Gangopadhyay, H. Temkin, Q.S. Pu, S.R. Liu, *Nanofluidic channels by anodic bonding of amorphous silicon to glass to study ion-accumulation and ion-depletion effect*, Talanta 68 (3) 659-665 (2006).

NANOFLUIDIC SIEVES FOR DNA SEPARATION USING COLLOIDAL CRYSTAL TECHNOLOGY

L.S.L. Cheung[1], K.P. Gerhardt[2], M.J. Wirth[3], and Y. Zohar[1]

[1]Department of Aerospace and Mechanical Engineering, [2]Department of Physiology, [3]Department of Chemistry, University of Arizona, Tucson, AZ 85721, USA

ABSTRACT

The fabrication of a novel nanosphere electrophoresis (NEP) microchip designed for DNA separation is described. A colloidal crystal technology, augmented by surface micromachining techniques, is utilized for patterning nanosphere-coated regions in microchannels to serve as an artificial sieving matrix. Fast and clear separation of DNA ladder is demonstrated a NEP device; furthermore, nanosphere-size dependent stacking effect and electrophoresis mobility are discussed.

Keywords: Nanofluidics, colloidal self-assembly, electrophoresis, DNA separation

1. INTRODUCTION

Microfluidic devices have shown tremendous advantage of miniaturization for performing analytical tasks. For example, separation of long DNA strands, difficult to achieve using the traditional agarose slab-gel method, has successfully been demonstrated in microchannels integrated with sub-micron mechanical structures [1]. However, separation of short DNA strands is difficult because the sub-micron spacing is not effective, and a sieving matrix with smaller pore size is required to obtain fast separation of short DNA fragments.

Colloidal crystal technology has been utilized to generate patterned nanospheres matrices with nano-scale pores in the range of 50-500nm [2]. Subsequently, electromigration of single DNA molecules through such structures has been carried out [3]; hooking events have been observed to be an important separation mechanism as DNA molecules temporarily move at a lower velocity. This suggests that colloidal crystal structures can serve as nanofluidics sieve for bioseparation. Indeed, successful DNA separation through a self-assembled colloidal matrix has recently been reported [4]. Here, we utilize this novel technology to fabricate NEP microchips for DNA electrophoresis. A few characteristics of DNA motion, accounting for electro-osmotic flow (EOF), such as pore-size dependent mobility and large DNA stacking phenomena are discussed.

2. NEP MICROCHIP FABRICATION

Highly uniform silica nanospheres about 270nm and 470nm in diameter were synthesized, as described elsewhere [5], while larger nano-spheres about 2000nm in diameter were purchased from Duke Scientific Co. The fabrication process is schematically illustrated in Figure 1. The nanospheres are first re-dispersed in an ethoxylated trimethylolpropane triacrylate (ETPTA) monomer, with 20% volume fraction, and 1% Darocur 1173 is added

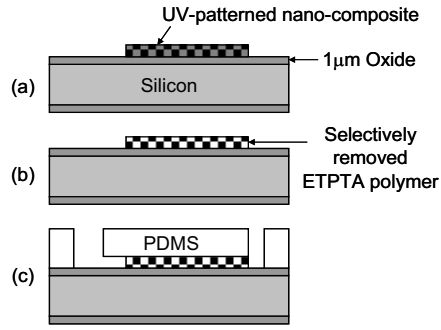

Fig 1. Schematic cross-sections for the fabrication of NEP microchips.

978-0-9798064-0-7/μTAS2007/$20©2007CBMS

as photoinitiator for UV-polymerization [2]. The solution is dispensed and spin-coated on a silicon substrate with a 1μm-thick oxide layer for electrical insulation. The ETPTA-nanospheres mixture is selectively pre-polymerized by exposure to 21mJ/cm^2 UV light (400nm wavelength) using a mask aligner. While the unexposed mixture is removed in acetone, further exposure to 5J/cm^2 UV light completes the polymerization resulting in a nanospheres-embedded nano-composite layer, Figure 1(a). The ETPTA polymer is selectively etched out in an oxygen plasma reactor with 4scfh flow rate and 750W for 5mins; thus, leaving only the nanosphere structure on the substrate, Figure 1(b), to serve as the separation sieve. Next, a PDMS film with matching grooves is aligned and bonded to the silicon substrate, Figure 1(c), forming a microchannel with the sieving matrix. The microchannel and nanofluidic sieve are about 15μm high and 320μm wide. A picture of a fabricated NEP device is shown in Figure 2(a). A SEM photo of the patterned nanofluidic sieve is shown in Figure 2(b), and a close up top view SEM image of the nanosphere structure prior to polymer etching is shown in Figure 2(c).

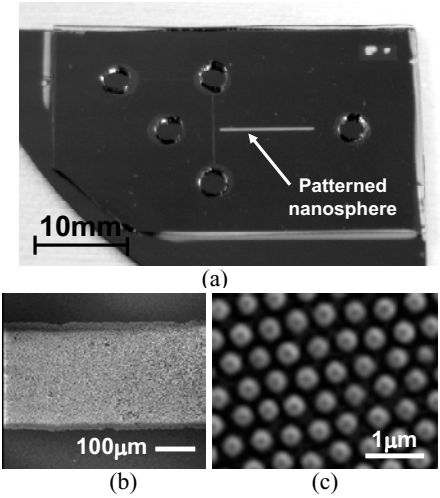

(a) (b) (c)

Fig 2. Pictures of a fabricated NEP device showing: (a) 15μm-high and 320μm-wide separation channel, (b) SEM image of the patterned nanosphere sieve, (c) close up SEM image of top nanosphere layer.



Fig 3. Separation of ϕX174 (HaeIII digest) DNA in a NEP microchip; (I) 72-310bp, (II) 602-1353bp.

3. RESULTS AND DISCUSSION

Nanosphere electrophoresis is conducted using ϕX174 DNA/Hae III digest, labelled with YOYO-1, in a 5×TBE buffer at pH 8.3 as shown by time elapsed fluorescence images in Figure 3; t=0 indicates the entrance of the DNA plug into the sieving matrix. Two bands, corresponding to (I) 72-310bp and (II) 602-1353bp, moving with different speeds along the separation matrix can be observed. The instantaneous fluorescence intensity profiles are plotted in Figure 4, where two separation peaks appear within a sieving distance of 800μm. The extracted migration velocity for each band increases linearly with increasing electric field as shown in Figure 5. Independent EOF velocity measurement, also plotted in Figure 5, allows calculation of the DNA electrophoretic mobility.

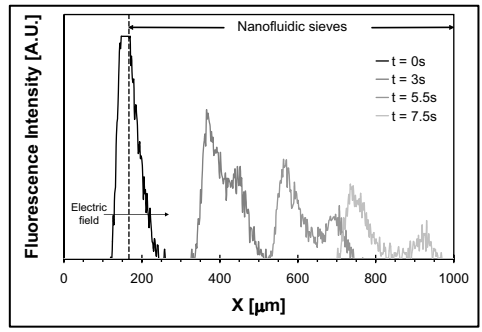

Fig 4. Fluorescence intensity plot of DNA plug at different times and locations along the separation channel corresponding to fig 3.

An important parameter dominating DNA kinetics within the nanofluidic sieving matrix is the ratio between the nanosphere and the DNA size. Although smaller nano-sphere is desired to enhance electrophoretic separation of short DNA strands; long DNA strands, however, may not be able to pass through a sieving matrix with very small pore size. A stacking phenomenon of large Lambda DNA (48kbp) is observed at the sieving matrix entrance as shown in the picture series in Figure 6. Integration of the light intensity at the nanofluidic sieve entrance after the DNA-plug passage, as shown in Figure 7, indicates that the stacking decreases with increasing nanosphere size. In contrast, small ϕX174 DNA (1.3kbp) migrates through all nanosphere sieves smoothly, with negligible molecule stacking for the 270nm nanosphere sieve. Moreover, the electrophoretic mobility of the smaller DNA fragments (ϕX174) is found to decrease monotonically with increasing nanosphere size within the tested range.

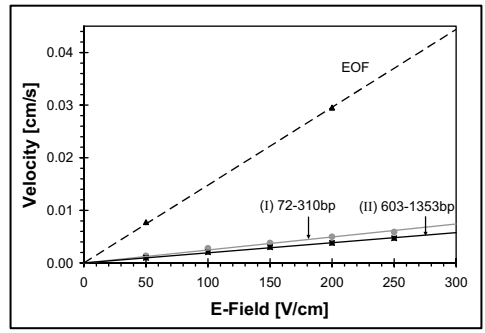

Fig 5. Measured migration velocity of EOF and ϕX174 DNA fractions (I and II) as a function of the applied electric field in a 270nm NEP chip.

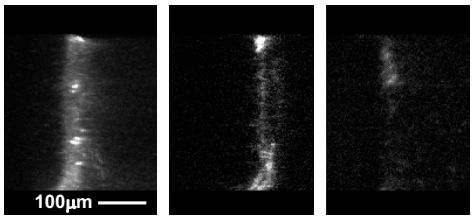

(a) (b) (c)

Fig 6. Lambda DNA (48kbp) stacking at the entrance to the nanofluidic sieves with different nanospheres size: (a) 270nm, (b) 470nm, and (c) 2000nm.

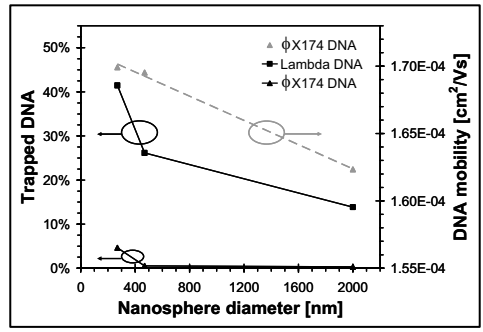

Fig 7. DNA stacking effect and electrophoresis mobility dependence on nanosphere size.

4. CONCLUSIONS

Nanosphere electrophoresis (NEP) microchips have successfully been fabricated utilizing colloidal crystal technology combined with standard patterning techniques. Fast electrophoretic separation of DNA ladder over a short sieving matrix length has been achieved. In contrast to smooth migration of short fragments, large DNA fragments are found to stack up at the entrance to the nanosphere sieving matrix. Indeed, consistently, the measured DNA electrophoretic mobility increases with decreasing pore size in the sieving matrix within the tested range.

REFERENCES

[1] N.Kaji, Y.Baba, et al., *Anal. Chem.*, **76**, p.15-22, 2004.
[2] P.Jiang and M.J.McFarland, *J.Am.Chem.Soc.*, **126**, p.13778-13786, 2004.
[3] H.Zhang and M.J.Wirth, *Anal. Chem.*, **77**, p1237-1242, 2005.
[4] Y.Zeng and D.J.Harrison, *Anal. Chem.*, **79**, p.2289-2295, 2007.
[5] G.H.Bogush, C.F.Zukoski IV, et al., *J. Non-Cryst. Solids*, **104**, p.95-106, 1988.

NANOPORE DEVICES FOR AC ELECTROKINETIC TRAPPING

Michelle L. Kovarik and Stephen C. Jacobson

Indiana University, USA

ABSTRACT

We report electrokinetic trapping of particles near the surface of a membrane with track-etched conical nanopores. The nanopore device integrated the membrane with the nanopores between two microchannels for fluid and sample delivery. By tuning the amplitude, frequencies, and DC offset of the applied potentials, we selectively trapped and released particles near the membrane surface. An advantage to using the conical nanopores is that steep field gradients can be generated easily, allowing small particles to be trapped efficiently.

Keywords: Nanofluidics, Nanopores, Electrokinetic Trapping

1. INTRODUCTION

Interest in microfluidic devices has increased over the past decade primarily because device miniaturization has led to a number of advantages, which include executing fast, efficient, high throughput assays, integrating multiple sample processing steps, and fabricating highly parallel device architectures [1]. As devices continue to shrink and approach the nanometer length scale, issues must be addressed regarding whether these systems are practical and which lessons from the microscale extrapolate to the nanometer regime. To develop functional nanofluidic systems, we are evaluating out-of-plane (nanopore) devices where transport is perpendicular to the device surface. The devices use a membrane with artificial pores sandwiched between two microfluidic channels. Artificial pores are robust, and sophisticated fabrication techniques can create pores on length scales comparable to those of protein pores. The pores can be formed by track-etching polymer membranes [2], isolation of a single carbon nanotube [3], nanomachining [4,5], and soft lithography [6].

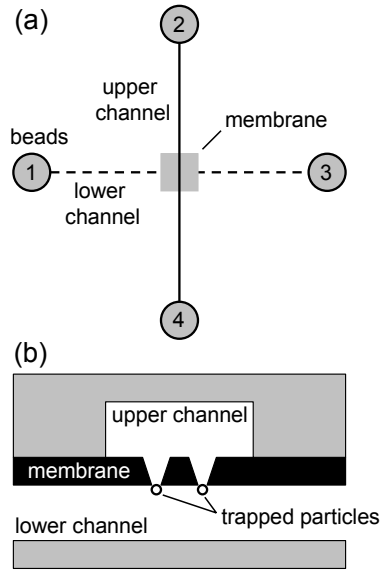

Figure 1. (a) Schematic of a nanopore device with a track-etched membrane positioned between upper and lower microfluidic channels. (b) Cross-sectional view of the microchannels and membrane with particles trapped at the nanopores.

2. EXPERIMENTAL

A schematic of the nanopore device is depicted in Figure 1a. Two poly(dimethyl-siloxane) (PDMS) substrates with a single microchannel cast in each were brought together with a poly(ethylene terephthalate) (PET) membrane positioned between them. Figure 2

978-0-9798064-0-7/μTAS2007/$20©2007CBMS

shows scanning electron microscope images of the track-etched conical nanopores in the PET membrane. The pores were 240 nm in diameter on the small side and 1.5 μm in diameter on the large side. As shown in Figure 1b, the membrane was positioned with the small side of the pore pointing toward the objective on an inverted microscope.

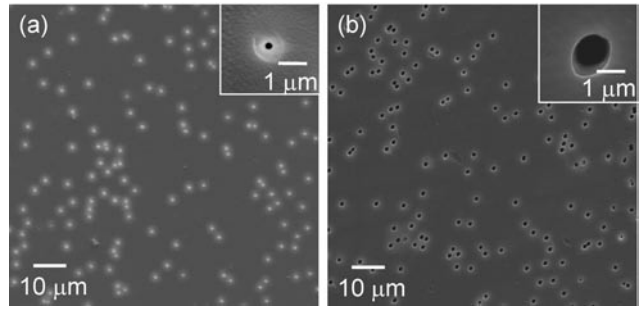

Figure 2. Scanning electron microscope images of a poly(ethylene terephthalate) (PET) membrane with track-etched conical nanopores. (a) The small side of the pores was 240 nm in diameter, and (b) the large side of the pores was 1.5 μm in diameter.

Figure 3a shows a white light image of the two microchannels intersecting with the membrane sandwiched between them. The dark circles in the image were the track-etched nanopores in the membrane, and the number of nanopores in the intersection was dictated by the width of the microchannels. The bead sample was transported to the cross intersection using a hydrostatic pressure difference between reservoirs 1 and 3. For the experiments, a square wave from 0 to 10 V was applied to the upper channel at frequencies from DC to 100 kHz to effect trapping. The lower channel, which contained the beads, was held at ground. This enabled the negatively charged beads to migrate toward the upper channel near the membrane.

3. RESULTS AND DISCUSSION

Figure 3b is a fluorescence image of 1 μm beads trapped at the nanopores following a 3 min accumulation time, using a frequency of 100 kHz. The beads were then released by reversing the applied potential (see Figure 3c). In Figure 4, variation of the number of beads trapped with frequency is shown. The number of beads accumulated at the membrane was

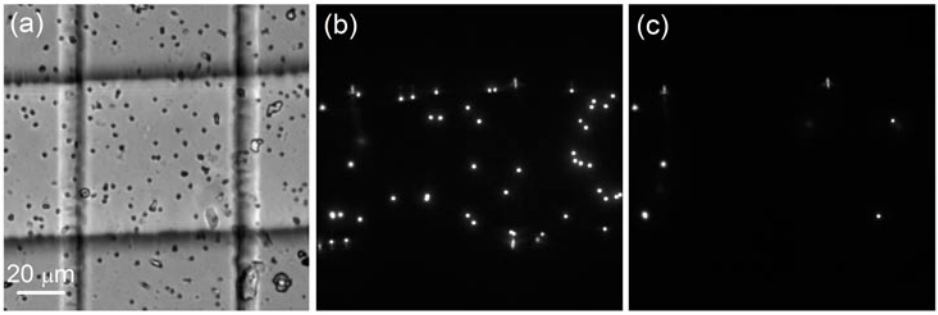

Figure 3. (a) Transmitted light image of two microchannels with a PET membrane sandwiched between them. (b) Fluorescence images of 1 μm beads (b) electrokinetically trapped and (c) released from the nanopores in (a).

normalized to the number trapped with a DC potential. The 1 μm beads trapped efficiently at frequencies ≥10 Hz, and the 200 nm beads trapped well at frequencies ≥1 kHz. The frequencies at which the beads accumulated corresponded well to the trapping frequencies expected for electrokinetic trapping. When trapping was attempted with a square wave with no DC offset (dielectrophoresis), the field gradient was not sufficient to induce trapping. By increasing the amplitude of the waveform, the trapping should transition from electrokinetic to dielectrophoretic. Having this combination of forces allows the separation to be tuned for a variety of systems. In addition, nanopores with smaller dimensions, e.g., 10-50 nm in diameter on the small side, can be used to trap and separate smaller particles such as proteins.

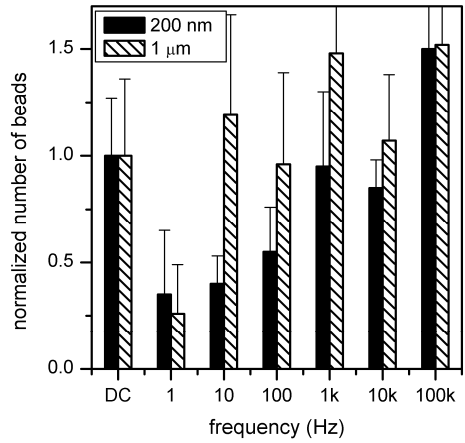

Figure 4. Variation of the normalized number of beads trapped at the nanopores with frequency. For frequencies ≥1 Hz, a square wave from 0 to 10 V was used.

ACKNOWLEDGMENT

This research was supported in part by Indiana University (IU) and by the Indiana METACyt Initiative of IU, funded in part through a major grant from the Lilly Endowment, Inc. This material is based in part upon work supported under a National Science Foundation Graduate Research Fellowship for M.L.K.

REFERENCES

[1] Whitesides, G.M. *Nature* **2006**, *442,* 368-373.
[2] Fischer, B.E.; Spohr, R. *Rev. Mod. Phys.* **1983**, *55,* 907-948.
[3] Henriquez, R.R.; Ito, T.; Sun, L.; Crooks, R.M. *Analyst* **2004**, *129,* 478-482.
[4] Li, J.; Stein, D.; McMullan, C.; Branton, D.; Aziz, M.J.; Golovchenko, J.A. *Nature* **2001**, *412,* 166-169.
[5] Uram, J.D.; Ke, K.; Hunt, A.J.; Mayer, M. *Angew. Chem. Int. Ed.* **2006**, *45,* 2281-2285.
[6] Saleh, O.A.; Sohn, L.L. *Nano Lett.* **2003**, *2,* 37-38.

REAL-TIME CONTROL OF NANOPORE WALL POTENTIAL FOR SINGLE-MOLECULE ANALYSES

AmirAli H. Talasaz[1,2], Thomas A. Zangle[3], Carolina Tropini[4], Reay Dick[2], Fabian Pease[1], Ronald W. Davis[2], Juan G. Santiago[3]

[1] Electrical Engineering Department, Stanford, CA
[2] Stanford Genome Technology Center, Stanford, CA
[3] Mechanical Engineering, Stanford, CA
[4] Department of Physics and Astronomy, University of British Columbia, Canada

ABSTRACT

We have demonstrated active control of the wall potential of a nanopore using capacitively coupled electrodes conformed to the nanopore. We have confirmed this behaviour using measurements of ionic current passing the nanopore and imaging of concentration polarization of fluorescent dyes in the region near the nanopore.

Keywords: Nanopores, wall potential, electric double-layer, single-molecule analysis

1. INTRODUCTION

Nanopore-based Coulter counter devices have been identified as offering unique opportunities for DNA sequencing [1], and label-free protein and viral detections [2]. However, the strong electric fields and field gradients associated with nanopore wall charge can interfere with translocation of biomolecules, or change the conformation of macromolecules during translocation. Additionally, interaction between the wall electric double-layers (EDLs), bulk liquid, and the electromigration of charged species can lead to modified biomolecule transport rates and/or adsorption and binding rates. These complexities can impede attempts to sequence DNA with single-base resolution or accurately detect proteins and protein activity.

2. THEORY

In this work, we present a nanopore device in which we actively modify wall charge to control and mitigate these effects. We demonstrate that nanopore wall potential can be

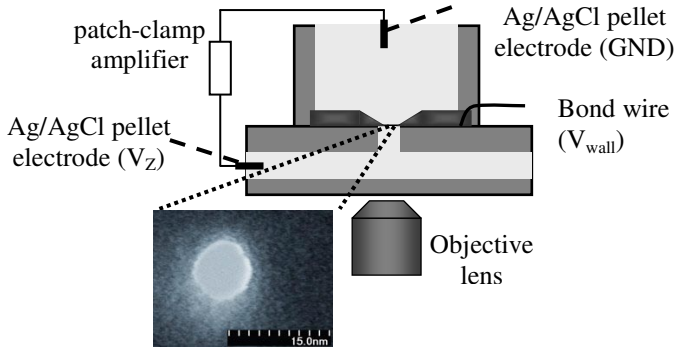

Figure 1. The nanopore fluidic coupling and imaging setup. Two electrodes are used for through pore potential (V_z) and a third electrode to control wall potential (V_{wall}). Insert is a TEM image (along pore axis) of the 10 nm diameter nanopore.

978-0-9798064-0-7/μTAS2007/$20©2007CBMS

actuated capacitively using metal film electrodes conformed to the nanopore and beneath an insulating layer. A fraction of wall electrode potential, $V_{wall}\ C_{alumina}/(C_{alumina}+C_{EDL})$, is applied to the EDL, changing the nanopore wall potential (C and V_{wall} are capacitance and applied potential).

3. RESULTS AND DISCUSSION

We fabricated synthetic nanopores in freestanding silicon nitride membranes using focused ion milling. Gold or chromium thin films are sputtered onto the membrane to reduce the pore diameter and serve as a nanopore wall electrode. The nanopore is then coated with a 3 nm thick Al_2O_3 insulating layer by atomic layer deposition. The completed pore structure is illustrated schematically in Fig. 2a. An SEM image of the nanopore is shown in Fig. 2b. We have demonstrated fabrication of 10 nm diameter and larger pores.

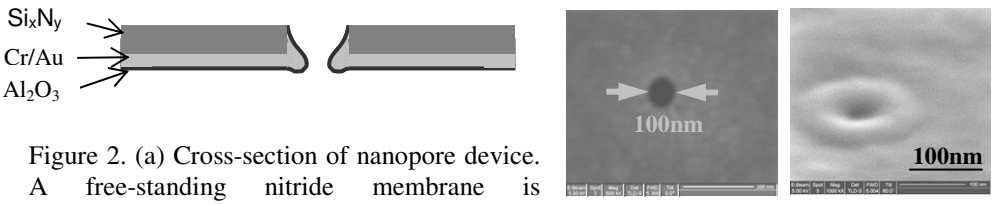

Figure 2. (a) Cross-section of nanopore device. A free-standing nitride membrane is conformally coated with gold or chrome and passivated with a 3 nm layer of alumina. Potential applied to the metal (V_{wall}) changes wall potential of the pore. (b) micrographs of a nanopore before and after gold sputtering. Final pore diameter here is 30 nm.

To demonstrate active control of nanopore wall potential, we measured ionic current passing through the nanopore as a function of wall electrode potentials, trans-pore potentials, electrolyte ionic strength and pH. As shown in Fig. 3a, the ionic current through the pore reaches a minimum value when the applied change in wall potential cancels the native surface charge of the alumina layer. Further experimental evidence is shown in Fig. 3b, where we show that ionic current rectification is controlled by applied wall potential.

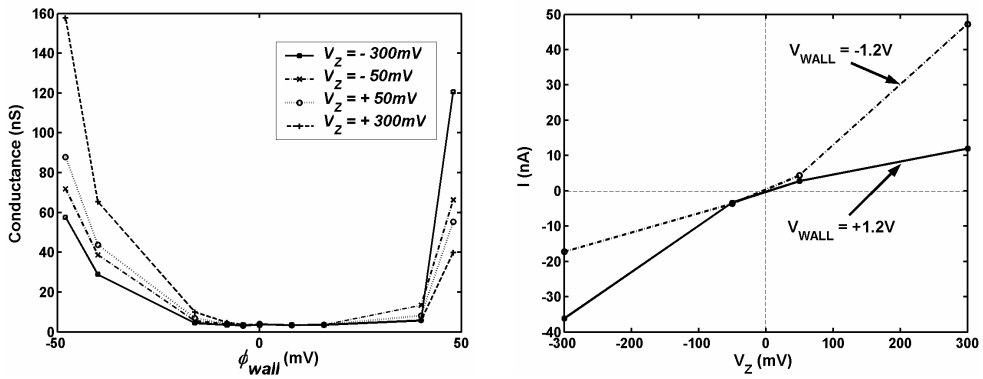

Figure 3. (a) Conductance through the nanopore vs capacitively applied changes in wall potential in 100mM KCl with pH 8. Conductance is minimized near the 10 mV applied wall potential (where applied potential cancels native surface charge). Results at pH 6 are qualitatively similar with a minimum near 15 m V. (b) Measured ionic current vs. voltages applied through the nanopore. The sign of the applied wall potential strongly affects current rectification (note slopes on either side of $V_z = 0$).

We have also performed a series of epifluorescence imaging experiments to quantify the effect of nanopore wall potential control on the translocation and concentration polarization of ionic fluorophores. We filled the pore device with 100 μM Alexa Fluor 488 (negative valence) to the top chamber (Fig. 1). We varied the pore wall potential via actuation of the thin film wall electrode from -4 to 4V while applying 20V across the pore to drive the dye through the nanopore. We captured images after current through the pore stabilized (~5 min). As shown in Fig. 4, we observe negligible concentration of dye when the wall electrode potential is zero or negative. In contrast, we measured a sharp increase in dye concentration when applied wall potential is positive. This behavior is consistent with the predicted direction of concentration polarization in the dye-containing top well of the pore device.

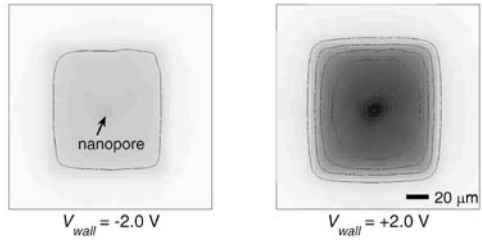

Figure 4. Images of translucent free standing nitride membrane (100 x 100 μm square) demonstrating that applied wall potential controls translocation and concentration polarization of dye. 50 nm nanopore is near the geometric center of the image and the upper well (the top and the far side of the membrane in Figure 1) contains 100 μM Alexa Fluor 488 for both conditions. For negative wall electrode potential, V_{wall}, relative to the bulk solution (left image), induced wall charge is negative and the concentration of Alexa Fluor 488 anion in the top well near the pore is measurably decreased by concentration polarization. For positive applied wall potential, wall charge is positive changing the polarity of concentration polarization and greatly increasing the concentration of dye in the top well in the vicinity of the pore (see high intensity spot near center on the right). Trans-pore potential, V_z was 20.0 V (electric field emerges out from the pore as visualized here) for both images. Contours are lines of constant fluorescence intensity and dark region denotes high fluorescence intensity. Both images are scaled to the same grayscale intensity. Images were taken with a 20X objective (NA = 0.4) with a 0.31X demagnifier after current through the pore had stabilized and captured.

4. CONCLUSIONS

Nanopores have the advantage of real-time, label-free electrical analysis of biomolecules. In this work, we demonstrate the ability to real-time control wall potential (and associated control of wall-molecule interactions). This control has important implications to the study of DNA sequencing and protein detection.

REFERENCES

[1] "Characterization of Nucleic Acids by Nanopore Analysis," D. W. Deamer, and D. Branton, Acc. Chem. Res., **35**, (2002).

[2] “Sensing protein molecules using nanofabricated pore,” A. Han, G. Schürmann, G. Mondin, R. A. Bitterli, N. G. Hegelbach, N. F. de Rooij, and U. Staufer, Applied Physics Letter, **88**, (2006)

IRON-OXIDE EMBEDDED SOLID LIPID NANO-VESICLES FOR MAGNETICALLY CONTROLLED DRUG DELIVERY

Ming-Huang Hsu and Yu-Chuan Su
Department of Engineering and System Science
National Tsing Hua University, TAIWAN

ABSTRACT

This paper presents the development of magnetic lipid nanoparticles that can serve as targeted delivery vehicles and release encapsulated drugs in a desired manner. The nano-vesicles are composed of multiple drugs and lipids, which are solid at body temperature while melted around 45 to 55 °C. Furthermore, nanometer-sized super-paramagnetic iron oxide particles are surface modified and dispersed uniformly in the lipid nanovesicles. In the prototype demonstration, it is verified that (1) the encapsulated iron oxide nanoparticles dissipate a large amount of heat while exposed to high-frequency magnetic fields and (2) the dissipated heat is capable of melting the lipid nanovesicles and accelerating the release of encapsulated drugs. As such, the presented lipid nanovesicles pioneer a new manipulating scheme for targeted and controlled drug delivery.

Keywords: Magnetic nanoparticle, Hyperthermia, Drug delivery, Lipid nanovesicle

1. INTRODUCTION

It has been well recognized that novel new drugs and associated delivery systems are equally important for achieving real progress in drug therapy [1, 2]. Solid lipid nano-vesicles, which are designed to alter the pharmacokinetics and bio-distribution of associated drugs, are particles of lipid matrices with drugs embedded and polymeric stabilizers on the surfaces [3, 4]. Based on this structure, a new scheme of integrating magnetic heating elements [5] for drug release control and hyperthermia enhancement is therefore developed.

2. PRINCIPLE

The structure of the proposed solid lipid nanovesicle is illustrated in Fig. 1. For targeted delivery, it is desired to (1) pack multiple drugs and ingredients into nanovesicles with desired sizes and surface properties, and (2) couple these nanovesicles with specific ligands to guide the delivery. In this work, lipophilic drug (tetracaine), fluorescent dye (Nile red), and iron-oxide (20 nm γ Fe_2O_3) nanoparticles are dispersed in melted lipid matrices, which are then emulsified in water to form solid vesicles once cooled down. The energy densities required to produce nanometer-sized emulsions are extremely high and can barely be achieved by few approaches such as high-pressure homogenization [6]. During the homo-genization process (as shown in Fig. 2), massive cavitational implosions are induced and the resulted enormous local temperature and pressure provide the desired power distribution for nano-emulsification [7]. For controlled delivery, the embedded iron-oxide nanoparticles function as heating elements that can be remotely energized to regulate the release of encap-sulated drugs. While exposed to alternating magnetic fields, these super-paramagnetic iron oxide nanoparticles periodically absorb and then dissipate magnetic energy into heat by means of Neel and Brownian rotations [5].

978-0-9798064-0-7/μTAS2007/$20©2007CBMS

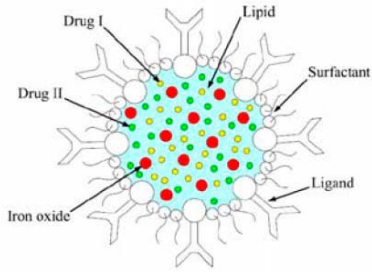

Fig. 1: Schematic of a solid lipid nanovesicle

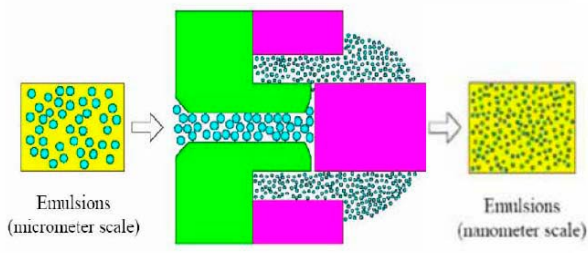

Fig. 2: High-pressure homogenization process

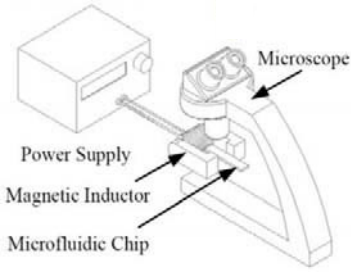

Fig. 3: Experimental setup

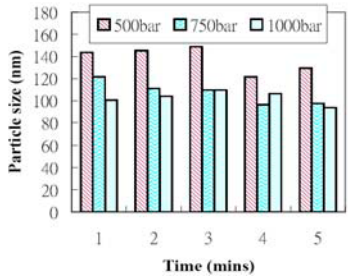

Fig. 4: Relationship between pressure, time, and particle sizes

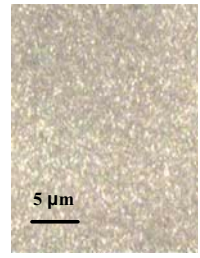

Fig. 5: Fluorescent image of nanovesicles

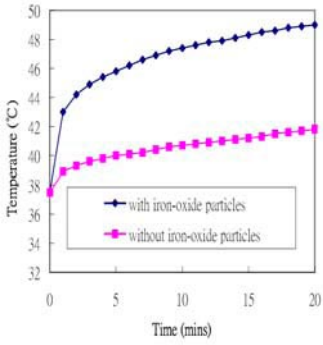

Fig. 6: Solution temp. while heated with/without iron oxide particles

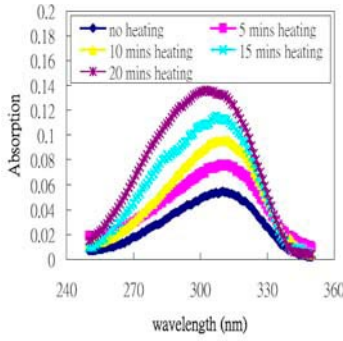

Fig. 7: UV/visible absorption shifts after heating

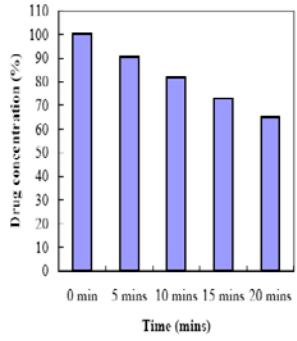

Fig. 8: Drug delivery profile

3. EXPERIMENTAL

To fabricate mono-disperse nanovesicles with desired sizes, a two-step emulsification process is employed. The lipid mixture is emulsified first using a heated microfluidic chip, and high-pressure homogenized afterward to form droplets of roughly 120 nm in diameter. Once solidified, the lipid nanovesicles provide stable protections for encapsulated drugs and iron oxide nanoparticles. The resulted colloidal solutions are stored at room temperature before further analysis, in which the particle sizes are determined by dynamic light scattering and the concentrations of embedded iron oxide are determined with an atomic absorption spectrometer to evaluate the encapsulation efficiency. To characterize the magnetic heating and delivery control, a setup (as shown in Fig. 3) including a high

speed power amplifier and an electric magnet are used to energize the iron-oxide nanoparticles with alternating magnetic fields up 60 kA/m at 25 kHz. Under a resolution-enhanced fluo-rescent microscope, the distribution of the encapsulated dyes (and therefore the nanovesicles) are observed as shown in Fig. 5. After minutes of heating, the temperatures and UV/VIS absorptions of the colloidal solutions are measured and analyzed.

4. RESULTS AND DISCUSSION

The average sizes of the resulted lipid nanovesicles range from 100 to 140 nm while process pressures vary from 1000 to 500 psi (as shown in Fig. 4). The background temperature in our heating experiments is set at body temperature (37 °C) and the resulted temperature rise in bulk solution is shown in Fig. 6, which indicates an 8 °C increase in 20 minutes. Under this circumstance, the heat dissipated from the embedded iron oxide nanoparticles melts the lipid nanovesicles. In our experiments, tetracaine is employed as the model drug and its concentrations (at 307 nm) are characterized as shown in Fig. 7, which indicates a rapid increase through the 20-minute heating period. Meanwhile, roughly 35% of the original encapsulated tetracaine is released from the nanovesicles as shown in Fig 8. Because the diffusion rate across lipid matrices is much higher in melted state than in solid state, a highly accelerated release of the encapsulated drugs is observed as expected.

5. CONCLUSIONS

We have successful demonstrated the fabrication and delivery control of magnetic lipid nanoparticles that can serve as targeted delivery vehicles. The nanovesicles, which contain multiple drugs and super-paramagnetic iron oxide particles, are solid at body temperature while melted around 45 to 55 °C. In our preliminary demonstration, it is verified that (1) the encapsulated iron oxide nanoparticles dissipate heat while exposed to alternating magnetic fields and (2) the dissipated heat can melt the lipid nanovesicles and accelerate the release of encapsulated drugs by hundreds of times. Based on these results, the presented lipid nanovesicles and the associated magnetic delivery scheme could potentially realize multi-modal and highly selective therapies for a variety of diseases.

ACKNOWLEDGEMENTS

This work is supported in part by the National Science Council of Taiwan (Grant number: NSC 95-2221-E-007-226.)

REFERENCES

[1] R. Langer, “Drug Delivery and Targeting,” *Nature*, vol. 392S, pp. 5-10, 1998

[2] T.M. Allen and P.R. Cullis, “Drug Delivery Systems: Entering the Mainstream,” *Science*, vol. 303, pp. 1818-1822, 2004

[3] R.H. Muller, K. Mader, and S. Gohla, “Solid Lipid Nanoparticles (SLN) for Controlled Drug Delivery - a Review of the State of the Art,” *European Journal of Pharmaceutics and Bio-pharmaceutics*, vol. 50, pp. 161-177, 2000

[4] W. Mehnert and K. Mader, “Solid Lipid Nanoparticles - Production, Characterization and Applications,” *Advanced Drug Delivery Reviews*, vol. 47, pp. 165-196, 2001

[5] S. Mornet, et al., “Magnetic Nanoparticle Design for Medical Diagnosis and Therapy,” *Journal of Materials Chemistry*, vol. 14, pp. 2161-2175, 2004

[6] S. Schultz, et al., ”High-Pressure Homogenization as a Process for Emulsion Formation,” *Chemical Engineering & Technology*, vol. 27, pp. 361-368, 2004

[7] K.S. Suslick, “Sonochemistry,” *Science*, vol. 247, pp. 1439-1445, 1990

FABRICATION OF MULTI-LAYERED CARBON NANOTUBE FILMS FOR LABEL-FREE DETECTION OF DNA HYBRIDIZATION

Youn-Kyoung Baek[1], Dae-Hwan Jung[1], Sang-Yup Lee[1], Yang-Kyu Choi[2] and Hee-Tae Jung[1]

[1]Department of Chemical and Biomolecular Engineering and
[2] Department of Electrical Engineering and Computer Science Korea Advanced Institute of Science and Technology, Korea

ABSTRACT

We immobilized the probe DNA oligonucleotides onto single wall carbon nanotube(SWNT) films and hybridized target DNA oligonucleotides with the complementary or non-complementary bases, in which SWNT films with a wide range of conductivities were prepared by vacuum filtration methods. Single strand DNA oligonucleotides were covalently attached to prepatterned films through amide bond formation using 1-ethyl-3-(3-dimethylaminopropyl)carbodiimide hydrochloride. Sensing ability of the DNA hybridization was demonstrated by investigating a change of response to linked DNA and its complementarity. We show that resultant DNA-attached CNT multilayer films are shown to exhibit good specificity for their potential use in biosensors.

Keywords: Carbon nanotube, Label-free, Biosensor, DNA hybridization

1. INTRODUCTION

Recent years have witnessed significant interest in biological applications of novel nanomaterials such as nanotubes with the motivation to create new types of analytical tools for life science and biotechnology. Single wall carbon nanotubes(SWNTs) are promising materials for highly sensitive bio-detection, since the electronic properties are more sensitive to change of charges on the sidewall[1]. Here, we report SWNT film immobilized with probe DNA molecules shows different signals for DNA hybridization according to the complementarity of DNA oligonucleotides. In contrast to previous methods, the fabrication of the DNA hybridized CNT films is very practical, and easily scaled up because it exhibit excellent specificity over large areas.

2. EXPERIMENTAL

2.1 Fabrication of multilayered carbon nanotube film-based electronic device

As-prepared SWNTs were purified, shortened, and polished in accordance with literature methods[2]. The SWNT films were prepared by simple method combining a transferring onto substrate with vacuum filtration[3]. Patterning of CNT films was conducted by photolithography technology coupled with developing process, followed by lift-off process for the construction of electrode[4].

2.2 Immobilization and Hybridization of DNA oligonucleotides to as prepared film

For the attachement of amine terminated DNA oligonucleotides, as prepared films were activated by the drop wise addition of 25 mM 2-[N morpholino] ethanesulfonic acid (MES) buffer solution containing 15 μM of N-hydroxysuccinimide (NHS), which was then left to

978-0-9798064-0-7/μTAS2007/$20©2007CBMS

incubate in a humidity chamber at 30 °C for 30 min. Following this, 4 μL of solution containing 75 μM of 1-ethyl-3-(3-dimethylaminopropyl)carbodiimide hydrochloride (EDC) and NH_2 terminated 20-base single strand DNA(ssDNA) was added to the activated film, and then the film was left to incubate for overnight at room temperature.
Hybridization was carried out using complementary-ssDNA and noncomplementary-ssDNA with Cy-5 label(10 μM, 5x concentrated standard saline citrate (SSC) buffer) in the condition of 42 °C chamber for overnight. The SWNT multilayer film was washed and rinsed with buffer solution, and then dried.

2.3. Chracterization

Images of SWNT films were taken at various magnifications using a field emission scanning electron microscope (XL30SFEG, Philips) equipped with a Schottky based field emission gun. To detect the immobilization and hybridization of DNA oligonucleotides, the fluorescence signals was performed on a ScanArray 5000 unit (Packard BioScience, BioChip Technologies LLC) and analyzed using the QuantArray 3.0 software package (GSI Lumonics, Billerica, U.S.A.). Electronic sensing was carried out by measuring current/voltage characteristics of the SWNT film through manual probe station (SUMMIT (11862B)) with semiconducting characterization system(Keithley 4200-SCS/F).

3. RESULTS AND DISCUSSION

High-density SWNT films were constructed via vacuum filtration method, creating stacks of SWNT layers, bound to amine slide glasses. A SEM investigation of the SWNT films confirmed that the methods produced uniform films with various coverage according to the amount of SWNT bundles(Figure 1). Probe DNA oligonucleotides were linked to the carboxylic acid funcionalized SWNT(cut in acid) surfaces via EDC catalytic amidation, followed by hybridization of target DNA oligonucleotides to the film. The scanned fluorescence intensity(Figure 2) revealed that probe DNA molecules were successfully linked on the SWNT surface and hybridized with Cy-5 labelled DNA oligonucleotides having fully matched bases and mismatched bases. The difference of each signals showed the selectivity of the probe DNA-functionalized SWNT films is sufficient to discriminate the mismatched DNA.
For the practical application of electronic sensors, the SWNT film was patterned by photolithography and e-beam lithography. Figure 3 shows typical optical microscopic images of an electrical device consisting of the patterned SWNT films bridging metal electrode pads. We have measured current versus voltage(I-V) characteristics of the bare SWNT film based electronic circuits and obtained a straight lines with constant slope under 2 V bias, indicating constant conductance corresponding to metallic behaviour.
After functionalizaion of probe DNA oligonucleotides onto CNT surface via covalent bonding, conductance of film was changed in the same electronic measurement condition. The electro-signal ($1-G/G_o$) response was obtained by calculating the ratio of conductance change between before and after immobilizing DNA oligonucleotides to conductance of bare SWNT film device. We show that the signals of spots linked by the probe DNA is stronger than those of the spots in the absence of DNA molecules(Figure 3).

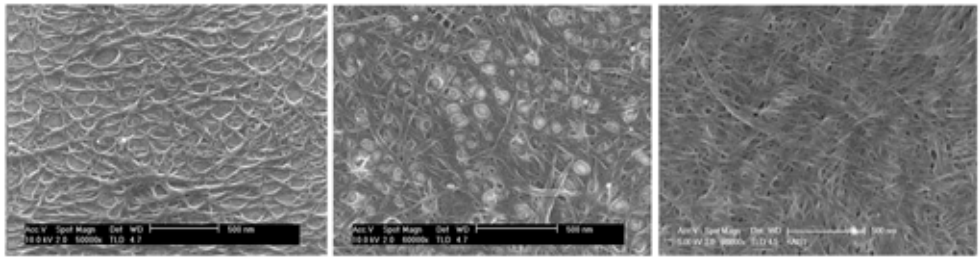

Figure 1. SEM images of multi-layered carbon nanotube films with various coverage according to the amount of SWNT bundles

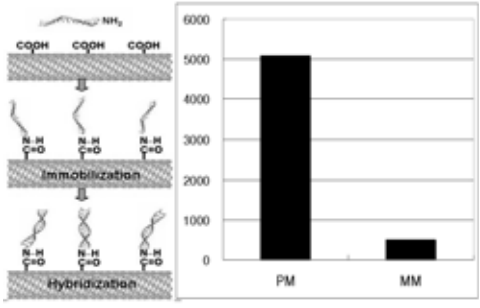

Figure 2. Scheme for the introduction of DNA moleucules to CNT surface and fluorescence detection results for the hybridization of complementary (PM; perfect match) and non complementary DNA oligonucleotide(MM: mismatch)

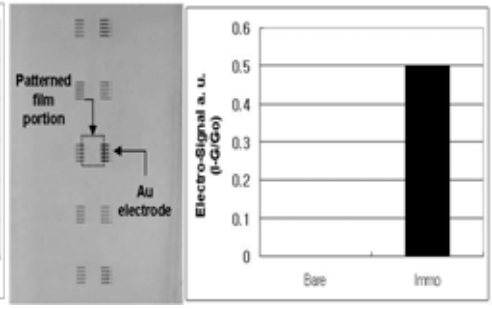

Figure 3. Optical image of an electronic sensor consisting of patterned SWNT films bridging Au electrode pads and electro-signals for the bare films and films immobilized by DNA oligonucelotides without labeling

5. CONCLUSIONS

Multilayered carbon nanotube films have the capability to role as a platform to attach DNA molecules to the nanotube surface, and play an important role in detecting immobilization of DNA without labelling. Compared to non-covalent attachment of DNA molecules, this covalent attachment approach can reduce noise from background signal. The electrical conductance changes in the presence or absence of DNA molecules might be attributed to the changes in surface charge of the nanostructures.

REFERENCES

[1] R. H. Baughman, A. A. Zakhidov, W. A. de Heer, "Carbon nanotube-the route toward applications", Science, Vol. 297, pp.787-792, (2002).

[2] K. J. Ziegler and Richard E. Smalley, "Controlled oxidative cutting of single-walled carbon nanotubes", J. Am. Chem. Soc., Vol. 127, pp.1541-1547, (2005).

[3] Z. Wu, Z. Chen, A. G. Rinzler, "Transparent, conductive carbon nanotube films", Science, Vol. 305, pp.1273-1276, (2004).

[4] D. H. Jung, M.S. Jung, H. T. Jung, "Carbon nanotube conducting arrays by consecutive amidation reactions ", Chemical Communications, Vol. 5, pp.526-527 (2004).

FABRICATION OF PDMS-BASED NANOCHANNELS FOR ENZYMATIC PROCESSING AND DETECTION OF BIOMOLECULES

Oliver Harnack, Ingeborg Hospach, Akio Yasuda
Materials Science Laboratory, Sony Deutschland GmbH,
Hedelfinger Str. 61, 70619 Stuttgart, GERMANY

ABSTRACT

We describe a simple route for creating nanofluidic structures for biomolecular analysis and processing. Nanochannels down to 140nm in width were fabricated by using combined ebeam and SU8 lithography, reactive ion etching, PDMS molding, and glass bonding. Then, 48 kbp long λ-DNA molecules, which were attached to polystyrene beads, could be trapped at micro-to-nano transitions and easily inserted into the nanochannels. By utilising this immobilisation approach we could investigate the activity of different DNA restriction enzymes such as Exo III, Sfo I, and Xba I in different spatial confinements.

Keywords: Nanofluidics, DNA-bead assemblies, enzymatic digestion, nanopores

1. INTRODUCTION

The manipulation and analysis of biomolecules on the level of only a very few analyte molecules will become an important requisite for the diagnosis of diseases at a very early stage, as well as for individual medicine, and furthermore for related applications such as DNA sequencing. Emerging nanobiotechnlogical approaches suggest exciting innovations for these fields. These often rely on the transfer of a biological process into an artificial, micro and nano-scaled environments. Our work is focussed on the realisation of a versatile micro and nano-fluidic platform for a carrier-mediated transfer of DNA to an immobilisation site and the controlled initiation of an enzymatic digestion process. In a future extension of the present device, the fragments of the digestion process could then be detected by using a single molecule detector, such as a pore protein [1].

2. FABRICATION AND DNA-MODIFICATION

For the device fabrication mix&match ebeam and SU8 lithography, molding, and glass bonding were utilised (Figure 1a). Firstly, an SiO_2/Si wafer master was patterned with nano-

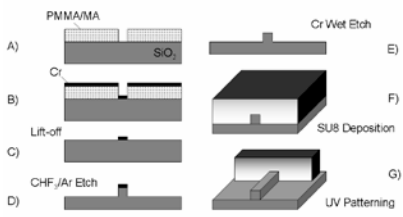

Figure 1a. Fabrication steps for the construction of a master for molding nanochannels with μ-fluidic terminals.

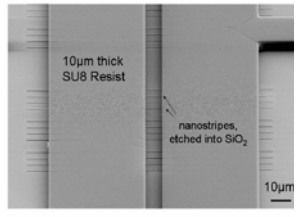

Figure 1b. SEM image of a SiO_2/Si master for PDMS molding step.

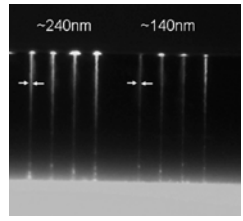

Figure 1c. PDMS nano-channels, filled with water containing FITC.

978-0-9798064-0-7/μTAS2007/$20©2007CBMS

stripes down to 140nm width and 250-500nm depth by applying ebeam lithography (Step A), Cr-mask deposition and reactive ion-etching (Steps B-E). Then, lines on a µm-scale for µ-fluidic interconnects were aligned and UV-exposed in an SU8 resist layer (Steps F,G). After PDMS molding using the master (Figure 1b) and subsequent bonding to glass, the resultant nanochannels could be completely filled with aqueous solutions (Figure 1c).
In order to reduce the effects of non-specific adsorption of biomolecules, we performed gas-phase silanisation on the freshly bonded nanochannels in PDMS/glass structures. We found that if we deposit methlysilanes then the levels of DNA adsorption on the device surface were considerably lowered. In order to accurately localise the DNA directly at the entrance of a nanochannel, we hybridized and ligated a biotin end-functionalized oligonucleotide to one 12-mer overhang of linear λ-DNA (Sigma) and then immobilized the 48 kbp long molecules onto 1.8µm large, streptavidin-coated polystyrene beads in a 1 M PBS buffer (Figure 2). In contrast to direct immobilisation methods to the channel walls, e.g. shown in [2], this method is useful to direct the DNA to a desired location inside the µ-fluidic device.

3. EXPERIMENTAL

These λ-DNA-bead assemblies were inserted into the µ-fluidic channels and selectively trapped at the µ-to-nano transitions by applying hydro-dynamic pressure. The attached DNAs were easily inserted and stretched either by hydro- dynamic flow (Figure 3, top) or by electric fields. The activity of different DNA restriction enzymes such as Exo III, Xba I, Sfo I on the DNA inserted inside the nano-scaled artificial structures was investigated by adding the corresponding enzymes (all New England BioLabs) at concentrations of 1 Unit/µl in the related enzyme buffer without the Mg2+ co-factor. After adding 10 mM Mg2+, Exo III begins to digest λ-DNA progressively base by base, while Xba I and Sfo I respectively cleave the λ-DNA at 24508 bp (approximately the centre of the strand) and at 45679 bp (close to the anchor point to the bead).

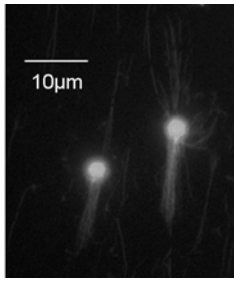

Figure 2. λ-DNA-poly-styrene bead assembly immobilised on a glass surface.

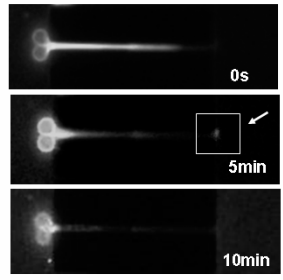

Figure 3. λ-DNAs digested by Exo III inside a 750nm wide and 500nm deep nano-channel. Scale bar = 10µm.

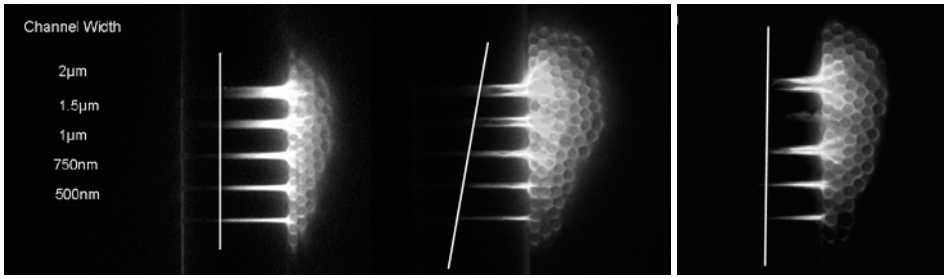

Figure 4. Trapped and stretched λ-DNA; (a) non-treated (left), (b) treated with Xba I for 2 hours (center), (c) treated for 16 hours (right). Channel widths are indicated on the left, the channel length was 20µm. The white lines approximate the ends of the DNA and are intended as guide for the eyes.

4. RESULTS, DISCUSSION, AND OUTLOOK

The results as presented in the fluorescence image in Figure 3 show that independently of the channel size Exo III digests the bundle of λ-DNA strands within approximately 10 minutes. However, in contrast to this, we found that the digestion activity of Xba I decreases with decreasing size of our nm-channels. Figure 4 shows the results of an Xba I digestion experiment over 16 hours. After 2 hours the digestion has proceeded well in the wider channels (Xba I cuts λ-DNA at about half length), while almost no change has occurred in the narrow channels (Figure 4b). Figure 4c shows the situation after 16 hours, where almost all DNA strands have the same length, suggesting that the digestion activity was considerably lower in the narrow channels. In the case of Sfo I, we could only observe a very small number of cleavage events, independently of the channel sizes. The cleavage site is very close to the carrier bead and thus may be not accessible if the DNA is partially wrapped around the bead. As indicated by the enhanced inset in Figure 3 (middle, white arrow), we usually observed an accumulation of fragments of the DNA digestion at the exit of the nano- channels. A further extension of our device structure is the integration of constrictions along the channels (Figure 5). In preliminary experiments we found that the nanochannels could indeed still be filled through such constrictions, and that furthermore the DNA did translocate. These findings give rise to the possibility of realising a nano-fluidic integrable Coulter counter in the form of a planar nanopore structure with applications such as DNA and protein detection.

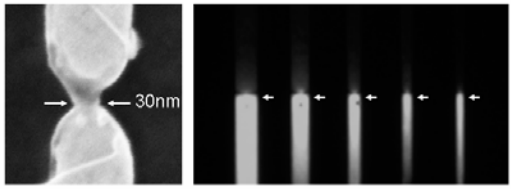

Figure 5. Integration of planar nanopores into PDMS nanochannels. Left: SEM image of constriction in Cr mask for defining master (Step C, Fig. 1a). Right: water (with FITC) diffuses through nm-sized pores in 2μm, 1.5μm, 1μm, 750nm, 500nm wide channels.

5. CONCLUSIONS

We have shown a straight-forward approach to the fabrication of PDMS-based nanochannels combined with microchannels. The capture of λ-DNA to polystyrene beads as carriers enables us to position the DNA with high accuracy inside μ-fluidic channels, directly at the entrance of nanochannels in which enzymatic processes can then be performed in a controlled manner. The activity of Exo III and Sfo I did not scale with the channel dimensions in the investigated range, whereas the restriction enzyme Xba I had a lower activity in the sub-1μm width channels. The nano-scaled design of our approach promises the future integration of single molecular sensors, such as nanopores or nanogaps.

ACKNOWLEDGEMENTS We thank Claire Basquin and Ulrich Keyser for fruitful discussions.

REFERENCES

[1] Y. Astier, O. Braha, and H. Bayley, *Towards Single Molecule DNA Sequencing*.., J. Am. Chem. Soc., 128(5), pp. 1705-1710, (2006).

[2] S. Matsuura et al. *Real-time observation of a single DNA digestion by λ exonuclease under a fluorescence microscope field*, Nucleic Acid Research, Vol. 29(16), pp. e79, (2001).

HYDRODYNAMIC FORCE CONTROL OF LAMINAR FLOW AS A NANO PROBING TOOL TO EVALUATE TORQUE OF SINGLE MOTOR PROTEIN

S. W. Lee[a], H. Kinoshita[a], T. Yamamoto[a], H. Noji[b], and T. Fujii[a]

[a] *Institute of Industrial Science, University of Tokyo,*

Fw-601, 4-6-1 Komaba, Meguro-ku, Tokyo, Japan

[b] *The institute of Science and industrial Research, Osaka University,*

8-1Mihogaoka Ibaraki Osaka Pref. Japan 567-0047

ABSTRACT

This paper presents an application of precisely controlled laminar flow to evaluate mechanochemical properties of a single motor protein using our previously developed microfluidic device, as our continuous effort to realize the platform device for future nanobiology.

Keywords: F_1-ATPase, microfluidics, single molecule study, multiple laminar flow

1. INTRODUCTION

In microfluidics-based biotechnology, the research to investigate hydrodynamic effects in proximity to surface has been mainly conducted for cultured cells, because the flow-induced shear stress is an important mechanical factor for cell culture [1]. Hydrodynamic force may exert negative influences to cell adhesion [2] and aggregation [3], and positive influences on endothelial cells and floating cells because those cells intrinsically influenced the flow of blood *in vivo* [4]. On the other hand, hydrodynamic effects on biomolecule have not studied broadly as cell level study, in part due to the difficulty of precise control of fluid motion in microspace and visualization of single molecule. There have been reported several applications using hydrodynamic effects on biomolecules such as stretching DNA to study protein-DNA interactions [5], chemical environmental control for single molecule study [6], mechanochemical characterization of a motor protein [7]. As an example of microfluidic operation for biomolecular study, we previously proposed and developed a chemical delivery method that supplies a chemical to a desired location by addressing the laminar flow carrying a desired chemical. Because this method intrinsically involves flow induced hydrodynamic effects to a target biomolecule, hydrodynamic effects in proximity to surface must be evaluated to ensure the availability of the laminar flow based chemical delivery.

In this work, we investigated hydrodynamic effects on a rotating single biomolecule of F_1-ATPase in a microfluidic device, as an extended study of our laminar flow based chemical delivery method. The flow velocity in proximity to the F_1-ATPase was obtained by Micro-PIV (particle image velocimetry) method. The hydrodynamic effects by varying flow velocities were evaluated by measuring the rotation speed of F_1-ATPase. As a result, we obtained the linear relation between flow speed and rotation speed of F_1-ATPase and discussed the availability of the chemical delivery using continuous laminar flow stream.

978-0-9798064-0-7/μTAS2007/$20©2007CBMS

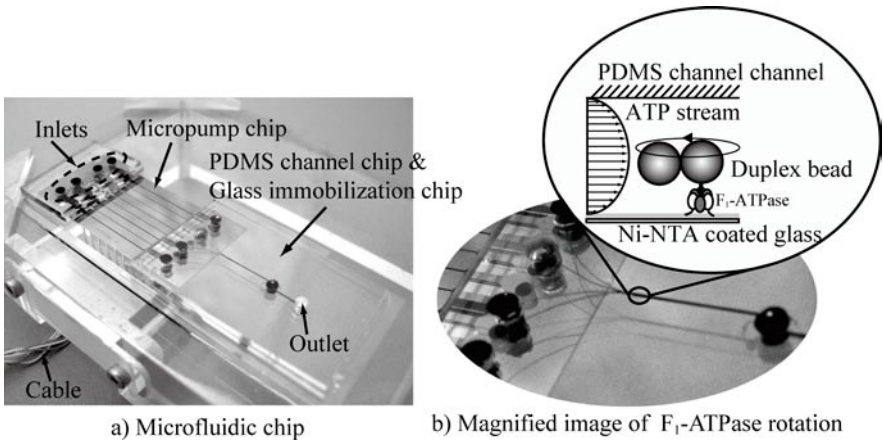

Figure 1 Microfluidic device for F_1-ATPase analysis

2. EXPERIMENTAL

The design of microfluidic device is followed by our previous one [8], in which the Si-based multi-channel micropump chip, the microchannel chip, and the Ni-NTA coated glass chip to immobilize any his-tagged proteins are assembled as shown in Fig. 1. The liquid injected from each input channel is controlled independently by the embedded micropump. This multiple input format can generate multiple laminar flows inside of the main channel, and can address any laminar flow to an arbitrary location with a certain flow velocity. The traverse translational velocity profile at a certain height of the microchannel was obtained by PIV method. Since the velocity profile of a laminar flow would be parabolic, the vertical velocity profile in proximity to the surface, where the target protein was immobilized, was derived from a traverse translational velocity profile by extrapolating a parabolic function.

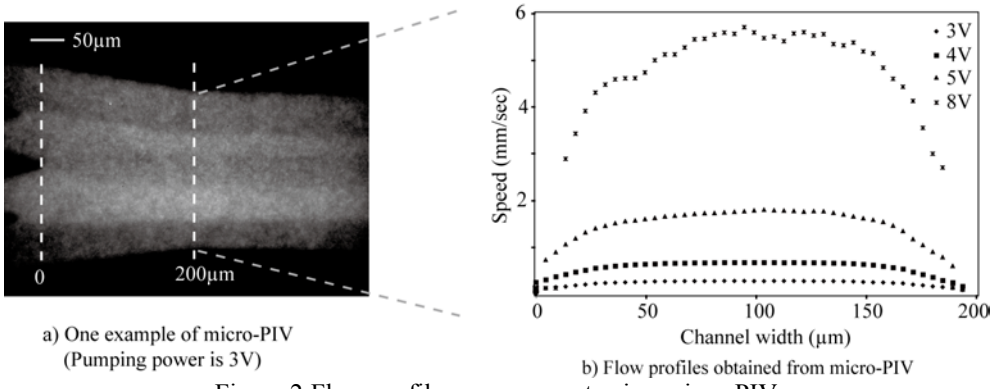

Figure 2 Flow profile measurement using micro-PIV

3. RESULTS AND DISCUSSION

Fig. 2 shows the particle images and the corresponding velocity profiles obtained by PIV measurements. The images are captured when all four micropumps were energized by the same pumping power at a time. The focal plane is adjusted at the center height of the channel, which corresponds to 30μm apart from the bottom surface. Fig. 3 a) shows the

time course of F_1-ATPase rotation at no-flow (A), 6.21μm/sec (B), 39.9μm/sec (C), and 59.8μm/sec (D) respectively. The corresponding rotation speeds are decreased 14% (B), 40% (C), and 99% (D) (Rotation stop) from the no flow condition (A). In order to find the relationship between the hydrodynamic force and the F_1-ATPase rotation speed, the rotational speed is obtained by the time derivation of Fig. 3 a) and plotted as a function of flow speed as shown in Fig.3 b). The rotation is not only clearly stopped when the flow velocity is over 59.8 μm/sec, but also stopped at slower velocities in the experiment (data not shown). We thus supposed that the critical flow velocity, which stops the rotation of F_1-ATPase, could be less than 59.8μm/sec; 59.8μm/sec could be an over speed. Therefore, we made the fitted line by neglecting 59.8μm/sec as shown in Fig. 3 b). The graph apparently shows linear correlation between the rotation speed of F_1-ATPase and the flow speed. This graph also leads the torque of F_1-ATPase that is 10.9 pN/nm, which is comparable to the value of 40 pN/nm in literature [7], which validate the accuracy of the measurement of the experiment. According to the result, any speed of flow stream will exert some hydrodynamic influence on the immobilized biomolecule, and suggest that the laminar flow based chemical delivery method requires careful attention to the side effects induced by flow.

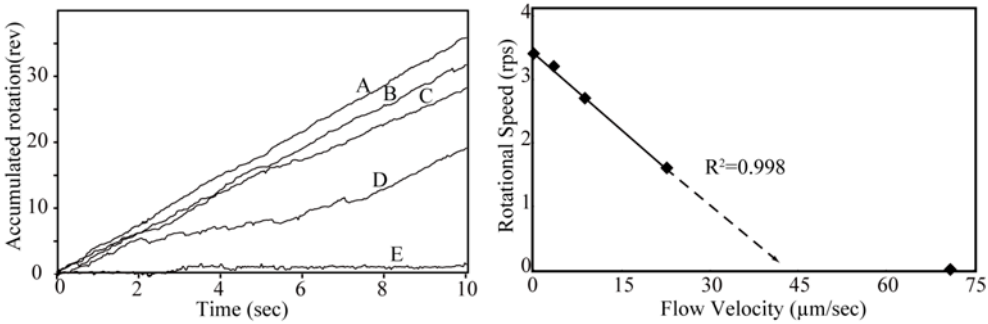

a) Time course of F_1-ATPase rotation with various flow velocities

b) Comparison of rotation and flow speed

Figure 3 Rotation of F_1-ATPase under different flow velocities

ACKNOWLEDGEMENTS

A part of this work has been performed in the Bioarchitect Research Program of the RIKEN Institute (Institute of Physical and Chemical Research). This work is partly supported by the Japan Society for the Promotion of Science, Bio-Oriented Technology Research Advancement Institution.

REFERENCES

[1] C. Yi, C.W. Li, S. Ji, and M. Yang, *Analytica Chimica Acta*, 2006, **560**, 1-23
[2] D.P. Gaver III and S. M. Kute, , *Biophysical Journal* ,1998, **75**, 721-733
[3] P. Snabre, M .Bitbol and P. Mills,, *Biophysical Journal,*1987 **51**, 795-807
[4] J. Ando, and A. Kamiya, , , *Jpn. Heart J.*,1996 37,19-32
[5] V. ram Dukkipati, et.al., *Nano Letters*, 2006, **6**, 2599-2504
[6] R. Yokokawa, et.al., *Nano Letters*, 2004, **4**, 2265-227
[7] H.Noji H and Yoshida M , J Biol Chem (2001) 276; 1665-1668
[8] S.W. Lee, et.al., *Enzyme. Microb. Technol.,*2006, **39**, 519-524

NANO ELISA SYSTEM FOR HIGHLY EFFICIENT AND SENSITIVE MOLECULAR RECOGNITION

Kazuma Mawatari[1], Ryu Kojima[2], Björn Renberg[2]and Takehiko Kitamori[1,2]
[1]Kanagawa Academy of Science and Technology (KAST), Japan
[2]The University of Tokyo, Japan

ABSTRACT

We report a novel method for highly efficient and sensitive molecular recognition by realizing ELISA (Enzyme-Linked ImmunoSorbent Assay) in nanospace for the first time. The nanofluidic system for nano ELISA is realized, and the basic principle of ELISA in nanochannels was verified.

Keywords: ELISA, Nanochannel, Thermal lens microscope, Single molecule

1. INTRODUCTION

Recently, a new method for understanding gene or protein expression at single cell level is increasingly desired in the fields of proteomics and metabolomics researches. One of the challenges is loss-less molecular recognition method with single molecule sensitivity in a large amount of co-existing molecules. One of the highly selective molecular recognition methods is immunoassay. Especially, ELISA method is usually utilized due to the high sensitivity coming from amplification reaction of dye molecules by an enzyme. Previously, we reported integration of the ELISA system on microchip and verified the excellent performance in very short analysis time and high sensitivity combining thermal lens microscope (TLM) which is our original ultra sensitive detector of non-fluorescent molecules [1] [2].

Further integration of ELISA in nanochannels seems to have several advantages. One is high sensitivity at single molecule level by combining TLM because amplified dye molecules are confined in nanochannels which increase the concentration of the dyes. In addition, we found approximately 4-time viscosity increase of water confined in nanochannels, which also increase the concentration due to the decrease of diffusion coefficient. Second is high efficiency due to the large surface-to-volume ratio, which leads to efficient immunoreactions without loss of analyte molecules. However, the basic method for ELISA in nanochannels has not been established.

In this presentation, we realized a nano-ELISA system for the first time to investigate these basic ideas.

2. EXPERIMENTAL

The basic principle of nano ELISA is illustrated in Figure 1. The dye concentration produced by an enzymatic amplification reaction following immunoreactions is measured by scanning TLM (488nm excitation), and the number of analyte in detection volume (~1μm^3) was determined. The nanofluidic system is shown in Figure 2. In ELISA, almost 10 kinds of reagents including washing solutions should be efficiently introduced without contamination. For this purpose, we fabricated a nanochannels (just in depth) for immunoreactions and microchannel for reagent reservoir. By a pressure controller, selective liquid introduction to the microchannel and nanochannels was realized (100 kPa

978-0-9798064-0-7/μTAS2007/$20©2007CBMS

and 500 kPa in liquid introduction for just microchannel and nanochannel filling, respectively). For filling each reagents in nanochannel, ~5 min (170 μm/s) was required considering the pressure drop. After introduction of substrates, the liquid is stopped and produced dyes were measured by scanning TLM. As an analyte, α-feto protein(AFP) was utilized for principle verification.

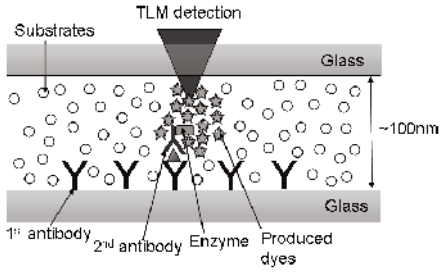

Figure 1. Illustration of principle of nano ELISA method

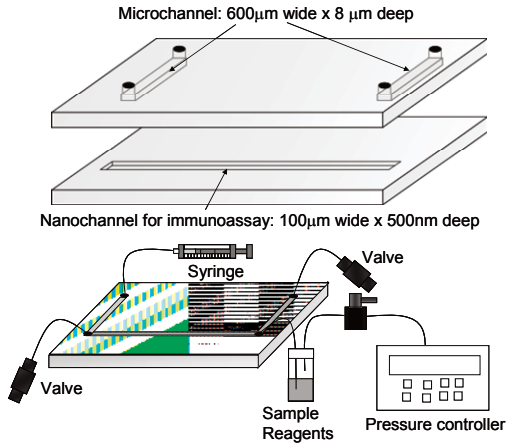

Figure 2. Illustration of micro/nano chip and the nanofluidic system

3. RESULTS AND DISCUSSION

At first, we investigated the principle of immunoreaction in nanochannel by observing a large number of analytes (10^7 molecules) in 100×350 μm area as shown in Figure 3. Fluorophores were labeled to second antibodies, and the immunoreactions were monitored by a fluorescence microscope. Clear difference in fluorescent intensity was observed for negative and positive controls. The weak fluorescent signals in negative control is due to nonspecific adsorption of analytes and second antibodies. From these results, principle of ELISA in nanochannel was verified.

Then, we investigated the performance in sensitivity by utilizing TLM detection. In this case, HRP is labeled to second antibodies, and the enzyme reactions with

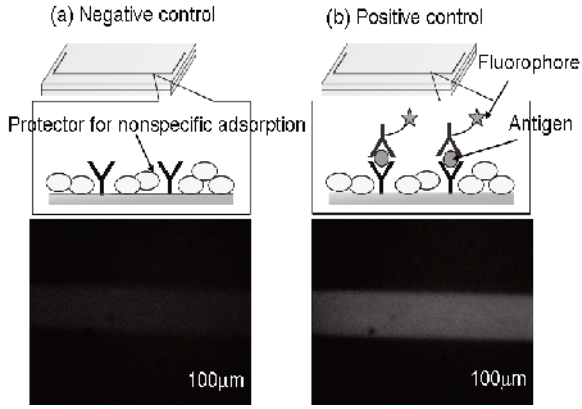

Figure 3. Principle verification of immunoreaction in nanochannel: (a) negative control, (b) 93μg/mL AFP.

substrates (TOOS) were monitored by scanning TLM. The result is shown in Figure 4. Assuming that all the antigens were captured by the antibodies, 840 analyte molecules in detection volume (~1μm^3) was successfully detected with signal-to-noise (S/N) ratio of approximately 96. The lower limit of detection (LOD) can be calculated to be ~20 molecules (S/N=2). This value is almost two-order lower than the values in micro ELISA method. Now, we are investigating the possibility of detecting single molecules by optimizing the conditions such as channel size, reaction time, substrate concentration, temperature, and so on.

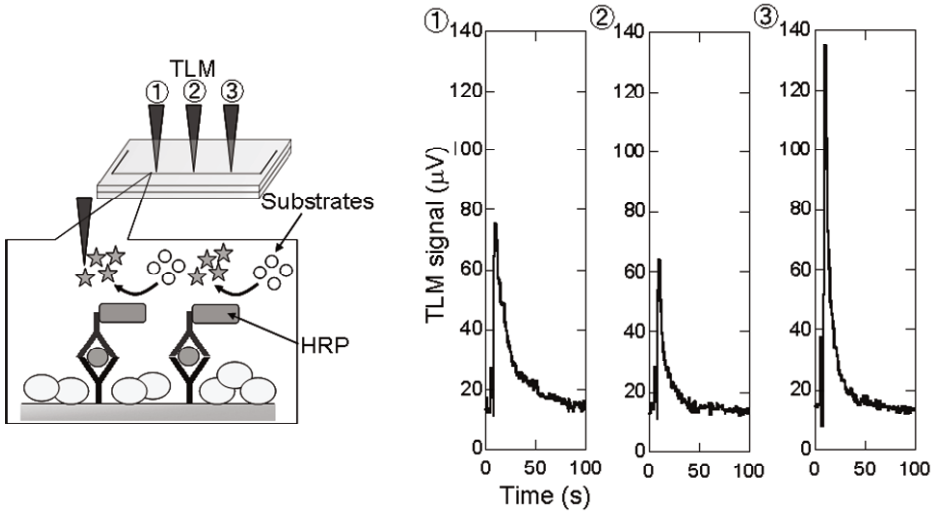

Figure 4. Performance of ELISA in nanochannel by scanning TLM detection.
(left: principle, right :result in three detection points)

4. CONCLUSIONS

We realized a nano ELISA system for the first time. The basic technologies were established, and the principle was successfully verified. As a result, excellent performance was shown in sensitivity. This novel method will be powerful molecular recognition tool at single molecule sensitivity in various analytical fields such as single cell proteomics.

REFERENCES

[1] T. Kitamori, M. Tokeshi, K. Sato, A. Hibara, "Thermal lens microscopy and microchip chemistry," Analytical Chemistry, 76, 52A (2004).

[2] M. Tokeshi, M. Uchida, A. Hibara, T. Sawada, T. Kitamori, “Determination of subyoctomole amounts of nonfluorescent molecules using a thermal lens microscope: Subsingle molecule determination,” Analytical Chemistry, 73, 2112 (2001).

PLASMON RESONANCE ENERGY TRANSFER SPECTROSCOPY (PRET)

Yeonho Choi,[†] Taewook Kang,[†] Gang L. Liu, Yitao Long, and Luke P. Lee

Department of Bioengineering, University of California, Berkeley, CA, USA, [†]Both authors contributed equally to this work

ABSTRACT

We demonstrate that gold nanoparticles (GNPs) with self-assembled monolayer (SAM) can function as all-optical nanoscale biomolecular detectors that monitor in situ resonant biomolecules, such as Cytochrome c. By tethering resonant biomolecules to Au nanoprobes, the binding events of Cytochrome c onto 50-nm Au nanoprobes yield characteristic spectral dips in scattering spectra of Au nanoprobes due to plasmon resonance energy transfer (PRET). The quenching dip depth of the single nanoprobe spectrum is found to be a function of incubation time (t) and concentration of Cytochrome c, which provides a real-time and nanoscale measurement and quantification of Cytochrome c.

Keywords: Plasmonic Resonance Energy Transfer, Gold Nanoparticle, Rayleigh Scattering, Cytochrome C

1. INTRODUCTION

Our understanding of biological systems is increasingly dependent on our ability to visualize and quantify biomolecules and biological events with high spatial and temporal resolution in the cellular context. Therefore, being able to observe process as biomolecular events proceed within a single living cell has great implications on our understanding of cell function and cellular diagnostics. Current fluorescent microscopy has photobleaching problem [1], interference from the emission spectrum of one label another label since multiple filter sets must be used for each corresponding fluorescent label, requiring multiple fluorescent labels to observe various biomolecules. However, recently we have developed a new method called Plasmonic Resonance Energy Transfer (PRET) nanospectroscopy by matching the electronic transition energy of a biomolecule matches and the plasmon resonance energy of nanoparticles [2].

Our strategy is focused on functionalization of GNPs with appropriate biomolecule receptors (Figure 1a). If the scattering spectrum of a single nanoparticle would change reversibly, quantitatively depending on both biomolecule (cytochrome c, cyt c) concentrations and the incubation time (Figure 1b), these conjugated GNPs would act as nanoscopic optical probes for dynamics of cyt c.

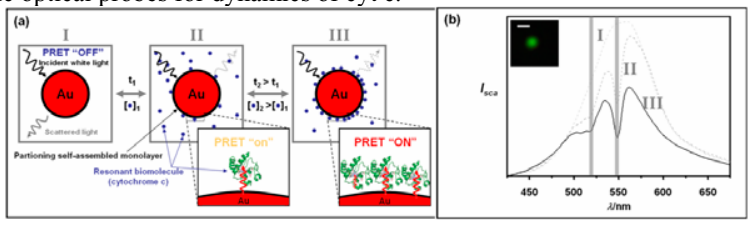

Figure 1. (a) Scheme of nanoscale local and in situ detection of resonant biomolecule using Au nanoparticle probes. (b) Representative time-resolved Rayleigh scattering spectra of the single PRET probe.

978-0-9798064-0-7/μTAS2007/$20©2007CBMS

2. THEORY

When white light is illuminated, a noble metal nanoparticle such as Au or Ag shows scattering peak at plasmonic renonance frequency (Fig. 2a). These scattering spectra can be modified by immobilized biomolecules onto the surface of nanoparticles. Especially, when these molecules have the absorptive characteristic near scattering peak of nanoparticles (Fig. 2b), some of scattering energy near absorbance peaks of conjugated biomolecules are easily transferred. As a result of this energy transfer, spectral quenching dips (Fig. 2c) can be generated in a scattering spectrum.

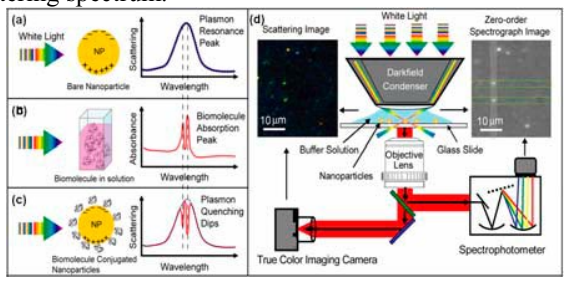

Figure 2. Schematic diagram of the mechanism of PRET and experimental set-up (a) representative Rayleigh scattering spectra from a single gold nanoparticle (b) absorbance properties of targeting biomolecules (cytochrome c) (c) typical scattering spectra from GNP conjugated with biomolecules by PRET (d) experimental configuration

3. EXPERIMENTAL

50nm spherical GNPs were immobilized on top of a cleaned glass slide using 3-mercaptopropyltrimethoxysilane (MPTMS). Freshly prepared GNPs on the glass slide was immersed into 1 mM 3-mercaptopropianic acid (MPA) for 12 hrs. White light (Xenon Arc lamp) is illuminated through a liquid-contact condenser lens (NA 1.2~1.4). The forward scattering light from each single GNP is collected by an objective lens (40x, NA 0.65) and sent to a CCD camera for image and spectrometer for spectra collection.

4. RESULTS AND DISCUSSION

Cytochrome C is chosen to show PRET because of its biological importance and optical absorption properties. The plasmon energy transfer from the GNPs to the immobilized cyt c is represented as spectral dips (520 nm and 550 nm) in the GNPs scattering spectra irrespective of the scattering maxima (Figure 3) and the positions of dips match with the absorption peak positions of cyt c.

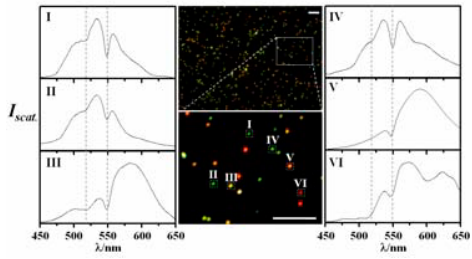

Figure 3. (center: top) Dark field image of Au nanoprobes on glass. The bar corresponds to 10 μm. (left & right) Rayleigh scattering spectra from the numbered Au nanoprobes in the figure (center: bottom) are represented after incubation with Cytochrome c.

As the incubation time increases, the scattering intensity of the dips gradually decreases, and reaches the equilibrium over 40 min. By replacing the cyt c solution to 50mM PBS, the scattering spectrum of the single GNP can be reversibly recovered. Figure 4 shows time course of the differential quenching dip change varying concentrations of cyt c. Interestingly, as the concentration of cyt c decreases, the response time to reach the equilibrium decreases. Figure 5 indicates normalized quenching dip depths at equilibrium as a function of concentration. Based on these results, optical detection limit for cyt c (operationally defined as 0.05 % change in the differential quenching dip) is found to be around 500 nM

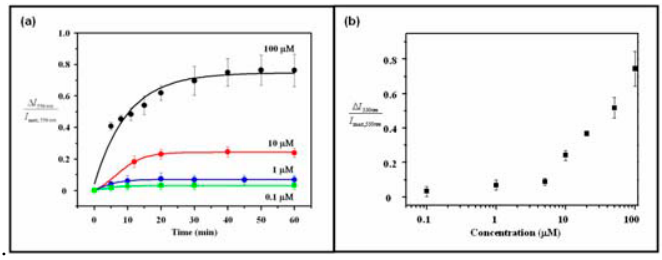

Figure 4. (a) Time course of the differential quenching dip change varying concentrations of Cyt c (b) Equilibrium differential quenching dip change as a function of Cyt c concentrations

5. CONCLUSIONS

In conclusion, we demonstrate that gold nanoparticles (GNPs) with partitioning self-assembled monolayer can function as all-optical nanoscale biomolecular detectors that monitor in situ resonant cyt c. The positions of the spectral quenching dips resulted from PRET reveal that the detected biomolecule is cyt c. By measuring the dip depths normalized by the maximum intensity, the concentrations can be quantitated down to 500 nM. We believe that these nanoscopic optical probes will have huge impacts on the fields of biomolecular and cellular imaging.

ACKNOWLEDGEMENT

This work was supported by a grant (code #: 05K1501-02810) from 'Center for Nanostructured Materials Technology' under '21st Century Frontier R&D Programs' of the Ministry of Science and Technology, Korea.

REFERENCES

[1] M. Bruchez, M. Moronne, P. Gin, S. Weiss, A. P. Alivisatos, Semiconductor nanocrystals as fluorescent biological labels, Science, 281, 2013 (1998).

[2] Y, Long, G. Liu, Y. Choi, T. Kang, L. P. Lee , Nanoscopic Biomolecular Absorption Spectroscopy Enabled by Single Nanoparticle Plasmon Resonance Energy Transfer, Nature Methods, under revision (2007).

PREPARATION OF CELL-SIZED LIPOSOMES ON SILICON: CONTROLLING LIPOSOME SIZE BY SURFACE MICRO-ENGINEERING

Maël Le Berre[1], Ayako Yamada[2], Yong Chen[1] and Damien Baigl[1]
[1]*Ecole Normale Supérieure, FRANCE*
[2]*Kyoto University, JAPAN*

ABSTRACT

We report on a novel method to prepare cell-sized liposomes with a controlled size distribution by using silicon substrates of various engineered surface properties. The electroformation method is used to swell liposomes from phospholipids films organized on various substrates. We studied the influence of surface homogeneity on lipid film organization and resulting liposomes size distribution. Then, we proposed a way to control size distribution by using silicon substrates with a silica insulating mask.

Keywords: liposome, electroformation, surface engineering, microfluidics

1. INTRODUCTION

Cell-sized liposomes (1-100 μm) are of great interest as cell models[1] or biochemical micro-reactors.[2] However, conventional preparation techniques lead to the formation of polydisperse liposomes.[3] Among them, electroswelling consist in swelling in a solution a phospholipids film, which has been dried on an electrode, using an AC electric field. In previous works, liposomes of controlled size were obtained using this method on patterned lipid films but could not be manipulated after preparation without loosing monodispersity.[4] Here, we show how silicon surface engineering can be used to control the size distribution of obtained liposomes. First, we present how chemical modification or microstructuration can modify the film organisation and the resulting size distribution. Then, silica microstructures are used to constrain the film and control the size of liposomes.

2. EXPERIMENTAL

For all experiments, a L-α-phosphatidylcholine (EPC) phospholipid solution in a 10:1 chloroform/methanol mixture was spread on a silicon substrate. After drying under nitrogen, the phospholipid film was organized into a stratified fashion corresponding to approx. 15 bilayers in avergage. (Figure 1A) A sucrose solution was then introduced between the phospholipid film and a transparent ITO counter-electrode. Under an AC field (2V, 10 Hz), the phospholipid film swelled to form liposomes containing the sucrose solution ('electroswelling', figure 1B *top*). After 10 h of electroswelling, a large amount of cell-sized liposomes were extracted and could be used for further manipulations. We characterized the obtained liposomes by phase contrast microscopy after 2h decantation in a glucose solution of same osmolarity. (Figure 1B *bottom*). From these images, size distribution was extracted with a custom-built image analysis software on approximately 10000 measured liposomes for each condition. Microstructures are etched in the silicon substrate after a photolithography step by a SF_6 reactive ion etching. For silica masked substrate, a 200nm thick SiO_2 layer is thermaly grown on silicon before the photolithography step and wet etched with buffered HF.

978-0-9798064-0-7/μTAS2007/$20©2007CBMS

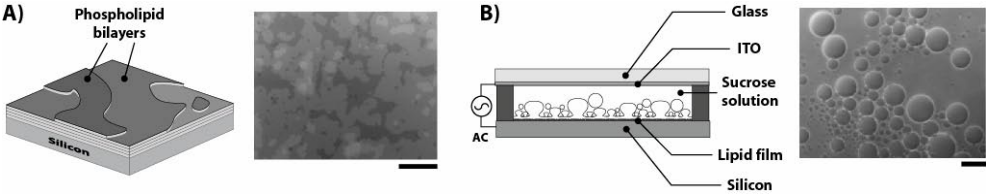

Figure 1. A) Scheme (top) and reflection microscopy image (bottom) of a phospholipid film on a Silicon substrate. B) Electroswelling setup (top) and typical phase contrast microscopy image of extracted liposomes (bottom). Scale bars are 50 µm.

3. RESULTS AND DISCUSSION

We studied the effect of the surface homogeneity of the Si substrate on the liposome size distribution. Figure 3B shows the size distribution of the liposomes obtained with three kinds of substrates: i) Si wafer used as received (native Si); ii) Si modified by a self-assembled monolayer of phenyl-triethoxysilane; iii) Si with microstructures etched by (Figure 3A). Compared to native silicon, the phenyl-modifed substrate leads to a smoother organization of the lipid film (almost no defects) and the formation of much larger liposomes in average. In contrast, the microstructured substrate induces a fragmentation of the lipid film (Figure 3A) and the generation of smaller liposomes. These results show that the liposome size distribution is directly correlated to surface chemical and topological homogeneity.

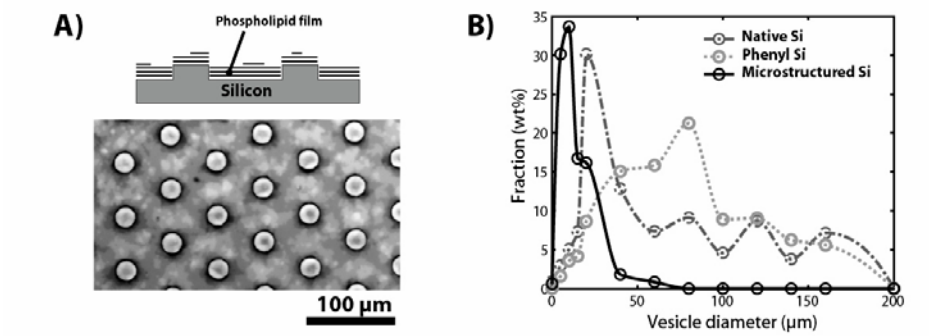

Figure 2. A) Scheme and reflection microscopy image of a phospholipid (EPC) film organized on a microstructured Substrate (hexagonal array of micropillars: height 150 nm, diameter 24 µm, pitch 60 µm). B) Distribution of vesicle sizes in fraction (wt%) of total lipid amount. Vesicles were obtained under the same conditions using various silicon substrates: native, phenyl modified, and with the microstructures of fig A). Solid lines are guidelines for the eyes.

However, in these experiments it is difficult to control liposome size precisely because all parts of the film contribute to the liposome formation. Therefore, we developed a new strategy to localize the electroswelling process with a micro-scale resolution. It consists of masking silicon with a patterned insulating silica layer (200 nm high) to localize the electroformation in the holes of the silica mask. Figure 3A shows the microscopy images of the lipid film and final liposomes on the different mask patterns. The liposome diameters

correspond approximately to the mask hole size, which is quantitatively confirmed by Figure 3B.

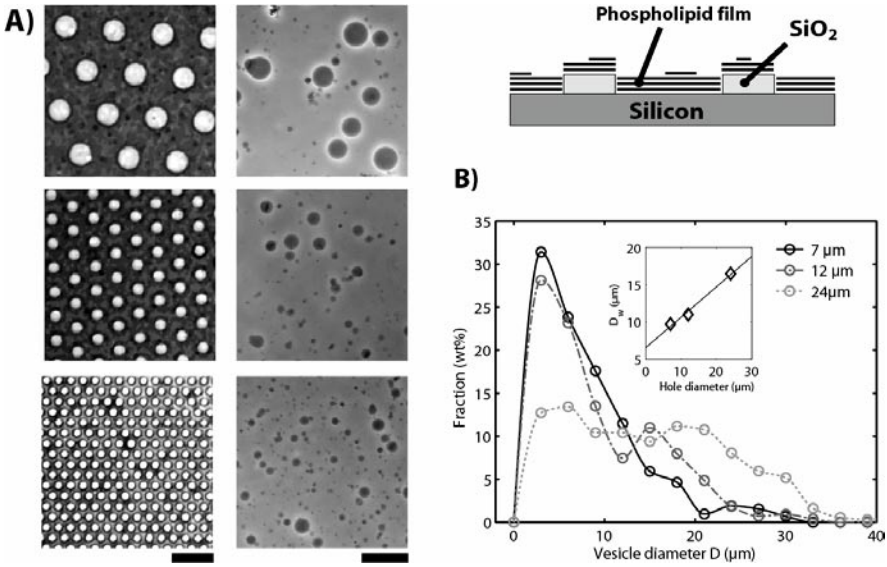

Figure 3. Effect of an insulating patterned mask of silica on the silicon substrate. A) Microscopy images show the film organization (left, reflection mode) and the resulting liposomes (right, phase contrast) for hole sizes of 24, 12, and 7 µm, respectively. Scale bars are 100 µm. B) Distribution of vesicle sizes in fraction (wt%) of total lipid amount and weight average diameter of liposomes D_W (inset) for silica masks of various hole sizes. Solid lines are guidelines for the eyes.

4. CONCLUSIONS

We demonstrated that surface micro-engineering is a promising strategy to prepare liposomes in a controlled way and that silicon is the adequate candidate as a new substrate for liposome electroformation.

ACKNOWLEDGEMENTS

This work was partially supported by the European Commission through project contract NABIS (NMP4-CT-2003-505311) and doctoral grants from EADS Foundation and DGA.

REFERENCES

[1] V. Noireaux and A. Libchaber, Proc. Natl. Acad. Sci. USA**,** 101, 17669 (2004)

[2] A. Karlsson, R. Karlsson, M. Karlsson, A. S. Cans, A. Stromberg, F. Ryttsen, and O. Orwar, Nature, 409, 150 (2001)

[3] M. I. Angelova and D. S. Dimitrov, Faraday Discuss. Chem. Soc., 81, 303 (1986)

[4] M. Le Berre, M. A Guedeau-Boudeville, Y. Chen, and D. Baigl, proc. of µTAS2006, 1399 (2006)

SIGNAL-GUIDED SEQUENTIAL ASSEMBLY OF NANO-BIO-COMPONENTS IN A COMPLETELY PACKAGED MICROFLUIDIC ENVIRONMENT

Xiaolong Luo, Angela T. Lewandowski, Hyunmin Yi, Gregory F. Payne, Reza Ghodssi, William E. Bentley and Gary W. Rubloff

University of Maryland, USA

ABSTRACT

This paper reports the signal-guided sequential assembly of labile nano-bio-components onto selected assembly sites within a completely packaged microfluidic environment. We demonstrate (a) the assembly of biologically active green fluorescence protein (GFP) and (b) sequential DNA hybridization on a chitosan scaffold at specific sites in a completely packaged microfluidic environment. Covalent conjugation through chitosan's amine groups provides for robust assembly of the biomolecules at specific sites. The spatial and temporal programmability of chitosan electrodeposition and biomolecule introduction to the microfluidic system provides a flexible platform for biomolecular sensing, synthesis, and metabolic engineering applications.

Keywords: Nano-bio-component, assembly, microfluidics, chitosan

1. INTRODUCTION

Robust and sequential assembly of labile nano-bio-components witin microfluidic devices is challenging. We report signal-guided sequential assembly of labile nano-bio-components onto selected assembly sites within a completely packaged microfluidic environment. We exploit an integrated device and package design [1] which supports programmable bio-component assembly at selected sites [2]. The aminopolysaccharide chitosan is utilized as the interfacial biofunctionalization material for (1) electric signal-guided electrodeposition of the chitosan scaffold onto a selected electrode under negative bias in the microfluidic channel, and (2) chemical signal-guided assembly of nano-bio-components onto chitosan scaffold either through *in situ* activation of a specifically engineered pro-tag on GFP or through glutaraldehyde activation of chitosan scaffold for sequential DNA hybridization.

2. EXPERIMENTAL METHODS AND RESULTS

We first demonstrate the assembly of biologically active green fluorescence protein (GFP) at a specific address in a completely packaged microfluidic channel. Fig.1(a) shows the prefabricated microfluidic device [1] used for signal-guided assembly of nano-bio-components. Fig.1(b) and (c) schematically show the signal-guided assembly of GFP onto a selected electrode within a microfluidic channel. First, in (b), a slightly acidic chitosan solution (pH<6.3) was introduced in the microchannel and electrodeposited on a negatively biased electrode. Next, in (c), we introduced into the microchannel a GFP solution containing tyrosinase, which activated a genetically engineered pro-tag on the GFP into active o-quinones to covalently bind to the amine groups of chitosan. Fig.2(a) shows the GFP fluorescence intensity on the assembly site increased with time and remained after buffer rinsing, confirming that the spatially selective assembly is covalently bonded. A

978-0-9798064-0-7/μTAS2007/$20©2007CBMS

control experiment shown in Fig.2(b) was performed without adding tyrosinase in the GFP solution. The fluorescence diminished substantially after buffer rinsing, indicating that its presence during flow was associated with weak non-specific bonding.

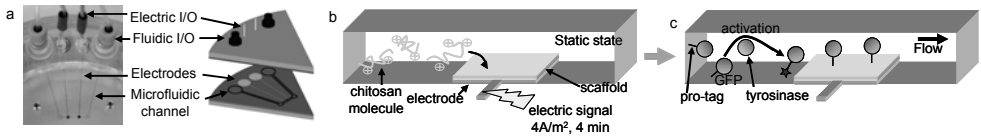

Figure 1: Microfluidic device and schematic flow of sequential protein assembly. (a) One of six microchannels of completely packaged microfluidic device, (b) chitosan assembly onto selected address within microchannel, (c) in situ tyrosinase activation and green fluorescence protein (GFP) assembly onto chitosan scaffold within microchannel.

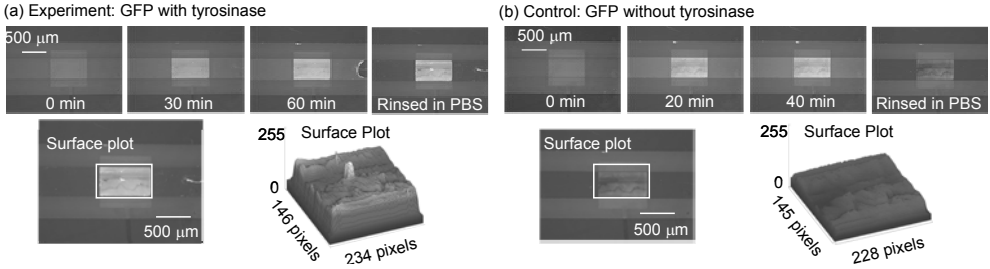

Figure 2: Fluorescent micrographs of assembly site during and after GFP assembly, and surface plot of rinsed assembly site. (a) Experiment: covalent assembly of GFP via in situ activation by tyrosinase, (b) control: no covalent assembly of GFP without tyrosinase activation.

Next, we demonstrate the sequential DNA hybridization on chitosan scaffold at specific sites in a completely packaged microfluidic channel. A schematic description of sequential DNA hybridization experiments in microfluidic devices is shown in Fig.3. First, chitosan solution was introduced into a microchannel and electrodeposited at a selected electrode. Second, glutaraldehyde was introduced to activate the electrodeposited chitosan for the probe single string DNA (ssDNA) to assemble onto the scaffold. After assembling the probe ssDNA, a mismatched ssDNA is introduced before transporting the matched target ssDNA to hybridize onto the probe ssDNA. The experiment results in Fig.4 show that the match target ssDNA was complementarily hybridized to probe ssDNA at the selected chitosan site, and the hybridization saturated within 15 minutes (Fig.5).

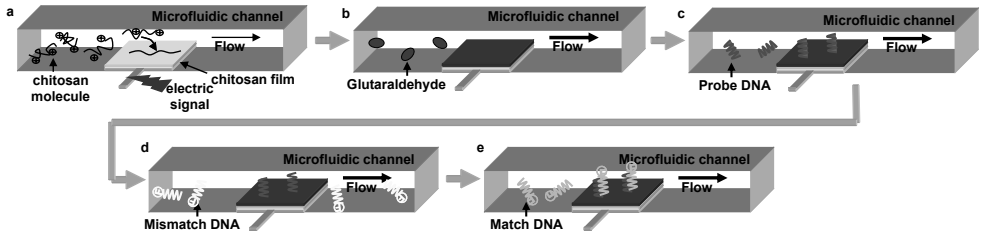

Figure 3: Schematic flow of sequential DNA hybridization in microfluidic device. (a) Chitosan assembly onto selected address, (b) Glutaraldehyde activation of chitosan scaffold, (c) probe ssDNA assembly onto activated chitosan surface, (d) introduction of mismatch target ssDNA, (e) introduction of match target ssDNA.

3. CONCLUSIONS AND DISCUSSIONS

This work demonstrates the assembly of labile nano-bio-components in a microfluidic device in a spatially and temporally selective manner while preserving the biological activity of the assembled components. The assembly is unique in that (a) the chitosan scaffold was electrodeposited at a selected site in microfluidic channels programmed by a simple electrical signal, (b) the model protein was covalently assembled onto the chitosan scaffold via enzymatic activation of the pro-tag of GFP, and (c) the target ssDNA is complementarily hybridized onto probe ssDNA on the patterned chitosan scaffold. This chitosan-mediated assembly is simple, robust and versatile. The signal-guided programmability is very attractive for precise assembly of biomolecules (e.g, expensive species such as enzymes) for multi-site designs and multi-step reactions bioMEMS applications in biosensing, biofabrication and metabolic engineering.

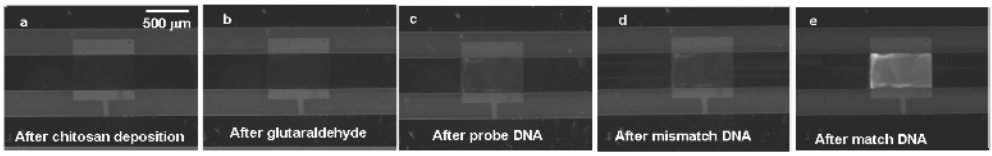

Figure 4: Bright field view and fluorescent micrographs of DNA hybridization site during the sequential hybridization process. (a) After chitosan electrodeposition, (b) after glutaraldehyde activation, (c) after probe ssDNA assembly, (d) after introduction of mismatch target ssDNA, (e) after introduction of match target ssDNA.

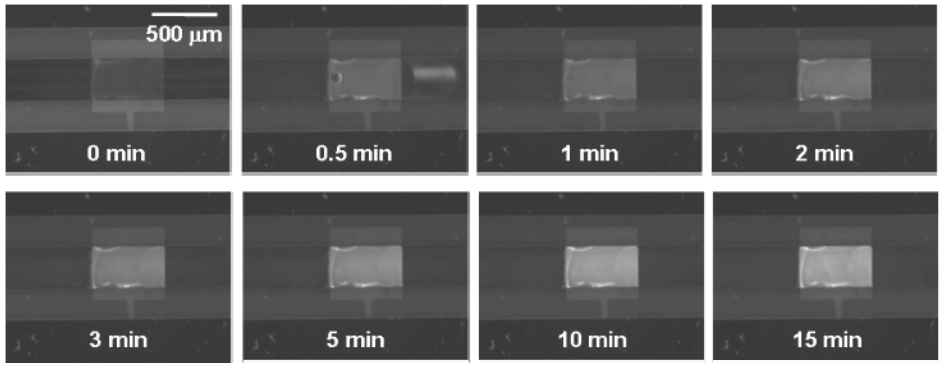

Figure 5: Sequential fluorescent micrographs during introduction of match target ssDNA to hybridize onto probe ssDNA on chitosan scaffold in microfluidic channel

ACKNOWLEDGEMENTS

This work is supported in part by the NSF MRSEC DMR080008, NSF IMI DMR0231291, NIST, and the Laboratory for Physical Sciences.

REFERENCES

1. J. J. Park, T.M. Valentine, R. Ghodssi, and G. W. Rubloff, The 9th International Conference on Miniaturized Chemical and Biochemical Analysis Systems (MicroTAS), Boston, MA, Oct 9-13, 2005.
2. J. J. Park, X. L. Luo, H. M. Yi, T. M. Valentine, G. F. Payne, W. E. Bentley, R. Ghodssi and G. W. Rubloff, *Lab on a Chip*, 2006, 6, 1315-1321.

SINGLE DNA/PROTEIN INTERACTION ANALYSIS USING QUANTUM DOT CONJUGATES AND MICROFLUIDIC SYSTEMS

D. Onoshima[1], N. Kaji[1,2], M. Tokeshi[1,2] and Y. Baba[1,2,3,4]

[1]Department of Applied Chemistry, Graduate School of Engineering, [2]MEXT Innovative Research Center for Preventive Medical Engineering, Nagoya University, [3]Health Technology Research Center, AIST, [4]Institute for Molecular Science, JAPAN

ABSTRACT

We have designed a microfluidic detection platform in which we can monitor and analyze single DNA/protein dynamic interaction using "single-molecule fluorescence tracing". The use of quantum dot (QD) labelling on DNA, polydimethylsiloxane (PDMS) microchip, micro patterning of active enzymes, and total internal reflection fluorescence (TIRF) microscope was successfully applied for nano-space experiments in micrometer-sized channels. We used this detection platform to observe the enzymatic reaction of restriction endonuclease (EcoRI) and measured the duration of its cleavage reaction.

Keywords: Quantum Dot, Polydimethylsiloxane, Micro Patterning, Total Internal Reflection Fluorescence Microscope

1. INTRODUCTION

The increased interest of scaled-down analytical processes has led to the development of various chip-based technologies in which bio-related analyses can be carried out more rapidly and precisely. Advances in such technologies have largely enriched the biophysical research approaches. The possibility of observing new bio-phenomena and obtaining detailed information about DNA unwinding [1] and mechanochemical transformation of F1-ATPase [2] are indeed possible examples. Therefore, adaptation of these single molecule approaches to lab-on-a-chip formats could provide a new class of research tools for the investigation of life processes. In this contribution, we show a simple device with a nano-space detection feature for evaluating DNA/protein interactions at a single molecule level (Figure 1).

2. EXPERIMENTAL

Fluidic micro-device consists of a flat glass substrate and a transparent PDMS material that has embossed micro-channels on its surface. PDMS structures were formed by conventional moulding procedures. By means of this fluidic structure, EcoRI was incubated and patterned as a slip onto an underlying planer glass substrate. The excess unbound proteins were washed out using water. For single DNA molecular imaging, CdSe/ZnS QD was attached to one end of λDNA (QD-λDNA), allowing prolonged real-time monitoring of single DNA behaviour.

Enzymatic cleavage reactions of immobilized EcoRI molecules were performed in the fabricated micro-channel. The injected sample solution can travel and reach the patterned EcoRI area through the channels that have laminar flow paths generated by the capillary pressure. Labelled DNA molecules running over the patterned EcoRI area were excited by TIRF system. Fluorescence images of reacting DNA molecules were recorded by a CCD

978-0-9798064-0-7/μTAS2007/$20©2007CBMS

camera at the video rate. The digestion products were analyzed using agarose gel electrophoresis.

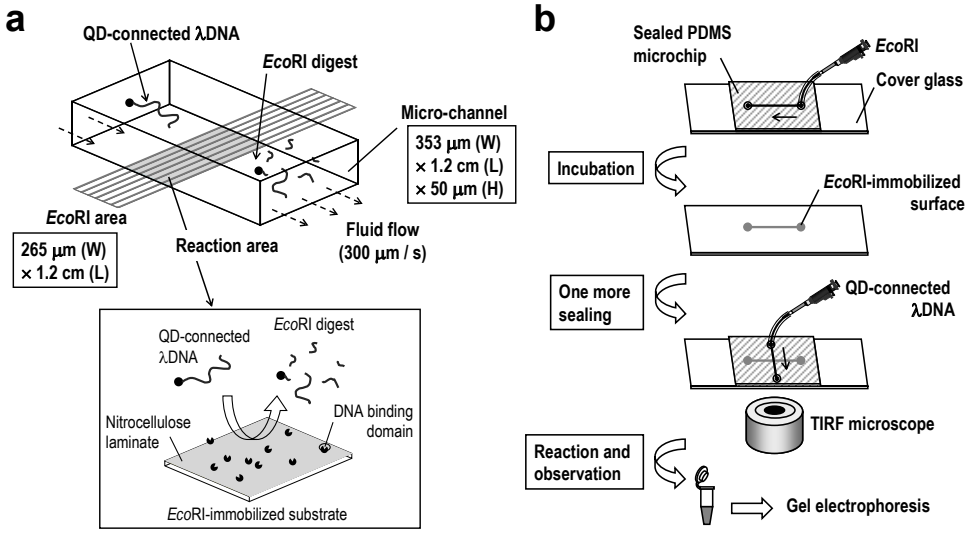

Figure 1. Strategy for real-time monitoring of enzymatic reactions on a surface (a) and procedure of the intersectional measurement on a glass substrate with PDMS microchip (b).

3. RESULTS AND DISCUSSION

TIRF technique allowed the DNA of interest to be highlighted within the evanescent field, and the enzyme reaction dynamics to be successfully measured as a function of time by tracing single QDs movements. Recorded videos were captured and further processed using analytical softwares. Figure 2 shows the direct observation of single QD-λDNA on the reaction area. The brightening QD sphere clearly traced the DNA motions. Time zero is defined as the first time of appearance of the QD-λDNA in the microscopic field. The position of each observed brightening QD was measured with respect to the center of the fluorescent spot and their moving velocities during reaction were calculated from the measured indices.

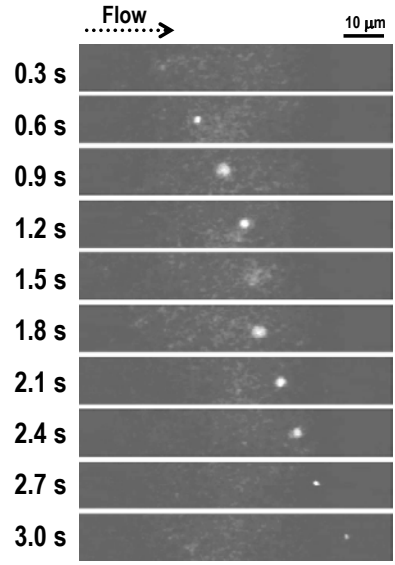

Figure 2. Sequential frames from a video recording of reacting QD-λDNA molecules.

As seen in Figure 3, the running QD slowed down from the flow rate and gradually built up speed again. This result indicates that the QD-λDNA was catched by EcoRI and the digestion products were released after the bond-breaking step. Time wise direct observation and subsequent statistical analysis of DNA movement were followed by gel electrophoresis analysis (data not shown). The duration of a cleavage reaction was defined in terms of the period of time in which the moving velocity of fluorescent spots kept within the standard speed obtained from the enzyme-free measurements (Figure 4).

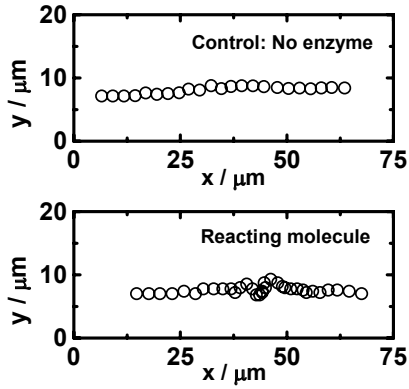

Figure 3. Indices for the movements of QD-λDNA in two different cases.

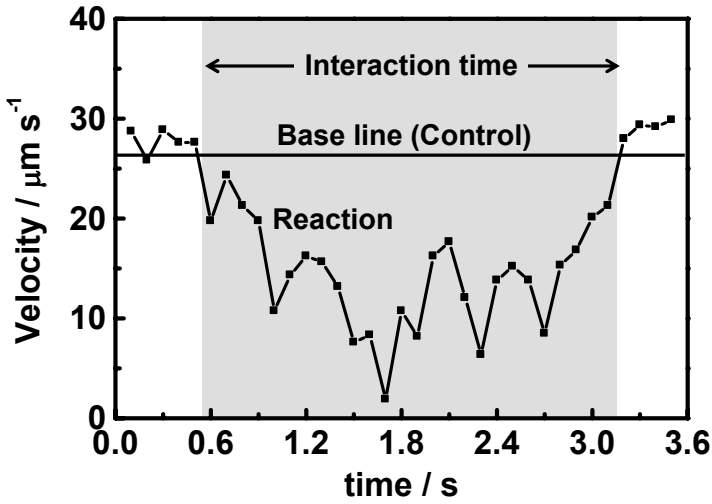

Figure 4. Time dependence of QD-λDNA speed on the reaction area.

4. CONCLUSIONS

Our results suggest that QD-λDNA and the introduced chip-based detection method to be a potential tool in studying single DNA/protein interactions. Consequently, this experiment set-up can be applied for future lab-on-a-chip systems engineered to use or analyse individual biomolecules.

REFERENCES

[1] P. R. Bianco et al., "Processive translocation and DNA unwinding by individual RecBCD enzyme molecules", Nature, Vol. 409, pp. 374-378 (2001).

[2] Y. Rondelez et al., "Highly coupled ATP synthesis by F1-ATPase single molecules", Nature, Vol. 433, pp. 773-777 (2005).

STRETCHING DNA IN SINGLE, EXTRA-LONG (1.5 cm) NANOFLUIDIC CHANNELS FABRICATED USING A NOVEL NANOIMPRINT MOLD

Xiaogan Liang[1], Keith J. Morton[1], Robert H. Austin[2] and Stephen Y. Chou[1]
[1]*Nanostructure Laboratory, Princeton University, Princeton, NJ, USA 08544*
[2]*Dept. of Physics, Princeton University, Princeton, NJ, USA, 08544*

ABSTRACT

We fabricated the first single centimeter long nanofluidic channel with continuous and uniform channel width (11 nm to 50 nm). The fabrication process uniquely combines the novel method for making imprint molds, nanoimprint lithography, and optional reactive ion etching. The key steps in the novel mold fabrication are anisotropic wet etching of (110)-oriented silicon and conformal edge deposition of mold material, which assure a continuous and uniform channel line. The continuous capillary flow through the entire channel verified the channel continuity over a centimeter-scale distance. We also demonstrated the stretching and transport of DNA strands in a single long nanochannel.

Keywords: Nanofluidics, nanofabrication, nanoimprint, Deoxyribonucleic acid

1. INTRODUCTION

A single, long (cm length), smooth, and uniform-width nanofluidic channel is needed for stretching and detecting individual DNA strands in rapid analysis and sequencing of their bases [1,2]. Fabrication of such devices is extremely difficult using conventional methods such as electron beam lithography (EBL) and reactive ion etching (RIE), due to two

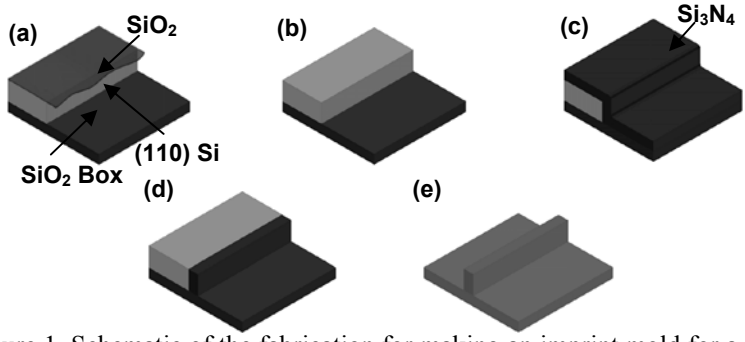

Figure 1. Schematic of the fabrication for making an imprint mold for a single, cm-long, uniform-width, continuous nanochannel. (a,b) Anisotropic wet etch of Si (110) surface of a SOI wafer; (c) conformal LPCVD of SiN_x; (d) CHF_3/O_2 RIE of SiN_x; (e) removal of (110) Si and final protruding via for imprint mold.

challenges: (1) line edge roughness generated in EBL and RIE can pinch-off long nanochannels; (2) the difficulty in keeping an electron beam tightly focused on a substrate over cm long distances (i.e.: conventional EBL is limited to a ~100 um and is incapable of stitching together a continuous narrow channel; and a fixed beam EBL on a scanning stage could also not keep the beam in good focus over cm lengths).

978-0-9798064-0-7/μTAS2007/$20©2007CBMS

We developed a new method for fabricating the single, long (3 mm - 1.5 cm), uniform width (10nm-50nm) continuous nanofluidic channels with ultra-smooth sidewalls, and demonstrate DNA stretching in such channels.

2. EXPERIMENTAL

The keys in the fabrication are first to use novel methods to create imprint molds with single long nanochannel devices, and then use imprint to duplicate the channels on a substrate. The novel mold fabrication method (Figure 1) consists of (a) wet crystalline anisotropic etching of (110) silicon to create a ridge with an atomically smooth surface (111); (b) conformal deposition of SiN_x by low pressure chemical vapor deposition (LPCVD); (c) CHF_3/O_2-based reactive ion etching (RIE) of SiN_x; and (d) removal of Si, to form protrusive SiN_x line. The orientation-dependant, crystalline anisotropic etching removes the edge roughness, and the conformal SiN_x deposition ensures a uniform and continuous channel regardless of the initial sidewall roughness. Figure 2 shows a cross-sectional SEM image of a mold bearing a 17 nm wide 1.5 centimeter long protrusive nanochannel pattern.

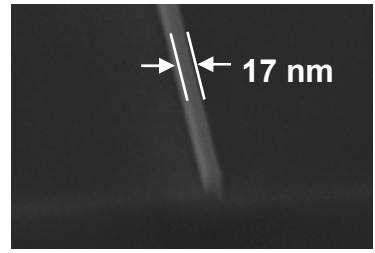

Figure 2. The cross-sectional SEM image of an imprint mold having a 17 nm wide, smooth, uniform, 1.5-cm-long single nanochannel pattern.

The final channel device is made by direct imprinting [3] of the mold in a functional material, which duplicates the smooth sidewall, uniform and continuous channel from the mold. This novel process either completely avoids the problematic EBL and RIE, or uses RIE only once. Figure 3 shows a single nanochannel imprinted directly into a Nanonex NXR-3020 UV-curable material layer (width: 17 ± 3 nm; length: 1.5 cm), which itself can be used as a nanofluidic channel. Four SEM images captured at different locations along the channel indicate that the standard variation of the channel width over a centimeter-scale length is within nanometer scale. Alternatively, this material can be used as an etching mask to faithfully transfer the long channel structure into other hard substrates (SiO_2) by a CF_4-based RIE. A 30 nm wide single nanochannel from a different master mold is shown in Figure 4 (a).

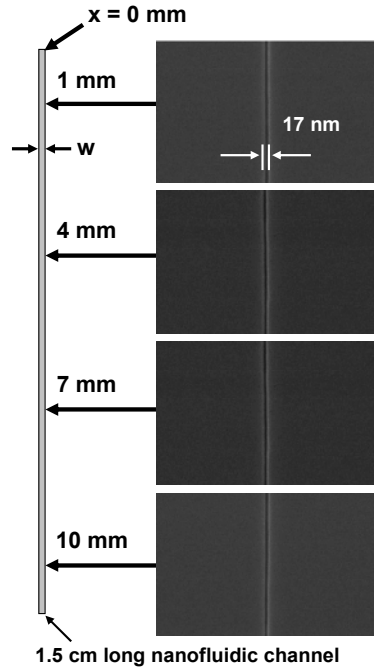

Figure 3. A 1.5-cm-long, uniform-width, continuous nanochannel directly imprinted in a UV-curable material layer. Four SEM images captured at different locations along the channel show the great uniformity of the channel width over a centimeter length (w = 17 ± 3 nm).

The RIE adds an edge roughness of ~5 nm.

3. RESULTS AND DISSCUSSION

After sealing the top of the long nanochannel with a transparent cover slip using quartz-quartz bonding, channel continuity was checked by continuous flow of fluorescent dye in DI water through the single nanochannel as shown in Figure 4(b). We also demonstrated DNA stretching and transport in the long nanochannel (Figure 5). Electrophoresis was used to move genomic length, fluorescently labeled T2 DNA (164 kbp) from a microchannel inlet into the nanochannel. The unconfined DNA coil in the microchannel is stretched as its moves into and through the nanochannel.

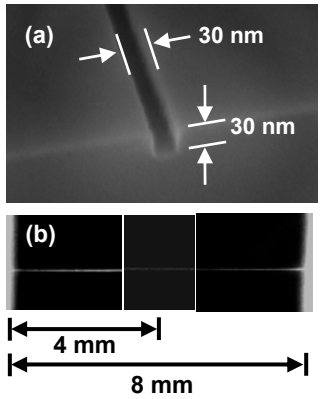

Figure 4. (a) The cross-sectional SEM image of a different 30 x 30 nm nanochannel transferred into a SiO_2 layer by CF_4/H_2 RIE. (b) Capillary flow with fluorescent dye into a 30 nm wide centimeter-long single nanochannel.

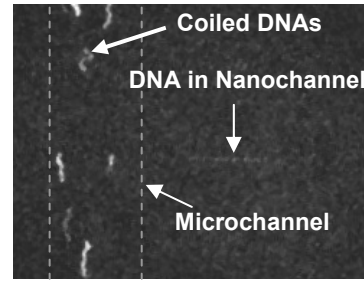

Figure 5. Time trace of a stretched T2 DNA moving through a 3 mm long, 50nm wide nanochannel. DNAs in the inlet microchannel are unconfined and remain in a coiled state.

4. CONCLUSIONS

The new approach we proposed has clearly demonstrated the fabrication of a single, narrow (17 nm or less), long (over 1.5 cm) and continuous fluidic-channel, and the transporting and stretching of DNAs in these channels. The new approach has removed a key obstacle in developing a variety of innovative bio/chemical sensors, particular single-stranded DNA sequencing devices.

REFERENCES

[1] J. Tegenfeldt, C. Prinz, H. Cao, S.Y. Chou, W. Reisner, R. Riehn, Y.M. Wang, E.C. Cox, J.C. Sturm, P. Silberzan and R. H. Austin, *Proc. Natl. Acad. Sci.*, 101, 30, July 27, 2004, pp. 10979–10983

[2] H. Cao, Z. Yu, J. J. Tegenfeldt, E. Chen, W. Wu, R. H. Austin and S.Y. Chou, *Appl. Phys. Lett*., 81, 1, July 2002, pp. 174-176

[3] S.Y. Chou, P. R. Kraus, P.J. Renstrom, *Science*, 272, 5258, 5 April 1996 pp. 85 - 87

WATER-VAPOR PERMEABILITY CONTROL OF PDMS BY DISPERSION OF COLLAGEN POWDER

Masatoshi Ishida*, Y. Kazoe**, Y. Sato** and Norihisa Miki**
*Ricoh, JAPAN, **Keio University, JAPAN*

ABSTRACT

Polydimethylsiloxane (PDMS) has been widely used for a material of μTAS devices due to the superior nature of manufacturability, chemical resistance, etc. This paper reports a new method to control the water-vapor permeability of PDMS by dispersing collagen powder. We designed and fabricated micro-fluidic devices to directly measure the amount of water-vapor permeating through PDMS and evaluated the effect of dispersed collagen. The water-vapor permeability of PDMS was successfully reduced by the dispersed collagen powder by 54%.

Keywords: Polydimethylsiloxane, Water Permeability, Collagen Powder, Polymer

1. INTRODUCTION

Polydimethylsiloxane (PDMS) has been widely used for a material of μTAS devices due to the superior nature of manufacturability, chemical resistance, etc. PDMS is known to allow permeation of gas and water-vapor. This characteristic was applied to efficient oxygen supply to liver cells cultivated in micro chambers [1] and power-free sample injection into micro fluidic devices [2]. Some applications, such as long-term experiments with aqueous samples, however, prefer to avert permeation of water-vapor through PDMS. This paper reports a new method to control the water-vapor permeability of PDMS by dispersing collagen powder. Collagen powder is considered to prevent the water-vapor from peameating through PDMS. We designed and fabricated micro-fluidic devices to directly measure the amount of water-vapor permeating through PDMS and evaluated the effect of dispersed collagen.

2. EXPERIMENTAL

We used commercially available collagen powder, Ergona (Matsuoka Chemical Co., Ltd.), which is much less costly than high-grade collagen for bio applications. The mean particle size is 8μm in diameter. The dispersion process is quite simple; mix collagen powder, PDMS (Dow Corning Toray, Silpot 184), and the curing agent and subsequently, cure the mixture at 60°C for 2 hours. The powder disperses into PDMS uniformly and PDMS becomes white and less transparent. Authors' group reported that manufacturability, which is represented by high precision molding and bonding capability to glass after treatment by oxygen plasma, mechanical strength and chemical resistance of PDMS was not deteriorated by the dispersed collagen powder [3].

We designed and fabricated a micro-fluidic device to directly measure the amount of water-vapor permeating through PDMS, as illustrated in Figure 1 and 2. The device contains a micro-channel and a large chamber (evaporation chamber). PDMS or collagen/PDMS membrane seals the upper side of the evaporation chamber. The channel and chamber are filled up with water. The difference in water height of 10mm provides a pressure difference between outside and inside the chamber. Water-vapor permeates

978-0-9798064-0-7/μTAS2007/$20©2007CBMS

through the membrane, which in turn, generates flow in the micro-channel. The volumetric flow rate in the channel represents the permeation rate of water-vapor through the membrane. The permeation flux is obtained by dividing the permeation rate by the area of the upper plane of the evaporation chamber. Note that the device is designed such that permeation through other planes of the chamber is negligible. We exploited micro particle image velocimetry (μPIV) utilizing submicron fluorescent particles to measure the flow velocity in the channel, as depicted in Figure 3. The permeation coefficient P is expressed as $P = Nt/\Delta p$, where P is permeation coefficient [cm^3 (STP)/cm s cmHg], N is permeation flux [cm^3 (STP)/cm^2 s], t is thickness of the membrane [cm], and Δp is the pressure difference between the outside and inside the evaporation chamber [cmHg].

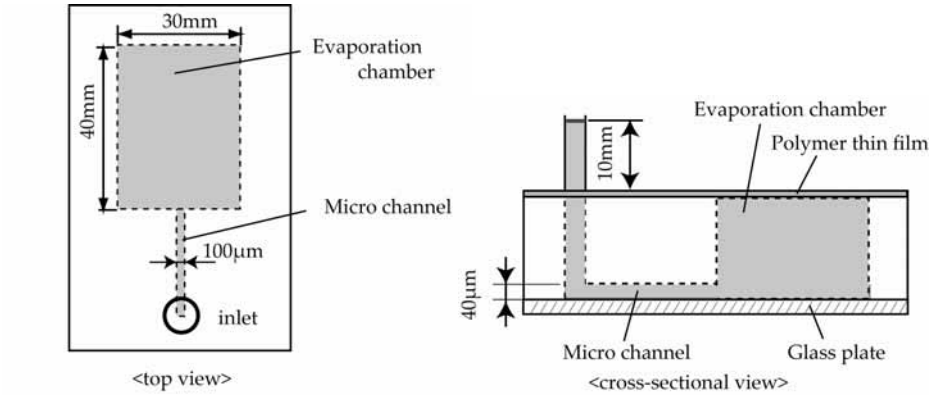

Figure 1. Micro-fluidic device to measure the permeating water-vapor through a polymer thin film.

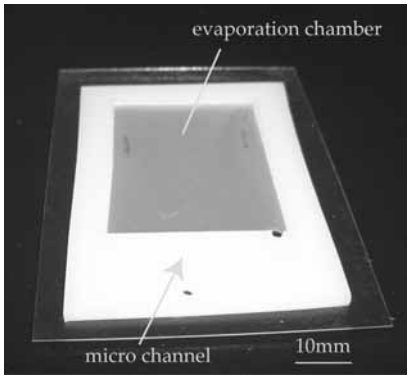

Figure 2. Photo image of the micro-fluidic device to measure water-vapor permeability. Collagen/PDMS is white and less transparent than pure PDMS.

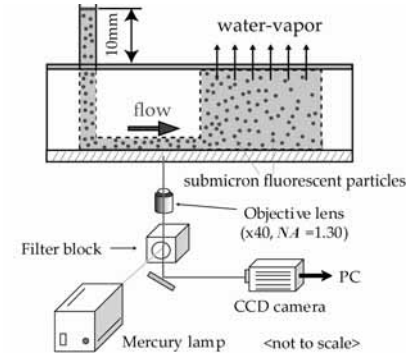

Figure 3. Measurement of the channel flow velocities by micro particle image velocimetry (μPIV). Submicron fluorescent particles were used to deduce the flow rate.

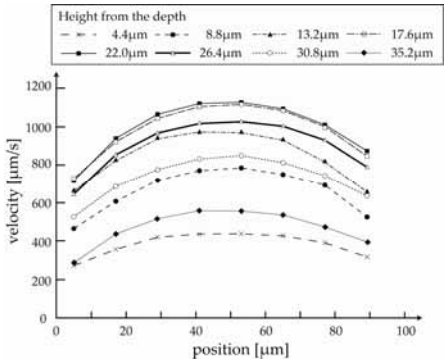

Figure 4. Flow velocities inside the micro-chamber of pure PDMS at various heights from the bottom.

Table 1. Permeate mass flux and permeation coefficient.

	PDMS	4 wt% collagen	8 wt% collagen
Mass flux [g/cm^2 s]	2.1×10^{-7}	1.5×10^{-7}	9.7×10^{-8}
Permeation Coefficient P [cm^3 (STP) /cm s cmHg]	2.0×10^{-4}	1.4×10^{-4}	9.2×10^{-5}
Ratio of P	1.0	0.70	0.46

3. RESULTS AND DISCUSSION

The experiments were conducted at 20 degrees Celsius and 40% RH. The flow velocities every 4.4μm in height and 12μm in width in the micro-channel were measured and integrated to deduce volumetric flow rate. Figure 4 depicts the flow velocities inside the micro-chamber of pure PDMS at various heights from the bottom. The parabola-shaped velocity profiles indicate the laminar flow in the micro channel. Table 1 depicts the permeated mass flux and permeability coefficient for pure PDMS, PDMS with 4wt% and 8wt% collagen. The experimental results showed that 4wt% and 8wt% of dispersed collagen reduced the water-vapor permeability by 30% and 54%, respectively.

4. CONCLUSIONS

The dispersion of collagen powder successfully controlled the water-vapor permeability of PDMS. 8wt% of dispersed collagen reduced the water-vapor permeability by 54%. The process of dispersing collagen powder into PDMS is quite simple and does not deteriorate the virtues of PDMS, such as manufacturability and chemical stability, only except the optical transparency. Collagen/PDMS can be readily applied to various μTAS devices to either exploit or prevent the water-vapor permeation.

ACKNOWLEDGEMENTS

This research was supported by The Center for Research Promotion, Keio University.

REFERENCES

[1] T. Leclerc, Y. Sakai, and T. Fujii, Biochemical Engineering Journal, 20, 143 (2004).
[2] K. Hosokawa, K. Sato, N. Ichikawa, and M. Maeda, Lab on a Chip, 4, 181 (2004).
[3] M. Ishida and N. Miki, Proc. of THE 23rd SENSOR SYMPOSIUM, 377 (2006).

AN EFFICIENT SURFACE MODIFICATION FOR SELECTIVE CONTROL OF CELL ATTACHEMENT USING PHOTOCHEMICAL REACTION

Kihoon Jang, Kae Sato, Tomohiro Konno,
Kazuhiko Ishihara, Takehiko Kitamori
The University of Tokyo, JAPAN

ABSTRACT

In this paper, we employed photochemical reaction for controlling the cell adhesion on the glass surface. The strategy is based on combining 2-Methacryloyloxyethyl phosphorylcholine (MPC) which is known to reduce non-specific binding, and photolabile linker (PL) for selective cell patterning. The MPC modified surface was irradiated through the MASK by UV and MPC were removed. After selective MPC cleavage, the cells only attached on UV illuminated region, which showed the selective surface control of cell attachment was performed using photochemical reaction.

Keywords: photochemical, adhesion, MPC, PL

1. INTRODUCTION

In recent, the interest of the cell-based microsystem has been increased to utilize as a powerful tool for performing basic biomedical research and clinical diagnosis. In these cellular researches, it is necessary to control the number of cells patterned on surface and the distance between cells for high efficient biological analysis. Therefore, biological surface modification[1-2] plays an important role in these cellular analysis to realize in a microchip. In this report, we have developed an efficient surface modification technique for regulating the cell adherence.

2. EXPERIMENTAL

Figure 1 illustrates the process to prepare the surface for selective cell culturing. The glass slides were precleaned in 0.1 M NaOH aqueous solution for 20 min at RT and then rinsed with deionized water and blown dry with nitrogen. The surface were aminated with 5%(v/v) 3-aminopropyltriethoxysilane (APTS) in Toluene for 2 h at RT, washed with Toluene, N,N-Dimethylformamide (DMF), deionized water vigorously and dried in vacuo. The aminated surface was then, coupled with 5mM Fmoc-photolabile linker [4-(4-(1-(9-fluorenylmethoxycarbonylamino)ethyl-2-methoxy-5-nitrophenoxy)-butanoic acid)], 10 mM benzotriazol-l-yloxy-tris(dimethylamino)phosphonium hexafluorophosphate (BOP), 1-hydroxy-benzotriazole (HOBt), diisopropylethylamine (DIEA) in DMF for 3 h at RT to prepare photo active surface, and then washed with DMF, deionized water, dried with nitrogen. After the coupling, 30% (v/v) acetic anhydride in Methylenechloride (MC) were used for 30 min to convert all the unreacted amino group to be inactivated, washed with MC, Ethanol, deionized water, and blown dry with nitrogen. Then, Fmoc were

978-0-9798064-0-7/μTAS2007/$20©2007CBMS

deprotected using 20% (v/v) piperidine in DMF for 30 min and then washed with DMF, deionized water, dried with nitrogen. The coupling of MPC was carried out in 0.1 M MPC,

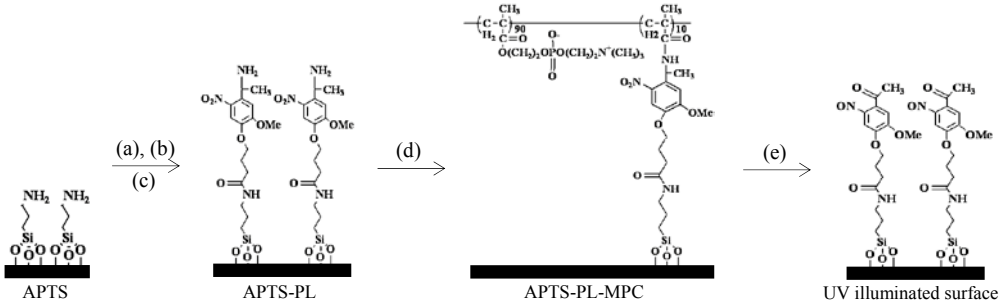

Figure 1. Preparation of photolabile linker-MPC modified surface: (a) Fmoc-photolabile linker (5 mM), BOP (5 mM), HOBt (5 mM), DIEA (5 mM) in DMF, (b) 30% (v/v) acetic anhydride in MC, (c) 20% (v/v) piperidine in DMF (d) MPC (10 mM), EDC (20 mM) in MOPS buffer (100 mM, pH 5.0), (e) UV (360 nm, 100 mW/cm^2) .

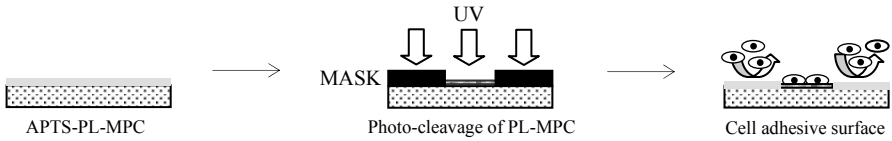

Figure 2. Schematic representation of the selective surface control of cell attachment.

0.2M 1-[3[(dimethylamino)propyl]-3-ethylcarbodiimide hydrochloride (EDC) in 0.1 M 3-Morpholinopropanesulfonic acid (MOPS) buffer (pH 5.0). In order to determine the optimal UV(360 nm, 100 mW) illumination time, the contact angle of the surface on UV illumination time was evaluated. After confirming the optimal UV irradiation time, UV was irradiated to the present surface, washed with deionized water, and then MC3T3-E1 cells (40×10^4cells/ml) were seeded on the surface and incubated at 5% CO_2 in 37℃.

3. RESULT AND DISCUSSION

Figure 1, 2 shows the schematic representation of preparing a cell controllable surface. Firstly, each step was confirmed by water contact angle (Figure 3, (a)). The coupling of Fmoc-PL on the aminated surface (APTS) was confirmed by the increasing of the water contact angle 52 degrees to 77 degrees (APTS-Fmoc PL). On deprotection of the Fmoc group, the water contact angle decreased 77 degrees to 63 degrees. After MPC were grafted to aminated surface, the contact angle was 14 degrees (APTS-PL-MPC), the hydrophilicity had increased rapidly. While UV was illuminated for 3 min (optimal UV irradiation was evaluated, figure 3b) the final contact angle was increased 14 degrees to 53 degrees, this result provide the MPC was removed and finally aromatic compounds were remained.

Next, after the preparing the surface, albumin-FITC and MC3T3-E1cells were introduced on each patterned surface. Figure 4 (b,c,d) shows the result of the cells cultured on surface between UV irradiated and not irradiated. The efficacy of a biomimetic polymer, MPC-grafted surface formed a resistant barrier for the protein and cell adherent. The cells were attached selectively on UV illuminated region where MPC were removed, as same pattern size as the photomask (Figure 4a), while cell adhesion was not found on the MPC remained area. MC3T3-E1 cells were patterned to relatively hydrophobic cleaved site of the surface selectively and the unattached cells were removed easily.

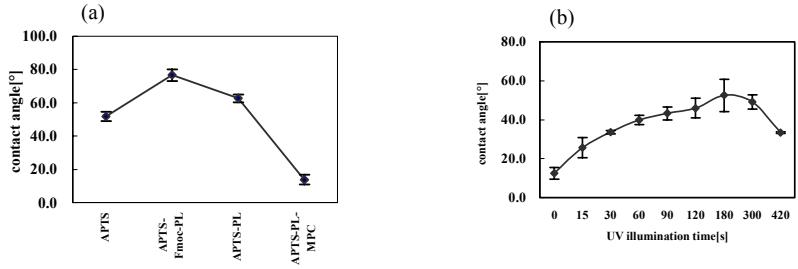

Figure 3. (a) Static water contact angles on modified glass surface. (b) Effect of UV illumination time on the contact angles of a glass surface modified with APTS-PL-MPC. The error bars represent standard deviations.

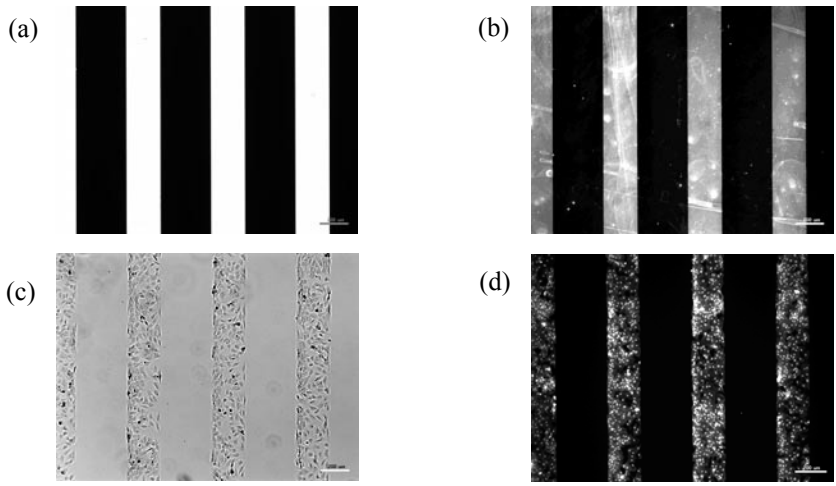

Figure 4. Proteins and cells patterned on glass surface after UV illumination. (a) UV irradiated region. (b) A Fluorescence image of albumin adsorbed on the glass surface. (c) MC3T3-E1 Cells patterned image after 12h after seeding. (d) Fluorescence merged image of cells; actin after rhodamine– phallo idin stain, nuclear after DAPI stain.

4. CONCLUSION

We have developed a new surface-treating method for regulating the cell attachment combined with MPC polymer and photolabile linker. By using UV illumination, the MPC were efficiently removed and the control of the cell attachment was achieved successfully. It was proved that the cells had a strong affinity to aromatic compound remained hydrophobic surface after the cleavage of the MPC after UV irradiation. Using the present approach used in this study, we still continuing to introduce a different types of cell patterning on the glass surface. This will be verified to be an effective and efficient to develop a fundamental cell based studies on analyzing the cell signaling and detecting two different types of cell interaction.

References

[1] Ying Luo, Molly S. Shoichet, *Nature materials*, 3, 249 (2004).
[2] Yasuhiko Iwasaki, Kazuhiko Ishihara, *Anal. Bioanal. Chem.*, 381, 534 (2005).

LOCAL SILICA COATING OF POLY(DIMETHYLSILOXANE) MICROCHANNELS

Jinhee Park, Miok Shin and Jong Hoon Hahn

Department of Chemistry, Pohang University of Science and Technology, South Korea

ABSTRACT

We developed a permanent surface coating method which integrates the advantages of poly(dimethylsiloxane) (PDMS) and glass as microchip materials. This method is based on the sol-gel process between PDMS surface and sol-gel solution containing the alkoxysilanes as a precursor and is able to create the silica coated PDMS. The most important point is the possibility of the local silica coating through corona discharge in only defined region of microchannel networks. Silica coated PDMS surface is uniform, hydrophilic and resistant to organic solvent. These improved properties provide the broaden applications as microfluidic devices.

Keywords: Corona discharge, local coating, PDMS, sol-gel

1. INTRODUCTION

Glass is popularly used as the microchip material because their properties in terms of hydrophilicity and optical transparency are pertinent to perform the analysis based on microchip. However, the fabrication process is time-consuming and requires the hazardous chemicals and clean room facilities. PDMS overcomes the disadvantages of glass using an inexpensive and easy replica molding method. Unfortunately its applications are limited due to the intrinsic properties such as the hydrophobicity and the low resistance to organic solvent and hydrophobic compounds [1]. Various surface modification methods are reported to reduce these defects of PDMS. Previous reports still show the instability and the limited applications and are invalid for local coating within microchannel network [2].

In our research, the sol-gel process is introduced to create permanently coated PDMS. Usually sol-gel process offers the inorganic gel that is transferred to glass through drying process at low temperature [3,4]. Furthermore local oxidation process using corona discharge in microchannel networks caused permanent and local silica coating. Figure 1 illustrates the crosslinking reaction between sol-gel and corona discharged PDMS.

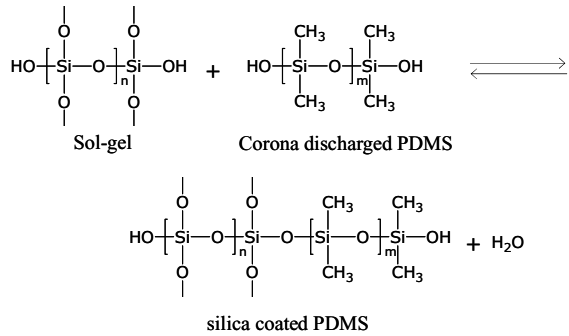

Figure 1. The coating mechanism between sol-gel and corona discharged PDMS.

978-0-9798064-0-7/μTAS2007/$20©2007CBMS

2. EXPERIMENTAL

For the local oxidation by corona discharge, PDMS were pierced with sharpened two thin Pt wires at the ends of local region where modification was to be done. One electrode functioned as electrical arc acceptor and another electrode was connected to ground. Corona discharge was treated at electrical arc acceptor using a Tesla coil. Potential difference between two electrodes extremely increased and the generated plasma flowed only through microchanneles between two electrodes (Figure 2).

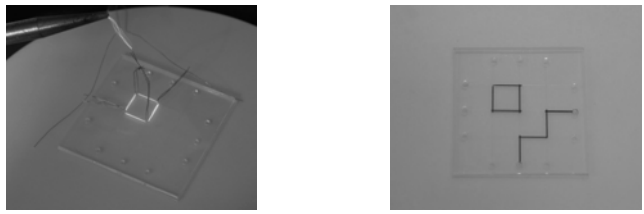

Figure 2. Corona discharge on defined region (left) and oxidized PDMS microchannels filled with aqueous red ink (right).

To prepare the sol-gel solution, tetramethylorthosilicate (TMOS), methyltrimethoxysilane (MTMS), ethanol and the D.I. water (0.01M HCl) was mixed at 1400 rpm for 5 hrs. The corona discharged microchannel was filled with sol-gel solution. After 10min, the remained sol-gel solution was extracted by flushing acetonitrile. The microchip was dried at the room temperature for 2 hours and then at 65℃ for 2 hours**.** Figure 2 shows the CCD image of locally modified PDMS microchannel and the SEM images which present slightly roughness but no cracks in silica coated PDMS microchannel.

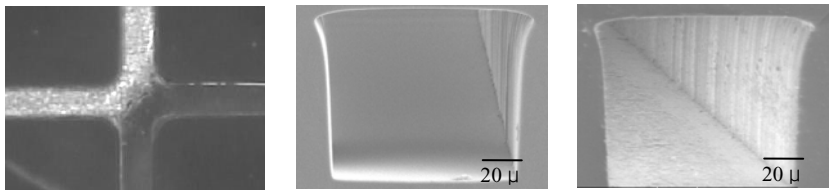

Figure 3. CCD image of locally silica coated PDMS microchannel (left).
SEM images of native (middle) and silica coated (right) PDMS microchannels.

3. RESULTS AND DISCUSSION

We examine the several properties of the silica coated PDMS. First, resistance to organic solvent and hydrophobic compound like BODIPY is prominently increased. In Figure 4, the absorption of the hydrophobic fluorescence is blocked and the swelling against to xylene is also reduced at silica coated PDMS microchannel [5].

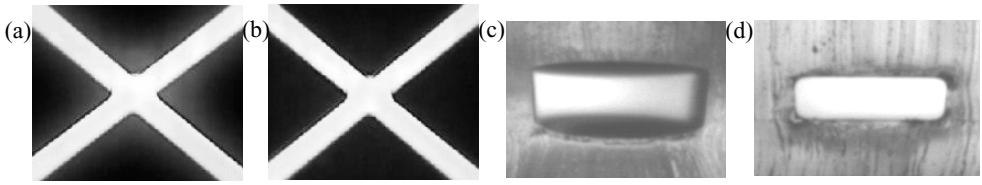

Figure 4. Fluorescence images of native after 20 min (a) and silica coated PDMS microchannel after 10 hr (b). CCD images of swelled native (c) and retained silica coated PDMS microchannel (d).

In contact angle measurements, silica coated PDMS has no alteration during 1 week, but corona discharged PDMS is rapidly changed. The contact angle of silica coated PDMS (76˚) means the acquirement of hydrophilic property compared with the native PDMS (103˚). Moreover the electroosmotic flow (EOF) mobilities of silica coated PDMS are 2 times higher than them of native PDMS in wide pH ranges. As the application of silica coated PDMS microchip, capillary gel electrophoresis (CGE) is performed which is limited to glass microchips in case of previous reports and all DNA fragments are separated within 5mins (figure 5).

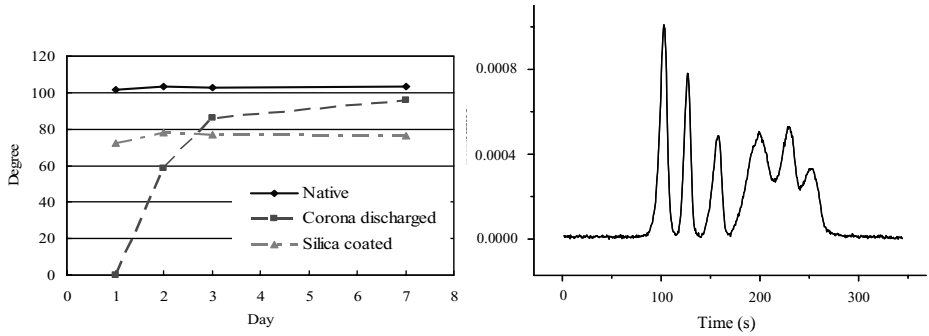

Figure 5. Contact angle results of native, corona discharged and silica coated PDMS surfaces (left). Separation of DNA fragments by CGE (right).

4. CONCLUSIONS

Modification based on sol-gel process provides the atmosphere like glass to PDMS microchannels. Increased hydrophilicity and reduced porosity of PDMS surface is reproducibly available using this method. In addition, the possibility of local coating could be practicable to the stepwise sample treatments such as enzyme reactions. In the whole, this simple and permanent modification technique has the potential to expand the applicable field of PDMS microchips into the chemical synthesis and bioassay in addition to chemical analysis.

REFERENCES

[1] H. Makamba, J. H. Kim, K. Lim, N. Park, and J. H. Hahn, *Surface Modification of Poly(dimethyl siloxane) Microchannels*, Electrophoresis, 24, pp. 3607-3619, (2003).

[2] H. Y. Chen, Y. Elkasabi, and J. Lahann, *Surface modification of confined microgeometries via vapour-deposited polymer coating*, JACS, 128, pp. 374-380, (2006).

[3] M. Kato, K. Sakai-Kato, T. Toyo'oka, *Silica sol-gel monolithic materials and their use in a variety of applications*, J. Sep. Sci., 28, pp. 1893-1908, (2005).

[4] G. T. Roman, and C. T. Culbertson, *Surface Engineering of Poly(dimethylsiloxane) microfluidic devices using transition metal sol-gel chemistry*, Langmuir, 22, pp. 4445-4451, (2006).

[5] J. Lee, M. J. Kim, H. H. Lee, *Surface modification of poly(dimethylsiloxane) for retarding swelling in organic solvents*, Langmuir, 22, pp. 2090-2095, (2006).

MICRO POST-STRUCTURED SURFACES FOR BUBBLE DETACHMENT

Sang Kug Chung[1], Ui-Chong Yi[2], and Sung Kwon Cho[1]*

[1]Department of Mechanical Engineering and Materials Science, University of Pittsburgh, USA, [2]Core MicroSolutions Inc., USA

ABSTRACT

This paper presents a novel approach that facilitates bubble detachment from solid surfaces. Arrayed micro posts were microfabricated on the surface, and their bubble detachment was examined and compared with the flat surface. A series of experiments showed that bubbles are more easily detached from the micro post-structured surfaces than from the flat surfaces of the same hydrophilic material.

Keywords: Micro Post-Structured Surface, Bubble, Detachment

1. INTRODUCTION

Bubble removal from solid surfaces is a critical issue in many applications, especially direct methanol fuel cells [1] and boiling process in micro gravity conditions [2] such as space crafts and cabins. Figure 1 illustrates how to lower the adhesion force F_A between the bubble and solid surface. The main idea is to lower the contact angle and shorten the length of the contact line by making the surface structured with micro posts. Many studies [3, 4] have reported that, when the surface is structured and covered with a hydrophilic material, the apparent contact angle ϕ (macroscopically defined on a structured surface) of bubbles and droplets on the structured surface can be dramatically lowered from the intrinsic contact angle θ (defined on a flat surface and intrinsically determined by surface material, not by surface structure). In this paper, this principle was applied to facilitate bubble detachment.

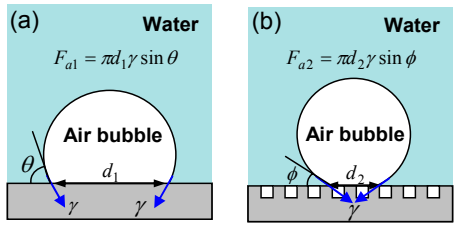

Fig. 1 Adhesion force F_a between bubble and solid surface. The adhesion force is proportional to the sine of contact angle and the length of contact line **(a)** flat surface, **(b)** post structured surface. $F_{a1} > F_{a2}$ since $\phi < \theta$ and $d_2 < d_1$. γ is the surface tension.

2. MICRO POST-STRUCTURED SUFACE

Shown in Fig. 2 are photos of the micro post-structured surface fabricated on a Si substrate. Arrayed micro square posts of 30 μm (L) × 30 μm (W) × 10 μm (H) with a spacing of 30 μm were fabricated using a DRIE process. Then, two different kinds of samples were prepared and tested: one covered with an Al layer ($\theta \approx 40^o$) and the other with a Parylene layer ($\theta \approx 86^o$). Figure 3 shows the contact angle change on each type of

978-0-9798064-0-7/μTAS2007/$20©2007CBMS

the sample. In both cases, ϕ becomes lower than θ, substantial change in the parylene-coated sample (Fig. 3b).

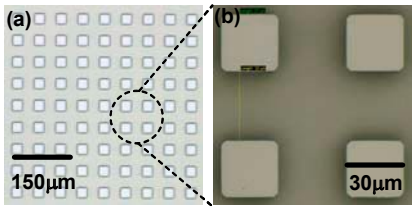

Fig. 2 Arrayed micro post structures on a Si substrate fabricated by photolithography and DRIE etching. **(a)** post dimension 30 μm (L) × 30 μm (W) × 10 μm (H) with a spacing of 30 μm **(b)** magnified view.

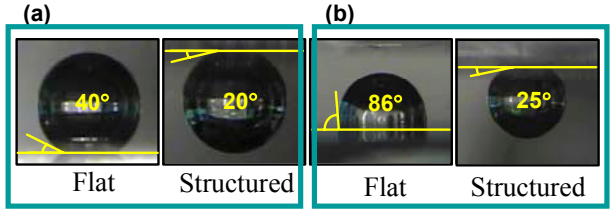

Fig. 3 Contact angle reduction by the structured surface **(a)** An aluminum layer is covered on both flat and structured surfaces. Contact angle changes from 40° to 20°. **(b)** A parylene layer is covered on both flat and structured surfaces. Contact angle changes from 86° to 25°. Contact angle reduction is more significant when a parylene layer is covered

3. EXPERIMENTAL SETUP

Figure 4 shows the bubble detachment experimental setup. Initially an air bubble was injected and sandwiched between two plates: the surface of the top plate is structured while the surface of the bottom plate is flat, but both are coated with the same layer: Al or Parylene. After the bubble becomes in contact with both the top and bottom plates, the top plate is slowly pulled up while the bottom plate is fixed. The detaching process was imaged by a CCD camera.

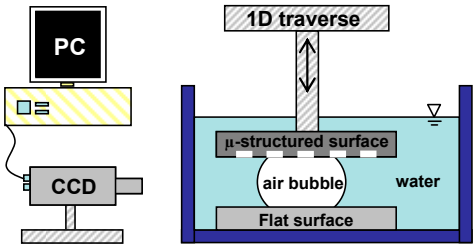

Fig. 4 Experimental setup for bubble detachment. An air bubble is sandwiched between the top structured surface and the bottom flat surface. The top plate is slowly pulled up. The CCD camera images the detachment process.

4. EXPERIMENTAL RESULTS

Figure 5 shows detachment results for Al coated surfaces. Two different bubble sizes were tested: 1 mm and 2.5 mm in diameter. The 1-mm bubble initially deposited on the top structured surface (Fig. 5a) is finally detached and transferred to the bottom flat surface, although the buoyancy force exerts the bubble towards the top surface, indicating that the micro structured Al surface has a lower adhesion force than the flat Al surface. However, for the 2.5-mm bubble, the buoyancy force (larger bubble) dominates over the difference of adhesion forces between on the two surfaces. As a result, the bubble remains on the top surface.

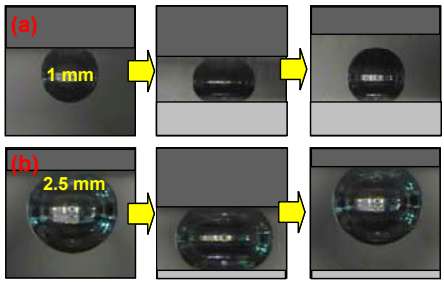

Fig. 5 Bubble detachment experiments on the aluminum coated samples: **(a)** 1-mm diameter air bubble is detached from the top structured surface and transferred to the bottom flat surface as the top plate moves up, although the buoyancy force exerts the bubble towards the top plate **(b)** 2.5-mm bubble is transferred to the top surface since the buoyancy force (larger bubble) dominates over the adhesion force difference between on the top and bottom surfaces.

Similar experiments were performed for the parylene-coated samples (Fig. 6a, b). Unlike the Al samples, the bubbles were always detached from the top structured surface and finally transferred to the bottom flat surface in the full range of tested bubble size (1 ~ 3 mm). This is because the contact angle reduction with a parylene layer is much larger than the one with an Al layer (Fig. 3). Meanwhile, when both top and bottom surfaces are flat, the bubble is always transferred to the top surface due to the buoyancy force (Fig. 6c).

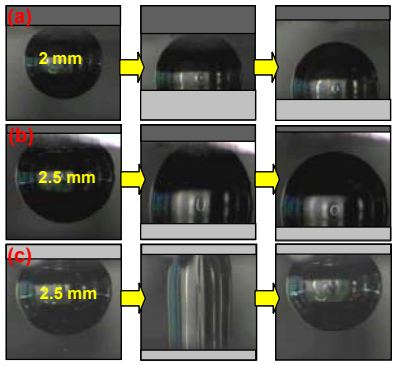

Fig. 6 Bubble detachment experiments on the parylene coated samples : **(a)** 2 mm bubble **(b)** 2.5 mm bubble. Bubbles always remain on the bottom flat surface regardless of bubble size since the adhesion force difference between on the top and bottom surfaces is larger than the buoyancy force. Note in Fig. 3 that contact angle change with parylene coating is larger than the one with Al coating. **(c)** Both the top and bottom surfaces are flat with a parylene layer. 2.5-mm bubble always remains on the top surface due to the buoyancy force (no adhesion force difference between on the top and bottom surfaces).

5. CONCLUSIONS

Bubble detachment on micro post-structured surfaces was examined and compared with the flat surfaces. The experiments demonstated that bubbles are more easily detached from the micro post-structured surfaces than from the flat surfaces of the same hydrophilic material.

ACKNOWLEDGEMENTS

The work was supported by the National Science Foundation (NSF ECS-0601470).

REFERENCES

[1] T. Schultz, S. Zhou, and K. Sundmacher, *Chem. Eng. Technol.*, Vol. 24 (12), pp. 1223-33, 2001.
[2] http://science.nasa.gov/headlines/y2001/ast07sep_2.htm
[3] J. Bico, C. Marzolin, and D. Quere, *Europhys. Lett.*, Vol. 47 (2), pp. 220-226, 1999.
[4] J. Lee, B. He, and N. A. Patankar, J. Micromech. Microeng., Vol. 15, pp. 591-600, 2005

SLIDING BEHAVIOR OF WATER DROPLETS SANDWICHED BETWEEN HYDROPHOBIC SURFACES

Shunsuke Suzuki*[1,2], Akira Nakajima*[1,2], Munetoshi Sakai[2], Ayako Hashimoto[2], Naoya Yoshida[2,3], Yoshikazu Kameshima[1,2] and Kiyoshi Okada[1]

[1]*Tokyo Institute of Technology, Japan*
[2]*Kanagawa Academy of Science and Technology, Japan*
[3]*The University of Tokyo, Japan*

ABSTRACT

The sliding behavior of water droplets sandwiched between Si plates treated by octadecyltrimethoxysilane (ODS) and fluoroalkylsilane (FAS) was observed by changing the plate's distance (D) and droplet mass (m). The sliding angle depended on D and m and the upper and bottom combination of surface. The internal fluidity of the sliding droplet was observed by particle image velocimetry method with the high-speed camera system. The molecular length of silane and its flexibility can affect affinity with water and the hydrodynamics at the interface.

Keywords: water, droplet, sliding, PIV, hydrophobicity

1. INTRODUCTION

Technologies related with hydrophobic coatings have been recognized of the importance for suppressing the solid-water interaction. Such coatings have been applied to various industrial items [1].

The water contact angle has been commonly used as a criterion for evaluating the static hydrophobicity of the surface, however it is inadequate for evaluating dynamic hydrophobicity: the sliding behavior of water droplets. To date, the sliding angle (the angle where a droplet can start to slide down on the solid surface) is commonly employed as a criterion for assessing the dynamic hydrophobicity. However, it does not include information on sliding velocity or acceleration of a water droplet at the solid surface. So far, the reports on sliding velocity or acceleration are limited [2-6]. We have studied sliding behavior of water droplets on Si treated by various silane agents [3-6]. However, almost previous studies were related on the opened system: a water droplet contacted with only one solid surface. In this study, we studied the sliding behavior of water droplets sandwiched between Si plates treated by octadecyltrimethoxysilane (ODS) and fluoroalkylsilane (FAS). And then the internal fluidity in the droplet was visualized by particle image velocimetry (PIV) method using a high-speed camera system.

2. EXPERIMENTAL

A Si (100) wafer (*n*-type; Aki Corp., Miyagi, Japan) was cut into 3 × 5 cm plates and cleaned using acetone and water. Vacuum ultraviolet (VUV) light was irradiated (λ=172 nm with a power density of around 7 mW cm^{-2}, UEM20-172; Ushio Inc. Inc., Tokyo, Japan) to the cleaned wafers for 10 min in air to form a homogeneous oxide layer. We used octadecyltrimethoxysilane (ODS, $CH_3(CH_2)_{17}Si(OCH_3)_3$, Aldrich, MI, USA) and 1*H*,1*H*,2*H*,2*H*-perfluorodecyltrimethoxysilane (FAS17, $CF_3(CF_2)_7CH_2CH_2Si(OCH_3)_3$,

978-0-9798064-0-7/μTAS2007/$20©2007CBMS

TSL8233; GE Toshiba Silicones, Tokyo, Japan) and trifluoropropyltrimethoxysilane (FAS3, $CF_3(CH_2)_2Si(OCH_3)_3$, KBM7103; Shinetsu Chemical Co., Japan) as coating agents. The Si plates were set into a glass container with either 0.02 mL (ODS, FAS17) or 0.04 mL (FAS3) and sealed with a glass cap under dry N_2 conditions. Then, the container was heated in an oven to 150 ^oC for 1 h (ODS, FAS17) or to 100 ^oC for 3 h (FAS3). After the heat treatment, the plates' surfaces were rinsed using flowing toluene, acetone, and water; then they were dried at 80 ^oC in air.

The water contact angle (WCA) of 4-mg water droplet and sliding angle (SA) of 30-mg water droplet were measured using commercial systems (Dropmaster 500, and SA-20; Kyowa Interface Science Co. Ltd., Saitama, Japan). The SA was measured by changing the plates' distance (D) from 1 to 4 mm and droplet mass (m) from 20 to 45 mg for the sandwiched droplet. The particle image velocimetry (PIV) method was applied for observing the internal fluidity of the droplet sliding between two hydrophobic plates at the slope surface (35°). A 35-μL water droplet containing 0.06mass% fluorescent particles (mainly polystyrene, 3 μm diameter, R0300; Duke Scientific Corp., CA, USA) was prepared using a micro syringe on the sample surface, which was tilted at 35°. A CMOS camera with a 1024×1024 pixel sensor resolution (1024PCI; Photron Ltd., Tokyo, Japan) was used for taking images for droplet's sliding. The two plates were set face-to-face on the slope with a space of 2.5 mm between the top and bottom surfaces. The sheet-shaped laser (Ar ion type, 1000 mW intensity; ca 200 μm width by the slit; Seika Corp., Tokyo, Japan) was emitted vertically to the interval space between these plates and was set to the center of droplet from the receding side during sliding. The details were described in Ref. [7].

3. RESULTS AND DISCUSSION

The WCAs were 100°±1, 107°±1 77°±1 on the Si plates treated by ODS, FAS17, and FAS3, respectively. The SAs were 10°±1, 10°±1 on the single plate treated by ODS, FAS17. The SAs of a 30-mg water droplet sandwiched between two parallel plates (ODS-ODS plates) were 12°±2 and 13°±1 at D=2.4, 1.0 mm. On the other hand, the SAs of the droplet between FAS17-FAS17 coatings were 11°±1 and 19°±4 at D=2.4, 1.0 mm. These results indicates that the water droplet between FAS17 coatings exhibits larger sliding angle than ODS coatings for D=1.0 mm even though the FAS17 coating possesses higher water contact angle. It is considered that FAS17 molecule has more rigid structure of the organic chain than ODS one [8]. The molecular length and its flexibility can affect affinity with water for the confined alignment. The internal fluidity of the droplet between the plates coated with ODS or FAS17 was visualized by PIV analysis (Fig. 1). The water droplet sandwiched between FAS/ODS became heterogeneous rolling fluid: the border of the twin flow was not the center between the plates. The ratio of the rolling motion and the slip motion depended on the chemical composition of the coatings. The larger slip motion is needed for higher sliding acceleration of the droplet.

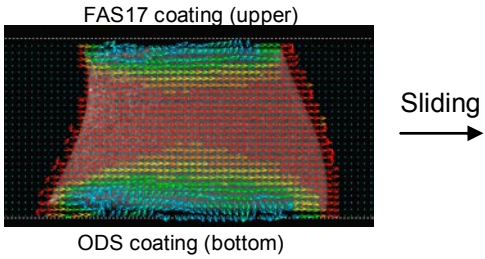

Figure 1. The internal fluidity of the water droplet sliding between FAS17-ODS coatings

4. CONCLUSIONS

In this study, we observed sliding behavior of water droplets sandwiched between two parallel plates with different silane coatings. The sliding angle of the droplet depends on the chemical composition of the solid surface and plates' distance. The internal fluidity of the droplet from the PIV analysis revealed that the different ratio of slip motion and rolling motion on the various coating surfaces. Thus, we could control the sliding behavior and the internal fluidity of the droplet by changing the surface chemical composition and the droplet's size and plate's distance.

ACKNOWLEDGEMENT

This work was partially supported by JSPS H17-08586.

REFERENCES

[1] A. Nakajima, J. Ceram. Soc. of Jpn., **112**, 533 (2004).
[2] N. Yoshida, Y. Abe, H. Shigeta, A. Nakajima, H. Osaki, K. Hashimoto, T. Watanabe, J. Am. Chem. Soc., **128**, 743 (2006).
[3] M. Sakai, J.-H. Song, N. Yoshida, S. Suzuki, Y. Kameshima, A. Nakajima, Lagamuir, **22**, 4906 (2006).
[4] S. Suzuki, A. Nakajima, M. Sakai, J.-H. Song, N. Yoshida, Y. Kameshima, K. Okada, Surf. Sci., 600, 2214 (2006).
[5] S. Suzuki, A. Nakajima, Y. Kameshima, K. Okada, Surf. Sci., **557**, L163 (2004).
[6] A. Nakajima, S. Suzuki, Y. Kameshima, N. Yoshida, T. Watanabe, K. Okada, Chem. Lett., **32**, 1148 (2003).
[7] M. Sakai, A. Hashimoto, N. Yoshida, S. Suzuki, Y. Kameshima, A. Nakajima, Rev. Sci. Inst. **78**, 045103 (2007).
[8] H. Murase, Ph.D. Thesis, The University of Tokyo, Tokyo, JAPAN, 1998.

SURFACE MODIFICATION WITHIN ENCLOSED POLYMER AND GLASS MICROFLUIDIC CHANNELS

Shaurya Prakash[1], Timothy M. Long[2], Jeffrey S. Moore[2], Mark A. Shannon[1]

[1] *Department of Mechanical Science and Engineering,*

[2]*Department of Chemistry, University of Illinois at Urbana-Champaign, Urbana, IL, USA*

ABSTRACT

Advances in chemical modification within enclosed poly(methyl methacrylate) (PMMA) microchannels using 'click' chemistry are reported. Successful modification was verified by X-ray photoelectron spectroscopy and static contact angle measurements. Flow imaging shows the ability to direct flows within microchannels based on control of surface charge or surface energy.

Keywords: 'Click' Surface Modification, Microchannels, PMMA, Glass, Capillary Electrophoresis, Microfluidics

1. INTRODUCTION

Applications for μ-TAS in electrophoretic separations, DNA and protein analyses, PCR, and protein extraction and purification require extensive interactions between microchannel surfaces and analytes due to high surface-area-to-volume ratios. Problems such as non-specific adsorption and reliable device performance have posed a challenge in developing μ-TAS. Many methods have been used to address these issues and to control flow characteristics, including manipulation of buffer concentrations, pH, and composition, application of radial electric fields, and surface modification using plasmas, laser ablation, and physisorbed surface layers [1, 2]. These μ-TAS often utilize electrokinetic flows within microchannels to achieve ideal plug flows for separating and manipulating chemical species within the fluid. The separation rates and resolutions within capillary or microchip electrophoretic (CE or MCE) systems are strongly affected by the surface ζ potentials, which need to be (1) uniform to achieve minimum deviations from ideal plug-like flow, and (2) adjustable for optimum separations of different species. The rate and direction of electroosmosis can be controlled by alteration of the surface ζ potential through chemical modifications; thereby affecting the separation resolutions directly.

The method reported here is distinct from past approaches. The current methodology, relying on self-assembled monolayers and 'click' chemistry, allows for: (i) a modular pathway for building surface scaffolds (ii) covalent attachment of pre-formed polymers to surfaces (iii) modification of confined surfaces within devices with a facile and robust scheme [3, 4]. This modular method to change and control surface chemistry within microfluidic channels provides the ability to: (i) manipulate effective surface charge and thus control the zeta potential (ii) control surface energies (iii) control the chemical composition of surfaces. The ability to alter surface properties in a systematic manner to produce desired flow characteristics can be a powerful tool for a separations technologist. The focus of this paper is to show the development of a robust technique to functionalize enclosed polymer microchannels.

978-0-9798064-0-7/μTAS2007/$20©2007CBMS

2. EXPERIMENTAL

A two-stage method for the surface functionalization of PMMA was developed; first, PMMA surfaces were activated by water-vapor plasma followed liquid or vapour phase modification with a terminal bromoalkyltrichlorosilane. Second, surface azides were introduced via S_N2 nucleophilic substitution with sodium azide followed by copper-catalyzed Huisgen 1,3-dipolar cycloaddition of functionalized alkynes to modify the surface through 1,2,3-triazole linkages. The cycloaddition reaction is referred in literature as 'click' chemistry [5]. The modified surfaces were surveyed by X-ray photoelectron spectroscopy (XPS) and static contact angle measurements to evaluate the effect of surface modifications.

3. RESULTS AND DISCUSSION

The modular method relying on bromine-terminated self-assembled monolayers (SAMs) and 'click' chemistry was shown to modify the surfaces of confined glass microfluidic channels [3]. In the same work, flow imaging showed that by changing the surface wall charge the direction of electroosmotic flow within microchannels can be controlled. In fact, by switching the polarity of surface charge from positive to negative, it was found that the direction of EOF could reversed [3]. In this paper, modification of PMMA surfaces is discussed.

Due to the low reactivity of the backbone esters in PMMA there exist few methods to modify the surface chemistry. Therefore, a suitable surface activation scheme is necessary. Such a scheme was developed and demonstrated in the past year [4]. Once the PMMA surface has been activated, the surfaces can be modified using the modular approach described above. XPS data shown in Fig. 1 confirms this surface modification of PMMA surfaces.

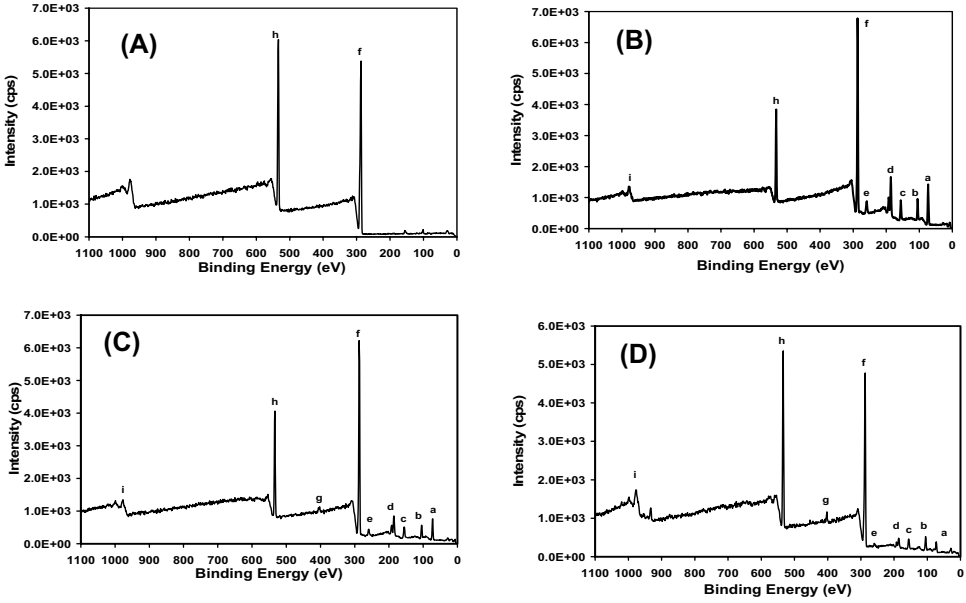

Figure 1: XPS of (A) untreated PMMA, (B) Br-PMMA, (C) azide-PMMA, and (D) PEG-PMMA. The peaks are shown as indicated: [a] Br (3d), [b] Si (2p), [c] Si (2s), [d] Br (3p), [e] Br (3s), [f] C (1s), [g] N (1s), [h] O (1s) [i] O (Auger).

Figure 1 confirms that the modular surface modification scheme can be implemented to functionalize PMMA surfaces. In the example shown, a poly(ethylene glycol) or PEG coating is applied to the PMMA surface. Such as surface could potentially be useful in reducing non-specific adsorption in biological applications of μ-TAS. The different surfaces tested were an untreated PMMA, PMMA functionalized with -Btr Octadecyltrichloro silane (OTS) functionalized, -F terminated, terminated with an azido group, and PEG. Table 1 summarizes the contact angle data for modified PMMA surfaces.

Table 1. Static Contact Angle

Sample	Contact Angle (°)
PMMA	64[4]
Br-PMMA	85[4]
OTS-PMMA	104[4]
F-PMMA	109
N_3-PMMA	75
PEG-PMMA	45

4. CONCLUSIONS

A robust, facile, and modular approach for building surface scaffolds of pre-formed polymers on PMMA surfaces has been desbcribed. Spectroscopic and contact angle data confirms successful surface modification.

ACKNOWLEDGEMENTS

The authors thank the National Science Foundation for financial support for the current research through the Science and Technology Center of Advanced Materials for the Purification of Water with Systems (WaterCAMPWS) under the agreement number CTS-0120978 and the Center for Nano-Chemical-Electrical-Mechanical Manufacturing Systems (Nano-CEMMS) under DMI-0328162. XPS is carried out in the Center for Microanalysis of Materials, University of Illinois, which is partially supported by the U.S. Department of Energy under grant DEFG02-91-ER45439.

REFERENCES

[1] J. Horvath, V. Dolník, *Polymer wall coatings for capillary electrophoresis*, Electrophoresis, **22**, 644-655 (2001).

[2] J.E. Melanson, N.E. Baryla, and C.A. Lucy, *Dynamic capillary coatings for electroosmotic flow control in capillary electrophoresis,* Trends in Analytical Chemistry. **20** 365-374 (2001).

[3] S. Prakash, T.M. Long, J.C. Selby, J.S. Moore, M.A. Shannon, *'Click' modification of silica surfaces and glass microfluidic channels*, Analytical Chemistry, **79**, 1661-1667 (2007).

[4] Long, T.M., S. Prakash, M.A. Shannon, and J.S. Moore, *Water-vapor plasma-based surface activation for trichlorosilane modification of PMMA,* Langmuir, **22**, 4104-4109 (2006).

[5] H.C. Kolb, M.G. Finn, K.B. Sharpless, *'Click' Chemistry: Diverse Chemical Function from a Few Good Reactions*, Angewandte Chemie, International Edition in English, **40**, 2004-2021 (2001).

ULTRA HYDROPHOBIC AND NANO POROUS PLANT LIKE SURFACES FABRICATED BY UV REVERSE SIDE EXPOSURE

Olaf Mertsch, Antje D. Walter, Ivo Rudolph, Daniel Schondelmaier and Bernd Loechel

Berliner Elektronenspeicherring-Gesellschaft für Synchrotronstrahlung m.b.H., Anwenderzentrum für Mikrotechnik (AZM), Germany

ABSTRACT

In this paper a new method for the production of ultra hydrophobic and plant like surfaces for the application in micro and nano fluidic systems will be presented. This method is based on a reverse side UV-exposure with some substantial changes in the exposure conditions. Plant like structures have been generated in the UV resist with wetting contact angles of approximately 140°. With an additional coating procedure of metallic thin films and self assembled monolayers (SAM) the contact angles was increased up to 165° with hysteresis values below 5°.

Keywords: wetting, contact angle, ultra hydrophobic surfaces, plant-like structures

1. INTRODUCTION

Wetting phenomena play a very important role in nature since millions of years now and receive more and more attention in research studies and technical applications today. Defined by the interactions between a fluid and a solid they determine if the fluid can spread on a surface, penetrate it or just easily run off. Mainly, surface morphologies that lead to the so called “Lotus Effect” are very important for self cleaning products like paintings, glass panels for applications in cars and buildings and for biological and medical systems [1]. In this special cases ultra hydrophobic surfaces with contact angles of more then 150° and hysteresis below 5° allow interesting solutions for MEMS and µ-TAS applications like self cleaning effects and self induced drop motion [2].The great advantage of the “Lotus Effect” is the generation of micro drops and thus the minimization of the sample volume as well as the surface contact between the fluid and the solid walls. Hence, nonspecific adsorption can be reduced drastically [3].

2. EXPERIMENTAL

Plant like structures and nano porous flat surfaces are generated via back side lithographic process by means of the exposure of a negative photo resist (SU 8) through an UV-permeable glass substrate. A standard silica glass mask or cost effective printed foil masks with periodical elements of specific structure widths in the micrometer range are used. We take glass of a certain thickness as substrate which additionally serves as a several hundred micrometer thick proximity gap between resist and mask (figure 1).

The important values for the creation of high aspect ratio micro structures or flat membranes are not given by the thickness of the resist matrix alone. Both the structure width and the structure distance on the mask become very important parameters for the diffraction effects behind the mask and thus for the final structure height (figure 2). The additional coating of metallic thin films serving as an adhesion layer for self assembled

978-0-9798064-0-7/µTAS2007/$20©2007CBMS

monolayers, are carried out with a standard PVD sputtering process. The monolayers themselves are generated by a dip coating procedure.

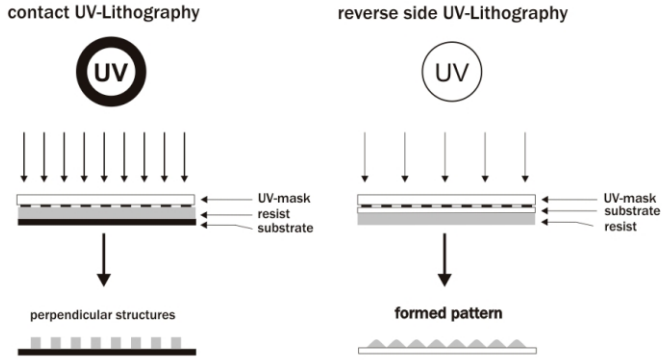

Fig.1: Comparison of the standard UV lithography and the reverse side exposure conditions used in the presented work.

3. RESULTS AND DISCUSSION

Some results of the back side exposure conditions are shown in figure 2. As a result of the diffraction pattern and the distance between the mask and the resist the structures turn into plant like shaped and tapered structures although the structures on the mask are perpendicular. Main consequence for this kind of structures is the reduction of the solid and fluid contact area.

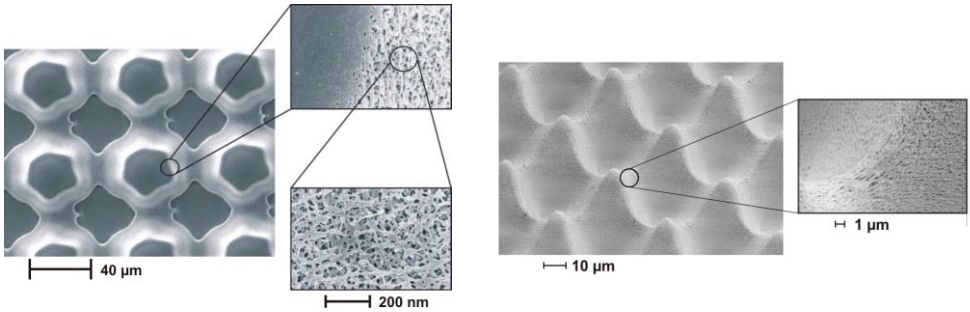

Fig.2: Detailed SEM pictures of lithographic plant like structures. The close-up views show the porous side walls of exemplary structures which cause contact angles above 160°.

Provoked by the shape and the chemical ingredients of the resist the water droplet are forced to drop shapes which lead to very high advancing contact angles in the range of 140° for the resist matrix alone. Unfortunately, because of the weak hydrophobic strange of the resist matrix, the receding of the water from such surfaces is almost impossible. That means the wetted surfaces stays wetted and the hysteresis turns out to be very high. Figure 3 shows some exemplary measurements. The unshaded medium-gray and dark-gray columns show the advancing and receding contact angles of tapered structures made of pure resist. The given fluid to solid contact area is related to the used perpendicular structures on the mask. The real contact area will be investigated later.

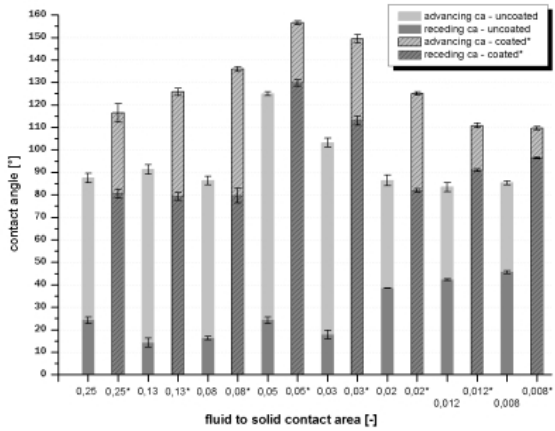

Fig.3: Comparison of advancing and receding contact angle by coated (shaded) and uncoated (unshaded) resist structures. The graph shows the increase in both angles and consequentially the decrease in contact angle hysteresis.

The very high hysteresis values can be reduced by coating the resist matrix with a self assembled monolayer, which further reduces the hydrophobic strength of the structures. Unfortunately, the tested SAM´s are not able to interact with the resist, hence an adhesion layer made of a metallic thin film was applied first. Result of this coating is a further increase of water contact angle on such surfaces and the reduction of contact angle hysteresis shown by the comparison of the shaded and unshaded columns in figure 3. The decrease in contact angle hysteresis to values of 5° as well as the increase in contact angle values of above 165° (figure 4) can be achieved by certain exposure conditions.

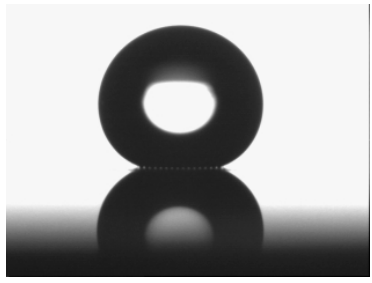

Fig.4: Example surface with a water drop and a contact angle of more than 160°. The drop is in the "fakir state" shown by the shaded structures directly underneath the drop.

4. REFERENCES

[1] Cerman, Z. et al., "Selbstreinigende Oberflächen und ihre Übertragung in die Technik – der Lotus-Effekt®", *Biol. Unserer Zeit*, vol. 34, pp. 290-296, 2004

[2] Daniel, S. et al., "Fast Drop Movements Resulting from the Phase Change on a Gradient Surface", *Science*, vol. 291, pp. 633-636, 2001

[3] Yoon, J.-Y., Garrell, R.L., „Preventing Biomolecular Adsorption in Electrowetting-Based Biofluidic Chips, *Anal. Chem.*, vol. 75, pp. 5097-5102, 2003

FABRICATION OF MICROCHANNELS WITH POROUS SILICON PILLARS FOR ON-CHIP LIQUID CHROMATOGRAPHY AND MICROREACTORS

V. Verdoold[1], W. De Malsche[1,2], G. Desmet[2] and J.G.E Gardeniers[1]

[1]MESA+ Institute for Nanotechnology, University of Twente, THE NETHERLANDS

[2]Department of Chemical Engineering, Free University of Brussels, BELGIUM

ABSTRACT

This paper describes the formation of porous silicon pillars for on-chip liquid chromatography and microreactors, by anodization in aqueous HF solution. The porous surface has a more than 5000-fold increase in surface area, with an average pore-size of 55±5 Å.

Keywords: Porous Silicon, Anodization, Liquid Chromatography, Pillar Array

1. INTRODUCTION

Mesoporous materials find many applications in chemistry, as e.g. catalyst supports in synthetic chemistry, stationary phases in HPLC, or membranes in separation processes. An elegant way to achieve the implementation of such materials in miniaturized chemical analysis and reaction systems is via anodization of silicon, which under specific conditions leads to the formation of porous silicon. Anodization can be carried out locally, e.g. in a microchannel, using special masking materials and photolithographic processes. An early example of the use of this material in a μTAS device was the development of enzymatic microreactors by Laurell and co-workers [1].

Here we report on the electrochemical treatment of silicon-micromachined ordered pillar columns. In chromatography, perfectly ordered pillars, compared to packed beds, have lower peak dispersion, because contributions caused by unequal liquid flow trajectories are reduced, giving very low theoretical plate heights [2,3]. In addition to this, when the pillars have a porous layer, the resulting large increase in surface area will increase the loadability and the retention coefficients of micromachined HPLC columns. Similarly, in catalytic microreactors, ordered columns will give a small residence time distribution, which improves the selectivity of chemical reactions. Porosity will give much higher conversion due to the larger surface-to-volume ratio.

2. EXPERIMENTAL

Microchannels containing pillars with a diameter of 5 or 10 μm were micromachined as described before [3], but in highly doped {100} silicon wafers (resistivity 0.001 Ωcm). A silicon nitride masking layer on top of the pillars, used in the deep reactive ion etching process to shape the pillars, was also used as a masking layer during the anodization process. After coating the backside of the wafer with aluminum to form an electrical contact, the wafer was anodized at a potential of 0.2V vs. SCE for 600 s in a 5% aqueous HF solution. The solution was purged with nitrogen to avoid entrapment of gas bubbles (e.g. hydrogen formed in the anodization

978-0-9798064-0-7/μTAS2007/$20©2007CBMS

process) in the pores. Figure 1 shows the resulting porous surface. The scallops visible on the pillars are a result of the reactive ion etching process.

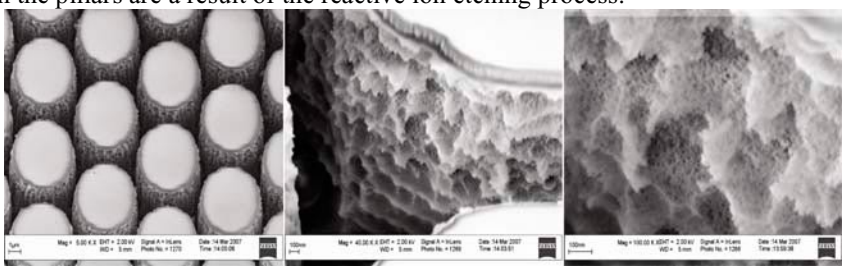

Figure 1: Scanning Electron Microscope (SEM) pictures of porous silicon pillars.

Figure 2 shows that the thickness of the porous layer on the pillars is 300 nm (with above mentioned settings) and that the layer thickness is uniform over the entire pillar height.

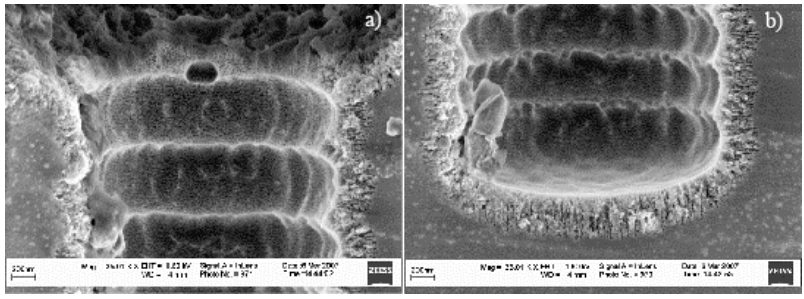

Figure 2. SEM's showing the uniform porous silicon layer thickness along the pillar surface: a) top, b) bottom of pillar

The latter can also be seen from figure 3, which is a top-view of a number of pillars. In this case the porous layer is ca. 1.5 µm thick. Figure 4 shows that pore propagation is along crystallographic directions.

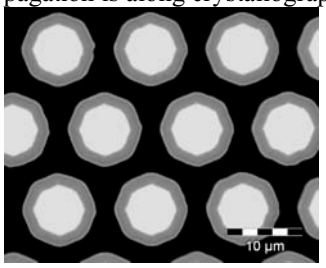

Figure 3. Optical microscopy top view of porous silicon pillar, with silicon nitride masking layer still present. Pillar diameter: 10µm. The darker grey layer is porous, the light grey is solid silicon.

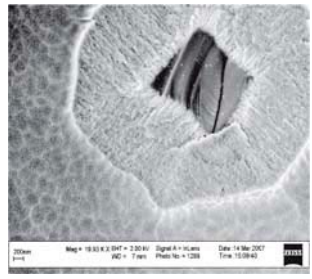

Figure 4. SEM picture of broken porous silicon pillar, showing that the pores follow crystallographic direction in the silicon.

3. RESULTS AND DISCUSSION

After anodization, the silicon wafer was anodically bonded to a Pyrex glass wafer, and a number of flow experiments were performed, similar to those reported in refs. [2,3]. Using a fluorescent dye (coumarine C480 dissolved in methanol), a theoretical plate height of 3.2 μm was found for the porous pillar column (pillar diameter 10 μm; no chromatographic coating applied; thickness of the porous zone 2 μm), which has to be compared with the plate height of 2 μm that was found for the non-porous pillars of the same configuration. BET analysis [4] was performed to characterize the porous surface. A BET surface area of 0.099 m^2/g was found for non porous, surface, and 509.3±26.5 m^2/g for the porous surface, thus a factor 5144 increase in surface area. BJH analysis [5] was performed to determine the pore-size distribution. A pore-size of 55±5 Å was found for the porous material for the applied anodization settings (anodized at a current of 100mA for 300 s in a 5 % aqueous HF solution).

4. CONCLUSIONS

This study shows that porous silicon can be a versatile material for on-chip liquid chromatography to increase loadability and retention coefficients and for microreactors. Via the BJH analysis a pore-size of 55±5 Å was found. A increase in surface area of at least 5000-fold was observed. For porous silicon pillars a plate height of 3.2 μm was measured and an increased retention coefficient was found.

ACKNOWLEDGEMENTS

This research was financially supported by IWT- Flanders within the NextChrom project.

REFERENCES

[1] J. Drott, K. Lindström, L. Rosengren and T. Laurell, "Porous silicon as the carrier matrix in microstructured enzyme reactors yielding high enzyme activities", J. of Micromech. Microeng., 7, 14 (1997).

[2] M. de Pra, W.Th. Kok, J.G.E. Gardeniers, G. Desmet, P.J. Schoenmakers, "Improving liquid chromatography efficiency: Channels structured with micro-pillars", Proc. MicroTAS 2005, Boston, Oct. 5-9, 2005, pp. 838-840.

[3] M. de Pra, W.Th. Kok, J.G.E. Gardeniers, G. Desmet, S. Eeltink, J.W. van Nieuwkasteele, and P.J. Schoenmakers, "Experimental study on band dispersion in channels structured with micro-pillars", Anal. Chem. 78, 6519 (2006).

[4] S. Brunauer, P.H. Emmet and E. Teller, “Adsorption of Gases in multimolecular layers”, J. of Am. Chem. Soc., 60 (2), 309 (1938)

[5] E.P. Barrett, L.G. Joyner and P.P. Halenda, “The determination of pore volume and area distributions in porous substrances. I. Computations from Nitrogen Isotherms”, J. of Am. Chem. Soc., 73 (1), 373 (1951)

A DIFFRACTION MOIRE BASED MICRO DOUBLE LAYERED CHIP FOR CELLULAR MECHANICS STUDY

Xiaoyu Zheng and Xin Zhang

Department of Manufacturing Engineering, Boston University, USA

ABSTRACT

This paper presents a moiré based micro chip for cellular mechanics study. We demonstrated that the double layered microscopic PDMS chip can be used to generate flexible moiré patterns that map the deflection of substrate consisting of micro polymeric pillar arrays thus correctly indicate the displacement and force distribution of the corresponding isolated cardiac myocytes. The magnification effect of moiré made a high sensitivity measurement far beyond the capacity of conventional measurement approaches, especially when the dimension of micro pillars becomes smaller and smaller and a higher sensitive sensing method is desired.

Keywords: Moiré, cardiac myocyte, PDMS (polydimethylsiloxane)

1. INTRODUCTION

Recently, researchers have been engineering polymer based periodic substratum for cell migration and cellular force measurement [1, 2]. The substratum ranges from thin elastomer films to micro beads or micro vertical pillar arrays which quantify the force evolution on cells upon their substratum. However, the determination of beads or pillar motion was only based on measurement of direct observation on each individual measuring unit via optical microscopy. Such method has several drawbacks. Firstly, it has to rely on the algorithm for determining the motion of each unit individually without knowing their initial state, which, on the other hand, could make the measurement problematic especially after fabrication, elastomer materials such as polydimethylsiloxane (PDMS), is distorted by stress, due to the contraction on curing of the elastomers and contact with a substrate. Such distortion could cause each individual sensor to distribute non-uniformly thus violate the assumption that the sensor was distributed evenly on the substratum and affect the accuracy of such measurement. Secondly, conventional tracking of each individual unit requires visibility of not only each individual unit but also their distortions. As a result, this method confines the sensors within micro meter domains due to the capacity determined by the microscope and camera, which requires that the sensors have very low stiffness to make the distortion distinguishable and may violate the linear load-displacement assumption when deflection is substantial.

2. THEORY

When light travels through a single layer of spatial periodic gratings it is diffracted into waves in different orders. Laser source produces approximate plane wave incident on periodic PDMS substrate which can be treated as transmittance grating. Image from transmittance gratings projected on bottom layer forms moiré patterns. The spatial periodicity or characteristic of top layer is slightly different from that of bottom layer so that after passing through the two layers interference pattern will be produced when

978-0-9798064-0-7/μTAS2007/$20©2007CBMS

patterns from respective layers are mixed as showed in Figure 1 (a), (b), (c), with bottom layers being gratings and dots patterns, respectively.

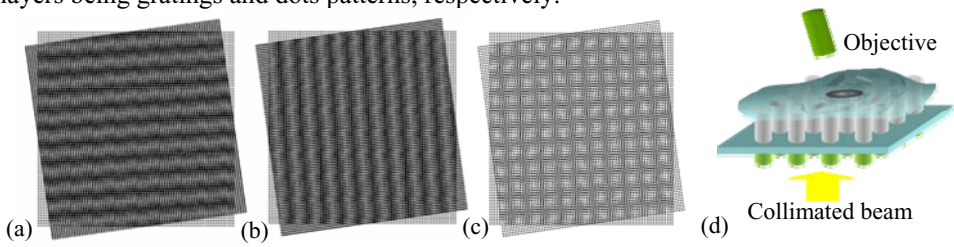

Figure 1. Principle of double layered diffraction moiré pattern (a) (1,0) Moiré pattern generated by periodic posts and gratings in Y direction. (b) (0,1)Moiré pattern generated by periodic posts and gratings in X direction. (c) 2-D Moiré pattern generated by double layered structures. (d) Diffraction moiré setup

The spatial periodicity of the moiré pattern and orientation are determined by the spatial periodicity and orientation of both the periodic structures and interference patterns. Such relation can be simplified and expressed as,

$$\begin{cases} D = \dfrac{a}{(1+a^2-2a\cos\theta)^{1/2}}d \\ \sin\varphi = \dfrac{\sin\theta}{(1+a^2-2a\cos\theta)^{1/2}} \end{cases} \quad (1)$$

where D is the periodicity of moiré fringe pattern, a is the ratio between periodicity of top layer and that of bottom layer, denoted as d. φ is the orientation of fringe pattern. θ is the angle between the two layers measured from stepper. Specifically, the orientation of top layer was adjusted to have a small angle (5º) with respect to one (X) direction of the periodicity of bottom layer, such that the periodicity of moiré pattern can be approximated as:

$$d_M \approx \frac{d}{|\theta|}, \sin\varphi \approx 1 \quad (2)$$

Therefore, the distortion in X direction of the generated moiré indicates the distortion of micro pillars in perpendicular (Y) direction and vice versa.

3. EXPERIMENTAL

We fabricated double layered chip by gluing of thin layers of PDMS with much higher stiffness on the bottom layer. As showed in Figure 1 (d), The top layer is the substratum consisting of each individual unit sensor such as pillars. The bottom layer consists of a pattern layer made of the same material but with a much higher rigidity which has slightly different scales than the top one and tilted by a small angle. A He-Ne 633nm laser was used as an imaging source that transmitted vertically through the plane of the substratum. A 10× to 50× objective and CCD camera was followed by the placement of the substratum. A circular aperture with 3 mm in diameter was mounted to increase the depth of focus. Upon saturation of laser, diffracted moiré pattern from the double layer was formed and visualized on monitor. The angle of the double layer was chosen such that orientations of

moiré pattern satisfies measurement needs which map the distortion of pillars or motion of beads in two orthogonal directions. Therefore, the information of initial state of periodic substratum can be visualized and the motion of every unit can be directly mapped in real time via diffracted moiré patterns.

4. RESULTS AND DISCUSSION

The two layered structure served as diffraction gratings through which microscopic displacement exerted on top of periodic pillars can be mapped. According to moiré theory, with the same periodicity on both periodic channels and pillars, under small angle approximation, the distortion of the diffracted moiré pattern is proportional to the deflection of micro pillars in perpendicular direction on the focusing plane. Figure 2 (a) shows distorted diffraction moiré pattern generated on micro chip where cardiac myocytes were cultured. Figure 2 (b) is the digitalized distorted diffraction moiré pattern from which the local distortion of micro pillar arrays in two perpendicular directions was derived. Finally, using elastic modulus from nanoindentation, the contraction force distribution shown in Figure 2 (c) was calculated.

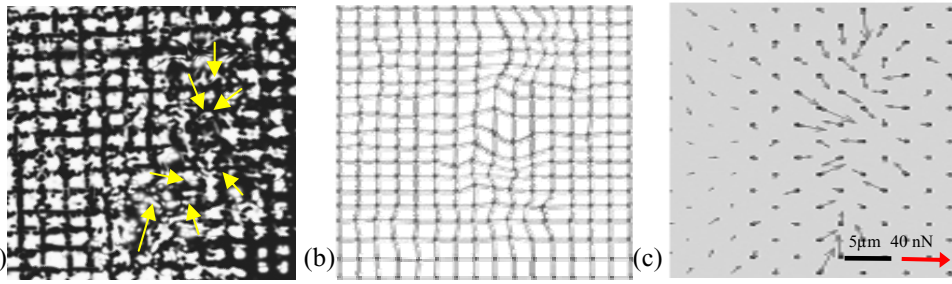

Figure 2. (a) Two-dimensional moiré pattern on double layered chip. Arrows shows derived cell contraction direction. (b) Digitalized two-dimensional undeformed moiré pattern by averaging the all the periodicities. The periodicity is 8μm. (c) Corresponding lateral force vector map on each individual pillars derived from the distortion distribution of the moiré pattern.

5. CONCLUSIONS

In this paper, a method for determination of microscopic deformation for periodic structure was implemented by virtue of double layered PDMS structures. By tuning different angles between each layer, different optical moiré pattern was generated and formed local deflection map of top layer due to fabrication failures and local cellular forces exerted on them.

ACKNOWLEDGEMENTS

This work is supported by NSF CAREER Award under Grant No. CMMI 0239163.

REFERENCES

[1] Y. Zhao and X. Zhang, *Cellular Mechanics Study in Cardiac Myocytes Using PDMS Pillars Array*, Sensors and Actuators A: Physical, vol. 125, pp. 398-404, (2006).

[2] J. L. Tan, J. Tien, D. M. Pirone, D. S. Gray, K. Bhadriraju, and C. S. Chen, *Cells Lying on a Bed of Microneedles: An Approach to Isolate Mechanical Force*, Proc Natl Acad Sci USA, vol. 100, pp. 1484-1489, (2003).

CAPILLARY-BASED MICROFLUIDIC FLOW INJECTION ANALYSIS BASED ON HIGH SENSITIVE LIQUID CORE WAVEGUIDE ABSORBANCE DETECTION

Lei Dong, Wen-Bin Du, Qun Fang*

Institute of Microanalytical Systems, Department of Chemistry, Zhejiang University, Hangzhou, China, 310058

ABSTRACT

A capillary-based flow injection analysis (FIA) system with liquid-core waveguide absorbance detection is described. A Teflon AF 2400 tubing was coupled with a fused-silica capillary with a wedge-shaped connecting interface, forming a high sensitive absorbance cell with minimal dead volume.

Keywords: Microfluidics, capillary, liquid-core waveguide, absorbance detection

1. INTRODUCTION

Recently, we have developed two capillary-based microfluidic analysis systems (CBMAS) [1, 2] to perform sequential injection analysis and high-speed capillary electrophoresis. Microfluidic operations including continuous sample introduction, reaction /separation and on-column detection were integrated on a short fused-silica capillary, showing advantages of automatic operation, low cost and high throughput. In this study, we attempted to broaden its application in high sensitive visible absorbance detection.

2. EXPERIMENTAL

The capillary-based microfluidic system is shown in Fig.1. Both ends of a Teflon AF tubing (20-mm long, 98-μm i.d., 375-μm o.d.) was cut into wedge-shape with an angle of 45°. The connecting ends of two fused-silica capillaries (100 μm i.d., 375 μm o.d.) were grinded into wedge shape to fit with the Teflon AF tubing as shown in Fig.1(A). The capillaries, Teflon AF tubing and optical fiber (400 μm o.d.) were connected with the aid of an elastic Tygon tube (200 μm i.d.) (as shown in Fig.1A), achieving a connection with minimal dead volume at the connecting interface.

An autosampling platform based on slotted-vial array[2] for sequential sample/reagents introduction is shown in Fig.1. Gravity was used to provide the driving force for flows in the microchannels. A 508-nm green LED was used as light source, positioned in front of the optical fiber without further focusing. A photodiode detector (OPT-301, Texas Instruments) was positioned at the outlet end of the optical fiber. The detection system was masked from ambient light with black adhesive box. LabVIEW (National Instruments) software was used to process signals.

3. RESULTS AND DISCUSSION

In this work, two connection approaches for the capillary and Teflon AF tubing with "T" shape and wedge shape interfaces (as shown in Fig.2) were tested. The connection with wedge shape interface showed lower dead volume and lower flow resistance.

978-0-9798064-0-7/μTAS2007/$20©2007CBMS

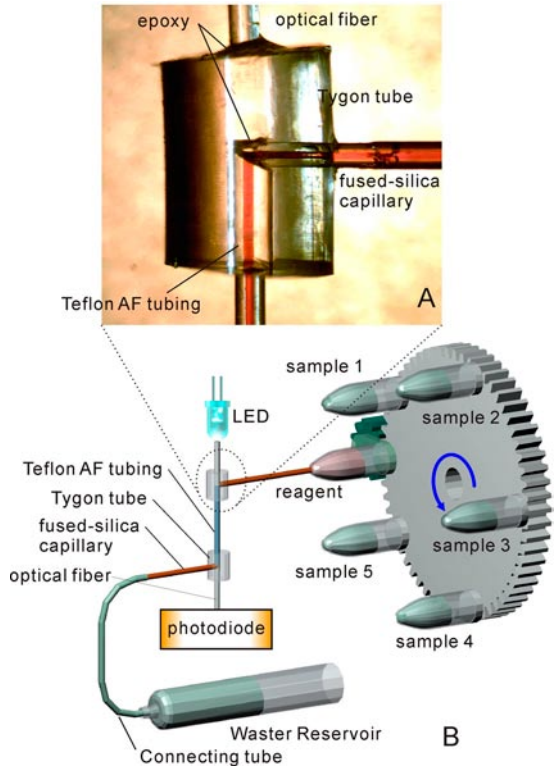

Figure 1. (A) Interface of the Teflon AF tubing and the capillary; (B) schematic diagram of the microfluidic system.

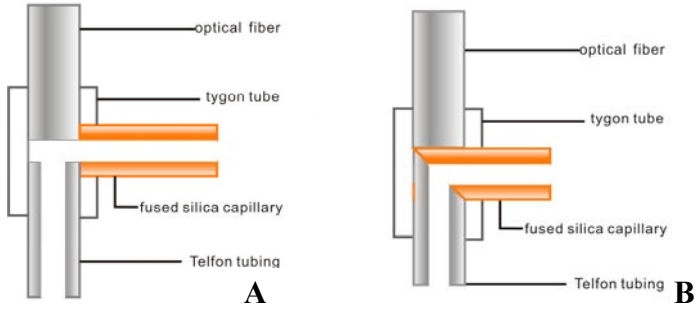

Figure 2. schematic diagram of interface of capillary Teflon AF tubing.and optical fiber (A) 'T' shape interface; (B) wedge shape interface.

The performance of the system was demonstrated using o-phenanthroline-Fe (II) complex as a model sample. Solution of o-phenanthroline and Fe(II) standard solutions were sequentially introduced into the capillary with a flow rate of 4.3 nl/min. The sample consumption was 4.3 nL with 1 s injection time. Absorbance response in the range 20~100 μM Fe (II) was linear (R^2=0.9972). The detection limit of Fe (II) was 0.1 μM.

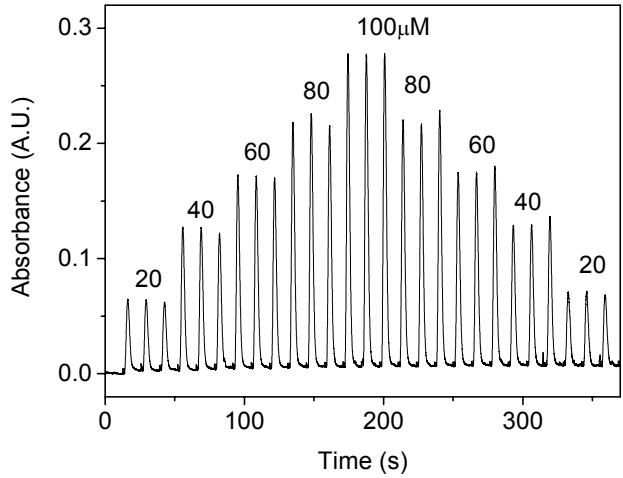

Figure 3. Typical recordings of sequentially injected of Fe(II) standard series .Concentration of Fe(II) for 1-5: 20, 40, 60, 80 and 100 μM; injection time: 1 s for standard solution and 12 s for carrier; flow rate: 4.3 nL/s.

4. CONCLUSIONS

In conclusion, we have successfully developed a CBMAS performing flow injection analysis with liquid-core waveguide flow cell, achieving high sensitive absorbance detection with low sample/reagent consumption. The connection approach between two capillarys with wedge shape interface was proved to be an effective approach to minimize interface dead volume. Such an approach could also be used to construct capillary-based microchannel networks for microfluidic systems.

ACKNOWLEDGEMENTS

This work was supported by the National Natural Science Foundation of China (Grant 20575059) and Ministry of Education (Grant NCET-05-0511).

REFERENCES

[1] J. Liu, Q. Fang, W. B. Du, *Chinese Journal of Anal. Chem.* **2005**, 33, 1799-1802.
[2] W. B. Du, Q. Fang, Z. L. Fang, *Anal. Chem.* **2006**, 78, 6404-6410.

CHARACTERIZATION OF LIGHT COUPLER-INTEGRATED PLASTIC SURFACE PLASMON RESONANCE SENSOR AND SYSTEM IN AQUEOUS AMBIENT

Hyeon-Bong Pyo[1], Moon Youn Jung[1], Seon Hee Park[1], Yong-Beom Shin[2], and Bong Hyun Chung[2]

[1] ICCL, ETRI, KOREA and

[2] BioNanotechnology Research Center, KRIBB, KOREA

ABSTRACT

We report experimental results using a plastic surface plasmon resonance (SPR) sensor and optical detection system in liquid phase. We designed and fabricated a plastic SPR sensor chip into which a light coupler is integrated, thereby no extra index matching medium is required. For absolute calibration of thickness change and multiplexed detection, we also developed an optical instrument, by which the SPR angle shift is represented in two-dimensional image for each channel.

Keywords: Surface plasmon resonance (SPR), cycloolefin copolymer (COC), SPR imaging, multiplexed detection

1. INTRODUCTION

SPR imaging technique has been widely employed by many research groups around the world, and has been an established methodology for the observation of biomolecular interactions on a solid surface [1, 2]. But one of the critical drawbacks in this intensity-measurement is that there is no information about absolute thickness (refractive index) change because what we see is rather a difference image (grayscale difference for each pixel) at a fixed angle and wavelength, where the difference intensity may change according to the wavelength, incident angle, and/or sensor layer structure.

In this paper we report a SPR imaging system in which a disposable plastic sensor chip is used, and the SPR angle shift is represented as a two-dimensional image. From cross-cut of the image, SPR curve is obtained, so the thickness change can be calibrated by fitting reflectivity curve as a function of incident angle for each channel.

2. EXPERIMENTAL

A detailed fabrication process of light coupler-integrated plastic surface plasmon resonance (SPR) sensor was described elsewhere [3]. In brief, a standard slide glass-sized, prism-integrated cycloolefin copolymer (COC) SPR chip was fabricated by injection molding (Figure 1), onto which plasmon-supporting Au layer was coated. For optimal sensor configuration and layer structure, we first figured out proper design parameters such as Au layer thickness and wavelength, while sensor material is fixed to COC (n=1.53). Dynamic range of the refractive index change is assumed to be n=1.33~1.36 which is usual in aqueous ambient (Figure 2). As a light source we chose a TM-polarized diode laser, with the center of wavelength at λ =850 nm. Series of injection-molded COC (Topas® TKX-0001) SPR sensors were used for the experiments, with the sensor configuration of COC/2

978-0-9798064-0-7/μTAS2007/$20©2007CBMS

nm Cr/48 nm Au layer. For liquid sample injection, a two-channel chamber which is made of PTFE with silicon O-ring was placed on top of the Au layer, and the flow rate was controlled by two syringe pumps. Series of video clips were obtained by a capture board for real-time monitoring, and stored as movie files on a personal computer. For end-point detection of the SPR angle shift, the cross-cut of captured image frame was used.

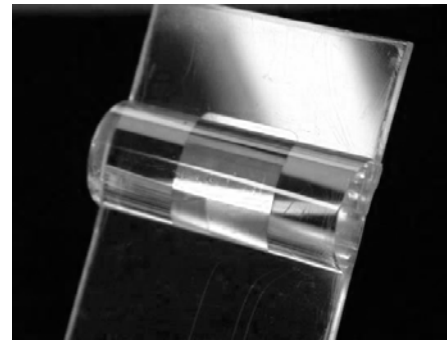

Figure 1. Fabricated plastic SPR sensor chip: Light coupler (prism) is integrated into sensor substrate, and plasmon-supporting Au layer was coated on the opposite side of the prism. Thickness of Cr (adhesion layer) and Au layer is 2 nm and 48 nm, respectively.

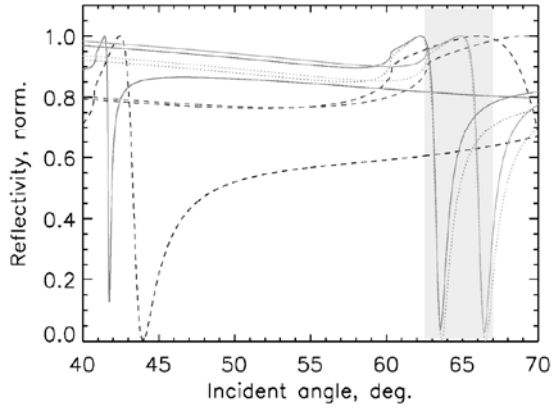

Figure 2. Calculated reflectivity of air, water, and ethanol at λ= 650 nm and at 850 nm: Assumed sensor substrate (as well as the prism) is cycloolefin copolymer (COC) with n=1.53. Filled region indicates the angle window that can be observed in our instrument, and is about $\Delta\theta$~4.5° (θ = 62.5°~67°). Solid line is SPR curve at 850 nm. For comparison, the same was calculated for 650 nm (dashed line). Dotted line shows more optimized condition for SPR sensor configuration, as the thickness of Au layer is reduced from 48 nm to 42 nm.

3. RESULTS AND DISCUSSION

Two dimensional view of SPR angle shift in air and in aqueous ambient is presented in Figure 3: Incident angle window is θ = 62.5°~67°. For comparison, reflected image of SPR sensor in air (n=1.00) is shown in Figure 3(a). Because SPR angle in air (θ_{SPR} ~ 41.8°) is by far below the angle window, there is no SPR dip "line" on the image. Figure 3(b) shows the same reflected image in water (n=1.33). Dark line corresponds to SPR dip in water at θ_{SPR} ~ 63.6°, see Figure 2. Both of SPR dip image in water (left) and in ethanol (right) on the same sensor chip was captured in Figure 3(c). Because the refractive index of ethanol (n=1.36) is higher than that of water, SPR dip line is shifted to the upper direction at θ_{SPR} ~ 66.4°. Figure 3(d) shows cross-cut of the SPR angle shift image Figure 3(c): Pixel averaged along the sample channel, and the refractive index change from n=1.33 (water) to n=1.36 (ethanol) corresponds to the change in pixel number from 63 to 203.

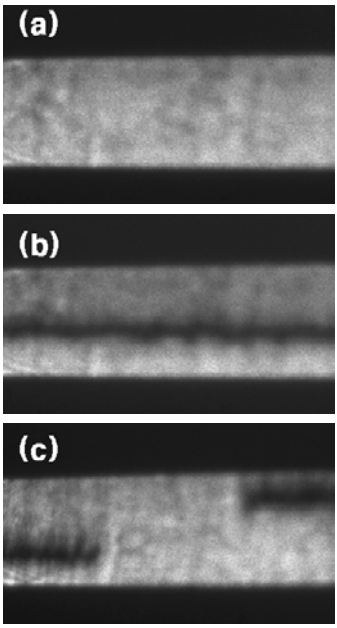

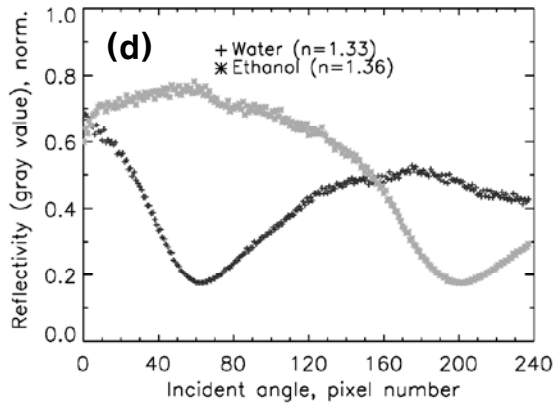

Figure 3. Two dimensional view of SPR angle shift in air and in aqueous ambient. (a) Reflected image of SPR sensor in air (n=1.00). (b) The same reflected image in water (n=1.33). (c) SPR dip image in water (left) and in ethanol (right) on the same sensor chip. (d) Cross-cut of the SPR angle shift curve, obtained from (c).

4. CONCLUSIONS

SPR imaging sensor system in which a light coupler-integrated plastic SPR sensor chip was used, is demonstrated. With the use of expanded beam of light, SPR angle shift was represented as SPR dip line in two-dimensional image, of which the cross-cut corresponds to the SPR curve.

ACKNOWLEDGEMENTS

Financial support by ETRI and by the Ministry of Information and Telecommunication (MIC) Korea , each under grant 06BB1100 and 07MB2700, is gratefully acknowledged.

REFERENCES

[1] Hyeon-Bong Pyo, Yong-Beom Shin, Min-Gon Kim, and Hyun C. Yoon, *Multichannel Surface Plasmon Resonance Imaging and Analysis of Micropatterned Self-Assembled Monolayers and Protein Affinity Interactions,* Langmuir, Vol. 21, pp. 166-171, (2005).

[2] Hye Jin Lee, Alastair W. Wark, and Robert M. Corn, *Creating Advanced Multifunctional Biosensors with Surface Enzymatic Transformations,* Langmuir, Vol. 22, pp. 5241-5250, (2006).

[3] Hyeon-Bong Pyo, Se Ho Park, Kwang Hyo Chung, and Chang Auck Choi, *Multiplexed polymer surface plasmon sensor with integrated optical coupler*, Proc. of SPIE Vol. 6007, SPIE, pp. 60070W-1-60070W-10, (2005).

MICROFLUIDIC ARRAY TO STUDY PROTEASE ACTIVITY

Digvijay A. Raorane[1], Frank Chen[2], Arun Majumdar[1]

1Mechanical Engineering Dept., Univ. of California, Berkeley, CA 94720, USA
2Lawrence Berkeley National Laboratory, Berkeley, CA 94720, USA.

ABSTRACT

We report the extension of the microcantilever based microfluidic platform to study the activity of serine protease. Serine proteases like Trypsin (digestive enzyme) play important role in the living organisms. This microfluidic array is label-free, multiplexed and requires small volumes of the analyte. The sensitivity of these microcantilevers combined with their fast response time has allowed us to study cleavage of substrates in the solution by surface-bound proteases and its inhibition. We have demonstrated the differential response for Trypsin protease at various substrate (Fibronectin fragment) concentrations. We are looking into the inhibition of Trypsin in the presence of SBTI (Soybean Trypsin Inhibitor).

Keywords: protease, label-free, microfluidic array.

1. INTRODUCTION

Microcantilevers have been widely used for the detection of molecular interactions in many biological sensing applications [1, 2]. Their extremely high surface-to-volume ratio permits detection of surface stresses which are too small to observe on a macroscale. Many groups have shown that processes like enzyme-substrate interactions induce a stress which causes the microcantilever to bend [3]. The microcantilever thereby converts a biochemical signal into a mechanical one. One can follow these surface processes by measuring the deflection of the microcantilever tip. We have utilized this phenomenon to study Trypsin activity.

2. MICROCANTILEVER ARRAY

We have developed microfluidic array to effectively perform experiments on multiple microcantilevers simultaneously [4]. These microcantilevers are bimorph comprising a 400μm silicon nitride beam with a gold layer ~20 nm thick as shown in figure 1. The exploded view shows a single well which contains 4 cantilevers. Each cantilever (100 μm^2) has a reflective paddle at its end. An optical detection method is used to measure the deflection of the microcantilever. In this method, a laser beam is projected onto the microcantilever array and the reflected beam emanating from the paddles of the microcantilever is captured onto a CCD. With the deflection of the microcantilever, the light is reflected to a different angle and strikes the CCD at a different position on its surface forming a spot. Using the thermal bimorph effect, one can convert the pixel movement of the spot on the CCD to the deflection/surface stress. Because the functional gold layer is 25 times thinner relative to the structural silicon nitride, we can use Stoney's formula to relate the surface stress in the gold layer to the cantilever tip rotation and deflection given in Eq. (1):

$$\Delta h = \frac{3\Delta\gamma(1-\nu_1)L^2}{E_1 t_1^2} \qquad (1)$$

978-0-9798064-0-7/μTAS2007/$20©2007CBMS

where $\Delta\gamma$ is the change in surface stress, ν_1 is the Poisson's ratio of the structural layer, E_1 is the Young's modulus of the structural layer, t_1 is the thickness of the structural layer, and L is the length of the cantilever.

By analyzing the CCD images, one can obtain the real time data for the cantilever deflection due to the biological reaction taking place on the surface of the cantilever. The deflection can then be converted into the surface stress.

3. EXPERIMENTAL

To demonstrate the use of the microcantilever to detect enzyme activity, we have studied the cleavage of substrate (Fibronectin fragment) with Tryspin. We begin by attaching Cysteamine (5mM in 1 X PBS) on the gold surface using gold-thiol chemistry. Glutaraldehyde (2.5% w/w) is then added to form amide bond with Cysteamine. Finally, Trypsin is immobilized on the microcantilever by covalently linking it to Glutaraldehyde as shown in figure 2 through the second amide bond.

When the substrate is injected in the well of the microcantilever chip, there is a large surface stress change. We varied the concentration of the Fibronectin fragment and observed the differential response of microcantilever. Higher the concentration of substrate, higher is the change in stress as shown in figure 3. In a control experiment, Lysine was added instead of protease to quench glutaraldehyde. When substrate was added afterwards, the microcantilever did not deflect as shown in figure 4. This is expected as there was no Trypsin present to cleave the substrate. In order to study inhibition, we injected SBTI (Soybean Trypsin Inhibitor) to the microcantilever immobilized with Trypsin. We didn't see any change in the stress level. In order to confirm the inhibition, we further injected substrate which did not lead to change in stress as shown in figure 5. This result confirmed the inhibition of active Trypsin enzyme by SBTI.

4. DISCUSSION AND CONCLUSIONS

We have developed micofluidic array to probe more complex systems such as detecting enzyme-substrate and enzyme-inhibitor interactions in label-free multiplexed way. We studied these interactions for Trypsin protease using Fibronectin fragment as substrate and SBTI as an inhibitor respectively. The response of microcanitlevers increased with increasing conc. of Fibronectin fragment. SBTI blocked the enzyme activity and hence microcantilevers showed no response. Thus, microcantilevers offer the characterization of activity of surface-bound-enzyme by detecting the stress changes associated with its interactions with substrate/inhibitor more readily than comparable techniques such as SPR or AFM.

REFERENCES

[1] "Translating biomolecular recognition into nanomechanics," J. Fritz, et al., Science, 288, pp.316 (2000).

[2] "Bioassay of prostate-specific antigen (PSA) using microcantilevers," G.H. Wu, et al., Nature Biotechnology, 19, pp.856 (2001).

[3] "Glucose biosensor based on the microcantilever," J.H. Pei, et al., Analytical Chemistry, 76, pp. 292 (2004).

[4] "A 2-D microcantilever array for multiplexed biomolecular analysis," M.Yue, et al., Journal of Microelectromechanical Systems, 13, pp. 290(2004).

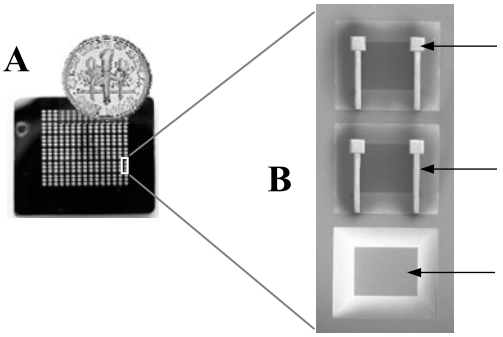

Figure 1. (a) MC array chip containing 2-D array of reaction wells (b) SEM picture: Single MC well.

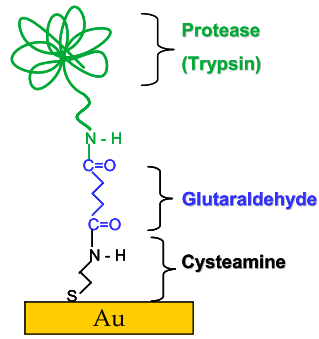

Figure 2. Conceptual diagram of immobilization of Trypsin with Gluteraldehyde and Cystamine.

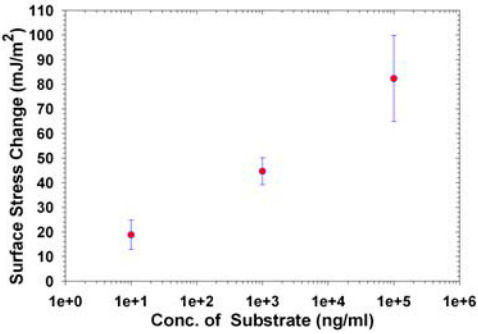

Figure 3. Surface stress change vs. conc. of substrate plot for Trypsin. MCs were prior functionalized with Trypsin using Glutaraldehyde & Cysteamine.

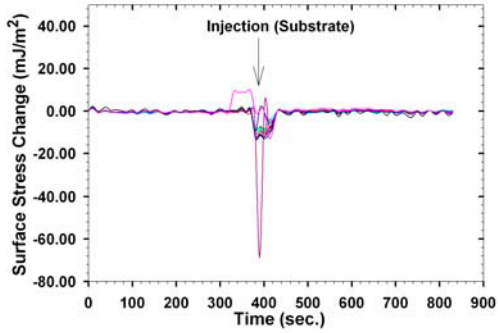

Figure 4. Insignificant deflection of MCs upon injection of substrate in absence Trypsin. MCs were prior functionalized with quenched Glutaraldehyde & Cysteamine.

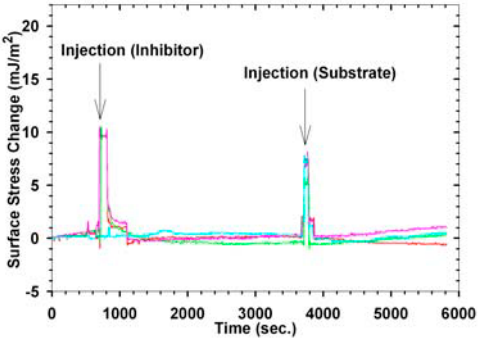

Figure 5. Insignificant deflection of MCs upon injection of inhibitor followed by that of substrate. MCs were prior functionalized with Trypsin using Glutaraldehyde & Cysteamine.

MULTI-TOTAL INTERNAL REFLECTION IN POLYDIMETHYLSILOXANE MICROFLUIDICS FOR ENHANCED ABSORBANCE DETECTION

Jack Sheng Kee[1,2] Daniel Puiu Poenar[2] and Levent Yobas[1]

[1]*Institute of Microelectronics, 11 Science Park Road, S117685, SINGAPORE*

[2]*Microelectronics Centre, School EEE, Nanyang Technological University, SINGAPORE*

ABSTRACT

This paper reports on multiple total internal reflections (MTIRs) of light in poly(dimethylsiloxane) (PDMS)-based microfluidics for enhanced absorbance detection.

Keywords: Polydimethylsiloxane, Absorbance detection, Total Internal Reflection

1. INTRODUCTION

Based on Beer-Lambert's law, the absorbance measurement for low concentration of analytes in a microfluidic channel is limited by the short optical path-length inherently associated with small microchannel width. To circumvent this drawback, multireflection of light has been employed in fluidic microchannels by utilising for the channel walls either mirror-like surfaces of silicon crystalline planes [1-3] or coating them with a metal layer [4]. In contrast with these previous attempts, we present multireflection of light by total internal reflection in a PDMS microfluidic chip with no reflective material coating.

2. THEORY

As depicted in Figure 1, MTIRs were attained by positioning the light input beam at an incident angle greater than the critical angle of the PDMS-air interface at the channel's sidewalls (θ_i=44.7° considering n_{PDMS}=1.42).

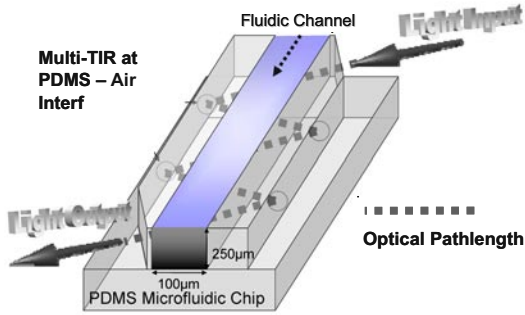

Figure 1. Schematic representation of MTIR in a microfluidic channel realized in PDMS.

3. EXPERIMENTAL

A PDMS microfluidic channel with cross sectional area of 100 µm (width) × 250 µm (height) was integrated with lateral grooves (1 mm long, 250 µm wide and deep) for the insertion of input & output optical fibers. The microchannels optical behaviour was simulated using ASAP™ and fabricated using soft lithography method with SU-8 photoresist as master mold. A PDMS cover layer with fluidic delivery holes was bonded to

978-0-9798064-0-7/µTAS2007/$20©2007CBMS

the channel using oxygen plasma treatment. A 635 nm pigtailed laser diode (Edmund Optics, Inc) was used as the light input and the light output was detected by a photodiode (Perkin Elmer. VTB8440B). Reflectivity measurements were carried out for incident angles of 40°, 45°, 48°, 50°, 53° and 55° using silicone oil as an index matching fluid. Brilliant blue (Sigma) of concentration from 0.1 μM to 500 μM was used in absorbance measurements for one, two and four TIRs in the channel. Absorbance measurement of haemoglobin from bovine serum was further demonstrated.

4. RESULTS AND DISCUSSION

Figure 2 demonstrates the MTIRs produced when the lateral grooves define an angle of 53° for the light input. Having no additional coating of reflective material, a low surface roughness (< 10-nm rms) of PDMS-air interface with optimized incident angle was crucial to ensure high reflectivity (Figure 3). Figure 4 confirms the feasibility of using high reflectivity PDMS-air interface (80% to 90%) for MTIRs in PDMS microchannel when incident angles >44.7°. As shown in Figure 5, the sensitivity of Brilliant Blue absorbance increases as the number of reflections increases while exhibiting an excellent linearity (R^2~0.99). Table 1 summarizes that an 18-fold increase in detection sensitivity was accomplished with the four TIRs as compared with the single TIR. The lowest limit of detection (LOD) of Brilliant Blue was found to be 1 μM for the four TIRs. Figure 6 corroborates the excellent agreement between the absorbance measurements of haemoglobin with Beer-Lambert's law.

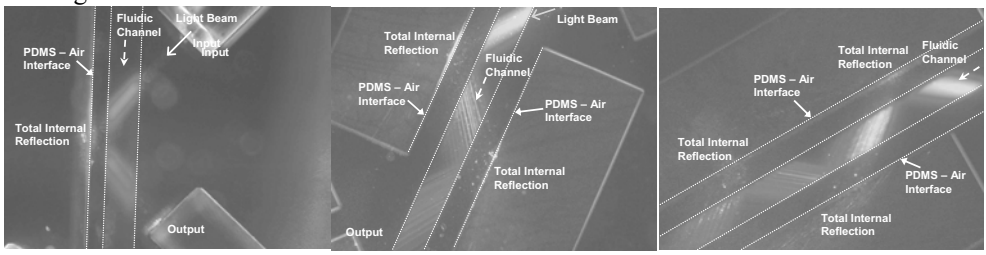

Figure 2. Images of TIR in PDMS with a) 1 Reflection, b) 2 Reflections and c) 3 Reflections.

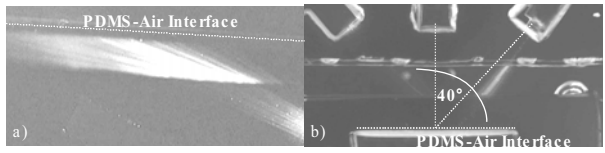

Figure 3. Unsuccessful TIR due to: a) Rough sidewall surface b) Incident angle < critical angle

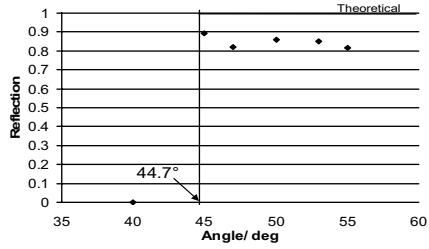

Figure 4. Reflectivity of the PDMS-air interface.

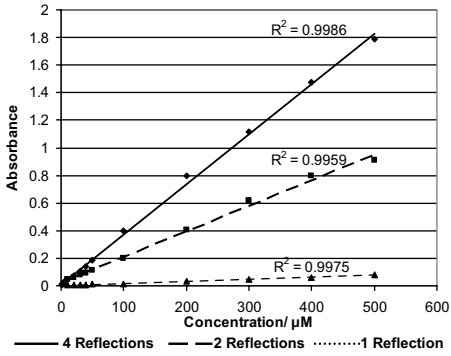

Figure 5. Absorbance measurement of Brilliant Blue with 1, 2 and 4 total internal reflections in the microfluidic channel.

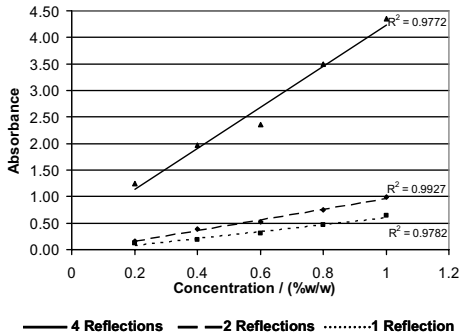

Figure 6. Absorbance measurement of haemoglobin

Table 1. Comparison of relative sensitivity for 1, 2 and 4 total internal reflections in the microfluidic channel for Brilliant Blue

Number of TIR	Optical Pathlength (µm)	Relative Sensitivity (slope)
1	750	1
2	1125	9
4	1875	18

5. CONCLUSIONS

In conclusion, the application of MTIRs in a PDMS microfluidic chip offers enhanced performance for absorbance measurement (lower detection limit and higher sensitivity) while retaining the low fabrication cost of the microfluidic chip in PDMS.

REFERENCES

[1] E. Verpoorte, A. Manz, H. Ludi, A.E. Bruno, F. Maystre, B. Krattiger, H.M. Widmer, B.H. van der Schoot and N. F. Rooij, "A Silicon Flow Cell for Optical Detection in a Miniaturised Total Chemical Analysis Systems," *Sensors and Actuators*, **6**, 66-70 (1992).

[2] R.M. Tiggelaar, T.T. Veenstra, R.G.P. Sanders, J.G.E. Gardeniers, M.C. Elwenspoek and A. van den Berg, "A light detection cell to be used in a micro analysis system for ammonia," *Talanta*, **56**, 331-339, (2002).

[3] H. Takao, T. Noda, M. Ashiki, K. Miyamura, K. Sawada and M. Ishida, "A silicon microchip for blood haemoglobin measurement using multireflection structure," *Proc. Micro Total Analysis Systems, Monterey, CA,* **363**, (2001).

[4] H. Salimi-Moosavi, Y. Jiang, L. Lestniers, G. McKinnon and D.J. Harrison, "A multireflection cell for enhanced absorbance detection in microchip-based capillary electrophoresis," *Electrophoresis*, **21** , 1291(2000).

NIR MICRO SPECTROMETRY OF CHEMICALLY AGGRESSIVE FLUIDS

Sylwester Bargiel[1], Jan Dziuban[1], Rafał Walczak[1], Paweł Knapkiewicz[1], Łukasz Nieradko[2], Anna Grzegorska[1], Bogdan Latecki[3]

[1]Faculty of Microsystem Electronics and Photonics, Wrocław University of Technology, POLAND
[2]Departement of Optics P.M. Duffieux, FEMTO-ST, University of Franche-Comté, FRANCE
[3]Institute of Electron Technology, POLAND

ABSTRACT

In this paper, the miniature corrosion resistant (including hot and concentrated sulphuric and nitric acids) near-infrared spectrometric system for in-line measurements of chemical and biochemical analytes is shown. Experimentally obtained absorbance/transmittance spectra of fluidic samples, for wavelengths in the range of 800-1700 nm, with high sensitivity of measurement, are presented.

Keywords: NIR spectroscopy, fiber-optic sensor, nitration reaction, microreactor

1. INTRODUCTION

The optical micro spectrometry is gaining increasing attention as the analytical method for continuous monitoring of analytes in the micro total analysis systems and microreactors [1-3]. However, the continuous analytical control of chemically aggressive reactants, for instance during nitration reactions of aromatic compounds in microreactors utilizing hot and concentrated sulphuric and nitric acids, is still unsolved.

Recently [4], we have shown the micromachined corrosion resistant silicon-glass cell. In this work we report the miniature NIR spectrometric system based on a minispectrometer and an optimized corrosion resistant detection cell with highly improved sensitivity.

2. EXPERIMENTAL

The detection cell. The cell is composed of silicon "body" covered with 0.3 μm-thick SiO_2 layer, 1.1 mm-thick Borofloat® 33 glass cover (Schott, Germany), and two multimode glass optical fibres (Figure 1a). Fluidic channel, optical cell, and two grooves for the positioning of optical fibers are micromachined by use of the DRIE method. The glass cover is anodically bonded to the silicon body. Two fibers, illuminating and collecting the transmitted light, are "isolated" from the fluidic channel by the perpendicular 20 μm-thick silicon walls, transparent for NIR light (Figure 1b,c). Thus, the aggressive fluids do not affect the fibers. The Borofloat® 33 and oxidized silicon are resistant against most of the chemical solutions (except HF acid and alkali solutions) and organic substances, what ensures high corrosion resistance of the detection cell. The silicon/glass chip of the detection cell with positioned SMA terminated fibers (Figure 1d) is epoxy glued to the PCB and packaged in a metal shock-resistant case. The case is equipped with standard fluidic connections (UpChurch, USA) (Figure 1e).

In order to increase NIR transmission through the optical cell, modified DRIE process has been applied leading to vertical side-walls and smoothing the surface of channels. Instead of the telecommunication fibers (62.5/125 μm), used in the older version of detection cell, laboratory-grade VIS/NIR fibers (Ocean Optics, USA) are used here.

978-0-9798064-0-7/μTAS2007/$20©2007CBMS

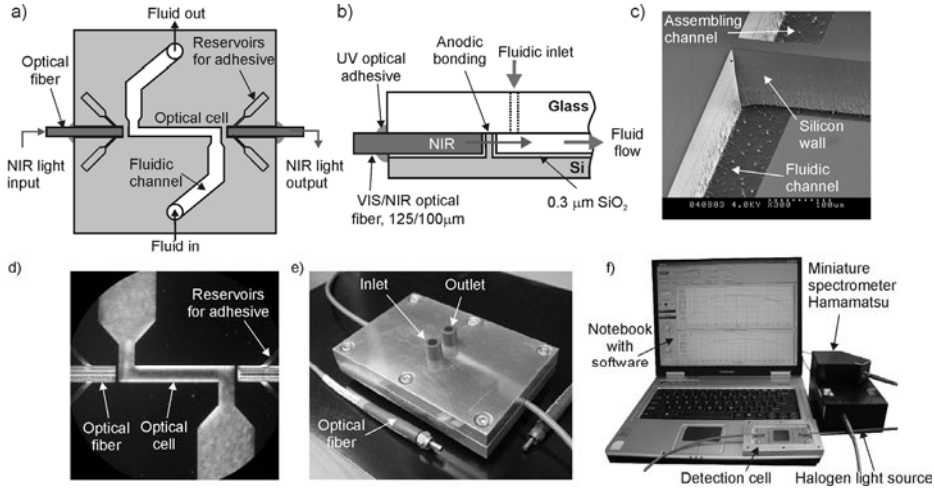

Figure 1. NIR spectrometric system: a) schematic of detection cell (top view), b) cross-section, c) SEM picture of DRIE etched channels and 20μm thick silicon wall, d) optical fibers assembled in grooves, e) detection unit with metal case and fluidic connections, f) miniature NIR system.

The fibers are characterized by the low NIR attenuation and the large core diameter (100 μm). The auxiliary channels (reservoirs) at the end of assembling grooves were etched to self-stop the capillary flow of an UV-curable optical adhesive.

NIR spectrometric system The NIR system is composed of a halogen light source (Optel, Poland), corrosion resistant detection unit with cell having path length of 5 mm, and a miniature array detector spectrometer C9406 (Hamamatsu, Japan) with spectral range of 800 – 1700 nm (Figure 1f). The advantage of this hand-held spectrometer, besides the lack of moving parts, is near real-time measurement of the whole NIR spectrum (10-90 ms). The system is controlled by a notebook with suitable software.

4. RESULTS AND DISCUSSION

The miniature spectrometric system has been tested experimentally by the measuring of NIR spectra of several samples including highly corrosive reactants of nitration reaction, petrochemical products, and beverage samples (red wine). Tests have shown that the intensity of the output optical signal, measured for control analytes, increased three orders of magnitude in comparison with the previously presented optical cell (Figure. 2a). Three absorption peaks of DI water, clearly visible at 955 nm, 1159 nm, and 1420 nm correspond well to the literature data (970 nm, 1438 nm, 1163 nm) [5]. The detection unit worked correctly at wide range of flow rates (0-300 ml/h) which confirms its mechanical robustness. The 24h test with cell filled with pure nitric acid followed by sulphuric acid showed a complete corrosion resistance of the detection unit. The spectra of pure nitric and sulphuric acids as well as their mixtures with deionized water were successfully obtained (Figure 2b). Thus, the desired chemical resistance of cell was achieved. It has been clearly shown that the microsensor recognizes properly different diesel oils and furnace oil as well as gasoline (Figure 2c). Concentration of ETOH in Porto red wine has been very well examined (Figure 2d).

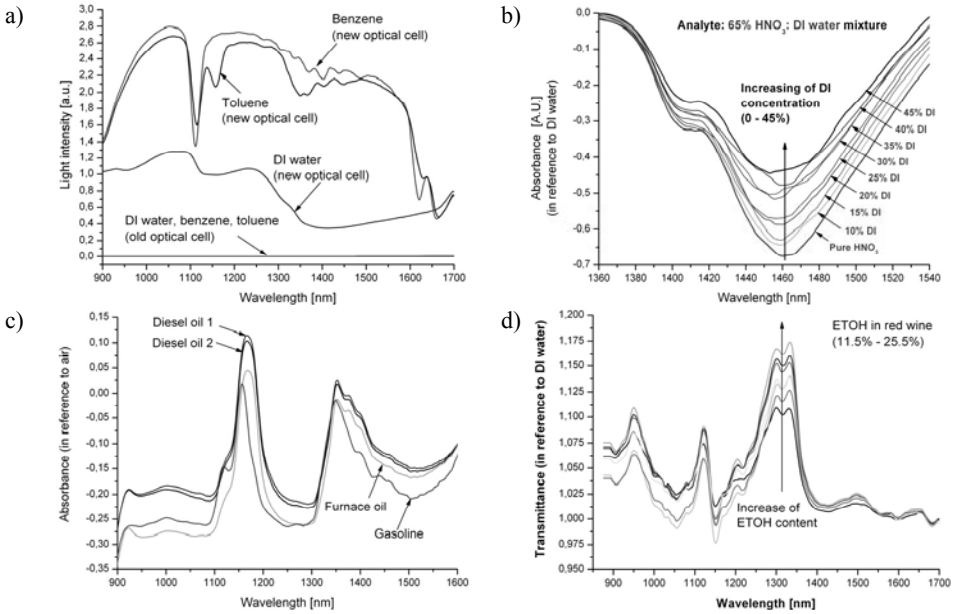

Figure 2. NIR spectra of fluidic samples: a) reactants of nitration reaction, b) pure nitric acid and its mixture with DI water, c) petrochemical products, e) Porto wine with different ETOH content.

5. CONCLUSIONS

Experimental results confirm the full applicability of the miniature corrosion resistant NIR spectrometric system for use in wide range of applications, e.g. μTAS, microreaction technology, biological/medical measurements. The maximal wavelength is limited by the properties of array detector applied in miniature Hamamatsu spectrometer. The use of longer NIR wavelengths is not limited by the detection unit itself.

ACKNOWLEDGEMENTS

This work was financed under NEPUMUC PR6 by the European Commission. We thank Jarosław Baszak of Hamamatsu Photonics Deutschland GmBH for help.

REFERENCES

[1] H. Lu, M.A. Schmidt, K.F. Jensen, *Photochemical reactions and on-line UV detection in microfabricated reactors*, Lab on a chip,1, pp. 22-28, (2001).

[2]M. Kölhed, B. Lendl, B. Karlberg, *On-line infrared detection in aqueous micro-volume systems*, Analyst, 128, pp. 2-6, (2003).

[3] R. Herzig-Marx, K.T. Queeney, R.J. Jackman, M.A. Schmidt, K.F. Jensen, *Infrared spectroscopy for chemically specific sensing in silicon-based microreactors*, Anal. Chem., 76, pp. 6476-6483, (2004).

[4] S. Bargiel, J. Dziuban, R. Walczak, P. Knapkiewicz, A. Górecka-Drzazga, *Corrosion resistant integrated optical microsensor for NIR spectroscopy and its application in microreactors*, Proc. of microTAS 2006, Vol. 1, pp. 741-743, (2006).

[5] Ch.V. Eddy, M.A. Arnold, *Near-infrared spectroscopy for measuring urea in hemodialysis fluids*, Clinical Chemistry 47:7, pp.1279–1286, (2001).

SIMULTANEOUS MEASUREMENTS OF NEAR-WALL VELOCITY AND WALL ZETA-POTENTIAL BY EVANESCENT WAVE ILLUMINATION

S. Miyakawa, Y. Kazoe and Y. Sato
Keio University, JAPAN

ABSTRACT

A simultaneous measurement technique of the near-wall electroosmotic velocity and the wall zeta-potential was developed by using the evanescent wave. Nano particle image velocimetry (nano-PIV) with submicron fluorescent particles and nanoscale laser induced fluorescence (nano-LIF) with fluorescent dye were used for the velocity and zeta-potential measurement, respectively. The images of particles (red fluorescence) and dye (green fluorescence) were captured by a 3CCD camera. The present study focused on the vicinity of the microchannel wall with uniform zeta-potential.

Keywords: Nanoscale, zeta-potential, electroosmotic flow, evanescent wave

1. INTRODUCTION

In order to achieve the precise flow control using electrokinetics in micro-TAS, it is critical to understand the relationship between the electroosmotic flow field and the distribution of wall zeta-potential, which is generated from the ion behavior in the microchannel and the surface chemical modification to the wall. The objective of the present study is to perform the simultaneous measurements of the electroosmotic velocity and the wall zeta-potential by using submicron fluorescent particles and fluorescent dye.

2. EXPERIMENTAL SETUP

Figure 1 illustrates a schematic of the evanescent wave illumination. Submicron fluorescent particles and fluorescent dye in the vicinity of the wall were excited by the evanescent wave, which was generated by total internal reflection of a laser beam with the wavelength of 488 nm. Since the fluorescent particles and fluorescent dye have different fluorescent wavelength as listed in Table 1 and 2, each fluorescence image was captured by a 3CCD camera separately. The near-wall electroosmotic velocity and the wall zeta-potential were measured by nano-PIV [1] with the fluorescent particles and nano-LIF

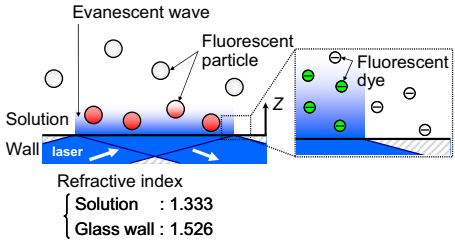

Figure 1. Schematic of the evanescent wave illumination.

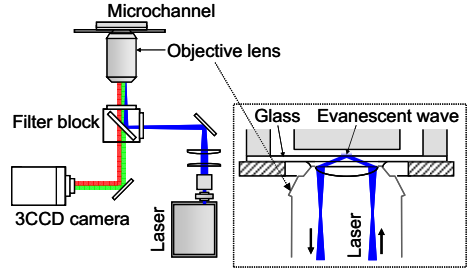

Figure 2. Schematic of the measurement system.

978-0-9798064-0-7/μTAS2007/$20©2007CBMS

Table 1. Properties of fluorescent particles

Diameter	(μm)	1.0
Volume concentration	(%)	0.2
Excitation wavelength	(nm)	488
Emission wavelength	(nm)	645
Mobility	(m^2/Vs)	5.58×10^{-8}

Table 2. Properties of fluorescent dye

Molecular weight	(Da)	643.41
Concentration	(μM)	30
Excitation wavelength	(nm)	494
Emission wavelength	(nm)	519
Fluorescence lifetime	(ns)	4.1

[2] with the fluorescent dye, respectively. The electroosmotic velocity was obtained by subtracting the particle electrophoretic velocity from the particle velocity [3]. The wall zeta-potential was obtained from the detected fluorescent intensity, because the fluorescence concentration near the wall was related to the zeta-potential by the Boltzmann distribution.

Figure 2 illustrates a measurement system comprised of an inverted fluorescent microscope, an optically pumped semiconductor laser, a 60× objective lens (NA = 1.45) and the 3CCD camera. The evanescent wave with the penetration depth of 74 nm was generated by total internal reflection of the laser beam at the glass-solution interface. The spatial resolution of nano-PIV and nano-LIF was 17.2 × 17.2 μm based on the size of reference window and 1.72 × 1.72 μm based on the pixel averaging per 8 × 8 to reduce the single pixel error, respectively. Prior to the measurement, the calibration experiments for nano-LIF were performed to estimate a relationship between the fluorescent intensity excited by the evanescent wave and the zeta-potential. The fluorescent intensity was measured at the uniform zeta-potential, which was prepared by adjusting the cation concentration in the solution.

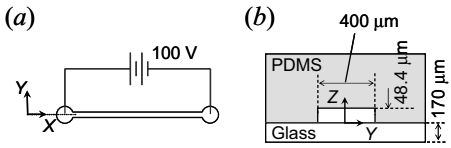

Figure 3. Schematic of the straight microchannel comprised of PDMS and borosilicate glass.

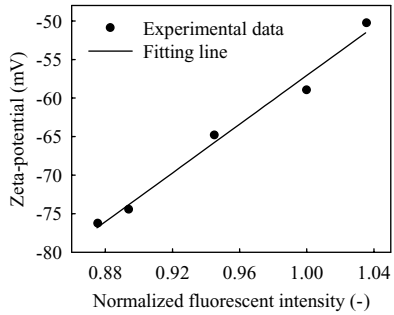

Figure 4. Calibration curve between the fluorescent intensity and the wall zeta-potential.

Figure 3 shows a schematic of the straight microchannel comprised of PDMS and borosilicate glass. A 5 mM HEPES solution with 0.5 mM NaCl, fluorescent particles and fluorescent dye was injected into the microchannel. A DC electric field of 17.2 V/cm was applied to induce electroosmotic flow. Measurements were performed in the vicinity of the glass wall.

3. RESULTS AND DISCUSSION

Figure 4 shows a calibration curve between the fluorescent intensity and the wall zeta-potential. The fluorescent intensity increases with increasing the zeta-potential. The measurement uncertainty of nano-LIF in 95% confidence level was 5.3 mV. Figure 5 shows the electroosmotic velocity vector map and the zeta-potential distribution, which were

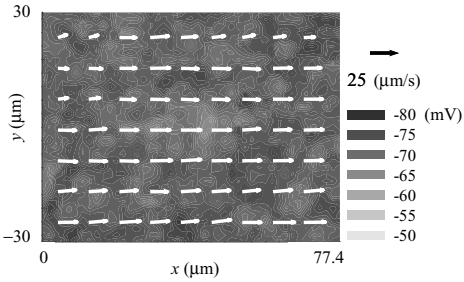

Figure 5. Electroosmotic velocity vector map by nano-PIV and two-dimensional zeta-potential distribution by nano-LIF.

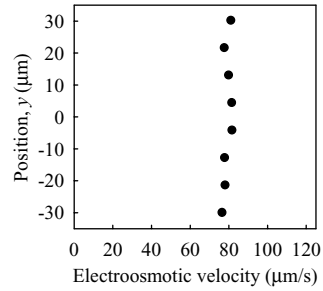

Figure 6. Profile of electroosmotic velocity in the Y-direction obtained by nano-PIV.

obtained by averaging 100 images. Figure 6 shows the electroosmotic velocity profile in the *Y*-direction, which was obtained by spatially averaging in the *X*-direction. The electroosmotic velocity was almost constant in the measurement area and the mean velocity was 79.3 μm/s. The zeta-potential also has the uniform distribution at the wall and the mean zeta-potential was −72.0 mV. It is noted that the electroosmotic velocity, which was estimated from the mean zeta-potential by the Helmholtz-Smoluchowski equation, was calculated to be 97 μm/s and approximately corresponds to that obtained by nano-PIV.

4. CONCLUSIONS

A simultaneous measurement technique of the near-wall electroosmotic velocity and wall zeta-potential was developed by using the evanescent wave. Measurements were performed in the vicinity of the wall with uniform zeta-potential. It is concluded that the near-wall electroosmotic flow field was generated depending on the wall zeta-potential. The future work will perform the measurement with nonuniform wall zeta-potential.

ACKNOWLEDGEMENT

This work is subsidized by the Grant-in-Aid for Young Scientists of the Ministry of Education, Culture, Sports, Science and Technology (MEXT) (No. 14702030 and No. 17686017). The second author is supported by the 21st COE for “System Design: Paradigm Shift from Intelligence to Life” from MEXT.

REFERENCES

[1] R. Sadr, M. Yoda, Z. Zheng and A. T. Conlisk, *An experimental study of electro-osmotic flow in rectangular microchannels*, J. Fluid Mech., **506**, pp. 357-367, (2004).

[2] Y. Kazoe and Y. Sato, *Nanoscale laser induced fluorescence imageing of zeta-potentil affected by ion motion in microchannel*, Micro-TAS 2006, **1**, pp. 101-103, (2006).

[3] Y. Sato and K. Hishida, *Electrokinetic effects on motion of submicron particles in microchannel*, Fluid Dynamics Research, **38,** pp. 787- 802, (2006).

SPR BIOSENSING COUPLED TO A DIGITAL MICROFLUIDIC SURFACE ACOUSTIC WAVE SYSTEM

E Galopin[1], M Beaugeois[2], F Lapierre[1], M Bouazaoui[2], JC Camart[1], V Thomy[1], B Pinchemel[2]

[1]*Institut d'Electronique, de Microélectronique et de Nanotechnologie (IEMN), UMR 8520, France*

[2]*Interdisciplinary Research Institute (IRI), FRE 2963, France*

ABSTRACT

Surface plasmon resonance (SPR) is now regarded as one of the most sensitive optical detection techniques for real time monitoring of binding interactions [1-2]. SPR is now also widely used to probe affinity and kinetic constants. However, if mass transport is low, diffusion limits reaction in terms of time scales and sensitivity, the measured response is virtually independent of the reaction rate and kinetic parameters can't be determined. An original solution is proposed, compared to generally used pressure driven flows. Efficiency of Surface Acoustic Wave (SAW) microstreaming coupled to SPR biosensing is considered, in order to improve the accuracy of kinetic parameter estimation in mass transport limited regime.

Key Words: Surface Plasmon Resonance, Biosensing, Droplet, Microstreaming

1. INTRODUCTION

The use of SAW at the liquid-solid interface in microdroplets is employed to favorably cope with mass transport issues, by providing streaming effects that enhance the interaction with the active surface [3]. SAW are generated by interdigited transducers laid on a top slide X-LiNbO3 substrate at 20 MHz. SAW micromixing [4] results from the absorption of the longitudinal pressure wave radiated into the droplet (Figure 1). In fact, the binding of an analyte to its immobilized ligand on the biosensing surface is a two step process, including the mass transport of the analyte to the sensing surface followed by the complexation which creates an analyte depleted zone. One can expect that SAW microstreaming maintains some fresh analyte at the surface and help overcome mass transport. Moreover, recorded SAW velocity fields dynamic is quite important (up to several hundreds of µm/sec) compared to other stirring methods, enabling to adapt to a large set of analyte/ligand interactions.

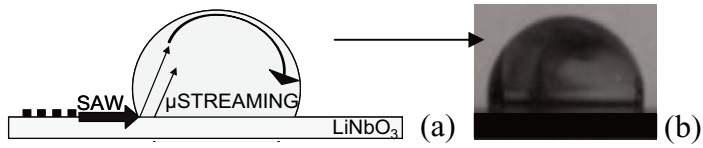

Figure 1. (a) Principle of SAW propagation at the substrate/ micro-droplet interface causing streaming effects and (b) Visualization of the streaming

SPR wave results from an evanescent field excitation of a thin metal film at a specific angle. For this resonance angle, the TM-polarized incident beam excites resonantly under total reflection the plasmon of the metal surface (Figure 2). The slightest change in refractive index is induced by reactions at the metal surface and results in a shift in resonance angle enabling to monitor in real time a biological interaction.

978-0-9798064-0-7/µTAS2007/$20©2007CBMS

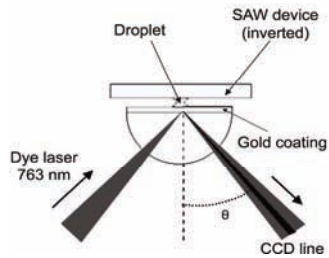

Figure 2. Experimental set-up comprising a $LiNbO_3$ Substrate on top slide, Au coated semi-cylindrical prism, and a droplet in which biomolecular interaction occur.

2. EXPERIMENTAL

Literature shows that SPR is highly sensitive to temperature due to the refractive index modification of the metal in particular [5]. Temperature elevation due to SAW excitation from top slide on SPR minimum position is studied. Several excitations are achieved in continuous and pulsed mode with various cyclic ratio r (Figure 2).

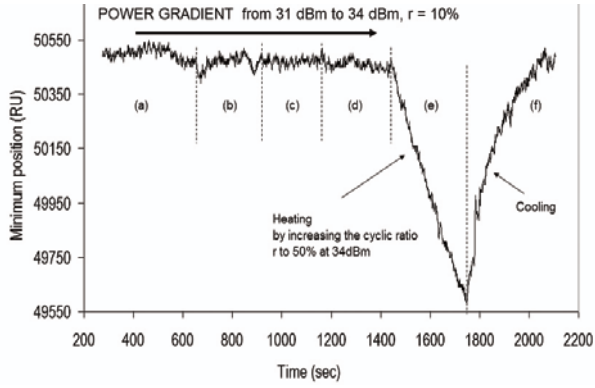

Figure 3. Evolution of SPR Min position as a function of SAW power in pulsed mode for a 3µl droplet: a) Stability test without SAW (b) P = 31dBm, r =10% (c) P = 31.5dBm, r = 10% (d) P= 34dBm, r = 10% (e) P = 34dBm, r=50% , (f) cooling

The recorded shift of the SPR minimum under SAW excitation and the calculated are of the same rank and confirm temperature elevation due to acoustical excitation. It is then shown that minimum position, and thus real time monitoring of reaction, is not affected by a SAW excitation in pulsed mode at 34 dBm with a cyclic ratio r of 10% for a 3µl droplet.

3. RESULTS AND DISCUSSION

Now that SAW excitation parameters comprising a pulsed excitation at 500Hz, 31 dBm, with a cyclic ratio of 10% have been adjusted to lead to micro-streaming effects without affecting SPR minimum position on 3µl water droplet, streptavidin binding on NHS activated carboxyl-terminated SAM's is obtained. Binding phenomena are compared under SAW micro-streaming and under static conditions. A first result of streptavidin binding on a NHS activated carboxyl-terminated SAM's is obtained (Figure 5) and shows that micro-streaming limits the effect of mass transport on the binding event. SAW

microstreaming, by maintaining some fresh analyte at the surface can help overcome mass transport limitations.

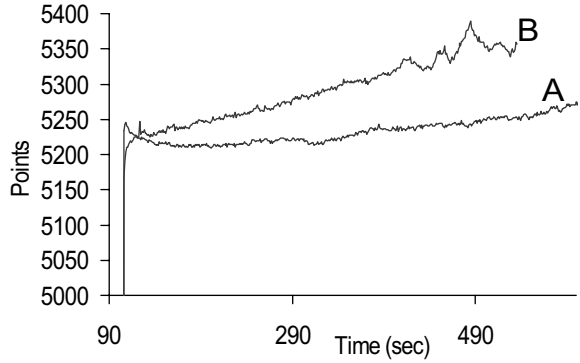

Figure 4. Streptavidin binding on a NHS activated carboxyl-terminated SAM's (A) under static conditions (B) under SAW micro-streaming

4. CONCLUSIONS

This work reports for the first time the use of acoustic SAW streaming coupled to SPR real time biosensing of analytes in microdroplets. It is shown in a first place that experimental conditions of digitalized microfluidics can be adapted to SPR biosensing in regards of the set up but also in regards of the expected temperature effects induced by SAW actuation. This work then exposes that an effective integrated micro-stirring can be monitored and evaluated by SPR, with a simple affinity reaction. A range of antibody/antigen couples presenting different kinetic parameters will be presented, in order to evaluate the advantages of the micro-streaming on different kinds of interactions.

ACKNOWLEDGEMENTS

The authors would like to acknowledge the "Institut de Recherche sur les Composants logiciels et materiels pour l'Information et la Communication Avancée" (IRCICA) as well as the "Pole de Recherche en MIcro-Optique" (PREMIO) Belgian-French Interreg III project for their support. FEDER (Fonds Européen de DEveloppement Régional) supported this work by equipment contribution.

REFERENCES

[1] "Surface plasmon resonance sensors: a review", J. Homola, S.S. Yee, G. Gauglitz, Sens. & Act. B, **54**, 3–15 (1999)

[2] "Biosensing with surface plasmon resonance: how it all started", B. Liedberg, C. Nylander, I. Lundstrom, Biosens. Bioelectron. 10 1-4 (1995)

[3] "Enhanced protein capture by ultrafast saw droplet µmixing", E. Galopin, A. Renaudin, V. Thomy, J.C. Camart, P. Tabourier, C. Druon, MicroTAS'06, 651-653 (2006)

[4] "Acoustic manipulation of small droplets", A. Wixforth, C. Strobl, Ch. Gauer, A. Toegl, J. Scriba, Z. Guttenberg, Anal. Bioanal. Chem., **379**, 982 (2004)

[5] "Temperature Effects on Surface Plasmon Resonance: Design Considerations for an Optical Temperature Sensor", S. Kaya Özdemir and G. Turhan-Sayan, Journal of lightwave technology, **21**, 805-814 (2003)

A BIOSENSOR BASED ON INTERDIGITATED ELECTRODES AND MICROSCOPIC MANIPULATION OF MAGNETIC PARTICLES

Zhengchun Peng[1], Peter Hesketh[1], William R Heineman[2], and Kathryn Kellar[3]

[1]*School of Mechanical Engineering, Georgia Institute of Technology, Atlanta, USA*
[2]*Department of Chemistry, University of Cincinnati, Cincinnati, USA*
[3]*Centers for Disease Control and Prevention, Atlanta, USA*

ABSTRACT

A particle-based electrochemical biosensor was developed by integrating patterned soft magnetic material (NiFe) with interdigitated array (IDA) electrodes. The NiFe patterns redirect the magnetic flux of a uniform field, thus creating field gradients which attract paramagnetic particles. The patterned NiFe features act as magnetic traps and were used to collect the enzyme labeled paramagnetic particles from a microchannel flow of particle suspension near to IDA electrodes, so that the enzyme product is generated in close proximity to the electrodes and thus increases sensitivity. The magnetic traps are designed in such a way that they can microscopically position particles among IDA electrodes without blocking the active electrode surface.

Key words: particle-based biosensor, magnetic traps, interdigitated electrodes

1. INTRODUCTION

Array microelectrodes exhibit a better signal/noise ratio than macroelectrodes because they not only minimize the noise associated with the double layer capacitance of the active area, but also enhance mass transfer due to nonlinear diffusion [1]. Among various array microelectrodes, the interdigitated type geometry has a relatively high reaction current, in addition to a high signal/noise ratio. Theoretical studies and experiments have both shown that redox cycling among IDA electrodes was more efficient with smaller electrodes due to shorter diffusion distance and more pronounced nonlinear diffusion [2]. However, IDA electrodes even in nanoscale have not reached the detection limit desired by many applications, particularly when used as a biosensor. Among other researchers, Yang and Zhang [3] have recently investigated the fundamental reasons that limit the performance of IDA electrodes. Their work indicates that the diffusion of redox couple from bulk to IDA surface is linear, regardless of the size of IDA electrodes. The nonlinear diffusion pattern is only present near the IDA surface when the size of the electrode becomes small. Therefore, while the mass transfer of the redox couple is faster and more directional towards the IDA surface of smaller electrodes, the supply from the bulk is still slow and not very directional, which limits the reaction current.

The principal objective of this work was to experimentally realize a highly sensitive biosensor that utilizes IDA electrodes to its best potential. According to the simulation results [3], the performance of such a biosensor can be improved by confining the electroactive species produced by a biological sample, such as enzyme, close to the IDA electrodes, instead of distributing them in the bulk solution. While many electrochemical biosensors immobilize the target onto the electrode surface so that the target-produced electroactive species are detected in proximity of the electrodes, we prefer to use the IDA electrode in combination with conjugated micro/nanoparticles, because particle-based assay

978-0-9798064-0-7/μTAS2007/$20©2007CBMS

gives rise to much more flexibility [4]. Due to its unique advantages, magnetic manipulation of particles through either external field or on-chip coils/circuits has been gaining increasing attention in many micro systems [5]. In this work, we make use of the interaction between magnetic particles and patterned soft magnetic material in order to trap the enzyme conjugated particles at the surface of IDA electrodes. Furthermore, we design the traps in such a way that they not only collect magnetic particles in a pressure driven microchannel flow, but also precisely position the particles in between the electrodes.

2. THEORY

A magnetostatics model (2D symmetric) was developed using COMSOL Multiphysics to study the attraction force between magnetic particles and soft magnetic materials such as $Ni_{80}Fe_{20}$. The result shown in Fig. 1A reveals that the NiFe strips focus the magnetic flux and re-distribute the flux of a uniform field. Thus, a local field gradient is created among the NiFe strips, as shown in Fig. 1B.

The field gradient can exert attraction force on a magnetic particle in proximity. The force on a magnetic particle inside a magnetic field is given by [5]:

$$F = \frac{\chi}{\mu_0} V (B \cdot \nabla) B \tag{1}$$

where V and χ are volume and susceptibilities of the particle, and B the field strength.

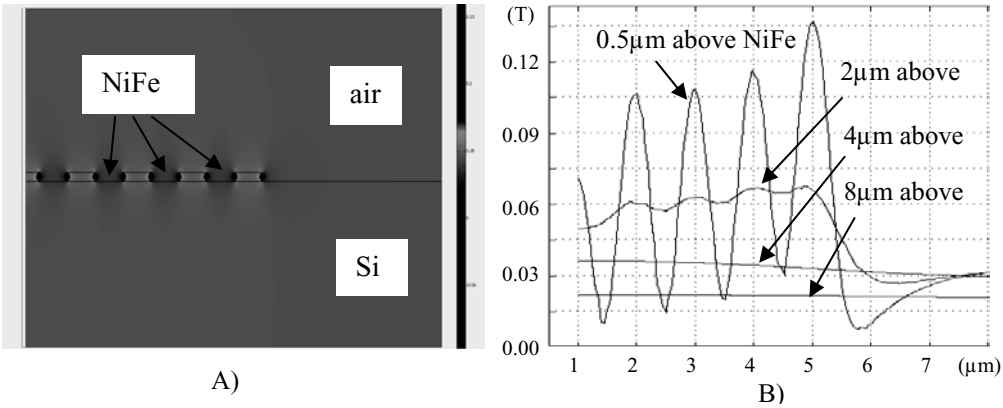

Fig 1. Magnetic flux density of NiFe strips subjected to a vertical field of 0.15T
A) Contour plot (the NiFe strips are 0.2μm thick and infinitely long in the direction into the paper); B) Cross-section plot along air-Si interface

3. SENSOR DESIGN AND FABRICATION

We believe that a highly sensitive particle-based biosensor can be realized by combining patterned NiFe material with IDA electrodes on the same chip, because the NiFe patterns can direct magnetic field to bring biologically conjugated magnetic particles very close to the IDA electrodes for detection. Two types of such combination can be designed for this purpose. For type I, the NiFe is defined in between IDA electrodes; while in type II, the IDA electrodes overlap with magnetic material (Fig. 2). In both designs, the electrodes and magnetic traps are insulated from each other, so that the NiFe are neither exposed to liquid sample nor electrical potential, both of which will lead to corrosion of NiFe. The electron beam lithography system (JBX-9300FS) was used to fabricate such devices in

submicron scale with tens of nanometer alignment accuracy. It is noted that, at the same dimension, type II device has advantage over type I in terms of redox cycling efficiency due to shorter spacing between electrodes. The device fabrication was completed after patterning Pt counter electrodes, Ag/AgCl reference electrode, and contact pads using UV lithography on the same wafer. Microfluidic channels were then integrated with the device.

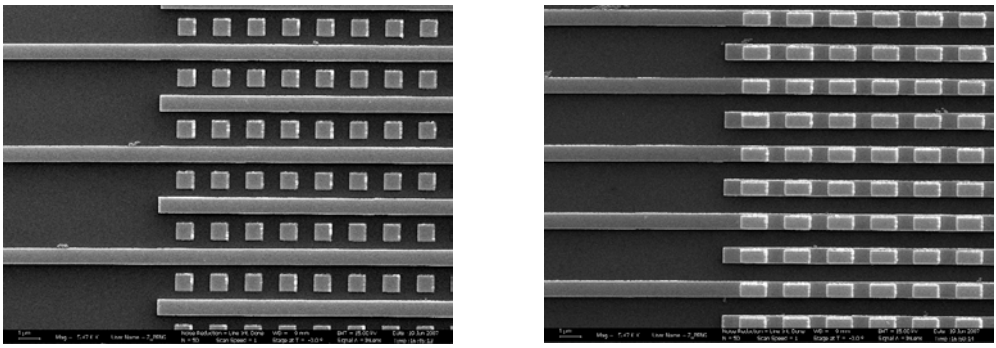

Fig 3. Magnetic traps (rectangles) integrated with electrodes (strips).
Left: Type I device (scale bar is 1µm); Right: Type II device (scale bar is 1µm)

4. RESULTS AND DISCUSSION

Experiments were carried out on both types of devices and both were capable of collecting 1µm Dynabeads® from microchannel flow of particle suspension at 1cm/sec. Shown in Fig. 4 is the particle trapped by a type II devices. As expected from the design, two neighboring traps interact with a single particle and the final location of particles is between two neighboring edges or corners of the NiFe patterns. This is because that the maxima of the field gradients are located at the edges of the traps (see Fig. 1B). As a result, the particles are held in between two adjacent electrodes. Thus, there were no beads blocking the active electrode surface by landing on top of the electrodes. This is advantageous over direct functionalization of electrodes which reduces the actual electrode surface and limits the electron transfer.

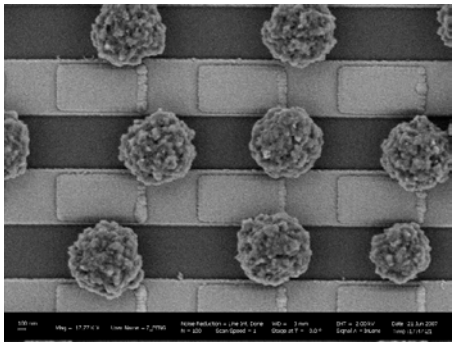

Fig 4. Trap 1µm Dynabeads among IDA (scale bar is 100nm)

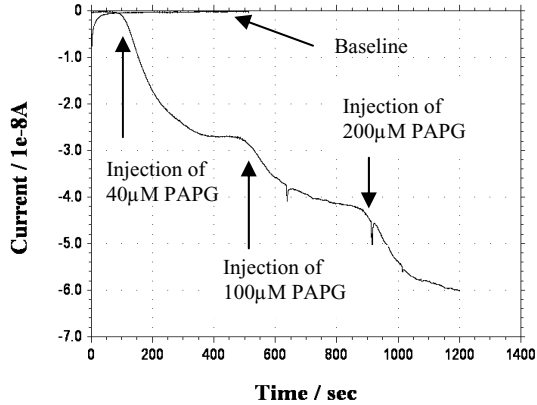

Fig. 5. IDA response to 1200 Dynabeads

Amperometric test followed the trapping of the β-Galactosidase labeled MyOne® Dynabeads. The sensor response of injecting the enzyme substrate, p-aminophenyl galactopyranoside (PAPG), with various concentrations is shown in Fig. 5. The enzyme product, p-aminophenol (PAP) was oxidized to p-quinone monoamine at 0.3mV vs. Ag/AgCl, and the electrochemical reversibility enabled to couple the enzyme labeling and effective redox cycling. The recorded signal corresponds to an estimate of about 1200 MyOne beads distributed among IDA electrodes as seen in Fig. 4. The sensor consists of 30 pairs of 0.8μm wide IDA electrodes with 0.8μm spacing and the length of the electrodes is 100μm. As far as the same surface area of both particles and electrodes is concerned, this device has shown much higher signal compared with our previous device [6], in which there were no magnetic traps integrated with the IDA electrodes.

5. CONCLUSIONS

We have improved the performance of IDA electrodes as a particle-based biosensor by combining magnetic traps with the IDA electrodes. Two types of trap-electrode combination were investigated. The carefully designed micro/nano magnetic traps not only collect enzyme labeled magnetic particles to IDA electrodes from a microchannel flow of particle suspension, but also precisely position them between IDA electrodes without blocking the actual electrode surface. This allows us to utilize submicron scale IDA electrodes to its best potential in terms of detecting small amount of molecules bound to magnetic particles.

ACKNOWLEDGEMENT

The financial support of the Georgia Tech/CDC seed grant and the kind help provided in the device fabrication by Georgia Tech MiRC staff are acknowledged. Special thanks go to MiRC Research Engineer Devin Brown for help with electron beam lithography.

REFERENCE

[1] A. J. Bard, J. A. Crayston, G. P. Kittlesen, T. V. Shea, M. S. Wrighton, "Digital simulation of the electro-chemical response of reversible redox couples at microelectrodes," *Anal. Chem.* vol. 58, 2321-1331, 1986;

[2] M. Paeschke, U. Wollenberger, C. Kohler, T. Lisec, U. Schnakenberg, R. Hintsche, "Properties of interdigital electrode arrays with different geometries," *Anal. Chim. Acta*., vol. 305, pp. 126-136, 1995

[3] X. Yang, G. Zhang, "The voltammetric performance of interdigitated electrodes with different electron transfer rate constants," accepted, *Sensor and Actuators (B).*

[4] E. Verpoorte, "Beads and chips: new recipes for analysis," *Lab on a Chip*, vol. 3, pp.60N-68N, 2003;

[5] N. Pamme, "Magnetism and microfluidics," *Lab on a Chip*, vol. 6, pp. 24-38, 2006.

[6] J. H. Thomas, S. K. Kim, P. Hesketh, H. B. Halsall, and W. R. Heineman, "Micro-bead-based electrochemical immunoassay with interdigitated electrodes," *Anal. Bioche*m., vol. 328, pp.113-122, 2004

ADAPTIVE NANOWIRES FOR SWITCHABLE MICROFLUIDIC DEVICES

E. Piccin[1], R. Laocharoensuk[2], J. Burdick[2], E. Carrilho[1] and J. Wang[2]
[1]*University of São Paulo, BRAZIL*
[2]*Arizona State University, USA*

ABSTRACT

This work demonstrates the use of adaptive functional nickel nanowires for switching on demand operation of microfluidic devices. Controlled reversible magnetic positioning and orientation of these nanowires at the microchannel outlet offers modulation of the detection and separation processes, respectively. The former facilitates switching between active and passive detection states to allow the microchip to be periodically activated to perform a measurement and reset it to the passive ("off") state between measurements. Fine magnetic tuning of the separation process (postchannel broadening of the analyte zone) is achieved by reversibly modulating the nanowire orientation (detector alignment) at the channel outlet.

Keywords: Electrochemical detection, nickel nanowires, CZE microchips, amino acids

1. INTRODUCTION

"Adaptive materials", whose function can be controlled via external (photonic or magnetic) stimuli, offer great promise for changing the operation of sensors or microchips in response to a specific need (event, opportunity, etc.) [1]. For example, magneto-switchable processes have been useful for on demand magnetic control of biosensing events [2]. Similarly, stimuli responsive nanowires have been employed for reversible magnetoswitchable control of electrochemical processes [3].

As will be illustrated below, adaptive nanowires can add an unique dimension to the operation of microfluidic devices, including control of the separation and detection processes. The use of adaptive nanowires for magneto-switchable microchip operation relies on placing, reorienting, and removing catalytic/magnetic nickel nanowires at the exit of the separation channel (Figure 1).

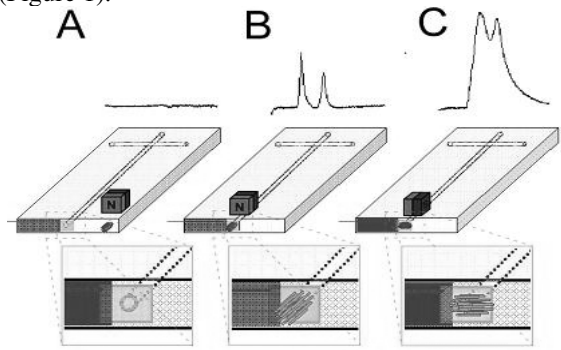

Figure 1. Schematic representation of the magnetoswitchable microchip detector based on adaptive nanowires. Magnetic control is used to position and reorient the nickel nanowires on the gold layer sputtered onto the outlet of the separation microchannel. Also shown (top) are corresponding electropherograms of a mixture without (A) and with the nanowires aligned in vertical (B) and horizontal (C) positions at the microchannel exit area.

978-0-9798064-0-7/μTAS2007/$20©2007CBMS

This allows magnetic switching between active and passive detection states as well as fine-tuning the microchip separation efficiency (peak resolution). The magnetic properties of nickel and its electrocatalytic activity toward aliphatic alcohols, carbohydrates, and amino acids [4] make nickel nanowires ideally suited for such adaptively controlled operation of microchip detection. Magnetic manipulations are particularly suitable for such adaptive microchip operation as they offer unique possibilities for controlling externally matters inside and outside a microchannel [5].

2. EXPERIMENTAL

The design of the Plexiglas holder, housing the separation chip and the detector, has been described previously [6]. The glass microchips were purchased from Microlyne Inc. (model MC-BF4-001, Edmonton, Canada). The separation channel was 65 mm in length (with effective length of 60 mm), while the injection channel was 10 mm long. The channels had a maximum depth of 20 μm and a width of 50 μm. Figure 1 displays the nanowires electrode assembly at the end of the separation channel. A thin gold film (200 nm), sputtered around the outlet of the separation channel, served as an electrical contact for the catalytic nickel nanowires during amperometric detection. An insulator ink was used for covering part of the gold layer, exposing an electrode area around 1.0 × 1.0 mm. Nickel nanowires were prepared by electrochemical deposition into the 200-nm-diameter nanopores of a 60-μm-thick alumina membrane template as described previously [3]. These particles (15-μm length) were oriented in either "vertical" or "horizontal" positions by changing the orientation of a cube-shaped magnet, which was placed on the top surface of the microchip (see Figure 1). A 90° rotation of the magnet corresponded to a 90° change in the orientation of the nanowires (Figure 1, B vs C). Switching of the microchip detector between the active (ON) and passive (OFF) states was accomplished by removing the cube magnet from its switching position and moving it to the side of the detection reservoir.

3. RESULTS AND DISCUSSION

The magnetic attraction and removal of the nanowires to and from the channel exit (Figure 1) allow microfluidic devices to be activated periodically to perform measurements and reset them to the passive (OFF) state between such measurements. Such reversible magnetoswitchable control of the microchip detection is illustrated in Figure 2A, which displays electropherograms for glucose obtained upon placement (ON) and removal (OFF) of the nanowires at the channel outlet. A well-defined glucose oxidation peak is observed in the presence of the nanowires at the channel outlet. In contrast, no signal is observed upon removing the nanowires. A relative standard deviation of 4.7% was estimated for the height of the six glucose peaks (of the three ON/OFF cycles), reflecting the reproducible placement and removal of the nanowire detection elements.

The adaptive nanowires also allow fine-tuning of the microchip separation through reversible modulation of the nanowire orientation at the channel outlet. Figure 2B demonstrates the influence of the nanowire detector orientation upon the separation performance in terms of peak width and symmetry. It displays electropherograms for a mixture of amino acids, with the nanowires placed in the vertical (a) and horizontal (c) orientations, as well as in the 45° alignment (b). Such behavior is attributed to postchannel broadening of the analyte zone associated with the different geometries and alignments of the nanowire detector assembly.

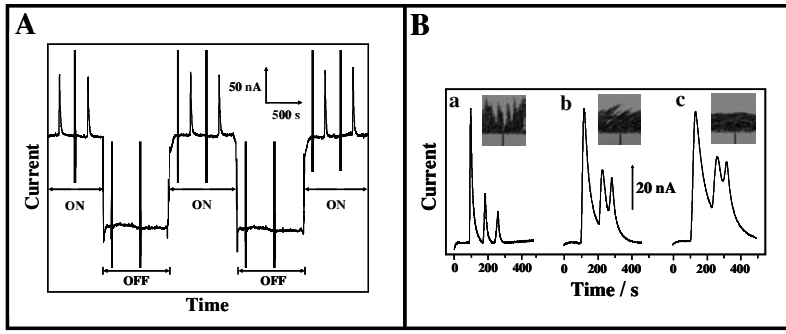

Figure 2. **(A)** Current-time recording for injections of 1 mM glucose obtained for reversible switching of the microchip detection by cyclic attraction ('ON') and removal ('OFF') of the nanowires to and from the channel exit. Separation medium, 35 mM NaOH; separation and injection potentials, + 1 kV; injection, 10 s; detection potential, +0.55 V (vs Ag/AgCl wire). **(B)** Tuning the separation efficiency of microchips through controlled orientation of the nanowires. Response for a mixture of amino acids containing 500 µM arginine, histidine, and glycine, with the nanowires in the 'vertical' (a) and 'horizontal' (c) positions, as well as in the 45° orientation (b). Separation and injection potentials, +700 V; detection, +0.55 V; injection, 5s; separation medium, 10 mM NaOH. Also shown (top) optical images of the nickel nanowires oriented in the three positions at the end of the channel.

The new nanowires-based adaptive microchip detection is highly reproducible. Analysis of a mixture of amino acids yielded reproducible electropherograms, with RSD (n = 5) (for peak height) of 1.91, 2.40, and 1.78% for histidine, arginine, and glycine, respectively. The concentration dependence was also examined by recording the electropherograms for samples containing increasing levels of arginine. Defined peaks, proportional to the amino acid concentration, were observed with correlation coefficient of 0.9985.

4. CONCLUSIONS

In this study we have demonstrated the use of adaptive nanowires for controlling on-demand the separation and detection processes in microfluidic devices. Other detector materials (e.g., Au, Pt) can be used in connection to nickel-based dual segment nanowires. Additional microchip functions, such as pretreatment or mixing, could also be controlled on demand using various external stimuli.

ACKNOWLEDGEMENTS

EP acknowledges fellowships from CAPES and CNPq. Supports from EPA, NSF and DOE.

REFERENCES

[1] R. Byrne, D. Diamond, *Nature Materials* **5**, 421 (2006).
[2] E. Katz, L.S. Haj-Ichia, A.F. Buckmann, I. Willner, *Angew.Chemie*. **41**, 1343 (2002).
[3] J. Wang, M. Scampicchio, R. Laocharoensuk, F. Valentini, O. Gonzalez-Garcia, J. Burdick, J., *J. Am. Chem. Soc.* **128**, 4562 (2006).
[4] I.G. Cassela, T.R. Cataldi, A. Salvi, E. Desimoni, *Anal. Chem.* **65,** 3143-3150 (1993).
[5] N. Pamme, *Lab on a Chip* **6**, 24 (2006).
[6] J. Wang, B. Tian, E. Sahlin, *Anal. Chem.* **71**, 3901 (1999).

RAPID, SEQUENCE SPECIFIC, REUSABLE ELECTRONIC DNA SENSOR IN MICROFLUIDIC DEVICES

E. Pavlovic[1], R.Y. Lai[2], B. Ferguson[3], J.S. Swensen[1], T.-T. Wu[4], R. Sun[4], A.J. Heeger[1], K.W. Plaxco[2], H.T Soh[1,3]

[1]Department of Materials, [2]Department of Chemistry and Biochemistry, [3]Department of Mechanical Engineering, University of California, Santa Barbara, CA,USA, [4]Department of Molecular and Medical Pharmacology, University of California, Los Angeles, CA, USA

ABSTRACT

We present an integrated E-Array chip for multi-target, electrochemical detection of DNA which is sensitive, specific, reagentless, reusable and selective enough to use directly in blood serum, soil and other complex media. The self-enclosed device allows *in situ* cleaning and preparation of the electrodes as well as probing for specific DNA sequences. Detection of DNA amplicons from the *H1N1* Human influenza virus was performed at a concentration of 400 nM. Signal uniformity across the three pixel electrode array inside the chamber is discussed.

Keywords: Electrochemistry, Biosensor, Microfluidics, DNA sensor

1. INTRODUCTION

Rapid, label-free, reagentless, and quantitative detection of DNA in a sequence specific manner has broad applications in point-of-use analysis. Toward this end, we have previously reported on the eDNA biosensor chemistry (Fig 1 a, b) which demonstrates high sensitivity (< 200 pM) in complex physiological solutions using bench-top instrumentation [1, 2]. In this work, we report on the full integration of the eDNA assay into a microfluidic

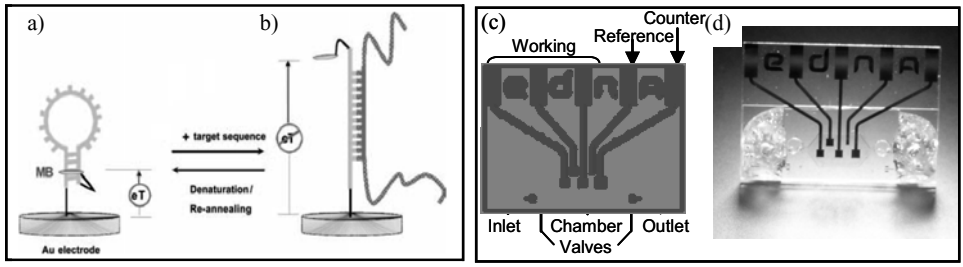

Figure 1: The eDNA sensor chemistry (a) Sequence specific DNA probes are immobilized on gold electrodes. Initially, the probes exhibit a stem loop conformation which permits facile electron tunneling between the reporter (Methylene Blue) and the electrode. (b)When the target DNA hybridizes to the probe, the resulting conformation inhibits electron tunneling which is measured through ACV. Denaturing the hybridized DNA returns the probe to its initial state, ready for reuse. **The E-Array device** (c) There are 3 working electrodes (Au) on which the probe DNA is immobilized, 1 counter electrode (Pt) and 1 reference electrode (Pt). (d) The devices measures 2.2 cm across and 1 cm wide. Input/output connections and microfluidic valves flank the electrochemical cell.

978-0-9798064-0-7/μTAS2007/$20©2007CBMS

platform (E-Array Chip) wherein the electrode preparation, probe immobilization, and detection of PCR amplicons from H1N1 Human Flu virus samples (detection sequence: 5'-CCA TGA GTT TGC AGT GA -3') is carried out in a self-enclosed, disposable device. Furthermore, to ensure the accuracy of the detection, we perform three redundant measurements from three independent working electrodes simultaneously that show reproducible detection results.

2. EXPERIMENTAL

The E-Array chip is an all-glass, electrochemical cell with 2 pneumatically driven, integrated PDMS valves used for fluidic metering (Fig 1 c, d). Within the chip, there are 3 working electrodes (Au) on which the probe DNA is immobilized, 1 counter electrode (Pt) and 1 reference electrode (Pt) that are fabricated through a standard process (Fig 2 A, B, C).

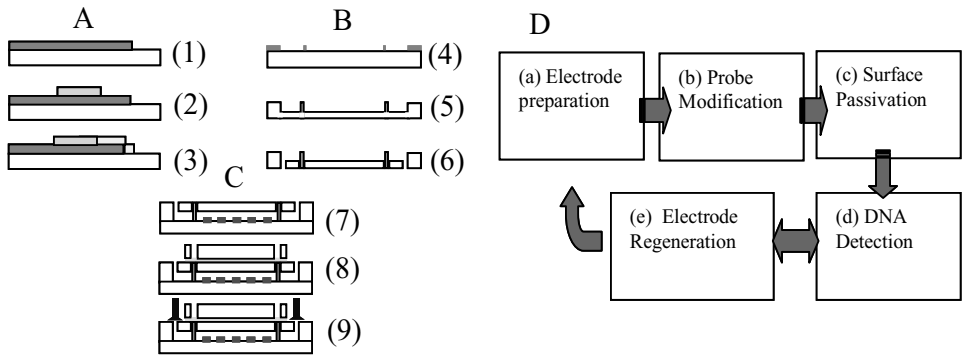

Figure 2:The E-Array fabrication process flow (A) Electrode substrate: (1) Evaporation of 1800Å of platinum (2) Sputtering of 4500Å SiO2 (3) Evaporation of 200Å Ti / 1800Å gold electrodes. (B) Chamber substrate: (4) CF4 plasma etch of the amorphous silicon sacrificial layer (5) HF etch of the glass 35µm deep, CF4 plasma etch of the remaining amorphous silicon (6) drilling of the inlet/outlet and valves hole. (C) Assembly of the substrates: (7) Bonding at 630°C (8) PDMS and manifold wafer valves assembly (9) microfluidic connector assembly. (D) **The Detection Assay** (a) The gold electrodes are thoroughly cleaned using cyclic voltammetry in 0.1 M H2SO4 and rinsed with DI (b)The DNA probe is adsorbed to the surface of the gold electrodes from a 2mM solution for 1 hour(c) The surface is passivated using a 2mM solution of 1-hydroxyhexaalkylthiol for 2 hours (d) The device is filled with a 0.9M NaCl and 0.09M sodium citrate pH 7.0 buffer, reduction scans are run before and after target hybridization (e) The target is released using DI rinse to regenerate the DNA probes. The E-Array is reuseable.

There are four major components of the assay (Fig 2 D): First, the working electrodes are prepared by cleaning with H_2SO_4 *in situ*. Then the probe DNA with Methylene Blue (MB) reporter molecules is immobilized to the working electrodes through Thiol chemistry. The exposed, unoccupied sites of the electrodes are passivated with 1-hydroxyhexaalkanethiol to prevent inadvertent redox reactions between the sample and the electrodes, which completes the biosensor preparation. Finally, the device is challenged with the analytes, and the resulting current signal from the eDNA sensors are measured through AC-voltammetry (ACV).

3. RESULTS AND DISCUSSION

Detection of PCR amplicons (concentration = 400nM) from the *H1N1* Human influenza virus in the E-Array device was performed by connecting the device to a commercial electrochemical work station (CHI Instruments). Reduction scans from working electrodes are acquired 5 and 25 minutes after the sample introduction, which showed a 51±4% and 59±4% change in the signal respectively (Figure 3).

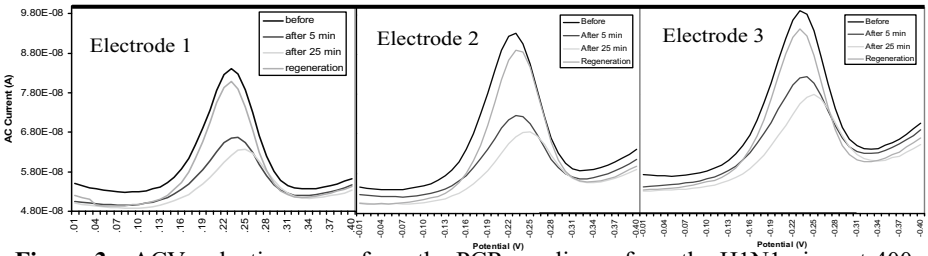

Figure 3: ACV reduction scans from the PCR amplicons from the H1N1 virus at 400 nM concentration from 3 integrated independent electrodes. Each graph illustrates the initial current amplitude before hybridization and the decreasing current amplitude, 5 minutes and 25 minutes after target injection. The corresponding signal change is 51±4% and 59±4% respectively.

The baseline of the reduction scans remained approximately constant during the entire experiment. ACV signal from the three independent electrodes within the chip were obtained simultaneously to ensure the accuracy of the measurements. The excellent agreement among the sensors confirms the robustness of the detection platform. The E-Array device is re-useable; the eDNA sensors can be regenerated by washing away the target DNA with DI water (Fig. 3).

4. CONCLUSIONS

We present a rapid, label-free, reagentless, sequence specific, electrochemical DNA sensor which is integrated in a self-enclosed, reusable device that is ideally suited for the continuous, rather than batch, monitoring of genetic materials. Combining the advantages of microfabrication and electrochemical biosensors demonstrates the viability an integrated biosensor system for its use for a range of applications including point of care diagnostics.

ACKNOWLEDGEMENTS

We thank the financial support from the ARO Institute for Collaborative Biotechnologies (DAAD1903D004), DARPA/DMEA-CNID grant H94003-05-2-0503 and DMEA90-02-2-0215. We thank Dr. Jim Sumner and Patrick Freudenthal for helpful discussions. Microfabrication was carried out in the Nanofabrication Facility at UC Santa Barbara.

REFERENCES

[1] C. Fan, K.W. Plaxco, and A.J. Heeger, *Electrochemical interrogation of conformational changes as a reagentless method for the sequence-specific detection of DNA*, PNAS **100** 9134–9137 (2003)

[2] R.Y. Lai, E.T. Lagally, S-Ho Lee, H. T. Soh, K.W. Plaxco, and Alan J. Heeger, *Rapid, sequence-specific detection of unpurified PCR amplicons via a reusable, electrochemical sensor,* PNAS **103** 4017–4021 (2006).

FABRICATION OF SENSETIVE ELECTRONIC SENSOR FOR LABLE-FREE DETECTION OF PROTEIN-PROTEIN INTERACTIONS

Ariel Cohen, Amihood Doron, Moran Horesh, Daniela Ullien, Mordehay Beraha, Udi Virobnik and Ilan Levy

Intel Research Israel, Intel Electronics, ISRAEL

ABSTRACT

Integration of active biological materials together with different type of sensitive transducers offers the possibility of generating highly sensitive, specific, selective and reliable biosensors. However, successful exploitation of this exciting possibility is highly dependant on a high volume manufacturing potential that will result in a low unit cost. Here, we present the first step into the fabrication of a low cost sensitive device with the potential future application in bio-sensing. We expect that the high sensitivity presented here will lay the foundations for the detections of diverse protein-protein interaction and that standard manufacturing process may enable various types of applications.

Keywords: Biosensor, Label-free, Field-effect device.

1. INTRODUCTION

Biosensors are normally composed of two main components; the sensing device and the sensing molecule. As a functional hybrid system, the biggest challenge is to optimize this system to benefit from coupling of the unique features of the bio-recognition event with the sensitive signal recognition and amplification potential of a sensing device [1]. This challenge had led in the last 30 years to the development of a diverse FED-based (field-effect device) devices with varied molecular selectivity [2-4]. The ability to detect biomolecular interactions is of extreme importance in medical diagnostics and most efforts in the last years were focused on sensors based on silicon nanowire [5]. However, the biggest drawback of this approach is the lack of industrial compatible manufacturing processes, such that will provide low manufacturing costs.

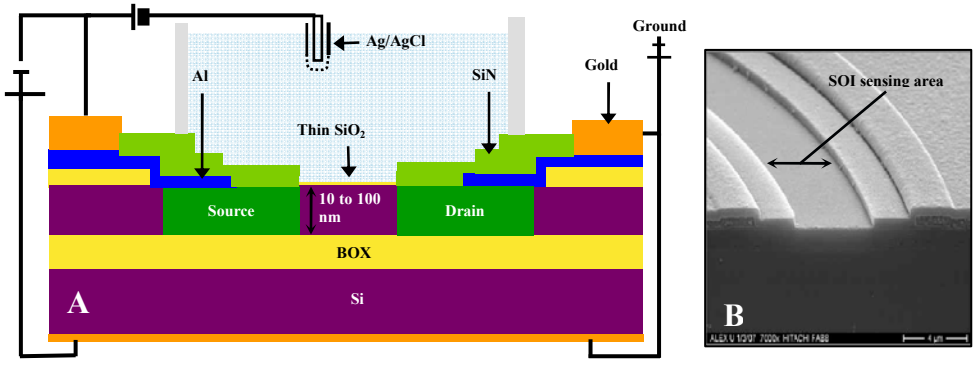

Figure 1: Schematic cross-sections of a sensing device with measuring setup (A) and top view SEM image (B). (A) Devices are based on thin, 10-100nm SOI layer covered by

978-0-9798064-0-7/μTAS2007/$20©2007CBMS

native oxide. The source/drain regions are protected by passivation layer. (B) The sensing area, or the 'gate', is shown in the SEM image bordered by drain/source regions on both sides. The metallization layer can be seen covered by passivation nitride layer.

2. EXPERIMENTAL

The sensor devices were fabricated on Silicon-on-Insulator (SOI) wafers and the schematic illustration is depicted in Figure 1. The SOI layer was gradually thinned down to 10nm using several oxidation and oxide removal steps. Pre activation of the native SiO_2 above the open gate (active area, see Figure 1B) was done by oxygen plasma and was followed by APTMS (3-trimethoxysilylpropyl amine) SAM (self assembly monolayer) deposition at room temperature. For the prostate specific antigen (PSA) sensing, anti-PSA antibodies were covalently attached to the APTMS SAM (Figure 2 B and C).

3. RESULTS AND DISCUSION

Device performance, as demonstrated in Figure. 2A, indicates that a 10nm thin SOI layer retains its single crystal properties throughout processing. Moreover, the presented n-type device is a depletion type with a negative threshold voltage of 0.2V. Therefore, it is possible to operate the device with V_{GS}=0V and to eliminate the need for a DC bias [6]. This in turn has direct effect on molecules as well as on the device reliability since the bias voltage induces leakage currents, drift and noise. The time response of I_{DS} under different pH values (Figure 2B) demonstrates a gate voltage change of ~20mV for one pH unit. The low drift currents resulted in a high signal to noise ratio.

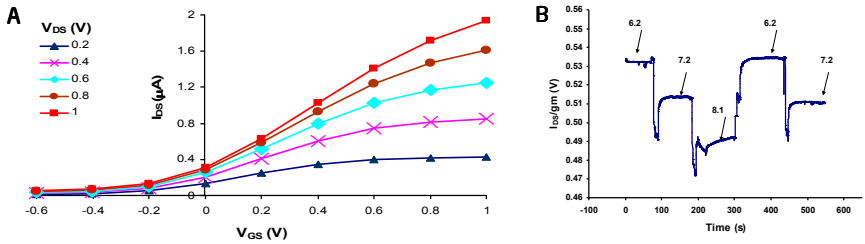

Figure 2: Characterization and pH sensitivity of a depletion type (n-type) transistor with a 10nm thin Si layer. (A) I_{DS} Vs. V_{GS} curves at different drain-source voltages. (B) I_{DS}/gm under different pH values (6.2, 7.2 and 8.1) (VGS = 0.4V and V_{DS} = 1V). The I_{DS} current was divided by gm in order to normalize the effect of pH change on the gate voltage. Changing one pH unit results with an equivalent of ~20mV in V_{GS}.

The next step was to test device sensitivity to PSA (prostate cancer biomarker) as a model system. Following covalent binding of anti-PSA antibodies to APTMS SAM layer, device was exposed to PSA in concentration as low as ~30pM. The significant difference between I/V curves following analyte application is shown in Figure 3. When a back-gate voltage (V_{BG}) was set to 4V, the current difference (ΔI_{DS}) due to PSA detection was ~0.1μA at V_{DS}=1V (Figure 3A). Moreover, the gain increased dramatically when the V_{BG} was set to 6V resulting in an ΔI_{DS} of 2.1μA. The clear difference in gain illustrates the potential of device modulation simply by using varied back-gate voltage biases. It eliminates the necessity to optimize device performance by a reference electrode which may cause leakage, noise and degradation of chip's surface.

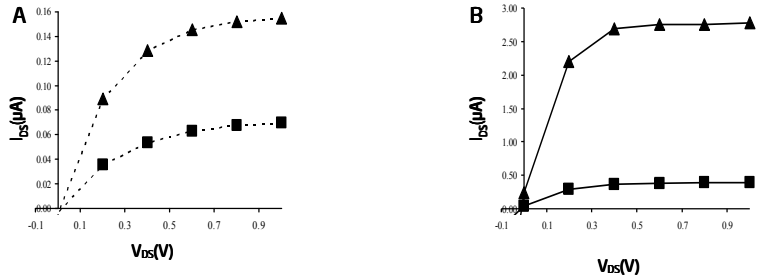

Figure 3: I_{DS} vs. V_{DS} curves of APTMS activated device covered with Anti-PSA antibodies as capturing molecules to PSA. The device was first exposed to buffer pH 7 (squares) and then to solution of 30 pM PSA (triangles) while measurements were taken at different V_{BG} biased voltages of (A) 4V and (B) 6V).

4. CONCLUSIONS

This preliminary study points to the potential application of a low-cost silicon-based FED in the field of biosensing. We have demonstrated that protein-protein interaction detection is feasible and anticipate that the ultra thin channel layer, the low noise and high sensitivity to pH values will lay the foundations for the detection of diverse molecular interactions.

REFERENCES:

[1] A.J. Killard and M.R. Smyth, *Creatinine biosensors: principles and designs*, Trends in Biotechnology. Vol. 18, pp. 433-437, October 2000.

[2] J.J. Xu, X.L. Luo and H.Y. Chen, *Analytical aspects of FET-based biosensors*, Frontiers in Biosciences. Vol. 10, pp. 420-430, January 2005.

[3] P. Bergveld, *Development of an ion-sensitive solid-state device for neurophysiological measurements*, IEEE Transactions on Biomedical Engineering., BME-17,70, 1970.

[4] M. Yuqing, G. Jianguo and C. Jianrong, *Ion sensitive field effect transducer-based biosensors*, Biotechnology Advances. Vol. 21, pp. 527-534, September 2003.

[5] F. Patolsky and C.M. Lieber, *Nanowire nanosensors*. Materials Today, Vol. 8, pp. 20-28, April 2005.

[6] A. Cohen, M.E. Spira, S. Yitshaik, G. Borghs, O. Shwartzglass and J. Shappir, *Depletion type floating gate P-channel MOS transistor for recording action potentials generated by cultured neurons*, Biosensor and Bioelectronics. Vol. 19, pp. 1703-1709, July 2004.

IMPEDANCE BASED FLOW-THROUGH BIOSENSOR FOR PARTICLE/CELL DETECTION

Karthik Sriram Lakshmi Narasimhan, Abdur Rub Abdur Rahman and Shekhar Bhansali

Bio-MEMS and Microsystems Laboratory, Department of Electrical Engineering, University of South Florida, 4202 E Fowler Ave ENB 118, Tampa, FL 33620, USA

ABSTRACT

This work reports on the development of a flow through biosensor capable of detecting particles and cells using a novel 16 microelectrode array, using impedance techniques. The impedance spikes caused by particles/cells are used for detection. Particles/cells were classified based on the magnitude of impedance spikes and the slope of the bode plots obtained from impedance spectroscopy measurements. The live cells were found to have impedance spikes, about 10 percent higher than that of dead cells.

Keywords: Microfluidics, microelectrodes, bioimpedance, impedance spectroscopy

1. INTRODUCTION

The objective of this work was to develop a flow through impedance based biosensor capable of detecting particles and cells using a novel 16 microelectrode array. Cells/particle detection plays an important role in the biological defense and food processing industries [1,2]. The current detection schemes are based on either electrical or optical methods. The electrical method is more preferred for portable applications, with the Coulter Counter being the widely used technique for particle/cell detection. The coulter counter works on the principle of electrical zone sensing, wherein the changes in electrical resistance along a fluid filled capillary tube, due to movement of cells/particles, is measured. Moreover, microfluidics based coulter counters offer advantages like, portability, lesser reagents and faster detection. Bioimpedance methods have also gained gradual acceptance due to their ability to characterise particles/cells apart from their detection.

In this work, the flow of the analyte solution being perpendicular to the electrodes gave rise to a uniform electric field across the flow channel. Thus, the position of the particle has little bearing on the sensitivity and accuracy of measurements made [3]. The sensor has been shown to be capable of detecting and characterising particles/cells based upon impedance measurements.

2. EXPERIMENTAL

The sensor was fabricated on a Pyrex glass substrate to minimize leakage currents. Figure 1 schematically illustrates the sensor fabrication process. Firstly, a negative resist was patterned on the substrate, followed by Cr/Au deposition and lift-off. Secondly, for a fluid flow, a 144 μm diameter hole was etched at the center of the microelectrode array using Laser Micromachining. Finally, Nanoport™ interconnects were attached on the glass substrate to connect the sensor to microfluidic pump, using SU-8 50 as an adhesive. The analyte solution was flown using a Harvard Apparatus syringe pump. The impedance measurements were carried out using an Agilent 4294A Impedance Analyzer in conjunction with a Cascade Microprobe Station between 10 kHz to 10MHz frequency range.

978-0-9798064-0-7/μTAS2007/$20©2007CBMS

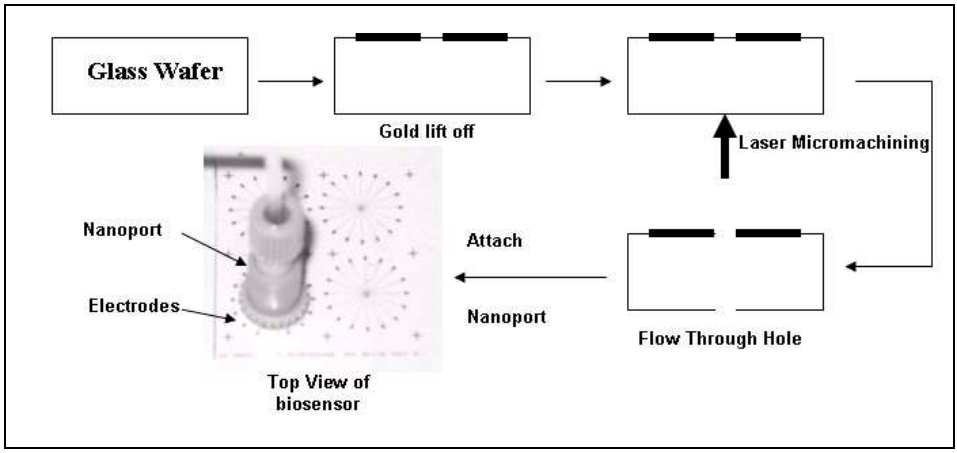

Figure 1. Process Flow for Sensor

Initially, the sensor was calibrated using polystyrene beads of different diameters (9.66 μm and 20 μm), suspended in PBS. Subsequently, the impedance of the analyte solution containing Melanoma-B cancer cells (with less than 0.01% dead cells), suspended in PBS along with 20 μm polystyrene beads was monitored for 10 sec. The sweep voltage and the frequency of 25 mV and 10 MHz were used availing focusing effect as demonstrated by Morgan et al [4]. The flow rate was held constant at 50 μl/s. Finally, the sensor was tested by flowing a solution containing both live and dead melanoma cancer cells. The ratio of dead to live cells was held greater than 0.2, under same experimental conditions.

3. RESULTS AND DISCUSSION

The impedance traces for the melanoma cells along with polystyrene beads are shown in figure 2(a). The impedance spikes falls into two levels, the lower level corresponding to polystyrene beads while the other representing melanoma cells. The impedance spectroscopy was performed with 10 data points to enable the system to perform the measurements while the relative position of the particle doesn't vary too much within the measurement time. This has a direct impact on the shape of the bode plots, composed of straight lines. The bode plot in figure 2(b) shows that the system is capable of differentiating between the polystyrene beads and melanoma cells using impedance spectroscopy based on the different slopes for the beads and melanoma cells.

The impedance spikes for the analyte solution consisting of live and dead melanoma cells are shown in Figure 2(c). Live cells exhibited larger impedance spikes. The impedance of the live cells was found to be higher than that of dead cells by about 10 percent. The slope of the bode plot (figure 2(d)) for live cells showed a marked difference from the slope obtained for the dead cells. The main reason for this change in impedance and difference in bode plot is due to the disintegration of the cell wall membrane and loss of cell constituents (ionic) as soon as the cell dies.

4. CONCLUSIONS

The ability of the sensor to detect and differentiate between particles and cells has been successfully demonstrated using impedance techniques. Future work will involve simultaneous multi-electrode measurements, which will aid in particle/cell imaging.

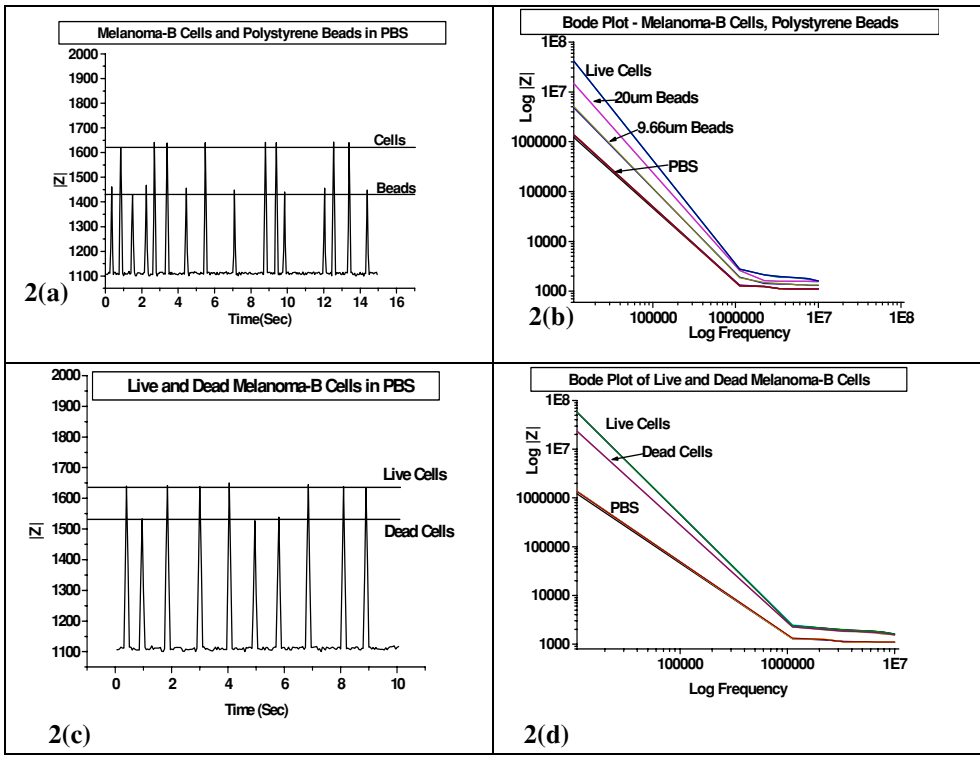

Figure 2. (a) Impedance trace of solution with cells and beads (b) Bode Plot for solution (c) Impedance trace of solution with live and dead cells (d) Bode plot for solution

ACKNOWLEDGEMENTS

This research was supported by the NSF Career Award Number 0239262.

REFERENCES

[1] J.Wu, Y.Ben and H.C.Chang, *Particle detection by electrical impedance spectroscopy with asymmetric-polarization AC electroosmotic trapping*, Microfluidics and Nanofluidics, 1, 161-167 (2005).

[2] S.M. Radke and E.C. Alocilja, *A High Density Microelectrode ArrayBiosensor for Detection of E. Coli O157:H7*, Biosensors and Bioelectronics 20 (2005) 1662– 1667.

[3] S. Gawad, L. Schild and Ph. Renauld, *Micromachined impedance spectroscopy flow cytometer for cell analysis and particle sizing*, Lab On a Chip, 1, 76 – 82(2001).

[4] H. Morgan, D. Holmes, N.G. Green, *High Speed simultaneous single particle impedance and fluorescence analysis on a chip*, Current Applied Physics, 6 (2006) 367– 370.

MICROWAVE COMPOSITIONAL ANALYSIS OF SOLVENT MATRICES IN MICROCAPILLARY MANIFOLD SYSTEMS

R. Göritz[1], A. Masood[1], O. Castell[1,2], D.A. Barrow[1], C. Allender[2] and A. Porch[1]

[1]*School of Engineering, Cardiff University, Cardiff, CF24 3AA, United Kingdom*

[2]*School of Pharmacy, Cardiff University, Cardiff, CF10 3NB, United Kingdom*

ABSTRACT

A compact, high *Q* microwave resonator (a 2.8 GHz copper hairpin) was used for in-situ compositional analysis of an acetonitrile:toluene solvent mixture within a PEEK microcapillary. Experimental results for the change in resonant frequency and transmitted power on resonance (both as a function of composition) were very close to those predicted using cavity perturbation theory from the known dielectric properties of the starting mixtures, measured separately using a coaxial reflectance probe. The combined measurements of resonant frequency shift and transmitted power allow very accurate (< 1% error) and fast (< 0.1s) compositional analysis of polar solvent mixtures.

Keywords: microwave resonator, dielectric measurement, solvent composition

1. INTRODUCTION

On-chip, non-invasive and fast compositional analysis of liquids is desirable in a diverse range of microchemistry applications, e.g. process control, but is generally unavailable. Microwave techniques have great potential for analysis of polar liquids owing to their strong interaction with microwave electric fields. Large liquid volumes (i.e. typically a few ml upwards) can be analyzed using a coaxial reflectance probe (e.g. [1]), but measurements of smaller volumes (i.e. a few μl or less) in arbitrarily shaped vessels and ducts are more problematic. Here, we use a quarter-wave copper hairpin resonator for in-situ analysis of a capillary containing mixtures of acetonitrile and toluene, selected as an initial evaluation system due to the large difference in molecular electric dipole moments.

2. EXPERIMENTAL DETAILS

A schematic diagram of the hairpin resonator package is shown in Figure 1. The hairpin was a 1 mm thick copper sheet, of width 20 mm, formed into a U-shaped configuration of length 25 mm and plate gap of 5 mm, of resonant frequency around 2.8 GHz when empty. This hairpin has the combined useful features of a high quality factor ($Q \approx 2000$) and small volume ($V \approx 1$ ml), resulting in highly sensitive dielectric characterization of any sample introduced within it. It was excited magnetically by a pair of loop-terminated, semi-rigid coaxial cables. The transmitted microwave power was measured in the frequency domain using an Agilent (HP) 8753 vector network analyzer. This hairpin resonator technique has been used extensively for non-destructive evaluation of the electrical properties of solids [2]. Here, we present a novel adaptation to interrogate a liquid-containing PEEK microcapillary, which passes through the open-end of the hairpin, where the microwave electric field is largest and approximately uniform in magnitude. Since the electric field decays very rapidly with distance outside of the hairpin plates, the measurement provides the average dielectric properties of the liquid contained in the 20 mm long section of capillary between the plates, corresponding to an active liquid volume of approximately 15 μl.

978-0-9798064-0-7/μTAS2007/$20©2007CBMS

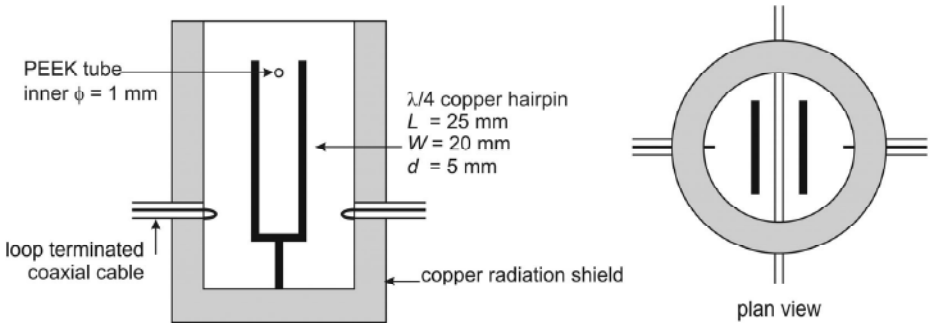

Figure 1. A schematic diagram of the hairpin resonator package. The resonant frequency when empty is approximately 2.8 GHz. The liquid sample (of active volume 15 μl) is injected into a PEEK microcapillary positioned at the region of maximum electric field at the open end of the resonator.

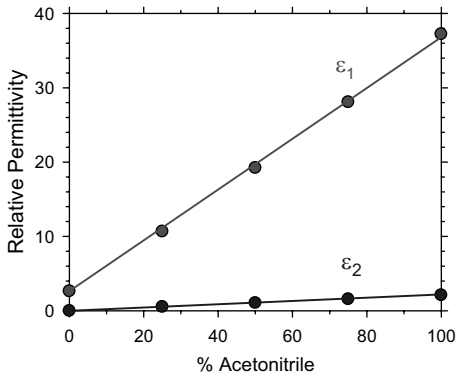

Figure 2. The polarisation ε_1 and loss ε_2 terms at 2.68 GHz of the relative permittivity of an acetonitrile:toluene mixture. Solid lines are the predictions of a simple linear mixing rule.

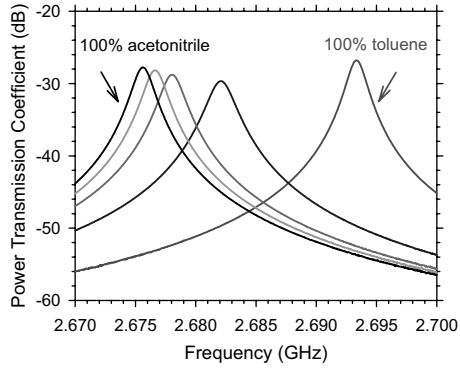

Figure 3. The transmitted power as a function of frequency for acetonitrile:toluene mixtures in the % proportions 100:0, 75:25, 50:50, 25:75 and 0:100 (in the sequence left to right).

3. RESULTS AND ANALYSIS

The real ε_1 and imaginary ε_2 parts of the complex relative permittivity of the component liquids were first measured in the range 2.5 – 3 GHz using a coaxial reflectance probe; the data at 2.68 GHz, appropriate for the experiments reported here, are shown in Figure 2. The measured resonance curves as a function of acetonitrile:toluene composition are shown in Figure 3, from which the resonant frequency and transmitted power at resonance (expressed in dB) were determined and are plotted in Figures 4 and 5, respectively. The resonant frequency decreased monotonically as the polar nature of the solvent mix increases. Also shown in Figure 4 is the theoretical prediction (using cavity perturbation theory) for a liquid-filled PEEK capillary, based on the measured dielectric properties of the component solvents (Figure 2). The peak transmitted power was minimized (i.e. loss maximized) for small proportions of acetonitrile (≈12%). This curious result is also entirely predicable by theory (the solid curve of Figure 5), its physical interpretation being the competition between the increased dielectric loss and the reduced internal electric field (by depolarization) within the solvent mixture as the proportion of acetonitrile was increased.

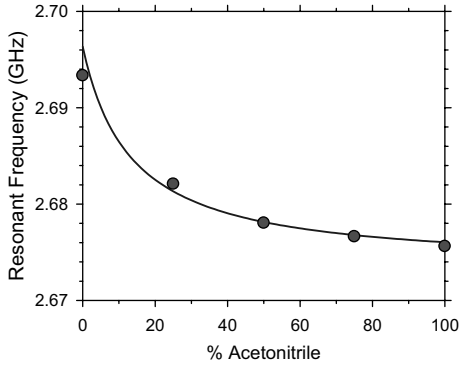

Figure 4. The resonant frequency as a function of composition. The theoretical dependence is shown by the solid line.

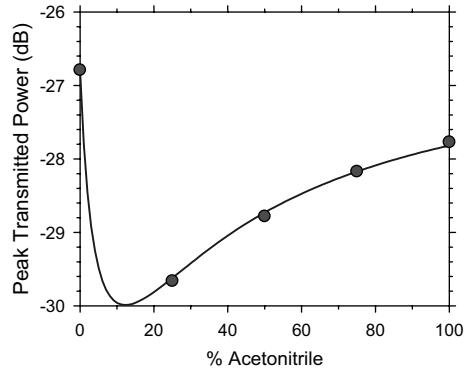

Figure 5. The peak transmitted power (in dB) as a function of composition. The theoretical dependence is shown by the solid line.

4. CONCLUDING REMARKS

There are multiple benefits of this resonant microwave technique over other methods. Firstly, it is fast, with data accumulation on a timescale of less than 0.1 s, thereby enabling compositional analysis in situations where fluid flow and/or chemical reaction are occurring. Secondly, it is non-destructive and applicable to arbitrarily-shaped sample volumes. Using the existing experimental set-up, the proportion of acetonitrile in toluene can be measured to an accuracy of $< 0.1\%$. This work complements works elsewhere on microanalysis involving microwave heating, e.g. polymerase chain reaction [3]. In the near future, we plan to enhance the sensitivity of the measurement system by using microwave host resonators (a) of smaller volumes, and (b) whose electric field is along the axis of the microcapillary, the latter leading to negligible depolarization. Regarding the size reduction (a), the measured sensitivity is inversely proportional to the volume occupied by the microwave electric field energy, so a reduction in effective volume from about 1 ml (as for the hairpin here) to about 1 μl (as can be achieved, for example, using a lumped element resonator whilst maintaining the same resonant frequency) can either give rise to a ×1000 enhancement of measurement sensitivity for the same sample volume, or a ×1000 sample volume reduction for the same measurement sensitivity. These next-generation resonators will enable characterization of microfabricated resonator-capillary systems of much smaller volumes, and/or of liquid mixtures whose components are more closely matched in terms of their molecular electric dipole moments (e.g. acetonitrile and water).

REFERENCES

[1] J.P. Grant *et al*., "A critical study of the open-ended coaxial line sensor technique for RF and microwave complex permittivity measurements", Journal of Physics E – Scientific Instruments, 22 (9) 757-770 (1989)

[2] M.J. Edmondson *et al*., "Can alkali metal doped zeolites be metallic? - Microwave conductivity of rubidium doped zeolite rho", Zeitschrift für Physikalische Chemie, 217 (8) 939-955 (2003)

[3] P.-A. Auroux *et al*., "Microfluidic method for thermal cycling by microwave dielectric heating", Proceedings of MicroTAS 2006, Tokyo, pp.1465-1467 (2006)

TECHNIQUE FOR MEASURING THE DIELECTRIC CONSTANT OF LIQUIDS AND GASES WITHOUT THE USE OF CALIBRATION STANDARDS

Hongshen Ma[1], Jeffery H. Lang[1], and Alexander H. Slocum[2]
[1]*Department of Electrical Engineering, Massachusetts Institute of Technology, USA*
[2]*Department of Mechanical Engineering, Massachusetts Institute of Technology, USA*

ABSTRACT

This paper presents the development of a method for measuring the dielectric constant of liquids and gases that does not require the use of calibration standards. This technique is based on precise adjustment of the separation between closely spaced spherical electrodes. By leveraging the dimensional accuracy of spheres and the accuracy of the adjustment mechanism, calibration-free measurements with 1% accuracy can be achieved.

Keywords: impedance spectroscopy, electrical detection, dielectric constant

1. INTRODUCTION

Electrochemical Impedance Spectroscopy (EIS) is an important detection technique in microTAS because of its favorable sensitivity limits, simple readout, and compatibility with portable devices [1-6]. A key problem in EIS detection is the extraction of the dielectric constant, ε, and conductivity, κ, from the measurable quantities of capacitance and conductance, which are related by a geometrical factor K_{cell}, and parasitic capacitance and conductance, C_0 and G_0, according to the equations,

$$C = \varepsilon / K_{cell} + C_0 \quad \text{and} \quad G = K_{cell} / \kappa + G_0 \qquad (1) \text{ and } (2)$$

Since accuracies better than 1% are required in many chemical analysis applications [7], the cell constant can be a major source of concern because of manufacturing variations, surface chemistry on the electrodes, and stray electric fields [5,7]. Existing conductivity meters typically address this problem by periodically calibrating the measurement apparatus using standard solutions with known values of ε and κ. This correction is often insufficient because parasitic capacitance and resistance is dependent on ε and κ, and as a result, the calibration is only valid if ε and κ of the sample and calibration fluid are similar [6]. In microchemical analysis systems, the use of calibration liquids is often impractical since the calibration fluid may irreversibly contaminate the microfluidic channels and the detection electrodes. This paper presents an EIS technique for measuring ε and κ using spherical electrodes with variable separations. The variable technique removes the effect of parasitic capacitance and conductance, and enables accurate measurements without requiring calibration standards. This technique is initially demonstrated in a meso-scale device. Microscale monolithic devices could eventually be fabricated using molding or embossing.

2. THEORY

The EIS technique presented here is based on the logarithmic relationship describing the capacitance between closely-spaced spherical electrodes:

$$C = \varepsilon_r \varepsilon_0 \pi r \log\left(2r / x\right) + C_0 \qquad (3)$$

978-0-9798064-0-7/μTAS2007/$20©2007CBMS

where ε_r is the relative dielectric constant, r is the sphere radius, x is the electrode separation, and $r \gg x$ [8]. The spatial derivative of C is inversely related to x such that,

$$\varepsilon_0 \pi r \left(\frac{dC}{dx} \right)^{-1} = \frac{x}{\varepsilon_r} \cdot \tag{4}$$

Thus, the value of ε_r can be determined from a plot of the left-hand side of (4) versus x. A parallel technique can be used to determine κ from the spatial derivative of G. Using the derivative of C and G to determine ε and κ removes the effect of parasitic capacitance and conductance that can produce systematic offsets in ε and κ. The accuracy of these measurements is ultimately derived from the geometry and position of the electrode spheres, which can be determined with high accuracy using known principles of precision machine design [9].

3. DESIGN AND FABRICATION

The electrodes are fabricated by depositing a 50nm Pt metal layer on a 9.525mm diameter silicon-nitride sphere (Cerbec Saint-Gobain: Grade 3) that act as the substrate material. The diameter of silicon nitride spheres are produced with extremely high accuracy, typically known to better than one part in 10^4. The sample liquid is constrained between two spherical electrodes and a sample chamber as shown in Figure 1. The electrodes are mounted on cylindrical shaft by a threaded clamp that double as electrical contacts to the Pt film. O-rings electrically isolate the shaft from the sample chamber and create a sealed liquid chamber. The shafts are mounted on a precision flexural stage, shown in Figure 2, which reduces the travel of a linear servo actuator with a transmission ratio of 190:1. As a result, the electrode separation can be adjusted in increments of 0.25nm with an overall range of 50µm. The shafts are electrically isolated from the flexural stage by a thin layer of polyimide tape. The relative position of the electrodes is measured using two capacitance sensors (Lion Precision) with 1nm resolution.

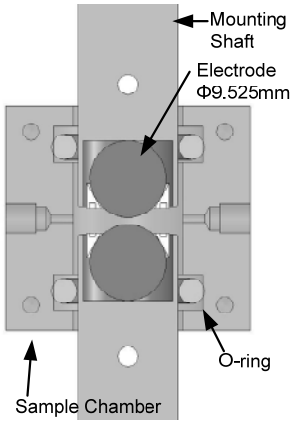

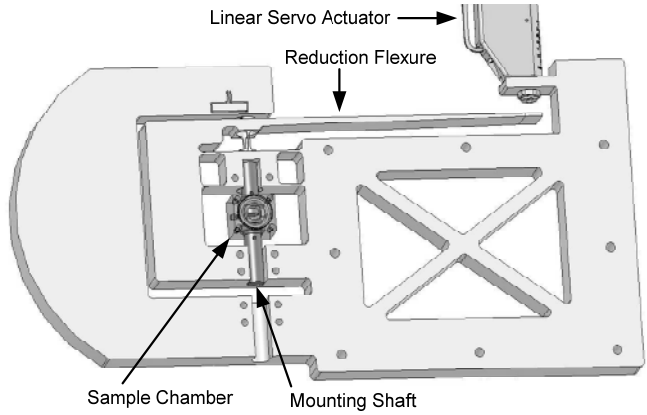

Figure 1 (left): Cross section of the sample chamber and electrodes; Figure 2 (right): flexure stage

4. RESULTS AND DISCUSSION

The proposed technique has been verified by measuring the dielectric constant of 2-propanol. The experiments were performed at 17.7°C, using degassed, anhydrous

2-propanol at 99.5% purity. An example data set is shown in Figure 3, where the x-axis indicates the electrode position measured by the capacitance probe, and the y-axis indicates the electrode separation derived from $-r\pi\varepsilon_0\Delta x/\Delta C$. The data show excellent correlation with theory. The value of ε_r, estimated using a least squares fit, is consistent with the known value at 17.7°C [10]. The distribution of the measured ε_r over 20 repetitions of the same experiment is shown in Figure 4. The results fall within ±1% of the known value and confirm the validity of this technique.

The variability of the data in Figure 3 increases with larger electrode separation since the value of ΔC is reduced in this region, resulting in a smaller signal-to-noise ratio. The raw fitted value for ε_r also carries an error of approximately +1.5%, which originates from the geometry of the electrode mounting shaft. This error can be reduced by changing the design of the mounting shaft to expose more of the spherical surface. A correction for this error has been applied to the data in this paper.

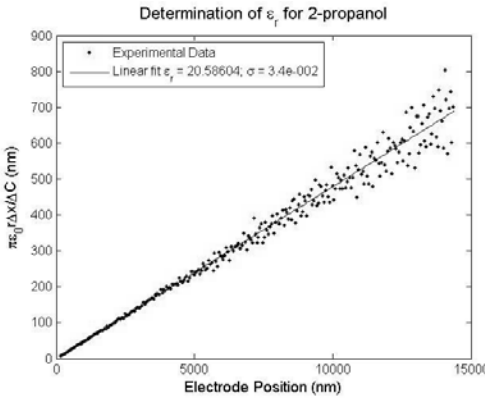

Figure 3: Measurements of ε_r for 2-propanol

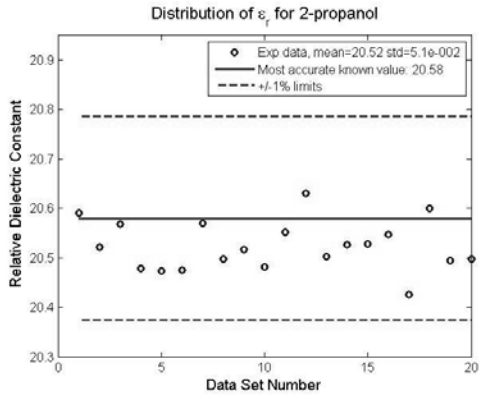

Figure 4: Distribution of ε_r for 2-propanol

ACKNOWLEDGEMENTS

This work has been supported by MIT's Center for Bits and Atoms under NSF Grant CCR-0122419. The authors would like to acknowledge Kurt Broderick and Mark Belanger for assistance with the fabrication of this device.

REFERENCES:

[1] B. Timmer, W. Sparreboom, *et al*, *Lab on a Chip,* **2**, 121 (2002).
[2] S. Gawad, K. Cheung, U. Seger, *et al*, *Lab on a Chip*, **4**, 241 (2003).
[3] T.G. Drummond, M.G. Hill, *et al*, *Nature Biotechnology*, **21**, 1192 (2003).
[4] J. Hong, D.S. Yoon, *et al*, *Lab on a Chip*, **5**, 270 (2005).
[5] V. Lvovich, C.C. Liu, *et al*, *Sensors and Actuators B*, **119**, 490 (2006).
[6] J.K. Duchowski, H. Mannebach, *Tribology Transactions*, **49**, 545, (2006).
[7] S.L. Shiefelbein, N.A. Fried, *et al*, *Rev. Sci. Instrum.*, **69**, 3308 (1998).
[8] L. Boyer, F. Houze, *et al*, *Journal of Physics D-Applied Physics*, **27**, 1504 (1994).
[9] A. Slocum, *Precision Machine Design*, Society of Manufacturing Engineers (1992).
[10] J. Barthel, R. Neueder, *Electrolyte Data Collection*, DECHEMA (1992).

TOWARD BACTERIA DETECTION ON CHIP: A BIOSENSOR BASED ON MAGNETOTACTIC BACTERIA AND IMPEDANCE SPECTROSCOPY

Zhao Lu, Ryan Denomme, Souleymane Bah and Sylvain Martel

NanoRobotics Laboratory, Department of Computer Engineering, École Polytechnique de Montréal, Montréal, CANADA. (correspondence: sylvain.martel@polymtl.ca)

ABSTRACT

The design, fabrication and preliminary results for a new class of biosensors based on magnetotactic bacteria (MTB), aimed at detecting pathogenic bacteria with significantly shorter detection periods, is presented. The MTB are used to push microbeads coated with phages or antibodies specific to the targeted bacteria. By controlling the swimming directions of the MTB with magnetic fields, controlled sweeps of the samples are achieved. Each microbead, being propelled by the flagella motor of the MTB, is then brought to a microelectrode array for detection by impedance spectroscopy. Finite Element Method (FEM) simulation and preliminary results presented in this paper demonstrate that 10 µm melamine beads can be detected with the proposed biosensor.

Keywords: Biosensor, Magnetotactic bacteria, Impedance Spectroscopy, MicraGEM

1. INTRODUCTION

Fast pathogen detection is a critical component of clinic diagnosis, disease control and the food industry. The conventional bacteria identification methods currently require hours, or even days, to accurately detect bacteria. This is especially evident at very low concentrations (early stages of bacteria growth), at which point detection is most vital. In previous work, we proposed to exploit magnetotactic bacteria (MTB) [1] as bio-carriers, in order to accelerate the detection procedure by binding the motile MTB to microbeads coated with antibodies or bacterial-phages. The swimming directions of the MTB are controlled by using a directional magnetic field [2], which induces a torque on a chain of embedded magnetosomes inside each MTB, acting like a compass. Under the control of external magnetic fields, the flagellated MTB propel the functional microbeads, effectively sweeping the aqueous sample [3, 4] to search for the targeted pathogenic bacteria. Then, the MTB transport the pathogenic bacteria to the microelectrodes array, where the variations in electric impedance are measured. The existence of a pathogen is indicated when the impedance variations increase beyond a certain threshold.

With the proposed approach, this biosensor offers several advantages. First, with the assistance of the MTB, active detection can be realized by transporting the targeted pathogenic bacteria to the microelectrodes, thus avoiding the long waiting time for the diffusion and duplication of bacteria required in current detection methods. This will greatly decrease the detection time required for a given sample and will increase detection sensitivity. Second, the use of the MTB as carriers as opposed to the similar approach of utilizing magnetic beads as carriers allows for much smaller power requirements. The power consumption for this biosensor will be significantly decreased because the minimum magnetic field required to effectively navigate the MTB can be as low as 3 Gauss, which can easily be achieved by small electrical currents flowing through specially designed micro-wires. This feature makes the future integration of the biosensor with the

978-0-9798064-0-7/µTAS2007/$20©2007CBMS

microelectronic sensing circuit and conventional CMOS technology feasible.

In this paper, the design and simulation of an impedance sensing platform based on the MicraGEM processes is discussed. The design and fabrication of planar microelectrodes used to verify the concept of detecting single cells or microparticles by impedance measurement are introduced. Preliminary experimental results indicate that a microbead, 10µm in diameter, can be detected by measuring the variations of impedance between a pair of planar electrodes.

2. METHODOLOGY, SIMULATION AND FABRICATION

The main structure of the microsystem is fabricated using the MicraGEM process provided by Micralyne. MicraGEM uses Pyrex glass as its substrate material. Two different microchannel depths, 10 and 12 µm can be etched into the Pyrex layer. A single crystal silicon layer (10µm) is anodically bonded to the Pyrex substrate to form the structural layer. Metal can be deposited on the Pyrex glass and on top of the single crystal silicon layer, which allows the creation of electrodes and/or electronic connections. In this process, we implement a microchamber (3mm × 3mm) and numerous microchannels (25µm × 10µm) on the Pyrex substrate. Microelectrodes (20µm × 20µm) for impedance measurement are patterned on the bottom of each microchannel. The single crystal silicon layer is used to seal the microchannels and the microchamber, and to form openings which provide inlets and outlets for sample injection. Metal microcoil arrays, used to generate the local magnetic field in the microchamber, are deposited on the top of the single crystal silicon layer. The local magnetic field generated by the microcoils can control the swimming direction of the MTB to realize the function of bacteria mixing and sorting. Since the MTB react to a very small magnetic field, only small DC currents are required when coupled with an insulation layer with a thickness of 10µm. The layout of the whole system is presented in Fig. 1. The fabricated microdevice is shown in Fig. 2.

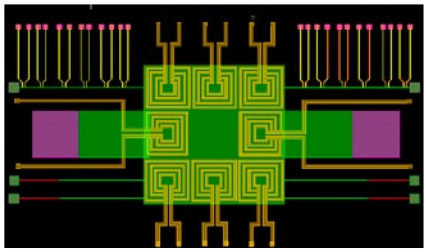

Figure 1. Schematics of the microchip

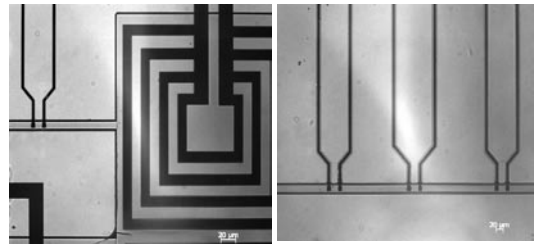

Figure 2. Microscopic pictures of Microelectrodes, microchannels and a microcoil

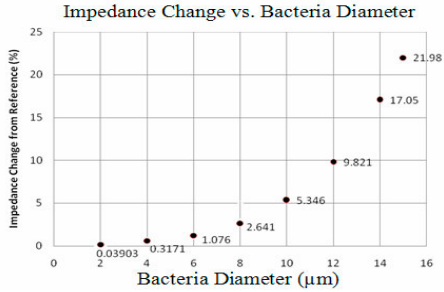

Figure 3. The impedance change from reference vs. bacteria size

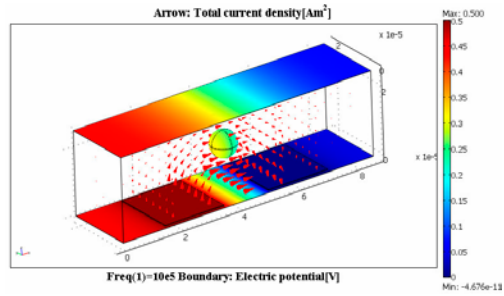

Figure 4. FEA simulation of a microbead between microelectrodes (20µm × 20µm)

FEM simulation shows that detection of a single bacterium or microparticle by measuring impedance variations between the microelectrodes is possible with this device. Fig. 3 shows a graph obtained from the FEM simulation that gives the increase in impedance from the reference signal as a function of bacteria diameter. Fig. 4 illustrates the FEM simulation of a single microparticle passing through a pair of embedded microelectrodes. This simulation allows investigation of the detection capabilities of our device. It is used to determine the device characteristics (electrode size, orientation, separation, and channel size) that are required to detect certain sizes of bacteria. This is imperative in order to construct a sensor that possesses adequate sensitivity to detect a single bacterium, yet being practical when performing fabrication and integration with an on-chip electronic sensing circuit.

3. EXPERIMENTAL RESULTS

In our preliminary experiments, an impedance analyzer (Agilent 4294A) is used to record impedance variations caused by the presence of bacteria or microparticles between a pair of microelectrodes embedded in a microfluidic device. As depicted in Fig. 5, navigation of MTB (with a microbead being attached to each bacterium) in the microchannel can be achieved by using external magnetic fields. Shown in Fig. 6, the preliminary experimental results indicate that variations of impedance caused by the microbeads can be detected by the dedicated microdevice. Issues such as mixing rate, binding efficiency and packaging will be addressed in more details with respect to the constraints of microfabrication and integration.

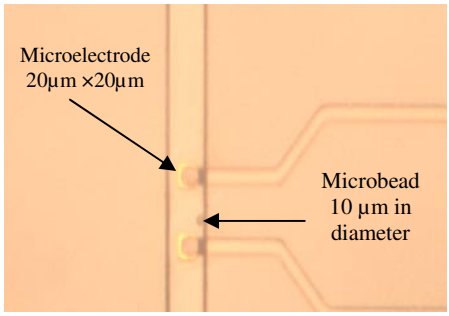

Figure 5. A 10 µm bead moving between Microelectrodes in the microchannel

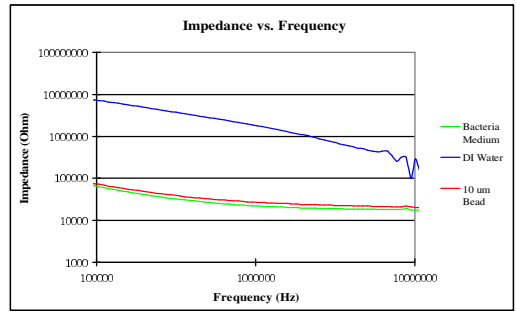

Figure 6. Impedance signal of the de-ionized water, bacteria medium, and a 10 µm bead in the bacteria solution over the signal range 0.1 MHz to 10 MHz.

REFERENCES:

[1] R. B. Frankel, D. A.Bazylinski, M. S. Johnson and B. L.Taylor, "Magneto-aerotaxis in Marine Coccoid Bacteria," *Biophysical Journal,* vol. 73, pp. 994-1000, (1997).

[2] S. Martel. C. Tremblay, S. Ngakeng, and G. Langlois, "Controlled Manipulation and Actuation of Micro-objects with Magnetotactic Bacteria," *Applied Physics Letters*, vol. 89, 233904, (2006).

[3] S. Martel, "Magnetotactic Phage-based Microrobotic Systems for the Detection of Live Bacteria", in *1st IEEE-RAS/EMBS Int. Conf. on Biomedical Robotics and Biomechatronics – BioRob,* Pisa, Tuscany, Italy, (2006).

[4] Z. Lu and S. Martel, "Preliminary Investigations of Bio-carriers Using Magnetotactic Bacteria", in *Proc. of the 28th Annual Int. Conf. of the IEEE Engineering in Medicine and Biology Society,* New York, USA, Aug. 30-Sept. 3, (2006).

LOW POWER IGNITION OF MICROPLASMA FOR VOLATILE ORGANIC COMPOUNDS DETECTION

D. C. Shin, K. W. Jo, M. G. Kim, S. Yang and J. H. Lee
Department of Mechatronics, GIST, South Korea.

ABSTRACT

This paper reports a portable 2.5-㎓ microwave-induced microplasma device for the detection of volatile orgarnic compounds gases based on optical emission spectroscopy. The minimal induced microwave powers required for igniting (37 dBm, 5W) and sustaining (29 dBm, 0.8W) of microplasma were experimentally determined under atmospheric air condition. Using the three types of volatile organic compounds (acetone, ethanol and methanol), it was found that the CN/CH emission peak ratio was relatively constant regardless of their concentrations for each compound. And the CN/CH emission peak ratio for the different types of compound showed significant differences with respect to the types of compound. On the other hand, the CO/CH emission peak ratio increased as the concentration of the each compound increased.

Keywords: 2.5-㎓ microwave-induced microplasma, optical emission spectroscopy, volatile organic compounds

1. INTRODUCTION

An optical emission spectroscopy (OES) has been widely used for detection of chemical species with an excellent selectivity [1]. There are several plasma sources, which are applicable to OES chemical detections including DC plasma, capacitively coupled plasma (CCP), inductively coupled plasma (ICP) and RF glow discharge [2]. However, these plasma sources still need a reduction of operating voltage (DC, CCP, ICP and RF), sputtering of electrodes (DC plasma) for portable chemical analysis. On the other hand, a microwave-induced microplasma (μ-MIP) can be utilized for long term operation because the plasma ignition requires relatively smaller power consumption even under atmospheric air condition with negligible sputtering effects [2]. This paper presents a portable μ-MIP device, which is utilizing a 2.5-㎓ split-ring resonator for the detection of gaseous volatile organic compounds (VOCs) based on conventional OES principle. In order to increase the electric field in a discharge gap (Figure 1), the proposed plasma device employed a half-wavelength split-ring resonator with a 100 ㎛ of a discharge gap where the microwave-induced microplasma is produced and confined [3].

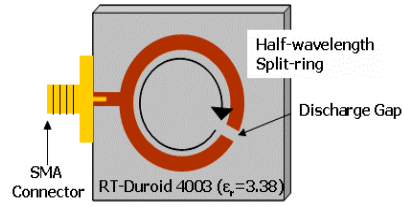

Figure 1. Schematic of split-ring resonator.

2. EXPERIMENTAL

A μ-MIP device was fabricated using conventional microfabrication processes including photolithograpy and Cu wet etching. Once the device is prepared, it was placed inside of a closed test chamber to allow stable measurement environment as shown in Figure 2. In this study, three types of electronic graded VOCs (acetone, ethanol and methanol) were used

978-0-9798064-0-7/μTAS2007/$20©2007CBMS

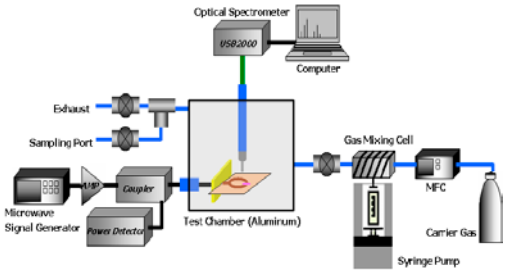

Figure 2. Schematic of the experimental setup for the gaseous VOCs detection using μ-MIP.

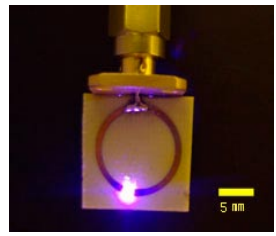

Figure 3. A photograph of the device showing the microplasma under the atmospheric condition.

with the purity higher than 99.9%. To infuse gaseous VOC into the device from the liquid VOC sample, the liquid VOC was vaporized using a wire-shaped heater and the vaporized VOC was transported into the mixing unit of the system by a syringe pump (PHD 2000, Harvard, Hollinston, USA). In the mixing unit, the concentration of the gaseous VOC is precisely controlled by mixing the vaporized VOC and the carrier gas (Ar) using a mass flow controller (MFC). Then the gaseous VOC sample was introduced into the μ-MIP device and then the device was ignited to produce VOC specific microplasma within the discharge gap. The emission spectrum of each VOC was obtained using a spectrometer (USB2000, Ocean Optics, Dunedin, USA). Figure 3 shows a photograph of the device demonstrating the microplasma generarted at the discharge gap under atmospheric air condition.

3. RESULTS AND DISCUSSION

The minimal induced microwave powers required for igniting (37 dBm, 5W) and maintaining (29 dBm, 0.8W) of microplasma were experimentally determined under atmospheric air condition. These minimal powers required are significantly smaller than the one reported [4]. In order to characterize the emission spectrum obtained from the device, three types of VOCs (ethanol-C_2H_5OH, acetone-CH_3COCH_3 and methanol-CH_3OH) were used. As a first step, the microplasma spectra of gaseous ethanol (500 ppm, 1000 ppm and 2000 ppm) were obtained to investigate the characteristic emission wavelength of the microplasma with respect to the concentration of gaseous ethanol. As shown in figure 4, the characteristic emission wavelength for each molecule (CN, CH, CO) does not change with the concentration of gaseous VOC and well agreed with the one previously reported [5, 6].

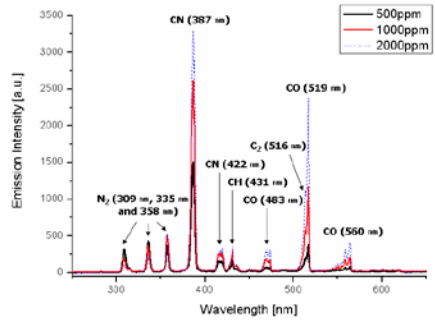

Figure 4. Emission spectra obtained for various concentration of gaseous ethanol.

In order to conduct detail investigation regarding the spectra of each VOC with respect to their types and concentrations, the emission peak intensities of CN, CO and CH were compared for each VOC. Figure 5 shows the intensity ratios of the "CN/CH" peaks with respect to the concentrations of acetone, ethanol and methanol. Each VOC shows the relatively constant CN/CH ratios regardless of their concentrations. And the CN/CH ratio

for different types of VOC shows significant differences with respect to the types of VOC. Figure 6 shows the intensity ratios of the "CO/CH" peaks with respect to their concentrations. In each VOC, the CO/CH ratio is increased as the concentration of the each VOC is increased.

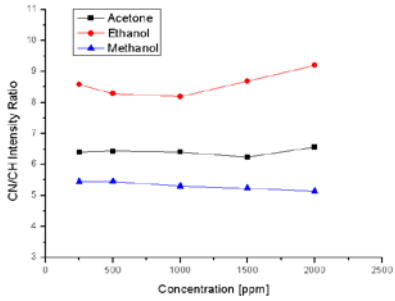

Figure 5. The intensity ratios of CN/CH for various concentration of VOCs.

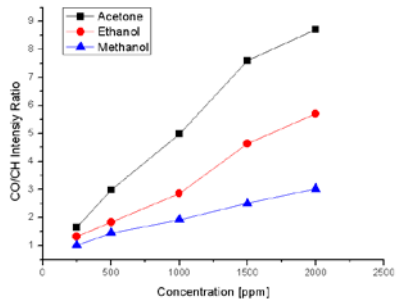

Figure 6. The intensity ratio of CO/CH for VOCs that linearly proportion to the concentration.

4. CONCLUSIONS AND FUTURE WORK

The microwave-induced microplasma generation device was successfully demonstrated with significantly smaller power consumption under ambient air condition. Under the present of VOC, the microplasma was also successfully produced. Based on the emission spectrum of the each VOC, it was observed that the CN/CH peak ratio is constant regardless of the concentration of the VOC and the CO/CH peak ratio increases with respect to the concentration of each VOC. Future work includes the characterization of other types of VOCs such as benzene, toluene and xylene for the applications of environmental monitoring.

ACKNOWLEDGEMENTS

This work was supported by the Korea Research Foundation Grant funded by the Korean Government(MOEHRD) (KRF-2005-202-D00179).

REFERENCES

[1] Jose A. C. Broekaert and Volker Siemens, "Some trends in the development of microplasmas for spectrochemical analysis", Anal Bioanal Chem., Vol. 380, pp. 185-189, (2004).

[2] Manuela Miclea and Joachim Franzke, "Analytical Detectors Based on Microplasma Spectrometry", Plasma Chem. Plasma Process, Vol. 27, pp. 205-224, (2007).

[3] F. Iza and J. Hopwood, "Split-ring Resonator Microplasma Microwave Model, Plasma Inpedance and Power Efficiency", Plasma sources Science and Technology, Vol. 14, pp. 297-406, (2005).

[4] Attila M. Bilgic, Edgar Voges, Ulrich Engel and Jose A. C. Broekaert, "A Low-power 2.45-㎓ microwave induced helium plasma source at atmospheric pressure based on microstrip technology", Journal of Analytical Atomic Spectrometry, Vol. 15, pp. 579-580, (2000).

[5] R. W. B. Pearse and A. G. Gaydon, "The Identification of Molecular Spectra", Chapman & Hall Lt., 4th ed., (1976).

[6] Robert S. Braman and Alexander Dynako, "Direct Current Discharge Spectral Emission-Type Detector", Analytical Chemistry, Vol. 40, No. 1, pp. 95-105, (1968).

MICROFLUIDIC THERMAL BIOSENSOR FOR BIOCHEMICAL REACTION

B. S. Kwak, B. S. Kim, J. S. Park, H. H. Cho, and H. I. Jung
Department of Mechanical Engineering, Yonsei University, South Korea

ABSTRACT

This paper presents a new design of silicon-based microfluidic thermal biosensor made by dual thermopiles and a microfluidic channel introducing a splitting and mixing of sample flow. Each thermopile consists of 26 Cr/Cu thermocouple pairs and electrodes of 50-μm width. The Seebeck coefficient's difference of each thermocouple is 19.97-μV/K, and the total sensitivity of thermopile is 519.22-μV/K. This dual-thermopile system enables the thermal biosensor to obtain reliable measurement data since it detects biochemical reaction and reference temperature simultaneously.

Keywords: Dual-thermopile, Microfluidic channel, Biochemical reaction

1. INTRODUCTION

Silicon-based thermal biosensors have been recently developed as techniques of MEMS and microfluidics progress. This miniaturized thermal sensor has many significant features about biochemical and clinical diagnostic applications: fast response times, no labeling or immobilization of reactants [1] and no need for a calibration system by using split-flow technique [2]. Our dual-thermopile based device has many advantages. First, it has self-compensation function. Second, it is capable of analyzing a few microliters of sample. Finally, our thermal sensor does not require a typical adiabatic vacuum surrounding.

2. THEORY

Thermocouple is a temperature sensor made of two dissimilar metal wires. The wires are joined at both ends and constitute two junctions. One of the junctions becomes a hot junction for heat generation, and the other a cold junction for a reference. A thermopile is an array of thermocouples connected together in series. A significant advantage of thermopile is that it can amplify the output voltage without amplifying device. In thermopile, the total voltage changes ΔV then increase to the more easily measureable level if n thermocouple junction pairs are connected in series; that is [3],

$$\Delta V = SAB \times n \times (Th - Tc) \quad (1)$$

where SAB (= SB − SA) is a relative Seebeck coefficient of two materials and (Th - Tc) is a temperature difference of two junctions. The Seebeck coefficients of Cr and Cu are 21.8 μVK^{-1} and 1.83 μVK^{-1} at 300 K, respectively [4]. The 26 junctions of thermopile are applied and consequently the integrated Seebeck coefficient is 519.22 μVK^{-1} at 300 K.

3. EXPERIMENTAL

To evaluate the microfluidic thermal biosensor, ascorbic acid was oxidized by ascorbate

978-0-9798064-0-7/μTAS2007/$20©2007CBMS

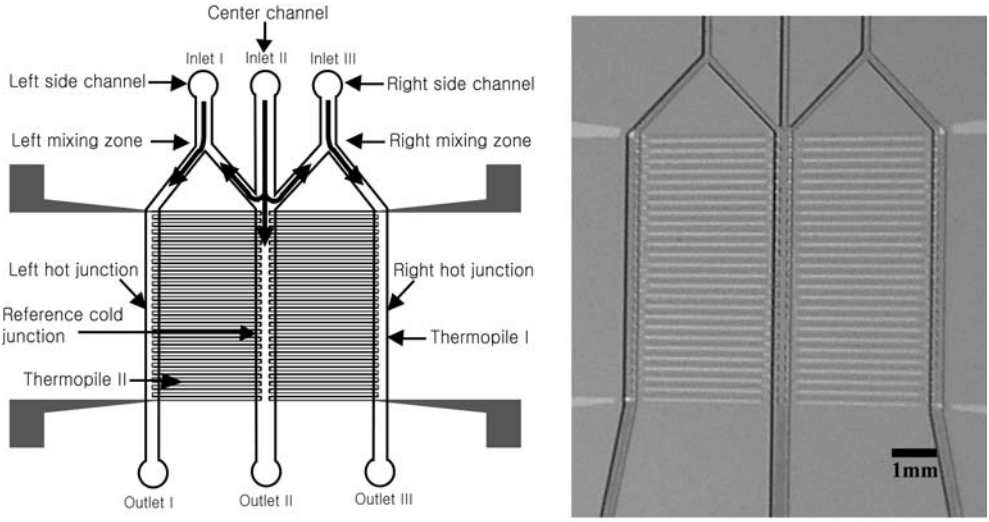

Fig.1 Illustration of thermal biosensor integrated in micro fluidic channel and its photographic image.

oxidase. This reaction is exothermic. The ascorbate oxidase of 125U/ml is prepared inwith phosphate buffer solution (PBS, pH 5.6) of 0.1-mmol /l. Four different concentrations (0.5, 1, 2, and 4 mmol/l) of L-ascorbic acid are prepared to measure the heat changes. We tried to verify the coincident response and sensitivity of dual thermopiles of our thermal biosensor. Figure 1 shows the microfluidic channel integrated with thermal biosensor. L-ascorbic acid of 2mM is injected into the left and right inlet with a flow rate of 1 μl/min. At the same time, ascorbate oxidase of 125 U/ml was injected into the center inlet with a constant flow rate of 6 μl/min. Thermopiles Ⅰ and Ⅱ simultaneously measure output voltages generated by the thermal difference between the hot and cold junctions. We also measured output voltages of thermal reaction by varying the concentration of substrate with constant concentration of enzyme. All experiments were performed at room temperature (22ºC).

4. RESULTS AND DISCUSSION

Figure 2 shows that dual thermopiles of our microfluidic thermal biosensor coincidently respond to the various flow-rates of L-ascorbic acid. One thermopile will be used for the reference sensor and the other for a measurement sensor. As shown in figure 3, the electrical signals were obtained from the reference and reaction sample for 10 minutes. The applied volumes of L-ascorbic acid and enzyme were about 10 μl and 60 μl, respectively. The maximum output voltage obtained from this experiment is around 25 μV. The sensitivity of microfluidic thermal biosensor is 519.22 μV/K, and the temperature change based on the maximum output voltage is 0.0481K.

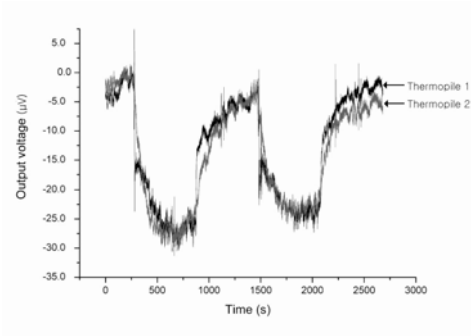

Fig. 2 Coincident output signals of dual thermopiles (left and right inlet: L-ascorbic acid of 2-mM, center inlet: ascorbate oxidase of 125-U/ml)

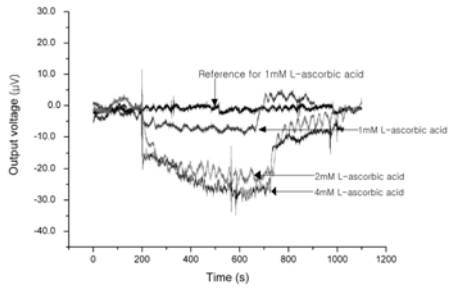

Fig. 3 Output signals that represent calories from the oxidation of L-ascorbic acid by ascorbate oxidase under a various concentrations of L-ascorbic acid.

5. CONCLUSIONS

We successfully demonstrated a dual-thermopile based microfluidic thermal biosensor which can measure a biochemical reaction and a reference temperature simultaneously. The use of dual-thermopile allows no requirement of typical adiabatic vacuum surrounding and a heater for the calibration of inlet samples. In addition, the microfluidic system was used for detecting accurate temperature of biochemical reaction with an order of ten microliters of samples.

ACKNOWLEDGEMENTS

This work was supported by Basic Research Program of the Korea Science & Engineering Foundation (Grant no. R01-2005-000-10160-0(2006)), ICBIN of Seoul R&BD program (Grant no. 10816) and National Core Research Center (NCRC) for Nanomedical Technology of the Korea Science & Engineering Foundation (Grant no. R15-2004-024-01001-0).

REFERENCES

[1] J. Lerchner, A. Wolf, G. Wolf, V. Baier, E. Kessler, M. Nietzsch and M. Krügel, *A new micro-fluid chip calorimeter for biochemical applications*, J. Thermochimica Acta, vol. 445, pp.144-150, (2005).

[2] S. I. Yoon, S. C. Park and Y. J. Kim, *A microcalorimeter based on split-flow microchannel for biochemical applications with no-calibration,* 20th EURO Sensors, Goteborg, Sweden, (2006)

[3] K. Verhaegen, K. Baert, J. Simaels and W. Van Driessche, *A High-throughput Silicon Microphysiometer*, J. Sensors and Actuators A: Physical, Vol. 82, Issues 1-3, Pages 186-190, (2000).

[4] J. P. Moore, R. K. Williams and R. S. Graves, *Thermal conductivity, electrical resistivity, and Seebeck coefficient of high-purity chromium from 280 to 1000K*, Journal of Applied Physics, Vol.48, No.2, pp.610-617, (1977).

SINGLE AND DOUBLE- SIDED SENSING WITH PIEZORESISTIVE MICROCANTILEVERS

Arnab Choudhury[1], Peter. J. Hesketh[1], Zhiyu Hu[1,2], Thomas G. Thundat[2]

[1]The George. Woodruff School of Mechanical Engineering, Georgia Institute of Technology, Atlanta, GA 30332, USA

[2]Bioscience Division, Oak Ridge National Laboratories, Oak Ridge, TN 37831, USA

ABSTRACT

Chemical sensing using microcantilevers is usually performed by functionalization of a single surface of the cantilever (single sided surface stress). The benefits of functionalization of both cantilever surfaces are discussed and a comparison of single and double-sided surface stress sensitivity is presented. Initial test results show that the surface stress sensitivities for these measurement modes compare well with theoretical estimates.

Keywords: Microcantilever, piezoresistive, surface stress, sensor

1. INTRODUCTION

Microcantilever-based surface stress sensors have been shown to be an effective and versatile platform for chemical and biochemical sensing [1]. Detection is based on measurement of surface stress, generated due to selective binding of the chosen analyte, to one side of the cantilever which has been functionalized (single-sided stress- SSS). Surface stress on a single surface (as opposed to both surfaces of the cantilever) results in cantilever deflection (Figure 1. A), which may be measured using optical, capacitive, piezoresistive or other methods. A basic assumption in these measurements is that the unfunctionalized surface does not interact with the analyte and no surface stress develops on this surface. Further, in most cases, the surface stress on the unfunctionalized surface cannot be verified without recourse to secondary calibration methods.

One solution to this problem is to functionalize both surfaces of the cantilever (double-sided stress measurement). Since no unfunctionalized surface is present, erroneous measurement, due to stress generation on the unfunctionalized surface, cannot occur. Double-sided surface stress (DSS) leads to an elongation or compression of the cantilever beam and these changes are difficult to measure via optical or capacitive methods, particularly in liquids. Piezoresistive or piezoelectric cantilevers can however be used for measurement of double-sided stress. In this work DSS measurement with piezoresistive microcantilevers is investigated.

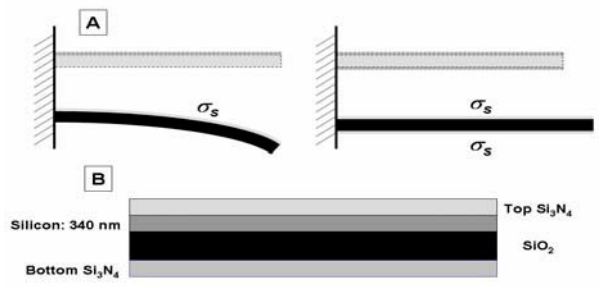

Figure 1: A) Cantilever deformation in SSS and DSS, B) Cantilever beam structure. (σ_s = surface stress)

978-0-9798064-0-7/μTAS2007/$20©2007CBMS

2. THEORY

This is the first report of experimental work on DSS measurement with piezoresistive cantilevers. Rasmussen et al. [2] have shown, theoretically, that DSS measurement may allow for higher stress sensitivity than SSS for single material piezoresistive cantilevers (Figure 2). An analytical model [3] was used to investigate surface stress sensitivity with DSS and SSS measurement in a multilayered cantilever structure (Figure 1. B). Figure 2 compares sensitivity in DSS and SSS measurement for different nitride encapsulation thickness (without the silicon dioxide layer). Clearly the ideal design for a DSS cantilever is achieved with a minimum thickness of nitride encapsulation.

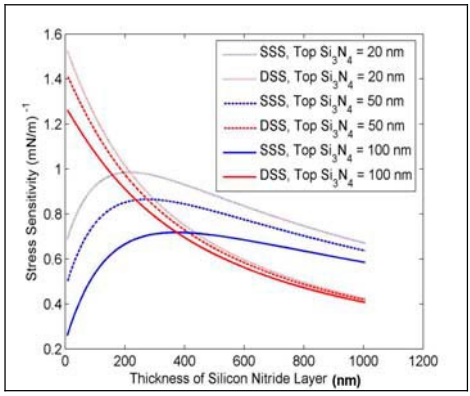

Figure 2: Calculated SSS and DSS surface stress sensitivity for varying bottom nitride thickness.

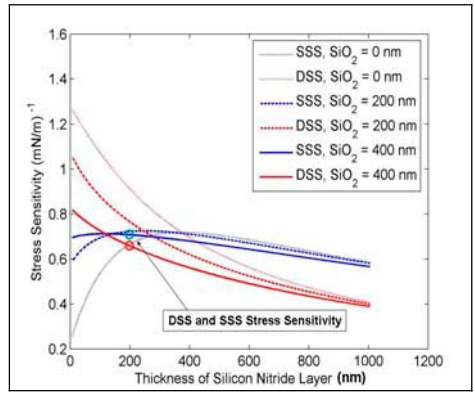

Figure 3: Calculated SSS and DSS surface stress sensitivity for the fabricated piezoresistive microcantilevers.

3. EXPERIMENTAL SETUP

In order to confirm these trends experimentally, we estimated the DSS surface stress sensitivity of sensors that had originally been developed for SSS measurement [3].

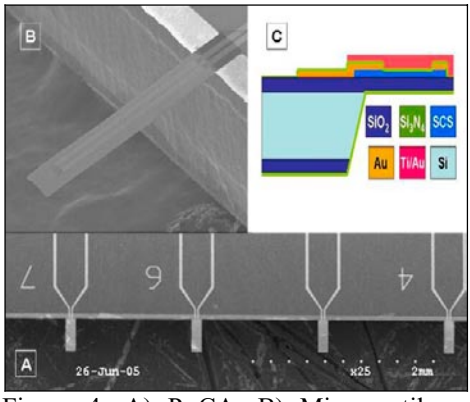

Figure 4: A) PμCA, B) Microcantilever with silicon piezoresistor, C) SSS cantilever cross-section (SCS = single crystal silicon)

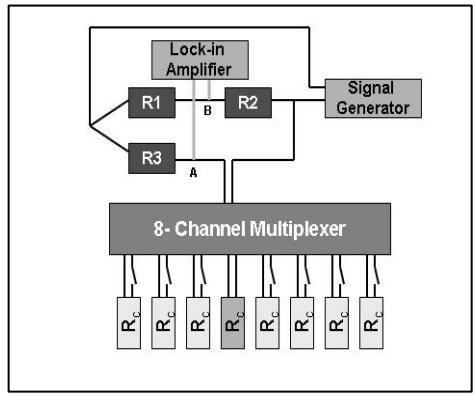

Figure 5: Low-noise measurement setup for measurement of multiple cantilevers.

DSS and SSS stress sensitivities of these cantilevers are expected to be near equal in magnitude (Figure 3). A 10-cantilever piezoresistive microcantilever array has been developed (Figure 4). In order to compare stress sensitivity using these measurement methods, two cantilevers were functionalized with 60 nm of gold (one double-sided and one single-sided). Also, an uncoated cantilever was used as a thermomechanical reference to filter noise due to thermomechanical and flow fluctuations present during the experiment. The cantilever array was assembled in a customized flow cell built utilizing stereolithography [4]. Measurements were made on a low-noise measurement setup (Figure 5) that can measure upto six cantilevers simultaneously.

4. RESULTS AND CONCLUSIONS

In tests with SSS measurement, cantilevers were exposed to 55 ppb of 6-mercapto-1-hexanol in nitrogen at 10 sccm at room temperature (Figure 6). A strong response was seen that corresponded to a surface stress of 96 mN/m. Initial tests to compare SSS and DSS measurement have been conducted successfully. A DSS response to 6-mercaptohexanol was observed. However, due to instrumentation issues, the signal-to-noise ratio in these measurements was not large and a quantitative comparison of DSS and SSS response could not be made. However the sensitivities for DSS and SSS appear to be similar as predicted by our theoretical estimates (Figure 3). Further, our current devices are not designed for optimal DSS measurement. Optimized DSS cantilever sensors will be fabricated once DSS measurement sensitivity has been successfully quantified.

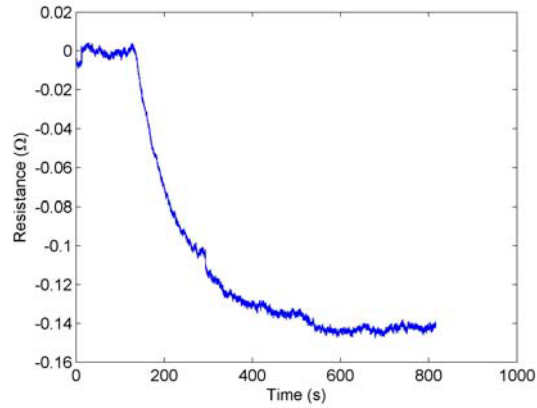

Figure 6: Single-sided response to 55 ppb of mercaptohexanol. The flow cell was purged with N_2 initially for 120s.

5. ACKNOWLEDGEMENTS

This research was supported by the Oak Ridge National Laboratory, managed by UT-Battelle, LLC, for the U.S. Department of Energy (DOE) under contract DE-AC05-00OR22725. Financial support from the DOE offices of Biological and Environmental Research is gratefully acknowledged. The authors would like to thank Robin Vujanic for his help in improving data acquisition programs for measurement and Guclu Onaran for valuable input towards establishing a working electrical measurement setup. Finally, we would like to thank the staff and members of the Georgia Tech MiRC cleanroom for their help and advice on improving the fabrication process.

6. REFERENCES

[1] T. Thundat, P. I. Oden, and R. J. Warmack, "Microcantilever sensors," *Microscale Thermophysical Engineering,* vol. 1, pp. 185-199, 1997.

[2] P. A. Rasmussen, A. V. Grigorov, and A. Boisen, "Double sided surface stress cantilever sensor," *Journal of Micromechanics and Microengineering,* vol. 15, pp. 1088-1091, 2005.

[3] A. Choudhury, P. J. Hesketh, T. G. Thundat, and Z. Hu, "A piezoresistive microcantilever array for surface stress measurement: curvature model and fabrication," *Journal of Micromechanics and Microengineering,* Submitted, 2007.

[4] A. Choudhury, P. J. Hesketh, Z. Hu, T. G. Thundat, "Low noise chemical detection with a Piezoresistive Microcantilever," *Transactions of the ECS*, vol 3, No. 10, pp. 473-482 2006.

DEVELOPMENT OF THE MODIFIED LIQUID-CRYSTAL-DISPLAY PROJECTOR DEVICE FOR FABRICATION OF SURFACE MICROPATTERNS AND MICROFLUIDIC CHANNELS

Jun Kobayashi, Kazuyoshi Itoga, Yukiko Tsuda, Masayuki Yamato, Akihiko Kikuchi and Teruo Okano

Institute of Advanced Biomedical Engineering and Science, Tokyo Women's Medical University, Japan

ABSTRACT

A newly developed device for exposure of micropatterns without the preparation of photomasks by a modified, commercially available liquid crystal display projector (LCDP) was reported. The new devise was equipped with XY positioning stages, sliding system for variable focal distance, and exchangeable objective lens, facilitating the exposure of micropattens with large area and variable resolution.

Keywords: Rapid Prototyping, Maskless, Liquid Crystal Display Projector, Photolithography

1. INTRODUCTION

Microfabrication techniques such as photolithography have been applied to micropatterning of polymers, biomolecules and cells [1]. However, most of microfabrication techniques require specialized equipment and the preparation of photomasks, resulting in costly and time-consuming processes. We have developed an all-in-one device by utilizing a commercially available LCDP for exposure of patterned images, which were generated on personal computer (PC), thorough the reduction lens [2-5]. Projection images are easily generated on PC monitors with commercial software, therefore special control software is not needed for lithographic pattern generation. This device facilitates preparation of micropatterned hydrogels [2], poly(dimethylsiloxane) (PDMS) microchannels [3, 4], and micropatterned cells [2-5] without the need for photomasks. The prototype of the modified LCDP, however, exposed only an image of 800×600 pixels with fixed resolution (10 μm/pixel).

The propose of this work is to develop a new device, which is equipped with XY positioning stages, sliding system for variable focal distance, and exchangeable objective lens (Figure 1). Resolution of exposed

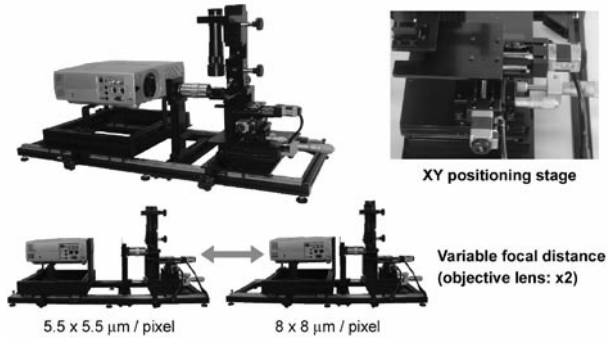

Figure 1.The modified liquid crystal display projector (LCDP) devise equipped with XY positioning stages, sliding lens system for variable focal distance, and exchangeable objective lens.

978-0-9798064-0-7/μTAS2007/$20©2007CBMS

micropatterns was easily varied by exchanging the objective lens and/or adjusting focal distance. Moreover, after the segmentation of a large mask image on PC, the images were repeatedly exposed with moving XY positioning stages and combined, resulting in the formation of micropatterns on large area. In this work, micropatterned cells with high resolution and microchannels on large area were fabricated.

2. EXPERIMENTAL

Fabrication of cellular micropatterns was achieved with this device according to previous report [5]. Briefly, polymerization of acrylamide was performed on silanized glass /micropatterned g-line positive-type photoresist. After the reaction, micropatterned photoresist was lifted off, resulting in a polyacrylamide–silane micropattern on the coverslip.

The procedure to fabricate PDMS microchannels is outlined in Figure 2. First, micropatterning of g-line negative photoresist on silicon wafer or silanized glass was performed by irradiation of visible light with the maskless LCDP device (Figure 2a). Second, PDMS microchannels are fabricated by pouring and curing PDMS prepolymer over the master (Figure 2b). Finally, product PDMS microchannels are sealed with a coverslip.

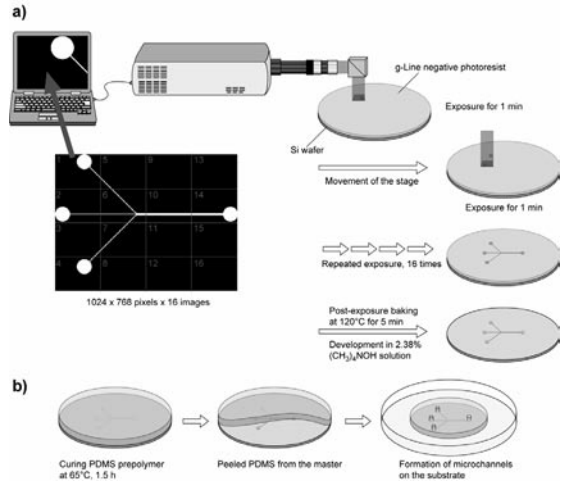

Figure 2. Fabrication of a microchannel master with the modified LCDP device (a) and PDMS microchannels (b).

3. RESULTS AND DISCUSSION

Figure 3 shows the fluorescent microscopy of micropatterned cells stained with Alexa488-conjugated phalloidin and ethidium homodimer-1. Cells seeded on the micropatterned surfaces attach and spread only on unpolymerized silanized glass surfaces. Micropatterned cells were cultured on 10 and 20 µm-wide lines, and 10 and 20 µm-square islands. With this device, the micropatterning of cells with 10 µm resolution, higher than the previous report [5], was achieved.

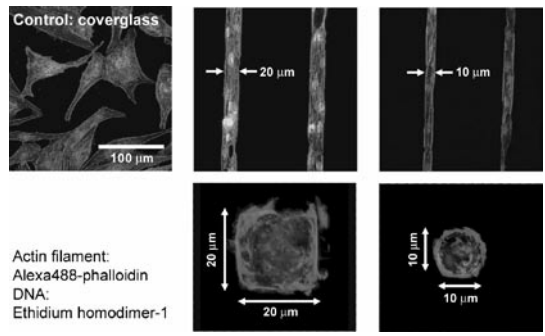

Figure 3. Micropatterned cells on 10 and 20 µm-wide lines, and 10 and 20 µm-square islands. Cells were stained with Alexa488-conjugated phalloidin for actin filaments and ethidium homodimer-1 for DNAs.

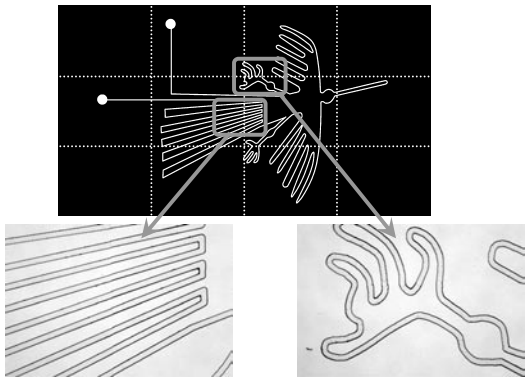

Figure 4. Microscopy of negative-photoresist patterns combined with segmented mask images.



Figure 5. Formation of PDMS microchannel with large area.

Negative-photoresist patterns combined with segmented mask images was observed by microscopy (Figure 4). Successful connection of negative-photoresist patterns on the boundaries between segmented mask images was achieved. PDMS microchannels were obtained using the micropatterned negative photoresist as the master. Finally, product PDMS microchannels are sealed with a coverslip and filled with the dye solution. No leaks were detected over the entire surfaces observed, so that fluid-tight boundary between the PDMS and coverslip was obtained (Figure 5).

4. CONCLUSIONS

A maskless approach using the modified LCDP device is considered to be a versatile approach for rapid prototyping of cellular micropatterns and microfluidic systems since the researchers create the individual designs based on their own purpose.

ACKNOWLEDGEMENTS

This work was financially supported by Formation of Innovation Center for Fusion of Advanced Technologies in the Special Coordination Funds for Promoting Science and Technology from the Ministry of Education, Culture, Sports, Science and Technology (MEXT), Japan, and Core Research for Evolutional Science and Technology (CREST), Japan Science and Technology Agency (JST), Japan.

REFERENCES

[1] A. Folch, M. Toner, Annu. Rev. Biomed. Eng., 2, 227 (2000).

[2] K. Itoga, M. Yamato, J. Kobayashi, A. Kikuchi, and T. Okano, Biomaterials, 25, 2047 (2004).

[3] K. Itoga, M. Yamato, J. Kobayashi, A. Kikuchi, and T. Okano, J. Biomed. Mater. Res., 69A, 391 (2004).

[4] J. Kobayashi, M. Yamato, K. Itoga, A. Kikuchi, and T. Okano, Adv. Mater., 16, 1997 (2004).

[5] K. Itoga, J. Kobayashi, M. Yamato, A. Kikuchi, T. Okano, Biomaterials, 27, 3005 (2006).

IN-BLOCK BONDING-LESS 3D MICROCHANNEL NETWORK FABRICATION IN PDMS

Marcin Juchniewicz, Olga Adamowicz, Michał Chudy, Artur Dybko, Zbigniew Brzózka

Warsaw University of Technology, POLAND

ABSTRACT

This paper reports a novel technology for bonding-less fabrication of 3D microchannels network in monolithic blocks of PDMS (poly(dimethylsiloxane)). The technology uses a capillary film, does not need expensive equipment and microchannels aligning. The matrix made of the capillary film was prepared in photolithography process and then molded inside PDMS block. The capillary film was removed from the block of crosslinked PDMS by washing it out. Fabricated devices were tested as a part of a microsystem for bilirubin determination.

Keywords: bonding, 3D, microchannels, PDMS

1. INTRODUCTION

Technologies commonly used in the microsystems fabrication almost always involve a bonding step. In many cases the bonding is difficult to perform and many failures occur. Also it is common that an equipment needed for the bonding is expensive. Presented method allows to eliminate bonding process from the fabrication of a microsystem. The technology makes usage of capillary films which are materials commonly used in screen printing technology. They consists of a support foil and a photosensitive emulsion layer. For testing stage we choose a method of bilirubin determination. Bilirubin is a bile pigment, normally found in serum as a result of red cell destruction. Bilirubin bound to albumin is transported into the liver where it is conjugated with glucuronide. Elevated serum bilirubin is indicative of impairment of the liver, hemolysis or obstruction of the biliery tract.

2. EXPERIMENTAL

A piece of a capillary film was stick with double adhesive tape to a stiff support (e.g. glass, plastic or metal plate). The support makes a further process of emulsion developing easier. Next, a photomask was placed on the top of the capillary film. As masks were used high resolution prints (3600 dpi) on a transparent foil. The capillary film was exposed through the mask to UV light with doses recommended by the producer. The exposed film was developed in a tap water stream. Developing process consist of 3 washing steps separated with drying. During the washing the capillary film was sprayed with a tap water and unexposed emulsion was removed. When contact of the emulsion with the water lasts too long, swelling occurs and defects appeared. To prevent this, the first washing step lasts no more than 30 seconds and each next step can not exceed 15 seconds. After each washing step the capillary films were immediately dried with nitrogen or air stream. Fully developed and dried capillary films were ready to use as a matrix for a microsystem. A 3-5 mm thick layer of a PDMS prepolymer was poured into mold. Partial crosslinking of the layer was achieved on a hot plate. The matrix made of the capillary film was transferred on the PDMS layer by pressing the developed capillary film to PDMS and gentle removing of a support foil. Emulsion layer of capillary film stuck to PDMS. At the ends of the pattern (future ends

978-0-9798064-0-7/μTAS2007/$20©2007CBMS

of the microchannels) the stainless steel tubes were placed to ensure the tubing connections (Fig. 1.). Steel tubes were also used for the preparation of an integrated fiber optic cell for absorbance and fluorescence measurements (Fig. 3.). Additional levels of the microchannels networks could be added easily by the preparation of the next not fully crosslinked layers of PDMS and transferring on them next parts of capillary film matrix. Then 3D network of microchannels was obtained. After preparation of all layers, the structure was poured with PDMS prepolymer which was then crosslinked. Then steel tubes were removed and distilled water was pumped into the microchannel to wet the capillary film matrix. The whole microsystem was frozen in liquid nitrogen. During defrosting PDMS started to be elastic, but emulsion soaked with water remained fragile. When PDMS was bent, the cracks in an emulsion appeared and the emulsion matrix broke into separate pieces. Those pieces were removed from the microchannel with distilled water, acetone or oil pumped with pulsing pressure.

4. RESULTS AND DISCUSSION

As a result the microsystem with the integrated optical cell and the microchannels inside monolithic block of PDMS was fabricated (Fig. 2,4). No oxygen plasma bonding process was used.

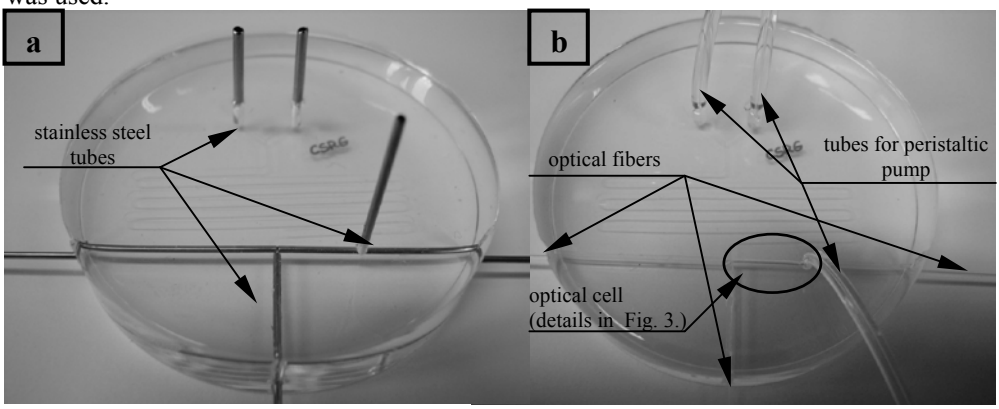

Fig. 1. Top view of the microsystem: a) microsystem with the stainless steel tubes inserted; b) microsystem after removing the steel tubes (tubes for peristaltic pump and optical fibers are connected).

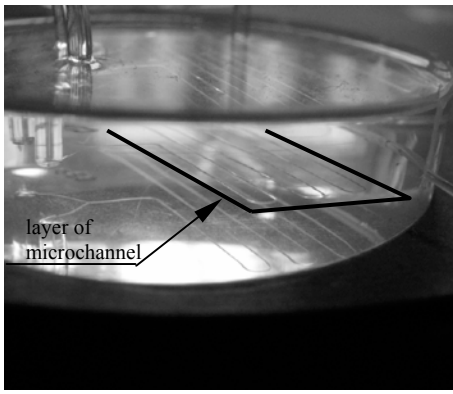

Fig. 2. Side view of the microsystem prepared without plasma bonding. A layer of the microchannel is shown.

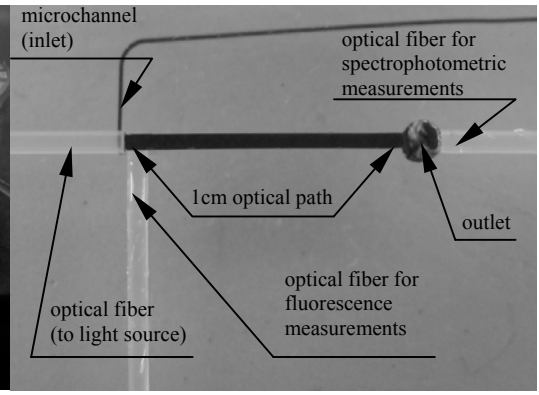

Fig. 3. Close-up of an integrated photometric cell prepared with the molded steel tubes. Both spectrophotometric and fluorometric measurements are possible.

SEM images of fabricated structures showed that cross section of microchannels is non ideal but close to rectangular (Fig. 4).

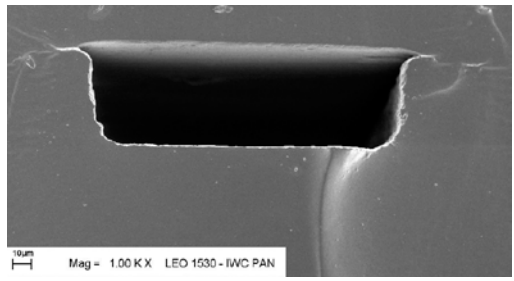

Fig. 4. Cross section of the microchannel (50x150 µm) prepared in a monolithic block of PDMS without plasma bonding.

Microsystems fabricated as described above were tested by the bilirubin determination. From three methods used in clinical analysis we choose and adapted one method. In this method, sulfanilic acid reacts with sodium nitrite to produce diazotized sulfanilic acid. In the presence of DMSO bilirubin reacts with diazotized sufanilic acid forming azobilirubin. The absorbance of the reaction mixture at 566 nm is directly proportional to the concentration of bilirubin. The reagent solution was prepared by mixing solutions of sulphanilic acid and sodium nitrite. Reagent and bilirubin solution in ratio v/v 1:1 were simultaneously pumped by a peristaltic pump into the microreactor. The reaction was carried out in the microchannel. Product of reaction was pumped to the flow cell and the absorbance measurements were carried out (Fig. 5.).

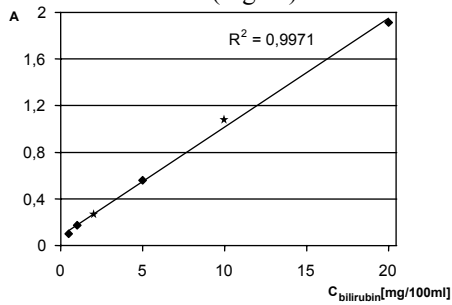

Fig. 5. Calibration curve for bilirubin concentration in standard solutions at wavelength λ = 566 nm (◆ - calibrants ⋆ - test samples)

5. CONCLUSIONS

Presented technology allows to fabricate bonding-less microsystems from PDMS. It is also possible to fabricate 3D networks of microchannels without need of expensive equipment. Although cross section of microchannels was non ideal, the bilirubin determinations performed in such microsystems were precise.

ACKNOWLEDGMENTS

This work was supported in part by The Ministry of Science and Information Society Technologies by a grant N 518 018 31/1006.

MECHANICAL MEASUREMENT OF DNA MOLECULE COMBINED WITH THE DNA TWEEZERS AND A WEDGE TYPE CANTILEVER

M. Hosogi[1], G. Hashiguchi[1], K. Ayano and H. Fujita[2]
[1] *Faculty of Engineering, Kagawa University, Japan*
[2] *Institute of Industrial Science, The University of Tokyo, Japan*

ABSTRACT

We have measured mechanical property of DNA wire using micromachined tweezers. In the experiment, we configured an atomic force microscope to the mechanical measurement of bridged DNA wires between the tweezers probes and utilized a special AFM cantilever having a knife-wedge shape tip with a very low spring constant for applying a loading force to the wire. Using the apparatus, a force curve was monitored under the several kinds of humidity level. The spring constant of the DNA wire was changed apparently by the humidity level. As demonstrated here, this method is useful for a mechanical evaluation technique of nano materials.

Keywords: DNA wire, DNA tweezers, wedge-type cantilever, humidity level

1. INTRODUCTION

Micromachining techniques based on IC-compatible fabrication technology have been applied to a great variety of micro-electro-mechanical systems (MEMS) through the integration of sensors and electronics in a chip-size system. Recent interest in nanotechnology requires a nanometer size device for handling nanoscale materials such as DNA molecule, which is one of the promising applications in nano-electro-mechanical systems (NEMS). A development of a measurement method for mechanical properties of biological molecule, such as DNA molecule and protein, is becoming increasingly important to the biophysical research field. A force curve measurements of DNA or protein have been reported so far [1-4]. However, effect of humidity level on the mechanical properties of the DNA molecule has not been reported. We have fabricated the micromachined DNA tweezers having a pair of opposing probes for retrieving the DNA molecules. Using the tweezers, we have demonstrated a retrieval of DNA and a principle of DNA modification by Pd nano particles, and measured its resistivity to evaluate the gauge factor [5, 6]. Here in this letter, we report a nano-Newton order force measurement for lambda DNA using an AFM cantilever and the micromachined DNA tweezers that we have originally fabricated. We evaluated the effect of the humidity on the spring constant of the DNA wire.

2. EXPERIMENTAL

Figure 1 shows a schematic diagram of a measurement for a force curve of the DNA wire bridged between the probe tips. The tweezers were attached to a tilting-stage and then set in the AFM system. An arbitrary deflection deformation can be given to the bridged wire by pressing using a cantilever. The net deflection displacement of the wire was detected by measuring deflection volume of a cantilever and a piezo-stage traveling distance in giving displacement to the wire. The measurements were conducted under the various humidity levels (27 ~ 60 %).

978-0-9798064-0-7/μTAS2007/$20©2007CBMS

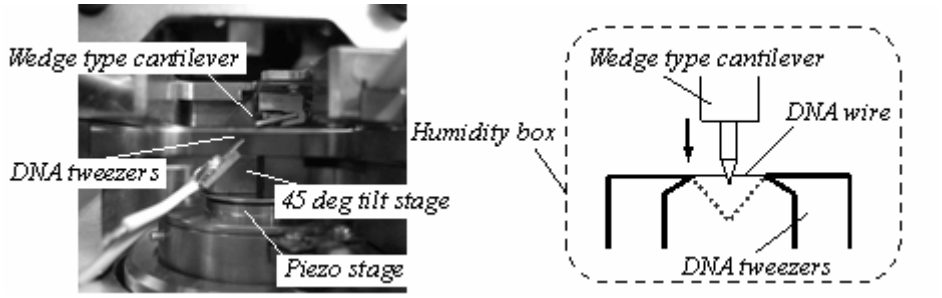

Fig.1 A schematic diagram of a measurement for a force curve of the DNA wire.

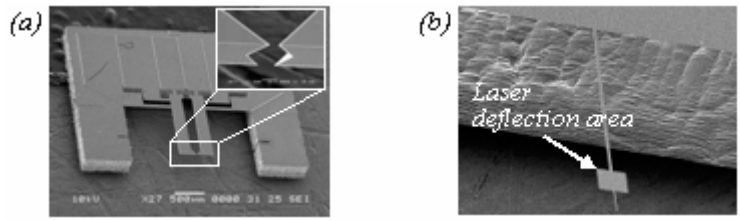

Fig.2 SEM images of the micromachined DNA tweezers and an AFM cantilever.

Figure 2 (a) and (b) show scanning electron microscope (SEM) images of the micromachined DNA tweezers and an AFM cantilever used in this study. The DNA tweezers has a pair of opposing probes, which are V-type probes (like claws) for retrieving the DNA molecules. Since the DNA wire were retrieved between the probes in the front side as shown in an inset figure in Fig.2 (a), it is possible to scan a shape of the bridged wire with the probe arm so as to know a center position of the wire. A DNA molecule has a feature of bonding its end to such metals as Al or Pt. For this reason, the DNA tweezers were coated with a 50 nm-thick Al film, which is deposited on the area of the probe arms and the electrode pads. We fabricated a new design AFM cantilever. The cantilever, which was made of 5 micro meter thick SOI wafer, is 1.5 micro meter in thickness and 560 micro meter in length and has an area for laser deflection. The spring constant was approximately 0.0064 N/m, which is soft enough to approach the nanoscale wire. As shown in Fig.2 (b), the front edge of the cantilever has a wedge configuration to keep contact easily on the wire while it is bending.

3. RESULTS AND DISCUSSION

The DNA wires having about 130 and 1070 nano meter in diameter were prepared for the force curve measurements as shown in Fig.3 respectively. Figure 4 show the force curves of each DNA wire, which were measured at 40 % humidity. In both force curves, the reaction force starts to increase at the cantilever contact point with the wire (loading process). Then the deformation of the wire made a milder recovery in the unloading process (unloading process); this indicates a viscoelastic deformation of the wire. Figure 5 shows the effect of humidity on the spring constant of each wire. The spring constant decreases as the humidity increases for each wire. As demonstrated here, this method is useful for a mechanical evaluation technique of nano materials.

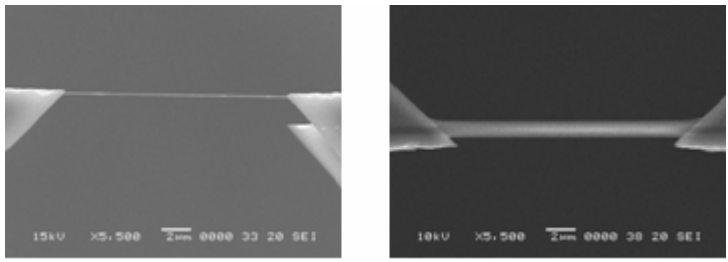

Fig.3 DNA wires having about 130 and 1070 nano meter thickness.

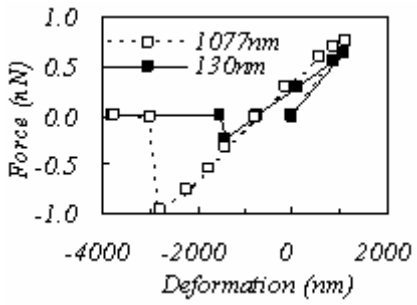

Fig.4 Force curves of DNA wire (1070 and 130 nm) at 40 % humidity.

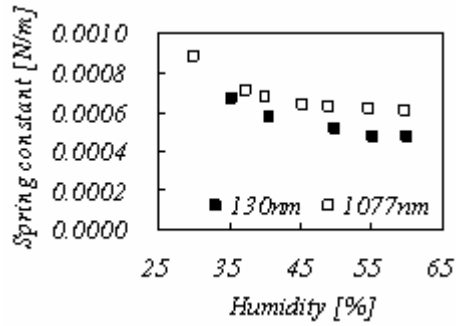

Fig.5 Effect of humidity on the spring constant of DNA wire.

4. CONCLUSIONS

We present a new method for evaluating a mechanical characteristic of nano materials such as DNA molecule using an AFM system, the micromachined tweezers and the wedge type cantilever. An AFM cantilever, which has 0.0064 N/m spring constant, was used for giving a minute displacement to the nano wire without breaking and the displacement was detected by an AFM system. In this paper, we showed a case of a mechanical measurement of lambda DNA wire.

REFERENCES

[1] C., Marko, J. F., Siggia, E. D. and Smith, S., *Entropic elasticity of lambda-phage DNA Bustamante*, Science 265, 1599–1600 (1994).

[2] Oberhauser, A.F., Marszalek, P.E., Erickson, H.P., and Fernandez, J.M, *The molecular elasticity of tenascin, an extracellular matrix protein*, Nature, 393, 181-185 (1998).

[3] Carrion-Vazquez M., A.F. Oberhauser, S.B. Fowler, P.E. Marszalek, S.E. Broedel, Jr. J. Clarke, and J.M. Fernandez., *Mechanical and chemical unfolding of a single protein*, Proc Natl. Acad. Sci. USA., 96, 3694-3699 (1999).

[4] M. Rief, J. Pascual,, M. Saraste, and H. Gaub, *Single Molecule Force Spectroscopy of Spectrin Repeats:Low unfolding forces in helix bundles*, J. Mol. Biol., 286, 553-561, (1999).

[5] G. Hashiguchi, T. Goda, M. Hosogi, K. Hirano, N. Kaji, Y. Baba, K. Kakushima and H. Fujita, *DNA manipulation and retrieval from an aqueous solution with micromachined nanotweezers*, Anal. Chem., 75, 4347-4350, (2003).

[6] M. Hosogi, G. Hashiguchi, M. Haga, T. Yonezawa, K. Kakushima and H. Fujita, *Electrical Conductivity of Lambda DNA–Pd Wire*, Jpn. J. Appl. Phys., 44, No.30, L955-L957, (2005).

PDMS MICROLENS ARRAY FABRICATION USING WATER DROPLETS

Shih-hui Chao[1,2], Robert Carlson[2] and Deirdre Meldrum[1,2]

[1] Microscale Life Sciences Center, University of Washington, USA and
[2]Department of Electrical Engineering, University of Washington, USA

ABSTRACT

We developed a novel method that uses water droplets as molds to fabricate large arrays of highly curved microlenses. The formation of water droplets is controlled by creating circular hydrophilic regions on a hydrophobic surface with microscale PLasma Activated Templating (μPLAT) [1-3], in which a physical mask is used to expose selected areas to air plasma to increase hydrophilicity. The new method dramatically improves the light gathering capacity of microlenses over traditional microfabrication methods with a minimum cost. These lens arrays can be easily integrated with lab-on-a-chip devices.

Keywords: Microscale plasma activated templating, soft lithography, microlens array

1. INTRODUCTION

The optical detection sensitivity of a lab-on-a-chip device can be improved through integration with high numerical aperture (NA) microlenses. Common microlenses are fabricated through circular patches of melted photoresist. However, those microlenses have limited NA because photoresist droplets have small contact angles and therefore low curvature. Here we present a new fabrication method that replaces photoresist droplets with patterned water droplets to achieve higher NA. The water patterns are generated by creating circular hydrophilic areas on hydrophobic surfaces through μPLAT.

2. FABRICATION PROCESS

The fabrication process is illustrated in Fig. 1, beginning with adhering a mask with a circular hole array to a silanized PDMS slab, followed by 1-minute air plasma treatment in Step (a). Then the mask is detached and placed the slab on ice to condense water in Step (b). Water droplets tend to coalesce into hydrophilic areas, with droplet edges pinned on the hydrophilic/hydrophobic interfaces. The duration determines the desired curvature of the lenses. In Step (c), uncured PDMS is poured on the slab then cured at 65°C. The new PDMS layer, having droplet-shaped cavities, can serve as concave lenses or a mold for convex lenses. For molding convex lenses, the mold substrate is silanized before lens molding in Step (d). After curing at 70°C for 3 hours, the newest PDMS convex lens layer can be peeled off from the mold and integrated with other lab-on-a-chip devices.

A demonstrative lens array was fabricated using a 75-mm diameter stainless steel screen with 400-mm holes as a μPLAT mask (Fig. 2a). The PDMS mold and final lens array are shown in Fig. 2b and 2c, respectively. The entire process took approximately seven hours, consisting primarily of curing and silanization. The cost for equipment (a plasma cleaner) and the cost of chemicals (water, 10 mL silane) are much lower than those of traditional microlens fabrication methods.

978-0-9798064-0-7/μTAS2007/$20©2007CBMS

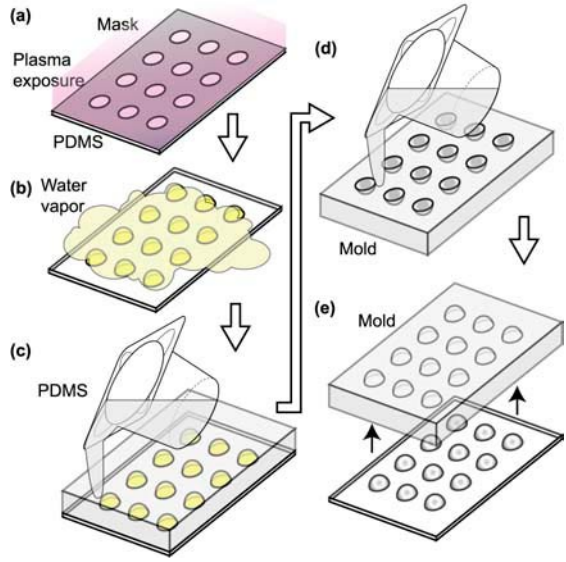

Figure 1: The fabrication steps of water droplet molding for microlens array.

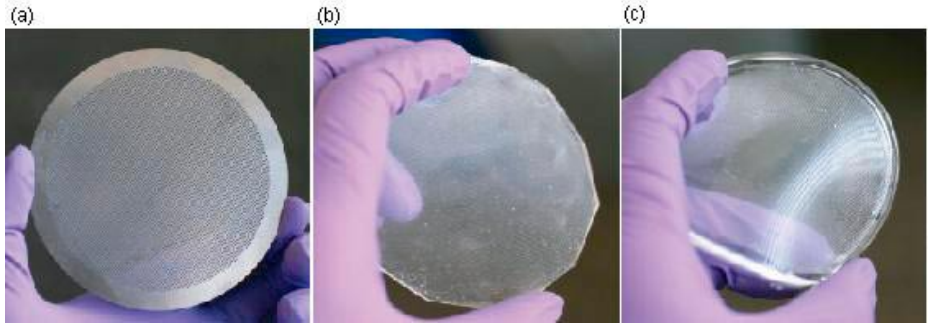

Figure 2. (a) μPLAT mask with 400 μm holes. (b) PDMS mold with concave lenses. (c) PDMS convex lens array.

3. RESULTS AND DISCUSSION

The μPLAT treated PDMS slab was kept in a condensation environment for 10 minutes. Figure 3 shows the profile of a produced lens in the array. The edge angle of the lens, resulted from the contact angle of the droplet, is 73.2°—much higher than that of photoresist (typically around 30°). The NA of this lens is twice those of photoresist based lenses when working without other optics, implying a 16x improvement in light gathering capacity under epi-fluorescence illumination. The NA of the lenses can be tuned by adjusting the amount of water loaded on the surface. However, condensing water for more than 10 minutes caused droplets in some adjacent hydrophilic areas to coalesce unstably.

Figure 4(a) shows the top view of a portion of the array, and Fig. 4(b) shows the ability of image magnification through these lenses when the PDMS lens layer was attached on a computer monitor.

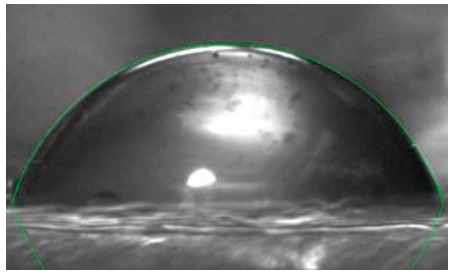

Figure 3. Side view of a microlens shows edge angle of 73.2°.

(a) (b)

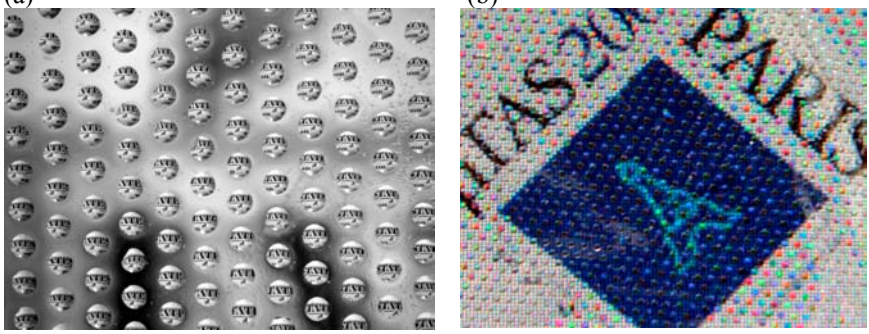

Figure 4. (a) Top view of a part of the array 25 mm above a US $20 bill, each lens shows the top of the White House. (b) The microlens array placed on a monitor showing the logo of μTAS2007 logo. The image of a single color of a pixel can be seen through each lens.

4. CONCLUSIONS

The new method enables general laboratories to fabricate PDMS microlens arrays with high optical qualities, low cost, fast turnaround time, and no hazardous waste. Future research will focus on integration with high content bio-optical lab-on-a-chip systems.

ACKNOWLEDGEMENTS

We acknowledge the support of the National Institutes of Health, National Human Genome Research Institute, Centers of Excellence in Genomic Science: Microscale Life Sciences Center, grant number 5 P50 HG002360-05, and grant number. 1 R01HG01497, and Fotofab Inc. for providing the free metal screen for μPLAT masking.

REFERENCES

[1]. Carlson, R. and Meldrum, D., *Electrostatic actuators composed of extensible graphite-PDMS composite membrane*. in microTAS. (2005).

[2]. Chao, S.H., Carlson, R., and Meldrum, D., *Soft lithography without using photolithography*. in microTAS. (2006).

[3]. Chao, S.H., Carlson, R., and Meldrum, D., *Rapid fabrication of microchannels using microscale plasma activated templating (uPLAT) generated water molds.* Lab on a Chip: DOI:10.1039/B618269K. (2007).

SU-8 BASED MICRONEEDLE FOR DRUG DELIVERY IN NANOMEDICINE APPLICATIONS WITH INTEGRATED ELECTRODES

Luis J. Fernández, Maria Tijero, Roman Vilares, Javier Berganzo, Kepa Mayora, F. J. Blanco

MEMS/MST Dept., Ikerlan S.Coop, Mondragón, SPAIN

ABSTRACT

In this work, we present the fabrication and first measurement results of SU-8 based microneedles with integrated electrodes. These devices were successfully packaged for their insertion in agarose gel, and the delivery of a saline solution was monitored by impedance change measurements.

Keywords: microneedle, SU-8, drug delivery, impedance monitoring

1. INTRODUCTION

Compared to the nowadays technology, where stainless steel needles are used, microneedles offer superior flexibility, considerable tissue damage reduction, and diminution of the pressure at the needle tip [1], which causes the backflow of the delivered drug along the path of the catheter for flow rates higher than 1 μl/min [2]. Although silicon based microfluidic needles have been developed during the last years [3-4], flexible materials such polymers have been recently proposed in order to minimize tissue damage, reduce the possibility of fracture, and increase biocompatibility [5]. Compared to other polymers, SU-8 shows better mechanical properties, lower water uptake and good biocompatibility. In this paper we present the fabrication of SU-8 microneedles and first measurement results for the impedance monitoring during the delivery of a saline solution into an agarose gel.

2. DESIGN AND FABRICATION

The design of the microneedles is presented in figure 1. The fluidic channel width ranges from 20 to 100 μm, and sensing electrodes are placed close to the channel outlets in order to monitor the drug delivery and its effect on the neural cells. The fabrication starts with a temporary bonding of a kapton film on top of a transparent substrate (figure 2.a), which will allow an easy release of the devices.

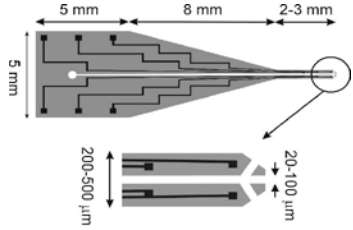

Figure 1. Schematic drawing of microneedle design

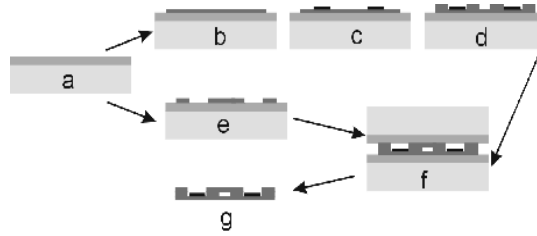

Figure 2. Fabrication process flow for SU-8 based microneedles

978-0-9798064-0-7/μTAS2007/$20©2007CBMS

Next, a 20 μm thick SU-8 layer is deposited and patterned (2.b). Metal electrodes are then deposited by sputtering (50 nm and 150 nm thick titanium and platinum respectively), and patterned by lift-off (2.c). Then, the SU-8 layer which will define the fluidic channel width (20-100 μm) and height (20-60 μm) is processed (2.d). Using another kapton substrate, a new layer of SU-8 (80-120 μm) is processed (2.e). By performing a bonding step between the SU-8 layers (2.f) the fabrication of the microneedle is completed. Finally, devices are manually released from the kapton film (2.g).

3. RESULTS AND DISCUSSION

Figures 3 and 4 show pictures of a typical fabrication result, and a SEM image of a microneedle tip respectively. As can be observed, the fluidic channel ends in three different outlets in order to prevent its occlusion.

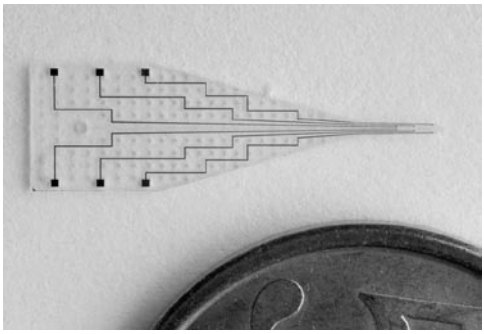

Figure 3. Top view picture of a finished microneedle

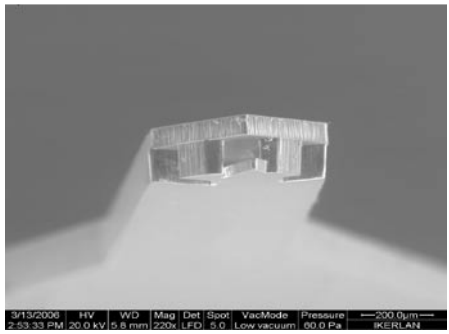

Figure 4. SEM pictures of a microneedle tip

Fluidic and electrical connections are achieved by an o-ring and 4 pins respectively, and the microneedle is perfectly held on by four screws to prevent any undesired displacement (figure 5). The insertion of a packaged SU-8 microneedle in agarose gel (0.6 % w/v) is shown in figure 6. Agarose gel was selected since it mimics the pressure-driven flow in brain tissue [4]. The SU-8 microneedles showed a perfect stiffness for the insertion.

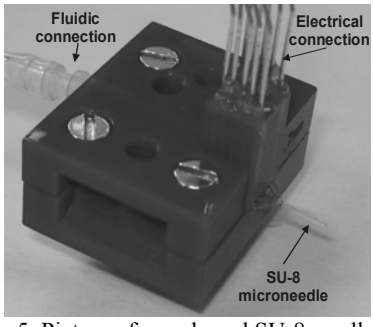

Figure 5. Picture of a packaged SU-8 needle.

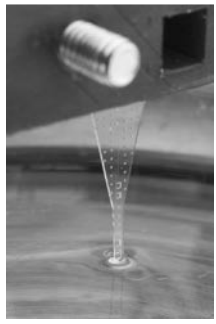

Figure 6. SU-8 needle packaged and inserted in agarose gel.

Water was delivered into the agarose gel at different flow rates (20, 40, 80 and 100 μl/min). Figure 7 shows that only when the flow rate is forced to exceed 80 μl/min backflow appeared in the form of flow peaks, while a successful response for the rest of flow rate values is obtained. First impedance monitoring experiments have been carried out, and preliminary results are shown in figure 8. As can be observed, an impedance reduction is obtained as a consequence of the presence of the saline solution in the agarose gel. Therefore, the sample delivery is confirmed by impedance measurements, which could be also used in the future to characterize possible cell response to specific drugs.

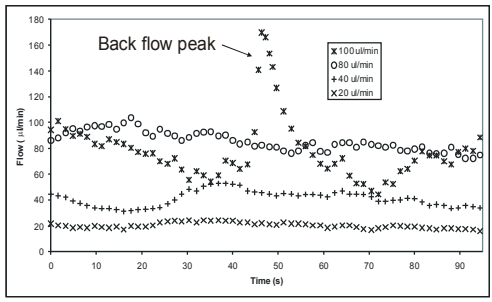

Figure 7. Different flow rates of water inserted in agarose gel by SU-8 microneedles with a 50x40 μm embedded channel.

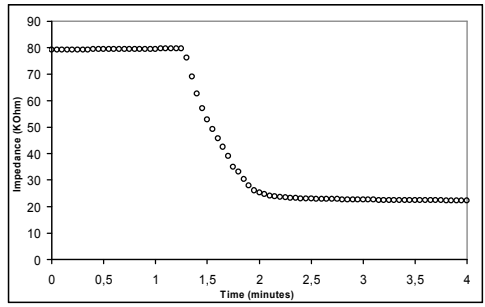

Figure 8. Impedance measurements while delivering a saline solution (0.9% of NaCl) in an agarose gel.

4. CONCLUSIONS

The fabrication of a microneedle completely made of SU8 polymer has been demonstrated. Higher flexibility and biocompatibility, together with a lower cost and reduced back flow risk are the main advantages of the proposed microneedles with respect to the state of the art. Measurement results show flow rates up to 80 μl/min without back flow effects, and drug delivery monitoring by means of impedance measurements.

REFERENCES

[1] Z. Chen et al., *A realistic brain tissue phantom for intraparenchymal infusion studies,* J. Neurosurg., **101**, pp. 314, (2004)

[2] M.Y. Chen et al., *Variables affecting convection-enhanced delivery to the striatum: a systematic examination ofrate of infusion, cannula size, infusate concentration, and tissue–cannula sealing*, J. Neurosurg., **14**, pp. 1215-1219, (2004). **90** (2), pp. 315, (1999)

[3] Neebes K. B. et al., *Fabrication and characterization of microfluiidic probes for convection enhanced drug delivery*, J. of Controlled Release, **111**, pp. 252, (2006)

[4] D. Papageorpiou et al., *A shuttered neural probe with on-chip flowmeters for chronic in vivo drug delivery,* J. MEMS., **15**, No 4, pp. 1025, (2006).

[5] Gabriela Voskerician et al., *Biocompatibility and biofouling of MEMS drug delivery device,* Biomaterials, **24**, pp. 1959-1967, (2003).

A MICROFABRICATED NANOPIPETTOR BASED ON ELECTROOSMOSIS

Shaorong Liu, Chang Kyu Byun and Qiaosheng Pu

Department of Chemistry & Biochemistry, Texas Tech University, Lubbock, TX 79407, USA

ABSTRACT

We present the results of our initial attempt to develop an electroosmosis-based nanopipettor to accurately pickup, transfer and deliver pL~μL solutions. The first version of this pipettor consists of a microfabricated EO pump, a polyacrylamide grounding interface, and a nL-pL pipet-tip. Good reproducibilities (RSD = 6% at 140 pL, 2% at 950 pL and 2% at 13 nL) and accuracies (9% at 0.13 nL, 4% at 1.0 nL and 3% at 10 nL) of this pipettor have been demonstrated. An excellent feature of an EO-driven pipettor is that it has no moving parts.

Keywords: Nanopipettor, electroosmotic pump, polyacrylamide grounding interface

1. INTRODUCTION

Minimizing the volumes of sample/reagent consumed in each assay is an effective means to reduce the overall analysis cost, which leads to a demand for small volume (*e.g.* nL) pipettors. Recently, increasing attention has been paid to investigate the behavior of individual cells. If one wishes to transfer solution to or from a single cell, a pL-pipettor is needed since the entire cell volume is commonly less than one nL. Pressure ejection[1,2] and iontophoresis[3,4] are capable of delivering solutions down to pLs, and instruments based on these technologies have been commercially manufactured.[5,6] However, because none of the above techniques can be used to accurately pick up solutions (a basic function of a pipettor), one cannot develop a pipettor out of these technologies. The state-of-the-art pipettors (*e.g.* Rainin pipette) is capable of handling liquids down to 100~200 nL, with an accuracy of ±12% at 200 nL,[7] and no commercial pipettors are available to accurately pick up, aliquot and transport solutions of less than 100 nL.

Electroosmotic (EO) flow has been employed to pump solutions in capillaries and micro-channels, and various pumps have been developed. EO Pumps have several unique features such as low stable flow rates, no moving parts, and convenience in adjusting the flow rate and flow direction. These features should enable us to develop an excellent nL-pL pipettor based on electroosmosis. Because EO flow goes with electric current, the solution outlet end is usually connected to an electrode. This arrangement will be practically inconvenient.

2. EXPERIMENTAL

Manufacturing of a polyacrylamide grounding interface. A 10-cm-long capillary (360 μm o.d. and 100 μm i.d.) was cut and its inner wall was cleaned by flushing the capillary with 1.0 M NaOH for 45 min, DI water for 15 min, and acetonitrile for 15 min. After the capillary was dried with N_2, the inner wall was reacted with a solution containing 0.4% (v/v) 3-(trimethoxysilyl)propyl methacrylate and 0.2% (v/v) acetic acid in acetonitrile at room temperature for 1 hour. Then, a degassed solution containing 2~12%T (%T stands for the total weight concentration acrylamide and bis in the solution), 3~7%C (%C represents bis concentration relative to acrylamide), 0.2% (v/v) TEMED and 0.1% APS was pressurized into the capillary, and remained inside the capillary at 4 ^{o}C overnight. After ~1

978-0-9798064-0-7/μTAS2007/$20©2007CBMS

cm of the capillaries at both ends were cut off and discarded, 50 mM sodium tetraborate was electrophoretically driven through the polyacrylamide inside the remaining capillary until a stable current was obtained. The above capillary was cut into ~1 cm a piece, and each piece serves as a polyacrylamide grounding interface.

Fabrication of an EO pump chip. A three-photomask process was used to make this device. Briefly (referring to Figure 1), one photomask was utilized to yield the semi-circular grooves on the top wafer, the second photomask for the semi-circular grooves on the bottom wafer, and the third photomask for the parallel shallow pump grooves. The radius of the semi-circular grooves was *ca*. 190 µm, and the dimension of the pump channels (24 in parallel) was 30 mm (length) x 200 µm (width) x ~1.5 µm (depth). The pump channels were evenly distributed with a center-to-center distance of 300 µm between two adjacent ones. The EO pump chip was produced after two wafers were aligned and thermally bonded.

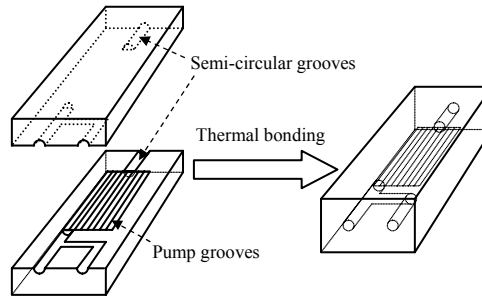

Figure 1. Schematic process to fabricate the pump part of an EO-driven pipettor.

Assembly of an EO-driven pipettor. Referring to Figure 2a, capillaries 1-3, having an i.d. of 150 µm, an o.d. of 375 µm, and lengths of 10 cm, 2 cm and 12 cm respectively, were inserted into the round channels of the pump chip, and secured in positions with silicone adhesive. The pipet-tip was another piece of capillary (~12-cm-long, 375-µm-o.d. and 100-µm-i.d.) with a taped tip (~1-cm-long). The taped tip was formed by pulling the capillary under a butane torch. At the very end of the tip the capillary had an o.d. of ~7 µm and an i.d. of ~5 µm. The pipet-tip was coupled with capillary 3 through a segment of tygon tubing. The polyacrylamide interface was incorporated between capillaries 2 and 4 as depicted in Figure 2b. Capillary 4 had an i.d. of 150 µm, an o.d. of 375 µm, and lengths of 5 cm,

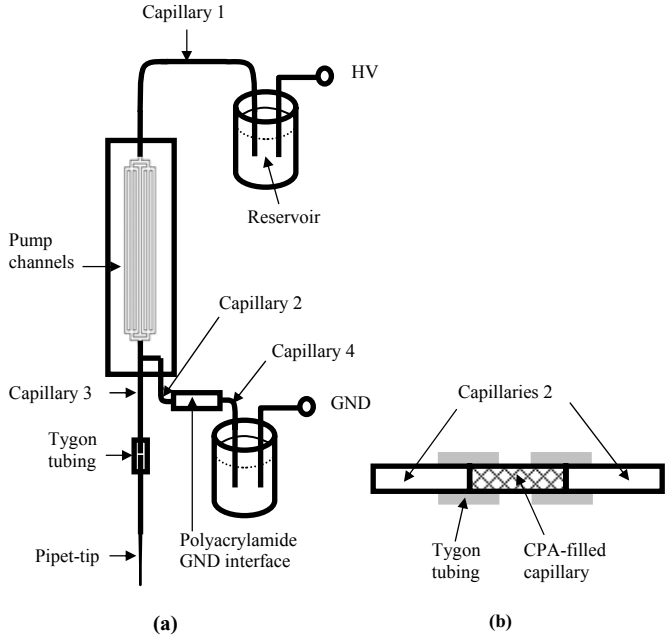

Figure 2. Schematic diagram of an EO-driven pipettor.
(a) Schematic configuration of an EO-driven pipettor, and (b) detailed structure of a polyacrylamide grounding interface. HV—high voltage, GND—ground/grounding, and CPA—cross-linked polyacrylamide.

but its i.d. can be increased and its length can be decreased in the next version of pipettors. During pipetting, a high voltage was applied to the free ends of capillaries 1 and 4 via two reservoirs containing 50 mM sodium tetraborate.

Pipettor operations. The pipet-tip was pre-filled with 50 mM sodium tetraborate by pumping the pump solution to the tip. Two operation modes were tested. Under operation mode A, a negative HV (e.g. -3.5 kV) was applied to capillary 1 for an extended period of time to aspirate ~500 nL of sample solution into the pipet-tip. The tip was rinsed by dipping it into and lifting it from a vial containing DI water for three times. Then, various aliquots of the solution were dispensed to different containers. Under operation mode B, a negative HV was applied to the pipettor temporarily to aspirate a desired amount of solution. The tip was rinsed by dipping it into and lifting it from a vial containing DI water for three times. The polarity of the HV was then switched (often the magnitude did not change) to dispense the solution. Normally, a dispense time of ~10% longer than the pipetting time was used to enable all aspirated solutions to be dispensed.

3. RESULTS AND DISCUSSION

Figure 3 presents an excellent linear relationship (r^2=0.999) between pipetted volume and pipetting time. It should be pointed out that all linear coefficients were within 0.999-1.000 when the total voltage applied to the pipettor was less than 3.5 kV. At higher voltages, the linear coefficient decreased progressively with an increasing voltage due to the growing Joule heating. The effect of Joule heating was further evidenced by the data presented in Figure 4. From 20-4000 V, the pipetted volume and the applied voltage had a reasonable good linear relationship (r^2=0.997), but an exponential curve clearly showed up as the voltage continuously increased.

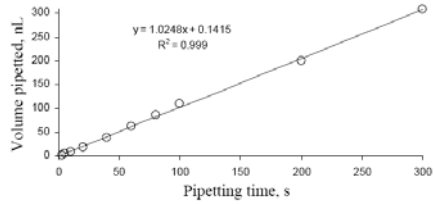

Figure 3. Pipetted volume vs pipetting time. The total applied voltage was 3.5 kV.

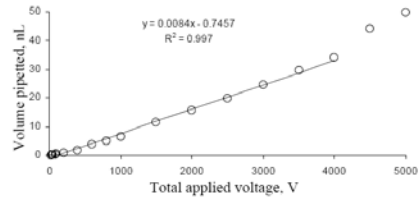

Figure 4. Pipetted volume vs total applied voltage. The pipetting time: 30 s.

4. CONCLUSIONS

We have for the first time developed an EO-driven nanopipettor, and demonstrated its feasibility to pipet nL-pL liquids with good accuracies and reproducibilities. An important specification of an EO-driven pipettor is its wide volume range of a single pipettor, *i.e.* ~100 pL to ~300 nL for the pipettor described in this paper. Because the major body of the pipettor is composed of a microfabricated chip and the associated capillaries, these pipettors can be highly parallelized with a common HV power supply. Combined with computer control, such tool can have great impact on high-throughput assays.

REFERENCES

1. Hanani, M. *J. Basic Clin Physiol Pharmacol.* **1997**, 8, 57-71.
2. McCaman, R. E.; McKenna, D.G.; Ono, J. K. *Brain Res.* **1977**, 136, 141-147.
3. Kalia, Y. N.; Naik, A.; Garrison, J.; Guy, R.H. *Adv. Drug Deliv. Rev.* **2004**, 56, 619–658.
4. Pikal, M. J. *Pharm. Res.* **1990**, 7, 118–126.
5. http://www.harvardapparatus.com; http://www.eppendorf.com
6. http://www.vyteris.com
7. http://www.rainin.com/pdf/ab15.pdf

A MULTILAYER SU-8 PROCESS FOR HIGH-DENSITY, STACKED MICROFLUIDIC SYSTEMS

C.A. Mousoulis and D.P. Papageorgiou
Northeastern University, USA

ABSTRACT

This paper describes a multi-layer SU-8 fabrication process with independent patterning and thickness selection for each structural layer. The selection is achieved through the use of a metal reflective coating between layers to optically decouple the top layer with the underlying layers. The method used to deposit the metal provides an additional degree of freedom in the formation of the stacked system by selecting if a thin layer of SU-8 will remain beneath the metal after development. This technique allows for high-density microfluidic systems with components such as microchannels, microvalves, micropumps and other microfluidic structures to be integrated together in three dimensions.

Keywords: SU-8, multi-layer, microfluidic, microchannels

1. INTRODUCTION

The fabrication of multi-layer microfluidic systems using CMOS-compatible processes has seen many approaches [1-3]. All are aimed at incorporating microfluidic structures and sensing elements to allow for in-vitro measurements and combine interconnected channels with reaction and mixing chambers, valves, optical, thermal and electric field sensors and actuators. Although the applications of these devices are of great importance, the numerous obstacles that occur during fabrication impede the production of sophisticated devices.

A material used with increasing popularity for the fabrication of embedded channels and microfluidic networks is the negative tone photopolymer SU-8. Some of the advantages of this permanent epoxy photoresist are its chemical inertness and biocompatibility, the near vertical sidewalls with high aspect ratio, and the transparency of polymerized SU-8 that permits for optical interrogation.

Reported multilayer SU-8 processes [1] only permit stacked features either on top of an already exposed feature or the use of substantially thinner SU-8 higher in the stack. Others require non standard fabrication tools [2] or a variety of photoresists [3]. The suggested method relies on standard fabrication tools and provides the option of selective interconnection between consecutive layers.

2. FABRICATION

Microfluidic structures are formed through the successive deposition and exposure of SU-8 2075 (MicroChem Corp) and deposition of a reflective metal layer. Since sputtering is used for the metal deposition, the UV light generated during the sputtering process is absorbed by the SU-8 and results in surface cross-linking. Although this effect can be used to isolate microchannels in adjacent layers, vias must be opened through the thin cross-linked layer for the developer to dissolve the undesired SU-8. These vias are dry etched

978-0-9798064-0-7/μTAS2007/$20©2007CBMS

using O_2/SF_6 assisted plasma [4]. The fabrication process is similar to the mask process by Guerin et al [5], except a SF_6/O_2 plasma is used for the selective interconnection of the microfluidic channels in adjacent layers. First, a layer of SU-8 2075 is spun-on, prebaked, and exposed (Figure 1a) using a filter to remove wavelengths below 350nm during exposure which eliminates the "T-topping" phenomenon and leads to vertical profiles and uniform polymerization [6]. Then, an aluminum layer with a thickness of 50nm is sputtered (causing a superficial polymerization of the underlying unexposed SU-8) (Figure 1b). Subsequently, a second layer of SU-8 is spun-on, prebaked, and exposed (Figure 1c). The top layer of photoresist is covered by a sputtered aluminum layer which is then patterned (Figure 1d). An O_2/SF_6 plasma is used to etch the superficial crosslinked layer of SU-8. Next, the unexposed SU-8 is developed (Figure 1e), and the aluminum layer is wet etched. Finally, after etching the revealed layers of crosslinked photoresist, the sample is dipped again in the developer and the last step is the removal of the remaining aluminum (Figure 1f).

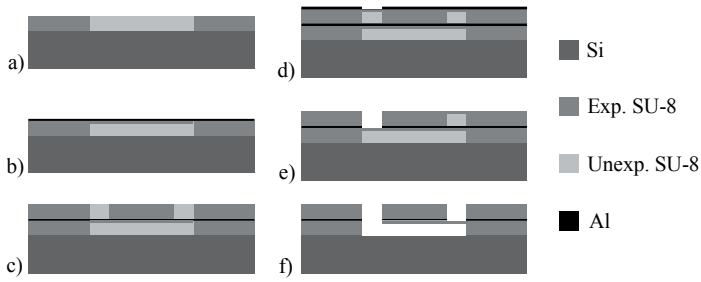

Figure 1. Fabrication process for selective interconnection of the microchannels.

Figure 2 shows images obtained by a Zygo 3D optical profiler of a fabricated double layer microchannel structure. The optical image (Figure 2, left) shows the overall structure which consists of a microfluidic chamber with channels running left and right in the bottom layer and a vertically aligned microchannel in the top layer. The corresponding surface map and profile (Figure 2, middle and right, respectively) highlight the fact that the adjacent layers of SU-8 are fluidically isolated from one another except where the vias have been formed.

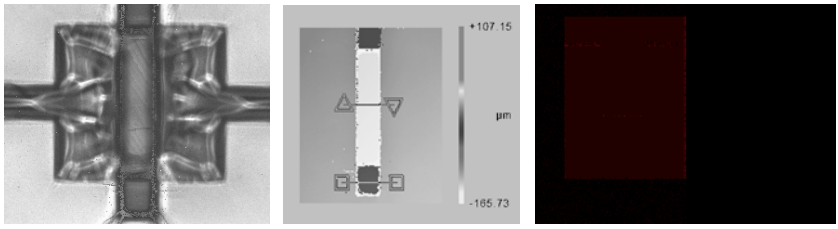

Figure 2. A three-dimensional microfluidic structure with the corresponding surface map and profile. The optical image (left) shows the chamber in the first layer with a connected microchannel running horizontally in the same layer, and a microchannel above running vertically. The surface map (middle) and profile (right) verify that the two layers are only connected at the vias.

Figure 3 shows a variety of structures which can be created using this process, and demonstrates the effectiveness of the reflective layer in preventing exposure of underlying layers. In Figure 3a, two layers of 75µm have been independently defined showing two surface channels patterned on top of two buried channels. Figure 3b shows a buried chamber with a connected channel in the depth, created in a two-layer process. The masking metal can also be seen and is an artifact of the cleaving of the devices.

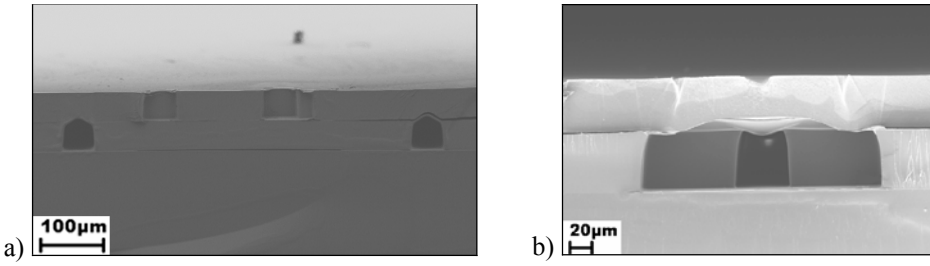

Figure 3. SEM pictures of microfluidic structures.

3. CONCLUSION

The demonstrated multilayer SU-8 process describes a method of forming 3-D structures that overcomes previous fabrication difficulties, like the superficial polymerization of the SU-8 layers during metal deposition steps. In addition, it is realized with the use of common fabrication tools, as opposed to other complex methods reported [1-3].

REFERENCES

[1] M. Agirregabiria, F. J. Blanco, J. Berganzo, M. T. Arroyo, A. Fullaondo, K. Mayora and J.M. Ruano-Lopez, *Fabrication of SU-8 multilayer microstructures based on successive CMOS compatible adhesive bonding and releasing steps*, Lab Chip., Vol. 5, pp. 545-552, (2005).

[2] H. Yu, O. Balogun, B. Li, T. W. Murray and X. Zhang, *Fabrication of three dimensional microstructures based on singled-layered SU-8 for lab-on-chip applications*, Sens. and Act. A, Vol. 127, pp. 228-234, (2006).

[3] P. Yao, G. J. Schneider and D. W. Prather, *Three-Dimensional Lithographical Fabrication of Microchannels*, J. Microelectromech. Syst., Vol. 14, pp. 799-805, (2005).

[4] G. Hong, A. S. Holmes and M. E. Heaton, *SU8 resist plasma etching and its optimisation*, Symp. on Design, Test, Integr. and Packag. of MEMS/MOEMS, pp. 268-271, (2003).

[5] L. J. Guerin, M. Bossel, M. Demierre, S. Calmes and Ph. Renaud, *Simple and low cost fabrication of embedded micro-channels by using a new thick-film photoplastic*, Proc. of Int. Conf. on Solid-State Sens. and Act. (Transducers 1997), Chicago, pp. 1419-1421, (1997).

[6] S. J. Lee, W. Shi, P. Maciel and S. W. Cha, *Top-edge profile control for SU-8 structural photoresist*, Proc. of 15th Univ./Gov./Ind. Microelec. Symp., pp 389-390, (2003).

AN OPTICALLY DRIVEN MICROPUMP USING A SPINNING DISK ROTOR

Shoji Maruo[1, 2] and Hiroyuki Inoue[1]
[1]*Yokohama National University, JAPAN*
[2]*PRESTO Japan Science and Technology Agency, JAPAN*

ABSTRACT

An optically driven micropump using viscous drag exerted on a spinning disk microrotor was developed. The disk microrotor (diameter: 10 μm), which has three columns as targets for the optical trap, is confined to a U-shaped microchannel. To pump fluid, the disk microrotor is rotated by a time-shared optical trapping technique. The flow field inside the U-shaped microchannel was analyzed using finite element method (FEM) based on the Navier-Stokes equation. The optimized micropump was fabricated using a two-photon microfabrication technique. The flow rate of the micropump agreed with simulation result obtained by FEM analysis.

Keywords: Optically driven micropump, two-photon microfabrication

1. INTRODUCTION

Lab-on-a-chip devices have attracted considerable attention for their ability to process reduced sample and reagent volumes, improving the throughput and efficiency of analysis and synthesis. Microfluidic devices such as micropumps and microvalves are set to play a major part in the further miniaturization and integration of lab-on-a-chip devices. However, since most previously developed micropumps are positive-displacement types using deformable membranes, it is difficult to reduce their size to below 100 μm. In addition, the pulsation of the positive-displacement pumps is harmful to high-precision chemical and biochemical process in the order of pL/min. These drawbacks make these pumps unsuitable for totally integrated microfluidic circuits.

There has been a great deal of interest in more promising methods of miniaturizing microfluidic devices to micrometer range by employing optically driven microfluidic elements, including micropumps, microvalves microstirrers, and a particle sorter [1-3]. In this paper, we propose a novel type of optically driven micropump using a spinning disk rotor. The optically driven micropumps can provide continuous ultralow flow on the order of 1pL/min without any pulsation, unlike other micropumps such as diaphragm pumps.

2. OPTICALLY DRIVEN MICROPUMP USING A SPINNING DISK ROTOR

Figure 1 shows a schematic of the micropump driven by the time-shared optical trapping technique. A disk microrotor, which has three columns as targets for the optical trap, is confined to a U-shaped microchannel. A three-point optical trap using a single laser beam enables the disk microrotor to be rotated without a shaft. The laser beam, focused on the right and left columns, is scanned circularly, while the central laser beam is focused on the center column. Since the optically trapped center column acts as the axis of rotation, the disk microrotor is stably rotated without a shaft. The rotation of the disk microrotor induces both a pressure gradient and flow along the curved channel. Although the pressure gradient is opposite to the desired flow direction, the viscous flow surrounding the rotor surmounts

978-0-9798064-0-7/μTAS2007/$20©2007CBMS

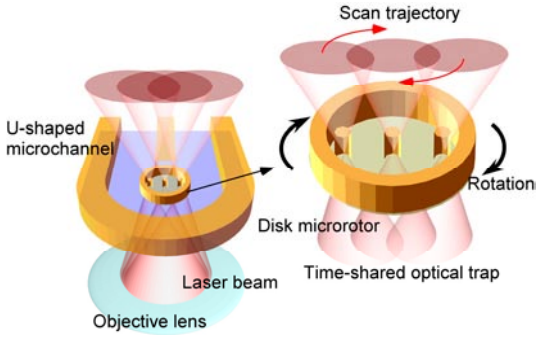

Fig. 1. Optically driven micropump using a spinning disk rotor

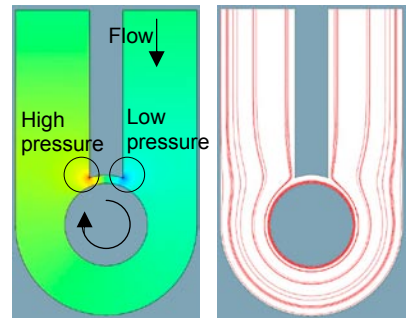

(a) (b)

Fig. 2. (a)Pressure field and (b)streamline of the optimized micropump

the resistance of the backpressure owing to the large viscous drag around the side of the rotor. In this micropump, the rotating disk microrotor provides continuous flow without pulsation. Steady continuous flow such as this is useful for continuous-flow chemical processes and the gentle sorting of biological samples.

3. SIMULATIONS AND EXPERIMENTS

To optimize the design of the micropump, the flow field inside the U-shaped microchannel was analyzed using the two-dimensional (2D) finite element method (FEM) based on the Navier-Stokes equation. In the simulation, the diameter of the disk microrotor was 10 μm. The pressure at the inlet and outlet of the linear channel was 0 Pa. To analyze the flow generated by rotating the disk microrotor, velocity was applied to the fluid around the disk rotor. The physical parameters such as viscosity agree with the parameters of glycol ether ester that was used in the following experiments.

The dependence of the maximum flow velocity of the laminar flow on the channel width was examined. The results indicated that a microchannel of approximately 9 μm width is suitable for a micropump with a 10 μm-diameter microrotor. Figure 2 shows the pressure field and streamlines of the micropump. By the optimization of the channel width, fluid can be transported in the forward direction owing to sufficient viscous force against the backpressure caused by the rotation of the rotor. At the linear regions of the U-shaped microchannels, a steady laminar flow is generated with a pressure gradient in the order of 10 mPa. This continuous laminar flow without pulsation is useful for continuous-flow chemical analysis and synthesis and gentle sorting of biological samples such as cells and proteins.

We fabricated a single-disk viscous micropump by means of two-photon microfabrication [4]. In this process, a femtosecond laser beam is focused and scanned inside a photopolymer to produce 3D microstructures. Both the microrotor (diameter: 10 μm) with three columns and the U-shaped microchannel were fabricated using the two-photon microfabrication system that we have previously developed. We demonstrated that the single-disk micropump can be used for pumping fluid and transportation of microobjects. Figure 3 shows a sequence of images taken at 2-s intervals showing the tracer particle being pumped through the channel with the disk microrotor being rotated at a speed

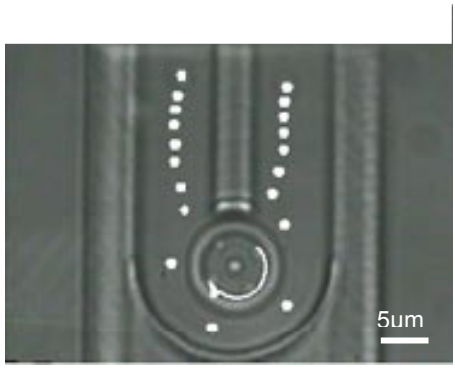

Fig. 3. Fluid transport in the optically driven micropump using a spinning disk rotor

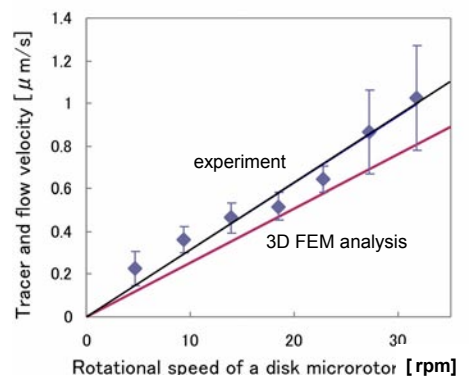

Fig. 4. Flow rate vs rotation speed of a spinning disk rotor

of 27 rpm. The tracer particle was entrained with the high flow velocity. The trajectory of the tracer particle movement was similar to the streamlines obtained by the FEM simulation shown in Fig. 2 (b). The flow velocity around the microrotor is higher than that of the linear microchannel, since the viscous drag around the microrotor is dominant.

Figure 4 shows the dependence of the flow velocity on the rotational speed of the microrotor. The flow velocity is proportional to the rotational speed of the microrotor. The measured flow velocity of the tracer particle agreed with the average flow velocity obtained by three-dimensional (3D) FEM analysis.

4. CONCLUSIONS

We have proposed a viscous micropump that consists of a spinning microdisk and a U-shaped microchannel. The single-disk micropump has numerous advantages, including simplicity, easy miniaturization, readily controlled flow velocity, production of continuous flow, and damage-free transportation of biological samples such as cells and proteins. The single-disk viscous micropump has potential for extensive use in lab-on-a-chip devices where steady continuous flows and damage-free transportation of biological samples are required.

ACKNOWLEDGEMENTS

This research was supported by a research grant from PRESTO, the Japan Science and Technology Agency, and a research grant from the Japan Society for the Promotion of Science (Exploratory Research and Scientific Research in Priority Areas: System Cell Engineering by Multi-scale Manipulation).

REFERENCES

[1] Alex Terray, et al., Science **296**, 1841 (2002).
[2] J. Leach, et al., Lab Chip **6**, 735 (2006).
[3] S. Maruo, et al. Appl. Phys. Lett. **89**, 144101 (2006).
[4] S. Maruo, Opt. Lett. **22**, 132 (1997).

ELECTRICALLY-ACTUATED PDMS MICROVALVES AND PUMPS FOR VLSI MICROFLUIDICS

Meng-Ping Chang[1], Tushar Bansal[2], and Michel M. Maharbiz[2]

[1]Department of Mechanical Engineering, [2]Department of Electrical Engineering and Computer Science, University of Michigan, USA

ABSTRACT

We present a polydimethylsiloxane (PDMS)-metal pump/valve technology that can actuate in liquid (water and oil) and air. The devices operate by AC electrostatic gap-closing (4-5 MHz 15-20 V) of a modified PDMS microchannel. The presented pump and valve process is compatible with standard PDMS microfluidics [1] and devices have actuation voltages low enough to be driven by a standard USB-interface microcontroller and IC amplifier, which makes possible the design of very-large-scale integration (VLSI) [6] microfluidics which requires no external pneumatic connections to operate.

Keywords: VLSI-microfluidics, polydimethylsiloxane, low power, micropump/valve

1. INTRODUCTION

Micropumps and valves are essential elements in Micro Total Analysis Systems (Micro-TAS); among various types pneumatic polymer-based pumps are the most popular found in most microfluidic systems [1, 2, and 3]. The electrostatic PDMS micropumps and valves we developed (Figure 1) can actuate water, oil, and air at low voltage. This makes possible the design of fluidic systems with many actuated components each driven by digitally synthesized control signals. Moreover, since the actuation is based on MHz frequency electrostatics, the devices: a) are scalable into the nanofluidic regime, and b) can be driven by conventional CMOS electronics.

2. THEORY

Electrostatic actuation is widely used in most dry MEMS devices. Using an AC driving signal in MHz frequency range it is applicable in wet environment because a) screening by electrical double layer is significantly reduced and b) electrolysis is avoided. Considering a membrane with a residual stress σ_R, the pull-in voltage can be expressed as [4, 5]:

$$V_{PI} = \sqrt{\frac{8k\left(g + t_{ox}\varepsilon_L/\varepsilon_{ox}\right)}{27\varepsilon_0\varepsilon_L A}\cdot\left(1+\frac{2\left(1-\nu^2\right)\sigma_R A}{9Et^2}\right)} \qquad (1)$$

where: k = spring constant; t_{ox} = oxide thickness; g = gap; ε_{ox}= oxide permittivity; A= capacitor area; ε_L = dielectric permittivity; ν = Poisson' ratio; E = Young's modulus, and t = membrane thickness. The calculated pull-in voltage of our device is about 16.6 volt.

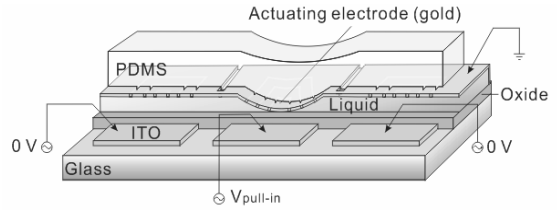

Figure 1. Conceptual View of the micropump

978-0-9798064-0-7/μTAS2007/$20©2007CBMS

3. EXPERIMENTAL

A. *Fabrication*

Figure 2 shows the fabrication flow of a basic valve. Indium tin oxide (ITO) electrodes (1000Å) were patterned and insulated by 4000Å PECVD oxide [2]. Oxide was etched to expose the contact pads. Photoresist (AZ-9260, 10 μm) was used as microchannel mold for subsequent metal and PDMS deposition. The metal layer was composed of Cr/Au/Cr (150/5000/150 Å) and the PDMS was Dow Corning WL-5351. The size of this PDMS-metal membrane was 300 μm by 300 μm. The total thickness of the PDMS-metal membrane was 7.2 μm. The embedded metal flexure formed the top capacitive plate and the ITO electrode formed the other.

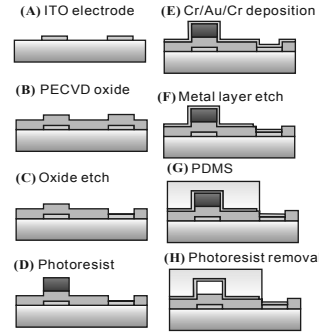

Figure 2. Fabrication

B. *Experiment Setup*

The circuit diagram is shown in Fig. 3. A programmable USB interfaced micro controller (BS1USB, Parallax) was used to control and provide a MHz signal (1.5 volt peak-to-peak) for actuation. This signal wass two-stage differentially amplified to 35-40 volt peak-to-peak by IC amplifiers (AD815), and switched by photovoltaic AC relays. All fluidic measurement was made with fluorescent microscopy (Figure 4). Flowrate was measured by particle imaging method on an inverted fluorescent microscope (Nikon TE2000-U). Pressure sensors (40PC150, Honeywell) were connected both upstream and downstream of the micro valve or pump to measure pressure difference across the devices.

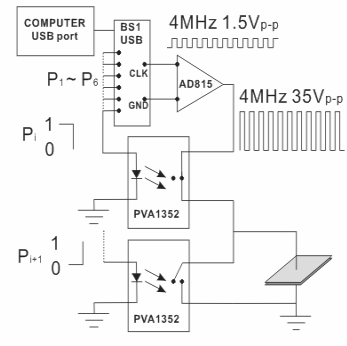

Figure 3. Circuit Diagram. Signals of P_i and P_{i+1} from BS1 are always out of phase.

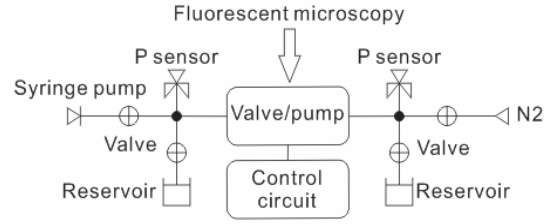

Figure 4. Fluidic measurement apparatus. A syringe pump is connected at the upstream to flush/fill the system prior to any test. The flow velocity is measured by detecting the displacement of 0.5 μm microspheres (PolySciences). A nitrogen bottle is used to provide backpressure for flowrate-pressure characterization.

4. RESULTS AND DISCUSSION

Figure 5a, b shows the basic valve operation. As the valve closed, the PDMS-metal membrane collapsed and the microspheres were either expelled or trapped by the valve. Expelled microspheres accumulated at the valve boundary. Pump and valve performance compares well with previous technologies [1, 3]. Our current devices can hold a 6 psi (41.37 kPa) pressure (Figure 5c). Figure 6a shows a three-valve peristaltic pump. Maximum pumping rate is 4.44 valve volumes/min (1 nL/min) at 1.6 Hz (Figure 6b), with an actuation voltage of 35 volt peak-to-peak at 5 MHz. After this critical frequency point

the flowrate decreases as pumping frequency increases. The peak current measured was less than 1 μA.

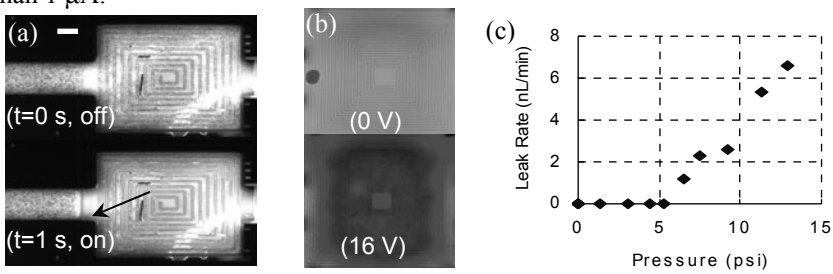

Figure 5. Valving characterization. (a) Inverted microscopy of open and closed valve. The valve was off at t = 0 s. Microspheres flow freely. The valve was actuated at t = 1 s. The PDMS-metal roof collapsed and the microspheres were trapped under the PDMS-metal membrane. When closed, the microspheres outside the valve chamber accumulated at the entrance of the valve chamber (arrows.) Scale bar, 20 μm. (b) Fluorescent image of fluorophore-filled open and closed valve showing valve deflection. (c) Leak rate vs. pressure. The valve is effective till the pressure is above 6 psi (41.37 kPa).

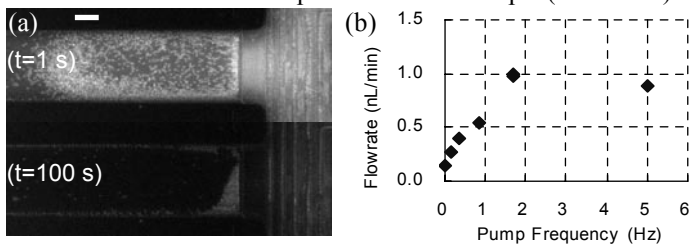

Figure 6. Pumping characterization. (a) Time frame pictures of free-flow pumping. Microspheres (diameter = 0.5 μm) were used for flow indication and flowrate measurement. The pump was activated (pump frequency = 1.6Hz) at t = 1 s. Scale bar, 20 μm. (b) Free-flow flowrate vs. pumping frequencies. The maximum flowrate (1nL/min) was achieved at 1.6Hz actuation.

5. CONCLUSIONS

A low-voltage electrostatic microvalves and pumps were designed and tested. These devices are compatible with PDMS-based microfluidics and complicated VLSI microfluidics.

ACKNOWLEDGEMENTS

The authors would like to thank the staff of Michigan Nanofabrication Facility (MNF). This work was funded by Center for Wireless Integrated Microsystems (WIMS).

REFERENCES

[1] M. A. Unger et al., Science, 2000, 288, 113-116.
[2] T. Bansal et al., Lab Chip, 2007, 7, 164-166.
[3] J. Xie et al., Lab Chip, 2004, 4, 495-501.
[4] B. Legrand et al., Appl. Phys. Lett., 2006, 88.
[5] P.-C. Hsu et al., Proc. MEMS 1998, 580-585
[6] T. Thorsen et al., Science, 2002, 298, 580-582

HIGH-FORCE LIQUID-GAP ELECTROSTATIC HYDRAULIC MICRO ACTUATORS

Hanseup Kim, Seunghyun Lee, and Khalil Najafi

Center for Wireless Integrated MicroSystems (WIMS ERC), University of Michigan, USA

ABSTRACT

This paper reports a capacitive electrostatic actuator that produces higher displacement (in and out of plane) and larger force than typical electrostatic actuators by utilizing a non-conducting liquid as its dielectric material. This new class of actuators utilizes the liquid dielectric for hydraulic amplification and force transfer. The liquid electrostatic actuator consists of two chambers, each forming a parallel-plate capacitor, filled with a non-conducting incompressible liquid. One chamber is compressed by pulling down a flexible membrane using electrostatic actuation, thus forcing the liquid under it to transfer into the other chamber. Such movement causes the other chamber's membrane to expand out of plane. Fabricated liquid-gap actuators with DI water as the working liquid have produced out-of-plane deflection of 36.7 and 16 μm from 2×2 and 1×1 mm^2 chambers, respectively, using 320V actuation voltage.

Keywords: Electrostatic actuation, hydraulic amplification, liquid gap actuator.

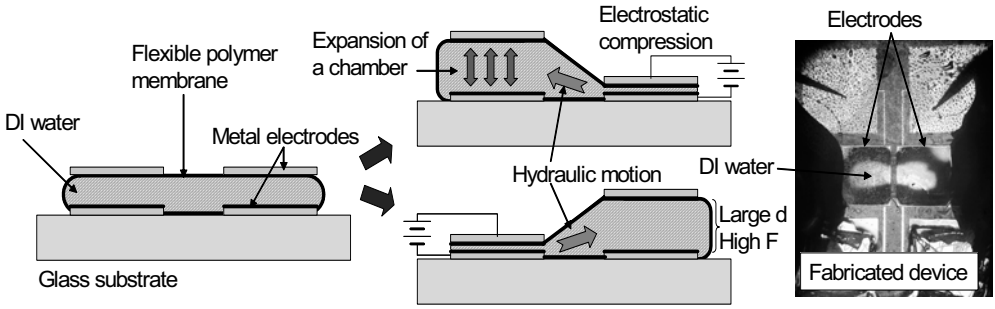

Figure 1. (Left and Center) Operation principle of a hydraulically-amplified electrostatic actuator and (Right) the fabricated actuator with encapsulated DI water inside.

1. INTRODUCTION

Electrostatic micro actuators have been widely used for numerous applications, such as gas micropumps [1], microvalves [2], and optical switching [3], because of their simple structure, high-speed operation, and compatibility with thin-film fabrication. However, typical air-gap electrostatic actuators produce limited force and deflection in the micro domain because the air gap distance, which determines the maximum deflection, cannot be too large to obtain sufficient mechanical force. Hydraulic actuators, on the other hand, have been used in numerous macro-scale applications and utilize incompressible liquids for hydraulic amplification and force transfer. Although electrostatic actuation in aqueous environments has been investigated [4], no micro devices that utilize non-conducting liquid for electrostatic actuation and hydraulic force transfer have been reported yet.

978-0-9798064-0-7/μTAS2007/$20©2007CBMS

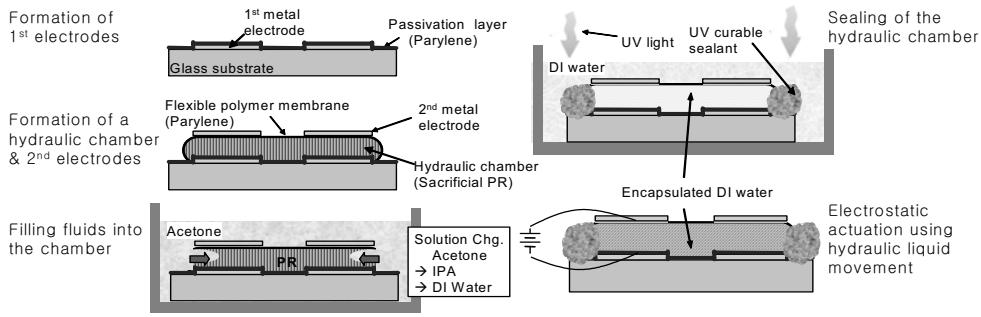

Figure 2. Fabrication process flow.

2. OPERATION

The liquid-gap electrostatic actuator consists of two liquid-filled chambers that are encapsulated together and connected through a fluid channel (Fig. 1). Each chamber has two metal electrodes separated by a sacrifical photoresist that is replaced by water. The top electrode is formed on a flexible polymer membrane that moves to the other during electrostatic actuation. The existence of the liquid in the gap serves two functions: 1) the large liquid dielectric constant produces a larger electrostatic force than is available in air-gap electrostatic actuators; and 2) the liquid acts as the hydraulic amplficiation fluid that transfers the large electrostatic force from one chamber to the other. The liquid-gap actuator can achieve larger electrostatic force using a larger relative permittivity of water (ε=80) than that of air (ε=1). The high electrostatic force is transferred through the confined liquid to the other side's chamber. The liquid-gap actuator achieves a large out-of-plane distance, since the maximum distance is determined by the transferred liquid volume instead of the gap between electrodes. The actuator also produces higher force by differentiating each chamber area. The resultant force from each chamber is determined by the area ratio between the two chambers, since the pressure in liquid is uniform and thus the actuation force is proportional to the areas of the chambers.

3. FABRICATION

A prototype liquid-gap electrostatic actuator has been fabricated on a glass wafer using surface micromachining and liquid encapsulation (Fig. 2). The first actuation electrode is patterned on a glass wafer by evaporating Cr/Au (300/4000Å), and then insulated with Parylene (0.5μm). Next, a sacrificial photoresist (6.5μm) is patterned to define the actuator chambers. A 2nd Parylene (3.5μm) layer is deposited to form a flexible moving membrane that encapsulates the chambers. Another metal layer is deposited and patterned to form the 2nd electrode on top of the flexible membrane. The whole device is then immersed into a series of liquids (Acetone, IPA, and DI water) to dissolve the sacrificial layer, release the actuation chambers, and fill the chambers with DI-water. Finally, the chamber is sealed in water using UV curable sealant, thus preventing trapping of air bubbles inside the chamber.

4. RESULTS AND DISCUSSION

Figure 3 shows the hydraulic movement of the fabricated actuators showing repeatable capacitance variations as one chamber collapses and the other expands (top-left). At each cycle one of the two chambers is compressed, and the corresponding capacitance changes as the liquid moves in or out of the chamber. Figure 3 (bottom-left) shows the capacitance

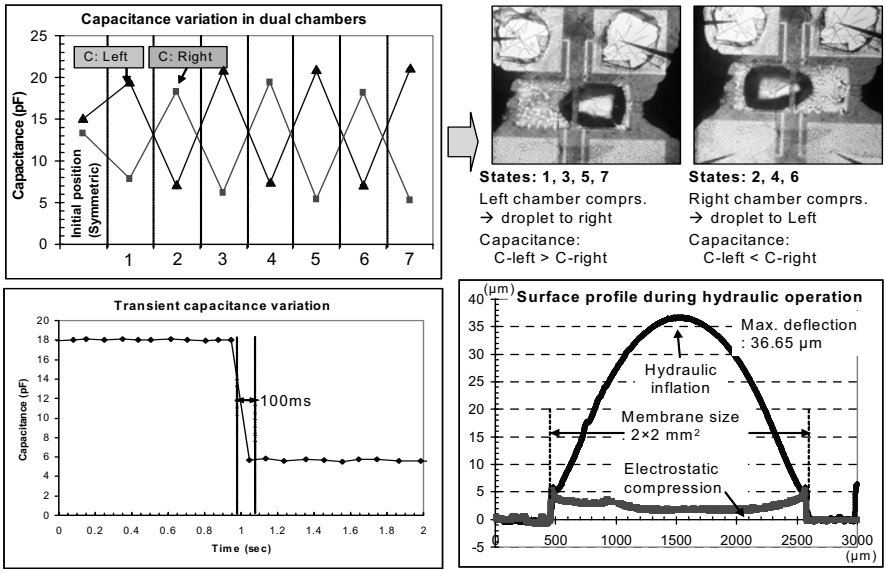

Figure 3. (Top-Left) Measured capacitance variation during bi-stable hydraulic electrostatic actuation and (Top-Right) pictures of the hydraulic actuator in motion. (Bottom-Left) Measured transient capacitance change using the LabView and HP4208 LCR meter: the hydraulic motion of a water droplet from one chamber (1×1 mm^2) to the other chamber of the same size takes place less than 100 ms. (Bottom-Right) Measured deflection and surface profile of a 2×2 mm^2 membrane during hydraulic inflation and electrostatic compression periods, respectively, using the Dektak surface profiler.

variation of one chamber that is electrostatically compressed, indicating faster than 100ms response time (limited by our measurement system). Figure 3 (bottom-right) shows the measured deflection and compression of a 2×2mm^2 membrane by hydraulic amplification and electrostatic actuation, respectively. The measured out-of-plane deflection was 36.7μm at an operation voltage of 320V.

5. CONCLUSIONS

We have demonstrated a liquid-gap electrostatic actuator where the hydraulic motion of a liquid medium amplifies the force and displacement produced using a parallel plate actuator. The fabricated device with a pair of 2×2 mm^2 chambers produces a large out-of-plane deflection of 36.7μm at 320V.

ACKNOWLEDGEMENTS

This project is funded by the Engineering Research Centers Program of the National Science Foundation under Award Number EEC-9986866.

REFERENCES

[1] H. Kim, A.Astle, K. Najafi, L.P. Bernal, and P.D. Washabaugh, MEMS '07, Kobe, Japan, 2007.
[2] X. Yang et al., JMEMS, v13, n4, pp. 676-687, 2004.
[3] S. Kwon, G.L. Liu, K.H. Joeng, and L.P. Lee, Optical MEMS '03, pp. 10-11, 2003.
[4] T.L. Sounart, T.A. Michalske, K.R. Zavadil, JMEMS, v14, n1, pp. 125-133, 2005.
[5] D.C. Roberts et al., JMEMS, v12, n1, pp. 81-92, 2003.

LARGE PANEL HOT ROLLER EMBOSSING FOR POLYMERIC MICROFLUIDIC DEVICES

S.H. Ng[1], Z.F. Wang[1] and N.F. de Rooij[2]

[1]Singapore Institute of Manufacturing Technology, SINGAPORE and
[2]Institute of Microtechnology, University of Neuchatel, SWITZERLAND

ABSTRACT

We developed a technique called hot roller embossing for the generation of large panel polymer substrates with imprinted microchannels. Measurements conducted on 100 µm features showed that the lateral dimensions could be replicated to within 2% tolerance, while over 85% of mould depth was embossed. Feature sizes down to 50 µm and feature depths up to 30 µm had been achieved.

Keywords: microfluidics, embossing, roller, polymer

1. INTRODUCTION

Large panel substrates have applications in microfluidics such as high throughput screening and large scale integration [1]. Large panel polymer substrates with embossed microchannels can be generated by hot roller embossing. Hence, the technique is also suitable for the mass production of smaller microfluidic devices. Its continuous film approach is compatible with other reel-to-reel processes such as gravure or flexo printing for the creation of conductive elements, and lamination for sealing and encapsulation. Some researchers [2] had performed roller nanoimprint lithography on thin (< 1 µm) coatings of photoresists spun on substrates limited to a couple of centimetres. In our approach (see Fig. 1(a)), a thermoplastic sheet or film is passed between two rollers. The top roller is a heated rigid mould while the bottom roller is a support roller. Heat is supplied to the embossing interface through the mould and a clamping pressure is applied between the two rollers. As the substrate passes between the rollers, the mould features are embossed into it. Preheating of the substrate can also be conducted before it is fed into the rollers. The process is different from hot embossing [3] where the polymer substrate is given ample time to heat up and cooling is carried out with force still applied.

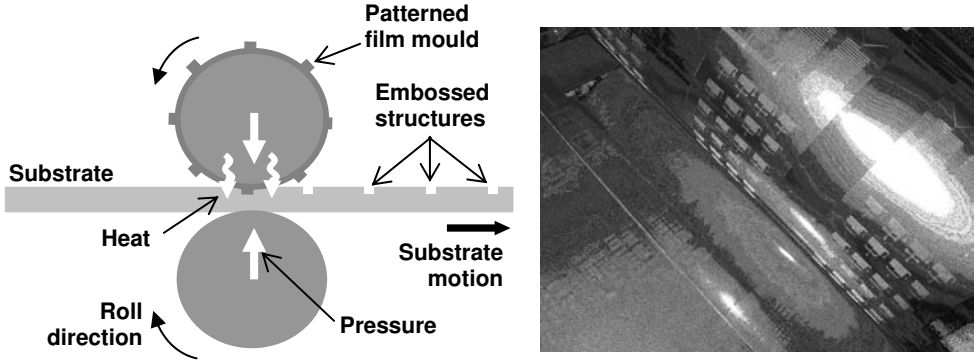

Figure 1. Hot roller embossing process.

978-0-9798064-0-7/µTAS2007/$20©2007CBMS

2. EXPERIMENTAL

A 50 µm thick nickel mould (see Fig. 1(b)) with raised micro features fabricated by electroplating, was wrapped around the top stainless steel roller that could be internally heated to 177 °C. A thermocouple connected to a temperature controller, was embedded into the roller. The machine had a web width of 45 cm and was capable of achieving a rolling speed of up to 6 m/min. Pneumatic pressure up to 6 bar provided the clamping force between the rollers. Polymethyl methacrylate (PMMA) sheets with 1.5 mm thickness were used in the experiments. The PMMA had a glass transition temperature of 105 °C measured from dynamic mechanical analysis.

3. RESULTS AND DISCUSSION

The primary parameters of the process are roller temperature, pressure and speed. As seen in Fig. 2, the embossed depths increased when pressure is increased or when the roller speed is reduced. In the graphs, the data points represent averages over 6 readings and the error bars are one standard deviation from the mean. The mould contained positive relief features occupying a small percentage of the mould base area. Hence, initial contact between the mould and the polymer happened at the top surface of the mould features. The mechanism is then similar to indentation where a higher contact pressure will result in a larger depth of penetration. The roller speed dictates the amount of time for transient heating of the surface of the polymer that contacts the mould. A slower speed will also allow a longer time for viscoplastic flow of the polymer material. As seen in Fig. 3, there is an optimal roller temperature (around 140 °C) in regards to the embossed depth. Below 110 °C, the embossed depth is less than 1 µm. Although the glass transition temperature of the PMMA is 105 °C, it is above 120 °C that the depth starts to increase rapidly peaking at ~140 °C. This is related to the pressure applied and roller speed that determines the heating time of the polymer. An interesting phenomenon is seen above 140 °C where the depth starts to decrease. This is a result of the partial reflow of the polymer material that has been heated up to a more fluidic state, as the mould separates from it. Measurements conducted on 100 µm features show that the lateral dimensions can be replicated to within 2% tolerance, while over 85% of mould depth is embossed. Figure 4 shows 100 µm width raised lines on the mould in comparison to the corresponding embossed PMMA microchannels. Feature sizes down to 50 µm and feature depths up to 30 µm have also been achieved.

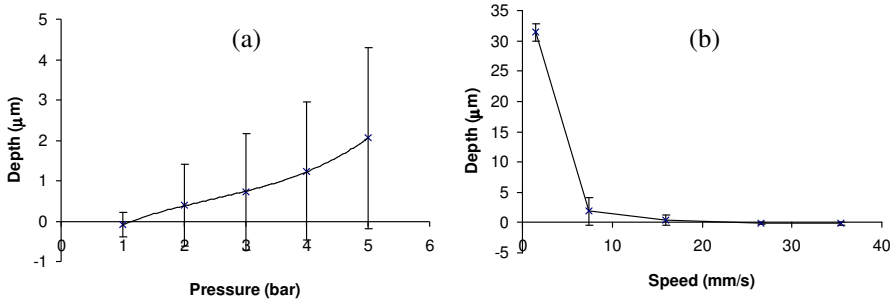

Figure 2. Pressure effect (a), Speed effect (b).

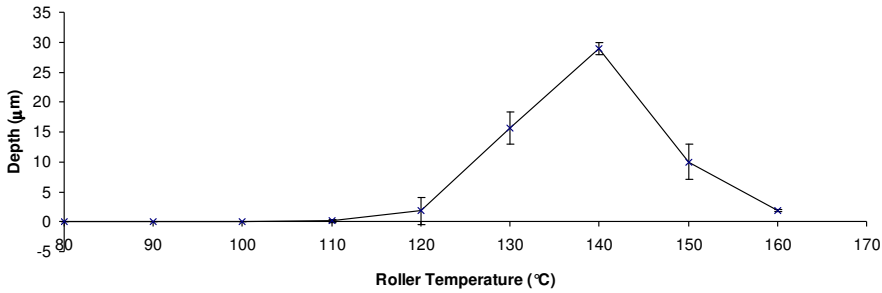

Figure 3. Temperature effect.

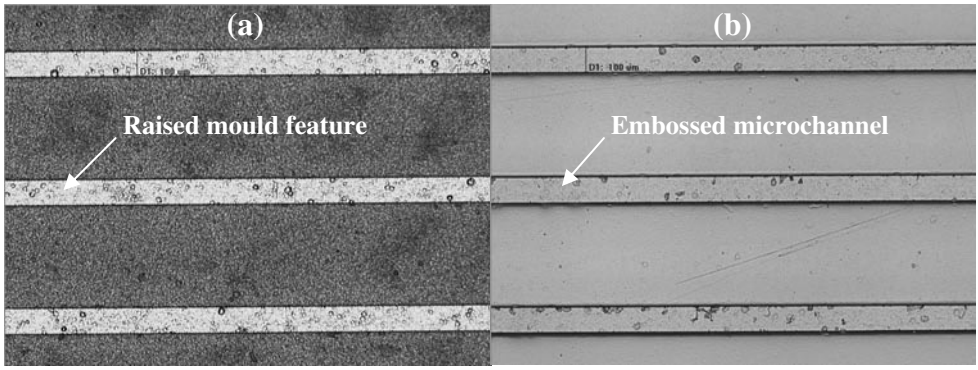

Figure 4. Mould features (a), Embossed PMMA (b).

4. CONCLUSIONS

Results showed that through control of process parameters, hot roller embossing could have the potential for mass production of large panel or continuous filmsubstrates and could be compatible with other reel to reel processes such as printing and lamination. In this research, feature size down to 50 µm and embossed depths of up to 30 µm had been demonstrated.

ACKNOWLEDGEMENT

This research is funded by the Agency for Science, Technology and Research (A*STAR), Singapore.

REFERENCES

[1] T. Thorsen, S. J. Maerkl, and S. R. Quake, *Microfluidic large-scale integration*, Science, 298, pp. 580, (2002).

[2] H. Tan, A. Gilbertson, and S. Y. Chou, *Roller nanoimprint lithography*, Journal of Vacuum Science Technology B, 16, pp. 3926, (1998).

[3] H. C. Scheer and H. Schulz, *A contribution to the flow behaviour of thin polymer films during hot embossing lithography*, Microelectronic Engineering, 56, pp. 311, (2001).

LOW POWER AND LOW COST TEMPERATURE AND FLUID CONTROL IN PDMS MICROFLUIDIC DEVICES

Robert Carlson and Deirdre Meldrum

Department of Electrical Engineering, University of Washington, Seattle, USA

ABSTRACT

On-chip control of fluids and temperature are critical capabilities for Micro Total Analysis Systems. Moreover, portable devices require pumps, valves, and heaters that operate within the constraints of a limited power budget. Using a combination of multilayer soft lithography and microscale Plasma Activated Templating (μ-PLAT)[1], we fabricate integrated electromechanical circuits in PDMS consisting of thermopneumatic valves for fluid control and thermocouples for *in situ* temperature measurement.

Keywords: μ-PLAT, thermopneumatic valve, peristaltic pump, thermocouple

1. INTRODUCTION

In this paper we demonstrate prototype integrated electromechanical circuits consisting of thermopneumatic actuators and a thermocouple array fabricated in silicone rubber (PDMS). Previous on-chip pumps in PDMS devices have required off-chip pneumatic connections for actuation and control or have utilized thermopneumatic[2] or electrostatic actuators[3] driven by electrodes fabricated using traditional microfabrication. The reliance of these devices on silicon components or off-chip pressure sources and solenoidal valves significantly impacts the cost of fabrication and use. We present devices that rely throughout on inexpensive materials and electronics.

2. THEORY

We exploit very simple physics – actuating a valve via thermal expansion of a working fluid (air, in this case), and thermovoltaic effects of material junctions – in integrated circuits containing as many as 8 total layers. While we have previously demonstrated temperature measurement with a resolution of ~.1 degree Celsius[1], the gold-graphite junctions presented here have a thermoelectric response too low (~3 mVolts per degree) for practical use and thus serve as placeholders in an engineering testbed. We have fabricated wires made of copper, palladium, and constantan (data not shown), which together with gold will eventually constitute the equivalent of K- and T-type thermocouples.

3. EXPERIMENTAL

Gold and graphite wires are fabricated as previously described[1]. Briefly, μ-PLAT is a process by which a stamp, usually PDMS cast from a photolithographically defined master, is used to protect a flat PDMS substrate during plasma exposure. The resulting chemical and physical patterns serve as a template for either deposition of powders or direct electroless deposition of metals.

We control heaters by a simple pull-down transistor circuit (not shown) and custom Labview code. The ~1 μm binder layer between the carbon thermocouple leads and the gold backbone consists of a 5:1 mixture of tertbutyl alcohol and uncured PDMS spun at 6000 rpm for 5 minutes and then cured at 60 degrees Celsius for 3 hours[4].

978-0-9798064-0-7/μTAS2007/$20©2007CBMS

4. RESULTS AND DISCUSSION

The circuit layers described here are plasma bonded to a multilayer PDMS structures containing a pressure vessel topped by a thin PDMS valve membrane and a sample channel. Driving the heater with 2-3 V causes the air inside the pressure vessel to expand, thereby closing the associated valve. We employ three such actuators as a peristaltic pump (Figure 1). Partial closure of valves at lower power, controlled via feedback from the thermocouples, should be useful for fluid metering.

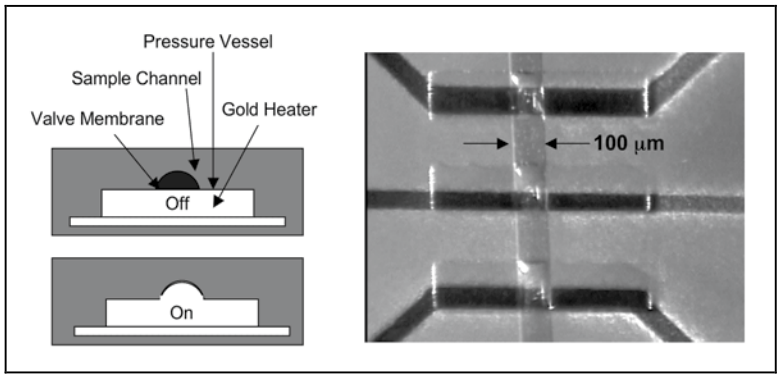

Figure 1. Left: side view schematic of pump design and function. Pump is surrounded by PDMS on all sides and fabricated on an inexpensive glass slide as a rigid substrate. Electrical connections presently consist of silver paint. Channel and pressure vessel are each approximately 16 μm high. Right: Video frame of all three valves caught closed during pumping of 10 μm fluorescent beads in food coloring; each heater consumes ~50 mW at a 100 ms duty cycle. Due to an error in printing the mask used to pattern the μ-PLAT stamp, the heater wires vary in width from the 50 μm design specification.

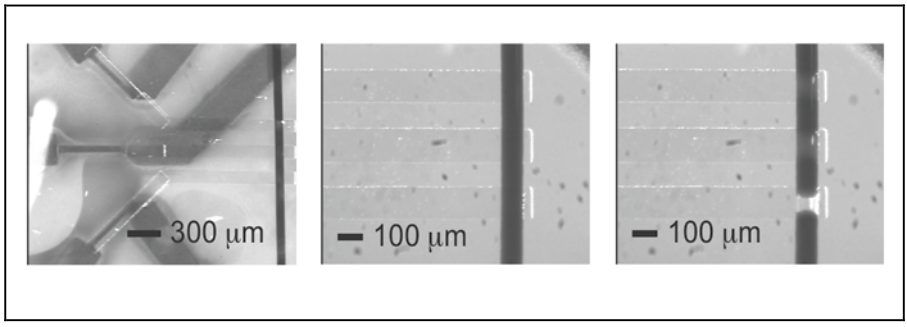

Figure 2. Second generation thermopneumatic pump showing a bellows later immediately above gold heaters, with a pneumatic relay layer above that runs beneath the sample channel. There is considerable thermal cross talk between the actuators; with only the bottom heater powered up, the top two actuators are both partially closed due to heating of their respective bellows.

Because the heaters are located immediately beneath the sample channel in the design shown in Figure 1, we observe an eventual heating of the sample by continuously active valves. Figure 2 demonstrates a complex, multilayer design that separates the heaters from

the sample by introducing a pneumatic relay layer between the bellows and the valve membrane. While an improvement over the original design, further work is required to optimize the dimensions of the bellows and pneumatic relays and also the spacing between the heaters; there is clear thermal crosstalk evident between heaters in this design that we hope to eliminate via by simply introducing a greater physical separation between them.

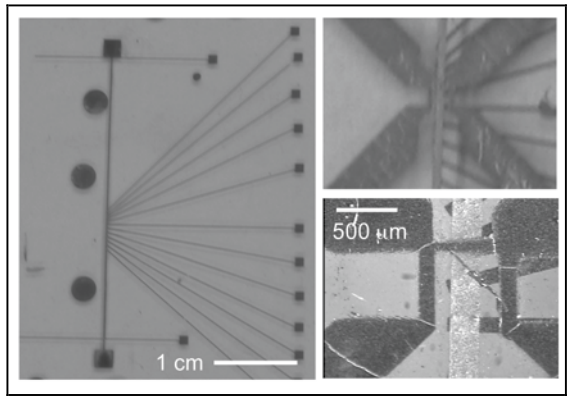

Figure 3. Left: Thermocouple array. Graphite electrodes are fabricated via μ-PLAT and then covered with a 1 μm binder layer of PDMS. A gold wire connecting the array with cold junctions is then produced via μ-PLAT and electroless deposition. Right top: A thermocouple array with a four-point gold heater electrolessly deposited over a 3 μm PDMS insulation layer, an 8-layer device. Right bottom: Close up of gold heater over thermocouple hot junction. AFM imaging of an insulation layer over a graphite wire suggests that connections between metal layers occur when gold is deposited across carbon peaks protruding through the thin PDMS layer.

5. CONCLUSIONS

We have demonstrated integration of thermopneumatic fluid control and prototype temperature measurement directly into PDMS structures. To our knowledge, we report here the first example of a microscale thermopneumatic pump fabricated solely in silicone rubber, and also the first example of electrical junctions formed across an insulating PDMS layer. Our present pump design pushes the current carrying limits of our gold heaters during high duty cycle operation. We believe this is primarily due to heat loss into the glass substrate. Incorporating the thermocouple array into a valve test bed will allow direct measurement of temperatures in situ and thus allow testing of hypotheses about heat flow.

ACKNOWLEDGEMENTS

We thank Joseph Chao, John Koschwanez, Michelle Entezari, and Barry Lutz.

REFERENCES

[1] R. Carlson, J. Koschwanez, and D. Meldrum, MicroTAS'05, pp. 672-674.
[2] M. Unger, *et al*., Science, **288**, pp113-116. N. Nguyen, et al., Trans ASME, **124**, pp. 384-392.
[3] T. Bansal, M. Chang, and M. Maharbiz, Lab Chip, 2007, **7**, 164 – 166.
[4] J. Koschwanez, R. Carlson, and D. Meldrum, Submitted to *Lab on a Chip*.

MICROFABRICATED IMPINGING JET MIXER FOR NANO PIGMENT PARTICLES

Takahiro Ezaki, Susumu Yasuda, Takayuki Teshima, Masao Majima and Takayuki Yagi

Canon Inc., 30-2, Shimomaruko 3-Chome, Ohta-ku, Tokyo 146-8501, JAPAN

ABSTRACT

This paper reports a novel micro mixer with no clogging for producing large volumes of nano pigment particles. The mixer is composed of vertical holes which jet small liquid leading to a collision of two streams in the air. The produced pigment dispersion had small particle (average particle diameter 53.7 nm) with narrow size distribution (standard deviation 20.3 nm). Highly precise distribution on the size of produced nano particles shows that the mixing in the air is well-controlled by our mixer.

Keywords: Impinging jet, mixer, nozzle, nano particle

1. INTRODUCTION

Micro mixers have a high potential for applications in the field of nano particle technology. Clogging is one of the important issues since nano particles are apt to attach to the side wall of micro channels. Therefore, past works have been done toward the prevention of clogging in channels [1, 2]. Impinging jet micro mixer is composed of two oblique nozzles which jet small liquid and lead to a collision of two streams in the air [3]. The mixer is useful for a particle generating process since it can avoid clogging. MEMS technology is suitable for producing the mixer since it can make uniformly hundreds of nozzles in high precision. However, it is difficult to make oblique nozzles for direct impinging in the air by planar micromachining. Therefore, our mixer is composed of vertical holes that have been designed to replace oblique nozzles.

2. DESIGN AND FABRICATION

Fig. 1 shows the schematic view of the microfabricated impinging jet mixer. The mixer consists of two ports, micro channels and micro nozzles. Liquid A and Liquid B are jetted and mixed in the air. The design of a pair of nozzles is shown in Fig. 2. Nozzle 1 is a round and vertical hole. Liquid A is jetted vertically from nozzle 1. The outlet of nozzle 2 is rectangle. Nozzle 2 is a non-straight flow path, so liquid B can be jetted obliquely

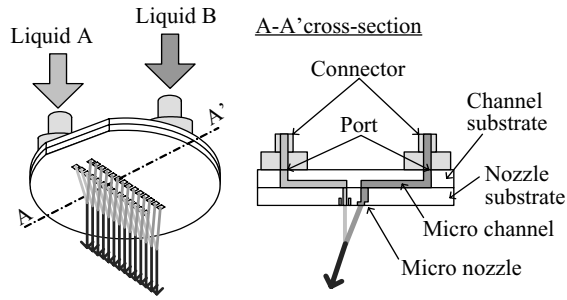

Figure 1. Schematic view of the microfabricated impinging jet mixer.

978-0-9798064-0-7/μTAS2007/$20©2007CBMS

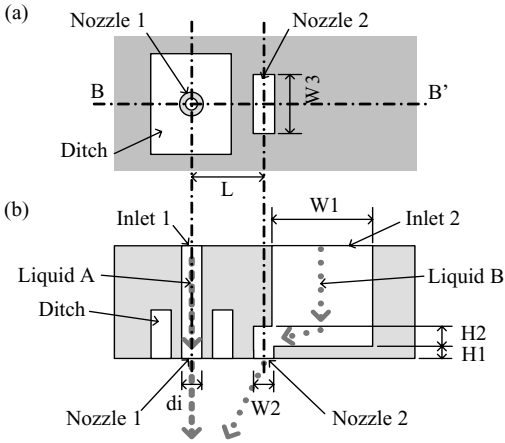

Figure 2. Geometry of a pair of nozzles: (a) top view of a pair of nozzles, (b) B-B' cross-section.

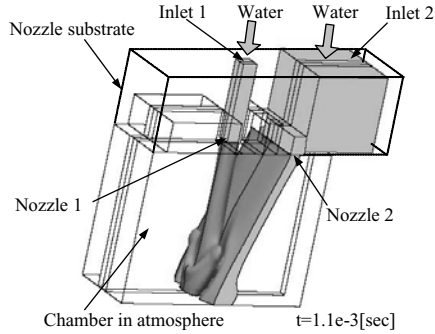

Figure 3. Two streams are impinging in a chamber in atmosphere. di=100 μm, H1=20 μm, H2=100 μm, W1=500 μm, W2=100 μm, W3=500 μm, L=350 μm, Inlet 1=0.1 MPa, Inlet 2=0.1 MPa.

at a certain designed angle. To ensure the collision of both liquid jets, the diameter di of nozzle 1 is smaller than the width W3 of nozzle 2. To prevent liquid A from flowing on the substrate and then mixing with liquid B, a ditch surrounding Nozzle 1 is formed.

In order to optimize the design, three-dimensional modeling of water flow was performed using a commercial computational fluid dynamics software package (CFD-ACE+) as shown in Fig. 3.

Fig. 4 shows the fabricated device. The features of the device were etched using deep-RIE. The nozzle substrate and the channel substrate were bounded by silicon fusion bonding. The mixer of Fig. 4 (c) is the same design as shown Fig. 3.

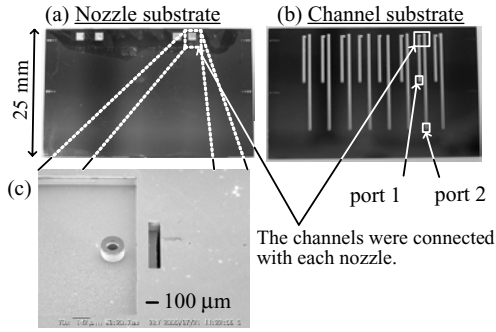

Figure 4. Eight types of a pair of nozzles were involved in the fabricated device.
(a) Nozzle substrate was made of SOI wafer.
(b) Channel substrate was made of Si wafer.
(c) SEM of a pair of nozzles.

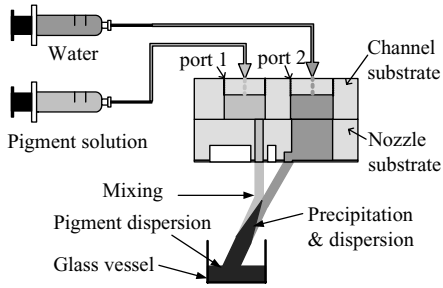

Figure 5. Micro reaction system using microfabricated impinging jet mixer.

3. EXPERIMENTAL

We applied the mixer to produce pigment dispersion. Fig. 5 shows the micro reaction system for pigment dispersion. In this study, C.I. Pigment Red 122 was chosen. The pigment dispersion was produced as follows. First, the pigment solution, including dispersing agent, was jetted by a syringe pump at 6.0 ml/min, and deionized water was jetted by a syringe pump at 9.0 ml/min. Secondly, the pigment solution impinged against the deionized water in air. Then, precipitation and dispersion occurred in air. Finally, the pigment dispersion was collected in a glass vessel. The experiment was conducted at room temperature. The particle size distribution was measured using a dynamic light scattering (DLS-7000, OTSUKA ELECTRONICS CO.,LTD.).

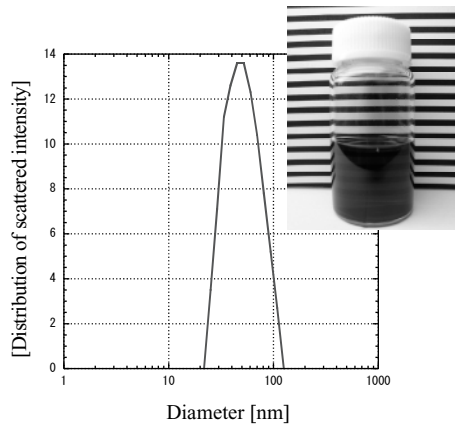

Figure 6. Particle size distribution obtained by micro reaction system. This picture shows the produced pigment dispersion of pigment concentration of 0.19 wt%.

4. RESULTS AND DISCUSSION

As shown in Fig. 6, the produced pigment dispersion had small particle (average particle diameter 53.7 nm) with narrow size distribution (standard deviation 20.3 nm), which features are difficult to be realized by the conventional pulverizing method. It is expected that the nano pigment particles enhance the performance of pigment ink and so on.

5. CONCLUSIONS

We proposed a novel impinging jet mixer for producing nano pigment particles. Highly precise distribution on the size of produced nano particles shows that the mixing in the air is well-controlled by our mixer.

REFERENCES

[1] M. Takagi, T. Maki, M. Miyahara and K. Mae, “Production of titania nanoparticles by using a new microreactor assembled with same axle dual pipe”, Chemical Engineering Journal, 101, pp. 269-276, 2004.
[2] H. Maeta, T. Sato, H. Nagasawa and K. Mae, “New Synthetic Method of Organic Pigment Nano Particle by Micro Reactor System”, Proceeding of the AIChE Spring National Meeting, Orlando, FL, USA, Apr.23-27,Session #98, 2006.
[3] V. Hessel, H. Lowe and T. Stange, “Micro chemical processing at IMM-from pioneering work to customer-specific services”, Lab on a Chip, 2, pp. 14N-21N, 2002.

SERIAL DILUTION CHIPS FOR ARBITRARY CONCENTRATION PROFILE AND APPLICATION FOR CYTOTOXICITY TEST

Choong Kim[1,2], Kang Sun Lee [1], Kyeong Sik Shin[1], Jong Hyun Kim[1], Kyu Jung Lee[2], Ji Yoon Kang[1], and Tae Song Kim[1]

[1] Korea Institute of Science and Technology, KOREA, [2] Korea University, KOREA

ABSTRACT

This paper proposes serial dilution microfluidic chips generating arbitrary (logarithmic or/and linear) concentrations for cytotoxicity. These concentrations were generated by adjusting the flow rate of converging two fluids at channel junctions. The desired dilution ratios are not affected by flow rate or diffusion length of molecules since it is influenced by only the ratio of two flow rate. The design flexibility of these chips is capable of satisfying customer's specifications on the concentration profile through the modification of microfluidic resistance network.

Keywords: serial dilution, linear, logarithmic, micromixer, cell toxicity

1. INTRODUCTION

Dilution is very tedious and laborious work but indispensable process in biological experiment. Especially, it is important to study the effect of drug concentrations on cell toxicity or cell differentiation in pharmacogenetics or chemosensitivity test [1] [2]. Recently, serial dilution chips based on molecular diffusion in laminar flows were reported to obtain concentration gradients with a single operation in a microfluidic device [3]. The diffusion-based dilution is, however, inevitably affected by molecular size, flow rate, and diffusion length. To overcome these problems, several dilution chips that are independent of flow rate were developed, but these chips were focused only linear profile or only logarithmic profile [3] [4] [5]. But, the dilution ratios that are required by users are neither linear profile nor logarithmic profile. Hence, we developed almost arbitrary concentrations (1, 1/2, 1/5 and 1/10) through the design of flow resistance network.

2. PRINCIPLES OF SERIAL DILUTION

After a chemical solution is diluted at the 1st intersection of buffer flow, the diluted fluid meets buffer solution again at the 2nd intersection. The concentrations of chemicals in the outlet chambers are defined by the relationship, $C_n/C_{n-1}=\eta_n$, where η_n is the dilution ratio at n^{th} intersection and C_n and C_{n-1} are the concentrations of nth and $(n-1)^{th}$ outlet chambers respectively. If the dilution ratios of all junctions are same, the concentrations of consecutive chambers are logarithmic (Figure 1).

When we adjust the nth dilution ratio, even linear concentration profile also can be achieved. As a demonstration of flexible dilution capability, the arbitrary profile (0.5, 0.2 and 0.1) was achieved by setting the dilution ratios as η_1=0.5, η_2=0.4, and η_3=0.5 using electrical circuit simulation (Figure 1).

978-0-9798064-0-7/μTAS2007/$20©2007CBMS

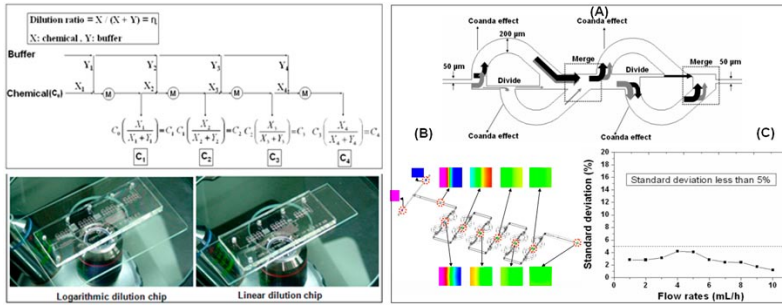

Figure 1. The principle of chip generating concentration gradient and photograph of dilution chip (logarithinc and linear)

Figure 2. The micromixer inserted serial dilution chip (a) schematic illustration of the principle of a micromixer; (b) cross-sections of the mixing pattern in the micromixer (simulation result) and (c) color intensity with the variation of flow rates.

3. EXPERIMENTAL

To measure the dilution ratio of the chip generating a linear concentration profile, the red-dyed and de-ionized water were injected. Microscopic images were captured using a Nicon Coolpix 4500 digital camera mounted on a Nicon SMZ-1500 stereomicroscope. MCF-7 human breast cancer cells (Korea Cell Line Bank, KCLB) were used in cytotoxicity and it was tested with mitomycin C (MC, Sigma-Aldrich, and M0440)). MC (30 μg/mL) was diluted 0.003, 0.03, 0.3, and 3.0 μg/mL by the logarithmic dilution device as well as consecutive manual pipetting to compare two results. All MTT assays were repeated three times.

4. RESULTS AND DISCUSSION

Only the adjustment of flow rate in the fluidic circuit, however, was not sufficient to implement serial dilution chip because the two merging laminar flows did not fully mixed before next intersection. Without mixer the dilution rate would be seriously affected by flow rate. Tesla mixer was inserted between intersections, where two fluids were divided and merged (Figure 2A). The fluids were fully mixed after 5 mixer sets in simulation (Figure 2B). In order to evaluate the realized micromixer, red dyed-and DI water were injected into the micromixer by a syringe pump. The mixing performance at flow rates of 6 and 60 are shown in Fig. 2C. As the flow rate increases, the mixing performance of the mixer can sustain almost 95% mixing performance over the wide range of flow rates as shown in Figure 2C. As a result, the mixer is sufficient to apply in dilution device.

In order to investigate the effect of flow rates in the linear dilution device, the red dye was diluted in DI water with various flow rates (Figure 3A). The average intensities of the red dye diluted in microfluidic chip was in good agreement with those of manual pipetting in spite of the change of flow rate (Figure 3B). The performance of dilution chip was verified by the quantification of BSA solution and cytotoxicity test of MCF-7 breast cancer cells. Figure 4 and 5 showed the compatibility of serial dilution chips with manual pipetting when the chemical was diluted logarithmically. If we connect logarithmic and linear dilution chip, a number of concentrations in wide range could be obtained as in Figure 6.

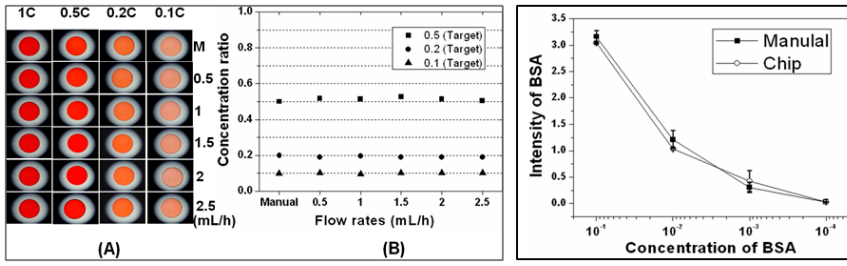

Figure 3. Color intensity with the variation of flow rates with linear dilution chip
Figure 4. with the spectroscopic quantification of BSA with logarithmic dilution chip

5. CONCLUSIONS

We proposed the principle that was not affected by flow rate or diffusion length of molecules and proved the proposed device could make the dilution all concentration user desires, in particular, linear and logarithmic dilution. The concentration profile from dilution devices were in good agreement with that from manual pipette method. If we connect logarithmic and linear dilution device, a number of concentrations in wide range could be obtained. We expect these serial dilution devices will be very useful in lots of biochemical experiments such as cancer drug dose testing, stem cell differentiation study, and drug sensitivity test.

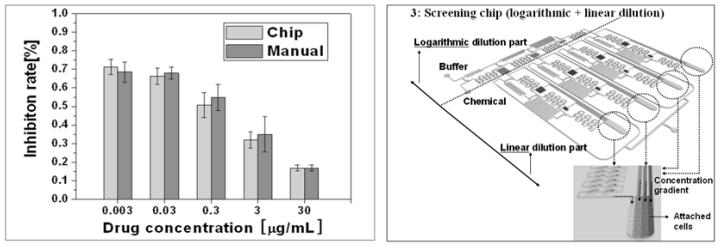

Figure 5. Comparision of cytoxicity in anticancer-drug-treated MCF-7 cell with logarithmic dilution chip
Figure 6. The screening chip of connected linear and logarithmic dilution chip

ACKNOWLEDGEMENTS

This research was supported by the Intelligent Microsystem Center (IMC; http://www.microsystem.re.kr), which is carrying out one of the 21st Century's Frontier R&D Projects sponsored by the Korea Ministry of Commerce, Industry and Energy

REFERENCES

[1] Sinqla DK, Sun B, Biochem. & Biophys. Res. Comm., 332, 135-141 (2005).
[2] Xulang Zhang et al, Biothecnol. Prog. 21. 1289-1296 (2005)
[3] Bong Geun Chung et al, Lab Cip, 5, 401-406 (2005)
[4] Kyle Campbell and Alex Groisman, Lab Chip, **7**, 264 – 272 (2007)
[5] Choong Kim et al, μTAS 06, 1160-1162 (2006)

TRANSPORTATION PERFORMANCES OF MICROMACHINED LINEAR BROWNIAN MOTORS

Ersin Altintas[1], Edin Sarajlic[1], Karl F. Böhringer[2] and Hiroyuki Fujita[1]
[1]CIRMM/IIS, The University of Tokyo, Meguro-ku, Tokyo, 153-8505 JAPAN
[2]The University of Washington, Seattle, WA 98195, USA

ABSTRACT

We report on microfabrication and experimental characterization of linear Brownian motors with a periodic 3-phase electrostatic rectification for unidirectional transport of nanobeads. The influence of spacing between the rectification electrodes on the motor performance is studied using two prototypes with respectively 2 µm and 4 µm electrode spacing. Results indicate that although the percentage of transported nanobeads in both prototypes is between 50 % and 60 %, the average speed of nanobeads decreases with increasing electrode spacing.

Keywords: Brownian motion, Brownian ratchet, nanobeads, rectification, transportation

1. INTRODUCTION

A Linear Brownian Motor (LBM) harvests random thermal fluctuations, so called Brownian motion, which is one of the dominating phenomena on the nanoscale [1, 2], to fuel transportation of nanoscopic particles. Recently, we have successfully devised the first LBM with a 3-phase electrostatic rectification and investigated its performance as function of the driving voltage [3].

In this paper we have further improved design of the 3-phase LBM by increasing the number of rectification electrodes from 6 in the previous to 33 in the current design allowing significantly larger transportation range. Furthermore, we have experimentally determined transportation performance of the motor

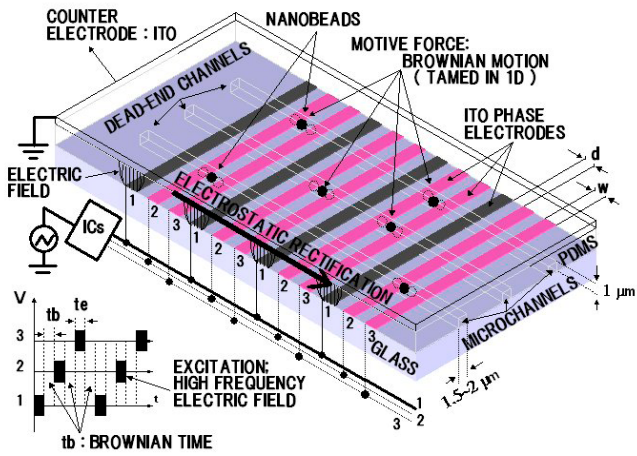

Figure 1. Improved micromachined linear Brownian motor (Micromachined LBM). 3D Brownian motion is tamed in microchannel and turned into 1D motion. 3-phase electrostatic field rectifies this random motion. (E-field is shown on the left side only. PDMS and glass are not to scale.
LBM2*2; w = d = 2µm, LBM24; 2w = d = 4µm. tb = te = 4 seconds)*

978-0-9798064-0-7/µTAS2007/$20©2007CBMS

as function of the electrode spacing.

The motor, schematically shown in Fig. 1, employs microchannels to limit the three dimensional (3D) random motion of nanobeads into 1D and equally spaced 3-phase electrodes for the rectification of the Brownian motion to accomplish unidirectional transport. During the rectification, as illustrated in Fig. 2, the electrostatic trapping force is not large enough to attract a bead directly from the adjacent inactive electrode, but is sufficiently large to counteract the Brownian force holding a bead on the active electrode. Therefore, a bead travels from one electrode to the next solely by Brownian motion, while the rectification in a certain direction only increases the probability that a bead will move in the same direction.

2. FABRICATION

Our experimental device, shown in Fig. 3, consists of a cover glass with ITO electrodes fabricated by a lift-off process. By shadow masking, Al was sputtered to provide pads for wire bonding. After lift-off, the samples were baked at 300 C for 4-6 hours to increase the conductance of ITO electrodes. Protecting the Al pads by a tape, OCD solution, which is hydrophilic, was spin-coated and baked for planerization of the surface. Approximately 100 µm thick PDMS sheet (500:50:1, Silicone elastomer:Curing agent:FZ-77) with 1 µm deep and 2 µm wide microchannels was fabricated [3]. Then, the sheet was punched for inlet, aligned and bonded on the cover glass before wire bonding. On the top of the PDMS sheet an ITO counter electrode is placed. A driving voltage of 0.5Vpp-1 MHz was applied to one phase for 4 s, (Fig. 2b). Before we switched it to another (Fig. 2d), we allowed 4 s without voltage for the motion of the particles (Fig 2c). We repeated this procedure in a cyclic manner (Fig. 1).

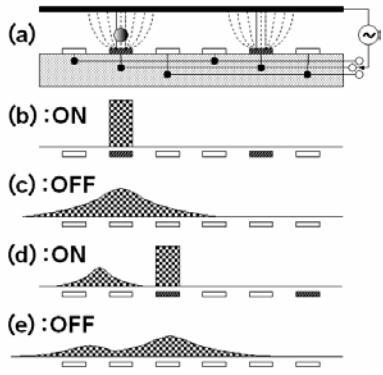

Figure 2. Principle of Brownian motor. 3-phase electrostatic rectification of Brownian motion provides net-motion. (a-b) Trapping of the bead. (c) Probability distribution. (d) Next phase and trapping. (e) Next probability distribution.

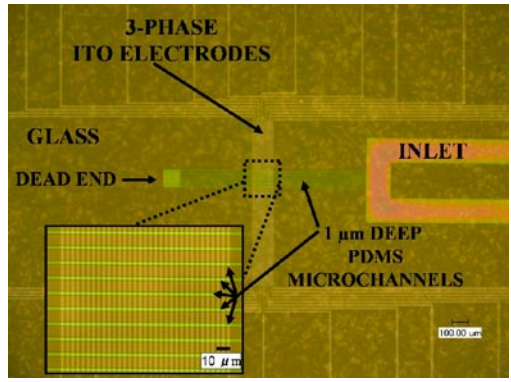

Figure 3. Fabricated device (LBM22, d = w = 2 µm). PDMS dead-end channels are aligned with 11 sets of 3-phase ITO electrodes.

3. RESULTS AND DISCUSSIONS

Fig. 4 shows the distribution of nanobeads in two prototypes of the 3-phase LBM after 2 minutes of transportation. The first prototype (LBM22) employs 2-µm-wide electrodes with 2 µm spacing while the second (LBM24) uses 2-µm-wide electrodes with 4 µm spacing. The graph shows a clear shift of the nanobeads in both prototypes transported in the rectification direction (+ direction). However, LBM22 has a mean of distribution of 5.62 µm, while LBM24 has 2.21 µm with a 0.55 µm measurement error (σ_{LBM22} = 11.28 and σ_{LBM24} = 10.57). Fig. 5 shows the performances of the motors in different regions of positive transportation. These show that LBM22 rectifies the Brownian motion of the nanobeads more efficiently due to smaller electrode spacing which is easier for particles to cross the spacing by Brownian motion.

4. CONCLUSIONS

Electrode spacing, or diffusion distance of particles, is an important parameter in the transportation performance of micromachined linear Brownian motor. Characterization is ongoing with other parameters such as viscosity of the medium, Brownian time (diffusion time) and excitation time.

ACKNOWLEDGEMENTS

The authors would like to thank to VDEC (VLSI Desing and Education Center), The University of Tokyo, for the fabrication of the masks.

REFERENCES

[1] R. D. Astumian, "Making Molecules into Motors", Sci. Am. V. 285, pp. 56-64, 2001

[2] P. Hanggi, F. Marchhesoni and F. Nori, "Brownian Motors". Ann. Phys. V.14, No.1-3, pp.51-70, 2005

[3] E. Altintas. K. F. Böhringer and H. Fujita "Micromachined Linear Brownian Motor: Net-unidirectional Transport of Nanobeads by Tamed Brownian Motion with Electrostatic Rectification", IEEE-MEMS Conference, pp. 839-842, Kobe, Japan, 2007

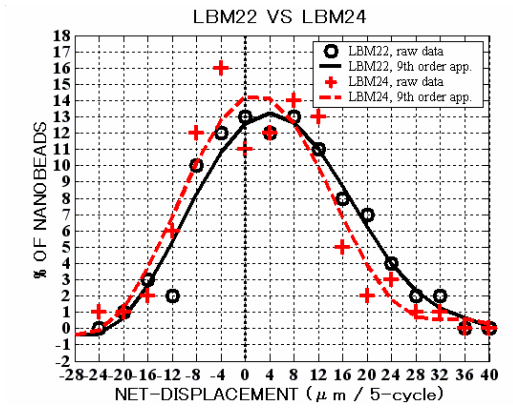

Figure 4. Rectified distribution of nanobeads in 2 different micromachined LBM. Displacements were calculated in 2 minute-videos. Values are rounded to nearest integer multiples of 4. (Approximations represent polynomial curve fittings. $Mean_{LBM22}$ = 5.62, $Mean_{LBM24}$ = 2.21)

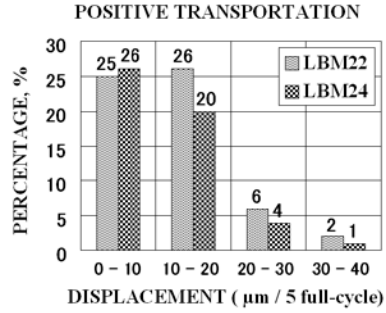

Figure 5. Performances of fabricated devices in different regions of transportation. LBM22 has a larger shift than LBM24.(% is out of total # of nanobeads.)

CMOS OPTICAL POLARIZATION ANALYZER CHIP FOR MICROCHAMBER AND MICROFLUIDIC SYSTEM

T. Tokuda, S. Sato, K. Kagawa, M. Nunoshita, and J. Ohta
Nara Institute of Science and Technology, JAPAN

ABSTRACT

We developed a CMOS optical polarization analizer designed to be implemented onto microchamber of microfluidic systems. A CMOS photosensor array with minolithically embedded metal grid structure was fabricated. The polarization analysis function of the fabricated sensor was demonstrated.

Keywords: CMOS sensor, Polarization Analysis, Microchamber, Microfluidic System

1. INTRODUCTION

A novel CMOS sensor chip with optical polarization analysis function is proposed and demonstrated. The CMOS microsensor is designed to be integratable with microchamber or microfluidic systems. A micro-structured metal grid polarizer is configured on CMOS optical sensor circuitry and polarization measurement was successfully demonstrated without any off-chip polarizer. Integrating the sensor chip into microchamber and microfluidic system, in situ optical measurements including polarization analysis can be performed in the microchemical systems.

2. DESIGN OF CMOS OPTICAL POLARIZATION ANALYZER

Fig. 1 shows concept of the present CMOS integratable microsensor chip for microchamber and microfluidic systems. The microsensor system will provide detailed information of the target system such as production yield, conductivity, electrochemical profile, etc. It will help us to totally control the system parameters such as flow speed, temperature, optical excitation, etc. Based on the concept, we designed a CMOS microsensor chip with optical polarization sensing function. Fig. 2 shows layout of the fabricated sensor. Specifications of the sensor chip are summarized in Table I. It should be noticed that we have designed the sensor chip with electrochemical sensing electrodes with current-sensing amplifiers.

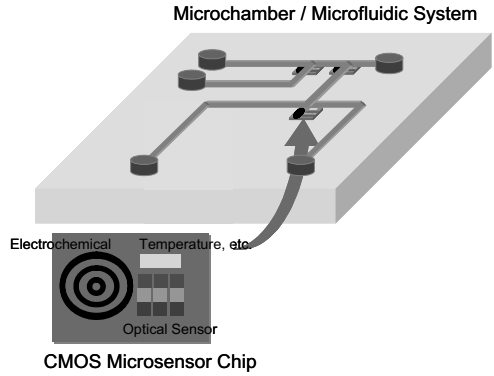

Figure 1. Concept of CMOS microsensor for Microchamber and Microfluidic system

Fig. 3 shows (a)schematic and (b)structure of the optical polarization analyzer. The sensing function is realized with a standard optical sensing circuitry called “3-transistor active pixel sensor” [1]. The polarization detection with on-chip polarizer is based on the

978-0-9798064-0-7/μTAS2007/$20©2007CBMS

reported idea [2], and the main feature of the present sensor is a monolithically embedded metal grid structure configured with a wiring layer of CMOS LSI. The inset of the Fig. 3(b) shows the structure of the metal grid implemented over the photodiode of the optical sensor. In the optical sensor array, three optical sensors (without grid, with a horizontal grid, and with a vertical grid) were designed as one measurement unit. Owing to this multi-sensor configuration, the optical polarization measurement can be performed with high reliability.

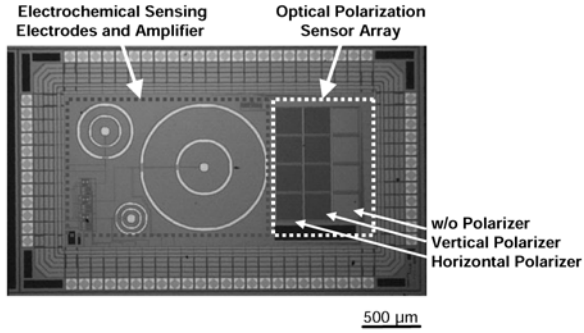

Figure 2. Layout of the fabricated sensor.

TABLE I. Specifications of the CMOS microsensor chip.

Technology	0.35µm 2-poly 4-metals Standard CMOS
Chip Size	3080 µm x 1880 µm
Optical Sensor	200µm x 200µm, 3 x 4 array
Metal Grid Polarizer	0.5 µm / 0.45µm line / space (0.95µm pitch)
Operation Voltage	3.3 V
Operational Amplifier	PMOS input 2-stage differential (single-end output)
Signal Output	Analog Voltage

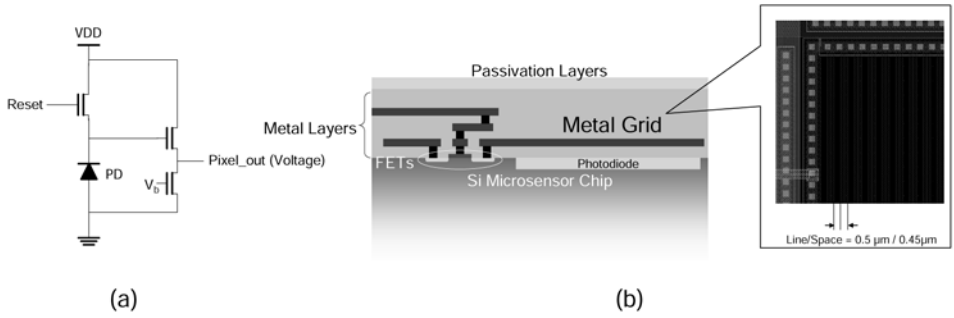

Figure 3. (a)Schematic and (b) structure of the optical polarization sensor.

3. CHARACTERIZATION OF THE FUNCTION

Fig. 4 shows typical result of polarization measurement. The fabricated sensor was illuminated with polarized light generated by LED with Glan-Thompson prism. The two traces are light intensities measured by photosensor with vertical and horizontal metal grid structure. The intensities are normalized by the intensity measured by the photosensor without grid structure. Polarization dependence due to the light source can be canceled and the polarization angle of the incident light (angle of then Glan-Thompson prism) was

accurately measured. This feature means that we can design simple measurement systems with LED-based light source. Fig. 5 shows suppression ratio in polarization analysis function. The suppression ratio of the on-chip grid polarizer is in the order of 10^0, and not as good as off-chip polarizer such as metal grid polarizer or Polaroid film. However, the multi-photosensor measurement scheme with orthogonal polarizer enables to separate signals corresponding to polarized and cross-talking light.

As shown in Fig. 3, coaxial electrodes and voltage controlling current sensing amplifier for on-chip electrochemical (voltammetric) measurements were also implemented on the sensor chip [3]. Characterization of the electrochemical measurement functions and integration of the chip onto microchemical systems are now undergoing and will be presented at the conference, too.

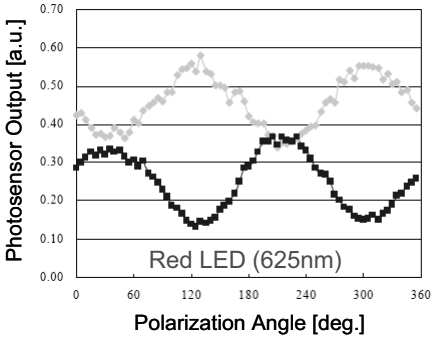

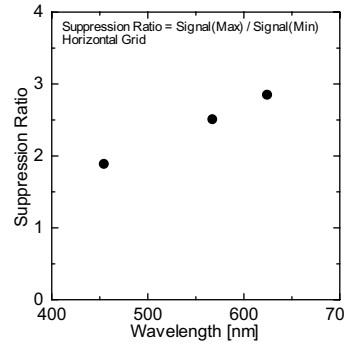

Figure 4(Left). Results of polarization measurement using the CMOS microsensor.
Figure 5(Right).Wavelength dependence of suppression ratio.

4. CONCLUSIONS

A novel CMOS photosensor chip whish is capable of polarization analysis was proposed and demonstrated. Taking a multi-sensor measurement scheme, we succeeded to measure polarization angle of the incident light, even rejection ratio of the embedded metal grid structure is in the order of 10^0.

ACKNOWLEDGEMENTS

This study was supported by Grants-in-Aid #18681024 from the Ministry of Education, Science, Sports and Culture.

REFERENCES

[1] E. R. Fossum, "Active pixel sensors - are CCDs dinosaurs ?," Proc. SPIE, 1900 (1993) 2-14.

[2] A. G. Andreou, and Z. K. Kalayjian, "Polarization Imaging: Principles and Integrated Polarimeters" IEEE Sensors Journal, 2 (2002) 566-576.

[3] T. Tokuda, K. Tanaka, M. Matsuo, K. Kagawa, M. Nunoshita, J. Ohta, "Optical and Electrochemical dual-image CMOS sensor for on-chip biomolecular sensing applications," Sensors & Actuators: A, in press.

IMPROVED WAFER-SCALE FABRICATION OF ALIGNED PDMS-GLASS MICROCHIPS WITH INTEGRATED ELECTRODES

Jiajie Li, Séverine Le Gac and Albert van den Berg

BIOS the Lab-on-a-Chip group, MESA+ Institute for Nanotechnology, The Netherlands

ABSTRACT

We report here on an improved fabrication process for the production of PDMS-based hybrid chips (e.g., glass-PDMS here) at the scale of a whole wafer and including an alignment step. This implies the production of a flat and even surface of PDMS so that the PDMS wafer can be used in dedicated equipment for alignment and bonding, as well as correcting/controlling the dimension variations of this elastomeric material upon temperature changes. We illustrate the applicability of this improved fabrication process for the production of microchips dedicated to electrical characterization of individual cells and the detection of apoptosis. PDMS-glass hybrid chips were fabricated for this purpose with an alignment precision down to 40 μm at the end of the process.

Keywords: PDMS-glass chips, aligned bonding, wafer-scale fabrication

1. INTRODUCTION

PDMS has become one of the most popular materials for microchips due to easy and low-cost fabrication [1]. Nonetheless, problems arise from its elastomeric nature, especially when alignment of two wafers is required: for instance, when chips include electrodes. PDMS presents dimension variations upon temperature change [1], it is soft and sticky, the PDMS layer is mostly uneven and not flat so that it is not compatible with the use of standard equipment for wafer alignment and bonding. The former aspect leads to misalignment errors of >700 μm across a 4"-wafer, ruining subsequently the alignment at the chip level. Therefore, bonding is done chip by chip under a microscope, and this precludes any mass production. We present here an improved fabrication methodology for PDMS-glass chips including electrodes with (i) the production of a flat/even layer of PDMS with controlled dimensions, (ii) alignment of the two layers at the scale of a whole wafer, (iii) bonding of the two aligned layers and (iv) dicing so as to release individual microchips.

2. EXPERIMENTAL

We focus here on PDMS-glass chips including electrodes for electrical measurement; the microfluidic network and the reservoirs are fabricated in the PDMS layer, while electrodes are supported on glass. Electrodes (Ta-Pt-Ta) are fabricated using a conventional procedure based on photolithography, metal sputtering and lift-off techniques. The PDMS layer is fabricated using conventional molding techniques against a silicon master [2]. Nonetheless, some slight changes are brought to the standard procedure. A flat and even surface with a fixed thickness is achieved by molding PDMS using a closed environment as illustrated on fig. 1: spacers are introduced below the mold and above the pre-polymer mixture to precisely yield a 2 mm PDMS layer. PDMS dimension variations are controlled and compensated by careful choice of the curing temperature and scaling the features on the mold to give final features with desired dimensions for the alignment step.

978-0-9798064-0-7/μTAS2007/$20©2007CBMS

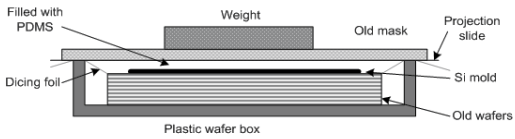

Fiure 1. Production of a PDMS layer with an even and controlled thickness using a closed environment.

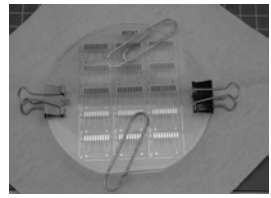

Figure 2. Photograph of the aligned wafers before bonding with the spacers and clips.

Following this, the two layers are aligned using dedicated equipment, and slightly pressed together. Spacers are introduced between the two wafers and clamps on them (see fig. 2) to keep the alignment during the O_2 plasma activation step of the surface. Finally, once bonded the chips are let at rest overnight and diced on the next day. The stack is introduced in dedicated equipment and a blade (parameters) is used to cut the glass side. Thereafter, the PDMS layer is cut manually using a sharp knife along the dicing lines.

4. RESULTS AND DISCUSSION

The critical part in this novel fabrication process is to accurately control the dimension changes in the PDMS. The first approach we have investigated here consists of avoiding any temperature change during the fabrication to alleviate any shrinkage/swelling of PDMS.

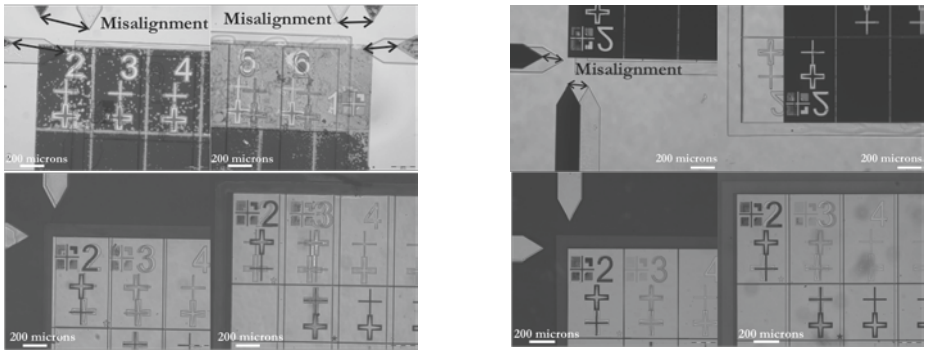

Figure 3. Controlling the dimensions of the PDMS features. *Top left*; misalignment when no care is taken (700 μm); *Top right*; alignment with curing at 20.2°C (510 μm); *Bottom left*; alignment with mold scaling up and curing at 60°C (79 μm); *Bottom right*; alignment with a combined approach (curing at 59.3°C) (35 μm). The two pictures for each experiment represent the two alignment zones on the edge of the 4"-wafer, scale bar of 200 μm.

The temperature for the alignment step being of 20.2°C, PDMS was cured for >24 h at this temperature. Unfortunately, results using this apparently attractive and straightforward methodology were not conclusive as a slight change of temperature leads to "big" dimension variations: for instance, a 1°C variation leads to >100 μm size changes. Moreover, keeping the temperature constant for > 24 h proved to be very difficult. The second approach is to compensate the shrinkage/swelling by scaling the mold accordingly. We determined the scaling factor to be used for a 4"-wafer (depending on the precise structures of the mold) and a curing temperature of 60°C. Results with this method were

much better: a 70 μm alignment accuracy was yielded on a 4"-wafer. Nonetheless, as we work with small features we targeted an alignment precision in the low 10 μm range. For that purpose, both methods were combined; the mold was initially scaled up, a first layer of PDMS cured at 60°C, and the curing temperature modified to further give almost zero dimension changes. This combined approach enabled us to reach down to 2-3 μm alignment accuracy, with routine values in the high 10 μm range.

Once PDMS dimensions are controlled, a glass and a PDMS wafers can be aligned and bonded, and chips diced. For these steps, standard procedures must be adapted according to the soft and sticky nature of the PDMS. After alignment, spacers are introduced between the wafers for proper activation of the surfaces and clips on them not to loose the alignment quality. Dicing is performed one day after bonding. Only the glass side is diced using dedicated equipment while the PDMS is cut with a sharp knife along the diced lines. Its elastomeric nature is not very compatible with the use of a blade, and dicing both layers simultaneously may result in damage in the bonding quality of the chips.

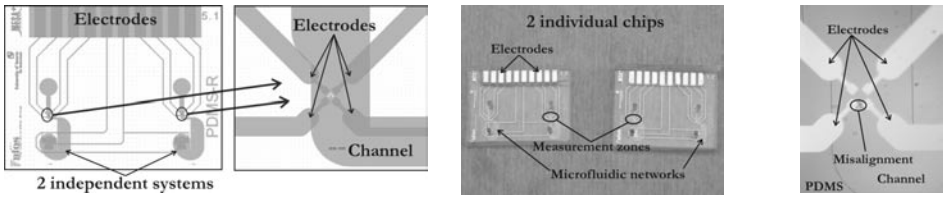

Figure 4. PDMS-glass hybrid chips. *From left to right*: Design of the chips (masks) showing a whole chip containing two independent devices as well as close-up view on the measurement area in the channel; Photograph of two finished chips; Close-up view on the electrodes of a finished chip (photo) (Note that the 3 PDMS pillars should be in the middle of the measurement zone).

Figure 4 represents both the design and the corresponding chips fabricated using this novel procedure. The chip also includes PDMS pillars in the measurement zone for trapping a cell for electrical measurements. Comparison of the mask drawing and the photo of the measurement area shows the shift of circa 40 μm in the alignment.

5. CONCLUSIONS

We have developed a novel and enhanced procedure for PDMS fabrication to produce hybrid glass-PDMS chips with alignment between the two layesr performed at the scale of a 4"-wafer. PDMS-glass chips including various electrodes have thereby been produced for electrical characterization of single cells.

ACKNOWLEDGEMENTS

The authors thank Jan W. van Nieuwkasteele and Johan G. Bomer for technical discussion and assistance. J.L. is supported by a graduate scholarship from the University of Twente.

REFERENCES

[1] Y. Xia, G. Whitesides, *Soft-lithography*, Angew. Chem., **37**, pp. 550 (1998).

[2] C. S. Effenhauser et al., *Integrated capillary electrophoresis on flexible silicone microdevices: Analysis of DNA restriction fragments and detection of single DNA molecules on microchips*, Anal. Chem., 69, pp. 3451 (1997).

DEMONSTRATION OF A TELEMETRIC SYSTEM USING GASTRIC-FLUID-UTILIZING MICRO BATTERY

Hikaru Jimbo and Norihisa Miki
Keio University, Japan

ABSTRACT

In order to realize more advanced and less invasive medical treatment, a variety of micro medical diagnostic devices have been studied. These devices have functions of diagnosis, clinical treatment and data transmission, all of which require effective power supply. This paper reports the gastric-fluid-utilizing micro battery (GMB) applicable for micro medical devices utilized in digestive organs, such as swallowable endoscopes. GMB utlizes Platinum and Zinc as the positive and negative electrodes, respectively, and the gastric fluid as the electrolyte. GMB successfully generated 0.34 mW (0.26 V, 1.3 mA) with 200 Ω external load. Power supply to a telemetric system was successfully demonstrated.

Key words: Micro Medical Device, Capsule Endoscope, Micro Battery, Gastric Fluid

1. INTRODUCTION

Recently, medical diagnosis and treatment using micro medical devices have been developed. They are swallowable or embedded in the human body. The power supply is one of the critical technologies to further enhance their performance. Currently we have two technologies, which are a small battery and radio power transmission. However, both of them have critical issues in terms of safety. The small battery contains chemicals poisonous to humans and radio power transmission affects other medical devices by the electromagnetic wave. Micro power sources for micro medical devices have been developed using MEMS technology (MicroElectroMechanical Systems). These technologies are termed as Power MEMS [1]. In application of power MEMS to micro medical devices, safety for human is the most critical issue. Power MEMS using in the human body have been widely studied. We consider that the key technology to satisfy the requirement is to exploit energy from the human body. For example, a chemical battery acquiring energy from human pee [2] was recently reported. These devices utilize the energy sources that originate from the human body and thus, are not harmful to humans.

In this paper, we propose a voltaic cell using the gastric fluid as the electrolyte for swallowable medical devices, such as a capsule endoscope. We term the GMB ("gastric-fluid-utilized micro battery"). The gastric fluid is safe for humans and rich in the stomach, where the swallowable medical devices work or pass. GMB proposed herein is designed to be small enough to fit the commercial capsule endoscope and be composed of only biocompatible materials.

2. THEORY AND DESIGN

Figure 1 shows the schematic diagram of GMB. GMB is one of the voltaic cells and generates electricity on the standard principle of the primary cell. The gastric fluid works as the electrolyte. It is rich and safe for humans in the stomach. Crucial issues are the size and safety for humans. The size of GMB is 10×10×4mm. Platinum and Zinc are employed as the positive and negative electrodes, respectively, taking account of biocompatibility. The theoretical voltage of GMB is 1.95V from the standard electrode

978-0-9798064-0-7/μTAS2007/$20©2007CBMS

potential [3]. PDMS is used for the casing, which is a biocompatible polymer. A rectangular parallelepiped filter made of porous ceramics is sandwiched between the electrodes to filter foreign materials as well as to hold the gastric fluid in GMB. Figure 2 shows the photo of GMB.

3. EXPERIMENTAL

We conducted the experiments with GMB using Simulated Gastric Fluid (SGF) as the electrolyte. SGF consists of 7.0 ml of HCl, 2.0 g of NaCl, 1000ml of water, and 349.1 mg of digestive enzyme pepsin [4]. GMB was dipped in the electrolyte for 30 seconds and taken out. Subsequently, the generated voltages by GMB were measured. We evaluated the load discharging characteristics and the I-V characteristics and demonstrate the power of GMB.

4. RESULTS AND DISCUSSION

Load-discharging characteristics are depicted in Fig. 3. GMB could generate the power for more than 10 hours, which are long enough to diagnose the digestive system given that conventional capsule endoscopes stay inside the body for about 8 hours after delivered from the mouth. Figure 4 shows current-voltage and current-power characteristics of GMB. The maximum power of 0.34 mW was achieved at the voltage of 0.26 V and the current of 1.3 mA with 200 Ω external load.

Several small and simple RF telemetric systems have been reported for wireless recording [5]. We designed the telemetric system, taking account of small size and simplicity. It is designed to transmit RF signals of 80MHz. We fabricated the telemetric system using SMD, a flexible polyimide board and an antenna (copper wire, 100μm in diameter). The board size is 10×25 mm. Figure 5 shows a photo of the fabricated telemetric system. To demonstrate the telemetric system, we used 3 cells GMB array connected in series. The array generated 0.87V, which is greater than required voltages of 0.82V for the telemetric system. The system successfully transmitted RF signals, which were collected by the antenna and acquired by an oscilloscope, which were found to be oscillating at a frequency of 80 MHz as designed.

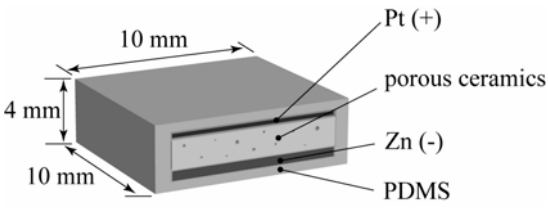

Figure 1. A schematic diagram ofGMB.

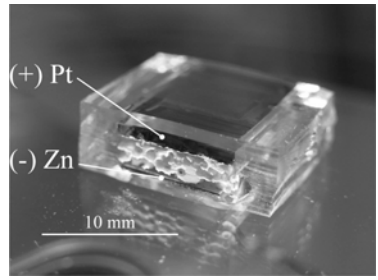

Figure 2. A photo of the fabricated GMB.

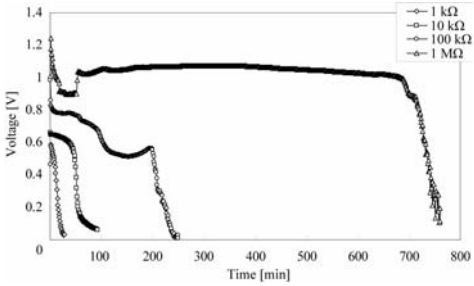

Figure 3. The load -discharging characteristics.

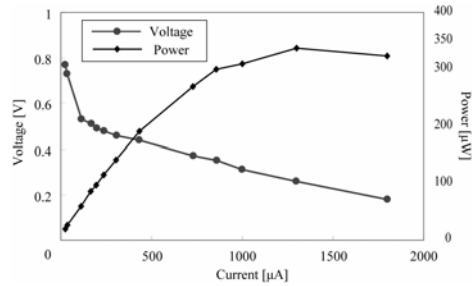

Figure 4. I-V characteristics.

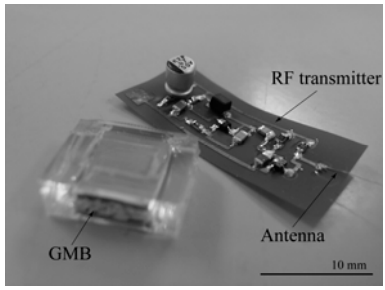

Figure 5. A photo of the telemetric system.

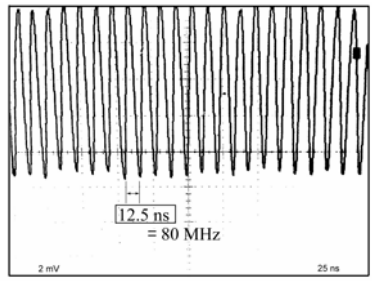

Figure 6. The oscillating signals.

5. CONCLUSIONS

GMB exhibited feasibility as a new, safe and effective battery for micro medical devices. GMB could even spin a small motor in another preliminary experiment. GMB can enhance the performance of the medical devices by offering additional functions, such as telemetry and mobility.

ACKNOWLEDGEMENTS

This research was supported by Electro-Mechanic Technology Advancing Foundation.

REFERENCES

1. "The Fourth International Workshop on Micro and Nanotechnology for Power Generation and Energy Conversion Applications (Power MEMS 2004)" S. Tanaka, JOURNAL OF MICROMECHANICS AND MICROENGINEERING, 15 , 9 (2005).
2. "Urine-activated paper batteries for biosystems" Ki B. Lee JOURNAL OF MICROMECHANICS AND MICROENGINEERING, 15, (2005).
3. "Hand book of batteries 2nd edn" D. Linden (1995).
4. " pH and concentrations of pepsin and trypsin in feeding tube aspirates as predictors of tube placement." N.A. Metheny, B.J. Stewart, L. Smith, H. Yan, M. Diebold and R.E. Clouse, JOURNAL OF PARENTERAL AND ETERNAL NUTRITION, 21, 5 (1997).
5. "A Radio-Telemetry System With a Shape Memory Alloy Microelectrode for Neural Recording of Freely Moving Insects" S. Takeuchi, I. Shimoyama, IEEE TRANSACTIONS ON BIOMEDICAL ENGINEERING, 51, 1 (2004).

STUDY OF CELL-CELL COMMUNICATION USING OPTICALLY ASSEMBLED 3D LIVING CELL MICROARRAYS

Winston Timp[1], Utkur Mirsaidov[2], Kaethe A. Timp[2], Mustafa Mir[2], Gregory Timp[2], Paul Matsudaira[1]

[1]Massachusetts Institute of Technolog, Cambridge, MA, USA and
[2]University of Illinois at Urbana-Chapaign, Urbana, IL, USA

ABSTRACT

Cell-cell signaling is an important, but experimentally elusive aspect of biology. In order to frame the experiment in the proper social context, the cells in question should be carefully positioned relative to each other. The cells should also be placed in a 3D environment, in order to both provide physiochemical cues and to ensure that the dominant mode of chemical transport is diffusive – as it is in most biological constructs. To that end, we have optically assembled heterotypic 3D microarrays of living cells encapsulated in hydrogel. Using these arrays, we have been able to study the dynamics of cell-cell signaling of bacteria on a single-cell level.

Keywords: Optical Trapping, Hydrogel, Cell Signaling, Gene Expression

1. INTRODUCTION

Previous work with cell signaling has been done in bulk, or with large scale patterning. Specifically, others have studied the effects of spatiotemporal signaling in bacteria[1], or eukaryotic cells[2]. These studies represent a great advance in the study of signaling and techniques of cell patterning yet are limited in the precision of cell placement. This prevents measurement at the single-cell level, where the most interesting stochastic processes may be studied[3].

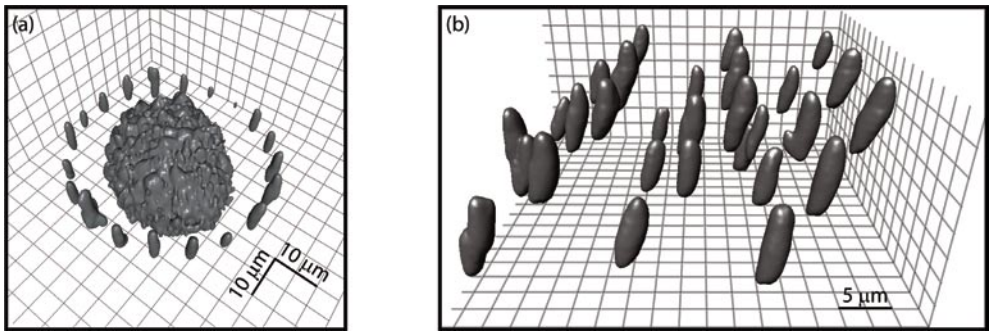

Figure 1: Examples of 3D Living cell Microarrays; Iso-surface reconstruction of : (a) S3T3 cell surrounded by a ring of P. aeruginosa bacteria; (b) 3x3x3 3D array of P. aeruginosa bacteria

In contrast, we have recently been able to use optical trapping in order to position cells with submicron accuracy in a three-dimensional array, then encapuslate them in a biomimetic hydrogel(Fig 1)[4]. Using this method, we now intend to attempt to study cell-cell signaling of a simple bacterial quorum sensing system. As most cell signaling studies,

978-0-9798064-0-7/μTAS2007/$20©2007CBMS

by the nature of their logistics, work on a bulk scale, our study has the advantage of looking at small numbers of cells, with complete control over their environment.

2. THEORY

For our signaling assay, we first take two different populations of E. Coli bacteria, from the same strain but containing different plasmids. The first type of cells, known as "senders", express red fluorescent protein (RFP) and the enzyme luxI under the control of the lac operon. LuxI is an enzyme from the V. Fischeri bacteria which catalyzes the synthesis of a signaling molecule, an acyl-homoserine lactone (AHL). The second type, known as "receivers", express green fluorescent protein (GFP) under the control of the lux operon, induced by the receipt of AHL.

In order to fully understand the cellular response, a model of the system was created. The microfluidic flow profile, as well as the convection/diffusion mass transport of the signal was simulated using a finite element method(FEM) (COMSOL Multiphysics). Protein production was coupled to the mass transport simulation, using a simple deterministic model based on mass-action kinetics. Using the simulation, parameters of each of the array loci were extracted using a best fit algorithm to match the fluorescent data.

3. EXPERIMENTAL

The two cell types are introduced into separate lanes of a microfluidic device, suspended in a pre-polymer solution of poly (ethylene glycol) diacrylate and photoinitiator. A third lane of clean pre-polymer mix was flowed between the cell lanes. Cells were snatched from the flow with optical tweezers and held in an array of time-shared optical traps, using the optical setup described previously[4]. A brief burst of 360nm light was used to polymerize the solution, encapsulating the cells in a hydrogel spot (Fig 2). The remaining cells were rinsed from the channel, and the sender cells induced with IPTG. This setup allowed us to observe the bacterial cells expressing fluorescent proteins in response to intercellular signals, prompted by external cues.

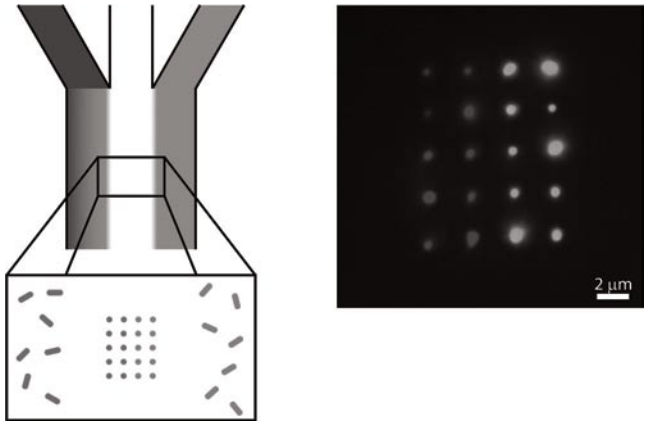

Figure 2: Schematic of microfluidic and method of heterotypic array assembly; Left channel has sender bacteria, right channel has receiver bacteria, center clear clean media.

4. RESULTS AND DISCUSSION

Using the described cellular positioning, we have been able to create 2D and 3D arrays of bacteria, and observe their ability to signal each other. First the red cells begin to fluoresce, corresponding with their production of AHL, then the green cells fluorescence is triggered.

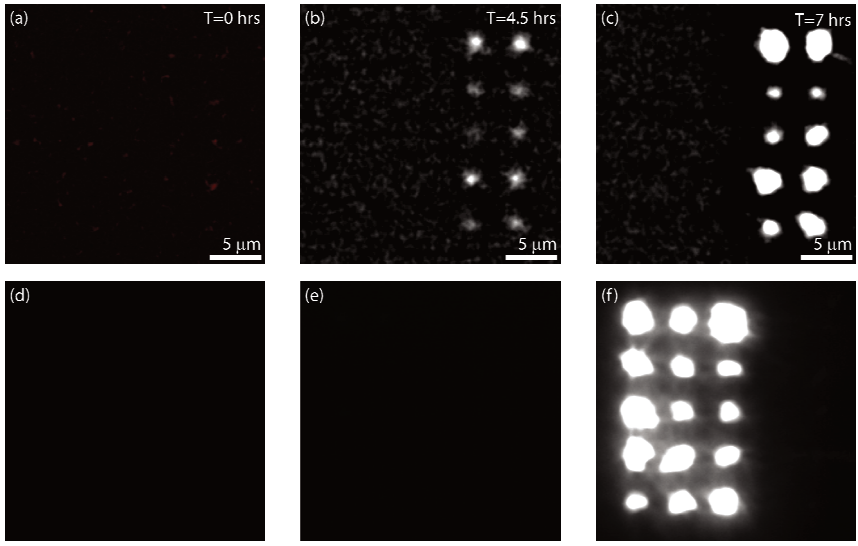

Figure 3: Signaling data and simulation: (a),(b),(c) Red fluorescence time-lapse data; (d), (e), (f) Green fluorescence time-lapse data.

5. CONCLUSIONS

Our study of the quorum sensing system in bacteria is only a beginning. This method can be used to study cell-cell interactions in eukaryotic cells, examining a variety of processes such as stem cell differentiation or cancer metastasis. By putting cells in an appropriate social context, while carefully controlling their microenvironment, it is possible to paint an enhanced picture of cellular behavior.

ACKNOWLEDGEMENTS

We acknowledge R. Weiss for contribution of some of the original plasmids.

REFERENCES

[1] Basu, S., et al., *A synthetic multicellular system for programmed pattern formation.* Nature, 2005. **434**(7037): p. 1130-1134.

[2] Albrecht, D.R., et al., *Probing the role of multicellular organization in three-dimensional microenvironments.* Nature Methods, 2006. **3**(5): p. 369-375.

[3] Di Carlo, D. and L.P. Lee, *Dynamic single-cell analysis for quantitative biology.* Analytical Chemistry, 2006. **78**(23): p. 7918-7925.

[4] Akselrod, G.M., et al., *Laser-guided assembly of heterotypic three-dimensional living cell microarrays.* Biophysical Journal, 2006. **91**(9): p. 3465-3473.

A LOW-DAMAGE CELL TRAPPING ARRAY FABRICATED BY SINGLE-MASK MULTIDIRECTIONAL PHOTOLITHOGRAPHY WITH EQUIVALENT CIRCUIT ANALYSIS

Takaaki Suzuki[1,2], Hideo Yamamoto[1], Masataka Ohoka[3], Isaku Kanno[1], Masao Washizu[2,4] and Hidetoshi Kotera[1,2]

[1]Kyoto University, JAPAN, [2]JST-CREST, JAPAN, [3]Advanced Software Technology and Mechatronics Research Institute in Kyoto, JAPAN and [4]University of Tokyo, JAPAN

ABSTRACT

In this paper, we propose a cell trapping array to simultaneously manipulate and treatment a great number of living cells with high-throughput and simple fluidic method. The array designed by the equivalent circuit simulation can immobilize a lot of cells on orifices without the damage due to local pressure gradient of high hydraulic resistance in embedded microchannels.

Keywords: Cell trapping array, photolithography, equivalent circuit

1. INTRODUCTION

Highly integrated microdevices show great promise for basic biomedical and pharmaceutical researches [1]. In particular, a cell manipulation system plays an important role to control the positioning and the treatment of the single cells [2]. In previous research literatures, the authors have proposed a novel simple fabrication method for a single cell analysis chip using double inclined UV lithography to expose a single layered SU-8 coated on a patterned mask [3], and demonstrated high-yield electroporation for living cells with the membrane impermeant substances [4]. In this paper, we design a novel structure for high-throughput cell trapping system with low damage by using the equivalent circuit analysis. Since the designed configuration has crossed/embedded microchannels and high density arrayed micro-orifices, which cannot be fabricated by the previous inclined lithography [3]. So, we propose a multidirectional –inclined/rotated– UV lithography for different kinds of functional components of the cell trapping array.

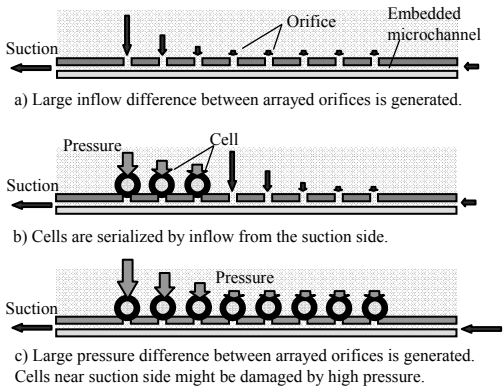

Figure 1. Cells behavior in cell array

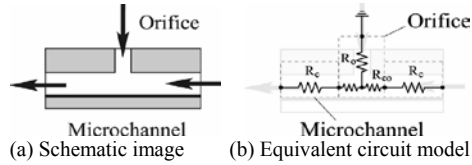

(a) Schematic image (b) Equivalent circuit model

Figure 2. Model of microchannel

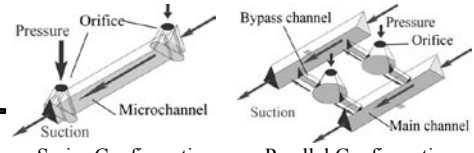

Series Configuration Parallel Configuration

Figure 3. Schematics of arrays

978-0-9798064-0-7/μTAS2007/$20©2007CBMS

2. THEORY

A schematic of cells behavior in commonly used cell trapping arrays driven by suction force is shown in Fig.1. In the handling of multiple cells by negative pressure of a syringe pump, the cells immobilized on orifices near the suction side are often damaged by the high pressure due to the hydraulic resistance in the embedded microchannels. So, we considered an equivalent circuit model as shown in Fig.2, and designed two types of embedded networks with series and parallel configurations as shown in Fig.3.

3. FABRICATION PROCESS

As the cell trapping array, the crossed/embedded microchannels and more than 10000 micro-orifices with 2μm diameter can be simultaneously fabricated by SIMPLE (SIngle-mask Multidirectinal PhotoLithography for Embedded network) process, which applies one spin-coating and one dipping development with inclined/rotated UV exposure using single-mask as shown in Fig.4. The SIMPLE process can simultaneously fabricated the curved microchannels and orifices from single mask as shown in Fig.5. The series and parallel arrays were fabricated by the SIMPLE process.

4. SUCTION TEST

To compare the series and parallel configurations as shown in Fig.6, we carried out a suction test. Figures 7 and 8 show the fluorescent images in process of suction tests when suction was applied from the bottom side of the image by one syringe pump, and cell immobilization rates, respectively. Since the parallel one realizes more unordered immobilization than the series one, the parallel configuration with bypass channels applies the equally suction force to the immobilized cells on each orifice by one syringe pump.

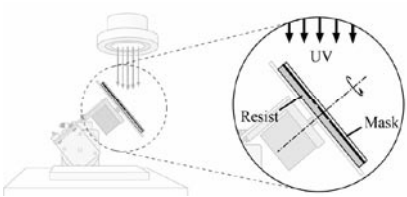

a) Schematic of photolithography machine

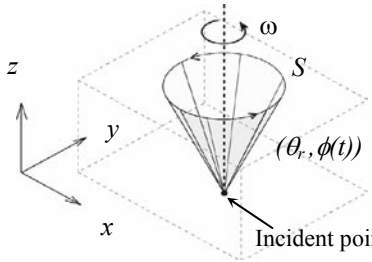

b) Exposed volume from one incident point

Figure 4. SIMPLE process

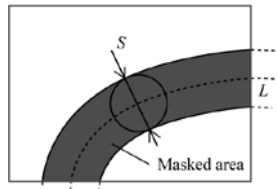

Mask pattern for curved microchannel

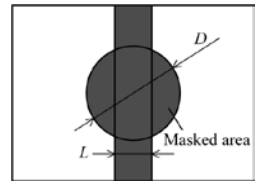

Mask pattern for orifice with microchannel

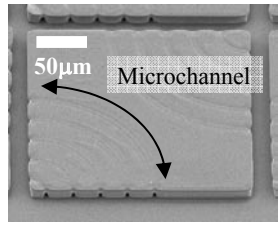

Curved microchannel

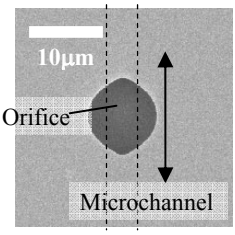

Microchannel with orifice

Figure 5. SEM images of fabricated components

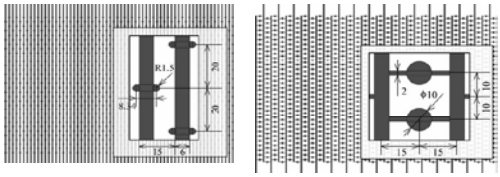

Series Configuration Parallel Configuration

Figure 6. Mask patterns for cell arrays

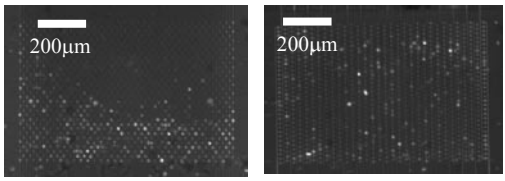

Series Configuration Parallel Configuration

Figure 7. Fluorescent images of ANS-stained cell immobilization on arrayed orifice (White dots are immobilized cells.)

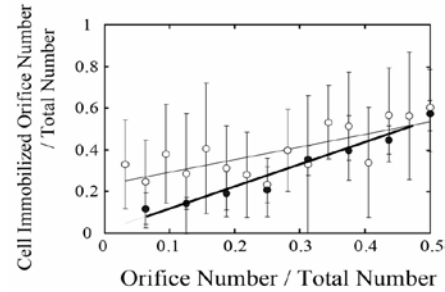

Figure 8. Cell immobilization rates with series / parallel configurations (● : Series, ○: Parallel configurations)

5. CONCLUSIONS

In this paper, we propose a cell trapping array to simultaneously manipulate and treatment a great number of living cells with high-throughput and simple fluidic method. As the cell trapping array, the crossed/embedded microchannels and more than 10000 micro-orifices with 2μm diameter can be simultaneously fabricated by the SIngle-mask Multidirectinal PhotoLithography for Embedded network (SIMPLE) process. By using the equivalent circuit analysis, the parallel configuration with bypass channels applies the equally suction force to the immobilized cells on each orifice by one syringe pump.

ACKNOWLEDGEMENTS

This study is a part of CREST of Japan Science and Technology Agency on the basis of research results supported in part by Mizuho Foundation for the Promotion of Sciences, Young Scientists (B) (No. 19760172), and Center of Excellence for Research and Education on Complex Functional Mechanical Systems (COE program) of MEXT, Japan.

REFERENCES

[1] J. Ei-Ali, P. K. Sorger and K. F. Jensen, *Cells on chips*, Nature, Vol.442, pp.403-411, (2006).

[2] M. Khine, A. Lau, C. I. Zanetti, J. Seo and L. P. Lee, *A single cell electroporation chip*, Lab on a chip, Vol.5, pp.38-43, (2005).

[3] T. Suzuki, T. Tokuda, N. Fujiwara, H. Yamamoto, I. Kanno, M. Washizu and H. Kotera, *Single-mask fabrication process for high aspect-ratio embedded microchannels with openings*, Proc. Micro Total Analysis Systems 2005, pp.1183-1185, (2005).

[4] T. Suzuki, H. Yamamoto, M. Ohoka, A. Okonogi, H. Kabata, I. Kanno, M. Washizu and H. Kotera, *High throughput electroporation microchip fabricated by single-mask inclined UV lithography*, Proc. Micro Total Analysis Systems 2006, pp.1498-1500, (2006).

ASYMMETRIC CELL DIVISION INDUCED BY MICROENVIRONMENT GEOMETRY

Manuel Théry[1,2], Andrea Jimenez-Dalmaroni[3], Victor Racine[1], Michel Bornens[1] and Frank Julicher[3]

[1] Institut Curie, Paris, France, [2] CEA, Grenoble, France, [3] M P I, Dresden, Germany

ABSTRACT

The orientation of the cleavage plane during cell division is defined by the position of the mitotic spindle. We showed using a combination of theory and experiments on micropatterns that spindle orientation in HeLa cells can be understood as the result of the action of cortical force generators, which interact with spindle microtubules and are activated by cortical cues [1]. We developed a simple physical description of this spindle mechanics, which allows us to calculate angular profiles of the torque acting on the spindle, as well as the angular distribution of spindle orientations. Our model accounts for the preferred spindle orientation and the shape of the full angular distribution of spindle orientations observed in a large variety of different cellular microenvironment geometries. Remarkably it correctly describes asymmetric spindle orientations, which are observed for certain distributions of cortical cues.

Keywords: micro-patterns, cell division, spindle orientation, theoretical model

1. INTRODUCTION

The architecture and adhesiveness of a cell microenvironment is a critical factor for the regulation of cell division in vivo. Cell division is governed by an internal transitory structure: the mitotic spindle. It is a bipolar array of filaments, the microtubules, which organise the mitotic chromosomes in a plate. The spindle poles interact with the cell periphery and position the chromosomes plate with respect to spatial cues in the cell membrane. The position of the spindle dictates the cleavage plane and the consequential positions of the two daughter cells. In vivo, the regulation of cell division is under the control of cell microenvironment [2]. Both soluble factors and contacts with neighbouring cells and with the extra-cellular matrix impinge on the temporal and spatial regulation of cell division [3, 4]. In particular, stem cells can either self-renew by dividing symmetrically or differentiate by dividing asymmetrically [2, 5].

2. THEORY

The adherent areas of cell microenvironment induced the formation of guiding cues for the mitotic spindle in the cell membrane (Figure 1) [6]. We assumed here that these cues put the astral microtubules of the spindle under tension. The torque associated to these tensions is responsible for spindle rotation and alignment with respect to the cell microenvironment geometry. The net torque exerted on the spindle is calculated by integrating the torques exerted by all the microtubules in contact with cortcal cues. This torque derives from a potential energy whose minima correspond to stable spindle orientations. Taking into account fluctuations as additional random torques with zero average, the system exhibits a distribution of spindle orientations which can be estimated numerically.

978-0-9798064-0-7/μTAS2007/$20©2007CBMS

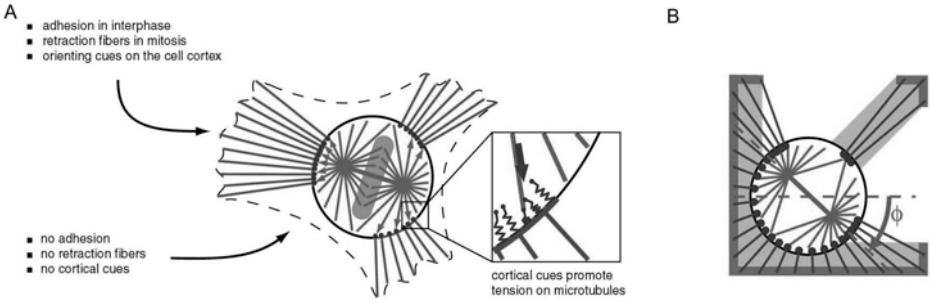

Figure 1. Adapted from [1]. **A**- Model description. Adhesion sites in interphase induce the formation of retraction fibers in mitosis. Molecular motors are activated at the top of these fibers and pull on the astral microtubules of the mitotic spindle. This torque induces spindle rotation and alignment with respect to adhesive microenvironment geometry. **B**- Calculation of retraction fibers (straight line) and cortical motors (small discs) spatial distributions for an arrow-shaped micro-pattern. The torque applied on the spindle is calculated for all spindle orientations.

3. EXPERIMENTAL

The orientation of the mitotic spindle in HeLa cells was studied experimentally on various fibronectin micropatterns for which we measured the angular distributions of spindle orientations during division. Micropatterns were made using classical microcontact printing technique on silanized glass coverslip passivated with poly-ethylene-glycol after the printing step [6]. Cell divisions were video-recorded in time-lapse phase contrast microscopy with an inverted microscope heated at 37°C. Using a motorized stage, we performed a multi-positions acquisition with a 3 minutes time-frame. Thereby we were able to record several hundreds of division in a few hours. Movies were automatically processed using a home-made analysis software based on image wavelet decomposition and image segmentation in order to detect cell shape changes during division [6].

4. RESULTS AND DISCUSSION

Based on micropattern geometries, we performed numerical simulations of our model. Our theory could correctly describe the most probable spindle orientation angle and furthermore could quantitatively account for the full shape of the angular distributions of spindle orientation. In addition, we found that some pattern geometries were able to induce asymmetric spindle orientation. In those cases spindle poles were not image from each other on both side of a symmetry axis of the pattern but aligned along the symmetry axis. Such spindle orientations place daughter cells in distinct configuration following division. We also described a configuration in which small variations can induce sharp transitions from symmetric to asymmetric spindle orientation in cells having quite similar shapes (Figure 2). Whereas the arrow-shaped patterns induced symmetric spindle orientation, crossbow-shaped pattern favoured asymmetric spindle orientations. Our model could account for this very sensitive behaviour of the spindle.

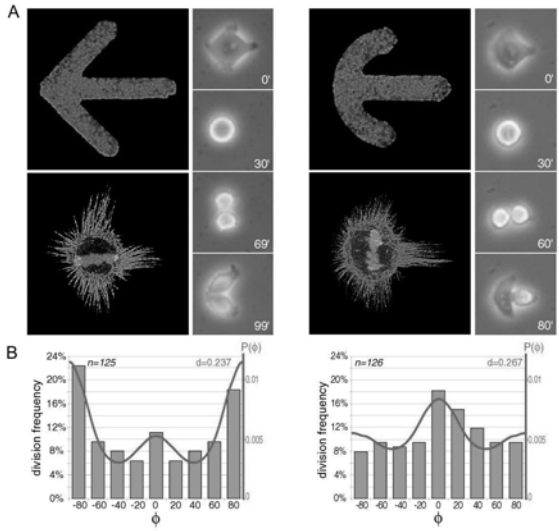

Figure 2. Adapted from [1]. **A**- Mitotic cells (actin and DNA staining, bottom) on two distinct fibronectin micropatterns (top) displaying a symmetric (left panel) and asymmetric (right panel) spindle orientation. Video-microscopy illustrates the similarity between the two daughter cells in the symmetric case (left panel) and their difference in the asymmetric one (right panel). **B**- Theoretical prediction of the angular distribution of mitotic spindle orientation (dark line) compared to experimental observations (histograms).

5. CONCLUSIONS

We showed that the geometrical information provided by the architecture of cell microenvironment is sufficient to guide cell division in culture. Our results suggest that the regulation of symmetric and asymmetric divisions of stem cells and thus their capacity to self-renew or differentiate could be controlled artificially in vitro by manipulating cell microenvironment geometry.

REFERENCES

1. Thery, M., et al., *Experimental and theoretical study of mitotic spindle orientation.* Nature, 2007. **447**(7143): p. 493-6.
2. Fuchs, E., T. Tumbar, and G. Guasch, *Socializing with the neighbors: stem cells and their niche.* Cell, 2004. **116**(6): p. 769-78.
3. Pugacheva, E.N., F. Roegiers, and E.A. Golemis, *Interdependence of cell attachment and cell cycle signaling.* Curr Opin Cell Biol, 2006.
4. Thery, M. and M. Bornens, *Cell shape and cell division.* Curr Opin Cell Biol, 2006. **18**(6): p. 648-57.
5. Morrison, S.J. and J. Kimble, *Asymmetric and symmetric stem-cell divisions in development and cancer.* Nature, 2006. **441**(7097): p. 1068-74.
6. Thery, M., et al., *The extracellular matrix guides the orientation of the cell division axis.* Nat Cell Biol, 2005. **7**(10): p. 947-53.

FLOATING ELECTRODE OPTOELECTRONIC TWEEZERS (FEOET): A NOVEL MECHANISM ENABLING OPTICAL MANIPULATION OF OIL IMMERSED AQUEOUS DROPLET

Sungyong Park[1], Chenlu Pan[1], Ting-Hsiang Wu[2], Sheraz Kalim[3], Michael Teitell[3] and Eric P.Y. Chiou[1]

[1] Mechanical and Aerospace Engineering, University of California at Los Angeles
[2] Electrical Engineering, University of California at Los Angeles
48-121 ENG. IV, 420 Westwood Plaza, Los Angeles, CA, 90095-1597, USA
[3] Pathology and Pediatrics, University of California at Los Angeles
675 Charles E. Young Dr. South, MRL 4-762, Los Angeles, CA 90095-1732

ABSTRACT

We report on a novel floating electrode optoelectronic tweezer (FEOET) that enables optical manipulation of oil-immersed droplets on a featureless photoconductive glass layer with direct optical images. This paper presents the concept, device structure, fabrication, numerical simulation, and proof-of-concept demonstration of this novel mechanism. We demonstrate that a 44 μW laser beam with an average intensity of 16.55 μW/mm^2 is able to transport a 750-μm oil immersed aqueous droplet at a speed of 82 μm/sec on a FEOET device. This promises FEOET to be an effective mechanism for massively parallel droplet manipulation.

Keywords: optical, dielectrophoresis, droplet manipulation, microfluidic devices.

1. INTRODUCTION

Manipulation of biological cells and micro/nano scale particles has recently attracted a lot of interests in microfluidic devices [1-4]. Optoelectronic tweezers (OET), as previously reported, allow for optical manipulation of single cells and microscopic particles sandwiched between an ITO electrode and a photoconductive electrode with direct optical images from incoherent light sources [5]. However, OET is optimized to work in an ionic medium with a conductivity between 10^{-3} to 1 S/m but is not able to provide optical modulation of electric field in electrically insulating biocompatible mediums such as oil. The FEOET device presented here enables, for the first time, optical manipulation of aqueous droplets in insulating oil with a low light intensity requirement and promises a powerful platform for parallel manipulation of a large array of oil-immersed water droplets with direct optical images.

2. DEVICE DESIGN AND WORKIGN MECHANISM

The structure of a FEOET device is illustrated in Fig. 1. It is fabricated by depositing two featureless a-Si:H layers, 500-nm undoped and 100-nm n$^+$, on a glass substrate. Two aluminum electrodes

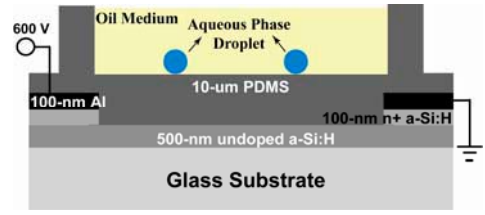

Fig. 1. FEOET device structure

978-0-9798064-0-7/μTAS2007/$20©2007CBMS

separated by a 1-cm gap are deposited at the two edges of the device using a lift-off method enabling electrical contact. The n^+ a-Si:H layer not covered by Al electrodes is etched away using RIE. A poly(dimethylsiloxane) PDMS chamber, filled with corn oil, is fixed on top of the undoped a-SiH layer, which houses the aqueous droplets. A 600 V DC bias is applied to the two aluminum electrodes to provide a lateral electric field across the whole device in both the oil and the a-Si:H layers. Since the aqueous droplets are much more conductive than the surrounding electrically insulating oil, an electric dipole is induced on each droplet under the application of a lateral electric field. Although the droplet induces a highly non-uniform electric field around itself, the droplet does not move due to dielectrophoresis (DEP) forces since the symmetric electric field pattern around a droplet results in a zero net force. However, when a light beam illuminates the photoconductive undoped a-Si:H layer at the edge of a droplet, it creates a light patterned virtual electrode which decreases the electric field strength at the illuminated site of the droplet. This phenomenon breaks the originally symmetric electric field pattern around a droplet and results in a non-zero net DEP force, which drives the droplet away from the light beam.

3. SIMULATION AND EXPERIMENTAL RESULTS

The working mechanism discussed in the previous section is verified by simulation and experimental results. Figure 2 shows the numerical simulation result of a two-dimensional electric field distribution in an oil medium under the illumination of a 70-um Gaussian laser beam. The local electric field near the illuminated spot is greatly decreased due to the light-patterned virtual electrode in the a-Si:H layer. When an aqueous droplet is immersed in the oil chamber, an electric dipole is induced by the water droplet as shown in Fig. 3(a). When a light beam illuminates the edge of a droplet, it decreases the electric field strength at the illuminated side and causes a non-uniform electric field distribution around the droplet. The net DEP force drives the droplet away from the light beam as indicated in Fig. 3(b).

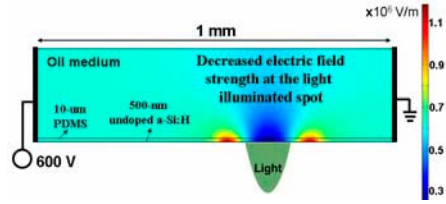

Fig. 2. Numerical simulation of the two-dimensional electric field distribution under the light illumination

Optically induced droplet manipulation has also been demonstrated experimentally. Fig. 4 shows the video snapshots demonstrating that a water droplet immersed in corn oil is repelled by a light spot as predicted in our simulation. Using a laser beam (532 nm, 4.35 mW) with a spot size of 2 mm, we can successfully drive a 750-µm droplet at a speed of 116 µm/sec. In addition, Fig. 5 shows that two droplets are driven to merge by a light beam. The optical power required to drive aqueous droplets on FEOET devices is low. Fig. 6 shows that a droplet can be driven at a

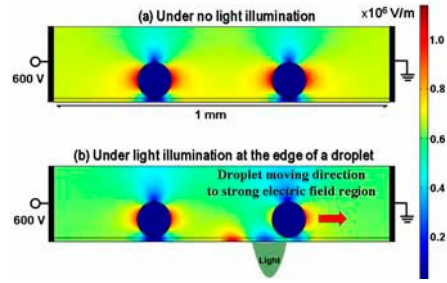

Fig. 3. Numerical simulation of the electric field distribution around two droplets. (a) Symmetric electric field distribution without light illumination. (b) Under light illumination, non-uniform electric field distribution around the droplet.

speed of 82 μm/sec even at an average light intensity of 16.55 μW/mm^2, promising the FEOET platform for massively parallel droplet manipulation.

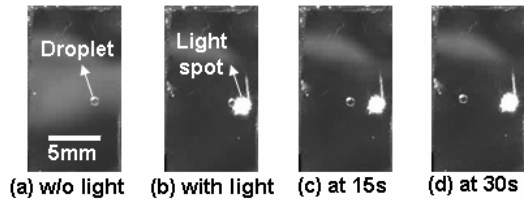

Fig. 4. Experimental results of the light-induced water droplet motion in corn oil medium.

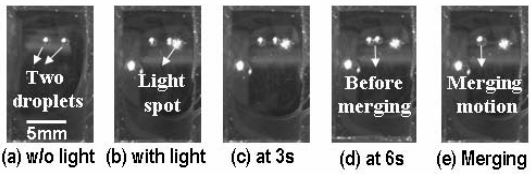

Fig. 5. Two-droplets merging motion induced by optical illumination.

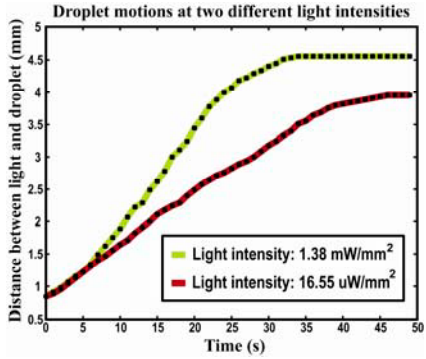

Fig. 6. Droplet position data at two different light intensities.

5. CONCLUSIONS

We have reported a novel floating electrode optoelectronic tweezer (FEOET) that enables, for the first time, optical manipulation of aqueous droplets in an electrically insulating oil medium with a light intensity as low as 16.55 μW/mm^2 on a proto-type device. The simple and flexible FEOET device allows droplet manipulation to be implemented in an open PDMS oil chamber. The simulation results demonstrate the mechanism of successful movement of an aqueous droplet using a light patterned virtual electrode. The virtual electrode decreases the electric field at the illuminated area to disrupt the originally symmetric field pattern around a droplet. The newly non-symmetric electric field induces a net non-zero DEP force thereby repelling the droplet away from the light beam illumination. Experimental results confirm the simulation results and demonstratedroplet movement, of a 750-μm droplet, using a laser beam (532 nm, 43.5 μW) with a spot size of 2 mm at a speed of 82 μm/sec. This promises FEOET as an effective mechanism for large scale, parallel droplet manipulations.

Acknowlegements: Special thanks to Prof. Tseng's group at UCLA Pharmacology.

REFERENCES

[1] C-M Ho, "Fluidics - The link between micro and nano science and technologies," *MEMS 2001, The 14th IEEE International MEMS Conference,* pp. 375-384, 2001.

[2] Y. Li, C. Dalton, H. Crabtree, G. Nilsson and K. Kaler, "Continuous dielectrophoretic cell separation microfluidic device," *Lab on a Chip*, 2007, 7, pp. 239–248.

[3] Martin Gijs, "Magnetic bead handling on-chip: new opportunities for analytical application," *Microfluidics and Nanofluidics,* Volume 1, November, 2004, pp. 22-40.

[4] V. Furdui and D. Harrison, "Immunomagnetic T cell capture from blood for PCR analysis using microfluidic systems," *Lab on a Chip*, vol 4, pp. 614–618, 2004.

[5] P. Y. Chiou, A. T. Ohta, and M. C. Wu, "Massively parallel manipulation of single cells and microparticles using optical images," *Nature*, vol. 436, pp. 370-372 , (2005).

A RAILED MICROFLUIDIC CHANNEL FOR MANIPULATION OF FINNED MICROTRAINS

Su Eun Chung[1], Hyunsung Park[2], Wook Park[1], Boyoung Kim[1], Kyoungsik Yu[3], and Sunghoon Kwon[1]

[1]*School of Electrical Engineering and Inter-university Semiconductor Research Center (ISRC), Seoul National University, SOUTH KOREA*

[2]*School of Electrical Engineering, Seoul National University, SOUTH KOREA, and*

[3]*Korea Electrical Engineering and Science Research Institute, SOUTH KOREA*

ABSTRACT

We propose and demonstrate a railed microfluidic channel and finned microstructures as a microscale analogy of trains on a monorail. Guided movement of polymeric microstructures in the microfluidic channel is demonstrated by fabricating grooves on the channel ('monorail') and finned microstructures connected to the groove structure ('trains'). The movement of the finned microtrains is controlled by the mechanical interaction between the guiding rail structure and the flow field in the microfluidic channel, which we envision adding important flexibility in microfluidic design.

Keywords: Microfluidics, Photopolymerization, Maskless lithography, Flow control

1. INTRODUCTION

The movement and migration of microparticles in microfluidic channels are important in a number of applications for micro total analysis systems. Techniques based on electrically [1] and magnetically [2] induced force have been extensively studied to control the movement of microstructures in fluidic environments. In this paper, we present a novel method of manipulating microstructures in the microfluidic channels with guiding grooves. In combination with an optofluidic maskless lithography technique for real-time synthesis of photopolymerized microstructures [3], the proposed technique provides a simple, yet powerful solution for generation, manipulation, and flow control of polymeric microstructures in the microfluidic channels.

2. DESIGN AND FABRICATION

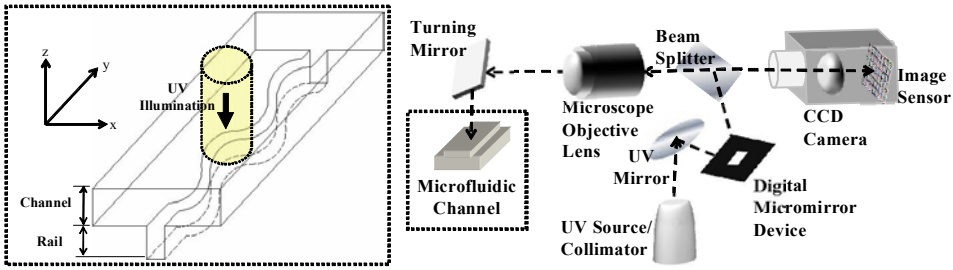

Figure 1. Schematic diagram of the maskless lithography setup (right) and the details of the railed-surface microfluidic channel (left inset). Finned microstructures fabricated by in-situ photopolymerization are bound to the guiding groove of the channel, and flow along the rail structure.

978-0-9798064-0-7/μTAS2007/$20©2007CBMS

Figure 1 schematically illustrates the optofluidic maskless lithography setup [3] and the concept of the railed microfluidics. We fabricate grooved microfluidic channels using a two-layer mold fabrication process described in Figure 2. The channel height and groove depth are 30 μm and 20 μm, respectively. By selectively polymerizing photocurable resin with a high-speed two-dimensional spatial light modulator, free-floating finned polymeric microstructures can be dynamically synthesized inside the railed microfluidic devices. Due to the mechanical interaction between the flow force and the guiding rail tracks, the polymerized two-layer microstructures will follow the rail. The two-layer channel structures can also be used to control the flow field inside the microfluidic channels [4].

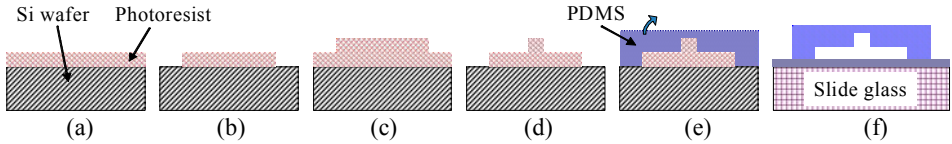

Figure 2. Fabrication process of a two-layer microfluidic channel with a guiding rail structure. (a) Photoresist (SU-8) coating on a silicon wafer. (b) Channel layer patterning. (c) Additional photoresist coating on top of the channel layer. (d) Rail-layer patterning. (e) Transferring the two-layer patterns to PDMS material. (f) Bonding the replica PDMS mold onto the PDMS-coated slide glass.

3. EXPERIMENTS AND RESULTS

Figure 3 shows dumbbell-shaped microstructures following a sinusoidally curved rail in a straight microfluidic channel. Although the flow field is straight, the movement of the synthesized polymeric microstructures bound on the rail follows the curved guiding rail. The snapshots of a rail-guided microstructure pushing a free-floating particle are also shown in Figure 3(b).

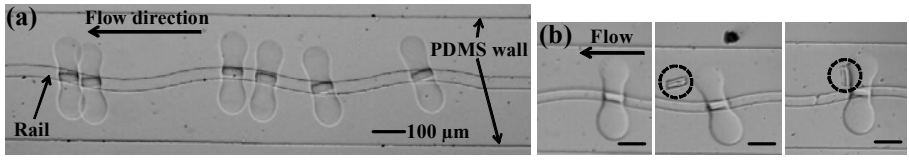

Figure 3. Dumbbell-shaped microtrains on a curved rail. (a) Movement of dumbbell-shaped microstructures on a sinusoidally curved rail. Although the flow field is straight inside the microfluidic channel, the railed microstructures trace the sinusoidal rail path. (b) A sequence of three microscope images of a fabricated dumbbell-shaped microstructure pushing and carrying a free-floating bar-shaped particle (dotted circle). All scale bars represent 100 μm.

Figure 4 demonstrates that the movement of the railed microstructures is mainly determined by the guiding rail track, not by the flow field per second. Polymeric microstructures fabricated off the rail (indicated by ① in Figure 4) don't have the fin structure, and, thus, follow the flow field. Due to the laminar flow characteristics, the position of a free-floating microparticle at the inlet channel determines which outlet channel it will go to at a junction. Approximately, microparticles at the lower half of the inlet go to the lower outlet channel (Figure 4 (d)), while microparticles at the upper half

flow straight (Figure 4 (h)). However, microstructures fabricated on the rail (indicated by ② in Figure 4) follow the rail path, and go to the lower output channel (Figure 4 (b-f)), despite that the free-floating microstructures at the similar locations flow straight.

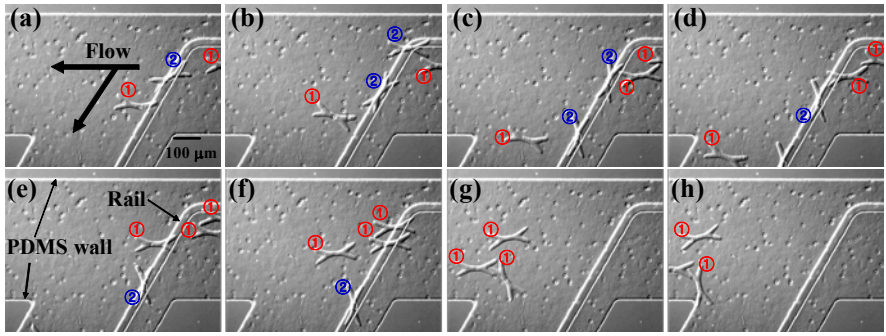

Figure 4. A sequence of differential interference contrast microscope images, comparing the transportation of photopolymerized microparticles on and off the guiding rail structure at a Y-branch junction. The finned polymeric microstructures remain on the guiding rail track, whereas other free-floating microstructures follow the flow field. In situ photopolymerized microstructures off and on the rail are labelled by ① and ②, respectively.

5. CONCLUSIONS

We have demonstrated that the railed microfluidic systems can manipulate the movement of in situ polymerized microstructures using the mechanical interaction between the original flow field and the guiding groove structures. In combination with dynamic fabrication of polymeric microstructures using maskless lithography [3] and assembly techniques [5], we envision that the demonstrated platform will find many interesting and innovative applications in biological or chemical assay requiring frequent solution exchange, and microparticle/cell manipulation in microfluidic environments.

ACKNOWLEDGEMENTS

This research is funded by the NANO Systems Institute-National Core Research Center (NSI-NCRC) program of Korea Science and Engineering Foundation (KOSEF), Korea.

REFERENCES

[1] P. C. H. Li and D. J. Harrison, "Transport, manipulation, and reaction of biological cells on-chip using electrokinetic effects," *Anal. Chem.* **69**(8), 1564-1568 (1997).

[2] H. Watarai, M. Suwa, and Y. Iiguni, "Magnetophoresis and electromagnetophoresis of microparticles in liquids," *Anal. Bioanal. Chem.* **378**(7), 1693-1699 (2004).

[3] S. E. Chung, W. Park, H. Park, K. Yu, N. Park, and S. Kwon, "Optofluidic maskless lithography system," Paper 3EA1.P, *Transducers 2007*.

[4] H. A. Stone, A. D. Stroock, and A. Ajdari, "Engineering flows in small devices: Microfluidics toward a Lab-on-a-Chip," Annu.Rev.Fluid Mech.**36**(1), 381-411 (2004).

[5] B. Kim, S. E. Chung, H. Park, W. Park, K. Yu, and S. Kwon, "Guided self-assembly of microlatches using railed microfluidics and optofluidic maskless lithography," accepted for presentation, *μTAS2007*.

METAMATERIALS FOR HYDRODYNAMICS: REFRACTION, FOCUSING AND BEAM STEERING FOR PARTICLES AND CELLS

K.J. Morton[1], O.K. Tsui[2], J.C. Sturm[1], R.H. Austin[3], S.Y. Chou[1]

[1]*Dept. of Electrical Engineering, Princeton University, USA*

[2] *Dept. of Physics, Boston University, USA*

[3]*Dept. of Physics, Princeton University, USA*

ABSTRACT

We show that it is possible to direct particles in a fluid much like rays of light in optics. We demonstrate refractive, focusing and dispersive elements for particles flowing through suitably constructed metamaterials: obstacle arrays with built-in asymmetry. We also configure these elements to address the problem of diffusion limited mixing in microfluidics. We show it is possible to cross dye or particle jets with a second particle stream and apply this concept to on-chip, continuous flow, "label & wash" of blood platelets. The unusual aspects of these *hydronic metamaterials* could be of great use for on-chip bio-particle mixing, separation and analysis.

Keywords: separation, mixing, concentration, cell handling

1. INTRODUCTION

The simplest hydronic element is based on deterministic lateral displacement (DLD) [1] of particles moving through an asymmetric obstacle course. As suspended particles transit an array of obstacles with its axis rotated relative to the direction of bulk fluid flow, they are separated by size with high resolution. Particles larger than a critical size move through the array at an angle to the flow, while smaller, sub-critical particles match the flow direction. Deterministic particle sorting has been successfully applied to a wide range of particle sizes and types using silicon, quartz and PDMS structures; from the separation of 100nm fluorescent beads in nanoimprinted devices [2] to the fractionation of whole blood (1um-30um diameter cells) into its components [3] using devices made with standard photolithography. With this basic hydronic element, we build up complex metamaterials for hydrodynamics and demonstrate novel, continuous flow handling of beads and cells. We show that a particle's path can be bent at an interface between two such elements and that particles can also be focused into hydrodynamic jets. We also cross two streams of different sized particles and label and rinse cells directly on-chip.

2. RESULTS AND DISCUSSION

A refractive hydronic element is shown in Figure 1. In this example, the metamaterial that fills the microchannel is a regular array of columns skewed at an angle ($+\alpha$) relative to the channel walls and fluid flow direction (Fig. 1b). Particles above a critical size move through the array at this angle until they reach an interface, in this case a ($-\alpha$) element, where they change direction (Fig. 1c). In Fig.1, the ($-\alpha$) element is downstream of the ($+\alpha$) element. If instead, these two elements are placed side-by-side they form a focusing

978-0-9798064-0-7/μTAS2007/$20©2007CBMS

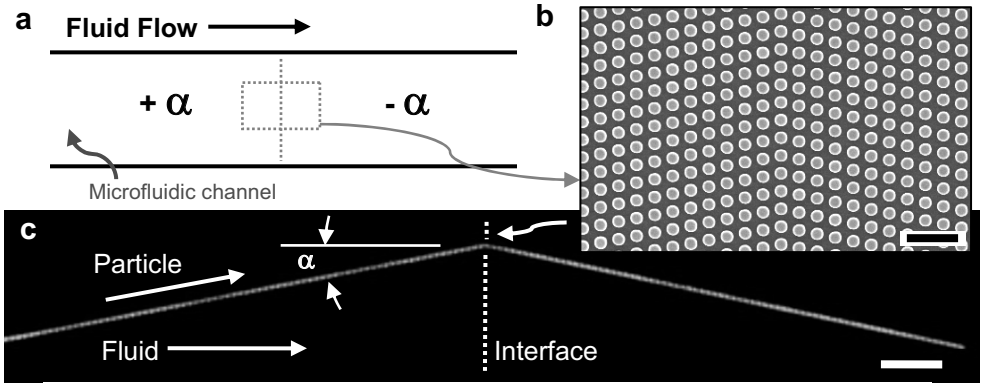

Figure 1. a) Schematic of a microfluidic channel filled with a structured asymmetric pillar array. Fluid flow direction is parallel to the channel walls, but particles larger than a critical size move along a trajectory defined by the array. b) SEM showing interface between +α and -α arrays (scale 30um.) c) Time trace of a single 3.0um fluorescent bead tracking at angle +α relative to the fluid flow and then changing direction at the interface (scale 100um).

element (+F) as shown schematically in Fig. 2a. Creating a hydrodynamic jet in a microfluidic channel typically requires carefully balancing flows across three input channels. Using the focusing element, we are able to create a narrow jet of particles easily from a single input (Fig. 2b) and concentrate species for downstream analysis. Figure 2c shows a complex metamaterial constructed by alternating focusing (+F) and dispersive (-F) elements of various focal lengths. The paths traced out by the particles moving through the device demonstrate that particles can be repeatedly manipulated according to the functionality of the hydronic elements in the structure.

We also apply these hydronic elements to address some fundamental challenges in micro-fluidics: mixing and separating particles in laminar fluid flow. Particle mixing in microfluidics is not efficient. Devices like the classic T mixer rely on large relative diffusion between different species and do not work well for particles with small diffusion coefficient such as cells. In Fig. 3a a particle in a simple hydronic element tracks along a diagonal path defined by the array and crosses a path traced by a smaller, sub-critical particle. Sub-critical particles follow

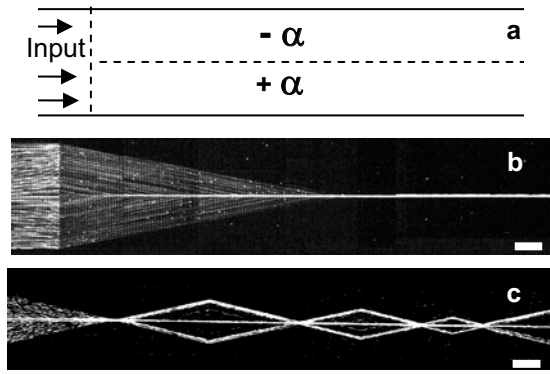

Figure 2. a) Microfluidic channel filled with -α arrays in the top half and +α in the bottom half to create a +F focusing elemen. b)Focusing particles from a single inlet into a concentrated jet. c)Beads propagating in a complex metamaterial constructed with alternating focusing (+F) and dispersive (-F) elements of varied focal lengths.

characteristic "zig-zag" paths as they move straight through the array following the overall fluid flow. Figure 3b shows a stream of particles tracking across a jet of smaller particles. Figure 3c shows the trajectory of a particle exiting a region of high dye concentration into a dye-free region, fully escaping the stream of continuously flowing dye. We extend these concepts to cell labeling and demonstrate on-chip, fluorescent labeling of blood platelets with fluorescent CD41a antigen which binds to the cell surface. Initially unlabeled platelets enter the chip, track across the dye stream, are labeled and then finally washed, exiting completely into the running buffer on the far side of the dye (Figure 3d).

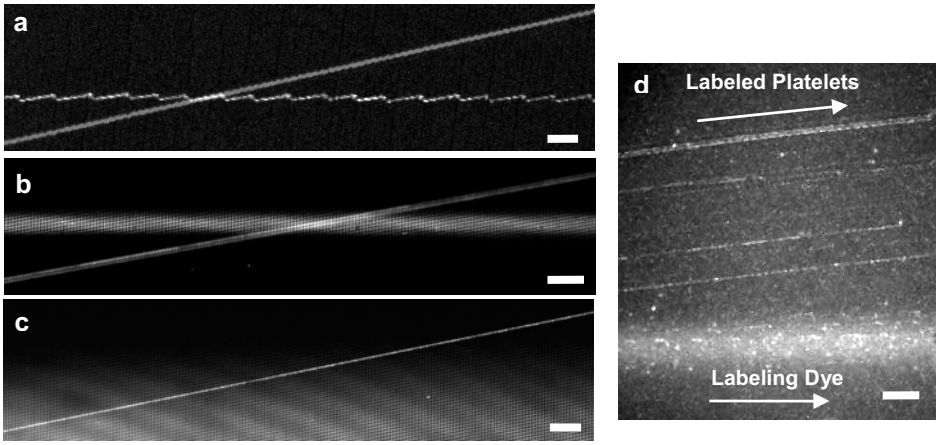

Figure 3. Particle jets crossing in simple +α hydronic elements. a) Single 3.0um bead (diagonal trace) tracking across the path of a 1.0um bead. The larger bead follows the array while the smaller bead is sub-critical and tracks in a "zig-zag" motion following the fluid flow straight through the array. b) Stream of 3.0um beads crossing a jet of 0.5um beads. c) Trajectory of 3.0um beads exiting a region of flowing fluorescent dye into dye-free fluid. d) On-chip "label & wash" of initially unlabeled blood platelets: The image shows newly labeled platelets after they emerge from the labeling stream and are washed in running buffer.

4. CONCLUSIONS

We constructed hydrodymamic metamaterials for microfluidic devices: arrays of posts tilted relative to the direction of fluid flow and assembled in various combinations that enable refraction of particle paths at interfaces and focusing of particles into a jet. The elements also provide a mechanism to steer beams of different sized particles across each other enabling continuous flow, on-chip cell handling, labeling and rinsing.

REFERENCES

[1] L.R. Huang, E.C. Cox, R.H. Austin and J.C. Sturm, Science, 304, 14 May 2004
[2] K.J.Morton, JC Sturm, RH Austin and SY Chou, Proc. MicroTAS 2006, Tokyo, Japan, pp 1014-1016, 2006
[3] JA Davis, DW Inglis, KJ Morton, DA Lawrence, LR Huang, SY Chou, JC Sturm, RH Austin, PNAS, Sept 2006

A FULLY INTEGRATED MICROFLUIDIC GENETIC ANALYSIS DEVICE FOR THE DETECTION OF BLOOD CANCERS

Lindsay A. Legendre[1], Daniel C. Leslie[1], Carleen J. Morris[1], Annelise Barron[3], Rebecca McClure[4] and James P. Landers[1,2]

University of Virginia Department of Chemistry[1] and Pathology[2], Charlottesville, VA 22904 USA

[3]Northwestern University, Department of Chemical Engineering, Evanston, IL 60208 USA

[4]Mayo Clinic, Division of Hematopathology, Rochester, MN 55905 USA

ABSTRACT

The work described here represents the development of a fully-integrated microdevice for clinical analysis in the diagnosis of T-cell lymphoma (TCL). Adapting the sample preparation steps to an integrated device involved optimization of both the PCR and DNA separation techniques that are currently used in in clinical labs. The time required to perform PCR was reduced by >7-fold (3 hours to 25 minutes) utilizing microchip-based non-contact heating. The DNA fragment separation was performed using a novel polymer formulation of (linear polyacrylamide/duramide), and successful integration of PCR with electrophoretic separation is presented.

Keywords: Integrated Microdevice, Cancer Detection, T-cell Lymphoma

1. INTRODUCTION

The pathogenesis of TCL frequently involves T-cell receptor (TCR) gene rearrangement, which can be detected by PCR amplification of select gene sequences. In normal individuals, the amplified PCR fragments represent a polyclonal lymphocyte population, while lymphoma patients display a monoclonal population These can be discriminated by electrophoretic separation (Figure 1A) where monoclonality appears as a few (1-3) uniformly-sized fragment(s) that predominate; while polyclonal T-cell expansions produce a distribution of fragment sizes with no predominant fragment(s). In clinical labs, DNA extraction is followed by a 3 hour PCR amplification and a 40 minute CE separation under single-stranded conditions and utilizing 4-color detection. While the automation associated with integration of sample preparation steps provides a significant advantage over traditional methods, any reduction in the analysis times associated with these lengthy processes is an additional benefit.

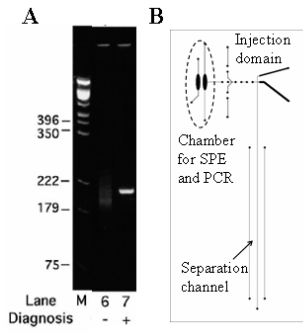

Figure 1. A) Gel electrophoresis of TCR-PCR products where Lane 6 is a negative, Lane 7 is a positive, and Lane M is a sizing standard. Image from reference [1]. B) The device design for the fully-integrated microchip.

978-0-9798064-0-7/μTAS2007/$20©2007CBMS

2. THEORY

While we have recently reported a fully-integrated device for the detection of bacteria [2], an integrated microfluidic genetic analysis device for rapid lymphoma detection must provide high-resolution separation of the amplified products and, consequently, a novel sieving polymer would be needed to discriminate and dissect out monoclonality. In addition, adaptation of the TCR-PCR to the microdevice format requires solid-phase extraction (SPE) of DNA in totally-aqueous conditions. Chitosan-coated magnetic beads provide such a phase eliminating PCR-inhibiting reagents, allowing DNA elution with the PCR master mix and eliminating DNA dilution [3].

3. EXPERIMENTAL

A microchip design can be seen in Figure 1B, illustrating the placement of the different sample processing domains. The microchip PCR was performed using non-contact thermocycling methods and, through tailoring the PCR protocol to the microchip, the time associated with thermocycling was reduced from 3 hours to 25 minutes. Of importance to developing an integrated microchip system for detecting the TCR gene rearrangements inherent to TCL, the separation method needed to be simplified to avoid further complicating microdevice design. A new co-polymer formulation of linear polyacrylamide (LPA) and 6 % poly-duramide was utilized for DNA separations to assist in discriminating between a positive or negative sample after the TCR-PCR. Use of this co-polymer in conjunction with a duramide coating for electroosmotic flow suppression [4] allowed for a double-stranded separation with the inclusion of a DNA intercalator for laser-induced fluorescence of the post-PCR products.

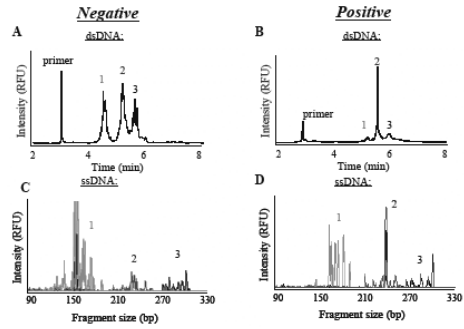

Figure 2. Comparison of DNA separation methods. Resultant electropherograms from positive (A, B) and negative (C, D) patient samples. The monoclonal product can be seen in the positive samples and labeled with "product" and the three polyclonal peaks in the negative samples are numbered. The microchip separations seen in A and C are double-stranded separations with single color detection represented by an "ME" while B and D are single-stranded DNA separations with 4-color detection, represented by a "CE".

4. RESULTS AND DISCUSSION

While simple PCR methods rely on either the absence or presence of a specified fragment, the TCR-PCR discriminates between a monoclonal or polyclonal cell population. Figure 2 shows the results of the separation currently performed in clinical labs with 4-color detection of single-stranded DNA (labelled as "CE" in the figure), compared to the simplified method which uses single color detection and a double stranded DNA separation (labelled as "ME"). The positive traces, shown in panels A and B, correspond to the same amplified sample analyzed by the two different separation techniques. The positive sample shows the presence of a strong, sharp peak, representative of a monoclonal cell population

while the broad peaks on either side of the sharp peak correspond to those labelled "1" and "3" in the single-stranded DNA separation. In the case of a negative sample, the electropherogram (C) shows the presence of three broad peaks, which result from the generation of multiple fragment sizes and represent a polyconal cell population; this is also illustrated in the single-stranded DNA separation electropherogram (D) in three different grouping of peaks, labelled with "1", "2", and "3". By eliminating the need for a single-stranded separation, the complication associated with on-chip chemical denaturation of the PCR products (i.e., with formamide) is avoided, and allows for direct injection of the PCR products from the PCR domain.

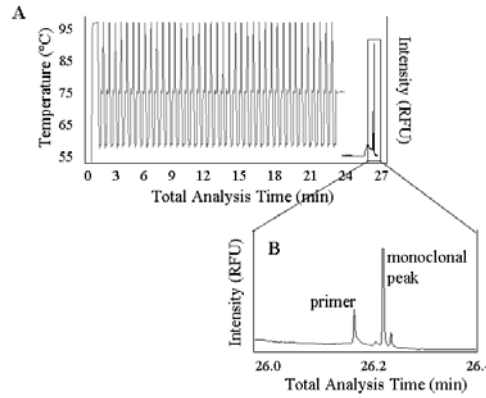

Figure 3. PCR-ME of a positive TCL sample. A) Shows the total analysis time for performing both PCR and ME. The thermocycling trace corresponds to the temperature axis on the left (shown in roughly 0-24 minutes) and the ME trace corresponds to the intensity axis on the right. B) Shows the ME trace magnified to distinguish the primer and products.

These two processes which requiring the most development, TCR-PCR and DNA separation, were further tested by performing the integration of non-contact PCR with double-stranded DNA separation using the LPA-co-duramide. Figure 3 shows the results from the integration of IR-PCR and the electrophoretic separation from a patient sample pre-determined to be positive for TCL – the time for performing the IR-PCR, and subsequent electrophoretic separation, has been reduced to under 30 minutes. The success of the method can be seen through the identification of the peak characteristic of a monoclonal cell population, labeled on the electropherogram.

5. CONCLUSIONS

Developing an integrated microdevice for the detection of TCL included extensive optimization of the processes currently used in the clinical lab, especially the PCR and DNA separation. Displayed here is the successful integration of these two processes requiring only the implementation of the DNA extraction method, which has been previously presented [3], to complete the system.

REFERENCES

[1] Munro, N. J., Snow, K., Kant, J. A., Landers, J. P. *Clin. Chem*., 1999, 45, 1906.

[2] Easley, C. J., Karlinsey, J. M., Bienvenue, J. M., Legendre, L. A., Roper, M. G., Feldman, S. H., Hughes, M. A., Merkel, T. J., Ferrance, J. P., Landers, J. P. *Proc. Natl. Acad. Sci. USA*, 2006, 109, 19272.

[3] Legendre, L. A., Cao, W., Ferrance, J. P., Landers, J. P. *Proc. Micro Total Analysis Systems*, 2006, 840.

[4] Albarghouthi, M. N., Buchholz, B. A., Huiberts, P. J., Stein, T. M., Barron, A. E., *Electrophoresis*, 2002, 23, 1429.

HYPERSPECTRAL AND SPATIAL MULTIPLEXING OF ULTRASENSITIVE IMMUNOASSAYS FOR DETECTING TOXIN EXPOSURE

A.V. Hatch, R.J. Meagher, D.S. Reichmuth, A.E. Herr, M.B. Sinclair, D.M. Haaland and A.K. Singh

Sandia National Laboratories, USA

ABSTRACT

We report on a diagnostic platform for rapidly detecting exposure to biotoxins. Through spatial and hyperspectral multiplexing, up to 32 ultrasensitive immunoassays can be performed simultaneously using a 1"-square microfluidic chip. Sub-picomolar sensitivity is achieved by on-chip sample preconcentration. Immunoassays for a panel of toxins and potential host response biomarkers have been developed.

Keywords: Immunoassay, Preconcentration, Electrophoresis, Portable Diagnostic

1. INTRODUCTION

Urgent need exists for developing next-generation clinical diagnostics devices for screening individuals exposed to biotoxins. These devices must be easy-to-use, automated and self-contained, and preferably, have a small footprint to allow use in point-of-care and point-of-incident settings. Early-stage or presymptomatic diagnosis of exposure is critical for effective treatment, but current assays of toxin exposure are slow and centralized at specialized labs [1]. To address these needs, we report on the development of a rapid multiplexed detection platform capable of performing 32 ultrasensitive immunoassays simultaneously in a single 1"-square chip with hand-portable instrumentation. The immunoassay format provides the high sensitivity (sub-pM) and specificity required for toxin exposure diagnosis using blood samples. Analyte detection via integrated mixing, preconcentration and PAGE separation is also rapid (5-20 minutes) and automated. The power of this immunoassay format was previously demonstrated for detecting protein markers of disease in saliva [2]. Spatial and hyperspectral fluorescence multiplexing enables 32 such assays simultaneously. We also report on assay development for a panel of toxins and host-response markers: Shiga, Ricin, SEB, Anthrax PA, TTC, TNF, IL6 and IL1β.

2. EXPERIMENTAL

Spatial Multiplexing: Chips were fabricated using methods described previously [2] but with much higher feature density for spatial multiplexing. Each immunoassay chip element includes loading, preconcentration, and separation gels photopolymerized within etched glass channels for fully automated analysis. Figure 1 shows an 8-element chip designed and fabricated for spatial multiplexing of assays. This design enables much faster loading of sample and reagents compared to previous work [2] with all 8 integrated immunoassay elements housed in approximately the same chip area used previously for a single assay.

Hyperspectral Multiplexing: In addition to spatial multiplexing, hyperspectral fluorescence detection enables multiple assays in each device element using a single excitation laser and a single set of emission optics [3]. A schematic of the detector is shown

978-0-9798064-0-7/μTAS2007/$20©2007CBMS

in Figure 2a. Multiple reporter dyes (one for each immunoassay) were excited simultaneously by a 488-nm laser and the emission was spectrally resolved using a prism and detected by a CCD. Multivariate curve resolution (MCR) algorithms allow rapid data extraction for multiple antibodies as shown in Figure 2b. Hyperspectral imaging with MCR analysis can eliminate interference from contaminant emission or autofluorescence resulting in higher quantitative accuracy relative to commercial microscopes [4]. Simultaneous resolution of many overlapping fluorophores is thus effective with a single laser line.

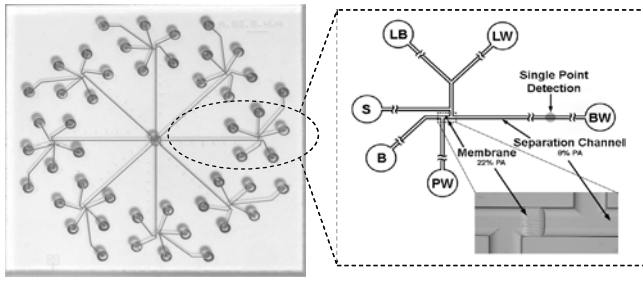

Figure 1. Spatial multiplexing with an 8-Element, 1"- square immunoassay chip filled with dye for visualization. Each immunoassay chip element (inset) contains photopolymerized loading, preconcentration/mixing, and separation gels to perform automated immunoassays. Separation of immune complexes is detected at a single point in each separation channel.

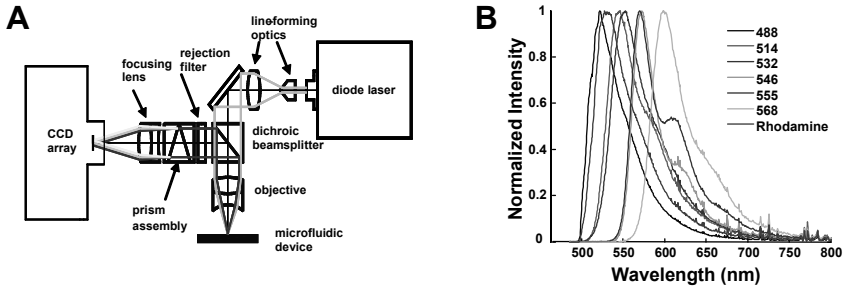

Figure 2. Spectral Multiplexing. A) Optics diagram of hyperspectral fluorescence detection. A single laser and CCD allow multiple assays simultaneously. The emission of uniquely-labeled antibodies is spectrally resolved and quantified by MCR analysis. B) A mixture of 7 different antibodies, each uniquely labeled, resolved simultaneously.

3. RESULTS AND DISCUSSION

Several toxin immunoassays were developed to form the basis of a diagnostic panel by selecting commercially available antibodies yielding the desired immunoassay response curve when mixed with relevant concentration ranges of toxin or host-response marker (Figure 3). Antibodies were labeled with dyes having unique fluorescence emission for hyperspectral multiplexing and sufficient 488-nm excitation. To achieve the detection sensitivity required for toxins with activity at extremely low concentrations, sample was preconcentrated on-chip [2, 5] prior to PAGE separation.

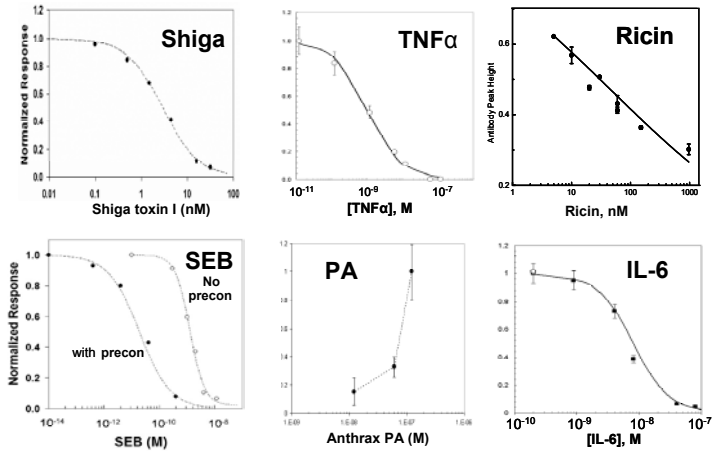

Figure 3. Immunoassay calibration curves for representative toxins and host response markers. Assay development for additional markers is ongoing. Samples are optionally preconcentrated to achieve the sensitivity required for diagnosis as shown for SEB, where calibration curves are for conditions with and without preconcentration.

4. CONCLUSIONS

This work establishes the necessary features of a toxin detection platform, namely ultrasensitivity, hand-portability, and rapid diagnosis (5-30 minutes) of multiple analytes for effective presymptomatic detection of exposure and intoxication.

ACKNOWLEDGEMENTS

This work was supported by the NIDCR (U01DE014961) and Sandia LDRD program. Sandia is a multiprogram laboratory operated by Sandia Corporation, a Lockheed Martin Company, for the US Department of Energy under contract DE-AC04-94AL85000.

REFERENCES

[1] E.A. Casman, "The Potential of Next-Generation Microbiological Diagnostics to Improve Bioterrorism Detection Speed" *Risk Analysis*, **24**, 521-536 (2004).

[2] A.E. Herr, A.V. Hatch, D.J. Throckmorton, H.M. Tran, J.S. Brennan, W.V. Giannobile, and A.K. Singh, "Microfluidic immunoassays as rapid saliva-based clinical diagnostics" *PNAS*, **104**, 5268-5273 (2007).

[3] M.B. Sinclair, D.M. Haaland, J.A. Timlin, and H.D.T. Jones, "Hyperspectral confocal microscope" *Applied Optics* **45**, 6283-6291 (2006).

[4] J.A. Timlin, D.M. Haaland, M.B. Sinclair, A.D. Aragon, M.J. Martinez, and M. Werner-Washburne, "Hyperspectral microarray scanning: impact on the accuracy and reliability of gene expression data." *BMC Genomics*, **6**, 72 (2005).

[5] A.V. Hatch, A.E. Herr, D.J. Throckmorton, J.S. Brennan, and A.K. Singh, "Integrated Preconcentration SDS-PAGE of Proteins in Microchips Using Photopatterned Cross-Linked Polyacrylamide Gels" *Analytical Chemistry*, **78**, 4976-4984 (2006).

NANOFLUIDIC PRECONCENTRATION DEVICE FOR SENSITIVE AND WIDE DYNAMIC RANGE IMMUNO-SENSING

Ying-Chih Wang[1,2], Vincent H. Liu[2], and Jongyoon Han[2,3]

[1]Dept. of Mechanical Engineering, [2]Dept. of Electrical Engineering and Computer Science, and [3]Department of Biological Engineering

Massachusetts Institute of Technology, Cambridge, MA 02139, USA

ABSTRACT

This paper describes a microfluidic immunoassay device with integrated preconcentration system, enabling the detection of various analytes (proteins) at low target concentrations with faster binding kinetics. It not only complements recent advances of novel immuno-biosensors, but also can be used to further enhance the most novel and advanced immuno-biosensor systems developed. The work has demonstrated significant sensitivity/kinetics enhancement by the preconcentration of antigens before the binding.

Keywords: Nanofluidics, preconcentration, immuno-sensing

1. INTRODUCTION

One of the key technological challenges in immuno-biosensing is its sensitivity and selectivity is inherently dependent on the properties of antibody-antigen pairs. Reliable detection becomes progressively harder and requires longer reaction time with lower target analyte concentrations, which are often the case in disease biomarker detection. While much progress has been made in the area of immuno-detection of proteins and other biomolecules, most of the existing techniques rely on the post-binding amplification (either physical or chemical) to enhance the signal created by the primary binding events. Therefore, the sensing would be still ultimately limited by the binding characteristics of primary antibodies. In this study, we have developed a novel strategy using electrokinetic pre-binding concentration. Instead of amplifying the signal after the primary immuno-reaction, we seek to enhance the concentration of the target molecule before the reaction using a unique molecular preconcentration device. The uniqueness of this novel method comes from the fact that the sensitivity, selectivity and kinetics of binding between the target analyte and the (primary) antibody are significantly enhanced, via an efficient preconcentration process before the binding. Because the number of target analytes near the binding site is increased via preconcentration, binding characteristics of primary antibody-antigen is directly improved, therefore leading to faster and more sensitive detection. We have demonstrated 500~1000 fold enhancements in sensitivity and much faster binding using a standard, bead-based immunoassay device over a molecular background.

2. EXPERIMENTAL

The idea was implemented by integrating nanofluidic preconcentrator and standard bead-based immunoassay in a microchip, therefore, the target concentration can be continuously increased at the site of primary immuno-binding by the concentrator. The nanofluidic preconcentrator applies the unique ion depletion force from charge-selective sub-50 nm nanofluidic channel to trap biomolecules in the adjacent microchannel (12x50 μm). To integrate the concentrator with immuno-sensors, capture (primary) antibodies were immobilized on streptavidin-labeled polystyrene beads and delivered to a predefined sample collection area of the preconcentrator. While the major limiting factor in low

978-0-9798064-0-7/μTAS2007/$20©2007CBMS

concentration analyte detection is posed by the quality of the antibody (binding constant, K_D), prolonged incubation time is unavoidable to reach sufficient primary binding. The presented integrated device can be used to address these issues by adjusting the analyte concentration and hence the reaction kinetics and sensitivity [1].

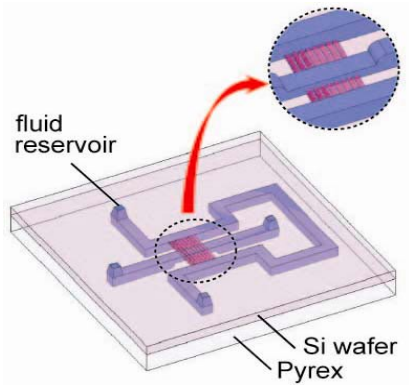

Figure 1. Schematics of the nanofluidic preconcentrator. The center sample channel is connected to the U shaped buffer channel by nanochannel arrays. The close view shows the nanochannels and bead trapping structure from the back side.

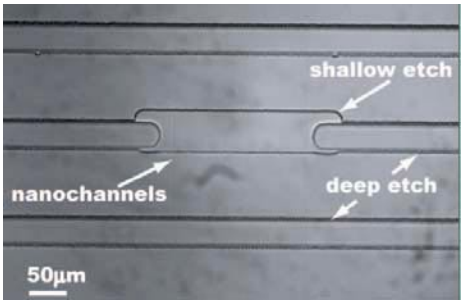

Figure 2. Bright field image of the nanofluidic channel array and bead trapping dam structure. The 40 nm deep nanochannel arrays have a width of 200 µm and are bridging microchannels 100 µm away from each other. As for the microchannels, except of the 5.5 µm shallow etches for bead trapping, all regions were etched to a 12 µm depth.

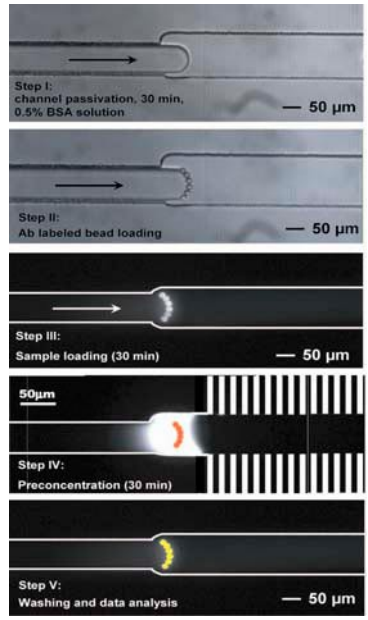

Figure 3. Bead loading, immunosensing and preconcentration procedure (target molecule R-phycoerythrin, false color images).

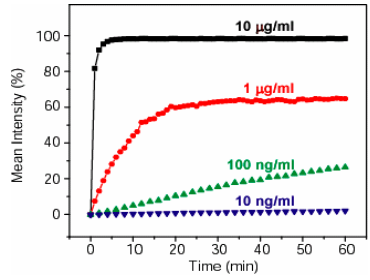

Figure 4 Binding kinetics of R-PE samples with various concentrations, the intensity represents the fluorescent signal from R-PE molecule captured on polystyrene beads.

3. RESULTS AND DISCUSSION

The novel electrokinetic preconcentration device was first published in 2006 [2], where we reported a million-fold biomolecule pre-concentration in a silicon-based nanofluidic system. Because the preconcentrator can increase the local biomolecule concentration by many orders of magnitude without complex buffer arrangement or in-line porous material, it allows direct coupling between the preconcentrator and the immuno-sensor.

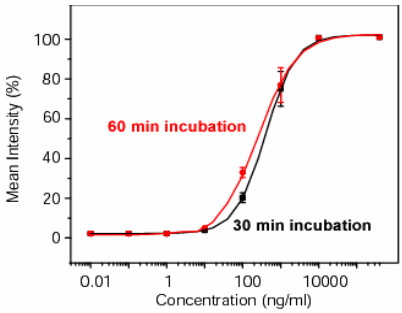

Figure 5 Dose response curves of R-PE molecule on anti-R-PE beads. As shown in the plot, longer incubation time can only slightly increase the signal intensity. Compares the responses between 30 min and 1 hr incubation, the detection limited (10 ng/ml) is not improved by 30 min longer incubations.

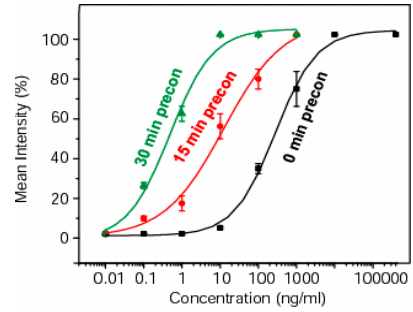

Figure 6 Plots shown the dose response of the immunoassay without preconcentration, with 15 min and 30 min preconcentration. Through maintaining a 30 min on-site preconcentration, this approach can lower the sensitivity limit by about 500 fold from 50 pM to sub 100 fM range. (with 10 µg/ml GFP as simulated molecular background)

Figure 1 is the layout of the device, which has nanochannel arrays on both side of the trapping region. **Figure 2** shows the image of the preconcentrator and the bead trapping area defined by two-step wetting etching process. The shallow microchannel was etched to a depth of 5.5 µm to hinder the 7.5 µm polystyrene beads (with anti-phycoerythrin labeled) and the deep microchannels were etched to a depth of 12 µm. The experimental procedure is shown in **Figure 3**. After channel passivation with BSA, beads and sample buffers where introduced before we started the preconcentration. In **Figure 4**, analytes with lower initial target concentration takes longer to reach binding equilibrium due to the diffusion-limited transport. **Figure 5** shows a 3 orders of magnitude dose response of the assay. In **Figure 6**, with a 30 min preconcentration we were able to enhance the immunoassay sensitivity by more than 500 fold from 50 pM to the sub 100 fM range. This was achieved with simulated molecular background in the sample solution, demonstrating possibility of detecting directly from complicated protein mixtures. Moreover, by adjusting the preconcentration time, we can tune the immunoassay detection range to cover 6 orders of magnitude concentration variation, which is critical for multiplexed detection of multiple target molecules.

4. CONCLUSIONS

As the system can be coupled to existing sensing and post-amplification techniques, it could be used to enhance the dynamic range of detection, binding kinetics, and sensitivity. We believe the integrated device can effectively address the most challenging detection issues in immuno-sensing. Moreover, the preconcentration system has been tested successfully for detection from serum samples with albumin and IgG depletion. Since the preconcentrator can concentrate target enzymes rapidly, it can also be used to probe various biochemical activities associated with human physiology.

ACKNOWLEDGEMENTS

This work was supported by NIH (GM68762, EB005743, CA119402).

REFERENCES

[1] P. R. Nair and M. A. Alam, *Applied Physics Letters* 88, 233120 (2006).
[2] Y.-C. Wang, A. L. Stevens, and J. Han, *Analytical Chemistry* 77, 4293 (2005).

PHOTO-PATTERNED MULTI-ENZYMATIC MICROREACTORS

Timothy B. Stachowiak[1,2], Timothy C. Logan[1], Douglas S. Clark[1], Frantisek Svec[2], and Jean M. J. Fréchet[1,2]

[1]Department of Chemical Engineering, University of California, Berkeley, USA and [2]Molecular Foundry, Lawrence Berkeley National Laboratory, Berkeley, California, USA

ABSTRACT

While enzymes have been used within microfluidic devices to enable a variety of biochemical applications, the complexity of confining multiple enzymes to distinct locations within a microfluidic system has thus far limited the development of multi-enzymatic reactors. In this work, we report a method for photo-patterning multiple enzymes on porous polymer monoliths within microfluidic channels to perform spatially-separated multi-enzyme reactions as well as to measure kinetic parameters of immobilized enzymes *in situ*.

Keywords: Polymer monolith, enzyme immobilization, photo-patterning, kinetics

1. INTRODUCTION

Porous polymer monoliths have been shown effective for creating many of the analytical components needed in an integrated system such as preconcentrators, chromatographic stationary phases, and immobilized enzymatic microreactors [1]. Monoliths with well-defined chemical and porous properties can be prepared directly within device microchannels using UV-initiated polymerization. Polymer monolith enzymatic reactors provide a higher surface area and enzyme loading than open channel devices [2], but in contrast to enzyme-loaded microbeads, monoliths do not require devices with auxiliary filling channels and/or microfabricated retaining structures [3].

In this work, enzymes were patterned on polymer monolith supports using a photografting technique to introduce reactive azlactone groups onto the surface of the monolith (Figure 1). An important benefit of photografting is that it is possible to pattern the location of grafted vinylazlactone chains, and subsequently the location of immobilized protein. Furthermore, multiple enzymes can be immobilized in different locations within a single device by repeating the azlactone photografting and subsequent enzyme immobilization process for each enzyme

2. EXPERIMENTAL

Poly(butyl methacrylate-*co*-ethylene dimethacrylate) polymer monoliths were photopolymerized in fused silica capillary columns. Poly(ethylene glycol) methacrylate (PEGMA) was photografted onto the surface of the polymer monolith to render it hydrophilic and prevent the non-specific adsorption of protein to the monolith surface, according to a previously reported procedure [4]. To enable the covalent immobilization of proteins, the surface of the polymer monolith was first activated by patterned photografting with the reactive monomer 2-vinyl-4,4-dimethylazlactone using a photografting solution consisting of 15 wt% vinyl azlactone and 0.22 wt% BP dissolved in a solution of 75:25 wt% *tert*-butanol:water. A photomask defined the areas grafted with azlactone chains.

978-0-9798064-0-7/μTAS2007/$20©2007CBMS

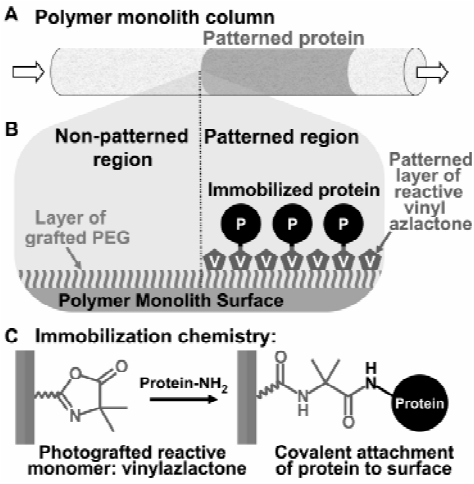

Figure 1. Schematic of the photo-patterning process. (A) Protein is immobilized to the polymer monolith surface in patterned regions within a microchannel. (B) PEG is grafted to the monolith surface to prevent non-specific protein adsorption. Vinyl azlactone is photo-patterned onto the PEG surface and activates the surface for protein immobilization. (C) Azlactone reacts with amines of proteins to form a covalent bond between the protein and the monolith surface.

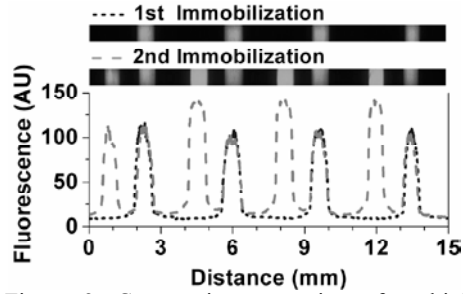

Figure 2. Consecutive patterning of multiple GFP patches on a polymer monolith. Each patch is ~750 μm in length.

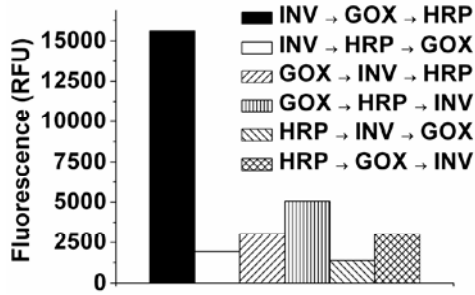

Figure 3. Directional synthesis with a three-enzyme system: INV, GOX, and HRP. Product fluorescence was measured with each possible arrangement of the enzymes.

Protein was then covalently immobilized onto the surface of a monolith already photografted with vinyl azlactone by pumping a protein solution through the monolith. The azlactone functionality reacts with the amine groups of proteins, forming a covalent bond between the protein and the support surface. This process was repeated for the immobilization of additional proteins on the monolith surface. A model multi-enzyme system was prepared using invertase, glucose oxidase, and horseradish peroxidase (HRP). The activity of HRP was monitored *in situ* by utilizing the fluorogenic substrate, Amplex Red, and monitoring the on-line production of fluorescent product.

3. RESULTS AND DISCUSSION

To enable effective patterning of enzymes on the monoliths, it was necessary to reduce non-specific protein adsorption by photografting the surface of the monolith with poly(ethylene glycol) methacrylate using a procedure we reported at μTAS '06 [4]. Optimizing immobilization conditions, including enzyme concentration and the inclusion of a non-ionic surfactant in the immobilization solution, further reduced nonspecific adsorption. The combination of these techniques enabled the successful photo-patterning of protein on monolith supports (Figure 2) and the creation of sequential multi-enzymatic reactors using two- and three-enzyme systems. A three-enzyme sequential reaction was performed using invertase, glucose oxidase, and horseradish peroxidase. All possible arrangements of the three enzymes were tested, but significant product formation was only observed when the enzymes were in the correct sequential order (Figure 3). Finally, to

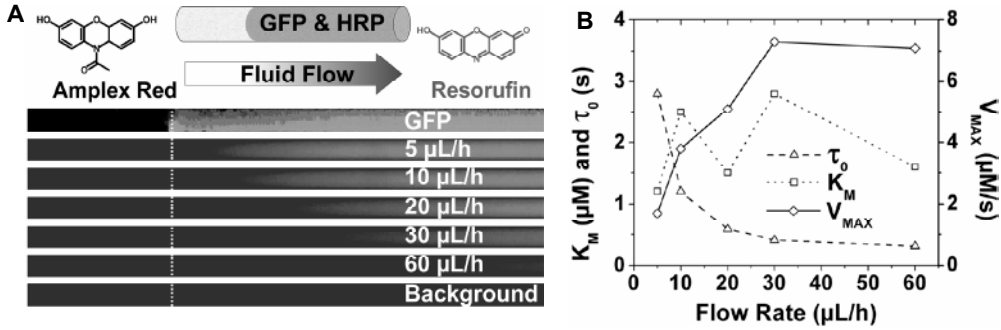

Figure 4. (A) Steady-state formation of fluorescent resorufin from Amplex Red catalyzed by photo-patterned HRP immobilized on polymer monolith. (B) Flow rate dependence of the observed kinetic parameters calculated from the fluorescence intensity profiles using the plug-flow reaction model.

measure the kinetics of immobilized enzymes, we measured the steady-state product profiles of the fluorescent reaction *in situ* and then analyzed the data using a plug-flow bioreactor model to determine the kinetic parameters (Figure 4). The Michaelis constant of 1.9 ± 0.7 µmol/L for horseradish peroxidase agrees with previously published values. The effects of mass-transfer limitations on the observed kinetic parameters were evident at relatively low flow rates but were absent at higher flow rates (cf. Figure 4B).

4. CONCLUSIONS

Photo-patterning enzymes on polymer monoliths provides a simple technique for preparing spatially localized multiple-enzyme micro-reactors capable of directional synthesis. Other potential applications of photo-patterned enzyme sequences include miniaturized analytical and diagnostic assays utilizing a specific order of reactions, high-throughput combinatorial biocatalysis in a microfluidic format, and the creation and investigation of artificial metabolic pathways *ex situ*.

ACKNOWLEDGEMENTS

Financial support of this work by the National Institute of Biomedical Imaging and Bioengineering, National Institutes of Health (EB-006133) is acknowledged with thanks. Work at the Molecular Foundry was supported by the Director, Office of Science, Office of Basic Energy Sciences, Materials Sciences and Engineering Division, of the U.S. Department of Energy under Contract No. DE-AC02-05CH11231

REFERENCES

[1] (a) Svec, F. *J. Chromatogr., B* **2006**, *841*, 52-64. (b) Stachowiak, T. B.; Svec, F.; Fréchet, J. M. J. *J. Chromatogr., A* **2004**, *1044*, 97–111. (c) Svec, F. *Electrophoresis* **2006**, *27*, 947–961.

[2] (a) Mao, H. B.; Yang, T. L.; Cremer, P. S. *Anal. Chem.* **2002**, *74*, 379-85. (b) Holden, M. A.; Jung, S. Y.; Cremer, P. S. *Anal. Chem.* **2004**, *76*, 1838-43.

[3] (a) Ku, B. S.; Cha, J. H.; Srinivasan, A.; Kwon, S. J.; Jeong, J. C.; Sherman, D. H.; Dordick, J. S. *Biotechnol. Prog.* **2006**, *22*, 1102-07. (b) Seong, G. H.; Crooks, R. M. *J. Am. Chem. Soc.* **2002**, *124*, 13360-61.

[4] Stachowiak, T. B.; Svec, F.; Fréchet, J. M. J. *Proc. Micro Total Analysis Systems* **2006**, *1*, 227-229.

SINGLE PARTICLE TRAPPING AND MELTING FOR FUNCTIONAL AND HIGH-RESOLUTION MODIFICATION OF PDMS MICROCHANNELS

Masashi Yamamoto[1], Masumi Yamada[2], Shizuka Fukushima[3], Masahiro Yasuda[1], Minoru Seki[1,3]*

[1]Osaka Prefecture University, 1-1 Gakuen-cho, Naka-ku, Sakai, Osaka 599-8531, JAPAN
[2]Tokyo Women's Medical University, 8-1 Kawada-cho, Shinjuku-ku, Tokyo 162-8666, JAPAN
[3]Chiba University, 1-33 Yayoi-cho, Inage-ku, Chiba 263-8522, JAPAN

ABSTRACT

We describe herein a surface modification scheme for PDMS microchannel with high resolution, via single-particle trapping and melting. In our previous study, we have reported a method for modifying microchannel by accumulating and melting multiple polymer particles[1]. To improve the resolution of modification, and to make the modified surface flat, single particles with functional group were trapped into particle-size wells formed on the bottom surface of a PDMS microchannel. The trapped particles were then melted by heating, and the functional group was transferred and immobilized onto the local surface of the microchannel. In this study, monodispersed polymer particles having epoxy groups were synthesized, and local surfaces with various shapes were accurately modified with a resolution of several micrometer. The flatness of the modified area was examined by confocal laser scanning microscopy. Also, by using two types of polymer beads with different diameters stepwise, the possibility of complex modification was successfully shown.

Keywords: Surface modification, PDMS microchannel, particle trapping

1. INTRODUCTION

Surface property of microchannel is essential to perform accurate fluid manipulation or biological analysis, due to the high volume-to-surface ratio. Several methods for local surface modification of microchannels have been hitherto developed using laminar flow control[2] or photo polymeri-zation[3,4]. In our previous study, we have developed a method for local surface modification of PDMS microchannel employing micro-particle accumulation and melting techniques[1]. However, the modified surface becomes concaved due to the void space of the accumulated particles, and

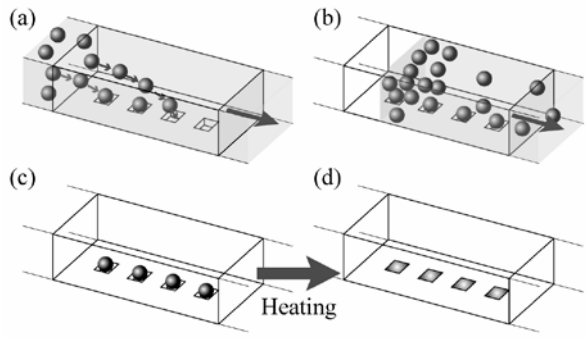

Figure 1. Schematic diagrams showing the procedure of local surface modification. (a)~(c) Particles are precipitated and trapped into the wells. (d) After trapping, particles are melted by heating, to immobilize the functional groups onto the local surface of the microchannel.

978-0-9798064-0-7/μTAS2007/$20©2007CBMS

the resolution was not sufficiently high. In this study, to overcome these shortcomings, we propose a scheme in which one site was modified with single micro-particle. The procedure of modification is shown in Fig. 1. When a particle suspension is introduced into a microchannel having particle-size wells on the bottom surface, single particles are trapped in the wells due to the interaction between the particle and well surfaces, surrounded by a proper medium. Then the trapped particles are melted, to stabilize the functional group onto the surface.

2. EXPERIMENTAL

Several types of monodispersed poly(styrene-glycidyl methacrylate) particles, which have epoxy group as a functional group, were synthesized via dispersion polymerization. The size of the particles was 3~7 μm, and they could be melted at ~150 °C. PDMS microdevices were fabricated by bonding two PDMS plates; one plate has the microchannel structure, and the other has microwells. The width, depth, and length of the channel were 200 μm, 150 μm, and 10 mm, respectively. Various types of microwells were employed, with sizes of 5~15 μm. Before introducing particles, channel surface was rendered hydrophobic by heating. Methanol was used as the career medium, and the particle behaviour was observed using a microscope. After trapping particles, the microdevice was heated at 200 °C to melt the particles. To examine the presence of the epoxy group on the local surface, the surface was treated with ethylene diamine and FITC.

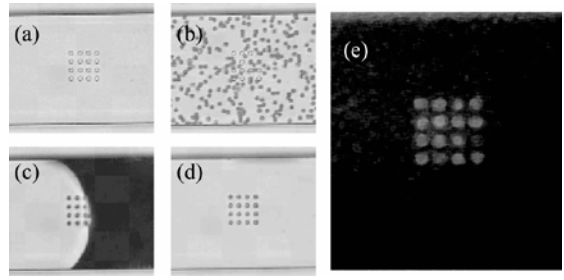

Figure 2. (a)-(d) Photographs showing the particle behavior; (a) before particle introduction, (b) flowing particles, (c) air introduction, and (d) trapped particles in 16 wells. (e) Fluorescent image of the modified region coupled with FITC, after melting the trapped particles. Τηε ωελλ διαμετερ ωασ 7 μm, and the channel width was 200 μm.

3. RESULTS AND DISCUSSION

Photographs of particle trapping in a microchannel with 16 wells are shown in Fig. 2 (a)-(d). Particles were specifically trapped into the wells, while non-specific particle adhesion onto the channel surface or channel corner was not observed. After melting the particles, the presence of the epoxy group was confirmed by staining the modified area using FITC (Fig. 2 (e)). Even when the number of wells was increased, the entire target sites could be modified by introducing particle suspension several times, as shown in Fig. 3. Also, modification of various-shape wells was demonstrated; Fig. 4 shows photographs of wells before and after particle

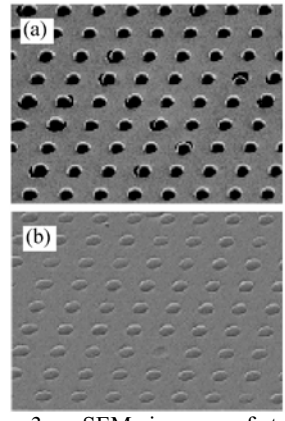

Figure 3. SEM images of trapped multiple single-particles (a) and melted particles (b). The diameter of wells was 7 μm. All of the wells were modified.

By designing optimal microwells, it was possible that to make roughness less than 300 nm; the surface profile could sufficiently be flat.

Then, stepwise trapping of different-size fluorescent particles using different size wells was examined, as shown in Fig. 5. Initially, a suspension of larger particles was introduced, to trap the large particles into the large wells, and then, suspension of smaller particles was introduced. Trapping of particles into multiple-size wells (Fig. 5 (a)-(d)) and Y-shaped wells (Fig. 6 (e)-(g)) was successfully performed, demonstrating the possibility for highly functional modification.

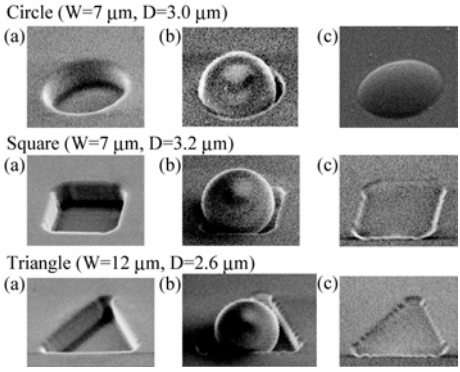

Figure 4. Modification of various shapes; (a) Before introduction, (b) trapped particles, and (c) melted-particle regions.

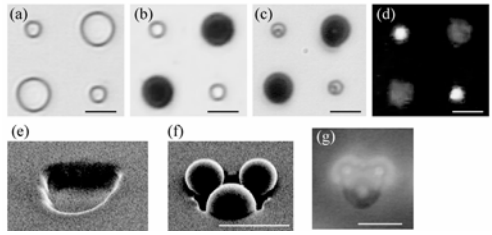

Figure 5. Surface modification using two types of particles with different diameters. (a)~(d) stepwise trapping of fluorescent particles into different-size wells. (e)~(g) Trapping of two types of particles into a Y-shape well. Larger particles were initially introduced. Scale bars, 10 μm.

4. CONCLUSIONS

We demonstrated a new scheme for local surface modification of PDMS microchannel with micrometer-order resolution, using micro-particles as the vector of functional groups. This scheme can be applied to pattern various chemicals in microchannel, which will be useful for cell micro-patterning or hydrophilicity/phobicity control.

ACKNOWLEDGEMENTS

This research was supported in part by Grants-in-aid for JSPS fellowship from JSPS and Scientific Research B (16310101) from the Ministry of Education, Science, Sports, and Culture of Japan.

REFERENCES

[1] N. Nonaka, M. Yamamoto, M. Yamada, M. Yasuda, M. Seki, *Proc. MicroTAS 2005*, Vol. 2, 758-760 (2005).
[2] B. Zhao, J. S. Moore, D. J. Beebe, *Anal. Chem.*, **74**, 4259-4268 (2002).
[3] S. Hu, X. Ren, M. Bachman, C. E. Sims, N. L. Allbriton, *Anal. Chem.*, **76**, 1865-1870 (2004).
[4] S. Lai, X. Cao, L. J. Lee, *Anal. Chem.*, **76**, 1175-1183 (2004).

EXTREME WATER-REPELLANT SURFACE ENABLED BY NANO-MICRO INTEGRATED TEXTURE

Yongjoo Kwon[1], Junkyu Choi[2], Neelesh Patankar[3] and Junghoo Lee[2]

[1]Nano System Institute – National Core Reaserch Center, Seoul National University, Korea
[2]School of Mechanical and Aerospace Engineering, Seoul National University, Korea and
[3]Department of Mechanical Engineering, Northwestern University, USA

ABSTRACT

A super hydrophobic surface is realized by forming double roughness on a silicon surface. A deep silicon etching and a gas phase isotropic silicon etching (XeF2) are used as the fabrication method for two different scales of roughness. Combination of these two techniques enables the uniform formation of double roughness on a silicon surface. The fabricated surface shows the tendency of preferring Cassie state [1] to Wenzel state [2] and a durable super hydrophobic property. Through a series of experiments, this study also offers a verification of the previous theoretical prediction [3] for the amplification of contact angle on a surface with double roughness.

Keywords: Nano roughness, Micro roughness, Double roughness, Super hydrophobic surface, Wenzel state, Cassie state, Contact angle, Contact angle hysteresis

1. INTRODUCTION

Reducing fluidic resistance has become an important issue for efficient control of micro fluid. One of the main streams for the attempt to reduce the flow resistance is to form a hydrophobic surface using roughness. A chemical surface treatment and micro or nano patterning have been used as methods to form roughness on a surface [4-7]. These approaches require submicron structures with high aspect ratio for hydrophobic surface which has low contact angle hysteresis [8]. Recently, forming a multiple roughness is proposed as a new method for roughness-based super hydrophobic surface [9,10]. Up to date, however, it has been a challenge to form adequate multiple roughness uniformly. We propose the combination of two etching techniques (Deep RIE and XeF2 Si etch) as an effective method to form a nano-micro integrated (double roughened) surface for a stable and hysteresis-free super hydrophobic surface.

2. FUNDAMENTAL

Cassie state in which a water droplet is completely lifted by the roughness structure is required for a super hydrophobic surface with low contact angle hysteresis [1]. There are several ways to fabricate the surface preferring the Cassie state. One of them is to form submicron scale structures with high aspect ratio [7]. These structures are, however, difficult to fabricate, and not durable. If an intrinsic contact angle (contact angle before forming the roughness) is made large enough, the surface will have an extreme hydrophobic property without the tall submicron structures [3]. For this, a self assembled monolayer (SAM) coating on the roughness can be considered, but is not enough to create a roughened surface that absolutely prefers the Cassie state. The essence of this study is to amplify the intrinsic contact angle using nano scale roughness to realize the Cassie state with simple micro scale roughness.

978-0-9798064-0-7/μTAS2007/$20©2007CBMS

3. FABRICATION & EXPERIMENTAL

The double roughness structure was produced in two steps. Micro-photolithography and Deep RIE (Plasma Therm) were used for the formation of a micro pillar structure on a silicon substrate. Then XeF2 etching (Tech Bank) was performed to generate the nano roughness on the surface of the pillars. Then the sample was coated with SAM. An image of a droplet on the fabricated surface was captured, and analyzed to find the contact angle. A tilting test was used to quantitatively compare the effect of the double roughness on reducing the hysteresis. The sample was tilted on a stage that can rotate. The tilting angle was recorded when the droplet starts to slip down.

4. RESULTS AND DISCUSSION

Figure 1 is a scanning electron microscope (SEM) image of the double roughness structure fabricated using the proposed method. Nano roughness uniformly covers not only the top of the pillar, but also the side walls, and the bottom substrate. Figure 2 (a) and (b) are the images of the droplet in contact with the single micro roughness and the double roughness respectively. While the single micro roughness is easily wet, the double roughness keeps the Cassie state with the largely amplified contact angle of 176°. Table 1 compares the calculated and the measured contact angles on the double roughness and the single micro roughness. From the values listed, it is shown that the measured contact angles for the double roughness are much larger than other cases. They are also in good accordance with the calculated ones.

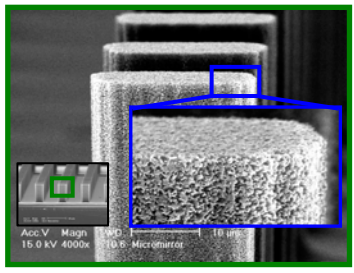

Figure 1. Fabricated Nano-Micro Hierarchical structure.

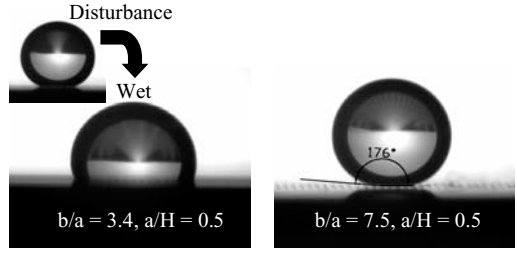

(a) Single Micro (b) Double

Figure 2. Contact angle on Single Micro roughness and Double roughness

Table 1. Contact angle and Tilting angles for the given surfaces (*b/a is value measured)

No roughness (Flat)			Nano roughness			Single micro roughness (a/H=0.5)				Double roughness (a/H=0.5)			
Contact angle		Tilting angle	Contact angle		Tilting angle	b/a	Contact angle		Tilting angle	b/a	Contact angle		Tilting angle
Calc.	**Meas.**		Calc.	**Meas.**		(of pillar)	Calc.	**Meas.**		(of pillar)	Calc.	**Meas.**	
-	**103°**	**Not slip**	-	**156°**	**10°**	1.5	151.1°	**152°**	**24°**	1.6	170.8°	**170°**	**2°**
-	-	-	-	-	-	2.3	158.2°	**155°**	**wet**	3.5	174.6°	**172°**	**1.5°**
-	-	-	-	-	-	3.4	163.7°	**160°**	**wet**	5.1	176.1°	**173°**	**1.4°**
-	-	-	-	-	-	4.7	167.4°	**wet**	**wet**	6.6	176.8°	**174°**	**0.6°**
-	-	-	-	-	-	5.6	169.2°	**wet**	**wet**	7.5	177.2°	**176°**	**< 0.6°**

Figure 4 is a graph derived from Wenzel and Cassie's equation for square pillar structure [6]. In this calculation the contact angle on the nano roughness was used as the intrinsic contact angle. As shown in the graph, the cosine value of the contact angle in Wenzel curve is almost always below '-1' (unreal region). This means the Wenzel state is energetically

impossible to reach, and the Cassie state dominates even when the aspect ratio is low (a/H = 2). Figure 5 shows a result of the tilting test. On the surface with the double roughness, the droplet started to slip at an extremely low tilting angle (0.6°). The droplet even shook due to a feeble vibration of laboratory floor. Figure 6 shows a result of the dropping test on the surface with double roughness. The light coming through the gap between the drop and the pillars confirms the theoretical prediction that there is no Wenzel state in the double roughness surface.

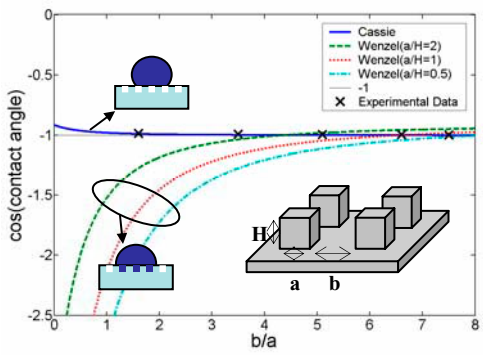

Figure 4. Wenzel & Cassie curve

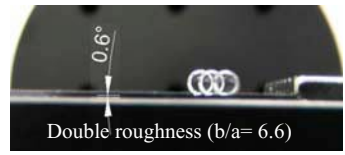

Figure 5. Tilting test on Double roughness

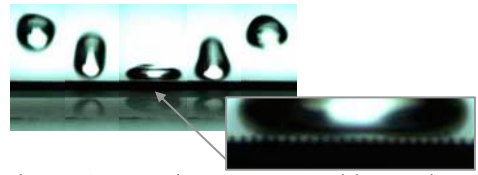

Figure 6. Dropping test on Double roughness

5. CONCLUSIONS

In this study, we realized the surface with the nano-micro integrated double roughness which has the Cassie state dominating at a large contact angle. The method of forming double roughness was developed by the combination of simple MEMS techniques. Through series of experiments, it was proved that the fabricated surface was in a stable hydrophobic state, and had very low contact angle hysteresis. Consequently, the validity of the theoretical prediction for the contact angle on a surface with double roughness was confirmed. This study shows that the combination of nano and micro elements can bring a totally new effect.

ACKNOWLEDGEMENTS

This work was supported by the NSI-NCRC program of KOSEF (R15-2003-032-01002-0(2006)), and Micro Thermal System Research Center (ERC) (R11-2001-095-03001-0).

REFERENCES

[1] Cassie A.B.D., S. Baxter, Trans. Faraday Soc., 1944, 40, 546.
[2] Wenzel, T. N. J., Phys. Colloid Chem. 1949, 53, 1466.
[3] Neelesh A. Patankar, Langmuir 2004, 20, 8209.
[4] Shibuchi, S., Onda, T., Satoh, N. & Tsuji,K., J. Phys. Chem 1996. 100, 19512-19517
[5] Chang-Hwan Choi, Chang-Jin Kim., PRL 96, 066001 (2006)
[6] He, B.; Patankar, N. A.; Lee, J., Langmuir 2003, 19 (12), 4999.
[7] Kim, J. and Kim, C. J., IEEE Conference on MEMS, Jan. 2002, pp. 479-482.
[8] Dussan, V. E. B. and Chow, R. T. P. J. Fluid Mech. 137, 1-29 (1983).
[9] Thangawng, A. L.; Lee, J., IMECE04, 2004; p 13.
[10] H. E. Jeong, S. H. Lee, J. K. Kim, and K. Y. Suh, Langmuir 2006, 22, 1640-1645

IN VITRO FERTILIZATION AND DEVELOPMENTS OF HEALTHY OOCYTES BY A DIELECTROPHORETIC SEPARATION CHIP

Wonjae Choi[1], Ji-Su Kim[2], Do-Hyun Lee[1], Deog-Bon Koo[2], Kyung-Kwang Lee[2] and Je-Kyun Park[1]

[1] Dept. of Bio and Brain Engineering, Korea Advanced Institute of Science and Technology (KAIST), KOREA and [2] Center for Regenerative Medicine, Korea Research Institute of Bioscience & Biotechnology (KRIBB), KOREA

ABSTRACT

We reports a new dielectrophoretic separation method of healthy oocytes for *in vitro* fertilization (IVF), utilizing their dielectrophoretic velocity difference based on castellated-shape electrodes. Under positive dielectrophoresis (DEP) condition of AC 3 V (15 s, 1 MHz), only normal oocytes are moved and separated effectively. Further analyses such as IVF and embryo development demonstrate that moved healthy oocytes have better developmental potential than stayed unhealthy oocytes. In addition, our method is comparable to conventional manual selection method.

Keywords: Dielectrophoresis, oocyte, *in vitro* fertilization, castellated-shape electrodes

1. INTRODUCTION

The choice of fertilizable oocytes is one of the important technical issues in IVF [1] (Figure 1). Conventionally, the selection of healthy oocyte has been manually conducted by a skilful expert with a microscopic observation one by one. The whole process is labor-intensive and time consuming. Although DEP is a favorable technique for the manipulation of biological cells, it has been used only for rotation experiments in embryology [2].

2. EXPERIMENTAL

An interdigitated castellated shape electrode was exploited for the DEP-based oocyte manipulation in a positive DEP condition (Figure 2). As the voltage is applied, a non-uniform electric field is generated. This resulted in the DEP to manipulate the oocytes. Each side of the castellated electrode was 500 μm, which was designed in consideration of normal size of oocyte. A pair of electrodes was fabricated using standard microfabrication

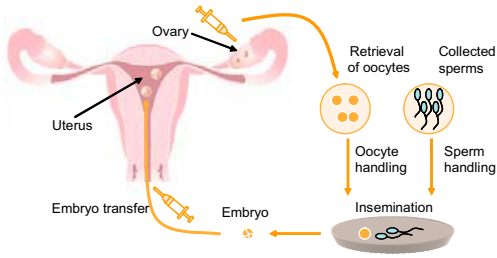

Figure 1. Schematic process of in vitro fertilization.

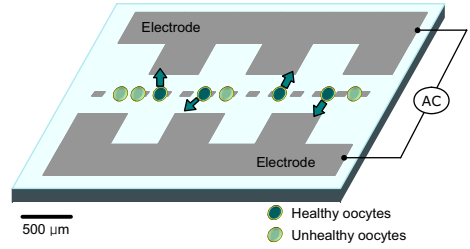

Figure 2. Configuration of dielectrophoretic separation chip for separating healthy oocytes.

978-0-9798064-0-7/μTAS2007/$20©2007CBMS

process as a thin-film Cr/Au electrode on a glass substrate. All DEP experiments were conducted using Zimmerman cell fusion medium.

3. DIELECTROPHORETIC MANIPULATION OF OOCYTES

Normal porcine oocytes were manipulated on the fabricated DEP separation chip with a condition of AC 3 V, 1 MHz and 15 s pulse (Figure 3). The moving direction of each oocyte was in a good agreement with the electric field simulation (Figure 4). As shown in Figure 5, normal oocytes moved faster than the abnormal oocytes, representing different DEP characteristics based on the intrinsic properties of oocyte. Here, abnormal oocytes were defined as oocytes cultured without medium for 3 days. For both group of oocytes, the dielectrophoretic velocities increase as the applied voltage increase. We select an optimum voltage of 3 V for oocyte selection experiments.

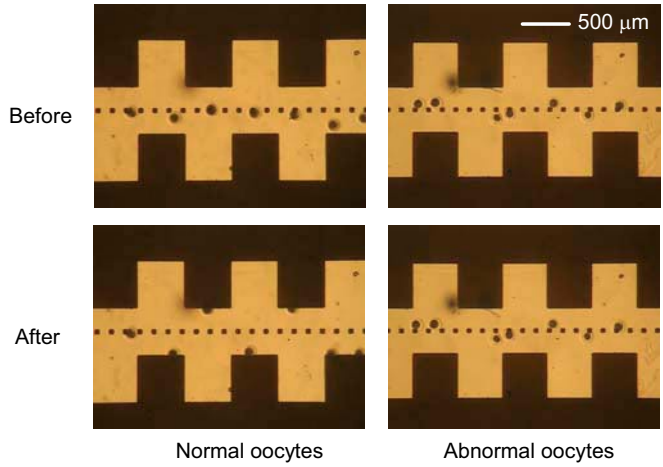

Figure 3. Examples of dielectrophoretic transportation of oocytes. Normal and abnormal porcine oocytes were manipulated by the same DEP condition (AC 3 V, 15 s pulse, 1 MHz).

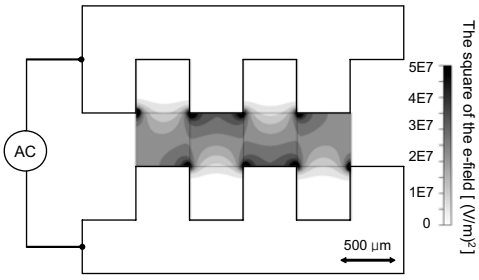

Figure 4. The simulated electric field distribution calculated by CFD solver (CFD-ACE+). The square of the electric field (E^2) is plotted because the DEP force is proportional to its gradient (∇E^2).

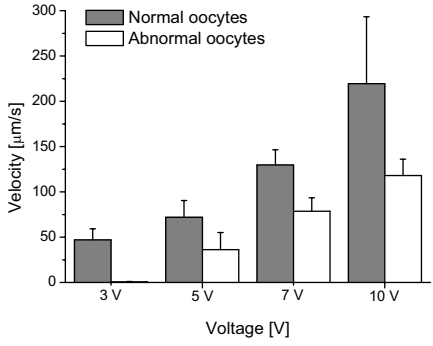

Figure 5. Effect of AC voltage on the dielectrophoretic velocities difference between normal and abnormal oocytes.

4. OOCYTE SELECTION AND ANALYSIS

In the oocyte selection experiment using unknown oocytes, the samples were collected as two groups; moved oocytes as healthy group and stayed oocytes as unhealthy group. The healthy group showed better potential than the unhealthy group (Figure 6). The staining data with other sample oocytes revealed that the embryos from the healthy oocytes have more fertilization competency (Table 1). Figure 7 shows an image of the developed blastocyst and a photograph of embryos of healthy and unhealthy oocytes, respectively. It is anticipated that our strategy based on the difference of DEP velocity can be useful to develop an automatic selection method for fertilizable oocytes, reducing human intervention in embryonic experiments.

Table 1. Comparison of embryo development after *in vitro* fertilization.

Group	Embryo number	No. of cells ICM [a]	TE [b]	Total
Control	17	7.6 ± 3.8	26.2 ± 9.4	34.3 ± 12.0
Healthy	21	7.3 ± 3.5	28.4 ± 9.2	35.6 ± 9.8
Unhealthy	9	3.9 ± 2.5	22.2 ± 3.8	26.1 ± 4.7

*Three replicates for this experiment were conducted. [a] ICM: inner cell mass. [b] TE: trophectoderm.

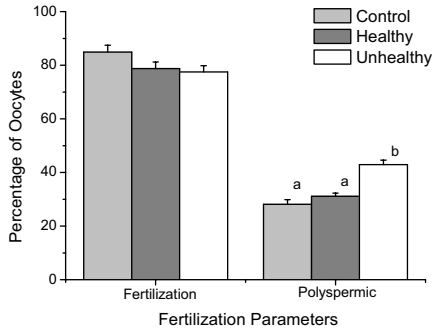

Figure 6. Comparison of fertilization parameter of selected oocyte group. The different superscripts a and b within columns represent significant difference (P<0.05). Values are mean ± standard deviation.

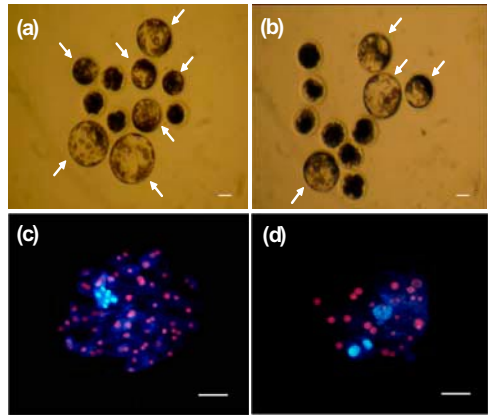

Figure 7. Photographs of embryos from (a) healthy and (b) unhealthy oocytes. Arrows indicate the blastocysts. (c) and (d) show differential staining images obtained from one of the developed blastocysts from healthy and unhealthy oocytes, respectively. Red: TE staining Blue: ICM staining. Scale bars are 50 μm.

REFERENCES

[1] R. S. Suh, N. Phadke, D. A. Ohl, S. Takayama and G. D. Smith, *Rethinking gamete/embryo isolation and culture with microfluidics*, Hum. Reprod. Update, 9, 451 (2003).

[2] J. Park, S. H. Jung, Y. H. Kim, B. Kim, S. K. Lee, J. O. Park, *Design and fabrication of an integrated cell processor for single embryo cell manipulation*, Lab Chip, 5, 91 (2005).

IMPEDANCE SPECTROSCOPY FOR LABEL-FREE DIFFERENTIAL LEUKOCYTE COUNTS

David Holmes[1], Julie Cakebread[2], Judith Holloway[2], Donna Davis[2] and Hywel Morgan[1]

[1] School of Electronics and Computer Science, University of Southampton, UK
[2] Southampton General Hospital, University of Southampton, UK

ABSTRACT

We present data from a microfabricated single cell impedance spectrometer. The device simultaneously measures the impedance and optical (fluorescence) properties of individual cells as they pass through the detection region on the chip. The impedance of the three main leukocyte sub-populations (monocytes, lymphocytes and neutrophils) of human blood was measured. The impedance data shows that the cells can be discriminated at frequencies of 2 and 5 MHz, implying that a 3-part differential analysis is possible.

Keywords: blood, dielectrophoresis, flowcytometry, single cell

1. INTRODUCTION

Impedance spectroscopy is a non-invasive technique which allows analysis of the surface and internal electrical and dielectric properties of cells and other particles [1-3]. In traditional impedance spectroscopy, the electrical properties of a cell suspension are measured using relatively large volumes (*circa* 100 µl). The measurement is therefore the average over several million cells. This represents a significant hurdle to the discrimination of cell sub-populations. To address these issues, we have developed a microfluidic device capable of the high-speed analysis of individual cells in rapid succession [4-6]. We demonstrate the ability of the device to distinguish, *based on impedance alone*, the leukocyte (white blood cell) sub-populations in human blood. Fluorescence analysis of the cells (currently the "gold standard") is performed simultaneously as the cells flow through the device to identify the individual cell types.

2. EXPERIMENTAL

Blood was obtained from healthy donors. Density gradient separation and magnetically activated cell sorting (MACS) was used to isolate the leukocyte sub-population (CD16+ (Neutrophils), CD14+ (Monocytes), CD3+ (T-lymphocytes)). Cells were suspended in PBS (2 mM EDTA and 0.5 % BSA). The medium was isotonic, with a conductivity of 1.2 $S.m^{-1}$. Cell concentration was adjusted to ~ 1 x 10^6 cells per ml reducing the probability of more than one cell being present in the detection region at any one time.

Cell samples were introduced into the device, and the cells flow through the chip under the influence of an externally applied pressure. Negative dielectrophoresis is used to focus cells into the centre of the channel [7, 8]. The cells then flow through a detection zone formed by two pairs of microelectrodes, where a differential impedance measurement is made. Optical measurements are made 100 µm down stream using free space optics and dual laser illumination at 488nm, 633nm and detection of fluorescent emission at 520nm, 633nm and >700nm. Optical and electrical measurements from individual cells are collected by high speed A/D card and processed on a PC. The system is shown in figure 1.

978-0-9798064-0-7/µTAS2007/$20©2007CBMS

Impedance measurements were performed over the frequency range 100 kHz – 20 MHz with applied signal amplitudes of 0.35 Vpp. A reference frequency was set at 503 kHz, 0.35 Vpp for all measurements. The sample flow rate was keep constant, so that the particle transit time through the measurement region was ~ 12 ms. This speed ensured that the DEP focussing was accurate when a signal of 5 Vpp at 8.3 MHz was applied to the focussing electrodes.

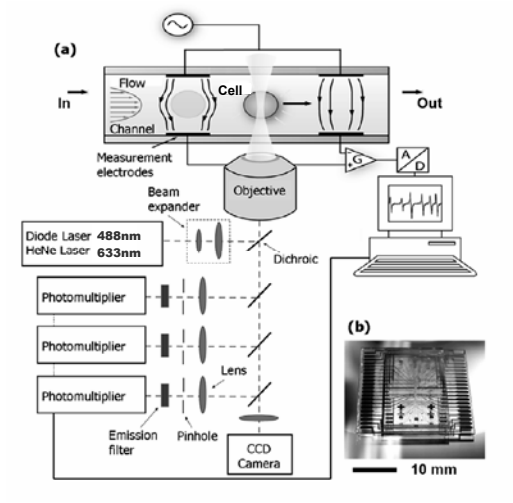

Figure 1 (a) Schematic diagram of the experimental setup showing the detection region of the chip and a simplified representation of the impedance and optical detection schemes. (b) Photograph of the chip.

3. RESULTS AND DISCUSSION

The impedance spectra for the individual leukocyte sub-populations is shown in figure 2. Data for a sample of 5.5 μm beads is shown for comparison. Data was determined using a population-averaged frequency sweep technique where two discrete frequencies were employed simultaneously. The low frequency reference was fixed at 503 kHz while the other frequency was swept. The ratio of the magnitudes of the swept and reference frequencies is termed opacity. This parameter factors out the influence of particle size and the position of the particle within the measurement zone. Opacity is calculated individually for each cell and approximately 1500 events are recorded at each frequency. The data in figure 2 shows that leukocyte discrimination is possible at frequencies of 2 and 5 MHz.

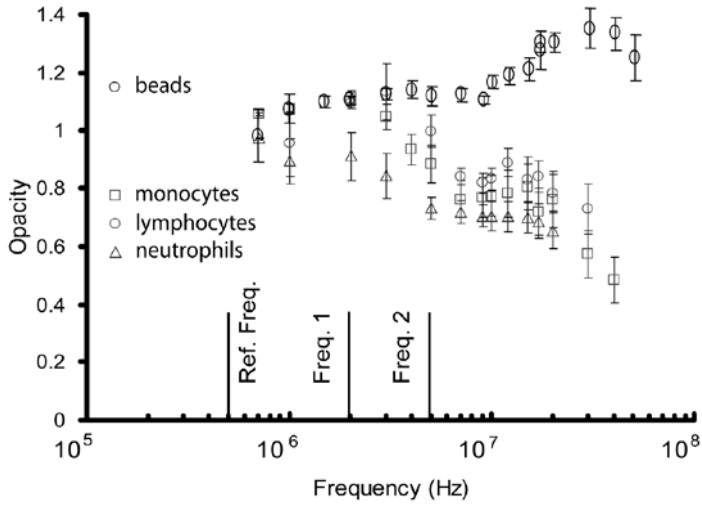

Figure 2 Opacity spectra for the three leukocyte sub-populations. Also shown is data from 5.5μm latex beads. The data shows that the three leukocyte sub-populations can be discriminated at frequencies of 2MHz and 5 MHz.

Mixtures of fluorescently labelled T-lymphocytes, monocytes and neutrophils were analysed on the device. The fluorescence signal from the individual cells was used to identify the cell type. The data is presented in figure 3 as an impedance scatter plot. The low frequency (0.5 MHz) signal gives a measure of the cell size. The different cell types appear in distinct regions on the plot demonstrating that the three population can be resolved.

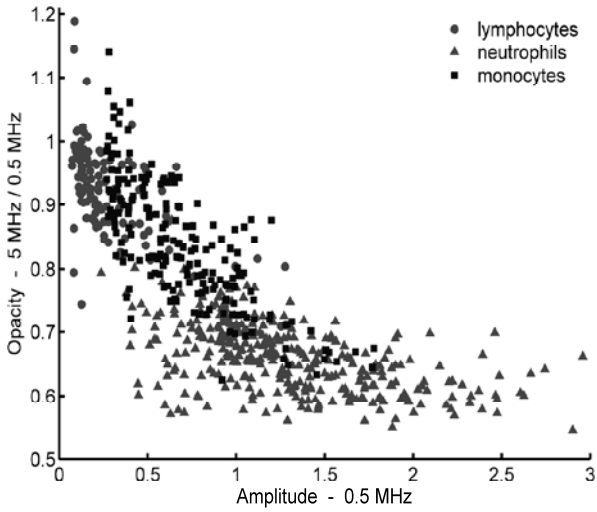

Figure 3 Scatter plot showing the distribution of neutrophils, monocytes and lymphocytes as measured at 5 MHz with reference frequency of 503 kHz. Cells are identified based on their fluorescent properties. Differences in the impedance properties of the cell types can be clearly seen.

4. CONCLUSIONS

An impedance micro-cytometer has been used to measure the electrical impedance of three different leukocyte sub-populations from human blood. The technique can measure differences in the dielectric properties of cells, demonstrating the feasibility of performing a 3-part differential count.

ACKNOWLEDGEMENTS

We acknowledge Philips Electronics for financial support and fabrication of devices.

REFERENCES

[1] H. Fricke. *J.Gen.Physiol.*, **9**, 137 (1925).
[2] K.S.Cole and R.H.Cole, *J. Chem. Phys.*, **9**, 341 (1941)
[3] H. Pauly and H.P. Schwan, *Z. Naturforsch*, **14**, 125 (1959).
[4] S.Gawad, L. Schild and P. Renaud, *Lab Chip*, **1**, 76 (2001).
[5] H. Morgan, D. Holmes, and N.G. Green, *Cur. Appl. Phys.* **6**, 367 (2006).
[6] H. Morgan, T. Sun, D. Holmes, S. Gawad and N.G. Green, *J. Phys. D: Appl. Phys.*, **40**, 61 (2007).
[7] D. Holmes, H. Morgan and N.G. Green, *Biosen. Bioelectron.*, 21, 1622 (2006).
[8] D. Holmes, J.K. She, P.L. Roach and H. Morgan, *Lab Chip*, (*in press* 2007) DOI: 10.1039/b707507n

SIMULTANEUOUS SORTING OF MULTIPLE BACTERIAL STRAINS USING DIELECTROPHORESIS

Unyoung Kim[1], Jiangrong Qian[1], Paul H. Bessette[2], Patrick S. Daugherty[2] and H. T. Soh[1,3]

[1]Department of Mechanical Engineering, [2]Department of Chemical Engineering, and [3]Department of Materials, University of California, Santa Barbara, USA

ABSTRACT

The process of sorting multiple biological targets (molecules, viruses, bacteria and mammalian cells) from complex sample mixtures *simultaneously*, is an important biotechnological capability. In this work, for the first time, we demonstrate the continuous dielectrophoretic sorting of multiple strains of bacteria (*E. coli*) based on their surface protein expression – a capability that has not been feasible in conventional, macro-scale systems. We describe the design and fabrication of the the Dielectrophoresis Activated Multi-target Sorter (DAMS), and report on its purity performance which can reach ~99% for each strain of bacteria starting from a binary mixture, in a single round of sorting.

Keywords: Dielectrophoresis, cell sorting, multi-target sorting, microfluidics

1. INTRODUCTION

Separation of biological cells based on surface marker expression from complex mixtures is a critical biotechnological capability. Previously, we presented the first marker specific separation of bacterial cells using dielectrophoresis (DEP) for a single strain of bacteria [1]. In this work, we demonstrate, for the first time, continuous DEP separation of multiple strains of bacteria (*E. coli*) based on their surface protein expression – a capability that has not been feasible in conventional, macroscale systems. The Dielectrophoresis Activated Multi-target Sorter (DAMS) is a one-input, multiple-output device, where a mixture of bacterial strains captured by different monoclonal antibodies (mAb) on polystyrene beads (PSB) enters the device, and then exits according to their surface protein expression (Fig 1a).

2. EXPERIMENTAL

The device is fabricated with polyimide channels in a manner similar to our previous work [1]. The top and bottom electrodes are patterned with 20 nm of Ti and 2000 nm of Au on top of glass wafers through e-beam evaporation. Then photo-sensitive polyimide is spun on the top and bottom substrates. Microfluidic channels are defined on this layer by photolithography using standard exposure tools, and developed. After drilling microfluidic vias on the top substrate by a computer-controlled milling machine and dicing of both substrates, the two pieces are aligned and bonded using a flip-chip aligner. Microfluidic inlets and outlets are manually fixed on the drilled vias using epoxy. For testing, the device is placed beneath the objective of an epifluorescence microscope and powered by a function generator through two card-edge, electrical connectors. Two dual-track programmable syringe pumps deliver the mixture and buffer fluid. The three outlets of the device are collected separately in centrifuge tubes.

978-0-9798064-0-7/μTAS2007/$20©2007CBMS

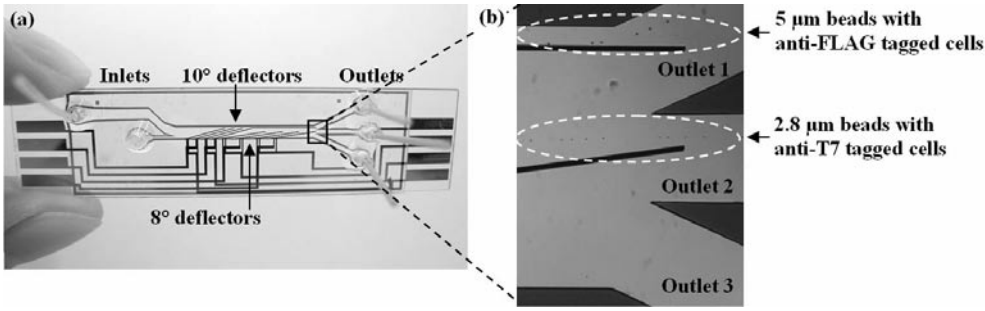

Figure 1. The Dielectrophoresis Activated Multi-target Sorter (DAMS) device: (a) Multiple sets of electrodes with two different angles enable simultaneous sorting of two target cells. (b) Anti-FLAG tagged cells (captured by the 5 μm beads) are deflected by the first set of electrodes and exit through outlet 1, and (c) Anti-T7 tagged cells (captured by the 2.8 μm beads) are deflected by the second set of electrodes and exit through outlet 2. Free, unlabeled cells exit through outlet 3 (not shown).

3. RESULTS AND DISCUSSION

DAMS uses multiple sets of DEP electrodes with different angles such that the balance of hydrodynamic and DEP forces cause different size of beads to elute through different outlets. For strain specific bacterial cell separation, two strains of *E. coli* are used: Strain A expresses the anti-FLAG binding peptide motif (RVKSNQDYKMSDPVR), and Strain B expresses anti-T7 binding peptide motif (GMAPMGPQMNLGRLW) on their cell surfaces [2]. Strain A is selectively captured by the anti-FLAG mAb immobilized on PSB (r=5 μm). Strain B is captured by anti-T7 mAb also immobilized on PSB (r= 2.8 μm). Thus, Strain A (captured by the 5 μm PSB) is deflected by the first set of electrodes and exit through outlet 1(Fig 1b, top), where as Strain B (captured by the 2.8 μm PSB) is deflected by the second set of electrodes, and exit through outlet 2 (Fig 1b, middle). Finally, the unlabeled, non-target cells are not deflected and thus flow through outlet 3 (Fig 1b, bottom).

The initial mixture of bacterial cells consisted of 60.6% Strain A and 39.4% Strain B as measured by flow cytometry (Fig 2a). The mixture was suspended in 0.1×PBS supplemented with 1% BSA to prevent agglomeration and adsorption of the particles on the electrodes of the DAMS. To prevent settling of the samples during sorting, the density of solution is adjusted to that of polystyrene beads (1.06 g/ml) with glycerol at a final concentration of 20% (vol/vol). When the flow pattern is stabilized within the DAMS device, a sine wave of 20 V peak-to-peak at 500 kHz is applied to the set of electrodes. The eluted samples from the three outlets were analyzed by flow cytometry after incubating the samples with fluorescently conjugated antibodies. Strain A was enriched to 99.8% in outlet 1(Fig 2b), Strain B was enriched to 98.7% in outlet 2 (Fig 2c) after 1 round of sorting.

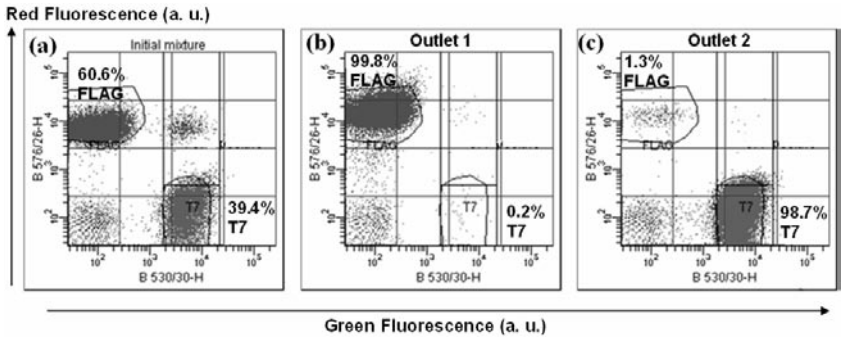

Figure 2. Multi-strain bacterial cell sorting with DAMS measured by flow cytometry. (a) The initial mixture consists of 60.6% Strain A and 39.4% Strain B. After 1 round of sorting, (b) Strain A is enriched to 99.8% in outlet 1, and (c) Strain B is enriched to 98.7% in outlet 2.

4. CONCLUSIONS

We demonstrate the first, surface marker specific, multi-target cell sorting using dielectrophoresis. The multiplexed-separation scheme described in this work is generalizable, and thus may be applied to a wide variety of applications where the simultaneous separation of multiple biological targets is required..

ACKNOWLEDGEMENTS

We thank the financial support from the ARO Institute for Collaborative Biotechnologies (DAAD1903D004), DARPA/DMEA-CNID grant H94003-05-2-0503. We thank Dr. Yanting Zhang, Sophia Kenrick, Marco Mina, and Gaurav Soni for helpful discussions. Microfabrication was carried out in the Nanofabrication Facility at UC Santa Barbara.

REFERENCES

[1] X. Hu *et al*, "Marker-specific sorting of rare cells using dielectrophoresis", PNAS Vol. 102, pp.15757-15761 (2005)

[2] P.H. Bessette *et al*, "Microfluidic library screening for mapping antibody epitopes", Anal. Chem. Vol. 79, pp.2174-2178 (2007)

GENTLE RETENTION OF CELLS IN A FOCUSING ULTRASONIC RESONATOR INTEGRATED IN A CHIP-BASED PERFUSION SYSTEM FOR CELL CHARACTERIZATION AND ON-CHIP CULTIVATION

J. Hultström Svennebring, O. Manneberg and M. Wiklund
Dept. of Applied Physics, Royal Institute of Technology, Sweden

ABSTRACT

Inside a microfluidic chip, lateral acoustic forces are obtained in an expansion chamber which focuses the sound field originating from an external transducer with a refractive element operating at 7 MHz. The chip system is designed for pre-alignment of cells in a straight inlet channel, followed by positioning and retention of cells in the expansion chamber. Trapped cells may be characterized using any kind of high-NA optical microscopy. Here, we demonstrate the use of conventional light transmission, phase contrast, dark-field and fluorescent microscopy imaging. The goal is to use the present device as a micro-bioreactor combined with optical characterization of individual cells.

Keywords: Acoustic, cell handling, focusing resonator, optical microscopy

1. INTRODUCTION

Ultrasonic standing wave (USW) technology is a promising tool for gentle cell handling in microfluidic chips [1]. Most USW chips utilize straight microchannels, in order to produce a plane standing wave between the channel walls [2-4]. While such systems primarily are efficient for continuous particle separation, retention systems require a lateral force component parallel to the fluid flow. For example, lateral forces can be obtained by a miniature transducer integrated in the microchannel, producing strong near-field gradients in the flow direction [5, 6]. In the present paper, we suggest an approach where lateral forces are obtained in an expansion chamber which focuses the sound field in the flow direction. The system is designed for pre-alignment in a straight inlet channel, followed by positioning and retention of cells in the expansion chamber. The purpose of the device is to serve as a miniature perfusion system for individual characterization of cells and on-chip cultivation.

2. EXPERIMENTAL ARRANGEMENT

The chip system, depicted in Fig. 1, consists of a dry-etched silicon structure sandwiched between two glass layers, and an external transducer with a refractive element placed on top of the chip for efficient coupling of ultrasound into the channel. By the use of single-frequency (~7 MHz) ultrasonic actuation, several manipulation functions are achieved simultaneously at different positions inside the chip depending on the channel geometry.

978-0-9798064-0-7/μTAS2007/$20©2007CBMS

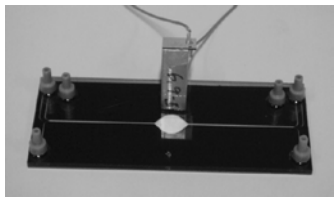

a

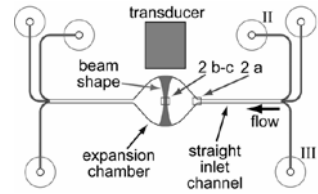

b

Figure 1. Photograph (a) and schematic (b) of the chip design featuring an expansion chamber actuated by the ultrasound transducer. The areas marked (2 a) and (2 b-c) are the imaged regions in Fig. 2. Injection of cells can be made in one or several of the inlet holes marked I, II and III, matching the three focused lines in Fig. 2 a.

In the straight inlet channel, manipulation in two dimensions is obtained by superposition of vertical and horizontal standing waves, both perpendicular to the flow, resulting in levitation and formation of three lines of cells, in the laminar flow from the corresponding inlet. In the expansion chamber, the curved reflecting walls create a focused horizontal standing-wave field superposed on the vertical levitating field, resulting in positioning and retention of cells in compact monolayer aggregates during perfusion of cell medium (see Fig. 3a). The USW modes in the expansion chamber are depicted in Fig. 2, where 10 µm polystyrene beads are used to visualize the pressure node pattern. Besides the focusing ability for generation of stronger lateral forces, the expansion chamber also has the advantage of reducing the flow velocity which in turn reduces the competing fluid drag force. Furthermore, the superposed fields guide the cells through the chip without any unwanted surface contact with the channel walls.

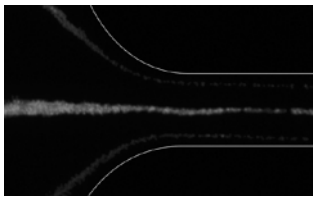

a

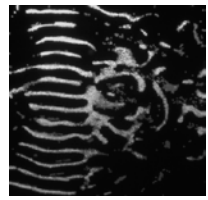

b

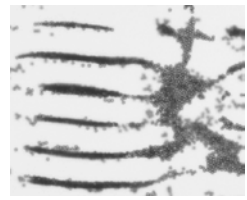

c

Figure 2. Visualization of the node pattern in the expansion chamber using 10 µm fluorescent beads with node-to-node distance ~100 µm. (a): Levitation and formation of three lines, picture shows the transition region between the straight inlet channel and the expansion chamber. The channel walls are outlined in white. (b-c): Pattern of retained beads at the center of the expansion chamber. In all images, the flow direction is from right to left.

3. CELL CHARACTERIZATION

Cells trapped in the expansion chamber may be studied and characterized using any kind of high-NA optical microscopy. In Fig. 3 and 4, we demonstrate the use of conventional light transmission, phase contrast, dark-field and fluorescent microscopy imaging of COS7E cells stained with the fluorescent viability indicator Calcein AM.

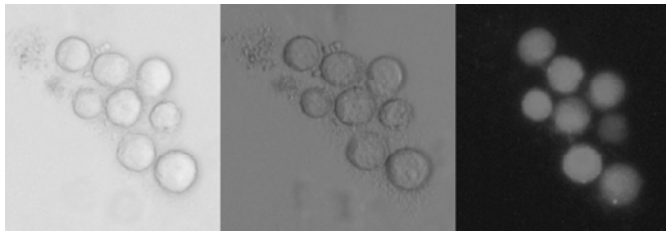

Figure 3. Positioned and retained COS7E cells (~10 μm) during perfusion of cell medium, visualized by transmitted light, phase contrast, and fluorescence microscopy (objective: 20X / N.A. 0.3). In all images, the flow direction is from right to left.

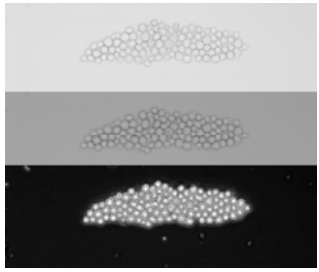

Figure 4. Positioned and retained COS7E cells (~10 μm) during perfusion of cell medium, visualized by transmitted light, phase contrast, and dark-field microscopy (objective: 20X / N.A. 0.3). In all images, the flow direction is from right to left.

When aiming for long-term (~days) cell retention and on-chip cultivation, it is important to maintain the biocompatibility of the system. Previous results include viability measurements and temperature control [1, 7]. In the present chip, the different microscopy techniques (cf. Fig 3 and 4) makes it possible to perform detailed optical characterization of cells without the need for toxic fluorescent labels. In the future, our device can be used as a micro-bioreactor with the option of individual cell monitoring and optical characterization.

REFERENCES

[1] J. Hultström *et al*, Ultrasound Med. Biol., **33**, 145-151 (2007).
[2] N.R. Harris *et al*, Sens. Actuators B, **95**, 425-434 (2003).
[3] T. Laurell *et al*, Chem. Soc. Rev., **36**, 492-506 (2007).
[4] M. Wiklund *et al*, Lab Chip, **6,** 1537-1544 (2006).
[5] T. Lilliehorn *et al*, Ultrasonics, **43**, 293-303 (2005).
[6] M. Evander *et al*, In: Proc. of μTAS 2006, 1055-1057 (Tokyo, Japan, 2006).
[7] J. Hultström *et al*, submitted manuscript (2007).

ON CHIP AFFINITY SELECTION OF ANTIBODIES USING ULTRASONIC STANDING WAVES

P. Augustsson, J. Persson, M. Ohlin and T. Laurell
Lund University, SWEDEN

ABSTRACT

A microfluidic particle wash chip was developed for efficient affinity selection and enrichment of specific binders from phage display libraries. Compared to commonplace manual washing procedures this device allows for complete automation of phage display selection, a method with great potential in high throughput proteomics.

Key words: Ultrasound, phage display, affinity extraction, antibodies

1. INTRODUCTION

Phage display [1] has become a leading method for isolating new binders from molecular libraries containing large sets of related but different molecules. It is likely to play an extensive role for the development of specific binders, often but not necessarily antibody-type molecules [2], against various targets (antigens). Such binders will e.g. allow for assessment of all components of the proteome, an approach important for efficient diagnosis, prediction and treatment of disease. Phage display is normally performed according to the following scheme. The antigen is immobilized to a surface, often in the form of a microbead. Following incubation, phage particles that display antigen-specific antibody fragments will be caught on the antigen coated surface. By washing away unbound phages, those phages displaying binders targeting the antigen are enriched and they can be used to produce the associated antibody fragments. The procedure of separating rare phages displaying antigen-specific binders from the large bulk of phage particles is a step that needs automation in order to allow isolation of specific binders to all members of proteomes, an effort central to ongoing strategic research consortia [3]. Current procedures are labor intense and require manual intervention, preventing high throughput approaches for development of specific binders by this technology.

Acoustic particle manipulation has shown great potential for particle washing in micro devices [4]. The governing force is the acoustic radiation force that is experienced by particles in a resonant acoustic wave field. The magnitude and direction of the force is dependent on the particle size, the acoustic properties of the particle relative to the carrier fluid and the strength and frequency of the applied field. The diversity in particle movement makes acoustic manipulation of particles suitable for various tasks such as washing, extraction, size sorting and density sorting. The washing performance of the earlier presented device was reported to be 95% relative to the input level of undesired material. Another chip, which performed multiple wash sequences in one channel, was reported to have a washing efficiency of 99% [5]. In many biomedical applications such as molecular affinity extraction (e.g. phage display) or cell staining, a washing efficiency of 99.9% or higher is required. It is also necessary to achieve high enough particle recovery in order to retain sufficient amount of specific binders.

In an effort to show the potential of acoustic particle manipulation in microfluidic devices for use in an automated phage display system, a chip was developed that could meet the demands regarding sample throughput, washing efficiency and bead recovery. This was carried out by combining design ideas from the two earlier presented devices and

978-0-9798064-0-7/μTAS2007/$20©2007CBMS

the performance was tested by washing samples of antigen-coated beads that had been incubated with phage particles displaying an antigen-specific antibody.

2. EXPERIMENTAL

Channels and inlet holes were KOH wet etched in <100> Silicon using commonplace UV-lithography and buffered HF for oxide removal. Borosilicate glass with drilled holes for fluid connections was anodically bonded to the Silicon to seal the channel and allow for visual inspection. The width of the two particle focusing segments of the channel was 375 μm with an aspect ratio of approximately 1:2. Short pieces of Silicone elastomer tubing were glued onto the chip for the fluid connections. For actuation of the ultrasound a 5 mm by 30 mm piezoelectric ceramic was glued onto the glass lid beside the channel structure. The frequency 2 MHz was chosen to create λ/2 resonance in the channel.

The fluids were pumped in and out from the system through Teflon tubing using syringes and syringe pumps. For the injection and removal of wash fluids a dual syringe pump was run in a push-pull configuration. The sample output was collected through an outlet open to atmospheric pressure into a test tube.

Phages displaying recombinant proteins were enriched on antigen-coated beads (Dynabeads M280, Invitrogen) with a diameter of 2.8 μm by mixing for 2 hours on rotator at room temperature. Elution of the bound phages was performed by mixing the beads in trypsin or hydrochloric acid. The phage particle numbers were subsequently analyzed by infecting *Escherichia coli* bacteria according to standard protocols at 37°C for 30 minutes. This was compared with the number of phages in the wash solution, which was determined in the same way. Bead concentrations before and after washing was analyzed using a coulter counter measuring the volume fraction of beads in the sample.

3. RESULTS AND DISCUSSION

To exploit the primary axial acoustic radiation force in the facilitation of automated phage display selection technology, a chip was developed with the intention of catching phages displaying specific binders and removing the bulk of non-bound phage particles. Phage particles were not by themselves focused by the acoustic radiation force. Rather, they remained in the part of the flow field into which they were injected. In contrast, microbeads could move under the influence of such forces. Phages displaying specific binders were retrieved with the microbead fraction if their antigen had been immobilized on the bead. In order to achieve high enough washing efficiency, the device performs two sequential cycles of acoustic carrier media particle transfer and washing. (Figure 1 b and c)

The presented two step microfluidic device could wash away phages particles from uncoated beads more efficiently than a four fold manual washing procedure. For antigen coated bead samples incubated with antigen-specific phage particles, the concentration of phages after wash and elution was 70 times that of uncoated bead samples (Figure 1 a). Studies of model systems indicate that more than an eighty thousand-fold enrichment of specific binders can be accomplished with the device. Selection of real phage-displayed antibody libraries has demonstrated that enrichment factors above one-thousand-fold can be achieved (Persson et al., manuscript in preparation), demonstrating the overall high performance of this approach in a real experimental setup. Loss of material in the system is minimal as recovery of beads was estimated to over 70%.

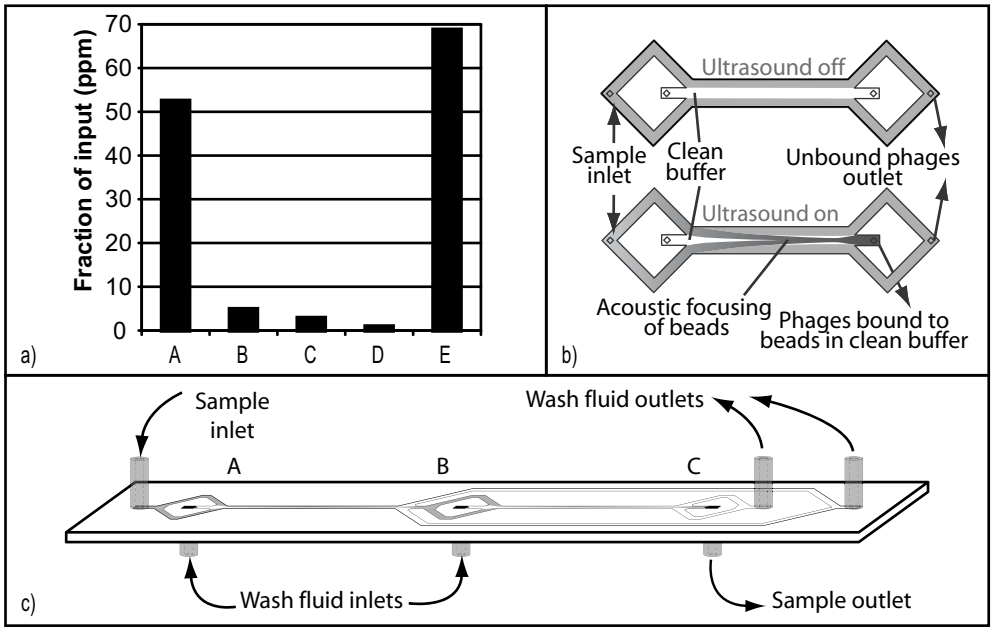

Figure 1: a) Histogram showing the concentration of phage particles in the washed samples as fraction of the input concentration. Bar A-C indicates 2, 3 and 4 times manual wash steps respectively, bar D indicate automated wash of uncoated beads and bar E indicate automated wash of antigen-coated beads after elution of phage particles. b) Principle of operation for a single step acoustic standing wave washing of beads. c) Schematic of the two step microfluidic device. Two narrow streams of sample are injected through the side inlets at A, separated by a stream of clean wash fluid in the center of the channel. The beads with the bound phages are acoustically focused towards the center of the channel A-B. At B the flow is split up into two waste outlets and a structure for passing along the focused beads to yet another wash step. The beads are again focused into fresh wash fluid between B and C and finally exit the channel through the center outlet.

5. CONCLUSIONS

This microfluidic design and extensions of it has the properties that allow it to be used in automated selection procedures not requiring manual steps involving e.g. centrifugation. We envisage that this technology will provide the basis for automation required to accomplish high throughput selection of specific binders by the state-of-the-art phage display technology.

6. REFERENCES

[1] J. McCafferty, A.D. Griffiths, G. Winter, D. Chiswell, Nature, 1990, 348, 552-554

[2] H.K. Binz, P. Amstutz, A. Plückthun, Nat Biotechnol, 2005, 23, 1257-1268

[3] M. Taussig *et al.* Nat. Methods, 2007, 4, 13-17

[4] F. Petersson, A. Nilsson, H. Jönsson and T. Laurell, Anal. Chem., 2005, 77, 1216-1221

[5] P. Augustsson, F. Petersson and T. Laurell, Proceedings of μTAS 2006 Conference, 2006, 627-629

FLUORESCENT ACTIVATED CELL SORTER USING ULTRASOUND STANDING WAVES IN MICRO CHANNELS

C. Grenvall, M. Carlsson, P. Augustsson, F. Petersson and T. Laurell
Department of Electrical Measurements, Lund University, SWEDEN

ABSTRACT

A microchip for ultrasonic fluorescent activated cell sorting (U-FACS) has been developed. The system extracts rare events from a complex bio-particle suspension. Fluorescent detection of single particles is used to activate acoustic translation of desired particles across a laminar flow profile to the collection outlet. Previous work has demonstrated acoustic driven carrier media exchange for cells in a continuous flow mode [1]. The current work expands this mode of operation to selective extraction of cells from a mixed environment aided by novel 2D-acoustic focusing.

Keywords: Ultrasound, FACS, Microfabrication, Acoustic particle separation

1. INTRODUCTION

Ultrasound standing wave particle manipulation is a robust way to handle bioparticles in microfluidic networks. The acoustic forces imposed on the cells have recently been proven harmless, enabling both successful in-chip culturing of cells in the acoustic standing wave field [2] and cell culturing post acoustic field exposure [3]. This paper reports the first proofs of two dimensional continuous flow acoustic focusing of particulate matter in micro channels. Aided by the 2D-focusing, rare event extractions of polystyrene beads in a micro channel are performed.

2. THEORY

When using fluorescence detection and acoustic force manipulation of single cells it is crucial to design for exact spatial positioning of the cells in the channel prior to acoustic translation. To facilitate single cell/particle selection by optical identification and acoustic manipulation a uniform cell velocity is prerequisite. Since fluid handling is performed in a parabolic flow profile a large distribution of particle velocities prevail, causing erroneous retention of the particles in the standing wave field. To reduce the velocity distribution of cells the chip was designed to perform a 2D acoustic focusing step prior to the subsequent fluorescent activated acoustic selection. This step brings particles into a well defined position in the parabolic flow profile, where the spatial velocity distribution is reduced. The position is determined by where the lateral and vertical standing wave nodes coincide.

3. EXPERIMENTAL

The current U-FACS design focuses particles along the sidewall of the separation channel prior to sorting. In order to accomplish 2D-focusing the channel dimensions matched a 3 $\lambda/2$ resonance criterion at 5 MHz, along the channel width, with a proximal pressure node approximately 75 um from the sidewall, figure 1. The depth of the channel simultaneously matched a $\lambda/2$ resonance criterion with a single pressure node at half distance between bottom and top of the channel. Acoustic particle sorting was performed by using a 2 MHz transducer down stream from the 2D-focusing regime, channel width set to $\lambda/2$ at 2 MHz.

978-0-9798064-0-7/μTAS2007/$20©2007CBMS

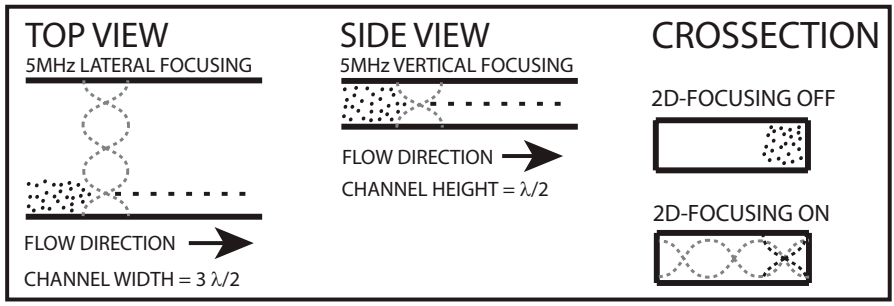

Figure 1. Schematic view of the 2D acoustic particle focusing. The right part shows the benefits of 2D-focusing with particles positioned in the coinciding nodes with ultrasound activated.

The outlet flow balance was set to direct the central zone of the flow to the collection outlet. Figures 2 and 3 show a continuous stream of particles 2D-focused and directed towards the (2) waste and (3) collection outlets. The particle switching time from the sidewall to the channel centre was observed to be less than < 20 ms with even less time needed to reach the centre from the 2D-lateral focusing path.

4. RESULTS AND DISCUSSION

Single particles were detected using a photomultiplier tube (PMT) positioned over the channel. The PMT activated the 2 MHz transducer, switching the detected particle into the collection outlet. A suspension of 6.2 μm FITC labelled and 8 μm unlabelled polystyrene beads was sorted. Initial FITC/unlabelled bead ratio was 1:50. The first testing of the U-FACS demonstrated a > 90% collection efficiency of FITC labelled beads as shown in figure 4.

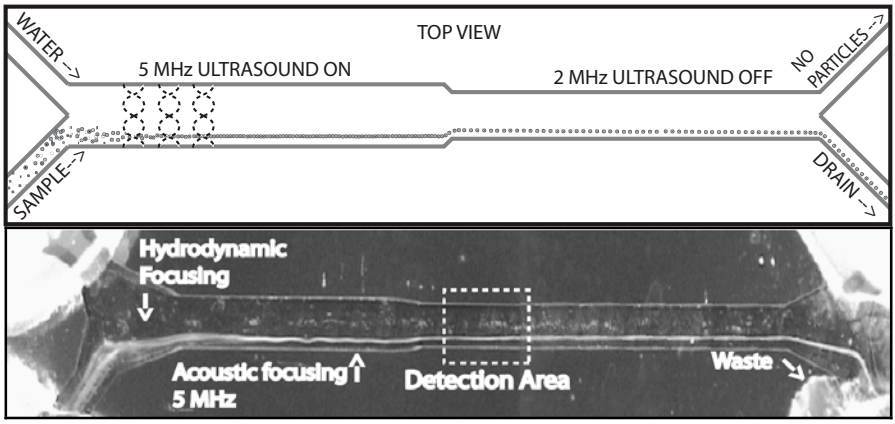

Figure 2 (upper). Schematic top view of 2D acoustic focusing (left side of the channel) with the 2 MHz acoustic sorting zone inactive (right side). Particles exit at the waste outlet. The lower part shows a microscope top view of the channel. An excess of particles is used to visualise the particles' trajectory.

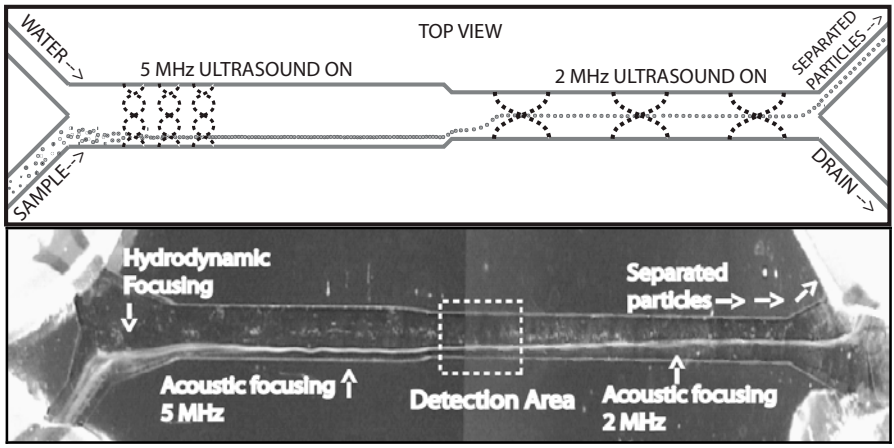

Figure 3 (upper). Schematic top view of 2D acoustic focusing (left side of the channel) with the 2 MHz acoustic sorting zone activated (right side). Particles exit at the collection outlet. The lower part shows a microscope top view of the channel. An excess of particles is used to visualise the particles' trajectory.

It is suspected that the microfluidic methods used when switching from calibration (start up) mode to operation mode cause the system to perform worse than what could otherwise be expected because of initial leakage into the collection outlet. An automatic valving system is being developed to solve this problem. The channel dimensions functions as expected but new outlet designs might result in improved collection efficiency.

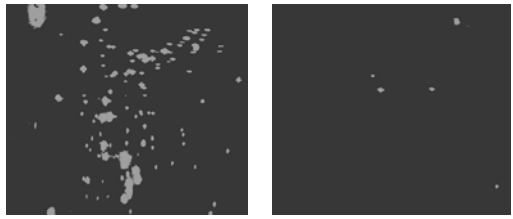

Figure 4. Particle concentration in the collection outlet container(left) and waste outlet container (right) viewed through a fluorescent (FITC) filtered microscope.

5. CONCLUSIONS

A U-FACS incorporating novel 2D-focusing was designed and fabricated. 6.2 µm FITC beads were sorted from a suspension with a 1:50 ratio of FITC/unlabelled beads. The initial tests of the U-FACS show good results and there are already several applications that could benefit from such an application. System performance is expected to be easily improved.

REFERENCES

[1] F. Petersson, A. Nilsson, C. Holm, H. Jönsson and T. Laurell, Anal. Chem, 2005, 77, 5 1216-1221

[2] M. Evander, L. Johansson, T. Lilliehorn, J. Piskur, M. Lindvall , S. Johansson, M. Almqvist, T. Laurell and J. Nilsson, Anal Chem, In press 2007

[3] J. Hultstrom, O. Manneberg, K. Dopf, et al, Ultrasound Med Biol 33 (1) 2007: 145-151

AUTHOR INDEX
Pages A1 – A22

KEYWORD INDEX
Pages A23 – A37

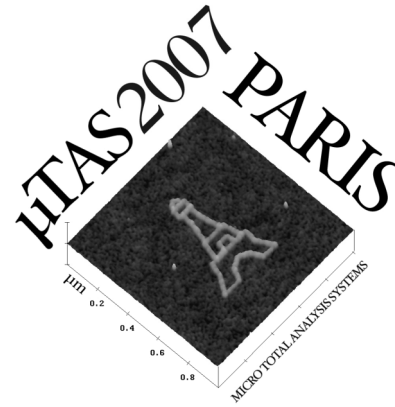

NOTES

Author Index

A

Abdelgawad, M. 327
Abe, K. 718
Abe, T. 787, 868
Abell, C. 143, 352
Abhyankar, V.V. 1550
Achard, J.L. 733
Adamowicz, O. 1711
Agabi, O. 730
Agache, V. 491
Agah, M. 239, 727
Agarwal, A. 607
Agirregabiria, M. 584
Agrawal, R. 518
Ahlford, A. 59
Ahn, C.H. 251, 482, 1420
Ahn, D.J. 421
Ahn, J.K. 1261
Ahn, Y. 503, 1324
Ajay, A. 140
Akagi, T. 1330
Akagi, Y. 1297
Akhmechet, R. 1225
Akiyama, Y. 433
Albrecht, A. 1387
Aldamiz-Echevarría, P. 584
Alexander, C. 146
Alexopoulos, L.G. 158
Al-Haq, M.I. 1459
Ali, S.A. 239
Aliabadi, R.M. 20
Allemand, J.-F. 236
Allen, D.J. 1559
Allender, C. 1689
Almqvist, M. 1372
Altamirano, J.C. 518
Altintas, E. 1750
Amashukeli, X. 254
Amatatongchai, M. 1164
Amin, A.M. 967
An, J.-Y. 1155
Anderson, P.D. 279, 1143
Andersson Svahn, H. 113, 688
Andreev, I.A. 470
Anhøj, T.A. 1071
Anraku, R. 1565
Anselmetti, D. 176, 242
Aoki, H. 1252
Aoki, T. 224
Aota, A. 871, 1213
Aoyagi, Y. 775
Arai, F. 467, 883
Arakawa, T. 224, 245, 862, 1360
Arata, H.F. 1240
Arrington, C. 560
Asai, H. 745
Asai, T. 868, 1565
Asano, T. 373
Asano, Y. 1053, 1384
Ashraf-Khorassani, M. 239
Atencia, J. 1336
Attia, R. 1146
Aubrey, A. 254
Auerswald, J. 1504
Augustsson, P. 1046, 1810, 1813
Auroux, P.-A. 1237
Austin, R.H. 131, 1622, 1777
Avian, J. 233
Ayano, K. 1714
Azioune, A. 1363
Azizi, F. 29, 919

B

Baba, T. 595
Baba, Y. ..... 65, 116, 309, 655, ... 781, 790, 841, 1003, ... 1176, 1207, 1402, 1565, 1619
Bablet, J. 476
Backhouse, C.J. 98
Bada, J.L. 254
Baek, Y.-K. 1598
Bah, S. 1695
Bahk, Y.K. 245
Baigl, D. 170, 1613
Baldrich, E. 1065
Bancaud, A. 910
Banerjee, A. 697
Bang, D.D. 59, 691
Bang, H. 1258
Bansal, T. 1732
Banu, S. 1264
Bao, J.-B. 44

Bao, N. 670
Bargiel, S. 1664
Barker, N.S. 110
Baroud, C.N. 336, 343
Barrett, A.G.M 261
Barrett, L.M. 318
Barron, A. 1780
Barrow, D.A. 1689
Barsotti, R.J. 991
Bart, J. 258
Barthès-Biesel, D. 880
Bartolo, D. 161, 1146, 1152
Bauer, J. 563
Bayiati, P. 92
Bazant, M.Z. 285
Bazargan, V. 355
Beaugeois, M. 1670
Becker, H. 1273
Beebe, D.J. . 146, 203, 1357, 1390, 1550
Beech, J.P. 1580
Bégin, F. 74
Begley, M.R. 288, 1489
Begolo, S. 1113
Belkin, S. 1049
Bengtsson, M. 1519
Benito-López, F. 264
Bentley, W.E. 784, 1616
Bentum, P.J.M. van 258
Ben-Yoav, H. 1049
Beppu, T. 625
Beraha, M. 1683
Berg, A. van den 206, 515, 676,
..... 928, 1201, 1243, 1756
Berganza, J. 584, 1720
Berganzo, J. 584
Bergeron, M.G. 74
Berry, S.M. 1134
Berthiaume, F. 164
Berthoumieux, H. 236
Bessette, P.H. 1804
Beuf, A. 901
Beusink, J.B. 676
Bhagavatula, S.K. 379
Bhagwat, A.R. 859
Bhansali, S. 1686
Bigot, S. 1504
Bilkova, Z. 637
Birtwell, S.W. 1264
Bishop, P.L. 251
Blagoi, G. 1027, 1071
Blanco, F.J. 1720
Blank, L.M. 715
Blatz, A. 724
Blazej, R.G. 949
Blossey, R. 1043
de Boer, H.L. 676
Böhringer, K.F. 1750
Boisen, A. 497, 1027
Boissinot, M. 74
Bonassar, L.J. 185
Bontoux, N. 1170
Boomhower, O. 1137
Borella, M. 349
Borgatti, M. 563
Bornens, M. 1768
Borno, R.T. 566
Bos, F. 1143
de Bot, V. 1547
Böttcher, L. 563
Bouazaoui, M. 1670
Boudreau, D.K. 74
Boukherroub, R. 1043
Bourgerette, A. 476
Bouzigues, C.I. 988
Brachet, A.G. 349
Bradley, D.D.C. 1164
Branch, D.W. 560, 1056
Branda, S.S. 1315
Bransky, A. 772
Braschler, T. 125, 494
Brask, A. 35
Bratton, D. 143
Braun, T. 563
Brener, I. 560, 1056
Brennan, J.S. 1315
Brennen, R. 554
Breslauer, D.N. 622
Brighenti, E. 721
Briscoe, T. 470
Brivio, M. 59, 1519
Broder, G.R. 1264
Broer, D.J. 1143
Brouzes, E.R. 113
Bruinink, A. 730
Bruus, H. 35
Brzózka, Z. 68, 1711

Bu, M. 59, 691
Buddharaju, K.D. 607
Bula, W.P. 1471
Buoncristiani, M. 721
Burdick, J. 1677
Burg, T.P. 1101
Burger, R. 1231
Burns, M.A. 628
Burrell, M. 1137
Byun, C.K. 1723

C

Cabrera, M. 901
Cakebread, J. 1801
Calemczuk, R. 173
Calleja, M. 497
Camart, J.C. 41, 294, 1043, 1670
Cambron, S.D. 1134
Camps, T. 910
Capurro, J.J. 1483
Carbonaro, A. 1173
Carlborg, C.F. 527
Carlen, E.T. 676
Carlson, R. 1717, 1741
Carlsson, M. 1813
Carofiglio, T. 1113
Carr, P.A. 200
Carrière, P. 901
Carrilho, E. 1677
Casals-Terré, J. 937
Castell, O. 1689
Castellan, G. 349
Celio, C. 811
Cha, B.H. 1267
Cha, J.M. 862
Cha, K.J. 907
Cha, M. 1122
Chabert, M. 598
Chabrol, C. 476
Chae, S.K. 1040
Chae, Y. 482
Chai, J.C.-K. 1562
Chang, C.C. 640
Chang, F. 742
Chang, J.K. 1258
Chang, K. 200
Chang, M.-P. 1732
Chang, T.C 62
Chansin, G.A.T. 1015
Chao, S.-H. 1717
Charbon, E. 1179
Chartier, I. 476
Charvet, G. 1080
Chatelain, F. 149, 491, 922, 1363
Chen, C. 1077
Chen, C.-Y. 1110
Chen, F. 1658
Chen, H. 1282
Chen, L. 29, 919, 1225, 1444
Chen, L. 200
Chen, P.-J. 518
Chen, W.-T. 62
Chen, Y. ..... 170, 276, 400, ... 832, 1170, 1583, 1613
Chen, Y.-Q. 5
Chen, Y.-T. 1119
Cheng, J.Y. 1279
Cheng, L.-J. 979, 1577
Cheong, T.K. 940
Cheow, L.F. 685
Chetouani, H. 149, 922
Cheung, L.S.L. 1586
Chiang, Y.-M. 991
Chiari, M. 1034
Chin, L.K. 1348
Chiou, A. 5
Chiou, E.P.Y. 1771
Chiu, C.H. 1279
Chiu, C.L. 1279
Cho, H. 1182
Cho, H.H. 1701
Cho, N.-G. 503
Cho, S.K. 300, 847, 913, 1634
Choi, D. 464
Choi, J. 1795
Choi, S. 215, 1486
Choi, W. 364, 1342, 1798
Choi, Y. 464, 1610
Choi, Y.H. 1294, 1538
Choi, Y.-J. 364, 877
Choi, Y.-K. 1598
Chokkalingam, V. 1534
Chou, S.Y. 1622, 1777
Choudhury, A. 1704
Chua, R. 188, 461, 694
Chudy, M. 68, 1711

Chun, H. 895
Chunara, R. 1101
Chung, A. 1225
Chung, B.H. 1655
Chung, C. 1258
Chung, C.-M. 5
Chung, J. 793
Chung, K. 1219
Chung, K.H. 218, 1294
Chung, S.E 1116, 1568, 1774
Chung, S.K. 300, 847, 913, 1634
Chung, T.D. 895
Clark, D.S. 1789
Clausen, C.H. 820
Clem, P.G. 560
Clicq, D. 248, 382
Cloarec, J.-P. 901
Coffinier, Y. 1043
Cohen, A. 1683
Cohn, R.W. 1134
Collard, D. 403, 415
Collé, E. 910
Cooper, R. 736
Cooper-White, J.J. 358, 946, 1453, 1495
Cordero, M.L. 343
Cordovez, B. 1225
Cosnier, M.-L. 476
Coulthard, S.M. 1107
Crane, M. 1219
Cretich, M. 1034
Croquette, V. 236
Cui, B. 442
Cui, X. 14
Cullen, C. 261

D

Dahan, M. 161
Dai, J. 646
Dame, G. 1246
Damin, F. 1034
Danger, G. 230, 823
Daniel, D. 940
Dao, D.V. 17
Darwish, N. 1065
Das, C. 1447
Daugherty, P.S. 1804
Dauphinot, L. 1170
Dauriac, V. 832
David, N. 476
Davis, D. 1801
Davis, R.W. 20, 1092, 1592
Davoust, L. 306, 925
Dayton, P.A. 191, 664
De Malsche, W. 248, 382, 1414, 1646
de Mello, A.J. ..... 261, 850, 1015, ... 1062, 1164, 1544
de Mello, J.C. 1164
De Moor, P. 248
De Palma, R. 23
De Stefano, L. 445
De Vroey, L. 1522
Decanini, D. 400
Declet, C. 997
Degertekin, F.L. 1336
Degré, G. 1152, 1480
Deguchi, K. 1098
Dekker, C. 385
Del Campo, F.J. 1065
Delaire, J. 324
Delamarche, E. 101, 1492
Delft, K. van 1201
Demierre, N. 125, 494
Denomme, R. 1695
Desai, S.P. 8, 448, 1104
Descroix, S. 832
Desmet, G. ... 248, 382, 682, 1414, 1646
Desportes, S. 324
Destro, F. 563
Detobel, F. 682, 1414
DeVoe, D.L. 640
Dextras, P. 1101
Dholakia, K. 470
Di Carlo, D. 709, 736, 1083
Di Carlo, G. 1034
Dick, R. 1592
Dimaki, M. 820
Dinnar, U. 772
Dittrich, P.S. 604, 766, 1556
Do, J. 251, 1420
Doll, J.C. 1107
Domansky, K. 167
Domenech, M. 146
Dong, L. 943, 1652
Dorfman, K.D. 997
Doron, A. 1683
Doyle, P. 1146

Doyle, P.S. 619
Drese, K.S. 613, 808
Du, W.-B. 1652
Du, W.B. 943
Duch, M. 937
Ducloux, O. 294
Ducrée, J. 1231, 1249, 1516
Dueck, M. 736
Dugas, V. 901
Dunoyer, N. 476
Dupont, R. 1363
Duxenneuner, M.R. 358, 946
Dybko, A. 68, 1711
Dyson, E.C. 1544
Dziuban, J.A. 691, 1664

E

Easley, C.J. 288, 1489
Ebin, L. 940
Eckhardt, A.E. 1559
Edahiro, J. 1321
Edel, J.B. 1015, 1062, 1544
Edwards-Lévy, F. 880
Egberink, R.J.M. 264
Eghbali, H. 248
Ehrenfreund, P. 254
Eichhorn, R. 242
Eick, S. 485
Eijkel, J.C.T . 515, 928, 982, 1201, 1243
Einfeld, W. 1300
Ek, P. 542
Elad, T. 1049
Elizalde, J. 524
Enoksson, P. 536
Erickson, D. 1225
Erlinge, D. 1372
Erson, A.E. 634
Estes, M. 1420
Esteve, J. 937
Estévez-Torres, A. 236
Evander, M. 1372
Evans, H. 339
Ezaki, T. 1744

F

Fajolle, D. 491
Falke, F.H. 1288
Faltin, B. 1516
Fan, Z.H. 1447
Fang, A.P. 400
Fang, J. 646
Fang, Q. 95, 943, 1652
Fang, Z.L. 646
Farrington, A. 254
Fedorov, A.G. 1336
Fei, J. 796
Fekete, V. 1414
Feldman, H. 303
Feng, H.H. 572, 1351
Ferguson, B. 122, 1680
Fernández, L.J. 524, 584, 1720
Fernandez, S. 236
Ferrance, J.P. 77
Feyereisen, K. 203
Fidalgo, L.M. 352
Fiechtner, G.J. 318
Fink, J. 1363
Fiola, M.-J. 74
Fischer, P. 358, 946
Fisher, J.S. 346, 1531
Fittipaldi, A. 721
Flaven, T. 476
Fletcher, D.A. 104, 616
Flyvbjerg, H. 1580
Foret, F. 50
Forry, S.P. 47, 964
Fouillet, Y. 349, 733, 925
Fournier, I. 41
Fraden, S. 370
Fradier, E. 901
Français, O. 324
Frank, Th. 1387
Franssila, S. 367, 569, 835, 1435
Franzke, J. 604, 766, 1556
Fréchet, J.M.J 1789
Freire, S.L.S. 327
Frey, O. 1288
Frisk, M.L. 1390
Fuchs, A. 491
Fuchter, M.J. 261
Fuentes, H.V. 817
Fuetterer, X. 613
Fujii, T. 152, 182, 844, 1604
Fujita, H. 403, 415, 745,
..... 1240, 1714, 1750
Fujiwara, K. 373

Fukuba, T. 844
Fukuda, T. 467
Fukushima, S. 1792
Fukuyama, N. 625
Fukuzawa, N. 844
Funatsu, T. 224, 1360
Fung, W.Y. 940
Furuberg, L. 673, 1513
Furui, K. 1053
Furutani, S. 179
Futamura, K. 439

G

Gaeta, A.L. 859
Gaitan, M. 1237
Gale, B.K. 643, 1131
Galitonov, G.S. 1264
Galopin, E. 294, 1670
Gambari, R. 563
Gantelius, J. 688
Gao, Z. 607
Gardeniers, H.J.G.E ..... 248, 258, 264, ... 382, 982, 1408, 1414, 1471, 1646
Garini, Y. 221
Gärtner, C 1273
Gavillet, J. 1504
Gavioli, R. 563
Gawad, S. 1086
Gazzola, D. 563
Geahlen, R.L. 670
Gebinoga, M. 1387
Gel, M. 512, 1375
Generelli, S. 164
Georges, A. 236
Gerhardt, K.P. 1586
Gershenfeld, N. 1216
Geschke, O. 820
Gessner, T. 1504
Gharizadeh, B. 20
Ghenim, L. 491
Ghodssi, R. 784, 1616
Ghosh, S. 859
Gianni, S. 721
Gijs, M.A.M. 730, 1179
Gillies, M. 1143
Gillot, F. 1240
Glezer, A. 1381
Gliére, A. 306
Glutz, L. 844
Go, J.S. 245, 862
Goda, T. 1031
Godley, L. 1173
de Goede, J. 1143
Gogolides, E. 92
Goh, S. 859
Gómez, E. 937
Gómez, M.V. 506
Gonzalez, R.L. 796
Goodman, M.B. 1107
Göritz, R. 1689
Gosse, C. 236
Grabowska, I. 68
Gratier, J. 306
Green, N.G. 826, 1086
Gregersen, M.M. 35
Greif, D. 176
Grenier, D. 324, 1522
Grenvall, C. 1813
Griffith, L.G. 167
Griffiths, S.K. 886, 970
Griss, P. 530
Groß, A. 1387
Grover, W.H. 892
Grunthaner, F.J. 254, 551
Grzegorska, A. 1664
Gué, A.-M. 910
Guenat, O.T. 164
Guerrieri, R. 563
Guillemaud, R. 1080
Gulliksen, A. 673
Guo, L.J. 979, 1577

H

Ha, J.B. 245
Haaland, D.M. 1783
Haapala, M. 569, 1435
Haasl, S. 536
Haeberle, S. 1231, 1516
Haguet, V. 149, 922
Hahn, J.H. 769, 1077, 1631
Hairer, G. 1474
Hamsten, C. 688
Han, D.-C. 1258
Han, J. 251, 811, 1198, 1786
Han, Y. 485
Han, Z. 80

Hansen, M.F. 35
Hansen, O. 1071
Harada, M. 955
Haraldsson, T. 527
Harashima, H. 781
Hardt, S. 808
Hardy, B.S. 1426
Harjee, N. 1107
Harnack, O. 1601
Harrison, D.J. 2, 44, 805, 1234
Hartberger, T.M. 77
Hashiguchi, G. 403, 415, 1714
Hashimoto, A. 1637
Hashimoto, M. 1318
Hashioka, S. 973, 1207
Hatch, A.V. 838, 1783
Hatsuzawa, T. 595
Hattori, A. 1565
Haubert, K. 1357
Hauschild, J.-P. 1185
Hawkins, B.G. 578
Haynes, C.L. 1009
He, M. 805
Heeger, A.J. 1192, 1680
Heineman, W.R. 1673
Hemmi, A. 1053
Henares, T.G. 427, 874
Heng, X. 14
Henkel, T. 1387
Hennion, M.C. 832
Herminghaus, S. 339, 931, 1534
Hernán, T. 985
Hernychova, L. 637
Herr, A.E. 1315, 1783
Herrmann, M. 661
Hesketh, P.J. 1673, 1704
Hettiarachchi, K. 191, 664
Hibara, A. 273, 430, 473, 601,
..... 871, 1018, 1213, 1574
Higuchi, T. 1285, 1501
Hiller, K. 1504
Hinestroza, J.P. 1465
Hirahara, S. 312
Hirai, Y. 1297
Hirano, K. 790, 1176, 1399, 1432
Hirota, N. 212
Hisamoto, H. 427, 874
Hishida, K. 209
Hizawa, T. 479
Ho, M.C. 1279
Ho, T. 1131
Hoang, V.H. 98
Hoel, A. 548
Höfemann, H. 242
Hoffmann, P. 1387
Hofmann, O. 1164
Högberg, C 1372
Hollfelder, F. 143
Holloway, J. 1801
Holmes, D. 1086, 1801
Homma, T. 1571
Hong, J. 454, 1015
Hong, J.S. 1477
Hong, L.-Y. 1456
Horesh, M. 1683
Horii, M. 451
Horiike, Y. 973, 1207
Horita, N. 212
Hosogi, M. 1714
Hosokawa, K. 26
Hospach, I. 1601
Hosseinkhani, H. 1378
Hosseinkhani, M. 1378
Hovig, E. 673
Hsieh, A.T.-H. 346
Hsiung, L.C. 1279
Hsiung, S.-K. 5
Hsu, C.Y. 1279
Hsu, M.C. 1279
Hsu, M.-H. 1595
H-Tok, J.B. 1192
Hu, Z. 1704
Hua, Y. 1234
Huang, C.-W. 1128
Huang, K.-J. 107
Huang, K.-S. 62, 700
Huang, S.-B. 1128
Huang, Y. 769
Huang, Y.-C. 700
Huang, Y.-H. 700
Hubalek, M. 637
Huber, D.E. 376
Hübner, J. 497, 1071
Huck, W.T.S 143, 352
Huebner, A. 143
Hukka, M. 1435

Huletsky, A. 74
Hulsen, M.A. 279
Hultström Svennebring, J. 1807
Hulvey, M.K. 1074
Humayun, M.S. 518
Hung, L.-H. 346
Hunt, A.J. 976
Hunt, B.D. 551
Hunziker, P. 101, 1492
Hwang, C.M. 778
Hwang, H. 131, 364, 877
Hwang, I.-H. 297, 1155
Hwang, J. 533
Hwang, K.S. 83, 631, 1267
Hwang, S.-Y. 503, 1324
Hwang, Y.W. 1342

I

Iafelice, B. 563
Ichikawa, N. 1037, 1158
Ichikawa, Y. 934
Ichiki, T. 1330
Ichimura, T. 1462
Idota, N. 430
Iino, R. 757
Ikami, M. 655
Ike, F. 1252
Ikeda, H. 955
Ikeda, M. 551
Ikeda, T. 1161
Ikeda, Y. 955
Ikeuchi, M. 1303
Ikuta, K. 1303
Iles, A. 212, 1270, 1378
Im, H. 1009
Imato, T. 1053
Ingebrandt, S. 485
Inman, W. 167
Inoue, H. 1729
Inoue, K. 1285
Ionescu-Zanetti, C. 724
Iribe, Y. 451
Irimia, D. 155
Ishibashi, R. 1423
Ishida, A. 1297
Ishida, H. 209
Ishida, M. 479, 1255, 1625
Ishida, T. 479
Ishida, Y. 306, 925
Ishido, T. 790, 1176, 1399, 1432
Ishihara, K. ..... 424, 436, 439, ... 500, 1031, 1291, 1628
Ishikawa, M. 790, 1176, 1399, 1432
Ishizuka, K. 649
Itoga, K. 1708
Iwase, E. 934
Iwata, R. 856

J

Jachimowicz, A. 1474
Jacobson, J.M. 200
Jacobson, S.C. 967, 1589
Jaenisch, R. 581
Jakobsen, M.H. 820, 1027
Jang, A. 251
Jang, J. 364
Jang, K. 1628
Jankovicova, B. 637
Janssen, J.W.G. 258
Jansson, T. 1417
Jarvius, J. 53, 994, 1306
Jarvius, M. 1306
Jary, D. 349
Javanmard, M. 1092
Jayashree, R.S. 1468
Jeandey, C. 149, 922
Jensen, K.F. 158, 952
Jensen, L.B. 820
Jeong, E.H. 862
Jeong, J.W. 282
Jeong, O.C. 557
Ji, H.M. 1351
Jia, G. 74
Jimbo, H. 1759
Jimenez-Dalmaroni, A. 1768
Jin, Y. 539
Jo, K.W. 1698
Joanicot, M. 1210
Joensson, H.N. 113
Johansson, H. 994, 1306
Johnson, E.A. 1390
Jokinen, V. 367
Jolicoeur, M. 164
Jones, A. 285
Jong, D.-S. 1110, 1279
Jorgensen, A.M. 1071

Ju, J. 1285
Juchniewicz, M. 1711
Julicher, F. 1768
Jullien, L. 236
Jullien, M.-C. 324, 548, 1522
Jun, C.H. 1294
Jung, B.H. 1655
Jung, D.-H. 1598
Jung, E. 563
Jung, H.-I. 1345, 1510, 1701
Jung, H.-T. 1598
Jung, I.-H. 533
Jung, M.Y. 218, 1294, 1655
Jung, S. 394

K

Kagawa, K. 1753
Kaigala, G.V. 98
Kaji, H. 787, 868, 1318
Kaji, N. 65, 116, 309, 655, 781,
..... 841, 1003, 1207, 1402, 1565, 1619
Kajita, A. 1252
Kakabakos, S.E. 92
Kalim, S. 1771
Kalkkinen, N. 1435
Kamei, K. 1309
Kameshima, Y. 1637
Kamiya, T. 787
Kan, T. 934
Kanai, M. 32
Kanie, T. 373
Kanamori, T. 1321
Kanda, K. 1498
Kaneki, N. 1053
Kang, I.S. 1477
Kang, J. 418
Kang, J.H. 703
Kang, J.Y. 330, 482, 1040, 1747
Kang, K.H. 1477
Kang, P.J. 282
Kang, T. 464, 1610
Kang, T.G. 279
Kang, T.J. 1122
Kanie, T. 373
Kanno, I. 1498, 1765
Kano, S. 1037
Karackattu, S. 167
Karlsen, F. 673
Kase, H. 1252
Kataoka, M. 65
Katayama, M. 373
Kauppila, T. 569
Kawai, K. 32
Kawai, T. 1021
Kawasaki, E. 47
Kawashima, T. 787, 1318
Kawata, H. 1297
Kazoe, Y. 889, 1625, 1667
Kee, J.S. 1661
Keenan, T.M. 203
Keimel, C. 1137
Kellar, K. 1673
Keller, S. 1027
Kenis, P.J.A. 590, 1468
Kentgens, A.P.M 258
Ketola, R.A. 569, 835, 1435
Kettelarij, A.J. 264
Keynton, R.S. 1134
Khan, S.A. 952
Khatavkar, V. 1143
Khine, M. 724
Khurana, T. 227
Kido, H. 74
Kihira, Y. 1450
Kikuchi, A. 433, 1708
Kikuchi, K. 1321
Kikukawa, Y. 137
Kikutani, Y. 955, 1450
Kilic, M.S. 285
Killeen, K. 554
Kim, B. 1568, 1774
Kim, B.S. 1701
Kim, C. 330, 1747
Kim, D. 1225
Kim, D.H. 1261, 1538
Kim, D.-P. 1456
Kim, D.S. 907
Kim, E.J. 421
Kim, H. 1735
Kim, H.-B. 916, 1213
Kim, H.C. 895
Kim, H.H. 658
Kim, H.J. 1261
Kim, H.-S. 1510
Kim, J. 643
Kim, J.-H. 1510

Kim, J.H. 330, 1747
Kim, J.H. 1339
Kim, J.-J. 364, 877
Kim, J.-M. 421
Kim, J.-S. 1798
Kim, K.C. 658, 862
Kim, M.-G. 1155, 1698
Kim, M.J. 1015
Kim, P. 1021
Kim, S.-H. 364
Kim, S.J. 1198
Kim, S.-J. 1345, 1510
Kim, S.K. 631, 1267, 1339
Kim, T. 1006
Kim, T.-J. 1345
Kim, T.S. 83, 330, 454,
..... 631, 1267, 1339, 1747
Kim, U. 1804
Kim, Y.C. 703, 1342
Kim, Y.H. 1122
Kim, Y.-H. 533
Kim, Y.J. 282
Kim, Y.-J. 533, 793, 1167
Kim, Z.H. 1339
Kimura, H. 152, 182
Kinoshita, H. 1604
Kirak, O. 581
Kirby, B.J. 185, 379, 578, 859, 1465
Kitagawa, F. 814, 1405
Kitamori, T. 53, 137, 273, 430,
..... 458, 473, 601, 625, 718, 799,
..... 871, 916, 955, 994, 1018, 1213,
..... 1423, 1450, 1565, 1574, 1607, 1628
Kjeldsen, B.G. 59
Klaunick, C. 1246
Klejwa, N. 1107
Klemm, R. 1273
Klenz, U. 1387
Kleparnik, K. 50
Klotzkin, D. 697
Knapkiewicz, P. 1664
Ko, S.H. 1477
Ko, Y.-J. 503, 1324
Kobayashi, I. 333, 1541
Kobayashi, J. 1708
Kogure, K. 781
Kohlheyer, D. 1243
Kojima, R. 1607
Kolari, K. 1435
Kole, A. 802
Koltay, P. 1149
Kong, D.S. 200
Konishi, S. 557
Konno, T. 424, 436, 1291, 1628
Koo, D.-B. 1798
Korecka, L. 637
Korin, N. 772
Kortmann, H. 715
Koster, S. 1333, 1547
Kostiainen, R. 569, 835, 1435
Kostner, S. 233, 739
Koszur, J. 691
Kotera, H. 1375, 1498, 1765
Kotiaho, T. 569, 835, 1435
Kotz, K.T. 155
Kou, S. 1525
Koudelka-Hep, M. 164, 1288
Kovarik, M.L. 1589
Kralj, J.G. 47, 964
Krämer, M. 1534
Krenkova, J. 50
Krishnamoorthy, G. 676, 1243
Krishnan, M. 391
Kristensen, A. 1580
Kubo, I. 179
Kulah, H. 634
Kumar, P. 640
Kumaresan, P. 122, 949
Kumemura, M. 403, 415, 745
Kung, C.F. 640
Kuo, C.-T. 1312
Kuo, T.S. 1531
Kurabayashi, K. 1012
Kuramoto, H. 781
Kuribayashi, K. 1222
Kuriyama, K. 1450
Kuroda, D. 841
Kurooka, K. 1098
Kurosawa, O. 512
Küttel, C. 494
Kutter, J.P. 808
Kuwana, K. 1095
Kuwano, H. 958
Kwak, B.S. 1701
Kwon, G.H. 397
Kwon, G.-H. 712

Kwon, R. 1107
Kwon, S. 1116, 1568, 1774
Kwon, T.H. 904, 907
Kwon, Y. 1795

L

Laachi, N. 997
Lafleur, J.P. 1441
Lagae, L. 23, 1369
Lagally, E.T. 1192
Lai, C.-W. 5
Lai, R.Y. 1680
Lai, Y.-S. 119
Lam, K.S. 122
Lam, L. 649
Lam, W.A. 616
Landegren, U. 1306
Landers, J.P. ... 77, 110, 288, 1489, 1780
Landry, D. 652
Lang, J.H. 1692
Lang, P. 1516
Lange, J.M. 820
Lao, I.K. 572
Laocharoensuk, R. 1677
Lapierre, F. 1670
Larsen, M.G. 817
Larsen, N.B. 1580
Larsson, C. 994
Latecki, B. 1664
Laurell, T. 1046, 1372,
..... 1417, 1810, 1813
Laureyn, W. 23, 1369
Laval, P. 1210
Lavella, G. 1396
Le Berre, M. 1613
Le Gac, S. 206, 1756
Le Nel, A. 50
Le Pioufle, B. 679
Le Saux, T. 236
Le Vot, S. 349
Le, N.C.H. 17
Lean, M.H. 802
Leclerc, E. 880
Lee, A.P. 191, 346, 664, 1024, 1531
Lee, B. 1182
Lee, B.-C. 1324
Lee, B.K. 1021
Lee, C. 572
Lee, C.H. 1040
Lee, D. 1119
Lee, D. 1294
Lee, D.-H. 1798
Lee, D.-S. 218, 853
Lee, E.-J. 712
Lee, E.S. 406, 464
Lee, G.-B. 5, 107, 1128
Lee, G.S. 421
Lee, H. 1279
Lee, H.-K. 793
Lee, H.L.T. 1068
Lee, H.Y. 1021
Lee, J. 394, 1122
Lee, J. 1795
Lee, J.H. 218
Lee, J.H. 1198
Lee, J.-H. 297, 509, 748, 1155, 1698
Lee, J.R. 330
Lee, J.Y 397, 961
Lee, K. 330
Lee, K.H. 397, 712, 961
Lee, K.J. 1747
Lee, K.-K. 1798
Lee, K.S. 1068, 1747
Lee, L. 14
Lee, L.P. 406, 464, 622, 709,
..... 736, 1083, 1182, 1610
Lee, M.C. 551
Lee, S. 482
Lee, S. 976
Lee, S. 1735
Lee, S.-H 503
Lee, S.H. 397, 712, 778, 961
Lee, S.-M. 83, 1267
Lee, S.-R. 1255
Lee, S.W. 1604
Lee, S.-Y. 1598
Lee, W.G. 1258
Lee, W.Y. 748
Lee, Y.-S. 83
Lefebvre, Y. 880
Legendre, L.A. 1780
Lehmann, U. 1179
Lehnert, T. 730
Lei, H.-Y. 107
Lemarchand, A. 236
Lemay, S.G. 385, 388

Leng, J. 1210
Lepioufle, B. 548
Leslie, D.C. 288, 1489, 1780
Lesuffleur, A. 1009
Lettieri, S. 445
Levenberg, S. 772
Levitan, J.A. 285
Levy , I. 1683
Lewandowski, A.T. 784, 1616
Li, C. 482
Li, J. 1756
Li, M. 769
Li, M.W. 1074
Li, P.C.H. 1282
Li, S. 610
Li, T.H. 104
Li, Y. 59
Li, Z. 409, 539
Liang, X. 1622
Liao, R. 128
Libera, M. 748
Lien, K.-Y. 107
Lim, C.S. 11, 1348
Lim, M.-H. 1167
Lim, M.H.M. 167
Lin, C.-H. 518
Lin, C.-M. 119
Lin, C.-T. 1012
Lin, H.-P. 62
Lin, L.A.G. 11, 1354
Lin, Q. 652, 796
Lin, Y.-C. 62, 700, 883
Lindner, A. 170
Lindquist, N.C. 1009
Lindstrom, H. 1378
Link, D.R. 113
Lissorgues, G. 1080
Littrel, R. 167
Liu, A.P. 104
Liu, A.Q. 11, 188, 461, 694,
..... 1059, 1348, 1354, 1438
Liu, C. 23, 1369
Liu, C.-H. 1312
Liu, C.N. 1195
Liu, G.L. 406, 1610
Liu, H.-P. 119
Liu, J. 640
Liu, K.-T. 1110
Liu, M.C. 1140
Liu, S. 418, 1723
Liu, V.H. 1786
Liu, W.-T. 1351
Liu, X.Y. 751
Livache, T. 173
Llamas Vidales, J.R. 167
Locascio, L.E. 47, 964, 1336
Lockhart, T. 361
Loechel, B. 1643
Logan, T.C. 1789
Lok, S. 1465
Long, T.M. 1640
Long, Y. 1182, 1610
Longo, M.L. 191, 664
Lopez-Garcia, M.D.C. 1357
Lou, X. 1192
Lu, C. 194, 670
Lu, H. 1219
Lu, J. 418
Lu, Q. 44
Lu, Z. 1695
Lübeck, T. 1387
Luo, L.-W. 140
Luo, X. 1616
Luo, X. 784
Luosujärvi, L. 569
Lutz, S. 1231, 1249, 1516

M

Ma, H. 1692
MacDonald, M.P. 470
Macka, M. 829
Maddalena, P. 445
Madjour, K. 1043
Madou, M.J. 74, 826
Maeda, E. 65
Maeda, M. 26
Maekawa, E. 427
Maeng, J.-H. 503, 1324
Maharbiz, M.M. 566, 1396, 1732
Mahmoudian, L. 1402
Mai, J. 610
Maier, W.F. 1534
Majima, M. 1744
Majumdar, A. 1658
Malaquin, L. 276, 400
Malic, L. 442

Malleo, D. 1083
Manage, D. 98
Manalis, S.R. 892, 1101
Manaresi, N. 721
Manessis, D. 563
Mani, A. 1204
Manneberg, O. 1807
Manz, A. 604, 766, 1556
Marchand, G. 476
Marche, P. 173
Marchiarullo, D.J. 110
Marggraf, U. 604
Markel, M.L. 376
Markesteijn, A.P. 221
Marko-Varga, G. 1046
Martel, S. 545, 1695
Martin, R.S. 1074
Martineau, I. 74
Martinez, F. 131
Martinez-Duarte, R. 826
Marty, B. 910
Maruo, S. 1729
Maruyama, H. 467
Mary, P. 1553
Mas, R. 1065
Masood, A. 1689
Mastrangelo, C.H. 29, 919, 1444
Masu, K. 973
Mathies, R.A. 254, 949, 1195
Matrozos, E. 92
Matson, C 997
Matsudaira, P. 1762
Matsui, K. 373
Matsumoto, I. 718
Matsumoto, K. 934, 1095
Matsumoto, S. 1037, 1158
Matsumoto, Y. 312, 757
Matsunaga, Y. 315
Matsushita, Y. 1462
Mawatari, K. 273, 473, 458,
..... 1450, 1565, 1607
Mayora, K. 524, 584, 1720
McBride, K.W. 89
McClure, R. 1780
McFarland, A. 1009
McKay, H.A. 628
Meacham, J.M. 1336
Meagher, R.J. 1783
Mecker, L.C. 1074
Medoro, G. 721
Meijer, H.E.H. 279
Meinhart, C.D. 291, 303
Meldrum, D.-R. 1717, 1741
Merani, V. 385
Mertsch, O 1643
Metz, T. 1149
Meyer, C. 385
Meyerhoff, M.E. 1396
Meyhofer, E. 1006, 1012
Meyrand, P. 1080
Meyvantsson, I. 146
Mielnik, M.M. 673, 1513
Miki, N. 312, 889, 1098, 1625, 1759
Mileros, K. 1372
Millunchick, J.M. 628
Mimura, S. 479
Min, B.G. 397
Min, J.K. 1258
Min, K.-I. 1456
Minamitani, H. 312
Minamitani, M. 1161
Minc, N. 575, 637, 742
Mindrinos, M. 155
Mir, L. 548
Mir, M. 1762
Mirkin, C.A. 1
Mirsaidov, U. 1762
Mistura, G. 1113
Mitchell, M. 1468
Miwa, Y. 315
Miyaji, A. 844
Miyakawa, S. 1667
Mizuno, J. 1405
Mizutani, F. 427, 874
Moehlenbrock, M.J. 1074
Mohamadi, M.R. 1402
Mohammadi, M. 545
Mol, T. 1143
Moldawer, L.L. 155
Molema, G. 1333
Molesin, S. 336
Mönch, I. 391
Monfort, L. 74
Monson, R.L. 1357
Moon, B.-P. 297
Moore, J.S. 1640

Moraes, C. 751
Morel, M. 161
Moreno, M. 1065
Morgan, H. ..... 826, 1083, 1086, ... 1089, 1264, 1801
Mori, T. 1297
Morikawa, S. 1252
Morin, H. 74
Morita, T. 56
Moriya, T. 1507
Morris, C.J. 1780
Morschhauser, A. 1504
Morton, K.J. 1622, 1777
Mortreux, J. 361
Mousoulis, C.A. 1726
Mukhija, D. 628
Mulder, P.P.M.F.A. 1333
Mulero, R. 1015
Müller, J. 1185
Muller, R. 125
Muller, S.J. 622
Münchow, G. 808
Muñoz, F.X. 1065
Munson, M.S. 47, 823
Murahara, H. 1003
Murata, A. 1462
Murata, M. 116
Murata, T. 1462

N

Nacapricha, D. 1164
Nagai, H. 179, 1176
Nagai, M. 745
Nagakura, T. 1303
Nagamune, T. 1252
Nagasaka, W. 1429
Nagasawa, S. 958
Nagata, H. 790, 1176, 1399, 1432
Najafi, K. 1735
Najmzadeh, M. 536
Nakabe, K. 315
Nakajima, A. 1637
Nakajima, H. 1053
Nakajima, M. 333, 775, 1541
Nakamura, H. 1222
Nakamura, S. 134
Nakanishi, H. 856
Nakano, K. 1053
Nakashima, Y. 706
Nakata, M. 757
Nakayama, T. 587
Nam, S.-W. 131, 1366, 1525
Nara, Y. 1360
Narasimhan, K.S.L. 1686
Nascimento, E. 494
Natali, M. 1113
Nawarathna, D. 122
Negoro, S. 373
Nemat-Gorgani, M. 1092
Nestler, J. 1504
Nevill, J.T. 736, 1083
Neylon, D.C. 1264
Ng, S.H. 1125, 1738
Nghe, P. 1152, 1480
Nguyen, N.-T. 1562
Nguyen, T.H. 652
Nichols, K.P. 982
Niclass, C. 1179
Nie, F.-Q. 829
Nieradko, L. 1664
Nieuwkasteele, J. van 1201
Nikaido, E. 757
Nikkhah, M. 727
Nilson, R.H. 886, 970
Nilsson, A. 1417
Nilsson, J. 1372
Nilsson, M. 53, 994, 1306
Nishino, K. 757
Nishizawa, K. 1291
Nishizawa, M. 787, 868,1318
Nisisako, T. 267, 595
Noh, H. 89, 1483
Noji, H. 587, 649, 757, 1604
Nonogi, M. 601
Nordström, M. 497
Nukada, K. 1303
Nunoshita, M. 1753
Nygren, A. 613

O

Oana, H. 197, 412, 512, 1000, 1375
Obata, Y. 1252
Oda, K. 473
Oda, T. 775
Offenhäusser, A. 485
Ogawa, J. 1498

Ogawa, R. 1207
Oh, J. 1483
Oh, S.-H. 1009
Oh, Y. 364, 877
Ohashi, T. 134
Ohi, S.-H. 122
Ohkohchi, N. 775
Ohl, C.-D. 206
Ohlin, M. 1810
Ohmori, H. 1285
Ohoka, M. 1765
Ohta, J. 1753
Ohuchi, M. 197
Okada, K. 1637
Okamoto, T. 844
Okano, T. 430, 433, 1708
Olabarria, G. 584
Oldani, C. 1034
Olesen, L.H. 35
Olguin, L.F. 143
Oliva, A.G. 494
Omata, M. 26
Omoto, Y. 309
Ong, W.-L. 140, 1528, 1562
Onoe, H. 934, 1222
Onoshima, D. 1619
Osato, K. 309, 1565
Ostmann, A. 563
Otsuka, K. 814, 1405
Otto, T. 1504
Owens, B. 167
Ozeki, E. 856

P

Padmanabhan, P. 1396
Paik, P.Y. 1559
Pais, A. 697
Pamme, N. 212, 1270
Pamula, V.K. 1559
Pan, C. 1771
Pan, J.-H. 346
Pan, J.-Z. 95
Pannacci, N. 361
Papageorgiou, D.P. 1726
Papautsky, I. 697
Pappaert, K. 382, 682
Parameswaran, M. 1282
Parekh, S.H. 104
Parikesit, G.O.F. 221
Paris, L.L. 670
Park, C.S. 282
Park, D.-H. 533
Park, H. 1116, 1568, 1774
Park, I. 409
Park, J. 1631
Park, J. 1258
Park, J.H. 282
Park, J.H. 1267
Park, J.-K. 215, 364, 703, 853, 877, 1342, 1486, 1798
Park, J.M. 904
Park, J.-S. 1510, 1701
Park, N. 1116
Park, S. 131, 1366, 1525
Park, S. 1771
Park, S.-C. 533
Park, S.H. 1294, 1655
Park, S.-H. 1456
Park, S.-J. 1342, 1456
Park, S.Y. 245
Park, W. 1116, 1568, 1774
Park, Y.D 397
Pärr, G.S. 1474
Pascual de Zulueta, M. 584
Patankar, N. 1795
Patel, K.D. 376
Paterson, L. 470
Paull, B. 829
Paumier, G. 910
Pausch, S. 1231
Pavlovic, E. 1680
Payer, K. 1101
Payne, G.F. 784, 1616
Pease, F. 20, 1092, 1592
Pedersen, S. 1071
Peh, X.L. 1351
Pei, R. 652
Pelletier, M.J. 551
Peltre, G. 832
Peng, K.-Q. 1528
Peng, Z. 1673
Pennathur, S. 376
Pépin, A. 400
Pereira Rodrigues, N. 152
Pérez-Castillejos, R. 937
Perozziello, G. 721

Perrais, V. 1080
Perry, S.L. 590
Persat, A. 56
Persson, A. 688
Persson, J. 1810
Peterson, D. 47
Petersson, F. 1813
Petrou, P.S. 92
Peyman, S. 1270
Peytavi, R. 74
Pfohl, T. 339
Phukan, A. 1137
Picard, F.J. .....
Piccin, E. 1677
Piel, M. 1363
Pietrocola, S. 1179
Pilarski, L.M. 98
Pinasco, P.G. 346
Pinchemel, B. 1670
Pinzón, J. 321
Pisano, A.P. 409
Plaxco, K.W. 1680
Player, A. 47
Plaza, F. 901
Plaza, J.A. 937
Plecis, A. 276, 1583
Plénat, T. 491
Plissonnier, M. 349
Poenar, D.P. 1661
Pól, J. 569, 1435
Pollack, M.G. 1559
Poo, M.-M. 763
Porch, A. 1689
Potier, M.-C. 1170
Potter, S.M. 1381
Poulichet, P. 324
Poulos, J. 1531
Pouteau, P. 733
Powell, A.K. 86
Prakash, M. 1216
Prakash, S. 1640
Pregibon, D. 619, 1146
Priest, C. 339, 931, 1534
Provin, C. 844
Pruitt, B.L. 1107
Psychari, E. 575
Pu, Q. 1723
Pyo, H.-B. 218, 853, 1294, 1655

Q

Qian, J. 1192, 1804
Qiu, Y. 128
Quinn, R. 254

R

Racine, V. 1768
Radu, C.G. 1309
Rahman, A.R.A. 1686
Ram, R.J. 1068
Ramadan, Q. 940
Rambani, K. 1381
Ranasinghe, R.T. 1264
Ranganathan, N. 140
Raorane, D.A. 1658
Ravula, S.K. 560
Raynal, F. 901
Reekmans, G. 23
Regehr, K. 146
Reginato, M.J. 89
Regtmeier, J. 242
Reichmuth, D.S. 1300, 1783
Reijme, M. 1143
Reimers, J.L. 59
Reinhoudt, D.N. 264, 506, 1471
Reisner, W.W. 1580
Renaud, P. 125, 494
Renberg, B. 1607
Renshaw, C.K. 859
Ressine, A. 1046
Revilla, F.D. 1089
Reyes, D.R. 1237
Reyne, G. 149, 922
Rhie, W. 1501
Riches, A.C. 470
Richmond, D.L. 104
Riegger, L. 1249
Ritzi, M. 613
Rivera, F. 349
Roach, P.L. 1264
Robert, L. 170
Roberts, G.W. 590
Rodd, L.E. 1495
Rodger, D.C. 518
Rodríguez, M.V. 524
Roeraade, J. 542
Roeser, T. 613
Ronaghi, M. 20, 1092

Rondeau, E. 1453
Rooij, N.F. de 1288, 1738
Ros, A. 176, 242
Rosenbluth, M.J. 616
Rosnerova, S. 637
Ross, D. 230, 823
Rossier, J. 1170
Rossteuscher, T.T.J. 273
Rostaing, H. 733
Rouabah, H.A. 826
Rouillard, A.D. 185
Roupioz, Y. 173
Rousseau, L. 324, 1080
Roussel, T.J. 1134
Rowlands, C. 850
Roy, E. 661
Ruano-López, J.M. 524, 584
Rubloff, G.W. 784, 1616
Rudolf von Rohr, Ph. 270
Rudolph, I. 1643
Russom, A. 155
Ryu, K. 300
Ryu, W.S. 131

S

Saarela, V. 569, 1435
Saati, S. 518
Saias, L. 575
Saiki, H. 856
Sakai, M. 1637
Sakai, Y. 152, 182, 309
Sakaki, N. 403, 415, 745
Sakakihara, S. 649, 757
Sakamoto, K. 856
Sakamoto, N. 134
Sakamoto, Y. 718
Saliba, A.E. 575
Salieb-Beugelaar, G. 1201
Salin, E.D. 1441
Salmon, J.-B. 1210
Salzet, M. 41
Samel, B. 530
Samitier, J. 1065
Samuels, M. 113
Samuelson, L. 985
Sandström, N. 530
Sano, T. 958
Sant, H.J. 1131
Santiago, J.G. 56, 227, 1204, 1592
Sarajlic, E. 1750
Sarrut, N. 306
Sasaki, M. 1450
Sasaki, N. 916
Sasamoto, Y. 1571
Satake, M. 775
Sato, H. 1571
Sato, K. 53, 137, 718, 1384, 1628
Sato, K. 53
Sato, M. 134, 958
Sato, S. 1753
Sato, T. 1037
Sato, Y. 209, 889, 1507, 1625, 1667
Sauter, F. 491
Sawada, K. 479, 1255
Schäfer, S. 485
Schasfoort, R.B.M. 676, 1243, 1408
Scheuring, S. 1188
Schlautmann, S. 676, 1243, 1408
Schlingloff, G. 1387
Schmid, A. 715
Schober, A. 1387
Schönberg, T. 542
Schondelmaier, D. 1643
Schönfeld, F. 321
Schumann, C.A. 766
Schwille, P. 391
Seemann, R. 339, 931, 1534
Seifert, W. 985
Seki, M. 898, 1228, 1297, 1792
Sekiguchi, T. 1571
Sekine, S. 787, 1318
Sekizawa, R. 427, 874
Selva, B. 324
Sénéchal, H. 832
Seo, J. 802
Serdy, J. 167
Sergio, M. 1179
Sert, C. 634
Setaro, A. 445
Shacham-Diamand, Y. 1049
Shackman, J.G. 823
Shah, J.J. 1237
Shah, P.J. 820
Shaikh, F.A. 71
Shamoto, E. 309
Shannon, M.A. 1640

Sharma, A.N. 379
Shaw, M.J. 1056
She, J.K. 1264
Shi, J. 400
Shim, J.-U. 370
Shimizu, H. 458
Shimoyama, I. 934, 1095
Shimura, K. 799, 1423
Shin, D.C. 1698
Shin, J. 1122
Shin, J.-S. 1167
Shin, K.S. 1747
Shin, M. 1631
Shin, S.J. 397, 961
Shin, S.-M. 297
Shin, Y.-B. 1655
Shinohara, H. 451, 1405
Shinohara, Y 65, 781
Shirasaki, Y. 224, 1360
Shoji, S. 32, 224, 245, 862,
..... 1360, 1405, 1571
Shokralla, S. 20
Shu, C.J. 1309
Shui, L. 928
Sibarani, J. 436
Sigman, J. 560
Sigurdson, M. 303
Sikanen, T. 835
Silva, T. 494
Sim, W.C. 282
Simmons, C.A. 751
Sinclair, M.B. 1783
Singh, A.K. . 318, 838, 1300, 1315, 1783
Singh, K. 658
Singh, N. 607
Sirevåg, R. 673
Sjödahl, J. 542
Skelley, A.M. 254, 581
Sklavounos, A. 110
Sköld, N. 985
Slocum, A.H. 1692
Slovakova, M. 637
Smadja, C. 50
Smela, E. 1327
Smith, A.E. 578
Sodunke, T.R. 89
Soh, H.T. 122, 1192, 1680, 1804
Soh, N. 1053
Sohn, L.L. 763, 1173
Solli, L.A. 1513
Sollier, E. 733
Solomon, M.J. 628
Sommer, G.J. 838
Song, J. 646
Song, W.Z. 11, 461
Song, Y.-A. 811, 1198
Song, Y.S. 1538
Soni, G. 291
Sorger, P. 158
Souteyrand, E. 901
Sparreboom, W. 515
Spicar-Mihalic, P. 667
Squires, T.M. 291
Srisa-Art, M. 1062, 1544
Srivastava, N. 1315
Stachowiak, J.C. 104
Stachowiak, T.B. 1789
Stauber, J. 41
Steigert, J. 1249
Steinmeyer, J.D. 566
Stellacci, F. 991
Stemme, G. 527, 530
Stetten, F. von 1231, 1516
Stevens, D.Y. 667
Stewart, G. 74
Stickel, A. 98
Stoeber, B. 355
Stojanovic, M. 652
Stone, H.A. 38
Streule, W. 1149, 1249
Strobl, J.S. 727
Studer, V. ... 161, 575, 1152, 1170, 1553
Sturm, J.C. 1777
Su, Y.-C. 1595
Subramanian, B. 940
Subramanian, K. 285
Sudor, J. 910
Sueyoshi, K. 814
Sugii, Y. 137, 871
Sugino, H. 224, 1360
Sugiura, S. 775, 1321
Sugiyama, S. 17
Suh, K.Y. 1021
Sukas, S. 634
Sumaru, K. 1321
Sun, C. 610

Sun, K. 778
Sun, R. 1680
Sun, T. 1086
Sun, Y 751
Sunahiro, S. 898
Sung, K.E. 628
Suraniti, E. 173
Surenjav, E. 339, 931
Suwa, K. 1161
Suzuki, H. 679, 1276
Suzuki, M. 451
Suzuki, N. 309
Suzuki, S. 1637
Suzuki, T. 1405, 1462, 1498, 1765
Svarnas, P. 1583
Svasek, P. 1474
Svec, F. 1789
Svendsen, C.N. 203
Svendsen, W. 820
Swensen, J.S. 1680
Syvänen, A.-C. 59

T

Tabata, K. 587
Tabeling, P. 361, 988, 1553
Tabrizian, M. 442, 661
Tachihara, A. 53
Tachikawa, K. 1556
Taddei, F. 170
Taff, B.M. 8, 448
Tai, Y.-C. 488, 518, 1140
Takahashi, T. 267
Takai, M. ..... 424, 436, 439, ... 500, 1031, 1291
Takamura, A. 868
Takamura, Y. 1429
Takao, H. 479, 1255
Takei, G. 1213
Takeo, M. 373
Takeuchi, S. .. 649, 679, 757, 1222, 1276
Takizawa, Y. 267
Talasaz, A.H. 20, 1092, 1592
Talen, W. 1143
Talreja, S. 590
Talu, E. 191, 664
Tamaki, E. 1574
Tamaki, S. 1459
Tamiya, E. 1429
Tan, S.-H. 1562
Tanaka, Y. ..... 53, 137, 994, ... 1176, 1306, 1399
Tandon, V. 379, 859
Tang, K.C. 140, 685
Tang, X. 80
Tanibata, H. 1462
Tarasow, T.M. 1192
Tatsumi, K. 315
Taverna, M. 50
Taylor, K.M. 1056
Taylor, L.T. 239
Teapal, J. 1201
Techaumnat, B. 1375
Tegenfeldt, J.O. 985, 1201, 1580
Teitell, M. 1771
Teo, C.Y. 685, 1351
Tepp, W.H. 1390
Terao, K. 1000
Teshima, T. 1744
Tezcan, D. 248
Thaitrong, N. 1195
Thery, J. 349
Théry, M. 1363, 1768
Thomy, V. 41, 294, 1043, 1670
Thorsen, T. 285
Thottethodi, M. 967
Throckmorton, D.J. 1300
Thundat, T.G. 1704
Thupil, A. 763
Thutupalli, S. 1137
Tian, W.-C. 1137
Tice, J.D. 590
Tidona, B. 270
Tiggelaar, R.M. 264
Tijero, M. 524, 1720
Timken, M. 721
Timp, G. 1762
Timp, K.A. 1762
Timp, W. 1762
Ting, T.-H. 1562
Tjeung, R.T. 1125
Toepke, M.W. 1550
Togo, M. 868
Tokeshi, M. 65, 116, 309, 655, 781, 841, 955, 1003, 1207, 1402, 1565, 1619
Tokuda, T. 1753
Tomizawa, Y. 1429

Tompkins, R.G. 155
Toner, M. 155, 619
Tong, J. 751
Toonder, J.M.J. den 279, 1143
Toriello, N.M. 1195
Torii, T. 267, 1459
Tovar, A. 1024
Trachsel, F. 270
Trau, D. 1528
Tresca, G. 721
Tropini, C. 1592
Tsao, C.W. 640
Tseng, F.G. 1411
Tseng, H.-R. 1309
Tserepi, A. 92
Tsuchiya, H. 1459
Tsuda, K. 1375, 1708
Tsui, O.K. 1777
Tsui, T. 185
Tsukahara, T. 430, 718, 1018, 1574
Tsuruta, T. 312
Tuomikoski, S. 835
Turnbull, J.E. 86

U

Uchiyama, K. 1053, 1450
Ueda, M. 865
Uemura, K. 333, 1541
Ueno, K. 1429
Ueno, M. 625
Ugaz, V.M. 71
Uhlén, M. 113, 688
Ukita, Y. 373
Ullien, D. 1683
Um, E. 853
Uozumi, Y. 625
Urban, G.A. 1246
Urbanski, J.P. 285
Urdaneta, M. 1327
Utsumi, Y. 373, 1161
Utz, M. 288, 1489

V

Vahey, M.D. 991, 1104
Vallès, E. 937
Vanapalli, S.A. 628
Vangelooven, J. 248, 382
Van Hummelen, P. 682
Varady, M. 1336
Varma, R. 518
Varnier, A. 491
Vawter, G.A. 1056
Velders, A.H. 506
Vellekoop, M.J. 233, 739, 1474
Verboom, W. 264, 1471
Verdoold, V. 248, 1646
Verdoy, D. 584
Veres, T. 442, 661
Verneuil, E. 343
Vernick, S. 1049
Verplanck, N. 41, 1043
Verpoorte, E. 1333, 1547
Vieider, C. 542
Viel, L. 1192
Vijaykumar, T.N. 967
Vilares, R. 1720
Villiers, M.-B. 173
Vineyard, L. 167
Viovy, J.-L. 50, 400, 575,
..... 598, 637, 1146
Virobnik, U. 1683
Vitalis, T. 1170
Vladisavljević, G.T. 1541
Voitel, J. 1513
Voldman, J. 8, 448, 581, 991, 1104
Vrillon, F. 476
Vukasinovic, J. 1381
Vulto, P. 1246

W

Wada, S. 1459
Wagner, C. 146
Wagner, J.B. 985
Wakida, S. 1176
Wal, P.D. van der 1288
Walczak, R. 691, 1664
Walter, A.D. 1643
Walter, J. 880
Wang, B. 796
Wang, H. 748
Wang, H.-Y. 194, 670
Wang, I.-L. 62
Wang, J. 670, 1677
Wang, S. 418
Wang, W. 539
Wang, X. 1164

Wang, Y. 919, 1444
Wang, Y.-C. 1786
Wang, Z. 1234
Wang, Z.F. 1125, 1738
Wapelhorst, E. 1185
Warrick, J. 146
Warrick, J.W. 1550
Wartena, R. 991
Washizu, M. 197, 412, 512,
..... 1000, 1375, 1765
Watanabe, E. 479
Watanabe, R. 412
Watarai, E. 500
Weidmann, M. 1246
Weigel, S. 730
Welle, R.P. 1426
Wells, J. 17
Wen, J. 77
Weng, Y.-C. 892
Weniger, M. 321, 613
Wereley, S. 967
West, J. 604
Westerweel, J. 221
Westlake, K. 1056
Wheeler, A. 327
White, V.E. 551
Whyte, G. 143
Widjara, J.E. 940
Wiesle, M. 730
Wijngaart, W. van der 527
Wijnperlé, D. 1201
Wiklund, M. 1807
Wilderbeek, H. 1143
Willaime, H. 361
Williams, R.S. 409
Willis, P.A. 254, 551
Windhab, E.J. 358, 946
Winkle, R. 850
Wirix-Speetjens, R. 23
Wirth, M.J. 1586
Wisztorski, M. 41
Witte, O.N. 1309
Wo, A.M. 119, 1110, 1279
Wolff, A. 59, 691, 1519
Wolfrum, B.L. 388
Won, D.G. 862
Wong, T.-N. 1562
Woolley, A.T. 817
Wootton, R.C.R. 261, 850
Wright, J.B. 1056
Wrobel, G. 485
Wu, B. 1396
Wu, L.-W. 700
Wu, L.Y. 709
Wu, P.-M. 251
Wu, R.-G. 1411
Wu, T.-H. 1771
Wu, T.-T. 1680
Wu, Y.-S. 1411
Wuite, G.J.L. 593
Wyżkiewicz, I. 68

X

Xie, Y. 919, 1444
Xu, D. 539
Xu, L. 170
Xu, Y. 424
Xu, Z.R. 646

Y

Yager, P. 667
Yagi, T. 1744
Yamada, A. 1303, 1613
Yamada, M. 898, 1792
Yamada, Y.M.A. 625
Yamagata, Y. 1252
Yamagata, Y. 1285
Yamaguchi, A. 757
Yamahara, R. 856
Yamahata, C. 403
Yamami, T. 754
Yamamoto, H. 1765
Yamamoto, K. 1297
Yamamoto, M. 1792
Yamamoto, T. 182, 844, 1604
Yamanishi, Y. 883
Yamato, M. 433, 1708
Yang, C. 14
Yang, C.H. 1279
Yang, C.J. 949
Yang, C.-S. 1411
Yang, D.H. 421
Yang, H. 327
Yang, K.S. 1261
Yang, S. 509, 1155, 1698
Yang, S.-Y. 107

Yano, H. 754
Yap, P.H. 11, 188, 461, 694,
..... 1059, 1348, 1354, 1438
Yap, Y.-F. 1562
Yarmush, M.L. 164
Yashima, E. 1565
Yasuda, A. 1601
Yasuda, M. 898, 1792
Yasuda, S. 1744
Yasuda, T. 706, 754
Yasui, T. 1207
Ye, L. 158
Yi, H. 1616
Yi, U.-C. 847, 1634
Yin, H. 554
Yobas, L. 140, 685, 1528, 1562, 1661
Yoganathan, N. 1282
Yokokawa, R. 17, 587
Yoo, S.-K. 509, 1155
Yoo, Y.S. 282
Yoon, D.H. 245
Yoon, E. 793
Yoon, H.C. 218
Yoon, H.-J. 83
Yoon, J. 1525
Yoon, S.H. 862
Yoon, S.-I. 1167
Yoon, S.K. 1468
Yoon, T.-H. 1456
Yorish, S. 1049
Yoshida, N. 1637
Yoshida, Y. 790, 1176, 1432
Yoshiki, A. 1252
Yoshimura, E. 718, 1384
Yotsuya, T. 1297
Young, I.T. 221
Yu, C. 940
Yu, H.-Z. 1282
Yu, K. 1116, 1568, 1774
Yu, Y.F. 188, 1059, 1354, 1438
Yu, Z.T.F. 1309
Yun, H. 1258
Yun, S.-S. 509, 1155
Yvert, B. 1080

Z

Zahn, P. 1246
Zalewski, D.R. 1408
Zangle, T.A. 1204, 1592
Zareian-Jahromi, M.A. 239
Zarnitsyn, V. 1336
Zauner, D.A. 497, 1071
Zauner, K.-P. 1089
Zeng, Y. 2, 805
Zengerle, R. 1149, 1231, 1249, 1516
Zent, A. 254
Zevenbergen, M.A.G. 388
Zhang, G.-J. 607
Zhang, H.D. 646
Zhang, J. 1447
Zhang, M. 158
Zhang, S. 200
Zhang, X. 128, 188, 461, 610, 694, 1649
Zhang, Y. 122
Zhao, Y. 521, 760, 847, 1137
Zheludev, N. 1264
Zheng, B. 80, 1393
Zheng, S. 488
Zheng, X. 1649
Zhi, Z.-L. 86
Zhou, J. 646, 1562
Zhou, W.-P. 1468
Zhou, X. 1393
Zhu, L. 1137, 1351
Ziegler, J. 101
Zimmermann, M. 101, 1492
Zohar, Y. 1586
Zou, Z. 251
Zoueshtiagh, F. 294
Zoval, J.V. 74
Zuiddam, M. 385

Keyword Index

A

Absorbance Detection 95, 1652, 1661
Alternating Current 1477
  Electrokinetics ..... 35, 285, ... 303, 1312, 1483
  Electrothermal Flow 916
Acoustic Effects 209, 1807
  Particle Separation 1813
  Streaming 300, 321
  Trapping 1372
Acrylamide 433, 649
Acrylic Acid Plasma 397
Active Droplet Control 1562
Active Mixer 916, 1143
Actuator(s) 745, 883, 1131
Adhesion 1628, 158
Adjustable Gap 542
Affinity Extraction 1810
Alginate Fiber 961
Aligned Bonding 1756
Alignment 1158
Allergen 637
Aluminium 563
Aluminum Oxide Membrane 643
Amino Acids 1677
Ammonia Gas 1450
Amperometric Detection 1074
Amplified Single Molecule 1306
Amylase Activity 65
Anisotropy 628
Annular Flow 955
Anodic Aluminum Oxide 1261
Anodic Bonding 1583
Anodic Stripping Voltammetry 251
Anodization 1646
Antibiofouling 424
Antibodies 113, 1810
Antibody/Antigen
  Microarray 173, 688
Anticancer Activity 1384
Antioxidants 1164
Apoptosis 128, 1330
APPI 569
Aptamer(s) 652, 1192
Aptasensor 652
Aqueous Two-Phase System 1538
Array Dependence 1207
Artificial Cilia 1143
Artificial Pore 1173
Assembly 1616
Asymmetric Inertial Migration 802
Asymmetric Reaction 1462
Asymmetric Through Holes 1541
Asymmetric Tubular
  Pinch Effect 802
Atomic Force Micropscopy
  (AFM) 1188
Atomic Vapor 859
Adenosine Triphosphate
  (ATP) 844, 1372
Automation 1219
Autosampler 892

B

Bacteria 1351
  Detection 1065, 1092
  Transport 545
  Cell 1510
Baker's Transformation 309
Bar Code 1, 1264
Batch Process 601
Bead 245, 503, 1522
Benzophenone 1363
Beurite Outgrowth 730
Bicomponent Extrustion 1465
Bilayer 679
Binding Assay 1544
Bioactivated Nanopores 20
Bioanalysis 1046, 1270
Bioassay 1384
Bio-Cell Characterisation 1556
Biochemical Reaction 1701
Biochemical Sensor 409
Biochip 17, 173, 679, 1354
Biocompatibility ..... 439, 1031, ... 1378, 1456
Biofilm 273, 748
Biofuel Cell 868
Bioimpedance 1686
Biolithography 820
Biological Imaging 161
Biologically Inspired 622

Bioluminescence 1049
Biomarker 254, 503
Biomaterial Encapsulation 853
Biomedical Implant 518
Biomedical Microdevice 563
BioMEMS 448, 658, 784
Biomolecular Interaction 676
Biomolecular Motor 1222, 1012
Biomolecule Delivery 1336
Biomolecule Manipulation 1429
Bioparticles 826
Biophysical Interrogation Techniques 86
Biorecognition Layer 436
Biosensor ..... 294, 485, 1089, ... 1098, 1101, 1288, 1390, ... 1598, 1670, 1680, 1683, 1695
Biotin-Streptavidin 1167
Bipolar Nanochannel 979
Bismuth Electrode 251
Blood 77, 470, 1801
  Cells 215, 488
  Fragmentation 733
  Lysis 1516
  Plasma 80, 706, 1486
Bonding 530, 1119, 1125, 1711
Botulinum Neurotoxin 1192
Break-Through Pressure 1489
Brownian Dynamics Simulation 991
Brownian Motion 388, 1750
Brownian Ratchet 1750
Bubble(s) 703, 952, 1149, 1634
Bubble Logic 1216
Buckling 742
Buoyancy 1294, 312
BZ Reaction 865

C

Caenorhabditis Elegans ..... 14, 131, ... 1107, 1219
Caco-2 Cell 182
Cage-Speed Separation 721
Calcium Signaling 1366
Cancer Detection 1780
Candida 74
Cantilever 497, 1101, 1714
Capillary Effects 367, 595
Capillary 101, 427, 943, 1149, 1652
Capillary Electrophoresis ..... 98, 817, ... 1077, 1161, 1195, 1408, 1640, 1677
Capillary Valve 1513
Capillary-Assembled Microchip 427, 874
Capsule Endoscope 1759
Carbohydrate and Protein Interactions 86
Carbon Dioxide 1462
Carbon Nanotube 1122, 1598
Cardiomyocyte 128, 1649
Cartridge 685
Cascaded Actuator 557
Caspase Activity 874
Cassie State 1795
Castellated-Shape Electrodes 1798
Catalysis 261, 625, 784
Cationic Coating 1234
Cavitation Bubble 206
CCD Camera 691
Cell(s) ..... 137, 143, 233, ... 598, 787, 808, 1333
  Adhesion 430, 485, 718, 1363
  Analysis 1348, 1279
  Assay 167, 736, 1309
  Cage 1327
  Counter 739
  Culture ..... 170, 182, 188, 461, ... 575, 700, 703, 709, ... 727, 1140, 1309, 1321
  Division 1768
  Encapsulation 775
  Focusing 318
  Free Layer 733
  Fusion 581, 1375
  Handling 1369, 1777, 1807
  Loading 1327
  Lysis 155, 409, 587, 1342
  Manipulation 512
  Mechanics 616
  Migration 610
  Morphology 1333
  l Motility 718
  Necrosis 164
  l Patterning 430, 1318
  Poration 206
  Processor 424
  Reprogramming 581

Separation 575, 1330, 1420
Sheet 433
Signaling 1315, 1762
Sorting ..... 122, 173, 330, ... 470, 793, 1804
Stimulation 1345
Surface Marker 113, 1173
Trapping Array 1765
Treatment 1336
Centrifugal Microfluidics ..... 179, 539, ... 733, 1231, 1516l
Acceleration 245
Chromatography 1441
Pumping 898
Ceramic 68
CFD (Computational Fluid Dynamics) 282, 1541
Channel Geometry 339
Chaotic Advection 904
Chaotic Mixing 279, 324, 901
Charged Species 970
Charge Transfer Technique ..... 479, ... 1255, 1255
Chemical Passivation 1065
Chemical Reactions 1534
Chemical Sensing 445, 1525
Chemical Signal 29
Chemical Stimulation 754
Chemiluminescence 1164, 1372
Chemotaxis 763, 766, 1324, 1366
Chiral Analysis 230
Chitosan 784, 1616
Chromosomal DNA 197, 1000
Ciliate 1366
Circulating Tumor Cells 613
Clinical Diagnosis 65, 77
Clinical Range 1267
C-MEMS 826
CMOS Sensor 1753
Coating 805, 1034, 1453
Coaxial Sheath Flow 1474
Co-Culture 146, 1318
Coflow 358, 946
Collagen Powder 1625
Collocated Monolithic Support Structure 248
Colloidal Self-Assembly 2, 1586
Combinatorial Chemistry 1387
Commercial Scanner 62
Complementary Metal Oxide Semiconductor 1179
Complete Engulfing 361
Concentration Effects ..... 763, 856, ... 1279, 1426, 1777
Condensation Effect 1176
Conducting Polymer 787
Conductivity 1692
Confined Polyelectrolytes 391
Confinement 805
Conformational Separation 790
Contact Angle 1477, 1643
Contact Guidance 610
Continuous Flow ..... 212, 919, ... 1270, 1273, 1528
Continuous Particle Separation 898, 1228
Continuous Separation 2, 125
Contrast Agents 664
Control Systems 850
Controlled Environment Bioreactor 715
Conversion of Segmented Flow to Parallel Flow 1213
Corona Discharge 1285, 1631
Cross-Channel 324
Cross-Polarization 697
Crystallization 590, 1210
Curved Channel 245
Cycloolefin Polymer 1655, 1405
Cylindrical Surfaces 1158
Cytochrome c 1610
Cytometry 14, 739

D

Dean Vortices 733
Deep X-Ray Lithography 373
Dendritic Amplification 26
Density Functional Theory 886
Density Sensor 536
Desorption 569
Detachment 1634
Detection 442
Development 203
Diabetes Mellitus 1303
Diagnosis 1, 59, 631, 673
Diamagnetism 212, 922

Dictyostelium 766
Dielectric Constant 1692
Dielectric Measurement 1689
Dielectric Microparticle 1176
Dielectrophoresis ..... 5, 8, 125, 221, ... 233, 318, 364, 403, 706, 715, ... 826, 877, 991, 1104, 1279, 1318, ... 1375, 1483, 1771, 1798, 1801, 1804
Dielectrophoretic Cages 721
Dielectrophoretic Parasite Detection 494
Diels-Alder 264
Differential Interference Contrast 458
Diffraction 71
Diffuser 297, 1501
Diffusion-Free Sampling 769
Digestion 649
Digital Microfluidics ..... 327, 346, 349, ... 572, 922, 1550, 1553, 1559
Digital Versatile Disk 739
Dipole Forces 877
Directed Sorting 1387
Direct-Write 1134
Disposable 530
Dissolution 1516
Distribution System 548
DNA ..... 1, 2, 56242, 415, ... 607, 841, 901, 985, 1201, ... 1237, 1432, 15801622, 1680
  Bead Assemblies 1601
  Condensation 1399
  Detection 71, 485
  Diagnosis 973
  Extraction 74, 643, 1231
  Hybridization 20, 442, 1598
  Microarrays 682
  Mutation 646
  Protein Interactions 593
  Purification 77
  Separation 997, 1161, 1414, 1586
  Stretching 391
  Tweezers 1714
  Wire 1714
DNA/RNA Extraction 1429
Dosing 1396
Double Emulsion(s) 361, 943
Double Layer 291
Double Roughness 1795
Drift 38
Drop-and-Sip 874
Droplet(s) .....113, 143, 294, 339, ... 346, 352, 598, 847, 853, ... 862, 925, 928, 931, 1040, ... 1059, 1062, 1210, 1528, 1531, ... 1538, 1544, 1553, 1562 1637, 1670
  Fusion 352
  Generation ..... 267, 333, 358, 943, ... 946, 949, 1231, 1541
  Microfluidics ..... 336, 343, ... 1556, 1562, 1771
Drug Assay 709, 1321
Drug Delivery ..... 104, 191, 194, ... 652, 1225, 1595, 1720
Dual Detection 68
Dual-Channel 1077
Dual-Thermopile 1701
DVD-Writer 1249
Dynamic Cantilever 83
Dynamic DNA/RNA Hybridization 1282

E

Early Response 158
EB Lithographic Polymerization 430
ECIS 128
EIS 128
Electric Double-Layer 1592
Electrical Detection 1092, 1692
Electroactive Microwells 1225
Electrochemical 856, 1680
  Cell Lysis 736
  Detection 1077, 1677
  Method 1318
  Sensor 476, 1021
Electrode(s) 787, 916, 982, 1686
Electroformation 1613
Electrohydrodynamics ..... 306, 925, ... 1510, 1538
Electrokinetic ..... 35, 185, 379, ... 1182, 1225, 1589
Electrolysis 1312, 1504
Electronic Paper 267
Electronic Sensing 1173
Electroosmosis Flow ..... 829, 886, 889, ... 1134, 1438, 1667, 1723

Electrophoresis ..... 65, 236, 400, 634, ... 724, 769, 808, 814, 835, 841, ... 985, 1074, 1207, 1330, 1402, ... 1405, 1423, 1447, 1586, 1783
Electrophoretic Purification 1246
Electroporation 194, 512, 670, 1339
Electrosonic Atomizer 1336
Electrospray ..... 542, 835, ... 1405, 1291, 1547
Electrospun Nanofiber Scaffold 397
Electrostatic Force 209
  Actuation 1735
  Deposition 1285
  Particle-Particle Interaction 877
Electrostretching 649
Electrothermal 303, 1483
Electrowetting ..... 306, 349, 640, 847, ... 925, 1043, 1477, 1559
Electrowetting on Dielectrics (EWOD) 913
ELISA 373, 661, 667, 1261
Embossing 1738
Embryonic Stem Cell 581, 772
Emergency 476
Emulsions 1459, 1534
Encapsulation 598, 961
Energy Scavenging 566
Enrichment 539
Enzymatic..... 113, 143, 784, 868
  Digestion 1601
  Reaction 1574
  Immobilization 1789
Epitope Extraction 637
Equivalent Circuit 1765
Erythrocytes 1372
Evanescent Field 1065
Evanescent Wave 17, 889, 1667
Evaporation 566
Expression Profiling 613
Extended-Nano Space 1018, 1574
Extraction 1553
Extrusion 604

F

F1-ATPase 1604
FACS 1813
Far Field 560, 1417
Fast Prototyping 1152
Feedback 850
Femtoliter Chamber 757, 976, 1003
Femtosecond Laser Machining 976
Fiber 622
Fiber Bragg Grating 1348
Fiber-Optic Sensor 1664
Field Constriction 1375
Field Effect Device 1683
Field Effect Transistor 485
Field-Flow 970
Filtration 215, 1351
Fission Yeast 742
Flagella 1222
Flexible Devices 327
FLIM 1062
Flow Control 321, 1774
  Cytometry ..... 11, 107, 125, 494, ... 670, 1258, 1315, 1801
  Focusing 598, 1465
  Lithography 619
  Measurement 276
  Stress 700
  Visualization 946
Flow-Through 667, 1559
Fluidic Capacitance 288
  Circuits 952
  Diodes 1489
  Handling 1288
  Instruction Set 967
  Resistance 288
Fluorescence 691
  Detection 17, 673, 1015
  Lifetime 1062
  Sensor 1068
Fluorescent Polydiacetylene Nanosomes 421
Fluoride 856
Fluorocarbon 92
Focusing 1204
Focusing Resonator 1807
Food Pathogens 691
Force Balance 134
Force Measurement 1095
Force Production 742
Force Sensor 1107
Forensic 721
Fourier Microfluidics 1444
Fourier Transform 236

Fractionation 970, 1408
Free-Flow Dielectrophoresis
Electrophorèse 221
Free-Flow Electrophoresis 811, 1243
Freeze-Drying 59
Frequency Response 288
FRET 1544
Fringe 1059
Frit 1435
Fuel Cell 1468

G
Gas Chromatography 239
Gas Partial Pressure 964
Gas Permeability 703
Gastric Fluid 1759
Gate Leakage 385
Gel Emulsion 339
Gel Microtube 775
Gene Assembly 200
Delivery 406
Expression 718, 1170, 1762
Synthesis 200
Therapy 781
General-Purpose Lab-On-a-Chip 967
Genetic Analysis 59, 1195
GFP 1240
Gigaseal 140
Glass Microchip 137, 264
Glucose 152
Glycoarrays 86
Gold Nanoparticle(s) 458, 464, 658
Gradient 203, 554
Grating 473
Growth Factor 146
Guar 358
Gynami Fluidic Signals 1444

H
Handheld 95, 1294
Head-On Devices 928
Heat Transfer 315
Heat-Controlled Microelectrode 218
Heating Resistance 324
Heavy Metal Ion 251
HeLa Cell 1345
Hematocrit 1249
Hepatic Metabolism 1384
Hepatitis B Virus 1261
Heteroduplex Analysis 634
Heterogeneous Buffer 790, 1432
High Pressure 264, 270
High Resolution 230
High Speed Sorter 224
High Throughput 143, 146, 751
Analysis 1544
Screening 619
Higher-Order Structures 197
HIV Screening 1258
hMSC 712
Hourglass 1110
Humidity Level 1714
Hybrid Technology 68
Hybridization 236, 376, 901
Hydraulic Amplification 1735
Hydraulic Inductance 952
Hydrodynamic Filtration 1228
Hydrodynamic Focusing 1474
Hydrodynamic Position Control 1571
Hydrodynamic Trapping 8, 581
Hydrodynamics 382
Hydrogel 1504, 1762
Hydrogel Beads 853
Hydrogenation 270
Hydrophilicity 439, 1119
Hydrophobic/Hydrophilic
Patterning 92
Hydrophobicity 379, 754, 1637
Hydrophoresis 215, 1486
Hyperthermia 1595

I
Imaging 1219, 1556
Immersion Refractometry 461
Immobilized pH Gradient 838
Immunoaffinity Chromatography 799
Immunoaffinity Positive Selection ... 155
Immunoassay 23, 26, 101, 107,
..... 303, 62, 655, 1024, 1252,
..... 1261, 1291, 1300, 1402, 1607, 1783
Immunodetection 20
Immuno-Gold Silver Staining 503
Immuno-Sensing 454, 1786
Impedance Spectroscopy 488, 494,
..... 1083, 1089, 1086,
..... 1686, 1692, 1695, 1720

Impinging Jet 1744
In Situ Analysis 230, 273, 694, 994
In Vitro Fertilization 1798
In-Cell Western 158
Indirect Detection 227
Infection 688
Influenza A 694
Inkjet 282
Innate Immunity 1315
Inorganic Polymer 1456
Insect Cyborg Sentinels 1225
Insulative Dielectrophoresis 578
Insulin 1303
Integrated
  Amperometric Microsensors 152
  In Situ Analyzer 844
  Microdevice 98, 1780
  Microflow Meter 1146
  Micropump 1288
  Positive and Negative
    Cell Sorter 1420
  Sample Preparation 1195
  Spectrometer 1071
  Waveguides 497
Interdigitated Electrodes 1673
Interface 306
Interface Adhesion Energy 1489
Interfacial Tension 871
Interferometry 1059
Intermittent Movement 1201
Intestinal Absorption 1384
Ion Sensitive Field Effect
  Transistor (ISFET) 479, 1255
Ion-Channel 491, 679
Ion-Depletion 895
Ionic Gradient Focusing 1583
Ionic Liquid Droplets 769
Ionic Rectifying Effect 979
Ionic Transistor 385
Ionization 542
Ion-Pair Reversed-Phase
  Chromatography 1414
Ion-Selective Membrane 1198
Ion-Selective Microelectrodes 164
Isocratic Elution 1414
Isoelectric Focusing 799, 832,
..... 838, 1423
Isoenzyme 65
Isolation 179, 403
Isotachophoresis 56, 227, 823, 1402
Isotonic Saline 312
IVF 1357

J
Janus 361
Jetting 1495

K
Kinase 670
Kinetics 590, 1471, 1789

L
Label-Free 494, 1083, 1095,
..... 1182, 1598, 1658, 1683
  Biosensing 1009
  Detection 20, 71, 176, 1092, 1243
  DNA Chips 421
Lab-on-a-Chip 59, 461, 643,
..... 676, 694, 1056, 1170,
..... 1351, 1504, 1513, 1562
Lab-on-a-Display 364
Laminar Flow 26, 766, 955, 1450, 1468
Laminated Membrane 551
Lamination 904, 1113
Laplace Pressure 601, 1213
Large-Area Patterning 2
Laser Ablation 1441
  Drilling 1110
  Fabrication 820
  Radiation Pressure 1507
  Trapping 1399
Layer-by-Layer 1528
Leakage Barrier 297
Leukemia 616
Leukocyte 137
Levitation 149, 922
Libraries 1104
Ligation 412
Light Scattering Theory 1354
Light-Control Micro-Pump
  System 1297
LightScribe 1249
Linear Amplification 47
Linear Motor 1501
Lipid 104
Lipid Bilayer 491

Lipid Nanovesicle 1595
Lipid Tubule 604
Liposome, Lipospheres .. 191, 934, 1613
Liquid Chromatography ..... 248, 554, ... 1435, 1646
Liquid Crystal Display Projector ... 1708
Liquid Dispensing 1393
Liquid Gap Actuator 1735
Liquid-Core Waveguide 95, 1652
Liquid-Liquid Extraction 327
Liquid-Liquid Interface 871
Liquid-Liquid Waveguide 11
Liquid-Liquid-Phase Electrospray 1547
Living Cell 161, 451, 461, 1354
Local Coating 1631
Local Pressure 1059
Local Reaction Control 934
Locomotion 1107
Logic Gates 1550
Longitudinal Chemical Concentration Gradient 1324
Lorentz Force 119
Low Power 1732
Low-Cost Optics 1249
Lymphocytic Choriomeningitis Virus 1252
Lyophilisate 1516

M

Mach-Zehnder Interferometer 454
MACS 330
Magnetic 685
  Beads 50, 107, 575, 661, 688
  Carrier(s) 637, 940
  Cell Sorting 1420
  Chain 279
  Glass Carriers 1387
  Nanoparticle 793, 1595
  Particle(s) 23, 1179, 1369
  Path 940
  Sensor 23, 1369
  Separation 122
  Traps 1673
Magnetically-Driven 883
Magnetophoresis ..... 149, 330, ... 1270, 1369
Magneto-Static FEA Analysis 937
Magnetotactic Bacteria 545, 1695
MALDI 41, 640, 1046
Manganese 844
Manipulation 339, 931, 1312
Maskless Lithography ..... 1116, 1568, ... 1708, 1774
Mass Spectrometry ..... 41, 44, 50, ... 554, 569, 835, 1234, 1405, 1435
Mast Cell Response 451
Materials Synthesis 859
Materials-Cell Interactions 500
Maximum Length Sequence 1086
MCF-10A 89
MCF-7 ..... 703, 1342
MDCK Cells 694
Mechanical Behaviour 745, 880
Mechanical Characterization 751
Mechanosensation 131
Mechanotransduction 185, 1107
Medical Implant 748
Medium Supply 1309
Membrane 1122, 1140
  Protein 595, 679, 1188, 1276
  Structure 1188
Membraneless 1468
MEMS ..... 239, 536, 937, ... 958, 1137, 1128, 1185
MEMS Tweezers 415
Mesophase 71
Metabolite Sensing 427
Metal-Ligand Complex 464
Micellar Electrokinetic Chromatography 814
MicraGEM 1695
Micro
  Battery 1759
  Column 1435
  Heater 1240
  Medical Device 1759
  Nozzle Array 775
  Orifice 512, 1375
  Post Structured Surface 1634
  Spectroscopy 1664
Microaperture 1110
Microarray(s) .. 74, 179, 333, 676, 1031, ... 1034, 1222, 1282, 1321, 1658
Microbubbles 191, 664
Microcalorimeter 1167

Microcantilever 631, 1267, 1704
Microcapsules 880
Microchamber 649, 1753
Microchannel(s) ..... 403, 545, 560, 934, ... 1012, 1345, 1459, 1498, ... 1640, 1701, 1711, 1726
Microchannel Emulsification 1541
Microchip ..... 188, 254, 506, 569, 613, ... 646, 1077, 1164, 1252, 1258, 1324
Microcirculation 880
Micro-Coils 940
Microcontact Printing 1198
Microdevice 584
Microelectrode Arrays 760, 1080
Microemulsion Polymerase Chain Reaction 949
Micro-Extractor 306
Microfabrication ..... 161, 512, 521, ... 742, 1813
Microfiber 545
Microfilter 503, 847
Microflow Regulator 937
Micro-Flow-Cell 856
Microfluidic
  Cell Culture 736
  Component 1152
  Computing 1216
  Control 883, 964
  Cytometer 1086
  Device(s) ..... 218, 197, 637, 706, ... 709, 898, 1228, 1342, 1366, 1771
  Disk 1137
  Flow 880
Microheaters 910
Microlens Array 1717
Micromechanics 521
Micrometer-Sized Particle 539
Micromixer ..... 29, 309, 312, ... 321, 904, 916, 1747
Micro-Molding in Capillaries 700
Microneedle 1155, 1720
Microparticle(s) 149, 212, 628, 1270
Micropattern(s) ..... 131, 185, 436, 787, ... 1333, 1363, 1619, 1768
Micropatterned Matrigel 89
Micropillars 134, 382, 832
Micropipette 751, 1128
Microporous Membrane 604
Micropump(s) ..... 5, 35, 285, 297, ... 300, 312, 315, 551, ... 1498, 1501, 1504, 1732
Microreactor 167, 270
Microring Resonator 1056
Microscale Plasma Activated Templating 1717, 1741
Microscope 14, 273
Microstreaming 1670
Microtools 883
Micro-Total Analysis System 829
Microtransfer Molding 89
Microtubules 1006
Microvalve(s) ..... 5, 32, 373, 524, 551, ... 754, 1131, 1195, 1447
Micro-Vortices 119
Microwave-Induced Microplasma . 1698
Microwave Dielectric Heating 110, 1237
Microwave Resonator 1689
Microwell 772, 1393
Microwires 1116
Miniaturized Solid Phase Synthesis 1387
Mitochondria Separation 224
Mixing ..... 318, 895, 901, 910, 913, ... 925, 1062, 1507, 1519, 1522, 1744
MLPA 613
Moiré 1649
Mold Process 1158
Molecular Crowding 1003
  Delivery 206
  Filter 1429
  Logic Gate 1525
  Manipulation 1000
  Sizing 1399
  Surgery 412
Monodisperse 346, 1459
Monolith 829, 1234
Monosaccharide 790
Morphology 361
Motile Sperm 1324
MPC 1628
MPC Polymer 1222, 1291
mRNA Amplification 673
Multi-Cell Sorting 1176
Multi-Channel 346, 451
Multi-Component Fibers 1571

Multi-Functional Envelope-Type Nano Device (MEND) 781
Multi-Layer 766, 1726
Multi-Layer Fabrication 47, 1113
Multi-Layered Device 1345
Multi-Level Microfluidics 817
Multi-Phase Flow ..... 871, 1348, ... 1450, 1453, 1538
Multiple Frequency Dielectrophoresis 1327
Multiple Laminar Flow 1604
Multi-Plexing 44, 1068, 1264, 1655
Multi-Sample Nucleic Acid Hybridization 1282
Multi-Target Sorting 1804
Multi-Well Tissue Culture Plates 167
Mutation Detection 634
Mutiplexed Immunoassay 330
Mycobacterium Smegmatis 578

N

Naked Eye Detection 688
Nano Particle 1098, 1285, 1744
Nano Roughness 1795
Nano-Bio-Component 1616
Nanobubble 379, 976
Nanocapillary 976
Nanochannel Chromatography 418
Nanochannel(s) ..... 385, 418, 473, ... 515, 979, 982, 1204, ... 1414, 1577, 1583, 1607
Nanocomposite 1122
Nanofabrication 515, 1264, 1622
Nanofiber 1291, 1465
Nanofilament 640
Nanofilters 997
Nanofluidic(s) ..... 221, 376, 979, ... 382, 385, 388, 391, 886, 988, ... 997, 1006, 1204, 1411, 1574, 1577, ... 1580, 1586, 1589, 1601, 1622, 1786
Nano-Gap Array 973
Nanohole Array 394, 1009
Nanoimprint 400, 1622
Nanomaterials 1378
Nano-Molding 1021
Nanoparticle(s) 1, 406, 991
Nanophotonics 1009
Nanopillar Chip 1207
Nanopipettor 1723
Nanoplasmonic Gold Nanoparticle 1610
Nanopore(s) ..... 862, 1015, ... 1589, 1592, 1601
Nanoporous Polymer 1300
Nanoscale 1667
Nanoslits 391, 1201
Nanosphere Lithography 394
Nanostructure 442, 718
Nanotube 985
Nanovelocimetry 988
Nanowell 1021
Nanowire 985, 1677
NASBA 673
Natural Convection 1294
Natural Nano-Structured Materials .. 445
Near Field 560
Near-Infrared 1664
Needle-Free 104
Neisseria Meningitidis 1167
Neurons 1080, 1396
Neuroprosthesis 730
Neutrophil 155
Nickel 524
N-Isopropylacrylamide 433
Nitration Reaction 1664
Nitric Oxide 1396
Nitrocellulose Membrane 667
NMR 258, 506, 1018
Noise Characteristics 479
Non-Equilibrium Transport 997
Non-Fluorescent Analyte 227
Nonlinear
  Capacitance 291
  Electrokinetics 285
  Optics 859
Non-Newtonian 1495
Non-Optical Lithographic Method ... 394
Non-Specific Adsorption 661
Nonspherical Droplets 333
Non-Symmetric Power Supply 1522
Non-Viral Gene Delivery 781
Nozzle 1744
Nucleation 1210
Nucleic Acid Hybridization 619
Numerical Simulation 315

O
OLED 697
Oligonucleotide 236, 376
On-Chip Catalysis 625
  Construction 781
  DNA Amplification 53
  Fluorescence Detection 697
  Gel Fabrication 775
  Labeling 769
  Mixing 1777
  Perfusion 182
  Purification 587
  Reference 1065
  Valving 1074
Online Concentration 1432
On-Site Analysis 1053
Oocyte 1798
Optical 1771
  Detection 1068, 1179
  Dielectrophoresis 572
  Electrowetting-on-Dielectric 572
  Emission Spectroscopy 1698
  Forcing 343
  Gradient Force 1176
  Manipulation 5, 470
  Microscopy 1807
  Trapping 1762
  Tweezers 116, 467, 1000, 1507
Optically Driven Micropump 1729
Optimisation 850
Optoelectronic Tweezers 364, 877
Optofluidic(s) 11, 14, 470, 572, 1116
Organelle Sorter 224
Organic Photodiodes (OPD) .. 697, 1164
Organic Transformation 625
Organotypic Cultures 1381
Oscillating Bubble 300, 913
Osmotic Pressure 1303
Osmotic Valve 1303
Osteoblast 748
Osteoproteogerin 658
Oxide-Free 607
Oxygen 152

P
Palladium Complex 625
Parallel Microreactor 1471
Parallelization 267, 1360
Partial Filling Technique 814
Particle Classification 533
  Focusing 1486
  Image Velocimetry (PIV) ..... 946, ... 1480, 1637
  Sampling 847
  Separation 802, 1438
  Trapping 1792
Particle-Based Biosensor 1673
Parylene 518, 1140
Passivation 524
Passive Synchronization 1216
Patch Clamp 140, 491, 1110
Pathogen/Bio Detection 1137
Particle Image Anemometry 276
Patterning 1510
Printed Circuit Board (PCB) ..... 1131, ... 1237, 1559
PDMS (Polydimethylsiloxane) ..... 530, ... 1037, 1360, 1649, 1711
PDMS (Polydimethylsiloxane) Container 1240
PDMS (Polydimethylsiloxane) Glass Chips 1756
PDMS (Polydimethylsiloxane) Membrane Deflection 1342
PDMS (Polydimethylsiloxane) Microfluidic Chip ..... 152, 176, ... 778, 1792
Polyethylene-Glycol (PEG) 1021
Peltier 1426
Penicillin Sensor 1255
Peptide 811
Perfusion Bioreactor 772
Perfusion Culture 1321, 1381
Peristaltic 315, 557, 685, 1741
Permanent Magnet 149, 922
pH 467, 790
pH Sensor 479
Phage Display 1810
Phase Inversion 778
Phase Separation 955
Phase-Change Material 1131
Phaseguides 1246
Phospholipid Polymer 424, 439, 500
Phosphorylation 134
Photocatalyst 1456, 1462
Photochemical 1628

Grafting 1031
Patterning 1053
Photoiniferter 436
Photolithography .. 448, 509, 1708, 1765
Photoluminescence 445
Photo-Oxidation 261
Photopatterning 1027, 1789
Photopolymerization ..... 655, 1113, ... 1116, 1146, 1568, 1774
Photoreaction 1462
Photothermal 273, 406, 458
Physarum 1089
Piezo-Copolymer (PVDF-TrFE) 482
Piezoelectric 1498
Piezoresistive 1101, 1704
Pillar Array 248, 1646
Pinched Flow Fractionation 1228
Pipe 1149
Pixelation 1556
Planar Lipid Bilayer 595, 1276
Plant-Like Structures 1643
Plasmonic Resonance Energy Transfer 464, 1610
PLGA Microfiber 778
Pluronic 355, 841
PMMA 1402, 1640
PNA 607
Pneumatic Valve 32
Point-of-Care 652
Poiseuille Flow 80
Polarizability 242
Polarization Analysis 1753
Poly(MPC) Brushes 436
Poly(N-Isopropylacrylamide) .. 218, 910
Polyacrylamide Gel 838, 1300
Polyacrylamide Grounding Interface 1723
Polydimethylsiloxane (PDMS) ..... 68, ... 116, 197, 370, 397, 521, 527, ... 557, 832, 1034, 1288, 1333, ... 1619, 1625, 1631, 1661, 1732
Polyelectrolyte 1122
Polyelectrolyte Encapsulation 1528
Polyelectrolytic Plug 895
Polymer 622, 1125, 1155, 1625, 1738
Actuators 1143
Biosensor 482
Fibers 1134
Functionalization 1027
Microcapsule 862
Microchips 817, 1273
Monolith 805, 1789
Physics 1580
Polymer Replica Molding 527
Polymerase Chain Reaction (PCR) ... 56, ... 98, 110, 584, 844, 1273, 1294
Polymer-Based 3D-Microfluidic Device 1297
Polymorph 1210
Polystyrene Bead 655
Porosity 805
Porous Polydimethylsiloxane Pump 907
Porous Polydimethylsiloxane Sponge 907
Porous Silicon 1646
Portable Diagnostic 1783
Potable Pump 907
Power-Free Microchip 26
Precise Pipetting 1128
Preconcentration ..... 829, 1006, 1182, ... 1198, 1411, 1583, 1783, 1786
Precursor Cell Differentiation 760
Pressure Measurement 38
Pressure Pulse 188
Pressure Valves 661
Pressure-Driven 754, 1574
Pre-Treatment Device 973
Printed Circuit Board 563
Probe DNA 973
Processor 1312
Programmable Microfluidics ... 793, 967
Protease 1658
Protein ..... 590, 811, 832, ... 1024, 1198, 1234, 1447
Analysis 799
Assay 587
Crystallization 943, 1393
Detection 409
Microarrays 92
Purification 1423
Sensor 1095
Separation 218, 1423
Interaction 1173
Proteomics 44, 50, 176, 1024, 1243
Proton Transfer 1018
Proximity Ligation 1306

PSA 1267
PTV 209
Pulsed Dielectrophoresis 415
Pump 685, 958
Purification 1426, 1429, 1553
PWM 29

Q
Quartz Crystal Microbalance (QCM) 500
Quantum Dot 1619
Quenching 445, 1471

R
Raman Spectroscopy 1071
Rapid Prototyping 1708
Rate Enhancements 264, 1471
Rayleigh Scattering 464, 1610
Reaction-Monitoring 258
Real Sample 584, 1267
Red-Blood Cells 38
Redox Cycling 388
Refractometry 473, 1348
Resonance Frequency 482, 631
Resonating Tube 536
Restriction Enzyme 412
Reverse Flow 35
Reversed Phase 248
Rheology 1480
Ribosome 796
RNA
  Extraction 1246
  Isolation 155
Roller 1738
Rotating Magnetic Field 279
Routing 1231
RT-PCR 691

S
Sacrificial 515
Sacrificial Etch 982
Sacrificial Layers 817
Salt Bridge 895
Salt Concentration 643
Sample
  Collection 1408
  Control 1513
  Preparation 98, 1315
  Stacking 823
Sandwich Assay 83
Secondary Flow 245
Segmented Flow 952
Selective Deposition 92
Selective Surface Modification 1031
Self Assembled Monolayer(s) 820, 1390
Self-Assembly 575, 862, 1098, 1568
Semi-Packed 239
Sensitivity Enhancement 83
Sensor 1113, 1704
Separation(s) ..... 38, 209, 221, 233, ... 242, 376, 808, 811, 826, ... 970, 1417, 1438, 1777, 1204
Sequential Micromixer 919
Sequentially Connected Semicircular Microchannel 539
Serial Dilution 1747
Serpentine Micromixer 904
Shear Banding 1480, 1495
Shear-Driven Fluidics 682
Sheath Flow 116, 1408, 1531
Sieve Electrode 730
Silica Particles and Nanoparticles ..... 83, ... 1258, 1534
Silicon 448, 491, 509, 1613
Silicon Beam 542
Silicon Mask 41
Silicon Microstructure 727
Silicon Nanowire(s) 409, 509, 607, 1043
Silicon Oxynitride 454
Silk 622
Silver Nanoparticles 62
Single Cell ..... 176, 179, 994, ... 1086, 1170, 1801
  Analysis 709, 715, 1083, 1306
  Assays 47
  Detection 739
  Electroporation 724
  Manipulation 8, 610
  Measurement 757
  Response 170
Single Enzyme 1003
Single Molecular Study ..... 403, 412, ... 415, 587, 593, 796, 994, ... 1399, 1592, 1604, 1607
Single Molecule Polymerase Chain Reaction 949

Single Photon Avalanche Diode 1179
Single-Nucleotide Polymorphism (SNP) 646
Skeletal Muscle 760
Slip 988, 1495
Soft Imprint 1152
Soft Lithography 131, 1717
Soft Matter 865
Soft Sensor 1146
SOI 1498
Sol Gel 1360, 1534, 1631
Soluble Factor 1309
Solvent 1125, 1689
Solvent Etching 1465
Sorting 1219, 1531
Spacers 227
Spacing Dependence 1207
Specific Binding 1095
Sperm 721, 1357
Spin Valve 23
Spindle Orientation 1768
Spiral Microchannel 1282
Split-Flow Microchannel 1167
Staphylococcus Epidermidis 748
Statistical Model 1012
Stem Cells 1378
Step 333
Stereolithography 1276
Stray Light Analysis 1049
Streaming 294
Stress 188
Stripline 258
Structural Instability 521
SU-8 ..... 367, 497, 584, 835, 982, 1000, ... 1027, 1119, 1264, 1720, 1726
Submicron Particle 1507
Sugar Leaching 907
Supercritical Fluids 270
Superhydrophobic 349, 1043, 1795
Superhydrophobic and Hydrophilic Patterning 1213
Supramolecular Chemistry 506
Surface Acoustic Wave(s) ..... 294, ... 958, 1285
Surface Conduction 291
Surface Engineering 1613
Surface Enhanced Raman Scattering (SERS) 1071, 1098, 1137, 1182
Surface Functionalization 820
Surface Machining 515
Surface Mobility 439
Surface Modification ..... 424, 601, 871, ... 889, 1024, 1037, 1640, 1792
Surface Patterning 352
Surface Plasmon Resonance (SPR) . 173, ... 442, 451, 676, 1009, ... 1053, 1243, 1297, 1655, 1670
Surface Stress 1704
Surface Topography 610
Surfactants 358
Suspended Microchannel Resonator 892
Sweeping 814
Switch 1531
Synthesis 850
Synthetic Biology 200
Systematic Evolution of Ligands by Exponential Enrichment 1192
Systems Biology 161, 170

T

Tapped Delay Line Filters 1444
Taurine 1432
T-Cell Lymphoma 1780
Teflon 551, 892
Temperature 467
  Control 715
  Gradient Capillary Electrophoresis 646
  Gradient Focusing 230, 823
Temperature Response 1240
Temperature-Controlled Microchannels 796
Tensile Loading 745
Textile 476
Theoretical Model 1768
Thermal Actuation 324
Thermal Channel Variation 355
Thermal Fusing 628
Thermal Lens Microscope ..... 1450, ... 1565, 1607
Thermocouple 1741
Thermocycling 110, 1237
Thermo-Electric Lysis 1246
Thermopneumatic 1155, 1741
Thermoresponsive 430, 910
Thick Brain Slices 1381

Three Dimensional ..... 309, 373, 727, ... 1140, 1158, 1711
Three-Dimensional Cell Culture 89
Three-Dimensional Optoelectronic Tweezers 364
Three-Dimensional Sheath Flow .... 224, ... 1571
Three-Dimensional Silicone Probes 1080
Tiling 919
Timer 1550
Time-Resolved Measurement 1565
Tip Streaming 336
Tissue Analysis 41
Tissue Engineering ..... 185, 760, ... 518, 778, 961
Titania Coatings 1378
Titanium 524
Titration 601
Topographical Structure 730
Total Internal Reflection 17, 1661, 1619
Toxicological Platform 164
Toxin 1390
Traction Forces 134
Transcriptome 47, 1170
Transdermal Injection 548
Transfection 194
Transferrin 1525
Translocation 670, 796, 931, 1015
Transmission Line 110
Transport 336, 1750
Transporter Protein 757
Trapping 119, 318
Triphasic Reactions 261
Trypan Blue 116
Trypsin 50
Tube 1149, 1501
Tumor Cells 488
Twist Ball 267
Two-Dimensional Separation 1447
Two-Phase Flow ..... 808, 853, ... 928, 934, 1547
Two-Photon Microfabrication 1729

U

Ultra Hydrophobic Surfaces 1643
Ultra Thin Layer 433
Ultra-Superhydrophobicity 1046
Ultrasonic Standing Waves (USW) . 560
Ultrasound 664, 1417, 1519, 1810, 1813
UV Curing 527
UV Light 1037, 1363

V

Valve(s) 32, 44, 892, 1492
Valveless 297
Vascular Model 137
Velocity Gradient 1438
Vertical Vias 527
Vesicle(s) 104, 1104
Virtual Impactor 533
Virus 1300
Viscosity 80, 955
Viscosity-Tunable Polymers 841
Vitamin K_3 868
VLSI-Microfluidics 1732
VOF (Volume of Fluid) 282
Volatile Organic Compounds 1698
Vorticella 745

W

Wafer-Scale Fabrication 1756
Wall Potential 1592
Water 1441, 1018, 1637
Water Octanol 1547
Water Permeability 1625
Water Permeation 370
Water Toxicity 1049
Waveguide(s) 859, 1068
Weir 8
Wet Computing 865
Wet Etching 509
Wettability 1037, 1459, 1492, 1643
Whole-Cell Biosensor 1049
Wormlike Micelles 1480

Y

Young's Modulus 1354

Z

Zeonor 578
Zero-Mode Waveguide 1015
Zeta Potential 379, 889, 1667
Zone Refining 1426
Zoonotic Infection 125

Micro Total Analysis Systems 2007

Micro Total Analysis Systems 2007
Volume 1

Proceedings of μTAS 2007
Eleventh International Conference on Miniaturized Systems for Chemistry and Life Sciences

Paris, FRANCE
7 – 11 October 2007

edited by

Jean-Louis Viovy
Institut Curie, FRANCE

Patrick Tabeling
Ecole Supérieure de Physique et de Chimie Industrielles (ESPCI), FRANCE

Stephanie Descroix
Ecole Supérieure de Physique et de Chimie Industrielles (ESPCI), FRANCE

Laurent Malaquin
Institut Curie, FRANCE

Sponsored by:
Chemical and Biological Microsystems Society





ISBN: 978-0-9798064-0-7 (2 Volume Set)
CBMS Catalog Number: 07CBMS-0001

Copyright and Reprint Permission: Abstracting of items in this volume is permitted with credit to the source. Authorization to photocopy items in this volume that carry a code at the bottom of the first page is granted by the Chemical and Biological Microsystems Society for internal or personal use, or the internal or personal use of specific clients, provided that the base fee of $20.00 is paid directly to the Chemical and Biological Microsystems Society. Instructors are permitted to photocopy isolated articles for educational classroom use without fee. For other forms of copying, reprint, or replication permission, write to the MicroTAS 2007 Conference at info@CBMSociety.org, c/o 307 Laurel Street, San Diego, California 92101-1630 USA or call 1-619-232-9499. All rights reserved. Copyright © 2007 by the Chemical and Biological Microsystems Society.

CBMS Catalog Number: 07CBMS-0001
ISBN: 978-0-9798064-0-7 (2 Volume Set)
ISSN: 1556-5890 (print)
ISSN: 1556-5904 (electronic)
Library of Congress Number: 2007934004

Copies of this volume are available for purchase. Please contact MicroTAS 2007 Conference, c/o 307 Laurel Street, San Diego, California 92101-1630 USA. Please contact the MicroTAS 2007 Conference at info@CBMSociety.org or call 1-619-232-9499 for ordering information.

PREFACE

The Eleventh International Conference on Miniaturized Systems for Chemistry and Life Sciences (in short, Micro Total Analysis Systems) is held this year in Paris at the "Cité des Sciences et de l'Industrie", following a now well established tradition of rotating between three continent families, the Americas, Asia/Oceania, and Europe/Africa. It combines leading research in microfluidics, micro- and nano-technology, material science, and chemistry, aimed at the development of miniaturized integrated devices with applications in chemistry, biology, and medicine. From the initial meeting in Enschede, The Netherlands, in 1994 the Conference has been growing steadily, and it broke the threshold of 1000 participants in Tokyo last year. This year's meeting marks the first time the newly formed Chemical and Biological Microsystems Society has acted as the primary sponsor for the Conference.

At the time of printing, it cannot be anticipated if the Tokyo record of about 1050 participants will be broken again, but the number of submitted abstracts, 980+, is the largest ever, as is the number of participating countries, around 40. This is a strong testimony to a steadily growing interest in the emerging fields of integrated microanalysis systems, microfluidics and bio-MEMS. This high number of abstracts, and their quality, has made the task of abstracts selection by the Technical Program Committee particularly challenging. In spite of this increase in the number of abstracts, the Committee has chosen to retain the format of 6 plenary sessions and two parallel tracks of 66 oral presentations, a format favourable for exchanges between participants from the very different scientific disciplines involved in µTAS Conferences. As a (difficult) comprise between the quality of the proposed abstracts, and the number of posters that one can reasonably consider in one session, the number of accepted posters has been increased this year to 520. These finite-time considerations, combined with the high submission rate, has made MicroTAS particularly selective, probably among the most selective Conferences in chemical and biological sciences. The Committee has full appreciation of the disappointment this has undoubtfully caused to researchers enthusiastic about sharing their results with the µTAS attendance, but we believe this makes the Conference particularly rewarding and time-valuable for all attendees.

In the Preface of µTAS 2006 proceedings, Prof. Kitamori noted that the number of submissions from Asia/Oceania exceeded for the first time submissions from either Americas or Europe/Africa. This is indeed the case again this year (388 from Asia/Oceania, 333 from Europe/Africa and 259 from Americas, respectively), confirming the strong interest of Asian countries for µTAS. In spite of a lower number of submissions, the maturity of the field in America is reflected by a high success rate, in particular for oral presentations.

The distribution of abstracts between subtopics remains rather equilibrated between application-oriented ones (Microsystems for Life Sciences, 307 abstracts, and Microsystems for Chemistry and Environment,138 abstracts) and methodology oriented ones (Microfluidics, 167, Nanotechnology, 76, Detection, 105, MEMS and NEMS technologies, 114). This confirms that in spite of an undoubtful evolution towards more and more mature and "industrial" products, fundamental development and innovation is still very vivid in the field.

In systems for life sciences, the very strong interest for cell handling and analysis systems revealed in Tokyo is sustained in Paris, confirming that microfluidics is seen by end-users as a major tool for cell biology and High Content Screening. Transposition of analytical methods to the "Microsystems" world also remains a strong trend, and the use of Microsystems for chemical synthesis and production, although still limited, in growing. On the methodological side, the development of microfluidic components and technologies remains very vivid, showing that the "toolbox" for μTAS engineers is still in demand of new ideas.

I would like to thank all of those who have helped organize the 2007 Conference. I am grateful to the Chemical and Biological Microsystems Society for sponsoring this meeting and express special thanks to its board members, in particular Profs. Jed Harrison and Mike Ramsey for their confidence and for responding rapidly and wisely to the numerous questions that arose during this year's organization. The Technical Program Committee (TPC) had this year a particularly difficult task for reading and evaluating 980+ abstracts and developing the final program, and we are extremely grateful to the TPC members and especially Prof. Thomas Laurell, head of the TPC, for achieving this task with dedication and high deontological standards. The Presidence and Services of Curie Institute also deserve our gratitude, for accepting to co-organize the 2007 session, and for dealing with administrative aspects of the organization on the French side.

I am also very grateful to my partners in the Local Organization Committee, Drs. Stéphanie Descroix and Patrick Tabeling, for their continuous contribution to the organization, planning and coordination of the Conference, and to Dr. Laurent Malaquin, for his help in the preparation of this Proceedings book. We are also indebted to the members of the Local Advisory committee for their advice and networking help.

I express my deepest gratitude to Katharine Cline and her staff at Preferred Meeting Management, Inc. for their absolute commitment to the success of this Conference, including putting together this proceedings book, and for sharing with us their immense experience in the organization of International Scientific Conferences. My group's assistant, Giuliana Carzedda, was also deeply committed in innumerable aspects of the Conference logistics on the French side, and she also deserves all our gratitude.

Equilibrating the budget of a Conference of this size in a city like Paris was not the least of challenges, and we are indebted to all industrial and institutional sponsors who supported the Conference. We express a particular gratitude to the Ile de France Regional Council (Conseil de Region Ile de France) for an outstanding contribution, which was essential to make the organization of this Conference possible. Last but not least, we thank all contributors and attendees, who make year after year MicroTAS such an outstanding event, by their lively participation, and this proceedings book a major scientific reference, by the quality of their contributions.

Jean-Louis Viovy
μTAS 2007 Chair
October 2007

PROGRAM COMMITTEE

Conference Chair
Jean-Louis Viovy ..... Institut Curie, FRANCE

Local Organizing Committee
Stephanie Descroix ..... ESPCI, FRANCE
Patrick Tabeling ..... ESPCI, FRANCE
Jean-Louis Viovy ..... Institut Curie, FRANCE

Technical Program Committee
Christopher S. Chen ..... University of Pennsylvania, USA
Zhao-Lun Fang ..... Zhejiang University & Northeastern University, CHINA
Stephen C. Jacobson ..... Indiana University, USA
Klavs F. Jensen ..... Massachusetts Institute of Technology, USA
Tae Song Kim ..... Korean Institute of Science and Technology, KOREA
Takehiko Kitamori ..... University of Tokyo, JAPAN
Jörg P. Kutter ..... Danmarks Tekiske Universitet, DENMARK
James Landers ..... University of Virginia, USA
Thomas Laurell ..... Lunds Universiteit, SWEDEN
Laurie E. Locascio ..... National Institute of Standards and Technology (NIST), USA
Andrew deMello ..... Imperial College London, UNITED KINGDOM
Petra Schwille ..... Technical University Dresden, GERMANY
Minoru Seki ..... Chiba University, JAPAN
Manabu Tokeshi ..... Nagoya University, JAPAN
Jean-Louis Viovy ..... Institut Curie, FRANCE

Advisory Committee
Armand Ajdari ..... ESPCI/CNRS, FRANCE
Dominique Collard .. Institute of Electronics and Micro-Electronics of Nanotechnologies, FRANCE
Andrew Griffiths ..... ISIS/ULP, FRANCE
Anne-Marie Gué ..... LAAS/CNRS, FRANCE
Patrick Huerre ..... Polytechnic School of Palaiseau, FRANCE
Mathieu Joanicot ..... Pessac, FRANCE
Jean-Yves Marzin ..... CNRS, FRANCE
Didier Roux ..... St Gobain, FRANCE

Board of Directors, Chemical and Biological Microsystems Society
Yoshinobu Baba ..... Nagoya University, JAPAN
Albert van den Berg ..... Universiteit Twente, THE NETHERLANDS
D. Jed Harrison ..... University of Alberta, CANADA
Klavs F. Jensen ..... Massachusetts Institute of Technology, USA
Takehiko Kitamori ..... University of Tokyo, JAPAN
Thomas Laurell ..... Lunds Universiteit, SWEDEN
Andreas Manz ..... Institute of Analytical Sciences, GERMANY
M. Allen Northrup ..... MicroFluidic Systems Inc., USA
J. Michael Ramsey ..... University of North Carolina, Chapel Hill, USA
Shuichi Shoji ..... Waseda University, JAPAN

CONTRIBUTORS AND EXHIBITORS

We gratefully acknowledge, at the time of printing these proceedings, the support of the following organizations to the Conference:

Biotray
cetoni GmbH Automation and Microsystems
Compagnie de Saint Gobain
The Dolomite Centre Ltd.
Epigem Limited
EU consortium ALLERGY-CARD
EU consortium NeuroTAS
Europractice
FLUIGENT
Institute of Microchemical Technology
Journal of Micromechanics and Microengineering (IOP Publishing)
Lab on a Chip (Royal Society of Chemistry)
LabSmith
LaVision GmbH
Little Things Factory GmbH
MEMStaff Inc.
MicroChem Corp.
microfluidic ChipShop GmbH
Micronit Microfluidics BV
OAI
Photron (Europe) Ltd.
Silex Microsystems
Societe Hydrotechnique de France
The Society for Chemistry and Micro-Nano Systems (Japan)
Takasago Electric, Inc.
Tronics Microsystems
VDI/VDE Innovation + Technik GmbH

PREVIOUS CONFERENCES

1994 - Enschede, THE NETHERLANDS
1996 - Basel, SWITZERLAND
1998 - Banff, Alberta, CANADA
2000 - Enschede, THE NETHERLANDS
2001 - Monterey, California, USA
2002 - Nara, JAPAN
2003 - Squaw Valley, California, USA
2004 - Malmö, SWEDEN
2005 - Boston, Massachusetts, USA
2006 - Tokyo, JAPAN

TABLE OF CONTENTS

Volume 1
Pages 1 – 918

Volume 2
Pages 919 – 1815



Day 1 - Monday, 8 October 2007

Plenary I

NANOTECHNOLOGICAL APPROACHES TO AMPLIFICATION IN BIOLOGICAL AND CHEMICAL DETECTION SYSTEMS 1
Chad A. Mirkin
Northwestern University, USA

Concurrent Session 1A1 - Cell Handling and Screening 1

HIGH-THROUGHPUT DNA MICROFRACTIONATOR USING SELF-PATTERNED LARGE-SCALE CRYSTALLINE NANOARRAYS 2
Y. Zeng and D.J. Harrison
University of Alberta, CANADA

CELL DELIVERY AND FIXING SYSTEM UTILIZING MICRO-PUMPS/ VALVES AND NEGATIVE-DEP DEVICES FOR ON-CHIP DUAL-BEAM OPTICAL TRAP APPLICATIONS 5
C.-W. Lai[1], S.-K. Hsiung[1], C.-M. Chung[1], Y.-Q. Chen[2], A. Chiou[2], and G.-B. Lee[1]
[1]*National Cheng Kung University, TAIWAN and*
[2]*National Yang-Ming University, TAIWAN*

DIELECTROPHORETICALLY SWITCHABLE MICROFLUIDIC WEIR STRUCTURES FOR EXCLUSION-BASED SINGLE-CELL MANIPULATION 8
B.M. Taff, S.P. Desai, and J. Voldman
Massachusetts Institute of Technology, USA

Concurrent Session 1B1 - Detection 1 (Optical)

OPTOFLUIDIC SPECTROMETER FOR MICROCHIP FLOW CYTOMETRY 11
W.Z. Song[1], L.A.G. Lin[1], A.Q. Liu[1], C.S. Lim[1], and P.H Yap[2]
[1]*Nanyang Technological University, SINGAPORE and*
[2]*DSO National Laboratories, SINGAPORE*

A COMPLETE ON-CHIP HIGH RESOLUTION MICROSCOPE SYSTEM BASED ON THE OPTOFLUIDIC MICROSCOPY METHOD 14
X. Cui, X. Heng, L. Lee, and C. Yang
California Institute of Technology, USA

A MONOLITHIC EVANESCENT EXCITATION (EE)-BASED BIOCHIP FOR HIGHLY-SENSITIVE AND REAL-TIME FLUORESCENT DETECTION 17
D.V. Dao, N.C.H. Le, R. Yokokawa, J. Wells and S. Sugiyama
Ritsumeikan University, JAPAN

Concurrent Session 1A2 - Immunodetection

DIRECT DETECTION OF BIOMOLECULAR INTERACTIONS WITH BIOACTIVATED NANOPORES 20
A.H. Talasaz, R.M. Aliabadi, B. Gharizadeh, S. Shokralla, M. Ronaghi, F. Pease, and R.W. Davis
Stanford University, USA

ULTRA-SENSITIVE MAGNETIC IMMUNOSENSING PLATFORM BASED ON THE COMBINED MANIPULATION AND DETECTION OF MAGNETIC PARTICLES 23
G. Reekmans, C. Liu, R. De Palma, R. Wirix-Speetjens, W. Laureyn, and L. Lagae
Interuniversity Microelectronics Center (IMEC), BELGIUM

ULTRASENSITIVE IMMUNOASSAY ON A POWER-FREE MICROCHIP WITH LAMINAR FLOW-ASSISTED SIGNAL AMPLIFICATION 26
K. Hosokawa, M. Omata, and M. Maeda
RIKEN, JAPAN

Concurrent Session 1B2 - Microfluidic Components

MICROFLUIDIC PWM GENERATION OF CHEMICAL SIGNALS 29
F. Azizi, L. Chen, and C.H. Mastrangelo
Case Western Reserve University, USA

EFFICIENT ADDRESSABLE FLUID CONTROL SYSTEM USING PNEUMATIC VALVE ARRAY 32
K. Kawai[1], M. Kanai[1,2], and S. Shoji[1]
[1]*Waseda University, JAPAN* and [2]*Shimadzu Corporation, JAPAN*

CHARACTERIZATION OF FLOW REVERSAL IN ANODICALLY BONDED GLASS-BASED AC ELECTROKINETIC MICROPUMPS 35
M.M. Gregersen, L.H. Olesen, A. Brask, M.F. Hansen, and H. Bruus
Technical University of Denmark, DENMARK

Plenary II

CELLULAR-SCALE HYDRODYNAMICS 38
Howard A. Stone
Harvard University, USA

Poster Session Microsystems for Life Sciences - Genomics & Proteomics

M1A ENHANCED SPATIAL RESOLUTION OF MALDI IMAGES USING SILICON MASKS 41
N. Verplanck[1], M. Wisztorski[2], J. Stauber[2], J.C. Camart[1], M. Salzet[2], I. Fournier[2], and V. Thomy[1]
[1]IEMN, FRANCE and [2]LNA, FRANCE

M2A INTEGRATION OF MONOLITHIC VALVES INTO MICROFLUIDIC DEVICE FOR PROTEOMIC ANALYSIS 44
Q. Lu, J.-B. Bao, and D.J. Harrison
University of Alberta, CANADA

M3A NON-PCR LINEAR AMPLIFICATION OF mRNA TOWARD SINGLE CELL WHOLE TRANSCRIPTOME ANALYSES 47
J.G. Kralj[1], A. Player[2], D. Peterson[2], S.P. Forry[1], M.S. Munson[1], E. Kawasaki[2], and L.E. Locascio[1]
[1]National Institute of Standards and Technology (NIST), USA and [2]National Cancer Institute/National Institutes of Health, USA

M4A ON-CHIP TRYPTIC DIGEST WITH DIRECT-COUPLING TO ESI/MS USING MAGNETIC NANOPARTICLES 50
A. Le Nel[1,2], J. Krenkova[3], K. Kleparnik[3], C. Smadja[2], M. Taverna[2], J.-L. Viovy[1], and F. Foret[3]
[1]Curie Institute, FRANCE, [2]Université Paris XI, FRANCE and [3]Institute of Analytical Chemistry-Brno, CZECH REPUBLIC

M5A SINGLE DNA MOLECULE DETECTION BY ON-BEAD ROLLING CIRCLE AMPLIFICATION IN A MICROCHIP 53
A. Tachihara[1], K. Sato[1], K. Sato[1], Y. Tanaka[2], J. Jarvius[2], M. Nilsson[2], and T. Kitamori[1]
[1]University of Tokyo, JAPAN and [2]Uppsala University, SWEDEN

M6A TOWARD ON-CHIP ISOTHERMAL POLYMERASE CHAIN REACTION 56
A. Persat[1], T. Morita[2], and J.G. Santiago[1]
[1]Stanford University, USA and [2]Ebara Research Co., LTD., JAPAN

Poster Session Microsystems for Life Sciences - Clinical Diagnostics

M7A A SIMPLE AND EFFICIENT METHOD FOR ON-CHIP STORAGE OF REAGENTS: TOWARDS LAB-ON-A-CHIP SYSTEMS FOR POINT-OF-CARE DNA DIAGNOSTICS 59
M. Brivio[1], Y. Li[1], A. Ahlford[2], B.G. Kjeldsen[1], J.L. Reimers[1], M. Bu[1], A.-C. Syvänen[2], D.D. Bang[1], and A. Wolff[1]
[1]Technical University of Denmark, DENMARK and [2]University Hospital, SWEDEN

M8A AN IMMUNOASSAY USING SILVER NANOPARTICLE, SILVER ENHANCEMENT AND A FLATBED SCANNER 62
K.-S. Huang, W.-T. Chen, I.-L. Wang, H.-P. Lin, T.C Chang, and Y.C-. Lin
National Cheng Kung University, TAIWAN

M9A DETERMINATON OF TOTAL AND PANCREATIC AMYLASE ACTIVITIES IN HUMAN BLOOD BY USE OF MICROCHIP ELECTROPHORESIS 65
E. Maeda[1], M. Kataoka[2], Y. Shinohara[1,2], N. Kaji[3], M. Tokeshi[3], and Y. Baba[2,3,4]
[1]University of Tokushima, JAPAN, [2]National Institute of Advanced Industrial Science and Technology (AIST), JAPAN, [3]Nagoya University, JAPAN, and [4]Japan Science and Technology Agency (JST), JAPAN

M10A HYBRID CERAMIC/PDMS MICROLAB WITH TWO INDEPENDENT DETECTION SYSTEMS FOR ON-LINE DIALYSIS' PARAMETERS MONITORING 68
I. Grabowska[1], I. Wyżkiewicz[2], M. Chudy[1], A. Dybko[1], and Z. Brzózka[1]
[1]Warsaw University of Technology, POLAND and
[2]Institute of Electronic Materials and Technology, POLAND

M11A LABEL-FREE OPTICAL DETECTION OF DNA BY REVERSIBLE ELECTRIC FIELD CONFINEMENT IN FREE SOLUTION 71
F.A. Shaikh and V.M. Ugaz
Texas A&M University, USA

M12A MICROFLUIDIC COMPACT DISC PLATFORMS FOR RAPID AND SENSITIVE DETECTION AND IDENTIFICATION OF *CANDIDA* YEASTS FROM BLOOD 74
I. Martineau[1], D.K. Boudreau[1], L. Monfort[1], F. Bégin[1], M.-J. Fiola[1], G. Stewart[1], H. Morin[1], A. Huletsky[1], R. Peytavi[1], F M. Boissinot[1], F.J. Picard[1], J.V. Zoval[2], H. Kido[2], G. Jia[2], M.J. Madou[2], and M.G. Bergeron[1]
[1]Université Laval, CANADA and [2]University of California, Irvine, USA

M13A MICROFLUIDICS FOR CLINICAL DIAGNOSTICS: DNA PURIFICATION FROM LARGE-VOLUME BLOOD SAMPLES USING A MICRO-TWO-DIMENSIONAL SOLID PHASE EXTRACTION SYSTEM 77
J. Wen, T.M. Hartberger, J.P. Ferrance, and J.P. Landers
University of Virginia, USA

M14A PDMS-BASED MICROLITER VISCOMETER FOR BLOOD PLASMA AND OTHER NEWTONIAN FLUIDS 80
Z. Han, X. Tang, and B. Zheng
Chinese University of Hong Kong, HONG KONG

M15A SENSITIVITY ENHANCEMENT OF THE NANOMECHANICAL DYNAMIC CANTILEVER BY TWO TYPES OF SANDWICH IMMUNOASSAYS BASED ON POLYCLONAL ANTIBODY AND POLYCLONAL ANTIBODY CONJUGATED SILICA NANOPARTICLES: FEMTOMOLAR PSA DETECTION AS MODEL STUDY 83
S.-M. Lee[1], K.S. Hwang[2], H.-J. Yoon[1], Y.-S. Lee[1], and T.S. Kim[2]
[1]Seoul National University, KOREA and
[2]Korea Institute of Science and Technology (KIST), KOREA

Poster Session Microsystems for Life Sciences - Microarrays

M16A GOLD SURFACE-BASED GLYCOARRAYS: A GENERIC PLATFORM FOR HIGH THROUGHPUT INTERROGATION OF CARBOHYDRATE-PROTEIN INTERACTIONS 86
Z.-L. Zhi, A.K. Powell, and J.E. Turnbull
University of Liverpool, UK

M17A MICROPATTERNED MATRIGEL FOR THREE-DIMENSIONAL EPITHELIAL CULTURES 89
T.R. Sodunke[1], K.W. McBride[2], M.J. Reginato[1], and H. Noh[1]
[1]Drexel University, USA and [2]Texas Tech University, USA

M18A PROTEIN PATTERNING THROUGH SELECTIVE FLUOROCARBON PLASMA-INDUCED DEPOSITION ON SILICON 92
P. Bayiati, A. Tserepi, P.S. Petrou, S.E. Kakabakos,
E. Matrozos, and E. Gogolides
NCSR "Demokritos", GREECE

Poster Session Microsystems for Life Sciences – Point of Care and Hand Held Devices

M19A A HANDHELD MICROFLUIDIC PHOTOMETER BASED ON LIQUID-CORE WAVEGUIDE ABSORBANCE DETECTION..... 95
J.-Z. Pan and Q. Fang
Zhejiang University, CHINA

M20A CLINICAL MOLECULAR DIAGNOSTICS USING AN INTEGRATED MICROCHIP WITHIN A FULLY PORTABLE PLATFORM..... 98
G.V. Kaigala, V.H. Hoang, A. Stickel, D. Manage, L.M. Pilarski,
and C.J. Backhouse
University of Alberta, CANADA

M21A FULLY AUTONOMOUS MICROFLUIDIC CAPILLARY SYSTEMS FOR FAST AND SENSITIVE SURFACE IMMUNOASSAYS 101
J. Ziegler[1,2], M. Zimmermann[1,2], P. Hunziker[1], and E. Delamarche[2]
[1]University Hospital Basel, SWITZERLAND and
[2]IBM Research GmbH, SWITZERLAND

M22A HIGH REYNOLDS NUMBER MICROFLUIDICS FOR DRUG DELIVERY 104
J.C. Stachowiak, T.H. Li, D.L. Richmond, A.P. Liu, S.H. Parekh, and D.A. Fletcher
University of California, Berkeley, USA

M23A IMMUNOASSAY UTILIZING MAGNETIC BEADS FOR RAPID VIRUS DETECTION IN THE MICROFLUIDIC FLOW CYTOMETER SYSTEM..... 107
S.-Y. Yang, K.-Y. Lien, K.-J. Huang, H.-Y. Lei, and G.-B. Lee
National Cheng Kung University, TAIWAN

M24A MICROWAVE-MEDIATED MICROCHIP THERMOCYCLING: PATHWAY TO AN INEXPENSIVE, HANDHELD REAL-TIME PCR INSTRUMENT..... 110
D.J. Marchiarullo, A. Sklavounos, N.S. Barker, and J.P. Landers
University of Virginia, USA

Poster Session Microsystems for Life Sciences - Cell Handling & Analysis

M25A BIOMARKER DETECTION BY ENZYMATIC AMPLIFICATION IN DROPLETS - TOWARDS HIGH THROUGHPUT DETECTION OF LOW COPY NUMBER CELL SURFACE BIOMARKERS 113
H.N. Joensson[1], E.R. Brouzes[2], M. Samuels[3], M. Uhlén[1], H. Andersson Svahn[1], and D.R. Link[3]
[1]Royal Institute of Technology, SWEDEN, [2]Harvard Medical School, USA, and [3]RainDance Technologies, USA

M26A CELL SORTING OF LIVE AND DEAD CELLS BY LASER RADIATION PRESSURE AND SHEATH FLOW IN MICROCHANNEL..... 116
M. Murata[1], N. Kaji[1], M. Tokeshi[1], and Y. Baba[1,2,3]
[1]Nagoya University, JAPAN, [2]National Institute of Advanced Industrial Science and Technology (AIST), JAPAN, and [3]Japan Science and Technology Agency (JST), JAPAN

M27A CELL TRAPPING VIA COUNTER-ROTATING MICRO-VORTICES 119
C.-M. Lin, Y.-S. Lai, H.-P. Liu, and A.M. Wo
National Taiwan University, TAIWAN

M28A CONTINUOUS MAGNETOPHORETIC ENRICHMENT OF RARE TUMOR CELLS 122
D. Nawarathna[1], P. Kurnaresan[2], Y. Zhang[3], B. Ferguson[1], S.-H. Oh[4], K.S. Lam[2], and H.T. Soh[1]
[1]University of California, Santa Barbara, USA, [2]University of California, Davis, USA, [3]CytomX, LLC, USA, and [4]University of Minnesota, USA

M29A CONTINUOUS SEPARATION OF CELLS IN A MICROFLUIDIC DEVICE USING LATERAL DIELECTROPHORESIS 125
N. Demierre, T. Braschler, R. Muller, and P. Renaud
Ecole Polytechnique Fédérale de Lausanne (EPFL), SWITZERLAND

M30A EIS-ASSISTED IMPEDANCE ASSAY FOR IN SITU MONITORING CARDIOMYOCYTE APOPTOSIS 128
Y. Qiu[1], R. Liao[2], and X. Zhang[1]
[1]Boston University, USA and [2]Harvard Medical School, USA

M31A ENHANCED LOCOMOTION *CAENORHABDITIS ELEGANS* IN STRUCTURED MICROFLUIDIC ENVIRONMENTS 131
H. Hwang[1], S.-W. Nam[1], F. Martinez[2], R.H. Austin[2], W.S. Ryu[2], and S. Park[1]
[1]Ewha Woman's University, KOREA and [2]Princeton University, USA

M32A ESTIMATION OF MECHANICAL ROLE OF INTRACELLULAR STRUCTURES IN SMOOTH MUSCLE CELLS BY USING TRACTION FORCE MEASUREMENTS 134
T. Ohashi, S. Nakamura, N. Sakamoto, and M. Sato
Tohoku University, JAPAN

M33A GLASS MICROCHIP-BASED BIOASSAY SYSTEM USING HUMAN ARTERIAL ENDOTHELIAL CELLS 137
Y. Tanaka[1], Y. Kikukawa[1], K. Sato[1], Y. Sugii[2], and T. Kitamori[1]
[1]University of Tokyo, JAPAN and [2]Kogakuin University, JAPAN

M34A HEAT-POLISHING INTEGRATED GLASS PATCH CAPILLARIES FOR ENHANCED GIGASEALS 140
W.-L. Ong, L.-W. Luo, A. Ajay, N. Ranganathan, K.C. Tang, and L. Yobas
Institute of Microelectronics, SINGAPORE

M35A HIGH-THROUGHPUT ENZYMATIC ASSAYS OF WHOLE CELLS ENCAPSULATED IN MICRODROPLETS 143
L.F. Olguin, A. Huebner, D. Bratton, G. Whyte, W. Huck, C. Abell, and F. Hollfelder
University of Cambridge, UK

M36A HIGH-THROUGHPUT μFLUIDIC CELLULAR ASSAYS 146
J. Warrick, K. Regehr, M. Domenech, I. Meyvantsson, C. Wagner, C. Alexander, and D.J. Beebe
University of Wisconsin, USA

M37A MAGNETOPHORETIC TRAPPING OF MICROPARTICLES 149
H. Chetouani[1,2], C. Jeandey[1], V. Haguet[1], F. Chatelain[1], and G. Reyne[2]
[1]Commissariat à l'Energie Atomique (CEA), FRANCE and
[2]Laboratoire de Génie Electrique de Grenoble, FRANCE

M38A MICROFLUIDIC BIOCHIP FOR THE ELECTROCHEMICAL CELL ACTIVITY ANALYSIS 152
N. Pereira Rodrigues, H. Kimura, Y. Sakai, and T. Fujii
University of Tokyo, JAPAN

M39A MICROFLUIDIC CASSETTE FOR RAPID ISOLATION AND PROCESSING OF LEUKOCYTE SUBPOPULATIONS FROM WHOLE BLOOD 155
K.T. Kotz[1], A. Russom[1], D. Irimia[1], M.N. Mindrinos[2], L.L. Moldawer[3], R.G. Tompkins[1], and M. Toner[1]
[1]Massachusetts General Hospital, Shriners Hospital for Children and Harvard Medical School, USA, [2]Stanford Genome Technology Center, USA, and [3]University of Florida College of Medicine, USA

M40A MICROFLUIDIC DEVICES FOR STUDYING THE RESPONSE OF ADHERENT CELLS UNDER SHORT TIME STIMULI TREATMENT 158
L. Ye[1], M. Zhang[2], L.G. Alexopoulos[2], P. Sorger[2], and K.F. Jensen[1]
[1]Massachusetts Institute of Technology, USA and
[2]Harvard Medical School, USA

M41A MICROFLUIDIC STICKERS FOR QUANTITATIVE STUDIES OF CULTURED CELLS 161
M. Morel[1], D. Bartolo[2], M. Dahan[1], and V. Studer[2]
[1]ENS, FRANCE and
[2]Ecole Supérieure de Physique et de Chimie Industrielles (ESPCI), FRANCE

M42A MICROFLUIDIC TOXICOLOGICAL PLATFORM FOR THE MONITORING OF EXTRACELLULAR IONIC ACTIVITIES 164
S. Generelli[1,2], F. Berthiaume[3], M.L. Yarmush[3], M. Jolicoeur[1], M. Koudelka-Hep[2], and O.T. Guenat[1]
[1]Ecole Polytechnique de Montréal, CANADA, [2]University of Neuchâtel, SWITZERLAND, and [3]Harvard Medical School, USA

M43A PERFUSED MULTIWELL TISSUE CULTURE PLATES FOR DRUG AND DISEASE MODEL DEVELOPMENT 167
K. Domansky[1], W. Inman[1], M.H.M. Lim[1,2], J. Serdy[1], B. Owens[1], S. Karackattu[1], J.R. Llamas Vidales[1], R. Littrel[1], L. Vineyard[1], and L.G. Griffith[1]
[1]Massachusetts Institute of Technology, USA and
[2]University of Cambridge, UK

M44A GROWTH RATE AND STRESS-RESPONSE ANALYSES OF MICRO-CONTACT PRINTED BACTERIAL ARRAYS AND SINGLE BACTERIA IN MICROFLUIDIC CHAMBERS 170
L. Robert[1,2], L. Xu[2], F. Taddei[1], Y. Chen[2], A. Lindner[1], and D. Baigl[2]
[1]Inserm U571, FRANCE and [2]Ecole Normale Superieure, FRANCE

M45A REAL TIME DETECTION OF CELL BINDING ON BIOCHIPS USING SPR IMAGING 173
Y. Roupioz[1], E. Suraniti[2], R. Calemczuk[2], T. Livache[2], P. Marche[2], and M.-B. Villiers[2]
[1]CNRS-CEA-UJF, FRANCE and [2]INSERM, FRANCE

M46A SINGLE CELL ANALYSIS BY NATIVE UV LASER INDUCED FLUORESCENCE DETECTION IN A PDMS MICROFLUIDIC CHIP 176
D. Greif, D. Anselmetti, and A. Ros
Bielefeld University, GERMANY

M47A SINGLE CELL ISOLATIONS BY TAMDEM MICROCHAMBERS ON A CENTRIFUGAL FLOW DEVICE 179
H. Nagai[1], S. Furutani[2], and I. Kubo[2]
[1]National Institute of Advanced Industrial Science and Technology (AIST), JAPAN and [2]Soka University, JAPAN

Poster Session Microsystems for Life Sciences - Tissue Engineering

M48A AN INTEGRATED MICROFLUIDIC SYSTEM FOR LONG-TERM CULTURE AND CONTINUOUS MONITORING OF INTESTINAL CELLS 182
H. Kimura, T. Yamamoto, Y. Sakai, and T. Fujii
University of Tokyo, JAPAN

M49A MICROPATTERNED HYDROGEL TISSUE SCAFFOLDS WITH CONTROLLED ELECTROKINETIC PROPERTIES FOR INVESTIGATION OF CHONDROCYTE MECHANOTRANSDUCTION 185
A.D. Rouillard, T. Tsue, L.J. Bonassar, and B.J. Kirby
Cornell University, USA

M50A PERIODIC PRESSURE PULSE GENERATOR IN CELL CULTURE CHIP 188
Y.F. Yu[1], X. Zhang[1], R. Chua[2], P.H. Yap[2], and A.Q. Liu[1]
[1]Nanyang Technological University, SINGAPORE and [2]DSO National Laboratories, SINGAPORE

Poster Session Microsystems for Life Sciences - Drug Discovery

M51A MANUFACTURE OF DUAL-LAYER MICROBUBBLE LIPOSPHERES AS DRUG DELIVERY VEHICLES IN MICROFLUIDIC DEVICES 191
K. Hettiarachchi[1], E. Talu[2], M.L. Longo[2], P.A. Dayton[2], and A.P. Lee[1]
[1]University of California, Irvine, USA an [2]University of California, Davis, USA

M52A MICROFLUIDIC ELECTROPORATIVE DELIVERY OF SMALL MOLECULES AND GENES INTO CELLS USING A COMMON DC POWER SUPPLY 194
H.-Y. Wang and C. Lu
Purdue University, USA

Poster Session Microsystems for Life Sciences

M53A CONTROLLING HIGHER-ORDER STRUCTURES OF GIANT GENOMIC DNA MOLECULES IN MICROFLUIDIC CHANNEL 197
H. Oana[1,2], M. Ohuchi[1], and M. Washizu[1,2]
[1]*University of Tokyo, JAPAN and*
[2]*Japan Science and Technology Agency (JST), JAPAN*

M54A MICROFLUIDIC GENE SYNTHESIS 200
D.S. Kong, P.A. Carr, L. Chen, K. Chang, S. Zhang, and J.M. Jacobson
Massachusetts Institute of Technology, USA

M55A MICROFLUIDIC GRADIENT GENERATOR FOR STEM CELL DIFFERENTIATION 203
T.M. Keenan, K. Feyereisen, C.N. Svendsen, and D.J. Beebe
University of Wisconsin, USA

M56A SONOPORATION OF SUSPENSION CELLS IN A MICROFLUIDIC FORMAT BY USE OF A SINGLE CAVITATION BUBBLE 206
S. Le Gac[1], A. van den Berg[1], and C.-D. Ohl[1,2]
[1]*University of Twente, THE NETHERLANDS and*
[2]*Nanyang Technical University, SINGAPORE*

Poster Session Microsystems for Chemistry and Environment – Separation Science

M1B CONTINUOUS AND SELECTIVE SEPARATION TECHNIUQUE OF SUSPENDED PARTICLES BY UTILIZING ACOUSTIC RADIATION AND ELECTROSTATIC FORCES 209
Y. Sato, H. Ishida, and K. Hishida
Keio University, JAPAN

M2B CONTINUOUS FLOW SORTING OF POLYMER MICROPARTICLES BY DIAMAGNETIC REPULSION 212
N. Hirota[1], A. Iles[2], and N. Pamme[2]
[1]*National Institute for Materials Science (NIMS), JAPAN and*
[2]*University of Hull, UK*

M3B CONTINUOUS SEPARATION OF WHITE BLOOD CELLS BY HYDROPHORETIC FILTRATION 215
S. Choi and J.-K. Park
Korea Advanced Institute of Science and Technology (KAIST), KOREA

M4B CONTROLLED PATTERNINGS OF THE TARGET PROTEINS BASED ON THE STRUCTURAL TRANSITION OF A HEAT-SENSITIVE POLYMER 218
D.-S. Lee[1], J.H. Lee[2], K.H. Chung[1], H.-B. Pyo[1], M.Y. Jung[1], and H.C. Yoon[2]
[1]Electronics and Telecommunications Research Institute (ETRI), KOREA and [2]Ajou University, KOREA

M5B FREE-FLOW DIELECTROPHORESIS - A NUMERICAL STUDY 221
G.O.F. Parikesit[1], A.P. Markesteijn[1], J. Westerweel[1], I.T. Young[1], and Y. Garini[1,2]
[1]Delft University of Technology, THE NETHERLANDS and [2]Bar-Ilan University, ISRAEL

M6B HIGH SPEED ORGANELLES SORTING MICROSYSTEM DRIVEN BY A SINGLE PRESSURE SOURCE 224
T. Aoki[1], Y. Shirasaki[2], T. Arakawa[1], H. Sugino[3], T. Funatsu[3], and S. Shoji[1]
[1]Waseda University, JAPAN, [2]Kazusa DNA Research Institute, JAPAN, and [3]University of Tokyo, JAPAN

M7B INDIRECT DETECTION AND SEPARATION OF NON-FLUORESCENT ANALYTES USING FLUORESCENT ISOTACHOPHORETIC SPACERS 227
T. Khurana and J.G. Santiago
Stanford University, USA

M8B MICROFLUIDIC TEMPERATURE GRADIENT FOCUSING FOR *IN SITU* CHIRAL AMINO ACIDS ANALYSIS ON MARS 230
G. Danger and D. Ross
National Institute of Standards and Technology (NIST), USA

M9B ON-CHIP CONTINUOUS CELL SEPARATOR USING POSITIVE AND NEGATIVE DIELECTROPHORESIS 233
J. Avian, S. Kostner, and M.J. Vellekoop
Vienna University of Technology, AUSTRIA

M10B POINT MUTATION DETECTION BY ON-CHIP DIFFUSION COEFFICIENT MEASUREMENT 236
A. Estévez-Torres[1], T. Le Saux[1], H. Berthoumieux[1], A. Georges[1], S. Fernandez[1], J.-F. Allemand[1], V. Croquette[1], A. Lemarchand[2], L. Jullien[1], and C. Gosse[3]
[1]Ecole Normale Supérieure, FRANCE, [2]Université Paris 6, FRANCE, and [3]LPN-CNRS, FRANCE

M11B SEMI-PACKED MICRO GAS CHROMATOGRAPHY COLUMNS 239
S.A. Ali, M.A. Zareian-Jahromi, M. Ashraf-Khorassani, L.T. Taylor, and M. Agah
Virginia Polytechnic Institute and State University, USA

M12B SEPARATION AND POLARIZABILITY OF DNA BY DIELECTROPHORESIS 242
J. Regtmeier, H. Höfemann, R. Eichhorn, D. Anselmetti, and A. Ros
Bielefeld University, GERMANY

M13B SIZE-SELECTIVE SEPARATION OF GLASS BEADS USING THE SECONDARY FLOW IN A CURVED MICROCHANNEL 245
J.B. Ha[1], D.H. Yoon[1], S.Y. Park[1], Y.K. Bahk[1], T. Arakawa[2], S. Shoji[2], and J.S. Go[1]
[1]Pusan National University, KOREA and [2]Waseda University, JAPAN

M14B USE OF MICRO- AND NANO-FABRICATED ORDERED PILLAR ARRAYS FOR PRESSURE-DRIVEN REVERSED PHASE LIQUID CHROMATOGRAPHY SEPARATIONS 248
W. De Malsche[1,2], H. Eghbali[1], D. Clicq[1], J. Vangelooven[1], D. Tezcan[3], P. De Moor[3], V. Verdoold[2], H. Gardeniers[1], and G. Desmet[1]
[1]Vrije Universiteit Brussel, BELGIUM, [2]Twente University, THE NETHERLANDS, and [3]IMEC, BELGIUM

Poster Session Microsystems for Chemistry and Environment – Environmental Analysis

M15B ENVIRONMENTALLY-FRIENDLY DISPOSABLE HEAVY METAL ION SENSORS USING PLANAR BISMUTH MICROELECTRODES FOR IN SITU ENVIRONMENTAL MONITORING 251
Z. Zou, A. Jang, P.-M. Wu, J. Do, J. Han, P.L. Bishop, and C.H. Ahn
University of Cincinnati, USA

M16B THE UREY INSTRUMENT: AN INTEGRATED END-TO-END *IN SITU* ANALYTICAL SYSTEM DESIGNED FOR THE ULTRA-SENSITIVE CHEMICAL DETECTION OF EXTANT OR EXTINCT LIFE ON MARS 254
F.J. Grunthaner[1], J.L. Bada[2], A.M. Skelley[3], R.A. Mathies[3], R. Quinn[4], A. Zent[4], P. Willis[1], X. Amashukeli[1], A. Farrington[1], A. Aubrey[2] and P. Ehrenfreund[5]
[1]California Institute of Technology, USA, [2]University of California, San Diego, USA, [3]University of California, Berkeley, USA, [4]NASA Ames Research Center, USA, and [5]Leiden Institute of Chemistry, THE NETHERLANDS

Poster Session Microsystems for Chemistry and Environment – Online Process Control

M17B A STRIPLINE BASED MICROFLUIDIC PROBE FOR NMR SPECTROSCOPY 258
J. Bart[1], J.W.G. Janssen[2], P.J.M. van Bentum[2], A.P.M Kentgens[2], and J.G.E Gardeniers[1]
[1]University of Twente, THE NETHERLANDS and [2]Radboud University, THE NETHERLANDS

Poster Session Microsystems for Chemistry and Environment – On-Chip Synthesis and Production

M18B A TRI-PHASE CATALYTIC MICROFLUIDIC REACTOR FOR THE GENERATION OF SINGLET OXYGEN USING A NOVEL IMMOBILISED *SECO*-PORPHYRAZINE CATALYST 261
C. Cullen[1], M.J. Fuchter[1], R.C.R. Wootton[2], A.G.M Barrett[1], and A.J. de Mello[1]
[1]Imperial College London, UK and [2]University of Cambridge, UK

M19B INFLUENCE OF PRESSURE ON DIELS-ALDER REACTIONS PERFORMED IN GLASS MICROREACTORS 264
F. Benito-López, R.M. Tiggelaar, A.J. Kettelarij, R.J.M. Egberink, J.G.E. Gardeniers, and D.N. Reinhoudt, and W. Verboom
University of Twente, THE NETHERLANDS

M20B MICROREACTOR FOR JANUS BEADS PRODUCTION USING MICROCHANNEL INTEGRATION TECHNIQUES..... 267
T. Torii[1], T. Takahashi[2], Y. Takizawa[2], and T. Nisisako[3]
[1]University of Tokyo, JAPAN, [2]Soken Chemical & Engineering Co., Ltd., JAPAN, and [3]Tokyo Institute of Technology, JAPAN

M21B SOLID CATALYZED HYDROGENATION IN A SI/GLASS MICROREACTOR USING SUPERCRITICAL CO_2 AS THE REACTION SOLVENT 270
F. Trachsel, B. Tidona, and Ph. Rudolf von Rohr
ETH Zurich, SWITZERLAND

Poster Session Microsystems for Chemistry and Environment

M22B OBSERVATION OF BIOFILM IN MICROCHANNEL WITH THERMAL LENS MICROSCOPY 273
T.T.J. Rossteuscher[1,2], A. Hibara[1,3,4], K. Mawatari[3], and T. Kitamori[1,3,4]
[1]University of Tokyo, JAPAN, [2]Technische Universität Müchen, GERMANY
[3]Kanagawa Academy of Science and Technology, JAPAN, and
[4]Japan Science and Technology Agency (JST), JAPAN

Poster Session Microfluidics - Fluid Mechanics & Modeling

M1C A PARTICULE IMAGE ANEMOMETRY TECHNIQUE FOR A NON INVASIVE, QUICK DETERMINATION OF AVERAGE FLOW RATES IN MICROCHANNELS 276
A. Plecis, L. Malaquin, and Y. Chen
LPN-CNRS, FRANCE

M2C CHAOTIC MIXING INDUCED BY A MAGNETIC CHAIN IN A ROTATING MAGNETIC FIELD 279
T.G. Kang, M.A. Hulsen, P.D. Anderson, J.M.J. den Toonder,and H.E.H. Meijer
Eindhoven University of Technology, THE NETHERLANDS

M3C COMPUTATIONAL SIMULATION OF DROPLET JETTING OF PIEZOELECTRIC DRIVEN INKJET HEAD WITH INK COMPRESSIBILITY 282
J.H. Park, W.C. Sim, Y.J. Kim, P.J. Kang, C.S. Park, Y.S. Yoo, and J.W. Jeong
Samsung Electro-Mechanics, KOREA

M4C ELECTROLYTE DEPENDENCE OF AC ELECTRO-OSMOSIS 285
M.Z. Bazant, J.P. Urbanski, J.A. Levitan, K. Subramanian, M.S. Kilic, A. Jones, and T. Thorsen
Massachusetts Institute of Technology, USA

M5C THE MECHANICS OF FREQUENCY-SPECIFIC MICROFLUIDIC NETWORKS 288
D.C. Leslie[1], C.J. Easley[2], J.P. Landers[1], M. Utz[1], and M.R. Begley[1]
[1]University of Virginia, USA and [2]Vanderbilt Medical Center, USA

M6C NONLINEAR PHENOMENA IN INDUCED-CHARGE-ELECTROOSMOSIS: A NUMERICAL AND EXPERIMENTAL INVESTIGATION 291
G. Soni, T.M. Squires, and C.D. Meinhart
University of California, Santa Barbara, USA

M7C SURFACE ACOUSTIC WAVE μSTREAMING TO ENHANCE BIOSENSING IN A DROPLET-BASED μTAS PLATEFORM 294
O. Ducloux[1], E. Galopin[1], J.-C. Camart[1], V. Thomy[1], and F. Zoueshtiagh[2]
[1]IEMN, FRANCE and [2]LML, FRANCE

M8C THEORETICAL AND EXPERIMENTAL INVESTIGATION OF THE VALVELESS MICROPUMP WITH A LEAKAGE BARRIER 297
I.-H. Hwang, B.-P. Moon, S.-M. Shin, and and J.-H. Lee
Gwangju Institute of Science and Technology (GIST), KOREA

Poster Session Microfluidics - Aliquoting, Mixing & Pumping

M9C A NEW MICROPUMPING PRINCIPLE BY ACOUSTICALLY EXCITED OSCILLATING BUBBLE 300
K. Ryu, S.K. Chung, and S.K. Cho
University of Pittsburgh, USA

M10C AC ELECTROKINETIC ENHANCEMENT FOR BIOSENSORS 303
M. Sigurdson, H. Feldman, and C. Meinhart
University of California, Santa Barbara, USA

M11C EWOD STABILIZATION OF TWO LIQUID STREAMS ALONG A MICROCHANNEL AND EHD-INDUCED ENHANCEMENT OF INTERFACIAL MASS TRANSFER 306
Y. Ishida[1], L. Davoust[2], A. Gliére[1], J. Gratier[1], and N. Sarrut[1]
[1]Minatec, FRANCE and [2]LEGI, FRANCE

M12C MICROMIXER BASED ON BAKER'S TRANSFORMATION 309
K. Osato[1], M. Tokeshi[1], N. Kaji[1], Y. Omoto[1], N. Suzuki[1], Y. Sakai[1], E. Shamoto[1], and Y. Baba[1,2,3]
[1]Nagoya University, JAPAN, [2] National Institute of Advanced Industrial Science and Technology (AIST), JAPAN, and [3]Japan Science and Technology Agency (JST), JAPAN

M13C MICROPUMP AND MICROMIXER BASED ON ELECTRICALLY INDUCED BUOYANCY 312
S. Hirahara, T. Tsuruta, Y. Matsumoto, N. Miki, and H. Minamitani
Keio University, JAPAN

M14C NUMERICAL STUDY ON FLOW AND HEAT TRANSFER CHARACTERISTICS OF PERISTALITIC PUMP 315
K. Tatsumi[1], Y. Miwa[1], Y. Matsunaga[2], and K. Nakabe[1]
[1]Kyoto University, JAPAN and [2]Osaka Prefecture University, JAPAN

M15C PARTICLE TRANSPORT AND MIXING IN MICRODEVICES WITH RIDGES 318
L.M. Barrett, G.J. Fiechtner, and A.K. Singh
Sandia National Laboratories, USA

M16C SLUG MIXING BY ACOUSTIC STREAMING IN LAB-CHIPS 321
F. Schönfeld, J. Pinzón, and M. Weniger
Institut für Mikrotechnik Mainz GmbH, GERMANY

M17C THERMAL ACTUATION FOR A CROSS-CHANNEL MICROMIXER 324
B. Selva[1], O. Français[2], L. Rousseau[3], P. Poulichet[3], S. Desportes[1], J. Delaire[1], D. Grenier[1], and M.-C. Jullien[1]
[1]ENS Cachan, FRANCE, [2]Ecole Supérieure de Physique et Chimie Industrielle, (ESCPI), FRANCE, and [3]Groupe ESIEE, FRANCE

Poster Session Microfluidics - Multi-Phase and Digital Microfluidics

M18C 3D DROPLET ACTUATION IN DIGITAL MICROFLUIDICS DEVICES: TOWARDS INTEGRATION WITH MASS SPECTROMETRY 327
S.L. Freire, M. Abdelgawad, H. Yang, and A. Wheeler
University of Toronto, CANADA

M19C FABRICATION AND CHARACTERIZATION OF MAGNETIC ALGINATE BEAD CARRIER FOR MULTIPLE SORTING OF CELLS OR MULTIPLEXED IMMUNOASSAY 330
K. Lee, C. Kim, J.R. Lee, J.H. Kim, J.Y. Kang, and T.S. Kim
Korea Institute Science and Technology, KOREA

M20C GENERATION OF MONODISPERSE NONSPHERICAL DROPLETS VIA MICROCHANNEL ARRAYS WITH A STEP 333
I. Kobayashi[1], K. Uemura[1], and M. Nakajima[1,2]
[1]National Food Research Institute, JAPAN and [2]University of Tsukuba, JAPAN

M21C GIANT DEFORMATIONS AND TIP-STREAMING FROM SHEARED DROPS 336
S. Molesin and C.N. Baroud
Ecole Polytechnique, FRANCE

M22C MANIPULATION OF MONODISPERSE GEL EMULSIONS IN MICROCHANNELS 339
E. Surenjav, H. Evans, T. Pfohl, C. Priest, S. Herminghaus, and R. Seemann
Max-Planck-Institute for Dynamics and Self Organization, GERMANY

M23C OPTICAL FORCING OF MICRODROPS: FLOWS AND TEMPERATURE FIELD CHARACTERIZATION 343
M.L. Cordero, E. Verneuil, and C.N. Baroud
Ecole Polytechnique, FRANCE

M24C POLYMER MICROSPHERE MASS PRODUCTION USING 128-CHANNEL DIGITAL FLUIDIC CHIP 346
A.T.-H. Hsieh, J.-H. Pan, P.G. Pinasco, J.S. Fisher, L.-H. Hung, and A.P. Lee
University of California, Irvine, USA

M25C SIOC AS A HYDROPHOBIC LAYER FOR ELECTROWETTING ON DIELECTRIC APPLICATIONS 349
J. Thery, M. Borella, S. Le Vot, D. Jary, F. Rivera, G. Castellan, A.G. Brachet, M. Plissonnier, and Y. Fouillet
CEA-Liten-Minatec, FRANCE

M26C SURFACE INDUCED DROPLET FUSION IN MICROFLUIDIC DEVICES 352
L.M. Fidalgo, C. Abell, and W.T.S Huck
University of Cambridge, UK

M27C THERMALLY TRIGGERED MODULATION OF FLOW CHANNEL GEOMTRY AND LAYOUT 355
V. Bazargan and B. Stoeber
University of British Columbia, CANADA

M28C UNIFORM DROPLET GENERATION IN SURFACTANTS/POLYMER/OIL SYSTEMS USING MACRO TO MICRO SCALED CO-FLOW CHANNELS 358
M.R. Duxenneuner[1,2], P. Fischer[2], E.J. Windhab[2], and J.J. Cooper-White[1]
[1]University of Queensland, AUSTRALIA and
[2]ETH Zurich, SWITZERLAND

M29C USING MICROFLUIDIC TECHNOLOGY TO PRODUCE DOUBLE EMULSIONS 361
N. Pannacci, T. Lockhart, J. Mortreux, P. Tabeling, and H. Willaime
Ecole Supérieure de Physique et de Chimie Industrielles (ESPCI), FRANCE

Poster Session Microfluidics

M30C ADSORPTION-FREE MICROPARTICLE MANIPULATION USING 3D OPTOELECTRONIC TWEEZERS COMPOSED OF DOUBLE PHOTOCONDUCTIVE LAYERS 364
H. Hwang[1], Y. Oh[1], J.-J. Kim[1], Y.-J. Choi[1], W. Choi[1], J.-K. Park[1], S.-H. Kim[2], and J. Jang[2]
[1]Korea Advanced Institute of Science and Technology (KAIST), KOREA and [2]Kyung Hee University, KOREA

M31C CONDITIONS FOR CAPILLARY FILLING IN MICROFABRICATED CHANNELS WITH HYDROPHILIC AND HYDROPHOBIC WALLS 367
V. Jokinen[1,2] and S. Franssila[2]
[1]University of Helsinki, FINLAND and [2]Helsinki University of Technology, FINLAND

M32C CONTROL OF THE PHASE BEHAVIOR OF AQUEOUS SOLUTIONS USING MICROFLUIDICS 370
J.-U. Shim[1] and S. Fraden[2]
[1]University of Cambridge, UK and [2]Brandeis University, USA

M33C VERTICAL MICROREACTOR WITH FLUID FILTERS CHARACTERIZED BY 3D-CAPILLARY-BUNDLE FOR HIGH-THROUGHPUT IMMUNOASSAY 373
Y. Ukita[1], T. Asano[1], K. Fujiwara[1], K. Matsui[1], M. Takeo[1], S. Negoro[1], T. Kanie[2], M. Katayama[2], and Y. Utsumi[1]
[1]University of Hyogo, JAPAN and [2]Sumitomo Electric Industries, Ltd., JAPAN

Poster Session Nanotechnology - Nanofluidics

M1D COUPLED FREE-SOLUTION SEPARATION AND ON-CHIP HYBRIDIZATION OF OLIGONUCLEOTIDES IN A NANOFLUIDIC DEVICE 376
D.E. Huber[1], M.L. Markel[1], S. Pennathur[2], and K.D. Patel[1]
[1]Sandia National Laboratories, USA and [2]University of California, Santa Barbara, USA

M2D ELECTROKINETIC AND ATOMIC FORCE MICROSCOPY CHARACTERIZATION OF INTERFACIAL VAPOR VOID PHENOMENA IN HYDROPHOBIC MICROFLUIDIC DEVICES 379
V. Tandon, A.N. Sharma, S.K. Bhagavatula, and B.J. Kirby
Cornell University, USA

M3D HIGH SPEED SHEAR-DRIVEN FLOWS THROUGH MICROSTRUCTURED 1D-NANO-CHANNELS 382
J. Vangelooven[1], W. De Malsche[1,2], K. Pappaert[1], D. Clicq[1], H. Gardeniers[2], and G. Desmet[1]
[1]Vrije Universiteit, BELGIUM and [2]University of Twente, THE NETHERLANDS

M4D IONIC CURRENTS IN METAL-GATED NANOCHANNELS AND CARBON NANOTUBES 385
C. Meyer, M. Zuiddam, V. Merani, S. Lemay, and C. Dekker
Delft University of Technology, THE NETHERLANDS

M5D MESOSCOPIC CONCENTRATION FLUCTUATIONS IN A NANOFLUIDIC DEVICE 388
M.A.G. Zevenbergen, B.L. Wolfrum, and S.G. Lemay
Delft University of Technology, THE NETHERLANDS

M6D SPONTANEOUS STRETCHING OF DNA IN A TWO-DIMENSIONAL NANOSLIT 391
M. Krishnan[1], I. Mönch[2], and P. Schwille[1]
[1]Technische Universität Dresden, GERMANY and [2]Leibniz Institute for Solid State and Materials Research, GERMANY

Poster Session Nanotechnology - Nanoengineering

M7D SUB-100NM LITHOGRAPHY WITH NANOSPHERES ARRAYED IN A TEMPLATE 394
S. Jung and J. Lee
Seoul National University, KOREA

Poster Session Nanotechnology - Nanobiotechnology

M8D ARGON AND ACRYLIC ACID PLASMA TREATED ELECTROSPUN NANOFIBER SCAFFOL 397
K.H. Lee[1], G.H. Kwon[2], S.J. Shin[2], J.Y. Lee[2], Y.D Park[2], B.G. Min[1], and S.H. Lee[2]
[1]Seoul National University, KOREA and [2]Korea University, KOREA

M9D HIGHLY PARALLEL FABRICATION OF MICROFLUIDIC CHIPS FOR LONG DNA MOLECULE SEPARATION 400
J. Shi[1,2], A.P. Fang[1], L. Malaquin[1], J.L. Viovy[3], A. Pépin[1], D. Decanini[1], and Y. Chen[1,2]
[1]CNRS, FRANCE, [2]ENS, FRANCE, and [3]Institut Curie, FRANCE

M10D ISOLATION OF DNA MOLECULE IN MICROCHANNEL AND SINGLE MOLECULE TRAPPING BETWEEN MICROELECTRODES 403
M. Kumemura[1], D. Collard[1], C. Yamahata[1], N. Sakaki[1], G. Hashiguchi[2], and H. Fujita[1]
[1]University of Tokyo, JAPAN and [2]Kagawa University, JAPAN

M11D LOCALIZED GENE REGULATION BY A REMOTE OPTICAL SWITCH 406
E.S. Lee, G.L. Liu, and L.P. Lee
University of California, Berkeley, USA

M12D SILICON NANOWIRE ARRAY AS A BIOCHEMICAL SENSOR/NANO-HEATER FOR POTENTIAL APPLICATIONS IN CELLULAR PROTEIN DETECTION 409
I. Park[1], Z. Li[2], A.P. Pisano[1], and R.S. Williams[2]
[1]University of California, Berkeley, USA and
[2]Hewlett-Packard Laboratories, USA

M13D SINGLE-MOLECULE LIGATION OF DNA AS A UNIT OPERATION FOR MOLECULAR SURGERY 412
R. Watanabe[1], H. Oana[1,2], and M. Washizu[1,2]
[1]University of Tokyo, JAPAN and [2]Japan Science and Technology, JAPAN

M14D TRAPPING OF SINGLE DNA MOLECULES BY MEMS TWEEZERS WITH PULSED DIELECTROPHORESIS 415
N. Sakaki[1], M. Kumemura[1], D. Collard[1], G. Hashiguchi[2], and H. Fujita[1]
[1]University of Tokyo, JAPAN and [2]Kagawa University, JAPAN

Poster Session Nanotechnology

M15D NANOCHANNEL CHROMATOGRAPHY - SEPARATIONS BASED ON THE UNEVEN DISTRIBUTIONS OF SPECIES IN NANOCHANNELS 418
S. Liu, J. Kang, S. Wang, and J. Lu
Texas Tech University, USA

Poster Session Materials - Innovative Chip Materials

M1E CONJUGATED FLUORESCENT NANOSOMES FOR A NOVEL LABEL-FREE MICROARRAY CHIPS FOR DNA ANALYSES 421
D.J. Ahn[1], E.J. Kim[1], D.H. Yang[1], G.S. Lee[1], and J.-M. Kim[2]
[1]Korea University, KOREA and [2]Hanyang University, KOREA

Poster Session Materials - Surface Modification and Characterization

M2E CHARGED PHOSPHOLIPID POLYMER SURFACES WITH HIGH CELL ADHESION RESISTANCE FOR CELL CHIP 424
Y. Xu, T. Konno, M. Takai, and K. Ishihara
Univerisity of Tokyo, JAPAN

M3E DEVELOPMENT OF ENZYME-RELEASE CAPILLARY FOR CAPILLARY-ASSEMBLED MICROCHIP TOWARDS MULTIPLE METABOLITE SENSING 427
T.G. Henares[1], E. Maekawa[1], F. Mizutani[1], R. Sekizawa[2], and H. Hisamoto[3]
[1]University of Hyogo, JAPAN, [2]Metaboscreen Co. Ltd., JAPAN, and [3]Osaka Prefecture University, JAPAN

M4E DIRECT POLYMERIZATION PATTERNING BASED ON EB LITHOGRAPHY FOR CONTROL OF CELL ADHESIVE ORIENTATION 430
N. Idota[1], T. Tsukahara[1,2], A. Hibara[1,2], T. Okano[3], and T. Kitamori[1,2]
[1]Japan Science and Technology Agency (JST), JAPAN, [2]University of Tokyo, JAPAN, and [3]Tokyo Women's Medical University, JAPAN

M5E FEATURES OF THERMORESPONSIVE POLYMERS GRAFTED ONTO HYDROPHILIC AND HYDROPHOBIC SURFACES AND APPLICATION OF THE SURFACES FOR RAPID RECOVERY OF THE CELL SHEET 433
Y. Akiyama, M. Yamato, A. Kikuchi, and T. Okano
Tokyo Women's Medical University, JAPAN

M6E NONBIOFOULING SURFACES AND MICROPATTERNED BIORECOGNITION LAYER ON POLYMERIC MATERIALS FOR HIGHLY SENSITIVE MICROARRAY BIOSENSORS 436
J. Sibarani, T. Konno, M. Takai, and K. Ishihara
University of Tokyo, JAPAN

M7E PHOSPHOLIPID POLYMER SURFACE SHOWING THEIR BIOCOMPATIBILITY RAPIDLY FROM DRY TO WATER ENVIRONMENT FOR MICROFLUIDIC DEVICES 439
K. Futamura, M. Takai, and K. Ishihara
University of Tokyo, JAPAN

Poster Session Materials - Nanostructured Materials

M8E NANOSTRUCTURE ENHANCED SURFACE PLASMON RESONANCE IMAGING DETECTION OF DNA HYBRIDIZATION 442
L. Malic[1], B. Cui[2], T. Veres[2], and M. Tabrizian[1]
[1]McGill University, CANADA and
[2]National Research Council (NRC), CANADA

M9E TOWARDS SELECTIVE OPTOCHEMICAL GAS SENSING BY LUMINESCENT MARINE DIATOMS 445
A. Setaro[1], S. Lettieri[1], L. De Stefano[2], and P. Maddalena[1]
[1]Universitá di Napoli Federico II, ITALY, and
[2]Unità di Napoli, ITALY

Poster Session Materials

M10E A PHOTOPATTERNABLE SILICONE FOR BIOMEMS APPLICATIONS 448
S.P. Desai, B.M. Taff, and J. Voldman
Massachusetts Institute of Technology, USA

Poster Session Detection Technologies - Optical

M1F APPLICATION OF HIGH RESOLUTION 2D-SPR IMAGER TO LIVING CELL-BASED ALLERGEN SENSING 451
M. Horii[1,2], H. Shinohara[1], Y. Iribe[1], and M. Suzuki[1]
[1]University of Toyama, JAPAN and [2]Toyama New Industry Organization, JAPAN

M2F DESIGN AND CHARACTERIZATION OF MACH-ZEHNDER INTERFEROMETRIC IMMUNOSENSORS OPERATING AT NEAR INFRARED 454
J. Hong[1] and T.S. Kim[2]
[1]Imperial College London, UK and
[2]Korea Institute of Science and Technology (KIST), KOREA

M3F DEVELOPMENT OF DIFFERENTIAL INTERFERENCE CONTRAST THERMAL LENS MICROSCOPE 458
H. Shimizu[1], K. Mawateri[2], and T. Kitamori[1,2]
[1]University of Tokyo, JAPAN and
[2]Kanagawa Academy of Science and Technology, JAPAN

M4F IMMERSION REFRACTOMETRY ANALYSIS OF LIVING CELLS IN MICROFLUIDIC CELL CULTURE CHIP 461
X. Zhang[1], R. Chua[2], P.H. Yap[2], W.Z. Song[1], and A.Q. Liu[1]
[1]Nanyang Technological University, SINGAPORE and
[2]DSO National Laboratories, SINGAPORE

M5F ION-SELECTIVE NANOPLASMONIC OPTICAL SENSOR 464
T. Kang, Y. Choi, D. Choi, E. Lee, and L.P. Lee
University of California, Berkeley, USA

M6F ON-CHIP pH AND TEMPERATURE SENSING WITH GEL-TOOL MANIPULATED BY OPTICAL TWEEZERS 467
H. Maruyama[1], F. Arai[2], and T. Fukuda[1]
[1]Nagoya University, JAPAN and [2]Tohoku University, JAPAN

M7F OPTOFLUIDIC BLOOD CELL SORTING 470
I.A. Andreev[2], A.C. Riches[2], T. Briscoe[2], L. Paterson[3],
K. Dholakia[2], and M.P. MacDonald[1]
[1]University of Dundee, UK, [2]University of St. Andrews, UK, and
[3]Heriot Watt University, UK

M8F REFRACTIVE INDEX DETECTOR FOR NANOCHANNEL USING ALTERNATIVE DIFFRACTION GRATING NANOCHANNEL 473
K. Mawatari[1], K. Oda[2], A. Hibara[2], and T. Kitamori[1,2]
[1]Kanagawa Academy of Science and Technology, JAPAN and
[2]University of Tokyo, JAPAN

Poster Session Detection Technologies - Electrochemical

M9F AN ELECTROCHEMICAL SENSOR INTEGRATED ON FABRIC 476
G. Marchand[1], M.-L. Cosnier[1], N. David[1], C. Chabrol[1], A. Bourgerette[1], F. Vrillon[1], T. Flaven[1], I. Chartier[2], J. Bablet[2], and N. Dunoyer[2]
[1]CEA LETI Minatec, FRANCE and [2]LITEN, FRANCE

M10F LOW-NOISE OPERATION OF CHARGE-TRANSFER-TYPE pH SENSOR USING CHARGE ACCUMULATION TECHNIQUE..... 479
E. Watanabe[1], T. Hizawa[1], S. Mimura[2], T. Ishida[3], H. Takao[4,5], K. Sawada[1,4,5], and M. Ishida[1,4,5]
[1]Toyohashi University of Technology, JAPAN, [2]HORIBA, Ltd., JAPAN, [3]Orimacky, Ltd., JAPAN, [4]Toyohashi University of Technology, JAPAN, and [5]Japan Science and Technology Agency (JST), JAPAN

M11F A FULLY INTEGRATED AND DISPOSABLE POLYMER BIOSENSOR USING MICRO DIAPHRAGM STRUCTURE OF PIEZO-COPOLYMER (PVDF-TrFE)..... 482
S. Lee[1,2], C. Li[1], Y. Chae[2], J. Kang[2], and C.H. Ahn[1]
[1]University of Cincinnati, USA and
[2]Korea Institute of Science and Technology (KIST), KOREA

M12F DIFFERENTIAL IMPEDANCE SPECTROSCOPY WITH AN ARRAY OF FIELD-EFFECT TRANSISTORS AS NOVEL BIOSENSOR CONCEPT 485
S. Ingebrandt, Y. Han, G. Wrobel, S. Eick, S. Schäfer, and A. Offenhäusser
Forschungszentrum Jülich, GERMANY

M13F DUAL FREQUENCY RESONANCE IMPEDANCE SPECTROSCOPY FLOW CYTOMETRY FOR BLOOD AND TUMOR CELLS 488
S. Zheng and Y.-C. Tai
California Institute of Technology, USA

M14F ELECTRICAL DETECTION OF ION CHANNEL ACTIVITY IN AN ARRAY OF SUSPENDED LIPID BILAYERS 491
A. Varnier[1], T. Plénat[1], L. Ghenim[1], D. Fajolle[2], V. Agache[2], F. Sauter[2], F. Chatelain[1], and A. Fuchs[1]
[1]Commissariat à l'Energie Atomique (CEA), FRANCE and
[2]CEA-LETI-Minatec, FRANCE

M15F IMPEDANCE SPECTROSCOPY ON A MICROFABRICATED FLOW CYTOMETER: LABEL-FREE DETECTION OF *BABESIA BOVIS* PARASITES IN BOVINE RED BLOOD CELLS 494
C. Küttel[1], E. Nascimento[2], N. Demierre[1], T. Silva[2], T. Braschler[1], A.G. Oliva[2], and P. Renaud[1]
[1]Ecole Polytechnique Fédérale de Lausanne (EPFL), SWITZERLAND and [2]Universidade Nova de Lisboa, PORTUGAL

Poster Session Detection Technologies

M16F CANTILEVER-BASED SENSOR WITH INTEGRATED OPTICAL READ-OUT USING SINGLE MODE WAVEGUIDES 497
M. Nordström[1], D.A. Zauner[1], M. Calleja[2], J. Hübner[1], and A. Boisen[1]
[1]Technical University of Denmark, DENMARK and [2]Institute of Microelectronics of Madrid, SPAIN

M17F DEVELOPMENT OF NOVEL CELL ANALYTICAL SYSTEM BASED ON HIGH SENSITIVE QCM SENSOR 500
E. Watarai, M. Takai, and K. Ishihara
University of Tokyo, JAPAN

M18F MICROFLUIDIC IMMUNOCHIP BASED ON ELECTRICAL DETECTION SYSTEM FOR CANCER BIOMARKER 503
J.-H. Maeng, Y.-J. Ko, Y. Ahn, S.-H. Lee, N.-G. Cho, and S.Y. Hwang
Hanyang University, KOREA

M19F SUPRAMOLECULAR CHEMISTRY IN AN NMR-CHIP 506
M.V. Gómez, D.N. Reinhoudt, and A.H. Velders
University of Twente, THE NETHERLANDS

Poster Session MEMS & NEMS Technologies - Micro and Nano-Machining

M1G A PHOTOLITHOGRAPHY-BASED SILICON NANOWIRE FABRICATION USING UNDERCUT ETCHING OF (110) SILICON WAFER FOR BIOSENSOR APPLICATIONS 509
S.-S. Yun, S.-K. Yoo, S. Yang, and J.-H. Lee
Gwangju Institute of Science and Technology (GIST), KOREA

M2G FABRICATION AND OPERATION OF A MICRO ORIFICE ARRAY CHIP WITH HIGH ELECTROPORATION EFFICIENCY 512
M. Gel[1], O. Kurosawa[2], H. Oana[1], and M. Washizu[1]
[1]University of Tokyo, JAPAN and [2]Advantec Co., JAPAN

M3G FAST ETCHING OF SACRIFICIAL GALVANIC COUPLED METALS FOR NANOCHANNEL FABRICATION: EXPERIMENTS AND THEORY 515
W. Sparreboom, J.C.T. Eijkel, and A. van den Berg
University of Twente, THE NETHERLANDS

M4G IMPLEMENTATION OF MICROFABRICATED SUTURE-LESS FLEXIBLE PARYLENE TISSUE ANCHORS ON MINIMALLY INVASIVE BIOMEDICAL IMPLANTS 518
P.-J. Chen[1], D.C. Rodger[1,2], S. Saati[3], J.C. Altamirano[3], C.-H. Lin[1], R. Agrawal[2,3], R. Varma[2,3], M.S. Humayun[2,3], and Y.-C. Tai[1]
[1]California Institute of Technology, USA, [2]University of Southern California, USA, and [3]Doheny Eye Institute, USA

M5G INVESTIGATION OF INTERSTRUCTURAL COLLAPSE OF PDMS MICROSTRUCTURES 521
Y. Zhao
Ohio State University, USA

M6G MAGNETIC MICROVALVE WITH BIOCOMPATIBLE SURFACES USING ELECTROCHEMICAL DEPOSITION AND PASSIVATION 524
M. Tijero[1], L.J. Fernández[1], J.M. Ruano-López[1], K. Mayora[1], M.V. Rodríguez[2], and J. Elizalde[1]
[1]Ikerlan S. Coop., SPAIN and [2]University of Basque Country, SPAIN

M7G RELIABLE BATCH MANUFACTURING OF MINIATURIZED VERTICAL VIAS IN SOFT POLYMER REPLICA MOLDING 527
C.F. Carlborg, T. Haraldsson, G. Stemme, and W. van der Wijngaart
Royal Institute of Technology, SWEDEN

Poster Session MEMS & NEMS Technologies - Microfluidic Components

M8G A LATERALLY OPERATING LIQUID ASPIRATION AND DISPENSING UNIT BASED ON AN EXPANDING PDMS COMPOSITE 530
B. Samel, N. Sandström, P. Griss, and G. Stemme
Royal Institute of Technology, SWEDEN

M9G A PARTICLE CLASSIFICATION CHIP FOR BOTH AIRBORNE AND LIQUID-SUSPENDED BIOLOGICAL PARTICLES 533
Y.-H. Kim, S.-C. Park, D.-H. Park, I.-H. Jung, J. Hwang, and Y.-J. Kim
Yonsei University, KOREA

M10G A STRAIGHT SILICON TUBE AS A MICROFLUIDIC DENSITY SENSOR 536
M. Najmzadeh[1], S. Haasl[2], and P. Enoksson[1]
[1]Chalmers University of Technology, SWEDEN and [2]Imego AB, SWEDEN

M11G CONTINUOUSLY MICROFLUIDIC CENTRIFUGATION IN SEQUENTIALLY CONNECTED SEMICIRCULAR MICROCHANNELS FOR MICROMETER-SIZED PARTICLE ENRICHMENT 539
D. Xu, W. Wang, Y. Jin, and Z. Li
Peking University, CHINA

M12G ELECTROSPRAY IONIZATION FROM A SILICON EMITTER WITH AN ADJUSTABLE GAP 542
T. Schönberg[1], P. Ek[2], J. Sjödahl[2], J. Roeraade[2], and C. Vieider[1]
[1]Acreo AB, SWEDEN and [2]Royal Institute of Technology, SWEDEN

M13G HIGH THROUGHPUT CONTROLLED BACTERIAL TRANSPORT USING GEOMETRICAL FLUIDIC MICROCHANNELS OR 3D MICROFIBERS STRUCTURES 545
S. Martel and M. Mohammadi
École Polytechnique de Montréal, CANADA

M14G MICROFLUIDIC DISTRIBUTION SYSTEM FOR HOMOGENEOUS INJECTION THROUGH A NEEDLE MATRIX 548
A. Hoel[1], L. Mir[2], B. Lepioufle[1], and M.-C. Jullien[1]
[1]ENS Cachan Antenne de Bretagne, FRANCE and
[2]Institut Gustave Roussy, FRANCE

M15G MONOLITHIC TEFLON MEMBRANE VALVES AND PUMPS FOR HARSH CHEMICAL AND LOW-TEMPERATURE USE 551
P.A. Willis[1], B.D. Hunt[1], V.E. White[1], M. Ikeda[1], M.C. Lee[1], M.J. Pelletier[2], and F.J. Grunthaner[1]
[1]California Institute of Technology, USA and
[2]Pfizer Global Research & Development, USA

M16G ON-CHIP MICROFLUIDIC GRADIENT GENERATION FOR NANOFLOW LIQUID CHROMATOGRAPHY 554
R. Brennen, H. Yin, and K. Killeen
Agilent Technologies, USA

M17G PERISTALTIC MICRO PUMP ACTUATED BY SINGLE INPUT SIGNAL 557
O.C. Jeong[1,2] and S. Konishi[3]
[1]INJE University, KOREA, [2]MEMS/NANO Fabrication Center, KOREA, and
[3]Ritsumeikan University, JAPAN

Poster Session MEMS & NEMS Technologies - Acoustic Devices

M18G PARTICLE POSITIONING IN MICROCHANNELS USING ULTRASONIC STANDING WAVES REINFORCED WITH RADIATED NEAR AND FAR FIELD PRESSURE WAVES 560
S.K. Ravula, D.W. Branch, J. Sigman, C. Arrington, P.G. Clem, and I. Brener
Sandia National Laboratories, USA

Poster Session MEMS & NEMS Technologies –
Hybrid Devices, Packaging, Components Interfacing

M19G ALUMINIUM PRINTED CIRCUIT BOARD TECHNOLOGY FOR BIOMEDICAL MICRO-DEVICES 563
B. Iafelice[1,2], F. Destro[3], D. Manessis[1], D. Gazzola[2], E. Jung[1], L. Böttcher[1], M. Borgatti[3], T. Braun[1], J. Bauer[1], R. Gavioli[3], R. Gambari[3], A. Ostmann[1], and R. Guerrieri[2]
[1]Fraunhofer Institute for Reliability and Microintegration (IZM), GERMANY, [2]Bologna University, ITALY, and [3]Ferrara University, ITALY

M20G ENERGY SCAVENGING FROM TRANSPIRATION: ELECTROSTATIC POWER GENERATION USING EVAPORATION-INDUCED BUBBLE MOTION 566
R.T. Borno, J.D. Steinmeyer, and M.M. Maharbiz
University of Michigan, USA

M21G MICROFABRICATED NEBULIZER CHIPS FOR ATMOSPHERIC PRESSURE PHOTOIONIZATION-MASS SPECTROMETRY 569
M. Haapala[1], J. Pól[1], T. Kauppila[1], L. Luosujärvi[1], V. Saarela[2], S. Franssila[2], R.A. Ketola[1,2], T. Kotiaho[1], and R. Kostiainen[1]
[1]University of Helsinki, FINLAND and
[2]Helsinki University of Technology, FINLAND

Poster Session MEMS & NEMS Technologies

M22G MANIPULATIONS OF BIO-MOLECULES INSIDE DISCRETE DROPLETS WITH DROPLET CONTROLS BY OPTICAL IMAGING 572
I.K. Lao[1], C. Lee[1,2], and H.H. Feng[1]
[1]Institute of Microelectronics, SINGAPORE and
[2]National University of Singapore, SINGAPORE

Concurrent Session 1A3 - Cell Handling and Screening 2

FERROFLUID PATTERN FOR GUIDING MAGNETIC BEADS SELF-ORGANISATION: APPLICATION TO AFFINITY CELL SEPARATION AND ON CHIP CELL CULTURE 575
A.-E. Saliba[1], E. Psichari[1], L. Saias[1], N. Minc[1], V. Studer[2], and J.-L. Viovy[1]
[1]Institut Curie, FRANCE and
[2]Ecole Supérieure de Physique et de Chimie Industrielles (ESPCI), FRANCE

HIGH-THROUGHPUT, CONTINUOUS-FLOW, DIELECTROPHORETIC SCREENING OF *MYCOBACTERIUM SMEGMATIS* IN COHERENTLY PATTERNED, POLYMERIC MICRO-CHANNELS 578
B.G. Hawkins, A.E. Smith, and B.J. Kirby
Cornell University, USA

STUDYING REPROGRAMMING OF SOMATIC CELLS VIA FUSION WITH EMBRYONIC STEM CELLS: A MASSIVELY PARALLEL DEVISE FOR CELL FUSION 581
A.M. Skelley, O. Kirak, R. Jaenisch, and J. Voldman
Massachusetts Institute of Technology, USA

Concurrent Session 1B3 - Integrated Systems

CONCENTRATION, LYSIS AND REAL-TIME PCR ON A SU-8 LAB ON A CHIP FOR RAPID DETECTION OF *Salmonella spp*. IN FAECES 584
M. Agirregabiria[1], D. Verdoy[2], G. Olabarria[2], J. Berganzo[1], J. Berganza[2], L.J. Fernandez[1], M. Pascual de Zulueta[2], K. Mayora[1], P. Aldamiz-Echevarría[2], and J.M. Ruano-López[1]
[1]Ikerlan S. Coop., SPAIN and [2]Gaiker-IK4, SPAIN

ON-CHIP SINGLE MOLECULE ASSAY DEVICE INTEGRATING CELL LYSIS AND PROTEIN EXTRACTION-PURIFICATION-ASSAY COMPONENTS FOR GENETICALLY ENGINEERED PROTEINS 587
T. Nakayama[1], K. Tabata[2], H. Noji[2], and R. Yokokawa[1,3]
[1]Ritsumeikan University, JAPAN, [2]Osaka University, JAPAN, and
[3]Japan Science and Technology Agency (JST), JAPAN

MICROFLUIDIC CHIPS FOR MEMBRANE PROTEIN CRYSTALLIZATION 590
P.J.A. Kenis, J.D. Tice, S.L. Perry, G.W. Roberts, and S. Talreja
University of Illinois, USA

Tuesday, 9 October 2007

Plenary III

A SINGULAR VIEW OF DNA TRANSACTIONS 593
Gijs J.L. Wuite
Vrije University, THE NETHERLANDS

Concurrent Session 2A1 - Multiphase and Digital Microfluidic 1

FORMATION OF ARRAYED PLANAR LIPID MEMBRANES BY THE ACCUMULATION OF UNIFORM AQUEOUS PLUGS IN A PSEUDO-POROUS MICROCHANNEL 595
T. Baba, T. Hatsuzawa, and T. Nisisako
Tokyo Insitute of Technology, JAPAN

SINGLE CELL ENCAPSULATION AND SORTING IN MICRODROPLETS USING PASSIVE HYDRODYNAMIC EFFECTS 598
M. Chabert and J.-L. Viovy
Institut Curie, FRANCE

MICROCHIP TITRATION BY UTILIZIGN LAPLACE VALVE 601
A. Hibara[1,2,3], M. Nonogi[1], and T. Kitamori[1,2,3]
[1]Univerisity of Tokyo, JAPAN, [2]Kanagawa Academy of Science and Technology, JAPAN, and [3]Japan Science and Technology Agency (JST), JAPAN

Concurrent Session 2B1 - Nanobiotechnology

MICROFLUIDIC ORGANIZATION OF LIPID TUBULE BIOREACTORS 604
J. West, U. Marggraf, A. Manz, J. Franzke, and P.S. Dittrich
Institute for Analytical Sciences (ISAS), GERMANY

HIGHLY SENSITIVE MEASUREMENT OF PNA-DNA HYBRIDIZATION USING OXIDE-FREE SILICON NANOWIRE SENSORS 607
G.-J. Zhang, A. Agarwal, K.D. Buddharaju, N. Singh, and Z. Gao
Institute of Microelectronics, SINGAPORE

PROBING CYTOSKELETON DYNAMICS WITH MULTI-DIRECTIONAL TOPOGRAPHICAL GUIDANCE 610
J. Mai, C. Sun, S. Li, and X. Zhang
University of California, Berkeley, USA

Concurrent Session 2A2 - Clinical Diagnostic 1

MICROFLUIDIC CHIP FOR RELATIVE QUANTIFICATION
OF mRNAs BY MLPA 613
T. Roeser[1], K.S. Drese[1], X. Fuetterer[1], A. Nygren[2], M. Weniger[1], and M. Ritzi[1]
[1]Institut fuer Mikrotechnik Mainz GmbH, GERMANY and
[2]MRC-Holland b.v., THE NETHERLANDS

BIOPHYSICAL FLOW CYTOMETRY FOR HEMATOLOGIC DISEASES 616
M.J. Rosenbluth, W.A. Lam, and D.A. Fletcher
University of California, Berkeley, USA

MULTIFUNCTIONAL BARCODED PARTICLES FOR
HIGH-THROUGHPUT MOLECULAR SCREENING 619
D.C. Pregibon[1], M. Toner[2], and P.S. Doyle[1]
[1]Massachusetts Institute of Technology, USA, and
[2]Massachusetts General Hospital and Harvard Medical School, USA

Concurrent Session 2B2 - On Chip Synthesis and Production

BIOLOGICALLY INSPIRED MICROFLUIDIC
SPINNING OF SILK FIBERS 622
D.N. Breslauer, S.J. Muller, and L.P. Lee
University of California, Berkeley, USA

INSTANTANEOUS CARBON-CARBON BOND FORMATION USING A
MICROCHANNEL REACTOR WITH A CATALYTIC MEMBRANE 625
Y. Uozumi[1], Y.M.A. Yamada[1], T. Beppu[1], N. Fukuyama[1],
M. Ueno[2], and T. Kitamori[2]
[1]Japan Science and Technology Agency (JST), JAPAN and
[2]University of Tokyo, JAPAN

MANUFACTURING OF MICROPARTICLES WITH CONFIGURABLE
SHAPE AND SEQUENCE ANISOTROPY BY FLUIDIC PROCESSING..... 628
K.E. Sung, S.A. Vanapalli, D. Mukhija, H.A. McKay, J.M. Millunchick,
M.J. Solomon, and M.A. Burns
University of Michigan, USA

Plenary IV

ACTUATING LAYER-EMBEDDED MICROCANTILEVER FOR
HIGHLY SENSITIVE BIOMOLECULE DETECTION 631
K.S. Hwang, S.K. Kim, and **Tae Song Kim**
Korea Institute of Science and Technology (KIST), KOREA

Poster Session Microsystems for Life Sciences - Genomics & Proteomics

T1A A PARYLENE BASED DOUBLE-CHANNEL MICRO-ELECTROPHORESIS SYSTEM FOR RAPID MUTATION DETECTION 634
S. Sukas, A.E. Erson, C. Sert, and H. Kulah
Middle East Technical University, TURKEY

T2A CHIP-BASED MAGNETIC BIOAFFINITY TECHNIQUE ADAPTED FOR QUALITATIVE ANALYSIS OF FOOD ALLERGENS 637
M. Slovakova[1], B. Jankovicova[1], S. Rosnerova[1], L. Korecka[1], N. Minc[2], J.-L. Viovy[2], L. Hernychova[3], M. Hubalek[3], and Z. Bilkova[1]
[1]University of Pardubice, CZECH REPUBLIC, [2]Institute Curie, FRANCE, and [3]University of Defense, Hradec Kralove, CZECH REPUBLIC

T3A ELECTROWETTING ON NANOFILAMENT SILICON FOR MATRIX-FREE LASER DESORPTION/IONIZATION MASS SPECTROMETRY 640
C.W. Tsao[1], P. Kumar[1], J. Liu[1], C.F. Kung[1,2], C.C. Chang[2], and D.L. DeVoe[1]
[1]University of Maryland, USA and [2]Academia Sinica, TAIWAN

T4A EVALUATION OF MICROFLUDIC DNA EXTRACTION SYSTEM USING A NANOPOROUS ALUMINUM OXIDE MEMBRANE 643
J. Kim and B.K. Gale
University of Utah, USA

T5A SLANTWISE RADIATIVE HEATING SYSTEM FOR TEMPERATURE GRADIENT CE DETECTION OF DNA MUTATION ON A MICROFLUIDIC CHIP 646
H.D. Zhang[1], J. Zhou[1], Z.R. Xu[2], J. Song[1], J. Dai[3], J. Fang[1], and Z.L. Fang[2]
[1]China Medical University, CHINA, [2]Northeastern University, CHINA, and [3]Shenyang Jianzhu University, CHINA

T6A VERSATILE ACRYLAMIDE-BASED MICROCHAMBERS FOR SINGLE MOLECULAR BIOLOGICAL ASSAYS AND ANALYSIS 649
L. Lam[1], S. Sakakihara[1], K. Ishizuka[1], S. Takeuchi[2], and H. Noji[1]
[1]Osaka University, JAPAN and [2]University of Tokyo, JAPAN

Poster Session Microsystems for Life Sciences - Clinical Diagnostics

T7A A MICROFLUIDIC AFFINITY APTASENSOR 652
T.H. Nguyen, R. Pei, M. Stojanovic, D. Landry, and Q. Lin
Columbia University, USA

T8A A NEW ON-CHIP PLATFORM FOR RAPID AND EASY-TO-USE IMMUNOASSAY 655
M. Ikami[1], M. Tokeshi[1], N. Kaji[1], and Y. Baba[1,2,3]
[1]Nagoya University, JAPAN, [2]National Institute of Advanced Industrial Science and Technology (AIST), JAPAN, and [3]Japan Science and Technology Agency (JST), JAPAN

T9A BIOMEMS FOR OSTEOPROTEOGERIN DETECTION WITH GOLD NANOPARTICLES 658
K. Singh, H.H. Kim, and K.C. Kim
Pusan National University, KOREA

T10A MICROFLUIDIC ELISA USING MAGNETIC BEADS AND PRESSURE VALVES TO REDUCE ASSAY NOISE 661
M. Herrmann[1,2], E. Roy[2], M. Tabrizian[1], and T. Veres[2]
[1]McGill University, CANADA and [2]Industrial Materials Institute, CANADA

T11A MULTI-ARRAY FLOW-FOCUSING DEVICES TO ACCELERATE PRODUCTION OF MICROBUBBLES FOR CONTRAST-ENHANCED ULTRASOUND IMAGING 664
K. Hettiarachchi[1], E. Talu[2], M.L. Longo[2], P.A. Dayton[2], and A.P. Lee[1]
[1]University of California, Irvine, USA and [2]University of California, Davis, USA

T12A PROGRESS TOWARD A FLOW-THROUGH MEMBRANE ELISA IN A MICROFLUIDIC FORMAT 667
P. Spicar-Mihalic, D.Y. Stevens, and P. Yager
University of Washington, USA

T13A RAPID DETECTION OF KINASE TRANSLOCATION AT THE SINGLE CELL LEVEL ON A MICROFLUIDIC CHIP 670
J. Wang, N. Bao, L.L. Paris, H.-Y. Wang, R.L. Geahlen, and C. Lu
Purdue University, USA

T14A STORAGE AND REACTIVATION OF ENZYMES IN A DISPOSABLE, SELF-CONTAINED LAB-ON-A-CHIP SYSTEM 673
A. Gulliksen[1,2], M.M. Mielnik[3], E. Hovig[4], F. Karlsen[1], L. Furuberg[3], and R. Sirevåg[2]
[1]NorChip AS, NORWAY, [2]University of Oslo, NORWAY, [3]SINTEF, NORWAY, and [4]The Norwegian Radiumhospital, NORWAY

Poster Session Microsystems for Life Sciences - Microarrays

T15A COMBINED LAB-ON-A-CHIP AND MICROARRAY APPROACH FOR BIOMOLECULAR INTERACTION SENSING USING SURFACE PLASMON RESONANCE IMAGING 676
G. Krishnamoorthy, J.B. Beusink, E.T. Carlen, S. Schlautmann, H.L. de Boer, A. van den Berg, and R.B.M. Schasfoort
University of Twente, THE NETHERLANDS

T16A HIGHLY PARALLELIZED LIPIDIC BILAYERS ARRAY FOR ION CHANNEL RECORDING 679
B. Le Pioufle[1,2], H. Suzuki[1], and S. Takeuchi[1,3]
[1]University of Tokyo, JAPAN, [2]ENS Cachan, FRANCE and [3]Japan Science and Technology, JAPAN

T17A RAPID HIGH-THROUGHPUT MICROARRAY ANALYSIS – A SHEAR-DRIVEN APPROACH 682
K. Pappaert[1], F. Detobel[1], P. Van Hummelen[2], and G. Desmet[1]
[1]Vrije Universiteit, BELGIUM and [2]VIB MicroArray Facility, BELGIUM

Poster Session Microsystems for Life Sciences - Point of Care and Hand Held Devices

T18A A DISPOSABLE MAGNETIC PLANAR PERISTALTIC PUMP FOR SELF-CONTAINED LAB-ON-A-CHIP (LOC) CARTRIDGE 685
L. Yobas, L.F. Cheow, K.C. Tang, and C.Y. Teo
Institute of Microelectronics, SINGAPORE

T19A BIOMAGNETIC BEAD BASED MICROFLUIDIC DEVICE FOR RAPID NAKED EYE FIELD DIAGNOSTICS OF CATTLE PNEUMONIA 688
J. Gantelius, C. Hamsten, A. Persson, M. Uhlen, and H. Andersson-Svahn
Royal Institute of Technology, SWEDEN

T20A CCD CAMERA-BASED OPTICAL READOUT SYSTEM FOR RT-PCR DNA ANALYZER: TOWARD RAPID AND CHEAP DETECTION OF PATHOGENS IN FOOD AND CLINICAL SAMPLES IN NANOGRAMS PER MILILITER CONCENTRATION OF DNA 691
R. Walczak[1,2], J.A. Dziuban[1,2], J. Koszur[1], A. Wolff[3], D.D. Bang[3], and M. Bu[3]
[1]Institute of Electron Technology, POLAND,[2]Wrocław University of Technology, POLAND and [3]Danish Technical University, DENMARK

T21A DIAGNOSIS-ON-A-CHIP: A MICROFLUIDIC PLATFORM FOR CELL CULTURE AND VIRUS ASSAYS 694
X. Zhang[1], R. Chua[2], P.H. Yap[2], and A.Q. Liu[1]
[1]Nanyang Technological University, SINGAPORE and [2]DSO National Laboratories, SINGAPORE

T22A ON-CHIP HIGH-SENSITIVITY FLUORESCENCE DETECTION SYSTEM USING CROSS-POLARIZATION AND ORGANIC THIN FILM DEVICES FOR A DISPOSABLE LAB-ON-A-CHIP 697
A. Banerjee, A. Pais, D. Klotzkin, and I. Papautsky
University of Cincinnati, USA

Poster Session Microsystems for Life Sciences - Cell Handling & Analysis

T23A A NEW METHOD FOR CELL CO-CULTURE USING MICRO-MOLDING IN CAPILLARIES TECHNOLOGY: STUDY OF CELL TRANSMIGRATION 700
Y.-C. Huang, Y.-H. Huang, K.-S. Huang, L.-W. Wu, and Y.-C. Lin
National Cheng Kung University, TAIWAN

T24A ANALYSIS OF PRESSURE-DRIVEN AIR BUBBLE ELIMINATION FOR A LARGE-AREA MICROFLUIDIC CELL CULTIVATING DEVICE..... 703
J.H. Kang[1], Y.C. Kim[1,2], and J.-K. Park[1]
[1]Korea Advanced Institute of Science and Technology (KAIST), KOREA and [2]Korea Institute of Machinery & Materials (KIMM), KOREA

T25A BLOOD PLASMA EXTRACTION FROM A MINUTE AMOUNT OF BLOOD USING DIELECTROPHORESIS 706
Y. Nakashima and T. Yasuda
Kyushu Institute of Technology, JAPAN

T26A LONG-TERM CYTOTOXIC DRUG ASSAY VIA SINGLE-CELL MICROFLUIDIC ARRAY 709
L.Y. Wu, D. Di Carlo, and L.P. Lee
University of California, Berkeley, USA

T27A CELL CHIP TO MONITOR THE INFLUENCE OF ELECTRIC FIELD ON THE HUMAN MESENDHYMAL STEM CELLS 712
G.-H. Kwon[1], K.H. Lee[2], E.-J. Lee[1], and S.-H Lee[1]
[1]Korea University, KOREA and [2]Seoul National University, KOREA

T28A CULTIVATION OF DIELECTROPHORETICALLY TRAPPED SINGLE CELLS UNDER OPTIMAL ENVIRONMENTAL CONDITIONS 715
H. Kortmann[1], L.M. Blank[1,2], and A. Schmid[1,2]
[1]Institute for Analytical Sciences (ISAS), GERMANY and [2]University of Dortmund, GERMANY

T29A DEVELOPMENT OF NANOSTRUCTURES FOR CELL ADHESION SURFACE AND BIOLOGICAL ANALYSES OF HUMAN CELLS CULTURED ON THE SURFACE 718
Y. Sakamoto, K. Sato, T. Tsukahara, T. Kitamori, I. Matsumoto, K. Abe, and E. Yoshimura
University of Tokyo, JAPAN

T30A DIELECTROPHORETIC SEPARATION OF HUMAN SPERMATOZOA FROM EPITHELIAL CELLS 721
G. Medoro[1], E. Brighenti[1], A. Fittipaldi[1], G. Tresca[1], S. Gianni[1], G. Perozziello[1], M. Timken[2], M. Buoncristiani[2], and N. Manaresi[1]
[1]Silicon Biosystems S.p.A., ITALY and [2]Department of Justice DNA Lab, USA

T31A ELECTROPHORESIS-ASSISTED ELECTROPORATION FOR EFFICIENT INTRACELLULAR SINGLE-CELL DELIVERY 724
C. Ionescu-Zanetti[1], A. Blatz[1], and M. Khine[2]
[1]Fluxion Biosciences, USA and [2]University of California, Merced, USA

T32A FIBROBLAST AND CANCER CELL BEHAVIORS IN THREE-DIMENSIONAL SILICON MICROSTRUCTURES 727
M. Nikkhah[1], J.S. Strobl[2], and M. Agah[1]
[1]Virginia Polytechnic Institute and State University, USA and [2]Edward Via Virginia College of Osteopathic Medicine, USA

T33A GUIDING OF NEURITE OUTGROWTH BY TOPOGRAPHICAL MICROSTRUCTURES AND MICROSIEVES 730
T. Lehnert[1], M. Wiesle[2], S. Weigel[2], O. Agabi[2,3], M. Gijs[1], and A. Bruinink[2]
[1]Ecole Polytechnique Fédérale de Lausanne (EPFL), SWITZERLAND, [2]EMPA, SWITZERLAND, and [3]Neuronics AG, SWITZERLAND

T34A HYDRODYNAMIC MICROSYSTEMS FOR NON-DILUTED BLOOD FRAGMENTATION 733
E. Sollier[1], H. Rostaing[1], Y. Fouillet[1], J.L. Achard[2], and P. Pouteau[1]
[1]CEA-LETI-Minatec, FRANCE and [2]INPG-LEGI, FRANCE

T35A MICROFLUIDIC CELL ANALYSIS PLATFORM: CELL CULTURE AND ELECTROCHEMICAL LYSIS 736
J.T. Nevill, R. Cooper, M. Dueck, D. Di Carlo, and L.P. Lee
University of California, Berkeley, USA

T36A LOW COST CYTOMETER BASED ON A DVD PICKUP HEAD 739
S. Kostner and M.J. Vellekoop
Vienna University of Technology, AUSTRIA

T37A MICROFABRICATED CONSTRAINTS FOR STUDYING FUNGI FORCE PRODUCTION 742
N. Minc and F. Chang
Columbia University, USA

T38A MICROFLUIDIC TENSILE LOADING SYSTEM FOR MEASUREMENT OF MECHANICAL PROPERTIES OF VORTICELLA 745
M. Nagai[1], M. Kumemura[1], N. Sakaki[1], H. Asai[2], and H. Fujita[1]
[1]University of Tokyo, JAPAN and [2]Waseda University, JAPAN

T39A MICROREACTOR MODEL FOR BIOFILM-ASSOCIATED INFECTION OF MEDICAL IMPLANTS 748
J.-H. Lee, H. Wang, M. Libera, and W.Y. Lee
Stevens Institute of Technology, USA

T40A PARALLEL MICROPIPETTE ASPIRATOR ARRAYS FOR HIGH-THROUGHPUT MECHANICAL CHARACTERIZATION OF BIOLOGICAL CELLS 751
C. Moraes, J. Tong, X.Y. Liu, C.A. Simmons, and Y Sun
University of Toronto, CANADA

T41A PRESSURE-DRIVEN MICROVALVE ARRAY FOR CONTROLLING CHEMICAL RELEASE TO CULTURED CELLS 754
T. Yasuda, T. Yamami, and H. Yano
Kyushu Institute of Technology, JAPAN

T42A RAPID DETECTION OF DRUG EFFLUX FROM SINGLE BACTERIAL CELL ENCLOSED IN FEMTOLITER CHAMBER ARRAY 757
R. Iino[1], K. Nishino[1], M. Nakata[1], E. Nikaido[1], Y. Matsumoto[1], S. Sakakihara[1], S. Takeuchi[2], A. Yamaguchi[1], and H. Noji[1]
[1]Osaka University, JAPAN and [2]University of Tokyo, JAPAN

T43A SKELETAL MYOBLAST PROLIFERATION AND FUSION REGULATED BY MICROELECTRODE ARRAYS 760
Y. Zhao
Ohio State University, USA

T44A STUDYING CELL CHEMOTAXIS USING A MICROFLUIDIC CONCENTRATION-GRADIENT GENERATOR 763
A. Thupil, M.-M. Poo, and L.L. Sohn
University of California, Berkeley, USA

T45A TOWARDS MULTI DIMENSIONAL CHEMICAL MANIPULATION OF LIVING CELLS: CHEMOTAXIS ANALYSIS OF SOCIAL AMOEBAE 766
C.A. Schumann, P.S. Dittrich, J. Franzke, and A. Manz
Institute for Analytical Sciences (ISAS), GERMANY

T46A USING IONIC LIQUID IN PL-SEGMENTED SAMPLING/FLUORESCENT LABELING/CE-LIF ANALYSIS ON A CHIP FOR SINGLE CELL ANALYSIS 769
M. Li, Y. Huang, and J.H. Hahn
Pohang University of Science and Technology, KOREA

Poster Session Microsystems for Life Sciences - Tissue Engineering

T47A A MICRO-WELL PERFUSION BIOREACTOR FOR HUMAN EMBRYONIC STEM CELL CULTURE 772
N. Korin, A. Bransky, U. Dinnar, and S. Levenberg
Technion, ISRAEL

T48A ENCAPSULATION OF LIVING CELLS INTO ALGINATE GEL MICROTUBE BY MICROFABRICATED NOZZLE ARRAY 775
S. Sugiura[1], T. Oda[2], Y. Aoyagi[2], M. Satake[3], N. Ohkohchi[2], and M. Nakajima[2]
[1]National Food Research Institute, JAPAN, [2]National Institute of Advanced Industrial Science and Technology (AIST), JAPAN, [3]University of Tsukuba, JAPAN, and [4]National Cancer Center, JAPAN

T49A MICROFLUIDIC DEVICE BASED BIODEGRADABLE MICROFIBER SCAFFOLD FABRICATION FOR TISSUE ENGINEERING APPLICATION 778
C.M. Hwang[1,2], K. Sun[1,2], and S.H. Lee[1,2]
[1]Korea Artificial Organ Center, KOREA and
[2]Korea University Medical Center, KOREA

Poster Session Microsystems for Life Sciences - Drug Discovery

T50A A MORE EXCELLENT CONSTRUCTION METHOD OF A MULTI FUNCTIONAL ENVELOPE-TYPE NANO DEVICE ON MICRODEVICE FOR GENE THERAPY 781
H. Kuramoto[1], N. Kaji[3], K. Kogure[6], M. Tokeshi[3], Y Shinohara[2], H. Harashima[6], and Y. Baba[3,4,5]
[1]Kanazawa University, JAPAN, [2]University of Tokushima, JAPAN, [3]Nagoya University, JAPAN, [4]National Institute of Advanced Industrial Science and Technology (AIST), JAPAN, [5]Japan Science and Technology Agency (JST), JAPAN, and [6]Hokkaido University, JAPAN

T51A ENZYME ASSEMBLY AND CATALYTIC ACTIVITY IN A REUSABLE BIOMEMS PLATFORM FOR METABOLIC ENGINEERING 784
X. Luo, A.T. Lewandowski, G.F. Payne, R. Ghodssi, W.E. Bentley, and G.W. Rubloff
University of Maryland, USA

Poster Session Microsystems for Life Sciences

T52A HYBRID MICROPATTERNS OF CELLS AND CONDUCTING POLYMERS 787
M. Nishizawa, T. Kamiya, S. Sekine, T. Kawashima, H. Kaji, and T. Abe
Tohoku University, JAPAN

T53A NOVEL HIGH-SENSITIVE DETECTION TECHNIQUE OF MONOSACCHARIDES OF GLYCOPROTEINS USING HETEROGENEOUS BUFFER ON MICROCHIP ELECTROPHORESIS 790
H. Nagata[1], Y. Yoshida[1], T. Ishido[1], Y. Baba[1,2], M. Ishikawa[1], and K. Hirano[1,3]
[1]National Institute of Advanced Industrial Science and Technology (AIST), JAPAN
[2]Nagoya University, JAPAN, and
[3]Japan Science and Technology Agency (JST), JAPAN

T54A PROGRAMMABLE MAGNETIC CELL SORTER FOR DIFFERENT SIZE USING LOCAL MAGNETIC FIELDS GENERATED BY CONTROLLING CURRENT UNDER EXTERNAL FIELD 793
J. Chung, H.-K. Lee, Y.-J. Kim, and E. Yoon
University of Minnesota, USA

T55A TRANSLOCATION OF THE RIBOSOME IN TEMPERATURE-CONTROLLED MICROFLUIDIC CHANNELS 796
B. Wang, J. Fei, R.L. Gonzalez, and Q. Lin
Columbia University, USA

Poster Session Microsystems for Chemistry and Environment – Separation Science

T1B AN INTEGRATED PROTEIN ANALYSIS CHIP: ON-CHIP COMBINATION OF IMMUNOAFFINITY CHROMATOGRAPHY AND ISOELECTRIC FOCUSING 799
K. Shimura and T. Kitamori
University of Tokyo, JAPAN

T2B ASYMMETRIC INERTIAL MIGRATION IN CURVILINEAR LAMINAR FLOWS FOR MICRO-SEPARATION 802
J. Seo, M.H. Lean, and A. Kole
Palo Alto Research Center, USA

T3B CONFINEMENT EFFECT ON THE STRUCTURE OF POLYMER MONOLITHS PHOTOPATTERNED WITHIN MICROCHANNELS 805
M. He, Y. Zeng, and D.J. Harrison
University of Alberta, CANADA

T4B CONTINUOUS SEPARATION OF PROTEINS AND CELLS BY TWO-PHASE ELECTROPHORESIS IN MICROCHANNELS 808
G. Münchow[1], S. Hardt[2], J.P. Kutter[3], and K.S. Drese[1]
[1]Institut für Mikrotechnik Mainz GmbH, GERMANY, [2]Leibniz Universität Hannover, GERMANY, and [3]Technical University of Denmark, DENMARK

T5B CONTINUOUS-FLOW PI-BASED SORTING OF PROTEINS AND PEPTIDES FOR ISOLATION OF BASIC PI RANGE MOLECULES 811
Y.-A. Song, C. Celio, and J. Han
Massachusetts Institute of Technology, USA

T6B DEVELOPMENT OF A NOVEL 5 WAY-CROSS MICROCHIP DEVICE FOR EFFECTIVE ON-LINE SAMPLE PRECONCENTRATIONS TOWARD HIGH PERFORMANCE ELECTROPHORETIC ANALYSIS 814
K. Sueyoshi, F. Kitagawa, and K. Otsuka
Kyoto University, JAPAN

T7B FABRICATION AND CHARACTERIZATION OF MULTILAYER POLYMER MICROFLUIDIC SYSTEMS WITH CROSSOVER CHANNELS 817
H.V. Fuentes, M.G. Larsen, and A.T. Woolley
Brigham Young University, USA

T8B FABRICATION OF POLYMERIC MICROSTRUCTURES TO CAPTURE CHROMOSOMES ON MONOLAYER OF ANTIBODIES 820
P.J. Shah, J.M. Lange, C.H. Clausen, M. Dimaki, L.B. Jensen, M.H. Jakobsen, O. Geschke, and W. Svendsen
Technical University of Denmark, DENMARK

T9B FIELD AMPLIFIED CONTINUOUS SAMPLE INJECTION (FACSI): A NEW METHOD FOR RAPID ANALYTE PRECONCENTRATION IN MICROFLUIDIC APPLICATIONS 823
M.S. Munson, J.G. Shackman, G. Danger, and D. Ross
National Institute of Standards and Technology (NIST), USA

T10B HIGHER EFFICIENCY AND THROUGHPUT IN PARTICLE SEPARATION WITH 3D C-MEMS DIELECTROPHORESIS 826
R. Martinez-Duarte[1], H.A. Rouabah[2], N.G. Green[2], M. Madou[1], and H. Morgan[2]
[1]University of California, Irvine, USA and [2]University of Southampton, UK

T11B INTEGRATING INDEPENDENT SILICA MONOLITH ELECTROOSMOTIC PUMPS FOR REAGENT DELIVERY AND SAMPLE PRECONCENTRATION IN A μ-TAS DEVICE 829
F.-Q. Nie, B. Paull, and M. Macka
Dublin City University, IRELAND

T12B MICROFABRICATED PLATFORM WITH MICROPILLARS FOR ELECTROPHORETIC SEPARATIONS 832
V. Dauriac[1,2], S. Descroix[1], H. Sénéchal[1], Y. Chen[2], M.C. Hennion[1], and G. Peltre[1]
[1]Ecole Supérieure de Physique et de Chimie Industrielles (ESPCI), FRANCE and [2]ENS, FRANCE

T13B MONOLITHICALLY INTEGRATED ELECTROPHORESIS MICROCHIP WITH ELECTROSPRAY IONIZATION MASS SPECTROMETRIC DETECTION 835
S. Tuomikoski[1], T. Sikanen[2], R.A. Ketola[2], R. Kostiainen[2], T. Kotiaho[2], and S. Franssila[1]
[1]Helsinki University of Technology, FINLAND and [2]University of Helsinki, FINLAND

T14B PH GRADIENTS IMMOBILIZED ON-CHIP FOR RAPID ISOELECTRIC FOCUSING 838
G.J. Sommer[1], A.K. Singh[2], and A.V. Hatch[2]
[1]University of Michigan, USA and [2]Sandia National Laboratories, USA

T15B VISCOSITY-TUNABLE POLYMER FOR MICROCHIP ELECTROPHORESIS OF DNA 841
D. Kuroda[1], N. Kaji[1], M. Tokeshi[1], and Y. Baba[1,2,3]
[1]Nagoya University, JAPAN, [2]National Institute of Advanced Industrial Science and Technology (AIST), JAPAN, and [3]Japan Science and Technology Agency (JST), JAPAN

Poster Session Microsystems for Chemistry and Environment – Environmental Analysis

T16B DEVELOPMENT OF INTEGRATED *IN SITU* ANALYZERS (IISA) FOR OCEANOGRAPHY APPLICATIONS 844
T. Fukuba[1], A. Miyaji[2], N. Fukuzawa[1], C. Provin[1], T. Yamamoto[1], L. Glutz[3], T. Okamoto[1], and T. Fujii[1]
[1]University of Tokyo, JAPAN, [2]Tokyo Institute of Technology, JAPAN, and [3]Ecole Polytechnique Federale de Lausanne (EPFL), SWITZERLAND

T17B MICRO PARTICLE SAMPLING ON MICRO-FABRICATED PERFORATED FILTER MEMBRANES 847
Y. Zhao[1], S.K. Chung[1], U.-C. Yi[2], and S.K. Cho[1]
[1]University of Pittsburgh, USA and [2]Core MicroSolutions, Inc., USA

Poster Session Microsystems for Chemistry and Environment – Online Process Control

T18B MICROFLUIDIC REACTION OPTMISATION USING INTELLIGENT FEEDBACK 850
C. Rowlands[1], R. Winkle[2], R. Wootton[1], and A. de Mello[2]
[1]Cambridge University, UK and [2]Imperial College London, UK

Poster Session Microsystems for Chemistry and Environment – On-Chip Synthesis and Production

T19B CONTINUOUS GENERATION OF PROTEIN CONTAINING HYDROGEL BEADS USING MICROFLUIDIC DROPLET-MERGING CHANNEL 853
E. Um[1], D.-S. Lee[2], H.-B. Pyo[2], and J.-K. Park[1]
[1]Korea Advanced Institute of Science and Technology (KAIST), KOREA and [2]Electronics and Telecommunications Research Institute (ETRI), KOREA

T20B ELECTROCHEMICAL MICRO-FLOW-CELL FOR RAPID AND EFFICIENT CONCENTRATION OF [^{18}F]FLUORIDE TO APROTIC SOLVENT FROM [^{18}O] WATER 856
R. Yamahara[1], H. Nakanishi[1], K. Sakamoto[1], H. Saiki[1], E. Ozeki[1], and R. Iwata[2]
[1]Shimadzu Corporation, JAPAN and [2]Tohoku University, JAPAN

T21B *IN-SITU* MICROFLUIDIC SYNTHESIS OF MATERIALS FOR NONLINEAR OPTICAL DEVICES: CONTROL OF ATOMIC VAPOR POPULATIONS IN MICROCHANNEL WAVEGUIDES 859
V. Tandon, S. Ghosh, A.R. Bhagwat, C.K. Renshaw, S. Goh, A.L. Gaeta, and B.J. Kirby
Cornell University, USA

T22B SIZE CONTROL OF NANO-PORES ON MICROCAPSULE FOR CONTROLLED RELEASE 862
D.G. Won[1], J.M. Cha[1], S.H. Yoon[1], E.H. Jeong[1], T. Arakawa[2], S. Shoji[2], K.C. Kim[1], and J.S. Go[1]
[1]Pusan National University, KOREA and [2]Waseda University, JAPAN

Poster Session Microsystems for Chemistry and Environment

T23B MICROFABRICATION OF SELF-OSCILLATING GELS FOR GEOMETRICAL CHEMICAL REACTOR NETWORKS 865
M. Ueda
RIKEN, JAPAN

T24B THE PERFORMANCES OF AN ENZYME-BASED MICROFLUIDIC BIOFUEL CELLS USING VITAMIN K_3-MEDIATED GLUCOSE OXIDATION 868
M. Togo, A. Takamura, T. Asai, H. Kaji, T. Abe, and M. Nishizawa
Tohoku University, JAPAN

Poster Session Microfluidics - Fluid Mechanics & Modeling

T1C RELATIONSHIP BETWEEN FLOWS AND SHAPES OF THE LIQUID-LIQUID INTERFACE IN MICRO COUNTER-CURRENT FLOWS 871
A. Aota[1], A. Hibara[1,2,3], Y. Sugii[4], and T. Kitamori[1,2,3]
[1]Kanagawa Academy of Science and Technology, JAPAN, [2]University of Tokyo, JAPAN, [3]Japan Science and Technology Agency (JST), JAPAN, and [4]Kogakuin University, JAPAN

T2C "DROP-AND-SIP" FLUID HANDLING TECHNIQUE FOR REAGENT-RELEASE CAPILLARY-BASED CAPILLARY-ASSEMBLED MICROCHIP (CAS-CHIP): MULTIPLE CELL LYSATE SAMPLE DELIVERY AND CASPASE-ACTIVITY SENSING..... 874
T.G. Henares[1], F. Mizutani[1], R. Sekizawa[2], and H. Hisamoto[3]
[1]University of Hyogo, JAPAN, [2]Metaboscreen Co. Ltd., JAPAN, and [3]Osaka Prefecture University, JAPAN

T3C ELECTROSTATIC PARTICLE-PARTICLE INTERACTIONS IN OPTOELECTRONIC TWEEZERS..... 877
H. Hwang, J.-J. Kim, Y. Oh, Y.-J. Choi, and J.-K. Park
Korea Advanced Institute of Science and Technology (KAIST), KOREA

T4C FLOW OF ARTIFICIAL MICROCAPSULES IN MICROCHANNELS: A METHOD FOR MEASURING MEMBRANE ELASTIC PROPERTIES 880
E. Leclerc[1], Y. Lefebvre[1], J. Walter[1], F. Edwards-Lévy[2], and D. Barthès-Biesel[1]
[1]CNRS-UMR, FRANCE and [2]CNRS-FRE, FRANCE

T5C MAGNETICALLY MODIFIED PDMS DEVICES FOR ACTIVE MICROFLUIDIC CONTROL 883
Y. Yamanishi, Y.-C. Lin, and F. Arai
Tohoku University, JAPAN

T6C MODELING ELECTROKINETIC TRANSPORT IN NANOCHANNELS: CLASSICAL POISSON-BOLTZMANN APPROACH MAY NOT BE SO BAD AFTER ALL 886
R.H. Nilson and S.K. Griffiths
Sandia National Laboratories, USA

T7C STRUCTURE OF ELECTROOSMOTIC MICROCHANNEL FLOW AFFECTED BY NONUNIFORM WALL ZETA-POTENTIAL 889
Y. Kazoe, N. Miki, and Y. Sato
Keio University, JAPAN

Poster Session Microfluidics - Aliquoting, Mixing & Pumping

T8C A MICROFLUIDIC AUTOSAMPLER WITH TRUE TEFLON VALVES: DESIGN AND APPLICATION TO SUSPENDED MICROCHANNEL RESONATOR MASS SENSORS 892
W.H. Grover, Y.-C. Weng, and S.R. Manalis
Massachusetts Institute of Technology, USA

T9C ACTIVE MICROMIXER BASED ON ION DEPLETION AND ENRICHMENT THROUGH POLYELECTROLYTIC FILTERS 895
H. Chun[1], H.C. Kim[2], and T.D. Chung[2]
[1]University of North Carolina, Chapel Hill, USA and
[2]Seoul National University, KOREA

T10C CENTRIFUGAL MICRODEVICE FOR CONTINUOUS AND SIZE-DEPENDENT SEPARATION OF PARTICLES 898
S. Sunahiro[1], M. Yamada[2], M. Yasuda[1], and M. Seki[1,3]
[1]Osaka Prefecture University, JAPAN,
[2]Tokyo Women's Medical University, JAPAN, and [3]Chiba University, JAPAN

T11C CHAOTIC MIXING IN A HELE-SHAW CELL, WITH APPLICATION TO DNA CHIP HYBRIDIZATION 901
F. Raynal[1], A. Beuf[1], F. Plaza[1], P. Carrière[1], M. Cabrera[1],
J.-P. Cloarec[1], V. Dugas[1,2], E. Fradier[1], and E. Souteyrand[1,2]
[1]Université de Lyon, FRANCE and [2]Rosatech, FRANCE

T12C CHARACTERIZATION OF THREE-DIMENSIONAL SERPENTINE MICROMIXERS: EFFECTS OF ROTATION, LAMINATION AND CHAOTIC ADVECTION 904
J.M. Park and T.H. Kwon
Pohang University of Science and Technology, KOREA

T13C DEVELOPMENT OF PORTABLE POROUS PDMS PUMP FOR MICROFLUIDIC LAB-ON-A-CHIP 907
K.J. Cha[1], D.S. Kim[2], and T.H. Kwon[1]
[1]Pohang University of Science and Technology, KOREA and [2]Chung-Ang University, KOREA

T14C ELECTROKINETIC MIXERS BASED ON STIMULI-RESPONDING SURFACES 910
G. Paumier[1], J. Sudor[1,2], E. Collé[1], B. Marty[1], A. Bancaud[1], T. Camps[1], and A.-M. Gué[1]
[1]University of Toulouse, FRANCE and [2]CEA/Léti, FRANCE

T15C OSCILLATING MOBILE BUBBLES FOR MICROFLUIDIC MIXING ENHANCEMENT 913
S.K. Chung and S.K. Cho
University of Pittsburgh, USA

T16C RAPID MIXING BY AC ELECTROTHERMAL FLOW 916
N. Sasaki[1], T. Kitamori[1,2,3], and H.-B. Kim[1,2,3]
[1]University of Tokyo, JAPAN, [1]Kanagawa Academy of Science and Technology, JAPAN, and [3]Japan Science and Technology Agency (JST), JAPAN

Poster Session Microfluidics - Multi-Phase and Digital Microfluidics

T17C AN ON-CHIP CONTINUOUS-FLOW SEQUENTIAL TILING MICROMIXER 919
Y. Xie, Y. Wang, F. Azizi, L. Chen, and C.H. Mastrangelo
Case Western Reserve University, USA

T18C DIAMAGNETIC LEVITATION BASED DIGITAL MICROFLUIDICS 922
C. Jeandey[1], H. Chetouani[1,2], V. Haguet[1], F. Chatelain[1], and G. Reyne[2]
[1]Commissariat à l'Energie Atomique (CEA), FRANCE and [2]Laboratoire de Génie Electrique de Grenoble, FRANCE

T19C DROP STIRRING FLOW UNDER EWOD AND EHD ACTUATION: A NEW STEP TOWARDS BIOLOGICAL SAMPLE PREPARATION 925
L. Davoust[1], Y. Fouillet[2], and Y. Ishida[2]
[1]CNRS, LEGI, FRANCE and [2]CEA-LETI-Minatec, FRANCE

T20C DROPLET GENERATION IN HEAD-ON DEVICES 928
L. Shui, J.C.T. Eijkel, and A. van den Berg
University of Twente, THE NETHERLANDS

T21C DROPLET-BASED MICROFLUIDICS AT HIGH DISPERSED-PHASE VOLUME FRACTIONS 931
C. Priest[1,2], E. Surenjav[1], S. Herminghaus[1], and R. Seemann[1]
[1]Max-Planck-Institute for Dynamics and Self-Organization, GERMANY and [2]University of South Australia, AUSTRALIA

T22C EXPERIMENTAL ANALYSIS OF LIPOSOME WATER TWO PHASE FLOW IN MICRO CHANNEL FOR LOCALIZING REACTION SYSTEM USING LIPOSOME 934
Y. Ichikawa, T. Kan, H. Onoe, E. Iwase, K. Matsumoto, and I. Shimoyama
University of Tokyo, JAPAN

T23C EXTERNALLY ACTUATED MAGNETIC FLOW REGULATOR FOR DISPOSABLE DRUG INFUSERS 937
M. Duch[1], J. Casals-Terré[2], J.A. Plaza[1], J. Esteve[1], R. Pérez-Castillejos[1], E. Vallès[3], and E. Gómez[3]
[1]Centro Nacional Microelectronica, SPAIN, [2]Technical Univeristy of Catalonia, SPAIN, and [3]University of Barcelona, SPAIN

T24C FAST AND HIGH RESOLUTION TRANSPORT OF MAGNETIC CARRIERS FOR MAGNETICALLY ASSISTED LAB ON A CHIP 940
Q. Ramadan[1], J.E. Widjara[2], T.K. Cheong[1], W.Y. Fung[2], B. Subramanian[1], L. Ebin[1], C.Yu[1], and P. Daniel[2]
[1]*Institute of Microelectroics, SINGAPORE and*
[2]*Nanyang Technological University, SINGAPORE*

T25C FLEXIBLE CAPILLARY-BASED SEQUENTIAL INTRODUCTION FOR MULTIPHASE DROPLET MICROFLUIDIC SYSTEMS 943
W.-B. Du, L. Dong, and Q. Fang
Zhejiang University, CHINA

T26C FLOW VISUALIZATION OF POLYMER/WATER/SURFACTANT DROPLETS IN OIL USING COFLOW AND FLOW-FOCUSING CHANNELS WITH μPIV TECHNIQUE 946
M.R. Duxenneuner[1,2], P. Fischer[2], E.J. Windhab[2], and J.J. Cooper-White[1]
[1]University of Queensland, AUSTRALIA and [2]ETH Zurich, SWITZERLAND

T27C MICROFABRICATED DROPLET GENERATOR FOR SINGLE MOLECULE PCR IN TUNABLE, MONODISPERSE EMULSIONS 949
P. Kumaresan, C.J. Yang, R.G. Blazej, and R.A. Mathies
University of California, Berkeley, USA

T28C OSCILLATORY BUBBLING IN A MICROFLUIDIC T-JUNCTION 952
S.A. Khan[1,2] and K.F. Jensen[3]
[1]National University of Singapore, SINGAPORE, [2]Singapore-MIT Alliance, and [3]Massachusetts Institute of Technology, USA

T29C TEMPERATURE DEPENDENT PHASE BEHAVIOR OF *N*-CYCLOHEXY L-2-PYRROLIDONE/WATER SYSTEM IN A MICROCHANNEL AND PHASE SEPARATION USING VISCOSITY DIFFERENCE 955
Y. Kikutani[1], H. Ikeda[1], M. Harada[2], Y. Ikeda[2], M. Tokeshi[3], and T. Kitamori[4]
[1]Kanagawa Academy of Science and Technology, JAPAN,
[2]Tokyo Institute of Technology, JAPAN, [3]Nagoya University, JAPAN, and
[4]University of Tokyo, JAPAN

Poster Session Microfluidics

T30C A NOVEL $LiNbO_3$ SURFACE ACOUSTIC WAVE PUMP ONTO MICRO CHANNEL WALL 958
T. Sano, M. Sato, H. Kuwano, and S. Nagasawa
Tohoku University, JAPAN

T31C FABRICATION OF ALGINATE FIBER USING MICROFLUIDIC DEVICE AND CELL ENCAPSULATION 961
S.J. Shin, K.H. Lee, J.Y Lee, and S.H Lee
Korea University, KOREA

T32C GAS PARTIAL PRESSURES CONTROLLED BETWEEN MICROCHANNELS 964
S.P. Forry, J.G. Kralj, and L.E. Locascio
National Institute of Standards and Technology (NIST), USA

T33C AQUACORE: A GENERAL-PURPOSE ARCHITECTURE FOR PROGRAMMABLE MICROFLUIDICS 967
A.M. Amin[1], M. Thottethodi[1], T.N. Vijaykumar[1], S. Wereley[1], and S.C. Jacobson[2]
[1]Purdue University, USA and [2]Indiana University, USA

Poster Session Nanotechnology - Nanofluidics

T1D RETENTION, PLATE HEIGHT AND RESOLUTION FOR CHARGED SPECIES TRANSPORT AND SEPARATION IN NANO-SCALE CHANNELS 970
S.K. Griffiths and R.H. Nilson
Sandia National Laboratories, USA

T2D DNA DIAGNOSIS CHIP INTEGRATING PRE-TREATMENT DEVICE AND NANO-GAP-ARRAY FOR INFECTIOUS DISEASE 973
S. Hashioka[1,2], K. Masu[1], and Y. Horiike[2]
[1]Tokyo Institute of Technology, JAPAN and
[2]National Institute for Materials Science, JAPAN

T3D FEMTO-LITER TRANSPORT IN 3D NANOCHANNELS MACHINED BY FEMTOSECOND LASER PULSES 976
S. Lee and A.J. Hunt
University of Michigan, USA

T4D IONIC RECTIFYING EFFECT IN BIPOLAR NANOCHANNELS 979
L.-J. Cheng and L.J. Guo
University of Michigan, USA

T5D NANOFLUIDIC CHANNELS IN SU-8 WITH INTEGRATED FLOOR AND CEILING ELECTRODES 982
K.P. Nichols, J. Eijkel, and H. Gardeniers
University of Twente, THE NETHERLANDS

T6D NANOFLUIDICS IN HOLLOW NANOWIRES 985
N. Sköld, T. Hernán, J.B. Wagner, W. Seifert, L. Samuelson, and J.O. Tegenfeldt
Lund University, SWEDEN

T7D PARTICLE IMAGE ANALYSIS: A NEW TOOL FOR THE EXPLORATION OF NANOFLUIDIC FLOWS 988
C.I. Bouzigues and P. Tabeling
Ecole Supérieure de Physique et de Chimie Industrielles (ESPCI), FRANCE

Poster Session Nanotechnology - Nanoengineering

T8D MODELING THE ELECTROKINETICS OF NANOPARTICLES FOR CONTROLLED ASSEMBLY 991
M.D. Vahey, R.J. Barsotti, R. Wartena, Y.-M. Chiang, F. Stellacci, and J. Voldman
Massachusetts Institute of Technology, USA

Poster Session Nanotechnology - Nanobiotechnology

T9D DNA DAMAGE ANALYSIS IN MICROFLUIDIC CHIPS 994
Y. Tanaka[1], H. Johansson[1], C. Larsson[1], J. Jarvius[1], T. Kitamori[2], and M. Nilsson[1]
[1]Uppsala University, SWEDEN and [2]University of Tokyo, JAPAN

T10D DNA NANOFILTRATION AT HIGH ELECTRIC FIELDS 997
N. Laachi[1], C. Declet[2], C Matson[3], and K.D. Dorfman[1]
[1]University of Minnesota, USA, [2]University of Puerto Rico, Mayagüez, PUERTO RICO, and [3]Mississippi State University, USA

T11D ISOLATION OF SINGLE CHROMOSOMAL DNA MOLECULE UNDER MICROSCOPE USING OPTICALLY-DRIVEN MICRO-BOBBINS 1000
K. Terao[1], H. Oana[2], and M. Washizu[2]
[1]Kyoto University, JAPAN and [2]University of Tokyo, JAPAN

T12D MOLECULAR CROWDING EFFECT ON ENZYMATIC REACTION IN A fL-MICROCHAMBER TO MIMIC CROWDED INTRACELLULAR ENVIRONMENT 1003
H. Murahara[1], N. Kaji[1], M. Tokeshi[1], and Y. Baba[1,2,3]
[1]Nagoya University, JAPAN, [2]National Institute of Advanced Industrial Science and Technology (AIST), JAPAN, and [3]Japan Science and Technology Agency (JST), JAPAN

T13D NANOFLUIDIC PRECONCENTRATION OF BIOMOLECULE ANALYTES USING MICROTUBULES 1006
T. Kim and E. Meyhofer
University of Michigan, USA

T14D REAL-TIME, LABEL-FREE PLASMONIC BIOSENSING USING PERIODIC NANOHOLE ARRAYS 1009
A. Lesuffleur, A. McFarland, H. Im, N.C. Lindquist, C.L. Haynes, and S.-H. Oh
University of Minnesota, USA

T15D STATISTICAL MODELS FOR BIOMOLECULAR SHUTTLES GLIDING IN MICROFABRICATED OPEN CHANNELS 1012
C.-T. Lin[1,2], E. Meyhofer[2], and K. Kurabayashi[2]
[1]National Taiwan University, TAIWAN and [2]University of Michigan, USA

T16D TOWARDS ULTRA-FAST PARALLEL DNA ANALYSIS: SUB-WAVELENGTH METALLIC NANOPORE ARRAYS FOR HIGH-THROUGHPUT SINGLE MOLECULE SPECTROSCOPY 1015
G.A.T. Chansin[1], R. Mulero[2], J. Hong[1], M.J. Kim[2], A.J. deMello[1], and J.B. Edel[1]
[1]Imperial College London, UK and [2]Drexel University, USA

Poster Session Nanotechnology

T17D NMR RELAXATION STUDIES ON THE PROTON TRANSFER DYNAMICS OF WATER CONFINED IN EXTENDED-NANO SPACES ON A CHIP 1018
T. Tsukahara[1,2], A. Hibara[1,3], and T. Kitamori[1,2,3]
[1]University of Tokyo, JAPAN, [2]Japan Science and Technology Agency (JST), JAPAN, and [3]Kanagawa Academy of Science and Technology, JAPAN

Poster Session Materials - Innovative Chip Materials

T1E MOLDED NANOWELL ELECTRODES FOR SITE-SELECTIVE SINGLE LIPOSOME ARRAYS 1021
P. Kim[1], B.K. Lee[2], H.Y. Lee[2], T. Kawai[2], and K.Y. Suh[1]
[1]Seoul National University, KOREA and [2]Osaka University, JAPAN

Poster Session Materials - Surface Modification and Characterization

T2E BIOMOLECULE IMMOBILIZATION ON AU SURFACES WITHIN A SEALED PDMS MICROSYSTEM 1024
A. Tovar and A.P. Lee
University of California, Irvine, USA

T3E NOVEL METHOD FOR CHEMICAL MODIFICATION AND PATTERNING OF THE SU-8 PHOTORESIST 1027
G. Blagoi, S. Keller, A. Boisen, and M.H. Jakobsen
Technical University of Denmark, DENMARK

T4E SELECTIVE SURFACE MODIFICATION FOR MICROARRAY ANALYSIS BY PHOTOCHEMICAL GRAFTING OF BIOCOMPATIBLE PHOSPHOLIPID POLYMER 1031
M. Takai, T. Goda, and K. Ishihara
University of Tokyo, JAPAN

T5E SURFACE DERIVATIZATION OF POLY(DIMETHYLSYLOXANE) BY CHEMISORPTION OF FUNCTIONAL COPOLYMERS 1034
M. Chiari, M. Cretich, F. Damin, G. Di Carlo, and C. Oldani
ICRM - C.N.R., ITALY

T6E SURFACE MODIFICATION OF PDMS BY UV LIGHT IRRADIATION 1037
S. Kano, S. Matsumoto, T. Sato, and N. Ichikawa
National Institute of Advanced Industrial Science and Technology (AIST), JAPAN

T7E THE EFFECT OF THE CONCENTRATION ON OIL DROPLET IN HYDROPHOBIC RECOVERY PDMS MICROCHANNEL 1040
S.K. Chae[1,2], C.H. Lee[2], and J.Y. Kang[1]
[1]Korea Institute of Science Technology, KOREA and [2]Yonsei University, KOREA

Poster Session Materials - Nanostructured Materials

T8E SUPERHYDROPHOBIC SURFACES: FROM IRREVERSIBLE TO REVERSIBLE ELECTROWETTING 1043
N. Verplanck[1], Y. Coffinier[2], K. Madjour[1], J.C. Camart[1], R. Blossey[2], R. Boukherroub[2], and V. Thomy[1]
[1]IEMN, FRANCE and [2]IRI, FRANCE

T9E ULTRAHYDROPHOBIC PROPERTIES OF POROUS SILICON FOR SURFACE BASED BIOANALYSIS 1046
A. Ressine, P. Augustsson, G. Marko-Varga, and T. Laurell
Lund University, SWEDEN

Poster Session Detection Technologies - Optical

T1F A NOVEL MICRO-FLUIDIC WHOLE CELL BIOSENSOR FOR WATER TOXICITY ANALYSIS USING BIOLUMINESCENCE DETECTION 1049
H. Ben-Yoav[1], S. Yorish[1], T. Elad[2], S. Vernick[1], S. Belkin[2], and Y. Shacham-Diamand[1]
[1]Tel-Aviv University, ISRAEL, [2]Hebrew University of Jerusalem, ISRAEL

T2F DEVELOPMENT OF PORTABLE SURFACE PLASMON RESONANCE SENSOR WITH MULTI DETECTION POINTS 1053
H. Nakajima[1], A. Hemmi[2], K. Furui[1], N. Soh[1], K. Nakano[1], Y. Asano[3], K. Uchiyama[3], N. Kaneki[4], and T. Imato[1]
[1]Kyushu University, JAPAN, [2]Mebius Advanced Technology Ltd., JAPAN, [3]Tokyo Metropolitan University, JAPAN, and [4]Muroran Institute of Technology, JAPAN

T3F INTEGRATED MICRORING-WAVEGUIDE RESONATOR BIOSENSOR ARRAYS 1056
I. Brener, J.B. Wright, K. Westlake, D.W. Branch, K.M. Taylor, M.J. Shaw, and G.A. Vawter
Sandia National Laboratories, USA

T4F MICRO-DROPLET INTERFEROMETRY FOR LOCAL PRESSURE MONITORING IN MICROFLUIDIC CHIPS 1059
Y.F. Yu[1], P.H. Yap[2], and A.Q. Liu[1]
[1]Nanyang Technological University, SINGAPORE and [2]DSO National Laboratories, SINGAPORE

T5F MONITORING MIXING DYNAMICS CONFINED WITHIN AQUEOUS MICRODROPLETS WITH 5 µs RESOLUTION 1062
M. Srisa-Art, A.J. deMello, and J.B. Edel
Imperial College London, UK

T6F OPTICAL GRATING COUPLER BIOCHEMICAL SENSORS WITH ON-CHIP REFERENCE 1065
N. Darwish[1], E. Baldrich[2], F.J. Del Campo[2], M. Moreno[1], F.X. Muñoz[2], R. Mas[2], and J. Samitier[1],
[1]Universitat de Barcelona, SPAIN and [2]CNM-CSIC, SPAIN

T7F OPTICAL MULTIPLEXING OF MULTIPLE FLUORESCENCE SENSORS FOR COMPACT LAB-ON-A-CHIP SYSTEMS 1068
K.S. Lee, H.L.T. Lee, and R.J. Ram
Massachusetts Institute of Technology, USA

T8F SURFACE ENHANCED RAMAN SPECTROSCOPY ON CHIP 1071
J. Hubner, T.A. Anhøj, S. Pedersen, D.A. Zauner, A.M. Jorgensen, G. Blagoi, and O. Hansen
Technical University of Denmark, DENMARK

Poster Session Detection Technologies - Electrochemical

T9F DEVELOPMENT OF A CEREBROVASCULAR MIMIC USING ON-CHIP VALVES, HYDRODYNAMIC FOCUSING, AND INTEGRATED MICROELECTRODES 1074
R.S. Martin, M.W. Li, M.K. Hulvey, L.C. Mecker, and M.J. Moehlenbrock
Saint Louis University, USA

T10F NOVEL DUAL-CHANNEL AMPEROMETRIC IN-CHANNEL DETECTION IN MICROCHIP CAPILLARY ELECTROPHORESIS 1077
C. Chen and J.H. Hahn
Pohang University of Science and Technology, KOREA

Poster Session Detection Technologies – Direct Electrical Detection and Impedancemetry

T11F NEW HIGH DENSITY 3D MEAS ASSOCIATED WITH AN INTEGRATED ELECTRONICS ACQUISITION SYSTEM (BioMEA™) 1080
L. Rousseau[1], V. Perrais[1], G. Charvet[2], R. Guillemaud[2], G. Lissorgues[1], P. Meyrand, and B. Yvert[3]
[1]Groupe ESIEE, FRANCE, [2]CEA-LETI, FRANCE, and [3]CNIC UMR, FRANCE

T12F EXAMINING CYTOTOXIC EFFECTS ON SINGLE CELLS USING AN IMPEDANCE SPECTROSCOPIC PLATFORM 1083
D. Malleo[1], J.T. Nevill[2], D. Di Carlo[2], L.P. Lee[2], and H. Morgan[1]
[1]University of Southampton, UK and [2]University of California, Berkeley, USA

T13F HIGH SPEED MULTI-FREQUENCY IMPEDANCE ANALYSIS OF SINGLE BIOLOGICAL PARTICLE USING MAXIMUM LENGTH SEQUENCES 1086
T. Sun[1], D. Holmes[1], S. Gawad[2], N.G. Green[1], and H. Morgan[1]
[1]University of Southampton, UK and
[2]Ecole Polytechnique Fédérale de Lausanne (EPFL), SWITZERLAND

T14F *PHYSARUM POLYCEPHALUM* ON A CHIP 1089
F.D. Revilla, K.-P. Zauner, and H. Morgan
University of Southampton, UK

T15F DETECTION OF BACTERIAL CELLS BASED ON MICRO-CHANNEL GATING 1092
M. Javanmard, A.H. Talasaz, M. Nemat-Gorgani, F. Pease, M. Ronaghi, and R.W. Davis
Stanford University, USA

Poster Session Detection Technologies

T16F MEASUREMENT OF BINDING FORCE BETWEEN A RECEPTOR-COATED PIEZORESISTIVE CANTILEVER AND A LIGAND-COATED SURFACE FOR PROTEIN CONCENTRATION SENSOR 1095
K. Kuwana, K. Matsumoto, and I. Shimoyama
University of Tokyo, JAPAN

T17F SITE-SELECTIVE DEPOSITION OF SILVER NANO PARTICLES FOR SURFACE ENHANCED RAMAN SCATTERING 1098
K. Kurooka[1], K. Deguchi[1], and N. Miki[1,2]
[1]Keio University, JAPAN and
[2]Kanagawa Academy of Science and Technology, JAPAN

T18F SUSPENDED MICROCHANNEL RESONATORS WITH INTEGRATED ELECTRONIC READOUT FOR BIOMOLECULAR AND SINGLE CELL ANALYSIS 1101
R. Chunara[1], T.P. Burg[2], K. Payer[2], P. Dextras[2], and S.R. Manalis[2]
[1]Harvard-MIT Division of Health Sciences and Technology, USA and
[2]Massachusetts Institute of Technology, USA

T19F VESICLE LIBRARIES - TOOLS FOR DIELECTROPHORESIS METROLOGY 1104
S.P. Desai, M.D. Vahey, and J. Voldman
Massachusetts Institute of Technology, USA

Poster Session MEMS & NEMS Technologies - Micro and Nano-Machining

T1G BIOLOGICAL MEASUREMENTS OF C. ELEGANS TOUCH SENSITIVITY WITH MICROFABRICATED FORCE SENSORS 1107
J.C. Doll, N. Harjee, N. Klejwa, R. Kwon, S.M. Coulthard, M.B. Goodman, and B.L. Pruitt
Stanford University, USA

T2G FABRICATION AND PHYSICS OF HOURGLASS-SHAPED MICROAPERTURE BY LASER DRILLING TECHNIQUE 1110
C.-Y. Chen, K.-T. Liu, D.-S. Jong, and A.M. Wo
National Taiwan University, TAIWAN

T3G FABRICATION OF A MICROFLUIDIC BEAD ARRAY SENSOR BY PHOTOPOLIMERIZATION AND LAMINATION 1113
S. Begolo[1], T. Carofiglio[1], G. Mistura[1], and M. Natali[2]
[1]Università di Padova, ITALY and [2]ICIS-CNR, ITALY

T4G FABRICATION OF HIGH ASPECT RATIO STRUCTURES IN MICROFLUIDIC CHANNEL USING OPTOFLUIDIC MASKLESS LITHOGRAPHY 1116
S.E. Chung[1], W. Park[1], H. Park[1], K. Yu[2], N. Park[1], and S. Kwon[1]
[1]Seoul National University, KOREA and
[2]Korea Electrical Engineering and Science Research Institute, KOREA

T5G NOVEL BONDING TECHNIQUE USING HYDROPHILIC SU-8 1119
Y.-T. Chen and D. Lee
National Cheng Kung University, TAIWAN

T6G ULTRA-THIN AND CONDUCTIVE MEMBRANES FOR NANOMECHANICAL TRANSDUCERS 1122
T.J. Kang, M. Cha, J. Shin, Y.H. Kim, and J. Lee
Seoul National University, KOREA

Poster Session MEMS & NEMS Technologies - Microfluidic Components

T7G A HIGH-PERFORMANCE BONDING TECHNIQUE FOR HOMOGENEOUS POLYMERIC MICROFLUIDIC DEVICES 1125
S.H. Ng, R.T. Tjeung, and Z.F. Wang
Singapore Institute of Manufacturing Technology, SINGAPORE

T8G A MICROFLUIDIC DEVICE FOR PRECISE PIPETTING 1128
C.-W. Huang, S.-B. Huang, and G.-B. Lee
National Cheng Kung University, TAIWAN

T9G A MICROFLUIDIC SWITCHBOARD 1131
H.J. Sant, T. Ho, and B. Gale
University of Utah, USA

T10G FABRICATION OF SUSPENDED ELECTROOSMOTIC MICROCHANNELS FROM SACRIFICIAL POLYMER FIBERS 1134
S.M. Berry, T.J. Roussel, S.D. Cambron, R.W. Cohn, and R.S. Keynton
University of Louisville, USA

T11G MICROFLUIDIC DISK SAMPLER FOR BIOLOGICAL DETECTION 1137
W.-C. Tian[1], Y. Zhao[1], S. Thutupalli[2], A. Phukan[2], C. Keimel[1], O. Boomhower[1], M. Burrell[1], and L. Zhu[1]
[1]GE Global Research Center, USA and
[2]John F. Welch Technology Center, INDIA

T12G MONOLITHIC MULTILEVEL MICROFLUIDIC NETWORKS WITH INTEGRATED MEMBRANE: APPLICATIONS FOR ON-CHIP CELL CO-CULTURE AND FABRICATION OF BIOMIMETIC CULTURE CHAMBER 1140
M.C. Liu and Y.C. Tai
California Institute of Technology, USA

T13G NATURE-INSPIRED ACTIVE MICRO-FLUIDIC MIXING USING ARTIFICIAL CILIA 1143
J.M.J. den Toonder[1,2], F. Bos[1,2], D.J. Broer[1,2], M. Gillies[1], J. de Goede[1], T. Mol[1], M. Reijme[1], W. Talen[1], H. Wilderbeek[1], V. Khatavkar[2], and P. Anderson[2]
[1]Philips Research Laboratories, THE NETHERLANDS and [2]Eindhoven University of Technology, THE NETHERLANDS

T14G SOFT MICROFLOW SENSORS 1146
R. Attia[1], D. Pregibon[2], P. Doyle[2], J.L. Viovy[1], and D. Bartolo[3]
[1]Institut Curie, FRANCE, [2]Massachusetts Institute of Technology, USA, and [3]ESPC, FRANCE

T15G STARTUBE: A NOVEL TUBE DESIGN FOR BUBBLE TOLERANT INTERCONNECTION IN FLUIDIC SYSTEMS 1149
T. Metz, W. Streule, R. Zengerle, and P. Koltay
University of Freiburg, GERMANY

T16G STICK AND FLOW: FAST SIMPLE PROTOTYPING METHOD FOR PERFORMANCE MICROFLUIDIC DEVICE 1152
D. Bartolo, G. Degré, P. Nghe, and and V. Studer
Ecole Supérieure de Physique et de Chimie Industrielles, FRANCE

Poster Session MEMS & NEMS Technologies – Hybrid Devices, Packaging, Components Interfacing

T17G ACTIVE POLYMERIC MICRONEEDLE ARRAY DRIVEN BY THERMOPNEUMATIC ACTUATOR FOR MICROFLUIDIC INTERFACE 1155
J.-Y. An, S.-S. Yun, I.-H. Hwang, S.-K. Yoo, M.-G. Kim, S. Yang, and J.-H. Lee
Gwangju Institute of Science and Technology, KOREA

T18G FABRICATION OF 3D MICROCHANNELS ON CYLINDRICAL SURFACES BY SINGLE MOLD PROCESS 1158
S. Matsumoto and N. Ichikawa
National Institute of Advanced Industrial Science and Technology (AIST), JAPAN

T19G STACKED STRUCTURE OF PMMA MICROCHANNELS FOR DNA SEPARATION FABRICATED BY DEEP X-RAY LITHOGRAPHY AND FUSION BONDING 1161
Y. Utsumi[1], T. Ikeda[2], M. Minamitani[2], and K. Suwa[2]
[1]University of Hyogo, JAPAN and [2]Fujipream Ltd., JAPAN

Poster Session MEMS & NEMS Technologies - Integration Strategies

T20G ON-CHIP ANTIOXIDANT CAPACITY SCREENING USING INTEGRATED LOW-COST ORGANIC PHOTODIODES 1164
X. Wang[1], M. Amatatongchai[1,2], D. Nacapricha[3], O. Hofmann[1], J.C. deMello[1], A.J. deMello[1], and D.D.C. Bradley[1]
[1]Imperial College London, UK, [2]Ubonrajathanee University, THAILAND, and [3]Mahidol University, THAILAND

Poster Session MEMS & NEMS Technologies

T21G AN INTEGRATED CALORIMETRIC BIOSENSOR AND ITS CHARCTERIZATION 1167
S.-I. Yoon[1], M.-H. Lim[2], J.-S. Shin[2], and Y.-J. Kim[1]
[1]Yonsei University, KOREA and [2]Yonsei University College of Medicine, KOREA

Concurrent Session 2A3 - Cell Characterization

INTEGRATING WHOLE TRANSCRIPTOME ASSAYS ON A LAB-ON-A-CHIP: A KEY APPROACH TOWARDS SINGLE CELL GENE PROFILING 1170
N. Bontoux[1,2], L. Dauphinot[1], T. Vitalis[1], V. Studer[1], Y Chen[2], J. Rossier[1], and M.-C. Potier[1]
[1]Ecole Supérieure de Physique et de Chimie Industrielles (ESPCI), FRANCE and [2]CNRS, FRANCE

CELL CHARACTERIZATION USING PROTEIN-FUNCTIONALIZED PORES 1173
A. Carbonaro[1], L. Godley[2], and L.L. Sohn[1]
[1]University of California, Berkeley, USA and [2]University of Chicago, USA

MULTI-CELL SORTING ON MICRO FLUIDIC CHIPS USING OPTICAL GRADIENT FORCE 1176
H. Nagata[1], Y. Yoshida[1], T. Ishido[1], H. Nagai[1], Y. Tanaka[1], S. Wakida[1], Y. Baba[1,2], M. Ishikawa[1], and K. Hirano[1,3]
[1]National Institute of Advanced Industrial Science and Technology (AIST), JAPAN, [2]Nagoya University, JAPAN, and [3]Japan Science and Technology Agency (JST), JAPAN

Concurrent Session 2B3 - Detection 2

PARTICLE-SHADOW TRACKING – COMBINING MAGNETIC PARTICLE MANIPULATION WITH *IN-SITU* OPTICAL DETECTION IN A CMOS MICROSYSTEM 1179
U. Lehmann, M. Sergio, S. Pietrocola, C. Niclass, E. Charbon, and M.A.M. Gijs
Ecole Polytechnique Fédérale de Lausanne (EPFL), SWITZERLAND

ELECTROKINETIC SERS SIGNAL AMPLIFICATION FOR LABEL-FREE BIOMOLECULAR DETECTION 1182
H. Cho, Y. Long, B. Lee, and L.P. Lee
University of California, Berkeley, USA

INORGANIC AND ORGANIC ANALYSIS BY A MICRO MASS SPECTROMETER 1185
E. Wapelhorst, J.-P. Hauschild, and J. Müller
Hamburg University of Technology, GERMANY

Wednesday, 10 October 2007

Plenary V

2-CHAMBER ATOMIC FORCE MICROSCOPE: TOWARDS A STRUCTURE/FUNCTION ANALYSIS OF MEMBRANE PROTEINS 1188
Simon Scheuring
Institute Curie, FRANCE

Concurrent Session 3A1 - Genomics and Proteomics

MICROFLUIDIC SCREENING OF APTAMER LIBRARIES 1192
X. Lou[1], L. Viel[1], J. Qian[1], E.T. Lagally[1], J.B. H-Tok[2], T.M. Tarasow[2], A.J. Heeger[1], and H.T. Soh[1]
[1]University of California, Santa Barbara, USA and [2]Lawrence Livermore National Laboratory, USA

INTEGRATED AFFINITY CAPTURE, PURIFICATION AND CAPILLARY ELECTROPHORESIS MICRODEVICE FOR QUANTITATIVE DOUBLE-STRANDED DNA ANALYSIS 1195
N.M. Toriello, C.N. Liu, N. Thaitrong, and R.A. Mathies
University of California, Berkeley, USA

HIGH-THROUGHPUT PROTEOMIC SAMPLE PRECONCENTRATION IN PDMS MICROFLUIDIC CHIP USING SURFACE-PATTERNED ION-SELECTIVE MEMBRANE 1198
J.H. Lee, Y.-A. Song, S.J. Kim, and J. Han
Massachusetts Institute of Technology, USA

Concurrent Session 3B1 - Nanofluidics

DNA MOVEMENT IN SUB-20 NM NANOSLITS 1201
G.B. Salieb-Beugelaar[1], J. Teapal[1], J. van Nieuwkasteele[1], D. Wijnperlé[1], J.O. Tegenfeldt[2], J.C.T Eijkel[1], and A. van den Berg[1]
[1]University of Twente, THE NETHERLANDS and [2]Lund University, SWEDEN

NOVEL DEVICE FOR ELECTROPHORETIC FOCUSING AND SEPARATION AT A MICROCHANNEL-NANOCHANNEL INTERFACE 1204
T.A. Zangle, A. Mani, and J.G. Santiago
Stanford University, USA

DNA SEPARATION BY SQUARE PATTERNED NANOPILLAR CHIPS 1207
T. Yasui[1], N. Kaji[1], R. Ogawa[2], S. Hashioka[2], M. Tokeshi[1], Y. Horiike[2], and Y. Baba[1,3,4]
[1]Nagoya University, JAPAN, [2]National Institute for Materials Science, JAPAN, [3]National Institute of Advanced Industrial Science and Technology (AIST), JAPAN, and [4]Japan Science and Technology Agency (JST), JAPAN

Concurrent Session 3A2 - Multiphase and Digital Microfluidic 2

MICROFLUIDIC TOOLS FOR INVESTIGATING KINETICS AND THERMODYNAMICS OF CRYSTALLIZATION PROCESSES 1210
P. Laval, J. Leng, M. Joanicot, and J.-B. Salmon
CNRS-Rhodia-Bordeaux 1, FRANCE

PHASE SEPARATION OF SEGMENTED FLOW BY THE PHOTOCATALYTIC WETTABILITY PATTERNING AND TUNING OF MICROCHANNEL SURFACE 1213
G. Takei[1], A. Aota[1], A. Hibara[1,2,3], T. Kitamori[1,2,3], and H.-B. Kim[1,2,3]
[1]University of Tokyo, JAPAN, [2]Kanagawa Academy of Science and Technology, JAPAN, and [3]Japan Science and Technology Agency (JST), JAPAN

SYNCHRONIZATION IN MICROFLUIDIC CIRCUITS 1216
M. Prakash and N. Gershenfeld
Massachusetts Institute of Technology, USA

Concurrent Session 3B2 - Active Bio-Based Devices

AUTOMATED AND INTEGRATED MICRO SYSTEM FOR HIGH RESOLUTION IMAGING AND HIGH-THROUGHPUT SORTING OF *C. ELEGANS* 1219
K. Chung, M. Crane, and H. Lu
Georgia Institute of Technology, USA

EUKARYOTIC FLAGELLA AS MOTILE TOOLS FOR MICROFLUIDIC DEVICES 1222
H. Nakamura[1], K. Kuribayashi[1], H. Onoe[1], and S. Takeuchi[1,2]
[1]University of Tokyo, JAPAN and [2]Japan Science and Technology Agency (JST), JAPAN

ELECTROACTIVE MICROFLUIDIC DEVICES FOR CONTROL OF INSECT CYBORG NEUROMUSCLAR SYSTEMS 1225
A. Chung, D. Kim, L. Chen, R. Akhmechet, B. Cordovez, and D. Erickson
Cornell University, USA

Plenary VI

CONTINUOUS PARTICLE CLASSIFICATION IN MICROFLUIDIC SYSTEMS 1228
Minoru Seki
Chiba University, JAPAN

Poster Session Microsystems for Life Sciences - Genomics & Proteomics

W1A AUTOMATION OF NUCLEIC ACID EXTRACTION BY A CORIOLIS-FORCE ACTUATED DROPLET ROUTER 1231
S. Haeberle[1], S. Pausch[1], R. Burger[1], S. Lutz[1], F. von Stetten[1,2], R. Zengerle[1,2], and J. Ducrée[1]
[1]HSG-IMIT, GERMANY and [2]University of Freiburg, GERMANY

W2A MICROCHIP-BASED SOLID-PHASE EXTRAXTION AND ENZYMATIC DIGESTION ON POROUS POLYMER MONOLITH FOR DIRECT ELECTROSPRAY MASS SPECTROMETRY 1234
Y. Hua, Z. Wang, and D.J. Harrison
University of Alberta, CANADA

W3A FAST AND HIGH EFFICIENT MICROFLUIDIC PCR BY MICROWAVE DIELECTRIC HEATING 1237
P.-A. Auroux, D.R. Reyes, J.J. Shah, and M. Gaitan
National Institute of Standards and Technology, (NIST), USA

W4A MILI-SECONDS ANALYSIS OF GREEN FLUORESCENT PROTEIN GFP IN fL CONTAINER HEATED BY MICRO FABRICATED THERMALDEVICE 1240
H.F. Arata[1], F. Gillot[2], and H. Fujita[1]
[1]University of Tokyo, JAPAN and [2]LIMMS-CNRS/IIS, FRANCE

W5A PROTEOMICS-ON-A-CHIP FOR BIOMARKER DISCOVERY 1243
R.B.M. Schasfoort, D. Kohlheyer, S. Schlautmann, J. Eijkel, and A. van den Berg
University of Twente, THE NETHERLANDS

W6A RNA EXTRACTION ON A CHIP BY COMBINED THERMO-ELECTRIC LYSIS AND ELECTROPHORETIC PURIFICATION 1246
P. Vulto[1], C. Klaunick[1], M. Weidmann[2], P. Zahn[1], G. Dame[1], and G.A. Urban[1]
[1]Ludwigs-Universität Freiburg, GERMANY and [2]University of Göttingen, GERMANY

Poster Session Microsystems for Life Sciences - Clinical Diagnostics

W7A AUTOMATED HEMATOCRIT MEASUREMENT AND PATIENT DATA LABELING BY A COMMERICAL DVD-WRITER WITH A LOW-COST OPTICAL ADD-ON 1249
L. Riegger[1], J. Steigert[1], S. Lutz[1], W. Streule[1], R. Zengerle[1,2], and J. Ducrée[2]
[1]University of Freiburg, GERMANY and [2]HSG-IMIT, GERMANY

W8A DETECTION OF EMERGING ZOONOTIC INFECTION IN MICE BY HIGH SENSITIVE MULTIPLEXED MICROFLUIDIC IMMUNOASSAY SYSTEM 1252
F. Ike[1], A. Kajita[1], H. Aoki[2], H. Kase[2], T. Nagamune[3], S. Morikawa[4], A. Yoshiki[1], Y. Obata[1], and Y. Yamagata[1]
[1]RIKEN, JAPAN, [2]Fuence Co. Ltd., JAPAN, [3]University of Tokyo, JAPAN, and [4]National Institute of Infectious Diseases, JAPAN

W9A HIGH PERFORMANCE PENICILLIN SENSOR USING CHARGE TRANSFER TECHNIQUE 1255
S.-R. Lee[1], K. Sawada[1,2], H. Takao[1,2], and M. Ishida[1,2]
[1]Toyohashi University of Technology, JAPAN and
[2]Japan Science and Technology Agency (JST), JAPAN

W10A MICROCHIP FLOWCYTOMETER USING FLUORESCENT SILICA NANOPARTICLES FOR HIV SCREENING 1258
H. Yun[1], J.K. Min[1], W.G. Lee[1], H. Bang[1], J. Park[2], C. Chung[2], J.K. Chang[2], and D.-C. Han[1]
[1]Seoul National University, KOREA and [2]NanoenTek, Inc., KOREA

W11A MICROFLUIDIC ELISA SYSTEM FOR THE DIAGNOSIS OF HEPATITIS B USING MICROWELLS MADE OF ANODIC ALUMINUM OXIDE 1261
K.S. Yang[1], H.J. Kim[2], J.K. Ahn[2], and D.H. Kim[1]
[1]Korea Advanced Institute of Science and Technology (KAIST), KOREA and
[2]Chungnam National University, KOREA

W12A MULTIPLEXED ANALYSIS USING NANO-BAR CODES 1264
H. Morgan, S. Banu, S.W. Birtwell, G.R. Broder, G.S. Galitonov, D.C. Neylon, R.T. Ranasinghe, J.K. She, N. Zheludev, and P.L. Roach
University of Southampton, UK

W13A NONSPECIFIC ADSORPTION MINIMIZED NANOMECHANICAL IMMUNOASSAY FOR APPLICATION TO ASSAY USING THE REAL SAMPLE 1267
K.S. Hwang[1,2], S.-M. Lee[1], B.H. Cha[1], S.K. Kim[1], J.H. Park[2], and T.S. Kim[1]
[1]Korea Institute of Science and Technology (KIST), KOREA and
[2]Korea University, KOREA

W14A PARALLEL MULTI-REAGENT STREAMS FOR A BIOASSAY ON SINGLE MAGNETIC PARTICLES IN CONTINUOUS FLOW 1270
S. Peyman, A. Iles, and N. Pamme
University of Hull, UK

W15A RELIABLE CONTINUOUS-FLOW PCR FROM POLYMERASE KITS AND ON-CHIP CELL EXTRACTED DNA 1273
H. Becker, R. Klemm, and C Gärtner
microfluidic ChipShop GmbH, GERMANY

Poster Session Microsystems for Life Sciences - Microarrays

W16A 3D MICROFLUIDIC CHIP FOR MEMBRANE PROTEIN ANALYSIS 1276
H. Suzuki[1] and S. Takeuchi[1,2]
[1]University of Tokyo, JAPAN and
[2]Japan Science and Technology Agency (JST), JAPAN

W17A CELLULAR STUDIES VIA DIELECTROPHORESIS-BASED CELLULAR MICROARRAY CHIP 1279
L.C. Hsiung[1], C.L. Chiu[1], C.H. Yang[1], A.M. Wo[1], H. Lee[1], D.S. Jong[1], C.H. Chiu[1], J.Y. Cheng[2], M.C. Ho[3], C.Y. Hsu[1] and M.C. Hsu[1]
[1]National Taiwan University, TAIWAN, [2]Academia Sinica, TAIWAN, and [3]National Taiwan University Hospital, TAIWAN

W18A HIGH-THROUGHPUT MICROFLUIDIC MICROARRAY HYBRIDIZATIONS CARRIED OUT IN SPIRAL CHANNELS ON A COMPACT DISC 1282
H. Chen, P.C.H. Li, H.-Z. Yu, M. Parameswaran, and N. Yoganathan
Simon Fraser University, CANADA

W19A MICRO XEROGRAPHY USING SURFACE ACOUSTIC WAVE ATOMIZER AND ELECTROSTATIC DEPOSITION 1285
J. Ju[1], Y. Yamagata[2], T. Higuchi[1], K. Inoue[3], and H. Ohmori[2]
[1]University of Tokyo, JAPAN, [2]RIKEN, JAPAN, and [3]Fuence Co., Ltd., JAPAN

Poster Session Microsystems for Life Sciences – Point of Care and Hand Held Devices

W20A MICROFLUIDIC STAND-ALONE DEVICE FOR THE CALIBRATION OF BRAIN-IMPLANTABLE BIOSENSOR MICROPROBES 1288
O. Frey[1], F.H. Falke[2], P.D. van der Wal[1], N.F. de Rooij[1], and M. Koudelka-Hep[1]
[1]University of Neuchâtel, SWITZERLAND and
[2]University of Twente, THE NETHERLANDS

W21A NANOSTRUCTURED PHOSPHOLIPID BIOINTERFACE FOR IMMUNOASSAY MICROCHIP INTEGRATED WITH PLASMA SEPARATION MEMBRANE 1291
K. Nishizawa, T. Konno, M. Takai, and K. Ishihara
University of Tokyo, JAPAN

W22A NATURAL CONVECTION DRIVEN HANDHELD PCR SYSTEM USING A DISPOSABLE POLYMER CHIP 1294
K.H. Chung, Y.H. Choi, C.H. Jun, D. Lee, H.B. Pyo, M.Y. Jung, and S.H. Park
Electronics and Telecommunications Research Institute, (ETRI), KOREA

W23A POLYMER-BASED THERAPEUTIC DRUG MONITORING CHIP WITH PERIODIC GOLD NANO-STRUCTURE FOR LOCALIZED SURFACE PLASMON RESONANCE SENSING 1297
Y. Akagi[1], K. Yamamoto[2], T. Yotsuya[3], A. Ishida[4], T. Mori[5], H. Kawata[3], Y. Hirai[3], and M. Seki[3,6]
[1]Sekisui Chemical Co., JAPAN, [2]Sekisui Integrated Research Co., JAPAN, [3]Osaka Prefecture University, JAPAN, [4]Kyoto Prefecture University, JAPAN, [5]Nara Medical University, JAPAN, and [6]Chiba University, JAPAN

W24A RAPID PEN-SIDE DIAGNOSTICS USING IMMUNOELECTROPHORETIC ASSAYS 1300
D.S. Reichmuth, S. Wang, D.J. Throckmorton, W. Einfeld, and A.K. Singh
Sandia National Laboratories, USA

W25A THE STUDY OF OSMOTIC VALVE FOR THE INSULIN THERAPY OF DIABETES 1303
T. Nagakura[1], K. Nukada[2], A. Yamada[2], M. Ikeuchi[3], and K. Ikuta[3]
[1]Osaka Electro-Communication University, JAPAN, [2]Okayama University, JAPAN, and [3]Nagoya University Graduate School of Medicine, JAPAN

Poster Session Microsystems for Life Sciences - Cell Handling & Analysis

W26A A MICROFLUIDIC CHIP FOR VISUALIZATION OF SINGLE MOLECULE INTERACTIONS *IN SITU* 1306
H. Johansson, M. Jarvius, Y. Tanaka, M. Nilsson, J. Jarvius, and U. Landegren
Uppsala University, SWEDEN

W27A A MICROFLUIDIC CHIP STUDYING THE EFFECT OF SOLUBLE FACTORS ASSOCIATED WITH THE MODES OF MEDIUM SUPPLY AND PERFORMING CELL ASSAYS 1309
Z.T.F. Yu, K. Kamei, C.J. Shu, C.G. Radu, O.N. Witte, and H.-R. Tseng
University of California, Los Angeles, USA

W28A A NOVEL MULTIFUNCTIONAL PROCESSOR FOR BIO-PARTICLES 1312
C.-T. Kuo and C.-H. Liu
National Tsing Hua University, TAIWAN

W29A MONITORING PROTEIN PHOSPHORYLATION DURING IMMUNE SIGNALING USING INTEGRATED MICROFLUIDIC FLOW CYTOMETRY 1315
N. Srivastava, J.S. Brennan, S.S. Branda, A.K. Singh, and A.E. Herr
Sandia National Laboratories, USA

W30A ARRANGEMENT OF CELLS WITHIN SEMI-CLOSED SPACE WITH MICROELECTRODE-BASED TECHNIQUE 1318
M. Hashimoto, S. Sekine, T. Kawashima, H. Kaji, and M. Nishizawa
Tohoku University, JAPAN

W31A CELL CULTURE MICROCHAMBER ARRAY WITH INDEPENDENT PERFUSION CHANNEL FOR PARALLEL DRUG TOXICITY ASSAY 1321
S. Sugiura, J. Edahiro, K. Kikuchi, K. Sumaru, and T. Kanamori
National Institute of Advanced Industrial Science and Technology (AIST), JAPAN

W32A CHEMOTAXIS-DRIVEN SEPARATION OF MOTILE SPERM BY LONGITUDINAL CHEMICAL CONCENTRATION GRADIENT IN MICROCHIP 1324
Y.-J. Ko, B.-C. Lee, J.-H. Maeng, S.-Y. Hwang, and Y. Ahn
Hanyang University, KOREA

W33A DIELECTROPHORETIC CELL MANIPULATION ENABLED BY PARASITIC TRAP CANCELLATION 1327
M. Urdaneta and E. Smela
University of Maryland, USA

W34A ON-CHIP EVALUATION EFFECT OF DRUG-INDUCED APOPTOSIS ON ELECTROPHORESIS MOBILITY OF HEK CELLS 1330
T. Akagi and T. Ichiki
University of Tokyo, JAPAN

W35A ENDOTHELIAL CELL PHENOTYPE ON GELATIN MICROPATTERNS COMPARED TO THAT IN MICROCHANNELS 1333
P.P.M.F.A. Mulder[1], S. Koster[1], G. Molema[2], and E. Verpoorte[1]
[1]*University of Groningen, THE NETHERLANDS and*
[2]*University Medical Center Groningen, THE NETHERLANDS*

W36A FABRICATION OF A DISPOSABLE ELECTROSONIC MICROARRAY IN THIOLENE AND PERFORMANCE CHARACTERIZATION FOR BIOMOLECULE DELIVERY 1336
J.M. Meacham[1], V. Zarnitsyn[2], M. Varady[2], J. Atencia[1], L. Locascio[1], F.L. Degertekin[2], and A.G. Fedorov[2]
[1]*National Institute of Standards and Technology (NIST), USA and*
[2]*Georgia Institute of Technology, USA*

W37A HIGH THROUGHPUT AND HIGH EFFICIENCY ELECTROPORATION CHIP WITH POLYELECTROLYTE CURRENT PATHS 1339
J.H. Kim[1,2], Z.H. Kim[2], T.S. Kim[1], and S.K. Kim[1]
[1]*Korea Institute of Science and Technology (KIST), KOREA and*
[2]*Korea University, KOREA*

W38A MECHANICAL CELL LYSIS USING PDMS MEMBRANE DEFLECTION IN A MICROFLUIDIC DEVICE 1342
Y.C. Kim[1,2], W. Choi[1], Y.W. Hwang[2], S.-J. Park[2], and J.-K. Park[1]
[1]*Korea Advanced Institute of Science and Technology (KAIST), KOREA and*
[2]*Korea Institute of Machinery & Materials (KIMM), KOREA*

W39A STIMULATION OF MAMMAUAN CELLS USING MICRO-BEAD IMPACT IN MICRO-BIOREACTOR 1345
T.-J. Kim, S.-J. Kim, and H.-I. Jung
Yonsei University, KOREA

W40A MULTIPHASE FLOW MANIPULATION FOR CONTINUOUS REFRACTIVE INDEX ANALYSIS OF SINGLE LIVING CELL 1348
L.K. Chin[1], A.Q. Liu[1], C.S. Lim[1], and P.H. Yap[2]
[1]Nanyang Technological University, SINGAPORE and
[2]DSO National Laboratories, SINGAPORE

W41A NANOFILTER FOR EFFICIENT BACTERIA TRAPPING AND DETECTION 1351
L. Zhu[1,2], X.L. Peh[1], C.Y. Teo[1], H.M. Ji[1], H.H. Feng[1], and W.-T. Liu[1]
[1]Institute of Microelectronics, SINGAPORE and
[2]National Institutes of Health, USA

W42A NON-CONTACT MEASUREMENT OF YOUNG'S MODULUS OF SINGLE LIVING CELL USING HYDROSTATIC PRESSURE IN A MICROCHAMBER 1354
L.A.G. Lin[1], Y.F. Yu[1], A.Q. Liu[1], and P.H. Yap[2]
[1]Nanyang Technological University, SINGAPORE and
[2]DSO National Laboratories, SINGAPORE

W43A OBSERVATIONS OF SPERM CELL BEHAVIOR IN A MICROFLUIDIC IN-VITRO FERTILIZATION DEVICE 1357
M.D.C. Lopez-Garcia[1], R.L. Monson[1], K. Haubert[2], and D.J. Beebe[1]
[1]University of Wisconsin, USA and [2]Vitae LLC, USA

W44A PARALLEL BIOPARTICLE SORTING WITH TGP SOLUTION IN 3-DIMENTIONAL MICROFLOW SYSTEM 1360
H. Sugino[1], Y. Nara[2], Y. Shirasaki[2], T. Arakawa[2], S. Shoji[2], and T. Funatsu[1]
[1]University of Tokyo, JAPAN and [2]Waseda University, JAPAN

W45A RAPID AND SIMPLE UV-DIRECTED MICROPATTERNING OF PROTEINS 1363
M. Théry[1], A. Azioune[2], J. Fink[2], R. Dupont[1], M. Piel[2], and F. Chatelain[1]
[1]Commissariat à l'Energie Atomique (CEA), FRANCE and
[2]Institut Curie, FRANCE

W46A CA^{2+} SIGNAL IS CONTROLLED BY RECEPTOR-MEDIATED ACTIVATION OF G-PROTEINS PATHWAY IN *TETRAHYMENA PYRIFORMIS* DURING CHEMOTAXES 1366
S.-W. Nam and S. Park
Ewha Woman's University, KOREA

W47A SIMULTANEOUS MANIPULATION AND DETECTION OF SINGLE CELLS USING MAGNETIC SENSORS 1369
C. Liu[1,2], W. Laureyn[1], and L. Lagae[1]
[1]Interuniversity Microelectronics Center (IMEC), BELGIUM and [2]Katholieke Universiteit Leuven, BELGIUM

W48A STUDY OF ATP-RELEASE FROM ACOUSTICALLY LEVITATED ERYTHROCYTES..... 1372
M. Evander, K. Mileros, C Högberg, D. Erlinge, M. Almqvist, T. Laurell, and J. Nilsson
Lund University, SWEDEN

W49A VERY HIGH YIELD ELECTRO CELL-FUSION BASED ON FIELD CONSTRICTION AT A MICROORIFICE..... 1375
K. Tsuda[1], M. Gel[1], H. Oana[1,2], B. Techaumnat[3], H. Kotera[2,4], and M. Washizu[1,2]
[1]University of Tokyo, JAPAN, [2]Japan Science and Technology Agency (JST), JAPAN, [3]Chulalongkorn University, THAILAND, and [4]Kyoto University, JAPAN

Poster Session Microsystems for Life Sciences - Tissue Engineering

W50A NANOPOROUS TITANIA FILMS FOR THE PROMOTION OF STEM CELL PROLIFERATION 1378
A. Iles[1], H. Hosseinkhani[2], M. Hosseinkhani[3], and H. Lindstrom[2]
[1]University of Hull, UK, [2]National Institute of Materials Science, JAPAN, and [3]Kyoto University Hospital, JAPAN

W51A THE UTILITY OF INTERSTITIAL, MICROFLUIDIC PERFUSION IN EXTENDED CULTURING OF THICK ORGANOTYPIC BRAIN SLICES..... 1381
J. Vukasinovic, K. Rambani, S.M. Potter, and A. Glezer
Georgia Institute of Technology, USA

Poster Session Microsystems for Life Sciences - Drug Discovery

W52A DEVELOPMENT OF A MICRO TOTAL BIOASSAY SYSTEM FOR ANTICANCER AGENT; ASSAY OF INTESTINAL ABSORPTION, HEPATIC METABOLISM, AND ANTICANCER ACTIVITY..... 1384
K. Sato, Y. Asano, and E. Yoshimura
University of Tokyo, JAPAN

W53A SYN&SORT – A CHIP BASED TOOL FOR COMBINATORIAL SYNTHESIS AND BIOLOGICAL SCREENING 1387
A. Schober[1], M. Gebinoga[1], A. Albrecht[1], T. Lübeck[1], T. Henkel[2], P. Hoffmann[2], U. Klenz[2], G. Schlingloff[4], Th. Frank[3], and A. Groß[1]
[1]Technische Universität Ilmenau, GERMANY, [2]Institute of Physical High Technology, GERMANY, [3]Little Things Factory, GERMANY, and [4]Nanomics Technologies GmbH, GERMANY

Poster Session Microsystems for Life Sciences

W54A A MICROFLUIDIC BIOSENSOR INTEGRATING SELF-ASSEMBLED PEPTIDE MONOLAYERS FOR THE DETECTION OF BOTULINUM NEUROTOXIN 1390
M.L. Frisk, W.H. Tepp, E.A. Johnson, and D.J. Beebe
University of Wisconsin, Madison, USA

W55A A MICROFLUIDIC DISPENSING SYSTEM FOR SCREENING PROTEIN CRYSTALLIZATION CONDITIONS 1393
X. Zhou and B. Zheng
Chinese University of Hong Kong, HONG KONG

W56A MICROFLUIDIC INTERFACES FOR LOCALIZED RELEASE OF NO INTO DEVELOPING RAT DORSAL ROOT GANGLIA 1396
G. Lavella, P. Padmanabhan, B. Wu, M.E. Meyerhoff, and M.M. Maharbiz
University of Michigan, USA

W57A SINGLE MOLECULE ANALYSIS OF CONDENSED DNA: MEASUREMENT OF CONDENSATION SPEED AND SINGLE MOLECULE SIZE USING LASER TRAPPING 1399
T. Ishido[1], H. Nagata[1], Y. Tanaka[1], M. Ishikawa[1], and K. Hirano[1,2]
[1]National Institute of Advanced Industrial Science and Technology (AIST), JAPAN and [2]Japan Science and Technology Agency (JST), JAPAN

Poster Session Microsystems for Chemistry and Environment – Separation Science

W1B 800 FOLD SIGNAL ENHANCEMENTS BY TRANSIENT ISOTACHOPHORESIS FOR IMMUNOASSAY OF HSA ON STANDARD CROSS CHANNEL MICROCHIPS 1402
M.R. Mohamadi[1,4], L. Mahmoudian[1], N. Kaji[1], M. Tokeshi[1], and Y. Baba[1,2,3]
[1]Nagoya University, JAPAN, [2]National Institute of Advanced Industrial Science and Technology (AIST), JAPAN, [3]Japan Science and Technology Agency (JST), JAPAN, and [4]Nagoya University Venture Business Laboratory, JAPAN

W2B APPILICATION OF CYCLOOLEFIN POLYMER CHIP DIRECTLY INTEGRATED WITH AN ELECTRONANOSPRAY TIP TO ELECTROPHORETIC SEPARATION AND MASS SPECTROMETRIC DETECTION 1405
F. Kitagawa[1], T. Suzuki[2], H. Shinohara[2], J. Mizuno[2], S. Shoji[2], and K. Otsuka[1]
[1]Kyoto University, JAPAN and [2]Waseda University, JAPAN

W3B DESIGN AND OPTIMIZATION OF FRACTION COLLECTOR FOR CAPILLARY ELECTROPHORESIS 1408
D.R. Zalewski, S. Schlautmann, R.B.M. Schasfoort, and H.J.G.E Gardeniers
University of Twente, THE NETHERLANDS

W4B ELECTROKINETIC BIO-MOLECULES PRECONCENTRATION AND SEPARATION BY MWCNTS FILTER IN NANOFLUIDIC CHANNEL 1411
R.-G. Wu, Y.-S. Wu, C.-S. Yang, and F.G. Tseng
National Tsing Hua University, TAIWAN

W5B FAST SHEAR-DRIVEN OLIGONUCLEOTIDE SEPARATION IN 1D-NANOCHANNELS 1414
F. Detobel[1], V. Fekete[1], W. De Malsche[2], H. Gardeniers[2], and G. Desmet[1]
[1]Vrije Universiteit, BELGIUM and
[2]University of Twente, THE NETHERLANDS

W6B IMPROVED ULTRASONIC MICRO ARRAY SEPARATION USING FAR FIELD ULTRASONIC EXCITATION 1417
A. Nilsson, T. Jansson, and T. Laurell
Lund University, SWEDEN

W7B INTEGRATED POSITIVE AND NEGATIVE CELL SEPARATION ON AN ON-CHIP MAGNETIC CELL SORTING SYSTEM 1420
M. Estes, J. Do, and C. Ahn
University of Cincinnati, USA

W8B ISOELECTRIC FOCUSING IN A MICRO CHAMBER ARRAY 1423
R. Ishibashi, T. Kitamori, and K. Shimura
University of Tokyo, JAPAN

W9B MICROFLUIDIC ZONE REFINING FOR SAMPLE CONCENTRATION 1426
R.P. Welle and B.S. Hardy
Aerospace Corporation, USA

W10B MODE TRANSITION & ITS MECHANISM OF RNA/DNA TRAP BY ELECTRIC AND HYDRAULIC FORCE FIELD IN MICROFLUIDIC TAPER SHAPE CHANNEL 1429
Y. Takamura[1], W. Nagasaka[1], K. Ueno[1], Y. Tomizawa[1], and E. Tamiya[1,2]
[1]Japan Advance Institute Science Technology (JAIST), JAPAN and
[2]Osaka University, JAPAN

W11B NOVEL ONLINE CONCENTRATION OF DNA TO SHORTEN MICROCHANNEL LENGTH USING HETEROGENEOUS BUFFER COMBINATIONS ON MICROCHIP ELECTROPHORESIS 1432
H. Nagata[1], Y. Yoshida[1], T. Ishido[1], M. Ishikawa[1], and K. Hirano[1,2]
[1]National Institute of Advanced Industrial Science and Technology (AIST), JAPAN and [2]Japan Science and Technology Agency (JST), JAPAN

W12B ON-CHIP LIQUID CHROMATOGRAPHY - ATMOSPHERIC PRESSURE IONIZATION - MASS SPECTROMETRY 1435
V. Saarela[1], M. Haapala[2], J. Pól[2], N. Kalkkinen[2], M. Hukka[2], K. Kolari[3], R.A. Ketola[2], R. Kostiainen[2], T. Kotiaho[2], and S. Franssila[1]
[1]Helsinki University of Technology, FINLAND,
[2]University of Helsinki, FINLAND, and
[3]VTT Technical Research Center, FINLAND

W13B PARTICLE SEPARATION VIA ADJUSTABLE VELOCITY PROFILE GENERATED BY EOF AND PRESSURE DRIVEN FLOW 1438
Y.F. Yu[1], P.H. Yap[2], and A.Q. Liu[1]
[1]Nanyang Technological University, SINGAPORE and
[2]DSO National Laboratories, SINGAPORE

W14B A MINIATURE CENTRIFUGAL CHROMATOGRAPHIC DEVICE FOR THE PRE-CONCENTRATION AND DETERMINATION OF LEAD IN AQUEOUS SAMPLES 1441
J.P. Lafleur and E.D. Salin
McGill University, CANADA

W15B SPECTRAL SEPARATIONS OF CHEMICAL SIGNALS WITH FOURIER MICROFLUIDICS 1444
Y. Xie, Y. Wang, L. Chen, and C.H. Mastrangelo
Case Western Reserve University, USA

W16B TWO-DIMENSIONAL PROTEIN SEPARATION IN A PLASTIC DEVICE WITH A MICROVALVE ARRAY 1447
Z.H. Fan, C. Das, and J. Zhang
University of Florida, USA

Poster Session Microsystems for Chemistry and Environment – Environmental Analysis

W17B ULTRA-TRACE GAS ANALYSIS SYSTEM OF AMMONIA IN CLEANROOM AIR 1450
K. Uchiyama[1], M. Sasaki[1], Y. Kihira[1], K. Kuriyama[1], Y. Kikutani[2], K. Mawatari[2], and T. Kitamori[3]
[1]Institute of Microchemical Technology, JAPAN, [2]Kanagawa Academy of Science and Technology, JAPAN, and [3]University of Tokyo, JAPAN

Poster Session Microsystems for Chemistry and Environment – On-Chip Synthesis and Production

W18B BIOPOLYMER COATED PARTICLE FORMATION UTILISING A MICROFLUIDIC DEVICE AND MULTIPHASE FLOW 1453
E. Rondeau and J. Cooper-White
University of Queensland, AUSTRALIA

W19B FABRICATION OF NOVEL INORGANIC POLYMER DERIVED MICROCHANNELS FOR MICROREACTOR APPLICATIONS 1456
T.-H. Yoon, L.-Y. Hong, S.-H. Park, K.-I. Min, S.-J. Park, and D.-P. Kim
Chungnam National University, KOREA

W20B PRODUCTION OF DOUBLE EMULSIONS ON ONE CHIP BY MODIFYING SURFACE PROPERTIES 1459
S. Tamaki, S. Wada, H. Tsuchiya, M.I. Al-Haq, and T. Torii
University of Tokyo, JAPAN

W21B PHOTOSYNTHESIS OF HIGH-VALUE ADDED COMPOUNDS IN A MICROREACTION SYSTEM 1462
Y. Matsushita[1], A. Murata[2], T. Murata[3], H. Tanibata[4], T. Suzuki[1], and T. Ichimura[1]
[1]Tokyo Institute of Technology, JAPAN, [2]Dainippon Screen MFG., Co., Ltd., JAPAN, [3]Mitsui Zosen Plant Engineering, Inc., JAPAN, and [4]Mitsui Engineering & Shipbuilding Co. Ltd., JAPAN

W22B SPATIALLY RESOLVED MICROFLUIDIC SOLVENT ETCHING OF BICOMPONENT EXTRUSION NANOFIBERS 1465
S. Lok, J.P. Hinestroza, and B.J. Kirby
Cornell University, USA

Poster Session Microsystems for Chemistry and Environment

W23B FUEL AND MEDIA FLEXIBLE AIR-BREATHING LAMINAR FLOW FUEL CELLS 1468
R.S. Jayashree, W.-P. Zhou, M. Mitchell, S.K. Yoon, and P.J.A. Kenis,
University of Illinois, USA

W24B MICROREACTORS FOR REACTION KINETICS MONITORING ON A CHIP - FROM SINGLE LINE TO MULTICHANNEL QUENCH-FLOW DEVICE 1471
W.P. Bula, D.N. Reinhoudt, W. Verboom, and H.J.G.E Gardeniers
University of Twente, THE NETHERLANDS

Poster Session Microfluidics - Fluid Mechanics & Modeling

W1C A NOVEL COAXIAL SHEATH FLOW DEVICE FOR SAMPLE FOCUSING 1474
G. Hairer, G.S. Pärr, P. Svasek, A. Jachimowicz, and M.J. Vellekoop
Vienna University of Technology, AUSTRIA

W2C ELECTROMECHANICAL ANALYSIS OF AC ELECTROWETTING OF A DROPLET 1477
J.S. Hong, S.H. Ko, K.H. Kang, and I.S. Kang
Pohang University of Science and Technology, SOUTH KOREA

W3C MICROFLUIDIC CHARACTERIZATION OF SURFACTANT SOLUTIONS 1480
G. Degré and P. Nghe
Ecole Supérieure de Physique et de Chimie Industrielles (ESPCI), FRANCE

W4C MOTION OF PARTICLES UNDER NON-UNIFORM AC FIELDS IN A MICROCHANNEL: ANALYSIS OF THE CONTRIBUTION OF AC ELECTROKINETIC FORCES 1483
J.J. Capurro, J. Oh, and H. Noh
Drexel University, USA

W5C SHEATHLESS PARTICLE FOCUSING BASED ON HYDROPHORESIS AND ITS APPLICATION TO BLOOD PLASMA SEPARATION 1486
S. Choi and J.-K. Park
Korea Advanced Institute of Science and Technology (KAIST), KOREA

W6C THE MECHANICS OF DEFORMABLE FLUIDIC DIODES: IMPLICATIONS FOR DESIGN AND PERFORMANCE 1489
D. Leslie[1], C.J. Easley[2], J.P. Landers[1], M. Utz[1], and M.R. Begley[1]
[1]University of Virginia, USA and [2]Vanderbilt University, USA

W7C VALVES FOR AUTONOMOUS MICROFLUIDIC CAPILLARY SYSTEMS 1492
M. Zimmermann[1,2], P. Hunziker[1], and E. Delamarche[2]
[1]University Hospital Basel, SWITZERLAND and
[2]IBM Research GmbH, SWITZERLAND

W8C WORM-LIKE SURFACTANT SOLUTIONS, FLOW INDUCED GELATION AND EFFECTIVE SLIP IN MICROCHANNELS 1495
L.E. Rodd and J.J. Cooper-White
University of Queensland, AUSTRALIA

Poster Session Microfluidics - Aliquoting, Mixing & Pumping

W9C A PIEZOELECTRIC ACTIVE MICROCHANNEL FOR FLUID TRANSPORT IN μTAS 1498
T. Suzuki[1], I. Kanno[1], J. Ogawa[1], K. Kanda[2], and H. Kotera[1]
[1]Kyoto University, JAPAN and [2]Advanced Software Technology and Mechatronics Research Institute, JAPAN

W10C DISPOSABLE DIFFUSER-VALVE MICROPUMP EXTERNALLY ACTUATED BY PRECISION LINEAR MOTOR 1501
W. Rhie and T. Higuchi
University of Tokyo, JAPAN

W11C ELECTROCHEMICAL MICROFLUIDIC PUMPS BASED ON SUPER ABSORBING POLYMERS 1504
J. Nestler[1], A. Morschhauser[1], K. Hiller[1], S. Bigot[2], J. Auerswald[3], J. Gavillet[4], T. Otto[5], and T. Gessner[1,5]
[1]Chemnitz University of Technology, GERMANY, [2]Cardiff University, UK, [3]CSEM Alpnach, SWITZERLAND, [4]CEA Liten, FRANCE, and [5]Fraunhofer IZM, GERMANY

W12C MICRO OPTICAL STIRRER FOR MIXING IN MICROCHANNEL FLOW 1507
T. Moriya and Y. Sato
Keio University, JAPAN

W13C PATTERNING OF BACTERIAL CELLS USING ELECTRO-HYDRODYNAMIC PRINTING 1510
J.-H. Kim, S.-J. Kim, H.-S. Kim, J.-S. Park, and H.-I. Jung
Yonsei University, KOREA

W14C SAMPLE METERING AND PARALLEL LIQUID PLUG ACTUATION FOR MULTIPLE BIOCHEMICAL ASSAYS 1513
M.M. Mielnik[1], J. Voitel[1], L.A. Solli[2], and L. Furuberg[1]
[1]SINTEF, NORWAY and [2]Norchip AS, NORWAY

W15C TOWARDS A COMPREHENSIVE CENTRIFUGAL PROCESS INTEGRATION BY ROTATIONALLY INDUCED LYOPHILIZATE DISSOLUTION AND CELL LYSIS 1516
S. Lutz[1], P. Lang[1], B. Faltin[2], S. Haeberle[1], F. von Stetten[2], R. Zengerle[1,2], and J. Ducrée[1]
[1]HSG-IMIT, GERMANY and [2]University of Freiburg, GERMANY

W16C ULTRASONIC MIXING IN POLYMER MICROFLUIDICS 1519
M. Bengtsson, M. Brivio, and A. Wolff
Technical University of Denmark, DENMARK

W17C USING ASYMMETRIC VOLTAGE SOURCES IN ELECTRO-HYDRODYNAMIC MICROMIXERS 1522
L. De Vroey[1], D. Grenier[2], and M.-C. Jullien[2]
[1]Université Catholique de Louvain, BELGIUM and [2]Université Européenne de Bretagne, FRANCE

Poster Session Microfluidics - Multi-Phase and Digital Microfluidics

W18C A MICROFLUIDIC PLATFORM FOR IMPLEMENTING MOLECULAR LOGIC GATE WITH FLUORESCENT CHEMOSENSORS 1525
S. Kou, S.-W. Nam, J. Yoon, and S. Park
Ewha Woman's University, KOREA

W19C CONTINUOUS-FLOW LAYER-BY-LAYER ENCAPSULATION WITH POLYELECTROLYTES THROUGH A MICROFLUIDIC DEVICE 1528
K.-Q. Peng[1,2], W.-L. Ong[1], L. Yobas[1], and D. Trau[2]
[1]Institute of Microelectronics, SINGAPORE and
[2]National University of Singapore, SINGAPORE

W20C DESIGN PARAMETERS FOR A 1XN MICRODROPLET SWITCH 1531
J.S. Fisher, T.S. Kuo, J. Poulos, and A.P. Lee
University of California, Irvine, USA

W21C DISCRETE MICROFLUIDICS: PRODUCTION OF SILICA PARTICLES WITH EMULSIONS 1534
V. Chokkalingam[1], C. Priest[1], M. Krämer[2], W.F. Maier[2], S. Herminghaus[1], and R. Seemann[1]
[1]Max Planck Institute for Dynamics and Self-Organization, GERMANY and
[2]Saarland University, GERMANY

W22C ELECTROHYDRODYNAMICALLY CONTROLLED GENERATION OF A SINGLE OR MULTIPLE DROPS IN THE MICROFLOW OF AQUEOUS TWO-PHASE SYSTEM 1538
Y.H. Choi, Y.S. Song, and D.H. Kim
Korea Advanced Institute of Science and Technology (KAIST), KOREA

W23C HIGH-PERFORMANCE PRODUCTION OF MONODISPERSE EMULSIONS USING MICROFABRICATED ASYMMETRIC THROUGH-HOLE ARRAY 1541
I. Kobayashi[1], G.T. Vladisavljević[2], K. Uemura[1], and M. Nakajima[1,3]
[1]National Food Research Institute, JAPAN, [2]Loughborough University, UK, and
[3]University of Tsukuba, JAPAN

W24C HIGH THROUGHPUT DROPLET-BASED DNA ASSAYS USING FLUORESCENCE RESONANCE ENERGY TRANSFER 1544
M. Srisa-Art, E.C. Dyson, A.J. deMello, and J.B. Edel
Imperial College London, UK

W25C LIQUID-LIQUID-PHASE ELECTROSPRAY IN MICROCHANNELS 1547
S. Koster, V. de Bot, and E. Verpoorte
University of Groningen, THE NETHERLANDS

W26C MICROFLUIDIC LOGIC GATES AND TIMERS 1550
M.W. Toepke, V.V. Abhyankar, J.W. Warrick, and D.J. Beebe
University of Wisconsin, USA

W27C MICROFLUIDIC QUANTITATIVE EXTRACTION IN DROPLETS 1553
P. Mary, V. Studer, and P. Tabeling
Ecole Supérieure de Physique et de Chimie Industrielles (ESPCI), FRANCE

W28C PIXELATION OF PLANAR BIOCHEMICAL SAMPLES: A NOVEL CONCEPT FOR MICROFLUIDIC IMAGING 1556
K. Tachikawa, P.S. Dittrich, J. Franzke, and A. Manz
Institute for Analytical Sciences (ISAS), GERMANY

W29C PROGRAMMABLE FLOW-THROUGH REAL-TIME PCR USING DIGITAL MICROFLUIDICS 1559
P.Y. Paik, D.J. Allen, A.E. Eckhardt, V.K. Pamula, and M.G. Pollack
Advanced Liquid Logic, USA

W30C THERMAL CONTROL OF DROPLET SIZE IN MICROCHANNELS 1562
N.-T. Nguyen[1], T.-H. Ting[1], Y.-F. Yap[1], T.-N. Wong[1], J.C.-K. Chai[1], W.-L. Ong[2], J. Zhou[1,2], S.-H. Tan[1,2], and L. Yobas[2]
[1]Nanyang Technological University, SINGAPORE and
[2]Institute of Microelectronics, SINGAPORE

Poster Session Microfluidics

W31C DYNAMICS MEASUREMENT OF STRUCTURAL CHANGE OF HELICAL POLYMER USING THERMAL LENS MICROSCOPY AND MICROFLUIDIC TECHNIQUE 1565
K. Osato[1], M. Tokeshi[1,2], N. Kaji[1], R. Anraku[3], T. Asai[3], A. Hattori[3], K. Mawatari[2], T. Kitamori[2,4], E. Yashima[1], and Y. Baba[1,5,6]
[1]Nagoya University, JAPAN, [2]Kanagawa Academy of Science and Technology, JAPAN, [3]Nippon Sheet Glass Co. Ltd., JAPAN, [4]University of Tokyo, JAPAN, [5]National Institute of Advanced Industrial Science and Technology (AIST), JAPAN, and [6]Japan Science and Technology Agency (JST), JAPAN

W32C GUIDED SELF-ASSEMBLY OF MICROLATCHES USING RAILED MICROFLUIDICS AND OPTOFLUIDIC MASKLESS LITHOGRAPHY 1568
B. Kim[1], S.E. Chung[1], H. Park[1], W. Park[1], K. Yu[2], and S. Kwon[1]
[1]Seoul National University, KOREA and
[2]Korea Electrical Engineering and Science Research Institute, KOREA

W33C MULTIPLE CORE-SHEATH LIQUID TRANSFER USING MATRIX ARRANGEMENT OF 3D SHEATH FLOWS 1571
H. Sato[1,2], Y. Sasamoto[1], T. Sekiguchi[1], T. Homma[1], and S. Shoji[1]
[1]Waseda University, JAPAN and
[2]Research Fellow of the Japan Society for the Promotion of Science, JAPAN

Poster Session Nanotechnology - Nanofluidics

W1D A NANOFLUIDIC-BASED ENZYMATIC REACTION ON A CHIP 1574
T. Tsukahara[1,2], E. Tamaki[1], A. Hibara[1,3], and T. Kitamori[1,2,3]
[1]University of Tokyo, JAPAN, [2]Japan Science and Technology Agency (JST), JAPAN, and [3]Kanagawa Academy of Science and Technology, JAPAN

W2D ASYMMETRIC IONIC CONDUCTANCE IN NANOCHANNELS 1577
L.-J. Cheng and L.J. Guo
University of Michigan, USA

W3D DIRECT VISUALIZATION OF DNA IN NANOCHANNELS 1580
W.W. Reisner[1,2], J.P. Beech[1], N.B. Larsen[2], H. Flyvbjerg[2], A. Kristensen[2], and J.O. Tegenfeldt[1]
[1]Lund University, SWEDEN and [2]Technical University of Denmark, DENMARK

W4D ELECTO-PRECONCENTRATION OF BIOMOLECULES IN NANOFLUIDICS: CONCENTRATION GRADIENT FOCUSING AT LOW AND HIGH IONIC STRENGTHS 1583
A. Plecis, P. Svarnas, and Y. Chen
LPN-CNRS, FRANCE

W5D NANOFLUIDIC SIEVES FOR DNA SEPARATION USING COLLOIDAL CRYSTAL TECHNOLOGY 1586
L.S.L. Cheung, K.P. Gerhardt, M.J. Wirth, and Y. Zohar
University of Arizona, USA

W6D NANOPORE DEVICES FOR AC ELECTROKINETIC TRAPPING 1589
M.L. Kovarik and S.C. Jacobson
Indiana University, USA

W7D REAL-TIME CONTROL OF NANOPORE WALL POTENTIAL FOR SINGLE-MOLECULE ANALYSES 1592
A.H. Talasaz[1], T.A. Zangle[1], C. Tropini[2], R. Dick[1], F. Pease[1], R.W. Davis[1], and J.G. Santiago[1]
[1]Stanford University, USA and [2]University of British Columbia, CANADA

Poster Session Nanotechnology - Nanoengineering

W8D IRON-OXIDE EMBEDDED SOLID LIPID NANO-VESICLES FOR MAGNETICALLY CONTROLLED DRUG DELIVERY 1595
M.-H. Hsu and Y.-C. Su
National Tsing Hua University, TAIWAN

Poster Session Nanotechnology - Nanobiotechnology

W9D FABRICATION OF MULTI-LAYERED CARBON NANOTUBE FILMS FOR LABEL-FREE DETECTION OF DNA HYBRIDIZATION 1598
Y.-K. Baek, D.-H. Jung, S.-Y. Lee, Y.-K. Choi, and H.-T. Jung
Korea Advanced Institute of Science and Technology (KAIST), KOREA

W10D FABRICATION OF PDMS-BASED NANOCHANNELS FOR ENZYMATIC PROCESSING AND DETECTION OF BIOMOLECULES 1601
O. Harnack, I. Hospach, and A. Yasuda
Sony Deutschland GmbH, GERMANY

W11D HYDRODYNAMIC FORCE CONTROL OF LAMINAR FLOW AS A NANO PROBING TOOL TO EVALUATE TORQUE OF SINGLE MOTOR PROTEIN 1604
S.W. Lee[1], H. Kinoshita[1], T. Yamamoto[1], H. Noji[2], and T. Fujii[1]
[1]University of Tokyo, JAPAN and [2]Osaka University, JAPAN

W12D NANO ELISA SYSTEM FOR HIGHLY EFFICIENT AND SENSITIVE MOLECULAR RECOGNITION 1607
K. Mawatari[1], R. Kojima[2], B. Renberg[2], and T. Kitamori[1,2]
[1]Kanagawa Academy of Science and Technology, JAPAN and [2]University of Tokyo, JAPAN

W13D PLASMON RESONANCE ENERGY TRANSFER SPECTROSCOPY (PRET) 1610
Y. Choi, T. Kang, G.L. Liu, Y. Long, and L.P. Lee
University of California, Berkeley, USA

W14D PREPARATION OF CELL-SIZED LIPOSOMES ON SILICON: CONTROLLING LIPOSOME SIZE BY SURFACE MICRO-ENGINEERING 1613
M. Le Berre[1], A. Yamada[2], Y. Chen[1], and D. Baigl[1]
[1]Ecole Normale Supérieure, FRANCE and [2]Kyoto University, JAPAN

W15D SIGNAL-GUIDED SEQUENTIAL ASSEMBLY OF NANO-BIO-COMPONENTS IN A COMPLETELY PACKAGED MICROFLUIDIC ENVIRONMENT 1616
X. Luo, A.T. Lewandowski, H. Yi, G.F. Payne, R. Ghodssi, W.E. Bentley, and G.W. Rubloff
University of Maryland, USA

W16D SINGLE DNA/PROTEIN INTERACTION ANALYSIS USING QUANTUM DOT CONJUGATES AND MICROFLUIDIC SYSTEMS 1619
D. Onoshima[1], N. Kaji[1], M. Tokeshi[1], and Y. Baba[1,2,3]
[1]Nagoya University, JAPAN, [2]National Institute of Advanced Industrial Science and Technology (AIST), JAPAN, and [3]Japan Science and Technology Agency (JST), JAPAN

W17D STRETCHING DNA IN SINGLE, EXTRA-LONG (1.5 cm) NANOFLUIDIC CHANNELS FABRICATED USING A NOVEL NANOIMPRINT MOLD 1622
X. Liang, K.J. Morton, R.H. Austin, and S.Y. Chou
Princeton University, USA

Poster Session Materials - Innovative Chip Materials

W1E WATER-VAPOR PERMEABILITY CONTROL OF PDMS BY DISPERSION OF COLLAGEN POWDER 1625
M. Ishida[1], Y. Kazoe[2], Y. Sato[2], and N. Miki[2]
[1]Ricoh, JAPAN and [2]Keio University, JAPAN

Poster Session Materials - Surface Modification and Characterization

W2E AN EFFICIENT SURFACE MODIFICATION FOR SELECTIVE CONTROL OF CELL ATTACHMENT USING PHOTOCHEMICAL REACTION 1628
K. Jang, K. Sato, T. Konno, K. Ishihara, and T. Kitamori
University of Tokyo, JAPAN

W3E LOCAL SILICA COATING OF POLY(DIMETHYLSILOXANE) MICROCHANNELS 1631
J. Park, M. Shin, and J.H. Hahn
Pohang University of Science and Technology, KOREA

W4E MICRO POST-STRUCTURED SURFACES FOR BUBBLE DETACHMENT 1634
S.K. Chung[1], U.-C. Yi[2], and S.K. Cho[1]
[1]University of Pittsburgh, USA and [2]Core MicroSolutions Inc., USA

W5E SLIDING BEHAVIOR OF WATER DROPLETS SANDWICHED BETWEEN HYDROPHOBIC SURFACES 1637
S. Suzuki[1,2], A. Nakajima[1,2], M. Sakai[2], A. Hashimoto[2], N. Yoshida[2,3], Y. Kameshima[1,2], and K. Okada[1]
[1]Tokyo Institute of Technology, JAPAN, [2]Kanagawa Academy of Science and Technology, JAPAN, and [3]University of Tokyo, JAPAN

W6E SURFACE MODIFICATION WITHIN ENCLOSED POLYMER AND GLASS MICROFLUIDIC CHANNELS 1640
S. Prakash, T.M. Long, J.S. Moore, and M.A. Shannon
University of Illinois, Urbana-Champaign, USA

W7E ULTRA HYDROPHOBIC AND NANO POROUS PLANT LIKE SURFACES FABRICATED BY UV REVERSE SIDE EXPOSURE 1643
O. Mertsch, A.D. Walter, I. Rudolph, D. Schondelmaier, and B. Loechel
Anwenderzentrum für Mikrotechnik, GERMANY

Poster Session Materials - Nanostructured Materials

W8E FABRICATION OF MICROCHANNELS WITH POROUS SILICON PILLARS FOR ON-CHIP LIQUID CHROMATOGRAPHY AND MICROREACTORS 1646
V. Verdoold[1], W. De Malsche[1,2], G. Desmet[2], and J.G.E Gardeniers[1]
[1]University of Twente, THE NETHERLANDS and
[2]Free University of Brussels, BELGIUM

Poster Session Detection Technologies - Optical

W1F A DIFFRACTION MOIRE BASED MICRO DOUBLE LAYERED CHIP FOR CELLULAR MECHANICS STUDY 1649
X. Zheng and X. Zhang
Boston University, USA

W2F CAPILLARY-BASED MICROFLUIDIC FLOW INJECTION ANALYSIS BASED ON HIGH SENSITIVE LIQUID CORE WAVEGUIDE ABSORBANCE DETECTION 1652
L. Dong, W.-B. Du, and Q. Fang
Zhejiang University, CHINA

W3F CHARACTERIZATION OF LIGHT COUPLER-INTEGRATED PLASTIC SURFACE PLASMON RESONANCE SENSOR AND SYSTEM IN AQUEOUS AMBIENT 1655
H.-B. Pyo[1], M.Y. Jung[1], S.H. Park[1], Y.-B. Shin[2], and B.H. Jung[2]
[1]Electronics and Telecommunications Research Institute (ETRI), KOREA and
[2]Korea Research Institute of Bioscience and Biotechnology (KRIBB), KOREA

W4F MICROFLUIDIC ARRAY TO STUDY PROTEASE ACTIVITY 1658
D.A. Raorane[1], F. Chen[2], A. Majumdar[1]
[1]University of California, Berkeley, USA and
[2]Lawrence Berkeley National Laboratory, USA

W5F MULTI-TOTAL INTERNAL REFLECTION IN POLYDIMETHYLSILOXANE MICROFLUIDICS FOR ENHANCED ABSORBANCE DETECTION 1661
J.S. Kee[1,2], D.P. Poenar[2], and L. Yobas[1]
[1]Institute of Microelectronics, SINGAPORE and
[2]Nanyang Technological University, SINGAPORE

W6F NIR MICRO SPECTROMETRY OF CHEMICALLY AGGRESSIVE FLUIDS 1664
S. Bargiel[1], J. Dziuban[1], R. Walczak[1], P. Knapkiewicz[1], L. Nieradko[2], A. Grzegorska[1], and B. Latecki[3]
[1]Wrocław University of Technology, POLAND, [2]University of Franche-Comté, FRANCE, and [3]Institute of Electron Technology, POLAND

W7F SIMULTANEOUS MEASUREMENTS OF NEAR-WALL VELOCITY AND WALL ZETA-POTENTIAL BY EVANESCENT WAVE ILLUMINATION 1667
S. Miyakawa, Y. Kazoe, and Y. Sato
Keio University, JAPAN

W8F SPR BIOSENSING COUPLED TO A DIGITAL MICROFLUIDIC SURFACE ACOUSTIC WAVE SYSTEM 1670
E. Galopin[1], M. Beaugeois[2], F. Lapierre[1], M. Bouazaoui[2], J.C. Camart[1], V. Thomy[1], and B. Pinchemel[2]
[1]IEMN, FRANCE and [2]Interdisciplinary Research Institute (IRI), FRANCE

Poster Session Detection Technologies - Electrochemical

W9F A BIOSENSOR BASED ON INTERDIGITATED ELECTRODES AND MICROSCOPIC MANIPULATION OF MAGNETIC PARTICLES 1673
Z. Peng[1], P. Hesketh[1], W.R. Heinemann[2], and K. Kellar[3]
[1]Georgia Institute of Technology, USA, [2]University of Cincinnati, USA, and [3]Center for Disease Control and Prevention, USA

W10F ADAPTIVE NANOWIRES FOR SWITCHABLE MICROFLUIDIC DEVICES 1677
E. Piccin[1], R. Laocharoensuk[2], J. Burdick[2], E. Carrilho[1], and J. Wang[2]
[1]University of São Paulo, BRAZIL and [2]Arizona State University, USA

W11F RAPID, SEQUENCE SPECIFIC, REUSABLE ELECTRONIC DNA SENSOR IN MICROFLUIDIC DEVICES 1680
E. Pavlovic[1], R.Y. Lai[1], B. Ferguson[1], J.S. Swensen[1], T.-T. Wu[2], R. Sun[2], A.J. Heeger[1], K.W. Plaxco[1], and H.T. Soh[1]
[1]University of California, Santa Barbara, USA and [2]University of California, Los Angeles, USA

Poster Session Detection Technologies – Direct Electrical Detection and Impedancemetry

W12F FABRICATION OF SENSETIVE ELECTRONIC SENSOR FOR LABLE-FREE DETECTION OF PROTEIN-PROTEIN INTERACTIONS 1683
A. Cohen, A. Doron, M. Horesh, D. Ullien, M. Beraha, U. Virobnik, and I. Levy
Intel Electronics, ISRAEL

W13F IMPEDANCE BASED FLOW-THROUGH BIOSENSOR FOR PARTICLE/CELL DETECTION 1686
K.S.L. Narasimhan, A.R.A. Rahman, and S. Bhansali
Univeristy of South Florida, USA

W14F MICROWAVE COMPOSITIONAL ANALYSIS OF SOLVENT MATRICES IN MICROCAPILLARY MANIFOLD SYSTEMS 1689
R. Göritz, A. Masood, O. Castell, D.A. Barrow, C. Allender, and A. Porch
Cardiff University, UK

W15F TECHNIQUE FOR MEASURING THE DIELECTRIC CONSTANT OF LIQUIDS AND GASES WITHOUT THE USE OF CALIBRATION STANDARDS 1692
H. Ma, J.H. Lang, and A.H. Slocum
Massachusetts Institute of Technology, USA

W16F TOWARD BACTERIA DETECTION ON CHIP: A BIOSENSOR BASED ON MAGNETOTACTIC BACTERIA AND IMPEDANCE SPECTROSCOPY 1695
Z. Lu, R. Denomme, S. Bah, and S. Martel
Ecole Polytechnique de Montreal, CANADA

Poster Session Detection Technologies

W17F LOW POWER IGNITION OF MICROPLASMA FOR VOLATILE ORGANIC COMPOUNDS DETECTION 1698
D.C. Shin, K.W. Jo, M.G. Kim, S. Yang, and J.H. Lee
Gwangju Institute of Science and Technology (GIST), KOREA

W18F MICROFLUIDIC THERMAL BIOSENSOR FOR BIOCHEMICAL REACTION 1701
B.S. Kwak, B.S. Kim, J.S. Park, H.H. Cho, and H.I. Jung
Yonsei University, KOREA

W19F SINGLE AND DOUBLE- SIDED SENSING WITH PIEZORESISTIVE MICROCANTILEVERS 1704
A. Choudhury[1], P.J. Hesketh[1], Z. Hu[1,2], and T.G. Thundat[2]
[1]*Georgia Institute of Technology, USA and*
[2]*Oak Ridge National Laboratory, USA*

Poster Session MEMS & NEMS Technologies - Micro and Nano-Machining

W1G DEVELOPMENT OF THE MODIFIED LIQUID-CRYSTAL-DISPLAY PROJECTOR DEVICE FOR FABRICATION OF SURFACE MICROPATTERNS AND MICROFLUIDIC CHANNELS 1708
J. Kobayashi, K. Itoga, Y. Tsuda, M. Yamato, A. Kikuchi, and T. Okano
Tokyo Women's Medical University, JAPAN

W2G IN-BLOCK BONDING-LESS 3D MICROCHANNEL NETWORK FABRICATION IN PDMS 1711
M. Juchniewicz, O. Adamowicz, M. Chudy, A. Dybko, and Z. Brzózka
Warsaw University of Technology, POLAND

W3G MECHANICAL MEASUREMENT OF DNA MOLECULE COMBINED WITH THE DNA TWEZEERS AND A WEDGE TYPE CANTILEVER 1714
M. Hosogi[1], G. Hashiguchi[1], K. Ayano[1], and H. Fujita[2]
[1]Kagawa University, JAPAN and [2]University of Tokyo, JAPAN

W4G PDMS MICROLENS ARRAY FABRICATION USING WATER DROPLETS 1717
S.-H. Chao, R. Carlson, and D. Meldrum
University of Washington, USA

W5G SU-8 BASED MICRONEEDLE FOR DRUG DELIVERY IN NANOMEDICINE APPLICATIONS WITH INTEGRATED ELECTRODES 1720
L.J. Fernández, M. Tijero, R. Vilares, J. Berganzo, K. Mayora, and F.J. Blanco
Ikerlan S. Corp., SPAIN

Poster Session MEMS & NEMS Technologies - Microfluidic Components

W6G A MICROFABRICATED NANOPIPETTOR BASED ON ELECTROOSMOSIS 1723
S. Liu, C.K. Byun, and Q. Pu
Texas Tech University, USA

W7G A MULTILAYER SU-8 PROCESS FOR HIGH-DENSITY, STACKED MICROFLUIDIC SYSTEMS 1726
C.A. Mousoulis and D.P. Papageorgiou
Northeastern University, USA

W8G AN OPTICALLY DRIVEN MICROPUMP USING A SPINNING DISK ROTOR 1729
S. Maruo[1,2] and H. Inoue[1]
[1]Yokohama National University, JAPAN and
[2]Japan Science and Technology Agency (JST), JAPAN

W9G ELECTRICALLY-ACTUATED PDMS MICROVALVES AND PUMPS FOR VLSI MICROFLUIDICS 1732
M.-P. Chang, T. Bansal, and M.M. Maharbiz
University of Michigan, USA

W10G HIGH-FORCE LIQUID-GAP ELECTROSTATIC HYDRAULIC MICRO ACTUATORS 1735
H. Kim, S. Lee, and K. Najafi
University of Michigan, USA

W11G LARGE PANEL HOT ROLLER EMBOSSING FOR POLYMERIC MICROFLUIDIC DEVICES 1738
S.H. Ng[1], Z.F. Wang[1], and N.F. de Rooij[2]
[1]*Singapore Institute of Manufacturing Technology, SINGAPORE and*
[2]*University of Neuchâtel, SWITZERLAND*

W12G LOW POWER AND LOW COST TEMPERATURE AND FLUID CONTROL IN PDMS MICROFLUIDIC DEVICES 1741
R. Carlson and D. Meldrum
University of Washington, USA

W13G MICROFABRICATED IMPINGING JET MIXER FOR NANO PIGMENT PARTICLES 1744
T. Ezaki, S. Yasuda, T. Teshima, M. Majima, and T. Yagi
Canon Inc., JAPAN

W14G SERIAL DILUTION CHIPS FOR ARBITRARY CONCENTRATION PROFILE AND APPLICATION TO CYTOTOXICITY TEST 1747
C. Kim[1,2], K.S. Lee[1], K.S. Shin[1], J.H. Kim[1], K.J. Lee[2], J.Y. Kang[1], and T.S. Kim[1]
[1]*Korea Institute of Science and Technology (KIST), KOREA and*
[2]*Korea University, KOREA*

W15G TRANSPORTATION PERFORMANCES OF MICROMACHINED LINEAR BROWNIAN MOTORS 1750
E. Altintas[1], E. Sarajlic[1], K.F. Böhringer[2], and H. Fujita[1]
[1]*University of Tokyo, JAPAN and* [2]*University of Washington, USA*

Poster Session MEMS & NEMS Technologies – Hybrid Devices, Packaging, Components Interfacing

W16G CMOS OPTICAL POLARIZATION ANALYZER CHIP FOR MICROCHAMBER AND MICROFLUIDIC SYSTEM 1753
T. Tokuda, S. Sato, K. Kagawa, M. Nunoshita, and J. Ohta
Nara Institute of Science and Technology, JAPAN

W17G IMPROVED WAFER-SCALE FABRICATION OF ALIGNED PDMS-GLASS MICROCHIPS WITH INTEGRATED ELECTRODES 1756
J. Li, S. Le Gac and A. van den Berg
University of Twente, THE NETHERLANDS

Poster Session MEMS & NEMS Technologies

W18G DEMONSTRATION OF A TELEMETRIC SYSTEM USING GASTRIC-FLUID-UTILIZING MICRO BATTERY 1759
H. Jimbo and N. Miki
Keio University, JAPAN

Concurrent Session 3A3 - Cell Arrays

STUDY OF CELL-CELL COMMUNICATION USING OPTICALLY ASSEMBLED 3D LIVING CELL MICROARRAYS 1762
W. Timp[1], U. Mirsaidov[2], K.A. Timp[2], M. Mir[2], G. Timp[2], and P. Matsudaira[1]
[1]Massachusetts Institute of Technology, USA and
[2]University of Illinois at Urbana-Champaign, USA

A LOW-DAMAGE CELL TRAPPING ARRAY FABRICATED BY SINGLE-MASK MULTIDIRECTIONAL PHOTOLITHOGRAPHY WITH EQUIVALENT CIRCUIT ANALYSIS 1765
T. Suzuki[1,2], H. Yamamoto[1], M. Ohoka[3], I. Kanno[1], M. Washizu[2,4], and H. Kotera[1,2]
[1]Kyoto University, JAPAN, [2]Japan Science and Technology Agency (JST), JAPAN, [3]Advanced Software Technology and Mechatronics Research Institute, JAPAN, and [4]University of Tokyo, JAPAN

ASYMMETRIC CELL DIVISION INDUCED BY MICROENVIRONMENT GEOMETRY 1768
M. Thery[1,2], A. Jimenez-Dalmaroni[3], V. Racine[1], M. Bornens[1], and F. Julicher[3]
[1]Institut Curie, FRANCE, [2]Commissariat à l'Energie Atomique (CEA), FRANCE, and [3]Max Plank Institute, GERMANY

Concurrent Session 3B3 - Detection 3

FLOATING ELECTRODE OPTOELECTRONIC TWEEZERS (FEOET): A NOVEL MECHANISM ENABLING OPTICAL MANIPULATION OF OIL IMMERSED AQUEOUS DROPLET 1771
S. Park, C. Pan, T.-H. Wu, S. Kalim, M. Teitell, and E.P.Y. Chiou
University of California, Los Angeles, USA

A RAILED MICROFLUIDIC CHANNEL FOR MANIPULATION OF FINNED MICROTRAINS 1774
S.E. Chung[1], H. Park[1], W. Park[1], B. Kim[1], K. Yu[2], and S. Kwon[1]
[1]Seoul National University, KOREA and
[2]Korea Electrical Engineering and Science Research Institute, KOREA

METAMATERIALS FOR HYDRODYNAMICS: REFRACTION, FOCUSING AND BEAM STEERING FOR PARTICLES AND CELLS 1777
K.J. Morton[1], O.K. Tsui[2], J.C. Sturm[1], R.H. Austin[1], and S.Y. Chou[1]
[1]Princeton University, USA and [2]Boston University, USA

Thursday, 11 October 2007

Concurrent Session 4A1 - Clinical Diagnostic 2

A FULLY INTEGRATED MICROFLUIDIC GENETIC ANALYSIS DEVICE FOR THE DETECTION OF BLOOD CANCERS 1780
L.A. Legendre[1], D.C. Leslie[1], C.J. Morris[1], A. Barron[2], R. McClure[3], and J.P. Landers[1]
[1]University of Virginia, USA, [2]Northwestern University, USA, and [3]Mayo Clinic, USA

HYPERSPECTRAL AND SPATIAL MULTIPLEXING OF ULTRASENSITIVE IMMUNOASSAYS FOR DETECTING TOXIN EXPOSURE 1783
A.V. Hatch, R.J. Meagher, D.S. Reichmuth, A.E. Herr, M.B. Sinclair, D.M. Haaland, and A.K. Singh
Sandia National Laboratories, USA

NANOFLUIDIC PRECONCENTRATION DEVICE FOR SENSITIVE AND WIDE DYNAMIC RANGE IMMUNO-SENSING 1786
Y.-C. Wang, V.H. Liu, and J. Han
Massachusetts Institute of Technology, USA

Concurrent Session 4B1 - Surface Modification and Characterization

PHOTO-PATTERNED MULTI-ENZYMATIC MICROREACTORS 1789
T.B. Stachowiak[1,2], T.C. Logan[1], D.S. Clark[1], F. Svec[2], and J.M.J Fréchet[1,2]
[1]University of California, Berkeley, USA and
[2]Lawrence Berkeley National Laboratory, USA

SINGLE PARTICLE TRAPPING AND MELTING FOR FUNCTIONAL AND HIGH-RESOLUTION MODIFICATION OF PDMS MICROCHANNELS 1792
M. Yamamoto[1], M. Yamada[2], S. Fukushima[3], M. Yasuda[1], and M. Seki[1,3]
[1]Osaka Prefecture University, JAPAN, [2]Tokyo Women's Medical University, JAPAN, and [3]Chiba University, JAPAN

EXTREME WATER-REPELLANT SURFACE ENABLED BY NANO-MICRO INTEGRATED TEXTURE 1795
Y. Kwon[1], J. Choi[1], N. Patankar[2], and J. Lee[1]
[1]Seoul National University, KOREA and [2]Northwestern University, USA

Concurrent Session 4A2 - Dielectrophoretic Cell Handling and Sorting

IN VITRO FERTILIZATION AND DEVELOPMENTS OF HEALTHY OOCYTES BY A DIELECTROPHORETIC SEPARATION CHIP 1798
W. Choi[1], J.-S. Kim[2], D.-H. Lee[1], D.-B. Koo[2], K.-K. Lee[2], and J.-K. Park[1]
[1]Korea Advanced Institute of Science and Technology (KAIST), KOREA and
[2]Korea Research Institute of Bioscience and Biotechnology (KRIBB), KOREA

IMPEDANCE SPECTROSCOPY FOR LABEL-FREE DIFFERENTIAL LEUKOCYTE COUNTS 1801
D. Holmes, J. Cakebread, J. Holloway, D. Davis, and H. Morgan
University of Southampton, UK

SIMULTANEUOUS SORTING OF MULTIPLE BACTERIAL STRAINS USING DIELECTROPHORESIS 1804
U. Kim, J. Qian, P.H. Bessette, P.S. Daugherty, and H.T. Soh
University of California, Santa Barbara, USA

Concurrent Session 4B2 - Acoustic Devices

GENTLE RETENTION OF CELLS IN A FOCUSING ULTRASONIC RESONATOR INTEGRATED IN A CHIP-BASED PERFUSION SYSTEM FOR CELL CHARACTERIZATION AND ON-CHIP CULTIVATION 1807
J. Hultström Svennebring, O. Manneberg, and M. Wiklund
Royal Institute of Technology, SWEDEN

ON CHIP AFFINITY SELECTION OF ANTIBODIES USING ULTRASONIC STANDING WAVES 1810
P. Augustsson, J. Persson, M. Ohlin, and T. Laurell
Lund University, SWEDEN

FLUORESCENT ACTIVATED CELL SORTER USING ULTRASOUND STANDING WAVES IN MICRO CHANNELS 1813
C. Grenvall, M. Carlsson, P. Augustsson, F. Petersson, and T. Laurell
Lund University, SWEDEN

Author Index A1

Keyword Index A23

TECHNICAL PAPERS

Volume 1
Pages 1 – 918

Volume 2
Pages 919 – 1815

